**Unified International Technical Conference on Refractories (UNITECR) 18th Biennial Worldwide Congress on Refractories**

26th – 29th September 2023
Germany | Frankfurt am Main | Kap Europa

UNITECR 2023

Deutsche Feuerfest Industrie e.V. — DFFI

European Centre for Refractories — ECREF

# PROCEEDINGS

# THE CARBON CHALLENGE

**Steps and leaps to master the future**

# SPONSORS

We would like to thank the sponsors who made it possible to develop UNITECR 2023 into a very special event. Whether it's important conference elements such as pens, pads or the conference bag, the events, the Welcome Evening or the Conference Dinner, all of this has been prepared even better for you with their support.

**REFRA**TECHNIK

RHI MAGNESITA

INTOCAST
EXPERTS ON FIRE.

ALMATIS

Bosai Europe GmbH
博赛欧洲有限责任公司

refractories
WORLDFORUM
Manufacturing & Performance of High-Temperature Materials

STEULER

MLR Mineralmühle Leun

EIRICH

# MEDIA PARTNERS

We would like to thank the media partners who helped us to publicize this UNITECR conference worldwide. With their support and also with the commitment in the social networks, UNITECR has grown into an outstanding event in 2023.

bulletin

CHNR
中国耐火材料

IMFORMED
Industrial Mineral Forums & Research

Institute of
Refractories
Engineers

IRON & STEEL REVIEW

25 STEEL & METALLURGY
A COMPLETE STEEL MAGAZINE

market
STEEL
PLATFORM ALL ABOUT METAL

Refractories Window
www.refwin.com
Global Refractories E-Business Platform

refractories
WORLDFORUM

stahl.

STAHL+
TECHNIK

ZKG
CEMENT
LIME | GYPSUM

# ORGANISATION

## UNITECR 2023

### HOST

Deutsche Feuerfest-Industrie e.V. (DFFI)
*German Refractory Association*

### ORGANIZATIONAL OFFICE

European Centre for Refractories gGmbH (ECREF)

Thomas Kaczmarek (Secretary General UNITECR 2023)

Dr. Christian Dannert (Secretary Scientific UNITECR 2023)

⊙ Rheinstrasse 58
56203 Höhr-Grenzhausen | Germany

☎ +49 2624 9433 125

✉ office@unitecr2023.org

### CONFERENCE VENUE

Kap Europa

⊙ Osloer Str. 5
60327 Frankfurt am Main | Germany

### UNITECR OFFICERS

Dr. Andus Buhr (UNITECR President)
Prof. Christos G. Aneziris (UNITECR Vice President, Chair of Scientific Committee)

### ORGANISATION TEAM

Prof. Dr. Christos G. Aneziris, Dr. Andus Buhr, Dr. Christian Dannert, Ulf Frohne-berg, Dr. Rainer Gaebel, Thomas Kaczmarek

### SCIENTIFIC COMMITTEE

Chairman: Prof. Dr. Christos G. Aneziris

**Raw Materials**
Dr. Christoph Wöhrmeyer

**Advances in Monolithic Technology**
Prof. Dr. Olaf Krause

**Refractories for Iron- and Steelmaking**
Prof. Dr. Helge Jansen

**Refractories for Non-Ferrous Metallurgy**
Daniel Cölle

**Refractories for Non-Metal Industries**
Dr. Stefan Postrach

**Modelling and Digitalization**
Rinus Siebring

**Education**
Dr. Dietmar Gruber

**Testing and Standardization**
Dr. Christian Dannert

**Basic Refractory Science and Technology Transfer**
Prof. Dr. Dr. h.c. Peter Quirmbach

### ADDITIONAL PUBLICATIONS IN „OPEN CERAMICS"

We have published a number of additional papers in a Special Issue titled „Ref-ractories for the Carbon Challenge" of the scientific journal „Open Ceramics". The Special Issue was edited by Prof. Olaf Krause (Koblenz University of Applied Sciences), Dr. Christian Dannert (Forschungsgemeinschaft Feuerfest e. V.) and Prof. Christos G. Aneziris (TU Bergakademie Freiberg). These papers are open access and can be viewed at **https://www.sciencedirect.com/journal/open-ceramics/special-issue/102HMR7RHH6**.

1

# WELCOME

**„The Carbon Challenge: Steps and Leaps to master the Future" is our motto at the UNITECR over the three days in Frankfurt – and for the coming years as we drive the transformation of our industry forward.**

During these days we will hear how the specialists want to further develop the path to $CO_2$ neutrality of our high-temperature industry, learn how we can reduce $CO_2$ emissions in the process and also give impetus to our customers. At UNITECR, experts, researchers and professionals from all over the world will come together to expand knowledge and find solutions to the challenges facing the industries.

An important aspect is the recycling economy to conserve limited resources and reduce the ecological footprint in the refractory industry. Regional value chains with close cooperation between suppliers, users and other stakeholders involved are essential. And there are already good examples of this.

There will be a leap in knowledge after this conference, which will be of enormous importance to all of us. We hope that you will experience inspiring presentations, exciting discussions and valuable networking opportunities during the conference. The UNITECR conference is known for its high-profile speakers and poster sessions. New are five panel debates on special topics that we have developed especially for this conference. Experience the exchange of opinions live and join the discussion.

Use this opportunity to expand your knowledge, exchange ideas with colleagues from the industry and discover new cooperation opportunities. We are confident that this conference will provide you with valuable insights and impulses for your work and research.

Prof. Dr. Christos G. Aneziris, as Vice-President of UNITECR 2023 and Chair of the Scientific Committee, and his team have ensured high quality and diversity. More than 250 papers will be presented in lectures or posters.

We both look forward to seeing you. Once again, welcome to the UNITECR Conference 2023. We wish you an inspiring and successful event.

We would like to thank all speakers, participants, exhibitors and organisers who have contributed to this event.

Dr. Andus Buhr
President UNITECR 2023

**Dr. Andus Buhr**
President UNITECR 2023

2

# TABLE OF CONTENTS

4

5

6

9

10

11

# 1  RAW MATERIALS

# DATA−BASED CARBON FOOTPRINT OF IMERYS SPECIALTY MINERALS FOR REFRACTORIES

S. Ranaivoharilala, N. Bunt, C. Wöhrmeyer
Imerys, Paris, France

## ABSTRACT

Refractory raw materials are the major contributor to the carbon footprint of unshaped refractories while for fired refractory bricks the firing process adds to the total carbon footprint. Significant energy and $CO_2$ emissions savings can be achieved by using monolithic refractories instead of fired bricks and a careful selection of raw materials can further reduce the total carbon footprint of refractory products. This paper will explain in detail the boundaries for the quantification of the $CO_2$ equivalents of Imerys specialty minerals for refractories. The analysis leads to product-specific scientific data-based $CO_2$ equivalents that allows a transparent calculation of the footprint of refractory products formulated with Imerys raw materials. This paper will concentrate on some Imerys specialty minerals and highlight the impact of different contributors on their carbon footprint, including the energy sources. Thanks to its effort to turn to low-emission energy supply, Imerys is capable of providing sustainable solutions and fulfilling its purpose to contribute to the decarbonization of the refractory value chain.

## INTRODUCTION

As part of its sustainability commitment, Imerys strives to develop minerals and expertise that deliver innovative, market-driven and sustainable solutions to society. For a few years now, a thorough assessment has been performed with the goal of understanding and further improving the sustainability profile of Imerys' existing and new solutions, including the specialty minerals manufactured for the refractory industry. First, this paper will detail the assessment methodology developed by Imerys, with a focus on the production step impact. Second, the evaluation outcomes of various minerals manufactured by Imerys, including chamotte, andalusite and white fused alumina, will be examined in view of the different carbon footprint contributors, namely the energy consumption. Advancing the sustainability goals of the refractory industry and their downstream users is one way Imerys is leading the challenge of caring for the planet through climate change mitigation by providing sustainable mineral solutions.

## IMERYS PORTFOLIO SUSTAINABILITY ASSESSMENT

Sustainability is anchored within Imerys activities, in a continuous improvement and long-term value creation approach. SustainAgility®, the program that structures sustainability within the Group, has been implemented based on the 2030 Agenda for Sustainable Development and major international framework agreements [1]. Delivering sustainable and high-quality solutions to its customers is one of the key ambitions of Imerys. SustainAgility Solutions Assessment (SSA) is the Group's methodology that screens and measures the sustainability of its portfolio and supports the development of its new solutions. Duly considering the World Business Council for Sustainable Development (WBCSD) guidelines for Portfolio Sustainability Assessments (PSA), it establishes a scientific, strong and reliable framework that considers the whole product's life cycle. The methodology results in a sustainability score, built on two specific factors called "Sustainable Value Creation", which is the balance between the economic value created and the environmental impact measured during the manufacturing stage, and "Market Alignment" which evaluates the sustainability benefits or challenges of the product in a specified application [2].

## IMERYS PRODUCT CRADLE-TO-GATE LIFE CYCLE ASSESSMENT

Life cycle assessment (LCA) is a technique used to identify, calculate and analyze the environmental and social impacts of a product or service over its life cycle. It takes into account the raw material production, acquisition, transformation, energy production, as well as the finished product use and end-of-life treatment. There are various manners to perform an LCA, including the conceptual, simplified or detailed approach. However, not all of the existing methods meet the ISO Standards. A conceptual LCA is the easiest technique as it only considers a limited qualitative inventory and results in qualitative findings focusing on the biggest impact contributors. A simplified LCA uses generic and standard data, and looks at the potential and/or most important life cycle stages and/or impacts. Conceptual and simplified LCAs are mainly used internally in order to support decision making, and their external use is meaningful provided that ISO Standards requirements are met. A detailed LCA is the more advanced approach and embeds a defined goal and scope, life cycle inventory or LCI (quantification of the inputs and outputs), life cycle inventory analysis or LCIA (understanding the importance of the impacts) and results interpretation (leading to the conclusions and recommendations) [3][4].

### Goal and scope

LCA is an integral part of Imerys' portfolio sustainability assessment. It has been used by the Group for many years, while ensuring continuous improvement, as a key instrument to measure and optimize the carbon footprint of its solutions [5]. As part of its SSA program, Imerys follows a detailed LCA approach and carefully aligns with the ISO 14040 and 1044 Standards on LCA "principles and framework" and "requirements and guidelines" respectively. This paper will look into the cradle-to-gate or manufacturing phase of the mineral, evaluated from the resource extraction and transformation ("cradle") until Imerys' gate ("gate"), meaning before the delivery step to the customer.

### Inventory: data collection

The cradle-to-gate system is modeled as exhaustively as possible with:

– primary data mainly: from Imerys quarries and factories' monitoring and measuring systems, which are the consumption and emission information related to the minerals extraction and transformation, and the packaging process,

– and secondary data: from external sources providing standard consumables and energy production and combustion data, as well as any other information not available at Imerys' level. The Group's main source of data is the ecoinvent database which is a repository that provides datasets on specific processes and their corresponding resource consumptions, emissions, products and wastes. The ecoinvent database covers multiple sectors globally and regionally and each dataset also contains LCIA results based on various assessment methods and impact categories [6]. The data, represented as input and output flows in the cradle-to-gate system are the:

– resources consumption (natural resources, consumables, energy),

– consumption of space (land occupation and transformation),

– production (products, coproducts, byproducts),

– wastes (mineral and process),

– emissions (to the air, water and soil).

Imerys also tracks energy-related indicators including: primary, non-renewable, renewable, fuel and feedstock energy.

**Inventory analysis: carbon footprint**
Imerys calculates and monitors a whole set of environmental and social impact indicators selected based on their relevance to the Group's activities, using a specific LCA tool. This paper will focus on the carbon footprint which evaluates the climate change impact by measuring the total amount of greenhouse gas (GHG) emissions generated by an individual, organization, event, service or product, over a 100-year time horizon. GHG emissions include carbon dioxide ($CO_2$), which is the reference gas, methane ($CH_4$), nitrous oxide ($N_2O$) and fluorinated gas (F-gases). Carbon footprint is expressed in $CO_2$ equivalents ($CO_2eq$) and is categorized into:
– scope 1: direct emissions from the company's factory, which are mainly the emissions from the fuels combustion or the carbon content of the raw materials,
– scope 2: indirect emissions from purchased energy sources, such as electricity or steam,
– scope 3: all the remaining indirect emissions from the whole value chain, including the raw materials upstream transportation or finished products downstream transportation, for instance.

**Cut-off rules, exclusions, allocations**
A cut-off criteria determines the quantity of flows or the environmental importance assigned to a process or system that is excluded. Imerys takes into account all the available inputs and outputs, allowing a cut-off ratio greater than 99% based on a mass criterion. Some stages are excluded from the life cycle inventory because of their irrelevant or insignificant impact: capital equipment, closing and rehabilitation of quarries, impacts of human activities onsite. Allocation procedure, which is the repartition of the inputs and outputs to the different products, is avoided as much as possible by using the dataset associated with each product. When needed, physical allocation - in contrast to economic allocation - is applied.

**CARBON FOOTPRINT OF SOME IMERYS MINERALS**
Product carbon footprint will consequently depend on the overall assessment approach, implying the assumptions, modeling and calculation methods. However, it is also impacted by the different transformation processes involved and the types and quantities of resources used, these latters being also dependent on diverse factors such as the geographical zone. According to ISO Standards, in order to ensure comparability of results, it is imperative to determine a functional unit defined as a quantified performance of a product system for use, which will be a reference to which the inputs and outputs are related [3]. For monolithic refractories, the carbon footprint will mainly be influenced by the choice of the raw materials which are the aggregates, binders and additives. The raw materials carbon footprint will be based on the extraction, production and transportation methods. Furthermore, the footprint will also be impacted by the energy sources and quantities required by the processes, such as blending and drying. For bricks, the carbon footprint will also be linked to the raw materials and manufacturing techniques, which involve the shaping and high-temperature firing of products made from formulations containing the refractory minerals. This paper will focus on the raw materials, as illustrated by some minerals manufactured by Imerys.

**Chamotte - France**
*Manufacturing description*
Chamotte is a calcined clay with a high proportion of alumina used in refractory applications as it resists extreme temperatures, operating conditions and corrosive environment. This section will focus on one of the Imerys' chamotte grades produced in France. The kaolinitic clay is extracted from Imerys quarries and transported by truck to the Imerys plant located 20 km away. The extracted clay is shredded, using electricity, and calcined in rotary

kilns between 1400°C and 1600°C, using electricity, fuel oil, biomass and biogas (both from waste) (Figure 1).

*Fig. 1: Imerys Chamotte manufacturing process.*
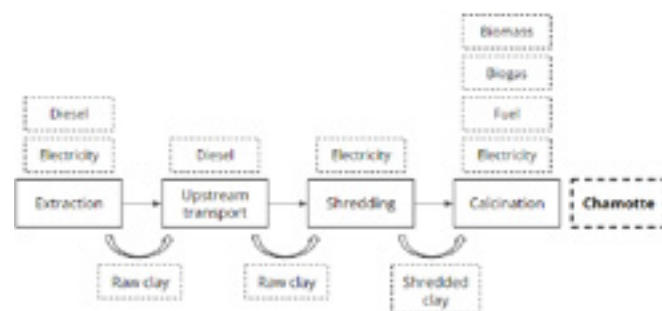


*Data sources and results*
For this system, 2020 primary data from Imerys plant and secondary data from the ecoinvent library were used. This chamotte grade has a carbon footprint of **251 kg CO2eq / ton**. All the impact comes from the energy production and use, and the calcination step is the highest contributor (Table 1).

Tab. 1: Carbon footprint breakdown in the manufacturing of the Imerys chamotte (France).

| Impact contributor | Extraction | Transport | Shredding | Calcination |
|---|---|---|---|---|
| Electricity | 0.1% | - | - | 0.9% |
| Diesel | 8.5% | 1.3% | 21.3% | - |
| Fuel oil | - | - | - | 56.1% |
| Biogas | - | - | - | 9.9% |
| Biomass | - | - | - | 1.9% |
| Total | 8.6% | 1.3% | 21.3% | 68.8% |

In the calcination step, the energy contribution of each source is as follows: biogas (40%), biomass (19%), fuels (37%), electricity (4%). Consequently, the usage of biogas and biomass has a substantial impact on the total carbon footprint of this chamotte. Using these renewable sources translates into a reduction of the total product carbon footprint of almost 50%, compared to a system operating solely with the fuel. As part of Imerys' target to mitigate climate change, a replacement of fossil fuels with biomass or low-emission energy sources is a key priority. This will have an impact on the Group's activities emissions but also the carbon footprint of its products. We should thus expect an improvement of Imerys chamottes' carbon footprint, which is already relatively low.

**Andalusite - France**
*Manufacturing description*
Andalusite is a rock-forming aluminosilicate mineral with a high alumina content used in the production of refractories. Imerys andalusite minerals are ideal solutions for fired and unfired refractory bricks and monolithics, thanks to their outstanding creep and high thermal shock resistance, as well as resistance to chemical attack, slag and metal penetration. This section will focus on one of one of the Imerys' andalusite grades called Kerphalite™ mined and treated in France. Kerphalite™ is a unique product due the separation processes involved in the beneficiation of this mineral. The andalusite ore is extracted from an open pit with a blasting process using explosives and transferred to the treatment plant located one kilometer away. The plant mainly uses electricity and natural gas as energy sources. Coproducts composed of fine dust emissions are introduced back into the production process, improving the mineral resource recovery. The ore is crushed, milled and beneficiated through a refining process composed of a classification with magnetic, densimetric and electrostatic separations to remove impurities. The purified product is then further dried, milled and packaged (Figure 2).

*Fig. 2: Imerys milled Kerphalite™ manufacturing process.*
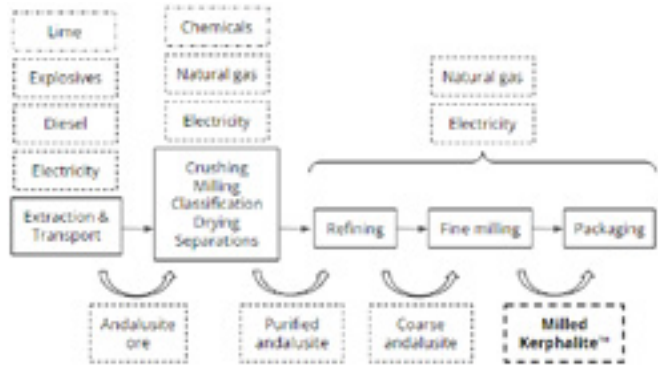


*Data sources and results*
For this system, 2021 primary data from Imerys plant and secondary data from the ecoinvent library were used. This milled Kerphalite™ has a carbon footprint of **312 kg CO2eq / ton**. Almost 80% of the carbon footprint comes from the energy production and use. The biggest impact contributor is the natural gas used in the process (Table 2).

Tab. 2: Carbon footprint breakdown in the manufacturing of the Imerys milled Kerphalite™ (France).

| Impact contributor | Extraction | Crushing to separations | Refining to packaging | Other |
|---|---|---|---|---|
| Electricity | 0.4% | 5.0% | 1.5% | 1.1% |
| Diesel | 10.8% | - | - | 2.1% |
| Natural gas | - | 52.1% | 3.1% | 3.5% |
| Explosives | 6.3% | - | - | - |
| Lime | 7.8% | - | - | 1.0% |
| Chemicals | - | 0.4% | - | 3.1% |
| Packaging | - | - | 1.8% | - |
| Total | 25.3% | 57.5% | 6.4% | 10.8% |

Electricity accounts for more than 20% of the energy consumption in the system. However, its impact is limited by the emission factor of the French grid mix, which is among the lowest in Europe and worldwide [7]. The replacement of natural gas with a low-emission energy source would further reduce the carbon footprint of this andalusite grade.

**White fused alumina - Austria**
Imerys is the world's largest producer of fused alumina. Fused aluminas are used in different industries including refractories, thanks to their great resistance to shocks, as well as thermal and chemical stability. The manufacturing process of this white fused alumina model includes the production and supply of calcined alumina (90% sourced from Europe), as well as graphite electrodes from China used in the electric arc furnace. The calcined alumina is smelted by electrothermal fusion in the furnace at temperatures of around 2000°C, before being crushed, milled, sieved, blended and packed (Figure 3).

*Fig. 3: Imerys white fused alumina manufacturing process.*
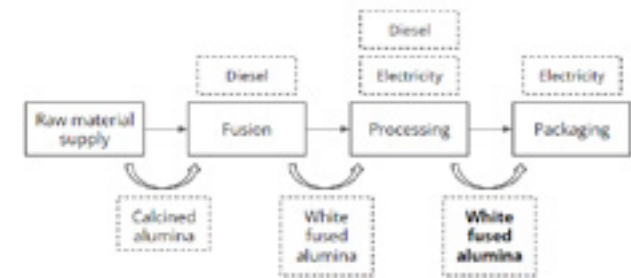


*Data sources and results*
For this system, 2021 primary data from Imerys plant and secondary data from the ecoinvent library were used. This standard white fused alumina grade has a carbon footprint of **1113 kg CO2eq / ton**. Alumina feedstock production and supply to Imerys represent more than 80% of the total impact.

Tab. 3: Carbon footprint breakdown in the manufacturing of the Imerys standard white fused alumina (Austria).

| Impact contributor | Raw material | Fusion to packaging |
|---|---|---|
| Calcined alumina | 82.4% | - |
| Graphite | 0.6% | 1.0% |
| Raw materials supply | 7.7% | - |
| Electricity (hydro) | - | 6.9% |
| Diesel | - | 0.3% |
| Packaging materials | - | 1.1% |
| Total | 90.7% | 9.3% |

The calcined alumina production has been modeled using information from the literature [8]. Fossil fuels production and combustion are the biggest carbon footprint contributors in the calcined alumina manufacturing (Table 4).

Tab. 4: Carbon footprint breakdown in the manufacturing of the calcined alumina (Europe) [8].

| Impact contributor | Raw material | Processing |
|---|---|---|
| Bauxite | 3.2% | - |
| Heavy fuel oil | - | 32.9% |
| Natural gas | - | 33.1% |
| Coal | - | 23.8% |
| Electricity | - | 6.8% |
| Diesel | - | 0.2% |
| Total | 3.2% | 96.8% |

The impact of the fusion and processing of the white fused alumina is highly reduced thanks to the usage of hydroelectric power in this Imerys Austrian plant, accounting for more than 99% of the energy used in the process. Consequently, the white fused alumina carbon footprint is impacted by the calcined alumina production and origin, but it may also differ more or less significantly based on the electricity used in the furnace, which depends on the factory location and thus its power sourcing. For instance, China's electricity emission factor ranges between 250 and 950 g CO2eq / kWh according to the region [9], which is around five to more than 20 times higher than the average of the European grids. A simulation has been performed with the same system and energy ratio but replacing the Austrian electricity model with a Chinese model (State Grid Corporation of China - SGCC) [6]. The results showed that a white fused alumina produced with this Chinese electricity model has a carbon footprint of around 6000 kg CO2eq / ton, which is more than five times higher than the one produced in the Imerys' Austrian factory.

**CONCLUSION AND OUTLOOK**

Product carbon footprint is influenced by multiple factors including the LCA method, raw materials origin or energy sources used in the processes. We could particularly see the role played by energy throughout the life cycle. It is important to note that carrying out product carbon footprint comparison is only valid if a functional unit has been clearly defined. As the downstream industries or customers to the refractory industry push forward to decarbonize, the contribution the refractory industry brings to this decarbonization will be assisted by the ability of raw material suppliers to provide high-quality low-carbon footprint solutions. Imerys is well positioned to help the downstream actors like the iron and steel, aluminum, cement, glass and the hydrocarbon

processing industries achieve their sustainability goals and help reduce their overall greenhouse gas emissions. These sustainability goals will continue to help us minimize the negative impact of manmade climate change on the planet. Unlocking the sustainable potential of minerals in a responsible way, using science-based targets and methodologies, choosing renewable energy sources like solar, hydropower and biomass, and last but not least developing new innovative products and processes targeting higher efficiency in production and during use in refractories for the high temperature industries will allow Imerys to assist its customers in reaching sustainability targets and helping to preserve the planet.

**REFERENCES**
[1]  Imerys, Annual Sustainability Report, 2022, p. 19
[2]  Imerys, Annual Sustainability Report, 2022, p. 46
[3]  ISO 14040, Environmental management - Life cycle assessment - Principles and framework, 2006
[4]  European Environment Agency, Life Cycle Assessment, A guide to approaches, experiences and information sources, Environmental Issues Series n°6, p.30
[5]  E. Henry-Lanier, M. Szepizdyn, C. Parr, The optimisation of the carbon footprint of calcium aluminate cement containing castables, 2015
[6]  https://ecoinvent.org/the-ecoinvent-database/
[7]  Carbon Footprint, Country-specific electricity grid greenhouse gas emission factors, 2023
[8]  S. Königshofer, Developing a model to calculate the carbon footprint of refractory products, University of Leoben, 2012
[9]  Shen Qu, Sai Liang, Ming Xu, $CO_2$ emissions embodied in interprovincial electricity transmissions in China, 2017

# SINTERING AND THERMO-MECHANICAL CHARACTERIZATION OF A NOVEL REFRACTORY GRADE BAUXITE

Noronha, Luiz Gustavo.
Bautek Minerais, Caldas, Brazil

Muche, Dereck Nills Ferreira.
Universidade Federal de São Carlos, São Carlos, Brazil

**ABSTRACT**

The global market for refractory grade bauxite (RGB) has been supplied by few players located in China and Guyana, mostly because of the chemical and mineralogical restrict specifications required for this class of material. When considering the mineralogical phases of the refractory grade bauxite, the main phases present higher content of corundum, tialite and mullite. Recently, a new Brazilian bauxite mine, located in Barro Alto, State of Goias, is capable of producing bauxite with higher $Al_2O_3$, low $Fe_2O_3$ and lower $TiO_2$ contents, than those available in the market. Herein, the present work focuses on the processing of the Brazilian RGB highlighting 2 main fronts: i) Improving the sintering of the bauxite to be able to attain the benchmark properties for bulk density and apparent porosity, approximately 3,2 g/cm³ and 9% respectively; ii) Comparing it with the global benchmarks (Guyanese and Chinese Refractory Grade Bauxite) in terms of chemical and mineralogical composition, and mechanical performance. Preliminary results so far, have shown that the Brazilian RGB develops only the mineralogical phases corundum and mullite, without the presence of tialite, with a density of ~3,3 g/cm³ and an apparent porosity lower than 10%, showing to be a promising candidate for refractory applications.

## INTRODUCTION

Bauxites are widely used as a source of aluminum and alumina in global production, with this market accounting for a significant portion of global production. However, bauxite has various other applications known as non-metallurgical applications. Among the non-metallurgical applications, the main use is as a refractory aggregate, which accounts for two-thirds of global production (excluding production for metallurgy)[1]. In the application as a refractory aggregate, bauxites are used in high-alumina refractories and can be part of the composition of shaped and monolithic refractories[2].

With refractory bauxite production controlled only by producers located in China and the Guianas [1], there is a need for new providers to achieve greater diversification and availability of the product globally. In recent years, due to several factors, production in the main producing country has been significantly reduced, which directly impacts the entire production chain. Therefore, the present study introduces a new source of material produced from the gibbsite ore in the region of Barro Alto, Goiás state, Brazil [3].

Bauxite can have two mineralogical sources, diaspore, predominant in China, and gibbsite, predominant in tropical regions such as the Guianas, India, and Brazil, and also, the contaminants that directly influence the properties of the final product, it is necessary to conduct a comprehensive analysis from the characterization of raw materials, the appropriate mineral processing, which greatly impact the quality of the final product [4], to the formation of the industrial sintered aggregate.

Refractory bauxites on the other hand, are specified to have low levels of contaminants, including iron oxides, titanium, alkali and alkaline earth minerals. This is due to the lower refractoriness found in bauxites with few impurities compared to the pure $Al_2O_3$-$SiO_2$ system [5], where even small contamination of titanium and iron significantly reduces the refractoriness of the material.

Typically, refractory bauxites have high refractoriness (~1840°C), but their refractoriness is reduced under load (1450-1550°C) due to impurities such as $TiO_2$ and $Fe_2O_3$, responsible for forming a liquid phase at these temperatures.

Secondary thermal expansion is another phenomenon that decreases the mechanical properties of refractories made from bauxites. Bauxites from specific regions in China have low secondary thermal expansion due to their low impurity content and unique phase change behavior in diaspore bauxites. In contrast, South American raw materials, mostly gibbsitic, exhibit a more significant occurrence of this phenomenon, making it harder to be used in high-alumina refractories applications, particularly when combined with refractory clays.[6]–[8]

Previous work on literature evaluated the impact of aggregate particle size in a refractory with 70% alumina composition. Fine bauxite fractions and coarse fractions, as well as fine and coarse alpha alumina, were analyzed. The study found that the use of fine fractions reduces the initial temperature of secondary volume increase. This is attributed to the easier dissolution of smaller bauxite particles, which accelerates the mullite formation process and volumetric expansion compared to coarser fractions of the same bauxite. The study also examined the influence of impurities present in bauxite compared to a refractory made with alpha alumina. It was observed that the behavior of the refractory resembled that of the bauxite in terms of secondary expansion only when contaminants like $Fe_2O_3$ and $TiO_2$ were included. [7], [9]

Caballero et al. [4] conducted a study to examine the influence of processing on the mechanical properties of bauxites, comparing South American and Chinese bauxites. Three processing methods were considered: direct sintering, grinding followed by pressing and sintering, and calcination followed by grinding, pressing, and sintering. Figure 1 shows the results that samples subjected to more complex processing had better mechanical properties, when compared to no processing ones. The maximum strength of South American bauxites, with no previous calcinantion (RBS and BSP) was significantly affected by the higher hydroxyl content compared to Chinese bauxites (RBC and BCP). The samples with the complete processing (BSPP and BCPP) were the ones with the better performance.
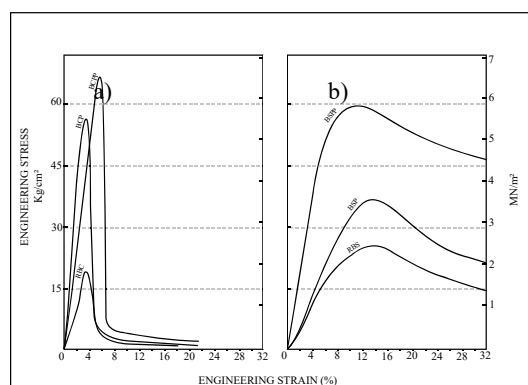


*Figure 1: Stress-strain curves at 1550°C for a constant load rate of 8,3 x 10 $^{-7}$ m/s. a) China samples b) South America Samples[4]*

The stress-strain curves revealed different behaviors for Chinese and South American bauxites. South American bauxites exhibited a toughening mechanism due to the presence of a needle-like mullite skeleton, which deflected cracks and increased toughness. Chinese bauxites, on the other hand, showed a brittle behavior due to the presence of alpha alumina. The tougher behavior of South American bauxites resulted from the more pronounced precipitation of secondary mullite, facilitated by the greater dissolution of unstable alpha alumina grains during sintering. In contrast, Chinese bauxites had more stable alpha alumina grains, therefore not been able to form as much secondary mullite.

Given the restrictions on high impurity levels and the available chemistry in the Barro Alto – GO bauxite deposit, a better understanding of the influence of iron oxide in refractory bauxite compositions is necessary. It has been observed that mullite and corundum have some susceptibility to enter solid solution with $Fe_2O_3$ by substituting $Al^{3+}$ cations with $Fe^{3+}$. Herein, Caballero and Aza [10] studied the influence of increasing iron content on the high-temperature mechanical properties of refractory bauxites. Analyzing the mineralogical composition of the samples, was observed that the addition of iron results in a considerable reduction in mullite content. It can be concluded that the addition of iron leads to the deterioration of refractory properties due to lower mullite formation and increased liquid phase formation.

The solubility of $TiO_2$ and $Fe_2O_3$ oxides, studied by Caballero and De Aza [11], [12], was analyzed in refractory bauxite compositions containing approximately 80% $Al_2O_3$ at different temperatures (1450 to 1700°C). The results of the solid solution concentrations of each mineralogical phase were analyzed using EDS. The solubility limit of each compound was determined for the main mineralogies present in refractory bauxite: corundum, mullite, and tialite. It can be observed that $Fe_2O_3$ exhibits solubility in all three major phases present in refractory bauxites. However, as the temperature increases, $Fe_2O_3$ tends to reduce its solubility in all compounds, reaching almost no solubility for tialite and mullite phases at 1700°C and 2% in weight for corundum.[7]

Considering the influence of alkalis on the composition and behavior of refractory bauxites, the study by Zhong et al. [13] analyzed that for every 1% of $K_2O$ present, there was a 7% increase in the glassy phase, a reduction of 15-20% in mullite content, and an increase of 8-13% of the corundum content. Therefore, with the addition of $K_2O$, the crack deflection mechanism generated by the presence of intragranular mullite around alumina grains is reduced. Based on the analysis of the quaternary phase diagram $Al_2O_3$-$SiO_2$-$Fe_2O_3$-$TiO_2$, it has been determined that while alkali and alkaline-earth oxides do not affect the phase relationship and crystallization sequence, their presence significantly influences the liquid formation temperature and its concentration at various temperatures.

In conclusion, two studies analyzed the production of refractory-grade bauxite using a blend of Brazilian gibbsite sources with low TiO2 content, similar to the ore present in this study. The South American bauxite exhibited thermomechanical properties similar to the standard product from Guyana and superior to the standard Chinese product. Considering the chemistry of the produced Brazilian bauxite, it had a high Fe2O3 content (+4.5%) and a relatively low TiO2 content (-1.5%). As a result, it predominantly generated Gibbsite and Mullite phases, with a lower formation of Hematite.[14], [15]

The present study will focus on the processing, characterization, and thermomechanical analysis of refractory-grade bauxite, exclusively using the Barro Alto - GO bauxite source. The production method will encompass the entire ideal ceramic processing, including initial thermal treatment, grinding, briquetting, and sintering. Additionally, after the thermal treatment of the gibbsitic ore, a magnetic separation process will be applied to achieve a higher-grade product with Al2O3 content above 90%, controlled Fe2O3 below 3.0%, and TiO2 content below 0.5%. These unique characteristics are specific to the RGB developed in this study.

## MATERIALS AND METHODS

For the preparation of bauxite samples from Barro Alto, Goiás, their initial step involved calcination at 1200°C in a rotary furnace. This process followed the recommended procedure [5], which includes a necessary thermal treatment prior to sintering. After calcination, the samples were subjected to magnetic separation to reduce the $Fe_2O_3$ content. The magnetically separated product was then ground to sizes of 0.150 mm and 0.075 mm and pressed at pressures of 40, and 80 MPa using a uniaxial press. The pressed bodies were fired in a static electric furnace at 1600°C, with a dwell time of 3 hours and a heating rate of 5°C/min. The sintered bodies were subsequently measured for apparent density and porosity in accordance with the ABNT NBR 8592 standard. X-ray diffraction analysis were conducted on the sintered gibbsitic bauxite samples from Barro Alto (BAUTEK R-90), along with the market bauxite samples (from Guiana and China). This analysis was performed using an Empyrean X-ray diffractometer equipped with a position-sensitive detector. The identification of crystalline phases was carried out by comparing the sample diffractogram with the PDF2 and ICSD databases from the International Centre for Diffraction Data. Quantification of the phases was carried out using the Rietveld method, employing crystal structures from the ICSD.

Benchmark refractory grade bauxite samples were obtained from two global suppliers, one from the Guianas (South America) and the other from China, both with reported $Al_2O_3$ contents above 88%. XRF analysis was performed on fused pellets using Panalytical equipment to confirm the composition of the market samples and the product made from the Barro Alto ore. Thermodynamic simulation was conducted using the FactSage software to evaluate the microstructural composition at different temperatures based on the oxide contents of each sample.

## RESULTS AND DISCUSSION

Table 1 depicts the results of the XRF analysis of the three samples, the bauxite from Barro Alto mine is described as BAUTEK R-90, the guianese bauxite is the BX GUIANA and the chinese one is the BX CHINA.

*Table 1: XRF Analysis of the three analyzed samples.*

| Sample | $Al_2O_3$ [%] | $Fe_2O_3$ [%] | $SiO_2$ [%] | $TiO_2$ [%] | $K_2O$ [%] |
|---|---|---|---|---|---|
| BAUTEK R-90 | 93.00 | 2,54 | 3,04 | 0,39 | 0,01 |
| BX GUIANA | 89,70 | 1,57 | 4,84 | 3,47 | 0,10 |
| BX CHINA | 86,70 | 2,01 | 4,62 | 3,48 | 0,26 |

Based on the XRF data provided in the table above, thermodynamic analyses were conducted to evaluate the possible phases present and the presence of a liquid phase at the proposed sintering temperature in this study.

Analyzing the data presented in Table 2 and Figure 2, it was observed that among the three bauxite samples, BAUTEK R-90 showed a lower formation of liquid at 1600°C and higher viscosity compared to BX CHINA and BX GUIANA, despite having a higher Fe2O3 content.

Additionally, from the analysis of

19

Figure 2, only corundum and mullite phases are detected in the BAUTEK R-90 sample. As observed, there is no presence of phases containing $Fe_2O_3$, as it tends to form solid solutions with the presented phases and high temperature [11], [12]. On the other hand, the benchmark samples showed the presence of the same two phases as well as some phases containing $TiO_2$, predominantly tialite.



Figure 2:FactSage analysis of the three analyzed samples

*Table 2: Liquid phase analysis of the three samples at 1600°C*

| Sample | Temperature [°C] | Liquid Phase [wt%] | Viscosity [mPa.s] |
|---|---|---|---|
| BAUTEK R-90 | 1600 | 2,1 | 449 |
| BX GUIANA | 1600 | 2,7 | 175 |
| BX CHINA | 1600 | 13,4 | 249 |

The presence of only corundum and mullite phases in BAUTEK R-90 indicates a lower formation of liquid phase at 1600°C, as seen in Table 2, compared to the other two samples, and a higher refractoriness for its composition compared to the others. To confirm the data obtained from thermodynamic simulation, X-ray diffraction analysis was performed, and the quantification of phases was carried out using the Rietveld refinment method and comparing to them crystal structures from the ICSD.

The phase composition of the analyzed bauxites, as shown in Table 3 and **Erro! Fonte de referência não encontrada.** , confirms the thermodynamic simulation previously conducted based on the XRF measurements. The BAUTEK R-90 sample exhibited only corundum and mullite phases. On the other hand, the Chinese and Guiana bauxites, due to their higher content of $TiO_2$, showed a lower concentration of these phases and the formation of tialite.



*Figure 3: XRD Analysis of the three samples. a) BAUTEK R-90; b) BX GUIANA; c) BX CHINA*
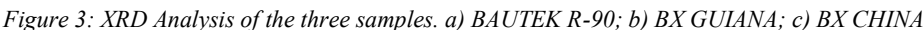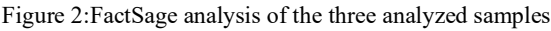
*Table 3: XRD Analysis of the three samples*

| Sample | BAUTEK R-90 | BX GUIANA | BX CHINA |
|---|---|---|---|
| Corundum ICDD 01-071-1123 | 86,00 | 72,00 | 83,00 |
| Mullite ICDD 98-002-8304 | 14,00 | 12,00 | 8,00 |
| Tialite ICDD 98-008-5054 | - | 16,00 | 8,00 |
| Hematite ICDD 98-007-0038 | - | - | 1,00 |
| Rutile ICDD 01-076-0319 | - | - | pp |

Figure 4 presents the apparent densities in relation to the established process variables (particle size and pressing pressure). It is observed that the variation in particle size did not result in a significant change in the density of the fired body. For a pressing pressure of 80 MPa, there was a density variation from 3.32 g/cm³ for particle size of 0.150 mm to 3.36 g/cm³ for particle size of 0.075 mm. On the other hand, it can be observed that the variation in pressing force had a significant influence on the sintering of the BAUTEK R-90 refractory bauxite, with the density varying from 3.07 g/cm³ to 3.36 g/cm³ for the product ground below 0.075 mm.
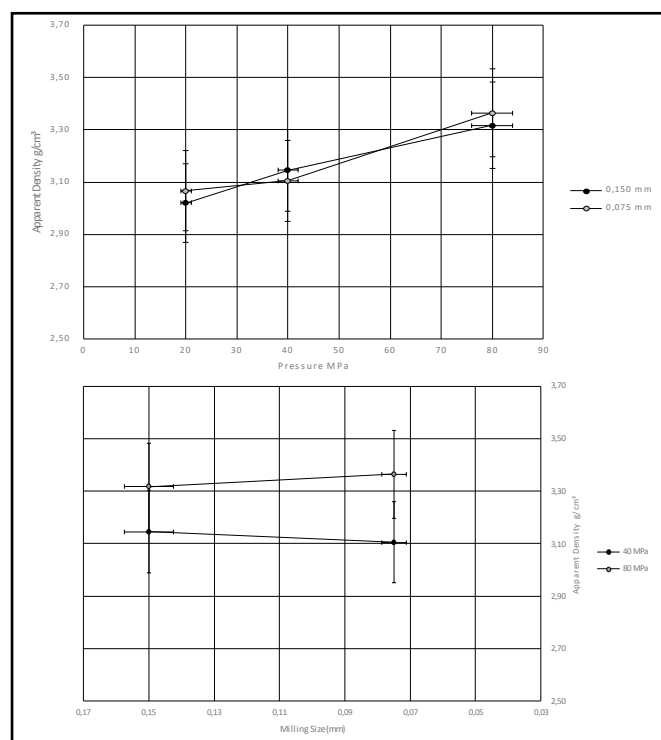


*Figure 4: Processing variables analysis for the sintering of the BAUTEK R-90*

## CONCLUSIONS AND NEXT STEPS

The results demonstrate that the refractory bauxite produced from Barro Alto ore exhibits a unique characteristic of not containing $TiO_2$ in its composition, unlike the Chinese and Guianese bauxites. It was also observed that for proper sintering, where the physical properties of the sintered product meet market standards, a processing route consisted of calcination, grinding, and pressing of the body is necessary before sintering with best results being attained under 0.150 mm of grinding size and 80 MPa of compaction pressure, exhibiting a promising rout for processing of this class of bauxites.

## REFERENCES

[1] Roskill Information Services Ltd., "Non-Metallurgical Bauxite and Alumina: Outlook to 2029," 2019.

[2] T. Hokii, *Refractories Handbook*. Tokyo, 1998.

[3] V. H. S. Moura, "Mineralogia e Geoquímica de Bauxitas de Barro Alto (Goiás): Considerações Genéticas," Dissertação de Mestrado, Univesidade Federal do Pará, Belém, 2019.

[4] A. Caballero, J. Requena, and S. De Aza, "Refractory Bauxites. How Processing Can Improve High Temperature Mechanical Properties," *Ceram Int*, vol. 12, pp. 155–160, 1986.

[5] A. Caballero, F. J. Valle, S. De Aza, and S. Castillo, "Contitution of Calcined Refractory-Grade Bauxites: An Interpretation," *Ceram Int*, vol. 11, no. 2, pp. 45–50, 1985.

[6] C. Pascoal and V. C. Pandolfelli, "Bauxitas refratárias: composição química, fases e propriedades - Parte I," *Cerâmica*, vol. 46, no. 298, pp. 76–82, Jun. 2000, doi: 10.1590/s0366-69132000000200005.

[7] C. Pascoal and V. C. Pandolfelli, "Bauxitas Refratárias: Composição Química, Fases e Propriedades - Parte II," *Cerâmica*, vol. 46, no. 229, pp. 131–138, 2000.

[8] D. Wang and L. Yu, "China Calcined Bauxite Market Production and Outlook," 2019. [Online]. Available: www.nhcl.com.cn

[9] T. D. Mcgee and C. M. Dodd, "Mechanism of Secondary Expansion of High-Alumina Refractories Containing Calcined Bauxite," *The American Ceramic Society*, no. Sixty-Second Annual Meeting, pp. 277–283, 1960.

[10] A. Caballero and S. De Aza, "Influencia del Oxido de Hierro Sobre Las Propriedades Mecanicas a Alta Temperatura de Las Bauxitas Refractarias (1)," *Boletín de la Sociedad Española de Cerámica y Vidrio*, vol. 26, pp. 117–121, 1986.

[11] A. Caballero and S. De Aza, "The System Al2O3-SiO2-TiO2-Iron Oxide in Air and its Practical Implications," *Science of Ceramics*, vol. 14, pp. 443–448, 1988.

[12] A. Caballero and S. De Aza, "The System Al2O3-SiO2-TiO2-Iron Oxide in Air to Understand the Constitution of Refractory Bauxites at High Temperatures," *UNITECR 89*, pp. 1642–1651, 1989.

[13] X. Zhong, G. Sun, and R. Yin, "Relationship of Creep Properties of Bauxite Refractories Microstructure," *Ceramics Engineering and Science Proceedings*, vol. 7, no. 1/2, pp. 314–323, 1986.

[14] A. L. Pereira, M. A. Reis, L. L. H. C. Ferreira, and P. M. Nakachima, "Brazilian refractory grade bauxite: A new alternative to refractories makers and users," *Ceramica*, vol. 65, pp. 40–46, Jan. 2019, doi: 10.1590/0366-6913201965S12611.

[15] V. G. de Oliveira, L. L. H. C. Ferreira, M. A. dos Reis, P. M. Nakachima, and A. L. Pereira, "Refractory Grade Bauxite: An Overview About the Effects of Different Bauxite Sources and Forming Processes on the Quality of the Material," *Global Journal of Researches in Engineering: A Mechanical and Mechanics Engineering*, vol. 19, no. 4, pp. 51–67, 2019.

21

# ALMATIS MISSION NEUTRAL REPRESENTS OUR SUSTAINABLE COMMITMENT TO THE REFRACTORY RAW MATERIALS INDUSTRY

Charles Compson
Almatis, Inc, Leetsdale, PA, USA

Andreas Buhr, Hans-Leo Groβ, Admir Skula
Almatis GmbH, Ludwigshafen, DE

**ABSTRACT**

There is increasing focus on carbon accounting and product carbon footprint throughout the value chain from mined materials to consumer goods. Pressure comes from legislators, financiers, end-users, customers and filters down through all supply chain partners. If the European steel & refractory market is to succeed in carbon reduction transformation, a key component will be transparency and understanding within that value chain. As a crucial alumina raw material supplier within that value chain, Almatis will provide a breakdown of the key components that impact our product carbon footprint and the role of Scopes 1,2 & 3 in determining a roadmap for the future. We will further outline our sustainability ambition, target commitments, strategic initiatives and areas of concern over the coming decade.

**SUSTAINABILITY INITIATIVE**

In September 2015, As part of the "*2030 Agenda for Sustainable Development*," the United Nations *17 Sustainable Development Goals* and their combined *169 associated targets* were announced. [1,2] This was stated as "a decision of great historic significance" and a "charter for people and plant in the twenty-first century", and a "...call-for-action for global governments, Parliaments, international institutions, local authorities, civil society, business & the private sector, the scientific and academic community - and all people."



*Figure 1: 17 UN Sustainable Development Goals (SDGs)*

At COP 21 in Paris, On December 12, 2015, the *Paris Agreement* on climate change was signed by 196 participants. [3] More than 70% of the world economies have now pledged their commitment to this binding international treaty. The treaty, as written "...aims to strengthen the global response to the threat of climate change, in the context of sustainable development and efforts to eradicate poverty, including by:

- Holding the increase in global average temperature to well below 2°C above pre-industrial levels and pursue efforts to limit the temperature increase to 1.5°C. This level is now commonly referred to as the *Science Based Targets Initiative (SBTi)*
- Increasing the ability to adapt to the adverse impacts of climate change and foster climate resilience and low greenhouse gas emissions in a manner that does not threaten food production
- Making finance flows consistent with a pathway towards low greenhouse gas emissions and climate-resilient development."

Out of this Treaty, many new goals & targets, government regulations and initiatives have been born. At COP25 in 2019, the *Climate Ambition Alliance* was announced. [4] This was another UN initiative, in an effort to "accelerate the necessary transformation to reach the goals of the Paris Agreement and stabilize the global temperature rise to 1.5°C." All members of the alliance committed to the same goal," achieving *carbon neutrality by 2050*.

**ALMATIS MISSION NEUTR*AL***

Almatis' commitment towards sustainability is our Mission Neutr*AL*. The mission is to provide the lowest delivered carbon footprint in the alumina industry to our core markets and is our long-term ambition towards a sustainable raw material industry. We further envision to lead the development & launch of lower carbon footprint products the advance a lower carbon economy.

Throughout Mission Neutr*AL*, we must impress short-term urgency within the context of a long-term outlook. It is essential that we align with all business & industry partners to ensure progressive targets and transparent reporting. Sustainability must not be just a corporate exercise, it is personal. Everyone must do their part to ensure that daily progress leads to lasting success. Our future generations depend on it.

Mission Neutr*AL* has three key areas:
- Neutr*AL* Ambition – Our vision and roadmap towards a carbon neutral business that delivers products with the lowest carbon footprint in the industry
- Neutr*AL* Commitment – Our strategic targets and initiatives to ensure that our business makes clear and determined progress in the Material Topic areas that are critical to our stakeholders
- NeutrAL Transparency – Our assurance that all critical data will be independently certified and our promise to report progress annually to stakeholders.

*Figure 2: Almatis Key Pillars of Mission Neutral Sustainability Strategy*

**SUSTAINABILITY STRATEGY**

Since the end of 2021, Almatis has been steadily progressing towards a clearly articulated NeutrAL Ambition. Together With our carbon accounting partner Ökotec and independent auditor GütCert, Almatis is certifying our corporate carbon footprint (CCF) and product carbon footprint (PCF). With our sustainability strategy partner, DNV Business Assurance, Almatis is building a sustainability strategy and will publish its first sustainability report.

Almatis program has been developed in alignment with global standards such as GRI (Global Reporting Initiative), SASB (Sustainable Accounting Standards Board), and the GHG (Green House Gas) Protocol and establishing Corporate Carbon Footprint (CCF) and Product Carbon Footprint (PCF) reporting. Together with our external partners, over the course of one year, Almatis developed a strategy and roadmap for carbon reduction, established its first corporate and product carbon footprint calculations and successfully passed audit verifications of our carbon accounting methodology and the carbon footprint of our European products.

From the 17 UN Sustainable Development Goals (SDG), seven were selected as being relevant for Almatis: #3 Good health and well-being, #7 Affordable and green energy, #8 Decent work and economic growth, #9 Industry, innovation and infrastructure, #10 Reduced inequalities, #12 Responsible consumption and production, #13 Climate action. After a base line study including the readiness analysis for Almatis, the "materiality" analysis was done. Materiality means here the "material" so relevant topics for the company for establishing the sustainability strategy and definition of targets and action plans. The global standards provide guidance for potential material topics, however, from these big lists of potential topics, it must be narrowed down and focused on about 6 key material topics, which are now being addressed appropriately in the strategy.

The result from internal and external evaluation is the materiality matrix, which enables the selection of those five resp. in our case six material topics for Almatis: Occupational Health & Safety, Employer Attractiveness, Sustainable Supply Chain Management, Energy and GHG Emissions, Environmental Performance, Innovation and R&D.



*Figure 3: Material topics in relation to selected UN sustainable development goals*

The proposed targets for each material area then are aligned with UNGC principles and specific SDGs and sub-SDG targets. Further, these have to be linked directly to a corporate strategy, so that metrics and actions plans are not in conflict. At Almatis, sustainability strategy is a part of our corporate strategy, embedded in all areas of the business. Examples of how this is outlined is given in figure 4.

23

**Respecting our People**

| Material Topic | UNGC Principle | UN SDG's |
|---|---|---|
| Occupational Health & Safety | | |
| • Total recordable injury rate per 200,000hrs<br>• Lost work days per year | **Principle 1** | |
| Employer Attractiveness | | |
| • Turnover rate<br>• Training hours completed | **Principle 6** | |

**Respecting our Planet**

| Material Topic | UNGC Principle | UN SDG's |
|---|---|---|
| Energy & GHG Emissions | | |
| • Implementation of renewable energy<br>• Reduction in Scope 1&2 emissions | **Principle 9** | |
| Environmental Performance | | |
| • Product life cycle assessments complete<br>• | **Principle 8** | |

**Respecting our business**

| Material Topic | UNGC Principle | UN SDG's |
|---|---|---|
| Sustainable Supply Chain | | |
| • Scope 3 emission reductions<br>• Supplier LCA assessments completed | **Principle 4** | |
| Innovation and R&D | | |
| • New products with a sustainable advantage<br>• Alternative & Bio-based fuel implementation | **Principle 9** | |

*Figure 4: Examples of sustainability metrics as part of Almatis corporate strategic directions.*

**CARBON ACCOUNTING**

Once the accounting methodology is established, all data must be compiled and evaluated for reporting specific material & packaging related product carbon footprints. The data collection is quite complex and requires cooperation and establishing data that is either coming from suppliers or else a reliable basis remains a huge challenge for determining an accurate and verifiable footprint calculation. GutCert audited and validated the method first, and then audited and verified the product carbon footprint reports and results. Fig. 5 gives an example of verified PCFs for Almatis sintered aggregate products and cement products. The carbon footprint of Almatis products is lower when compared to public available figures for competitive white aggregates, which is a significant benefit to the general EU refractory industry that has, up to now, been using significantly higher figures.

*An example of NeutrAL Transparency in practice – the independently certified product carbon footprint values for Ludwigshafen Aggregates and Rotterdam Cement.*
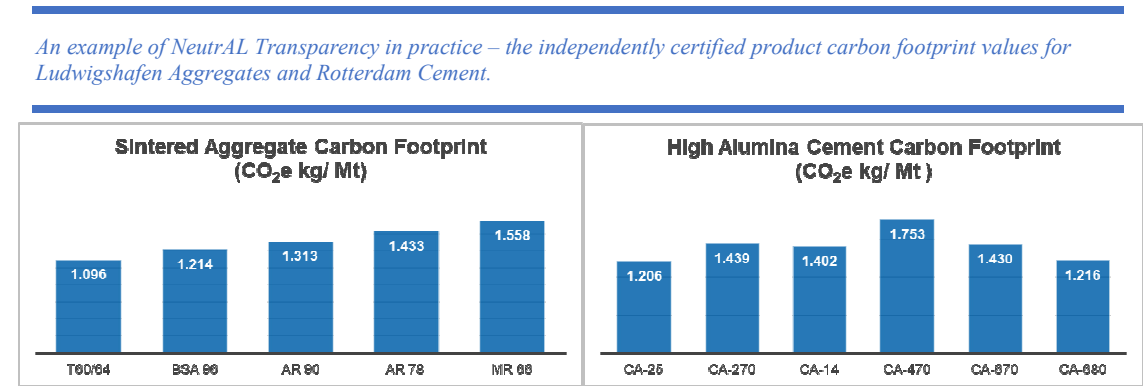
*Figure 5: EU Product Carbon Footprint (PCF) examples*

The carbon accounting methodology can be extrapolated and shared with other operations around the world and utilized for faster calculation and therefore also audit and verification. This process is underway, with the target to have 95% of products verified by 2024.

**PRODUCT INNOVATION WITH SUSTAINABLE ADVANTAGE**

Future product & process developments must focus on having a sustainable advantage. Almatis is committed to future products having a sustainable advantage in 1 of our 6 material topic areas outlined in figure 3. In recent years, the reduction of thermal losses in the steel making process is continuously gaining momentum, and cyclical used vessels such as the steel ladle are of special interest. The heat which is lost from the hot face during the empty stage in ladle cycling depends on the thermal properties of the ladle lining, which are the heat capacity, related to the density, and the thermal conductivity. For alumina-spinel-based, carbon-free linings, the heat losses are 10-15K lower when compared to magnesia-carbon bricks, which can save specific cost per tonne of steel in the magnitude of the refractories lining costs of the ladle! Almatis is developing a lower density aggregate than tabular alumina which will further reduce such heat losses and also reduces the weight of the refractory lining.

CA-SYNC cement was developed to overcome challenges in the production of pre-cast shapes with an inner core such as well blocks, seating blocks, EAF delta sections, and others. Due to the inherent setting shrinkage taking place when the cement phases are hydrating, the time window for removing the inner core is rather short, e.g. 20 min for regular 70% alumina cement whereas it is more than an hour for CA-SYNC. If the core is removed too late, microcracks are induced which lead to macrocracks during drying and yield losses in production. CA-SYNC helps to improve production efficiency and saving energy.

In China, the use of chromium oxide in purging plugs still is very common, though the synthetic chromium oxide is expensive and the disposal of chromium containing refractories waste can become an issue as it is in many cases already in the rest of the world. Extended investigations including thermal shock and slag resistance testing have proved that E-SY 88 reactive alumina can replace chromium oxide in such formulations without compromising hot properties and slag resistance, and the thermal shock resistance is even improved.

Another example from outside the refractories industry is Almatis TR 150, a crystalline silica free polishing alumina as alternative to natural based Tripoli for industrial polishing of aluminum and brass. Tripoli has been classified carcinogenic due to its crystalline silica content. TR 150 provides a safe alternative with equivalent or better performance than the crystalline silica counterpart and is a safe, sustainable solution for the future.

**CONCLUSION**

Almatis' mission is the be the chosen partner in alumina-based products and solutions. Almatis Mission NeutrAL means a long-term ambition and commitment towards a sustainable future. Our target is to supply alumina products with the lowest delivered carbon footprint in order to help advance our industry and the global community. We have achieved verified product carbon footprints for our European sintered aggregate products and cements, and for most European calcined and reactive aluminas. These are just stepping stones in a path toward understanding our carbon impact, stablishing the baseline of our product carbon footprint and the foundational structure behind our sustainability strategy.

**REFERENCES**

[1] Transforming our world: the 2030 Agenda for Sustainable Development | Department of Economic and Social Affairs (sdgs.un.org/2030agenda)
[2] THE 17 GOALS | Sustainable Development (sdgs.un.org/goals)
[3] https://unfccc.int/process-and-meetings/the-paris-agreement/the-paris-agreement
[4] https://cop25.mma.gob.cl/en/climate-ambition-alliance/

25

# MANAGING PERFORMANCE OF CALCINED ALUMINAS THROUGH MANUFACTURING PROCESS MODIFICATIONS

Carl Zetterström, Jerome Contat, Paul Soler, Johnson Lee
Alteo, Gardanne, France

**ABSTRACT**

The characteristics of calcined alumina impact greatly on the behaviour of refractory castables and the final refractory properties in application. Calcined aluminas are typically described by a chemical analysis, the specific surface (BET) and the particle size distribution (PSD), and these in turn depend on the manufacturing process.

Over the last century, Gardanne plant has been a major actor in the world of alumina manufacturing using the Bayer process, which consists in dissolving bauxite and precipitating an alumina hydrate. In 2022, the Bayer process in Gardanne was partially closed, and instead alumina hydrates are sourced on the market and used for the manufacturing of Calcined Aluminas.

Following the modifications to the manufacturing process, extensive work was done in order to ensure the quality and stability of the products, independently of variations in the properties of the alumina hydrates. Work was carried out to achieve the same quality of calcined alumina in terms of chemistry, BET and PSD of the alumina powder, while using alumina hydrates having varying characteristics, and furthermore also evaluating the impact from the calcined alumina on the behaviour of refractory castables.

## INTRODUCTION

Alteo, located in Gardanne, France, is a prominent alumina manufacturer with a rich history in the industry. For over a century, the company has been at the forefront of producing high-quality alumina and related products. With its roots dating back to 1894, Alteo has consistently demonstrated its expertise and commitment to excellence.

The company's journey began with the creation of the worlds first industrial Bayer process, and a few years later was integrated with the Pechiney industrial group.

Over time, the company expanded its operations, optimizing its production processes and diversifying its product portfolio. Today, Alteo is recognized as a leading global supplier of specialty aluminas for the refractory market as well as a wide range of industries such as technical ceramics, lithium-ion batteries and abrasives.

The Gardanne plant has consistently invested in research and development to enhance its product offerings and stay at the cutting edge of alumina technology. The company has developed innovative solutions and tailored products to meet the specific needs and requirements of its diverse customer base. With a strong emphasis on sustainability, Alteo has also made significant strides in reducing its environmental impact and promoting responsible practices throughout its operations.

Through its dedication to quality, innovation, and sustainability, Alteo has earned a reputation for reliability and excellence in the alumina industry. The company continues to evolve and adapt to the changing market dynamics, driving forward the development of new applications for alumina and supporting its customers' success worldwide.

In 2022, as a logic step in Alteo's continuous focus on specialty aluminas, the Bayer process was replaced by external sources of alumina hydrates. The purpose of this paper is to give some insight into the vast program of testing and validation that was issued in order to guarantee that our products would maintain the high standards our customers have come to expect, and that defines our brand.

## MANUFACTURING OF ALUMINA

*The Bayer Process*

The initial step in manufacturing alumina for the purpose of refractory materials always starts with the Bayer process. Alumina hydrate is extracted from the mineral ore Bauxite in the Bayer Process which involves a dissolution of bauxite in soda and precipitation and drying of hydrates as a white crystalline powder.

One of the significant factors driving the global alumina hydrate market is the ever-increasing demand for aluminium metal. The construction sector also contributes to the demand for alumina hydrate due to its use in fire-retardant materials, ceramics, and glass manufacturing.

*Calcination of alumina hydrate*

The hydrate is calcined in a rotary furnace. In the first step of calcination, de-hydration occurs transforming the hydrate into a highly disorganized structure of pure alumina, during this step the specific surface (BET) increases drastically to numbers above 300 $m^2/g$. A schematic of the influence on BET during calcination is represented in *Fig 1*. While temperature increases during the calcination, and depending on the initial structure of the hydrate, its particle size and the rate of decomposition, the alumina will morph through different types of transition alumina before reaching the most stable state which is the alpha-alumina crystal structure [1]. Starting from the alumina hydrate gibbsite, $Al(OH)_3$, this usually follows two routes: (a) gibbsite-boehmite-$\delta$-$\gamma$-$\theta$-$\alpha$-$Al_2O_3$ or (b) gibbsite-$\chi$-$\kappa$-$\alpha$-$Al_2O_3$ [1] [2]. The former is supposedly more common, but both can happen simultaneously, and some different parameters can be beneficial for one route or the other. While this transformation goes on, the BET gradually decreases down to below 1 $m^2/g$. The temperature required to transform the transition alumina into alpha-alumina takes place above 1200°C, even if route (b) is at a slightly lower temperature than (a). Nevertheless, it's possible to decrease this temperature significantly independently of route, by use of additives, such as nucleation seeds ($\alpha$-$Al_2O_3$, $\alpha$-$Fe_2O_3$) [3] [4] and mineralizers [5] [6]. Furthermore, after it is formed, the alpha-alumina crystal will grow and typically reaches a size of between 2 to 3 µm in highly calcined products. This is important because the crystal size will be a natural limit for the particle size during milling. It can be mentioned here that for transition alumina, the BET is mostly a measure of calcination degree, while for hard calcined products the BET becomes a measure mainly related to particle size.

*Fig. 1: Impact of Calcination Temperature on BET*
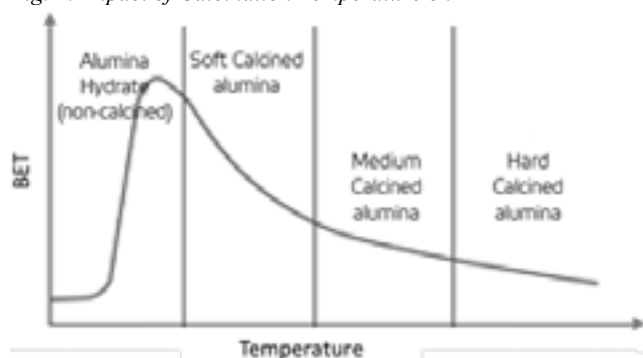


In commercial products, aluminas are referred to as "calcined" and "reactive". The distinction between these two words will be found in the degree of calcination. Typically, products that are "hard"

calcined, where the transformation to alpha-alumina is almost complete, specific surface is very low and the crystal size is large are what we call "calcined". Reactive aluminas are made from a combination of slightly higher BET, and particularly a smaller crystal size which allows for smaller particle size. It's the combination of BET and particle size that make the product more reactive.

*Milling stage*

The final stage in manufacturing of alumina for refractories consists in the milling. Various processes exist including continuous and batch processes, ball milling, air jet and wet grinding. As mentioned, the alpha-alumina crystal size plays an important role in the milling. In fact, the milling process consists in breaking apart agglomerations of individual crystals, but its virtually impossible to break the actual crystal. In highly calcined products, the crystal size is typically in the range of 2 to 3 μm, and most ground high calcined products will have a particle size between 3 and 6 μm.

**MATERIALS AND METHODS**

In the framework of finding a new raw material source, multiple different sources of alumina hydrate, were obtained and evaluated. Part of this work is presented in this paper. The hydrates are evaluated as such for their chemical properties, granulometry and morphology. The calcined products are characterized according to their BET, crystal size (sd50R), particle size distribution (PSD) and chemical composition. The applicative performance is evaluated by the flow properties in concrete (standard recipe in Tab. 4) and mechanical properties after firing. All externally sourced hydrates (EH-1 to EH-10) are compared to the historical hydrate from the internal Bayer process of Gardanne (AH). The chosen refractory formula is a relatively pure recipe with minimal impurities added from the aggregates. This way the maximum impact from chemical impurities, particularly soda, from the calcined alumina is expected to be observed.

**RESULTS AND DISCUSSION**

**Characterisation of Hydrates**

Tab. 1: Chemical Analysis of Alumina Hydrates

| Hydrate | $H_2O$ | ld50 | $Na_2O$ tot | CaO | $SiO_2$ | $Fe_2O_3$ |
|---|---|---|---|---|---|---|
| | [%] | [μm] | [ppm] | [ppm] | [ppm] | [ppm] |
| AH | 3,1 | 111 | 1000 | 105 | 35 | 95 |
| EH-1 | 4 | 130 | 2800 | 40 | 90 | 75 |
| EH-2 | 1,2 | 140 | 2300 | 130 | 60 | 105 |
| EH-3 | 5 | 115 | 2100 | 20 | 60 | 80 |
| EH-4 | 4,2 | 106 | 2300 | 130 | 50 | 100 |
| EH-5 | 5,5 | 125 | 2350 | 240 | 35 | 40 |
| EH-6 | 3,9 | 116 | 2300 | 115 | 75 | 185 |
| EH-7 | 4,9 | 77 | 2100 | 105 | 165 | 125 |
| EH-8 | 9,3 | 129 | 500 | 60 | 25 | 55 |
| EH-9 | 1,3 | 80 | 1450 | 295 | 100 | 55 |
| EH-10 | 5,8 | 122 | 2950 | 225 | 60 | 45 |

The main impurity of alumina hydrates is soda from the Bayer process, and the measured content in most externally sourced hydrates are higher than the historical Gardanne hydrate. This has an impact on the calcination which is discussed later.

Fig. 2: Color variation of hydrates and Fe2O3 content in [ppm]



| EH-8 (55) | AH (95) | EH-6 (185) |
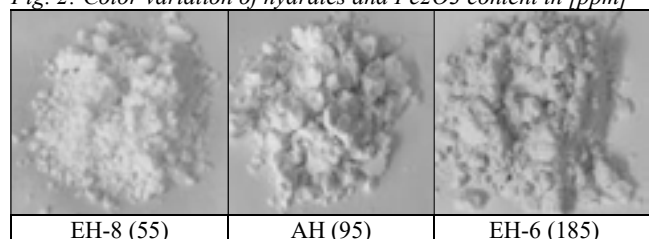
Second important impurity to consider in Tab. 1 is the iron content. Several applications of aluminas are sensitive to iron and it also has an impact on the color/whiteness of the hydrate, turning it slightly reddish. An example is given in *Fig 2*.

A third important factor is related to the PSD. Increased amounts of small particles, (small ld10), will impact the flow of the particles in the furnace and it is believed to improve the alphanisation of the alumina by promoting the route (b) of alphanisation.

Finally, the morphology of the hydrates was also investigated, and they can be classified according to two typical cases: large crystals in a blocky shape or agglomerates of small crystals in a mosaic type of geometry. Only two hydrates are of the blocky type: AH and EH-4, all other hydrates are mosaic type. This property was studied in some depth. It will be shown later that the impact from the morphology of hydrates on properties of "high" calcined aluminas is low to insignificant. It can have a small influence on lower calcined products, ie. reactive aluminas. To give an example, SEM pictures of these differences are shown in *Fig 3*. However, for the case of reactive aluminas in Gardanne, all hydrates independently of origin, are dissolved and reprecipitated in the Bayer installations. The resulting hydrate is identical to the historical product. This is done primarily for the sake of chemical properties but simultaneously eliminates any difference in morphology, whether it has an influence or not.

Fig. 3: Hydrate Morphology, SEM x1000, bottom scale = 10μm



| AH | EH-3 |
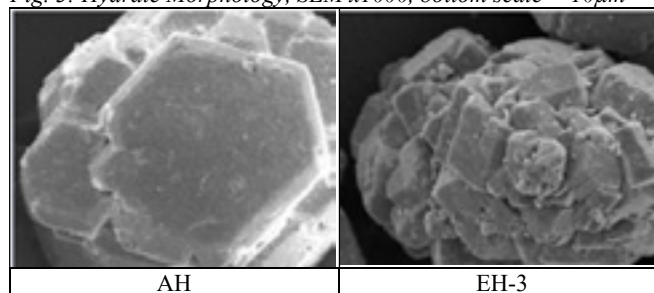
**Characterisation of Calcined Alumina**

The target set in order to compare the different hydrates is to reach the same BET compared to the historical hydrate AH.

Fig 4.: BET vs Temperature for different hydrates
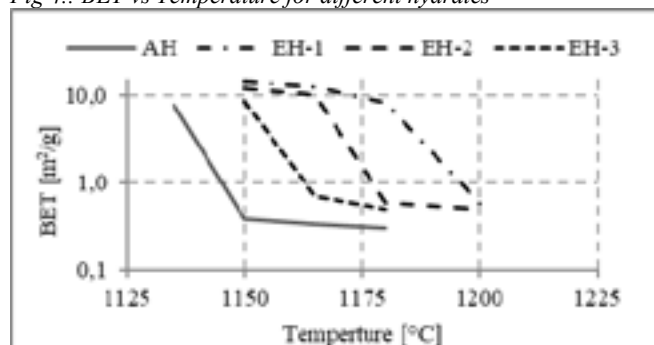


It is observed in *Fig 4*, that during the calcination of different hydrates, the alphanisation takes place at higher temperature when the soda content is higher. The variation is roughly up to 50°C difference. The reason for this is thought to be that the soda ion is relatively large and takes up a lot of space in the alumina crystal structure, thereby physically obstructing movement of atoms into other configurations, notably the alpha structure. Furthermore, this variation in transformation temperature is mentioned in literature [7] and can be observed via thermogravimetric analysis thanks to an exothermic peak related to the alpha transformation. The calcined alumina (C) properties are shown in Tab. 2 here below

Tab 2: Hard Calcined Alumina properties from respective hydrate

| Calcined Hydrate | d10 | d50 | d90 | BET | sd50R | Na$_2$O | CaO | SiO$_2$ | Fe$_2$O$_3$ |
|---|---|---|---|---|---|---|---|---|---|
| | [µm] | [µm] | [µm] | [m$^2$/g] | [µm] | [ppm] | [ppm] | [ppm] | [ppm] |
| CAH | 14 | 81 | 142 | 0,48 | 2.60 | 1950 | 165 | 60 | 150 |
| CEH-1 | 16 | 102 | 185 | 0,46 | 3.30 | 4150 | 105 | 175 | 130 |
| CEH-2 | 17 | 100 | 181 | 0.49 | 2.80 | 3450 | 270 | 185 | 160 |
| CEH-3 | 20 | 85 | 148 | 0,49 | 2.65 | 3000 | 70 | 125 | 115 |

There is an additional impact from the soda, and/or from the higher required calcination temperature, which is an increased crystal size (sd50R). The variation is not insignificant but is still within a normal range in comparison to historical production data over longer periods. As a property of the calcined alumina, a larger alpha crystal size is probably a positive attribute, however, it has a negative impact on the milling time, as can be seen in Tab. 3.

*Morphology of medium calcined alumina*
*Fig 5: SEM pictures of medium calcined hydrates at x1000 and x20.000, bottom scales = 10µm and 1µm respectively*



AH — EH-1



EH-2 — EH-3
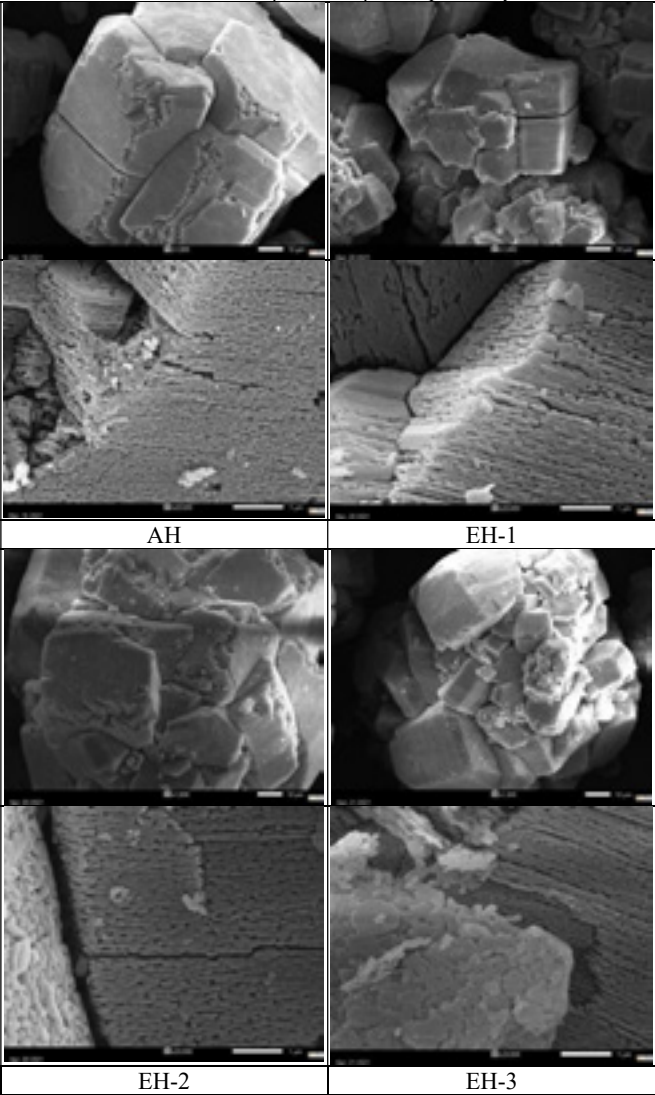
After calcination to a BET of 12m$^2$/g, one can still distinguish the morphology of the initial hydrate. It is most probably not of importance and is definitely not visible in milled products.

*Morphology of hard calcined alumina*
*Fig 6.: SEM pictures of hard calcined alumina at x500 and x5.000, bottom scale = 50µm and 5µm respectively*



AH — EH-1



EH-2 — EH-3
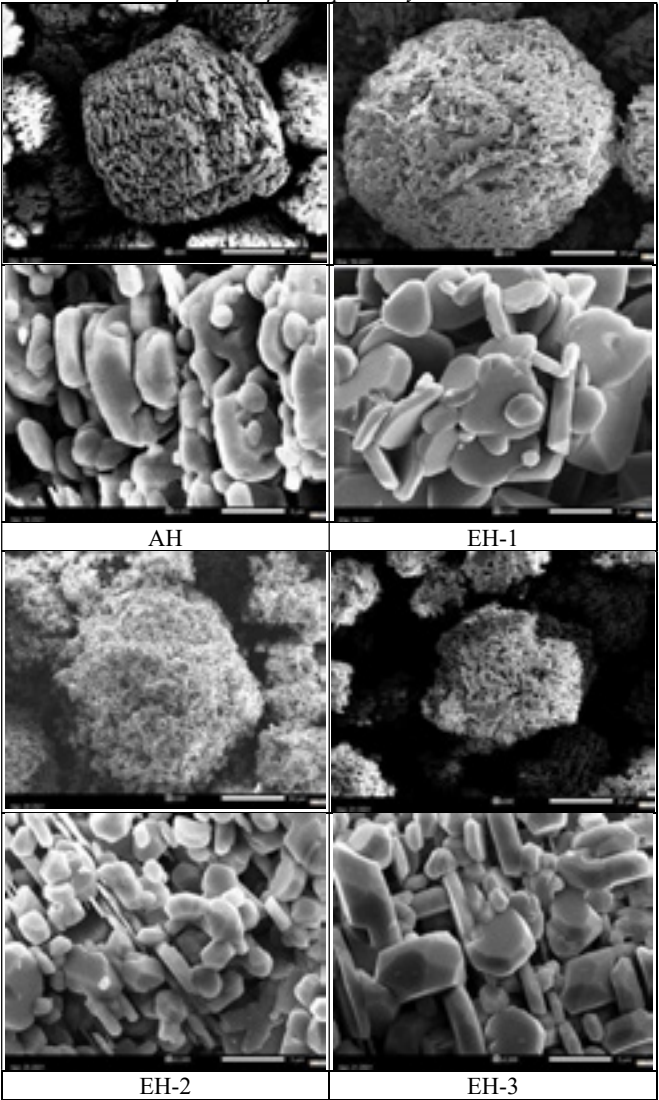
After "hard" calcination down to a BET of below 1m$^2$/g, the initial morphology of the hydrate is unrecognizable. Only the chemical composition of the hydrate is of real importance.

**Characterisation in Application**
The calcined alumina obtained from each respective hydrate were milled to 5µm (Tab. 3) and used in the standard refractory self-flow formula (Tab. 1) for evaluation of application performance.

Tab 3: Hard Calcined Milled Alumina properties

| Calcined and Milled Hydrate | d10 | d50 | d90 | Milling time |
|---|---|---|---|---|
| | [µm] | [µm] | [µm] | [min] |
| CMAH | 1,9 | 5 | 12,9 | 53 |
| CMEH-1 | 2,2 | 5 | 11,5 | 150 |
| CMEH-2 | 2 | 5 | 14,6 | 75 |
| CMEH-3 | 2,12 | 5,1 | 13,2 | 55 |

28

Tab. 4: Standard Refractory Formula for Application Tests

| Raw Material | Specification | [%] |
|---|---|---|
| Tab Alumina | 0-6 mm | 80 |
| CAC | 70% Alumina | 5 |
| Calcined Alumina | Various tested | 6 |
| Reactive Alumina | PFR20 | 4 |
| Reactive Alumina | PFR | 5 |
| Dispersant | PCE | 0,2 |
| Water | | 4,5 |

*Fig 7* shows the flow properies of the concrete using the different hard calcined and milled aluminas.

*Fig 7: Flow measurement of standard formula*
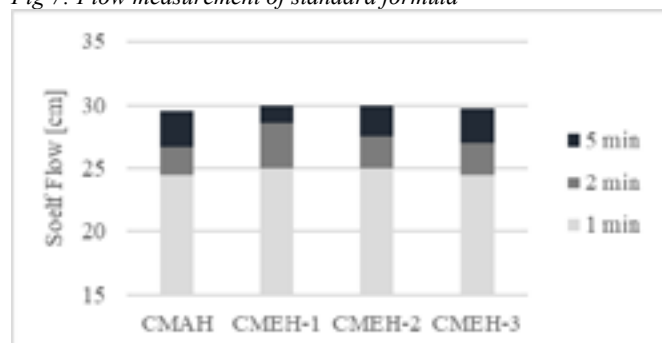


There is no visible impact on flow between any of the aluminas. The one property that is generally associated with flow behaviour is the particle size distribution. In this case all aluminas have been ground down to 5μm and the flow is near identical. In other words, we don't see any influence from for example the soda content on flow properties of castable.

*Fig 8: Porosity and Density of standard formula*
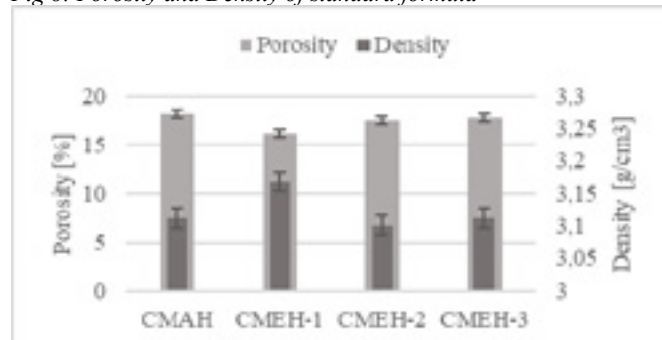


*Fig 9: CCS and MOR of standard formula after firing at 1600°C*
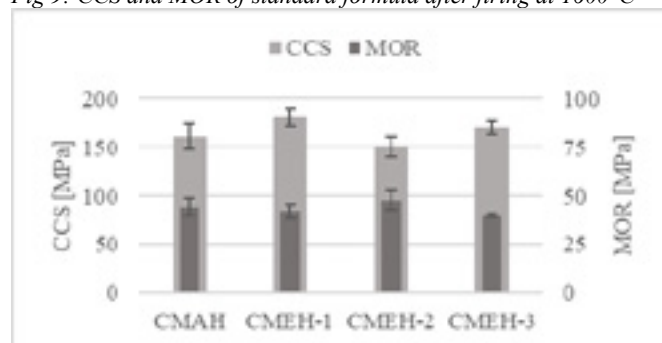


While we see some variations on porosity and density of the obtained concrete slabs after casting. This variation is within what we normally see in concretes. The one alumina that is somewhat different is CMEH-1 where a lower porosity is obtained. We don't believe this is significant.

Lastly, cold crushing strength (CCS) and modulus of rupture (MOR) was measured. All samples are very good and comparable to each other. No significant difference can be attributed to the calcined alumina. A slightly higher value for CMEH-1 is most probably related to the higher density that was obtained with this alumina in this specific series of test.

**CONCLUSION**

Various tests were carried out calcining and milling alumina starting from several different sources of alumina hydrates. It was observed that variations exist in both morphology and chemistry of the hydrates.

The morphology of hydrates could be described as falling into two different types, large crystals in blocky shape or small agglomerated crystals. This morphology remains observable after calcination to $12 m^2/g$ but becomes indistinguishable after "hard" calcination to $1 m^2/g$.

The behaviour of the hydrate during calcination varies depending on the chemistry, specifically the soda content. With higher soda content, the calcination temperature needs to be increased by up to 50°C depending on the % in order to obtain an equivalent specific surface of the calcined alumina. Following the variations in calcination temperature, and/or due to the chemical composition, a varying alpha alumina crystal size is observed which impacts the milling time in order to obtain iso D50 for aluminas calcined from different hydrates.

Results were shown from three different hydrates that had been calcined and milled to close to identical powder properties. The in-application performance was equivalent for all products and in comparison to historical calcined alumina from hydrates of the Gardanne Bayer process.

Managing the performance of the final calcined alumina product finally relies on the capacity and expertise to adapt the calcination and milling processes according to the varying chemical properties of the hydrates.

Any hydrate can be dissolved and reprecipitated, which allows for making of a hydrate identical to historical Gardanne products in terms of both chemistry and morphology, this is the case for all current reactive aluminas in the portfolio for refractory products.

**REFERENCES**
[1] B. Castel, Les alumines et leurs applications, (1990), 17-21
[2] V.J.Ingram Jones, R.Slade, T.W.Davies, J.C.Southern, S.Salvador, Dehydroxylation sequences of gibbsite and bohemite: study of differences between soak and flash calcination and of particle-size effects, J.Mater.Chem.6 (1) (2006) 73–79.
[3] R.B. Bagwell, G.L. Messing, Effect of seeding and water vapor on the nucleation and growth of α-Al2O3 from γ-Al2O3, J.Am.Ceram.Soc.82 (4) (1999) 825–832.
[4] Y.Saito, T.Takei, S.Hayashi, A.Yasumori, K.Okada, Effects on amorphous and crystalline SiO2 additives on γ-Al2O3-to-α-Al2O3 phase transitions, J.Am. Ceram. Soc.81(8) (1998) 2197–2200.
[5] Z.D. Zivkovic,N.Pacovic,M.Filipovic,The effect of AlF3 on the calcination of aluminium hydroxide, Thermochim. Acta 32 (1979) 181–188.
[6] K. Daimon, E. Kato, Morphology of corundum crystallized by heating mixture of η-Al2O3 and AlF3, J.Cryst.Growth 75 (1986) 348–352.
[7] L.D. Hart, Alumina Chemicals, p 99-108: T.J. Carbone, Production processes properties and applications for calcined and high-purity aluminas. 102

29

# INFLUENCE OF MINERAL COMPOSITION ON THE PROCESSING OF IRON−RICH BAUXITE RAW MATERIALS BY USING HYDROCHLORIC ACID LEACHING

Alena Stein, Almuth Sax and Peter Quirmbach

Institute for Integrated Natural Sciences, Technical Chemistry and Corrosion Sciences, University of Koblenz, Koblenz, Germany

## ABSTRACT

Bauxite is an essential raw material for the refractory industry, but it can only be used with sufficient raw material quality. For the classification of bauxite as refractory grade, first of all the chemical composition is crucial and especially the $Fe_2O_3$ content should be < 2 wt%. The global availability of suitable qualities will, however, become increasingly problematic in the future, which is made clear by the European Commission's classification of bauxite as a critical raw material in 2020. Therefore, it is already of great importance to develop strategies that make different bauxite raw materials, for example those rich in iron, accessible for the refractory industry. In this study, it is demonstrated that a beneficiation of iron-rich bauxite raw materials can be carried out by an acid leaching process. For this purpose, raw material grades of different chemical and mineralogical composition are leached in hydrochloric acid and their $Fe_2O_3$ and $Al_2O_3$ contents are compared before and after leaching. In addition, the findings of powder X-ray diffraction measurements (PXRD) to determine mineralogical composition before and after leaching are used to draw conclusions about the leachability of various iron and aluminum minerals in bauxite. These findings, in conjunction with methodologies for determining optimal leaching conditions, complete the understanding of the effectiveness of bauxite processing using hydrochloric acid leaching.

## INTRODUCTION

Bauxite is a residual or sedimentary rock in which the content of aluminum, iron or titanium oxides and/or hydroxides is higher than 50 % by weight and the aluminum minerals dominate over the iron and titanium minerals [1]. Because of its natural formation, bauxite is not a clearly defined mineral of a particular composition. Different bauxites exhibit large differences in both chemical and mineralogical composition. Generally, a chemical composition of 50–80 wt-% $Al_2O_3$, 0–10 wt-% $SiO_2$, and 0–30 wt-% $Fe_2O_3$ is assumed [2], but this is not binding. Especially the iron oxide content varies greatly and influences various properties of the material. In terms of mineralogical composition, the aluminum minerals commonly identified in bauxite are gibbsite, boehmite, and diaspore [2–5]. These form the major phase. The iron-bearing minerals hematite, goethite, maghemite, magnetite, ilmenite, or chamosite are often present as minor phases. Other minerals are for example kaolinite, as well as a variety of other iron- and aluminum-substituted silicates, quartz, anatase, and rutile [4, 6, 7].

Depending on its composition, bauxite can be used for different applications [3]. In the EU, for example, applications include aluminum production at about 90 %, chemical production at about 2 %, use as an abrasive at about 2 %, use in the cement industry at about 3 %, and use as a refractory at about 3 % [8].

The use of iron-rich bauxites is particularly problematic for the refractory industry. Since too high iron contents in the raw material have a strong negative influence on the refractoriness as well as the CO resistance, only raw materials with low $Fe_2O_3$ (< 2 wt-%) can be used. At the same time, the $Al_2O_3$ content in the raw material should be as high as possible (about 80–85 wt-%) [9–13]. For this reason, it is useful to process previously unusable raw materials by reducing the $Fe_2O_3$ content [12, 13].

In the past, there have been several studies on the processing of bauxites and other raw materials by using hydrometallurgical processes [12, 13]. In particular, acid leaching with hydrochloric acid has been shown to be a method with great potential [14–16]. In this context, studies on the kinetics of the dissolution process of different (pure) iron minerals or different iron minerals in bauxite have also

been carried out repeatedly [14–22]. However, the findings obtained vary widely depending on the study and usually relate only to the single mineral studied or to specific leaching conditions such as a particular acid concentration or leaching temperature. In order to specifically investigate the leachability of minerals present in bauxites, different bauxite minerals were leached in this study and their chemical and mineralogical compositions were compared before and after leaching. The focus was on the iron and aluminum minerals present as well as the $Fe_2O_3$ and $Al_2O_3$ contents before and after leaching.

## MATERIALS AND METHODS

### Bauxite raw material

In this study, three different bauxites, Na1, IMF2 and IMC2 were investigated. All three bauxites have different optical appearances (especially color) and differed in their origin. Na1 and IMF2 are European bauxites, while IMC2 is a Chinese one.

### Bauxite leaching

The leaching of the bauxites was carried out on a laboratory scale in a three-neck round bottom flask with reflux condenser. The temperature was set with a tempered oil bath and controlled with an additional thermometer in the flask [23]. First, V = 50 mL or V = 400 mL of hydrochloric acid (HCl) of the desired concentration c(HCl) were added to the flask and heated to the leaching temperature T with stirring. Once the temperature T was reached, m = 10–20 g of bauxite corresponding to the desired solid-acid ratio s/a of grain size GF was added and the leaching time t was started. After completion of the leaching time t, the solid was separated from the acid by a sieve and a centrifuge and was washed with demineralized water to pH neutrality. Drying of the solid took place at T = 40 °C in a drying oven.

The factor settings used for leaching for each bauxite are shown in Tab. 1. Selection of the factor settings was based on computerized statistical design of experiments (DOE) after individual model development and fitting for each bauxite. The detailed procedure is explained in [23] and [24]. The settings used are the conditions at which the lowest $Fe_2O_3$ content was obtained for the respective bauxite by leaching.

Tab. 1: Factor settings of leaching experiments.

| Bauxite | c(HCl) in mol/L | s/a in g/L | T in °C | t in min | Grain fraction GF |
|---------|-----------------|------------|---------|----------|-------------------|
| Na1 | 11,69 | 100 | 90 | 300 | 2.36–3.35 mm |
| IMF2 | 12,00 | 100 | 90 | 180 | < 1.25 mm |
| IMC2 | 6,50 | 100 | 60 | 300 | < 1.25 mm |

### Chemical characterization

For the chemical characterization of the bauxites used, X-ray fluorescence analyses were performed before and after leaching. The X-ray fluorescence (XRF) analyses were performed quantitatively on lithium tetraborate melt tablets in accordance with DIN EN ISO 12677. A Bruker wavelength dispersive spectrometer was used for this purpose. For sample preparation, all samples were ground with the Pulverisette 0 from the company Fritsch (mortar and ball made of hardened stainless steel).

**Mineralogical characterization**

Mineralogical characterization of the samples before and after acid leaching was performed by X-ray powder diffraction (PXRD). PXRD measurements were performed on a Bruker D8 ADVANCE with Cu-Kα radiation and subsequently analyzed using DIFFRAC.EVA V6.0 software, the Crystallography Open Database [25], and the ICDD PDF-4+ 2022 database. Semi-quantitative analysis was performed by Rietveld refinement using TOPAS V6 software. For preparation, the samples were also ground with the Pulverisette 0.

**RESULTS**

**Chemical characterization**

The results of the chemical analyses of the three bauxite raw materials used as well as the leached samples can be seen in Tab. 2, Tab. 3 and Tab. 4. All percentages refer to the ignited substances. The $Al_2O_3$ contents of all samples have increased due to acid leaching, while the $Fe_2O_3$ contents have decreased significantly. In the case of bauxite Na1, it is also noticeable that both the $SiO_2$ and $TiO_2$ contents are significantly higher after leaching (?). In the case of IMC2, the $SiO_2$ content has also risen strongly as a result of the leaching.

Tab. 2: Contents of the main components present in Na1 in wt.-% (based on the ignited substance).

| component | $Al_2O_3$ | $SiO_2$ | $Fe_2O_3$ | $TiO_2$ | LOI (1,025 °C) |
|---|---|---|---|---|---|
| Na1 [24] | 61.17 | 3.01 | 31.27 | 3.83 | 24.56 |
| Na1-HCl | 81.87 | 6.39 | 1.41 | 9.52 | 28.30 |

Tab. 3: Contents of the main components present in IMF2 in wt.-% (based on the ignited substance).

| component | $Al_2O_3$ | $SiO_2$ | $Fe_2O_3$ | $TiO_2$ | LOI (1,025 °C) |
|---|---|---|---|---|---|
| IMF2 [24] | 64.30 | 5.02 | 23.99 | 2.96 | 13.45 |
| IMF2-HCl | 87.23 | 5.97 | 2.66 | 3.50 | 14.21 |

Tab. 4: Contents of the main components present in IMC2 in wt.-% (based on the ignited substance).

| component | $Al_2O_3$ | $SiO_2$ | $Fe_2O_3$ | $TiO_2$ | LOI (1,025 °C) |
|---|---|---|---|---|---|
| IMC2 [24] | 61.90 | 5.54 | 25.52 | 3.30 | 15.71 |
| IMC2-HCl | 82.05 | 9.17 | 2.52 | 4.57 | 13.60 |

**Mineralogical characterization**

Fig. 1, Fig. 2 and Fig. 3 show the measured X-ray diffractograms of the bauxites before and after leaching. The characteristic peaks of the associated phases are marked respectively.

The X-ray diffraction pattern of Na1 shows that goethite and hematite are present as iron phases prior to leaching. The main Al phase is gibbsite ($\gamma$-Al(OH)$_3$). This high proportion of gibbsite causes the comparatively high loss on ignition (see Tab. 2). After leaching, especially the peaks characteristic for hematite ($\alpha$-Fe$_2$O$_3$) are no longer visible and also the peaks assigned to goethite ($\gamma$-FeO(OH)) have lost considerably in intensity. This becomes especially clear in the enlarged section in Fig. 1.
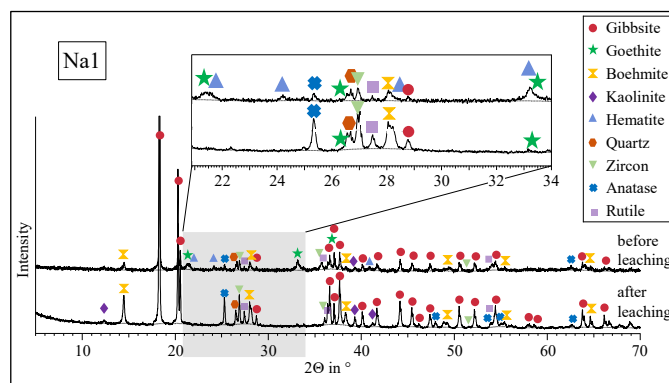


*Fig. 1: PXRD diffractogram of Na1 before and after leaching. According to [24].*

From the X-ray diffractogram of IMF2 in Fig. 2, it is clear that this bauxite contains diaspore ($\alpha$-AlO(OH)) as the main mineral. Furthermore, boehmite ($\gamma$-AlO(OH)) is clearly identified as an aluminum mineral present. The iron minerals are hematite, goethite and ilmenite. After leaching, the intensity of the peaks characteristic of hematite, goethite and ilmenite (FeTiO$_3$) is much lower, so that they can hardly be identified. Boehmite and anatase (TiO$_2$) associated peaks show a significantly higher intensity at the same time. It is also noticeable that calcite (CaCO$_3$) present in the raw material seems to be completely removed after leaching.
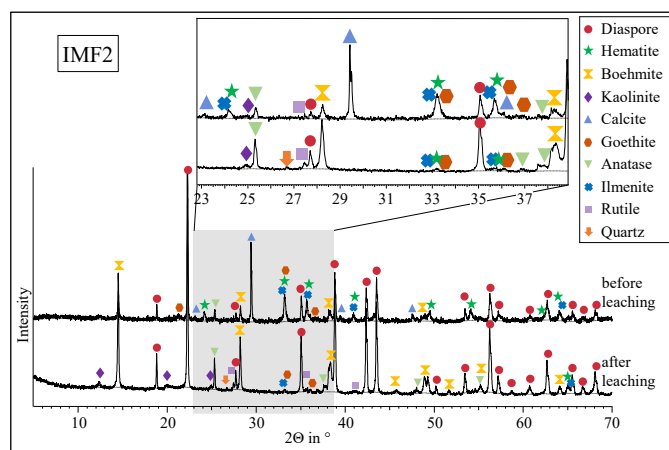


*Fig. 2: PXRD diffractogram of IMF2 before and after leaching. According to [24].*

The X-ray diffraction pattern in Fig. 3 shows a very complex mineral composition of the bauxite IMC2. The main Al mineral is diaspore. As iron minerals goethite, hematite and magnetite (Fe$_3$O$_4$) can be identified in small amounts. Furthermore, iron occurs as a substituent in small amounts in the numerous different silicates present, such as epidote ((Ca$_2$Al$_{2,16}$Fe$_{0,84}$)(SiO$_4$)$_3$(OH)), yoderite ((Al$_{2,84}$Fe$_{0,16}$Mg)O$_2$(SiO$_4$)$_2$), clinozoisite (Ca$_2$Al$_{0,79}$Fe$_{0,21}$Al$_2$[O$_2$(SiO$_4$)(Si$_2$O$_7$)]), chamosite ((Mg$_{5,036}$Fe$_{4,964}$)Al$_{2,724}$(Si$_{5,70}$Al$_{2,30}$O$_{20}$)(OH)$_{16}$) and lizardite (Mg$_{2,79}$Fe$_{0,15}$Al$_{0,06}$)(Si$_{1,84}$Al$_{0,16}$)O$_5$(OH)$_4$). After leaching, only minor changes can be seen in the X-ray diffractogram. The intensity of the peak characteristic of the pure iron minerals goethite and magnetite only decreased. Hematite can no longer be identified after leaching. At the same time, the intensity of the peaks characteristic of diaspore has increased significantly.

31
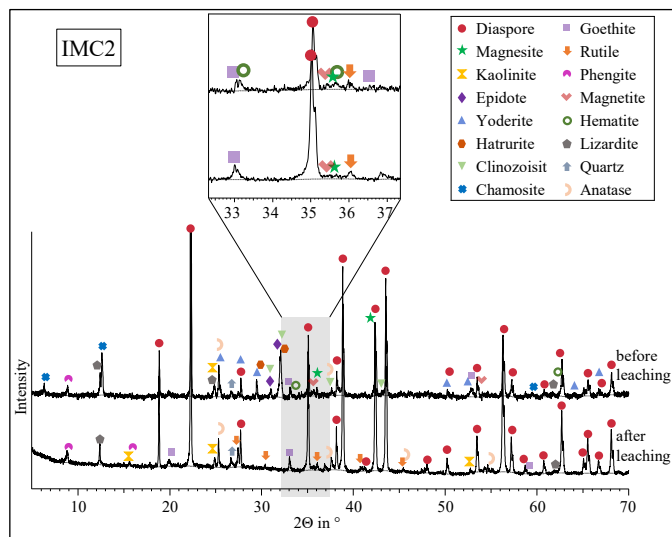
*Fig. 3: PXRD diffractogram of IMC2 before and after leaching. According to [24].*

## DISCUSSION

The results of the chemical and mineralogical analyses of the three bauxites investigated show overall that hardly any aluminum minerals are dissolved during the leaching process. This is evident from the higher intensities of the corresponding peaks in the X-ray diffractograms and from the increased $Al_2O_3$ contents after leaching in all three bauxites. Likewise, the results show that hematite in particular is dissolved during the leaching process. Hematite was identified in all of the bauxites examined prior to leaching, while it was not detectable, or only in very small amounts, after leaching. The goethite contents also appear to have decreased in all three bauxites. However, larger proportions are still present here after leaching compared to hematite.

It is remarkable that after leaching the lowest $Fe_2O_3$ content was obtained at Na1 although the $Fe_2O_3$ content was highest there in the raw material. The results of the X-ray powder diffraction indicate in this context that this is due to the apparently good solubility of hematite in hydrochloric acid. In the case of the bauxites IMF2 and IMC2, in addition to hematite and goethite, ilmenite and magnetite could be identified, respectively, which were also partially dissolved by the hydrochloric acid but can still be detected after leaching. On the other hand, especially IMC2 contains many Fe-substituted silicates, whereby iron is incorporated firmly into foreign crystal lattices. This iron can hardly be reached despite the optimal leaching conditions and therefore remains in the bauxite even after leaching. As a result, the $Fe_2O_3$ content is comparatively high even after leaching, although hardly any characteristic peaks of the iron minerals can be seen in the X-ray diffraction pattern.

The strongly increased $SiO_2$ and $TiO_2$ contents in Na1 after leaching additionally indicate that significant portions of gibbsite were dissolved by the acid leaching. This could additionally indicate that gibbsite bauxites are overall more attacked than diasporic bauxites during the leaching process. As a result, iron components trapped in the bauxite or present as a substituent would also be better removed, resulting in a lower $Fe_2O_3$ content after leaching.

## CONCLUSIONS

Chemical and mineralogical analyses of different bauxites before and after acid leaching were used to investigate the influence of the bauxite composition on the leaching result.

It was observed that hematite in particular can be well dissolved from the bauxite by the acid. Iron constituents that are incorporated as substituents in the crystal lattice of other minerals, in contrast, can hardly be dissolved by the acid. The results have further shown that gibbsite bauxites can be leached better than diasporic bauxites due to

the lower resistance of gibbsite to hydrochloric acid. This means that lower $Fe_2O_3$ contents can be obtained by leaching at optimum parameters. At the same time, however, the $SiO_2$ and $TiO_2$ content in the raw material increases due to the dissolution process of gibbsite.

## REFERENCES

[1] Bárdossy, G. Karst Bauxites. Bauxite Deposits on Carbonate Rocks. Developments in Economic Geology 14. Elsevier Scientific Publishing Company, Amsterdam, Oxford, New York, 1982.

[2] Niggli, P. and Niggli, E. Gesteine und Minerallagerstätten. Zweiter Band: Exogene Gesteine und Minerallagerstätten. Lehrbücher und Monographien aus dem Gebiete Der Exakten Wissenschaften, Mineralogisch-Geotechnische Reihe. Birkhäuser, Basel, 1952.

[3] Sukla, L. B., Pattanaik, A., Pradhan, D. 2019. Advances in Beneficiation of Low-Grade Bauxite. In *Light Metals 2019*, C. Chesonis, Ed. The Minerals, Metals & Materials Series. Springer, Cham, Schweiz, p. 3–10. doi:10.1007/978-3-030-05864-7_1.

[4] Meyer, F. M. Availability of Bauxite Reserves. Natural Resources Research 13 (3), 2004, p. 161–172.

[5] Arnold, B. Von Rubinen und Implantaten. Aluminiumoxid und seine vielfältige Welt. Technik im Fokus. Springer, Berlin, 2018.

[6] Aquino, T. F. de, Riella, H. G., Bernardin, A. M. Mineralogical and Physical–Chemical Characterization of a Bauxite Ore from Lages, Santa Catarina, Brazil, for Refractory Production. Mineral Processing and Extractive Metallurgy Review 32 (3), 2011, p. 137–149.

[7] Kuys, K., Ralston, J., Smart, R., Sobieraj, S., Wood, R., Turner, P. S. Surface characterisation, iron removal and enrichment of bauxite ultrafines. Minerals Engineering 3 (5), 1990, p. 421–435.

[8] European Commission. 2020. Study on the EU's list of Critical Raw Materials (2020). Factsheets on Critical Raw Materials. doi:10.2873/92480.

[9] Oliveira, V. G. de, Curimbaba Ferreira, L. L. H., dos Reis, M. A., Nakachima, P. M., Pereira, A. L. Refractory Grade Bauxite: An Overview about the Effects of different Bauxite Sources and Forming Processes on the Quality of the Material. Global Journal of Researches in Engineering: A 19 (4), 2019, p. 51–67.

[10] Swain, R., Padhy, L. N., Bhima Rao, R. Beneficiation Studies on Bauxite Mining Waste: A Value Addition for Refractory Industries. Iranian Journal of Materials Science & Engineering 8 (3), 2011, p. 37–49.

[11] Salmang, H., Scholze, H., and Telle, R. Keramik. 7., vollständig neubearbeitete und erweiterte Auflage. Herausgegeben von Rainer Telle. Springer, Berlin, Heidelberg, 2007.

[12] Papassiopi, N., Vaxevanidou, K., Paspaliaris, I. Effectiveness of iron reducing bacteria for the removal of iron from bauxite ores. Minerals Engineering 23 (1), 2010, p. 25–31.

[13] Schönwelski, W. Possible Solutions for the global shortage of refractory bauxite. Refractories Worldforum , 2009, p. 17–19.

[14] Zafar, Z. I. Determination of semi empirical kinetic model for dissolution of bauxite ore with sulfuric acid: Parametric cumulative effect on the Arrhenius parameters. Chemical Engineering Journal 141 (1-3), 2008, p. 233–241.

[15] Dissanayake, D., Mantilaka, M., Silva, R. T. de, Silva, K. de, Pitawala, H. Laterite and its potential as an alternative-bauxite. Cleaner Materials 1 , 2021, p. 100016.

[16] Cui, L., Guo, Y., Wang, X., Du, Z., Cheng, F. Dissolution kinetics of aluminum and iron from coal mining waste by hydrochloric acid. Chinese Journal of Chemical Engineering 23 (3), 2015, p. 590–596.

[17] Valeev, D., Pankratov, D., Shoppert, A., Sokolov, A., Kasikov, A., Mikhailova, A., Salazar-Concha, C., Rodionov, I.

Mechanism and kinetics of iron extraction from high silica boehmite–kaolinite bauxite by hydrochloric acid leaching. Transactions of Nonferrous Metals Society of China 31 (10), 2021, p. 3128–3149.

[18] Olanipekun, E. A kinetic study of the leaching of a Nigerian ilmenite ore by hydrochloric acid. Hydrometallurgy 53 (1), 1999, p. 1–10.

[19] Mergen, A., Bilen, M., Büyükburc, A., Gündüz, M. Kinetics of Leaching of Boehmitic Bauxite of Konya-Turkey with Hydrochloric Acid. Silicates Industriels 67 (6–7), 2002, p. 75–80.

[20] Mergen, A. Production of sintered high alumina refractories from Turkish bauxite ore. British Ceramic Transactions 103 (1), 2004, p. 42–46.

[21] Paspaliaris, Y., Yiouli, Y., Patermarakis, G. Reaction kinetics for leaching of iron oxides in boehmitic bauxite by hydrochloric acid. Transactions of the Institution of Mining and Metallurgy, Section C (98), 1989, p. C21-C25.

[22] Majima, H., Awakura, Y., Mishima, T. The Leaching of Hematite in Acid Solutions. Metallurgical Transactions B 16 (1), 1985, p. 23–30.

[23] Stein, A., Sax, A., Quirmbach, P. Iron leaching from nonrefractory grade bauxite: Individual process optimization and prediction by using DOE. International Journal of Ceramic Engineering & Science 4 (2), 2022, p. 112–118.

[24] Stein, A. 2023. Entwicklung eines chemischen Raffinationsverfahrens zur Aufbereitung unterschiedlicher Naturbauxite unter Verwendung computergestützter statistischer Versuchsplanung. Dissertation, Universität Koblenz.

[25] Crystallography Open Database. Open-access collection of crystal structures of organic, inorganic, metal-organic compounds and minerals, excluding biopolymers. http://www.crystallography.net/cod/index.php.

33

# FROM LAB TO PLANT – FROM MINE TO REFRACTORY BRICKS: MAKING USE OF A NEW DOLOMITE RAW MATERIAL SOURCE IN EUROPE

C. Ebner, M.-A. Müller, M. Marout, J.-F. Stenger
RHI Magnesita GmbH, Technology Center Leoben, Leoben, Austria

T. Müller
Veitsch-Radex GmbH&Co OG, Dolomite Resource Center Hochfilzen, Hochfilzen, Austria

## ABSTRACT

A previously not commercially used dolomite mine in Hochfilzen, Austria has recently been developed to produce high-quality dead burnt dolomite for basic refractory bricks and mixes. The extremely high purity of dolomite from this mining site normally demands a 2-step process and profound raw material research has been undertaken to provide a simplified process. Main target was to produce high-purity high-density dead burnt dolomite in a single-step rotary kiln process. In extensive laboratory and industrial trials, the kiln parameters and sintering additives were optimised and the suitability for brick and mixes production was confirmed and yielded products which at a minimum display similar physical properties and superior chemical composition when compared to the current standard raw material from shaft kiln processes. This paper summarizes the journey of raw material development and gives some insights about the implementation in refractory production. In addition, some performance related details of the resulting refractory products will be provided.

## INTRODUCTION

Doloma-based refractory bricks for high-quality stainless-steel production have been used with great success for many decades now [1,2]. The main base raw material for such products, the mineral dolomite ($CaMg(CO_3)_2$) which is converted to doloma (or sintered dolomite/doloma sinter/dead burned dolomite = $CaO+MgO$) during raw material production has mainly been formed from calcite deposits by diagenetic processes in the upper earth's strati [3,4]. It is abundantly available in large quantities, refractory application, however, has special requirements strongly narrowing down the useful part for high-temperature applications. The scarcity of appropriate carbonatic rock deposits and the developments in production technology of doloma-based raw materials as well as recent spikes in energy prices have influenced the search for new raw material sources in terms of ecological and economical aspects. Deposits which formerly had not been utilizable are now gaining importance and their exploitation has been made possible only by new developments in the field of raw mineral mining and refractory aggregate production. In this proceeding the economic utilization of a formerly unused dolomite mine in central Europe is summarised covering all steps from raw material development and production to refractory goods manufacturing and field application.

## RAW MATERIAL DEVELOPMENT

### From lab to plant

Dolomite raw material from a mine situated in the west of Austria was subjected to extensive investigations in terms of sinterability, densification and the potential use of appropriate additives supporting an economically viable firing process. The mine formerly had not been commercially exploited for refractory raw material production as the extremely high purity of its carbonate rocks prevented sufficiently high densification without using excessive amounts of energy. By explorative drillings on site the high quality of the dolomite stone was re-confirmed along with a predicted lifetime for the mine exceeding 50 years.

First attempts to make use of this mine dating back to the 80ies of last century led to the conclusion that an expensive 2-step process of dolomite calcining in a low-temperature shaft kiln followed by briquetting and re-firing in a high temperature shaft kiln would have been needed to provide dense and well sintered dead burned doloma (DBD).

30 years later, however, the approach was revived, and a multinational team of research and production experts started to design experiments investigating into a cost-efficient one-step approach by making use of new insights gained from other raw material research areas. Target of these lab trials was to provide sintered dolomite with a density of at least 3.15 to 3.20 g/cm³ and an overall flux level between 1.7 and 2.2% in the final raw material which is an excellent starting point for high-quality refractory products. Direct comparison with the former standard doloma raw material coming from a shaft kiln process was done to benchmark the resulting refractory material [5].

The tests clearly showed potential of designing a single-step process in a modern rotary kiln by using additives which can promote sintering of dolomite-based minerals [6,7]. These successful trials subsequently paved the way for first scale up tests in already existing rotary kilns to confirm the findings. Raw stone from the mine was sized to a grain size dimensionally corresponding to the needs of final dead burned dolomite. By doing so, the efforts for crushing grains down to the size needed for refractory formulations can be minimised. Results from the laboratory trials could be validated and the resulting doloma raw material showed higher density than the former raw material from shaft kilns while the impurity level could be kept below other commercially used raw materials (table 1).

*Table 1: Density and impurity levels of doloma raw materials from old shaft kiln process and new rotary kiln process. Taken from [5].*

|  |  | New source | Old source |
|---|---|---|---|
| $Al_2O_3$ | % | 0.4 | 0.4 |
| $SiO_2$ | % | 0.2 | 0.8 |
| $Fe_2O_3$ | % | 0.9 | 0.7 |
| Bulk density | g/cm³ | 3.20-3.25 | 3.18 |

Notably, the $SiO_2$ content of the resulting sinter dolomite was exceptionally low and, considering the low alumina level, a very low share of low melting phases was expected for the final product. Iron oxide was mainly found inside the periclase crystals and only small amounts of well-dispersed interstitial phases were found in mineralogical investigations. Periclase crystals had an average size of 10-15 μm which is in the range of other doloma raw materials [Fig. 1].
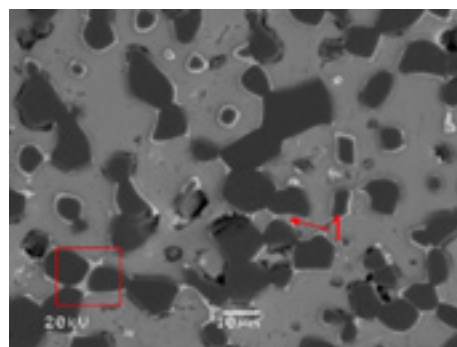


*Fig. 1: Microstructure of sinter dolomite showing well distributed interstitial phases (red square) and small amounts of iron-containing phases (red arrow). Reprinted from [5] with permission.*

Due to the switch from shaft kiln to the rotary kiln process another benefit could be realised: The dense outer layer of doloma grains beholds a clear advantage for hydration resistance, one of the major drawbacks of lime-containing refractory materials [Fig. 2].
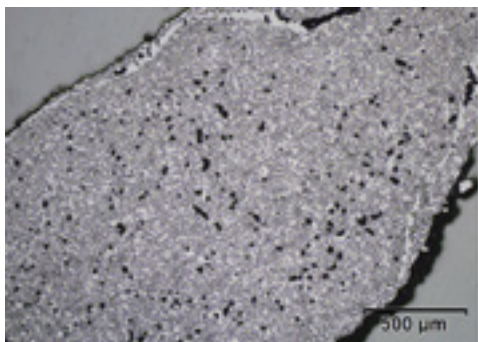


*Fig. 2: Polished section of a doloma grain from the new rotary kiln process showing a dense outer layer and low porosity on the inside. Black spots represent pores. Reprinted with permission [5].*

The higher iron content as compared to the former shaft kiln material had another effect on the final material by giving it a much darker colour as depicted in figure 3 where macrographs of both materials are shown next to each other.



*Fig. 3: Doloma grains from the new rotary kiln process [left] and the former shaft kiln process [right] showing darker colour due to higher iron oxide levels. Reprinted from [5] with permission.*

Comparative hydration tests which were done on both, the new and the former doloma raw material, showed significant improvement of hydration resistance for the rotary kiln material due to the higher density and the lower surface porosity providing a protective layer against water attack (table 2 and [8]).

*Table 2: Hydration susceptibility of rotary and shaft kiln doloma tested under autoclave conditions of 120 °C with 100% RH and a pressure of 1.6 bar. Taken from [5].*

| | | Shaft kiln doloma crushed and sieved 1-5 mm | Rotary kiln doloma | |
|---|---|---|---|---|
| | | | uncrushed and sieved 1-5 mm | crushed and sieved 1-5 mm |
| Weight gain | % | 2.5 | 0.9 | 1.2 |
| Hydration susceptibility | % | 16.7 | 2.1 | 5.1 |

Based on the very successful and promising outcome of the lab and plant trial sets, a significant investment into a new raw material centre including mining, automatic transportation from the mine to the sinter plant and a new state-of-the-art rotary kiln was approved. The construction works for the rotary kiln were completed in 2021 and raw material production was started right away. Raw material transportation from sinter plant to brick production plants was switched from predominant truck delivery to train transfer resulting in improved energy and $CO_2$ efficiency.

## IMPLEMENTATION OF NEW DOLOMA RAW MATERIAL IN BRICK PRODUCTION

### From mine to refractory bricks-Testing of the new raw material in production environment

Preceded by successful large scale raw material production trials and thorough lab testing of the resulting doloma raw material, brick production trials were initiated to learn more about the material's behaviour in a brick production environment. The higher iron content of the new rotary kiln material was identified as a potential risk of higher shrinkage during the firing step. This was supported by former trials done with another doloma-based raw material with a similar $Fe_2O_3$ content in which severe deformation and tilting of the brick columns on the tunnel kiln car were observed [Fig. 4].



*Fig. 4: Severely deformed bricks on kiln car due to high iron levels in raw material. Reprinted from [5] with permission.*

Precautions to prevent kiln blockage by falling bricks were taken by a pyramid-like setting of the bricks produced with the new doloma raw material [Fig. 5].



*Fig. 5: Pyramid-like setting pattern to prevent bricks from falling and blockage of tunnel kiln. Reprinted from [5] with permission.*

However, the bricks did not show excessive shrinkage or deformation after firing and the switch from one material to the other could be done in a rather uncomplicated and straight-forward manner. Before full implementation, extended production testing for fired as well as unfired (tempered) refractory bricks was done.

### Property evaluation of fired refractory bricks

Thorough investigation of mineralogical features and physical hot properties showed at least similar, in many cases even superior properties for density, porosity and cold crushing strength when the new rotary kiln material-based bricks were compared to the ones produced with the former shaft kiln doloma raw material. All relevant data are shown in tables 3 and 4.

*Table 3: Typical chemical composition of fired doloma bricks produced with former shaft kiln sinter doloma and with newly developed rotary kiln material. Taken from [5].*

| Product type (shaped) | Fired doloma | Fired doloma | Fired magdol | Fired magdol |
|---|---|---|---|---|
| Type of raw material | Rotary kiln doloma | Shaft kiln doloma | Rotary kiln doloma | Shaft kiln doloma |
| Chemical analyses | Wt.% | Wt.% | Wt.% | Wt.% |
| MgO | 40.1 | 40.2 | 56.5 | 57.7 |
| $Al_2O_3$ | 0.37 | 0.56 | 0.28 | 0.41 |
| $SiO_2$ | 0.22 | 0.91 | 0.32 | 0.79 |
| CaO | 58.3 | 57.7 | 42.0 | 40.4 |
| MnO | 0.11 | 0.09 | 0.10 | 0.09 |
| $Fe_2O_3$ | 0.86 | 0.54 | 0.75 | 0.57 |

*Table 4: Typical physical properties of fired doloma bricks produced with former shaft kiln sinter doloma and with newly developed rotary kiln material. Taken from [5].*

| Physical test results | | | | | |
|---|---|---|---|---|---|
| Test method | Unit | | | | |
| Bulk density | g/cm³ | 3.01 | 3.00 | 3.02 | 3.00 |
| Apparent porosity | Vol% | 11.5 | 12.0 | 11.7 | 12.2 |
| Cold crushing strength | MPa | 80 | 70 | 70 | 60 |
| HMOR @ 1400 °C | MPa | 2.3 | 2.3 | 1.9 | 1.7 |
| HMOR @ 1500 °C | MPa | 1.6 | 1.8 | 1.6 | 1.7 |
| CMOR @ RT | MPa | 19.3 | 14.5 | 17.0 | 9.5 |

Special emphasis was put on to the thermomechanical behaviour which was determined by means of creep-in-compression tests carried out at 1500 °C with an applied load of 0.2 MPa. Figure 6 clearly illustrates the advantage of the new raw material showing significant reduction in load-related deformation at high temperatures.
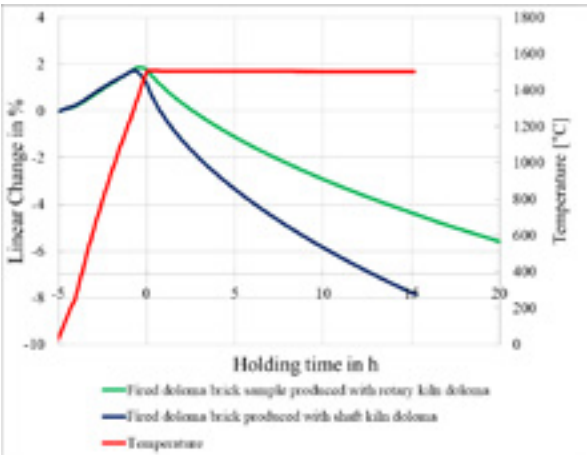


*Fig. 6: Creep-in-compression tests of refractory brick samples produced with rotary kiln material (green) and shaft kiln material (blue).*

Low silica levels in doloma-based refractory bricks are generally seen as a benefit, especially when it comes to resistance against silica-based slags which are predominantly used in AOD converter processes. To provide evidence for this assumption, finger shaped brick samples produced with the newly developed and samples with the former shaft kiln-based doloma raw material were subjected to slag corrosion tests in an induction furnace employing an aggressive synthetic silica-rich AOD slag with a low C/S ratio of ~1.2. Testing temperature was kept at 1650 °C for a test duration of 3 h. Results showed superior slag resistance of the rotary kiln-based brick samples, mainly due to the raw material's lower silica content but also due to higher bulk density and lower porosity [Fig. 7 and table 3]. The samples on the right-hand side had a significantly higher remaining thickness. Quantitative measurement of thickness was prevented due to complete disintegration by phase change of dicalcium silicate during sample cooling.



*Fig. 7: Finger-shaped slag testing samples after slag corrosion tests. Brick samples prepared with shaft kiln doloma material (left) and rotary kiln doloma having higher bulk density and lower silica levels (right).*

**Property evaluation of tempered refractory bricks**

Benefits coming from higher density, lower porosity and improved hydration resistance showed even more benefit of the newly developed rotary kiln doloma material. It is assumed that higher hydration resistance of raw material has significant influence on the overall properties. Comparative properties of resin bonded straight doloma bricks are summarised in tables 5 and 6.

*Table 5: Typical chemical composition of tempered doloma bricks produced with former shaft kiln sinter doloma and with newly developed rotary kiln material. Taken from [5].*

| Type of product (brick) | Tempered resin bonded | Tempered resin bonded |
|---|---|---|
| Type of raw material | Rotary kiln doloma | Shaft kiln doloma |
| Chemical analyses | Wt.% | Wt.% |
| MgO | 42.0 | 41.8 |
| $Al_2O_3$ | 0.4 | 0.5 |
| $SiO_2$ | 0.3 | 0.7 |
| CaO | 56.4 | 56.4 |
| MnO | 0.1 | 0.1 |
| $Fe_2O_3$ | 0.8 | 0.4 |
| Total carbon content | 4.8 | 5.5 |
| Residual carbon content | 3.1 | 3.2 |

Table 6: *Typical properties of tempered resin bonded doloma bricks produced with former shaft kiln sinter doloma and with newly developed rotary kiln material. Taken from [5].*

| Physical test results | | | |
|---|---|---|---|
| Test method | Unit | | |
| Bulk density | g/cm³ | 2.95 | 2.86 |
| Apparent porosity | Vol% | 3.9 | 5.6 |
| Cold crushing strength | MPa | 100 | 87 |
| Bulk density after coking@1000 °C | g/cm³ | 2.87 | 2.79 |
| Apparent porosity after coking @1000°C | Vol% | 12.8 | 14.8 |
| Cold crushing strength after coking @1000 °C | MPa | 40 | 38 |
| HMOR @ 1400 °C | MPa | 2.8 | 3.9 |
| HMOR @ 1500 °C | MPa | 3.1 | 2.7 |
| CMOR @ RT | MPa | 21.0 | 17.4 |

**LARGE SCALE RAW MATERIAL PRODUCTION, ENERGY & ADDITIVE OPTIMIZATION**

Production of doloma with the new rotary kiln in Austria made a good development in 2022 and sustainably stabilised in 2023. The quality of DBD could be kept on high levels regarding all relevant parameters. Like many other fields, the energy crisis also hit the refractory industry in 2022/2023, especially in highly energy-intensive processes like raw material production requiring temperatures above 2000 °C. With all this in mind, considerations were made to look for more cost-effective sintering additives than the ones used so far. Obviously, the target was to keep the high quality of the product at the same levels. A screening of possible alternatives provided among others a recycling material from refractory products. The selected materials were evaluated for sintering simulation tests in a lab rotary kiln.

The results with recycling material addition looked promising enough to initiate a large-scale trial in the sinter plant. One of the additive silos was filled with the new recycling material and a smooth overlapping switch from the standard material to the new one was made using the dosing conveyor belts. Regular analysis of the dolomite sinter chemistry and bulk density safeguarded the quality of the product.

This first large-scale trial lasted only for a few days and the influence of dust recycling back into the kiln feed with possible aggregation of certain compounds could not be evaluated. Density levels, however, were well above the target [Fig.8] and chemical composition was still very good.
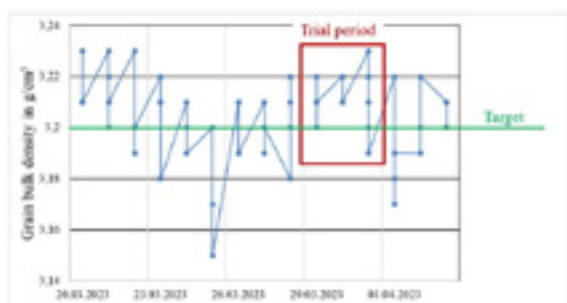


Fig. 8: *Grain bulk density of doloma before, during (red square) and after trial.*

Therefore, a longer trial was scheduled lasting for around one month. This trial confirmed the good results from the first one and, most importantly, did not show any negative effects coming from kiln dust recycling. Since then, the production has been switched to the new recycling material-based additive providing benefits for the cost of sinter dolomite.

**CONCLUSIONS**

A high-quality supply of sintered dolomite has recently been set up in Western Austria by making use of a high-quality dolomite mine through implementing a newly designed one-step rotary kiln process using sintering additives. Raw material and process development were started with extensive lab trials followed by scale-up trials and thorough testing of raw materials in lab and production plant environment. Since the start of the sinter plant, several optimization steps have led to improved energy efficiency and cost structure by introduction of new additives, recycled materials, and side-products. Main benefits of the rotary kiln process and the resulting doloma raw material over the former shaft kiln process and material are:

1. Cost-efficient and highly flexible single-step process allowing for changes in fuel as well as dosing of different additives and recycled materials.
2. Higher density of dolomite sinter and very low surface porosity significantly improving hydration resistance.
3. Extremely low silica content and overall low flux level in final doloma.
4. Improved density and porosity of bricks produced with rotary kiln doloma.
5. Improved slag resistance of bricks produced with the new raw material as compared to bricks produced with the former shaft kiln raw material.

By implementing this new process, the future supply of high-quality doloma and doloma-based refractory products from Europe has been secured for the next decades to come. Continuous improvements of feeding raw materials and fuel usage will lead to higher energy and mining efficiency at the same time keeping the good performance level of the final products.

**REFERENCES**
[1] Wei, Z. Choice and application of refractories for AOD furnace, Naihuo Cailiao/Refractories. 36, 2002, p. 224–225, 228.
[2] Buhr, A., Refractories for steel secondary metallurgy, CN-Refractories 6, 1999, p. 19–30.
[3] Koeshidayatullah, A., Al-Sinawi, N., Swart, P.K., Boyce, A., Redfern, J., Hollis, C. Coevolution of diagenetic fronts and fluid-fracture pathways. Scientific Reports 12, 2022, p. 9278-9287.
[4] Warren, J. Dolomite: occurrence, evolution and economically important associations. Earth-Science Reviews 52, p. 1-81.
[5] Ebner, C., Mueller, M.-A., Mueller, T., Eckstein, W., Kappel, M., Stenger, J.-F. Bulletin 106, p. 106-111.
[6] Duvigneaud, P.-H., Derie, R. and Naessens, Influence de l'oxide de fer sur la croissance des oxydes de calcium et de magnesium dans la dolomite calcinee. Revue international des hautes temperatures es des refractaires 1972, 9, 313–324.
[7] Koval, E.J., Messing, G.L., Bradt, R.C. Effects of Raw Material Properties and $Fe_2O_3$ Additions on Sintering of Dolomites. Ceramics and Composites 1984, 63 (2), p. 274-277.
[8] Gosh, A., Tripathi, H.S. Sintering Behaviour and Hydration Resistance of Reactive Dolomite. Ceramics International 2011, 38, p. 1315-1318.

37

# DESIGNING ECO-FRIENDLY ALTERNATIVE TO THE MAGNESIA-CHROMITE AGGREGATES

O. H. Borges, F.G. Coury, D.N.F. Muche, V.C. Pandolfelli

Federal University of Sao Carlos, Graduate Program in Materials Science and Engineering, Sao Carlos-SP, Brazil.

## ABSTRACT

Due to its outstanding thermomechanical and corrosive performance, electrofused magnesia-chromite aggregates (EMCA) have been consistently applied to refractory compositions since the beginning of the 20th century. Notwithstanding the performance of refractories containing this raw material, the rising environmental and safety concerns have been driving the replacement of chrome-containing compositions by greener alternatives as this type of refractory can generate a highly toxic by-product ($Cr^{6+}$), suppressing landfilling and recycling. However, finding eco-friendly and affordable alternatives to EMCA remains a challenge. Firstly, there is a lack of understanding of the mechanisms that give rise to its good performance and, secondly, conventional formulation criteria can hardly account for the microstructure complexity of this raw material. In this work, multiple electron-microscope-based techniques, such as EBSD and EDS, were used to assess EMCA microstructural features and a mechanism to explain their generation was proposed. Based on the latter and with the aid of thermodynamic calculations, the concepts of designing compositionally complex ceramics were applied to find eco-friendly alternatives to EMCA. From the 154 simulated systems, the 4 most promising compositions were experimentally produced and characterized at a laboratory scale. Although kinetics aspects still must be addressed, Cr-free EMCA mimetized microstructures were obtained, highlighting that this design approach can be used to support the development of novel raw-material that can better merge performance, cost and eco-friendliness.

## INTRODUCTION

The search for refractory systems capable of withstanding the complex solicitations (*e.g.* thermal shock, corrosion, erosion) is a constant demand in high-temperature industries[1]. To address such a scenario, refractories containing electrofused magnesia-chromium aggregates (EMCA) have been broadly applied since the 1960s[1]. In these systems, which fit into the compositionally complex ceramic classification[1], the predominant phases are periclase and a solid solution based on a complex spinel obtained by combining different types of spinel structures ($AB_2O_4$-type phases, in which A represents a divalent cation and B a trivalent one)[2]. This complex structure results in excellent resistance to corrosion and slag penetration[2]. Additionally, although the literature does not report in detail the driving force for this phenomenon, the high number of preferentially oriented microcracks formed on the EMCA microstructure gives rise to a material with good flexibility and thermal shock damage resistance.

Besides its outstanding corrosion and thermal shock damage resistance, EMCA has received little attention from the scientific community in recent decades, which can be attributed to its toxicity (mainly due to the formation of hexavalent chromium). Thus, greater efforts have been made to study safer systems, especially based on $MgAl_2O_4$, as alternatives to replace EMCA, but equivalent performance in applications such as in RH degassers has not yet been achieved[3]. Consequently, there is a lack of understanding of the mechanisms that lead to EMCA properties, especially related to its high thermal shock damage resistance.

Aiming at understanding the mechanism that leads to their features, multiple techniques were used in this work to assess the microstructure of commercially-available EMCA. Based on that and using thermodynamic calculations (CALPHAD), the concepts of designing compositionally complex ceramics[4] were applied to find eco-friendly alternatives to this chromium-containing raw material. Some of the most promising compositions were then processed by electrofusion in lab-scale arc furnace equipment and their resulting microstructures were analysed.

## EXPERIMENTAL PROCEDURE

Microstructural characterization was firstly conducted for commercially-available electrofused magnesia-chromium aggregates (FMCR 18-20, $d_{50}$ = 3 mm, Chenglong, Liaoyang, China). The as-received samples were embedded in a polymeric resin, cut to expose their sectioned surface, ground using SiC-based sandpaper, and polished in AutoMet (model Phoenix Beta, Buehler, USA) using polycrystalline diamond paste with particle sizes ranging from 15 μm to 0.25 μm (MetaDi Medium Concentration, Buehler, USA). The diamond-polished samples had their microstructure assessed by backscattered electrons imaging (BSE) coupled with energy-dispersive X-ray spectroscopy (EDS) on a scanning electron microscope device (Inspect S50, Thermo Fisher Scientific, USA). To avoid charging artefacts, the latter analysis was conducted on golden-coated surfaces (Balzers SCD 004, Bal-Tec, Switzerland). The crystallographic orientation of the EMCA phases was assessed by electron backscattered diffraction technique (30 kV, Inspect S50, FEI, USA). Thermodynamic calculations were carried out in Equilib module of FactSage software (FToxid and FactPS databases, version 6.4, CRCT, Canada) using the EMCA chemical composition (X-ray fluorescence, MagiX PRO, Malvern Panalytical, UK) to assess its solidification path.

Aiming at finding eco-friendly alternatives to the chromium-containing material, the same thermodynamic approach was used to assess the solidification path of binary, ternary or quaternary spinel systems (available in the aforementioned database) together with 66.4 wt% of MgO, giving rise to 154 distinct systems. This MgO content was selected because it is the same as that presented by the reference material (EMCA). To allow a better comparison among the simulated systems, they were ranked considering 5 key indicators, which will be presented later in this work. This ranking showed four systems with similar features to those presented by EMCA, thus, they were selected as the most promising and experimentally processed in a lab-scale arc melter (MAM-1, Edmund Buehler, Germany). To enable their electrofusion in this equipment, the raw materials presented in Tab. 1 were dispersed in a ball-milling with alumina balls for 2h and moulded into small (~ 1 cm³) uniaxially-pressed (~ 60 MPa) pieces, avoiding powder aspersion during electric arc opening.

Tab. 1: Composition of the four selected electrofused systems in a lab-scale arc melter.

| Composition | MgO | FeO | Fe₂O₃ | Al₂O₃ | NiO | Ni₂O₃ |
|---|---|---|---|---|---|---|
| | | | wt% | | | |
| 1 | 69.54 | 5.59 | 24.87 | - | - | - |
| 2 | 66.40 | 11.27 | 8.35 | 5.33 | - | 8.65 |
| 3 | 71.12 | 4.21 | 18.70 | 5.97 | - | - |
| 4 | 70.01 | 3.22 | 14.30 | 9.13 | 3.34 | - |

These pressed pieces were placed inside the electric arc melter and the melting process took place for ~ 90 seconds. Compared with the industrial electrofusion process, the lab-scale equipment imposes distinct processing conditions, such as much higher cooling rates (the samples cool down within seconds). Therefore, to bring them closer to the thermodynamic equilibrium, the as-fused samples were annealed for 5h at 1500 ºC in a conventional electric heated furnace (Lindberg/Blue M, Thermo Fisher Scientific, USA). After that, the microstructure of the annealed samples was assessed by BSE/EDS and XRD (D8 Focus, Bruker, Germany).

## EXPERIMENTAL PROCEDURE

Firstly, the microstructure of the commercially-available EMCA was analysed by BSE coupled with EDS (see Fig.1), highlighting that the aggregate is formed by a magnesium-oxide matrix

containing nodular precipitates with oxygen, magnesium, chromium, aluminium and iron as its main elements. Using the CALPHAD-based FactSage software, the mean composition of the two distinct regions was used as input for the thermodynamic calculation. The result indicated that the EMCA should be comprised of a complex spinel solid solution (spinel[SS]) with the chemical formula $(Mg_{0.865}Fe_{0.135})(Al_{0.099}Cr_{0.877}Fe_{0.024})_2O_4$, surrounded by a periclase solid solution $[(Mg_{0.991}Cr_{0.006}Fe_{0.003})O]$ matrix. XRD analysis (not presented here) attested the formation of both phases, in line with previously reported works. Additionally, image analysis software was used to measure the mean diameter of the spinel precipitates, which was $15 \pm 2$ μm.

Although the mineralogical composition and the microstructure of EMCA have already been reported in the literature, the mechanism that leads to the cracking behaviour seen in the microscopy (Fig.1) remains unclear. Thus, microcrack generation due to thermal expansion mismatch between distinct ceramic phases during the cooling process was considered. By using the approach proposed by Luchini *et al.*[5] and considering the properties of the spinel[SS] and periclase extracted from the literature (further information on these calculi is described in[6]), the minimum precipitate diameter ($d_c$) to generate microcracking in this system was calculated as 2.3 μm. As the average spinel size measured in the EMCA ($15 \pm 2$ μm) is considerably bigger than this value, microcracking due to thermal expansion mismatch is, indeed, expected. However, although the thermal expansion mismatch accounted for the highly cracked microstructure of the EMCA, it does not explain their crack orientation pattern, which plays a key role in the outstanding flexibility of this raw material. To assess the mechanism that leads to this oriented microcracking, EBSD analyses were conducted.
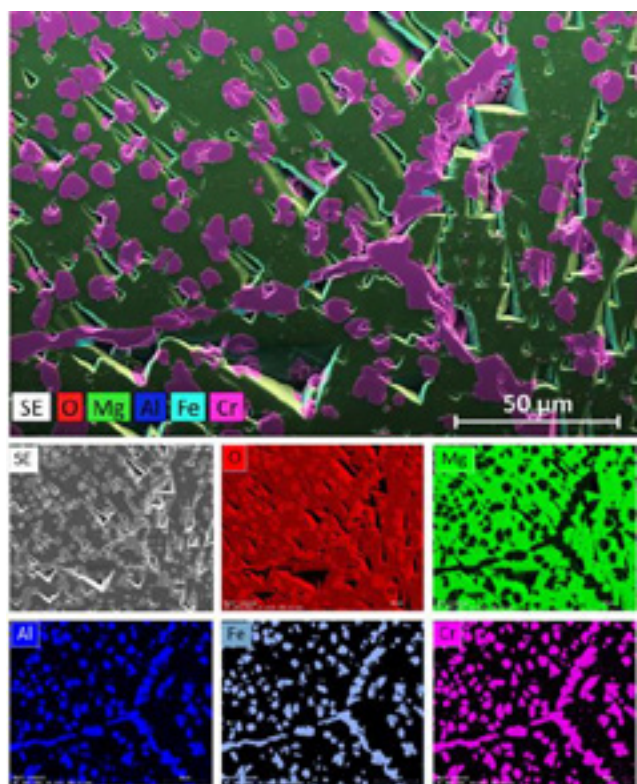


Fig. 1: Morphology and elementary mapping of the EMCA microstructure assessed by scanning electron microscopy coupled to energy dispersive spectroscopy. Extracted from [6] with Elsevier permission (nº 5573751435544).

Due to the unevenness of the surface, generated by the distinct hardness between the spinel and periclase ($H_{Vickers's}$ typically varying from 5.3 GPa to 8.6 GPa and 12 GPa to 16 GPa, respectively), no Kikuchi lines were detected for the former, however, the analysis could be conducted for the MgO matrix. Evaluating the obtained results (displayed in Fig. 2), the formation

of distinct MgO grains inside the aggregates was attested, giving rise to intergranular flaws, likely generated by solidification defects, at their interfaces (marked as F). Besides them, oriented cracks were observed within the MgO grains (marked as C). The post-processing software was used to determine their relative orientation, revealing a good fit with the {110} family of crystallographic planes, which are the MgO slip planes, whereas {100} are the cleavage ones. Additionally, the intersection among the oriented microcracks formed triangular slits (marked as S). These two features – cracks on slip planes instead of cleavage planes and the formation of triangular cracks – are in agreement with the cracking mechanism proposed by Zener and further described by Stroh[7]. According to these authors, crack nuclei are induced by a pile-up of edge dislocations that are halted at an obstacle, such as precipitates. In the case of MgO, non-homogeneous deformations (as those generated by thermal expansion mismatch) induce the pile-up of edge dislocations, resulting in crack nucleation at the {110} family of planes and triangular slits at the crack intersection, similar to what was observed for the EMCA[8].
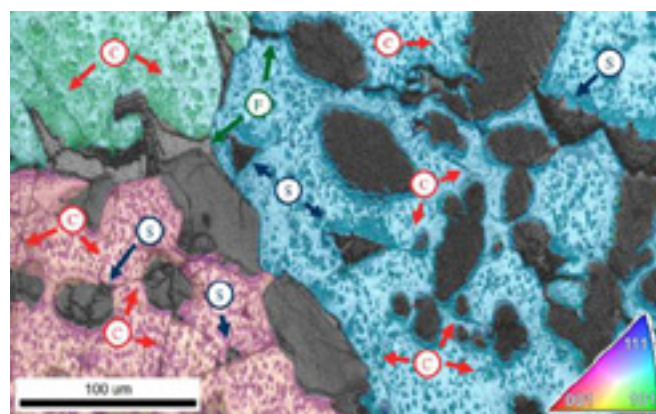


Fig. 2: Microstructure of EMCA assessed by EBSD. The colours indicate the MgO orientation. Intergranular flaws, oriented cracks and triangular slits are highlighted as F, C and S, respectively. Extracted from [6] with Elsevier permission (nº 5573751435544).

Therefore, the microcrack orientation pattern established in the EMCA – and that gives rise to their flexibility – is attributed to the Zener-Stroh crack mechanism triggered by the stress generated due to the thermal expansion mismatch between the MgO and the complex spinel. Thus, the properties and geometry of the spinel precipitates play a key role in promoting such a structure as it will affect, (a) the thermal-induced stress level and, (b), act as dislocation barriers. At first sight, all these features seem to be feasible to obtain in a nontoxic and simpler system, such as a magnesia-rich MgO-Al$_2$O$_3$ composition. However, previous works showed that instead of spinel precipitates in a MgO matrix, this system presents the formation of periclase and spinel grains separately, which halts attaining preferentially oriented microcracks. Thus, to understand the role played by the chromite mineral on the formation of its microstructure, the solidification path of the EMCA and MgO-Al$_2$O$_3$ system were assessed by thermodynamics calculations carried out in the FactSage software. The solidification seen in Fig. 3 explains the distribution of phases in the EMCA (Fig.1), pointing out that the chromium addition plays a key role by enabling the formation of a MgO[SS] at high temperatures, which exsolves a spinel[SS] as the material cools down.

The results discussed so far pointed out the mechanism and key features responsible for the formation of the EMCA microstructure and, consequently, good thermomechanical properties. To do this, a system capable of forming a broad solid solution with MgO at high temperature, but exsolving a second phase presenting a lower thermal expansion coefficient, as internal precipitates with mean size higher than the critical value to induce fracture by thermal expansion mismatch is required to trigger the Zener-Stroh cracking mechanism, leading to highly oriented microcrack formation. This

intricate set of features explains why finding other compositions to replace the EMCA is so difficult, especially using the traditional selection paradigm. Therefore, the compositionally complex ceramic (CCC) selection approach was used to assess promising alternatives that could mimetize the EMCA but without containing chromium addition. The validated systems of FactSage 6.4 gave rise to a total of 154 compositions, which were ranked by taking 5 key indicators into account: (i) the periclase decay step; (ii) whether any gas was predicted to be generated up to 2800 ºC; (iii) the solidification interval; (iv) the $\Delta\alpha$ between the periclase and the spinel formed; and (v) the temperature of the first liquid formation.
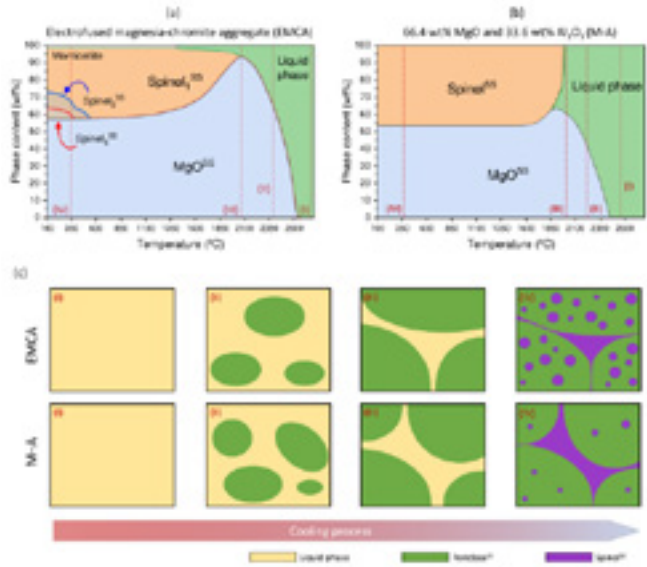


Fig. 3: EMCA (a) and M-A (b) solidification path assessed by FactSage. The drawings (c) presented a schematic representation of the microstructure at different temperatures. Extracted from [6] with Elsevier permission (nº 5573751435544).

According to these indicators and considering the reference values, 4 systems stood out as promising compositions to mimetize EMCA, as depicted in Tab. 2 (the values for all the 154 evaluated systems can be checked in[6]). At first, it is worth noticing that no Zn-containing system was selected, which is attributed to the high partial pressure of this element, resulting in gas formation at temperatures close to 2400 ºC. Secondly, all selected compositions presented Fe additions, which was observed to display a similar role of Cr, also presenting a high solubility in periclase at high temperatures and able to exsolve a spinel structure during cooling.

Tab. 2: Indicator values for the EMCA and the four most promising compositions to mimetize it.

| Composition | MgO decay (wt%) | Gas formation | Solidification interval (ºC) | $\Delta\alpha$ (%) | First liquid formation (ºC) |
|---|---|---|---|---|---|
| EMCA | 40.4 | No | 450 | 42.9 | 2200 |
| 1 | 38.6 | No | 525 | 67.3 | 2200 |
| 2 | 34.0 | No | 550 | 37.8 | 2125 |
| 3 | 36.4 | No | 575 | 38.2 | 2100 |
| 4 | 34.5 | No | 550 | 38.2 | 2100 |

Although this computer-based selection method is valuable to guide the search for alternative eco-friendly compositions to replace the EMCA without performance losses, it must be experimentally validated to check its accuracy. Therefore, compositions 1 to 4 were processed in a laboratory-scale arc melter, which allows the production of small electrofused pieces (~ 1 cm³). Due to the processing conditions imposed by this equipment (especially high cooling rates), which are distinct from the industrial ones, the as-fused samples were annealed for 5 h at 1500 ºC to bring them closer to the thermodynamic equilibrium. Aiming at assessing the mineralogical phases for each system, annealed samples were

grounded and the resulting powder was analyzed by XRD. Fig. 4 shows the X-ray diffractogram, highlighting the regions of 2θ next to 35.5 º and 43 º, where the most intense spinel and periclase peaks are located, respectively. By indexing the profiles, one can notice that just these two phases were identified, as the content of contaminants was lower. The highlighted peaks show significant changes for the spinel phase, remaining quite constant for periclase. This trend was expected as the systems were designed to present distinct spinel[SS] compositions, whereas the periclase matrix is very similar, and is almost fully comprised by MgO. Moreover, quantitative mineralogical content indicated that all samples presented spinel content ranging from 34 wt% to 36 wt%, which is quite close to the values estimated using EDS data collected in the internal region of the grains of compositions 1 to 4 (see Fig. 5), especially considering the inherent uncertainty related to these experimental techniques.
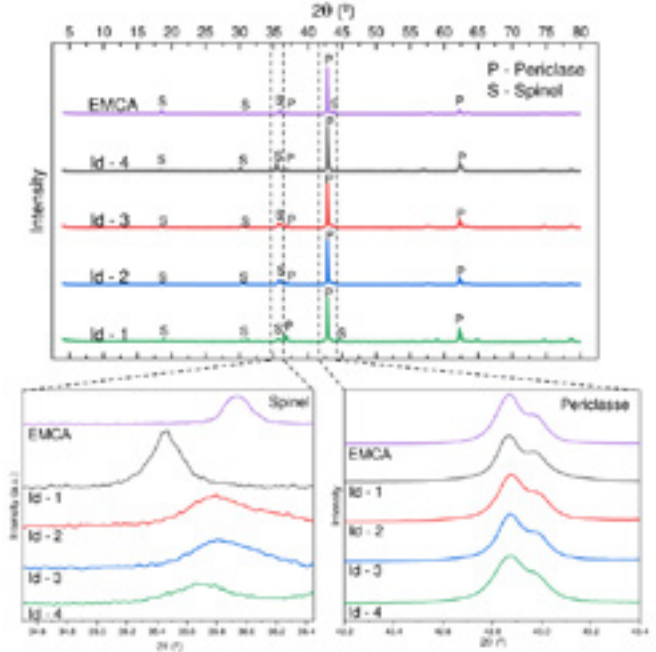


Fig. 4: X-ray profile of the EMCA and compositions 1 to 4 after the annealing treatment. Extracted from [6] with Elsevier permission (nº 5573751435544).

However, the XRD analyses does not provide information regarding phase distribution and the presence of minor contaminating phases, thus the compositions were further analyzed by SEM in the BSE coupled with energy dispersive X-ray spectrometry (EDS), depicted in Fig. 5. Comparing the general morphological aspects similar trends could be observed for the four compositions:

(i) Solidification defects were detected in the samples, which are assigned to the high solidification interval (> 500 ºC) present by all compositions and the high cooling rates imposed by the lab-scale arc melter. In the industrial process, the compositions are produced in a block geometry that is subsequently broken and milled to give rise to the aggregates, which usually withdraws such solidification defects from the final microstructure.

(ii) The microstructures presented some contamination mainly located at the periclase grain boundaries. The lighter color in the image indicates the presence of heavier elements in these regions, which were identified as calcium and tungsten that originated from the MgO raw material and the W-based electrode used in the melting process, respectively.

(iii) All compositions underwent the formation of a periclase matrix with spinel precipitates. The EDS data coupled with thermodynamic calculations were used to assess the phase content of some selected regions showing that the grains are formed by ~ 40 wt% of spinel and ~ 60 wt% of periclase.
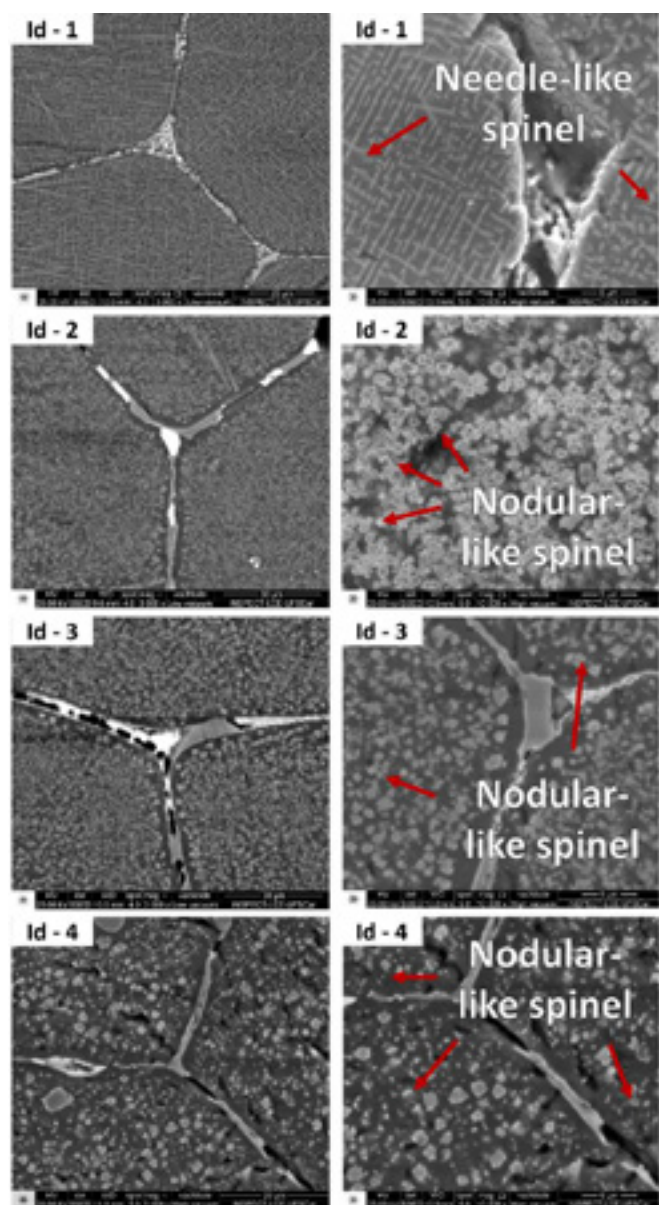
Fig. 5: Backscattered electron images of compositions 1, 2, 3 and 4. Extracted from [6] with Elsevier permission (nº 5573751435544).

However, obtaining a microstructure with MgO grains with spinel precipitates is a required but not sufficient condition to achieve a highly flexible material mimetizing the EMCA. Taking a closer look at the microstructure of compositions 1 to 4, the distinct morphology of the second phase stood out. For composition 1, a needle-like spinel structure was observed, whereas, for the other, nodular-like geometries were detected. Their sizes were assessed using image processing software (ImageJ, version 1.53t), which pointed out 0.9 μm, 1.4 μm and 2.5 μm as the mean equivalent diameter of the precipitates in compositions 2, 3 and 4, respectively. Not coincidentally, composition 4 presented the highest number of cracks, as bigger precipitates lead to higher stresses on the periclase matrix. Nevertheless, even for composition 4, the mean spinel size was considerably below the 15 μm presented by commercially produced EMCA, resulting in less crack generation than expected. In this sense, it is worth highlighting that the thermodynamic approach used in this analysis does not take kinetics into account. Thus, the larger spinel size observed in the EMCA (see Fig. 1) could be attributed to the much lower cooling rates applied in the industrial manufacturing of this raw material (electrofused blocks usually take close to 7 days to completely cool down) compared to that imposed by the laboratory-scale arc melter. To address such issues and understand whether the selection method should also consider the temperature of spinel formation or if this variable could be neglected for industrially produced aggregates, electrofusing these compositions in larger scales would be needed and its on course.

## CONCLUSIONS

In this work, multiple electron-microscope-based techniques were used to assess EMCA microstructural features. BSE coupled with EDS highlighted that the aggregate comprises a magnesium-oxide matrix containing nodular-like precipitates. The mean size of the precipitated spinel was measured as $15 \pm 2$ μm, which is above the critical diameter to induce microcracking due to thermal expansion mismatch in this system. However, such cracking is not randomly distributed and EBSD was used to assess its pattern, unveiling a good fit with the {110} family of crystallographic planes. Therefore, the microcrack orientation pattern in the EMCA could be attributed to the Zener-Stroh crack mechanism triggered by the stress generated due to the thermal expansion mismatch between the MgO and the complex spinel. Based on this mechanism and with the aid of thermodynamic calculations, the concepts of designing compositionally complex ceramics were applied to find eco-friendly EMCA alternatives. From the 154 simulated systems, the four most promising compositions were experimentally produced using a laboratory-scale arc melter and characterized by XRD and BSE/EDS. Although kinetics aspects still must be addressed, Cr-free EMCA-inspired microstructures were obtained, highlighting that this design approach can be used to support the development of novel raw-material that can better merge performance, cost and eco-friendliness.

## ACKNOWLEDGMENTS AND OTHER INFORMATION

## REFERENCES

1. Wang, E., Luo, C., Chen, J. & Hou, X. High-performance chromite by structure stabilization treatment. *J. Iron Steel Res. Int.* **27**, 169–179 (2020).

2. Xu, T. *et al.* Corrosion mechanisms of magnesia-chrome refractories in copper slag and concurrent formation of hexavalent chromium. *J. Alloys Compd.* **786**, 306–313 (2019).

3. Horckmans, L., Nielsen, P., Dierckx, P. & Ducastel, A. Recycling of refractory bricks used in basic steelmaking: a review. *Resour. Conserv. Recycl.* **140**, 297–304 (2019).

4. Wright, A. J. *et al.* From high-entropy ceramics to compositionally-complex ceramics: a case study of fluorite oxides. *J. Eur. Ceram. Soc.* **40**, 2120–2129 (2020).

5. Luchini, B., Sciuti, V. F., Angélico, R. A., Canto, R. B. & Pandolfelli, V. C. Critical inclusion size prediction in refractory ceramics via finite element simulations. *J. Eur. Ceram. Soc.* **37**, 315–321 (2017).

6. Borges, O. H., Coury, F. G., Muche, D. N. F. & Pandolfelli, V. C. Eco-friendly design of complex refractory aggregates as alternatives to the magnesia-chromite ones. *J. Eur. Ceram. Soc.* (2023) doi:10.1016/j.jeurceramsoc.2023.06.023.

7. Stroh, A. N. The formation of cracks as a result of plastic flow. *Proc. R. Soc. London. Ser. A. Math. Phys. Sci.* **223**, 404–414 (1954).

8. Armstrong, R. W. Dislocation pile-ups: from {110} cracking in MgO to model strength evaluations. *Mater. Sci. Eng. A* **409**, 24–31 (2005).

# DEVELOPMENT OF NOVEL DBM PORTFOLIO FOR STEEL, CEMENT AND GLASS REFRACTORIES

Matheus, Moraes, Gustavo, Nogueira, Graziella, Pacheco, Pedro, Almeida, José Alvaro, Sardelli
RHI Magnesita, Contagem, Brazil

Jacob, Kerr
RHI Magnesita, York, United States of America

**ABSTRACT**
The verticalization of refractory producers, with sustainable exploitation of mineral reserves, and the development of alternatives for Chinese raw materials are important topics for the industry. RHI Magnesita is investing in a new rotary kiln on its Brazilian plant, located in Brumado, and more than a cost-reduction target, the optimization of its magnesite reserves and the production of value-added products were prioritized. Therefore, novel high-quality DBMs were developed with characteristics to supply steel, cement, and glass refractories. The research focused on an innovative production process, strengthening RHI Magnesita vertical integration and delivering to the market sustainable products. This article explores the DBMs development process, including lab, pilot and industrial trials, as the refractory trials for the selected product lines. Finally, the reference DBMs are compared to the new portfolio according to product properties and sustainability impact.

**INTRODUCTION**
The dead burned magnesia (DBM) is one of the most important raw materials for refractory production. Bricks and monolithics based on this refractory aggregate are produced for steel, cement, glass, non-ferrous metals, and other key industries [1].
Nevertheless, each application has a different wear mechanism and the DBM characteristics directly influence the performance of the final product.
For steel applications, the DBM needs different features according to the application. Some examples are relative high grain bulk density (GBD) and low thermal conductivity for the safety lining of different vessels, high purity, GBD and periclase crystal size in ladle and electric arc furnace (EAF) bricks, right amount of fluxes for a good sinterability and low corrosion in EAF mixes, low cost, chemical compatibility and correct particle size distribution (PSD) for repair mixes and, finally, low-cost, compatible chemistry, necessary porosity and PSD for tundish mixes [2,3,4].
For cement, especially in the burning zone, high GBD, controlled lime to silica ratio (C/S) and high purity are desired, avoiding chrome oxide addition to the DBM aiming to increase GBD [5,6].
Finally, in glass application, low iron content, high GBD, low C/S (<1), particularly due to a low CaO content, and high purity are desired for high performance [7,8].
RHI Magnesita, out of its plant in Brumado (Brazil), produces two DBM grades. The M30B is a high-purity and high-GBD DBM for brick applications, produced in double step firing being sintered in a pressurized shaft kiln in temperatures surpassing 2200°C. The M10, in turn, is a medium grade and intermediate density DBM mainly used for mixes but with brick applications, produced in single step firing using a conventional shaft kiln at 1850°C. This paper describes the development process of new qualities especially linked to a new rotary kiln being installed in this Brazilian plant [9].

**NEW GRADES DESIGN**
The development of the new DBMs for Brumado plant was motivated by the investment on a state-of-the-art rotary kiln, with a process specifically designed to take advantage on the two magnesite mines (figure 1) being operated at this site and other deposits on the vicinity with mining rights granted to RHI Magnesita.

The new DBMs were designed to reduce the stripping ratio, increase the process yield and use ores that couldn't be used due to operational restrictions from the shaft kilns and technical constrains from the current specs. These features lead to a more sustainable process, increasing the life of mine (LOM), reducing landfilling, and improving the cost-competitiveness of the complete site operation.
The development process was divided in three steps. First the differences in kiln technology and how the exploit the upsides of the new rotary kiln are explored. Secondly, the characteristics expected of new DBMs for each application is described. Finally, the process design features, and properties of the new raw materials are detailed.


*Fig. 1: Pedra Preta (left) and Pomba (right) mines from RHI Magnesita in Brumado-BR.*

**DIFFERENCES ON KILN TECHNOLOGY**
The conventional shaft kiln technology (as the one used to sinter M10 in Brumado, figure 2) in comparison to a rotary kiln (new kiln being installed in the same plant) has the advantage of a low specific energy consumption and a more flexible control on the residence time, normally capable of operating with longer retention period. Nevertheless, it has strong limitation on the particle size to be fed and for ores prone to decrepitation (breaking down inside of the kiln), since the gas permeability is utterly important for a proper operation in this case which the kiln is almost fully filled with material [9].
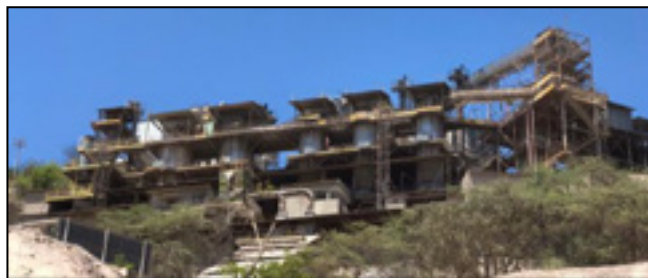

*Fig. 2: Vertical shaft kilns from RHI Magnesita in Brumado-BR.*

The rotary kiln (figure 3 presents the rotary kiln operated by RHI Magnesita in Turkey to produce DBM), in turn, operates with a low filling rate and the gas is transported above the material. This characteristic gives more flexibility for the feedstock, allowing finer particles to be fed and the ore breakage inside of the kiln does not have a strong impact on the operation parameters.
The downside of the rotary kiln is the less efficient heat transfer and higher thermal dissipation, increasing the specific energy consumption compared to the shaft kiln. However, the total cost is reduced, as the productivity is higher, workforce is reduced and

alternative fuels can be applied (gas, liquid and solid). Another point of attention for the rotary kiln is the dedusting system capacity and dust return to the process. With finer material being fed and the breakage of original feedstock due to decrepitation and the tumbling effect of rotary kiln, the dust load can be as high as 30% of the feed rate (even higher in some cases). Hence, a robust dedusting system to handle this load combined to a proper system and strategy for recirculation is necessary to increase productive and improve energy efficiency.



*Fig. 3: Rotary kiln from RHI Magnesita in Eskişehir-TR.*

Therefore, the new rotary kiln in Brumado open new possibilities for feedstocks never explored due to technology restrictions and alternative DBMs started to be explored to be supplied to different market applications.

## NEW DBMs AND TARGETED APPLICATIONS

The new DBMs were developed to improve the deposit utilization and increase the value generation. The first DBM described is an intermediate grade and density, targeting to combine high decrepitation ores and accommodate higher silica and iron oxide for steel application. Secondly, a higher grade DBM was developed for EAF hearth construction mixes, with increased density and controlled silica content. Finally, a high grade DBM with low iron content and low C/S for glass and cement applications is detailed.

## DBM M9

The DBM M9 was designed to combine different ore sources to maximize the mine utilization and increase the life of mine, without loosing performance on target applications. The main modification compared to the M10 is a slightly higher $SiO_2$ and $Fe_2O_3$ content, keeping the same density and particle size for refractory application. With this modification, combined to others debottlenecking provided by the rotary kiln technology, the estimated LOM for Pedra Preta was increased from 47 years to more than 120 years, considering the current geology dataset. Figure 4 illustrates the increase on ore recovery due to the modifications (consequence of DBM M9 and the other DBMs, combined to the kiln characteristics.)



*Fig. 4: Increase in ore recovery due to technology and product design.*

This intermediate grade was designed to be supplied to repair mixes, tundish mixes and EAF mixes, for ramp construction and hearth repair. For these markets a cost-competitive alternative is necessary, but the right chemistry must be achieved, not too pure

that would hinder a quick sintering on the application and controlled fluxes to prevent early wear. Additionally, the process must be able to generate both coarse fractions (>2mm) for the EAF products and fines (<1mm) for repair and tundish mixes without excessive chemistry segregation.

Finally, the density should not be high for these applications since a certain reactivity is still desired for the quick sintering and, especially for tundish and EAF hearth repair, lower thermal conductivity is desired. Nevertheless, if the GBD is too low and the material is still not stable, high shrinkage might be observed, leading to cracks formation reducing the thermomechanical stability and increasing infiltration. Therefore, the right balance on properties must be achieved. Figure 5 show trials successfully carried out with this new DBM concept, with similar application behaviour, specific consumption, and operational time.



*Fig. 5: DBM M9 applied to EAF wall hot repair mix (left) and tundish work lining (right) on RHI Magnesita products.*

## DBM M25F

The DBM M25F was developed to be used in EAF hearth construction, replacing the top-grade DBM (M30B) that is normally combined to high-lime and iron-rich DBMs to improve sinterability. The two key aspects for this application are keeping the $SiO_2$ content low (combined a high MgO grade), to prevent corrosion by slag in the EAF cycles, and provide a proper sintering of the hearth, more intense in the upper portion to generate mechanical strength but gradually decreasing for the lower portions to accommodate the impact of the kiln feeding material and reduce the temperature on the anode (due to the lower thermal conductivity of the mix). Figure 6 exemplify the lab trials carried out to evaluate the application of this DBM on EAF heart mixes, checking for linear change (PLC) and crushing strength (CCS) upon different firing temperatures. The results were very similar to the reference and field trials will be carried out as soon as the volume necessary is available for industrial utilization.
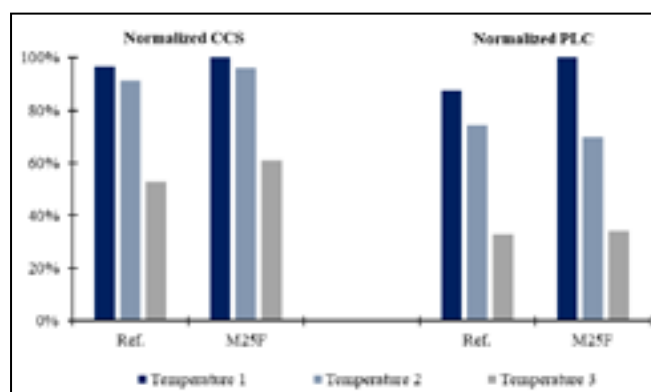


*Fig. 6: Tested properties of M25F applied to EAF hearth mix.*

## DBM M25S

For glass application, the low iron content is necessary to avoid inclusions on the desired product, while the forsterite present as a secondary phase is important for sulphate attack resistance. Additionally, a good creep behaviour is key for a long-lasting product. Finally, complex shapes are necessary for the kilns and a controlled expansion upon firing, still in the refractory production,

is necessary to reduce the scrap generation, keep production costs and quality under control.

The M25S was designed to cope with these demands, the silica content balanced to generate the necessary forsterite and reduce the thermal expansion that would be observed for a top-grade DBM being applied in the same product. Figure 7 exhibits glass bricks successfully produced with M25S and shipped to customers and its microstructural analysis with the M25S grain highlighted.
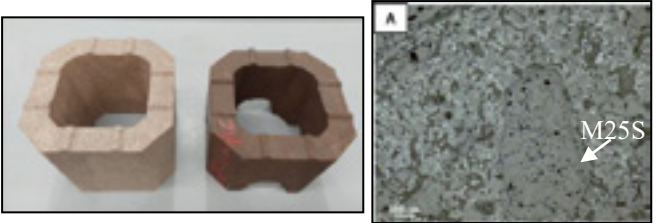


Fig. 7: Glass checker brick produced with M25S and its microstructure.

Another application being studied for M25S is cement bricks for the intermediate zone, exposed to a lower temperature as an opportunity to replace top-grade DBM without loss on performance. With the same objective, this DBM is being tested for magnesia-chrome bricks for non-ferrous metals applications and for tundish furniture in steel production.

## DBM PRODUCTION PROCESS DEVELOPMENT

In order to achieve the targeted properties on the DBM and produce a cost competitive high-grade DBM from a macro-crystalline magnesite in a rotary kiln, an innovative process was developed.

This process was designed combining different stages of pre-processing, binders, and sintering additives. For each DBM, different pre-processing set-ups were tested combined to sintering trials at different temperature levels, assess the feasibility to be produced in a rotary kiln. The sintering trials were carried out first in a batch furnace and, for selected conditions, using a pilot rotary kiln, both present at RHI Magnesita R&D Centre in Brazil. Figure 9 shows the batch and pilot rotary kilns used for the trials.
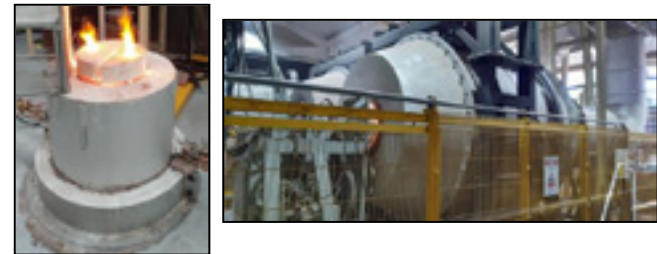


Fig. 8: Batch (left) and pilot rotary (right) kilns at RHI Magnesita R&D Centre Brazil.

The main challenges faced in the process development were to achieve the grain bulk density necessary for brick application and preserving the coarse fraction after the tumbling effect promoted in the rotary kiln.

Initially, the sintering process was explored, evaluating alternative process parameters combined to firing temperature to achieve the grain bulk density goal. Figure 9 illustrate the development steps for the M9, M25S and M25F according to the adjustments.

To evaluate the particle size after the rotary kiln, trials were carried out in the pilot device and the product of was compared to the M30B, the reference for coarse grain generation. In this analysis, two assessments were carried out after the binders and sintering additives were optimized.

First, the particle of the kiln product (run of kiln – ROK) without processing compared to the reference, also without processing. In the second step, both samples were crushed and their PSD were compared after processing. Figure 10 presents the results for the M25 DBM class compared to M30B for ROK and after crushing.
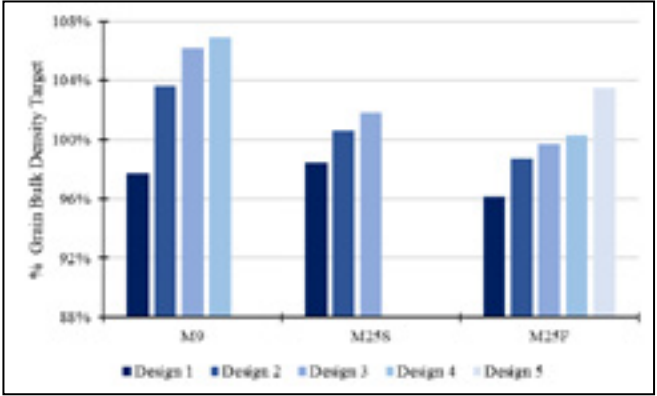
Fig. 9: Grain bulk density evolution according to parameter set-up on batch sintering trials.
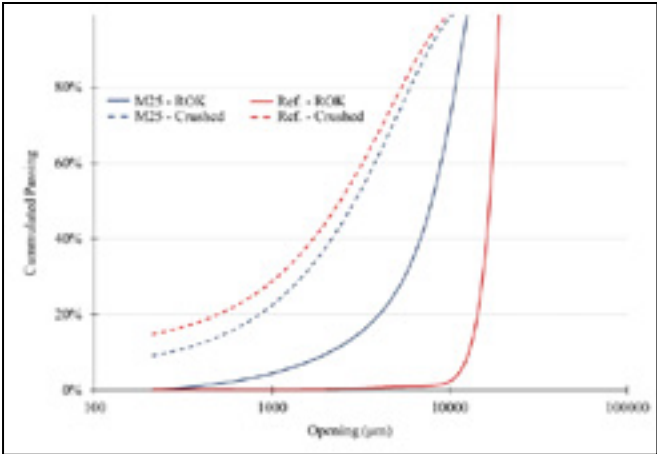


Fig. 10: Particle size distribution of new DBM class compared to reference.

Despite having a finer particle size distribution after the kiln processing, the M25 class DBM has a very similar PSD after a single crushing stage, within the coarse size fraction generation range for brick application.

Considering the firing results and process alternatives evaluated, an innovative plant design could be stablished combining the desired specs for each DBM to a cost-effective processing route.

## PORTFOLIO CHARACTERISTICS

Table 1 is elaborated to compare the different DBMs developed with the regular products, giving an overview of the new portfolio to be produced out of Brumado.

Tab. 1: New DBM portfolio and properties

| DBM | M9 | M10 | M25F | M25S | M30 |
|-----|-----|-----|------|------|-----|
| GBD | + | + | ++ | ++ | +++ |
| MgO | + | + | ++ | ++ | +++ |
| SiO2 | ++ | + | + | ++ | - |
| Fe2O3 | ++ | ++ | + | - | - |
| CaO | - | - | - | + | + |
| C/S | - | - | - | - | ++ |

Considering this new portfolio, and the state-of-start technology rotary kiln being implemented, the Brumado DBM production in Brazil is prepared to supply competitive amd high-performance refractory raw materials for a wide varity of applications, reafirming the importance of this plant for the global supply and improving its sustainability for the long-term.

## CONCLUSIONS

Taking advantage on the RHI Magnesita knowledge on the full production chain of refractories, new dead burned magnesia grades

were developed to increase the value and sustainability of its Brumado plant in Brazil.

The new DBMs were designed to have the desired characteristics of each targeted market, in steel, glass and cement industries. To achieve the properties, trials were carried out in lab, pilot and industrial scale, evaluating the process design and impact on downstream processes.

For all new DBMs, M9, M25F and M25S, the desired chemical and physical properties could be achieved. Combined to this results, refractory trials were successfully carried out, in some cases even considering customer application.

With this new portfolio, RHI Magnesita strengthen its backward integration and Brumado plant improve its cost-competitiveness and sustainability, expanding the pool of applications and potential customers for the high-quality DBMs produced at this site.

**REFERENCES**

[1] Chowdhury A.A., Rasul M.G., Khan M.M.K. Thermodynamic processes and characterisation of dead burned magnesia: a review. Recent Advances in Energy and Environment, 2010, p. 344-349.

[2] Kujur M.K., Roy I., Kumar K., Chintaiah P., Ghosh S., Ghosh N.K. Raw materials for manufacturing of superior quality MgO-C bricks. Materials Today: Proceedings, 5(1), 2018, p. 2359-2366.

[3] Nanda S., Choudhury A., Chandra K.S., Sarkar D. Raw materials, microstructure, and properties of MgO–C refractories. Journal of European Ceramic Society, 43, 2023, p.14-36.

[4] Kerr J., Hanna A., Moraes M.N. Development of an innovative electric furnace hearth. Proceedings: UNITECR 2022.

[5] Gonçalves G.E., Pacheco G.R.C., Brito M.A.M., Cabral S.L., Lins V.F.C. Influence of magnesia in the infiltration of magnesia-spinel refractory bricks by different clinkers. REM, 68 (4), 2015, p. 409-415.

[6] Gotod K., Lee, W.E. The "Direct Bond" in Magnesia Chromite and Magnesia Spinel Refractories. Journal of the American Ceramic Society, 78(7), 1995, p.1753-1760.

[7] İzmirlioğlu B., Yılmaz S. Glass melting furnace refractories and refractory related defects. Journal of Chemical Technology and Metallurgy, 50 (4), 2015, p.404-410.

[8] Meynckens J.P., Cherdon, B. Environmental Impact for Regenerators Materials Selection in Soda-Lime Flat Glass Furnaces. Advanced Materials Research, 39-40, 2008, p.619-624.

[9] Drnek T., Moraes M.N., Bonadia P. Overview of magnesite. Journal of refractory innovations, 2018, p.14-22

# AN ECO–FRIENDLY APPROACH TO PURIFY NATURAL MAGNESITE AND TO DENSIFY SINTERED MAGNESIA

Zongchun Yu, Northeastern University, Shenyang 110000, China
Li Wang, Zhaoqing Li, Xu Han, Wenjun Sun, Dongda Dongke Drying & Calcining Technology Co., Shenyang 110000, China
Zongqi Guo, Presenter, guozongqi@xauat.edu.cn, Xi'an University of Architecture and Technology, Xi'an 710055 &
Liaoning Fenghua Industries Corporation, Yingkou 115100, China

## ABSTRACT

High-grade magnesite raw ore for DBM97 production became rare in China after a frenzy of mining for over 30 years. But the demand for high-purity sintered magnesia grows in high temperature industries that accompanies volatile components. Some attempts have been made for the purification and densification from the flotation of low-grade natural magnesite, flash calcination in suspension calciner, and sintering in extraordinarily high temperature shaft kiln. In this work, a novel eco-friendly approach is developed, based on a pilot plant with the capacity of 40 t/d, to calcine natural magnesite grading as low as 40% MgO, to carry out three levels of watering treatments removing Si-, Fe- and Ca- components and hydrating MgO (gaining >90% $Mg(OH)_2$), to calcine magnesium hydroxide for active MgO in suspension calciner, and finally to burn high purity magnesia to high densification. MgO hydration process is highlighted with the pivotal parameters of hydrating duration and temperature. The calcined caustic magnesia obtained has high activity of < 20 s with citric acid. Dead burnt magnesia reaches the purity of > 97.5% MgO and the bulk density of > 3.4 $g/cm^3$, from low grade natural magnesite, in industrial potential.

## 1. INTRODUCTION

A plentiful resource of natural magnesite deposits lies in the northeast of China, with 3,115 million tonnes and 26% of global reserves [1,2], where various grades of refractory magnesia have been dominantly supplying the global demand of high temperature industries [3]. After high grades of magnesite are merely mined and traditional manufacturing processes of magnesia are performed for over 30 years, critical technologies of magnesite calcination and purification are being developed, as well as sintering approaches to the magnesia densification [4,5].

In order to remove more than 50% $CO_2$ from magnesite, light calcination must be firstly made in the magnesia manufacturing process, which produces caustic calcined magnesia (CCM). As the most widely used technology (China), about 1500 reverberatory furnaces are being run in Liaoning province with the production capacity of over 10 million tonnes CCM per year. This is a typical fixed bed calcination reactor, in which the calcination occurs at a temperature in the range from 1,000 °C to 1,300 °C. Only large size magnesite lumps in 30–80 mm are adopted to allow gas flow from bottom to top in reverberatory furnace and to ensure the combustion space for fuel gas and the transportation channels for emitted gases, which makes the calcinating time elongated up to 3–5 h and a low production capacity of maximumly 30 tonnes per day. A mass of small-size magnesite generated during mining are abandoned. On the other hand, over-burning on lump surface and insufficient-burning in the inner core occur, resulting in unstable quality and low activity of CCM. In general, the drawbacks of reverberatory furnace are high energy consumption, bad feedstock adaptability, long reaction time, unsteady CCM quality, low CCM activity and severe environmental pollution [6,7]. Due to the reducing availability of high-grade magnesite, dozens of flotation magnesite lines have been built in last 10 years to upgrade low-grade magnesite fines. A flash calcining technology is developed as suspension calciner for calcining floated magnesite powders.

As a traditional manufacturing route, lumps of magnesite are calcined in a reverberatory furnace to produce caustic calcined magnesia, and CCM briquettes are sintered in a shaft kiln to produce dead burnt magnesia (DBM97). Mainly due to low activity of CCM from

reverberatory furnace, the bulk density of DBM97 is in the range between 3.24 and 3.30 $g/cm^3$. The purified magnesite powders after floating can be calcined in multiple hearth furnace for CCM production and the DBM98 briquettes have the optimal bulk density of 3.36 $g/cm^3$. While floated magnesite is calcined in a suspension calciner, the bulk density of DBM98 can reach 3.42 $g/cm^3$ [8]. In these cases, all high purity magnesia briquettes have to be sintered at ultra-high temperature of 1,950–2,100 °C in shaft kiln. Additionally, impurity of iron-component is hardly removed in the flotation process if iron ions enter MgO lattice.

The most common beneficiations are carried out by dense-media separation, magnetic route and flotation process. The potential pollution exists during flotation process of magnesite purification because a lot of chemicals are used. There are no appropriate solutions to deal with 20–30% tailings of magnesite floatation. In some deposits of magnesite ore, the impurities are strongly bound to the crystalline structure, for instance, Fe ions in MgO crystals. An eco-friendly approach has been developed for purification and densification, firstly to calcine low grade magnesite, then to hydrate CCM for separating the suspension of magnesium hydroxide from $Ca^{2+}$ and precipitating Al-, Fe- and Si-components. After de-watering of magnesium hydroxide suspension, the paste of magnesium hydroxide is dried and calcined in the system of suspension calciner to have secondary CCM, which is sintered at various temperatures for densification.

## 2. EXPERIMENTAL PROCEDURE

Low grades of magnesite ore are used as raw material for purification. Their chemical analyses are listed in Table 1.

*Tab. 1: Chemical analyses of magnesite ore used for purification*

| Magnesite sample | MgO wt% | $Al_2O_3$ wt% | $Fe_2O_3$ wt% | CaO wt% | $SiO_2$ wt% | LOI wt% |
|---|---|---|---|---|---|---|
| No. 1 | 81.43 | 0.67 | 2.17 | 9.15 | 6.57 | 49.50 |
| No. 2 | 86.74 | 0.57 | 1.80 | 4.82 | 6.07 | 48.96 |
| No. 3 | 83.28 | 0.69 | 1.78 | 8.26 | 6.07 | 47.05 |
| No. 4 | 89.10 | 0.50 | 1.30 | 3.47 | 5.08 | 48.55 |
| No. 5 | 88.97 | 0.55 | 1.30 | 3.50 | 4.68 | 48.02 |

The flow chart from raw magnesite ore, calcining, hydrating and purifying, secondary calcining to sintering is shown in Figure 1. Raw magnesite ore is crushed and ground to 90% below 200 mesh.

1) Magnesite calcination: Magnesite powders are fed to the suspension calciner by 1.6 t/h, to have 0.7 t/h primary CCM.
2) First stage hydration: primary CCM is put into a water tank with agitating vane. After 1 hour, suspension solution of MgO and magnesium hydroxide is generated. Undecomposed magnesite, grains and contamination are removed from suspension solution by precipitation.
3) Second stage hydration: Suspension solution overflows from first tank to second tank with heating instrument and stirrers. The temperature of suspension solution is adjusted according to increasing solution quantity. Entire hydration is completed in this stage, which takes 2 hours at the temperature of 90–100 °C. The impurities of $SiO_2$ and $Fe_2O_3$ are precipitated to reduce their contents on the levels of $SiO_2$ < 0.15% and $Fe_2O_3$ < 0.25%.

4) Chlorination stage: magnesium hydration solution flows to third tank and remains certain temperature of 90–100 °C. By adding hydrochloric acid and/or $MgCl_2$, CaO is solved in the solution for separation. Finally, at least 90% Mg $(OH)_2$ is acquired in the solution.

5) Calcining magnesium hydroxide powders: After de-watering, magnesium hydroxide powders are calcined in a suspension calciner, to produce secondary CCM.

6) Briquetting and sintering: Secondary CCM briquettes are sintered at the temperatures of 1,400°C, 1,500°C and 1,600°C for 5 hours in maffle furnace, 1,650°C, 1,700°C and 1,750°C for 5 hours in tunnel kiln.



*Fig. 1: Flow chart of magnesia purification and densification*

## 3. RESULTS AND DISCUSSION

### 3.1 Flash decomposition in suspension calciner

The flow chart of magnesite calcination is shown in Figure 2. Magnesite powders with the size of < 200 mesh are fed into dryer to mix with hot exhausted gas for removal of free water. The material is reversely flowed with hot gas to heat up itself and finally separated by multiple stage cyclones. The airstream and solid materials are in reverse flow. After calcinating, CCM powders are cooled and separated also by multiple stage cyclones, from the top of which the exhausted gas is expelled. CCM falls down to storage tank.

The concentrates paste is dried at 450 °C by reversely flowing hot gas coming from the calciner. The dried concentrates (the moisture <1%) are separated in three stages cyclones, and then fed into the lower portion of the suspension calciner. The magnesite concentrates are calcined at the temperature of 680–850 °C in the flowing movement from the bottom to the top, with hot gas, which takes about 3 seconds. Again, caustic calcined magnesia is separated by three-stage cyclones and then stored in silos with eco-friendly production. Natural gas is consumed in 1,950–2,100 m³/h, combusted with air of 40,000 m³/h and later cooled with air of 50,000 m³/h. It is a new generation of the magnesite calciner with some preferred characteristics. 1) Instantaneously calcining magnesite with the homogeneous mixture of solid and gas, as well as the large specific surface for dissociation; 2) Continuous operation, ensuring stable activity of CCM; 3) Entirely closed system under negative pressure and multiple stages separation, being eco-friendly, high productivity.
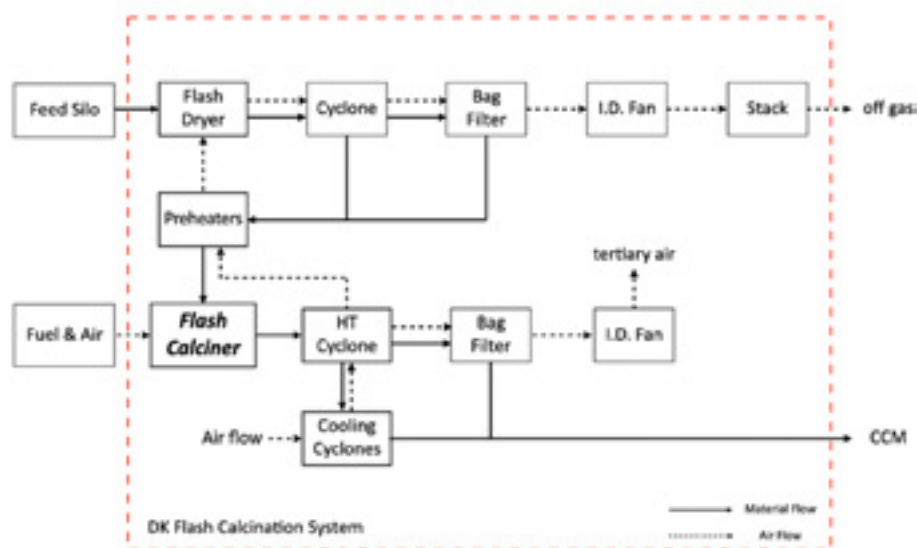


*Fig. 2: Flow chart of suspension calcination process*

The illustration and principle of suspension calciner are displayed in Figure 3, where the temperature and pressure are graphed. Fuel is completely combusted to yield high temperature gas (up to 1,400 °C), which is drawn into cyclone accelerator to mix with preheated magnesite powder. The particle size is smaller than 200 mesh. The large particles mostly receive radiation transfer heat because of high centrifugal force in spiral motion, while the small particles have more convection transfer heat. Therefore, due to high specific surface area, the particles in swirl movement are exposed to radiate heat and transfer heat within calciner. Flowed with hot gas in conjugate movement of 7–12 seconds, and moved in a route of 80–130 m, magnesite particles complete overall decomposition in the following equation, by absorbing radiate energy.

$$MgCO_3 \rightarrow MgO + CO_2$$
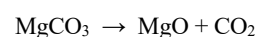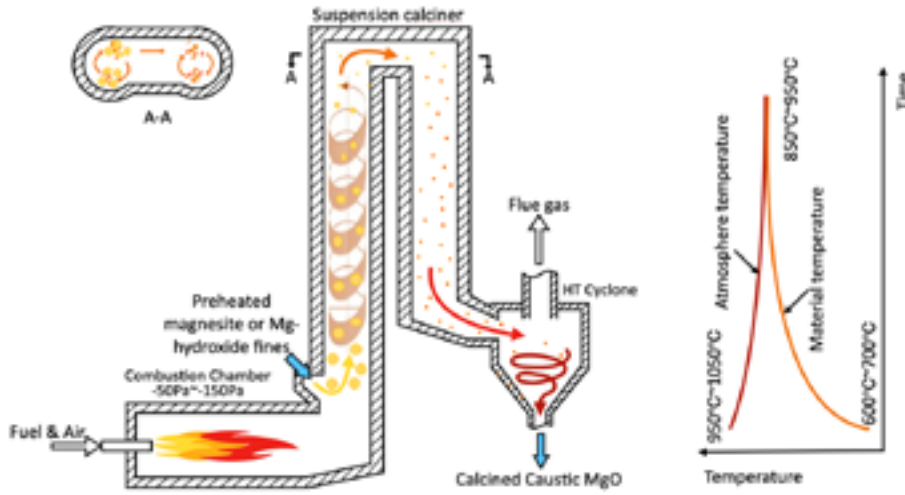
*Fig. 3: Illustration and principle of suspension calciner*

The calciner is operated under the negative pressure between –90 Pa and –150 Pa. The loss on ignition is controlled with the limit of 2% for primary CCM.

After hydration and purification, most of primary CCM have been transformed to magnesium hydroxide, which needs to be calcined in suspension calciner again. Eventually, secondary CCM is obtained, according to the following equation.

$$Mg(OH)_2 \ \rightarrow \ MgO + H_2O$$
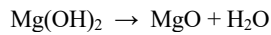
The physical and chemical properties of secondary caustic calcining magnesia are listed in Table 2. Compared to the chemical composition in Table 1, secondary CCM have been significantly purified, which upgrades low grades of natural magnesite for manufacturing high grade of sintered refractory magnesia.

*Tab. 2: Physical and chemical properties of secondary CCM*

| No. | MgO wt% | Al$_2$O$_3$ wt% | Fe$_2$O$_3$ wt% | CaO wt% | SiO$_2$ wt% | Size* μm | Ac** s |
|---|---|---|---|---|---|---|---|
| 1Se | 97.68 | 0.15 | 0.19 | 1.39 | 0.59 | 28.30 | 15 |
| 2Se | 96.57 | 0.15 | 0.19 | 1.46 | 0.55 | 29.55 | 17 |

*Particle size, D$_{90}$; **Activity: Reaction time with citric acid.

### 3.2 Purification in hydration process

After grinding and calcining raw ore of magnesite, primary CCM is purified in three stages, as shown in Figure 4.
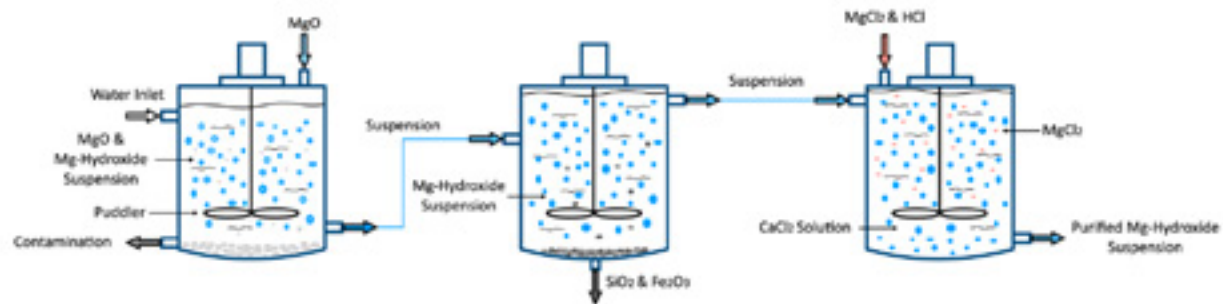


*Fig. 4: Hydration and chlorination of primary CCM for purification*

In the first tank, primary CCM is in hydrating process to form a suspension of magnesium hydroxide and to precipitate undecomposed magnesite and contamination at room temperature. While the suspension is moved to the second tank, most of CCM would complete hydration at 90–100 °C.

$$MgO + H_2O \rightarrow Mg(OH)_2$$
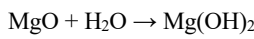
Most of Si- and Fe- components are precipitated on the bottom of the second tank. When the suspension is drawn to the third tank, hydrochloric acid and/or MgCl$_2$ are fed to react with Ca(OH)$_2$ to form CaCl$_2$ in the solution. The following reactions take place in the third tank. In this way, CaO content is reduced in the suspension of magnesium hydroxide.

$$Mg(OH)_2 + HCl \ \rightarrow \ MgCl_2 + H_2O$$

$$MgCl_2 + Ca(OH)_2 \ \rightarrow \ Mg(OH)_2 + CaCl_2$$

$$Ca(OH)_2 + HCl \ \rightarrow \ CaCl_2 + H_2O$$
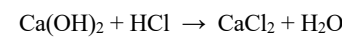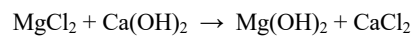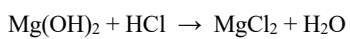
The chemical compositions of magnesium hydroxide from the second tank and from the third tank are listed in Table 3, which proves the approaches of purification are really functional.

The suspension of magnesium hydroxide, out of the third tank, is de-watered to have the paste, which is dried and calcined in the suspension calciner for secondary caustic calcined magnesia.

*Tab. 3: Chemical analyses of magnesium hydroxide powder*

| Treatment | MgO wt% | Al$_2$O$_3$ wt% | Fe$_2$O$_3$ wt% | CaO wt% | SiO$_2$ wt% | LOI wt% |
|---|---|---|---|---|---|---|
| Hydrating | 67.00 | 0.08 | 0.04 | 4.00 | 0.20 | 28.30 |
| Chlorinating | 68.88 | 0.06 | 0.12 | 0.86 | 0.33 | 29.55 |

### 3.3 Sintering of CCM

Low-grade magnesite is firstly calcined in a suspension calciner and the acquired caustic magnesia is hydrated to precipitate the impurities of $Al_2O_3$ and $Fe_2O_3$ from magnesium hydroxide suspension solution. The chlorination is then carried out to dissolve $Ca(OH)_2$ to $CaCl_2$ to reduce CaO content. After de-watering, magnesium hydroxide is calcined in the suspension calciner to produce secondary caustic magnesia.

A commercial CCM is collected for sintering comparison, which is made by magnesite flotation and calcination process. Its compositions are 97.75% MgO, 1.44% CaO, 0.48% $Fe_2O_3$, 0.33% $SiO_2$. Both CCM powders are compacted and sintered in a muffle furnace (1,400 °C, 1,500 °C, 1,600 °C) and a tunnel kiln (1,650 °C, 1,700 °C, 1,750 °C). Apparent porosity and bulk density of magnesia are displayed in Figures 5 and 6, as a function of sintering temperature. The process of calcination, hydration and chlorination, secondary calcination and sintering is called as 3-step firing. The flotation, calcination and sintering route is named as 2-step firing. It can be seen in Figure 5 that the apparent porosity is near linear reduction and down to < 2% by 3-step firing, and decreased at lower temperature and on the same level (near 10%) at higher temperature by 2-step firing.
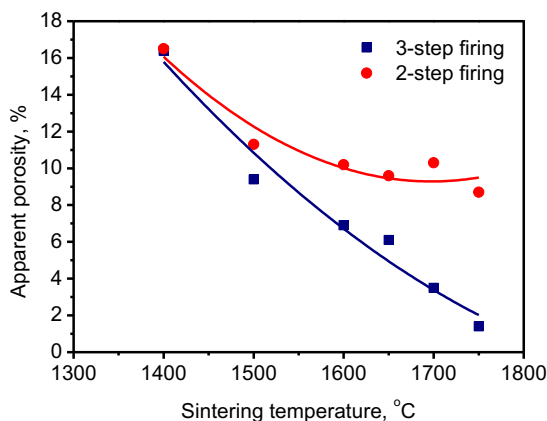


*Fig. 5: Apparent porosity of magnesia as a function of sintering temperature*

As shown in Figure 6, the influence of sintering temperature on densification is more significate by three-step firing than 2-step firing. By hydrating and 3-step firing process, the magnesia density reaches 3.43 $g/cm^3$ after sintering at 1,750 °C, but the bulk density of magnesia directly from magnesite maximally attains the density of around 3 $g/cm^3$. It is the similar results to previous lab experiment [4].

It is hard to densify magnesia directly from natural magnesite. Only possibility is to sinter magnesia at the temperature range of 1,950–2,100 °C in a shaft kiln. Through hydration beneficiation process, it is possible to sinter and to densify magnesia at ordinarily high temperature of 1,750 °C.
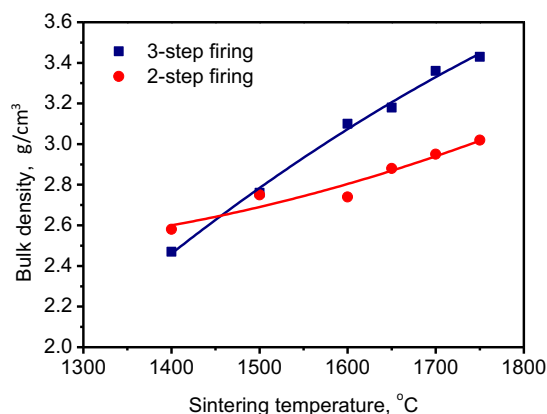


*Fig. 6: Bulk density of magnesia as a function of sintering temperature*

### 4. CONCLUSION

An eco-friendly approach is developed to purify low-grade magnesite by hydrating primary calcined magnesia and precipitating impurities of Ca-, Fe- and Al-components. The resulted magnesium hydroxide powders are calcined again to acquire secondary calcined magnesia, which is compacted and sintered at various temperatures (1,400 °C–1,750 °C). By hydrating caustic calcined magnesia for precipitating impurities and firing in three steps, high purity and density of DBM97.5 have been produced at the ordinarily high temperature.

**REFERENCES:**
[1] Wilson, L: Global magnesite resources and production. Magmin Conference 2015. Athens, Greece, 18–20 May 2015.
[2] Ministry of Natural Resources, PR China: Mineral Resources. Beijing, Geological Publishing House, October 2018.
[3] O'Driscoll M: The new world of China's mineral supply. Refractories Worldforum 11(4), 2019, p. 54–57.
[4] Guo Z, Ma Y, Rigaud M: Sinterability of macrocrystalline and cryptocrystalline magnesite to refractory magnesia. International Journal of Ceramic Engineering and Science 2(6), 2020, p. 303–309.
[5] Guo Z, Bi D, Ma Y, Sun Z: Approaches to high-grade sintered magnesia from natural magnesite. China's Refractories 29(3), 2020, p. 7–12.
[6] Ba H, Bai L, Zhao W, Ma Y, Yin X: Review on preparation and processing of caustic calcined magnesite. Conservation and Utilization of Mineral Resources 37(1), 2017, p. 84–89.
[7] Li J, Zhang Y, Shao S, Zhang S, Ma S: Application of cleaner production in a Chinese magnesia refractory plant. Journal of Cleaner Production 113, 2016, p. 1015–1023.
[8] Guo Z, Bi D, Sun S: Purification and densification of sintered magnesia from natural macrocrystalline magnesite in China. Refractories Worldforum 13(3), 2021, p. 67–71.

49

# ENHANCED PERFORMANCE OF FREE CAO IMPURITY CONTAINING MAGNESIA WITH AL$_2$O$_3$–TIO$_2$ COMPOSITE POWDER

Yibiao Xu*, Yawei Li, Zhenzhen Li

The State Key Laboratory of Refractories and Metallurgy, Wuhan University of Science and Technology, Wuhan, PR China

## ABSTRACT

Free CaO impurity containing magnesia has intrinsic shortcomings of poor resistance to hydration and thermal shock. Here, a novel approach, the introduction of $Al_2O_3$-$TiO_2$ composite powder, is proposed to enhance the performances of such magnesia in this work. The results showed that with increasing the composite powder, $CaTiO_3$ and $Mg_{1+x}Al_{2(1-x)}Ti_xO_4$ phases were sequentially formed at MgO grain boundaries, which affected the microstructure and properties of the specimens. the addition of $Al_2O_3$-$TiO_2$ enhanced the MgO grains growth and conversion of free CaO to $CaTiO_3$, and therefore weight gain rate of the specimens after hydration test reduced from 0.212 % to 0.097 % with increasing $Al_2O_3$-$TiO_2$ from 0 wt% to 7 wt%. The formed intergranular $CaTiO_3$ and $Mg_{1+x}Al_{2(1-x)}Ti_xO_4$ phases reduced the thermal expansion coefficient and induced the crack deflection, which thus siginifically improved the thermal shock resistance the specimens.

## INTRODUCTION

Magnesia is a refractory raw material widely used in industrial metallurgical furnaces owing to its high refractoriness and excellent corrosion resistance to basic slag [1]. In China, magnesia produced by cryptocrystalline magnesite usually exhibits high chemical stability and excellent thermo-mechanical properties due to the infinitesimal $SiO_2$ and $Fe_2O_3$ impurities. However, this kind of magnesia shows low hydration resistance due to the presence of free CaO [2]. Besides, magnesia raw material has intrinsic shortcoming of poor thermal shock resistance (TSR),which would shorten service life of the magnesia based refractories [3]. To improve TSR of the magnesia, several researches have been carried out in recent years. Zou et al. [4] prepared magnesia aggregates with the introduction of nanosized $Al_2O_3$. They found that the formation of $MgAl_2O_4$ phase reduced the pore size and enhanced the ceramic bonding, thus improving TSR of the magnesia aggregates. Our previous work introduced $ZrO_2$ to high purity magnesia and found that $ZrO_2$ grains would distribute at the MgO grain boundaries and perform pinning effect, which caused the crack deflection and therefore enhanced the TSR [5]. More recently, Zhao et al [6] reported that the introduction of $Al_2TiO_5$ as second phase in the magnesia matrix could effectively reduce the thermal expansion coefficient and thus improved the residual bending strength of the magnesia after three thermal cycles.

Based on the above work, it was expected that for the free CaO containing magnesia, the performance could be enhanced by the combination of $Al_2O_3$ and $TiO_2$. For one hand, the thermodynamic calculations presented in **Fig. 1** demonstrated that free CaO would preferentially react with $TiO_2$ forming high melting point phase $CaTiO_3$ (2000°C), which could eliminate the free CaO and effectively improve the hydration resistance [7]. On the other hand, $MgAl_2O_4$ and $Al_2TiO_5$ may be generated in the magnesia at elevated temperature, contributing to the superior TSR of such material [4, 6]. Therefore, in order to fully utilize the advantages of $Al_2O_3$ and $TiO_2$, micro-sized $Al_2O_3$-$TiO_2$ composite powder was added into free CaO containing magnesia in the present work and its effects on sintering behavior, phase compositions, microstructure, hydration resistance, and TSR of such refractory raw material were studied in detail.
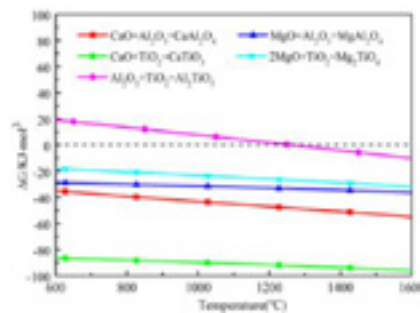


*Fig. 1 Gibbs free energies for reactions of MgO-CaO-Al$_2$O$_3$-TiO$_2$*

## EXPERIMENTAL

The raw materials are light burned magnesia powder ($D_{50}$= 15.1 μm, MgO ≥ 96.06 wt%; 0.97wt% CaO, 0.05 wt% $SiO_2$, 0.07 wt% $Fe_2O_3$) and reagent grade $Al_2O_3$-$TiO_2$ composite powder consisting of 50 mol% $Al_2O_3$ and 50 mol% $TiO_2$. The specimens with various amounts of composite powder (0, 1, 3, 5, 7 wt%) were ball-milled for 6 h and named as MAT0, MAT1, MAT3, MAT5 and MAT7, respectively. Subsequently, the mixtures were dried, screened, and pressed into specimens with dimensions of Φ50mm×20mm under 100 MPa. Finally, all these specimens were sintered at 1600 °C for 3 h in an electric furnace in air.

The bulk density and apparent porosity were measured by Archimedes's Principle. The phase composition and microstructure were determined by X-ray diffraction (XRD, X'Pert Pro, Philips, Netherlands) and scanning electron microscope (SEM, Nova 400 NanoSEM, FEI Company, USA), respectively. The thermal expansion of the specimens was tested in Ar atmosphere by a thermal dilatometer (Anter Corp., Pittsburgh, PA). The flexural strength (3 mm×4 mm ×34 mm) before and after thermal shock tests (ΔT=1100°C, oil quenching) was evaluated by three-point bending method [5]. During hydration resistance, specimens with size of Φ20 mm×10mm were put in an autoclave and heated till the pressure reached 0.14 MPa at 134 °C. After maintaining for 3 h, the specimens were dried in an oven at 110 °C. The percentage weight gains were used to characterize the hydration resistance [8].

## RESULTS AND DISCUSSION

Fig.2 exhibits the phase compositions of the specimens after treated at 1600 °C. Only periclase phase could be found in specimen MAT0 due to its low impurity content. In specimen MAT1, apart from periclase, $CaTiO_3$ compound could be detected. With further increasing the amount of $Al_2O_3$-$TiO_2$, a composite spinel phase identified as $Mg_{1+x}Al_{2(1-x)}Ti_xO_4$ was generated, which was a solid solution formed by interdiffusion between $Mg_2TiO_4$ and $MgAl_2O_4$ [9]. Besides, as shown in Fig. 2b, the diffraction peaks of the composite spinel shifted toward lower angles as the composite powder amount increased, demonstrating that more $Mg_2TiO_4$ with a larger cell volume diffused into $MgAl_2O_4$ [10].
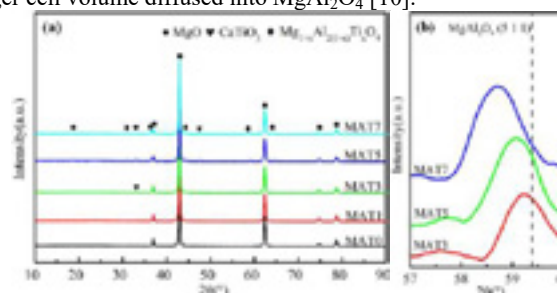


*Fig. 2 XRD patterns of the specimens after firing at 1600°C*

SEM images of the specimens are shown in Fig. 3. For specimen MAT0, the MgO grain size was small and some pores with a size of 2-6μm could be found. Free CaO and tiny $Ca_2Fe_2O_5$ could also be observed in the matrix, although they were not detected in the XRD patterns. As for specimen MAT1, the amounts of free CaO and $Ca_2Fe_2O_5$ reduced dramatically, whereas $CaTiO_3$ together with trace $CaAl_2O_4$ was generated at the boundaries. In the specimens MAT3, MAT5 and MAT7, apart from periclase and $CaTiO_3$, $Mg_{1+x}Al_{2(1-x)}Ti_xO_4$ solid solution could be observed, whose amount increased continuously with the $Al_2O_3$-$TiO_2$ content. Furthermore, as shown in Table 1, with increasing composite powder content, the size of both MgO grains and pores in the specimens showed an increase tendency. The mean MgO grain size of specimens MAT0 to MAT7 was 20.3, 34.1, 38.8, 49.6 and 43.8 μm, respectively. Correspondingly, the mean pore size increased from 1.2 μm in specimen MAT0 to 6.4 μm in specimen MAT7.

It can be proposed that when 1 wt% $Al_2O_3$-$TiO_2$ was added to magnesia, the CaO impurity firstly reacted with $TiO_2$ to form $CaTiO_3$ and part of the residual CaO would then combine $Al_2O_3$ to generate $CaAl_2O_4$. As the composite powder was 3 wt% or higher, all free CaO transformed into $CaTiO_3$ phase, while the $Al_2O_3$ together with residual $TiO_2$ would react with MgO to produce $MgAl_2O_4$ and $Mg_2TiO_4$ respectively, which in turn formed the $Mg_{1+x}Al_{2(1-x)}Ti_xO_4$ solid solution. The above reactions promoted mass transfer andMgO grain growth, whereas the pores were not eliminated further due to their agglomeration and growth at the MgO boundaries. Therefore, as shown in Table 1, the addition of $Al_2O_3$-$TiO_2$ had no obvious effect on the relative density.

Fig. 4a shows the flexural strength of the specimens and their residual strength after thermal shock tests. As the $Al_2O_3$-$TiO_2$ increased from 0 wt% to 7 wt%, the flexural strength decreased constantly from 161.4 MPa to 106.8MPa. Since all specimens had similar density, the reduction in flexural strength was probably attributed to the coarsening of MgO grains and pore size [11]. However, after the thermal shock tests, compared with specimen MAT0, specimens with composite powder possessed both higher residual flexural strength and residual flexural strength ratio (Fig. 4b), indicating the effective enhancement in TSR. Based on the thermoelastic theory, TSR of the composites is closely related to the thermal expansion coefficient. Fig. 5 revealed that specimens with more composite powder obtained lower thermal expansion coefficient. This was mainly because MgO ($13.8 \times 10^{-6}$/K) had higher thermal expansion coefficient than that of $CaTiO_3$ ($12.2 \times 10^{-6}$/K), $MgAl_2O_4$ ($7.8 \times 10^{-6}$/K) and $Mg_2TiO_4$ ($10.1 \times 10^{-6}$/K). As a result, less surface thermal stress would be produced in the specimens with higher composite powder, which contributed to improving the TSR. Again, the crack propagation behavior is another key factor affecting TSR [12]. As shown in Fig. 6, transgranular fracture occurred when the specimen MAT0 was subjected to thermal stress. However, for the specimens with composite powder, the $CaTiO_3$ and $Mg_{1+x}Al_{2(1-x)}Ti_xO_4$ phases induced the crack deflection and intergranular fracture gradually became the main fracture mode. The crack deflection could increase the crack path and absorb more fracture energy, leading to the enhancement of the TSR [13].
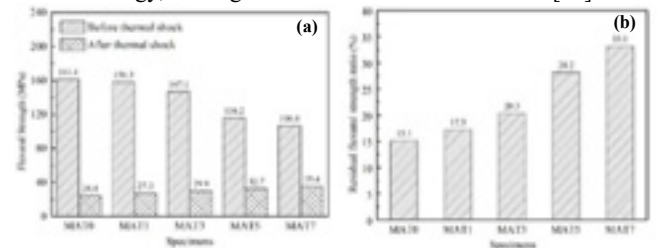
*Fig. 4 Strength, residual strength and its ratio of the specimens*
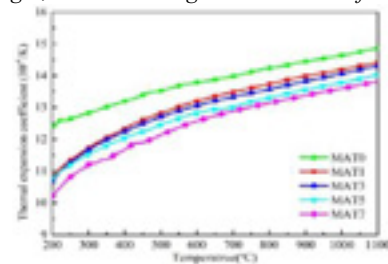
*Fig. 5 Thermal expansion coefficient of the specimens.*

*Fig. 3 SEM micrographs of the specimens after firing at 1600℃*

Table 1: Mean grain size, mean pore size and relative density

| Index | Grain size (μm) | Pore size (μm) | Apparent porosity (%) | Relative density (%) |
|---|---|---|---|---|
| MAT0 | 20.3 | 1.2 | 0.7 | 95.8 |
| MAT1 | 34.1 | 3.2 | 0.6 | 94.9 |
| MAT3 | 38.8 | 3.9 | 0.6 | 95.1 |
| MAT5 | 49.6 | 6.5 | 0.5 | 95.3 |
| MAT7 | 43.8 | 6.4 | 0.5 | 95.6 |
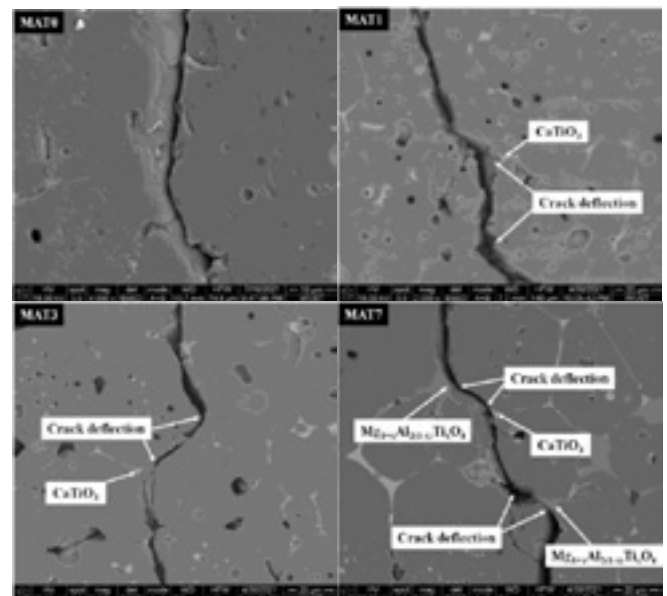
*Fig. 6 Crack propagation in the specimens after thermal shock tests*

After the hydration test, the weight gain rate of the specimens is shown in Fig. 7. It can be found that the weight gain rate decreased from 0.212 % to 0.156 % when 1 wt% $Al_2O_3$-$TiO_2$ was introduced, and further reduced to 0.107 % as the composite powder increased to 3 wt%. With further increasing the composite powder content, the weight gain rate of the specimens showed a negligible change. Specimens MAT3, MAT5 and MAT7 exhibited an obvious improvement in hydration resistance, whose weight gain rate was approximate half that of the pure MgO specimen. XRD patterns of the specimens after the hydration test are shown in Fig. 8. In specimen MAT0, the characteristic diffraction peaks of newly formed $Ca(OH)_2$ hydrated products could be detected. As for the specimens with composite powder, the diffraction peaks of the $Ca(OH)_2$ phase disappeared completely. Besides, the diffraction peak intensity of $Mg(OH)_2$ hydrated product decreased sharply when the composite powder increased from 0 wt% to 3 wt% but had a negligible change with further increasing the content of composite powder. Fig. 9 presented the SEM image of the specimens after the hydration test. For specimen without composite powder, plenty of granular $Ca(OH)_2$ and lamellar $Mg(OH)_2$ hydrated products were formed on the outer surface, demonstrating the occurrence of serious hydration reactions. The hydration processes preferentially occurred in the CaO grains, which resulted in formation of cracks on the surface and sustained hydration of CaO and MgO in the inner part of the specimen [7]. As 1 wt% composite powder was added into the magnesia, obvious decrease in the amount of both $Ca(OH)_2$ and $Mg(OH)_2$ could be found. As for specimens MAT3, MAT5 and MAT7, only a trace of $Mg(OH)_2$ hydrated product could be observed on their outer surface, indicating the effective suppression of the hydration processes. These XRD and SEM observations were entirely consistent with the results of weight gain rate shown in Fig. 9.

Combining the hydration test results with the phase and microstructure evolutions, the significant improvement in hydration resistance by adding $Al_2O_3$-$TiO_2$ could be proposed. i) Due to the increased MgO grain size and decreased grain boundaries, diffusion channels for water vapor into the inner part of the specimens declined, which retarded the hydration processes [14]. ii) The free CaO transformed into high hydration resistant phase $CaTiO_3$, eliminating the CaO hydration and effectively improving the hydration resistance of the raw material [7].
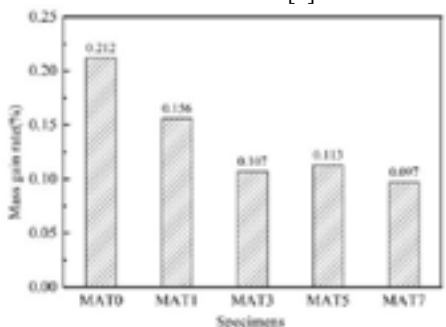


*Fig. 7 Mass gain rate of the specimens after the hydration test*
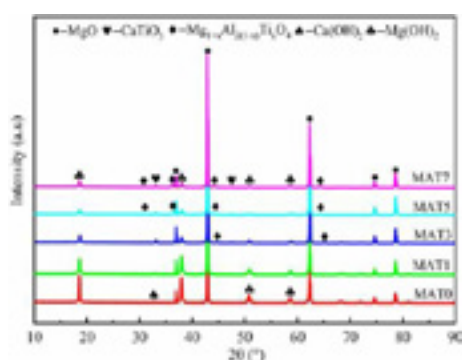


*Fig. 8 XRD patterns of the specimens after the hydration test*
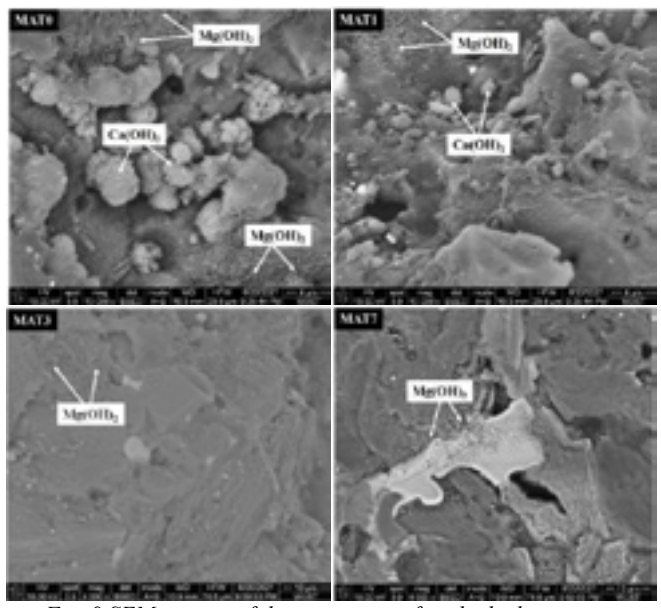


*Fig. 9 SEM images of the specimens after the hydration test*

## CONCLUSIONS

The effects of $Al_2O_3$-$TiO_2$ composite powder on the sintering behavior, phase composition, microstructure, hydration resistance, and TSR of free CaO containing magnesia were investigated in the present study. The main conclusions can be drawn as follows:

(1) With increasing the composite powder, $CaTiO_3$ and $Mg_{1+x}Al_{2(1-x)}Ti_xO_4$ phases were sequentially formed at MgO grain boundaries, which promoted MgO grain growth but had little effects on the density owing to the agglomeration of pores. Due to the conversion of free CaO to $CaTiO_3$ and MgO grains growth, hydration resistance of the specimens was improved effectively by introducing the composite powder.

(2) The addition of $Al_2O_3$-$TiO_2$ composite powder reduced the flexural strength of the magnesia due to the coarsening of MgO grains and increase of pore size. However, TSR of the specimens improved gradually with the composite powder content attributing to the reduction in thermal expansion coefficient and occurrence of crack deflection.

## REFERENCES

[1] Zhu T, Li Y, Jin S. Microstructure and mechanical properties of MgO-C refractories containing graphite oxide nanosheets (GONs)[J]. Ceramics International 39 (3), 2013, p. 3017-3025
[2] Chen M, Lu C, Yu J. Improvement in performance of MgO-CaO refractories by addition of nano-sized $ZrO_2$[J]. Journal of the European Ceramic Society 27 (16), 2007, p. 4633-4638
[3] Mohapatra D, Sarkar D. Effect of in situ spinel seeding on synthesis of MgO-rich $MgAl_2O_4$ composite[J]. Journal of Materials Science 42 (17), 2007, p. 7286-7293.
[4] Zou Y, Gu H, Huang A, et al. Characterisation and properties of low-conductivity microporous magnesia based aggregates with in-situ intergranular spinel phases[J]. Ceramics International 47 (8), 2020, p. 11063-11071.
[5] Mi Y, Xu Y, Li Y. Fabrication and thermal shock behavior of $ZrO_2$ toughened magnesia aggregates[J]. Ceramics International 47 (3), 2021, p. 26475-26483.
[6] Zhao J, Hao X, Wang S. Sintering behavior and thermal shock resistance of aluminum titanate ($Al_2TiO_5$)-toughened MgO-based ceramics[J]. Ceramics International 47, 2021, p. 26643-26650
[7] Ghasemi-Kahrizsangi S, Dehsheikh H, Karamian E. A comparative evaluation of the addition impact of nanometer-sized tetravalent oxides on the performance of Doloma-Magnesia ceramic refractories[J]. Ceramics International 44 (2), 2018, p. 2058-2064

[8] Xu T, Su Y, Shi T. Improving hydration resistance of MgO-CaO ceramics by in situ synthesized $CaZrO_3$ coatings prepared using a non-hydrolytic sol[J]. Ceramics International 47 (2), 2021, p. 2165-2171

[9] Petrova M, Mikirticheva G, Novikova A. Spinel solid solutions in the systems $MgAl_2O_4$-$ZnAl_2O_4$ and $MgAl_2O_4$-$Mg_2TiO_4$ [J]. Journal of Materials Research 12 (10), 1997, p. 2584-2588.

[10] Yang X, Lai Y, Zeng Y. Spinel-type solid solution ceramic $MgAl_2O_4$-$Mg_2TiO_4$ with excellent microwave dielectric properties[J]. Journal of Alloys and Compounds 898 (25), 2021, p. 162905.

[11] Bucevac D, Omeraevi M, Egelja A. Effect of YAG content on creep resistance and mechanical properties of $Al_2O_3$-YAG composite[J]. Ceramics International 46 (10), 2020, p. 15998-16007.

[12] Liao N, Jia D, Yang Z. Enhanced mechanical properties, thermal shock resistance and oxidation resistance of Si2BC3N ceramics with Zr-Al addition[J]. Materials Science and Engineering A 725, 2018, p. 364-374.

[13] Shi S, Cho S, Goto T. Ti and $SmAlO_3$ co-affected $Al_2O_3$ ceramics: Microstructure, electrical and mechanical properties[J]. Journal of Alloys and Compounds 835, 2020, p. 155427.

[14] Dehsheikh H, Ghasemi-Kahrizsangi S, Karamian E. Hydration resistance improvement of doloma particles using different nanoparticles [J]. Ceramics International 45 (6), 2019, p. 7390-7396.

SHORT COMMUNICATIONS

# THE PREPARATION OF ELECTRICAL−GRADE MAGNESIA FROM MICROCRYSTALLINE MAGNESITE

Zhixun Li*, Xiaoli Tian, Runtang Feng,Tianqing Li
Puyang Refractories Group Co.,Ltd, Puyang, Henan 457100, PR China

**ABSTRACT**
The preparation of electrical grade magnesia from microcrystalline magnesite in the Sichuan Tibet area is made by melting at 2800 ℃ in an electric arc furnace. Then broken and sorted according to content from MgO. High-temperature electrical grade magnesia powder was prepared by crushing, screening, iron removal, modification, and other processes.After studying its properties. The results show that the flow rate of the prepared high-temperature electrical grade magnesia powder is 150 ± 20s/100g, compaction density is 2.34 ± 0.05g/cm$^3$. In this process, the higher the MgO content, the better the corresponding electrical performance.

The electrical grade magnesium oxide prepared based on 98.5% MgO grade fused magnesia has a tube meter load of 12w/cm$^2$, the current is less than 0.30 mA, and the insulation withstand voltage strength is greater than 2500v. The durability test show that the leakage current of each electrical grade magnesium oxide decreases slightly and tends to be stable with the extension of the test time.

The high-temperature electrical grade magnesia powder prepared from Sichuan Tibet microcrystalline magnesite by electric melting has excellent electrical properties and is attributed to the unique ultra-low Fe$_2$O$_3$ content characteristics of the microcrystalline magnesite.

**KEY WORDS:** Microcrystalline magnesite, electrical-grade magnesia,leakage current

**INTRODUCTION**
Magnesite is a main natural mineral raw material in the refractory industry[1-2]. According to the different crystalline states, it is generally divided into crystalline magnesite with complete cleavage and amorphous magnesite with dense structure, high hardness and colloidal form[3]. Magnesite in the Sichuan-Tibet area is called microcrystalline magnesite because it has dense, fine, smooth, hard and brittle texture, uniform ceramic-like macrostructure, typical lattice constant and complete crystal morphology[4]. It has the characteristics of high purity and low iron content. Electrical grade magnesium oxide is an electrically fused magnesium oxide produced by melting Magnesite at high temperature in an electric arc furnace. It is crushed and matched with different particle sizes (mesh size) according to a certain proportion. It is directly or modified and used in tubular electric heating elements as an insulating medium for heat conduction at high temperatures. It has excellent insulation performance and thermal conductivity[5]. The application of electrical grade magnesium oxide is very wide. For civil use, it is mainly applicable to high-grade stainless steel tubes such as microwave oven tubes, Bread machine tubes, oven heating tubes, and Ingley tubes. High-end products can also be used to produce insulation materials in fields such as aviation, aerospace, and nuclear power[6]. Relying on the high purity and low iron properties of Sichuan-Tibet microcrystalline Magnesite, electrical grade magnesia is prepared, and expect to obtain products with superior electrical performance and high-cost performance.

**1. EXPERIMENT**
**1.1 Experimental materials**
The microcrystalline magnesite in the Sichuan-Tibet is fused in an electric arc furnace at 2800~3000℃, and the resulting magnesium oxide was FM985, FM98, FM975, FM97 and FM965 after breaking and sorting. The chemical composition is shown in Table 1. It can be seen that the microcrystalline magnesite has a high purity and extremely low iron content.

Tab. 1: Chemical composition of the fused magnesium oxide and magnesite

| | Chemical composition/% | | | | | |
| --- | --- | --- | --- | --- | --- | --- |
| | SiO$_2$ | Al$_2$O$_3$ | Fe$_2$O$_3$ | CaO | MgO | Loss |
| Magnesite | 0.25 | 0.02 | 0.03 | 0.70 | 47.25 | 51.72 |
| FM 985 | 0.35 | 0.01 | 0.03 | 1.04 | 98.52 | 0.02 |
| FM 98 | 0.39 | 0.03 | 0.05 | 1.35 | 98.14 | 0.03 |
| FM 975 | 0.43 | 0.03 | 0.06 | 2.05 | 97.39 | 0.03 |
| FM 97 | 0.69 | 0.04 | 0.07 | 2.71 | 96.42 | 0.05 |
| FM 965 | 1.01 | 0.05 | 0.08 | 2.76 | 96.06 | 0.03 |

**1.2 Experimental method**
High temperature electrical grade magnesium oxide powder were obtained by crushing, screening, removing iron, and adding organic silicon and silicate additives to FM985, FM98, FM975, FM97, and FM965, respectively. Their physical and electrical properties were detected.

**1.3 Test method**
Chemical composition analysis: This experiment uses the PANalytical fluorescence spectrum analyzer produced by Panaco to analyze the chemical composition of microcrystalline Magnesite and fused magnesia in the Sichuan Tibet area.

Flow rate(F.R) and tap density (T.D): F.R and T.D refer to the density measured with AP901122 tap densimeter made in the USA. The method is to put 100g of magnesium oxide into a density meter 3 # Ford cup and measure the flow time and density.

Electrical performance: Electrician-grade magnesium oxide samples are filled into electric heating tubes and made into standard components. After heat treatment at 1050 ℃, they are lowered to room temperature. Electrical properties such as thermal insulation that withstand voltage strength and leakage current are tested under the corresponding tube meter load.

**2. RESULTS AND DISCUSSION**
**2.1 Effect of raw materials on physical and electrical properties**
High-temperature electrical grade magnesium oxide powder was prepared from raw materials with different magnesium contents and standard components were prepared. After heat treatment at 1050 ℃, the leakage current was tested at a tube meter load of 11w/cm$^2$ (with a detection time of 20 minutes). The physical properties and leakage current of electrical-grade magnesium oxide powder are shown in Fig. 1.



(a)

(b)



(c)
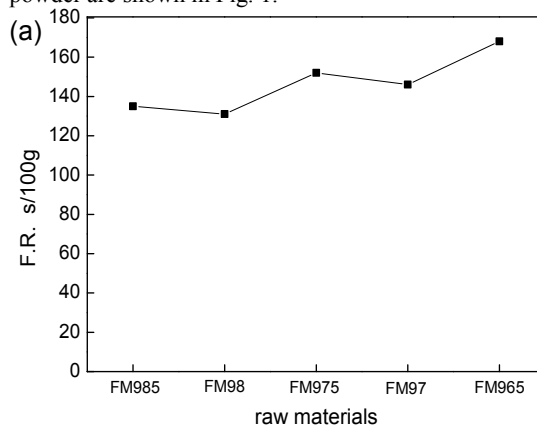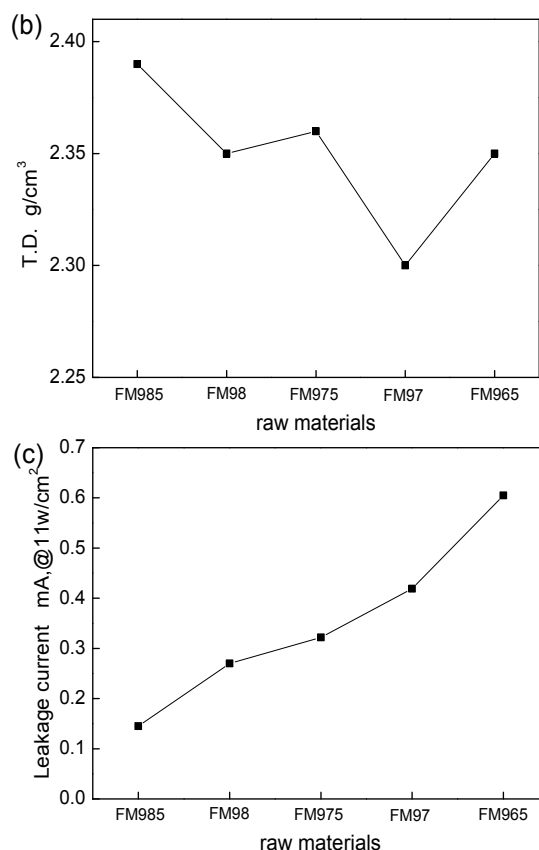
*Fig.1 Effect of raw material type on physical indexes:(a)Flow rate;(b) Tab density;(c)Leakage current*

From Fig.1 a and b, it can be seen that the high-temperature electrical grade magnesium oxide prepared from raw materials with different magnesium contents has a flow rate of $150\pm20s/100g$ and a tap density of $2.34\pm0.05$ g/cm$^3$. Fig. 1 c shows that at a tube meter load of 11w/cm$^2$, the leakage current increases with the decrease of magnesium content in the raw material, indicating that the higher the magnesium content, the better its electrical performance.

**2.2 Impact of tube meter load on electrical performance**
The high-temperature electrical grade magnesium oxide powder prepared from FM985 was tested for its electrical performance under different tube meter loads (with a detection time of 20 minutes) as shown in Fig .2.

(a)



(b)
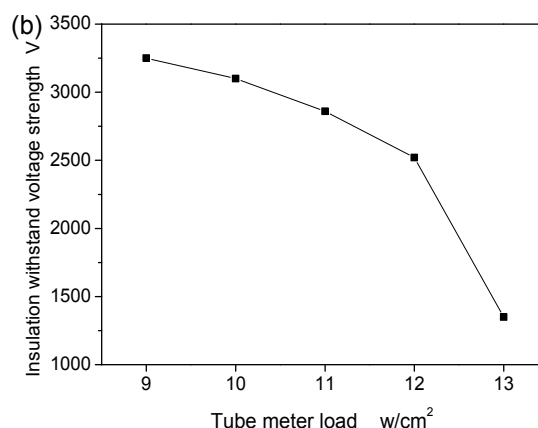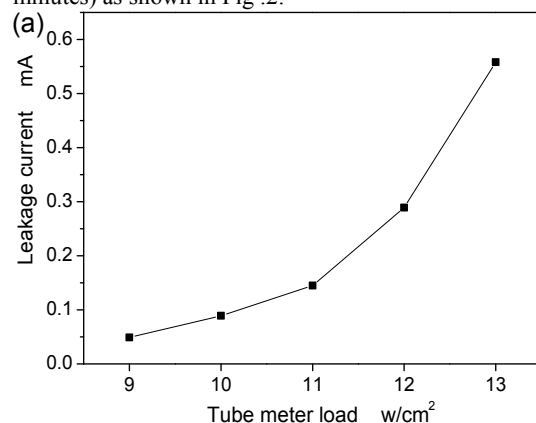


*Fig.2 Impact of tube meter load on electrical performance：(a)Leakage current;(b)Insulation withstand voltage strength*

In Fig. 2, the electrical grade magnesium oxide powder prepared with FM985 has an increase in tube meter load from 9w/cm$^2$ to 12w/cm$^2$, the leakage current from 0.049mA to 0.291mA, a gradual decrease in insulation withstand voltage strength from 3250V to 2520V, an increase in tube meter load from 12w/cm$^2$ to 13w/cm$^2$, a sharp increase in leakage current from 0.291mA to 0.558mA, and a rapid decrease in insulation withstand voltage strength from 2520V to 1350V. Therefore, the high-temperature electrical grade magnesium oxide prepared with FM985 has a tube meter load of less than 12w/cm$^2$, a leakage current of no more than 0.3mA, and an insulation withstand voltage strength of more than 2500V. Higher tube meter load has potential safety risks.

**2.3 Durability test**
The standard component is made of electrical grade magnesium oxide using FM985 as the raw material. As the tube meter load of 12w/cm$^2$ ,it is continuously tested for 10080 minutes, and the leakage current value is recorded as shown in Fig. 3. a. The 0-60 minute portion is enlarged, as shown in Fig. 3. b.

(a)



(b)
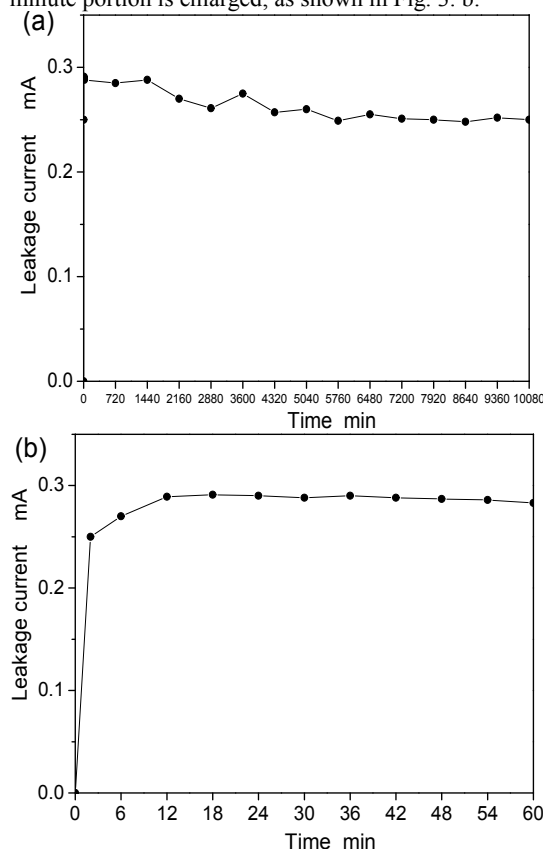


*Fig.3 FM985 Durability test:(a)for 10080min; (b)for 60min*

In Fig. 3. a, with the increases of testing time, the leakage current of the standard components prepared with electrical grade magnesium oxide gradually decreases and tends to stabilize. Fig.3.b shows that the leakage current rapidly increased 2 minutes before the test, reaching a maximum of 0.292mA in about 12 minutes, and then stabilized.

The high temperature electric grade magnesia powder prepared by electric melting of Sichuan-Tibet microcrystalline Magnesite has excellent electrical properties, thanks to its microcrystalline Magnesite with unique ultra-low $Fe_2O_3$ content. The characteristics of low iron effectively reduce the leakage current during the use of electric heating components and increase their withstand voltage performance.

## 3. CONCLUSIONS

The flow rate of high-temperature electrical grade magnesia powder prepared from Sichuan Tibet microcrystalline Magnesite is $150 \pm 20s/100g$, and the compaction density is $2.34 \pm 0.05g/cm^3$. The higher the content of magnesium oxide, the better the corresponding electrical performance.

The electrical grade magnesium oxide prepared using FM985 has a tube surface load of $12w/cm^2$, a current of less than 0.30 mA, and an insulation withstand voltage strength greater than 2500v. As the testing time prolongs, the leakage current slightly decreases and tends to stabilize.

High temperature electrical grade magnesia powder prepared by electrofusion of Sichuan-Tibet microcrystalline Magnesite has excellent electrical properties and its attributed to the unique ultra-low $Fe_2O_3$ content characteristics of the microcrystalline magnesite.

## REFERENCES

[1]  Q. Hu.Production and application of magnesium compounds [M].Beijing Chemical Industry Press，2004：11-77.

[2]  Z, Gao. He, L. Ma.Crystallographic characterization and thermal decomposition behavior of high purity microcrystalline magnesite[C]//2012 national magnesium salt industry annual meeting and founding meeting of magnesium compound branch，2012：57-61.

[3]  G. Hu，X. Zhang，F. Wei，et al.Flame retardant synergism of rubber and $Mg(OH)_2$ in EVA composites[J]. Polymer,2007,48:2537 -2541.

[4]  H. Xu, X. Deng. Preparation and properties of superfine $Mg(OH)_2$ flame retardant[J]. Transactions of Nonferrous Metals Society of China，2006,16（2）:488-492.

[5]  JB/T 8508-1996, Electrical grade magnesium oxide[S].

[6]  H. Su, G. Ren,S Wang. A high-temperature resistant, highly hydrophobic, and hydroelectric grade magnesium oxide powder and its preparation method.[P]. Liaoning: CN109835927B,2021-09-17.

SHORT COMMUNICATIONS

# EFFECT OF CALCINATED CONDITIONS ON THE PREPARATION OF HIGH-LY ACTIVE MAGNESIUM OXIDE FROM MICROCRYSTALLINE MAGNESITE

XuePei, Wang[1], Xiaoli TIAN[1]
1.Puyang Refractories Group Co., Ltd (PRCO), Puyang, 457100, PR China

## ABSTRACT

The effect of magnesite, calcination time on the activity of magnesia was studied using microcrystalline magnesite from Tibet as raw material. The activity of magnesium oxide was determined by iodine absorption value method. The chemical compositions, phase compositions and microstructure of the magnesium oxide with different iodine absorption value were analyzed by XRF, XRD and SEM. The results indicated that the magnesium oxide obtained the lower activity prepared at lower or higher calcinated temperature. When the particle size of the ore was 3-1 mm and the calcinated temperature was 600 °C for 4 hours, the highly active magnesium oxide with iodine absorption value up to 160 mg/g was prepared successfully. The relationship between the crystal morphology and the iodine absorption value of the magnesium oxide prepared under different conditions was established.

**KEY WORDS**：High active; magnesium oxide; calcination time; iodine absorption value

## INTRODUCTION

In recent years, with the development of technology, the demand for refractory materials in the steel and metallurgical industries has been increasing [1-2].Microcrystalline magnesite is one of the raw materials for refractory production and the main source of magnesium. It has the advantages of high purity and less impurities. Magnesium oxide (MgO) is an ionic compound belonging to the cubic crystal system, Fm3m space group.The activity of magnesium oxide refers to its ability to participate in chemical or physical processes, which can be expressed by the iodine absorption value (adsorption performance index). The greater the activity of magnesium oxide, the greater the iodine absorption value [3].When the iodine absorption value is 120-180 mg/g, it is called highly active magnesium oxide, when the iodine absorption value is 50 ~ 80 mg/g, it is medium active magnesium oxide, and when the iodine absorption value is 19 ~ 43 mg/g, it is low active magnesium oxide.Highly active magnesium oxide has the characteristics of small grain size and large specific surface area, which is conducive to promoting the solid-state reaction [4].As a new type of adsorption material, it also has great application prospects in wastewater treatment [5].In this work, the effect of calcination time on the activity of magnesia was studied by iodine adsorption method using Xizang microcrystalline magnesite as raw material, in order to provide reference for the preparation of high activity magnesia.

## 1. EXPERIMENTAL PART

### 1.1 Reagents and instruments

Experimental reagents include carbon tetrachloride, (AR, Tianjin Fengchuan Chemical Reagent Technology Co., LTD.);Iodine, anhydrous ethanol (AR, Tianjin Yongda Chemical Reagent Co., LTD.);Potassium iodide (AR, Tianjin Kaitong Chemical Reagent Co., LTD.);Sodium thiosulfate (AR, Tianjin Hengxing Chemical Reagent Manufacturing Co., LTD.);Deionized water (homemade).

The phase composition of the sample was detected by PANalytical X'pert Pro diffractometer.The microstructure of the samples was observed by JEOLJSM-6360 scanning electron microscope.Kang's oscillator (Jintan Xicheng Xinrui Instrument Factory);The iodine adsorption value was detected according to the national standard HG/ T3928-2012 "Industrial Active Light magnesium Oxide".

### 1.2 Experiment

**Preparation of magnesium oxide**

The microcrystalline magnesite with particle size of 1-3 mm was put into a Muff furnace, and the calcination time was set for calcination after the temperature was raised to 600 °C.After cooling to room temperature, the product is sifted 100 mesh after vibration grinding and set aside.

**Activity determination of magnesium oxide**

Determination of iodine adsorption value: accurately weigh about 1 g sample, pour 50 mL iodide carbon tetrachloride (I-CCl₄) solution, shock on the oscillator for 25 min, and then quickly move the solution in the bottle to the stopper colorimetric tube, cover the stopper tightly, and stand in the dark for more than 10 min until the solution is clarified.Remove 10 mL of clear iodine-carbon tetrachloride, place it in 250 mL conical bottle, add 20 mL potassium iodide ethanol solution, and titrate with sodium thiosulfate standard titration solution until colorless solution is the end point.At the same time, a blank experiment was carried out according to the following steps: Remove 10 mL iodide-carbon tetrachloride solution, place it in 250 mL conical bottle, add 20 mL potassium iodide ethanol solution, and titrate with sodium thiosulfate standard titration solution until colorless solution was the end point.

The iodine absorption value is measured by $x_1$, and the value is expressed in milligrams of iodine per gram of magnesium oxide ($mgI_2/gMgO$), calculated according to formula (1) :

$$\chi_1 = \frac{(V_2 - V_1)cM}{m(10/50)} \qquad (1)$$

Formula:
$V_1$: The value of sodium thiosulfate standard titration solution volume consumed by titration test solution, in milliliters (mL);
$V_2$: The value of the volume of sodium thiosulfate standard titration solution consumed by titrating the blank test solution, in milliliters (mL);
c: The exact value of the concentration of sodium thiosulfate standard titration solution, in moles per liter (mol/L) (c=0.1 mol/L);
m: The value of the mass of the sample, in grams (g);
M: The number of moles of iodine in grams per mole (g/mol) (M=126.9)

The arithmetic mean of the parallel determination results was taken as the determination results, and the absolute difference between the two parallel determination results was not more than 0.5 mg/g.

## 2. RESULTS AND DISCUSSION

### 2.1 Chemical composition and phase composition of highly active magnesium oxide

The raw material used in the test is Xizang microcrystalline magnesite, and its chemical composition after heat treatment with different calcination time is shown in Table 1.It can be seen that the main component is MgO, which has high purity and belongs to low-silicon and low-iron magnesite. With the extension of calcination time, the content of MgO gradually increases and the LOSS value gradually decreases.

Tab. 1: Chemical composition of highly active magnesium oxide after different calcination time.

57

| Time | SiO$_2$ | Al$_2$O$_3$ | Fe$_2$O$_3$ | TiO$_2$ | CaO | MgO | Loss |
|------|------|------|------|------|------|------|------|
| 1h | 0.34 | 0.07 | 0.04 | 0.04 | 1.45 | 68.80 | 29.26 |
| 2h | 0.36 | 0.14 | 0.05 | 0.05 | 1.76 | 71.27 | 26.37 |
| 3h | 0.34 | 0.15 | 0.03 | 0.04 | 1.57 | 74.37 | 23.5 |
| 4h | 0.25 | 0.03 | 0.03 | 0.06 | 1.86 | 89.59 | 8.18 |
| 5h | 0.32 | 0.08 | 0.04 | 0.06 | 2.04 | 90.43 | 7.03 |
| 6h | 0.51 | 0.19 | 0.04 | 0.02 | 2.23 | 93.49 | 3.52 |

Figure 1 shows the XRD patterns of active magnesia at different calcination times. Compared with the standard PDF cards (45-0946 and 08-0479), it can be determined that the main crystal phases are cubic crystal system MgO and trigonal rhombohedral system MgCO$_3$, and a small amount of Ca impurities exist in the form of dolomite CaMg(CO$_3$)$_2$, which is consistent with the high purity obtained by chemical analysis.With the extension of calcination time, the diffraction peak intensity of MgO is stronger, the diffraction peak intensity of MgCO$_3$ is lower, and the peak shape of each peak tends to be sharp, indicating that magnesite is more fully transformed into oxide, the crystallinity of magnesium oxide gradually increases, and the structure becomes denser.
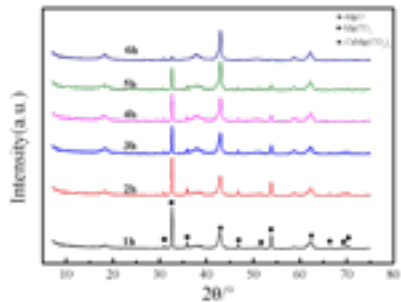


*Fig. 1: XRD patterns of MgO at different calcination time.*

## 2.2 Microstructure of highly active magnesium oxide

Figure 2 shows the SEM spectrum of active magnesium oxide for 4 h calcination time. It can be seen from the graph that its morphology is spheroidal, the average particle size of magnesium oxide is about 38 nm, the maximum particle size is 55 nm, and the minimum particle size is 25 nm. The distribution is relatively uniform, the dispersion is good, and the agglomeration is small, which promotes the activation of the lattice.
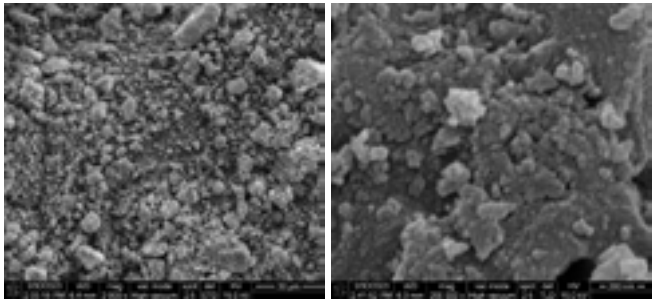


*Fig. 2: SEM images of active MgO for calcination time 4h.*

## 2.3 Influence of calcination time on LOSS

Figure 3 shows the relationship between different calcination time and LOSS of active magnesium oxide. It can be observed that when calcination time is 1h, the LOSS value reaches 29.26 % at the highest level, and gradually decreases with the extension of calcination time. At 6 h, the LOSS value reaches the lowest level of 3.52 %, with the highest MgO content, indicating that calcination is sufficient.
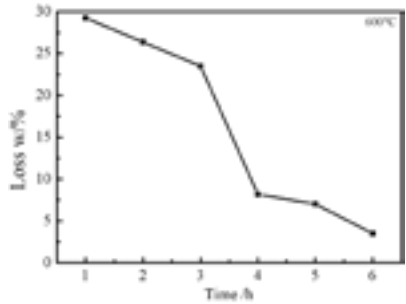


*Fig. 2: LOSS of active MgO at different calcination times*

## 2.4 Effect of calcination time on iodine adsorption value

The activity of MgO increases with the extension of *calcination* time. As shown in Figure 4, When calcination time reaches 4 h, the activity of MgO product obtained from the calcination of magnesite raw material is the highest, and the adsorption value of iodine is 160 mg/g. When calcination time exceeds 4 h, the activity of MgO decreases with the extension of calcination time.This indicates that the crystallization of the product is getting better and better, the crystal shape tends to be complete, and the activity begins to decrease.The activity of magnesium oxide also has a great relationship with the defects on the crystal surface, the better the crystallinity of the crystal, the more complete the crystal, the smaller the surface defect, the lower the activity of magnesium oxide[6].
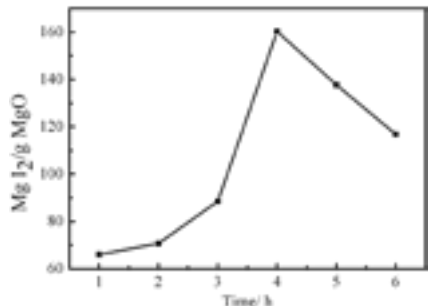


*Fig. 4: Effects of calcination time on the Iodine absorption value activity of MgO*

## 3. CONCLUSIONS

Using magnesite as raw material, it was calcined at 600 ℃ and held for different time to prepare highly active magnesium oxide. Taking iodine absorption value as sample activity target, when holding time was 4 h, its distribution was more uniform, its dispersion was better, and the highest iodine absorption value was 160 mg/g, meeting the requirement of highly active magnesium oxide.

## REFERENCES

[1] Li Yuzhe, Xu Na, Li Yannan, et al.Effect of light-fired magnesia activity on the compactness of sintered magnesia [C]// 2019 National Academic Exchange Conference on Fire-resistant Raw Materials.Chinese Society of Metals and Steel Luoyang Refractory Research Institute Co., LTD., 2019.

[2] Luo Ming, Yu Yan, Ma Zheng, et al.Effect of sintered magnesia addition amount on properties of Al$_2$O$_3$-SiC-C brick.Ring [J]. Refractory Materials, 2016,50 (3) : 225-227.

[3] CUI Xin, DENG Min.Preparation method of magnesium oxide, measurement method of activity and hydration [J].Silicate bulletin, 2008, 27 (1) : 6.

[4] Peng Qiang, Guo Yuxiang, QuDianLi, etc.Preparation of high-activity light-fired magnesia by suspension calcining of magnesite [J]. Refractories, 2017, 51(4):4.

[5] Gu Yawei, Yin Shiqiang, Zhu Xifeng, et al.Study on treatment of chromium-containing wastewater by activated magnesium oxide [J]. Inorganicchemicalsindustry, 2015, 47(4):15.

[6] WANG S Ping.Study on the preparation and adsorption properties of highly active magnesium oxide [D]. Tianjin University.

# TAILOR–MADE POLYCARBOXYLATE ETHERS TO IMPROVE PROPERTIES OF CASTABLE MIX DESIGNS

Joachim Riedmiller, Alexander Ganss, BASF Construction Additives GmbH, 83308 Trostberg, Germany

## ABSTRACT

For about 30 years polycarboxylate ethers (PCEs) are widely known as a family of tailor-made dispersants for castables containing calcium aluminate cement, reactive alumina, microsilica and aggregates improving their water reduction, wetting, and setting. By using these types of dispersants, the castables benefit from improved properties such as reduced porosity, prolonged lifetime, increased density, and strength combined with a significantly improved workability [1].

We will show how specific PCEs in combination with adequate raw materials interact and can be used to formulate custom tailored castables according to specific requirements.

PCEs are highly valuable, essential ingredients to develop and manufacture new, enhanced refractory materials.

## DISPERSING MECHANISM

The general structure of a PCE could be described as a brush having an anionic backbone containing carboxylic groups and several non-ionic sidechains made of polyethylene glycol. As soon as such molecules come closer to positively charged surfaces, such as cement grains, they will adsorb on them due to the interaction with the anionic part of the molecules and leave the outer particle sphere covered with protruding non-ionic sidechains. This arrangement is the basis for a superior dispersing power compared to purely electrostatic dispersants, such as sodium tripolyphosphate or polyacrylic acid (figure 1). The polymer side chains allow an additional long-range repulsive interaction between the inorganic surfaces according to an electrosteric dispersing mechanism leading to a creamy rheology of well-dispersed particles in high solid suspensions.
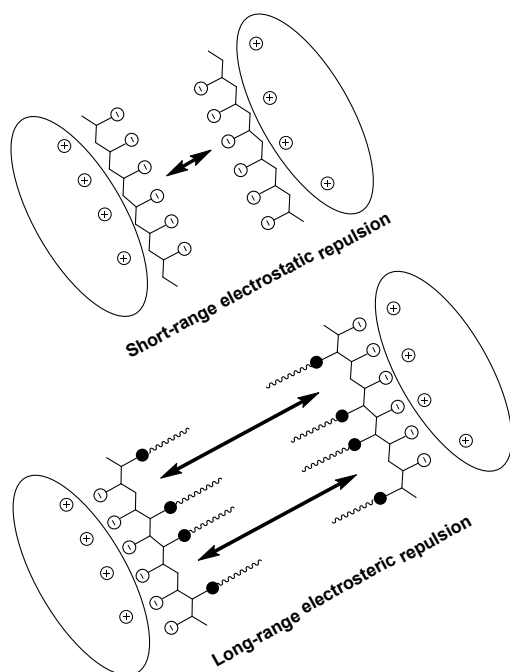


Fig. 1: Long-range electrosteric dispersing mechanism of PCE.

## POLYMER SYNTHESIS

Beside the general dispersing mechanism, the advantage of PCEs lies in the wide structural variety achieved by monomer selection, synthetic route, and polymer design leading to optimized water reduction, flowability, strength development, adjustment of set time and wetting for refractory mix designs. Sometimes the combination of several polymers or the addition of further additives provides special features such as retardation or acceleration, slump retention and robustness towards microsilica or hydrophobic particles.

One of the most common ways to synthesize PCE for refractory applications is a copolymerization of performance-relevant mono-mers, carboxylic acids and macromonomers containing the poly-ethylene glycol side chain. Alternatively, it is possible to connect the sidechain in a second step which is called grafting (figure 2). Depending on the synthetic route, the PCEs differ in their polymer structure and there are possibly restrictions for the application of additional monomers.
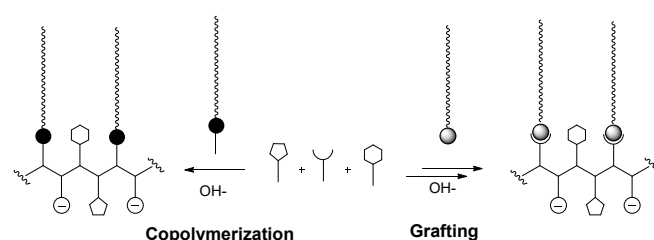


Fig. 2: PCE synthesis via different routes

Once a composition of monomers and a suitable synthetic route has been selected, the systematic variation of three parameters finetunes the further polymer properties (figure 3). The sidechain length of the macromonomer influences for example retardation, robustness of flow, slump retention and heat of hydration. Charge density affects the affinity towards inorganic surfaces due to the adsorption speed and therefore the wet-out time. The molecular weight is responsible for the overall dispersing power which determines dosage efficiency.
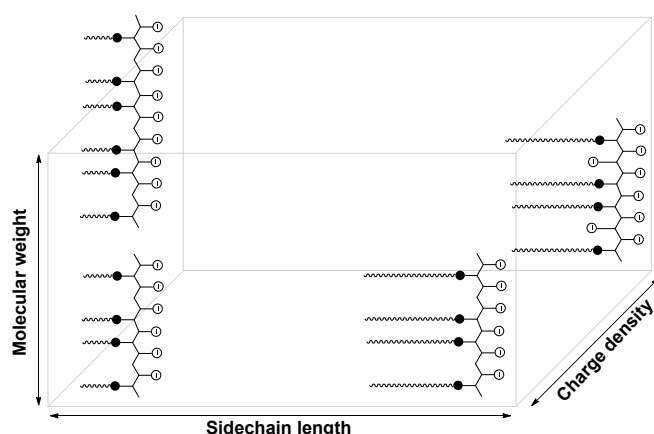


Fig. 3: Parameters providing structural variety of PCE

Modern PCE dispersants can be structurally optimized for applications in the refractory and ceramic industry with monitored purity in terms of their thermo-oxidative degradation.

## BENEFITS OF TAYLORED PCEs FOR CASTABLE MIX DESING

PCEs play a key role in the mix design of modern castables at a water amount between 4-6 %. Only such a low water amount guarantees the best castable performance with high mechanical strength, wear and chemical resistance and optimal hot properties. Thereby the workability of the material remains at a very high level. The

combination of good workability and best performance of a modern castable would not be achievable without a high-performance dispersant.

**SELECTED PCEs**

Three different PCE structures were selected for testing in a castable: a PCE with short sidechains (PCE-S), a PCE with medium sidechains (PCE-M), and a PCE with long sidechains (PCE-L). The design of the three different PCEs is optimized for the raw materials used in the refractory application (molecular weight, charge density, spacer).
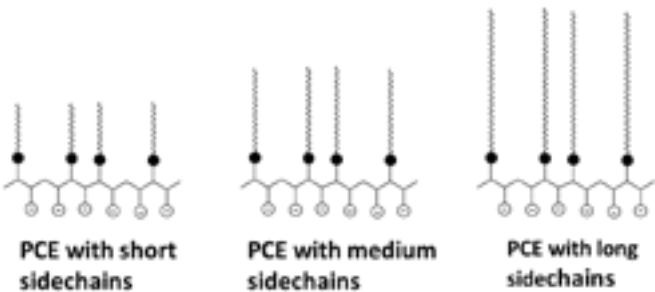


Fig. 4: Schematic molecular design of the used PCEs

**TEST CASTABLE**

A low cement vibration castable was selected for the test series. The table below shows its composition:

Tab. 1: Castable composition

| Raw material | Type | Amount |
|---|---|---|
| Tabular Alumina | 0-6 mm | 84 % |
| Alumina | D50 = 3.5μm | 12 % |
| High Alumina cement | 70 % $Al_2O_3$ | 5 % |
| PCE var | PCE-S or PCE-M or PCE-L | 0.1 % |
| Water | | 4.5 % |

Three mixes were tested using the castable with the composition given in Tab. 1. To reduce the water to 4.5% and still have a good workability, each one of the three PCEs was added to the mix in an amount of 0.1% by weight of dry mix.

**TEST RESULTS FOR CASTABLE**

*Vibrational Flow*

The vibrational flow was measured with a vibrational table and a cone (100 mm x 70 mm x 50 mm).

With PCE-S a good flow of 21.9 cm after 5 minutes can be achieved. After 60 minutes the flow is slightly increased (22.8 cm). PCE-M has a moderately higher initial flow with 23.4 cm. After 60 minutes, the flow drops to 21.4 cm. PCE-L has the largest initial flow with 25.2 cm. The drop in flow, is not as prominent as with PCE-M, with less than 1 cm after 60 minutes.

The dosage efficiency of the PCE depends on the sidechain length of the polyethylene glycol. The longer the sidechain the more dosage efficient is the PCE. Shorter sidechains mean less dosage efficient. On the contrary the less dosage efficiency leads to a better slump retention over time.

An additional advantage of PCEs with shorter sidechains is the robustness towards raw material fluctuations and water deviations which is less prominent compared to the PCE with longer sidechains.
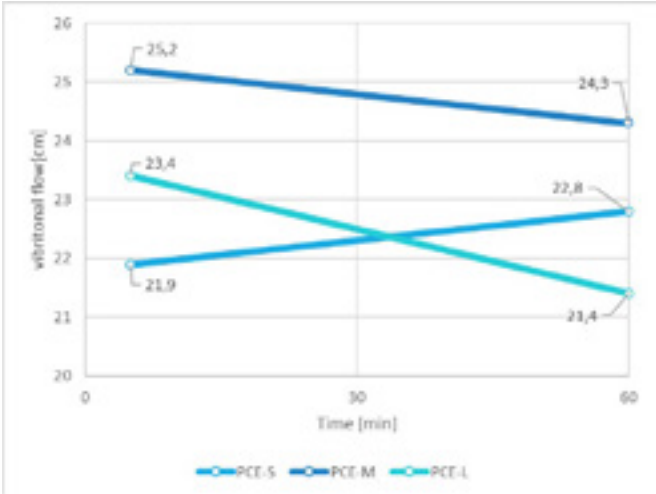


Fig. 5: Vibrational flow of test castable with selected PCEs

*Castable Setting and Strength Development*

The setting behaviour was measured by the exothermal method (EXO). Details of the method and the terminology were described by Gierisch et al. [2].

The different PCEs influence the setting of the castable significantly. In figure 6 the EXO1_ Start and EXO_Max times are given in hours and minutes. The PCE with long sidechains is the least retarding PCE. The PCEs with medium and short sidechains show a significantly stronger retardation. By choosing the right PCE, the setting and therefore the workability time can be adjusted. In colder environment, a less retarding PCE can be preferable, whereas in warmer environments a more retarding PCE can be beneficial.

Furthermore, the maximum exothermal heat (EXO_Max) is also strongly influenced by the selected PCE. The PCE with the long sidechain shows the shortest EXO_Max time. According to Kockegey-Lorenz al. [1], the EXO_Max time correlates with the strength, which is necessary for demolding of the castable and sufficient strength to transport pre-cast shapes. A shorter sidechain corresponds with shorter demolding times, which is a big advantage in handling of the hardened castable.
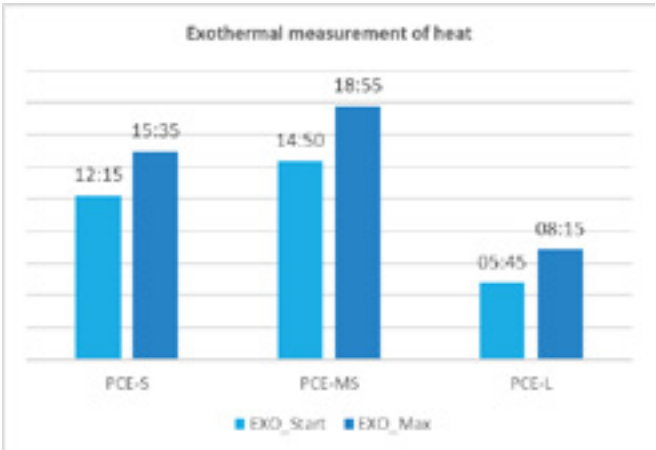


Fig. 6: Exothermal data of hydration

Cold crushing strength (CCS) and cold modulus of rupture (CMoR) were measured after 24h curing at 20°C. This is also commonly referred to as green strength.

The CCS and the CMoR show a direct correlation to the length of the sidechain of the PCE (Fig. 7). The longer the sidechain, the higher the strength. The explanation is, that the PCE with longer sidechains do not cover the surface of the cement as densely as shorter sidechains, hence they hinder each other more and move the PCEs further apart. As a result, the water can reach the surface in shorter time. The hydration of the cement is therefore faster and leads

to a better strength development due to the earlier formation of hydration phases.
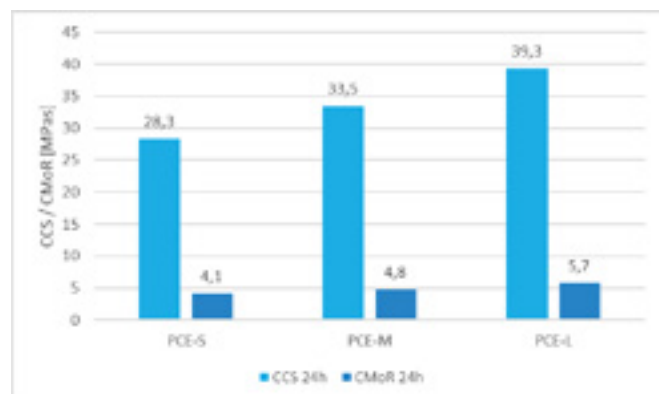


Fig. 7: Cold crushing strength and cold modulus of rupture

## PCE FOR HYDROPHOBIC RAW MATERIALS

Dispersing raw materials with a hydrophobic surface can be very challenging. Materials with hydrophobic character are mainly carbon-containing raw materials like silicon carbide or micronized or flaky graphite. Further, metal oxides like for e.g., chromium oxide. show a hydrophobic character of the surface. If some percentages of e.g., carbon is incorporated in a castable, and a standard dispersant is added, the typical spots of non-wetted and non-dispersed particles occur, which are swimming on top of the mix (Fig. 8). The application of a modified PCE dispersant can significantly reduce this effect in carbon-containing mixes. Introducing of long polyether sidechains and hydrophobic groups into the backbone of polycarboxylate ether provide a more hydrophobic character. Incorporating of such a product into a castable mix will minimize mixing times and improve the wettability of hydrophobic components. The component is better dispersed, which leads to better overall performance. The effect of such a special PCE design is shown in a castable with carbon black. No unwetted and no undispersed particles can be observed with the optimized PCE (Fig. 8).

| Unwetted spots with a standard PCE for refractory | Good wetting a with specially designed PCE |
|---|---|
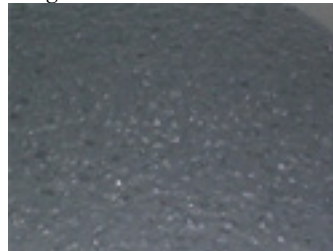


Fig. 8: Left side: insufficient dispersion of carbon black. Right side: homogeneous dispersion of carbon black

## PCE FOR MICROSILICA CONTAINING CASTABLE

A common mix design of castable includes microsilica as a matrix filler in an amount of 3-8%. Castable with these amounts of microsilica cannot be dispersed well or at all with standard PCEs. The reason is the PEG sidechains which interact with the surface of the microsilica. This interaction leads to partial flocculation of the particles and prevents a proper dispersion. Therefore, the flow is reduced or even killed. With the design of a special PCE with very short sidechains and special anchor groups, the problem can be overcome.

In the mix design of the castable from Table 1, 5% of alumina was replaced by microsilica Elkem 971 U. The water amount is kept constant at 4.5%.

If the PCE-S is used in this castable, no vibrational flow is detectable (Fig. 9). 10 cm vibrational flow means the diameter of the used cone. With a specially designed PCE for microsilica (PCE-MS), a good vibrational flow of 20.5 cm can be achieved. The flow at 60 minutes is still at 19.8 cm. The workability and casting of the castable with microsilica is therefore possible and easy.
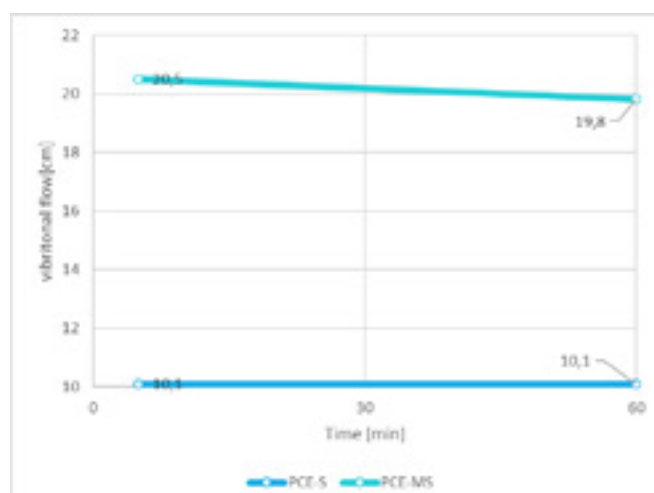


Fig. 9: Vibrational flow of microsilica containing castable with selected PCEs

An acceptable mixing time of the refractory concrete is guaranteed due to the wet-out time of 170 seconds. This is often critical with microsilica-containing castable and is heavily influenced by the used dispersant.

The dispersant has also a strong influence on the workability time and the setting of the castable. The EXO1_Start corresponds to the end of workability which is 80 min for PCE-MS. The EXO_Max is with 20 hours and 10 minutes in the range that the castable can be demolded after 24 hours.

## CONCLUSIONS

Polycarboxylate ethers specially developed for the refractory application play a key role in the design of a modern castable. Without efficient dispersants it is not possible to reduce the water content in castable to 4-5%. This lowest possible water content leads to a high density, low porosity, high strength, and optimal hot properties. A good workability and setting time are thereby obtained. Without the optimization of the PCE structure, an adequate performance in refractory applications would not be possible.

By choosing the appropriate PCE the desired properties of the castable can be set. Wet-out time, flow retention, workability time at different temperatures and strength development can be adjusted. In addition, the choice of the dispersant depends on the type of raw materials used and is the key to optimize the properties of the castable.

All the various influencing factors must be understood to develop and use the optimal dispersant for refractory applications.

## REFERENCES

[1] Seyerl von J. Chemical Additives for Castables, UNITECR 2011, Kyoto, Japan

[2] Gierisch, D.; Buhr, A.; Dutton, J.; Hösler, M.; Franz, B. Aging behaviour of Alphabond and Calcium Aluminate Cement bonded castables. 49th International Colloquium on Refractories, Aachen, Germany, 2006, 137-142

[3] Kockegey-Lorenz R, Andreas Buhr A, Schmidtmeier D, Zhongkai T, Zacherl D, Chatterjee S, Dutton J. The value of additives in refractory castables – castables without silica fume USB-Stick UNITECR2015 – 14th Biennial Worldwide Congress

# INNOVATIVE APPROACHES FOR ENERGY-INTENSIVE PRODUCTION PROCESSES OF SHAPED REFRACTORY PRODUCTS FOR THE STEEL INDUSTRY

Daniel Cölle, Michael Dombrow, Lutz Reißberg, Bastian Vesenberg
EKW GmbH, Eisenberg, Germany

Peter Schwalb
Hagenburger Feuerfeste Produkte GmbH, Grünstadt, Germany

**ABSTRACT**

An overview is provided of consistent use of resource-efficient raw materials for the production of functional components for the secondary steel metallurgy, e.g. ingot casting, pouring nozzles.

In recent years, the incorporation of regionally available raw materials in particular into existing production processes has proven to be promising, both from a technological and an economic point of view. In this context, the product-specific carbon footprint is of particular importance, which is also discussed in association with its complexity in calculative considerations.

# INSIGHTS ON NUMERICAL MODELS TO PREDICT POTENTIAL RECYCLABILITY OF SPENT REFRACTORIES FROM STEEL MAKING INDUSTRY

Andrea Salerno[a,b,*], Martiniano Picicco[a], Lionel Rebouillat[c], Nicolas Tessier-Doyen[b], Elsa Thune[b], Severine Romero Baivier[a], Marc Huger[b]

[a]Vesuvius group plc, Department of Advanced Refractories
[b]Univ. Limoges, Institut de Recherche sur les Céramiques, UMR CNRS 7315, F-87000 Limoges, France
[c]Pyrotek, Isomag-America

## ABSTRACT

The present study is part of the CESAREF (Concerted European action on Sustainable Applications of REFractories) doctoral network started in late 2022. The aim of the consortium is the contribution to scientific breakthroughs inherent to refractories for steel making sector thanks to transversal competences deriving from academic and industrial realities. European green deal and circular economy targets set by EU for 2025 are also related to the massive consumption of refractory materials in the steel industry. Operative lifetimes of refractories range from hours to several months depending on their role. As a result of increasingly tightened policies and disposal costs, and due to recent supply chain shortages, end-of-life refractories recovery and recycling practices are receiving great attention. Some of the core requirements for sustainability and circularity are the reduction of open-loop and down scaling strategies, to maintain refractory materials value as long as possible, of the end-of-life materials. Over the years application of numerical models has proved to be a useful strategy for researchers facing in-use issues related to refractory materials. In this study, different finite element models (FEM) applied to end-use refractories are discussed to understand their suitability for potential recyclability prediction. Thermomechanical characterization of prior- and post-use materials allow to identify the critical issues related to numerical models' development. The comparison between empirical results and the appropriate numerical model allow us to identify suitable pathways to improve refractories sustainability.

## CONTEXT

There has always been an intricate connection between society's evolution and raw materials. In fact, the common partitioning of prehistoric periods occurs through the raw materials that enabled progress: stone, bronze, and iron ages. Although advances in materials and technologies have aided development and welfare distribution, unfettered consumption and overexploitation of resources remains a driver for conflicts, geopolitical tensions, and environmental damage. Thus, we are looking for technological solutions to ensure progress, and at the same time make our way of life more sustainable by decoupling economic growth from resources use.

The recent European Union directive regarding wastes introduced a hierarchic strategy to be adopted for waste reduction and circularity improvement.[1] The preference order established by the directive is set as: prevention, re-use, recycle, recovery, disposal. Furthermore, circular economy growth is one of the strategic targets of EU's Green Deal for ensuring raw materials' solid supply chains.[2]

One of the main sectors involved in the green transition is the iron and steel industry, for which ambitious sustainability targets have been set for 2050. Starting from the iron ore to get the final product an energy intensive process is needed. World average data reports $CO_2$ emissions equal to 2 tons per ton of steel produced.[3] That is why EU is strongly pushing steel producers towards more efficient and lower energetically intensive production processes. Hence, projects such as CESAREF (Concerted European actions on Sustainable applications of REFractories) are put in place receiving great attention from the academic and industrial sectors. CESAREF is a big European consortium of universities and companies acting together with the aim of training different doctorate students on excellent science to create breakthroughs in the field of refractory materials for the steel industry.

## INTRODUCTION

Steel embodies a vast class of iron alloys containing carbon in the range between 0.002 and 2.14 wt.%. Steel making occurs through the casting process and nowadays the most used method is the continuous casting, counting for more than the 96% of total steel produced.[3] A modern continuous casting system is composed by three main parts: the ladle, the tundish, and the cooling zone (figure 1). A ladle is a big reservoir of liquid steel (able to contain from tens to several hundred tons of liquid steel) which is then poured into the tundish. The tonnage of the ladle corresponds to one heat, and the number of heats performed with one tundish corresponds to one sequence. The tundish acts as reservoir of molten steel and distributes the liquid metal into the multiple casting molds where steel solidification starts. The tundish stores a small amount of molten steel while dispensing part of this latter elsewhere with general purpose to regulate flow and achieve a steady output with intermittent inputs.

The tundish has the roles of molten steel distribution, buffering, flow control, purification, and heat loss limitation. To nicely exploit the above-mentioned functions many refractory materials are used in the tundish:

- refractories to control and homogenize the liquid metal flow in the vessel (dams, wires, impact pads, purging plugs);
- refractories to enable the steel to move safely with no oxidation limiting material and energy losses from one reservoir to the following, these products can be submerged entry shrouds (SES), submerged entry nozzles (SEN), stoppers, and slide gates;
- refractories to separate and isolate the external steel shell from the molten steel ensuring safety and energy savings, these materials are called lining refractories.
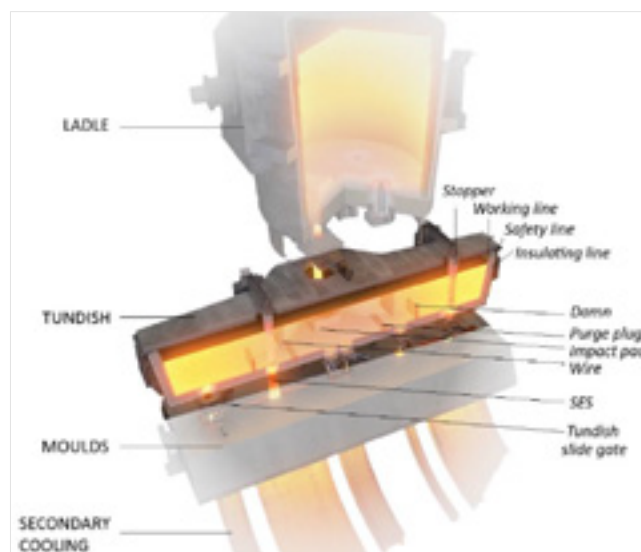


*Figure 1: elements in the continuous casting process for steel production and some of the refractory parts used for the tundish. Reproduced with the courtesy of Vesuvius plc.*

Commonly the lining refractories can be distinguished depending on their position: the working lining is directly in contact with steel and slag, the permanent lining, in between working and insulating lining, is supposed to compensate stresses and to allow operations safeness in case of working line failure; and insulating lining reduces heat exchange between the previous linings and metallic shell. Some of the above-mentioned refractories are highlighted in figure 1 and various refractory products, grouped by their applications, principal functions, main failure mechanisms, average lifetimes, and some of the possible refractory composition that are commonly used, are provided in table 1.

## STRATEGY AND PERSPECTIVES

The thermo-mechanical behavior of most of the refractory materials during operative conditions is complex and difficult to determine and foreseen. The reasons behind are their nonlinear responses to stimuli derived, in part, from heterogeneous nature and harsh operative conditions. Due to that, reliable investigations to improve refractory products lifetime require the combination of experimental analysis and computational methods, such as finite element analysis (FEA).[4,5]

Additionally, to tackle waste production, the re-use and recycling practices need to be fully exploited. In the former case, re-use, the ageing of key thermomechanical properties of the refractories during usage can be assessed and deployed, in combination with the operative conditions severity, into an adapted Failure Modes, Effects, and Criticality Analysis (FMECA). The purpose is to obtain qualitative and quantitative reliable information on the lifetime of the refractory product for a particular application. Furthermore, end-of-life refractories recycling is another key step related to sustainability. During spent material sorting, compositional evaluation, sieving, and other pivotal steps, great bottlenecks must still be overcome. On top of the technical recycling passages, a proper algorithm able to predict profitability has not been developed yet. Hence, this project will focus on the adaptation of a Multi Criteria Decision Approach (MCDA) for refractories sorting based on their intrinsic characteristics, to define recycling convenience.

### Experimental characterization and numerical modelling

Refractory materials are, for definition, supposed to resist high temperatures, chemically aggressive conditions, and various mechanical stresses. It is possible to discriminate between stress and strain-controlled loads.[6] The first are the function of the structure's geometry and its density. The latter, strain-controlled loads, can derive from thermal expansions, creep, or structural constraints. They are function of the material's properties, as for example the thermal expansion coefficient, Young's modulus, Poisson's ratio, thermal conduction, porosity, and others.[4] Refractories for steel-making industry are primarily exposed to thermal loads and, as a response, most of them undergo in softening enhancing the plastic behavior at high temperatures. This is the reason why a strong focus will be given in this project to the key thermomechanical properties variation and elastoplastic laws governing the materials behavior. In particular, attention will be paid on the evolution of thermomechanical properties from prior to after usage state. Identification of the pivotal properties and simulation, through the proper yielding function, of the material behavior, are crucial priorities to enhance the performance of the products, hence tackling the prevention step of circularity.

Refractory materials for tundish linings will be at the center of the research. For example, insulating boards composed mostly of vermiculite will be investigated. Previous works, on the carbon pick-up of similar material utilized in the ladle, identified the thermal properties degradation triggering factors. Densification, impurities diffusion, secondary phases formation, and permanent shrinkage are expected phenomena that will be experimentally assessed during this research's post-mortem experimental characterization.[7] These key properties are also related to the operative conditions such as thermal enhanced diffusion, compressive and shear stresses due to lining system's architecture, but also to the cyclical thermal gradients related to continuous charge-discharge steps. Hence, it is possible to consider periodic fatigue cycles and the proper finite element model is needed not only to identify the magnitude and location of the critical loads (thermal and mechanical), but also to further extrapolate their impact on properties degradation.

Over the years, many yield functions have been developed to explain the plastic behavior and consequent failure of various material classes. The Mohr-Coulomb, Tresca, von Mises, and Drucker-Prager are some of the most known criteria describing specific materials' yielding under particular conditions.[8,9] These above-cited yield laws show some critical drawbacks such as the necessity to evaluate shear and tensile yielding stresses to define ranges of applicability, the approximation to homogeneous material's properties, and the non-exhaustive behavior prediction in certain regimes. For these reasons, over the years, several yield criteria have been proposed. In particular, Bigoni D. and Piccolroaz A. developed a modulable criterion for which is possible to modify the yield function.[10] The model is based on a phenomenological based yield criterion (the yield function is directly obtained from interpolation of experimental data) valuable in predicting the mechanical behavior also of ceramic materials

*Table 1 : Overview of products, functions, properties, failure mechanisms, lifetime, and some of the compositions for tundish's refractories.[4,6,7,14]*

| | APPLICATION | PRINCIPAL FUNCTIONS | MAIN FAILURE MECHANISMS | LIFETIME | COMMON COMPOSITION |
|---|---|---|---|---|---|
| Steady flow control | Dam/wire/multilayer filters | Ensure uniform liquid steel flow and temperature distribution also preventing inclusion flow | Corrosion<br>Erosion<br>Thermal shock | 5-20 heats | Alumina-magnesia-carbon<br>Alumina-silica-carbon<br>High purity alumina/magnesia |
| | Impact pad | Control molten steel from ladle impact and reduce inclusions spread | Corrosion<br>Erosion<br>Thermal shock | 5-20 heats | High alumina or magnesia<br>Alumina-magnesia spinel<br>Magnesia-chrome |
| Flow control | Submerged Entry Nozzle (SEN)<br>Submerged Entry Shroud (SES) | Feed molten steel from tundish to mold, suppress oxidation and nitrogen pickup, reduced heat loss | Corrosion<br>Thermal shock<br>Clogging | 10-30 hours | Alumina-silica-carbon (body)<br>Magnesia-carbon (seat SEN)<br>Zirconia-graphite (sleeve SES) |
| | Tundish slide gate | Control liquid steel flow rate from tundish to molds | Bore hole erosion<br>Surface abrasion<br>Steel infiltration | 5-10 heats | High alumina/magnesia<br>Alumina-magnesia spinel<br>AZC (alumina-zirconia-carbon) |
| Lining | Working line | Contain molten steel ensuring operations quality and safety | Corrosion<br>Cracks propagation<br>Spalling | 5-20 heats | High purity alumina/magnesia<br>Zirconia-carbon (slag line)<br>Magnesia-Chrome |
| | Insulating line | Reduce the thermal diffusion in steel shell and energy losses | Permanent shrinkage/densification<br>Tensile/compressive failure<br>Working/safety lines failure | 20 heats - 1 sequence | Vermiculite<br>Alumina-silica fibers<br>Magnesium-silicate |

sensitive to pressure. The flexibility shown by the criterion is appreciated in the field of refractories since, during their processing and working conditions, many changes occur.

**Fatigue and Failure Modes, Effects, and Criticality Analysis**

Experimental and numerical modeling are not always sufficient for failure prediction and materials' behavior foreseen. Commonly, lifetime evaluation is a complex practice in the field of refractories used in continuous casting process due to their heterogeneous nature, complex geometry, and strong variety of stresses to which they are subjected. Additionally, the possible failure mechanisms associated to a particular product in a specific application are not due to a single parameter. Different failure mechanisms can be observed for the same refractory application. Although in recent years, the research on refractories has made great strides obtaining strongly performant materials, few researchers have applied the fatigue theory to refractory materials. This kind of analysis is widely used in many engineering fields to predict the lifetime of ductile materials such as metals. Examples are the Goodman-Haigh and Gerber diagrams frequently adopted by structural engineers in case of low- and high-cycle fatigue cases. Previous studies on refractory materials have reported several mechanical failure mechanisms under cyclic loadings. The identification of preferential cracks propagation paths, damage saturation, cracks coalescence and interlocking, and grains relocation mechanisms are a result of fatigue inside the material.[11] Furthermore, the turning point has been the link of these individuated energy dissipation mechanisms with the key thermomechanical properties of the material to define the lifetime of the material.[12]

Failure Mode, Effects, and Criticality Analysis, FMECA, is a strategy adopted in the last century to assess the operativity and reliability of a product through inductive reasoning. Essentially, the analysis consists in individuating the ways or modes in which the product could fail, understand the consequences of such failures on the products operativity and on the overall system, and finally define criticality and severity levels for each of the individuated failures and related effects.[13] The adaptation of this approach could enable a more rigorous and statistic treatment of failure analysis allowing the incorporation of fatigue in the investigation. The frame of this strategy is to improve the utilization of a product enhancing the re-use by identifying the proper actions to reduce waste generation. In this context, it is possible to perform both qualitative and quantitative analysis because of the integration of significance measure through criticality analysis. By generally adapting the quantitative evaluation of each $i$-th failure mode, the related criticality number, $C_i$, can be defined as:[13]

$$C_i = \alpha_i \beta \lambda_n t \qquad (1)$$

It is worth specifying each of the parameters composing the equation. The failure mode ratio $\alpha_i$ can be defined as the probability (expressed in decimal fraction) that the product or a part of it will fail in the $i$-type mode. It represents the diverse ways a system or a part of it fails. This number is statistically derived and is given as a percentage of the total observed failures. The condition probability, $\beta$, of operational failure represents the probability that the identified failure mode will cause the product failure due to the ageing or degradation of the key properties related to the identified $i$-type failure mode. The component failure rate $\lambda_n$ represents the number of particular $n$-parts of the product which are subjected to the $i$-type failure mechanism. At last, $t$ corresponds to the total operational time the product has been utilized.

Afterwards, a severity classification of the operational conditions is built. To do so, the numerical modeling already performed will assist the purpose. The outputs from Finite Element Analysis are the maps of stresses, strains, pressures, and other parameters. From these, is then possible to quantify operative conditions severity. Comparing the output fields to the experimentally determined key properties of the material prior usage, it is possible to classify the severity in four categories: negligible, marginal, critical, and catastrophic. Finally, the lifetime space (figure 2), including a criticality function proper for the product in the specific application, represents the link between severity conditions and probability of occurrence, or criticality number, for each system's failure modes and parts. Four different levels can be thus defined related to the fatigue and the lifetime of the material: i) unacceptable criticality, the product is considered no more suitable for that specific application, ii) high criticality, the product can be considered in necessity of repair (at the specific $n$-part) before further use, iii) and iv) moderate or low criticality, the product's resulting properties can be considered appropriate for an additional life cycle, thus tackling re-use target.

**Multi criteria approach for refractories recycling**

As previously said, during steel production the smelted material passes into several furnaces and vessels. Each of these containers has its own type of refractories used for specific needs. Thus, at first glance, the collection sorting and categorizing step is one of the first bottlenecks for refractories waste recycling. An additional blocking point in refractories recycling consists in the crushing/pulverization of the materials to remove impurities or better homogenize the end-of-life materials. But, besides these steps, it is strictly necessary from an environmental point of view and for energy and resources usage, to identify the convenience of recycling. Thus, it is important also to distinguish recycling practices. Indeed, two ways of recycling exist: closed-loop and open-loop. In closed-loop recycling, the value of the waste is considered not far from primary raw materials' value. Hence, it is possible to reprocess the materials and reintroduce them in the same circle of production. Conversely, in open-loop recycling, the operative conditions lead the material to a dramatic change resulting in lower value with respect to the primary raw materials. This latter case is common for all the refractories recycling practices put into operation currently. In literature, many cases of open-loop recycling can be found. Most of the postmortem refractories are recycled in roadbeds, slag additives or conditioners, aggregates for clinker and for the cement industry, and as soil neutralizers and flowerbeds.[14] It is evident that the closed-loop recycling has the potential to hold end-use materials' value and functionality constant. Furthermore, closed loop recycling contributes in a significant way to the development of

65
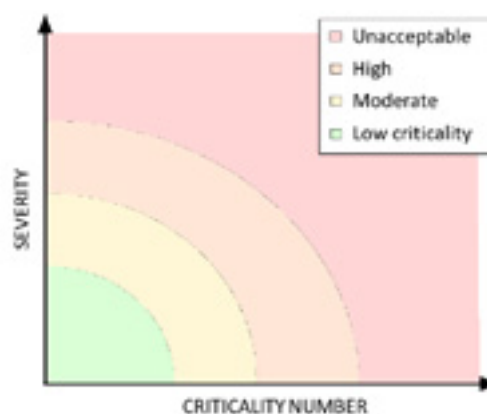


*Figure 2: Criticality space representing the criticality number and the severity relation defining refractory product's lifetime.*

circular economy. That is why the development of more powerful strategies may help in keeping up the value of the spent material as much as possible. Since there is a wide variety of aspects to consider, a multiple criteria decision analysis could be the key. After processing, refractory materials can have, for example, oxides and/or elemental impurities, steel residues, crystallographic phases developed during the operations, structural instabilities, morphological variations. Thus, it is necessary to assess the additional properties and specifications for the end-of-life material that can have an impact on further applications if inserted in a specific refractory formulation. To distinguish between valuable compositions in terms of purity, economic value, possible resulting thermomechanical properties in a refractory product, or other parameters, an interesting approach may be the adoption of multi criteria decision approach (MCDA). This latter is a strategical method to evaluate the best option or the set of more convenient options in the framework of problems involving many variables. In brief, the multi criteria problem can be mathematically seen as the need of maximization for a global value function, $U_{d_{(g_l)}}$, dependent on a marginal value function of the $x$-component possessing a certain $l$ attribute, $u_{(d_{(g_l)})}$, and the relative attribute weight, $p_l$:

$$U_{(u_d)} = \sum_{l=1}^{s} p_l u_{(d)} \tag{2}$$

where $d_{(g_l)}$ corresponds to the evaluation vector of the $x$-component with $l$-th attributed in the level $g$.

With this strategy, a study has been recently performed on the feasibility of the application of a linear multicriteria decision analysis coupled with an on/off criteria to sort spent refractories, also in the frame of sustainable targets. [15] The study proved the good versatility of the method and the possibility of its adaptation to end of life refractories case. Big rooms for improvement are still needed and a proper adaptation to the case of recycling is necessary but a glimpse of feasibility has been observed.

## CONCLUSIONS

European Green Deal has set big technological and scientific challenges for steel making sector to achieve sustainability, circularity, and environmental impact requirements for 2050. CESAREF consortium aims to help in creating breakthroughs in the field of refractory materials for steel making transferrable also to other sectors. For this research, focus will be put on the refractory materials for the tundish linings. One of the possible strategies to tackle the European challenges considering as reference key steps, the waste hierarchy can be the identification of the key properties to be assessed depending on the refractory application requirements. The tested properties may be used as inputs in numerical simulations to obtain a clear view of failure and yielding phenomena occurring in refractories. Furthermore, key properties aging, obtained from the comparison of pre- and post-usage refractories, linked with fatigue theory could help refractory producers in more rigorous evaluation of products lifetime. The dependency of properties degradation, operational conditions, and statistical information may be considered for an adapted Failure Modes Effects and Criticality Analysis to obtain reliable qualitative and quantitative investigations of the refractory materials conditions. Moreover, a linear algorithm has been proposed and further tests in that way will be presented soon to optimize it for specific cases. Besides prevention and re-use, to tackle recycling in literature, a large variety of cases have been observed in the frame of open-loop recycling. Hence, big efforts are needed to progress in closed-loop recycling. Many factors must be considered to efficiently solve the recycling reliability problems related to the spent refractory materials. To take forward this bottleneck, a Multi Criteria Decision Analysis (MCDA) has been proposed. This latter approach has recently proved to be efficient for refractories wastes disposal in sustainable framework. Therefore, it opened possibilities for its adaptation in the case of reliable and predictive recyclability determination.

## REFERENCES

[1] European Parliament, C. of the E. U. Directive 2008/98/EC of the European Parliament and of the Council of 19 November 2008 on waste and repealing certain Directives (Text with EEA relevance). (2008).

[2] Volckaert, A. Raw materials for refractories: The European perspective. in Proceedings of the Unified International Technical Conference on Refractories, UNITECR 2013 (2014). doi:10.1002/9781118837009.ch197.

[3] World Steel Association. Steel Statistical Yearbook 2022. (2022).

[4] Schacht, C. A. Refractories handbook. Refractories Handbook (2004). doi:10.1201/9780203026328.

[5] André, D., Levraut, B., Tessier-Doyen, N. & Huger, M. A discrete element thermo-mechanical modelling of diffuse damage induced by thermal expansion mismatch of two-phase materials. Comput Methods Appl Mech Eng 318, (2017).

[6] Harbison & Walker. HARBISON-WALKER Handbook of Refractory Practice. www.hwr.com (2005).

[7] Vitiello, D., Nait-Ali, B., Tessier-Doyen, N., Rebouillat, L. & Smith, D. S. Thermal conductivity of porous refractory material after aging in service with carbon pick-up. Open Ceramics 11, (2022).

[8] Chen, W. F. & Han, D. J. Plasticity for Structural Engineers. Plasticity for Structural Engineers (1988). doi:10.1007/978-1-4612-3864-5.

[9] Robert M. Jones. Deformation theory of plasticity. (Bull Ridge Publishing, 2009).

[10] Davide Bigoni & Andrea Piccolroaz. Yield criteria for quasibrittle and frictional materials. Int J Solids Struct (2004).

[11] Andreev, K., Yin, Y., Luchini, B. & Sabirov, I. Failure of refractory masonry material under monotonic and cyclic loading – Crack propagation analysis. Constr Build Mater 299, (2021).

[12] Gao, J. et al. Numerical Analysis of Fracture Failure Behavior of Refractory Lining in Coal-Water Slurry Gasifier. ACS Omega 7, 18041–18051 (2022).

[13] Robert Borgovini, Stephen Pemberton & Michael Rossi. Failure Mode, Effects and Criticality Analysis (FMECA). (1993).

[14] Hanagiri, S. et al. Recent improvement of recycling technology for refractories. Nippon Steel Technical Report (2009).

[15] Spyridakos, A. et al. Waste Classification of Spent Refractory Materials to Achieve Sustainable Development Goals Exploiting Multiple Criteria Decision Aiding Approach. Applied Sciences (Switzerland) 12, (2022).

# CARBONIZED WOOD AND SUNFLOWER SEED HULL PELLETS AS A SUBSTITUTION FOR NATURAL GRAPHITE FOR THE PRODUCTION OF MGO−C REFRACTORIES

Patrick Gehre*, Alexander Kitze, Christos G. Aneziris
TU Bergakademie Freiberg, Institute of Ceramics Refractories and Composite Materials, Freiberg, Germany

Stefan Guhl, Martin Gräbner
TU Bergakademie Freiberg, Institute of Energy Process Engineering and Chemical Engineering, Freiberg, Germany

## ABSTRACT
Refractories based on MgO are the dominating lining materials for vessels in steelmaking and refining plants. To preserve limited resources and establish regional raw material supply chains, alternative resources for graphite are required. Pellets from sunflower seed hull and wood were converted into carbon and added to a MgO-C batch. After hardening and carbonizing the MgO-C samples, their phase composition, microstructure, cold crushing strength, refractoriness under load, and oxidation resistance were investigated. The addition of carbonized wood and sunflower seed hull pellets reduced the CCS due to an inhomogeneous microstructure. The RuL is at the same level as the reference samples. The addition of carbonized biomass pellets has in particular a positive effect on the oxidation resistance, resulting in 30 % less carbon oxidation of wood pellet coke compared to carbon black at 1600 °C.

## INTRODUCTION
Refractories based on MgO and C are the dominating lining materials in steel making and refining plants, like basic oxygen furnaces (BOF), electric arc furnaces (EAF), and steel ladles [1]. The MgO and carbon raw materials are bonded by high carbon-containing pitch or resin and may contain some metallic powder as antioxidants to protect the carbon from oxidation. Due to the carbon portion, MgO-C bricks possess excellent thermal shock resistance by the increased thermal conductivity and reduced thermal expansion as well as a microstructure-flexible binding characteristic of the carbon bond. Carbon also reduces the slag corrosion due to the non-wettability resulting in a reduced interaction and infiltration depth. Furthermore, carbon serves as a pressing aid during production, whereby the open porosity of MgO-C bricks is greatly reduced in comparison to fired MgO bricks. Hence, carbon plays a key role in the production of MgO-C refractories. The refractory industry is by far the largest consumer of natural graphite, accounting for approximately 46 % of global consumption of 947,000 t in 2018 [2]. Natural flake graphite is commonly used as a carbon carrier since it is the most stable modification of carbon [3]. Due to the resulting low surface energy of the flakes, their reaction potential is very low and is poorly wetted by all kinds of liquids such as slags and molten metals. A further advantage of graphite is its structural high oxidation resistance [4]. Recent investigations showed an improvement in MgO-C bricks by partially replacing flake graphite with expanded graphite [5,6]. However, the expanded graphite has a high specific surface, which limits the amount to less than 1 % without reducing the oxidation resistance. Carbon black is another main carbon source for refractories. However, carbon black is only limited used in MgO-C due to its low primary particle size. The low particle size increases the amount of liquid binder needed to be added to the batch and has lower oxidation resistance, but enables an optimal pore filling of the bricks resulting in higher corrosion resistance. New types of MgO-C have been developed using nano carbon black, especially for the production of MgO-C with low carbon content. The nanometer carbon black favours the dispersion of carbon particles, which filled the tiny spaces, pores, and gaps in the matrix between the MgO particles and thus improves the properties [7–9]. The predicted surge in demand for natural graphite by the growing battery industry marks serious competition in raw material supply for the refractory industry. But this can be a great opportunity for the refractory industry to focus on alternative carbon sources. In this regard, carbon black was partially replaced by wood and sunflower seed hull pellet coke and the impact of the carbonized biomass on the properties of MgO-C was investigated. The use of biomasses, which are zero $CO_2$ emission resources that only release the amount of $CO_2$ that was picked up during their lifetime, as a carbon source in MgO-C refractories would support the refractory industry in their effort in establishing regional raw material supply chains, saving fossil raw materials, and reducing the $CO_2$ emission.

## MATERIALS AND METHODS
Representative subsamples of the pellets were ground to particle sizes below 200 µm. During a long-term pyrolysis (carbonization) at 750 °C for 2 h (heating rate of 10 K·min-1), the biomass raw materials were thermally converted in the absence of air (nitrogen atmosphere) to liquid products such as pyrolysis oils, which were evaporated and had left the retort furnace, and solid secondary products such as pyrolysis coke including ash. The latter can serve as a carbon source in a refractory mixture. Next to MgO-C with the carbonized wood and sunflower seed hull pellets, MgO-C with carbon black and nano carbon black, respectively, were prepared as reference materials. All compositions contain coarse flaky graphite as a fixed carbon source. The compositions are displayed in table 1.

Tab. 1: Composition of the test specimen.

| Raw material | Composition (wt.-%) | | | |
|---|---|---|---|---|
| | MgO-C_CB | MgO-C_nCB | MgO-C_WP | MgO-C_SFSH |
| MgO 98 2-4 mm | 17.0 | 17.0 | 17.0 | 17.0 |
| MgO 98 1-2 mm | 29.7 | 29.7 | 29.7 | 29.7 |
| MgO 98 0-1 mm | 34.3 | 34.3 | 34.3 | 34.3 |
| MgO 98 powder | 16.8 | 16.8 | 16.8 | 16.8 |
| Graphite NFL | 1.1 | 1.1 | 1.1 | 1.1 |
| Carbon black N991 | 1.1 | - | - | - |
| Nano CB N-220 | - | 1.1 | - | - |
| Wood pellets coke | - | - | 1.1 | - |
| Sunflower seed hull pellets coke | - | - | - | 1.1 |
| Powder resin | 1.5 | 1.5 | 1.5 | 1.5 |
| Liquid resin | 1.5 | 1.5 | 1.5 | 1.5 |
| Hardener | 0.3 | 0.3 | 0.3 | 0.3 |

The raw materials used for the preparation of the MgO-C samples were the in-house produced wood (WP) and sunflower seed hull

pellets (SFSH) cokes, magnesium oxide with a purity of 98 % (QMAG, Parkhurst, Australia), flaky graphite NFL (Graphit Kropfmühl AG, Hauzenberg, Germany), carbon black MT Thermax N-991 Powder (Lehmann & Voss & Co.KG, Hamburg, Germany), and nano carbon black N-220 (Penta Carbon GmbH, Haltern am See, Germany). Liquid resin 9308-FL, powder resin 0235 DP, and hexamethylenetetramine hardener (all Hexion, Duisburg, Germany) were used as binders. The liquid resin was heated up to 70 °C in a temperature control unit and added to the coarse MgO fractions. After mixing for 5 minutes, the MgO powder, carbon sources, powder resin, and hardener were added and mixed for another 5 minutes to achieve a homogeneous distribution of the raw materials in the mixture. After the mixing process, cylinder-shaped samples with a height of 50 mm and a diameter of 50 mm were pressed with a uniaxial press and an applied pressure of 120 MPa. After pressing, the samples were hardened by a three steps thermal treatment with a maximum temperature of 180 °C. Afterwards, the samples were placed in SiC retorts, covered by petrol coke (0.2–2 mm, Müco, Essen, Germany), and carbonized in an electrically heated furnace at 1000 °C for 5 h.

The density and open porosity of the carbonized samples have been analysed according to EN 993-1 using toluol as the test medium. The microstructure has been examined utilizing an SEM equipped with EDS (Philips XL 30 ESEM FEG, Eindhoven, The Netherlands). The phase composition of milled powders of the samples after carbonization was performed by X-ray diffraction analysis (XRD) using a PHILIPS diffractometer (CuKα-radiation, K-alpha1 [°A] = 1,54060), whereas the evaluation and the portion of phases were calculated by Rietveld refinement method using the High-Score Plus 4.8 software (Malvern Panalytical B.V./NL). The cold crushing strength (CCS) has been evaluated using the TIRATest 2420 machine (TIRA, Schalkau, Germany) according to EN 993-5 with a 100 kN load cell. The loading rate was 2 mm·min-1 till a preload of 10 N and henceforward 1 N·mm2·s 1 till a maximum load of 100 kN or a dF of 50 % (load drop after reaching maximum load FH). The determination of the refractoriness under load (RuL) was carried out according to DIN EN 993-8 up to 1600 °C with a constantly applied load of 0.2 MPa under an oxidizing atmosphere with a heating rate of 10 K·min-1. One of the main focuses of the work is the impact of biomass coke on the oxidation resistance, as it has been found, that potassium causes an increase in the Boudouard reaction rate in the temperature range of 800–1200 °C [10]. For the oxidation resistance test, the cylindrical samples were placed in an electrically heated furnace (heating rate of 10 K·min-1) under ambient conditions at 1600 °C with 2 minutes of dwell time. During the test run, the weight loss of the samples was detected by a scale. Additionally, the samples were cut into halves and the degree of oxidation (area of carbon combustion $C_{loss}$) was calculated by

$$C_{loss}=(A_s-A_c)\cdot A_s^{-1}\cdot 100\ \% \qquad (1)$$

with the initial sample area $A_s$, and the area of carbon-containing sample portion $A_c$, both detected using a digital light microscope (VHX-2000 D, Keyence International, Mechelen, Belgium).

## RESULTS AND DISCUSSION
### Microstructure, phase composition, and physical properties of MgO-C with different carbon raw materials

None of the applied carbon sources (carbonized wood and sunflower seed hull pellets, carbon black, and nano carbon black) showed a negative effect on the manufacturing of the MgO-C samples. For instance, no differences in the mixing process, sticking at the pressing tools, or sticking of petrol coke at the samples could be observed. In the SEM, at low magnification, no significant differences in the microstructure of the samples with varying carbon sources could be detected. The microstructure consists of coarse and fine MgO grains, flaky graphite, and a MgO-

and carbon-containing matrix. Differences in the homogenization or a distinct pore-filling effect compared to the MgO-C reference material could not be observed. Within the MgO grains, for instance, monticellite (CaO·MgO·SiO2 – CMS) as a single impurity and CMS enclosing a FeP-rich phase together with merwinite (3CaO·MgO·2SiO2 – $C_3MS_2$) could be detected. The carbonized wood pellet coke grains appear very porous, which results from the loss of the volatile components of the biomass pellet.

Due to its comparatively low accuracy, no differences in the phase composition of the MgO-C samples by the addition of different carbon sources could be detected with the XRD method. The X-ray diffraction spectra show intense peaks of MgO and carbon. Secondary phases with a low peak intensity are calcium magnesium silicate impurities of the MgO raw material such as monticellite, merwinite and iron-containing phases. Potassium-containing phases originating from the biomass coke ash could not be detected with the XRD method and hence would represent a portion with an amount of far below 1 wt.-%.
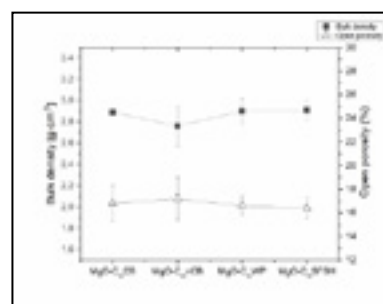


*Fig. 1 Bulk density (black squares) and open porosity (triangle) of the MgO-C samples after carbonization at 1000 °C.*

Figure 1 displays the bulk density and open porosity of the MgO-C samples after carbonization at 1000 °C. The reference MgO-C material with carbon black as a fine graphite source has a bulk density of 2,89 g·cm-3 and an open porosity of 16.8 %. The addition of nano carbon black slightly reduces the density to 2.76 g·cm-3 and increases the porosity to 17.2 %. In contrast, with the addition of carbonized wood and sunflower seed hull pellets, respectively, no significant change in the density and porosity compared to the MgO-C reference material is detectable. Hence, the amount of the added porous wood pellets coke is too low to have a negative impact on the porosity of the whole MgO-C sample. Additionally, the volatile components of the cokes would have left the system through the pore channels during the carbonization of the MgO-C samples without generating additional porosity

### Thermomechanical properties of MgO-C with different carbon raw materials
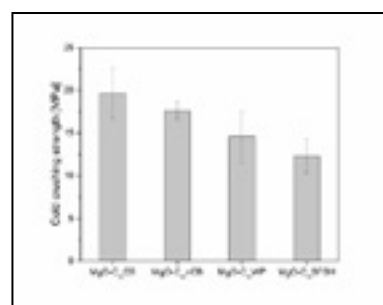


*Fig. 2: Cold crushing strength of the MgO-C samples after carbonization at 1000 °C.*

Figure 2 shows the cold crushing strength of the samples with different carbon sources after the carbonization at 1000 °C. The reference MgO-C sample with 1.1 wt.-% carbon black addition has the highest CCS of 19.65 MPa. Even if the addition of 1.1 wt.-% carbonized wood and sunflower seed hull pellets doesn't have a notable effect on the bulk density and open porosity, a significant decrease in the cold crushing strength could be detected. Here, a trend is notable, that the carbonized SFSH pellets with a lower amount of carbon and higher amount of ash result in an even lower CCS of 12.36 MPa compared to the carbonized wood pellets (14.56 MPa). The lower CCS of sample MgO-C_SFSH compared to the reference sample MgO-C_CB could be explained by the lower amount of carbon in the raw material (approx. 96 wt.-% in carbon black vs. 85 wt.-% in the carbonized SFSH), which is vital in the degree of the carbon-bond.

However, this doesn't explain the lower CCS of the sample MgO-C_WP with the carbonized wood pellets with a similar carbon content to carbon black. But the WP coke has a higher $d_{50}$ grain size of 150 μm compared to carbon black of 57 μm, which will reduce their contribution to the bonding. The CCS of the sample MgO-C_nCB with nano carbon black addition queues with 7.64 MPa between the reference sample and the biomass-based carbon sources.

Table 2 summarizes the results of the RuL testing. The MgO-C samples with carbon black and nano carbon black haven't shown compression until the maximum test temperature of 1600 °C, which underlines the very high refractoriness of MgO-based refractories. As expected, the addition of 1.1 wt.-% wood pellet coke with an ash content of 2.76 wt.-% slightly reduces the refractoriness, whereby the maximum elongation has been reached at a temperature of 1595 °C ($T_{00}$). The first characteristic temperature of the RuL testing ($T_{01}$) of sample MgO-C_WP is above the maximum testing temperature of 1600 °C, indicating still very good refractoriness. Also as expected, the sunflower seed hull pellet coke with a higher ash content of 10.45 wt.-%, which predominantly contains potassium, has an impact on the refractoriness of MgO-C, resulting in a maximum elongation at 1584 °C. But again, a $T_{01}$-value could not be detected, which means that the softening doesn't occur suddenly but takes place over a longer range of increasing temperature. With $T_{01}$-values above 1600 °C, the samples MgO-C_WP and MgO-C_SFHS exhibited very good refractoriness. Especially in the case of sample MgO-C_SFHS containing about 0.06 wt.-% $K_2O$, this is a positive finding. Hence, the biomass coke won't remarkably lower the maximum operating temperature of MgO-C.

Tab. 2: Maximum elongation $dL_{max}$ and its temperature ($T_{00}$) of the MgO-C samples after the RuL testing.

| Sample | $dL_{max}$ (%) | $T_{00}$ (°C) |
|---|---|---|
| MgO-C_CB | >1.85 | >1600 |
| MgO-C_nCB | >1.79 | >1600 |
| MgO-C_WP | 0.983 | 1594.5 |
| MgO-C_SFSH | 0.969 | 1583.5 |

**Impact of carbon raw materials on the oxidation resistance of MgO-C**
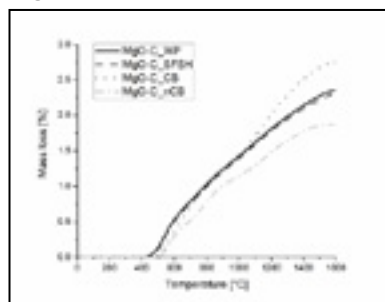


*Fig. 3: Mass loss of the samples during heating to 1600 °C.*

In figure 3, the mass loss of the samples during heating to 1600 °C is displayed, which is equivalent to the loss of carbon and hence the resistance against oxidation. The starting temperature of the oxidation of the carbon and its degree is complex and strongly depends on the type and modification of the carbon such as being present as crystalline graphite or in an amorphous state, the grain size and the specific surface of the raw material, the carbon-bond type, and the microstructure (porosity) of the composite [11]. The oxidation of the porous wood pellet coke (Sample MgO-C_WP) starts at a temperature of 418 °C, whereas the sunflower seed hull pellet coke in sample MgO-C_SFSH start to oxidize at 447 °C, the carbon black in the reference sample MgO-C_CB at 491 °C, and the nano carbon black in sample MgO-C_nCB at 520 °C, respectively. All samples exhibited a comparatively high oxidation resistance indicated by not being fully oxidized during the oxidation test. Sample MgO-C_nCB with nano carbon black showed not only the latest starting temperature of oxidation but also the highest resistance against oxidation with a total mass loss of 1.87 %. The biomass pellet cokes exhibited a similar oxidation resistance with a mass loss in the range of 2.3-2.35 %. But taking the higher amount of fixed carbon into account, the porous wood pellet coke has some advantages in oxidation resistance compared to the sunflower seed hull pellet coke. Furthermore, both samples with biomass coke had a higher oxidation resistance than the reference sample MgO-C_CB, where a mass loss of 2.75 % was detected. Next to the mass loss, the oxidized area $C_{loss}$ as an additional degree of oxidation resistance was detected. After cutting the cylinders after the oxidation resistance testing, no significant differences are visual. Table 3 lists the area of carbon combustion calculated using Eq. 1 (mean value of both cut cylinder halves) and additionally summarizes the starting temperature of carbon oxidation and mass loss. Based on the light microscope evaluation, sample MgO-C-nBC with nano carbon black addition showed an oxidized area of 8.9 % and hence the highest oxidation resistance. Sample MgO-C_WP containing the coarse porous wood pellet coke exhibited an oxidized area of 10.8 %. The lowest oxidation resistance was identified at the reference sample MgO-C_CB (15.0 %) and sample MgO-C_SFSH (16.5 %).

Tab. 3: Area of carbon combustion ($C_{loss}$), temperature of starting carbon oxidation ($T_{ox}$), and mass loss of the samples during heating to 1600 °C.

| Sample | $C_{loss}$ (%) | $T_{ox}$ (°C) | Mass loss (%) |
|---|---|---|---|
| MgO-C_CB | 15.0 ± 1.5 | 491 | 2.75 |
| MgO-C_nCB | 8.9 ± 1.5 | 520 | 1.87 |
| MgO-C_WP | 10.8 ± 1.0 | 418 | 2.35 |
| MgO-C_SFSH | 16.5 ± 1.6 | 447 | 2.30 |

**CONCLUSIONS**

The carbonization of wood pellets results in a porous coke with a $d_{50}$ particle size of 150 μm, a carbon content of 94.78 wt.-% and 2.76 wt.-% of a $SiO_2$, and CaO-rich ash. The sunflower seed hull pellets coke is fine-grained with a $d_{50}$ of 57 μm and is composed of 84.92 wt.-% carbon and 10.46 wt.-% of ash containing approx. 50 wt.-% $K_2O$. The addition of 1.1 wt.-% of the alternative carbon sources hadn't influenced the manufacturing, the microstructure, and the phase composition. Also, no significant change in the density and porosity compared to the MgO-C reference material by using carbonized wood and sunflower seed hull pellet coke could be detected, whereas the nano carbon black slightly increases the open porosity from 16.8 to 17.2 %. However, compared to carbon black, the wood pellet and sunflower seed hull coke reduce the CCS of MgO-C by 25 to 35 % due to higher particle size or lower amount of carbon, respectively. As expected, the addition of 1.1 wt.-% wood pellet coke or sunflower seed hull pellet coke with an ash content of 2.76 and 10.46 wt.-%, respectively, slightly reduces the refractoriness, but with $T_{01}$-values above 1600 °C, both samples surprisingly exhibited very good refractoriness. Especially in the case of sample MgO-C_SFHS containing about 0.06 wt.-% $K_2O$, this is a positive finding. Both biomass cokes start to oxidize at lower temperatures than carbon black and nanometer carbon black but exhibited still a comparatively high oxidation resistance. Sample MgO-C-nBC with nano carbon black addition showed the highest oxidation resistance. The lowest oxidation resistance was identified at the reference sample MgO-C_CB and sample MgO-C_SFSH. Thus, the results show, that for MgO-C with a low amount of C, the carbon black could be replaced by biomass coke without a significant reduction of the properties. An ideal biomass coke for the refractory industry shouldn't be porous and should exhibit a particle size below 40 μm, a high carbon content of more than 95 wt.-% and a low ash content of less than 30 wt.-% with a minor amount of alkalis. Biomass cokes which meet these requirements will be appropriate to replace parts of the natural graphite portion of a MgO-C batch, which would support the refractory industry in their effort in establishing regional raw material supply chains, saving fossil raw materials, and reducing $CO_2$ emission.

**REFERENCES**

[1]     Hasanbeigi MAT, Lynn K. Price A. The state–of-the-art clean technologies (SOACT) for steelmaking handbook, 2010.

[2]     R.I. Services, Natural and Synthetic Graphite: Global Industry Markets and Outlook, Roskill Information Services Limited, 2012.

[3]     Tanabe T, Niwase K, Tsukuda N, Kuramoto E. On the characterization of graphite. Journal of Nuclear Material 191–194, 1992, p. 330–334.

[4]     Hahn JR. Kinetic study of graphite oxidation along two lattice directions. Carbon N. Y. 43, 2005, p. 1506–1511.

[5]     Zhu T, Li Y, Jin S, Sang S, Wang Q, Zhao L, Li Y, Li S. Microstructure and mechanical properties of MgO-C refractories containing expanded graphite. Ceramics International 39, (2013, p. 4529–4537.

[6]     Mahato S, Pratihar SK, Behera SK. Fabrication and properties of MgO-C refractories improved with expanded graphite. Ceramics International 40, 2014, p. 16535–16542.

[7]     Behera SK, Sarkar R. Low-carbon magnesia-carbon refractory: Use of N220 nanocarbon black. International Journal of Applied Ceramic Technology 11, 2014, p. 968–976.

[8]     Zhu T, Li Y, Sang S, Jin S, Li Y, Zhao L, Liang X. Effect of nanocarbon sources on microstructure and mechanical properties of MgO-C refractories. Ceramics International 40, 2014, p. 4333–4340.

[9]     Liu B, Sun JL, Tang GS, Liu KQ, Li L, Liu YF. Effects of nanometer carbon black on performance of low-carbon MgO-C composites, Journal of Iron Steel Research International 17, 2010, p. 75–78.

[10]   Lindstad T, Syvertsen M, Ishak RJ, Arntzen HB, Grøntvedt PO. The influence of alkalis on the Boudouard reaction. 10th International Ferroalloys Congress, 2004, p. 261–271.

[11]   Cho GH, Kim EH, Li J, Lee JH, Jung YG, Byeun YK, Jo CY. Improvement of oxidation resistance in graphite for MgO-C refractory through surface modification. Transaction of the Nonferrous Meal Society of China (English Ed) 24, 2014, p-s119–s124.

70

# SQUARING THE CIRCLE: CHALLENGES & OPPORTUNITIES IN RECYCLING REFRACTORY MINERALS

Mike O'Driscoll

IMFORMED, Epsom, United Kingdom

The strive towards the Circular Economy has boosted the evolution of recycling industrial waste, and spent refractories are no exception. The drive for sustainability has increased the potential of recycling refractory minerals as technical and economic challenges in their sourcing, processing, cost, and distribution receive growing attention and solutions. While refractory recycling is not new, it is now fast becoming a mainstream activity, even a necessity, rather than its previous perception as an esoteric sideshow. There are several drivers for recycling refractory minerals, among which are overreliance on limited sources, increasing challenges and costs in opening new mines, and logistics. The upshot is that a new supply chain option of recycled refractory minerals is now evolving to meet both market demand and environmental expectations. At the same time it has also encouraged growth in a parallel sector developing and supplying technology and equipment for refractory recyclers. Although there is much interest in recycling, it still remains a fledgling sector, with a small but expanding group of pioneers, regional contrasts, and with many challenges. Some big players are only just starting to get into action, while many others are still assessing their strategic approach. Today's waste sources will be tomorrow's new mineral resources, and the refractory industry needs to make this happen. This paper will outline the current status, the main players, and spotlight the key challenges and opportunities in recycling refractory minerals.

# LATEST ADVANCED DEVELOPMENTS IN THE IMPLEMENTATION OF CIRCULAR ECONOMY STRATEGY IN THE REFRACTORY WASTE MANAGEMENT

Aintzane Soto, David Maza, Miguel Ángel Mangas, Sidenor Investigación y Desarrollo S.A, Basauri, Spain.

## ABSTRACT

The reinforcement of the environmental policies that started taking place during last decades, has pushed steel producers to implement Circular Economy criteria in their waste management. However, in the case of refractory waste, a great part of it is still being dumped into landfills, since the valorisation solutions developed for every kind of refractory waste are not thoroughly implemented.

In Sidenor, the research work developed through internal continuous improvement projects and the European LIFE 5RefrAct and RFCS E-CO-LadleBrick projects, has allowed to implement systematically the Circular Economy 4R Model in the routine of the refractory waste management. This approach includes advanced solutions for every kind of refractory waste considering the potential "Reduce", "Reuse", "Remanufacture" and "Recycle" available alternatives.

On the one hand, several laser based technological equipment have been tested in Sidenor´s plant in order to optimise the ladle life and thus, "Reduce" the amount of refractory waste that is generated. Commercial equipment allow to have information about the wear rate in hot conditions and it can be joined with the process variables in order to optimise and extend the life of the refractory lining.

On the other hand, for the different kind of refractory waste generated in the meltshop, a number of innovative "Reuse", "Remanufacture" and "Recycle" applications have been identified and implemented in the routine, taking into account the economic and environmental benefits associated to them. A Decision Algorithm has also been developed to assess the selection of the best valorisation alternative in every case.

**Keywords:** refractory waste, bricks, Circular Economy, 4R Model, laser, thickness, valorisation.

## INTRODUCTION

The economic system known as Circular Economy that aims at minimising waste, has been widely integrated and applied in the steel sector, specifically in the valorisation of Electric Arc Furnace (EAF) slag, EAF dust, Ladle Furnace (LF) slag or iron scale. However, hardly any work has been developed in the management of refractory waste, at least in a systematic and integral way.



*Fig. 1: Teardown of the ladle in Sidenor*

Considering the potential for valorisation of spent refractories (see the waste condition in Fig. 1), in 2012 Sidenor meltshop operational staff found a very unexplored and unexploited market. At that moment, in Sidenor only the 7% of refractory waste was valorised, while the rest was directly sent to landfill. This scenario seemed to be similar in the rest of the steelworks, and prompted the research of possible actions that could lead to increase the valorised percentage.

This is how Sidenor started a continuous improvement initiative with the aim of minimizing the refractory waste disposal in landfills. At first, a working group involving staff from the Steelworks and the Environmental and Purchasing departments was created. At that time, from the total amount of refractory waste generated (Fig. 2), the recoverable fraction corresponded to MgO-C bricks and High Alumina waste (bricks and ladle consumables).
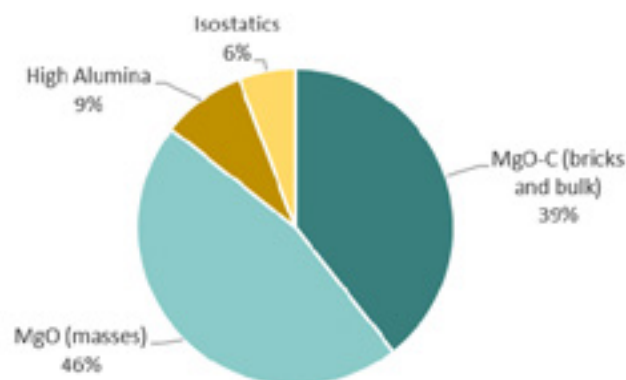


*Fig. 2: Refractory waste distribution*

With the aim to increase the recoverable fraction, Sidenor initiated in 2017 the local ISOVAL project (co-funded by IHOBE, the Basque Government Environmental Department) valuing the waste from the Isostatic refractory parts.

Considering that MgO masses (not recoverable so far) accounted for almost half of the refractory waste generated in the steelworks, Sidenor started in 2018 the coordination of the European project 5REFRACT LIFE Programme, where, in cooperation with refractory manufacturers such as MAGNA or Refralia, developed high value added refractory products incorporating a significant amount of recycled refractory. It included solutions for the Magnesia-Carbon and High Alumina waste (increasing the value added with respect to the previous solutions), and for the Isostatic scraps and Magnesia masses.

In parallel to this work, Sidenor also started in 2019 another coordination work related to the European RFCS project E-CO-LadleBrick, where, according to the 4R model, combined a Reduction of the volume of Magnesia-Carbon waste by means of monitoring the ladle refractory consumption with a laser developed by Tecnalia (via remaining brick thickness optimisation), with new processes for Reusing, Remanufacturing and Recycling the ladle spent bricks. The final optimized application came from an expert decision algorithm performed by the FGF and the LCA studies done by the Danish company 2.0 LCA Consultants.

## CIRCULAR ECONOMY IMPLEMENTATION

The main actions that were required to start implementing the Circular Economy model in the refractory waste management in Sidenor, are the following:

1) Adopt the 4R model: Reduce, Reuse, Remanufacture and Recycle.

2)  Separate the waste directly in its points of generation: through containers in a devoted colour, labelled with the name of each type of waste for the small volumes, and a bunker separated with walls and its corresponding labelling for the large volumes.

3)  Include all the partners in the value chain: refractory manufacturers, external valorisation agents and steel producers.

## 1R: Reduce

To reduce the amount of waste generated in the meltshop, specifically in the case of MgO-C bricks from the ladles, the useful life of the bricks must be extended as much as possible. To do so, and always working on safe conditions, it is necessary to optimize the consumption of refractory material during the processes involved in the steelworks.

First, it is necessary to know the wear rate of the refractory lining during its operation, at high temperature conditions. So far, the only information available was the remaining refractory thickness measured after the selective demolition of the ladles, in cold conditions, and after the end of their useful life. The problem is that this does not allow the life of the ladle to be extended or reduced depending on the process conditions.

To monitor the remaining refractory thickness of the ladles during the operation, in the E-CO-LadleBrick project, Tecnalia developed a low cost 3D laser scanner. Due to some process limitations, within the project, it was necessary to use a commercial equipment to obtain a significant amount of immediate measurements (Fig. 3) with which to make decisions. In the case of Sidenor, Ferrotron's LaCam Mobile equipment was rented for 3 months.
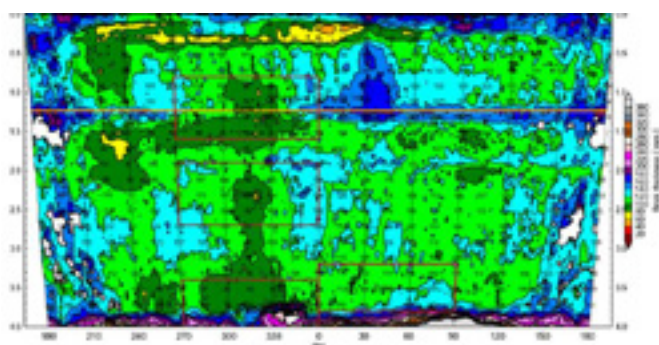


*Fig. 3: Ladle remaining thickness measurements with the Ferrotron equipment*

Thanks for the knowledge of the remaining thickness in every point inside the ladle, heat by heat, it was possible to analyse the effect of the secondary metallurgy operating variables on the wear, and thus build a Machine Learning predictive model of refractory wear in ladles.

## 2R: Reuse

Bearing in mind the environmental and economic impact of the valorization of refractory waste, it is important to search for the biggest amount of refractory waste to be internally reused (without any processing operation on the waste involved).

As a usual practice, Magnesia-Carbon and Alumina spent bricks obtained from the EAF and LF lining are separated and palletised in a systematic way, and placed in a specific area inside the meltshop for the pallets disposal.

MgO-C bricks are directly reused in application such as the EAF Pre-Wall, the emergency ladle, the EAF wear lining reparation and the upper rows or the slag pot lining. In the case of Alumina bricks,

they can be reused in the ladle tapping spout or in the lining of the pits built for cooling or safety purposes in the meltshop.

## 3R: Remanufacture

This alternative requires a processing operation by an external valorisation agent and the consequent return of the transformed reclaimed refractory to be used again in the meltshop. For that reason, the Purchasing department of Sidenor contacted and negotiated with different waste companies to apply the necessary processing of the material to be used in a new application.

As a remanufacture application can be highlighted the EAF breast (Fig. 4), replacing the usual mixture material composed of dolomite lime and magnesia masses, by a transformed Magnesia base new recycled and more efficient refractory at lower cost. Other alternatives could be the routes, the pavements, EBT filling, backfiller in the ladles, the vacuum shield filling or slag formers and conditioners.



*Fig. 4: EAF Breast remanufactured refractory*

## 4R: Recycle

Most of the refractory waste that could not be internally reused, or remanufactured for a different use in the steelworks, was definitely sent to an external valorisation agent that, after some transformations, delivered the material to other companies (mainly refractory manufacturers) in order to make a different product. This is the case of the MgO-C in bulk (including the finest parts), the alumina consumables, the isostatics and the MgO masses.

With MgO-C in bulk and with the MgO masses, a new gunning product incorporating up to 70% of refractory waste was developed and industrially employed in the EAF slag line gunning and in the ladles top ring gunning. Other Magnesia base materials were also produced for the EAF steepbank or the EAF breast.

In the case of Alumina waste and Isostatics, a new recycled refractory concrete incorporating up to 65% of spent material was produced. This new product is already implemented in the routine in applications like the ladle lip, the ladle lip segments, the Continuous Casting cooling chamber or the tundish lids.

## CONCLUSIONS

The excellent and coordinated work performed in Sidenor during the last 11 years in this field, has positioned our company as a

73

world benchmark in the Refractory Waste Management, reaching global refractory recovery levels over 95%.

In addition, all of the valorisation solutions that were developed and summarized in this paper, are currently implemented in the routine in the meltshop of Sidenor.

It was also demonstrated that the methodology applied required the commitment of managers and employees in the adequacy of the facilities and procedures in order to achieve a correct segregation of the different refractory waste and the further employment of the recycled products.

It was also of paramount importance to allocate more resources and to bet on new ambitious research projects where, with the collaboration of refractory experts, it could be possible to continue investigating and exploring other non-recoverable fractions, like some years ago happened with the MgO masses (successfully recycled for the first time by Sidenor).

## AKNOWLEDGEMENTS

## REFERENCES

All the information contained in this paper is own source.

# ESTABLISHING CIRCULAR ECONOMY FOR REFRACTORIES IN CEMENT APPLICATIONS BY ADVANCED RECYCLING TECHNOLOGIES

Sandra Königshofer, Martin Geith,
RHI Magnesita GmbH, Leoben, Austria.

## ABSTRACT

RHI Magnesita is committed to sustainability and the establishment of a circular economy for the refractory industry. However, extending recycling strategies and the use of secondary raw materials can be challenging due to the manifold of used products in tailor-made lining concepts for various industries withstanding tremendous conditions. Consequently, spent refractory bricks are subjected to intensive material alteration and infiltration, matrix conversion and microstructural changes. Further considering mixed storage of different breakout materials, adhering impurities, and adjacent lining materials, it becomes evident that sorting and cleaning is crucial. Typically hand sorting is still the standard to allocate spent refractory bricks into different secondary raw material categories. This paper illustrates how the 3.5-year ReSoURCE (Refractory Sorting Using Revolutionizing Classification Equipment) project funded by the EU in June 2022, led by RHI Magnesita, aims to innovate the full process chain of refractory recycling by the development of an automated sorting system with AI-supported multi sensor equipment as its core technology. Focussing on the example of the recycling of spent refractory bricks from cement rotary kilns, representative sampling, material characterization and appropriate treatment will be presented that allows RHI Magnesita to provide sustainable products with significantly lower carbon footprint and to support customers from cement industry in reducing $CO_2$ emissions.

## THE RESOURCE PROJECT

Establishing a circular economy for the refractory industry by extending recycling and the use of secondary raw materials is indispensable. The reuse of spent refractories by the refractory producers is already a standard for selected product types of certain industries with no significant level of contamination, and the recycling business itself has continuously grown during the last years. However, to further extend the use of, especially high-quality, secondary raw materials and to develop innovative and economic recycling technologies is challenging for different reasons. One complication is that within a lining multiple refractory product types with different chemistries are combined individually for each customer to achieve the required performance. During service the original installed refractories wear because of occurring stresses or dissolve due to the harsh process conditions and environments of the customer's process. Besides, refractories are subjected to material alteration and infiltration, matrix conversion and microstructural changes. When considering the complex mix of remaining materials, including impurities stuck to their surface and materials nearby, it becomes clear that hand sorting often provides the most effective method of processing these materials. However, manual sorting is strongly dependent on the experience of trained personnel, who classify the material based on visually recognizable secondary characteristics such as colour or particle shape, and can only be used for the sorting of the coarse particle size fraction of spent refractory bricks (~ >80 mm). The finer parts (~ <80 mm), currently manually unsortable, are either landfilled, used as metallurgical additive or raw meal addition. Automated sorting per se, potentially capable of determining also primary characteristics such as chemistry, is a standard processing method for several mining applications and conventional recycling branches (e.g., glass, plastics) already. However, reliable automated sorting solutions for this intricate task of refractory recycling could not be established so far. Hence, a multitude of proof-of-principle trials have been performed by RHI Magnesita, confirming the need

for combining different sensor technologies as commercially available sensor-based sorting solutions were not able to achieve the required product qualities. Therefore, RHI Magnesita has initiated the ReSoURCE project and applied for the Horizon Europe funding program together with a team of globally leading technology partners (LSA GmbH, Norsk Elektro Optikk AS, Innolas Laser GmbH, Fraunhofer ILT, Montanuniversität Leoben, SINTEF AS, CPI Centre for Process Innovation Ltd, Crowdhelix Ltd.). The project with an overall budget of 8.5 million EUR was funded by the European Union totalling 6 million EUR and aims to revolutionize the entire process chain of refractory recycling by introducing AI-supported multi-sensor sorting equipment as the central technology. Combining laser-induced breakdown spectroscopy, hyperspectral imaging and 3D object recognition with optimized pre-processing, and automated ejection systems will lay the foundation to set a new state-of-the-art for refractory sorting. Besides allowing a fast integration in the present established daily business, during this 3.5-year project a reliable and robust sorting system will be developed that allows to handle the entire particle size fractions by building two demonstrator units to sort the breakout materials precisely. On top further possible application areas for residues will be explored. ReSoURCE aims to improve the current recycling situation by increasing the share of recycled material reusable in refractories from 15 % to about 37.5 %, decreasing landfilling from 30 % to 5 % and enhancing downcycling from 5 % to 7.5 %. Reaching these ambitious goals will lead to massive annual $CO_2$ reductions (up to 800 kilo tonnes), energy savings (up to 760 GWh) and saving in landfill capacity (up to 800 kilo tonnes) in the European Union (see Figure 1). The continuous monitoring of the economic and ecologic benefits by techno-economic analysis and life cycle assessment will ensure the green and digital transformation of the refractory recycling value chain. [1], [2]
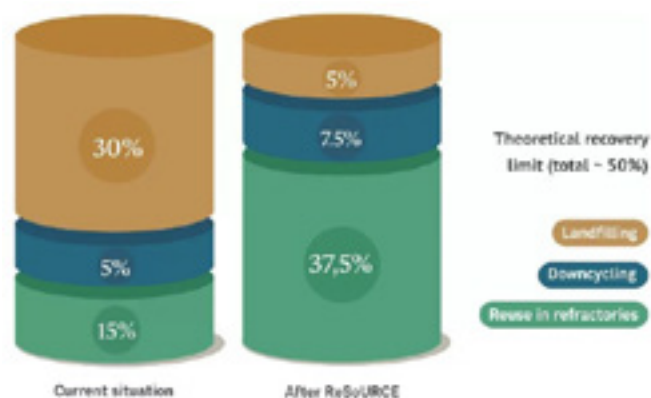


*Fig. 1: Ambitious goals set in the ReSoURCE project [1].*

## RECYCLING OF SPENT REFRACTORY BRICKS FROM CEMENT ROTARY KILNS

One of the first tasks in ReSoURCE, was the selection of appropriate breakout materials as feedstock based on the evaluation of the refractory market in terms of volumes, availability, and lining compositions to determine materials having the highest impact regarding environmental and economic benefits to be used during the project. Here, spent cement rotary kilns bricks proved to

be one of the most suitable choices with high potential for refractory recycling as large quantities in sufficient quality are readily accessible on an annual basis with a high number of installed aggregates worldwide. This was also confirmed at on-site visits of cement producers by evaluating the breakout procedure during their winter repairs. Furthermore, sustainability and the associated reduction of $CO_2$ emissions play a key role in the cement industry, and environmental friendly refractories will contribute to decarbonize their supply chain and related scope 3 emissions. It is well known that spent refractories from cement rotary kilns contain substantial process-related contaminations, such as high levels of Na, K, S or Cl originating from the clinker primary raw materials [5] or the enhanced use of alternative fuels, especially in Europe. The evaporation of related volatile phases in the burning zone of the kiln in conjunction with the transport into cooler kiln areas connected with the formation of recondensation products lead to the formation of so-called alkali-sulphate-circles. Therefore, spent cement rotary kiln bricks are infiltrated with alkali salts (-sulphates and -chlorides), even penetrating the pore structure of the refractories. To tackle these challenges that diminish quality, and to enhance recycling practices to be able to offer sustainable solutions to cement customers, RHIM has pioneered a patented treatment method. [3], [4]

**Representative sampling**

An extensive material characterization is the foundation for the development of innovative processing methods. For performing such detailed investigations, representative samples of these inhomogeneous breakout material streams are required. Spent refractories can differ considerably from the originally produced refractory material. For instance, they are subjected to intensive material alteration and infiltration, which affects the chemical and mineralogical composition and leads to matrix conversion and microstructural changes from the hot to the cold face. Moreover, after dismantling often large tonnages of mixed product types in different size fractions and of a different degree of contamination are stored together in outdoor material boxes without weather protection. Consequently, all these circumstances effect the reliability and validity of the analytical results of the samples for quality control and material characterization purposes. Hence, finding appropriate sampling procedures is a declared target of the ReSoURCE team. To draw representative samples certain instructions and standards exist that were evaluated to be applicable for this special case of spent refractories. Sampling should be done randomized and follows a probabilistic approach, so that every grain has theoretically the same probability of becoming part of the representative sample. The prerequisite for this is that the entire quantity of the material to be sampled is accessible. Thus, the entirety of the breakout material (in this case about 50 tons) was spread out and a sampling scheme was created depending on the size of the heap by dividing the grid area into subsections. Based on data from initial inspection, the particle size of the spent bricks was determined and the number of individual samples and their quantity to take within the subsections was calculated. Before combining the individual samples to one combined sample, several steps of sample processing and splitting were performed for each sample. The described sampling scheme and the sampled sections are shown in Fig. 2. [6]
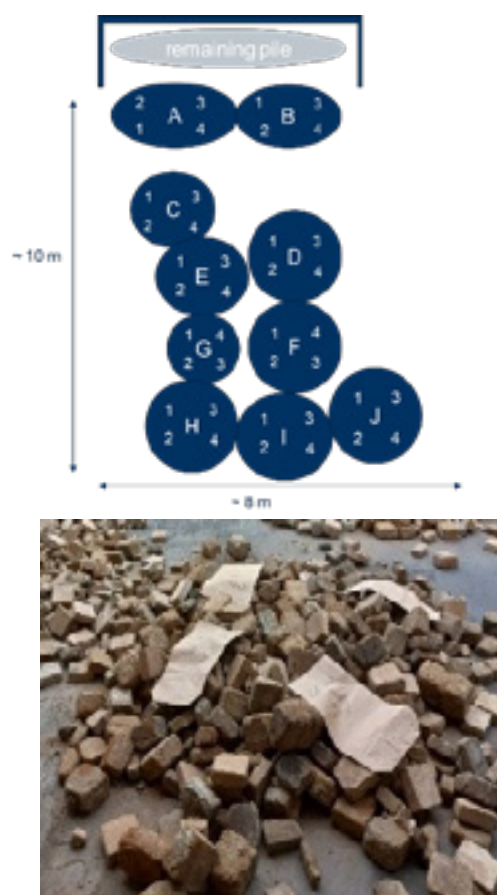


*Fig. 1: Sampling scheme (top) and sampled sections (bottom).*

**Chemical and mineralogical material characterization**

The performed investigations and analyses for the chemical and mineralogical characteristics proved, as expected, that the sampled breakout material consists of different magnesia-spinel based product types, typically installed in cement rotary kilns. The major components of the combined sample are MgO >80 % and $Al_2O_3$ ~10 %, and the main mineral phases are periclase, and spinel. As concerns the degree of infiltrated alkali salts the total amount of $Na_2O$, $K_2O$, $SO_3$ and Cl varied up to ~8 % in examined brick sections of the hot, middle and the cold face. Tab. 1 gives an overview about the chemical analysis of the combined sample, taken from the cement rotary kiln breakout material. It is clearly visible that additionally to the main refractory oxides infiltration by alkali-sulphates and alkali-chlorides can be detected.

Tab. 1: Average analysis of cement rotary kiln recycling material from representative sampling, 1) analysis by XRF, 2) elementary analysis.

| components | [wt%] |
|---|---|
| MgO [1] | 85.5 |
| $Al_2O_3$ [1] | 8.6 |
| CaO [1] | 1.4 |
| $SiO_2$ [1] | 0.8 |
| $Fe_2O_3$ [1] | 1.8 |
| MnO [1] | 0.07 |
| LOI | 3.8 |
| Na [2] | 0.1 |
| K [2] | 2.0 |
| SO3 [2] | 0.8 |
| Cl [2] | 1.0 |

The chemical analysis was confirmed by detailed microscopic investigations of polished sections by incident light and SEM, showing besides magnesia and spinel as main mineral phases the

presence of chloride- and sulphate-bearing reaction phases (alkali salts) in Fig. 3-5, e.g., sylvite (KCl), calcium-langbeinite ($K_2Ca_2(SO_4)_3$), arcanite ($K_2SO_4$), anhydrite ($CaSO_4$), aphthitalite $K_3Na(SO_4)_2$.
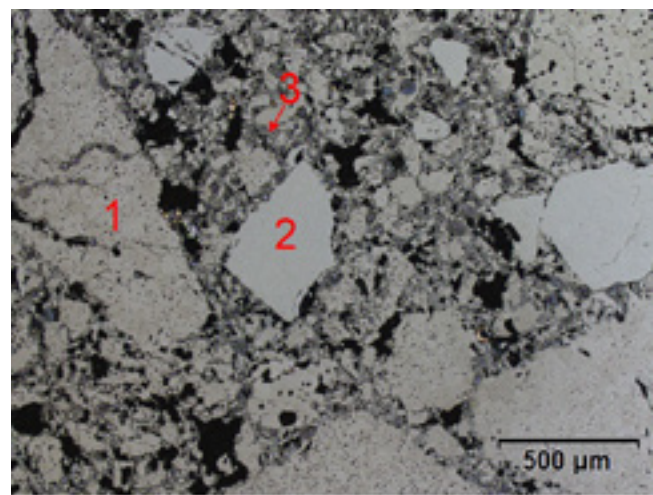


*Fig. 3: Microscopical overview of a cement rotary kiln recycling material: magnesia (1). spinel (2). alkali salt (3).*
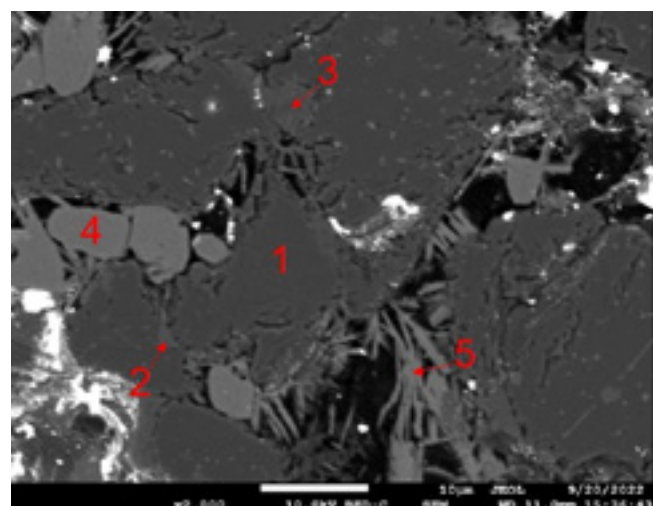


*Fig. 4: Detail of cement rotary kiln recycling material by SEM: periclase (1), spinel solid solutions (2), forsterite (3), calcium sulphate (4) and calcium-langbeinite (5).*
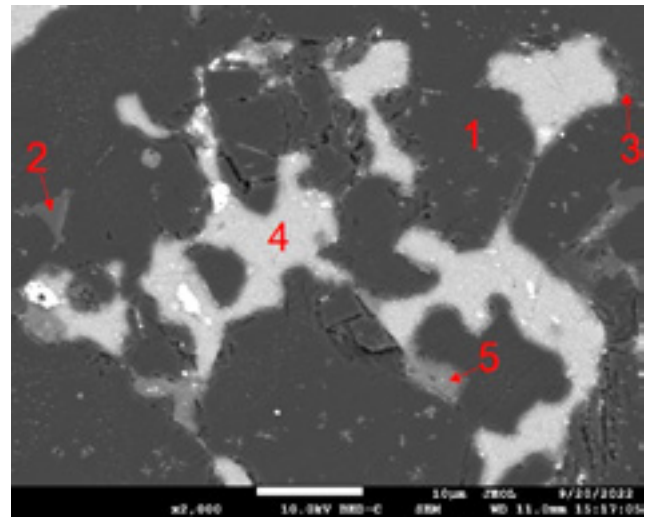


*Fig. 5: Detail of cement rotary kiln recycling material by SEM: periclase (1), spinel solid solutions (2), forsterite (3), sylvite (4) and arcanite (5).*

Hence, for the development of the ReSoURCE's automated sorting equipment, material characterization is of key importance for the definition of sorting criteria and classes as well as for validating the accuracy and performance of the sorting equipment.

**Developed and patented treatment method [3]**
As stated previously, usually spent cement rotary kiln bricks are infiltrated with alkali salts and therefore exceed the specifications as concerns the limit values for the contents of Na, K, Cl and S. (see chem. analysis in Tab.1). Thus, these have been considered unsuitable for the use as recycling materials in the past due to the negative influence on the brick properties and related brick production problems. For this reason, RHI Magnesita has developed a patented treatment method to minimize the alkali salt contamination of spent cement rotary kiln bricks and to enable the reuse as recycling materials for high-quality brick brands. R&D Leoben carried out comprehensive studies on spent bricks from different European cements plants, showing a diverse degree of contamination and included contaminants, with the result that a treatment by washing was most promising as the vast majority of contaminants, as described in the material characterization section before, proved to show a good water solubility. Various lab trials and parameter studies towards the development of an effective and efficient washing procedure were conducted with crushed material. The efficiency increased with decreasing particle size and improved process execution. For the effectiveness the appropriate water quantity and washing time, also considering the saturation limit of water by adjusted process control, are decisive. Fig. 6 provides an overview on the achieved alkali salt reduction, whereby an overall reduction of ~70 % of all salts could be achieved. On closer examination of the reduction of the individual constituents, it revealed that the washing treatment was most efficient for chloride-bearing phases and lower for sulphate-bearing phases explicable by their lower water solubility.
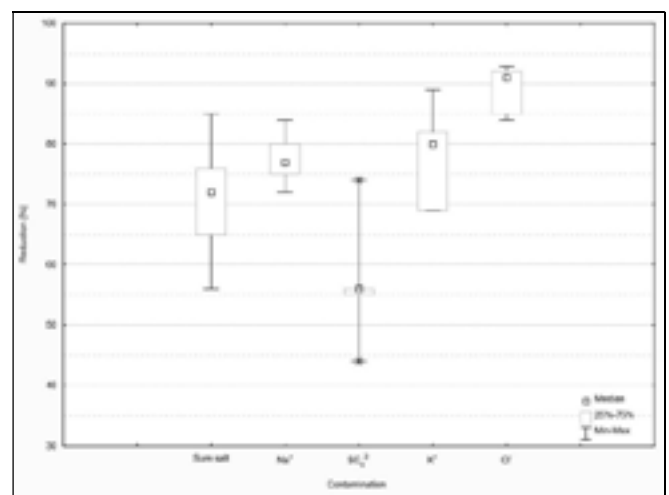


*Fig. 6: Alkali salt reduction for the washing of five different spent cement rotary kiln bricks (0-5 mm) [3].*

The washed material and the untreated material were used for brick production trials, applying the same recipe (20 % recycled material) and process parameters (firing at 1,600 °C in a tunnel kiln), in comparison to standard bricks only consisting of primary raw materials. With increasing content of recycling material, also problems during brick production could be observed (e.g., bricks sticking together, evaporation of volatiles, crack formation) leading to the defined value of 20% recycling content tested in these trial series. Bulk density (BD), open porosity (OP), cold crushing strength (CCS), and refractoriness under load (RuL) were measured to assess the physical properties of the produced bricks. Tab. 2 shows that due to the application of the newly developed and patented washing process, the physical properties could be

improved compared to the untreated material, and also no problems during brick production could be observed. Bricks containing untreated recycling material showed a decrease of the BD, an increase of the OP and reduced RuL (T0) compared to bricks containing virgin raw material or washed material. This enhancement is caused mainly by the reduction of volatile substances and low melting phases. In comparison to the untreated material, especially the RuL (T0) reached similar values to the standard bricks. The CCS values of the bricks were within the usual range of the standard production of this brand for all investigated samples.

Tab. 2: physical brick properties comparing washed with untreated material and standard bricks [3].

| Recycled material content | BD [g/cm³] | OP [%] | CCS [MPa] | RuL T0 [°C] |
|---|---|---|---|---|
| virgin raw materials (0%) | 2.95 | 15.3 | 68 | 1,520 |
| untreated material (20%) | 2.90 | 17.6 | 65 | 1,396 |
| washed material (20%) | 2.93 | 16.2 | 77 | 1,502 |

## ESTABLISHMENT OF A CIRCULAR ECONOMY – THE ANKRAL LC SERIES

Circular economy will be one of the main drivers to significantly reduce $CO_2$ in the refractory industry, as the energy-intensive primary raw material production has by far the highest impact on the product's carbon footprint. The use of washed secondary raw material in the ANKRAL LC (low carbon) series paves the way to products with significantly lower $CO_2$ footprint without compromising technical requirements and specifications by the partly substitution of primary raw materials, such as magnesia. However, to establish circular economy and to ensure the high-quality of recycled materials, customer collaboration is required, as depicted in Fig. 7 RHI Magnesita actively assists cement plants when breaking out the lining. Separate and dry storage of different brick types after demolition is preferred to support manual sorting and cleaning at RHI Magnesita's recycling hubs before the recycled materials are re-introduced to the brick production process. [4]

While the described solutions provide satisfactory results, the projected strong growth of recycling demand in future makes it inevitable to work on the next generation of recycling technologies. Automated sensor supported sorting of various grain size fractions will not only allow to increase the feedstock availability but will as well indicate contamination levels required for further optimization of the subsequent post-treatment.

## CONCLUSIONS

There's no question that one of the biggest challenges the industry faces today is decarbonization. RHI Magnesita is taking the initiative to reduce $CO_2$ emissions to provide diverse customers with sustainable products. The automated sensor-based sorting will be pivotal in significantly boosting recycling volumes in the future, all while maintaining the quality of secondary raw materials and thereby also the performance of the recycling containing final product.

Due to the enormous complexity of this task, RHI Magnesita has established the ReSoURCE project, aiming to redefine the standard for refractory sorting and leverage this new technology to benefit related processes. Ensuring a consistent, representative sampled supply of feedstock materials is critical for realizing these innovative steps.

The significance of thorough R&D work becomes evident when considering RHI Magnesita's ANKRAL LC series. This is a prime example of how one can achieve high-quality secondary raw materials, which will be crucial in further enhancing the recycling content in refractory products.

## ACKNOWLEDGEMENTS

## REFERENCES

[1] https://www.project-resource.eu
[2] Königshofer S., Kohlmaier S., Leitner, A.: Increasing the use of secondary raw materials by the processing of spent refractories. BHM Berg- und Hüttenmännische Monatshefte, Volume 168, Issue 4, April 2023, p. 188-193.
[3] Klitzsch M., Geith M., Setting new standards for circular economy in the cement industry, Proceedings TMS Rewas Conference
[4] Klitzsch M., Krischanitz, R., Telser, H.: RHI Magnesita is Leading the Way to a Circular Economy in the Refractory Industry, Bulletin The Journal of Refractory Innovations, 2021 p. 12-14.
[5] Harrisson, A. M.: Constitution and Specification of Portland Cement, Lea's Chemistry of Cement and Concrete, 2019, p. 87–155.
[6] Feucht F., Sedlazeck P., Friedrich K., Sattler T., Pomberger R., 2023. At the beginning of Project ReSoURCE, Deutsche gesellschaft für Abfallwirtschaft e.V. DGAW, 12. Wissenschaftskongress, Abfall- und Ressourcenwirtschaft, Hamburg; innsbruck university press 2023, pp.217 – 219; DOI: 10.15203/99106-095-6.



Fig. 7: The cement industry as example for the already established circular economy approach of RHI Magnesita. [4]

# INVESTIGATION OF THE INFLUENCE OF IMPURITIES TYPICAL IN SECONDARY RAW MATERIALS ON THE BEHAVIOR OF HIGH ALUMINA CASTABLES – PART I: DESIGN OF THE CASTABLES, SETTING PROPERTIES AND HIGH TEMPERATURE FRACTURE BEHAVIOR

Laura Erbar, Katharina Sarnow, Olaf Krause
Koblenz University of Applied Sciences, Höhr-Grenzhausen, Germany

Erwan Brochen, Michael Kaminski, Christian Dannert
Forschungsgemeinschaft Feuerfest e. V. at the European Centre for Refractories, Höhr-Grenzhausen, Germany

Jacek Podwórny, Karolina Dudek, Magdalena Kujawa, Robert Kusiorowski
Institute of Ceramics and Building Materials, Refractory Division, Gliwice, Poland

## ABSTRACT

Forced by economic, ecologic, or even legal causes, refractory producers want to, need, or must increase the use of secondary raw materials. It is unclear, however, how impurities which are being carried over into refractory materials from secondary raw materials influence the behavior of those refractory materials, either during the processing state or during their use in high temperature environments.

The research was carried out using a primary high alumina raw material that was selectively spiked with typical elements found in secondary raw materials. These artificially spiked raw materials were processed into cement-free high alumina monolithics by 1:1 substitution of the corresponding high alumina matrix fraction in the formulation. Regardless of the impurity, the rheology and setting behavior of the developed model refractory castables showed a very high degree of comparability with the reference material. Comparable workability allowed the production of comparable test pieces for hot wedge splitting tests. The effects on high temperature fracture behavior observed in this study can therefore be attributed solely to the impurities.

## INTRODUCTION

The literature indicates that impurities, even at low concentrations, have a significant effect on the thermal behavior of high alumina monolithic materials [1, 2]. Due to the production process, iron, titanium, and silicon are typically present in concentrations below 0.1 wt.-% (traces). Secondary high alumina raw materials are expected to contain higher levels of impurities due to previous industrial use. In particular, calcium is significantly enriched in secondary raw materials, as Ca is a major component of metallurgical slags.

A first attempt to assess the effect of sodium on high alumina calcium aluminate cement-bonded refractories was made by Alex et al. [1]. They found that monolithics spiked with up to 1 wt% Na by the addition of sodium acetate show significant changes in the thermal evolution of the calcium aluminate phases, causing increased expansion of the materials, which significantly degraded the properties of the castables. Möhmel [2] shows that considerably higher impurity concentrations can actually improve the thermal stability and thermo-mechanical properties of high alumina monolithics, depending on whether the critical impurities are present in the coarse grains or in the matrix.

However, due to a lack of publications that take a systematic approach, it remains unclear how impurities from secondary raw materials affect the high temperature performance of refractories. It is not clear which processes cause changes in high temperature performance.

### Research method

The aim of this work is to spike cement-free monolithics with impurities as found in recycled raw materials, but in a controlled scientific procedure. During the previous use(s) of recycled high alumina raw materials, impurities will either have formed mixed oxides (e.g., hibonite in the presence of Ca), beta-alumina (in the presence of Na) or if impurities are present in higher concentrations, melt/glass phases. These reactions are therefore simulated in a controlled laboratory environment by mixing pure fine primary alumina (< 45 µm) with varying amounts of impurities (Na, Ti, Si, Ca, and Fe in oxidic form up to 2 wt%), homogenizing and pelletizing the mixtures and sintering them at 1600 °C. The sintering temperature refers to the average process conditions during the steel production. The sintered materials are then ground to a fraction of 0 to 45 µm, which is the typical open fine grain fraction in the matrix composition.

The intention was to create precursors with as many different mineralogical conditions as possible but making them involve a substantial amount of work. FactSage® was used to determine the critical amounts and mixtures of the impurities and to predict the reactions that occur in this concentration range. The precursors then substituted tabular alumina (0-45 µm) in the formulation of the model refractory castable. The influence of these spiked precursors on the working and setting properties (slump flow test and ultrasonic velocity measurement) and high temperature behavior (wedge splitting test) of the monolithics was systematically investigated.

Further thermomechanical investigations are the content of "Part II: Influence on thermomechanical behavior" of this research topic [3].

## EXPERIMENTAL SETUP AND SAMPLE TREATMENT

### Spiked alumina raw materials (precursors)

Refractory materials consist of a large range of particle sizes. Impurities are being enriched in the fine (matrix) fractions. The matrix behaves differently compared to the coarse-grain fraction and the matrix mainly controls the properties of a high performing refractory material what is especially critical for monolithics where the proportion of matrix is higher compared to shapes materials as reported by Samanta et. al. [4]. Therefore, a matrix component material was selected as basis material to be spiked with impurities. A tabular alumina in the matrix fraction of 0-45 µm ($d_{50}$ = 10 µm) was finally chosen, which is a typical open fine grain fraction in the matrix composition. The spiked materials (precursors) consist of 98 wt% alumina (0-45 µm fraction) and 2 wt% of impure material and were completely tailored in terms of the amount and type of the introduced impurities. Na, Ti, Si, Ca, and Fe were identified as common impurities. They were therefore selected for the present investigation based on their importance and relevance to the research objective.

The presence of impurities in the matrix increases the amount of the liquid phase. FactSage® was used to determine the critical concentration and mixing ratios of the oxidic components of the before mentioned elements using ternary or four component systems with alumina as the main component. The calculation was used to find the ratio where the highest amount of liquid phase will be formed when the temperature is above 1600 °C as the sintering temperature of the precursors was set to 1600 °C to simulate an application temperature to ensure the relevant phase transformations comparable to secondary raw materials. The final precursor formulations and measured $d_{50}$ values of the spiked materials thereof are listed in Tab. 1.

Tab. 1: Calculated composition (highest amount of liquid phase at 1600 °C) of selected five precursors; 98 wt% $Al_2O_3$ and 2 wt% in total of two or three of the oxides of the selected impurities ($Na_2O$, $TiO_2$, $SiO_2$, CaO and $Fe_2O_3$) and their $d_{50}$ values measured by laser granulometry.

| Component | wt% | | | | |
|---|---|---|---|---|---|
| | 2CS | 2NS | 2FC | 2FCS | 2TCS |
| $Al_2O_3$ | 98 | 98 | 98 | 98 | 98 |
| CaO | 1.0 | - | 0.7 | 0.7 | 0.9 |
| $SiO_2$ | 1.0 | 1.6 | - | 0.3 | 0.8 |
| $Na_2O$ | - | 0.4 | - | - | - |
| $Fe_2O_3$ | - | - | 1.3 | 1.0 | - |
| $TiO_2$ | - | - | - | - | 0.3 |
| *Sum* | *100* | *100* | *100* | *100* | *100* |
| $d_{50}$ in µm | 14.88 | 18.87 | 22.03 | 18.64 | 17.77 |

### Castable design

The reference monolithic material (MHA-REF) chosen is a self-flowing, cement-free (hydratable alumina bonded – Alphabond 300), high alumina castable with a maximum grain size of 3 mm. The formulation contains different types of alumina raw materials supplied by Almatis GmbH, Germany. Using the prepared precursors (Tab. 1), five corresponding spiked model castables were developed by substituting the 0-45 mm pure tabular alumina grain fraction 1:1 with one of the precursors (Tab. 2). Calculated on the basis of the composition the resulting amount of impurities brought in the castable by the precursor is 0.18 wt%. All castables were mixed in an intensive mixer with the same water and dispersing agent content.

Tab. 2: Recipes of the reference castable MHA-REF and the impure formulations MHA-2CS, MHA-2NS, MHA-2FC, MHA-2FCS and MHA-2TCS, where the TA fraction 0-45 µm has been replaced by the precursors 2CS, 2NS, 2FC, 2FCS and 2TCS.

| Component | MHA-REF | MHA-* |
|---|---|---|
| | wt% | wt% |
| Tabular alumina (T60/64) 0.2-3 mm | 57 | 57 |
| 0-0.2 mm | 12 | 12 |
| 0-45 mm | 9 | - |
| Precursor (*2CS, 2NS, 2FC, 2FCS or 2TCS) 0-45 mm | - | 9 |
| Calcined alumina (CTC20) | 10 | 10 |
| Reactive alumina (RG4000) | 7 | 7 |
| Alphabond 300 | 5 | 5 |
| *Sum* | *100* | *100* |
| Water | 6.3 | 6.3 |
| Disp. agent PCE (Castament FS60) | 0.15 | 0.15 |

### Analysis of working and setting properties

The rheological properties of the resulting self-flowing castables were analyzed using the slump flow test. The use of a digital camera during the measurement allows a time dependent (10 min) investigation of the traditional slump flow test setup based on ISO 1927-4 as reported by L. Klein and O. Krause [5].

The time-dependent curing and setting behavior of the different refractory castables was investigated using ultrasonic velocity measurements according to the IP8-measuring system of the company UltraTest GmbH - Dr. Steinkamp & Büssenschütt, Germany. Curing conditions were 20 °C and 95 % relative humidity for 48 hours.

### Analysis of high temperature fracture behavior

The wedge splitting test (WST) was used to monitor and quantify the stable fracture process of test specimens to assess the ability of the castable to resist damage acc. to the description by Brochen et.al. [6]. 1000 °C and 1250 °C were identified as the temperatures of interest for the comparison of the materials investigated, as a drastic change in the energy required to fracture this cement-free high alumina castable is assessed between 1000 °C and 1250 °C.

## RESULTS AND DISCUSSION

The rheological investigations showed a correlation between the end of flow (stoppage time) and the slump flow diameter, confirming that lower viscose mixtures show a higher flow rate if the PSD is properly adjusted. There was only one exception. Mixture MHA-2FC had the smallest final spread but took almost the longest. This is probably due to the highest $d_{50}$ value of the corresponding precursor 2FC (Tab. 1). The setting and curing behavior measured by ultrasonic velocity is comparable for all castables and has no technological influence on the preparation of the castable. These results confirm the assumption that the ions are no longer water-soluble and are already bound by the sintering process of the precursors at 1600 °C. On the other hand, the addition of impurities to the castables leads almost systematically to a deterioration in their high temperature mechanical properties and a reduction in their damage tolerance (ductility). A notable exception is the combination of Fe and Ca (MHA-2FC), which appears to toughen the material and increase its ductility. From the FactSage® calculations a correlation with the expected formation of the lowest liquid phase content at the test temperature of 1250 °C can be seen.

## CONCLUSIONS

In the present work no significant effects of the systematically spiked raw materials on the working properties and curing of the investigated refractory castables were found. Due to the sintering of the precursors at 1600 °C, all ions are bound and are no longer water-soluble and therefore have no influence on the flow and setting properties of the castables. The slight variations observed are most likely due to the different particle size distributions of the precursors which in turn have a significant influence on the flow behavior, as can be clearly seen in the case of MHA-2FC. Nevertheless, the workability and setting behavior were comparable to the pure high alumina reference material.

The situation was different for the high temperature fracture behavior where the addition of the precursors reduced the mechanical properties and decreased the ductility of the material, as emphasized by the results of the wedge splitting tests. The only exception was the material containing the precursor with Fe and Ca (MHA-2FC), which formed the least amount of liquid phase at the temperature investigated and therefore toughened the material. From the results it will be possible to obtain an indication of the mutual proportions of impurities for which the deterioration of the high temperature fracture behavior will not be critical.

## REFERENCES

[1] Alex, J.; Vandeperre, L.; Touzo, B.; Parr, C.; Lee, W. E.: Effect of Sodium on Microstructures and Thermoelastic Properties of Calcium Aluminate Cement–Bonded Refractories. J. American Ceramic Society 99 (3), (2016), p. 1079–1085.

[2] Möhmel, S.; Weissenbacher, M.; Kurz, B., Joubert, O.: The influence of different raw materials on the behaviour of low cement castables. Proc. UNITECR 2015, Wien (2015).

[3] Podwórny, J.; Dudek, K.; Kujawa, M.; Kusiorowski, R.: Investigation of the role of impurities typical in secondary raw materials on the behaviour of high alumina castables - part II: Influence on thermomechanical behaviour. Proc. UNITECR 2023, Frankfurt (2023).

[4] Samanta, A. K.; Sathpathy, S.; Arimitsu, E.; Tsuyuguchi, K.; Panda, P. B.; Shankha Chatterjee: The Role of Matrix Aluminas on the Properties of High Performing Refractory Castables. Proc. UNITECR 2017, Santiago de Chile (2017).

[5] Klein L, Krause O.: Automatic Image Analysis of the Slump Flow and Comparison to Rheometrical Measurements with the Ball Measuring System. 59th International Colloquium on Refractories 2016, Aachen (2016).

[6] Brochen, E.; Dannert, C.; Holleyn, F.; Krause, O.; Rathaj, M., Podwórny, J.; Dudek, K.: Matrix design in high alumina refractory castables – Part II: Assessment of the brittle-ductile transition temperature and ways to influence it. Proc. UNITECR 2019, Yokohama (2019).

# INVESTIGATION OF THE ROLE OF IMPURITIES TYPICAL IN SECONDARY RAW MATERIALS ON THE BEHAVIOUR OF HIGH ALUMINA CASTABLES – PART II: INFLUENCE ON THERMOMECHANICAL BEHAVIOUR

*Jacek Podwórny. Karolina Dudek. Magdalena Kujawa. Robert Kusiorowski*
Łukasiewicz-Institute of Ceramics and Building Materials. Refractory Materials Center. Gliwice. Poland


*Erwan Brochen. Christian Dannert*
Forschungsgemeinschaft Feuerfest e. V. at the European Centre for Refractories. Höhr-Grenzhausen. Germany


*Olaf Krause. Laura Erbar. Katharina Sarnow*
Hochschule Koblenz. Höhr-Grenzhausen. Germany

## ABSTRACT
The present work investigated the effect of relatively small additions of impurities originating in secondary raw materials on the thermomechanical properties of alumina castables bonded with active alumina. Castable compositions containing impurities for testing were selected on the basis of predictions from thermochemical calculations of their phase composition and the formation of large amounts of liquid phase at the temperature of 1600 °C. Viscosity of the emerging liquid phase was also calculated. The selected alumina castables with impurities from the systems: $CaO$-$SiO_2$. $Na_2O$-$SiO_2$. $Fe_2O_3$-$CaO$. $Fe_2O_3$-$CaO$-$SiO_2$ and $TiO_2$-$CaO$-$SiO_2$ were tested for thermomechanical properties by analysing the effect of impurities on refractoriness under load (RUL) creep in compression (CiC) and resonant frequencies and damping changes versus temperature (RFDA). Real composition of tested material via high temperature X-ray diffraction (HT-XRD) were verified. The obtained results indicate that impurities introduced into the refractory castables in a total amount of 0,18 wt.% (2 % in the fraction 0-45 µm) and in the most unfavourable ratio from the point of view of phase equilibria have an observable effect on the properties of the material at elevated temperature. The obtained results show that in the case of introducing impurities into the material with mutual proportions of shares limiting the formation of the liquid phase. It will be possible to maintain the thermomechanical properties of alumina castables at a satisfactory level (compared to the pure one) from the industrial process perspective in which it will be used. The obtained results shed new light on the possibilities of the conscious use of secondary raw materials in refractory monolithics technology.

## INTRODUCTION
Due to the depletion of natural resources and an overall endeavour to manage natural resources sustainably, there is a need to increasingly use recycled materials. In the case of refractory materials, which are used in various industries, the reuse of refractory materials after decommissioning of worn refractory linings as secondary raw materials is not easy. Refractory producers face a classic and basic dilemma to have to select between high purity, usually more expensive and less available raw materials that are expected to promote high temperature performance, or lower grad, less expensive raw materials, including secondary sources (i.e. recycled materials) but deem to lead to lower refractoriness. More broadly, refractory producers need reliable data on the influence of impurities on the high temperature performance of refractory products in order to develop formulations suitable for specific applications with targeted refractoriness and tailored admissible level of impurities, and hence promote the use of recycled raw materials.

On the whole, refractory industry need to better understand of how critical impurities (in terms of nature and concentration) affect the thermomechanical stability at high temperature, and of how and when a certain level of impurities will lead to malfunctions of the refractories in use.

The aim of this work was therefore twofold. To determine how critical impurities (in terms of nature, concentration and interaction) affect the high temperature performance of refractories and to better understand the high temperature performance of refractories.

## TESTED MATERIALS
For the needs of the project, synthetic materials (precursors) imitating secondary raw materials with compositions, or more precisely, mutual proportions of impurity oxides were produced and sintered at 1600 °C. The compositions of the precursors were chosen regarding their most , the most unfavourable from the point of view of the temperature of formation of the liquid phase in the material, its quantity and viscosity.

The selection of these compositions was based on thermochemical calculations in the equilibrium state using FactSage program. Based on these calculations, 5 precursors were prepared (compositions listed in table 2), which were then introduced into the reference material MHA-REF (chemical composition present Table 1). The matrix fraction 0-45 µm (tabular alumina) with the amount of 9 wt.% was substituted 1:1 by the precursor material. The sum of impurity oxides in these spiked alumina's was 2 wt.% and resulted in 0.18 wt.% relative to the whole castable formulation. The castable design is described more detail in the Part I paper of the research topic. The phase compositions of the reference material and the precursors measured by X-ray diffractometry are presented in table 3.

*Tab. 1: Chemical composition of reference material MHA-REF.*

| LoI | [%] | 0.80 |
|---|---|---|
| $SiO_2$ | [%] | 0.02 |
| $Al_2O_3$ | [%] | 98.59 |
| $Fe_2O_3$ | [%] | 0.04 |
| $TiO_2$ | [%] | < 0.01 |
| MnO | [%] | 0.01 |
| CaO | [%] | 0.04 |
| MgO | [%] | 0.02 |
| $Na_2O$ | [%] | 0.21 |
| $K_2O$ | [%] | < 0.01 |
| $P_2O_5$ | [%] | < 0.01 |
| SUM | [%] | 99.74 |

*Tab. 2:* Composition of precursors with impurities.

| Identification | CaO | $Na_2O$ | $SiO_2$ | $Fe_2O_3$ | $TiO_2$ | $Al_2O_3$ (198 43 µm) |
|---|---|---|---|---|---|---|
| 2CS | 1 | - | 1 | - | - | 98 |
| 2NS | - | 0.4 | 1.6 | - | - | 98 |
| 2FC | 0.7 | - | - | 1.3 | - | 98 |
| 2FSC | 0.7 | - | 0.3 | 1.0 | - | 98 |
| 2TSC | 0.9 | - | 0.8 | - | 0.3 | 98 |

*Tab. 3: Phase compositions of the reference material and the 5 precursors (XRD).*

| MHA-REF | $Al_2O_3$ (corundum), $\beta$-$Al_2O_3$, amorphous $Al_2O_3$ |
|---|---|
| 2CS | $Al_2O_3$ (corundum), $\beta$-$Al_2O_3$, $CaAl_{12}O_{19}$ (hibonite), $NaAlSiO_4$ (nepheline) |
| 2NS | $Al_2O_3$ (corundum), $\beta$-$Al_2O_3$, $NaAlSiO_4$ (nepheline), $NaAlSiO_4$ |
| 2FC | $Al_2O_3$ (corundum), $\beta$-$Al_2O_3$, $CaAl_{12}O_{19}$ (hibonite) |
| 2FCS | $Al_2O_3$ (corundum), $\beta$-$Al_2O_3$, $CaAl_{12}O_{19}$ (hibonite), $NaAlSiO_4$ (nepheline) |
| 2TCS | $Al_2O_3$ (corundum), $CaAl_{12}O_{19}$ (hibonite), $NaAlSiO_4$ (nepheline), $CaTiO_3$ (perovskite) |

## TESTING METHODS

### Refractoriness under Load (RuL) and Creep in Compression (CiC)

The high temperature performance of refractory products is basically assessed using the testing standards EN ISO 1893: Determination of refractoriness under load, and EN 993 - 9: Determination of creep in compression. Both testing standards are carried out with the same testing equipment and similar testing procedure. A cylindrical refractory sample is subjected to a constant load (0,2 MPa) while increasing the temperature (5 °C.min$^{-1}$) in air. The deformation (height) of the sample is recorded continuously, usually with the differential method. For the determination of refractoriness under load (RuL), the test is stopped once a prescribed deformation is attained, typically 5% of its initial length ($T_{0.5}$). For the determination of creep in compression (CiC), once a specified temperature of the sample has been reached, the temperature is maintained constant for a given time. The deformation of the sample at this constant temperature over time is then recorded. In both tests, temperatures corresponding to a characteristic degree of deformation are identified from the deformation against temperature/time curves.

In the present study, the testing conditions specified in the standards were extended. Variable load conditions were selected and applied on cylinders ($\phi$35 x 50 mm) with an axial hole of $\phi$12 mm. The measurements were performed in a NETZSCH 421 device heated by an electric furnace. For CiC measurements, the test pieces were heated to $T_{0.5}$ - 100 °C, $T_{0.5}$ °C, $T_{0.5}$ + 100 °C at a rate of 5 K/min and three different loading forces (0.2, 0.8 and 1.2 MPa).

### Resonant Frequencies and Damping Analysis (RFDA)

The Impulse Excitation Technique (IET) was used for the non-destructive determination of the elastic properties. The Young's modulus was determined dynamically by resonance frequency and damping analysis according to ASTM E1876-15, ISO 12680-1, EN 843-2. This method allows the frequency and damping parameters of the vibration to be determined. Damping represents the absorption and dissipation of energy by the material. Here, the relationship between the change in modulus of elasticity in a temperature range depending on their refractoriness under load, based on the criterion $T_{0,5}$ - 100 °C, has been determined.

The dimensions of the specimens were 25 x 35 x 150 mm, the heating and cooling rate was set at 3 K/min and the specimens were soaked at the maximum temperature for 2 hours to achieve an equilibrium state in the material at the temperature T0.5 - 100 °C. Each test was repeated twice.

### Fracture energy

The fracture energy was measured using the three-point bending method up to high temperature (Hot Modulus of Rupture / Netzsch HMOR422) for prismatic test pieces (25 x 25 x 150 mm) with a notch depth of 7 mm and a 0.5 mm width and a loading rate of 20 µm/min. The system's deformation was corrected for all measurements.

### Creep in Compression (CiC) based on the Norton-Bailey concept

The CiC was measured under variable load conditions in a NETZSCH 421 device heated with by an electric furnace.

The test pieces were prepared in the shape of a cylinder of dimensions $\phi$35 x 50 mm with an axial hole with a diameter of $\phi$12 mm. The test pieces were heated to $T_{0.5}$ - 100 °C,. $T_{0.5}$ °C,. $T_{0.5}$ + 100 °C at a rate of 5 °C/min and three different loading forces (0.2, 0.8 and 1.2 MPa).

### Scanning electron microscopy (SEM/EDS)

Microstructure analysis was performed using a TESCAN Mira 3 LMU electron microscope equipped with an Energy Dispersive Spectrometer (EDS) from Oxford Instruments. Images were collected using secondary electron (SE) and backscattered electron (BSE) detectors. The measurements were carried out on the samples coated with a 5 nm of Cr layer using a Quorum Q150T instrument.

### RESULTS AND DISCUSSION

The temperature of the appearance of the first drop of the liquid phase for the investigated materials as well as the amount and viscosity of the melt in the temperature range 1200 to 1300 °C are given in Table 4. The formation of the liquid phase is one of the reasons for the reduction of the refractoriness under the load, and especially $T_{0.5}$, of the investigated materials. It was found that during the first test all materials displayed significantly reduced refractoriness under load (Table 5) compared to corundum castables, even the reference material which contained no impurities (fluxes) and consisted mainly of alumina (Table 1). The repetition of the RuL measurements on the same test pieces showed that the refractoriness under load, in each case, increased by up to several hundred degrees after the second heating (table 5 and figure 1). This indicates that the amount of the liquid phase is not the only and the main factor influencing the thermomechanical properties of these materials. Reactive alumina and its sinterability play an equally important role in this type of material.

Studies of the microstructure of the samples show that in order to give the material high refractoriness, a bonded microstructure and growth of alumina grains in the matrix must occur (Figure 2). Loading the test piece which contain reactive alumina with 0.2 MPa (standard RuL tests) during the formation of the appropriate microstructure in the castable is destructive to the material, and the liquid phase appearing in the system at a certain temperature further affects the deterioration of thermomechanical properties. The influence of the phenomenon of the formation of the material microstructure during the first firing is also evident in other studies of the thermomechanical properties [1]. Figure 3 shows an example of the temperature dependence of the changes in the flexural vibration frequency and damping of the MHA-2TCS material during heating and cooling to the temperature $T_{0,5}$ -100 °C. The observed changes with temperature, particularly visible in the damping values, are most likely the result of changes occurring in the microstructure of the material: sintering, crystal growth, melting and crystallisation from the liquid phase, opening and closing of microcracks. Different mechanisms of cracking during this process are illustrated in figure 4. Table 6 shows the changes in the Young's modulus obtained in the RFDA test performed to the temperature $T_{0.5}$ -100 °C. The results also show that only the MHA-REF had a higher Young's modulus after the test than at the beginning. It decreased for the spiked materials. It was also found that spiked materials had a twice as high Young's modulus after setting and drying, proving that impurities introduced into the material also play a role in the setting process of the castables.

The results of the determination of the fracture energy obtained by the three-point bending method show that all the spiked materials have inferior properties compared to the reference material at the temperature of $T_{0.5}$ (figure 5). Below this temperature, the composition of the impurities may lead to improvement of the thermomechanical properties. Taking into account that

unfavourable combinations of compositions of impurities were introduced into the tested materials in order to produce as much of the liquid phase as possible at high temperature (eutectic compositions), it is possible, that by moving the composition away from the eutectic, the detrimental effects of impurities near the working temperature will be much more limited.

Tab. 4: The temperature of the appearance of the liquid phase in individual systems and its amount and viscosity.

| | First drop of liquid phase, ºC | Amount of liquid phase, g | Viscosity of liquid phase | | |
|---|---|---|---|---|---|
| | | 1250 °C | 1200 °C | 1250 °C | 1300 °C |
| MHA-REF | 1249 | 0.1 | - | 3.1 | 1.6 |
| MHA-2CS | 1087 | 1.6 | 93.8 | 35.7 | 15.5 |
| MHA-2NS | 920 | 3.2 | 48879 | 13595 | 4917 |
| MHA-2FC | 1217 | 0.2 | 1.9 | 0.3 | 0.2 |
| MHA-2FCS | 1087 | 1.6 | 53.4 | 2.1 | 0.7 |
| MHA-2TCS | 1082 | 2.0 | 50.3 | 16.1 | 6.7 |

Tab. 5: Refractoriness under load after the first and the second heating of the same samples.

| | $T_{0.5}$ °C First run | $T_{0.5}$ °C Second run |
|---|---|---|
| MHA-REF | **1410** | **>1700** |
| MHA-2CS | 1360 | 1390 |
| MHA-2NS | 1360 | 1630 |
| MHA-2FC | 1420 | >1700 |
| MHA-2FCS | 1360 | 1600 |
| MHA-2TCS | 1370 | 1630 |
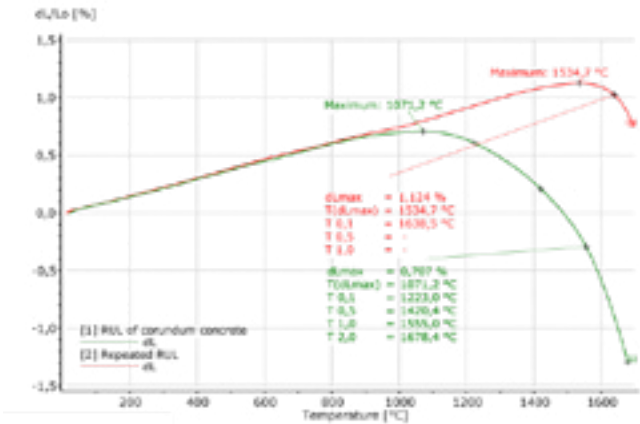


Fig. 1: Refractoriness under load after the first and the second heating of the same samples; as an example: reference material MHA-REF.
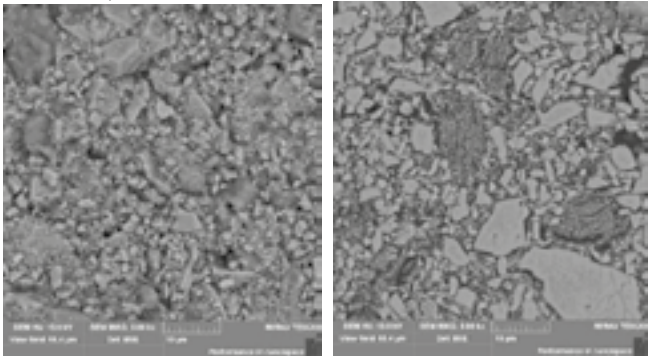


Fig. 2: Microstructure of the reference material with active alumina in the matrix after drying at 100 °C (left) and bonded microstructure after sintering at 1420 °C (right). Alumina grain growth is clearly visible.
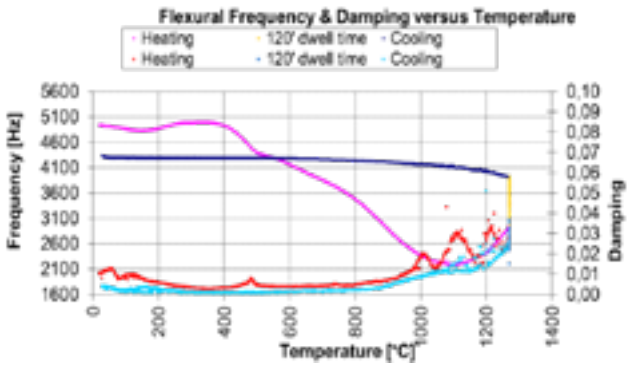


Fig. 3: Temperature dependence of the frequency of flexural vibrations and damping of the MHA-2TCS material.
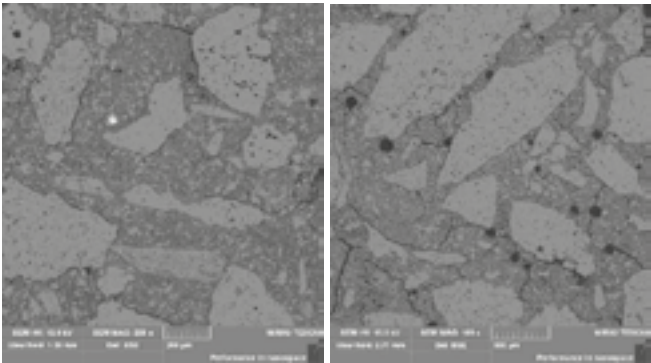


Fig. 4: Different mechanisms of microcrack formation in MHA-2FCS material with dominant cracks around the coarse alumina grains at the matrix boundary (left) and MHA-REF material with dominant cracks in the matrix (right).

Tab. 6: Changes in the Young's modulus measured by RFDA after heating and cooling to the temperature $T_{0.5}$ -100 °C and the results of a subjective description of the micro-cracks formed at the testing conditions.

| | E modulus in GPa before test | E modulus in GPa after $T_{0.5}$ -100 °C | SEM microcracks observation | |
|---|---|---|---|---|
| | | | Before test | After RFDA |
| MHA-REF | 32 | 40 | Invisible | Numerous. mostly on the grain/matrix border |
| MHA-2CS | 62 | 53 | Numerous. at the grain/matrix interface and through the matrix itself. of various lengths | Single long at the grain/matrix interface and single shorter through the matrix itself |
| MHA-2NS | 74 | 53 | Numerous. at the grain/matrix interface and through the matrix itself. of various lengths | Very numerous. on the grain/matrix border and through the matrix itself |
| MHA-2FC | 74 | 67 | Numerous. at the grain/matrix interface and through the matrix itself. of various lengths | Very numerous. at the grain/matrix interface and through the matrix itself. often through numerous spherical pores |
| MHA-2FCS | 74 | 53 | Single. short | Moderately numerous. mainly at the grain/matrix interface and also visible through the grains themselves |
| MHA-2TCS | 74 | 53 | Numerous. at the grain/matrix interface and through the matrix itself. of various lengths | Numerous. mainly through the matrix. sporadically at the grain/matrix boundary |
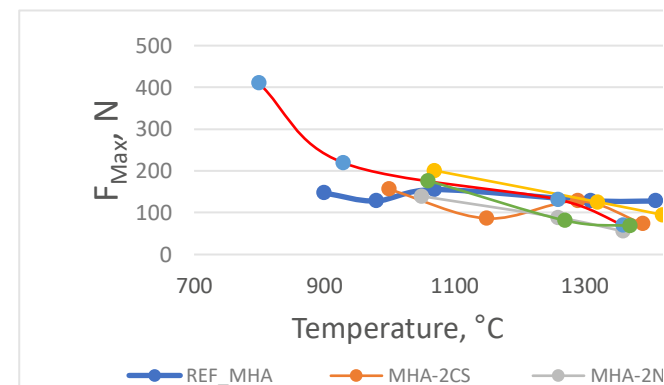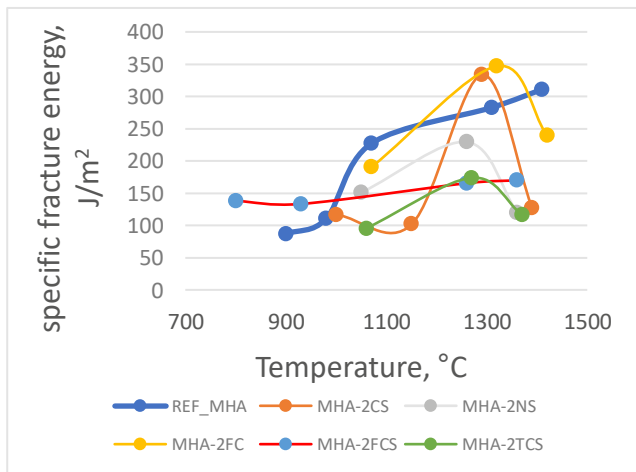
Fig. 5: Evolution of the specific fracture energy and bending force before fracture as a function of the temperature (the maximum temperature corresponds to $T_{0.5}$ for each material).

Creep rate was also measured using a newly developed method based on the Norton-Bailey concept and works [2, 3] to identify the different stages of creep. The first two stages of creep described by the Norton-Bailey theory were identified in these studies. Despite the application of the maximum load allowed by the capabilities of the testing equipment, i.e. 1.2 MPa, the third stage of creep of the tested materials leading to their destruction was not observed (figure 6). In some cases, when using a heavy load at T0.5 and T0.5 +100 °C, the tests had to be stopped due to excessive strain beyond the measuring range of the device (figure 7). The fact that the material has not failed up to this point is indicative of the extensive thermoplastic properties of the material and is the most likely explanation for the lack of a failure step for the material subjected to mechanical stress.
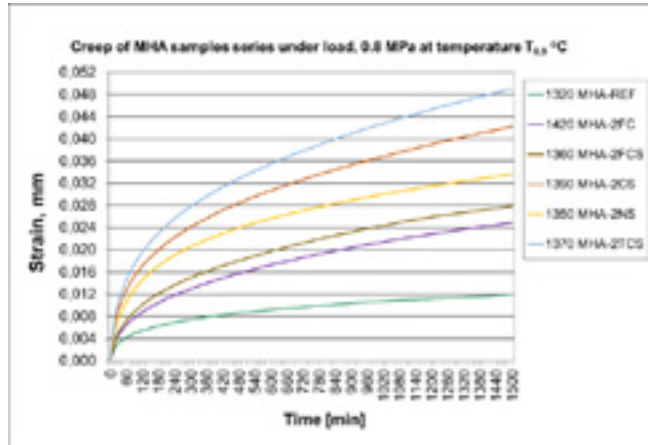


Fig. 6: Creep rate of MHA castables under load, 0.8 MPa at a temperature of $T_{0.5}$.
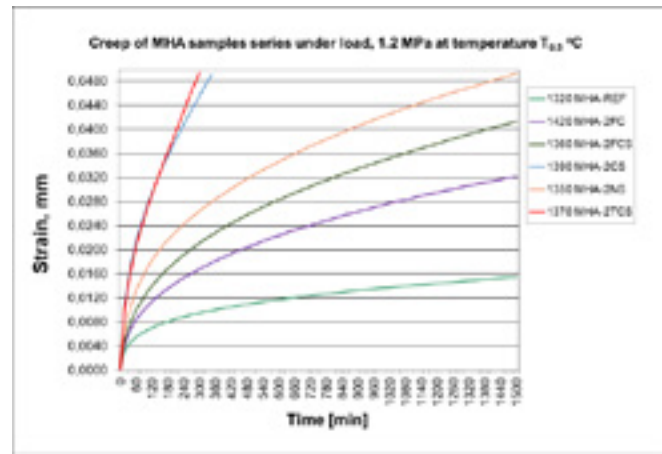


Fig. 7: Creep rate of MHA castables under load, 1.2 MPa at a temperature of $T_{0.5}$.

## CONCLUSIONS

The introduced impurities affect the mechanics of cracking and facilitate the sintering of the tested materials at low temperature by forming of small amounts of liquid phase. This also affects the thermomechanical properties of the tested materials.

However, the active alumina binder plays an important role in the sintering process allowing the material to sinter at low temperatures. This has an impact on the sintering process of the alumina castables tested. The material is in a viscoplastic state during the sintering process.

The conclusion from these studies is that processes such as grain growth in the material matrix and the formation of ceramic bonds, which increase the thermomechanical strength of the tested materials, do not keep up with the effects caused by the applied load. This is a valuable clue that materials of this type, i.e. on active bonding with alumina, should not be use in those applications where there is a high mechanical load during initial heating.

The combination of impurities selected in these studies represent the most unfavorable cases in terms of thermomechanical properties due to liquid phase formation. However, the obtained results show that it should be possible to deduce mutual proportions of impurities for which the deterioration of thermomechanical properties should not be critical.

## ACKNOWLEDGEMENTS

## REFERENCES

[1]   Luza A. P , Gomesb D. T, Pandolfellia V. C. Maximum working temperature of refractory castables: do we really know how to evaluate it? Ceramics International 43(12), (2017), p. 9077–9083, DOI: 10.1016/j.ceramint.2017.04.053

[1]   Jin S, Harmuth H, Gruber D. Compressive creep testing of refractories at elevated loads—Device, material law and evaluation techniques. Journal of the European Ceramic Society, 34(15), (2014), p. 4037–4042, DOI: 10.1016/j.jeurceramsoc.2014.05.034

[3]    Samadi S, Jin S, Gruber D, Harmuth H, Schachner S. Statistical study of compressive creep parameters of an alumina spinel refractory. Ceramics International 46(10), 2020, p. 14662-14668, DOI: 10.1016/j.ceramint.2020.02.267

85

# THE PROPERTIES OF MGO–C REFRACTORIES WITH A NEW RECYCLED MGO–C RAW MATERIAL

Tae hwa Lee*, In kyung Bae, Yong moon Cho

Refractory solution group, Basic material Research center, POSCOFUTUREM

110, Sinhang-ro, Nam-gu, Pohang-si, Gyeongsangbuk-do, Republic of Korea

## ABSTRACT

Recently, one of the main topics in refractory research is eenvironmental issues related to waste treatment and resource recycling, as is research in other industries. Especially, much interest have focused on the recycling of MgO-C refractories. It can be used as raw materials for refractories according to processing methods, and their use is expanding. In the case of the MgO-C refractory spent, the remaining Al and C must be treated for recycling. Al remaining during the reuse process causes structural collapse due to hydration and C weakens the bond of refractories.

In this study, the properties of MgO-C refractories with a new recycled MgO-C raw material which shows better MgO purity and physical properties compared to the existing recycled raw material were investigated. From this research, we could obtain a high-quality MgO-C refractories with same or similar corrosion resistance and structural spalling resistance. In addition, by applying the recycled MgO-C as a raw material in the MgO-C refractory, it was possible to achieve the effect of reducing manufacturing costs and virtuous cycle of resources at the same time.

## INTRODUCTION

In steelmaking processes, such as the blast furnace, electric furnace, and ladle, high refractoriness is required, leading to the predominant use of MgO-C refractory materials as the lining bricks. However, over time, the surface of these refractory bricks gets eroded and the residual amount decreases, resulting in a loss of their refractory function. As a result, after a certain number of uses, the bricks need to be replaced with new ones, thereby generating a significant amount of waste refractory materials, which poses environmental issues.[1][2] Many refractory companies are making efforts to reuse waste refractory materials. To minimize waste, recycling waste refractory materials is the most appropriate approach. However, when using MgO-C refractory materials without pre-treatment, issues such as cracking and damage occur during refractory manufacturing. This limits the amount of material that can be effectively recycled, resulting in only a small quantity being reused, while the rest finds other applications. For instance, waste refractory materials have been incorporated into slag in steelmaking processes or included in the non-standard composition of repair and reuse materials for refractory linings. However, such usage is inherently limited, and there is still a need for separate investment to manufacture new refractory bricks using fresh raw materials. Waste MgO-C refractory can be produced as a raw material by supplying high-temperature steam. The residual Al and $Al_4C_3$ within the refractory materials are stabilized as $Al_2O_3$ under high-temperature steam conditions, preventing structural collapse when reusing them as refractory material. The treatment with steam preserves the form of the refractory product.[3] This indicates that areas where small-sized raw materials or carbon materials are agglomerated remain intact, which can lead to a decrease in the density and strength of the final product. Additionally, residual Al and $Al_4C_3$ that have not fully reacted through steam treatment can result in weakened bonding strength during subsequent refractory manufacturing. These issues contribute to the limited usage quantity of regenerated materials produced through steam treatment. To address the issues with steam-treated waste MgO-C regenerated materials, it is possible to remove carbon and unstable metallic components. This removal ensures that the raw materials do not cause cracking and structural collapse during MgO-C refractory manufacturing and usage. Regenerated materials produced through this method exhibit chemical stability, but they suffer from the problem of non-uniform density and chemical composition among individual particles. The inclusion of a matrix in aggregate materials, leads to a reduced density and MgO purity compared to MgO clinkers. Such non-uniformity among different raw materials becomes a contributing factor to the degradation in quality of refractories where regenerated materials are used.

In this study, carbon and metal oxides were removed from the MgO-C refractory, resulting in the production of regenerated material similar to new MgO feedstock. This regenerated material maintains high purity and density, ensuring no degradation in the quality of the refractory. As a result, the use of regenerated materials in refractories is increased while achieving comparable performance to that of fresh MgO-C refractories in actual furnace applications.

## EXPERIMENT

### Experimental procedure

Characteristics of the raw materials for MgO-C refractories manufacturing are as follows:

- Fused Magnesia MgO 97.5%(FM) in the grain size fractions 0–1, 1–3, and 3–5 ㎜

- Graphite, flakes, ≥98% carbon basis

- Alumium powder, ≥99%

- Phenilic Resin (Resol)

- MgO-C recycled Materials (RA, RB1, and RB2 in the fractions 0-4 ㎜)

Phenolic resin was utilized as a binder in this study. The Fused Magnesia(FM) and Recycled materials(RA, RB1 and RB2) can be seen in *Fig. 1*. The recovered MgO-C is crushed and processed to create refractory raw materials(*Fig. 2*).[4] RA is produced through a high-temperature steam treatment process. During this process, the Al and $Al_4C_3$ present inside the raw materials are converted to $Al_2O_3$. Manufactured through the process, RB1 and RB2 do not contain carbon components. *Fig. 3* presents microscopic images of the produced raw materials. Each sample was embedded in epoxy resin, polished, and observed under a JSM-7610F scanning electron microscope. The chemical compositions of the FM and three recycled products were measured using S8 TIGER(Bruker). The density of the materials was measured according to Archimedes' principle, and the apparent porosity values were obtained using the same measurement method. Table. 1 presents the measured values for the characteristics of the raw materials. RA, as shown in Fig. 3, has a similar structure to refractory materials, with fines and graphite adhered to large aggregate particles.[5] The binder that existed between the raw materials is lost, and $Al_4C_3$ is converted to $Al_2O_3$, resulting in a decreased bond strength in the matrix portion. RB1 forms porosity by removing graphite in the fines and contains
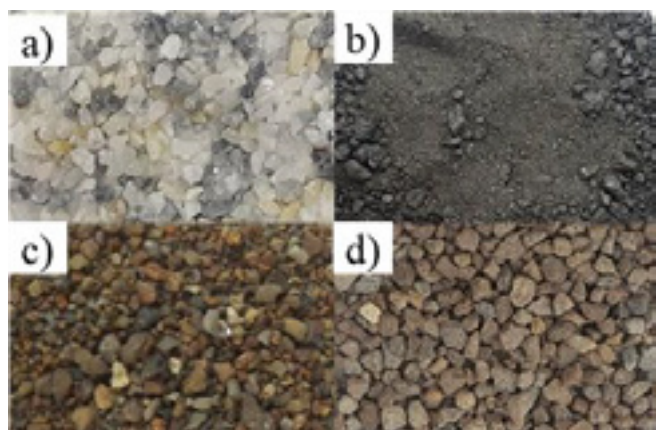
*Fig. 1: The appearance of the raw materials a) FM  b) RA  c) RB1 d) RB2*
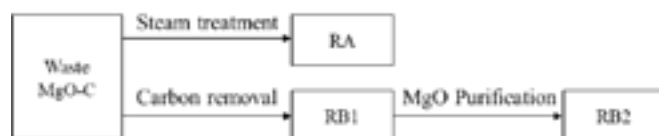


*Fig. 2: A manufacturing process for recycled raw materials utilizing spent MgO-C refractories*

Al$_2$O$_3$ and SiO$_2$ derived from the antioxidant. RB2 has minimal fines and is primarily composed of aggregates.
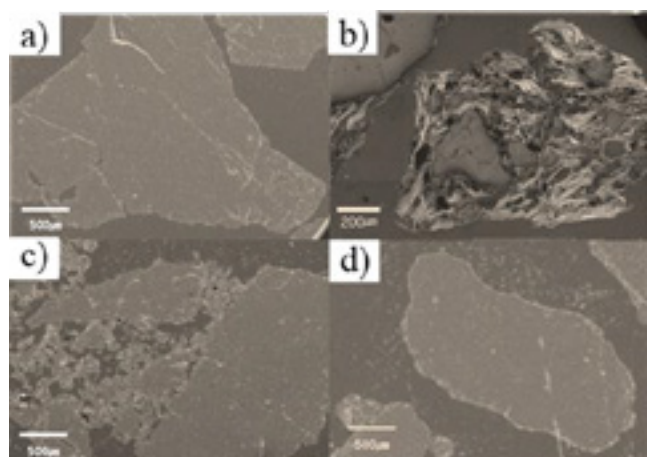


*Fig. 3: The microscopic images of the produced raw materials. a) FM  b) RA  c) RB1  d) RB2*

Tab. 1: The measured values for the characteristics of the raw material

| | Density (g/m³) | Porosity (%) | Chemical composition (%) | | | |
|---|---|---|---|---|---|---|
| | | | MgO | Al₂O₃ | SiO₂ | TC |
| FM | 3.46 | 3.2 | 97.5 | 0.2 | 0.4 | - |
| RA | 2.89 | 8.5 | 74.2 | 5.5 | 0.6 | 17.5 |
| RB1 | 3.32 | 5.7 | 93.2 | 2.7 | 1.5 | - |
| RB2 | 3.44 | 2.9 | 96.3 | 1.4 | 0.7 | - |

**Experimental method**

Based on the mixture formula of the MgO-C currently being used, a test blend was designed. Due to the inclusion of graphite in the recycled raw material (RA), the graphite content was adjusted in the mixture formula. The formula for manufacturing bricks, which includes graphite, antioxidants, and binders, can be found in Table. 2.

The raw materials were mixed using a laboratory-scale Irich mixer. Subsequently, they were manufactured by applying uniaxial pressure in a 3200-ton press to obtain specimens with dimensions of 800 x 50 x 50 ㎤. The molded products were subjected to a temperature treatment at 180℃ for 24 hours in ambient air. After curing and after coking, the bulk density of the specimens was determined from the mass and geometric dimensions. The apparent porosity values were also obtained by the last-mentioned measurements. And CCS were conducted by subjecting cubic-shaped specimens to uniaxial pressure.

Tab. 2: Mixture formulations and resulting content of recycled material

| Composition (%) | Desination | | | | | | |
|---|---|---|---|---|---|---|---|
| | A | B-1 | B-2 | C-1 | C-2 | D-1 | D-2 |
| FM | 81 | 74 | 65 | 72 | 62 | 72 | 62 |
| RA | | 10 | 20 | | | | |
| RB1 | | | | 10 | 20 | | |
| RB2 | | | | | | 10 | 20 |
| Graphite | 17 | 15 | 14 | 17 | 17 | 17 | 17 |
| Aluminum | 2 | 2 | 2 | 2 | 2 | 2 | 2 |
| Phenilic Resin | 3.5 | 3.5 | 3.5 | 3.5 | 3.5 | 3.5 | 3.5 |

A specially designed apparatus was devised for the evaluation of corrosion resistance. The specimens were machined into disc shapes and were rotated along the vertical axis, subjected to chemical and physical corrosion by molten slag. After being subjected to an hour-long test at 1650℃ with a C/S ratio of 1 slag, they were subsequently discharged from the rear. This process was repeated 10 times over a duration of 10 hours(*Fig. 4*)
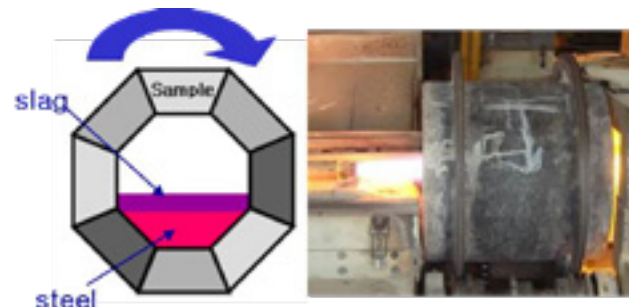


*Fig. 4: Schematic representation of the rotating corrosion test*

**RESULTS AND DISCUSSION**
**Lab test**

Table. 3 shows the properties of MgO-C specimens after curing and coking. An increase in the content of recycled raw materials leads to a decrease in density. This trend is more pronounced in specimens using RA and RB1 compared to RB2.

Tab. 3: The measured values for the mechanical properties after curing(after coking)

| Properties | Desination | | | | | | |
|---|---|---|---|---|---|---|---|
| | A | B-1 | B-2 | C-1 | C-2 | D-1 | D-2 |
| Bulk Density (g/m³) | 2.97 (2.87) | 2.94 (2.83) | 2.92 (2.82) | 2.96 (2.96) | 2.94 (2.83) | 2.96 (2.86) | 2.95 (2.84) |
| Apparent porosity (%) | 1.6 (10.1) | 3.2 (11.0) | 2.0 (11.2) | 1.9 (10.4) | 2.0 (10.7) | 2.8 (10.4) | 2.1 (10.6) |
| CCS (kg/m³) | 544 (305) | 462 (236) | 439 (225) | 508 (246) | 443 (236) | 533 (284) | 470 (254) |

The decrease in density can be attributed to the increase in porosity. Fig.3 shows that both RA and RB1 have a significant amount of porosity within the raw material particles. This high

porosity of these raw materials is maintained in the final product even after the pressing, curing, and coking stages. Unlike sintered refractories, MgO-C refractories primarily utilize FM raw materials, with a low possibility of material consolidation occurring before usage. The utilization of recycled raw materials with high porosity can lead to a decrease in the compressive strength of refractories. [6]

Tab. 4: The measured values for the corrosion rate

| | Desination | | | | | | |
|---|---|---|---|---|---|---|---|
| | A | B-1 | B-2 | C-1 | C-2 | D-1 | D-2 |
| corrosion rate (mm/ch) | 0.79 | 0.88 | 1.01 | 0.84 | 0.88 | 0.81 | 0.80 |
| corrosion rate index | 100 | 112 | 128 | 106 | 111 | 102 | 101 |

The results in Table. 4 demonstrate that the corrosion resistance is enhanced when RB2 is applied compared to RA/RB1. The corrosion on the refractory surface of the furnace occurs due to a combination of chemical and physical factors. RB2, after undergoing a purification process, achieves high purity and can effectively suppress chemical corrosion even under conditions with low alkalinity slag.[7] Additionally, the low porosity and reinforcement of the matrix contribute to increased resistance against mechanical erosion.

**Field test**

*Fig.5* shows the appearance of MgO-C bricks containing RB2 after their use in Ladle equipment. The specimen exhibited similar corrosion resistance to conventional MgO-C bricks. Even when applied to MgO-C refractories containing a low amount of graphite as a raw material, they showed comparable performance to the conventional product. When RB2 was added to MgO-C for RH applications at a 20% level, it was verified that excellent residual performance was achieved with minimal spalling(*Fig.6*).

As described above, it has been confirmed that MgO-C bricks utilizing refined recycled materials can be used for actual furnaces, with the potential for further enhancement of their functionality in the future.
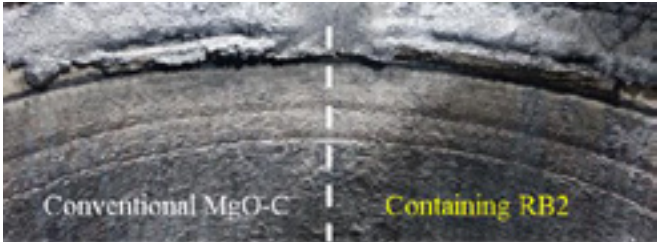


*Fig. 5: The appearance after conducting a performance test of MgO-C bricks containing RB2 in ladle equipment: the boundary between conventional MgO-C bricks and RB2-containing MgO-C bricks*
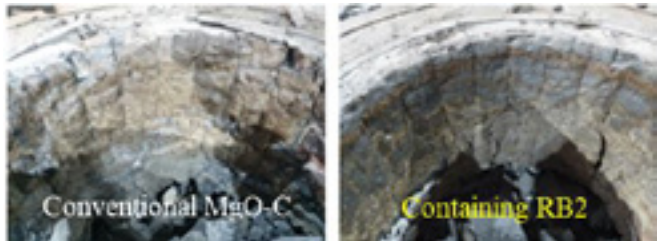


*Fig. 6: The appearance after conducting a performance test of MgO-C bricks containing RB2 in RH*

**CONCLUSIONS**

The differences in processing methods for recycling MgO-C refractory raw materials were investigated, and the resulting substitutions were evaluated. Regenerated materials treated with steam to remove reactivity were found to contain carbon, allowing for a reduction in graphite addition. However, the high porosity of the raw materials affected the final quality. Simply combusting graphite to address this issue resulted in carbon removal but exposed structural weaknesses in the raw material. When using refined raw materials with removed graphite and increased structural and chemical stability, there were no major issues in replacing pure FM. Tests are being conducted to apply a higher content of these materials and improve manufacturing yields.

**REFERENCES**

[1] T. C. Avelar, Recycling practices of crushed MgO-C bricks and dolomite sinter fines used as a slag conditioning additive in the EAF, Waste Management and the Environment 163, 2012, p.25-269

[2] Jei-Pil Wang, Basic Study on the Recycling of a Waste MgO-C Refractory Material as a Flux for EAF Steelmaking. Resources Recycling 30 (6), 2021, p.53-60

[3] Kirsten Moritz, Magnesia-carbon refractories from recycled materials. composites. Ceramic Enginneering & Science 29(3), 2021

[4] Kyei-Sing Kwong and James P. Bennett, RECYCLING PRACTICES OF SPENT MgO-C REFRACTORIES. Journal of Minerals & Materials Characterization & Engineering, 30(6), 2002, p.69-78

[5] Yu Zhang, Junfeng Chen, The microstructure evolution and mechanical properties of MgO-C refractories with recycling Si/SiC solid waste from photovoltaic industry. Ceramics International, 44(14), 2018, p.16435-16442

[6] Siddhartha Nanda, Raw materials, microstructure, and properties of MgO–C refractories: Directions for refractory recipe development. Journal of the European Ceramic Society, 43(1), 2023, p.14-36

[7] Seungwook Lee, The effect of C content in MgO–C on dissolution behavior in CaO–SiO2–Al2O3 slag. Ceramics International, 48(18), 2002, p.26984-26991

# TECHNICAL CHALLENGES FOR RECYCLING PROCESSING AND UTILIZATION RAMP−UP

Matheus, Moraes, Gustavo, Nogueira
RHI Magnesita, Contagem, Brazil

Alexander Leitner
RHI Magnesita, Leoben, Austria

Barbara Zocratto
RHI Magnesita, Rotterdam, Netherlands

## ABSTRACT

Recycling usage can bring several benefits including less dependency of imported raw-materials, cost reduction and proposition of a circular solution for the customers. Nevertheless, the carbon footprint reduction has been the key driver for the utilization ramp-up, fostering technical development of refractories producers and the implementation of a sustainable portfolio for refractory users. This paper presents an overview on the technical challenges currently faced to boost recycling utilization rates, from pre-sorting during dismantling, to refractory classes selection and contaminants removal or stabilization, finally discussing on preparation for product application.

## INTRODUCTION

The contribution of refractory linings to steel and cement carbon footprint is relatively small [1], being most of the efforts of those industries linked to new production processes and carbon capture, utilization and storage – CCUS (scope 1 emissions [2]) [3,4]. Nevertheless, once the novel processes are implemented, scope 3 emissions [2] will represent most of the emissions and refractories would turn into one of the main contributors.

Therefore, some refractory consumers are already demanding products with lower carbon footprint, quantifying its content, with safe application and reduced environmental impact, including waste management.

Recycling is a key strategy to cope with these market demands, ensuring emissions reduction from raw material production and closing the loop of by-products management. The raw material aggregate represents from 70 to 90% of the refractory's $CO_2$ emissions [1]. Additionally, from the refractory producer perspective, it is one of the shortest-term solutions to move ahead with eco-friendly products, once changes in production process and CCUS depends on technologies still under development, solutions for legislation disputes, and a long time frame for implementation [5,6,7].

Table 1 shows the carbon footprint of selected refractory raw materials, representing the potential reduction on emission upon their replacement [8].

Tab. 1: Refractory Raw Materials $CO_2$ Footprint

| Raw Material | Estimated $CO_2$ Footprint (t/t) |
|---|---|
| Dead Burned Magnesia | 1,5 – 1,9 |
| Fused Magnesia | 2,6 – 5,0 |
| Chamotte | 0,7 |
| Silicon Carbide | 5,8 |
| Calcined Alumina | 0,7 |
| Tabular Alumina | 2,9 |
| Brown Fused Alumina | 1,0 – 1,2 |
| White Fused Alumina | 1,0 – 1,3 |
| Recycling | <0,1 |

While carbon footprint reduction is an important benefit for recycling utilization, there are other advantages both for refractory consumers and producers. By using recycling, the raw material supply chain can be simplified, reducing the dependency on imported goods and the complexity and risks linked to it. Moreover, closing the loop for the product life cycle reduces the amount of residues to be disposed, leading to lower costs for landfilling and waste management. Finally, refractory companies with advanced recycling strategies can propose to customers full circular contracts, a competitive advantage for a market demanding environmentally sustainable products [8,9].

## CHALLENGES FOR RECYCLING PROCESSING AND UTILIZATION

The amount of recycling to be used in a refractory composition is dependent on the proper dismantling and sorting at the source, quality and selectivity of its processing, and the original raw materials being replaced.

The recycling process until its final utilization back to refractories can be separated in sub-processes for a better illustration. Firstly, the dismantling at the refractory consumer (and spent refractory generator) is carried out and an initial sorting per equipment being relined may be performed, alongside magnetic separation and screening to remove small particles normally contaminated with impurities and difficult to process on the downstream processes. The next step is the logistics to a recycling processing facility. Inside the recycling processing facility, the sorting of different material families is carried out for a more stable and proper chemical and mineralogical composition. After the separation, different beneficiation steps might be necessary, as carbides hydration, salts solubilization and magnetic particles removal. Finally, with the materials in proper quality and homogeneity, the particles are comminuted and sized for the suitable addition on refractory formulations, usually engineered to replace virgin raw materials without impacting product performance.

The challenges of each process step are commented and illustrated, while examples of solutions being explored by the industry are presented.

### Refractory Lining Dismantling

The refractory lining dismantling process and sorting has a strong influence on the quality and complexity on the recycling downstream processes. The better the selectivity during the dismantling processes, separating the refractory families according to the lining project, the higher the quality and therefore the recycling utilization can be maximized. This is especially important in cases where the recycling materials are difficult to sort out from each other and the chemistry is a limitation due to the cross-contamination. An example of this situation is the steel ladle recycling.

The lining concept of a steel ladle often comprises magnesia-carbon and alumina-magnesia-carbon bricks in different positions (steel and slag lines). With a selective dismantling these different families can be separated by the brick position directly at the site. However, if everything is broken down and sent to the recycler all together, the sorting among those bricks mixture is very difficult and the cross-contamination limits the usage at a new refractory product.

A selective dismantling would contribute for a better circularity and lower carbon footprint of refractories. Nevertheless, most of the

consumers are still prioritizing a fast dismantling in order to quickly return the equipment for operation, normally using a contractor not impacted by a higher or lower recyclability.

Therefore, the selective dismantling is an opportunity to improve the recycling utilization, but a compromise must be reached among availability of the vessel and quality of separation, even better if performed by a company targeting both speed and material separation quality.

**Logistics and Legislation**

One important challenge for recycling is the transport distance from the spent material generation to the recycling processer and finally to the recycling user. The economic feasibility of the spent refractory utilization has a strong dependency on the cost and complexity of this supply chain.

In countries and regions with significant distance among the refractory users and producers (e.g., United States and Brazil) the logistic cost is an important factor, especially when the material losses throughout the recycling processing are relatively high.

Another challenge faced is the cross-border transport of the materials, especially if they are considered hazardous waste. Some spent refractories are classified as such and face limitations to cross borders between countries, even if it's further processed to stabilize the material and to be used to reduce carbon emissions.

Therefore, it is necessary to evaluate and discuss specific legislation for recycling processes, simplifying (and in some cases even allowing) the supply chain of spent refractories since the processing and producing site locations are rather limited.

Additionally, the adoption of incentives and carbon taxation will help to improve the recycling competitiveness, which will become a key factor with the advance of utilization. The higher demand for recycling will lead to sourcing in further places, increasing logistic cost, and more elaborated processing to remove contaminants, increasing processing expenditures.

**Sorting of Recycling**

The sorting of spent refractories in different recycling groups is the most important and most used processing step, guaranteeing the material chemical and mineralogical homogeneity.

The vast majority of refractory recycling companies rely on manual sorting processes. In almost every new dismantling received at the plant, a sample of each spent refractory with distinct visual characteristic is collected and sent for chemical and mineralogical analysis. According to the results, a selection instruction is built, and the sorters are trained for the specific lot received. After selection, a new analysis is made on the lots to ensure quality and release for the downstream processes (or decide on blending or reprocessing in case the results are not according to the specification). Figure 1 shows a sorting plant in Brazil.



Fig 1 – Spent recycling sorting plant in Brazil.

A key development invested by recycling companies is on automated sorting processes. The benefits from this breakthrough technology are the better quality of separation (allowing to sort materials not possible by visual inspection), increased productivity and cost competitiveness, especially for regions with high labor cost. Additionally, finer particles (<80mm) could be sorted, not possible with the current manual process due to financial and technical constrains.

Automated sorters are available commercially for other industries, as mining and electronic waste. The sensors use color, for visible and NIR (near infra-red) wavelength ranges and chemistry, with XRT (x-ray transmission) and LIBS (laser induced breakdown spectroscopy) sensors [10].

Nevertheless, conventional devices present constrains that prevents a direct utilization for refractory recycling. Firstly, the carbon content which is part of the formulation of a significant volume of available materials, cannot be sorted simply by color and the carbon and impurities disturb the response for the XRT sensor, drastically reducing the sorting efficiency.

Secondly, most of the devices can only separate the feedstock in two product streams, while most of the spent materials received comprises five to ten different material types. Fitting a two streams equipment to multiple products increases the complexity of the flowsheet, set-up time, and material handling, finally reducing the productivity and increasing investment and cost.

Another limitation for the current technology is the necessity of removing any fine material covering the coarse fraction, normally adopting water sprayed screening. This additional step brings another complexity for the plant design, and for refractories susceptible for hydration as magnesian and dolomitic bricks, would make the process unfeasible.

Therefore, the current studies are targeting automated methods which surpasses these limitations from out-of-the-shelf equipment, improving yield, quality and economics of recycling.

**Stabilization and Beneficiation of Recycling**

The stabilization and removal of undesired mineralogical phases from recycling particles is essential to increase or even allow its utilization. A few classical examples of contaminants are alkali salts from cement kilns bricks, slag and steel infiltration from steel spent refractories, and magnesia carbon bricks containing aluminum carbide from the original aluminum powder added as antioxidant [11,12].

For the alkali salts and carbides contamination, the challenge is to mechanize the process for a higher productivity, lower lead-time and reduced footprint for high tonnage plants. The current method relies on spraying water over piles of material and wait for days, some cases months, until the reaction or dissolution takes place (Fig 2). Moreover, it is necessary a good control to prevent hydration (besides the aluminum hydration) or that hydrated particles do not reach the refractory production. Preventively, drying at temperatures surpassing 300°C are adopted to ensure proper treatment, increasing the processing cost.



Fig 2 – Water spraying process for aluminum carbide stabilization.

For steel and metallic particles removal, magnetic separators are normally used. However, when oxides and non-magnetic alloys contaminate the recycling grains, specific development is necessary for their removal.

**Engineering of recycling containing products**

After separation, contaminants removal and quality determination, the recycling grains are prepared for utilization and a proper product design is necessary to achieve similar performance replacing virgin raw materials by recycling grains.

A common challenge is to define how many and which size fractions can be used back into refractories. For a proper particle packing, similar sizes to the original raw materials are preferred, however the amount of silos available is an usual constrain for the implementation. Hence, a compromise is searched reducing the amount of different sizes, but also limiting the maximum replacement for a good particles packing.

Another design constrain is the variation in chemistry from recycling grains. Despite the processing steps and quality controls, the specs for a secondary raw material are normally broader than for a virgin one, since a recycling grain is a piece of the originating brick and its mix of raw materials. It is expected higher variation for a secondary material, being a task for the product developer to surpass the challenge imposed by this natural difference.

A final example of difference to be addressed in the product design is the grain density and porosity. Normally the virgin raw materials present higher density than recycling aggregates, leading to the necessity of adjusting processing and pressing parameters to achieve similar brick green density. In addition, for fired bricks, the combination of different chemistry, particles packing, and aggregate density might lead to adjustments on the temperature profile to achieve similar ceramization.

Therefore, the research and development capability of a refractory producer is directly linked to its capacity to increase recycling utilization, especially for increased recycling rates, since the market is demanding lower $CO_2$ footprint but similar product performance. Once achieved the refractory composition, it is important to report on the product datasheet the final carbon footprint, giving awareness and transparency to the customer to decide among the product options. Fig 3 exemplifies a recycling containing brand from RHI Magnesita.

Fig 3 – Technical datasheet with product carbon footprint.

**RESULTS OF MAJOR REFRACTORY COMPANIES**

Two of the most important refractories companies have included recycling on their strategic targets and published the results on their sustainability reports. Fig 4 displays the results presented by RHI Magnesita and Vesuvius [13,14].

RHI Magnesita has demonstrated strong development on their recycling rate, combining strategic push from the executive management team, product development drive, process innovation and novel business models. As a result, already in 2022, the target set for 2025 (10% recycling rate) was surpassed.

It is important to notice the decision of the market leaders on including recycling targets for the company shareholders report (10% until 2025 for RHI Magnesita and 7% until 2025 for Vesuvius), reinforcing to the market the importance of the topic and driving initiatives to foster recycling adoption by refractory consumers.
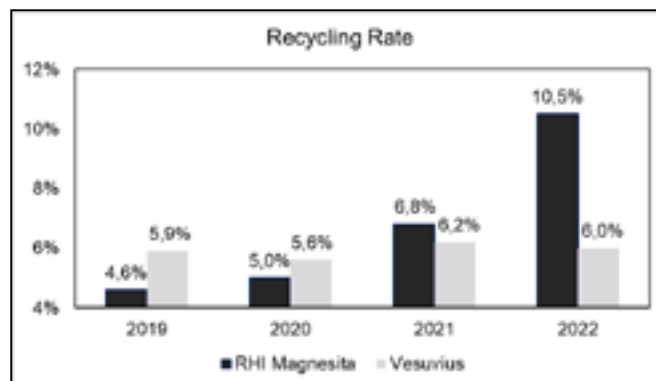
Fig 4 – Reported recycling rate result of RHI Magnesita e Vesuvius.

**CONCLUSIONS**

The recycling utilization is one of the quickest and most cost-effective strategies to reduce the carbon footprint of recycling products. Additionally, by closing the loop, the amount of material to be landfilled and controlled is reduced.

To improve the recycling rate and contribute to this essential goal, technological constrains need to be addressed and novel business models need to be elaborated to improve the material availability and quality.

In the dismantling, a compromise among refractory user, service provider and recycling company is necessary to extract the full potential from the spent material, ideally with a circular business model integrating refractory supply and recycling return to the producer.

Sorting is the major focus in the current set-up. Finding an automated process is essential to support significant increase in recycling rates, simplifying the material handling, improving the overall yield and improving quality. Additionally, the development of sensors specific for refractory recycling challenges is key to sort out among the different spent materials, overcoming the limitations from out-of-the-shelf equipment.

Another necessary technology upgrade is for the stabilization of undesired mineralogical phases and removal of contaminants. The mechanization of existing processes is key to increase productivity, reduce lead-time and guaranteeing quality, at the same time reducing the necessary footprint for the production upscaling.

Additionally, engineering refractory products containing recycling grains is a task that demands research and development capability and process know-how to use available resources at production plant, taking advantage of the benefits of a lower product $CO_2$ footprint without impacting performance. Limitation in silos and modification on process parameters to keep similar product properties demand creativity from the refractory development team, attempting to increase recycling content without major investments, increased production complexity and keeping cost-competitiveness. Finally, logistics and limitations of supply chain imposed by legislation to spent materials is a topic to be addressed, currently reducing the competitiveness of recycling compared to primary raw materials. Adoption of incentives and carbon taxation are necessary for high recycling consumption, which will demand higher expenses for transportation and more complex processing steps.

The major refractory producers have set targets for recycling rate, demonstrating a trend in the industry to migrate to lower carbon footprint products. RHI Magnesita has already achieved its target for 2025, surpassing 10% already in 2022, benefiting from a strong strategic focus, investment and synergies with different companies along the recycling supply chain.

## REFERENCES

[1]    Strubel, S. Developing a model to calculate the carbon footprint of refractory products. 2012, Montanuniversität Leoben (Master Thesis).

[2]    Anquetin T., Coqueret G., Tavin B., Welgryn L. Scopes of carbon emissions and their impact on green portfolios. 2022, Economic Modelling, 115, 105951.

[3]    Fan, Z., Friedmann, S.J. Low-carbon production of iron and steel: Technology options, economic assessment, and policy. 2021, Joule, 5:4, pp. 829-862.

[4]    Kildahl H., Wang L., Tong L., Ding Y. Cost effective decarbonization of blast furnace – basic oxygen furnace steel production through thermochemical sector coupling. Journal of Cleaner Production, 389, 2023, p.1-7.

[5]    Moraes M.N., Nogueira G.G.R., Silveira F.T. Desafios técnicos no processamento de reciclados. Proceedings: ALAFAR conference 2022.

[6]    Agrinier P., Bonijoly D., Farret R., Favre E., Duong M. H., Kalaydjian F., Pironon J., Birat J., Czop V., David M., Marliave L, Gresser R., Le Thiez P., Sonnois L., Van Der Beken A., Czernichowski I., Moisan, F. The capture, transport, geological storage and re-use of CO2 (CCUS) - Strategic roadmap. 2011, Agence de l'environnement et de la maitrise de l'energie.

[7]    Poretti F., Stengler E.  The climate roadmap of the European Waste-to-Energy sector - The path to carbon negative. Proceedings: International Conference on Greenhouse Gas Control Technologies 2022.

[8]    Moraes M.N., Nogueira G.G.R., Lopez M., Silveira F.T., Bonadia, P. Refractories recycling - challenges and opportunities in a path towards CO2 footprint reduction. 2022, Proceedings: EMECR - International Conference on Energy and Material Efficiency and CO2 Reduction in the Steel Industry.

[9]    Schutte M. Refractory recycling earning your environmental brownie points. 2010, Proceedings: Refractories 2010 Conference, The Southern African Institute of Mining and Metallurgy, pp. 75-86.

[10]   Knapp H, Horckmans L, Bouillot F, Fricke-Begemann C, Makowe J, Ducastel A. Sensor-based identification of spent Refractory Bricks. 2015, Proceedings: XVI BMP Congress, pp. 279-284.

[11]   El-Attar M.M., Sadek D.M., Salah A.M. Recycling of high volumes of cement kiln dust in bricks industry. 2016, Journal of Cleaner Production, pp. 1-10.

[12]   Moriz K., Dudczig S., Endres H.G., Herzog D., Schwarz M., Schöttler L., Veres D., Aneziris C.G. Magnesia-carbon refractories from recycled materials. 2021, Ceramic Engineering and Science, 4:1, pp. 53-58.

[13]   RHI Magnesita Sustainability Report. 2022.

[14]   Vesuvius Sustainability Report. 2022.

# A NEW APPROACH TO ACHIEVE ROBUST AND EASY TO USE NCC

Frédéric Lacoue*, Quentin Collomb, Chunfeng Liu, Christoph Wöhrmeyer
Imerys S.A., Paris, France
* Presenting author

## ABSTRACT

The key drivers for the development of silica sol based No Cement Castables (NCC) over the last two decades are their fast drying ability and the in-situ formation of an almost pure mullite matrix composition at high temperature. It then leads to faster onsite installation/repair and a high refractoriness and thermal shock resistance that improve durability of such castables [1, 2]. Nevertheless, the main drawbacks of this solution compared to the largely used calcium aluminate binder, are the more difficult control of setting, low green mechanical strength, the need to handle a temperature sensitive liquid product at the job site. To overcome some of these drawbacks of silica sol, small amounts of magnesia or calcium aluminate are commonly added in formulations. Magnesia is introduced as a gelling or coagulating agent for faster structuration while small amount of cement allows to increase green mechanical strength [3, 4, 5]. From there, this study will show that calcium aluminate could be, as well, a suitable binder to formulate NCC castables with equal or less than 0.2 wt% CaO as required by the classification. This solution doesn't require a separate liquid colloidal binder, works simply with water and provides similar robustness and formulation flexibility as traditional ultra-low cement castables (ULCC).

## INTRODUCTION

A bauxite refractory castable formulation is used to compare different binders such as commercial colloidal silica, calcium aluminate Secar® 71, and a new calcium aluminate based laboratory prototype LP660. For each binder, flow behaviour, structuration kinetics, and physical properties after curing and drying are investigated. Dry-out behaviour is also compared through macro thermo gravimetric analysis on 10 cm$^3$ cubes. Hot properties such as refractoriness under load and hot modulus of rupture are also compared. The matrix mineral composition of the castables is analysed by X-ray diffraction to qualitatively assess mullite formation after calcination.

## EXPERIMENTAL PROCEDURE

### Model formulas

In this study, all binders are tested in castables with the same particle size distribution of bauxite aggregates, the same amount of water and the same silica content (Table 1). Then, same open porosity is expected after complete drying. As dried powder, Secar® 71 and LP660 are added in the same amount in ULCC and NCC-1K formulas. In NCC-2K, commercial silica sol used is Ludox 50TM and consists of 50 wt% SiO$_2$ nanoparticles. Then, 10 wt% of Ludox entirely replaces micro silica and brings 5 wt% of needed water. Additional 0.5 wt% of water is required to keep the same amount of liquid between all formulations. Main changing parameter within this benchmark is CaO content from almost 0 wt% for NCC-2K to 0.75 wt% for ULCC. The value for the NCC-1K is placed just below the standard limit for a no cement castable (i.e. ≤0.2 wt %).

### Test methods and equipments

- Flow decay: measured after 4 minutes mixing of raw materials with water. The sample is placed and tamped in a trunconic ASTM mould (inner diameter of 100 mm at the bottom, 70 mm at the top and 50 mm height). Then the mould is removed and the sample is vibrated for 30 seconds with an amplitude of 0.5 mm on a Sinex table. The resulting diameter of the sample is measured in three different positions. The flow value is the average of the three measurements expressed in % increase versus the initial 100 mm base diameter. Flow decay is given by repeating the test after 30 and 60 minutes.

- Ultrasonic profiles: measured with the Ultratest IP8 during castable curing at 20°C for 24 hours.
- Mechanical strength: cold compressive strength is measured according to NF EN196-1 after 24 hours curing under 20°C, 90% relative humidity and after drying at 110 °C for another 24 hours.

Tab. 1: Bauxite model castables.

| Raw materials (weight%) | ULCC | NCC-1K | NCC-2K |
|---|---|---|---|
| Calcined Bauxite 0-6 mm | 85 | 85 | 85 |
| Calcined alumina | 7,5 | 7,5 | 10 |
| Micro Silica Elkem 971U | 5 | 5 | 0 |
| **Secar® 71** | **2,5** | | |
| **LP660** | | **2,5** | |
| **Silica Sol Ludox TM-50** | | | **10** |
| **Total** | 100 | 100 | 100 |
| **Dispersants/Retarders** | | | |
| NaTPP | 0,08 | | |
| Darvan7S | | 0,05 | |
| Citric Acid | | 0,02 | |
| Darvan811D | | | 0,1 |
| MgO DBM | | | 0,03 |
| **LDPE Fibers** | | **0,1** | |
| **Added water** | | **+5,5** | **+0,5** |
| **Estimated CaO w%** | **0,75** | **≤0,2** | **0,0** |

- Open porosity: determined by water immersion according to Archimedes' method.
- Permeability: discs of 100 mm in diameter and 25 mm height, have been prepared by casting into a plastic mould followed by curing at 20°C, 90% relative humidity. A permeameter has been used to measure the air permeability. From the pressure change in the chamber over time and the sample dimensions, the average permeability K has been calculated. Results are expressed in mDarcy as explained in [6].
- X-Ray Diffraction (XRD): performed on a Bruker D8-Advance diffractometer under Cu radiation in the 2Θ range 5°-80° using samples milled less than 100μm.
- Hot modulus of rupture are done on samples with following dimensions, 40x40x160mm$^3$. Samples are first calcined at 1450°C for 5 hours. Measurements are done at 1450°C with a heating rate of 5°C/minute and a holding time of 30 minutes.
- For refractoriness under load, cylinders with following dimensions are prepared: 50mm±0.5mm in diameter, 50mm±0.5mm in height, and a centred hole of ~12mm in diameter. After a first calcination at 1450°C during 5 hours, measurements are done with 5°C/minute heating rate and a load of 0.2MPa.

## RESULTS AND DISCUSSION

### Rheology and structuration

As a reminder and in order to compare later drying ability of the samples, the three formulations are casted with the same amount of water. Figure 1 shows it was possible to adjust a very similar flow behavior for these three formulations with the help of different commonly used dispersant, accelerator and retarder. Having this property allows to ensure a proper placing of the samples during casting for the further mechanical strength development. However, previous tests adding Ludox silica sol and micro silica in the same formula failed to find an adjustment of the additives to get a good flow behavior and a satisfactory structuration kinetics. This confirms that the use of colloidal silica is very sensitive and not trivial. This is

93

why the best compromise finally retained is that one with 10 wt% Ludox 50, but without the use of micro silica.
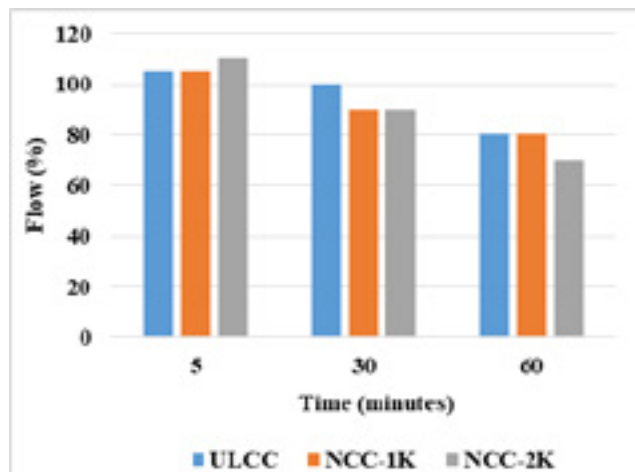


*Fig. 1: Flow values for the different castables.*

Structuration kinetics between the castables are quite different depending on the binder used. Figure 2 clearly shows that the structuration of NCC-2K bonded with colloidal silica starts earlier than NCC-1K, but progresses more slowly. The velocity signal reaches a maximum value of only 2300 m/s despite the high amount of silica sol used. Besides, the use of magnesia as a gelling agent only allows to adjust the starting point of signal increase but not its maximum value. This indicates the efficiency limit of silica sol as a binder. On the contrary, the ultrasonic propagation speed in NCC-1K reaches within a few hours up to 3000 m/s, indicating a noticeable structuration of the castable that can be easily controlled by citric acid as a retarder. As expected, ULCC ultrasonic profile is faster and higher due to the presence of calcium aluminate in a higher quantity.
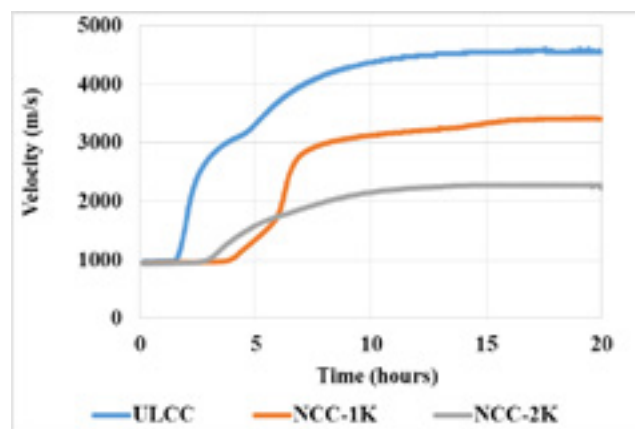


*Fig. 2: Ultrasonic profiles.*

After a drying at 110°C according to table 2, water loss and open porosity values for ULCC castable indicate the lowest free water release from the sample at this step. At higher drying temperature, the amount of bonded water in calcium aluminate hydrates will release from the sample and will contribute to the increase of apparent porosity to a similar value as NCC-2K. For NCC-1K, a higher water loss and intermediate value of porosity indicates higher amount of free water and lower amount of calcium aluminate hydrates compared to ULCC. As for ULCC, by increasing the drying temperature, the open porosity should increase by the same order of 18% like NCC-2K. In the case of silica sol, water loss is only 4.8%, probably due to mass measurement error between demoulding and drying step as a small part of water may release from the sample. On the other hand, porosity is already at maximum. These results, in static conditions at 110°C along 24hours, already show the different drying behaviours between these formulas depending on the different kinds of bonding system involved. Macro thermo gravimetric

analyses will complete these results in dynamic conditions over a wider range of temperature.

Tab. 2: water loss and porosity after drying at 110°C

| Samples | Water Loss (wt%) | Apparent Porosity (%) |
|---------|------------------|-----------------------|
| ULCC | 4,4 | 14,2 |
| NCC-1K | 4,9 | 16,6 |
| NCC-2K | 4,8 | 18,3 |

**Drying ability**

The drying behaviour of the castables is compared through a macro thermo gravimetric analysis with the help of the equipment below (figure 3). Samples are casted in a cubic mould of 10 cm side with a thermocouple inside, near its centre. After a curing of 24 hours under 90% relative humidity and demoulding, the sample is then placed in a kiln and suspended on a balance by the thermocouple. A steel box prevents damage to the kiln in case of explosion.
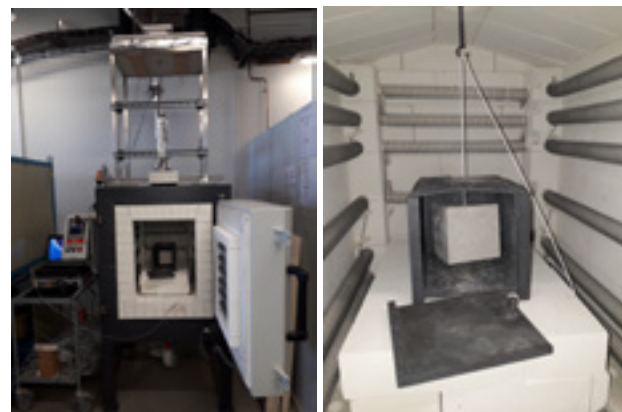


*Fig.3: macro thermogravimetric equipment and sample mounting.*

By simultaneously controlling the kiln temperature and measuring the mass of the sample, the macro thermo gravimetric curves are obtained as shown in figure 4. To test repeatability of the experiment, 3 trials are usually done for each formula with a heating rate of 300°C/hour until 600°C. As a reminder, table 2 indicates a mass loss between 4.4 and 4.9 wt% after 24 hours at 110°C for all samples. On figure 4, NCC-2K curve confirms the same mass loss of water and complete drying in the ebullition range of temperature (i.e. 4.5 wt% around 110°C). On ULCC and NCC-1K curves, mass losses are respectively around 1 wt% and 1.8 wt% in the same range of temperature. This already indicates the slower release of water vapour for these two formulations compared to NCC-2K. In parallel, this is well correlated with low permeability values measured at 110°C on figure 5, while NCC-2K already exhibits more than 5 mDarcy. In case of NCC-2K, release of boiling water directly creates high permeability in the castable due to bonding mechanism of colloidal silica. In case of ULCC and NCC-1K, presence of crystalline hydrates from hydration reactions before drying and from in-situ hydration reactions during drying under different hydrothermal conditions [6], lead to a lower permeability (figure 5) and prevent free water to release easily from the castable. Indeed, while temperature is increasing on figure 4, ULCC curve shows the lowest slope of mass loss and drying process is only complete after around 280°C, once free water and bonded water from calcium aluminate hydrates have released. NCC-1K curve shows a higher slope of mass loss and complete drying is done at around 200°C. This is well correlated with the increase of permeability between 110 and 200°C for NCC-1K (figure 5), in which free and bonded water can be released from the castable slightly more easily than ULCC for which permeability values keep very low. We assume NCC-1K castable presents higher values of permeability due to a lower amount of crystallised hydrates compared to ULCC. But, from our experience during the technical development of Refpac® Mipore product [7], these values are not enough to ensure safe drying at very high heating rate without spalling or explosion. Therefore, a second formulation of NCC-1K is also tested with Mipore permeability enhancement concept and shown as NCC-1K Mipore curve on figure 4. The result

clearly shows the same behaviour as NCC-2K with a main mass loss in the ebullition temperature range. Figure 5 also confirms the increasing of permeability values compared to NCC-1K with a value of around 3 mDarcy.
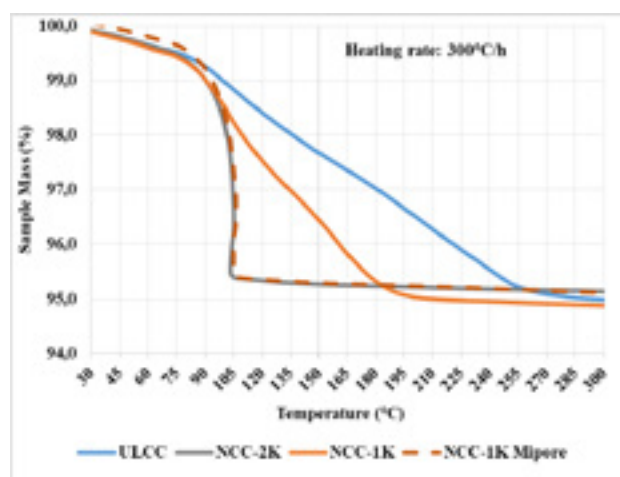


Fig.4: mass of 10 cm3 cubes versus inner temperature.
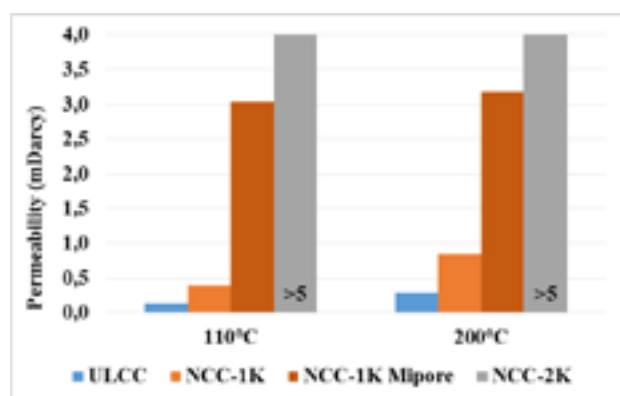


Fig.5: permeability measurements after 110 and 200°C.

Figure 6 shows the cubes after the drying experiments until 600°C. On one hand, ULCC and NCC-1K are free of cracks, on the other hand NCC-2K cube shows large cracks on sides and bottom. As it concerns NCC-1K Mipore only small and few cracks are noticeable. In the case of NCC-2K, these cracks should be due to initial low mechanical strength just after demoulding (figure 7) while a high amount of water is released from the sample during drying period until 105-110°C. In other words, the kinetic of the increase in mechanical strength is slower than the kinetic or mass transfer of the water vapour release from the sample, which leads to the formation of cracks. To avoid this, heating rate must be adapted to more usual values like 50°C/hour. In NCC-1K Mipore formula where cracks form in a lesser extent, higher initial mechanical strength must help in supporting this high water vapour release at ebullition temperature. Similarly, a slower heating rate should avoid this. Finally, due to the low permeability depending on calcium aluminate bonding in ULCC formula, free water is more difficult to remove during drying. Then, ULCC formula will need the highest temperature for a complete drying that occurs around 280°C. Nevertheless, as calcium aluminate cement develops strong mechanical strength, the formula is able to support high pressure increase from water vapour inside porosity, limiting the risk of explosion. As NCC-1K develops slightly higher permeability compared to ULCC, removing free water is easier and will require a lower temperature as the complete drying is done at around 200°C. On the other hand as it develops lower mechanical strength, the risk of steam spalling is still present in case of too fast pressure increase. Thus, a drying with an adapted heating rate is recommended. In the end, NCC-2K and NCC-1K Mipore will require the lowest temperature for complete drying, as in both cases, it occurs at 100-110°C, and where the risk of high steam pressure build-up is

low. Systems like colloidal silica as well as LP660 with Mipore concept are able to develop bonds with low dehydration temperature and creating high permeability. Then, spalling or explosion risk is much lower, but cracks formation can still be an issue in case of too high heating rate due to lower mechanical strength compared to ULCC.
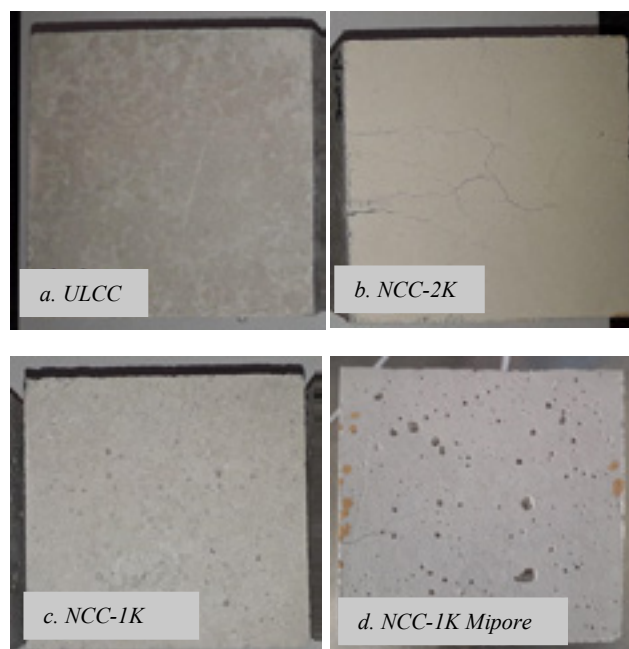


Fig.6: Cubes after drying until 600°C.
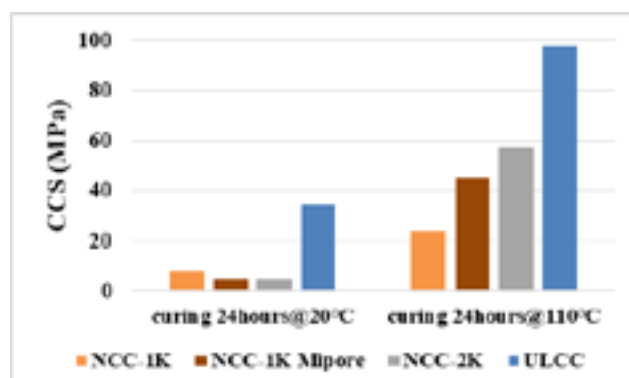


Fig.7: Green and dried Cold Compressive Strength on 3x3x16cm³ specimens.

**Thermo-mechanical properties**

Beside a fast drying ability, another key expectation for a binder is its compatibility with hot properties of a castable. In addition to the other raw materials used in a refractory castable, the binder itself can have a great impact on refractoriness, thermal shock and maybe corrosion resistance. It is well known that a good approach to improve hot properties is to limit calcium content brought by the nevertheless very useful calcium aluminate cement [8]. Figure 8 confirms low values of hot modulus of rupture in both cases, after a curing of 110°C or after a first calcination at 1450°C, for ULCC samples compared to NCC-1K and NCC-2K. These ones exhibit similar results in both cases. Same trend is also confirmed through refractoriness under load on figure 9. For every rates of deformation of the samples, ULCC shows lower temperature values indicating its lower refractoriness. NCC-1K has a very close behaviour compared to NCC-2K, indicating an almost similar refractoriness. These tests confirm the low impact of less than 0.2 wt%CaO in NCC-1K compared to castable NCC-2K.
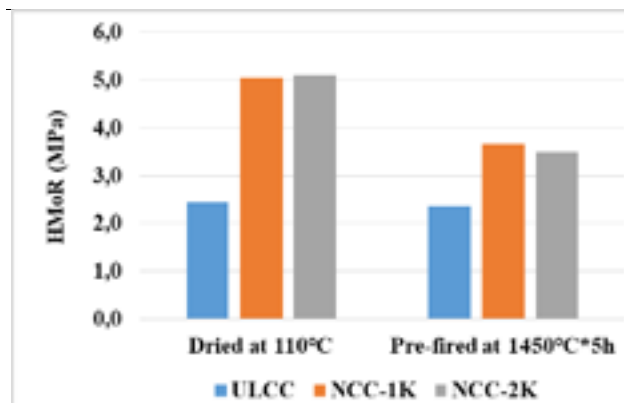
*Fig.8: Hot Modulus of Rupture (HMoR) at 1450°C after drying and after calcination at 1450°C during 5h.*
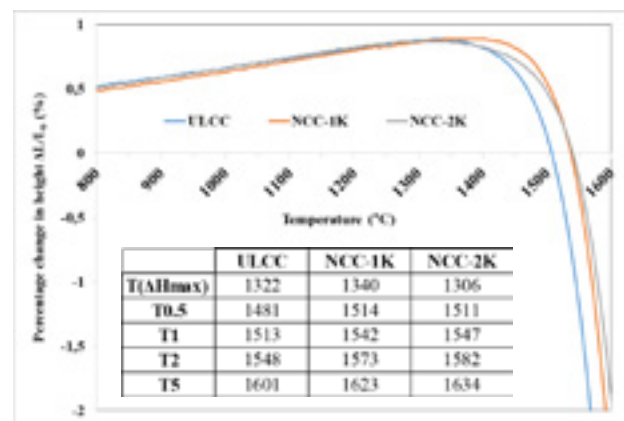


*Fig.9: Refractoriness under load after calcination at 1450°C during 5h.*

96
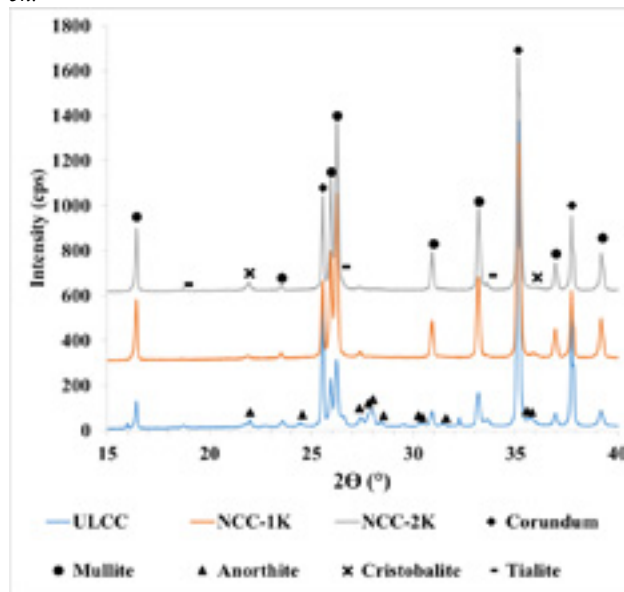


*Fig.10: XRD diagrams of fine fraction of castable (<100µm) after calcination at 1400°C during 6h.*

Finally, XRD diagram for ULCC sample on figure 10 clearly shows the presence of anorthite after cooling due to approximately 0.75 wt% of calcium oxide. The presence of anorthite with a low melting temperature is well in accordance with refractoriness under load and hot modulus of rupture results. XRD diagrams for NCC-1K and NCC-2K don't reveal the presence of anorthite and exhibit much higher mullite compared to ULCC. Still presence of cristobalite also indicates that mullite formation is not totally complete at 1400°C. Small differences noticed on refractoriness under load results

between NCC-1K and NCC-2K over 1550°C should come from differences in quantity, composition, and viscosity of the liquid phase. Also, difference in distribution and reaction of the liquid phase inside the fine matrix of the castables, between small crystals of mullite and nature of excess alumina particles, should affect high temperature property. Additionally, it is to notice that with only 5 wt% of micro silica in our castable formulations, we may not have maximized mullite formation.

## CONCLUSIONS AND PERSPECTIVES

The dry powder NCC-binder prototype LP660 shows robust properties for setting and flow ability compared to colloidal silica which needs magnesia as a setting accelerator. Although it seems contradictory, this calcium aluminate based LP660 prototype concept shows the possibility to use it as binder for no cement castables. It creates sufficient green strength comparable to silica sol/gel, but in a more predictable and shorter time frame. Under fast drying conditions, a castable requires a good compromise between mechanical strength development and creation of permeability to support release of high water vapor pressure. The use of the LP660 prototype in NCC-1K under fast drying conditions (300 °C/h) showed intermediate behavior compared to ULCC and NCC-2K. Nevertheless, lower heating rates are recommended to avoid steam explosion, especially for thicker linings and big precast shapes. Moreover, the combination of LP660 prototype with Mipore permeability enhancement concept showed that similar drying profile like colloidal silica can be reached. Concerning the thermomechanical properties, the usage of LP660 gave nearly the same results as the NCC-2K which is using a silica sol/gel bond. This demonstrates that 0.2 wt% CaO in a castable are not detrimental to the refractoriness. Nevertheless, this low presence of calcium oxide in combination with other impurities like $TiO_2$ and $Fe_2O_3$ coming from bauxite fine powder, as well as the amount of $SiO_2$ in that kind of matrix formulation, will be further studied to better understand its impact on mullite and liquid formation at high temperature.

## REFERENCES

[1] M. R. Ismael, R.D. dos Anjos, R. Salomão and V.C. Pandolfelli: Colloidal silica as a nanostructured binder for refractory. July/August 2006 Refractories Applications and News, Volume 11, Number 4.

[2] R.D. dos Anjos, M.R. Ismael, I.R. de Oliveira, V.C. Pandolfelli : Workability and setting parameters evaluation of colloidal silica bonded refractory suspensions. CeramicsInternational34(2008)165–171

[3] Hong Peng, Bjørn Myhre: Microsilica-Gel Bonded Refractory Castables with Improved Set-Behaviour and Mechanical Properties. Refractories WORLDFORUM 7 (2015)

[4] A.P. Luz, M.H. Moreira, M.A.L. Braulio, C. Parr, V.C. Pandolfelli : Drying behavior of dense refractory ceramic castables. Part 1 – General aspects and experimental techniques used to assess water removal : Ceramics International Volume 47, Issue 16, 15 August 2021, Pages 22246-22268.

[5] A.P. Luz, M.H. Moreira, R. Salomão, M.A.L. Braulio, V.C. Pandolfelli : Drying behavior of dense refractory castables. Part 2 – Drying agents and design of heating. Ceramics International Volume 48, Issue 3, 1 February 2022, Pages 2965-2987

[6] C. Wöhrmeyer, C. Parr, J-M. Auvray, M. Lievin, E. Frier: https://www.researchgate.net/publication/313077635_The_imp act_of_hydration_and_dehydration_conditions_on_the_permea bility_of_LCC_systems.

[7] C. Wöhrmeyer, J.-M. Auvray, C. Zetterström: Dry out of dense refractory castables via use of permeability enhancing active compound. 59th ICR, Aachen, 2016

[8] Lei Xu, Yang Liu, Min Chen, Nan Wang : An accurate correlation between high-temperature performance and cement content of the high-alumina refractory castables. Ceramics International Volume 48, Issue 15, 1 August 2022, Pages 22560-22566

# WHAT IS REALLY IN THERE? CLASSIFICATION OF AROMATIC COMPOUNDS IN CARBON-BASED REFRACTORY BONDS BY HIGH-RESOLUTION MASS SPECTROMETRY AND MULTIVARIATE STATISTICS

Julia Doll, Ali Masoudi Alavi, Peter Quirmbach
University of Koblenz, Koblenz, Germany

## ABSTRACT

Carbon is used in different configurations in refractory materials because of its property-enhancing effects, such as increased thermal shock resistance and wear reduction. In this context, organic carbon in particular is frequently criticized for its partly carcinogenic and mutagenic impact on human health, which arises especially in the presence of PAH. But despite decades of research, there is still no standardized analytical strategy for the detailed investigation of the complex organic phases in refractory materials apart from the analysis of some single defined compounds. Therefore, in this work, a non-target analytical strategy for characterization and classifications of refractory materials is presented. This is particularly challenging because the organic phase in these materials is often present in only a very small proportion and along with many other substances so that highly sophisticated analytical methods have to be used. The focus in this work is on the generation of a large amount of high-quality data using high resolution time-of-flight mass spectrometry as well as a targeted reduction, evaluation and interpretation of these data using multivariate statistical approaches. In addition to the clear classification of the materials based on their structure and chemical composition, characteristic features of each sample could be identified and extracted to provide a comprehensive understanding of the investigated refractories in order to evaluate their quality and even foresee their behavior in the future.

## INTRODUCTION

Carbon has been used in refractory materials for a long time due to its property-improving effect. These include, in particular, a wear reduction by reducing the infiltration depth of melts and slags, an improvement in thermal shock resistance by increasing thermal conductivity while reducing thermal expansion, as well as a characteristic structural flexibility. Carbon is introduced into the microstructure through two forms. On the one hand, through inorganic carbon carriers, such as graphite or carbon black, on the other hand, in the form of organic binders, such as synthetic resins or pitches. The latter are increasingly the focus of attention of authorities, industry and science due to their known hazardous properties to health and the environment. However, despite decades of research, the exact chemical composition of these carbon mixtures has still not been fully clarified. This deficit is particularly caused by their complexity. In addition to the large number of compounds, their structural and chemical similarity as well as their largely non-volatile character are particularly challenging [1–3]. In addition, the complex carbon mixtures in the field of refractory applications are precisely not present isolated. Instead, they are a minor component of a refractory batch, which further increases the complexity of the sample. However, in the analysis of refractory materials, the focus of previous studies has been predominantly on maintaining and optimizing the chemical, mechanical, and thermal properties of refractory systems while reducing harmful emissions by combining and substituting different binders [4–9] and characterizing oxide and non-oxide inorganic constituents [10]. In contrast, a characterization of the organic constituents of already manufactured refractory materials has hardly been carried out. Therefore, in this work, the organic phase of refractory materials will be investigated in more detail. For this purpose, three MgO-C samples were first analyzed by DIP-HR-TOFMS, which in previous studies showed great potential to overcome the listed challenging properties [11–14]. For example, the studies showed a decrease in the effective boiling temperature of the analytes from

T = 330-350 °C [12–14], which can be attributed to the reduced pressure in the system during the measurement. In addition, an applied temperature gradient and the high resolution of the mass spectrometer were able to separate the analytes and thus reduce the complexity of the samples [12]. However, since this method leads to a large amount of data, a reduction was performed using multivariate statistical methods such as hierarchical cluster analysis (HCA) and principal component analysis (PCA) to classify the samples based on their organic phases and extract characteristic structural features.

## EXPERIMENTAL

### Sample material

In this work, three magnesia-carbon bricks MgO-C with a graphite content of 10 wt.-% and different binders with a content between 2.5 wt.-% and 3.0 wt.-% were analyzed. In MgO-C1, a mixture of fused magnesia and sintered magnesia was used as raw material. In MgO-C2 and MgO-C3, only fused magnesia served as raw material. All bricks were dried at T = 200 °C. For further analysis, the MgO-C bricks were first coarsely crushed and then finely ground for t = 10 min using a Pulverisette 0 vibratory micro mill (Fritsch, Idar-Oberstein, Germany).

### High-resolution mass spectrometry, DIP-HR-TOFMS

The samples were analyzed by high-resolution time-of-flight mass spectrometry (HR-TOFMS) on a Pegasus GC-HRT 4D (Leco, St. Joseph, USA) with an equipped direct inlet system (DIP, SIM GmbH, Oberhausen, Germany). Approx. m = 5 mg of the solid samples were transferred to the ion source without any further sample preparation and heated with a temperature gradient to T = 400 °C and a dwell time of t = 3 min, resulting in a total analysis time of t = 540 s. Seven replicates were measured for each sample.

### Data processing and statistical analysis

DIP-HR-TOFMS data were processed with home-build Matlab scripts (R2020b, The MathWorks, Natick, USA). Briefly each detected feature was assigned to a molecular formula $C_cH_hN_nO_oS_s$ based on its exact mass with $2 \leq c \leq 100$, $2 \leq h \leq 100$, $0 \leq n \leq 2$, $0 \leq o \leq 2$ and $0 \leq s \leq 1$ and a maximum number of three heteroatoms. If no assignment was possible within an error window of 5 ppm, the corresponding feature was removed. The assigned features then served as input for further statistical analysis.

For statistical analysis, the abundance data were first normalized to total intensity and then power transformed to reduce heteroscedasticity. For hierarchical cluster analyses (HCA), with Ward's minimum variance algorithm and Euclidian distance as metric, the intensities were mean centered.

To investigate differences in bricks, a supervised principal component analysis (PCA) was performed. For this purpose, significantly different *m/z* were extracted by ANOVA with p = 0.05 followed by Bonferroni correction. The extracted ions intensities were then mean centered and served as input to PCA.

## RESULTS AND DISCUSSION

### Chemical and structural investigation of the samples

The mean relative mass accuracies and assignment ratios of the data processing of the seven replicate measurements with the associated sample standard deviations are shown in Tab. 1.

97

*Tab. 1: Assignment rate, relative mass accuracy and standard deviations after data processing*

|  | MgO-C1 | MgO-C2 | MgO-C3 |
|---|---|---|---|
| **Assignment rate in %** | 83.8 (± 1.5) | 77.6 (± 12.5) | 78.2 (± 2.2) |
| **Relative mass accuracy in ppm** | 2.03 (± 0.03) | 1.60 (± 0.09) | 1.81 (± 0.05) |

The contour plots in Fig. 1 show the m/z of the ions as a function of analysis time. The color scale represents the intensity normalized to the total ion current. Sum spectra were obtained by adding the intensities per m/z over the total analysis time, while the ion current describes the added intensity per second.
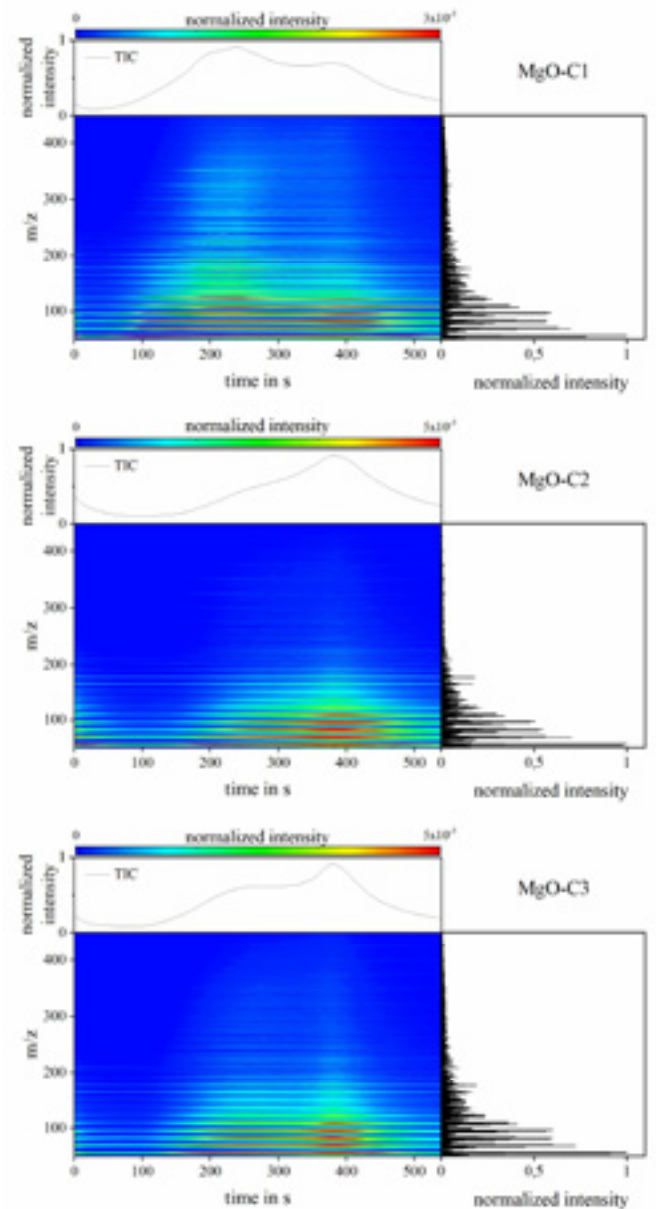


*Fig. 1: Contour plots with normalized intensities of detected m/z as a function of analysis time, total ion currents (TIC) as a function of analysis time and sum spectra over the entire measurement [14]*

In all samples, ions with m/z < 120 are detected directly at the beginning of the measurement, before the intensity of the total ion current decreases again. In the further course of the measurement, two peaks of the TIC can be observed. For MgO-C1, these are clearly separated and occur at t = 240 s and t = 390 s. In the case of MgO-C2 and MgO-C3, an overlapping occurs, with the first peak occurring as

the shoulder of the maximum. Overall, it is evident that ion currents of these two samples are very similar, in contrast to MgO-C1. This is also reflected in the contour plots. In MgO-C2 and MgO-C3, mainly ions with m/z < 200 are measured over the entire measurement period, while in MgO-C1, especially between 150 s < t < 450 s, higher molecular weight ions up to m/z < 400 also appear with low intensities. Over the entire measurement, MgO-C1 shows the highest average m/z with m/z 183 ± 16, followed by MgO-C3 with m/z 140 ± 7 and MgO-C2 with m/z 118 ± 7. It is remarkable that in none of the samples a strong increase of the maximum m/z with increasing measurement time and thus increasing temperature can be observed. Even at the end of the measurement, mainly ions with *m/z < 120* appear with strong intensities, indicating a strong fragmentation or thermal decomposition of the contained compounds.

To investigate the chemical composition, the detected compounds were assigned to a compound class on the basis of their integrated heteroatoms N, O, and S. Fig. 2 shows the distribution of all assigned mass traces in the three different samples as the mean value of the seven replicates. In all samples, more than 70 % of all detected features are attributed to ions without integrated heteroatom. The largest difference between the samples is observed in the intensity distribution of the heteroatomic compound classes. MgO-C2 shows higher relative intensities of the oxygen-containing compounds of classes O and O₂ compared to MgO-C1 and MgO-C3. In contrast, in MgO-C1 and MgO-C3, ions with a nitrogen and a sulfur atom, respectively, are also detected in higher intensities than in MgO-C2.
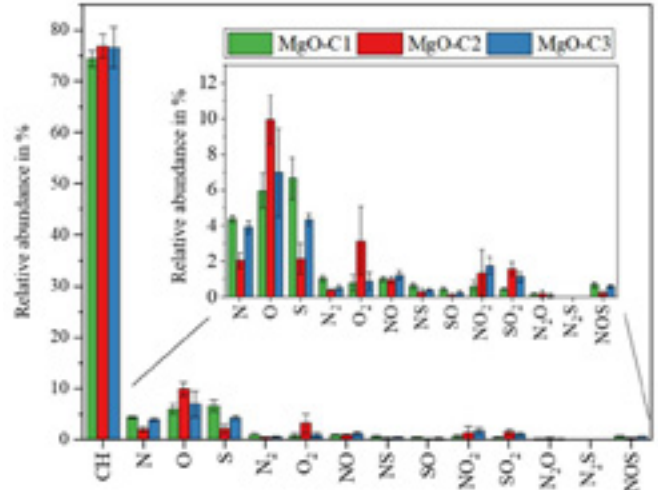


*Fig. 2: Normalized intensities of all assigned compound classes for the three samples studied. The error bars show the sample standard deviations of the seven replicates. [14]*

In summary, the results indicate a very similar structure for all samples. At the same time, differences in molecular mass distribution and elemental composition can be observed. Furthermore, comparatively high standard deviations of the relative abundances of the individual compound classes can be observed within the samples in the seven replicate measurements. On the one hand, this can be explained by the low mass fraction of the organic phase and the associated low intensities. On the other hand, it has to be considered that the samples are crushed refractory products based on natural raw materials. Even if a complete pulverization and homogenization of the sample was aimed at in the course of the sample preparation, variances in the sample composition of the individual replicates cannot be excluded. Taken together, this makes it difficult to intuitively determine significant differences and makes the use of statistical methods essential for a reliable classification of MgO-C samples.

**Classification by multivariate statistical data analysis**
Fig. 3 shows the result of the hierarchical cluster analysis (HCA) of all assigned ions with all variables mean centered. This data preparation leads to the fact that the intensities of the individual variables have a direct influence on the model. A cophenetic correlation

98

coefficient of $c_{coef} = 0.73$ confirms an adequate reproduction of the data set by the applied cluster model. The seven replicates of MgO-C1 are clustered together by the model and are also clearly separated from the other two samples. However, this unsupervised cluster analysis is not able to distinguish between the samples MgO-C2 and MgO-C3. This is in good agreement with the results of the contour plots, which also showed a visually greater similarity between these two samples. At the same time, this also shows that intense ions occur with comparable intensities in both samples. These compounds are therefore neither suitable for classification nor as characteristic structural elements, but rather overlap such elements. Therefore, to reduce the data to potential classifiers, an ANOVA was performed. This reduced the original 725 features to 299 potential classifiers. Only the potential classifiers extracted by ANOVA were then used as input for a supervised principal component analysis to determine characteristic structural elements for each sample.
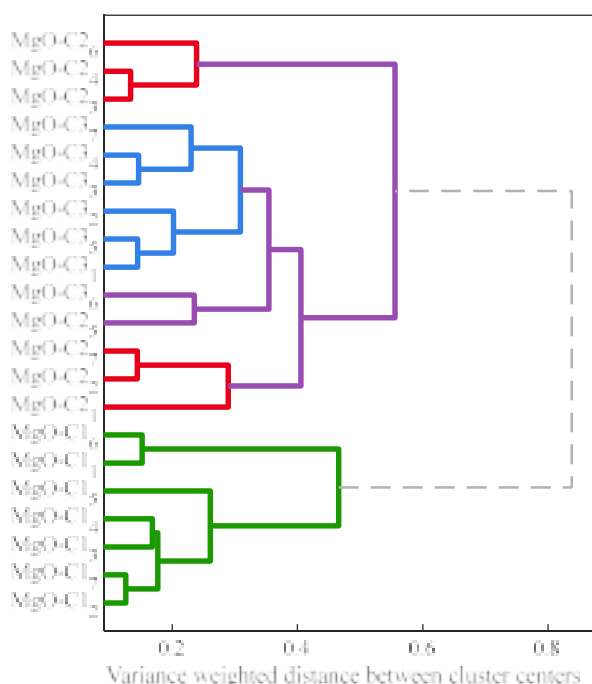


Fig. 3: Dendrogram of hierarchical cluster analysis (HCA) of the three MgO-C bricks and their seven replicates, using the mean-centered DIP-HR-TOFMS data as input. [14]

The results of the principal component analysis (PCA) are shown in the form of biplots in Fig. 4 and Fig. 5. Here, the scores are represented by black diamonds and the loadings by circles. The color coding shows the different properties of each variable, such as its number of DBE (Fig. 4) or its association with a particular compound class (Fig. 5). A clear clustering of the three MgO-C samples and their seven replicates can be seen. The first principal component clearly separates MgO-C1 from MgO-C2, while the separation of MgO-C3 is additionally based on the second principal component. The color highlighted loadings in Fig. 4 show a distinctive influence of the number of double bond equivalents on the classification of the MgO-C samples. Almost all features with DBE $\geq 10$ have a strong negative influence on the first principal component and are thus correlated with MgO-C1. This is in good agreement with the higher average molecular mass of this sample compared to the other two.
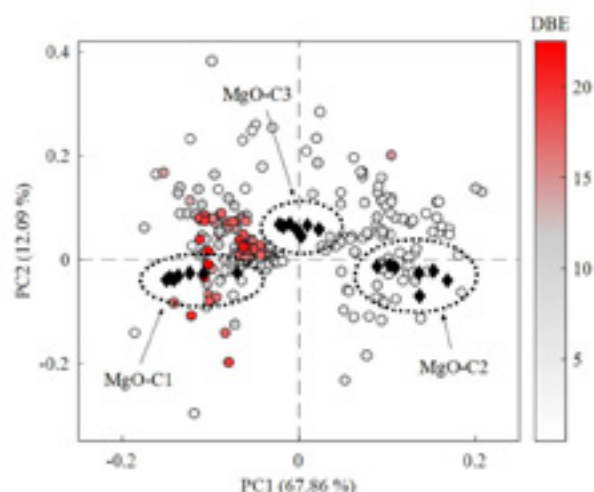
Fig. 4: Biplot of the scores and loadings of principal component analysis (PCA). The color scale classifies the features according to their number of DBE. [14]

In addition to molecular size, individual compound classes are also essential for distinguishing the samples. Fig. 5 shows that, apart from four features, all oxygen-containing compounds are located in the right half of the biplot and thus have a positive influence on PC1. Furthermore, compounds of the $O_2$-class additionally show an exclusively negative influence on PC2. This proves a strong positive correlation of oxygen compounds with MgO-C2. In contrast, sulfur-containing features have an exclusively negative influence on PC1 and are thus significant for MgO-C1. When analyzing the S-compounds, it can be observed that they are predominantly organic compounds with DBE $> 9$. Features of the N-class are only observed in the upper two and the lower left quadrants of the biplot. This proves the negative correlation of nitrogenous features with the sample MgO-C2, whose scores occur exclusively in the lower right quadrant. Overall, these results are in good agreement with the relative abundances of the compound classes in the respective samples shown in Fig. 2.
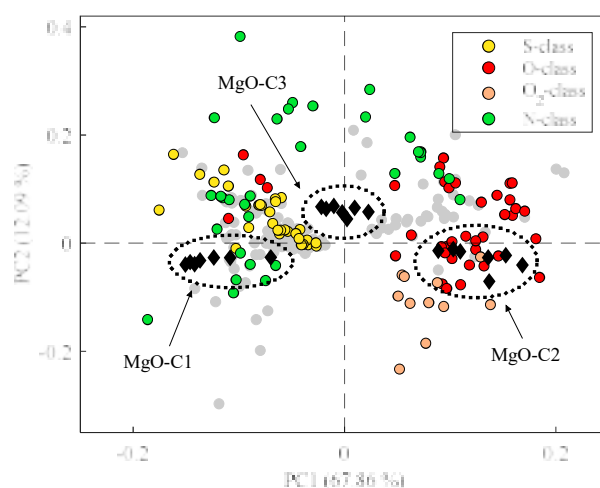
Fig. 5: Biplot of the scores and loadings of principal component analysis (PCA). Features with a major influence on the first two principal components are highlighted in color, classified according to their substance classes. [14]

## CONCLUSIONS

Multivariate statistical methods such as HCA und PCA for the analysis of complex DIP-HR-TOFMS data represents a powerful tool for characterization and classification of refractory materials. It was shown that the investigated refractory products can be distinguished without any doubt despite the low mass fraction of the organic phase and a basically similar structural composition. By applying a supervised PCA, it was also possible to identify and extract characteristic structural features of each sample. In addition to the size of the aromatic system, heteroatomic structures in particular were of major importance in distinguishing the samples.

## REFERENCES

[1]    M. Zander und G. Collin, „A review of the significance of polycyclic aromatic chemistry for pitch science", *Fuel*, Jg. 72, Nr. 9, S. 1281–1285, 1993.

[2]    M. Zander, „On the composition of pitches" (en), *Fuel*, Jg. 66, Nr. 11, S. 1536–1539, 1987, doi: 10.1016/0016-2361(87)90014-7.

[3]    J. R. Kershaw, „The Chemical Composition of a Coal-Tar Pitch", *Polycyclic Aromatic Compounds*, Jg. 3, Nr. 3, S. 185–197, 1993, doi: 10.1080/10406639308047870.

[4]    C. G. Aneziris, d. Borzov, J. Ulbricht, J. Suren und H. Dern, „Phenolic Resins with Carbo-Resin Additions for Improved MgO-C Refractories", *KEM*, 264-268, S. 1767–1770, 2004, doi: 10.4028/www.scientific.net/KEM.264-268.1767.

[5]    C. G. Aneziris, U. Klippel, W. Schärfl und V. Stein, „Functional Refractory Material Design for Advanced Thermal Shock Performance Due to Titania Additions", *Applied Ceramic Technology*, Jg. 4, Nr. 6, S. 481–489, 2007.

[6]    G. Bock, M. Hampel, S. Dudezig und C. G. Aneziris, „Application of bitumen based binders for production of MgO-C-refractories".

[7]    G. Buchebner, R. Neuboeck und S. Grassegger, „Carbon-Bonding - a New Milestone on Low Emission Magnesia-Cabon Bricks" in *UNITECR 2001*, Cancun, 2001, S. 324–335.

[8]    L. Jun, L. H. Xia und F. Haixia, „Influence of carbores binder on the strength of Magnesia-Carbon materials" in *Advances in Engineering Research*, Bd. 27, *3rd International conference on material, mechanical and manufacturing engineering (IC3ME 2015): Guangzhou, China, June 27-28, 2015*, M. Fong, Hg., Amsterdam: Atlantis Press, 2015, S. 1815–1820.

[9]    T. Kuffa, G. Sucik und D. Hrsak, „The influence of carbon materials on the properties of MgO refractories", *Materials and Technology*, Jg. 39, Nr. 6, S. 211–213, 2005.

[10]   A. H. de Aza, F. J. Valle, P. Ortega, P. Pena und S. de Aza, „Analytical Characterization of a Magnesia-Graphite Refractory", *J American Ceramic Society*, Jg. 89, Nr. 5, S. 1704–1708, 2006, doi: 10.1111/j.1551-2916.2006.00975.x.

[11]   J. Doll, A. Masoudi Alavi und P. Quirmbach, „Comparative analytical characterization of two carbonaceous binders used in refractory materials" in *Unified International Technical Conference on Refractories (UNITECR 2022): 17th Biennial Worldwide Congress on Refractories : Chicago, Illinois, USA, 15-18 March 2022*, 2022.

[12]   J. Doll, A. Masoudi Alavi und P. Quirmbach, „High-Resolution Mass Spectrometry and Multivariate Statistics: A Powerful Tool for the Characterization and Discrimination of Refractory Materials", *Refractrories Worldforum*, Jg. 15, Nr. 1, 2023.

[13]   U. Käfer *et al.,* „Direct inlet probe - High-resolution time-of-flight mass spectrometry as fast technique for the chemical description of complex high-boiling samples", *Talanta*, Jg. 202, S. 308–316, 2019.

[14]   J. Doll, „Entwicklung einer Non-Target-Analysestrategie zur Untersuchung komplexer Kohlenstoffgemische aus dem Bereich feuerfester Anwendungen". Dissertation (eingereicht), Institut für Integrierte Naturwissenschaften, Universität Koblenz, Koblenz, 2023.

# REFRACTORY CEMENTS CONTAINING ZR AND SR AS ALTERNATIVES TO THE CACS DESIGNED FOR THE PRODUCTION OF HIGH PERFORMANCE MONOLITHIC REFRACTORIES

**Dominika Madej**
AGH University of Science and Technology, Faculty of Materials Science and Ceramics,
Department of Ceramics and Refractories, al. A. Mickiewicza 30, 30-059 Kraków, Poland
dmadej@agh.edu.pl

## ABSTRACT

In connection with the development of the manufacture of monolithic refractories containing zirconium dioxide it has become necessary to carry out investigations into the hydraulic binder systems containing $ZrO_2$. One of these systems is $CaO$-$SrO$-$Al_2O_3$-$ZrO_2$ (C-S-A-Z), especially in the regard the components of high melting point. Thus, complementary experiments of X-ray diffraction analysis (XRD) and scanning electron microscopy (SEM) were used to analyse the properties of state-of-the-art cements belonging to the C-S-A-Z system. Strontium zirconium aluminate cement and strontium calcium zirconium aluminate cements were prepared as multiphase materials. Moreover, strontium aluminate cement with high content of $SrAl_2O_4$ as the main clinker phase was prepared by milling and calcination of the equimolar mixture of strontium carbonate and aluminium oxide. This work also compare the properties of $SrAl_2O_4$-bonded alumina-based castables, and of the equivalent castables containing calcium aluminate cement (CAC).

*Keywords: refractories, special inorganic cements, castables, microstructure, synthesis, new solutions for monolithics*

## INTRODUCTION

Calcium aluminate cement (CAC) is the most widely used binder for monolithic refractories, especially castables [1]. During the hydration process, calcium aluminates CA, $CA_2$ and $C_{12}A_7$ (C=CaO, A=$Al_2O_3$) undergo hydration and form a network of hydration products in the matrix, connecting fillers i.e. the fines and the refractory aggregates [2]. This process is crucial for development of the high-quality cement-based monolithics.

An increasing tendency to use the monolithic refractories over the past decade has been accompanied with the parallel trend of the improvement of cement-containing castables by introducing Zr-containing compounds, e.g. $ZrSiO_4$, $CaZrO_3$, $ZrO_2$ or AZS and AZ materials (A=$Al_2O_3$, Z=$ZrO_2$, S=$SiO_2$) as aggregates or modifying binder systems by introducing Zr, Sr or Ba elements [3-6]. In this regard, the system of $CaO$-$SrO$-$Al_2O_3$-$ZrO_2$ (C-S-A-Z) will form large group of hydraulic binders under the aegis of this project.

### Motivation and goal of this work

Thus, in this study, composite cements belonging to the S-A-Z, C-S-A-Z and S-A systems were obtained and evaluated as alternatives to CACs for use in the refractory monolithic technologies, especially castables.
Thus, the main goals of this work are:
- to synthesize and investigate new cements belonging to the S-A-Z, C-S-A-Z and S-A systems,
- to investigate and compare the properties of alumina-based castables made of CAC or strontium monoaluminate (S-A)-containing cement.

## EXPERIMENTAL PART

### Synthesis

For the preparation of refractory cement clinker (Table 1), stoichiometric quantities of $SrCO_3$, $Al_2O_3$ and $ZrO_2$ (sample $S_7A_3Z$); $CaCO_3$, $SrCO_3$, $Al_2O_3$ and $ZrO_2$ (sample $C_{3.5}S_{3.5}A_3Z$); $SrCO_3$ and $Al_2O_3$ (sample SA) were used. The powders were then ball milled using monoclinic zirconia balls for 1 h at a speed of 400 r/min. After milling, the batches were pressed at 50 MPa, to produce cylindrical green compacts of about 20 mm diameter. These cylindrical-shaped samples were heated at 2°C/min and calcined at 1300°C for 10 h. After calcination, samples were

crashed using mortar and pestle. The crashed powders were again ball-milled for 1 h, pressed and sintered at sintered at 1500°C for 1 h ($S_7A_3Z$ sample), at 1430°C for 10 h ($C_{3.5}S_{3.5}A_3Z$ sample), and at 1550°C for 10 h (SA sample) to obtain sintered bodies. Moreover, commercially available calcium aluminate cement Górkal 70 from Górka Cement was also used in further investigations.

*Table 1. Composition of samples.*

| Sample abbreviation* | Composition |
|---|---|
| $S_7A_3Z$ | $7SrO \cdot 3Al_2O_3 \cdot ZrO_2$ |
| $C_{3.5}S_{3.5}A_3Z$ | $3.5CaO \cdot 3.5SrO \cdot 3Al_2O_3 \cdot ZrO_2$ |
| SA | $SrO \cdot Al_2O_3$ |
| CAC70 | Commercially available calcium aluminate cement Górkal 70 from Górka Cement |

*C=CaO, S=SrO, A=$Al_2O_3$, Z=$ZrO_2$

### Castables preparation

The raw materials for alumina-based castables are different sizes of tabular alumina, spinel AR90 and reactive alumina from Almatis, microsilica 971 from Elkem, calcium aluminate cement Górkal 70 (CAC70) from Górka Cement (Trzebinia, Poland) or strontium aluminate cement (SA) synthesized under laboratory conditions and additives. Details of these compositions are listed in Table 2.

*Table 2. The composition of $Al_2O_3$-based castables (wt. %).*

| Raw materials | CAC70-Castables | SA-Castables |
|---|---|---|
| Tabular alumina 0.2-6 mm | 50.86 | 50.86 |
| Spinel AR90 0-0.5 mm | 20.89 | 20.89 |
| Electrocorundum < 0.1 mm | 6.31 | 6.31 |
| Reactive alumina | 15.5 | 15.5 |
| Reference CAC Górkal 70 | 5.35 | - |
| As-synthesized SA cement | - | 5.35 |
| Microsilica 971 | 1.09 | 1.09 |
| Additives | 0.1 | 0.1 |
| Water | 4.5 | 4.5 |

The castable compositions were weighted, dry and wet homogenized, poured in a mold and compacted through vibration. Then, samples were kept in the molds for 24 h to set completely and then they were removed from the molds, dried at 110°C for 24 h and heat treated at 1500°C for 10 h.

### Sample preparation and methods of investigation

The microstructure of the $S_7A_3Z$, $C_{3.5}S_{3.5}A_3Z$ and SA cement clinkers was characterized by SEM-EDS method. For this purpose, the scanning electron microscopy NOVA NANO SEM 200 of FEI, equipped with a EDS system of EDAX was used. Samples were embedded in resin, cut, grinded, polished and coated with carbon to be conductive and then examined. The clinkers were crushed and milled to obtain fine powders, with particle size below 63 µm. Phase identification for the as-synthesized $S_7A_3Z$, $C_{3.5}S_{3.5}A_3Z$ and

SA cement clinkers was carried out using X-ray diffraction (XRD) on a ProPANalytical X'Pert X-ray diffractometer, with Cu Kα radiation (λ = 0.15418 nm), with 0.02° per step and 3s time per step (2theta range from 10° to 50°).

The CAC70-Castables and SA-Castables heat treated at 1500°C for 10 h were investigated in term of their physical properties including apparent porosity (AP), cold modulus of rupture (CMOR) and cold cursing strength (CCS) according to the procedures presented in the PN-EN ISO 1927-6:2013-06 standard.

One of the most important instrument for the analysis of microstructural characteristics of castables was the scanning electron microscope (SEM). For this purpose, the samples were cut, immersed in resin, grinded, polished and coated with carbon.

## RESULTS

### Phase composition and microstructure of cement clinkers

XRD patterns for the as-synthesized the $S_7A_3Z$, $C_{3.5}S_{3.5}A_3Z$ and SA cement clinkers are shown in Figs 1, 3 and 6, respectively. The main crystalline phases identified in the $S_7A_3Z$ clinker, were $Sr_3Al_2O_6$, $SrAl_2O_4$ and $SrZrO_3$ (Fig. 1). The $C_{3.5}S_{3.5}A_3Z$ sample contains $(Ca,Sr)_3Al_2O_6$, $SrAl_2O_4$, $SrZrO_3$ and $CaZrO_3$ (Fig. 3), whereas the SA sample was found as monophase (Fig. 6).
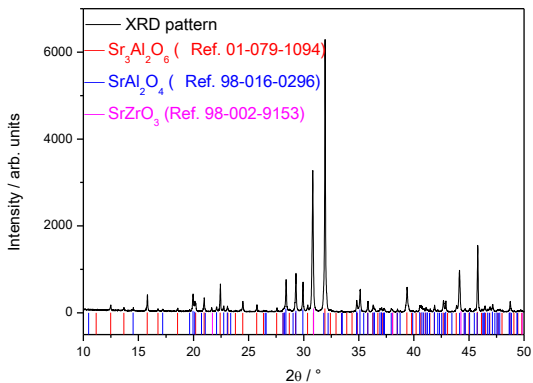


Fig. 1. XRD pattern of the $S_7A_3Z$ sample after sintering at 1500°C for 1 h.
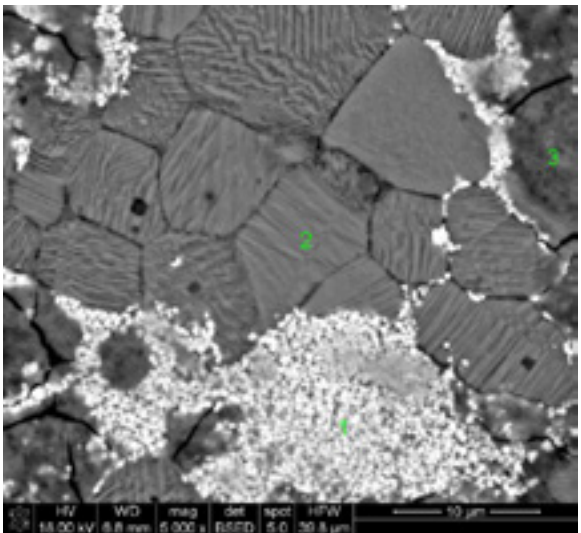


Fig. 2. SEM image of microstructure of the $S_7A_3Z$ sample after sintering at 1500°C for 1 h. EDS analysis: 1-$SrZrO_3$, 2-$SrAl_2O_4$, 3-$Sr_3Al_2O_6$.

Moreover, Fig. 5 compares (a) the XRD peaks corresponding to $SrZrO_3$ and $(Sr,Ca)ZrO_3$ in the samples $S_7A_3Z$ and $C_{3.5}S_{3.5}A_3Z$, respectively, and (b) XRD peaks corresponding to $SrAl_2O_4$ and $(Sr,Ca)Al_2O_4$ in the samples $S_7A_3Z$ and $C_{3.5}S_{3.5}A_3Z$, respectively.

As it can be noticed in Fig. 5, the XRD peaks shifts revealed features between two samples $S_7A_3Z$ and $C_{3.5}S_{3.5}A_3Z$. It can be seen that the main XRD peaks of $SrZrO_3$ and $SrAl_2O_4$ slightly shifted toward higher angles in the $C_{3.5}S_{3.5}A_3Z$ sample, suggesting decreased of the unit cell volume of $(Sr,Ca)ZrO_3$ and $(Sr,Ca)Al_2O_4$, when compared to the pure $SrZrO_3$ and $SrAl_2O_4$ in the $S_7A_3Z$ sample. This is attributed to the much larger ionic radius of $Sr^{2+}$ (132 p.m.) compared with $Ca^{2+}$ (114 p.m.).
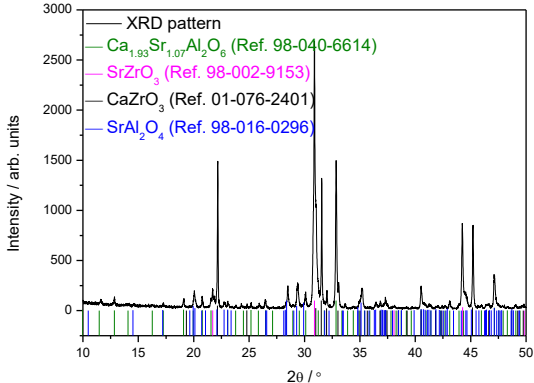


Fig. 3. XRD pattern of the $C_{3.5}S_{3.5}A_3Z$ sample after sintering at 1430°C for 10 h.
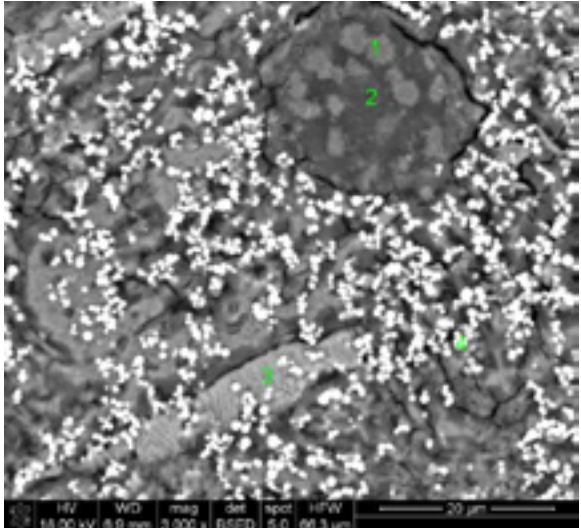


Fig. 4. SEM image of microstructure of the $C_{3.5}S_{3.5}A_3Z$ sample after sintering at 1430°C for 10 h. EDS analysis: 1,2-$(Ca,Sr)Al_2O_6$ with different compositions, 3-$(Ca,Sr)Al_2O_4$, 4-$(Sr,Ca)ZrO_3$.
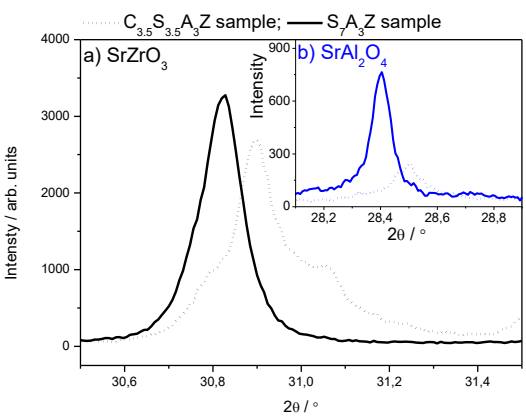


Fig. 5. (a) XRD peaks corresponding to $SrZrO_3$ and $(Sr,Ca)ZrO_3$ in the samples $S_7A_3Z$ and $C_{3.5}S_{3.5}A_3Z$, respectively. (b) XRD peaks corresponding to $SrAl_2O_4$ and $(Sr,Ca)Al_2O_4$ in the samples $S_7A_3Z$ and $C_{3.5}S_{3.5}A_3Z$, respectively.
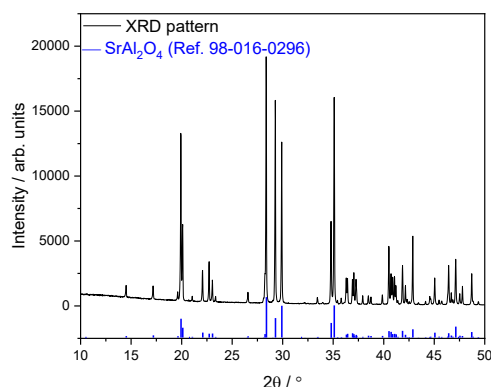
Fig. 6. XRD pattern of the SA sample after sintering at 1550°C for 10 h.
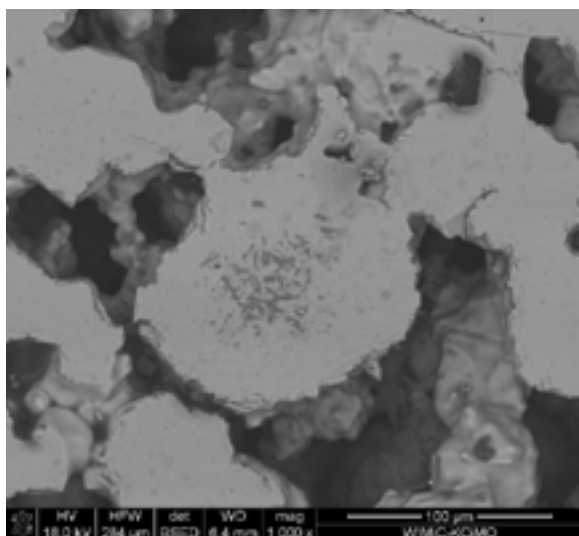


Fig. 7. SEM image of microstructure of the SA sample after sintering at 1550°C for 10 h.

SEM was used to characterize clinkers produced under laboratory conditions. SEM images for the as-synthesized the $S_7A_3Z$, $C_{3.5}S_{3.5}A_3Z$ and SA cement clinkers are shown in Figs 2, 4 and 7, respectively. The composition of the raw materials and conditions of synthesis greatly affect the clinker microstructure, and the distribution and sized of the phase grains. SEM revealed the phases in the $S_7A_3Z$ clinker, which include $Sr_3Al_2O_6$ and $SrAl_2O_4$ (coarse and fine), and agglomerated and partially sintered particles of $SrZrO_3$ (Fig. 2). On the other hand, Zr-rich phases were homogeneously distributed throughout the $C_{3.5}S_{3.5}A_3Z$ matrix (Fig. 4).

### Physical properties and microstructure of castables

The physical and mechanical properties of the two castables heat-treated at 1500°C are listed in Table 2. It can be seen that both the mechanical properties and apparent porosity of the alumina-based materials depends on the cement type.

Table 2. Physical and mechanical properties of the castables heat-treated at 1500°C.

| Samples | AP / % | CMOR / MPa | CCS / MPa |
|---|---|---|---|
| CAC70-Castables | 15.75 | 40.54 | 152.98 |
| SA-Castables | 17.80 | 30.62 | 222.82 |
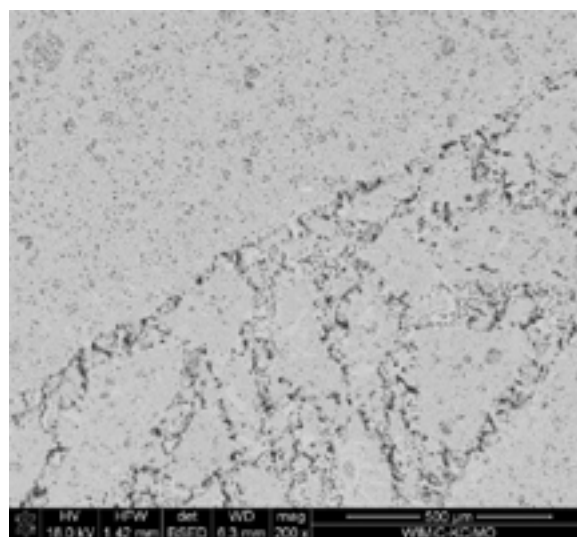


Fig. 8. SEM image of microstructure of the CAC70-Castables after firing at 1500°C for 10 h.
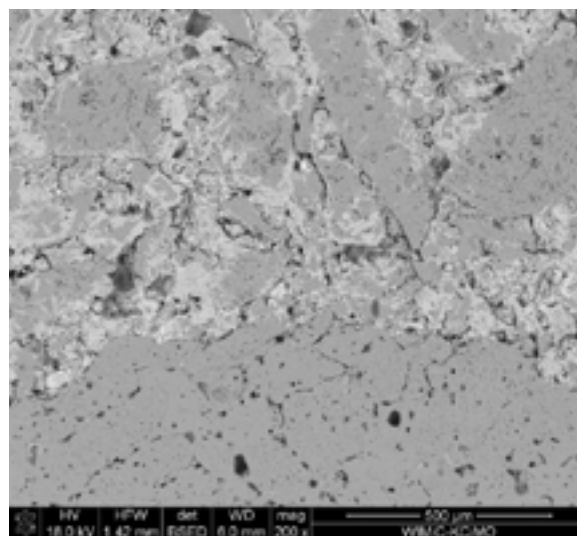


Fig. 9. SEM image of microstructure of the SA-Castables after firing at 1500°C for 10 h.

SEM images for the as-synthesized the CAC70-Castables and SA-Castables after firing at 1500°C for 10 h are shown in Figs 8-9, respectively. The cement type affects the microstructure of the bonding interfaces between the matrix and aggregates in castables.

### CONCLUSIONS

A group of novel cements from the S-A-Z, C-Sr-A-Z and S-A systems was proposed and investigated. The strontium zirconium aluminate, strontium calcium zirconium aluminate and strontium monoaluminate cements were successfully synthesized by a two-step solid state reaction route and characterized by XRD and SEM-EDS.

The as-synthesized S-A cement was used to prepare alumina-based castables. The properties of $SrAl_2O_4$-bonded alumina-based castables, and of the equivalent castables containing calcium aluminate cement (CAC) were stablished. The SA-Castables exhibit better results in terms of CCS.

**REFERENCES**

[1]	Madej D, Kruk A. Tracing the early and long-term hydration of fast setting cementitious material ($Ca_7ZrAl_6O_{18}$) and calcium aluminate cement (CAC) pastes by means of electrochemical impedance spectroscopy and other methods. Construction and Building Materials 164, 2018, p. 94-102

[2]	Kruk A, Madej, D. A new approach to time-resolved electrochemical impedance spectroscopy using the Impedance Camera to track fast hydration processes in cement-based materials. Measurement 205, 2022, 112199

[3]	Madej D, Sieroń K, Kruk A. Synthesis and performance of aluminous cements containing zirconium and strontium as alternatives to the calcium aluminate cements designed for the production of high performance refractories. Cement and Concrete Composites 130, 2022, 104518

[4]	Madej D, Kruk A. Monitoring hydration of Sr-doped calcium zirconium aluminate $(Ca,Sr)_7ZrAl_6O_{18}$ cement via electrochemical impedance spectroscopy (EIS) and supported techniques. Construction and Building Materials 206, 2019, p. 307-320

[5]	Madej D, Rajska M, Kruk A. Synthesis and hydration behaviour of calcium zirconium aluminate powders by modifying co-precipitation method. Ceramics International 46(2), 2020, p. 2373-2383

[6]	Madej D, Silarski M, Parzych S. Design, structure, microstructure and gamma radiation shielding properties of refractory concrete materials containing Ba- and Sr-doped cements. Materials Chemistry and Physics 260, 2021, 124095

# THE BINDING OF NON−CEMENT REFRACTORY CASTABLES USING THE TECHNOLOGY OF *IN−SITU* SOL−GEL FORMATION

Michel Cichocki, Joachim Angelkort, Natalie Fröse, Storm Higgins, Manfred Knoll, Marcel Mix

Intocast AG, Westpreußenstr. 30, 47809 Krefeld, Germany

michel.cichocki@intocast.com

**Abstract**

In recent years, silica sol solutions have been increasingly used as cement-free binders in refractory unshaped products. The silica sol solutions are aqueous colloidal dispersions of nanoscale amorphous $SiO_2$ particles. Compared to conventional high alumina cement-bonded concretes, the silica sol-bonded products are characterized by good alkali and acid resistance. The main advantage, however, is that no calcium aluminate hydrate phases are formed during the setting process and thus these concretes can be heated much faster.

A major disadvantage of silica fume solutions is that they must be stored in separate containers, protected from frost and light. To avoid this, a new system in which the silica sol formation takes place "in-situ" in the refractory matrix is introduced. For this purpose, a microscale amorphous $SiO_2$ powder is mixed directly into the refractory mass. By adding water, the silica sol formation is generated within the matrix. This eliminates many of the major disadvantages of using aqueous silica sol solutions. The addition of < 1.0 % of this binder leads to good green strengths of the refractory castable. To compare the binding of cement-free and cement-containing refractories, the physical and chemical properties of a nearly pure alumina product was tested. For this purpose, all tests were carried out on the cement containing products and their non-cement counterparts bonded by liquid sol-gel or by the in-situ sol-gel formation. Furthermore, an example of application will be given proving the efficiency of the in-situ sol-gel technique for practical use.

**Introduction**

The most common binding system for unshaped refractories is based on calcium-aluminate-cement (CAC) which involves the formation of low melting phases like for example anorthite during firing [1, 2]. Therefore, a reduction of the CAC content is desirable. To achieve this, various alternative binding systems like the gel bindings were investigated in the past [3, 4]. The technique of gel binding is known since the 1990's and is mostly used in ultra-low cement castables (ULCC) and no-cement castables (NCC) [3, 5]. Instead of gaining the green strength by the hydration of CACs forming calcium alumina hydrates in sol-gel bonded systems the strength is achieved by creating a 3D-network by polymerization of amorphous silica particles immersed in water. Commonly a dispersion of $SiO_2$ in water is used as sol-gel for casting. This leads to lower green strength after drying [6]. After firing at temperatures above 900 °C, however, the strength of sol-gel bonded castables is higher than the one observed in cement-containing bonding systems [3]. Due to the absence of calcium hydrate phases during setting, the refractory castable can be heated at a higher rate [7, 8]. Furthermore, sol-bonded products show a higher alkali and acid resistance compared to cement bonded ones. The downside of using sol-gel as binder is its complex storing in separate canisters for liquids. To avoid the difficult storage of the silica fume solutions due to its vulnerability to light and frost, < 1 % microscale amorphous silica powder can be added to the mixture [9]. By casting it with water, a process of "in-situ sol-gel" formation occurs and leads to a sufficiently high green strength. This binding system can be applied to any kind of raw material-based refractory mix, and due to the low addition of silica powder, results in a pure chemical composition that does not impact the melting temperature of the refractory.

**Methods**

A high alumina thixotropic ULCC product was used as reference and modified to a NCC variant using a liquid sol-gel (NCC-L) and to another NCC variant by adding a microscale amorphous silica powder (NCC-P). After hydration, the microscale amorphous $SiO_2$ powder in combination with fine MgO as a gelling agent accounted for a binding in an otherwise pure $Al_2O_3$ system (Table 1). Consequently, the $SiO_2$ and MgO content is slightly raised, and the CaO content is lowered compared to the ULCC. In case of the NCC-L, a sol-gel with the composition of 30 % $SiO_2$ and 70 % water was added to the modified base recipe (Table 1). Compared to the NCC-L, the $SiO_2$ content in the NCC-P is 1.5 % lower, which leads to a $SiO_2$ content of below 1.0 % in the NCC-P (Table 2).

*Table 1: Composition of the tested products*

|  | **Raw material** | **Mixing agent** |
|---|---|---|
| **ULCC** | alumina, CAC (0.45 %) | 4.5 % water |
| **NCC -P** | alumina, fine MgO, fine SiO2 | 5.4 % water |
| **NCC-L** | alumina | 7.0 % sol-gel (30 % silica, 70 % water) |

Three bars and one cylinder were casted for each recipe. These were dried at room temperature as well as at 110 °C for 24 h, respectively. Afterwards two of the samples were burned at temperatures of 1000 °C and 1500 °C. All three bars of each product were used to measure the PLC (permanent linear change), the CCS and CMOR by using a standard test machine from Form+Test.

Pieces of each bar were pulverized and investigated via X-ray diffraction (XRD) measurements. For this purpose, a PANalytical X'Pert[3] diffractometer with a Cu $K_\alpha$ X-ray tube was used.

For the refractory under load measurement, the casted cylinders were pre-fired at 1000°C for 24 h and polished on the surface. The measurement was performed with a machine from Netzsch Gerätebau GmbH with a uniaxial pressure of 0,2 $N/mm^2$ during constant heating.

*Table 2: Chemical composition of the tested high alumina product with CAC, sol-gel and in-situ sol-gel after drying (110 °C, 24 h).*

| **Oxide** | **ULCC** | **NCC-P** | **NCC-L** |
|---|---|---|---|
| **Al2O3** | 99.0 | 98.7 | 97.4 |
| **SiO2** | 0.0 | 0.4 | 1.9 |
| **CaO** | 0.4 | 0.0 | 0.0 |
| **Na2O** | 0.3 | 0.4 | 0.4 |
| **MgO** | 0.1 | 0.4 | 0.1 |

105

*Table 3: Phase compositions of the samples ULCC, NCC-P and NCC-L after firing at different temperatures.*

| Binding system | Temp / °C | corundum | β-alumina | hibonite | mullite | others |
|---|---|---|---|---|---|---|
| ULCC | 110 | 95.4 | 3.8 | - | - | 0.7 |
| | 1000 | 94.3 | 4.4 | - | - | 1.3 |
| | 1500 | 90.5 | 3.9 | 5.4 | - | 0.2 |
| NCC-P | 110 | 96.0 | 3.8 | - | - | 0.1 |
| | 1000 | 96.4 | 3.2 | - | - | 0.2 |
| | 1500 | 97.8 | 0.8 | - | - | 1.3 |
| NCC-L | 110 | 96.0 | 3.7 | - | - | 0.2 |
| | 1000 | 96.0 | 3.6 | - | - | 0.2 |
| | 1500 | 97.7 | 0.5 | - | 1.4 | 0.2 |

## Results and discussion

According to the X-ray diffraction patterns, the samples ULCC, NCC-P and NCC-L consist of 95.4 % - 96.0 % corundum and 3.7 % - 3.8 % β-alumina. After firing, the amount of corundum in the ULCC decreases from 95 % to 91 % and increases from 96 % to 98 % in the cement-free samples NCC-P and NCC-L. The latter is accompanied with the decrease of β-alumina to nearly 0 %. Beside this, the ULCC formed $CA_6$ (hibonite) consuming the cement phases at 1500 °C whereas in the NCC-L the relatively high amount of $SiO_2$ leads to the formation of mullite. None of these phases can be observed in significant amounts in the sample NCC-P due to the high purity of the system (Table 3). In contrast to that, a small amount of $SiO_2$ and $MgAl_2O_4$ (spinel) can be found due to the use of MgO as a gelling agent.

Due to the formation of calcium aluminate hydrate phases, the green strength of the ULCC is higher than that of the NCCs. Compared to the NCC-P, the green strength of the NCC-L is slightly higher. This is probably caused by the higher initial amount of silanol groups (Si-O-H) in the sol-gel compared to the powder (Figure 1, Figure 2).

After firing at 1000 °C, the CCS and CMOR of the cement-containing ULCC become lower than the ones of the NCCs, which is related to the decomposition of the CAH phases. The NCC-L has a significantly higher $SiO_2$ content compared to the NCC-P and thus the sintering temperature is lowered due to the lower melting point. For the same reason, the CCS and CMOR of the NCC-L are higher than the ones of the NCC-P (Figure 1, Figure 2).

With further increase of the temperature to 1500 °C, the CCS and the CMOR of the ULCC increases due to the formation of hibonite and the CCS overcomes those of the NCCs. In contrast to that, no large increase in the strength of the NCC-L can be observed (Figure 1, Figure 2). This can be also related to the high $SiO_2$ content, which not only lowers the sintering temperature, but also decreases the melting point. Without the high amount of $SiO_2$, melting occurs at a higher temperature. Thus, the strength of the NCC-P increases due to the sintering of the nearly pure $Al_2O_3$. This effect leads to a higher CMOR of the NCC-P compared to the NCC-L and ULCC (Figure 1, Figure 2).

The increase in the strength of the ULCC at 1500 °C is also related to a volume expansion at 1400 °C measured by the refractory under load test (Figure 3). This expansion might be related to the formation of hibonite. The NCC-L shows a lower refractoriness compared to the NCC-P (Figure 3). This can also be explained by the relatively high content of $SiO_2$ of approx. 2 % in the NCC-L compared to the NCC-P. Therefore, a suitable strength and refractoriness can be achieved in a nearly pure $Al_2O_3$ system with a $SiO_2$ content of < 1 %.
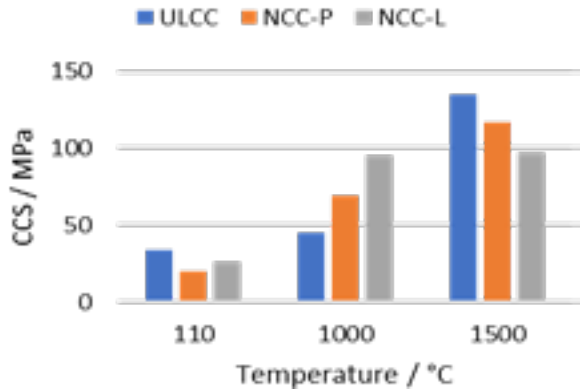


*Figure 1: Cold crushing Strength (CCS) of the tested ULCC, NCC-P and NCC-L castable.*
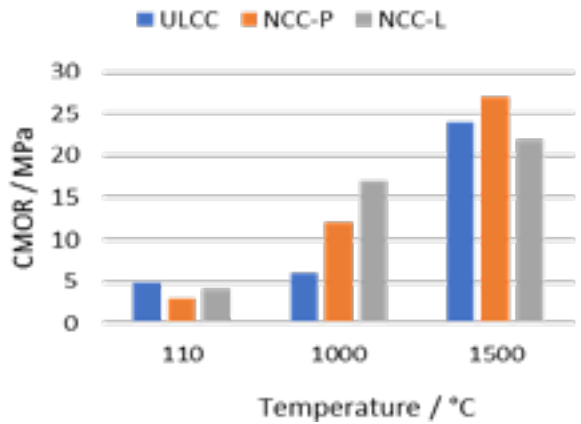


*Figure 2: Cold modulus of rupture (CMOR) of the tested ULCC, NCC-P and NCC-L castable.*
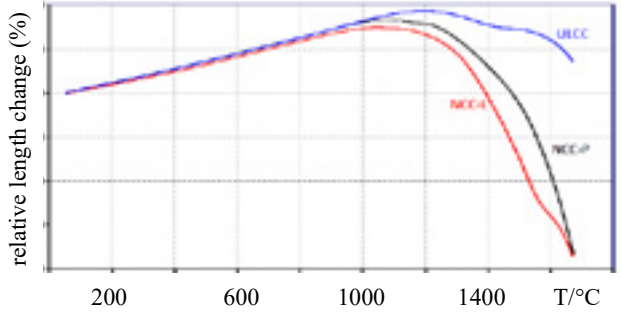


*Figure 3: Refractory under load measurement of the analyzed ULCC and the NCC variants with sol-gel and the in-situ sol-gel components.*

Apart from productions on a laboratory scale, the product based on the in-situ sol-gel binding has been used for casting well blocks in different shapes and dimensions, ranging from 370 mm to 470 mm in height and 360 mm in wide with a cylindrical hole with a diameter ranging from 118 mm to 199 mm (Figure 4). After casting and drying for 24 hours, the NCC-P showed sufficient green strength for demolding. In its application the NCC-P was used with a durability of 52 to 57 heating cycles at a plant site, which is comparable to the performance of spinel-containing alumina products.

Apart from this, the in-situ sol-gel binding system offers the advantages of using solely water for casting. Thus, the installation procedure is comparable to castables with a cement-based binding system. If $SiO_2$ is added as a powder and not as liquid sol-gel, the binder is already included in the dry-mixture and no temperature-

controlled storage of supplementary canisters is required. This saves storage space, reduces energy costs and simplifies the transport.

Furthermore, this binding system can be adapted to any products based on MgO, $SiO_2$ or $Al_2O_3$. This includes qualities from chamotte to high alumina raw materials. Even SiC can be added to the system. Further investigations of the in-situ sol-gel bindings system and adaptations to different applications are ongoing and will be discussed in the future.
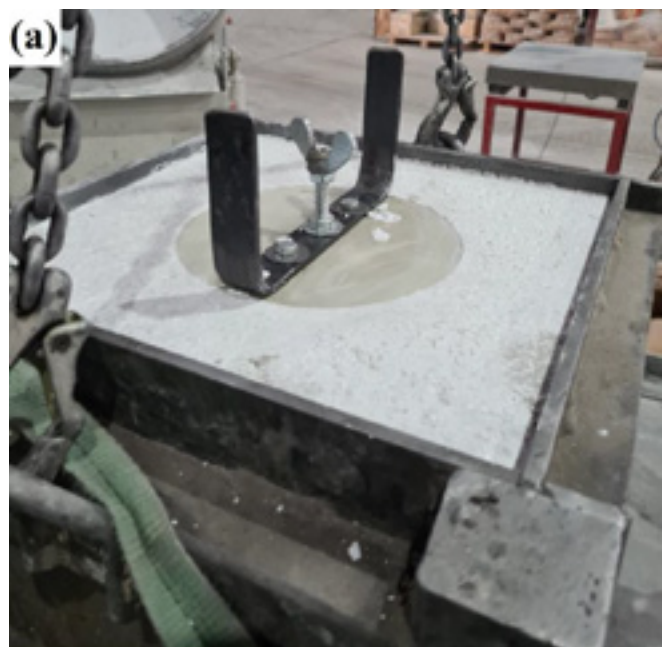




*Figure 4: Well block casted from NCC-P mass (a), NCC-P well block after demolding (b)*

## Conclusions

Besides the conventional binding system based on calcium-aluminate-cements, sol-gel can be used as an alternative approach. Disadvantages associated with the liquid sol-gel can be avoided by mixing a microscale silica powder in the dry-mixture initiating an in-situ formation of the sol-gel by adding water to the product. Compared to the liquid sol-gel, a significantly smaller $SiO_2$ amount of < 1.0 % is already sufficient to establish an adequate green strength through the silica powder addition. Due to the lower $SiO_2$ content, the number and the total amount of low-melting phases is diminished leading to higher refractoriness of the in-situ sol-gel bonded sample in a nearly pure $Al_2O_3$ system.

Based on the service live of the in-situ sol-gel bonded well blocks, the addition of the microscale silica is suitable for the intended application and thus can be used as an alternative to cement. In contrast to the use of the liquid sol-gel binder, the dry-mixture containing the microscale amorphous $SiO_2$ powder only needs water for casting, making the installation practice comparable to conventional cement-containing products. This delivers an "all-in-bag" solution for cement-free castables.

## References

[1] D. Zemánek, L. Nevřivová, "Use of the Sol-gel Method for Production of No Cement Castables", Special Concrete and Composites 2020, AIP Conf. Proc. 2322, 020004-1 – 020004-6, 2020

[2] R. Sarkar, J. Srinivas, "Effect of Cement and Sol Combined Binders on High-Alumina Refractory Castables", refractories WORLDFORUM 8, 73-78, 2016

[3] B. Myhre, "Gel Bonding in Refractory Castables. New Insights in the making of refractory castables that have high density, high refractoriness, ease of firing and good placeability", 6th international symposiun on refractories, Zhenzhou, China, Oct. 18-20, 2012

[4] A. Singh, R. Sarkar, "High alumina castables: a comparison among various sol-gel bonding systems", Aust Ceram Soc 53:553-567, 2017

[5] H. Peng, B. Myhre, "Microsilica-gel bonded refractory castable with improved setting behaviour and mechanical properties." Refractories World Forum, vol. 3, 69-75, 2015

[6] S. Badiee, S. Otroj, "NON-CEMENT REFRACTORY CASTABLES CONTAINING NANO-SILICA: PERFORMANCE, MICROSTRUCTURE, PROPERTIES", Ceramics-Silikáty 53 (4), 297-302, 2009

[7] T. Schemmel, H. Jansen, B. Kesselheim, U. Kremer, "Nanobond – the New Cement Free Castable for Quick Lining and Fast Repairing", refractories WORLDFORUM 4, 89-92, 2012

[8] K. Beimdiek, B. Kesselheim, H. Klischat, T. Schemmel, "Zementfreie Feuerfestbetone für spannungsreduzierende Gefüge", Giesserei-Praxis 5, 2019

[9] M. Knoll, N. Fröse, Feuerfestmasse und Bindemittel dafür, Verfahren zur deren Herstellung sowie Verwendung, Patent Offenlegungsschrift DE 102019001214 A1, 2020

# 2   ADVANCES IN MONOLITHIC TECHNOLOGY

# NOVEL COLLOIDAL SILICA TECHNOLOGY FOR MGO–CONTAINING REFRACTORIES – PART 1: ANTI–HYDROXYLATION BINDER

Rafael Salomão, Leandro Fernandes
São Carlos School of Engineering, Materials Engineering Department, University of São Paulo, São Carlos, Brazil

Andreas Sundblom, Peter Greenwood
Nouryon AB, Göteborg, Sweden

Isabela Santos Martinatti, Paulo Roberto Teruo Tiba
Nouryon South America, Jundiaí, Brazil

## ABSTRACT

This study combined fine MgO sinter with a novel aqueous dispersion of colloidal silica whose particles were surface modified with an epoxysilane agent. Their engineered surface reactivity produced self-flowing fine MgO sinter-colloidal-silica suspensions of easy mixing and suitable workability. Reference compositions containing plain water and conventional unsilanized colloidal silica were prepared and tested under the same conditions. After mixing, casting, and curing, the reactions between colloidal silica and MgO formed a packed $Mg_5Si_8O_{20}.8H_2O$ (magnesium silicate hydrate hydrate or talc) coating over MgO particles' surfaces hindering further hydroxylation and preventing their volumetric expansion. Therefore, the cast structures attained displayed suitable strength for demolding (12 MPa flexural strength) and safer drying (no explosive spalling). During thermal treatment up to 1600°C, silica particles softened and promoted viscous flow favoring MgO grains' densification. After sintering, the microstructure attained comprised dense MgO grains (84 % relative density) surrounded by small portions of $Mg_2SiO_4$ (2 wt%).

## INTRODUCTION

MgO-containing and colloidal silica-bonded are important classes of refractory castables. The former shows high refractoriness and resistance to corrosion by slag [1], whereas the latter involves straightforward mixing, curing, and drying processes [2]. However, their combination in a same system has not been synergistic so far. The hydroxylation reaction MgO particles experience during mixing releases $Mg^{2+}$ ions and triggers the colloidal silica gelling mechanism [3]. Therefore, whereas small additions of MgO (0.01-0.1 wt%) gradually harden typical high-alumina colloidal silica-bonded castables in a 1-hour time, solid amounts greater than 0.1-0.2 wt% instantaneously set the system hindering its homogenization and casting (Fig. 1a) [4]. Nevertheless, the potential for technological applications of colloidal silica-bonded MgO-containing castables suggests efforts to making such systems compatible are worthy [5].

Towards overcoming the poor workability drawback, authors investigated a novel grade of colloidal silica whose silanol groups at particles' surfaces were carefully modified with an epoxy silane-based coupling agent (gamma-glycidoxypropyltrimethoxysilane, GPTMS) [6]. The epoxy-ring opening reaction that occurred during the surface modification process resulted in a diol functionality at the end of each silane group, providing them with a hydrophilic character and superior steric stabilization in comparison to conventional unsilanized grades. As a consequence, high-solid load suspensions of fine MgO sinter particles could be prepared without instantaneous gelling [7,8].

In this study, aqueous suspensions of MgO sinter (MS) containing up to 17 wt% of silanized colloidal silica (SCS) were prepared and evaluated regarding mixing, dispersion, flowability, and workability. After casting and curing, the investigation focused on how SCS particles affected MgO hydroxylation. Drying behavior and evolution of physical properties (flexural strength, total porosity, and phases formed) and microstructure were evaluated during isothermal treatments from 120°C up to 1600°C. Reference compositions prepared with plain water and an equivalent unsilanized colloidal silica grade (similar particle diameter, solid load) were also tested under the same conditions.

## EXPERIMENTAL

Raw materials: fine MgO sinter (MS, High-Purity M30, RHI-Magnesita, Brazil; $D_{50} = 8$ μm, 98.3 wt% MgO), silanized colloidal silica (SCS, Levasil FX401, Nouryon, Sweden; $D_{50} = 11$ nm, 40 wt% of solids), unsilanized colloidal silica (UCS, Levasil CS40-222; $D_{50} = 9$ nm, 40 wt% of solids), and distilled water. The following three compositions were tested: a) 83 wt% of MgO sinter and 17 wt% of silanized colloidal silica (MS+SCS, 6.8 wt% of solid $SiO_2$, 0.95 MgO molar ratio), b) 88 wt% of MgO sinter and 12 wt% of distilled water (MS+$H_2O$, silica-free reference), and c) 83 wt% of MgO sinter and 17 wt% of conventional unsilanized colloidal silica (MS+UCS, 6.8 wt% of solid $SiO_2$).

After mixing (paddle mixer, 1000 rpm, 3 min), three sets of samples were prepared. The first remained in a closed vessel at 60°C for free-flowability measurements for up to 1 h; the second was cast as 70 mm length × 16 mm diameter cylinders for geometrical total porosity and three-point flexural strength tests, remaining 24 h at 60°C in a closed environment, 24 h at 60°C in a ventilated environment, and dried at 120°C overnight. Isothermal treatments were applied from 300-1600°C (1°C.min$^{-1}$ up to 300°C, 1 h hold, 2°C.min$^{-1}$ up to maximum temperature, 3 h hold; cooling rate of 5°C.min$^{-1}$ down to 800°C and 10°C.min$^{-1}$ down to room temperature). The third set was cast as 40 mm × 40 mm cylinders for drying tests and hydroxylation degree ($W_H$, wt%) and apparent volumetric expansion (AVE, %) measurements. They remained in a humid environment for up to 7 days at 60°C. Fractured green dried and sintered samples were observed by scanning electron microscopy and crystalline phases were identified by X-ray diffraction. References [1,3,8,9] describe the techniques.

## RESULTS AND DISCUSSION

The addition of MS to UCS led to its instantaneous gelling and the production of a flocculated material unsuitable for casting (Fig. 1a); the mixture with SCS, on the other hand, resulted in a highly fluid stable suspension (Figs. 1b and 2).
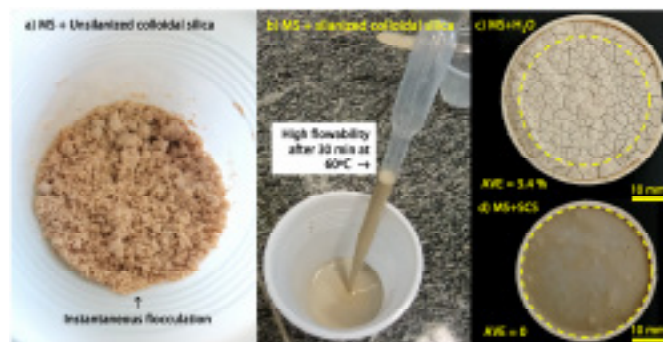


*Fig. 1: As-produced aqueous suspensions of MgO sinter with a) unsilanized colloidal silica or b) silanized colloidal silica; samples for AVE measurements (3 days, 60°C, [1]): MgO mixed with c) plain water (MS+H₂O) or d) silanized colloidal silica (MS+SCS).*

After mixing, the composition with SCS remained highly fluid and castable (FFI > 100 %) for up to 20 min longer than the silica-free reference even when the testing temperature was 60ºC. As discussed elsewhere, such a behavior was due to interactions amongst the positive charges at MgO particles' surfaces and the anionic character of SCS. The formation of a surface coating of $Mg_5Si_8O_{20}.8H_2O$ resulted in a system with high negative Zeta potential levels, and, hence, good stability [8].
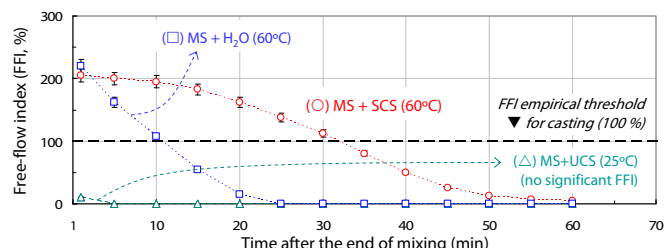


*Fig. 2: Free-flow index for MgO sinter (MS) suspensions prepared with plain water (MS+H2O), silanized colloidal silica (MS+SCS), or unsilanized colloidal silica (MS+UCS) kept at 60ºC for up 1 h.*

Such protective coating remained (Fig. 3a) during 7-days curing and, therefore, samples prepared with SCS showed significantly lower hydroxylation degree ($W_H$) levels and no damages by apparent volumetric expansion (AVE) in comparison to the silica-free reference (Figs. 1c and 4). The anti-hydroxylation behavior also produced lower total porosity and higher flexural strength samples after drying and isothermal treatments (Fig. 5)
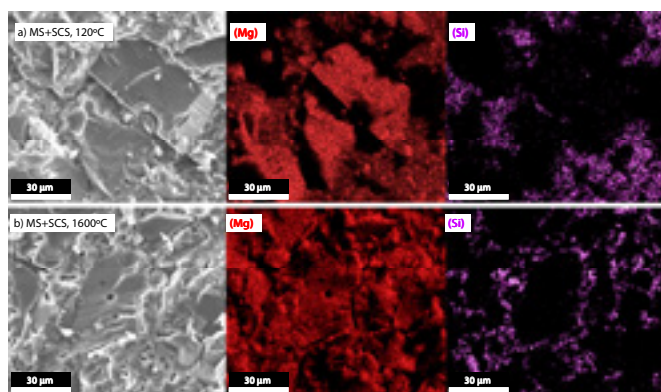


*Fig. 3: SEM/EDX images of a) green dried (120ºC) and b) sintered samples (fractured cross-section highlighting elemental analysis).*
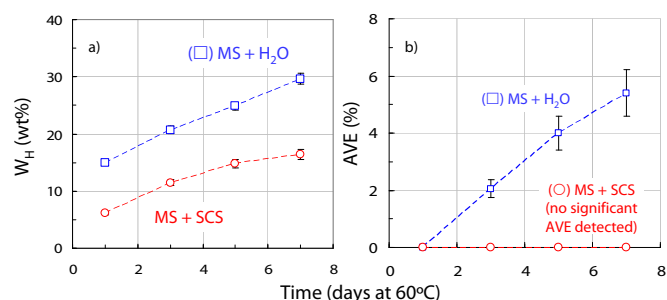


*Fig. 4: a) Hydroxylation degree ($W_H$) and apparent volumetric expansion (AVE) for MgO sinter suspensions ($H_2O$ or silanized colloidal silica, SCS) after up to 7 days at 60ºC.*

The silica-free reference samples showed an intense strength reduction as the temperature of isothermal treatment increases above 120ºC due to the decomposition of the bridging points formed by magnesium hydroxide ($Mg(OH)_2$) particles during curing time [9]. Above 900ºC, the initial stages of sintering reduced total porosity and typical strength values were attained up to 1600ºC. Regarding SCS-bonded samples, on the other hand, strength increased continuously with the temperature of isothermal

treatment, attaining final levels slightly higher than those observed for the silica-free reference.

During sintering, $Mg_5Si_8O_{20}.8H_2O$ collapsed and evolved to $Mg_2SiO_4$ (forsterite). Rietveld quantification revealed a 98-2 wt% $MgO-Mg_2SiO_4$ ratio. Since the theoretical $MgO-Mg_2SiO_4$ maximum ratio was 17.3 wt% and no $SiO_2$-based crystalline phases were detected, most of the $SiO_2$ originally from SCS must have remained as a non-crystalline third phase amongst the other two (Fig. 3b)
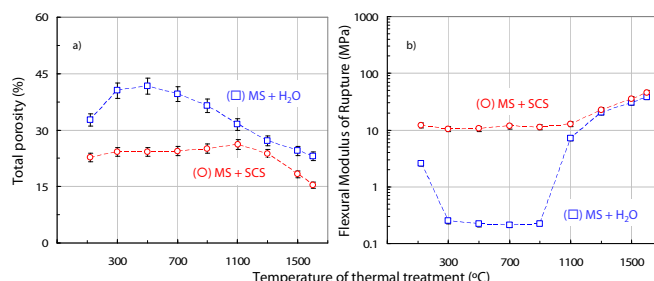


*Fig. 5: a) Total porosity and b) flexural modulus of rupture for suspensions of MgO with water (MS+H2O) or silanized colloidal silica (MS+SCS) after isothermal treatments (120-1600ºC)*

## CONCLUSIONS

The combination of fine MgO sinter particles with an aqueous dispersion of silanized colloidal silica (0.95 MgO-SiO2 molar ratio) produced suspensions of high flowability and workability (approximately 30 min at 60ºC). During curing and drying, the formation of a protective coating of magnesium silicate hydroxide hydrate ($Mg_5Si_8O_{20}.8H_2O$ or talc) prevented damages caused by MgO hydroxylation. No explosive spalling occurred during drying. After isothermal treatments, the samples' flexural strength increased continuously due to the reduction in total porosity. The final microstructure after sintering contained dense grains of periclase ($\alpha$-MgO) surrounded by a thin layer of forsterite ($Mg_2SiO_4$) and non-crystallized $SiO_2$.

## REFERENCES
[1] Salomão, R., Bittencourt, L.R.M., Pandolfelli, V.C. A novel approach for magnesia hydration assessment in refractory castables (2007) Ceram. Inter. 33 (5), pp. 803-810.
[2] Banerjee, S., Recent developments in monolithic refractories (1998) Am. Ceram. Soc. Bull. 77 (10), pp. 59-63.
[3] Ismael, M.R., Salomão, R., Pandolfelli, V.C. Refractory Castables Based on Colloidal Silica and Hydratable Alumina (2007) Am. Ceram. Soc. Bull. 86 (9), pp. 58-61.
[4] Cai, M., Liang, Y., Nie, J., Yin, Y., Ju, M., Zhang, Q. Colloidal silica-bonded MgO-CaO hot gunning mixes: Characterization of physical properties, microstructure, and gunning performance (2019) Ceram. Inter. 45 (17), pp. 22426-22431.
[5] Roy, J., Chandra, S., Maitra, S. Nanotechnology in castable refractory (2019) Ceram. Inter. 45 (1), pp. 19-29.
[6] Greenwood, P., Gevert, B. Aqueous silane modified silica sols (2011) Pigment & Resin Tech. 40 (5), pp. 275-284.
[7] Martinatti, I.S., Tiba, P.R.T., Greenwood, P.H.J., Salomão, R. Colloidal silica-bonded MgO-containing refractory castables (2022) European Patent (Pending) 364.1484EP.
[8] Salomão, R., Martinatti, I.S., Fernandes, L., Sundblom, A., Greewood, P., Tiba, P.R.T. Novel silanized colloidal silica-MgO self-flowing dispersions with improved hydroxylation resistance (*in press*, J. Eur. Ceram. Soc., 2023).
[9] Salomão, R., Pandolfelli, V.C., Fernandes, L. Designing high-temperature thermal insulators based on densification-resistant *in situ* spinel (2020) J. Eur. Ceram. Soc. 41 (4), pp. 2923-2937.

# INVESTIGATING THE MGO CASTABLE'S HYDRATION MECHANISM BY HYDRATABLE ALUMINA SUBSTITUTION FOR CALCIUM ALUMINATE CEMENT, AND PHASE FORMATION AT HIGH TEMPERATURE USING NANO–MGAL$_2$O$_4$ ADDITIVES

AmirAbbas Nourbakhsh [1], Reza Davoudian Dehkordi[2], Mozhdeh Jalali [1], Najmeh Lotfian[1], Mahsa Masoud [1] Hossein Rafiei Boroujeni [2], Marzieh Nourbakhsh [3], Amir Hossein Nourbakhsh[1], Hamed Fathi[1].

1-Arvin Dirgodaz Vijeh Sepano company, Isfahan Science and Technology Town, Isfahan, Iran.
2-, Mehrgodaz Refractory Company, Sefiddasht, Chaharrmahal and Bakhtiari, Iran.
3-Institute Für Ziegelforschung Essen Am Zehnthof 197, 45307 Essen, Germany.

## ABSTRACT
In spite of all positive features of magnesia as a refractory material, the hydration of MgO and formation of Brucite are the main obstacles in using magnesia in monolithic refractories. To overcome this problem, the substitution of calcium aluminate cement for hydratable alumina (HA), and Nano MgAl$_2$O$_4$ addition on magnesia spinel castable have been investigated. The magnesia spinel castable has been prepared in presence of dead burned magnesia, reactive alumina, binders (calcium aluminate cement and hydratable alumina), and 6 wt.% water. The hydration resistance of castables investigated in sequential pH at 25 °C. Then, 0-5 wt.% of Nano-spinel, synthesized by citrate-nitrate route, substituted for part of fine magnesia. The optimized sample were fired between 1250 and 1700 °C, then characterized by TGA, XRD, SEM. Physical and mechanical properties of optimized sample have been investigated by PLC, AP, CCS, and thermal gravimetric according to ASTM C113 and C20 standards. The results approved that magnesia hydration could be reduced by replacing CAC with HA as a binder. The optimized amount of hydratable alumina was 5% according to TGA analysis. The reason is that HA addition could decrease castable's pH, and motivate Hydrotalcite phase formation on the surface of MgO that could decrease MgO hydration. Also, results showed that using HA cement with 3 wt.% Nano-spinel additive not only increased hydration resistance, but also encouraged spinel formation at 1500 °C which increased thermal shock resistance and mechanical properties during the application of refractories.

**Keywords:** Magnesia Spinel, Hydratable Alumina, Nano MgAl2O4, Castable, Monolithic Refractories.

## INTRODUCTION
Refractory castables containing MgO are prone to material cracking because of their tendencies to react with water and form Mg(OH)$_2$ which could lead to volumetric expansion. Some researches indicate that the formation of hydrotalcite-like phases in this refractory could help the creation of more permeable castable structure by crystalline layers of Mg(OH)$_2$ and Al(OH)$_3$ which are separated by water molecules. Besides, the electric charges are neutralized by the anion located between the lamellas [1]. MgO and hydratable alumina interaction could produce hydrotalcite-like phases. To be more precise, Al(OH)$_3$ and Mg(OH)$_2$ reaction in aqueous medium form the hydrotalcite-like compounds [2]. It has been observed that the in situ hydrotalcite formation showed the higher mechanical strength than hydratable alumina-free compounds after curing. It has also been pointed out that hydrotalcite-like phases act as a binder. The outstanding roll of these compounds related to the formation of MgAl$_2$O$_4$ spinel. Calcium alumina cement (CAC) and hydrated alumina (HA) are the most commonly used binders in the formulation of castables. When alumina-calcium (CAC) cements are mixed with water, the cement is rapidly hydrated and various alumina-calcium hydrates with different morphologies are formed. Hydrated alumina castables behave like calcium alumina cement castables and require some water and similar additives. The curing mechanisms in both types of binders (CAC, HA) are based on hydration reactions in which the hydration of magnesite and the apparent volumetric expansion

(AVE) are influenced by the type and amount of binder. Also, due to the presence of CaO in the bond, the possibility of phases formation with low melting point is high. Hydratable alumina (HA) is a binder that commonly used for the situation where the CaO is not desirable. In this regard, the magnesia castables of the cement-free Forsterite bond (MgO-Al$_2$O$_3$-SiO$_2$ system) was investigated and the addition of micro silica was suggested in order to curing the castable magnesia refractory. Micro silica and magnesia form a hydrated gel in the presence of water and cause the curing of the refractory body [3]. Besides, the effect of hydrated alumina as a binder on the physical and mechanical properties of castable magnesia in spin-bond magnesia castables showed that the optimum amount of hydrated alumina in the refractory body is 5%. Also, the optimum amount of in-situ spinel formed for magnesium base mass was estimated to be about 25%. The hydraulic binders (calcium alumina cement and hydrated alumina cement) and changing the amount of these binders influence the magnesite hydration, pH, volumetric expansion, mechanical strength and porosity. Apparent volume expansion (AVE) is significantly affected by the type and amount of binder used in the composition. By replacing the hydrated alumina with cement and formation of hydrotalcite on the particle surface, both the hydration of magnesite and volumetric expansion halted. Also, the mechanical strength was at least 2.5 times higher than similar compounds containing cement [4].

This research addressed the role of calcium aluminate cement (CAC) and hydratable alumina (HA) as binders and evaluated the effect of Nano-spinel (MgAl$_2$O$_4$) addition as a nucleant agent on hydration behaviour of magnesia. In this regard, the MgAl$_2$O$_4$ Nano-spinel powder was synthesized by citrate-nitrate method. The distinct properties of Nano-spinel alumina-magnesia showed that the deleterious effects of magnesia hydration were greatly minimized.

## EXPERIMENTAL PROCEDURE
### Materials
Magnesium nitrate (Mg (NO$_3$)$_2$.6H$_2$O), aluminium nitrate (Al (NO$_3$)$_3$.9H$_2$O), citric acid (HOC(COOH)(CH$_2$COOH)$_2$) and ammonia solution (NH$_4$OH,30%) were used to synthesis MgAl$_2$O$_4$ spinel and provided by Merck Co., Ltd. All of the reagents used were analytical grade without further purification and all the aqueous solutions were prepared using deionized water. Commercially available magnesia (OMS, china), reactive alumina (Alcan, UK), hydratable alumina (Actibond 2005) and calcium aluminate cement (Secar 71) (Kerneos, France) sources also were used in this research.

### Synthesis of nanocrystalline magnesium aluminate spinel
Nano-sized MgAl$_2$O$_4$ spinel powders were synthesized through the citrate-nitrate route. A stoichiometric amount of magnesium nitrate and aluminium nitrate were dissolved in deionized water, and then a Citric acid as chelating-fuel agent added to the solution. The molar ratio of citrate to metallic ions in the solution was maintained at 0.5:1. Citric acid as a chelating agent binds metallic ions (Al$^{3+}$ & Mg$^{2+}$) and prohibits precipitation of solution during pH changing. Besides, Citric acid helps the progression of synthesis at a relatively low temperature. The solution was homogenized using a

magnetic stirrer for 1h at room temperature. pH of the solution was adjusted to six by adding ammonia. Then, the gel was heated at 110 °C for 24 h in an electric oven to get a pale yellowish mass. The obtained mass was ground into powder by a pestle and then fired at 900 °C with 10 °C/min heating rate and soaking time of 1 h [5].

## Sample preparation
The castable's composition was determined using Dinger&Funk equation [6]:

$$CPFT=100[(d^q-d_s^q)/(D^q-d_s^q)] \qquad (1)$$

Where CPFT is Cumulative Present Finer Than, D represent Maximum grain size, d is grain size, $d_s$ shows the Minimums grain size, and q is constant coefficient. The constant coefficient in these samples was 0.26. 5 wt.% of hydratable alumina as well as 5% wt.% of calcium aluminate cement was used as a binder. Varying content of alumina-magnesia Nano sized spinel were selected to be between 1 to 5 wt.% and the remaining amounts of reactive alumina and magnesia to form 25% of the spinel phase were calculated and experimental activities were performed accordingly. Based on Tables 1 and 2 contents, dry raw materials were mixed and then water was added to the required amount of 6 wt.% to form different batches of Nano composition. Also, the pH of the samples was recorded every 10 seconds for 4 hours at room temperature (25 ℃).

Table 1: Sample's composition containing Hydratable Alumina as a binder in magnesia castables

| Total wt.% spinel =25 | | | | | | | |
|---|---|---|---|---|---|---|---|
| | Particle size | H0 | H1 | H2 | H3 | H4 | H5 |
| SM | 0.25-4 | 71.33 | | | | | |
| Rest | 0-0.25 | 28.67 | | | | | |
| HA | | 5 | | | | | |
| SM | | 10.74 | 10.46 | 10.18 | 9.90 | 9.61 | 9.33 |
| RA | | 12.93 | 12.21 | 11.49 | 10.77 | 10.06 | 9.34 |
| N.Sp | | 0 | 1 | 2 | 3 | 4 | 5 |

SM: Sintered Magnesia, HA:Hydratable Alumina, RA: Reactive Alumina, N.Sp: Nano-spinel.

Table 2: Sample's composition containing CAC as a binder in magnesia castables.

| Total wt.% spinel =25 | | | | | | | |
|---|---|---|---|---|---|---|---|
| | Particle size | S0 | S1 | S2 | S3 | S4 | S5 |
| SM | 0.25-4 | 71.33 | | | | | |
| Rest | 0-0.25 | 28.67 | | | | | |
| CAC | | 5 | | | | | |
| SM | | 9.30 | 9.01 | 8.73 | 8.44 | 8.16 | 7.88 |
| RA | | 14.37 | 13.66 | 12.94 | 12.23 | 11.51 | 10.79 |
| N.Sp | | 0 | 1 | 2 | 3 | 4 | 5 |

SM: Sintered Magnesia, CAC: Calcium Aluminate Cement, RA: Reactive Alumina, N.Sp: Nano-spinel.

The samples were pressed into 5*10 mm cylindrical shape and were situated in refrigerated incubator shaker for 24h at 8 ℃. Hydration tests were performed on samples that were kept in a humid environment at 50 °C for seven days. Drying test were recorded on MgAl$_2$O$_4$ Nano spinl up to 600 °C with a heating rate of 10 °C/min and the percentage of weight loss (dw/dt, %wt/min) versus the temperature axis was evaluated in drying behaviour studies. Then, by selecting the optimal sample and in order to investigate the effect of temperature on the properties of castables, cubic samples (30*30*40) were prepared. After leaving the mold,

the samples were placed in the open air for 24 h and then in a dryer at 110 ° C for 24 hours. Then they were tempered at 1250, 1400, 1550, and 1700 °C with heating ratio of 5 °C /min.(summarized)

## Characterization
Samples morphology was observed by Philips CM10 transmission electron microscopy (TEM) and VEGA II TESCAN scanning electron microscope (SEM) equipped with EDS. To determine the crystallite phases of compounds X-ray diffraction (XRD) patterns were reported by Philips XPERT X-ray diffractometer with Cu kα radiation. In order to investigate the reactions that take place during firing and also to determine the approximate starting temperature of the reactions and the type of compositions, simultaneous thermal analysis (STA) Labsys-Setaram was used with a temperature capability up to 1600 ° C. The reference material in this experiment was alumina powder. Plant material was also made of alumina. pH meter (691 model, metrohm, Switzerland) was used to evaluate the pH during the experimental process.

## RESULTS AND DISCUSSION
### Phase composition and microstructural analysis of Nano-sized MgAl2O4 spinel
The XRD pattern of the as-prepared sample after heat treatment at 900 °C is shown at Figure.1. the spinel phases of MgAl$_2$O$_4$ had four main peaks, which can be ascribed to (440) and (511), (400), and (311) diffraction planes. The sharp diffraction peaks of MgAl$_2$O$_4$ indicates the good crystallinity. Besides, the intensity of his MgO peak against the spinel is negligible.
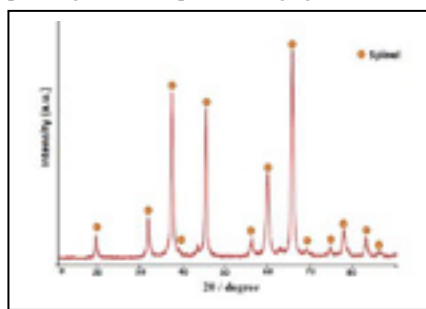


Fig.1: XRD pattern of the MgAl2O4 spinel powder calcined at 900 °C.

The morphology of Nano spinel was characterized by TEM (Figure .2). The image of the synthesized powder at 900 °C exhibited polycrystalline spinel with a crystal size of about 24 nm. The observed results are in good agreement with the crystallite size calculated by the Scherer equation.
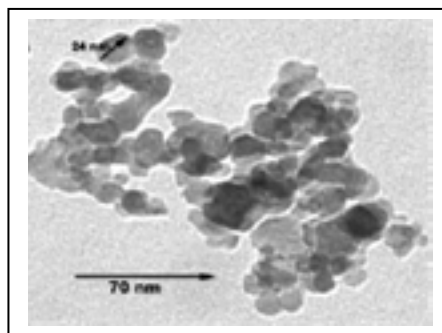


Fig.2: TEM images of MgAl$_2$O$_4$ Nano-spinel powder calcined at 900 °C.

### Hydration resistance Investigation
#### pH investigation
pH changes of castables after mixing with water is an influential factor on magnesia hydration. Figure .3 and 4 shows the pH graphs versus time of samples containing calcium aluminate cement and hydratable alumina with different values of magnesia after mixing at 25 ℃, respectively. Lower amount of pH represents lower hydration of magnesia. The initial pH of samples was about 9.5 (before hydration) that increased smoothly and reached the maximum (about 11.3) after 30 minutes.
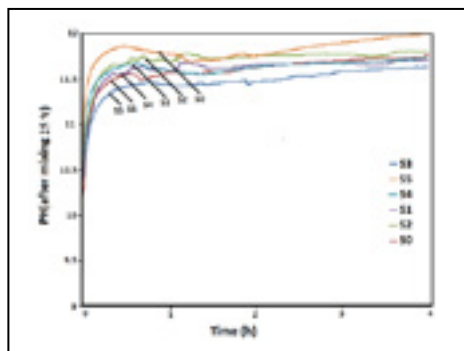
*Fig.3: pH value after mixing (at 25°C) of MgO containing castables prepared with CAC and different amounts of MgAl₂O₄ nanosized.*

Castables containing CAC in comparison with samples containing HA had the higher pH value of about 11.9 that could be caused by generation of $Al^{3+}$, $Ca^{2+}$, and $OH^-$ in water. In other words, when the binder is constant, increasing of Nano-spinel additive up to 3% caused decreasing of magnesia hydration.
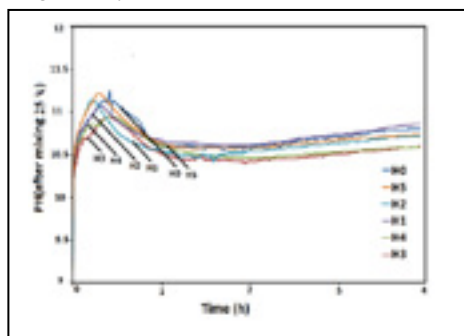


*Fig.4: pH value after mixing (at 25°C) of MgO containing castables prepared with HA and different amounts of MgAl₂O₄ nanosized.*

CAC released OH- in the water and as a result pH of castable increases greatly during the hydration. Due to the chemical equilibrium shifting principle, this excess of $OH^-$ ions favours the magnesia hydration, as shown in Eq (2):

$$Ca\,(AlO_2)_2 + 4H_2O \rightarrow Ca^{2+} + 2Al(OH)^{4-} \tag{1}$$

$$Al(OH)_4 \rightarrow Al^{3+} + 4OH^- \tag{2}$$

$$MgO + H_2O \rightarrow MgOH^+ + OH^- \rightarrow Mg(OH)_2 \tag{3}$$
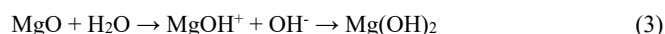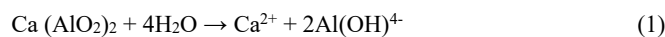
One of the main effects of CAC in comparison with HA addition in magnesia containing castables was the increase of the brucite formation rate due to the high alkaline environment. CAC hydration begins a few hours after mixing, whereas, for magnesia, it can last for days. Therefore, magnesia castables containing HA was selected for further investigation because its hydration was less than those of CAC.

*Thermal gravimetric analysis (TGA) investigation*
Thermogravimetric analysis (TGA) was carried out between 25–600 °C to investigate the thermal behaviours of Hydratable Alumina, MgAl₂O₄ Nano-spinel, and castables containing HA as binders and different amount of Nano size spine after 7days drying at 50 °C in environment. The TGA curves of all the synthesized samples are presented in Figure.5. The mass loss rate is categorized to three main peaks. Mass loss resulting from the removal of adsorbed water is observed from 25 to 150 °C. The mass loss in the 150–350 °C range resulted from the removal of Hydratable Alumina [7]. The continued weight loos from 350 to 600 °C is due the MgO and Nano-spinel hydration. This investigation shows that magnesia hydration was greatly reduce by replacing CAC with HA as binder and enhances the amount of nanosized MgAl₂O₄ up to 3%. This behaviour can be attributed to two main causes: firstly, the HA addition did not change the pH values of castable that could affect MgO hydration. Therefore, the driving force of magnesia hydration was not significantly increased. Secondly, the combination of magnesia and HA results in formation of

hydrotalcite (*HDTC*). The HDTC is preferably formed on the surface of the magnesia particles where the $Mg^{2+}$ concentration is
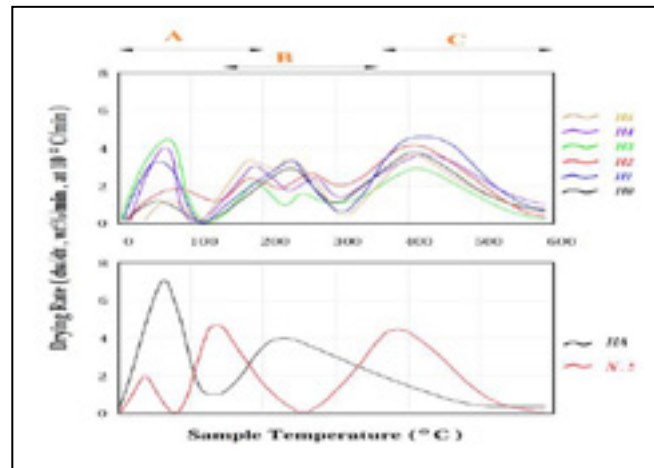


higher.

*Fig.5: Thermal gravimetric (10 °C/min) of HA, Nano-spinel MgAl₂O₄, castable containing 5wt.% of HA and different amounts of HA.*

Because of HDTC low solubility in alkaline environment and the hydrogen bonds, a protective coating on the surface of the magnesia particles is formed that can halt the hydration reaction and simultaneously bonding the castable's matrix particles strongly together. Replacing the calcium alumina cement (CAC) with hydrated alumina (HA) as a binder and nanosized alumina-magnesia spinel addition up to 3 wt.%, result in the great reduction of magnesia hydration and eliminating its effects. In sample H3 the lowest pH value was obtained. Graphs of mass loss versus temperature show that at temperatures below 200 °C large amount of water was removed from the sample and sample encountered with the high mass loss. Additionally, peaks in the range of 15 to 350 emerged due to the presence of hydrated alumina and Nano-spinel. At a temperature of 350 to 600 °C, the presence of 3% Nano-spinel caused minimum decomposition of brucite and reduced the hydration of magnesia. The low pH of this sample reduced the rate of brucite formation due to the less alkaline environment.

*XRD analysis investigation*
Also, X-ray diffraction pattern of samples containing different amount of the MgAl₂O₄ (Figure.6) indicates that increase of MgAl₂O₄ up to 3% causes the enhancement of HDTC formation; therefore, decreased the hydration of magnesia.
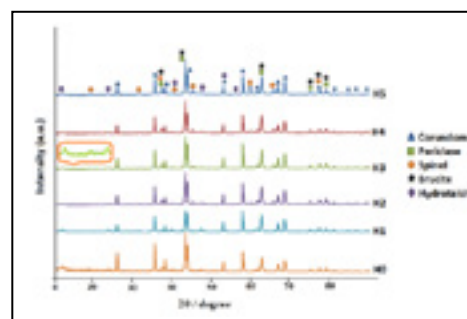


*Fig.6: XRD pattern of castables containing hydratable alumina with different amount of Nano-spinel MgAl₂O₄.*

**Physical, phase analysis and microstructure of optimized sample at different temperature (sample H3)**

*Physical investigation of sample H3 at different temperature*
The PLC results suggest that two mechanisms may be involved that are the expansion due to spinel phase formation and/or shrinkage due to sintering process. Based on the opposed mechanism the PLC results showed 2.24 % expansion in sample which fired at 1250 °C

that could be caused from spinel formation, while the sample showed 3% shrinkage by increasing the temperature up to 1400 °C. The sample showed 20% shrinkage, which could be due to solid sintering of sample, by increasing the temperature up to 1700 °C. Also, the bulk density of sample was enhanced by increasing the temperature, which can be the result of good sintering of sample.

*XRD analysis of sample H3 in different temperature*
The phase structure of the sintered H3 at variable temperatures was investigated using the X-ray diffraction technique (Figure 7). The X-ray diffraction pattern of the samples indicates the formation of spinel ($MgAl_2O_4$) and periclase (MgO) phases, which shows increase in intensity with increasing temperature. Very weak corundum peaks ($Al_2O_3$) appeared for H3 sample sintered at 1250°C; This could be attributed to formation of spinel phase in higher temperature.
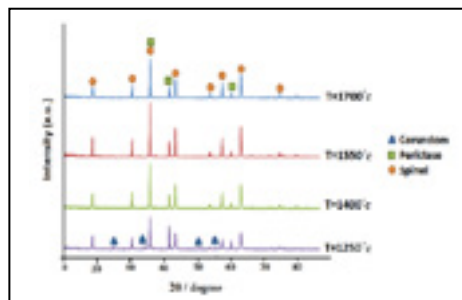


*Fig.7: XRD patterns of H3 at different temperatures*

According XRD patterns, no wide peak that indicates the formation of amorphous compounds during sintering was observed that could be because of solid state sintering. However, due to the possibility of existence of small amounts of amorphous phases, the samples were examined by SEM electron microscopy.

*Microstructure investigation of sample H3 in different temperature*
The SEM images of samples sintered at 1700 °C (Figure 8) shows that there is direct bond contact between grains, and no liquid phase formation was observed which was determined by XRD analysis confirming the H3 dense structure. The results showed that with increasing the temperature from 1250 to 1700 °C and due to the growth of crystals and also the reduction of voids, the dominant mechanism could be Solid State Sintering. The absence or very low amount of low melting point phases in the composition cannot affect the thermodynamic properties of the castables.
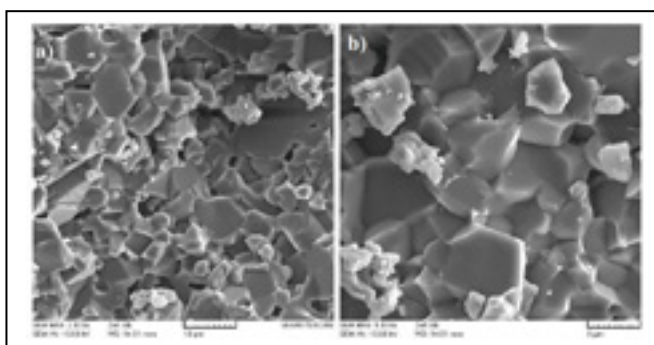


*Fig.8: SEM microstructure of sample H3 fired at 1700 °C.*

**CONCLUSIONS**
Magnesium aluminate spinel has been prepared by Citrate-Nitrate route. In addition, the effect of nanosized $MgAl_2O_4$ spinel on MgO hydration and HA binder was investigated. The XRD and TEM results showed that the $MgAl_2O_4$ phase was formed successfully. The replacement of CAC by hydratable alumina showed distinctive pH results. In fact, the changes of pH value indicated that the effect of Magnesia hydration decreased in the castables prepared using HA as binder and 3 wt.% of nanosized spinel ($MgAl_2O_4$) in the matrix of MgO. It was also found that Magnesia hydration was affected by the generation of hydrotalcite (HDTC) in the surface of castables. The improved hydration properties of magnesium castables can be attributed to the addition of hydrated alumina along with Nano-spinel. This work indicates that the Hydratable Alumina binder has more practical values that CAC.

**REFERENCES**
[1]Adak, A., S. Saha, and P. Pramanik, *Synthesis and characterization of MgAl₂O₄ spinel by PVA evaporation technique.* Journal of materials science letters, 1997. 16(3): p. 234-235.

[2]Pan, X.-L., et al., *Mesoporous spinel MgAl₂O₄ prepared by in situ modification of boehmite sol particle surface: I Synthesis and characterization of the unsupported membranes.* Colloids and surfaces A: Physicochemical and engineering aspects, 2001. 179(2-3): p. 163-169.

[3]Walling, S.A. and J.L. Provis, *Magnesia-based cements: a journey of 150 years, and cements for the future?* Chemical reviews, 2016. 116(7): p. 4170-4204.

[4]Luz, A., et al., *Drying behavior of dense refractory ceramic castables. Part 1–General aspects and experimental techniques used to assess water removal.* Ceramics International, 2021. 47(16): p. 22246-22268.

[5]Saberi, A., et al., *Chemical synthesis of nanocrystalline magnesium aluminate spinel via nitrate–citrate combustion route.* Journal of Alloys and Compounds, 2008. 462(1-2): p. 142-146.

[6]Sarkar, R., *Particle size distribution for refractory castables: a review.* Interceram-International Ceramic Review, 2016. 65(3): p. 82-86.

[7]Salomão, R., et al., *Hydratable alumina-bonded suspensions: evolution of microstructure and physical properties during first heating.* Interceram-International Ceramic Review, 2017. 66: p. 28-37.

115

# NOVEL COLLOIDAL SILICA TECHNOLOGY FOR MGO−CONTAINING REFRACTORIES − PART 2: „IN SITU" SPINELIZATION

Rafael Salomão, Leandro Fernandes
São Carlos School of Engineering, Materials Engineering Department, University of São Paulo, São Carlos, Brazil

Andreas Sundblom, Peter Greenwood
Nouryon AB, Göteborg, Sweden

Isabela Santos Martinatti, Paulo Roberto Teruo Tiba
Nouryon South America, Jundiaí, Brazil

## ABSTRACT

This study used a novel aqueous dispersion of silanized colloidal silica (SCS), whose particles' surfaces were modified with an epoxysilane–based coupling agent, as liquid medium and binder for $MgO$-$Al_2O_3$-containing suspensions. Fine calcined alumina and magnesia sinter particles were dispersed in CS to form a 65 vol% solids suspension. Silica-free compositions containing calcium aluminate cement and hydratable alumina were also tested. After mixing, the SCS-suspension showed low viscosity and suitable workability. After curing, the formation of a thin protective coating of magnesium silicate hydrate (MSH) prevented MgO hydroxylation and improved bonding strength amongst particles, generating green-dried structures of significant flexural strength (8 MPa). During initial heating, the decomposition of MSH and the softening of amorphous silica particles reduced the expansion of spinel formation. After sintering, the final structure showed high flexural strength (73 MPa) and a microstructure comprised of large and regularly-shaped spinel crystals surrounded by a thin amorphous silica layer.

## INTRODUCTION

*In situ* magnesium spinel ($MgAl_2O_4$)-containing castables are chief materials for steelmaking due to their high refractoriness and corrosion and thermal shock resistance. Despite their technological importance, such materials present two significant drawbacks. Due to the high density of the initial reactants (MgO, 3.5 $g.cm^{-3}$; $Al_2O_3$, 4 $g.cm^{-3}$), the formation of $Mg(OH)_2$ (2.4 $g.cm^{-3}$), during curing and drying, and $MgAl_2O_4$ (3.2 $g.cm^{-3}$), during sintering, can cause significant volumetric expansion and mechanical damages to the structure [1,2]. This study proposes a simultaneous solution for both problems based on the use of a novel grade of colloidal silica whose silanol groups at particles' surfaces were modified with an epoxy silane-based coupling agent (gamma-glycidoxypropyltrimethoxysilane, GPTMS) [3,4]. The epoxy-ring opening reaction that occurred during the surface modification process resulted in a diol functionality at the end of each silane group, providing them with a hydrophilic character and leading to superior steric stabilization, in comparison to conventional unsilanized grades [5]. Therefore, high-solid load suspensions of fine MgO sinter particles can be prepared without instantaneous gelling (Fig. 1a).
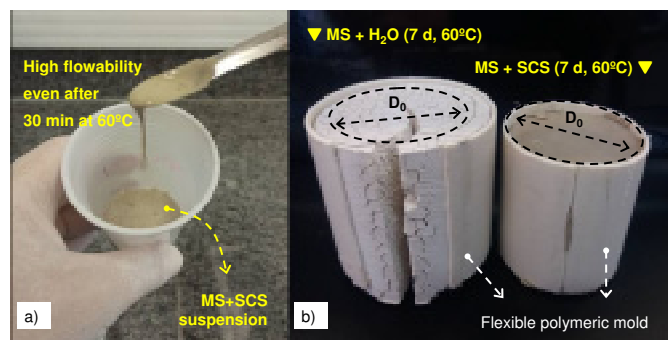


Figure 1: a) MS+SCS suspension: remaining fluid after 30 min at 60ºC; b) apparent volumetric expansion test for $MS+H_2O$ or MS+SCS samples (7 days, 60ºC, humid environment) [3].

The reactions between dissolved $MgOH^+$ ions and siloxanes groups of the silanized colloidal silica (SCS) produced a thin protective coating of magnesium silicate hydroxide hydrate ($Mg_5Si_8O_{20}.8H_2O$) at the surfaces of MgO particles [3,4]. Besides hindering further hydroxylation reaction and apparent volumetric expansion (Fig. 1b), it significantly enhanced the flexural strength and rigidity of the structure after thermal treatment from 120ºC up to 1600ºC. During sintering, part of the $SiO_2$ present in the system produced a small portion of $Mg_2SiO_4$, which improved densification and gain of strength. No significant traces of crystalline $SiO_2$ were detected.

In this study, aqueous mixtures of fine calcined alumina and MgO sinter were prepared to produce stoichiometric spinel and bonded with the same volumetric amount of calcium aluminate cement (CA), hydratable alumina (HA), or silanized colloidal silica (SCS). The large fraction of MgO (30 wt%) employed highlights the potential damages caused by the apparent volumetric expansion of MgO hydroxylation and *in situ* formation of spinel. The hydraulic binders were tested as references, whereas CA is widely used in refractory castables due to its versatility and competitive costs, HA is well known as an effective anti-hydroxylation-calcium-free binder for MgO-containing systems [6,7].

## EXPERIMENTAL

Raw materials: fine MgO sinter (MS, High-Purity M30, RHI-Magnesita, Brazil; $D_{50}$ = 8 µm, 98.3 wt% MgO), calcined alumina (AA, E-sy 1000, Almatis, USA; $D_{50}$ = 1.5 µm, 99.7 wt% $\alpha$-$Al_2O_3$), hydratable alumina (HDA, Alphabond 300, Almatis, USA; $D_{50}$ = 7.6 µm, 99.4 wt% $\alpha$-$Al_2O_3$ after calcination 1000ºC); calcium aluminate cement (CAC, EL70, Elfusa GE, Brazil; $D_{50}$ = 2.0 µm, 70 wt% $Al_2O_3$); silanized colloidal silica (SCS, Levasil FX401, Nouryon, Sweden; $D_{50}$ = 11 nm, 40 wt% of solids), dispersant (Castment FS20, BASF, Germany, 0.1 wt% dry-basis), distilled water. Three compositions were prepared with the same equimolar $MgO/Al_2O_3$ ratio and a similar volumetric ratio of water (35 vol%) and solid binder (10 vol.%) (Table 1).

Table 1: Compositions tested.

| Raw materials | Compositions (wt.%/vol.%) | | |
|---|---|---|---|
| | MS_AA_HDA | MS_AA_CAC | MS_AA_SCS |
| MS | 22.17/17/.06 | 22.00/17.26 | 22.31/16.95 |
| AA | 54.63/37.38 | 53.50/37.32 | 56.66/38.29 |
| Binder | 10.23/10.24 | 11.79/10.14 | *8.37/10.72 |
| Water | 12.97/35.32 | 12.71/35.29 | **12.66/34.05 |

*Solid $SiO_2$ particles and **water from SCS

After mixing (paddle mixer, 1000 rpm, 3 min), the samples were cast as 70 mm length × 16 mm diameter cylinders for total porosity and three-point flexural strength tests, 40 mm length × 40 mm diameter cylinders for drying and apparent volumetric expansion (AVE) tests, and 8 mm length × 6 mm diameter cylinders for dilatometric analysis. They remained for 24 h at 60ºC in a closed environment and for 24 h at 60ºC in a ventilated environment before drying at 120ºC overnight and sintering (1ºC.$min^{-1}$ up to 400ºC, 1 h hold, 2ºC.$min^{-1}$ up to 1500ºC, 3 h hold; cooling rate of 5ºC.$min^{-1}$ down to 800ºC and 10ºC.$min^{-1}$ down to room

temperature). The crystalline phases formed were identified by X-ray diffraction and microstructure was observed in fractured samples by scanning electron microscopy. Refer to [1,2,7] for a detailed description of the techniques.

## RESULTS AND DISCUSSION

In comparison to the SCS-free samples, those containing SCS showed suitable flowability and remained fluid for approximately 30 min at 60ºC (Fig. 2a). Differently from the combination with unsilanized anionic colloidal silica, no instantaneous gelling occurred [8-10]. The formation of a negatively charged and protective coating of magnesium silicate hydroxide hydrate at the surface of MgO particles prevented further dissolution and ensured flowability [3].
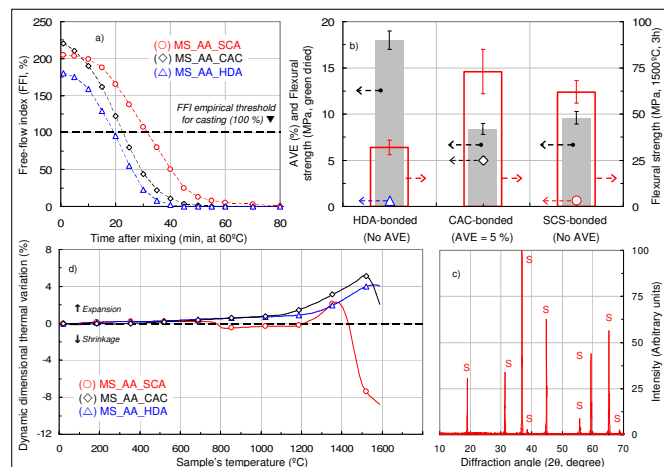


Figure 2: a) Free-flow index, b) flexural strength (green dried; after sintering) and AVE (3 days, 60ºC), c) XRD for MS_AA_SCS after sintering (1500ºC, 3h; S=Spinel, $MgAl_2O_4$), d) dimensional thermal variation for samples containing different binders.

For the same reasons, during the curing and drying steps, no significant apparent volumetric expansion was observed for samples bonded with HDA and SCS, whereas for the CAC-bonded one, severe cracking started after 24 h (Fig. 2b). Similarly to SCS, the combination of MS and HDA is hydroxylation-resistant due to the formation of a protective coating of hydrotalcite $(Mg_6Al_2(CO_3)(OH)_{16}.4H_2O)$ [7]. After sintering, the SCS-bonded ones displayed a microstructure comprised of large crystals of spinel (Fig. 2c) surrounded by a non-crystalline $SiO_2$-based phase (Fig. 3).
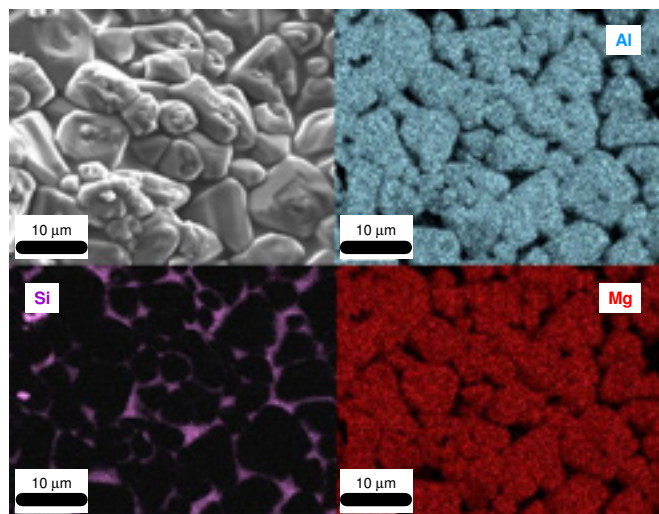


Figure 3: SEM/EDX image of fracture cross-section for MS_AA_SCS after sintering (1500ºC, 3h).

The HDA-bonded sample showed a significant volumetric expansion and experienced a strong densification resistance due to the spinel formation, as observed elsewhere (Fig. 2c) [2], whereas the CAC-bonded one exhibited the formation of liquid phases and densification after an initial expansion that followed $CaAl_{12}O_{19}$ reaction [7]. The presence of soft and non-crystalline $SiO_2$-based phases produced three interesting effects. First, it reduced the volumetric expansion of spinel; second, the high mobility of $Mg^{2+}$, $Al^{3+}$, and $O^{2-}$ ions through it favored the densification and construction of large crystals, thus leading to intense porosity reduction. Such aspects, which are technologically interesting regarding thermal shock and corrosion resistance, are currently under investigation in the Authors' research group.

## CONCLUSIONS

The composition comprised of calcined alumina, MgO sinter (MS), and silanized colloidal silica (SCS) showed suitable workability for mixing, casting, and drying. In comparison to the reference samples prepared with calcium aluminate cement (CAC) or hydratable alumina (HDA), those bonded with CS showed similar or higher flexural strength and much lower hydroxylation degree for MgO. Such behavior was associated with the formation of a magnesium silicate hydroxide hydrate at the surface of MgO particles, hindering their hydroxylation and strengthening the structure. After sintering, CA and MS reacted to form spinel. Lower levels of expansion and total porosity were verified in the CS-bonded samples due to the softening action of amorphous $SiO_2$. The final microstructure comprised large and well-built spinel crystals surrounded by a thin layer of non-crystalline $SiO_2$. The low total porosity levels, the compactness of the structure, and the large size of spinel crystals suggest such a composition is highly likely to be corrosion-resistant. This aspect is currently under investigation in the Authors' research group.

## REFERENCES

[1] Salomão, R., Bittencourt, L.R.M., Pandolfelli, V.C. A novel approach for magnesia hydration assessment in refractory castables (2007) Ceram. Inter. 33 (5), pp. 803-810.
[2] Salomão, R., Pandolfelli, V.C., Fernandes, L. Designing high-temperature thermal insulators based on densification-resistant in situ spinel (2020) J. Eur. Ceram. Soc. 41 (4), pp. 2923-2937.
[3] Salomão, R., Martinatti, I.S., Fernandes, L., Sundblom, A., Greenwood, P., Tiba, P.R.T. Novel silanized colloidal silica-MgO self-flowing dispersions with improved hydroxylation resistance (2023) J. Eur. Ceram. Soc. 43 (13), pp. 5691-5705.
[4] Martinatti, I.S., Tiba, P.R.T., Greenwood, P.H.J., Salomão, R. Colloidal silica-bonded MgO-containing refractory castables (2022) European Patent (Pending) 364.1484EP.
[5] Greenwood, P., Gevert, B. Aqueous silane modified silica sols (2011) Pigment & Resin Technology 40 (5), pp. 275-284.
[6] Salomão, R.; Ismael, M.R., Pandolfelli, V.C. Hydraulic binders for refractory castables: Mixing, curing and drying. (2007) Ceram. For. Intern. 84, pp. 103-108.
[7] Salomão, R., Pandolfelli, V.C. The role of hydraulic binders on magnesia containing refractory castables (2009) Ceram. Inter. 35 (8), pp. 3117-3124.
[8] Banerjee, Subrata Recent developments in monolithic refractories (1998) Am. Ceramic Soc. Bulletin 77 (10), pp. 59-63.
[9] Ismael, M.R., Salomão, R., Pandolfelli, V.C. Refractory Castables Based on Colloidal Silica and Hydratable Alumina (2007) Am. Ceram. Soc. Bull. 86 (9), pp. 58-61.
[10] Cai, M., Liang, Y., Yin, Y., Ju, M., Zhang, Q. Colloidal silica-bonded MgO-CaO hot gunning mixes: Characterization of physical properties, microstructure, and gunning performance (2019) Ceram. Inter. 45 (17), pp. 22426-22431.

# THE *IN-SITU* SPINEL FORMATION IN A MAGNESIA ALUMINA CASTABLE AND THE EFFECT OF SELECTED ADDITIVES ON THE PROPERTIES OF THE CASTABLE

J. Angelkort, M. Cichocki, S. Higgins, Y. Lakotta-Weinhold, N. Fröse, M. Mix
Intocast AG, Westpreußenstr. 30, 47809, Krefeld, Germany
email address: joachim.angelkort@intocast.de

**Short Communication**

Additions of sintering agents in refractory materials can help to promote the in-situ spinel formation. In this comparative study, four sintering agents (namely sodium polyphosphate, microsilica, titania and zirconia) were tested in a magnesia alumina castable to probe their influence on spinelization. It was found that castables containing one of the additives formed a significantly larger amount of spinel than additive-free reference samples burned at the same temperature (1200 °C and 1500 °C, respectively). Among the tested additives, sodium polyphosphate proved to be the most suited agent to enhance the amount of spinel in the castable. Consistently, dilatometric measurements showed that a phosphate addition affects a strong increase of the linear thermal expansion with an onset of the expansion occurring already ~100 °C below the starting temperature of the spinelization in the reference sample. Moreover, phosphate-containing castables experienced during the burning process a much larger volume expansion and a larger weight loss than the reference sample and possessed, in comparison to the latter, a lower mechanical strength after burning. The large swelling and the distinctively larger weight loss of the phosphate-containing samples are regarded as indications for a vaporization of parts of the sodium phosphate on heating.

In the microsilica-containing sample burned at 1500 °C, silicate phases were found to cover the surface of periclase grains. These layers shielded the interior of the MgO grains from a chemical attack and seemingly counteracted the progress of the spinalization.

An addition of 1 wt% of the $TiO_2$-containing additive led to a lowering of the formation temperature of spinel by ~20°C compared to the reference sample. A heat treatment of the $TiO_2$-containing castable at 1500 °C resulted in a strong increase of the mechanical strength of the castable.

The addition of the $ZrO_2$-containing additive was associated with an increase of the thermal stability of the castable. The $ZrO_2$ addition was found to exert a positive impact on the spinel formation at a temperature of ~1200 °C and above. The effect is presumably caused by fine $ZrO_2$ particles, a few micrometers in size, serving as nuclei for the spinel formation.

# A NOVEL APPROACH TO DEVELOP SUSTAINABLE CEMENT-FREE MAGNESIA CASTABLES

Hong Peng

Materials Innovation, Elkem Silicon Products Development, Kristiansand, Norway

*Email: hong.peng@elkem.com

## ABSTRACT

Magnesia (MgO)-rich castables are not commonly used in the steel-making industry due to the reaction between magnesia and water, which forms brucite ($Mg(OH)_2$) during mixing, curing, and drying. This reaction causes volume expansion and cracking, commonly known as "slaking." In this paper, the advantages of using cement-free MgO castables are reviewed from an environmental standpoint. These advantages include: i) easy installation and energy savings compared to MgO bricks, ii) direct reduction in CO2 footprint due to the substitution of the cement binder with microsilica, and iii) easy recycling of the spent MgO castable thanks to the absence of $Ca^{2+}$ from calcium aluminate cement. The focus of the study was on understanding the role of microsilica in MgO castables. Microsilica not only serves as a silica-gel binder ($MgO-SiO_2-H_2O$) to replace calcium aluminate cement, but also functions as a powerful anti-hydration agent to prevent brucite formation. Furthermore, the impact of the dimensions of specimens and drying agents on water removal of industrial-scale samples (up to 80kg) of a selected MgO castable was investigated using a unique macro thermo-balance (macro-TGA). The results indicate that it is possible to develop a close-to-reality drying profile for industrial-scale samples. Perfect 600kg blocks of cement-free MgO castables with enhanced properties have been produced with no cracking after drying. Finally, a novel approach is proposed to produce cement-free MgO castables involving using microsilica-gel as a binder in combination with a proper drying agent and adopting a more accurate drying profile.

## 1 INTRODUCTION

Magnesium-containing refractories, mainly bricks, are commonly used in ladles and tundishes in the steelmaking industry due to their high refractoriness and excellent corrosion resistance to alkaline slag. The continuous improvement of refractory materials is driven by the requirements and needs of many industries, particularly the steel industry, which accounts for approximately 70% of the market as the largest end-user of refractory products. As a result of increasing $CO_2$ emissions and the costs associated with the European Green Deal, industries are facing the pressing challenge of remaining competitive by investing in breakthrough technologies to decarbonize and reduce energy consumption, while continuously improving production efficiency. In refractory technology, the most notable trend in recent years has been the increasing use of amorphous or unshaped products. There is significant potential to convert shaped magnesia refractory materials to magnesia castable due to the advantages of relatively low raw material costs, energy savings, shorter installation times, and easier maintenance.

Refractory castables containing MgO, whether formed in situ or preformed spinel ($MgAl_2O_4$)-containing cement-bonded refractory castables (LCC), have been developed for ladle applications due to their excellent corrosion resistance to basic slag and good thermomechanical properties [1]. Refractories are essential for iron and steel production. However, the

potential for reducing $CO_2$ emissions through the selection of refractory material and design aligned to each application area is often underestimated. Optimal refractory solutions can extend operating times and prevent unscheduled furnace stops. Over the last 40 years, many papers have presented castables based on MgO; however, development seems to be mainly focused on MgO-containing systems and lab-scale results, and magnesia-rich castables are not widely used in steel-making industries. One of the major challenges is that magnesia reacts with water to form brucite ($Mg(OH)_2$) under mixing, curing, and dry-out. The formation of brucite causes volume expansion and subsequent cracking, a phenomenon commonly referred to as "slaking" [2]. Earlier research has demonstrated that the interaction between MgO and microsilica ($SiO_2$) prevents slaking.

In 1989, Elkem started developing a binder system for basic castables based on the reaction between MgO fines, microsilica ($SiO_2$), and water. An important observation was that no slaking occurred at 6% microsilica addition in lab-scale samples [3]. Since then, considerable research has been conducted to understand and solve the hydration problems of MgO in castables [4-7]. Various technologies have been reported to inhibit and/or prevent brucite formation by using microsilica as an anti-hydration agent, fibers as a drying agent to accelerate water evaporation, and optimizing additives and water addition to minimize water available for brucite formation after placing. However, most studies on the hydration of MgO described above are focused on "MgO-containing" castables, such as spinel-magnesia castables with cement. Little work has been done on MgO-rich cement-free castables, and few studies on actual-size MgO castables have been reported.

At ALAFAR 2012, Hong et al. presented preliminary results using an additive package designed to promote the sustainable bond system $MgO-SiO_2-H_2O$ for cement-free MgO castables, and to produce crack-free large pieces [8]. Recently, it has been observed that microsilica not only acts as a gel binder but also suppresses the hydration process of MgO during curing and drying. The types of additives, microsilica content and drying agents have a strong impact on flowability and slaking. Systematic studies based on both lab and industrial-scale specimens confirm that crack-free, cement-free MgO castables using $MgO-SiO_2-H_2O$ can be made. A 3wt% dosage of microsilica is necessary for producing lab-scale specimens, while more microsilica is needed for industrial-scale use. The combination of microsilica (up to 8%) and a specialty product (SIOXX®-Mag, Elkem) and a proper drying agent appears to be an efficient anti-hydration solution for MgO castables [9-14].

Microsilica, also known as condensed silica fume or silica fume, is an amorphous sub-micron silicon dioxide that has a spherical shape. It is produced by collecting and treating the fumes/smoke released during the production of ferrosilicon and silicon metal, as shown in Fig.1. The process involves reducing high purity quartz in electric arc furnaces at temperatures over 2,000 ºC using coal, coke, and wood chips as reduction materials. The smoke is drawn through cooling pipes, a

pre-collector, and a cyclone to remove coarse particles that may have been carried over from the furnace. It is then blown into specially designed baghouse filters where the microsilica is collected. By removing silica fume from smelting furnace smoke, a visible pollution problem is eliminated and the microsilica is turned into a useful product in various fields such as concrete and refractory castables since the 1970's.
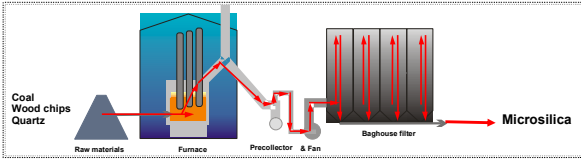


*Fig. 1 Schematic drawing of production at a smelter using electric arc furnaces to produce Si-met or ferrosilicon alloy.*

The carbon footprint of microsilica, also known as silica fume, can vary depending on the production process and the source of raw materials used. However, the production of microsilica generates a significant low carbon footprint compared to other cementitious materials, such as Portland cement. Euroalliages advocacy has allocated a zero C-footprint for microsilica. The use of microsilica in various industrial segents, such as concrete and refractory, is one of the most impressive examples of "from pollution to solution," as exemplified in Fig. 2.
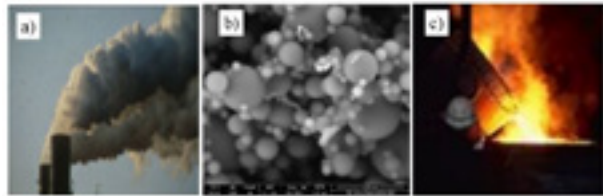


*Fig. 2 The forms and its application of microsilica. A) pollution as smoke, b) morphology of microsilica under SEM, and c) refractory castable containing microsilica for steel production.*

Microsilica is an ultrafine powder that primarily consists of spherical amorphous (non-crystalline) silicon dioxide ($SiO_2$) with an average particle size of 150nm (Fig. 2b). When microsilica-gel bonding is used instead of cement bonding, the refractory castable not only exhibits improved hot-properties but also reduces $CO_2$ footprint. Hence, it is worthwhile to explore the use of microsilica-gel as a binder for MgO castables from both technical and environmental perspectives.

There are several solutions to produce sustainable MgO castables, including:

1. Use of cement-free binders: The use of cement-free binders, such as microsilica-gel, can reduce the carbon footprint of MgO castables and enable easy recycling of spent castables.
2. Optimization of drying conditions: The drying conditions of castables need to be optimized to prevent cracking and eventually fast dryout. This can be achieved by adopting a more accurate drying profile and using a proper drying agent [12, 13].
3. Recycling of spent refractories: Spent refractories can be recycled and used as raw materials in the production of new refractories, reducing waste and conserving resources.
4. Development of new technologies: new technologies, such as nanotechnology, can be used to develop sustainable MgO castables with improved properties and reduced environmental impact.
5. Use of renewable energy: The use of renewable energy sources, such as solar or wind power, in the production of MgO castables can reduce the carbon footprint and improve sustainability.

The use of cement-free MgO castables offers several advantages, including improved thermal-shock and slag resistance against basic slag, easy installation, and energy savings compared to MgO bricks. Additionally, the substitution of cement binder with microsilica reduces the direct $CO_2$ footprint. Furthermore, spent MgO castable can be easily recycled thanks to the forsterite from the interaction between MgO and $SiO_2$ and no $Ca^{2+}$ from calcium aluminate cement.

However, producing crack-free large objects of MgO castables is challenging due to brucite formation during the curing and drying process, especially for industrial-scale samples. This paper focuses on understanding the roles of microsilica in MgO castables. The EMMA program was used to design the MgO mixes with different q-values, and the impact of drying agent and specimen dimensions on water removal of industrial-scale samples (up to 80kg) was investigated using a unique macro thermo-balance (macro-TGA).

This work has led to a better understanding of the MgO hydration mechanism and ultimately, a solution to develop microsilica-gel bonded MgO castables. By understanding the roles of microsilica in MgO castables, producers can develop more sustainable castables that are crack-free, environmentally friendly, and energy-saving.

## 2 EXPERIMENTAL
### 2.1 Mix design
Table 1 displays the mix design of magnesia castables with an $MgO$-$SiO_2$-$H_2O$ binder. Castable SF-8 and SF-6 are self-flowing mixes with q-values of 0.24 and 0.25, respectively. The mix with a q-value of 0.28 is a vibration castable labelled VF-6. The main raw materials used are synthetic dead burned MgO of different fractions (Nedmag 99, labelled Synthetic DBM) and microsilica (Elkem Microsilica® 971). SioxX-Mag, designed specifically for magnesia castables, is used as a dispersant at a dosage of 2%, bringing the silica content of the mixes to a total of 6% for SF-6 and VF-6 and 8% for SF-8. To understand their dry behavior and produce industrial-scale blocks, MgO mixes of SF-8 and VF-6 with 0.1% drying agent (EMSIL-DRY®, Elkem, Norway) were also produced. The water dosage remains at 5.5% for all mixes.

Table 1: Mix design of MgO castables.

| | | SF-8 | SF-6 | VF-6 |
|---|---|---|---|---|
| Synthetic DBM | (0-5mm) | 65 | 63 | 71.5 |
| | 100 mesh | 6 | 10 | 11 |
| | 325 mesh | 19.5 | 19.5 | 10 |
| ELKEM MICROSILICA® | 971U | 7.5 | 5.5 | 5.5 |
| SioxX®-Mag | | 2 | 2 | 2 |
| Water | | 5.5 | 5.5 | 5.5 |
| q-value | | 0.24 | 0.25 | 0.28 |

### 2.3 Sample preparation and characterization
The dry components were mixed for 4 minutes in a mixer, and then water was added. The castable was wet mixed for an additional 6 minutes. Self-flow and vibration-flow were measured using the flow-cone described in ASTM C230 (with a height of 50mm, not 80mm as described in EN 1402-4:2003). The self-flow value is the percentage increase of the diameter of the fresh mix measured 90 seconds after removing the cone. The castable was then cast into 40x40x160mm moulds for Cold Crushing Strength (CCS) and Cold Modulus of Rupture (CMOR) measurements. The moulds were kept at 20oC at >90% RH for 24 hours before de-moulding and then dried at

110oC for 24 hours. All lab-scale small prisms were crack-free. To investigate the thermal behavior of 300mm cubes (approximately 80kg), a unique macro thermo-balance capable of measuring industrial-sized samples (Macro-TGA, Elkem, Norway), as shown in Figure 3, was used. The heating schedule was 20 to 450°C at 50°C/hr, and cooling from 450 to 20°C at 50°C/hr. During heating, the 80kg cube was put in a steel net cage to prevent damage to the furnace wall if an explosion occurs. The mass loss of the specimen was recorded
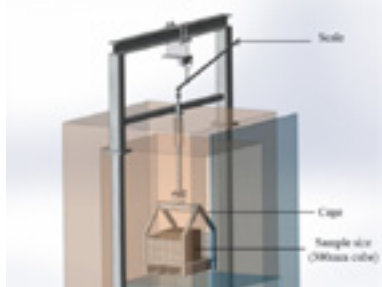


Fig. 3: Schematic drawing of the industrial-scale thermo-balance (Macro-TGA).
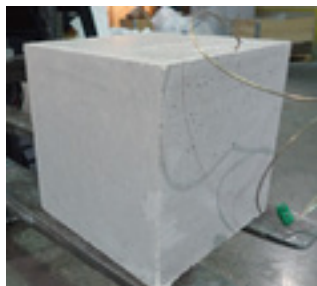


Fig. 4: A 300mm cube with embedded thermocouple in the centre of the specimens to monitor the temperature during the heat-up process.

The mass loss, temperature in the centre of the cube and in the furnace is recorded. The drying rate at time $t_i$ is calculated using the derivative of the $W$ (wt%) parameter, which represents the cumulative fraction of water released during the heat-up, according to the expressions:

$$W=100\% \times (M_0 – M)/(M_0 - M_F) \qquad (1)$$

$$(dW/dt)_i = (W_i – W_{i-10})/(t_i – t_{i-10}) \qquad (2)$$

Where $M$ is the instantaneous mass recorded at time $t_i$ during the heating stages of the samples, $M_0$ is the initial mass and $M_F$ is the final (dry) mass of the sample.

## 3 RESULTS AND DISCUSSION
### 3.1 Hydration behaviour of MgO in industrial-scale samples
To investigate the MgO hydration behavior and possible cracking of large blocks, different sizes of MgO castable with 6% and 8% microsilica (no drying agent) were produced.

Small blocks (300x300x150mm) of MgO castable with 6% microsilica were produced first (SF-6 and VF-6, Table 1). After being demolded after one day, all the blocks were found to be perfect, with no cracks observed. After curing for another day in air, all the blocks were dried at 150°C for 12 hours. Figure 5 displays the MgO blocks after drying, and all of the blocks appear to be perfect, with no cracks observed after drying.
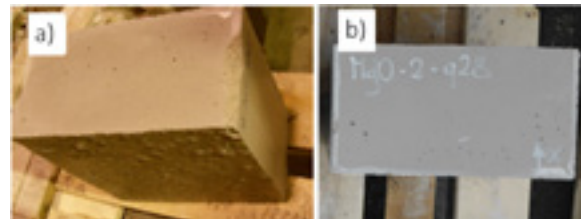


Fig. 5: Blocks (~38kgs, 300x300x150mm) after dry-out at 150°C for 12hrs (dry-out profile I): a) SF-6 and b) VF-6. The block of SF-8 was also perfect.

Next, blocks with double the thickness (300mm, ~75kg) were produced (as seen in Figure 6). SF-8 with 8% microsilica did not crack, while the others with 6% microsilica cracked. SF-6 had small cracks, and VF-6 had larger cracks. It is evident that the amount of microsilica and the thickness of the samples have a strong impact on the hydration of MgO and subsequent cracking of the dried larger blocks.



Fig. 6: Cubes (~75kgs, 300mm) after dry-out at 150°C for 12hrs: a) SF-6: 6% microsilica, b) SF-8: 8% microsilica, c) VF-6%: 6% microsilica.

To understand the MgO hydration mechanism, samples from the center of ~75kg blocks of SF-6 and SF-8 were used for a mineralogical phase analysis using XRD and SEM characterization. Figure 7 presents the XRD patterns. The SF-6 with 6wt% microsilica contains mainly periclase (MgO) and small amounts of brucite. In SF-8 with 8wt% microsilica, only periclase is observed, and no brucite phases could be detected. The major difference in composition between SF-6 and SF-8 is the microsilica content; 6% and 8%, respectively. Furthermore, no magnesia silicate hydrate (M-S-H) could be detected in the two samples, indicating that the M-S-H has poor crystallinity.
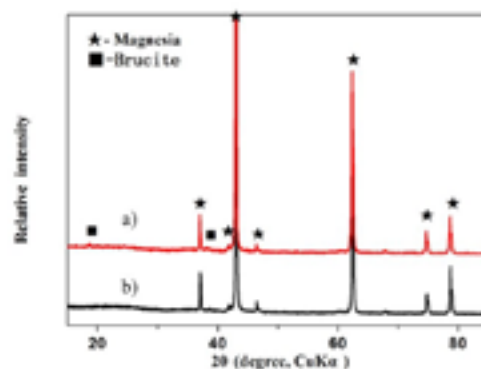


Fig. 7: XRD patterns of cubes (~75kgs, 300mm) after dry-out at 150°C for 12hrs: a) SF-6: 6% microsilica, b) SF-8: 8% microsilica.

Figures 8 and 9 display the SEM microstructures of the fractured surfaces of SF-6 and SF-8, respectively. In Figure 8, $Mg(OH)_2$ crystals can be observed as fibrous rosettes exhibiting a trigonal crystal system (hexagonal scalenohedral). In this case, 6% microsilica appears to be sufficient to fill all gaps/pores for close packing and good flow. However, this is not enough to cover all the surfaces of MgO. Some MgO fine powder in the matrix will contact water during the placement

process and be hydrated to a certain extent to form brucite. When 8% microsilica was used (Figure 9), all the surface of the magnesia was covered, and hydration of the magnesia was prevented so that brucite was not visible.
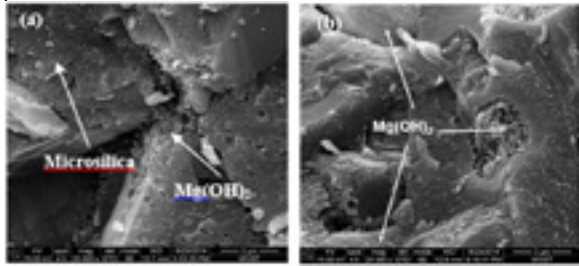


Fig. 8: SEM micrographs of fractured surfaces of SF-6 with 6% microsilica after dry-out at 150°C for 12hrs.
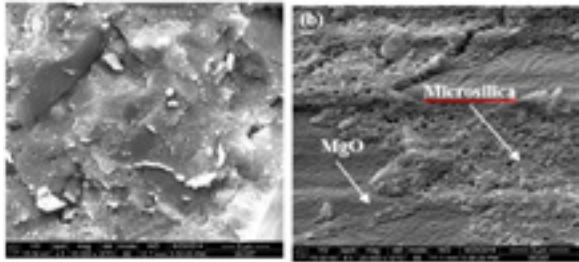


Fig. 9: SEM micrographs of fractured surfaces of SF-8 with 8% microsilica after dry-out at 150°C for 12hrs.

Based on the results presented in Figures 7 to 9, a higher dosage of microsilica appears to be an effective way to prevent and/or slow down brucite formation during the curing and drying process. When 6% microsilica is used, MgO hydration is significantly reduced, resulting in crack-free lab-scale prisms and blocks with dimensions of 300x300x150mm, as water evaporates relatively quickly. However, when larger blocks with a thickness of 300mm are produced, cracking may occur during the dry-out process. Increasing the microsilica content (e.g., 8wt%) seems to be a viable alternative.
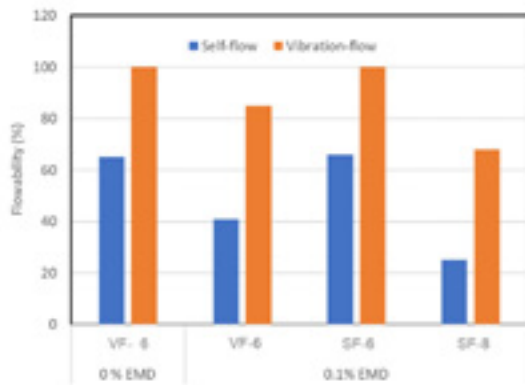
Fig. 10: Effect of drying agents on self-flow and vibration-flow of castables.

### 3.2 Flowability and mechanical strength
The results from a previous study showed that the flowability of MgO mix is greatly affected by the type of drying agent used [14]. When EMSIL-DRY® (EMD) was used instead of polypropylene fiber (PP-fiber), the self-flow value of VF-6 mix increased from approximately 12% to approximately 44%, while the vibration-flow value remained similar.
In this context, Figure 10 summarizes the results of self-flow and vibration-flow measurements for MgO mixes containing either 6% or 8% microsilica, with and without EMSIL-DRY® (EMD). The introduction of EMD only slightly reduced both

self-flow and vibration-flow values, and the mixes were still able to be easily cast with the same amount of water as the reference mixes.
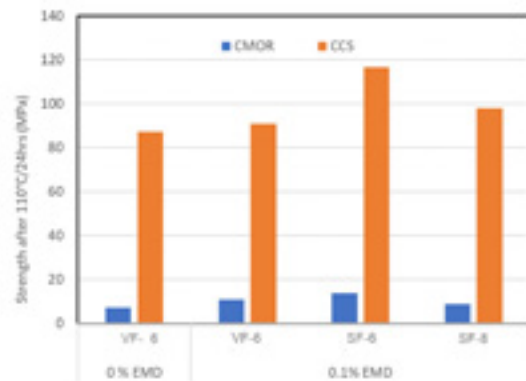


Fig. 11: Effect of drying agents on mechanical properties after drying at 110°C for 24hrs.

In this section, Figure 11 shows the compressive strength (CCS) and cold modulus of rupture (CMOR) of the samples after being dried at 110°C for 24 hours. The CCS and CMOR values of the SF-6 (q=0.26) series were slightly greater than those of the VF-6 series. Additionally, it was observed that the type of drying agent used did not significantly affect the mechanical strength of the samples after drying.

### 3.3 Mass loss and drying rate evaluation by industrial-scale Macro-TGA
In order to understand how drying agents affect the thermal behavior of large specimens (weighing around 75kg and measuring 300mm cubed) and to improve the drying process, a special macro-thermo-balance (Macro-TGA) was used to measure the percentage of mass loss (%) and the drying rate (dw/dt, %/min) during the heating process. The heating schedule involved a temperature range of 20 to 450°C, with a rate of 40°C per hour.
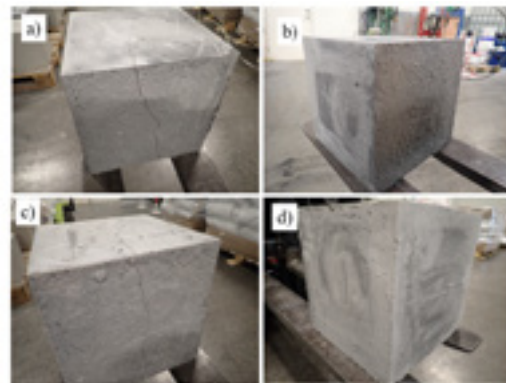


Fig. 12: Cubes (~75kgs, 300mm) after Macro-TGA: a) SF-8 with 0% EMD, b) SF-8 with 0.1%EMD, c) VF-6 without EMD and d) VF-6 with 0.1% EMD.

Figure 12 displays photographs taken after the Macro-TGA measurement. With 0.1% EMD, both the SF-8 and VF-8 blocks were in perfect condition, while the reference samples without EMD had cracks. Additionally, it was observed that the 75kg SF-8 block was in perfect condition after being dried at 150°C for 12 hours (as shown in Figure 6B). This confirms that the drying process significantly affects water removal and the formation of cracks.
Figures 13a and 13b show the mass loss (%) and drying rate (dw/dt) versus core temperature of the samples, respectively.

Compared to the reference sample without EMD, the samples containing EMD showed faster dewatering and a lower temperature for maximum dewatering rate in the temperature range of 100-300°C. The Macro-TGA results indicate that EMD contributes to faster dewatering in the early stage of the firing process, primarily due to its low melting point. This leads to lower steam inside the block and less water available for brucite formation, subsequently reducing the risk of cracking caused by brucite formation.
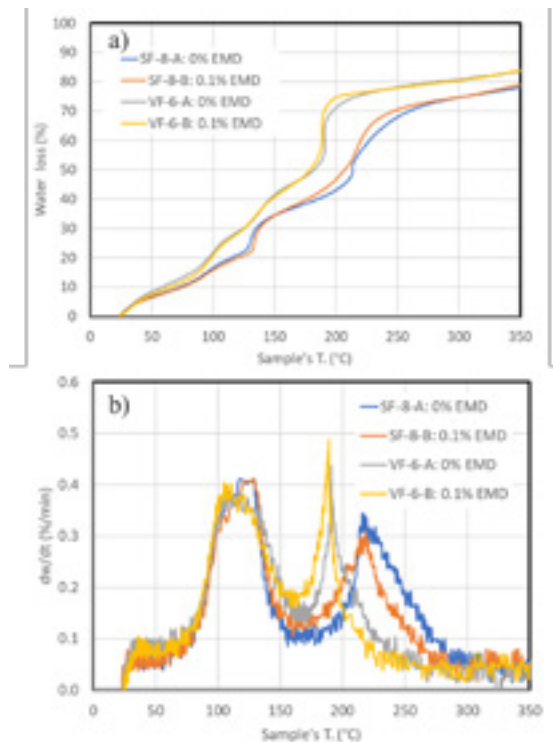


*Fig. 13 Drying behaviour of LCC containing drying agents using Macro-TGA. A) Mass loss, and B) Drying rate (dw/dt).*

The temperature at the center of the blocks was also measured and plotted as a function of the furnace temperature, as shown in Figure 14. Two "plateaus" were observed for all samples, at sample temperatures of approximately 130°C and 200°C, respectively. The corresponding oven temperatures ranged from approximately 220°C to 320°C, respectively. Therefore, the following drying profile is recommended to produce larger blocks of SF-8 and VF-6:

i) Room temperature to 220°C, 30°C/hr, and hold at 220°C for 5 hours.

ii) 20°C to 320°C, 50°C/hr, and hold at 320°C for 8 hours.

iii) Turn off the furnace and allow it to cool.
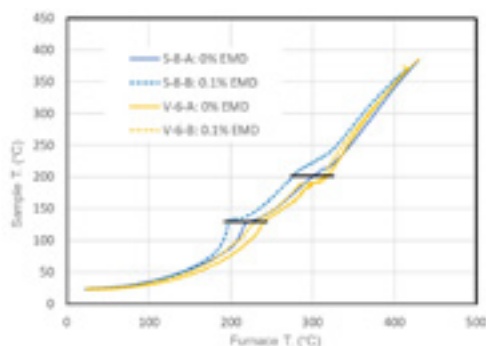


*Fig. 14 Sample T. in the center of block plotted as a function of furnace temperature under Macro-TGA test.*

By following this drying profile, the risk of cracking caused by brucite formation can be significantly reduced, resulting in less failure of MgO castable.

### 3.4 "Real-size" industrial-scale specimens

To evaluate the effect of microsilica content and drying agent on crack formation, two series of blocks of SF-8 and VF-6, weighing approximately 600kg with dimensions of 900x900x270mm, were cast with varying dosages of EMD. Here, 10% DBM (325mesh) was replaced by calcined alumina (Table 1), based on the request of a customer. The blocks were demolded after one day and air-cured at ambient temperature before the dry-out process began. A thermocouple was embedded in the center of the specimens to monitor the temperature profile. The optimized drying profile recommended above based on Macro-TGA measured input was applied.

Figures 14a to 14d present photos of the blocks of two series of SF-8 and VF-6 with varying dosages of EMD after drying. The typical pattern of crack formation due to brucite formation damage was observed in the SF-8 block without EMD and the VF-6 block with 0.05% EMD. This crack forms around the center of the castable and propagates to the surface. This can be explained as an "autoclave effect" inside the castable. For larger blocks, internal vapor pressure is generated, which favors the formation of brucite in this area. This reaction causes a dramatic expansion of the internal volume of the sample.
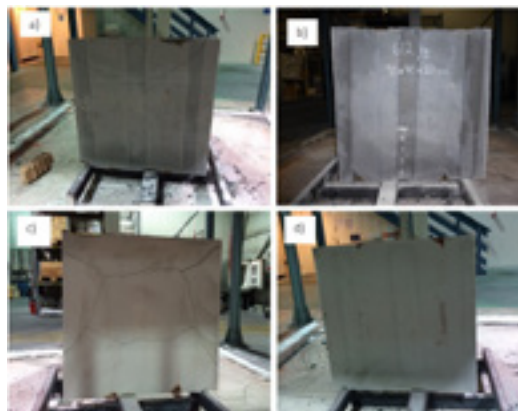


*Fig. 14: Blocks (~600kgs, 900x900x270mm) dried at 320°C for 8hrs. a) SF-8, no drying agent, b) SF-8, 0.1% EMD, c) VF-6, 0.05% EMD, and d) VF-6, 0.1% EMD.*

Furthermore, it was observed that cracking in VF-6 containing 6% microsilica + 0.05% EMD was much more severe than in SF-8 containing 8% microsilica and no EMSIL-DRY™. This confirms that for larger industrial samples, more microsilica is required to prevent brucite formation. When EMSIL-DRY® was increased to 0.1%, both the SF-8 and VF-6 samples produced perfect blocks after drying, with no cracks observed. These results demonstrate the effectiveness of using EMSIL-DRY® to prevent brucite formation and subsequent cracking in large industrial-scale MgO castables.

These results demonstrate the importance of using microsilica and drying agents to prevent the formation of brucite and subsequent cracking in industrial-scale MgO castables. By understanding the mechanisms of crack formation, producers can develop more effective drying profiles and refine their formulations to produce high-quality, crack-free industrial-scale MgO castables.

### 4 CONCLUSIONS

The future of refractory technology is focused on developing long-lasting, energy-saving, environmentally-friendly, low-carbon, and functional combinations through research and

innovation. This paper investigates the impact of microsilica dosage (q-value) on the hydration behavior of MgO in industrial-scale blocks using SEM and XRD. Additionally, the drying profile is optimized using Macro-TGA. Microsilica serves not only as a binder ($MgO-SiO_2-H_2O$) but also as a potent anti-hydration agent, preventing the formation of brucite. The result is the production of cement-free magnesia castables with low $CO_2$ footprint bonding (micro-silica-gel bonding) without any issues.

This study also offers a solution for developing crack-free industrial-scale MgO castables using a microsilica-gel binder, controlling MgO hydration, and applying a tailor-made drying profile. However, further research is necessary for continued innovation and advances from both environmental and technological perspectives. Several approaches should be pursued, such as selecting magnesia raw materials with a reduced $CO_2$ footprint, using recycled magnesia material, simultaneously developing refractory formulation, and bonding systems, and collaborating with refractory producers and end-users to develop application-oriented solutions. By pursuing these approaches, the refractory industry can continue to innovate and improve while meeting the demands of a changing world.

**REFERENCES**

1. E.Y. Sako, M. A. L. Braulio, V. C. Pandolfelli, "The corrosion and microstructure relationship for cement-bonded spinel refractory castables, Ceram. Int. 382177–2185 (2012).
2. Y. Watanabe, T. Ono, T Yukinawa and S. Sakamoto, "Development and Application of Monolithic Refractory Containing Magnesia Clinker", Proc. 2nd. Int. Conf. Refr. Tokyo, Japan. 1987. p. 494-506.
3. Sandberg, B, Mosberg, T., "Use of microsilica in binder systems for ultra-low cement castables and basic, "cement-free" castables". Advances in Refractories Technology. Vol. 4. 1989. p. 245 – 258.
4. Wagner M. Silva, Christos G. Aneziris, and Modestino A. M. Brito, "Effect of Alumina and Silica on the Hydration Behavior of Magnesia-Based Refractory Castables". J. Am. Ceram. Soc., 94 [12], 2011. p. 4218–4225.
5. Rafael Salomão and Victor C. Pandolfelli, "Microsilica Addition as an Antihydration Technique for Magnesia-Containing Refractory Castables". American Ceramic Society Bulletin, Vol. 86, No. 6, 2007. p. 9301-9306.
6. Rafael Salomão, L.R.M. Bittencourt, V.C. Pandolfelli, "A novel approach for magnesia hydration assessment in refractory castables". Ceram. Inter., 33(5), 2007. p. 803-810.
7. T. M. Souzaa, A.P.Luza, T. Santos, D. C. Gimenesa, M. M. Migliolia, A. M. Correab, and V.C. Pandolfelli, "Phosphate chemical binder as an anti-hydration additive for Al2O3–MgO refractory castables." Ceramics International Vol 40, 2014. p. 1503–1512.
8. H. Peng, B. Myhre and M. Luo, "New additive packages for self-flowing high-alumina and MgO based refractory castables". Proc ALAFAR 2012, Cancun, Mexico, Nov. 5-8, 2012.
9. B. Myhre, H. Peng, and M. Luo, "Cement free MgO castables Part I, flow, setting and slaking". Proc. UNITCER'13, Canada, 2013. p. 881-886.
10. H. Peng and B. Myhre, "The road map of hydration behaviour off MgO based refractory castables". Proc ALAFAR 2014, Santiago, Chile. Oct. 28-31, 2014.
11. H. Peng, B. Myhre, and L. Ning, "Development of cement-free basic castables by controlling MgO hydration behaviour." Proceeding of UNITECR, Vienna, Austria, Sept. 16-18, 2015
12. Hong Peng, Bjørn Myhre, "Drying behaviour and explosion resistance of refractory castables." ICR (62st International Colloquium on Refractories, Aachen, Germany, pp30-34, Sept. 2019
13. Hong Peng, Bjørn Myhre, "Cracking of mgo based castables – a challenge of the past?" ICR (63st International Colloquium on Refractories, Aachen, Germany, pp30-34, Sept. 2020
14. Hong Peng, "Fast dry-out of cement-free mgo based castables." ICR (64st International Colloquium on Refractories, Aachen, Germany, pp30-34, Sept. 2021
15. EMMA (Elkem Materials - Mixture Analyzer) software, free download at: http://www.materials.elkem.com/

# DRY HIGH-PERFORMANCE MATERIALS IN THE CHANGE OF TIME

Bojan Damjanovič, Aleksandra Veličevič
EKW-Kremen d.o.o., Šentjernej, Slovenia

Erik Kurtscheid, Daniel Cölle
EKW GmbH, Eisenberg, Germany

**ABSTRACT**

The so-called dry mixes represent an extremely important species of unshaped refractory ceramics for serving monolithic lining concepts in a wide range of industries that are, however, essentially based on the metallurgical melting process. Even a normative definition of dry material exists according to ISO 1927-1:2012: "These are materials which are specially designed for dry application by vibration, "vibro-compaction" or ramming. The dry mixes achieve maximum densification during installation, making it possible to remove the template either before or after heating. These materials may have a temporary bond, but are ultimately ceramic bonded."

A comprehensive introduction to the "specific world" of dry materials with an historical overview and focus on fundamental, classificatory aspects of raw material geology and mineralogy is presented. The latest regulations within the continuous REACH discussion require a targeted response from the refractory industry and are interpreted as an opportunity to generate progressive approaches to solutions. Dry mixes are also experiencing a modernized design and are characterized by new structural characteristics which are identified and critically discussed on the basis of well-chosen examples.

The article would like to conclude with discussions of a couple of actual metallurgical problems and proposed solutions from exemplary industrial and engineering end-users and at the same time provide an outlook on future problems and approaches to solutions for the integration of dry mixes in modern monolithic refractory linings of industrial systems.

125

# ASSESSMENT OF THERMAL–MECHANICAL STRESS DAMAGE MECHANISMS OF MONOCARBONATE BONDED ALUMINASPINEL CASTABLES BY HIGH–TEMPERATURE WEDGE SPLITTING TEST

Ning Liao, Wenjing Liu, Yawei Li, Shengli Jin

The Key Laboratory of Refractories and Metallurgy, Wuhan University of Science and Technology, Wuhan, 430081, China

National-Provincial Joint Engineering Research Centre of High-Temperature Materials and Lining Technology, Wuhan, 430081, China

## ABSTRACT

The hydration behavior of calcium aluminate cement (CAC) greatly affects the structures and properties of the CAC bonded alumina-spinel castables, especially the mechanical properties and thermal shock resistance. Therefore, we investigated the specific influences of characteristic hydrates ($CAH_{10}$, $C_2AH_8$, and $C_3AH_6$), the curing, the heating temperatures on the evolutions of nano and micron-sized pore structures of castables through mercury intrusion porosimetry (MIP) combined with micro-CT scanning technology, where the corresponding fractal dimensions were calculated to determine the complexity. Furthermore, more stable hydrates such as $C_4AcH_{11}$, and $Mg_4Al_2(OH)_{16}(CO_3)\cdot 4H_2O$ were elaborately designed based on thermodynamic calculation of hydration (GEMS). Finally, the fracture behaviors were characterized by wedge splitting test (WST) both at room temperature and high temperature to better evaluated the thermal shock resistance of castables in practice.

## 1 INTRODUCTION

Refractory castables are widely used as furnace lining materials owing to their energy efficiency, adaptability, excellent integrity, and high efficiency [1].CAC, as one of the commonly used hydraulic binders for refractory castables, has higher green strength and excellent thermomechanical properties compared to other binders. In fact, the mechanical properties, phase composition, and microstructure evolution of the castables are associated with the early hydration of CAC and the formation of various calcium aluminate phases [2]. Recently, there have been extensive discussions about the effects of CAC hydrates on the properties of castables. It has been widely accepted that there are three kinds of hydrates of CAC, i.e., $CaO\cdot Al_2O_3\cdot 10H_2O$ ($CAH_{10}$), $2CaO\cdot Al_2O_3\cdot 8H_2O$ ($C_2AH_8$), and $3CaO\cdot Al_2O_3\cdot 6H_2O$ ($C_3AH_6$). Our previous study has confirmed that plate-like hydrate $C_2AH_8$ could construct highly homogeneous $CA_6$ after high-temperature treatment, resulting in a more complex and homogeneous pore structure, hence acquiring excellent comprehensive properties [3].

However, metastable phases (C-A-H, C/A$\leq$2) inevitably transform during the conventional curing and drying stages, and the process is accompanied by the increase of pores and the decay of strength (Fig.1) [4]. Therefore, designing stable plate-like hydrates to inhibit hydrates transformation has been a promising solution. Luz [5] et al. added $CaCO_3$ to cement pastes, resulting in improved volume stability and early strength owing to the formation of monocarbonate ($C_3A\cdot CaCO_3\cdot 11H_2O$, $C_4AcH_{11}$) instead of $CAH_{10}/C_2AH_8$. Besides, $C_4AcH_{11}$ was confirmed as a plate-like and stable phase even though sufficient water was available in the hydration system, which distinguished it from $C_2AH_8$. However, it is worth noting that the generation of hydrates with high C/A ratios ($C_2AH_8$, C/A=2 and $C_4AcH_{11}$, C/A=4) was inevitably accompanied by the precipitation of substantial amounts of $AH_3$ [6]. Its stronger pore-filling effect is further deteriorating the permeability of the CAC-bound castables, resulting in an explosion risk. Therefore, the generation of stable plate hydrates together with the consumption of $AH_3$ in the system is the focus of the hydrates design.

Based on the GEMs thermodynamic calculations (Fig.2), MgO was added into the CAC system containing carbonate, and the reaction of $AH_3$ with MgO induced the hydrate hydrotalcite (M-A-H). M-A-H was demonstrated to be a lamellar structure, and its generation not only solved the problem of reduced permeability but also contributed to the improvement of early bonding strength. This paper presents carbonate and MgO to modify and design hydration products and further assess the effect of early hydration on alumina-spinel castables' pore structure and resistance to thermomechanical stress damage.
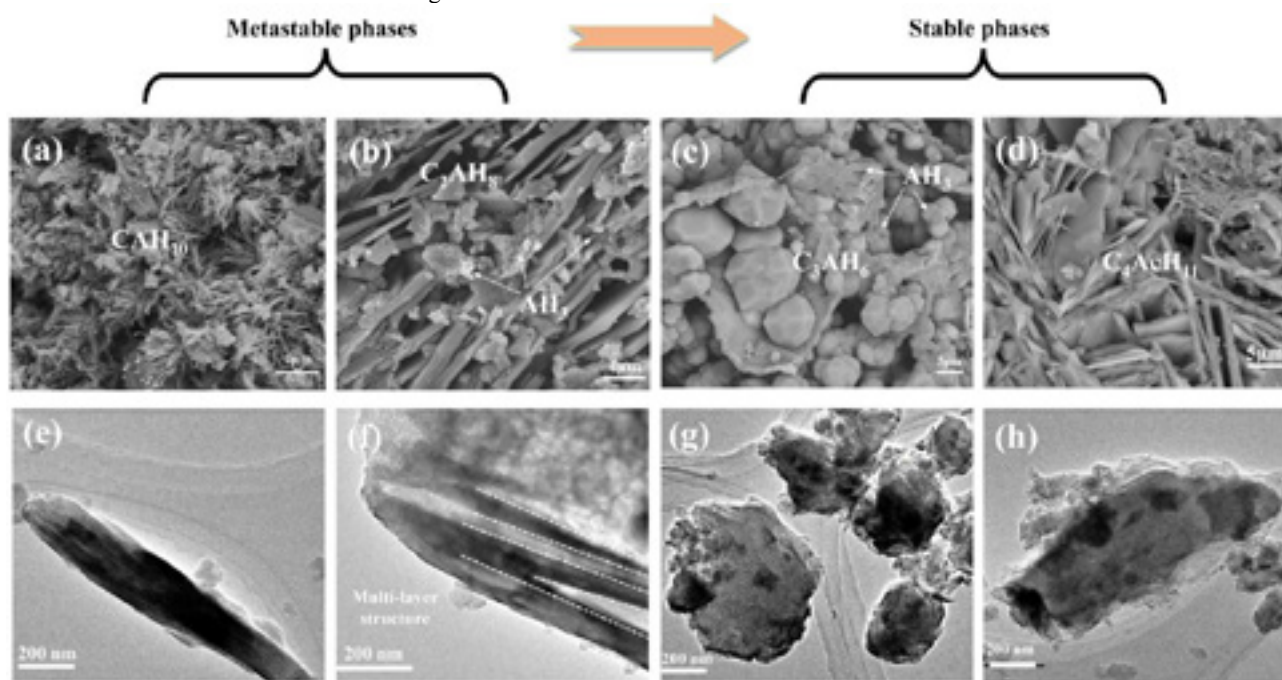


*Fig.1 Microstructures of characteristic hydrates: (a, e) $CAH_{10}$, (b, f) $C_2AH_8$, (c, g) $C_3AH_6$, (d, h) $C_4AcH_{11}$.*
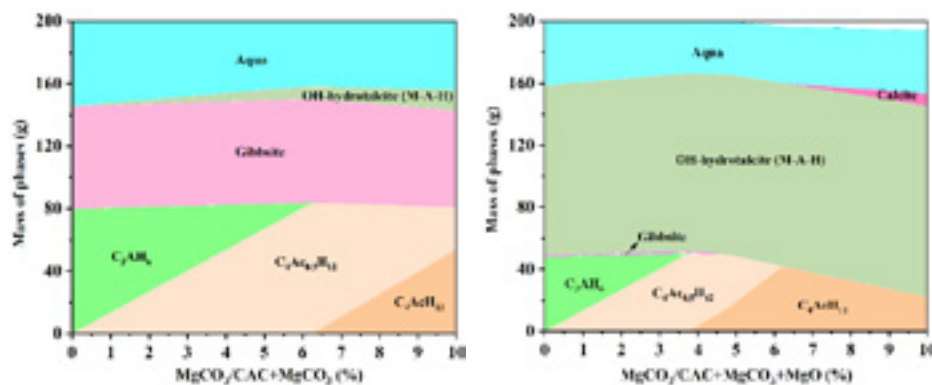
*Fig. 2 Stable phase assemblages based on GEMs model.*

## 2 MATERIALS AND METHODS

### 2.1 Preparation of hydration samples and alumina-spinel castables.

Nanoscale $CaCO_3$, Mg-Al hydrotalcite, and $MgCO_3$ compounded with MgO were added to the CAC hydration systems, and the detailed preparation procedures can refer to our previous work [3]. The raw materials used for the castables are tabular alumina aggregates, tabular alumina powder, $\alpha$-$Al_2O_3$ powder, spinel powder, CAC binder (Secar 71), and nanoscale $CaCO_3$/ Mg-Al hydrotalcite/ $MgCO_3$ compounded with MgO, the specific compositions and preparation of castables are also referred to previous work [7].

### 2.2 Test and Characterization.

For hydration samples, the phase compositions were identified by powder X-ray diffraction analysis using a Philips X' Pert PRO diffractometer. The microstructures were observed using field-emission scanning electron microscopy. The hydrates and the degree were analyzed using differential scanning calorimetey. The early setting behavior of castables was monitored in real time using ultrasonic velocity testing. The modulus of rupture (CMOR), cold crushing strength (CCS), and apparent porosity (AP) of castable specimens was evaluated. Additionally, the center part of the castables was cut into some cubes with a side length of ~5 mm for mercury intrusion porosimetry. The high-temperature wedge splitting test of specimens pre-fired at 1600 °C was loaded at a rate of 0.5 mm/min for unidirectional compression at 1400 °C, the test procedures and device can refer to the literature [8].

## 3 RESULTS AND DISCUSSION

Fig. 3 indicates that the predominant hydrates of the R sample cured at 25 °C for 1 d were plate $C_2AH_8$ and with tiny amounts of prismatic $CAH_{10}$ and $AH_3$. The NCc sample with nanoscale $CaCO_3$ showed distinct diffraction peaks at $2\theta$ angles of ~12° and ~23°, which matched with the monocarbonate-$C_4AcH_{11}$. SEM results confirmed that the morphology of $C_4AcH_{11}$ was a plate and constituted interlocking structures. For the MAH sample with Mg-Al hydrotalcite, the main hydrates were $C_2AH_8$ and $C_4AcH_{11}$, and the morphology of both hydrates was typical plate structure. While the hydrated sample with $MgCO_3$ and MgO was cured at 40 °C for 12 h and then at 80 °C for 12 h. The results verified the feasibility of the two-step curing, which induced the formation of nanoplate $Mg_4Al_2(OH)_2(CO_3)\cdot 3H_2O$ along with the stable micrometer plate $C_4AcH_{11}$. Both the addition of carbonate-containing additives and the two-step curing led to a significant decrease in the diffraction peaks of the CA and $CA_2$ compared to the R sample, i.e., a significantly increased degree of CAC hydration.

127
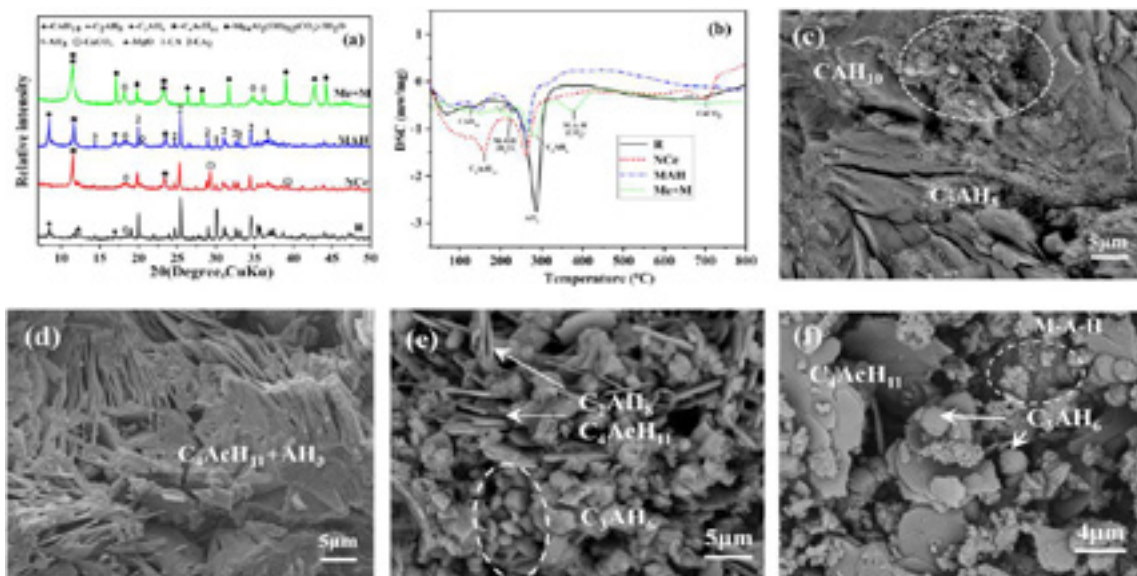


*Fig.3 XRD patterns (a) DSC (b), and SEM of hydration samples.*

The early hydration of CAC determines its bonded castables setting behavior and green strength. Fig. 4 indicates that an earlier increase in the velocity was detected in the specimens of castables with the addition of nanoscale $CaCO_3$ and hydrotalcite (earlier setting behavior). This is ascribed to the fact that nanoscale $CaCO_3$ and hydrotalcite provide more nucleation sites to accelerate the CAC hydration. It also confirmed that the plate-like hydrate $C_4AcH_{11}$ played a similar and better reinforcement role as $C_2AH_8$.
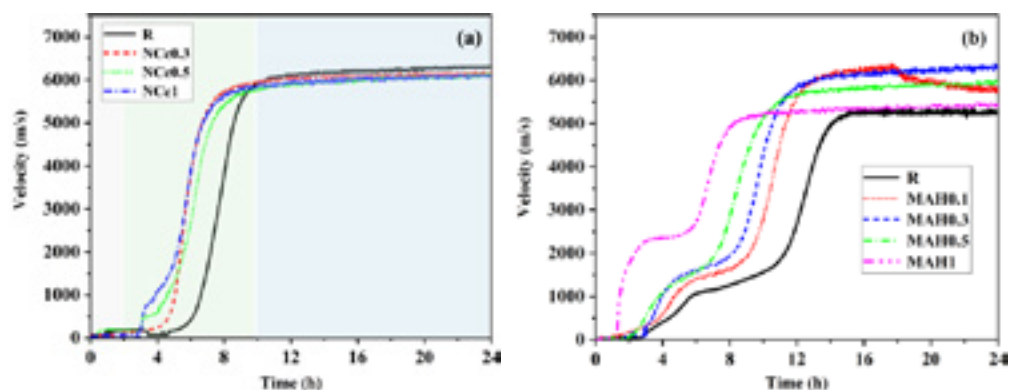
Fig. 4 Ultrasonic wave velocity vs. time of castables containing nanoscale CaCO₃ (a) and microscale hydrotalcite (b).

Fig. 5 exhibits that the R sample had larger pores and pore connectivity. Furthermore, more detailed, R sample had larger plate $CA_6$ grains, while for NCc sample, the pore was refined and the morphology of $CA_6$ gradually changed to small and elongated structure, owing to CaO sources being well dispersed and high reactivity (Fig. 5e). Additionally, the similar refinement of the pore structure was verified when the additive of $MgCO_3$ compounded with MgO was added. Furthermore, $CA_6$ encrusted microcrystalline spinel structure was formed in the matrixes (Fig. 5f).
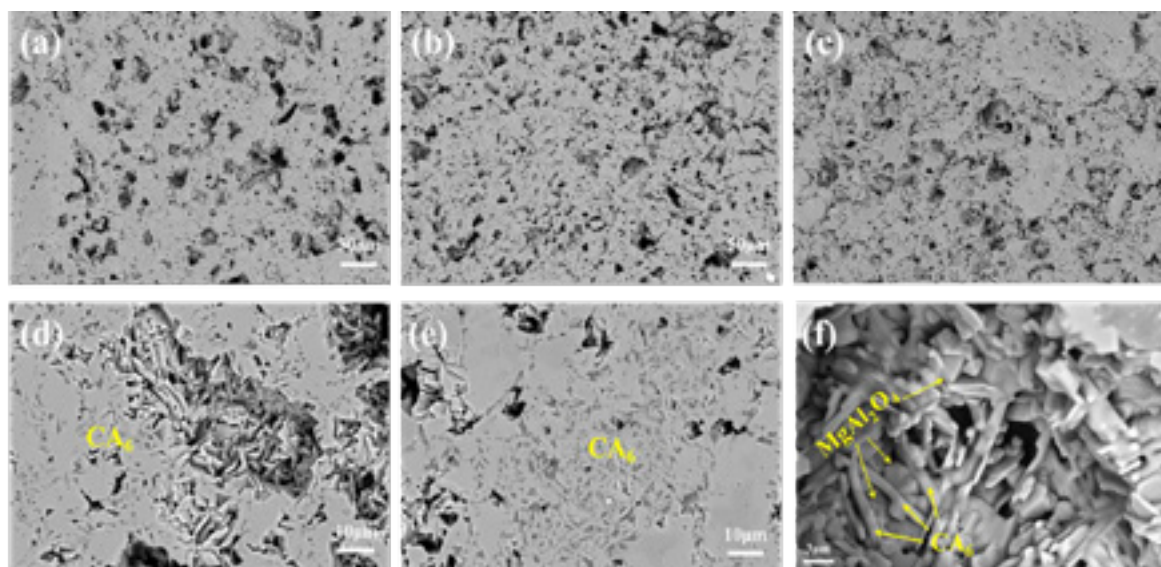


Fig. 5 SEM of castables treated at 1600 °C: (a, d) R sample, (b, e) NCc sample, (c, f) Mc+M sample.

Mercury intrusion porosimetry to assess pore size up to 5 nm~800 μm, as shown in Fig. 6. Obviously, the pores with a diameter range of 1~10 μm were significantly increased with the increase of nanoscale $CaCO_3$, attributed to the pore structure constructed by the interlocking of elongated $CA_6$. Similarly, the addition of Mg-Al hydrotalcite significantly increased the proportion of <10 μm pores along with a reduction of 100~100 μm. Additionally, the addition of $MgCO_3$ compounded with MgO was favorable to increase the pores of 10-100 nm and decreasing the micropores (100~800 μm) after drying and firing.
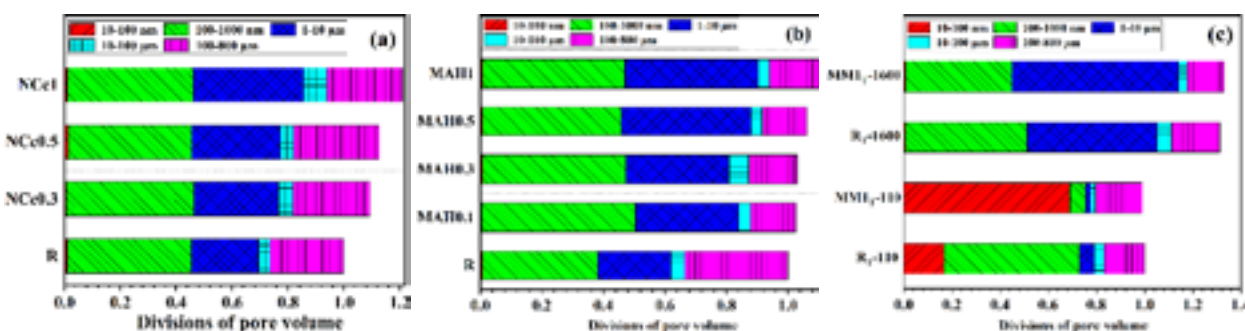


Fig. 6 Divisions of pores volume of castables treated at 1600 °C based on MIP.

Noteworthily, the high-temperature wedge splitting test presented more interesting fracture behavior at 1400 °C as shown in Fig.7. Distinguished from the room temperature test, all specimens presented nonlinear fracture behavior, and the vertical loads reduced from ~2500 N to ~600 N. Furthermore, the specimens with nanoscale $CaCO_3$ showed larger vertical displacements up to 6~7 mm and exhibited better resistance to crack propagation (with smaller load-dropping rate and larger vertical displacements). It indicated that the CAC-bonded castables exhibited stable crack propagation and excellent toughness fracture characteristics at high temperature. Again, it demonstrated that the addition of nanoscale $CaCO_3$ can play a strengthening and toughening role in castables. Comprehensively, a distinctive feature of the load-displacement curves was that the fracture curves showed high peak loads and narrow ultimate displacements at room temperature, whereas the curves assessed at 1400 °C were dramatically different, lower maximum loads and larger ultimate displacements.
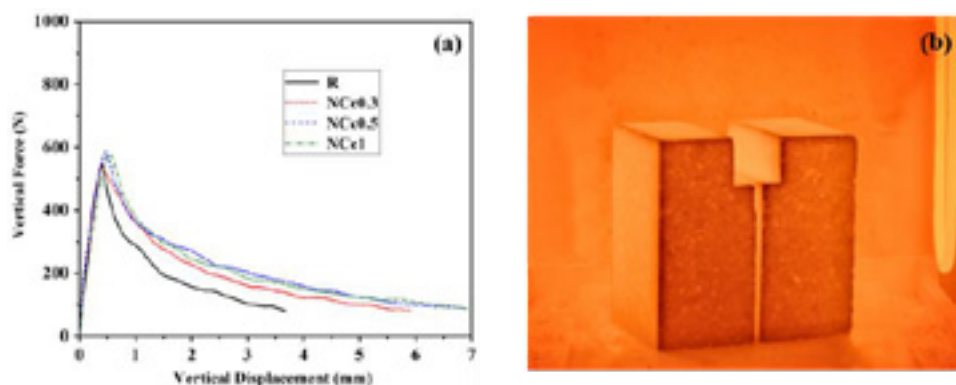
*Fig. 7 Vertical force-displacement curves (b) and of alumina-spinel castables evaluated at 1400 °C.*

Additionally, based on the 2D images scanned by Micro-CT, crack damage identification and evaluation were further performed (Fig.8). The results demonstrated that the crack paths of the specimen R were mainly within the matrixes (69.9%), together with 30.1% through the aggregates. With the addition of nanoscale $CaCO_3$, the cracks were induced through aggregates owing to the reinforcing effects of the elongated network-$CA_6$ in matrixes, and the reducing percentage of cracks through the matrixes was well-verified (~66%). However, there was also the fact that the percentage of cracks through the matrixes of specimen containing 1% nanoscale $CaCO_3$ was rebounded compared to NCc0.5 specimens. The results were related to the increase of total porosity which slightly weakened the matrixes, but it still exhibited matrixes reinforcement.
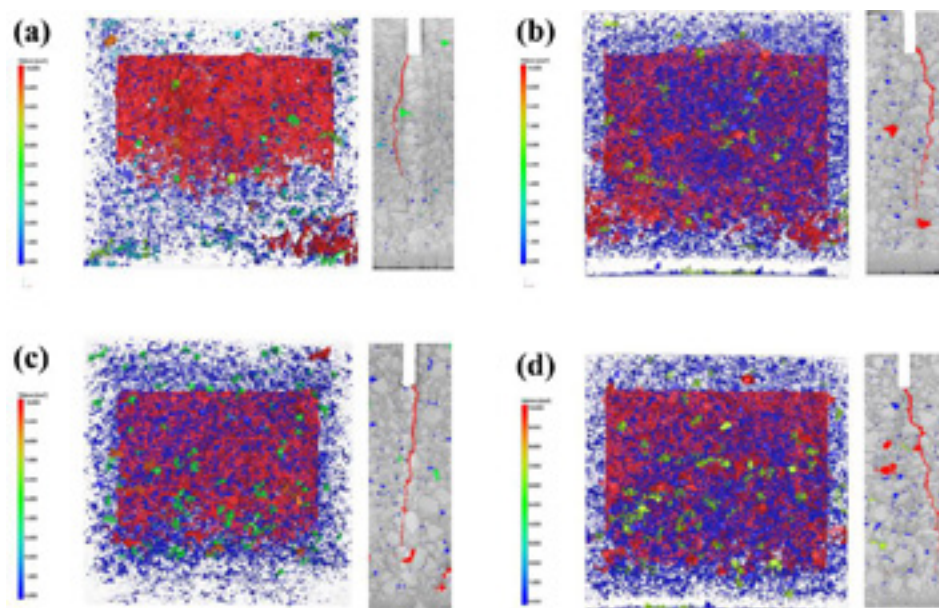


*Fig. 8 Cross-sections in different directions and 3D photo of samples after high-temperature splitting tests.*

## 4 CONCLUSIONS

The generation of plate-like hydrates ($C_2AH_8$, $C_4AcH_{11}$ and $Mg_4Al_2(OH)_{16}(CO_3)\cdot 4H_2O$) together with proper hydration degree contributed to higher bonding strength after demolding and thereafter heat treatments. Meanwhile, these hydrates were conducive to the construction of multistage porous structures, which facilitated the consume of elastic energy stored in the crack tip and induced crack propagation within the matrixes and along aggregate-matrix interfaces. These works provided a new solution to enhance thermal shock resistance of CAC bonded castables.

## REFERENCES

[1] L. Xu, D. Zhang, Y. Liu, M. Chen, N. Wang, Comparison of microstructure, thermo-mechanical property and corrosion resistance of bauxite-corundum refractory castables reinforced by two approaches, Ceram. Int. 47(10) (2021) 13660-13668.

[2] N. Liao, W. Liu, J. Yang, M. Nath, Y. Dai, L. Pan, Y. Li, In-depth investigation of pore structure and fracture behavior of CAC bonded alumina-spinel castables treated at 110 ~ 1600 °C, Ceram. Int. (2022).

[3] W. Liu, N. Liao, M. Nath, Y. Li, Y. Dai, L. Pan, Effects of characteristic hydrates on the pore structure and fracture behavior of CAC bonded alumina-spinel castables, Construction and Building Materials 389 (2023).

[4] Y. Zhang, G. Ye, W. Gu, D. Ding, L. Chen, L. Zhu, Conversion of calcium aluminate cement hydrates at 60°C with and without water, J. Am. Ceram. Soc. 101(7) (2018) 2712-2717.

[5] A.P. Luz, V.C. Pandolfelli, $CaCO_3$ addition effect on the hydration and mechanical strength evolution of calcium aluminate cement for endodontic applications, Ceram. Int. 38(2) (2012) 1417-1425.

[6] J. Goergens, R. Belli, C. Schulbert, F. Goetz-Neunhoeffer, Influence of different $CA_2$/CA-ratios on hydration degree, $AH_3$ content and flexural strength investigated for a binder formulation of calcium aluminate cement with calcite, Cem. Concr. Res. 165 (2023).

[7] W. Liu, N. Liao, M. Nath, Z. Ji, Y. Dai, L. Pan, Y. Li, I. Jastrzębska, J. Szczerba, Effects of curing time on the pore structure evolution and fracture behavior of CAC bonded alumina-spinel castables, Ceram. Int. 48(17) (2022) 25000-25010.

[8] S. Jin, H. Harmuth, Asymmetric creep modeling of common refractory ceramics with high temperature wedge splitting test, Engineering Fracture Mechanics 252(1) (2021) 107819.

# USE OF NOVEL REFRACTORY DESIGN AND INSTALLATION TECHNIQUES FOR IMPROVED ENERGY EFFICIENCY IN IRON AND STEEL AND OTHER ENERGY INTENSIVE INDUSTRIES

James G. Hemrick
Oak Ridge National Laboratory, Oak Ridge, USA

Manoj K. Mahapatra
University of Alabama – Birmingham, Birmingham, USA

## ABSTRACT

This work describes a US Department of Energy funded program which unites key players to develop and deploy new technologies aimed at increasing energy efficiencies while reducing their overall energy and environmental footprint. The research brings together a vertically integrated collaborative team consisting of the end user (US Steel), material producers/suppliers (Allied Mineral Products and Reno Refractories), raw material suppliers (American Metallurgical Services, Minerals Manufacturing), and research organizations (Oak Ridge National Laboratory, National Energy Technology Laboratory and University of Alabama-Birmingham) with the objective of designing and producing new refractory materials. Design and production criteria are based on novel aggregates, improved particle packing, and engineered surface textures. In addition, the recycling and use of spent refractory materials has been investigated resulting in development of a novel installation technique that utilizes additive manufacturing technology and existing refractory shotcrete technology. The combination of these new technologies will improve the energy, environmental, and economic efficiencies of the steel industry while reducing the environmental footprint. The developed technology is potentially applicable to additional energy intensive industries including cement, glass, pulp and paper, and non-ferrous metals processing.

## BACKGROUND

Oak Ridge National Laboratory (ORNL) has a history of being one of two federal laboratories (the other being the National Energy Technology Laboratory (NETL) who is also a partner on this project) actively involved in refractory ceramic research for the improvement of the energy efficiency of energy intensive industrial processes. Successful past projects related to refractory ceramics have been carried out utilizing the unique capabilities and facilities housed at ORNL and have involved both the advanced characterization of existing materials and the development and implementation of new materials for numerous industrial applications including the analysis of fusion cast refractories for more energy efficient oxy-fuel glass furnaces, identification and evaluation of refractory materials for black liquor gasification in the pulp and paper industry, development of multifunctional metallic and refractory molten metal handling materials used in the steel/aluminum/copper/special alloy industries, development of nano-scaled interpenetrating phase composites for industrial and vehicle applications, development and testing of refractories for coal gasification, and the development of novel refractory materials for high alkali and high temperature environments including aluminum, black liquor, coal gasification, and lime kiln environments.

It is the goal of this project to address the estimated 80% of the total energy usage in the steel industry (shown in Tab. 1) which can be directly affected by improved refractory technology by building on previous work to develop and implement improved monolithic refractory ceramic materials with longer lifetimes resulting in an increase in thermal efficiency of key processes in the steel industry and providing an incremental increase in time before refractory lining materials require maintenance. A near-term goal of 2% and a long-term goal of up to 10% overall energy savings due to improved refractory materials is sought relating to over 17 TBtu/Yr (2% goal) and 85 TBtu/Yr (10% goal) in the steel industry, with additional benefits possible if iron foundries are included.

Tab. 1. Energy Savings Possible Through Refractory Improvements

| Industry | NAICS codes | Total TBtu/year* | Usage affected by refractories | | Energy savings goals for improved refractories (TBtu/Yr) | |
|---|---|---|---|---|---|---|
| | | | % | TBtu/Yr | Near-term 2% | Long-term 10% |
| Iron and Steel Mills | 3311111 | 1,065 | 80% | 852 | 17.04 | 85.20 |
| Iron Foundries | 331511 | 48 | 80% | 38 | 0.77 | 3.84 |

## PROJECT FOCUS

This project focuses on the design of refractory ceramic materials used in applications such as blast furnace linings, electric arc furnace (EAF) linings and metal transport vessels (ladles, tundishes, etc.) utilized in the steel industry. Current refractory lining systems for the vessels of interest generally consist of brick or monolithic ceramic materials. In the case of brick, the installation of these materials is highly labor and time intensive. Additionally, the failure of a single region of the lining can lead to widespread failure of the lining as surrounding bricks rely on each other to remain in place, and the many joints between the bricks offer paths for corrosive liquids and vapors to penetrate the lining. Monolithic refractory lining systems (like those being proposed in this project) have the advantage of faster installation methods (casting, gunning, shotcreting) and elimination of the joints between the bricks that offer paths for corrosion. Additionally, monolithic materials are generally installed in continuous panels or complete rings removing the reliance of bricks on their local neighbors for lining integrity. While brick linings have traditionally been favored in many steel applications, monolithic refractories are recently finding use due to improvements and innovations such as no-cement binder systems and improved properties.

Depending on the vessel of interest, refractory lining systems can last for several years (in the case of blast furnaces and EAF) or can be completely replaced as often as weekly or monthly (transfer vessels such as ladles or tundishes). In between complete refractory relines, vessels will be patched as

needed (daily, weekly, or monthly) using monolithic repair material which is gunned, shotcreted, or applied by hand as a coating. In this project we will address primary lining materials, as opposed to repair materials, although the technology being developed could be applied to these repair systems. This project will not only address the energy savings goals above but will also aim to provide an incremental increase in time before the material requires maintenance as shown in Tab. 2 for several example vessels.

Tab. 2. Process Vessel Lifetime Improvement Goals

| Process Vessel | Normal Outage Period for Maintenance | Target Outage Period for Maintenance |
|---|---|---|
| Blast Furnace | 6 months | 12 months (2X) |
| Electric Arc Furnace | 6 months | 12 months (2X) |
| Metal Transfer Ladle | 1 month | 3 months (3X) |
| Tundish | 2 weeks | 6 weeks (3X) |

**PROJECT PROGRESS HIGHLIGHTS**

This project is entering the third and final year. In the first year of the project, the approach taken was to utilize artificial intelligence/machine (AI/ML) learning resources at ORNL, not currently available or widely utilized by the refractory industry, to optimize particle packing and mix composition, along with surface topology, in an effort to produce materials with greater densities (20%), lower permeabilities (10%), and greater chemical inertness resulting in stronger, more corrosion resistant and longer lasting linings. This translates into installed linings being replaced less frequently (reducing process down times, the need to cool and reheat process vessels, and the need to produce and install new refractory materials) and allowing for higher energy efficiency of the process as the insulating value of the lining is maintained as the refractory lining is not degraded as quickly.



Fig. 1: Example ASCENDS data set (input table) and correlation analysis output.

The ASCENDS (Advanced data SCiEnce toolkit for Non-Data Scientists) AI/ML tool developed at ORNL was evaluated for use in educated refractory design. This tool allows the advantage of training of various machine learning models from a spreadsheet-type dataset. Predictions can then be made from trained surrogate models without additional coding. Work under this project was carried out with datasets put together from information previously collected at ORNL and additional data sets provided by refractory partners used as input tables to "train the model". This information was then used to produce correlation tables which were used for model predictions (output tables). Although some information could be gathered from this exercise and the use of this tool (which was used to guide refractory development and design for the remainder of the project), it was determined that larger data sets are needed to fully utilize the capabilities of such AI/ML methods for future refractory design.
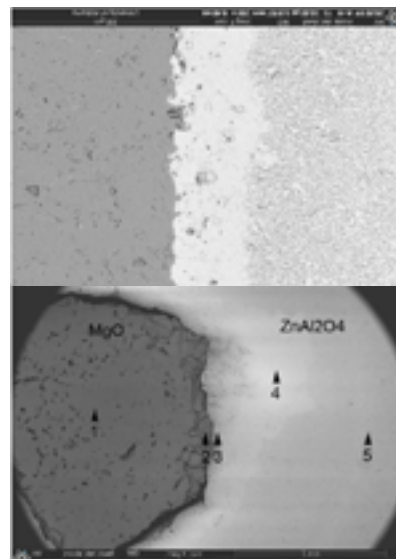


Fig. 2: Scanning electron micrographs of new $ZnAl_2O_4$ material.

The primary new material system developed under this project is a zinc aluminate ($ZnAl_2O_4$) system based on funded and co-advised graduate student and undergraduate student research work at the academic partner University of Alabama – Birmingham (UAB). This system appears to be a viable candidate for replacing existing alumina- and spinel-based systems in the current applications of interest. Several papers regarding this material and its application have been published [1][2] along with the associated dissertation work [3]. Advantages of this new material include intimate bonding of the aggregate with traditional monolithic refractory matrices, favorable thermal expansion behavior, and good corrosion resistance to molten metal and slag. Incorporation of this material into relevant industrial refractory formulations is being undertaken by the refractory industrial partners and samples will be prepared for suitable applications and industrial validation during the final year of the project.

Additionally, the use of recycled raw materials was investigated during the first year of the project and continued into the second year as a means to further improve the energy, environmental, and economic efficiency of the produced materials and targeted processes. Recycling has been a topic of consideration in both the steel industry, as they look for ways to dispose of waste materials after a furnace rebuild, and in the refractory industry, as they look for alternative raw material sources and possible cost reductions. It has also been a topic of academic research as nearly 35 million tons per year of raw materials are consumed worldwide for the manufacture of refractory materials for the iron, steel, other non-ferrous metals, cement and glass industries [4]. According to Industrial Mineral Forums and Research "Mineral Market Matrix", refractories rank 10th out of the 26 leading markets for industrial minerals, consuming 24 different industrial minerals. The economic viability, along with feasibility of

131

using such materials has been problematic in the past due to issues regarding material sorting, material purity, material cost, and material supply [5]. Technical issues include contamination by metal inclusions and corrosive species of the refractory material being processed, comingling of individual refractory raw materials, and the cost of recycled materials relative to equivalent primary raw materials.



*Fig. 3: Recycled raw material from a steel delta.*

The use of recycled refractory materials has taken two paths under this project. The first is led by industrial partner American Metallurgy Services regarding investigations into possible waste streams from the steel industry and their use as raw material streams to produce new refractory materials. It has been estimated from current work that the processed recycled materials being produced could be as much as 50% cheaper when substituted for virgin raw materials. Currently, about 1,500 pounds of crushed calcined bauxite from used steel deltas and several hundred pounds of tabular alumina from other sources has been processed. Opportunities to try this material in industrial refractory mixes are currently being investigated and trialed. A new industrial process is currently being patented from this work as well.
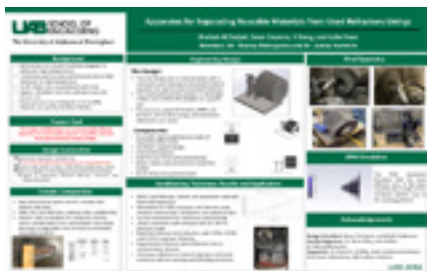


*Fig. 4: UAB senior design project.*

In conjunction with the above work, a senior design project was funded at academic partner University of Alabama – Birmingham (UAB) to investigate low-cost mechanical separation of salvaged refractory material from steel slag and waste after tear out. This project resulted in the development of a simple apparatus utilizing grit blasting and rotary separation techniques that successfully demonstrated separation of refractory waste streams from metal inclusions and waste.

The second recycled material pathway involves the development of recycled alumina and magnesia/alumina spinel aggregate materials sutiable for use in the steel industry by a new industrial partner Evergreen Alumina [6]. The production of this aggregate is based on a new recycled raw material source from the aluminum industry previously not utilized (currently 100% landfilled). Preliminary characterization efforts have been undertaken on this recycled raw material and the processed material which will potentially be used for aggregate production. It is also being introduced to the refractory producers for testing in monolithic refractory mix formulations and is hoped to be trialed in industrial trials later in the project.



*Fig. 5: Examples of shotcrete and novel installation geometries.*

In the second year of the project efforts also focused on the development of a novel installation technique that takes advantage of additive manufacturing technologies currently under development at ORNL's Manufacturing Demonstration Facility (MDF) for ceramic and metallic systems and extending the use to refractory ceramic systems (large aggregate, pumpable mixes) based on knowledge of commercial scale refractory shotcrete technology. Such a method is hoped to increase the rate of installation of these refractory materials, reduce the manpower required for installation of these materials, increase the accuracy of the installation, and allow for novel installation geometries not possible by traditional installation techniques.

Advances in additive concrete manufacturing techniques are relevant here, along with large scale additive processes developed and implemented by the ORNL MDF [7][8]. These techniques can be married with existing industrial technology for the shotcreting of refractory ceramic systems currently being employed and widely utilized by the project industrial partners. One example of advances that can be introduced through the use of AM is graded structuring. This would allow for having different conditions at the free surface/slag line, in the freeboard above the liquid and in the liquid containment space of a steel containing vessel or furnace. Conceptually, one might print a cellular insulating lightweight structure from recycled materials in the freeboard, then at the slag line print a dense corrosion resistant engineered refractory and in the liquid contact area a combination of high density at the hot face with low density insulating material behind it.



*Fig. 6: ORNL SKYBAAM system.*

The ORNL MDF staff identified two possible platforms for this application. The first is the ORNL SKYBAAM (Sky Big Area Additive Manufacturing) cable-hoisted construction 3D printing technology designed for concrete installation, but which could possibly be modified to accommodate refractory gunning or shotcrete mixes. This system utilizes a gantry system to introduce a large print head for computer-controlled application of cementitious materials on a large scale.

*Fig. 7: ORNL OCILOW system.*

The second and preferred platform is the ORNL OCILOW (Off-Centered In-Line Omni-directional Wheels) omnidirectional vehicle which is a programmable steerable platform with up to 10,000-pound payload on which a standard shotcrete or gunning hose assembly could be mounted for computer controlled refractory installation. This system is currently being retrofitted to meet our project needs. It is currently planned to modify this platform for use in a demonstration in conjunction with the project refractory partner Reno Refractories to shoot a test vessel surface or panel when they are in the area servicing a local client with the demonstration either being performed at the ORNL MDF or at the local customer site.

The third year of the project will focus on further refining and characterizing the materials and processes developed during the first two years and validating commercially produced (by our refractory industrial partners) samples of these materials and methods through industrial trials of at partner locations. Operational trials of up to six months are hoped for, along with acerated laboratory trials.

## CONCLUSION

The successful completion of the project will result in new materials and technologies not only appropriate for improving the productivity and energy efficiency of the iron and steel industry, but also multiple other energy intensive industries such as non-ferrous metals, cement, glass, and pulp and paper. Not only will the lifecycle energy of the produced products in these industries be improved, but environmental benefits will also be seen through reduced fuel usage and the use of recycled raw materials and advanced technology and research methods only available at national laboratories and universities will be leveraged into industrial settings.

## ACKNOWLEDGEMENTS

## REFERENCES

[1] S. Mandal, J.G. Hemrick, and M.K. Mahapatra, "Zinc aluminate ($ZnAl_2O_4$) refractory aggregates: Dilatometric sintering studies and thermal expansion coefficient," Journal of the European Ceramic Society, 42:6244-6254, https://doi.org/10.1016/j.jeurceramsoc.2022.06.058, (2022).

[2] S. Mandal, J.G. Hemrick, and M.K. Mahapatra, "Impact on aggregate/matrix bonding when a refractory contains zinc aluminate instead of spinel and magnesia-chrome," Journal of the American Ceramic Society, http://doi.org/10.1111/jace.19214, (2023).

[3] S. Mandal, "Investigation of Zinc Aluminate as a Refractory Material," PhD Dissertation, University of Alabama – Birmingham, (2022).

[4] "Recycling refractories: entering a new era," Informed 2016, Industrial Mineral Forums and Research, (2016).

[5] L. Horckmans, P. Nielsen, P. Dierck, and A. Ducastel, "Recycling of refractory bricks used in basic steelmaking: A review," Resources, Conservation & Recycling 140, 297–304, (2019).

[6] P. Ormond, R. Robbins, and J. Hemrick, "Industrial Waste to Value in the Circular Economy," Proceeding of the 58th Symposium on Refractories, St. Louis, Missouri, March (2023).

[7] P.C. Chesser, P.L. Wang, J.E. Vaughan, R.F. Lind, and B.K. Post, "Kinematics of a Cable-Driven Robotic Platform for Large-Scale Additive Manufacturing," Journal of mechanisms and robotics, 14 (2), (2021).

[8] M. Borish, B.K. Post, A. Roschli, P.C. Chesser, L. Love, and K.T. Gaul, "Defect Identification and Mitigation Via Visual Inspection in Large-Scale Additive Manufacturing," Journal of Materials, 71 (3), 893-899, (2018).

# INFLUENCE OF THE TYPE OF PHOSPHATE ADDITIVE ON THE SETTING KINETICS OF CA CEMENT BONDED REFRACTORY CASTABLES WITH SPECIAL REGARD TO THE RESULTING PH VALUE

J. Kasper, M. Bastian, C. Dannert

Forschungsgemeinschaft Feuerfest e. V. at the European Centre for Refractories, Höhr-Grenzhausen, Germany

## INTRODUCTION/RESEARCH APPROACH

A recent study showed that an increased S-(T)PP concentration (sodium (tri)polyphosphate) as dispersing agent in a refractory castable resulted in a distinctly earlier onset of the main hydration of CA cement (which corresponds to a shorter dormant period) [1] and the specific reasons for this behaviour were questioned. One recent theory comprises that the dormant period results from the formation of an Al-O-H passivation layer on CA cement particles by the depletion of $Ca^{2+}$ [2-4]. This Al-O-H-rich passivation layer then has to go through an aging process [2, 3] to enable a further dissolution of CA cement and thus the overall hydration reaction of CA cement. Kasper put up for discussion that differences of the pH value during the dormant period reasonably explain the length of the dormant period: an increased pH value increases solubility and probably also the rate of solution of the Al-O-H passivation layer in the pore water. Therefore, the subsequent main hydration, which causes the final and major increase in green strength, will be accelerated or decelerated, depending on the pH value. At neutral pH values, the solubility of the passivation layer is low and a retarded aging of the passivation layer on CA cement particles is present. At higher pH values, the solubility of the passivation layer is being increased and an accelerated aging of the passivation layer on CA cement particles is present. The acceleration resp. retardation of the aging of the passivation layer corresponds to a change of the hydration velocity of refractory castables [5-6, 7].

Since the phosphate component becomes ineffective by its complexation with $Ca^{2+}$ [8, 9] during coagulation of the matrix suspension, one could argue that the remaining part of S-(T)PP in solution, the $Na^+$ ions, may provoke the accelerating behaviour if the S-(T)PP concentration is being increased. Especially, since pure phosphoric acid results in a strong retardation of the hydration reaction of CA cement [10]. The amount of $Na^+$ introduced by S-(T)PP may be varied by two measures: Firstly, the chain length of the phosphate influences the concentration of $Na^+$ in solution at a constant S-(T)PP concentration. Secondly, the concentration of $Na^+$ can be varied by the S-(T)PP concentration itself. It is assumed that these changes of the $Na^+$ concentration may be responsible for provoking the changes of the length of the dormant period of the CA cement hydration in the presence of S-(T)PP, by changing the pH value and the corresponding dissolution kinetic of the Al-O-H passivation layer.

The aim of this study was to investigate how the pH value during the dormant period of the CA cement hydration changes, and how this pH value shortens or prolongs the dormant period in dependence of the $Na^+$ concentration. Subsequently, the theory of a pH dependent solubility of the Al-O-H passivation layer shall be confirmed and the influence of the concentration of $Na^+$, as a measure for the shift towards dissolved NaOH by the complexation of phosphate by $Ca^{2+}$, shall be determined.

## MATERIALS AND METHODS

Setting experiments were conducted on alumina-based model refractory castables (coarse grains up to 3 mm, all alumina raw materials supplied by Almatis). CA cement (Secar71, imerys) was used as binder. Different types of S-(T)PP (Chemische Fabriken Budenheim) and citric acid were used as dispersing agents, retarder and accelerator respectively. The water content was chosen to achieve a flow value between 210 and 250 mm (medium to good flow at a water content of 6 wt.-%, vibration according to ISO 1927-4). Only with a high concentration of S-TPP of 0.2 wt.-%, a higher water content of 6.3 wt.-% was needed to achieve a sufficient flow of 190 mm.

The refractory castables were mixed in batches of 3.5 kg using a compulsory mixer (kitchen aid professional) for 3.5 min (0.5 min dry and 3 min wet).

The setting kinetics were investigated using pH value measurements and gave information about the pH value of the pore solution of the refractory castables during setting in a direct comparison to the events which were identified by measuring the sonic velocity, especially about the pH value during the dormant period. Sonic velocity (data presented in Open Ceramics peer review paper) was measured to correlate pH value increases with the period of main hydration of CA cement within the refractory castables.

## RESULTS

The pH value of the pore solution of the refractory castables during setting due to differing chain lengths of the phosphate molecule and differing concentration of S-(T)PP is displayed in Fig. 1. The correlation between the pH during the periods of constant pH and the time when the pH value starts to increase is displayed in Fig. 2. The following observations could be made:

- The pH value was found to increase in distinct steps: A low S-(T)PP concentration (0.1 wt.-%) results in a three-parted increase of the pH value for all phosphate chain lengths with two intermediate periods of constant pH value. The third increase of the pH value corresponds to the main hydration. At high S-(T)PP concentration (0.2 wt.-%), the pH value increases in two steps with one intermediate period of constant pH value. The second increase of the pH value corresponds to the main hydration.

- General speaking, at low S-(T)PP concentrations the pH value increases less compared to high S-(T)PP concentrations. This results in a retarded aging of the passivation layer (lower solubility) at a low S-(T)PP concentration and in an accelerated aging of the passivation layer (higher solubility) at a high S-(T)PP concentration. The chain length of the S-(T)PP plays a less important role.
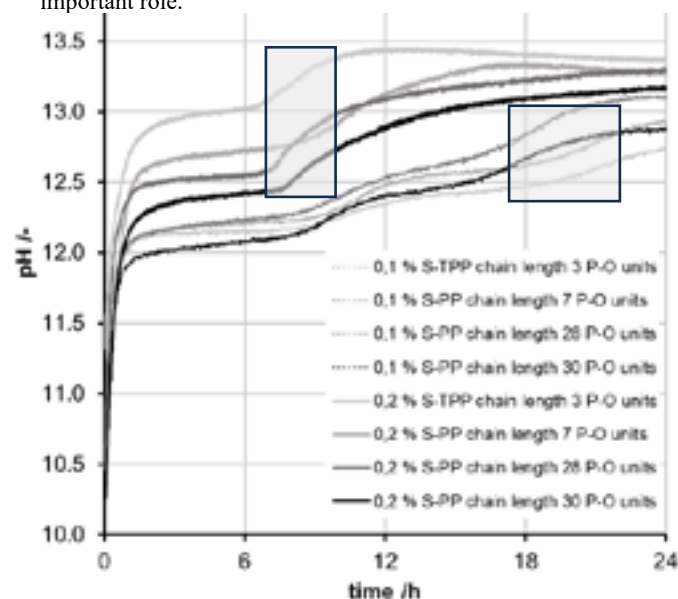


*Fig. 1 pH value of the CA cement bonded refractory castables during setting, differing concentration of S-(T)PP (0.1 and 0.2 wt.-%) and chain length (3, 7, 28 and 30 P-O units) resp. $Na^+$ concentration, grey boxes indicate time intervall of main hydration.*

- The final increase of pH value is linearly correlated to the final increase of sonic velocity (main hydration, data presented in Open Ceramics peer review paper). This implies that the final increase of the pH value is indirectly related to the increase of strength by the precipitation of hydrate phases.
- The periods of constant pH value can be differentiated into two regions (Fig. 2, grey background and white background): The pH value stays below 12.2 and no hydration of CA cement takes place after this period and the pH value exceeds 12.4 and hydration takes place directly after this period ended. The differentiation supports the assumption of Kasper et al. of a pH-dependant solubility of the Al-O-H passivation layer on CA cement particles as the reason for the dormant period [6, 11]. Nevertheless, additional effects seem to be present which influence the length of the dormant period of the CA cement hydration beyond the pH value: Above pH of 12.4, there is no clear correlation between the pH value directly before the occurrence of the main hydration and the time when main hydration takes place (final increase of the pH value and final increase of sonic velocity).
- Only the higher $Na^+$ concentrations of 0.15 to 0.22 (resulting from 0.2 wt.-% S-(T)PP) result in a direct hydration of CA cement between 8-11 h. At the lower $Na^+$ concentrations between 0.08 and 0.12 (resulting from 0.1 wt.-% S-(T)PP), a further final increase of the pH value, additional to the slight increase of the pH value at 10/11 h, has to take place between 18-22 h to provoke the immediate hydration of CA cement.
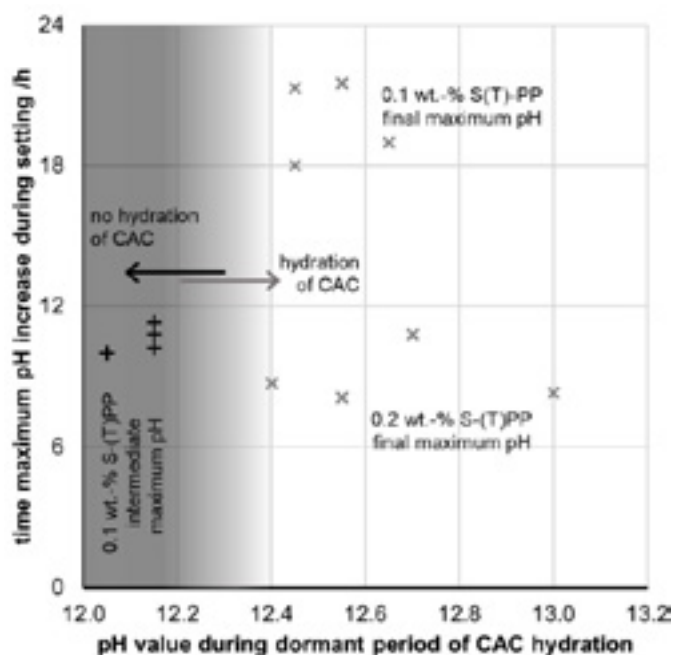


Fig. 2 pH value during the 1st/2nd period of constant pH value vs. time of increasing pH value of the pore solution of the refractory castables during setting, parameter S-(T)PP concentration, grey - region no hydration of CA cement, white - region hydration of CA cement.

**CONCLUSION**

Finally, there is a noticeable correlation between an increasing $Na^+$ concentration from S-(T)PP and the time where the pH value finally increases and the main hydration takes place. The initial assumption that the remaining free $Na^+$ ions provoke an increased pH value resulting in a faster dissolution of the Al-O-H passivation layer, a corresponding shorter dormant period and accelerated main hydration of the CA cement seems reasonable. Nevertheless, the connection of setting kinetics with the $Na^+$ concentration could be better. This implies that there are effects like remaining free phosphate molecules or the ionic strength of the pore solution which may influence the hydration reaction of CA cement further. However, the theory of a pH-dependent solubility of the Al-O-H

passivation layer as the reason for the length of the dormant theory is strengthened [6, 11].

**REFERENCES**
[1] J. Kasper, M. Bastian, C. Dannert, The role of the pH value on the setting of CA cement bonded refractory castables containing phosphate, citric acid AND Li2CO3, Proc. 65th ICR 2022, 57-60.
[2] F. Goetz-Neunhoeffer, Kinetics of the hydration of calcium aluminate cement with additives, ZKG Intern. 58/4 (2005), 2-9.
[3] F. Goetz-Neunhoeffer, Modelle zur Kinetik der Hydratation von Calciumaluminatzement mit Calciumsulfat aus kristallchemischer und mineralogischer Sicht, habilitation thesis, FAU Erlangen-Nürnberg, 2006.
[4] S. R. Klaus, J. Neubauer, F. Goetz-Neunhoeffer, How to increase the hydration degree of CA - the influence of CA particle fineness, Cem. Con. Res. 67 (2015), 11–20, https://doi.org/10.1016/j.cemconres.2014.08.001.
[5] J. Kasper, C. Dannert, A. Koch, O. Krause, Dispersion and stiffening behavior of matrixsuspensions of refractory castables in the presence of impurities, Proc. 64th ICR 2021, 81-84.
[6] J. Kasper, Modellbildung zum Abbindeverhalten von PCE-verflüssigten und CA-Zement gebundenen Feuerbetonen, PhD-thesis University Koblenz, 2021.
[7] O. Krause, D. Tischer, J. Kasper, C. Dannert, The influence of the water-to-cement ratio on the formation of CA hydrate phases in refractory castables after water addition, Proc. 59th ICR 2016, 148-151.
[8] K. Jono, E. Maeda, K. Sorimachi, Reaction between Alumina Cement and Phosphate, J. TARJ 20 (2000), 66.
[9] L. Brecević, H. Füredi-Milhofer, Precipitation of calcium phosphates from electrolyte solutions V. The influence of citrate ions, Calcif. Tiss. Intern. 28 (1979), 131–136, https://doi.org/10.1007/BF02441231.
[10] T. Manninger, D. Jansen, J. Neubauer, F. Goetz-Neunhoeffer, The retarding effect of phosphoric acid during CAC hydration, Cem. Con. Res. 122 (2019), 83–92, https://doi.org/10.1016/j.cemconres.2019.04.020.
[11] J. Kasper, M. Bastian, C. Dannert, M. Thiel, O. Krause, How does the pH-value influence the setting kinetics of hydraulically bonded refractory castables?, 60th ICR 2017, 44-47.

135

# INFLUENCE OF DEFLOCCULANTS ON THE HYDRATE PHASE FORMATION AND TECHNOLOGICAL PROPERTIES OF CAC−BONDED CASTABLES DURING THE FIRST HEATING PROCESS

Bettina Noll, Thekla Stein, Olaf Krause
University of Applied Sciences, Koblenz, Germany

Ralf Simmat
Forschungsgemeinschaft Feuerfest e. V., Höhr-Grenzhausen, Germany

## ABSTRACT
Until now the mechanism and conditions of growth and decomposition of calcium aluminate cement hydrate phases (CAH-phases) that determine the drying behaviour of calcium-aluminate bonded castables are not sufficiently understood. This paper focuses on the influence of different deflocculants (polyphosphate, acrylate, polycarboxylate ether) on the formation of hydrate-phases and their impact on the development of the technological properties of Medium Cement Castables during first heating. To improve the understanding on the hydrate phases CAH-phase formation and decomposition, the investigation of the technical properties (flexural strength and open porosity) of the castables at various temperatures during first heating was combined with high resolution SEM, XRD phase analysis and pore size analysis. Flexural strength was found to develop differently with increasing temperature depending on the type of the used dispersing agent. Considerable influence of the deflocculants on the pore sizes was detected. SEM imaging reveals the differences in shape and size of the formed hydrate CAH phases.

## INTRODUCTION
During the first heating of a castable spalling may occur when the internal pore pressure exceeds the material strength. Studies conducted on cement limes or simplified castable mixes already stated which hydrate phases are formed under defined ambient conditions and at which temperatures hydrate phases are thermally decomposed [1,2,3]. However, said findings do not incorporate the entire composition and microstructure of castables. Deflocculants significantly influence the forming of CAH-phases as discussed in this paper. They also affect the thermal evolution of the pore structure and consequently the permeability of the castable. Low permeability leads to increasing pore pressure during the first heating of the castable and the boiling point of water shifts to higher temperature. It has to be considered that the resulting hydrothermal conditions may stabilize cement hydrate-phases to higher temperatures.

## MATERIALS AND METHODS
For the evaluation of the temperature dependent changes of technological properties of CAC-bonded castables, three modifications of a model MCC containing 90 wt.-% alumina and 10 wt-% CAC were developed using three different types of deflocculants: Each deflocculant affects the workability of the castable in a specific way, requiring different amounts of deflocculant and water. These were adapted accordingly for the following types of castable mixes:

**(a) MCC-P+C:**    0.15 wt.-% sodium polyphosphate (Budit 4H) [1]
0.02 wt.-% citric acid [1],
6.50 wt.-% deionized water

**(b) MCC-A:**    0.30 wt.-% acrylate (KX2314) [2],
6.50 wt.-% deionized water,

**(c) MCC-PCE:**    0.06 wt.-% polycarboxylate ether (Castament FS60, BASF, Germany),
4.8 wt.-% deionized water,

[1] Chemische Fabrik Budenheim KG, Germany
[2] Zschimmer & Schwarz GmbH & Co. KG, Germany;
[3] BASF SE, Germany

Thermal analysis by the Method of Monotonic Heating (MMH) [4] and Thermal Gravimetric (TG) analysis were conducted after a curing period of 48 h at 20 °C and 95 % relative humidity. Flexural strength of freeze-dried prismatic test pieces was tested after curing and after subsequent heating up to 5 temperature levels that were selected to frame temperature ranges in which mineral phase changes were detected by MMH and TG. The halved prisms and fragments thereof were used to determine open porosity (water absorption method), pore size distribution (mercury intrusion porosimeter), size and habitus of the developed hydrate phases (FE-SEM) and mineral phase composition (XRD-Analysis).

## RESULTS AND DISKUSSION
### MMH and TGA
The signals detected in MMH and TGA indicate the ebullition of water and the thermal decomposition of hydrate phases under hydrothermal conditions, similar to those described by Simmat et al. for LC castables. These were investigated using the same test procedure as described here for the MC castables [5]. Exothermic signals at ~100 °C were attributed to the thermally induced rapid hydration of relict CAC remaining after the curing process. Endothermic reactions above ~130 °C are related to the thermal decomposition of different hydrate phases: $CAH_{10}$, dicalcium aluminate hydrate ($C_2AH_x$), katoite ($C_3AH_6$), gibbsite ($AH_3$) and boehmite (AH). The correlation of the endothermic signals in the MMH curves with the thermal decomposition of discrete hydrate phases in the castables has already been described in [5]. The assignment of the signals in MMH was carried out based on plausibility under consideration of known hydrate phases and their temperatures of thermal decomposition as documented in the literature [6]. The relation of these dehydration temperatures to the signals in the MMH-curves is not straightforward, because the stated temperatures have been determined on cement limes, but not on full-scale castables. The low permeability of the dense castables allows the formation of high vapour pressure in the pore structure during the initial heating. The high vapour pressure can stabilise hydrate phases to higher temperatures.

Distinct signals in the form of sharply increasing curves of $a_{eff.}$ were interpreted as the end of the ebullition of free water. At the temperature at which this endothermic process was completed, the heating rate in the sample immediately increased, causing an increase in $a_{eff.}$. This temperature was found to be higher than 150 °C in all samples, indicating hydrothermal conditions prevailing in the pores of the castables.

The temperatures of MMH signals related to the decomposition of hydrate phases for each type of MC-castable are given in table 1.

Tab. 1: Temperatures of MMH-signals attributed to the decomposition of hydrate phases for different types of MCC.

| decomposing hydrate phase | MCC-A Temp. [°C] | MCC-P+C Temp. [°C] | MCC-PCE Temp [°C] |
|---|---|---|---|
| $AH_3$ | 270 | [1] | 290 [2] |
| $CAH_{10}$ | [1] | 130 | [1] |
| $C_2AH_x$ | 155 | 170 | 175 |
| $C_3AH_6$ | 320 | 320 | 320 |
| AH | [1] | 530 | 530 |

1) not detected 2) origin of signal not yet clarified, provisionally interpreted as the decomposition of gibbsite

**Mineral phase Analysis (XRD)**

Significant differences in the mineral phase composition of castables prepared with varying deflocculants are detected after curing. All types of MCC show an increased hydrate phase content after heating to 130 °C but the mineral phase composition develops differently:

**MCC-A**: Only a small amount of hydrate phases ($CAH_{10}$ and $AH_3$) is detected after curing. $CAH_{10}$ is no longer detected at 130 °C but considerable amounts of $AH_3$ and $C_3AH_6$ are evident. The $AH_3$ proportion gradually decreases in the following temperature levels, whereas the $C_3AH_6$ proportion remains stable up to 250 °C but is extinct at 300 °C.

**MCC-P+C:** After curing the gibbsite content is higher than in MCC-A and additionally some $C_3AH_6$ is found. At 130°C $C_3AH_6$ and $AH_3$ are the predominating hydrate phases with traces of $CAH_{10}$ and $AH$. The $C_3AH_6$ content increases with rising temperature up to 250 °C, whereas $AH_3$ is reduced. Instead $AH$ forms a growing part of the hydrate phases. The increasing weight share of the summarized hydrate phases gives evidence of an ongoing hydration process up to 250 °C. At 355 °C $C_3AH_6$ is no longer detected in MCC-P+C.

**MCC-PCE:** After curing the hydrate phase composition is similar to MCC-P+C but with a higher content of $C_3AH_6$. After heating to 130 °C $C_3AH_6$ and $AH_3$ are the prevalent hydrate phases. Compared to MCC-P+C a higher amount of $AH_3$ is detected. The transformation of $AH_3$ to $AH$ occurs later than in MCC-P+C, whereas $C_3AH_6$ decomposes at lower temperature, resulting in $AH$ as the predominant hydrate phase at 300 °C.

**Technical properties**

After curing the examined types of MCCs show widely deviating open porosity (OP), ranging from 2.4 % (MCC-PCE) to 14.6 % (MCC-A). During first heating of the castables a similar increase of OP is observed for all MCCs. MCCs prepared with varying types of deflocculant show specific patterns in pore size distribution. After curing the median pore diameter in MCC-A (~0.2 µm)=is larger than in the other types of MCC (~0.1 µm) examined in this study and increases during first heating. Opposed to this, pores in MCC-P+C and MCC-PCE remain small throughout the heating process.

As depicted in *Fig. 1* the tested MCC modifications show different levels of flexural strength after curing. This can be attributed in part to the detrimental effect of high open porosity on the tensile strength. Differing curve progression with rising temperature substantiates an additional influence due to the differing strength of the hydraulic bond developing within the castable.
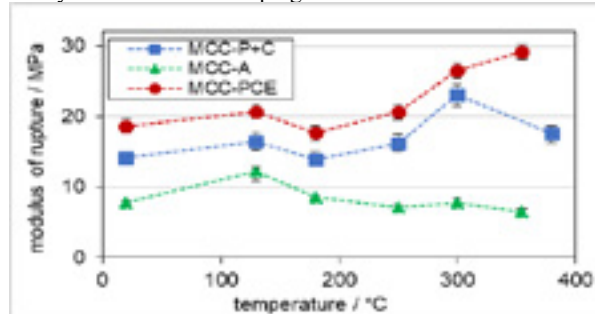


*Fig. 1: Modulus of Rupture (MoR) for each type of MCC after 48 h curing at 20 °C and after subsequent short-time heating to the indicated temperature, followed by freeze drying. Depending on the type of dispersant MoR develops differently with increasing temperature above 180 °C*

**Microscopy**

Depending on the used deflocculant high resolution microscopy revealed considerable differences in the shape and size of the hydrate phases formed during the curing step and their evolution at different temperature steps. After curing mainly clusters of long prismatic crystal shapes and very few tabular crystals are visible in MCC-A. MCC-P+C shows prismatic and tabular crystals and a matrix partly compacted by a gel-like phase. In MCC-PCE very small prismatic crystals are visible only at higher resolution. After the first heating step (130 °C) a complete change in the hydrate phase habitus can be observed. In MCC-A the granular matrix is now interspersed with some tabular hydrate phases. In MCC-P+C and MCC-PCE densely packed large prismatic crystal shapes are prevalent at 130 °C. Through the 180 ° and 250 °C heating steps these prismatic crystals are replaced by a network of intergrown tabular crystals.

**Conclusion**

The results show that deflocculants have significant influence on the formation and decomposition of hydrate phases during the first heating and consequently on the drying behaviour. These results only apply to the liquefiers used in combination with the specific corundum refractory concrete and are not to be standardised.

Using the method of monotonic heating different decomposition temperatures of hydrate phases have been observed. The signal in the range from 150 – 180 °C related to the decomposition of $C_2AH_x$ is shifted to higher temperature in castables with low open porosity. This is attributed to the prevailing hydrothermal conditions. The observed dehydration temperature of $C_3AH_6$ at ~320 °C is not affected by differences in porosity.

XRD analysis confirmed deviations in the mineral phase composition after curing and at five preselected temperature steps depending on the used deflocculant. Heating of the castables leads to a thermally induced rapid hydration of relict clinker phases forming predominantly katoite and gibbsite in all examined castable modifications. The liquefier has a significant effect on the pore structure of the castable, thus affects the thermal decomposition of the hydrate phases. Only in castables with low open porosity the transformation of gibbsite to boehmite is observed.

Flexural strength is typically used to indicate the resistance of castables against spalling. In CAC-bonded castables, this is determined firstly by the quality of the interparticle bonds, which are strengthened by the growth of interlocking hydrate phases, and secondly by the influence of porosity. Both aspects are strongly affected by the type of dispersing agent utilized in the preparation of deflocculated castables.

**REFERENCES**

[1] Götz-Neunhoeffer, F.: „Modelle zur Kinetik der Hydratation von Calciumaluminatzement mit Calciumsulfat aus kristallchemischer und mineralogischer Sicht", Habilitation, FAU Erlangen-Nürnberg, 2006. Erlanger Forschungen, Reihe B • Naturwissenschaften und Medizin 29, ISBN: 3-930357-78-X, ISSN: 0174-6081

[2] Scrivener, L., Capmas, A.: Calcium Aluminate Cements. Chapter 13 in „LEA's Chemistry of Cement and Concrete." 4th ed. Edited by Peter C. Hewlett, John Wiley and Sons New York, 1998

[3] Köhler A., Neubauer J., Götz-Neunhoeffer F.:Phase changes during the drying of calcium aluminate cement bond castables – the influence of curing and drying conditions In: Cement 7 (2022), S. 100020 ISSN: 2666-5492, DOI: 10.1016/j.cement.2021.100020

[4] Simmat, R. et al.: In-situ determination of sintering processes in refractory materials by the method of monotonic heating (MMH). UNITECR 14th, Vienna, Austria, Sept. 15th – 18th 2015, p. 58, DOI/URN: urn:nbn:de:101:1-201506294612

[5] Simmat, R. et al.: Influence of deflocculants on the behavior of calciumaluminate bonded refractory castables, proceedings of ICR2022, Aachen, Germany, Sept. 28th – 29th 2022, pp 132-135

[6] Cardoso, F. A., Innocentini, M. D. M., Akiyoshi, M. M., Pandolfelli, V. C., 2004. Effect of curing time on the properties of CAC bonded refractory castables, Journal of the European Ceramic Society 24, pp. 2073-2078. DOI: 10.1016/S0955-2219(03)00371-6

# IMPACT OF NANO ADDITIVES ON THE PERFORMANCE OF LOW CEMENT REFRACTORY CASTABLE

R. Boris*, V. Antonovič, J. Malaiškienė, R. Stonys

Laboratory of Composite Materials, Vilnius Gediminas Technical University, Lithuania

**ABSTRACT.**

The use of nano additives has attracted great interest due to the impact on the hydration of calcium aluminate cement (CAC) and possibilities to change the properties of refractories.

In this work, the properties of low cement castable (LCC) with 0; 0.3; 0.5 and 0.8% of nano-silica (NS) and combined superplasticizer (0.2%) with the CAC content of 7.0 wt% were investigated. The physical, mechanical, and thermal properties of the castables after thermal treatment (105, 800, 950, 1100 and 1200°C) were determined. The SEM results obtained show a positive effect of NS on the formation of the structure during its hardening. Modification of the binder with nano-additives results in a more densified structure, as a result, a lower total porosity and a higher amount of the smallest pores in the microstructure formation of the LCC. NS was found to increase density, cold crushing strength and thermal shock resistance of LCC; reduces shrinkage, and the optimal NS content was found to be 0.5 wt%.

**Keywords:** low cement castable, nano-silica, microstructure, properties.

## INTRODUCTION

The global production of refractories was estimated to total approximately 45-50 million tons per year. Furthermore, it is expected that the prospects of market's growth will further extend and increase the use of refractory materials [1]. It is important to create and investigate refractory castables, because of their increasing applications and the requirements for the quality of them. A substantial increase in the quality of the new generation of refractory castables can be achieved by reducing the cement content, adding nano and micro additives, and applying effective deffloculants [2]. Nanotechnology plays an important role in the development of cementitious materials [3]. Due to investigations the use of nanomaterials in refractory castables have a great interest in the following aspects: obtaining more unique properties by suppressing the conversion of hydrates [4], improving the bonding, densification, durability of materials (better thermal shock resistance), higher cold crushing strength, control of cracks, etc. depend on the formation of nano and microstructure [5,6]. Studies of nanostructures in refractory materials, in which CAC is used, have not been studied as widely as has been done in the case of Portland cement systems [7,8]. In particular, only a small amount of adding nano-silica mitigated the conversion from metastable phases to stable phases, improving early age strength, durability and decreasing compressive strength loss [4]. Therefore, adding nano particles could improve the castable properties, as long as the nano agglomeration problem is kept under control. There is still an interesting field for investigating the influence of nano additives on the behaviour of properties and microstructure of CAC-based LCC. Furthermore, these castables have valuable properties, such as high density and strength and lower shrinkage [9,10]. Recently, the use of nanosized particles has increased in many refractory-related ceramic applications with the aim of filling even the void space between the micrometre-sized particles and improving the formation of a more densified structure, which is the most important parameter in the function of high performance castable.

The aim of this work was to determine the effect of nano-silica on the structure formation, physical, mechanical and thermal properties of the low cement castable. According to our knowledge, the influence of nano-silica as an admixture has been studied to a small extent on the impact on the CAC hydration and conversion processes and the modification of the properties of castables. This work is the first step in comparative investigations of the possibilities of using these admixtures in refractory castable.

## MATERIALS AND METHODS

The following materials were used to make the samples:

Calcium aluminate cement Gorkal-70 (G70) (chemical composition, mass %: $Al_2O_3$—71.0; CaO—28.0; $SiO_2$—0.5, and $Fe_2O_3$—0.4. Blaine surface area 450 $m^2$/kg) manufactured by Górka Cement Sp. zo.o. (Poland). Microsilica (MC) RW-Fuller (chemical composition, mass %: $SiO_2$—96.06, $Al_2O_3$—0.2, $Fe_2O_3$—0.05, C—0.6, CaO—0.25, MgO—0.4, $K_2O$—1.2, $Na_2O$—0.1, and $SO_3$—0.35) manufactured by RW Silicium GmbH (Germany). Reactive alumina (RA) CTC 20 (chemical composition, mass %: $Al_2O_3$—99.7; $Na_2O$—0.12; $Fe_2O_3$—0.03; $SiO_2$—0.03; and CaO—0.02. Blaine surface area 2100 $m^2$/kg) manufactured by Almatis (Germany).

Bauxite filler (BF; chemical composition, mass %: $Al_2O_3$—81.7; $SiO_2$—10.0; $TiO_2$—4.4; $Fe_2O_3$—2.4; CaO—0.5; $P_2O_5$—0.3; $K_2O$—0.3; MgO—0.2; $ZrO_2$—0.2; $Na_2O$—0.04; and $SO_3$—0.02) of 0-1; 1-3mm was used as a filler (Stanchem, Poland).

The compositions were prepared using the two mixed superplasticizers. Nano-silica (NS) properties: purity 99.8%, particle surface area 202 $m^2$/g, size of grains: 10–30 nm (Sigma-Aldrich Chemie GmbH, Germany) [11,12].

Low cement castables according to the guide recipe given in Table 1 have been prepared by mixing all dry components in a Hobart mixer for five minutes. The NS particles were dispersed in water for 5 min at 400 W, 22 kHz (in an ultrasonic dispergator UZDN-2 T). Furthermore, the resulting suspension was cooled to a temperature 21±1∘C; and the prepared suspension was poured into the castable, after the addition of water, the mixing was continued for another five minutes.

**Table 1.** Compositions (mass %) of the castables tested.

| The mark of composition | G70 (%) | MC+RA (%) | BF (%) | NS* (%) | Superplasticizers* (%) | Water* (%) |
|---|---|---|---|---|---|---|
| LC0 | 7 | 29 | 64 | 0 | 0.2 | 6.5 |
| LCNS1 | 7 | 29 | 64 | 0.3 | 0.2 | 6.5 |
| LCNS2 | 7 | 29 | 64 | 0.5 | 0.2 | 6.5 |
| LCNS3 | 7 | 29 | 64 | 0.8 | 0.2 | 6.5 |

* — above 100%, calculated according mass of dry materials.

The samples for the physical and mechanical properties tests according to LST EN ISO 1927-(5-6):2013 were fired at 105, 1100 and 1200°C. The ultrasonic pulse velocity (UPW) of the castable was established using „Pundit 7" (Germany).

The porosity of the samples was investigated by a mercury intrusion porosimetry (MIP) Quantachrome Poremaster 33/60 (USA).

The samples for thermal shock resistance (TSR) tests were fired at 800°C and 950°C. The destruction of the material was estimated by means of changes of ultrasonic pulse velocity and compressive strength.

The microstructure analysis of the materials was performed with a SEM JEOL SEM-7600F scanning electron microscope (Japan).

## RESULTS AND DISCUSSION

The effect of nano-silica on the density, UPW and CCS of bauxite based LCC were tested. Investigations show that NS has slight effect on the density of castables after drying at 100 °C (~2650 kg/m$^3$), and after thermal treatment at different temperatures (at 1100 °C – ~2620 kg/m$^3$ and at 1200 °C – ~2600 kg/m$^3$) (Fig. 1, a). The difference in the average density values compared to the control sample exceeds 1 to 2%. However, it was found that the UPWs of the castable samples with 0.5% of NS are higher. Considerably UPW values exceeds 7 to 10% compared to the control sample (Fig. 1, b).



a)                                                                          b)
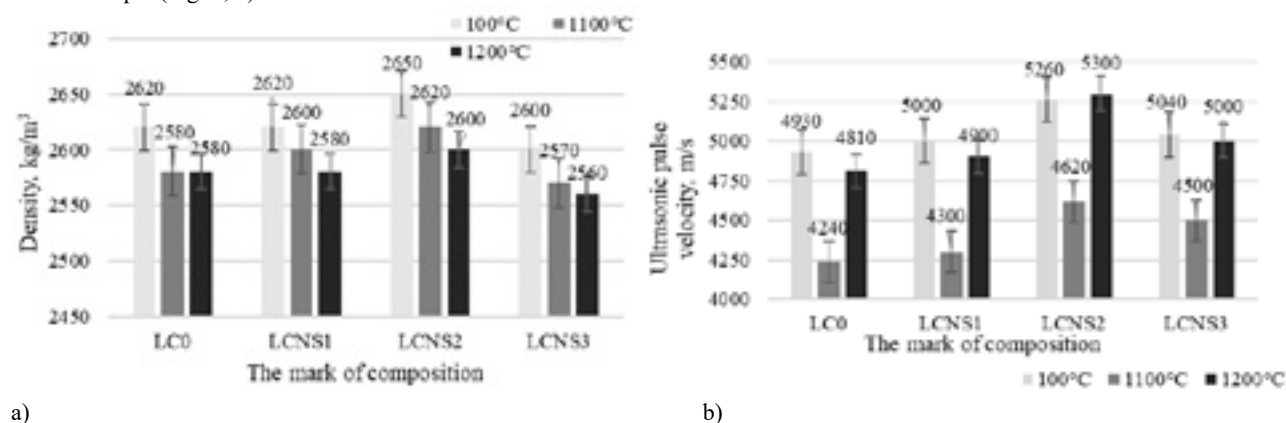
**Fig. 1.** The density (a) and ultrasonic pulse velocity (b) of castable samples after thermal treatment

The results of mechanical testing showed (Fig. 2) that a NS dosage of 0.5% had a significant effect on the CCS of the castable samples (LCNS2). The cold crushing strength strength of LCNS2 was the highest (213 MPa and 205 MPa) compared to the castable control specimen LC0 (185 MPa and 164 MPa). It was found that depending on the addition of 0.5% of NS after firing at 1100°C and 1200°C, the CCS increased by 15-25%, compared to the CCS of the control sample. It was found [13] that the total content of high activated of nanometres and micrometres SiO$_2$ can promote the sintering between the particles, reinforcing the structure of the castable and, as a result, creating an improvement in strength after thermal treatment. In practice the higher CCS leads to the higher erosion resistance of castable and prolonged life time. The tendency of decreasing in CCS up to 1200°C for tested castables may occur due to the dehydration of CAC.
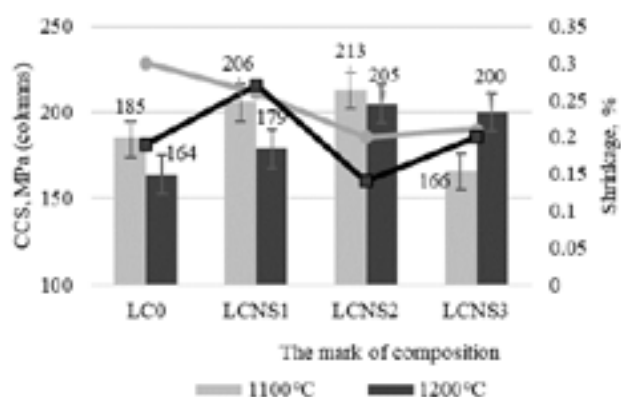


**Fig. 2.** Cold crushing strength and shrinkage of the castable samples after thermal treatment

The microstructure of the CAC-based control matrix and containing nano-silica after firing at 1100 °C is shown in Figure 3. The microstructure analysis of the characteristic matrix with NS (Fig. 3 c, d) reveal the formation of a more compaction structure and microstructurally smaller pores are visible after thermal treatment. A more porous structure of the control binder was observed (Fig. 3 a, b). Different sorts of the investigations refractories with nano additives suggested that NS influences the hydration behaviour of CAC by facilitating the growth of hydration products, has structure modification properties, the microstructure is more stable and providing the nucleation site [12,13]. The samples shrinkage tests after firing at temperatures of 1100°C range from 0.15 to 0.31%.

139
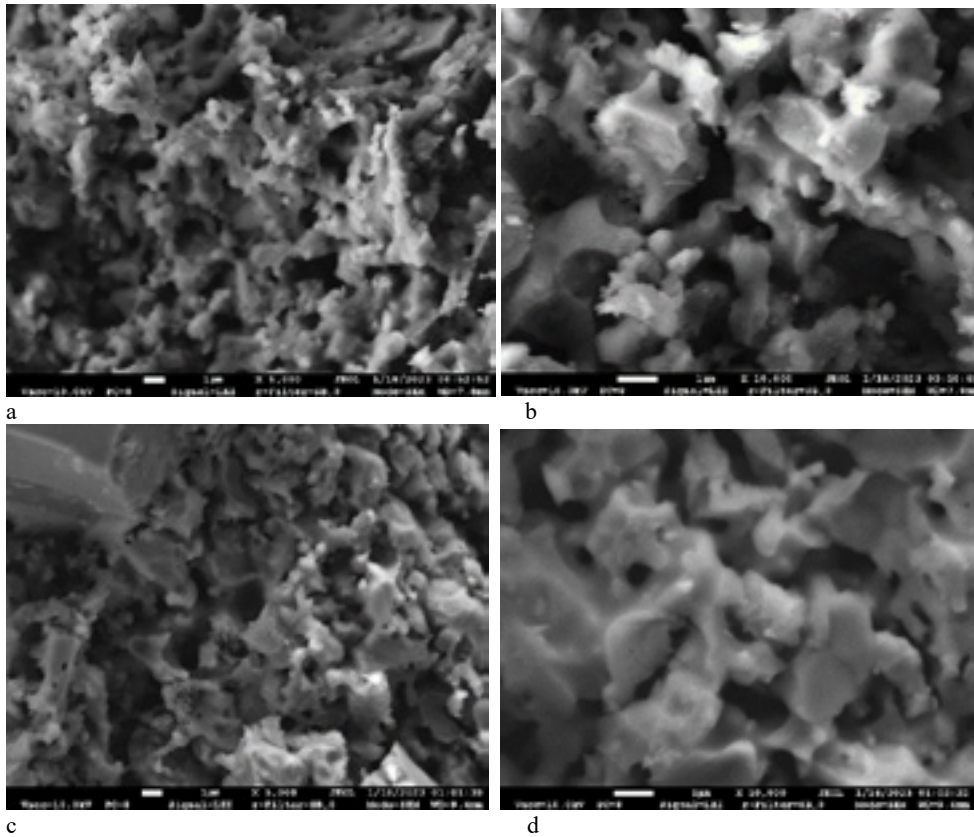
**Fig. 3.** The microstructure of the a, b - LC0; c, d – LCNS2 sample after thermal treatment at 1100ºC

Measurements of the pore size distribution (Fig. 4) in characteristic castable samples (LC0 and LCNS2) were performed. The pore volume of ~0.1µm size was higher in the samples containing NS (0.5 %), which involves an increase in the pore volume by ~1.5 times. The more pronounced number of smaller pores (~0.1µm size pores) in the samples modified with NS agrees with the results of the SEM analysis (Fig. 3 c, d). The results of both analyses show that the samples with NS have more small pores than the reference sample (LC0). These microstructural results are consistent with the literature [13], which can be attributed to dehydration after firing which produces porosity with smaller pores.
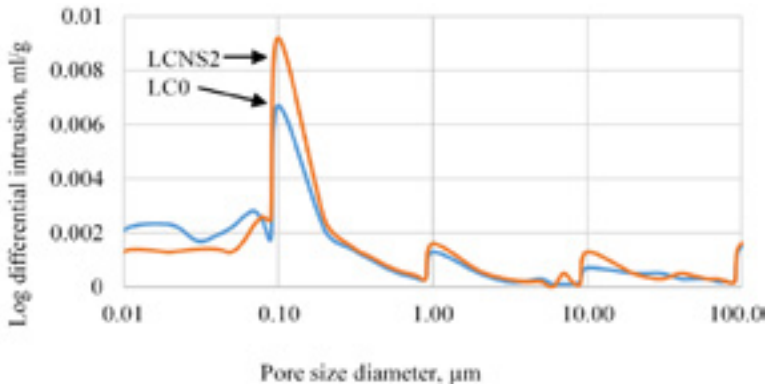


**Fig. 4.** Results of the pore size distribution of LC0 and LCNS2 (0.5% of nano silica)

The thermal shock resistance of the castable samples was evaluated by cyclic firing of the samples at a temperature of 800°C (1st methodology) and subsequent cooling between two metal plates cooled by water and according to the 2nd – firing at a temperature of 950°C and cooling in water. After 7 heating and cooling cycles, the residual bending and cold crushing strengths were determined (Fig. 5, a). The drop in UPW after firing is typical for refractory castables: the discontinuity of the microstructure increases as a result of thermal cycling. The curves of ultrasonic pulse velocity in the castable samples tested during thermal cycling are shown in Figure 5 (b). The bigger decrease in the velocity of the ultrasonic pulse corresponds to a larger number of microcracks and other discontinuities developed in the material during thermal cycling and, respectively, a lower material capacity to withstand thermal shocks. The highest residual CCS values (more than 1.5 times) and the lower decrease in UPW were obtained in castable LCNS2 with 0.5% of NS admixture compared to the control sample.

a)                                                                                      b)
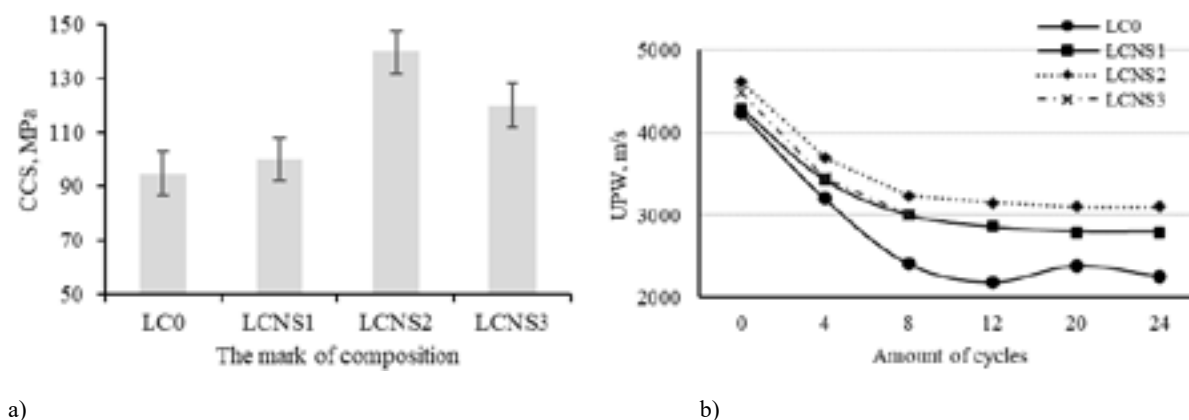
**Fig. 5.** Thermal shock resistance of castable samples: a - variation of CCS and bending strength after 7 heating-cooling cycles at 800°C, b - variation of ultrasonic pulse velocity after thermal cycling at 950°C

As clearly indicated by the above results, the castable with nano-silica addition exhibit higher residual strength, UPW, and as a result better thermal shock resistance. This may be attributed to the nano- and micro-particles that fill the gaps and pores in the matrix forming an optimum packing mode and can also react with $Al_2O_3$ that forms an in situ mullite ceramic bonding phase, improves the strength of the castables after thermal treatment [14]. Therefore, adding NS to refractory castable which improve better mechanical, thermal properties, and exhibited higher amount of the smallest pores, in general, could extend the service life. Some statements require experimental confirmation and such castables will be the subject of research in the future.

**CONCLUSIONS**

In the present work, the effect of nano-silica on the microstructure, physical, mechanical properties, and thermal shock resistance behaviour of low-cement refractory castable with bauxite filler was studied. The following conclusions were drawn from the results of the experimental research described in this paper:

1. It was found that nano-silica influence more compacted matrix formation, which was observed during microstructural analysis, and, in terms of material matrix continuity, can be considered as a formation of smaller uniformly distributed cavities of regular shape.
2. The tested castable exhibits a sufficient strength, with more small pores which results in a good thermal shock resistance. This study showed that even a small quantity of certain additives might significantly modify their mechanical properties through different mechanisms, such as densified structure and smaller pores formation. Because the nano-silica has the most significant influence on the mechanical behaviour, further studies will treat this type of additives in more detail.

**REFERENCES**

[1] https://www.researchandmarkets.com/report/refractories#tag-pos-1. Global Refractories Market Size, Segments, Outlook, and Revenue Forecast by Product Type, Form, Alkalinity, End User, Region, 2022-2028.
[2] Tomšu, F, Palčo, Š. Refractory Monolithics versus Shaped Refractory Products. Interceram 66(1), 2017, p. 20-23.
[3] Middendorf, B, Singh, N. Nanoscience and nanotechnology in cementitious materials. Cement International 4, 2006, p. 80-86.
[4] Son, HM, Park, SM, Jang, JG, Lee, HK. Effect of nano-silica on hydration and conversion of calcium aluminate cement. Construction and Building Materials 169, 2018, p. 819-825.
[5] Antonovič, V, Pundienė, I, Stonys, R, Čėsnienė, J, Kerienė, J. A review of the possible applications of nanotechnology in refractory concrete. Journal Civil Engineering Management 16(4), 2010, p. 595–602.
[6] Shiri, S, Abbasi, M H, Monshi, A, Karimzadeh, F. A study on mechanical and physical properties of monocalcium aluminate cement reinforced with nano-$SiO_2$ particles. Composites: Part B 56 (2014) p. 30–33
[7] Singh, LP, Karade, SR, Bhattacharyya, SK, Yousuf, MM, Ahalawat, S. Beneficial role of nano-silica in cement based materials – A review. Construction and Building Materials 47, 2013, p. 1069–1077.
[8] Malaiškienė, J, Costa, C, Banevičienė, V, Antonovič, V, Vaičienė, M. The effect of nano SiO2 and spent fluid catalytic cracking catalyst on cement hydration and physical mechanical properties. Construction and Building Materials 299, 2021, p. 124281.
[9] Karamian, E, Monshi, A. Influence of additives on nano-SiC whisker formation in alumina silicate–SiC–C monolithic refractories. Ceramics International 36, 2010, p. 811-816.
[10] Diaz, L.A., Torrecillas, R. Hot bending strength and creep behaviour at 1000–1400 °C of high alumina refractory castables with spinel, periclase and dolomite additions. Journal of European Ceramic Society 29, 2009, p. 53-58.
[11] Antonovič, V, Aleknevičius, M, Keriene, J, Pundienė, I, Stonys, R. Investigating the hydration of deflocculant calcium aluminate cement-based binder with catalyst waste. Journal of Thermal Analysis and Calorimetry 2012, 109, p. 537–544.
[12] Boris, R, Wilińska, I, Pacewska, B, Antonovič, V. Investigations of the influence of nano-admixtures on early hydration and selected properties of calcium aluminate cement paste. Materials 2022, 15(14), p. 49-58.
[13] Nouri-Khezrabad, M, Braulio, MAL, Pandolfelli, VC, Golestani-Fard, F, Rezaie, HR. Nano-bonded refractory castables, Ceramics International 39(4), 2013, p. 3479–3497.
[14] Quanli, J, Ju, Z, Ying, Z, Gaoyang, J, Xinhong, L. Effect of microsilica addition on the properties of colloidal silica bonded bauxite-andalusite based castables. Ceramics International 2018, 44, p. 3064–3068.

141

# AN HOLISTIC VIEW AND BENEFITS BASED ON A PLANNED CIRCULATING FLUIDIZED BED BOILER CASTABLE LINING DESIGN

M. A. L. Braulio[1], C. Linhares[2], J. R. Cunha[2], A. J. Maxwell[3], D. Whiteman[3], V. C. Pandolfelli[4]

[1]4Cast, Sao Carlos, Brazil [2]Alcoa, Sao Luis, Brazil [3]Alcoa, Pinjarra, Australia [4]UFSCar, Sao Carlos, Brazil

## ABSTRACT

Changing the refractory lining concept for any high-temperature equipment is not a straightforward task. It involves many steps, including materials' selection, design adjustments, new procurement specifications, contractor application training, and so on. This work illustrates how this process took place for a circulating fluidized bed boiler in an alumina refinery, aiming to reduce the total overhaul time by decreasing the curing and drying time. This objective was attained by replacing cement-bonded castable by phosphate-based ones. Firstly, the selected materials were tested in lab conditions, to guarantee that the change would not affect the lining performance and equipment reliability. After that, pilot trials were conducted in selected boiler areas to evaluate the materials' behavior under operating conditions. Later, during the next overhaul, the new materials were applied in the whole maintenance selected regions, ensuring a reduction from the original 64h to 48h in the dry out curve. The benefits of this modification were various: higher productivity (additional 16h of steam production), lower need to use an external contractor to manage the drying step, shorter curing time (5h for the phosphate-bonded castable versus 24h for the cement containing ones), increase in the products' shelf life (from 6 to 18 months), lower amount of product's types (2 instead of 4) and financial savings. Because of this systemic approach, it is not only expected shorter overhauls but also greater intervals between two consecutive maintenance halts, pointing out the advantages of a suitable materials' selection.

## INTRODUCTION

Circulating fluidized bed boilers (CFB's) are used for steam and power generation, covering nearly all types of solid fuels, such as coal and biomass. The combustion technology delivers high efficiency and reliability, allowing almost complete combustion with lowest emissions ($CO_2$, unburned carbon in ash, $SO_2$ and $NO_2$). The coque particles are suspended in a hot, bubbling fluidity bed of ash and other particle materials (sand, limestone, etc.). The system requires jets of air, which are blown to provide the oxygen for combustion. The fuel is burnt at temperatures ranging from 750 to 1000°C. Fig. 1 presents a schematic representation of the CFB operating mode [1], in which high pressure air lifts the bed material and keeps it in suspension. For circulation, the particles of coal, ash and bed materials are carried to the upper areas and into the cyclone, where the separation of the heavier particles from the gas takes place, returning later to the furnace for recirculation. Meanwhile, the hot gases go out of the boiler.

Due to the high speed of the particles' circulation, the refractory lining is mainly subjected to erosion. In this case, the refractory wear occurs due to the impact of the particles on the material, causing its surface removal. Parameters such as the particles' size, density, hardness, and speed, as well as the castables' microstructure (sort of aggregates, binder, etc.) and toughness affect the degree of damage that is generated [2, 3]. Typical lining damage profiles observed in the boiler vessels (lower and upper furnace regions) are shown in Fig. 2.
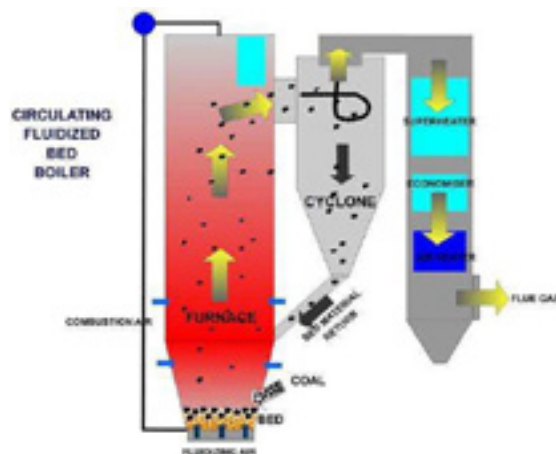


Fig. 1: Schematic view of a CFB boiler operating conditions.
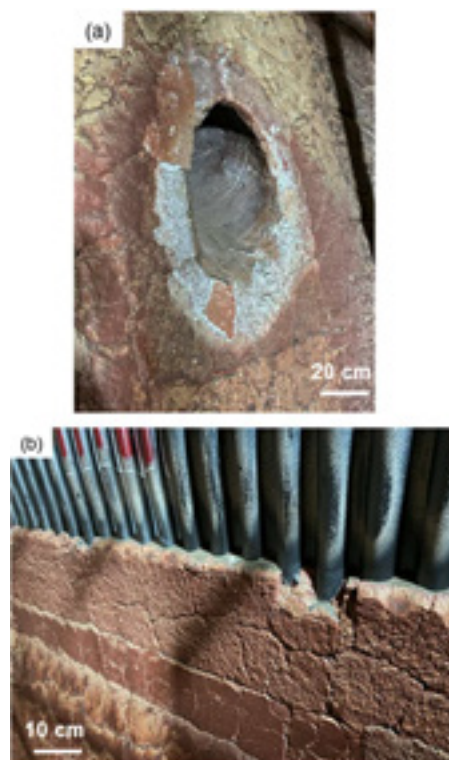


Fig. 2: Erosion wear in (a) the lower and (b) the upper furnace areas.

Besides erosion, the furnace region is submitted to temperature changes, generating thermal stresses mainly in the lower region, where the burners are located. For this sort of refractory damage, crack branching, cracked corners with a 45° degree and structural spalling are usually detected. The thermo-mechanical stresses are caused by the differential expansion or shrinkage along the refractory lining thickness, caused by thermal gradients. During cooling, the lining surface cools down faster than the inner part, leading to a tensile state. Conversely, during heating, the surface expands to a

greater extension than the inner region, resulting in a compressive state [4]. Fig. 3 illustrates the cracking profile and the lining wear caused by thermal shock in the CFB furnace area.



*Fig. 3: Refractory lining spalling due to thermal shock damage.*

Typical CFB projects involve the use of conventional refractory products, such as high alumina bricks, high alumina (chamotte, mullite, bauxite) cement-bonded castables, and lightweight insulation. Different installation methods are used (ramming, gunning, casting) depending on the area geometry, available room for application and required properties. In this concept, the dry out process is a slow and lengthy process. Therefore, if an unexpected halt takes place and the same material is used, resuming the operations takes longer. Furthermore, usual shut-down intervals are of 12 months and the period of downtime is limited (between 2 and 4 weeks). To fulfill this requirement of restarting the process as soon as possible, phosphate-bonded castables are an interesting alternative. This sort of material can ensure easy placing, fast setting and heat up, coupled with suitable erosion and thermal shock resistances [5].

Taking these aspects into account, this work focused on replacing typical castables bonded with calcium aluminate cement by phosphate-bonded materials. A holistic approach, involving initial lab evaluation, followed by pilot trials and then final implementation involves a longer but trustful procedure, to ensure that the changes would not impart a negative effect on equipment operations. In the end, positive results in terms of reducing the shut-down time and increasing the CFB boiler productivity were attained, indicating that the technical and management decisions were worthy.

**METHODOLOGY**

Four steps were conducted before the full lining replacement:

1. Materials selection and testing in lab scale: the current cement-bonded castables (CAC - vibratable - VB, self-flowing - SF and ramming - RAM) had their erosion and thermal shock resistances evaluated in the lab, following the ASTM C704-15 and C1171 standards, respectfully. The vibratable and self-flowing castables are high alumina products (72 wt% $Al_2O_3$, containing tabular alumina and mullite in their composition, 1.4 wt% CaO, density of 2.65 g/cm$^3$, Calderys). The ramming castable has higher alumina content (85 wt% $Al_2O_3$, containing calcined bauxite, and 2.3 wt% CaO, density of 2.9 g/cm$^3$, Morgan Thermal Ceramics). The phos-bond (PHOS) options (Thermbond, Alkegen) were also tested in the lab. The vibratable (VB) castable is a high alumina product (85 wt% $Al_2O_3$ and 4 wt% $P_2O_5$, density of 2.8 g/cm$^3$). The self-flowing (SF) material has less alumina (61 wt% $Al_2O_3$, 1.80 wt% CaO and 0.05 wt% $P_2O_5$, density of 2.5 g/cm$^3$) and is cast with water. Even though,

it was developed to provide fast setting and dryout as typical phos-bond composition. The ramming (RAM) phos-bond composition is also high alumina (80 wt% $Al_2O_3$ and 4 wt% $P_2O_5$, density of 2.9 g/cm$^3$). For the erosion resistance, the samples were fired at typical boiler operating temperatures (600, 800 or 1000°C for 5 hours) and evaluated at room temperature. The thermal shock tests were conducted on samples fired at 1000°C for 5 hours and submitted to thermal cycles of 15 minutes (cooling and heating) under a thermal gradient of 975°C. The ramming castables were only evaluated for the erosion resistance as they are applied in a specific region of the boiler, at the upper furnace region, where erosion is the only predominant wear mechanism.

2. Technical discussions among Engineering, Operations and Manufacturer teams: after approving the materials in the lab, some meetings took place to raise the operational issues and limitations and decide on the new dry out curve.

3. Field trial tests: the new castables were installed in pilot panels in different boiler regions (upper and lower furnace, close to the burners) to evaluate the performance under operational conditions.

4. Final assessment and decision: after evaluating the behavior in the field and other important parameters such as castables' shelf-life, cost-benefit, and potential savings.

**RESULTS AND DISCUSSION**

Fig. 4 presents the erosion results of the CAC-bonded castables and the alternative PHOS-bond options. For all the material types (vibratable - VB, self-flowing - SF and ramming - RAM), the phos-bond castables showed a relevant improvement in the erosion resistance (lower eroded volume) when increasing the firing temperature. Conversely, the CAC-containing options did not change too much this property as a function of the temperature, as the calcium aluminate phases require temperatures above 1000°C to be generated and provide ceramic bonding. At typical boiler operating temperatures (800 to 1000°C), all phos-bond options showed excellent erosion resistance and, thus, were approved for the field testing.
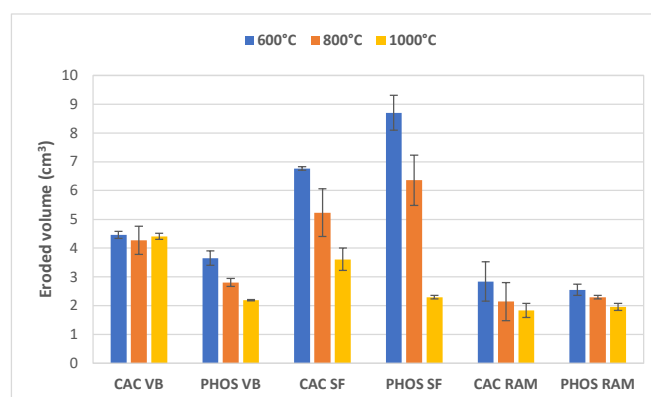


*Fig. 4: Erosion resistance for CAC or PHOS-bonded castables, after firing at distinct temperatures.*

Regarding the thermal shock resistance, the phos-bond castables also had a better behavior (Fig. 5). Both materials presented higher absolute elastic modulus coupled with lower percentual loss as function of the number of thermal cycles. The relative elastic modulus (% loss) indicates the degree of thermal shock damage caused by cracking formation. The higher the loss, the greater the number of defects that are generated during the thermal cycling. Due to the suitable lab results, the materials were approved for pilot tests in the boiler.

143
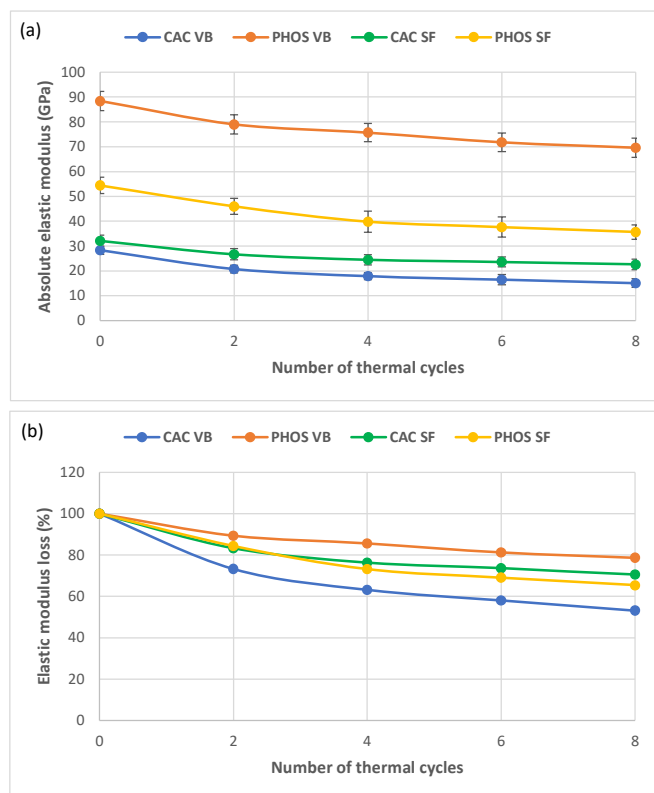
*Fig. 5: (a) Absolute and (b) relative elastic modulus for CAC or PHOS-bonded castables, after 8 cycles of thermal shock under a thermal gradient of 975°C.*

While waiting for the plant trial, the technical team had several discussions with the processing area and the manufacturer to figure out the best way to conduct the heat up curve, based on the lining thickness and overall amount of applied material in a typical boiler maintenance shutdown. It is well known that controlling the heat up of a CFB boiler, without using external burners provided by external contractors, is not an easy task due to its size and design. Nevertheless, as phos-bond castables can withstand higher heating rates, it was confirmed that the procedure could be managed by the processing team, using the boiler burners and the typical heat up process. The proposed dry out curve (Fig. 6) was shorter than the one typically used for the CAC-containing castables, leading to a faster return to operations (reduction of 16 hours).

The approved materials were then applied in different sections of the boiler to evaluate its performance under the operating conditions. The ramming version (PHOS RAM) was installed in a typical area where erosion is severe (kick-out section, upper furnace), during an emergency shutdown (with no dryout curve) and as a patching material as well, for partial repairing of a burner (lower furnace region). Fig. 7 shows the details of these applications. The self-flowing version (PHOS SF) was also analyzed in a plant trial (Fig. 8), in two different areas: next to the burners and close to the second air nozzles. It is worth mentioning that this SF castable can also be shaped using vibration by decreasing the water content. Considering this aspect, it was then selected instead of the vibratable version (PHOS VB) originally evaluated in the lab. This would reduce the number of materials to be purchased for the boilers overhaul, easing the acquisition and transportation logistics (no need to use phosphoric acid liquid for this case - mixed with water).
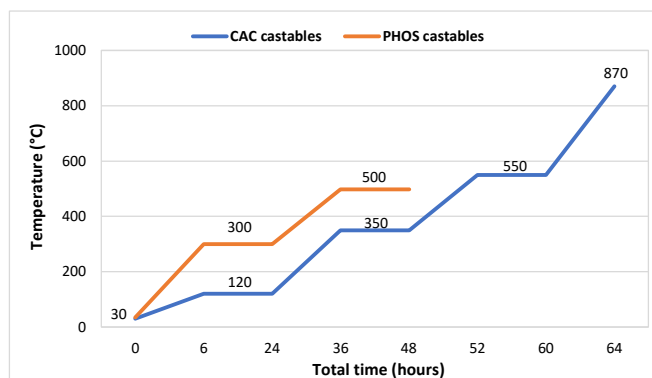


*Fig. 6: Reduction of the dry out / heat up curve time when changing CAC-bonded castables by PHOS-bond ones.*
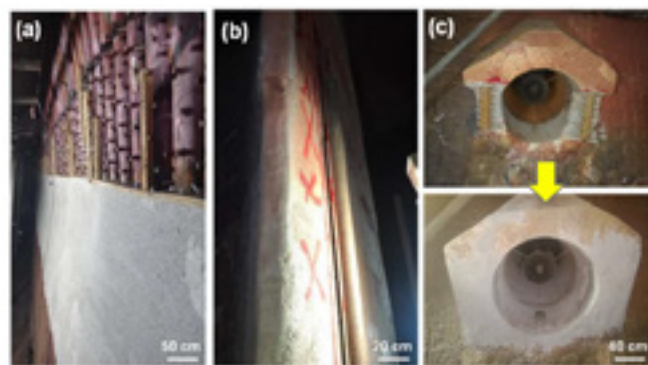


*Fig. 7: Applications of the ramming phos-bond castable: (a) on the kick out area (high erosion wear), (b) during an emergency shutdown and (c) as patching material (partial burner repair).*



*Fig. 8: Applications of the self-flowing phos-bond castable: next to the burners (lower furnace) and close to second air nozzles.*

After four months of operations, the boiler had an emergency halt, and it was possible to evaluate the performance of the PHOS SF material (Fig. 9). The panels applied below the burner (to assess the thermal shock resistance) and near the second air nozzles (to assess the erosion resistance) presented no signs of degradation, pointing out the suitable performance during its use in the boiler. The ramming castable (PHOS RAM) was applied in different opportunities during emergency halts as it could also be used as a patching option. During these evaluations, it has also been approved for the major boiler overhaul.

Taking these results into account, it was decided to move forward with the refractory lining concept change, which resulted in various benefits:

- Decrease in the dry out curve from 64 to 48 hours;

- Reduction in the castables' curing time (5 hours for the PHOS-bond versus 24 hours for the CAC-containing);

- Increase in the products' shelf life (18-24 months for the PHOS-bond versus 6 months for the CAC-containing);

- Cost reduction with gas purchasing due to shorter boiler offline time;

- No need of an external contractor to conduct the first part of the dry out curve (100% managed by the operations);

- Decrease in the number of castables required for the overhaul (4 types for the CAC castables, there was another one used in low volume for some specific areas that was not evaluated in the lab, versus 2 types for the PHOS-bond compositions);

- The PHOS-bond castables are available in Brazil, making the logistics easier in case of emergencies. The CAC-containing castables are imported;

- The high performance observed in the lab and in the plant for the selected materials also indicates the possibility of increasing the lining working life, minimizing the need for maintenance and associated costs.
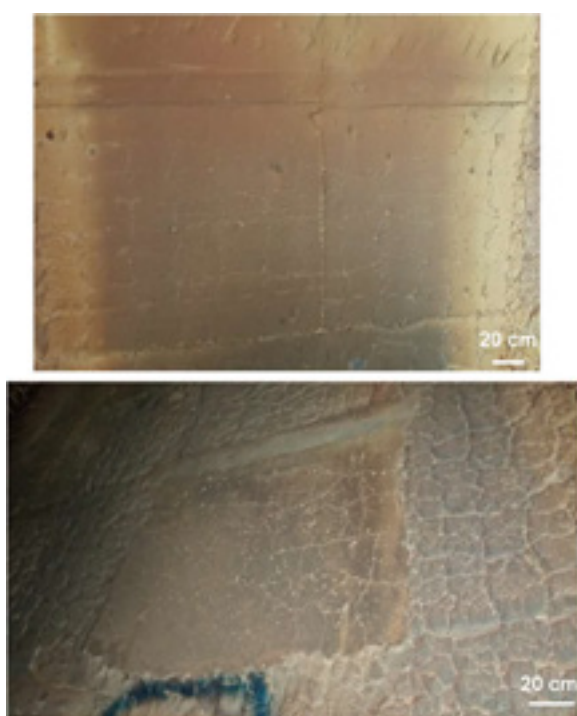


*Fig. 9: No relevant wear was identified in the refractory lining (extensive cracks or thickness reduction), after a campaign time of 4 months.*

## FINAL REMARKS

Proper refractory selection is key for maintenance and operational advances. Changing calcium aluminate cement castables by phosphate-based ones, although increasing the purchasing costs, led to outstanding achievements: faster curing and drying, faster return to operations and cost reductions. The holistic approach ensured a safe and well-designed development, enhancing the boiler reliability and productivity.

## ACKNOWLEDGMENTS

## REFERENCES

[1] How circulating fluidized bed boilers work? Bright Hub Engineering. https://www.brighthubengineering.com/power-plants/26547-how-does-a-circulating-fluidized-bed-boiler-work. Accessed in July 2023.

[2] Wiederhorn, S. Erosion of castable refractories. Refractories Applications 2 (1), 1997, 2-6.

[3] Wiederhorn, S., Hockey, B. J. Effect of material parameters on the erosion resistance of brittle materials. Journal of Materials Science 18, 1983, 766-780.

[4] Hasselman, D. P. H. Unified theory of thermal shock fracture initiation and crack propagation in brittler ceramics. Journal of the American Ceramic Society, 52 (11), 1969, 600-604.

[5] Luz, A. P., Braulio, M. A. L., Pandolfelli, V. C. Refractory castable engineering. Chapters 4 and 6, Göller Verlag, 2015.

# INFLUENCE OF SINTERING ADDITIVES AND SOL−GEL BONDING AGENTS ON WORKABILITY AND FLEXURAL STRENGTH OF CEMENT FREE CASTABLES

L. T. Ibarra, M. Thiesen and O. Krause
Koblenz University of Applied Sciences, Höhr-Grenzhausen, Germany

E. Brochen and C. Dannert
Forschungsgemeinschaft Feuerfest e. V. (FGF) at the European Centre for Refractories (ECREF), Höhr-Grenzhausen, Germany

S. Abdelouhab, C. Lang, C. Delmotte and V. Vandeneede
BCRC-INISMa, Belgian Ceramic Research Center, Mons, Belgium

## ABSTRACT

A few decades ago, no cement castables (NCCs) were a real novelty with increasing papers published on the so-called sol/gel bonded castables for now to be stablished industrially. In the present study, among other things, the effect of the remaining pore water on the development of green strength was investigated and is put up for discussion. An important part of the work was the comparison of new $SiO_2$-free sol biding systems with the established silica sol binding system. The different binding systems are compared concerning their workability using different rheological tests like the flow cone test and regarding the hardening of these NCCs, ultrasonic velocity measurements were used.

## 1. INTRODUCTION

To overcome the drawbacks related to calcium aluminate cements, colloidal silica has been recently used as bonding agent. In addition to the faster drying and the improvement to the thermomechanical resistance, especially in acidic environment compared with materials containing calcium aluminate cements, they also present an increase in thermomechanical resistance at elevated temperatures (750°C-1500°C) due to possible formation of mullite when micro-silica is adding in the starting mixture [1-4]. However, in basic environment such as numerous steel process, the increase in micro-silica content or the presence of amorphous silica from the silica binder decreases the corrosion resistance. It is because of micro-silica or amorphous colloidal silica binder which can react with CaO or MgO contained in the slags or dust by forming low melting point or glassy phases [5]. To avoid such issues other colloidal binders for refractory castables were tested in the literature such as alumina, spinel, mullite and boehmite sols. The results of these studies have indicated similar or even higher thermomechanical and thermochemical properties for castables bonded with alternative colloidal binders [6]. In this context, this study investigates the effect of the use of different sintering additives in high alumina vibrating refractory castables on early age mullite formation and the effect of the use of different alternative high solids colloidal binders compared to those described in the literature on high temperature properties.

## 2. MATERIAL AND METHOD

### 2.1 Materials

Two different base compositions were used in this study, a fine variant (F) and a coarse variant (C) and an industrial reference (IN). The fine version was evaluated using commercial silica sol and different additives (0,1%): $TiO_2$ (FT), boehmite powder (FB) and $MgF_2$ (FM). Furthermore, the behaviour of this variant without any binding agent (FN) was analysed. To evaluate the effect of the different colloidal suspensions, the coarse variant was used.
To improve the workability time showed by the composition containing boehmite sol, it was decided to produce a composition without spinel (since Mg present may lead to a more basic value of pH producing the collapse of the nanoparticles). In this new composition (CBS2) all matrix components were substituted by tabular alumina with a particle size of 0-0,045 mm.

Tab. 1: Castable composition in wt.%.

| Component | F | FT | FB | FM | FN | C | CBS | CBS2 | CSP |
|---|---|---|---|---|---|---|---|---|---|
| Tab. alumina | | | | | | | | | |
| 3-6 mm | 5 | 5 | 5 | 5 | 5 | 23 | 23 | 23 | 23 |
| 1-3 mm | 10 | 10 | 10 | 10 | 10 | 20 | 20 | 20 | 20 |
| 0,5-1 mm | 10 | 10 | 10 | 10 | 10 | 10 | 10 | 10 | 10 |
| 0,2-0,6 mm | 5 | 5 | 5 | 5 | 5 | | | | |
| 0-0,5 mm | 18 | 18 | 18 | 18 | 18 | 15 | 15 | 15 | 15 |
| 0-0,2 mm | 20 | 20 | 20 | 20 | 20 | | | | |
| 0-0,045 mm | 10 | 10 | 10 | 10 | 10 | | | 30 | |
| AR78 | | | | | | 10 | 10 | | 10 |
| E-SY2000 | 20 | 20 | 20 | 20 | 20 | 20 | 20 | | 20 |
| Silica Sol | 5 | 5 | 5 | 5 | | 5 | | | |
| Boehmite Sol | | | | | | | 5 | 2,5 | |
| Spinel Sol | | | | | | | | | 5 |
| $TiO_2$ | | 0,1 | | | | | | | |
| Boehmite | | | 0,1 | | | | | | |
| $MgF_2$ | | | | 0,1 | | | | | |
| Dispersant | 0,1 | 0,1 | 0,1 | 0,1 | 0,1 | 0,1 | | | 0,1 |
| Water | 2,5 | 2,5 | 2,5 | 2,5 | 2,5 | 1,5 | 1,5 | 6,4 | 1,5 |

Tab. 2: Sol suspensions.

| Sol reference | Max. particle size (nm) | pH stabilisation | Solid content (wt.%) | Zeta potential |
|---|---|---|---|---|
| Commercial silica sol. | 15 | 10 | 30 | |
| Boehmite* | 45 | 3 | 20 or 30 | +29,3 |
| Spinel* | 500 | 9 | 20 or 30 | -40 |

*Developed by the Belgian Ceramic Research Centre (BCRC-INISMa in Mons, Belgium).

### 2.2 Methods

The mixing procedure was conducted with an intensive mixer (R05, Maschinenfabrik Gustav Eirich) and a stand mixer (KitchenAid 5KSM7990XESL 325 W). The fine compositions were mixed using the intensive mixer with 1-minute dry mixing at the lowest rpm possible and 3-minute wet mixing at 450 rpm. For the coarser compositions the stand mixer with lower mixing energy was used.
After mixing, the slump flow was determined using a metal conical mould for vibratable castables (according to DIN 1927-4). The mould was filled within an interval of 30 seconds, afterwards the mould was lifted and the castable was vibrated for 60 seconds. At the end the diameter of the slump was recorded. The setting process was analysed using a ultrasound measuring system. (Tester IP-8, Ultratest GmbH).
The castables were casted in bar moulds with measurements of 40x40x160 mm. The samples were left to cure in open air conditions for 24 hours and then left to dry at 110°C for 24 hours. Then they were sintered at different temperatures. The burned samples were milled and their mineralogical composition was investigated with X-ray diffraction technique.
Cold modulus of rupture tests (CMoR) were conducted after demoulding (green state), drying (110°C for 24 hours) and burning/sintering the samples at 800 °C, 1000 °C, 1100 °C, 1200 °C, 1400 °C and 1600 °C using a three-point bending measuring

146

device from Franz Wohl & Partner Prüfmaschinen GmbH. The microstructural characteristics of one of the samples presenting a higher value of CMoR were evaluated using field emission scanning electron microscopy (JEOL JSM-7200F).

To analyse the pore water effect, bar samples were stored at 25 °C with a relative humidity of 60% for five days. The test was conducted by measuring the CMoR after 5, 24, 36 and 72 hours, then weighing the samples and then again after drying at 110 °C for 24 hours to calculate the rest water.

## 3. RESULTS AND DISCUSSION

### 3.1 Effect of additives on fine composition
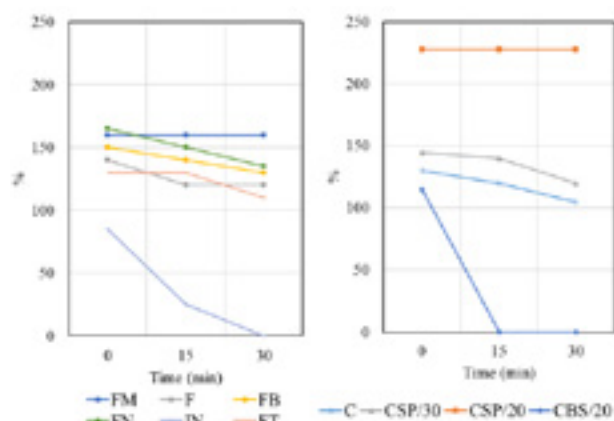


*Fig. 1: Two-dimensional slump flow values at 0, 15 and 30 minutes after mixing.*

The different additives showed no significant effect on the workability of the fine composition, meaning that with time no significant change in consistency was observed within the 30 minutes after mixing (see left diagram from fig. 1).
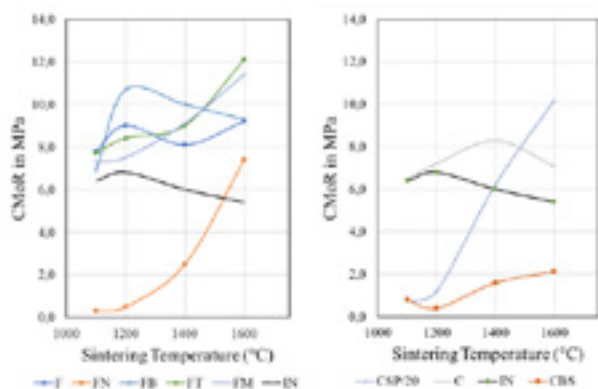


*Fig. 2: CMoR values after different sintering temperatures with a dwell time of 1 hr. Fine composition with different sintering additives (left); comparison different bonding agents (right).*

Tab. 3: CMoR values (MPa) after sintering samples at different temperatures.

| T(°C) | F | FN | FB | FT | FM | IN | C | CBS |
|-------|-----|-----|------|------|------|-----|-----|-----|
| 1100 | 7,8 | 0,3 | 6,9 | 7,7 | 7,3 | 6,4 | 6,5 | 0,8 |
| 1200 | 9,0 | 0,5 | 10,7 | 8,4 | 7,5 | 6,8 | 7,2 | 0,4 |
| 1400 | 8,1 | 2,5 | 10,0 | 9,0 | 9,1 | 6,0 | 8,3 | 1,6 |
| 1600 | 9,2 | 7,4 | 9,3 | 12,1 | 11,4 | 5,4 | 7,1 | 2,1 |

The results of the CMoR measurements are reported in Figure 2. In order to make a better comparison, a formulation without silica sol (FN) and a silica sol bonded commercial castable (IN) were

subjected to the test. With the drying and sintering temperatures 110 °C and 800°C respectively, no significant difference between the modulus of rupture values of the compositions with different additives can be noted. After burning the samples at 1000 °C, the MgF$_2$, containing castables (FM) shows a higher strength value. It has been previously found that MgF$_2$ promotes densification and grain growth in certain types of ceramics which may be the cause for this behaviour at this temperature [7]. At the sintering temperature of 1200 °C a peak corresponding to the composition with 0,1% boehmite (FB) can be observed. Similar behaviour has been already reported in the literature [8]. At the temperature of 1600 °C the highest modulus of rupture value corresponds to the composition with TiO$_2$ (FT), which can be explained by the fact that TiO$_2$ favours an abundant liquid phase during sintering, leading to a higher degree of densification of the sample [9].
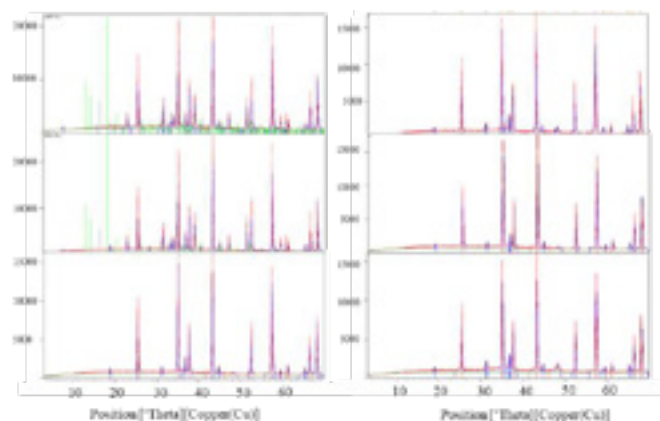


*Fig. 3: XRD Diagrams of (from top to bottom) compositions FT, FB and FM after sintering at 1100 °C for 1 hr (left) and 1200 °C for 5 hrs (right).*

The investigations with X-Ray diffraction were conducted on the samples that were fired at 1200 °C with a dwell time of one hour. In the composition containing TiO$_2$, it is clearly showed that gibbsite and mullite are present in the samples. Concerning the composition with MgF$_2$, it can be observed that spinel is present in the composition. The latter can explain the higher cold modulus of rupture reported previously in this firing temperature range (Fig. 2 left diagram). Figure 3 shows the X-ray diffraction diagrams corresponding to the same compositions, but after sintering at 1200 °C with a dwell time of 5 hours. In all of three of them, a small amount (between 7 and 8%) of spinel can be found. For this reason, the composition containing titania was evaluated with FE-SEM (Fig. 4). Besides the presence of beta alumina, no evidence of spinel could be found with this technique.
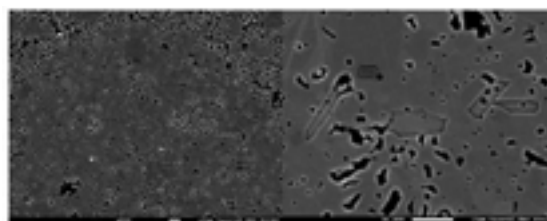


*Fig. 4: FE-SEM images of a sample of the composition with TiO$_2$ after sintering at 1200 °C for 1 hr.*

### 3.2 Effect of different sol suspensions on coarse version (C)

The slump flow test was performed right after mixing, and after 15 and 30 minutes to determine the workability time of this variations of the castables. The results are shown in Fig. 1 (right diagram).

The commercial silica sol and the spinel sol with 30% solids, produce similar values due to the similar pH (10 and 9 respectively) and equal solid content. The spinel sol with 20% solids, produce no

change in the slump flow value as time increased, which may indicate longer periods of time for the samples to be ready to demould. This can be endorsed with the results from the in Figure 8. The results show that the composition with commercial silica sol develops enough placement properties after 24 hours after being casted, whereas for the samples containing spinel sol 20% solids it takes more than 48 hours to develop enough strength to be demoulded.
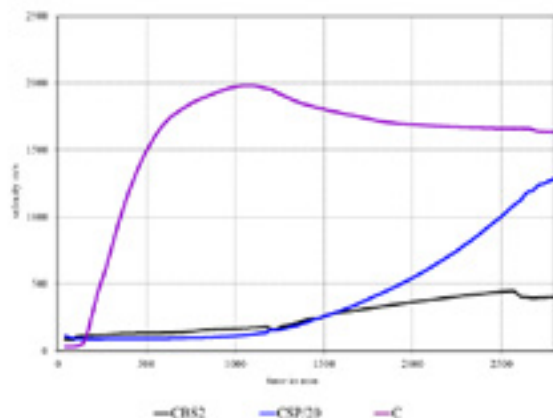


*Fig. 4: Setting process diagram comparing the coarse composition with commercial silica sol (30 % solids, pH 10), spinel sol (20% solids, pH 9) and boehmite sol (20% solids, pH 3).*

The ultrasound diagrams (Fig. 4) show that, compared to silica sol, both boehmite and spinel sol containing castables require a longer time (more than 24 hours) to show good setting properties. This may be due to the lower solid content of this castables. Samples corresponding to the composition CBS showed to have better demoulding properties than those of CBS2, so within the workable timeframe, further samples with the composition CBS were casted for further investigations.

The pore water investigation (Fig. 5) shows a slight increase in green strength of the samples containing 0,1% of MgO. This may indicate that MgO is promoting the setting mechanism of silica nanoparticles, as stated in the literature [10], by favouring the generation of $Mg(OH)_2$, generating a higher green strength.
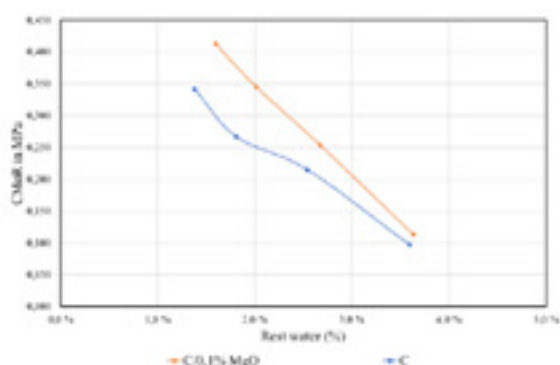


*Fig. 5: Diagram of CMoR against pore water content (%w) comparing E2C composition, with and without 0,1% MgO (dead burned magnesia).*

Fig. 2 (right diagram) compares the cold modulus of rupture of the compositions with different sol suspensions against the fine version, an industrial reference and the coarse version. At temperatures below 1600 °C the compositions containing silica sol (F and C) present higher CMoR values, even than the industrial

reference. The composition containing spinel sol with 20% solids show very low values at the temperatures of 1100 and 1200 °C, similar to the composition containing pseudo-boehmite sol (20% solids). This may be due to the lower solid content of the castables.

## CONCLUSIONS

The sintering additives have no significant effect on the cold modulus of rupture of the fine version of the castable after the analysed burning temperatures below 1600 °C, only at this last temperature an important difference can be noted. Nevertheless, when comparing the variation of the castable with no binder, meaning no silica sol, show lower values of CMoR. The silica sol thus leads to a densification of the structure because of liquid phase sintering, which leads to higher cold compressive strengths. It was confirmed that for these specific formulations the pH value has a very important role on the workability of the castables, meaning that for the coarse composition a basic sol suspension with at least 30% of solid content produces a workability time of at least 30 minutes and good placement properties.

## REFERENCES

[1] Ismael MR, Valenzuela FAO, Polito LA, Pandolfelli VC. Thermo-mechanical properties of colloidal silica-containing castable. Cerâmica 2007:314–8.

[2] Ismael. Colloidal silica as a nanostructured binder for refractory castables. Refract. Appl. New. 2006;11(4):16.

[3] Ismael MR, Ramal Jr FT, Pandolfelli VC. Sol de sílica como agente ligante para concretos refratários. Cerâmica 2006;52(321):82–7.

[4] Ismael MR, Salomão R, Pandolfelli VC. Otimização do uso de sol de sílica como agente ligante para concretos refratários. Cerâmica.

[5] Demin EN, Sarychev AV, Urazova GV. Refractory Cement-Free Castables: Properties and Potential Uses in Metallurgy. Refract Ind Ceram 2005;46(3):159–61.

[6] Singh AK, Sarkar R. High alumina castables: a comparison among various sol-gel bonding systems. J Aust Ceram Soc 2017;53(2):553–67.

[7] Nečina V, Hostaša J, Pabst W, Veselý M. Magnesium fluoride (MgF2) – A novel sintering additive for the preparation of transparent YAG ceramics via SPS. Journal of the European Ceramic Society 2022;42(7):3290–6.

[8] Kwon S, Messing GL. Constrained densification in boehmite–alumina mixtures for the fabrication of porous alumina ceramics. Journal of Materials Science 1998;33(4):913–21.

[9] Vlad EM, Buzduga RV, Buzduga MD, Caloian V, Plopeanu EF, Pandelescu C et al. Experimental research on the effect of additives on the sintering process of alumina-based refractory materials. J. Phys.: Conf. Ser. 2021;1781(1):12066.

[10] dos Anjos RD, Ismael MR, Oliveira IRd, Pandolfelli VC. Workability and setting parameters evaluation of colloidal silica bonded refractory suspensions. Ceramics International 2008;34(1):165–71.

# HIGH TEMPERATURE INNOVATIVE ZIRCONIA–ALUMINA RAMMING MASS

Ph. D. Valeriy V. Martynenko*, Ph. D. Iryna G. Shulyk, Dr. Sc. Volodymyr V. Prymachenko, Ph. D. Pavlo O. Kushchenko

Ukrainian Research Institute of Refractories named after A.S. Berezhnoy, Kharkiv, Ukraine

## INTRODUCTION

The high demand for carbon black on the world market is due to its unique ability to increase the strength and wear resistance of synthetic rubber. The most effective in this capacity are active grades of carbon black, for the production of which it is necessary to increase the temperature in the combustion chamber of reactors for carbon black production to 1900 ºC and above, meanwhile the higher temperature the higher percentage of quality products [1]. In the JSC "URIR named after A.S. Berezhnoy" a technology of ramming masses based on zirconia stabilized by $Y_2O_3$, CaO or combined stabilizing additives CaO and MgO on a phosphate bond, which provide the service temperature up to 2450, 2350 and 2250 ºC, respectively, has been developed and their production has been mastered [2–5]. These refractory materials are successfully used in the combustion chambers lining of industrial carbon black reactors and other high-temperature equipments with oxidizing gas environment.

In the reaction zone of reactor with operating temperature up to 1850 ºC and reducing atmosphere, the refractories containing ~ 99 % $Al_2O_3$ or alumina with addition of 5–12 % $Cr_2O_3$, which are developed and produced in JSC "URIR named after A.S. Berezhnoy", are used [6].

Considering the above, as well as the service conditions at the boundary of combustion and reaction zones of the carbon black reactors - erosion wear and corrosion from high-speed gas flows and droplets of sprayed process feedstock, a variable oxidizing to reducing gas environments, and aggressive effects of alkaline additives introduced into the process feedstock to regulate the quality of produced carbon black - it was advisable to carry out research to develop a special zirconia-alumina ramming mass for this area of the reactor lining.

## EXPERIMENTAL PART

The initial materials for research were fused stabilised zirconia containing 94.0 % $ZrO_2$ and 5.80 % CaO (hereafter stabilised zirconia), monoclinic zirconia containing 98.52 % $ZrO_2$ and alumina containing 99.65 % $Al_2O_3$ (α-$Al_2O_3$ ~ 98 %).

To study the influence of alumina additive amount on the main properties of ramming mass samples based on zirconia stabilized by calcium oxide on a phosphate bond, four compositions were made. The basic composition is zirconia ramming mass, in which the coarse aggregate is represented by stabilized zirconia with a maximum grain size of 5 mm, matrix — vibro-milled zirconia (stabilized and monoclinic). The next batch compositions differed from the basic composition by fact that they contained in matrix vibro-milled alumina in the amount of 5 %, 10 % and 15 % instead of vibro-milled zirconia. The batches were moistened with orthophosphoric acid with a density of 1.7 $g/cm^3$, taken in the amount of 4.2 % (2.6 % $P_2O_5$).

The studied samples were formed on a hydraulic press at a pressure of 100 $N/mm^2$. Determination of the main properties was carried out on samples-cylinders with diameter 36 and height 36 mm (CCS) and 50 mm. Drying of the samples was carried out at 110 ºC in a desiccator. Heat treatment of the samples was carried out at 200, 800, 1200, 1400, 1600, 1700, 2000, 2100 ºC with keeping at each of these temperatures within 2 hours.

The physical and chemical properties of the samples were determined by standard methods. Open porosity, apparent density of the heat-treated samples were determined according to DSTU ISO 5017:2014, CCS — according to DSTU ISO 10059-1:2018, thermal shock resistance (1300 ºC – water) — according to GOST 7875.0-2018. Chemical composition of the initial materials was determined by the chemical analysis method according to acting standards.

Analysis of phase composition was carried out on diffractometer DRON-2.5 in radiation Cu-Kα (with Ni-filter)[1].

## RESULTS AND DISCUSSION

The study of main properties dependence of the ramming mass samples based on stabilized zirconia on the alumina additive amount showed that with increasing of this additive content from 5 to 15 % CCS of the samples regardless of their heat treatment temperature is ~ 1.5 times higher than that of the samples without additive, while an apparent density of the samples with additive somewhat decreases and their open porosity slightly increases compared with the samples without additive. Thermal shock resistance of the samples practically does not change with the alumina introduction (amounts to 5 and 6 heat changes of 1300 ºC – water without and with alumina additive, respectively).

Taking into account of the obtained results, the samples containing 10 % of alumina additive are optimal in terms of properties after firing at 1600 ºC: open porosity — 15.9 %, CCS — 62 $N/mm^2$, linear dimensions change — 1 %. Further tests were carried out on the samples of this composition.

Due to the fact that the carbon black reactor is put into operation within 9–12 days after the refractory lining has been made, the change of main properties (Figure) and phase formation in the developed zirconia-alumina lining material depending on heat-treatment temperature in the range of 200—2100 ºC was studies.

Analysis of the data presented in the Figure shows that the studied samples properties change as the heat treatment temperature increases, as follows:
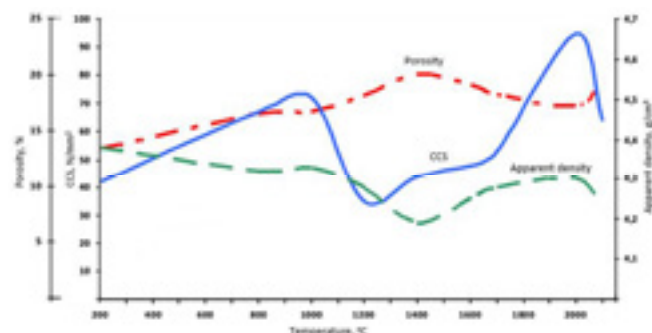


*Fig.* The main properties dependence of the ramming mass samples based on stabilized zirconia with 10 % alumina additive on the heat treatment temperature

– at 200 ºC — the samples have quite high strength (42 $N/mm^2$) and the lowest values of open porosity and relatively high apparent density (13.4 % and 4.38 $g/cm^3$);

– 200–800 ºC — the samples strength increases significantly and amounts to 67 $N/mm^2$, their open porosity increases from 13.4 % to 16.5 %, and apparent density decreases from 4.38 $g/cm^3$ to 4.32 $g/cm^3$;

– 1200–1400 ºC — CCS of the samples decreases to 35–44 $N/mm^2$, open porosity increases and apparent density decreases (accordingly 18.1–20.0 % and 4.28–4.19 $g/cm^3$);

– 1400–1700 ºC — CCS of the samples increases to 53 $N/mm^2$ and their open porosity changes and makes up 18.2 % against 18.1 and 20.0 % for the samples fired at 1200 and 1400 ºC accordingly, and their apparent density — 4.28 $g/cm^3$ against 4.28–4.19 $g/cm^3$;

– 1700–2000 ºC — hardening of the samples (CCS – 95 $N/mm^2$), as well as decreasing of open porosity and increasing of apparent density in comparison with the analogous characteristics of the

---

[1] Carried out by V.V. Varganov.

samples fired at temperature 1700 ºC, namely from 18.2 to 17.2 % and from 4.28 to 4.30 g/cm$^3$, respectively, are observed;

– 2000–2100 ºC — decrease in the samples strength (to 64 N/mm$^2$), as well as an increase in their open porosity from 17.2 to 19.5 % and a decrease in apparent density from 4.30 to 4.23 g/cm$^3$ are observed, compared to these properties of the samples fired at 2000 ºC. A slight melting of the sample surface is also observed.

At the same time, the samples strength after firing in the temperature range of 200–2000 ºC remains high enough to ensure the structural strength of a lining.

The phase composition dependence of the zirconia-alumina ramming mass samples on the heat treatment temperature in the range 200–2100 °C was also studied. This study showed the change of $ZrO_2$ phases during heat treatment in the presence of $Al_2O_3$ and $P_2O_5$ and the effect of these processes on the ramming mass properties. It was found that phase composition of samples after heat treatment at 200 and 800 °C is represented by cubic and monoclinic $ZrO_2$ (accordingly ~ 68–70 % and ~ 18—20 %), as well as glass phase and zirconium, calcium and aluminium phosphates (~ 8–10 %) formed by the interaction of $P_2O_5$ with components of the sample batch. These phosphates act as bond and harden the samples structure. The most complete interaction of $P_2O_5$ with cubic $ZrO_2$ occurs in the temperature range 1200–1400 ºC, which appears in a significant destabilization of cubic $ZrO_2$ phase (whose amount varies from 70 to ~ 35 %). At that time, monoclinic $ZrO_2$ amount increases to ~ 51–53 % and total content of glass phase, zirconium, calcium and aluminium phosphates and the resulting calcium aluminates increases to ~ 11–13 %. It is accompanied by a decrease of the samples strength (CCS varies from 62–72 to 35–44 N/mm$^2$), which remains sufficient to maintain the structural strength of a lining. The destabilization process of cubic $ZrO_2$ phase ends at 1700 ºC (content, %: cubic $ZrO_2$ ~ 28–30; monoclinic $ZrO_2$ ~ 58–60; glass phase, the above phosphates and aluminates ~ 11–13). Increasing of heat treated temperature of the samples from 1700 to 2000 ºC causes the decomposition of aluminium, calcium and zirconium phosphates and leads to the $ZrO_2$ re-stabilization with the cubic $ZrO_2$ phase formation (which amount increases to ~ 33–35 %). The above processes contribute to densification and hardening of the samples structure. Further increasing of temperature from 2000 to 2100 ºC results in the melting of sample surface due to $Al_2O_3$ melting at 2050–2070 ºC.

As a result of this research it has been established that the maximum service temperature of a lining made of the developed zirconia-alumina ramming mass should not exceed 2000 ºC. During phase formation in the temperature range of 200–2000 ºC, the ramming mass strength is high enough to ensure structural strength of the lining in service.

The developed zirconia-alumina ramming mass has been successfully applied at one of the carbon black plants for the lining making on the boundary of combustion chamber and reaction zone of industrial carbon black reactors.

## CONCLUSIONS

The influence of alumina additive amount on the main properties of ramming mass samples based on zirconia stabilized by calcium oxide on a phosphate bond has been studied. It was shown the samples containing 10 % of alumina additive are optimal in terms of properties: content, wt. %: $ZrO_2$ + $HfO_2$ — 83.52, CaO — 3.86; porosity — 15.9 %, CCS — 62 N/mm$^2$, linear dimensions change — 1 %; thermal shock resistance (1300 ºC – water) — 6 heat changes.

The phase formation processes and main properties of the zirconia-alumina ramming mass samples based on a phosphate bond heat-treated in the temperature range 200—2100 ºC have been studied. The changes of $ZrO_2$ phases during heat treatment in the presence of $Al_2O_3$ and $P_2O_5$ and the effect of these processes on the ramming mass properties were shown. It was found that the most complete interaction of $P_2O_5$ with cubic $ZrO_2$ occurs in the temperature range 1200—1400 ºC, it is appeared in a significant destabilization of cubic $ZrO_2$ phase and accompanied by a decline in the samples strength. The destabilization process of cubic $ZrO_2$ phase ends at 1700 ºC. Increasing of heat treated temperature of the samples from 1700 to 2000 ºC causes the decomposition of aluminium, calcium and zirconium phosphates and leads to the $ZrO_2$ re-stabilisation. These processes contribute to densification and hardening of the samples structure. Further increase of temperature from 2000 to 2100 ºC leads to some melting of sample surface.

It is found that during phase formation in the temperature range of 200—2000 ºC, the lining strength made of the zirconia-alumina ramming mass is high enough to ensure its structural strength in service. In view of the above, the maximum service temperature of the lining made of the developed zirconia-alumina ramming mass must not exceed 2000 ºC.

The developed ramming mass has been successfully applied at one of the carbon black plants for the lining making on the boundary of combustion chamber and reaction zone of industrial carbon black reactors.

## REFERENCES

[1] Razd'yakonova, G. Dispersed carbon. OmGTU Publ., Omsk, 2013

[2] Primachenko, V, Martynenko, V, Shulik, I et al. Ramming mix and products from zirconium oxide stabilized by yttrium oxide used for lining high temperature reactors. Stahl und Eisen spec. (9), 2005 p. 134–137.

[3] Primachenko, V, Martynenko, V, Shulik, I et al. Unshaped and Shaped Refractories for Carbon Black Production Reactors Lining. Proc. of 6th International Symposium of Refractories. Zhengzhoy, China, 2012 p. 272–275.

[4] Primachenko, V, Martynenko, V, Shulik, I et al. Investigation of $Y_2O_3$-stabilized Zirconia Ramming Mix after Service in Carbon Black Reactor. Proc. UNITECR-2013 Congress, Victoria, Canada 2013 p. 1116—1121.

[5] Martynenko, V, Primachenko, V, Shulik, I et al. Advanced ramming mix based on fused zirconia stabilized by combined additives of CaO and MgO for lining of carbon black production reactor. China´s Refractories (3), 2017 p. 1–7

[6] Primachenko, V, Martynenko, V, Shulik, I et al. Alumina-chromium oxide refractories and low-cement chrome-containing alumina castable for service in reactors for carbon black production. New refractories (4), 2009 p. 44.

# DEVELOPMENT OF CEMENT FREE DRY-GUNNING MIX AND ITS APPLICATION TO ACTUAL FURNACES

Shiho Takeuchi *, Shuto Azukizawa, Kazushige Watanabe, and Yasutaka Yoshimi

MINO CERAMIC CO.,LTD., Nagoya, Japan

## 1. INTRODUCTION

### 1-1. Cement free dry-gunning mix

Castables have such advantages as they can be installed relatively easily without the need for skilled techniques and also installed even in complex shapes compared to shaped refractories. The castable installation generally include pouring installation and gunning construction in terms of its method. Compared to pouring installation, gunning installation does not require formwork and has the advantage of higher installation efficiency. Gunning installation can be roughly divided into dry-gunning installation and wet-gunning installation. In the installation setup, dry-gunning installation is superior in terms of ease of workability, while wet-gunning installation is superior in terms of quality of installation body.

With regards to binders for castables, alumina cement is generally used but the calcia component in its binder reacts with foreign components such as alkali components and acid gases derived from treated materials and fuels. Furthermore, castables containing a certain amount of alumina cement are inferior in denseness and strength compared to fired bricks. Therefore, in the 1970s, low cement castables with reduced alumina cement content were developed by using the dispersion and agglomeration of fillers with particle sizes ranging from a few microns to submicrons as a method of strength development.

However, these low cement castables have the disadvantage that they are dense and lack the air permeability, making them prone to explosion when heated. Generally, it is possible to prevent explosion by slowing down the temperature rise rate and lengthening the drying time, but there will be issues with longer installation period and increased use of burner fuel. As this situation requires castables with high air permeability that can be dried in a short period of time, various cement free castables have been developed with improved air permeability in recent years.

This paper presents a cement free dry-gunning mix using silica sol as a binder. We have investigated the effects of types of silica sol and amount of clay raw material added on the air permeability, the strength, and workability of the cement free dry gunning mix and also reported the result after a service in an actual furnace.

### 1-2. Mechanism of explosion

In the drying process, dry of castables starts from the heating of the sample surface. After that, as the surface temperature rises, the inside temperature gradually rises due to heat conduction, and the water in the castables evaporates. Water vapor diffuses through pores, but vapor pressure inside the castables increases due to ventilation resistance if water vapor is hard to flow. If water vapor pressure inside the castables becomes greater than the strength of construction body, it occurs crack and explosion.

### 1-3. Improvement of explosion resistance using silica sol

The silica fine particles in the silica sol are negatively charged and dispersed, but when mixed with the powder in refractory materials, they gelatinize and aggregate under the influence of counter ions derived from the powder, resulting in bonding. On that occasion, microcracks are created, which provide an escape route for water vapor during drying of castables, thereby improving the air permeability. Additionally, cement free dry-gunning mixes using silica sol as a binder have the advantage of being less likely to explode due to the low crystalline water content.

## 2. EXAMINATION OF SILICA SOL

The properties of cement free dry-gunning mixes using silica sol are considered to be greatly influenced by the types of silica sol, such as pH, the average particle size, and the solid concentration.

### 2-1. Evaluation method

Table 1 shows the composition of the samples used in the evaluation. Samples were prepared in a bench scale test and the amount of silica sol added was adjusted to achieve the same degree of softness in each sample. Evaluated were the air permeability, the bending strength at room temperature, and the workability. The samples for air permeability measurement were casted in $\varphi 50mm \times 50mm$ mold, cured for more than 24 hours at room temperature and demolded. The air permeability was measured for the cured samples and the samples heated at 110 ºC $\times$ 24 hours. The samples for bending strength measurement were casted in 160 mm $\times$ 40 mm $\times$ 40 mm mold, cured for more than 24 hours at room temperature and demolded. The bending strength at room temperature was measured for the cured samples and the samples heated at 110 ºC $\times$ 24 hours by the 3-point bending test. In addition, dry-gunning tests were conducted using dry gunning equipment (Sika's Aliva-237), assuming a ceiling section. Figure 1 shows the appearance of the dry-gunning test. Figure 2 shows a schematic view of the dry-gunning test assuming a sidewall section. Dry powder materials are generally conveyed with pressurized air, mixed with pressurized silica sol by a separate system at the nozzle tip, and installed by spraying. The workability was evaluated in terms of moisture range, and dust generation, etc. The moisture range refers to the range of the amount of silica sol that can be mixed with the material at the nozzle tip during dry-gunning, and the wider it is, the better the workability.

Table 1 Details of samples used in the evaluation

| | | | DG1 | DG2 | DG3 |
|---|---|---|---|---|---|
| Raw materials | Chemical composition / mass% | Al$_2$O$_3$ | 72 | | |
| | | SiO$_2$ | 23 | | |
| Silica sol | Solid concentration / mass% | | 40 | 30 | 30 |
| | Average particle size / nm | | α | α | 0.7α |
| | pH | | 8～11 | | |



Fig.1 Appearance of dry-gunning test.
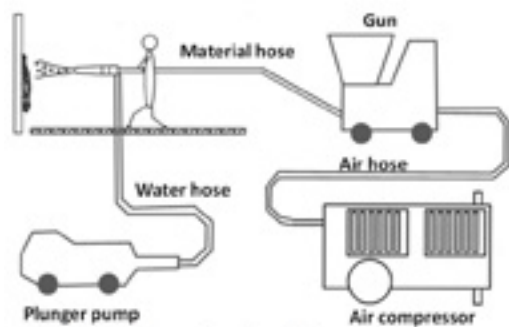
Fig.2 Schematic view of dry-gunning test.

## 2-2. Results and discussion

### 2-2-1. Solid concentration of silica sol

Figure 3(a) and 3(b) show the results of the air permeability and the bending strength at room temperature respectively when the solid concentration of silica sol is varied. The results are shown as an index with the measured value after curing of DG2 being 100. As seen in the graph, the air permeability was greater at higher the solid concentrations of silica sol. This would be due to the higher amount of silica particles derived from the silica sol in the sample, which increased the amount of microcracks generated during gelation. Additionally, the bending strength at room temperature was greater at higher solid concentration of the silica sol. This can indicate that the silica particles in the silica sol act as a filler to fill the spaces between the aggregates of the castables, thereby improving the filling properties of the samples and increasing their strength.



(a) Air permeability



(b) Bending strength at room temperature
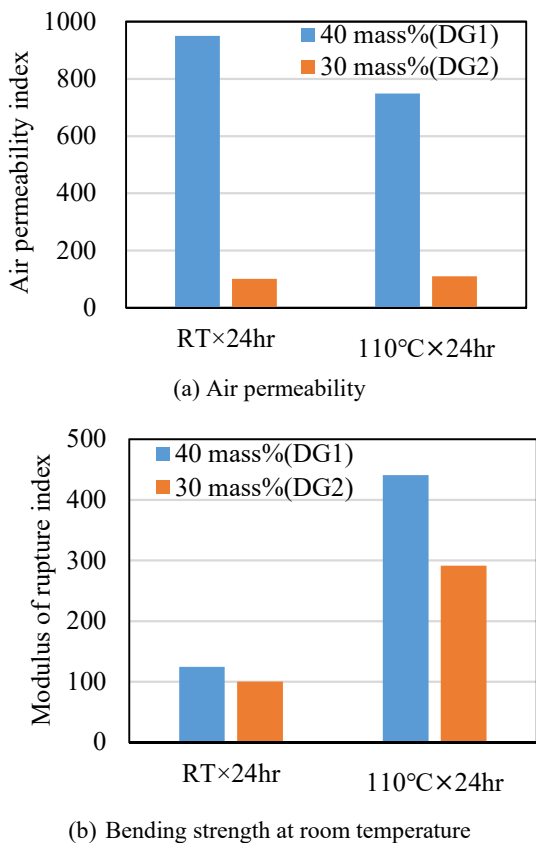
Fig.3 Results of the air permeability and the bending strength at room temperature when the solid concentration of silica sol is varied

### 2-2-2. Average particle size of silica sol

Figure 4(a) and 4(b) show the results of the air permeability and the bending strength at room temperature respectively when the average particle size of silica sol is varied. The results are shown as an index with the measured value after curing of DG2 being 100. As

seen in the graph, the air permeability was greater for the smaller the average particle size. When silica sol with the same solid concentration is used, it is considered that the smaller average particle size has a larger specific surface area, resulting in a larger volume shrinkage associated with gelation and more microcracks. In addition, the bending strength at room temperature was smaller for the smaller average particle size. As mentioned earlier, this would be due to the greater volume shrinkage caused by the smaller average particle size and the spread of microcracks.



(a) Air permeability



(b) Bending strength at room temperature
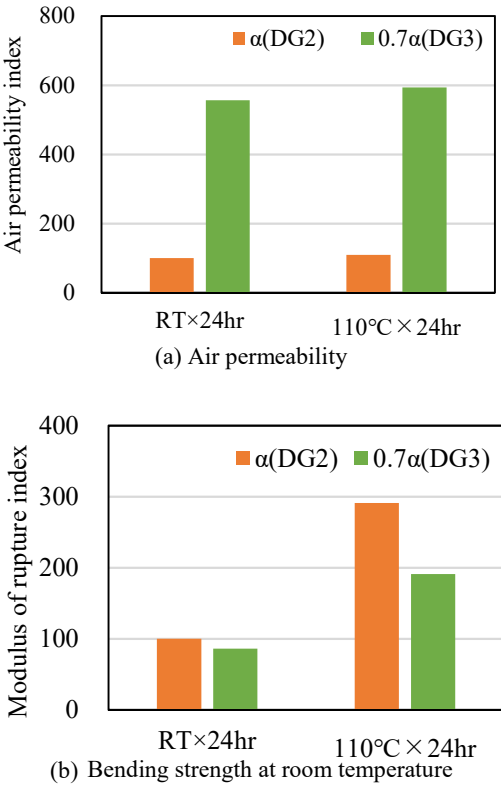
Fig.4 Results of the air permeability and the bending strength at room temperature when the average particle size of silica sol is varied.

### 2-2-3. Workability

Table 2 shows the results of the dry-gunning test with different types of silica sols. The workability in dry-gunning test demonstrated good results, but nozzle clogging occurred in DG1 using silica sol with 40 mass% solid concentration. Because silica sols with higher solid concentrations are more viscous, DG1 was considered more viscous in its mixture with the powder than DG2 and DG3.

Table 2 Results of dry-gunning test with different types of silica sols

| | | DG1 | DG2 | DG3 |
|---|---|---|---|---|
| Silica sol | Solid concentration / mass% | 40 | 30 | 30 |
| | Average particle size / nm | $\alpha$ | $\alpha$ | $0.7\alpha$ |
| | Viscosity / mPa·s | $3\beta$ | $\beta$ | $\beta$ |
| Workability | Adhesiveness | ○ | ○ | ○ |
| | Dust generation | ○ | ○ | ○ |
| | Nozzle clogging | × | ○ | ○ |
| | Moisture range | ○ | ○ | ○ |

## 3. EXAMINATION OF THE AMOUNT OF CLAY RAW MATERIAL

Since the application of clay raw materials is essential for adhesion with dry-gunning mixes, the effect of the amount of clay raw material A added on the air permeability was investigated.

## 3-1. Evaluation method

Table 3 shows the composition of the samples used in the evaluation. The total amount of fines less than 75 µm in each sample was kept constant, and the amount of silica sol added was adjusted to achieve the same degree of softness in each sample. The same procedure as in the Section 2 was used to measure the air permeability, the bending strength at room temperature, and to conduct the dry-gunning test evaluate the workability.

Table 3 Details of samples used in the evaluation

| | | | DG4 | DG5 | DG6 | DG7 |
|---|---|---|---|---|---|---|
| Raw materials | Chemical composition / mass% | $Al_2O_3$ | 72 | | | |
| | | $SiO_2$ | 23 | | | |
| | Amount of clay raw material A added / mass% | | 1 | 2 | 3 | 4 |
| Silica sol | Solid concentration / mass% | | 30 | | | |
| | Average particle size / nm | | α | | | |
| | Amount of addition / mass% | | 14.7 | 14.9 | 15.4 | 15.7 |

## 3-2. Results and discussion

### 3-2-1. Amount of clay raw material

Figure 5 shows the results of the air permeability as an index with the measured value after curing of DG4 being 100. The air permeability of DG6 and DG7 was comparable, but the air permeability tended to increase with the addition of a larger amount of clay raw material A. Additionally, a tendency for the amount of silica sol added to increase with an increase in clay raw material A was observed. Considering clay raw materials have high water retention properties, the increase in the amount of silica sol added could be due to the water retention properties of clay raw material A. The increase in the amount of silica sol added is considered to have increased the amount of silica particles that contributes to gelation and improved the air permeability. Figure 6 shows the results of the bending strength at room temperature for DG6 and DG7, which had comparable air permeability, expressed as an index with the measured value after curing of DG6 being 100. The bending strength at room temperature was higher for DG6 with a smaller amount of clay raw material A than for DG7, which could be caused by the increased water content derived from the silica sol in DG7.
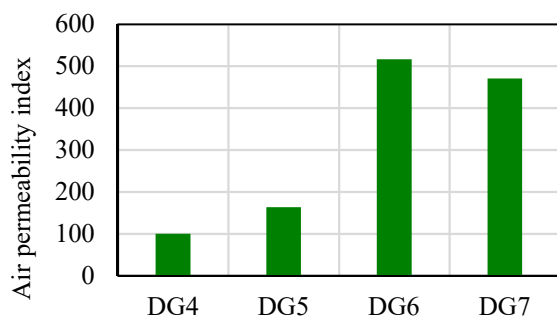


Fig.5 Results of the air permeability measurement after curing at room temperature in the study of clay raw materials for varying amounts of clay raw material A added.
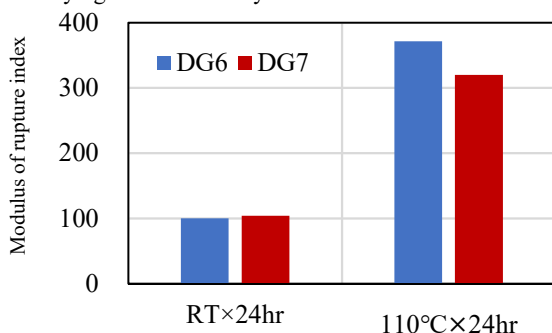


Fig.6 Results of the bending strength at room temperature after curing at room temperature and after drying at 110°C for varying amounts of clay raw material A added.

### 3-2-2. Workability

Table 4 shows the results of the dry-gunning tests for DG6 and DG7. DG6 had a narrow moisture range and dust generation was observed, while DG7 had a sufficient moisture range, no dust generation or nozzle clogging was observed, and the workability was good. DG7 is considered to have a sufficient moisture range due to the large amount of clay raw material A with water retention properties.

Table 4 Results of dry-gunning test with different amounts of clay raw material A added

| | DG6 | DG7 |
|---|---|---|
| Amount of clay raw material A added / mass% | 3 | 4 |
| Adhesiveness | ○ | ○ |
| Dust generation | △ | ○ |
| Nozzle clogging | ○ | ○ |
| Moisture range | △ | ○ |

## 4. CEMENT FREE DRY-GUNNING MIX PROPERTIES

Based on the above considerations, a cement free dry-gunning mix based on DG7 was developed. Since the developed dry-gunning mix is expected to have improved explosion resistance and alkali resistance, we evaluated its explosion resistance and alkali resistance. We also inspected the conditions for installation and drying, and performance in an actual furnace.

### 4-1. Explosion resistance

The test method
· Sample size 60×60×60mm with thermocouple at the center.
· Casting in cast mold.
· Curing for 24 hours.
· The sample into the electric furnace was maintained at 400 °C.
· The temperature inside the sample was measured.
· The temperature change inside the sample is shown in Fig. 7.

The evaluation method
· The surface temperature of the sample into the electric furnace maintained at 400 °C rises. After that, the internal temperature of the sample rises because heat is gradually transferred from the surface to the inside (Fig. 7, section ①)
· Heat energy is used as latent heat to change water to vapor. The internal temperature of the sample rises gradually. (Fig. 7, section②)
· The evaporation of water is completed. Heat energy is used to only heat the sample. The sample is heated up faster. (Fig. 7, section ③)
· $t$ °C is a temperature at the inflection point that moves from section ② to section ③. E MPa (Saturated water vapor pressure) is calculated by the following formula (1).

$$E(t) = 6.11 \times 10^{\frac{7.5t}{237+t}} \times 10^{-4} \qquad (1)$$

Assuming that the vapor in the sample was saturated at temperature ($t$), the maximum vapor pressure in the sample was evaluated as $E(t)$.

Table 5 shows the calculated vapor pressure inside the sample. The inside vapor pressure of the developed dry-gunning mix was 0.18 MPa, which was smaller than that of the low cement dry-gunning mix (0.73 MPa), confirming the improved explosion resistance.

153
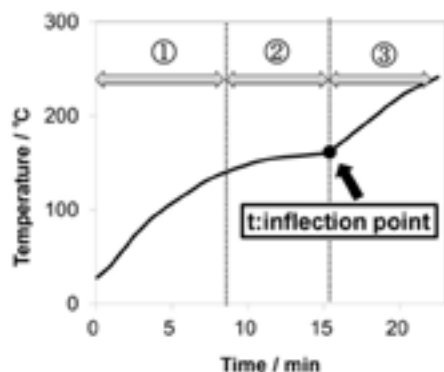
Fig.7 Example of temperature change inside a sample due to heating.

Table 5 Results of internal vapor pressure test

| | Temperature at inflection point / ℃ | Saturation vapor pressure / MPa |
|---|---|---|
| Developed dry-gunning mix | 117 | 0.18 |
| Low cement dry-gunning mix | 165 | 0.73 |

**4-2. Alkali resistance**

Dry-gunning mixes are generally applied in incinerators. Since the main damage factor is structural spalling caused by alkali attack from foreign components, the alkali resistance of the developed dry-gunning mix was evaluated.

Figure 8 shows a schematic view of the sample used in the alkali resistance evaluation. The samples prepared in the bench scale test were heated at 1000 °C or 1100 °C and filled with sodium carbonate and potassium sulfate as reactants in the space inside the samples. Samples filled with sodium carbonate were heated at 1000 °C × 10 hours, and potassium sulfate samples were heated at 1100 °C × 10 hours. The evaluation was based on the change in appearance of the cut surface of the samples after the test. Table 6 shows the infiltrated area of the reactants in the developed dry-gunning mix, expressed as an index with the measured value of the alumina cement dry-gunning mix as 100. The amount of alkali infiltration in case of both sodium carbonate and potassium sulfate was reduced compared to the conventional alumina cement dry-gunning mixes, confirming improved alkali resistance. The developed dry-gunning mix is considered to have excellent alkali resistance because it does not contain CaO derived from alumina cement.
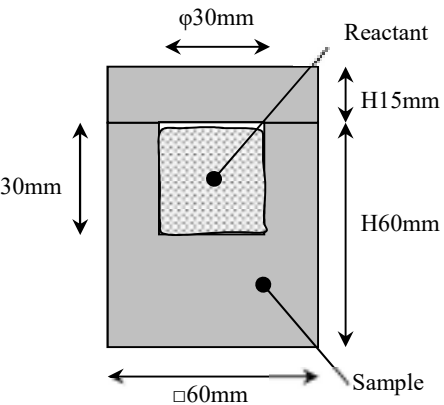


Fig.8 Schematic view of sample for alkali resistance test.

Table 6 Results of alkali resistance test

| | | Developed dry-gunning mix | Alumina cement dry-gunning mix |
|---|---|---|---|
| Infiltration index | Sodium carbonate | 39 | 100 |
| | Potassium sulfate | 98 | 100 |

**4-3. Actual furnace result**

Figure 9 shows the developed dry-gunning mix applied to the side walls of the secondary combustion chamber of an incinerator. There were no problems with the workability including dust generation and moisture range, and the same equipment and procedures as conventional dry-gunning mixes was used by only replacing the water with silica sol. In addition, it was possible to dry without exploding in less than half the time of conventional dry-gunning mixes. No damage was observed that would interfere with furnace operation after approximately six months of use, indicating stable service life.




(a) Before installation      (b) During installation



(c) After installation
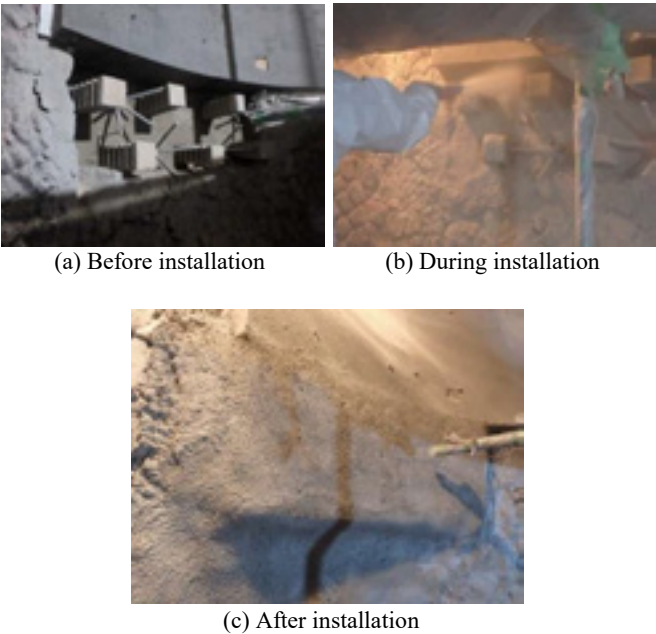
Fig.9 Appearances of actual furnace installation.

**5. CONCLUSION**

In this study, a cement free dry-gunning mix using silica sol as a binder was developed, and its explosion resistance was confirmed to be improved from that of conventional low cement dry-gunning mixes. It was confirmed that the developed dry-gunning mix can be installed in actual furnaces using the same equipment and procedures as conventional dry-gunning mixes, and that the drying time can be reduced.

Shortening the drying time not only shortens the construction period and improves the operating efficiency of the furnace, but also reduces the amount of burner fuel used in the drying process. Since cement is not used, it is expected to contribute to the SDGs by reducing $CO_2$ emissions generated in the cement manufacturing process.

**REFERENCES**

[1] TARJ, Refractory notebook revision edition 12, 2015, p.209
[2] C. Hirate, S. Kawaguchi, H. Chiba, M. Ohno, "Development of Explosion Resistant Refractory Castables for Rotary Kilns", Proc. UNITECR 2019, 2019, p.723-726
[3] M. Komatsu, H. Nishida, "Use of silica sol", Gypsum & Lime No. 232, 1991, p.47-58
[4] S. Takeuchi, H. Toda, H. Chiba, Y. Yoshimi, "Development of Cementless Dry Gunning Mix", Taikabutsu 73 (3), 2021, p.107
[5] S. Azukizawa, A. Hakamada, S. Takeuchi, K. Watanabe, H. Toda, Y. Yoshimi, "Development of Cementless Dry Gunning Mix and Its Application to Furnaces, "Taikabutsu 74 (3), 2022, p.112

# HOW THE COMPOSITION OF SELF−FLOWING REFRACTORY CASTABLES INFLUENCES THEIR RHEOLOGICAL PROPERTIES

Marcel Bastian, Maren Sollbach, Johannes Kasper, Christian Dannert
Forschungsgemeinschaft Feuerfest e. V. at the European Centre for Refractories, Höhr-Grenzhausen, Germany

Ashish Pokhrel, Olaf Krause
Koblenz University of Applied Sciences, Höhr-Grenzhausen, Germany

**ABSTRACT**
Numerous, sometimes contradicting factors which influence the rheological properties of refractory castables are listed as state of the art. Some authors report a predominant influence of the rheology of the matrix suspension, while others mention an exclusive correlation between the aggregate composition and the rheology of refractory castables. Again others describe that all the raw materials of a refractory castable together determine the rheology of it. As a result, improving the rheological properties of refractory castables is not as straightforward as it could be.
To gain new knowledge, the matrix suspensions, the aggregates and the overall compositions of refractory castables were modified and the resulting changes of their rheological properties were determined. This was done by measuring the shear rate dependent viscosity of these castables, using a novel lifting sphere viscometer. It was shown that the matrix composition and the aggregates are responsible for the rheology of refractory castables. The rheology of refractory castables is much more complex than assumed and depends on all the raw materials used and their properties. It is demonstrated that negative rheological effects like strong dilatancy or high viscosity can be suppressed by changing the matrix composition, the aggregates, or both. Consequently, there is a large toolbox available to improve the rheological properties of refractory castables.

**INTRODUCTION**
The rheological properties of refractory castables define their behaviour in processing like mixing, pumping, casting and levelling. These in turn are responsible for the quality of the lining or prefabricated part made from the castable. Since there are specific shear rates present at each processing, it is necessary to evaluate the rheological properties like the dynamic viscosity in dependence of the shear rate. A rheogram can be generated as a result, which allows the prediction of the behaviour in processing. If the rheological properties are unsuitable or maladjusted for the processing, the castables are not easily processable and defects in the dried castable may occur that reduce their service life.

Therefore, it is necessary to understand how specific components of the composition of refractory castables influence their rheological properties during processing. **INFLUENCING FACTORS OF THE RHEOLOGY OF CASTABLES**
How and how intense the components of castables influence their rheological properties has not been described uniformly. Some studies indicate that only the matrix components influence the rheological properties of castables, while others highlight the influence of the aggregates. Again others showed that both the matrix and the aggregate composition, respectively the whole composition, is responsible for the rheology of the castables. Some authors advise to change the composition and the fraction of the matrix to adjust the rheological properties of the castable. A finer particle size distribution was reported to lead to an optimisation of flowability and mixability [1]. A more multimodal composition of the matrix components was also reported to reduce the dynamic viscosity of a slurry made of the matrix components of a castable. This reduction directly effects the flowability of the castable, which is increasing with decreasing viscosity [2], [3]. A coarsening of the particle size distribution or an increasing amount of the fine materials was reported to result in castables with a stronger dilatancy [4] [5]. Others describe a strong influence of the rheological properties of a refractory castable from the overall composition of the aggregates of the castable. They describe that the particle size distribution of the aggregate fraction has an optimum in regard to the rheology. That implies that the rheological properties can be adjusted by changes in the aggregate fraction [6]. However, all the studies on castables were carried out with measuring methods that do not allow the description of the rheological fundamentals, like spread flow, or error prone methods like impeller rheometers.
So far, it is not fully understood how the overall composition of self-flowing refractory castables influences their rheological properties.

**MATERIALS AND METHODS**
**Materials**
*Castables for the rheological investigations*
Nine different refractory castables were used (table 1).

Tab. 1: Variation of the raw materials in the castables (in wt.-%). The variations in the raw materials in relation to the base materials V1, V2 and V3 are highlighted in italics.

| Raw material | V1 | V1-2 | V1-3 | V2 | V2-2 | V2-3 | V3 | V3-2 | V3-3 |
|---|---|---|---|---|---|---|---|---|---|
| T60 3-6 mm | 19 | *17* | *17,5* | 19 | *17* | *17,5* | 19 | *17* | *17,5* |
| T60 1-3 mm | 17 | *15* | *15,5* | 17 | *15* | *15,5* | 17 | *15* | *15,5* |
| T60 0,5-1 mm | 14 | *16* | *16,5* | 14 | *16* | *16,5* | 14 | *16* | *16,5* |
| T60 0-0,5 mm | 15 | *17* | *17,5* | 15 | *17* | *17,5* | 15 | *17* | *17,5* |
| T60 -45 µm | 13 | 13 | 13 | 13 | 13 | 13 | 13 | 13 | 13 |
| CT9FG | | | | 5 | 5 | *4,5* | | | |
| CT800FG | | | | 5 | 5 | *4,5* | | | |
| NO 725-10 | 10 | 10 | *9* | 3,5 | 3,5 | *3* | 7 | 7 | *6* |
| NO 713-10 RF | 7 | 7 | *6* | 3,5 | 3,5 | *3* | 10 | 10 | *9* |
| Secar71 | 5 | 5 | 5 | 5 | 5 | 5 | 5 | 5 | 5 |
| FS 60 | 0,1 | 0,1 | 0,1 | 0,1 | 0,1 | 0,1 | 0,1 | 0,1 | 0,1 |
| water | 5 | 5 | 5 | 5 | 5 | 5 | 5 | 5 | 5 |
| Description | medium fine matrix castables | | | coarse matrix castables | | | fine matrix castables | | |

The castables vary in the coarse fraction, in the matrix composition or in their overall composition. The three base materials V1, V2 and V3 contained the same amounts of different tabular aluminas T60 (from 6 mm to 45 µm), while the calcined (CT 9 FG and CT 800 FG, Almatis, Germany) and reactive alumina products (NO 725-10 and NO 713-10 RF, Nabaltec, Germany) were varied in terms of type and concentration/content. The castables specific surface areas were V2 >> V1> V3, so the castables based on V2 were the coarsest.

In these three base materials V1, V2 and V3 (abbreviated "VX"), the overall content of the tabular alumina aggregate fraction (all Almatis, Germany) was kept constant for the variationVX-2, but the amount of the sand fraction was increased, and of the coarse fraction (> 1 mm) was decreased. As a result, the particle size distribution was only varied in the aggregate fraction.

In the castables variations VX-3, the content of the aggregate fraction was raised, while the content of the matrix composition was decreased.

The contents of water (5 wt.-%) and superplasticizer (0,1 wt.-%) (Castament FS 60, BASF, Germany) were kept constant.

*Castables for the manipulation of the dilatancy by adaption of the aggregates*

Since only the castables based on V2 showed a pronounced dilatancy, the dilatancy was manipulated only for these castables. For that reason, the matrix was kept constant to V2, while the aggregate particle size distribution was changed. Therefore 4 wt.-% of the finer sand fraction (0-0,5 mm) was substituted by the coarser one (0,5-1 mm). In the coarse grain fraction, 4 wt.-% of the finer material (1-3 mm) were also substituted by the coarser one (3-6 mm). The contents of water (5 wt.-%) and superplasticizer (0,1 wt.-%) (Castament FS 60, BASF, Germany) were kept constant.

**Methods**
*Rheological investigations*
The rheological measurements were carried out with a novel lifting sphere viscometer. This novel viscometer is able to determine the fundamental rheological value of dynamic viscosity of refractory castables <u>in dependence of the shear rate</u> [7]. Commonly, the consistency of refractory castables is determined by spread flow. For the comparison of the rheological fundamental units with a, in the refractory research and industry well known method, the flowability was investigated by spread flow according to DIN EN 1402-4. Both measurements were done directly after the mixing process.

*Cold crushing strength - CCS*
The CCS was characterized based on the standard DIN EN 1402-6. The castables were stored in a climate cabinet at 20 °C for 24 h. The relative humidity was greater than 90 %. The CCS was determined immediately after the 24 h in the climate cabinet.

**RESULTS**
**Rheological investigations**
The rheological properties of the nine different refractory castables are presented in figure 1. On the left, the results from investigating the medium fine matrix castables V1/V1-2/V1-3 are depicted. The basic material V1 shows a relatively low dynamic viscosity at low shear rates, that decreases at first and then raises again with an increasing shear rate. The castable with the higher amount of the sand fraction (V1-2) shows, for the medium fine matrix castables, the highest dynamic viscosity at low shear rates, which is nearly 50 % higher than that of the basic material. As the shear rate increases, the dynamic viscosity drops sharply and increases again. Except for the viscosity at low shear rates, the dynamic viscosity of this castable (V1-2) is nearly similar to the standard castable V1. The dynamic viscosity of castable V1-3 (lower matrix content) at the lowest shear rate is rated between V1 and V1-2. With increasing shear rate, the dynamic viscosity is initially nearly constant, then increases linearly. The coarse matrix castables (V2/V2-2/V2-3) all show at first a drop, then an exponential increase of the dynamic viscosity with increasing shear rates (figure 1, middle). The basic material V2 shows the lowest dynamic viscosity, the castable with the higher sand content (V2-2) a higher and the castable with the lower matrix content (V2-3) the highest dynamic viscosity. All of these three castables exhibit qualitatively a very similar progression of the shear rate dependant dynamic viscosity. The exponential increase of the dynamic viscosity at high shear rates indicates a high dilatancy.

On the ride side of figure 1, the shear rate dependant dynamic viscosity of the fine matrix materials (V3/V3-2/V3-3) is shown. The progression of the dynamic viscosity of the basic castable (V3) and the castable with the higher amount of sand (V3-2) is nearly identical. The dynamic viscosity is decreasing first, then linearly increasing with increasing shear rates. The dynamic viscosity of the castable with the lower amount of matrix (V3-3) behaves almost like the two others, but the initial decrease of the dynamic viscosity is more pronounced. In this minimum, the dynamic viscosity is similar to those of the other castables (V3, V3-2), while lower or higher shear rates result in a higher dynamic viscosity compared to V3 and V3-2.
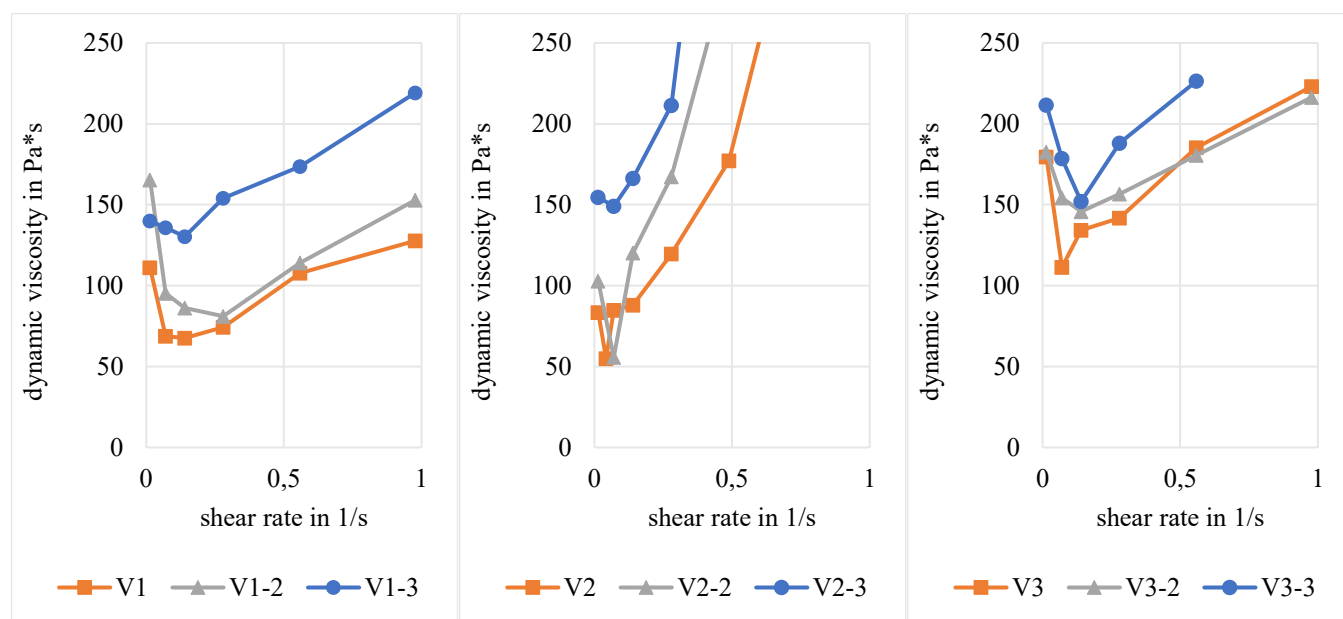


Fig. 1: Dynamic viscosity of the castables in dependence of the shear rate. Left: Medium fine matrix castables. Middle: Coarse matrix castables. Right: Fine matrix castables.

The results of the rheological studies represent the dependency of the rheological behaviour from the matrix, the aggregates and the overall composition of the castables. Looking at different castable matrix compositions shows a strong influence on the dynamic viscosity (V1 compared to V2 compared to V3). Changes in the composition of the aggregates (V1-2 compared to V2-2 compared to V3-2) lead to different influencing intensities on the dynamic viscosity, depending on the matrix components. A change in the overall composition (reduced matrix content / V1-3 compared to V2-3 compared to V3-3) generally results in the highest dynamic viscosity of all castables, except the dynamic viscosity at the lowest shear rate (0.013965 1/s) of castable V1-2. These results indicate a very complex rheology which depends on all components and can be influenced by variations in the aggregates, in the matrix or both.

Figure 2 illustrates the dynamic viscosity in dependence of the shear rate of the castables with the coarse matrix. The graph demonstrates that the dynamic viscosity at high shear rates is nearly identical for the basic material V2 and the castable with the higher sand content (V2-2), although the dynamic viscosity of castable V2-2 is higher at medium shear rates. The dynamic viscosity of the castable with the lower matrix content (V2-3) rises significantly stronger with increasing shear rate and takes on values more than twice as high at the highest shear rate. This means a significantly higher degree of dilatancy. Since the shear rate while pumping a refractory castable during installation is high, all of these castables should display a low or impossible pumpability. This means that such castables cannot be processed on customer construction sites.
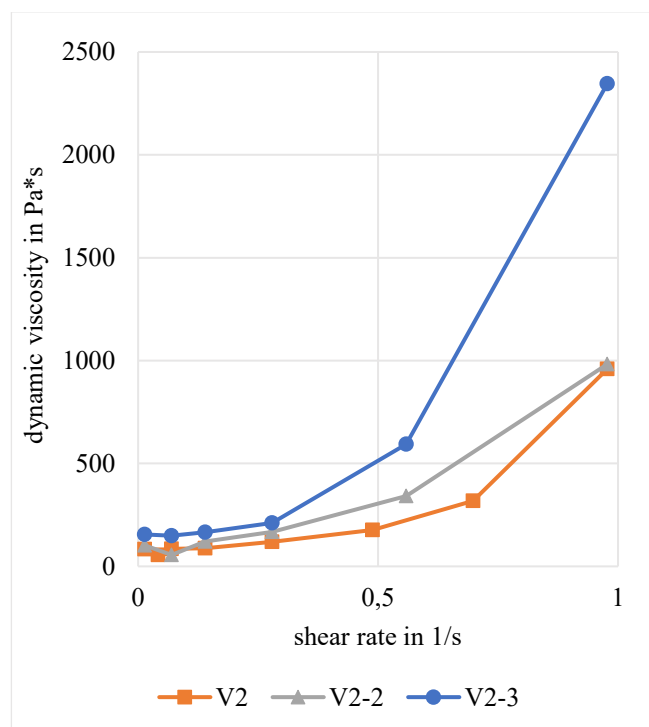


*Fig. 2: Dynamic viscosity of the castables in dependence of the shear rate of the coarse matrix castables V2/V2-2/V2-3.*

Figure 3 illustrates the dependency of the spread flow of the castables in dependency of the dynamic viscosity at the lowest measured shear rate (0.013965 1/s). Since the viscosity at low shear rates is connected to the yield stress, the spread flow is directly connected to the dynamic viscosity at 0.013965 1/s. With increasing dynamic viscosity, the spread flow decreases linearly. The coefficient of determination of a potential linear regression is sufficient but not extraordinary. One reason is the high error of the determination of the spread flow (approximately ± 10 mm). Additionally, the connection between those two values will only exist if a castable reaches his final spread within two minutes. If the castable did not reach its final spread, the measured data would be faulty.
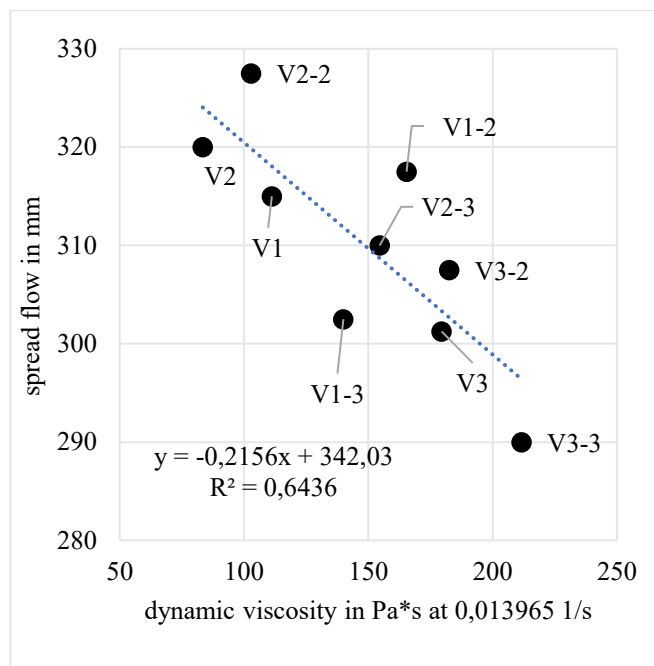


*Fig. 3: Spread flow in dependence of the shear rate dependant dynamic viscosity of the castables.*

**Manipulation of the dilatancy by adaption of the aggregates**

Figure 4 shows the shear rate dependant dynamic viscosity of two castables with a coarse matrix. While V2 exhibits an extraordinary dilatancy, the dilatancy of V2 mod is mostly supressed. The difference between those two castables is only the particle size distribution in the aggregate fraction. V2 mod had a coarsened sand and coarse grain fraction. This means that the dilatancy of refractory castables can also be manipulated by changing the aggregate fraction of the castable, while keeping the matrix composition constant. This in turn opens the possibility to manipulate the rheological behaviour by changing only the matrix composition, only the aggregate composition or the overall composition. The dynamic viscosity in low shear rate areas is nearly identical for both castables, which should lead to similar material properties like strength and porosity caused by similar flowability and compactability.

157
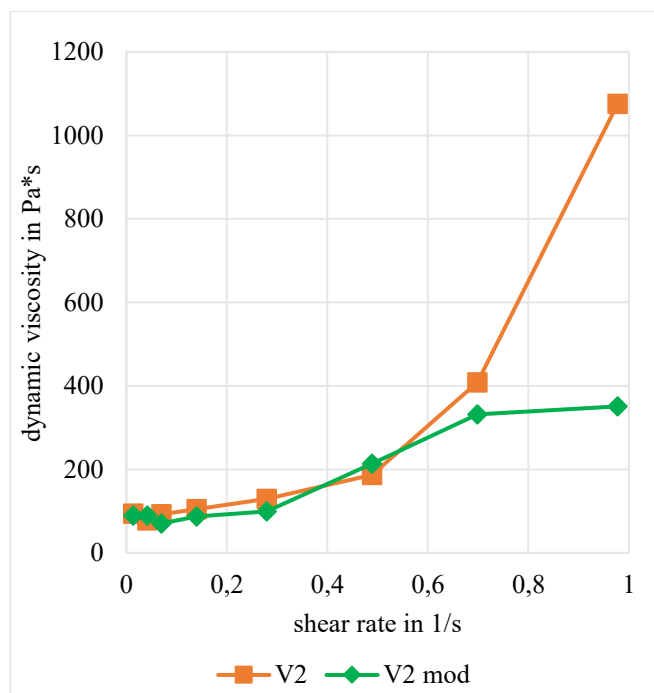


*Fig. 4: Shear rate dependant dynamic viscosity of the coarse matrix castables with focus on the dilatancy.*

The CCS of the two castables was determined to prove whether the change in the composition of the sand and coarse grain fraction influences the CCS of the castable (figure 5). The variation of the composition in the sand fraction and the coarse grain fraction has no influence on the CCS after 24 hours curing in the climate cabinet at a temperature of 20 °C and a relative humidity greater than 90 %.
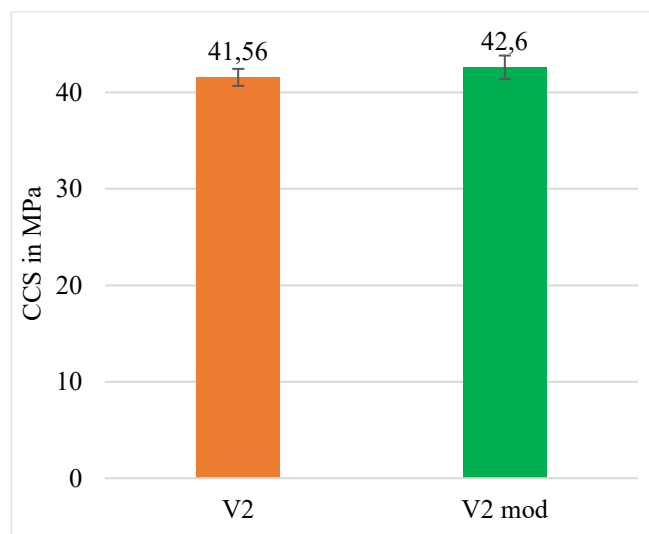


*Fig. 5: CCS of the basic coarse matrix castable V2 (left) and the castable "V2 mod" with coarsened sand and coarse grain fraction (right).*

The evaluation of the CCS of these two castables demonstrate that the dilatancy of the castables can be changed without influencing material properties like green strength. This in turn allows to make a castable pumpable without negatively affecting the important green properties.

## CONCLUSIONS

Nine refractory castables with varying composition of the matrix, the aggregate fraction or both were rheologically investigated using a novel lifting sphere viscometer and by measuring the spread flow. It has been shown that:

1.  The matrix composition has a major influence on the shear rate dependant viscosity of the refractory castables.
2.  The aggregate composition also has a significant influence on the shear rate dependant viscosity of the refractory castables.
3.  The intensity of these influences of the rheological properties by the aggregate composition depends on the matrix composition and vice versa.

As a result, the shear rate dependant dynamic viscosity of the castables depends on the overall composition of the castable and each component influences the rheological properties in its own way. This means that there are several opportunities to adjust the rheological properties of refractory castables as required.

Since the influence of variations in the composition of the castables cannot be predicted, one must evaluate it with a suitable method like the novel lifting sphere rheometer. Otherwise, it is not possible to describe the rheological properties and predict the behaviour of the castable in processes like flowing, levelling, pumping and mixing.

The castables with the coarse matrix showed a strong dilatancy, thus the dynamic viscosity exponentially increased with an increasing shear rate. These castables are not pumpable and the mixing process may result in a higher wear of the mixing tool. It was demonstrated that a change in the matrix components from coarse to a medium fine or a fine matrix results in a castable without dilatancy. In many cases the matrix is adjusted to the final use of the refractory castables at high temperatures. Therefore it should be investigated, whether the dilatancy can be supressed by changing the aggregate components.

A coarsening of the sand fraction and the coarse grains leads to a massive reduction of the dilatancy. Despite the change in the composition of the aggregate fraction, the green strength of the castable was unchanged. Such changes create a refractory castable with much improved rheological properties in point of dilatancy, without exerting a negative effect on the green properties like CCS.

All in all, every component in the refractory castables defines its shear rate dependant dynamic viscosity. It is possible to change the rheological behaviour of refractory castables by varying the matrix composition, the aggregate composition or both. Therefore, many possibilities are present with which the rheological properties can be adjusted to the requirements while processing.

## ACKNOWLEDGEMENTS

## REFERENCES
[1]  Kiennemann J, Chabas E, Ulrich C, Dumont D. The Role of Granulometry and Additives in Optimising the Alumina Matrix in Low Cement Castables. refractories WORLDFORUM 9 (4), 2017 p. 77-82.
[2]  Farris R J. Prediction of the Viscosity of Multimodal Suspensions from Unimodal Viscosity Data. Transactions of the Society of Rheology 12 (2), 1968, p. 281-301.
[3]  Schnabel M, Buhr A, Dutton J. Rheology of High Performance Alumina and Spinel Castables. refractories WORLDFORUM 4 (2), 2012, p. 95-100.
[4]  Hu C, de Larrard F. THE RHEOLOGY OF FRESH HIGH - PERFORMANCE CONCRETE. Cement and Concrete Research 26, 1996, p. 283-294.
[5]  K. Watanabe, M. Ishikawa und M. Wakamatsu, „Rheology of Castable Refractories, TAIKABATSU OVERSEAS 9 (1), 1989, p. 41-53.
[6]  ACI Committee 238. Report on Measurements of Workability and Rheology of Fresh Concrete - ACI 238.1R-08. American Concrete Institute, 2008.
[7]  Bastian M, Kasper J, Danner C., Pokhrel A, Ibarra-Plata L T, Krause O. Measurement of the dynamic viscosity of refractory castables – Interaction between slurry and aggregates. Proceedings of the 65th, 2022, p. 49-52.

# DEVELOPMENT OF A PRINTABLE ALUMINA−BASED COMPOSITION OF REFRACTORY CASTABLE FOR 3D PRINTING PRESHAPED PARTS

Sandra Abdelouhab

BCRC-INISMa, Belgian Ceramic Research Center, Mons, Belgium

## ABSTRACT

Thanks to its high versatility, additive manufacturing is used in many fields such as powder metallurgy, polymers, ceramics and recently in the field of civil engineering.

In the field of refractories, this shaping approach, based mainly on material extrusion, has not yet been adopted whereas it has a significant potential. Indeed, it offers the possibility of producing parts with complex geometries which are difficult to achieve by conventional techniques while avoiding the use of formworks/moulds whose costs from a few hundred to several thousand euros. In addition, a reduction in production costs, environmental and societal impacts can be considered via the reduction of labour and waste, controlled consumption of raw materials via the topological optimisation of parts as well as the reduction of risks on site.

To allow the emergence of this approach in this field, key scientific barriers have to be overcome, especially in the formulation, implementation, and characterization of these materials. This is the purpose of this current study by developing a printable formulation of an alumina based refractory castable. This tailored formulation must have pumpability, extrudability and buildability properties, mandatory for the printability characteristics of such materials. The parts produced by material extrusion will be characterised in terms of thermomechanical performance after printing and firing at high temperature and compared to similar parts obtained by conventional techniques.

## INTRODUCTION

Since the invention of the first 3D printer in 1983, the development of this additive manufacturing technology has been very fast and is currently widely used in several fields, including biomedical applications, jewellery, automotive or aerospace [1].

More recently, the material extrusion technology has been implemented in the building sector as now it is possible to print an entire building with this technique. In the field of refractory materials, this 3D printing technique has not yet been widespread. However, with making a parallel with civil engineering concretes, the use of this technology applied to refractory precast products suggests the same benefits as those in the field of building sector, namely [2]:

- Economic, with a lower time and cost production: usually castable shaping is done with formworks. For refractory pre-shaped parts, formworks can cost from a few hundred to several thousand euros when they are not standardised;
- Environmental, with the reduction of raw material consumption: the 3D-printing process allows a better control of the required material amount for the part construction. This contributes to the waste reduction in addition with the formwork-free construction and less dust generation compared to traditional methods;
- Social, by the reduction of arduous human labour and risk on site through the process automation.

Moreover, this 3D printing technology allows the generation of complex shape designs at a better cost than current casting methods. To print a pre-shaped part, a digital model is firstly created either with a CAD like modelling software or by a 3D scanning of the object. Next, this digital model is sliced by a dedicated software. Finally, a digitally controlled device builds the object slice-by-slice. For the 3D concrete printing (3DCP), the most common used technique is the layered material extrusion [3] even though selective powder binding method have also been reported [4].

For the extrusion method, typically a well-designed cementitious mixture is pumped through a nozzle mounted either on cartesian system or a robotic arm. Based on the 3D digital model, the printing head moves in order to extrude various filament shapes depending on nozzle shape with a printing speed of 50-500 mm/s. To produce refractory pre-shaped parts with the use of 3D extrusion printer, the refractory mix has to meet specific rheological requirements. Indeed, as for printable civil engineering formulations, printability characteristics are prerequisites:

- Pumpability, which is the ability of the cementitious ink at "fresh" state to be conveyed from the wet material tank to the extrusion nozzle via a pipe under the pump action;
- Extrudability, which means the ability of the cementitious ink to be extruded easily under the form of a continuous filament without clogging or segregation during this phase;
- And finally, buildability, which represents the ability of the printed cementitious ink to support the weight of the upper layers without excessive creep of the lower layers or printed element.

When the formulation combines these 3 properties, the cementitious ink is considered printable. However, these rheological characteristics remain antagonistic. While stiffness and cohesiveness are requested for buildability to support the weight of subsequent layers and limit the deformation of the printed layers, a high flowability is requested for pumpability and extrudability [5]. This highlights the whole issue of the composition and formulation of such printable materials, for which an optimum has to be found between flowability and stiffness/cohesion in order to simultaneously satisfy the properties of pumpability, extrudability and buildability.

In this context, the goal of this study was to develop a refractory cementitious ink formulation gathering the printable characteristics. To reach out this goal, this formulation development has been considered through mainly:

- the characterisation of 3D commercial cementitious inks printable with a large-scale 3D printing device without stiffness additives at the printing nozzle;
- a literature review on refractory gunning mixes.

## MATERIALS AND METHODS

### Materials

*Commercial cementitious inks:* For the development of refractory cementitious ink, two commercial civil engineering cementitious inks have been characterised: 704 CLAVEX + HP mortar (704 CL+HP) and SIKACRETE – 751 3D (751 SI-3D). These commercial inks are printable with a cartesian large-scale 3D printing system (Mini Printer Pro supplied by CONSTRUCTION 3D society). The buildability of 704 CL+HP material is limited as it can quickly present an excessive part deformation or a structural collapse. The second one, 751 SI-3D presents a higher buildability. The table 1 reports the main characteristics of both commercial cementitious inks indicated in the product data sheet.

Tab. 1: Main characteristics of commercial cementitious inks.

| Sample reference | 704 CL+HP | 751 SI-3D |
|---|---|---|
| Maximum grain size | 0 - 2 mm | 0 - 1 mm |
| Density (g/cm³) | 2.2 | 2.14 |
| Water content for a plastic consistency | 11% | 18% |
| Setting times at 20 °C | 6 h – 7 h | 45 min – 60 min |
| Practical use life after extrusion (start of the fresh material stiffness) | 60 min | 15 min |
| CCS (MPa) at 28 days | 60 | 50 |
| MOR (MPa) at 28 days | 12 | 10 |

159

*Material selection for the refractory cementitious ink (3D-RCI):* The following raw materials have been used for the formulation of the refractory cementitious ink: tabular alumina (3 – 1 mm, 1 – 0.5 mm, 0.5 – 0 mm, 0.6 – 0.2 mm, 0.2 – 0 mm - ≤ 0.045 mm; Almatis), reactive alumina (RG4000, Almatis) and calcium aluminate cement (Secar 71, Imerys).

As the 3D printing equipment considered to further print the 3D-RCI material, does not allow the addition of a stiffness agent directly after the extrusion at the printing nozzle, the dry refractory mix has to contain a stiffness agent to ensure an early age stiffness development. It will ensure the refractory ink buildability. However, the stiffness development has to be slow enough to avoid pipeline clogging and short enough to avoid a structural deformation or collapsing. The stiffness agent used in this study was a BASF additive.

A water reducing agent was also used to optimise the start of the stiffness development and the water content in the starting mixture. Indeed, due to its plasticizer effect, it allows to decrease the water content required for a good flowability and in the meantime, it influences the early age of the stiffening development as it has retarding properties. A BASF plasticizer was used in this study as a water reducing agent.

*Experimental procedure for the fresh material preparation:* The commercial cementitious inks were prepared according to the recommendations of the technical data sheets.

For the developed refractory cementitious ink, a dry mixing of the raw material was performed for 2 minutes then the required water content was added to mixture and the mixing was carried out for a further 3 minutes. An Eirich mixer, R02/E type, with a star rotor was used with a rpm range between 450 for the dry mixing and 750 for the wet mixing.

## Characterisation methods

*Bulk Density (BD) and Apparent Porosity (AP):* The bulk density and the apparent porosity of the castable samples were measured according to Archimedes' principle in relation with the standard EN ISO 1927-6.

*Flow-cone test:* The pumpable consistency was characterised by means of a flow-cone test. The fresh wet mix was placed in a cone shape mould with standard dimensions (Hagerman cone). After the flow of the material under its own weight, the largest diameter (D1) and the diameter perpendicular to it (D2) were measured. The flow value (F) is given by the following relationship:

$$F\ (\%) = \frac{\left(\frac{D_1 + D_2}{2}\right) - D_{inf}}{D_{inf}} \times 100 \qquad \text{Equation 1}$$

Where $D_{inf}$ is the lower diameter of the cone, which is 100 mm. The upper diameter is 70 mm and height 60 mm.

*Gun test:* As there are no actual standards for extrudability testing, a manual gun device with a 20 mm circular nozzle diameter was used to assess the extrudability of cementitious inks at laboratory scale. The material was defined as extrudable when it squeezed out of the printing nozzle in a continuous manner while maintaining the required dimensional accuracy and layer quality without causing any clogging or segregation. The manual gun used in this study is shown on figure 1.



*Fig. 1: Picture of the device used for manual gun tests*

*Ultrasonic wave transmission measurements:* The material buildability can be assessed through the characterisation of the setting properties determined by ultrasonic wave velocity evolution. Indeed, the increase of the ultrasonic velocity indicates the increase of the stiffness or the mechanical resistance of the material [6]. In this study, the setting properties of all cementitious inks were characterised by using ultrasonic wave transmission measurements performed with a FreshCon system developed at the University of Stuttgart [7]. The FreshCon system consists in a specific mould (for castable or mortar) equipped with two piezoelectric transducers (one transmitter and one receiver). A computer equipped with a data acquisition card is linked to a piezoelectric high voltage pulser to generate a high voltage short rectangular wave (typically 800 V with a pulse width between 2.5 and 5 μs). A wide band ultrasonic (mechanical) wave is generated and picked up by the receiver of which the signal is amplified after traveling through the material. The software automatically computes the travelling time from the transmitter to the receiver and deduces the velocity of the wave. More detailed information on this device can be found in [7].

*Mechanical test:* Format D samples, according the standard EN ISO 1927-6, have been casted with the 3D-RCI composition, cured during 48 h and dried 24 h at 110°C. Cold modulus of rupture (CMOR) and cold crushing strength (CCS) tests have then been performed with samples thus prepared. For each mechanical trial, three samples have been tested.

## RESULTS

### Formulation of the 3D printing refractory mix

For the formulation development of a refractory cementitious ink, the first targeted, among the three characteristics needed to obtain a printable mix, has been the pumpability. For that, a literature review on shotcreting refractory castables has been carried out, focusing especially on the relationship between the castable ability to be pumped and their particle size distribution. This review revealed that to enhance the pumping ability of the shotcreting castable, the ratio between the coarse grains and fine particles has to be optimised. If the mix presents an excess of aggregates, collisions between particles and friction forces will be enhanced, resulting in an increase of the pumping pressure. The mix will also have low cohesion or a greater tendency to segregate during the transport in the pipeline. At the contrary, if the mix presents an excess of fine particles, the mixture will become less fluid during pumping, which will lead to the clogging of the pumping pipe [8].

To determine the optimum ratio between fine and coarse grains to obtain good pumping properties, authors [9] first formulated three compositions of refractory castables according to the Andreasen's model [10] with q coefficients 0.21, 0.26 and 0.31. The rheological behaviour of these three refractory castables was characterised by measuring the torque as a function of the rotation speed of their mixing tool. Tests have been carried out with and without volume restriction, the latter simulating the flow in a pipe during pumping. The results indicated that the rheological behaviour of castable compositions with q values 0.21 and 0.31 was dilatant for tests without volume restriction then became Newtonian for tests with volume restriction. For the composition, with a q value 0.26, exhibited a pseudo-plastic or a rheo-fluidifying rheological behaviour for tests with or without volume restriction [9].

This pseudo-plastic of rheo-fluidifying behaviour is required when a fluid is subjected to an increase in a shear stress, as it is the case during pumping. Indeed, the resistance of the fluid flow tends to stabilise or even decrease with increasing stress for a rheo-fluidifying rheological behaviour. The pseudo-plastic behaviour for castable compositions with q value 0.26 has been confirmed by authors for the use of different maximum grain size [11].

Based on the literature results, a 3D printing refractory mix was designed according to the Andreasen's model with a q value 0.26. The table 2 reports the cementitious ink composition with the different proportions of each component in weight percentage.

Tab. 2: Refractory ink composition (wt %)

| Tabular alumina | T 60 (1-3) mm | 25 |
|---|---|---|
| | T 60 (0.5-1) mm | 5 |
| | T 60 (0.2-0.6) mm | 10 |
| | T 60 (0-0.5) mm | 15 |
| | T 60 (0-0.2) mm | 15 |
| | T 60 (0-0.045) mm | 13 |
| Reactive Alumina | RG4000 | 10 |
| CAC | SECAR 71 | 5 |

This 3D refractory printing mix designed corresponds to a LCC castable according to the CaO content in the composition. (1.5 wt%). A BASF stiffness agent (0.1 wt%) has been added to the dry mixture.

**Flow-cone test results**
After the cementitious ink design, the water content has been determined thanks to the flow-cone test to obtain a pumpable formulation: obtention of a plastic consistency. Firstly, the flow-cone tests have been performed on commercial cementitious inks to establish a flow value range for a plastic consistency. Table 3 reports pictures of commercial materials obtained after adding the mixing water content recommended by the supplier for a plastic consistency and their flow under their own weight after the cone removal. The test results indicate a flow value of 35% and 45% respectively for 751 SI-3D and 704 CL+HP. To obtain approximately the same flow value for the 3D refractory cementitious ink (3D-RCI), a water content close to 8% was needed. This water content led to a flow value of 40% for the 3D-RCI material. A picture after the flow-cone test is also reported on table 3 for the 3D-RCI ink.

Tab. 3: Flow-cone test results

| Sample | Water content (%) | F (%) | Picture |
|---|---|---|---|
| 704 CL+HP | 10 | 45 | |
| 751 SI-3D | 18 | 35 | |
| 3D-RCI | 8 | 40 | |

**Results of ultrasonic wave transmission measurements**
To go further on the development of the refractory cementitious ink formulation, characterisation of the setting properties has been performed to determine the elapsed time between the mixing water addition in the dry mix and the time when the system began to stiffen. The knowledge of this elapsed time is extremely important for the 3D printer as there is no addition possibility of a stiffness accelerator at the printing nozzle. If this elapsed time is too short, there is a risk that the material will stiffen in the pipe during transport, causing the clogging pipe. If the time interval is too long, the material may not be suitable for buildability, with the lower layers collapsing under upper layers.
To suitable adjust the stiffness development of the 3D-RCI material, firstly those of commercial materials, has been determined by using ultrasonic wave transmission measurements and then compared to the developed ink.
The Figure 2 reports the ultrasonic wave velocity evolution through the materials 704 CL+HP, 751 SI-3D and 3D-RCI. During experiment, the temperature profile of each material was also recorded as it allows the setting time detection.
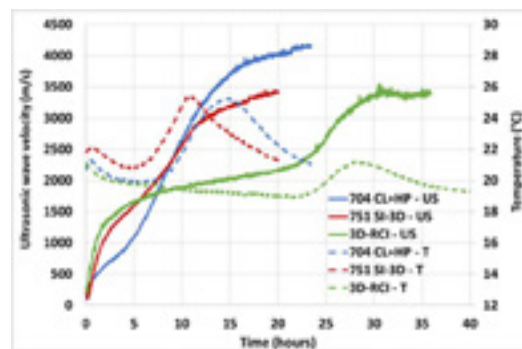


Fig. 2: Ultrasonic wave velocity and temperature over time

For both commercial materials, the ultrasonic wave signal is detected about 20 or 25 minutes after the water addition in the dry mixture whereas it is about 10 minutes for 3D-RCI material. It corresponds to the beginning of a first increase of the ultrasonic wave velocity. Then a second increase of the wave velocity can be defined corresponding to the material setting. The beginning of this second increase is related to the start of the temperature rise inside the material, and the end of the increase of the wave velocity to the exothermic peak. The first increase of the wave velocity is then defined as the material stiffness. For both commercial inks, the setting material occurs just after the stiffness whereas it is not the case for the developed ink. Its setting occurs few hours later.
Comparing both commercial inks, their velocity curves indicate a higher acceleration of the wave velocity at early age for 751 SI-3D than for 704 CL+HP. As the wave velocity value can be related to the mechanical resistance of the materials [6], at early age it signifies, 751 SI-3D material has a higher mechanical resistance than 704 CL+HP explaining its higher buildability. The 3D-RCI material exhibits the same behaviour at early age as those of 751 SI-3D. However, as the wave velocity signal of 3D-RCI ink appears about 10 minutes after the water addition, this result highlights the fact that its stiffness appears too fast and could induce a clogging of the pipe before its extrusion.
To delay the beginning of 3D-RCI ink stiffness, the content of the stiffness agent has been firstly decreased. It induced only an early age of the setting period but not a delay of the stiffness one. Therefore, a water reducing agent has been added to the dry mixture also acting as stiffness retardant. An optimum ratio between the water reducing agent and the stiffness agent had to be found to obtain an appropriate setting curve corresponding to a ratio of 0.75. Moreover, as the water reducing agent is a plasticizer, its addition in the mixture has decreased the mixing water content down to 7% without a degradation of the flow properties at early age. The flow value of the optimised composition was the same as those of the first formulation: 40%. The ultrasonic wave velocity and temperature over time of the optimised formulation are presented on figure 3.
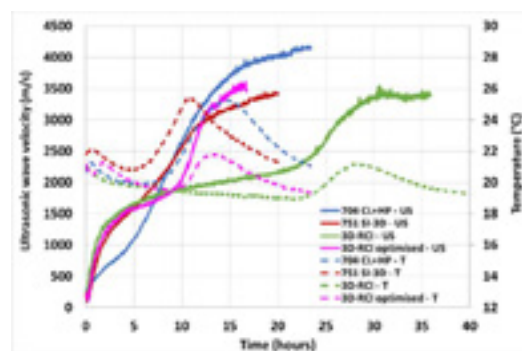


Fig. 3: Ultrasonic wave velocity and temperature over time for 3D-RCI, 3D-RCI optimised, 704 CL+HP and 751 SI-3D

The setting behaviour of the optimised 3D-RCI optimised ink is close to 751 SI-3D ink. Indeed, the stiffness starts approximately at the same time, about 20 minutes after the mixing water addition.

Moreover, the evolution of the wave velocity during the stiffness phase is the same for both materials signifying the same buildability if the consistency is mastered during the 3D printing at large scale.

**Gun tests**

The gun test has been used to assess the material extrudability at lab scale. In the meantime, the buildability has been also evaluated by manually printing 4 or 5 stacked layers. Both commercial inks have been tested with also the optimised 3D-RCI material. Pictures of the manually printed parts are shown on table 4.

Tab. 4: Pictures of the manually printing parts

| Sample reference | Picture during printing | Picture of the parts after printing |
|---|---|---|
| 704 CL+HP |  |  |
| 751 SI-3D |  |  |
| 3D-RCI |  |  |

These manual tests have indicated that the developed refractory ink is extrudable and buildable at lab scale: it was possible to squeeze out of the gun nozzle filaments and to stack several layers without a flow of the lower layers.

**Physical and mechanical characterisation of the developed ink**

As the printable refractory composition thus developed seems to be promising for a large-scale printing test, firstly, 4/4/16 samples were produced according to refractory standards to determine the apparent porosity (AP), the bulk density (BD) and the MOR and CCS of 3D-RCI material after a drying at 110°C. The average results of each test are reported on table 5.

Tab. 5: Physical and mechanical characteristics of 3D-RCI materials

| Sample reference | BD (g/cm³) | AP (%) | MOR (MPa) | CCS (MPa) |
|---|---|---|---|---|
| 3D-RCI | 2.88 | 19.7 | 8.10 | 34.57 |
| 3D-RCI optimised | 2.94 | 17.9 | 10.36 | 40.7 |
| 6S71B [12] | / | 8 | 24 | / |

The AP and BD results of 3D-RCI materials show an improvement of the density, porosity, and green mechanical properties for the optimised formulation. It is probably due to the use of the water reducing agent allowing a decrease of the water addition from 8% down 7% without a deterioration of flow properties at early age. The MOR average value is lower and the average AP value higher than those found in the literature for a high alumina LCC castable composed from Andreasen's model with a q value of 0.26 [12], maybe due to no vibration applied on 3D-RCI samples.

**CONCLUSIONS**

In this study, a 3D printable refractory cementitious ink has been formulated. To reach out a such goal, the strategy adopted was firstly to design a pumpable mix according to the literature review on shotcreting castables. Then, the contents of the mixing water, the stiffness additive and water reducing agent have been optimised to obtain suitable extrudability and buildability properties according to the 3D concrete equipment which will be further used to print the refractory ink. These last optimisations have been achieved through manual gun tests and ultrasonic wave velocity measurements. The developed mix corresponds to a classical LCC castable according to the CAC content.

Although such a 3D printable mix has been developed and its printability has been demonstrated at lab scale, large-scale printing tests need to be carried out. In addition, a great deal of works remains to be done. One of them concerns a deeper rheological characterisation of the printing castable with also the mechanical characterisation at the green state and at high temperature of samples collected from printed parts. The influence of the printing parameters also needs to be studied: nozzle speed, pump flow, slice thickness, …

Upcoming future investigations will be undertaken along these guidelines. An upgrade of the composition by using larger coarse grains (up to 6 mm) or the adding of viscosity modifying agent (VMA) to improve the thixotropic behaviour, may also be of a great interest.

**REFERENCES**

[1] S.H. Huang, P. Liu, A. Mokasdar, L. Hou, Additive manufacturing and its societal impact: a literature review, Int. J. Adv. Manuf. Technol. 67, 2013, p. 1191–1203, https://doi.org/10.1007/s00170-012-4558-5

[2] J. Xiao, G. Ji, Y. Zhang, G. Ma, V. Mechtcherine, J. Pan, L. Wang, T. Ding, Z. Duan, S. Du, Large-scale 3D printing concrete technology: Current status and future opportunities, Cem. Concr. Compos., 2021, 104115, http://dx.doi.org/10.1016/j.cemconcomp.2021.104115

[3] Buswell RA, de Silva WRL, Jones SZ, Dirrenberger J. 3D printing using concrete extrusion: a roadmap for research. Cem Concr Res, 112, 2018, p. 37–49

[4] M. Xia, B. Nematollahi, J. Sanjayan, Compressive strength and dimensional accuracy of Portland cement mortar made using powder-based 3D printing for construction applications, First RILEM Int. Conf. on Concrete and Digital Fabrication-Digital Concrete 2018, Springer, Cham 2018, p. 245–254, https://doi.org/10.1007/978-3-319-99519-9_23

[5] Gosselin C, Duballet R, Roux P, Large-scale 3D printing of ultra-high performance concrete-a new processing route for architects and builders. Mater Des, 100, 2016, p. 102–109

[6] D. Tischer, O. Krause, J. Kaper and C. Dannert, The formation velocity of CA hydrate phases in refractory castables after water addition, Proceeding 342, Unitecr 2015

[7] H. W. Reinhardt and C. U. Grosse, Continuous monitoring of setting and hardening of mortar and concrete, Construction and Building materials, 18, 2004, p. 145-154

[8] M. Koga, I. Takita, M. Kataoka, K. Kawasaki: « New wet spray method for castables. », Taikabtsu Overseas, 19 [3], 1999, p. 14-20

[9] R. G. Pileggi, V. C. Pandolfelli: « Rheology and particle size distribution of pumpable refractory castables », Am. Ceram. Soc. Bull., 80 [10], 2001, p. 52-57

[10] A. H. M. Andreasen, J. Andersen: « Über die beziehung zwischen kornabstufung und zwischenraum in produkten aus losen körnern (mit einigen experimenten) », Kolloid Z., 50, 1930, p. 217-228

[11] R. G. Pileggi, E. T. Ramal Jr., A. E. Paiva, V. C. Pandolfelli: « High performance refractory castables: particle size design», Refractories Application and News, 8 [5], 2003, p. 17-21

[12] A. P. Luz, M. H. Moreira, C. Wöhrmeyer, C. Parr, V. C. Pandolfelli, Drying behavior optimization of dense refractory castables by adding a permeabililty enhancing active compound, Ceramics International, 45, 2019, p. 9048-906

# ADAPTATION OF THE CONTOUR–CRAFTING PROCESS TO REFRACTORIES AND INVESTIGATION OF MATERIAL PROPERTIES AFTER THE 3D PRINTING PROCESS

Florian Holleyn*, Lee Klein, Sinje Zimmer, Olaf Krause

Hochschule Koblenz, Höhr-Grenzhausen, Germany

## ABSTRACT

Traditional casting of refractory materials requires the use of complex and costly moulds. Years ago, the construction industry took first steps to develop Additive Manufacturing (AM) of building concrete, also known as 3D printing. It became clear very quickly that AM offers new degrees of freedom in geometric complexity and abilities of adjustment. So far, however, 3D printing processes are not yet state of the art regarding refractory monolithics.

It was necessary to develop a suitable printing technology as it is not yet available. A further challenge was to develop printable refractory castables, whereby pumpability and the volume stability after printing (stiffening, setting, hardening) are key issues. A major challenge in the future is to provide a system that is easy to use and wins over with regard to its cost-efficient and rapid processing.

We report on our state of the art as we have achieved it within the framework of the foundation of the competence centre, 3D-Keramik in Höhr-Grenzhausen.

The paper shows first steps towards implementation of AM in the refractory industry. Test pieces of printable castables that were successfully developed could be manufactured with a 3D printing device, that was also developed in the project.

Material properties like strength and open porosity are examined. It also will be worked out how the internal structure in contour crafted specimen influence the isotropic technological properties.

In further, it will be figured out that the homogeneity of pre-shaped monolithics could be optimized by optimizing the printing paths.

## INTRODUCTION

Years ago, the construction industry in civil engineering undertook first efforts to develop construction concretes that enables Additive Manufacturing (AM) of large three-dimensional shapes. Components now can even be designed using hollow structures to save raw materials in comparison to traditional monolithic fabrication. Additionally, those hollow structures can be used, for example, to install water tubes, cooling channels or electrical wires [1]. It was successfully proved that AM offers new degrees of freedom in geometric complexity and abilities of adjustment compared to traditional methods. When using Contour-Crafting (CC) time and money can be saved, because AM virtually works without time consuming and therefore expensive formworks. It appears straight forward that AM should be also applied in the refractory industry. Especially in the field of large, prefabricated members like electric arc furnace lids or tundishes AM has a high potential to overcome complex mould production and allows very easily customized design adoption.

At the first glance, AM in civil engineering already has been proved as a feasible technique that allows printing of entire buildings [2, 3], however, meets its limits, because till now solely mortar like concretes with no coarse grains are processed. Thus, from this state of art it can be concluded that concretes can be toughen for AM, but the progress that was made for civil engineering concrete could not be transferred to refractory castables. This is due to the fact, that the nature of refractory castables is entirely different in terms of water addition (approx. 5 wt.-% instead of 20 to 25 wt.-%), a much higher density of the raw material with approximately 3,6 g/cm³ and a much lower content of cement (only 5 % wt.-% in case of LCC). Therefore, for AM of refractory castables material development needs an entirely re-thinking where the shotcreting process can be seen as a good starting point in this development. To enable the refractory industry to build large, prefabricated members, the authors applied successfully for the Establishment of a competence centre for additive manufacturing of inorganic-non-metallic materials that is founded by the Rhineland-Palatinate Ministry of Economic Affairs (MWVLW) and the European Fund for Regional Development (EFRE).

Due to the described characteristics of refractory concrete, the 3D printers used in the construction industry cannot be used. As a result, the structure of a large-scale CC setup had to be rethought.

For the material properties clear targets are defined. The castables must be pumpable. A dimensional stability after extrusion for a distinct and rigid layer formation is inevitable when several layers of refractory concrete must be printed to produce complex component geometries. Hence the castables rheology must be adjusted precisely using different process additives and combinations thereof. In particular, dispersing agents and gelling agents are used, because they allow to gain plastic properties. A long working time is inevitable. This makes on the other hand setting agents as accelerators necessary that are added immediately at the tip of the printing head to achieve a sufficient volume stability of the printing strands.

From technological side, different parameters must be considered when building a large-scale 3D-printer setup and which special features play an important role in the actual printing process. To produce true to size members all variations of the printing process, especially the printing path must be coordinated.

This paper follows on from our work that we presented and published at a previous conference [4,5] and is a scale-up of the results presented at that time. It reports on our state of the art as we have achieved it within the framework of the foundation of the competence centre, 3D-Keramik in Höhr-Grenzhausen. First steps are shown towards implementation of AM in the refractory industry. Test pieces of printable castables that were successfully developed could be manufactured with a large-scale 3D printing device, that was also developed in the project.

Material properties like strength and open porosity are examined. It is also worked out how the internal structure in contour crafted specimen influence the isotropic technological properties.

In further, it is figured out that the homogeneity of pre-shaped monolithics could be optimized by optimizing the printing paths.

### Printable castables with clear focus on targets of material properties

Exact material property targets for printable refractory castables were defined within this project and still published [5]. A key issue for the execution of CC is the pumpability of the castable. The layer wise printing of refractory castables needs a perfect adjustment of the particle size distribution and the right combination of additives. The interplay of all components enables pumpability, a low tendency for particle segregation, also under pressure, dimensional accuracy after printing, a sufficient working time and green strength. In further, accelerators can be used as setting agents and could be added immediately after the extrudate leaves the printing nozzle.

### Large-scale 3D printer

The development and evaluation of the large-scale printer used for this investigation (Fig. 1) was part of the project [4]. In order to produce the components in a sufficient size using the CC process, a robotic arm from ABB Robotics was installed as a manipulator to move the print head in an area of approx. 2.5 x 2.5 x 2 m (l x w x h). Due to the high specific density of the raw materials,

"dry-mix" systems as already established on the market and optimized for the CC of concrete do not work properly and therefore cannot be used. The printer set-up was configured based on solitary components where the mixing and pumping devices are already in use for refractory castables. An 80 l EIRICH mixer (Maschinenfabrik Gustav Eirich GmbH) was used as mixing device, as this type of mixer allows degrees of freedom in terms of a distinct adjustment of mixing power that is inevitable to adjust the rheological properties of the printable castables. In addition, this device allows reproducible results and is already used for a long time in smaller dimensions within the working group. After the mixing process, a pump unit (Mader GmbH) transports the material to the print head, which could be moved in a three-dimensional space in the dimensions mentioned above. The pump unit was chosen because it belongs already to the state of art for the processing of shotcrete material. Both the hose and the nozzle were chosen to be as small as possible (hose inner diameter 35 mm, nozzle opening 15 mm). This dimensional set-up allows the printing of refractory castables with a maximum grain size of 3 mm.

However, printing jobs can be carried out in a continuous process. While the first batch is being printed, another batch can already be homogenized in the mixer and then added to the pump unit and printing process can be continued without interruption.



*Fig. 1: Process chain of Contour-Crafting (from r. to l.): After homogenization by using an intensive mixer, a concrete pump transports the material to the manipulator to create components weighing up to 400 kg in a three-dimensional space.*

**Motion control**

The entire CC process is subject to a large number of factors which can significantly influence the printing result. Extrusion speed, layer thickness, traversing speed and finally also the way in which the individual layers are built up influence the shape and thus also the technical properties of the printed component. Since the large printer is an experimental setup, the individual components (casting agent and additive pump, robot arm, intensive mixer) are not yet coordinated with each other, or the controls cannot yet be combined to implement the process via a central control system. A software update from ABB has recently made it possible to convert CAD files, i.e. the basic information about the appearance of the files to be printed, via a slicing program into machine code that the robot arm understands. Of course, certain geometric details can also be defined in this way, such as the thickness of the individual print layers or the structure of the component itself. This greatly simplifies the programming of the robot arm movements, but the integration of pump control and the addition of additives, as described above, is still missing. To achieve full automation and take full advantage of the ABB software, it must be possible, for example, to stop or, at best, even reverse the material feed if the position of the print nozzle changes during a print job so that the material does not run out. Of course, the output files of a slicer program do not take into account that the system is not yet fully automated, so the print files must be designed with CAD in such a way that the slicer program has no option but to define the print path in the desired way.

For example, to contour a cuboid, the program would suggest solid outer layers with a defined fill pattern. However, this would require the print head to stop at one point and start printing at another. To avoid this, the print path is defined in CAD using the above criteria to create an endless print path, as shown in Fig. 2 with an alignment of the subsequent layers at 180° angles. Other print schemes could represent subsequent layers at 90° or 45° angles. Layer thickness, traverse and extrusion speed, and the overall structure of the CC part must be coordinated to avoid layer formation and defects and to produce a part that is as homogeneous as possible.

To achieve this target, the extrusion speed and thus also the pump pressure, the traverse speed and the layer thickness must be synchronised, always considering the viscosity of the castable and the current printer setup (pump head and hose diameter as well as nozzle diameter). Defects and layer formation can be counteracted by over-extrusion, i.e. forced extrusion of the extrudate into one another by increasing the extrusion speed while maintaining the same travel speed or by slowing down the travel speed while maintaining the same extrusion speed, or by varying the layer thickness.
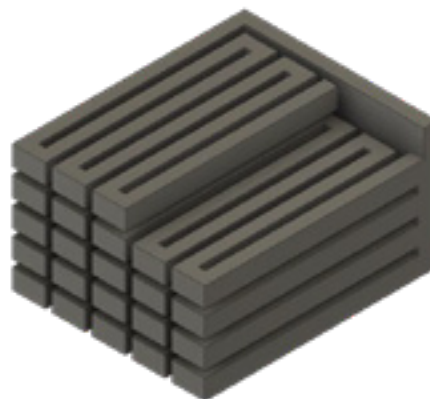


*Fig. 2: CAD design of five layers of a cuboid (350 mm x 290 mm). Endless print path without any stoppage of material flow, carried out with a printing path by alignment of the subsequent layers in a 180° angle.*

**EXPERIMENTAL PROCEDURE**
**Castable preparation**
For the experiments high-alumina cement bonded castables with a maximum grain size of 3 mm was developed (Tab. 1). The workability of this castable was proven by experiments with two different laboratory 3D printing devices [5]. As a bonding phase 5 wt.-% CA-cement (70 wt.-% $Al_2O_3$) from Imerys S.A., Oberhausen, Germany is added, therefore the castables can be addressed as LCC. A polycarboxylate ether (PCE) (BASF SE, Ludwigshafen, Germany) was used as dispersant. The different alumina fractions were provided by Almatis GmbH, Ludwigshafen, Germany.

Multifil-fibers (< 6 mm) from Elkem, Oslo, Norway were used to improve the volume stability of the castable and to enable a faster dry-out after printing and setting. Methyl cellulose as rheological stiffening agent was used to reduce the castables viscosity and to provoke a kind of plastic behaviour. An interlayer adherence agent from BASF SE, Ludwigshafen, Germany was used in all mixes to accomplish a good interlocking of the printed layers. $Li_2CO_3$ from Carl Roth GmbH & Co. KG, Karlsruhe, Gemany was used as an accelerator for a faster setting in case of cement bonded castables. The castables were mixed in an 80 l intensive mixer (Eirich GmbH & Co. KG, Hardheim, Germany). A star agitator in co-current flow for all experiments was used. Castables were mixed 1 min dry with a rotation speed of 44 rpm and 7 min wet with a rotation speed of 177 rpm. The mixing vessel rotates with 16 rpm. The water demand was set to 7,3 wt.-%.

**Test piece manufacturing and treatment**

A cuboid with a dimension of 350 mm x 290 mm was built by layer-on-layer construction (10 layers in x-, y-axis and 5 layers in z-axis) with the large-scale printer (Fig. 1) after the scheme shown in Fig. 2. The manufacturing was carried out with a printing path by alignment of the subsequent layers in a 180° angle. The real printing process can be seen in Fig. 3. 60 kg of raw material was homogenized and then added into the pump unit to be delivered to the print head. The actual printing process was started manually on both the pump and the ABB robot, and the print path was also programmed manually. $Li_2CO_3$ as setting accelerator was added directly added at the tip of the nozzle using an additive pump.

Test pieces for CMoR according to ISO 1927-5 (160x40x40 mm) Format D prisms were cut out. The sampling positions are marked in Fig. 4. Four test pieces were manufactured in print direction (180° angle) and another four test pieces were prepared at a 65° angle to get clues about the influence of a diagonal offset.

The cuboid was cured at room temperature, after cutting the test pieces were dried at 110 °C for 48 h and sintered at 1500°C with a dwell-time of 2 h.

Tab. 1: Composition of printable high-alumina model-castable, cement containing.

|  | CAC 3 mm |
| --- | --- |
| **Component** | **wt.-%** |
| Tabular alumina | |
| 1-3 mm | 15 |
| 0.5-1 mm | 18 |
| 0.2–0.6 mm | 16 |
| 0–0.2 mm | 19 |
| Reactive alumina | 27 |
| CA cement (70 wt.-% $Al_2O_3$) | 5 |
| **Sum** | **100** |
| Water | 7,3 |
| Multifil-fibers | 0.1 |
| Dispersing agent (PCE) | 0.15 |
| Methyl cellulose | 0.1 |
| Interlayer adherence agent | 0.05 |

**Experimental setup**

CMoR of two test pieces each was measured after drying at 110°C and after sintering at 1500 °C (dwell = 2 h). Open porosity was measured according to Archimedes by water buoyancy weighing.

**RESULTS AND DISCUSSION**

As shown on a smaller scale in former investigations [5] it was possible to upscale the experiments and print a true to size cuboid with the dimensions of 350 mm x 290 mm by layer-on-layer construction (10 layers in x-, y-axis and 5 layers in z-axis) with the self-developed castable CAC 3 mm in combination with $Li_2CO_3$ as an accelerator with the also self-developed large-scale printer.

The printed cuboid cut into two halves is envisaged in Fig. 5. The inner structure of the built layer on layer construction against print direction can be seen. Strands can be obtained that still own their extrusion shape with large casting cavities in between. The printing path could be changed to close those gaps mechanically by using a narrower path of the nozzle in x-, y- and z-direction and thus pressing the extruded strands more into each other. The single strands of the extrudate indicate that the viscosity of these castable is adequate to build out discrete strands. The castable is stable enough to withstand the weight of the subsequent layers and a discrete layer on layer formation can be manufactured. The printed member contains coarse grains of tabular alumina up to 3 mm and it is visible that these coarse grains are homogenously dispersed within the member as well as in every single strand.



Fig. 3: Printing process of a cuboid with a dimension of 350 mm x 290 mm by layer-on-layer construction (10 layers in x-, y-axis and 5 layers in z-axis) with the large-scale printer after the scheme shown in Fig. 2. $Li_2CO_3$ was used as setting accelerator and directly added after nozzle exit.
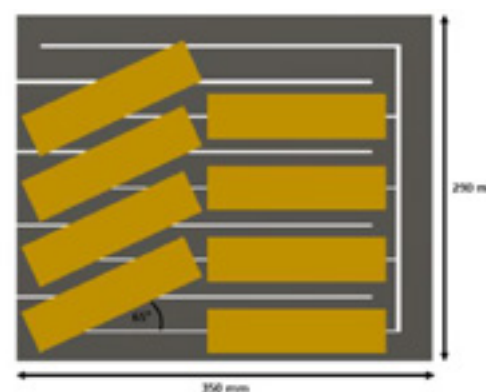


Fig. 4: Schematic top view and sampling positions within the cuboid (Fig. 3) of four test pieces, manufactured in print direction (180° angle) and another four test pieces at a 65° angle to get clues about the influence of a diagonal offset.

A cut test piece (180° angle), to show the inner structure of built layer on layer construction in print direction can be seen in Fig. 6 (l.). Here individual layers could not be identified. The grains and particles seem homogeneously dispersed and no big pores or cavities are evident to observe. A low tendency for segregation is obvious that can lead to prefabricated members with a high homogeneity.

Fig. 6 (r.) represents the fracture surface of the same test piece after measuring the bending strength. The sample section shows partially separate not well interlocked strands that still own their extrusion shape with large casting cavities in between. $Li_2CO_3$ leads to a volume stability, but acceleration has must be adjusted to enable a cavity free prefabricated member. Also, a more perfect inner structure could be achieved by optimising the printing path.

Fig. 7 shows the evolution of the CMoR and open porosity of CAC 3 mm. Test pieces 180° and 65° angle are pretreated at different temperatures (110 °C and 1500 °C). CAC 3 mm prepared at an angle of 180° delivers a strengths value of 4.5 MPa and an open porosity of 12.6 % at 110 °C. Sintered at 1500 °C the CMoR is 21.1 MPa and the porosity is 29.4 %. The same castable prepared at an angle of 65° shows a CMoR of 4.4 MPa at 110 °C and a porosity of 14.4 %. The strength is 15.8 MPa if sintered at 1500 °C and the porosity is 29.6%. The sampling with regard to orientation in the cuboid and the print path (180° and 65° angle) should be considered. Dried at 110 °C CMoR and open porosity do not seem to be significantly affected in these studies presented. If sintered at 1500 °C, 180° angle samples show a slightly higher strengths than those prepared at 65°. An explanation could be given by a slightly higher tendency for delamination of the layers due to the skew. In

general, the values of CMoR are lower and those of the open porosity are higher compared to conventionally produced members by moulding technique. Further material development could be necessary depending on the application of the manufactured components. However, the open porosity values are likely to be not only real porosity but also cavities due to the printing process. The values could therefore possibly be corrected downwards.
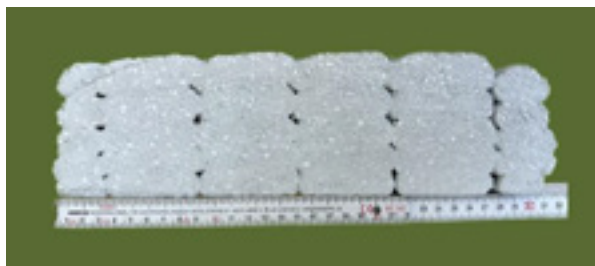


Fig. 5: Cut cuboid, to show the inner structure of built layer on layer construction against print direction.



Fig. 6: Cut test piece (180° angle), to show the inner structure of built layer on layer construction in print direction (l.) and fracture surface of cut test piece (180° angle), to show the inner structure of built layer on layer construction (r.).

Considering the images of the cut cuboid in Fig. 5 and the test piece prepared therefrom in Fig. 6 and the results of the measurement of CMoR in Fig. 7 it can be concluded that the additives must be adjusted more carefully, to achieve a homogenous material that is stable enough to keep its volume stability. Although stable layer formation is desirable, discrete strands will not allow homogeneously printed parts with the desired dimension. In general, the test pieces show lower values of strength compared to conventionally produced ones by moulding technique. This can be explained by more defects like cavities caused due to quite discrete strands standing on top of each other. However, this can be counteracted with a better printer setup when the individual layers were printed more into one another during the printing process by reducing the traverse path of the printer nozzle in x-, y- and z-axis (over-extrusion). A more homogeneous inner structure without cavities could be achieved and less defects in their inner structure could lead to higher values of strengths.
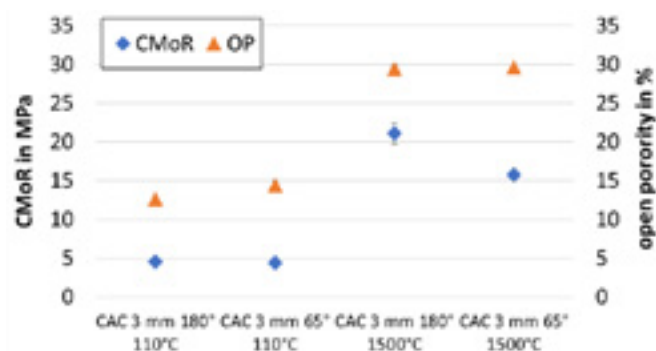


Fig. 7: CMoR and open porosity of castable CAC 3 mm (65° angle and 180° angle test pieces), dried at 110°C and sintered at 1500°C for 2h.

## CONCLUSIONS

In this contribution we envisaged first success in the development of castables that are suitable for CC as well as development of a large-scale 3D printer. It was possible to upscale former experiments [4,5] and print a true to size cuboid.

We figured out, that pumpable castables must be adjusted precisely regarding their grain size and particle size distribution, water demand and additive system and thus their rheology. The use of suitable additives in a precisely adjusted concentration is inevitable to gain the wanted properties of printable castables. Stiffening agents in a defined concentration are necessary to achieve shear thinning rheological behavior that allows a good pumpability but also an increasing viscosity after leaving the printing nozzle to achieve a sufficient volume stability and to produce near net shape members. Accelerator agents are mandatory to achieve a rapid setting of the concrete. The strength evolution must be high enough to withstand the weight of the subsequent layers. However, the right dosage must be still be optimized.

Another very important point is the printing process itself, especially the printing path and the movement of the printing head and thus the nozzle in x-, y- and z-direction. This influences the material properties CMoR and open porosity. Gaps and printing cavities provoke higher open porosities and lead to defects that lower the strengths. In order to produce homogeneous parts, the extrusion speed and thus also the pump pressure, the traverse speed and the layer thickness must be synchronised, always taking into account the viscosity of the castable and the current printer setup Defects and layer formation could be counteracted by over-extrusion, i.e. forced extrusion of the extrudate into one another.

It can be concluded in general that the end-shape printing of large members with a smooth surface and homogeneous material properties like those that are obtained by the conventional moulding technique is a complex interplay of both materials properties and printing process.

In further investigations other printing schemes should be tested, where the application of the layers is changed. Possible variations represent an alignment of the subsequent layers not carried out as in this version at an 180° angle, but at a 90° or 45° angle. The influence on resulting materials properties should be considered.

Microscopic as well as computer tomographic investigations should be carried out to to examine the inner structure and layer formation in more detail.

## ACKNOWLEDGEMENT

## REFERENCES

[1] Pfeiffer, S., Stephan, D., Dorn, T., Hirsch, T.: State of the art and perspectives of 3D printing in construction, Drymix Mortar Yearbook, 3D Special, 2019.

[2] Ma, GW., Wang, L., Ju, Y.: State-of-the-art of 3D printing technology of cementitious material – AN emerging technique for construction, Sci China, Technological Sciences, 60 (2017).

[3] Bos, F., Ahmed, Z., Justinov, E., Salet, T.: Experimental exploration of metal cable as reinforcement in 3D printed concrete, Materials, 10(11), 1314 (2017).

[4] Klein, L., Holleyn, F., Zimmer, S., Krause, O.: Research and development of new 3D printing technologies and adaption of the Contour-Crafting process to refractories, Part I: Basics of the printing process and Contour-Crafting setup, 65nd ICR 2022.

[5] Holleyn, F., Klein, L., Zimmer, S., Krause, O.: Research and development of new 3D printing technologies and adaption of the contour-crafting process to refractories, Part II: Castable Development, 65nd ICR 2022.

# EFFECT OF FIRING TEMPERATURE ON THERMO-MECHANICAL PROPERTIES OF LOW CEMENT CASTABLES

Sougata Roy, Subhadeep Chatterjee, Minakshi Dash, Arup Kumar Samanta, Yoshihiro Mizuma, Sunanda Sengupta, P. B. Panda
TRL Krosaki Refractories Limited, Belpahar-768218, Odisha (India)

## ABSTRACT

Due to several advantages of Monolithics, particularly castables, its consumption is increasing day-by-day in different applications replacing bricks. In castables, cement is responsible for developing strength after installation followed by curing and firing. However, the presence of CaO coming from cement restricts the thermo-mechanical properties of castables, specially for low cement castables having microsilica in matrix. Several works have been conducted to improve the thermo-mechanical properties while reducing the cement content or introducing different binders replacing cement. In different applications, some of the items are too complicated and larger in shape which is quite difficult to manufacture in pressed route. In addition, to avoid additional activities and unable to maintain proper pre-firing schedule at application sites, most of the users prefer to use precast and pre-fired (PCPF) items for critical applications which not only provide quick installation but also give consistent performance. Due to criticality and larger in shape, it is not always possible to pre-fire the items at high temperatures to develop required thermo-mechanical properties which are important from the viewpoint of application.

In the present work, two types of castable have been considered where one is designed with microsilica in matrix and other is without microsilica. Different thermo-mechanical properties like HMOR, PLC, RUL etc. are measured after firing the samples at different temperatures. The relation of thermo-mechanical properties with firing temperatures is explained while development of different mineralogical phases as well as changes in microstructure through different techniques e.g., XRD, SEM, EDAX etc.

## INTRODUCTION

Refractory castables as a kind of high-temperature composite, have the several advantages like easy installation, enery savings, suitable for partial repairing and to make monolithic structure. One of the essential component for castables is calcium aluminate binder which gives good workability at the time of application. However, the high-temperature mechanical properties like HMOR[1] of castables depends upon the formation of different mineralogical phases specially $CA_6$. The degree of $CA_6$ formation, its shape and location of formation are also responsible for high-temperature properties. Presence of matrix components and the formation of other liquidus phases strongly affect the high temperature properties. Basically, there are two types of castable. One is with microsilica in matrix and other without microsilica. In both the cases there is formation of $CA_6$ phase[2] but its shape is different and ultimately affect the mechanical properties.

Pre-firing temperature also plays a vital role as different mineralogical phases are formed during pre-firing which contribute better high-temperature thermo-mechanical properties.

## EXPERIMENTAL

Two types of castable are designed in this study having $\sim$ 90% $Al_2O_3$. One is having microsilica in matrix and other is without microsilica. The base raw materials are WTA, sillimanite. Two different kinds of dispersing agents were used for two types of castable. Samples were fired at 1200, 1400 & 1600$^0$C to measure the CCS. To understand the effect of pre-firing temperature on HMOR, samples were pre-fired at 300, 600, 900, 1200, 1300, 1400, 1500 and 1600$^0$C before measuring HMOR at 1450$^0$C. HMOR was also measured for those samples just after drying at 110$^0$C for 24 hours. To identify the formation of mineralogical phases after firing at different temperatures, XRD was done. Development of microstructure was carried out by SEM along with EDAX. RUL of all samples was measured after firing at different temperatures to understand the effect of pre-firing temperature on RUL.

## RESULTS & DISCUSSION

In Table-1, batch formulation for two types of castables is shown. "SF90" batch doesn't have microsilica whereas "LC90" batch is having microsilica in matrix.

**Table 1: Batch formulation**

| Raw Materials | SF 90 | LC 90 |
|---|---|---|
| WTA | 69 | 80 |
| Sillimanite | 16 | 5 |
| Microsilica | 0 | 5 |
| Calcined Alumina | 0 | 5 |
| Reactive Alumina | 10 | 0 |
| HAC | 5 | 5 |
| Dispersant A | 0 | 0.1 |
| Dispersant B | 0.1 | 0 |

CCS for all samples was measured after firing at 1200, 1400 and 1600$^0$C including after drying at 110$^0$C for 24 hours. The variation of CCS is shown in Fig.1. It has been observed that there is no significant variation in CCS between two types of castable.
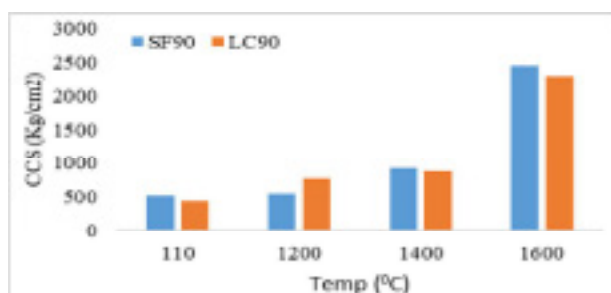


*Fig.1: CCS for two types of castables*
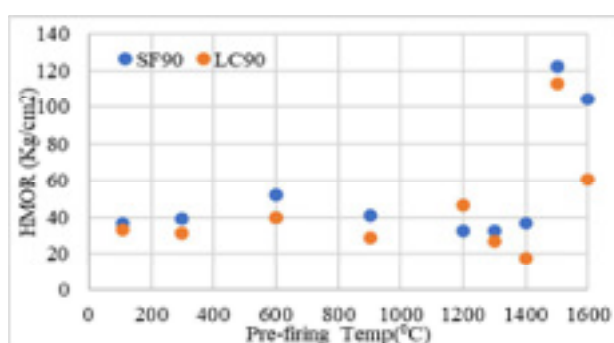


*Fig.2: HMOR measured against different pre-firing temperature*

Variation in HMOR is plotted in Fig. 2 measured at 1450$^0$C as a function of pre-firing temperature. It has been clearly observed that there is no significant effect in HMOR between two types of castable on pre-firing temperature till 1500$^0$C. However, a wide diffence in HMOR is observed when samples were pre-fired at

$1600^0$C. Another important observation is the values of HMOR, till pre-firing temperature of $1400^0$C, all values are almost similar. However, it has incresed significantly when samples were pre-fired at $1500^0$C. The significant increase in HMOR is basically the formation of $CA_6$ phase and its orientation. Below $1500^0$C, formation of $CA_6$ is not significant and therefore HMOR values were in lower side. The HMOR value of LC90 is showing significantly low when pre-firing temperature was $1600^0$C. This is due to formation of different low eutectic compounds as LC90 samples are having microsilica in matrix.

XRD patterns of both samples pre-fired at different temperatures were also analysed. As an example, patterens after firing at $1500^0$C are shown in Fig. 3 and 4. SF90 sample is having significant amount of sillimanite but it is fully disappeared at $1500^0$C. Sillimanite may dissociates to form mullite which is another reason for high HMOR.
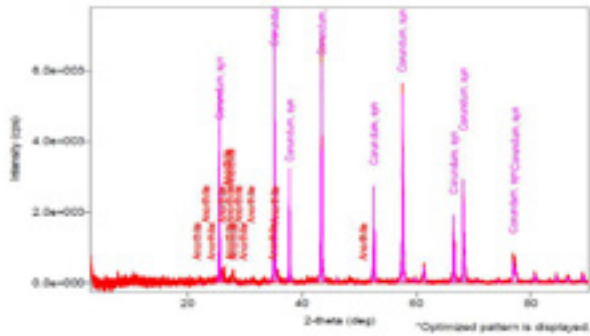


*Fig.3:XRD of SF90 after pre-firing the sample at $1500^0$C*
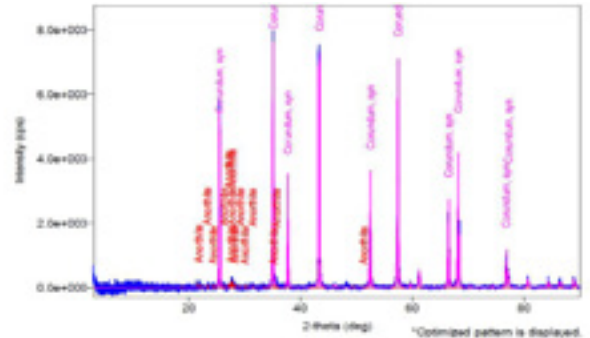


*Fig.4:XRD of LC90 after pre-firing the sample at $1500^0$C*

SEM analysis was carried out after firing the samples at $1500^0$C and it is shown in Fig. 5. In both the cases there are significant grain growth. However, the grain growth is higher in LC90 samples. Probably, the formation of liquid phases accelerate the grain growth mechanism. The EDAX behaviour is shown in Fig. 6.
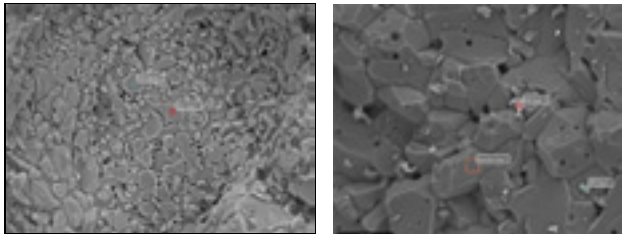


*Fig.5:SEM analysis for SF90 (Left) and LC90(Right)*

RUL is another important high temperature thermo-mechanical property for refractory. This property was measured for both the samples after each pre-firing temperature. The behaviour of RUL after pre-firing at $1500^0$C is shown in Fig. 7 and 8.
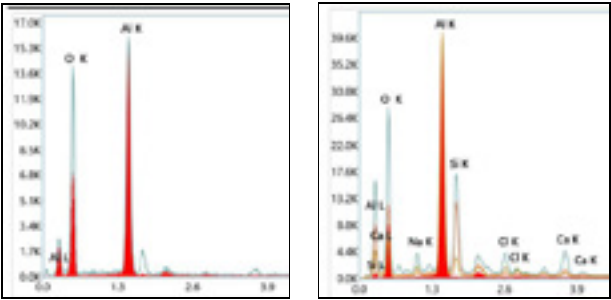


*Fig.6:EDAX of SF90 (Left) and LC90 (Right)*
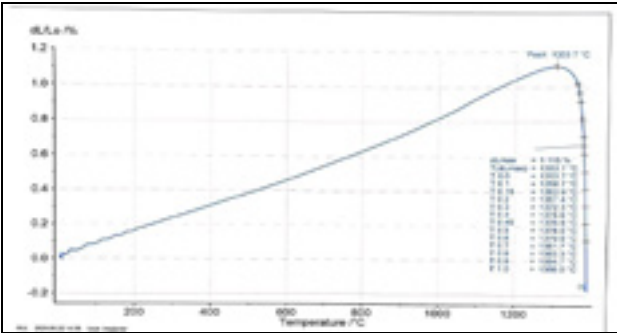


*Fig.7:RUL of SF 90 measured after firing the sample at $1500^0$C*
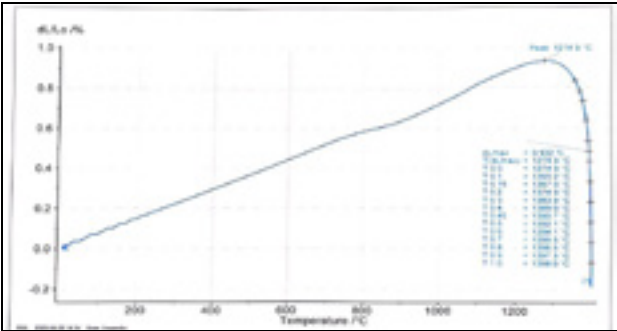


*Fig.8:RUL of LC 90 measured after firing the sample at $1500^0$C*

## CONCLUSIONS

High temperature thermo-mechanical properties of castables depend on several factors like matrix design, pre-firing temperature, formation of $CA_6$ phase and its shape etc. It has been observed that there is no significant effect on pre-firing temperature till $1400^0$C for both the samples having microsilica in matrix and without microsilica. However, there is significant increase in HMOR for both samples after pre-firing at $1500^0$C. This is due to formation of different mineralogical phases like $CA_6$, mullite and others. HMOR is observed significantly low while pre-fired it at $1600^0$C for LC90. Due to presence of microsilica, different low eutectic compounds formed while pre-firing at $1600^0$C resulting in low HMOR against SF90 having no microsilica. This study also indicates to decide the pre-firing temperature for PCPF items to achieve best high-temperature thermo-mechanical properties.

## REFERENCES

1. F. Wang, Xiangeheng LI, Pingan Chen, Girish Madhav Kale, Boquan Zhu. "The adjustment of $CA_6$ morphology and its effect on the thermos-mechanical properties of high temperature composites. Journal of the Ceramic Society of Japan 126 (12), 2018

2. X Liu, B. Andreas, B. Gunter. Refractories, 1, 01-06, 2006

# DESIGN OF SELF–FLOW CASTABLE USING SIOXX (TM) – FLOW AND ITS AGEING ANALYSIS IN TROPICAL CONDITION

Ankita Mishra, Arindam Mukherjee, Hong Peng
Elkem South Asia Pvt Ltd, Nagpur, India

## ABSTRACT

Modern installation techniques like pumping or shotcreting are gaining popularity with refractory users and manufacturers. The rheological behavior of the castables is important to obtain optimum placement properties and to improve the performance of refractory monolithic in the application. Low cement self-flow monolithic are often faced with challenges of reduced flow during installation at site. Such challenges are increased manifold with the ageing of castable, and with varying climatic conditions - which limits the storage life of castables and application. In this work, a low cement self-flow castable mix is designed using SioxX™-Flow to achieve optimum initial self-flow and working time for the application. The rheological properties with SioxX™-Flow are compared with commercially available other dispersants. The effect of ageing (6 months) on the castable properties when stored at site was also studied.

## INTRODUCTION

In the late 1990s, Low cement self-flowing castables joined the family of refractory monolithics. Due to the ease of application over vibration castable, self-flow castables gained demand in the market. A self-flow castable can be used in shotcreting installations, where refractory aggregates, binders & dispersing agents are premixed in a mixer with water and pumped through a nozzle. At the end of the nozzle, setting accelerator is added to reduce rebound losses. But the mix must remain plastic in nature for trowelling or levelling of the surface. Similarly, in pumping castables the wet mix is directly transported through piston pump at the application site. Hence, for good self-flowing castable, rheological properties are a key factor. Often, the loss in flow is compensated by more addition of water, which leads to grain segregation, prolonged setting time, higher porosity after firing and longer curing time to avoid explosion during preheating.

The rheology of castables is affected by particle size distribution, selection of dispersant and hardening time controller (i.e accelerator or retarder, water to matrix ratio, sequence of water addition, ambient temperature at the time of application and storage or ageing condition of castable). In this work, a low cement self-flow castable mix is designed using SioxX™-Flow to achieve optimum initial self-flow and working time for the application. The rheological properties with SioxX™-Flow are compared with commercially available other dispersants. The effect of ageing on the castable properties when stored at site was also studied.

## EXPERIMENTAL WORK

### Castable mix design

Indian grade bauxite (90% $Al_2O_3$) is selected for coarse to midsize aggregate, fine matrix includes reactive, calcined alumina, bauxite fines and tabular alumina fines. Calcium alumina cement (70% $Al_2O_3$) selected as hydraulic binder, microsilica 971U (97% $SiO_2$, origin Norway) was used as silica fume.

Here, three dispersants are selected to compare the rheology of the castable, Mix-A with SioxX™ -Flow, which is a microsilica-based dispersant for low cement and ultra-low cement system, Mix- B with lab grade sodium hexametaphosphate (SHMP) and Mix C with polycarboxylate ether based additive (Castament FS 20). Details of formulation is shown in table 1.

Table 1 Composition of self-flow castable

| Raw Material | Mix-A | Mix-B | Mix-C |
|---|---|---|---|
| Bauxite 3-5mm | 10 | 10 | 10 |
| Bauxite 1-3mm | 28 | 28 | 28 |
| Bauxite 0-1mm | 15 | 15 | 15 |
| Tabular Alumina 0.2-0.6mm | 10 | 10 | 10 |
| Bauxite 200 mesh | 11 | 11 | 11 |
| CT 800SG | 8 | 8 | 8 |
| CA14M | 5 | 5 | 5 |
| MS 971U | 6 | 7 | 7 |
| CL 370 | 6 | 6 | 6 |
| Dispersant –SioxX™-Flow | 1 | | |
| Dispersant –SHMP | | 0.2 | |
| Dispersant –FS 20 | | | 0.075 |
| Setting Retarder-Boric acid | | 0.05 | 0.1 |
| | 100.0 | 100.52 | 100.175 |

During the application of self-flow castable, flow decay is an important factor, as it has to flow over long distances inside a pipeline and face high shear rates and restricted volume. The wet mix must maintain fluidity without clogging the pipe, segregation of grains.

## 2.2 Experimental procedures

### Mix preparation

To conduct comparative study of placement properties of three additives, trial batches of 6kg prepared. To measure the flowability up to 60min and ageing analysis up to 6 months at frequency Day 0, 7, 14, 30, 60, 90 and 180 days. Investigation of ageing was performed using microsilica 971U. All the raw materials were mixed in a planetary mixer as per the composition and mixed with water 6.5% in two steps (80% addition of water to achieve mix wet-out & rest 20% to achieve self-flow). The reason of fixing 6.5%water is discussed in 2.3. The total mixing time for castable is 5min. Dry mix & water temperature was maintained at 22±2°C during all trials.

### Flow measurement and casting

To measure the flowability of castable i.e self-flow and vibration flow, flow cone (ASTM C230) used. Wet mix sample poured in flow cone, levelled it to surface, cone is removed and then due to gravity, the castable spread on the flat surface. After the spread of the castable up to 30s, diameter is measured using vernier calliper. Similarly, the vibration flow is measured after 15s of vibration using a vibration table. To measure the flow after 30min and 60min, the castable is poured into a zip lock bag and secured from evaporation. Hardening time is measured through ultra-sonic IP 8 tester, where hardening time is determined by the propogation of ultrasonic waves through the material. With time, castable loses its plasticity & gets hardened. Therefore, the velocity of sonic waves increases. Deviation in curve of Sonic velocity (m/s) vs Time (min), initial and final set of the castable is estimated.

To understand the impact of ageing, all 21 batches were packed in a 25kg HDPE bag with additional inner liner and stored in a warehouse, where no temperature and humidity conditioning facility is available, to replicate the site condition. Thrice a day the

169

ambient temperature and the humidity of warehouse were measured using hygrometer and recorded.

### 2.3 Determination of optimum water demand and selection of dispersants

To determine the optimum water demand of the refractory mix, Mix-A trials conducted with water addition of 8%, 7% and 6.5%. With 6.5% of water, desired wet-out time and self-flow of castable achieved as per table 2.

Table 2 Self-flow with different water addition

| Mix-A | Targets | Water addition 8% | Water addition 7% | Water addition 6.5% |
|---|---|---|---|---|
| Wet-out time (s) | <90 | 37 | 60 | 70 |
| Initial Self-Flow_F0(%) | ≥100 | 118 | 110 | 108 |

Further study was conducted at 6.5% of water addition to compare the self-flow up to 30 min with SHMP and FS 20, without any use of setting time controller which is shown in table 3.

Table 3 Comparison of self-flow with different additive

| | Targets | Mix-A | Mix-B | Mix-C |
|---|---|---|---|---|
| Wet-out time (s) | <90 | 70 | 70 | 129 |
| Initial Self-Flow_F0(%) | ≥100 | 108 | 78 | 85 |
| 30min Self-Flow_F30(%) | ≥80 | 86 | 61 | 34 |
| Setting time (min) | | 140 | 100 | 95 |

As Mix-B and Mix-C could not achieve the desired flow without retarder, trials conducted with Citric acid, tri-sodium citrate and Boric acid, where with optimal dosage of boric acid (>99.5% $H_3BO_3$) offered better results.

### RESULTS AND DISCUSSION

#### 3.1 Flowability

Rheological properties with SioxX™-Flow in Mix-A achieved without any addition of retarder whereas with SHMP in Mix-B and with FS-20 in Mix-C of Boric acid (BA) is added with dose of 0.05% and 0.1% respectively. Following are the initial results of flow comparison with microsilica 971U with different additives in table 4.

Table 4 Self-flow with different additives

| | Targets | Mix-A (SioxX™-flow) | Mix-B (SHMP + BA) | Mix-C (FS-20 + BA) |
|---|---|---|---|---|
| Wet-out time (s) | <90 | 80 | 145 | 120 |
| Initial Self-Flow_F0(%) | ≥100 | 107 | 79 | 90 |
| 30min Self-Flow_F30(%) | ≥80 | 97 | 65 | 88 |
| 60min Self-Flow_F60(%) | ≥60 | 80 | 38 | 62 |
| Setting time (min) | < 420 | 290 | 1000 | 450 |

### 3.2 Ageing Analysis

Investigation of the change in rheology of low cement castable is important due to the presence of high alumina cement, microsilica, dispersants and set controller additives, which are more prone to interact with each other and alter the castable behaviour. Fig 1 shows the plot of ambient temperature and relative humidity of the storage facility over the period of 180days.
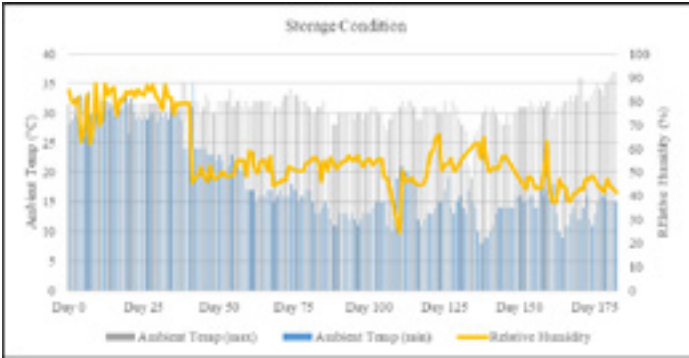


*Fig. 1 Plot of avg. ambient temperature and relative humidity*



*Fig.2 Storage facility for ageing analysis*

On the day of the trial, dry castables were mixed in a planetary mixer for 1 min, to break any agglomerates formed during storage. Impact of ageing of 180 days on wet-out time and flowability in all mixes are shown in Fig 3 to Fig 6.



*Fig. 3 Impact of aging on wet-out time for all mixes*

Wet-out time of mix with SioxX™-Flow(80s) is lower than SHMP(145s) and FS-20(120s) on Day-1. With increase in storage days, gradual increase in wet-out time observed in Mix-A to 5min on 180th day, whereas in Mix-B and C increase in wet-out time is rapid up to 60days (>200s) and reached 195s and 312s on 180th day respectively
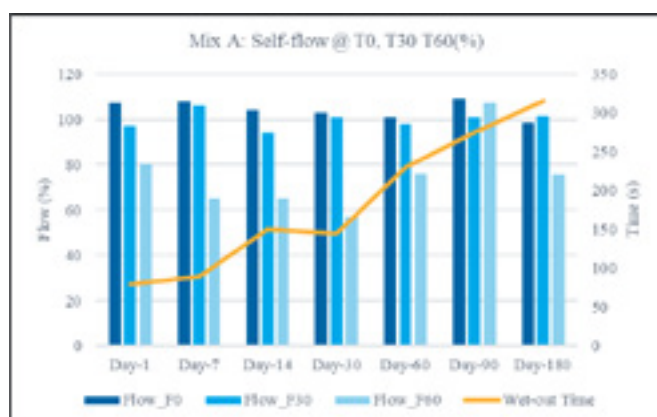
*Fig. 4 Impact of ageing on wet-out and flow in Mix-A*



*Fig. 5 Impact of ageing on wet-out and flow in Mix-B*
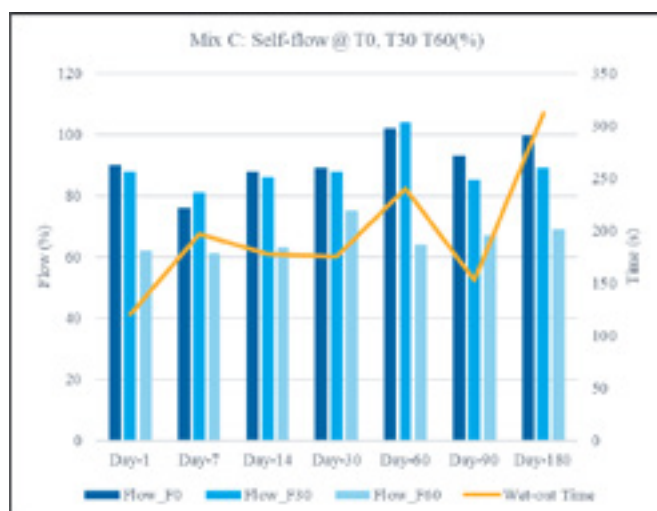


*Fig. 6 Impact of ageing on wet-out and flow in Mix-C*

Mix-A self-flow on day-1, immediate after mixing (F0), after 30min (F30) and after 60min (F60) are aligned with target. After 30 days, flow decay (at 30 min & 60min) declined. After 180 days, although the wet out time increased, self flow is close to target.

Mix-B self flow on day-1 is below target for self flow. With ageing, no improvement in flow observed and after 60days samples were found difficult to flow and at the same time high in setting time.

Mix-C self flow on day-1 , immediate after mixing (F0), was below target but offered working time upto 60min. With ageing, wet out time increased , inital flow and workability remain unaffected.
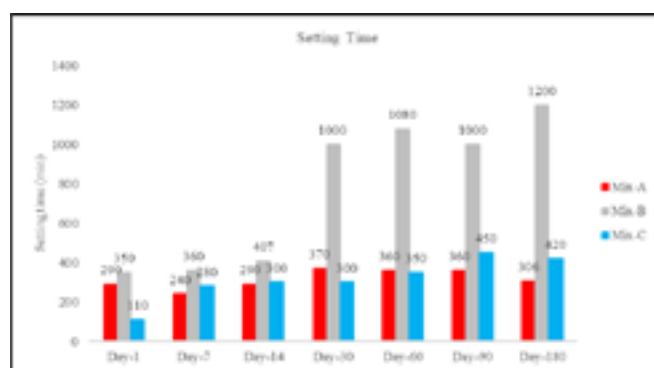


*Fig. 7 Impact of ageing on wet-out and flow in Mixes*

During the application, the loss in plasticity helps in better sticking of the castable on surface. Optimum setting time helps quick installation and change over on site. Mix-A and Mix-C indicate the apt thickening time & setting time, which enable the mix to coagulate, but flow and stick onto the surface, providing high strength and low porosity. Mix-B indicates short thickening and long setting, which will not allow flow and proper sticking of the castable Additionally, long setting hinders the panel removal or demoulding. After 180 days, Mix-B setting time is approximately 50hr, after demoulding of casted sample crack observed in samples. Mix-C 7hr and Mix-A 5hr, which indicated that with SioxX™-Flow, effect of ageing is not significant.

## CONCLUSIONS

a) Selection of admixture / dispersants is important to achieve suitable flow and working time for application of self-flow monolithics. SioxX™ - Flow with 1% dosage in a well-designed self-flow mix demonstrates superior initial flow and workability compared to other dispersants.

b) SioxX™- Flow can eliminate the small quantities of dispersants / retarders and reduces variability of refractory mix design.

c) A mix of reactive alumina-silica fume-hydraulic binder-dispersant is more susceptible to ageing, which may increase wet-out time and setting as well to reduce working time. Mix with SioxX™- Flow demonstrates superior and stable ageing behavior as compared to other dispersants. With 6months of

## REFERENCES

[1] X. Zhou, K. Sankaranarayanane, M. Rigaud, Design of bauxite-based low-cement pumpable castables: a rheological approach, Ceramics International 30 (2004) 47–55.

[2] A. Hundere, B. Myhre, C. Odegard, B. Sandberg, Wet shotcreting refractory castables with varying cement content, in: XIII Conference on Refractory castables Nov. 4-5, 1998, Prague, Czech Republic

[3] B. Mhyre, B. Sandberg, A. Hundere, Flow and flow decay of refractory castables, in 3rd India International Refractories Congress 1998. Calcutta.

[4] R. Sarkar, A. Satpathy, High Alumina Self-flow Castables with Different Binder refractories Worldforum 4 (2012)

[5] B.Myhre, Particle Size Distribution and its relevance in refractory castables, in: 2nd India International Refractory Congress 1996, New Delhi

[6] R.G. Pileggi, Y.A. Marques, D. Vasques Filho, A.R. Studart, V.C. Pandolfelli, Wet shotcrete for refractory castables, Am. Ceram. Soc. Bull. 81 (10) (2002) 51–56.

# MICROSTRUCTURE DESIGN OF A MORE SUSTAINABLE ALUMINA–SPINEL REFRACTORY CASTABLE

Kwasi Addo, Boateng[1,2], Jean-Michel, Auvray[1], Christoph, Wöhrmeyer[1]
[1]Imerys S.A., Paris, France

Nicolas, Tessier-Doyen[2], Elsa, Thune[2], Marc, Huger[2]
[2]Université de Limoges, IRCER, UMR CNRS 7315, 12 rue Atlantis, 87068, Limoges, France

## ABSTRACT

Alumina-spinel based refractories are excellent furnace linings due to high refractoriness and superior corrosion and slag penetration resistance. Tabular alumina aggregates have been popularly used in alumina-spinel refractories due to their high purity, high melting point and volume stability at high temperatures. Nevertheless, white fused alumina (WFA) aggregates were also considered in this work in the quest to propose a new microstructural design for refractory materials with improved thermo-mechanical properties. The influence of WFA aggregates on the porosity, physical property, microstructure and thermal shock resistance (TSR) of calcium aluminate bonded castables (M-TA resp. M-WFA) were investigated. Calcium hexa-aluminate phases ($CA_6$) were formed along the borders of tabular and white fused alumina aggregates at 1500 °C but in denser layers around white fused aggregates. Residual modulus of elasticity after one and five thermal shocking cycles are comparable for both M-TA and M-WFA castables regardless of original strengths after sintering. Interestingly, residual modulus of rupture for M-WFA castables remains higher than that of M-TA castables after one and five thermal cycles.

## INTRODUCTION

Alumina-spinel castables have been long used in several areas of the steelmaking process including ladle lining [1]. Two types of alumina are widely produced for refractory applications comprising tabular alumina (TA) and white fused alumina (WFA). Nevertheless, tabular alumina has been the main alumina aggregates used in alumina-spinel ($Al_2O_3$-$MgAl_2O_4$) castables. Due to significant amount of closed pores (about 5 vol%.) evenly distributed, tabular alumina is believed to improve thermal shock resistance compared to castables containing white fused alumina [2]. Additionally, tabular alumina consists of elongated, tablet-shaped crystallites with lower open pores than that of white fused alumina grains which are angular shaped [3]. The difference in morphology and particle porosity is mainly due to the different processing routes, that is sintering and electrofusion for tabular and fused alumina respectively. With sodium impurities unevenly distributed and concentrated more at grain boundaries, the deficiency of the large and dense crystallites of white fused alumina in thermomechanical behaviour compared to tabular alumina-based spinel refractories is not well understood. The work reported in this paper seeks to investigate the correlations between microstructural changes and thermomechanical properties of alumina-spinel castables containing tabular (M-TA) and white fused alumina (M-WFA) at high temperatures.

## MATERIALS AND EXPERIMENTAL PROCEDURE
### Raw materials

Tabular alumina, TA (Almatis, Germany) and White Fused Alumina, WFA (Imerys, Germany) were used as the main alumina aggregates (coarse, medium and fines) in the castables. Calcium aluminate cement (CAC, Secar® 71, France) as binder, reactive alumina (P152SB, Alteo, France) and a chemical additive (Peramin® AL200, Imerys, France) as dispersant add up to the castable composition.

The characteristics of tabular alumina and white fused alumina aggregates are given in Table 1. The determination of the apparent densities, open porosities and water absorption of the alumina aggregates was done using the Archimedes method.

Tab. 1: Properties of tabular and white fused alumina aggregates.

| Property | Tabular Alumina | White Fused Alumina |
|---|---|---|
| Apparent density, g/cm³ | 3.6 | 3.5 |
| Open porosity, % | 4.3 | 9.9 |
| Water absorption, % | 1.2 | 3.7 |
| Shape | Blocky | angular |
| $Al_2O_3$, % | 99.9 | 99.8 |
| $Na_2O$, % | 0.3 | 0.3 |

### Castable preparation

Table 2 shows the two types of alumina-spinel castables prepared: (i) one containing tabular alumina aggregates (TA) and (ii) the other containing white fused alumina aggregates (WFA). Both formulations were cast into prisms of 160x30x30 mm³. Castables were cured (at 20 °C, 100 % RH) for 48 h, dried at 110 °C for 24 h and fired at 5 °C/min up to 1100 °C, 1300 °C and 1500 °C for 6 h.

Tab. 2: Compositions of castables, wt%.

| | M-TA | M-WFA |
|---|---|---|
| **Tabular Alumina** | | |
| 3-6 mm | 33 | - |
| 1-3 mm | 16 | - |
| 0.3-0.6 mm | 6 | - |
| 0-0.3 mm | 5 | - |
| **White Fused Alumina** | | |
| 3-5 mm | - | 33 |
| 1-3 mm | - | 16 |
| 0.2-0.5 mm | - | 6 |
| 0-0.2 mm | - | 5 |
| **Sintered spinel** | | |
| 0.5-1 mm | 9 | 9 |
| 0-0.5 mm | 4 | 4 |
| 0-0.09 mm | 10 | 10 |
| **Reactive Alumina** | 11 | 11 |
| **CAC Secar® 71** | 6 | 6 |
| **PCE Peramin® AL200** | + 0.1 | + 0.1 |
| **Water** | + 4.1 | + 4.1 |

### Testing methods

Apparent porosity measurements based on the Archimedes method were performed using water as the immersion liquid. 3-point bending tests were used to measure the modulus of rupture for castables after curing, drying and firing. To interpret the microstructural evolution of the castables fired at 1500 °C, scanning electron microscopy (SEM) studies were carried out with the equipment Quanta FEG 250. Regarding the thermal shock tests, pre-fired samples (1500 °C for 6 h) were subjected to a total of five heating and cooling cycles. Samples were placed in the furnace already heated at 950 °C for 2 h. Afterwards, the samples were removed and air-cooled naturally to room temperature. For each cycle, the damage caused by the thermal cycling was evaluated by elastic modulus measurements (E) *via* frequency resonance at room temperature with the Grindosonic® MK7. Modulus of rupture (MoR) tests were carried out to evaluate the residual strength after thermal cycles.

## RESULTS AND DISCUSSION
### Castable properties
Lowest and highest porosities in both castables were measured after treatment at 110 °C and 1500 °C respectively. The apparent porosities in M-WFA are higher compared to M-TA castables (see Figure 1). However, there is a slight decrease in porosity in M-TA at 1300 °C. One of the reasons for higher porosities in M-WFA castables can be partly attributed to higher open porosities in white fused alumina aggregates.
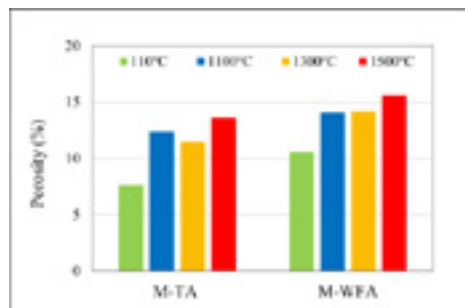


Fig. 1: Apparent porosity of the tabular (M-TA) and white fused (M-WFA) alumina based castables after drying at 110 °C and different firing temperatures.

Modulus of rupture are relatively low and comparable in both M-TA and M-WFA castables up to 1300 °C. At 1500 °C, both castables have high modulus of rupture but more significant in M-TA castables as seen in Figure 2.
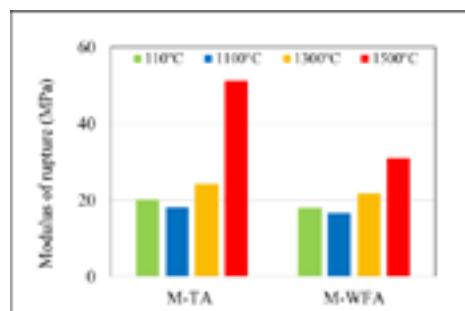


Fig. 2: Modulus of rupture of tabular (M-TA) and white fused (WFA) alumina based castables after drying at 110 °C and different firing temperatures.

### Microstructure
SEM images show the presence of hibonite ($CA_6$) at the borders of the alumina aggregates for both M-TA and M-WFA castables as shown in Figure 3. Despite overall higher open porosities in WFA aggregates, they look WFA aggregates look denser at macroscale compared to TA aggregates but are embedded in a matrix containing bigger pores.
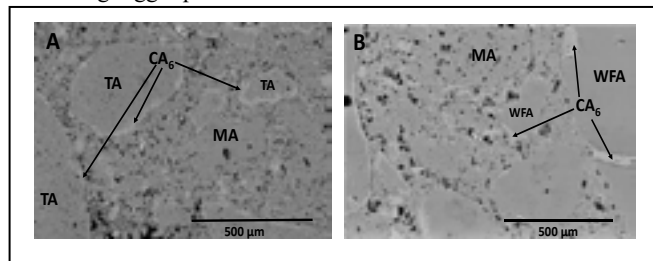


Fig. 3: SEM micrographs of A) tabular and B) white fused alumina-based spinel castables sintered at 1500°C.

However, $CA_6$ seems to be evenly distributed along the tabular alumina aggregates. In M-WFA castables, $CA_6$ tends to form on discrete parts on the surface of the aggregate but in denser layers than in M-TA castables.

### Thermal Shock
M-TA and M-WFA castables show a gradual loss in modulus of elasticity after thermal shock cycles. The residual modulus of elasticity were comparable for both M-TA and M-WFA castables regardless of original strengths after sintering (Figure 4).
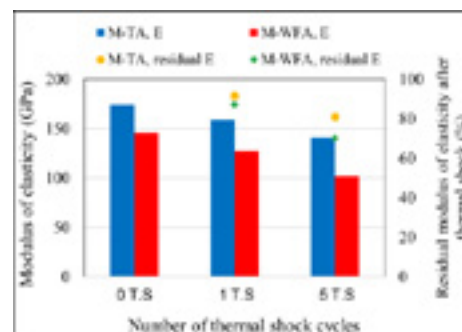


Fig. 4: Modulus of Elasticity of the tabular (M-TA) and white fused (M-WFA) alumina based castables after sintering and thermal shock cycles.

The modulus of rupture after sintering is significantly higher for M-TA than M-WFA castables at 1500°C. Likewise, after the first thermal cycle, M-TA castables experiences a bigger drop in strength compared to M-WFA castables. Surprisingly, the residual modulus of rupture for M-WFA castables remains a little higher than that of M-TA castables after one and five thermal cycles.
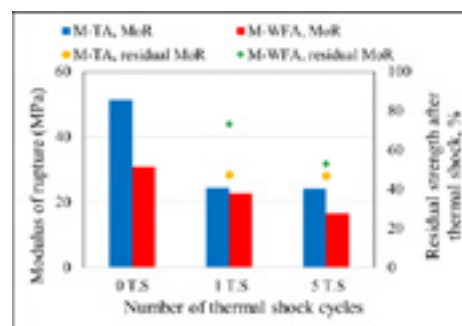


Fig. 5: Modulus of Rupture of the tabular (M-TA) and white fused (WFA) alumina based castables after sintering and thermal shock cycles.

## CONCLUSIONS
This work shows the significant influence in castable properties at high temperatures comparing the two types of alumina aggregates. Higher modulus of elasticity and rupture could be related to the less porous and dense microstructure of M-TA castables. Thermal shocking results show a higher elastic modulus and residual elastic modulus in M-TA castables after five thermal cycles. Conversely, M-WFA castables exhibit a lower modulus of rupture but a higher residual modulus of rupture of about 50 % after five thermal cycles.

## REFERENCES
[1] Braulio, M. A. L., Rigaud, M., Buhr, A., Parr, C., & Pandolfelli, V. C. (2011). Spinel-containing alumina-based refractory castables. Ceramics International, 37(6), 1705-1724.

[2] Büchel, G., Liu, X., Buhr, A., & Dutton, J. (2007). Review of tabular alumina as high performance refractory material. Interceram Refractories Manual, 6-12.

[3] Schaffӧner, S., Dietze, C., Mӧhmel, S., Fruhstorfer, J., & Aneziris, C. G. (2017). Refractories containing fused and sintered alumina aggregates: Investigations on processing, particle size distribution and particle morphology. Ceramics International, 43(5), 4252-4262.

## Deutsches Institut für Feuerfest und Keramik GmbH

Deutsches Institut für Feuerfest und Keramik GmbH



The laboratory is accredited by DAkkS under registration number **D-PL-17672-01-00** after **DIN EN ISO / IEC / 17025:2005** and is able to carry out more than 100 standardized resp. specific test methods. In the process chemical, physical and mineralogical methods as well as selected high temperature measuring procedures are used according to the standards and rules of **DIN, EN, ISO, ASTM API, JIS ABNT, CIR**, etc.



Focussed on maximum customer orientation promptness and reliability are the main attributes of the manner of functioning of DIFK Gmbh since more than 25 years. The experienced and consequently trained staff works together with best possible equipment of a modern laboratory. The consulting of the international customers for productive selection of the most suitable measuring methods is the focus of dialog to retain customer satisfaction.

Head of Laboratory: **Dr.-Ing. Thomas Deinet**

📍 Rheinstr. 58
56203 Höhr-Grenzhausen
Germany

✉ info@difk.de

📞 +49 2624 94 33 200

🌐 www.difk.de

---

## Deutsches Institut für Feuerfest und Keramik GmbH

Deutsches Institut für Feuerfest und Keramik GmbH



**DIFK Deutsches Institut für Feuerfest und Keramik GmbH** is an independent and international operating test laboratory for testing of refractory raw materials, refractory products like bricks, castables, insulating materials and functional parts and in the case of damage the testing of refractory systems.





**Standardized Testing**

**Technical Advice**

**Customer Solutions**

**International Services**

# WHAT IF WE DID NOT HAVE TO DRY TROUGH AND RUNNERS CASTABLES ANYMORE?

Heloisa D. Orsolini; Eric Y Sako; Douglas F. Galesi; Bianca M. G. Silva, Wiliam Alves

Shinagawa Refratários do Brasil, Vinhedo, Brazil

**ABSTRACT**

The constant increase in demand has imposed to the steel industry an intense search for high productivity. Following this trend, the use of monolithic refractories is growing significantly, allowing shorter installation times and consequently greater availability of equipment. The main disadvantage of this class of material is the need for long drying times during its application. In this work, an entirely novel binder system for monolithic refractories is proposed, aiming at the reduction and potential elimination of the drying step during trough and runners repairs. For this purpose, this binder system was evaluated in an $Al_2O_3$-SiC-C castable and compared with the two most used commercial binders: calcium aluminate cement and colloidal silica. The results showed that this system successfully produced a permeable gel-like microstructure, which led to an excellent drying behavior, even in the most aggressive heating conditions, without damaging the product's mechanical, oxidation and corrosion resistance. In the field, runners have already operated successfully using the new binder without any drying step, maintaining their performance with the benefit of a drastic reduction in repair time. Such positive results highlighted that the use of such exclusive binder could lead to the avoidance of up to 500 tons of $CO_2$ emitted into the atmosphere annually per blast furnace.

## INTRODUCTION

The global scenario is challenging for steel producers. The low quality of raw materials, as well as the need for low coke rate and the search for green steel and high competitiveness have increased the stress and pressure for productivity and stability. Therefore, there is a search and incentive to develop products that facilitate and eliminate production steps that bring risks, uncertainties and increase manufacturing stresses.

In this trend, Shinagawa Brasil has developed a new line of monolithic products for trough and runners that do not require drying: the BestDrying[TR] refractories. The working lining refractories in this equipment, which are in direct contact with the pig iron and slag, are traditionally monolithic materials as they allow a fast installation rate, ensuring shorter repair times and consequently higher productivity for the blast furnaces. One of the main issues when it comes to monolithic materials is the drying time required during their application. This is a determining factor in the choice of the binder used for these materials. Historically, the most used binder for monolithic refractories is calcium aluminate cement (CAC), due to its elevated green mechanical properties, suitable cost-benefit, and high chemical stability when in contact with molten metal and slag. The increase in temperature during refractories operation results in morphological and volume changes of the unit cell of the hydrated phases generated during reaction of the hydraulic cements.[1] These changes are caused by the gradual loss of water molecules generating embrittlement of the microstructure and increased internal stresses (vapor pressure). If the generated pressure exceeds the material's mechanical strength, a serious damage on the just-installed material occurs, leading to loss of the refractory integrity, risks of explosion and accidents involving operators and a large financial loss. To minimize these risks, the refractory industry has been using long heating curves for the castable dry-out, so that the dehydration of the cement can gradually take place. When large volumes of castable are applied (general repairs) the required drying time reaches several hours, accounting for approximately 30% of the total trough and runners repair time. In general, such drying stages are carried out using natural gas burners, which results in a significant consumption of this fossil fuel and, consequently, in the emission of greenhouse gas impacting on the carbon footprint of the final steel.

As an alternative to cement and its inherent drying issues, another type of binder widely used for refractory castables is colloidal silica (CS). Whereas hydraulic cements provide castables with mechanical green strength via the formation of crystalline hydrates, colloidal silica fulfills this role by forming a 3D network of permeable structure, which guarantees a much easier drying step, with less risk of explosion [2]. However, the presence of silica in most commercially applied refractories causes the generation of a low viscosity glassy phase resulting in reduced refractoriness and low resistance to chemical attack. Moreover, the use of colloidal silica as binder also generates a castable with challenging workability, due to the instability of the colloidal suspension, besides requiring additional transportation costs.

Therefore, the objective of this study was to develop an innovative and high-performance line of products (BestDrying[TR]) which is easy to dry without bringing along the drawbacks related to the increased silica content. By the introduction of such novel technology in the market, a significant reduction on the drying curves, and consequently on the natural gas consumption, is expected during the casting house repair procedures, leading not only to a higher trough availability, but also to lower $CO_2$ emission rates, increased productivity, operational stability, and safety.

## MATERIALS AND METHODS

To fulfil the objectives proposed in this work, a standard formulation of through and runners castable ($Al2O3$-SiC-C) was used as the reference for the comparative evaluation of the new proposed system (BestDrying[TR]) with the two most traditional binder systems: calcium aluminate cement (CAC) and colloidal silica (CS), as highlighted in Table 1. The amount of colloidal silica used was selected to ensure similar levels of flowability for all castables in the study.

Tab. 1: Formulation of the materials evaluated in this work containing three different binders: calcium aluminate cement (CAC), colloidal silica (CS) and the newly developed BestDrying[TR].

| Raw Material (%wt) | Calcium Aluminate Cement (CAC) | Colloidal Silica (CS) | BestDrying[TR] |
|---|---|---|---|
| Alumina | 56 | 56 | 56 |
| Silicon Carbide | 25 | 25 | 25 |
| Carbon sources | 3 | 3 | 3 |
| CAC 70% $Al_2O_3$ | 2 | - | - |
| CS 40% solids | - | 10 | - |
| BestDrying[TR] system | - | - | 2 |
| Others | 14 | 14 | 14 |

The material's workability was determined by two different measurements: the flowability after mixing and the setting time at 60°C. These two tests are very important as they directly influence the final quality of the samples, as well as the applicability and performance of the refractory at field. The flowability directly influences the material's ability to flow and occupy all cavities and spaces of the region where it will be applied. The setting time determines how much time is required for the material to completely harden and to develop enough mechanical strength to allow the mold to be withdrawn. These properties present crucial importance during the through and runners repair, as they affect the final quality of the working lining, mainly its surface finishing and porosity. The flow values were obtained according to the NBR 13320 standard, where the castable is poured into a mold with well-defined diameter and the flowability is measured after removing the

mold and vibrating the material, comparing the original and the final diameters. For this test, the castable was obtained using a planetary mixer by performing the processing step according to an internal mixing procedure. The same procedure was used to produce samples for permeability, cold crushing strength and fast drying tests.

For permeability measurements, disc-shaped samples measuring approximately 5,7 cm in diameter and 2,1 cm in thickness were tested in an experimental apparatus for permeability using ambient air as the fluid. Tests were performed on three samples of each composition and two tests were performed on each sample. The Darcian permeability or viscous constant ($k_1$) was obtained using the Forchheimer's equation. [3]

To analyze the microstructure formed during the curing step of the proposed new binder system, scanning electron microscopy (SEM) evaluation was performed on polished and gold-coated cubic specimens (2 cm) of the castable after molding and curing at room temperature.

The cold compressive strength was measured according to the NBR 11222 standard. Prismatic samples (160mm x 40mm x 40mm) were casted and after 24 hours curing at ambient temperature, the samples were dried at 110°C and fired at 1450°C at reducing atmosphere, cooled down and tested.

For the fast-drying test at lab scales, 100mm x 100mm cylinders were prepared and cured for either at room temperature for 24h or at 60°C for 3h or 6h and immediately exposed to a temperature of 1000°C for 30 minutes. For the industrial scale test a 500mm x 600mm x 700mm block was molded, cured for 24 hours at room temperature, and directly inserted into a gas burner oven programmed to reach 400°C in a very short time (2h30min). For both lab and industrial tests, a visual inspection was carried out in the samples to check the presence of any damages generated during the fast-drying procedure, such as cracks, chipping, and/or explosion. Only the formulations with no issues during the laboratory test were tested on an industrial scale.

The castable containing the novel binder system was also installed in some casting houses in a Brazilian steel mill to run pilot trials and confirm the results attained at lab scale. The initial field tests were performed in three stages. The first stage consisted of a 50% reduction of the traditional drying curve used in the runners after repair, while in the second stage a 75% shorter curve was performed, finally, the last step consisted of eliminating the drying curve.

## RESULTS
### Laboratory and industrial scale results

Table 2 presents the water (or colloidal silica) content, the flow values, and the setting time at 60°C for the three evaluated formulations. Calcium aluminate cement-bonded castables, in general, present good workability, with very suitable flowability (165 mm) and setting time (100 min). The colloidal silica-bonded castable, as expected, showed an unstable behavior, with flow rate of 154 mm and setting time of 45 min, even using 10% of colloidal silica which provides a residual water content of 6%. The material bonded by the new BestDrying[TR] system showed very similar characteristics to the reference CAC castable, pointing out that this new solution would not bring any issues during the material installation at field.

Tab. 2: Water and Colloidal Silica Content, Flowability and Setting Time at 60°C for CAC, CS and BestDrying[TR] castables.

| Material | Water / Colloidal Sílica Content (%) | Flowability (mm) | Setting Time - 60°C (min) |
|---|---|---|---|
| CAC | 5,6 | 165 | 100 |
| CS | 10 | 154 | 45 |
| BestDrying[TR] | 5,6 | 165 | 110 |

CAC and BestDrying[TR] castables were prepared using water, while CS were prepared using 40%-solids colloidal silica.

The presence of hydrated crystalline phases in the CAC-bonded formulation resulted in very low permeability over the entire temperature range (110-400°C), with a permeability constant ($k_1$) always equal to or less than $0,1.10^{-14}$ (Figure 2). As also expected, and previously reported [2], the permeability results illustrate the benefits of colloidal silica, which helps to generate a more permeable structure when compared to CAC. However, although representing the state-of-the art technology, the $k_1$ values of the CS material was still not as high as the one attained by the very special structure formed by the BestDrying[TR] bonding system, which resulted in a castable with extreme levels of permeability, showing a $k_1$ constant up to two orders of magnitude greater than the CAC formulation.
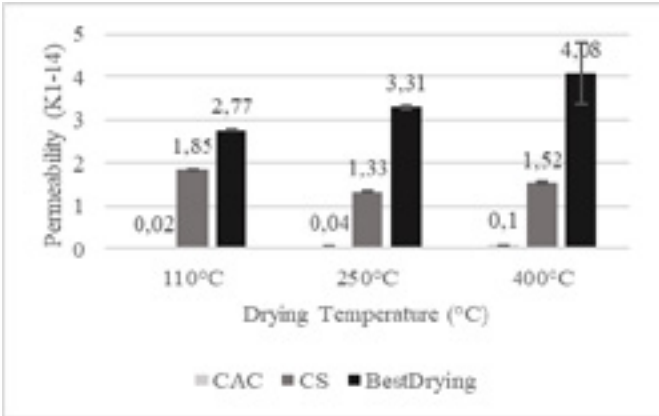


*Fig. 1: Permeability test comparing the permeability constant k1 of CAC, CS and BestDrying[TR] binders treated at different temperatures (110°C, 250°C and 400°C).*

To better understand the differences in the microstructural evolution of CAC and BestDrying[TR] during the castable curing step, scanning electron microscopy (SEM) analyses were conducted with samples of both formulations (Figure 2). For the CAC composition (Figure 2.a), it is possible to observe the presence of countless needled crystals, resulting from the CAC hydration process and responsible for providing green mechanical strength to the sample. Numerous hydrated phases can be formed during the hydration of CAC ($CAH_{10}+AH_3$(gel), $C_2AH_8+AH_3$(gel/crystal), $C_3AH_6+AH_3$(crystal)), and their formation tendency is dependent on the time, temperature, and water content present in the medium. [4] When observing the microstructure of the BestDrying[TR] - bonded castable (2.b)), it is possible to notice a completely different structure, where an interconnected gel structure is formed throughout the material, with the absence of needle-like crystalline phases. This difference presents a direct impact on the permeability results presented above for the two materials.
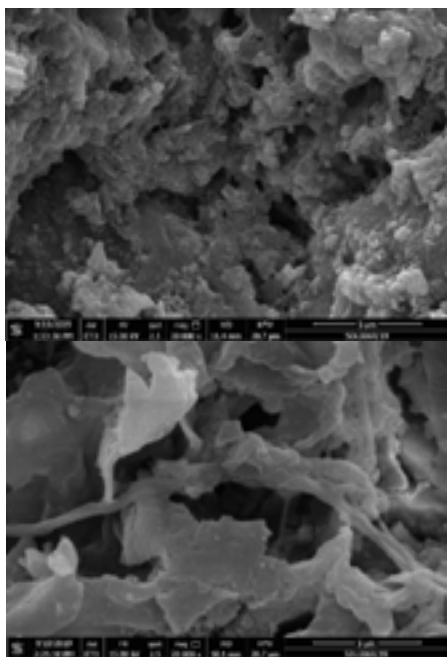
*Fig. 2: Scanning electron microscopy of the formulation bonded by a) CAC, showing the presence of several needled phases, resulting from the cement hydration process; and b) BestDrying^{TR}, with the formation of a gel structure that permeates the entire sample and the absence of crystalline hydrates.*

Although it is not a direct demand during use, the mechanical strength is an important parameter for trough and runner materials, as it determines, together with permeability, the drying resistance of the material. Usually when increasing the permeability of a refractory, the mechanical strength is lost, resulting in poor resistance to drying and making the development of a fast-dry material a very tough task. However, that issue was successfully overcome for the new proposed binder (Fig. 3.), as it was able to show proper mechanical strength both after drying (110°C) and firing (1450°C), with values close to those presented by the standard CAC-bonded formulation. The samples prepared with colloidal silica also presented high CCS values, but that was associated with the use of higher amount of binder required for an adequate flowability. As permeability is a property directly related to porosity, it is natural that the system with greater permeability presents greater porosity, however, the BestDrying^{TR} system was carefully developed so its greater porosity did not affect its performance in the field, as will be seen below.
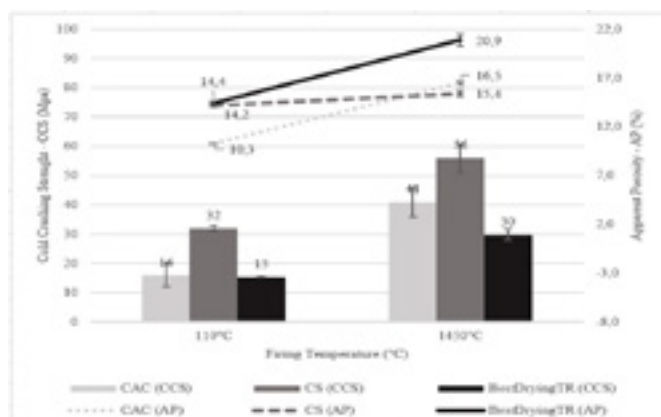


*Fig. 3: Cold Crushing Strength (MPa) and Apparent Porosity (AP) of the castables bonded with CAC, CS and BestDrying^{TR} after dried at 110°C and fired at 1450°C.*

The drying resistance, as mentioned above, is a result of the combination of permeability and mechanical strength. If the water

vapor is not properly released in a non-permeable structure and generates a high internal pressure which overcomes the material's mechanical resistance, it will not resist and will fail during the drying step. Therefore, an efficient fast-drying material should present high permeability, which will facilitate water vapor release, and high mechanical strength so that the internal pressure will always be lower than the castable's bonding structure.

As can be observed in Table 4, the CAC-bonded castable presents good mechanical strength, but poor permeability resulting in a material with difficulty in drying, which failed catastrophically and exploded during the tests. The CS castable, despite showing higher permeability than the CAC one, still did not present enough combination of properties and it was also damaged during the critical drying test. As a result of the very high permeability and adequate mechanical strength, the BestDrying^{TR} material did not present any external or internal damage after the fast-drying test.

Tab. 3: Fast-drying tests results presented by the castable bonded by CAC, CS and BestDrying^{TR} after curing at room temperature for 24 hours and then exposed to 1000°C for 30 minutes. Only the BestDrying^{TR}-bonded material resisted.

| Time | CAC | CS | BestDrying^{TR} |
|---|---|---|---|
| 24 hours of curing |  |  |  |
| | Severely damaged | Damaged | No damage |

After successfully going through all the validation steps in the lab scale, an industrial test was performed for the BestDrying^{TR} formulation using a 500 mm x 600 mm x 700 mm block, in order to evaluate if the drying resistance of the material could be affected by any volume effect. The block passed the industrial fast-drying test again without presenting any damage in its structure, as shown in Fig. 4, indicating that the BestDrying^{TR} binder system proved to be extremely resistant to quick drying procedures, regardless the material volume.



*Fig.4. Industrial scale block of approximately half a ton prepared with BestDrying^{TR} bonded castable after fast drying test.*

Regarding the main properties for trough and runners' materials at high temperatures, such as the oxidation and corrosion resistances, the BestDrying^{TR} bonded castable also showed excellent results. Fig. 5 depicts the oxidation and corrosion behavior of the three evaluated formulations, where one can note that the engineered microstructure developed by the new binder during curing guarantees a low oxidation rate and low corrosion rate, even with high porosity values, which will allow it to keep good performance during use.

177
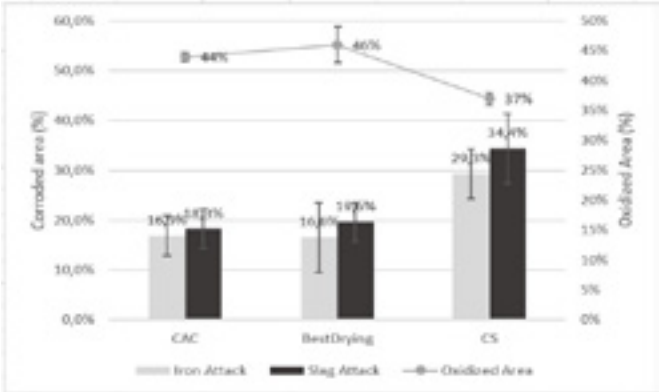
*Fig. 5. Corrosion and Oxidation tests results of the evaluated formulations. Note the similar performance of CAC and BestDrying[TR] materials and lower performance of the CS one, mainly in contact with slag.*

**Field Tests**

Castables from the BestDrying[TR] portfolio has been successfully applied in different steel houses around Brazil, with approved results in the following general scenarios:

Tab. 3: General scenarios of field tests using BestDrying[TR] refractories in Brazil.

| Trough and Runners | Drying Curve Applied | Drying Evaluation | Campaign Performance (In terms of specific consumption) |
|---|---|---|---|
| Slag Runner | 0% (eliminated) | Successful | Successful |
| Pig Iron Runner | 0% (eliminated) | Successful | Successful |
| Main Trough | 50% | Successful | Successful |
| Entire Casting House (including skimmer, tilting runner…) | 50% | Successful | Ongoing campaign |

In all the tests carried out, the BestDrying[TR] refractories did not show any anomalies during the drying stage, as well as at the start of operation. During the inspections, the materials showed standard wear, without any point of attention. At the end of the campaign, in all the equipment tested, the BestDrying[TR] refractories showed wear levels compatible with standard cement-bonded refractory, allowing the maintenance of the specific consumption standards already practiced.

The excellent results collected in the field, as shown in Tab.3, allowed to proceed the next steps, which includes running the casting house after eliminating the drying curve of both the main trough and the secondary runners. In addition, it was possible to calculate the benefits of customers by eliminating the necessity of drying trough and runners in their plants. In a two-main trough blast furnace with a daily production of 7500 tons in which the productivity must be reduced by 10% during the repair period (tap-to-tap operation in only one main trough), 7000 tons of pig iron could be recovered, with a financial return of $700,000, the non-use of 51.520 Nm³ of natural gas and the non-emission of 100.000 tons of $CO_2$ into the atmosphere per blast furnace during a full campaign.

**CONCLUSIONS**

Motivated by the urgent need to increase equipment availability, reduce risk and stress in the casting house, this work aimed to characterize and analyze in the field the new line of monolithic refractories without drying developed by Shinagawa. That was possible by obtaining a binder system with an open microstructure

and without crystalline hydrate that produces a refractory with high permeability and easy water removal. In addition, the novel technology also maintained good workability, mechanical strength, resistance to oxidation and corrosion. In the field, BestDrying[TR] products are adding up achievements, with slag and pig iron runners operating without any drying and the main troughs already reaching 50% reduction of the drying curve, while maintaining the specific consumption level presented by the line material. Eliminating drying in the main trough is the next step, and the sky as the limit.

**REFERENCES**
[1] Lee WE, Vieira W, Zhang S, Ghanbari Ahari K, Sarpoolaky ndH, Parr C. Castable refractory concretes. International Materials Reviews 46 (3), 2001, p. 145-167.
[2] Ismael MR, Salomão R, Pandolfelli VC. Refractory Castables Based on colloidal silica and hydratable alumina. American Ceramic Society Bulletin 86(9), 2007, p. 58-62.
[3] Innocentini MDM, Pandolfelli VC. Issues concerning the evaluation of permeability in refractory concretes with Darcy and Forchheimer equations. Cerâmica. 45 (292), 1999, p. 61-67.
[4] Garcia JR, Oliveira IR, Pandolfelli VC. Hidration process and the mechanisms of retarding and accelerating the setting time of calcium aluminate cement. Cerâmica. 53, 2007, p. 42-55.

# ONLINE DRYING MONITORING SYSTEM FOR REFRACTORY CASTBLES

Thekla Stein, Olaf Krause
University of Applied Sciences, Höhr-Grenzhausen, Germany

Wolfgang Taute, Michael Höft
Kiel University, Kiel, Germany

## ABSTRACT

The careful drying of refractory castable is a crucial step before the final implementation in the industrial process. If not executed correctly it can lead to spalling and even to the destruction of the material and the surrounding installation. Due to the challenging temperature level (up to 600 °C) and the marginal water amount in the material, there is no electronic sensor online monitoring system available yet to control the progression of the drying process in situ. Thus, the drying procedure is based on empirical values only.

Microwave resonators are commonly used to detect moisture in the temperature range from 20 °C to 130 °C in various industrial fields. A new design designated to withstand the temperature range up to 600 °C was developed by Kiel University. A first series of tests was performed at the University of Applied Sciences in Koblenz to understand the system's capabilities and limits in detecting water in castable material during the drying process. It was expected that during heating the evaporation of water and the dehydration of the hydrate phases within the material will influence the resonating frequency and result in a widening of the frequency bandwidth. Simultaneously with the changes in the microwave field the weight loss of the material was monitored. By linking the new approach of observing the resonating frequency with the weight loss as a well understood indicator [1] for the drying progress, the suitability of a microwave resonator as a drying monitoring system for refractory castables will be validated.

## INTRODUCTION

In refractory applications, the physical and the chemical bonded water in the castable needs to be removed prior to the first use. If it is not carefully removed, the developing vapor phase in the pores and the related pressure build up can exceed the material strength. In this case the material disintegrates, and the dreaded spalling occurs [2].

The physical bonded water contained in the pores of a refractory castable is removed in a temperature range up to 200°C. The water chemically bonded in cement hydrates phases is released in a temperature range from 200 °C to 600 °C [3]. Thus, the available commercial systems to monitor the drying progress are not suitable for refractory materials and the harsh environment in the applicating industry.

In various industries like food, paper and concrete, microwave resonators are a commonly used method to measure the humidity [4, 5]. Due to the long experience with such resonators, they provide reliable data about the humidity in real-time and they have proven to detect small changes in humidity independent on the density of the material [6]. Most commercially available systems are designed for an application temperature close to the evaporation of water (max. 130 °C) under atmospheric pressure. An application for higher temperature is not commercially available.

To develop a microwave sensor capable to measure at high temperatures would close a monitoring gap in the industrial process control. The application temperature of the existing microwave resonators is limited by the heat resistance of the solder joints and the delicate electrical parts like cables and other electronic components which are necessary for the proper functioning of the sensor.

Another challenge for the measurement in a high temperature environment is that all electrical properties are temperature dependent. Thus, temperature will influence the measurement result and a distinction between wanted measurement and inevitable temperature effect is necessary. Hauschild et al. [7] measured the complex permittivity at 1000 °C of solid materials. The knowledge about the material's complex permittivity at higher temperature is necessary to distinguish the thermal influences on the material properties from those of the decreasing humidity and dehydration of castables. Prior to this study this is still unknown for castables and a blank reading needs be performed to differentiate between the thermal influences on the material and the change in water content. In case the developed microwave resonator proves to be valid, the missing data can be generated by performing a relevant amount of test series.

When successfully developed a microwave resonator suitable for high temperature has a major potential of saving energy and time in the industrial castable application processes (for example steel production) and the enhancement in safety for the workers.

## METHOD

In an electrical field water molecules will orientate according to the field polarisation, due to the dipole molecule structure. The necessary energy for the reorientation of the water molecules is taken from the electromagnetic field energy. Simultaneously the propagation speed of an electromagnetic wave is reduced. Dielectric solid materials also influence the propagation speed and the field energy [8]. Depending on the construction of the electromagnetic field excitation, the penetrated material and the chosen frequency, the electrical field forms resonances. Resonances are highly sensitive to changes in material humidity due to the ongoing field penetration [9]. The resonator is operated in transmission mode, i.e. the resonator is coupled in series to two coaxial ports [10]. The resonance frequency and its bandwidth can be determined by the frequency sweep of the scattering parameter S21 [10] and will change depending on the humidity in the material. The S21 value is the transmission coefficient between port 1 and 2 of the used VNA (Vector network analyser) [10]. In case the dielectric properties are known and well understood, the change in propagation speed and field energy and their impact on the resonances can be used to determine the humidity of a material.

For this work a microwave resonator was constructed by Kiel University. The resonator head is completely made of brass and can withstand temperatures up to 700 °C. The resonator head is attached to two long coaxial brass tubes for an inductive coupling arrangement of the two port measurements. The sensitive electrical cables need to have enough distance to the heating source to avoid a thermal decomposing of this sensitive parts. The operating frequency range is 0.6 GHz to 1.6 GHz. The dimension of the sample and the constructed resonator are specifically designed to form resonance in the investigated material, thus the dimensions and the distance between resonator and sample must be maintained to achieve reproducible results. The resonances are evaluated by a Lorentz curve fitting [11].

To identify the thermal impact on the resonator during the heat-up, the resonator measurement method must be based on a blank measurement (measurement without sample). For the presented system this cannot be achieved in the usual way. The material parameters (i.e. its dielectric properties) and the temperature dependence of the same are not sufficiently known. Thus, the drying (release of physical bond pore water) and dehydration (decomposing of hydrate phases) cannot be distinguished from the impact which the thermal influence are having on the material and likewise on the test station and in consequence on the results. To overcome that lack of knowledge every sample is heated up twice.

179

During the first heat-up, the drying and the dehydration occurs. In the second heat up, the sample is already free of water and all changes in the detected signals can be linked to thermal influences either on the material or the testing station.

The base of the testing station is a scale to measure the weight change during the experiment. On top of the scale a heating plate is located, that can achieve a maximum temperature of 600 °C and initiates the drying and dehydration of the castable. A metal container (tube closed on one side by a welded-on plate) is placed on the heating plate. Inside this metal container the castable sample is centrally positioned. The inductive coupling arrangement for the excitation of the microwave resonator is located above but without direct contact to the sample and emits a microwave field in the sample (Fig. 1).
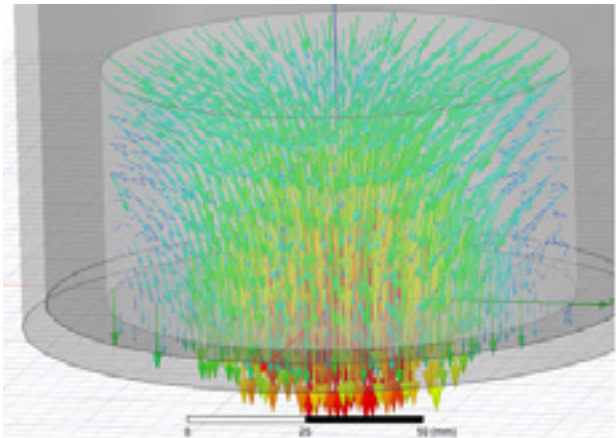


*Fig. 1: Microwave field simulation for the resonating frequencies 0,99 GHz. The light grey cylindric shape represents the castable sample. The partially shown cylindric shapes represent the surrounding metal container. The coloured lines indicate the electric field of this eigenmode.*

During the measurement the weight loss of the sample is detected by the scale, the VNA (Vector network analyser) is determining the parameters of the microwave field. The temperature is not measured in the sample, because a thermocouple would strongly disturb the microwave field. Thus, the temperature is measured at the heating plate surface.

**EXPERIMENTAL PROCEDURE**

**Sample treatment**

The investigated material (Tab. 2) was mixed in a compulsory mixer and casted into cylindric shape (diameter 100 mm and height 50 mm). For the preliminary tests the castable represented in Tab. 2 was used. The treatment of the samples was altered for the preliminary test series. All samples were stored in a climatic chamber at 20 °C and 95 % humidity for 48 hours, to ensure stable conditions and a stable hydrate phase growth after mixing. Thereafter they were divided in two groups (Tab 1).

*Tab. 1. Sample treatment for preliminary test series*

| Sample nomenclature | Climatic chamber 20 °C and 95 % humidity | Drying chamber 110 °C |
|---|---|---|
| Sample A | 48 h | 24 h |
| Sample B | 48 h | - |

Sample A one did not receive a further treatment prior the drying test. Sample B was stored for 24 h in a drying chamber at 110 °C to remove the pore water before testing. The heating rate generated by the heating plate for all tests was 60 K/h. For all samples the heat treatment was performed twice in succession. The first heat-up

resulted in the sample's drying and dehydration. The second heat-up was used as a blank reading to eliminate the thermal influences on the measured results.

*Tab. 2: Castable recipe*

| Component | Addition wt % |
|---|---|
| Tabular Alumina 0 – 3 mm | 78 |
| Calcined Alumina | 10 |
| Reactive Alumina | 7 |
| CA-Cement | 5 |
| Dispersant | 0.15 |
| Water / % | 5.20 |

**Determination of the suitable resonance**

Before performing investigation the refractory castable the suitability of the resonance must be evaluated. Two samples were prepared and tested (see Sample treatment). The pore water in sample A was dried out at 110 °C. In sample B the pore water and the hydrate bond water remained. The heating rate was set at 60 K/h with a dwell time of 3 hours. In Fig. 2 the results for sample A are represented. The S21 value is shown vs. the frequency. The frequency sweep covers the range from 0.6 GHz to 1.6 GHz.
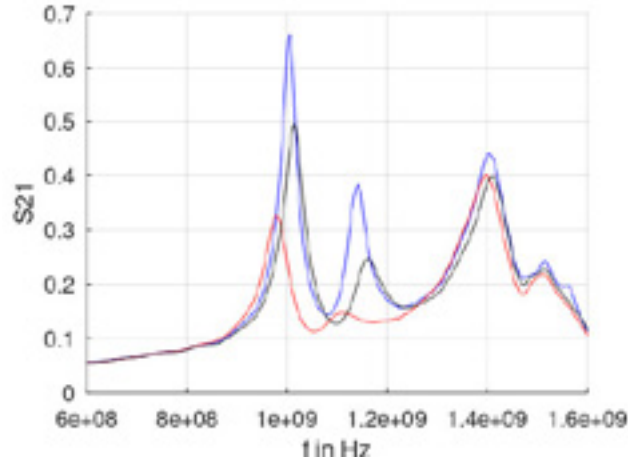


*Fig. 2: Results for sample A cured 48 h at 20 °C and 24 h at 110 °C. The measurement of S21 value of the frequency band over the frequency sweep is shown in the diagram. The pore water was dried out at 110 °C. The dehydration was performed in the test station. The red curve represents the resonance frequencies for the hydrated sample. The black curve represents the signal in the middle of the heat treatment. The blue curve represents the dehydrated sample after the completed heat treatment.*

The three different curves represent three different drying states of the sample. The red curve shows the results for the sample at the beginning of the heat treatment. The chemical bonded water in the hydrate phases is still intact. The black curve represents the middle of the heat treatment, and the blue curve represents the status for the dehydrated sample after the heat treatment. For three frequencies a resonance is formed, at 0.99 GHz, at 1.15 GHz and at 1.4 GHz each recognizable as peaks for the S21 value.

In Fig. 3 the results for sample B are represented. The S21 value is shown vs. the frequency. Again, the frequency sweep covers the range from 0.6 GHz to 1.6 GHz. The three different curves represent three different drying states of the sample. The red curve shows the results for the sample at the beginning of the heat treatment. The physical bonded pore water and the chemical bonded water in the hydrate phases are still present. The black curve represents the middle of the heat treatment, and the blue curve represents the status for the dehydrated sample after the heat treatment. Resonances are formed at 0.99 GHz, at 1.15 GHz and at 1.4 GHz each recognizable as peaks for the S21 value for the black

and the blue curve. The red curve only shows a resonance at 1.4 GHz. The development of the red curve does not show the resonances at 1.15 GHz and 0.99 GHz.
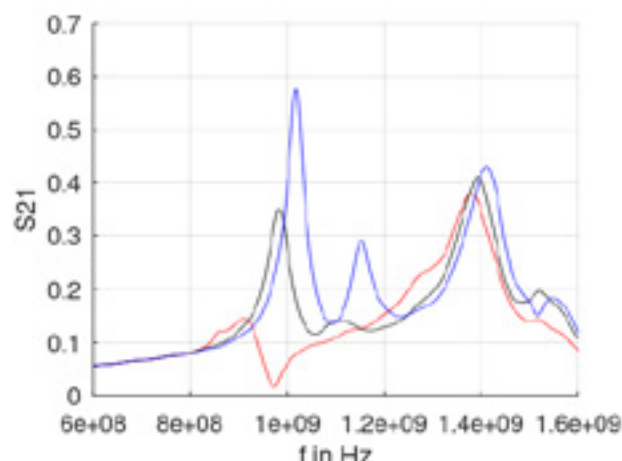


*Fig. 3: Results for sample B cured 48 h at 20 °C. S21 value of the frequency band over the frequency sweep. The pore water and the hydrate phases were intact at the beginning of measurement and the related heat treatment. The red curve shows the first signal of the sample with intact pore water and hydrates phases. The black curve shows the middle of the heat treatment. The blue curve shows the sample after the heat treatment was completed.*

**Conclusion about suitable resonance for further test series**

For sample A and sample B the resonance at 1.4 GHz does not show significant changes in dependence of the humidity and cannot be used to determine the drying or the dehydration of the castable. The resonance at 1.15 GHz shows for sample A and sample B a drastic change depending on the humidity. The bandwidth of the red curve for the untreated sample A is too broad for a curve fitting evaluation and the peak of the resonance is shifting strongly. For sample B in the completely undried status the resonance is not visible in the curve. Thus, this resonance is not suitable for further investigations.

For sample A the resonance 0.99 GHz is suitable for a Lorentz curve fitting. Sample B in an undried status is not suitable for a Lorentz curve fitting at this frequency. With enhancing drying progress, the resonance at 0.99 GHz for sample B becomes more defined and suitable for a curve fitting.

The main difference between sample A and B is the physical bonded porewater. The sample B contains primarily physical pore water and a relatively small amount of chemical bonded water in the hydrate phases. The influence of pore water on the microwave resonator is too dominant for the chosen design and frequency span for a suitable evaluation. This leads to the conclusion that the resonance at 0.99 GHz cannot monitor the pore water dry-out completely, due to the high amount of water at the beginning of the drying process. The preliminary tests show that dehydration of a castable in the presented test station can be determined with a sufficient accuracy at the frequency 0.99 GHz.

Thus, the frequency 0.99 GHz will be used for the further investigation of dehydration progress in the castable material.

**RESULTS FOR DRYING MONITORING OF A CASTABLE**

After identifying the suitable resonance for the new testing station, a series of tests was performed to investigate the drying progress in castables. The samples were prepared and treated as described in the chapter, Sample treatment. The investigated material was mixed according to the recipe shown in Tab. 2. Before the testing procedure the sample was stored in a climatic chamber at 20 °C for 48 h and in a drying chamber at 110 °C for 24 h. The heating rate in the testing station was set at 60 K/h until it reached a maximum of 600 °C. The maximum temperature was maintained for 3 h,

followed by a passive cooling phase. Due to the complex data the common link between the parameters are the measurements points (N) (0 to 10,000 for a complete heat-up session). Thus, all the represented results show the measurement points at the x-axis.
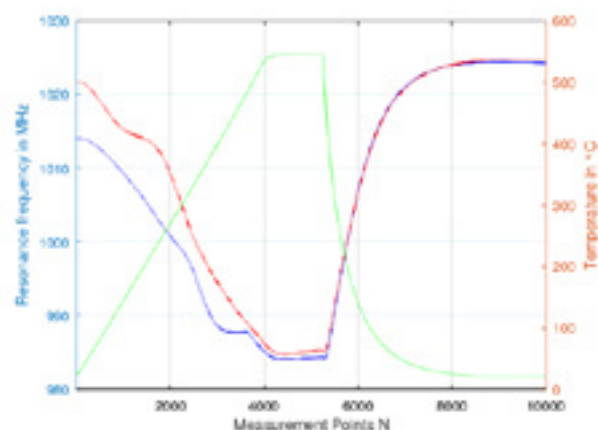


*Fig. 4: Resonance frequency for the consecutive heat-ups vs. measurement points. The blue line represents the first heat-up. The red line represents the second heat-up. The green graph indicates the temperature development during both measurements.*

In Fig. 4 the resonance frequency is presented at the left y-axis and the temperature of the heating plate at the right y-axis. The blue graph represents the resonance frequency for the first heat up. The red graph represents the second heat up of the castable sample. The green line indicates the temperature development during the measurement. The data is linked to the number of measurement points. The different parameters are saved by different devices and the link over the measurement points is the most suitable one for the used evaluation software. The temperature increases till the measurement point 4000. From there on it remains stable at 550 °C till measurement point 4600. Due to the passive cooling the temperature drops rapidly and reaches room temperature at measurement point 8000. During the heating the resonance frequency drops for the first and the second heat-up. During the dwell time the resonance frequency shows a continuous development. As soon as the heating plate is turned off and the cooling starts, the resonance frequency rises in reverse proportion to the temperature.
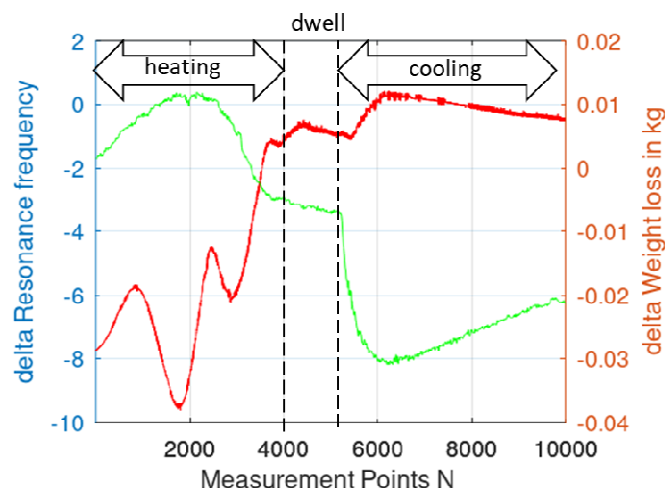


*Fig. 5: The red curves represent the delta from the resonance frequency form Fig. 4. In green the weight loss due to the water transport out of the sample is presented. The x-axis shows the measurement points for the test. The heating, dwell and cooling phase is indicated in the diagram.*

Fig. 5 shows the delta of the resonance frequencies between first and second heat-up presented in Fig. 4 and the weight loss of the

181

sample during the heat up. The measurement points on the x-axis are identical to Fig. 4. The heating, dwell and cooling phase are indicated in the diagram. During the heating phase the delta of the resonance frequencies increases with a drop in the signal at measurement point 1900 (the related temperature is approximately 220 °C). The weight loss curve shows an increase in weight at the beginning of the heating phase and a decreasing weight from measurement point 2100 on. During the dwell time the delta resonance frequencies rises at first and has a more linear development afterwards, likewise the weight loss. As soon the heating is turned off and the passive cooling is initiated the delta resonance frequencies increases in invers proportional to the weight loss till measurement point 6000. From there on both develop linear.

## DISCUSSION

By linking the delta resonance frequency with the weight loss, the castable dehydration is monitored with two systems and leads to evaluable results (Fig. 5). The apparent sample weight increases at the beginning of the heating phase. The convection flow around the scale is most likely responsible for this effect and a constant weight loss at the beginning of the measurement can be assumed. Shortly before reaching the maximum applied temperature the progression of the weight loss curve shows an inflection point and the weight loss progresses much slower afterwards. The difference in weight loss progress can be interpreted as a twostep dehydration process. Because the temperature is only measured at the surface of the heating plate the values cannot be linked to the temperature in the material. Thus, a specific identification of the different dehydrations processes and the decomposition of the related hydrate-phases is not possible. Also, the heating plate temperature is set at 600 °C, but the thermocouple only measures a maximum temperature of 500 °C. Therefore, it would be necessary to improve the thermal insulation of the test station.

The delta resonance frequencies show minima at the measurement point 1900 (220 °C) and at 3000 (400 °C). The change in the resonance frequencies can be interpreted as an increase in the amount of water molecules that interfere with the electromagnetic field. The increase in water molecules occurs because the decomposing of the hydrate phases releases water inside the material. The weight loss decreases in a linear way till measurement point 3800 (500 °C) Thus the weight loss is not directly linked to the decomposing of the hydrates phase. The time needed to transport the water from the sample inside to the surface is way dependant. Thus, the weight loss decrease is delayed compared to the decomposing of the hydrate phases indicated by the delta resonance frequencies. At the beginning of the cooling phase, the apparent weight drops dramatically. This effect is related to the collapse of the convection flow around the scale. The cooling also effects the resonance frequency. This needs to be evaluated by further experiment.

## CONCLUSIONS

For the newly developed testing station the resonance at 0.99 GHz has proven to be suitable for the monitoring of the dehydration of castables. The drying of physical bond water cannot be monitored because the high amount of pore water influences the resonance frequency too strongly for a valid interpretation. Thus, the sample needs to be treated at 110 °C before the measurement in the testing station.

To minimise the thermal influences on the measured signal the sample was heated up twice consecutively and the delta of the two measurements was calculated. Both resonance frequencies in Fig. 4 are strongly influenced by the temperature change. The delta resonance frequency in Fig. 5 does not show this influence and the assumption, that the thermal influence on the results can be eliminated by consecutive heat up is proven correct.

The resonance frequency is also affected by cooling. The cause of that effect needs to be evaluated by further experiments. Also, the

knowledge about the dielectric properties of refractory castables during the heat treatment is not sufficient for a final interpretation of the results and needs further investigation.

## OUTLOOK

By looking at the state of art is was expected that the detection of the physical bonded water and the dry-out of the pore water would be possible (already successfully implement for different materials [4,5] till 130 °C). The detection of the chemical bonded water and the decomposing of the hydrate-phases was never monitored before by a microwave resonator and results were unpredictable. The newly develop microwave flied resonator has proven to monitor the decomposing of hydrate-phases. Based on the presented work the next step would be to develop a system that is able to monitor the drying of the physical bonded water likewise the decomposing of the hydrate-phases. Due to the existing knowledge on monitoring physical water till 130 °C the construction of such is within reach.

## REFERENCES

[1] Czechowski, J.; Majchrowicz, I.: "Microwave and conventional treatment of low cement high- alumina castables with different water-to-cement ratio; Part II Dehydration, Ceramic International 44, 2018

[2] Luz, A.P.; Moreira, M.H.; Braulio, M.A.L.; Parr, C.; Pandofelli, V.C.: "Drying behavior of dense refractory ceramic castables. Part 1- General aspects and experimental techniques used to assess water removal"; Ceramic International 47 (2021) 2246-22268

[3] Peng, H.; Myhre, B.: "New insight into dry-out behaviour and explosion resistance of refractory castables", ICR Aachen (2018) 92 – 96

[4] Peters, J.; Taute, W.; Bartscher, K.; Döscher, C.; Höft, M.; Knöchel, R., Breitkreutz, J.: "Design, development and method validation of a novel multi resonance microwave sensor for moisture measurement"; Analytica Chemica Acta 961 (2017) 119 – 127

[5] Tretau, A.; Wagner, R.; Bonitz, F.; Shahri, A.: „Materialspezifische Feuchtebestimmung während der Ziegeltrocknung"; Ziegelindustrie International 5/2020

[6] Knöchel, R.; Taute, W.; Döscher, C.: "Stray field ring resonators and novel trough guide resonator for precise microwave moisture and density measurements"; Meas. Sci. Technol. 18 (2007) 1061 – 1068

[7] Hauschild, T.; Knöchel, R.: "Measurement of complex permittivity of solids up to 1000 °C"; IEEE MTT-S Digest 1996

[8] Fleisch, D.; Kinnaman, L.: "A student's guide to waves", Cambridge University Press, 2015

[9] Peters, J.; Taute, W.; Stern, F.; Döscher, C.; Höft, M.; Knöchel, R., Breitkreuz, J.: "Multi-Resonance Microwave Sensor for Moisture Monitoring: Review and Prospects", 13th International Conference on Electromagnetic Wave Interaction with Water and Moist Substances (ISEMA), Kiel, Germany, 2021, 1-5, doi: 10.1109/ISEMA49699.2021.9508282

[10] Pozar, D. M.: „Microwave Engineering", 4th edition, John Wiley & Sons, New York, USA, 2011

[11] Nimtz, G.: „Mikrowellen: Einführung in Theorie und Anwendung", Pflaum-Verlag, Berlin, 2001

# PERMEABILITY–ENHANCING DRYING ADDITIVES – A PERSPECTIVE FROM *IN–SITU* ANALYSIS

Murilo Henrique Moreira[1], Alessandro Tengattini[2, 3], Stefano Dal Pont[2], Victor Carlos Pandolfelli[1]

[1] Federal University of São Carlos (UFSCar), Materials Engineering Department,
Rod. Washington Luiz, km 235, São Carlos, SP, 13565-905, Brazil.
[2] CNRS, Grenoble INP, 3SR, Université Grenoble Alpes, 38000 Grenoble, France
[3] Institut Laue-Langevin (ILL), 71 Avenue des Martyrs, 38000 Grenoble, France

## ABSTRACT

The drying process of hydraulic bonded refractories represents a crucial bottleneck to the widespread adoption of this significant class of materials. Mitigating the risk of explosive spalling is of paramount importance as it entails extended heating procedures, resulting in substantial $CO_2$ emissions and reduced end-user productivity. To minimize the occurrence of such explosions, two commonly deploying strategies involve the utilization of semi-empirically defined temperature plateaus and the incorporation of permeability-enhancing additives. Among these later, polymeric fibers have emerged as a preferred choice due to their cost-effectiveness and efficacy. Nevertheless, despite the ability to tailor various properties such as fiber melting temperature and melt viscosity, the underlying mechanisms by which these synthetic materials enhance permeability remain not clearly understood. Hence, the present study proposes the use of neutron tomography to provide insights into the influence of these fibers on the drying process. Notably, alterations in the velocity of the drying front and moisture accumulation were quantified. The anticipated outcomes of this investigation encompass advancing fundamental understanding of these mechanisms, providing practical guidelines to optimize the potential of polymeric fibers in averting explosive spalling, thereby inducing safer and faster drying processes for refractory castables.

## INTRODUCTION

Drying is a process in which water is extracted from a partially or completely saturated porous material through various mass transport mechanisms, such as the diffusion of water molecules and capillary pressure driven flow [1]. These phenomena occur due to gradients in pressure, temperature, concentration or a combination thereof, leading to the removal of moisture from the material [1].

This process can even occur at room temperature depending on the environmental relative humidity thanks to the imbalance in the partial pressure of water vapor between the gaseous mixture present within the material's porous structure and the one in its surroundings. An analogous behavior is observed when washed laundry is hanged for drying after washing.

In the context of refractory castables, where quick procedures to reach operational conditions is essential, the intrinsic permeability is low, the structures have significant dimensions, and water is also present as free and combined forms, thermal gradients are frequently employed to control and induce faster water withdrawn [1, 2].

Still, this is the most time-demanding stage within the refractory castables processing route, impacting directly the costs with energy consumption and, most importantly, the production halt of products that involve high temperature processes [3].

The risk of explosive spalling, which refers to the sudden and destructive failure of the refractory castable which arises from the combined effects of pressurized water vapor trapped within the material's pores and thermomechanical stresses [4], is the main reason for the extended time length of the drying stage, as the use of slower heating rates and temperature plateaus prescribed by semi-empirical laws are the most common strategies to ensure safe drying of the lining [1, 2].

As shown by Cunha et al. [5], the aforementioned strategies result in large energy consumption and may actually be an overconservative approach. A distinct line of development on this matter is the study of composition optimization to mitigate the risk of pressurization and, ultimately, explosive spalling [6]. This can be carried out through the incorporation of polymeric fibers into the castable composition, which increases its intrinsic permeability during the heating process.

Much has been theorized about the mechanisms of permeability enhancement of the compositions containing fibers. For instance, Zhang et al. [7] have proposed that the inclusion of polypropylene fibers may induce the formation of microcracks due to thermal expansion differences between the polymer and the castable matrix. On the other hand, Innocentini and colleagues have proposed that the enhancement could arise from the melting of the fibers and their subsequent burning out [8]. However, as highlighted by the recent review by Mohammed [9], the precise manner in which these additives improve the spalling behavior of concrete remains elusive.

This leads to a conundrum: even though synthetic polymers can be meticulously tailored to have properties that fulfill multiple concurrent requirements, a definitive guideline regarding the specific attributes that the optimal drying additive should possess is currently lacking.

The efforts to study this class of additives include: i) permeability measurements [8]; ii) differential scanning calorimetry (DSC) characterization of the fibers' behavior during heating [7]; iii) thermogravimetry analysis (TGA) of the compositions or the additives themselves [1]; iv) explosion tests (TGA performed with high heating rates in equipment designed to withstand extreme conditions) to assess their effectiveness to prevent explosive spalling [1]; and v) electronic micrography analysis after the drying process, which cannot determine which microstructure features were originated during the test, or the cooling, or even in the sample preparation [7].

More recently, Stelzner et al. [11] investigated the moisture transport and reconfiguration (determined by the bonding state of water) in high-performance concrete (HPC) either with or without PP-fibers using X-ray-CT and $^1H$ NMR. Results showed that the samples with the permeability-enhancing additive exhibited a faster drying front. Moreover, the dried zone (DZ) after the heating procedure was 40% longer in the PP-containing sample, and the total moisture content at the samples' bottom increased by approximately 5 vol.% and 2 vol.% for the fiber-free composition and the containing one, respectively, after heating. However, the study did not compare different additives, and the mechanisms behind the increase in permeability were not thoroughly discussed.

Barakat et al. [12] explored the drying process of refractories incorporating polymeric fibers through NMR experiments. It was found that the increased permeability during fiber melting speed-up the water removal and reduced both the drying front temperature and the resulting maximum pressure. However, the results didn't quantify the water distribution or fiber placement. Recently, neutron tomography was used to observe directly the drying of refractory castables providing unequivocal proof of the accumulation of water that occurs at the innermost position of the sample, also known as the "moisture clog phenomenon" [13]. Additionally, the heating rate effect on the moisture clog was studied and it was found out that higher heating rates resulted in a faster and longer lasting water accumulation at the innermost position of the sample [14].

Thus, the current work aims to apply neutron tomography in-situ observation methods to compare the behavior of refractory compositions with different types of fibers.

## MATERIALS AND METHODS

The current study considered high alumina castable compositions with 5 wt. % of calcium aluminate cement, consisting of tabular alumina and calcined and reactive $Al_2O_3$. As a drying additive, polypropylene, polyethylene or cellulose fibers were added and the detailed castables compositions can be found in Table 1. It should be noted that changes in the water content were necessary to ensure similar levels of flowability for the samples with distinct fibers and the reference material without any drying additives. Also, the weight percentage of the fibers was different as the cellulose fiber is less dense than its synthetic counterparts, and it was decided to maintain the volumetric fiber content constant for all different additives tested.

Tab. 1: High alumina refractory castables compositions considered in the current study.

| Raw Materials | | 5CAC (wt.%) | 5CAC-PP (wt.%) | 5CAC-PE (wt.%) | 5CAC-Cel (wt.%) |
|---|---|---|---|---|---|
| Tabular Alumina (Almatis) | AT 6-3 | 18 | 18 | 18 | 18 |
| | AT 3-1 | 10 | 10 | 10 | 10 |
| | AT 1-0.5 | 11 | 11 | 11 | 11 |
| | AT 0.6-0.2 | 9 | 9 | 9 | 9 |
| | AT 0.2-0 | 16 | 16 | 16 | 16 |
| | AT<45 | 10 | 10 | 10 | 10 |
| Calcined and reactive alumina | CL370, Almatis | 11 | 11 | 11 | 11 |
| | CT3000SG, Almatis | 10 | 10 | 10 | 10 |
| Calcium Aluminate Cement | Secar 71, Imerys | 5.0 | 5.0 | 5.00 | 5.00 |
| Drying Additive | PP, supplied by RHI-Magnesita | - | 0.1 | - | - |
| | PE, Emsil-Dry, Elkem | - | - | 0.1 | - |
| | Cellulose, Suzano | - | - | - | 0.2 |
| Distilled Water | | 4.5 | 4.7 | 4.6 | 5.4 |
| Dispersant | Castement FS60, Basf | 0.2 | 0.2 | 0.2 | 0.2 |

The castables without additives, with PP and PE fibers, were obtained following the standard protocol of pre-mixing the powders for 1 minute in a regular rheometer. Next, the water was added, and the composition was mixed for an additional 3 minutes. The sample with cellulose fibers was obtained using a different methodology. As its mechanism is based on the swelling of the fibers, before the castable preparation, half of the water added to the composition was mixed with the cellulose fibers in a bench mixer for 5 minutes. After that, the mixture of water and cellulose was added to the castable, following similar protocols to the ones used for the other compositions.

Afterwards, the compositions were cast in dense alumina cylindrical ceramic casings with internal diameters of 3.6cm and 5cm high with open ends (the bottom part was closed with adhesive tape during casting and curing) for the neutron tomography tests. The experimental layout of the in-situ drying tests is present in Figure 1. The sample is dried from an infrared heater placed close to its top surface. The heating rate applied was 20°C/min up to 600°C, with a plateau afterwards for 30 additional minutes. The whole setup is fixed on a turntable table with screws. To fill the gap between the sample and the Teflon container, and to avoid lateral heating, a thermal insulator is used. Regarding the sample, Figure 3 b), shows

a slice of the neutron tomography highlighting the impermeable ceramic casing. Finally, it should be noticed that the samples were placed in the opposite direction of the casting.
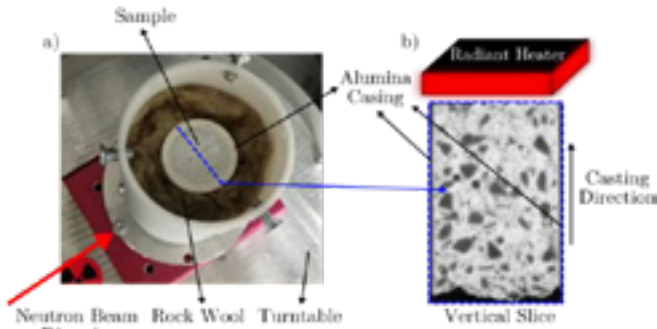


*Fig. 1: (a) Experimental set up for the neutron tomography test in the NeXT equipment at Institut Laue-Langevin (ILL) and (b) vertical slice of the 3D reconstruction of the neutron tomography of the sample showing the alumina casings.*

The neutron tomographies were acquired using the NeXT instrument at the Institut Laue-Lavengin (ILL). The true spatial resolution was around 190 µm whereas the time interval between two successive tomographies was 58.5s, as described in the tests reported by Tengattini et al. [15]. After the tests, the 3D volumes were reconstructed using the Feldkamp filtered back projection using a commercial software (X-act, by RX Solutions).

Considering the post-processing of the images, the drying front progression used for calculating the sizes of the dried zones (DZ) volumes was obtained through a gradient based algorithm, visually described in Figure 2.
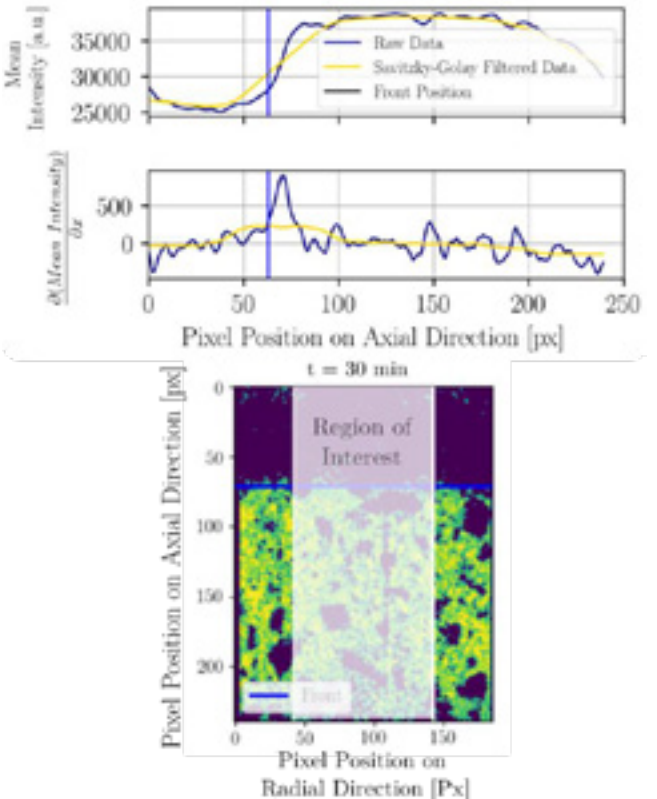


*Fig. 2: Drying front position detection algorithm. Firstly, the mean of the intensity value on the radial direction was calculated inside the region of interest, then a Savitzky-Golay filter was used to reduce the noise of the data. Finally, the minimum of the derivative of the radial mean intensity with respect to the height defined the drying front position, which is represented by the blue line (notice how it is defined by the maximum of the yellow line on the derivative plot).*

A different method also used to quantitatively analyse the evolution of the water content during drying was the calculation of the normalized intensity evolution over slices of the sample. This is calculated using the ratio between the intensity of an image at a given moment and the median of the first 10 tomographies (representing the initial state before drying).

**RESULTS AND DISCUSSION**

The mass loss between the sample preparation and the experiment execution (the storage aging mass loss) and after the test is summarized in Table 2. It is possible to see that all samples lost between 2 wt.% to 7 wt.%, regardless of the composition.

Tab. 2: Summary of the water loss of each sample. All percentages are calculated as a fraction of the total water added in each composition.

| Test | Composition | Storage Aging Mass Loss (wt.%) | Experiment Mass Loss (wt.%) |
|------|-------------|-------------------------------|-----------------------------|
| 1 | 5CAC | 3.1% | 9.4% |
| 2 | 5CAC | 4.2% | 7.5% |
| 3 | 5CAC-PP | 3.3% | 14.4% |
| 4 | 5CAC-PP | 4.4% | 17.6% |
| 5 | 5CAC-PE | 3.0% | 15.4% |
| 6 | 5CAC-PE | 2.2% | 14.5% |
| 7 | 5CAC-Cel | 5.9% | 20.7% |
| 8 | 5CAC-Cel | 3.5% | 21.9% |

Direct comparisons between different samples using the data of Table 2 are not possible as the tests did not have the exact same duration, nonetheless, an overall trend can be identified when considering the experiment water removal, with the reference 5CAC composition without any additive displaying the smallest amount of water removed, followed by the PE and PP samples. The samples with cellulose were the ones with the highest quantity of water lost during the drying test.

In order to draw a clear comparison between the different tests, a relative time scale, $t_r$, is considered, in which the initial time is defined by the start of the drying front progression obtained through the methodology depicted in Figure 2. Axial slices of the normalized intensity sample are shown in Figure 3. It is possible to see that the sample with no additives (5CAC) was indeed the one with the smallest dried region (the area characterized by a smaller normalized intensity - in blue - at the top of the sample).

The evolution of the mass transport within the composition containing PP fibers showed a more intense drying between $t_r = 0$ min and $t_r = 12$ min, however, the size of the dried zone (DZ) remained similar to the 5CAC composition. At the end, the DZ is roughly 1.5 times bigger than the one seen on the sample with no additives.

The 5CAC-PE sample showed a moisture distribution at $t_r = 12$ min similar to the reference composition. This might highlight a permeability enhancing mechanism that starts later when compared to what is seen for the 5CAC-PP and 5CAC-Cel. The final condition shows a larger DZ than 5CAC, suggesting that the water removal rate increased over time. Moreover, the dried zone is not as intense as the other compositions containing additives.

Finally, 5CAC-Cel shows a fast and intense drying that proceeds with a constant water removal rate, as the DZ is the largest at both $t_r = 12$ min and $t_r = 20$ min and it has the smallest values of normalized intensity.

To further investigate these observations, quantitative analyses considering the relative drying volume percentage are presented in Figure 4. The reference composition was the one where the water removal was the slowest. For instance, it took around 30 minutes to reach the 20% of relative drying volume. That mark was reached after only 18 minutes for the 5CAC-PP, 13 minutes for 5CAC-PE and 10 minutes for the 5CAC-Cel. This is directly linked to the different mechanisms of actuation of the fibers.
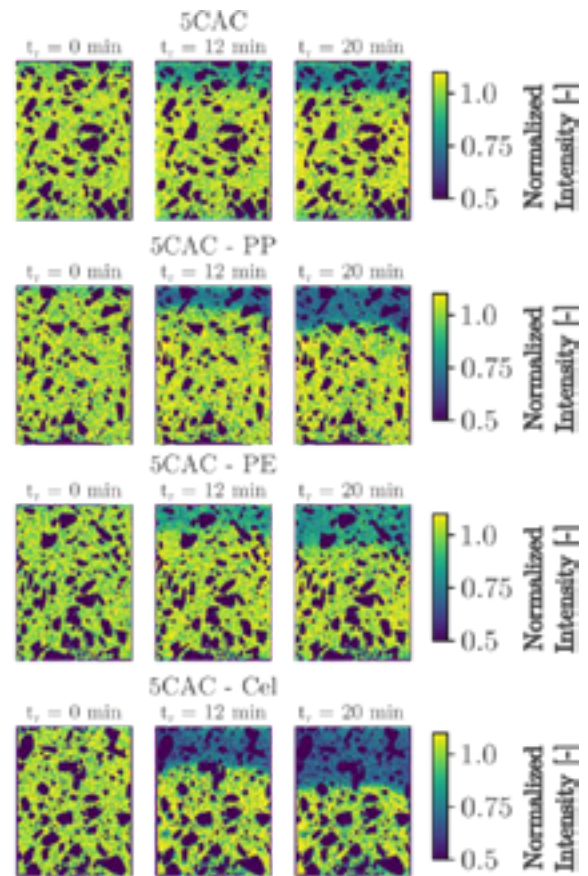


Fig. 3: Normalized intensity at 0 min, 12 min and 20 min of relative time, $t_r$. This temporal scale considers the initial time ($t_r = 0$ min) as the beginning of the drying front progression detected by the gradient based algorithm.

It is known that cellulose can lead to higher permeability even before reaching 110º C [6], due to the removal of water from the swelled fibers, thus leading to a faster water withdrawn at presumably smaller temperatures. Polypropylene and polyethylene, on the other hand, depend on thermally-activated changes of their state that take place at higher temperatures [6, 7, 8], leading to the initial behavior closer to the reference one. After that, the permeability increases and the process is faster than in the 5CAC samples.
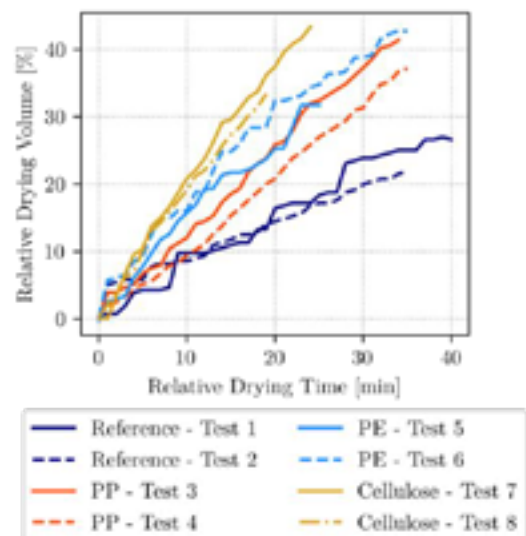


Fig. 4: Relative drying volume versus the relative drying time for all compositions. The dried volumes were obtained from the drying front position detection algorithm presented in Figure 2.

185

To investigate the influence of fibers on the moisture clog, the evolution of the normalized average gray value within a disk of the sample was analyzed, as shown in Figure 5. Among the compositions studied, the 5CAC composition exhibited a more prolonged moisture accumulation period (marked by gray values higher than the initial ones), while the 5CAC-cellulose composition showed a shorter duration. However, the total moisture accumulation was slightly more intense and occurred at a significantly faster rate. This observation indicates that the enhanced moisture transport occurs in both directions, towards the hot surface and into the center of the sample. The increased permeability, though, eases the rapid withdrawal of this accumulated moisture, before dangerous higher temperatures are reached, resulting in a faster and safer drying process. Similar behavior was observed for samples containing polypropylene (PP) and polyethylene (PE) fibers.
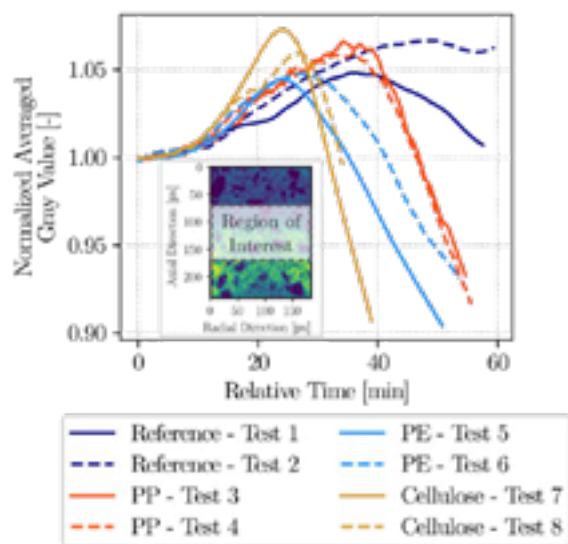


*Fig. 5: Normalized averaged gray value evolution for the central disk of the sample, shown in the inset.*

Thus, when considering unidirectional drying, additives that rely on mechanisms that are triggered at too high temperatures might actually be not as beneficial, as the entrapment of moisture can still take place in the colder regions of the refractory castable and potentially induce explosive spalling.

## CONCLUSIONS

The understanding of the drying process in refractories castables holds great potential for reducing the carbon footprint of the processing of these materials, thanks to the long drying curves, which are often overly conservative. Efforts to provide safe and efficient drying of refractory castables entail cheap and readily available additives that won't affect any of the required properties during their use.

Polymeric fibers have emerged as the most promising and widely adopted choice. Thus, the objective of this study was to investigate the impact of various permeability-enhancing additives from an unprecedented perspective. By employing neutron tomography, the drying process of compositions with polypropylene, polyethylene, cellulose fibers, or with no additives was observed in real-time.

It was found out that the 5CAC sample was the one with the smallest drying zone after the test followed by 5CAC-PP and 5CAC-PE. 5CAC-Cel was the one with the largest portion dried, indicating faster water removal with a constant drying rate. The moisture clog observed when cellulose was used was also the largest one observed, while being the shortest one in duration. The composition with no additive showed the longer lasting moisture accumulation.

In future works, modifications in the current methodology will be explored to enable the direct examination of the thermal behavior of fibers, aiming at uncovering the underlying mechanisms responsible for the increase of the castables' permeability. Once these mechanisms are better understood, synthetic fibers could be engineered to enhance their effectiveness, or alternative natural fiber options could be explored based on similar mechanisms. This approach would further contribute to greener practices, ensuring secure and faster drying processes.

## REFERENCES

[1] da Luz A. P., et al., Drying behavior of dense refractory ceramic castables. Part 1 – General aspects and experimental techniques used to assess water removal. Ceramics International, 47 (16), 2021, p. 22246-22268

[2] Palmer, G., et al., The accelerated drying of refractory concrete – Part 1: a review of current understanding. Refractories Worldforum, 6 (2), 2014, p. 75–83

[3] da Luz A. P., et al., Drying behavior optimization of dense refractory castables by adding a permeability enhancing active compound. Ceramics International, 45 (7), 2019, p. 9048-9060

[4] Moreira, M. H., et al., Main trends on the simulation of the drying of refractory castables - Review. Ceramics International, Elsevier, 47 (20) p. 28086-28105 (2021)

[5] Cunha, T. M., et al., A simple methodology based on numerical analysis for the drying curve design of a castable lined steel ladle. Open Ceramics, 13, 2023, p.100330

[6] da Luz A. P., et al., Drying behavior of dense refractory ceramic castables. Part 2 – Drying agents and design of heating schedules. Ceramics International, 48 (1), 2022, p. 2965-2987

[7] Zhang, D., Hai Tan, K., Effect of various polymer fibers on spalling mitigation of ultra-high performance concrete at high temperature. Cement and Concrete Composites, 114, 2020, p. 103815

[8] Innocentini, M., et al., Permeability of fiber-containing refractory castables. American Ceramic Society Bulletin, 81 (7), 2002, p. 34

[9] Mohammed, H. et al., Heat-induced spalling of concrete: A review of the influencing factors and their importance to the phenomenon. Materials, 15 (5), 2022, p. 1693

[11] Barakat, A. J. et al., The effect of permeability enhancement on dry-out behavior of CA- and microsilica gel-bonded castables as determined by NMR. Ceramics International, 46 (9), 2020 p. 13556-13568

[12] Stelzner, L., et al., Thermally-induced moisture transport in high-performance concrete studied by X-ray-CT and 1HNMR, Construction and Building Materials, 224, 2019, p. 600–609

[13] Moreira, M. H., Dal Pont, S., Tengattini, A., Luz, A. P., Pandolfelli, V. C. Experimental proof of moisture clog through neutron tomography in a porous medium under truly one-directional drying, Journal of The American Ceramic Society, 105 (5), 2022, p. 3534-3543

[14] Moreira, M. H., Dal Pont, S., Tengattini, A., Pandolfelli, V. C. Heating rate effect on the moisture clog while drying refractory castables: A neutron tomography perspective, Journal of The American Ceramic Society, 106 (3), 2023, p. 1706-1715

[15] Tengattini, A., Dal Pont, S., Cheikh Sleiman, H., Kisuka, F., Quantification of evolving moisture profiles in concrete samples subjected to temperature gradient by means of rapid neutron tomography: Influence of boundary conditions, hygro-thermal loading history and spalling mitigation additives. Strain, 56 (6), 2020, p. e12371

# PRACTICAL EXPERIMENTATION AND MODEL DEVELOPMENT FOR THE DRYING OF MONOLITHIC REFRACTORY CASTABLES

Matthew Lambert[1]; Dana Goski[1]; Luke Gritter[2]; Kyle Koppenhoefer[2]

[1]Allied Mineral Products, LLC, Columbus, OH, United States; [2]AltaSim Technologies, LLC, Columbus, OH, United States

The presence of liquid in refractory ceramic protective linings can be detrimental or dangerous to many industrial processes. The removal of this liquid, usually water, via heating of monolithic refractory ceramics is a critical first step for their in-service use post-installation. If not carefully performed, however, temperature increases can lead to a build-up of steam pressure within the refractory due to a lack of steam escape pathways. If the pressure increases to above the refractory strength, the material can mechanically fail and spall. The physical properties of refractory ceramics, such as strength, permeability, and thermal conductivity, can be important variables that will determine the likelihood of an explosive spalling event. Using small scale experimental data and extensive numerical relationships from literature as input to a COMSOL Multiphysics model, the temperature and pressure evolution within a refractory monolithic material can be estimated. Medium and large scale experimentation can be used for nominal comparison and validation of the modelling results

# NUMERICAL MODELLING ANALYSES OF STEEL LADLE WEEP HOLE EFFICIENCA

T. M. Cunha[(1)], M. H. Moreira[(1)], J. G. P. Silva[(2)], R. A. Angélico[(3)], V. C. Pandolfelli[(1)]

(1) Federal University of Sao Carlos, Graduate Program in Materials Science and Engineering, Sao Carlos, SP, Brazil
(2) Federal University of Sao Carlos, Department of Mechanical Engineering, Sao Carlos, SP, Brazil
(3) University of Sao Paulo, Department of Aeronautical Engineering, Sao Carlos, Brazil

## ABSTRACT

Refractory castable drying is a key processing step where explosive spalling can happen if the combination of generated vapor pressure within the material's pores and the thermomechanical stresses exceeds its mechanical strength. Therefore, to avoid major problems, refractory producers usually select conservative heating schedules. To attain lower energy consumption and faster drying, deeper analysis considering the material's composition and heating profiles can be carried out via computational simulations. Additionally, in the context of refractory castables applied for the lining of steel ladles, the drying process can be improved with the help of weep holes in their metallic shells. To the authors` knowledge, studies considering the effectiveness of weep holes in the decision-making process involving this equipment have not been reported in the reviewed literature. Nevertheless, refractory producers commonly adopt them based on experimental observations and their practical efficiency. In this context, this study aims to carry out computational simulations to highlight the behavior of a steel ladle lining drying designed with weep holes. The simulations enabled a better understanding of the pressure build-up and moisture flow to optimize the drying step without detrimental side effects.

## INTRODUCTION

The steelmaking industry relies on using of steel ladles for holding and conducting secondary refinement on steel. Because this process takes place at high temperatures, refractory linings are employed at the interface between the metallic shell and the transported material. These linings act as a barrier to prevent both thermal loss, liquid leakage and corrosion. [1].

In recent years, there has been a notable transition from the utilization of pre-shaped refractory bricks to monolithic working layers within the steelmaking industry [2]. This shift is driven by the numerous advantages offered by monolithic working layers, which include, but are not limited to, the absence of expansion joints and greater design flexibility in terms of shape and in some instances, higher installation rate. [1, 3].

However, in the process of obtaining the castable from powdered raw materials, water and additives are typically added. This addition acts both as a mixing medium and the required formation of hydrates when considering hydraulic binders, leading to an increase in green strength [3]. Consequentially, it is crucial to remove the water through a controlled heating schedule. Failure to do so may lead to the accumulation of vapor within the material's porosity, resulting in a pressure buildup. This process poses the risk of explosive spalling of the lining, which can cause damage to equipment and personnel. Thus, lasting maintenance time and loss of productivity may occur [4] thanks to overconservative and long heating protocols.

In previous studies conducted by the research group, methodologies for optimizing the heating schedule were examined. However, they have a limitation in terms of how much the heating rate can be increased before reaching a maximum threshold [5].

Therefore, this work focuses on exploring an alternative approach to drying through the numerical evaluation of incorporating weep holes into the metallic shell, which can release water through through the cooler surface of the ladle. Typically, these holes are manually drilled into the shell by operators and are commonly applied in the industry [6].

However, despite their widespread use, there is limited information available in the literature regarding general practices of weep hole design. Minimal details are provided, such as the importance of maintaining cleanliness and the typical diameter of the drilled holes [7]. Additionally, in case of lining failure, the likelihood of liquid metal pouring accidents poses an optimization task between increasing the number of weepholes while still keeping the security of the process. Thus, numerical modelling is proposed as a tool to assess the effect of weepholes on the drying behavior of refractory castables.

For such analysis, the mesh used in this study was initially generated using gmsh. Following, the FEniCS python library was employed for solving a numerical problem of drying using the finite-element methodology. The objective was to simulate the water removal process from the refractory castable lining of a steel ladle wall, evaluating the moisture vapor pressure and temperature at each point. The presence or absence of weep holes in the metallic shell was considered during the evaluation. Post-processing was conducted using tools such as numpy, matplotlib and scipy. These particular tools were selected for their open-source nature and large community users, reliability and efficiency.

## MATERIALS AND METHODS
### Material and Properties

The material considered for the simulations is a high alumina calcium aluminate cement-based castable, with a 5%wt content of this cement. The composition of the material is summarized in the Table 1.

Tab. 1: 5CAC castable composition.

| Raw Material | Mass Fraction (%) | Supplier |
| --- | --- | --- |
| Tabular Alumina (< 5 mm) | 74 | T-60, Almatis |
| Calcinated Alumina | 11 | CL370, Almatis |
| Reactive Alumina | 10 | CT30000SG, Almatis |
| CAC | 5 | Secar 71, Imerys Aluminates |
| Dispersant | 0.2 | Castament FS60, BASF |
| Water | 4.5 | - |

The particle size distribution of the material was adjusted using the Andreassen model with a packing coefficient of 0.21. Subsequently, the powder was homogenized with water and a dispersant using a home-made rheometer [8]. The resulting mixture was then shaped into samples for various tests, including:

1. TGA (Thermogravimetric Analysis) samples: cylinders with dimensions of 50 mm in height and 50 mm in diameter.
2. Three-point bending test samples: rectangular prisms with dimensions of 25 mm x 25 mm x 150 mm, following ASTM C583-15 standard with a loading rate of 12.9 N/s
3. Thermal conductivity measurement samples: rectangular blocks with dimensions of 233 mm x 114 mm x 64 mm, measured by the hot wire method, ISO 8894-2.
4. Permeability at room temperature measurement samples: cylinders with 25 mm height and 50 mm in diameter, following ASTM C577.
5. Density: small cylinders for the measurement using Archimedes methodology, as outlined in the ASTM C830-00 standard.

After shaping, the samples were cured for 24 hours at 30°C and 90% relative humidity. Following, all samples except the TGA ones were subjected to firing at temperatures ranging from 300°C to 500°C with 5 hours dwell time.

By conducting these measurements, the required physical properties were obtained to accurately define the material's constitutive laws in the numerical simulation.

Both thermal conductivity and permeability are crucial parameters for the numerical simulation [9]. The thermal conductivity evolution was evaluated at various temperatures, and the resulting behavior was fit to a polynomial curve to obtain a temperature-dependent law.

Regarding permeability, the method to obtain an extrapolation of the high temperature behavior can be found in [10].
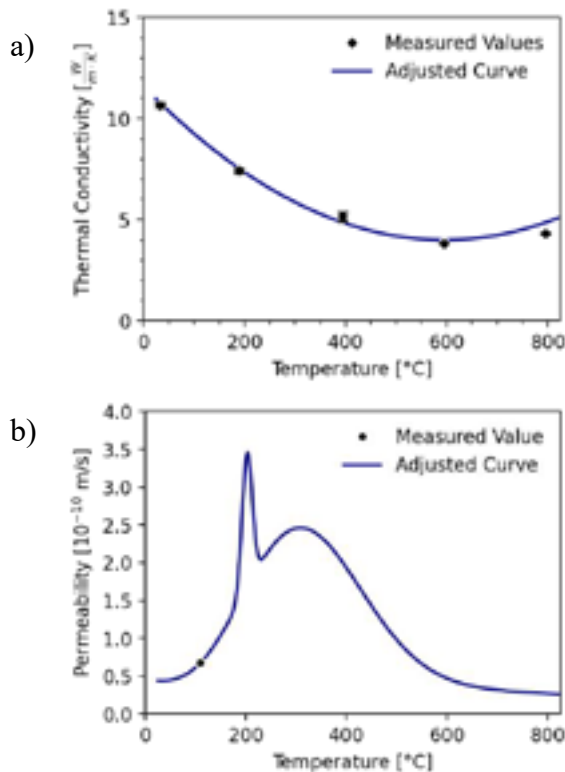


Fig. 1: a) Thermal conductivity as a function of temperature. b) Extrapolation of the permeability curve. The measured value at room temperature is highlighted by a black point, whereas the methodology for the acquiring of the rest of the curve can be found at [10].

To compare the vapor pressure obtained by the numerical simulation with the local mechanical strength, a parameter called the "resistance ratio" was introduced, and it is defined as the ratio between the local vapor pressure and the local triaxial stress strength of the material. To assess the material resistance, the mechanical stress obtained from the three-point bending tests was converted to the resistance ratio using the method described in Figure 2.

Additionally, two different hydraulic conductivity values were assumed for the different layers of the material. For the permanent layer a value of 1e-8 m/s was considered whereas for the insulating one, 1e-6 m/s. These values were chosen to represent the permeability properties of each respective layer in the numerical simulation.

**Geometry and Meshing**

The chosen geometry for this study is the section of a wall from a steel ladle, as depicted in Figure 3. Its design is based on the works by Santos et al. [1]. To implement it and generate a mesh,

the gmsh software was used. Initially, a basic geometry was generated, considering the following thicknesses: 200 mm for the working layer, 50 mm for the permanent layer, and 34 mm for the insulating one, as the wall illustrated in Figure 3.
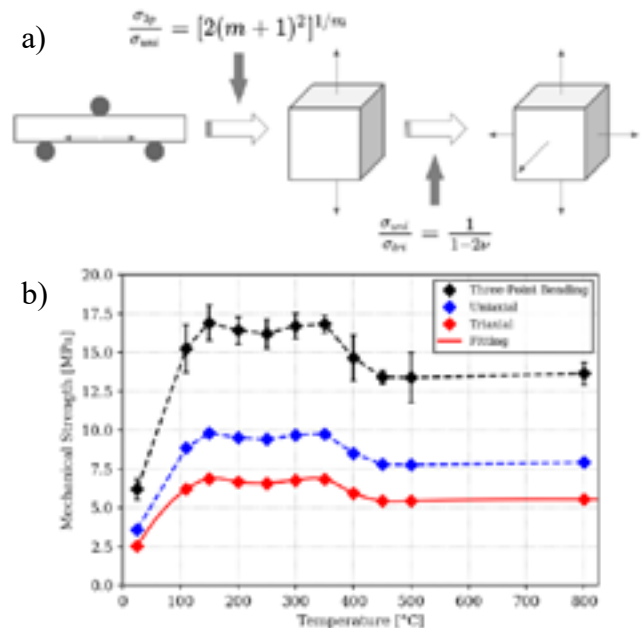


Fig. 2: a) Conversion schedule of the strength from three-point bending test (3p) to uniaxial (uni) to triaxial (tri). b) Values obtained in each of these steps. [5, 10]
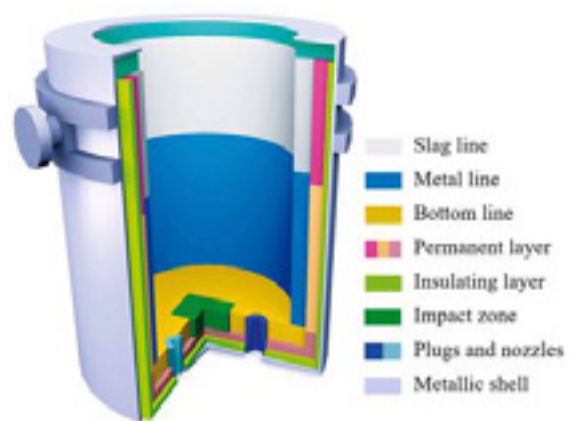


Fig. 3: Schematic for a steel ladle, displaying the many layers in which this work was based at [1].

Previous studies conducted by the research group have observed that the thermal gradient in the metallic shell is relatively low due to its high thermal conductivity. As a result, it was found that this specific layer could be replaced by a Dirichlet boundary condition on the cold face. This approach offers several benefits, including easier manipulation of results and faster simulation times.

In the study, a 2 cm weep hole was incorporated into the ladle shell identifiable in Figure 4 as a more refined zone located on the ladle's rightmost face and the white face color of the polygons.

Local refining techniques were implemented in the interface zones between the different layers. Additionally, near the weep hole, this strategy was also employed. The purpose of it was to reduce the local moisture velocity computing error, as larger elements can lead to larger pressure gradients.

Figure 4 presents the meshed geometry, specifically representing a quarter of a weep hole and the adjacent region.
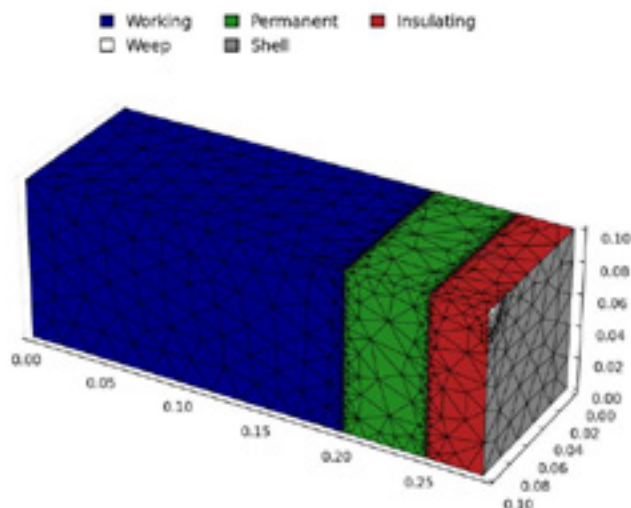
*Fig. 4: Meshing of the selected geometry, units are in meter.*

For the final geometry, the boundary conditions enforce symmetry on the side planes of the ladle sample. Specifically, the larger sides of the ladle, measuring 284 mm x 100 mm in Figure 4, exhibit symmetry. As shown in Figure 5, the weep holes are arranged in a square mesh pattern with a distance of 200 mm between the centers of the weep holes.
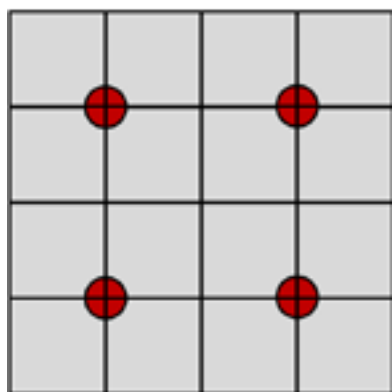


*Fig. 5: Representation of simulated geometry. Black lines identify the symmetry planes whereas the red circles are the weep holes.*

**Simulation setup and post-treatment**

The problem at hand was solved using the FEniCS python library, which provides a finite element environment for numerical simulations. The model is based on the works by Bazant [11] and Gong [12], which consider a single flowing phase percolating through the materials porosity. Further details about the specific numerical model and its application can be found in previous publications by the research group [5, 10].

In the simulation, the heating conditions were applied to the hot face, which corresponds to the interface between the working layer and hot air. This was achieved using Dirichlet boundary conditions. On the other hand, the cold face (where the weep hole is located) was subjected to cooling by convection and radiation. Surface mass transfer was allowed at the hot face and also at the weep hole when it was present, while the remaining portion of the cold face, representing the metallic shell, was assumed impermeable.

Because the model considers a single flowing phase, local refinement was implemented between the different layers to enhance numerical convergence. The properties assigned to the working layer were measured from the reference material, whereas the properties for the permanent and insulating layers were adapted from the work by Santos et al. [1];

The simulations have an initial temperature of 25°C which is gradually increased at a rate of 100°C/h on the hot face until

reaching 825°C. This temperature profile was applied to assess the impact of the presence or absence of the weep hole on the drying process of castable.

For post-processing, the meshio, numpy, and scipy libraries were employed to compute water content and velocities. Water content was calculated based on the current pressure and temperature, whereas the velocity was determined using the pressure gradient according to Darcy's law. The obtained data were visualized using matplotlib, which served as a tool for data visualization and analysis.

**RESULTS AND DISCUSSION**

Following the completion of the simulations, the results were extracted and analyzed as described earlier. Figure 6 illustrates the evolution of the maximum pressure at each time step over the time. In the early stages of the drying process, there is no significant difference observed between the simulations with and without the weep hole. This is due to the drying front being located closer to the hot face, resulting in minimal moisture flow towards the colder regions, where the effect of the weephole's presence is the largest.

As the drying process progresses, the pressure gradient at the drying front leads to the accumulation of moisture within the cooler zones of the ladle wall, which, in turn, triggers the moisture clogging. This effect is highlighted by the significant pressure peak in the red curve, which reaches values exceeding 20 MPa. This peak indicates the formation of localized high-pressure vapor region within the ladle wall as a result of moisture accumulation.
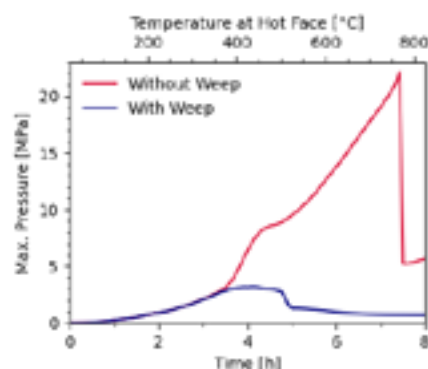


*Fig. 6: Evolution of the maximum pressure for each geometry as a function of time.*

This phenomenon occurs when the drying front transfers humidity from hotter zones to cooler ones, causing water to readsorb into the inner regions of the castable lining. It can happen in any monolithic wall setup, but it is more pronounced when the cold face lacks permeability for moisture transportation. Without it, water accumulates, leading to higher pressures and potential issues like damage to the vessel. Therefore, weep holes provide a controlled means of moisture transportation, diminishing the accumulated pressure and the risk of explosion of the lining.

In the present model, which considers a single flowing phase, it is not possible to define the specific physical state of water. However, it is feasible to observe the accumulation of free adsorbed water or changes in local relative humidity, as supported by experimental observation [13].

In Figure 7, the water content evolution in each layer is shown, normalized to the initial content. With the temperature increase, the sample with a weep hole experiences faster drying of free adsorbed water, while the sample without a weep hole only redistributes the water in the cooler zones, resulting in a minimal difference in total adsorbed water in the body. Between 200°C and 400°C, structural water is released, but trapped moisture leads to increased adsorption and the overall water content. As free water dries up, vapor pressure decreases, and higher temperatures result in a quick water withdrawal due to pressure gradients.
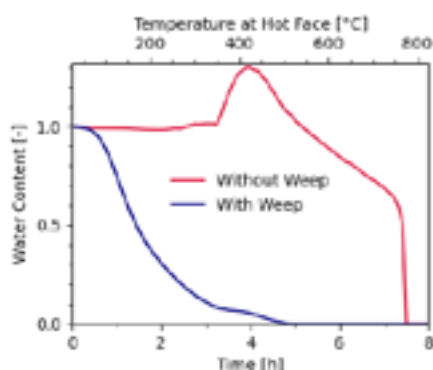
*Fig. 7: Evolution of the free adsorbed water for each geometry as a function of time. The peak in the red curve indicated the phenomenon of moisture clogging.*

Figure 8 illustrates the calculated exit velocity at the hot surface. The presence of a weep hole reduces the velocity in this zone, as moisture can exit through the opposite side of the lining. Conversely, the absence of a weep hole leads to slightly higher and delayed velocity peaks, resulting from the limited withdrawal of trapped moisture. Additionally, non-zero velocity values at the early stages of drying for the design without a weep hole indicate that there is moisture exiting through the heated surface in the same way it is being released in the lining with the hole. This suggests that water is being transferred in the cooler zones at a similar rate, indicated by the low variance in the total free water content as shown in Figure 7, as a decrease should be expected if water was not being adsorbed within that region.
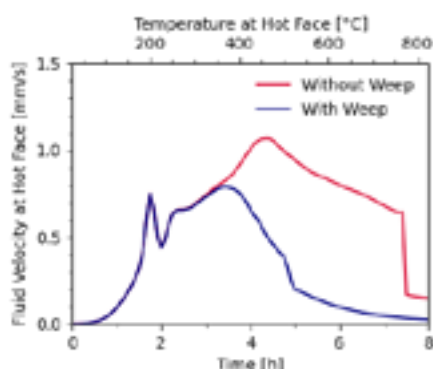


*Fig. 8: Evolution of the fluid velocity at the hot face for each geometry as a function of time.*

## CONCLUSIONS

In this study, the drying process of a steel ladle wall was analyzed and the effect of weep holes on moisture transfer was evaluated. Using numerical simulations based on the finite element methodology, the pressure, water content and exit velocity of water during the drying process was assessed.

The simulations showed that weep holes played a crucial role in enhancing moisture removal. In the absence of it, water accumulated in cooler zones, lead to pressure peaks and the phenomenon of moisture clogging, whereas their presence prevented such accumulation and reduced the pressure buildup.

The water content evolution analysis indicated that the presence of such holes resulted in the drying of free adsorbed water, whereas in their absence moisture was redistributed to cooler zones. Structural water released during the drying process increased the overall water content due to adsorption in trapped moisture zones.

Furthermore, the exit velocity of the fluid on the heated linint surface was examined. Weep holes allowed moisture release through the opposite side of the lining, reducing the velocity observed in the heated surface. Conversely, without weep holes,

higher and delayed velocity peaks were observed, indicating limited and delayed withdrawal of trapped moisture.

In summary, the current study highlights the significant influence of weep holes on moisture transfer during the drying of a steel ladle wall. The findings provide an uprecendeted analysis that can enable valuable insights for optimizing ladle lining design and maintenance, helping to improve the efficiency and safety of the drying of castables as well as increase the overall productivity in the steelmaking industry.

## REFERENCES

[1] Santos M., Moreira M., Campos M., Pelissari P. I., Angélico R., Sako E., Sinnema S., Pandolfelli V. C., Enhanced numerical tool to evaluate steel ladle thermal losses, Ceramics International 44, 2018.

[2] Schacht C., Refractories Handbook, CRC Press, Hoboken, 2004.

[3] Luz A. P., Bráulio M. d. A. L., Pandolfelli V. C., Refractory Castable Engineering, 2015.

[4] Moreira M., Pont S., Ausas R., Luz A. P., Cunha T., Parr C., Pandolfelli V. C., Main trends on the simulation of the drying of refractory castables - review, Ceramics International 47, 2021, 28086–28105.

[5] Cunha, T. M., Moreira, M. H., Santos, M. F., Angélico, R. A., Pandolfelli, V. C. A simple methodology based on numerical analysis for the drying curve design of a castable lined steel ladle. In Open Ceramics 13, 2023, 100330.

[6] Moore, R. C., Shotcreting monolithic steel ladle linings at Dofasco. 29 21-27.

[7] Sengupta, P. Refractories for the Cement Industry. Springer International Publishing, 2020.

[8] Pileggi R., Pandolfelli V., Paiva A., Gallo J., Novel rheometer for re- fractory castables, American Ceramic Society Bulletin 79, 2000, 54–58.

[9] Moreira M. H., Ausas, R. F., dal Pont S., Pelissari P. I., da Luz, A. P., Pandolfelli, V. C., Towards a single-phase mixed formulation of refractory castables and structural concrete at high temperatures. International Journal of Heat and Mass Transfer 171, 2021, 121064.

[10] Cunha, T. M., Moreira, M. H., Santos, M. F., Luz, A. P., & Pandolfelli, V. C.. Drying behavior of steel-ladle lining refractory castables under continuous heating rate. In Ceramics International 48, 2022, 1142–1151.

[11] Bažant, Z. P., & Thonguthai, W. Pore pressure in heated concrete walls: theoretical prediction. In Magazine of Concrete Research 31, 1979, 67-76.

[12] Gong, Z.-X., & JluJumdar, A. S. A Model for Kiln-Dryins of Refractory Concrete Slabs. In Drying Technology 11, 1993, 1617–1639.

[13] Stelzner, L., Powierza, B., Oesch, T., Dlugosch, R., Weise, F., Thermally-induced moisture transport in high-performance concrete studied by X-ray-CT and 1HNMR, Construction and Building Materials, 224, 2019, 600–609.

# MICROWAVE SINTERING OF ZNO–CONTAINING *IN–SITU* SPINELIZED ALUMINA–BASED CASTABLES

Borges, O.H.; Cardoso, A. L. F.; Moreira, M. H.; Klein-Gunnewiek, R. F.; Pandolfelli, V.C.

Federal University of Sao Carlos, Graduate Program in Materials Science and Engineering, Sao Carlos-SP, Brazil.

## ABSTRACT

Matching industrial activity and environmental protection is one of the toughest challenges of the 21st century. As high consumers of fossil-based materials, refractory manufacturers are consistently seeking processes that can provide higher energy efficiency. In this sense, using microwaves for ceramic sintering has shown significant advantages compared with the conventional route (based on electrical or natural gas heating), reducing lead time, enhancing mechanical properties, and demanding less power. However, this method has been underexplored for such application due to the lack of knowledge about refractory phases capable of effectively interacting with this type of electromagnetic radiation. Thus, this work addressed the potential of applying ZnO as a microwave absorber in $Al_2O_3$-based refractories, comparing microwave-sintered castables with electric-heated ones thermally treated up to 1700 ºC. Although presenting a relatively high vapor pressure, the content of ZnO (11.4 wt%) remained stable at all temperatures applied in the electric-heated furnace, whereas significant evaporation was detected for samples microwaved above 1300 ºC. The mechanisms related to this behavior and strategies to avoid it are discussed. On top of that, the microwave sintering method showed benefits such as higher densified microstructure with open pores remaining homogeneously scattered in the matrix, enhanced mechanical properties at room temperature, 26-fold faster lead time, and roughly-estimated 70%-lower energy consumption. Thus, this sintering method might be a promising alternative to increase the efficiency of refractory manufacturing, lowering environmental impacts and production costs.

## INTRODUCTION

In a world with finite natural resources and where energy production fundamentally relies on the burning of fossil fuels, fulfilling the upcoming energy demand (47 % increase by 2050), ensuring environmental protection is considered one of the greatest challenges of this century[1]. Regardless of introducing new non-polluting energy sources, it is believed that such a balance cannot be achieved without increasing the efficiency of the currently-used processes[1]. Accounting for close to 12 % of all energy consumed worldwide[2], special attention must be given to industrial processes operating at high temperatures, such as the conventional sintering of ceramic materials. In this procedure, temperatures usually between 1000 ºC and 2000 ºC are applied for several hours to compact powder systems aiming at inducing the formation of ceramic bonds between the particles[2]. Aiming at speeding up the sintering step and minimizing the energy consumed for it, different techniques have been developed in recent decades, such as microwave sintering[2]. However, to be effective, this technique relies on the presence of phases capable of interacting with microwaves, converting the electric and/or magnetic fields into thermal energy, or even directly enhancing the diffusion process of the sintering mechanisms. These aspects depend on the materials' dielectric and magnetic properties and, for a broadly used ceramic oxide range (*e.g.* $Al_2O_3$, MgO and $SiO_2$) that are transparent to microwave at room temperatures, they do not allow microwave heating without using susceptors[3]. However, scaling up this sintering process to massive production, as is the case of refractories, remains a challenge[3]. Thus, adding microwave-absorbing compounds may foster using this sintering method for refractories and, as indicated by Bhattacharya and Basak[4], zincite (ZnO) is a promising candidate due to its suitable microwave absorption.

Notwithstanding the changes led to the castables' properties, recent studies[5,6] pointed out the feasibility of applying ZnO in alumina-based castables as these oxides react at intermediate temperatures (~ 800 ºC) forming a spinel-like phase with interesting properties (*e.g.* high refractoriness and low coefficient of thermal expansion). In this work, microwave-sintered ZnO-containing alumina-based vibrated castables were produced at different temperatures. Some of their key properties, microstructural features and energy demanded for sintering were assessed and compared to their conventionally fired counterparts.

## EXPERIMENTAL PROCEDURE

The vibrated castables analysed in this work were produced with a packing distribution according to the modified Andreasen's model (q = 0.26) and following the procedure described in[5]. Calcined and tabular alumina (CL370 and T60/T64, Almatis, Germany) were used as $Al_2O_3$ sources, whereas 11.4 wt% of ZnO (analytical grade, Basile Química, Brazil) was added to induce the formation of 23.1 vol% (25.7 wt%) of $ZnAl_2O_4$ after firing. The castables were bonded with 6 wt% of calcium aluminate cement (CAC, Secar 71, Imerys Aluminates, France) and dispersed using 0.2 wt% of a commercial surfactant (Castament FS60, BASF, Germany), as shown in Tab. 1.

Tab. 1: Overall castable composition.

| Raw material | wt% |
|---|---|
| Tabular alumina (<6 mm) | 77.6 |
| Calcined alumina (CL370) | 5.0 |
| Calcium aluminate cement | 6.0 |
| ZnO | 11.4 |

This dry mixture was firstly homogenized for 5 minutes in special rheometer equipment designed to process refractory castables, followed by the addition of 3.8 wt% of distilled water. The fresh suspension was molded into bars (25 mm x 25 mm x 150 mm), cured in a climatic chamber (VC 2020, Vötsch, Germany) for 24 h under 50 ºC and 80 % of relative humidity, dried at 110 ºC for another 24 h, and calcined at 600 ºC for 5 h.

The calcined samples were then sintered at different temperatures up to 1600 ºC using a conventional electric furnace (model BF51314C, cavity capacity of 2.5 L, Lindberg/blue, USA) or up to 1700 ºC in microwave equipment (model MS6K, multimode cavity, 2.45GHz, useful cavity capacity of ~ 3 L, Cober Electronics, USA) with effective power (also referred to as non-reflected or forward power) up to 4 kW and silicon carbide as susceptors[4]. In the former case, a constant heating rate of 2 ºCmin$^{-1}$ and a dwell time of 5 h was applied, whereas for the latter, 50 ºCmin$^{-1}$ up to 1100 ºC and 20 ºCmin$^{-1}$ above it, and dwell time of 15 minutes at the selected temperature, was used. To ensure proper temperature control, a type-B thermocouple (Thermo Fisher Scientific, USA) or a pyrometer (MA2S, Marathon Series, Raytek, USA) were applied in the conventional and microwave equipment, respectively. Moreover, the electric power required for the set firing schedule in both furnaces was tracked down using the potentiometer embodied in each piece of equipment (BF51314C and MS6K, for the electric and microwave furnaces, respectively).

The previously described sintering conditions gave rise to the nomenclature system, depicted in Tab. 2. After the sintering step, all samples had their mass loss assessed with an analytical balance (model TS400D, Ohaus, USA). Young's modulus was measured by the non-destructive sonic resonance technique (Scanelastic equipment, ATCP Physical engineering, Brazil). Cold modulus of rupture (CMOR) was carried out in MTS 810 equipment (MTS Systems, USA) under 3-point bending (ASTM C133 – 97) and

using 8 specimens for each sintering temperature. Quantitative mineralogical content was conducted by applying Rietveld's refinement (Topas software, version 4.2, Bruker, USA) on the X-ray diffraction patterns (D8 Focus, Bruker, Germany) obtained for grounded samples. Open porosity and density were evaluated by the immersion method based on Archimedes' principle and using kerosene as liquid media (ASTM C830-00). Based on the samples' density and the theoretical density considering the quantitative phase content (XRD), the total porosity was estimated. The microstructure of some selected samples was evaluated by scanning electron microscopy (Inspect S50, FEI, USA) coupled with an energy-dispersive X-ray spectroscope (EDS). Additionally, thermodynamic calculations (FactSage 6.4, CRCT, Canada) were carried out to assess the oxygen partial pressure ($pO_2$) inside the microwave cavity during the sintering.

Tab. 2: Nomenclature used for the distinct sintering methods.

| Firing Method | Maximum temperature | Nomenclature |
|---|---|---|
| Electric furnace | 1150 ºC | EF-1150 |
| | 1300 ºC | EF-1300 |
| | 1500 ºC | EF-1500 |
| Microwave | 1150 ºC | MW-1150 |
| | 1300 ºC | MW-1300 |
| | 1500 ºC | MW-1500 |
| | 1700 ºC | MW-1700 |

**RESULTS AND DISCUSSIONS**

Aiming at addressing the effect of the sintering method on the microstructure of the castable, the total and open porosity were measured and are depicted in Fig. 1. For conventional firing, it could be seen that the increase in the thermal treatment temperature resulted in a decrease in both open and total porosity, especially in the former. Additionally, for the same sintering process a general trend between total and open porosity could be seen (indicated by the red dotted line), in which the total porosity scales with the open porosity. This behaviour is expected for this traditional sintering technique as the densification process will usually act similarly on open and closed pores located among the particles (whereas pores within the grains require much higher energy to be eliminated), reducing their amount[3].
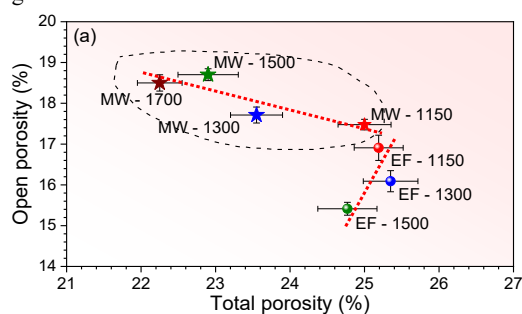


Fig. 1: Open and total porosity of rupture for conventional (EF) and microwave (MW) sintered castables. Adapted from Ref. 12 with Elsevier permission (nº 5577640295991).

As higher heating rates favoured the densification process rather than grain coarsening, a more significant reduction in both types of pores was expected for microwave sintering[7]. Nevertheless, for these samples, the increment in the sintering temperature led to a significant total porosity decrease, as expected, but with an open porosity increase. Therefore, although more effective to densify the castable composition evaluated in this work, the microwave heating technique also induced a higher number of open pores. It is worth highlighting that this additional open porosity is not necessarily detrimental to the castables' properties. On one hand, if they are small and well dispersed, these open pores can induce fracture energy increase by crack branching and/or increasing the crack tip curvature radius[8]. On the other hand, if coarse and preferentially

located, this open porosity will act as critical defects and paths for slag infiltration, reducing the mechanical and corrosion resistances. To evaluate the impact of each sintering condition on the mechanical properties of the castable, Youngs' modulus (E) and cold modulus of rupture (CMOR) tests were carried out and are presented in Fig. 2.
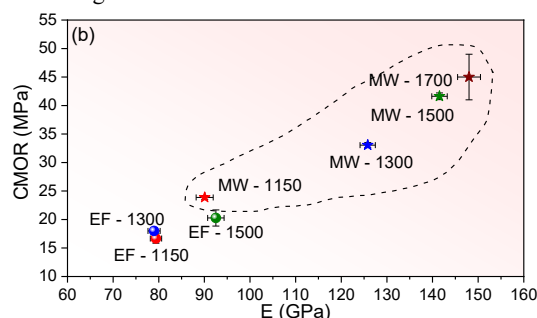


Fig. 2: Elastic modulus and cold modulus of rupture. Adapted from Ref. 12 with Elsevier permission (nº 5577640295991).

Analysing these results, one can see a clear relationship between E and CMOR for both sintering techniques. Additionally, although increasing the sintering temperature resulted in enhanced mechanical properties for conventional and microwave-sintered samples, this effect was much more significant for the latter. The joint analyses of Fig. 1 and Fig. 2 points out, as expected, that the total porosity plays a major role on the mechanical strength. Therefore, the significant densification led by microwave sintering resulted in samples with higher E and CMOR, which is attributed to the higher heating rate and enhanced ion diffusion induced by this sintering technique[2]. Note that the samples sintered by microwave radiation at 1150 ºC for 15 minutes presented equivalent strength to those conventionally fired at 1500 ºC for 5 hours. Thus, while the conventional sintering (1500 ºC) lasted 17.5 h to complete the firing schedule, the microwave heating (1150 ºC) required less than 40 minutes to produce castables with similar E and CMOR, which is twenty-six-fold faster.

Besides the time saving, the energy consumption to manufacture the specimens was also highly impacted by the firing method. Fig. 3 shows the energy required to run the sintering procedure in the electric furnace (2 ºCmin$^{-1}$ up to 1500 ºC and 5h of dwell time) and in the microwave one (50 ºCmin$^{-1}$ up to 1100 ºC and 20 ºCmin$^{-1}$ above it, with a dwell time of 15 minutes). Analysing it, one can see that the conventional furnace demanded 3.5 kWh per sample, whereas the microwave consumed 1 kWh per sample, which is ~ 70 % lower. This higher efficiency can be attributed to the lack of energy loss for heating up the air and insulating refractories inside the microwave equipment. Conversely, in conventional heating, all the systems (air and refractories included) will reach high temperatures, implying higher energy losses[2].
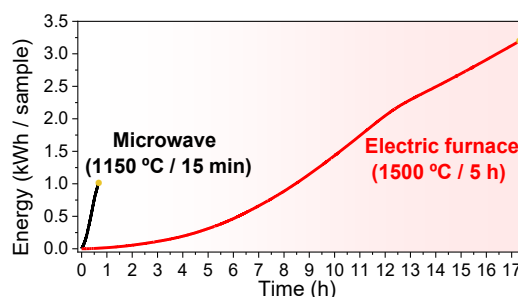


Fig. 3: Energy demanded for each bar sample to be sintered (● denotes the end of the firing process). Adapted from Ref. 12 with Elsevier permission (nº 5577640295991).

Therefore, to reach equivalent E and CMOR in the analysed system, the microwave sintering (1150 ºC / 15 min) was 26-fold faster and 70 % more energy-efficient that the conventional electric-heated equipment (1500 ºC / 5 h). Although these are eye-catching features, it is worth noticing that suitable E and CMOR are

just two of several other key properties that must be fulfilled by the refractory material, depending on the application. Therefore, further analyses are required to assess the feasibility of applying such a sintering technique to a broad production of refractories. Moving forward on these characterizations, the microstructural changes resulting from the distinct sintering methods were evaluated by BSE/SEM, depicted in Fig. 4, of samples thermally treated at 1150 ºC and 1500 ºC. It is worth noticing that the comparison between samples produced by both sintering techniques must consider that the microwaves electromagnetic fields affect samples' thermodynamic stability and enhance the ion mobility[9]. On top of that, the quite distinct heating rate used for each sintering technique also helps to induce different microstructures, as previously reported by several other authors[3].
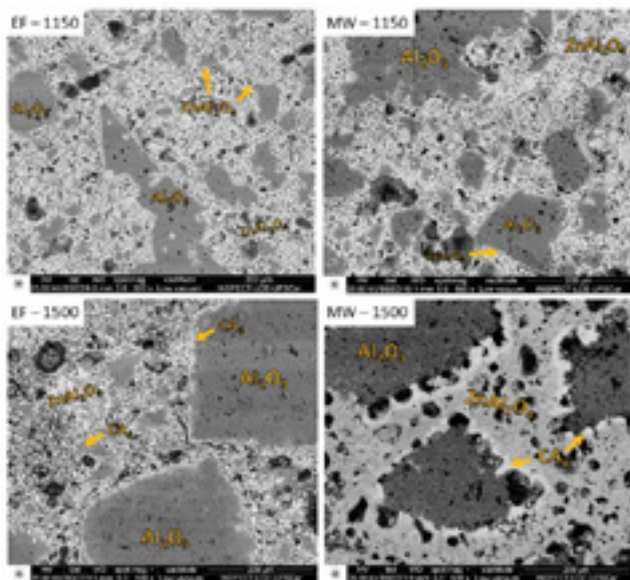


Fig. 4: Microstructure of samples sintered at 1150 ºC or 1500 ºC assessed by SEM/BSE. Adapted from Ref. 12 with Elsevier permission (nº 5577640295991).

Initially, firing at 1150 ºC by both sintering methods resulted in similar microstructures comprised of well-defined alumina aggregates with $ZnAl_2O_4$ formed in the matrix, which also presented several pores and undensified regions attributed to the significant Kirkendall effect undergone by this composition[5]. As the temperature increases to 1500 ºC, some distinctions between the heating methods stand out. In tune with total porosity analysis (Fig. 1), the conventionally fired samples remained with a less densified gahnite-based matrix. Moreover, at 1500 ºC, the samples also presented acicular-grown calcium hexaluminate ($CaO·6Al_2O_3$ or $CA_6$) as a result of the calcium aluminate cement (CAC) addition. On the other hand, for the microwave sintering, heating at 1500 ºC led remarkable microstructural changes, with nodular-like $CA_6$ formation in a highly densified matrix containing spherical pores. These types of microstructures agree with the porosity results presented in Fig. 1, in which the microwave sintering was more effective to reduce total porosity, but induced the formation of a higher number of open pores.

Aiming at assessing the mechanism that led to this open porosity increase for the microwave sintering, calcined samples had their mass loss analyzed after subsequent thermal treatments, as shown in Fig. 5 (a). At temperatures in the range of 1150 ºC up to 1500 ºC, no appreciable mass loss was detected for conventionally fired samples, which is assigned to the lack of organic or hydrated phases, as they were decomposed in the calcining step. However, the mass loss faced by microwave-heated samples stood out. Firing at 1500 ºC and 1700 ºC in the microwave equipment resulted in a mass decrease of 1.3 wt% and 4.3 wt%, respectively. To track down the causes of these mass losses, quantitative XRD analyses were conducted and Fig.5 (b) depicts the changes in gahnite content for the conventionally- or microwave-heated samples.
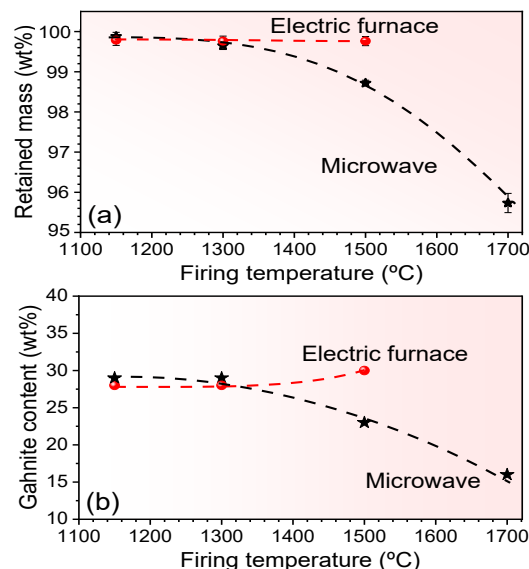


Fig. 5: (a) Mass variation after firing; (b) $ZnAl_2O_4$ (gahnite) content measured by quantitative XRD. Adapted from Ref. 12 with Elsevier permission (nº 5577640295991).

Conversely to the conventional firing, in which gahnite was stable at all analyzed temperatures, the microwave heating led to partial gahnite decomposition at 1500 ºC and 1700 ºC. Moreover, as no other Zn-containing phase was detected and the reduction in $ZnAl_2O_4$ content took place along with alumina content increase, gahnite decomposition could have happened by the Zn volatilization, which was withdrawn from the spinel structure as gaseous zinc, leaving $Al_2O_3$ behind. The zinc removal from the spinel structure was already studied in the literature, especially applied to zinc recovery from the blast furnace dust, which presented up to 5 wt% of zinc ferrite ($ZnFe_2O_4$) and gahnite ($ZnAl_2O_4$) in its composition[10]. Nevertheless, in that dust, zinc volatilization just takes place close to 1300 ºC at reducing atmospheres[10]. Although neither the electric furnace nor the microwave equipment had a controlled atmosphere, the latter presented susceptors made out of silicon carbide, which could be oxidized at high temperatures leading to a reducing environment inside the microwave chamber.

To evaluate this hypothesis, a piece of the silicon carbide susceptor used for a single sintering (1500 ºC / 15 min) in the microwave equipment [a picture of distinct pieces before and after such thermal treatment can be seen in Fig. 6] had its transversal sectioning evaluated by SEM, depicted in Fig. 6. A $SiO_2$ layer on the surface of the SiC susceptor was observed and its mean thickness measured was 64.9 µm. Based on this oxidative reaction zone, a $pO_2$ down to $10^{-15}$ atm and $10^{-13}$ atm are foreseen by the thermodynamic simulation to be formed inside the microwave chamber at 1500 ºC and 1700 ºC, respectively. Therefore, although experimental measurements are required to precisely determine the real $pO_2$-value during the microwave sintering, it can be inferred that the SiC oxidation will lead to a reducing atmosphere inside the microwave chamber during sintering.
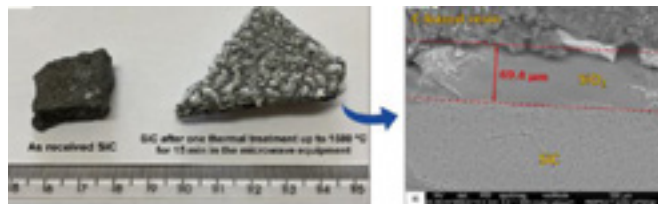


Fig. 6: Distinct SiC-based susceptors pieces before (as received) and after the microwave treatment up to 1500 ºC for 15 minutes under uncontrolled atmosphere, and SEM image of the $SiO_2$ layer formed on the SiC susceptor surface after one heating at 1500 ºC for 15 minutes. Adapted from Ref. 12 with Elsevier permission (nº 5577640295991).

As previously discussed, well-distributed small pores in the highly densified matrix of the castable are not necessarily undesirable. However, for some applications in which the castable will be in contact with molten media (slag or metal), these open pores can increase the susceptibility to corrosion. Thus, a likely strategy to merge the high strength (E and CMOR) provided by the microwave sintering at higher temperatures (> 1300 ºC) with the minimization of the open porosity is attained by applying a purging gas flow inside the microwave chamber to reduce the SiC oxidation, avoiding the formation of a reducing atmosphere during the firing procedure. To assess such an approach, argon (Ar, analytical grade) was used to continuously purge the microwave chamber (flux of 1.5 L min$^{-1}$) when heating at 1500 ºC for 15 min, resulting in the castable microstructure depicted in Fig. 7. Although not fully avoided, the porosity created due to ZnO volatilization was minimized and the mean size of the pores was reduced. Compared to the samples fired at the same temperature and dwell time, but without atmospheric control, lower mass loss after sintering (0.65 wt% vs. 1.3 wt%), a decrease in the total and open porosity (21. 2 % and 16.4 % vs. 22.9 % and 18.7 %, respectively), higher E (154 GPa vs. 142 GPa) and improved CMOR (48 MPa vs. 41.4 MPa), were achieved. Moreover, another interesting aspect was the formation of the $ZnAl_2O_4$ phase within the alumina aggregates. Thus, conversely to the microstructure obtained for the microwaved samples (1500 ºC / 15 min) in an uncontrolled atmosphere, the gahnite formed inside the alumina aggregates could be preserved in a saturated argon environment.
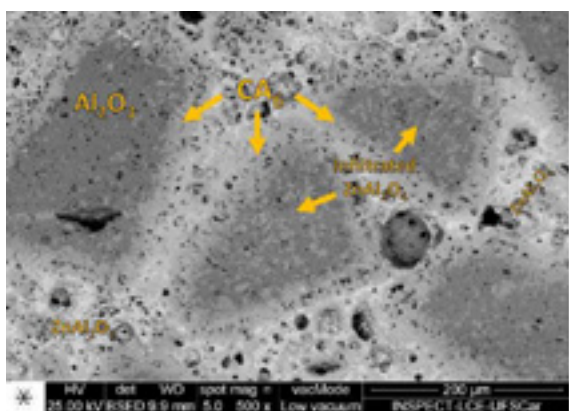


Fig. 7: Microstructure (SEM/BSE) of microwaved samples processed at 1500 ºC for 15 minutes under a controlled atmosphere (Argon, 1.5 L min$^{-1}$). Adapted from Ref. 12 with Elsevier permission (nº 5577640295991).

These results indicate that the zinc volatilization was minimized by controlling the atmosphere during the microwave sintering, but it was not completely halted. Two non-mutually exclusive mechanisms could explain such behaviour: (i) the electromagnetic microwave fields imposed on the sample at high temperatures may change the thermodynamic stability of zinc in the structure (it is worth noticing that all thermodynamic calculations were conducted considering no electromagnetic fields due to the lack of data under such conditions); (ii) the gas flux applied (1.5 L min$^{-1}$) increased the $pO_2$ during the sintering, but it was not enough to avoid the formation of a reducing atmosphere. The evaluation of such a hypothesis requires further analysis, however, for the second case, replacing silicon carbide susceptors by oxide materials could be a suitable way to avoid a reducing atmosphere during the microwave sintering procedure[4]. In this sense, some promising alternatives are being evaluated.

## CONCLUSIONS

The feasibility of applying microwave sintering to ZnO-containing alumina-based castables bonded with CAC was assessed using SiC susceptors up to 1700 ºC with a dwell time of 15 minutes. To enable comparisons, conventionally fired samples were produced in an electric furnace after sintering for 5h at selected temperatures. Due to the higher heating rate and enhanced ion mobility provided by the microwave technique, denser (lower total porosity) and stronger (higher E and CMOR) samples were produced in a much faster and 70% less energy consuming sintering procedure. The microwave processing also induced an increase in open pore content, as shown by SEM micrographs. The pores were relatively small in size and homogeneously scattered in the matrix of the castable, which could positively impact some thermomechanical properties. Despite these worthwhile aspects, mass loss and quantitative XRD indicated zinc volatilization for microwave samples heated above 1300 ºC in air. When a purging inert gas flux was applied to the microwave sintering up to 1500 ºC, mass losses were significantly decreased, corroborating the hypothesis that a reducing atmosphere is fostering such ZnO volatilization. Therefore, even though some parameters must be optimized, the present work highlights that microwave radiation could be applied to thermally treat some pre-shaped refractory compositions, leading to environmental, productivity and performance benefits.

## REFERENCES

1. U.S. Energy Information Administration. The International Energy Outlook. at (2021).
2. Ibn-Mohammed, T. *et al.* Decarbonising ceramic manufacturing: a techno-economic analysis of energy efficient sintering technologies in the functional materials sector. *J. Eur. Ceram. Soc.* **39**, 5213–5235 (2019).
3. Oghbaei, M. & Mirzaee, O. Microwave versus conventional sintering: A review of fundamentals, advantages and applications. *J. Alloys Compd.* **494**, 175–189 (2010).
4. Bhattacharya, M. & Basak, T. Susceptor-assisted enhanced microwave processing of ceramics - a review. *Crit. Rev. Solid State Mater. Sci.* **42**, 433–469 (2017).
5. Borges, O. H., Sardelli, J. A. P., Pagliosa Neto, C., da Luz, A. P. & Pandolfelli, V. C. ZnO and MgO as inducers of spinel-like phase formation on alumina-based castables. *J. Eur. Ceram. Soc.* (2022) doi:10.1016/j.jeurceramsoc.2022.08.030.
6. Sardelli, J. A. P., Borges, O. H., Neto, C. P. & Pandolfelli, V. C. Is the *in-situ* $ZnAl_2O_4$ formation an alternative for magnesia-alumina spinel zero-carbon shaped refractories? *Ceram. Int.* (2023) doi:10.1016/j.ceramint.2023.06.119.
7. Barsoum, M. W. *Fundamentals of ceramics*. (IOP, 1997).
8. Coates, C. & Sooklal, V. *Modern Applied Fracture Mechanics*. (CRC Press, 2022). doi:10.1201/9781003052050.
9. Laughlin, D. E. Magnetic transformations and phase diagrams. *Metall. Mater. Trans. A* **50**, 2555–2569 (2019).
10. Wang, W. *et al.* Effect of $CaCO_3$ on volatilization of self-reduced zinc from blast furnace dust. *J. Iron Steel Res. Int.* **29**, 1404–1411 (2022).
11. Jacques Poirier & Michel Rigaud. *FIRE Compendium Series: Corrosion of refractories - the fundamentals*. (Göller Verlag, 2017).
12. Borges, O. H., Cardoso, A. L. F., Moreira, M. H., Klein-Gunnewiek, R. F. & Pandolfelli, V. C. Conventional and microwave-assisted sintering of ZnO-containing CAC-bonded alumina-based refractory castables. *J. Eur. Ceram. Soc.* (2023) doi: 10.1016/j.jeurceramsoc.2023.06.063.

195

# ONE SIDED DRYOUT DEGRADATION

Joshua Sayre, Jeffrey Bogan, HarbisonWalker International, Pittsburgh, USA

## ABSTRACT

Dryout of monolithic products is the last step of a successful installation. Depending on the nature of the dryout; steam and internal pressures can degrade the mechanical properties of a product even before the material is put into service. In extreme cases, the lining spalls and needs reconstructed. While a spalled lining is an obvious, mechanical properties of a lining that has not spalled may be decreased that can reduce the linings service life without any visual evidence of damage. Studying the residual properties of samples from panels dried from one side, degradation in mechanical properties were observed that influence the rate at which lining can be heated up.

## INTRODUCTION

One of the key attributes of a successful monolithic refractory installation is the dryout or the removal of the water. The water takes two forms within a monolithic product either physical or chemical, bound in cement hydrates. Two typical situations occur upon dryout either the lining survives the dryout and is put into service, or the material can spall and thus require removal or additional repair. However, even if the lining has not spalled the lining may have been degraded on dryout from the introduction of cracks and potentially reducing the life span of the lining. Refractory producers recommend following carefully controlled dryout profiles to maximize the performance of a lining. These profiles take into lining configurations and factor in a degree of safety to reduce any degradation to the material.

Calcium aluminate cement (CAC) bonded refractories dominate the monolithic refractory products due to their relative ease of installation, green strength, and suitable properties. Upon installation, the CAC forms four major hydration products: free water (100°C), $7C_3AH_6$ (227°C), $C_3AH_6$ (277°C), and $C_3AH_{1.5}$ (549°C). As the temperature of the lining increases; steam possesses an exponential increase in pressure with temperature. If the pressure exceeds the strength of the material, cracks will form, and the material can catastrophically fail. Cracks can also be formed by the differential thermal expansion due to the transient heat wave through a refractory upon the initial heat-up. Any cracks can cause permanent detrimental reduction in mechanical strength, because steam pressure cannot be relieved quickly through crack propagation without catastrophic spalling. Organic dryout fibers are utilized to help form channels to increase the permeability of the product and allow for the successful dryout.

The work here focuses on the cracks and observable changes based on different dryout rates utilized in one sided dryouts. The goal is to better understand how faster one side dryouts permanently degrade the mechanical properties of a lining

## TEST PROCEDURES

Samples of 46cm x 30.5cm x 20cm were formed inside a metal shell with 101.6cm solid sides (see Fig 1 & Fig 2). The samples were either cast, gunned, or rammed into place. After curing, the test pieces were placed into the door of a gas fired kiln. Three Type-K thermocouples were used to monitor the test panels inside the door of the kiln: two on the front face and one thermocouple mounted in the back of the panel.

Three types of products were chosen to perform the one-sided dryout testing: lightweight gunite mix, 60% alumina low cement dense gunite mix, and 85% alumina phosphate plastic mix. Three samples (23cm x 11.5cm x 5cm) were cut from each panel representing the hot surface, intermediate surface and back (see Fig

3). A set of standard samples were reheated using standard heating rates for property testing - cut before reheating.

The kiln ramp rate was varied depending on the product and desired testing. The lightweight product had the most testing performed: 55°C/hr, 167°C/hr (2x), 277°C/hr, and 417°C/hr. (See Fig 4). One 166°C/hr run experienced a rapid heat-up with an excursion straight to 204°C before aligning with the set point for the kiln. The low cement dense castable was tested at 111°C/hr and the 85% alumina phosphate plastic at 277°C/hr. All pieces were ramped to 815°C and held for 16 hours before cooling at 55°C/hr.



Fig. 1: Gunned sample formed inside shotbox



Fig. 2: Sample removed from Wood forms. Note the metal casting that makes up the shell of the panel.
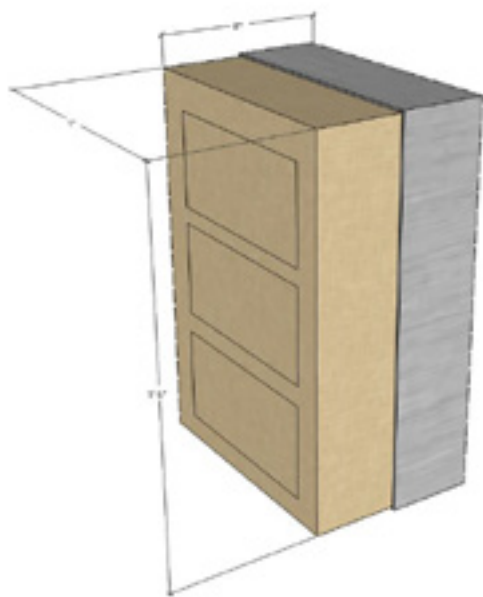
Fig. 3: Schematic of the Samples Cut from the Prepared Panels
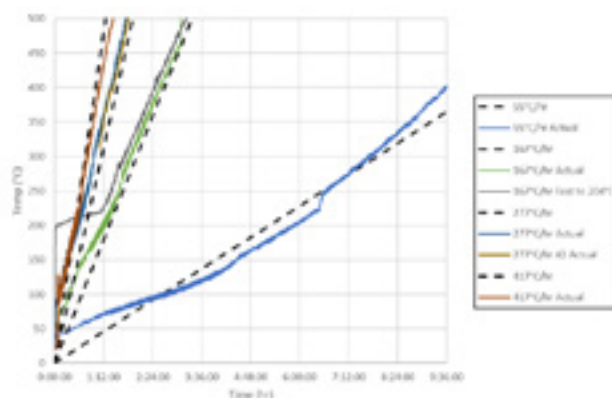


Fig 4: Kiln Profile of Heat-ups for the lightweight gunite mix.

## RESULTS AND DISCUSSION

The concern with increasing the ramp rate is degradation in the mechanical properties of materials due to the increase in cracking as steam escapes due to the physical and chemical water contained in the refractory[1-3]. An additional degradation most likely can occur due to the differential thermal expansion of the material with faster heat-ups with extreme cases being thermal shock. Combining these two forces together can lead to increased cracking and degradation of the final properties of the monolithic lining. When examining the degradation of the lightweight castable this became the focal point of the analysis.
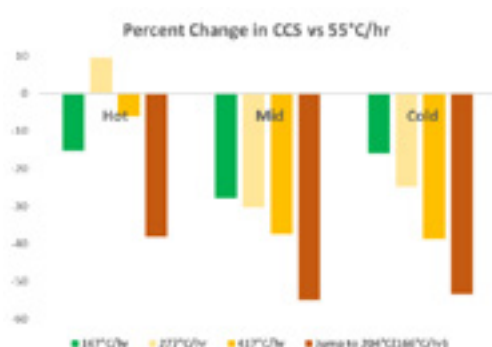


Fig 5: Percent Change in CCS from 55°C/hr to faster dryout rates for 1.28 g/cc LW Gun Mix

With each increasing ramp rate, the resulting CCS shifted lower with the 417°C/hr ramp rate resulting in over a 1/3 reduction in CCS strength after ramping the simulated lining (See Fig 5). No visible cracks were apparent. The observed trends in MOR did not align with the shifting ramp rate, which likely indicates the degradation due to the dryout is less apparent in MOR since this is more related to internal macro crack generation for a middleweight refractory. The sample that experienced a rapid excursion to 204°C before adjusting the temperature profile exhibited the highest loss in CCS due to the extreme excursion. While not targeted to be part of the analysis, this provided very insightful data on very rapid heating rates because these types of excursions are not uncommon due to the difficulties of maintaining low temperatures with process heaters versus utilizing specifically designed excess air burners for dryout.

Shifting to the dense 60% alumina gunite mix, a 167°C ramp rate caused extensive cracking that didn't affect the CCS as much as the MOR (see Table 1). While the CCS did decrease by 10-20%, the MOR decreased between 50-65%. The cracking emanated from the hot face of the block, which is likely the difference between the larger percent drop in MOR versus the lower percent drop in CCS. While the cracks will leave a permanent reduction in the mechanical properties, they may be acting as channels for moisture to escape the castable.

Table 1: 60% Alumina Dense Gunite Mix After 167°C/hr. STD is 55°C/hr samples dried separately

| 815°C | | | |
|---|---|---|---|
| | STD | Hot | Mid | Cold |
| Density (g/cc) | 2.26 | 2.23 | 2.23 | 2.22 |
| MOR (MPa) | 10.4 | 3.7 | 5.0 | 7.3 |
| CCS (MPa) | 54.1 | 47.6 | 44.6 | 44.3 |

Rammed 85% alumina phosphate plastic also produced significant degradation in mechanical properties when heated at 417°C/hr. Phosphate plastics are often recommended to be heated at faster rates due to their typical usage as patches and phosphate bonding. Phosphate bonding does not produce permeability reducing hydrate phases and contains less water that needs to be removed. However, phosphate bonded materials still require a controlled dryout. The phosphate materials go through a softening as phase changes occur with the final crosslinking occurring after 250°C. Due to the softening and lower strength until reaching the desired temperature, the transient heating conditions through the block led to cracking that radiated with the temperature profile through the block. This isn't surprising as layers of material would have changing phases and varying strength creating stress planes within the mix. The degradation yielded a 75% reduction in CCS and 90% reduction in MOR (see Table 2).

Table 2: 85% Alumina Phosphate Plastic Testing After 417°C/hr

| 815°C | | | |
|---|---|---|---|
| | STD | Hot | Mid | Cold |
| Density (g/cc) | 2.62 | 2.38 | 2.41 | 2.28 |
| MOR (MPa) | 10.3 | 1.5 | 2.1 | 1.7 |
| CCS (MPa) | 44.3 | 13.1 | 11.0 | 9.2 |

197

## CONCLUSIONS

Monolithic dryout is a critical aspect of a successful installation. While the focus of most dryout testing and analysis is on successfully removing the water and surviving; the work presented here identified cracking from the heat-up causing permanent degradation in the mechanical properties of the lining with accelerated heat-ups in one-sided drying situations. The faster the heat up rate the greater the strength loss even without catastrophic failure occurring. A lightweight gunning mix was able to be dried out at an accelerated rate due to the high porosity/permeability (higher water) nature of the mix with only minimal strength degradation. For a dense castable and phosphate bonded ram mix, 38°C/hr is still recommended. This aligns with most fired brick manufacturer recommendations due to the inherent concerns with thermal expansion and lowering the chance of cracks.

## REFERENCES

[1] Salomao, R., Pandolfelli, V., "Dryout temperature-vapor pressure profile of polymeric fiber containing refractory castables," Ceramics Intl 39, pp.7217-7222, (2013).

[2] Hipps, D.L. and J.B. Brown, "Internal Pressure Measurements for Control of Explosive Spalling in Refractory Castables," Am. Ceram. Soc. Bull., 63[7] 905-910 (1984)

[3] Bogan, J., "Dryout of refractory castables," The 39th Symposium on Refractories, St Louis Section Meeting, April 9-10, (2003).

# OBSERVATIONS ON THE STRENGTH AND DRYING PERFORMANCE OF SOLCAST CASTABLES

Antti Piippo, Kyösti Ruotanen, Niko Poutiainen
Bet-Ker Oy, Ylivieska, Finland

Eetu-Pekka Heikkinen, Ville-Valtteri Visuri
Process Metallurgy Research Unit, University of Oulu, Finland

## ABSTRACT

Colloidal silica has been used as a CaO-free binding system over a long time. The drawback of colloidal silica castable has been the low green strength and long setting times compared to CAC-based castable [1]. Yaghoubi et al. found that siloxane bond formation increases when CAC is added to colloidal silica-bonded castable [2]. CAC as the setting agent showed good green strength in the castable [2]. Development has been done with various SolCast castables to increase green strength but to still have good drying properties. Drying is usually the longest and the most critical process observed when heating refractory lining to process temperature. The development of high steam pressure may lead to explosive spalling and mechanical damage to the refractory lining [3]. Luz et al. [3] wrote a review article about theoretical aspects related to the drying process, the influence of the phase transformations derived from the binder additives and the experimental techniques to assess the water removal from consolidated castable pieces [3]. Industrial scale drying tests were done with various CAC amounts and different heating curves. The optimum CAC had good green strength but didn't weaken drying properties. A rapid drying curve was found for 400kg precast shapes without drying damage.

## INTRODUCTION

Monolithic materials have developed a lot but still these products require special attention during their curing, drying and firing stages. [3] Drying is the most critical process for monolithic lining since the reduced permeability of lining may lead to explosive spalling or mechanical damage. [4] Steam pressure buildup can be avoided by applying more permeable lining. [4] Colloidal silica-bonded castables have higher permeability compared to calcium aluminate cement (CAC) bonded castables and are thus known for their good drying properties. [1]

There has been a lot of research on the differences between CAC and colloidal silica. [1] Low green strength and long setting time has been the drawback for colloidal silica castables. [2] Yaghoubi et al. [2] found that siloxane bond formation increases when CAC is added but this may affect the workability of castable. Nouri-Khezrabad et al. [5] studied effects of CAC and hydratable alumina (HA) addition to colloidal silica-bonded castable and found out CAC+HA had the most positive impact on the green strength. Nonetheless HA has poor drying properties and this will hinder good drying properties of colloidal silica-bonded castable. CAC addition showed good green strength for the castable. [5]

Still it is not clear what is the optimum amount of CAC addition to have good drying properties and to have higher green strength for the castable. In this study industrial-scale drying experiments were carried out to find out optimum CAC addition and efficient drying curve for practical applications.

## MATERIALS AND METHODS

### Studied materials

Drying tests were carried out in two stages. First, tests with alumina castables with different amounts of CAC were conducted. Various tests were carried out on these alumina castables. Later, drying tests were made to alumina-silicate castables with fixed CAC amounts but with different drying curves. All the castables with colloidal silica and CAC were formulated using the Alfred packing model with q = 0.28.

Castable compositions for alumina castable can be seen in Table 1. The amount of fine tabular alumina varies to achieve the same particle size distribution for all of the castables. Tabular alumina, calcined alumina and calcium aluminate cement were supplied by Almatis. The magnesia content of dead burned magnesia was 90.5%. Used dispersants and retarders were sodium polyacrylate, boric acid and sodium tripolyphosphate. The consistency and fluidity of the mixtures were determined according to ASTM 860. The material was mixed dry for 4 minutes and 4 minutes after colloidal silica and water addition. Specimens for testing were cast under vibration.

Alumina silicate castable aggregates were chamotte and bauxite with a fixed CAC amount of 0.5 wt-%.

Tab. 1: Castable composition (wt-%)

|  | 0 | 0.5 | 1 | 1.5 |
|---|---|---|---|---|
| Tabular alumina (Almatis) | 84.8 | 84.3 | 83.8 | 83.3 |
| Calcined alumina (Almatis) | 12.9 | 12.9 | 12.9 | 12.9 |
| DBM | 0.2 | 0.2 | 0.2 | 0.2 |
| CAC 70% (CA-14 Almatis) | 0 | 0.5 | 1 | 1.5 |
| Colloidal silica suspension (40 wt.% solids) | 2% solids | 2% solids | 2% solids | 2% solids |
| Dispersant | 0.1 | 0.1 | 0.1 | 0.1 |
| Water (wt. %) | 3.5 | 3.5 | 3.5 | 3.5 |

### Experiments

Specimens (160x40x40 mm) were cured first at 20°C for 24h and then at 110 °C for 24h. Thermal treatment at 1600 °C was performed for 2h with Entech SF 6/17-S. The oven was heated to 1600 °C for 2h and the cooling was passive. Cold crushing strength (CCS) was determined according to EN 933-5:2018 with Pilot Controls 50-C92C22. Density and permanent linear changes (PLC) during the thermal treatments were determined according to ISO 1927:2012. Weight loss was determined between temperatures 110 °C and 1600 °C. Weight loss was calculated according to Eq. 1.

$$\text{Weight loss \%} = (W_{\text{Before firing}} - W_{\text{After firing}}) / W_{\text{Before firing}} \qquad (1)$$

The drying tests were performed using Nabertherm Mod W1500/A. Heating rate was 50 °C/h from 20 °C to 500 °C. Hold time was 12 h at 500 °C, and the furnace was allowed to cool to ambient temperature. Specimens for drying test were cast into 500x500x500mm mold. A thermoelement was installed during casting to the center of specimens.

199

Two test series were made: small-scale in the laboratory and industrial-scale drying tests. Small-scale tests were made only for alumina castables. Industrial-scale drying tests were made to get practical results from the drying. The surface area of laboratory-scale samples is too big to have practical results out of drying tests. The analyses conducted are tabulated in Table 2 along with relevant test specifications.

Tab. 2: Overview of analysis methods.

| Test series | Laboratory scale | Industrial scale | Note |
|---|---|---|---|
| Cold Crushing Strength | X | | EN 933-5:2018 |
| Density | X | | ISO 1927:2012 |
| Permanent Linear Change | X | | ISO 1927:2012 |
| Weight Loss | X | | Equation (1) |
| Casting properties | X | X | ASTM 860 |
| Drying properties | | X | 0.5m × 0.5m × 0.5m cube |

## RESULTS AND DISCUSSION

### Physical tests

Table 2 shows a compilation of the physical tests conducted. Results of CCS, density, PLC and weight loss are presented in Table 3. The values shown represent averages from three samples. CAC addition affects the low-temperature cold crushing strength. The addition of more than 1% of CAC has a clear effect on CCS at 20 °C. Differences in CCS at 110 °C and 1600 °C are minor, and variation, especially at 1600 °C, was extensive. CAC doesn't have a significant effect on CCS at higher temperatures since different sintering reactions have a greater effect. A decrease in density can be seen when CAC addition increases. The reason for this is the higher density of tabular alumina compared to CAC but also higher porosity in the castable when CAC is used. This result is in line with the results by Gao et al. [6]. There are minimal differences in PLC and weight loss, but there is no trend with increasing CAC amount. There were no differences in the flowability and workability between castables.

Tab. 3: Measured properties oft he castables

| T (°C) | Property | 0 | 0.5 | 1 | 1.5 |
|---|---|---|---|---|---|
| 20 | CCS (MPa) | 22.08 | 22.72 | 33.87 | 33.23 |
| 20 | Density (kg/m$^3$) | 3.10 | 3.08 | 3.08 | 3.05 |
| 110 | CCS (MPa) | 47.00 | 41.61 | 56.68 | 63.13 |
| 110 | Density (kg/m$^3$) | 3.05 | 3.04 | 3.04 | 3.02 |
| 1600 | CCS (MPa) | 180.99 | 157.02 | 167.13 | 171.94 |
| 1600 | Density (kg/m$^3$) | 3.15 | 3.15 | 3.14 | 3.12 |
| 1600 | PLC (%) | −1.30 | −1.50 | −1.43 | −1.45 |
| 1600 | Weight loss (%) | 0.30 | 0.27 | 0.33 | 0.37 |

### Drying tests

The drying tests were conducted for 0.5m × 0.5m × 0.5m cube elements in an furnace while the temperature of the pieces and the furnace was measured. The measured temperatures and heating rates are presented in Figures 3 and 4, respectively. Photos of the elements after drying are presented in Figure 5. The temperature difference between furnace control and temperature measurement from the furnace atmosphere was detected. The maximum temperature for the drying test was 460°C, while the average recorded heating rate was 41.11 °C/h, a value somewhat lower than the aimed heating rate of 50 °C/h.

The results of the drying tests indicate that the CAC content increases the damage to the castable when the heating rate is high. Damage occurs even in the element where 0.5% CAC was used. Damage occurs when vapor pressure inside the element becomes higher than the strength of the castable. The sample with 0% CAC content had the steadiest heating rate of the samples. Only between 110°C and 140°C the heating rate slowed down due to the ebullition of water. A steady heating rate indicates that there are no restricting reactions from CAC to the ebullition of water.

Damage to the samples occurred when temperatures were between 300 °C to 400 °C. Wang et al. [7] found out that at this rapid dehydration stage from 220 °C to 340 °C Young's modulus decreases by approximately 50% compared to the room temperature when CAC is used as a binder.
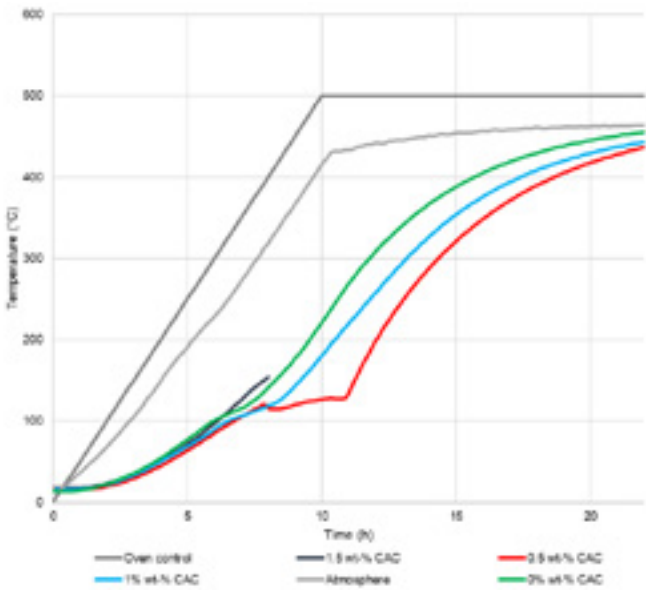


*Fig. 1: Temperature measurements from the drying test.*
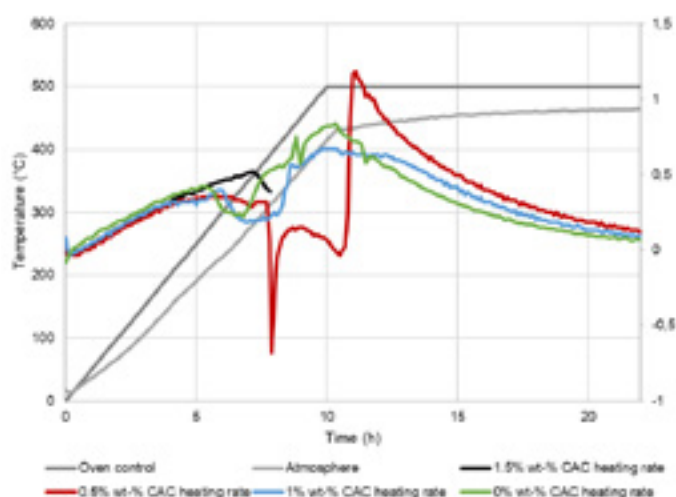
Fig. 2: Heating rates of samples on the drying tests.



Fig. 4: Drying test results with 0.5% CAC content and 25 hours drying time.



Fig. 3: Drying test results for 400kg pieces with different amounts of CAC: a) 0 wt-%, b) 0.5 wt-%, c) 1 wt-%, and d) 1.5 wt-%



Fig. 5: Element after 30-hour drying time with 0.5 wt-% CAC content.

A successful drying process is important when good results are wanted in practice. Even hair cracks that are formed during drying degrade the performance of refractory lining. Results from the alumina castable drying bring out possibilities of energy saving and better productivity with shorter drying times. Consequently, drying tests were continued with a fixed amount of 0.5 wt-% CAC. Aggregates in this mix are bauxite and chamotte, and DBM was not used, but otherwise, these castables are comparable. 0.5 wt-% CAC addition was used since it was found that CAC acts well as an accelerator for the colloidal silica binder. Binding was more robust compared to DBM, where setting time was more volatile. These additional drying trials are intended to find the optimal drying curve for the castable. The first drying was done in 30 hours up to a maximum temperature of 400 °C. Results from this drying are presented in Figure 4. Ebullition temperature can be seen from the temperature measurement since temperature isn't rising during ebullition. Ebullition temperature in the test was between at 170°C indicating high steam pressure inside the cube. After drying, there were no cracks or other damage in the cube element (see Figure 5).

The next drying trial was only 16 hours long, and the maximum temperature was set to 300 °C. Since the CAC amount is low, there are low amounts of alumina hydrates in the castable, and it is not necessary to heat the castable up to 400 °C. Results from this drying are presented in Figure 6. Ebullition temperature in this test was at 195 °C which is significantly higher compared to the previous test. After drying, there were no cracks or other damage in the cube element (see Figure 7).

201
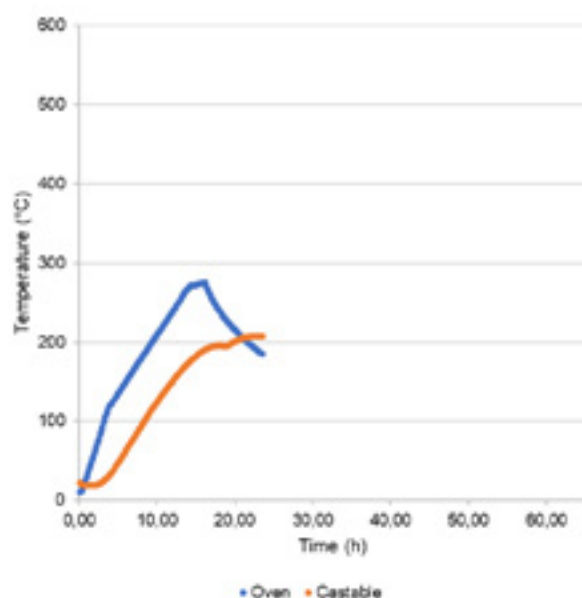
*Fig. 6: Drying test results with 0.5% CAC content and 16 hours drying time.*

202
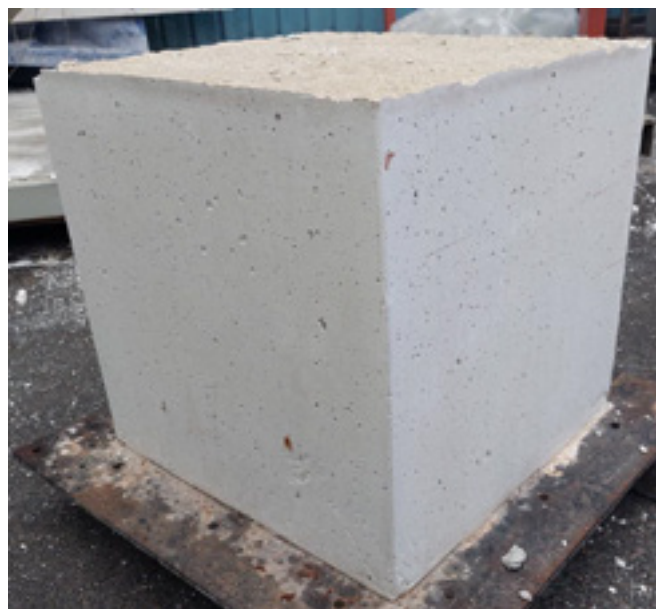


*Fig. 7: Element after 16-hour drying time with 0.5 wt-% CAC content.*

Drying trials with a fixed amount of CAC did not result in cracks or other damage and were thus considered successful. The employed drying time of 16 hours is very short for this kind of element with a width of 0.5 metres. Most of the applications for this kind of castable can be dried with the employed drying curve. Ebullition of water finishes actually after the drying curve is already terminated and the passive cooling of the oven is going on, which can be seen in Figure 6. Ebullition temperature is about 190 °C in the latest test which indicates high pressure inside the element. The strength of the element is enough to withstand this internal pressure.

## CONCLUSIONS

Results from this research clearly state the benefits of colloidal silica-bonded castables. 0.5 wt-% CAC amount was found to be a robust accelerator for the colloidal silica, and it also presents some strength development for the castable. Drying trials were conducted successfully with this low amount of CAC without any damage or cracks in the elements. Elements were so large (0.5m × 0.5m ×

0.5m cube) that practically almost all of the corresponding applications could be dried with this short 16-hour drying curve. Differences in the higher temperatures were not found in the alumina castables.

## REFERENCES

[1] M. Nouri-Khezrabad, M. A. L. Braulio, V. C. Pandolfelli, F. Golestani-Fard, and H. R. Rezaie, "Nano-bonded refractory castables," Ceramics International, vol. 39, no. 4. pp. 3479–3497, May 2013. doi: 10.1016/j.ceramint.2012.11.028.[4

[2] H. Yaghoubi, H. Sarpoolaky, F. Golestanifard, and A. Souri, "INFLUENCE OF NANO SILICA ON PROPERTIES AND MICROSTRUCTURE OF HIGH ALUMINA ULTRA-LOW CEMENT REFRACTORY CASTABLES," 2012.

[3] A. P. Luz, M. H. Moreira, M. A. L. Braulio, C. Parr, and V. C. Pandolfelli, "Drying behavior of dense refractory ceramic castables. Part 1 – General aspects and experimental techniques used to assess water removal," Ceramics International, vol. 47, no. 16. Elsevier Ltd, pp. 22246–22268, Aug. 15, 2021. doi: 10.1016/j.ceramint.2021.05.022.

[4] A. P. Luz, M. H. Moreira, R. Salomão, M. A. L. Braulio, and V. C. Pandolfelli, "Drying behavior of dense refractory castables. Part 2 – Drying agents and design of heating schedules," Ceramics International, vol. 48, no. 3. Elsevier Ltd, pp. 2965–2987, Feb. 01, 2022. doi: 10.1016/j.ceramint.2021.10.190.

[5] M. Nouri-Khezrabad, A. P. Luz, V. R. Salvini, F. Golestani-Fard, H. R. Rezaie, and V. C. Pandolfelli, "PaPers Novel Engineering Route to Improve the Green Mechanical Properties of Nano-Bonded Refractory Castables," 2015.

[6] S. Gao et al., "Effect of CAC content on the strength of castables at temperatures between 300 and 1000 °C," Ceram Int, vol. 46, no. 10, pp. 14957–14963, Jul. 2020, doi: 10.1016/j.ceramint.2020.03.024.

[7] Y. Wang, X. Li, B. Zhu, and P. Chen, "Microstructure evolution during the heating process and its effect on the elastic properties of CAC-bonded alumina castables," Ceram Int, vol. 42, no. 9, pp. 11355–11362, Jul. 2016, doi: 10.1016/j.ceramint.2016.04.058.

# EFFECT OF CURING TEMPERATURE AND CURING TIME ON THE PROPERTIES OF LOW CEMENT BONDED CORUNDUM – SPINEL CASTABLES FOR WELL BLOCK

Sisi Zhang, Guotao Liu, Guojie Liu, Zongzhe Li

Puyang Refractories Group Co., Ltd., Puyang, China

## ABSTRACT

This study involved an investigation of the influence of curing temperature and curing time on the properties of low cement bonded corundum-spinel castables for well block. The physical properties of the castables treated at different temperatures and the HMOR at 1500℃ were compared after short-term curing at 35℃, 45℃ and 55℃ for 4h, 6h and 8h, respectively. The structure evolution of specimens under different curing conditions were studied by SEM. The results showed that the CMOR and HMOR were unexpectedly the highest after curing at 35℃. The strength of cement bonded castables depends on cement hydration products, but the completion of the hydration reaction requires a certain temperature and time, and the generation of new hydration products may destroy the original structure, and then show differences in performance. This work provides guidance for the curing condition of the well block production.

## INTRODUCTION

Low cement bonded corundum-spinel castable has been widely used in different areas as working lining like steel ladle as well as in different prefabricated refractory items like well block, seating block due to its excellent thermal stability[1-2]. In practical manufacture process, due to the limitations of workers' working time and work efficiency, under normal circumstances, the demoulding time of the well block will not exceed 16 hours. Therefore, the curing step of the well block is critical. Calcium aluminate cements (CAC) is used as binder agents for low cement bonded corundum-spinel castable, providing relatively fast green mechanical resistance [3-5]. Reactions between CAC and water lead to the formation of diverse hydrated phases, which also results in difference at drying and firing stage. Additionally, this process mainly depend on the curing time and temperature [6-7], which is this work focused on, the effect of short curing time(4h, 6h and 8h) and temperature(35℃, 45℃ and 55℃) for the low cement bonded corundum-spinel castable is investigated to provide guidance for the curing condition of the well block production.

## EXPERIMENTAL

The main raw materials used in the experiment are corundum(Haicheng, China) with various article sizes (6-3mm, 3-1mm, 1-0mm and 325mesh), calcium aluminate cement (CAC, Secar 71, Kerneos, Tianjin, China), α-alumina powder(Almatis, Qingdao), spinel powder and additives. The chemical compositions and partical size of main raw materials are shown in Tab.1. All samples used in this work had the same initial composition. The aggregates and matrix were first mixed in a mortar mixer for 3 min, and then water was added to continue the mixing for another 3 min. After that, the prismatic samples were casted to a size of 40mm× 40mm× 160mm under vibration. The curing experiments took place at three temperatures, 35℃, 45℃ and 55℃, and for each temperature, the samples were cured for 4h, 6h and 8h to simulate a real production environment. The samples were labelled A-B, where A stands for the curing temperature, and B stands for the curing time. After curing, the samples were dried in a 110℃ chamber for 16h and then fired at 1600℃ with a holding time of 3h for basic performance tests. The hot modulus of rupture (HMOR) was carried out at 1500℃ with a holding time of 0.5h (using specimens pre-fired at 1600℃ for 3h). In order to analyse the microstructure of the castables at different treatment, the castable fracture was observed under SEM.

Tab.1: Chemical compositions and partical size of raw materials

|          | Al₂O₃ | CaO   | MgO  | SiO₂ | Na₂O | D₅₀ |
|----------|-------|-------|------|------|------|-----|
| Secar 71 | 69.50 | 29.50 | 0.31 | 0.31 | 0.20 | 12.68μm |
| CL370    | 99.86 | 0.03  | 0.04 | 0.00 | 0.02 | 2.57μm |

## RESULTS AND DISCUSSION

### Physical properties and mechanical properties

The curing samples were investigated because they should correspond to green bodies that are placed in the oven once they are firm enough to be demoulded. Fig.1 and Fig.2 present the CMOR and CCS of specimens after curing for various temperatures and time, Fig.3 and Fig.4 show their strength after drying. As can be seen that the green strength of specimens cured at 35℃ for 4h is sufficient for demoulding. And as expected, the demoulding strength increased with the raise of curing temperature and curing time. However, after dying at 110℃, the strength presents an unexpected different trend, the CMOR and CCS decreases with the temperature rising. This goes against a lot of research, and the possible cause may relate to the formation and destruction of hydrate products. The hydration products in the specimen aggrandized with the increase of curing temperature and the extension of curing time, which might introduce different phase composition as prevailing in the inner part. The compact cohesion and continuous distribution of large number of hydration products are cemented between the aggregate and fine particles, which is conducive to the improvement of the strength of the specimen after demoulding. After short time curing, the specimens were immediately heated to 110℃ for drying treatment, and the incomplete hydrated CAx continued to undergo hydration reaction, lead to the continuous increase of strength. However, the hydration products like CAHx decomposed rapidly when the temperature rose sharply, result in structural damage. As more hydration products are generated, theoretically the strength loss caused by dehydration and decomposition of hydration products will be more serious[8-9], thus the strength of specimens cured at 55℃ is lower than that of 35℃.
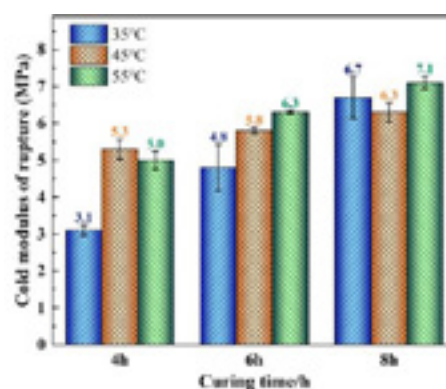


*Fig.1: The CMOR of specimens after curing*
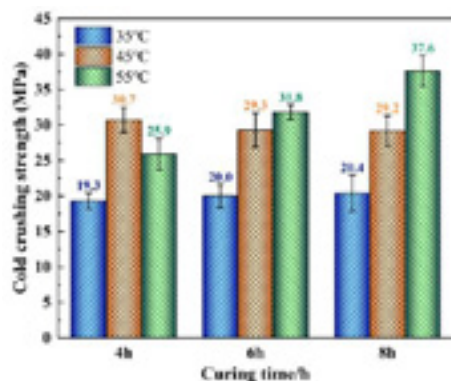
*Fig.2: The CCS of specimens after curing*
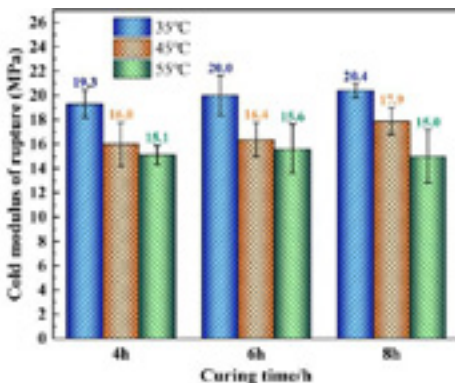


*Fig.3: The CMOR of specimens after drying*
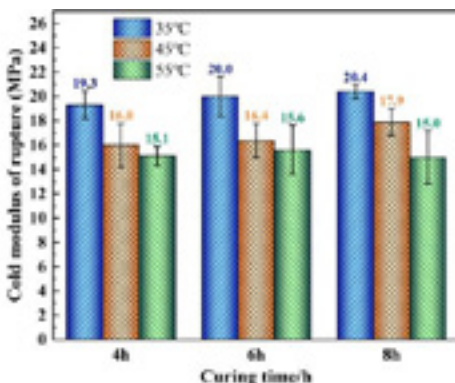


*Fig.4: The CCS of specimens after drying*

The bulk density and the apparent porosity after demoulding and drying are displayed in Tab.2. Under the same curing temperature, the bulk density of the sample increases with the prolonging of curing time, while the apparent porosity decreases. This can be attributed to the continuous formation and crystallization of hydration products. As for the specimens cured at different temperatures, no apparent regularity was found.

Tab.2: The BD and AP of specimens after drying

| Curing temperature | Curing time | Bulk density(g/cm$^3$) | Apparent porosity(%) |
|---|---|---|---|
| 35℃ | 4h | 3.20±0.01 | 11.9±0.2 |
| | 6h | 3.21±0.00 | 11.9±0.1 |
| | 8h | 3.24±0.02 | 9.6±0.2 |
| 45℃ | 4h | 3.18±0.01 | 12.1±0.4 |
| | 6h | 3.20±0.01 | 9.8±0.2 |
| | 8h | 3.20±0.00 | 10.0±0.1 |
| 55℃ | 4h | 3.18±0.01 | 11.9±0.3 |
| | 6h | 3.21±0.02 | 9.9±0.1 |

| | 8h | 3.20±0.01 | 9.0±0.1 |
|---|---|---|---|

The early curing conditions will affect the formation and crystallization of hydration products, and furthermore, cause the variations in sintering and microstructure of materials after high temperature treated [10]. Fig.5 and Fig.6 dipicted the CMOR and CCS of specimens fired at 1600℃ respectively. Interestingly, it's observed that specimens cured at 35℃ obtained highest strength, and there was a gradual decline with the raise of curing temperature especially for the short time curing of 4h.
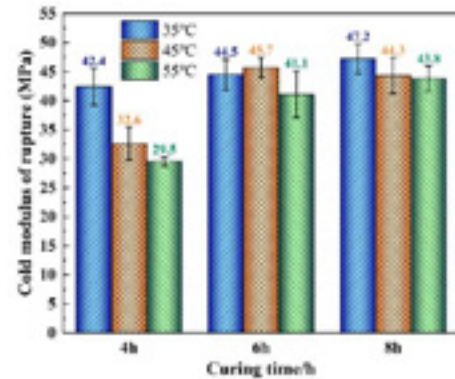


*Fig.5: The CMOR of specimens after firing at 1600 ℃*
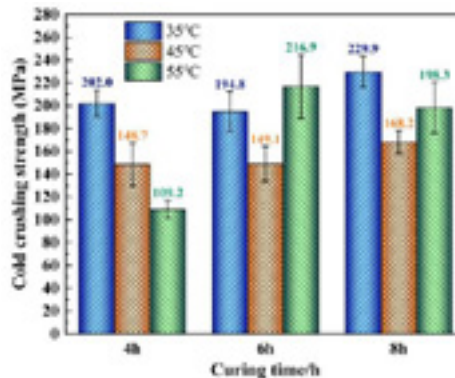


*Fig.6: The CCS of specimens after firing at 1600 ℃*

The bulk density, apparent porosity and permanent liner change of the specimens after high temperature firing are shown in the Tab.3, with slight difference. It can be seen that the overall bulk density of the sample after curing at 35℃ is higher, and the apparent porosity is lower, which indicates a more compact structure. Yet the permanent liner change was still expansion, owing to the formation of CA$_6$ crystals by calcium aluminate cement [9], which will be discussed later.

Tab.3: The BD and AP of specimens after firing at 1600℃

| Curing temperature | Curing time | Bulk density(g/cm$^3$) | Apparent porosity(%) | PLC/% |
|---|---|---|---|---|
| 35℃ | 4h | 3.13±0.01 | 16.9±0.1 | 0.37±0.04 |
| | 6h | 3.14±0.00 | 16.7±0.1 | 0.31±0.02 |
| | 8h | 3.13±0.01 | 17.0±0.2 | 0.28±0.03 |
| 45℃ | 4h | 3.12±0.01 | 17.2±0.3 | 0.21±0.02 |
| | 6h | 3.12±0.01 | 17.3±0.1 | 0.37±0.01 |
| | 8h | 3.11±0.00 | 17.6±0.3 | 0.38±0.04 |
| 55℃ | 4h | 3.08±0.01 | 18.2±0.2 | 0.38±0.05 |
| | 6h | 3.11±0.02 | 17.5±0.1 | 0.20±0.01 |
| | 8h | 3.10±0.01 | 17.4±0.3 | 0.17±0.01 |

The HMOR at 1500°C for 0.5h is shown in Fig.7. Similarly, specimens cured at 35°C gained higher HMOR, and the variation trend is consistent as before.
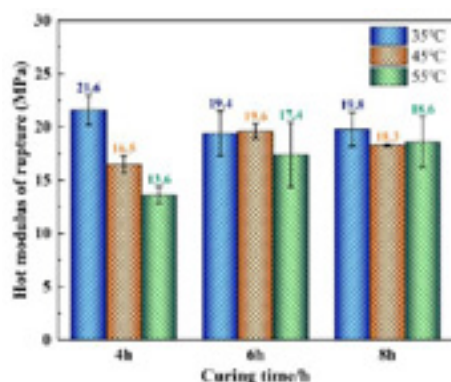


*Fig.7: The HMOR of specimens pre-fired at 1600 ℃*

**Microstructures**

To better understand the variation of the performance for specimens, the microstructure of the fracture was observed. The SEM images of specimens after drying at 110°C are illustrated in the Fig.8 and Fig.9. It can be seen that with the increase of curing temperature, the pores inside the castable become larger and more numerous, and a less compact structure can be observed. This is because the more hydration products generated in the early stage, the more structural damage caused by the decomposition of hydration products after drying, which further confirms the difference in the performance of the specimens after drying. The magnification images displayed in Fig.9 show that cubic aluminum micro-powder particles and hydration products were coated on the surface of cement particles at the fracture of the specimen, and flaky hydration products were filled in the pores. With the increase of curing temperature, less flaky hydration products can be observed due to their decomposition [8].
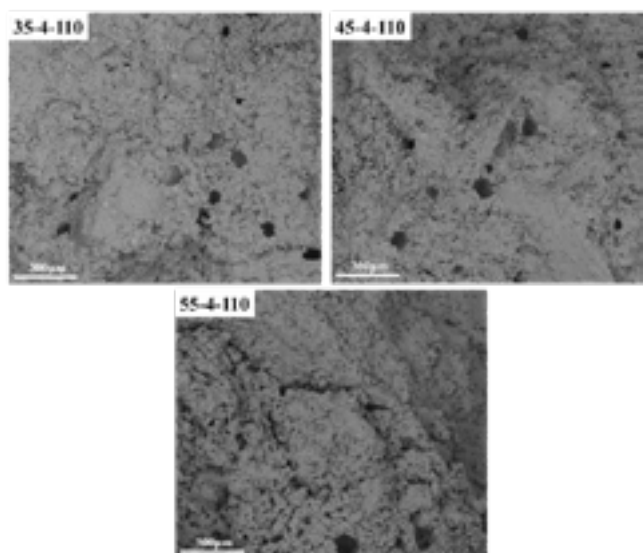


*Fig.8: The SEM images (200× magnification) of specimens after drying*
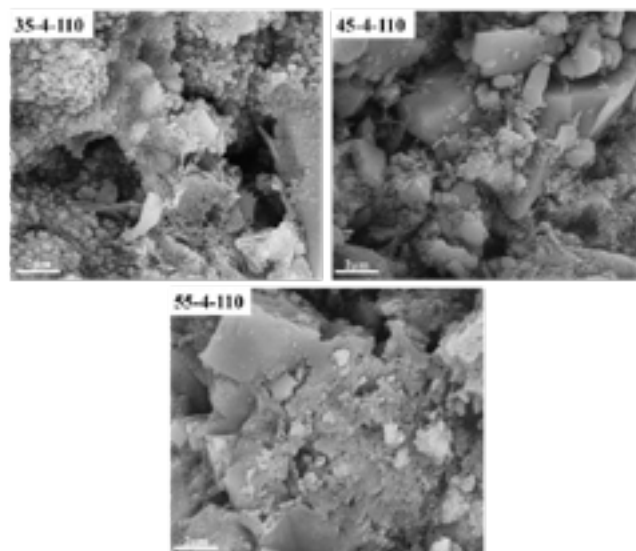


*Fig.9: The SEM images (20000× magnification) of specimens after drying*

Fig.10 and Fig.11 provide the microstructure of the specimens after firing at 1600°C. As is shown in the graphs that there are pores in the fracture surface, and the size of pores tends to slightly increase with the increase of curing temperature. This may explain the higher strength of specimen 35-4 after high temperature treatment. In the magnification images(Fig.11), extensive columnar $CA_6$ are generated in the voids, interlacing with each other to form an interlocking structure. On the one hand, the reaction is an expansion reaction, that's why the PLC shows swelling; and on the other hand, the $CA_6$ crystals form a staggered network structure to block the void inside the castable, result in the densification of the materials, which is of great benefit to the strength and high temperature performance of castable [10].
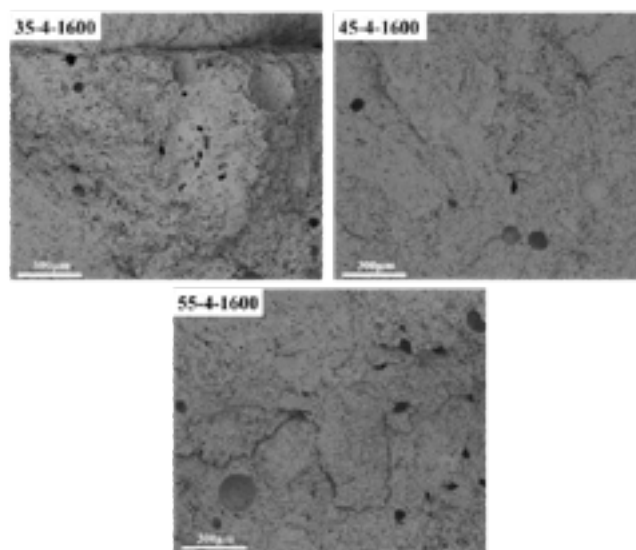


*Fig.10: The SEM images (200× magnification) of specimens after firing at 1600 ℃*

205
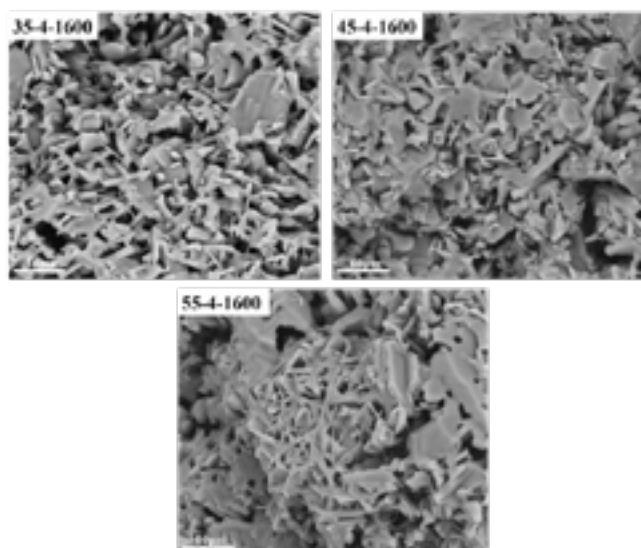
*Fig.11: The SEM images (5000× magnification) of specimens after firing at 1600 ℃*

## CONCLUSIONS

The castable with a size of 40mm×40mm×160mm made in this experiment, when the cement content of 5wt%, cured at 35℃ for 4h has obtained sufficient demoulding strength, and the performance is a little better than that of the sample cured at 55℃ under the same conditions. This is related to the rapid hydration reaction that occurs inside the castable during short time curing and the damage of the structure caused by rapid decomposition of the hydration products after drying. The formation and decomposition of the hydration products in the early stage will also affect the formation and structure of the crystalline phase after high temperature firing, thus lead to the difference in performance.

What is remarkable is that in practical production applications, the dimension of our refractory products such as the well block and the seating block, is significantly larger compare to the laboratory test sample (shown in Fig.12 is 360mm×360mm×380mm well block), and the water vapor in the castable will travel a longer distance and exist for extended period, result in more complex hydration reaction. Generally, the curing temperature and time of the product in the curing kiln is determined according to the material system, the type and content of the binder in the formula and the weather conditions. The well block combined with low cement corundum spinel castables manufactured by our company can obtain sufficient strength after curing at 35℃ for 6-12 hours, which can save energy and improve efficiency at the same time. Moreover, the performance can also be guaranteed.

## REFERENCES

[1] Abilio P. SilvaAna M. SegadaesDeesy G. Pinto. Effect of particle size distribution and calcium aluminate cement on the Theological behaviour of all-alumina refractory castables. Powder Technology: An International Journal on the Science and Technology of Wet and Dry Particulate Systems, 226, 2012.

[2] Tobias Dorn , Oliver Blask , Dietmar Stephan. Acceleration of cement hydration-A review of the working mechanisms, effects on setting time, and compressive strength development of accelerating admixtures. Construction and Building Materials, 323, 2022.

[3] Rafael Salomao˜ , Mirian A. Kawamura, Ana B.V. Emilio, Jos´e Sakihama, Ana M. Segadaes. Calcium aluminate cement in castable alumina: From hydrate bonding to the in situ formation of calcium hexaluminate. Ceramics International, 47, 2021, p. 15082-15093.

[4] Y. Wang, B. Zhu, X. Lin, P. Chen. Effect of dispersants on the hydrate morphologies of spinel-containing calcium aluminate cement and on the properties of refractory castables. Ceramics International, 42 (1), 2016, p. 711-720.

[5] Koehler A , Neubauer J , Goetz-Neunhoeffer F .Phase changes during the drying of calcium aluminate cement bond castables － the influence of curing and drying conditions - ScienceDirect[J].Cement, 2022.

[6] N. Li, X. Wang, Y. Mu, R. Zhang, L. Zhu, G. Ye. Mechanical property and phase evolution of the hydrates of CAC-bonded alumina castables during drying at 110℃. Construction and Building Materials, 266, 2023.

[7] Fábio A. Cardoso, Murilo D.M. Innocentini, Mario M. Akiyoshi, Victor C. Pandolfelli. Effect of curing time on the properties of CAC bonded refractory castables. Journal of the European Ceramic Society, 24(7), 2004, p. 2073-2078.

[8] W. Liu, N. Liao, Mithun Nath, Y. Li, Y. Dai, L. Pan. Effects of curing time on the pore structure evolution and fracture behavior of CAC bonded alumina-spinel castables. Ceramics International, 2023.

[9] Rafael Salomao˜, Mirian A. Kawamura, Ana B.V. Emilio, Jos´e Sakihama, Ana M. Segadaes. Calcium aluminate cement in castable alumina: from hydrate bonding to the in situ formation of calcium hexaluminate. Ceramics International, 47, 2021, p. 15082-15093.

[10] Oliveira, I. R., Ortega, F. S. , Pandolfelli, V. C. . Hydration of CAC cement in a castable refractory matrix containing processing additives. Ceramics International, 35 (4), 2009, p.1545-1552.

206



*Fig.12: Well block for 180MT steel ladle*

# IMPACT OF CURING TEMPERATURES AND DRYING UNDER HYDROTHERMAL CONDITIONS ON PHASE COMPOSITION AND MICROSTRUCTURE OF CEMENT BONDED CASTABLES

Andreas, Koehler, Sebastian, Klaus
Almatis GmbH, Ludwigshafen, Germany

Stefan, Kuiper
Almatis B.V., Rotterdam, Netherlands

Jerry, Dutton
Stourbridge, United Kingdom

Friedlinde, Goetz-Neunhoeffer
Friedrich-Alexander-Universität Erlangen-Nürnberg, Germany

## ABSTRACT

During drying of modern highly dispersed cement bonded castables, hydrothermal conditions appear because the water cannot evaporate fast enough from the bulk of the dense castable body. Under such high pressure conditions, problems such as explosive spalling can arise. Different curing temperatures lead to the formation of different hydrate phases and accordingly, different microstructures can develop in the hardened material. Under hydrothermal conditions, the original hydrate phases can transform into new hydrate phases, but still leave a footprint of the initial microstructure behind. This study presents the changes in porosity and mineralogical composition of a refractory castable model system under hydrothermal conditions depending on the curing temperature (5, 23 and 40 °C).

Quantitative X-ray diffraction (QXRD) measurements show that different hydrate phases are formed during curing, while $C_3AH_6$ and boehmite are formed in the same quantities after hydrothermal treatment in an autoclave at ~11 bar/180 °C. Although the mineralogical composition after autoclaving is not different, the three samples differ in their microstructure. Mercury intrusion porosimetry measurements reveal that although the total porosity after autoclaving is the same, the 40 °C samples have a higher proportion of large pores. SEM images also show that the appearance of $C_3AH_6$ in the 40 °C autoclaved samples varies, which originates from the starting phase composition and microstructure after curing.

## INTRODUCTION

High performance refractory castables are formulated to give a high density matrix . In the production of castables, a mixture of different types of aggregates, fine components, additives and a binding phase is mixed with water and poured into a mould. In the first step, the hydration/curing step, the binder phase, typically calcium aluminate cement (CAC), reacts with the water and after a certain period of time sufficient green strength is achieved so that the body can be demoulded. The castable body is then dried with the aim of removing the remaining unreacted and crystalline water from the body before the castable can be used in the final high-temperature application. The drying step is particularly critical as problems such as cracking or even explosive spalling can occur. These issues arise because modern highly dispersed cement bonded castables are so dense that the water cannot easily leave the green body when heated and the steam that potentially forms causes an increase in pressure inside the castable. This increase in temperature and pressure can cause hydrothermal conditions, which lead to a change in the hydrate phases that have been formed during hydration. The hydration of CAC is extremely temperature dependent. This affects the reaction speed, the formation of different hydrate phases and also the microstructure. At low temperatures (<20 °C) $CAH_{10}$ is typically formed [1,2]. It can be stable even up to 30 °C [3], but typically at moderate temperatures $C_2AH_x$ and $AH_3$ are formed [2,4]. The amount of $H_2O$ in $C_2AH_x$ can vary [5,6,7]. However, it is most usually referred to as $C_2AH_8$. $AH_3$ has a gibbsite-like structure and its crystallinity can vary from amorphous to nano and microcrystalline [3,8]. Its crystallinity increases with increasing temperature and time. At higher temperatures the thermodynamically stable calcium aluminate hydrate $C_3AH_6$ is formed in addition to $AH_3$ [2,3,9].

Depending on the temperature during the curing step, different hydrate phases are formed and a different hydration progress is reached. This material is then affected by the hydrothermal processes, which also leads to different microstructures, i.e. porosity and permeability. This study therefore aims to determine which mineral phases are formed when hydrothermal conditions occur in a calcium aluminate cement bonded castable and how the initial curing temperature affects the phase composition and microstructure.

## MATERIAL AND METHODS

All samples that were investigated in this study had the same initial composition (40 wt.% calcium aluminate cement and 60 wt.% alumina filler). The 40 wt.% CAC used in this study is a significantly higher amount of calcium aluminate cement than is typically used in modern castables. This large amount was chosen to better visualise the effect of the cement and the hydrate phases that form during hydration and hydrothermal conditions. For the same reason, a very simplistic system with only one alumina filler was chosen. A commercial 70% $Al_2O_3$ CAC (Almatis CA14-S) was used. The main phases in the cement are CA and $CA_2$, but also some $\alpha$-$Al_2O_3$. The alumina filler (Almatis tabular alumina T60/T64 <45 µm) consisted of corundum with traces of $\beta$-$Al_2O_3$ ($NaAl_{11}O_{17}$) (Fig. 1 start). The dry mixture was homogenized with deionized $H_2O$ and then cured for 48 h at 5, 23 or 40 °C. When solid the sample was then transferred to a PTFE-lined stainless-steel autoclave for the hydrothermal experiments. After autoclaving, the samples were analysed using X-ray diffraction (XRD), scanning electron microscope (SEM) and mercury intrusion porosimetry (MIP). The XRD measurements were carried out with a D8 Advance diffractometer (Bruker). The quantitative phase composition was determined by applying the G-factor method [10] to Rietveld data [11] using quartz as an external standard. Back-scattered electron (BSE) imaging and energy dispersive X-ray (EDX) spectroscopy were used for microstructural characterization of the samples. BSE imaging and EDX analysis were carried out at a 12 kV acceleration voltage and 1.6 nA electron current using a high-resolution field emission SEM. The mercury intrusion measurements (MIP) were carried out with a Poremaster 60 (Quantachrome). The smallest measurable pore diameter was 3.6 nm. The sample preparation and the methods used in this study are described in more detail in the publications by Koehler et al. [12,13].

## RESULTS AND DISCUSSION

### Phase composition after curing and autoclaving

The mixture of calcium aluminate cement and alumina filler was hydrated for 48 h at 5, 23 and 40 °C in a closed system to make sure no water can leave the samples during hydration. The phase composition before (start) and after hydration is shown in Fig. 1. A different degree of hydration of the clinker phases CA and $CA_2$ is reached after 48 h. Also different calcium aluminate hydrates are

207

formed. At 5 °C, only $CAH_{10}$ was formed as a crystalline phase. The clinker phases, especially $CA_2$, reacted only slightly at this temperature. In the samples hydrated at 23 °C, $C_2AH_8$ and $AH_3$ are also formed together with some $CAH_{10}$. At this temperature more CA and also some $CA_2$ have reacted. At 40 °C both clinker phases have completely reacted and $C_3AH_6$ and $AH_3$ are formed. All three samples show a different phase composition and hydration progress after 48 hours. These samples were then placed in the autoclave at 180 °C and ~11 bar for 12 h to simulate the hydrothermal conditions that can occur during the heating step of refractory castables.



Fig. 1: Phase compositions of the samples after curing for 48 hours at 5, 23 and 40 °C. Start column: phase compositions of the paste before curing.
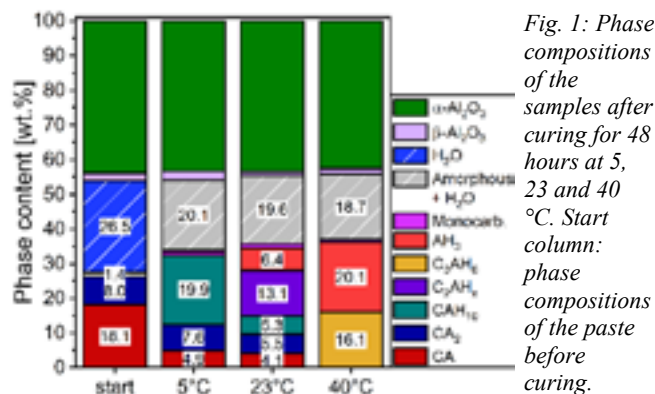
After autoclaving all samples have exactly the same phase composition (Fig. 2). They consist of 18.4 ± 0.2 wt.% $C_3AH_6$ and 19.4 ± 0.4 wt.% boehmite (AlOOH) plus the unreacted alumina. In the 5 and 23 °C samples, $C_3AH_6$ was formed from the remaining unreacted CA and $CA_2$, and also from the conversion of $CAH_{10}$ and $C_2AH_8$, due to the hydrothermal conditions. In the 40 °C samples, $C_3AH_6$ was already present after curing and was not formed first in the autoclave. In contrast, the boehmite was newly formed in all three samples, transforming entirely from $AH_3$ in the 40 °C sample and from different sources in the 5 and 23 °C samples. It can be concluded that regardless of the initial composition, $C_3AH_6$ and boehmite are formed as stable phases under these hydrothermal conditions. This is in line with the results of Jensen et al. [14] and Auvray et al. [15] who observed the formation of $C_3AH_6$ and boehmite in a $CaO$-$Al_2O_3$ system under hydrothermal conditions.



Fig. 2: Phase compositions of the samples hydrated at 5, 23 and 40 °C after autoclaving at ~11 bar/ 180 °C.
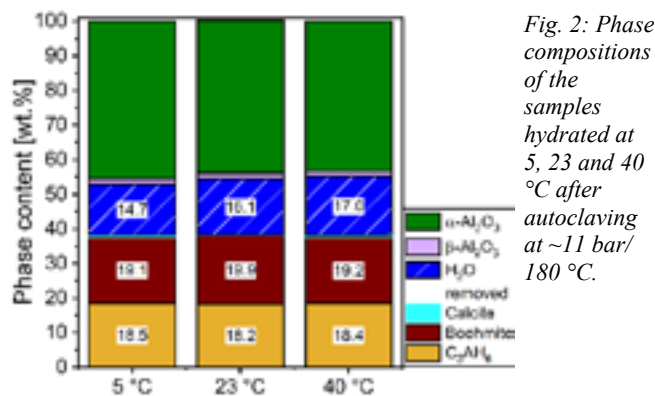
The development of the phase composition with increasing temperature and pressure was also determined using a 23 °C cured sample as an example. (Fig. 3). At 120 °C/ 2.0 bar all hydrate phases have already converted to $C_3AH_6$ and $AH_3$. While $C_3AH_6$ stays stable with increasing temperature and pressure, $AH_3$ is converted to boehmite at ~140 °C. From 160 to 180 °C no change can be observed. This is consistent with the results of Serena et al. [16] who showed in a thermodynamic modelling that from 140 °C/ 3.6 bar $AH_3$ is converted into boehmite, which then remains stable up to 300 °C. This means that the formation/conversion into $C_3AH_6$ happens first and then, at higher temperature and pressure, the formation of boehmite takes place.



Fig. 3. Phase composition development of a sample hydrated at 23 °C with increasing temperature and pressure.
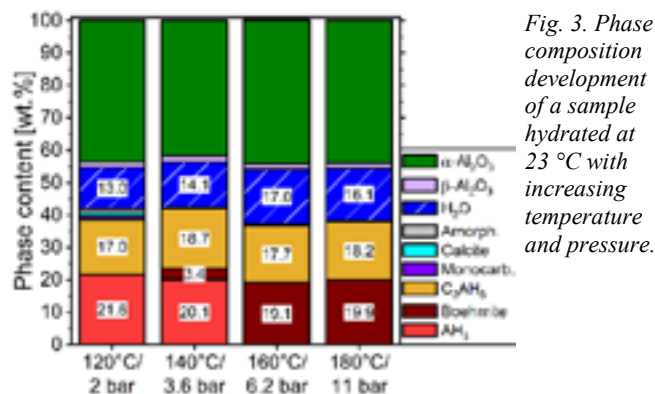
The evaluation of the XRD analyses of the curing samples shows that a completely different phase composition is produced at different hydration temperatures. However, due to hydrothermal conditions, exactly the same hydrate phases are formed in the same quantities from 120 °C. This means that the original phase composition has no effect on the final phase composition once hydrothermal conditions occur. However, the question arises whether the microstructure formed during hydration influences the final microstructure produced by the hydrothermal conditions.

**Microstructure after autoclaving**

SEM images in combination with EDX analysis were taken of 5, 23 and 40 °C samples after autoclaving to identify the mineral phases and image their morphology and microstructure. An overlay of the Ca- and Al-element distribution by EDX analysis enables the three phases ($Al_2O_3$, $C_3AH_6$ and boehmite) occurring in the autoclaved samples to be distinguished. A 5 °C autoclave sample is shown as an example in Fig. 4. The minerals in the 23 and 40 °C samples look similar to the 5 °C sample. The largest amount in the sample is $\alpha$-$Al_2O_3$, with $C_3AH_6$ present as larger aggregates.



Fig. 4: Overlay of Ca, Al and BSE images of a 5 °C autoclave sample. Green phase: $C_3AH_6$, light blue: $Al_2O_3$, dark blue: boehmite, black: pores.
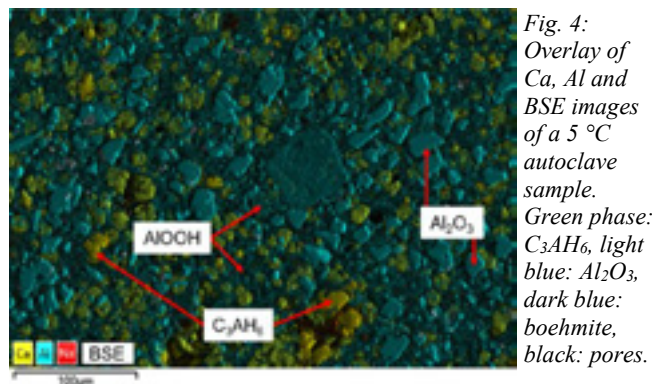
Boehmite has a fine-grained sheet-like structure (Fig. 5) and is located between the bigger alumina and $C_3AH_6$ crystals. Since boehmite is newly formed due to hydrothermal conditions, the crystal appearance is similar in each sample. This leaf-like structure can also be observed when boehmite is hydrothermally synthesised [17]. While boehmite, corundum (dense and sharp edged) and $C_3AH_6$ (massive irregular aggregates) appear similar in the 5, 23 and 40 °C autoclaved samples, the microstructure observed in the SEM images differs.
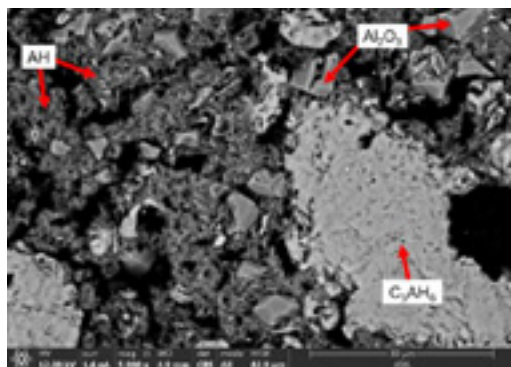
*Fig. 5: SEM-BSE image of a 40 °C autoclave sample.*

Fig. 6 shows two examples of SEM-BSE images of an autoclaved 5 °C sample (top image) and a 40 °C sample (bottom image). The 5 °C and 23 °C samples are very similar and both differ in the same way from the 40 °C samples. The pores coloured red in these images show that the pores in the 40 °C autoclaved sample are significantly larger and more heterogeneously distributed than in the 5 °C (and 23 °C) sample. On the other hand, the pores of the 5 °C sample are smaller in average but more evenly distributed.
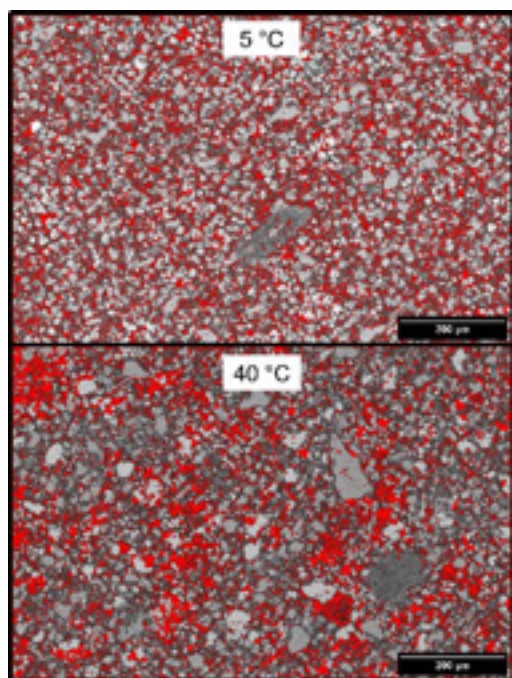


*Fig. 6: Large-area segmented SEM-BSE images of 5 °C (top) and 40 °C (bottom) autoclave samples with pores coloured in red. Both SEM images have the same scale.*

Another difference between the 5/23 °C and the 40 °C autoclave sample is also evident in the appearance of $C_3AH_6$ (Fig. 7). While the $C_3AH_6$ aggregates are smaller and more evenly distributed in the 5/23 °C autoclave samples, they are clearly much larger in the 40 °C autoclave samples. The amount of $C_3AH_6$ however, is the same, as shown by the XRD analyses (Fig. 2). The difference in the $C_3AH_6$ is explained by the fact that after curing for 48 h at 40 °C CA and $CA_2$ were reacted completely and the maximum amount of $C_3AH_6$ was already formed during hydration. $C_3AH_6$ was formed at 40 °C curing temperature in the paste, where the material is still plastic and growth is not hindered. On the other hand, $C_3AH_6$ is formed in the 5/23 °C samples from the remaining clinker phases and from conversion of the metastable hydrate phases $CAH_{10}$ and $C_2AH_8$ only due to the hydrothermal conditions. When these conditions occur, or when the samples enter the autoclave, they are already solidified and the growth of $C_3AH_6$ to bigger grains is only possible to a certain extent.
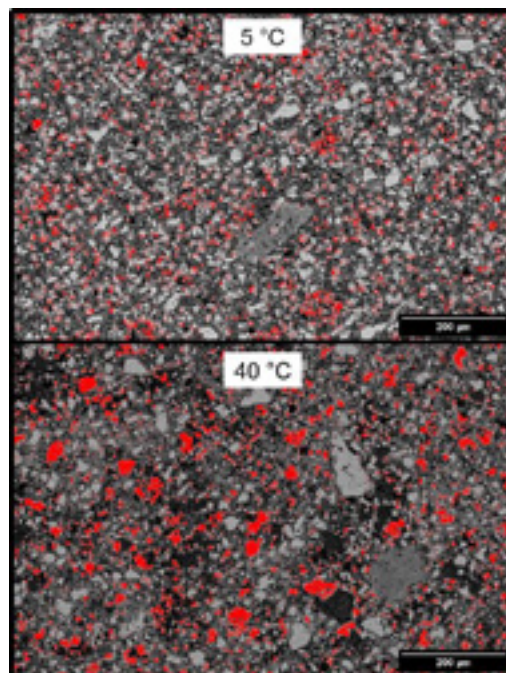


*Fig. 7: Large-area segmented SEM-BSE images of 5 °C (top) and 40 °C (bottom) autoclave samples with $C_3AH_6$ coloured in red. Both SEM images have the same scale.*

To verify the differences in porosity that were observed in the SEM images, MIP measurements were performed on the autoclaved samples. The total porosity and bulk density are exactly the same in all three samples (Tab. 1). This was to be expected, as the chemical and mineralogical composition of these samples is exactly the same and no change in volume of the samples could be observed due to the autoclaving process. The rather low bulk density (1.69 g/cm³) and rather high total porosity (~43 %) in our study can be explained by the chosen water/cement ratio used in the investigated mixtures. In technical refractory castables, the total porosity would be significantly lower due to a lower cement and water content and also a better balanced particle size distribution of the matrix material. Nevertheless, the effect of curing temperature on the pore size distribution is present (Fig. 8), albeit on a smaller scale.

Tab. 1. Bulk density and total porosity after the autoclaving 12 h at ~11 bar/ 180 °C determined with MIP.

| Temperature | Bulk density [g/cm³] | Total porosity [%] |
|---|---|---|
| 5 °C | 1.69 ± 0.01 | 42.8 ± 0.3 |
| 23 °C | 1.69 ± 0.01 | 44.1 ± 1.2 |
| 40 °C | 1.68 ± 0.02 | 43.3 ± 0.7 |

The pore size distribution (Fig. 8) shows that all three autoclaved samples exhibit a pore diameter maximum of ~1 μm. The 40 °C sample, however, has a significantly lower peak than the 5/23 °C sample and instead a second maximum at ~3 μm. The 40 °C autoclaved samples have less fine pores but a proportion of large pores that does not appear in the 5/23 °C samples. The results of the MIP measurements match the observations of the SEM images. Although hydrothermal conditions result in the same phase composition ($C_3AH_6$, AlOOH and α-$Al_2O_3$) regardless of the initial composition, the microstructure of the samples differs. The reason for this is that the curing conditions (in this case the temperature) already create a different microstructure, of which a "footprint" remains in the samples despite hydrothermal conditions and the resulting phase transformations.

The proportion of larger pores (2-10 μm) that only appears in the 40 °C autoclave samples can be explained by the initial phase composition after curing. At high hydration temperatures, a large amount of $C_3AH_6$ and $AH_3$ is formed after a short time. Of the calcium aluminate hydrates, $C_3AH_6$ has the least amount of $H_2O$ incorporated into its structure. It also has the highest density (2.53 g/cm³) [18]. As a result, the water after curing is located in either very crystalline phases or remains as "free"/unbound water in the pores. When hydrothermal conditions occur, the already formed $C_3AH_6$ remains stable and only the $AH_3$ converts to boehmite,

releasing additional water. This leads to additional porosity. Thus, the microstructure is not particularly altered by hydrothermal conditions.

In contrast, the microstructure of castables that are cured at low/moderate temperatures changes significantly as soon as hydrothermal conditions arise. After curing, these samples consist of $CAH_{10}$ (1.78 g/cm$^3$), $C_2AH_8$ (1.95 g/cm$^3$) [18], low crystalline or amorphous $AH_3$ and unreacted clinker phases. The microstructure is more complex, with fewer large pores, because of these different, less crystalline and less dense hydrate phases. The microstructure is probably less permeable and could additionally prevent the water from leaving the castable body during heating, which then leads to steam pressure and therefore hydrothermal conditions. When these conditions occur, the phase composition changes completely to $C_3AH_6$ and boehmite. However, the microstructure with finer pores remains.
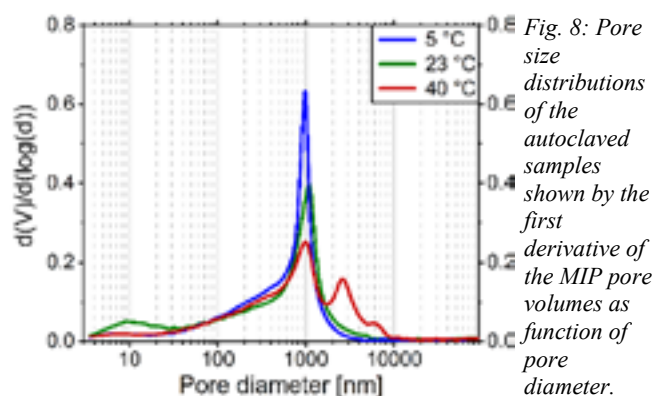


*Fig. 8: Pore size distributions of the autoclaved samples shown by the first derivative of the MIP pore volumes as function of pore diameter.*

## CONCLUSIONS

Curing calcium aluminate cement bonded castables at different temperatures leads to the formation of different mineral phases, resulting in different microstructures. Hydrothermal conditions can occur if water cannot leave the castable body fast enough during drying/heating. Under these conditions the stable phases $C_3AH_6$ and boehmite are formed from all hydrate and remaining clinker phases. While the mineral composition, bulk density and total porosity are exactly the same, when these conditions occur, the microstructure of the high temperature hydrated samples differ from the low and medium temperature samples. Castables that already consist of $C_3AH_6$ after curing due to high temperatures (40 °C) have significantly larger pores and do not change as much if hydrothermal conditions arise. Since samples cured at low/moderate temperature already contain smaller pores after curing and retain them under hydrothermal conditions, it can be concluded that these castables are more prone to explosive spalling or other pressure related problems.

## REFERENCES

[1] F.G. Buttler, H.F.W. Taylor, The system CaO-Al$_2$O$_3$-H$_2$O at 5°, J Chem Soc. (1958) 2103–2110.

[2] R.N. Edmonds, A.J. Majumdar, The hydration of monocalcium aluminate at different temperatures, Cem Concr Res. 18 (1988) 311–320.

[3] B. Lothenbach, L. Pelletier-Chaignat, F. Winnefeld, Stability in the system CaO-Al$_2$O$_3$-H$_2$O, Cem Concr Res. 42 (2012) 1621–1634.

[4] A. Capmas, D. Menetrier-Sorrentino, D. Damidot, Effect of temperature on setting time of calcium aluminate cements, Calcium Aluminate Cements. (1990) 65–80.

[5] B. Raab, Synthese und Charakterisierung nanoskaliger hydraulisch hochreaktiver Phasen des Portland-und Tonerdezements, Hallesches Jahrbuch Für Geowissenschaften/Beiheft. 26 (2013).

[6] F. Hueller, J. Neubauer, S. Kaessner, F. Goetz-Neunhoeffer, Hydration of calcium aluminates at 60° C–Development paths of C$_2$AH$_x$ in dependence on the content of free water, Journal of the American Ceramic Society. 102 (2019) 4376–4387.

[7] J. Goergens, A. Koehler, F. Goetz-Neunhoeffer, Calibration and quantitative analysis of C$_2$AH$_x$ (2CaO·Al$_2$O$_3$·xH$_2$O) by Rietveld refinement combined G-factor method, Cem, Concr. Res. 158

[8] F. Hueller, C. Naber, J. Neubauer, F. Goetz-Neunhoeffer, Impact of initial CA dissolution on the hydration mechanism of CAC, Cem Concr Res. (2018).

[9] R.B. Peppler, L.S. Wells, The system of lime, alumina, and water from 50 °C to 250 °C, J Res Natl Bur Stand (1934). 52 (1954) 75.

[10] D. Jansen, F. Goetz-Neunhoeffer, C. Stabler, J. Neubauer, A remastered external standard method applied to the quantification of early OPC hydration, Cem Concr Res. 41 (2011) 602–608.

[11] B.H. O'Connor, M.D. Raven, Application of the Rietveld refinement procedure in assaying powdered mixtures, Powder Diffr. 3 (1988) 2–6.

[12] A. Koehler, J. Neubauer, F. Goetz-Neunhoeffer, Phase changes during the drying of calcium aluminate cement bond castables–the influence of curing and drying conditions, Cement. (2022) 100020.

[13] A. Koehler, C. Rößler, J. Neubauer, F. Goetz-Neunhoeffer, Phase and porosity changes in a calcium aluminate cement and alumina system under hydrothermal conditions, Ceram Int. 49 (2023) 4659–4667.

[14] T.R. Jensen, A.N. Christensen, J.C. Hanson, Hydrothermal transformation of the calcium aluminum oxide hydrates CaAl$_2$O$_4$·10H$_2$O and Ca$_2$Al$_2$O$_5$·8H$_2$O to Ca$_3$Al$_2$(OH)$_{12}$ investigated by in situ synchrotron X-ray powder diffraction, Cem Concr Res. 35 (2005) 2300–2309.

[15] J.M. Auvray, C. Zetterström, C. Wöhrmeyer, H. Fryda, C. Parr, C. Eychenne-Baron, Dry-out simulation of castables containing calcium aluminate cement under hydrothermal conditions, in: Proceedings of the Unified International Technical Conference on Refractories (UNITECR 2013), John Wiley & Sons, 2014: p. 159.

[16] S. Serena, M.A. Raso, M.A. Rodriguez, A. Caballero, T.J. Leo, Thermodynamic evaluation of the Al$_2$O$_3$–H$_2$O binary system at pressures up to 30 MPa, Ceram Int. 35 (2009) 3081–3090.

[17] Y. Liu, D. Ma, X. Han, X. Bao, W. Frandsen, D. Wang, D. Su, Hydrothermal synthesis of microscale boehmite and gamma nanoleaves alumina, Mater. Lett. 62 (2008) 1297–1301.

[18] W. Kurdowski, Cement and concrete chemistry. Springer Science & Business, 2014.

# CO$_2$–FOOTPRINT REDUCTION IN DRY TUNDISH WEAR LINING INSTALLATION WITH RESPECT TO REFRACTORY MATERIAL AND ELECTRICAL EQUIPMENT (EMOULD) TECHNOLOGY

Robert Fechner, Malte Kreuels, Emine Sari
WEERULIN GmbH, Mülheim an der Ruhr, Germany

Sven Karrasch, Manuel Schmitz
thyssenkrupp Steel Europe AG, Duisburg, Germany

Thorsten Bierkämper,
BIERKÄMPER Engineering, Hamm, Germany

Martin Goedecke,
SIEVERING GmbH & CoKG, Mülheim an der Ruhr, Germany

## ABSTRACT

In general two different lining concepts exist for the wear lining of modern continuous casting tundishes: wet gunning and dry mix. Both concepts have specific advantages and disadvantages.
The dry mix technology has been standard in thyssenkrupp plants Beeckerwerth and Bruckhausen for more than 20 years. The reduction of energy consumption and the reduction of CO$_2$ emissions could be achieved in part by switching from wet spray to dry mix. The last continous caster changed to dry mix at thyssenkrupp Steel in 2015. The thin slab caster changed after some years of parallel wet spray usage. In the second step, the heavy 90 DBM was successfully replaced by the light magnesia to reduce the consumption quantities per tundish. The light magnesia product has been used and established in both plants since 2012. The aim of this work is to prove that it is possible to cast the same grades and sequences with a new European olivine-based formulation, which has a much lower carbon footprint than magnesia (and light magnesia) in production and transport. The objectives are to first optimize the dry mix product for thyssenkrupp and then implement field trials to change the technology of baking the dry mix with today`s hot air mould to eMould, an electrical heating solution, to save even more CO$_2$ emissions, time and energy in the future.

## PROCESS FROM WET SPRAY TO DRY MIX

The use of wet gunning mixes for the tundish wear lining has a long history in the steel industry. The quality of a lining depends on the individual skill of the supplier, employees and the drying equipment employed in order to heat out approximately 25-30% water, equivalent to 250-300l of water per ton. This consumes a high amount of energy and time. Favorable insulating properties, low material consumption, as well as the non-necessity of pre-drying are usually attributed to this type of refractory material, when the possibility of spraying on hot permanent lining is given. The fact that no pre-drying is required, usually depends on the thickness of the sprayed wear lining. Disadvantages have been ascribed to the presence of water and SiO$_2$, originating from the binders. Water can readily affect the hydrogen pick up during casting. Wet gunning mixes are currently available which contain solely SiO$_2$-free binders and which are inherently different from conventional wet gunning mixes with regard to the reduction potential.[1]

With the dry mix, it is possible to achieve lower hydrogen pick up over the long term on average, due to stable dry material conditions, lower lining costs are incurred and the plants achieve higher tundish availability. The disadvantages consist of lower insulation properties, due to higher densities resulting in higher consumption, and the necessity of baking prior to casting. Thyssenkrupp was able to reduce the disadvantage of the 90 DBM (bulk density 1.80-1.90 g/cm³) dry-mix by switching from heavy to light magnesia (bulk density 1.40-1.50 g/cm³) product in 2012. This step has reduced the consumption of the material nearly 20% per tundish and the CO$_2$ footprint from 3100kg (90 DBM) to 1100.2kg (light magnesia) CO$_2$ per ton raw material, which is a scope 3 emission. The technical data of the plants as well as the current consumption quantities of dry mix material are shown here in Table 1.

Tab. 1: Technical informations about the plants OX I and OX II

| Steel plants | OX I | OX II | |
|---|---|---|---|
| Annual production capacity [t] | 5,2 Mio. | 5,4 Mio. | |
| Main steel grades | 33% Thin-plated 40% Thin-slab 13% Silicon grades | 40% ULC + IF Steel 43% High-strength steel 10 % Sheet Others | |
| CCM*[quantity] | SGA 3 | SGA 1 | SGA 2 |
| Tundish capacity in liquid steel [t] | 86 | 75 | 75 |
| Lining thickness bottom [mm] | 30-40 | 30-35 | 30-35 |
| Lining thickness wall [mm] | 30 | 30 | 30 |
| Consumption per tundish in heavy DBM [kg] | 3300 | 2700 | 2700 |
| Consumption in light weight magnesia [kg] | 2700 | 2200 | 2200 |
| Ø casting sequences [Ladle] | 4.5 | 4.5 | 5.4 |

*CCM = Continues casting machine

With the bulk density of 1.50-1.60 g/cm³, the olivine based mix had a 4.5% higher material consumption, equivalent to 100kg per tundish in the trials at the plants OX 1 and OX 2. This surplus in consumption was not included in following CO$_2$ savings calculation, as the final consumption per tundish is not yet validated.

## SWITCHING FROM LIGHT 90 DBM TO OLIVINE BASED DRY MIX PRODUCT

The calculating of the carbon footprint of refractories starts with the raw materials. It must be taken into account how much CO$_2$ the suppliers generate during the production of one ton of raw material. In this case for example, the Chinese supplier currently generates 3.1 tons of CO$_2$ in the production of one ton 90 DBM.[2] As climate-neutral fuels are used for the production of "light megnesia", the CO$_2$ amount is about 1.1 tons per ton of raw material.[3] The transport distances for the raw materials as well as the values for the production of one ton of dry-mix must also be taken into account when calculating the emission values. It is possible to further reduce these CO$_2$ amounts even further by trying to economically integrate European raw material sources into the formulations. In this project we are replacing 2/3 of light magnesia DBM with European olivine. The supplier from Europe creates only 0.007 ton CO$_2$ per ton of olivine production.[4]

The results of the carbon footprint calculation for the production of 1 ton dry mix are shown in the table 2.

Tab. 2: $CO_2$ calculation for 1 ton dry mix at WEERULIN GmbH

|  | DBM 90 China dry mix [kg $CO_2$ / t] | Light magnesia China dry mix [kg $CO_2$ / t] | 100% Olivine Norway based mixed dry mix [kg $CO_2$ / t] |
|---|---|---|---|
| Transport | 79.30 | 52.50 | 21.87 |
| Production raw material | 3,100 | 1,100 | 7 |
| Mixing at Weerulin | 5 | 5 | 5 |
| **Total** | **3,184.3** | **1,157.5** | **33.87** |
| **Savings of $CO_2$ per t dry mix** | **0** | **2,026.80** | **3,150.43** |

Replacing heavy 90 DBM with 100% Olivine saves approx. 3151kg per ton (Tab. 2). Assuming up to a 2/3 exchange of DBM with olivine in the recipe 2100kg of $CO_2$ per ton of dry mix is saved. With an annual consumption of approx. 13000 tons material corresponds to a total savings of 27300 tons $CO_2$ emission per year for the thyssenkrupp plants OX 1 and OX 2. Assuming that the change would be based on 100% light magnesia dry mix, the total consumption per year would be only 10400 tons and therefore the change to the olivine based dry mix would end up saving 745kg $CO_2$ per ton refractory material or approx. 7750 tons of $CO_2$ per year.

Thyssenkrupp`s feedback shows that the lining of the tundish with the olivine based dry mix has been successful with no negative effects reported so far. There was no increase in loose material after baking in the bottom. The wall construction was very stable, good baking behavior, no abrasion. The same casting sequences with olivine based were achieved without any problems. There was no significant wear in the slag zone. The quality requirements could be met. The metallurgical effects in produced grades are currently being assessed.

**COMPARISON OF ENERGY CONSUMPTION**
The best amount of energy required for the baking process of the dry mix is 200°C. Based on the experience Weerulin and Sievering, the energy requirement was calculated on average per 1m² area of working lining (regardless of the tundish form) for the products in Table 2. In this calculation, only the energy demand for gas consumption during baking was taken into account. The energy consumption of the electrical auxiliary (cooling/air fan) of the hot air mould system is not included in these values.

When drying with the hot air mould, the energy requirements were determined for the products with heavy 90 DBM, light 90 DBM and the olivine based dry mix. The same calculations were then used for the eMould and compared Table 3 below.

Tab. 3: Determination of the energy requirements for the dry-mix masses in comparison with the baking technology

| Energy requirement | Hot air mould [in MJ/m²] | eMould [in MJ/m²] |
|---|---|---|
| Heavy 90 DBM dry mix | 144 | 19 |
| Light DBM dry mix | 144 | 21 |
| Olivine based dry mix | 147 | 23 |
| Average | 145 | 21 |
| **Energy efficiency** | **11%** | **73%** |

The energy efficiency of the energy used per m² to bake, which is converted into heating of the mould, is mathematically only 11% for the hot Air mould and 73% for the eMould. This study showed that an energy saving of 85% could be achieved with the eMould. In addition, the manifold delivery process could be $CO_2$ free if purely renewable electricity is used.

By using the eMould, additional huge time savings can be achieved in the baking process of the tundish compared to the hot air mould. This in turn has a major influence on the overall setting time of a tundish and thus increases the number of the tundishes available in the plants. The time required for one baking cycle (baking + cooling) is 120 min. for OX 1 and 90 min. for OX 2. By using the eMould, the time required can be reduced to 30 min. per baking cycle in total. This results in savings of 4575 hours for OX 1 and 4800 hours for OX 2 per year (Fig.1). [5]
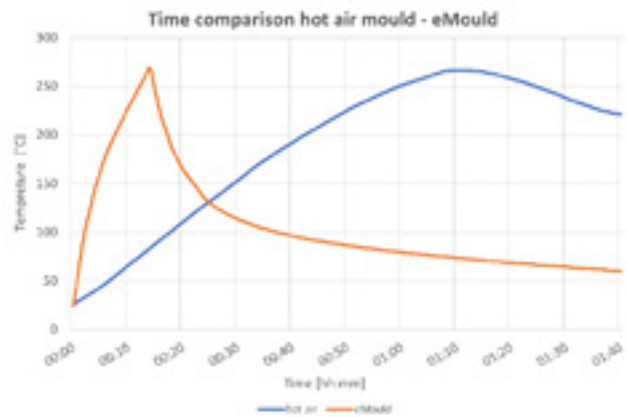


*Fig. 1: Backing time comparison hot air mould to eMould*

Another disadvantage of the hot air mould is the uncontrollable heat distribution within the mould. The simulation results (Figure 2) show the heat distribution in comparison to eMould. In order to bring the cold spots of the hot air mould to the target temperature, more energy is required, which in turn can lead to the formation of unwanted hot spots.
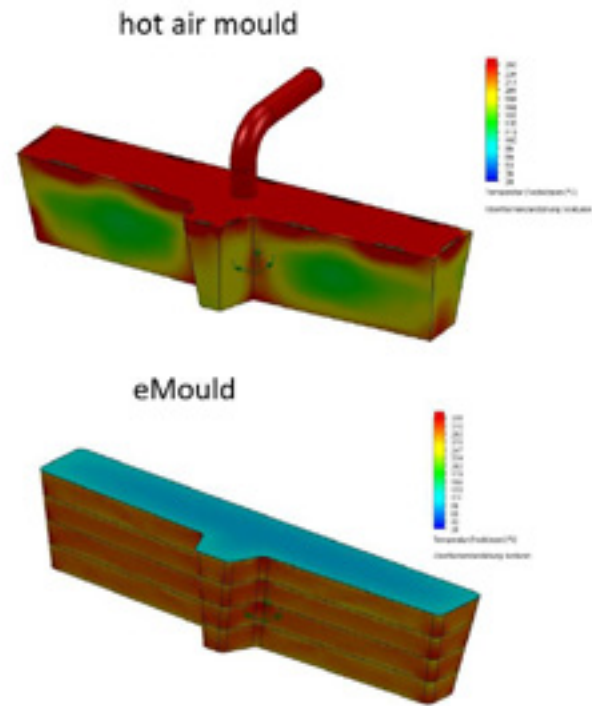


*Fig. 2: Heat distribution in the moulds*

With the eMould, a maximum ΔT of 10 Kelvin is possible and the complete baking process is controllable. Ramps and holding points can be combined with each other as desired (Fig.3).[5]
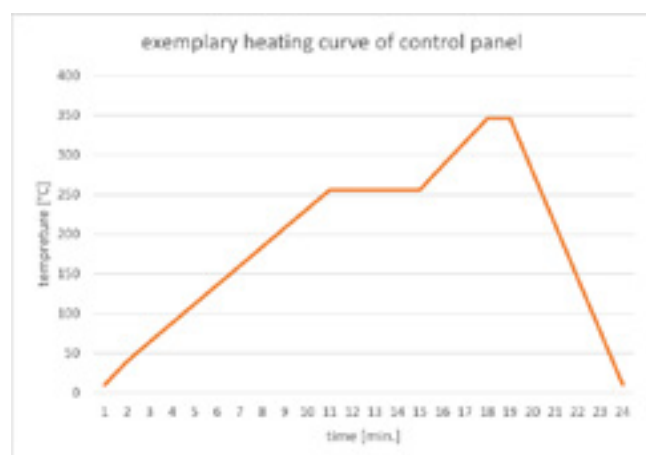


Fig. 3: Heating curve of control panel eMould

In the experiment with the eMould prototype, homogeneous heating of the eMould was successfully demonstrated. As shown in Figure 4 – thermal image, the tundish could be baked in 15 min. and the eMould could be pulled without problems after only 10 min. cooling time.
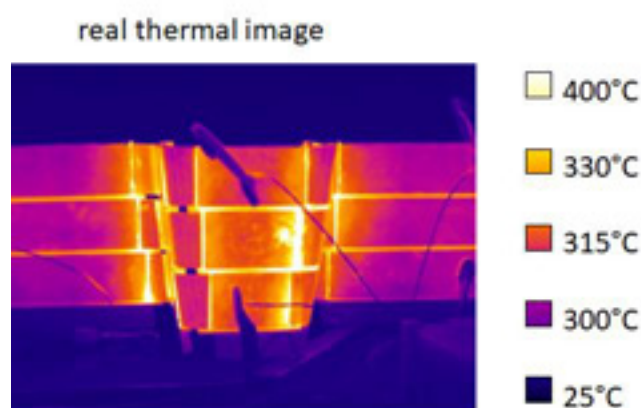


Fig. 4: eMould thermal image on baking temperature



Fig. 5: Baked dry mix in lap test with eMould

For energy savings, the type of electricity used must still be taken into account, and the value listed here for energy savings must be corrected by the corresponding factor. In the case of electricity generated from renewable sources, the transmission losses must be calculated. In the case of electricity from cogeneration, the efficiency of the power plant must be taken into account. With a total of 7850 baking processes per year, energy savings per baking

process of 0.764 MWh are calculated with the eMould. This means an annual energy saving of 5997 MWh equivalent to approx. 600000 Nm³ of natural gas compared to the hot air mould.[5]

Further savings in energy consumption were achieved at the OX 1 and 2 plants by converting the heat up process on the casting platform. This was already done many years before by switching from heating the entire tundish to heating the strands with the chimney technique. The energy consumption is in the range of 1 – 2 GJ (3,6 GJ ≙ 1 MWh) per tundish. The holding at a maximum temperature of 1200°C consumes 1 GJ per hour. The rest of the tundish starts off relatively cold (Fig. 6).
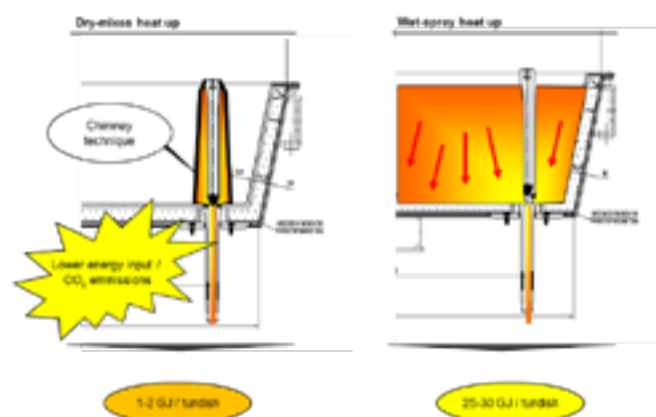


Fig. 6: For dry mixes merely special areas (tundish nozzles) require a heating process.

As can be seen from Fig. 6 the energy balance is clearly favorable for the dry mix in comparison to wet spray tundish practice. Additionally it is increasing the number of tundishes available due to the lower time for baking. Finally, the cold start up practice is again favorable with respect to reduced $CO_2$ emissions (Fig. 7).



Fig. 7. Dry mix after baking thyssenkrupp Steel with the chimney technique

**CONCLUSIONS**
Practical trials with the olivine based dry mix compound in thyssenkrupp Steel plants OX 1 and OX 2 have shown that the use of this product is technically possible. The metallurgical effects in produced grades are currently being assessed. In comparison to conventional heavy 90 DBM dry mixes, which are still in use in the market, the olivine based dry mix material provides a consumption saving of approx. 15-20% and a total $CO_2$ reduction of up to 27300 tons per year. Even in comparison with the more modern light magnesia dry mix, the $CO_2$ savings sum up to 7750 tons. The

213

material consumption in the trials indicates a 4,5% higher consumption, but is matter of further improvements. According to this trial the future changeover from hot air mould to eMould, the plants will be able to achieve together an annual energy savings compared to hot air mould of 7850 baking processes per year, energy savings per baking process of 0.764 MWh are calculated with the eMould. This means an annual energy saving of 5997 MWh equivalent to approx. 600000 Nm³ natural gas compared to the hot air mould. Thyssenkrupp will also save approx. 4575 hours for OX 1 and 4800 hours for OX 2 in baking time. Which means a total saving with the eMould of approx. 9375 hours together in both plants and a much higer tundish availability.

This work has clearly shown that by adapting the recipes and increasing the use of European raw materials in combination with the use of eMould, high $CO_2$ emission savings are possible in the area of the tundish working lining.

**REFERENCES**
[1]    Bradley MJ. Overview of tundish dry vibe technology. MPT International 2, 2008. p. 70-72.
[2]    Liang Zhao, Junsheng Feng, Hui Dong. Analysis of carbon footprint and reduction approach of magnesia production in China. In: Journal of cleaner production, Volume 334, 01.02.2022, 130194
[3]    The European Magnesite/Magnesia Industry: enabler in the transition to a low-carbon economy, January 2020, European Association of Mining Industries, Metal Ores & Industrial Minerals Avenue de Tervueren 168, box 15, 1150 Brussels, Belgium www.euromines.org
[4]    Sibelco Nordic AS, CO2 Emission calculation
[5]    T. Bierkämper, Research project for the development of the eMould. Mould-Tec.com
[6]    Calculator - CO2-CALCULATOR (carboncare.org)

# INVESTIGATION OF THE DRYING BEHAVIOR OF LOW CEMENT CASTABLES

Uwe, Klippel, Patrick, Malkmus
Calderys Deutschland GmbH, Neuwied, Germany

Steffen, Möhmel
Imerys Villach GmbH, Villach, Austria

**ABSTRACT**

Monolithic refractory castables still comprise a hydraulic bond in the vast majority of the cases despite of many new developments for chemical as well as non-cement castable (NCC) binders in the last decade. In particular deflocculated dense castables of the low cement castable (LCC) range can be considered as the workhorse in this field. The drying of such monolithic deflocculated dense refractory linings during the first heat up maintained to be a challenge while complying with constantly increasing market demands for simpler procedures and quicker drying regimes. Quite a few publications have been released on this topic for the last ten years, indeed. However, mostly either the product is altered in regard to its bond nature and/or harsh steam spalling test conditions were investigated to qualify new product types in regard to their spalling resistance. This paper, however, introduces a simple laboratory scale test setup to study and iteratively improve the drying schedule of a given castable lining to deliver both: enhancing the drying effectiveness in avoiding steam spalling as well as the drying efficiency in releasing physically and chemically bonded water as quick as possible. The influence of the matrix and the bond is showcased by an experimental design comprising self-compacting and vibro-casting LCC's either with or without silica fume in combination with or without drying fibers, respectively.

**INTRODUCTION**

Since the beginning and rise of deflocculated low cement castables five decades ago [1] the performance of such hydraulically bonded monolithic refractory concretes has been significantly enhanced through improved particle size distributions and incorporation of submicron particles such as silica fume [2-4]. Nevertheless, the drying of deflocculated hydraulically bonded castables is still considered as the major drawback among minor disadvantages in comparison to competing bonding mechanisms such as chemical, colloidal or other no cement castable bonds until today [5]. The common practice of incorporating drying aids, e.g. organic fibers, to enhance the permeability and, thus, supporting the removal of water steam during drying, has been investigated and reported throughout the years and is still under investigation today [6-13]. The incorporation of drying aids or modifications of the bond nature [14-17] were accompanied by further investigations on the mechanisms of the drying process to qualify materials for their respective drying ability or sensitiveness in regard to steam spalling [18-22]. Eventually, further developed experimental setups gave way to analyse the drying process for actual heat up curves and lining configurations including approaches of conducting simulations of the same [23-28].

Consequently, the experimental pressure-temperature-mass (PTM) setup, presented earlier [18, 21], was upgraded by applying a programmable heating plate as temperature source for the reason of offering a simple and robust laboratory method. As a result, the impact of various factors on the drying effectiveness to prevent catastrophic steam spalling as well as drying efficiency to remove physically and chemically bonded water from the hydraulically bonded refractory castable lining was studied. Complementary to the refractory castable type as a common factor, the speed as well as the design of heat up curves (HUC), e.g. ramp-and-hold and/or continuous ramp, were investigated. Results of the applied method are presented and discussed exemplarily for vibro-casting as well as self-compacting LCC formulations following the suggestions of Schnabel et al. [29] and are compared against their physical properties such as pore size distribution as well as air permeability.

**EXPERIMENTAL**

Generally, ALMATIS white tabular alumina (WTA) was used to formulate both: the vibro-casting as well as the self-compacting castable formulations (table 1-2). ELKEM 971U microsilica (MS) was applied as silica fume source whereas super ground reactive alumina CT 3000 SG from ALMATIS was used for silica fume free formulations. Additionally, fine ground calcined alumina MR30A from HINDALCO was incorporated into self-compacting castable formulations. Eventually, CA-14 W calcium aluminate cement (CAC) in combination with either the dispersant ADS1 or M-ADS1 from ALMATIS completed the formulations. BAUMHÜTER 2.8dtex monofilament shortcut polypropylene (PP) fibers in 6mm length were employed as drying aids.

The consistency of the freshly made castable was determined according to EN 1402-4 with the 80 mm tall cone all times. Specimens were made, temperature treated and characterized according to EN 1402-5 and EN 1402-6, respectively. The air gas permeability, µ, was measured at room temperature according to EN 1402-8. The pore size distribution was determined through mercury (Hg) intrusion method in accordance with DIN ISO 15901-1 with a Micromeritics AutoPore IV.

The PTM setup of Meunier et al. [18-19] was enhanced by an IKA C-MAG HS 7 CONTROL programmable heating plate regulated by an extra thermocouple attached to the hot face of the Ø 190 mm and 150 mm tall cast body. Two different HUC's were applied. The configuration of the steam pressure sensors and the thermocouples remained as same as lastly reported ten years ago [21].

215

Tab. 1: Vibro-casting castable formulations used

| Material \ Code | C | C-F | C-S | C-SF |
|---|---|---|---|---|
| | wt.% | | | |
| WTA 3-6 mm | 25 | 25 | 25 | 25 |
| WTA 1-3 mm | 25 | 25 | 25 | 25 |
| WTA 0.5-1 mm | 10 | 10 | 10 | 10 |
| WTA 0-0.5 mm | 15 | 15 | 15 | 15 |
| WTA 0-0.3 mm | 3 | 3 | 3 | 3 |
| WTA 0-0.45 mm | 10 | 10 | 10 | 10 |
| CAC CA-14 W | 5 | 5 | 5 | 5 |
| CT 3000 SG | 6 | 6 | | |
| ADS 1 | 1 | 1 | | |
| M-ADS 1 | | | 1 | 1 |
| MS 971U | | | 6 | 6 |
| PP Fiber | | 0.05 | | 0.05 |

Tab. 2: Self-compacting castable formulations used

| Material \ Code | SF | SF-F | SF-S | SF-SF |
|---|---|---|---|---|
| | wt.% | | | |
| WTA 3-6 mm | 30 | 30 | 30 | 30 |
| WTA 1-3 mm | 10 | 10 | 10 | 10 |
| WTA 0.5-1 mm | 10 | 10 | 10 | 10 |
| WTA 0-0.5 mm | 22 | 22 | 22 | 22 |
| WTA 0-0.45 mm | 5 | 5 | 5 | 5 |
| CAC CA-14 W | 5 | 5 | 5 | 5 |
| MR 30A | 12 | 12 | 12 | 12 |
| CT 3000 SG | 6 | 6 | | |
| ADS 1 | 1 | 1 | | |
| M-ADS 1 | | | 1 | 1 |
| MS 971U | | | 6 | 6 |
| PP Fiber | | 0.05 | | 0.05 |

Tab. 3: Physical and mechanical properties of the investigated refractory castable formulations (table 1-2)

| | H₂O | iSF | iVF | ρ | | πₐ | | WA | | CCS | | MOR | | μ | | Φ₅₀,ₕₘ | |
|---|---|---|---|---|---|---|---|---|---|---|---|---|---|---|---|---|---|
| | wt.% | % | % | g·cm⁻³ | | vol.% | | wt.% | | N·mm⁻² | | N·mm⁻² | | 10⁻¹⁶ m² | | μm | |
| ϑ / °C | 20 | 20 | 20 | 400 | 110 | 400 | 110 | 400 | 110 | 400 | 110 | 400 | 110 | 200 | 400 | 110 | 400 |
| C | 4.3 | ✕ | 160 | 3.2 | 11 | 14 | 3.5 | 4.3 | 85 | 84 | 11 | 8 | 18.2 | 16.8 | 26.3 | 0.12 | 0.05 |
| C-F | 4.3 | ✕ | 95 | 3.1 | 13 | 17 | 4.1 | 5.3 | 85 | 87 | 12 | 11 | 11.4 | max | max | 0.11 | 0.06 |
| C-S | 4.3 | ✕ | 135 | 3.1 | 11 | 13 | 3.4 | 4.2 | 141 | 176 | 15 | 26 | min | 0.5 | 2.0 | 0.03 | 0.05 |
| C-SF | 4.3 | ✕ | 100 | 3.0 | 11 | 15 | 3.6 | 5.1 | 146 | 171 | 16 | 23 | 0.5 | 9.0 | max | 0.03 | 0.05 |
| SF | 5.0 | 165 | ✕ | 3.1 | 13 | 16 | 4.2 | 5.0 | 54 | 64 | 7 | 6 | 23.5 | 26.5 | 30.7 | 0.15 | 0.05 |
| SF-F | 5.0 | 70 | 175 | 3.1 | 13 | 16 | 4.1 | 5.2 | 74 | 72 | 12 | 9 | 17.1 | max | max | 0.12 | 0.05 |
| SF-S | 5.0 | 155 | ✕ | 3.0 | 12 | 14 | 3.8 | 4.6 | 99 | 146 | 13 | 21 | 0.7 | 0.9 | 2.0 | 0.03 | 0.04 |
| SF-SF | 5.0 | 50 | 165 | 3.0 | 12 | 15 | 3.8 | 4.9 | 99 | 134 | 13 | 20 | 0.6 | 4.7 | max | 0.03 | 0.05 |

H₂O: gauging water, iVF: initial vibro-flow, iSF: initial self-flow, ϑ: pre-treatment temperature, ρ: bulk density, πₐ: open porosity, WA: water absorption, CCS: cold crushing strength, MOR: modulus of rupture, μ: air permeability $k_1$ at 5 bar, Φ₅₀,ₕₘ: average pore size diameter

## RESULTS

The castable formulations according to table 1-2 were analyzed for their placement characteristics as well as physical and mechanical properties (table 3). The given average values are simply of informative character and were subjected to a deviation of about 10%. Though, the quantity of applied drying aid PP fibers was with about 1.5 kilograms per cubic meter concrete considerably low; the placement behavior of both: the vibro-casting (C-F, C-FS) as well as the self-compacting (SF-F, SF-SF) formulations was impacted significantly. The respective self-compacting castables had to be subjected to vibro-casting to obtain specimens, eventually. Figure 1 shows exemplarily the visible effect of PP fiber decomposition in generating fine pores at around 10 μm pore size diameter such as already reported by Meunier et al. [8].

Due to the submicron silica fume addition with an about 40 percent lower density than its reactive alumina counterpart, the well-known matrix densification took place for formulations such as C-S, C-SF and SF-S, SF-SF, respectively, visible by the cumulative pore size distribution in figure 2 and by the average pore size diameter, Φ₅₀,ₕₘ given in table 3.

The air permeability, μ, remains about one magnitude behind when comparing silica fume bearing formulations with silica fume free formulations (table 3). The effect of silica fume appeared to be dominant over the different castable types and their respective difference in matrix volume share, i.e. either C or SF. Air permeability values indicated with "max" refer to more than 110·10⁻¹⁶ m² whereas "min" represents less than 0.5·10⁻¹⁶ m².

## Pressure-Temperature-Mass Test Results

The castable formulations were subjected to the aforementioned PTM test procedure with two different heat up curves:

N°1: RT → 43 K/h → 150°C → 12 h → 150°C → 9 K/h → 350°C
N°2: RT → 43 K/h → 150°C → 6 K/h → 350°C

N°1 represents the initial phase of a commonly applied ramp and hold drying curve procedure and N°2 refers to the also commonly applied continuous ramp philosophy whereas both share the first segment until reaching 150°C. However, the new heating plate was lacking heating performance in kilowatts, hence, the specimen did not reach the maximum temperature of 350°C as targeted.

Table 4 summarizes the results for the acquired maximum relative pressures and associated temperatures for given formulations, heat up curves as well as distances from the hot face (depth s). Figures 3-6 show the pressure pattern over heat up time as well as the dewatering by weight loss, -Δm. The temperature profile over the lining depth is given exemplarily for the HUC N°1 and N°2 by figure 3 and 4, respectively. The lower permeability of silica fume containing formulations contributed to significantly higher relative pressures. PP fibers did effectively decrease these pressures to avoid steam spalling. The occurrence of maximum relative pressure peaks after the hold at 150°C (figure 3 and 5) revealed an ineffectiveness of such a hold to prevent steam spalling. Comparing both HUC results, it appears that N°1 shows a decreased efficiency of water removal per time as reported by Fey et al. [24-26].



Fig. 1: Incremental pore size distribution by Hg intrusion method
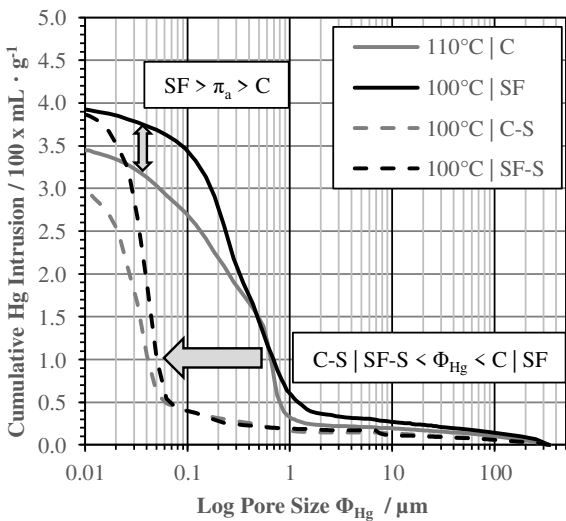


Fig. 2: Cumulative pore size distribution by Hg intrusion method

Tab. 4: Results of PTM Test concerning maximum rel. pressure at a given time, temperature and depth from the hot phase per HUC

| s | Heat Up Curve N°1 \| Ramp & Hold | | | | | | | | Heat Up Curve N°2 \| Continuous Ramp | | | | | | | |
|---|---|---|---|---|---|---|---|---|---|---|---|---|---|---|---|---|
| | 40 mm | | 60 mm | | 80 mm | | 100 mm | | 40 mm | | 60 mm | | 80 mm | | 100 mm | |
| | $p_{max}$ | $\vartheta_{Pmax}$ | $p_{max}$ | $\vartheta_{Pmax}$ | $p_{max}$ | $\vartheta_{Pmax}$ | $p_{max}$ | $\vartheta_{Pmax}$ | $p_{max}$ | $\vartheta_{Pmax}$ | $p_{max}$ | $\vartheta_{Pmax}$ | $p_{max}$ | $\vartheta_{Pmax}$ | $p_{max}$ | $\vartheta_{Pmax}$ |
| | bar | °C | bar | °C | bar | °C | bar | °C | bar | °C | bar | °C | bar | °C | bar | °C |
| C | 2 | 129 | 2 | 171 | 4 | 175 | 3 | 168 | 2 | 143 | 4 | 166 | 5 | 172 | 5 | 178 |
| C-F | 1 | 110 | 1 | 161 | 3 | 167 | 4 | 168 | 2 | 141 | 2 | 149 | 5 | 173 | 5 | 179 |
| C-S | 21 | 240 | 20 | 230 | 18 | 229 | 12 | 230 | 18 | 236 | 21 | 230 | 15 | 230 | 7 | 234 |
| C-SF | 12 | 218 | 11 | 195 | 6 | 207 | 5 | 200 | 5 | 185 | 5 | 184 | 3 | 197 | 4 | 205 |
| SF | 4 | 191 | 6 | 185 | 7 | 188 | 5 | 185 | 3 | 159 | 5 | 168 | 6 | 182 | 6 | 187 |
| SF-F | 4 | 176 | 6 | 173 | 7 | 181 | 6 | 186 | 5 | 168 | 6 | 173 | 7 | 178 | 7 | 187 |
| SF-S | 18 | 235 | 20 | 230 | 17 | 231 | 8 | 235 | 16 | 220 | 17 | 218 | 16 | 220 | 14 | 221 |
| SF-SF | 8 | 213 | 14 | 207 | 12 | 202 | 4 | 204 | 8 | 191 | 10 | 196 | 7 | 195 | 5 | 207 |

s: depth from hot phase, $p_{max}$: maximum relative pressure at depth s, $\vartheta_{Pmax}$: temperature at $p_{max}$ and depth s
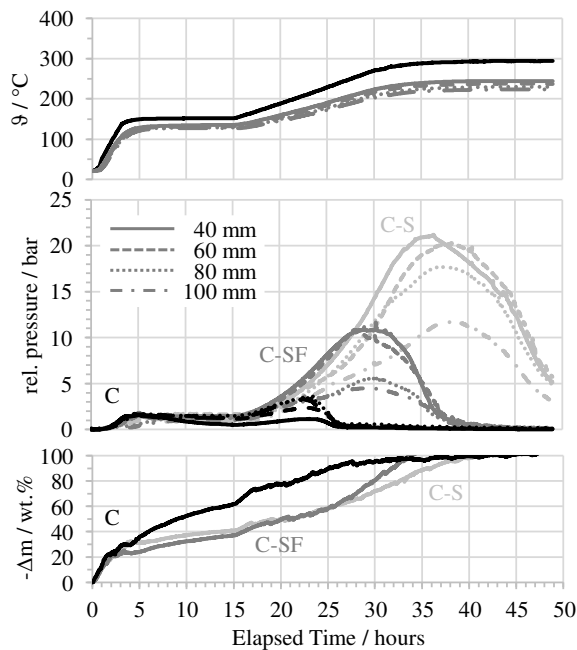


Fig. 3: PTM Results for HUC N°1, C, C-S and C-SF
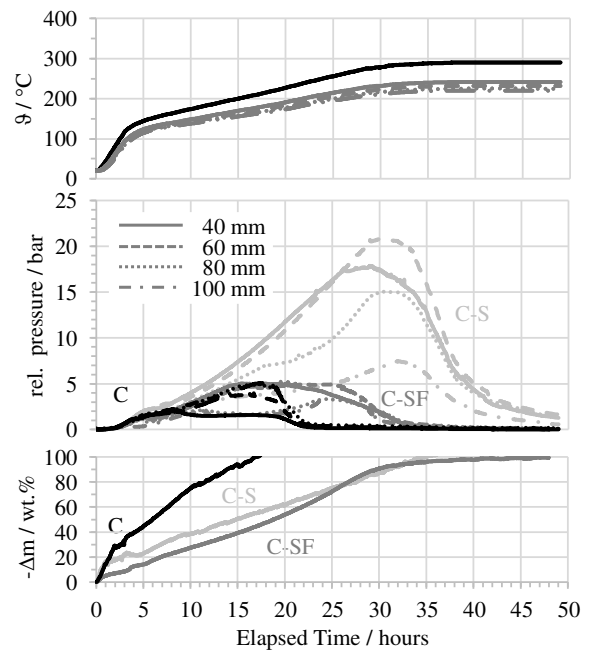


Fig. 4: PTM Results for HUC N°2, C, C-S and C-SF
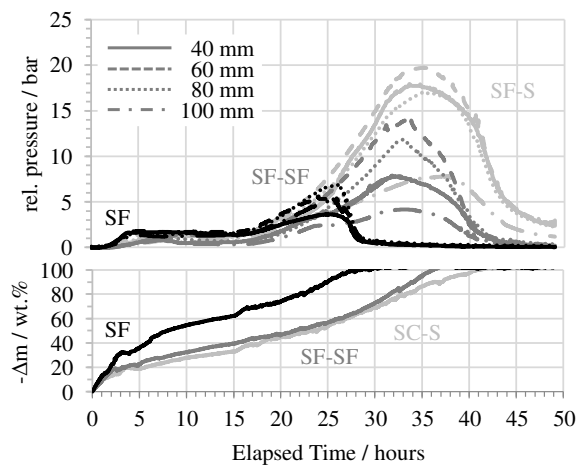


Fig. 5: PTM Results for HUC N°1, SF, SF-S and SF-SF
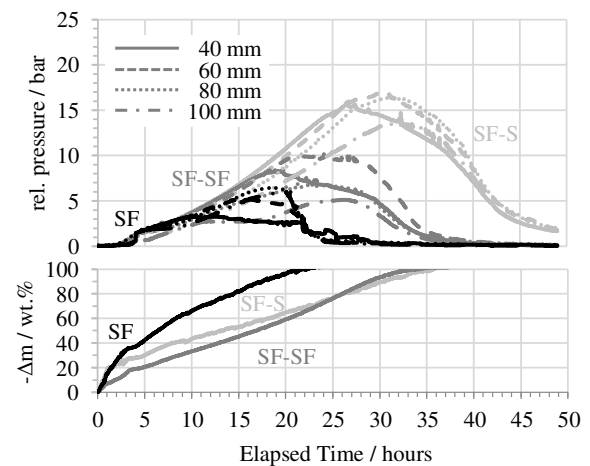


Fig. 6: PTM Results for HUC N°2, SF, SF-S and SF-SF

Silica fume free LCC formulations, (C, SF), appeared not in need for further drying aids in this investigation. Neither showed their respective PP fiber containing counterparts (C-F, SF-F) further improvements and are, thus, not shown. The reason is seen in their sufficient air permeability already at 110°C (table 3) to evacuate the water steam properly without contributing to high steam pressures. To quantify the difference in drying speed, v, the difference of weight loss at 80 wt.% and the already reached weight loss value at

217

150°C in conjunction with the respective elapsed time was used to calculate the values in table 5. Interestingly, the ramp design recorded regularly higher drying speeds versus the hold design. This is traced back to the determined temperatures at peak steam pressures in table 4 which indicate that a hold temperature of 150°C is simply insufficient to create a meaningful pressure to push the water steam out of the lining. The ramp design, however, was reaching an isotherm of about 180-200°C earlier in time, hence, advancing the water removal. Comparing the pressure build-up occurrence during the second ramp with 9 K/h in HUC N°1 and 6 K/h in HUC N°2 shows a pressure flattening for N°2 in particular for silica fume and PP fiber containing formulations (C-SF, SF-SF). Thus, a ramp design appeared to be safer in avoiding steam spalling in this study. Generally, silica fume bearing formulations recorded lower drying speeds as well as the highest pressures (-S, -SF).

Tab. 5: Drying speed per formulation and heat up curve

| Code | C | C-F | C-S | C-SF | SF | SF-F | SF-S | SF-SF |
|---|---|---|---|---|---|---|---|---|
| | average dewatering speed v / wt.% · h⁻¹ | | | | | | | |
| HUC N°1 | 2.8 | 2.8 | 1.9 | 2.1 | 2.5 | 2.5 | 2.1 | 2.2 |
| HUC N°2 | 5.6 | 3.9 | 2.4 | 3.0 | 4.0 | 3.5 | 2.3 | 2.9 |

**CONCLUSIONS**

The modified PTM setup delivered significantly more information about the behavior of refractory castables during the initial heat up than the usually performed material qualification methods. Besides the ability to support materials optimization to avoid steam spalling, the method gives also way to incrementally improve the heat up curve design with considerably low efforts. Consequently, the method contributes to enhancements in drying of monolithic refractories, in particular for hydraulically bonded castables with their references across high temperature applications and industries.

**REFERENCES**

[1] L. Prost, A. Pauillac: Hydraulically setting refractory compositions. US3802894A (1974) and FR6934405A (1969)

[2] B. Myhre: Microsilica in alumina based ultralow-cement castables. The effect of microsilica additions on flow. XXIII ALAFAR Congress, Puerto Vallarta, Mexico (1994)

[3] B. Myhre, A.M. Hundere: The use of particle size distribution in development of refractory castables. XXV ALAFAR Congress, San Carlos de Bariloche, Argentina (1996)

[4] F. Tomšů, S. Palčo: From conventional refractory castables to actual high-quality hydraulic bonded products – development during the last forty years. InterCeram: International Ceramic Review 60 (2011), p. 202-207

[5] C. Parr, J.M. Auvray, M. Szepizdyn, C. Wöhrmeyer, C. Zetterstrom: A Review of Bond Systems for Monolithic Castable Refractories, Refractories Worldforum 7 (2015) 2, p. 63-72

[6] J.M. Canon, T.P. Sandler, J.D. Smith, R.E. Moore: Effect of organic fiber addition on the permeability of refractory concrete, Proceedings of 5th UNITECR (1997), New Orleans, USA, p. 583–592

[7] R. Salomão, V.C. Pandolfelli, L.R.M. Bittencourt: Advances on the understanding of the role of polymeric fibers as drying additives for refractory castables. Proceedings of 9th UNITECR (2005), Orlando, USA, p. 816-820

[8] P. Meunier, L. Ronsoux: Permeability and dehydration of refractory castables. Proceedings of 9th UNITECR, (2005), Orlando, p. 799-803

[9] M.D.M. Innocentini, R. Salomão, C. Ribeiro, V.C. Pandolfelli, R.P. Rettore, L.R.M. Bittencourt: Permeability of fiber-containing refractory castables – part 1, American Ceramic Society Bulletin 81 (2002) 7, p. 34-38

[10] R. Salomão, F.A. Cardoso, M.D.M. Innocentini, V.C. Pandolfelli, L.R.M. Bittencourt: Effect of polymeric fibers on refractory castable permeability. American Ceramic Society Bulletin 82 (2003) 4, pp. 51–56

[11] H. Peng, B. Myhre: Dring behaviour and explosion resistance of no-cement refractory castables. Refractories Worldforum 11 (2019) 4, p. 62-66

[12] A.P. Luz, M.H. Moreira, R. Salomão, M.A.L. Braulio, V.C. Pandolfelli: Drying behavior of dense refractory castables. Part 2 – Drying agents and design of heating schedules. Ceramics International 48 (2022) 3, p. 2965-2987

[13] H.Peng, B. Myhre: Improved explosion resistance of low cement refractory castables using drying agents. International Journal of Ceramic Engineering and Science (2022), p. 1–8

[14] J. Soudier: QD NCC: Quick drying no cement castables. A novel non-cementitious mineral bond permitting extreme rapid dry out of monolithic refractory linings. Proceedings of 12th UNITECR (2011), Kyoto, Japan, 1-D-17.

[15] P. Malkmus, P. Meunier, J. Soudier: Time, energy and cost saving during monolithic refractory lining installation by combining quick dry technology and gunning technics. Proceedings of 13th UNITECR (2013), Victoria, Canada, p.1007-1012

[16] M. Nouri-Khezrabad, M.A.L. Braulio, V.C. Pandolfelli, F. Golestani-Fard, H.R. Rezaie: Nano-bonded refractory castables. Ceramics International 39 (2013), p. 3479 – 3497

[17] U. Klippel, J. Soudier, J. Lee, A Wahyu: Colloidal silica sol bonded castables for high temperature applications. China's Refractories 24 (2015), p. 51-56.

[18] P. Meunier, J.-C. Mindeguia, P. Pimienta: Mass, temperature and pressure measurements during the dry out of refractory castables. Proceedings of 51st International Colloquium on Refractories, Aachen, (2008), p. 95-98

[19] P. Meunier, J. Soudier: The drying of refractory castables: from tests to models. Proceedings of 11th UNITECR (2009), Salvador, Brazil, p. 221-224

[20] A.P. Luz, M.H. Moreira, M.A.L. Braulio, C. Parr, V.C. Pandolfelli: Drying behaviour of dense refractory ceramic castables. Part 1 – General aspects and experimental techniques used to assess water removal. Ceramics International 47 (2012) 16, p. 22246-22268

[21] P. Meunier, P. Ermtraud: Methods to assess the drying ability of refractory castables. Proceedings of 13th UNITECR (2013), Victoria, Canada, p. 959-964

[22] G. Palmer, J. Cobos, J. Millard, T. Howes: The accelerated drying of refractory concrete - part I: a review of current understanding. Refractories Worldforum 6 (2014) 2, p. 75-83

[23] G. Palmer, J. Cobos, J. Millard, T. Howes: The accelerated drying of refractory concrete - part 2 numerical modelling. Refractories Worldforum 6 (2014) 4, p. 89-97

[24] K.G. Fey, I. Riehl, R. Wulf, U. Gross: Pressure driven heat-up curves - a numerical and experimental investigation. International Journal of Thermal Sciences 113 (2017), p. 1-9

[25] K.G. Fey, I. Riehl, R. Wulf, U. Gross: First heat-up of 1D multi-layer walls and 2D geometries consisting of refractory concrete. International Journal of Thermal Sciences 116 (2017), p. 159-171

[26] K.G. Fey, I. Riehl, R. Wulf, U. Gross: Experimental and numerical investigation of the first heat-up of refractory concrete. International Journal of Thermal Sciences 100 (2016), p. 108-125

[27] M.H. Moreira, S. Dal Pont, R.F. Ausas, T.M. Cunha, A.P. Luz, V.C. Pandolfelli: Direct comparison of multi and single-phase models depicting the drying process of refractory castables. Open Ceramics 6 (2021) 100111, p. 1-17

[28] M.H. Moreira, S.Dal Pont, R.F. Ausas, A.P. Luz, T.M. Cunha, C. Parr, V.C. Pandolfelli: Main trends on the simulation of the drying of refractory castables - review. Ceramics International 47 (2021) 20, p. 28086-28105

[29] M. Schnabel, A. Buhr, J. Dutton: Rheology of high performance alumina and spinel castables. Refractories Worldforum 4 (2012) 2, p. 95-100

# A NOVEL TYPE OF ANTI–SPALLING NATURAL STRAW FIBERS FOR REFRACTORY CASTABLES

Minghua Zhang, Micael Larsson, Edina Alibasic, Ronald Robles
Höganäs Borgestad AB, Sweden

## ABSTRACT

With the coaction of internal pressure created by water vapor and thermal stress triggered by temperature gradient, cement based castables are prone to structural damage and even explosive spalling during dry-out process; thus to cut down the service life of refractory linings and cause economic loss. Here a novel type of natural plant fibers is introduced in terms of castables' anti-spalling property. The permeability of conventional castables and ultra-low cement castables are tested and presented in combination of the novel fibers and polypropylene (PP) fibers. The results demonstrate those natural plant fibers are functional with enhanced permeable properties and lower risk of spalling. Moreover, laboratorial and industrial practices have confirmed that those fibers make cement based castables excellent anti-spalling during quick dry-out.

## INTRODUCTION

### 1. Natural Plant Fibers

Nature created materials is the natural fibers which are abundantly available, eco-friendly and have renewable in their behavior. The cultivation and on growing harvesting and primary processing conditions to extract the fiber will dictate the homogeneity.

The use of natural fibers is now in demand compared to synthetic fibers as awareness and awareness of the environment is raised among individuals. There are plenty of trees for the fiber production of various trees such as hemp, banyan, neem, palmyra, jute, sisal, banana, etc. As here it is transformation of the waste material into raw material for the composites.

Plant fibers are hydrophilic owing to the presence of functional groups such as hydroxyl in their structure. Therefore, plant fibers absorb a considerable amount of moisture from the surrounding environment. The moisture absorption capacity of plant fibers depends mainly on their chemical composition and crystallinity. Plant fibers are generally composed of cellulose, often in combination with other components such as lignin. Plant fibers are classified according to their source in plants.

- Bast or stem fibers, derived from the fibrous bundles in the inner bark of plant stems.
- Leaf fibers, which run lengthwise through the leaves of monocotyledonous plants.
- Seed-hair fibers, such as cotton.

### 2. Anti-spalling agents for refractory castables

After the castable has been installed and hardened, there are two types of water remaining: physical water and chemical water. Both must be removed before the refractory material can be used in service.

Heat needs to be applied to remove both types of water. The physical and chemical water is released at certain critical temperatures during the dry-out which are as follows:

- Removal of free water: 100°C
- Dehydration of major cement phases: 220°C, 270°C and 549°C.

All water must be removed in a controlled manner and dry-out schedules should pay attention to these critical temperatures.

When water turns to steam there is a volume expansion of approximately 1,600 times. This increase in volume causes high pressures within the lining. At each critical temperature there is a high potential for developing internal pressures that could exceed the strength of the refractory castable and cause the material to spall.

This physical disintegration of the castables often occurs at temperatures between 100 and 300 °C, where water is released in a combined process of (i) evaporation of free water and (ii) dehydration of the calcium-aluminum-hydrates.

The refractory producers have identified several countermeasures that allow a more secure first heat-up, where water (vapor) is released at lower temperatures if CAC is reduced to a minimum in the formulation.

Over the past few decades, with the use of organic fibers, which are known to melt at temperatures below 200 °C, a straightened pore structure introduces additionally permeable pathways that permit easier vapor release toward the surface of the castable.

One of the action mechanisms of the polymeric fibers is activated during the softening and melting of the filaments. The first permeable paths will be formed by the deformation of the molten polymer using the pressurized water vapor generated inside the ceramic microstructure. After the fibers' decomposition, the overall permeability of the castables increases when interconnections are generated between regions presenting different permeability and the formed channels themselves [1-6].

Thereby, polymeric fibers are added to act as sacrificial agents and their effectiveness will depend on the physicochemical properties of the selected polymers. This route may provide the development of refractory castables with more permeable microstructures, reducing the explosions likelihood of these dense materials during drying.

### 3. Permeability & Darcy's Law

Permeability is part of the proportionality constant in Darcy's law which relates discharge (flow rate) and fluid physical properties (e.g. viscosity), to a pressure gradient applied to the porous media. Darcy's Law for incompressible fluids (linear flow) is given below:

$$v = \frac{k}{\mu}\frac{\Delta P}{\Delta x} \qquad (1)$$

Therefore;

$$k = v\frac{\mu \Delta x}{\Delta P} \qquad (2)$$

Where:

$v$-is the superficial fluid flow velocity through the medium (m/s)

$k$ -is the permeability of a medium (m$^2$)

$\mu$- is the dynamic viscosity of the fluid (Pa·s)

$\Delta P$ -is the applied pressure difference (Pa)

$\Delta x$ -is the thickness of the bed of the porous medium (m)

In naturally occurring materials, the permeability values range over many orders of magnitude. Deviating from Darcy's linear law, the porous flow characteristics obey a non-linear law in a low-permeability porous medium, the viscosity of the porous flow fluid, and the permeability values of fluid are not constants. This study uses Darcy's linear law only.

## EXPERIMENTAL SECTION

### 1. Mixes Design

Table 1 shows the composition of the ultra-low cement castables. Guyana bauxite were used as aggregate, and calcium alumina cement, fume silica and a superfine aluminosilicate binder were used as matrix. With or without special plant fiber were used to compare the flowability and permeability. Table 2 shows the

219

overall composition of the conventional cement Tabular based castables.

Tab.1: Mix design of bauxite based ultra-low cement castables (wt %)

| Ultra-low Cement Castables | Flow ULC 851 | Flow ULC 851-1 |
|---|---|---|
| Plant fiber | 0 | 0.2 |
| Bauxite Guyana | 81 | 81 |
| Calcined alumina | 10 | 10 |
| Microsilica | 5 | 5 |
| Cement 70 | 1 | 1 |
| Superfine $Al_2O_3$-$SiO_2$ binder | 3 | 3 |
| Total | 100 | 100.2 |
| Final water addition% | 6 | 6 |
| Wetting time Sec. | 50 | 45 |
| Self flow% T0 | 158 | 165 |
| Self flow% T30 | 145 | 141 |

Tab.2: Mix design of tabular alumina based conventional castables (wt %)

| Conventional Castable | CC95 | CC95-1 | CC95-2 |
|---|---|---|---|
| Plant fiber | 0 | 0.27 | 0.27 |
| Polypropylen Fiber | 0.06 | 0.06 | 0 |
| Tabular Alumina | 70 | 70 | 70 |
| Cement 80 | 30 | 30 | 30 |
| Total | 100.06 | 100.33 | 100.27 |
| Final water addition % | 9.5 | 9.5 | 9.5 |

## 2. Permeability Testing
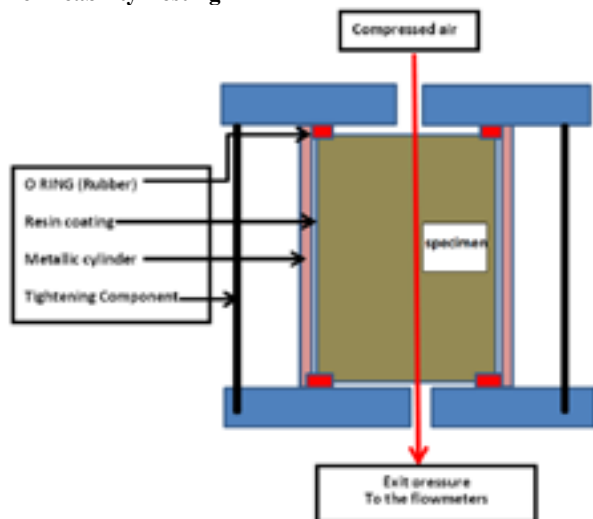


*Fig. 1: Schematic representation of permeability tester fabricated in laboratory*

The apparatus fabricated and used for measuring permeability is illustrated in Figure 1. The castables specimens, treated at different temperatures were coated with a thermosetting resin on the side surface. This is to prevent the gas leak though side surfaces while measuring permeability.

Compressed air at a pressure of 0.5 to 6.5 bars is passed through the specimen to measure the flow rate of gas (ml/min or l/min). Darcy's Law is applied to evaluate the permeability of the material. In this study, the exit pressure is supposed as a standard atmosphere and omitted. Therefore, compressed air at a pressure

of 0.5 to 6.5 bars could be considered as a pressure gradient or difference.

## RESULTS AND DISCUSSION

### 1. The permeability of Bauxite based ultra-low cement castables with different treated temperatures

In the really practice, castable refractories containing superfine aluminosilicate binder has had lower porosity and permeability, explosive spalling during dry-out has been an ongoing problem. Thus mixes of bauxite based ultra-low cement castables in Table 1 was selected to measure the permeability in terms of different treated temperatures.

Figure 2 unmistakably demonstrates that with the plant fibers, the castable held a great streak of success in improved permeability at all temperatures range from ambient temperature to 1600°C; in comparison to without plant fiber one, especially in the lower temperatures.



*Figure 2 The permeability of Flow ULC 851 with/without special plant fiber after treated at different temperatures*

### 2. The permeability of tabular alumina based conventional castables with different treated temperatures

As shown in Figure 3, castable CC95 with polypropylene fibers indicated higher permeability at 220°C, 320°C and 400°C thermal treatment, despite the lower permeability level after thermal treatment at 600 °C.
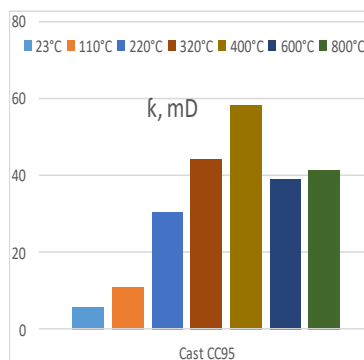


*Figure3 The permeability of conventional castable CC95 with regular Polypropylene fiber at different temperatures*

Comparison with polypropylene fibers, the special plant fibers cannot make significant permeability till 400°C despite higher permeability after 110°C, as illustrated in Figure 4.
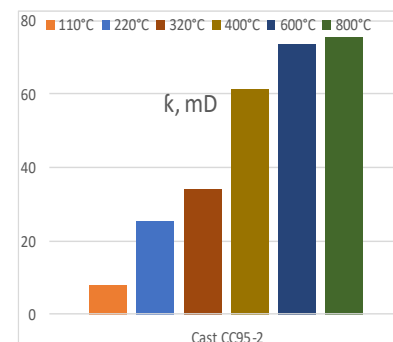


*Figure 4 The permeability of conventional castable CC95-2 with plant fiber at different temperatures*

Combing with special plant fibers and polypropylene fibers, CC95-1 castable has demonstrated optimal permeability after PP fiber molten at 170°C as revealed in Figure 5.
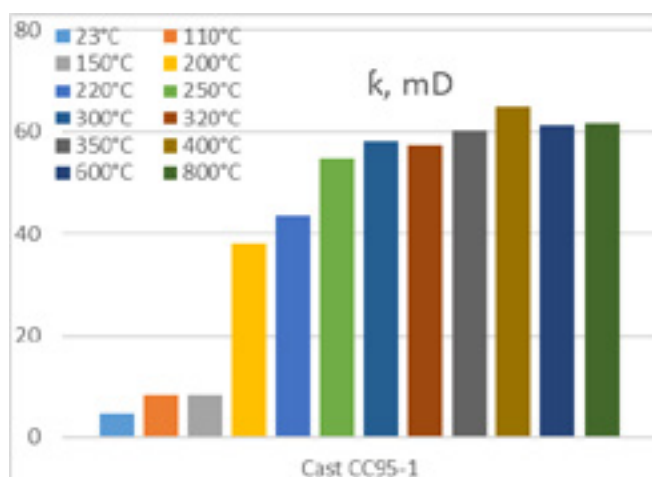


*Figure 5 The permeability of conventional castable CC95 with regular PP fiber and plant fiber at different temperatures*

These results present great technological relevance due to two aspects. Firstly, it was shown that the plant fibers could be used as feedstock to produce drying agents for refractory castables. Secondly, due to the permeability increase dramatically after 170°C, the total drying time during castables' dry-out schedule can be significantly reduced, as well as the risks of explosive spalling.
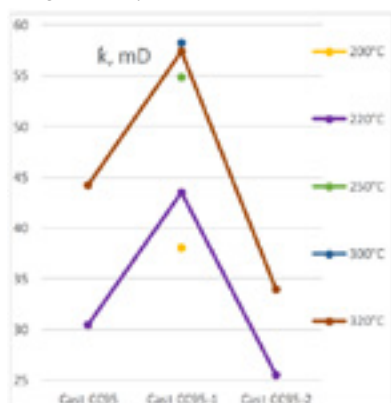


*Figure 6 Comparison of the permeability among conventional castables with different fibers between 200°C and 300°C critical temperatures*

Furthermore, in the high risk of explosion temperature extent as shown in Figure 6, combination of plant fibers and polypropylene fibers, the conventional cement castable CC95-1 has demonstrated ideal permeability.

### 3. Plant Fiber Analysis

Plant fibers are generally composed of cellulose, often in combination with other components. The main constituents of the plant fibers are cellulose, hemicelluloses, lignin, pectin, and wax. The composition of fibers depends on the geographic location where the plants are grown up.

**Plant fibers TG and DTG analysis**
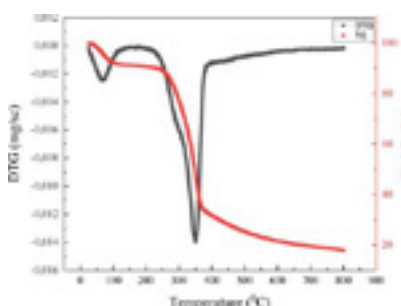


*Figure 7 Typical TG and DTG curves of the natural fibers* [7]

The thermal behavior of plant fibers was studied through TG and DTG curves provided in Figure 7. The initial thermal decomposition of fiber sample was observed at 60°C which is mainly due to the loss of moisture through evaporation. The second stage of thermal degradation of plant fibers was observed to occur between 250°C and 300°C associated with a mass loss of 20% could be attributed to thermal depolymerization of hemicelluloses. The major sharp peak at 350°C showed a major mass loss of about 60% occurred due to the thermal degradation of cellulose.

The peak observed in DTG curve within temperature 400°C to 650°C indicated the thermal depolymerization of wax and thermal degradation of lignin present in the plant fibers. The complex aromatic molecular structure of lignin makes it thermally more stable.

The results showed that the plant fibers were thermally stable up to 250°C. From 250°C to 350°C, the plant fibers were most unstable thermally.

Those temperature extent made an adaption to the drawbacks of using cement castables that explosive spalling around 200–300°C while the plant fibers were used as ant-spalling agent.

**Fibers Morphological Analysis**

A bauxite based castable with 0.25% plant fobers was casted. After 24 hrs curing in air, a sample was prepared for optical microscope measurement.
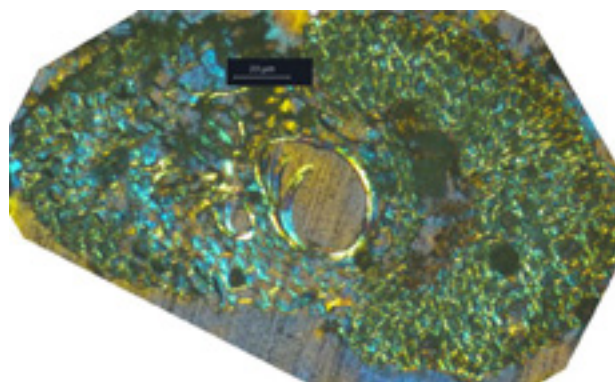


*Figure 8 Optical microstructure image of the natural plant fibers within castable after 110°C for 24 hours*
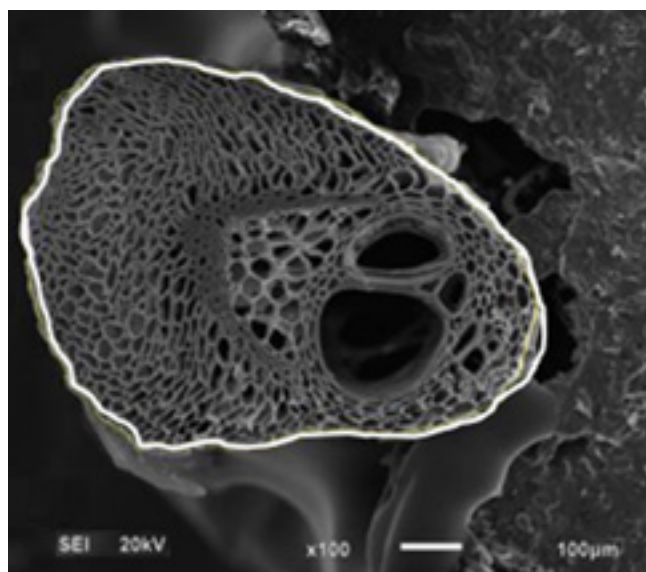


*SEM image of the fiber cross sectional area*
*Figure9 The fiber cross sectional area using the SEM micrographs in ImageJ*

The plant fiber had a structure in which each fiber had numerous individual fiber cells along the length. The fiber cells were composed of four main parts, which were the primary wall, the secondary wall, the tertiary wall, and the lumen. The fiber cells were joined together by means of hemicellulose and lignin, and they are called the middle lamella [7].

The morphology of plant fiber differed in the amount of main voids (or main lumens) that were used to transport the cell sap, i.e., watery fluid that circulated through the plant and carries food and other substances to various tissues.

The microstructural observation performed in plant fibers showed that there are main voids with many small voids. Those voids will become channels to leave vapors whenever castables were heating.

## 4. Laboratorial and industrial trial: explosion resistance testing

Laboratory testing was done by two cuboids. Each one about ~2.7 kg (100 × 100 × 100 mm), casted by CC95 and CC95-1 which containing special plant fiber and polypropylene fiber.

Those two cuboids cured at room temperature for 24 h, de-molded, and dry at room temperature for another 24 hours.

A liquefied petroleum gas (LPG) burner was used to flame the cuboids.

Finally, CC95 cuboid was exploded and CC95-1 was not.

Industrial practices have been done through the applications in cement kilns, mining grate kilns and steel lades.

Generally, drying monolithic refractory means executing a thermal cycle that starts at ambient temperatures and follows a curve specified by the manufacturer.

Eventually, the castable blocks containing plant fibers has remained intact and demonstrated excellent ant-spalling resistance; in spite of all other low cement castables were exploded.

## CONCLUSIONS

- Regarding superfine aluminosilicate powder bonded ultra-low cement castables, the special plant fibers are effective very well for overall temperatures range from room temperature to even more than 800°C which enable to have much higher permeability.
- Regarding conventional cement castables, special plant fibers cannot make higher permeability till 400°C compared with polypropylene fibers.
- Combination of special plant fibers & polypropylene fibers makes conventional cement castables avoiding dangerous explosive temperature extent (200-300°C).
- Laboratorial and industrial trials have confirmed that those special plant fibers work excellently for quick drying castables without any risk of explosive spalling.

## REFERENCES

[1] Hong Peng, Bjørn Myhre: Drying behavior and explosion resistance of refractory castables, 62th International Colloquium on Refractories 2019 Aachen, Germany (pp.30-33)

[2] R.Salomãoa, V.C.Pandolfellib, Anti-spalling fibers for refractory castables: A potential application for recycling drinking plants, Ceramics International Volume 46, Issue 9, 15 June 2020, Pages 14262-14268

[3] Nader Kazemi, Reasons for crack propagation and strength loss in refractory castables based on changes in their chemical compositions and micromorphologies with heating: special focus on the large blocks, Volume 7, 2019-Issue 2 (109-126)

[4] Peng H, Myhre B. Improved explosion resistance of low cement refractory castables using drying agents. Int J Ceramic Eng Sci. 2022; 4:84–91.

[5] Barakat A, Pel L, Adan OCG, Mhyre B, Peng H. The effect of permeability enhancement on dry-out behavior of CA- and microsilica gel-bonded castables as determined by NMR. International Ceramics. June 2020; 46:13556–68.

[6] B.P. Bezerra, A.P. Luz, R. Salomão, V.C. Pandolfelli. Low-melting-point polymeric fiber performance as drying additives for refractory castables. Ceramic International Volume 48, Issue 3, 1 February 2022, Pages 3504-3514

[7] Christian Ganser ·June 2011 · Diploma thesis. Surface characterization of cellulose fibers by atomic force microscopy in liquid media and under ambient conditions. The Institute of Physics Montanuniversität Leoben, Austria

## Panel 1

**DFFI**

Deutsche Feuerfest Industrie e.V.

# Refractory Organisations in Höhr-Grenzhausen ——

## The Business Association

The German Refractory Association (Deutsche Feuerfest-Industrie e.V. | DFFI), founded in 1949, represents and advances the interests of German manufacturers operating in the industry.

The Association collaborates in networks to promote the economic and technological evolution of its member companies by putting forward the jointly adopted positions in both political and societal contexts.

The Association gives a strong voice to the refractory industry – a sector largely dominated by small and medium-sized enterprises.

- Advocacy | Network | Perception
- Environment | Climate | Energy
- Raw Material | Recycling
- Knowlede | Education | Career

### Refractory Organisations in Höhr-Grenzhausen

| | |
|---|---|
| Deutsche Feuerfest Industrie e.V. | Deutsches Institut für Feuerfest und Keramik GmbH |
| Forschungs-Gemeinschaft Feuerfest e.V. | European Centre for Refractories |

## Panel 2

**DFFI**

Deutsche Feuerfest Industrie e.V.

# Refractory Organisations in Höhr-Grenzhausen ——



DFFI-Board
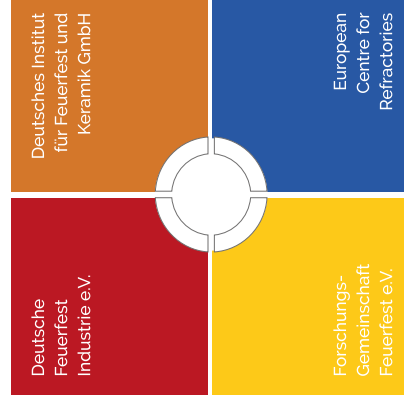
## Service and Performance

The German Refractories Association represents and pursues the politico-economic interests of its member companies vis-à-vis public authorities and government bodies in both national and European contexts. The Association covers a broad spectrum of issues and activities: It provides comprehensive support and guidance in all matters pertaining to raw materials supply security, environment and energy policy as well as tax, law, research and technology, including questions relating to standardisation.

Major German companies and international brand leaders have joined the Association, which for its part is a member of the national and European network of associations.

## The Benefit

- Information about current technical and economic policy developments with special attention to the interests of the refractory industry.
- Creation of legally secure statistics on the development, sales and consumption of refractory products, personnel costs, fuel and energy consumption, development of raw material prices and market developments in the customer industries
- Refractory committee work on technical and environmental issues and participation in BBS, BDI or DIN and ISO.
- European Cooperation (PRE and Cerame-Unie) is bundled and in dialogue with the European Institutions. World trade and regulatory issues are discussed in the World Refractories Association (WRA).

Managing Director: **Thomas Kaczmarek**

- Rheinstr. 58
  56203 Höhr-Grenzhausen
  Germany
- +49 2624 94 33 100
- info@dffi.de
- www.dffi.de

SHORT COMMUNICATIONS

# EFFECT OF H₂O₂ ADDITION AN ANTI-EXPLOSION PERFORMANCE OF ALUMINA BASED CASTABLES BONDED BY HYDRATABLE ALUMINA

Wang Zhanmin, Wang Huan, Feng Haixia, Cao Xiying, Cao Yingnan, Liu Jun
State Key Laboratory of Advanced Refractories, Sinosteel LIRR, Luoyang 471039, China

## ABSTRACT

Effect of $H_2O_2$ addition on explosive resistance of alumina based castables bonded by hydratable alumina was investigated in present paper. In order to improve the explosive resistance of the castables, 0.025%, 0.050%, 0.075%, 0.100% and 0.125% (w) $H_2O_2$ were introduced to the castables respectively. Explosive resistances were tested of the specimens cured at room temperature for 12 h at 450, 500, 550, 600, 650, 700, 750 and up to 800°C in order. Apparent porosity, bulk density, cold modulus of rupture, cold crushing strength, air permeability and pore size distribution were determined by specimens cured, dried and heat treated at different temperature. The results show that with the increase of $H_2O_2$ addition, explosive resistances of castables increase, average pore diameters increase, and bulk density, CMOR and CCS decrease gradually. The appropriate amount of $H_2O_2$ should be controlled within 0.075%.

**Key words:** Hydratable alumina; alumina castable; $H_2O_2$; explosive resistance; air permeability; pore size distribution

## INTRODUCTION

Alumina cement using in castables will bring CaO to castables, which affects the hot properties and performance of castables [1]. This problem does not exist when hydratable alumina is used as the binder[2] for castables. However, the hydration products of hydratable alumina show low density and easily block pores, thus resulting in poor permeability of castables, and it rapidly dehydrates at 300-500 °C to form a large amount of water vapor [3], which lead to explosive spalling of hydratable alumina bonded castables during heating.

At present, the main method to improve the explosive resistance of castables is to introduce anti-explosion additives such as aluminum powder, organic fibres, azoformamide and aluminum lactate [4]. However, there are also many problems for these additives [5-9]: aluminum powder easily leads to expansion or cracking of castables, and the hydrogen produced shows the risk of combustion and explosion in case of fire; organic fibres are difficult to disperse evenly in castables; azoformamide easily creates a lot of cracks in castables; and aluminum lactate forms permanent cracks in castables and affects the corrosion resistance.

$H_2O_2$ can spontaneously decompose into water and $O_2$ at room temperature, which is an environment friendly foaming agent [10-11]. In present work, $H_2O_2$ was introduced as the anti-explosion additives of hydratable alumina bonded corundum castables, and the effect of the $H_2O_2$ addition on the physical properties and explosive resistance of the castables was investigated.

## EXPERIMENT

### Raw Materials

The raw materials used for experiments included white fused alumina (5-3mm, 3-1mm, 1-0mm and≤0.074mm), activated ultrafine α-$Al_2O_3$ ($d_{50}$=1.198μm), microsilica ($d_{50}$=0.268μm), hydrogen peroxide solution ($H_2O_2$=30mass%), hydratable alumina powder (d50=2.4μm), and sodium hexametaphosphate. Table 1 shows the chemical composition of the raw materials used.

Table 1 Chemical composition of raw materials used/mass%

| | $Al_2O_3$ | $SiO_2$ | $Fe_2O_3$ | CaO | $K_2O$ | $Na_2O$ |
|---|---|---|---|---|---|---|
| White fused $Al_2O_3$ | 99.40 | 0.05 | 0.15 | | | 0.20 |
| Ultrafine α-$Al_2O_3$ | 0.40 | 96.77 | 0.10 | 0.20 | 0.26 | 0.29 |
| Microsilica | 99.38 | 0.13 | | | | 0.19 |

## Specimen Preparation and Testing

Specimen preparation procedure includes: batching the raw materials according to Table 2, hand mixing for 2-3min in a plastic bag, putting them into a mixing pot and dry mixing for 90s, adding water and wet mixing for 150s, adding hydrogen peroxide solution and stirring for 15s, then putting into mold and vibrating for 120s for the specimens with sizes of 40mm×40mm×160mm, 50mm×50mm×50mm and φ50mm×50mm.

Table 2 Formulations of specimens /mass%

| | | H₀ | H₁ | H₂ | H₃ | H₄ | H₅ |
|---|---|---|---|---|---|---|---|
| White fused alumina | 5-3 mm | 18 | 18 | 18 | 18 | 18 | 18 |
| | 3-1 mm | 30 | 30 | 30 | 30 | 30 | 30 |
| | 1-0 mm | 18 | 18 | 18 | 18 | 18 | 18 |
| | ≤0.074 mm | 25 | 25 | 25 | 25 | 25 | 25 |
| Mcrisilica | | 2 | 2 | 2 | 2 | 2 | 2 |
| Ultrafine α-$Al_2O_3$ | | 2 | 2 | 2 | 2 | 2 | 2 |
| hydratable alumina | | 5 | 5 | 5 | 5 | 5 | 5 |
| Sodium hexametaphosphate | | 0.2 | 0.2 | 0.2 | 0.2 | 0.2 | 0.2 |
| Deionized water | | 5 | 5 | 5 | 4.9 | 4.9 | 4.9 |
| Hydrogen peroxide solution | | 0 | 0.025 | 0.050 | 0.075 | 0.100 | 0.125 |

The specimens of 50 mm×50 mm×50 mm were cured at room temperature for 12 h and demoulded. The explosion resistance tests were carried out at 450, 500, 550, 600, 650, 700, 750 and 800 °C according to GB/T 36134-2018. The explosion resistance temperature and explosion time of the specimens were recorded. When two specimens in a group explode, the shorter explosion time is taken as the explosion time of the group. When the explosion resistance temperature of two groups of specimens is the same, the specimen with longer explosion time has better explosive resistance.

The rest specimens were cure at room temperature for 24h and then demoulded, dried at 110°C for 24h, and fired at 1400°C for 3h in the air atmosphere. The permanent linear change of the specimens was measured, the apparent porosity and the bulk density were determined according to YB/T 5200-1993, the cold modulus of rupture was determined according to GB/T 3001-2007, the cold crushing strength was determined according to GB/T 5072-2008, the air permeability was determined according to GB/T 3000-1999, and the pore size distribution was tested by the mercury intrusion method.

Specimens without aggregates were prepared by procedure: batching the raw materials according to Table 3, mixing and demoulding according to the same process as above, curing at room temperature for 24h, demoulding and dry at 110°C for 24h. The pore size distribution and the pore structure parameters of the specimens were determined by the mercury intrusion method.

Table 3 Formulations of specimens without aggregates /mass%

| | h₀ | h₁ | h₂ | h₃ | h₄ | h₅ |
|---|---|---|---|---|---|---|
| White fused alumina (≤0.074 mm) | 73.53 | 73.53 | 73.53 | 73.53 | 73.53 | 73.53 |
| Microsilica | 5.88 | 5.88 | 5.88 | 5.88 | 5.88 | 5.88 |
| Ultrafine α-$Al_2O_3$ | 5.88 | 5.88 | 5.88 | 5.88 | 5.88 | 5.88 |
| Hydratable alumina | 14.71 | 14.71 | 14.71 | 14.71 | 14.71 | 14.71 |
| Sodium hexametaphosphate | 0.59 | 0.59 | 0.59 | 0.59 | 0.59 | 0.59 |
| Deionized water | 14.7 | 14.7 | 14.7 | 14.7 | 14.7 | 14.7 |
| Hydrogen peroxide solution | 0 | 0.074 | 0.147 | 0.221 | 0.294 | 0.368 |

The microstructure of the specimens was observed and analyzed by a scanning electron microscope.

## RESULTS AND DISCUSSIONS

### Microstructure

Figure 1 shows the SEM photos of specimens H1, H3 and H5 fired at 1400℃. It can be seen that circular pores are generated by $H_2O_2$ decomposition in the three specimens. With the increases of the $H_2O_2$ additions, the size and the number of circular pores increase.
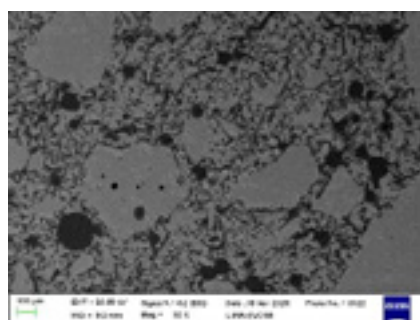


(a) Specimen H1
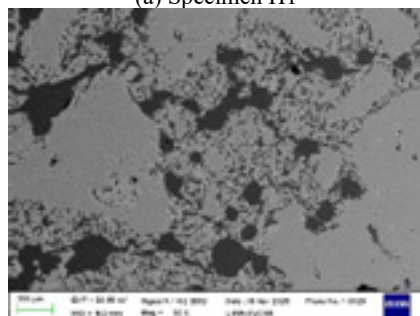


(b) Specimen H3
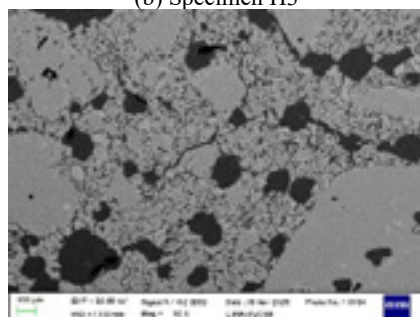


(c) Specimen H5

Fig. 1 SEM photos of specimens H1, H3, and H5 fired at 1400℃

### Air Permeability

Table 4 shows the air permeability of the specimens after demoulding, drying at 110℃ or firing at 1400℃. It can be seen that with the increases of the $H_2O_2$ additions, the permeability values of the specimens after demoulding, drying or firing gradually increase. This is because that the number of pores generated by foaming increases, and the average distance between pores shortens, which smooths the connection between pores. With the increases of the $H_2O_2$ additions, the permeability differences between the dried specimens and the demoulded specimens increases gradually because of the increasing permeability potential.

Table 4 Air permeability of specimens after demoulding, drying and firing

| $\times 10^{-15}$ /m$^2$ | H$_0$ | H$_1$ | H$_2$ | H$_3$ | H$_4$ | H$_5$ |
|---|---|---|---|---|---|---|
| After demoulding | 0.23 | 0.76 | 1.02 | 3.44 | 5.62 | 6.83 |
| After drying at 110℃ | 0.30 | 1.50 | 1.84 | 4.41 | 6.88 | 8.20 |
| After firing at 1400℃ | 130.12 | 143.37 | 180.95 | 211.45 | 342.75 | 356.31 |

## Pore Size Distribution

The pore size distribution of the specimens without aggregates after drying is shown in Fig. 2, and the pore structure parameters are shown in Table 5. It can be seen from Fig. 2 (a) that the main peak of the specimens is in the 0.1-2μm range, but the peak of the specimens added with $H_2O_2$ is lower and moves to the right compared with that of specimen h0. Moreover, with the increases of the $H_2O_2$ additions, an obvious peak appears in the 5-20 μm range for specimens h3, h4, and h5. It can be seen from Fig. 2 (b) that with the increases of the $H_2O_2$ additions, the cumulative distribution curves of the specimens gradually rises, especially in the 1-20 μm range. It can be seen from Table 5 that with the increases of the $H_2O_2$ additions, the total pore volume of the specimens increases gradually; the total pore surface area increases at first and then decreases; and the average pore size decreases at first and then increases significantly. This is because that with the increases of the $H_2O_2$ additions, the numbers of pores formed by $H_2O_2$ foaming increase, leading to the increase of the total pore volume. The less $H_2O_2$ additions, the smaller pore size of the specimens is, so the pore surface area increases. However, with more $H_2O_2$ addition, excessive pores gather and link to form larger pores. When the total pore volume does not increase more, the total pore surface area decreases. The average pore size is calculated through dividing 4 times the total pore volume by the total pore surface area.
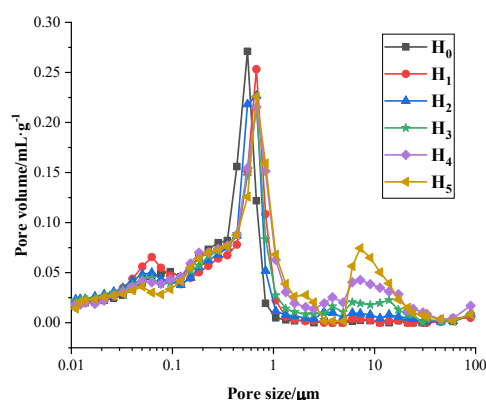


(a) Differential distribution
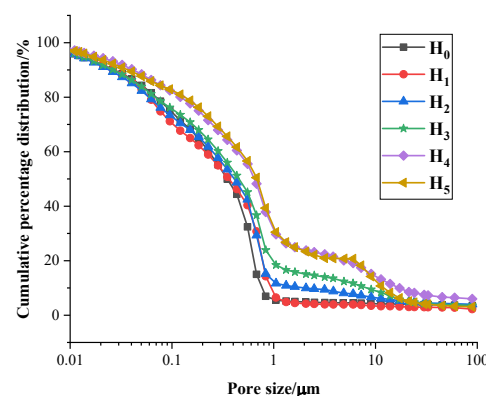


(b) Cumulative distribution

Fig. 2 Pore size distribution of specimens without aggregates after drying

Table 5 Pore structure parameters of specimens without aggregates after drying

| | h$_0$ | h$_1$ | h$_2$ | h$_3$ | h$_4$ | h$_5$ |
|---|---|---|---|---|---|---|
| Total pore volume /(ml·g$^{-1}$) | 0.138 | 0.139 | 0.146 | 0.153 | 0.182 | 0.187 |
| Total pore surface area /(m$^2$·g$^{-1}$) | 7.47 | 7.70 | 8.21 | 7.94 | 7.32 | 7.22 |
| Average pore size /nm | 73.7 | 72.2 | 71.3 | 77.1 | 99.3 | 103.6 |

The pore size distribution of the specimens containing aggregates fired at 1400℃ is shown in Fig. 3. It can be seen that the specimens without $H_2O_2$ have a single peak pore size distribution; the specimens with $H_2O_2$ additions show a double peak pore size distribution, and the second peak continuously moves to the right with the increasing $H_2O_2$ addition, indicating that the numbers of large pores and the average pore size gradually increase. However, the distribution curves of the specimens move to the right compared with those of the specimens without aggregates, indicating that their pore size is larger than that of the specimens without aggregates, which is due to the larger pores formed by the accumulation of aggregate particles.
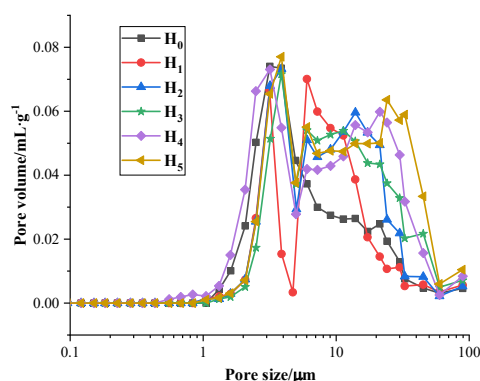


(a) Differential distribution
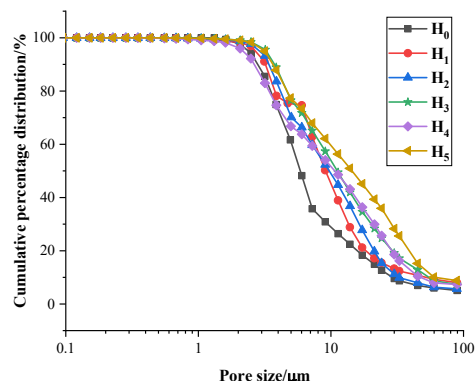


(b) Cumulative distribution

Fig. 3 Pore size distribution of specimens containing aggregates fired at 1400℃

**Physical Properties**

Figure 4 shows apparent porosity and bulk density of the specimens after demoulding, drying and firing as well as permanent linear change after firing at 1400℃. It can be seen that with the increases of the $H_2O_2$ additions, apparent porosity of the specimens after demoulding, drying and firing increases gradually, bulk density decreases gradually, and permanent linear shrinkage of the specimens after firing at 1400℃ slightly increases.

The cold modulus of rupture and the cold crushing strength of the specimens after demoulding, drying and firing are shown in Fig. 5. It can be seen that with the increases of the $H_2O_2$ additions, the cold modulus of rupture and the cold crushing strength of the specimens after demoulding, drying and firing decrease gradually. This is because the strength of the specimen is positively related to its density and densification.
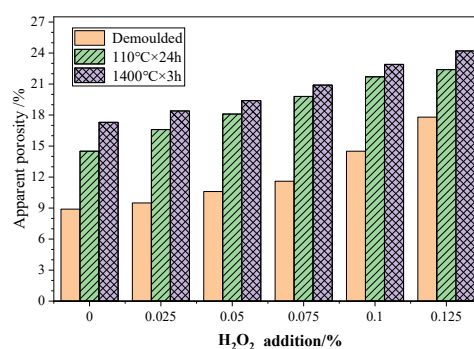


(a) Apparent porosity
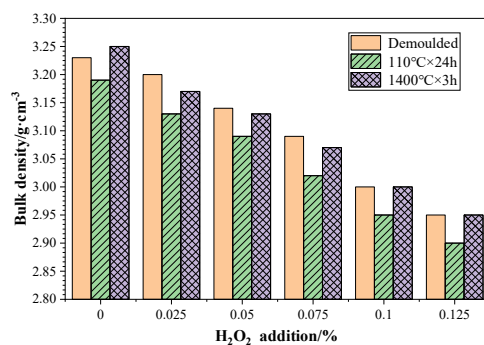


(b) Bulk density
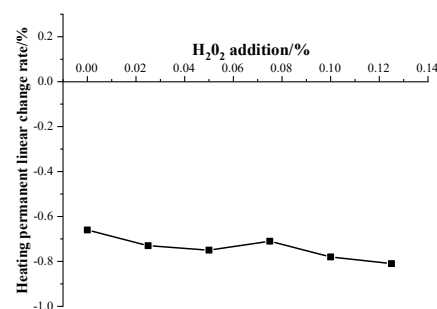


(c) Permanent linear shrinkage of specimens after firing at 1400℃

Fig. 4 Apparent porosity and density of specimens after demoulding, drying and firing as well as permanent linear change after firing at 1400℃

**Explosive Resistance**

Table 6 shows the results of explosive resistance of the specimens after curing for 12 h in moulds at room temperature. It can be seen that the explosive resistance temperature of specimens H0, H1, H2, H3, H4 and H5 is 450, 500, 500, 550, 650 and 750 ℃ respectively, which increase nearly with the increases of the $H_2O_2$ additions. Although specimens H1 and H2 have the same explosive resistance temperature of 500℃, specimen H2 shows longer explosion time than specimen H1, and only one piece of specimen H2 explosive spalling. The explosive resistance of the specimens is in the order of H5>H4>H3>H2>H1>H0, that is, they are really enhanced with the increases of the $H_2O_2$ additions.

The mechanism of $H_2O_2$ addition to improve the explosive resistance of castables can be described as follows: the foaming effect of $H_2O_2$ increases the porosity of castables, which enlarges the space for holding the water vapor generated during heating thus slows down the increase rate of water vapor pressure and reduces the water vapor pressure peak; and when the numbers of pores increase, the average distances between pores shorten, speeding up the escape of water

vapor. Both of them are beneficial to improve the explosive resistance of castables.
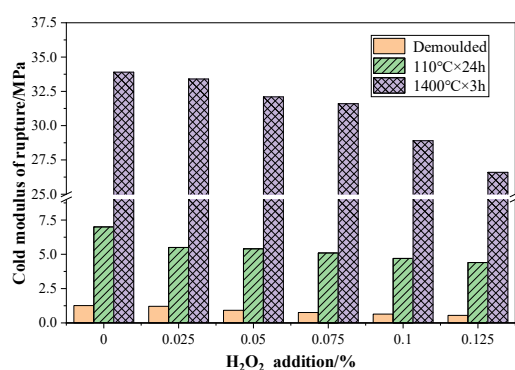


(a) Cold modulus of rupture
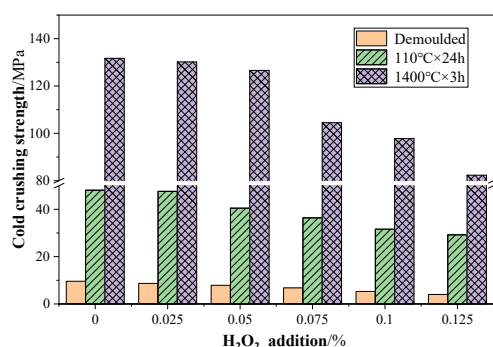


(b) Cold crushing strength

Fig. 5 Cold modulus of rupture and cold crushing strength of specimens after demoulding, drying and firing

Table 6 Explosive resistance temperature of specimens after curing for 12h at room temperature

|  | $H_0$ | $H_1$ | $H_2$ | $H_3$ | $H_4$ | $H_5$ |
|---|---|---|---|---|---|---|
| 800°C | — | — | — | — | — | ×× (146s) |
| 750°C | — | — | — | — | — | OO |
| 700°C | — | — | — | — | ×× (182s) | OO |
| 650°C | — | — | — | — | OO | OO |
| 600°C | — | — | ×× | ×× (220s) | OO | OO |
| 550°C | — | ×× (257s) | O× (314s) | OO | — | — |
| 500°C | ×× (326s) | OO | OO | OO | — | — |
| 450°C | OO | OO | OO | — | — | — |

Note: — means no test, O means no explosion, × means explosion, and the data in brackets are the explosion time.

**CONCLUSIONS**

With the increases of the $H_2O_2$ additions, explosive resistance temperature of the castables. With the increases of the $H_2O_2$ additions, average pore size gradually increases of the castables, and bulk density, CMOR and CCS decrease gradually.

Appropriate $H_2O_2$ additions can improve remarkably explosive resistance of alumina castables bonded by hydratable alumina. By comprehensive consideration, the appropriate $H_2O_2$ addition shall be controlled around 0.075%.

**REFERENCES**

[1] Li Ye, Liu Kun, Ding Dafei. Effect of curing temperature on intermediate temperature properties of calcium aluminate cement bonded corundum castables. Naihuo Cailiao (Refractories, in Chinese), 53(5), 2019, p363-366

[2] G. Ye, T. Troczynski. Hydration of hydratable alumina in the presence of various forms of MgO. Ceramics International, 32(3), 2006, p257-262

[3] Nana Xu, Yuanbing Li, Shujing Li, Hailu Wang, Ruofei Xiang, Si Ouyang. Hydration mechanism and sintering characteristics of hydratable alumina with microsilica addition. Ceramics International, 45(11), 2019, p13780-13786

[4] Cai Manfei, Nie Jianhua, Yin Guoheng, Liang Yonghe, Yin Yucheng. Influence of anti-explosive agents on performance of corundum–spinel castables. Journal of Ceramics (in Chinese), 38(6), 2017, p862-867

[5] Zhang He, Wu Yang, Gao Hongyue. Study on different types of anti-explosion fiber. Refractories & Lime (in Chinese), 44(5), 2019, p13-15

[6] Zhiqiang Wang, Xiangcheng Li, Boquan Zhu, Zhongxing Lei, Xiaoqian Peng, Yulong Wang. Analysis on mechanism of explosive spalling resistance of aluminum powder on ladle corundum-based refractory castable. Ceramics International, 46(11), 2020, p18958-18964

[7] Huang Yufei, Wang Zhanmin, Cao Xiying, Li Shaofei, Zhang Jun, Zhu Zhu. Effect of bonding mode and specimen dimension on explosion temperature during heating of bauxite based castables. Naihuo Cailiao (Refractories, in Chinese), 46(2), 2012, p111-113

[8] Wang Guangqiang, Chen Wangxue. Effects of some factors on spalling resistance of Al2O3-SiC-C castables. Refractories & Lime (in Chinese), 43(5), 2018, p10-13

[9] Yichong Li, Huizhong Zhao, Han Zhang, Dunxiang Pan, Yunkang Feng, Yuangao Li, Xinquan Wang, Yindong Guo. Enhancement and explosion-proof mechanism of aluminum fiber addition in Al2O3-SiC-C castables for iron runner. Ceramics International, 45(17), 2019, p22723-22730

[10] Liu Jun, Qi Wei, Liu Runqing, Tian Yue. Research on the relationship between compressive strength and air-void characteristics of foamed concrete with hydrogen peroxide as foaming agent. Concrete (in Chinese), 27(5), 2016, p. 1-4

[11] Zhou Kun, Tan Bin, Li Yuping, Yu Xiuyong. Foaming of hydrogen peroxide and its application in manufacturing light concrete. Sichuan Building Materials (in Chinese), 46(2), 2020, p. 4-5

# NEW METHOD FOR THE DETERMINATION OF THE DYNAMIC VISCOSITY OF CASTABLES

Marcel Bastian, Johannes Kasper, Christian Dannert
Forschungsgemeinschaft Feuerfest e. V. at the European Centre for Refractories, Höhr-Grenzhausen, Germany

Ashish Pokhrel, Olaf Krause
University of Applied Sciences Koblenz, Höhr-Grenzhausen, Germany

**ABSTRACT**

The workability of refractory castables determines the quality of linings or prefabricated parts made thereof. It is their rheology, particularly the shear rate-dependent dynamic viscosity that defines the workability of refractory castables during various processes such as flowing, levelling, compaction, casting, and pumping. Traditionally, the rheology of refractory castables is assessed through the spread flow test, which is a quick and simple method but does not provide quantified rheological data, including shear rate-dependent viscosity. Consequently, there is a significant gap in our understanding of the rheological properties of refractory castables, impeding the optimization of lining and prefabricated part quality.

To address this issue, a novel method has been developed to determine the shear rate-dependent (dynamic) viscosity of refractory castables. This method employs a lifting sphere rheometer to measure viscosity and utilizes a coupled CFD-FEM analysis to determine the prevailing shear rate during the measurement. By integrating these techniques, comprehensive rheological data for refractory castables can be obtained.

This innovative approach provides a means to accurately measure rheological properties of refractory castables. With this knowledge, the quality of linings and prefabricated parts can be optimised.

## INTRODUCTION

Refractory castables are increasingly being utilized in high-temperature operational units [1]. The rheological properties of these castables, influenced by their composition and processing technique, play a crucial role in defining their processing characteristics. It is essential to adjust these rheological properties according to the specific processing method, such as vibrocasting or self-levelling. Failure to do so can result in sedimentation or voids within linings or prefabricated parts made from the castables, which ultimately reduce their service life. The performance of a refractory castable during service primarily depends on its rheological properties during processing [2, 3, 4]. Insufficient rheological properties can lead to diminished performance or even complete failure of the monolithic structure [5].

The DIN EN ISO 1927-4 standard is commonly used for determining the rheological properties of refractory castables. In the case of self-flowing refractory castables, a cone is filled with the castable, lifted, and the resulting spread diameter is measured after two minutes. For vibrocasting castables, the cone is filled under vibration for 30 seconds. Then, it is lifted, and the castable is vibrated for an additional 30 seconds. Both vibration processes have an amplitude of 0.5 mm and a frequency of 50 Hz. However, a significant challenge with methods that measure spread or slump is the inability to obtain rheological properties based on shear rate, shear stress, or viscosity during the measurement. Consequently, these properties cannot be adjusted and optimized using such measuring methods [6]. As a result, different materials can show the same test result when measuring spread even though their rheological behaviour during processing (such as pumping, compacting, flowing) may vary greatly, because the measurement only represents processing equivalent to spread flow after a certain time. Flowing speed during flow or behaviour in high shear rate areas cannot be obtained. This means that castables may be entirely unsuitable for certain processing techniques despite their seemingly good values of spread flow.

### Challenges in measuring the shear rate dependant viscosity of refractory castables

The major problem with the evaluation of the fundamental rheological units of refractory castables is the coarse components of the castable, since standardized rheometers only allow a gap size (and thus particle diameters) of about 100 μm. Other rheometers, mostly developed for the construction industry, display significant sources of error [6, 7, 8, 9, 10, 11]. No method had been available before with which the shear rate dependant dynamic viscosity of castables could be measured.

### New approach for measuring the shear rate dependant viscosity of refractory castables

The set-up of the new approach is based on a lifting sphere rheometer. A sphere is positioned at the bottom of a test container which is then filled with a refractory castable. The measuring sphere is connected to a force sensor through a cable. The force sensor is attached to a linear motor axis, with which the sphere is lifted through the castable at a defined lifting speed. In the experiment, a predefined speed is set and the force needed to lift the sphere through the castable is measured. Considering the geometric design of the sphere and the measuring container as well as the lifting speed and measured force, one is able to calculate the dynamic viscosity of the castable. The force without lifting and during lifting is measured, to directly calculate the friction force by subtraction the force without motion from the force with motion. This simplifies the Stokes law for the determination of the dynamic viscosity to Eq. 1.

$$\eta_F = \frac{F_R * (1 - 2,1 * \frac{r_P}{R_W})}{6 * \pi * r_P * v_s} \tag{1}$$

With the friction force $F_R$, the radius $r_P$ of the sphere, the radius $R_W$ of the container and the lifting velocity $v_S$. The term in the brackets describes the Faxensche wall correction, which integrates the interaction of the fluid with the container wall into the equation.

The determination of the prevailing shear rate during a measurement of the dynamic viscosity has been a notable challenge and was overcome by CFD-FEM analysis, integrating the dynamic viscosity, density, and lifting speed. The shear rates during measurements with different experimental parameters were then calculated. The results demonstrated a significant correlation between shear rate and lifting velocity, with dynamic viscosity and castable density having a minor impact. This significant finding paved the way for developing a comprehensive database that describes the shear rate in relation to these experimental parameters. The database encompasses a wide range of lifting velocities (1 - 100 mm/s), densities (2500 - 3500 kg/m³), and dynamic viscosities (0.5-5000 Pa*s) as depicted in Figure 1. Notably, when considering errors smaller than 4 % arising from ignoring the influence of dynamic viscosity and density, the shear rate can be calculated based only on the lifting velocity. This implies that the shear rate can now be controlled and predetermined during a measurement by utilizing the correlation between shear rate and lifting speed. Consequently, this enables a controlled measurement of dynamic viscosity in castables, as the shear rate can be effectively regulated during the measurements.

228
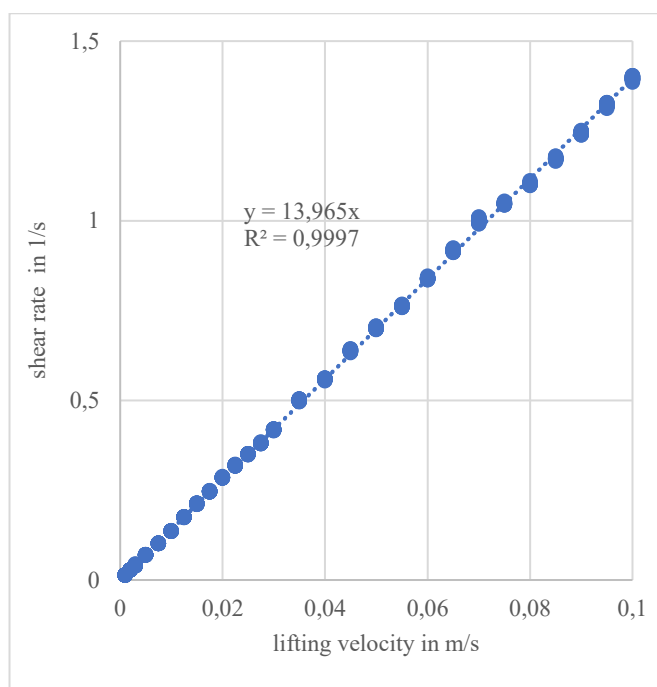
Fig. 1: Shear rate in dependence of the lifting velocity, calculated with the CFD-FEM. The datapoints are a set of points which represent all dynamic viscosities and densities.

## Rheological behaviour – influencing factors

It is necessary to separately describe the influencing factors on the rheological properties for two different material classes, self-flowing castables and vibrocasting castables. Excluding the mixing process, the composition of the castables (of both classes) is mainly responsible for the rheological behaviour. The vibration parameters, amplitude and frequency, also define the rheological properties while processing the vibrocasting castables. Depending on the type of composition (coarser or finer PSD) a change in the amplitude or frequency during vibrocasting leads to a different rheological respective flowing behaviour. Therefore, a method for the determination of the shear rate dependant viscosity of the castables is required, that allows the description of the rheological properties under vibration [12, 13, 14].

## MATERIALS AND METHODS
### Materials
*Matrix suspensions (cement free)*
For the evaluation and verification of the new method, three castable matrix suspensions were investigated (Table 1). Their compositions regarding the calcined (CT 9 FG and CT 800 FG, Almatis, Germany) and reactive alumina products (NO 725-10 and NO 713-10 RF, Nabaltec, Germany) were varied in terms of type and concentration/content, whereas the sum of concentration/content of these materials was kept constant. The contents of water and superplasticizer (Castament FS 60, BASF, Germany) were always kept constant. The particle size distribution from coarse to fine was S2 >> S1>S3.

Tab. 1: Castable matrix suspensions.

| Raw material | S1 in wt.-% | S2 in wt.-% | S3 in wt.-% |
|---|---|---|---|
| T60 -45 µm | 51,4 | 51,4 | 51,4 |
| CT 9 FG | 0 | 14,3 | 0 |
| CT 800 FG | 0 | 14,3 | 0 |
| NO 725-10 | 28,6 | 10 | 20 |
| NO 713-10 RF | 20 | 10 | 28,6 |
| Castament FS 60 | 0,3 | 0,3 | 0,3 |
| Water | 15,7 | 15,7 | 15,7 |
| Matrix particle size distribution | medium fine | coarse | fine |

*Self-flowing castables (cement free)*
The matrix suspensions ("S1", "S2" and "S3", abbreviated as "Sx") were loaded with tabular alumina aggregates (T60 0-0.5 mm, 0.5-1 mm, 1-3 mm, 3-6 mm, Almatis, Germany). The proportion of water to matrix suspension as well as the proportion of water to superplasticizer remained constant. Table 2 shows the compositions of the "coarse dispersions" ("CDx"), which are equal to cement free castables.

Tab. 2: Self-flowing castables (cement free).

| Raw Material | CD1 in wt.-% | CD2 in wt.-% | CD3 in wt.-% |
|---|---|---|---|
| T60 3-6 mm | 19 | 19 | 19 |
| T60 1-3 mm | 17 | 17 | 17 |
| T60 0,5-1 mm | 14 | 14 | 14 |
| T60 0-0,5 mm | 15 | 15 | 15 |
| Matrix | 35 (S1) | 35 (S2) | 35 (S3) |
| Castament FS 60 | 0.1 | 0.1 | 0.1 |
| Water | 5.5 | 5.5 | 5.5 |
| Matrix particle size distribution | medium fine | coarse | fine |

*Vibrocasting castable*
One vibrocasting castable ("VC") had the following composition with a particle size distribution with a q-value of 0.34: 26.1 wt.-% T60 3-6 mm, 17.5 wt.-% T60 1-3 mm, 17.5 wt.-% T60 0.5-1 mm, 10.4 wt.-% T60 0-0.5 mm, 13.4 wt.-% T60 0-0.3 mm, 4.1 wt.-% T60 -45 µm (all Almatis, Germany), 6.1 wt.-% NO 713-10 RF (Nabaltec, Germany) and 5 wt.-% Secar 71 (Kerneos, France). As additives NTTP (0.1 wt.-%) and citric acid (0.005 wt.-%) were added. The water content was 6.8 wt.-%.

*Sample preparation*
The matrix suspensions were mixed with a Vollrath stirrer for about 20 minutes. The castables were dry mixed for 0.5 minutes and subsequently mixed for 5 minutes after water addition (batches of 5 kg).

## Methods
*Rheological measurements*
Rheological measurements of the matrix suspensions with a standardized rheometer as reference were carried out with a coaxial cylinder rheometer (Malvern Kinexus Pro+) C 25 SW1177.
The shear rate dependant dynamic viscosities of the matrix suspensions and castables were determined with the new lifting sphere rheometer with coupled CFD-FEM (CFD-FEM database). The materials under investigation were filled into a cylindrical test container with a diameter of 90 mm up to a height of 150 mm. A sphere with a diameter of 15 mm was positioned at the bottom of the test container before starting the measurement and then lifted up with a constant lifting velocity of 3 mm/s ($\approx$ 0.042 1/s), meaning a constant shear rate during the experiments. The force required for lifting was measured and the dynamic viscosity was calculated from this. For the vibrocasting castables, the measurements were done during vibrocasting with an amplitude of 0.6 mm and frequencies of 30, 50 and 70 Hz.

## RESULTS
### Verification of the method
Firstly, the new method was verified and the reproducibility was proven for matrix suspensions of refractory castables (cement-free). Therefore, the shear rate-dependent viscosity of the matrix suspensions S1 (Figure 1), S2 (Figure 2), and S3 (Figure 3) was determined using a standardized rheometer (Figures 1-3, solid green lines) and the new lifting sphere rheometer. For the new lifting sphere rheometer, the calculation of the shear rate was also performed using various formulas from the literature, of which only the most applicable results according to Noor are presented (Figures 1-3, orange lines with "X") [11]. Additionally, CFD-FEM

229

was employed to determine the shear rate (Figure 1: red triangles, Figure 2: blue triangles, and Figure 3: red triangles) in the same experiment. In all measurements, the dynamic viscosity exhibited a more or less regressive decrease with increasing shear rates. When compared to shear rate evaluations based on the previously known formula of Noon (orange lines with "X"), the calculation of shear rate using CFD-FEM (triangles) showed excellent agreement with the results obtained from measurements using the standardized rheometer. Furthermore, the shear rate-dependent dynamic viscosities of the three "S1" measurements demonstrated outstanding reproducibility. These tests verified the new method for use with matrix suspension of refractory castables and validated its reproducibility.
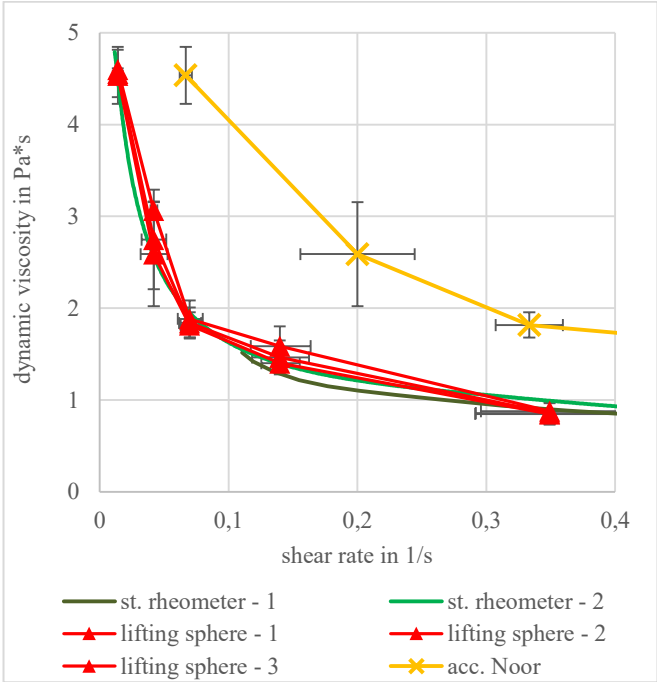


Fig 1: Shear rate dependant viscosity of S1 (medium fine matrix). The X represent the determination of the shear rate according to the formula used by Noor and Uomoto [11].
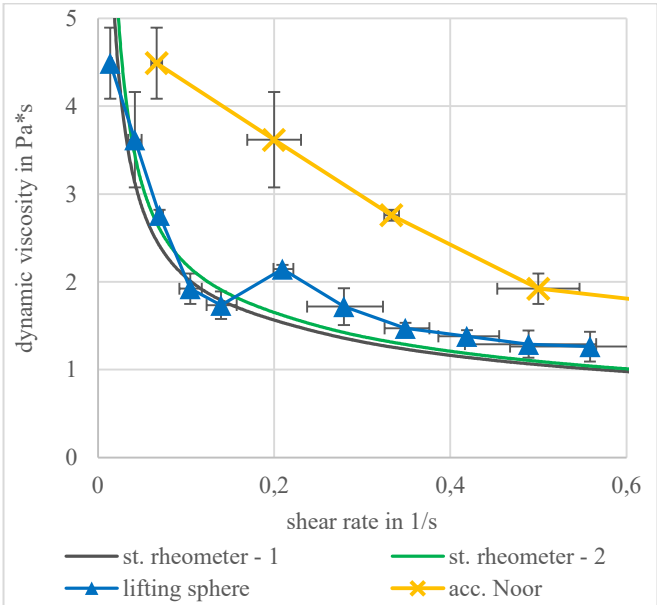


Fig 2: Shear rate dependant viscosity of S2 (coarse matrix). The X represent the determination of the shear rate according to the formula used by Noor and Uomoto [11].
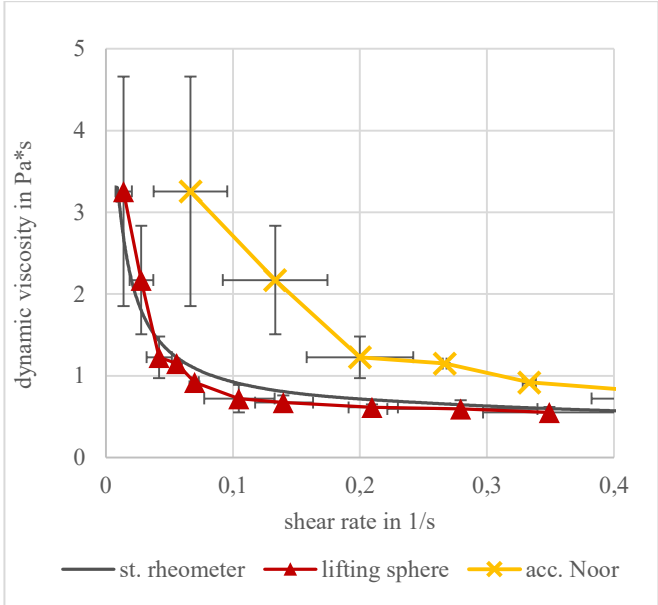


Fig 3: Shear rate dependant viscosity of S3 (fine matrix). The X represent the determination of the shear rate according to the formula used by Noor and Uomoto [11].

**Determination of the rheology of self-flowing castables**

Figure 4 illustrates the shear rate dependant viscosity of the three self-flowing castables, measured with the new lifting sphere rheometer. The castable with the medium fine matrix (CD1) exhibits a moderate dynamic viscosity at the lowest measured shear rate, which regressively decreased up to a shear rate of about 0.1 1/s and then increased linearly up to a shear rate of about 1 1/s. In comparison the castable with the coarse matrix (CD2) showed a low dynamic viscosity at low shear rates, but also a regressive decrease of the dynamic viscosity in the same range of shear rates as CD1. However, the dynamic viscosity then exponentially increased with increasing shear rate, which represents a strong dilatancy. The castable with the finest matrix (CD3) behaved similar to CD1 but showed nearly two times higher dynamic viscosities at low shear rates.
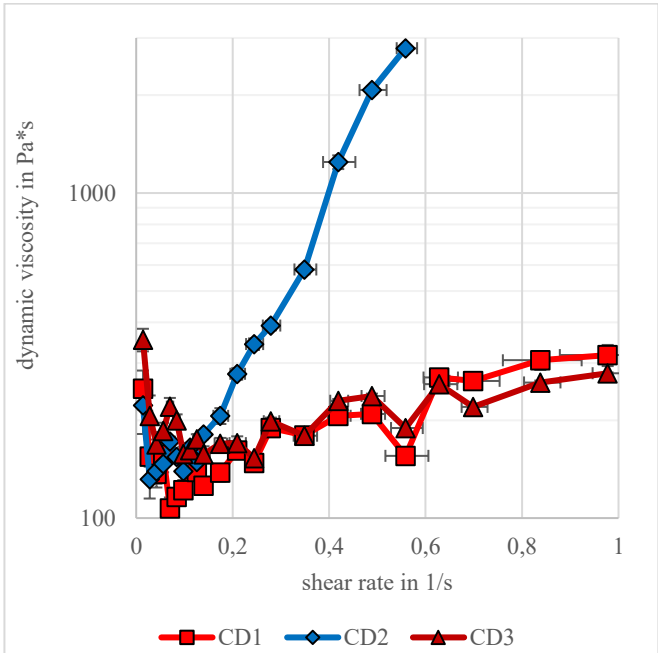


Fig 4: Shear rate dependant viscosity of the self-flowing cement free castables.

**Determination of the rheology of vibrocasting castables**

The influence of the vibration frequency on the dynamic viscosity of vibrocasting castables at a low shear rate of 0.042 1/s is represented in Figure 5. At a low vibration frequency of 30 Hz, the cable for lifting the sphere tore. This in turn indicates a dynamic viscosity of at least 80000 Pa*s and leads to an unprocessable castable. At a vibration frequency of 50 Hz, the dynamic viscosity is 150 Pa*s, so a good flowability and processability is expected. A further increase of the vibration frequency leads to a strongly rising dynamic viscosity of the castable up to a value of about (10000 Pa*s). This also renders such a castable impossible to process.

The rather large error at the measurement of low dynamic viscosities in low shear rate areas results from the vibration itself respectively the vibration of the cable for lifting the sphere and will be addressed in further research work.
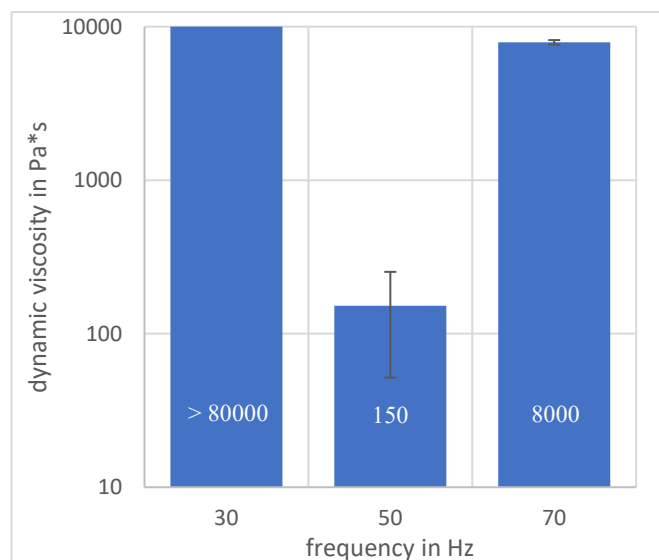


*Fig 5: Dynamic viscosity of VD at a lifting velocity of 3 mm-s (0.042 1/s) and a vibration amplitude of 0.6 mm in dependency of the frequency.*

**CONCLUSIONS**

A new method for determining the shear rate dependent viscosity of castables has been successfully verified and is available for rheological measurements of self-flowing and vibrocasting castables.

Reproducibility and verification experiments conducted on matrix suspensions of castables have demonstrated excellent agreement with measurements obtained using standardized rheometers.

The composition of the matrix plays a major role in determining the shear rate dependent viscosity of castables and can be utilized as a tool for rheology control. By employing the new method, it becomes possible to measure and assess these variations in rheological behavior.

Additionally, the new method has facilitated the evaluation of the impact of shear rate dependent viscosity during the vibration of castables. Among the vibration parameters, the vibration frequency strongly influences the rheological behavior of castables. This observation indicates that different vibration parameters in the laboratory and on installation sites may result in different rheological behaviors of castables, potentially leading to variations in the quality of prefabricated parts or linings.

Using the newly developed database for determining the shear rate during dynamic viscosity measurements with the lifting sphere rheometer, it is now possible for others to replicate the new method. This advancement enables quality assurance and research and development departments within the refractory sector to measure the shear rate dependent viscosity of refractory castables casted through self-flowing or vibration. Consequently, this provides an opportunity for improved quality assurance, faster optimization of existing castables, and the development of new innovative castables.

**OUTLOOK**

The errors encountered during the measurement of dynamic viscosity in castables during vibration will be addressed in further research work that aims at investigating the impact of vibration parameters and castable compositions on rheological properties.

**REFERENCES**

[1] Petzold, A.; Ulbricht, J.: Feuerbeton und betonartige feuerfeste Massen und Materialien, 1994, Deutscher Verlag für Grundstoffindustrie, Leipzig, Stuttgart.

[2] Ferrara, L.; Cremonesi, M.; Tregger, N.; Frangi A.; Shah, S.: On the identification of rheological properties of cement suspensions: Rheometry, Computational Fluid Dynamics modelling and field test measurements. Cement and Concrete Research, 2012, Vol. 42, pp. 1134-1146.

[3] Ferraris, C.; Obla, K.; Hill, R.: The influence of mineral admixtures on the rheology of cement paste and concrete. Cement and Concrete Research, 2001, Vol. 31, pp. 245-255.

[4] Ferraris, C. F.; Brower, L. E.; Banfill, P. F. G.; Beaupré, D.; Chapdalaine, F.; de Larrard, F.; Domone, P.; Nachbaur, L.; Sedran, T.; Wallevik, O.; Wallevik, J.: Comparison of concrete rheometers: International tests at LCPC (Nantes, France) in October, 2000. NIST Interagency/Internal Report (NISTIR) – 6819, 2001.

[5] Wallevik, O.; Wallevik, J.: Rheology as a tool in concrete science: The use of rheographs and workability boxes, Cement and Concrete Research, 2011, Vol. 41, pp. 1279-1288.

[6] Banfill, P. F. G.: RHEOLOGY OF FRESH CEMENT AND CONCRETE. Rheology Reviews 2006, 2006, pp. 61-130.

[7] Ferraris, C. F.; Geiker, M.; Martys, N. S.; Muzzatti, N.: Parallel-plate Rheometer Calibration Using Oil and Computer Simulation. Journal of Advanced Concrete Technology, 2007, Vol. 5, Nr. 3, pp. 687-697.

[8] Wallevik, O. H.; Feys, D.; Wallewik J. E.; Khayat, K.: Avoiding inaccurate interpretations of rheological measurements for cement-based materials. Cement and Concrete Research, 2015, Vol. 78, pp. 100-109.

[9] Hočevar, A.; Kavčič, F.; Bokan-Bosiljkov, V.: Rheological parameters of fresh concrete - comparison of rheometers. GRAĐEVINAR, 2013, Vol. 65, Nr. 2, pp. 99-109.

[10] Ferraris, C. F.; Martys, N. S.: Relating Fresh Concrete Viscosity Measurements from Different Rheometer. Journal of Research of the National Institute of Standards and Technology, 2003, Vol. 108, Nr. 3, pp. 229-234.

[11] Noor, M. A.; Uomoto, T: Rheology of high flowing mortar and concrete, 2004, Materials and Structures, Vol. 37, pp. 513-521.

[12] Bastian, M.; Kasper, J.; Dannert, C.; Pokhrel, A.; Ibarra Plata, L. T.; Krause, O.: Measurement of the dynamic viscosity of refractory castables – interaction between slurry and aggregates, 2022, Proceedings of the International Colloquium on Refractories.

[13] Banfill, P. F. G.; Yongmo, X.; Domone, P. L. J.: Relationship between the rheology of unvibrated fresh concrete and its flow under vibration in a vertical pipe apparatus. Magazine of Concrete Research, Bd. 51, Nr. 3, pp. 181-190, 1999.

[14] Safawi,M. I.; Iwaki, I.; Miura, T.: The segregation tendency in the vibration of high fluidity concrete. Cement and Concrete Research, Bd. 34, pp. 219-226, 2004.

231

# RHEOLOGY OF REFRACTORY CASTABLES – PART 1: A NOVEL 3D SPREAD FLOW MEASURING DEVICE ALLOWS TO DETERMINE MORE PRECISELY THE WORKABILITY OF REFRACTORY CASTABLES

*O. Krause[1], A. Pokhrel[1], L. T. Ibarra Plata[1], M. Kakavand[1]
1 Koblenz University of Applied Sciences, Höhr-Grenzhausen, Germany

M. Bastian[2], C. Linden[2], C. Dannert[2]
2Forschungsgemeinschaft Feuerfest e.V., Höhr-Grenzhausen, Germany

**ABSTRACT**

This article describes a method for improved evaluation of the slump flow according to ISO 1927-4. While the normative method solely compares the averaged diameter of the slump cake with the initial value after a fixed time span, the improved method allows to record three-dimensional pictures over the entire test time. In particular, the height-dependent flow rate and flow velocity can be determined.

This work now shows that considerably more findings can be obtained from this rather simple experiment, if the time dependant spread flow is recorded with a 3D camera. In addition, this part shows how the temperature of the ready mixture, which varies depending on the raw material temperature, affects the rheological properties. The article shows clear differences in the flow behaviour in a temperature range from 21 to 30°C.

**Introduction**

Refractory castables are complex mixtures of granulations of refractory raw materials with grain sizes between approx. 0.1 μm and 6 mm, a binder, and chemical additives [1], [2]. The chemical additives, especially dispersing agents, exert a considerable influence on the rheological properties of refractory concretes.

Refractory castables are homogenised with water in compulsory mixers and then placed in a mould or behind a formwork. This is done by self-flowing, vibration or spraying. Refractory castables can also be pumped.

Depending on the placement method, the refractory castables are subjected to very different shear rates on the process side, ranging from < 0.1 1/s (self-flowing) to 100 1/s (pumping) [3]. In order to be able to adjust the flow behaviour of a refractory castable for the different types of placement, it is therefore of great importance to be able to measure the rheological properties of refractory castables as a function of the shear rate. The rheological properties are crucial for the successful use of refractory castables in the respective application, as they determine the performance of the lining [4], [5], [6]. Poorly adjusted rheological properties lead to reduced performance and even material failure [7], [11]. It is therefore crucial to adjust the rheological properties of refractory castables to the respective processing procedure. For this purpose, the rheological parameters, especially the shear rate-dependent viscosity, must be known.

The most common method in the refractory industry for determining the rheological properties is the determination of the consistency by means of spread-flow according to ISO 1927-4. The standard defines (in the case of self-flowing refractory concretes), a funnel mould with a height of 80 mm, a lower diameter of 100 mm and an upper diameter of 70 mm, which is filled with the refractory castable and placed on a firm base with the opening facing downwards. The funnel is then pulled away upwards and the spread of the refractory concrete after 2 minutes is determined as the average diameter of the pile. Disadvantages: The measurement is a semi-quantitative single-point measurement that cannot reproduce rheological parameters [7], [9], [10], [11]. No shear rate can be specified for the method and the method is limited to the maximum flow rate of the refractory concrete. Another problem is that the flow conditions (e.g. shear rate) during the expansion of the refractory concrete are completely unknown. Thus, the rheological parameters of refractory castables cannot be investigated so far.

This work is intended to show that considerably more findings can be obtained from this rather simple experiment if the entire course of the run-out is recorded with a 3D camera as a function of time. This results in the height-dependent flow velocity as additional values, from which the dynamic viscosity can also be derived in principle, provided that the height-dependent material pressure (hydrostatic pressure) exerted on the refractory concrete can be simulated exactly over the entire course of the test. The results show that this time-dependent method provides significantly more information about the flow properties of refractory concretes.

For this purpose, a cement free coarse grain dispersion was used to demonstrate the capabilities of this time-resolved method.

**MATERIAL AND METHODS**

**Material**

The investigations were carried out on a coarse-grain dispersion, CD6, which does not contain any cement, as the initial aim here is to ensure that the rheological behaviour is not influenced by the setting process of the cement phase. In particular, it should be emphasised here that the early formation of cement hydrate phases leads to stiffening, but also that the change in pH due to the solution of $Ca^{2+}$ ions influence the rheological properties. This ensures that only the particle size distribution in combination with the plasticiser, in this case Castament® FS60, determines the rheological properties.

The coarse grain dispersion, CD6, belongs to a development series of a total of 10 formulations that were developed within the framework of a 2-year IGF project, whereby here the matrix components were permuted in their concentration but kept the same in total. Two further coarse grain dispersions will be discussed in more deepens in the second part of this contribution [12]. The specific surface area varies between 1.29 and 4.93 $m^2$/g. CD 6, at 2.32 $m^2$/g, is in the coarser range of offset variations. CD6 has a low dynamic viscosity at a low shear rate. This increases exponentially with increasing shear rate. This reflects a pronounced dilatant rheological behaviour for this offset. All coarse grain dispersions have been developed to have self-flowing properties.

Coarse grain dispersion, CD6, consists of different grades of tabular alumina T60 (from 6 mm to 45 μm, Almatis, Germany). The matrix components contain four grades of calcined alumina that allow to adjust a variety of matrix compositions that lead to 10 permutations with specific surface of the matrix components. Namely CT 9 FG, CT 800 FG, (Almatis, Germany) NO 725 10, and NO 713 10 RF (Nabaltec, Germany) were used in different proportions over the entire set of coarse grain dispersions. In this study solely CD6 was used (table 1).

Tab. 1: Composition of coarse grain dispersion, CD6

| Raw Materials | CD6 | Raw Materials | CD6 |
|---|---|---|---|
| T60 3-6 mm | 19 | NO 725-10 | 3,5 |
| T60 1-3 mm | 17 | NO 713-10 RF | 3,5 |
| T60 0,5-1 mm | 14 | CT9FG | 5 |
| T60 0-0,5 mm | 15 | CT800FG | 5 |
| T60 0-0.045mm | 18 | FS60 | 0,1 |
| | | Wasser | 5,5 |

## Methods

*Preparation of coarse grain dispersions*

To ensure a proper mixing, an intensive mixer (type R02, Eirich GmbH & Co. KG, Germany) was used with a stick agitator and simultaneous rotation with a rotation speed of 200 rpm, which corresponds approximately to the energy input of a planetary mixer as recommended by ISO 1927. The mixing time was variated to investigate the properties of the coarse dispersions under different energy input.

A total of 9 mixtures of 5 kg each were produced, differing only in the storage temperature of the raw materials (15, 22, 25°C) and the mixing time. All mixtures were premixed dry for 1 minute and then homogenised for 2, 3 or 4 minutes after adding water. With increasing mixing time, the temperature of the processable mass increases linearly (see figure 1). The resulting processing temperatures can be found in table 2.

Tab. 2: raw material storage temperature (T initial), wet mixing time and resulting temperature after mixing.

| T initial | 15 | 15 | 15 | 22 | 22 | 22 | 25 | 25 | 25 |
|---|---|---|---|---|---|---|---|---|---|
| wet mixing time | 2 | 3 | 4 | 2 | 3 | 4 | 2 | 3 | 4 |
| T after mixing | 21 | 23 | 25 | 26 | 28 | 30 | 26 | 28 | 29 |
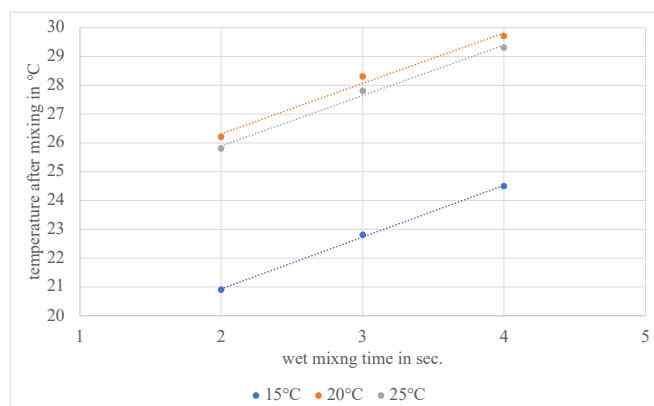


*Fig. 1: Temperature after mixing. With increased mixing time the temperatures after mixing increase almost linearly. The shift in temperature is due to different initial temperatures.*

*Measurement procedure and device for 3D-slump flow*

The recording of the 3D-slumpflow is realised with an image processing platform and integrated area camera with a projection field size of 250 x 250mm. Here, a 3D point cloud is generated by means of fringe projection, the combination of high-speed camera and structured light from eight projectors, included in model CV-H1X, provided by Keyence Cooperation (fig 1). This process virtually eliminates shadowing effects and reflection artefacts. Following the recording of the test specimen to be analysed, the image data is evaluated by the controller and the integrated image processing software. With the help of tools such as the determination of the diameter and the height of the body, but also the recording of the 3D topography as well as a self-developed function for the calculation of the percentage area growth based on binary representation of the image data, the flow process of the castables is recorded and documented (fig. 3). The collected data is output for further evaluation via a connected mass storage device or direct PC connection with the controller of the image processing platform.

*Calculation of rheologic parameters by using the Image processing platform and integrated area scan camera*

In order to be able to characterise the rheological parameters of castables, it is necessary to determine the flow velocity and the resulting shear rate. It is assumed here that the spreading of the mass is uniformly circular.

The calculation of the flow velocity as a function of the time-dependent height is carried out according to formula 1.

$$V_i = (d_i+1-d_i)/2(t_i+1-t_i) \tag{1}$$

with $v_i$ = flow velocity at time $t_i$ in m/s; $d_i+1 - d_i$ = difference of the yield value of two successive measuring points in m, $t_i +1 - t_i$ = time difference of two consecutive measuring points in s.

To determine the shear rates, the time-dependent flow cake height recorded by the measuring system is required. Since the use of coarse grain (3-6mm) causes measurement deviations in relation to the average height, the values are averaged accordingly and used to calculate the shear rates. The formula for determining the shear rates is shown in formula 2.

$$\Upsilon = v_i/ h_i \tag{2}$$

With $\Upsilon$ = shear rate at time $t_i$ in s$^{-1}$; $h_i$ = flow cake height at time $t_i$ in minutes

In addition, the weight force is a driving force in the course of the flow process and can be calculated as the hydrostatic pressure acting on the mass for the entire duration of the experiment.

The hydrostatic pressure is determined most simplified according to formula 3.

$$p_{hydrost.} = h_i \cdot g \cdot \rho_{castable} \tag{2}$$

with $h_i$ = flow cake height at time $t_i$; g = acceleration due to gravity in ms$^{-2}$; $\rho_{castable}$ = Bulk density of the mass in kgm$^{-3}$
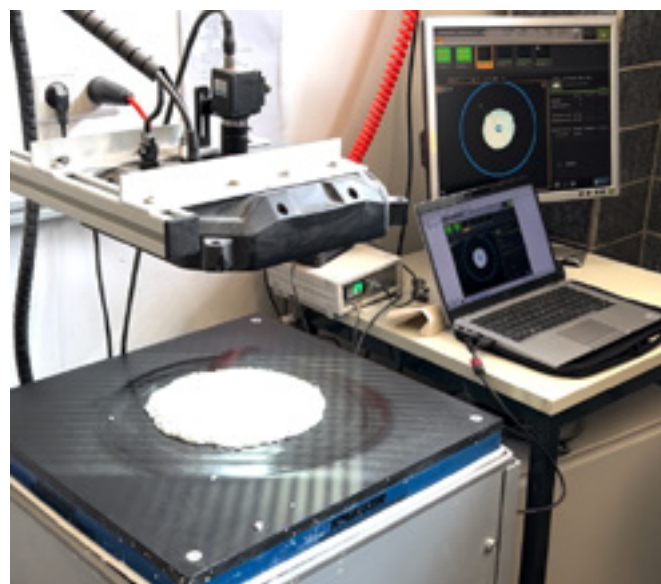


*Fig. 2: Acquisition of the 3D point cloud is generated by means of fringe projection, the combination of high-speed camera and structured light from eight projectors, included in model CV-H1X, provided by Keyence Cooperation*

The bulk density required for determining the hydrostatic pressure is obtained by recording the liter weight immediately after the mixing process and then converting it to the required density.

To be clear, the shear rate dependent viscosities that can be calculated in this way are about 100 times higher than those obtained by Bastian et al. [13] with the lifting sphere rheometer, which has already been implemented as a very suitable method for refractory concretes. The actual problem is based on the fact that the hydrostatic pressure changes dynamically over the whole course of the test and therefore requires a much more complex computational model that will be worked out in the coming two years. Nevertheless, the results of the shear rate-dependent viscosities derived from the 3D spread flow are comparable and can describe the flow behavior of refractory castables with a significantly higher resolution. Even if the determination of the dynamic viscosity does not yet seem realistic, the time-dependent observation of the outflow of coarse-grained dispersions can have

233

great advantages for the development of refractory concretes. For example, the height-dependent flow velocity is a valuable parameter that can be used to make rheological properties more tangible.
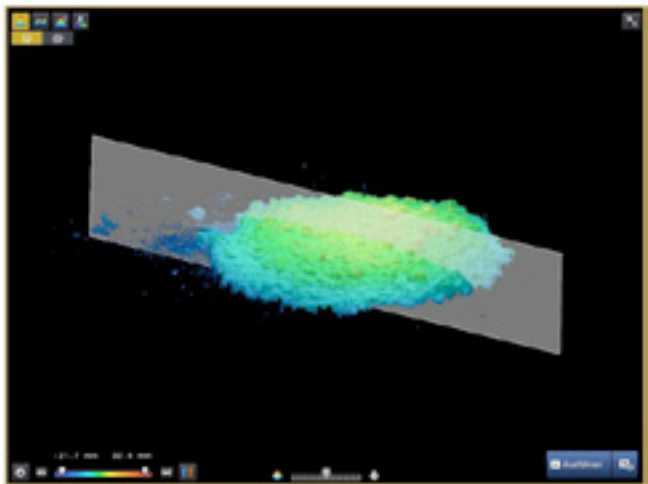


*Fig. 3: Acquisition of the 3D topography of a castable in false colour representation with contour line*

### RESULTS AND DISCUSSION

The first part of this two-part article focused on the influence of the temperature of the castables after mixing. In order to obtain a wider range of temperatures, the materials were stored at different temperatures, resulting in variable temperatures ranging from 21 to 30°C (Table 1, Figure 1). From Figure 4 it can be seen that the average flow rate varies between 218 and 271 mm after 120 seconds. Similar trends can be seen when the spread flow is measured at 10, 20 and 30 seconds, of course with lower spread values. In general, the spread values increase with increasing temperature of the castables.

With a little good will, a linear relationship can also be seen here that is independent of the time of measurement. This is a little surprising at first, since a higher flow velocity is actually to be assumed at the beginning, since the weight should still have a much stronger influence here due to the greater height of the mass. Especially if one assumes that masses with a higher temperature should have a lower viscosity, this should have the effect of a faster flow in the first seconds.
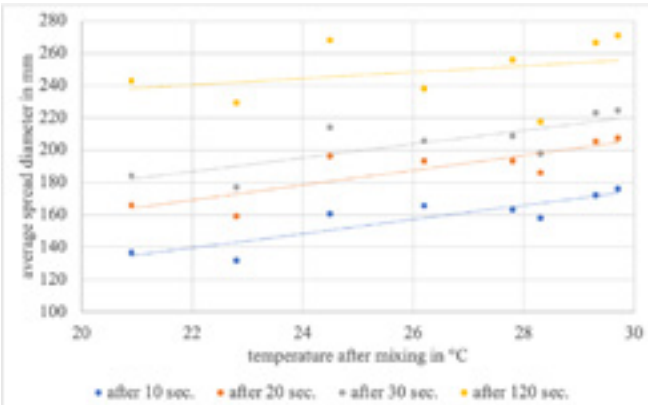


*Fig. 4: Average spread diameter after 10, 20, 30 and 120 sec as a function of temperature after mixing. The last value corresponds to the specifications of ISO 1927.*

However, this becomes visible when the flow velocity of the masses is deducted instead of the average diameter. Here it becomes clear that the flow velocity is naturally highest at the beginning (after 10 seconds) and increases with the mass temperature. After 30 seconds, this trend reverses, indicating that

the masses with the highest initial velocity have already lost so much height after 30 seconds that there is no longer enough pressure on the material. The flow velocity at the beginning, i.e. with a high shear rate, therefore has a decisive influence on the further course of the spread flow and correlates here with the dynamic viscosity. As described at the beginning, a coarse grain dispersion was selected here that has a low dynamic viscosity at low shear rates, but which increases exponentially at higher shear rates. This becomes clear when the shear stress is plotted against the shear rate. Figure 6 also shows that the shear thickening property of the coarse grain dispersion decreases with increasing temperature and becomes close to Bingham flow behavior when the mass temperature exceeds 26°C after mixing. The yield stress also decreases systematically with increasing mass temperature (Figure 7).
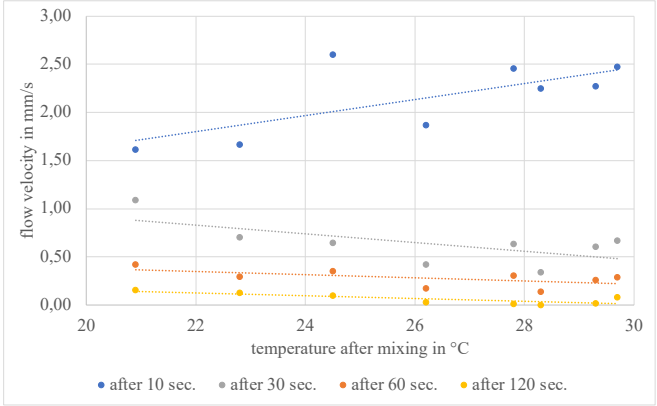


*Fig. 5: Flow velocity after 10, 20, 30 and 120 sec as a function of temperature after mixing.*
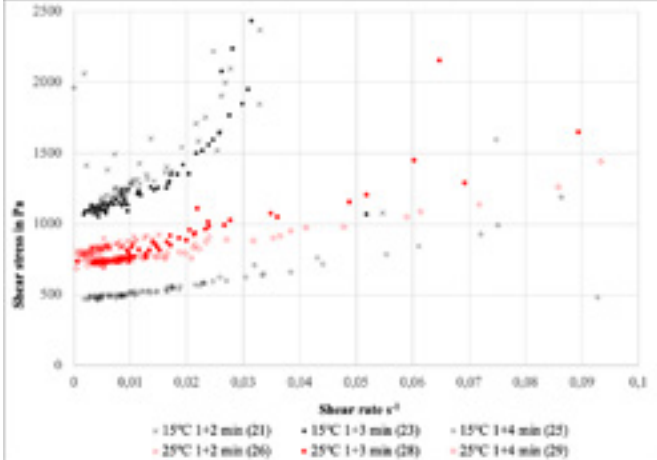


*Fig. 6: Shear rate plotted against the shear stress. The colours indicate the initial temperature prior to mixing. The symbols indicate the mixing time and additionally the initial temperature. In brackets the temperatures after mixing are given. To keep the graph clear, the measurement series was not shown here, where the initial temperature of the mass was 22°C.*

### CONCLUSIONS

First, it is not surprising that the rheological properties are temperature dependent. With increasing mass temperature, the viscosity of the mass decreases and in the present case the masses increasingly show Bingham flow behavior with increasing temperature, while at low temperatures they show shear thickening properties. The yield stress also decreases with increasing temperature. This relationship can already be deduced from the average flow rate, which has values between 218 and 271 and also increases systematically with the material temperature. However, the 3D slump flow measurement system as presented here achieves

a new order of magnitude in the resolution of the rheological processes that take place during the slump flow test.

In the present work, a coarse-grain dispersion with a specific surface area in the matrix grain range of 2.32 m²/g was deliberately selected, which at 20°C exhibits a clearly shear-thickening behavior, which, however, loses significance with increasing temperatures. The coarse grain dispersion is thus already in a range where one can no longer speak of an optimal matrix grain structure. Whether adjustments in the matrix design will lead to less temperature-sensitive dispersions remains open at this point and will be investigated in subsequent work.
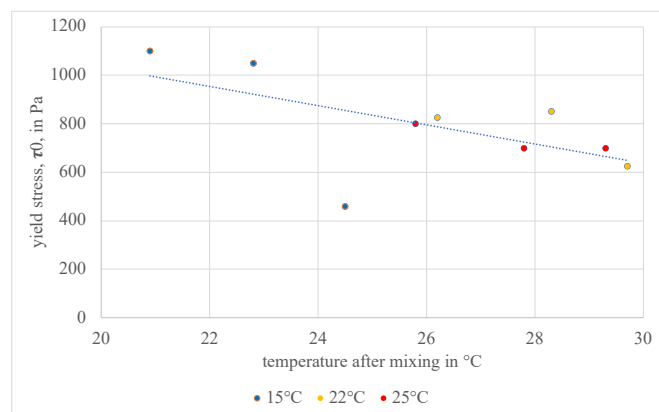


*Fig. 7: Dependence of the yield stress on the mass temperature after mixing. Different colours indicate different initial temperatures prior to mixing.*

Basically, however, this work reveals a dilemma. Rheological investigations on coarse grain suspensions and refractory castables must be temperature corrected. Otherwise, even the spreading factor according to ISO 1927 does not lead to reliable results. No indication of the mass temperature after mixing severely limits an objective evaluation of the rheology. Even if the mixing procedure is standardized (1 minute dry and 4 minutes wet, according to ISO 1927), the masses may heat up to different degrees depending on the particle size design. Causing an apparent improvement in material properties to be registered when more heating occurs, which is then falsely attributed to an improvement in particle size distribution. Furthermore, it must be noted here that in the case of cement addition, higher temperatures lead to a higher dissolution rate of the cement particles, which either favors solidification by coagulation due to an increase in the pH value and also leads to a more rapid precipitation of the cement hydrate phases. Then, of course, the flow behavior deteriorates dramatically.

## ACKNOWLEDGEMENTS

## REFERENCES

[1] P. P. C. Evangelista und C. Revais, Control of formulation and optimization of self flow castables based on pure calcium aluminates. Kerneos Technical Paper, Presented at ALAFAR 2000, 2000.

[2] W. Lee, W. Vieira, S. Zhang, K. Ghanbari Ahari, H. Sarpoolaky und C. Parr, Castable refractory concretes. International Materials Reviews, Bd. 46, Nr. 3, pp. 145-167, 2001.

[3] J. Reed, Principle of ceramic processing, New York: JOHN WILEY & SONS, INC., 1995.

[4] H. Wallevik, D. Feys, J. Wallewik und K. Khayat, Avoiding inaccurate interpretations of rheological measurements for cement-based materials. Cement and Concrete Research, Bd. 78, pp. 100-109, 2015.

[5] L. Ferrara, M. Cremonesi, N. Tregger, A. Frangi und S. Shah, On the identification of rheological properties of cement suspensions: Rheometry, Computational Fluid Dynamics modeling and field test measurements. Cement and Concrete Research, Bd. 42, pp. 1134-1146, 2012.

[6] Y. Pivinskii, „Rheology in Ceramic an Refractory Technlogy. Principal Concepts and Rheological Models," Ogneupory, Bd. 3, pp. 7-15, 1994.

[7] H. Wallevik und J. Wallevik, „Rheology as a tool in concrete science: The use of rheographs and workability boxes. Cement and Concrete Research, Bd. 41, pp. 1279-1288, 2011.

[8] P. Banfill, Rheology of fresh cement and concrete. Rheology Reviews, Bde. %1 von %261-130, 2006.

[9] F. Rubio-Hernández, J. Velásquez-Navarro und L. Ordóñez-Belloc, Rheology of concrete: a study case upon the use of the concrete equivalent mortar. Materials and Structures, Bd. 46, pp. 587-605, 2013.

[10] N. Roussel, Correlation between yield stress and slump: Comparison between numerical simulations and concrete rheometers results. Materials and Structures, Bd. 226, pp. 107-113, 2006.

[11] C. Ferraris, L. Brower, P. Banfill, et al., Comparison of concrete rheometers: International tests at LCPC (Nantes, France) in October 2000. NIST Interagency/Internal Report (NISTIR) – 6819, 2001.

[12] O. Krause, A. Pokhrel, L. T. Ibarra Plata, M. Kakavand, M. Bastian, C. Linden, C. Dannert, Rheology of refractory castables – PART 2: Influence of the mixing energy input in terms of mixing time and velocityon the spread measured with a new 3D-spread-flow device with special regard towards the ambient working conditions, UNITECr 2023, Frankfurt, this proceeding.

[13] M. Bastian; J. Kasper; C. Dannert et al.: Measurement of the dynamic viscosity of refractory castables: interaction between slurry and aggregates. 65th International Colloquium on Refractories 2022: The future transformation of the process industry; September 28th and 29th, 2022. Höhr-Grenzhausen: ECREF European Centre for Refractories gemeinnützige GmbH 2022 S. 49 - 52

235

# THERMO–MECHANICAL BEHAVIOR OF ALUMINA–MAGNESIA CASTABLES AND ITS LINING LIFETIME SIMULATION

Yajie Dai[1], Fei Wang[3], Ning Liao[1], Wen Yan[1], Yawei Li[1]

[1]The State Key Laboratory of Refractories and Metallurgy, Wuhan University of Science and Technology, 430081, China
[3]School of Resources and Civil Engineering, Northeaster University, 110819, China

## ABSTRACT

Due to the advantages of high temperature strength, thermal shock resistance and corrosion resistance, the alumina-magnesia castables is considered to be an optimal lining material for sidewall of steel ladles. The castables is installed without pre-sintering, whose thermo-mechanical properties vary with temperature during the pre-heating process and metallurgical service. The castables at different thermal stages shows distinct sensitivity to temperature fluctuation. In this study, the influence of heat treatment temperature and heating/cooling rate on the thermo-mechanical properties as well as fracture behaviour of alumina-magnesia castables is investigated using uniaxial compressive test equipped with a high frequency induction heating system and Brazilian test combined with digital image correlation. Meanwhile, the temperature-dependent Elastic modulus, thermal expansion coefficient and thermal conductivity are measured for alumina-magnesia castables at different thermal stages. The evolution of thermo-mechanical behavior and its dependence on instant thermophysical has been simulated using FLAC3D. It is seen that the brittleness and mechanical strength of alumina-magnesia castables increases with heat treatment temperature due to the better sintering and formation of calcium hexaluminate and spinel phases. Without fully relaxation of residual stresses, the stiffness increases while the strength decreases after fast heating of 200 °C/min. The same castables after different thermal treatments show disparate mechanical responses to cooling rates. Meanwhile, the simulation from pre-heating period to metallurgy operation period using real-time properties provide a more realistic understanding of lifetime thermo-mechanical behavior for castable linings.

## KEYWORDS

Alumina-magnesia castables, thermal stages, calcium hexaluminate, thermo-mechanical behavior, modelling

## INTRODUCTION

Alumina-magnesia castables are adopted as an optimal lining material for sidewalls below the slag line of steel ladles, because of its good high-temperature strength, thermal shock resistance and corrosion resistance [1]. After production, the castables experience curing, drying, pre-heating and service processes (teeming-holding-tapping cycles). Alumina-magnesia castables sustain severe thermal shock during teeming/tapping processes. The thermal shock resistance of castables is often studied by the evolution of residual mechanical parameters after quenching [2]. Besides the quenching process, most thermo-mechanical tests are performed with a slow heating scenario (e.g. 5°C/min). The in-situ mechanical behaviour of castables under high-speed thermal fluctuation and its systematic correlation with service processes should be further studied.

Meanwhile, with the hydration/dehydration, constituents' reactions, phases formation and microstructure evolutions during thermal processes, the thermophysical properties of castables are highly temperature dependent. For typical cement-bonded alumina-magnesia castables, the decomposition of hydrates mainly takes place above 200 °C up to 550-660 °C [3]. The calcium aluminate ($CaO \cdot Al_2O_3$, CA) and calcium dialuminate ($CaO \cdot 2Al_2O_3$, $CA_2$) form at 900 °C and 1000-1200 °C [4]. The in-situ formation of calcium hexaluminate ($CaO \cdot 6Al_2O_3$, $CA_6$) and spinel ($MgAl_2O_4$) take place above 1200 °C [5]. These two ceramic phases contribute to the higher corrosion resistance, high-temperature strength and thermal shock resistance by forming the ceramic bond and strong interlocking. It is apparent that the thermo-mechanical behavior of alumina-magnesia castables varies during firing and service with respected to temperature and time.

The steel ladle consists working lining, safety lining, insulating lining and metallic shell. Besides the lining materials themselves, the thermo-mechanical behavior of steel ladle has also been investigated for reproducing the thermal loss and stress/temperature fields at different thermal processes. For example, the drying stage of castables, which is crucial for the integrality of lining due to the inner vapor pressure, has been simulated to demonstrate the influence of lining geometries and drying scenarios [6]. The thermal modelling has also been performed for pre-heating processes with the consideration of the lid for heat preservation, heat radiation/convection, non-steady state heat conduction and so on [7]. Advanced numerical tool has been developed as well for simulating the thermal evolution in service cycles [8]. However, the effect of castables at different thermal stages with distinct material properties and the continuous evolution of thermo-mechanical behavior for steel ladle from pre-heating to service with temperature-dependent properties are less clarified.

This study analyses the thermo-mechanical behaviour and evolution of thermophysical properties with respected to temperature of alumina-magnesia castables during the pre-heating treatment and the first casting cycle, represented by the specimens after drying, decomposition of hydrates and sintering. The sensitivity of castables to heating and cooling rate is studied via uniaxial compressive tests during fast heating and Brazilian tests afterwards including digital image correlation (DIC) monitoring at room temperature. Besides, the dynamic thermophysical properties are assigned to an axisymmetric numerical model to simulate the thermo-mechanical behavior of castable lining with different properties and evolution of stress/temperature distribution in transient state. The work aims to demonstrate the variation of thermo-mechanical failure pattern of alumina-magnesia castables with the consideration of temperature dependent properties from pre-heating period to metallurgy operation period and provides a basic understanding of the impact of different thermal scenarios.

## MATERIAL AND INVESTIGATION METHODS
### Castables preparation

The composition of alumina-magnesia castables comprises tabular corundum aggregates and powder (98.85wt% $Al_2O_3$), $\alpha$-$Al_2O_3$ powder (99.3 wt% $Al_2O_3$, $d_{50}$=4.1 μm) and fused magnesia powder (98 wt% MgO). The used binder is calcium aluminate cement with the commercial name of "Secar 71"($\leqslant$50 μm, 70.47 wt% $Al_2O_3$, 28.08 wt% CaO). The water-reducing agent is polycarboxylate amphoteric surfactant (FS60, BASF). The dry components were mixed with 4.2 wt% of distilled water. After well mixing, the castables were poured into the steel molds for forming the cylindrical samples with a diameter of 50 mm and height of 100 mm. For better degasification of the samples, the castables were added stepwise during the vibro-molding process. Additionally, some prismatic samples were also molded for basic mechanical tests. All the specimens were cured at 25 °C with 75% humidity for 24 h, and then dried at 110 °C for 24 h in the oven. The cured and dried samples were respectively fired at 1000 °C and 1400 °C for 3 hours. According to different thermal treatment temperatures, the samples were denoted as L, M and H referring to low (110 °C), medium (1000 °C) and high (1400 °C) temperatures. These target temperatures represent the castables at different life stages: i) after drying process, ii) after pre-heating process and iii) at the first service cycle. The applied representative materials at different thermal stages and its application in heating scheme of outer surface of working lining for numerical simulation can also be seen in Fig. 1.

*Fig.1: Representative materials and heating scheme for simulation*
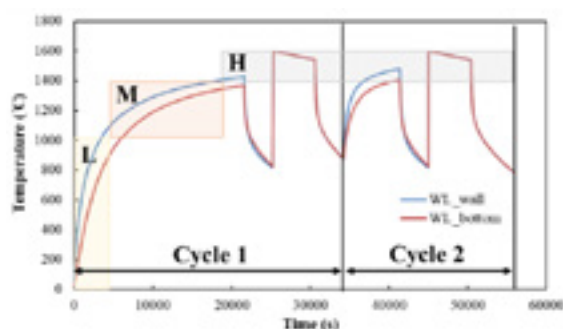
## Mechanical laboratory tests

Usually, high-temperature mechanical tests of refractories are performed with slow heating rates. To measure the high-temperature mechanical properties after fast heating caused by metallurgy thermal operations, the induction heating equipment with a frequency of 20 kHz was coupled with a universal testing machine. An infrared thermometer was placed as monitor and controller for judging heating or temperature maintenance. A target temperature of 1200 °C was applied using two different heating rates: regular (10 °C/min) and high speed (200 °C/min). Both heating scenarios had a dwell time of 30 minutes at target temperature for achieving an uniform temperature distribution across the specimen with diameter of 50 mm under heat flux on the outer surface. The specimens were uniaxially loaded with a loading rate of 0.5 mm/min after reaching homogeneous temperature distribution within the volume.

To study the impact of cooling rate on fracturing process of castables, the disc specimens with geometry of $\phi 50$ mm$\times$20 mm were cooled inside (slow cooling) or outside (fast cooling) the furnace to room temperature after fast heating scenario. Brazilian test was performed for the specimens after cooling. To avoid stress concentrations at the loading points, the arc jaws with radii of 1.5 times the disc specimens were used as loading blocks for a velocity controlled Brazilian tests with a loading rate of 0.05 mm/min. For monitoring the fracture processes, a CCD digital camera with a resolution of 2452 x 2056 pixels$^2$ was positioned in front of the specimens. Surface images are recorded with a frequency of 1 image/second during the whole test. The front face was painted with a white-black random speckle pattern. For both the uniaxial compressive tests and the Brazilian tests, three samples are used for each kind of specimen.

## Numerical methodology

In this study, numerical simulation of thermal analysis was performed by the continuum based Finite Difference code FLAC3D (Itasca, 2020). The variables involved in heat conduction in FLAC3D are related through the energy-balance equation and transport laws derived from Fourier's law. A simplified steel ladle consisting four lining layers was modelled as shown in Fig. 2. The monolithic alumina magnesia castables is applied in working lining and its assigned temperature-dependent thermophysical parameters (Elastic modulus, thermal conductivity and thermal expansion coefficient) are from the laboratory measurements. The rest less sensitive parameters with temperature are adopted from litterature or neglected. The assigned properties of high alumina bricks (Permanent lining, PL), the alumina insulator (Insulation layer, IL) was adopted from the work of Santos et al. [10]. A quarter of the steel ladle was built under the assumption of symmetry conditions.

Since the existing pores and microcracks usually make the refractory materials inhomogeneous, the statistical method using the Weibull distribution was adopted to representing the heterogeneity. The heterogeneity is becoming smaller with increasing shape factor *m*. In this study, *m*=45 was used to characterize the heterogeneity of the WL, PL, and IL, and the steel shell was set as homogeneous material. Afterwards, the

heterogeneous numerical elements were assigned with the temperature-dependent constitutive laws. The Mohr-Coulomb strength criterion with tension cut-off was used as failure criterion and the Mohr-Coulomb model was extended by strain-softening functions to accurately simulate the behavior under/after thermal loading due to the loss of brittleness at high temperatures.



*Fig.2: Steel ladle model with different functional layers*
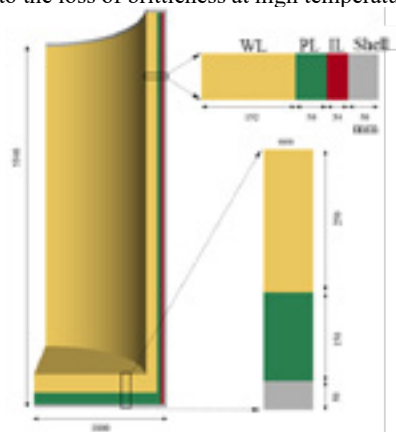
## Results

### Evolution of thermo-physical properties with temperature

The characterizations by X-ray diffraction and scanning electron microscopy show that the corundum and periclase are the fundamental phases of alumina-magnesia castables (Fig. 3). The high-temperature ceramic phases $CA_6$ and spinel are formed in specimen H, while small amount of CA and $CA_2$ phases presents in specimen M. The newly formed phases locate in the matrix due to the in-situ reactions between alumina and calcium oxides as well as with magnesia. The $CA_6$ and spinel phases have similar thermal expansion coefficient as corundum, which results in good thermal compatibility. Meanwhile, the $CA_6$ has a plate-like morphology and contributes to the construction of strong interlocking between $CA_6$ and spinel. Due to the remarkable volume expansion during the formation of high-temperature phases and the ceramic bond, the apparent porosity, strength and ultrasonic velocity increase with the thermal treatment temperature: L<M<H.



*Fig.3: XRD patterns (a) and SEM microstructure (b)*
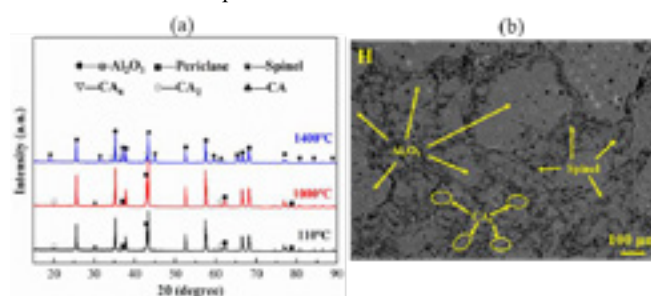
With different thermal treatment, the alumina-magnesia castables specimens show distinct evolution of thermal expansion coefficient and elastic modulus with temperature (Fig. 4). The stiffness of alumina-magnesia castables (presented by elastic modulus) decrease in order of H>M>L. The ceramic phases and their interlocking favor the high-temperature mechanical resistance. With less microstructure evolution and damage accumulation, the elastic modulus of specimen H decreases slightly with temperature up to 1200 °C and no obvious attenuation exhibits during heating-cooling cycle. The elastic modulus of specimen M and L decrease with temperature and a lessening of the decrease followed by an increase above 1050 °C is observed. Between 200 °C and 350 °C, a strong decrease of elastic modulus of specimen L occurs due to the dehydration of calcium aluminates hydrates. With the microstructure variation, the room temperature elastic moduli of specimen M and L after thermal cycle significantly reduce.

237

The specimen H is quite linearly expanded with temperature as no further phase transformation occurs after fully reaction during material preparation. With the existence of ceramic phases ($CA_6$ and spinel) and strong bonding, the H shows highest thermal expansion below 1100 °C, while that of M is also higher than L with the presence of certain amount CA and $CA_2$ in matrix. The crystallization of CA at this temperature range has slight effect on the thermal expansion, which turns in to high-temperature calcium aluminate phases with further temperature increase. Above 1100 °C, the specimen M and L exhibit high volume expansion because of the accumulated formation of $CA_2$ and spinel. The $CA_2$ reacts afterwards with the alumina for the formation of $CA_6$, which results in the further expansion. Part of the calcium oxide has already reacted with alumina during the firing of specimen M at 1000 °C. Thus, the volume expansion rising of specimen L is the most significant with the high amount of new phases formation. The thermal conductivities of three kinds of specimens also increase with temperature.
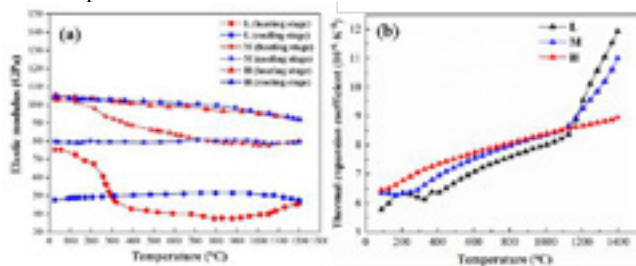


*Fig.4: Evolution of elastic modulus (a) and thermal expansion coefficient (b) with respect to temperature*

**Dependence of fracture behaviour on heating and cooling rate**

Fig. 5(a) exhibits the stress-displacement curves of the uniaxial compressed specimens under 1200 °C experienced fast (200 °C/min, denoted as -f and solid lines) and slow (10 °C/min, denoted as -s and dash lines) heating procedures. With the formation of high ceramic phases and better sintering, the uniaxial compressive strengths UCS of H and M exceed 80 MPa. No softening behaviour is observed for fired specimens under this stress level, only some isolated small cracks occur on the surface of H while massive cracks are generated in M. It can be assumed that compressive strength of H is higher than that of M. The UCS of dried specimen L-f is 69.6 MPa and a slight-nonlinear yielding behaviour appears right before reaching the peak load and the brittle failure. The lateral deformation of specimen L-f is small and the specimen shows a clear shear failure, whose inclined fracture surface is rough and loose. The static Young's modulus E can be calculated from the slope of the stress-displacement curves, which is used for characterizing the material stiffness. The static E increases in the order L < M < H. One should be aware that the static E of specimen H-f (40 GPa) is much smaller than the dynamic one, due to the different determination methodology and compliance of the mechanical tests.

The stiffnesses for specimens with slow heating are smaller than those with fast heating. During fast heating, less microstructure relaxation is allowed, which results in higher residual thermal stresses and stiffer mechanical response. With the existence of high-temperature ceramics phases $CA_6$ and spinel, the H has better high-temperature mechanical properties. During slow heating to 1200 °C, further densification and thermal reactions occur in specimens L and M. The maximum load of L-s is higher than for L-f. All three types of loaded specimens have only fine cracks as documented for H without forming significant macro-cracks or ruptures after slow heating, suggesting a smaller degree of damage. The fast heating rate up to 200 °C/min acts as an in-situ thermal shock and results in significant UCS reducations, but a much less difference in stiffness.

The castable lining experiences drying, pre-heating, first operation cycle (teeming-holding-tapping), re-heating and successive operation cycles till repair or service termination. It undergoes severe cold shock during tapping and unexpected shut down. Before a thorough discussion of the difference between H, M and L, the tensile failure of specimen H, which represents the alumina-magnesia castables at the first operation cycle, is firstly investigated. The Brazilian tests are performed at room temperature for three types of H: the original one without further heat treatment as H-O, the one fast heated to 1200 °C and air quenched as H-F and the one slowly cooled in the furnace as H-S. Their force-displacement curves are shown in Fig. 5(b). The forces continuously increase with applied displacement followed by an abrupt failure after reaching the maximum load. The quasi-linear increase and abrupt dropping of forces imply a predominant brittle failure of all specimens of H. The average strengths and their standard deviations are listed in the table. The cold shocked specimens H-F have the lowest strength and reveal some visible nonlinearity (softening) near the peak region. This manifests the generation of primary damage in H-F during fast cooling. It is similar for H-S but with less reduction of strength and non-obvious nonlinearity.



| Strength | Origin | Fast cooled | Slow cooled |
|---|---|---|---|
| **H** | 11.25±0.69 | 9.31±0.9 | 10.21±1.22 |
| **M** | 4.87±0.79 | 4.17±0.6 | 4.1±0.26 |
| **L** | 3.05±0.32 | 3.33±1.21 | 3.44±1.22 |
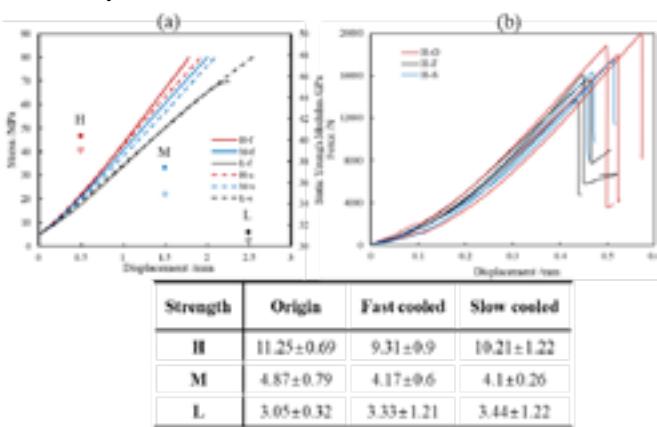
*Fig.5: Stress-displacement curves under UCS (a) and Brazilian test (b), average tensile strength (table)*

To better illustrate the influence of damage induced by different cooling strategies on tensile failure under Brazilian test, DIC analysis is performed. The strain evolution of specimen H with and without thermal shock is shown in Fig. 6(a). The horizontal strain component $\varepsilon_{xx}$ is adopted as indicator for crack opening in the horizontal direction. Due to the high strength and brittleness, almost no micro-crack development for H-O is observed before reaching the maximum load. With the high amount of elastic energy stored within the bulk of H-O, the disc specimens are split into two halves shortly after the peak load (indicated by the high displacement difference before and after load peak in Fig. 6(b)).

During slow cooling in furnace, some fine micro-cracks are induced in H-S, which cause the earlier damage in the pre-peak region and the development of a more complicated crack network. With the gradual energy release during the fracture process zone development, a milder and narrower crack opening is observed at peak for H-S. H-F shows similar failure behaviour as H-S and H-F. However, with a severe cold shock (fast cooling), a larger initial crack exists in H-F. Instead of forming a fracture process zone like in H-S, a further opening of the initial crack is observed in the pre-peak region. Due to the tensile stress accumulation in the Brazilian disc, the primary crack propagates along the direction of the vertical diameter, which is different from the initial crack path induced by the cold shock. As a consequence, the change of horizontal opening displacement for H-F is stronger than that of H-S, but still much lower than that of H-O due to less stored elastic energy.
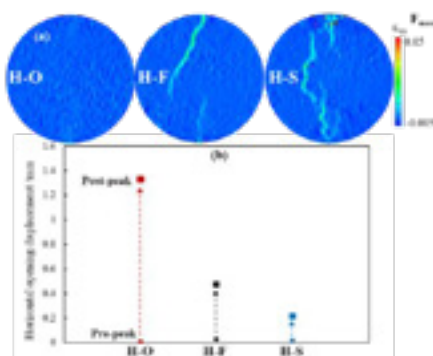
*Fig.6: Strain map of specimen H after different heat treatment (a) and variation of crack opening displacement (b) at load peak*

**Simulation of stress and temperature distribution**

To better understand the impact of temperature-dependent thermophysical parameters, a series of sensitivity analysis was conducted. In this case, five parallel models with same geometries were created, with three of them having all parameters inputted as temperature independent except for the parameter being analysed (conductivity, expansion and Young's modulus). The fourth model has all parameter as temperature dependent (model "all" as in Fig. 8), while the fifth model serves as a completely temperature independent reference (model "Noun"). The "stress ratio" and "displacement ratio" are defined as the ratio between values of the target models and that of the reference model. Ratio over 1 means a growth in temperature-induced stress or displacement, ratio between 0 and 1 means a reduction, and negative ratio indicates the change from tensile to compressive stress. The stress and displacement variations are acquired along a scanline, which is the horizontal line drawn from heated surface of WL to shell (Fig. 7).

The temperature-dependent thermal conductivity is the predominant factor of temperature distribution, which is related to the subsequent thermal expansion and deformation. As it is seen, the results of model "cond" are close to that of mode "all". Meanwhile, the stress ratio of model "expan" varies a lot along the scanline, as remarkable volume expansion tends to take place at higher temperature, which is restrained by the surrounding lower temperature region and incurs a great compressive stress to high temperature region. Compared to other two parameters, the model with temperature-dependent Young's modulus has less undulant changes with distance from heated surface. Meanwhile, with the softening at higher temperature, the Young's modulus and thermal expansion have offset each other in the simulation results of stress and deformation. The maximum principal stress and displacement ration in the PL, IL and steel shell are more or less stable.
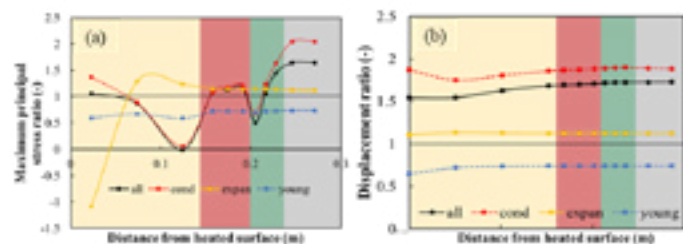


*Fig.7: Stress (a) and displacement(b) ratios of target models at the end of pre-heating*

Figure 8 shows the plasticity states of the five parallel models after two metallurgy cycles. The outer surface of WL experiences the most severe thermal shock and highest temperature, which could be damaged by the shear stress. The discrete tensile stress can also occur due to the local thermal mismatch related to the heterogeneity. Meanwhile, the most plastic deformation induced by the tensile stress locate in the permanent lining. Compared with the plasticity state of "Noun" model, the damage is much more severe in the model with the temperature-dependent parameters, which implies the necessity to consider the dynamic evolution of

properties with time and temperature for achieving realistic thermos-mechanical investigation.
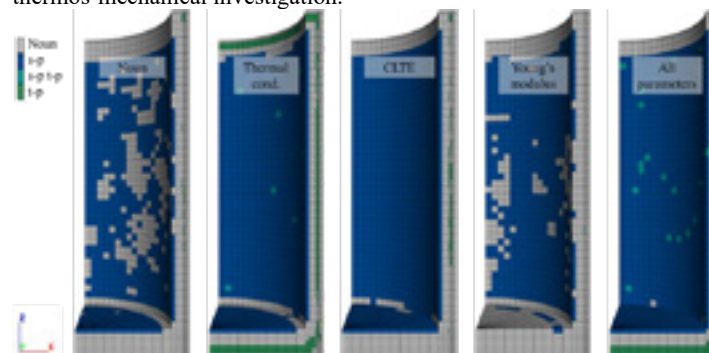


*Fig.8: Plasticity states for five parallel models at the end of two metallurgy cycles (Legend: s and t: shear and damage, p: failure accumulated in the past, None: no damage )*

**CONCLUSIONS**

By experimental characterization and numerical modelling, the dependence of thermophysical properties on time and temperature and its influence on the thermomechanical behavior of alumina-magnesia castables has been studied. Main conclusions are:

(1) The brittleness and mechanical strength of alumina-magnesia castables increase with heat treatment temperature due to the better sintering and formation of ceramic phases. Without full relaxation of residual stresses, the stiffness increases while the strength decreases after fast heating of 200 °C/min. Meanwhile. the same castables after different thermal treatments show disparate mechanical responses to cooling rates.

(2) The thermophysical parameters evolve with temperature and piecewise change with the thermal processes. The sensitivity analysis of parallel simulations demonstrates that the thermal conductivity is the most influential parameter, as it dominants the temperature distribution and affects the succeeding thermal expansion and deformation. The increase of thermal expansion coefficient and decrease of Young's modulus with temperature counterbalance the deformation of linings.

(3) Compared with the modelling using temperature-independent parameters, the model with temperature-dependent thermophysical parameters exhibits more severe shear damage in the outer surface of working lining and tensile stress induced plasticity in permanent lining.

**REFERENCES**

[1]    Kumar, S., Sarkar, R. (2022). Alumina spinel castable for steel ladles: An overview. Int. J. App. Ceram. Tec., 1-14.

[2]    Luz, A. P., Santos Jr, T., et al. (2013). Thermal shock damage evaluation of refractory castables via hot elastic modulus measurements. Ceram. Int., 39(6), 6189-6197.

[3]    Luz, A. P., Moreira, et al. (2021). Drying behavior of dense refractory ceramic castables. Part 1-General aspects and experimental techniques used to assess water removal. Ceram. Int., 47(16), 22246-22268.

[4]    Bareiro, W. G., de Andrade Silva, F., et al. (2018). The influence of alumina content on the chemical and mechanical behavior of refractory concretes fired at different temperatures. Constr. Build. Mater., 187, 1214-1223.

[5]    Auvray, J. M., Gault, C., Huger, M. (2007). Evolution of elastic properties and microstructural changes versus temperature in bonding phases of alumina and alumina–magnesia refractory castables. J. Eur. Ceram. Soc., 27(12), 3489-3496.

[6]   Schmitt, N., Berthaud, Y., et al. (2004). Damage of monolithic refractory linings in steel ladles during drying. British Ceram.Trans., 103(3), 121-133.

[7]    Glaser, B., Görnerup, M., Sichen, D. (2011). Thermal modelling of the ladle preheating process. Steel Res. Int., 82(12), 1425-1434.

[8]   Santos, M., Moreira, M., et al. (2018). Enhanced numerical tool to evaluate steel ladle thermal losses. Ceram. Int., 44(11), 12831-12840.

239

# RHEOLOGY OF REFRACTORY CASTABLES – PART 2: INFLUENCE OF THE MIXING ENERGY INPUT IN TERMS OF MIXING TIME AND VELOCITY ON THE SPREAD MEASURED WITH A NEW 3D-SPREAD-FLOW DEVICE WITH SPECIAL REGARD TOWARDS THE AMBIENT WORKING CONDITIONS.

O. Krause[1], A. Pokhrel[1], L. T. Ibarra[1] Plata *M. Kakavand[1]
[1] Koblenz University of Applied Sciences, Höhr-Grenzhausen, Germany

M. Bastian[2], C. Linden[2], C. Dannert[2]
[2] Forschungsgemeinschaft Feuerfest e.V., Höhr-Grenzhausen, Germany

## ABSTRACT

Appropriate mixing of monolithic materials is inevitable for a proper installation of refractory monolithics. Without in-depth knowledge about this important step refractory installations are prone to premature break down with unwanted and expensive down times. With the help of a 3D-spread flow device it is possible to quantify the effect of inappropriate mixing and how not precisely adjusted grain size distributions may contribute to this. It is still under investigation how the grain size distribution especially in the matrix grain fraction affect the complexity of mixing.

However, at this point of research it already can be stated that the grain size distribution is susceptible to the mixing velocity and mixing time and if not appropriate even susceptible to the ambient conditions. It could be figured out that the ambient conditions affect the dynamic viscosity in certain matrix combinations remarkably. To substantiate this assertion model castables were developed that solely were altered in the proportions of reactive and calcined alumina concentrations and therefore in their specific surface. While the first part describes the method of 3D-spread-flow and the temperature dependence of the rheological properties [1], the second part shows by way of example three coarse-grain dispersions that differ from the real refractory concrete only in that no cement was added to the material. The coarse grain dispersions in turn differ in the specific surface area of the matrix components, whereby a very coarse, a medium and a very fine matrix composition was considered with 2.32 4.06 4.94 m$^2$/g.

## Introduction

Refractory concretes are complex mixtures of granulations of refractory raw materials with grain sizes between approx. 0.1 µm and 6 mm, a binder, and chemical additives [2], [3]. The chemical additives, especially dispersing agents, exert a considerable influence on the rheological properties of refractory concretes.

Refractory castables are homogenised with water in compulsory mixers and then placed in a mould or behind a formwork. This is done by self-flowing, vibration or spraying. Refractory concretes can also be pumped.

Tab. 1: Composition of coarse grain dispersions that vary in the matrix particle compositions leading to specific surface areas that are given in m$^2$/g.

| Raw Materials | all | Raw Materials | CD1 | CD6 | CD10 |
|---|---|---|---|---|---|
| T60 3-6 mm | 19 | NO 725-10 | 10 | 3.5 | 7 |
| T60 1-3 mm | 17 | NO 713-10 RF | 7 | 3.5 | 10 |
| T60 0.5-1 mm | 14 | CT9FG | 0 | 5 | 0 |
| T60 0-0.5 mm | 15 | CT800FG | 0 | 5 | 0 |
| T60 0-0.045mm | 18 | FS60 | 0.1 | 0.1 | 0.1 |
| water | 5,5 | spec. Surf. area | 4.06 | 2.32 | 4.94 |

Each component of refractory castable influences its rheological properties [3]. A differentiation must be made between the individual classifications of the raw materials into fine (0-100 µm), medium (0.1-1 mm) and coarse (> 1 mm) grains. Medium and coarse grains can be summarised as aggregates [4]. The aggregates and their grain size distribution clearly influence the viscosity of refractory concretes. This is due to interlocking, friction and movement of the aggregates during flow. The general consensus is that aggregates exert a considerable influence on the rheology of coarsely dispersed fluids [5], [6], [7], [8], [9], [10].

For this purpose, a cement free coarse grain dispersions were used that differ in the specific surface area of the matrix components, whereby a very coarse, a medium and a very fine matrix composition was considered with 2.32 4.06 4.94 m2/g. The purpose of this article is to show how the rheological properties change with different mixing times (1 minute dry and 2, 3 and 4 minutes wet) and three different mixing speeds (200, 450 and 700 rpm).

## MATERIAL AND METHODS
### Material

The investigations were carried out on three coarse-grain dispersions, CD1, CD6, and CD10 which does not contain any cement, as the initial aim here is to ensure that the rheological behaviour is not influenced by the setting process of the cement phase. In particular, it should be emphasised here that the early formation of cement hydrate phases leads to stiffening, but also that the change in pH due to the solution of $Ca^{2+}$ ions influence the rheological properties. This ensures that only the particle size distribution in combination with the plasticiser, in this case Castament® FS60, determines the rheological properties.

Said coarse grain dispersions, belongs to a development series of a total of 10 formulations that were developed within the framework of a 2-year IGF project, whereby here the matrix components were permuted in their concentration but kept the same in total. The specific surface area varies between 1.29 and 4.93 m$^2$/g. All coarse grain dispersions have been developed to have self-flowing properties.
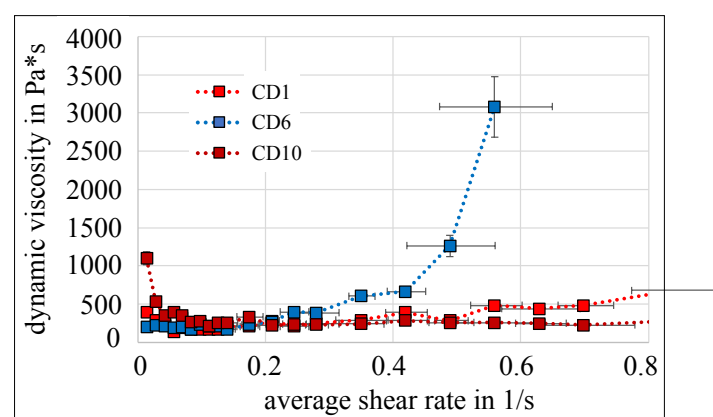


Fig. 1: Effective dynamic viscosity of the cement-free refractory concretes or coarse dispersions as a function of the mean shear rate. The dynamic viscosity was determined with the lifting sphere rheometer, as developed by Bastian and the shear rate was calculated by means of CFD-FEM simulation.

This paper focus on three coarse grain dispersions, CD1, CD6 and CD10, that cover a distinct range of matrix grain size distribution from coarse to fine with specific surfaces 2.32 (CD6), 4.06 (CD1) 4.94 m2/g (CD10).

All coarse grain dispersions consist of different grades of tabular alumina T60 (from 6 mm to 45 µm, Almatis, Germany). The matrix components contain four grades of calcined alumina that allow to adjust a variety of matrix compositions, namely CT 9 FG, CT 800 FG, (Almatis, Germany) NO 725 10, and NO 713 10 RF (Nabaltec, Germany) were used in different proportions over the entire set of coarse grain dispersions (table 1).

Figure 1 describes the shear rate dependent dynamic viscosity of these three coarse grain dispersions as there were recorded by Bastian et al. by using the lifting sphere rheometer which is described in [11], [12]. The shear rate-dependent dynamic viscosity of these coarse grain dispersions varies massively with the composition of the slurry phase. The medium-fine matrix of the coarse grain dispersion (GD1) results in a medium dynamic viscosity at low shear rates and a lower dilatancy, if any, at higher shear rates. The coarse grain dispersion with the coarse matrix (GD6) has a low dynamic viscosity at low shear rates. This increases exponentially with increasing shear rate. This reflects a pronounced dilatant rheological behaviour. If the matrix of the refractory concrete (GD10) is very fine, a high viscosity is pronounced at low shear rates. As the shear rate increases, the dynamic viscosity decreases and remains at a low level.
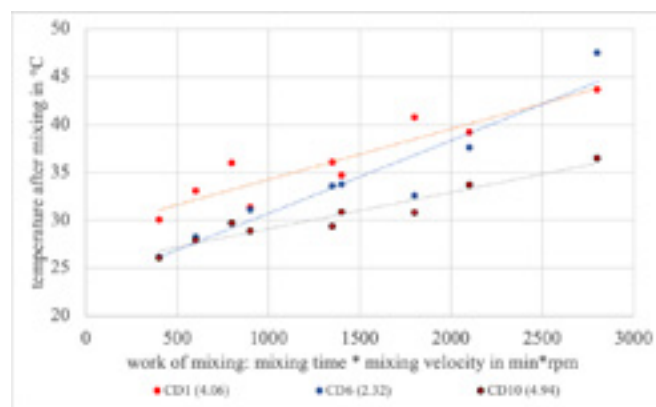


Fig. 2: Temperature after mixing correlated with the work of mixing, which is defined in simplified terms as the product of the mixing speed and the mixing time. With increased work of mixing the temperatures after mixing increase almost linearly.
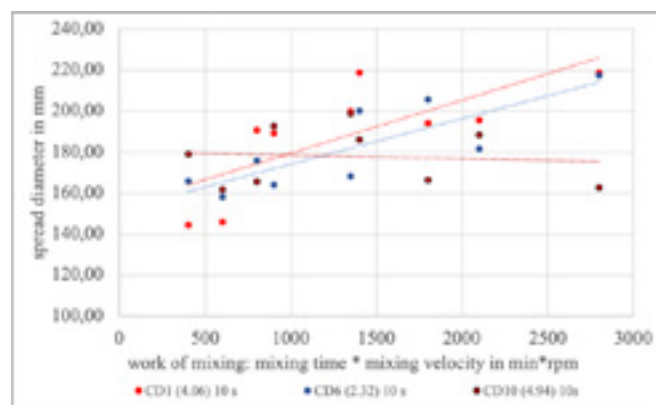


Fig. 3: The mean diameter of the spread flow after 10 seconds is plotted against the mixing work.

### Methods

*Preparation of coarse grain dispersions*

To ensure a proper mixing, an intensive mixer (type R02, Eirich GmbH & Co. KG, Germany) was used with a stick agitator and simultaneous rotation with a rotation speed of 200, 450 and 700 rpm. 200 rpm corresponds approximately to the energy input of a planetary mixer as recommended by ISO 1927. All mixtures were premixed dry for 1 minute and then homogenised for 2, 3 or 4 minutes after adding water. A total of 9 mixtures of 5 kg each were produced for every coarse grain dispersion.

*Measurement procedure and device for 3D-slump flow*

The recording of the 3D-slumpflow is realised with an image processing platform and integrated area camera with a projection field size of 250 x 250mm. Here, a 3D point cloud is generated by means of fringe projection, the combination of high-speed camera and structured light from eight projectors, included in model CV-H1X, provided by Keyence Cooperation as described in part one of this contribution [1].
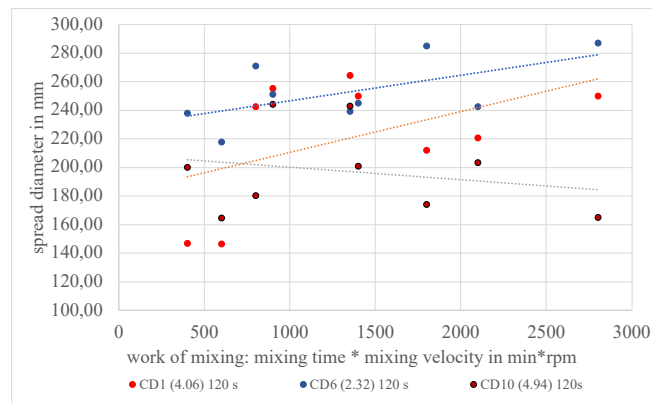


Fig. 4: The mean diameter of the spread flow after 120 seconds is plotted against the mixing work.

### RESULTS AND DISCUSSION

While the first part of this article dealt with the temperature influence of the rheological properties of coarse-grained dispersions, the dependence of the rheological properties on the mixing energy input and on the grain structure of the matrix is investigated here on the basis of three selected compositions.

Since all 27 tests carried out (9 for each coarse grain dispersion) differ individually in their production before the spread-flow is recorded, namely in the mixing energy input, it is first important to take a closer look at the heat absorbed by friction of the particles. Figure 2 therefore relates the temperature after mixing to the mixing work. The mixing work is assumed to be a very simplified product of the mixing time and the mixing speed, which at least means that the mixing energy input can be used as a value without being quantified exactly. Figure 2 then shows a near linear correlation of the work of mixing with the temperature after mixing. This is not particularly surprising at first, since the energy input is controlled by the mixing time and the mixing speed. However, it is remarkable that the coarse-grain dispersion, CD6, absorbs significantly more friction heat, although CD1 absorbs more heat with less mixing work. However, DC1 and CD10 basically react similarly to the increasing mixing energy input. The deviating heat absorption of the coarse grain dispersion, CD6 can be attributed to the significantly higher viscosity at high shear rates, as described above. It is still important to mention here that the absolute temperatures are less important than the linear increase with the mixing energy input, the slope of which differs significantly in the case of CD6. The final temperature depends strongly on the raw material temperature before mixing. The results imply that CD1 were processed at higher ambient conditions.

If the spread flow after 10 and 120 seconds is plotted against the work of mixing, the positive trend shows that the result is also influenced by the heat absorption due to mixing. If one takes a closer look at both diagrams, it becomes clear with a little effort that CD 6 after 10 seconds hardly differs from the other two coarse-grain dispersions, but after 120 seconds it tends to lead the others resulting in larger average diameters in the spread flow. Since there is also quite a high scatter of results within the coarse grain dispersions, it is not really opportune to enter trend lines. However, they do open up the possibility of guiding the eye a little. Except for CD10, the finest variant, a positive trend generally implies the temperature dependence of the flow. In general, CD10 is cooler during processing, so that at least the lower spread flow can be

explained by this. However, the almost linear temperature increase with different mixing work should also lead to a positive correlation for CD10, if non-matrix-dependent influences must be taken into account more strongly here. In principle, further investigations must be carried out in the future to gain a better understanding.

In order to make the large amount of data somewhat clearer, only one mixing time (4 minutes wet) and two different mixing speeds are considered in figure 5. If the shear rate is plotted against the shear stress, it is immediately apparent that the yield stress value, $\tau_0$, is dependent on the mixing speed. The lowest values are measurable for the coarse grain dispersion, CD6, whereby a higher mixing speed significantly reduces $\tau_0$. The high mixing speed also leads to a moderate increase in shear stress with increasing shear rate. The mass becomes less viscous, which in turn is primarily due to the influence of temperature. The mass is about 14°C warmer after mixing at 700 rpm (compare table 2). CD1, on the other hand, shows a comparable yield stress at both mixing speeds, whereby the temperature difference here is only 7.7 K. The yield stress, however, is significantly higher than that of the CD1. However, the yield stress is remarkably higher than for CD6. Again, it can be seen that the high mixing speed leads to a moderate increase in shear stress with increasing shear rate. The slopes are comparable for both coarse grain dispersions depending on the mixing energy. The coarse grain dispersion, CD10, behaves somewhat differently.

First of all, it should be noted that CD10 has a significantly higher yield stress than CD1 and CD6, although the temperatures for both mixtures are at least comparable to GD10. In addition, it should be noted that less mixing energy leads to a lower yield stress and therefore behaves differently to CD1 and CD6. Furthermore, the mass mixed at 700 rpm shows no significant dependence on the shear rate in shear stress.

If we compare this result with figure 1 and the corresponding description, it becomes clear that both results can be linked to each other. As described, CD6 exhibits negligible dynamic viscosity at low shear rates, while CD1 and CD10 show a shear thinning behavior, although this is more pronounced for CD10. This also explains why the yield stress is noticeably higher for CD1 and very clearly higher for DC10.

Basically, it is not surprising that the viscosity decreases with increasing temperature after mixing. Nevertheless, one can recognize differences between the coarse-grain dispersions presented here that relate to the mass structure of the matrix. Figure 6 again extends the consideration to the different mixing times (1+2 and 1+4 minutes) and all mixing speeds are considered (200, 450 and 700 rpm). While an almost linear relationship can be observed for CD6, this appears to be more complex for CD1 and CD10. There is no linear relationship here. On the one hand, this can be attributed to the more complex behavior of both masses at low shear rates (fig. 1), on the other hand, more work needs to be invested in the 3D-spread flow method in order to better substantiate the significance of the measurement results.

Tab. 2: Temperatures after mixing for 1 minute dry and 4 minutes wet at velocities of 200 and 700 rpm.

| Disspersion | Mixing velocity | Temperature after mixing in °C |
|---|---|---|
| CD 1 | 200 rpm | 36.0 |
|  | 700 rpm | 43.7 |
| CD6 | 200 rpm | 29.7 |
|  | 700 rpm | 47.5 |
| CD10 | 200 rpm | 29.7 |
|  | 700 rpm | 36.5 |

## CONCLUSIONS

Within the framework of a two-year research project, a total of 10 coarse grain dispersions were developed, which differ only in the grain structure of the matrix. From these 10, three were selected for this work, which cover a representative range from coarse to fine with specific surface areas of 2.32 (CD6), 4.06 (CD1) and 4.94 m2/g (CD10).

In general, it can be stated that the 3D spreading flow provides significantly more information about the rheological behavior of coarse-grained dispersions than simply an average spread-flow after a given time. By constantly measuring the slump flow, practically from the first second to the end (here 150 seconds), the change in height and diameter over time can be documented. This makes it possible to determine shear rates and evaluate them. Even the shear stress can be calculated, although, as already described in part 1 [1], a suitable model must still be developed that dynamically simulates the hydrostatic pressure over the entire test period. Shear stress values as reported in this paper are unrealistically high and do not match the results obtained with the lifting sphere rheometer. Nevertheless, the results are suitable to show differences in a direct comparison.
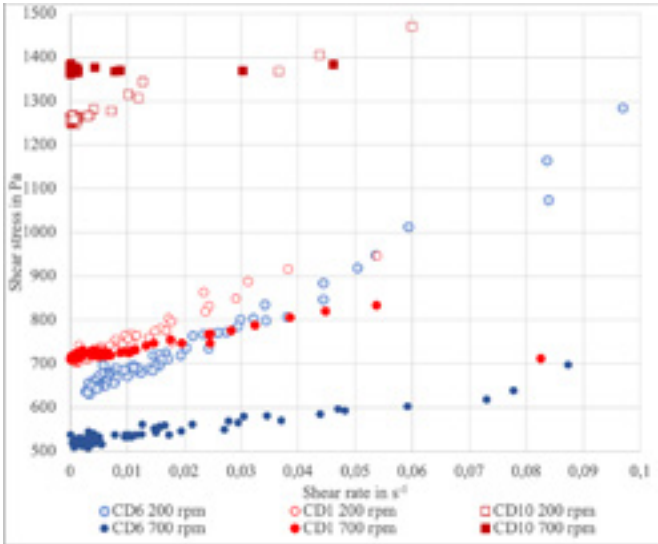


*Fig. 5: Shear rate plotted against the shear stress. The colours indicate the nature of the coarse grain dispesion, CD1, 6 and 10. The number of results is reduced to two mixing velocities, 200 and 700 at a single mixing time of 4 minutes wet mixing. The calculation of shear rate and shear stress is reported in part 1 of this contribution [1]*
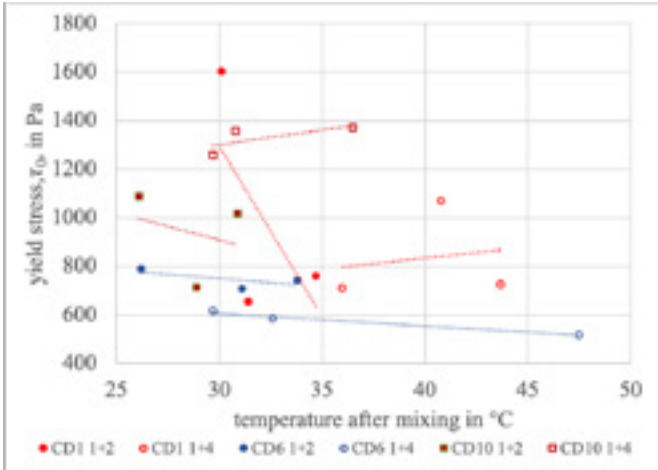


*Fig. 6: Yield stress plotted against the temperature after mixing. The colours indicate the nature of the coarse grain dispersion. The symbols indicate the mixing time, 1+2 and 1+4 (1 minute dry, x minutes wet). For every kind of symbol three values are shown, that could be distinguished from left to right by the mixing energy input (200, 450 and 700 rpm)*

Differences within individual coarse-grain dispersions are mainly due to the temperature of the masses, which is caused by different mixing energy input.

Nevertheless, the results show that the coarse grain dispersions behave differently, which was already described by Bastian using the lifting sphere rheometer [11], [12]. In particular, CD1 and CD10 show a high viscosity at low shear rates, which could also be confirmed with the 3D spread flow (fig. 5). However, the temperature-dependent relationship to viscosity is less clear for both coarse grain suspensions (fig. 6). Sometimes the yield stress even increases, which is particularly true for GD10. Since this is especially true for long mixing times (1+4), it could also be that water evaporates during mixing, to which the fine-grain dispersions react more sensitively, since they have a larger grain surface and thus require more water for wetting. In addition, it can be shown that differences in the particle size distribution of the matrix obviously have different capacities to absorb heat through qualitatively different friction and thus show clear differences in the mass temperature after mixing. It can be stated that coarser particles may generate more friction than fine particles.

The results presented here show that the relationships are complex and have not yet been understood in depth and require further research. In the following investigations, the seven coarse-grain dispersions will also be included in order to obtain a clearer picture of the interaction of the matrix composition with the flow behavior.

In principle, however, it can be stated that a higher mixing energy input reduces the viscosity of the coarse-grain dispersions, whereby the temperature increase plays a decisive role. It should be noted, however, that the addition of cement only allows a moderate temperature increase without provoking too early stiffening.

The project will be continued within the framework of a new IGF project, which will make it possible, for example, to keep the temperature comparable after mixing.

Finally, it should be mentioned that with relatively little additional effort, considerably more information can be extracted from a routine test, which is practically always carried out as part of the refractory castable development. So far, tests have only been carried out on self-flow castables, but a transfer to vibratory concretes is possible without any problems, if not even easier, since with self-flow castables the flow begins immediately after the cone is pulled and measurement data cannot be obtained until the cone and hand are out of the picture.

## REFERENCES

[1] O. Krause, A. Pokhrel, L. T. Ibarra Plata, M. Kakavand, M. Bastian, C. Linden, C. Dannert, Rheology of refractory castables – Part 1: A novel 3D-spread-flowmeasuring device allows to determine more precisely the workability of refractory castables, UNITECr 2023, Frankfurt, this proceeding.

[2] L. Ferrara, M. Cremonesi, N. Tregger, A. Frangi und S. Shah, „On the identification of rheological properties of cement suspensions: Rheometry, Computational Fluid Dynamics modeling and field test measurements," Cement and Concrete Research, Bd. 42, pp. 1134-1146, 2012.

[3] C. Ferraris, K. Obla und R. Hill, „The influence of mineral admixtures on the rheology of cement paste and concrete," Cement and Concrete Research, Bd. 31, pp. 245-255, 2001.

[4] S. Otroj, M. Bahrevar, F. Mostarzadeh und M. Nilforoshan, „The effect of deflocculants on the self flow characteristics of ultra low-cement castables in Al2O3-SiC-C system," Ceramics International, Bd. 31, pp. 647-653, 2005.

[5] P. P. C. Evangelista und C. Revais, „CONTROL OF FORMULATION AND OPTIMIZATION OF SELF-FLOW CASTABLE BASED ON PURE CALCIUM ALUMINATES," Kerneos Technical Paper, Presented at ALAFAR 2000, 2000.

[6] T. Erdem, K. Khayat und A. Yahia, „Correlation Rheology of Self-Consolifdating Concrete to Correspondending Concrete-Equivalent Mortar," ACI Materials Journal (Technical Paper), Bd. 106, Nr. 2, pp. 154-160, 2009.

[7] C. Begemann, D. Cotardo, T. Schack und L. Lohaus, „Mischungsstabilität fließfähiger Betone - rheologische Messungen zur Bestimmung des Einfusses von Leim, Mörtel und Gesteinskörnung," Rheologische Messungen an Baustoffen 2018 - Tagungsband zum 27. Workshop und Kolloquium, pp. 112-124, 2018.

[8] D. Han, J. Kim, J. Lee und S.-T. Kang, „Critical Grain Size of fine Aggregates in the View of the Rheology of Mortar," International Journal of Concrete Structures and Materials, Bd. 11, pp. 627-635, 2017.

[9] M. Petrou, K. Harries, F. Gadala-Maria und V. Kolli, „A unique experimental method for monitoring aggregate settlement in concrete," Cement and Concrete Research, Bd. 30, pp. 809-816, 2000.

[10] J. Yammine, M. Chaouche, M. Guerinet, M. Moranville und N. Roussel, „From ordinary rheology cocnrete to self-compacting concrete: A transition between frictional and hydrodynamic ineractions," Cement and Concrete research, Bd. 38, pp. 890-896, 2008.

[11] M. Bastian; J. Kasper; C. Dannert et al.: Measurement of the dynamic viscosity of refractory castables: interaction between slurry and aggregates. 65th International Colloquium on Refractories 2022: The future transformation of the process industry; September 28th and 29th, 2022. Höhr-Grenzhausen: ECREF European Centre for Refractories gemeinnützige GmbH 2022 S. 49 – 52

[12] M. Bastian; O. Krause et al. Abschlussbericht zum Forschungsvorhaben IGF Nr. 21830 N, Entwicklung neuer praxisnaher Methoden zur Messung der scherratenabhängigen dynamischen Viskosität für die Ermittlung des Einflusses der Zusammensetzung und des Mischprozesses auf die rheologischen Eigenschaften von Feuerbetonen, in preparation.

243

OUR OPERATING TEMPERATURE?

HOT AS HELL.

THE INTOCAST GROUP OF EXPERTS

CARBOOX    Dolomite Franchi    ΞXUS    MAPEKO    SLOVMAG

www.intocast.com

INTOCAST
EXPERTS ON FIRE.

# 3 REFRACTORIES FOR IRON- AND STEELMAKING

# END OF PETROLEUM TAR BINDER, NEW GENERATION OF TAP-HOLE CLAY. FORMALDEHYDE AND PAH FREE TECHNOLOGY

Thierry Joly, VESUVIUS EUROPE – Advanced Refractories, Lyon, France
Roger Isenbarger, Stephen Draper, VESUVIUS USA – Advanced Refractories, Pittsburgh, USA

**ABSTRACT**
Taphole clay (THC) is used to control the iron tapping stream and hearth liquid levels in the blast furnace. THC consists of a solid part and a binder phase. Vesuvius has launched a major program to develop THCs that are safe for health and the environment. In a previous publication [1], the study carried out on the substitution of phenolic resins led to the development of a phenol-free, formaldehyde-free, and PAH-free material for the European market. The study presented here concerns the substitution of tars (coal or petroleum) used in NAFTA and the development of a Formaldehyde-free and PAH-free material.

**INTRODUCTION**
THC needs to fulfill functions as described [2] and [3]:
1) The plasticity should be compatible with the mud gun characteristics. The THC should exhibit high density after plugging. The shelf life is also an important parameter.
2) The degree of sintering must be balanced between being sufficient to resist to the top gas pressure and have no deterioration of the mushroom, against not being excessive to allow taphole opening without difficulties.
3) The THC should have high resistance to erosion by hot metal and slag then corrosion by slag. The THC should allow proper hole enlargement at the time of tapping to ensure removal of slag and manage the level of the liquid inside the blast furnace.
4) To ensure the THC volume stability at all temperatures of usage (in the taphole sleeve during curing, at high temperature during tapping), change in volume must be expansile.
5) Close adhesion of newly injected taphole clay to the residual THC applied previously is essential.
6) During the design processing, the THC must consider the environment and taking care of the health of the users.

In NAFTA, the legislation does not prohibit the use of coal tar, the choice of clean or dirty solutions depends on the environmental policy applied in each company.

## 1. CHOICE OF THE BINDER
The choice of binder consists in proscribing coal or petroleum tar, which contains PAHs (Table 1) harmful to human health [4]

| PAH | Carcino genicity | Coal Tar (ppm) | Petroleum Tar (ppm) |
|---|---|---|---|
| Naphthalene | D | $8.2 \times 10^3$ | $1 \times 10^3$ |
| Acenaphthylene | D | | |
| Acenaphthene | NA | $3.9 \times 10^3$ | $2.8 \times 10^2$ |
| Fluorene | D | $2.1 \times 10^3$ | $1.6 \times 10^2$ |
| Phenanthrene | D | $6.6 \times 10^3$ | $7.4 \times 10^2$ |
| Anthracene | D | $1.7 \times 10^3$ | $2.1 \times 10^2$ |
| Fluoranthene | D | $4.2 \times 10^3$ | $2.3 \times 10^2$ |
| Pyrene | NA | $3.3 \times 10^3$ | $5 \times 10^2$ |
| Benzo[a] anthracene | B2 | $1.4 \times 10^3$ | $2.6 \times 10^2$ |
| Chrysene | B2 | $1.3 \times 10^3$ | $2.7 \times 10^2$ |
| Benzo[b] Fluoranthene | B2 | $1.3 \times 10^3$ | |
| Benzo[k] Fluoranthene | B2 | $5.5 \times 10^2$ | |
| Benzo(a)pyrene | B2 | $1.2 \times 10^3$ | $1.9 \times 10^2$ |
| Indeno[1,2,3-cd] pyrene | B2 | $5.9 \times 10^2$ | |
| Dibenzo[a,h] anthracene | B2 | $2.1 \times 10^2$ | |
| Benzo[g,h,i] perylene | D | $6 \times 10^2$ | |
| Sum | | $3.7 \times 10^4$ | $3.9 \times 10^3$ |

*Table 1: PAH in coal and petroleum tars. B2 "possibly carcinogenic to humans"; D "unclassifiable as to carcinogenicity"; NA Not Available*

Similarly, the use of phenolic resins containing volatile organic compounds such as phenol or formaldehyde is undesirable. The new generation of binder system contains no PAHs or formaldehyde, making it the cleanest solution on the market. To select the adequate binder, constraints are divided in three main categories: raw materials that are not REACH or GHS regulation sensitive; production orientation by providing a solution which is

not impacting the manufacturing speed or reliability, then customer oriented by providing a solution which is fitting the current protocols used with the standard systems.

## 2. EXPERIMENTAL PROCEDURE
The experimental approach was carried out in four stages:
1) The study followed the development of the European New Generation [1] duplicated the solution in NAFTA.
2) Rheology study performed in comparison with the petroleum tar product (Anton Paar MCR 302 Rheometer).
3) Thermogravimetric analysis launched to search for a behavior close to that of petroleum tar (STA 409 Netzsch).
4) Selected binder tested during several field trial to assess the real situation.

## 3. RESULT and DISCUSSION
### 3.1 Rheological study
A series of samples was tested by a rheology approach, only the retained solution compared to petroleum tar is presented. The concept is to present a close match for the viscosity in regard with the petroleum tar. The retained solutions has carbon adjustments to keep an equivalent fixed carbon rate between the petroleum tar and Eco-Friendly binder change. This addition of carbon impacts the rheological behavior of the selected solution.

Viscosities of the blends were determined at three different temperatures (25, 45 and 65 ºC).

Figure 2 and Figure 3 are respectively showing the viscosity evolution of petroleum tar then Eco-Friendly binders at different temperature and share rate (1 s$^{-1}$ and 100 s$^{-1}$).
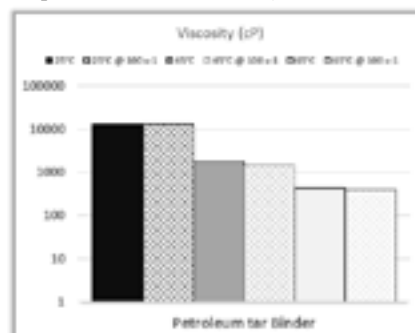


*Fig. 2: Evolution of petroleum tar viscosity in regards with temperatures.*
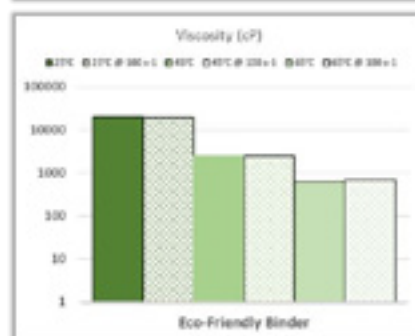


*Fig. 3: Evolution of Eco-Friendly binder viscosity in regards with temperatures.*

Although the viscosity values differ between the two systems, they are very close and indicate compatibility of the Eco-Friendly binder with the THC mix.

This was also supported by the Hershel-Bulkley Index [5] as described in the Figure 4. Parameter p which is the Hershel-Bulkley index, is indicated for describing the behavior of the flow for both systems:

- p < 1: shear thinning.
- p > 1: shear thickening.
- p = 1: Bingham behavior.
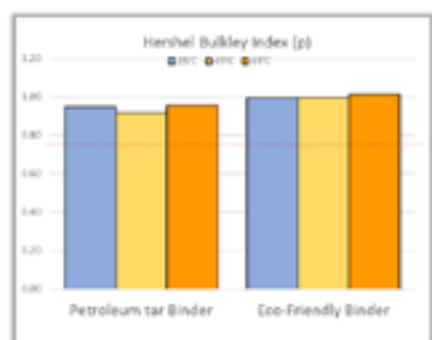


*Fig. 4: Hershel-Bulkley Index (p) at different temperature (25, 45, 65°C) show the shear-thinning behavior of the binders.*

Both systems have the same behavior as illustrated by the Herschel-Bulkley index with p < 1.

The binders were also evaluated as a function of viscosity (fig. 5).
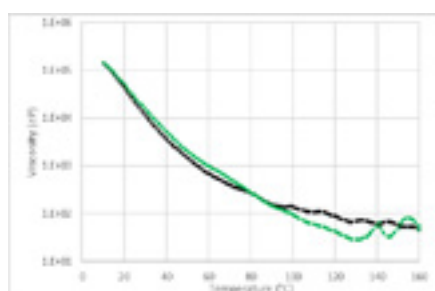


*Fig. 5: viscosity in function of temperature between Petroleum tar binder (curve in black) and Eco-Friendly binder (curve in green).*

Up to 90 °C, both binders behave equally well; viscosity gradually decreases with temperature. Around 90 °C, petroleum tar begins to stabilize its behavior while the Eco-Friendly continues to decrease in viscosity until approximatively 130 °C, when it begins to stiffen. At this level, the carbonaceous additions of the Eco-Friendly binder governs the rheological behavior.

In conclusion of the study for the rheology part, one solution was selected. Indeed, the Eco-Friendly system is presenting the closest behavior to the petroleum tar from all the first possibilities.

### 3.2 Thermogravimetric study

To further characterise the binder blends, TGA under non-oxidizing atmosphere based on argon was conducted. The experimental conditions are a progressive rise in temperature (without thermal pre-treatment) up to 1450 °C at 5 °C per minute, without step and under argon atmosphere (Figure 6).
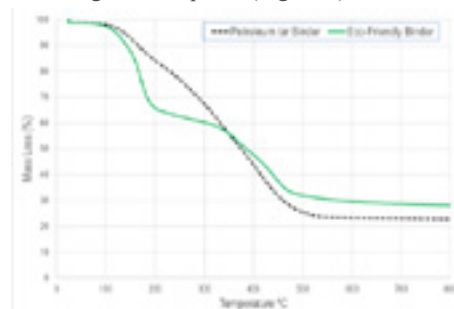


*Fig. 6: TGA of Petroleum tar binder (black curve) and Eco-friendly binder (green curve).*

As explained in the section 3.1, the Eco-Friendly binder consists in a blend of a liquid and some carbon. We observe a rapid loss of mass at low temperatures and a stabilization between 200 and 400 °C (effect of added carbon). The new system of binder degasses more quickly than the petroleum tar at low temperatures. This allows to consider a short dwell time but also indicates a THC which will have sufficiently evacuated its volatile matters not to generate splashing by outgassing at the time of the taphole opening and reduces wet taphole conditions.

### 3.3 Extrusion Pressure

The evolution of the extrusion pressure by a Marshall Test as a function of the sample' temperature is provided (Figure 7).
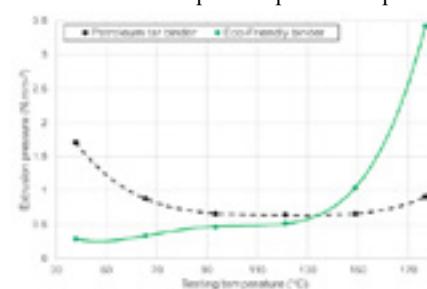


*Fig. 7: Extrusion pressure given by a Marshall test of Petroleum tar binder (black curve) and Eco-friendly binder (green curve).*

The stable extrusion pressure as a function of the temperature allows an easy use of the developed THC mix, it is possible to initiate the cure as early around 130°C. This reduces the holding time of the mudgun on the taphole face compared to the petroleum tar bonding system.

### 3.4 Physical properties of THC

Table 3, shows the main physical characteristics of the two THC after firing at 1093 °C (2000 °F) in a reducing atmosphere for 5 hours. The Eco-Friendly binder is presenting a higher mechanical strength for a lower open porosity in comparison with the petroleum tar bonded system, this is aligned with an improved performance on customer site.

| THC product | Rammed Density (k.gm$^{-3}$) | Fired Density (k.gm$^{-3}$) | CCS (N.mm$^{-2}$) | Apparent Porosity (%) | Volatile Loss (%) |
|---|---|---|---|---|---|
| Petro. tar | 2400 | 2130 | 8.3 | 30.5 | 8.6 |
| Eco-F. Binder | 2370 | 2100 | 13.9 | 24.0 | 9.7 |

*Table 3: Main characteristics of a taphole mixes made with Petro Tar and Eco-Friendly binder.*

### 3.5 Field Trial

In NAFTA, Eco-Friendly binder has replaced petroleum tar bonded system in all Vesuvius formulations. The new materials perform better in the mud gun with better injection stability, an easy cleaning and limited loss of THC per plugging. The tapping performance is at least equivalent to the petroleum tar system. Customers noticed the decreasing of organic smell and black smoke. Opening is easy, typical drill duration took between 60 and 90 seconds. A fast firing rate with a faster release of volatiles than the petroleum tar leads to limited spatter at the beginning of the tap. The taphole length is consistently at the top of the range. At one of our main customers the quantity injected is reduced and cuts specific consumption by at least 17%.

### 4. CONCLUSION

The Eco-Friendly Binder has zero formaldehyde and zero PAH contents. Application in the field shows equivalent or increased performance. Eco-Friendly Binder does not require any reworking of the THC formulation, so it can be easily substituted for conventional binder for all currently supplied materials.

### REFERENCES

[1] Joly, T and all, "Next generation of taphole clay, formaldehyde and PAH free technology". ICR 2022.

[2] Ribeiro,A.S, "Analise sistemica das massas de tamponamento para altos-fornos". PhD Thesis, Universidade federal de Sao Carlos, 2010

[3] Muroi,N. "New taphole mud for blast furnace", Taikabutsu Overseas, Vol.19, n°3, pp 24-27, 1999

[4] Dandajeh H.A and all, "Influence of combustion characteristics and fuel composition on exhaust PAHs in a compression ignition engine", Energies 2019, 12, 2575.

[5] Mud and Debris Flow – HEC-RAS Mud and Debris Flow. https://www.hec.usace.army.mil/

# COMPARATIVE STUDY BETWEEN COAL TAR PITCH AND LOWER POLYCYCLIC AROMATIC HYDROCARBON (PAH) ALTERNATIVE BINDERS FOR USE IN TAPHOLE CLAYS

I.J. Cameron[a], S. Ramjee[b], A.M. Garbers-Craig*[a], [a,b]University of Pretoria, South-Africa

## ABSTRACT

The conventional binder used in taphole clay is high volatile coal tar pitch (CTPht) or a similar low softening point pitch which poses great health and environmental risks due to the polycyclic aromatic hydrocarbon (PAH) present in the binder. Less toxic or non-toxic (lower PAH content) alternatives that have been identified as substitutions are distilled coal tar, petroleum-based phenolic pitch, waxy (paraffin) crude oil, and wood-based tars which are derived from the Kraft process. The behaviour of the CTPht was evaluated with respect to its rheological properties (Newtonian behaviour, thermal stability), its thermal behaviour (using thermogravimetric analysis, TGA-DTG) as well as its chemical composition (using gas chromatography mass spectroscopy, GC-MS) to identify critical binder properties. The proposed alternative binders were then evaluated against the critical binder properties of the CTPht and the most suitable alternative proposed.

## INTRODUCTION

The binder systems conventionally used in taphole clays are either pitch bonded (high-temperature coal tar pitch, CTPht), resin bonded (phenolic resole resin) or a combination binder that contains both coal tar pitch and phenolic resin [1] [2] [3]. The CTPht has unique fluid properties that make it a favourable binder for taphole clays. These properties include viscoelasticity, which ensures mixing of the binder with the aggregate and matrix at low temperatures (<50 °C) during the manufacturing process. The binder also allows for good plastic behaviour during ageing of the clay. The use of CTPht in taphole clays allows for a thermoplastic clay to be formed that ensures a transition-free sintering zone between the new clay that is rammed into the tap hole and the previously sintered clay in the tap hole [1] [4] [5].

The major disadvantage of CTPht is the toxicity due to the presence of polycyclic aromatic hydrocarbons (PAH) in the fluid of which the 16-EPA-PAH species are identified Group I carcinogens [6]. The permissible exposure limit (PEL) identified by the US environmental protection agency (EPA) for the 16-PAH species in air is 0.2 mg/m$^3$ during an 8-hour period [7]. In order to eliminate this exposre to humans in contact with the material, alternative binders are evaluated which include processed and synthetic coal tar pitch with lower PAH content, petroleum-based mesophase-forming pitch, and waxy oil, as well as wood-based tars from three different sources, i.e., beechwood, pinewood and a vegetable source. The work in this paper describes the characteristics and behaviour of the model taphole clay binder, CTPht, and compares the alternative bidners with lower PAH content to it.

## MATERIALS & METHODS

The binders that were selected for evaluation with their respective designation and origin are shown in Table 1.

*Tab.1: Alternative binders identified for comparison evaluation to coal tar pitch (CTPht)*

| Binder name | Group |
|---|---|
| CTPht, 20P, EcoP | Coal tar |
| CWO, PCWO, MP | Petroleum |
| Tar-BW, Tar-PW | Wood-based |
| Tar-Veg | Vegetable |

## Gas chromatography mass spectroscopy (GC-MS)

The volatile species in each of the samples were evaluated by gas-analysis using GC-MS. Both targeted and untargeted analyses were done to (1) determine the concentration of each of the 16-EPA-PAH species in the sample (targeted), and (2) determine the remainder of the species in the sample (pseudo-quantitatively, untargeted). The samples were prepared in both hexane and toluene, and the results reported are for the toluene solvent. For the targeted analysis a pesticide standard containing the 16-EPA-PAH was used to construct concentration diagrams, which were then used to determine the concentrations in the samples. The same procedure was used for the untargeted analysis however, concentration diagrams were not constructed but only used for identification. The pseudo-quantification was done on the chromatographs. An 6890N Agilent with inert XL EI/CI mass selective detector, coupled with e CTC Analytics PAL auto-sampler, was used. A non-polar Rxi-5Sil MS capillary column was used for the samples.

## Thermogravimetric analysis (TGA)

The volatilization study on each of the samples was done using a Hitachi STA 7300 TGA coupled with a differential scanning calorimeter (DSC), using TA 7000 interpretation and measuring software. 30μL alumina crucibles were used, with sample size 5-10 mg. The samples were heated from 50-800 °C in a nitrogen atmosphere (flow rate = 20mL/min) at a rate of 10°C/min.

## Rheology

For the rheology evaluations the binders were tested for (1) isothermal rotation at 45 °C (Newtonian fluid behaviour), (2) temperature sweep in rotation to determine thermal stability from 30-150 °C at a heat rate of 5 °C/min. The rheometer used was an Anton Paar Physica MCR 501 equipped with both a cone-plate measuring system and a Peltier 200 temperature control system. For the cone-plate system, a 0,5°, 50 mm diameter sized spindle was used, and the samples were heated in air. For interpretation, RheoCompassRM software was used.

## RESULTS AND DISCUSSION

### Gas chromatography mass spectroscopy

The targeted analysis results of each of the binders were used to determine the total PAH content (16-EPA-PAH) species and calculate the benzene equivalent [8]. The results from the GC-MS targeted analysis are shown in Table 2. The beechwood and pinewood tar sample results are not shown in Table 2 due to the samples not containing any of the 16-EPA-PAH species. The coal-based binders, especially 20P, showed the highest toxicity with respect to total PAH. The EcoP had the lowest PAH content and BE-value among the coal-based binders. The petroleum binders all had PAH contents an order of magnitude lower than the coal-based ones. The processed crude wax oil was the least toxic binder of the petroleum binders. The wood-based binders showed to lowest toxicity with both beechwood and pinewood tars not containing any carcinogenic 16-EPA-PAH species.

### Thermal analysis (TGA)

Thermal analysis was used to determine the average mass loss during a specific temperature range in order to compare the degree of volatile release and how suddenly it occurs. The reference binder had the lowest average mass loss (0,28 g / °C) over a temperature range of ΔT ~ 310 °C. The closest alternative was the EcoP, with an average mass loss of 0,21g / °C at ΔT ~ 398 °C compared to the reference. The 20P had a higher average mass loss over a shorter temperature range. The pinewood and vegetable tar had similar average mass losses to the 20P over a comparable temperature range (ΔT ~200). The petroleum-based binders had the highest

average mass losses, ranging from 0,96-0,97 g / °C over a short temperature range (ΔT ~ 100 °C).

*Tab.2: Targeted analysis results showing calculated total PAH and BE-value*

| Binder | Total PAH (ppm) | Benzene equivalent, BE (%) |
|--------|-----------------|----------------------------|
| CTPht | 13737,1 | 1,67 |
| 20P | 19918 | 1,80 |
| EcoP | 8491 | 0,18 |
| CWO | 906,8 | 0,03 |
| PCWO | 43,02 | 0,03 |
| MP | 1525,1 | 0,30 |
| Tar-Veg | 126,16 | 0,02 |

**Rheology**

All binders were evaluated for their Newtonian behaviour, and all binders, except for CWO, showed Newtonian behaviour. The shear-thinning behaviour of the CWO is probably due to the presence of residual moisture in the sample, as it is an unrefined version of the wax oil. The thermal stability of the binders is shown in Figure 1. The results show that, except for Tar-Veg and Ta-PW, the binders are homogeneous mixtures that maintain their molecular structure during heating. There is a correlation between extrusion pressure and workability, wherein binders with higher viscosities require higher extrusion pressures to extrude the clay [9]. The Tar-BW has the closest thermal stability and change in viscosity with temperature compared to the reference binder. It has a slightly higher starting viscosity, which can be mitigated by incorporating a lower viscosity liquid as a plasticizer to slightly lower the viscosity. The MP binder has the highest decrease in viscosity during heating while still maintaining its molecular structure at higher temperatures. The Tar-PW and Tar-Veg binders did not maintain thermal stability and are not considered favourable alternatives to CTPht, as thermal stability is a critical property of binders.
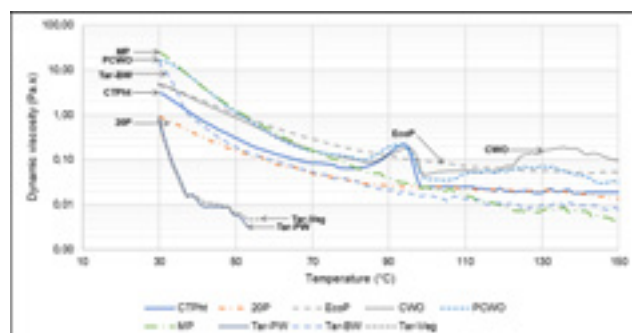


*Fig. 1: Rheological thermal stability of various binders*

**Overall ranking of binders**

The analytical evaluations were used to rank the alternative binders according to their suitability to replace CTPht as a binder in taphole clay. Table 3 shows the binders and their rankings, based on composition, thermal analysis, and rheology.

*Tab.3: Overall ranking of alternative binders based on the compositional, thermal, and rheological evaluations*

| Position | Overall rank |
|----------|--------------|
| 1 | Tar-BW |
| 2 | CWO |
| 3 | MP |
| 4 | PCWO |
| 5 | EcoP |
| 6 | 20P |
| 7 | Tar-PW |
| 8 | Tar-Veg |

The rankings are listed from top to bottom, with the most suitable binders at the top and the least suitable at the end. The selection criterion for ranking was a combination of lowest total PAH value, and good dynamic viscosity and thermal stability for manufacturing and green strength development. The most suitable binder to replace CTPht is the beechwood tar (Tar-BW). The other bio-based binders were ranked lowest due to limited dynamic viscosity thermal stability. The coal-based binders were also ranked low due to their high toxicity levels. The petroleum-based binders were the closest alternatives, besides the Tar-BW, to replace the CTPht, with the CWO and MP ranking as the second and third alternatives, respectively.

**CONCLUSIONS**

The selection of alternative binders to CTPht was carried out by using compositional and toxicity measurements (GC-MS), thermal behavior (TGA) and rotational rheology to evaluate the flow characteristics, and dynamic viscosity thermal stability of each binder. The GC-MS targeted analysis showed that the binder with the highest total PAH content to be 20P, while Tar-PW and Tar-BW exhibited the lowest toxicity among the binders. Some of the petroleum-based binders (CWO, PCWO) also exhibit low toxicity compared to the coal-based alternatives. The variation in thermal stability between the binders was 0,21-0,96 g / °C. The petroleum wax-based binders having the highest mass loss over a short temperature range, while the coal-based binders exhibited the lowest mass loss over a wide temperature range. This behavior is similar to that of the reference binder. The dynamic thermal stability assessment indicated that all binders, except for Tar-PW and Tar-Veg, had good thermal stability and have the potential to replace CTPht. From the analytical evaluations and comparison to the behavior of the reference binder, Tar-BW has shown to be the most favorable binder for replacing CTPht in taphole clay.

**REFERENCES**

[1] L. Nelson and R. Hundermark, "The 'tap-hole' - key to furnace performance," The Journal of the Southern African Institute of Mining and Metallurgy, vol. 116, no. 2, pp. 465-490, 2014.

[2] R. Hsissou, R. Seghiri, Z. Benzekri, M. Hilali, M. Rafik and A. Elharfi, "Polymer composite materials: A comprehensive review," Composite structures, no. 262, pp. 2-15, 2021.

[3] E. Sharp and R. Harper, "Resin bonded taphole closure refractory product". Canada Patent CA2124488A1, 29 November 1994.

[4] P. Sarika, P. Nancarrow, A. Khansaheb and T. Ibrahim, "Bio-based alternatives to phenol and formaldehyde for the production of resins," Polymers, no. 12, pp. 1-24, 2020.

[5] Z. Katovic, "Curing of resole-type phenol-formaldehyde resin," Journal of applied polymer science, vol. II, pp. 85-93, 1967.

[6] B. Mazumder, "Coal-derived industrial carbons," in Coal science and engineering, Woodhead publishing, 2012, pp. 344-370.

[7] Agency for toxic substance and disease registry (ATSDR), "Polycyclic aromatic hydrocarbons (PAH)> What are the standard and regulations for exposure?," 1 July 2013. [Online]. Available: https://www.atsdr.cdc.gov/csem/polycyclic-aromatic-hydrocarbons/standards_and_regulations_for_exposure.html. [Accessed 06 April 2023].

[8] E. Andreikov, I. Amosova and M. Pervova, "Determining the content of polycyclic aromatic hydrocarbons in industrial samples of coal tar and pitch," Coke and chemistry, vol. 51, no. 8, pp. 321-325, 2008.

[9] I. Cameron, "Investigating premature ageing of blast furnace taphole clay containing a resole resin and liquid pitch binder," University of Pretoria, Pretoria, 2021.

# DEVELOPMENT OF HIGH PERFORMANCE TAP HOLE CLAY

Tuhin Patranabish, Kazi Asif Ahmed, Saumen Sinha and Indra Nath Chakraborty
Calderys India Refractories Limited

**ABSTRACT:**

Taphole Clay (THC) related challenges increase with the increased BF productivity, quality variation of iron ore and cost of refractory raw materials**.** Addressing these issues has all along been a problem since the changes THC undergoes, after injection, inside a Blast Furnace (BF) is never known. Decisions regarding THC formulation design are always based on speculation. In this paper we report the development of THC, for big and jumbo furnaces, following a thermodynamic approach. Influences of THC raw materials were evident in thermodynamic calculation results as well as corrosion of the refractory, by a representative BF slag, during laboratory Induction furnace corrosion study. Corrosion of the THC, observed during induction furnace interaction study, was correlated with the quantum of liquid as well as the minerals formed during THC - Slag interaction and viscosity of the liquid formed.

The THC formulations were optimized based on thermodynamic results and the same has been used successfully in Big and Jumbo BF.

**INTRODUCTION:**

Colloquially Big and Jumbo Blast Furnaces (JBF) are defined as those with capacities in the range of 6000 - 9500 and > 9500 Ton/Day, respectively. Good health and reliable operation of the tap hole are essential for smooth functioning as well as achieving the desired lifespan of BF. Nowadays Jumbo BF operations are very challenging due to the high productivity target, deterioration of the input raw material quality, especially iron ore and cost reduction target.

The expectation of BF operators, from THC, are plugging without any leakage and back flushing, smooth TH opening, i. e. only with drill bit without hammering or oxygen lancing, no increase in TH diameter during slag as well as metal casting, consistent TH Length, no slag delay and no spitting during casting. Achieving these targets requires correct THC formulation as well as its quality consistency. Controlled drainage rate, with required Cast Duration (CD), depends on the stability of the Mushroom and controlled erosion of TH pipe formed by the THC used for closing after the completion of slag - metal tapping operation.

CD is defined as the total drainage time of Metal and Slag after opening of TH. The same, depends on the mushroom stability and TH Pipe erosion rate during drainage of metal and slag. Mushroom stability depends on several factors, e. g. THC formulation, THC binder system as well as mixing process during its production and THC workability / plasticity. BF operation practice, including plugging, also plays a significant role in THC performance. In today's context the designed THC should not get corroded under high slag rate, high slag basicity and slag with >1.0% MnO.

In general, Ferro silicon nitride (FSN) and silicon carbide (SiC) are seen as essential constituents of THC for its acceptable performance, e. g. desired CD. [1] Concentration optimization of these constituents is vital for attaining the targeted THC performance parameters. During this work, FactSage 8.2, a chemical thermodynamic software and database [2], has been utilized to optimize the characteristics as well as minimize the quantum of liquid formed during THC - slag interaction, at lower FSN and SiC concentrations in THC formulation. The FactSage THC - slag interaction results have been verified in the laboratory by Induction furnace Finger Test (FT). The optimized THC formulation has been tried in a 12000 TPD BF. This paper reports the THC formulation optimisation process using FactSage, laboratory induction furnace and field trial results

**EXPERIMENTAL:**

Conventional THC constituents were used for calculation of THC - slag / metal interaction by FactSage equilibrium phase proportion as well as laboratory induction furnace THC - slag interaction. Numerous THC - slag interaction data were generated, by using FactSage, for THCs with varied (SiC + FSN) concentrations and Alumina to silica ratios. The chemistry of shortlisted THC compositions, used for the FactSage calculation, are reported in Table I.

Primary focus has been given on (SiC + FSN) concentration. THC A is the conventional formulation for JBF. The process adopted for formulation adjustment is reported in Table II.

FactSage was used to see the impact of temperature on 70% THC and 30% JBF slag mix as well as 70% THC and 30% JBF Hot Metal (HM) mix. FactPS, FToxide, FTmisc, FTOxCN (only for solid phases) was used to do the calculation for this subject topic. Calculations were done for an interaction temperature of 1500 $^0$C.FactSage predicts the concentrations as well as compositions of gas, liquid and solid of the aforementioned interactions.

**Table** Ⅰ Chemistry of THC formulae

| Formula | Al2O3+SiO2+C | SiC+FSN |
|---|---|---|
| THC A | X | Y |
| THC B | X+Δx1 | Y-Δy1 |
| THC C | X+Δx2 | Y-Δy2 |

**Table** Ⅱ THC Formulae Chemistry Balance

| Product | Chemistry balance |
|---|---|
| THC B | Δx1=Δy1 |
| THC C | Δx2=Δy2 |

Typical slag chemistry of JBF, where the field trial was conducted, are reported in Tables III.

Table IV reports the typical HM chemistry of the aforementioned JBF. The accuracy of factsage equilibrium prediction for this type of mix was verified by laboratory induction furnace FT. For FactSage calculation as well as laboratory induction furnace FT, the slag and HM, reported in Table III and IV, respectively, were used.

The test specimens, for induction furnace FT, were of cylindrical shape for avoidance of corner breakage. 70% metal and 30% Slag, on weight basis, were used for the test. The molten liquid temperature was maintained between 1498°C to 1520°C. Samples were dipped partially into the molten liquid. The sample holder was rotated from a control panel at a speed of 5 rpm. After the completion of the test, samples were cooled down. The corrosion was measured along the diameter of the cylinders. The reduction in diameter, in comparison to the initial specimen diameter, has been reported as refractory wear.

**Table III** Jumbo BF Slag

| Constituent Concentration, % | | | | | | | | |
|---|---|---|---|---|---|---|---|---|
| $SiO_2$ | $Al_2O_3$ | CaO | MgO | MnO | FeO | $TiO_2$ | $Na_2O$ | S |
| 35.07 | 18.26 | 35.84 | 6.82 | 1.32 | 0.37 | 0.82 | 0.33 | 0.59 |

**Table I**V Hot metal chemistry in %

| Fe | Mn | Si | C |
|---|---|---|---|
| 94.5 | 0.5 | 1.0 | 4.0 |

The Green and 1300 $^0$C / 3 hrs coked bulk density data were generated for THC A,THC B and THC C. The apparent porosity (AP), volatile matter (VM) and cold crushing strength (CCS) were measured after curing the test specimens in reducing atmosphere at 1300 $^0$C for 3 hrs. All the data were generated using internal test procedures.

**RESULTS AND DISCUSSION:**
Figure 1 shows FactSage predicted mineral, liquid and gas concentrations of 70% THC - 30% JBF slag interaction at 1500 $^0$C . Apart from gas and liquid, the major constituents of the predicted solid phases are SiC, $CM_2A_8$ [3] and $CA_2$ where C, M and A are CaO, MgO and $Al_2O_3$, respectively. $CA_2$ is a refractory phase. The formation of $CM_2A_8$ is significant, which is a solid solution of $CA_6$ and MA(spinel) [3]. $CA_6$, like spinel, can accommodate a varied range of atoms in its crystal structure.[4] As a result $CA_6$ also can modify the slag characteristics as well as the slag corrosion behavior. The $CM_2A_8$ concentration follows the following trend.

THC C > THC B > THC A

THC C is expected to offer greater resistance to the slag attack owing to higher $CM_2A_8$ concentration. The concentration of in situ formed (secondary) SiC, after interaction with slag, also follows the same trend. In situ SiC formation has been explained in greater detail in one of the following sections.

It is prudent to mention that THC A had the highest concentration of (SiC + FSN) whereas the same for THC C was the lowest (Table I). The predicted liquid phase follows a trend reverse to that for SiC phase, i. e. least for THC C and is highest for THC A, though THC C has the highest oxide concentrations (Table I). The liquid concentration, thus, is controlled by the amount as well as ratios of the THC oxide constituents.

Figure 1 also illustrates the concentrations of the THC - slag interacted gas phase. Concentrations of gas formed after interactions are comparable for all the three formulations.

Carbon monoxide (CO) and Nitrogen ($N_2$) are the major gas constituents. CO originates from the oxidation of carbonaceous constituents of the THC formulation. $N_2$ originates from the dissociation of FSN as per reaction 1. [1]

$$3Fe + Si_3N_4 \longrightarrow 3FeSi + 2N_2 (g) \qquad (1)$$
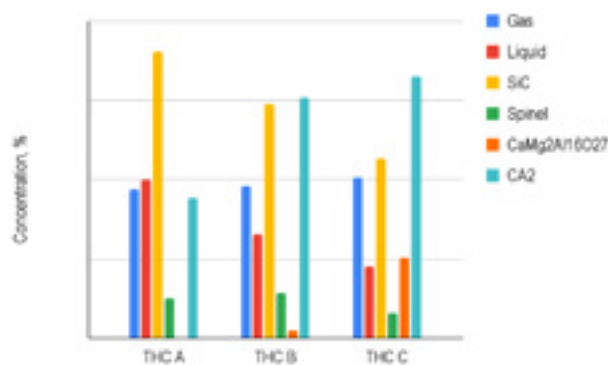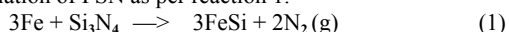


***Fig 1*** *FactSage results of THC - Slag Interaction at 1500 $^0$C*

Figure 2 illustrates the yields of 70% THC - 30% HM interaction at 1500 $^0$C. The yields are fairly similar to those observed for THC - slag interactions. Like THC - slag interaction, the constituents of the gas yields are $N_2$ and CO. The solid yields of the interaction are the constituents of the virgin THC, except for the $Al_2OC$ - AlN phase. Apart from slag, THC - HM interaction at 1500°C also yields an iron rich liquid termed as Fe- liquid. The concentration of Fe - liquid varies in a narrow range, viz. between 34.64 to 34.87 %.
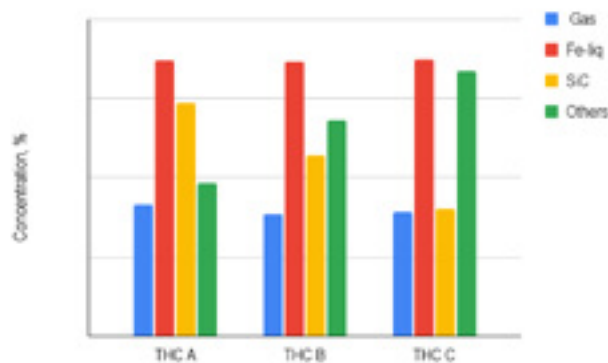


***Fig 2*** *FactSage results of THC-HM Interaction at 1500 $^0$C*

Figure 3 shows the viscosity of liquid, formed during THC - slag interaction, has been calculated based on the liquid chemistry predicted by FactSage. In reality viscosity of the solid - liquid mix should have been considered. [4] The liquid yield of THC - slag interaction, however, is too low for accurate determination of Solid - Liquid mix viscosity. Only liquid viscosity, hence, has been considered for discussion of the results. The viscosity of the liquid formed by virtue of interaction follows the following trend.

THC C > THC B > THC A

It is evident that the viscosity variation of the liquid formed during slag interaction with different THC, however, is marginal. In the interaction equilibrium phase proportion, liquid concentration for THC C is significantly lower. As a result, the effective viscosity of Solid - liquid mix would be significantly higher for THC C - slag interaction equilibrium phase proportion. These aspects of THC C are expected to play a significant role in determining the resistance to slag attack.

251
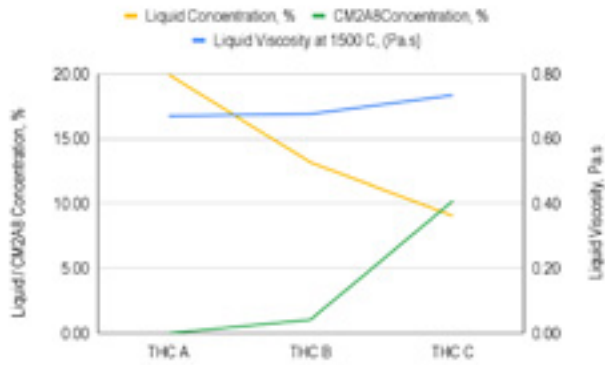
**Fig 3** *Viscosity of the liquid formed during THC - Slag Interaction at 1500 $^0C$*

Figure 3 also illustrates the concentration of $CM_2A_8$ during interaction with slag.

When the SiC content of the THC - slag interaction equilibrium phase proportion is higher than that in the starting THC - slag mix, it is obvious that SiC had formed during the aforementioned interaction. The increased SiC concentration has been defined as secondary / in situ formed SiC. In situ SiC formation occurs by virtue of the reaction 2. [1] FeSi of equation 2 originates from reaction 1.

$$FeSi + C \longrightarrow SiC + Fe \qquad (2)$$

Secondary SiC formation has also been observed for THC - HM interaction. The quantum of secondary SiC formation, however, is lower compared to THC - slag interaction. It may, thus, be speculated that part of the SiC of THC is dissolved in the HM during the interaction.

Figure 4 illustrates the impact of Alumina to Silica (A to S) ratio of THC formulation on the quantum and viscosity of the liquid formed during interaction with slag at 1500 $^0C$. It is evident from the results that increased A to S ratio lowers the concentration of the liquid formed as well as increases the viscosity of the liquid. Additionally, increased A to S ratio also increases the secondary SiC formation. The combined effect of all these aspects is expected to improve slag attack resistance of THC.

It is also obvious from Figure 4 that the increase of A to S ratio also enhances $CM_2A_8$ formation as well as slag corrosion resistance. The combined effect of A to S modification on liquid concentration as well as its viscosity, $CM_2A_8$ formation and secondary SiC formation, is reflected on the slag resistance.
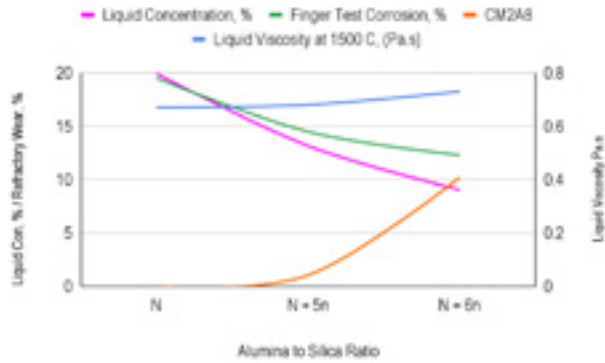


**Fig 4** *$Al_2O_3$ / $SiO_2$ ratio impact on liquid characteristics formed during THC - Slag interaction at 1500 $^0C$*
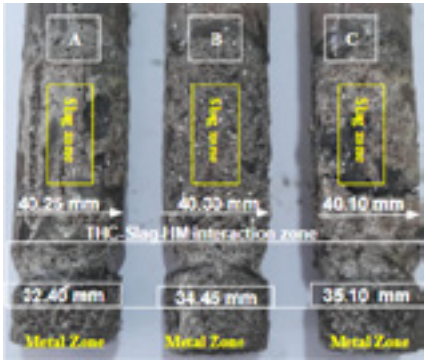


**Fig 5** Appearance of Finger Test Specimens after Interaction with slag - HM mix at 1500 $^0C$

It is apparent from Figure 5 that THC C, which has the least concentration of (SiC + FSN), offers the best resistance to slag attack. Apart from the aforementioned ingredients of THC formulations, adjustment of A to S ratio, thus, also influences THC slag resistance.

Figure 6 illustrates the Green BD and 1300 $^0C$ / 3 hrs cured BD of the THC formulations (A,B,C) which were shortlisted based on FactSage calculations. The results show that the change in the composition, in terms of ingredient concentrations as well as their type, does not alter the product density.

Figure 7 illustrates the VM, AP and CCS of the shortlisted compositions. Here again the differences in these properties are marginal.

**FIELD TRIAL APPLICATION RESULTS :**

All three FactSage result based shortlisted THC formulations were manufactured through the same manufacturing process. After aging, all the three THCs were used in a JBF. Table V reports the observations made during the field trial of THCs. During this study, the quantity of THC used for plugging and CD were the primary performance determining parameters. The quantity used for plugging was lowest for THC C, whereas CD for this formulation, however, was the highest compared to the other trial formulations. Higher CD indicates that the wear of the mushroom formed by THC C is minimal. This fact corroborates with the observation made during laboratory induction furnace corrosion tests.
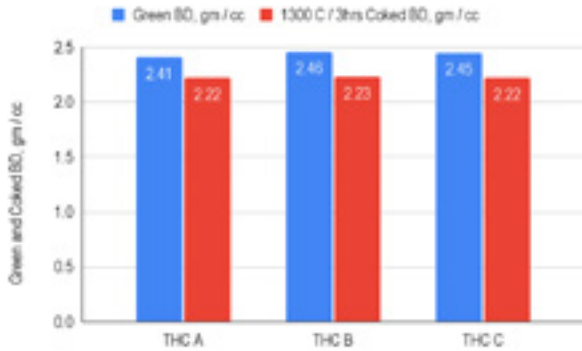


**Fig 6** *Green Bulk density and 1300 $^0C$ / 3 hrs Coked Bulk density*
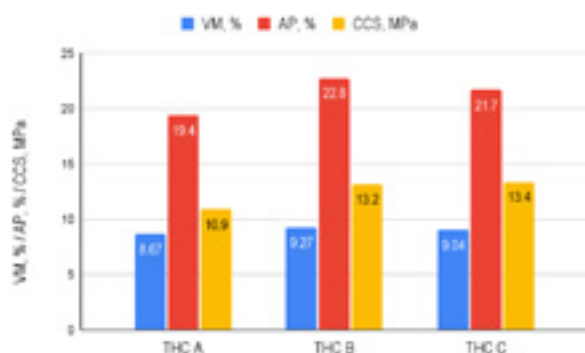
***Fig 7*** *Apparent Porosity (AP),Volatile Matter (VM) and 1300 ⁰C / 3 hrs Cured Cold Crushing Strength (CCS)*

It is evident from the field trial results that for THC C, the average HM temperature was higher by ~ 15 ⁰C. It also is well known that the chemical reaction rate accelerates exponentially with increasing temperature. Even with such adverse operating conditions, i. e. higher BF operating temperature, THC C, which had the lowest (SiC + FSN) concentrations, has yielded the best performance. It also is evident that the liquid phase concentration and the liquid viscosity predicted by FactSage, for THC - slag interaction, as well as laboratory induction furnace FT results can be taken as a good indicator for the resistance of THC to slag attack during their usage in the field. The role of evolved gasses, viz. $N_2$ and CO, on the slag attack resistance, however, is not very clear. It is speculated that the evolved gasses form a barrier between THC and slag and thus, the interaction between THC and slag is reduced. The other plausible role of evolved gasses could be that they get generated within the THC pores and thus, the slag penetration is reduced.

**Table** V **Corrosion Test and site performance data**

| Product | HM Temperature Range, ℃ | Plugging Quantity, Liter | Average (minutes) | Finger Test Corrosion, % |
|---|---|---|---|---|
| THC A | 1486 - 1523 | 180 | 146 | 19.5 |
| THC B | 1475 - 1522 | 185 | 178 | 14.5 |
| THC C | 1500 - 1532 | 176 | 181 | 12.3 |

**CONCLUSION:**
FactSage thermodynamic software predicted THC - slag interacted liquid characteristics, viz. its quantum and viscosity, is a good indicator for the field performance of THC. Usage of FactSage software, for THC formulation optimisation, virtually eliminates time consuming as well as expensive conventional route for formulation optimisation. It appears that the THC formulation should be so adjusted that THC - slag interaction yields lowest liquid concentration, highest liquid viscosity at highest possible A to S ratio of the THC formulation. It is obvious from this work that FactSage can be used for generation of these data without carrying out any laboratory experiment. Laboratory induction furnace FT also reveals that control of these parameters reduces the THC wear by slag. Lesser THC corrosion, during its interaction with slag, is reflected in longer CDs during BF tapping.
The work also reveals that the concentrations of (SiC + FSN) can be optimized by using the FactSage software. Apart from the concentrations of these critical constituents, A to S ratio of THC formulations play a significant role, by influencing secondary SiC

formation, in controlling the THC wear in JBF and as a result increases the CD. The calculation reveals that $N_2$ and CO gases evolve during interaction of THC with slag as well as HM. The impact of these evolved gasses on the THC wear, however, could not be deciphered during this work.

**REFERENCE:**
1)  Daisuke Tanaka,Tatsuya Kageyama and Akihito Kajitani, "Influence of Heating Time on Taphole Mix properties", Journal of the Technical Association of Refractories, Japan, 39 [4] 250 - 255 (2019)

2)  http://www.factsage.com/fs82_news.htm

3)  Synthesis of CaO·2MgO·8AlO (CMA) and its slag resistance mechanism, Junhong Chen , Haiyang Chen , Wenjun Mi , Zheng Cao , Bin Li , Guangqi Li

4)  Exploring the limits of Fe3+ solid solution in calcium hexaluminate, P. G. de la Iglesia[1], O. García‑Moreno[2], J. L. Menéndez[1], R. Torrecillas[1], J. F. Marco[3],

5)  Shinichiro Haruki, Sohei Sukenaga, Noritaka Saito and Kunihiko Nakashima, "Viscosity Estimation of Spherical Particles Dispersed Suspension", High Temp. Mater. Proc., 30 405–409 (2011) (DOI 10.1515/HTMP.2011.062)

# BEHAVIOR OF CARBON-BASED BINDERS FOR BLAST FURNACE TAPHOLE CLAYS FOCUSED ON ENVIRONMENT, SAFETY, AND PERFORMANCE

Tomás Moreira de Oliveira, Aloísio Simões Ribeiro, Paschoal Bonadia Neto
RHI Magnesita, Contagem, Brazil

Eduardo Henrique Martins Nunes
Universidade Federal de Minas Gerais, Belo Horizonte, Brazil

**ABSTRACT**

The liquid binder plays an essential role in taphole clay composition to guarantee its properties such as plasticity, adhesion, corrosion/erosion resistance, and ease of drilling during use in blast furnaces. Additionally, the binder also has a major role concerning environmental and safety aspects. Several studies have been carried out on taphole clay binders, but it is not common to find an in-depth comparative analysis between the different existing types. In this study, four commercially available carbon-based binders were investigated, namely a traditional coal tar pitch, a novolak phenolic resin, a low benzopyrene coal tar pitch, and a petroleum-based binder. This study aimed to understand the key properties of each taphole clay binder and how they affect the refractory mix regarding environmental, safety, and performance aspects. Specific tests to evaluate binders were carried out and associated with taphole clay properties.

## 1 INTRODUCTION

Taphole clays are plastic refractory materials used to seal blast furnace tapholes at the end of the tapping operation. They are made from various solid raw materials in different grain sizes, which are agglomerated by the addition of a liquid binder. This liquid material is very important for taphole clays to obtain their properties such as plasticity, adhesion, corrosion/erosion resistance and ease of drilling. Additionally, the binder has a major role concerning environmental and safety aspects. For this reason, taphole clay binders have been the subject of several recent studies[1-4].

One of the main binders in used is coal tar pitch, but it is a toxic material. Due to the high presence of polycyclic aromatic hydrocarbons (PAHs), especially benzopyrene (BaP), coal tar pitch is carcinogenic[5-7], which has motivated the development of alternative binders. These include phenolic resins, coal tar pitches with low benzopyrene content and petroleum-based binders.

Although taphole clay binders are an important topic, it is not common to find an in-depth comparative analysis of the different types available. In addition, there is no adequate reference about key properties to be evaluated in binders for taphole clays. In this study, four types of binders available on the market were characterized: traditional coal tar pitch, novolac phenolic resin, low benzopyrene coal tar pitch, and a petroleum-based binder.

## 2 OBJECTIVES

Understand the key properties of each taphole clay binder and how they affect the performance of the refractory mix.

## 3 MATERIALS AND METHODS

### 3.1 Materials

Table 1 shows the identification and description of each product evaluated in this study. The selected binders were a conventional coal tar pitch, a low-benzopyrene coal tar pitch, a petroleum-based binder, and a phenolic novolac resin.

Tab. 1: Identification and description of the analyzed binders.

| Identification | Description |
|---|---|
| CTP | Traditional coal tar pitch |
| ECTP | Eco coal tar pitch with low benzopyrene |
| PNR | Phenolic novolac resin |
| PBB | Petroleum-based binder |

### 3.2 Brookfield viscosity

The Brookfield viscometer measures fluid viscosity at given shear rates and temperatures, which is a measure of a fluid's resistance to flow. The viscometer rotates a sensing element (spindle) in a fluid and measures the torque required to overcome the viscous resistance to the induced motion. In this test, spindle number 21 was used, and viscosity was measured at 30, 40, 50, 60, 70, 80, and 90 °C.

### 3.3 Curing test with parallel plate rheometer

The equipment used for this analysis was an Anton Paar / MCR 102 parallel plate rheometer. In this test, the viscosity of the binder was measured as the sample was heated to evaluate the curing behavior of the binder. The measuring system used for the curing test was a 25 mm disposable plate. The deformation used was 0.1% with a 1 Hz frequency. The samples were heated from 40°C to 400°C at a rate of 3 °C/min.

### 3.4 Thermogravimetric analysis

Thermogravimetric analysis (TGA) was performed using a TGA Discovery thermobalance. The binders were heated from room temperature to 800 °C at a rate of 10 °C/min. Nitrogen was used as the purge gas at a flow rate of 25 mL/min to avoid oxidation. TGA was used to determine mass loss as a function of temperature, examining the release of volatiles and residual carbon from the binders.

### 3.5 Gas chromatography coupled with mass spectrometry and a flame ionization detector

The equipment used for this analysis was a Thermo Scientific Trace 1310 GC with a TSQ 8000 Evo Triple Quadrupole Mass Spectrometer and Ionization Flame. This test was used to analyze PAHs from CTP, ECTP, and PBB, and free phenol and formaldehyde from PNR, which according to the literature[5-11] are the most common compounds analyzed in this type of binders to check their hazardousness.

For the determination of the content of PAHs, about 100 mg of the binder samples were extracted with a mixture of tetrahydrofuran/toluene (4: 6 ratio) using bath ultrasonics. The samples were then filtered, and an aliquot was taken for purification by solid phase extraction (SPE) using the dichloromethane/pentane mixture (4: 6 ratio). After the extraction step, the extracts obtained were subjected to analysis by gas chromatography with mass spectrometry (GC/MS) and flame ionization (FID) detectors. The following analytical standards were used for quantification of PHAs and process control: PAH standard solution, deuterated PAH internal standard solution (mixture of naphthalene d8 (NAP d8), acenaphthene d10 (ACE d10), phenanthrene d10 (PHE d12), chrysene d12 (CHR d12) and perylene d12 (PER d12)) and decafluorobiphenyl (DBF) injection standard solution.

For the determination of the content of free phenol and formaldehyde, about 10g of the phenolic resin was extracted with diethyl ether after neutralization with concentrated sulfuric acid. After the extraction step, the extract obtained was subjected to analysis by GC/MS and FID. Phenol and formaldehyde standard solutions were used to quantify free phenol and formaldehyde in the sample.

# 4 RESULTS AND DISCUSSION

## 4.1 Brookfield viscosity

Table 2 gives the Brookfield viscosity of each binder analyzed in this study in mPa.s and % relative to the value at 30 °C. Some values could not be measured, because the viscosity was too low to be detected by the equipment. ECTP is the material with higher values and PBB with lower. Binders with higher viscosity have been reported for improving the plasticity of taphole clays, which gives longer and good texture inside the taphole under hot conditions, resulting in a stable mushroom (taphole clay wall formed inside the blast furnace hearth)[12]. However, it is well known that the viscosity is something that can easily be adjusted during the production of the binder according to the needs of the taphole clay producer.

Another important feature is that PNR showed a lower decrease in viscosity relative to the initial value measured at 30°C compared to the other binders. This behavior suggests that the plasticity of taphole clays produced with PNR should be less sensitive to temperature variations within the mudgun for this temperature range (30-90°C), which would increase plasticity stability over injections at different temperatures.

Tab. 2: Brookfield viscosity as a function of temperature of each binder in mPa.s and % relative to the value at 30 °C.

| Temperature (°C) | Brookfield viscosity (mPa.s) | | | |
|---|---|---|---|---|
| | CTP | ECTP | PBB | PNR |
| 30 | 1980 | 13860 | 1175 | 1645 |
| 40 | 708 | 2295 | 252 | 757 |
| 50 | 216 | 612 | 123 | 366 |
| 60 | 126 | 267 | * | 201 |
| 70 | * | 139 | * | 130 |
| 80 | * | * | * | * |
| 90 | * | * | * | * |
| Temperature (°C) | Brookfield viscosity (%) | | | |
| | CTP | ECTP | PBB | PNR |
| 30 | 100 | 100 | 100 | 100 |
| 40 | 36 | 17 | 21 | 46 |
| 50 | 11 | 4 | 10 | 22 |
| 60 | 6 | 2 | * | 12 |
| 70 | * | 1 | * | 8 |
| 80 | * | * | * | * |
| 90 | * | * | * | * |
| *Out of detection limit | | | | |

## 4.2 Curing test with parallel plate rheometer

The results from the curing test with a parallel plate rheometer can be seen in Figure 1. PNR presented a behavior that is significantly different from the other binders. Due to the curing of the novolac resin, there is a sharp increase in its viscosity at 128°C, whereas all other binders only show a significant increase in viscosity at temperatures above 300°C. This increase in viscosity is related to the curing of the binder and explains why resin-bonded taphole clays cure faster than tar-bonded clays, as reported by some authors[2, 12, 13].

ECTP presented an increase in viscosity in two steps. At 280°C the viscosity starts to increase, but at 313°C the values decrease and do not increase again until 343°C. The first complex viscosity increase (280 °C) is believed to be related to the release of volatiles from the solvents of the binder, while the decrease at 313 °C is probably related to the softening point of the pitch, which has been combined with the solvents to produce the binder. Pitch passes through a thermoplastic phase when heated to pyrolysis temperature[10, 14-16]. The increase in viscosity at 343 °C represents the final consolidation of ECTP in the solid state.

CTP and PBB showed an increase in viscosity in one step, starting at 367 °C for CTP and 316 °C for PBB. The petroleum based-binder starts its hardening process at a lower temperature when compared to the coal tar-based material, but it shows an improvement in hot plasticity when compared to the resin-based binder.

CTP is the binder that can keep its liquid form for a longer time and comparing its behavior with PNR, the differences in the properties of the taphole clays with these two binders are better understood. During and after plugging, pitch-bonded taphole clays are able to maintain plasticity for a longer period of time as they are heated (slow curing process), while resin-bonded mixes have a faster curing process that leads to a rapid loss of plasticity[2, 12, 13]. These characteristics improve injectability of pitch-bonded material, but at the same time increase the chance of having gas pocket over drilling and unstable flow of hot metal and slag from the blast furnace over tapping if time between taps is short[13, 17].
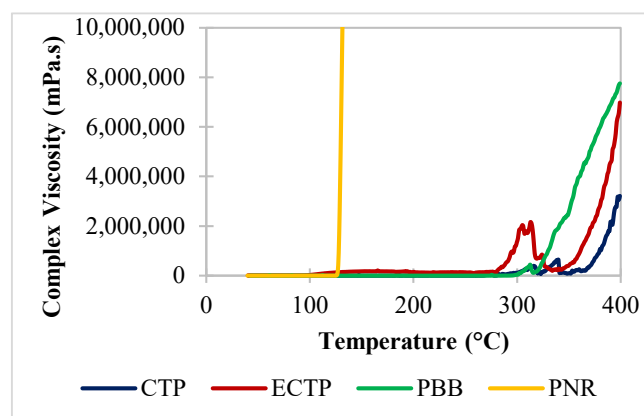


Fig. 1: Curing test with parallel plate rheometer results with each binder.

## 4.3 Thermogravimetric analysis

Figure 2 shows the results for TGA of each binder sample over heating in a non-oxidizing atmosphere. The most important information analyzed from the graph was the final residual carbon at 800 °C and the way that volatiles were released for each binder.

With greater residual carbon, higher corrosion resistance is expected, as higher amount of carbon that has low slag wettability[18] fills the porous of the refractory. The order of products that had more residual carbon from highest to lowest is PNR (38.0 %), ECTP (26.0 %), CTP (18.0 %) and PBB (11.2 %). Thus, although this is not the only binder property to affect corrosion resistance, higher resistance to hot metal and slag attack is expected for the taphole clays produced with the binders containing higher residual carbon. The lower capacity of carbon fixation of petroleum-based binders that was reported by some authors[10] was also seen in this TGA analysis.
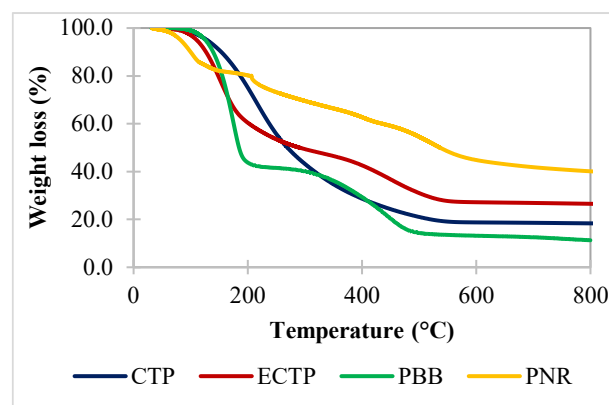


Fig. 2: TGA results for each binder analyzed in a non-oxidizing atmosphere.

255

Regarding volatiles release behavior, it is known that the release of these gases in lower temperatures together with fast curing favors crack formation in taphole clay mushroom[2]. Figure 3 shows the derivative of the curves from the TGA test, and PNR, as expected, was the binder that showed the first peak of weight loss at a lower temperature (103 °C), followed by ECTP (152 °C), PBB (175 °C) and CTP (216 °C). Since PNR also has fast curing, a taphole clay with this resin would be more subjected to crack formation due to gas release pressure in a structure that is already solid.
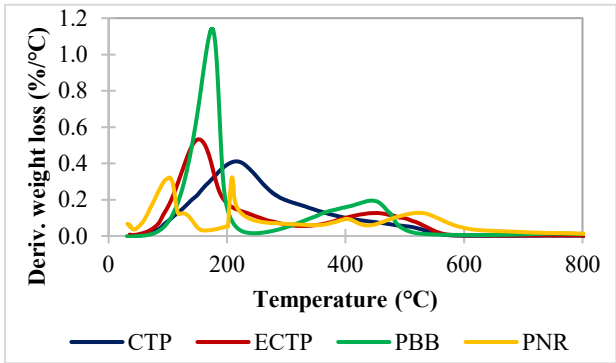


*Fig. 3: Derivative from TGA results with each binder analyzed in a non-oxidizing atmosphere.*

### 4.4 Gas chromatography coupled with mass spectrometry and a flame ionization detector

The results from GC/MS are presented in Table 3 and Table 4. PAHs were analyzed for CTP, ECTP and PBB and free-phenol and formaldehyde were analyzed for PNR. As expected, CTP is the binder with the highest amount of BaP (611 ppm) associated with a high level of total PAHs (38428 ppm), which makes it more harmful to human health. Although BaP from CTP is much lower than what has been found in the literature (10000-15000 ppm[10]), it is still higher than 50 ppm, which is the limit for not being considered a dangerous working material according to TRGS 551[7].

Tab. 3: PAHs of CTP, ECTP and PBB analyzed by GC/MS.

| PAH (ppm) | CTP | ECTP | PBB |
|---|---|---|---|
| Naphthalene (NAP) | 9771 | 7708 | 0 |
| Acenaphthylene (ACY) | 66 | 296 | 44 |
| Acenaphthene (ACE) | 5707 | 13141 | 32 |
| Fluorene (FLU) | 2594 | 3242 | 10 |
| Phenanthrene (PHE) | 7707 | 3300 | 157 |
| Anthracene (ANT) | 1289 | 503 | 275 |
| Fluoranthene (FTL) | 3971 | 5801 | 7 |
| Pyrene (PYR) | 3104 | 4115 | 42 |
| Chrysene (CHR) | 577 | 425 | 27 |
| Benzo[a]anthracene (BaA) | 628 | 462 | 25 |
| Benzo[j]fluoranthene (BjF) | 788 | 367 | 12 |
| Benzo[k]fluoranthene (BkF) | 158 | 90 | 9 |
| Benzo[b]fluoranthene (BbF) | 292 | 159 | 22 |
| Benzo[e]pyrene (BeP) | 380 | 198 | 15 |
| Benzo[a]pyrene (BaP) | 611 | 289 | 16 |
| Indeno[l,2,3-cd]pyrene (IND) | 358 | 156 | 18 |
| Dibenzo[a,h]anthracene (DahA) | 114 | 58 | 8 |
| Benzo[g,h,i]perylene (BghiP) | 313 | 165 | 20 |
| **Total** | 38428 | 40475 | 739 |

Tab. 4: Free-phenol and formaldehyde of PNR analyzed by GC/MS.

| Compound (%) | PNR |
|---|---|
| Phenol | 0.82 |
| Formaldehyde | N.D. |
| ***N.D.: Not detected*** | |

ECTP showed better values for BaP (289 ppm), but was still higher than 50 ppm. Besides that, the total PAHs of ECTP (40475 ppm) was the highest, which makes it a reasonably hazardous material. The only binder with less than 50 ppm BaP and low total PAHs was PBB, which had 16 ppm BaP and 739 ppm total PAHs. As expected, based on literature review[10-11], PBB contains much lower levels of PAHs than conventional coal tar pitch.

Similar to PBB, PNR showed GC/MS results (Table 4) of a binder with a lower risk to human health. Some standards classify the resins containing more than 5 wt. % of free-phenol as toxic[19], and PNR contains only 0.8 % of free-phenol, with no amount of formaldehyde detected by the equipment.

### 4.5 Key binder properties for taphole clay application

With all results that were presented and discussed for binder characterization it was possible to define some parameters that would be important to evaluate in binders for taphole clays and the expected taphole clay properties that would be influenced by these binder characteristics. Table 5 shows the description of each of these parameters and the influenced taphole clay properties. It is always important to check the behavior of the binder mixed in the taphole clays, but a first analysis of the pure binder can already show important information about the expected behavior in the final refractory, which could be useful e.g., when searching for new binders to be used in taphole clays.

Table 6 presents a summary of the results obtained for each studied binder and can be used as a reference for future studies. When thinking about substituting CPT for more eco-friendly options, ECTP is the most similar binder. PNR has much faster curing, which means that a taphole clay produced with it should require much more care over taphole plugging to avoid difficulties over injection and crack formation in the mushroom. On the other hand, PBB has low residual and for that reason less erosion and corrosion resistance are to be expected from the taphole clay produced with it.

Tab. 5: Important characteristics of binders for taphole clays.

| Property | Description | Influenced taphole clay properties |
|---|---|---|
| Viscosity at 50 °C | Brookfield viscosity measured at 50 °C. | Plasticity and texture inside the taphole. |
| Viscosity variation over temperature | Level of Brookfield viscosity variation measured from 30 to 90 °C. | Plasticity sensitivity to temperature variation within the mudgun. |
| Curing temperature | Binder hardening temperature during curing test with parallel plate rheometer. | Hardening speed during heating. |
| Residual carbon | Residue from TGA. | Erosion and corrosion resistance. |
| Beginning of weight loss | Temperature of the first peak of TGA derivative curve. | Tendency to crack formation inside the taphole. |
| Total PAH's | Sum of PAH's measured with GC/MS. | Toxicity. |
| BaP | BaP measured with GC/MS. | Toxicity. |
| Free phenol and formaldehyde | Free phenol and formaldehyde measured with GC/MS. | Toxicity. |

Tab. 6: Important characteristics of the analyzed binders for taphole clays.

| Property | CTP | ECTP | PBB | PNR |
|---|---|---|---|---|
| Viscosity at 50 °C | 216 | 612 | 123 | 366 |
| Viscosity variation over termperture | High | High | High | Medium |
| Curing temperature | 360 | 340 | 320 | 130 |
| Residual carbon | 18.0 | 26.0 | 11.2 | 38.0 |
| Beginning of weight loss | 216 | 152 | 174 | 103 |
| Total PAH's | 38428 | 40475 | 739 | N/A |
| BaP | 611 | 289 | 16 | N/A |
| Free phenol | N/A | N/A | N/A | 0.8 |
| Free formaldehyde | N/A | N/A | N/A | N.D. |

*N/A: Not applicable*

*N.D.: Not detected*

## 5 CONCLUSIONS

The conclusions are as follows:

(1) The analysis of the pure binders already contains significant amount of information regarding their expected behavior when added to taphole clays. With all results that were presented and discussed it was possible to define some parameters that would be important to evaluate in binders for taphole clays (viscosity at 50 °C, viscosity variation over temperature, curing temperature, residual carbon, beginning of weight loss, total PAH's, BaP, free phenol and free formaldehyde) and the expected taphole clay properties that would be influenced by these binder characteristics.

(2) Based on the results and discussion from binder characterization, ECTP is the material most similar to CTP. PNR has much faster curing, which means that a taphole clay produced with it should require much more care over taphole plugging to avoid difficulties over injection and crack formation in the mushroom. On the other hand, PBB has low residual and for that reason less erosion and corrosion resistance are to be expected from the taphole clay produced with it.

## 6 REFERENCES

[1] Oliveira, T., Silva, W., Bassalo, H., Ribeiro, A., Brito, M. Comparison between different taphole clays for metal tapholes of Fe-alloy reduction furnaces. In: UNITECR, 16, 2019, Yokohama, p. 640-643.

[2] Otsubo, Y., Ushijima, Y., Yonemoto, K., Kitazawa, Y. Development of taphole clay with new generation resin binder. In: UNITECR, 16, 2019, Yokohama, p. 540-543.

[3] Miyajima, S. Rheological behavior of organic binders for blast furnace taphole clay. In: UNITECR, 16, 2019, Yokohama, p. 11-14.

[4] Kim, T.W., Lee, J.H., Go, J.S., Kim, W.G. Development of high-performance eco-friendly tap-hole clay (THC) with carbonized organic matter. In: UNITECR, 16, 2019, Yokohama, p. 552-555.

[5] Wang, L., Yin, Y., Qiu, W., Liang, Y., Ruan, G., Zhao, L. Effects of pitch addition on the properties of environmental-friendly tap-hole clay. Journal of the Ceramic Society of Japan 125 (1), 2017, p. 12-18.

[6] Stendera, J.W., Hershey, R.A., Biever, G.G. Challenges to improving the environmental and health safety characteristics of tap hole clay. In: UNITECR, 13, 2013, Victoria, p. 445-449.

[7] Boenigk, W. et al. Pechstämmige Bindemittel für Feuerfest-produkte –Eigensschaften, Problemeund Perspektiven. In: FEUERFEST-SEMINAR (VDEH-SEMINAR 71/94), 1994, Bad Neuenahr.

[8] Zoglmeyr, G. Technical and environmental aspects of the use of phenolic resins in modern-day refractories. Interceram: Int. Ceram. Rev. 42, 1993, p. 145-149.

[9] Pagliosa, C. et al. Next MgO-C for steel ladle: Zero emission brick. In: AISTECH, 2017, Nashville, p. 3569-3575.

[10] Hampel, M.; Anerizis, G.C. Carbon-bonded refractories - characterization of interaction between binder and graphite. In: INTERNATIONAL COLLOQUIUM ON REFRACTORIES, 49, 2006, Aachen, p. 21-25.

[11] Dolmatov, L.V.; Kutukov, I.E.; Serkovskaya, G.S. Petroleum binders and impregnating materials - substitutes for highly toxic coal products. Chem. Tech. Fuels Oils 38 (2), 2002, p. 135-137.

[12] Ushijima, Y. et al. Taphole Clay for Blast Furnace. In: AISTECH, 2004, p. 187-193.

[13] Bassalo, H.C., Bittencourt, L.R.M. Massas de tamponamento para furos de corrida de altos-fornos - tipos, projeto de desenvolvimento e adequação às condições operacionais. In: XXXII SEMINÁRIO DE REDUÇÃO DE MINÉRIO DE FERRO, 32, 2002, Vitória, p. 349-357.

[14] Ewais, E.M.M. Carbon based refractories, J. Ceram. Soc. Jap. 112 (10), 2004, p. 512-532.

[15] Gardziella, A.; Pilato, L.A.; Knop, A. Phenolic Resins: Chemistry, Applications, Standardization, Safety and Ecology. 2. ed. rev. Germany: Springer, 2000. ISBN 978-3-642-08484-3.

[16] B. Rand, B. McEnaney, Carbon binders from polymeric resins and pitch, Part I - Pyrolysis behaviour and structure of the carbons, Brit. Ceram. Trans. J. 84, 5 (1985) 157-165.

[17] Mitsui, H., Toritani, Y., Yamane, T., Yamasaki, S., Ogushi, Y., Kawakami, T. Recent developments in tap hole mud for blast furnaces. In: INTERNATIONAL COLLOQUIUM ON REFRACTORIES, 31, 1988, Aachen, p. 98-102.

[18] Cooper, C.F. Chemistry and Industry. 18. ed., 1982, 678 p.

[19] LUZ, A.P. et al. Thermosetting resins for carbon-containing refractories: Theoretical basis and novel insights. Open Ceramics, [S. l.], v. 3, p. 1-22, 2020.

# IMPROVEMENT OF AL$_2$O$_3$–SIC–C BRICKS OF THE HOT METAL LADLE

Kazuma Hashimoto, Koji Yamada, Yasuhiro Yamada
Nippon Steel Corporation, Tokyo, Japan

Shinsaku Takahara and Katsuhiro Ishimoto
Krosaki Harima Corporation, Fukuoka, Japan

## ABSTRACT

The life of hot metal ladles was short at Nagoya Works, Nippon Steel, because Al$_2$O$_3$–SiC–C bricks at the ladle sidewall fell in the last stage of operation. The falling of the bricks was caused by the damage to the joints of the bricks, whereas parts other than the joints were not damaged. We investigated used sidewall bricks to understand the mechanism of joint damage. We developed a new Al$_2$O$_3$–SiC–C brick. The investigation of the used bricks revealed that the molten slag infiltrated the joint mortar and corroded the mortar and brick. Furthermore, the molten slag infiltrated through the cracks caused by the lack of residual expansion of the bricks. Therefore, we applied a new expansible raw material to the Al$_2$O$_3$–SiC–C brick to control residual expansion. Laboratory evaluation confirmed that the developed brick exceeded conventional bricks in terms of residual expansion and corrosion resistance. We adopted the developed brick to hot metal ladle sidewall. Consequently, the life of hot metal ladle was increased by 20%, and the refractory cost was reduced by 17 %.

## BACKGROUND AND PURPOSES OF IMPROVEMENT ACTIVITIES

### Role of hot metal ladle in Nagoya Works

Hot metal transported from a blast furnace by a torpedo car is poured into a hot metal ladle along with a small amount of blast furnace slag. After charging the hot metal into the optimizing refining process (ORP) converter furnace, the Si, P, and S components are removed. Subsequently, the hot metal is recharged into another convert furnace for decarburization. In this steel refining process, a hot metal ladle is used as a transport vessel for hot metal from a torpedo car to an ORP converter furnace.

### Refractory relining specifications and repair pattern of hot metal ladle

The specifications of the hot metal ladle refractory relining are shown in figure 1. The free board and slag line portions of the hot metal ladle wall are relined with Roseki (pyrophyllite)–SiC bricks that are characterized by high durability against the mechanical impact caused by the demolishing work of the adhering metal. The metal line portion of the hot metal ladle is relined with Al$_2$O$_3$–SiC–C bricks (hereinafter referred to as ASC bricks) with superior erosion resistance against blast furnace slag. Among the five (5) hot metal ladles, three (3) ladles are generally operated, with one (1) ladle on stand-by and another one (1) ladle under refractory maintenance repair. In refractory maintenance repair, all wear bricks are newly relined after approximately 2000 heats of operation at the end of their service life without any intermediate repair work.
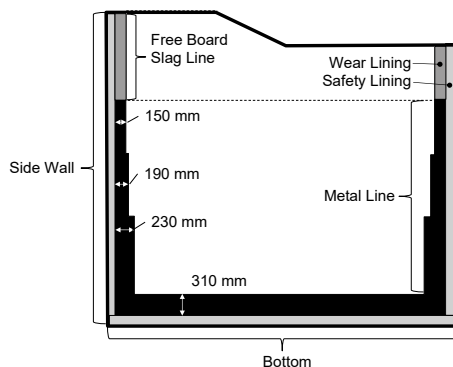


*Fig. 1: Hot metal ladle relining specifications.*

### Confronting issues of hot metal ladle refractory

Figure 2 shows the surface appearance of the wear bricks in a hot metal ladle that was scheduled for the entire refractory repair work after 2060 heats of operation. Localized wear at the brick joints is clearly observable. When the localized wear at the brick joints is further advanced, the worn bricks drop off owing to the deficiency of mutual support by wedges. Because of this wear pattern, worn bricks must be relined before they are completely outworn; in other words, under the condition in which a relatively large amount of thickness remains in their major portion, the service life of hot metal ladles is insufficient. In addition, irregularities in the surface appearance of worn bricks because of this wearing pattern make it difficult to detect the exposure of permanent bricks caused by the dropping off of worn bricks that may lead to a possible risk of hot metal leakage. Under the aforementioned circumstances, a series of improvement activities is performed to achieve cost reduction of a hot metal ladle refractory by suppressing localized wear at brick joints and minimizing hot metal leakage incidents by introducing a temperature monitoring system on the hot metal ladle steel shell.



*Fig. 2: Surface appearance of wear bricks at 2060 heats of service life.*

## SERVICE LIFE EXTENSION OF HOT METAL LADLE

### Quantitative wear measurement with 3D profile meter

As a first step in the investigation of the wear mechanism, a quantitative measurement of the wear amount of the wear bricks at various relining positions was performed. In the past, the remaining thickness was measured using a rule on used worn bricks retrieved from several relining positions of a hot metal ladle when its refractory maintenance work was scheduled. Because this manual measurement was time-consuming and measuring all relined wear bricks was difficult, three-dimensional (3D) profile meter (hereinafter referred to as PFM) using a lazar ray was introduced. The major specifications of the introduced PFM are listed in table 1. The PFM was set in a refractory maintenance yard for the profile

Tab. 1: Specifications of 3D profile meter system (PFM) for hot metal ladle refractory.

| Item | General Specification |
|---|---|
| Type | Mobile |
| Scannning time | 15 min |
| Range | 35 m (max.) |
| Measurement accuracy | ±5 mm |

measurement of hot metal ladles and other hot metal and molten steel transport vessels under cooled down conditions. The profile measurement of one transport vessel with $+/-$ 5 mm of measurement accuracy took 15 min. With prior profile measurements of the permanent brick surface of the transport vessel, measurement errors caused by steel shell deformation can be cancelled and corrected. In short, the introduced PFM enabled quick quantitative profile measurements of wear bricks relined in all transport vessels for hot metal and molten steel.

**Investigation study on wear mechanism**
First, the wear pattern of wear bricks, that is, the influence of the relined position on the wear amount, was investigated on a hot metal ladle whose refractory maintenance was scheduled after 2060 heats of operation. A vertical wear pattern profile of the hot metal ladle refractory measured with the PFM is shown in figure 3, along with the typical remaining thicknesses of the wear bricks and the calculated wear rate at major portions. The thinnest remaining
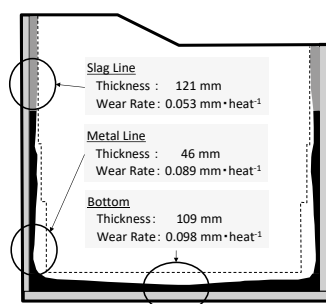


*Fig. 3: Vertical wear profile of hot metal ladle refractory at 2060 heats of service life.*

thickness of the wear bricks was observed at the metal line in the lower part of the side wall with 46 mm of remining thickness. Notably, owing to the smallest remaining thickness, wear bricks relined at the metal line in the lower part of the side wall tended to drop off and regulate the service life of the entire hot metal ladle refractory. The most severe wear rate was observed at the ladle bottom, followed by at the lower part of the side wall, where wear bricks were subjected to a relatively strong impact by hot metal discharged from the torpedo car along with the blast furnace slag. The lowest wear rate was observed at the slag line. Second, used wear bricks relined at the metal line in the lower part of the side wall, by the wear amount at which the service life of the hot metal ladle refractory is generally regulated, were closely observed. The cross section of a wear brick retrieved from the lower part of the side wall is shown in figure 4. The sampled wear brick exhibited a smooth hot
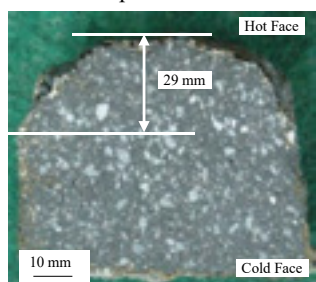


*Fig. 4: Cross section of a used conventional wear brick.*

surface without internal cracks or peel-off damage. However, localized wear was clearly observed on both sides of the brick, namely, at both brick joints, with a considerably larger wear amount than that at the center position by 29 mm. Therefore, the symmetrical localized appearance of brick wear at both brick joints was not caused by corner cracks initiated by the wedge effect between adjacent relined bricks. Figure 5 shows a microstructure image obtained by electron probe micro analyzer (EPMA), and element distribution mapping of the brick joint area. The hot face of the wear brick corner was eroded by the slag, and the erosion depth at the left-side brick corner was greater than that of the mortar adhering to the
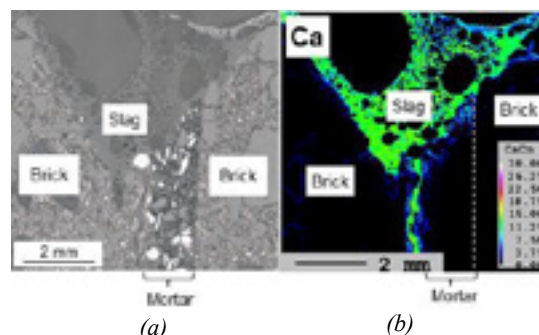


*Fig. 5: Microstructure of a wear brick near the joint area.*
*(a) Optical reflecting micrograph.*
*(b) EPMA analysis.*

right-side brick. Slag penetration into the gap generated between the mortar and wear brick was observed with Ca element mapping. This slag penetration inferred that joint breakage occurred during the hot metal receiving operation. Based on the aforementioned results, the wear mechanism schematically illustrated in figure 6 can be inferred. First, the mortar was forcibly shrunken by expanding the wear bricks during the hot metal receiving operation. When the temperature was reduced after hot metal discharge, joint breakage occurred because of the insufficient permanent linear expansion of the wear bricks to compensate for the forcibly shrunken mortar. During subsequent hot metal reception, the slag could penetrate the gaps generated by mortar breakage. In association with the deepening of depressions at localized eroded brick joints, turbulence in hot metal and/or slag flow at brick joints became increasingly prominent, accelerating localized erosion. This inferred wear mechanism concluded that imparting sufficient permanent linear expansion to wear bricks and improving their erosion resistance were effective. Precedent studies [1–3] reported that localized wear at brick joints was suppressed by improvement of permanent linear expansion of bricks. Focusing on the aforementioned two characteristics of hot metal ladle wear bricks, improved wear brick materials were developed.
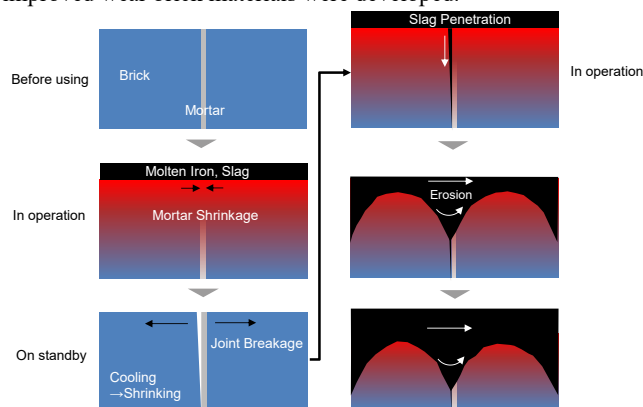


*Fig. 6: Presumed mechanism for localized wear at the brick joint.*

**Development of a new wear brick material**
The specific value of permanent linear expansion at which localized wear at the brick joints was sufficiently suppressed was examined. The specific value of permanent linear expansion of the wear brick at which joint breakage can be prevented can be calculated using Equation (1).

Permanent linear expansion [%] >100×(Joint thickness [mm]×Permanent linear expansion of mortar [%]/100)/Wear brick dimension [mm]                    (1)

When inserting specific figures for a practical operation, namely, 2 mm of mortar thickness, 66 mm of short side dimension of wear brick, and 30 % of permanent linear expansion of mortar, into equation (1), 0.91 % of critical value for permanent linear expansion of wear brick is calculated. To achieve this specific value of

259

permanent linear expansion, new wear brick materials were developed. Two types of wear brick materials, sample materials 1 and 2, onto which sufficient permanent linear expansion and improved erosion resistance were imparted, were developed. The

Tab. 2: Blending compositions of new ASC sample materials.

| | | Conventional | Sample1 | Sample2 |
|---|---|---|---|---|
| Chemical composition / mass% | Al$_2$O$_3$ | 55 | 47 | 56 |
| | SiO$_2$ | 19 | 27 | 18 |
| | SiC | 8 | 8 | 8 |
| | C | 15 | 15 | 15 |
| Expansible material index / - | A | a | 1.5a | - |
| | B | - | - | b |

blend compositions of sample materials 1 and 2 are summarized in table 2. An increase in the permanent linear expansion of sample material 1 was intended by increasing the added amount of expansive raw material A. However, another expansive raw material, B, was applied for sample material 2. To ensure the oxidation resistances of the brick material, blend compositions of SiC and C applied to conventional wear bricks were adopted for the two types of sample materials. The permanent linear expansion, thermal spalling resistance, and erosion resistance of the sample materials were evaluated, along with those of conventional wear bricks. The permanent linear expansions of the three types of refractory materials were measured with differential refractoriness under a load test. Sample specimens under 0.2 MPa of constant load were heated up to and maintained at 1400 °C for 3 h, and to prevent oxidation, internal atmosphere of the furnace was substituted with Ar gas on a steady basis, followed by gradual cooling. After complete cooling, the dimensions of the sample specimens were measured to calculate the permanent linear expansion. The comparative test results are shown in figure 7. Compared with the target value of 0.91 %, the
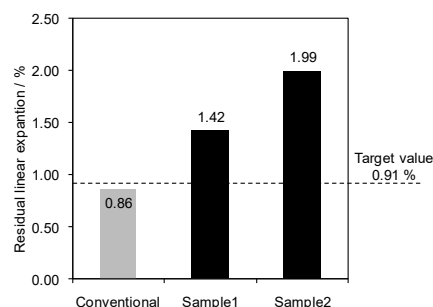


Fig. 7: Comparison of permanent linear expansion.

conventional wear brick exhibited a permanent linear expansion of 0.86 %. In contrast, sample materials 1 and 2 exhibited permanent linear expansions of 1.42 % and 1.99 %, respectively, that were sufficiently larger than the target value.

The erosion resistances of three types of refractory materials were evaluated with a rotary erosion test, in which sample specimens were eroded by an erosive agent with 1.1 basicity (C/S) at 1500 °C for 1 h. After repeating the erosion test five times, the amount of erosion was measured to calculate the erosion index. The erosion test results are shown in figure 8, where an erosion index of 100 represents the conventional wear brick. Compared with the conventional wear
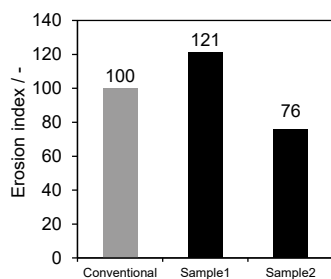


Fig. 8: Comparison of the erosion index observed in the erosion.

brick, sample material 1 exhibited a worse erosion index of 121, whereas sample material 2 exhibited a better erosion index of 76.

Thermal spalling resistances of three types of refractory materials were evaluated by repeating a spalling test 10 times. In that test, cubic sample specimens, with 50 mm on a side, were rapidly heated by inserting into an electric furnace whose inner temperature was maintained at 1200 °C for 15 min, followed by water cooling for 5 min. After a series of thermal spalling tests, the total length of the cracks initiated in the sample specimen was measured to calculate the crack length index that was normalized with 50 mm of a side length. Figure 9 presents a comparison of the crack length indices of the sample specimens. Both sample materials 1 and 2 exhibited superior thermal spalling resistance to the conventional wear brick. In conclusion, sample material 2 was definitely superior to the conventional wear brick in all the characteristics required for hot metal ladle relining. Based on this conclusion, a practical application of the wear brick made of sample material 2 was conducted.
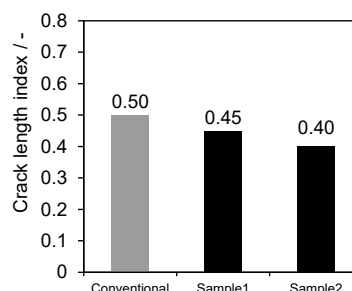


Fig. 9: Comparison of the crack length index observed in the thermal spalling test.

**Practical application of the newly developed wear brick**

Wear bricks made of sample material 2 were relined in the lower part of the side wall in the hot metal ladle, by wear amount at which the service life of hot metal ladle is generally regulated. The surface appearances and a cross section of new wear bricks relined in the lower part of the side wall in the hot metal ladle that operated for the 1978 heats of hot metal transportation, are shown in figure 10 and figure 11, respectively. As shown in figure 11, the localized wear depth at the brick joints was reduced to 11 mm from 29 mm in conventional wear bricks. Despite the significant permanent linear expansion of the new wear brick, no corner cracks caused by the



Fig. 10: Surface appearance of new ASC wear bricks at 1978 heats of service life.
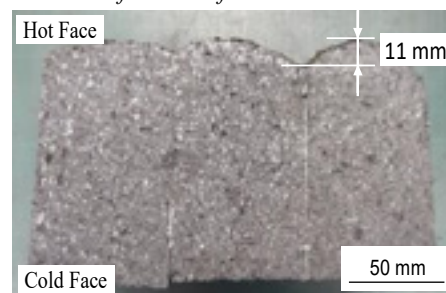


Fig. 11: Cross section of the used wear brick made of sample material 2.

wedge effect were observed. Owing to the suppression of localized wear at the brick joints, as shown in figure 12, the wear rate of the new wear brick improved by 31 %. Consequently, as shown in figure 13, the average service life of the hot metal ladle relined with the new wear bricks was extended by approximately 20 %, and the unit refractory cost consumption was reduced by 17 %.
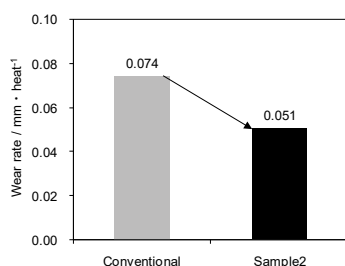


*Fig. 12: Comparison of the wear rates of conventional and sample2.*
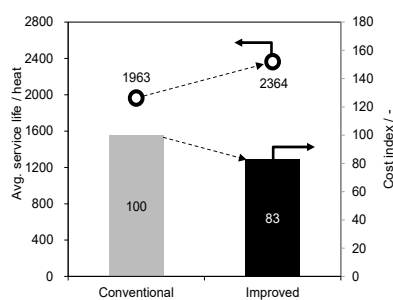


*Fig. 13: Change in the hot metal service life and unit cost consumption index.*

## INTRODUCTION OF MONITORING SYSTEM ON HOT METAL LADLE

### Confronting issues of online hot metal ladle inspection

Despite the suppression of localized wear at brick joints, a new wear brick surface in a hot metal ladle is still accompanied by irregularities; hence, the exposure of permanent bricks can be overlooked during visual inspection. Therefore, a hot metal ladle monitoring system was introduced to improve the accuracy of the hot metal ladle management system. Online maintenance on a hot metal ladle has been conventionally performed by combining visual inspection of the brick surface appearance by an operator and careful weight management, but the maintenance accuracy is unsatisfactory, and relatively large scattering exists. By introducing a ladle steel shell temperature monitoring system, which is broadly applied for teeming ladles, an improvement in the daily hot metal ladle maintenance accuracy was achieved.

### Introduction of the Steel Shell Temperature Monitoring System

The layout of the hot metal ladle steel shell temperature monitoring system is shown in figure 14. A set of observed thermal images is shown in figure 15. The entire sidewall of the hot metal ladle steel shell was monitored using three (3) cameras, and the ladle bottom was monitored using one (1) camera. A monitoring display was placed in the operating room to monitor the photographed thermal images at any time. When the photographed steel shell temperature exceeded a threshold value, a warning light was automatically activated along with an alarm sounding. As supposed steel shell temperature at 50 mm of remaining thickness of relined wear brick in hot metal ladle, 400 °C and 350 °C were set as threshold values for the sidewall and bottom, respectively. In accordance with the information provided by the steel shell temperature monitoring system, hot metal ladle refractory maintenance could be scheduled before exposure of the permanent brick without the risk of hot metal leakage incidents.
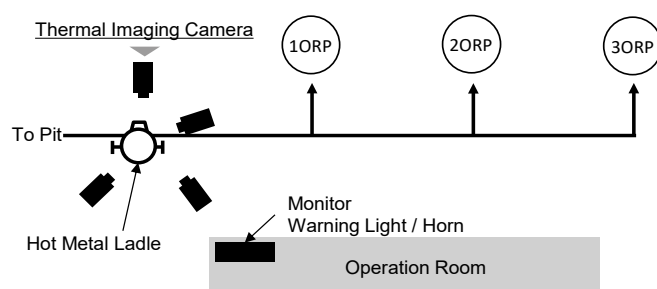


*Fig. 14: Layout of the hot metal ladle steel shell temperature monitoring system.*
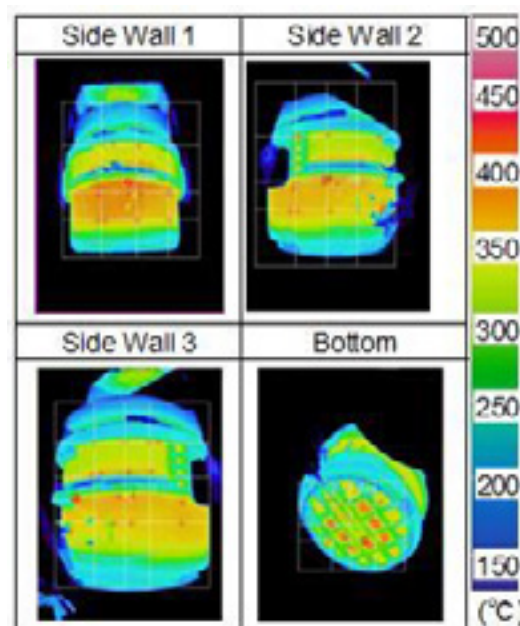


*Fig. 15: Thermal images of hot metal ladle steel shell.*

## CONCLUSIONS

With a series of activities for extending the service life of the hot metal ladle in Nagoya Steel Works, the following performances were achieved.

1. By utilizing a 3D PFM, precise measurement of the remaining thickness of wear bricks relined in a hot metal ladle was enabled.
2. The mechanism of localized wear at the brick joints was clarified by investigating the damage patterns of wear bricks relined in a hot metal ladle.
3. A New ASC brick with a sufficiently large permanent linear expansion and improved erosion resistance was developed and applied in practical operation. Owing to the suppression of localized wear at the brick joints materialized by the newly developed ASC brick, the service life of the hot metal ladle was extended by 20 %, with a 17 % reduction in unit refractory cost consumption.
4. By introducing a hot metal ladle steel shell temperature monitoring system, the concern of hot metal leakage incidents was almost eliminated.

## REFERENCES

1) Sato, T., Shintani, H., Kawakami, T. *Taikabutsu*. 41 (11), 1989, 594
2) Kataoka, K., Sato, T., Kifune, I. *CAMP-ISIJ*, 5, 1992, 237
3) Taira, H., Nakao, A., Nakamura, Y., Matsui, T. *Taikabutsu*, 47 (8), 1995, 405
Figure 1-15 and table 1, 2 are reproduced from the proceedings of The 7th Symposium on Refractories for Iron and Steel, 2019, 38-47 with the permission of the owner.

261

# REDUCTION OF HEAT LOSS IN STEELMAKING PROCESS

Kai Taniguchi *, Yuta Hino, Hisahiro Matsunaga
JFE Steel Corporation

## Abstract

In JFE Steel Chiba Works, torpedo car has been used to transport hot metal from the blast furnace to the steelmaking workshop. In many cases, the hot metal pre-treatment has been used by the flux injection to the hot metal in torpedo car to remove impurities such as Si and P. During pre-pretreatment, the liquid slag was adhered on the wear bricks at the roof of torpedo car. As a result, the bricks were corroded.

In order to extend the service life of the torpedo car refractory, the upper part of the outer steel shell of the torpedo car was cooled with water mist to reduce the brick corrosion rate.

At first, a heat transfer analysis was conducted to verify the effect of the reduction of the brick surface temperature by cooling the steel shell.

Secondary, rotary slag test was performed to evaluate the influence of the brick surface temperature on the brick corrosion rate.

Based on the above investigations, an experiment, in which the upper part of the outer steel shell was cooled with mist, was conducted.

## 1. Introduction

Torpedo car is the vessel to carry out the pretreatment as well as to transport hot metal from the blast furnace to the converter. The wear of the roof brick has been severe. Since the liquid slag was adhered on the wear bricks at the roof of torpedo car during pretreatment. As a result, the bricks were corroded. **Fig.1** shows a schematic diagram of the damage morphology of roof bricks. The roof bricks are heated by post combustion flame.

In this study, a technology to reduce the wear rate of the roof bricks by cooling the steel shell with water mist was developed.
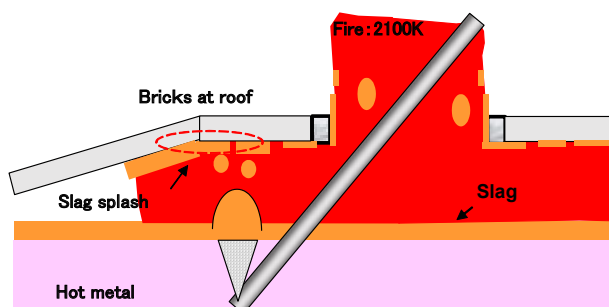


**Fig. 1 Schematic diagram of the damage morphology of roof bricks**

## 2. Heat transfer analysis
### 2.1 analysis condition

A two-dimensional unsteady heat transfer analysis was performed to evaluate the effect of cooling. The general structural analysis code MARC 2008 r1 was applied to the treatment of the cross section of the torpedo car as a 1/2 symmetrical model.

As an improvement to reduce the hot face temperature of wear brick, the following two methods were thought. The one was to make the safety lining bricks material higher conductivity by changing the refractory lining. The another was to cool the steel shell forcibly. Regarding the improvement of the thermal conductivity of safety lining bricks, there is a concern that the deformation of the safety lining bricks may occur due to the increase of the temperature. Therefore, two cases of simulation were conducted, namely the wear bricks had full thckness and 0 mm. It was thought that this might cover all the refractory linings of the torpedo car in operation. **Table 1** shows analysis cases.

In addition to the case of the combination of safety lining bricks and castable, the case of the combination that the safety lining brick material was the same as the wear bricks were evaluated. The thickness of the wear brick was assumed as the two cases; an initial thickness and 0 mm. **Fig. 2** shows the refractory lining of torpedo car. The material properties specified thermal conductivity, specific heat and density for each temperature. The thermal conductivity of the hot metal is given by taking the stirring of the hot metal into consideration in order not to decrease the temperature due to the radiation.

It was assumed that that the torpedo car was operated in a single cycle of empty, hot metal tapping, transportation, pretreatment, transportation, and discharge. Here, it was assumed that hot metal should be taken a radiant heat source, and the convection heat transfer by the contact with hot metal could not be negligible.

The boundary conditions were set by dividing into 3 conditions: empty, with hot metal (hot metal tapping, transportation, and discharging), and conducting pretreatment. Steel shell cooling was performed in the process of pretreatment. Heat transfer from the outside surface of the steel shell was estimated to be $1,000 \text{W} \cdot \text{m}^{-2} \cdot \text{K}^{-1}$ as the heat transfer coefficient of the steel shell when cooled with water [1]. The heat transfer coefficients and ambient temperature were determined in each case.

Heat transfer calculations were repeated up to five cycles until the temperature stabilized.

| | Safety brick material | Cooling of steel shell | Thickness of wear brick |
|---|---|---|---|
| CASE 1 | Conventional | None | Initial brick |
| CASE 2 | Conventional | Done | |
| CASE 3 | High thermal conductivity | None | |
| CASE 4 | High thermal conductivity | Done | |
| CASE 5 | Conventional | None | 0mm |
| CASE 6 | Conventional | Done | |
| CASE 7 | High thermal conductivity | None | |
| CASE 8 | High thermal conductivity | Done | |

**Table 1 Analysis case for heat transfer.**
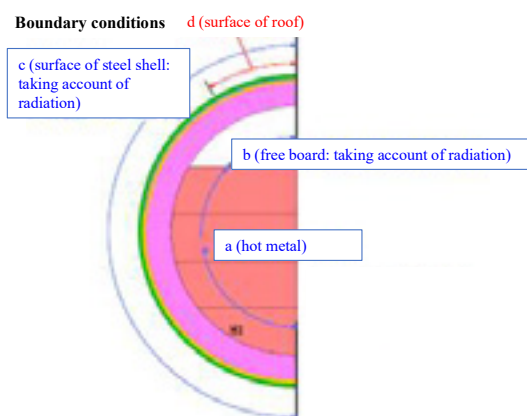


**Fig. 2 Schematic diagram of lining.**

## 2.2 Result of heat transfer analysis

The steel shell temperature distribution was obtained by heat transfer analysis. **Fig. 3** shows the change of temperature with time in the CASE 1,2,3 and 4 at the new wear brick. When CASE 1 was compared with CASE 3, the maximum temperature of the barks increased from about 450 K to 550 K because the thermal conductivity of the safety lining bricks became higher. Comparing CASE 4 with CASE 3, the temperature of the iron skin increased during the period from the completion of the pre-treatment to the discharge in all cases and the maximum temperature was shown just before the discharge although the temperature of the iron shell in the pre-treatment decreased due to the cooling of the steel shell. Although the figure doesn't show in this manuscript, the calculation has been done in the case that the work block was worn. The maximum temperature of the CASE 7 without cooling in the linings with modified safety lining bricl materials was 928 K, and even the case of the CASE 8 in which the steel shell was cooled could only be lowered to 913 K. The steel shell of the torpedo boat is made of heat-resistant steel and has a maximum endurance temperature of 723 K. When the torpedo car was used with worn wear bricks, deformation of the steel shell might occur.

Therefore, it could be difficult to detect the exposure of safety lining bricks by visual inspection. Therefore, the use of the wear brick material as safety ling brick was given up.

Next, the change of the hot surface temperature of refractory is shown in **Fig. 4**. The hot surface temperature reduction effect by the steel shell cooling by 7.4 K (in the case of new brick) and 20.6 K (in the case of worn brick) were obtained in 1 cycle on average. If the average thickness of worn bricks in torpedo cars is assumed to be 2/3 of the thickness of new bricks, the effect of lowering the thermal surface temperature of worn bricks can be expected to be 11.8 K.
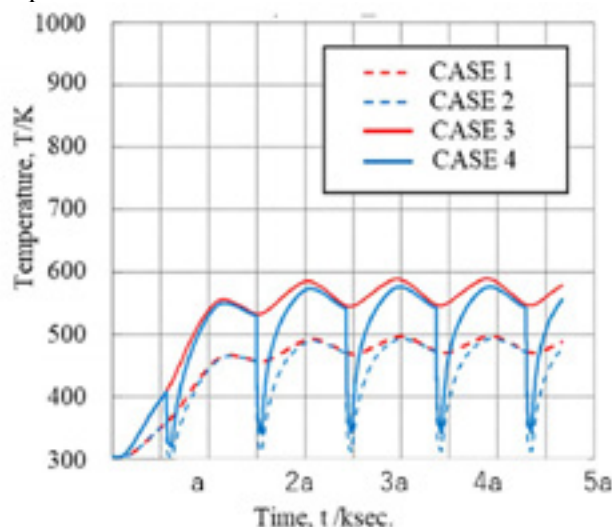


**Fig. 3    The steel shell temperature.**
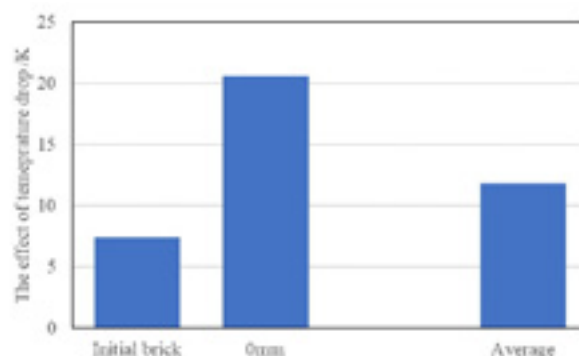


**Fig.4 The estimated result of temperature drop.**

## 3. Rotary Slag Testing
### 3.1 experimental procedure

A rotary slag test was caried out to evaluate the temperature dependence of the corrosion rate. Two kinds of safety lining bricks were prepared, and the same wear bricks were evaluated. To raise the hot face temperature, the safety lining refractory and a high-performance insulating material were used behind wear brick as a role of insulation and, and to lower the hot face temperature, an MgO-C brick was used behind wear brick.

263

Temperature and time for the test were 2073K × 4 h, and the slag was changed every one hour. The surface temperature was measured with a radiation thermometer during the test. The corrosion rate was calculated by dividing the difference in refractory thickness before and after the experiment by the experimental time.

### 3.2 Result and discussion of rotary slag testing

Considering the corrosion rate obtained in the rotary slag test, when the thermal conductivity of the backside was higher, the surface temperature was lower, and the wear rate was also lower.

The corrosion rate was evaluated assuming the mass transfer of alumina in the slag should be the rate controlling step by using the following equations expressed with Eqs(1) to (6). [2]

$$J = \left(\frac{D}{\delta}\right) \cdot (N_s - N_b) \tag{1}$$

$J$: mass flux $(g \cdot cm^{-2} \cdot s^{-1})$
$D$: diffusion coefficient $(cm^2 \cdot s^{-1})$
$\delta$: the thickness of boundary layer (cm)
$N_s$: saturated alumina content $(g \cdot cm^{-3})$
$N_b$: alumina content in liquid slag $(g \cdot cm^{-3})$

$$\rho \cdot B_f \left(-\frac{dr}{dt}\right) = B_f \cdot J \tag{2}$$

$\rho$: density of refractory $(g \cdot cm^{-3})$
$B_f$: interfacial area $(cm^2)$

$$V = k \frac{\rho_b}{\rho} \cdot \frac{\Delta(Al_2O_3)}{100} \tag{3}$$

V: corrosion rate of refractory $(m \cdot s^{-1})$
$\rho$: density of refractory $(g \cdot cm^{-3})$
$\rho_b$: density of liquid slag $(g \cdot cm^{-3})$
$k$: mass transfer coefficient $(m \cdot s^{-1})$

$$k = \frac{D}{\delta} \tag{4}$$

$$k = exp\left(-\frac{E_k}{RT}\right) \tag{5}$$

A: constant $(m \cdot s^{-1})$
$E_k$ : apparent activation energy $(J \cdot mol^{-1})$
R: gas constant $(=8.31 \ J \cdot mol^{-1} \cdot K^{-1})$

$$ln \ k = ln \ A - \frac{E_k}{RT} \tag{6}$$

The density $\rho$ of the refractory was measured from a sample taken from the hot surface side of the brick after usage. The density of the molten slag $\rho_b$ was obtained from the literature. [3] The saturated $Al_2O_3$ concentration of the slag was calculated using

FACTSAGE 7.2®. The value of the corrosion rate obtained in the rotatory slag test was used for the evaluation of mass transfer coefficient.

The Arrhenius plot of the mass transfer coefficient k of the refractory is shown in **Fig.5**. Since a good linear relationship was confirmed, the apparent activation energy was calculated from the slope of the regression line. The apparent activation energy was determined as 367 kJ· mol$^{-1}$. This value was almost similar to the apparent activation energy of CaO-SiO$_2$-Al$_2$O$_3$ slag (338 kJ・mol$^{-1}$) obtained by the same method as the result of the rotary slag test[2]. Then, this relationship was extrapolated to the low temperature side, and the reduction effect of wear rate by the steel shell cooling was estimated. The hot surface temperature of wear brick in actual torpedo car was set as 1673 K, and when the steel shell was cooled, the operating surface temperature was set at 1661.2 K using the reduction of 11.8 K obtained from the heat transfer analysis in Chapter 2. As a result of calculating the effect of reducing the wear rate by cooling the steel shell, it was found that 20% of the wear reduction effect could be expected.
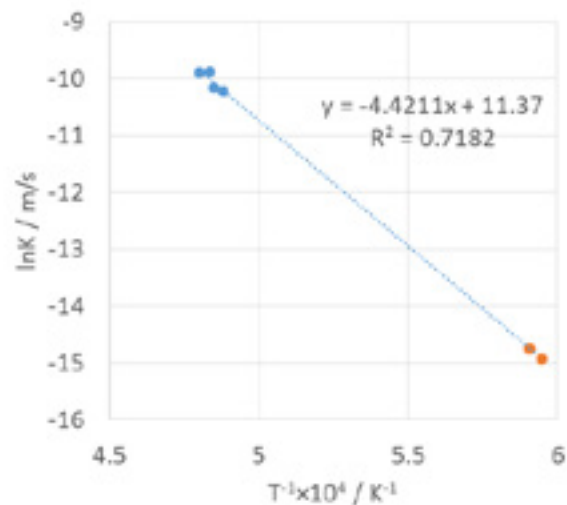


**Fig. 5 The Arrhenius plot of the mass transfer coefficient k of the refractory.**

### 4. Demonstration experiment
### 4.1 experimental procedure

A water-cooling system for the Torpedo car was installed in hot metal pre-treatment centre in JFE Steel Workshop. The steel shell has been cooled from the start to the end of the treatment to reduce the corrosion rate of the wear refractory. The mist was sprayed to the top area of steel shell of torpedo car and the steel shell was cooled by the heat of vaporization. The area of about 2 m$^2$ where the wear rate was especially high was cooled by 6 nozzles. Cooling was carried out using a nozzle which sprayed a mist of 60-80 μm by water droplets at a

cooling water density of 10L·m$^{2-1}$·min$^{-1}$. The mist discharge direction was adjusted so that the cooling water did not enter the hot metal from the furnace mouth. And the flow rate was set so that the water did not spill to the line through the steel shell side surface. Also, the cooling water pipe was not exposed to radiation heat from the torpedo car mouth passing under the equipment. **Fig. 6** shows the torpedo car under cooling.

To evaluate the validity of the heat transfer analysis, the temperature of the steel shell before and after cooling was measured by a thermo-viewer. The corrosion rate of the refractory was calculated as the corrosion of the refractory during the repair period, which was divided by the number of cycles.



**Fig. 6    Torpedo ladle furnace under cooling..**

### 4.2 Result and discussion

**Fig. 7** shows the results of heat transfer analysis and measurement result. The actual steel shell temperature drop was almost similar to the results of heat transfer analysis, which was reduced by 100K. **Fig. 8** shows the corrosion rate of wear bricks. The wear rate was reduced by 10% (from 0.56 mm・ch$^{-1}$ to 0.50mm・ch$^{-1}$). Steel shell cooling was performed for 50% of all operations.
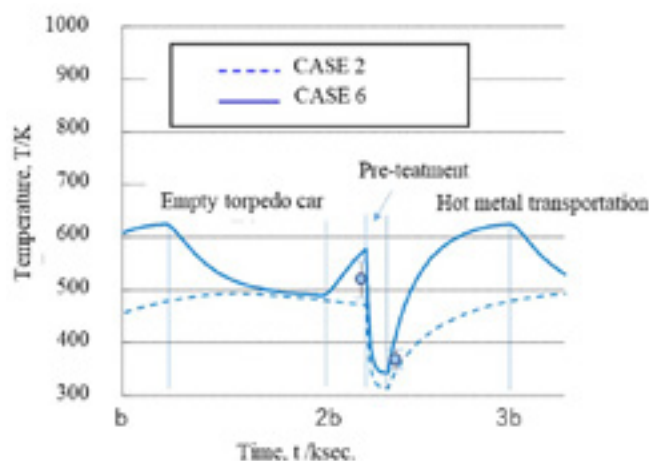


**Fig. 7 The temperature before and after the treatment.**
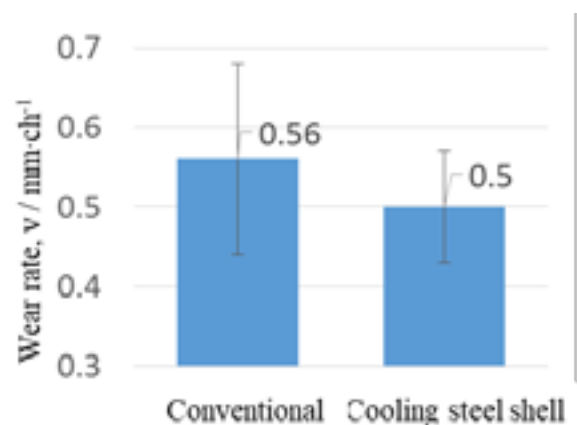


**Fig. 8    The erosion rate of roof bricks.**

The corrosion rate reduction of 10% in the actual plant test could be corresponded to the corrosion reduction effect of 20%, which was assumed in the laboratory, considering the execution rate of cooling of 50%.

## 5 Conclusions

In order to reduce the wear rate of wear bricks of torpedo car refractory, the mist cooling of the steel shell was carried out. As a result of the heat transfer analysis, the reduction effect of hot surface temperature was −11.8K. The relationship between the surface temperature obtained in the rotary slag test and the wear rate was evaluated assuming the mass transfer rate of alumina in the slag should be the rate controlling step, and the apparent activation energy $E_k=367kJ・mol^{-1}$ was obtained. Assuming the reduction of the hot surface temperature by cooling the steel shell as -11.8 K, 20% of reduction in wear rate could be expected. Wear rate of wear refractory in the actual plant test was reduced by 10%. This can be explained as the effect of cooling, taking the 50% of the steel shell cooling experiments conduction into consideration.

### References
1) "Forced cooling of steel" ISIJ, Tokyo 8,58,59 (1978).
2) S. Taira et.al.: Tetsu to Hagane vol.81 [1]16-21 (1995)
3) Handbook of properties of molten iron and slag, ISIJ, Tokyo 22-31 (1972)

# SELF–HEALING MICROSTRUCTURE: THE UTMOST REFRACTORY TOUGH–NESS MECHANISM

Eric Y Sako; Heloisa D. Orsolini; Felipe C. Carreri; Douglas F. Galesi; Bianca M. G. Silva, Wiliam Alves.

Shinagawa Refratários do Brasil, Vinhedo, Brazil

## ABSTRACT

Refractories are often exposed to thermal variations during their operational cycle, such as in torpedo cars and iron ladles, where molten metal is loaded and unloaded at a high frequency basis. Dealing with that aggressive thermal shock is not straightforward and the most common approach for these materials is to optimize the carbon sources, increasing the thermal conductivity of the bricks and reducing the thermal gradient between the hot and cold faces. If, on one hand, the material becomes more resistant to thermal shock damages, on the other hand, its higher conductivity imposes a negative consequence: higher thermal loss during operation. In this work, inspired by intelligent microstructures with the ability to adapt to the most severe environmental conditions, an innovative approach was evaluated, aiming at obtaining an Al2O3-SiC-C brick formulation designed to present a self-healing behavior, without variation in the carbon sources or content. The new developed structure successfully regenerated the cracks initiated during thermal cycles, resulting in an even tougher material after thermal shock tests. Other properties such as mechanical, oxidation, and corrosion resistance also showed promising results, pointing out the birth of a smart self-healing technology, able to completely change the role of refractories in thermal cyclic operations.

## INTRODUCTION

The steel production chain has been going through a transition process towards a descarbonized future, where a large variety of actions are under consideration [1]. Although most of them are predicted to be fully implemented before no less than two decades, others are already in place in the ironmaking sector, involving both the use of different fuel mixes and the addition of new metallic charges. Additionally, steel producers have been looking for opportunities to reduce energy losses and $CO_2$ emissions in process beyond the Blast-Furnace operations [2].

The refractory lining is directly responsible to keep the heat inside the equipment and prevent any metal temperature drop. Nonetheless, in some cases, such role becomes challenging as the refractory material must also withstand very aggressive thermal cycles, as in the case of torpedo cars and hot metal ladles. A classical approach to reduce the thermal damage is by adding carbon sources, mainly graphite, in the refractories' structure so that the heat is easily transferred through the material and a lower thermal stress is generated. As a side-effect, however, more energy is lost by thermal conductivity by the refractory walls, which is undesirable for the sustainability commitments of steel producers [3].

In this scenario, where avoiding the cracks generated by thermal cycles are not straightforward, a different perspective is needed and the right question to be asked is: what if we could recover such cracks during operation?

Self-healing mechanisms are quite largely explored in the polymers field, where, for instance, small capsules containing a setting agent are included in the materials structure [4]. When a crack reaches them, the capsules are broken and a hardening reaction takes place between the base material and the additive which is now available, promoting the complete sealing of the crack area. Likewise, a new class of concretes for building construction was also developed with biomineralization ability. In these materials, bacteria are introduced so that they can metabolically produce minerals to help repair cracks and damage to the concrete [5].

Although those self-healing mechanisms are well-known and proved to work efficiently, they are still limited to room temperature conditions. At very high temperatures, such as the ones contemplated during the steel process operations, the usual components incorporated to induce self-healing mechanisms in those materials are no longer functional. The main purpose of this work was, then, to investigate and develop an entirely novel high temperature self-recovery mechanism, based on nature-like phenomena adapted to refractory structures, giving birth to the utmost toughness mechanism ever seen.

## MATERIALS AND METHODS

### Materials

The introduction of the new self-healing mechanism was evaluated in a Al2O3-SiC-C brick, frequently used as the torpedo car lining material. In order to mimic the healing behavior of living creatures, the regular ACS microstructure was reengineered in such a way that it could smartly interact with the just-generated crack and seal it, just like the human tissue heals a fresh wound with the formation of a new tissue layer. For this purpose, a combination of two non-organic recovery agent was added to the torpedo car formulation, as show in Tab. 1. The reference ACS recipe (SRB REF) was selected due to its benchmarking performance in the market.

Tab. 1: ACS brick formulations evaluated in this work, in wt%. SRB REF is the Shinagawa reference brick in the market. SRB SH stands for the newly developed SELF-HEALING technology.

| Raw-material | SRB REF | SRB SH |
|---|---|---|
| Coarse $Al_2O_3$ | 55,0% | 55,0% |
| Fine $Al_2O_3$ | 13,0% | 13,0% |
| SiC + C | 13,0% | 13,0% |
| Binder | 4,0% | 4,0% |
| Anti-oxidants | 2,0% | 2,0% |
| Self-healing additives | - | 5,0% |

### Self-healing evaluation

For a better observation of the presence of eventual self-healing mechanisms, cyclic thermal shock tests were conducted for both formulations, using three prismatic samples (160mm x 40mm x 40mm) of each composition, pre-fired at 1450°C for 5h at reducing conditions. Each cycle started with placing the samples originally at room temperature (30°C) into a pre-heated furnace (1200°C), leading to an aggressive heating shock. After leaving them there for 30 minutes, the cycle ended by returning the pieces to room temperature for more 30 minutes, inducing a cooling stress. This step was repeated for sixteen times and, every two cycles, the modulus of rupture (MoE) of the samples were measured to follow any variation in the material's structure along the test.

Once the recovering benefits could be proved, a scanning electron microstructural (SEM) analysis were performed to identify the presence of healed cracks in the damaged samples of the SRB SH composition. The cracks in the SRB REF material were also investigated for comparison's sake.

### Performance evaluation

One of the project assumptions is that the introduction of a self-healing mechanism in the refractory's microstructure would not

damage any of the other properties and, therefore, compromise the well-know performance of Shinagawa's bricks for torpedo car. The following properties were then evaluated for the two formulations (SRB REF and SRB SH):

- Open porosity and apparent density: evaluated by using the Archimedes technique in kerosene, following the ASTM Standard C380;
- Modulus of rupture: carried out under three-point bending tests (ASTMC 583) using prismatic samples (160 mm x 40 mm x 40 mm);
- Corrosion tests: conducted in a rotary furnace, in a two-cycle process, where a mix of blast-furnace slag and pig iron was used (80% slag + 20% pig iron);
- Oxidation resistance tests: carried out according to the following procedure → cubic samples of 50 x 50 x 50mm were placed inside a pre-fired furnace at 1000°C, under oxidizing atmosphere, so they could go through an aggressive oxidation process. They were withdrawn after 6h or 24h and, after cooling down, they were cut and the cross-sections were used for measuring the oxidized layer.

For all the above-mentioned tests, samples were previously fired at 1000°C or 1450°C, for 5h, at reducing atmosphere.

**RESULTS AND DISCUSSION**

The results obtained during the cyclical thermal shock tests are shown in Fig. 1. It is possible to observe that the reference material (SRB REF) confirmed its denomination as the benchmarking product, with a very good performance after 16 thermal cycles. A small decrease in the Modulus of Elasticity is perceived after the two first cycles (~15%), indicating the formation of minor damage in the structure, with no more further deterioration, which, in other words, means that the SRB REF composition was well designed to sustain the initial thermal shock damage and gurantee a stable performance. The new developed formulation (SRB SH) also presented the same initial behavior, with the generation of thermal cracks in its microstructure. Nonetheless, better than just supressing the damage propagation along the the test, its smart microstructure was able to interact with the new cracks and progressively seal them as further thermal cycles were applied to the samples. As the test was concluded, the last MoE measurement presented an amazing result: its value was entirely recovered to the level of the original, non-damaged structure.
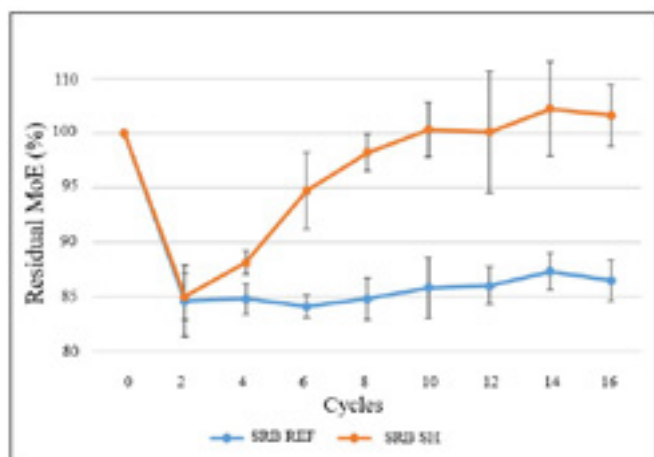


*Fig. 1. Residual Moduli of Elasticity (MoE) as a function of thermal shock cycles for SRB REF and SRB SH formulations.*

After the test, the samples of SRB REF and SRB SH were collected and used for a microstructural evaluation in order to identifiy and compare the cracks situation at both materials. Fig. 2 (a) shows the SEM image obtained for the SRB REF material using topographic

effects, where it is easy to point out the generated crack between a coarse grain and the matrix. Due to a well designed grain size distribution and proper thermal properties, the crack was succesfully deflected and stopped, enabling a stable behavior along the thermal cycles, as seen in the previous graph. In the microstructure of the SRB SH material (Fig. 2 (b)), one may also observe the same crack pattern between the matrix and coarse grains. The main and most important difference is that such crack is visually sealed with a new phase that was formed during the following thermal cycles by the activation of the self-healing agents in the microstructure when they interacted with the propagating crack.
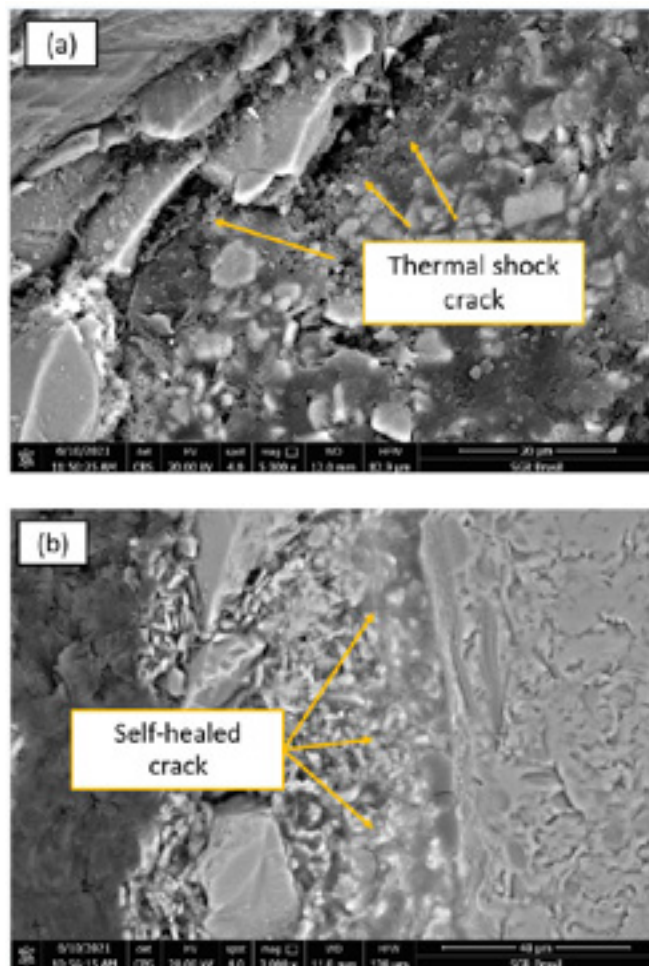


*Fig. 2. Micrograph of (a) SRB REF and (b) SRB SH samples, obtained by SEM after sixteen thermal shock cycles.*

This innovative smart mechanism was responsible to restore the microstructure original condition and, therefore, could be used to implement a new series of $Al_2O_3$-SiC-C bricks virtually inmunne to thermal cyclic damages. For that, it is also important to verify other important physical and chemical properties in order to check whether the introduction of such new structure could lead to a non-expected side-effect. Fig. 3, 4 and 5 presents, respectivelly, the apparent density, apparent porosity and hot modulus of rupture for both materials after firing at 1000°C and 1450°C for 5h at reducing atmosphere.

267
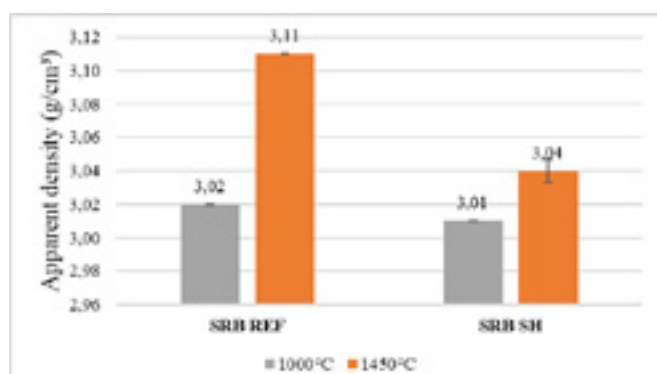
Fig. 3. Apparent density of SRB REF and SRB SH samples after firing at 1000°C and 1450°C.
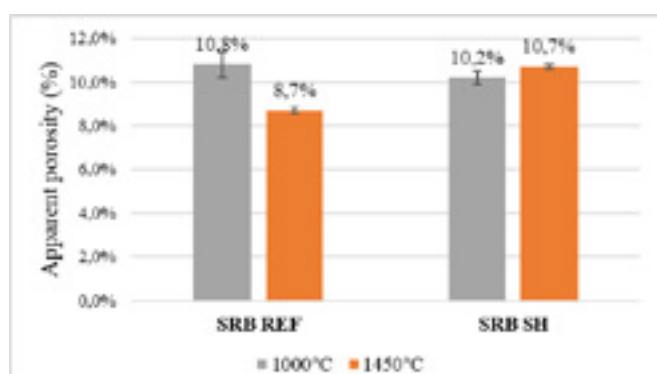


Fig. 4. Apparent porosity of SRB REF and SRB SH samples after firing at 1000°C and 1450°C.
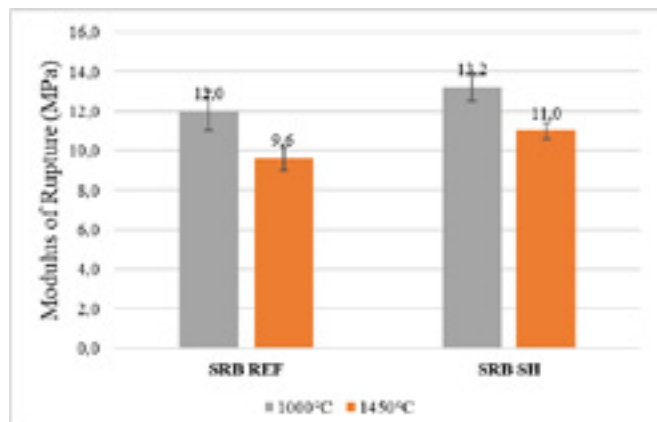


Fig. 5. Modulus of rupture of SRB REF and SRB SH samples after firing at 1000°C and 1450°C.

Due to the difference composition of the brick's matrix and, consequently, to the new phase structures which are formed at high temperatures, the new SRB SH samples presented slight differences in the density and porosity values after firing at 1450°C. However, it is relevant to note that, despite of those differences, the new self-healing material presented a cohesive and well bonded structure, as the MoR values were entirely compatible with the benchmarking reference ones.

Besides keeping almost the same values for the basic physical properties, the introduction of the smart self-healing mechanism in the SRB SH material also led to an improvement of the corrosion resistance, as observed in Fig. 6 and 7. As the refractory corrosion takes place via the infiltration of metal and slag through voids and deffects in the material, a high-temperature sealing system may clearly help to block possible infiltration paths and to prevent chemical dissolution inside the brick.
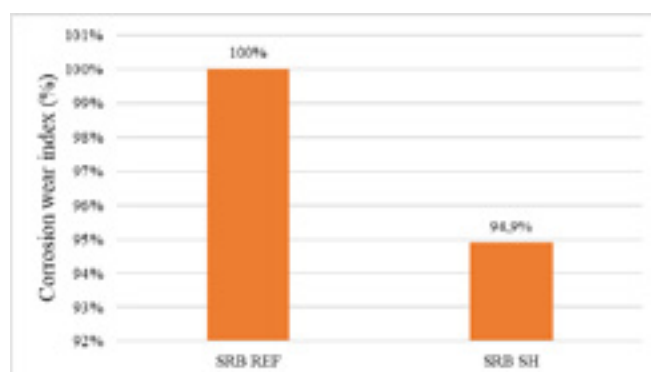


Fig. 6. Corrosion wear index of SRB REF and SRB SH samples.



Fig. 7. Cross-sextion of SRB REF and SRB SH samples after the corrosion test.

Finally, Fig.8 presents the measurements of the oxidized area of SRB REF and SRB SH samples after exposition of 6h and 24h in air. Once again, the presence of the self-recovery additives did not affect the material's oxidation resistance and, actually, the smart sealing process could again have helped to slightly decreased the oxidation process for the SRB SH material.
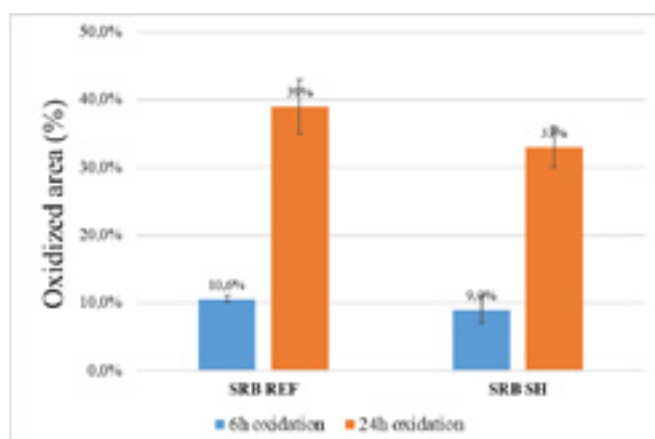
*Fig.8. Oxidation resistance results after 6h and 24h for SRB REF and SRB SH samples.*

## CONCLUSIONS

Aiming at reducing the energy losses in the steel manufacturing process while also increasing the lifetime of refractories applied at high thermal cyclical areas, an exclusive smart self-healing structure was developed and introduced in a $Al_2O_3$-SiC-C torpedo car brick composition. The new mechanism was able to interact promptly with the cracks generated during thermal shock processes, activating the self-healing agents, and completely sealing the crack area. This innovative process induced a total recover of the original structure of the material and its modulus of elasticity returned to values as high as the pre-thermal shock condition. As neither the physical properties nor the corrosion and oxidation resistances were affected by this new smart structure, a very promising future is expected for refractories materials with the rise of such utmost and nature-inspired toughness mechanism.

## REFERENCES

[1] Managi, S., Kaneko, S. Iron and Steel Indusry – Dialogue on European descarbonisation strategies. https://doi.org/10.4337/9781849803434.00015.

[2] Barati, M., Esfahani, S., Utigard, T. Energy recovery from high-temperature slags. Energy 36, 5440-5449. https://doi.org/10.1016/j.energy.2011.07.007

[3] Chen, E. S., Fréchette, M. H. Thermal and thermomechanical evaluation of high-strength insulation in steelmaking ladle, 79th Steel. Conf. Proc., ISS, 457-463 (1996).

[4] Yu, D.W., Meure, S., Solomon, D. Self-healing polymeric materials – a review. Progress in polymer science 33, 479-522 (2008).

[5] Wiktor, V., Jonkers, H.M. Quantification of crack-healing in novel bacteria-based self-healing concrete. Cement and concrete composites 33, 763-770 (2011).

# RECYCLING OF AL$_2$O$_3$–SIC–C REFRACTORY BRICK FOR REPAIRING TORPEDO LADLE CAR

SeongYeol, Kim, SeokJu, Jang, SungHyun, Lee, SeungDeuck, Lee, JeongSeob, Kim
Hyundai Steel Company, Dangjin-Si, South Korea

ByoungWook, Jung
Korea Refractories Company, Dangjin-Si, South Korea

**ABSTRACT**

Torpedo ladle car is the main apparatus for transporting the molten iron produced in the blast furnace. $Al_2O_3$-SiC-C refractory bricks were mainly used for the working lining of torpedo ladle cars and have excellent slag resistance, abrasion resistance and thermal shock resistance. When the torpedo ladle car was used up to a certain life, the used $Al_2O_3$-SiC-C refractory bricks are replaced for repairing. At this time, the amount of waste generated is about 2,000 tons per year in Hyundai Steel, and it is necessary to develop technology for recycling the used refractory brick. Therefore, in this study, recycled $Al_2O_3$-SiC-C refractory bricks were used for repairing torpedo ladle car to develop refractory recycling technology. The torpedo ladle car was repaired by shotcrete method with a certain life cycle. Recycled $Al_2O_3$-SiC-C refractory bricks were mixed with shotcrete refractories and compared with torpedo ladle cars that were repaired without recycled materials. When compared after about 100 heat of use, a slight peeling off was observed in the torpedo ladle car with the recycled Al2O3-SiC-C refractory bricks. However, the residual of refractory were similar when comparing the residual using 3D scanning equipment. In addition, the erosion rate difference of refractory was less than 3% when directly measured using a tool after using about 250 heat. In conclusion, it was confirmed that the shotcrete with recycled $Al_2O_3$-SiC-C refractory bricks was used without any problems until the next shotcrete repair period.

**INTRODUCTION**

$Al_2O_3$-SiC-C refractories were characterized by excellent thermal shock resistance, good abrasion resistance and non-sticking slag. So, $Al_2O_3$-SiC-C refractory brick are mainly used for torpedo ladle car lining. Torpedo ladle car play a vital role in transporting the molten iron from blast furnace.



*Fig. 1. Shotcrete repair in torpedo ladle car*

Torpedo ladle car are repaired by the shotcrete method when a low lifespan are used and by completely replacing the $Al_2O_3$-SiC-C brick when used over a high lifespan. Fig. 1 shows shotcrete repair in torpedo ladle car. At this time, about 2,000 tons of spent $Al_2O_3$-SiC-C refractory brick are generated and wasted each year in Hyundai Steel.

Thus, it is necessary for steel and refractories industries to develop research of recycle refractory waste materials. In this study, wasted $Al_2O_3$-SiC-C brick that was used in torpedo ladle car was recycled and investigated whether it could be applied to shotcrete refractory for torpedo ladle car.

**EXPERIMENTAL PROCEDURE**
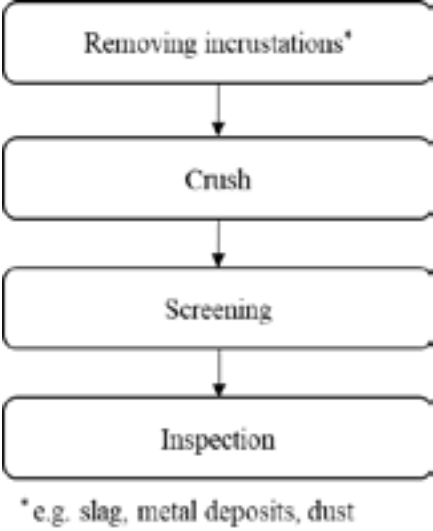


*Fig. 2. Recycling method of spent Al2O3-SiC-C brick*

Recycled raw material was obtained as shown Fig. 2. Firstly, incrustations such as slag, metal deposit and dust on the $Al_2O_3$-SiC-C brick in torpedo ladle car were removed. And then, the materials were crushed using jaw crusher. Crushed materials were screening to obtain desired particle size. Finally, moisture of the recycled raw materials were inspected. If the materials had 0.3% over, that were dried for 24hour. Table 1 shows the chemical composition of recycled raw material. In order to investigate whether the recyclied $Al_2O_3$-SiC-C brick can be added as a shotcrete refractory material, tests were performed by adjusting the content of recycled raw materials. And then the field test was conducted by the optimal ratio of recycled raw materials.

Tab. 1: Chemical composition of recycled $Al_2O_3$-SiC-C raw materials

| Classification | | Value |
|---|---|---|
| Chemical composition (%) | $Al_2O_3$ | 64.5 |
| | $SiO_2$ | 8.7 |
| | $Fe_2O_3$ | 0.9 |
| | $CaO$ | 0.3 |
| | $Na_2O+K_2O$ | <0.8 |

To investigate the optimal ratio, physical properties and thermal properties were compared according to the ratio of recycled $Al_2O_3$-SiC-C raw materials addition as shown in Table 2. The samples of pysical properties test (40 mm × 40 mm × 160 mm) were cured at 25 °C for 24 h, and then dried at 110 °C for 24 h. Physical properties(cold modulus of rupture (CMOR), The cold crushing strength (CCS) and bulk density) were measured with dried sample and heat-treated sample at 1,500°C for 3h. Erosion test was performed using a blast furnace slag with $CaO/SiO_2$ = 1.21 on a rotary corrosion tester.

Tab. 2: Composition accroding to recycled Al₂O₃-SiC-C raw materials addition

| Raw material | R0 | R1 | R2 |
|---|---|---|---|
| Recycled ASC brick(%) | 0 | α | 2 α |

Table 3 shows the field test conditions by applying optimal ratio to shotcrete refractories for torpedo ladle car. Each test was conducted twice. The torperdo ladle car was divided into two sides (Side M and D), and shotcrete with recycled Al₂O₃-SiC-C raw materials was applied to one side, and shotcrete of not including recycled Al₂O₃-SiC-C raw materials was applied to the other side. Then, after using about 100 heat, the remaining refractory was measured through laser sccaning system.

Tab. 3: Field test conditions

| Classification | Side M | Side D |
|---|---|---|
| 1st test (2EA) | R1 (α%) | R0 (0%) |
| 2nd test (2EA) | R0 (0%) | R1 (α%) |

**RESULT AND DISSCUSSION**

Table 4 shows the physical properties of shotcrete refractory mixed with recycled raw material. Bulk density increases as the content of recycled raw material increases. This result was because impurities with high specific gravity such as FeO remained in the recycleid raw material. In the case of CCS and CMOR, as the content of recycled raw materials increases, it tends to decrease gradually. The reason was due to the low purity of the material due to impurities in the recycled raw materials. In the case of permanent linear change, there was no change at 110°C, but it showed a tendency to increase after heat-treatment at 1500°C. This was presumed to be because impurities such as CaO in the recycled raw material reacted at high temperatures.

Tab. 4: Physical properties according to recycled raw material content

| Physical properties | | R0 | R1 | R2 |
|---|---|---|---|---|
| 110°C × 24h | Bulk density | 2.49 | 2.53 | 2.57 |
| | CCS(kgf/cm²) | 450 | 425 | 412 |
| | CMOR(kgf/cm²) | 94 | 88 | 86 |
| | PLC(%) | 0.01 | -0.01 | -0.01 |
| 1,500°C × 3h | Bulk density | 2.47 | 2.49 | 2.52 |
| | CCS(kgf/cm²) | 1630 | 1390 | 1265 |
| | CMOR(kgf/cm²) | 193 | 188 | 160 |
| | PLC(%) | 0.12 | 0.20 | 0.22 |

Fig. 3 shows the erosion test results. Erosion test results show a tendency for corrosion resistance to decrease (corrosion index increase) as the recycled raw material increases. Similar to the pysical test result, it seems that the corrosion resistance decreased like this because the impurities affected the shotcrete refractory. therefore, The field test was conducted with the composition of R1 because the properties of R1 and R0 were not significantly different.
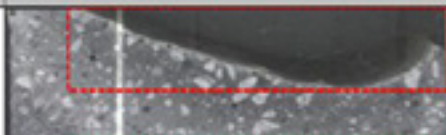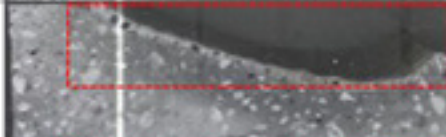


*Fig. 3. Rotational erosion test piece cross section with recycled raw materials*



*(a)*



*(B)*
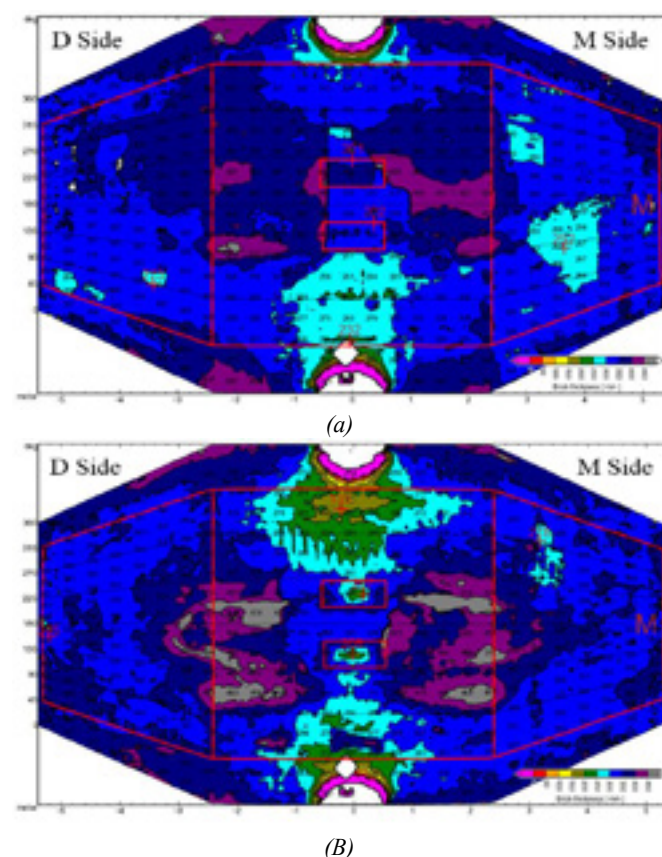
*Fig. 4. Laser scanning result of first field test: (a) test 1 and (b) test 2*

Fig. 4 shows the results of the first field measured by laser scanning equipment after using about 100 heat. In the first test, shotcrete with recycled raw materials was repaired to the M side. As a result of the test, it was confirmed that there was some peeling on the M side, but it seems similar with D side. After using 250 heat, The inside of the Torpedo ladle car was observed and it was confirmed

that there was peeling on the M side compared to the D side like laser scanning result. It was shown Fig. 5. However, when directly measured after 250 heat, the erosion rate of M side was 3% higer than D side.



*(a)*



*(b)*
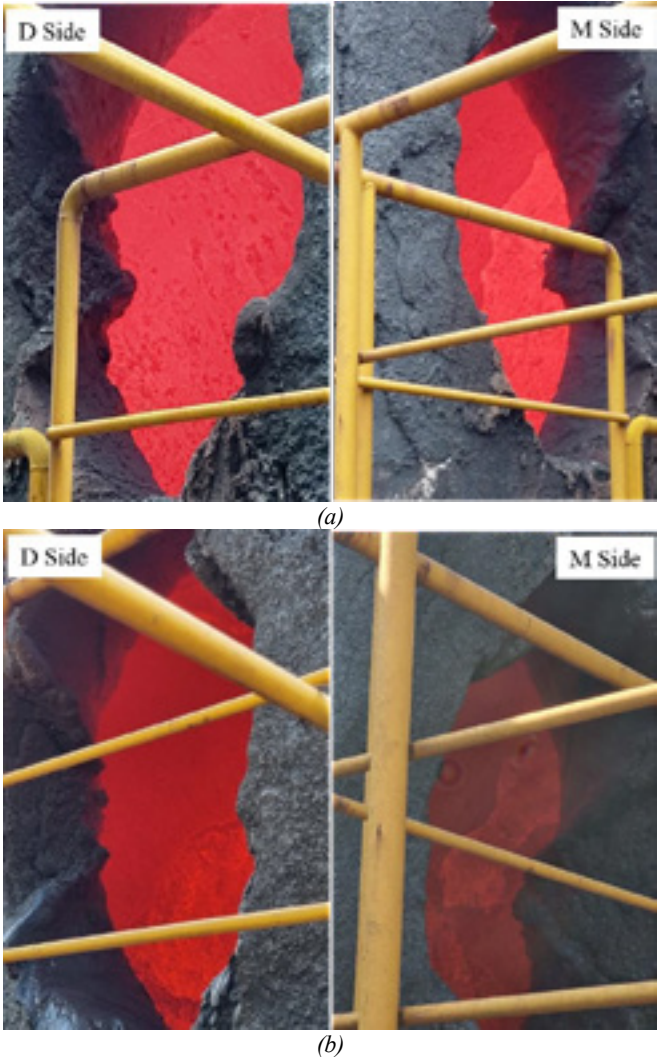
*Fig. 5. First field test result after using 250heat: (a) test 1 and (b) test 2*

Laser scanning result of the second field test was shown in Fig. 6. In the second test, shotcrete with recycled raw materials was repaired to the D side. As a result of the test, in the second test, some peeling occurred on the M side after using 100 heat, and the remaining refractory brick on the D side was better.



*(a)*



*(b)*
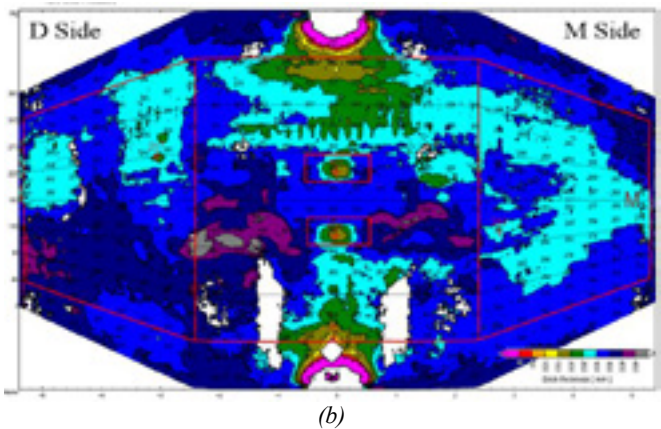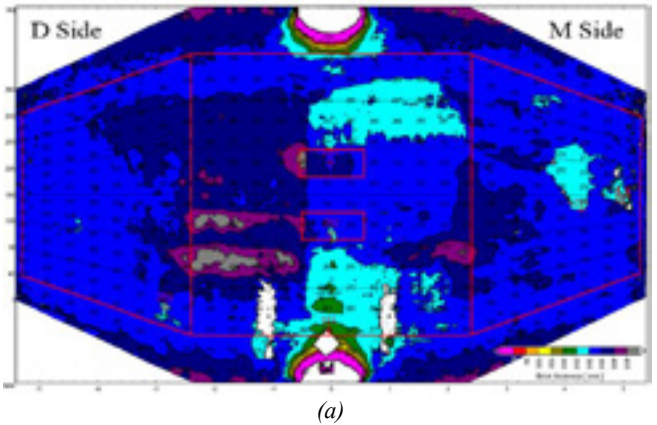
*Fig. 6. Laser scanning result of Second field test: (a) test 1 and (b) test 2*



*(a)*



*(b)*
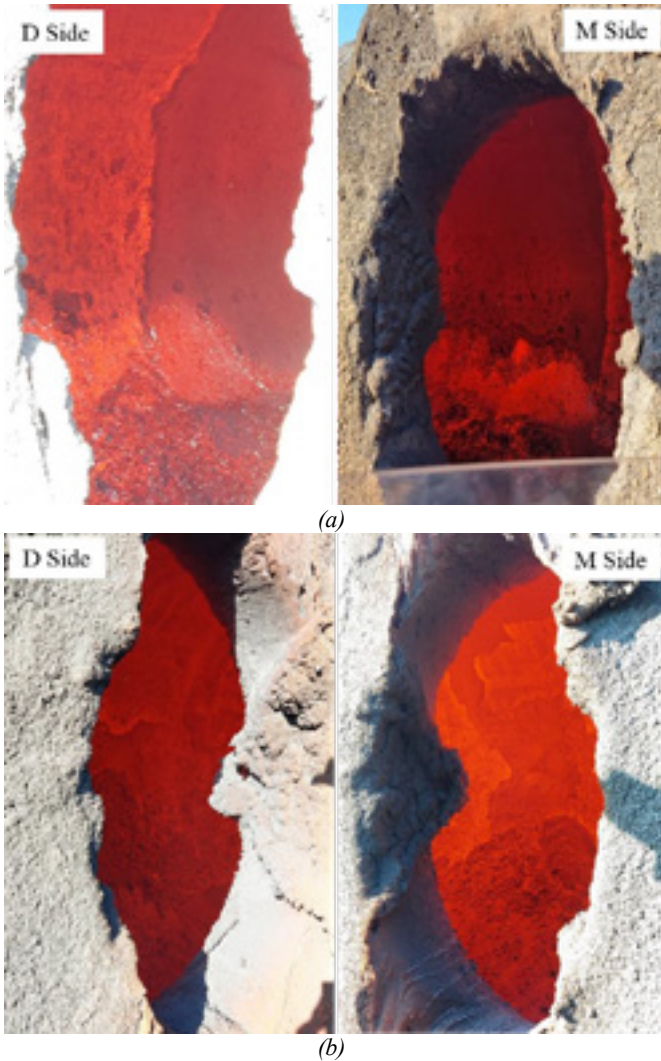
*Fig. 7. Second field test result after using 250heat: (a) test 1 and (b) test 2*

The second field test result was shown in Fig. 7. Second test also can be confirmed that peeling-off of shotcrete refractory on the M side after using 250heat. Therefore, it was assumed that this result came out because the damage on the M side during use was more severe than the effect of recycled raw material. When direcytly mesured after 250 heat, the erosion rate of M side was 2% higer than D side. In conclusion, although shotcrete refractory with recycled $Al_2O_3$-SiC-C raw material affects physical and thermal properties, it can be used in the field by adjusting the content. And also, it was confirmed that the shotcrete with recycled raw material

was used without any problems until the next shotcrete repair period.

## CONCLUSIONS

The problem of handling waste refractories in the steel and refractory industry was a major issue, and research on refractory recycling was needed worldwide. In this study, shotcrete refractory was mixed with recycled $Al_2O_3$-SiC-C brick to confirm the possibility of using of spent $Al_2O_3$-SiC-C bricks used in torpedo ladle cars. In order to repair the shotcrete refractory with recycled raw material in torpedo ladle car, the physical and thermal properties were confirmed by adjusting the content. As a result, the physical strength and erosion resistance decreased due to the impurities present in the recycled raw material, and the field test was conducted by the shotcrete refractory with $\alpha\%$ recycled raw material as the optimal content. In the field test, the torpedo ladle car was divided into two sides and repaired with shotcrete with recycled raw material mixed to only one side. As a result of the field test, after using 100 heat, the M side was slightly inferior in both the 1st and 2nd tests in laser scanning, but after using 250 heat, the erosion rate showed a difference of about 2-3%. In conclusion, it was confirmed that recycled $Al_2O_3$-SiC-C raw material can be used in the shotcrete refractory for Torpedo ladle car, and additional research is needed by increasing the content in the future.

## REFERENCES

[1]    Jorge, M, A review on recycling of refractories for the iron and steel industry. In proceedings of the UNITECR 2017 15th Biennial Worldwide Congress, Santiago, Chile, 26–29 September 2017.

[2]    Liesbeth, H, Peter, N, Philippe, D, Antoine, D. Recycling of refractory bricks used in basic steelmaking: A review. Resource, Conservation & Recycling 140, 2019, p. 297-304

# REFRACTORY LINING MATERIAL IN IRON MAKING PROCESS – AN OVERVIEW WITH  DEVELOPMENT AND CHARACTERISATION STUDY OF CRITICAL PROPRIETIES

Ranjan Dey, S. Panneerselvam, C. Natarajan,  Subhasis Gangopadhyay,  N. Thiagarajan, C. R. Manoj Kumar, Prabhakar Jha, Prantik Ghosh, V.T. Eswar, S.Velappan, B.R. Pai, Nimit Chowdhury, Sourav Naskar, K.Suresh, G.Kathiravan, Prashanta Mandal, Imran Khan, Saimon Ray
**Carborundum Universal Limited**, Chennai, India

## ABSTRACT

Blast Furnace ironmaking process is currently the dominant process for providing steelmaking raw materials worldwide. However, the blast furnace process relies heavily on metallurgical coke and involves coke-making and sintering operations, which often attract serious environmental concerns. Therefore, Direct Reduction and Smelting Reduction technologies using non-coking coal or other gases as reducing agents to replace metallurgical coke have emerged as alternative routes for iron production. Due to the vast difference in operating conditions between these processes, requirement of suitable refractory lining and critical parameters also vary to a large extent.

Silicon Carbide based refractories with different bond system e.g. Silicon Nitride, SiAlON have been established as most suitable lining refractory in the critical area of blast furnace over the years. The major advantage of Silicon Carbide Refractory with Silicon Nitride and SiAlON bonding are Alkali Resistance, Oxidation Resistance, Thermal Conductivity, Thermal Shock Resistance, Abrasion Resistance etc.

For direct reduction of iron in shaft furnace process using natural gas, high alumina refractory specifically for bustle port and the wall requires superior Refractoriness Under Load and Creep resistance properties.

Characterisation of developed refractories for lining of blast furnace, Smelting Reduction and gas based DRI shaft kiln has been discussed here.

## EVOLUTION OF IRON MAKING PROCESS

Historically ironmaking was more an art than a science as it began in Egypt, India, China and in Europe. Early iron producers learned this art over many generations through training and practices. By mid-nineteenth century, scientific innovations and improvements became primary approach in iron smelting.

This practice and innovation has come a long way in 4000 years. The transition from sponge iron produced in Catalon forges to liquid iron produced in Stuckofen, Flussofen and then through charcoal blast furnaces were significant milestones in advancement of iron smelting process.

Then came the change from cold blast, charcoal furnaces to hot blast, coke furnaces in the mid-1800s which brought iron making into the modern era. Better understanding of iron-making reactions and improved equipment evolved into the hard-driving furnace operation centered in the 1880s to 1900s. Finally, the revolution in scientific applications to iron smelting, installation of sophisticated equipment and advent of electronically controlled systems augmented blast furnace iron making into current state. Catalon Forge, Charcoal based BF  and current BF are shown in Fig.1.

Blast furnaces are estimated to have been responsible for over 4% of global greenhouse gas emissions between 1900 and 2015, but are difficult to decarbonize.

Smelting Reduction (SR) processes were developed as an viable alternative for blast furnace in producing hot metal. These processes combine the gasification of non-coking coal with the melt reduction of iron ore. As alternative to blast furnace process, smelting reduction is economical and environment friendly.

In smelting reduction, Hot metal is produced in two stages. Ores are partly reduced in the first step, final reduction and meting takes place in secold stage. Some of the common processes are COREX
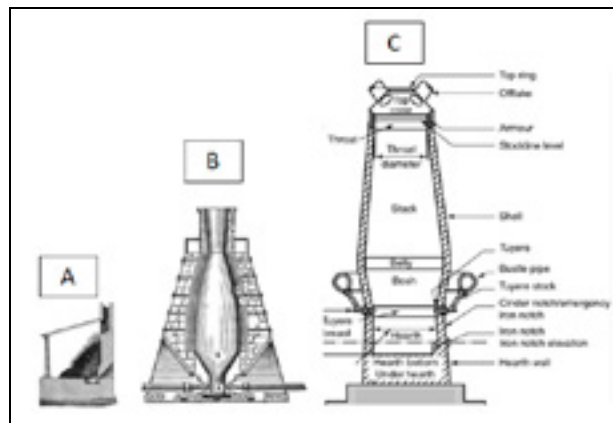


*Fig. 1. (A) Catalon Forge, (B) Charcoal based BF, (C) Current BF*

[Coal Reduction Process], FINEX [Direct use of fine ore], DIOS [Direct Iron Smelting], AUSMELT [Australia Smelting], HISMELT, ROMELT, PLASMASMELT etc.

Steelmakers have also found that a combination of the different processes could be fundamentally utilized to develop new processes that could compete with the productivity and quality of the BF hot metal, more economically competitive and finally environmentally friendly.

The COREX and FINEX technology (shown in Fig. 2) are major economic and ecologic industrially realized alternative to the blast furnace route for the production of hot metal.
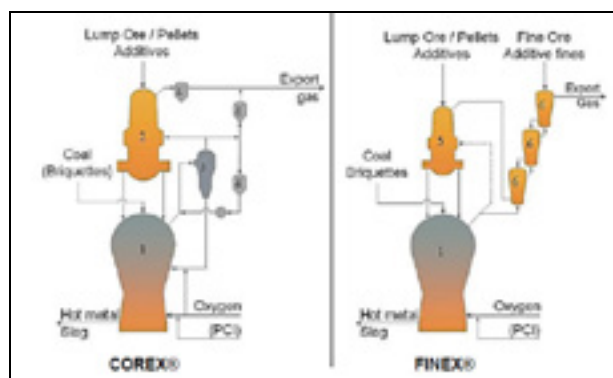


*Fig.2. Corex® and Finex® process flow sheets; 1) melter-gasifier, 2) reduction shaft,3) hot gas cyclone,4) process gas scrubber,5) hot compacted iron bin, 6) fluidized bed reactor (Wieder, et al., 2009)*

Advantages of this process are following:
- Substantial reduction in investment costs compared with conventional blast furnace steelmaking process
- Production cost less up to 25% compared with a blast furnace
- Outstanding overall environmental compatibility, due to reduction in CO2 generated per ton of iron production
- Use of COREX export gas for a wide range of applications
- Use of a wide variety of iron ores, coals and elimination of coking
- Hot-metal quality suitable for all steel applications
- Combined production of DRI possible.

Development of suitable Refractory and improvement played major role for long campaign life of BF, DRI and Smelting-reduction.

## BLAST FURNACE LINING APPLICATION AND DEVELOPMENT OF SUITABILE REFRACTORIES

In the Upper Stack, resistance to abrasion from downward moving ore, pellet, sinter is the major function for the lining refractory. NBSiC is good option over High Alumina

In the lower stack, refractory lining need to withstand reducing effect of carbon monoxide, alkali vapours, zinc and aluminium penetration and oxidation from carbon dioxide at temperatures as high as 820 Deg. C over and above abrasion. Also as the burden moves, thermal shock can be extreme in the lower stack. NBSiC and SiAlON-SiC is found to be very suitable.

In the Bosh, Slag and molten iron dribbled down as the blast furnace mass descends. Erosion and abrasion of Refractories are very severe. Here Modulus of Rupture (MOR), generally equated by refractory engineers as a good indication of high temperature abrasion resistance. Here the SiAlON-SiC brick meets overall requirement of high MOR and alkali attack resistance.

In the Mantle or Belly region, conditions are extremely severe. There is a change of direction in the descending charge causes tremendous abrasion. Carbon monoxide and alkali attack is more severe as there is less slag coating for protection. Occasional violent thermal shock occurs with burden shifts. Hot strength (modulus of rupture and refractoriness under load) of SiAlON-SiC is a key for longer life of the lining.

In the Tuyere Bowls, in addition to hot air and steam oxidation, attack from alkali & zinc vapour, tremendous erosion and corrosion by molten iron and slag directs to selection of SiAlON-SiC. Thermal conductivity of the SiAlON-SiC brick is sufficiently high to freeze and hold a slag coating in this area.

In the hearth, many blast furnaces have Carbon based lining, however to extend the hearth life and to save energy addressing good resistance to iron and slag, reducing chance of infiltration of hot metal; keeping isotherm of 1150 °C close to the working hot surface, SiAlON-Corundum lining in the hot face together with high creep resistance Mullite are considered for Ceramic Pad.

## REFRACTORY LINING IN THE CRITICAL ZONE OF SMELTING-REDUCTION (SR) PLANT

**Typically in Melter-Gasifier of SR Plant, following zonal refractory configurations are considered**

Above Tuyere Band and Charbed Zone : SiAlON-SiC
Calming Zone : SiAlON-Corundum
Dome Nozzles : NBSiC
Hearth Ceramic Pad : Mullite, Corundum
Stave Inserts/ Dust Burner : NBSiC, SiAlON-SiC

Study conducted by Xiaoge Wang[3] et. al showed that the maximum average erosion of refractory lining bricks happened in the drip zone. Its surface was mainly affected by slag erosion and mechanical scour of slag.

## CHARACTERISATION OF CRITICAL PROPERTIES

Present work carried out to make improvement in desired properties and samples drawn from bulk manufactured lots of NBSiC, SiAlON-SiC, SiAlON-Corundum. Following properties are evaluated :
-   Resistance to Alkali
-   Thermal Conductivity
-   Resistance to Carbon Monoxide
-   Abrasion Resistance
-   Refractoriness under Load
-   Microstructure Analysis

Addressing critical application at Hearth with Ceramic Pad, Creep under Compression evaluated for Mullite based products.

**Effect of Alkali Attack:**

Resistance to Alkali is evaluated in line with Bethlehem test. Samples of 150x25x25 mm. kept inside a steel tray, filled with technical grade $K_2CO_3$ powder all around. This steel tray closed with a lid kept inside a refractory sagger, filled with coke breeze all around and closed with a refractory lid. This sagger heated in a laboratory furnace at 950°C for 3 hours. After every cycle, samples were cleaned and same process with new $K_2CO_3$ and calcined pet coke repeated for three cycles. Modulus of Rupture (MOR) test is carried out before and after test as per ASTM C 133. Samples and chamges in MOR are shown in Fig.3 & Tab.1 respectively.



*Fig. 3 : Samples after three cycles of Alkali Test*

Tab.1: Chamges in MOR after Alkali test (Also refer graphs below)

| Samples | Average Variation in MOR (%) after Alkali attack |
|---|---|
| NBSiC | -13.2% |
| SiAlON - SiC | -9.3% |
| SiAlON - Corundum | -30.2% |
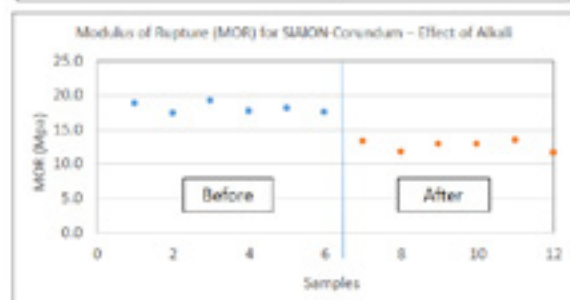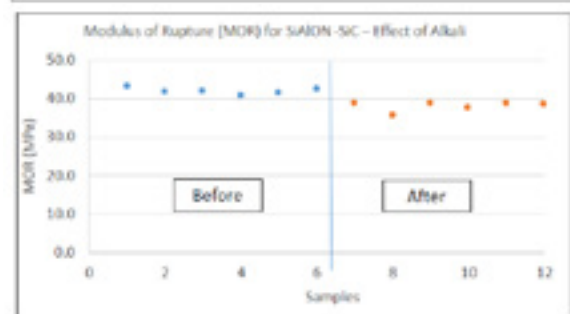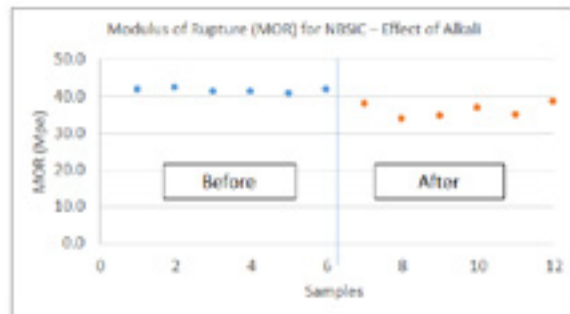
**Thermal Conductivity**
Test data by hotwire (parallel wire) method, EN ISO 8894-2 is shown in Tab. 2

Tab. 2. Thermal Conductivity (values in W/m.$^o$K)

| Temp. ($^o$C) | NBSiC | SiAlON-SiC |
|---|---|---|
| 350 | 22.0 - 24.0 | 16.0 - 20.0 |
| 700 | 19.0 - 21.0 | 13.0 - 16.0 |
| 1000 | 15.0 - 18.0 | 11.0 - 13.0 |

**Resistance to Carbon Monoxide (CO):**
Disintegration of refractories under CO evaluated as per ASTM C 288 for NBSiC and SiAlON-SiC. All were found unaffected / classified as A category. Images of test samples are shown in Fig. 4 and Fig. 5 respectively.



*Fig. 4 : NBSiC  Unaffected / Class A*



*Fig. 5 : SiAlON-SiC Unaffected / Class A*

**Abrasion Resistance :**
Evaluation carried out following ASTM C 704. Samples after test and result is shown in Fig. 6 & 7  respectively.
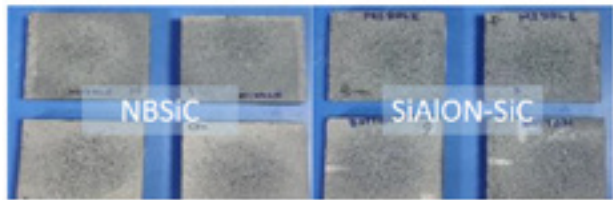


*Fig. 6.  NBSiC & SiAlON-SiC samples after abrasion test*
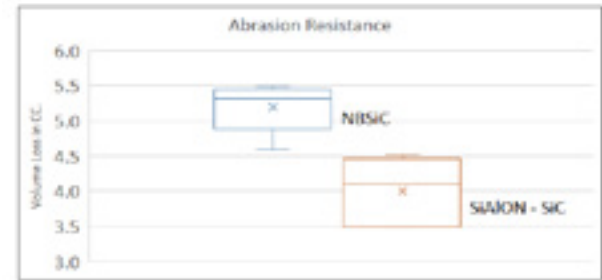


*Fig.7.  Abrasion resistance of NBSiC & SiAlON-SiC*

**Refractoriness under load (RUL)**
Test carried out as per ISO 1893 (DIN EN 993-8) under protecting gas (N$_2$), T05/T1/T2/T5 for NBSiC and SiAlON-SiC is found > 1674$^o$C (Dmax at 1674$^o$C = 0.62%) and >1660$^o$C (Dmax at 1505$^o$C = 0.52%) respectively. RUL curves is shown in Fig. 8.
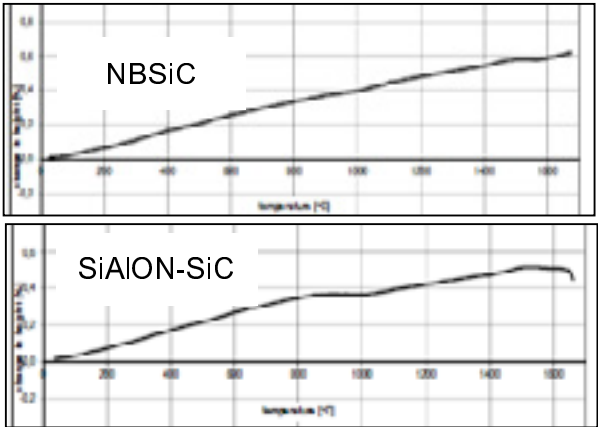


*Fig. 8. RUL curves for NBSiC & SiAlON-SiC*

**Microstructure analysis**
Scanning Electron Microscopy (SEM) shown below in Fig. 9 & 10.
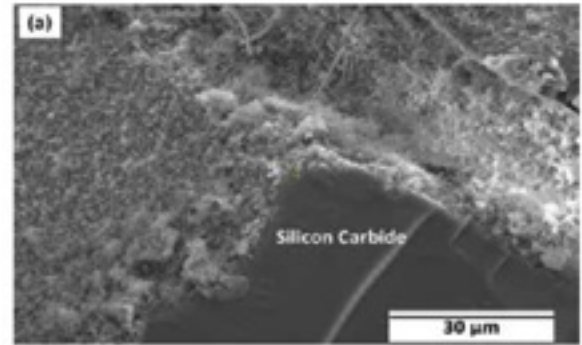


*Fig. 9. SEM image of NBSiC showing SiC grain with both granular and fibrous nature of Si$_3$N$_4$ bond matrix*
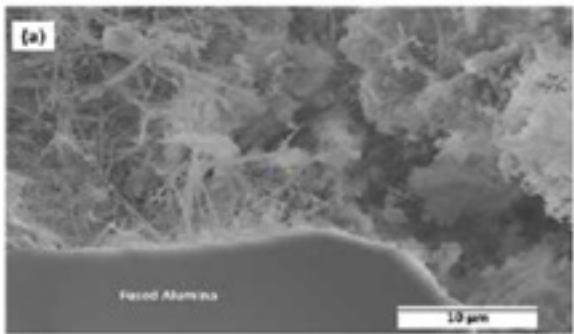


*Fig. 10. SEM image of SiAlON-SiC showing Fused Alumina grain with  SiAlON+Nitride bond matrix (primarily fibrous in nature)*

**Resistance to Creep under compression**
W.r.t severe load bearing application in Ceramic Pad, Creep under compression test carried out as per EN 993-9, shown in Tab, 3.

Tab. 3 : Creep under Compression for Mullite grades

| | Mullite (based on Andalusite + Fused Mullite) | High Purity Mullite (based on Fused Mullite) |
|---|---|---|
| At 1450 deg. C / 5 – 25 Hrs. | - 0.268 % | - 0.019 % |
| At 1550 deg. C / 5 – 25 Hrs. | - 0.532 % | + 0.001 % |
| At 1600 deg. C / 5 – 25 Hrs. | - | + 0.008 % |

## DRI PROCESSES

Direct reduction of iron (DRI) ore has been an alternative solution to the BF process to provide the steelmaker the opportunity to utilize raw materials without the need for sintering and cokemaking. Several alternative ironmaking processes have been developed and commercialized. Among various DRI processes (shown in Fig. 10 ), Shaft furnace route with natural gas (or other reducing gases) has become a major DRI manufacturing method[2].



*Fig. 10. DRI Processes with Coal & Gas as reducing agent*

For direct reduction of iron in shaft furnace process using natural gas, high alumina refractory specifically for bustle port and the wall requires superior Hot strength properties i.e. Hot Load Deformation Creep resistance, Refractoriness Under Load, Resistance to CO etc.

### Hot Load Deformation

W.r.t severe load bearing application in the bustle port blocks, test carried out as per ASTM C 16.
Deformation at 3000 $^{o}$F (i.e. at 1650$^{o}$C) / 100 Hrs. is 0.68 %
Deformation at 2400 $^{o}$F (i.e. at 1316$^{o}$C) / 50 Hrs. is < 0.10 %

### Resistance to Creep under compression

Addionally this test carried out at 1550$^{o}$C/ 50 Hrs. as per DIN EN 993-9.  Deformation observed during 5 – 50 Hrs. is 0.044 %

### Resistance to Carbon Monoxide:

Disintegration of refractories under carbon monoxide evaluated as per ASTM C 288 for (a) burnt phosphate bonded high alumina brick and low iron Insulation Firebricks (b) grade 23 and (c) grade 28. All were found unaffected / classified as A category.
Images of test samples are shown in Fig. 11.
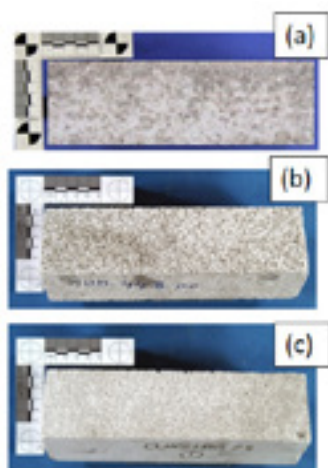


*Fig.11. Images of refractories after exposure to CO [All Unaffected / Class A]*

## Corrosion test under H$_2$-atmosphere

To ascertain condition of  high alumina refractory in highly reducing condition, carried out this test at 1350°C/ 100 Hrs. Changes in physical dimension, cold crushing strength (EN 993-5) and modulus of rupture (EN 993-6) data obtained before and after exposure to H$_2$. Images of samples and test data shown in Fig. 12 and Tab. 4 respectively.
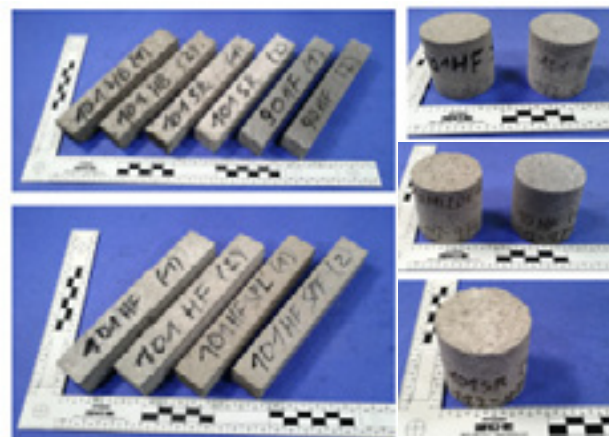


*Fig. 12. High Alumina refractory samples after H$_2$ exposure*

Tab. 4. Changes in strength properties after H$_2$ exposure

| Under H2 Atm., 1350 Deg. C/100 Hrs. | Changes in Strength | |
| --- | --- | --- |
| | Cold Crushing Strength | Modulus of Rupture |
| +90% Alumina Refractory. | Approx. - 28 % | Approx. - 30 % |
| +99.5% Alumina .Refractory (Various compositions / fired at different Temp.) | -26% to +2 % | -12 % to +40 % |

## CONCLUSIONS

NBSiC, SiAlON- SiC and SiAlON-Corundum are well established in zonal lining of Blast Furnace, Smelting-Reduction Furnace owing to their superior properties like alkali resistance, resistance to CO, Hot Strength properties, Abrasion resistance, Thermal conductivity etc. while high creep resistant Mullite and Corundum serves the critical areas of Ceramic Pad, Bustle port etc.

With new generation Green DRI process becomes a reality, iron ore pellets will be reduced by green hydrogen in direct reduction process. Reduction occurs in a solid state at a lower temperature. Development of suitable refractories and Effect of Ccorrosion Analysis in H2 atmosphere at appropriate temperature will be a major step forward in the selection of superior refractory in the journey  and making positive contribution to our environment.

### REFERENCES

[1]    Evolution of Blast Furnace Ironmaking – Ispatguru
[2]    2021 WORLD DIRECT REDUCTION STATISTICS – Compilation by Midrex Technologies.
[3]    Modelling of Trace Material Flow Distribution in a Melter Gasifier based on Thermodynamic Multiphase Equilibrium Calculations by Andreas Spanlang et. al., 2018
[4]    Research on corrosion mechanism of refractory lining in drip zone of COREX melting gasifier by Xiaoge Wang, Pengcheng Li, Huili Sun and Shitao Song.
[5]    COREX® + MIDREX AN IDEAL CONCEPT FOR ECONOMIC AND ENVIRONMENTAL FRIENDLY STEEL PRODUCTION by Christian Böhm, Gerhard Fritsch, Wolfgang Sterrer & Johann Wurm.

For queries/ details, kindly Mail: deyranjan@cumi.murugappa.com

277

# TRADITIONAL REFRACTORY DESIGNS REPLACED BY INNOVATIVE REFRACTORY SOLUTIONS IN HOT BLAST STOVES

F. van Laar, B. Hansen, J. Carreau
Allied Mineral Technical Services, Columbus, OH, USA

B. Byerman, B. Eschbach
Burns Harbor, Burns Harbor, IN, USA

**ABSTRACT**
This paper will discuss novel repair methods for refractory systems in Hot Blast Stoves. The failure of refractory systems in a fast-paced industry creates demand for reliable repairs that offer the shortest timeline. Therefore, innovative solutions must improve the refractory design and installation methods to repair older, traditional refractory systems promptly. An alternative design with monolithic materials was successfully implemented in 2020 and 2021 at stove D1 and D3, and currently stove C4 at Burns Harbor. Failure of the traditional (brick) hot stove refractory system led to the casting of a complete monolithic dome and large sections of the walls. A post-construction analysis will demonstrate the validity and feasibility of the design.

**INTRODUCTION**
In July of 2020 Stove D1 suffered a catastrophic failure where the dome shell separated from the cylindrical portion of the stove. The dome refractories as well as approximately twenty feet of the checkers, ring wall and combustion chamber walls were significantly damaged. Stove inspections were ordered for the remaining three hot blast stoves to ensure that the furnace could operate on a three-stove operation. Hot endoscopic inspections for Stoves D2, D3 and D4 were performed in August of 2020. Repairing these stoves with traditional refractory systems using alumina and/or silica brick shapes would mean long lead times for engineering, procuring and manufacturing the standard and special shape bricks. Refractory suppliers were uncertain on actual delivery dates with estimates at over one year. Suppliers struggled with overseas raw materials and unpredictable shipping port delays. Clearly, Stove D1 must be repaired and online immediately with other material options before another stove could be taken offline for repairs. Therefore, Allied Minerals Technical Services LLC offered an innovative and proven solution to repair the stove refractories with the use of in-place castable pours. The in-place castable pours was selected for the following reasons:

i.    Material availability (in stock).
ii.   Short lead times compared to brick for unplanned repairs (Brick 1yr+).
iii.  Shorter construction period (ability to cast large panels at once.)
iv.   The castable design alleviates stress build-up in dome (Patent # US9194013B2).
v.    Tighter gas restriction in the partition wall by means of a significant reduction in mortar joints.
vi.   The ability to adjust the castable according to site conditions.

As the construction was finishing up on D1 (6 months after the failure) the total cost for in place castable was comparable to that of conventional refractory shapes. The castable design would again be implemented on Stove D3 once Stove D1 was completed and back on-line. The success of the castable repair on Stoves D1 and D3 lead to the decision to repair Stove C4 with in place castable as well. This paper will discuss the difference between castable and brick, castable design features, and construction techniques that make a castable repair option not only feasible, but a preferred option.

**HIGH SIGMA EVENT DESCRIPTION**
On the morning of July 16th, 2020, Blast Furnace D Stove No. 1 (D1) suffered a catastrophic failure at the connection of the cylinder and dome of the hot blast stove. Stove refractory was blown out of the top of the stove as the dome failed at the base circumferential rim. This violently distributed ~2000°F refractory brick across a vast area destroying equipment, burning wire trays, and taking away hydraulic controls from top charging, gas cleaning and stove functionality. No injuries were sustained but the potential for a life-threatening injury was substantial. Blast Furnace D was taken offline safely as it was isolated from the utilities and the uncontrolled fire at the top of the open hot blast stove D1 was dramatically minimized.

**CASTABLE VS. BRICK**
**Engineering and Logistics**
There is a clear advantage to using castable material over alumina or silica bricks when time is a factor. Designing a repair using castable requires less engineering and a shorter lead time to secure and manufacture the material. Using alumina and/or silica bricks requires engineering to ensure the bricks fit the designed radius. With castable, this engineering is eliminated and the castable follows the existing walls and formwork without cutting brick. Figure 1 below shows an example of a combustion chamber repaired using an alumina castable.
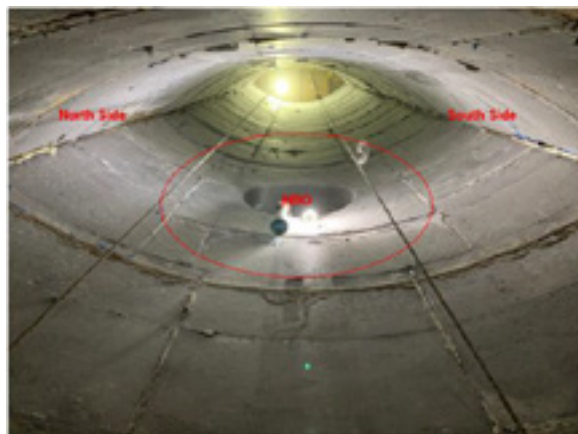


*Fig. 1: Complete castable combustion chamber*

**Expansion**
Traditional brick refractory systems can either use a panel construction or plastic packs for expansion. Both designs use mortar between the alumina bricks along with radial expansion provisions. This is a viable solution if designed and installed properly. However, upon cooling of hot blast stoves in which the refractory systems have failed, inspections have shown that using plastic as expansion provisions with mortar does not always work as intended. The expansion designed in panel construction has proven to show more longevity and less issues than the plastic pack design. If the expansion allowances are not followed correctly during construction, the panels can become unlocked allowing large sections of the combustion chamber walls to collapse. The telescopic brick used for expansion can crack at the tongue causing the panels to unlock (Figure 2).
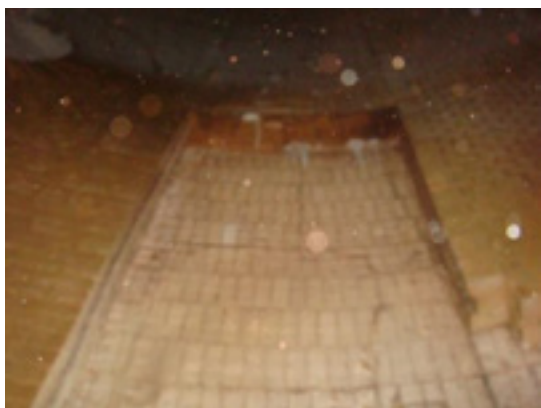
*Fig. 2: Panels unlocked due to cracked telescopic bricks at the tongue*

For castable stove designs, the combustion chamber walls are cast in large sections using a tongue and groove system to lock-in the panels. Expansion joints are placed between panels to absorb the growth of the castable in the radial direction to minimize the stress in the lining (refer to Figure 1). Furthermore, using castable eliminates the need for mortar joints, which are common deficiencies in traditional refractory systems when they are not applied correctly. Mortar joints that are not evenly applied to the brick's surfaces can create localized stress points on the refractory bricks as the refractory system expands and the pressure between each brick increases. Finally, the use of castable eliminates gaps between bricks that result from poor installation and/or design which cause localized hot spots on the shell.

### Installation

Installing bricks in traditional refractory systems is also labor intensive. The number of different brick shapes and different types of materials required for the installation requires a large lay down area and a competent expeditor to stage the bricks properly for installation. Monolithic materials come in powder form and are mixed with water on-site before being pumped into place between forms. The castable must be kept dry and above freezing to install correctly. Generally, once the pouring starts on one level, the formwork can begin on the next level. Installation of castable materials is straight forward once the formwork is in place. Figure 3 shows an example of how an original brick lining can be tied into a new castable lining.
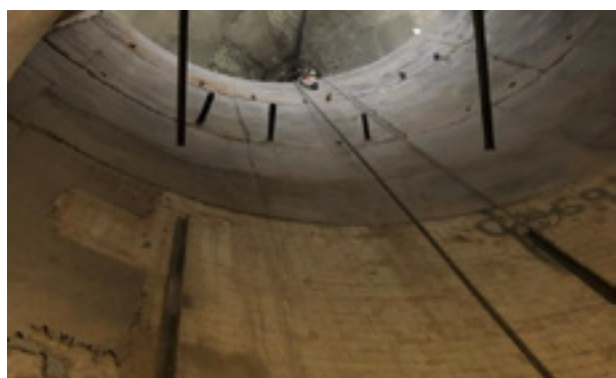


*Fig. 3: Castable pours integrated with existing brickwork*

### Material Properties

It is important to first note that the chemical, physical and mechanical properties of a material will vary depending on the supplier (higher % of andalusite versus lower % of andalusite and mullite/bauxite). Table 1 shows a chemical composition comparison between a typical high alumina brick and castable.

Tab. 1: Typical chemical composition of a high alumina brick and castsable

| Constituent | High Alumina Brick (%) | Alumina Castable (%) |
|---|---|---|
| $Al_2O_3$ | 65 | 62 |
| $SiO_2$ | 33 | 35 |
| CaO | N/A | 2 |
| $Fe_2O_3$ | 1 | 0.7 |
| $TiO_2$ | 0.3 | N/A |

The alumina and silica content are similar in both brick and castable. The differences arise in manufacturing and result in differing physical and mechanical properties, as shown in Table 2. Typical values are shown.

Tab. 2: Typical physical and mechanical properties of a high alumina brick and castable.

| Property | High Alumina Brick | Alumina Castable |
|---|---|---|
| Density (kg/m$^3$) | 2500 | 2680 |
| Porosity (%) | 18 | 16 |
| Cold Crushing Strength (MPa) | 40 | 64 |
| Modulus of Rupture (MPa) | 14 | 14 |

The andalusite-based alumina castable shows superior physical and mechanical properties. The castable has a higher density and lower porosity compared to the high alumina brick. Furthermore, the cold crushing strength is 60% higher than the alumina brick. The decreased porosity in the alumina castable improves its strength, load bearing capacity and corrosion resistance, however, reduces the thermal conductivity and thermal shock resistance. Therefore, while there are advantages to be gained by using castable instead of brick, there is also a compromise to be made. Materials are selected based on the conditions in the different zones of hot blast stoves to account for this in castable stove designs.

Some important properties for stove wall materials are creep and thermal shock resistance. The specific Allied andalusite castable was designed for stove internals. Table 3 below shows the results from an application-specific thermal shock test which indicates the relative difference between samples. A higher number indicates large loss in material strength, while a lower number indicates the material retained strength. The Allied andalusite-based castable proved superior to the other traditional andalusite-based stove bricks tested by a factor of 3 to 5. This material performs well in the lower combustion chamber due to the temperature fluctuations imposed by the flame.

Tab. 3: Thermal shock test results.

| Sample | Thermal Cycling Test Strength Loss (% of original) |
|---|---|
| Supplier A | 94.9% |
| Supplier B | 69.0% |
| Supplier C | 58.5% |
| Allied Andalusite-Based Castable | 19.9% |

The creep testing at the dome temperature for andalusite castable is an important part of the design. Samples were selected for creep testing during the repair of Stove D1 and D3. Table 4 shows the results.

Tab. 4: Creep test results per ASTM standards C-832.

| | Sample 10 Stove D1 | Sample 7 Stove D3 | Sample 11 Stove D3 |
|---|---|---|---|
| % Reduction of height of the sample under load at 1400°C after 20-50 hours | 0.27 | 0.34 | 0.34 |

The results show that the material is in a very good range with typical brick specifications and working conditions for these stoves.

## INSTALLATION / CONSTRUCTION

The stove refractory demolition began immediately with internal steel workers to provide an assessment of the remaining stove refractory. A field assessment was completed on Stove D1 to ensure the overall condition was satisfactory for rebuild. The objective was to salvage the 10-year-old checker column. A high-level scope of work was defined with the understanding that it was probable that additional issues would be discovered in the remaining refractories. Refractory in the combustion chamber required repairs in various areas and degrees in the hot face linings, crushed combustion wall intersections (Figure 4), burner inlet and hot blast outlet arches required repairs and design upgrades. Allied provided basic design changes including poured monolithic lintels arches and nozzles along with wall panel sections that tie-into to the existing refractory.

A contractor was selected in September 2020 and a construction plan was developed with much discussion regarding forms. All parties agreed to use a combination of wood forms and engineered scaffold which allowed for field adjustments to the existing conditions by the carpenters and bricklayers. The contractor began a slow methodical demolition with jack bracing down the combustion well with input from the operations and engineering departments (Figure 5). While demolition continued, the dome forms were under fabrication off-site (Figure 5). The first major cast was the burner inlet at the bottom of the combustion chamber. The nozzle back-up wall and hot face were made in two pours: one for the bottom section and one for the top section (Figure 6). The hot face walls were cast in sections with each pour approximately eight feet in height. The hot face pours continued up the combustion chamber until the bottom of the dome skewback pour. The various dome ring pours required a maze of form supports with the monolithic skewback pour being the largest at 96,000 pounds. The dome ring pours gradually reduced in size until the dome plug was the final pour (Figure 6). While installing the dome materials, the formwork in the combustion chamber was removed and a final inspection was completed for the poured walls.
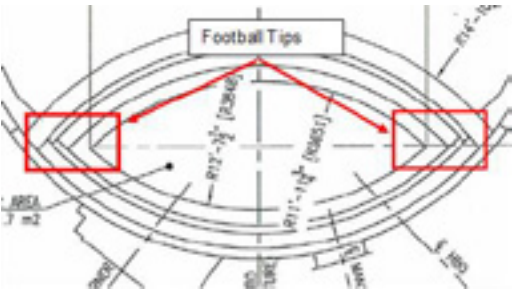


Fig. 4: "Football tips" of the combustion chamber.
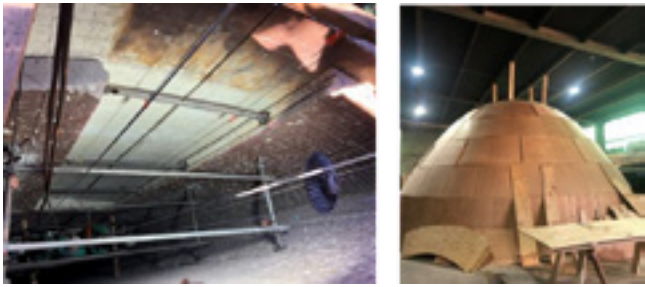


Fig. 5: Bracing the existing walls during demolition (left) and fabrication of the dome forms (right).



Fig. 6: Burner inlet pour (left) and complete castable dome (right).

## POST-REPAIR ANALYSIS

D1 stove was returned to service after a sufficient heat up / dry out in January of 2021. At the end of July 2021, an inner dome inspection was completed by Fosbel and Allied. Four videos were captured during this inspection and overall, the cast design of the inner dome proves to be holding up very well. Thermal scans were also performed on domes of stoves D1 and D3 during operation post-repair. The shell temperatures are in range with design calculations and are in an acceptable range for operation and validate the integrity of the repair. See Figure 7.
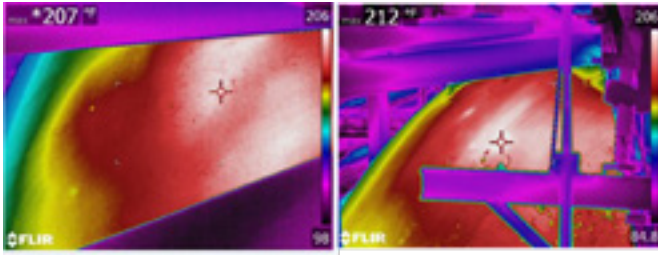


Fig. 7: Post-repair thermal scans of dome shell, stove D1 (left) and stove D3 (right).

The dome and stack temperature were compared before and after the repairs of stove D1 and D3.

Tab. 5: Dome and waste gas process temperature before and after the repairs of stove D1 and D3.

| | Stove D1 | | Stove D3 | |
|---|---|---|---|---|
| | Before Repair February 2021 | After Repair February 2022 | Before Repair February 2021 | After Repair February 2022 |
| Dome Temperature °F / °C | 2220 / 1216 | 2450 / 1343 | 2180 / 1193 | 2550 / 1400 |
| Waste Gas Temperature °F / °C | 525 / 274 | 535 / 279 | 540 / 282 | 530 / 277 |

**CONCLUSIONS**

In summary, a castable stove repair is superior to traditional brick designs for the following reasons:

  i.    Less engineering required.
  ii.   Shorter lead time to secure and manufacture the material.
  iii.  Ability to cast large panels at once.
  iv.   More functional expansion design due to panel construction.
  v.    Superior thermal shock properties compared to traditional andalusite bricks.
  vi.   Ability to retain strength under load at elevated temperatures (creep resistance).
  vii.  Eliminates the need for mortar joints, which are common deficiencies in stove construction if not applied correctly.
  viii. Helps to prevent short circuiting through the division wall (no bed or head joints).
  ix.   Can easily be tied into existing brick designs.

Burns Harbor management is confident in the new castable design. Enough so that three full stove repairs have been completed with this design and the current plan is to have four total castable designed stove repairs (two on each furnace).

# CORROSION MECHANISMS OF AL$_2$O$_3$–SIC–SIO$_2$–C REFRACTORY CASTABLES BY IRON AND SLAG BASED ON POST–MORTEM ANALYSIS OF INDUSTRIAL SAMPLES

Sina Darban[1], Laurent Cassayre[2], Simon Chiartano[3], , Laurie Lacarrière[1], Martin Cyr[1], Cédric Patapy[1], Pascal Prigent[3]

[1]Laboratoire Matériaux et Durabilité des Constructions, INSA/UPS Génie Civil, Université de Toulouse, CEDEX 04, 31077 Toulouse, France
[2] Laboratoire de Génie Chimique, Université de Toulouse, CNRS, INP, UPS, 31077 Toulouse, France
[3] TRB, 69150 Decines Charpieu, France

**ABSTRACT**
The Al$_2$O$_3$-SiC-C or (ASC) castables are used in the main runners of blast furnaces. Most of the published papers are focused on the laboratory corrosion tests due to the difficult access to the post-mortem samples of ASC castables. However, investigating the post-mortem samples is a key factor for reducing the wear of ASC castables. In this study, the microstructure of post-mortem samples located in working linings were investigated by SEM /EDS. The thermodynamic simulations were carried out in different systems such as slag/refractory and iron/refractory using the FactSage software. The SEM/EDS results showed formation of low melting phases such as gehlenite, anorthite, as well as spinel solid solutions in the matrix and calcium dialuminate near the alumina aggregates. The thermodynamic simulations showed that the slag and iron are prone to react with alumina and silicon carbide, respectively.

## 1. Introduction
To understand the corrosion mechanisms of ASC castables, it is informative to perform the corrosion tests in laboratory conditions. Nevertheless, the conditions (atmosphere, temperature, heating rate) of the laboratory tests can be far from industrial conditions. Therefore, investigating the post-mortem samples that were exposed to the real industrial conditions could be interesting to achieve better understanding of the real needs for improving the next generation of refractory materials. The study on the post-mortem ASC castables, especially, in the various zones of the runner is determinant of their lifetime. Comparing the post-mortem samples of ASC castables located in the working linings of the runner could give important information regarding their chemical and mechanical degradations.

As such, this research is focused on the corrosion mechanism of ASC castables by implementing the post-mortem analysis as well as thermodynamic computations. For this means first the microstructure of the post-mortem samples of ASC castables from different (turbulence, middle, non-turbulence) zones of the main runner were investigated by SEM/EDS. Next, the thermodynamic simulations were performed with the FactSage commercial software. Based on the principle of the main runner of blast furnace, the thermodynamic computations investigated phase equilibria with presence of slag or iron in contact with ASC castables at high temperature as well as during the cooling steps.

## 2. Materials and method
### 2.1 Slag and refractory castable
Tab. 1 shows the chemical composition of blast furnace (BF) slag used in this study. The major components are (wt.%) SiO$_2$ 37.2, CaO 34.4, Al$_2$O$_3$ 14. The minor components are (wt.%) MgO 8.8, K$_2$O 1, SO$_2$ 0.9, TiO$_2$ 0.7, MnO 0.6, Na$_2$O 0.6, FeO 0.4. Based on CaO/SiO$_2$ the percentage of the basicity is around 0.9 % which indicate that the BF's slag is an acidic slag.

Tab. 1: Chemical composition of blast furnace slag.

| Components | wt.% |
|---|---|
| SiO$_2$ | 37.2 |
| CaO | 34.4 |
| Al$_2$O$_3$ | 14 |
| MgO | 8.8 |
| K$_2$O | 1 |
| SO$_2$ | 0.9 |
| TiO$_2$ | 0.7 |
| MnO | 0.6 |
| Na$_2$O | 0.6 |
| FeO | 0.4 |
| Others | 1.4 |
| Sum | 100 |
| %B (CaO/SiO$_2$) | 0.9 |

The mineralogical composition of ASC castables is shown in Tab. 2 The major components of the castable are (wt.%) 60-65 alumina aggregates (0-1 mm,1-3 mm, 3-5 mm, 5-10 mm), 15-25 silicon carbide (0-200 μm, 0-1mm), 8-15 fine alumina (3-6 μm). The minor components are (wt.%) 2-3.5 carbon, 1-2.5 cement, 0-2.5 silica fume, 0.5-3 antioxidants, and 0.1-0.2 additives for flowability and setting time.

Tab. 2: The chemical composition of Al$_2$O$_3$-SiC-C castables.

| Components | wt.% |
|---|---|
| alumina aggregates | 60-65 |
| Silicon carbide | 15-25 |
| Fine alumina | 8-15 |
| Carbon | 2-3.5 |
| Cement | 1-2.5 |
| Silica fume | 0-2.5 |
| Antioxidants | 0.5-3 |
| Additives | 0.1-0.2 |

### 2.2 Selection of the post-mortem bricks of the main runner
The post-mortem Al$_2$O$_3$-SiC-C (ASC) castables are received from the industrial partner of this project. According to Fig.1 (b) the (post-mortem) samples are (from top to bottom) called slag line (sample 1), slag/metal line (sample 2), and metal line (sample 3). Samples A-1 and A-2 were investigated from turbulence (A) zone.
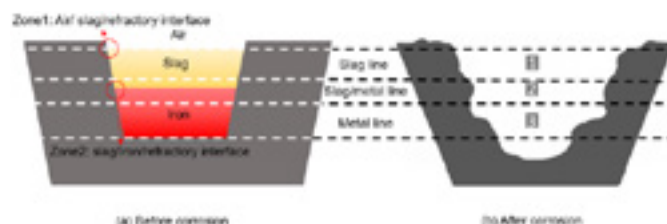


Fig. 1: *Schema of main runner of blast furnace before (a) and after (b) corrosion. The runner is divided into air/slag/refractory (zone 1) and slag/iron/refractory (zone 2). The post-mortem samples selected from slag line (1), slag/metal line (2), metal line (3).*

### 2.3 Thermodynamic simulations with FactSage software
The commercial software FactSage® v8.2 [1] was implemented for the high temperature thermodynamic calculations. The calculation consisted in adding an increasing amount of slag in a system composed initially of pure ACS castable, in order to calculate the nature and amount of the phases resulting from the equilibrium, and thus simulate the corrosion reactions. The temperature was 1550 °C, and the pressure was 1 atm.

## 3. Results and discussion

Fig. 2(a, b) shows the SEM images with lower and higher magnification of the hot face of the sample A-2, respectively. The sample A-2 was positioned in the slag/metal transition area during the lifetime of the main runner. Fig. 2(a) shows that the crystallized slag is mainly made of gehlenite ($Ca_2AlSiO_7$). The in-situ spinel particles with rectangular shapes are present in the interaction within the infiltrated zone. On the right upper side, the titanium particles accumulated near the spinel ($MgAl_2O_4$) particles. The thin interaction zone between slag and alumina aggregate is shown in Fig. 2(b). A layer of calcium dialuminate ($CA_2$) is formed along the alumina aggregate [2].



Fig. 2: *SEM-BSE mode images of hot face of sample A-2, low magnification (a) and high magnification (b).*

Fig. 3 shows the main stable phases during the addition of slag to 100 g of ASC castables at 1550 °C, where the amount of slag was increased from 0 g to 50 g by step of 5. These calculations aim to represent the reaction of slag infiltrating into the refractory. It could be observed that without slag in the system (i.e. for the x-axis value of 0 in Fig. 3), the calculation predicts the presence of two major phases, $Al_2O_3$ and SiC, as well as small amounts (about 3 g) of anorthite ($CaAl_2Si_2O_8$) and mullite ($Al_6Si_2O_{13}$). These two later phases are probably not representative of the ASC castable's initial phase distribution, but, due to their low concentration, we considered they could be disregarded. Furthermore, these minor phases tend to disappear in contact with small amount of slag.

Increasing the amount of slag causes the amount of alumina ($Al_2O_3$) to decrease from about 70 g to 30 g. This means that the infiltration of slag can induce the dissolution of large amounts of alumina aggregates. Conversely, the content of silicon carbide (SiC) is constant, which means that silicon carbide cannot dissolve into the slag. For high amounts of slag (above 30 g for 100 g of refractory), the formation of minor secondary phases (calcium hexaluminate ($CaAl_{12}O_{19}$), and spinel ($MgAl_2O_4$)) is predicted. The detection of such phases in corroded materials could then be an indicator of a strongly corroded zone.
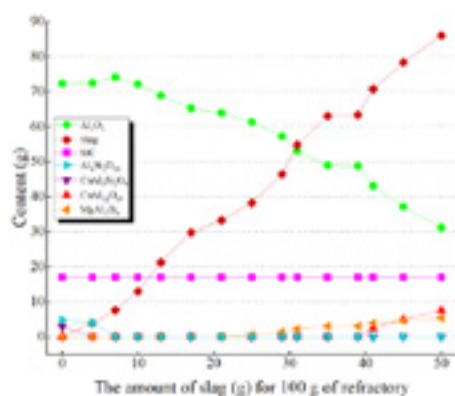


Fig. 3: *Predicted stable phases in the refractory+slag system at 1550 °C.*

Here, microstructural analysis of hot face region (Fig. 2) and the thermodynamic results of slag/refractory system (Fig. 3) are in line with each other. Regarding sample A-2, the thermodynamic results are in accordance with experimental SEM/EDS results.

The SEM images showed that the calcium dialuminate ($CA_2$) as well as spinel grains are present in the hot face. Based on the FactSage results, by increasing the content of slag in the ASC castables, both calcium hexaluminate and spinel were formed at 1550 °C in the final steps. Also, they were formed during the cooling procedure of slag-ASC castable. The mechanism of formation of calcium aluminates e.g., CA, $CA_2$, $CA_6$ is extensively explained in [3], [4] and it is not in the domain interest of this study.

According to the thermodynamic results, the calcium hexaluminate should form at 1550 °C, when large amount of slag reacts with alumina. Furthermore, it is also a stable phase during the cooling steps, due to the infiltration of $Ca^{+2}$ ions from the slag side into the calcium dialuminate layer. Nevertheless, our examinations (Fig. 2) showed that calcium dialuminate layer was formed around the alumina aggregates of sample A-2 rather than the hexaluminate phase, indicating that the system did not reach equilibrium because of the protective role of $CA_2$.

The SEM image in Fig. 2(b) showed that the anorthite and gehlenite were formed in the infiltrated matrix of sample A-2 that are in accordance with the thermodynamic simulations showed in Fig. 3. According to the thermodynamic results, during the cooling of slag, first the anorthite started to form at 1500 °C and the gehlenite appeared at 1100 °C. Hence, it is concluded that the formation of ternary phases such as gehlenite and anorthite is in the infiltrated matrix is progressed during the cooling of slag and not at the working temperature.

## CONCLUSIONS

Obtained experimental results were compared with those simulated by the thermodynamic software of FactSage. It was found that the simulated results correlated with the obtained results from the microstructural characterizations of the post-mortem samples of ASC castables.

The presence of gehlenite, anorthite, solid solutions of spinel were confirmed in the infiltrated regions of the matrix of post-mortem sample A-2 that were located in the slag/iron transition area of the working lining in the main runner.

According to the thermodynamic results the slag was mainly reacted with alumina from the refractory side and not silicon carbide or carbon.

## REFERENCES

[1] Bale, Christopher W., E. Bélisle, Patrice Chartrand, S. A. Decterov, G. Eriksson, Aïmen E. Gheribi, K. Hack et al. "Reprint of: FactSage thermochemical software and databases, 2010–2016." *Calphad* 55 (2016): 1-19.

[2] Braulio, M. A. L., AG Tomba Martinez, A. P. Luz, C. Liebske, and V. C. Pandolfelli. "Basic slag attack of spinel-containing refractory castables." *Ceramics International* 37, no. 6 (2011): 1935-1945.

[3] de Bilbao, Emmanuel, Mathieu Dombrowski, Henry Pilliere, and Jacques Poirier. "Time-resolved high-temperature X-ray diffraction for studying the kinetics of corrosion of high-alumina refractory by molten oxides." *Corrosion Science* 139 (2018): 346-354.

[4] Darban, Sina, Camille Reynaert, Maciej Ludwig, Ryszard Prorok, Ilona Jastrzębska, and Jacek Szczerba. "Corrosion of Alumina-Spinel Refractory by Secondary Metallurgical Slag Using Coating Corrosion Test." *Materials* 15, no. 10 (2022): 3425.

283

# DEVELOPMENT OF HIGH-PERFORMANCE SILICA REFRACTORY WITH LOW RESIDUAL QUARTZ FOR COKE OVEN BATTERIES

D. Banerjee, J. P. Nayak, B. Ghosh, P. Das, H. Nagata, S. Sengupta, H. Sehgal, P. B. Panda

TRL Krosaki Refractories Ltd., Jharsuguda, Odisha, India

## ABSTRACT

Silica bricks have always been the standard refractory used in the construction of coke oven batteries for over a few decades now. With technological advancements, production challenges and requirements of longer campaign life of batteries, new and improved qualities of silica refractories have now been in great demand over the last few years. To meet these requirements, high-performance silica bricks have been developed with optimum amount of residual-quartz content.

Residual-quartz (RQ) in silica bricks plays a very crucial role in determining the life of the refractories, as well as the campaign period of coke oven batteries. RQ is basically the low-quartz phase in fired silica bricks which has not converted into high temperature sTable phases during firing. This undergoes transformations during heating up of the batteries, causing volume expansions, thus resulting in cracks and subsequent destabilization of the refractory structure. Lower the residual-quartz content, lesser will be the expansion in the refractory lining work of the batteries while heating, ensuring maintenance of a proper and an optimum battery heating curve with no fluctuations.

In the present article, the authors have elaborated the development of high-performance silica refractory with low RQ content 1-1.5%. The product has been designed using high-purity quartzite, selecting high-grade mineralizers and additives. The production process followed highly modernized equipment like high-capacity inclined mixer machine, automatic hydraulic presses and tunnel kiln designed to fire silica bricks. The developed product has been supplied to some of the leading steel plant's coke oven rebuilding job and is running successfully.

## MATERIALS AND PROCEDURE

### Selection of Raw Materials

Silica refractories are produced from chemically pure quartzite with $SiO_2$ content >97%. Naturally, quartzite comes in two variants namely coarse crystalline (hardened chemically) and crypto crystalline (hardened tectonically)[1]. With various internal trials, suitable source of medium to coarse crystalline quartzite was identified from Chuinpally, India having desired properties like silica greater than 99%, very low amount of fluxing agents, good thermal behavior, and ease of conversion to higher temperature form.

Materials which accelerate the conversion from low temperature form to high temperature polymorphic form are called mineralizers. Transformation process of quartz to tridymite and cristobalite is sluggish in nature because it involves bond breaking and bond formation (reconstructive transformation). To optimize the conversion of quartz into tridymite & cristobalite, without affecting the high temperature properties, combination of various mineralizers (lime, iron oxide and other calcium containing binder) were used. Types of mineralizers, their composition and method of addition to the mix were chosen based on the result of internal trials. According to Dale's theory, lime slurry (hydrated lime) loses

its physical moisture within 200°C and at around 400°C, it starts decomposing to form anhydrous lime and with increase in temperature to 800°C, reaction between nascent lime and fine silica starts and forms $CaO-SiO_2$ bonding phase in the refractory aggregates and further increase in the temperature to 1250°C-1300°C, liquid starts forming in the $CaO-SiO_2$ system in the presence of impurities like $Fe_2O_3$, $Al_2O_3$, $TiO_2$ etc. The basic mechanism of transformation involves dissolution of quartz in the $CaO-SiO_2$ liquid system and precipitation of cristobalite crystals from the liquid[2].

Tab. 1: Typical data of quartzite chosen for this development.

| Components | % | Quartzite Firing Analysis (fired at 1440°C, 36 hours soaking) | |
|---|---|---|---|
| $SiO_2$ | 99.01 | AP % (before firing) | 0.6 |
| $Al_2O_3$ | 0.42 | AP % (after firing) | 12.3 |
| $Fe_2O_3$ | 0.37 | BD (g/cc) (before firing) | 2.63 |
| CaO | 0.06 | BD (g/cc) (after firing) | 2.01 |
| $Na_2O+K_2O$ | 0.06 | ASG (before firing) | 2.64 |
| $TiO_2$ | Trace | ASG (after firing) | 2.30 |
| LOI | 0.10 | % of phase conversion (based on ASG) | 13.02 |

Fig. 1: Microstructure of a typical quartzite grain showing medium to coarse crystalline structure; average crystal size: 390μm - 400μm.
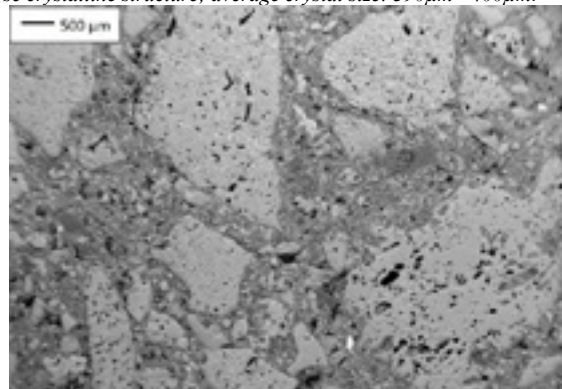


Fig. 2: Tridymite and Cristobalite phases well observed in burnt quartzite, suggesting good amount of phase conversion in raw material.
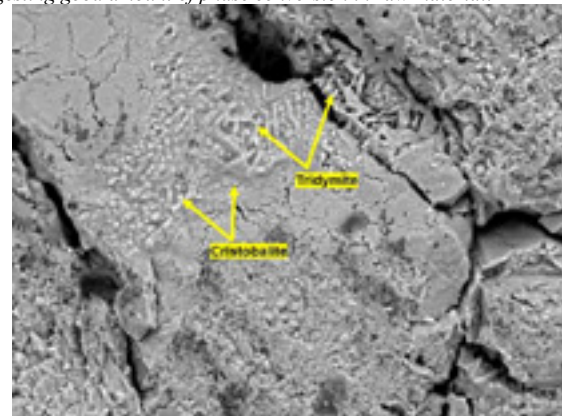
**Manufacturing Process**

*Washing, Grinding & Screening of Quartzite*

Quartzite lumps received from the mines are washed, dried, hand-picked and fed into jaw crusher for grinding and then into secondary crusher to get desired size fractions of coarse, fines and by magnetic separator system (using strong electromagnets) and then these materials are transferred to the silos.

*Batching & Mixing*

Balance car collects the raw material from silos according to the specified batch composition and charged into high intensity inclined EIRICH mixer machine which ensures mixing with high productivity and homogeneity. Mineralizers, organic green binders, and special additives (for high grade KS quality bricks) are added to prepare the workable mix.

*Pressing*

The mix is pressed in PLC-controlled high capacity 1600 Ton SACMI automatic hydraulic presses in metal molds. Complicated shapes are pressed in electric screw presses. Consistent green properties are ensured with careful monitoring of mix granulometry, moisture and binder content.

*Drying & Firing*

Natural drying of molded bricks is followed by tunnel drying and duration of drying depends on the weight of the brick.

Dried bricks are set on the cars, small bricks are placed on the top and bigger bricks are set on the bottom and are arranged in such a way that maximum area is exposed for the conduction and convection to take place for uniform firing thereby ensuring maximum transformations into the required phase and consistent properties of finished bricks.

Firing silica bricks is the most critical step in its manufacturing because of the polymorphic transformation of silica associated with moderate to high volume changes at different temperatures. As high as 4-5% linear expansion takes place due to these high temperature phase transformations. Firing curve is selected based on the thermal properties of raw material in a way to maximize conversion of quartz into tridymite and minimize residual quartz to the range of 1-1.5 % or lesser. At around 600°C slow cooling is required to accommodate any volume changes because of presence of residual quartz ($\beta$-quartz to $\alpha$-quartz).

Ried Hammer designed, gas fired, long tunnel kiln equipped with PLC controlled preheating, firing and cooling zone is used for the firing of the green dried silica bricks. Firing curve is maintained as designed by Ried Hammer. Firing temperature of silica bricks depends on the desired final phase (cristobalite/tridymite) in the brick. For tridymite, soaking temperature is maintained in the range of 1430°C-1450°C. Temperatures of different zones are digitally monitored for better RQ control and consistency in finished products.

*Inspection & Dispatch*

Each lot of the bricks passes through stringent quality check. ISO-5022, ISO-9001, DIN-1089-1 [3] are followed to carry internal quality checks.

Fig. 3: Flow chart depicting the manufacturing process of silica refractories.



**Characterization**

Following apparatus and methods were used for testing raw materials and finished products.

1. Chemical Analysis by XRF as per DIN 51001
2. Physical properties (AP, BD, ASG) as per DIN 51056
3. Microstructure by ZEISS EVO 18 Scanning Electron Microscope
4. Creep-in-compression by Netzsch Hot load Furnace as per DIN 51053 (part-2)
5. RUL test as per DIN 51064
6. PCE test as per DIN 51053 (part-1)
7. Abrasion resistance test as per DIN 50148
8. CCS test as per DIN 51067 (part-1)
9. RTE as per IS 1528-1991 (part-11)

Tab. 2: DIN 1089-1 standard and TRLK test.

| Properties | Grades as per DIN 1089-1 | | | TRLK Test Results | | |
|---|---|---|---|---|---|---|
| | KN | KD | KS | SCW KN | SCW KD | SCW KS |
| **Chemical Analysis (%)** | | | | | | |
| SiO₂ (min) | 94.50 | 95.00 | 95.00 | 95.32 | 95.48 | 96.01 |
| Al₂O₃ (max) | 2.00 | 1.50 | 1.50 | 0.46 | 0.42 | 0.43 |
| Fe₂O₃ (max) | 1.00 | 1.00 | 1.00 | 0.82 | 0.75 | 0.71 |
| CaO (max) | 3.00 | 3.00 | 3.00 | 2.21 | 2.26 | 2.23 |
| Alkali (max) | 0.35 | 0.35 | 0.35 | 0.06 | 0.12 | 0.11 |
| **XRD Analysis** | | | | | | |
| % RQ (max) (coarse crystalline) | 6.00 | 6.00 | 6.00 | 0.92 | 0.87 | 0.84 |
| % RQ (max) (crypto crystalline) | 1.50 | 1.50 | 1.50 | | | |
| **Physical Properties** | | | | | | |
| AP % (max) | 24.5 | 22.0 | 22.0 | 21.0 | 19.4 | 16.8 |
| BD (g/cc)* | - | - | - | 1.84 | 1.86 | 1.88 |
| A.S.G.* | - | - | - | 2.33 | 2.34 | 2.32 |
| CCS (N/mm²) (min) | 28.0 | 35.0 | 45.0 | 32.0 | 41.0 | 52.0 |
| **% Creep at 1450°C with load at loading rate of 2kg/cm²** | | | | | | |
| Z₅₋₂₅ (max) | 0.12 | 0.12 | - | 0.03 | | |
| Z₂₅ (max) | 0.35 | 0.35 | - | 0.09 | | |
| **Other physical, thermal & thermo-mechanical properties** | | | | | | |
| RUL (tₐ) °C (min) | 1640 | 1650 | 1650 | 1670 | 1670 | 1680 |
| PCE (SK) (min) | 31 | - | - | +31 | +31 | +31 |
| Abrasion (mm) (max) | - | - | 4.50 | - | - | 2.86 |
| RTE*(% at 1000°C) | - | - | - | 1.26 | 1.25 | 1.23 |

*Additional testing (apart from DIN specification).*

285

## RESULTS AND DISCUSSIONS

The properties of different grades of silica refractories as per internationally recognized DIN 1089-1 standard and test results of developed high performance silica bricks at author's plant have been shown in Table-2. Apart from DIN 1089-1, additional characterization like RTE has also been carried out.

### Chemical Analysis

As observed from Table-2, the alumina and alkali content which deteriorate the high temperature properties of silica brick, are well below the permissible limit and this result shows that selected quartzite is suitable for high performance silica refractory.

### Mineralogy

During heating up of silica refractory, high amount of residual quartz (RQ) gives higher thermal expansion and so to keep the expansion value low, the brick should have low residual quartz [4]. Mineralizers, ease of conversion of raw materials, firing temperature and soaking period control the amount of RQ in silica brick. In the long run of application of silica brick in coke oven where application temperature is in the range of 1200°C-1380°C, following phenomenon occurs: 1) conversion of cristobalite into tridymite which results in positive expansion and 2) lattice contraction of tridymite particles which may result into maximum 0.3% negative expansion in the silica brick [5]. To counterbalance the effect of negative expansion, some amount of RQ should be present in the silica refractory.

### Physical Properties

Granulometry was adjusted to achieve high green bulk density and use of optimized combination of mineralizers helped in sintering which subsequently resulted in high bulk density and sufficiently low apparent porosity (as per DIN standard) and accordingly improvement in compressive strength was observed. High dense silica bricks improve the thermal conductivity, thus improving the efficiency of coke oven batteries by reducing the coking time.

### High Temperature Properties

PCE & RUL values were found to be well above standard value. High value was achieved by using purer raw materials having extremely low content of fluxing agents, thus ensuring minimal formation of viscous liquid at relatively low temperature and good high-temperature properties.

Creep-in-compression determines the long-term life of silica refractory in the coke oven. It gives an idea about the deformation of brick under load at high temperature. Excellent creep resistance quite below the specified value was found for silica bricks manufactured at author's plant. Creep test curve for KD quality has been shown with the testing condition in Fig-4.

### XRD Analysis for RQ Content Determination

XRD analysis of the samples were done to determine the residual quartz content. From Table-2, it is seen that RQ content is well within norms. This was achieved due to careful selection of quartzite having medium to coarse crystalline crystal structure with average crystal size in the range of 390μm - 400μm, and by maintaining a stable firing curve during the entire firing process with enough soaking period to ensure maximum conversion of quartz to tridymite and cristobalite.

Low level of residual quartz ensures very low and minimal volume changes due to displacive transformations ($\alpha\leftrightarrow\beta$ phase transformations) during application, thus ensuring good structural integrity of the refractory structure over the long-life cycle of coke oven batteries.

### Microstructure

Microstructure images of TRLK developed KD, KN, KS quality silica refractory by SEM have been shown in figures Fig. 5-6, Fig. 7-8, and Fig. 9-10 respectively.

*Fig. 4: Creep test curve of TRL SCW KD.*

*Fig. 5: KD quality brick showing tridymite and glassy phase formation in the matrix region and conversion of fine silica grain into cristobalite.*



*Fig. 6: KD quality brick showing well distributed and balanced tridymite and cristobalite phases.*
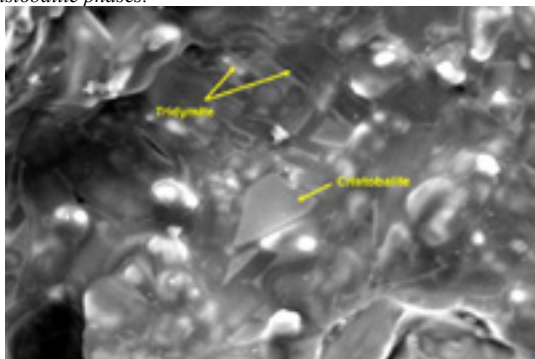


*Fig. 7: KN quality bricks showing tridymite and glassy phase in matrix part.*
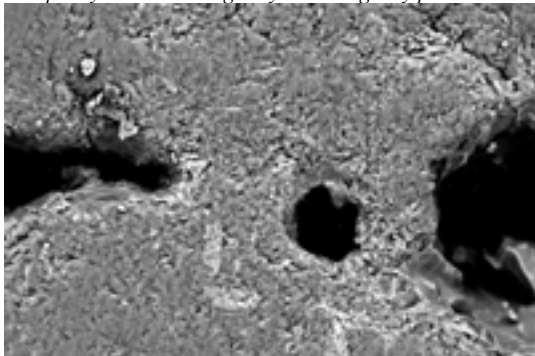


*Fig. 8: KN quality bricks showing coarse silica grain converted to cristobalite.*
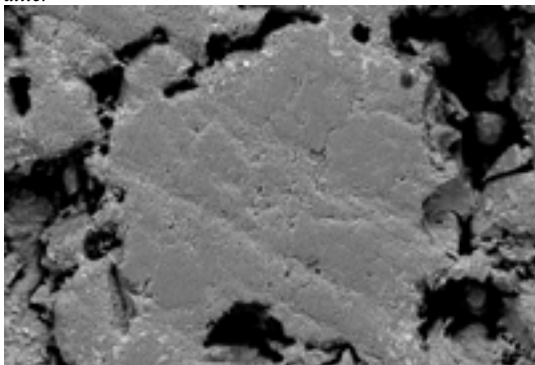


*Fig. 9: KS quality bricks showing well-formed grain boundaries.*
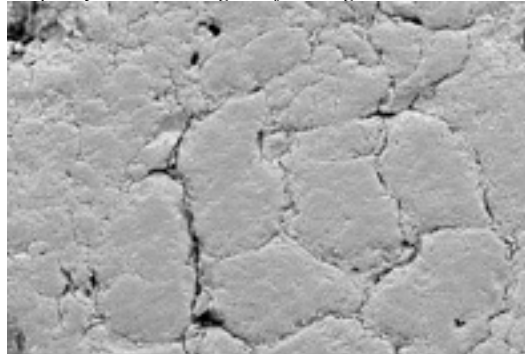


*Fig. 10: Special additive grain in KS quality bricks; increases abrasion resistance of oven sole bricks.*



## CONCLUSION

High performance silica refractories with improved properties like lower residual quartz, high creep resistance, high density and optimum distribution of tridymite and cristobalite phases have been developed at author's plant meeting the internationally accepted specification like DIN 1089-1. The selection of appropriate grade of high purity quartzite, optimum combination of mineralizers and binders and state-of-the-art manufacturing technology has resulted in improved quality of silica bricks which have been supplied globally to steel plants for modern and high-efficiency coke oven battery construction, and have been running successfully.

## REFERENCES

[1] Stanislav Dvorak: *Development and Production of High-Density Silica for Coke Oven;* IRMA Journal Vol. XXXXVI, No 2, June 2013.

[2] R Sarkar: *Refractory Technology: Fundamentals and Applications*.

[3] DIN 1089-1: *Refractories for Use in Coke Ovens Part 1: Silica Bricks; Requirements and Testing*, Feb 1995.

[4] P. Sahu, N. Sahoo: *Improvement of Silica Refractory for Modern Coke Oven;* IRMA Journal, Volume-2, Jun 2013.

[5] F. Brunk: *Silica Bricks for Modern Coke Oven Batteries;* COKE MAKING.

287

# ONLINE REPAIRING OF BLAST FURNACE TROUGH TO ENHANCE HOT METAL THROUGHPUT

Arup Kumar Samanta*, Sougata Roy, Subhadeep Chatterjee, Amit Banik, Yoshihiro Mizuma, Sunanda Sengupta, P. B. Panda

TRL Krosaki Refractories Limited, Belpahar-768218, Odisha (India)

## ABSTRACT

In the field of Iron making, new technologies are being adopted for improving the quality of hot metal and to increase the productivity. Many integrated steel plants are gradually increasing their Blast furnace capacity to achieve higher productivity with lower rate of coke consumption, in turn, energy consumption. To make such advancement successful, running of trough without interruption is imperative to continue the supply chain of hot metal. Thus, it is becoming a big challenge for refractories technologists to further increase the hot metal throughput before taking a shut down for repair works. To address this, improvement in castable quality is not sufficient, rather, online repairing is the most beneficial technique to further extend refractory life with minimum down time. Moreover, cracking in trough is a common issue due to intermittent operation and frequent hot metal discharge which restrict to get expected hot metal throughput. Online repairing not only extends the throughput and controls the specific consumption of refractories but also protects the trough from metal leakage due to cracking.

In the present work, one new trough repairing material is developed by careful selection of base raw materials and special additives suitable for wide variation of temperature range. The removal of moisture was studied at temperatures ranging from $(200 – 500^{0}C)$ along with strength development. The blasting/explosion behaviour was examined at $1000^{0}C$ and $1300^{0}C$. The developed material is used in several integrated steel plants and the performance is satisfactory in terms of extended hot metal throughput.

## INTRODUCTION

The iron ores which were not very rich in Fe (Iron) and having high impurities of other metallic elements (like Mn) and oxides (like $Al_2O_3$) have not been used earlier days in BF operations. However, with increase of production facilities supplies of good quality iron ore are becoming expensive for iron making.

While using good quality iron ores the MnO content varies from 0.2 to 0.5% in slag. But it may go upto 3% while using low grades iron ore. The MnO present in slag affects the refractory through different mechanisms. It forms several low eutectic compounds[1] with other oxides like $Mn_2Al_4Si_3O_{18}$ ($1180^{0}C$), $Mn_3Al_2Si_3O_{12}$ ($1200^{0}C$), $MnSiO_3$ ($1293^{0}C$), $Mn_2SiO_4$ ($1347^{0}C$) and lowering the viscosity of the slag. It also increases the wettability of refractory surface while changing the wetting angle below $90^{0}$ between solid and liquid.

Under the present circumstances, usages of iron ores with high manganese oxides, the frequency of repairs of normal $Al_2O_3$- SiC-C bearing trough castables has increased many folds with decreased reliability of performance. But frequent shutdown of trough is not permitted from the view point of Blast furnace operation. Therefore, *Online* repairing of blast furnace trough is only the solution to enhance the trough throughput. So, the need is to design a good repairing material which can be used *Online* by gunning. There are several advantages while repairing trough without taking shut down like cracks are filled up with gunning after trough discharge, no metal penetration through the affected areas and no formation of any rat/dent hole after discharge. Additionally, it is safe, user friendly and easy to install. No need to arrange manpower for repairing cracks or localize affected areas and finally life of trough can be stretched to a certain limit while keeping minimum corrosion/erosion of original working lining castable.

## EXPERIMENTAL

The present trough repairing material is having some shortcomings specifically it is not suitable when there is wide variation of trough surface temperature at the time of application by gunning as it is based on high alumina cement. The major issue is blasting/explosion followed by chipping out. To avoid this issue two more recipes are designed without high alumina cement and introducing several additives. It has been observed that the trough temperature varies between $200^{0}C$ to $500^{0}C$ before applying the repairing material through gunning. Blasting or explosion is basically due to presence of moisture inside the repairing material and hence blasting can be avoided if moisture is removed before tapping the hot metal in trough. To understand the presence of residual moisture, the rate of removal of moisture in the temperature range of $200^{0}C$ to $500^{0}C$ was studied upto 90 minutes along with development of strength. The blasting cum explosion tendency was studied while putting the samples inside the furnace at $1000^{0}C$ and $1300^{0}C$ for 30 minutes.

## RESULTS & DISCUSSION

The recipe of existing repairing material along with two trial recipes are shown in Table.1. In case of two trial recipes there is no high alumina cement binder rather several non-hydraulic binders are introduced.

Table:1 Recipes of existing and trial through repairing material

| Raw Materials | Trough Gun | Trial - 1 | Trial - 2 |
|---|---|---|---|
| HAC binder | 3.5 | 0 | 0 |
| Additive - 1 | 1.8 | 4.8 | 2.4 |
| Additive - 2 | 0 | 0.5 | 0.25 |
| Additive - 3 | 2 | 0 | 0 |
| Additive - 4 | 0.05 | 0 | 0 |
| Additive - 5 | 0.5 | 0 | 0 |
| Additive - 6 | 0.7 | 1.2 | 0.6 |
| Organic fibre | 0.25 | 0.2 | 0.2 |
| Others | 93 | 97 | 94 |

In Fig.1, removal of moisture at $200^{0}C$ is shown with the time duration of 30, 60 and 90 minutes. The strength development was studied while measuring the CCS. The same is shown in Fig.2 at $500^{0}C$. The observations both at $200^{0}C$ and $500^{0}C$ are same.
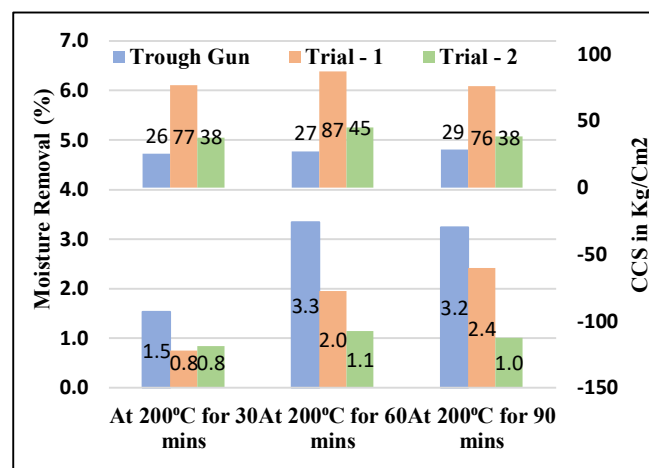


*Fig.1: Moisture removal and sgtrength development at $200^{0}C$*

For existing trough gun, there is maximum moisture removal at both the temperatures as it is having high alumina cement binder. On the other hand, strength development is highest for Trial -1 material.
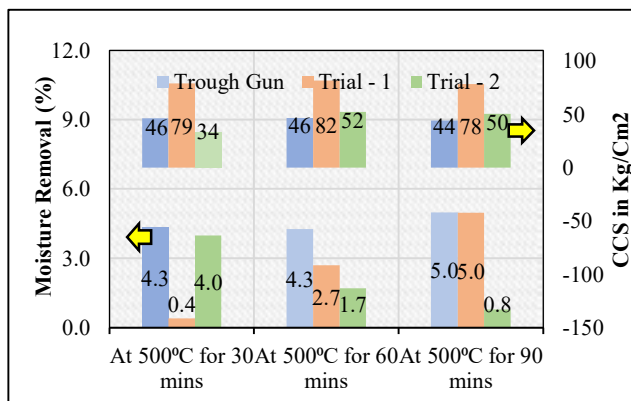


*Fig.2: Moisture removal and strength development at 500$^0$C*

The blasting tendency was studied at 1000$^0$C and 1300$^0$C and the appearance of samples is shown in Fig.3 after conducting the test at 1300$^0$C. Both at 1000$^0$C and 1300$^0$C there is damage in existing sample whereas Trial-1 and Trial-2 samples are almost in good condition. However, slight damage is observed in Trial-1 sample at 1300$^0$C. But Trial-2 sample is in good condition. Therefore, considering the blasting tendency, Trial-2 sample is showing the best results.



*Fig.3: Samples appeatance after blasting test at 1300$^0$C*

Considering the strength development and blasting/explosion tendecy, Trial -1 material was applied in an integrated steel plant in two troughs (T-1 & T-2). The appearance of trough before application and after application is shown in Fig.4. The appearance of trough after repairing is very smooth and all the cracks are filled up with the repairing material.



*Fig.4: Appearance of trough before (Left) and after application (Right) of repairing material*

The application details like thickness build up approximate rebound loss, material used and throughput after each gunning is shown in Table.2. The hot metal throughput acheived after gunning with repairing material is shown in Table.3
From our previous experience and data we have calculated the total erosion of working lining to achieve the certain hot metal through put. The same is compared when repairing material was applied. While applying the repairing material there is significant reduction in erosion is observed and it is shown in Table.4.

Table 2: Details parameters while using trough repairing material

| Parameter | T1 Trough | | | T2 Trough | | |
|---|---|---|---|---|---|---|
| Campaign | 1st | 2nd | 3rd | 1st | 2nd | 3rd |
| Life in THM | 117841 | 153718 | 189615 | 82724 | 100852 | 201821 |
| Qty used (MT) | 2 | 1.5 | 1.1 | 1.2 | 1 | 1.2 |
| Rebound Loss (%) | 8 | 9 | 9 | 8.5 | 9 | 8.5 |
| Thickness build up (mm) | | | | | | |
| Impact Area | 90-100 | 70-80 | 60-70 | 60-80 | 60-80 | 60-80 |
| Others area | 50-60 | 50-60 | 30-40 | 40-50 | 30-40 | 40-50 |

Table 3: Hot metal throughput with repairing material

| Trough No | Trough life (Throughput in MT) | | |
|---|---|---|---|
| | Gunning started at | Final life at the end of the campaign | Gunning life |
| T1 | 117841 | 189615 | 71774 |
| T2 | 82724 | 201821 | 119097 |

Table 4: Details parameters while using trough repairing material

| Trough | Distance From Taphole in Mtrs | Lower corrosion of working lining castable (mm) | |
|---|---|---|---|
| | | Slag Line | Metal Line |
| T1 | 2 | 48/33 | 33/55 |
| | 6.5 | 45/31 | 51/43 |
| | 9.5 | 34/22 | 36/12 |
| | 12.5 | 19/41 | 34/30 |
| T2 | 2 | 84/90 | 85/67 |
| | 6.5 | 52/60 | 50/48 |
| | 9.5 | 63/49 | 53/46 |
| | 12.5 | 26/46 | 51/36 |

**CONCLUSIONS**
Due to high productivity of blast furnace, it is not permitted to allow frequent shutdown of trough for intermediate repairing. Online repairing by suitable material is the solution to stretch the life of trough. There is wide variation in temperature observed in trough before applying the repairing material and therefore the material should be designed which can be applied without any blasting or explosion. In general, several repairing materials are available with high alumina cement as binder. However, these materials are having some issues when there is variation in temperatures at the time of application. The newly designed material is designed with several additives and has already been applied at several integrated steel plants and gives satisfactory performance.

**REFERENCES**
1. H. B. Zuo, C. Wang, C. F. Xu, J, L. Zhang and T. Zhang, "Effects of MnO on slag viscosity and wetting behaviour between slag and refractory". Iron making and Steel making, July 2015.

289

# INFLUENCE OF PITCH TYPE ON PROPERTIES OF BLAST FURNACE TROUGH CASTABLE

Takuma Kangawa*, Kenji Suzuki and Takashi Iida
Shinagawa Refractories Co., Ltd.

**ABSTRACT**

The influences of pitch type on the physical properties of blast furnace trough castable refractories were investigated by focusing on softening point and QI (quinoline-insoluble) content among the various characteristics of pitch powder.

When pitch powders of identical starting materials and preparation method with various softening points, were used, the hot modulus of rupture as well as corrosion resistance was lowered in accordance with an increase in softening point. When different types of similar softening point levels pitch powders with different starting materials and preparation methods, were used, the hot modulus of rupture and corrosion resistance were higher. In accordance with the increase in the QI content of the pitch powder, irrespective of pitch type, the hot modulus of rupture and corrosion resistance of the castable refractory sample was lowered.

QI signifies heavy pitch components with molecular weight exceeding 1200. QI components have been confirmed to inhibit infiltration or penetration of pitch into small pores in refractory bodies. It is inferred that, since pitch powder with low QI content tends to be diffused evenly and broadly into refractory bodies, associated with reinforcement of refractory structure by extensive carbon bond formation, both the hot modulus of rupture and corrosion resistance of castable refractory are improved.

## 1. INTORODUCTION

As a blast furnace trough castable refractory, Al2O3-SiC-C castable refractory is generally applied using carbon black and/or pitch powder as the carbon resource. Since pitch powder is used as a raw material for various kinds of refractory products, its influences on the characteristics of refractory products have been reported aboundingly [1,2]. In many of these reports, attention is put on the softening point of pitch powder, because a correlation can be found between the softening point of pitch powder and various properties of refractories in many cases. However, there are some experiment results which are not explainable by the softening point of pitch powder. In this study, focusing on other characteristics of pitch powder, the influences of pitch type on the properties of blast furnace trough castable refractories were investigated.

## 2. EXPERIMENT METHOD

### 2.1 Sample preparation

Table 1 shows the characteristics of pitch powders used in this study. Pitch powder A20，A25，A30 and A35 (which are collectively called A pitch) were prepared from a certain starting material and the softening point of each pitch powder was varied by applying different heat treatments. The starting materials as well as preparation methods used for pitch powders B and C were different from those for pitch powder A. Table 2 shows the blend compositions of the test samples. Al2O3-SiC-C castable refractory containing 19 mass% SiC and 1 mass% carbon black was used as a base, six different pitch powders were blended so that samples exhibit similar level of fixed carbon content.

Tab. 1: Properties of pitch powders

|  | A20 | A25 | A30 | A35 | B | C |
|---|---|---|---|---|---|---|
| Softening point / °C | 200 | 250 | 300 | 350 | 235 | 280 |
| Fixed carbon / mass% | 77 | 80 | 83 | 87 | 83 | 80 |
| QI / mass% | 24 | 42 | 51 | 62 | 11 | 23 |

Tab. 2: Blend composition of Al$_2$O$_3$-SiC-C castable refractory samples

| Additive pitch | | A 20 | A 25 | A 30 | A 35 | B | C |
|---|---|---|---|---|---|---|---|
| Chemical composition / mass% | Al$_2$O$_3$ | 72 | | | | | |
| | SiC | 19 | | | | | |
| | C | 3 | | | | | |
| Amount of carbonaceous materials / mass% | Carbon black | 1 | | | | | |
| | Pitch | 2.6 | 2.5 | 2.4 | 2.3 | 2.4 | 2.5 |

### 2.2 Hot modulus of rupture

The hot modulus of rupture of castable refractory samples was measured in order to study the influence of pitch type on mechanical strength. The Raw material mixture shown in Table 2 was mixed with a certain amount of water, followed by casting in a 40x40x160 mm mold. After curing at 30°C for 24 hours, the samples were demolded and dried at 110°C for 24 hours. Afterwards, the samples were fired at 1000°C for 3 hours in a coke breeze. The hot modulus of rupture of the fired samples was measured at 1000°C in a nitrogen atmosphere.

### 2.3 Corrosion resistance

In order to study the influence of pitch type on corrosion resistance, a rotary drum corrosion test was conducted on castable refractory samples at 1600°C for 5 hours with blast furnace slag (C/S = 1.2) as corrosive agent, which was exchanged every 1 hour.

## 3. RESULTS

### 3.1 Hot modulus of rupture

The relation between pitch powder softening point and hot modulus of rupture is shown in Fig. 1. The relation between the QI (quinoline-insoluble) content of pitch powder and hot modulus of rupture is shown in Fig. 2. The hot modulus of rupture is lowered in accordance with increase of softening point of A pitch powder. Both B and C pitch powders, with softening points similar to that of A pitch powder, exhibit higher values of hot modulus of rupture than A pitch powder. In accordance with the increase in the QI content of the pitch powder, the hot modulus of rupture is lowered.

### 3.2 Corrosion resistance

The relation between the softening point of pitch powder and the corrosion index is shown in Fig. 3. The relation between the QI content of the pitch powder and corrosion index is shown in Fig. 4. The corrosion index is steadily increased in accordance with the increase in softening point of A and B pitch powders. However, C pitch powder, with a softening point similar to that of A pitch powder, exhibits a bigger corrosion index. The corrosion index increased in accordance with the increase in the QI content of the pitch powder.
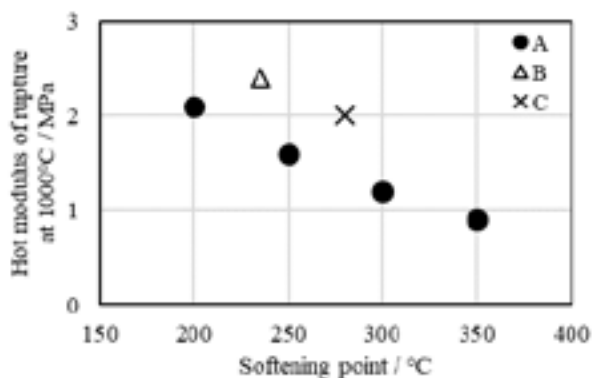
*Fig.1 Relation between softening point of pitch powder and hot modulus of rupture at 1000°C*
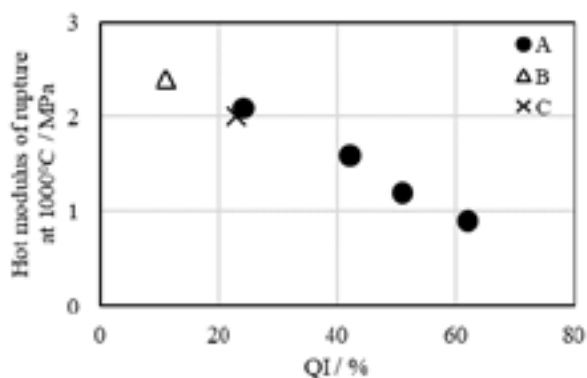


*Fig.2 Relation between QI of pitch powder and hot modulus of rupture at 1000°C*
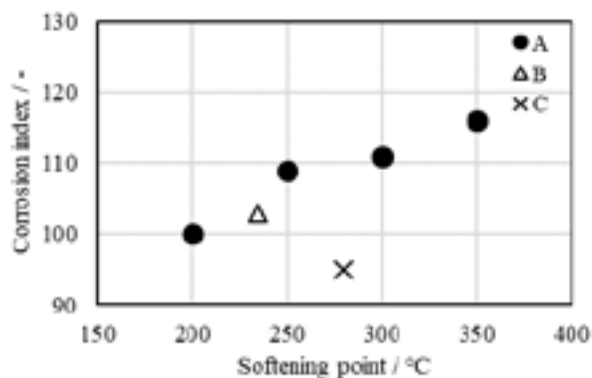


*Fig.3 Relation between softening point of pitch powder and corrosion index.*
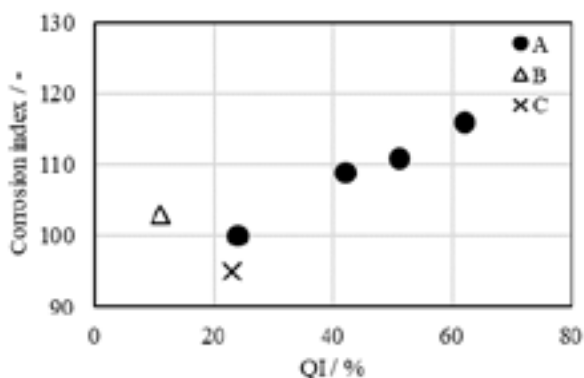


*Fig.4 Relation between QI content of pitch powder and corrosion index*

## 4. DISCUSSION

A correlation observed between the softening point and properties of castable refractory samples were affirmed in A pitch powders, of which the starting material and preparation method were identical. However, pitch powder B and C exhibited different experimental results which deviated from the relation observed in A pitch powders. Taking the QI content of the pitch powder into consideration, in accordance with the increase in the QI content of the pitch powder, irrespective of pitch type, the hot modulus of rupture and corrosion resistance of the castable refractory sample was lowered. The QI content signifies the content of heavy components in pitch with molecular weights exceeding 1200. It is well known that QI components inhibit infiltration or penetration of pitch into small pores in the refractory body [3]. It is inferred that, since pitch powder with low QI content can be easily diffuse into pores in the refractory body, a carbon bonded structure is evenly and broadly formed in the refractory body, associated with high hot modulus of rupture.

The dissolution of Al2O3-SiC-C castable refractory into blast furnace slag is composed of the following series of events; (1) infiltration of slag into refractory body, (2) oxidation of SiC by infiltrating slag associated with formation of SiO2, and (3) dissolution of refractory into formed low melting point SiO2 phase [4]. Taking into account such a corrosion mechanism, the influence of pitch powder QI content on castable refractory corrosion resistance can be summarized as follows. Since pitch powder with low QI content tends to be diffused into the refractory structure, carbon bond formation materializes in a broad area of the refractory body. As a result, such carbon bonded structure is hardly wetted by molten blast furnace slag and slag penetration into the refractory structure is effectively suppressed. It can be concluded that, since suppresion of slag penetration into the refractory body decelertes the dissolution rate of refractory into blast furnace slag, castable refractories blended with low QI content pitch powder exhibit improved corrosion resistance.

## 5. CONCLUSIONS

A correlation was observed between the QI content of pitch powder and properties of castable refractory through investigating the influences of pitch powder characteristics on properties of blast furnace trough castable refractory. It was indicated that, in accordance with lowering the QI content of pitch powder, pitch components can diffuse more evenly and broadly into the refractory body structure. This results in a reinforced refractory structure attained through carbon bond formation.

## REFERENCES
[1]  K. Jyono, E. Maeda, K. Nakai and T. Yoshida : *Taikabutsu* , 55 [11], 530-531 (2003)
[2]  Y. Hoshiyama, O. Nomura, H. Nishio and K. Ichikawa : *Taikabutsu* , 48 [1], 35-41 (1996)
[3]  H. Okamoto, K. Fujii and F. Ikeda : *Taikabutsu* , 57 [5], 252-261 (2005)
[4]  M. Iida and K. Ogura : *Taikabutsu , 62 [4], 175-184 (2005)

# UNDERSTANDING HOW THE BINDER SYSTEM INFLUENCES THE PROPERTIES AND PROCESS PERFORMANCE INDICATORS OF TAPHOLE CLAYS

I.J. Cameron[a], A.M. Garbers-Craig*[a], [a]University of Pretoria, Pretoria, South-Africa

## ABSTRACT

The use of conventional high-volatile coal tar pitch as a binder in taphole clays has notoriously been under scrutiny for replacement with non-toxic alternatives. The health and environmental impacts associated with the use of coal tar pitch (CTPht) have led to investigations into obtaining suitable non-toxic (free from polycyclic aromatic hydrocarbon, PAH) or less toxic alternatives (lower PAH-containing) to CTPht. In order to propose alternatives to CTPht, the binder-related features of the clay, as well as associated process performance indicators need to be considered. There are certain key properties of the taphole clay that are required during the process stages of ramming (closing of the taphole), drilling (opening of the taphole), and tapping. But while these processes are proceeding, the integrity of the taphole must be maintained throughout. This paper discusses the role of the binder system on the performance of the taphole clay during each of these process stages, and how these performance criteria can be measured and evaluated.

## LITERATURE

### Process and performance indicators

The main function of taphole clays is to form a semi-permanent seal that can withstand the conditions inside a smelting vessel (mechanical load and gas pressure) until the seal is opened to release the molten mixture inside the smelter or furnace. The three main taphole clay processes are ramming, which involves closing the furnace with a clay mass through the use of a mud gun; tapping, which involves emptying the furnace by opening it using either mechanical or oxidation methods; and protection, which involves preserving both the inside and surrounding area to the taphole [1] [2]. For each of these processes, there are performance indicators that are used to evaluate the process efficiency, and linked to these performance indicators are taphole clay features and properties. These relationships are shown in Figure 1.
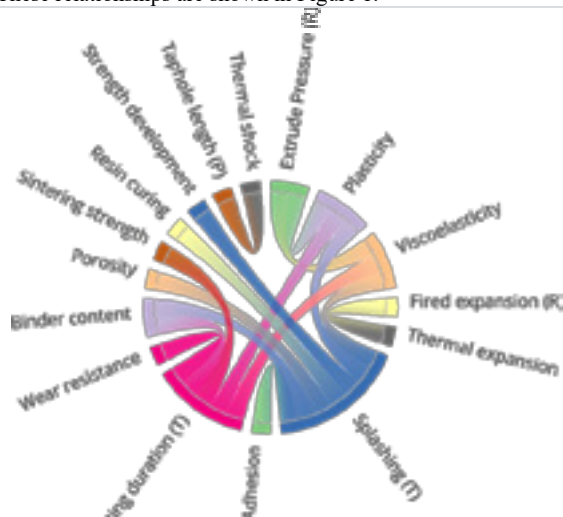


*Fig. 1: Relationships between taphole clay processes, performance indicators and clay features (R – ramming, T – tapping, P-protection) [1] [2] [3] [4] [5] [6] [7] [8]*

### Performance indicators for ramming process

The main objective of ramming is to properly close the taphole and ensure that a seal is maintained throughout the operation of the furnace. The two performance indicators for ramming the clay are the mud gun extrusion pressure and the expansion of the clay upon heating [1]. The clay features related to the extrusion pressure are the rheology of the clay during ageing and heating. For the expansion of the clay, movement in both the ramming direction and the radial direction is critical, which depends on the constitution of the clay (type of aggregate used like pyrophyllite and kyanite). The expansion of the clay influences the plasticity of the clay, and this is one of the critical clay features [1]. With insufficient expansion of the clay, from aggregates, the plasticity of the clay in the injection direction and direction perpendicular is reduced. This can be evaluated through the compressive strength of the clay, clay extrusion simulation by means of Marshall Extrusion Pressure (MEP) [9] evaluations, visual inspection of clay spreadability, and clay compactability evaluated by means of workability measurements. The workability and MEP of a blast furnace taphole clay are shown in Figure 2 [9]. The importance of achieving a plateau in both workability and MEP after ageing, as observed for Clay B in Figure 2, determines process stability through reduced mud gun pressure variation during ramming. A low extrusion pressure ensures that taphole clay material is moved further along into the mud gun which increases the taphole clay length, while good compaction ensures the clay attains the required strength. Both factors are related, where the decrease in workability during ageing, results in an increase in MEP.
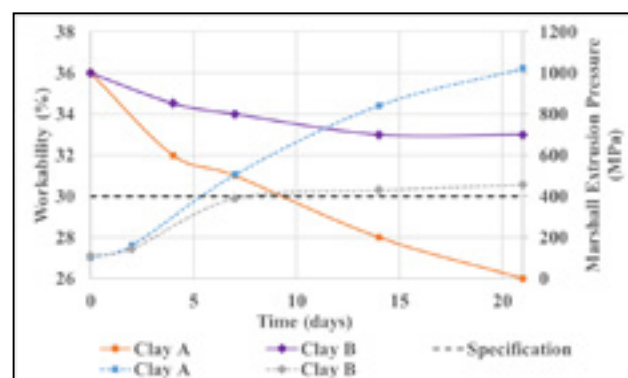


*Fig. 2: Taphole clay plasticity results of blast furnace clay workability and MEP ageing (Clay A – synthetic coal tar pitch & phenolic resin binder, Clay B – crude coal tar pitch binder) [9]*

### Performance indicators for tapping process

The main objectives of the tapping process are to allow easy discharge of molten material from the taphole, stable flow rate of material from the taphole, minimal slag splashing, reduced refractory consumption (including waste from the mud gun) and a reduced workforce (labour) due to the risk of injury close to the tap hole [1] [2] [3] [4]. The performance indicators for the tapping process include efficient drilling practices, measured through the drilling time, the casting duration (time from opening of the taphole to closure of the taphole) and slag/metal splashing.

#### Drilling practice

The requirements for efficient drilling practice are short drilling times without implementing additional measures such as vibration assist on the drill to open of the tap hole. The opening of the tap hole should result in a stable flow rate of molten material from the tap hole to minimize damage to the taphole area due to increased heat flux or erosion. The drilling ability is strongly influenced by the durability of the clay, i.e., sintering strength and the sintering strength is influenced by the taphole clay plasticity, adhesion (drying ability), and strength development [1]. With high plasticity, the taphole clay will have a resulting high spreadability [1],

allowing the clay to move further along the axial direction of the taphole and prevent accumulation of molten material. This accumulation of molten material on the inner part of the tap hole, where clay material should have occupied, can lead to drilling difficulties [5] and longer drilling times. The high adhesion of the clay ensures a high sinterability [1] of the clay through limiting low temperature volatilization that increases the viscosity of the binder (drying ability), to reduce voids or cracking in the clay when heated inside the tap hole. The high adhesion of the clay increases wear resistance and prevents material from entering the clay matrix or breaking it down through penetration and erosion. Controlling both the adhesion of the clay and strength development largely relies on the phenolic resin used in the clay [9] [13] [14]. For improved high temperature strength development of the clay, early strength development (<300°C) is important which is largely controlled by the phenolic resin in the case of phenolic resin containing clays. During cross-linking of the phenolic resin when heated, volailization occurs up to the decomposition temperature of the resin. This increased volatilization of the phenolic resin lowers the adhesion of the clay by premature drying of the binder [15].

*Casting duration*
The casting duration is the time between tapping and ramming, i.e., when the melt is transported away from the furnace into ladles or cast directly. The casting duration is largely determined by the molten flow rate, and this influences the wear rate of the taphole refractory. The sintered clay inside the tap hole needs to erode to an extent, during tapping, for two main reasons: to ensure the same amount of clay is rammed for the next heat (taphole length) and to maintain the casting duration by allowing small increases in flow rate during casting. The degradation of the refractory is due to extreme heat fluxes, thermal shock, and corrosion [5]. Depending on the smelting practice, one of these usually dominates the degradation of refractories [10]. These factors need to be limited to the tap hole and surrounding areas. The casting duration is also influenced by the plasticity of the clay, the binder quantity, and sintering strength (Figure 1). Regarding plasticity, it is crucial to maintain a low extrusion pressure, high compaction of the clay, and good spreadability to ensure limited corrosion and erosion of the taphole refractory including the taphole clay. If the plasticity of the clay is not sufficiently high, the casting duration will decrease (due to insufficient movement of the clay into the taphole), but the corrosion rates of the surrounding taphole area will be high [1] [6] [11]. To achieve the desired casting duration, sufficient sintering strength needs to be maintained with low porosity to limit penetration [1] of molten material and thereby reduce corrosion [12].

*Slag/metal splashing*
There are certain taphole clay features that are important for reduced slag splashing, which includes high plasticity, optimized binder content, fast curing speed of the binder, good adhesion, and strength development [9], [13]. Limiting the binder content reduces the volatile gas turbulence behind the tap hole and ensures less erosion of the tap hole. The strength development of a taphole clay needs to increase by 0,5% of the starting compressive strength, and the strength gain should not be too high, as this would complicate drilling operations [9].

**Protection of taphole clay materials**
The protection of the taphole clay is complex and influenced by several features, but the most important is the wear resistance of the clay, which is largely influence by its plasticity [14]. Having a high plasticity (compressive strength) [1] will ensure that long taphole clay lengths are maintained, and erosion of the taphole refractories are reduced [14].

**CONCLUSIONS**
There exists a relationship between the taphole processes, performance indicators, and clay characteristics. These factors need to be optimized for each individual operation. Both the processes- and performance indicators depend on the clay characteristics that should be controlled to ensure good taphole practices (ramming, drilling, tapping) and maintain the integrity and longevity of the tap hole. The taphole clay characteristics that need to be considered when altering binders include plasticity, wear resistance, binder quantity, open porosity of the clay, curing speed of the clay, adhesion, and strength development.

**REFERENCES**

[1] Y. Otsubo, A. Yamasaki, Y. Tanaka and T. Matsunaga, "High Performance Taphole Clay For Blast Furnace,", Report, TRL Krosaki Refractories Limited, Odisha, India, 2010.

[2] A. Gupta, K. Banerjee, P. Bharath, S. Kumar and K. Arun, "Properties and performance of a mud gun mass (tap hole clay) with respect to the stable application of the product in blast furnace," in *Interceram - refractories manual*, Bellary, India, 2014. Pp 307 – 311.

[3] I. Nolet, "Tapping of PGM-Ni mattes: an industry survey," in *The Southern African Institute of Mining and Metallurgy Furnace Tapping Conference 2014*, Johannesburg, South Africa, 2014. Pp 223 – 232.

[4] S. Nightingale, L. Wells, F. Tanzil, J. Cummins and B. Monaghan, "Assessment of the structural development of resin bonded taphole clay,", Report, University of Wollogong, Wollogong, 2006.

[5] L. Nelson and R. Hundermark, "The 'tap-hole' - key to furnace performance," in *The Southern African Institute of Mining and Metallurgy Furnace Tapping Conference 2014*, Johannesburg, 2014. Pp 1-32.

[6] W. Beek and T. Goff, "An overview of the design, operation, and maintenance practices relating to tap-hole management of a PGM smelting furnace," in *The Southern African Institute of Mining and Metallurgy Furnace Tapping Conference*, Johannesburg, 116 (2014). Pp 27 – 34.

[7] S. Dash, "Development of improved tap hole clay for blast furnace tap hole," Department of ceramic engineering, MTech thesis, Rourkela, 2009 . Pp 2 – 9.

[8] A. Pretto and L. Lindstad, "Health-Friendly Plugging Replair Paste," in *Turnace tapping 2022*, California, 2022. Pp 375 – 387.

[9] I. Cameron, "Investigating premature ageing of blast furnace taphole clay containing a resole resin and liquid pitch binder," MEng thesis, University of Pretoria, Pretoria, 2021. Pp 1 - 39.

[10] L. Thomson, "Monitoring, repair, and safety practices for electric furnace matte tapping," *The southern african institute of mining and metallurgy furnace tapping conference,* pp. 87-95, 2014.

[11] P. Geyer and Z. Halifa, "Blast furnace tapping practices at ArcelorMittal South-Africa, Vanderbijlpark Works," *The Southern African Institute of Mining and Metallurgy Furnace Tapping Conference,* pp. 97-112, 214.

[12] A. Campbell, K. Pericleous and M. Cross, "Modelling of freeze layers and refractory wear in direct smelting process,", PhD thesis, Centre of numerical modelling and process analysis, Greenwich, 2002. Pp 1 – 14.

[13] E. Sako, D. Galesi, C. Leao, F. Rodrigues, A. Souza, J. Roy, M. Kitamura and T. Horiushi, "High-performance taphole clay: A key for blast furnace hearth protection and a tool for cost reduction," *Iron and Steel Technology,* pp. 1-6, 2018.

[14] T. Kageyama, M. Kitamura and D. Tanaka, "Eco-friendly High Performance Taphole Mix," Shinagawa Refractories co. ltd, Tokyo, 2005.

[15] K. Matsatsugu, "Optimizing taphole clay technology," Shinagawa Refractories , Tokyo, 2014.

293

# European Centre for Refractories gGmbH

## ICR — International Colloquium on Refractories

**SCIENTIFIC CONFERENCE AND TRADE FAIR**

The International Colloquium on Refractories ICR® is a world-renowned event held annually in the city of Aachen. The event consists of a scientific conference, a trade fair for refractory companies and suppliers of raw materials, machinery, services and knowledge to the refractory industry, and of a varied supporting programm and social event.

Two days of scientific presentations and posters covering all aspects of the latest refractory research (raw materials, processing, refractory materials, applications and recycling)

Trade fair for refractory companies, customer and for suppliers of raw materials, machinery, services and knowledge to the refractory industry.

- Knowledge Transfer
- Education and Training
- Scholarships
- European Networking

Managing Directors: **Dr. Christian Dannert | Thomas Kaczmarek**

- Rheinstr. 58
  56203 Höhr-Grenzhausen
  Germany
- +49 2624 94 33 130
- info@ecref.eu
- www.ecref.eu

---

# Refractory Organisations in Höhr-Grenzhausen

## European Centre for Refractories gGmbH

- Operation of a European competence centre for refractory materials and technologies
- Promotion of education and further training in the field of refractories
- Organization and realization of scientific seminars, colloquia and similar events
- Talent programmes with the awarding of grants and awards for scientific work in the field of refractory products
- Steering of standardization activities

**International Colloquium on Refractories**
Congress, Trade Fair and Social Event

**Seminar**
Refractories – Key Technology and its Applications

**Refractory Innovation Days**
Research and Development, Funding Programmes

**Awareness and Relevance**
Websites and Social Media

# SHORT COMMUNICATIONS

# AL$_2$O$_3$–SIC–C CASTABLE DEVELOPMENT WITH IMPROVED OXIDATION RESISTANCE

ByoungWook Jung[1*], TaeWan Kim[1], JaeNyung Heo[1], KwangHo Shin[2]

[1]Korea Refractories Company, Dangjin, South Korea
[2]Hyundai Steel Company, Dangjin, South Korea

## ABSTRACT

The castable primarily used in the slag zone of a blast furnace runner is composed of Al$_2$O$_3$-SiC-C materials. Major types of damage to the slag zone include wear owing to the efflux of molten iron, erosion from slag reactions, and the oxidation and spalling of the castable caused by cyclic exposure to molten iron and air. To enhance the operational stability of a blast furnace and increase throughput, it is necessary to improve oxidation resistance under an oxidizing atmosphere and enhance mechanical strength and erosion resistance against efflux. Given their low wettability with molten slag and high thermal conductivity, silicon carbide (SiC) and carbon—the primary raw materials of castables—are widely used as refractories in blast furnace runners. One drawback, however, is that carbon is prone to oxidation. This study, therefore, reviewed the optimal carbon addition rate depending on SiC content and experimentally compared physical and thermal characteristics using tests involving various types and amounts of oxidation inhibitors. We evaluated oxidation resistance by producing specimens of the same size and performing oxidation firing at temperatures similar to operating conditions. We evaluated erosion resistance using blast furnace slag (C/S=1.17~1.21) in a rotation corrosion test. The results showed that increasing the appropriate amounts of SiC and carbon improved oxidation resistance. This improvement was attributed to the suppression of carbon oxidation as more SiO$_2$ film formed at high temperatures owing to the increase in SiC. By adjusting the types and ratios of boron-based oxidation inhibitors, we achieved superior oxidation and erosion resistance compared with existing solutions. However, the overuse of oxidation inhibitors could lead to reduced fluidity of the product and property degradation; thus, tests were conducted with optimal amounts. When boron-based oxidation inhibitors were applied, excellent oxidation resistance was achieved owing to the densification of the structure caused by the formation of B$_2$O$_3$ and C and the formation of an oxidation inhibition layer through B$_2$O$_3$ melting. Based on the test results, we applied the product to Blast Furnace No. 3 at H Steel Mill in South Korea. This achieved an 8% improvement in erosion rate and a 30% reduction in repair volume compared with the existing product.

## 1. INTRODUCTION

Al$_2$O$_3$-SiC-C (hereafter, ASC) castables are refractories widely used in areas such as the main runner of a blast furnace and both the iron and slag runners. This is because of their superior resistance to thermal shock and excellent erosion resistance against slag [1]. Silicon carbide (SiC) and carbon, the primary raw materials of ASC castables, are chosen for their low wettability with molten slag and high thermal conductivity, which make them suitable for most blast furnace runners [2, 3]. However, because of harsh operating conditions created by efforts to increase both the refractory usage lifespan and blast furnace output, the features of ASC castables need improvement, especially in the slag zone where conditions are the most severe. The major types of damage to slag zone castables include wear owing to the efflux of molten iron, erosion, and the oxidation and spalling of the castable caused

by cyclic exposure to molten iron and air [4–6]. Fig. 1 shows the types of damage occurring in the slag zone during actual use. Compared with the metal zone, the erosion rate is substantially higher, and there is also damage attributable to spalling caused by oxidation. To extend the lifespan of the slag zone, it is necessary to improve oxidation resistance and enhance erosion resistance against slag [7, 8].



Fig. 1. Slag zone damage during main runner usage

In this study, we selected the optimal ratio of SiC to carbon in ASC materials and evaluated oxidation and erosion resistance according to the types and amount of oxidation inhibitors. A field test was conducted with a product whose hot properties had been improved. Analysis of the residual and repair volumes after the test showed an 8% improvement in the erosion rate and a 30% reduction in repair volume compared with the existing product.

## 2. EXPERIMENTAL PROCEDURE

The first test was conducted with four samples by increasing the SiC content and changing the SiC–carbon ratio based on the existing mixture C, as shown in Table I. In the second test, after selecting the SiC–carbon ratio with the best properties in the first test, we configured the mixture depending on the types and amount of oxidation inhibitors, as shown in Table II.

Table I.Composition of raw materials based on SiC–carbon ratio

| Raw materials | C | C1 | C2 | C3 |
|---|---|---|---|---|
| Al$_2$O$_3$ | 63 | 49 | 49 | 49 |
| SiC | 24.5 | 40 | | |
| Carbon | 3.5 | 2.5 | 4.5 | 6.5 |
| SiC–carbon ratio | 7.0 | 16.0 | 9.0 | 6.0 |

Table II. Composition based on the type and amount of oxidation inhibitors

| Raw materials | C | Oxidation inhibitor: A | | | Oxidation inhibitor: B | | |
|---|---|---|---|---|---|---|---|
| | | A1 | A2 | A3 | B1 | B2 | B3 |
| $Al_2O_3$ | 63 | 49 | | | | | |
| SiC | 24.5 | 40 | | | | | |
| Carbon | 3.5 | 6.5 | | | | | |
| Oxidation inhibitor | - | $\alpha$ −0.5 | $\alpha$ | A +0.5 | $\beta$ −0.5 | $\beta$ | $\beta$ +0.5 |

The main characteristics of oxidation inhibitors A and B are known to enhance erosion and oxidation resistance by forming a denser structure through the production of $B_2O_3$ and C and by forming an oxidation inhibition layer by $B_2O_3$ melting.

First, since the properties of castables can significantly change depending on the raw materials and oxidation inhibitors, leading to altered flowability, we evaluated flowability to determine the optimal amount to be added. To compare the hot properties of each test sample, we produced samples 60 mm X 60 mm X 60 mm in size for oxidation resistance evaluation, let them harden at room temperature for 24 hours, and dried them at 110°C for another 24 hours. We then fired them in an oxidizing atmosphere at 1,450°C for three hours and evaluated their oxidation resistance by calculating the total and non-oxidized areas. Based on the evaluation, we selected mixtures with excellent oxidation resistance and performed an erosion test using blast furnace slag with CaO/SiO2=1.17~1.21 in a rotary corrosion tester.

## 3. RESULTS

### 3-1. Impact According to SiC–Carbon Ratio

We maintained the particle size composition and designed it to be equivalent to the existing mixture C. Hence, the amount of water added and the fluidity index were at the same level as shown in Fig. 2.
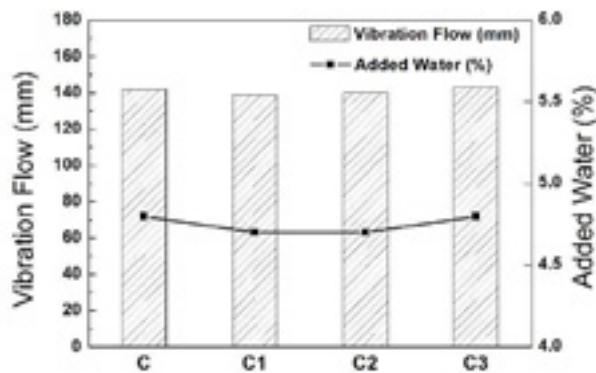


Fig. 2. Flowability evaluation according to SiC–carbon ratio

Fig. 3 shows the results of the oxidation resistance evaluation. We found that oxidation resistance improved as the SiC and carbon content increased. This can be attributed to an increase in the amount of $SiO_2$ film formed at high temperatures as the SiC content increased, suppressing oxidation and the impact of the densification of the matrix area.
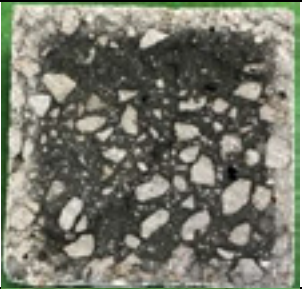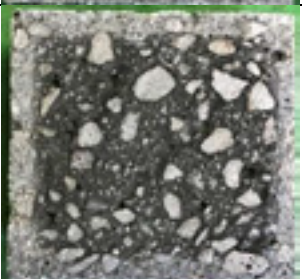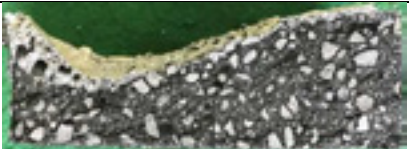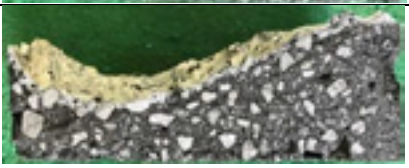
| | Cross-sections | Oxidation rate (%) |
|---|---|---|
| C |  | 32.6 |
| C1 |  | 31.7 |
| C2 |  | 28.8 |
| C3 |  | 26.7 |

Fig. 3. Evaluation of oxidation resistance according to the SiC–carbon ratio

As shown in Fig. 4, the erosion resistance evaluation results revealed the following order: C3 > existing >= C2 > C1. Therefore, from the evaluation according to the SiC–carbon ratio, we selected the C3 mixture—which yielded 18.1% and 4% improvements in oxidation resistance and erosion resistance, respectively—to further investigate the application of oxidation inhibitors.

| Cross-sections | Sample and corrosion index |
|---|---|
|  | C 1.00 |
|  | C1 1.07 |

| | | C2<br>1.02 |
| | | C3<br>0.96 |
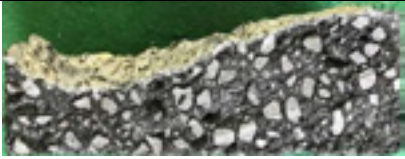
Fig. 4. Evaluation of erosion resistance according to SiC–carbon ratio

### 3-2. Impact based on the type and amount of oxidation nhibitors

When a large amount of oxidation inhibitors were added, we observed reduced workability and decreased pot life owing to rapid product settling in all cases. As shown in Fig. 5, we determined that A3 and B3 were unsuitable for field application owing to property degradation and construction issues caused by excess moisture. Thus, they were excluded from the oxidation and erosion resistance evaluations.
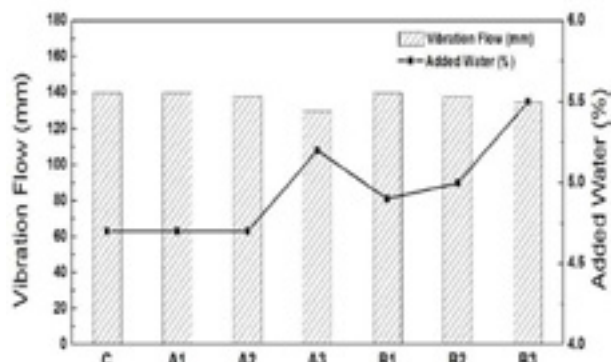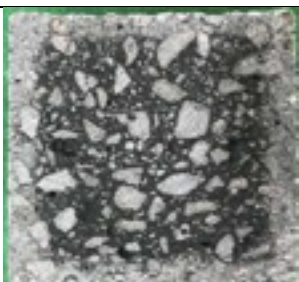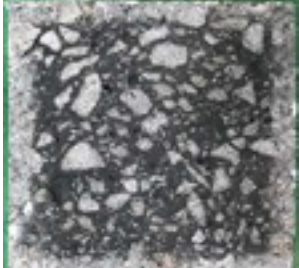
Fig. 5. Flowability evaluation

Fig. 6. shows the results of the oxidation resistance evaluation after applying oxidation inhibitor A. For A2, we observed a 35% enhancement in oxidation resistance compared with the existing level.

| | Cross-sections | Oxidation rate (%) |
|---|---|---|
| C | | 34.3 |
| A1 | | 25.7 |

| | Cross-sections | Oxidation rate (%) |
|---|---|---|
| A2 | | 22.3 |
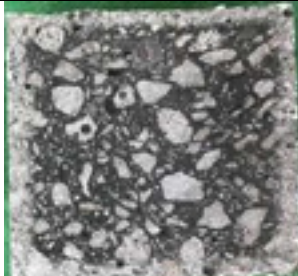
Fig. 6. Evaluation of oxidation resistance after applying oxidation inhibitor A

Fig. 7. shows the results of the oxidation resistance evaluation after applying oxidation inhibitor B. The order of oxidation resistance was B2 > B1 > existing product. For B2, we observed a 34.6% improvement in oxidation resistance compared with the existing level.
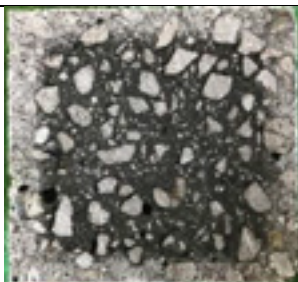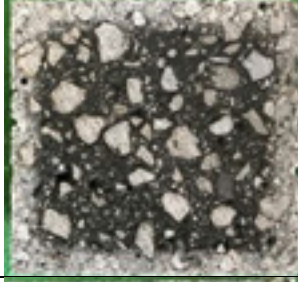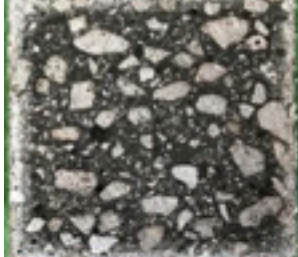
| | Cross-sections | Oxidation rate (%) |
|---|---|---|
| C | | 34.7 |
| B1 | | 31.7 |
| B2 | | 22.7 |

Fig. 7. Evaluation of oxidation resistance after applying oxidation inhibitor B

We found that the application of both oxidation inhibitors A and B improved oxidation resistance. Based on the evaluation results, we selected C and the mixtures with the best oxidation resistance (i.e., A2 and B2) for the erosion resistance evaluation. The A2 mixture showed a 21% improvement in erosion resistance while C2 remained similar to the existing level. Fig. 8 shows the results.

| Cross-sections | Sample and corrosion index |
|---|---|
|  | C 1.00 |
|  | A2 0.79 |
|  | C2 0.97 |

Fig. 8. Evaluation of erosion resistance after applying oxidation inhibitors

The mixture with increased SiC and a SiC–carbon ratio of 6, along with the application of oxidation inhibitor A, demonstrated excellent results in both oxidation and erosion resistance. Finally, we selected the A2 mixture for the field test.

## 4. FIELD TEST

For the field test, we applied the developed product to the main runner slag zone of Blast Furnace No. 3 at H Steel Mill in South Korea. The developed product and the existing product were used in equal quantity and throughput. Table III and Fig. 9 show the results. Compared with the existing product, our developed product resulted in an 8% improvement in the erosion rate and a 30% decrease in repair volume after use.

Table III. Comparison of remaining amounts and repair volume after completion

| | Existing product | Developed product | Notes |
|---|---|---|---|
| Throughput (tons) | 250,000 tons | 250,000 tons | - |
| Minimum remaining (mm) | 250 | 300 | ↑20% |
| Erosion rate (mm/1000 tons) | 1.76 | 1.61 | ↑8% |
| Repair material usage (ton) | 18.5 | 13.0 | ↓30% |

| Existing product | Developed product |
|---|---|
|  |  |
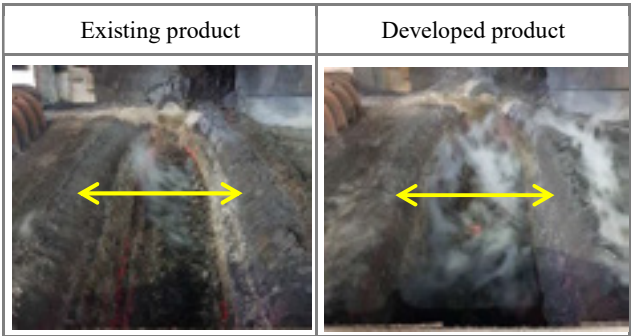
Fig. 9. Status of existing product and test product after completion

## 5. CONCLUSION

In this study, we sought to extend the slag zone lifespan of a blast furnace main runner by improving its oxidation resistance. We evaluated oxidation and corrosion resistance according to increases in SiC and the SiC–carbon ratio in the ASC material. We also adjusted the application and proportion of oxidation inhibitors according to the optimal SiC–carbon ratio. The conclusions are as follows:

1) With the increase of SiC content, the amount of $SiO_2$ film formed at high temperatures increased, leading to improved oxidation resistance. The best erosion resistance was observed using a mixture with a SiC–carbon ratio of 6.

2) When the boron-based oxidation inhibitor A was applied to the mixture, which had increased SiC and a SiC–carbon ratio of 6, we noted improvements of 35% and 21% in oxidation resistance and erosion resistance, respectively, compared with the existing product. It was crucial to control the amount of oxidation inhibitors added since excessive addition could lead to property degradation from excess moisture and construction issues.

3) We conducted a field test in the main runner slag zone using the developed product mixture. According to the results, the erosion rate improved by 8% owing to enhanced oxidation resistance compared with the existing product, and the volume of repair material used decreased by 30%. This made it possible to use the main runner more stably and improve the volume of repair material used. These outcomes can be attributed to improved oxidation and corrosion resistance through using the optimal SiC–carbon ratio and the application of oxidation inhibitors.

## REFERENCES

1. A. Chen, Y. Fu, "Oxidation resistance of andalusite-bearing $Al_2O_3$–SiC–C castables containing reduced anti-oxidant", Ceramics Int., 47 (2021) 14579–14586.
2. N. Prompt, E. Ouedraogo, "High temperature mechanical characterization of an alumina refractory concrete for Blast Furnace main trough: Part I. General context", J. Eur. Ceram. Soc. 28 (2008) 2859–2865.
3. N. Prompt, E. Ouedraogo, "High-temperature mechanical characterization of an alumina refractory concrete for Blast Furnace main trough: Part II. Material behavior", J. Eur. Ceram. Soc. 28 (2008) 2867–2875.
4. V. Pillin, R. Sarkar, "Effect of spinel content on the properties of $Al_2O_3$-SiC-C based trough castable", Ceram. Int. 42 (2016) 2969-2982.
**5.** L. Hong and V. Sahajwalla, "Investigation of in-situ chemical reactions of Al2O3-SiC-SiO2-C refractory and its interactions with slag", ISIJ Int. 44 (2004) 785–789.
6. D. Yang, Y. Liu, H. Ding, Z. Huang, "Influence of β-sialon/Ti(C, N) powders on the corrosion and oxidation resistance of zero-cement $Al_2O_3$-SiC-C refractory castables", T. Indian Ceram. Soc. 74 (2015) 22–28.
7. A.S. Gokce, C. Gurcan, S. Ozgen, S. Aydin, "The effect of antioxidants on the oxidation behaviour of magnesia-carbon refractory bricks", Ceram. Int. 34 (2008) 323–330. 8. C.F. Chan, B.B. Argent, W. E. Lee, "Prediction of the effect of additives on slag resistance of A12O3-SiO2-SiC-C bond phases in air", Calphad 27 (2003) 115–125.

# SHORT COMMUNICATIONS

# INNOVATION IN CARBON FOOTPRINT REDUCTION AND SUSTAINABILITY IN THE MANUFACTURING OF INSULATION FIREBRICKS FOR LINING OF BLAST FURNACE STOVE

C. Natarajan, Ranjan Dey, S. Panneerselvam, S. Velappan, B. Raghavendra Pai, PM. Sivaram
Carborundum Universal Limited, Chennai, India

## ABSTRACT

Hot Blast Stove [HBS] is used to preheat air used in the Blast Furnace. HBS works as counter current regenerative heat exchanger which consists cylindrical steel structures lined with different kind of refractories includes Fire clay, Alumina, Silica and Insulation Fire bricks [IFB] having low bulk density, higher porosity and lower thermal conductivity.

IFB are manufactured by mixing the organic material such as saw dust, expandable polystyrene. Upon firing, organic material is burnt out and leaving pores in the finished bricks. These organic material burning have several negative environmental impacts due to release of harmful substances and generation of greenhouse gases. In order to have the sustainability & lesser carbon foot print, an innovative pore forming technology is introduced in the manufacturing of Insulation bricks.

Trials are carried out in ASTM 26 grade Insulation bricks in existing and new process for study purpose.

## IFB EXISTING MANUFACTURING PROCESS :

Insulating Fire bricks are made through different manufacturing process such as hand moulding, extrusion and slurry casting & slinger process. For this study, ASTM 26 grade is manufactured through slurry casting.

In the slurry casting process, expandable polystyrene is used as pore former.

This process consists of mixing refractory raw materials in appropriate proportion with expandable polystyrene and water and poured in the moulds and dried followed by Firing and finished with cutting operation.

## PROCESS FLOW CHART [Existing casting process]



## FOAMING PROCESS

In this process, the refractory slurry is prepared. The foaming agent is diluted with water and air and further mixed with refractory slurry. The slurry sets around the foam bubbles and this paste have sufficient strength to maintain its shape around the foam bubbles. It entrains 30-35 % of air by volume into the slurry and as a results low density foam structure is obtained.

Quality of the structure depends upon quality and type of foam used. Foaming agent is a material that facilitates formation of foam as surfactants. When foaming agent is added into the water in foam generator with proportion 1:30 to 1:40, a foam is generated.

## PROCESS FLOW FOR IFB MANUNFACTURING THROUGH FOAMING PROCESS



The bricks manufactured through existing process and foaming process are studied for various physical properties such as Pore size, Bulk Density, Apparent Porosity, Cold Crushing Strength and Thermal Conductivity.

## PORE SIZE

Pore size of foam based bricks are half the smaller in size which makes the product made out from foams are having micropores compared to existing process route product. These micropores helps to reduce the thermal conductivity
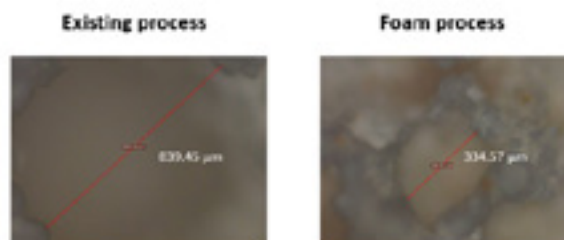


## BULK DENSITY

Existing process range: 0.84 to 0.88 g/cc. Foam process range : 0.82 to 0.86 g/cc.
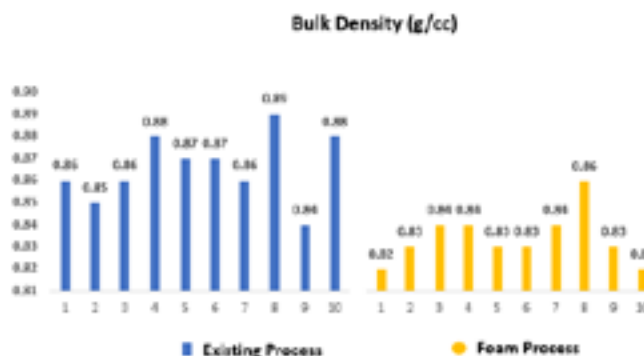
## COLD CRUSHING STRENGTH

Existing process range : 1.7 to 2.1 Mpa. Foam process range : 2.3 to 2.5 Mpa.



Cold Crushing Strength (Mpa)
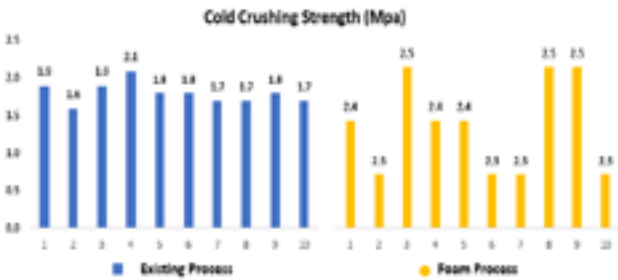
## APPARENT POROSITY

Existing process range: 61 to 68.3 %. Foam process range : 58.0 to 63.2 %



Apparent Porosity (%)

## THERMAL CONDUCTIVITY



Thermal Conductivity (W/mK)
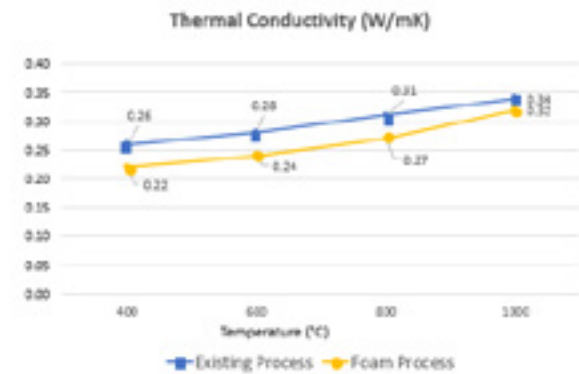
## CARBON FOOT PRINT REDUCTION

Expandable polystyrene is derived from fossil fuels, primarily petroleum, and burning it involves the combustion of these carbon-based materials. The combustion process releases the carbon atoms present in polystyrene, combining them with oxygen from the air to form carbon dioxide.

The exact amount of $CO_2$ emissions produced from burning polystyrene can vary depending on factors such as the composition of the polystyrene, the efficiency of the combustion process, and the conditions under which it is burnt. However, as a general estimate, burning one kilogram of polystyrene can release approximately 3.3 kilograms of $CO_2$ emissions.

It's important to note that the environmental impact of polystyrene extends beyond just its $CO_2$ emissions from burning. The production of polystyrene also involves the extraction and refining of petroleum, which contributes to greenhouse gas emissions and other environmental concerns. Additionally, the disposal of polystyrene waste, whether through burning or other means, can have detrimental environmental effects, as discussed earlier

In the Foam process $CO_2$ emission is not experienced.



For 1 ton of ASTM 26 Mfg. CO2 emission [kg]
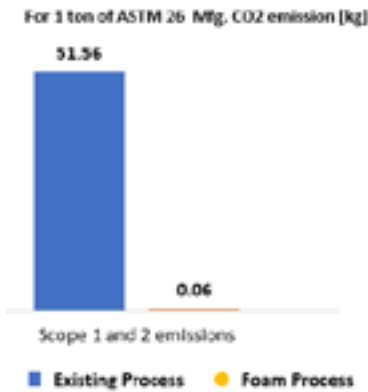
## CONCLUSIONS

The Insulating bricks produced through Foam process shows lower Bulk Density & Higher Mechanical strength and Lower Thermal Conductivity due to presence of appropriate pore size distribution.

In the regular process the $CO_2$ emission is 51.56 Kg of per ton of Insulation bricks where as in Foam process the emission is 0.06 Kg only.

The foaming agent is made from plants that are more readily available and easier to cultivate.

Processes based on foam are sustainable and good to the environment in terms of lesser carbon foot print

## REFERENCES

[1]   Sepulveda, P.Binner,J.G.P : Processing of Cellular ceramics by foaming and in situ polymerization of organic monomers. J.Europ.Ceram Soc.19(1999) 2059-2066

[2]   Woyansky, J.S.Scott, C.E.MinnearW.P Processing of porous ceramics Am.Ceram Soc Bull. 71(1992) [11] 1674-1682

[3]    Tang, F.et al: Preparation of porous materials with controlled pore size and porosity. J Europ Ceram Soc 24(2004) [2]341-344

[4]    Sach .J.: Seifert H. Foamed concrete technology: Possibilities of thermal insulation at high temperature. Cfi/Ber DKG 76 (1999) [9]23-30

# SHORT COMMUNICATIONS

# DEVELOPMENT OF A NOVEL TAPHOLE CLAY WITH TOXICITY-FREE AND ODOR-LIGHTEN

Shougo Miyajima, Yuji Ootsubo, Katsumi Morikawa, Kiyoshi Goto, and Takashi Matsunaga.
Krosaki Harima Corporation, Kitakyushu, Japan

## ABSTRACT

Taphole cray is a key thermoplastic material to facilitate smooth filling from the taphole and to protect blast furnace hearth from erosion damage by molten pig iron or slag. As the plasticizer and the binder for the taphole clay, coal tar has been conventionally used widely due to its excellent thermal stability with high rate of carbon residual. In the usage of the coal tar, however, a serious deterioration of the working environment such as the carcinogenicity of polycyclic aromatic hydrocarbons (PAHs), the toxicity of volatile organic compounds, and the emission of bad odors with smoke. The taphole clay with the developed phenolic resin as the substitutin for the coal tar has exhibited better thermo plasticity than the taphole clay with the conventional phenolic resin, bringing in an expectation of improvement in plugging into the taphole when it applied practically in the blast furnace. The new taphole clay is also easy to handle with an excellent thermal stability, using the taphole clay working environment is significantly improved with elimination and lightnening of various burdens on the carcinogenicity, the toxicity and the odor/smoking.

## BACKGROUND

Figure 1 shows schematic image of a plugging process of the taphole clay. Plugging excutes using a clay gun with required of typically $200 \sim 500$kg taphole clay consumption. Such a large amout of the clay is for plugging intended to protect the inner wall of the blast furnace. The thermoplastic characteristics of the taphole clay is quite important to cover the inner wall of the blast furnace during plugging. Furthermore, extreme gap of temperature from 60 °C (taphole clay) to >1500°C (inner side of the blast furnace) tend to cause crack generation in the filled taphole clay. Stable and safety tapping of the pig iron through the taphole is an earnest requirement without cracking in the taphole clay during plugging. Coal tar is known as its superior thermoplastic property with slow volatilization by containing thermally stable wide variety of PAHs. Due to high toxicity and environmental harmfulness of the PAHs, in many countries they are prohibited or limited the usage of coal tar as refractory binder when the phenolic resin as substitute for coal tar is used for the taphole clay binder, rapidly hardening after filling into the blast furnace is an advantage to prevent cracking. However such early hardening property of the resin bonded clay often causes poor workability of the clay because of the difficulty of precise temperature control of the clay in actual operation. There are several patents to claim on some methods controlling the hardening property of the clay to solve this contradictory issues[1, 2]. Additionally, from the point of volatilization property of the heated resin bonded clay, there are several patents to claim on the enhancement of the volatilization behaviour of the clay for decreasing inner pressure after filling in the blast furnace[3, 4]. Those attempts for the resin bonded clay are aimed to the thermoplastic and volatilization properties to imitate those of the coal tar bonded clay. Our development policy also followed the previous attempts and aimed to develop thermally stable resin bonded clay realizing fine workability comparable to the previous attempts the coal tar bonded clay without toxicity and odor/smoking.

## CHARACTERISTICS AND CONCLUSION

Tab.1 shows hazardous component contained in the binders for taphole clays. Vaporized phenol from the resin bonded taphole clays was measured at approximately 70 °C by using Kitagawa gas detector tube; which can detect the concentration from 0.5 to 25ppm.
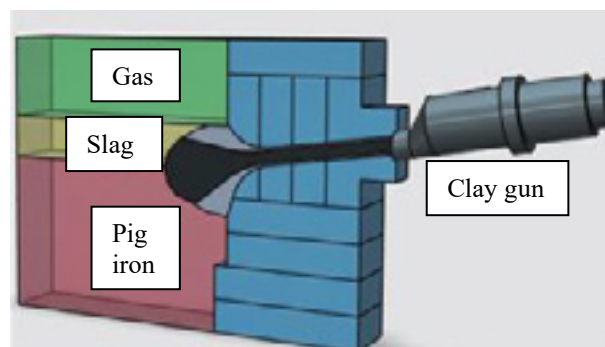


*Fig.1:Schematic image of a plugging process of taphole clay.*

Tab.1: Properties

| Binder property | Coal tar | Conventional resin binder | Developed resin binder |
|---|---|---|---|
| Carcinogen / ppm (Benzo[a]pyrene) | 7000 | Free | Free |
| Free phenol / % | — | >1% | <1% |
| Odor / ppm (Vaporized phenol) | — | >25 | Free |
| Taphole clay property | Coal tar | Conventional resin binder | Developed resin binder |
| Plugging | ++++ | + | +++ |
| Taphole depth | +++ | ++ | +++ |
| Tapping time | +++ | ++ | +++ |
| Handring | ++++ | + | +++ |
| Rapid hardening | + | ++++ | +++ |

Developed resin binder was free from both of carcinogen and vaporized phenol. Plugging performance of the developed clay was also compared with those of coal tar clay and conventional resin bonded clay as shown in Tab.1. Figure 2 shows comparison of hardening behaviour for each taphole clay with an uniaxial compression test at constant ambient temperatures. At 300 °C, developed taphole clay kept plasticity like a coal tar bonded clay in contrast, the conventional resin bonded clay hardened quickly. At 500 °C, the developed clay hardened quickly next to the hardening of conventional resin bonded clay. In contrast, coal tar bonded clay remained plasticity in the same time span. Such intermediate properties of the developed resin bonded clay between the coal tar and the conventional resin bonded clay is ideal for practice usage. Figure 3 shows schematic image of plugging test system[5] and Figure 4 shows results of plugging test of taphole clay after 3h calcination in the furnace. From the results of image analysis (use Image J software) for sectional image of specimens after plugging test, the developed resin bonded clay showed 2.2% of crack area close to the value of coal tar bonded clay. Uniformly filled plugging body shown in the cross section view gave us expectation to realize the satable tapping.

## REFERENCES
[1] Jap. Patent Application 1973-094708
[2] Jap. Patent Application 2021-187979
[3] Jap. Patent Application 2010-254497
[4] Jap. Patent Application 2011-132555
[5] Jap. Patent Application 2009-228047
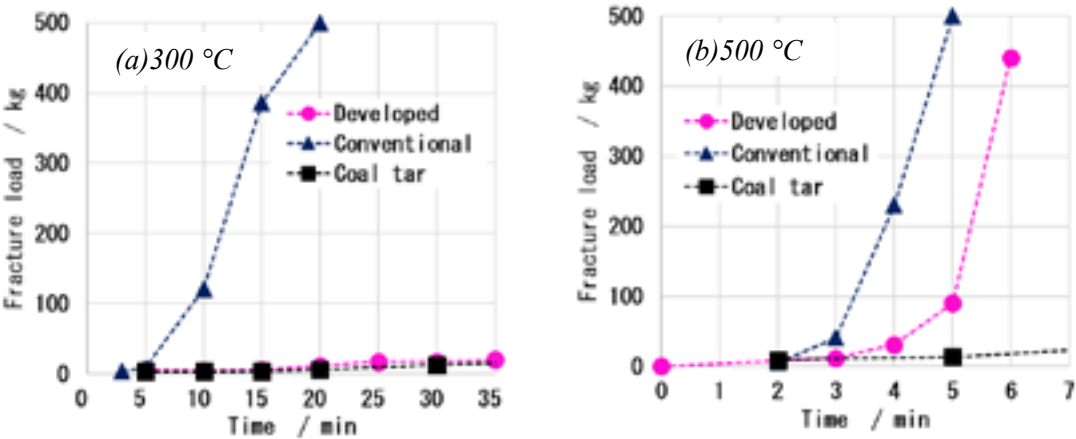
*Fig.2:Comparison of hardening behaviour for taphole clays which contains three kind of binders (d=50mm, h=50mm cylindrical shaped specimen) at temperature of (a)300 °C and (b)500 °C.*
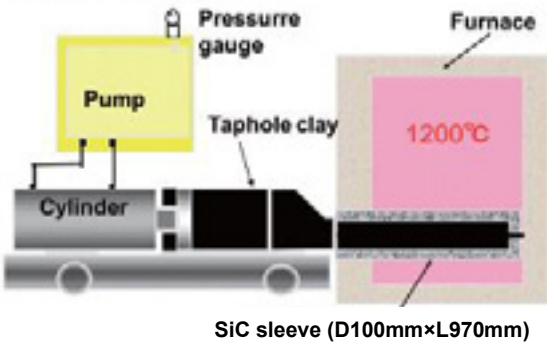


*Fig.3:Schematic image of plugging test system.*



*Fig.4:Results of plugging test of taphole clay with crack analysis.*

302

# REFRACTORY INNOVATIONS UNDER THE TARGET OF CARBON DIOXIDE PEAKING AND CARBON NEUTRALITY IN CHINA

Li Hongxia

Sinosteel Luoyang Institute of Refractories Research Co., Ltd., Luoyang 471039, China

**Abstract:**

Based on the target of carbon peak and carbon neutrality in China, the situation of carbon reduction and green development of the main high temperature industries under the background of double carbon will be introduced. The new technologies for the reduction of pollution and carbon in the iron and the key points of technological innovation of metallurgical refractories will be emphasized. The challenges and opportunities for refractories industry under the double carbon targets will be analyzed. The main innovation directions of refractories will be also pointed out.

Keywords: carbon peak; carbon neutrality; technological innovation of refractories; carbon reduction and green development

## 1 The development of the main high temperature industries served by refractories under the background of double carbon

At the Leaders' Climate Summit, President Xi Jinping announced that China will strive to achieve a carbon peak by 2030 and carbon neutrality by 2060. Carbon peak refers to the peak of greenhouse gas emissions in the country, and carbon neutralization refers to the balance between carbon production and carbon consumption, so as to achieve zero carbon load. China's commitment to achieve the time from carbon peak to carbon neutrality is far shorter than all the time of developed countries, which requires China to make arduous efforts. The '14th Five-Year Plan' is the critical period and window period for carbon peak. According to the decision-making and deployment of the central government, China will focus on building a clean, low-carbon, safe and efficient energy system. Actions to reduce pollution and carbon emissions in key industries will be implemented. Green low-carbon technology will achieve an important breakthrough. Green low-carbon policy and market system will be perfected. Green low-carbon life will be further advocated. Ecological carbon sink capacity will be improved.

According to statistics, in 2019, China's manufacturing industry accounted for 27.2 % of GDP. The total output value of typical process industries including petrochemical, chemical, iron and steel, non-ferrous, building materials, wafer manufacturing and other industries accounted for 51.98 % of the total annual output value of national enterprises.

The large-scale process manufacturing industry had caused huge carbon emissions, of which the $CO_2$ emissions of the basic raw material industry accounted for 70.0 %. The output of pig iron, crude steel, alumina, cement, ten kinds of non-ferrous metals, petrochemical and chemical industries with high carbon emissions in China's has ranked first in the world for many years. This is one of the main reasons why China's energy consumption per unit of GDP was 130 % of the world average and carbon emissions accounted for 28 % of the world's total. According to calculation, in order to make the energy consumption per unit GDP reach the world average level, China needs to reduce the consumption of 1 billion tons of standard coal every year. Therefore China 's energy saving and carbon reduction potential is huge. Therefore, high temperature industries such as electric power, iron and steel, non-ferrous metals, chemical industry and building materials are the key areas of energy saving and carbon reduction in China. At present, these high carbon emission industries have formulated and promoted carbon peak and carbon neutrality action plan and technology roadmap. Driven by the huge pressure of carbon neutrality and capacity reduction, the industry and product structure have been comprehensively adjusted, and scientific and technological innovation has been fully exerted, which promote the completion time of carbon peak and carbon neutrality ahead of the original schedule (2030 and 2060).

Refractories is an important support and indispensable part of high temperature industry. Its industrial development and technological innovation are closely related to the development of key high temperature industries and the path of energy saving and carbon reduction technology. The development of refractories is full of opportunities and challenges under the background of double carbon.

## 2 The development of iron and steel industry and the scientific and technological innovation of refractories for metallurgy under the goal of double carbon

China's refractories production ranks first in the world, and more than 70% of it is used in the metallurgical industry, which runs through metallurgy. The development and technological innovation of refractory industry depend on the development of iron and steel industry, technological innovation and technological progress.

According to statistics, China's pig iron and crude steel production in 2020 were 887.52 million tons and 1053 million tons respectively, an increase of 4.3 % and 5.2 % respectively. China 's steel production emits more than 1.96 billion tons of $CO_2$ per year, accounting for about 15 % of the total national greenhouse gas emissions [1], ranking second in the carbon emissions of the industry. The carbon reduction pressure of the iron and steel industry is huge, and it is the key area to reduce carbon emissions.

At the beginning of 2021, China Baowu Iron and Steel Group Co., Ltd. took the lead in releasing the goal of achieving carbon peak and carbon neutralization in advance to the society [2]. Strive to achieve carbon peak in 2023 by optimizing management and improving efficiency. Strive to reduce carbon emissions by 30% in 2025 and 30% in 2035 through technological innovation and process optimization. Strive to achieve carbon neutrality in 2050 through the path of process revolution and process reengineering. Baowu put forward the idea of green low-carbon development led by green development. The greenization of steel production process is realized by low-carbon metallurgy and intelligent manufacturing. The green use process of steel products is realized by high-quality products. Finally, contribute to the construction of carbon neutral society.

Hbis group has also issued a low-carbon green development action plan in the steel industry [3]. In 2021, a low-carbon metallurgical roadmap was released. In 2022, carbon will peak. In 2025, carbon emissions will be reduced by more than 10 % from the peak. In 2030, carbon emissions will be reduced by more than 30 % from the peak. In 2050, carbon neutrality target will be realized.

The energy saving and emission reduction of the steel industry is inseparable from technological innovation. China Baowu has explored and practiced the mode of low-carbon innovation and development and has made breakthroughs in non-blast furnace ironmaking technology. The OY furnace of non-blast furnace ironmaking process was built in Bayi Iron and Steel Co., Ltd. Based on the in-depth understanding and practice of COREX-3000, the technical research and re-innovation of non-blast furnace ironmaking process were carried out. In addition, China Baowu also built a low-carbon metallurgical innovation test platform. In 2019, the 430 $m^3$ blast furnace in Bayi was reconstructed into a hydrogen-rich carbon-circulating oxygen blast furnace, which, together with OY furnace and other auxiliary process equipment, became an innovative test platform for low-carbon metallurgy in Baowu. It was completed and put into operation on July 15, 2020. In 2020, the first stage test target of 35 % blast oxygen content was achieved, which broke through the oxygen-enriched smelting limit of traditional blast furnace. In addition, as early as August 2015, the original Baosteel Group proposed a metallurgical-coal chemical coupling theory and new process ideas. Those ideas closely combined metallurgical processes and chemical processes to convert metallurgical gas into chemical products for carbon sequestration, which can greatly reduce carbon dioxide emissions.

Hbis group has vigorously implemented hydrogen metallurgy technology, taking the lead in building the world's first 1.2 million

303

tons of hydrogen metallurgy production demonstration line in Zhangjiakou, Hebei Province, and building 1.2 million tons of production lines in Tangshan and Handan respectively. The demonstration and application of CCUS (carbon capture, utilization and storage) technology research and development was accelerated. The development and application of technologies such as imitation mantle molten iron bath was promoted.

The $CO_2$ emissions from the ironmaking process account for 70 % of the total emissions of the steel industry. Therefore, the ironmaking process is the key process for the steel industry to break through energy conservation and carbon reduction. About non-coking ironmaking, the University of Science and Technology Beijing and Jianlong Group proposed a new technology of hydrogen-based smelting reduction ironmaking (CISP), which avoided sintering and coking processes and realized the direct feeding of powder ore into the furnace. The process has strong adaptability to mineral powder and can deal with high phosphorus ore, vanadium titanium ore and so on. In the report of "Near net shape manufacturing technology under the background of carbon neutralization, "Academician Mao Xinping [4] introduced the SuSteel project proposed by the VAI in 2016. The project uses plasma hydrogen as fuel and reducing agent to realize direct steelmaking of iron ore, which can continuously produce crude steel without traditional steelmaking process. The technologies involved in this process include hydrogen plasma torch melting furnace, tail gas preheating and pre-reduction of iron ore.

At present, the research on new technology of non-coking ironmaking is a hot topic at home and abroad, mainly including high proportion pellet blast furnace ironmaking, low carbon ironmaking of full oxygen and hydrogen-rich blast furnace, gas-based shaft furnace hydrogen-rich direct reduction ironmaking, hydrogen-rich direct reduction ironmaking based on low rank coal, hydrogen-based smelting reduction ironmaking, and biomass ironmaking technology [5].

In addition, in China's steel industry, low $CO_2$ emissions of electric furnace short process accounted for less than 10%, far lower than the United States 62%, the European Union 39%, Japan 22% of the development level, also lower than the global average of 25.2%. The increasing amount of waste steel resources in Chinese society has provided favorable conditions for the development of short-process electric furnace steelmaking. It has become a consensus in the industry to promote the development of electric furnace steelmaking in China in an orderly manner. New steelmaking technologies include electric furnace steelmaking, $CO_2$ instead of $N_2$/Ar converter low-blowing technology cycle [5], cross-industry co-production technology and near-net-shape casting and rolling green low-carbon technology.

In summary, the iron and steel industry focuses on the following six key low-carbon metallurgical technologies in terms of how to reduce $CO_2$ emissions. 1) seeking the large-scale self-digestion of $CO_2$ in the long-process steel process [4]. 2) changing the steel manufacturing process and developing the short process electric furnace steelmaking and near net shape casting and rolling technology. 3) using non-fossil hydrogen metallurgy to reduce $CO_2$ emissions from the source. 4) applying metallurgical-coal chemical coupling to smelt direct reduction iron, exploring ironmaking to achieve negative carbon emissions. 5) researching and developing high-quality steel materials to improve life and reduce consumption. 6) Improving energy efficiency and reduce emissions through energy substitution and smart manufacturing.

Therefore, in order to achieve pollution reduction, carbon reduction and high-quality green development in the iron and steel industry, refractories should focus on the following six studies.

1) Study on long-life refractories for non-blast furnace ironmaking. Non-fossil hydrogen metallurgy technology should be paid attention to, including gas-based shaft furnace reduction and hydrogen-based smelting reduction ironmaking, full-oxygen hydrogen-rich blast furnace low-carbon ironmaking, biomass ironmaking etc.

2) Study on green functional refractories for converter furnace, electric furnace and refining technology. The bottom blowing of converter can effectively reduce the carbon and oxygen accumulation and improve the purity of molten steel. However, it will cause serious damage to the refractory at the bottom of the converter, especially when the life of the bottom blowing powder is less than 2000 heats. The new steelmaking technology for high-quality steel production makes the service environment of refractories more extreme and complex, including higher temperature, slag, molten metal, gas corrosion, mechanical wear, more severe thermal shock, higher pressure and high temperature vacuum. These harsh service environments pose a challenge to refractory workers.

3) Study on refractory for high quality steel efficient continuous casting. At present, the problems existing in the casting of high-quality steel include carburization (ultra-low carbon steel) and non-metallic inclusions, among which the problems of high-quality steel such as cord steel, bearing steel and rare earth steel are the most serious. Excessive alloying elements such as Mn, B, Ti, and rare earth lead to a decrease in the corrosion life of functional refractories, which will affect production efficiency. The submerged entry nozzle is easy to be blocked when casting Ti, Al and rare earth steel, which will affect the quality of steel. A series of high performance refractories for high quality superalloy production need to have better service performance.

4) Study on high quality refractory for near net shape continuous casting (ESP, thin strip continuous casting and amorphous thin strip production). Such as submerged entry nozzle, flow distribution nozzle, side sealing plate, nozzle, etc.

5) Study on a series of high-performance energy-saving refractory for thermal management of metallurgical high temperature devices.

6) Study on high value utilization of refractory and metallurgical slag.

## 3   Challenges and opportunities of refractory industry

A series of policies related to double carbon goal, green development, smart manufacturing, development and safety will further drive the technological innovation of high-temperature industry and promote the emergence of revolutionary high-temperature new technologies, which will greatly promote the technological innovation and industrial transformation of refractories. In addition, the calculation of carbon footprint in the whole life cycle of materials and the establishment of low-carbon green standards will make the development of refractory industry face great challenges and will also be full of opportunities and vitality. But in general, with the realization of the goal of high temperature industrial carbon peak and technological innovation, the general trend of the development of refractories is to reduce the quantity and increase the quality.

From the perspective of double carbon goal and low-carbon green high-quality development, there are some outstanding problems in China's refractory industry. The export of refractory raw materials in China accounts for a high proportion in the world, including various grades of magnesia, silicon carbide, brown corundum, white corundum, etc., resulting in high carbon emissions. The output of refractories in China is the first, among which the proportion of amorphous materials is low, the export volume of high energy consumption ordinary silicon bricks is large, and the proportion of green high quality materials is relatively low. The product structure needs to be further optimized. The manufacture of refractories is mainly based on fossil energy such as natural gas, which causes high carbon emissions. The energy efficiency and waste heat utilization rate of refractory manufacturing process need to be further improved. The utilization rate of refractories after reuse needs to be further improved.

Under the background of carbon neutrality and rapid development of new technologies in high temperature industries, the refractory industry is facing severe challenges. Carbon peak and carbon neutrality are not only the choice of technology, but also the reform of development right and development mode. Therefore, the refractory industry must: 1) implement new development concepts such as energy conservation and emission reduction, low-carbon green; 2) adhere to supply-side structural reforms, study raw material

decarbonization, energy reduction/decarbonization, production and manufacturing process decarbonization; 3) further improve energy efficiency and improve carbon sink capacity. The realization of the double carbon goal, the decarbonization of policies and regulations will gradually strengthen, decarbonization legislation, carbon quota, carbon trading, carbon tax, carbon negative list, carbon planning and so on will be stronger than the progress of science and technology in the short term, which needs the industry to attach great importance to.

In order to achieve low-carbon emission and carbon neutrality, the refractory industry also needs to deeply adjust the industrial layout and structure, not only to be close to raw materials but also to the market: 1) backward production capacity and high energy consumption equipment should be eliminated; 2) alternative raw materials for low-carbon emissions; 3) high life and functional materials should be developed to reduce resource and energy consumption; 4) key technologies for energy conservation and emission reduction should be developed and non-fossil clean energy should be used to improve energy efficiency; 5) The process flow should be optimized to promote smart manufacturing and green manufacturing; 6) the export of high-carbon emissions raw materials such as primary processing raw materials and low-end products should be curbed; 7) the technologies of carbon absorption and carbon consumption should be developed.

## 4 The direction of technological innovation in refractory industry

In order to comply with the high-end and intelligent manufacturing of high-quality carbon-reducing green development in the steel industry, refractories should achieve scientific and technological innovation. Firstly, we should focus on reduction and develop high-performance, long-life and lightweight products. Secondly, we should focus on functionalization and develop materials that are conducive to the production of high-quality steel and improve the energy efficiency of high-temperature industry. Thirdiy, we should focus on green environmental protection and develop environment-friendly, ecological and recyclable refractories with pollution reduction and carbon reduction. Fourthly, we should focus on the componentization of materials and improve the online detection and intelligent level of refractories. Science and technology of refractories should be considered from the aspects of material composition, structural design, preparation technology and material application engineering.

The first is the research of carbon reduction of raw materials. The main task is to innovate the preparation process of refractory raw materials. Alternative raw materials for low carbon emissions should be developed. The green calcination and enrichment and utilization technology of $CO_2$ of magnesite and dolomite based on product gas recycling should be developed. New heating technologies with low carbon emission should be developed to improve the efficiency of raw material preparation. Systematic research on replacing fused raw materials with lightweight high-strength microporous aggregates and sintered raw materials should be carried out. New green inorganic binders should be developed to replace organic binders with high carbon emissions such as phenolic resin and asphalt. Surfactants such as green additives and water reducer should be developed. Based on the innovation of raw material value chain of recycling, the proportion of high-quality recycling of used refractories should be improved. We should focus on improving the comprehensive utilization rate of low-quality raw materials. The improvement of comprehensive utilization rate of low-quality raw materials Attention should be paid to the improvement of comprehensive utilization rate of low-quality raw materials. The technology of replacing refractory raw materials with solid waste such as metallurgical slags is developed.

The second is the study of advanced high-temperature materials and the study of material components. The integrated design of structure and function should be innovated, and the research on cross-scale material compounding, gradient structure compounding, layered structure compounding and surface modification from nanometer to millimeter should be carried out to realize the optimal regulation of high temperature mechanical properties, thermal physics and functionality of materials. Long-life structure function integration high-temperature and high-transmittance wavelength furnace lining materials for new heating technologies and high-performance furnace lining materials for plasma heating, and refractories for waste incineration and industrial hazardous waste harmless treatment equipment should be studied. The key technologies of energy saving and emission reduction should be developed, and high performance and long-life green high temperature insulation materials should be developed to improve energy efficiency. To assist the field of new energy, new refractories with high efficiency, long life and green for coal gasification, and with high thermal shock resistance and high thermal insulation function for gas turbines should be studied. The innovation of multi-disciplinary cross-integration should be carried out, and materials, high temperature sensors, radar monitoring and computational simulation should be integrated to make high temperature materials modular and component-based, so as to maximize the online monitoring and service life of refractories.

The third is refractories evaluation and method innovation. The coupling mechanism of heat, force and corrosion medium of refractories under high temperature and complex service environment should be studied, and the service failure model and database should be established to predict the service life and service behavior, which provides a basis for the research and development of new and efficient refractory materials for different environments. The research on design and preparation of new materials based on the design of gradient materials and microstructure control should be carry out, and combining with thermodynamic simulation calculation, material genetic engineering and laboratory high temperature simulation verification to provide technical support for the development of a series of green refractory materials with excellent service behavior, long life and reliability. Finally, the synergistic improvement of key properties such as thermal shock resistance, permeability resistance, corrosion resistance and functionality of refractory materials is realized.

The fourth is the development of carbon reduction of preparation technology. The research on uniform forming and near net-shape preparation of refractories including complex shape of aggregates.should be carry out to solve the key common technology of structural functionalization, lightweight and complex shape material preparation of refractory materials. New equipment for shaped product to improve efficiency and reduce energy consumption should be researched and developed. New sintering technology and equipment, such as the use of microwave sintering technology, plasma sintering and other new technologies should be researched and developed. The energy consumption and heat loss of the process should be reduced, and intelligent manufacturing should be promoted to optimize the manufacturing process of refractory materials.

The fifth is to do a good job in carbon reduction infrastructure research. The calculation of the carbon footprint of refractories should be carry out by life cycle assessment (LCA). The carbon emissions of the industry should be accounted and verified. The total carbon emissions of the industry should be checked and ratified. The carbon market mechanism and carbon emission management should be improved. A series of standards for low-carbon development in industries such as carbon emission accounting standards should be formulated. These are the basic work to improve energy efficiency and low-carbon green development, are also green passes to enter the service industry, and play a major role in promoting the development of low carbon technology and standardizing market order to realize the greening of the whole life cycle of refractories and promote the high-temperature industry to achieve the target of carbon peak and carbon neutrality in China.

## References

[1] Ruiyu Y. Understanding of Carbon Peak and Carbon neutrality in Iron and Steel Industry. Founding Conference of Low Carbon Work Promotion Committee of Iron and Steel Industry

305

and Seminar on Low Carbon Development Path of Iron and Steel Industry, Shanghai, China, April 21-23, 2021.

[2] Guodong X. The practice and innovation of green low-carbon development in China Baowu. Founding Conference of Low Carbon Work Promotion Committee of Iron and Steel Industry and Seminar on Low Carbon Development Path of Iron and Steel Industry, Shanghai, China, April 21-23, 2021.

[3] Yiren L. Low-carbon green development path of Hbis group under the vision of carbon neutrality. Founding Conference of Low Carbon Work Promotion Committee of Iron and Steel Industry and Seminar on Low Carbon Development Path of Iron and Steel Industry, Shanghai, China, April 21-23, 2021.

[4] Xinping M. Near net shape manufacturing technology under the background of carbon neutrality. High-end forum of near net shape manufacturing technology. Zhangjiagang City, Jiangsu Province, China, April 23-25, 2021.

[5] Rong Z. Carbon dioxide green crystallization steelmaking technology and its application. China's 2021 Special Metallurgy Award.

# NEW WAYS TO DESTROY REFRACTORIES – THE FUTURE OF GREEN STEELMAKING!

Thomas (Tom) Vert, Strategic Refractory Consulting Inc., Hamilton, ON, Canada.

## ABSTRACT

The "Carbon Challenge" that we are all trying to address is a major change in refractory customer manufacturing processes. Changes in steel plants to move to "green" steel will include removal or major modification of coke ovens, blast furnaces (BF) and basic oxygen furnaces(BOF); a shift to electric furnace (EAF) steelmaking with possible oxygen addition, direct reduced iron (DRI), liquid iron, hot briquetted iron (HBI); and the injection of hydrogen into any or all of these processes and/or any combination of all of the above!

A natural move from BOF wear rates of approximately 0.2mm/heat to EAF wear rates of 1mm/heat alone will increase refractory consumption regardless of any of the other technologies. The engineered move to each of the above changes and combinations thereof will increase the wear mechanisms of the refractories by an unknown factor also. Higher gangue ratios in DRI, use of EOF or Conarc furnaces, in the EAF technical space will raise major wear challenges to the refractories being used. And of course, it is still very early to see what the addition of high temperature hydrogen and/or steam as a byproduct will do!

This paper will attempt to predict the future of wear mechanisms and wear rates of "green steelmaking" with the prediction that no matter what...we will find new ways to destroy refractories! (and of course, new refractories to withstand these changes)

## WHAT IS GREEN STEEL?

Essentially, green steel is the manufacturing of steel without the use of fossil fuels.  So-called "green hydrogen" is one solution that could help reduce the steel industry's carbon footprint.

Hydrogen is labelled according to the source of underlying energy carrier used to produce the $H_2$ and whether carbon capture and storage (CCS) is employed, with green hydrogen as the ultimate goal.

With steel production making up ~7% of the world production of CO2, it is imperative to meet the climate change challenge, to reduce the use of fossil fuel usage.

As can be seen in Figure 1, the easiest and fastest way to meet this challenge is to move from BF/BOF production to EAF production[1].
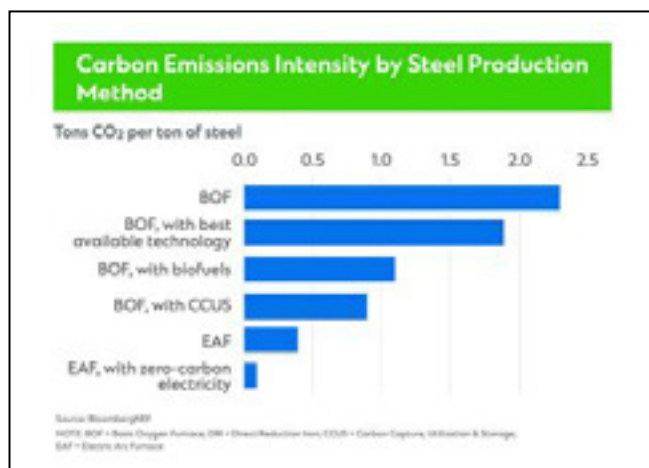


Figure 1: Carbon emission intensity by steel production method[1].

A nice visual I like to use is the one from Midrex which shows the journey to green steel from the current state, as seen in the Figure 2[2].
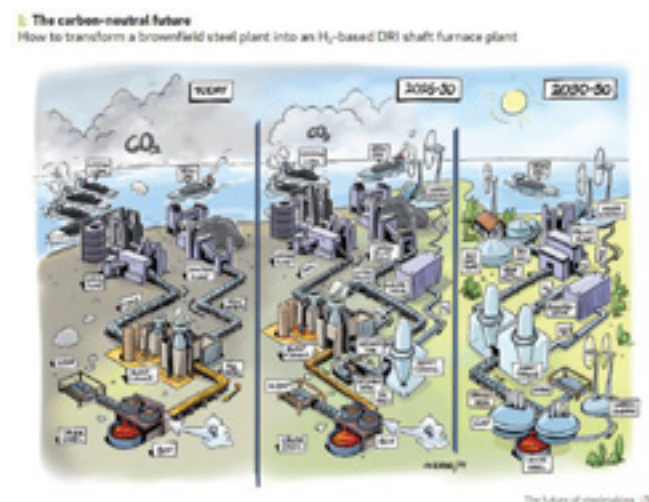


Figure 2: Journey to green steel from the current state[2].

There are also numerous other pilot processes out there (e.g., HyBrit, Boston Metal, etc.) that may be a part of the solution, however, it is this author's opinion that the EAF will be the backbone of green steel future!

## HOW DO YOU WEAR OUT REFRACTORIES?

Refractories are worn by a combination of mechanisms which are summarized as "TMC".  TMC stands for thermal (T), mechanical (M) and chemical (C) wear mechanisms.  The general checklist that makes up the "TMC" analysis is shown in Table 1.

Table 1: TMC Wear Mechanisms

| Main Mechanism | Sub-Mechanism | Examples |
|---|---|---|
| **Thermal** | Peak temperature (T) | Tapping temperatures |
| | Thermal shock (delta T): Frequency and amplitude of changes | Heats/day and long outages |
| **Mechanical** | Impact | EAF door cleaning, force of scrap impact |
| | Abrasion | Stirring energy |
| | Applied stress | Mass of bricks sitting on the lowest layer of bricks (BOF stadium) |
| **Chemical (and Thermo-Chemical)** | Dissolution | Slag matrices attacked by chemically aggressive slags – especially at high temperatures |
| | Penetration | Fluid slag penetration |
| **Thermo-Mechanical** | Strain of thermal expansion | Expansion of lining |
| **Thermo-Mechanical (and Chemical)** | Spalling of the penetrated zones | Thermal expansion mismatch of penetrated zone vs virgin material |

A key to this analysis is also to evaluate from a refractory perspective. Refractory specialists are used for this as metallurgists usually understand the steelmaking process but do not understand refractory properties, and therefore cannot appreciate the effect of the former on the latter.

Besides to understand the refractories wear it is important to analyze current wear rates and predict them in the future.

## CURRENT WEAR RATES OF REFRACTORIES IN EACH PROCESS

### Blast Furnace Production

Refractories for blast furnaces include the initial lining (including stoves), repairs every 2 years on average (shotcrete and/or gunning and/or brick and/or castable repairs) (Table 2). Note that taphole clay is a metallurgical consumable and not a refractory so is therefore no included. Also, torpedo cars and/or hot metal ladles are not included as it is very plant layout dependent on wear rates but is not high enough to change the premise of this paper.

Table 2: BF Refractory Usage (no taphole clay)

| Initial lining (one time) | 1,000,000 | kg |
|---|---|---|
| Lining repairs every 2 years | 20,000 | kg |
| Trough refractories (~0.5kg/t) | 750,000 | kg |
| 20 year total kg usage | 16,200,000 | kg |
| Annual HM production | 1,500,000 | Tonnes |
| 20 year total HM production | 30,000,000 | Tonnes |
| Total BF refractory kg/t | 0.54 | kg/tonne |

Modern blast furnaces are a blend of carbon, silicon carbide, high alumina silicon carbide and high alumina bricks with zoning for key wear mechanisms.

Over time the trend has been to increase the usage of carbon and silicon carbide (SiC) type products to resist the high thermal loads and cycling in a modern BF operation. With a normally pressurized reducing atmosphere, the risk of oxidation has been low, and the lifetime of these refractories has increased. Modern carbon inclusive shotcrete materials have led to major increase in repair life. This has led to an increase in BF refractory life from 3 to 5 years in the 1980's to talk of a "perpetual" lining in future, with lives of over 20 years already documented without major relines.

### Basic Oxygen Furnace Production

Refractories for BOF's include the initial lining, the safety lining, gunning repairs and taphole changes are presented in (Table 3.)

Table 3: BOF Refractory Usage

| Area | kg/t | kg |
|---|---|---|
| Safety Lining | 0.01 | 14,727 |
| Working Brick | 0.09 | 141,029 |
| Gunning Repairs | 1.00 | 1,500,000 |
| Tapholes | 0.01 | 15,000 |
| Total Campaign Refractory usage | 1.11 | 1,670,756 |
| BOF Campaign Lifetime | 5,000 | - |
| BOF Average Heat Size | 300 | - |
| BOF Campaign Tonnage | 1,500,000 | - |
| Total BOF Refractory Usage | 1.11 | - |

Modern BOF's are mainly a blend of magnesia carbon brick, with zoning for key wear mechanisms (e.g., charge pad, trunnions, bottoms, etc.)

BOF life is highly dependent on operating and repair practices. USA BOF's have historically used slag splashing as a way to push BOF life to over 20,000 heats, though with the downside of lack of bottom stirring which adds other metallurgical costs including a higher usage of deoxidants.

Repair materials include basic gunning materials as well as patching with slags, used bricks, and/or bulk patching materials.

### Electric Arc Furnace Production

Refractories for EAF's include the initial lining, fettling and gunning repairs as well as taphole changes are presented in Table 4.

Table 4: EAF Refractory Usage (AC Furnace)

| Area | kg/t | kg |
|---|---|---|
| Hearth / Fettling | 1.50 | 225,000 |
| Working Brick | 0.60 | 90,000 |
| Gunning Repairs | 1.00 | 150,000 |
| Tapholes | 0.03 | 4,500 |
| Total Campaign Refractory usage | 3.13 | 469,500 |
| EAF Campaign Lifetime | 1,000 | - |
| EAF Average Heat Size | 150 | - |
| EAF Campaign Tonnage | 150,000 | - |
| Total EAF Refractory Usage | 3.13 | - |

Modern EAF's are mainly a blend of magnesia carbon brick, with zoning for key wear mechanisms (e.g., hot spot, above EBT, door area, etc.)

EAF life is highly dependent on operating and repair practices, even more so than the BOF. The variations on EAF sizes (from 20 tonnes to over 300 tonnes) as well as type (AC, DC, EOF, Conarc, etc.) make them very hard to generalize actual kg/tonne usage. The above calculations are for an average of AC type furnace.

From experience it is known that wear rates and higher refractory usage result from the following designs:

DC < AC < Shaft < EOF < Conarc

The major difference is in the amount of fettling and gunning repair required and again is highly dependent on foamy slag operations (which can cure many metallurgical sins!)

Wear rate is also affected by the type of scrap/iron charge from 100% scrap to large pieces of cold iron (from BF hot metal dumping) to HBI, DRI and even hot metal charging (up to 30% of the metallic charge. Note that the effect of these materials will be discussed more in the future state section.

## PREDICTED WEAR MECHANISMS/RATES OF REFRACTORIES IN EACH PROCESS WITH GREEN STEEL

### Blast Furnace Production

In the future, it is predicted that those companies that continue to utilize blast furnaces will try to inject hydrogen as one of the fuels. It is well known that hydrogen produces more water compared to other hydrocarbon fuels and may result in water vapor being present in the furnace atmosphere, which can lead to increased refractory corrosion for certain refractory compositions[3]. Modern day blast furnaces are composed of a combination of carbon, silicon carbide and alumina bricks with similar containing monolithic repair materials. The effect of $H_2$ and or $H_2O$ in these furnaces will lead to degradation of the refractory lining by the chemical reactions, as presented in equations 1 to 4:

| | |
|---|---|
| $2H_2 + C = CH_4$ | Eq. 1 |
| $2H_2 + SiC = Si + CH_4$ | Eq. 2 |
| $2H_2O + 2C = CO + CH_4$ | Eq. 3 |
| $2H_2O + SiC = SiO_2 + CH_4$ | Eq. 4 |
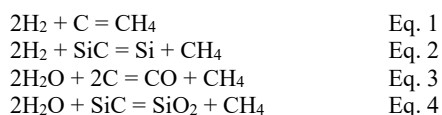
The blast furnace maintains as much as possible a reducing atmosphere when stable and under pressure, however, there are numerous times when the furnace is open to atmosphere for repairs and/or inspections. Also, water can enter the furnace through stave and/or plate leaks and/or snow/ice during winter months. All of these conditions will lead to higher wear rates, but it is unknown how high these wear rates may go.

It is this author's opinion that the initial lining wear rates for BFs with hydrogen injection will at least double due to the nature of attack mechanisms and operational conditions. Future predictions for refractory usage are presented in Table 5.

Table 5: BF Refractory Usage (no taphole clay) – FUTURE

| | | |
|---|---|---|
| Initial lining (one time) | 1,000,000 | kg |
| Lining repairs every **1 year** | **50,000** | kg |
| Trough refractories (~0.5kg/t) | 750,000 | kg |
| 20 year total kg usage | **17,000,000** | kg |
| Annual HM production | 1,500,000 | Tonnes |
| 20 year total HM production | 30,000,000 | Tonnes |
| Total BF refractory kg/t | **0.57** | kg/tonne |

It can be seen in Table 5 that overall wear rate only increases from 0.54 to 0.57kg/t due to the main refractory usage being in the BF troughs.

The key drop in refractory consumption, however, will be the major drop in the number of blast furnaces online which is expected to decrease at least 50% though this will vary widely by region due to economics, as seen in Figure 3[4]. For example, all North American steelmakers except Cliffs have committed to a switch to EAF production by 2040.
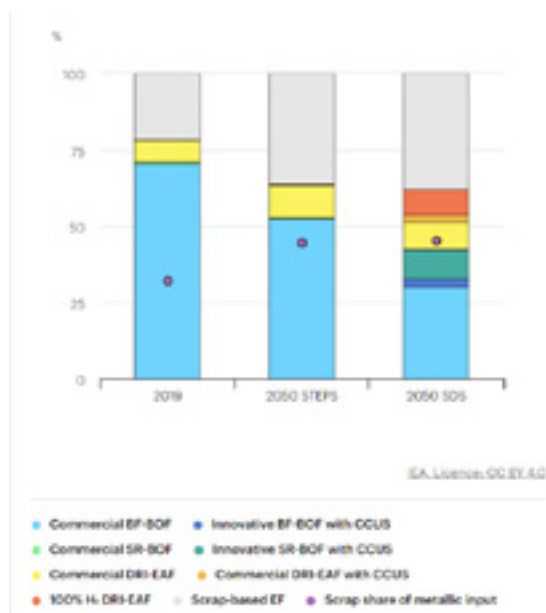


Figure 3: Global crude steel production by process route and scenario: 2019 to 2050[4].

**Basic Oxygen Furnace Production**

There is no mention at the current time of injecting hydrogen into the BOF and therefore there is assumed to be little change to wear rates of the BOF refractories.

As discussed with BF's, the key change in refractory consumption, will be the major drop in the number of oxygen furnaces online which is expected to drop by at least 50% though this will vary widely by region due to economics[4].

**Electric Arc Furnace Production**

Refractory wear for EAF's will increase in the future due to a combination of four factors:

1. Increased usage of combination oxygen/EAF furnaces such as EOF, Conarc and/or oxygen injection from bottom tuyeres.
2. Higher use of DRI/HBI and even liquid hot metal to meet final customer metallurgical requirements.
3. Injection of hydrogen into the EAF.
4. Usage of hot metal from other processes into the furnace.

Four factors will lead to an increase in refractory wear and usage, as follow:

1. As stated earlier in this paper, from experience it is known that wear rates and higher refractory usage result from the following designs:

    DC < AC < Shaft < EOF < Conarc

    As steel plants move to EAF's and push the envelope to meet stringent final customer demands for the move to more destructive designs will be natural. It is also expected that bottom stirring will be used with argon or potentially with oxygen to increase the process speed and lower tap to tap times. All of these will lead to higher refractory consumption.
2. The move to higher amounts of HBI, DRI and even hot metal charging will also lead to higher wear rates. It has been stated that the amount of higher quality DRI/HBI is dropping and therefore gangue materials will increase. This will lead to longer processing times, higher slag ratios and therefore more refractory issues.
3. Injection of hydrogen into the EAF with associated free $H_2$ and potentially $H_2O$ will again lead to refractory wear as the magnesia carbon brick will be destroyed quickly and need repairs. If the carbon is decreased in the brick, then the amount of thermal spalling will increase so for now there are not solutions to this challenge.

Table 6 shows this author's "crystal ball" projection of the >50% increase expected in refractory consumption!

Table 6: EAF Refractory Usage Future State (AC Furnace)

| Area | kg/t | kg |
|---|---|---|
| **Hearth / Fettling** | **2.00** | 300,000 |
| **Working Brick** | **1.20** | 180,000 |
| **Gunning Repairs** | **1.50** | 225,000 |
| Tapholes | 0.03 | 4,500 |
| Total Campaign Refractory usage | 4.73 | 709,500 |
| EAF Campaign Lifetime | 1,000 | |
| EAF Average Heat Size | 150 | |
| EAF Campaign Tonnage | 150,000 | |
| **Total EAF Refractory Usage** | **4.73** | **51% increase** |

**FUTURE REFRACTORY SOLUTIONS**

So, if the future will include some combination of more EAF's, more hydrogen, longer processing times and more aggressive slags, etc., than how do refractory designers move forward?

309

It should be noted that all refractory companies have started to work on the effects of hydrogen injection and what to do.

Some key work has been done and the key points are summarized as follows:

- From the Ellingham diagram, presented in Figure 4[5], it is possible to see that alumina, chromia and titania are the key oxides that are less affected by hydrogen at steelmaking temperatures.
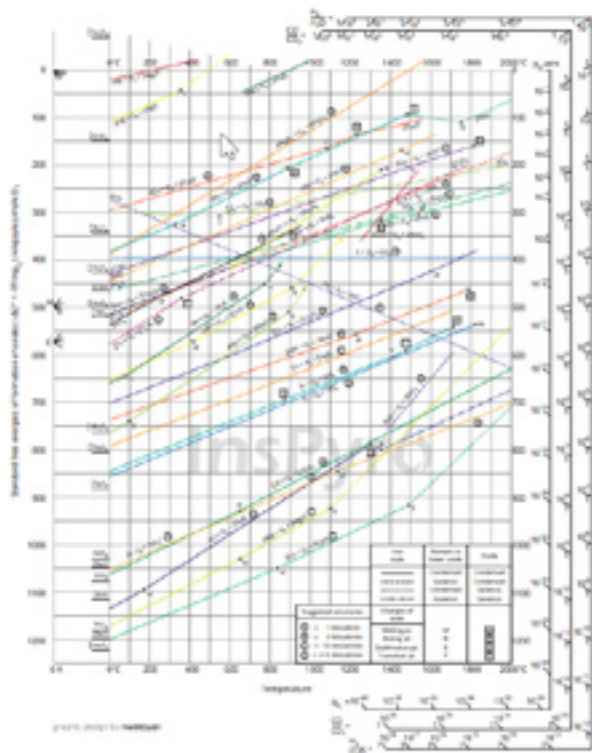


Figure 4: Hydrogen Ellingham diagram[5].

This explains why very high purity alumina has been used in hydrogen atmospheres over time in other non-ferrous industries and why it is the refractory of choice in modern injection capable DRI facilities.

This will not be good enough for usage in an EAF of course as the carbon in the magnesia carbon brick, and the magnesia for basic slags are needed for survival.

Potential options are low carbon magnesia through the use of nano-carbon technologies, some forms of spinel (though chrome 6+ is still a major issue), or high temperature calcium aluminates (like hibonite).

We look forward to seeing the development of technologies to combat the newer and more aggressive steel plant processes!

**CONCLUSIONS**

1. "Green" Steelmaking will result in a shift from the BF/BOF route to the EAF route over the foreseeable future in order to get large gains in decarbonization.
2. The new process route will result in an increase of refractory usage by at least 90%. This is because the BF/BOF route uses 1.65kg/tonne and the EAF route uses more than 3.13kg/tonne.

3. The EAF route itself will generate additional refractory consumption due to process route, raw material, and injection changes towards more hydrogen.

**REFERENCES**

[1] https://www.sc.com/en/feature/ironing-out-chinas-plan-carbon-neutral-steel-production/
[2] https://www.rolandberger.com/en/Insights/Publications/It-s-time-for-steelmakers-to-reduce-emissions.html
[3] Carniglia, S.C and Barna, G.L., Handbook of Industrial Refractories Technology: Principles, Types, Properties and Applications, Noyes Publications/William Andrew Publishing, LLC, USA, (1992).
[4] https://www.iea.org/reports/iron-and-steel-technology-roadmap
[5] https://inspyro.be/reduction-with-hydrogen-ellingham-diagram/

# TRANSFORMATION TO HYDROGEN-BASED STEEL MAKING AND REFRACTORY CHALLENGES AT THYSSENKRUPP STEEL EUROPE AG IN DUISBURG

K. Kursch, Dr. B. Kohnen, Dr. M. Weinberg, thyssenkrupp Steel Europe AG, Duisburg

**ABSTRACT**

In 2045 tkSE wants to be climate neutral. To reach the goal the existing blast furnaces have to be replaced by direct reduction plants and smelters.

The change will be challenging for the plant site as well as for the refractory material. tkSE wants to use hydrogen gas for the production of up to 2,5 mio to/ a hot metal.

Already in 2019 tkSE started the first researches and development projects for new refractory materials together with several suppliers, universities, external labs and other industrial cooperation partners.

The behaviour of different materials under hydrogen atmosphere as well as under a mixed gas atmosphere with H2 and NG are investigated. Another big field of investigation is the smelter technology which works under a reducing atmosphere. Melting down a big amount of DRI (direct reduced iron) with an almost blast-furnace-like slag is not a common operation and also a challenging operation for the refractory.

## 1 INTRODUCTION

At tkSE AG, one blast furnace will be replaced by a DR (direct reduction) plant plus two smelters in the future. In one plant, 2.5 million tons per year of CO2-reduced hot metal are to be produced by melting $H_2$-reduced DRI (direct reduced iron). Due to structural conditions, tkSE has decided to use a SAF (submerged arc furnace) or ESF (electric smelting furnace) for the production instead of a conventional EAF (electric arc furnace). Due to the significantly lower power density compared to a conventional EAF, large melting units are required: in detail, the size of one smelter will be about 400 $m^2$.

tkSE would like to retain the steel mill route, including the conventional converter process, so that the almost carbon-free DRI produced will have to be carburized in the smelter.

On the one hand, this approach enables one-to-one production for all conventional grades in the steel mill produced by tkSE, i.e. the customer can rely on the usual quality. On the other hand, the slag produced by melting the DRI in the SAF has a similar chemical composition to conventional blast furnace slag, so that the cement and building materials industries, as customers of the granulated slag, can also continue to be supplied without restriction. Thus, no slags are produced, which can only be used as lump slag in road construction.

However, due to this plant combination tkSE faces completely new challenges with regard to the refractory lining of the above-mentioned aggregates.

## 2 H₂ – CORROSION IN DR-PLANTS

The DR plant planned by SMS is to be operated in the future, after a ramp-up period (natural gas operation), first with mixed gas (natural gas and $H_2$) and finally with 100 % $H_2$. In the plant, DRI will be produced under overpressure at gas inlet temperatures of up to 1100 °C. This process produces combinations of reactive gases, as well as hot water vapor.

### 2.1. Laboratory scale studies

In order to be able to assess the extent of possible damage by $H_2$ to the refractory lining, tkSE has already started testing different raw materials and products under operating conditions together with various institutes trand refractory suppliers at the end of 2019. An important project in this context is the RUHL (refractories under hydrogen load) project led by the University of Koblenz-Landau. In these tests, potential refractory products from Almatis, Refratechnik Steel and Steuler KCH are examined under varying conditions. Due

to extremely long delivery times for new test units, it has only been possible to test the materials in a pure $H_2$ atmosphere at various temperatures. Mixtures of water vapor and hydrogen could therefore not be tested so far.

Here, tkSE is paying particular attention to corundum-based materials, since this material represents a standard for DR systems currently in operation.

The corundum concrete described below, based on brown fused corundum, was subjected to 100% $H_2$ at 1200 °C for 200 h. This test was performed with three different specimens, each placed at different positions in a gas purging furnace, so that positioning effects on the strength of corrosion could be minimized.

After treatment, the concrete bar was prepared for examination under a scanning electron microscope. When viewing the polished surface, it is noticeable that macroscopically, unlike specimens of other materials, no corrosion zone is visible (Fig. 1).
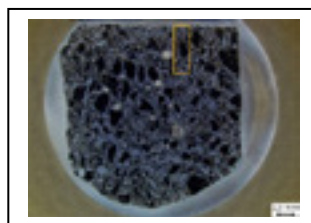


*Fig. 1: Section of corundum concrete for SEM analysis.*

By means of element mapping, however, it can be shown beyond doubt, that the Si content decreases strongly towards the hot side (Fig 2).
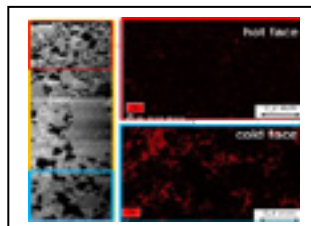


*Fig. 2: EDX - Mapping for Si - distribution in the marked area.*

The physical properties also show a clear structural damage due to $H_2$ attack. The corundum concrete exhibits the lowest weight loss of all tested materials (Fig. 3), but shows the highest loss of cold bending strength with approx. 50 % (Fig. 4).
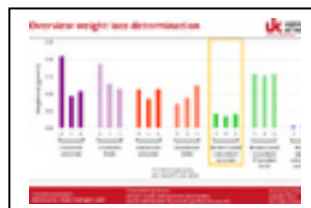


*Fig. 3: Overview weight loss*
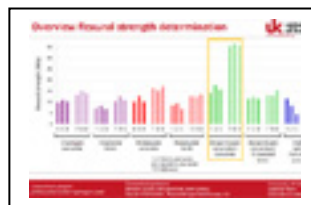


*Fig. 4: Overview cold bending strength*

### 2.2. Results from practice

From other industrial plants with comparable conditions, samples from refractory linings were examined internally by tkSE. Some of them had been in use for many years. These are andalusite bricks with 35-40 % $SiO_2$ content.

In the cracking reactor of the Claus plant, an aggregate of the gas treatment of the coking plant, conditions with 1120 °C, 5 - 8 % $H_2$ and water vapor are similar to those in DR plants. Investigations of samples which were installed in a plant for five years each show a partly massive damage of the microstructure of the bricks (Fig. 5)

311

*Fig. 5: H₂-destroyed grate of the fission reactor v. 2018*

The specimens show the same corrosion mechanism as the laboratory specimens (Figs. 6 and 7): $H_2$ dissolves the silicate components from the microstructure on the hot side, reacts with $SiO_2$ to form $H_2O$ and $SiO$, which outgasses from the microstructure and leaves pores. Through these, new hydrogen can penetrate further into the structure and continue the process. What remains is a corundum fringe on the stone surface and a completely mullitic transformed microstructure inside.



*Fig. 6: Depletion of SiO₂ towards the hot side of 2018*
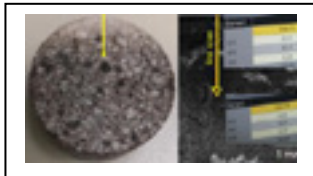


*Fig. 7: Depletion of SiO₂ towards hot side of 2020*

The examination of the strength showed that, although the microstructure was heavily attacked, the stone surprisingly exhibited a higher cold compressive strength than in the as-delivered condition (Fig. 8). The reason for this is not yet clear. It is assumed in the literature, that the combination of the outgassing SiO with water vapor forms a kind of gel on cooling and that this strengthens the microstructure again. [1].
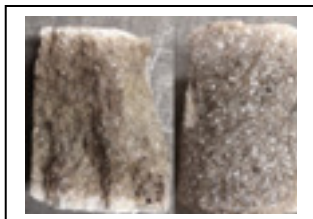


*Fig. 8: KDF specimen with 99 and 117 MPa (unused 70-100 MPa)*

Refractory samples from a cowper were also examined (andalusite bricks, operating temperature approx. 1300 °C, 5-10 % $H_2$). Here, too, the same wear and corrosion pattern were found. Under the microscope, also secondary corundum could be found on the hot side, which would also be attacked and dissolved by $H_2$ in the further course. (Fig. 9)
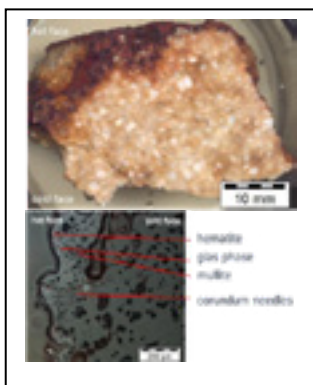


*Fig. 9: Ground cowper brick with sec. corundum on the hot side*

### 3 CHALLENGES FOR SAF WEAR LINING

In the new melting units, the heat for melting the DRI is introduced via the slag to a greater extent than in EAFs. To get the DRI liquid, this process needs about 1650 °C operating temperature. Together with a slag basicity of 1.1 and reducing conditions, the FF lining is highly stressed. A conventional EAF lining will not withstand these conditions for a long time.

### 3.1. Laboratory scale studies

For carburization tests in a test furnace, it was necessary to investigate different FF materials for the melting vessel. For this purpose, crucibles were made from different materials and filled with blast furnace slag and DRI. Thus prepared, they were heated for 20 h at 1650 °C (later operating temperature of the smelter) under a slightly reducing atmosphere. The results show that most of the tested materials would not have reached 10 h operating time.

Initially, bricks were tested that are also in use elsewhere at tkSE and perform very well there, as well as the grade used as the standard lining for the test vessel. Figs. 10-12 list the crucibles that showed the best resistance.

Only three crucibles of the stone products reached 20 h of exposure without breaking through laterally, but here the microstructure is also heavily infiltrated and at least washed out.



*Fig. 10: Mg-Cr (20 % Cr₂O₃), slag is completely infiltrated*
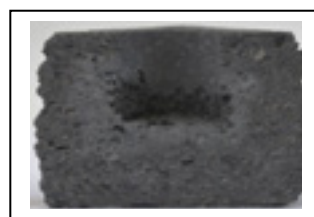


*Fig. 11: Al-C-SiC (10 % SiC), DRI and slag completely infiltrated, microstructure heavily washed out*



*Fig. 12: Andalusite, DRI not, slag little infiltrated, microstructure on the right almost broken through*

The microstructure of a pure corundum stone was completely destroyed (Fig. 13+14).



*Fig. 13+14: Corundum stone with 99% Al₂O₃, completely infiltrated and broken through*

As well as a corundum mullite stone with 9 % $SiO_2$, or a C-corundum chromite stone with 10 % $Cr_2O_3$ (Fig. 15+16).



*Fig. 15: Corundum mullite stone*
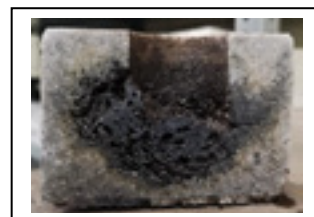
*Fig. 16: C-corundum chromite stone*

The results for the monolithic products are also sobering. Even a corundum concrete, which has been used for decades (at least 15 years) in the blast furnace floor as a prefabricated part, was completely destroyed after 20 hours (Fig. 17).
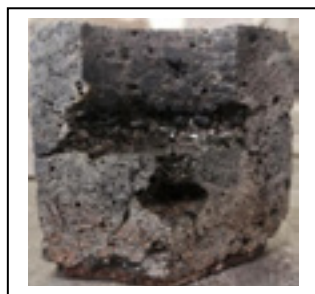


*Fig. 17: Corundum prefabricated concrete of the blast furnace floor*

These results lead to the conclusion, that the use of a freeze lining in the slag zone will be of elementary importance for the high durability of the selected furnace design.

## 4  SUMMARY

DR –Plant:
*   refractory samples of comparable plants all show a strong attack, up to a massive damage of the microstructure by $H_2$
*   The refractory material of future DR plants should have a minimum content of $SiO_2$

Smelter:
*   Conditions in a smelter used for hot metal production (acid slags with basicity of 1.1, 1650 °C, reducing atmosphere) are highly aggressive for the lining
*   Conventional EAF refractory concepts cannot be easily adapted, partly because of the reducing atmosphere
*   Freeze lining is of high importance for the durability of the refractory of a smelter

Next Steps:
➢   Tests must be carried out with mixed gases and hot water vapor
➢   Samples from DR facilities already operating in a conventional manner are to be examined
➢   Temperature gradient existing in real application due to freeze-lining requires modified tests
➢   New refractory products must be developed in close cooperation with the suppliers over the next two years

## REFERENCES

[1] "Hydrogen-silica reactions in refractories", M.S. Crowley, research and development dept. American Oil Co., Whiting Ind., Ceramic Society Bulletin, Vol. 49, 1969

[2] "Hydrogen-silica reactions in refractories – Part II", M.S. Crowley, research and development dept. American Oil Co., Whiting Ind., Ceramic Society Bulletin, Vol. 50, 1970

[3] "The reduction of silica and mullite in hydrogen", Chung-I Chen, B.S, M.S., Ohio State University, 1979

[4] AV – Nr. 141/18, " Appraisal and examination of the used andalusite grid stones of Clausanlage 1", Baaske, Häußler, thyssenkrupp Steel Europe AG

[5] AV – Nr. 146/21, " Examination of the used samples from the cowper", Rzepka, thyssenkrupp Steel Europe AG

[6] „Hydrogen attack in the auxiliary recovery unit", Baaske, Mertke, 2021, thyssenkrupp Steel Europe AG

[7] „Consortial projekt - Refractories under hydrogen load", Isabelle Henn, Universität Koblenz, results from March 2023

# DECARBONISATION OF STEEL INDUSTRY AND ITS IMPACT ON FUTURE SLAG

Olena Volkova, Institute of Iron and Steel Technology, TU Bergakademie Freiberg, Freiberg, Germany

## ABSTRACT

The current transformation of the steel industry is presented. The latest and planned measures for $CO_2$ reduction in steel production are exhibited. Two possible production routes, hydrogen-based direct reduction with an electric arc furnace (DR-EAF) and hydrogen-based direct reduction with a basic oxygen furnace via a smelter (DR-smelter-BOF) are explained. Possible changes in future slag and metallurgical treatment, such as desulphurisation and dephosphorisation, are addressed.

## INTRODUCTION

Steel is an indispensable material in our modern society. In 2022, 1878.5 million tons of crude steel were produced worldwide [1]. Only in Germany last year, 36.8 million tons of crude steel were manufactured [2]. This makes Germany the largest steel producer in the European Union. The most important German steel producers with the largest output are thyssenkrupp Steel Europe AG, ArcelorMittal Germany Holding GmbH, and Salzgitter AG.

Today, steel is usually produced mainly in two ways: an integrated route using raw materials (iron ore, limestone, coal, etc.), and a secondary route based on the re-melting of metal scrap. For the integrated route, often called as the primary route, $CO_2$ gas in the amount of 1,880 kg/t crude steel is directly emitted from the coke plant, sinter plant, blast furnace (BF), basic oxygen furnace (BOF), and following continuous casting and forming processes [3]. Herewith, BF has the highest share of $CO_2$ emissions.

With the scrap-based secondary steelmaking route, often called as the electric arc furnace (EAF) route, only a portion of the $CO_2$ emissions is directly associated with the production site. Meanwhile, the most of $CO_2$ emissions are attributed to the generation of electrical energy, which serves as the main source of heating in this route. For instance, crude steel from the EAF route emitted 410 kg/t, assuming the $CO_2$ emissions for the electrical energy production of 300 g-$CO_2$-eq/kWh [3]. If the $CO_2$ load of the electrical energy increases, the $CO_2$ emissions of the secondary steelmaking route would increase immediately. Depending upon the source, the generation of 1 kWh of electrical energy produces 295 to 1005g of $CO_2$ [4]. According to [5], the average $CO_2$ load of electrical energy in the last 5 years was 473 g-$CO_2$-eq/kWh in Germany and 819 g-$CO_2$-eq/kWh in Poland.

Direct reduced iron (DRI) production began its commercial introduction in the late 1950s [6]. DRI was seen as a niche material for use in EAF applications, where large quantities of steel were not required or where sufficient scrap stocks were not available [6]. Currently, about 4.8% of total steel production is made through the direct reduction (DR)-EAF route, using predominantly natural gas, and thus producing lower $CO_2$ emissions compared to the integrated route [7]. For example, the $CO_2$ emissions from DR-EAF route were calculated as 993kg/t crude steel [3]. The top 5 DRI producing countries in 2021 were India, Iran, Russia, Saudi Arabia, and Mexico [8].

The EAF route provides approx. 28% of world steel, accounting only for 8% of the $CO_2$ emissions generated by the steel industry [4]. On the other hand, the integrated route produces almost 72% of steel but is responsible for 92% of the $CO_2$ emissions [4]. In total, the iron and steel industry is the second largest global industrial $CO_2$ emitter, contributing 7-9% of global $CO_2$ emissions [9].

In 2011, a roadmap to achieve a competitive low-C economy in Europe by 2050 was developed [10]. It shows that European industries will have to reduce their $CO_2$ emissions by 80-95% in absolute terms by 2050 compared to 1990 levels, which is a significant challenge. The answer to this challenge is the development and implementation of key pathways for $CO_2$ reduction, such as smart C usage (SCU) and C direct avoidance (CDA) in the iron and steel industry.

SCU includes incremental actions/optimisations for the conventional primary route of steel production and $CO_2$ reduction, involving end-of-pipe technologies, such as $CO_2$ capture and storage (CCS) and C capture and usage (CCU). Examples of SCU are actual processes and technologies developed recently, such as Carbon2Chem from thyssenkrupp steel Europe [11], Steelanol from ArcelorMittal together with Primetals, LanzaTech, and E4tech [12]. CDA includes the scrap-based secondary route of steel production (electric furnace) and the Fe ore-based direct reduction electric furnace route with natural gas and/or hydrogen as a reducing agent, avoiding the use of coal and coke.

Unfortunately, there is a shortage of scrap to fully meet the demand for iron and steel via the EAF route [5]. Moreover, this route cannot be used for all steel grades due to quality restrictions. For example, the production of flat products is still hardly possible in EAFs [13]. The production of manganese-free high-silicon electrical steels is also hardly conceivable via this route. Copper (Cu), Tin (Sn), Chromium (Cr), Molybdenum (Mo), and Nickel (Ni) contaminations of scrap are a vital problem for EAF production of several grades of steel, Fig. 1. In 2019, the average copper content of scrap was 0.34 mass%, exhibiting a clear increase from 0.22 mass% Cu in 1982, and is expected to rise further with continued recycling [4].
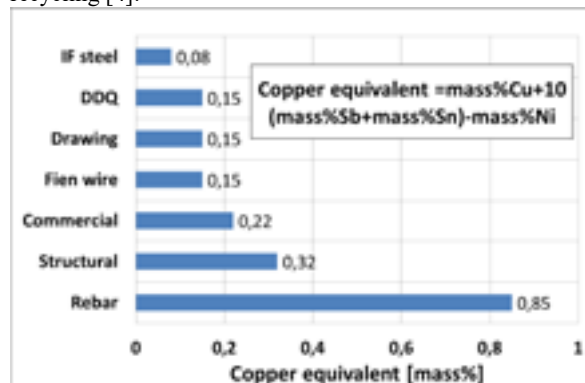


Fig. 1: Copper equivalent for different steel groups (adapted from [14]).

Examples of CDA are planned, developed, and researched projects, such as SALCOS® from Salzgitter AG [15], HYBRIT® from SSAB/LKAB/Vattenfall [16], and H2Future from voestalpine [17], etc. Thereby, the conventional blast furnaces will be replaced with direct reduction units, involving hydrogen ($H_2$) as a reducing agent.

## HYDROGEN STEELMAKING

Using $H_2$ as a reducing agent is not a new concept. Direct reduction with a high proportion of $H_2$ has been proven in a MIDREX Shaft Furnace [6]. The Ferrominera Orinoco MIDREX Plant in Venezuela used a steam reformer, resulting in an $H_2$/CO molar ratio in a range from 3.3 to 3.8 [6]. For comparison, in a MIDREX process with natural gas, the typical reducing gas consists of 55 mol% $H_2$ and 36 mol% CO. In 1986, several test campaigns utilized a very high hydrogen content ($H_2$/CO=4.2) [6] in one pilot plant. However, the main aim of today's transformation processes in steelmaking is the renouncement of coal and natural gas and a complete transition to the use of $H_2$ in iron production.

### Two ways of steelmaking with hydrogen

Currently, there are two strategies for implementing hydrogen-based steelmaking, Fig. 2:

- One-step process includes direct reduction unit with EAF (DR-EAF-route), and
- Two-step process contains direct reduction unit, smelter, and BOF (DR-smelter-BOF-route).

The one step process (DR-EAF) with natural gas (NG) direct reduction is the most widespread strategy, especially in countries rich in NG, such as Saudi Arabia, United Arabic Emirates (UAE), Iran, and Mexico [18]. The two-step process (DR-smelter-BOF) with coal based direct reduction has proven to be successful in processing ilmenite- or titanomagnetite-based sponge iron, e.g., in South Africa or New Zealand [18].

In their decarbonization strategies, steelmakers such as ArcelorMittal Germany Holding GmbH [19] and Salzgitter AG [20], rely on the one-step process strategy for implementing hydrogen-based steelmaking. Thereby, capacity of EAF can be up to 250 tons of tapping mass. But Germany's largest steelmaker, thyssenkrupp Steel Europe AG is developing the two-step process [21]. The reasons for the different decisions will be elucidated further.
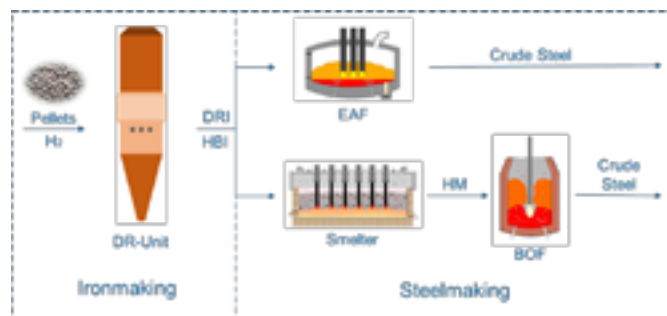


*Fig. 2: Two strategies for implementing hydrogen-based steelmaking*

Depending on the iron content, iron ore can be classified as [5]:
- high grade iron ore, if its Fe content exceeds 65 mass%,
- medium quality, if its Fe content is from 58 mass% to 65 mass%, and
- low-grade iron ore with Fe content less than 58 mass%.

Typical impurities of iron ore are $SiO_2$, $Al_2O_3$, CaO, MgO, MnO, $P_2O_5$, $TiO_2$, $V_2O_3$, and sulphur. The amount of impurities (gangue) is different for different grades of iron ore. The low grade one can contain more than 19 mass% of gangue, whereas iron ore with Fe>67 mass% (high grade) has less than 3mass% gangue [5].

Most gangue oxides cannot be reduced with hydrogen in direct reduction units, remaining as oxides in DRI (direct reduced iron), Fig. 3. Depending on the degree of metallization, a minor fraction of iron can also remain as an oxide in DRI. As DRI is melted in EAF, gangue oxide and unreduced iron form slag, to which other slag formers, such as lime, dololime, or $SiO_2$ holders/formers, should be added in order to achieve the desired chemical composition and desired basicity ($CaO/SiO_2$) of the slag. The use of iron ore with high gangue content within the one-step process (DR-EAF) leads to an increase in slag amounts in EAF, higher consumption of slag formers (flux), higher electrical energy usage, and increased refractory wear. All these issues contribute to the increased operation costs for the EAF. For example, when using iron ore with 58 mass% of Fe and 19 mass% of gangue, assuming a degree of metallization during DR of 90% and metallic yield in EAF of 95%, more than 530 kg of slag/t crude steel would be produced only from DRI. This simple calculation does not take into account the use of a binder by pelletizing, e.g., bentonite, or the addition of slag formers for necessary metallurgical tasks. Because of this, the total amount of gangue in oxide pellets for DR-EAF process should not exceed 3-4 mass% [22]. Tab. 1 shows the practical and preferred chemical quality for iron ore for the one-step process. However, only a small percentage of global seaborne iron ore (about 3%) comes close to these requirements [7].

The two-step process was proposed for processing DRIs from low grade ores. Specifically, as the first step, a submerged arc furnace (SAF), i.e., a smelter, is utilized to melt and accomplish final reduction. Then, the melt is refined in a BOF. This technological route, involving a split into two separate units, enables efficient separation of the melt from the slag within the first step by the

smelter. Furthermore, the slag obtained from the smelter may be further used for the cement industry [5].

Tab. 1: Chemical composition limits for iron ore by one-step process (DR-EAF), (adapted from [22])

| Sources | Practical limits [mass%] | Preferred limits [mass%] |
|---|---|---|
| Fe | 66.0 min | 67.0 min |
| $SiO_2+Al_2O_3$ | 3.5 max | 2.0 mas |
| CaO | 2.5 max | - |
| MgO | 1.0 max | - |
| $P_2O_5$ | 0.03max | 0.015max |
| S | 0.025 max | 0.015 max |
| $TiO_2$ | 0.35max | 0.15 max |
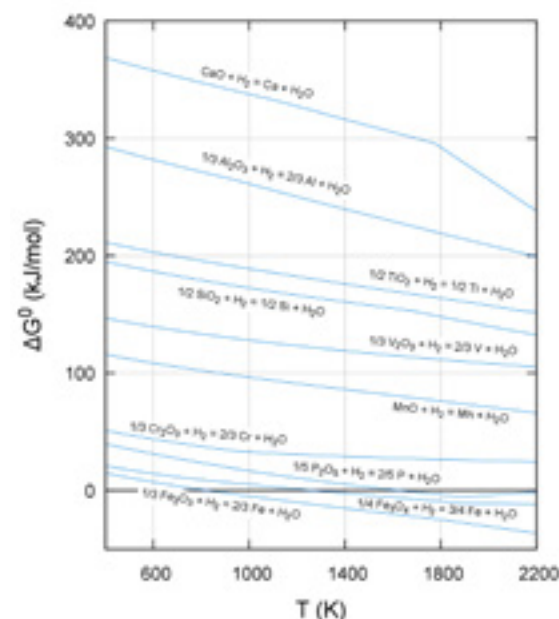


*Fig. 3: Change of the standard Gibbs free energy for reactions of hydrogen with different oxides of iron ore. Calculated with FactSage 7.2 (FtOxid, all database)*

The disadvantage of the two-step process is a need of two metallurgical units, leading to elevated operation costs. The benefits of the two-step process are:
- possibility of using low-grade iron ore,
- using existing periphery of an integrated steel plant (BOF, casting ladles, ladle furnaces, vacuum degassers, stirring station, and continuous caster),
- ability to produce a wide range of steels, with strict requirements for chemical composition,
- usage of smelter slag for the cement industry.

Many integrated steel plants in the world, as well as in Germany, operate with a tapping mass capacity of 300-400 tons from BOF. The two-step process is expected to be especially attractive for these large-scale units.

Smelter is still named differently by various authors and companies. For instance, the following terms can be found in the literature: submerged arc furnace (SAF), open bath furnace (OBF), or open slag bath furnace (OSBF). Smelter configuration can be circular or rectangular. A rectangular furnace design, considering inner dimensions of 36 x 14 m and six-in-line electrodes (Soederberg electrodes), can reach annual production rates of up to 1.5 Mt/year of DRI charges to the smelter [5]. The electrodes are submerged in the DRI and carbon mixture, resulting in melting upon the application of Joule heat to the burden. A circular smelter, for production capacity of 0.9 Mt/year, having an internal shell diameter of 20m, MgO conductive lining, and three 1700 mm Soederberg electrodes, was presented in [23]. When compared to EAF, the smelter is expected to have a much longer campaign life,

lowering logistic measures of relining (crane, building, frequent downtime, etc.) [24]).

In addition, a larger area of bath surface leads to a lower slag rise. The operation costs for Soederberg electrodes are less than those for graphite electrodes [24]. Tab. 2 provides a comparison of these two strategies.

Tab. 2: Comparison of one- and two-step process strategies for implementing hydrogen-based steelmaking (adapted from [5] and [24])

| | DR-EAF | DR-Smelter-BOF |
|---|---|---|
| **Iron ores** | High grade iron ore pellets | Flexibility for using low grade iron ore pellets |
| **Charge materials** | From 100% scrap to 100% DRI, depending on target steel quality | 100% DRI in smelter, scrap as coolant in BOF |
| **Slag** | Foaming slag with minimum weight and basicity of 1.6 to 1.8, maintaining EAF yields and refractory wear | **Smelter:** slag with low basicity of approx. 1.0; use of existing slag granulation facilities. **BOF:** Typical BOF slag with basicity of 3.6 and higher |
| **Slag usage** | Only minor application known for such slag, worst case: landfilling of the slag is required | **Smelter:** usage in cement industry. **BOF:** Typical usage of BOF slags, higher P content might also allow extended use as fertilizer |
| **Metallic Yield** | High slag amount in combination with high FeO content of the slag results in high Fe losses and thus low yield | **Smelter:** reducing atmosphere in smelter and long setting time ensure low Fe and FeO contents of slag. **BOF:** High FeO content of slag but low slag amount. High metallic yield for the two-step process |
| **Metallurgical tasks** | Limited possibility of Dephosphorization. Desulfurization after EAF during secondary metallurgy | **Smelter:** very good desulfurization. Desulfurization of hot metal before BOF. **BOF:** Very good dephosphorization |

The transformation process to direct reduction assumes many variations in possible technological solutions. Competing companies for steelmaking facilities offer their customers diverse systems. For instance, Tenova and Danieli have jointly developed the ENERGIRON technology, which attracted one of the largest German steel companies, Salzgitter AG (signed a memorandum of understanding, MOU, in 2022) to build a new plant. Accordingly, the plant is designed to have an annual capacity of 2.1 million tons of directly reduced sponge iron [25]. Alternatively, MIDREX technology is attracting new investments. Both technologies for DRI production involve the shaft furnace; however, MIDREX operates at lower pressures compared to ENERGIRON and utilizes a reduction gas generated in an external reformer. Another technology in the DRI market is HYFOR (Hydrogen-based Fine Ore Reduction) developed by Primetals. The world's first HYFOR pilot plant fabricates DRIs from fine concentrates of iron ore after beneficiation. Notably, no additional agglomeration, such as sintering or pelletizing, is required. This approach allows the processing of iron ore concentrate fines that are 100% smaller than 0.15 mm in particle size. Furthermore, it can handle a broad range of ores, including but not limited to hematite and magnetite [26].

## Impact of strategies for implementing hydrogen-based steelmaking on future slag

In contrast to the BF, a DR unit does not separate gangue from iron ore. The gangue is brought into a melting unit within DRI and ends up in the slag after melting. This increases a demand for slag formers and energy consumption. Thereby, an amount of slag formed in EAF via the DR-EAF-route and its chemical composition depend on:

- iron ore grade (gangue oxides: amount, type) and binder used for pelletizing,
- metallization degree in DR-unit,
- charged mixture of materials (DRI, scrap),
- scrap quality,
- added slag formers,
- metallic yield and produced steel quality.

The slag in EAF has a high FeO content, which lowers its desulfurization ability. Desulfurization takes place in a casting ladle during secondary metallurgy on a ladle furnace (LF), stirring stand, or vacuum degassing (VD/VOD) after deoxidation and decarburisation. This can lead to an extended steel processing in a ladle, increased heat losses, increased taping temperatures, an increase in heating during LF, and to an increase of ladle refractory wear.

For proper slag foaming in EAF, no CaO-rich slag should be adjusted, which, together with poorer mixing conditions of EAF compared to BOF, limits dephosphorization. The $Al_2O_3$, $TiO_2$, and $V_2O_3$ from gangue and binder would end up in EAF slag and further worsen dephosphorization [27].

In Tab. 3, the amount and chemical composition of the slags from the conventional scrap-based EAF route and DR-EAF route are compared. The values for the DR-EAF route are from [18], where they were obtained using the mass- and energy balances model by FactSage[tm]. As a results, the higher amount of slag is exhibited for the DR-EAF route.

Tab. 3: Comparison of steelmaking slags for conventional scrap-based route and one-step process strategies for implementing hydrogen-based steelmaking (* quality steel)

| | EAF, scrap-based route* [28] | EAF (DR-EAF-route) | |
|---|---|---|---|
| | | High-quality DRI [18] | Low-quality DRI [18] |
| **Slag [kg/t-CSt]** | 100-200 [29] | 207 | 496 |
| **CaO [mass%]** | 20-35 | 30 | 31 |
| **SiO$_2$[mass%]** | 10-20 | 19 | 19 |
| **Al$_2$O$_3$[mass%]** | 5-15 | 9,6 | 6,2 |
| **MgO [mass%]** | 4-7 | 10 | 10 |
| **FeO [mass%]** | 30-50 | 31 | 32 |
| **CaO/SiO$_2$** | 1-3.5 | 1.6 | 1.6 |

Tab. 4: Comparison of ironmaking slags for conventional integrated route and two-step process strategies for implementing hydrogen-based steelmaking

| | BF [30] | Smelter | |
|---|---|---|---|
| | | High-quality DRI [18] | Low-quality DRI [18] |
| **Slag [kg/t-HM]** | 150-300 [31] | 94 | 276 |
| **CaO [mass%]** | 37-42 | 46 | 37 |
| **SiO$_2$ [mass%]** | 32-38 | 38 | 33 |
| **Al$_2$O$_3$ [mass%]** | 10-15 | 13 | 17 |
| **MgO [mass%]** | 6-12 | 1.4 | 11 |
| **FeO [mass%]** | <1 | 1.3 | 1.1 |
| **CaO/SiO$_2$** | 0,97-1,3 | 1.2 | 1.1 |

The amount of slag formed in a smelter and its chemical composition would depend only on iron ore grade, gangue oxides, binder used for pelletizing. The smelter slag would have the

chemical composition near to BF slag, Tab. 4. This slag would have high desulfurization ability and can be used in the cement industry.

**Processing magnetite ore without oxidising**

Enrichment of magnetite ore via magnetic separation is generally more efficient than that of hematite ore. However, magnetite ($Fe_3O_4$) has lower reducibility compared to hematite ($Fe_2O_3$) [4]. From this reason, magnetite would be converted to hematite before charging into a reduction unit. Herewith, pellets from magnetite ore undergo the oxidation roasting process, encompassing four different stages: drying, preheating (800-900°C), induration (1200-1350°C) and cooling. Purohit et al [4, 32] reported an increase in magnetite reducibility through combining magnetite with lime. Specifically, thermal treatment (approx. 950°C to 1000°C) with fluxes and other additives transforms magnetite to an intermediate reducible form, exhibiting a formation of the $CaFe_3O_5$ phase. This new phase is highly beneficial for increasing the further reducibility and mechanical strength of pellets. As a result, up to 150 kg $CO_2$/t crude steel can be saved [4].
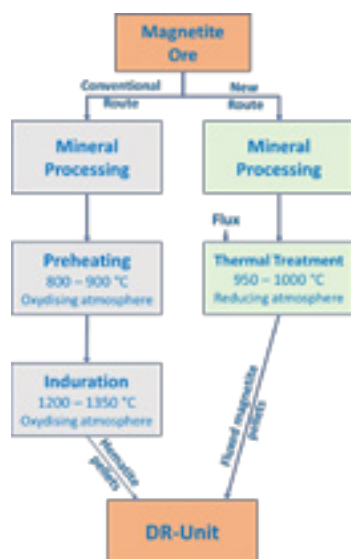


*Fig. 4: Magnetite ore processing route (adapted from [4])*

**CONCLUSIONS**

Steel industry is again in transformation. It will become $CO_2$ neutral in the future. The ongoing transformation of the steel industry introduces new challenges and consequently new tasks for further research. These include the design of iron ore pellets, smelter design, recycling of new slags, refractory design for new steelmaking processes, and more. Currently, manufacturing steel in a completely carbon-free manner remains a significant technological challenge. The Electric Arc Furnace (EAF) requires carbon for proper mixing through the formation of CO bubbles, for slag foaming to reduce energy consumption and refractory wear, and for alloying. Small quantities of carbon will also be used in the smelter. Nevertheless, it is probable that new solutions will be discovered for these issues.

**REFERENCES**

[1] https://www.stahl-online.de/stahl-online-news/weltrohstahlproduktion-2022-zurueckgegangen/#:~:text=Die%20Rohstahlerzeugung%20der%2064%20L%C3%A4nder,t%20zur%C3%BCck, 09.06.2023

[2] https://www.stahl-online.de/medieninformationen/rohstahlproduktion-in-deutschland-im-jahr-2022/, 09.06.2023

[3] Luengen H.B. Wege zur Minderung von CO2-Emissionen in der Stahl- und Eisenindustrie in Europa. August 2020 Stahlinstitut VDEh, Duesseldorf

[4] Brooks G.A, Hornby S.A. Alternate routes to green steel. Steel Times International, 46 (1), 2022, p. 33-37

[5] Wimmer G, Rosner J, Fleischanderl A. Two steps towards net zero carbon. Steel Times International, 46 (3), 2022, p.58-61

[6] Astoria T, Hughes G, Mizutani N. Moving from natural gas to hydrogen. Steel times International, 47 (1), 2023, p. 40-45

[7] https://ieefa.org/sites/default/files/2022-06/Iron%20Ore%20Quality%20a%20Potential%20Headwind%20to%20Green%20Steelmaking_June%202022.pdf, 19.06.2023

[8] https://www.midrex.com/wp-content/uploads/MidrexSTATSBook2021.pdf, 20.06.2023

[9] https://app.electricitymaps.com/zone/DE, https://app.electricitymaps.com/zone/PL, 19.06.2023

[10] https://eur-lex.europa.eu/LexUriServ/LexUriServ.do?uri=COM:2011:0112:FIN:en:PDF, 19.06.2023

[11] https://www.thyssenkrupp.com/de/carbon2chem, 19.06.2023

[12] http://www.steelanol.eu/en, 19.06.2023

[13] Grummes F. Rapider Technologiewechsel in der Volksrepublik? Stahl und Eisen 139 (7-8), 2019, p. 66

[14] Vucinic B, Suber M. EAFs maintain BOF liquid quality. Steel times International, 46 (5), 2022, p. 47-52

[15] https://salcos.salzgitter-ag.com/de/salcos.html, 19.06.2023

[16] https://www.ssab.com/de-de/fossilfrei#ffs, 19.06.2023

[17] https://www.voestalpine.com/group/en/media/press-releases/2019-11-11-h2future-worlds-largest-green-hydrogen-pilot-facility-successfully-commences-operation/, 19.06.2023

[18] Pfeiffer A, Wimmer G, Wurm J, Schenk J. Processing low-grade Direct Reduced Iron –Definition and comparison of melting strategies. EOSC&CTSI 2022: 9th European Oxygen Steelmaking Conference. 6th Clean Technologies in the Steel Industry. 17-22 October 2022, Aachen, Germany

[19] https://germany.arcelormittal.com/News-und-Medien/, "Auf dem Weg zum grünen Stahl", 25.06.2023

[20] https://salcos.salzgitter-ag.com/de/, 25.06.2023

[21] https://www.thyssenkrupp-steel.com/de/unternehmen/nachhaltigkeit/klimastrategie/, 25.06.2023

[22] https://www.midrex.com/wp-content/uploads/Midrex-2019-DFM4QTR-Final.pdf, 19.06.2023

[23] Cavaliere P, Perrone A, Silvello A, Stagnoli P, Duarte P. Intergration of Open Slag Bath Furnace with Direct Reduction Reactors for New-Generation Steelmaking, Metals 12, 2022, 203

[24] Duarte P. Decarbonising the steelmaking industry. Steel Times International, 45 (1), 2021, p.44-46

[25] Steel Times International, 46 (3), 2022, p. 24

[26] https://www.primetals.com/press-media/news/hyfor-pilot-plant-under-operation-the-next-step-for-carbon-free-hydrogen-based-direct-reduction-is-done, 25.06.2023

[27] Neubert L, Kovtun O, Kreschel T, Volkova O. Phosphorus partition between liquid crude steel and high-basicity basic oxygen furnace slags containing V2O5. Metallurgical and Materials Transaction b 54B (6), 2023, p. 1524-1531

[28] Markus H.P, Hofmeister H, Heußen M. Die Lech-Stahlwerke in Bayern- ein modernes Elektrostahlwerk und seine Schlackenmetallurgie. InThome-Kozmiensky K.J, Versteyl A. Schlacken aus der Metallurgie. TK Verlag, Neuruppin, 2011, p. 67-88

[29] Pfeifer H. In Heine K-H. (Ed.), Elektrostahlerzeugung," Verlag Stahleisen, Düsseldorf, 1997, p.112-127

[30] Babich A, Senk D, Gudenau H.W. Ironmaking. Verlag Stahleisen, Düsseldorf, 2016, p. 285

[31] Yang Y, Raipala K, Holappa L. Ironmaking. In Seetharaman S. (Ed.) Treatise on Process Metallurgy, Industrial Processes, Part A, 3, 2014Elsevier, ISBN: 978-0-08-096088-6, p. 2-88

[32] Purohit S, Brooks G.A, Rhamdhan M.A, Pownceby M.J, Scarlet N. Alternate Route for Processing Magnetite for Lower Carbon Footprint Ironmaking through Lime – Magnetite Pellets Containing CaFe3O5.Ironmaking and Steelmaking 47 (6), 2020, p.674-685

317

# INNOVATIVE DESIGN AND INSTALLATION TECHNIQUE FOR SLAG DOOR OF CONARC FURNACE – A UNIQUE APPROACH FOR PERFORMANCE HIKE-UP

Prof. Dr. Helge Jansen, Dr. Thomas Schemmel*, Dr. Ujjwal Sengupta, Yarra Prasad, Dr. Murugesan Sathiyakumar & Dr. Debasish Chandra
Refratechnik Steel GmbH, Düsseldorf, Germany, steel@refra.com

ABSTRACT

More vigour refractory design for critical application in steel plant operation plays an important role to control final performance. A smart way of performance augmentation to achieve low specific refractory consumption by suitable refractory quality, lining design and right application/installation practice should be attempted. This paper deals in identification of critical area followed by suitable solution of CONARC furnace to achieve higher performance. CONARC furnace may be sub-divided into micro-zones based on criticality and operational parameters – and slag door has found to be the most critical area due to thermo-mechanical and chemical stresses especially during slag cleaning. An attempt has been made for designing and making a pre-engineered shape cluster at slag door area of CONARC furnace to achieve high structural strength to eliminate brick damage and fall during running, targeting higher and consistent lifetime. Special focus has been made to improve abrasion resistance while designing and special installation technique to address thermo-mechanical issue during operation. A suitable design of refractory, its quality and its installation for good structural strength is thereby most important. Such unique approach has been successfully used in an Indian steel plant. The success based on a case-study has validated the effectiveness of the thought process and the development as well in order to reduce specific refractory consumption.

INTRODUCTION

Apart from operational parameters in any specific steel melting shop[1], appropriate design and installation are the important success keys to achieve high refractory performance. Challenge for the refractory designers is to establish an effective corelation between refractory performance, installation design, shop operational parameters and quality of refractories. Proper corelation helps correct choice of quality to get the intended performance. Each steel plant has their standard operating practices, which may not be largely favourable to refractory lifetime in general. Therefore, designing refractory to suit the existing shop operating practice and logistics should be the approach of refractory designer to move hand-in-hand with the user in order to achieve intended lifetime. Apart from providing the effective product for improvement, proper installation of the product becomes very important. So, refractory designers and manufacturers often acts as a total solution provider which starts from designing refractory and ends up with the intended performance as per shop floor demand.

DEVELOPING MOTIVATION FOR AN INNOVATIVE APPROACH

Performance of refractories is the final measurement of success of a refractory supplier in front of any customer. Performance issues acts as motivation for improvement or development of products,

approaches, or processes as a scope of improvement.

Existing performance issues of CONARC furnace in steel melting shop are –

- Inconsistent performance with uncertainty of lifetime
- Difficulty in planning at shop floor to achieve targeted production with desired productivity and minimum down time
- Sudden failure resulting unsafe situation
- High specific consumption of refractories

EXISTING MECHANISM FOR PERFORMANCE LIMITATION

Like all high temperature process vessels, CONARC furnace also has different zones (Fig. 1) with respect to its unique criticality and quality requirements. They are bottom, side wall, slag door, co-jets, hot spot, and nose. In slag door area slag deposition is quite common phenomenon as after slag draining, it sticks to the refractory of slag door by temperature drop resulting increase in viscosity[2].
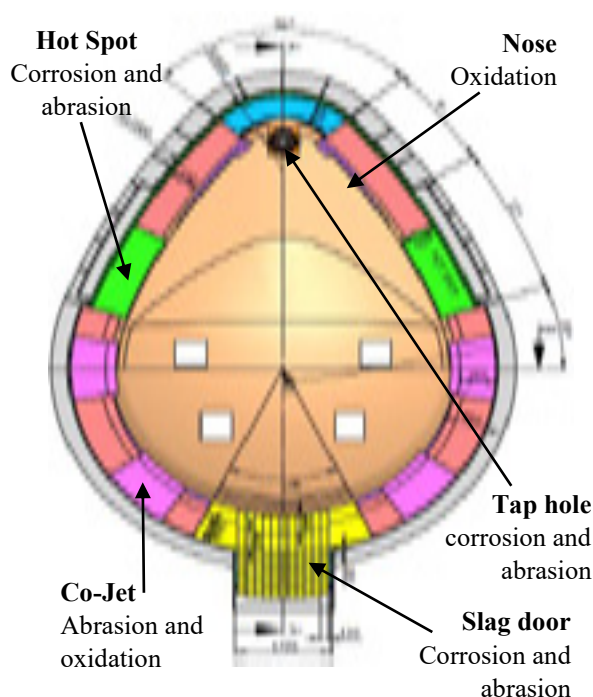


Fig 1: Major zones and challenges for refractories in CONARC furnace

The deposition needs to be cleaned intermittently, mostly by mechanical means (say, by using forklifts). Probable mechanical impacts from back side loosens the slag door lining structure due to obvious reason. It was observed that the long bricks used to come out from working lining and fall inside furnace during campaign, limiting the lifetime potential of refractory. This forces intermittent on-line repairs with refractory masses, which not only incur financial loss but also results inconsistent lifetime pattern as well as higher specific consumption of refractory masses with productivity loss which is not desirable. Additionally, it also results un-utilisation of high life potential of other zones.

HOW WE THOUGHT…. THE ROADMAP

It is inevitable that slag temperature comes down after slag dumping followed by metal tapping which increases the viscosity of slag, deposited on slag door refractories-create jamming and difficult to clean smoothly without disturbing refractories and its structural stability. It is also inevitable that for cleaner operation and better control, operators keep on cleaning that area manually by poking with forks of a forklift. This process results inconsistent performance due to many uncontrolled factors.

Special considerations while design –

- To increase unit weight of brick, it is to be pre-assembled structure of different big blocks with interlocking design expected to have better resistance to abrasion by mechanical abuse during slag cleaning in comparison to existing practice.
- To design better brick-to-brick locking
- Blocks are to be installed by special glue at site to have better structural strength.
- User-friendliness by lifting arrangement for individual assembly conforming site facilities
- Size of the blocks by pre-assembling were designed to optimize easy handling, user-

friendly installation, and improvement of structural strength in staggered manner.

Such big blocks are more resistant in loosening from working lining due to higher weight with proper locking during installation and bond formation between blocks by special glue influenced by thermal effect during operation. The assembly has been done by special refractory glue and the joints have tested and found high strength after curing during production process (Fig. 2).
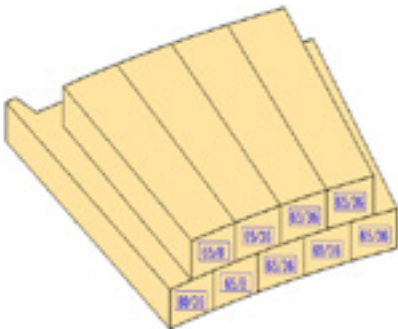


Fig. 2: Brick assembly in production process with special refractory glue
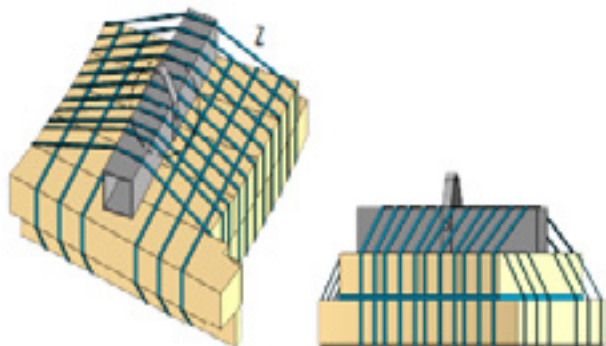
Fig. 3: Brick assembly lifting arrangement designed for easy handling during installation

Lifting arrangement (Fig. 3) has been also designed to have user-friendly installation. Additionally, from the schematic diagram (Fig. 4), pre-assembled structure design clearly indicates the basic concept for improved structural strength of slag door.
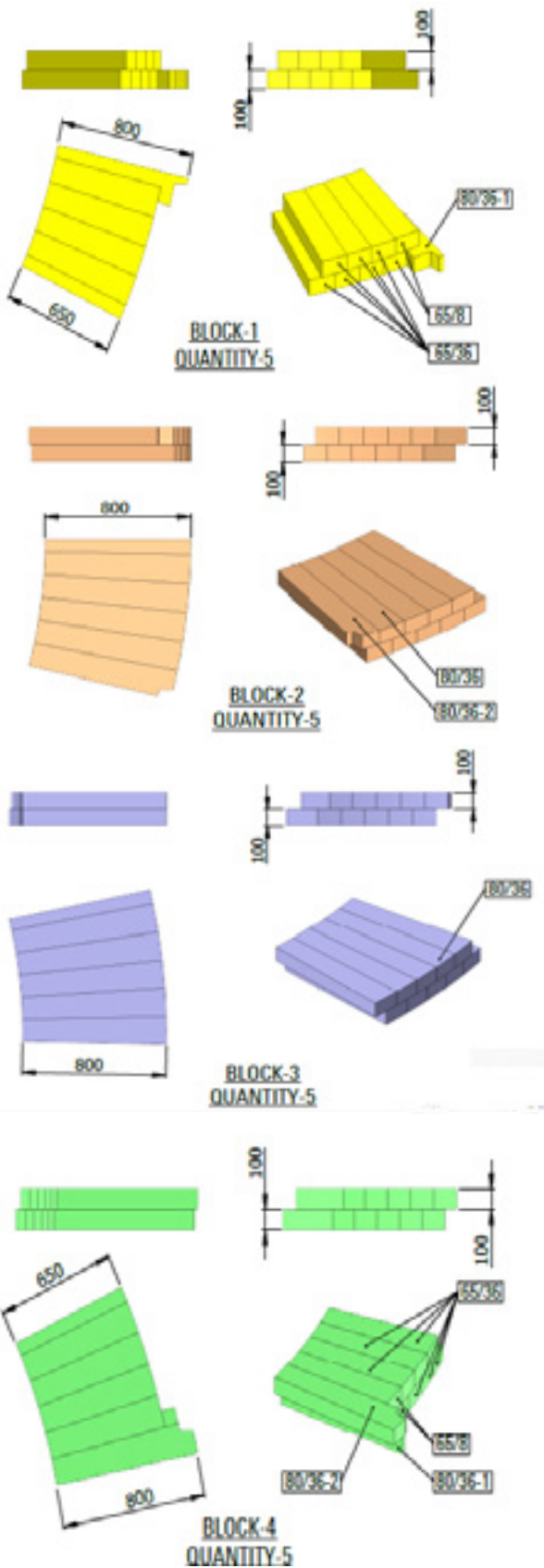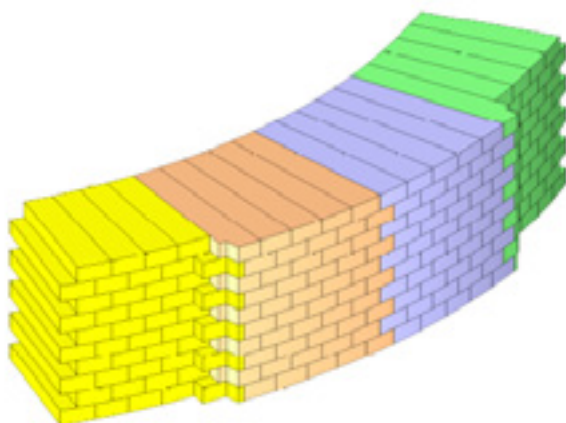
Fig. 4: Brick pre-assembled structure design and total assembly

Quality of refractory has been designed in a unique way to optimise between resistance to abrasion, corrosion by slag and thermal spalling by judicious combination of dosage of flaky graphite with high purity magnesia.

Table 1: Refractory quality contributes to performance

| Corrosion by slag | Slag door is used to drain slag, corrosion in brick rather stimulate slag sticking; hence better non-wetting character is required |
|---|---|
| Thermal spalling resistance | Slag door is exposed in thermal stress continuously during the total campaign lifetime-hence graphite plays important role for to improve resistance to thermal cycling |
| Resistance to abrasion | Periodic slag draining, mechanical aberration in cleaning-high strength product is required |
| Optimization of flaky graphite & high purity magnesia | Both raw materials have discrete roles but physical properties are opposite; balancing them in recipe is the design challenge for optimum performance |

Property data of the brand has been tabulated in Table 2.

MANUFACTURING PROCESS AND INSTALLATION

Designed shapes were pressed in high-capacity hydraulic press followed by efficient tempering to achieve high bulk density and low AP with high CCS- both as such and after coking which indicates proper carbon bond in the product. The bricks are then glued during production as per the design (Fig. 2). The assembled bricks are then packed according to the BLOCK numbers for easy identification & installation. The lifting arrangements (Fig. 2) for all assembled blocks are placed as designed and strapped. The concept was tried to prove the worth of the same in an Indian integrated steel plant. The pre-assembled blocks were installed in slag door of CONARC furnace as per the design without any difficulties (Fig. 4). Perfect design includes exact shell profile, and the execution was also satisfactory without any adjustments. High level of dimensional accuracy made things even easier. Performance was found to be quite encouraging. Table 2: Property data of the brand

Table 2: Brand property data

| Physical Properties | As supplied | Coked ASTM C831 |
|---|---|---|
| Bulk Density [g/cc] | >3.00 | >2.95 |
| Apparent Porosity [Vol-%] | <4 | <10 |
| Cold Crushing Strength [N/mm$^2$] | >40 | >20 |
| Carbon Content [Wt-%] | >11 | |
| **Chemical Analysis of Magnesia** | | |
| MgO [%] | >97.8 | |
| Al$_2$O$_3$ [%] | < 0.2 | |
| Fe$_2$O$_3$ [%] | < 0.6 | |

PERFORMANCE AND EVALUATION:

It is obvious that operational parameters have the paramount importance (Table 3) over refractory performance. The performance was satisfactory and shown in Table 4. Due to robust design the refractory, mass consumption is also lower by

approximately 15 t in a single campaign and the lifetime has been improved by >8%.

PERFORMANCE FEEDBACK

A few glimpses of photographs (Fig. 5 & 6) during installation are shown below for better understanding.



Fig. 5: Photograph of installed blocks

Fig. 6: Photograph of installed blocks

Major operational parameters with respect to the specific field trial are as flows:

Table 3: Major Operational Parameters of CONARC furnace during the campaign

| Operational Parameters | |
|---|---|
| Heat Size [t] | 188 |
| Holding time [min] | 60 |
| Arcing time [min] | Arcing 20-22, Blowing 30-35 |
| Tapping $O_2$ [ppm] | 900 |
| Lining Thickness [mm] | 650 |
| Number heats/day | 20 - 22 |
| **Slag Chemistry** | |
| CaO [%] | 30 - 35 |
| MgO [%] | 8 - 12 |
| $SiO_2$ [%] | 10 - 12 |
| FeO [%] | 25 - 30 |

Table 4: Performance detail of trial in CONARC furnace

| Lifetime (heats) | 387 |
|---|---|
| Repair | No repair at Slag Door |
| Gunning consumption standard In trial | 0.5 kg /Ton LM |

The furnace was terminated by plan without any issue of slag door damage. No sign of loosening of slag door structure was observed during operation of full campaign.

The benefits for such design are as follows –

i. Reduction in gunning mass consumption by more than 27%. This has good impact on overall commercials as the gunning mass consumption at slag door area had the lion share

ii. Overall improvement of campaign life by more than 7%

iii. Consistent lifetime, which is safe and predictive from operation point of view

SUMMARY AND CONCLUSION:

Innovative design in slag door of CONARC furnace has proved its efficiency for higher lifetime in CONARC furnace. The salient features of design and performance are as follows:

i. Optimized size of block design to have good resistance to abrasion during slag cleaning

ii. Efficient interlocking between blocks

iii. Unique glue to impart better locking during installation

iv. Better structural strength

v. Quality of refractory has been designed in tailor made way to take care of all issues in slag door

vi. Less specific consumption of gunning mass and proper utilization of other zones to achieve higher lifetime observed in field trial in an Indian steel plant

Finally, it may be concluded that it is possible to design slag door with smart technology to take care of operational issues leading low specific consumption of refractory.

REFERENCE:

i. Robin JM, Y Berthaud, et al, "Thermo-mechanical behavior of magnesia-carbon refractories", British ceramic transactions, Volume 97 (1988), PP 1-10

ii. Ioana A, Semenescu A, Marcu D, Pollifroni M, Březinová M (2015) "Some aspects about product management of electric arc furnace elements", Appl Mech Mater 809:1319–1324

# NOVEL MICROPOROUS MGO–BASED HIGH–TEMPERATURE THERMAL INSULATOR

Rafael Salomão, Leandro Fernandes

São Carlos School of Engineering, Materials Engineering Department, University of São Paulo, São Carlos, Brazil


Luís Carlos Simão

Fibertechnic Ltda., Valinhos, Brazil

## ABSTRACT

This study addresses the development of a novel MgO-based thermal insulator (Nanoxtherm®) whose temperature-resistant microporous structure was engineered to introduce controlled packing flaws amongst their highly asymmetric particles during the compacting. Hard-burnt MgO and dolomite particles were dry-mixed with exfoliated expanded aluminum phyllosilicate and fibers, before being sprayed with colloidal silica. The mixture was uniaxially pressed as boards ($400 \times 100 \times 20$ mm) and dried overnight (120ºC). Samples were thermally treated at different temperatures (120-1100ºC) for the evaluation of their physical properties (compression strength, rigidity, permanent dimensional thermal variation, solid density, total porosity, thermal conductivity), crystalline phases, and microstructure. The microporous microstructure generated during pressing was not significantly affected by thermal treatment below 1100ºC. Samples' thermal conductivity, total porosity, and compression strength varied between 0.20-0.14 W.(m.K)$^{-1}$, 54-56 %, and 29-15 MPa in the 200-1000ºC temperature range, respectively.

## INTRODUCTION

Microporous refractory ceramics are effective thermal barriers for high-temperature insulation due to a useful combination of features. Their microstructure contains pores with a careful balance between volumetric fraction (50-80 %), diameter distribution (0.5-5 microns), and geometry and degree of interconnection (ideally isolated spheres) [1]. The solid ceramic phase surrounding such functional pores shows significant corrosion and densification resistance for avoiding microstructure changes, extending materials' service life, and preventing maintenance operations. In comparison to ceramic fiber-based insulators, microporous refractories show straightforward manufacturing and installation and do not produce hazardous particulate debris [2]. They also show lower thermal conductivity and diffusivity above the temperature range at which heat loss by infrared radiation becomes significant (600-800ºC).

Several combinations of raw materials and processing techniques result in microporous ceramic structures. As an example, the addition of organic particles (e.g., starch and other synthetic polymers) or foams to stable particles' suspension produces cellular ceramics whose total porosity levels can be as high as 90 % [2]. On the other hand, aqueous dispersions of $\alpha$-$Al_2O_3$, solid inorganic porogenic agents ($\alpha$-$Al(OH)_3$, $Mg(OH)_2$, $CaCO_3$), and binders ($\rho$-$Al_2O_3$, calcium aluminate cement) formed castable systems which evolve to microporous refractories of $\alpha$-$Al_2O_3$, $Al_9Si_3O_{13}$, $MgAl_2O_4$, and $CaAl_{12}O_{19}$, after sintering. Since such compounds are intrinsically densification-resistant, they are good candidates for applications that require long exposures to high temperatures [3-6].

This study employed a novel approach based on the production of controlled packing flaws during compacting for generating a microporous MgO-based (MMB) thermal insulator with a large fraction of micropores and preventing their disappearance during service at high temperatures (Nanoxtherm®) [7]. Mixtures of different types of ceramic raw materials containing a large fraction of inner pores and comprised of highly asymmetric particles were shaped as boards by uniaxial pressing assisted by a bonding spray of colloidal silica. In comparison to the other porogenic methods presented, the strategy shows energy-saving straightforward processing, since the structures produced require no previous thermal treatment to attain sufficient strength and porosity for use.

## EXPERIMENTAL

Flat boards of Nanoxtherm® ($400 \times 100 \times 20$ mm) were produced dry-mixing as-received coarse dolomite (($Mg.Ca)CO_3$) and hard-burnt magnesia (MgO) particles with inorganic and polymeric fibers and exfoliated expanded aluminum phyllosilicate (($Mg,Fe^{2+},Fe^{3+})_3(Al,Si)_4O_{10}(OH)_2.4H_2O$). After receiving a short spray of colloidal silica, the mixture was uniaxially pressed (50 MPa, 60 s) and dried overnight at 120ºC. The main boards were then sliced as $100 \times 40 \times 20$ mm prisms and $20 \times 20 \times 20$ mm cubes. Before and after isothermal treatment (200-1100ºC, 2ºC.min$^{-1}$ heating rate, 5 h hold, 10ºC.min$^{-1}$ cooling rate), the samples' dimensions and mass were measured for the calculation of geometric total porosity and permanent dimensional thermal variation. Solid density was measured by Helium pycnometer method in equivalent samples after grounding and cubic samples were used for cold-crushing strength measurements. Fractured surfaces were observed by optical stereoscopic and scanning electron microscopy and the samples' thermal conductivity was measured by the calorimetric method (200-1100ºC). The crystalline phases formed were identified by X-ray diffraction.

## RESULTS AND DISCUSSION

The structure attained after pressing showed a heterogeneous microstructure containing two phases. In the follicular one (Figs. 1a-c), the lamellar particles of phyllosilicate are oriented perpendicularly to the pressing direction surrounding the granular one comprised of MgO and dolomite particles (Figs. 1d-f).
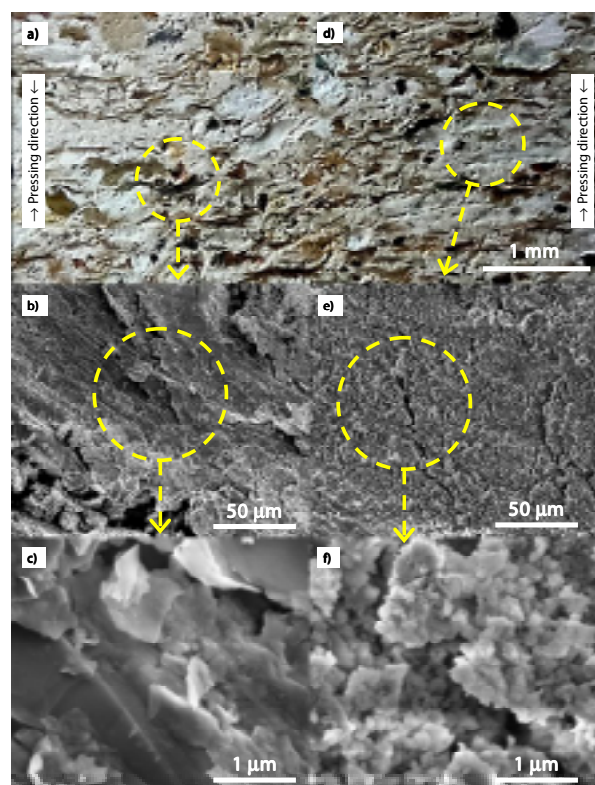


*Fig. 1: Cross-section of as-produced f MMB thermal insulator (Nanoxtherm®): a-c) follicular and d-e) granular phases.*

In comparison to other studies, significantly higher levels of total porosity (54 %) and compression strength (28 MPa) were observed for green-dried samples (Figs. 2a-b) before any thermal treatment. Differently from [3-5] in which porogenic mechanisms were triggered by dehydroxylation reactions, the very small pores observed at the cross-section of the MMB structure were formed due to packing flaws during pressing. Therefore, after the early drying stages, the material is already highly porous and can behave as a thermal insulator.
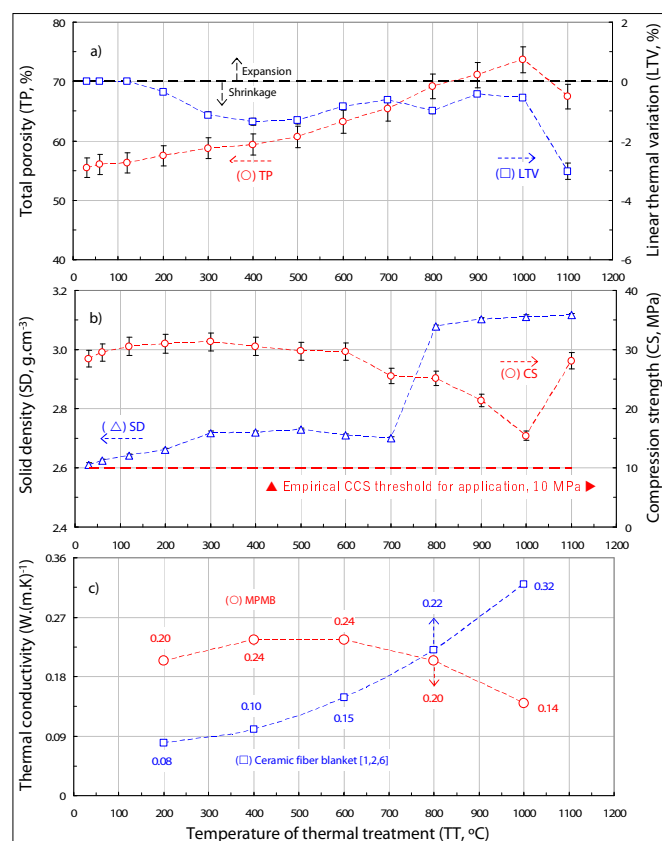


*Fig. 2: Evolution of physical properties of microporous MgO-based thermal insulator with thermal treatment up to 1100ºC.*

An increase in the thermal treatment temperature of up to 700ºC promoted no significant changes in TP, dimensions, CS, and thermal conductivity (Fig. 2c). The XRD results (not shown here) showed no significant chemical reaction occurred up to that temperature. In the 700-1000ºC range, the decomposition of phyllosilicate and $CaCO_3$ promoted an increase in their solid density. Since those particles were inserted in a non-reactive and rigid MgO scaffold, their volume reduction increased the pore content of the structure [3]. Above 1000ºC, early sintering and formation of small portions of the liquid phase (Fig. 3) led to a densification-related shrinkage and gain of strength. Such results suggest 1100ºC is the maximum temperature of use for the composition in contact with a primary source of heat.
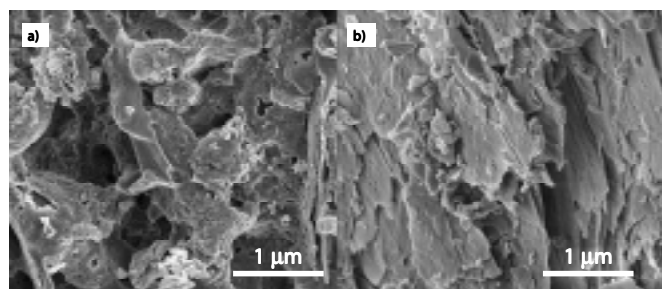


*Fig. 3: Cross-section of MMB thermal insulator of follicular (a-c) and granular (d-e) phases after 5 h at 900ºC.*

Interestingly, a significant reduction in thermal conductivity followed the microstructure changes, and a total porosity reduction was observed between 900-1100ºC, differing from the behavior observed for ceramic fibers blankets, which showed higher thermal conductivity as temperature increased. Such behavior indicates refractory structures containing micropores can scatter infrared electromagnetic heat waves, which are the dominant heat transfer mechanism above 600ºC. In the same temperature range, fiber blankets were less effective in block heat flow due to their excessive pore fraction, which increases the mean free path for photons throughout the structure. Besides superior thermal insulation capacity for the same lining thickness, the novel microporous MgO-based material showed excellent compression strength despite its large pore fraction. Such a synergetic combination of useful properties is due to the fact that the ceramic particles employed show intrinsically high refractoriness and their inter-particle pores are densification-resistant and Taylor-made for scattering heat waves in a wide temperature range.

## CONCLUSIONS

This present study addressed the characterization of a novel microporous MgO-based thermal insulator (Nanoxtherm®) which presented two strategies for thermal insulation. In the first and most significant one, controlled compacting flaws promoted by highly asymmetric phyllosilicate particles became pores of sub-micrometric dimension after demolding and, during the initial heating, the decomposition of hydroxyl-carbonated compounds generated pores at the particles' surfaces. Therefore, up to 600ºC, the large fraction of thin pores reduced thermal conduction through phonons. Secondly, between 600-1100ºC, the slight total porosity reduction observed also favored photon scattering, reducing the thermal conduction that occurred by irradiation of infrared waves. In comparison to other classes of insulators, such as ceramic fiber blankets, the low thermal conductivity and high compression strength levels observed enable his novel material to be employed as self-supporting thinner insulating linings in steel ladles and runners and as other pieces of equipment for primary aluminum processing, petrochemical units, and cement kilns.

## ACKNOWLEDGEMENTS

## REFERENCES
[1] Salomão, R., Oliveira, K.S., Fernandes, L. Tiba, P., Prado, U.S. Porous refractory ceramics for high-temperature thermal insulation – Part 2: The technology behind energy saving (2021). Interceram – International Ceramic Review 71 (1), pp. 38-50.

[2] Salomão, R., Fernandes, L. Tiba, P., Prado, U.S. Porous refractory ceramics for high-temperature thermal insulation – Part 3: Innovation in energy saving (2021). Interceram – International Ceramic Review 71 (3), pp. 30-37.

[3] Souza, A.D.V., Salomão, R. Evaluation of the porogenic behavior of aluminum hydroxide particles of different size distribution in castable high-alumina structures (2016). Journal of The European Ceramic Society 36 (3), pp. 885-897.

[4] Salomão, R., Pandolfelli, V.C., Fernandes, L. Designing high-temperature thermal insulators based on densification-resistant *in situ* spinel (2020). Journal of The European Ceramic Society 41 (4), pp. 2923-2937.

[5] Costa, L.M.M., Sakihama, J., Salomão, R. Characterization of porous calcium hexaluminate ceramics produced from calcined alumina and microspheres of Vaterite (μ-$CaCO_3$) (2018). Journal of The European Ceramic Society 38 (15), pp. 5208-5218.

[6] Zacherl, D., Schnable, M., Buhr, A., Kockegey-Lorenz, R., Dutton, J. Advantages of calcium hexaluminate in a corrosive environment (2011). Refractories Worldforum 3 (4), pp. 87-94.

[7] https://www.fibertechnic.com.br/ (accessed in June 30th 2023).

# NEXT GENERATION ELECTRIC ARC FURNACE GUNNING PRODUCTS FOR IMPROVED SUSTAINABILITY

C. Gurcan[*,1], Y. Zeybek[1], C. Daly[2], A. McCormack[2]

1.Minteq-Asmas, Kocaeli, Turkey

2. Minteq Europe Limited, Cork, Ireland

## ABSTRACT

Consumption of Electric Arc Furnace (EAF) basic monolithic gunning refractory products will increase with the projected green steel transformation from Blast Furnace-Basic Oxygen furnace (BF-BOF) route to Direct reduced Iron-Electric Arc Furnace (DRI-EAF) route. Dead Burned Magnesia (DBM) is the primary raw material used in the basic monolithic gunning refractory products. Production of DBM from magnesite ore significantly contributes to the greenhouse gas (GHG) emissions. One sustainability approach is to replace the DBM with recycled refractory materials to reduce the carbon footprint of the monolithic gunning products. However, the availability of these recycled materials is limited, and process requires significant investment on the refractory waste sorting systems to control the quality. The approach in this study explores the use of a sustainable and low carbon footprint natural mineral in a monolithic EAF gunning product. Results showed that this approach could reduce GHG emissions by around 30% compared to a standard gunning material comprising only DBM. Mechanical and physical characterization, slag corrosion tests supported with thermochemical simulations and electron microscopy, demonstrated that a product using the natural refractory mineral could exhibit refractory properties comparable to a gunning material comprising only DBM.

## INTRODUCTION

The Iron and steel industry has a significant role on carbon neutrality to achieve the Paris climate agreement's long-term temperature goal of limiting global temperature increase to well below $2^0C$, while pursuing efforts to limit the increase to 1.5 °C. The Global steel industry is responsible for around 11% of global carbon dioxide ($CO_2$) emissions and 7% of global Greenhouse gas (GHG) emissions [1,2]. According to the World Steel Association figures, 28.2% of the crude steel was produced by Electric Arc Furnace (EAF) route and 71.5% was produced from Blast Furnace – Basic Oxygen Furnace (BF-BOF) route in 2022 [3]. Steel decarbonization scenarios of International Energy Agency (IEA) estimate that EAF steel production to double in next 30 years and become the dominant steelmaking technology in the world, as it offers a wider range of decarbonization options compared to the BF-BOF steelmaking to meet mid-century net zero emission goals [1,2].

Magnesia (MgO) based refractory products are the primary refractory materials used in the working lining of both BOFs and EAFs. Demand on these refractories will continue to increase as the steel demand is projected to rise 30% by 2050 [4]. On the other hand, transformation of the steelmaking route from BOF to EAF would result in the additional increase in the consumption of MgO-based refractories because of the expected increase in Direct Reduced Iron (DRI) usage in the commercial EAF processes and with the introduction of new DRI-EAF based technologies like 100% Hydrogen ($H_2$). The DRI-EAF is an important technological pathway for the carbon neutral steel sector with over 15 projects officially announced in Europe for roll out up to 2030 [5].

Dead burned magnesia (DBM) and fused magnesia (FM) are the main raw materials used in the MgO-based refractory products used in EAFs. In 2021, world production capacity of DBM and FM from magnesite ore was $8.85 \times 10^3$ kilotons and $2.15 \times 10^3$ kilotons respectively [6]. DBM production from magnesium carbonate ore ($MgCO_3$) significantly contributes to the GHG emissions which is mainly caused by carbonate decomposition ($MgCO_{3(s)}$ + heat = $MgO_{(s)}$ + $CO_{2(g)}$) and fossil fuel combustion. As a benchmark for natural low-iron DBM production, direct emissions for a modern gas-fired shaft furnace are around 1.65 t CO2-eq/t MgO, while for an old coal-fired shaft furnace, these emissions could increase to around 2.50 t CO2-eq/t MgO [7].

Magnesia containing shaped and unshaped basic refractories are the most widely used refractories in the steel industry. They also have the highest environmental impact among the refractories used in the steelmaking furnaces due to the higher carbon footprint of the virgin raw materials (DBM & FM) used and higher amount of spent refractory waste generation after use. Spent refractories are mostly recycled by using them in open-loop applications such as roadbed aggregates and slag conditioners. Closed-loop recycling of spent refractories is increasing and has potential to generate more economic and environmental benefits by replacing the virgin raw materials. Targets to lower cost and increase sustainability of the refractory products have created a strong demand for closed-loop refractory recycling [8]. However, the supply of these recycled spent refractories is limited and estimated to cover only 7% of the raw material demand for refractories. Since the supply is limited, the price of these recycled aggregates has started to increase in the recent years due to the higher demand in the market. On the other hand, spent refractory waste management market is still under development to meet the quality requirements from refractory producers. To meet these requirements, production processes for recycled aggregates will require higher investment cost sophisticated sorting systems for proper removal of slag, iron, and other impurities to avoid variations in the aggregate quality [9].

Electric arc furnaces have still the highest refractory wear among the steelmaking furnaces. Specific consumption of MgO based refractories in a modern scrap based EAF can be reduced to around 2.0 kg/ton steel in average with application of good refractory maintenance practices. MgO based monolithic hot gunning repair materials play an important role in refractory maintenance to extend the furnace lifetime, to decrease overall refractory costs and finally increase productivity. Another advantage of these hot gunning repair materials is the utilization of higher percentage of recycled aggregates to reduce the carbon footprint of the products for sustainability. However, as outlined in the previous paragraph availability of these recycles is limited at present.

As an alternative approach for the improved sustainability of refractory products and EAF steelmaking, the purpose of this study is to characterize and evaluate refractory properties of an experimental EAF hot gunning product that use a lower carbon footprint natural mineral.

## MATERIALS

Two different silicate bonded EAF hot gunning products designated as A and B were examined and compared. Product A contains only DBM. Product B has a forsteritic type natural refractory mineral as a partial replacement to DBM to reduce the carbon footprint of the product. Table 1 shows chemistries of the products together with the relative carbon footprint of the products calculated based on the direct emissions from DBM usage.

As part of the study two different types of industrial EAF slag sampled before tapping were used for evaluation of slag-refractory interaction. Slag 1 was from an EAF charged with 30% scrap-70% DRI that produce high carbon rebar and construction steel grades. Slag 2 was from an EAF charged with 100% scrap that produce low carbon specialty steel grades. Chemistry and basicity of the slags are shown in table 2.

Tab. 1: Chemistry (on ignited basis) and relative carbon footprint of experimental gunning products

|  | Product A | Product B |
|---|---|---|
| Composition | DBM | DBM / Mineral |
| Chemistry | % | % |
| MgO | 88.6 | 74.9 |
| CaO | 1.8 | 1.8 |
| SiO$_2$ | 6.2 | 17.8 |
| Fe$_2$O$_3$ | 1.8 | 3.8 |
| Al$_2$O$_3$ | 0.9 | 0.6 |
|  | % | % |
| Relative carbon footprint[1] | 100.0 | 70.3 |

[1]: Calculations are based on direct emissions from DBM. Product A that composed to have only DBM is referenced as 100%.

Tab. 2: Chemistry and basicity of the slag 1 and slag 2

|  | EAF Slag 1 | EAF Slag 2 |
|---|---|---|
| Chemistry | % | % |
| MgO | 11.8 | 4.1 |
| Al$_2$O$_3$ | 5.5 | 5.1 |
| SiO$_2$ | 19.7 | 10.2 |
| CaO | 27.7 | 35.5 |
| TiO$_2$ | 1.2 | 0.4 |
| MnO | 2.0 | 4.6 |
| Cr$_2$O$_3$ | 0.2 | 1.1 |
| FeO | 29.9 | 38.1 |
| Basicity |  |  |
| B2 | 1.40 | 3.48 |
| B4 | 1.57 | 2.59 |

B2 = CaO/SiO$_2$, B4 = (CaO+MgO)/(SiO2+Al$_2$O$_3$)

## METHODS

Mechanical characterization of the refractory gunning samples was performed by hot modulus of rupture (HMOR) and cold crushing strength (CCS) tests, with variations in temperature ranging from 1000 °C to 1600 °C. Additionally, physical properties such as permanent linear change (PLC) and apparent porosity (AP) were determined from samples treated under the same temperature range.

Static slag corrosion test (cup test) was used to evaluate slag corrosion of the gunning samples. Samples were filled into cylindrical steel moulds by casting with 10% water to form hollow refractory cups. Cups were first dried at 110 °C for 24 hours and then pre-fired at 1200 °C for 3 hours before the corrosion tests. After pre-firing, each cup was filled with 40 g of pulverized slag up to the middle of the hole and then fired at 1600 °C for 3 hours to complete the corrosion test. The test cups were dissected for the visual examination of the slag penetration into samples. Slag penetration area was calculated by using the Image J software. Scanning electron microscopy supported with energy-dispersive X-ray spectroscopy (SEM/EDS) was used for mapping of the interacted zones between samples and molten slag. Thermochemical simulations were performed by using "Equilib" module of FactSage 7.0 to simulate counter-cross inter-diffusion reactions at interface between refractory gunning samples and slags. "Phase Diagram" module was used to estimate the monoxide saturation in the slags. FToxide database was selected for both modules to forecast the possible solid and liquid solution phase formations. Viscosity module was also used the calculate the viscosities of the slags.

## RESULTS AND DISCUSSION
### Mechanical and physical properties

The HMOR test results (figure 1a) indicated that both product A and product B had high and similar strength values at 1000⁰C and 1100 ºC. However, their strength suddenly dropped at 1200 °C and continued decreasing as the temperature increased. Product A's strength decreased at a faster rate than product B's when transitioning from 1100 °C to 1200 °C and stayed relatively stable between 1200 °C to 1500 °C before it reached its lowest value at 1500 °C. Product B showed higher strength values at all temperatures after 1200 °C compared to product A and a sharp decrease after 1300 °C was noted until it reached its lowest value at 1500 °C.

The CCS test results (figure 1b) showed a linear change in the strength values of product A at temperatures ranging from 1000 °C to 1600 °C. Product B also had a linear increase in strength values between 1000 °C-1400 °C, but a slight decrease was observed after 1400 °C. Product B had higher strength values between 1000 °C-1400 °C compared to product A, before strength values for both of the products reached to very close numbers at 1600 ºC.
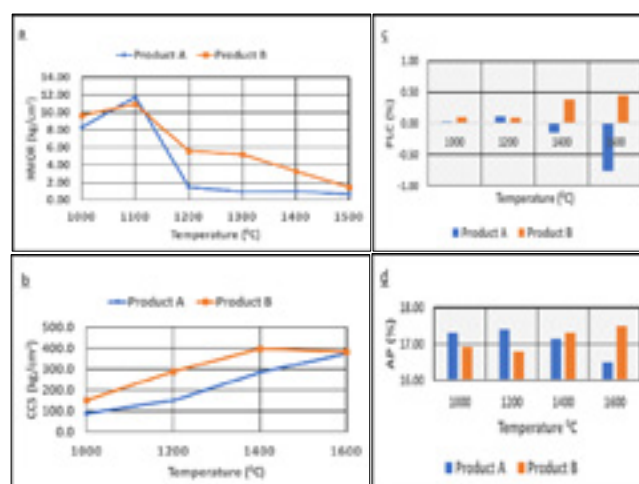


Fig. 1: (a) Hot modulus of rupture (HMOR), (b) Cold crushing strength (CCS), (c) Permanent linear change (PLC) and (d) Apparent porosity (AP) of the samples in the temperature range from 1000 °C to 1600 °C.

PLC and AP test results are given in figure 1c and figure 1d. According to the results, product B showed a positive PLC at temperatures after 1200 °C, while product A showed a negative PLC. As a result of these changes in the PLC, an increase in the AP of product B was observed for temperatures between 1400 °C and 1600 °C, while the AP of product A decreased. The reason for the thermal expansion in Product B is that the SiO$_2$ in the mineral used in its composition is converted into forsterite (Mg$_2$SiO$_4$) by reacting with the MgO in the DBM used. This conversion and the additional sintering resulted from this conversion allowed product B to have higher HMOR and CCS strength values than product A in the temperature range of 1200 °C to 1400 °C. However, at temperatures after 1400 °C, the AP increase in product B decreased its strength and the strength values of both products were found to be close to each other at 1600 °C with strength of product B was still slightly higher.

### Slag corrosion cup tests

After conducting slag corrosion tests, the cross-sectional surfaces of the samples (figure 2) were examined. Overall, it was observed that slag 1 caused less penetration compared to slag 2. This is evident from figures 2a and 2c, where slag 1 remained still in the cup while Slag 2 almost completely penetrated and rarely remained in the cup, as seen in figures 2b and 2d. The calculated slag penetration areas shown in figure 2 revealed that there is no considerable difference found on the corrosion profiles of product A and product B when reacted with both type of slags.

327
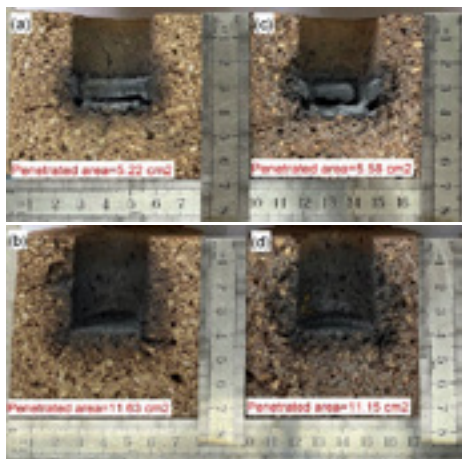
*Fig. 2: Slag penetration into samples after slag corrosion cup test at 1600 °C for 3 hours, (a) Product A – Slag 1 (b) Product A – Slag 2 (c) Product B – Slag 1 (d) Product B – Slag 2*

MgO saturation lines calculated by Factsage for both slag 1 and slag 2 are shown in the phase diagram in figure 3. Diagram indicated that slag 2 is in the undersaturated region in terms of MgO dissolution. However, slag 1 is in the saturated region. In addition, the viscosity values calculated by Factsage presented in figure 3 confirmed that slag 2 (0.124 Poise) has considerably lower viscosity than slag 1 (0.327 Poise). Given its high fluidity and insufficient MgO saturation, slag 2 caused more penetration and corrosion in the samples than slag 1.

*Fig. 3: MgO saturation lines of slags at 28% CaO and 35% CaO in the system $CaO-SiO_2-FeO-MgO-5\%Al_2O_3$ and slag viscosities calculated by Factsage at 1600 °C 1 atm.*

To better understand the mechanisms behind the slag corrosion, the interaction of each gunning sample with slag 1 and slag 2 was evaluated separately by thermochemical simulations and SEM/EDS examinations.

**Interactions of Product A with Slag 1 and Slag 2**

According to the thermochemical simulations in figure 4a and b, when slag mass % increases at 1600 °C, the percentage of the solid monoxide phases MgO (MeO_A#1) and solid forsterite (Fo) in product A decreases linearly and continues to dissolve in the liquid phase (SLAGA#1). During this dissolution MgO reacts with the FeO in the slag to form a secondary solid phase called magnesiowustite (MW) as symbolized as FeO (MeO_A#1) in the graphs.

Comparison of the two interactions shows that MW solid phase in product A- slag 2 graph reaches its maximum value at a slag mass ratio of 50% (figure 4b), while product A-slag 1 graph shows a higher starting point of MW phase dissolution at a slag mass ratio of 70% (figure4a). This is because of the higher FeO content of slag 2 compared to slag 1 (table 2) and explains why slag 2 caused higher dissolution of MgO from product A compared to slag 1 in the slag corrosion cup tests. Another important difference between two

interactions is the presence of the FeO(MeO_A#1) and MgO (MeO_A#1) phases in solid form in the graph for slag 1 on the 100% slag axis, while complete dissolution of these phases is observed in the graph for slag 2 which also indicates the higher corrosive behaviour of slag 2.
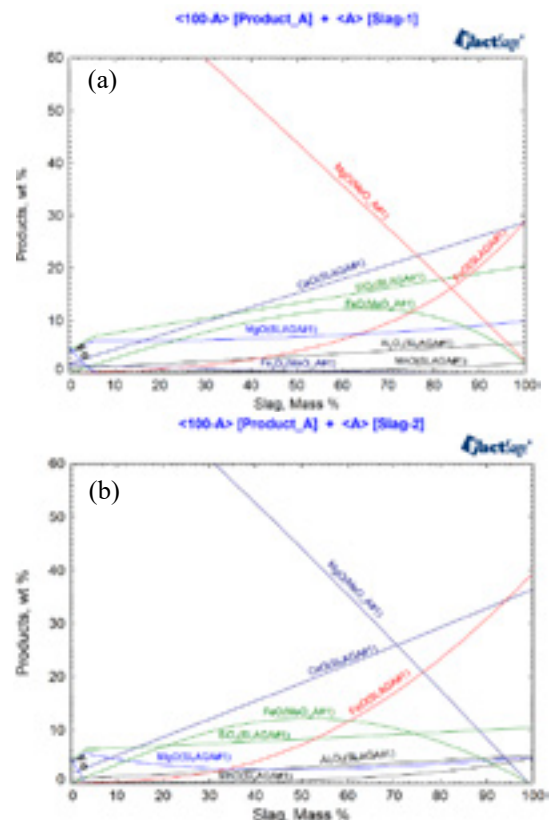


*Fig. 4: Percentage of products (phases) formed versus slag-refractory mass ratio in the refractory-slag system at 1600 °C 1 atm determined by Factsage (a) Product A – Slag 1 reaction, (b) Product A – Slag 2 reaction.*

Figure 5 shows SEM images and EDS analysis of the slag-refractory interaction zones for product A-slag 1 (figure 5a) and product B-slag 2 (figure 5b). Iron (Fe) was mapped in blue colour on the images for better distinction between the interacted zones. EDS analyses were performed on three zones marked in yellow on the images with zone 1 serving as the initial reaction area between refractory and slag, zone 2 as the intermediate reaction area and zone 3 as the refractory zone. High levels of Mg and Fe were detected in zones 1 and 2, together with other elements (Ca, Si, Al and Mn) mostly originating from the slag. It was also observed that Fe content increased from zone 3 (refractory) towards zone 1 where the initial
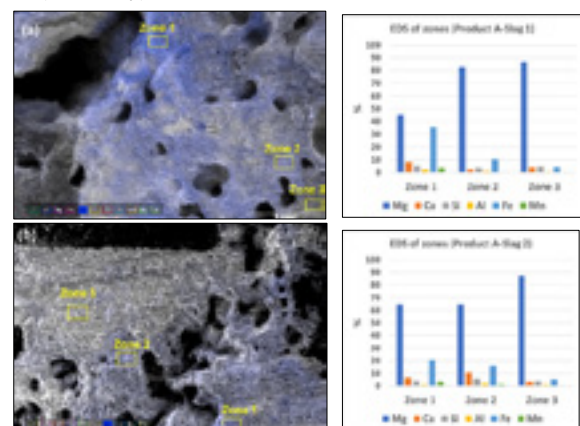


*Fig. 5: SEM images and EDS analysis of the interacted zones on the samples after slag corrosion test, (a) Product A – Slag 1, (b) Product A – Slag 2*

reaction with slag and refractory had occurred. These findings are in line with the MW formation shown in corrosion models predicted by the Factsage thermochemical simulations given in figure 4.

**Interactions of Product B with Slag 1 and Slag 2**
According to the thermochemical simulations in figure 6a and 6b, the corrosion modeling of product B shows differences compared to Product A given in the previous section. The main reason for this difference is the higher forsterite ($Mg_2SiO_4$) phase presence resulting from the use of refractory mineral in product B. Simulations in graphs showed that with the increase in the percentage of slag, the solid forsterite (Fo) dissolves and passes into the liquid phase (SLAGA#1). Complete dissolution of the forsterite occurs at a slag mass ratio of 26% for the slag 1-product B reaction (figure 6a), while this dissolution occurs at a slag mass ratio of 18% for the slag 2-product B reaction (figure 6b). This difference explains why Slag 2 caused more corrosion in product B compared to Slag 1. During forsterite dissolution some of the MgO in the forsterite is transformed into the solid MW phase by reacting with the FeO in the slag, while some of it passes into the liquid phase with the SiO2 in the forsterite.
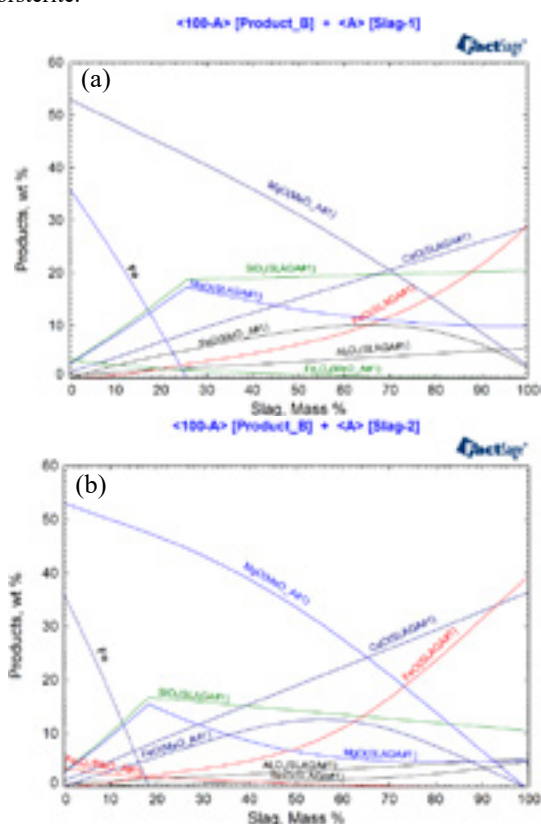


*Fig. 6: Percentage of products (phases) formed versus slag-refractory mass ratio in the refractory-slag system at 1600°C 1 atm determined by Factsage (a) Product B – Slag 1 reaction, (b) Product B – Slag 2 reaction.*

As seen in the SEM images and EDS analyses given in Figure 7, high percentage of Silicium (Si) was detected in the regions where the first interaction with the slag and refractory took place (zone 1). This confirmed forsterite dissolution in slag which was also predicted with the thermochemical simulations. In addition, in the areas where slag penetration took place, refractoy grains that were not fully dissolved (zone 2 and zone 3) in the slag were also detected. The Mg and Si peaks detected in EDS scans indicated that the chemistry of these grains are in line with the to the forsteritic type of composition and some Ca and Fe were also found on the grain boundiries which is an indication of grain dissolution started in the slags (zone 2 and zone 3 in figure 7a).
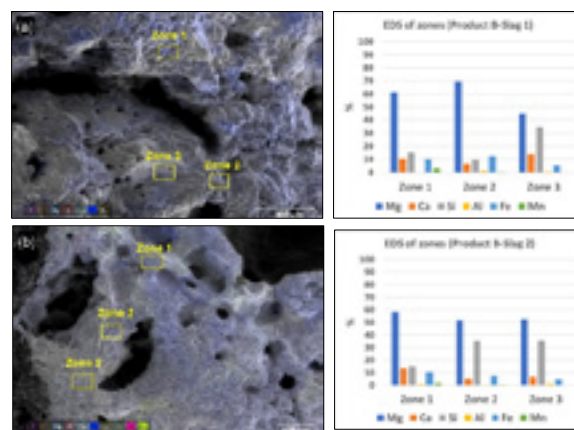


*Fig. 7: SEM images and EDS analysis of the interacted zones on the samples after slag corrosion test, (a) Product B – Slag 1, (b) Product B – Slag 2*

**CONCLUSIONS**
This study has shown that the utilization of a lower carbon footprint natural mineral in EAF gunning products is viable option in improving sustainability. Product B, which contains the lower carbon footprint mineral has given a 30% reduction in GHG emissions. This lower carbon footprint product displays notable refractory properties with good high temperature strength, physical properties, and slag corrosion resistance when compared to a standard gunning material comprising only DBM.

The study has revealed that product B exhibited higher HMOR and CCS than product A at temperatures ranging from 1200 °C to 1600 °C, with a slighlty higher AP at 1600 °C due to the thermal expansion in product B related to forsterite formation. Although product B has a higher AP than product A at 1600 °C, the slag penetration areas of both products were found to be similar, and MgO stauration and viscosity of the slags were the significant factors in slag corrosion of both products. The thermodynamic simulation outcomes were consistent with corrosion test results and SEM/EDS investigations, with the formation of magenesiowustite (MW) and forsterite dissolution determined in the slag refractory interaction zones.

Further research is intended to gain a more in-depth understanding of the corrosion mechanism. It is also proposed to carry out field trial assesments in different EAF operating conditions to understand the performance of the Product B.

**REFERENCES**
[1] Swalec C, Shearer C. Pedal to the Metal. Global Energy Monitor, June 2021
[2] Hasanbeigi A. Steel Climate Impact. Global Efficiency Intelligence, April 2022
[3] World Steel in Figures. World Steel Association, May 2023
[4] Fostering Effective Energy Transition. World Economic Forum, May 2022
[5] https://www.industrytransition.org/green-steel-tracker/, Leadit
[6] U.S. Geological Survey (USGS), 2021
[7] Szednyj I, Brandhuber D. Stand der Technik zur Kalk, Gips und Magnesiaherstellung. Report, 2007
[8] Horckmans L, Nielsen P, Dierckx P, Ducastel A. Recycling of refactory bricks used in basic steelmaking:A review. Resources, Conservation & Recycling, 140, 2019, p. 297-304
[9] Moritz K, Brachhold N, Hubálková J, Schmidt, G, Aneziris C.G. Utilization of Recycled Material for Producing Magnesia–Carbon Refractories. Ceramics, 6, 2023, p. 30–42.

329

# REFRACTORY SOLUTIONS TO "THE CARBON CHALLENGE"

*Yawei Li, Ning Liao, Shaobai Sang*

The Key Laboratory of Refractories and Metallurgy, Wuhan University of Science and Technology, Wuhan, 430081, China
National-Provincial Joint Engineering Research Centre of High-Temperature Materials and Lining Technology, Wuhan, 430081, China

## ABSTRACT

Nowadays the global demand to lower $CO_2$ emission brings new opportunities and challenges to the refractory industries. Refractories as traditional materials are much concerned by its end users of high temperature industries, such as iron and steel making, cement producers. Of course, the transformation to green, lower $CO_2$ emission and new technologies in these high temperature processes will bring much impact on the refractory materials and lining concept of the furnaces. In present paper, several solutions are addressed to the above challenges, including recycling of solid wastes into lightweight mullite aggregates, optimization of cement bonded unshaped refractories and application of layered structure compounds into carbon containing refractories.

## 1 INTRODUCTION

Refractories are key materials for high temperature industries, such as cement, metallurgy, and petrochemical. In fact, the $CO_2$ emission of these conventional industries plays an important role for the global carbon emissions. Therefore, it is of great importance to design superior refractories to tackle the carbon emission challenges. Generally, several solutions are proposed: 1) recycling of solid waste as raw materials for high value-added refractories 2) reducing carbon sources from carbon containing refractories; 3) promotion of the application of monolithic to reduce $CO_2$ emissions during production, application and recycle after use.

Recently, much attention was paid on the above topics. As for recycling of solid waste or mineral tailings, especially for aluminosilicate, much effort were spent on preparation of dense or lightweight mullite clinkers by utilizing coal gangue, fly ash, and kyanite tailings, etc. In addition, the green and low carbon technologies to produce cement bonded unshaped refractories were widely used in many high temperature applications due to their good handleability, high green and hot strengths. In most cases, CaO content should be reduced for better high temperature performances of unshaped refractories. Therefore, several additives with high specific surface area, such as zeolite, M-S-H, hydrotalcite are proposed to stimulate the hydration of cement phases and subsequently optimize the comprehensive properties.

For carbon containing refractories, nano carbon technology can reduce the total carbon content while improving the elevated temperature properties, especially the thermal shock resistance. More recently, investigations focus on the replacement of traditional graphite flake with layered structure compounds, including BN, $Ti_2AlC_3$ and $Cr_2AlB_2$. These compounds have much better oxidation resistance and their by-product during structure transformation could further enhance the refractories, similar to graphite's well-known deformation, strengthening and toughening mechanism.

In present paper, we summarize several research works from our group regarding the topic of green and low-carbon refractories.

## 2 SOLUTIONS TO $CO_2$ CHALLENGES

### 2.1 Recycling of solid wastes into lightweight mullite aggregates

As a matter of fact, million tons of aluminosilicate solid wastes are dumped every year globally. One promising application is the recycling of valuable alumina and silica and make them into mullite-based materials (mostly used below 1500°C due to certain impurities). For our works, the chemical compositions of raw materials are listed in Table 1. As a reference, 95.6% grade III bauxite and 4.4% microsilica (named as M) are mixed and fired at 1400-1600 °C for 3h. In comparison, new batch with 51% grade III bauxite, 34 % fly ash and 15% reactive alumina powders (named as M-F) are prepared [1]. The microstructures of obtained specimens are shown in Fig.1. The mullite crystal size increases with the rise in temperature, and the fly ash containing specimens (M-F) present remarkable growth of mullite. Therefore, it is reasonable to see that the specimens M-F have higher strengths than those of the specimens M. In addition, the higher firing temperature brings no further contribution to the enhancement due to the abnormal growth of mullite and the generation of more liquid phase. Consequently, the proper developed mullite structure contributes to optimized/refined pore structure and thus decreases the thermal conductivity to a certain content, where the lowest value reaches 0.616 W/(m·K) (at 1000 °C) for the fly ash containing specimens fired at 1500 °C. It should be noted that the firing temperature above 1500 °C would increase the thermal conductivity significantly due to the enhanced liquid sintering behaviour.

Table 1. Chemical composition of raw materials (wt.%).

| Raw material | $SiO_2$ | $Al_2O_3$ | $Fe_2O_3$ | CaO | MgO | $K_2O$ | $Na_2O$ | $TiO_2$ | LOI |
|---|---|---|---|---|---|---|---|---|---|
| Grade III bauxite | 26.94 | 55.97 | 1.74 | 0.15 | 0.25 | 0.36 | 0.03 | 2.65 | 11.28 |
| Fly ash | 50.52 | 36.84 | 3.13 | 4.07 | 0.56 | 0.25 | 0.07 | 1.23 | 2.77 |
| Coal gangue | 45.48 | 34.88 | 0.37 | 0.89 | 0.15 | 0.11 | 0.01 | 0.52 | 17.58 |
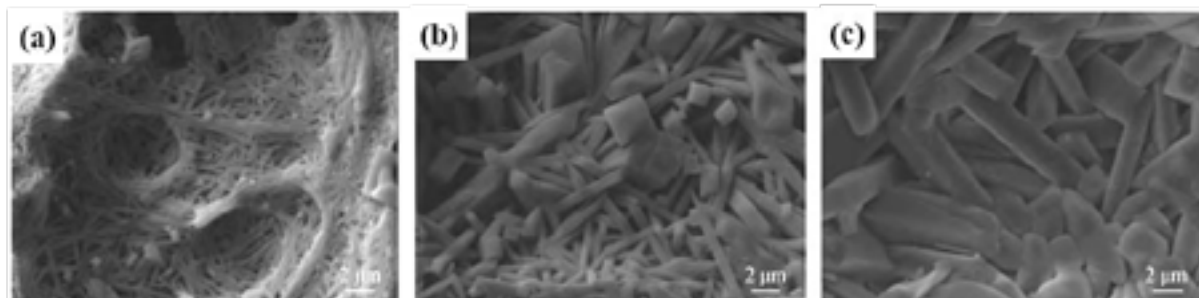


*Fig. 1: Microstructures of the obtained mullite specimens fired at: 1400 °C (a), 1500 °C (b), 1600 °C (c).*
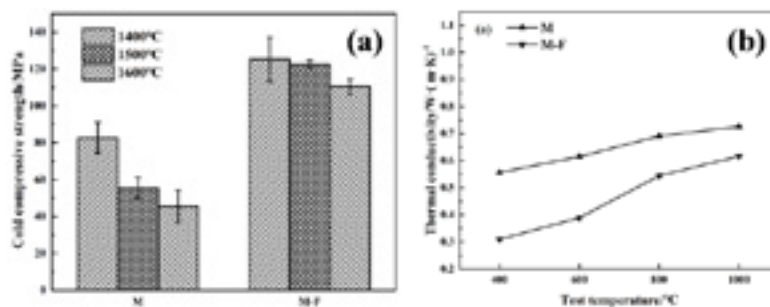
*Fig. 2: Mechanical properties of different specimens (a) and thermal conductivity of obtained mullite specimens at 1500 ℃ (b).*

Furthermore, the combination of coal gangue and fly ash is also feasible to prepare lightweight mullite with low thermal conductivity. Three batches with coal gangue : fly ash : reactive alumina ratio at 60:10:30, 50:20:30, and 40:30:30 (named as F10, F20 and F30, respectively) were fired at 1500 ℃ for 3 hours. The results (Fig.3) show that the increase of fly ash promotes the growth of mullite, while it also improves the thermal conductivity from 0.512 W/(m·K) to 0.719 W/(m·K) (at 1000 ℃). Therefore, the content of fly ash should be elaborately designed to achieve lower thermal conductivity with good mechanical properties.
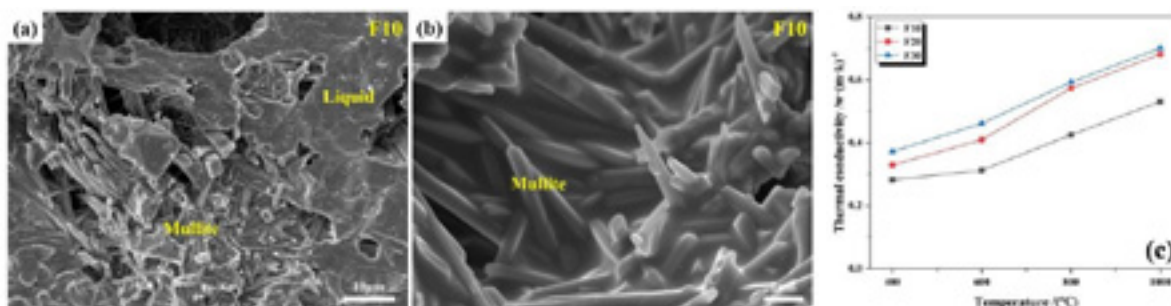


*Fig. 3: Microstructure (a, b) and thermal conductivity (c) of mullite specimens fired at 1500 ℃.*

In addition, kyanite is regarded as one of important aluminum silicate ($Al_2SiO_5$) minerals in refractory field, which accompanies volume expansion during the heating-up process and exhibits excellent alkali attack resistance due to the structure feature of mullite-high silica glass phase after its complete mullitization [2]. In our experiments, zircon containing kyanite tailings ( 54.01%$Al_2O_3$, 33.13%$SiO_2$ and 7.63% $ZrO_2$) were used to prepare lightweight mullite at 1400-1650 ℃. The phase composition indicates that kyanite finishs its mullitization process at 1400 ℃ and zircon decomposes into $ZrO_2$ and $SiO_2$ above 1500 ℃. Consequently, lightweight mullite and high silica glass composite with a great number of close pores (nearly 20%) can be prepared at 1600 and 1650℃ (Fig.4). Additionally, the alkali attack test (in mass change ratio) shows mullite and high silica glass composite has good potassium vapor alkali attack resistance (Fig.5).
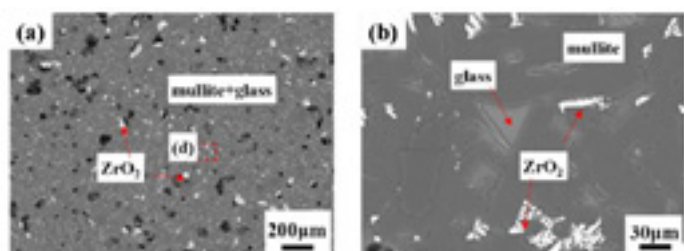


*Fig. 4: Microstructure of lightweight mullite specimens fired at 1650 ℃.*  *Fig. 5: Relationship between porosity and alkali attack on specimens.*
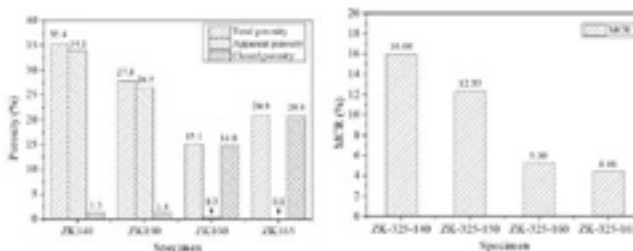
## 2.2 Optimization of cement bonded unshaped refractories

Calcium aluminate cement (CAC) is an important binder for unshaped refractories with the advantages of excellent green strength, good handleability, and good high temperature properties. In fact, the hydrates in cement hydration process determine the early strength, microstructure evolution and comprehensive properties [3]. Generally, metastable $CAH_{10}$, $C_2AH_8$ hydrates will transform into stable $C_3AH_6$ and $AH_3$ (Fig.6), resulting in deteriorated mechanical properties and coarser pore structures [4]. In the last decades, researchers have been trying to stimulate the formation of stable and laminar hydrates such as $C_2AH_8$ and to hinder the formation of granular $C_3AH_6$ ones. As for the formation of $C_2AH_8$, our previous works find out that silicates such as zeolite can stimulate the hydration of cement and induce the formation of $C_2AH_8$ (Fig.7) [5]. Similar to $C_2AH_8$, $C_4AcH_{11}$ as another similar layered structure compound, can enhance remarkably the performances of castables because it could construct the most complicated pore structure both at early stage and elevating temperatures. Our recent work finds out that Mg-Al hydrotalcite (M-A-H) can accelerate the hydration and stimulate the formation of $C_4AcH_{11}$. Besides, another layered structure compound, magnesium silicate hydrate (M-S-H), can promote the hydration of cement and the formation of $CAH_{10}$ and $C_2AH_8$. With the combination of M-S-H with CAC, the mechanical properties of lightweight mullite castables can be further improved (Fig.8). In order to further reduce the thermal conductivity, the air entrainer is also incorporated. The results show that the introduction of 0.01% or 0.02% of air entrainer can remain a high strength, while further optimized pore size distribution (especially between 4~40 μm) can be obtained. With the presence of abundant close pores, the thermal conductivity is obviously reduced, where the lowest one for the 0.02% of air entrainer containing castables can be 0.601 W/(m·K).
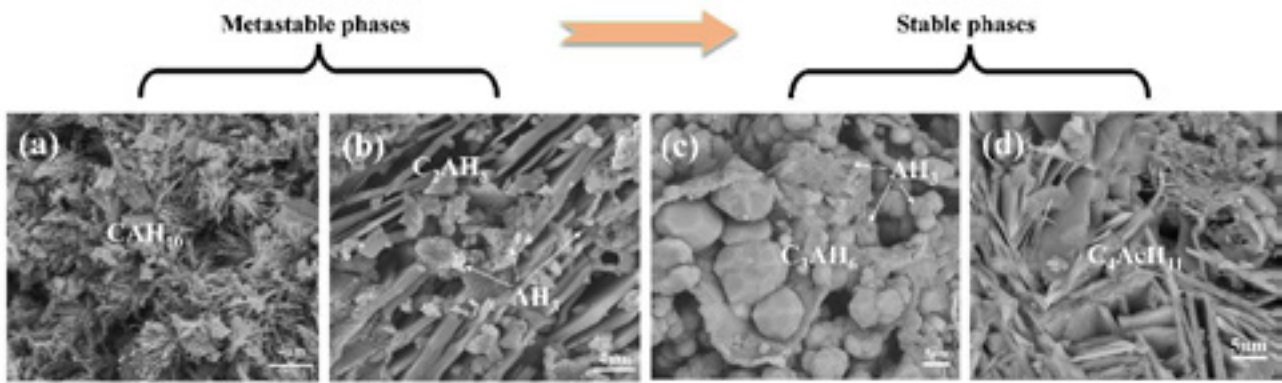
*Fig. 6: Characteristic hydrates from CAC cement.*
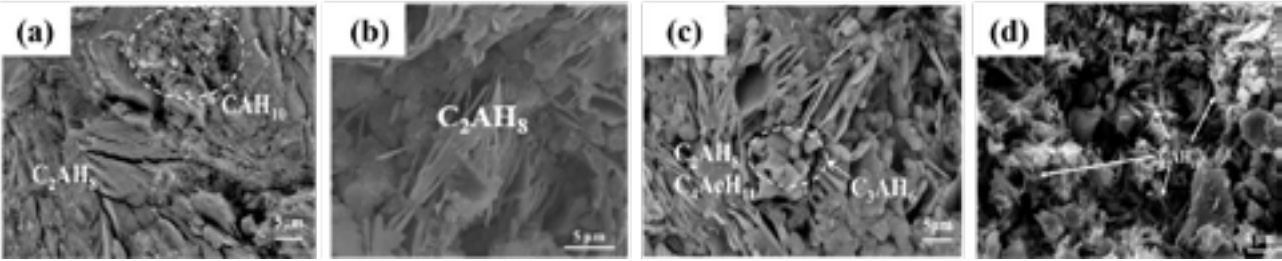


*Fig. 7: Microstructures of different additives incorporated CAC pastes: reference (a), zeolite (b), Mg-Al hydrotalcite (c), and M-S-H (d).*
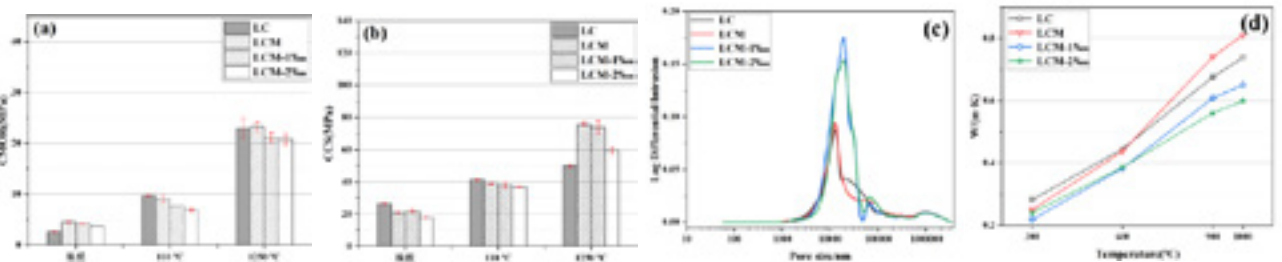


*Fig. 8: Mechanical properties (a, b), pore size distribution (c) and thermal conductivity (d) of lightweight mullite-based castables.*

### 2.3  Application of layered structure compound into carbon containing refractories

Carbon containing refractories were widely used as functional component for converter, ladle, and continuous casting. The presence of carbon mainly in form of graphite is important for thermal shock resistance and slag corrosion resistance. However, the drawbacks are the poor oxidation of graphite and risk of carbon pick up in clean steel-making process. Therefore, many efforts were made to reduce carbon content in refractories. At the beginning of 21$^{st}$ century, nano structured matrixes were proposed by the addition of nano carbon and oxides into refractories, which include nano carbon black, carbon nanotubes, graphene, expanded graphite, *in-situ* catalytic growth of nano carbon and whiskers, nano alumina, and spinel powders. These additives can reduce total carbon content and dramatically optimize the thermal shock resistance and toughen the refractories by the aid of crack bridging, crack deflection, and whisker pull-out mechanisms.

Recently, non-carbon-based compounds with layered structure, such as *h*-BN [6], $Ti_2AlC_3$ [7] and $Cr_2AlB_2$ [8] were used to replace flaky graphite (Fig.9). These compounds could improve oxidation resistance while their layered structure toughened the mechanical properties. Howerver, the toughening mechanisms are completely different from each other. BN remains its structure even at high temperature, while $Ti_2AlC_3$ transforms into a mullite-$Ai_2TiO_5$-TiC/$TiO_2$ core-shell structure. Similarly, scattered BN, $Cr_2O_3$, and $Cr_3C_2$ was generated within the matrix with the addition of $Cr_2AlB_2$ (Fig.10). These structure transformations contribute to obviously optimized pore structure and induce the growth of whiskers, which eventually improve the fracture behaviours of alumina-carbon refractories. As shown in Fig.11a, the introduction of 0.5 wt.% BN (Fig.11a) can improve the displacement of $Al_2O_3$-C refractories remarkably, while the further increase of BN can still increase the toughness and remain good strength. Besides, the addition of 1 wt.% $Ti_2AlC_3$ contributes to larger displacement (2.6 mm to 3.5 mm) and all the three batches obtain comparable fracture loads (Fig.11b). It should be mentioned that excess addition of these layered structure compound would decrease the bonding strengths like conventional graphite flake.
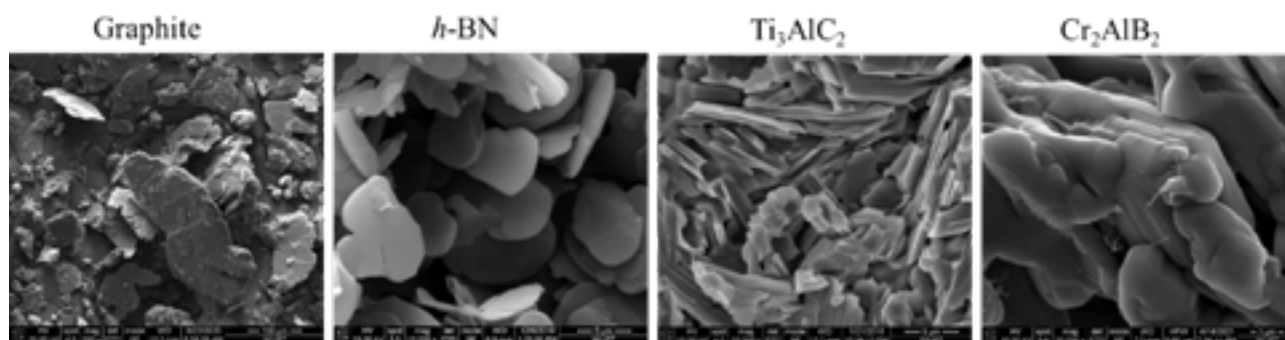
*Fig. 9: Microstructure of several additives with layered structure.*
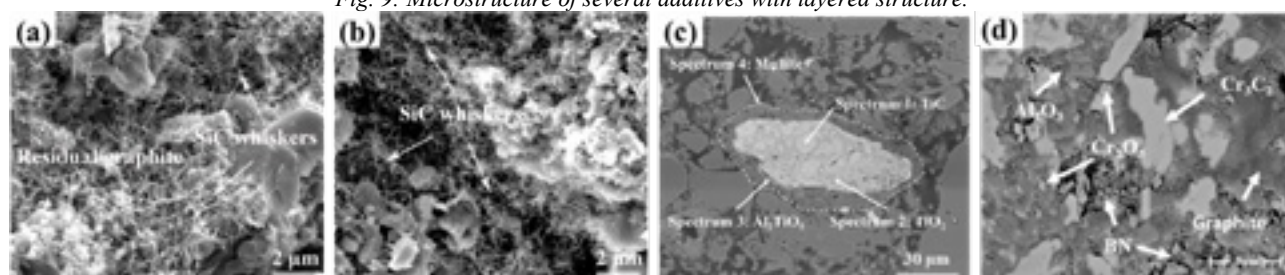


*Fig. 10: Microstructure of $Al_2O_3$-C refractories (1400 °C*3h) with addition of graphite (a), BN (b), $Ti_2AlC_3$ (c) and $Cr_2AlB_2$ (d) respectively.*
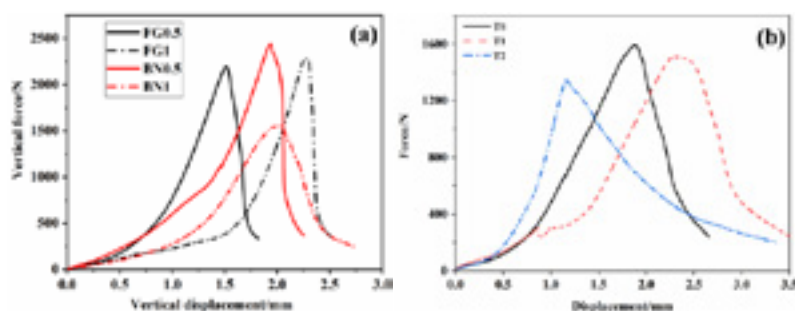


*Fig. 11: Load-displacement curves of $Al_2O_3$-C refractories (1400 °C*3h, room T wedge splitting test) with addition of graphite, BN (a), and $Ti_2AlC_3$ (b).*

## 3. CONCLUSIONS

Refractory technologies can contribute significantly to reducing global $CO_2$ emission. Recycling of coal gangue, fly ash, and kyanite tailings can be adopted to prepare lightweight mullite clinkers for low thermal conductivity refectory products. As for carbon containing refractories, several non-oxides such as BN, $Ti_2AlC_3$ and $Cr_2AlB_2$ could replace flaky graphite in order to remarkably improve the thermal shock resistance as well as oxidation resistance. Besides, as for the unshaped castables, the additives such as zeolite, M-S-H, and M-A-H with high specific surface area and different functional groups would accelerate the hydration of CAC and induce the formation of layered structure hydrates $C_2AH_8$ and $C_4AcH_{11}$, which decrease the demand of cement and improve the high temperature properties.

## REFERENCES

[1]. Chen Fuwen, Sang Shaobai, Wan Zhuofu, Ma Yuzhou, Liao Ning. Effects of fly ash and firing temperature on structure and properties of bauxite-based lightweight mullite materials. Bulletin of the Chinese Ceramic Society, 2023, 42(4): 1488-1495.

[2]. Wang Zhifeng, Li Yawei, Ma Shulong, et al, Alkali attack resistance of mullite-high silica glass composite materials prepared from kyanite tailings,Refractories, 2023 (In Chinese)

[3]. Liu Wenjing, Liao Ning, Nath Mithun, Ji Zixu, Dai Yajie, Pan Liping, Li Yawei, Jastrzębska Ilona, Szczerba Jacek. Effects of curing time on the pore structure evolution and fracture behavior of CAC bonded alumina-spinel castables. Ceramics International 48 (2022) 25000-25010.

[4]. Liao Ning, Liu Wenjing, Yang Jingwei, Nath Mithun, Dai Yajie, Pan Liping, Li Yawei. In-depth investigation of pore structure and fracture behavior of CAC bonded alumina-spinel castables treated at 110 ~ 1600 °C. Ceramics International 48 (2022) 33763-33772.

[5]. Shan Jiangbo, Li Yawei, Liao Ning, et al, Critical roles of synthetic zeolite on the properties of ultra-low cement bonded $Al_2O_3$-SiC-C castables, Journal of the European Ceramic Society, 40 (2020) 6132–6140.

[6]. Ji Zixu, Liao Ning, Li Yawei, et al. Effect of h-BN on the microstructure and fracture behavior of low carbon $Al_2O_3$-C refractories. Ceramics International 47 (2021) 29900-29907.

[7]. Liu Gengfu, Liao Ning, Li Yawei, Zhang Yang, Ji Zixu, Zhu Tianbin. Influence of $Ti_3AlC_2$ addition on water vapor resistance of low-carbon $Al_2O_3$-C refractories. Int J Appl Ceram Technol. 2022; 1-12.

[8]. Zhang Yang, Li Yawei, Liao Ning, et al, Structural evolution of $Cr_2AlB_2$ powder and its effect on properties in $Al_2O_3$–C refractories at high temperature,  Journal of the Chinese Ceramic Society,2023,51(3)579-588(In Chineses).

# PREFABRICATED SLAG DOOR SOLUTION – TO SOLVE A WELL-KNOWN OBSTACLE TO INCREASE EAF PERFORMANCE

Bernd Buchberger*, Dietmar Jammernegg, Mario Valdes, Andreas Viertauer,
Mayerton Refractories Ltd, UK
Sreedharan Unni Chakkungal, Asif Ahmad, Muhammad Abubaker
National Steel CO. LTD., KSA

## ABSTRACT

One of the bottlenecks for high performance of EAFs is extended refractory wear in the slag door area. This often limits the lifetime of the complete vessel. Problems are mainly related to grade selection, lining process/installation, and process conditions.

To overcome this issue Mayerton developed solutions with preassembled slag doors. The given example describes the implementation of such a slag door at National Steel (NASCO) in Saudi Arabia. NASCO is operating a split type EAF, which gives the opportunity to place such a preassembled slag door into the furnace.

Detailed engineering of the overall situation of the EAF (condition of furnace shell, installation equipment in steel plant, space for the block) is mandatory and has to be taken into account. For the correct choice of the refractory grade the knowledge of process parameters is essential as well. Specifics about the refractory detail engineering, grade selection, installation and performance results will be given in-depth in the paper.

## INTRODUCTION

Under the umbrella of Al Ittefaq Steel Products Cooperation. (ISPC), National Steel Cooperation. (NASCO) was established in 2004 with an annual capacity of 0.5 million metric tonnes (MT) of steel billets. Since then, NASCO has strategically enhanced its capacity to achieve 1.0 million MT production in 2014 through technical upgrades to maintain the quality and meet the increasing demand.

NASCO is a steel melt shop that produces steel billets for the ISPC group. They mainly produce construction steel grades through EAF-LF-CCM route. Steel scrap and direct reduced iron (DRI) are used. A state of the art, highly productive EAF with continuous DRI feeding system and advanced auxiliary equipment to ensure consistent production of quality steel is the primary facility. Novel is that an induction furnace (IF) with twenty ton capacity runs in combination with the EAF to increase overall output in a cost-effective manner. One ladle furnace (LF) is taking care for refining to ensure the desired quality is achieved. The steel is cast at a four strands billet continuous casting machine (CCM) with very high level of automation capable of producing billet sections of 130 mm to 180 mm[1]. The product mix spans from low-, medium- to high carbon grades. The official equipment manufacturer was Siemens-VAI.

The EAF is producing 24 – 28 heats per day. Due to the planned plant utilization and planned maintenance stops the lifetime is around 400 heats. After the end of the campaign the whole furnace is taken out with a heavy crane and replaced by a newly relined or repaired vessel which is directly taken into operational mode. One of the obstacles to extend the lifetime and to reduce the number of maintenance cycles is the high pre-wear at the slag door.

RESULTS AND DISCUSSION

The EAF is lined in a common lining configuration. Above the three layers of permanent lining which are fired magnesia bricks a hearth ramming mass for the bottom and banks is placed. The side wall is lined with different MgO-C grades in respect of balanced lining, especially for the hot spot areas.
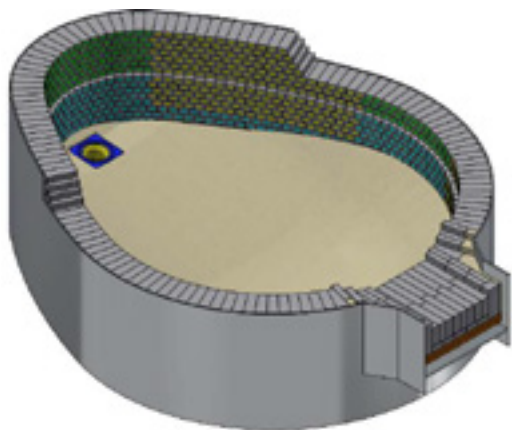


Fig 1. Lower shell of the EAF with refractory lining included.

The slag door area is the clearly defined weak point and is the main reason to take the furnace out of operation due to high pre-wear compared with the rest of the lining. Notable is the additional downtime for gunning the slag door area. It was decided to select a new refractory material together with a custom-fit engineered slag door solution.

Refractory selection:

For choosing the best refractory material in an EAF, especially in the slag door area, several facts have to be taken into account: The atmospheric conditions as this area has a close contact to the normal atmosphere outside the furnace, thermal shocks and regular contact with slag. On the one hand high carbon content would increase resistance against slags but would on the other hand decrease oxidation resistance of the material. Antioxidants increase corrosion resistance but decrease hot strength of the refractory material.

The finally chosen refractory grade is based on the furnace operating conditions. The chosen material is based on high purity fused magnesia (FM 98) with a C/S ratio >2, a carbon content of around 15%, and a resin bond. For restrengthening the brick structure a well-known combination of metal powders was added to the brick (metallic Al and Si)[2,3], dense pressing of the bricks was chosen as the densifying method to prevent steel and slag infiltration into the brick's microstructure. For the final assembly of the slag door the single bricks were glued with a glue based on polyurethane with oxidic additions to give a maximum strength to the final piece part. The preassembly assures a perfect fit of every single brick in this critical area, avoiding steel or slag penetration into brick joints.

Slag door detail engineering:

There are some main facts to consider. Most importantly, the upper part must be separably from the lower part of the kiln shell. This gives the opportunity to set a prefab solution into the furnace from above. Furnace steel shells which have been in operation for several years normally show thermos-mechanical deformation. This deformation has to be considered for the detailed design engineering.

NASCO runs an EAF split type vessel which gives the opportunity to set a preassembled slag door solution in one piece with a crane into the furnace during maintenance or refractory rebuilt. Figure 2a shows the slag door refractory design with the handling slings. The jamb bricks (Fig. 2b) will be settled separately after setting the block to close the gap to the wall lining (Fig. 1).

(a)                          (b)
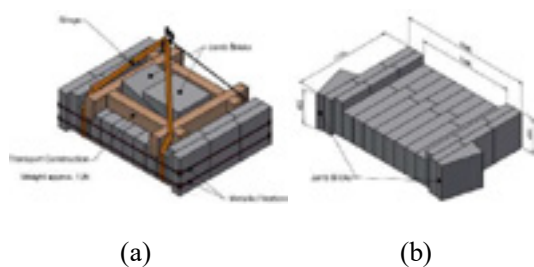
Fig. 2. (a) Prefab slag door with lifting slings,
(b) with jamb bricks set in place.

Before setting the prefab slag door into its final place the flatness of the surface was checked (Figure 3 a). To avoid steel and slag penetration in the horizontal gap between standard lining and the prefab block it was decided to use a mortar between the seating pad and the prefab block (Figure 3 b).



(a)                          (b)

Fig. 3 (a) check the flatness, (b) mortar patching.

Figure 4 depicts the prefab block manipulation on the lifting device before setting. It has to be noticed that the mortar layer brings an additional benefit for the fine adjustment of the block due to the reduced friction.



Fig. 4. Setting in place the preassembled slag door block.

Essential for the stable mechanical fixation are large vertical pilar bricks, which are set left and right of the slag door block (Figure 5 a and b). The necessary tolerances/gap between the pilar bricks, jam bricks and upper shell are essential for mounting the upper shell and to compensate the brick elongation during furnace operation (Figure 6). The gap between bricks and water cooled panels was closed with conventional patching mortar.



(a)                          (b)
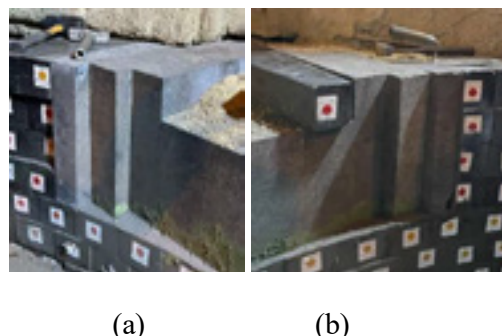
Fig. 5. after setting the upper shell (a) left and (b) right pillar bricks were set as connection to the wall lining.



Fig. 6. Prefab slag door solution after mounting the upper shell.

The complete newly relined furnace with the prefab slag door went into operation directly after completion of the maintenance on October 12th 2022. The EAF campaign duration was scheduled for exactly 3 weeks with high plant utilization with very limited time for gunning. Figure 7 gives an impression about the furnace refractory after 20 heats while Figure 8 shows the status at 338 heats after gunning.

336
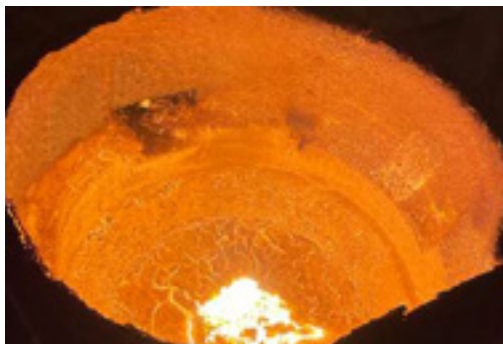
Fig. 7. EAF after 20 heats.



Fig. 8. EAF after 338 heats.

The furnace was taken out of operation after 422 heats. The expectation of achievable lifetime, maintenance service activities and residual lining thickness was more than fulfilled. Figure 9 shows the lower shell area after dismantling from the upper shell with the slag door directly before wrecking. The remaining thickness of the prefab slag door would allow additional approximately >100 heats. This positive result with the residual thickness is the ignition to modify the whole lining configuration to extend the planned EAF operation.



Fig. 9. After demounting the upper shell – lower shell with slag door area.

In a further trial the target of 450 heats has been reached without any problems in the slag door area.

CONCLUSION

Besides safe handling and fast mounting the prefabricated slag door solution showed its main benefit – debottlenecking a critical area of refractory service life and therefor extend the furnace operation with reduced downtime for gunning which led to higher plant productivity and reduced OPEX. Nevertheless, the right choice of the refractory material was essential as well.

ACKNOWLEDGEMENT

REFERENCES

1. Homepage www.ispc.com.sa/National-Steel-Co.aspx
2. Z. Shumao et al, "Effects of Antioxidants Particle Size on Oxidation Resistance of MgO-C Refractory", Key Engineering Materials, Vol. 821, pp. 452-456, (2019).
3. G. Routschka, "Handbook of Refractory Materials" 3rd Edition, pp. 449-452, (2001).

337

# IMPROVE FURNACE LIFETIME AND OPERATIONAL SAFETY BY ROBOTIC GUNNING REPAIR

Christian Wolf, Velco GmbH, Velbert Germany

## ABSTRACT

The hot gunning repair of furnaces, ladles, RH degasser snorkels is a well-established procedure to increase the refractory lifetime and avoid break outs. However during the repair, the aggregate will not be available for production. It is the steelmaker's intention to reduce the time loss for the gunning repair, and to perform the repair efficient and with the highest standards for operational safety. This paper describes the recent developments in robotic gunning with the help of integrated TV cameras and laser scanners.

## LADLES

The refractory wear at ladles is mainly in the slag zone and the lip area. At plants with secondary metallurgy the slag zone wears out even more quickly. Sometimes the top of the lining, the lip ring, becomes damaged due to slag removal with a breaking out machine. Consequently, a ladle can be put back into operation very quick after a hot gunning repair focussed only on the slag zone. The most convenient location to carry out a hot repair is the tilting stand, where the slide gate is repaired. It is possible to use a manual gunning lance but this results in high physical stress for the worker.

When using a gunning robot the gunning repair is:

- Quicker, because of higher gunning rates.
- More efficient, because of the well directed jet.
- Easier because there is no physical stress for the worker.

Velco has built different solutions for this task, depending on the plant layout and if the ladle is in horizontal or vertical position. One version is a fixed installation consisting of a rotating lance that can move in and out, running on a beam structure. For each repair stand one robot is required (Fig. 1)



Fig. 1 Stationary ladle gunning installation

The second version is a gunning lance which is mounted on an electric trolley that can drive from a parked position to one, or more repair positions. Fig. 2 shows a manipulator at a ladle with a liquid content of approximately 150t of steel, for the repair of ladles which are in a tilting stand, at voest alpine in Linz, Austria.



Fig. 2 Mobile lance trolley for ladle gunning

## ELECTRIC ARC FURNACES

In the past 25 years Velco has supplied 22 gunning robots for electric arc furnaces. However, due to the different layouts of the melt shops no two robots are alike. It has to checked for collisions with T&P robot, oxygen lance or door ram.

In between the vessel exchange sequences, hot gunning is the preferred solution to keep the furnace operative. When using hand lancing a pipe of typically 6 to 8m in length is introduced through the slag door. The gunning rate is only 60 to 80 kg/min. Handling the pipe is hard work and not all areas at the furnace can be reached, especially close to the slag door.

There is the option to install a CCTV camera in the gunning head (Fig. 3), so that it is possible to watch and record the gunning repair. The operator can stay safely in the pulpit.
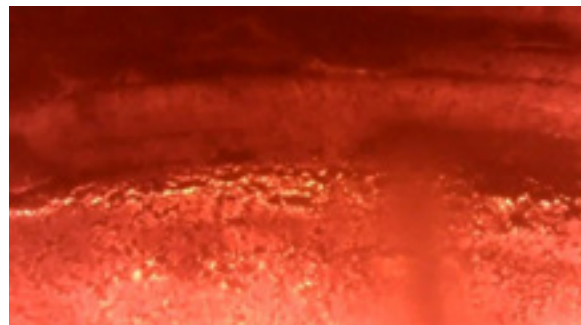


Fig. 3 Video of gunning with Camera in gunning robot head

The new design developed in 2021 is called METOP. It has a pure mechanical lift system by an electro-mechanical cylinder. No hydraulic required Fig. 4.



Fig. 4 new design of Metop

Next step of improvement is the use of pre-programmed gunning programs. The operator can pre-select areas to be gunned on a touch screen. He can save different gunning programs depending on the gunning strategy and furnace life. The robot then automatically repairs only the selected locations (Fig. 5)



Fig. 5 Zone selection for automatic gunning

Lucchini Industries Steel Plant in Lovere /Italy was looking for a new gunning manipulator to improve operational safety, but had no space near the electric arc furnace. They decided for the crane held gunning manipulator PNEUTOP. Which is parked approx. 40m away from the furnace in a special structure. For the gunning repair, the manipulator is picked up by the overhead crane (Fig.6) and lowered from the top into the furnace. The PNEUTOP is connected to a pressure vessel machine.



Fig. 6 PNEUTOP robot moved by a crane

The refractory gunning material is supplied in BIG BAGs that are filled into the pressure vessel via a filling hopper. Via a radio remote control the operator moves the lance to the desired location, starts and stops the pressure vessel machine and controls the gunning water flow.

Using the gunning manipulator the repair is quicker and the operational safety is improved (Fig. 7) .



Fig. 7  hot gunning repair with PNEUTOP

**LASER SCANNER**

In cooperation with IMSI (Industrial Measuring Systems Inc., Toronto, Canada) it has been developed a design where a high speed laser scanner with its own swing arm is attached to the boom of the gunning robot.
The laser arm is mounted very compact onto the gunning robot boom and requires no extra space on the shop floor. During parking and gunning operation the laser and the arm  head towards the robot base. Only for the measurement the arm swings over the furnace shell (Fig. 8a, b). The laser is protected against heat and dust by enclosures, heat shields and air cooling. The laser scans the shape of the refractory lining, compares with the initial brick lining and gives recommendations where gunning should take place. So the gunning repair can be performed automatically.

Fig. 8 a, b Gunning robot with laser scanner arm in parking, resp. scanning mode

## RH-DEGASSERS

The high quality demands of the automobile industry, leads to an increase in the proportion of melts routed via the vacuum degasser. Snorkel lifetime is an important factor in achieving high availability, of the RH-degasser. Due to the reaction with steel and slag, the snorkel wears out both internally and externally. Often the outside lining is damaged by slag removal with scrapers or de-bricking machines. It is of primary importance to keep the system safe and to avoid break outs of hot metal, but the service time is limited as the sequences of the steel plant have priority. Any unplanned exchange of the snorkels should be avoided. Outside gunning is a common practice. However, the workplace is exposed to heat and the operator likes to stay away from the snorkel, so the gunning is not always well directed and has high rebound losses.

Some steel plants have a service car to which a platform for hand gunning is attached. So the distance is smaller and the rebound lower. Nevertheless, inside gunning is not possible because of the danger of dripping hot steel or slag from the RH-vessel.

Hence, using a gunning robot is beneficial for outside repairs, because the gunning is better directed and the physical stress on the workers is eliminated. A robot is essential for the inside repair of the RH snorkel. If gunning is performed well, consumption is in the range of 0.5kg/t steel. Typically gunning takes place after 6 to 8 treatments.

Most robots have two gunning lances, one for inside and one for the outside repair. Lances and lifting arm are based on a frame that can rotate by 180° (Fig. 9 a, b). One lance can repair the inside of snorkel A, while the other is doing the outside repair of the snorkel B. When this is finished, the main base rotates, so snorkel A is repaired on the outside and snorkel B is repaired on

the inside.
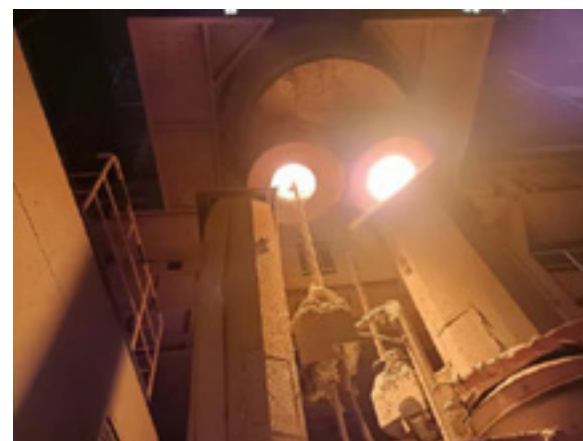




Fig .9 a, b Gunning manipulator with 2 lances

The advantage of placing the scraper and the gunning robot on the same service car is the time saving in handling. The complete operation of snorkel cleaning and inside/outside gunning can be performed in approx. 12 -15 min. (Fig 10).
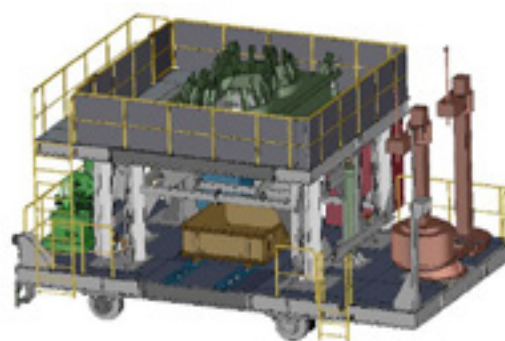


Fig. 10 service car with scraper and gunning robot (picture SMS group)

For the inspection and documentation of the wear pattern it is possible to attach a camera on the robot (Fig. 11). Instead of the inner gunning lance, a water cooled camera is driven into the snorkel. A video can be made of the snorkel or the lower vessel area. Using positioning encoders, the area of robot in the video can be exactly determined (Fig. 12). The video can be stored and the wear can be documented. By this process the lifetime can be optimised. The inspected areas can be precisely repaired with the robot.



Fig. 11 water cooled inspection camera



Fig. 12 Inside picture of RH-snorkel

The operator can either use automatic programmes or may control the maintenance process via a radio remote control (manually).

**CONCLUSIONS**

Gunning robots help to increase productivity and the safety of the refractory brick lining. In combination with cameras and laser scanner they bring a new level of operational safety to the steel mill.

341

# EFFECT OF MAGNESIA GRAIN SIZE COMPOSITION ON INTERNAL PORE STRUCTURE IN MAGNESIA CARBON REFRACTORY BRICKS

Tetsuya Furukawa, Gaku Shimada and Eiji Ishihara
Shinagawa refractories Co., Ltd., Bizen, Japan

## ABSTRACT

The permeability of MgO-C brick is highly influenced by its pore structure, a three-dimensionally connecting complex structure. It was indicated in the author's previous study that the permeability of MgO-C brick is influenced by not only the apparent porosity but also other factors. The particle size distribution coefficient corresponding to the Fuller index of the Andreasen's equation is defined as the apparent q value ($q_{AP}$). Relations between $q_{AP}$ and the specific surface area of inner pores as well as the tortuosity factor of pores were examined in this study. It was clarified that there exists a correlation between the $q_{AP}$ value and specific surface area of inner pores as well as between the $q_{AP}$ value and tortuosity factor of pores. The tortuosity factor of pores was found to be the parameter which most considerably influences the permeability of MgO-C brick.

## INTRODUCTION

One of the deterioration mechanisms of MgO-C brick which is exposed to elevated temperatures is oxidation-reduction reaction between MgO and C, namely, MgO-C reaction. A series of reactions which were proposed by R. J. Leonards et al. [1] in the earliest investigation study work on MgO-C reaction are (1) decomposition of MgO to Mg and O, (2) attachment of generated oxygen (O) on C surface, (3) generation of CO on C surface and (4) reduction of MgO by generated CO gas. In each reaction the transfer of gas components, attachment/detachment of gas components and interface reactions are engaged.

A backscattered electron image of MgO-C brick structure is shown in Fig. 1. MgO-C brick structure is composed of magnesia particles, scaly graphite and a great number of pores with various sizes which are extended in magnesia and graphite particles.
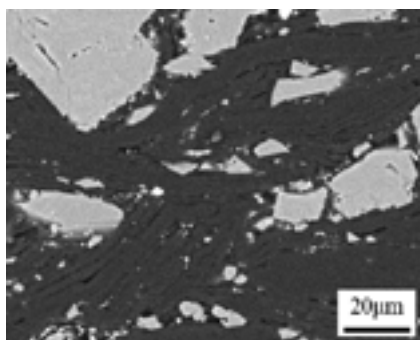


*Fig. 1: Backscattered electron image of MgO-C brick structure*

Influenced by the morphological feature of being composed of magnesia and graphite particles, as well as by particle size distribution and the filling factor of raw materials, these pores are three-dimensionally connected to demonstrate a complex pore structure. The pore structure influences the ease of internal gas movement, which is indexed with a parameter of "permeability" expressed with equation (1) [2], [3].

$$K_p=\varepsilon^3/2\tau^2 S_v^2(1-\varepsilon)^2=f(\varepsilon, \tau^{-2}, S_v^{-2}) \tag{1}$$

Where,
  $K_p$: Permeability[m$^2$]
  $\varepsilon$ : Apparent porosity
  $\tau$: Tortuosity factor of pores
  $S_v$: Specific surface area of inner pore[m$^2$/m$^3$]

While, as expressed with equation (2), tortuosity factor of pores, $\tau$, is defined as the ratio between actual distance and shortest distance.

$$\tau=l_e/l \tag{2}$$

Where,
  $\tau$: Tortuosity factor of pores
  $l_e$: Actual distance[m]
  $l$: Shortest distance[m]

Controlling the pore structure in MgO-C brick is thought to be quite important with the prospect of lowering permeability contributing to suppression of MgO-C reaction. Relations between apparent q value ($q_{AP}$) and various physical properties of MgO-C brick examined in the authors' previous study presented at the UNITECR 2022 by G. Shimada et al. [4] by introducing particle size distribution expressed as apparent q value ($q_{AP}$), which is defined referring to the Fuller index in Andreasen distribution [5], one of the theoretical formulas used for filling particle bodies. As shown in Fig. 2 and Fig. 3, it was clarified that, in accordance to lowering of $q_{AP}$, the permeability of MgO-C brick was lowered and a marked change was observed in the apparent porosity of MgO-C brick at approximately 0.28 of $q_{AP}$.
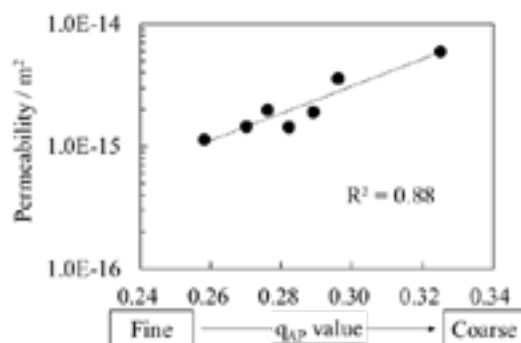


*Fig. 2: Relation between $q_{AP}$ value and permeability [4]*
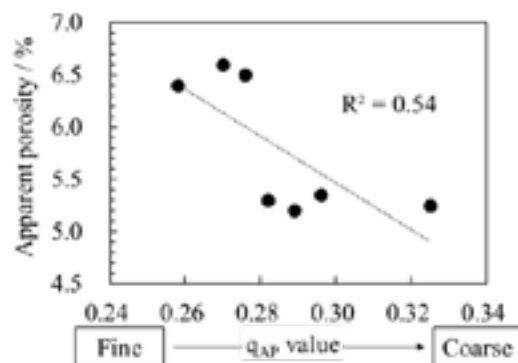


*Fig. 3: Relation between $q_{AP}$ value and apparent porosity [4]*

Since lowering the permeability of MgO-C brick, which was observed in the previous study work, cannot be explained simply by change of apparent porosity, it is inferred that permeability is influenced by other factors of pore structure expressed in right-hand side of equation (1). In addition to the apparent porosity, influences of other parameters of pore structure, namely, specific surface area of inner pores and tortuosity factor of pores, on

permeability of MgO-C brick were studied by examining relations between $q_{AP}$ and these parameters.

## EXPERIMENT

Five (5) different MgO-C brick samples were prepared with varying particle size distributions of raw material MgO particles. Blend compositions of each MgO-C brick sample are comparatively shown in Fig. 4, along with particle size distribution, which, similarly to the previous study work, is expressed as apparent q value ($q_{AP}$). Portions of fine and middle particle size magnesia particles in each MgO-C brick sample were elaborately adjusted so that MgO-C brick samples A-E exhibit around 0.28 of $q_{AP}$, at which a marked change in apparent porosity was observed in the previous study.

| Coarse → Fine | | | | | |
|---|---|---|---|---|---|
| Sample name | A | B | C | D | E |
| $q_{AP}$ | 0.289 | 0.282 | 0.276 | 0.270 | 0.258 |
| MgO — Coarse grain (Upper 1mm) | a | a-c | a-2c | a-3c | a-5c |
| MgO — Fine grain (Under 1mm) | b | b+c | b+2c | b+3c | b+5c |
| C | Fixed amount | | | | |
| Binder | Changed by surface area of MgO | | | | |
| Additive | Fixed amount | | | | |

a: 0~40, b: 40~80, c: 0~5

*Fig. 4: Blend compositions of MgO-C brick samples*

Each MgO-C brick sample was prepared by a combination of raw material mixing with high-speed mixer and shaping with uniaxial pressing machine. After firing the MgO-C brick samples embedded in coke breeze at 1500°C, their physical properties, specific surface area of inner pores and tortuosity factor of pores, were evaluated. These physical properties were measured by mercury porosimetry in accordance with JIS R1655 (Test methods for pore size distribution of fine ceramic green body by mercury porosimetry). The specific surface area of the inner pores ($S_v$) and tortuosity factor of pores ($\tau$) of each MgO-C brick sample were calculated with equation (3) and equation (4), respectively.

$$S_v = -Y_s \Sigma P \Delta V / W_s \gamma \cos\theta \tag{3}$$

$$\tau = \{D_{avg}^2 / 96 K_p (1 - Y_s V_{tot}/W_s)\}^{1/2} \tag{4}$$

Where
$S_v$: Specific surface area of inner pore[m²/m³]
P: Injection pressure of mercury[N/m²]
V: Injection volume of mercury[m³]
$\gamma$: Surface energy[N/m]
$\theta$: Contact angle[deg]
$Y_s$: Apparent density of sample specimen[g/m³]
$W_s$: Weight of sample specimen[g]
$\tau$: Tortuosity factor of pores
$D_{avg}$: Weighted average pore size[m]
$K_p$: Permeability[m²]
$V_{tot}$: Whole volume of injection mercury[m³]

## RESULTS

The relation between the apparent q value ($q_{AP}$) and specific surface area of the inner pores is shown in Fig. 5.
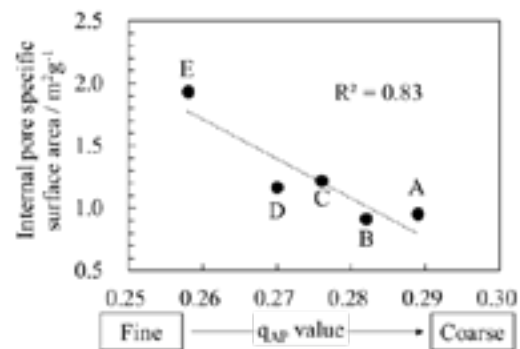


*Fig. 5: Relation between $q_{AP}$ value and specific surface area of inner pores*

In association with the lowering of $q_{AP}$, the specific surface area of the inner pores in the MgO-C brick sample increased with a strong correlation. The relation between $q_{AP}$ and the tortuosity factor of the pores is shown in Fig. 6.
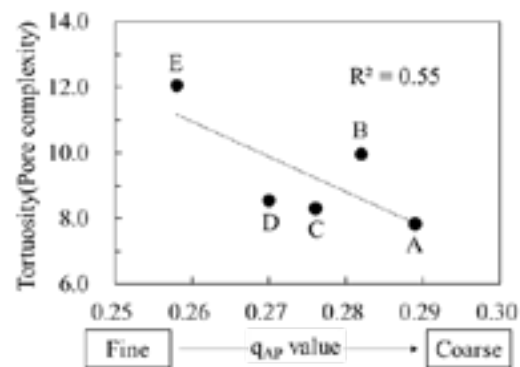


*Fig. 6: Relation between $q_{AP}$ value and tortuosity factor of pores*

In accordance with the lowering of $q_{AP}$, the tortuosity factor of the pores increased with moderate correlation.

## DISCUSSION

Equation (1) indicates that permeability is in proportion to apparent porosity and permeability is in inverse proportion to the squared value of the specific surface area of inner pores and tortuosity factor of pores. That is, permeability of MgO-C brick is influenced by its apparent porosity as well as by its specific surface area of inner pores and tortuosity factor of pores. The relation between permeability and specific surface area of inner pores is shown in Fig. 7, and the relation between permeability and tortuosity factor of pores is shown in Fig. 8.
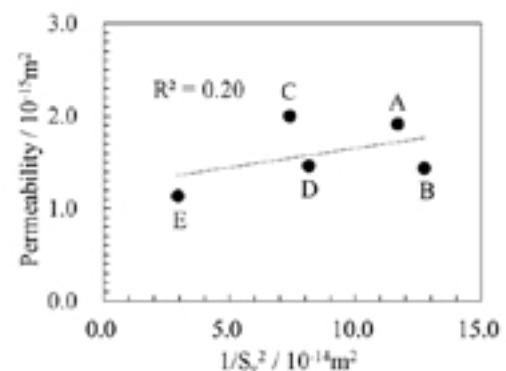


*Fig. 7: Relation between specific surface area of inner pores and permeability*
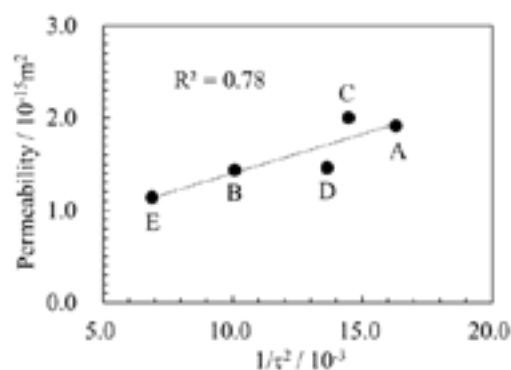
*Fig. 8: Relation between tortuosity factor of pores and permeability*

Both figures affirm that permeability of MgO-C brick is in inverse proportional to the squared value of both specific surface area of inner pores and tortuosity factor of pores. When comparing the correlation of these two factors, it can be concluded that influence of the tortuosity factor of pores on permeability is bigger than that of the specific surface area of inner pores. It is safe to conclude that the highest influencing factor on permeability of MgO-C brick is the tortuosity factor of pores.

**CONCLUSIONS**

The follwing are conclusions attained in this study

- The specific surface area of the inner pores
  increases with a strong correlation to the lowering the $q_{AP}$ value.

- The tortuosity factor of pores increases with
  moderate correlation to the lowering the $q_{AP}$ value.

- The permeability of MgO-C brick is influenced by
  the apparent porosity,specific surface area of
  inner pores and tortuosity factor of pores.
  The highest influencing factor on permeability is
  the tortuosity factor of pores.

**REFERENCES**

1) R. J. Leonard, R. H. Herron :
   J. Am. Ceram. Soc., 55 [1], 1-6 (1972)
2) Kozeny. J. :
   S. B. Akad. Wiss. Wien, Abt. IIa, 136, 271-306 (1927)
3) P. C. Carman : Trans. Inst. Chem. Eng., 15, 150-166 (1937)
4) G. Shimada, T. Furukawa, E. Ishihara, A. Iida :
   "Reduction of gas permeability of MgO-C brick by optimizing
   particle size distribution", UNITECR Proceedings (2022)
5) A. H. M. Andreasen, J. Andersen :
   Kolloid Zeit., 50, 217-228 (1930)

# DEVELOPMENT OF INTEGRATED METHODS FOR HOT REPAIR OF CONVERTER LINING BASED ON MAGNESIAN MATERIALS OF "GIR–REFRACTORIES"

G.G. Nemsadze, PJSC «CUVCIF "General Investment Resources «GIR» (Kyiv, Ukraine);
K.N. Sharandin, GIR-ENGINEERING LLC (Dnipro, Ukraine);
A.N.Smirnov, Physical-Technological Institute of Metals and Alloys, National Academy of Sciences of Ukraine (Kyiv, Ukraine);
R.A. Dzhodzua, PJSC «CUVCIF "General Investment Resources «GIR» (Kyiv, Ukraine);
D.V. Ryaby, GIR-ENGINEERING LLC (Dnipro, Ukraine);
M.S. Goryuk, Physical-Technological Institute of Metals and Alloys, National Academy of Sciences of Ukraine (Kyiv, Ukraine);

**ABSTRACT**

One of the most important strategies for the development of converter steel production technology is achieving high resistance of the working lining, which corresponds to the minimum unit cost of refractories and eliminates the downtime associated with repairs [1,2].

The choice of the optimal lining treatment system during a campaign is formed, ultimately, for reasons of reducing unit costs and process requirements [3,4].

When assessing the prospects for the development of the refractory market for steel-smelting complex of Ukraine, we can assume the further development of the tendency to reduce the specific consumption of refractories per 1 ton of steel by increasing the operational durability of the converter's linings. This is evidenced by indicators of persistence in Europe, Japan, China and the United States, one and a half to two times or more surpassing the average indicators achieved in Ukraine.

Modern technologies allow performing "hot" repairs of the converter lining without its decommissioning during the working campaign. The main methods of refractory restoration: gunning (semi-dry, flare), patching (molded products, masses), remaining (modified) slag blowing with nitrogen [5-7].

Such methods, as a rule, are not long-lasting (5-35 minutes) and, with considerable efficiency, keep up the rhythm of the production process in the workshop.

By results of laboratory researches the hot repair self-flowing mass "GIR-RB-X" and flux-modifier "GIR-MBF" on the basis of secondary, domestic raw materials, were developed.

Obtained results were employed for the improvement of skull coating process and hot repairing method of the converter lining at several metals works of Ukraine.

Industrial tests of the self-flowing, hot repair magnesium mass, and flux-modifier on lining of heavy-load converters in the conditions of PJSC "DMK" and PJSC "MK "Azovstal" are carried out.

The LLC "GIR-Engineering» company organized serial production of self-flowing magnesium mass "GIR-RB-X" brand and magnesium flux-modifier "GIR-MBF" brand on production capacities in Ukraine (Dnipro region)

## Introduction

Nowadays, at least two dominating approaches to the production run of converters refractory lining, are existent. One of them ("North-American") is based on the principle of continuous maintenance of the refractory lining and assuring its maximum permissible lifetime, so-called "everlasting lining". The second ("European") approach of steelmaking process is principally focused on the maximum steel output through minimum heat cycle. In this respect, all maintenance activities on the refractory lining are minimized and rigidly scheduled. Converter lining lifetime with this approach, amounts to 5-7 thousand heats. Ukraine steelmaking companies have embraced "European" approach with particular modifications into the maintenance strategy, specifically, scheduling of specially treated slag splashing by nitrogen. The method of local hot repairs BOF lining using magnesium self-flowing masses is also widely used.

It is known that the converter refractory work is subject to uneven wear during the campaign. This is due to a number of factors, the main of which are the corrosive effect of slag and the erosive effect of the circulation flows of the gas-slag-metal emulsion. Due to the characteristics of the hydrodynamics of the converter process and the specificity of its cyclicity (filling-sampling-discharge), i.e. constant tilting of the unit with products of melting, zones of advanced wear of the lining are formed. These are mainly the zones of the lower bell, the trunnions zones, the drain zone and the tap zone. A diagram of the zone masonry of the converter and an example of the topography of the uneven wear of the lining is presented in Figure 1.
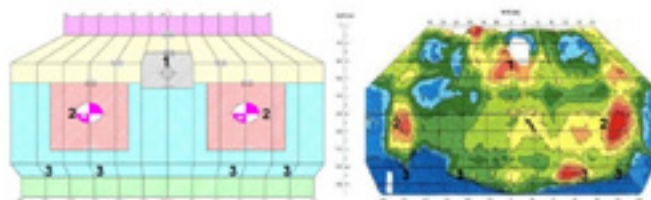


*Fig. 1: Zonal lining of a 350 - ton converter and an example of non-uniformity of wear: 1 - tap area; 2 - axle zones; 3 - zone of the lower cone. Color on topography - residual lining thickness: blue - max, red - min.*

One of the most efficient technologies for increasing the lifetime of BOF refractories all over the lining is "Slag Splashing". Slag coating on the lining surface exercised by means of nitrogen jets that splash specially treated slag with special magnesium flux-modifiers / additives during 2-8 min. This skull serves as a consumable refractory layer – "secondary lining", which protects BOF refractory brickwork against adverse process factors (wear). Chemical and mineralogical composition of the splashing slag, is thoroughly selected for particular manufacturing conditions of the given enterprise. The selection of the optimum slag composition, is normally based on the concentration of two compounds: iron oxide $FeO_x$ and magnesium oxide MgO, which is followed by the selection of the required low-melting and high-melting phases mix. Low-melting phases secure firm binding of the slag and the refractory, while high-melting phases promote the "backbone" formation assuring its strength and refractory properties.

There are two main methods of hot repairing the most "difficult" areas of advanced wear of the trunnions and tap-hole zones lining. This is a method of gunning (semi-dry, flare) and patching by self-spreading mass. At the same time, gunning is carried out using special equipment, which requires preparation and adjustment before the operation, which entails considerable time costs that disrupt the production schedule. So, the time spent on gunning, comes to 30-50 minutes. Often, saving time (reducing exposure time, reducing mass consumption) for such an operation adversely affects the quality of repair and reduces the durability of the restored section.

The most promising alternative to the gunning of local wear, which does not require special equipment and personnel training, is a patching by self-spreading, magnesium masses.

The raw-material base of Ukraine metals sector, is notable for the absence of high-quality magnesium raw materials. The solution to this problem is the development of manufacture using secondary magnesium raw-material for slag-forming mixes and repair masses.

345

**Procedures for evaluation of slag physical properties meant for skull coating**

Skull layer formation is governed by certain thermophysical conditions, among those are thermal field distribution of the primary and "secondary" lining (heat removal), volume ratio of solid phases, thermal effect of solidification, temperature range of melting, adhesion, etc. Slag viscosity, its amount, lance design, its height above the bath level, liquid bath depth, blowing modes, etc., exert profound influence on the skull layer formation [8].

The offered procedure on qualitative evaluation of physical and chemical properties of the skull layer, comprises 4 steps.

At the first step, emphasis was laid on the preparation of refractory "pads" samples that model the facility lining. To attain adequate resemblance to the refractory material surface, the samples were annealed in the furnace to enable surface carbon release and simulate the first wear stage. The annealing process was exercised by thermal-cycling method (1000↔1600 °C) for 1 hour (2-3 thermocycles) in the oxidizing medium. Further, the "pad", under converter process temperatures, was soaked with slag, to simulate the second wear stage of the refractory. Finally, the required (similar) refractory surface was obtained, akin to the actual surface susceptible to wear in the course of converter campaigns. Figure 4.1. shows outer appearance of the refractory pad treated sample of 30x30x30 mm.



*Fig. 2: Treated refractory pad modelling converter lining (30x30x30 mm), A – depth of slag penetration into the refractory.*

Activities at the second step included immediate modification of the BOF slag by a number of magnesian materials of different chemical and mineralogical composition. Figure 3. represents the second step in the graphic form.
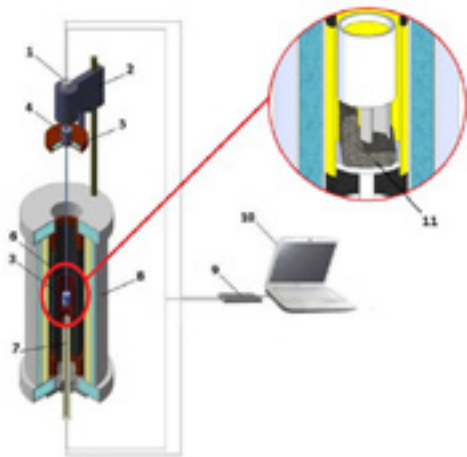


*Fig. 3: Overview of the equipment employed in the second modelling step. 1 – electrical motor; 2 – rack; 3 – molybdenic shaft with spindle; 4 – bearing assembly; 5 – copper water-cooler; 6 – molybdenic crucible with molten slag; 7 – thermocouple; 8 – Tamman furnace; 9 – logging unit with analog-digital converter; 10 – computer, 11 – refractory sample – pad.*

Basic slags exhibit low viscosity at steelmaking temperatures (1550–1650°C). Basic slags viscosity raises together with the increase of CaO content and MgO content in particular. A substantial rise in the slag apparent viscosity is observed at the presence of 1-5 mm non-dissolved particles (e.g.,periclase "grains") bringing about a marked increase of internal friction. Figure 4. demonstrates empirical relation between the viscosity of final converter slag and the volume of dispersed solids ("grains").
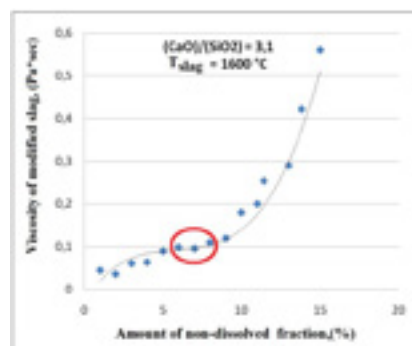


*Fig. 4: Relation between treated slag viscosity and non-dissolved "grains" volume (WT %).*

It is evident from the diagram that the increase in the volume of dispersed solid (non-dissolved) phase in the slag, results in the viscosity growth. At reaching some 6-8% by the "grain" phase, the slag displays "satisfactory" viscosity for splashing process. Whereas at gaining 10% and over by the "grain" phase, a dramatic rise in the slag viscosity occurs, stemming from the melt heterogenization. These data correlate well with the physical (cold) modelling of splashing process as considered above.

Based on the studies performed at this step, we have formulated a conceptual approach to physical and chemical properties of modifying fluxes meant for treating slag to be further splashed. Thus, the presence of low-soluble components in magnesium-containing materials at the amount of 0.65-0.35 (WT %), min. 80% of those having 2-6 mm fraction, promotes their uniform distribution over the entire volume of the molten slag as early as within first seconds of nitrogen purging. It is attained thanks to the presence of readily-soluble, fine components in the material that contribute to the dispersion of additions. The said additions upon coming into contact with the slag, are assimilated (dissolved) in a speedy manner, thus increasing MgO content in the slag. This ratio of low-soluble and readily-soluble components leads to the formation of a considerable amount of high-melting ferritic phases in the treated slag, and formation of a firm "backbone" in the cooled skull layer due to non-dissolved fractions – "grains".

To verify and corroborate the above-mentioned approach to slag modification for further splashing, the third step dealt with the evaluation of adhesion of the treated skull to periclase-carbon refractories. The adhesion was assessed in terms of limiting wetting angle of the "pad" by a slag droplet, as we as thermal resistance (low fusibility) of the cooled layer.

The diagram representation of the third simulation step is given in Figure 5.
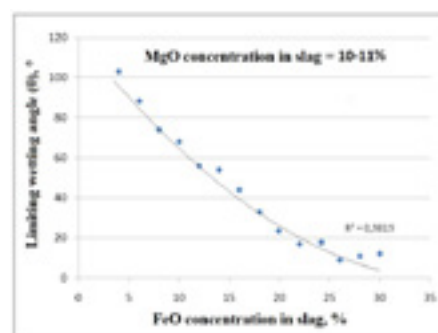


*Fig.5: Relationship of the limiting wetting angle and FeO content in the slag.*

On a treated refractory corner heated to temperature of a converter lining prior to purging (1500°C), Figure 6 (a), a droplet of modified slag was placed. By means of dimensional scaling of photo- and video-recordings of the wetting process, limiting wetting angles of slag droplets of various chemical composition, were determined.

It has been established that the main parameters guiding the wetting, are FeO and MgO content in the slag.
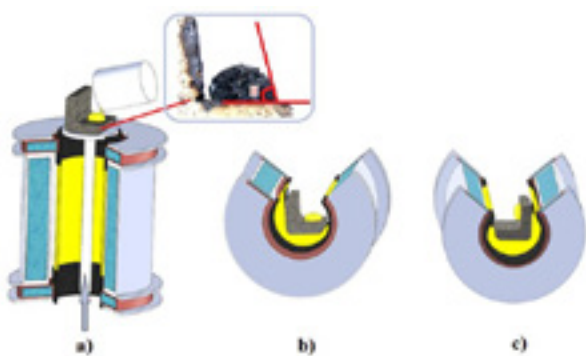
*Fig. 6: Schematic representation of skull layer adhesion to the refractory "pad".*

As such, at FeO content of over 25% and MgO content of 6-7%, the wetting angle is under 10°, i.e., very small (nearly no wetting). With FeO content decrease, wetting angle grows and at some 5% FeO content, it is averaging 90°. It is noteworthy that the rise in MgO content in the slag, results in the wetting decline of periclase-carbon material, herewith, the degree of wetting angle elevation, depends heavily on the slag oxidation. At FeO content of 25%, MgO content gain from 6 to 16% brings about wetting angle increase from 10 to 25°, at FeO content of 15%, similar MgO content gain would cause wetting angle change to 90°.

Together with support of limiting wetting angle (θ) that reflects efficient "bonding" of the skull with the lining surface, we have managed to achieve high refractoriness of the protective layer. To estimate the temperature range of treated skull layer melting, the "pad" sample with a slag droplet thereon, was put into a horizontal heating furnace. In addition, the "corner" was placed in the horizontal position (Fig. 6 (b)). Once the design temperatures (1550 – 1650°C), were reached, the sample was turned at 90° angle, thus simulating vertical wall of the converter lining (Fig. 6 (c)). By means of continuous photo- and video-recordings, concurrently with temperature assessment, the evaluation of the skull lifetime within the temperature range of converter heat, was performed.

Figure 7 illustrates a skull layer sample with high adhesion characteristics to the refractory and high thermal resistance.
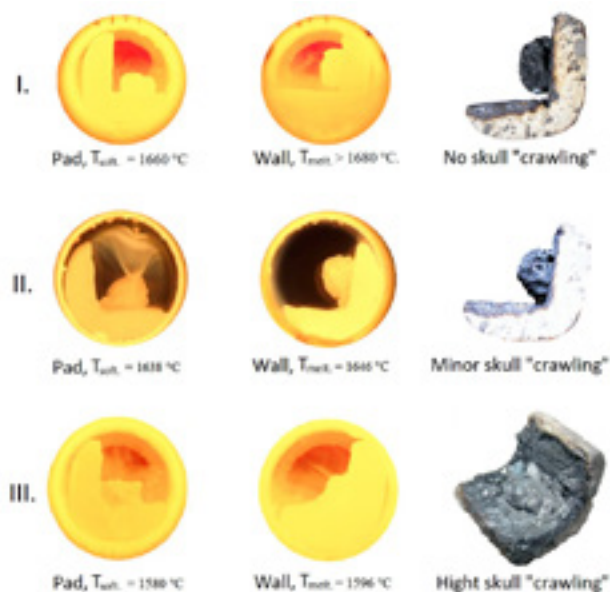


*Fig. 7: Skull layer behaviour in the melting temperature range. I. – high adhesion and low fusibility (>1680°C; II. – high adhesion, low refractory properties (1646°C), minor skull "crawling" is reported; III. – low adhesion, unsatisfactory refractory properties (1596°C), skull "crawling".*

As indicated in the figure 7 (I.) *(flux-modifier "GIR-MBF" brand)*, at attaining high temperatures at the final stage of the converter heat (1680°C and over), the skull layer sample has not reached the melting point and has not lost the adhesion to the "corner", i.e., the "crawling" of the protective layer is not reported. On the second case (figure 7 (II.)) near 1638 °C, observed the surface melting of skull sample, and rise of temperature to 1646 °C led to minor skull "crawling" down to vertical wall. Unsatisfactory quality of skull sample shown on fig. 7. (III.). The sample of modifier slag in the range of 1580 – 1596 °C is fully crossed in liquid phase and trickle down.

This result can reasonably prove the quality of the skull layer and demonstrate the correctness of the agent chemistry selection to be used for slag modification before splashing.

As mentioned earlier, the optimum slag chemistry is attained upon reducing FeO content and supersaturating slag with MgO. Slag oversaturation with MgO has a fundamental importance for slag treatment before splashing, since it binds Fe oxides into high-melting magnesia-ferrites displacing low-melting calcium ferrites.

Slag solidification (loss of mobility) and skull formation are reported when the volume ratio of solid phases solidifying therein, crosses the boundary required for their percolation, thus forming robust framing within the molten slag. Consequently, the "penetration" of solid components from the modifying agent into the slag ("under-dissolved grains"), enhances this process.

Experiments have shown that the optimum slag composition is reachable upon reducing FeO content down to 13-15%, slag oversaturation with MgO to 10-12% and introducing of low-soluble fractions (2-6 mm) of 6-8% weight ratio into the modifying agent. This correlation secures adequate volume of high-melting phases, while the presence of non-dissolved fractions (low soluble components) in the slag, results in the formation of the "binding backbone" within the skull layer. It is attributable to the origination of the protective skull layer featured with wear-resistance, mechanical strength, and high adhesion to the refractory lining surface.

Based on the obtained results, flux-modifier "GIR-MBF" brend for final converter slag was developed and tested in the industrial environment, the flux-modifier being of magnesia-based, produced from available domestic materials comprising both low-soluble and readily-soluble components. With regard to the above mentioned, 2-6 mm fractions made up min. 80% of the total volume of low-soluble components.

As a result, industrial testing modifier additives to optimize the cost and implementation of the developed "mini-regulations" in PJSC "MK AZOVSTAL" overall, the total consumption of magnesium materials for melting (at the end of the campaign 2000- 2936 heats.) was reduced by 20 % (compared to the beginning), and decrease unit costs of steel production at 0,85 \$/t

**Procedures for evaluation of self-flowing magnesium mass for local hot repair BOF lining**

In order to test and optimize the physico-chemical properties of the welding mass, a technique has been developed. A unit for the experiments was a rotary-type heating furnace. The layout and appearance of the experimental installations is presented in Fig. 8.
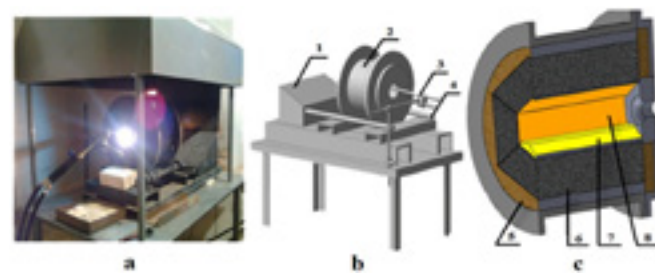


*Fig. 8: General view (a) and installation diagram (b, c) of an experimental test bench of a rotary type furnace: 1 - engine;*

347

*2 - furnace body; 3 - gas-oxygen burner, 4 - drive shaft; 5 - heat insulation; 6 - periclase-carbon lining (converter refractories); 7 - welding mass of the "GIR-RB-X" brand; 8 - working surface of the refractory (impregnation with melting products);*

The experimental research methodology was divided into three stages.:
- *first stage;* preparation of refractory samples for patching. Melting in the cavity of the furnace slag metal emulsion. The temperature of the liquid bath is 1630°C. Forced wear of the internal space was carried out by rotating the furnace around its axis with a frequency of 10-12 revolutions/min. The uneven wear of the internal space was achieved by tilting the furnace relative to the horizontal axis. Prolonged contact (3.5 hours) of the working surface with a slag-metal emulsion imitated erosion and corrosion wear of a periclase-carbon brick with infiltration of liquid smelting products into the refractory, which corresponded sufficiently to the mechanisms of wear in actual conditions of converter smelting. After rendering adequate properties of the working surface of the refractories, they moved to the second stage - patching the worn area with the "GIR-RB-X" developed mass.
- *second stage;* filling with the repair weight of the zone ahead of wear. Before filling the mass into the cavity of the furnace, the melting products tapped. The temperature of the working space after the melting tapping is 1450°C. The mass was fed in heat into the inner space on the worn area of the lining. Mass consumption per operation is 0.5 kg.
The test of the "mobility" of the mass was evaluated when the furnace was rotated around the horizontal axis by reversing it in two directions by 45°. The filling of the worn area occurred evenly, without premature sintering of the mass. Then the furnace was returned to its original position and held for 15 min, until the sample was fully heated and sintering (Figure 9 a)).



*Fig. 9: a) - uniform filling of the worn area, b) - patching after reheating and erosion-corrosive wear.*

The degree of mass adhesion after sintering to the surface was evaluated by rotating the furnace around a horizontal axis. The mass was sintered in a dense monolith with a lining, did not crumble and did not flake off.
- *third stage;* reheating of the furnace to a working temperature of 1630°C; testing of erosion and corrosion resistance of the welding mass.
After evaluating the adhesive properties and sintering rate, the workspace was reheated to the converter melting temperature. At the same time, new portions of metal and slag were loaded into the working space before the formation of a liquid bath (1/3 of the internal volume of the furnace) 4-5 kg. Continuous rotation of the furnace with slag-metal emulsion lasted for 1 hour, to simulate the erosive and corrosive wear of the patching conglomerate. Then the products of melting were tapped again from the furnace. The appearance and residual amount of the patching mass after reheating and wear of the slag metal emulsion is shown in Fig. 9 b). After a qualitative assessment of the behavior of the patching mass, the degree of its adhesion to the periclase-carbon brick, the sintering time and corrosion and erosion resistance, the furnace was cooled to room temperature. The inner lining was dismantled and the sintered mass was separated from the surface of the refractory. After mechanical preparation of the sample conglomerate, the compressive strength was measured on a laboratory press. As a

result, this parameter amounted to 38.5 MPa, which fully satisfies production requirements and corresponds to the indicator of foreign analogues. Figure 5 shows a sample of a sintered "GIR-RB-X" mass conglomerate after destruction by a press.



*Fig 9: A sample of a "GIR-RB-X" mass conglomerate*

Figure 5 shows the dense structure of the sample of the welding mass, which is also confirmed by the number of large fragments after destruction by the press. Strength at compression (after sintering 1600 ° C) not less then 35 MPa.
Based on the tests, the following results were obtained on PJSC "Kamet-Steel". Specific consumption of the repair mass was 0.089 kg/ton, with the standard - 0.092 kg/ton

## CONCLUSIONS
A unique technique for assessing the physico-chemical properties of a slag coating modified with various additives has been developed.
Based on the obtained results, flux-modifier "GIR-MBF" brend for final converter slag was developed and tested in the industrial environment, the flux-modifier being of magnesia-based, produced from available domestic materials comprising both low-soluble and readily-soluble components. With regard to the above mentioned, 2-6 mm fractions made up min. 80% of the total volume of low-soluble components.
Based on the developed methodology using available domestic raw material, a self-flowing magnesium hot repair mass "GIR-RB-X" brand has been developed.
The main quality indicators of the material are as follows: - grain size distribution; grading fraction of 0-8 mm, selected so as to ensure the most dense packing of grains after sintering. - chemical composition; MgO content 80-85 % by mass (on ignition basis) to ensure maximum erosion resistance after sintering.

## REFERENCES
[1]   Smirnov A., V European conference on the steel production using oxygen, Steel 2006, №10, pp. 25-28.
[2]   Serdyukov A., Tonkushin A., Smirnov A., Modern lining for the heavy-load oxygen converters, Metal and casting of Ukraine, 2010, №9-10, pp.4-7.
[3]   Lamm R., Vintiens P. Use of technology 3-d laser scanning in the capacity of process tool in the converter plant, Proceeding of 8 congress of the steelmakers, 2002, pp. 97-102.
[4]   Nemsadze G.G, Sharandin K.N. BOF Lining Lifetime Improvement. Monograph. – Donetsk: GIR-INTERNATIONAL – Nord Press. 2014. – 135 p.
[5]   Smirnov O. Evolution conditions of final BOF slag on the efficiency of slag splashing technology / O. Smirnov, A. Tonkushin, K. Sharandin // 5th International Congress on the Science and Technology of Steelmaking. Dresden, Germany, 1-3 october. 2012. – pp. 1216-1225.
[6]   Nemsadze G. Evolution conditions of end BOF slag on the effectively slag splash-ing technology / Nemsadze G., Smirnov A., Sharandin K. // Proceedings of International Colloquium on Refractories. Eurogress, Aachen, Germany. September 26-27, 2018. – CD-print.
[7]   Nemsadze G. Converter layer hot repair process using the «GIR-RB-X» magnesium mass developed by the «GIR-ENGINEERING» LLC / Nemsadze G., Smirnov A., Dzodzhua R, Sharandin K. // Proceedings of International Colloquium on Refractories. Eurogress, Aachen, Germany. September 25-26, 2019. – CD-print.
[8]   Luomala M., Fabritius T. M. J., Virtanen E. O., etc. Physical model study of selective slag splashing in the BOF // ISIJ Int., 2002, vol. 42, 1219-1224.

# SHORT COMMUNICATIONS

# DEVELOPMENT OF LOW CO₂ EMISSION REPAIR MATERIAL AT BASIC OXYGEN FURNACE (BOF) APPLICATION

Patrícia Alves Silva de Resende Brum, Vladnilson Peter de Souza Ramos, Douglas Fernando Galesi, Ariovaldo do Nascimento, Haysler Apolinário Amoroso Lima, Hamilton Cesar Guimaraes of Shinagawa Refractories, Vinhedo, Brazil

## ABSTRACT

Steel market across the globe is increasingly facing a decarbonization challenge due to the pressure to reduce its carbon footprint and have more sustainable processes and products. Step forward, steel producers have the mission to estimate, evaluate and establish economically and technologically feasible plan to decrease carbon dioxide emissions. Shinagawa Refractories' strategy is aligned to prioritize projects which are focused on these sustainable guidelines. In a Basic Oxygen Furnace (BOF), the corrosion caused by high FeO content slag and high oxidation are the most critical conditions for maintenance of refractory lining integrity. Because of all technologies and innovations taken by Shinagawa, the durability of refractory products applied at BOF lining is improved and it is possible to reduce the quantity of repair material throughout the campaign which leads carbon dioxide emissions reduction. The present work will show the significant in one of our customers results of low CO₂ emission basic repair material applied in BOF with gain in performance related to flowability, adhesion to work lining and curing time.

## INTRODUCTION

The expansion of more technological processes increases the pressure on steel producers claiming for higher quality products consistent with the rise of restricted sustainability measures. Refractories products has a relevant position on steelmaking industry due to its effect on manufacturing costs and product quality as they are applied on harsh operating environments to endure high temperatures and wear conditions [1].

Steel production needs high amount of energy, and it is responsible for 11% of overall global carbon emissions [2]. In the 21st century, climate change is the most important concern for steel producers and as it was agreed at the aims of Paris Agreement [3] the steel industry is committed to reduce greenhouse gas emissions in a short time to achieve a climate neutral world by 2050 from its operations and the use of its products.

Blow Oxygen Furnace (BOF) is a crucial step at steelmaking process, as it is defined as an asset whose availability directly impacts steel mills productivity. A BOF with low production level led to a series of undesirable consequences, such as higher number of cycles of available BOFs, an increase on demand for steel heating up processes consuming energy and a lower final product yield. Currently, one of the factors with the greatest impact on BOF availability is the maintenance of refractory lining. Regularly steel mills have 2 or 3 BOF equipment and, if 1 of them stops its operation to change refractory lining, it means a reduction of 33 to 50% in the steel production. Normally, this replacement time is in between 60 and 100 hours, having a significant impact on production. In addition, hot repair techniques for refractory lining consume equipment downtime, between 40 and 100 minutes, and therefore it also impacts on asset availability [4].

The wear of the working lining of BOF converters is associated with the characteristics of the material of the refractory lining, the slag and steel of the BOF, in addition to the interaction between them, also temperature and oxidizing atmosphere inside BOF.

The most common refractory lining repair technique performed to reduce the wear rate is hot repair which can be divided into slag splashing, slag coating, pouring and projection. In these processes there is a formation of a protective layer (coat) that will be effective against all wear mechanisms (abrasion, corrosion, erosion and thermoclase). A correct operation will provide this result, avoiding the removal of this layer and, in fact, contributing to the formation of a protective layer. Hot repair technique should be selected based on the wear mechanisms present in each region. Considering operational parameters, the lowest cost and shortest time countermeasures are preferred, as they lead to greater availability of the asset for production, since productivity is the factor with the greatest impact from a refractory point of view on operating costs in a plant BOF [4].

Even Magnesia-Carbon (MgO-C) bricks are widely used in BOF due to their desirable resistance to chemical corrosion and mechanical stresses, hot repair is required to improve the total lifetime of the converter lining. Traditionally, the application for hot repair BOF and ladle slag line have been filled with basic dry gunning mixes since the 1970s, when mostly phosphate-bonded materials were utilized. A continuously growth on lower-carbon steel demand has caused severe operating conditions to converters as previously mentioned on this paper. Therefore, MgO bricks and repairing mixes needed to be redesigned [5,6].

When the hot repair mix is applied into the BOF at high temperature it is needed some time to burn up the volatile matters with an origin on carbon content coming from raw materials used on the mix composition. A defined quantity of fumes emission can be originated from this volatile burning which reduction is the main propose of this paper. Hot repairing mix presented on this paper was developed to maintain the required properties of its compatibility with MgO-C bricks and allowing self-flowing application. But most important focus is on lowering suspended particles and gases emissions.

## MATERIALS AND METHODS

### Formulation

The composition of basic self-flow mix was based on its compatibility with basic bricks to allow the hot repairing and it was formulated using high grade calcined magnesia of different grain sizes to contribute not only for densification but also to endorse good fluidity needed to product installation. To guarantee the increase of mechanical resistance at high temperatures, some additives were incorporated in the formulation.

Table 1 presents chemical composition results of the basic self-flow mix in which % of MgO and other compounds were performed following the ABNT NBR 12860 standard. Carbon content was measured at Combustion Analyser LECO CS230CH.

Tab. 1: Chemical composition of basic self-flow mix for hot repair

| Composition | % |
|---|---|
| MgO | 88.5 |
| C | 7.0 |
| Others | 4.5 |

### Physical Properties

Prismatic samples (160 mm x 40 mm x 40 mm) were obtained by performing the mixing step according to an internal mixing procedure. After moulding, the samples were baked at 200°C and 1,400 °C at reducing atmosphere, cooled down and tested. Apparent Density and Apparent Porosity were conducted according to the ABNT NBR 16661 standard. Cold compressive strength and module of rupture tests were conducted at Universal Testing Machine KRATOS (model: KE-30.000/E MP) according to ABNT NBR 10059 and 5014, respectively.

### Hot Modulus of Rupture (HMOR)

The Hot Modulus of Rupture (HMOR) measurements were conducted following ASTM C583 standard under three-point bending tests at 1,400°C. The samples were moulded in a prismatic format (150 mm x 25 mm x 25 mm), heated at 1,400 °C and in reducing atmosphere during the test.

349

**Rheology of mix**

Fluidity is an important property for self-flow mix as great quantity of mix needs to flow correctly and be deposited to cover the worn area of BOF refractory lining for repairing. During BOF operations for steel refining, after converter tapping, the temperature inside it is between 1,200 °C and 1,400 °C and when the curing of hot repair mix is concluded the temperature lowered to 1,000°C. Because of that conditions, thermal fluidity of the repair mix was fixed at 1,000°C [6].

**Field Tests**

After lab trials, two pilot trials were conducted in a BOF (denoted here as BOF#A) with a capacity of 220 ton of a Brazilian steel producer, aiming to validate developed mix performance at field conditions. Total quantity was 1,500 kg divided in two big bags of 750 kg each. Hot repair mix was installed with the help of a crane's arm to put the mix big bag inside the converter.

**RESULTS AND DISCUSSION**

Table 2 presented the results of physical properties measured after baking at 200 °C and after heating at 1,400 °C conducted at basic self-flow mix for hot repair.

Tab. 2: Physical and rheological properties of basic self-flow mix after baking at 200 °C and after heating at 1,400 °C.

| Properties | Basic Self-Flow Mix |
|---|---|
| | After baking at 200 °C |
| Apparent Density (g/cm³) | 2.43 |
| Apparent Porosity (%) | 19.3 |
| Cold Crushing Strength (MPa) | 15.1 |
| Module of Rupture (MPa) | 4.4 |
| | After heating at 1,400 °C |
| Apparent Density (g/cm³) | 2.39 |
| Apparent Porosity (%) | 26.6 |
| Cold Crushing Strength (MPa) | 11.1 |
| Module of Rupture (MPa) | 2.0 |
| HMOR (MPa) | 9.42 |
| Self-flow (mm) | 173 |
| Self-flow after 15 beats (mm) | 190 |

Table 1 shows that basic self-flow mix presented good properties of density and porosity with expected results after curing and heat treatment which are in accordance with other basic hot repair mixes developments [6,7]. The basic mix also shows great mechanical properties on both temperatures and the most important a high hot module of rupture which can indicate a good field performance of enduring mechanical impact of liquid metal on BOF converters.

Figure 1 presents the aspect of the mix after self-flow test and demonstrate the good thermal fluidity after a test at 1,000°C which indicates a good workability of this hot repair mix with a good potential to be applied at converters refractory lining.
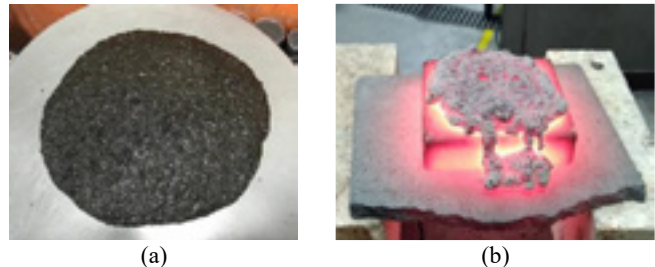


Fig. 1: (a) Self-flow test; (b) Thermal flow at 1,000 °C.

At first field test, 1 big bag of 750kg of mix were put at tapping area of converter and, after 90 minutes curing time, it was sintered maintaining attached at correct region for 16 heats, as shown in Figure 2. For the second trial, 1 big bag of 750 kg of the mix was put at the same region, but after 120 minutes curing, it was attached for 42 heats (Figure 3). In both scenarios, fluidity and adherence at refractory wall were validated.
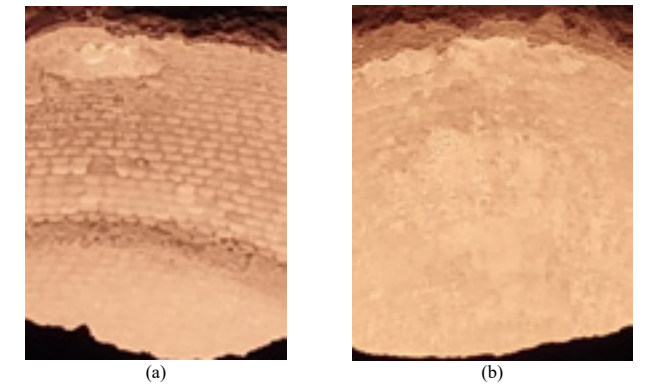


Fig. 2: First field trial (a) BOF#A tap region before hot repair; (b) Basic self-flow mix adhered after 16 heats.
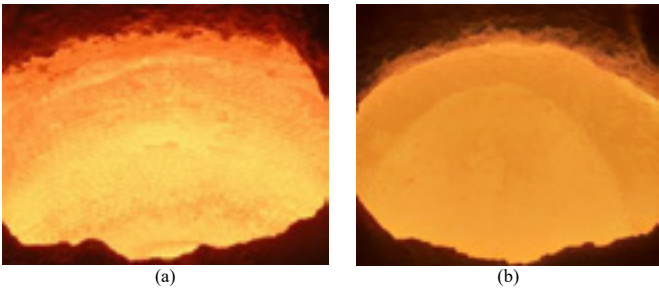


Fig. 3: Second field trial (a) BOF#A tap region before hot repair; (b) Basic self-flow mix adhered after 42 heats.

**CONCLUSIONS**

High mechanical resistance at high temperatures (HMOR) and thermal fluidity properties of basic self-flow mix presented in this paper were measured in lab scale but also validated by an excellent performance field trial. Not only the good workability and sintering of hot repair mix were noticed but also a reduction on articulate emissions by steelmaking company's workers as positive feedback, achieving one of main purpose of mix this product development. Shinagawa Refractories has a continuously efforts to reduce not only the particulate material, as well as to decrease carbon footprint and $CO_2$ emissions of hot repair mix.

**REFERENCES**

[1] TAKEUCHI, T., TAKI, N. "Progress and Future Prospects of Refractory technology of Nippon Steel Corporation". Nippon Steel Technical Report. No. 125. Dec. 2020.

[2] M'barek BB, Hasanbeigi A, Gray M. "Global Steel Production Costs: A country and plant-level cost analysis." Transition Zero. 2022. p. 1-35.

[3] United Nations – Climate Change. "The Paris Agreement". 2015. Available from: https://unfccc.int/process-and-meetings/the-paris-agreement/the-paris-agreement.

[4] Auad, M.V. Desenvolvimento de modelo para cálculo de adições no processo de slag splashing e slag coating de um Basic Oxygen Furnace (BOF). UFMG, Belo Horizonte, 2018.

[5] K. Asano, "Recent Trends in Refractory Technologies for BOFs in Japan," Interceram, 6–12 (2004).

[6] PAGLIOSA, C., PANDOLFELLI, V.C. "R2U-Ready-To-Use Castables". American Ceramic Society Bulletin, Vol. 87, No. 1. 2008.

[7] BUYUNGSU, K., et al. "The development of hot repair mix for BOF". UNITECR'09 Proceedings. 2009.

# STEEL LADLE LINING MANAGEMENT: COMPARISON BETWEEN DIFFERENT MAINTENANCE TECHNOLOGIES TO INCREASE PERFORMANCE, REDUCE REFRACTORY CONSUMPTION AND WASTE DISPOSAL OF USED MATERIALS

Luca Folco, Alan Kranjc, Seven Refractories d.o.o. Divača, Slovenia

## ABSTRACT

Nowadays steel ladle is the main vessel for secondary metallurgy, and this means that long service life and stable performance play a key role on final quality and quantity of produced steel.

During the years have been proved that zoning the different areas of the steel ladle, with specific refractory materials, it is the most effective and safe approach, optimize the service life and currently steelmakers rely basically on two concepts of refractory lining.

Most of them trust on bricks (MgO-C, AMC, Doloma, etc), that give good high temperature resistance, strong slag protection, easy heating up and reliable service life.

Others have switched to monolithic solutions based on alumina-spinel, with high thermal stability, good hot strength, excellent resistance to thermal spalling, low carbon pick and lower thermal conductivity important for production of ULC steels and energy savings respectively.

Both concepts have problem of uneven wear of refractories at different zones.

Higher corrosion of slag zone, high wear in impact zone, blocked purging plugs and need for their replacement. Therefore, at these stoppages, decision needs to be made to replace complete lining in low wear zones and consequently loosing high amount of perfectly good material or to continue with existing lining and risk potential breakthrough.

Repair with sprayable materials emerges as a good solution to increasing number of heats before complete relining is needed and assures low risk of breakthrough. This can be done with shotcrete, which gives very good performance, but requires expensive equipment or gunning where performance of installed material is much lower or new emerging technology called ShotGun that shows much higher performance than gunning at lower installation cost compared to shotcrete. It promises to be a good option specially for smaller steel shops, where slightly higher performance of shotcrete just cannot outweigh its limitations.

## INTRODUCTION

Steel ladles play a critical role in steel production, serving as vessels for transporting liquid steel through various stages of secondary metallurgy. The refractory lining of these ladles is subjected to chemical, thermal, and mechanical wear during the refining processes. Making it essential to carefully select type of refractories, installation technique, and maintenance of the lining. There is no one-size-fits-all solution due to the wide-ranging requirements set by steel shop managers, including durability, balanced performance, low consumption, resistance to slag attack, safety, ease of installation, quick heating-up, capacity optimization, insulation properties, flexibility, and cost-effectiveness. Finding the best compromise with those complex requirements is a continuous challenge.

While MgO-C bricks have long been favoured for ladle lining due to their high-temperature resistance and reliable service life, the steel industry is increasingly recognizing the potential of alumina-spinel monolithic refractories. Research conducted over two decades ago revealed that these monolithic products not only compete with traditional lining materials but also offer additional benefits, such as increased ladle capacity and reduced thermal losses. [1]

Recent reports and articles have further supported these findings, highlighting the advantages of alumina-spinel monolithic refractories. Lower operating costs and improved consistency in carbon content, particularly for ultralow carbon steels, make these refractories appealing to steelmakers seeking enhanced efficiency and higher-quality steel production. Furthermore, transitioning from MgO-C bricks to alumina-spinel monolithic refractories can contribute to a reduction in $CO_2$ emissions, both during refractory production and operation, making it an environmentally sustainable choice. Another advantage of monolithic refractories is their ability to minimize waste generation by allowing targeted repairs instead of complete demolition and relining, optimizing resource utilization in the steelmaking process. [2] [3] [4] [5]

**Summary of article from 2020**

A previous article presented at ICR 2020 showcased Seven Refractories' innovative cyclic shotcreting repair technique for steel ladle management. This summary provides a connection between the new advances and the previous work. [6]

The cyclic shotcreting repair approach involves applying protective layers of monolithic castable onto an existing brick lining in a repetitive manner. By combining the advantages of monolithic and brick linings, this method offers a flexible and reliable solution for ladle lining repair.

The shotcreting technique, known for its flexibility and ability to create refractory linings with similar technical features as traditional casting methods, is utilized in this application. A castable mix is sprayed at high pressure onto the surface, where it rapidly sets, allowing for targeted repairs without complete demolition and relining.

A comparison between the typical brick lining cycle and the cycle with shot repair reveals the advantages of the shotcreting application. (Tab.1.) Without steel zone repair, the slag line can be replaced only once before complete relining becomes necessary. However, with shot repair in the steel zone, the slag line can be changed multiple times before complete relining is required.

The shotcreting application extends the campaign life of ladles, reduces specific consumption and costs, all while maintaining the use of traditional brick linings. The shotcreting layer takes on wear, while the original bricks remain intact.

This technology offers significant benefits, including prolonged ladle campaign life, easy visual wear control, and reduced waste of refractory lining. It leads to substantial reductions in specific consumption and operational costs without compromising the availability, reliability, and safety of ladle management.

In conclusion, the cyclic shotcreting repair technique provides a cost-effective and efficient solution for extending the lifespan of steel ladle working linings while capitalizing on the advantages of both monolithic and brick linings.

## MORE EXAMPLES OF IMPLEMENTATION OF SHOTCRETE REPAIRS

Since 2020, shotcreting repair has become a standard solution applied in numerous steelworks. The increased number of ladles repaired has led to the optimization of cleaning techniques, installations, and heating curves, resulting in more reliable ladle management. This article presents the results obtained from two steelworks.

On average, the slag line bricks are replaced after approximately 40 heats. Ladle then survive another 40 heats. The ladle then continues to operate for another 40 heats. However, at around 82 heats, the bricks in the steel zone become too worn to complete another slag zone cycle, resulting in the complete demolition of the ladle. In the new campaign life cycle, the introduction of two repairs in the steel zone and two replacements of slag zone bricks extends the ladle's campaign life by 50%. (Tab.2)

| Phase | Standard Procedure | Shotcreting Application |
|-------|--------------------|------------------------|
|  | Description | Description |
| 1 | New brick lining (complete) | New brick lining (complete) |
| 2 | First part of the campaign<br>Number of heats = N1 | First part of the campaign<br>Number of heats = N1 |
| 3 | Ladle out of service<br>Change of the slag line bricks<br><br>- **HEATING-UP** | Ladle out of service<br>Change of the slag line bricks<br><br>- **CLEANING of the application surface**<br>- **SHOTCRETING on steel zone brick lining**<br>- **HEATING-UP** |
| 4 | Second part of the campaign<br>Number of heats = N2 | Second part of the campaign<br>Number of heats = N2 |
| 5 | Ladle out of service<br>Total brick lining demolition<br>New brick lining (complete) | Ladle out of service<br><br>**AVOID TOTAL DEMOLITION of bricks lining**<br>**AVOID NEW BRICKS LINING**<br><br>Change the slag line<br><br>- **CLEANING of the application surface**<br>- **SHOTCRETING on steel zone brick lining**<br>- **HEATING-UP** |

Tab. 1: Comparison between the standard steel ladle life cycle and the one with included shotcrete repair.

**Steelworks 1**

| Capacity of steel ladle | 350 t |
|-------------------------|-------|
| Nr. of ladle campaigns (2020-23) | 350 |
| Tonnage of bricks for steel zone | 26,5 t |
| Tonnage of bricks for slag zone | 14,3 t |
| Avg. quantity of Shot material per repair | 4 t |
| Nr. of heats without repair | 82 |
| Nr. of heats with 2 repairs | 123 |

Tab.2. Average performance of steel ladles in steelworks 1

**Steelworks 2**

| Capacity of steel ladle | 160 t |
|-------------------------|-------|
| Nr. of ladle campaigns (2020-23) | 690 |
| Tonnage of bricks for steel zone | 16 t |
| Tonnage of bricks for slag zone | 6,3 t |
| Avg. quantity of Shot material per repair | 3 t |
| Nr. of heats without repair | 100 |
| Nr. of heats with 2 repairs | 185 |

Tab.3. Average performance of steel ladles in steelworks 2

On average, the slag line bricks in Steelworks 2 are replaced after approximately 60 heats in the ladle. The ladle then continues to operate for another 40 heats. However, at around 100 heats, the bricks in the steel zone become too worn, resulting in the complete demolition of the ladle. In the new campaign life cycle, the implementation of two repairs in the steel zone and two replacements of slag zone bricks extends the ladle's campaign to an average of 185 heats, representing an 85% increase. (Tab.3)

From these values, we can calculate the specific consumption of refractories used for the steel ladle wall per ton of produced steel. (Tab.4a, 4b)

| Capacity of steel ladle | 350 t steel ladle | |
|-------------------------|-------------------|--|
|  | Standard practice | Shotcreting application |
| Quantity of produced steel | 28700 t | 43050 t |
| Tonnage of refractories used | 55,1 t | 77,4 t |
| Refractories used per t of steel | 1,92 kg | 1,80 kg |

Tab.4a. Production of steel and tonnage of refractories per steel ladle in steelworks 1

| Capacity of steel ladle | 160 t | |
|-------------------------|-------|--|
|  | Standard practice | Shotcreting application |
| Quantity of produced steel | 16000 t | 29600 t |
| Tonnage of refractories used | 28,6 t | 40,9 t |
| Refractories used per t of steel | 1,79 kg | 1,38 kg |

Tab.4b: Production of steel and tonnage of refractories per steel ladle in steelworks 2

| Capacity of steel ladle | 160 t | |
|-------------------------|-------|--|
|  | Standard practice | Shotcreting application |
| Number of ladles per year | 219 | 118 |
| Total quantity of refractories | 6256 t | 4836 t |
| Quantity of refractory waste | 1877 t | 1238 t |

Tab. 5: Total number of ladles, tonnage of refractories, and waste per year in Steelworks 2

Knowing the yearly production for Steelworks 2, which is 3,5 million tons of steel, we can calculate the number of required ladles per year, the total amount of refractories needed for the steel ladle wall, and the amount of waste considering that the ladle is demolished when the bricks reach 30% of their original thickness. These numbers reflect significant savings in the cost of refractories, increased availability of steel ladles, and reduced waste generation. (Tab.5)

*Fig. 1: Pictures of steel ladle during complete campaign*
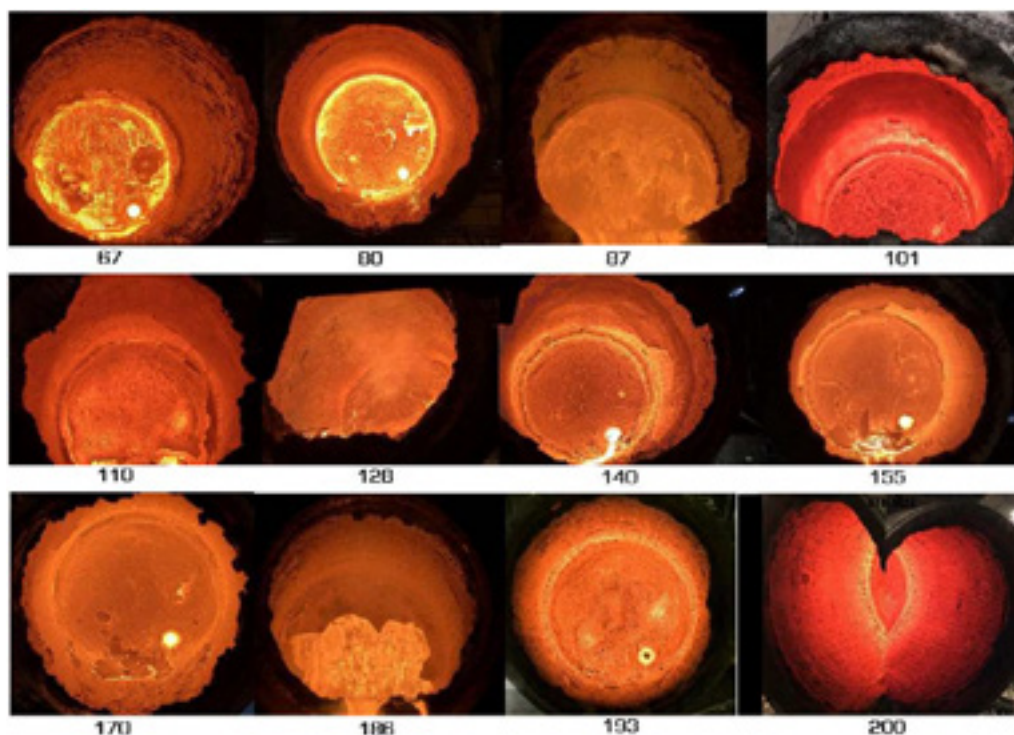
## NEW INSTALLATION METHOD – SHOTGUN

Shotcreting is a versatile monolithic application technique where a castable mix is sprayed onto a surface at high pressure, rapidly setting in place. It offers exceptional flexibility, allowing it to be used in various locations regardless of complex geometries. Crucially, shotcreting achieves refractory linings with comparable technical features to traditional vibrating casting methods, particularly in terms of mechanical parameters. However, shotcreting is typically not used for small repairs due to the higher cost of equipment, longer preparation time, and increased cleaning requirements after installation. These limitations are easily overcome by larger steelworks where the number of steel ladles and the quantity of installed material are high, and top-of-the-line performance is expected. On the other hand, for smaller steel mills, these limitations can be a dealbreaker, hindering them from modernizing their steel ladle management. To assist them in moving into the future, Seven Refractories has developed a new installation technique and material that allows for the utilization of gunning machines to apply similarly performing material as shotcrete.
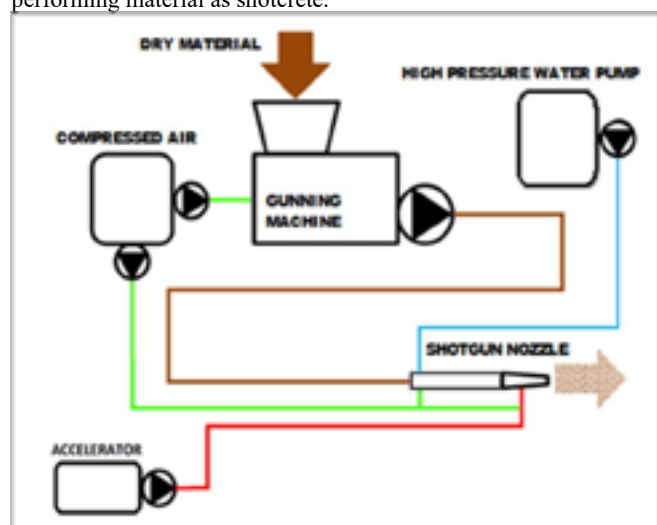


*Fig. 2: ShotGun system*

This led to the development of the SHOTGUN system (*Fig. 2*), which includes a modified gunning machine, high-pressure water pump, compressed air source, accelerator pump, and a special ShotGun nozzle developed by Seven Refractories. (*Fig. 3*) [7]. This system eliminates the need for a planetary mixer and shotcrete pump, which take up a lot of space and are costly, while also significantly reducing setup time and man power. Since water is added at the nozzle, there is no need for cleaning hoses, and there is no wasted material that would normally be left in the mixer, pump, and pipes.



*Fig. 3: New ShotGun nozzle*

The existing Seven Shot material was not fully compatible with the new installation system, requiring a material that is dry pumpable without separation and can be wetted out in a short amount of time. As a result, the particle size distribution and additives were modified, giving rise to a new family of Seven ShotGun products. A comparison of physical properties between the two products shows that both have high CCS (Cold Crushing Strength) values, especially at operating temperatures. The permanent linear change (PLC) is relatively constant and far from the critical value of -1.5%. Although there is a slight reduction in CCS for ShotGun, the values are still sufficiently high, and the less negative PLC reduces the stress experienced by the material.
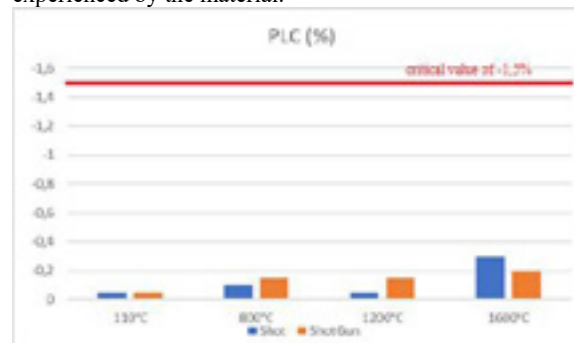


*Fig. 4a: Comparison of PLC between Shot and ShotGun*

353
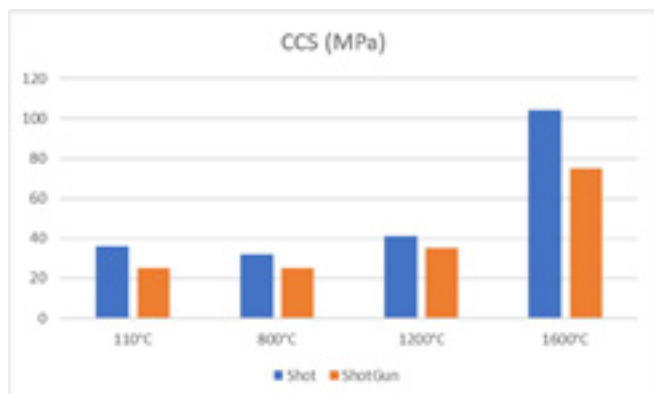
*Fig. 4b: Comparison of CCS between Shot and ShotGun*

## RESULTS FROM INDUSTRIAL TRIALS OF SHOTGUN

### Steelworks 3

A bottleneck during the standard campaign was wear in the steel zone of the ladle. The application of the ShotGun solution during the replacement of slag zone bricks extended the campaign until the bottom and slag zones became the limiting factors for the steel ladle's life cycle. This has been confirmed in several steel ladle campaigns. With this solution, all zones reach their end of life at the same time, which is a crucial parameter in economical calculations for all refractory linings and significantly reduces the amount of wasted material.



*Fig.5: Steel ladle repaired with ShotGun*

## CONCLUSIONS

After years of experience, shotcrete repairs for steel ladles have proven to be an effective solution. These repairs extend the service life of ladles, reduce waste, and decrease material consumption per ton of steel. As a result, operating costs are lowered, and the environmental impact is reduced. Furthermore, the repair process helps equalize the life cycles of different zones within the ladles, resulting in reduced refractory waste.

The introduction of the new ShotGun solution has made these benefits more accessible and easier to implement. Laboratory tests have shown only minimal reductions in physical values, ensuring high-quality repairs. Initial feedback from the field has been positive, particularly for smaller steel mills seeking to optimize their steel ladle performance. We are confident that further industrial trials will establish ShotGun as a reliable installation technique, enabling steel producers to transition towards a greener and more efficient future.



*Fig. 6: Steel ladle repaired with ShotGun during operation*

## REFERENCES

[1] A. Buhr, Refractories for Steel Secondary Metallurgy. CN-Refractories Vol.6 No.3, 1999

[2] J. Vatanen, Monolithic Ladle Lining in a 3-Cnverter-Shop Steel Academy seminar – Steel Ladle Lining 2022

[3] Ir. Rinus Siebring, Economics in Refractory Usage, Steel Academy seminar – Steel Ladle Lining 2022

[4] A. Buhr, Trends in Clean Steel Technology and Steel Ladle Lining, Steel Academy seminar – Steel Ladle Lining 2022

[5] Akselrod LM, Garten V. An alternative lining of steel ladles: technical and economic aspects. Ferrous Metallurgy. Bulletin of Scientific, Technical and Economic Information. 2018;(12):72-80

[6] G. Copetti, L. Folco, Steel Ladle Management: An Integrated View of the Challenges in Resistance, Environmental Impact, and Economic Issues. Feuerfestkolloquium Aachen, 2020

[7] European patent EP3858491 - International publication number WO 2020/040665

# THE EFFECT OF MGO−C REFRACTORY MATERIALS ON THE INCLUSION POPULATION WITHIN STEEL

Florian Kerber, Nora Brachhold, Christos G. Aneziris,
TU Bergakademie Freiberg, Institute of Ceramics, Refractories and Composite Materials, Freiberg, Germany

Volker Stein, Thomas Schemmel, Helge Jansen,
Refratechnik Steel GmbH, Research and Development, Düsseldorf, Germany

## ABSTRACT

Among others, the refractory lining material in steel ladles is a potential source for the formation of non-metallic inclusions, which requires in-depth knowledge of the interactions of refractory lining materials with the steel melt and the inclusion population. Within this work, the behavior of different grades of MgO-C refractory materials in contact with liquid steel at 1600°C and 1680°C was studied in detail via immersion tests. The immersed specimens were characterized in terms of their exterior and chemical alteration. Moreover, the inclusion population in the solidified steel samples was investigated particular with regard to the inclusion size distribution using automated feature analysis. Phase analysis of characteristic inclusions were performed using electron back scatter diffraction.

The formation of oxide structures was observed at the specimens' surface, including a coherent MgO layer, spinel containing crystal-like structures and phases from the quaternary $CaO-Al_2O_3-SiO_2-MgO$ system. The amount of accompanying phases correlated with the proportion of such phases in the primary refractory material, i.e. the grade of the used MgO raw materials. These phases further appeared to influence the layer growth and the formation of crystal-like structures. Only at an immersion temperature of 1680 °C the formation of larger bubbles was observed at the specimens' surface irrespective of their MgO grade.

The main inclusions detected in the solidified steel samples were crystalline $Al_2O_3$ inclusions, amorphous Mn-Si-Al-O inclusions and complex inclusions consisting of an amorphous Mn-Si-Al-O matrix with crystalline $Al_2O_3$ and/or $MnTiO_3$ precipitations. Both the MgO grade of the refractories and the steel melt temperature significantly influenced the total number of inclusions detected, the types of inclusions present and particularly their size distributions. Here, a lower MgO grade resulted in the formation of less but larger $Al_2O_3$ inclusions.

## INTRODUCTION

The occurrence of non-metallic inclusions (NMIs) in solidified metals is a research topic of high interest for several decades [1]. Because of their detrimental impact on the metallic properties, there is an ongoing demand for controlling the population of non-metallic inclusions in the steel melt. Here, the goal is to limit their frequency to the lowest possible level by keeping their size distribution, morphology and chemical composition under control.

Several NMI formation mechanisms are already known, such as the deoxidation process [2]. Alternatively, complex NMIs have been reported to form by the mutual collision of pre-existing NMIs, which was previously observed for MgO or MgO-rich spinel NMIs and liquid $CaO-SiO_2-MgO-Al_2O_3$ NMIs [3].

Among others, also the refractory lining material is a potential source for the formation of non-metallic inclusions [4]. Such materials, which are in direct contact with the steel melt, are a potential source of NMI formation by their erosion [5]. Conversely, they also possess the ability to influence pre-existing NMIs through chemical or mechanical interactions [6]. Nowadays, MgO-C refractories are used in BOF or ladle linings based on their superior thermomechanical properties including excellent thermal shock resistance, resistance against hot erosion and corrosion resistance [7].

Recently, MgO-C refractory materials with different MgO grade were investigated in contact with a steel melt via immersion tests carried out in a steel casting simulator [8]. The same materials were utilized for immersion tests at a higher temperature, i.e. 1680°C [9].

This work summarizes and connects these recently published results focusing also on the characterization of the immersed specimens. Although the influence of the immersed MgO-C refractories on the NMI frequency has been intensively discussed, the formation of the characteristic NMIs and their exact phase composition have not yet been investigated. Based on these studies, the previously observed NMIs were in-depth analyzed in this work. Structure and composition analyzes of different NMI species were carried out proposing possible formation and modification mechanisms of NMIs. In addition, the inclusion size distribution of the most observed inclusions, i.e. alumina NMIs were studied in more detail related to the MgO grade of the immersed MgO-C refractories and the immersion temperature.

## EXPERIMENTAL

Bar-shaped specimens of different MgO-C refractories with a carbon content of 10 wt% were subjected to immersion tests carried out in steel casting simulator (Systec, Germany) schematically shown in Fig. 1. The chemical composition of the used MgO-C refractories after coking is shown in Tab. 1, while details regarding the refractory specimen preparation were reported in a previous work [8].

*Tab. 1: Chemical composition of the MgO-C refractories determined by X-ray fluorescence spectroscopy in wt%; carbon excluded*

| Grade | MgO | CaO | $Al_2O_3$ | $SiO_2$ | $Fe_2O_3$ |
|---|---|---|---|---|---|
| G90 | 89.83 | 2.90 | 0.26 | 5.51 | 1.27 |
| G98 | 97.55 | 0.81 | 0.29 | 0.43 | 0.65 |

Approximately 38 kg of 42CrMo4 steel was inductively melted in an alumina/alumina-magnesia spinel crucible. After reaching the target temperature of 1600 °C or 1680 °C, non-metallic inclusions were generated intentionally be oxidizing and deoxidizing the melt using $FeO/Fe_2O_3$ powder (0.5 wt% related to the steel mass) and metallic Al (0.05 wt% based on the steel mass), respectively. The MgO-C specimen was then immersed into the steel melt for 30 minutes. Finally, the steel melt was cooled freely to room temperature after the immersed specimen was removed.
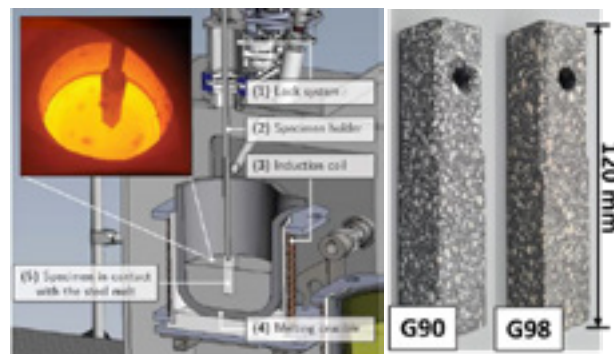


*Fig. 1: Steel casting simulator used for the immersion tests.*

After the melting trials, steel samples ($40 \times 40 \times 12$ mm³) were cut from the solidified steel blocks and analyzed with regards to the non-metallic inclusion population. The immersed specimens were analyzed using optical microscopy, scanning electron microscopy, energy-dispersive X-ray spectroscopy and X-ray diffraction.

Manually selected characteristic NMIs were analyzed by scanning electron microscopy (SEM, AMBER, Tescan, Brno, Czech Republic) with energy dispersive X ray spectroscopy (EDS, Bruker Nano GmbH, Berlin, Germany). In addition, phase analyzes were performed using electron backscatter diffraction (EBSD, Bruker Nano GmbH, Berlin, Germany).

**CONCLUSIONS**

This work investigated the behavior of MgO-C refractories with different MgO grade in contact with an Al-deoxidized steel melt at 1600 °C and 1680 °C and their influence on the population of non-metallic inclusions. Characteristic non-metallic inclusions observed after the immersion tests were intensively studied.

It was shown that the behavior of MgO-C refractories in contact with a steel melt differed depending on their MgO grade and the temperature during the immersion. All specimens were covered by a coherent MgO layer containing accompanying phases from the primary refractory material. The frequency of these phases was dependent on the specimens MgO grade, increasing with decreasing MgO grade. A higher proportion of such phases appeared to densify the newly formed coherent layer hampering layer growth and the formation of crystal-like $MgO/MgAl_2O_4$ structures.

The analysis of the structures and compositions of different inclusion species revealed the presence of various types, including crystalline, amorphous, and complex inclusions that contained both crystalline and amorphous phases. The complex inclusions consisted of an amorphous Mn-Si-Al-O matrix, along with various crystalline phases such as $Al_2O_3$, $MnAl_2O_4$ and/or $MnTiO_3$. The formation of amorphous Mn-Si-Al-O inclusions was attributed to the oxidation of the steel melt, while pure crystalline corundum inclusions resulted from both the oxidation and deoxidation processes. The shapes of the alumina inclusions varied, possibly due to variations in aluminum and oxygen supersaturation in the steel melt during their formation. Complex inclusions were suggested to form through the precipitation on existing inclusions and the mutual collision of pre-existing inclusions, facilitated by the non-wetting behavior of solid alumina inclusions in the steel melt.

The size distribution of the crystalline $Al_2O_3$ inclusions was related to the MgO grade of the previously immersed specimen. Here, a lower MgO grade, i.e. a higher proportion of accompanying phases in contact with the steel melt, resulted in a shift of the inclusion size distribution towards a larger inclusion size.

**REFERENCES**

[1] L. Zhang, B.G. Thomas, State of the art in evaluation and control of steel cleanliness, ISIJ International 43 (2003) 271–291. https://doi.org/10.2355/isijinternational.43.271.

[2] André Luiz Vasconcellos da Costa e Silva, The effects of non-metallic inclusions on properties relevant to the performance of steel in structural and mechanical applications, Journal of Materials Research and Technology 8 (2019) 2408–2422. https://doi.org/10.1016/j.jmrt.2019.01.009.

[3] Y. Liu, Y. Zhang, L. Zhang, Y. Ren, P. Shen, Y. Luo, Formation Mechanism of Complex Oxide Inclusions in 55SiCr Spring Steels, steel research int. 89 (2018) 1700277. https://doi.org/10.1002/srin.201700277.

[4] L. Chen, W. Chen, Y. Hu, Z. Chen, Y. Xu, W. Yan, Effect of Al antioxidant in MgO-C refractory on the formation of Al2O3-rich inclusions in high-carbon steel for saw wire under vacuum conditions, Ironmaking & steelmaking 45 (2018) 272–279. https://doi.org/10.1080/03019233.2016.1261245.

[5] K. Wasai, K. Mukai, A. Miyanaga, Observation of inclusion in aluminum deoxidized iron, ISIJ International 42 (2002) 459–466. https://doi.org/10.2355/isijinternational.42.459.

[6] Z. Deng, M. Zhu, Du Sichen, Effect of Refractory on Nonmetallic Inclusions in Al-Killed Steel, Metallurgical and Materials Transactions B 47 (2016) 3158–3167. https://doi.org/10.1007/s11663-016-0746-2.

[7] C.G. Aneziris, S. Dudczig, M. Emmel, H. Berek, G. Schmidt, J. Hubalkova, Reactive filters for steel melt filtration, Advanced Engineering Materials 15 (2013) 46–59. https://doi.org/10.1002/adem.201200199.

[8] F. Kerber, T. Zienert, J. Hubálková, V. Stein, T. Schemmel, H. Jansen, C.G. Aneziris, Effect of MgO Grade in MgO–C Refractories on the Non-metallic Inclusion Population in Al-Treated Steel, steel research international 93 (2022) 2100482. https://doi.org/10.1002/srin.202100482.

[9] F. Kerber, P. Malczyk, V. Stein, T. Schemmel, H. Jansen, C.G. Aneziris, Influence of the MgO grade in MgO-C refractory material and steel melt temperature on the inclusion population in Al-treated steel, Int J Ceramic Engine & Sci 4 (2022) 102–111. https://doi.org/10.1002/ces2.10119.

# A NOVEL MEMBER IN THE CMA-FAMILY OF AGGREGATES CREATING MORE SUSTAINABLE A-MA STEEL LADLE REFRACTORIES

C. Wöhrmeyer, R. Soth, M. Lievin, R.M. Mineau, E. Frier, V. Germain, C. Liu, X. Ma, J.M. Auvray

Imerys S.A., Paris, France

## ABSTRACT

This paper explores new refractory aggregate compositions and microstructures in the $CaO-MgO-Al_2O_3$ (CMA) system. MagArmour (MagA) is a microporous CMA-aggregate that is designed for application as dopant to MgO-C bricks where amongst other effects it can replace antioxidants like Al and Si metals. But it has also shown positive effects as addition to alumina spinel (A-MA) castables and gunning mixes in terms of thermal shock resistance (TSR). However, the application in castables is limited to relatively small addition rates due to the apparent porosity of the MagA aggregate (25-35 vol. %). It impacts the water requirement so that the full potential of this concept can only be exploited to a small extent in castables. To further build on this positive experience concerning the TSR this study investigates which aspect contributes most to it, the micro porosity of the aggregates or their composition within the CMA-system. It was found within the perimeter of tested materials that some alterations of the aggregate composition have a more significant impact on thermal shock resistance than significant modifications of the porosity of the aggregates. With this it was possible to design new CMA aggregates that are on one hand fully compatible with application requirements in bricks and in castables, in the latter especially with respect to their rheological requirements, and on the other hand provide the resistance to the harsh steel ladle conditions, both in terms of thermal shock and corrosion resistance.

## INTRODUCTION

Alumina-spinel (A-MA) refractories are well known products for steel ladle applications providing excellent refractoriness and corrosion resistance. Although already improved compared to pure alumina refractories due to a small thermal expansion mismatch between alumina and spinel [1], their thermal shock resistance is still significantly inferior to products based on mullite or mullitized andalusite since mullite has a very low coefficient of thermal expansion [2]. However, to minimize interactions with steel, higher amounts of silica containing phases are not desired in direct contact with high quality steel [3]. An improvement of the TSR of A-MA dry-gunning mixes has been reported with the introduction of MagArmour (MagA), a porous aggregate consisting of micro spinel crystallites and hydraulic calcium aluminate phases [4]. However, applied in castables, the water demand increased, and furthermore, without adjusting the matrix composition, shrinkage after firing at 1500 °C may occur. The aim of the present study is to continue the aggregates development in the CMA system by further understanding the underlying mechanism that led to the improved thermal shock resistance of MagA. In this regard the attempt is to investigate which aspect plays a bigger role for the TSR within the CMA system, the micro-porosity of the aggregate or its composition. This then leads to the development of a new generation of CMA-aggregates that combine the positive aspects in terms of thermal shock resistance with a high level of corrosion resistance and enable the universal application in A-MA refractories, including castables, gunning mixes, and bricks.

## TEST MATERIALS

To investigate the effect of the composition of aggregates from the CMA system vs their porosity on the thermal shock resistance of alumina spinel castables, two different aggregate compositions (CMA1 and CMA2) and variants in terms of their apparent porosity (26 and 4 vol.% for CMA1 resp. 6 vol.% for CMA2) have been prepared (Tab. 1). CMA1-26 corresponds to the original MagArmour product of Imerys, France. The composition and apparent porosity of the tabular alumina and the magnesium aluminate (MA) spinel aggregates used in this study are shown as well in Tab. 1.

Tab. 1: Composition and apparent porosity of different refractory aggregates.

| | | MA Spinel | Tab. Alu. | CMA1-26 (MagA) | CMA1-4 | CMA2-6 |
|---|---|---|---|---|---|---|
| $Al_2O_3$ | wt, % | 76 | 99.6 | 69.8 | 69.8 | 77.6 |
| MgO | wt. % | 23 | | 19.0 | 19.0 | 18.9 |
| CaO | wt. % | 0.3 | | 10.4 | 10.4 | 3.0 |
| Ap. Po | vol. % | 3 | 3 | 26 | 4 | 6 |

Aggregates of the fractions 0-1, 1-3 and 3-6 mm have been produced by crushing the synthesized clinkers. SEM backscattered micrographs of the CMA1-26, CMA1-4, and CMA2-6 aggregates can be seen in Fig. 1. The micrograph of CMA1-26 has been taken at a higher magnification due to the smaller crystal size inside the grain structure, mainly consisting of (dark grey) spinel (Sp) and a smaller portion of CA (light grey) and CA2 (grey) phases. Contrary to that, CMA1-4 and CMA2-6 contain larger primary crystals with an assemblage of mainly spinel in both cases, but CA and CA2 as secondary phases in case of CMA1-4 and mainly CA2 in case of CMA2-6. While in case of CMA1-26 the high amount of micro pores are clearly visible (black), the other two aggregates clearly exhibit much less porosity.
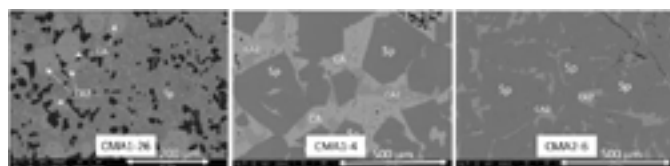


*Fig. 1: Microstructures of different aggregates from the CMA system.*

These aggregates have been applied in three different alumina spinel castables. In model formulation type A (Tab. 2) the objective was to keep the total amount of spinel in the recipe close to the 23 % of spinel in the reference formulation (REF-A-SP). Consequently, the amount of added pure MA spinel in the fraction 0-1 mm has been reduced when 20% CMA1-26, CMA1-4 or CMA2-6 have been added. The difference has been compensated with a reduction of tabular alumina.

Tab. 2: Model castable formulation type A with 20 % CMA aggregates and reference model castable formulation REF-A-SP.

| wt. % | | REF-A-SP | CMA1-26A | CMA1-4A | CMA2-6A |
|---|---|---|---|---|---|
| CMA1-26 | 1-6 mm | | 12 | | |
| CMA1-26 | 0-1 mm | | 8 | | |
| CMA1-4 | 1-6 mm | | | 9 | |
| CMA1-4 | 0-1 mm | | | 11 | |
| CMA2-6 | 1-6 mm | | | | 13 |
| CMA2-6 | 0-1 mm | | | | 9 |
| Tab. Alu | 1-6 mm | 49 | 40 | 40 | 39 |
| Tab. Alu | 0-1 mm | 11 | 14 | 14 | 17 |
| MA spinel | 0-1 mm | 23 | 9 | 9 | 7 |
| React. Alu | d50 = 1.5 μm | 11 | | | |
| Secar 71 | | 6 | | | |
| Permount Al 200 | | 0.1 | | | |
| Total | | 100.1 | 100.1 | 100.1 | 100.1 |
| Water addition | | 3.25 | 3.75 | 3.25 | 3.25 |

A second set of model formulations (type B) is using 20 % CMA-aggregates only in the fraction >1 mm as replacement for tabular alumina (Tab. 3). Consequently, the total amount of spinel is higher than in REF-A-SP (23 %) and reaches approximately 35 % in

357

CMA1-26B and CMA1-4B, while CMA2-6B reaches a spinel content of 40 %.

Tab. 3: Model castable formulation type B with 20 % CMA aggregates and reference model castable formulation REF-A-SP.

| wt. % | | REF A-SP | CMA1-26B | CMA1-4B | CMA2-6B |
|---|---|---|---|---|---|
| CMA1-26 | 1-6 mm | | 20 | | |
| CMA1-4 | 1-6 mm | | | 20 | |
| CMA2-6 | 1-6 mm | | | | 20 |
| Tab. Alu. | 1-6 mm | 45 | 29 | 29 | 29 |
| Tab. Alu. | 0-1 mm | | 11 | | |
| MA spinel | 0-1 mm | | 23 | | |
| React. Alu. | d50 = 1.5 μm | | 11 | | |
| Secar® 71 | | | 6 | | |
| Peramid® Al 200 | | | 0.1 | | |
| Total | | 100.1 | 100.1 | 100.1 | 100.1 |
| Water addition | | 3.25 | 4.75 | 3.5 | 3.5 |

Finally, a third set of model formulations (type C) has been tested where all the tabular alumina fractions >1 mm have been replaced by the different CMA aggregates (Tab. 4). Here the focus was on the question to which extent a very high spinel content and at the same time a very high total CaO content in the castable, both introduced through the CMA aggregates, would still give interesting thermomechanical properties. These C-type castables are now in fact rather spinel-alumina castables as they contain approximately 55 % spinel (CMA1-26C and CMA1-4B) and 60 % spinel (CMA2-6C), respectively. It also need to be mentioned that the CMA1-26C and CMA1-4C contain a very high lime content, between 6 and 7 % CaO, roughly twice as much as CMA2-6C and about four times more than the reference REF A-SP.

Tab. 4: Model castable formulation type C with 49 % CMA aggregates and reference model castable formulation REF A-SP.

| wt. % | | REF A-SP | CMA1-26C | CMA1-4C | CMA2-6C |
|---|---|---|---|---|---|
| CMA1-26 | 1-6 mm | | 49 | | |
| CMA1-4 | 1-6 mm | | | 49 | |
| CMA2-6 | 1-6 mm | | | | 49 |
| Tab. Alu. | 1-6 mm | 49 | | | |
| Tab. Alu. | 0-1 mm | | 11 | | |
| MA spinel | 0-1 mm | | 23 | | |
| React. Alu. | d50 = 1.5 μm | | 11 | | |
| Secar® 71 | | | 6 | | |
| Peramid® Al 200 | | | 0.1 | | |
| Total | | 100.1 | 100.1 | 100.1 | 100.1 |
| Water | | 3.25 | 7.5 | 4.5 | 4.5 |

## TEST METHODS

Physical properties (castable bulk density, apparent porosity, permanent linear change, modulus of rupture, crushing strength) have been determined at room temperature on hardened castable prisms (30 x 30 x 120 mm$^3$) after 24 h curing at 20 °C followed by 24 h drying at 110 °C, and after firing in a chamber furnace at different temperatures (800, 1100, 1400, 1600 °C) with a dwell time of 5 h.

Thermal shock tests have been carried out in accordance with NF EN 993-11 on prisms with the following dimension: 230x54x63 mm$^3$ (format B). Prior to the thermal shock tests the prisms have been pre-fired at 1600 °C (6 h), the temperature that is expected during the application in a steel ladle. For the thermal shock test itself the samples are put into a furnace that is pre-heated at 950 °C where they remain during 30 min to ensure an even temperature distribution within the prism. Then they are removed from the electric oven, placed on a steel plate and exposed to a jet of air (20°C). After this first quenching, the procedure is repeated 4 times. Subsequently, after the last quenching, the residual cold modulus of rupture (MOR) is determined and compared with a sample of the same material (and sample size) that has not undergone this quenching procedure. The thermal shock resistance is defined by the percentage of the residual MOR compared to the MOR of the non-quenched specimen.

Static cup corrosion tests have been carried out using castables, pre-fired at 1600 °C for 6 h. The refractory cup (inner diameter 5 cm) has been filled with 376 g of steel (structural carbon steel

AX48, containing 0.5 % C, 0.65 % Mn, <0.4 % Si, and <0.035 % S and P, respectively. A synthetic slag powder (40 g) with composition as shown in Tab. 4 was added. The corrosion test was conducted in a chamber furnace at 1500 °C for 6 h.

Tab. 5: Composition of slag used for corrosion test (wt. %).

| CaO | SiO$_2$ | Al$_2$O$_3$ | MgO | Fe$_2$O$_3$ | MnO | SO$_3$ | TiO$_2$ | Na$_2$O+ K$_2$O |
|---|---|---|---|---|---|---|---|---|
| 42.6 | 32.7 | 10.1 | 7.0 | 3.1 | 1.2 | 2.1 | 0.5 | 0.6 |

## TEST RESULTS

### Water demand and vibration flow

For all formulations (Tab. 2-4), water addition was adjusted to achieve a similar initial vibration flow value, in the range between 100 – 120%, directly after 4 minutes wet mixing. The lowest water demand was observed with the reference formulation (REF A-SP). This can be attributed to the low apparent porosity of the tabular alumina aggregates. As expected the high porosity in CMA1-26 leads to a higher water demand, especially when the content in the formulation is high (type C). This aspect is significantly improved with CMA1-4 and CMA2-6, both giving low water demands in formulation types A and B and a moderate increase in formulation type C compared to the CMA-free reference.

### Castable bulk density reduction

Since spinel has a lower density than corundum, a reduction of the castable bulk density is one of the desired effects when increasing the total amount of spinel through the addition of CMA aggregates since it will reduce material consumption and potentially as well the heat loss through the refractory lining, thus creating a more sustainable solution during usage in steel ladles. As can be seen in Fig. 2a, the reduction of bulk density is minimal when the total amount of spinel remains constant (type-A formulations). Only the impact of the higher porosity of CMA1-26 leads here to a more significant decrease (4 %) due to the additional grain porosity and the higher water demand. In formulation type-B (replacement of tabular alumina only) the difference is somewhat more pronounced compared to type-A mixes but still remains at low level (2 % density reduction) for the CMA aggregates with low porosity, while it is significantly higher for the CMA1-26 containing formulation that exhibits a 8 % density reduction versus the reference formulation without CMA (Fig. 2b). The biggest effect has been observed with the highest addition rates for all CMA-aggregate types, ranging from 6-8 % density reduction for the low-porous CMA-versions to 18 % for CMA1-26 (Fig. 2c) where the lower spinel density and the high grain porosity create a double effect.
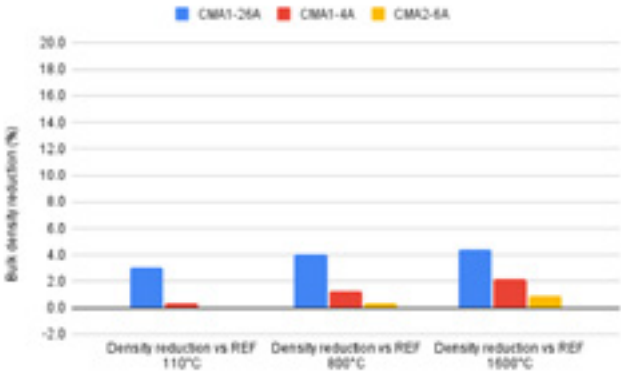


Fig. 2a: Reduction of bulk density of CMA-containing castables (type A) versus REF A-SP.
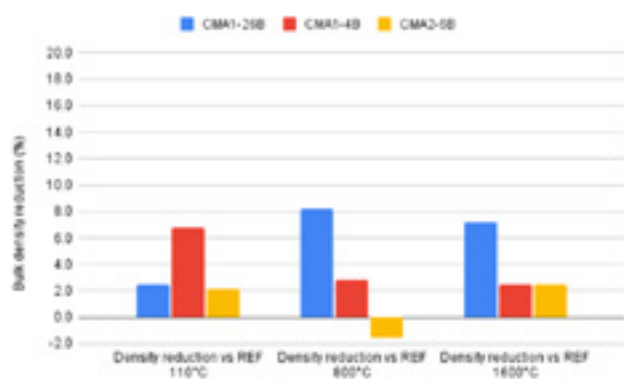
*Fig. 2b: Reduction of bulk density of CMA-containing castables (type B) versus REF A-SP.*
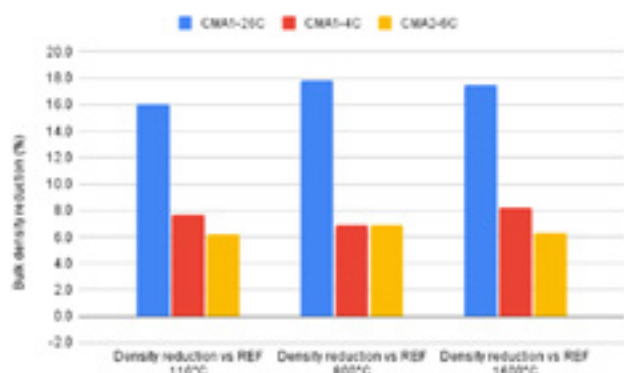


*Fig. 2c: Reduction of bulk density of CMA-containing castables (type C) versus REF A-SP.*

**Permanent linear change (PLC) after the first castable firing**

One important parameter for an application in a steel ladle is the volume evolution of the refractory material during the first heat-up. The experience has shown, that refractories with a slightly positive PLC, for example alumina-magnesia castables (expansive spinel + CA6 formation at high temperature), bring a potential performance advantage over alumina-spinel castables. The latter typically exhibit only a small expansion related to CA6 formation or even show a slight shrinkage. Almost all tested formulations in this study remained within a very small shrinkage or expansion window between -0.2 and +0.2 % for all firings up to 1600 °C. However, it was noticed that the reference formulation and the formulation types A and B with CMA1-26 tended more to a small shrinkage at 1400 and 1600 °C as shown exemplary for the type A formulations (Fig. 3a) while the formulations with CMA1-4 and CMA2-6 showed small levels of expansion. For formulation type C (Fig. 3b) only CMA1-4 exhibited a somewhat higher expansion (0.4 %) while all others showed small shrinkage at 1400 and 1600 °C, with no significant difference between those formulations.



*Fig. 3a: Permanent linear change of type-A formulations.*



*Fig. 3b: Permanent linear change of type-C formulations.*

**Thermal shock resistance**

The most interesting results in this study are related to the performance in the thermal cycling test. As expected the reference formulation gets significantly affected, mainly already after the first shock and loses almost 90 % of its initial modulus of rupture (MOR) after 5 thermal cycles. As already reported in other publications [4], also these test series confirm that with CMA1-26 (MagArmour) the MOR after firing is lower than the reference, but achieves after five thermal cycles in absolute terms a higher MOR than the reference. It keeps between 18 and 42% of the initial MOR with the higher value for the higher addition rate (formulation type C). So the question was if this is related just to the higher micro porosity in MagArmour, or related to the different aggregate compositions. From these tests one can conclude that mineralogy is playing the dominant effect since also the dense version (CMA1-4) exhibits excellent thermal shock resistance, and even better than CMA1-26, with retention rates between 30 and 50% and again with the higher values for the type-C mixes. Contrary to that the CMA2-6 aggregates with their higher $Al_2O_3$ and lower CaO content but similar low porosity as CMA1-4, perform in a similar way as the reference in terms of relative remaining MOR but with even lower absolute values after the 5 thermal cycles. This was also confirmed by some additional experiments where the CMA2 composition was modified towards higher apparent porosity (up to 30%) which did not result in a higher thermal shock resistance.
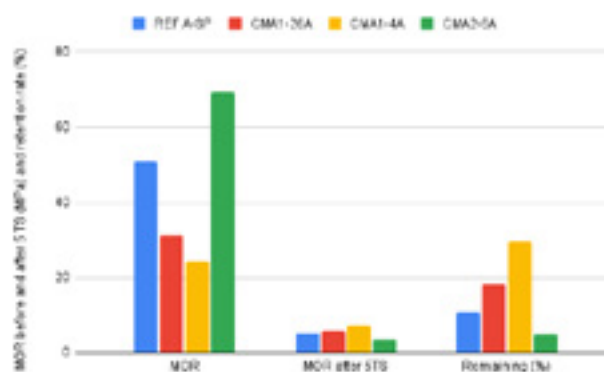


*Fig. 4a: Modulus of rupture of type-A recipes after firing at 1600 °C, after additional 5 thermal shock cycles, and retention rate.*

359
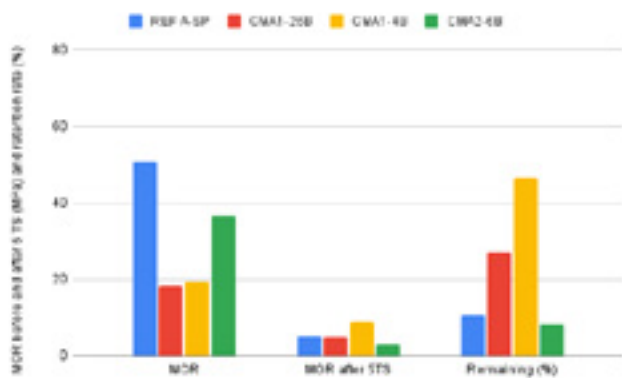
*Fig. 4b: Modulus of rupture of type-B recipes after firing at 1600 °C, after additional 5 thermal shock cycles, and retention rate.*
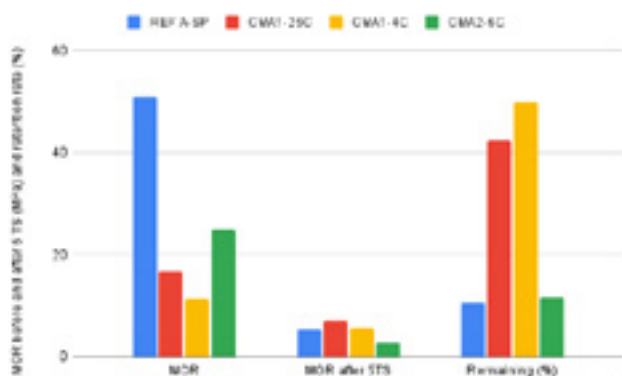


*Fig. 4c: Modulus of rupture of type-C recipes after firing at 1600 °C, after additional 5 thermal shock cycles, and retention rate.*

360
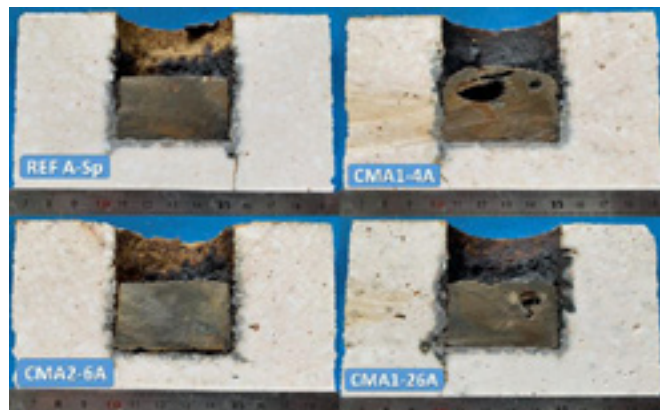


*Fig. 5: Cup corrosion tests at 1500 °C, 6 h, with 376 g steel and 40 g slag (C/S=1.3, Fe2O3 = 3.1 %).*

**Corrosion resistance**

For a first quick evaluation some cup tests with steel and slag have been conducted with the type A formulations to evaluate if there would be an obvious difference in corrosion resistance between those mixes, that had constant total spinel content, but somewhat different CaO contents, and differences in grain porosity, especially in case of CMA1-26A. Fig. 5 shows the cross sections of the cups after the test at 1500 °C (6 h). It is obvious that castable CMA1-26A with its higher open porosity (14.5 vol. % after firing at 1600°C vs 12.2 vol. % for REF A-SP) shows a higher slag penetration. But both CMA1-4A and CMA2-6A with porosities close to 13% after firing at 1600°C resist the slag attack in a quite similar good way as the reference REF A-SP. Further tests are ongoing to evaluate the corrosion resistance also with a dynamic corrosion test and for the other formulation types.

## SUMMARY AND CONCLUSION

This study has investigated different alumina spinel model castables containing different versions of aggregates from the calcium magnesium aluminate system in comparison with a classical alumina spinel model castable based on tabular alumina and magnesium aluminate spinel. The study has confirmed that employing the microporous aggregate CMA1-26 (MagArmour) one can achieve superior TSR versus the reference material. However, the water demand and open porosity of the castable is increasing with this concept and thus the corrosion resistance is impacted. The modified CMA aggregates in terms of chemistry and porosity have shown that the impact of chemistry and with that the phase assemblage plays a more important role for the TSR than the micro porosity of the aggregates. A newly designed aggregate (CMA1-4) with a much lower porosity versus CMA1-26, but the same composition, has resulted in the best thermal shock resistance while keeping corrosion resistance at a similar good level as the reference material for the formulation type-A. Another effect of the employment of CMA-aggregates is that they reduce the material requirement for a given furnace design, thus safe material, but potentially also energy and contribute to a more sustainable steel production. Overall, so far the new CMA1-4 version resulted in the best compromise between resistance against thermal shock, corrosion and reduction of density. Further investigations are ongoing and will be reported in the future.

## REFERENCES

[1] Da Luz A, Braulio M, Pandolfelli V. Refractory castable engineering. F.I.R.E. compendium series, Göller Verlag, p. 499, 2015

[2] Schneider H, Eberhard E. The thermal expansion of mullite. J. Am. Cer. Soc. Vol. 73 (7), 1990, p. 2073-2076

[3] Poirier J. A review: influence of refractories on steel quality. Metall. Res. Technol. 112, article No. 410, 2015

[4] Wöhrmeyer C, Gao J, Szepizdyn M, Graddick S, Liu C. Designed porous aggregates – a solution for more sustainable steel ladle refractories. Unitecr 2022, Chicago, USA

# CASTABLE MATRIX CONCEPT FOR ROBUST BEHAVIOUR IN STEEL LADLE BOTTOM REPAIR

G. Rojek, M. Sułkowski, M. Klewski ArcelorMittal Refractories, ul. Ujastek 1, 30-969 Krakow, Poland

D. Bednarek – ArcelorMittal Dąbrowa Górnicza, Al. Józefa Piłsudskiego 92, 41-308 Dąbrowa Górnicza, Poland

Dr. A. Buhr, Almatis, Lyoner Strasse 9, 60528 Frankfurt am Main, Germany

D. Schmidtmeier, Almatis, Giulinistrasse 2, 67065 Ludwigshafen, Germany

J. Dutton, 3 Silverdale Gardens, DY8 5NU Stourbridge, United Kingdom

## ABSTRACT

When installing new well blocks, seating blocks for purging plugs, or impact pads in steel ladle bottom, self-flowing mixes are usually used for filling the gap between the bottom bricks and the pre-cast shapes. As the material demand is relatively low for these installations, smaller and less powerful mixers or even simple manual mixing procedures are used instead of high intensity refractory mixers. The mixing behaviour of castables strongly depends on the matrix formulation.

In general, the mixes can show shorter or longer wet-out times and softer or more dilatant consistency. An easy mixing behaviour is particularly important with this type of castable to prevent over-watering the mix on site and therefore jeopardizing the performance in use.

The paper describes suitable matrix formulations for this purpose and also practical experience and results.

## INTRODUCTION

A ladle bottom at ArcelorMittal Dabrowa Gornicza is lined with AluMagCarbon bricks with a pre-cast well block (Fig. 1). After 30 heats, the well block is replaced by a new one in a cold repair and replaced again after 50 to 60 heats. In order to close the joint between the well block and the bricks, a self-flowing castable is used as a better alternative to a ramming mix. The castable enables a faster and more reliable installation because less manual work is required.
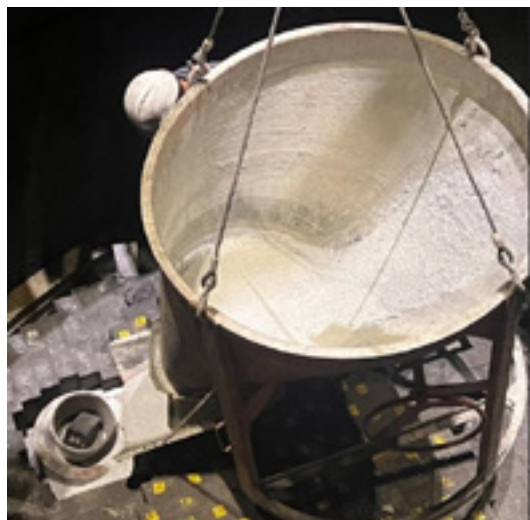


*Fig. 1: Trial in ArcelorMittal Dabrowa Gornicza*

A castable with good self-flowing properties completely fills the joint and degasses without need for vibration. A low cement corundum-spinel castable is used to achieve the desired wear resistance in the ladle bottom. Adding spinel to the alumina mix improves properties such as thermal shock resistance, slag penetration and corrosion resistance.

Alumina-spinel castables are characterized by a hot modulus of rupture (HMoR) in the range of 20-30 MPa. The increase in strength is due to the formation of a strong bond between the $CA_6$ phase, hibonite, and alumina or spinel grains during sintering at higher temperatures. At a higher temperature (1400-1700°C) in the CaO-$Al_2O_3$-MgO ternary system, ternary CAM phase is also formed. With increasing temperature, the amount of this phase increases at the expense of alumina grains, spinel and the $CA_6$ phase. CAM has a platy hexagonal shape and grows into alumina grains, strongly connecting the matrix with the aggregates, resulting in high hot strength. [1,2] Alumina-spinel castable is used for precast shapes for example purging plugs, well-blocks and lances or for in-situ monolithic linings of steel ladles. In secondary metallurgy it is used for RH-snorkel and ladle cover and lip-ring. In the steel ladle bottom, it is used to fill the gap between bottom bricks and precast shapes.

Only a small amount of castable is required to line the joint between the bottom bricks and the well block. Therefore only small, less powerful mixers are used. Sometimes even manual mixing must be sufficient. It is important that the castable can cope with such sub-optimal mixing conditions and is designed for fast wet out behaviour, low dilatancy during mixing and handling, and low stickiness of the mix.

Particle size distribution determines the rheology of the castable. The degree of self-flowing is determined by the grain size below 100 μm, and more specifically below 45 μm, because the smallest fraction predominantly determines the flowability [3]. Three types of reactive alumina were used in the study: monomodal, bimodal and spinel-containing bimodal reactive alumina E-SY 2000. The bimodal distribution is composed of a finer and a coarser fraction, which results in a higher density and therefore lower porosity of the mix [4]. The E-SY 2000 has a special particle size distribution designed for easy mixing behaviour, fast wet out and low dilatancy of the mix for easy handling on site.

Due to the fact that this work focuses on rheological properties, it is worth adding that it is mainly reactive alumina that decides and controls the flow and also the type and development of bonds. The works of other authors also focused on flow (approx. 250mm), wet out time tests, where 45s was achieved as the lowest result [5]. E-SY was also used in the research, which allowed comparable spreading results to be achieved with a much lower mixing water content (4 wt.%). It's not easy to find articles that discuss the issues in industrial tests, so the work focuses mainly on the practical properties.

The purpose of this study was to create an alumina-spinel self-flowing castable with a modified matrix which meets the requirements of easy application in industrial conditions. This can be confirmed during tests in the steelworks and in the laboratory by short wet out time and ball drop test. It should have a long setting time, which allows application of the castable between well-blocks without risk of flow decay during transport to the steel ladle. In our research we compare three basic recipes that differ in the content and type of matrix alumina and AR78 spinel, which affect the thermomechanical strength and, in particular, the rheological properties.

## MATERIALS AND METHODS

The following raw materials were used for the research: ALMATIS Tabular Alumina T60/T64 in various fractions (3-6 mm, 1-3 mm, 0.5-1mm, 0-0.3 mm, -45 and -20MY). Each recipe had 5 wt.% of cement with a long setting time. Samples contained alumina rich spinel AR78 in two fractions (0-0.5 mm and -90MY) with a total of 17 wt.% plus 1 wt.% additives.

The most important variable is the use of different grades of reactive alumina. Mix (A) contains 13 wt.% of bi-modal $Al_2O_3$, mix (B) contains 13 wt.% of mono-modal $Al_2O_3$ and mix (C) contains reactive alumina with spinel E-SY 2000 in total 20 wt.%, to compensate for the reduced amount of spinel.

The castables were prepared in the laboratory initially by dry mixing for 1 minute, then, after adding the appropriate amount of water, wet mixing for 4 minutes. The wet out time, flow, ball drop test, and exothermic reaction during cement setting (EXO method) were measured. Industrial trials of the one selected mix were carried out at AM Dabrowa Gornicza for joint filling around the well block in the steel ladle bottom.

For flow testing (PN-EN ISO 1927-4:2013-06) a metal cone with dimensions 80x100 was used and filled with castable. The flow was measured 2 and 20 min after wet mixing.

Wet out time is a test that shows how quickly a material combines with water to form a wet mass. The result is the time measured from adding water to observing the wetting of the material. The shorter the time, the easier the material mixes. This also applies in industrial conditions.

In the ball drop test, a steel ball (110g, 30 mm diameter) falls from a height of 1 m into the castable in the mixing bowl. The result of the test is the time measured from the moment the ball is released until it is completely immersed in the mix [3]. A short immersion time is a quantitative indicator of the softness of the mix, which is important for easy installation on site. The ball drop test is a very simple but important method which shows different behaviour of castables with regard to stiffness caused by dilatancy. High dilatancy is a big negative for the handling of castables on site. This often causes excess water to be added by the operators which, in turn decreases the performance of the lining in use. The challenge is therefore to create a castable with the lowest possible water requirement combined with lowest dilatancy.

Test bars with dimensions of 64x64x240mm were made using each recipe. Firstly, samples were dried at 110°C/24h and then fired at 450°C/5h or 1570°C/5h respectively. Open porosity and bulk density (993-1:2019-01), cold crushing strength (EN 196-1:2005) and cold modulus of rupture (EN 993-5:2019-01), PLC (PN-EN ISO 1927-6:2013-06) were measured. Samples for HMoR had dimensions of 25x25x148 mm (PN-EN 993-7), and were dried at 110°C/24h and pre-fired at 1500°C/5h. The test was carried out at 1450°C.

**Tab. 1:** Compositions of castables

| Castable<br>Components | | A | B | C |
|---|---|---|---|---|
| Tabular Alumina | | 64 | 64 | 66 |
| Cement | | 5 | 5 | 5 |
| Reactive alumina bi-modal | | 13 | - | - |
| Reactive alumina mono-modal | Wt. % | - | 13 | - |
| Reactive alumina E-SY 2000 | | - | - | 20 |
| Spinel AR78 | | 17 | 17 | 9 |

## RESULTS AND DISCUSION

### Rheological properties

After 20 minutes all test castables show good self-flow behaviour without flow decay (Tab. 2). Castables B and C need 0.2% less water to achieve the desired flow value.

Wet out time is similar for all castables. In the ball drop test, castable C clearly obtained the best result.

The EXO results are shown in Table 2 and Figure 3. Start 1 indicates the end of workability and flow. Start 2 shows when hydration of cement and strength development start. Exo Max shows the point when sufficient green strength for demoulding is achieved. Comparison of the results from EXO test shows the longest setting time was achieved with castable C. This allows for a longer time for castable application in industrial conditions.

**Tab. 2:** Wet castable properties.

| Properties | | A | B | C |
|---|---|---|---|---|
| Water [%] | | 5.0 | 4,8 | 4,8 |
| Flow [mm] 2 min | | 237,5 | 238,1 | 236,5 |
| Flow [mm] 20 min | | 232,5 | 240,1 | 242,5 |
| Wet out time [s] | | 35 | 35 | 30 |
| Ball drop test [s] | | 15 | 15 | 6 |
| EXO | Start 1 / min | 348 | 234 | 402 |
| | Start 2 / h | 11,2 | 8,7 | 13,1 |
| | Exo Max / h | 13,2 | 10,6 | 15,3 |
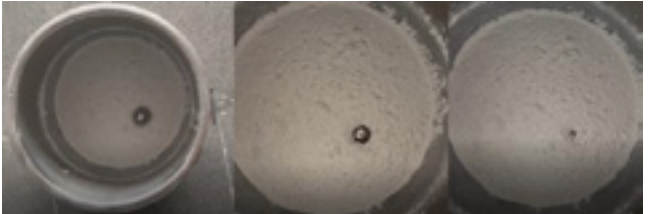


**Fig. 2:** Ball drop test
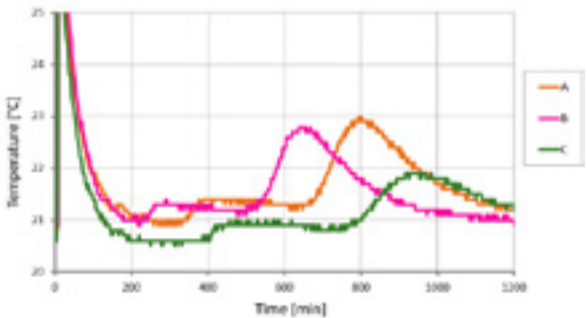


**Fig. 3:** EXO test for castable samples

### Thermo-mechanical properties

Figure 4 shows bulk density (a) and open porosity (b) for the castable samples at different temperatures. For each sample density decreases and porosity increases with increasing temperature. The typical values for alumina-spinel castables are approximately $3 \text{ g/cm}^3$. Open porosity at 1500°C can reach up to 20% [3].

a)



b)
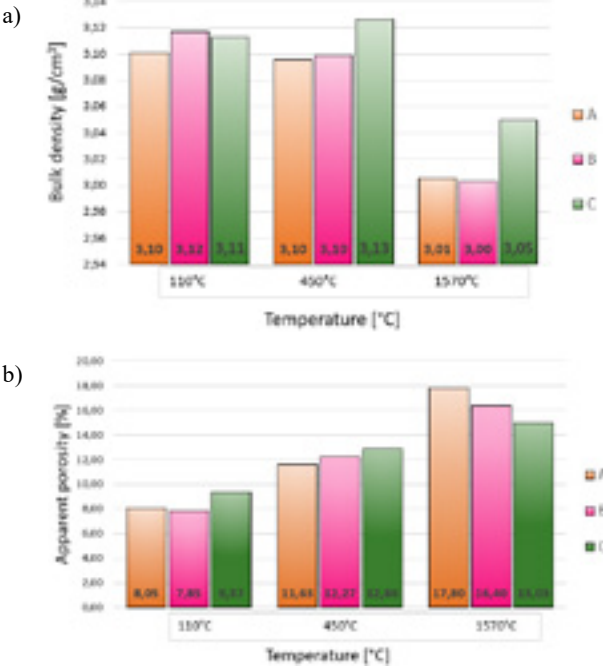


**Fig. 4:** Bulk density (a) and open porosity (b)

Fig. 5 shows permanent linear change at 110, 450 and 1570°C. All samples achieved slight expansion at 1570°C. To sum up alumina-spinel castables are stable and deviations in dimensions are not significant.
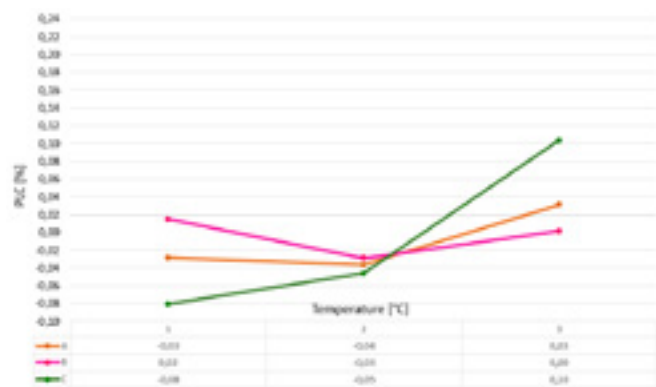


**Fig. 5**: *Change linear dimensions for castable samples*

Fig. 6 shows cold modulus of rupture, and Fig. 7 cold crushing strength. All materials show a significant effect of temperature increase on the strength of the material.
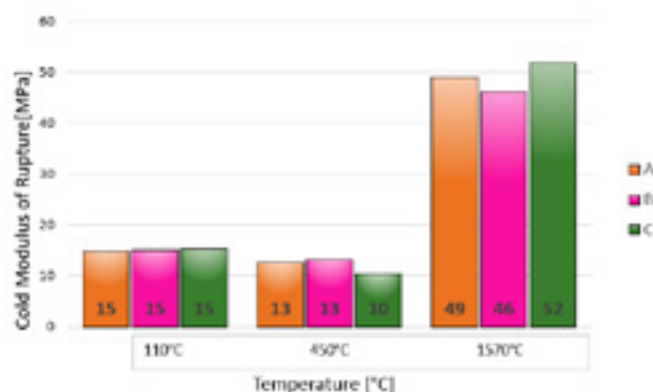


**Fig. 6**: *Cold Modulus of Rupture for castable samples*
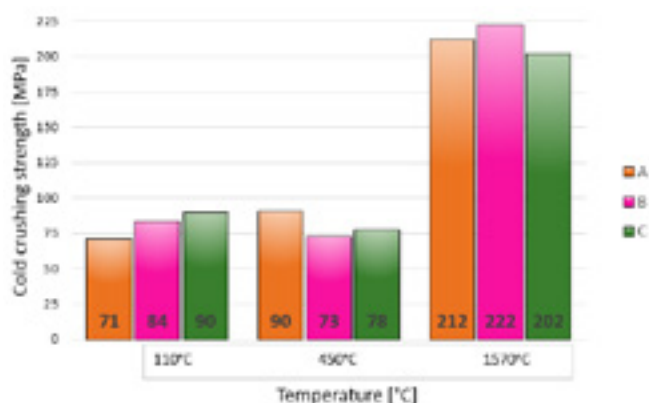


**Fig. 7**: *Cold Crushing Strength for castable samples*

The castable is used in a highly erosive environment in the steel ladle bottom. Therefore hot modulus of rupture was carried out at a temperature of 1450°C (Fig. 8) as an indicator of erosion resistance at high temperature. High hot strength values were obtained, which prove the high resistance of the material even in difficult conditions. Each of the samples obtained >30MPa. The highest result was observed for sample C. This may be due to the type of reactive alumina. In its composition, E-SY 2000 contains super fine spinel, which is more reactive and enables better sintering. [6]
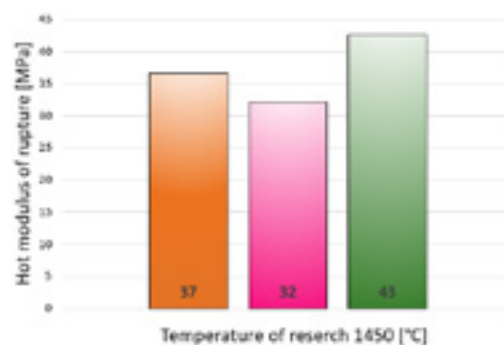


**Fig. 8**: *HMoR for castable samples*

## PRACTICAL EXPERIENCES

After analysis of the above results, sample C was selected for the industrial trial. Figure 1 shows application of castable around the well-block in the steel ladle bottom in Dabrowa Gornicza. Initially the product was dry mixed and then the specified amount of water was added. The total mixing time was approximately 6 minutes. Because of the short wet out time of max 30s, the operators rely on the castable behaving normally and therefore not add additional water. Long setting time and consistency of the mix (doesn't stick to the blades or to the walls of the mixer) allows for smooth and reliable application.

The desired lining life performance is achieved at ArcelorMittal Dabrowa Gornicza, and the joint lining is never the root cause for early repair of the bottom. However the wear of the well block defines the maintenance pattern.

## CONCLUSIONS

Joint lining between bricks and well block in the bottom is important for the performance of the entire ladle bottom lining. Self-flowing corundum spinel castable with spinel-containing bimodal reactive alumina type E-SY 2000 has shown good performance at AM Dabrowa Gornicza. The developed castable shows low water demand, fast wet out, low dilatancy as tested by the ball drop test, and low stickiness. Mixing and installation in the steelplant works well without problems even in sub-optimal conditions, and has become the standard practice. The desired lining life is achieved by the wear resistant corundum spinel low cement castable.

363

## REFERENCES

[1] Ch. Schacht "Refractory Handbook" 2004 by Marcel Dekker
[2] S. Klaus, A. Buhr, M. Bauer, m. Göbbels, J. Dutton: Formation of hexa-aluminate solid solution phases in spinel containing castables – mineralogical investigations in the system CaO-Al2O3-MgO, 62. International Colloquium on Refractories 2019, Aachen, 90-94.
[3] R.W. McConnell, G. Büchel, A. Buhr, R. Kockegey-Lorenz, D. Gierisch: E-SY Aluminas – The new solution for Pumpability of silica-free high performance tabular alumina and spinel castables, UNITECR 2005, Orlando/USA, 424-428
[4] A. Lak, A. F. Thunemann, M. Schilling, F. Ludwig "Resolving particle size modality in bi-modal iron oxide nanoparticle suspensions" Journal of Magnetism and Magnetic Materials, Vol 380, April 2015
[5] R. Kockegey-Lorenz, D. Schmidtmeier, A. Buhr, D. van Garsel, J. Dutton "E-SY alumina for easy to use high-performance castable" 52nd ICR Aachen, 2009, 86-88
[6] R. Kockegey-Lorenz, A. Buhr, D. Zacherl, B. Long, S. Hayashi, J. Dutton: Review of Matrix Aluminas for Refractory Formulations, UNITECR 2011, Kyoto, Japan, paper 2-B2-9

# APPLICATION OF UNBURNED MAGNESIA BRICKS
# FOR STEEL SECONDARY REFINING PROCESSES

Yuya Tomita, Takahiro Anan, Kiyoshi Goto and Katsumi Morikawa
Krosaki Harima Corporation, Kitakyushu, Japan

## ABSTRACT

In the steel refining processes, magnesia carbon or magnesia chrome bricks have been widely used conventionally as refractories for holding molten steel to be refined due mainly to satisfy the material requirement for high corrosion resistant. However, magnesia carbon bricks and magnesia chrome bricks have heat loss and hexavalent chromium formation problems, respectively. A novel unburned magnesia brick have been developed for use in the steel secondary refining process that contains neither graphite nor chromium, in light of future environmental issues. As a notifying point of the developed brick, the high temperature corrosion resistance against iron oxide, FeO was superior to the conventional magnesia-carbon and -chromite bricks. Thus, newly developed environmentally friendly unburned magnesia brick will be contributing not only in the reduction of $CO_2$ and carbon neutrality but also in the elimination of chromium.

## INTRODUCTION

Magnesia carbon (MgO-C) bricks and magnesia chrome (MgO-$Cr_2O_3$) bricks with high corrosion resistance are used widely in the secondary refining processes of steel. The development of chromium-free material is examined as a countermeasure against the problem that magnesia chrome bricks easily react with alkaline components in the molten steel and produce harmful hexavalent chromium compound [1 - 4].

In future, the challenge for $CO_2$ reduction and carbon neutrality will be required more keenly for industrial world. MgO-$Cr_2O_3$ bricks are fired at temeratures higher than 1700 °C, and a large amount of carbon dioxide is emitted during production. An unburned MgO-$Cr_2O_3$ brick tempered at 200 °C for the secondary refining was examined and reported to have corrosion resistance equivalent to that of fired MgO-$Cr_2O_3$ bricks [5], [6] .

Since the MgO-C bricks contain flake graphite, there are concerns about heat dissipation into the atmosphere due to increased thermal conductivity and carbon leaching into the molten steel. It was reported that applying low graphite MgO-C bricks to the converters, the heat loss could be reduced by 17 % with improved durability of the brick [7].

Considering these situations, we also have examined to develop an unburned magnesia brick for the secondary refining without containing neither chromium nor graphite. In the present study, the characteristics of the developed bricks were investigated, together with the effect of heat loss control when used in an actual furnace.

## EXPERIMENTAL PROCEDURE

### Test Materials

The unburned magnesia (MgO) bricks without containing graphite and MgO-C bricks with the graphite contents of 1, 3, and 5% were named materials A to D, respectively. They were chosen as test materials together with material E of a direct bonded MgO-$Cr_2O_3$ brick for comparison, as shown in **Table 1**. Raw materials powders for the test materials A to D were mixed with both suitable amounts of phenol resin as binder, and some antioxidant agent, molded and formed to 230×100×110mm shape bar using a vacuum hydraulic press, then dried at 250°C for 5h to prepare the test samples.

### Test Method

*Density and Porosity*

Bulk density and porosity were measured based on JIS R 2205. The measurements were carried out for each sample for materials A to D after drying and after firing at 1400°C for 3h under the reducing atmosphere as shown in **Table 2**. As a comparision the direct bonded magnesia chrome brick (E) after fired was also evaluated.

*Thermal Property and Corrosion*

The thermal conductivity was measured at 800 °C using the heat flow method in the specimen after the firing at 1400 °C for 3h.

**Figure 1** shows a schematic of the apparatus and method of high-temperature Fe-oxide corrosion test. The test was carried out by a method in which a specimen, which had been reduced and fired at 1400 °C for 3h in advance, was heated to 1750 °C and held for 30min, oxygen was blown from a steel lance, and the brick was corroded by the Fe-oxide formed with heat generated by oxidation reaction in th the lance tip under a high temperature [8]. The degree of corrosion was evaluated by measuring the amount of errosion in a cut surface of the specimen after the corrosion test and in addition to the microstructure observation in the cross section of the specimen at the vicinity of corroded surface after the high temperature Fe-oxide test. Assessment of the corrosion behavior was performed by two methods; a direct measurement of the amount of corrosion and an analysis of microstructural observation of corroded surface. In the former assessment, measured amount of corrosion for each sample was converted to corrosion index to compare the amount relatively by setting the amount of corrosion for MgO-$Cr_2O_3$ to 100. Microstructural observation as an another assessment, was carried out in the specimen obtained from the cross section of the sample for each material at the vicinity of corroded surface using scanning electron microscope (SEM) including detail analysis using EPMA (Electron probe micro-analyzer).

Tab. 1: Composition of test materials A~E

| Material | | A | B | C | D | E |
|---|---|---|---|---|---|---|
| (Category) | | MgO | MgO-C | | | MgO-$Cr_2O_3$ |
| Composition / mass% | MgO | 100 | 99 | 97 | 95 | 54 |
| | $Cr_2O_3$ | - | - | - | - | 31 |
| | $Al_2O_3$ | - | - | - | - | 7 |
| | C(Graphite) | - | 1 | 3 | 5 | - |
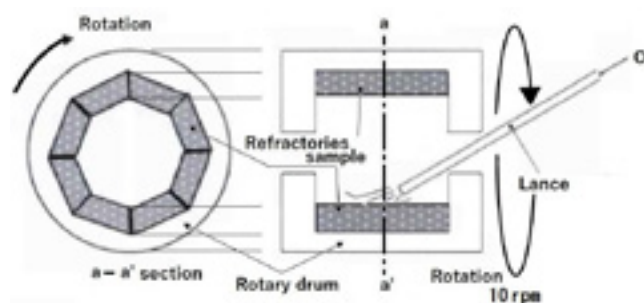


*Fig. 1: Schematic image of high temperature Fe-oxide test.*

## EXPERIMENTAL RESULTS AND DISCUSSION

### Bulk Density and Apparent Porosity

**Table 2** shows the physical properties of materials (A-D) after dried and after fired at 1400 °C for 3h and material (E) after firing as a conpmarision. **Figure 2** shows the variations of bulk density (a), apparent porosity (b) with amount of graphite addition for both dried and fired states.

First, the bulk density showed a tendency to increase with the graphite addition for the amount up to 1% then, decrease with exceeding addition to 1% for both dried and fired states. Next, the apparent porosity tended to decrease with increase in the graphite addition for after dried states, and showed almost constant value in the case of the addition exceeding 1%, though it slightly decreased with the graphite addition for after fired states.

Tab. 2: Bulk density and porosity of materials A~ E

| Material<br>Density/Porosity | A<br>MgO | B<br>MgO-C | C | D | E<br>MgO-Cr$_2$O$_3$ |
|---|---|---|---|---|---|
| Bulk density<br>/ × 10$^3$kg·m$^{-3}$ | 3.14<br>(3.15) | 3.14<br>(3.16) | 3.12<br>(3.15) | 3.08<br>(3.10) | 3.27 |
| Apparent porosity<br>/ % | 9.0<br>(5.4) | 8.3<br>(4.3) | 8.2<br>(3.5) | 8.3<br>(3.0) | 15.6 |

(   ) : After drying
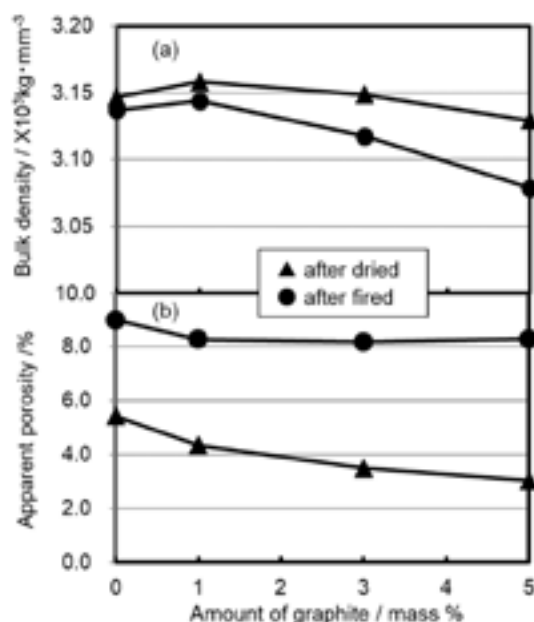


Fig. 2: Variations of bulk density (a) and apparent porosity \ (b) with amount of graphite addition for both dried and fired states.

**Thermal Conductivity and High Temperature Corrosion**
The dependences of the graphite addition amount on the thermal conductivity at 800°C and the corrosion index in the high temperature Fe-oxide test are shown in **Figure 3** (a) and (b), respectively. Decreasing the graphite content, the thermal conductivity lowers to the minimal value with 0% addition, resulting in the 50% reduction from the value with 5% graphite. The thermal conductivity value of the material without graphite is almost the same value of the direct bonded MgO-Cr$_2$O$_3$ brick.
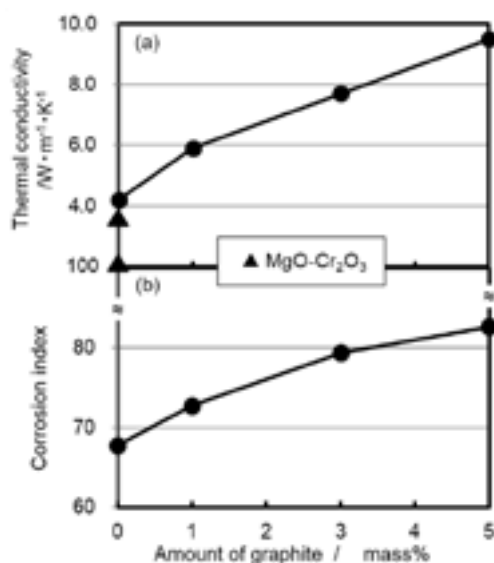


Fig. 3: Variation of thermal conductivity (a) and corrosion index obtained by the high temperature Fe-oxide test (b) with amount of graphite addition.

Supposing the corrosion index of the magnesia chromite specimen as 100, the index of MgO-C bricks was much lower than that of the magnesia chromite brick and the index lowered with decreasing the graphite indicating the improvement in the corrosion resistance.
The corrosion resistance of the MgO-C bricks after firing has been reported to be affected by the porosity in the manner in which the corrosion resistance became higher with lowering the porosity [9]. As shown in the **Figure 3** (b), the corrosion resistance against Fe-oxide at high temperature was improved in the bricks without graphite, although the porosity after firing was higher than in the other bricks. To investigate the reason why this occurred, we have carefully observed the microstructure at the vicinity of corroded test surface of the specimen after high temperature Fe-oxide test.

**Microstructure of Corroded Surface of Bricks**
**Figure 4** shows the microstructures at the vicinity of corroded test surface of the cross section after high temperature Fe-oxide test for materials with (a) 5 %, (b) 0 % graphite and (c) the direct bonded MgO-Cr$_2$O$_3$ brick.
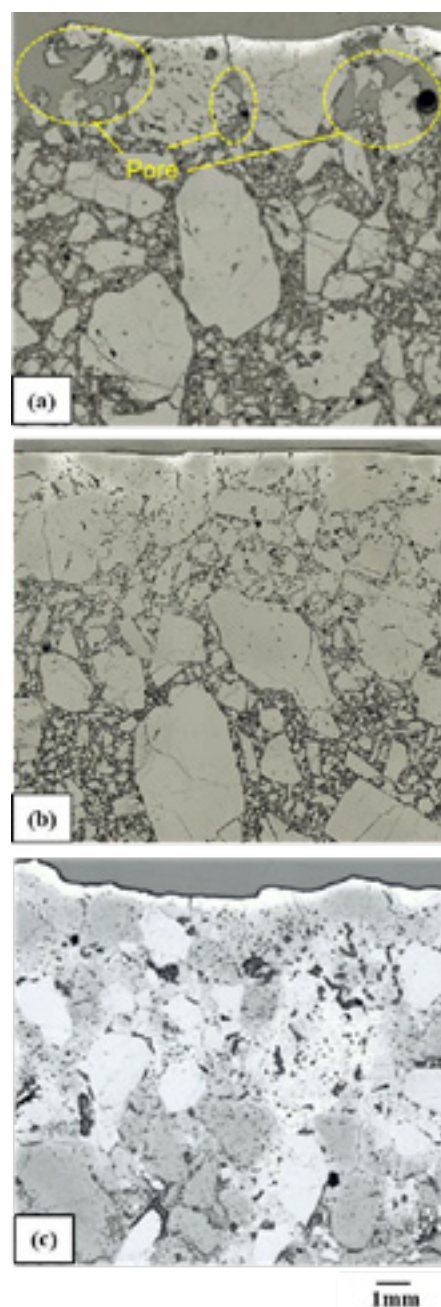


Fig. 4: Microstructure of the cross section of the specimen at the vicinity of surface after high temperature Fe-oxide corrosion test for materials A, D and E for (a), (b) and (c), respectively.

365

Although formation of MgO clinker on the corroded test surface is observed, in both materials with graphite of 5 %(a) and 0 %(b) the clinker has poor continuity by intervening the pores. In the case of (a) large pore formed by corrosion with MgO-C reaction. On the other hand, in the case of (b), no large pore in the layer of MgO clinker is observed on the corroded test surface, and there is durable connecting layer was reserved. The formation of the pores due to MgO-C reaction in the specimen inside under the clinker layer was also significantly suppressed in the case of (b) compared with that of (a). Thus, it was apparent that the material without graphite showed higher corrosion resistance than those with graphite by preventing the clinker layer formed in the corroded surface from the penetration of Fe-oxide and the dispersion of Mg with MgO-C reaction, protecting the inside under the layer.

In the case of (c), which had the worst corrosion resistance test results, no large pore was observed on the corroded test surface like as the case of (b). On the other hand, the shape of the aggregate in the material E (c) was observed to be indistinct, unlike both the materials A (b) and D (a).

To investigate the difference in erosion between the materials A (b) and E (c), EPMA was used to analyze the microstructure. **Figure 5** shows the state of the hot surface of for both materials A (a) and E (b) after the Fe-oxide test. Focusing on the elemental distribution of iron, it was observed that in the A (a), the iron remained on the hot surface, while in the E (b), the iron infiltrated into the interior of the structure. Thus, the material A (a) was considered to have improved corrosion resistance where the infiltration of iron was more controlled than in the material E (b) .
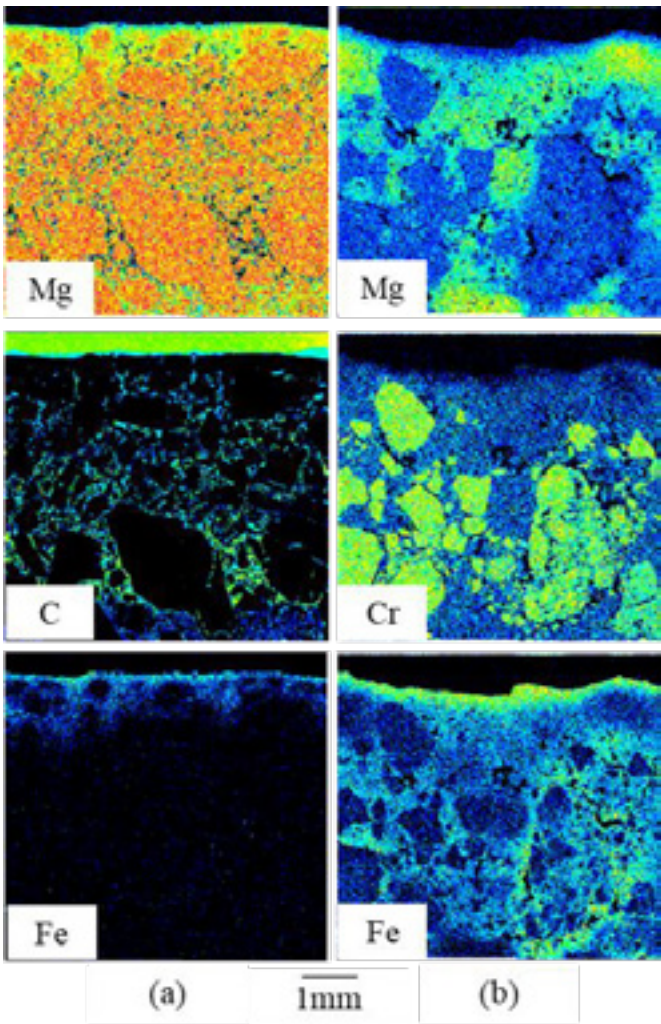


*Fig. 5: EPMA analysis of the materials A (a) and the E (b) after the Fe-oxide test.*

## Possible Improvement of Heat Dissipation

The heat conduction in the steady state was calculated on the assumption that four materials shown in the **Table 1** were applied respectively to the vessel wall (wear brick) in the lower vessel of the typical RH degasser. **Figure 6** shows the cross sectional view of the lower vessel of the RH degasser (a) and the part of area surrounded by the broken line was simplified to a model cylinder with (b), showing also layer composition of the vessel wall. 2500 mm height and 1000 mm distance from the center to the surface of the wear brick for the calculation. In addition, **Table 3** shows thickness and thermal conductivity for 4-layer materials composing the wall as a calculation condition. The measured values shown in **Figure 3** (a) were used as the thermal conductivity of 4 materials in the **Table 3** (1).
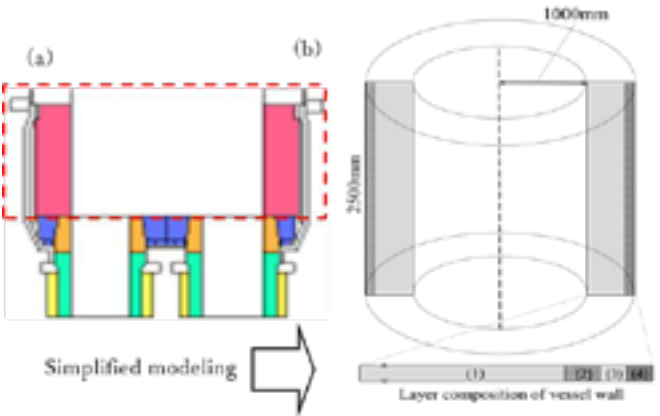


*Fig.6 : Cross sectional view of the lower vessel of the typical RH\* degasser(a) and the part of area surrounded by the broken line was simplified to a model cylinder(b) with wall composed by 4-layer materials shown in Table 3.   (\*RH: Ruhrstahl Heraeus degassing process)*

Tab. 3: Condition for calculation of heat conduction in vessel wall

| Layer composition of wall | | Thickness /mm | Thermal conductivity, $\lambda$ /W·m$^{-1}$·K$^{-1}$ |
|---|---|---|---|
| (1) | Wear brick(inner) | 450 | 4.0~9.5(MgO-C brick, see Fig.3(a)) |
| (2) | Permanent brick | 50 | 3.0 |
| (3) | Insulating brick | 30 | 0.1 |
| (4) | Steel shell (outer most) | 30 | 40.0 |

Assuming steady heat conduction, heat release from the steel shell of the outermost layer in the vessel wall shown in **Figure 6** (b), is estimated for the case that the inner and outer surface sides are contacting with 1600 ℃ molten steel and 25 ℃ air, respectively, and the emissivity of the steel shell as 0.85.

For 4 materials in the **Table 1**, the estimated both temperature of external steel shell and heat flux are shown in **Figure 7** as a function of graphite amount in the materials. As shown in the **Figure 7**, the temperature of steel shell lowered with the graphite content, and the temperature for the material without graphite was lower than that for the 5%graphite content by about 16℃. Heat flux reduced also with the graphite content as shown in **Figure 7**, and the heat flux for the material without graphite decreased by about 13% compared with that for the 5% graphite content.

In the estimation performed so far, the heat release was calculated with the constant thickness of wear brick as 450mm. In actual operation, however, the wear brick must be thinned with time due to erosion of molten steel. Thus, assuming that the brick is thinned to 100mm at a constant rate, the temperature of both external shell and heat flux are calculated for the 4 materials with taking account of thinning of the wear brick during operation, as shown in **Figure 8**(a) and (b). As apparent in the figure, when the wear brick becomes

100mm thickness, the temperature of external shell and heat flux increased from those for the original thickness of 450mm by about 30% and about 75%, respectively.
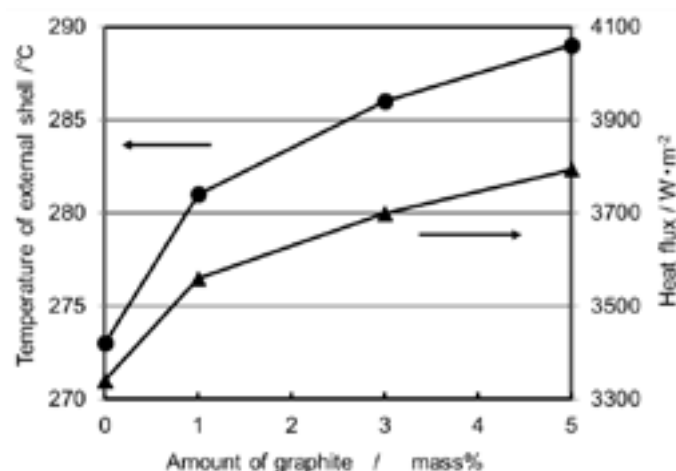


*Fig.7 : Variations of temperature of exteranal steel shell, and heat flux with amount of graphite addition.*
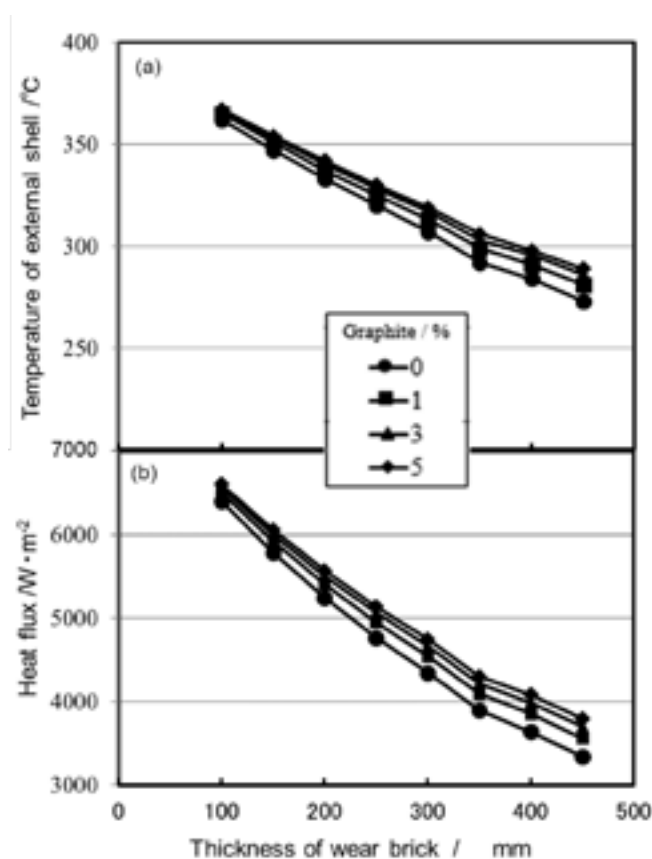


*Fig.8 : Variations of temperature of exteranal steel shell (a), and heat flux (b) with thickness of wear brick for 4-kind of MgO-C system materials*

Next, the accumulated heat radiation from the lower vessel of the RH degasser, Heat transfer amount Q was calculated using the equation (1) as shown in **Figure 9**, when the 4 materials are applied to the wear brick of the vessel wall. As the assumption, total life of the lower vessel is considered as 350ch with 30 min each.

$$Q = h_c \cdot S \cdot (T_s - T_a) + \sigma \cdot \varepsilon \cdot S \cdot (T_s^4 - T_a^4) \qquad (1)$$

Where, $h_c$ is convective heat transfer coefficient of external surface: $1.16 \times 10^{-5}$ W/mm$^2$ · K$^{-1}$, S is area of heat transfer, $T_s$ and $T_a$ are temperatures of surface of the wear bricks and outside air, respectively, σ is Stefan Boltzmann constant:$5.67 \times 10^{-14}$ W/mm$^2$ · K$^4$ and ε is emissivity of the steel shell: 0.85.

The accumulated heat radiation decreased with decreasing graphite content, and the heat radiation of the brick without containing the graphite was about 10% lower than that with 5% graphite content as shown in **Figure 9**.
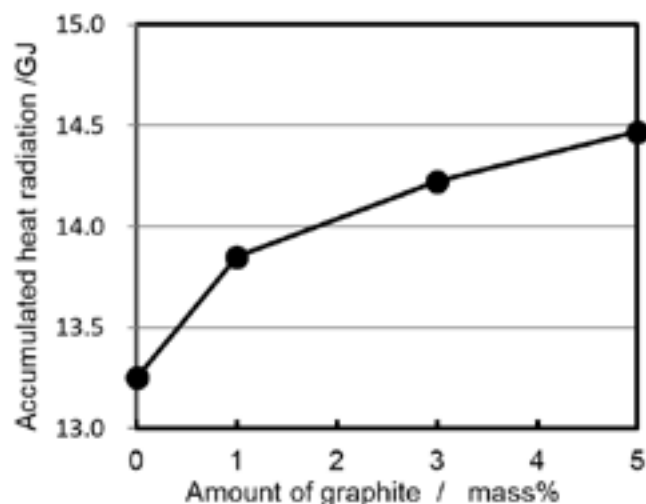


*Fig.9 : Accumulated heat radiation of the lower vessel of RH degasser estimated for the cases of 4 MgO-C materials used as the wear brick of the furnace.*

## SUMMARY

The characteristics of unburned graphite-free magnesia bricks were confirmed to be lower bulk density, higher porosity, and lower thermal conductivity in comparison with the bricks containing graphite. In addition to the expected suppression of the heat loss, due to low thermal conductivity, the unburned graphite-free magnesia brick showed higher corrosion resistance against Fe-oxide at high temperature than the MgO-C (graphite) bricks. Thus, in the practical use of the unburned graphite-free magnesia brick, the steel making process is expected to be improved by increasing durability of refractories for the secondary refining, by decreasing the environmental loading through both CO$_2$ reduction and chromium eliminations from the refractories, and by minimizing the opportunity of the steel to pick-up carbon from the refractories.

## REFERENCES

[1] Nakamori, Y., et al. Application of chrome-free brick to side wall of RH-lower vessel. Taikabutsu 49(8), 1997, p.478-479

[2] Shimizu, K., et al. Chrome-free brick applied to lower vessel of RH degasser. Taikabutsu 53(2),2001, p.84-85

[3] Anan, T., et al. Corrosion resistance and mechanism of bricks for secondary furnace. Taikabutsu 67(3), 2015, p.166

[4] Ghosh, G., et al. Development of chrome free brick for RH degasser. Proc. UNITECR 2009, p.80

[5] Pagliosa, C., et al. Novel tempered MgO-Cr$_2$O$_3$ bricks with zero C binder for RH degasser. Proc. UNITECR 2019, p.137-140

[6] Borges, B., et al. Zero carbon tempered MgO-Cr$_2$O$_3$ bricks for RH degassers : advances from customers' trials. Proc. UNITECR 2022, p.112

[7] Tanaka, M., et al. Nano-tech. MgO-C bricks for converters to minimize the heat loss. Proc. UNITECR 2011, 2-E-18

[8] Fuchimoto, H., et al. Result of high temperature oxgen Fe-oxide corrosion test of bricks used for RH. Taikabutsu, 52(3), 2000, p.136-137

[9] Matsudo, H., et al. Influence of porosity after heat treatment on the corrosion resistance of MgO-C bricks. Taikabutsu, 66(3), 2014, p.145

367

# APPLICATION OF HIGH−CALCIUM MAGNESIA IN LADLE BRICK AND ITS PURIFICATION EFFECT ON MOLTEN STEEL

Xiaoli TIAN[1,2,3], Zhixun LI[1,2], Runtang FENG[1,2], Tianqing LI[1], Cheng LIU[1], Xiangdong XING[3]

1. Puyang Refractories Group Co. Ltd., Puyang 457100, China
2. PRCO Qinghai High-tech Material Co.,Ltd. Haidong 810700, China
3. Xi'an University of Architecture and Technology, Xi'an 710055, China

**ABSTRACT**

With high-calcium fused magnesite produced by Tibetan microcrystalline magnesite in China and graphite as main raw materials, aluminum powder、 silicon powder and silicon carbide powder as antioxidants, and phenolic resin as binder, a new type of high-calcium magnesia-carbon brick was prepared after mixing, molding and drying. Then its physical and chemical properties were tested. To investigate the influence of the new high-calcium magnesia-carbon brick on molten steel quality in smelting process, a high-temperature vacuum tube furnace was adopted, the smelting temperatures were 1550℃ and 1600℃, and the smelting times were 20min, 40min, 60min, 80min and 100min. The comparison experiment between new high-calcium magnesia-carbon brick and traditional magnesia-carbon brick was conducted for the second smelting of 45 steel. By comparing the change characteristics of molten steel composition and inclusions before and after smelting, the purification of S and P elements and the removal of inclusions by the new high-calcium magnesia-carbon brick were explored. The results show that: 1) The new high-calcium magnesia-carbon brick produced with high-calcium fused magnesia has a CaO content of about 5wt%, and its physical properties are equivalent to those of traditional magnesia-carbon brick; 2) The purification of S and P elements in steel by the new high-calcium magnesia-carbon brick is obviously higher than traditional magnesia-carbon brick, and the removal rate of S and P can separately reach 14.58% and 19.41% under the melting condition of 1600℃×40min. 3) The new high-calcium magnesia-carbon brick has obvious removal effect on the number and size of inclusions in steel.

**KEY WORDS**：Tibetan microcrystalline magnesite; high-calcium fused magnesite; new high-calcium magnesia-carbon brick; purify molten steel; remove inclusions

## INTRODUCTION

Magnesia-carbon brick is a common material of ladle. The main raw materials are magnesia, graphite, resin and antioxidant. Traditional magnesia-carbon brick has the advantages of high temperature resistance, good slag corrosion resistance and thermal shock resistance.

Magnesium-calcium refractories not only have good chemical stability to molten steel and good slag corrosion resistance, but also can purify molten steel[1-2].

The crystal structures of MgO and CaO are NaCl-type structures, belonging to face-centered cubic lattice, cubic crystal system and Fm-3m space group [3].

The lattice constant of MgO is 0.4211nm, the theoretical density is about 3.58g/cm3, and the melting point is 2800℃. MgO has good corrosion resistance, but its thermal stability is poor. So, it is easy to be infiltrated and eroded by slag. The lattice constant of CaO is 0.4810nm, the theoretical density is about 3.582g/cm3, the melting point is 2572℃. CaO has a small thermal expansion coefficient at high temperature and low saturated steam pressure. And the structural spalling resistance and slag resistance are excellent.

At the same time, CaO easily reacts with $SiO_2$ in molten slag to generate $C_2S$ and $C_3S$. These products have high melting point and high viscosity, which can improve the viscosity of slag. Thus it becomes easy for slag to hang on the surface of working layer to form a covering layer, which can block pores and effectively slow down the penetration of slag into bricks, and then protect refractories from being corroded by molten slag. Finally, the slag resistance of the material is improved. At the same time, the covering layer makes the furnace lining not directly contact with air. This reduces carbon oxidation. Moreover, CaO has high chemical activity and can effectively absorb [Al], [S], [P] and other impurities in molten steel. In addition, the existence of free CaO makes magnesia-calcium-carbon brick have good slag corrosion resistance to high alkalinity, and the slag alkalinity is low in the initial stage of refining. Free CaO can improve the slag alkalinity on the surface of working lining brick and then reduce the chemical corrosion of slag.

Based on the above theory, this paper firstly prepares a new type of high calcium magnesium carbon brick with high calcium magnesia compared from Tibetan microcrystalline magnesite (Western CHINA ) as raw material, in order to improve the purification effect of ladle brick on molten steel; Then, to investigate the influence of new high-calcium magnesia-carbon brick on the quality of molten steel in the smelting process, a high-temperature vacuum tube furnace was used to select different smelting process conditions, and a comparative experiment was carried out between new high-calcium magnesia-carbon brick and traditional magnesia-carbon brick, and 45 steel was used for secondary smelting, and the characteristics of molten steel composition before and after were compared. The interaction mechanism between new high calcium magnesium carbon brick and molten steel is analyzed, and the purification law of molten steel is explored.

## 1. EXPERIMENTAL PROCEDURE

### 1.1 Raw materials

The main raw materials are ordinary magnesia and Tibetan high calcium magnesia, and their chemical compositions are shown in Table 1.

Tab.1: chemical compositions of magnesia

| Magnesia | ω/% | | | |
|---|---|---|---|---|
| | SiO₂ | Fe₂O₃ | CaO | MgO |
| Ordinarymagnesia A | 0.58 | 0.61 | 1.76 | 97.05 |
| Tibetan high-calcium magnesite B | 0.51 | 0.42 | 6.03 | 92.85 |

### 1.2 Sample preparation

Traditional magnesia-carbon bricks and new magnesia-carbon bricks with high calcium content were made from three kinds of magnesia and graphite in Table 1, aluminum powder, silicon powder and silicon carbide powder as antioxidants and phenolic resin as binder, respectively, after mixing, molding and drying, and their physical and chemical properties were tested. The results are shown in Table 2.

Tab.2: Properties of two kinds of magnesia-carbon bricks

| Brick | chemical composition ω/% | | | | | physical properties | |
|---|---|---|---|---|---|---|---|
| | CaO | MgO | C | SiO₂ | Al₂O₃ | B.D. | CCS |
| A | 1.88 | 86.37 | 8.01 | 2.02 | 2.03 | 2.99 | 35.9 |
| B | 5.01 | 83.43 | 8.01 | 2.01 | 2.02 | 3.01 | 35.7 |

### 1.3 Experimental process

A high-temperature vacuum tube furnace (model CQL16-60, as shown in Figure 1) was adopted in order to investigate the influence of new high-calcium magnesia-carbon brick on the quality of molten steel during smelting.

While the smelting temperature was set to 1,550℃ and 1,600℃, and the smelting time was set to 20min, 40min, 60min, 80min and 100min.

The secondary smelting experiment was conducted on 45 steel with new high-calcium magnesia-carbon brick and traditional magnesia-carbon brick.

By comparing the change characteristics of molten steel composition and inclusions before and after smelting, the purification effect of new high calcium magnesium carbon brick on [S] and [P] elements in steel and the removal of inclusions were explored.



*Fig.1: high-temperature vacuum tube furnace*

## 2. RESULTS & DISCUSSION

### 2.1 Effect of high calcium magnesium carbon brick on sulfur in steel

The effect of magnesia-carbon brick on sulfur in steel under different smelting conditions was shown in Figure 2.

It can be seen that，

1) Under the melting condition of 1550℃, the highest desulfurization rate is only 2.17% when using traditional magnesia-carbon brick A, while that is 5.38% when using high calcium magnesia-carbon brick B.

2) Under the condition of melting at 1600℃, the highest desulfurization rate is only 7.29% when using traditional magnesia-carbon brick A, while that is 14.58% when using high calcium magnesia-carbon brick B.

3) Compared with traditional magnesia-carbon brick, high calcium magnesia-carbon brick has obvious desulfurization effect.

It is considered that, there is some free CaO in the new high calcium magnesium carbon brick compared with traditional magnesia-carbon brick. when melting, the free CaO component in the new high calcium magnesium carbon brick will react with [S] in molten steel as follows:

$$[S]+(CaO)\rightarrow(CaS)+[O] \tag{1}$$

CaS will adhere to the surface of refractories, forming a dense sulfide layer. Moreover, the concentration of CaS gradually increases with the extension of reaction time, and a dense reaction layer is formed. Part of the reaction layer falls off due to the stirring of molten steel, and CaS will enter the steel to form inclusions or gradually enter the slag for removal.



（a）1550℃ （b）1600℃
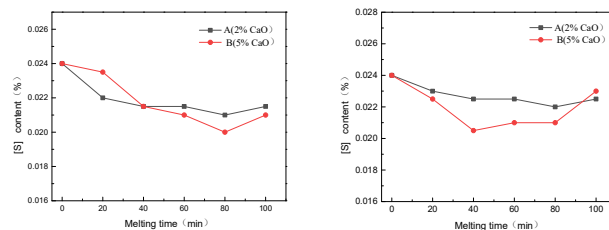
*Fig.2: Effect of magnesia-carbon brick on sulfur in steel under different melting conditions*

### 2.2 Effect of high calcium magnesium carbon brick on phosphorus in steel

The effect of magnesia-carbon brick on phosphorus in steel under different smelting conditions was shown in Figure 3. It can be seen that，

1) Under the melting condition of 1550℃, the highest dephosphorization rate is only 9.7% when using traditional magnesia-carbon brick A, while that is 14.5% when using high calcium magnesia-carbon brick B.

2) Under the melting condition of 1600℃, the highest dephosphorization rate is 16.1% when using traditional magnesia-carbon brick A, while that is 19.4% when using high calcium magnesia-carbon brick B.

3) Compared with traditional magnesia-carbon brick, high calcium magnesia-carbon brick has obvious dephosphorization effect.

It is considered that, when the new high calcium magnesium carbon brick is used for smelting, the free CaO component in the brick will react with [P] in molten steel as follows:

$$2[P]+5[O]=(P_2O_5) \tag{2}$$

$$(P_2O_5)+4(CaO)=(4CaO \cdot P_2O_5) \tag{3}$$

Therefore, the new high calcium magnesium carbon brick has good dephosphorization effect when melting.



（a）1550℃ （b）1600℃
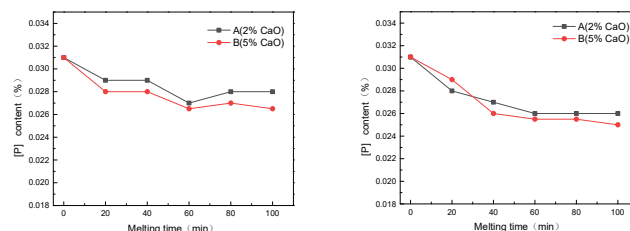
*Fig.3: Effect of magnesia-carbon brick on sulfur in steel under different melting conditions phosphorus*

### 2.3 Effect of high calcium magnesium carbon brick on the change of inclusion quantity in steel

The effect of magnesia-carbon brick on Quantity and area ratio of inclusions in steel under different smelting conditions was shown in Figure 4. It can be seen that,

1) Under the melting condition of 1550℃, the reduction ratio of the Inclusion quantity in steel is 28.3% when melting with traditional magnesia-carbon brick A, while that is 29.7% when melting with high calcium magnesia-carbon brick B.

2) Under the melting condition of 1600℃, the reduction ratio of the Inclusion area in steel is 25.1% when melting with traditional magnesia-carbon brick A, while that is 29.1% when melting with high calcium magnesia-carbon brick B.

369

（a）1550℃       （b）1600℃
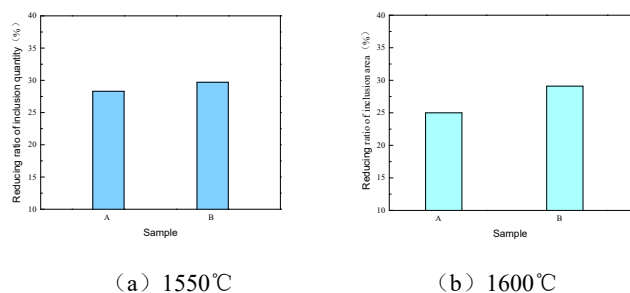
*Fig.4: Effect of magnesium carbon brick on the inclusion quantity in steel under different melting conditions*

Figure 5 shows the distribution of inclusions in the original steel sample. The selected 45 steel is with low cleanliness and high inclusion content. So many banded inclusions can be observed, and the distribution is relatively dense as a whole.

Figure 6 shows the distribution of inclusions in steel samples after melting with new magnesia-carbon brick B. It can be seen that the number of inclusions in steel is obviously reduced and the inclusion distribution transformed into sporadic point distribution after melting.



*Fig. 5: Banded distribution of typical inclusions in original steel samples*
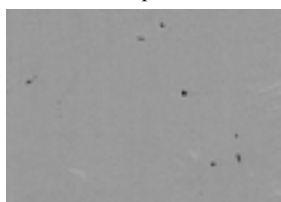


*Fig.6: Distribution of Inclusions in Steel Samples after Melting*

*（1600℃×40min）*

Above all, compared with the traditional magnesia-carbon brick, the high calcium magnesia-carbon brick significantly improves the reduction ratio of the number of inclusions and the area of inclusions in steel. That is, the effect of removing inclusions in steel is stronger.

## 2.4 Effect of high calcium magnesium carbon brick on size distribution of inclusions in steel

Figure 7 shows the influence of magnesia-carbon brick on the size distribution of inclusions in steel under different melting conditions (small particle inclusions with a diameter of 1-3 μ m; Large particle inclusions, diameter > 3 μ m), it can be seen that,

1) Under the melting condition of 1550℃, compared with the traditional magnesia-carbon brick A, the reduction ratio of small particle inclusions in steel is basically the same, but the reduction ratio of large particle inclusions in steel is significantly improved.

2) Under the melting condition of 1600℃, compared with the traditional magnesia-carbon brick A, the reduction ratio of small particle inclusions and large particle inclusions in steel is basically the same.

In summary, compared with the traditional magnesia-carbon brick, when high calcium magnesium carbon brick is used for smelting, the size of inclusions in steel is obviously reduced; while the reduction ratio of small particle inclusions in steel is basically

the same, but the reduction ratio of large particle inclusions is obvious.



（a）1550℃       （b）1600℃
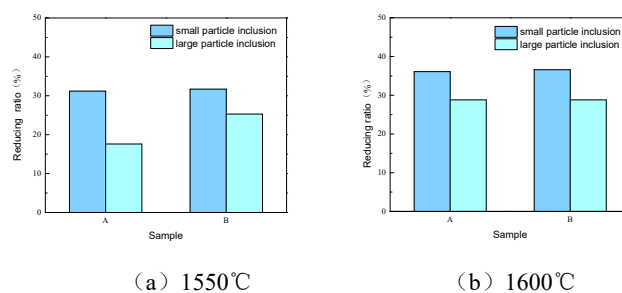
*Fig.7: Effect of magnesium carbon brick on the inclusions size under different melting conditions*

## CONCLUSIONS

1) The new high-calcium magnesia-carbon brick produced with high-calcium fused magnesia has a CaO content of about 5wt%, and its physical properties are equivalent to those of traditional magnesia-carbon brick;

2) The purification of S and P elements in steel by the new high-calcium magnesia-carbon brick is obviously higher than traditional magnesia-carbon brick, and the removal rate of S and P can separately reach 14.58% and 19.41% under the melting condition of 1600℃×40min.

3) The new high-calcium magnesia-carbon brick has obvious removal effect on the number and size of inclusions in steel.

## REFERENCES

[1] LI Nan, KUNAG Jiacai. Study on Dephosphorization of Basic Refractory. Refractories, 2000,34(5):249—251.

[2] TIAN Lin，ZHANG Hongying. Influence of MgO-CaO Refractory on Impurity of IF Steel [J]. Journal of Anshan University of Science and Technology，2006, 29(3): 239-241.

[2] CHEN Zhaofeng，YANG LIxia．Inorganic non-metallic materials science[M]．Xi'an,Northwestern Polytechnical University press，2022.12.

# STEEL LADLE: CAPACITY INCREASE, LINING CONCEPTS AND RECYCLING EXPERIENCE OVER 25 YEARS

Reinhard Exenberger, Georg Grimm
voestalpine Stahl Gmbh, Linz, Austria

## ABSTRACT

The annual production in Linz has grown from 3.6 mt/a in 1998 to almost 5.3 mt/a in 2023. To provide these figures, an increase of the heat weight from 151,2 t/heat to 178t/heat had been necessary. When we had been changing the LD vessels to bigger sizes in 2001 and 2009, we also had to purchase new ladle vessels to handle the bigger heat size. To relax the pressure in the daily converter production, we procured bigger steel shells in 2022 again.

Whilst changing the steel ladle vessels, we realized modifications to the lining concepts, for an increase of ladle capacity. We gained experience with brick lined and monolithic ladles.

Regarding refractory breakout material we relied on our decades of experience in recycling. Magnesia breakout has been recycled to Magnesia Carbon bricks in the inhouse brick plant, whereas fine grains from the bag filters have been charged into the LD vessel as Magnesia carrier. Alumina breakout has been recycled into slag formers for the secondary metallurgy.

## STEEL PRODUCTION AT VOESTALPINE LINZ

voestalpine is a globally active group and represented by 500 companies that produce, process, and further develop high-quality steel products in 50 countries on all 5 continents. The headquarter is in Linz/Austria. There is the group's biggest steel plant as part of an integrated mill for flat steel production. The production facilities of the melting shop and the caster area are three hot metal desulfurization stands, one hot metal mixer with a capacity of 2000 t, three LD vessels with a capacity of 180 t/heat, four ladle furnaces, four RH degassers, one double strand slab caster and four single strand slab casters (figure 1). It is worth mentioning, that there is a brick plant for Magnesiacarbon bricks located in Linz.
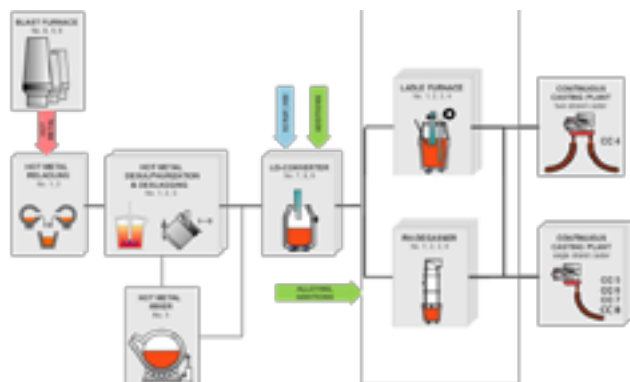


Fig. 1: Production facilities

The annual production increased over several ups and downs from 3.6 mt/a in BY 1998 to 5.3 mt/a in BY 2023, where the daily production increased from 65,7 heats per day to 83,4 heats per day (figure 2).



Fig. 2: Annual production and heats per day.

To increase the heat size from 151,2 t to 178 t over the years, we exchanged the LD vessels in 2002 and 2009. The ladle vessels were exchanged in 2002, 2009 and 2022 (figure 3) and the lining concepts were adjusted again and again.
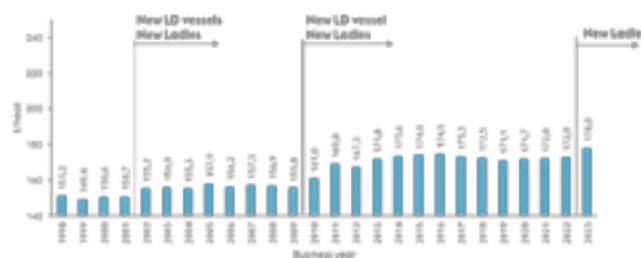


Fig. 3: Heat size

## STEEL SHELLS AND REFRACTORIES

The lining has developed in refractory quality and dimensions.

Starting in 2001, the steel ladle was lined with a high alumina vibration castable in the bottom and the wall and Magnesiacarbon bricks in the slag line. It was usual, to reline the wall every second slag line and bottom campaign. The thickness of the bottom sloped down from 300 mm to 250mm towards the teeming hole. The thickness of the wall was chosen increasing from 167 mm below the slag line to 204 mm above the bottom. The slag line was a balanced mix of 3P, 4P and 5P shapes (figure 4). The average heat size was appx. 151 t/heat with a bottom lifetime of 119 heats on average between 1998 and 2001.
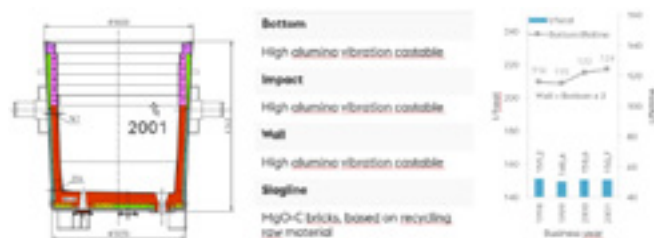


Fig. 4: Steel ladle until 2001

All steel shells were so deformed that we decided to purchase a new ladle fleet in 2001. Since a bigger heat size provided a higher daily production, we used the opportunity to increase the diameter of the shell by 80 mm and the height by 40 mm. The dimensions of the lining were almost the same as in the ladle before. The thickness of the bottom sloped down from 350 mm to 250 mm towards the teeming hole. The wall thickness was increasing from 171 mm below the slag line to 193 mm above the bottom and the slag line was a balanced mix of 3P, 4P and 5P shapes again. The wall was relined every second bottom and slag line campaign. This resulted in a capacity increase of about 5 tons per heat, the average heat size was about 156 tons at lifetime of 117 heats (figure 5).

371
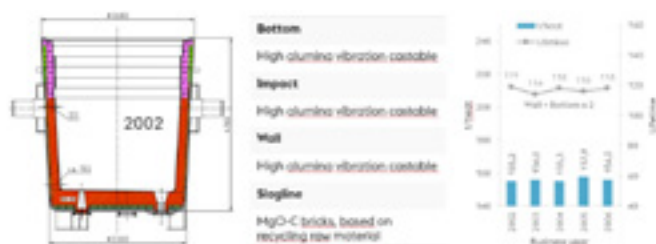
*Fig. 5: Steel ladle from 2002 to 2009*

Because of the startup of a third RH-Degasser in 2007, freeboard became more and more significant. To increase it by 150mm, we reduced the thickness of the wall from 171 mm in 2002 to 106 mm in 2007. Then we had to reline the wall every bottom- and slag line campaign. Spinel forming castables in the wall and Spinel containing, self-flowing castables in the bottom were established in 2005. In the bottom impact we changed from spinel containing castables to AMC bricks in in 2007. To compensate the weak point in the wall just above the bottom and the bucket deformation of the steel shell, we had to adapt the mould of the wall to balance the lining. The average lifetime was close to 125 heats (figure 6).



*Fig. 6: Steel ladle, adjustment to +150mm freeboard*

A further decision to increase the heat size again, leaded into the change of LD-Vessels and bigger ladles in 2010. The diameter of the steel shell was increased further 90 mm. Concerning the lining, we went on with the good experience of the ladle fleet before. The wall thickness was chosen by 110 mm below the slag line and 136 mm above the bottom without reinforcement, while the impact AMC bricks measured 300mm and the bottom 250 mm. The slag line was balanced again with 3P, 4P and 5P shapes. From 2010 to 2012 the average heat size was166 t, the ladle lifetime 116 heats.

When the oldest continuous caster which was limited to 155 tons per heat was shut down in 2013, a capacity close to 173 tons per heat was ensured. The lining lifetime was 104 heats from 2013 to 2022 (figure7).
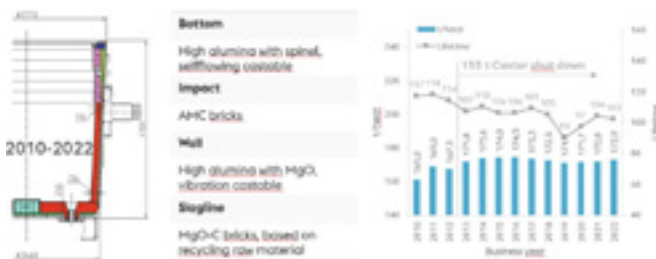


*Fig. 7: Steel ladle from 2010 to 2022*

In 2010 we also made trials with brick lined walls. We choose our inhouse Magnesia Carbon bricks based 100% recycled Magnesia, and cut 5P bricks in half, what ended in a wall thickness of appx. 107 mm (figure 8).
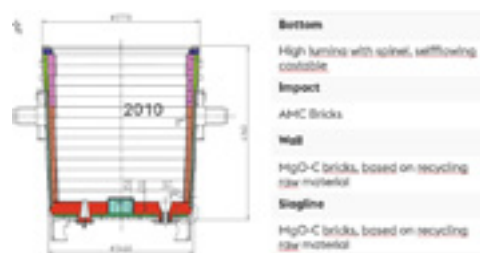


*Fig. 8: Brick lined ladle 2010*

The lifetime of the lining was comparable to the monolithic wall. We compared metallurgical parameters from ULC heats. The Carbon Content showed an insignificant increase (figure 9a) and the Total Oxygen Content as indicator for steel cleanliness was equal (figure 9b).
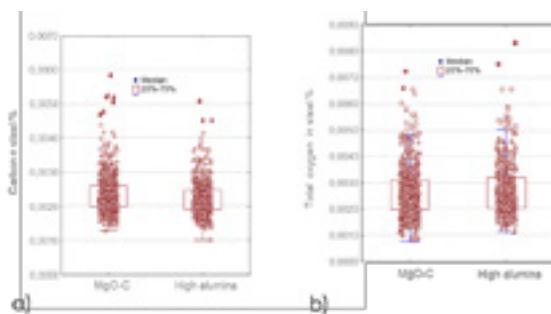


*Fig. 9: Carbon and total oxygen in ULC Steel*

Because the thermal conductivity of MgO-C is higher, we made some simple steady state calculations to estimate the increase of the temperature on the steel shell. By changing the wear lining from high alumina to MgO-C the calculation showed a temperature increase from 377°C to 415°C with the usual 40mm bauxite safety lining and 13 mm vermiculate insulation layer (figure 10a, figure 10b). Since we wanted an equal temperature, we had to add a lightweight brick layer of 20 mm. The calculation showed 367°C (figure 10c).



*Fig. 10: Steady state heat transfer*

The electric power consumption was interesting, too. We compared one steel grade, that required intensive treatment in secondary metallurgy. In case of MgO-C bricked walls we had a consumption of 38,3±8,0 kWh/t$_{Crude\ steel}$ while high alumina lined ladles needed 33,7±7,0 kWh/t$_{Crude\ steel}$ (figure 11).
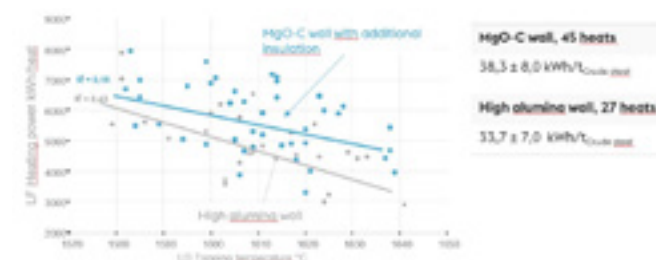


*Fig. 11: Electric power at LF for HIC Steel Grade*

It must also be added that we lost filling weight due to the additional insulating layer. This meant a capacity loss of two tons. The wear lining bricks had to be backfilled. When breaking out the ladle, we found sticky backfill material on the safety lining, which became more and more after each campaign. This resulted in the need to reline the safety lining every 3 to 4 campaigns. This is about 4 times as much as a monolithic wall.

In 2022 we had to produce 98 heats per day in full production, to reach our production goals. That was very difficult to achieve. With more ladle capacity we could have relaxed the situation. We decided to purchase bigger ladles again. This had become possible, because we had to exchange the crane runway girders before and increased their carrying capacity.

The limiting factors for the ladle steel shell were the trunnion spacing and the total height of the lade. To gain more capacity, we reduced the taper of the steel shell and shortened the legs. This resulted in an increase of 50 mm in height and 80 mm in the lower diameter.

What about refractories? Wall thickness was chosen uniform by 150 mm. Bottom impact AMC bricks measured 350mm and the bottom 270 mm. The slag line was balanced again with 3P and 4P shapes. Since the lipring of the new steel shell must support the static load of the ladle, we have been protecting it with a self-flowing steel needle enforced concrete based on high alumina.

The average heat size is 178 t, the average lifetime 104 heats (figure 12). Daily production has eased somewhat. The new target figure at full production is 94 instead of 98 heats now.
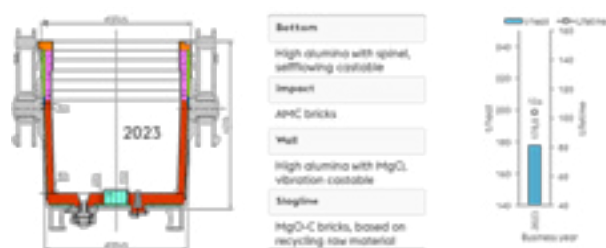


*Fig. 12: Steel ladle from 2023*

## REFRACTORY BALANCE

To present a representative material balance, I refer to the lining concept of the monolithic ladle that was in use from 2013 to 2022. The figures reflect the average for approx. 3000 linings. A similar balance can be expected for the current ladle.

A new lining requires 0.7 t of impact bricks, 6.1 t of floor concrete, 8.7 t of wall concrete and 6.8 t of slag zone bricks.

For relining, 100% of the impact and slag zone bricks are replaced. In the bottom, 3.7 t of concrete and in the wall 6.2 t of concrete are re-casted. The amounts of wear and breakout for high alumina are roughly estimated from the laser scan (figure 13a), the amounts of MgO-C are obtained from weighing reports. High alumina breakout can be quantified at appx 6,5 t/ladle, MgO-C at 2,9 t/ladle (figure 13b). The specific consumption in the impact is 0.04 kg/t, in the bottom 0.21kg/t, in the wall 0.24 kg/t and in the slag zone 0.38 kg/t (figure 13c).
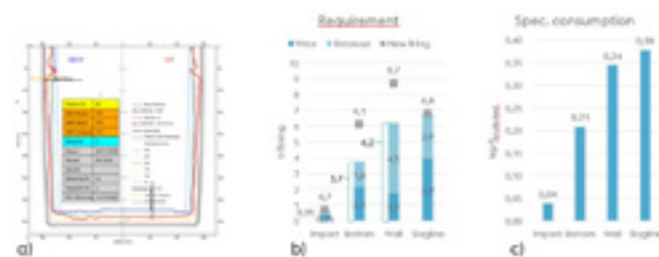


*Fig. 13: Refractory balance*

## RECYCLING

Recycling has a long tradition in our plant. Concerning the steel ladle, we separate MgO-C and Alumina breakout at our breakout stand (picture 1).



*Pic. 1: Ladle breakout stand*

*Magnesia Carbon*
In the slag line, we install about 2030 t/a of Magnesia Carbon bricks. The breakout can be estimated at 850 t/a, which is 42% of the original quantity. Of this, 560 t/a are used as recycled material for brick production, which is 28% of the original quantity. The remaining 14% is used as MgO carrier in the LD vessel (figure 14).
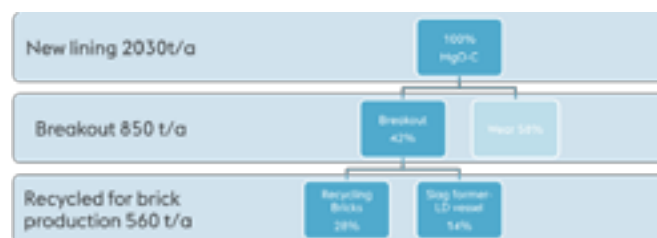


*Fig. 14: Recycling balance MgO-C*

*High alumina*
Our annual demand for high alumina materials for new linings and relinings amounts to 3350 t/a. Of this, 1930 or 57% is breakout, of which 1640t/a, or 48% is processed as slag former for the secondary metallurgy in the inhouse recycling department. The remaining 9% is passed on to the cement industry (figure 15).



*Fig. 15: Recycling balance high alumina*

## CONCLUSIONS

To accompany the capacity increases, it was necessary to purchase LD-vessels and new ladles. The ladle lining has been adjusted several times. The monolithic lining has proven itself in the wall.

MgO-C breakout has been used for production of recycled bricks in the in-house brick factory and as MgO carrier in the LD crucible. Alumina excavated material has been processed into slag formers in the in-house recycling center and a small portion has been passed on to the cement industry.

373

# ECO-TAB – A NEW ALUMINA AGGREGATE FOR STEEL LADLE LINING

Sebastian Klaus, Andreas Buhr, Hans-Leo Groß,
Almatis GmbH, Frankfurt, Germany

Dagmar Schmidtmeier
Almatis GmbH, Ludwigshafen, Germany

Wouter Zwijnenburg
Almatis B.V., Rotterdam, The Netherlands

Jerry Dutton
Stourbridge, Great Britain

## ABSTRACT

ECO-TAB® is a new alumina refractory aggregate with lower density when compared to the globally produced Tabular Alumina T60/T64 (3.3 vs. 3.55 g/cm³). The business case for the development of this new aggregate is based on its application in a steel ladle wear lining. Two factors are relevant here. The heat capacity and the thermal conductivity of the wear lining material are important for reducing the thermal losses of steel into the refractory lining during the thermal cycling of the ladle whilst in use. With lower heat capacity and thermal conductivity of the lining, the heat losses while the ladle is empty can be reduced and accordingly the heat losses from the steel to the refractory lining later. In addition, a lower density and weight of the refractory lining enables lower materials demand and higher tapping weight of steel into the ladle when the maximum crane weight in the steel works becomes the limiting factor during the ladle campaign. Firstly, the volume is the limiting factor but with increasing refractory wear, the crane weight then becomes the new limiting factor. ECO-TAB® contributes to energy saving, capacity improvement, and reduced material consumption through lower weight of the refractory lining.
The paper discusses the material properties and application testing of the new aggregate including induction furnace slag testing and thermal conductivity.

## INTRODUCTION

Tabular Alumina is known for its exceptional thermal and mechanical properties. It has high refractoriness, which means it can withstand very high temperatures without undergoing significant deformation or melting. This makes it suitable for various high-temperature applications and is therefore a very common synthetic aggregate used in a number of applications for steel making refractories such as steel ladle linings, impact pads, sliding gates, nozzles and purging plugs.
One key physical parameter for Tabular Alumina is it's density, also called BSG (bulk specific gravity). It is common knowledge in the refractory industry that the higher the density of the aggregates, the better the quality. However, for the steel ladle where a thermal cycling process is applied during emptying and refilling, the density of aggregate used in the steel ladle lining influences two key factors, the thermal and weight factors.

### Thermal factor

Fig. 1 shows the temperature change in the refractory lining of a steel ladle from empty to full as discussed by Ogata et al. [1].
After emptying the ladle, the hot surface of the working lining has cooled down to 800°C, as indicated in the graph. During filling and teeming, the refractory working lining temperature increases up to 1550-1600°C, resulting in energy transfer from the liquid steel to the cooler refractory lining leading to a reduction in steel temperature.
The main reasons of heat loss in the refractory lining during standard operation of a steel ladle are heat radiation and heat storage. The radiation at the steel shell can effectively be reduced by installation of insulating refractories or optimisation of the thermal conductivity of the applied refractories.

The dashed area in Fig. 1 corresponds to the heat storage ($\Delta Q$) as defined in equation (1).

$$\Delta Q = W C_p \Delta T = \rho V C_p \Delta T \qquad (1)$$

Considering the equation above, we can conclude that a reduction of heat losses by heat storage can be achieved either by reduced density ($\rho$) of the working lining or by decreasing it's volume ($V$). $W$ represents the weight and $C_p$ the constant specific heat capacity.
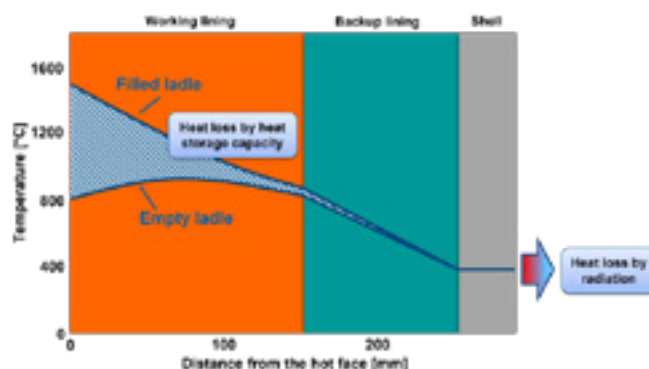


Fig. 1: Schematic drawing of the temperature change in the refractory lining of a steel ladle during operation. Drawing after [1]

Volume reduction of the working lining is often limited. A balance needs to be achieved between optimising thermal and mechanical stability whilst at the same time maximising the number of heats per ladle. The density of the refractory lining is defined by the raw materials used and the processes applied to manufacture the lining. High density raw materials are commonly used to reduce wear during application.
The costs for the loss of 1K steel temperature is considered to be in the range of 0.05 – 0.1 € per ton of steel [2]. In times of energy crisis these costs can be easily doubled.
As confirmed by Tata Steel IJmuiden [3] the costs of 1K loss per ton of steel has been €0.05. However, the current costs are expected to be in the range of €0.14 /mt steel, considering the increased energy and $CO_2$ prices.

### Weight factor

In addition, a lower weight of refractory lining enables a higher tapping weight of steel into the ladle when the maximum crane weight in the steel works becomes the limiting factor during the ladle campaign. Initially, the volume is the limiting factor but with increasing refractory wear, the crane weight becomes the new limit instead.

### ECO-TAB®

ECO-TAB® is a new alumina refractory aggregate with lower density when compared to the conventional Tabular Alumina aggregate T60/T64. The thermomechanical stability of refractory formulations is maintained at reduced bulk heat capacity leading to energy saving opportunities.

The typical physical parameters for a regular T60/T64 Tabular Alumina and ECO-TAB® are listed in Tab. 1.

Tab. 1: Typical physical parameters of T60/64 Tabular and ECO-TAB®.

|  |  | T60/T64 | ECO-TAB® |
|---|---|---|---|
| Typical density (BSG) | g/cm³ | 3.55 | 3.3 |
| Typical apparent porosity | % | 2 | 11 |
| Typical water absorption | % | 0.5 | 3.5 |
| Al₂O₃ content | % | 99.5 | 99.5 |

It is worthwhile mentioning that the lower density is not achieved by a change in chemistry but by proprietary modifications during the production process to achieve the designed microstructure. ECO-TAB® is as volume stable as Tabular T60/T64 at steelmaking temperatures.

**EXPERIMENTAL**
Refractory castables based on regular Tabular T60/T64 and ECO-TAB® were produced and investigated with regard to physical properties and wear resistance. Tab. 2 shows the mixture of the vibratable spinel containing castables and Tab. 3 of the vibratable spinel forming castables. In the latter, 0.5% silica fume was added to compensate for the expansion due to in-situ spinel formation.
The water demand was adjusted to achieve similar flow properties and curing of the test bars was performed at 20°C for 24h.

Tab. 2: Composition of spinel containing test castables.

|  | VIB-SC-TAB [%] | VIB-SC-ECO [%] |
|---|---|---|
| **Tabular T60/T64; 0.5 – 6 mm** | **55** | |
| **ECO-TAB®; 0.5 – 6 mm** | | **55** |
| Spinel AR 78; 0.020 – 0.500 mm | 27 | 27 |
| Reactive Alumina | 13 | 13 |
| 70% CAC | 5 | 5 |
| Dispersing Aluminas | 1 | 1 |
| Water demand | 4.5 | 6.0 |

Tab. 3: Composition of spinel forming test castables.

|  | VIB-SF-TAB [%] | VIB-SF-ECO [%] |
|---|---|---|
| **Tabular T60/T64; 0 – 6 mm** | **76** | |
| **ECO-TAB®; 0 – 6 mm** | | **76** |
| MgO; Nedmag DIN 70 | 5 | 5 |
| Silica Fume | 0.5 | 0.5 |
| Calcined and Reactive Alumina | 17 | 17 |
| 70% CAC | 1.5 | 1.5 |
| Dispersing Aluminas | 1 | 1 |
| Water demand | 5.0 | 6.2 |

The refractoriness under load, thermal conductivity and induction furnace corrosion tests were performed at the German refractory institute in Höhr-Grenzhausen.

**RESULTS**
**Microstructure investigations of ECO-TAB®**
The typical microstructure of ECO-TAB® is shown on the right side of Fig. 2. The pore structure is more pronounced and finely distributed when compared to regular T60/T64 Tabular. Also, the grain size is smaller than for Tabular.
A pore size analysis was performed using the image processing software ImageJ [4] for 32 SEM images to ensure statistical value. The average pore size of 2.6 $\mu m^2$ is smaller than that of Tabular. The major difference is shown in the area of the images covered by pores. For ECO-TAB® an average of 7.2% is covered by pores, whereas for Tabular it is only 2.5%.
This optical and two-dimensional method to investigate the porosity shows a lower porosity for ECO-TAB® when compared to the bulk density (BSG) test using the normal water absorption method.

However, the primary focus here was to investigate the pore size within the material.
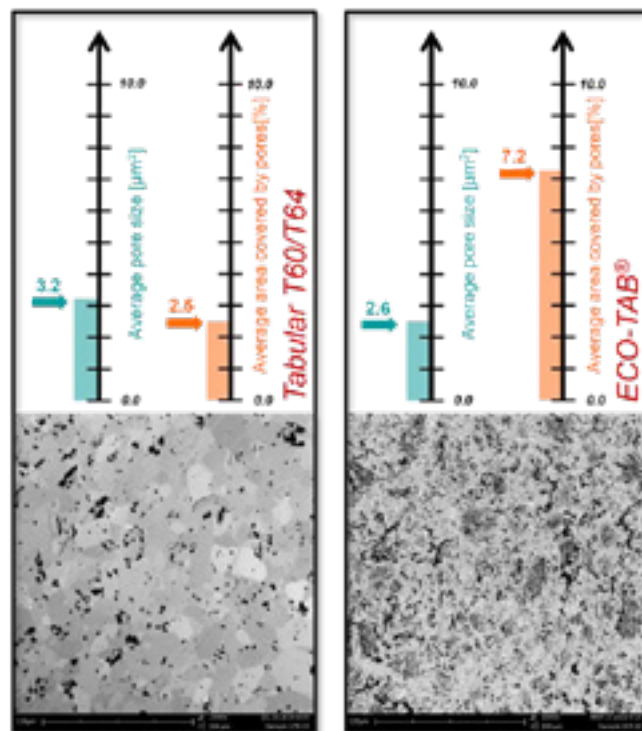


Fig. 2: Image based pore size analysis of ECO-TAB® in comparison to Tabular T60/T64. 1000x magnification.

**Physical properties of refractory castables**
The cold crushing strength (CCS) and cold modulus of rupture (CMoR) for the spinel containing castables is shown in Fig. 3. In the cured state (20°C / 24h) the strength for regular T60/T64 Tabular and ECO-TAB® is very similar. For the other temperatures ECO-TAB® is slightly lower in strength but still clearly exceeding the minimum level of 30 MPa CCS for steel ladle applications. Both castables show the typical drop in strength at 1000°C due to the dehydration of calcium aluminate hydrates.
Strength data for the spinel forming castables is shown in Fig. 4. Here, T60/T64 Tabular and ECO-TAB® show very similar results for all temperatures tested.
It is reported that an increase in water demand of only 1% can already reduce the strength properties by 50% [5]. Although, the water demand for the ECO-TAB® containing castables had to be increased by 1.5% and 1.2% respectively, the strength properties are not negatively affected. This can be explained by the fact that the additional water is absorbed by the higher porosity in ECO-TAB® whilst not weakening the matrix bond.
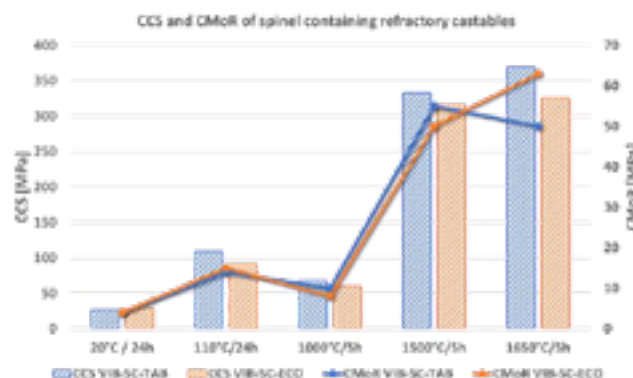


Fig. 3: Cold crushing strength (CCS) and cold modulus of rupture (CMoR) of spinel containing test castables.

375
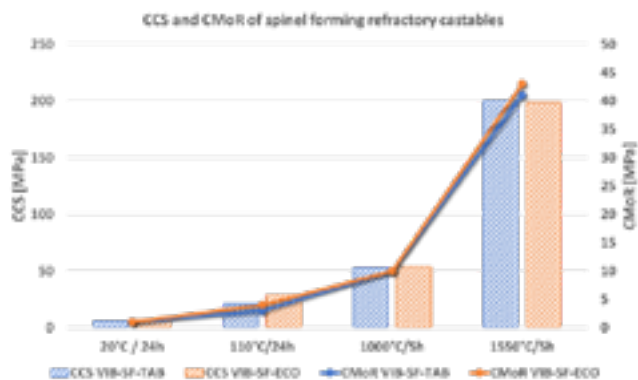
Fig. 4: Cold crushing strength (CCS) and cold modulus of rupture (CMoR) of spinel forming test castables.

The dashed bars in Fig. 5 and Fig. 6 represent the density evaluation of the dried and sintered test castables. The castables based on ECO-TAB® exhibit on average approximately 5% less bulk density (0.15 g/cm³ lower) than Tabular based castables. Fired at high temperature the difference decreases and the ECO-TAB® castables remain at ~0.1 g/cm³ lower density.

The permanent linear change as shown in the solid lines is lower for the ECO-TAB® castables, especially when fired at 1650°C or 1550°C respectively. The increased shrinkage of ~0.5% during firing is assumed to be due to the slightly increased sinter reactivity of ECO-TAB® when compared to the dense aggregate T60/T64.
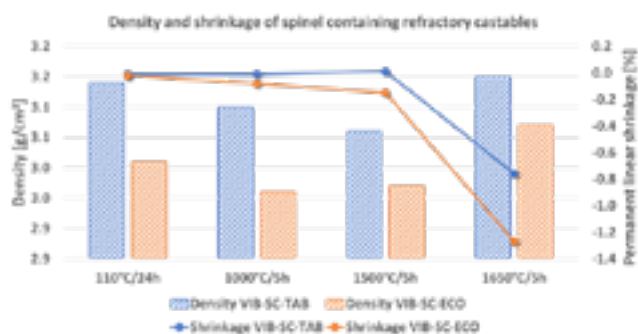


Fig. 5: Density and shrinkage of spinel containing refractory castables.

The spinel forming castables exhibit higher total positive permanent linear shrinkage due to the expansion by spinel formation during heat treatment. In addition, the castable based on ECO-TAB® shows lower expansion than the castable based on T60/T64.
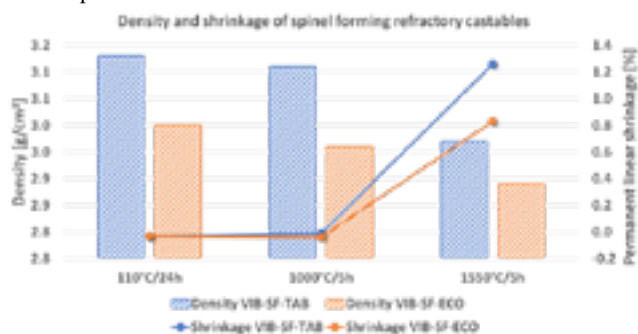


Fig. 6: Density and shrinkage of spinel forming refractory castables.

The thermal conductivity for the spinel containing test castables measured by the hot wire method is shown in Fig. 7. The castable based on ECO-TAB® exhibits approximately 10% lower thermal conductivity for the full range of tested temperatures.
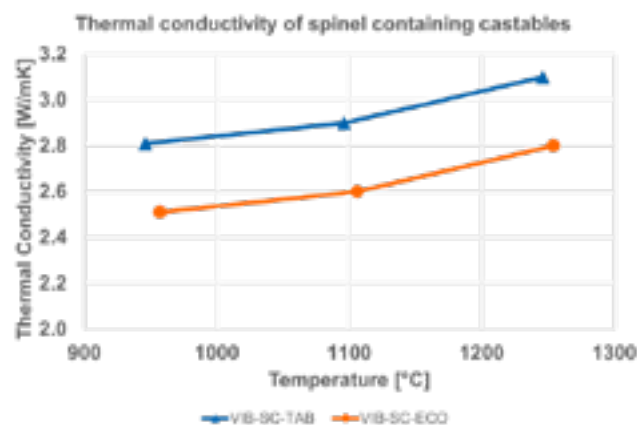


Fig. 7: Thermal conductivity for the test castables measured by hot wire method; samples pre-fired at 1000 °C / 5 h.

**Refractoriness under load of spinel containing refractory castables**

For the measurement of the refractoriness under load (RUL) the spinel containing refractory castable test bar was pre-fired at 1000°C with a holding time of 5h. The results for a constant pressure of 0.2 MPa and heating rate of 5 K/min are shown in Fig. 8.
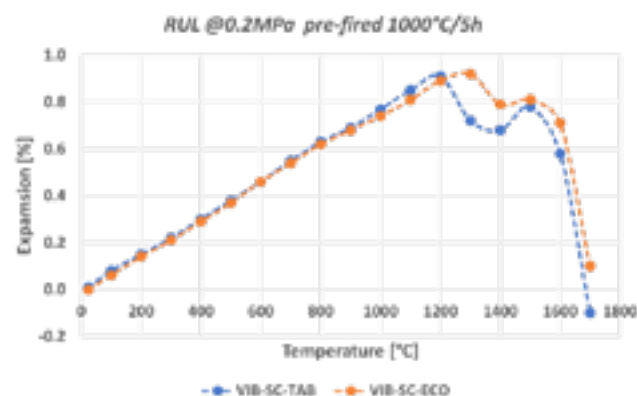


Fig. 8: Refractoriness under load of the spinel containing test castables.

The expansion curves of T60/T64 Tabular and ECO-TAB® show very similar results. The point of maximum expansion ($D_{max}$) is at a higher temperature (1283°C) with ECO-TAB®.

**Induction furnace corrosion tests of refractory castables**

In order to judge the feasibility in application, a corrosion test was conducted in an induction furnace. The test setup has the advantage of being as close as possible to real life conditions in the steel ladle. The test segments were cured at 20°C for 24h and pre-fired to 1000°C with a 5h holding time. The position of the segments in the induction furnace is shown in Fig. 9.



Segment 1 & 1a: VIB-SC-TAB

Segment 2 & 2a: VIB-SC-ECO

Segment 3 & 3a: VIB-SF-TAB

Segment 4 & 4a: VIB-SF-ECO
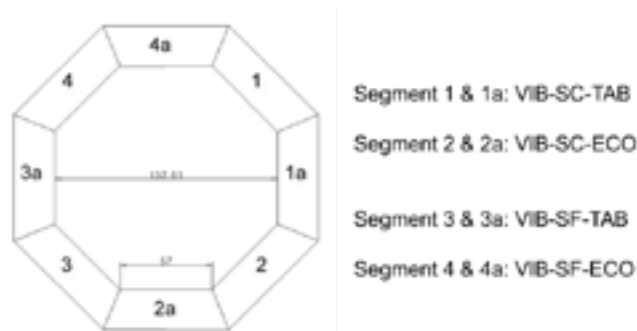
Fig. 9: Schematic drawing of segmentation for the induction furnace corrosion test.

The test was performed at 1600°C for 2h with 14 kg of ST52 steel and 750 g of a synthetic slag typical for Al-killed steel (Wt%: CaO 41.5; Al$_2$O$_3$ 38.5; SiO$_2$ 5.0; MgO 5.0; FeO 6.0; MnO 4.0). The slag was exchanged after 1 hour.

The post-mortem segments are shown in Fig. 10 and the corresponding depth of corrosion in Tab. 4. It can be seen that the depth of corrosion at the Marangoni convection zone [6] is very similar for all type of tested castables.
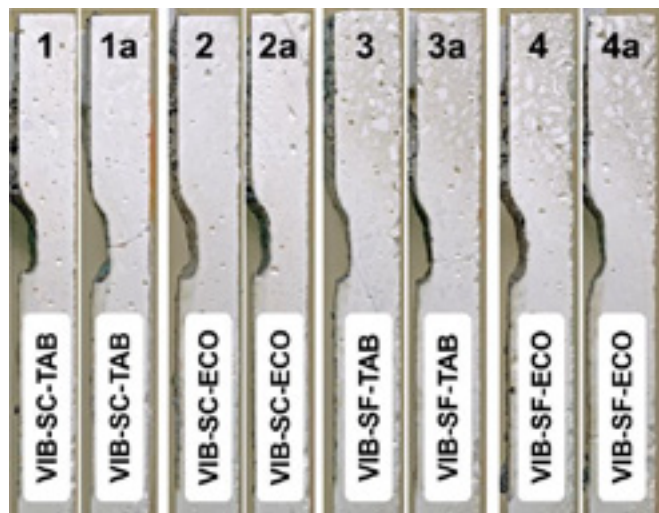


Fig. 10: Images of castable test segments after corrosion test.

Tab. 4: Depth of corrosion of tested castable segments.

|  | VIB-SC-TAB | VIB-SC-ECO | VIB-SF-TAB | VIB-SF-ECO |
|---|---|---|---|---|
| Corrosion depth [mm] | 7.15 | 7.25 | 5.80 | 6.65 |

The slag infiltrated area is very visible in the polished sections as shown in Fig. 11. The dark area on the left side of each segment is remaining slag. The infiltrated area can be separated into two zones. Zone I is characterised by a brownish colour. During infiltration, the Fe and Mn content in the slag decreases leading to loss of the brownish discoloration of the refractory material (zone II). The depth of infiltrated area is very similar in the castables based on ECO-TAB® and Tabular T60/T64.

It can be concluded, that despite the significantly higher porosity of ECO-TAB®, the slag resistance of the refractory castables is very comparable.

Back scattered electron (BSE) images were taken to further investigate the reaction of the aggregate grains with the infiltrated slag. The BSE image of the area highlighted in the polished section in Fig. 11 depicts the cooled slag on the left side and infiltrated refractory castable on the right side (Fig. 12).

The solidified slag shows zonation with higher Fe contents at the hot side (white area) which remained at the surface during cooling after completion of the test.
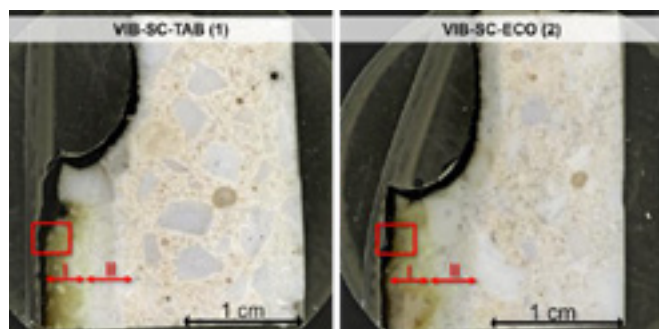


Fig. 11: Polished segments of VIB-SC-TAB (1) and VIB-SC-ECO (2) used for SEM investigations.
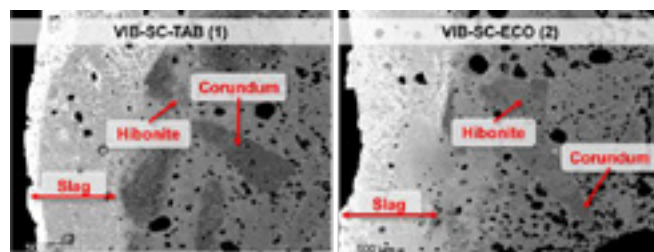


Fig. 12: BSE images of segments (1) and (2) close at the slag zone.

The fine matrix is completely infiltrated by the slag, whereas coarse alumina grains remain (dark grey phase). The Tabular Alumina T60/T64 grains in the left image show some conversion to Hibonite (CaO·6Al$_2$O$_3$) at the surface of the grains in contact with the infiltrated matrix (lighter grey phase). This reaction is the result of calcia availability provided by the infiltrated slag. The ECO-TAB® grains as shown on the right image show more pronounced formation of Hibonite, hence higher reactivity. However, the depth of infiltration and the resistance of the castables against corrosion is not affected.

## CONCLUSIONS

This paper introduces ECO-TAB®, a new alumina aggregate with reduced density of ~3.3 g/cm$^3$ compared to ~3.55 g/cm$^3$ for regular Tabular Alumina T60/T64. Advantages in steel ladle linings are reduced energy losses by lowered heat capacity and thermal conductivity. In addition, the lower weight of the refractory lining enables lower material demands and higher tapping weight of steel into the ladle when the maximum crane weight in the steel works is the limiting factor.

Despite the lower aggregate density of ECO-TAB®, application tests with relevant castables show no difference in strength or refractoriness compared to the reference castable based on Tabular T60/T64. Corrosion tests reveal slightly higher reactivity of the ECO-TAB® grains in contact with slag infiltrated matrix but without any negative effect on corrosion or infiltration depth.

ECO-TAB® contributes to energy saving, capacity improvement, and reduced material consumption through lower weight of the steel ladle refractory working lining while maintaining end application performance.

## REFERENCES

[1] M. Ogata, M. Namba, S. Uchida and E. Maeda, "Saving Energy by using Working-lining Refractories with Low Thermal Conductivity," *Journal of the Technical Association of Refractories, Japan,* pp. 181-184, 2015.

[2] A. Buhr, R. Bruckhaus and R. Fandrich, "The Steel Industry in Germany - Trends in Clean Steel Technology and Refractory Engineering," *refractories WORLDFORUM,* pp. 57-63, 2016.

[3] P. v. Beurden, "The value-in-use of steel ladles and the role of a thermal efficiency from a modelling perspective," in *Steel meets Refractory*, 2021.

[4] M. Abramoff, P. Magalhaes and S. Ram, "Image Processing with ImageJ," *Biophotonics International,* pp. 36-42, 2004.

[5] S. Klaus, *Steel Academy Seminar "Refractory Technology I",* 2023.

[6] J. Pötschke and C. Brüggmann, "Premature Wear of Refractories due to Marangoni-Convection," *Steel Research International 83(7),* 2012.

# RECYCLATE–CONTAINING MAGNESIA–CARBON REFRACTORIES – INFLUENCE ON THE NON–METALLIC INCLUSIONS IN STEEL

Kirsten Moritz, Florian Kerber, Steffen Dudczig, Gert Schmidt, Christos G. Aneziris
Technische Universität Bergakademie Freiberg, Institute of Ceramics, Refractories and Composite Materials, Freiberg, Germany

Thomas Schemmel, Helge Jansen
Refratechnik Steel GmbH, Düsseldorf, Germany

Matthias Schwarz
Deutsche Edelstahlwerke Specialty Steel GmbH & Co. KG, Siegen, Germany

## ABSTRACT
In this study, the influence of different contents of recycled magnesia-carbon (MgO-C) material in MgO-C refractories on the non-metallic inclusions in steel was investigated. Recyclate-containing MgO-C samples and a recyclate-free reference material were tested in contact with a 16MnCr5 steel melt and a slag on the top of the melt. By means of a subsequent automated feature analysis of the solidified steel, MnS and $Al_2O_3$-MnS inclusions were found to be the predominant ones. No negative influence of the recyclate, neither with regard to the number nor the size of the inclusions, was detected.

## INTRODUCTION
MgO-C refractories are widely used in the steel industry, mainly as wear lining material in converters, electric arc furnaces, and steel treatment ladles. This is due to beneficial properties such as high thermal shock resistance and low slag infiltration depths [1, 2]. However, the production of the raw materials sintered and fused magnesia from magnesite as their main source is energy-intensive and associated with high $CO_2$ emissions [3]. The partial replacement of virgin raw materials with MgO-C recyclates is therefore of great interest and provides economic advantages as well. The possibility of producing MgO-C materials that have suitable physical, mechanical, and thermomechanical properties using recyclates has been demonstrated (for example in Ref. [4]), but little is known about the influence of the recyclates on the non-metallic inclusions in steel. This issue is very important because such non-metallic inclusions, depending on their properties (such as size, hardness, and morphology) can significantly impair the steel properties [5].
In the present work, MgO-C refractory samples having different recyclate contents, with two different recyclates being used, were subjected to a steel melt in a steel casting simulator. Slag was added onto the melt. After the experiment, the non-metallic inclusions in the solidified steel were analyzed.

## MATERIALS AND METHODS
Following raw materials were used for preparing MgO-C refractory samples:
- MgO-C recyclate R94A1 (3–6, 1–3, and 0–1 mm) or R92A4.5 (3–5, 1–3, and 0–1 mm),
- Chinese fused magnesia FM97 (3–5, 1–3, and 0–1 mm),
- fine-grained Chinese fused magnesia FM96DIN,

with the recyclates and fused magnesia being provided by Horn & Co. Minerals Recovery GmbH & Co. KG, Germany, and
- graphite NFL90/92 (Quingdao Kropfmuehl Graphite, China).

Starting from a recyclate-free reference mixture, the weight ratio between the recyclate and the fused magnesia FM97 was increased in three steps—from 0:100 to 50:50, 80:20, and finally 100:0. The carbon content as sum of graphite NFL90/92 and carbon introduced by the recyclate was adjusted to approximately 10 wt% in each case. The corresponding recyclate contents of the MgO-C materials were 0, 40, 65, and 82 or 83 wt% (in the case of the samples containing recyclate R94A1 and R92A4.5, respectively).
After preparing the raw material mixtures, which also contained a combination of carbonaceous binders, test bars with dimensions of 150 mm x 25 mm x 25 mm were produced by uniaxial pressing,

cured at 180 °C, and coked at 1000 °C with 5 h holding time under reducing conditions (for more information see [6]).
Using ground samples after burning out the carbon, the chemical composition of the refractory materials was analyzed by X-ray fluorescence analysis (XRF) in an XRF spectrometer S8 Tiger II (Bruker).
Tests in a steel casting simulator (Systec, Germany) were performed. One MgO-C sample per test was fixed in an $Al_2O_3/MgAl_2O_4$ crucible, 16MnCr5 steel was filled into the crucible and melted by increasing the temperature to 1650 °C. Thirty minutes after reaching this temperature, a crushed slag, whose main components were CaO (54 wt%), $Al_2O_3$ (24 wt%), $SiO_2$ (8 wt%), and MgO (6.5 wt%), was added. Steel and slag were provided by Deutsche Edelstahlwerke Specialty Steel GmbH & Co. KG, Germany. After a time of 60 min at 1650 °C, the heating was switched off. All experiments took place under argon atmosphere.
Samples of the solidified steel were taken and examined by an automated feature analysis using a scanning electron microscope equipped with energy dispersive X-ray spectroscopy (ASPEX PSEM eXpress, FEI, USA) to determine the non-metallic inclusions contained. The inclusions were classified by chemical composition and by size, the latter using the maximum inclusion diameter ($D_{I,max}$) and the square root of the inclusion area ($\sqrt{A_I}$). Population density functions were calculated according to Equation 1.

$$PDF = \frac{n_I(h_{ab})}{h_b - h_a} \qquad (1) [7]$$

$n_I(h_{ab})$     inclusion number per unit of area in a given bin
$h_b - h_a$     bin width

## RESULTS
Figure 1 shows the non-metallic inclusions classified by their chemical composition. The steel samples investigated were designated according to the MgO-C material used in the test, with "RI" representing the R94A1 recyclate, "RII" the R92A4.5 recyclate, and "FM" the FM97 fused magnesia. The designation "0R-100FM" stands for the reference test with the recyclate-free MgO-C material.
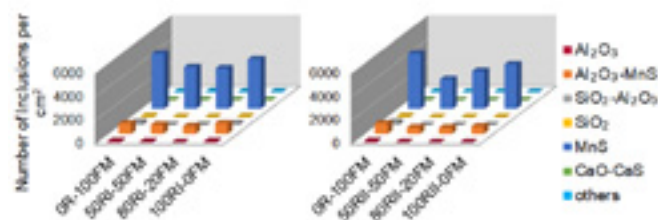


*Fig. 1: Inclusions in the solidified steel from the experiments with MgO-C samples containing recyclate RI (a) or RII (b) in comparison with the test using the recyclate-free MgO-C.*

The majority of the detected inclusions were assigned to the MnS and $Al_2O_3$-MnS classes. MnS inclusions are formed during solidification of the steel [8]. They may even be beneficial to some extent because they improve the steel's machinability [9]. By

contrast, hard and brittle oxide inclusions such as $Al_2O_3$ are the most detrimental, especially for fatigue strength [5]. The steel samples contained only a few pure $Al_2O_3$ inclusions. Instead, existing $Al_2O_3$ inclusions apparently served as nuclei for the precipitation of MnS according to a mechanism known from the literature [10], resulting in complex $Al_2O_3$-MnS inclusions.

Both recyclates did not lead to an increase in the number of inclusions compared with the experiment using the recyclate-free reference material (see Fig. 1).

The size distribution of the inclusions was similar in all steel samples. However, a trend to a lower number of larger inclusions in the steel samples from the experiments with recyclate-containing MgO-C was observed for the sum of the $Al_2O_3$ and $Al_2O_3$-MnS classes, especially in the case of the tests with MgO-C containing the recyclate RII (see Fig. 2). This trend, which had to be verified by further tests, might be explained by the decreasing content of the impurities $SiO_2$, CaO, and $Fe_2O_3$ in the MgO-C material with increasing proportion of recyclate (Table 1). It is consistent with similar results obtained in recent studies using industrially produced MgO-C refractories with varying degrees of MgO purity [11, 12]. There it was assumed that the impurity phases from the MgO-C material interact with the molten steel and promote the agglomeration and sintering of $Al_2O_3$ inclusions.

The size of the MnS inclusions was less effected by the recyclate content of the refractory material.
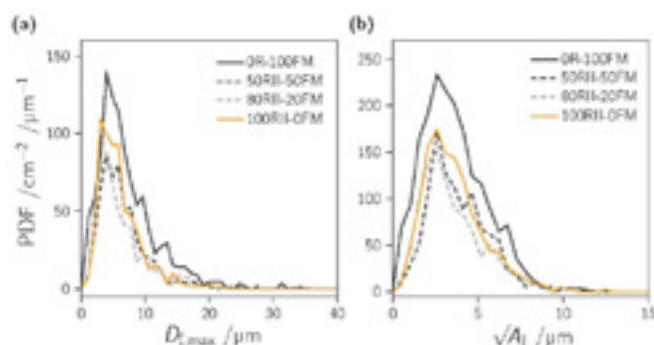


*Fig. 2: Population density function of $Al_2O_3$ + $Al_2O_3$-MnS inclusions vs. the maximum inclusion diameter (a) and the square root of the inclusion area (b) in the solidified steel from the experiments with MgO-C samples containing the recyclate RII in comparison with the test using the recyclate-free MgO-C.*

Table 1: Content of magnesia and the main impurities in the refractory materials containing the recyclate RII compared with the recyclate-free reference material (analyzed after burning out the carbon).

| MgO-C material | MgO | $Al_2O_3$ | $SiO_2$ | CaO | $Fe_2O_3$ |
|---|---|---|---|---|---|
| | (wt%) | | | | |
| 0R-100FM [6] | 95.6 | 0.46 | 1.16 | 1.75 | 0.80 |
| 50RII-50FM | 94.6 | 1.93 | 1.08 | 1.41 | 0.70 |
| 80RII-20FM | 94.3 | 2.55 | 0.93 | 1.32 | 0.69 |
| 100RII-0FM | 94.1 | 3.12 | 0.80 | 1.16 | 0.62 |

## CONCLUSIONS

The investigation of recyclate-containing MgO-C samples in contact with molten 16MnCr5 steel and a slag did not indicate any negative influence of the recyclate on the steel cleanliness in terms of non-metallic inclusions. Especially in the case of one of the two recyclates used, there was rather a trend towards a smaller number of larger inclusions for the classes $Al_2O_3$ + $Al_2O_3$-MnS.

These results refer to the first use of the refractory material. The influence of the recyclate in the case of repeated contact between the refractory and the molten steel is to be investigated in further studies.

## REFERENCES

[1] Buchebner G, Barthel, H. Magnesia-carbon bricks. In: Routschka G, Wuthnow H (Eds.), Pocket manual refractory materials: design, properties, testing; third edition. Vulkan-Verlag GmbH, Essen, Germany, 2008, pp. 183–193

[2] Ewais EMM. Carbon based refractories. J. Ceram. Soc. Jpn. 112, 2004, pp. 515–532

[3] Zhao L, Feng J, Dong H. Analysis of carbon footprint and reduction approach of magnesia production in China. J. Clean. Prod. 334, 2022, 130194

[4] Ludwig M, Śnieżek E, Jastrzębska I, Prorok R, Sułkowski M, Goławski C, Fischer C, Wojteczko K, Szczerba J. Recycled magnesia-carbon aggregate as the component of new type of MgO-C refractories. Constr. Build. Mater. 272, 2021, 121912

[5] Zhang L, Thomas BG. Inclusions in continuous casting of steel. In: XXIV National Steelmaking Symposium, Morelia, Mich., Mexico, 2003, pp. 138–183

[6] Moritz K, Brachhold N, Hubálková J, Schmidt G, Aneziris CG. Utilization of recycled material for producing magnesia–carbon refractories, Ceramics 6, 2023, pp. 30–42

[7] van Ende M-A, Guo M, Zinngrebe E, Blanpain B, Jung I-H. Evolution of non-metallic inclusions in secondary steelmaking: Learning from inclusion size distributions. ISIJ International 53, 2013, pp. 1974–1982

[8] Vasconcellos da Costa e Silva AL. The effects of non-metallic inclusions on properties relevant to the performance of steel in structural and mechanical applications. J. Mater. Res. Technol. 8, 2019, pp. 2408–2422

[9] Ånmark N, Karasev A, Jönsson PG. The effect of different non-metallic inclusions on the machinability of steels. Materials 8, 2015, pp. 751–783

[10] Wakoh M, Sawai T, Mizoguchi S. Effect of S content on the MnS precipitation in steel with oxide nuclei. ISIJ International 36, 1996, pp.1014–1021

[11] Kerber F, Zienert T, Hubálková J, Stein V, Schemmel T, Jansen H, Aneziris CG. Effect of MgO grade in MgO–C refractories on the non-metallic inclusion population in Al-treated steel. Steel Res. Int. 93, 2022, 2100482

[12] Kerber F, Malczyk P, Stein V, Schemmel T, Jansen H, Aneziris CG. Influence of the MgO grade in MgO-C refractory material and steel melt temperature on the inclusion population in Al-treated steel. Int. J. Ceramic Eng. Sci. 4, 2022, pp. 102–111

379

# EFFECT OF DIFFERENT CARBON SOURCES ON ULTRA LOW CARBON BRICKS FOR STEEL APPLICATIONS

Sérgio Luiz Cabral Silva, Laura Falco Paiva Carvalho, Sophia Vieira Macedo.
RHI Magnesita, R&D, Contagem, Brazil

Edmilson Dias Gonzaga, Sérgio Eustáquio Soares.
RHI Magnesita, Technical Marketing & Solutions, Contagem, Brazil

## ABSTRACT

It is evident that the demand for lower carbon-footprint materials in the steelmaking industry tends to increase due to environmental concerns and operational demands, such as the need for lower shell temperatures resulting in energy savings and lesser thermal stresses in the equipment's structure. In addition, the ever-increasing quality control in special steels production demands processes that minimizes the carbon pick-up effect. Therefore, among the relevant strategies to meet such needs, Ultra-Low Carbon (ULC) bricks, used as an alternative to traditional MgO-C brick products (with such high carbon content) and MgCr bricks, are being developed. The ULC brick technology (retained carbon $\leq$ 1.8 %wt) has been validated and is currently being applied in steel production processes, presenting similar or even better performance, if compared to the originally used refractories. Despite its considerably low carbon content, the product can fulfill the thermomechanical behavior and corrosion resistance needed for steel processing. This performance is made possible through the usage of special carbon sources. This paper aims to show how these different carbon sources affect ULC bricks properties.

## INTRODUCTION

MgO-C refractory bricks are extensively used in various iron and steelmaking equipment, including mainly LD converters, electric-arc furnaces and steel ladles. Its satisfactory performance for such applications can be attributed to the association of the basic ceramic material's capacity of maintaining its physical and chemical stability under high-temperature conditions with the carbon addition providing excellent thermomechanical properties and low wettability by slags. Therefore, this class of refractory has outstanding slag infiltration and thermal shock resistances, which contributes to lower wear rates.

Although this kind of product has been successful thus far, conceptual changes need to be made to align it with market tendencies. It is evident that demands of different natures push the refractory industry to lower the amount of carbon used. Among them, cleaner steel productions require less carbon, lesser $CO_2$ emissions and higher energy savings, which in turn incentivizes the use of refractories that both have lower carbon footprint and that are less thermally conductive to reduce shell temperatures. Additionally, special high purity steel productions for specialized applications require carbon content in the final product as low as less than 0.005 %wt [1] and, as such, carbon pick-up effects caused by high-temperature diffusion between the lining and molten steel during processing must be minimized.

One of the strategies often implemented to avoid carbon related issues is the use of fired refractories such as MgCr and doloma bricks in steel ladles and RH Degassers. However, these products are more susceptible to slag infiltration, which in turn causes structural spalling due to the difference in coefficient of thermal expansion between infiltrated and non-infiltrated brick regions, leading to uneven and higher lining wear rates. Moreover, the absence of carbon results in stiffer bricks, which have considerably worse thermomechanical properties and lower resistance to crack formation, and thus requires much lower preheating and cooling rates for operation. Besides, the production of fired bricks incurs higher energy costs compared to unfired ones, making the final product more expensive for the steel industry.

Aiming to take advantage of what MgO-C technology offers while meeting the industry's decarbonization expectations, several studies in the last years have consolidated the ULC technology. It is important to notice that simply reducing the amount of carbon added to traditional bricks does not yield adequate results [2].

By using special carbon sources associated with specific binder systems and additives, it was possible to create new ULC bricks with less than 1.8 %wt fixed carbon content while maintaining satisfactory thermomechanical properties, avoiding spalling, and presenting good performance when compared to the originally used linings that can have up to 12 %wt carbon content. This product line, ensuring minimal carbon pick-up, is currently used in steel ladles for secondary treatment of special steels requiring less than 25 ppm of carbon content [1].

Given the technological success of ULC bricks and the steel industry's requirements for continuous improvement, it is important to keep developing this technology and look for ways of reducing the carbon content even further. Such advancements are likely to result in longer lining lifetime, as well as in partial replacement of less environmentally friendly bricks, such as MgCr ones.

As such, this paper aims to explore how different carbon sources affect ULC bricks properties. More specifically, four different kinds of carbon sources with varying morphologies, surface areas, and ashes content were tested in current ULC formulations. The main interest properties include the physical properties after curing and coking, thermal shock resistance and relaxation tests.

## EXPERIMENTAL PROCEDURE

### Carbon sources characterization

In order to characterize the different carbon sources used, all four of them were submitted to surface area analysis through Brunauer-Emmett-Teller (BET) tests, morphology analysis by scanning electron microscopy (SEM), oxidation behavior evaluation by thermogravimetric tests using a LECO TGA 701 thermogravimetry analyzer (10 °C/min heating rate, under oxidizing atmosphere, until 1000 °C). The loss on ignition (LOI), moisture, fixed carbon, volatiles and ash content were also measured using LECO TGA 701.

### Brick specimens' production and heat treatments

Tested formulations can be seen in Table 1. Most of the compositions use commercially available carbon sources, except C4 and C6 that contains an experimental material (CS4). These carbon sources are added in an amount of < 1.0 %wt. All formulations have the same phenolic resin type resole as binder and use the same type of MgO (a fused magnesia FM98 from China). Compositions C5 and C6 are equivalents to C2 and C4 with the use of antioxidant additives to evaluate their interaction with the different carbon sources.

Tab. 1: Compositions adopted for the experimental procedure.

|  | C1 | C2 | C3 | C4 | C5 | C6 |
|---|---|---|---|---|---|---|
| FM 98 | X | X | X | X | X | X |
| Carbon Source | CS1 | CS2 | CS3 | CS4 | CS2 | CS4 |
| Additive 1 | + | + | + | + | + | + |
| Additive 2 | - | - | - | - | + | + |
| Resin | + | + | + | + | + | + |

It is essential to ensure that all mixing and pressing equipment are thoroughly cleaned before the bricks production, in order to avoid carbon contamination from previous batches. Then, the raw materials with adequate particle size distribution are mixed with the

phenolic resin in a determined mixing sequence. The mixing has been adjusted to obtain good dispersion and homogenization of the components, especially of the carbon sources, contributing to better overall properties. Afterwards, the material is hydraulically pressed with a maximum pressure of 170 MPa.

Once conformed, the samples are cured at 200 ºC for 6 hours. Additionally, some of the samples were coked at 1400 ºC for 5 hours and others at 1100 ºC for 8 hours to simulate the temperature conditions of refractory use while avoiding oxidation.

## MgO-C bricks tests

The samples cured and coked at 1400 ºC were submitted to bulk density (BD), apparent porosity (AP), modulus of rupture (MOR), cold crushing strength (CCS), dynamic modulus of elasticity (MOE) tests. Other additional experiments made with the cured samples were carbon content and relaxation tests while thermal shock resistance (TSR) and hot compression strain (HCS) tests were conducted with specimens coked at 1100 ºC and 1400 ºC respectively. The bricks' carbon content was obtained using a LECO CS 200 equipment.

BD and AP tests are based on NBR-6220 using the Archimedes principle. MOR was obtained using a 3-point bending test in a Kratos device (KE 3000 MP) with a loading speed of $(60 \pm 10)$ N/s and spacing between the supports of 100 mm. The CCS was measured according to NBR 6224 using 50 mm diameter and 50 mm height cylinders with rectified faces. The specimens were compressed with an increasing vertical load rate of $(200 \pm 0.1)$ kgf/s until crack formation.

The dynamic modulus of elasticity was obtained according to NBR-11222 by propagating an ultrasonic wave through the biggest dimension of the sample and measuring the time taken by the wave to cross the material. Therefore, MOE values can be used to evaluate the refractory's internal microstructure, as the presence of microcracks, and different phase formations, since overall components distribution affects the wave propagation.

The relaxation test measures the stress developed by the sample itself (cylinder with 35 mm diameter and 50 mm height) in the first heating cycle of a steel ladle lining. The cured samples were placed in a Material Testing System (MTS) 810 equipment and subjected to a heating rate of 5 °C/min in inert atmosphere keeping the bars fixed after touching the sample. Then, the force generated by the sample's tendency to expand while heated is measured by the equipment's sensor until the sample failure or until a maximum standard tension of 40 kN is reached.

The hot compression strain (HCS) test is conducted in the same MTS equipment used for the relaxation test but using cylindric samples of 25 mm of diameter and 50 mm height with rectified faces. The samples are previously coked at 1400 ºC for 5 h. During the test, a heating rate of 5 ºC/min under inert atmosphere is applied until reaching a stable temperature of 1400 ºC for at least 15 minutes. Once the temperature is stabilized, a force is applied at the rate of 0.2 mm/min and their deformation is measured by sensors located perpendicularly to the specimen until critical failure.

The specimens coked at 1100 ºC were used in a thermal shock resistance (TSR) test. The different coking temperature was chosen as a way of simulating the preheating process in steel ladles for this test. During the test, (160 x 40 x 40) mm³ bricks are wrapped in a nickel foil and heated to 1200 ºC with a dwell time of 30 minutes and cooled to room temperature on top of a steel plate refrigerated with water. This process is repeated 20 times and the MOE is measured at the beginning of the test as well as at the end of the 1st, 3rd, 5th, 10th, 15th and 20th cycles. Analyzing the evolution of the residual modulus of elasticity, which is the comparison between the current MOE value and the one from before the cycles, it is possible to observe structural changes caused by the thermal stresses.

## RESULTS AND DISCUSSION
### Carbon sources characterization

The LOI, moisture, fixed carbon, volatiles, ash content and specific surface area (SSA) of each carbon source are described in Table 2. The main differences are the LOI (comparing the first 3 sources to the last one) and the SSA, playing an important role in the material's distribution in the brick's matrix.

Tab. 2: Carbon sources characterization results.

| Carbon source | CS1 | CS2 | CS3 | CS4 |
|---|---|---|---|---|
| LOI (%) | 97.8 | 99.9 | 99.8 | 45.8 |
| Fixed carbon (%) | 96.1 | 98.5 | 97.6 | 42.1 |
| Volatiles (%) | 1.70 | 1.43 | 2.19 | 3.63 |
| Ash (%) | 2.25 | 0.06 | 0.10 | 54.20 |
| SSA (m²/g) | 1.86 | 9.32 | 18.31 | 37.24 |
| XRD | Graphite | Graphite | Graphite | MgO Graphite |

CS4 has the highest ash content among the carbon sources because this material is constituted by nano carbon tubes (nCT) deposited on a MgO substrate. The materials' oxidation behavior can be observed in Figure 1, and it is possible to associate the oxidation resistance to each material's SSA. CS4 starts to oxidize at a lower temperature (~ 500 ºC) due to its higher SSA, while CS1 presents the opposite behavior, starting the oxidation process at ~ 700 ºC. Such a lower oxidation resistance for the CS4 means that the Al and/or Si powder would not be effective to protect this carbon source against oxidation, since it oxidizes at lower temperatures than the metallic powders themselves [2].
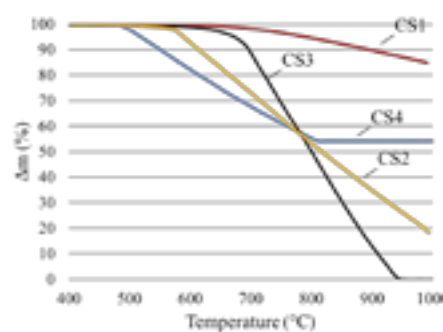


*Fig. 1: Relative weight loss profile comparison.*

The morphology of the carbon sources can be observed in Figure 2. The SEM images show a flake structure for CS1, which justifies its small SSA and higher oxidation resistance. CS2 and CS3 present leaf-like morphology, and the CS4 presents nanotubes morphology - what confirms the higher SSA reported. The average diameter of the nCT is in the range of 20-40 nm.
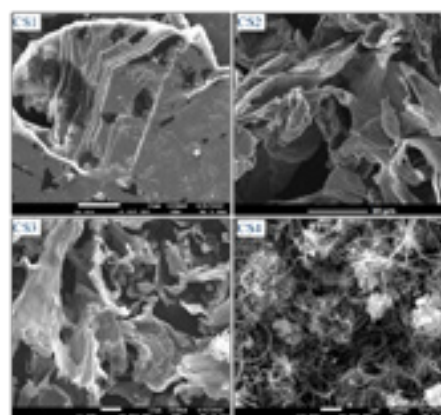


*Fig. 2: Carbon sources SEM images.*

### Brick's Characterization After Curing and Coking.

Table 3 shows the results of the cured samples using the different carbon sources (C1-C4). It is possible to say that the investigated physical properties are mainly affected by the SSA of the carbon source. As the SSA of the carbon source increases, it is observed a

tendency to decrease the BD, MOE, MOR and CCS, and increase the AP. The total carbon content and the fixed carbon are according to the expected range. The composition C4 presented the lowest fixed carbon, which could be explained by the higher volatile content of this carbon source.

Tab. 3: Results after curing at 200 °C/6h.

|  | C1 | | C2 | | C3 | | C4 | |
|---|---|---|---|---|---|---|---|---|
|  | Avg | SD | Avg | SD | Avg | SD | Avg | SD |
| BD (g/cm³) | 3.18 | 0.01 | 3.17 | 0.01 | 3.09 | 0.01 | 3.08 | < 0.01 |
| AP (%) | 5.94 | 0.33 | 5.73 | 0.5 | 9.17 | 0.54 | 9.62 | 0.14 |
| MOR (Mpa) | - | - | 26.2 | 1.7 | 19.6 | 3.7 | 10.7 | 2.0 |
| CCS (Mpa) | 88.4 | 9.1 | 83.4 | 8.7 | 73.9 | 7.1 | 71.2 | 12.8 |
| MOE (GPa) | 113.0 | 5.1 | 119.5 | 4.0 | 86.9 | 2.2 | 53.0 | 1.6 |
| Fixed C (%) | 1.76 | - | 1.62 | - | 1.5 | - | 1.46 | - |
| Total C (%) | 2.88 | - | 2.86 | - | 2.59 | - | 2.64 | - |

The results after coking are shown in Table 4. The trend observed for the variables was similar to the samples after curing. The MOE of the sample using the carbon source with the lowest SSA (C1) was 61 GPa, while for the sample using the carbon source with the highest SSA (C4) the MOE was 14 GPa. Taking the lower MOE after coking, it was expected that composition C4 could have the better thermal shock resistance among all the evaluated compositions. On the other hand, a higher SSA, as shown before, means a lower oxidation resistance, which could impair other important properties for this type of material.

Tab. 4: Results after coking at 1400 °C/5h

|  | C1 | | C2 | | C3 | | C4 | |
|---|---|---|---|---|---|---|---|---|
|  | Avg | SD | Avg | SD | Avg | SD | Avg | SD |
| LV (%) | -0.16 | 0.02 | -0.14 | 0.01 | -0.2 | 0.02 | -0.24 | 0.01 |
| VV (%) | -0.74 | 0.02 | -0.65 | 0.04 | -0.88 | 0.06 | -1.16 | 0.02 |
| BD (g/cm³) | 3.12 | 0.01 | 3.11 | 0.02 | 3.07 | 0.04 | 3.06 | 0.02 |
| AP (%) | 10.81 | 0.27 | 11.20 | 0.56 | 12.09 | 1.08 | 12.49 | 0.55 |
| MOR (Mpa) | - | - | 5.7 | 0.1 | 2.4 | 0.1 | 1.3 | 0.2 |
| CCS (Mpa) | - | - | 29.5 | 2.7 | 26.8 | 5.1 | 21.4 | 3.2 |
| MOE (GPa) | 61.1 | 2.7 | 55.6 | 3.1 | 36.2 | 5.2 | 14.0 | 2.3 |

Therefore, to control the oxidation rate (and improve the thermal shock resistance) of the ULC bricks, an additive was tested in compositions C5 and C6; the results are shown in Tab 5. The additive does not seem to affect the properties after curing but they do have an effect after coking. The compositions with the additive show a higher MOR, CCS, MOE and a lower coked porosity if compared to their versions without additives. For the similar compositions without additive (C2 and C4), the coking process causes a decrease of the MOR, CCS and MOE. While the same pattern can be seen for the mentioned properties in composition C5, composition C6 presents an increase of MOE with the coking process (from 74 GPa to 110 GPa). Therefore, the effect of the additive is in the way to increase the MOR, CCS and MOE and to reduce the coked porosity compared to the coked values in its absence, which helps to increase the brick's corrosion resistance. However, the final word in terms of the effect of the different carbon sources and the use of the additive will come from analyzing the thermomechanical properties discussed in the next topics.

**Thermomechanical and oxidation test results**
The relaxation test results for the compositions with each carbon source (C1 to C4) is shown in Figure 3. It is possible to identify an overall tendency of higher force produced by the heated sample with lower carbon SSA. Additionally, the samples with lower bulk density and higher apparent porosity after curing (C3 and C4) are also the ones that better performed in this test.
This result is consistent with the expected behavior, since more empty spaces and surface area of malleable material within the brick's internal structure allow for better tension accommodation.

Tab. 5: Test results of C5 and C6 (compositions with additive).

|  | After Curing | | | | After coking (1400 °C/5h) | | | |
|---|---|---|---|---|---|---|---|---|
|  | C5 | | C6 | | C5 | | C6 | |
|  | Avg | SD | Avg | SD | Avg | SD | Avg | SD |
| BD (g/cm³) | 3.18 | 0.01 | 3.04 | 0.01 | 3.13 | 0.01 | 3.08 | 0.01 |
| AP (%) | 5.73 | 0.21 | 9.53 | 0.42 | 10.00 | 0.30 | 11.20 | 0.17 |
| MOR (Mpa) | 27.4 | 2.0 | 12.8 | 0.7 | 11.6 | 0.4 | 8.7 | 0.2 |
| CCS (Mpa) | 88.8 | 9.3 | 128.0 | 6.9 | 58.0 | 1.8 | 92.7 | 19.0 |
| MOE (GPa) | 126.4 | 3.0 | 74.2 | 4.2 | 114.4 | 4.4 | 110.6 | 1.3 |
| Fixed C (%) | 1.84 | - | 1.60 | - |  |  |  |  |
| Total C (%) | 3.03 | - | 3.00 | - |  |  |  |  |

Particular attention is drawn to composition C4, which yielded an excellent result considering the low amount of carbon used. As such, it could be expected that refractories made with carbon source CS4 would present very little or absent spalling during the equipment's pre-heating step.
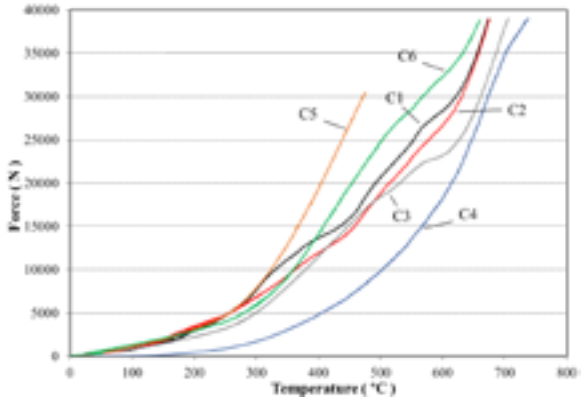


*Fig. 3: Relaxation test results for each carbon source composition.*

Another interesting observation is that, although the carbon sources from compositions C2 and C3 have a 2-fold difference in SSA, their force generation when heated is relatively similar in intermediate temperatures. One hypothesis to explain such behavior is that the carbon source morphology has a significant impact on tension accommodation that is not necessarily dependent on the surface area it generates, as both compositions have a leaf-like morphology. However, by introducing the additive, compositions C5 and C6, the force increased compared to the similar ones without additive (C2 and C4). This behavior is not well understood so far, but it was replicated in prior testing.
The stress-strain curve obtained at 1400 ºC can be seen in Figure 4. As the driving stress factor in steel ladles is related to strain caused by thermal expansion, instead of load-bearing [3], it is necessary to analyze the presented data accordingly by observing the maximum stress related to the strains that would be caused by thermal expansion in an operational situation.
The results show a clear pattern of higher maximum stress values for compositions with carbons of lower SSA and higher strain in the point of maximum stress for compositions with higher SSA carbon sources. This could indicate, for example, that sample C1 has worse thermomechanical behavior, as it develops higher tensions in its internal structure when submitted to relatively low strains. By associating these results with the relaxation test, it seems that carbon source CS1 is not efficient enough in the matter of tension dissipation to be used in such low amounts, while the other three are viable options, being carbon source CS4 the more promising of them.
Regarding the thermal shock resistance test, which can be seen in Figure 5, initially only compositions without additives (C1 to C4) were tested. Curiously, the results obtained were the exact opposite of the hypothesized based on information gained from the relaxation and hot compression strain data, being composition C1 the one which kept most of its structural integrity throughout the thermal shock cycles and C4 being the worst one.
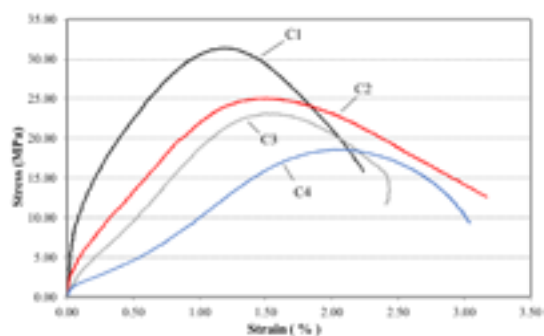
*Fig. 4: Stress-strain curves at 1400 ºC for each composition.*



*Fig. 6: Cross section of the samples without and with additives after 20 thermal shock cycles.*
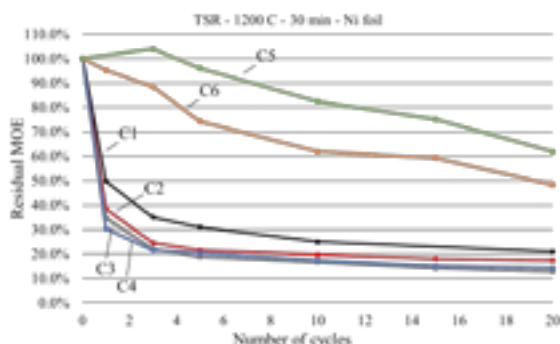


*Fig. 5: Thermal shock resistance results for each carbon source composition and two compositions with additives.*

Upon visual inspection of the samples' longitudinal cross sections, it become evident that the nickel foil method was not sufficient to prevent oxidation, Figure 6. Analyzing the observed discoloration, it was clear that the specimens suffered oxidation with proportional intensity of their carbon source oxidation rate previously defined. Therefore, compositions using carbon sources with high SSA (C4) have shown the worst results. As such, it is understood that this thermal shock resistance test reflects more the structural changes, caused by the oxidation process and further internal damage (developed due to the lack of carbon) than the real thermomechanical behavior of the brick during operation in a reducing condition of being submerged in slag or molten steel.

In order to further verify this observation and to try to analyze thermal shock resistance, two of the compositions that underperformed (C2 and C4) were altered to include antioxidant additives in the same amount (becoming C5 and C6 respectively). The results showed an excellent performance, indicating that the evaluated carbon sources, when present in low amounts, were able to satisfactorily distribute compression and tensile forces caused by fast and repeated thermal expansion and contraction. However, it was evident that a certain level of oxidation was still present and more intense for composition C6 (higher SSA carbon source.), as seen in Figure 6. Therefore, it is interesting to note that even if the mass of carbon used in the samples was the same, carbon source 4 seems to require higher amounts of antioxidants to reach its full thermomechanical potential expected for this test.

Once again, it is important to emphasize that, during operation in steel ladles, the MgO-C placed on the metal and slag lines have limited contact with oxygen gas, being the preheating step the most critical one in this regard, which happens in lower temperatures than during steel treatment. Therefore, it is not expected that MgO-C bricks after being used present the level of oxidation seen after the thermal shock test, which purposefully reproduces extremely harsh conditions for the material.
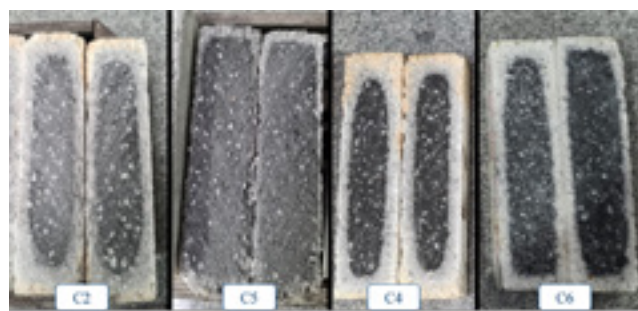
## CONCLUSIONS

The different carbon sources characterization successfully showed several key distinctions between them. Among the most important, there is a significant SSA variation, up to a 20-fold difference between the lower and higher obtained values, and three kinds of morphology (flake, leaf-like and carbon nanotubes) were identified. These properties, in turn, lead to the observed varied behavior for the ULC bricks. Carbon source 1 showed a high MOE after coking at 1400 ºC for 5 hours, high stresses developed in both relaxation and HCS tests and low strain at the point of maximum stress in the latter. These are strong indicators that CS1 is not efficient enough in the matter of tension dissipation to be used in such low amounts, even if it seems to be the most oxidation resistant composition without additives. The use of special carbon sources 2, 3 and 4 presented satisfactory physical properties and thermomechanical behavior. Carbon source 4 shows exceptional results in most tests, indicating that even lower amounts of it could be used in further testing. Although carbon source 4 is very promising in the path of refractory decarbonization, thermal shock tests associated with visual inspection revealed that higher amounts of antioxidants are necessary to prevent the brick's oxidation if compared to other sources with lower SSA and oxidation rates. Therefore, carbon sources 2 and 3 show themselves as good compromises between performance and oxidation resistance for situations in which oxidation may be a significant factor (such as operations with high intermittency and long preheating time periods) and in which the excessive use of antioxidants is undesired due to possible cost disadvantages.

## REFERENCES

[1] Silva SLC, Brito MAM, Hill K, Gueguen E, Ducastek A. Development of ultra-low carbon bricks for ultra-low carbon content steels. 59th International Colloquium on Refractories 2016.

[2] Behera, S. and Sarkar, R. Nano carbon containing low carbon magnesia carbon refractory: an overview. Protection of Metals and Physical Chemistry Surfaces 52 (3), 2016, p. 467 – 474.

[3] Schacht, C.A. Refractory linings – Thermomechanical design and applications. Marcel Dekker, Inc. New York, 1995.

# UNFIRED ZERO C BRICK FOR ENERGY SAVINGS AND PERFORMANCE INCREASING OF METAL LINE FOR STEEL LADLE

Carlos Pagliosa, Marcelo Borges, Leandro Martins, Bruno Laidens, Haylander Avila, RHI MAGNESITA, Contagem, Brazil

## ABSTRACT

As the requirements for steel quality have become increasingly strict with strong demand for high strength and high toughness steel plates, increased number of customers are concerned about carbon pick up. A new generation of unfired zero carbon refractories was developed to replace firing and carbon bonded bricks, reducing $CO_2$ footprint with performance increasing. Steel ladle lining plays an important role on the energy consumption during the production and the refractory lining design contributes to minimize thermal bath loss and shell temperature. This work presents the development of the unburned Alumina-Magnesia technology with a unique microstructure for better heat scattering with energy savings and customers' performance compared to resin bonded bricks.

## INTRODUCTION

The iron and steel industry are one of the most energy-intensive worldwide and accounts for around 21% of global industrial energy use and about 24% of industrial $CO_2$ emissions. Global steel production has more than doubled between 2000 and 2018. The energy use and greenhouse gas (GHG) emissions of the steel industry is likely to continue increasing because of the higher demand for steel, particularly in developing countries, due to infrastructure constructions and the higher output for cleaner steels [1].

Clean steel encompasses a multitude of concepts that are based on fulfilling customer requirements and can be produced in many ways depending on the existing equipment. A common feature of all clean steel production is a tight process control along with continuous monitoring. The major remaining issues to be addressed are disturbances that occur in industrial reality. This requires continuous improvements in processes and equipment on one hand and further development of quality assurance systems for full size control of any possible detrimental effects on the other hand [2].

To meet an increasing demand for cold-rolled (CR) steel sheets of improved mechanical properties, and to cope with the change of the annealing process from a batch-type to a continuous process, it is necessary to establish a technique for making ultralow carbon (ULC) steel. Particularly, for an economical manufacture of extra deep drawing or high tensile strength CR steel sheet with superior deep drawing properties, it is essential to obtain ULC molten steel with a C-concentration lower than 20 ppm for the steelmaking process. ULC steel is widely used for the automotive industry [2,3].

The composition, quantity, and size distribution of non-metallic inclusions (NMI) in steel, determine the quality and performance in application. Over the past decade, ULC steel, also referred to as interstitial free (IF) steel, has been used in automobile parts because of the excellent formability. However, the high quantity of inclusions, especially larger ones, can cause a deterioration of surface properties. In addition to the low C (< 30 ppm) and the low N (< 30 ppm) requirements for obtaining an extraordinary formability and providing a non-aging property, a constraint over the maximum inclusion size (< 100 μm) is also required for ULC steels [4].

The ULC molten steel is produced by two decarburization steps: 1) in the BOF for reducing the C concentration to approximately 300 ppm, and 2) in the ladle, where vacuum decarburization in the RH, under reduced partial pressure of CO (carbon monoxide) gas is obtained. Passing the initial quick decarburization period, when C

and O (oxygen) are abundantly available, the decarburization rate becomes stagnant after a few minutes in the RH degasser. To further bring the C down, O must be injected into the liquid steel to speed up the decarburization reaction. Such O injection contributes to the higher concentration of dissolved O in liquid steel after degassing. Consequently, aluminium addition is necessary for complete deoxidation of the ULC steel. This results in the generation of a large number of indigenous $Al_2O_3$ (alumina) inclusions after the deoxidation step in the ladle. However, inclusion agglomeration due to Brownian motion, Stokes collision and liquid steel bath turbulence followed by flotation lead to the inclusion removal [4,5].

The last decarburization process takes time to reach the desired C-content, which results in a drop in the steel temperature, which is offset by increasing the BOF tapping temperature, leading to higher steel cost, and placing higher demands on the refractory material, mainly in the secondary metallurgy [5].

The secondary metallurgy is a high energy-intensive step in steelmaking process as it requires an accurate match of the composition and temperature of the molten metal during the ladle refining. So, the steel ladle lining plays an important role on the energy consumption of the process, as the refractory thermal properties are strictly related to the ladle ability to keep constant the bath temperature. Aiming to improve the energy efficiency, reducing costs and the environmental impacts, a different approach in working lining material is necessary [6].

The iron and steel industry that carry out high temperature processes, require advanced energy solutions for efficiently heat management during their processing. Steel makers have been looking for new strategies and solutions to decrease the energy consumption, due to the growing demands for steel products and the reduction in the environment impacts. Most of the green solutions will depend on the proper design of the refractory linings in all furnaces and machinery, suppressing the molten metal heat losses and reducing the specific refractory consumption per ton of steel. Also, controlling and monitoring the thermal state of the process is essential to ensure the final product quality and to guarantee the steel mill operational flow [2,3].

A major challenge in modern industry is to guarantee the competitiveness with observance of environmental requirements. Steel ladle lining plays an important role on the energy consumption during the steel production and the refractory lining design contributes to minimize thermal bath loss and shell temperature. A new generation of unfired zero carbon refractories was developed with two specific approaches: 1) replacement of firing bricks reducing $CO_2$ footprint and 2) replacement of carbon containing bricks with performance increasing. Bricks can be used in working linings with a unique microstructure with better heat scattering and similar thermomechanical properties. This work presents customers' performance compared to traditional products highlighting energy savings.

## ZERO CARBON BRICK TECHNOLOGY

Ladle lining configurations are most based on the customer's operational cycle and the type of the steel shop. Anyway, is possible to distinguish common refractory specifications for barrel or metal line. For integrated steel shops tempered bricks ($Al_2O_3.MgO.C$ – AMC or $MgO.Al_2O_3.C$ – MAC) are most used.

This aim of this paper is to present original solutions for energy savings products replacing the conventional approach used as working lining, to maximize shell temperature reduction.

Zero carbon unfired brick technology is based on the development of a new binder system with a surface treatment on fines of the composition, enabling that the raw materials develop a binder effect. No resin or pitch is added enabling zero C-pickup on the production of ULC steel. This novel binder can be applied for most of refractories, as basic and alumina bricks. Basic bricks cover products with dead burned magnesia (DMB), fused magnesia (FM) and magnesia-crome (MgO-Cr). Alumina bricks cover all range of the products from 45% to 95% alumina content, making this binder very flexible to plant production. All bricks are delivered to the customer just after tempering, that can range from 170 to 250°C, the same as carbon binder bricks [7].

Replacement of carbon containing products, mainly for the barrels of steel ladles has some advantages summarized as follow:
1. No pollutant binder.
2. No oxidation of the bricks during pre-heating or during the ladle campaign.
3. In situ spinel formation for joint closing for the safety and working brick linings.
4. No carbon pick-up for ULC steel production.
5. Energy saving: reduction of shell temperature and bath temperature loss due lower thermal conductivity compared to conventional carbon bonded bricks.
6. Easy for recycling as no carbon or antioxidants are in the composition.
7. Performance increase in most of the cases when carbon bricks were replaced by this technology.

To meet the requirements for the ULC steel quality with strong demand for high-strength and high-toughness plates, some customers demand a zero C brick for metal line. Steel ladles are subjected to high temperature effects, aggressive slags, long-lasting metal holding time, and many refining factors that require high-quality refractory products. Usually, the current refractory solution is a fired brick based on alumina-magnesia compositions and fired over 1500 °C prior to delivery, forming magnesia-alumina (MA) spinel ($MgO.Al_2O_3$). This new phase presents unique properties as follow: 2135 °C melting point, high mechanical resistance at high temperatures, better corrosion resistance against basic slags than alumina aggregates, low thermal expansion value, similar thermal shock resistance as alumina, high stability under vacuum and environmentally friendly, with no risks of chrome-bearing products Few customers also consent on standard products such as AMC and MAC bricks, although, natural graphite and the C from the binder system have been identified as potential sources for C-pickup [8-10].

Unfired alumina-magnesia bricks were developed as a technological alternative for the barrel of the ladles for any C-steel grade but with an additional benefit for ULC steel for avoiding C pickup. Although, all customers can take benefit of the reduction of the shell temperature due to the low thermal conductivity of the brick. Spinel $MgO.Al_2O_3$ formation still occurs during ladle operation with an expansive reaction for joints closing, that can prevent metal and slag infiltration, better corrosion resistance and operational safety. Thermodynamic simulation performed in this work was based on the minimization of the free energy of the system to find out the nature of the solid, liquid, and gaseous phases, as well as its chemical composition and reaction rate at the thermodynamic equilibrium [11]. Simulation was carried out using FactSage (version 8.1) and it is presented in figure 1. Phase development shows a preformed spinel to counter act corrosion resistance since the beginning of ladle operation and spinel forming as the vessel has been soaked by molten steel. This expansion reaction will promote joint closing to avoid liquid infiltration and

guarantee safety operational conditions and performance increasing.
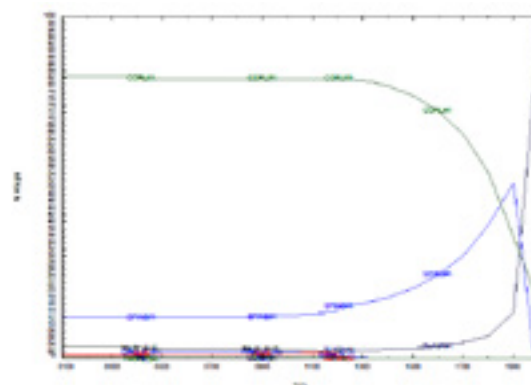


*Fig. 1. Phase evolution predicted by the thermodynamic simulations for the zero carbon unfired brick.*

Table 1 shows the chemical, physical and mechanical properties of the conventional barrel design brick (referred as MAC) and the zero carbon unfired brick (referred as AM-K).

Tab 1. Chemical physical and mechanical properties of the conventional barrel design brick (MAC) and the zero carbon unburned brick (AM-K).

| | MAC | AM-K |
|---|---|---|
| $Al_2O_3$ (%) | 22.8 | 94.7 |
| MgO (%) | 74.8 | 4.7 |
| C (%) | 6.7 | Zero |
| Binder | Resin | New binder |
| Antioxidant | Yes | Zero |
| **After Tempering 180 °C** | | |
| Bulk Density (g/cm³) | 2.94 | 3.33 |
| Apparent Porosity (%) | 10.0 | 8.4 |
| Cold Crushing Strength (MPa) | 65 | 57 |
| Elastic Modulus (GPa) | 63 | 52 |
| **After coked 1000 °C** | | |
| Bulk Density (g/cm³) | 2.88 | 3.27 |
| Apparent Porosity (%) | 14.8 | 15.8 |
| Permanent Volumetric Expansion (%) | -0.54 | 0.15 |
| Cold Crushing Strength (MPa) | 50 | 43 |
| Elastic Modulus (GPa) | 24 | 25 |
| Slag corrosion[1] (%) | 82 | 21 |
| **After coked 1400 °C** | | |
| Bulk Density (g/cm³) | 2.79 | 3.16 |
| Apparent Porosity (%) | 17.1 | 17.2 |
| Permanent Volumetric Expansion (%) | 4.16 | 2.19 |
| Cold Crushing Strength (MPa) | 41 | 48 |
| Elastic Modulus (GPa) | 19 | 71 |

Bulk density of AM-K product was higher than MAC brick at all temperatures due to a higher proportion of raw materials with fewer defects and impurities. The apparent porosity of the AM-K product had a similar behaviour to MAC, mainly after firing at 1400 °C. The main reasons for increasing porosity in MAC were the burning of volatiles and formation of the spinel phase. For the zero C product (AM-K) the predominant factor was only the formation of the expansive spinel phase. Due to differences in the binder system, AM-K brick showed higher cold crushing strength (CCS) after

firing at 1400 °C, while the MAC product had slightly higher CCS after tempering and at 1000 °C.

Regarding the elastic modulus, the AM-K product showed improved behaviour after being exposed over 1400 °C due to the higher sintering capability compared to the MAC brick and resulting in smaller number of internal defects. This fast sintering also has consequences for much better result for corrosion index due to a physical barrier that is formed at hot face and for the spinel formation.

AM-K brick presented a positive volumetric expansion at 1000 °C and 1400 °C. Brick-joint closure started earlier than MAC product during the ladle operation, preventing the penetration of liquid metal. Also, at 1400 °C, the expansion value of the AM-K is lower when compared to the MAC product, then less stress is generated in the barrel bricks.

**Example 1 – Customer A – Ladle 350t**

Figure 2 shows the results of average performance after the roll-out of this novel zero carbon concept in the operational cycle of melt shop. Steel ladles with AM-K lining showed 23% better average performance when compared to MAC lining. A significant remaining thickness was also noticed during tear-out. Over the years, MAC brand presented an average ladle life of approximately 96 heats and a remaining safety thickness of 40 mm. AM-K bricks are achieving 130 heats with a remaining thickness of 70 mm.



*Fig. 2. Average performance comparison between MAC and AM-K lining with the zero carbon technology concept.*

One of the most significant benefits accomplished by the AM-K lining was the lower bath temperature loss. More than 220 steel temperature samples were taken just prior to the ladle leaving the first secondary metallurgy station and just after it arrived in the second station. A comparison between both linings was made and the results are shown in figure 3. A decrease of 8% was achieved in bath temperature loss, which lead to a lower consumption of raw materials by the customer for maintaining the desired temperature, also creating a significant impact in energy savings.
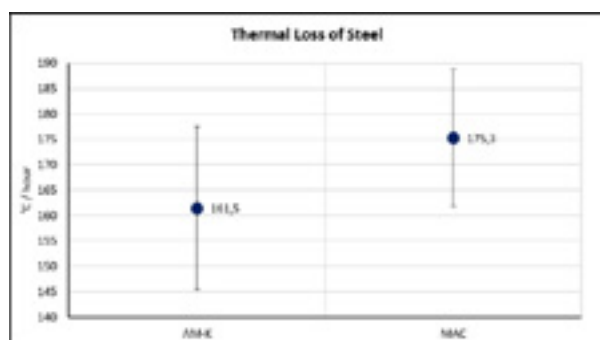


*Fig. 3. Comparison of bath temperature loss for MAC and AM-K linings with the zero carbon technology concept.*

Figure 4 shows an example of the visual inspection of AM-K linings at the end of the ladle campaign. No drawbacks were noticed during the whole cycle.
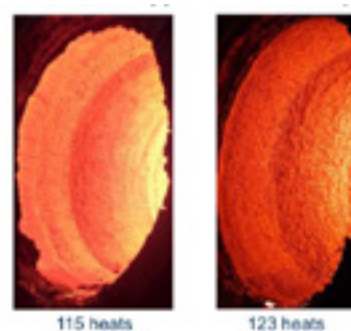


*Fig. 4. Examples of the visual inspection of two ladles at the end of the campaign of AM-K linings with the zero carbon technology concept.*

**Example 2 – Customer B – Ladle 320t**

Evaluation was conducted with a direct comparison of MAC and AM-K linings at the same steel ladle in order to guarantee the same operational conditions in both products during the whole campaign. Figure 5 shows the barrel assembling. Zero carbon brick lining is easily identified. Figure 6 shows both products after 180 heats, with a better coating and insolation protection for the AM-K.

Shelf temperature was monitored using infrared camera during the campaign to measure the benefits of this technology, as shown in figure 7. Total measurements were 49 shots that presented an impressive average shelf temperature reduction of 28°C (82.4 °F), also a direct benefit for energy savings. Figure 8 presents the laser scan on the ladle at 180 heats. Lowest remaining thickness for the both products were as follow: 47mm for MAC against 87mm for AM-K bricks.



*Fig. 5: Ladle barrel assembling for customer trial with MAC and AM-K lining with the zero carbon technology concept.*



*Fig. 6: Ladle barrel after 180 heats, with a better coating and insolation protection for the AM-K lining with the zero carbon technology concept.*
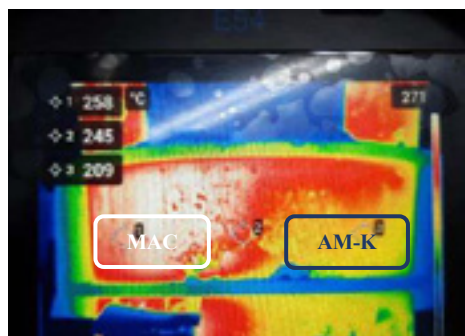
*Fig. 7: Shell temperature measurement by infrared camera after the first heat - point 1: MAC brick and point 3: AM-K brick*
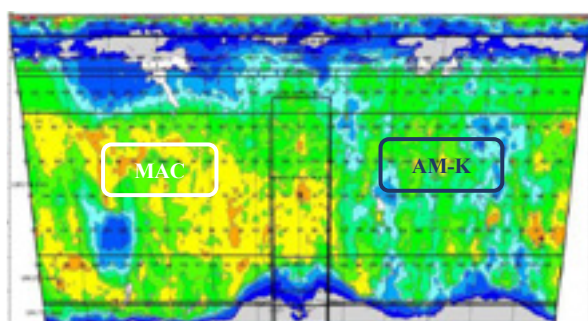


*Fig. 8: Laser scan on the ladle at 180 heats - right side: MAC brick and left side: AM-K brick.*

## SUMMARY AND CONCLUSIONS

A new generation of unfired zero carbon refractories was developed for replacement of firing bricks and carbon containing ones, with lower $CO_2$ footprint during fabrication, easy recyclability and a fast sintering process development on customer's site.

This novel binder can be applied for most of basic and alumina refractories products, making this technology very flexible to plant production and attending wide spread of customer's demand.

Customer's trials showed better performance for the working line with expressive shell temperature reduction due to the better heat scattering related to porous distribution, highlighting the potential of the this zero carbon technology for saving energy at real application's on the steel shops.

## REFERENCES

[1]  1.  A Hasanbeigi, C Springer, E Global – How clean is the U.S. steel industry? An International Benchmarking of Energy and CO2 Intensities, 2019 - aciercanadien.ca
[2]  Wünnenberg, K. IISI study on clean steel. La Revue de Métallurgie-CIT. Octobre 2005, 687–692.
[3]  Lee, S., Saito, Y., Park K. and Shin D.H. Microstructure and mechanical properties of ultralow carbon IF steel processed by accumulative roll bonding process. Material Transaction. 2002, 43, 9, 2320–2325.
[4]  Pande, M.M., Guo, M., Dumarey, R., Devisscher, S. and Blanpain, B. Determination of steel cleanliness in ultra low carbon steel by pulse discrimination analysis-optical emission spectroscopy technique. ISIJ International. 2011, 51, 1778–17871.
[5]  Sumida, N., Fujii, T., Oguchi, Y., Morishita, H., Yoshimura, K. and Sudo, F. Production of ulta low carbon steel by combined process of bottom blow converter and RH degasser. Kawasaki Technical Report. 1983, 8, 69–76.
[6]  M. F. Santos1, M. H. Moreira, M. G. G. Campos, P. I. B. G. B. Pelissari, R. A. Angelico, E. Y. Sako, V. C. Pandolfelli. Steel ladle energy saving by refractory lining design. Proceedings UNITECR 2017, Santiago, Chile.
[7]  Pagliosa, C., Sardelli, J.A., Melo, B., Borges, M., Cavalcante, C., Mejia, E. - Energy Efficiency Refractory Bricks for Steel Ladle Linings. Proceedings AISTech 2023.
[8]  Pagliosa, C., Campos, A., Freire, N. and Loeffelholz, M. MAC bricks for steel ladle – Novel Technology to Metal Line. Proceedings AISTech 2013,1, 796–801.
[9]  Sainz, M.A., Mazzoni, A.D., Aglietti, E.F. and Caballero, A. Thermomechanical stability of spinel (MgO-Al2O3) under strong reducing conditions. Materials Chemistry and Physics. 2004, 86, 399–408.
[10]  Aksel, C., Rand, B., Riley, F. L. and Warren, P. D. Thermal shock behaviour of magnesia-spinel composites. Journal of the European Ceramic Society. 2004, 24, 2839–2845.
[11]  Luz, A.P., Tomba Martinez, A.G., Braulio, M.A.L and Pandolfelli, V.C. Thermodynamic evaluation of spinel containing refractory castables corrosion by secondary metallurgy slag. Ceramics International. 2011, 37, 1191–1201.

387

# IMPROVED SLAG CORROSION RESISTANCE OF MGO−C REFRACTORIES FOR LADLE SLAG LINE

Tianbin Zhu [a, b, *], Weijie Guo [a, b], Yawei Li [a, b]

[a]The State Key Laboratory of Refractories and Metallurgy, Wuhan University of Science and Technology, Wuhan 430081, China

[b]National-provincial Joint Engineering Research Center of High Temperature Materials and Lining Technology, Wuhan University of Science and Technology, Wuhan 430081, China

## ABSTRACT

The influence of calcium magnesium aluminate (CMA) aggregate on the slag corrosion resistance of MgO–C refractories was investigated by the induction furnace tests and the sessile drop test. The results showed that $CaAl_2O_4$ in CMA converted into low melting phases when facing slag, while spinel diffused into the refractory-slag interface. The Al-containing liquid phase melted from $CaAl_2O_4$ increased the Al content of slag, increasing the proportion of indirect dissolution, forming more spinel and decreasing the corrosion rate. Furthermore, the spinel and liquid slag formed solid-liquid mixture at the interface, increasing the viscosity and promoting the formation of protective slag layer, which avoided direct contact between slag and refractory. The combined use of CMA aggregate and silicon carbide showed better corrosion resistance because silicon carbide increased the oxidation resistance and inhibited the decarburized layer, while the FeSi alloy and higher viscosity also enhanced the slag corrosion resistance of refractory.

## INTRODUCTION

Since 1970s, MgO–C refractories had been widely used as lining material for ladle slag line because the low wettability of graphite with slag gave such refractories excellent slag corrosion resistance [1].

With the development of metallurgy technology, the high scrap ratio metallurgy was regarded as important method to reduce $CO_2$ emission and consume fast-growing scrap output [2-3]. However, with the large-scale applicant of high scrap ratio, the service life of refractory lining reduced. Increasing the scrap ratio makes slag contain more impurities, changing the chemical compositions and reducing the viscosity of slag. To adapt high scrap ratio metallurgy, it is necessary to develop new kind of MgO–C refractories with better slag corrosion resistance.

Previous research showed that calcium magnesium aluminate (CMA) aggregate, a newly-developed porous aggregate, had positive effect on the slag corrosion resistance of various refractories. Preisker *et al.* [4] investigated the formation of protective slag layer through finger test and static cup tests, finding that the brownmillerite-rich phase promoted the formation of protective slag layer in MgO–CMA–C refractories. However, the formation of such layer may be influenced by the testing condition and the compositions of the slag. The static cup test used in previous works did not well simulate the violent turbulent motion of slag/steel in the ladle, and the slag with different chemical composition may change the phases in protective slag layer, causing different corrosion behavior of refractories.

In present work, influence of CMA aggregate on the MgO–C refractories was comprehensively studied by induction furnace slag tests. The suitable addition of CMA was also obtained by combined use of CMA and silicon carbide. The sessile drop test was used to further investigate the corrosion behavior of CMA aggregate. Thermodynamic calculation was applied to the corrosion behavior analysis to further explain the slag corrosion process. Based on Einstein-Roscoe equation and thermodynamic calculation, the viscosity of protective slag layer as well as the formation mechanism of such layer were explained in details.

## EXPERIMENTAL

The raw material of CMA cylinder samples was CMA powder (200 mesh). To prepare the CMA cylinder samples (φ50 mm × 10 mm), 50g CMA powder with 5g binder (30 wt% phenolic resin) were pressed under 150 MPa. Then the CMA cylinder samples were cooked at 1600°C for 3 h to sinter. As for MgO-C refractories specimens, raw materials were CMA aggregates (3-1 mm and 1-0 mm), fused magnesia (5-3 mm, 3-1 mm, 1-0 mm and 180 mesh), silicon carbide (1-0 mm and 200 mesh), flake graphite (100 mesh), carbon black (100-700 nm), pitch powder (Carbores P, 85 wt% carbon), $B_4C$ powder (325 mesh), aluminum powder (180 mesh) and liquid phenolic resin (36 wt% carbon yield). The formulations of MgO-C refractories are shown in Tab. 1.

Tab. 1: Formulations of MgO–C specimens

| Raw materials | R | C | S | CS |
|---|---|---|---|---|
| Fused magnesia | 96.7 | 91.7 | 91.7 | 86.7 |
| CMA aggregates | / | 5 | / | 5 |
| Silicon carbide | / | / | 5 | 5 |
| Antioxidants | 0.8 | 0.8 | 0.8 | 0.8 |
| Carbon | 2.5 | 2.5 | 2.5 | 2.5 |
| Phenolic resin | +4 | +4 | +4 | +4 |

Apparent porosity (AP) and bulk density (BD) were obtained by Archimedes principle. CMOR and HOMR were measured by three points bending tests. For CMOR, the tests carried out at room temperature; for HMOR, samples were cooked at 1400 °C for 30 min in reducing atmosphere. The specimens were tempered at 1600 °C for 3h

to test oxidation resistance. The oxidation index (OI) was the ratio of oxidized area to total area of the section. The sessile drop method was used for the corrosion behavior of CMA cylinder. 5 g slag and the cylinder sample were tempered at 1600 °C for 10 min. Then, corroded specimens were cut along the central line. To evaluate the slag corrosion resistance of the MgO–C refractories with CMA aggregates and silicon carbide, induction furnace slag tests was used. The rectangular samples were embedded into the castable crucible. The crucible was fixed in the induction furnace, and cylindrical No. 45 low-carbon steel (φ90 mm × 130 mm) melted at 1600 °C. After complete melting of the steel, 75 g slag was poured into the crucible and the corrosion time was 30 min. The automobile plate slag (Angang Steel Group Limited, Anshan, China) was used in this work, and its chemical compositions are shown in Tab. 2.

Tab. 2: Chemical compositions of the slag

| $SiO_2$ | $Al_2O_3$ | FeO | CaO | MgO | $CaF_2$ | MnO |
|------|------|------|------|------|------|------|
| 9.90 | 32.24 | 8.48 | 33.73 | 8.20 | 4.57 | 1.33 |

## RESULTS AND DISCUSSION

### Properties of MgO–C refractories

Tab. 3 represents the apparent porosity (AP), bulk density (BD), hot modulus of rupture (HMOR) and oxidation index (OI) of MgO–C refractories. With the addition of CMA aggregates, the bulk densities of specimens with CMA aggregates decreased while the apparent porosity slightly increased. A slight decrease in HMOR of specimens with CMA aggregates could be observed due to the formation of liquid phase in CMA aggregate at high temperature. The specimens without silicon carbide had poor oxidation resistance (Fig. 1). The OI of specimens with CMA aggregates was slightly lower than those without them, which was related to the higher apparent porosity.

Tab. 3: Properties of MgO–C refractories

| | AP (%) | BD (g/cm³) | HMOR (MPa) | OI (%) |
|------|------|------|------|------|
| R | 5.2±0.3 | 3.14±0.02 | 14.2±0.2 | 85.73 |
| C | 5.9±0.8 | 3.11±0.02 | 13.2±0.8 | 89.98 |
| S | 6.0±0.7 | 3.12±0.02 | 14.1±1.7 | 64.97 |
| CS | 8.1±0.7 | 3.03±0.02 | 13.4±0.7 | 72.92 |



*Fig. 1: Oxidzied specimens: (a)R, (b)C, (c)S, (d)CS*

### Visual inspection of corroded refractories

Fig. 2 shows the images of corroded specimens after induction slag tests. As shown in Fig. 3, the corrosion area of specimen R was the largest (78.84 mm²), and the corrosion area of specimen C and S were 62.10 mm² and 54.14 mm² respectively. As shown in Fig. 4, protective slag layer could be observed at the corroded area, and it was porous with thickness of 2 mm for specimen CS.
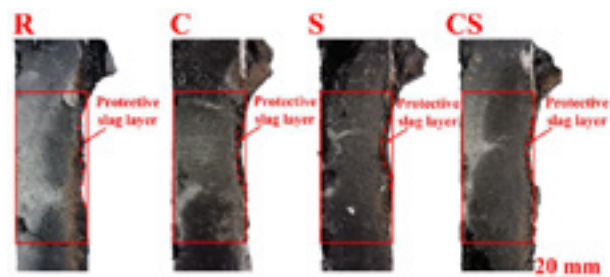


*Fig. 2: Images of corroded specimens*
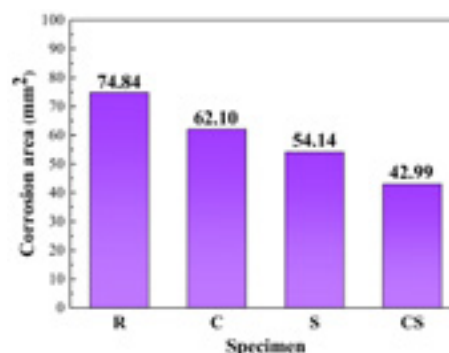


*Fig. 3: Corrosion area of different specimens*
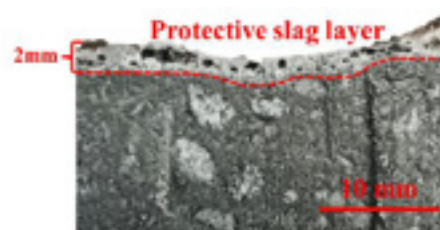


*Fig. 4: Images of protectvie slag layer of specimen CS*

### Microstructure of corroded refractories

The microstructure of corroded specimens was presented at Fig. 5. Decarburized layer could be found at specimen R and C due their poor oxidation resistance. For specimen S and CS, no obvious infiltration layer or decarburized layer existed, and a slightly corroded CMA aggregate was observed at the slag-refractory interface of specimen CS. The SEM images of protective slag layer were shown in Fig. 6. Main compositions of protective slag layer were low-melting phase and spinel. Tab. 4 shows the EDS results of metal. Obviously, for specimen C without silicon carbide, Fe and MnO were the main compositions of the metal, while the FeSi could be found for specimen CS with silicon carbide, indicating that silicon carbide powder converted FeO into FeSi. Obviously, the slag layer was solid-liquid mixture instead of pure liquid.
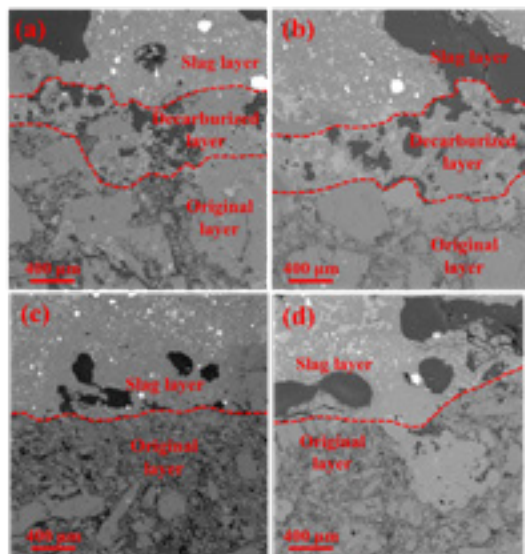
*Fig. 5: Microstructure of corroded specimens: (a)R, (b)C, (c)S, (d)CS*
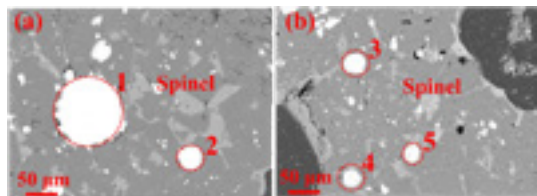


*Fig. 6: Microstructure of slag layer: (a)C, (b)CS*

Tab. 4: EDS area analysis results

| Specimen | Area | Possible phases |
|----------|------|-----------------|
| C | 1-2 | Fe, FeO, MnO |
| CS | 3-5 | FeSi, Fe, FeO, MnO |

**Corrosion behavior of CMA cylinder**

To comprehensively demonstrate the corrosion behavior of CMA aggregate, the sessile drop test was used in this work. Fig. 7 shows the images of corroded CMA cylinder specimen. The slag was melted and spread on cylinder, and it tended to flow along the side. The slag coating was porous, and the brown corroded area could be observed at the contact surface of cylinder.



*Fig. 7: Corroded CMA cylinder specimen*

Fig. 8 presents the microstructure of corroded CMA cylinder. Obviously, the slag-CMA interface was seriously corroded, and porous slag could be observed above the CMA cylinder. Since both CMA and slag contain Mg, Ca, and Al elements, Fe and Si were selected to analysis the ending of the penetration. Fig. 8b shows the microstructure

of corroded interface. The slag-CMA interface was not smooth due to the corrosion of slag, and CMA at the edge was disintegrated. Fine particles remained at interface, which were mainly spinel (Points 1-5) according to Tab. 5. Few amount of Fe was dissolved in spinel, meaning that $Mg(Al, Fe)_2O_4$ was formed. At the outer side of slag (Points 6-8), low melting phases including gehlenite could be observed, which were compositions of the slag after cooling. Fig. 8c shows the corroded area of CMA cylinder. The $CaAl_4O_7$ (Points 11, 12) and spinel (Points 13, 14) could be detected due to their higher stability against slag. Ca-containing phases (Points 9, 10) including Gehlenite and FeO could be observed inside the CMA, which were corroded low melting phases after the infiltration of the slag. The $CaAl_2O_4$ phase could not be detected because it converted into low melting phases and melting into liquid phase.
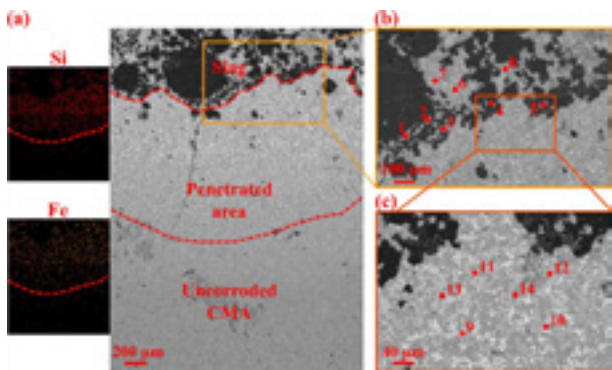


*Fig. 8: Microstructure of corroded CMA cylinder (a), CMA-slag interface (b) and penetrated area (c)*

Tab. 5: EDS point analysis results

| Area | Point | Possible phases |
|------|-------|-----------------|
| Interface | 1-5 | $Mg(Al, Fe)_2O_4$ |
| Slag | 6-8 | Gehlenite, FeO, $Ca_2SiO_4$ |
| CMA | 9-10 | Gehlenite, FeO |
| | 11-14 | $CaAl_4O_7$, $Mg(Al, Fe)_2O$ |

When facing the slag, the $CaAl_2O_4$ in CMA was firstly converted into corroded phases like gehlenite. Those phases were mainly low melting phases, making the structure of CMA unstable at high temperature, thus the CMA at the interface was disintegrated. After the disintegration of CMA, the spinel particles diffused into the slag, which could remain stable at the slag-CMA interface.

**Thermodynamic calculation**

The thermodynamic calculation results of MgO–C refractories were shown in Fig. 9 and Tab. 6. The specimen with CMA aggregates (C and CS) had more spinel compared with the specimens without CMA aggregates (R and S). A part of spinel was from the CMA aggregates, and a part was formed as the product of the indirect dissolution of periclase. The MgO in refractories reacted with the $Al_2O_3$

in the slag, formed intermediate solid phase instead of directly diffused into slag following Fick's first law. As a result, the direct dissolution was inhibited and the proportion of indirect dissolution was increased. The specimens with silicon carbide (S and CS) could found solid FeSi alloy. FeSi was formed through the reaction between silicon carbide and FeO. The infiltrability of FeSi was lower compared with $Fe^{2+}$ in the slag due to its poor wettability with the refractory. The addition of silicon carbide also increased the oxidation resistance of the specimens, thus no decarburized layer was observed in S and CS.
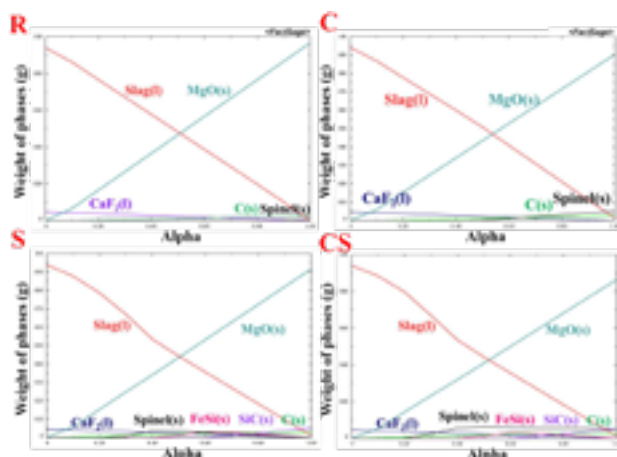


Fig. 9: Calculation results of MgO–C refractories

Tab. 6: Maximum spinel and FeSi amounts of different specimens (g)

| Specimen | Maximum Spinel Amount | Maximum FeSi Amount |
|----------|----------------------|---------------------|
| R | 0.62 | / |
| C | 4.96 | / |
| S | 3.57 | 3.09 |
| CS | 6.04 | 3.09 |

The protective slag layer was solid-liquid mixture instead of pure liquid phase. Therefore, in present work, Einstein-Roscoe equation was used to calculate the viscosity of liquid-solid mixture (Fig. 10).
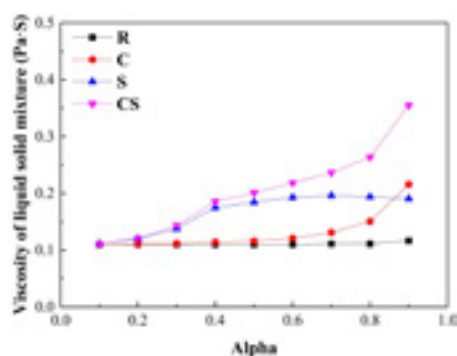


Fig. 10: Viscosity of liquid-solid mixture

For specimens with silicon carbide (S and CS), the viscosity gradually rose at the *Alpha* range of 0.10-0.40 because the formation of

FeSi alloy decreased the contents of $Fe^{2+}$ in the slag. For specimens with CMA aggregates (C, CS), the viscosity dramatically increased at the *Alpha* range of 0.60 to 0.90, which was nearly same as the range of spinel formation, indicating that the spinel significantly contributed to the increase in the viscosity of liquid-solid mixture.

Therefore, at the refractory-slag interface, liquid slag mixed with spinel and FeSi and formed a highly viscous solid-liquid mixture. The high viscosity of such mixture decreased the infiltrability of the slag, thus no infiltration layer was observed in corroded specimens. The viscous solid-liquid mixture also promoted the formation of protective slag layer, which avoided the direct contact between slag and refractories and increased the slag corrosion resistance of refractory.

**CONCLUSIONS**

(1) When facing the slag, the $CaAl_2O_4$ in the CMA aggregate were converted into Al-containing liquid phases, which increased the Al content of the slag, promoted the formation of spinel and enhanced the indirect dissolution of MgO–C refractories. After the disintegration of the CMA, the original spinel component in CMA aggregate diffused into the slag-refractories interface.

(2) The spinel and liquid slag formed high viscous solid-liquid mixture at the slag-refractory interface. The high viscosity of solid-liquid mixture decreased the penetration ability of the slag, while the mass transport from the refractories to slag was also inhibited by it. Furthermore, the protective slag layer avoided direct contact between liquid slag and refractories.

(3) Combined use of CMA aggregate and silicon carbide for MgO–C refractories had better slag corrosion resistance. The silicon carbide further increased the viscosity of liquid-solid mixture. The enhanced oxidation resistance inhibited the formation of porous decarburized layer, lessening the channels for slag penetration.

**REFERENCES**

[1] Q.L. Chen, Y.W. Li, T.B. Zhu, Y.B. Xu, Y.J. Li, X.Y. Wang. Improved thermal shock resistance of MgO–C refractories with addition of calcium magnesium aluminate (CMA) aggregates. Ceramics International 48(2), 2022, p. 2500-2509.

[2] S. Pauliuk, T. Wang, D.B. Müller, Environ. Sci. Technol. Moving toward the circular economy: The role of stocks in the Chinese steel cycle. Environmental Science & Technology 46, 2012, p. 148-154.

[3] C. Ryman, M. Larsson. Reduction of $CO_2$ emissions from integrated steelmaking by optimised scrap strategies: Application of process integration models on the BF–BOF system, ISIJ international 46, 2006, p. 1752-1758.

[4] T. Preisker, P. Gehre, G. Schmidt, C. G. Aneziris, C. Wöhrmeyer, C. Parr. Kinetics of the formation of protective slag layers on MgO–MgAl2O4–C ladle bricks determined in laboratory, Ceramics International 46(1), 2020, p. 452-459.

# INTERACTION OF MOLTEN SECONDARY METALLURGICAL LADLE SLAG WITH MGO–C REFRACTORIES

Anton Yehorov, Xingwen Wei, Olena Volkova, TU Bergakademie Freiberg, Freiberg, Germany

Marcel Mix, Natalie Froese, INTOCAST AG, Ratingen, Germany

## ABSTRACT

The present work experimentally studied the corrosion behavior of MgO-C ladle refractory exposed to molten slag during steel refining. The corrosion of ladle refractories, especially at the slag line, causes issues that require maintenance and repair and can even lead to melt outages.

## INTRODATION

Carbon bonded ceramics are in high demand in iron and steelmaking industries as the refractory material [1,2]. The addition of carbon into the oxides is considered as the beneficial approach to enhance its thermal properties such as thermal shock resistance, thermal conductivity, minimize the corrosion, and erosion process of the liquid slags, i.e. due to the low wettability of graphite to the liquid slags [3–5].

Magnesia-carbon refractory materials (MgO-C) is the most widespread carbon bonded ceramic for steelmaking industry. They are applied as a lining material in steel ladles, basic oxygen furnaces (BOF), electric arc (EAF) furnaces, and casting furnaces [6–8]. The service life of refractory material can vary from type steelmaking. This is strongly correlated the factors such as: temperature, pressure, atmosphere, and chemical reactivity of the melt. Changing these production conditions could enhance the carbon oxidation, the increasing of open porosity, and the dissolution of MgO grains into slag [9–11]. All of this phenomena lead to a decrease of life time of the refractory [12].

Normally, when the steel ladle is preheated above 500 °C, carbon from the MgO-C refractory material reacts with oxygen in the pores and form $CO_2$-gas on the surface of the refractory [13].

Subsequently, as the $CO_2$ temperature rises, the $CO_2$ gas reacts further with carbon to form CO gas. This type of reaction is called direct carbon oxidation.

However, above 1400 °C an indirect carbon oxidation takes place in the MgO-C refractory. This reaction involves the reaction between MgO and carbon, found in resin and graphite, resulting in the formation of Mg and CO gases [14–17].

The oxidation process not only increases the weight loss of the refractory material, but also enhances the open porosity. Open porosity represents the effective volume of pores within the refractory that can be penetrated by melt. An increase in the open porosity of the refractory has a negative effect on the corrosion resistance of the refractory in contact with molten slags and metals.

Corrosion in MgO-C can be divided into three stages [14]:

1 – The penetration of the melt into the hot surface of the refractory material. If the temperature of the refractory falls below the solidus temperature of the melt, the melt freezes and penetration stops.

2 - If the melt does not freeze, it penetrates the capillaries of the refractory. The melt penetrates the refractory material through the capillary infiltration, which affects the refractory matrix. Infiltration usually occurs when there are large temperature gradients from the hot surface to the cold surface of the refractory material.

3 - Refractory material is impregnated with melt to such an extent that the core is held together by the melt as the matrix corrodes.

According to the increased requirements, a change in the chemical composition of the steel or process leads to a change in the chemical composition of the slag. These changes directly affect the ability of the slag to dissolve the refractory, and the thermophysical properties of the slag. The penetration and infiltration of refractory material by the melt is influenced by the open porosity, wetting angle of the refractory, viscosity, surface tension, and contact time, **Equation 1**[18–21].

$$l^2 = \frac{r \cdot \sigma \cdot \cos\theta}{2\eta} \cdot t \qquad \text{Equation 1}$$

where r (m) is the open pore radius of refractory, σ (N/m) is the surface tension of the slag, θ is the contact angle between the slag and refractory, η (Pa·s) is the slag viscosity, t (s) is the contact time and l (m) is the infiltration depth.

Hence, a combination of high viscosity, low surface tension, open porosity, and appropriate contact angle serves to minimize the infiltration of slag into the refractory and subsequent dissolution [18]. Besides, temperature also has a great influence on MgO-C refractory wear, with increasing temperature, the viscosity values decrease and the maximum dissolution of MgO in the slag increases. This allows the slag to penetrate deeper into the refractory and actively dissolve its grains, weakening the entire structure.

Borges et al. studied the addition of sodium to desulphurisation slags and showed the sodium addition to calcium-aluminium silicates increases the dissolution of MgO grains and reduces the life of the steel ladle [22]. Guo et al. investigated the effect of VOD (Vacuum Oxygen Decarburization) slag with 15 wt% $Al_2O_3$ content on the refractory material MgO-C at 1650 °C and low oxygen partial pressure [23,24]. Later on, a porous MgO layer was formed on the sample surface instead of a dense MgO layer. This indicates that under these experimental conditions, Mg gas oxidation from molten oxides is not complete. Such porous MgO layer in industrial and turbulent conditions is not effective for slowing down the slag infiltration into the refractory material. The authors also argued that at temperatures above 1650 °C, the oxidation of MgO-C by atmospheric oxygen or metal oxides in the slag is limited and the main reaction of decarburization of refractory is indirect carbon oxidation in MgO + C. Liu et al. observed direct and indirect dissolution of MgO particles in a low basicity $CaO-Al_2O_3-SiO_2$ slag. He demonstrated that the dissolution rate of MgO increases with increasing slag temperature and decreases strongly with increasing MgO concentration in the slag [25]. Wang et al. investigated the dissolution rate of MgO solids in synthetic ladle slag. According to their experimental results, the increase of $Al_2O_3$ and MgO in slag decreases the dissolution rate of MgO due to the formation of magnesia spinel layer at the interface, and the increase of $CaO/SiO_2$ basicity also increases the dissolution rate of solid MgO in slag [26]. Several studies have demonstrated that when slags containing $Al_2O_3$ come into contact with MgO-C refractories, the surface of the refractory forms a protective layer of magnesian spinel. This magnesian spinel layer acts as a barrier, inhibiting the infiltration of slag [27–29].

The present study is a logical continuation of two previous studies, where the effect of $SiO_2$ addition on changes of thermo-physical properties of slag and the interaction between refining slag with $CaO/Al_2O_3$ ratio 1:1 on refractory MgO-C material [7,30]. In this study, the focus was on evaluation of corrosion of MgO-C material with altered $CaO/Al_2O_3$ (C/A) ratio in the slag. This study helps to better understand the effect of C/A and $SiO_2$ in secondary metallurgy slag on refractory corrosion in magnesia-carbon refractory material.

## MATERIALS AND METHODS

The MgO-C samples with 13 wt% of residual carbon based on phenolic resin with adding of Carbores P and 2 wt% of metallic aluminium as an antioxidant, see Table 1. Before the corrosion test, the MgO-C samples catted off from industrial refractory brick with the size 30x30x100 mm. In the upper part of each sample drilled a

25 mm deep hole for installation of $Al_2O_3$ holder. After cementing of the $Al_2O_3$ holder into sample body, the MgO-C samples were dried 12 hours at 120 °C.

Table 1. The constituent of MgO-C refractory (wt%).

| MgO | SiO₂ | CaO | Fe₂O₃ | Al₂O₃ | C | Al |
|-----|------|-----|-------|-------|---|-----|
| **97.5** | 0.6 | 1.2 | 0.6 | 0.1 | 13 | 2 |

The target slags were mixed from industrial slag formers: lime and alumina carrier. The partial size of the slag formers was under 100 μm. All the slags were dried in a desiccator for 24 hours at 120 °C before and after mixing.

According to the $CaO/Al_2O_3$ (C/A) ratio the slags can be divided into: High-$Al_2O_3$, Cleanness, and Desulfurization slag, Table 2. C/A ratio is the parameter, determinate the task of the secondary metallurgical slag. Slag compositions with C/A-ratio < 1 appear after deep deoxidised steel and steels with high aluminium content. In the case of C/A= 1, the slag has a refining function to agglomerate non-metallic inclusions out of the steel. Slag with C/A> 1 and up to 2 has desulphuration function in steel production processing. The increased MgO content in the High-$Al_2O_3$ slag is related to its content in the alumina carrier. Also the Table 2 contains the viscosity values of these three slags at 1650 °C from the previous publication [30].

Table 2. Chemical composition of ladle slags (wt%) and viscosity values (mPa*s) at 1650 °C.

|  | **High-Al₂O₃** | **Cleanness** | **Desulfurization** |
|---|---|---|---|
| CaO | 30.09 | 43.33 | 59.77 |
| Al₂O₃ | 53.86 | 43.33 | 30.06 |
| SiO₂ | 1.05 | 1.08 | 0.98 |
| MgO | 13.91 | 11.00 | 8.12 |
| Fe₂O₃ | 0.99 | 1.16 | 0.99 |
| MnO | 0.1 | 0.1 | 0.08 |
| CaO/Al₂O₃ | 0.56 | 1.00 | 1.99 |
| Viscosity (mPa*s) | 1777.24 | 100.29 | 70.32 |

The MgO-C corrosion test carried out according to the Finger Testing method, a schematic description of setup is shown in Fig. 1. A pre-dried slag of about 1000 g. melted in a graphite crucible (130 mm height x 80 mm inner diameter) in an induction furnace. After reaching the target temperature, the melt is held for at least 30 minutes at the constant temperature for the homogenization.

At the other hand, the MgO-C sample was carbonised in a metal box under graphite powder for 60 minutes at 1000 °C. Right after carbonisation, the MgO-C samples were immersed into the molten slag for 60 minutes.
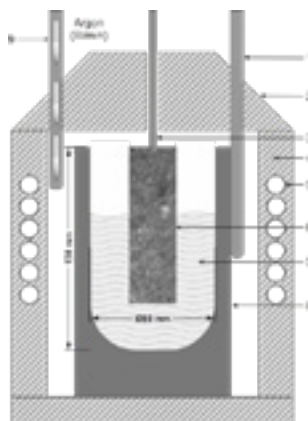


Fig. 1. Induction furnace for finger testing:
1-side thermocouple
2- ceramic top cover,
3- corundum rod,
4- furnace,
5- induction coil,
6- MgO–C sample,
7- molten slag,
8- graphite crucible
9- argon supply

At the end of holding time, the MgO-C samples were removed from the slag and cooled in the air, see Fig. 2. The slag solidified on the sample immediately when the sample left the molten slag,

and forming a dense layer on the MgO-C surface. Afterward, the samples were embedded epoxy resin and cut crosswise to a thickness of 10 millimetres for optical and SEM- analyse.
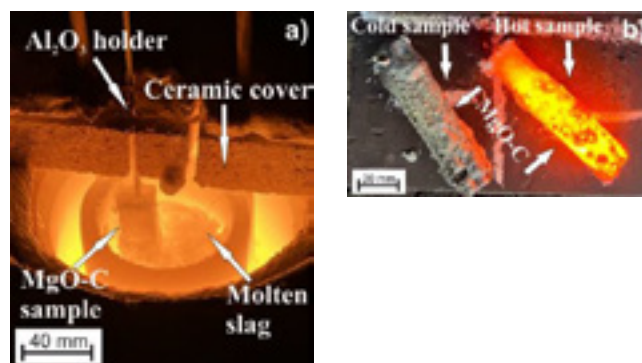


Fig. 2. Finger testing: a) immersion of MgO-C sample in molten slag; b) cooling of samples in the air.

## RESULTS AND DISCUSSION
### Surface analyses of MgO-C

Fig. 3 represents photos of the MgO-C refractory samples immersed in the molten slag at 1650 °C for 60 minutes. After the finger testing experiments, the slag layer was observed to adhere on the surface of the refractories. The thickness of the refractory surface adhered slags was related to wettability of the refractory to the slags, hence, the factors such as the temperature, the roughness, and the porosity of the refractory, and the thermophysical properties of the slags, i.e. surface tension and viscosity of the slag could play an influential role. The present investigation focused on the utilization of a singular type of refractory material as the immersion sample. Consequently, the primary roughness and porosity were assumed to be identical among the specimens. As a result, the depth of corrosion emerged as the determining factor influencing the thickness of the adhered slags. The subsequent analysis considered the influence of viscosity and surface tension on the corrosion process, with specific attention given to the anticipated viscosity value.

The upper part of the refractory material above the slag was oxidised. Compared to the primary MgO-C refractory, the areas that were not in contact with the slag turned from dark to grey. The protective gas employed in the experiments, namely Argon 5.0, contained a minor concentration of oxygen (2-3 ppm oxygen). The oxygen content within the gas initially interacted with the carbon residing on the surface of both the refractory material and the graphite crucible, fostering a reducing atmosphere characterized by the presence of CO gas. Subsequently, the CO gas further reacted with carbon, ultimately yielding $CO_2$ gas.

Furthermore, a part of the slag was found to be pulled up to the non-immersed part of the refractory to the decarbonised layer. The height of the pulled up liquid slag (h) can be expressed by Jurin's law [31] as depicted in Equation 2. Clearly, the factors such as surface tension, contact angle, and density of the liquid slag could directly affect the h, consequently they also affect the contact area between liquid slags and refractory, namely the corrosion area. The degraded MgO from the side of refractory to the side of liquid slags could change the factors (surface tension, density, and also the contact angle).

$$h = \frac{2\gamma \cos\theta}{\rho g r_0}$$

Equation 2

where h is the height of the top of the layer to the liquid surface (m); θ is the contact angle of the liquid on the crucible wall; γ is the surface tension of the liquid (mN·m-1); ρ is the density of the liquid (kg·m-3); g is the gravitational acceleration and $r_0$ is the crucible radius (m).
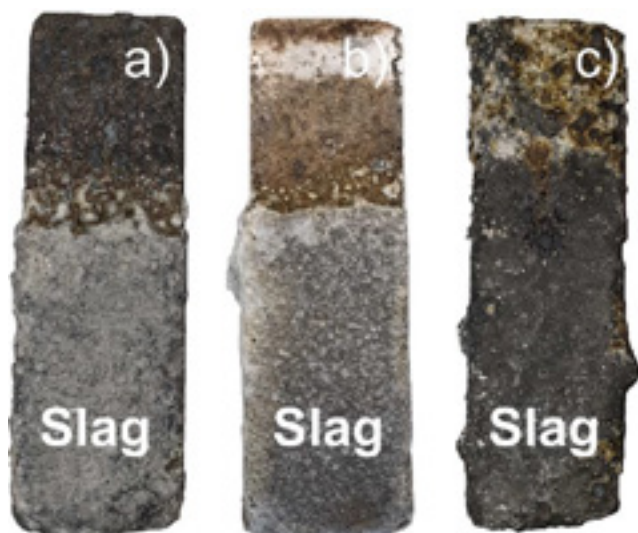
**Fig. 3** Photographs immersed MgO-C refractory in the slag melts: a) High-Al$_2$O$_3$ b) Cleanness, and c) Desulfurization

**Microstructure analyse**

Fig. 4 shows the MgO-C sample after contact with the molten High-Al$_2$O$_3$ slag. This slag has a high viscosity of 1777 mPa*s at 1650 °C. Because of this high slag viscosity, no visible slag infiltration can be seen. Cracks and ducts in the refractory remain free of slag since the high viscosity of the slag prevents the infiltration of slag into the refractory. Nevertheless, the residual slag build-up on the refractory is up to 2.3 mm.
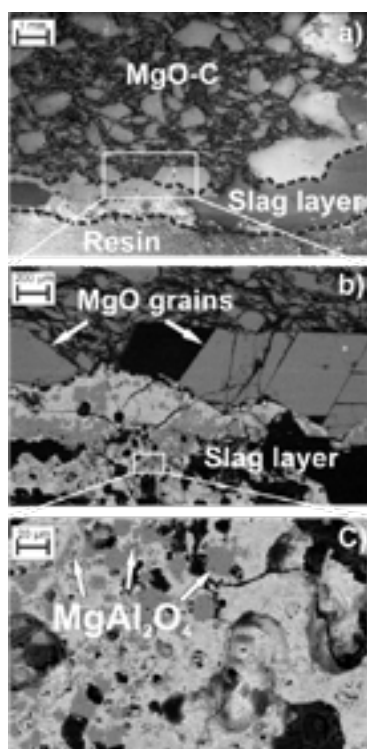
**Fig. 4.** Cross section of MgO-C after 60 minutes contact with High-Al$_2$O$_3$ slag at 1650 °C.

This is a partially dissolved surface layer of the refractory as well as a cured slag layer on the surface. The slag layer is very dense, which during cooling caused numerous pores and slag cracking. The slag contains high amounts of magnesia spinel, which also increases the risk of slag infiltration into the refractory. The large amount of Al$_2$O$_3$ in the slag can break up the MgO grains to form more spinel, which makes the infiltration into the refractory even worse. The SEM-EDX analysis found a large amount of magnesia spinel in the slag and on the refractory surface.
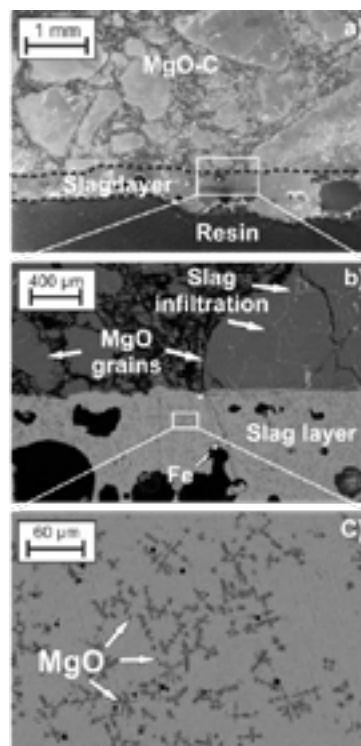


**Fig. 5.** Cross section of MgO-C after 60 minutes contact with cleanness slag at 1650 °C.

Fig. 5 shows the refractory material in a cleanness slag. Its viscosity at 1650 °C is seventeen times less (100 mPa*s) than the previous High-Al$_2$O$_3$ slag. These values are sufficient to infiltrate the slag into the refractory material, through the capillaries, and to crack the grains. The total slag layer on the refractory surface was 1.7 mm. Also a massive of the solid particles of MgO in the slag were found. This suggests that the slag in this composition cannot dissolve MgO grains due to its saturation in the slag. Such solid dendrites can be released when the slag is cooled on a hot refractory, when the MgO solubility in the slag decreases as the temperature decreases.
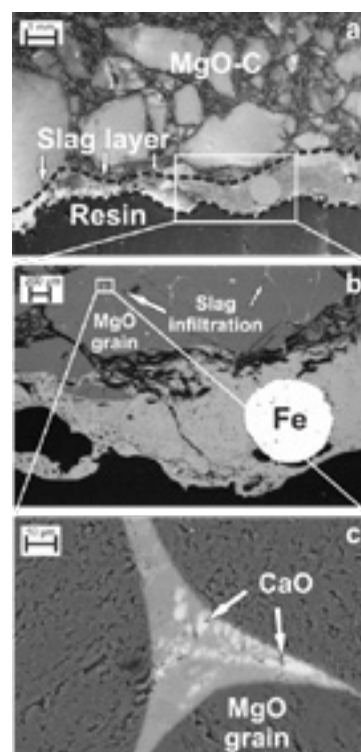


**Fig. 6.** Cross section of MgO-C after 60 minutes contact with desulfurization slag at 1650 °C.

Fig. 6 shows MgO-C after contacting with the desulphurising slag. The depth of the slag layer is 1.57 mm due to the low viscosity 70mPa*s of the slag. In picture b), a spherical reduced iron with a diameter of 0.91 micrometre is observed. Although this slag does not contain more than one percent FeO, it is reduced to pure iron and agglomerated into a single sphere on contact with the refractory carbon. Due to the low viscosity this slag is infiltrated deep into the refractory. Infiltration is more active in areas where there is no carbon. These are often splits in the MgO grains, where the slag is infiltrated by the droplet effect. As the slag contains a large amount of CaO, its maximum allowable solubility in the slag drops and it is isolated separately as CaO solid.

## CONCLUSIONS

In present work, the effect of different slags on the MgO-C refractory was investigated. The different C/A-ratio in the slag affected the capability of the slag to dissolve the MgO-grain, and prevented slag infiltration into the refractory:

1. Slag infiltration into the MgO-C refractory was not detected at a viscosity of more than 100 mPa*s.

2. Although high-$Al_2O_3$ was reacted with the refractory, it could dissolve the MgO grains to form $MgAl_2O_4$.

3. Cleanness slag has low viscosity values, which lead them infiltrate deeper into the MgO-C refractory. At the same time, dissolution of MgO grains was not possible due to their saturation in the slag.

4. The desulphurized slag has the lowest viscosity index, because of its infiltration into the refractory the deepest. Solid CaO is released from the solidified slag as it is saturated with it.

## REFERENCES

[1] X. Wei, E. Storti, S. Dudczig, A. Yehorov, O. Fabrichnaya, C.G. Aneziris, O. Volkova, The interaction of carbon-bonded ceramics with Armco iron, J. Eur. Ceram. Soc. (2022). https://doi.org/10.1016/J.JEURCERAMSOC.2022.04.058.

[2] S. Jansson, V. Brabie, P. Jönsson, Corrosion mechanism of commercial MgO-C refractories in contact with different gas atmospheres, ISIJ Int. 48 (2008) 760–767. https://doi.org/10.2355/isijinternational.48.760.

[3] H. Zielke, T. Wetzig, C. Himcinschi, M. Abendroth, M. Kuna, C.G. Aneziris, Influence of carbon content and coking temperature on the biaxial flexural strength of carbon-bonded alumina at elevated temperatures, Carbon N. Y. 159 (2020) 324–332. https://doi.org/10.1016/j.carbon.2019.12.042.

[4] J. Poirier, A review: Influence of refractories on steel quality, Metall. Res. Technol. 112 (2015). https://doi.org/10.1051/metal/2015028.

[5] Z. Liu, J. Yu, X. Yang, E. Jin, L. Yuan, Oxidation resistance and wetting behavior of MgO-C refractories: Effect of carbon content, Materials (Basel). 11 (2018). https://doi.org/10.3390/ma11060883.

[6] W. da Silveira, G. Falk, Production of MgO-X Refractory Material with Cellular Matrix by Colloidal Processing, Low Carbon Econ. 03 (2012) 83–91. https://doi.org/10.4236/lce.2012.323012.

[7] A. Yehorov, G. Ma, O. Volkova, Interaction between MgO–C-bricks and ladle slag with a 1:1 CaO/Al2O3 ratio and varying SiO2 content, Ceram. Int. 47 (2021) 11677–11686. https://doi.org/10.1016/j.ceramint.2021.01.007.

[8] S.K. Sadrnezhaad, Z.A. Nemati, S. Mahshid, S. Hosseini, B. Hashemi, Effect of Al antioxidant on the rate of oxidation of carbon in MgO-C refractory, J. Am. Ceram. Soc. 90 (2007) 509–515. https://doi.org/10.1111/j.1551-2916.2006.01391.x.

[9] R. Sarkar, Refractory Technology, 2016. https://doi.org/10.1201/9781315368054.

[10] E.M.M. Ewais, Carbon based refractories, J. Ceram. Soc. Japan. 112 (2004) 517–532. https://doi.org/10.2109/jcersj.112.517.

[11] T. Bahtli, D.Y. Hopa, V.M. Bostanci, N.S. Ulvan, S.Y. Yasti, Corrosion behaviours of MgO-C refractories: Incorporation of graphite or pyrolytic carbon black as a carbon source, Ceram. Int. 44 (2018) 6780–6785. https://doi.org/10.1016/j.ceramint.2018.01.097.

[12] D.A. Brosnan, Corrosion of refractories, 2004. https://www.jurispro.com/files/documents/doc-1066205184-article-1609.pdf.

[13] T.L. Dhami, O.P. Bahl, B.R. Awasthy, Oxidation-resistant carbon-carbon composites up to 1700 °C, Carbon N. Y. 33 (1995) 479–490. https://doi.org/10.1016/0008-6223(94)00173-W.

[14] B. yue Ma, X. ming Ren, Z. Gao, F. Qian, Z. yang Liu, G. qi Liu, J. kun Yu, G. feng Fu, Influence of pre-synthesized Al2O3–SiC composite powder from clay on properties of low-carbon MgO–C refractories, J. Iron Steel Res. Int. 29 (2022) 1080–1088. https://doi.org/10.1007/s42243-021-00653-8.

[15] M.A. Faghihi-Sani, A. Yamaguchi, Oxidation kinetics of MgO-C refractory bricks, Ceram. Int. 28 (2002) 835–839. https://doi.org/10.1016/S0272-8842(02)00049-4.

[16] S.K. Sadrnezhaad, S. Mahshid, B. Hashemi, Z.A. Nemati, Oxidation mechanism of C in MgO-C refractory bricks, J. Am. Ceram. Soc. 89 (2006) 1308–1316. https://doi.org/10.1111/j.1551-2916.2005.00863.x.

[17] S. Nanda, A. Choudhury, K.S. Chandra, D. Sarkar, Raw materials, microstructure, and properties of MgO–C refractories: Directions for refractory recipe development, J. Eur. Ceram. Soc. 43 (2023) 14–36. https://doi.org/10.1016/j.jeurceramsoc.2022.09.032.

[18] W.E. Lee, S. Zhang, Melt corrosion of oxide and oxide-carbon refractories, Int. Mater. Rev. 44 (1999) 77–104. https://doi.org/10.1179/095066099101528234.

[19] S. Jansson, V. Brabie, P. Jonsson, Corrosion mechanism and kinetic behaviour of MgO-C refractory material in contact with CaO-Al2O3-SiO2-MgO slag, Scand. J. Metall. 34 (2005) 283–292. https://doi.org/10.1111/j.1600-0692.2005.00748.x.

[20] S.N. Silva, F. Vernilli, S.M. Justus, O.R. Marques, A. Mazine, J.B. Baldo, E. Longo, J.A. Varela, Wear mechanism for blast furnace hearth refractory lining, Ironmak. Steelmak. 32 (2005) 459–467. https://doi.org/10.1179/174328105X48160.

[21] W. Huihua, W. Channa, X. Yingjun, J. Kun, Q. Tianpeng, T. Jun, W. Deyong, Induced Electro-Deposition of High Melting-Point Phases on MgO-C Refractory in CaO-Al 2 O 3 -SiO 2 -(MgO) Slag at 1773 K, High Temp. Mater. Process. 38 (2019) 396–403. https://doi.org/10.1515/htmp-2018-0035.

[22] R.A.A. Borges, G.F.B. Lenz e Silva, A statistical and post-mortem study of wear and performance of MgO-C resin bonded refractories used on the slag line ladle of a basic oxygen steelmaking plant, Eng. Fail. Anal. 78 (2017) 161–168. https://doi.org/10.1016/j.engfailanal.2017.03.020.

[23] M. Guo, S. Parada, P.T. Jones, J. Van Dyck, E. Boydens, D. Durinck, B. Blanpain, P. Wollants, Degradation mechanisms of magnesia-carbon refractories by high-alumina stainless steel slags under vacuum, Ceram. Int. 33 (2007) 1007–1018. https://doi.org/10.1016/j.ceramint.2006.03.009.

[24] M. Guo, S. Parada, P.T. Jones, E. Boydens, J. V. Dyck, B. Blanpain, P. Wollants, Interaction of Al2O3-rich slag with MgO-C refractories during VOD refining-MgO and spinel layer formation at the slag/refractory interface, J. Eur. Ceram. Soc. 29 (2009) 1053–1060. https://doi.org/10.1016/j.jeurceramsoc.2008.07.063.

[25] J. Liu, M. Guo, P.T. Jones, F. Verhaeghe, B. Blanpain, P. Wollants, In situ observation of the direct and indirect dissolution of MgO particles in CaO-Al2O3-SiO2-based slags, J. Eur. Ceram. Soc. 27 (2007) 1961–1972. https://doi.org/10.1016/j.jeurceramsoc.2006.05.107.

[26] D. Wang, X. Li, H. Wang, Y. Mi, M. Jiang, Y. Zhang, Dissolution rate and mechanism of solid MgO particles in synthetic ladle slags, J. Non. Cryst. Solids. 358 (2012) 1196–1201. https://doi.org/10.1016/j.jnoncrysol.2012.02.014.

[27] X. ming Ren, B. yue Ma, S. ming Li, H. xia Li, G. qi Liu, W. gang Yang, F. Qian, S. xian Zhao, J. kun Yu, Comparison study of slag corrosion resistance of MgO–MgAl2O4, MgO–CaO and MgO–C refractories under electromagnetic field, J. Iron Steel Res. Int. 28 (2021) 38–45. https://doi.org/10.1007/s42243-020-00421-0.

[28] M. Yan, Y. Li, H. Li, Y. Sun, H. Qin, Q. Zheng, Preparation and ladle slag resistance mechanism of MgAlON bonded Al2O3 -MgAlON-Zr2Al3C4-(Al2CO)1-x(AlN)x refractories, Ceram. Int. 45 (2019) 346–353. https://doi.org/10.1016/j.ceramint.2018.09.173.

[29] T. Preisker, P. Gehre, G. Schmidt, C.G. Aneziris, C. Wöhrmeyer, C. Parr, Kinetics of the formation of protective slag layers on MgO–MgAl2O4–C ladle bricks determined in laboratory, Ceram. Int. 46 (2020) 452–459. https://doi.org/10.1016/j.ceramint.2019.08.282.

[30] A. Yehorov, X. Wei, M.R. Bellé, O. Volkova, Influence of SiO 2 -adding on the thermophysical properties and crystallization behaviour of ladle slags , Steel Res. Int. (2023). https://doi.org/10.1002/srin.202300173.

[31] T. Shyrokykh, X. Wei, S. Seetharaman, O. Volkova, Vaporization of Vanadium Pentoxide from CaO-SiO2-VOx Slags During Alumina Dissolution, Metall. Mater. Trans. B. 52 (2021) 1472–1483. https://doi.org/10.1007/s11663-021-02114-9.

395

# HIGH DURABILITY LADLE TREATMENT LANCE FOR STEEL SECONDARY REFINING

Keisuke Yamada*, Yoshihiro Sasatani, Akira Nomura
Krosaki Harima Corporation, Kitakyushu, Japan

Takafumi Sato, Shunsuke Matsui
Nippon Steel Corporation, Futtsu, Japan

## ABSTRACT
A new material was developed for the LT lance to endure in the high temperature corrosive environment with high spalling resistance, by suppressing expansion of spinel with reduced magnesia content and densifying with reduced water content using a novel dispersant. The material exhibited both low apparent porosity and residual expansion with keeping an appropriate strength at temperatures higher than 1200°C, together with high thermal spalling resistance. Thus, a parameter, crack index determined by the thermal spalling test was closely correlated with the thermal shock damage resistance and the fracture energy. The developed lance was successfully applied actually to the secondary refining process of stainless steel with increased durability both in the average life and cumulative immersion time in the molten steel.

## INTRODUCTION
Secondary refining of steel in the ladle has been implemented widely with the LT lance which is inserted and blows argon or nitrogen gas into the molten steel to maintain its uniformity in composition and temperature [1]. Major factors affecting on the life of the lance are considered to be corrosion at the slag line as well as crack extension and peeling-off the tip part of the refractories, so the lance must be required to endure in the condition of high temperature corrosive environment with high spalling resistance [2]. In order to decrease the peeling of the refractories covering the steel tube during immersion, we aimed to reduce the thermal expansion of the refractories at higher temperature corresponding to that of the molten steel. In addition, by densifying and strengthening the refractories covering the tubes, we have also aimed to improve the total rigidity of the lance. The LT lance was installed to the ladle with vertical configuration as shown in **Fig.1**, where the one end of the lance was fixed to a beam of the upper structure of the ladle and the other end was immersed to blow gas into the molten steel with three ports perforated in the side wall of the lance slightly upper position from the tip end. Three ports for discharging gas give rise to a rotational moment during blowing the gas. (Although the moment does not generate when the gas blow rate from the three ports is always constant, the gas blow rate varies in the port by port with difference in the state of damaging the refractories around the port.) In the configuration described in the figure, the rotational moment exerted at free end generates a torsional stress in the lance. If the rigidity of the lance (the strength of the refractories) is lower than the torsional stress, the longitudinal cracking of the refractories covering the steel tube will be induced.

In the present study, in order to improve the durability of the LT lance, we aimed to develop the material having both low apparent porosity and residual expansion with keeping an appropriate strength at high temperatures over 1200°C, together with high thermal spalling properties.

## EXPERIMENTAL PROCEDURE
### Test Materials
**Table 1** shows raw material particle size, composition and required water content for the castable refractories sample of the materials A, B and C, respectively. The A is a conventional material, and the B and C are newly developed materials. For the B and C, the dispersant type was changed from that for the A. By changing the type of dispersant, the required water content for mixing castables of the B and C (for Y) could be reduced from the A (for X) with 5.8% to 4.5%. The amount of magnesia in the C decreased by 0.5a% from that in the A, and increased the same amount of alumina with same particle size. The permanent linear change, modulus of rupture, compressive strength and apparent porosity of each sample were measured after drying at 110°C or firing at 1000, 1200 and 1500°C for 3h.

### Thermal Shock Test
We evaluated the material A (conventional) and material C (developed). The A was evaluated by adding f % of stainless steel fiber. In order to investigate the effect of the amount of stainless steel fiber on the heat-resistant spalling properties, the C was evaluated by adding 0 to f % of the fibers as shown in **Table 2**.

**Figure 2** shows a schematic image of the equipment for thermal shock test [3]. In the test, one side (heating surface) of the sample with prismatic shape was quickly heated by a propane-oxygen gas burner. The thermal insulation brick with longer side of the heating side of the sample was arranged on the front of the heating side to prevent the burner flame from going around to the other sides. In one of the side surface other than the front heating surface, there is a temperature gradient from high in the front heating surface to low in back side surface, originating thermal stress to give strain to the sample. The photographs were taken in such side surface with certain interval. The side surface is covered by the heat insulating material which is removed just at the timing of the photographing to prevent
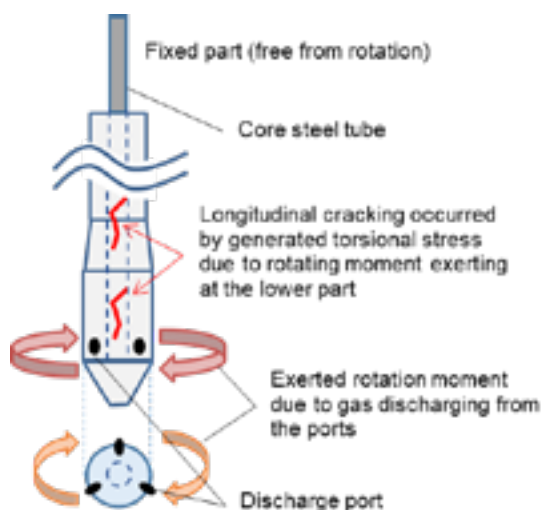


*Fig. 1 Possible mechanism for occurrence of longitudinal cracking in the refractories of the LT lance.*

Tab. 1 Raw material particle size, composition and required water content of the castable refractories sample

( / mass%)

| Raw material / particle size ( / mm) | | Material | A | B | C |
|---|---|---|---|---|---|
| | | | Conventional | Developed | |
| | | Type of dispersant | X | Y | |
| Al$_2$O$_3$ | / +1 | Aggregate | 45 | | |
| Al$_2$O$_3$ | / 0.1~1 | | 27.5 | | |
| Al$_2$O$_3$ | / -0.1 | Matrix | b | | b+0.5a |
| MgO | | | a | | 0.5a |
| Others | | | c | | |
| Water | | | 5.8 | 4.5 | |

(a,b,c : constants)

Tab. 2 Addition of stainless steel fiber to the materials A and C

( / mass%)

| Material | A | C | | | |
| --- | --- | --- | --- | --- | --- |
| | Conventional | Developed | | | |
| Stainless steel fiber | f | 0 | 0.25f | 0.5f | 0.75f | f |

(f : constant, 1 < f < 5)
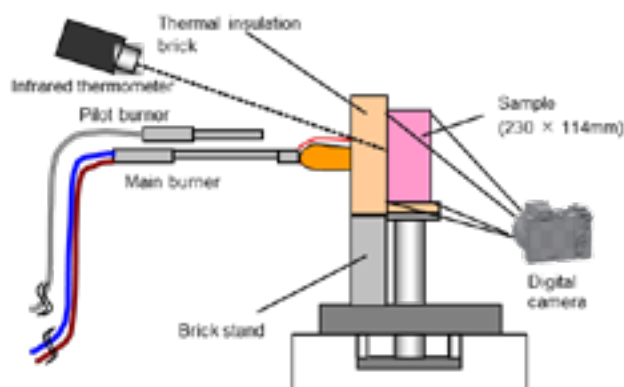


*Fig. 2 Scheme of experimental set-up for thermal spalling test equipment.*
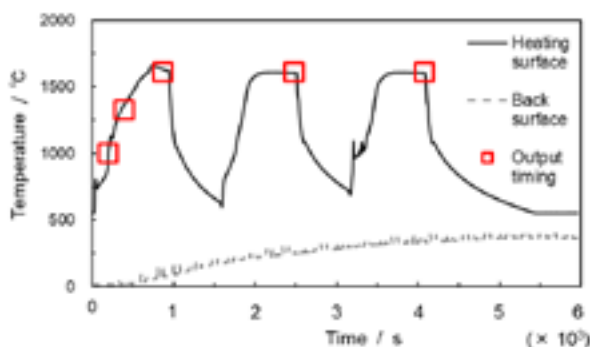


*Fig. 3 Heating schedule of test samples and measured temperature at both heating and back surfaces.*

the sample cooled from unfavorable direction. Then, amount of strain was calculated from the displacement before and after deformation due to thermal stress and the initial length by processing the image data of the sample using the digital image correlation method [4]. It is possible to evaluate crack width and length quantitatively in the method, since increase in the calculated strain is reflected in initiation and propagation of the crack.

The sample was 230 × 114 × 65mm prismatic shape, with heat treatments of drying at 110°C for 24h, and then firing at 1000°C for 3h. The heating front surface of the thermal spalling test was 230 × 65mm, and the side surface photographed by a digital camera was 230 × 114mm. An example of the temperature change given to the sample is shown in **Fig. 3** where the temperature was raised to 1600°C at the heating rate of 200 °C/min, kept for 10min, and then cooled for 10min. The thermal cycle was repeated three times in the test. The strain distribution kept count at the timings of 201s and 402s after the start of heating, 871s after the first holding at 1600°C for 10min, 2479s after the second holding at 1600°C for 10min, and 4079s after the third holding at 1600°C for 10min, respectively, with the photographing interval of 67s.

**Corrosion Resistance Test**
Corrosion resistance was evaluated using a rotary drum erosion test apparatus. Slag with C/S (CaO/SiO$_2$) = 3 was charged into the furnace held at 1600°C, heated for 30 min, and then the slag was discharged. After repeating the treatment 10 times, the center of the specimen was cut and the amount of corrosion was measured. We evaluated the material A (conventional) and material C (developed) adding f % of stainless steel fiber.

**RESULTS AND DISCUSSIONS**
**Physical property**
**Figure 4** shows the results of measurement in the linear expansion **(a)**, apparent porosity **(b)**, modulus of rupture **(c)**, and compressive strength **(d)** for all the samples with each heat treatment condition. As seen in the figure, the reduction in the spinel formation due to decreasing addition of magnesia succeeded in suppressing permanent linear change of the C fired both at 1200 and 1500°C. The strengths of developed materials fired in each temperature were higher than those of the A. Especially, the strength increase was remarkable in the materials fired at both 1000 and 1200°C. The developed materials with fired at each temperature had low apparent porosity due to their lowered water content in the green state. Especially, in the C densification was achieved by not only reduction in water content but suppression in permanent linear change by reducing the formation of spinel at firing temperatures higher than 1200°C. As the results, the higher strength was also achieved in the C, finally. Then, we try to check the ability of the developed materials to suppress cracking in the actual use through the thermal shock test.

**Thermal Spalling Resistance**
**Figure 5** shows the strain distributions counted at each timing shown also in **Fig.3** for all the samples tested. The crack index, as one of the measures of the thermal spalling resistance, was determined as the ratio between the total sum of strains higher than 2% in whole detecting positions and whole number of the detecting positions by calculating the amount of strain in all directions (both x and y) in the strain distribution shown in **Fig.5**.
**Figure 6** shows the calculated crack index at the output timing shown in the **Fig.3** for all the samples tested. Comparing the A (conventional) and the C (developed) both with f % stainless steel fiber, the C had smaller crack index at all the timings detected, showing apparently superior thermal spalling resistance to the A.

397
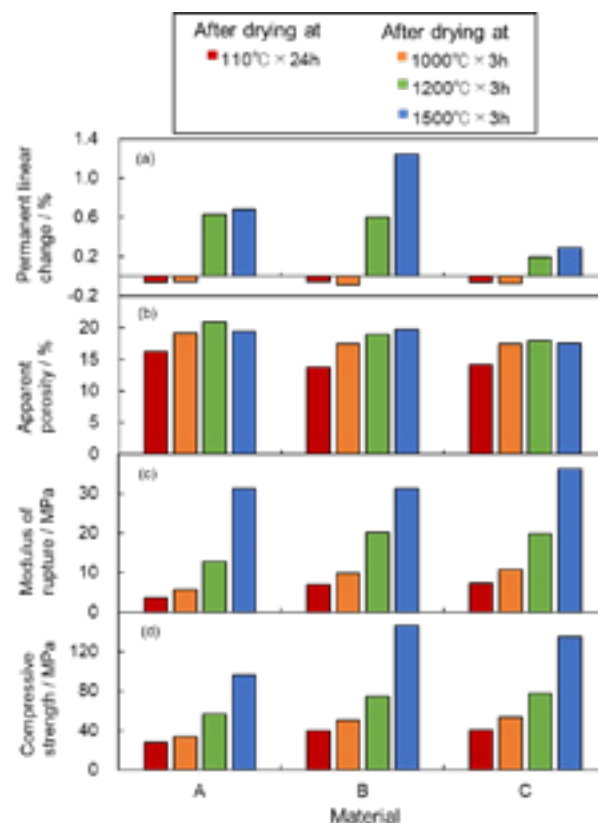


*Fig. 4 Measured properties of (a) permanent linear change, (b) apparent porosity, (c) modulus of rupture and (d) compressive strength for materials A, B and C with various heat treatment conditions showing above the figure.*

**Figure 7** shows the relationship between the crack index at 4079s (after the third holding at 1600℃ for 10min) and the amount of stainless steel fiber added. Since there was a strong correlation between the crack index and the amount of the stainless steel fiber for the C, the usefulness of the stainless steel fiber addition to the refractories for the lance was able to be confirmed.

We investigated the correlations between the calculated crack index determined by the thermal spalling test and various indices representing thermal shock resistance [5]: thermal shock fracture resistance $R$, thermal shock damage resistance $R''''$ and Crack stability index $R_{st}$, as well as, fracture energy $\gamma$.

The equations expressing them are shown below;

$$R = \frac{S(1-\nu)}{E\alpha} \qquad (1)$$

$$R'''' = \frac{E\gamma}{S^2(1-\nu)} \qquad (2)$$

$$R_{st} = \left(\frac{\gamma(1-\nu^2)}{E\alpha^2}\right)^{\frac{1}{2}} \qquad (3)$$

where, $S$:modulus of rupture, $E$:modulus of elasticity, $\gamma$:fracture energy (measured by three-point bending test of notched specimen), $\nu$:poisson's ratio, $\alpha$:thermal expansion coefficient. (Values for $S$, $E$ and $\gamma$ were measured in sample fired at 1000 °C for 3 h).

**Figure 8 (a)~(d)** shows the relationships of the calculated crack index at 4079s to the fracture energy and the three indices representing thermal shock resistance. Although there was no strong correlation of the $R$ with the crack index **(a)**, the other two indices for thermal shock resistance $R''''$ and $R_{st}$ correlated strongly with the crack index **(b, c)**. The fracture energy $\gamma$ has also strong correlation with the crack index **(d)**. The strong correlations of the $R''''$ and the $R_{st}$ with the crack index depended on the fracture energy $\gamma$ which constitutes both equations for the $R''''$ and the $R_{st}$. Therefore, controlling of the fracture energy $\gamma$ is important for suppressing the crack. It was also proven in the C that the increase in amount of the stainless steel fiber was quite effective to improve the $R''''$, $R_{st}$ and $\gamma$.



*Fig. 7 Effect of stainless steel fiber addition on the crack index at 4079s.*





*Fig. 5 Shift of strain distribution with time on the thermal shock test for all the samples.*
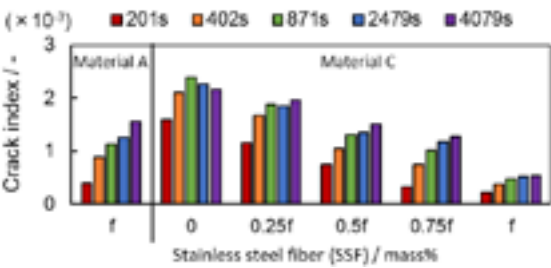


*Fig. 6 Comparison of calculated crack index at the timings shown in the figure for all the samples tested.*
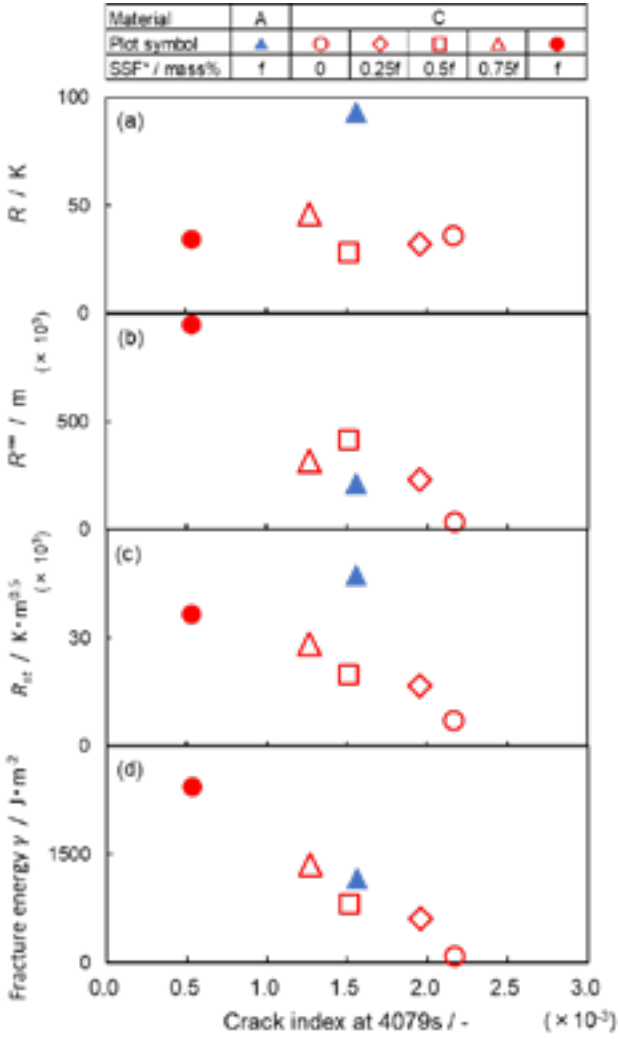


*Fig. 8 Correlation of the crack index at 4079s with various parameters of (a) R, (b) R'''', (c) Rst and (d) fracture energy.*

**Corrosion Resistance**

**Figure 9** shows the results of erosion investigation using a rotating drum type erosion test apparatus. When base material A is set to 100 for the index, the index for the material C is shown in the figure together with the appearances of the cut surface after the test. Although there was concern that the corrosion resistance of the C would decline because of its lower magnesia content compared to the A, a slight improvement in corrosion resistance was achieved by the densification in the green state due to decreased water content.

**TEST IN ACTUAL OPERATION**

The material C with f % stainless steel fibers, exhibited a high performance in the laboratory thermal shock test with the lower crack index and high corrosion resistance, was used in actual operation.

The developed LT lance was used in first actual operation, and marked an improved performance in both service life and cumulative immersion time of 16ch and 120min (conventionally 11.1ch and 88min), respectively. **Figure 10** shows some views of the LT lance after use. Deep and large longitudinal and ring cracks occurred frequently in the conventional lance were not observed in the developed one. The reason for determining the exchange of the lance changed from cracking to the corrosion of the slag line. **Figure 11**

compares the durability of the developed lance in the actual operation at n = 26 with that of conventional one. It has an improved durability with the average life from 11.1 to 18.0ch, and the average cumulative immersion time from 88 to 121min compared to the conventional one. Since the developed LT lance had excellent durability, it became to be used steadily in the actual operation.



*Fig. 11 Comparison of cumulative immersion time and life for the developed LT lance with the conventional one.*

| Material | A | C |
|---|---|---|
| Corrosion index | 100 | 93 |
| Cross sectional view | | |



*Fig. 9 Cross sectional view of the sample after corrosion resistance test.*
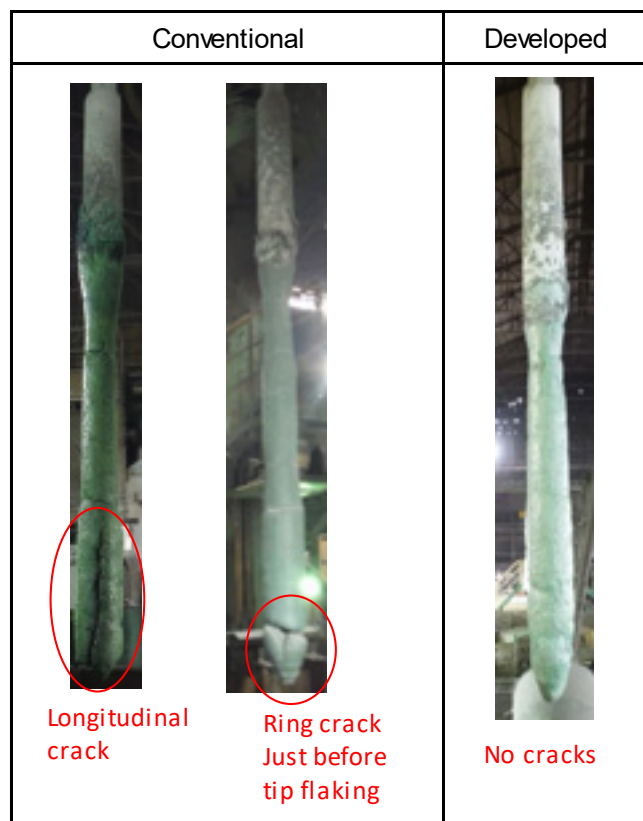


*Fig. 10 Views of conventional and developed LT lances after use in actual operation.*

**CONCLUSIONS**

The developed ladle treatment (LT) lance became to be used steadily in the actual operation as the result of efforts to reduce cracking at the vicinity of the tip, with achieving the following improvements in the material from the conventional one.

(1) Both lower permanent expansion change and apparent porosity, with higher strength at the temperatures higher than 1200°C, were achieved by suppressing the spinel expansion due to decrease in the magnesia content.

(2) Superior thermal spalling properties were also achieved by processing mentioned above with making the crack index determined by the thermal shock test correlates strongly with the thermal shock damage resistance $R''''$ and the fracture energy $\gamma$.

(3) An equivalent or rather better corrosion resistance was achieved by lowering the apparent porosity with decreasing the water content in the green state.

(4) The durability of the LT lance in the actual operation increased the average life and cumulative immersion time significantly by as much as about 60% and 40%, respectively.

(5) The decreased cracking at the vicinity of the tip in the lance resulted in alteration of the reason for exchange the LT lance from the cracking of tip to the corrosion of slag line.

**REFERENCES**

[1] Ribeiro, B. A. B., et al. Numerical comparison of the efficiency of gas injection through lances and plugs. Proc. UNITECR 2009, p.246-249

[2] Samantha, A. K., Sinha, R. K., Chattopadhyay, A. K. Development of desulphurization lance – an Indian experience. Proc. UNITECR 2003, p.369-372

[3] Tsuji, Y., et al. Thermal shock resistance of monolithic refractories with coarse grained aggregates under constraint condition. Proc. UNITECR 2019, p.895-898

[4] Kamio, H. Digital image correlation method for analyzing the deformation behavior of the refractories. Proc. UNITECR 2011, 2-B1-02

[5] The Technical Association of Refractories of Japan (TARJ). Refractories Handbook, revised edition 12(in Japanese), 2015, p.86, p.101-102

# GRAPHENE ADDED CARBON MGO-C FOR SLAG ZONE IN STEEL LADLE

Goutam Ghosh, Navneet Sinha, Sujat Ali Khan, Prasanta Panigrahi, Brijender Singh

Tata Steel Ltd, Jamshedpur, India

## ABSTRACT

Magnesia carbon (MgO-C) refractories are widely used in iron and steel industries due to its excellent corrosion resistance to basic slag. There are limitations in quantity of Carbon, (mainly by using natural flaky graphite), beyond a threshold limit, as it adversely impacts coked properties, thermal conductivity and Carbon pick-up by steel. To mitigate this adversity, in recent past, there have been several approaches to use of Nano-particle carbon, as it has been reported to have improved the thermos-mechanical properties of MgO-C, by suitably modifying the binding structure. In Tata Steel, Graphene (TSG), as a form of nano-carbon particle was used to develop improved quality MgO-C for the slag zone in the steel ladle. The objective was to get improved oxidation resistance, corrosion resistance, and hot bending strength of MgO-C. The developed bricks were tried in the steel-making shop ladles slag zone. Aluminum killed steel ladle slag showed the lowest corrosion when Graphene added MgO-C brick was used in slag zone. The new class of graphene added magnesia carbon brick has a lower wear rate compared to regular quality of magnesia carbon bricks.

Keywords: Magnesia carbon, corrosion, oxidation, performance

## INTRODUCTION

In modern steel making process, magnesia carbon refractory plays a significant role in the most critical areas like secondary steel making steel ladle and BOF Convertor. Development of high-performance magnesia carbon bricks has been the focus of the steel plant for improved production efficiency and lower cost of steelmaking. Carbon in form of graphite is key element for slag resistance and high temperature strength.
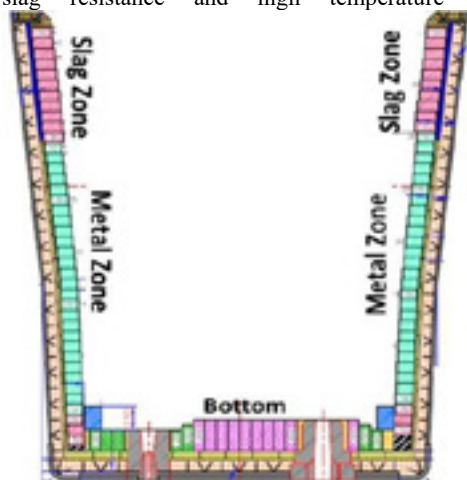


Fig. 1: Steel ladle pictorial view

To enhance the role of carbon a study was initiated to use Graphene as a partial substituted material for formation of nano bonding system in magnesia carbon material. Literature shows that the addition of nano carbon in the magnesia carbon quality forms additional carbides bonds in the matrix. There are various sources such as graphene, carbon nano tube, carbon black of the nano carbon for the magnesia carbon bricks. Addition of graphene provides additional advantage due to structural similarity with the graphite material. This paper illustrates the developmental work of Graphene added magnesia carbon brick for ladle slag zone. The study tries to explore the influence of graphene on thermomechanical properties and corrosion behabour of Mag-C through laboratory experimental setup and field trials in ladle. In Fig 1 schematic picture of steel ladle is shown.

## EXPERIMENTAL PROCEDURE

Magnesia Carbon bricks were manufactured using high purity fused magnesia, 97% Fixed Carbon graphite, Al and Si metal powder as antioxidant and graphene as a source of nano carbon. For laboratory evaluation bricks are produced in 100 Kg Eirich mixture machine and 600 Ton electric screw press. These bricks properties are evaluated in laboratory. The manufacturing process used the same industrial production resource, as for production of regular MgO-C bricks.

Physical and chemical characterisation of bricks were done by several techniques. Chemical analysis of the samples was done using Inductively coupled plasma mass spectrometry (ICP-MS) method. Bulk density (BD) and apparent porosity (AP) were determined by both DIN EN 993-1(DIN 51056) standard and Tata Steel standard. Hot modulus of rupture (HMOR) was determined in HMOR machine (Make: Netzsch) according to ISO 5013: 1985 standard. Thermal expansion measurement was done in dilatometer (TA Instrument) up to $1400^0C$ temperature according to ISO/FDIS 16835. Slag corrosion conducted in dynamic condition in induction furnace (make: Inductotherm) with steel ladle slag for 60 minutes dipping time at 1650 degree C temperature as per Tata Steel standard.

## RESULTS AND ANALYSIS

### Graphene properties

Table 1: Properties of the Tata Steel, Graphene (TSG)

| Parameter | Tata Steel, Graphene (TSG) |
|---|---|
| Appearance | Flakes |
| Number of layers | $\leq 15$ |
| Bulk Density (g/cm3) | 0.04 – 0.06 |
| Thermal Stability | 590 °C (in air), 870 °C (in inert) |
| Elemental Analysis (%) | C (91-95), O (3-5), S (0.1- 0.4) and H (0-1.5) |

The appearance of the Tata Steel graphene is flake like appearance with less than 15 layers of carbon. The bulk density of the graphene is 0.04 to 0.06 gm/cc. The

graphene is oxidized in 590$^0$C in air and 870$^0$C in inert atmosphere. The graphene contains C (91-95), O (3-5), S (0.1- 0.4) and H (0-1.5).

**Chemical and physical properties**
Chemical and physical properties of the materials are analyzed to understand the change behabour of the materials as shown in table 2 and table-3 respectively. The as such and coked porosity of the existing and graphene added magnesia carbon material is similar. Bulk density in as such and coked condition in both the sample is similar in value.

Tab. 2: Chemical analysis of existing and graphene added magnesia carbon bricks

| Test element (Weight %) | Existing magnesia carbon | Graphene added magnesia carbon |
|---|---|---|
| Al$_2$O$_3$ | 3.70 | 3.65 |
| MgO | 91.64 | 91.05 |
| CaO | 1.46 | 1.20 |
| Fe$_2$O$_3$ | 1.01 | 2.09 |
| SiO$_2$ | 1.51 | 1.25 |

Tab. 3: Physical properties of existing and graphene added magnesia carbon bricks

| Sample | Existing magnesia carbon | Graphene added magnesia carbon |
|---|---|---|
| AP as received (%) | 3.12 | 2.26 |
| AP after coking at 1000C/2hrs (%) | 8.18 | 17.35 |
| BULK DENSITY (gm/cc) | 3.03 | 3.04 |
| BD after coking at 1000°C/2 hrs (gm/cc) | 2.97 | 3.00 |
| CCS As received (kg/cm2) | 433 | 456 |
| CCS after coking 1000°C/2 hrs (kg/cm2) | 345 | 364 |

**Hot bending strength**
As shown in the Fig. 2, HMOR value of the graphene added bricks have improved over the existing bricks. Graphene is having the plate like structural similarity of

with the graphite material. The plate like structure of the graphene helps in formation of the reactive phases.
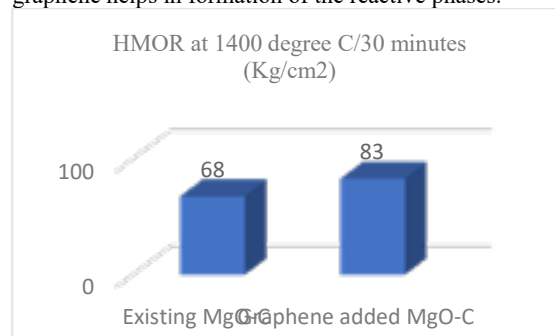


Fig. 2: HMOR of magnesia carbon bricks

**Corrosion resistance**
This slag corrosion test had been done with steel ladle slag at 1600°C with magnesia carbon bricks with a soaking time of 0.5 hours. The induction furnace dip test was done with sample size of 40x40x180mm. This arrangement provides slag to flow over the materials at high temperature. From the pictures in Table 4 we can visualize that the MgO-C brick is getting oxidized from the outer surface. Details measurement of corrosion is given in table 4. Corrosion resistance of the graphene added magnesia carbon is better than the existing magnesia carbon bricks.

Tab. 4: Corrosion of existing and graphene added magnesia carbon bricks

| Sample details | Existing magnesia carbon | Graphene added magnesia carbon |
|---|---|---|
| Pictures of the samples after corrosion test | | |
| Corrosion (%) | 5.9 | 3.9 |
| Visual Observation | Medium groove formation | Low groove formation |
| Ranks | 1 | 2 |

Table 4 shows the photographs of corroded sample after slag corrosion test where a neck formation corresponds to the penetration depth. Slag penetration was found to be minimum for graphene added magnesia carbon bricks. The corrosion index of the two samples is given in table 4. Corrosion index shows graphene added magnesia carbon bricks have better corrosion properties than other sample

of same quality. The relative improvement of corrosion behabour is more for graphene added magnesia carbon bricks sample compared to existing magnesia carbon sample.

**Thermal expansion value**

The thermal expansion is an essential data point for design of refractory structure, and it is important parameter which plays a role in thermal shock resistance. Reversible thermal expansion curve was obtained with the help of push rod dilatometer from room temp to 1400˚C. The heating rate was 5℃/min. Fig 3 shows that there is not much difference in the thermal expansion values of existing and improved quality magnesia carbon bricks.
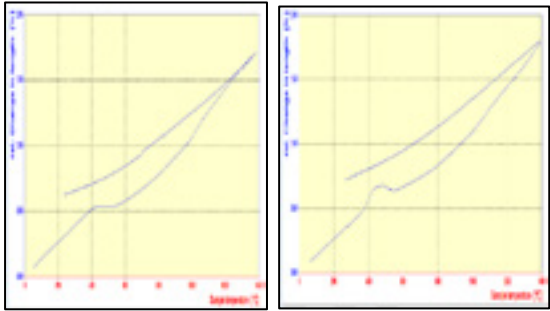


Fig 3: Thermal expansion curve of existing and graphene added magnesia carbon bricks

**APPLICATION IN STEEL LADLE**

Magnesia carbon bricks with graphene addition is manufactured in the plant and installed in the slag zone of 8 ladles in the Al- killed steel making shop. The relining of graphene added magnesia carbon bricks picture given in Fig. 4.
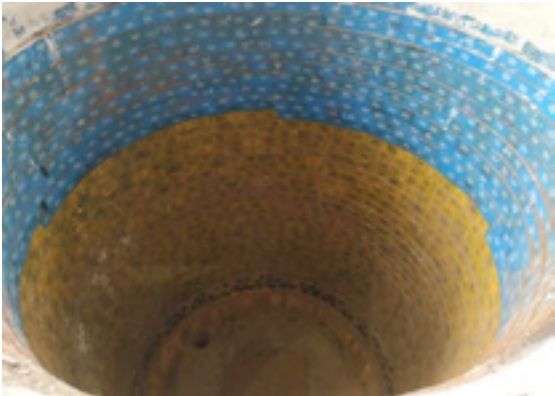


Fig 4: Steel ladle relining

The scan report of the steel ladle after the campaign is given in Fig. 5 which shows erosion of the trunnion zone of steel ladle slag zone. The condition of ladle during the operation was observed normal as shown in the picture 6. During relining of the ladle, the used graphene added magnesia carbon bricks was observed to have less oxidation during use as shown in Fig. 7. The trial performance is shown in the Table 5 which shows a trend of around 10-20% performance improvement of the graphene added magnesia carbon bricks over existing magnesia carbon bricks.

Tab. 5: Performance of graphene added magnesia carbon

| Area | Erosion rate (mm/ heat) | left over thickness (mm) | Erosion rate (mm/heat) |
|---|---|---|---|
| Steel ladle slag zone (average erosion) | 1.10 | 67.90 | 1.46 |
| Steel ladle slag zone (maximum erosion) | 1.61 | 35.00 | 2.05 |
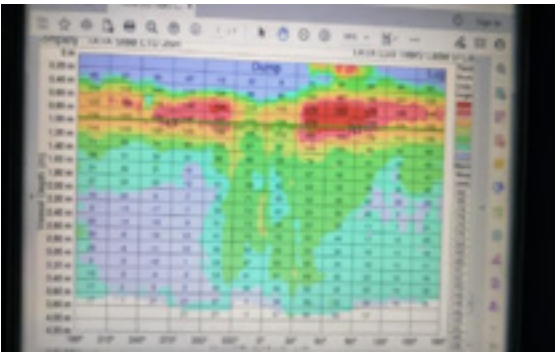


Fig. 5: Scan report after campaign



Fig. 6: Condition of ladle during operation



Fig. 7: Ladle condition during dismantling

**CONCLUSION**

The conclusions of the work are:

1. Addition of graphene in magnesia carbon bricks have the potential for improving the key performance determining properties like hot strength, elasticity and corrosion resistance.

2. Optimization of quantity of graphene addition plays a significant role in magnesia carbon properties. Further development in this regard to be continued with respect to quantity and types of graphene.

3. Details analysis reveals that formation of the carbides in presence of reactive graphene.

4. Plant trial of the graphene added magnesia carbon bricks in steel ladle slag zone shows slight improvement in the performance. More trials with various recipes of graphene in steel ladle to be done to further improvement in the performance.

**REFERENCES**

[1] Yamaguchi, A., Control of oxidation reduction in MgO-C refractories. Taikabutsu Overseas, 1984, 4(1), 332-337

[2] Nobuhiro Maruoka, Arira Ishikawa, Hiroyuki Shibata and Shin-ya Kitamura, Competitive Dissolution of MgO from Flux and refractory, UNITECR 2011, Vol-3, 1-E-17

[3] Shingo Umeda, Tadashi Ikemoto and Kiyoshi Goto; Effect of thermal treatment on corrosion resistance of magnesia carbon converter bricks, UNITECR 2011, Vol-3, 1-E-16

[4] Dr Michel RIGAUD, Advanced seminar on refractories for steelmaking, Mechanism of wear, Page-70, September 25-26, 2007

# EFFECTS OF CALCIUM MAGNESIUM ALUMINATE BINDER ON PROPERTIES OF ALUMINA–MAGNESIA CASTABLES FOR STEEL LADLE

Kun Ming Chen*, Chia Hung Kuo, Tung Hsin Su

New Materials Research & Development Dept., China Steel Corporation, Taiwan, Republic of China

## Abstract

The starting material of the alumina-magnesia castables contains $Al_2O_3$ and $MgO$, which formed the alumina-magnesia spinel phase during high temperature service. This phase formation consequently resulted excessive expansion and cracking that lead to poor performing castables. The main purpose of this study is to observe the improvements in the properties of alumina-magnesia castables by adding Calcium-Magnesium-Aluminate (CMA) binder and reducing MgO powder addition. Corrosion resistance was defined by the deepest penetration depth of molten steel. The experiment results revealed that steel corrosion resistance was enhanced as CMA binder increased when comparing to original alumina-magnesia castables. However, addition of CMA binder had no significant improvement on thermal shock resistance. Furthermore, corrosion behavior was observed in 0% and 2% CMA binder samples through microstructural analysis. Corrosion was firstly occurred in the matrix region and then the aggregate area could have been exposed during high temperature service which resulted in spalling and reduced performance. It was also found that 2% CMA binder added sample had a distinct interface layer. Further analysis by SEM/EDS showed that the refractory interface layer was mainly alumina-magnesia spinel phase. This spinel phase could block the continuous penetration of molten steel. In this study, refractory matrix area was enhanced by the addition of CMA binder into the castables, thereby improved the ladle lifespan.

## Introduction

The production technology of clean steel has been developed rapidly [1], which made secondary refining of steel ladles extremely important in recent years. In addition, the steel types also tend to be diversified and the tapping temperature is correspondingly increased, resulting a more stringent conditions for ladles. Therefore, the refractory material "Alumina-Magnesia Castables" used on the ladle working lining has to satisfy the essential requirements: (1) Excellent peeling resistance, (2) High resistance to iron oxide corrosion, (3) Good resistance to steel penetration, (4) Well thermal shock resistance, (5) High strength. The alumina-magnesia castables are mainly composed of aggregates and powders. The main materials for the aggregates are fused white corundum, brown corundum, and sintered tabular corundum. The fine powder includes alumina powder, magnesia powder, calcium aluminate cement, silica powder, and various additives, etc [2-5]. The most critical property of alumina-magnesia castables is the corrosion resistance of molten steel. Poor corrosion resistance may reduce ladle lifespan and increase the cost of steelmaking. In severe cases, it could even cause safety accidents such as steel leakage. The starting material of the alumina-magnesia castables contains $Al_2O_3$ and $MgO$, which would form the alumina-magnesia spinel phase during high temperature service. This phase formation consequently resulted excessive expansion and cracking that lead to poor performing castables [6]. Recently, a new type of cement "Calcium Magnesium Aluminate (CMA) Binder" was developed by Kerneos, which contains both calcium aluminate and alumina-magnesia spinel phases. Q. Chen et al. introduced CMA binder into magnesia carbon ladle bricks and obtained significant improvements on thermal shock and corrosion resistance [7]. Therefore, the main purpose of this study is to add CMA binder into alumina-magnesia castables and simultaneously reduce the amount of MgO powder to inhibit excessive expansion, thereby improve the performance of alumina-magnesia castables.

## Experimental Procedure

The composition of alumina-magnesia castables in this study is divided into two particle size categories, aggregates (size>200mesh) and fine powder (size≤200mesh). Aggregate uses white corundum with purity≥99%, and its particle size includes 5~8mm, 3~5mm, 1~3mm and 0.075mm~1mm. The fine powder uses α-$Al_2O_3$ micropowder (purity≥99%, D50≤5um), MgO powder (purity≥90%, particle size≤200mesh), micro-silica (purity≥97%, particle size≤1um), calcium aluminate cement ($Al_2O_3$≥70%, CaO≤30%) and dispersant. In addition to the above mentioned raw materials, this study added a new type of cement "Calcium Magnesium Aluminate (CMA) Binder" developed by Kerneos. It contains both calcium aluminate and alumina-magnesia spinel phases, and its chemical composition is $Al_2O_3$ (69~72%), CaO (7.5~10.5%), and MgO (19~22%). The experiment adds CMA binder while reducing the amount of MgO powder to keep the chemical total amount of MgO in the castables at 6%. In this study, the addition of CMA binder were 0%, 0.5%, 1%, 1.5%, and 2%, as shown in Table 1.

In terms of sample preparation, the raw materials are first proportionally prepared per design for aggregates, powders and additives. The raw materials are loaded into a blender (Hongda, JD-402) with appropriate amount of water added and stired for 3 minutes. The mixture was poured into the mold and held for 24 hours. After demoulding, the samples were dried in an oven at 110°C for 24hrs and then heat-treated at 1500°C/3hrs to set for analysis. Analysis process include (1). Measuring the fluidity of castable materials by jumping table method with reference to ASTM C1446-19; (2). Measuring the bulk density (BD) and the apparent porosity (AP) with a density tester (Precondar, XQK-04); (3). Using a universal testing machine (Hung-Ta, HT-2402) to measure the modulus of rupture (MOR) at room temperature with reference to ASTM C583-15; (4). Using a crushing strength tester to measure the cold crushing strength (CCS) at room temperature with reference to ASTM C133-97; (5). Referring to ASTM C1171-05 to define the thermal shock resistance. The experimental conditions increase the temperature to 1000°C/15min, then take the samples out to room temperature for 15min as a cycle, a total of 5 cycles. MOR is measured before and after the thermal shock test and then convert the recession rate; (6). Referring to JIS R2214 to carry out the steel penetration resistance. In this study, medium carbon steel block was selected and the test condition was 1600°C/3hr; (7). Using polarizing optical microscope and scanning electron microscope (SEM/EDS) for microstructure analysis and erosion mechanism. In addition, the sample with better steel penetration resistance was selected to investigate the influence of steelmaking conditions. The operating conditions were 1600°C±50°C and maintained for 4±1 hours.

*Tab. 1: Formula table of alumina-magnesia castables with different additions of CMA binder*

| Sample | CMA-(0) | CMA-(1) | CMA-(2) | CMA-(3) | CMA-(4) |
|---|---|---|---|---|---|
| Aggregates | 70% | 70% | 70% | 70% | 70% |
| CMA | 0% | 0.5% | 1% | 1.5% | 2% |
| MgO | 6% | 5.9% | 5.8% | 5.7% | 5.6% |
| Other Powders | 24% | 23.6% | 23.2% | 22.8% | 22.4% |

## Results and Discussion

(1) Fluidity and physical properties

The Fluidity becomes extremely important for alumina-magnesia castables since the main construction method is to pour into the working lining at the bottom and wall of the ladle. Poor

fluidity tend to create holes or gaps after pouring. These defects increase the risk of steel leakage during the ladle carries molten steel. Fig. 1 shows the effect of adding CMA binder on the fluidity of alumina-magnesia castables. The results revealed that the fluidity of castables increased with the addition of CMA binder, which is beneficial to ladle construction. The effect of adding CMA binder on the physical properties of aluminum-magnesium castables is shown in Tab. 2, including permanent line change rate (PLC), modulus of rapture (MOR), cold crushing strength (CCS), apparent porosity (AP) and bulk density (BD). It was found that the addition of CMA binder had no significant effect on MOR, CCS, AP and BD, but PLC decreased with the increase of CMA binder addition. The reason could be due to the replacement of MgO powder by CMA binder in this study while maintaining the total chemical composition of MgO at 6wt%. It reduced the expansion caused by the process of forming spinel phase ($MgAl_2O_4$) from MgO and $Al_2O_3$ after the temperature of heat treatment reached over 1200°C. This help improving the excessive expansion and cracking of the working lining of ladle.
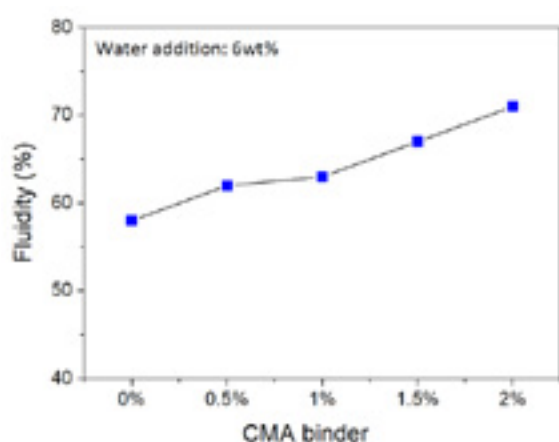


*Fig. 1: Effect of adding CMA binder on fluidity of castables*

*Tab. 2: Effect of adding CMA binder on the physical properties*

| Sample | Physical properties (@1500°C/3hr) | | | | |
|---|---|---|---|---|---|
| | PLC (%) | MOR (MPa) | CCS (MPa) | AP (%) | BD (g/cm³) |
| CMA-(0) | 1.93 | 28.7 | 78.3 | 23.2 | 2.88 |
| CMA-(1) | 1.91 | 26.4 | 77.9 | 23.1 | 2.87 |
| CMA-(2) | 1.88 | 28.0 | 81.7 | 23.0 | 2.89 |
| CMA-(3) | 1.84 | 27.0 | 79.4 | 23.8 | 2.86 |
| CMA-(4) | 1.81 | 27.3 | 79.7 | 23.2 | 2.89 |

(2) Steel penetration resistance and thermal shock resistance

Alumina-magnesia castables is mainly used as the working lining for carrying molten steel in ladle Therefore, the steel penetration resistance is its most critical performance. In this study, the castables was poured into a mold to make a cup-shaped sample. After demoulding and drying, a steel block was put into the sample and then heat-treat at 1600°C/3hr. Next, the cooled sample is cut in half and the deepest penetration depth at the bottom (smaller-the-better) is measured as a criterion for judging the steel penetration resistance. The effect of adding CMA binder on the steel penetration resistance of alumina-magnesia castables is shown in Tab. 3. The deepest penetration depths of samples CMA-(0) to CMA-(4) are 12.1mm, 11.7mm, 11.1mm, 10.7mm and 10.2mm in sequence. The appearance of the sample after cutting is depicted in Fig. 2. The results indicated that the steel penetration resistance was enhanced as CMA binder increased when comparing to original alumina-magnesia castables. The thermal shock resistance of the castables is also one of the evaluation indicators because the operation of the ladle has frequent temperature alternation. The judgment method is by measuring the MOR before and after the thermal shock test to convert the recession rate (smaller-the-better).

The results of adding CMA binder on thermal shock resistance of alumina-magnesia castables is shown in Tab. 4. It revealed that the addition of CMA binder had no significant improvement on thermal shock resistance.

*Tab. 3: Effect of adding CMA binder on the steel penetration resistance of alumina-magnesia castables*

| Sample | Deepest penetration depth |
|---|---|
| CMA-(0) | 12.1 mm |
| CMA-(1) | 11.7 mm |
| CMA-(2) | 11.1 mm |
| CMA-(3) | 10.7 mm |
| CMA-(4) | 10.2 mm |
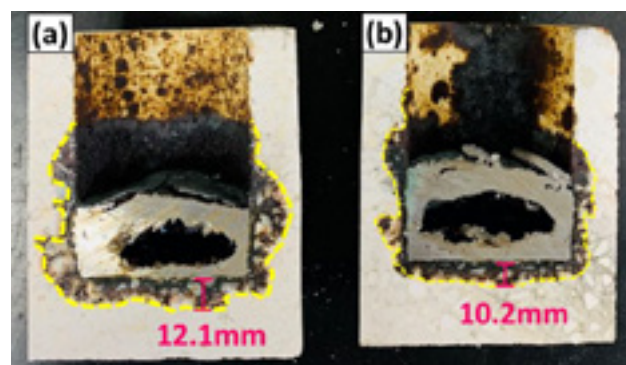


*Fig. 2: Cross-sectional photos of the samples for steel penetration resistance. (a). CMA-(0); (b). CMA-(4)*

*Tab. 4: Effect of adding CMA binder on thermal shock resistance of alumina-magnesia castables*

| Sample | Before test MOR (MPa) | After test MOR (MPa) | Recession rate (%) |
|---|---|---|---|
| CMA-(0) | 28.7 | 12.8 | 55.4 |
| CMA-(1) | 26.4 | 11.5 | 56.4 |
| CMA-(2) | 28 | 12.6 | 55.0 |
| CMA-(3) | 27 | 12.2 | 54.8 |
| CMA-(4) | 27.3 | 12.4 | 54.6 |

(3) Microstructure observation and erosion mechanism discussion

Among the above properties including fluidity, physical properties and steel penetration resistance, the sample CMA-(4) performed best. Therefore, samples from the experimental group CMA-(4) and the control group CMA-(0) were subjected to microstructure analysis to investigate the effect of adding CMA binder on alumina-magnesia castables. The polarizing optical microscope observation is shown in Fig. 3. The results found that CMA-(4) has a more obvious interface (orange area) than CMA-(0). It is speculated that this zone is mainly composed of Al-Mg spinel phase, which prevents further diffusion of the steel penetration area into the normal area. The penetration of molten steel into the refractories will cause qualitative changes in the composition and structure near the interface and accelerate the damage of the refractories. The penetration damage is directly proportional to the porosity of the castables. Furthermore, even the chemical composition of the castables is similar while the penetration rate is significantly different due to its varied structure. If the castables can produce obvious and thicker alumina-magnesia spinel phase at the interface, it can effectively block the further penetration of molten steel. Alumina-magnesia spinel phase is a dense structure with high melting point. In order to verify the above inference, SEM and EDS mapping were used to analyse the interface layer, as exhibited in Fig. 4. It verified that alumina-magnesia spinel phase does exist in the interface layer. Combined with the polarizing optical microscope observation results in Fig.3, CMA-(4) had a more obvious interface with alumina-magnesia spinel structure than CMA-(0).

405

Samples were taken from the interface area of CMA-(0) and CMA-(4) for XRD analysis. XRD Result is shown in Fig. 5. Fig. 5-(a) shows that while the main phases of CMA-(0) and CMA-(4) are corundum ($Al_2O_3$) and alumina-magnesia spinel ($MgAl_2O_4$), there are still traces of iron oxide ($Fe_2O_3$) and periclase ($MgO$) detected from the sample. Figure 5-(b) is the peak of spinel (311) plane. By comparing CMA-(0) and CMA-(4), CMA-(4) has an obvious peak shift which is caused by lattice distortion. The supposed cause is that the iron oxide produce from the oxidation of molten steel and then solid-solute into the alumina-magnesia spinel structure, as shown in the following reaction:

$$FeO + MgAl_2O_4 \rightarrow (Fe,Mg)O \cdot (Fe,Al)_2O_3$$

The lattice distortion is created as the atomic radius of Fe (156pm) being larger than that of Al (118pm) and Mg (145pm). It revealed that iron oxide was more solid-dissolved in the alumina-magnesia spinel at the interface area of CMA-(4). The XRD result is echoed with the microstructural observations.
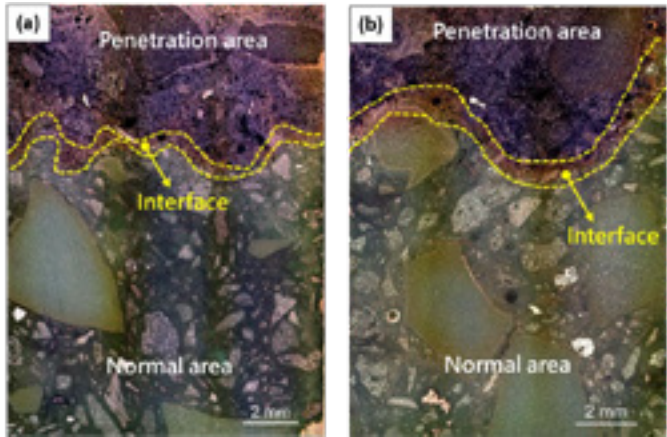


*Fig. 3: Observation of polarizing optical microscope analysis. (a). CMA-(0); (b). CMA-(4)*
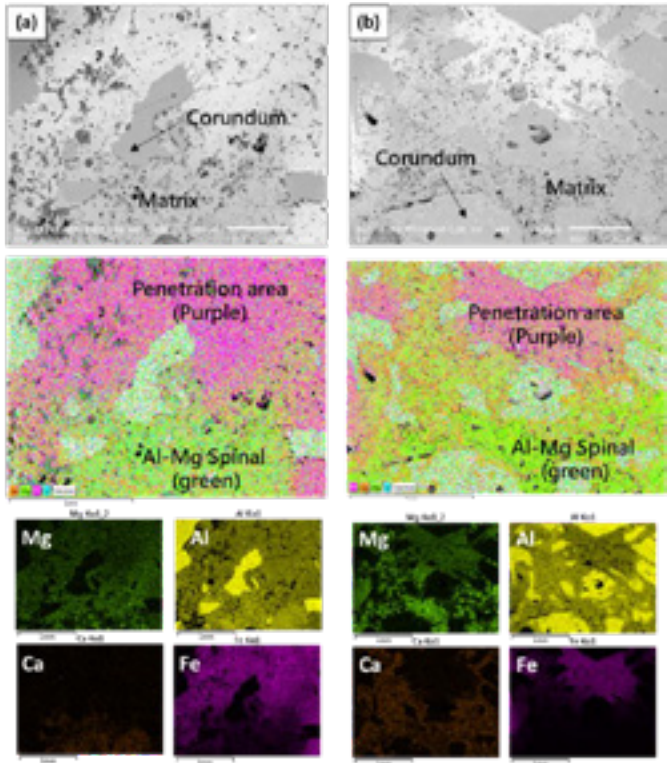
*Fig. 4: SEM and EDS mapping analysis at the interface. (a). CMA-(0); (b). CMA-(4)*
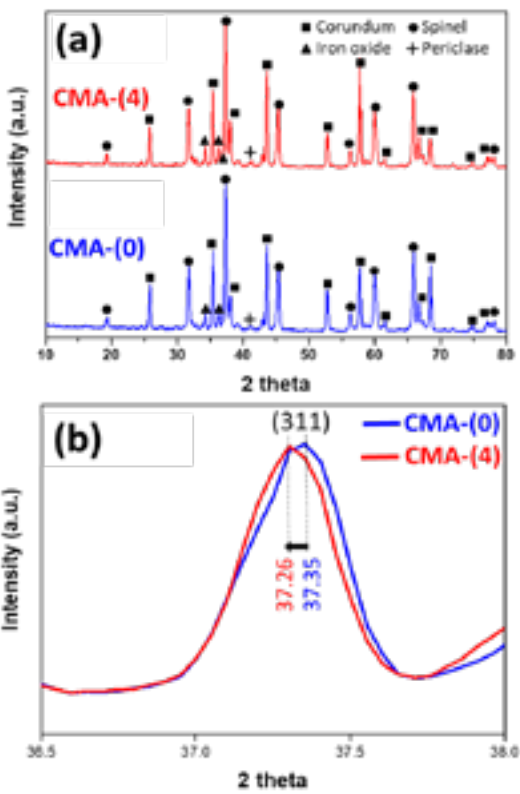


*Fig. 5: XRD analysis of interface area*

The alumina-magnesia castables is mainly used as the working lining of ladle to carry molten steel, but it is still possible to contact with slag. The overall hypothesis of penetration and corrosion mechanism is illustrated in Fig. 6. A circulation cycle formed when the molten steel/slag reacts with the alumina-magnesia castables to form low melting point phases such as CA ($CaAlO_4$) and CA2 ($CaAl_2O_7$) [9] and adhere to the surface of the refractories. These low-melting substances penetrate and erode the castables. The new reactive layer adheres to the old layer to thicken the reactive layer and cause spalling. This cycle makes the residual thickness of the alumina-magnesia castables thinner. Furthermore, the matrix area of the aluminia-magnesia castables was found to be eroded first before the aggregate area is exposed. If the matrix area is eroded aggressively, the aggregate area will spall into molten steel/slag. In this study, the refractory matrix area was enhanced by the addition of CMA binder into the castables, thereby improved the ladle lifespan.
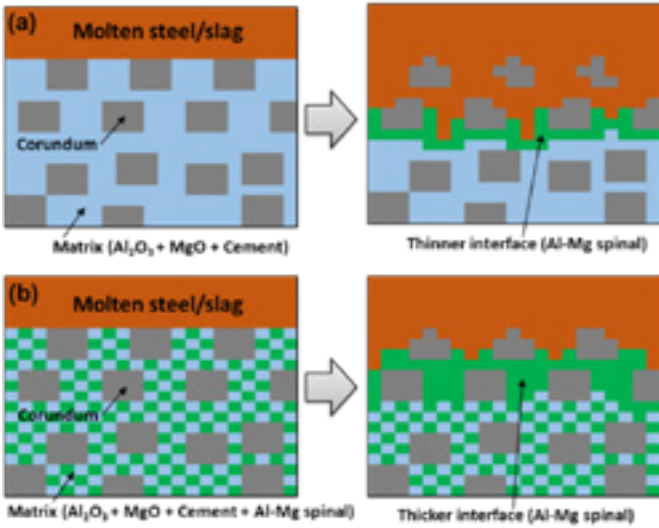


*Fig. 6: Hypothesis of penetration and corrosion mechanism. (a). CMA-(0)；(b). CMA-(4)*

**(4) Influence of steelmaking conditions on steel penetration depth**

The general operating condition for contacting molten steel in each round of steel ladle from the basic oxygen furnace (BOF) to the tundish is about 1550~1650°C and holding for 3~5 hours. In this study, the CMA-(4) with better steel penetration resistance was selected to investigate the influence of steelmaking conditions on the penetration depth of molten steel. The heat treatment condition is 1600°C±50°C for 4±1 hours. The result is exhibited in Fig. 7 and the formula obtained by linear regression of the experimental data is listed below. The deepest penetration depth of molten steel is $\Delta d$, the heat treatment temperature is T, and the heat treatment time is t.

If T=1550°C, $\Delta d = -0.1t^2 + 1.4t + 5.9$
If T=1600°C, $\Delta d = -0.15t^2 + 1.85t + 6$
If T=1650°C, $\Delta d = -0.05t^2 + 1.45t + 7.6$

The result revealed that since the coefficient value of $t^2$ was negative, which indicated that the steel penetration increased with the prolongation of the heat treatment time. However, the magnitude of penetration depth becomes smaller with the prolongation of heat treatment time. Furthermore, the depth of penetration of molten steel increases significantly with the increase of heat treatment temperature, which means the effect of operating temperature on penetration of molten steel is much greater than the effect of time. In order to increase the service life of the alumina-magnesia castables, the operating temperature and the time of the molten steel in the ladle should be reduced as much as possible under the premise of meeting the production conditions. If the operating conditions of the steel plant are difficult to change, it is recommended to use alumina-magnesia castables with better steel penetration resistance as the working lining in ladle.
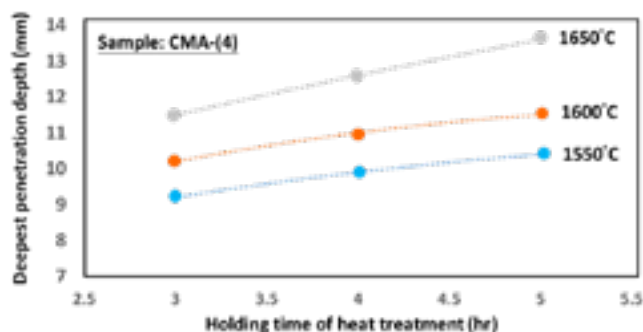


Fig. 7: Influence of steelmaking conditions on penetration depth.

**Conclusions**

Improvements were traced in the properties of alumina-magnesia castables by adding Calcium-Magnesium-Aluminate (CMA) binder and reducing MgO powder addition. The steel penetration resistance was enhanced as CMA binder increased when comparing to original alumina-magnesia castables. However, the addition of CMA binder has no significant improvement on thermal shock resistance. The corrosion behavior was firstly occurred in the matrix region and then the aggregate area could have been exposed during high temperature service which resulted in spalling and reduced performance. It was also found that CMA binder added sample has a distinct interface layer (alumina-magnesia spinel phase), which was analyzed by SEM/EDS. This spinel phase could block the continuous penetration of molten steel. In this study, the refractory matrix area was enhanced by the addition of CMA binder into the castables, thereby improved the ladle lifespan.

**References**

[1] Y. Wang, A. Huang, M. Wu, H. Gu, orrosion of alumina-magnesia castable by high manganese steel with respect to steel cleanness, Ceramics International, 45 (2019) 9884-9890.
[2] M.A.L. Braulio, L.R.M. Bittencourt, V.C. Pandolfelli, Selection of binders for in situ spinel refractory castables, Journal of the European Ceramic Society 29 (2009) 2727-2735.
[3] M.A.L. Braulio, G.G. Morbioli, D.H. Milanez, V.C. Pandolfelli, Calcium aluminate cement source evaluation for Al$_2$O$_3$–MgO refractory castables, Ceramics International, 37 (2011) 215–221.
[4] Schacht, C.A., Refractories Handbook. Marcel Dekker, Inc., New York, (2004).
[5] Chen, S.K., Cheng, M.Y., Lin, S.J., Ko, Y.C., Thermal characteristics of Al$_2$O$_3$-MgO and Al$_2$O$_3$-spinel castables for steel ladles. Ceram. Internat. 28 (2002) 811-817.
[6] Braulio, M.A.L., Milanez, D.H., Sako, E.Y., Bittencourt, L.R.M., Pandolfelli, V.C. 廿 Expansion behavior of cement-bonded alumina-magnesia refractory castables. Amer. Ceram. Soc. Bull. 86 (2007) 9201–9209.
[7] Q. Chen, Y. Lia, T. Zhu, Y. Xu, Y. Li, X. Wang, Improved thermal shock resistance of MgO–C refractories with addition of calcium magnesium aluminate (CMA) aggregates, Ceramics International, 48 (2022) 2500-2509.
[8] E. Clementi, D.L.Raimondi, W.P. Reinhardt, J. Chem. Phys, 38 (1963), 2686.
[9] D.A Jerebtsov, G.G Mikhailov, "Phase diagram of CaO–Al2O3 system", Ceramics International, 27 (2011) 25-28.

# CHROME FREE BAKED MAGNESIA BRICK – A REALLY ENVIRONMENTALLY FRIENDLY PRODUCT FOR RH DEGASSERS

Patrícia Alves Silva de Resende Brum, Vladnilson Peter de Souza Ramos, Douglas Fernando Galesi, Ariovaldo do Nascimento, Haysler Apolinário Amoroso Lima, Hamilton Cesar Guimaraes of Shinagawa Refractories, Vinhedo, Brazil

## ABSTRACT

The companies' commitment to zero $CO_2$ emissions by 2050 has promoted a huge effort in the search for alternatives to replace conventional products, aiming to drastically reduce the carbon footprint. In refractory industry, for example, materials produced at low temperatures have been researched to replace high temperatures fired bricks, with significant $CO_2$ emissions in their processing. This is the case of $MgO-Cr_2O_3$ products, used as refractory lining at RH degassers. In addition to the environmental appeal for $CO_2$ reduction, the elimination of chromium is also a pursued objective, mainly due to the possibility of contamination of the environment by $Cr^{+6}$. Additionally, new possibilities for safe recycling can be explored with the absence of chromium. This work presents the efforts in the development of unfired Cr-free alternative refractories for application in RH degassers, to contribute with environmentally friendly products.

## INTRODUCTION

Currently around 70% of consumed refractories in the world are used by the steel industry, of which 1/3 are consumed during secondary refining operations [1]. The introduction of continuous casting, the growing demand for "ultra clean" steels [2] and the increased use of scrap as a raw material require additional treatment steps. Degassing – the main example of which is the Ruhrstahl Henrichshutte (RH) process – is one of these additional stages, incorporated for the elimination of hydrogen, carbon and oxygen, in addition to the homogenization of liquid steel.

Evidently, the stability of the refractories lining inside of equipment for steel refining is crucial for cleanliness of the final product, which includes minimizing its wear and eventual incorporation of refractory particles into the metal bath. In addition, the correct selection of lining material extends the operating cycle of the asset and avoids interruptions in production. For this, understanding the wear mechanisms of refractories subject to RH Degasser operation is essential.

Despite its performance when it comes to high corrosion resistance as a result from direct bonding between chromium ores and magnesium aggregates through which the grains are predominantly joined by a solid-state diffusion mechanism, current magnesia-chrome refractory linings have been replaced due to the toxicological and environmental risks associated with $Cr^{6+}$. Aiming at finding a potential substitute, compositions containing spinel $MgO\cdot Al_2O_3$ have been the focus of multiple studies to verify their applicability in industrial processes such as steel degassing (RH [3], VOD [4]), copper refining [5] and cement production [6].

Focusing mainly on thermal shock and corrosion, this work proposes to compare laboratory trials results between a proposal of new product unfired and based on $MgO-Al_2O_3$ without chromium in its composition with current fired with chromium content in RH operation. Initially, an exposition will be made of the physical-chemical, thermal and mechanical properties to which the lining is submitted during the industrial process. Based on these mechanisms, the experimental results of thermal shock and corrosion resistance tests will be discussed.

## EXPERIMENTAL PROCEDURE

Following the purpose of this paper to evaluate a more environmentally friendly product as an alternative to standard fired magnesia-chrome containing materials, a composition (here named as U1 presented on Table 1) of high-grade fused magnesia, high MgO content magnesia sinter and fused spinel of different grain sizes were made as the proposed formulation. Grain sizes of mentioned raw materials was defined to provide an optimized grain

sized distribution and higher densification. Due to thermal cycles and high FeO content slag the refractory lining of RH Degassers are submitted, two main properties of the product are necessary to achieve good field performance: high thermal shock resistance and high corrosion resistance. Aiming at having a product with high performance in both properties, ceramic additives were used in the mix and a chemical binder, activated at lower temperatures (below 500 °C), was used to provide non-fired bricks, in order to reduce $CO_2$ emissions.

Table 1 also presents two different chemical analysis of direct-bonded $MgO-Cr_2O_3$ products as commercial references, currently applied as RH Degassers lining: CR1 for lower vessel critical areas, such as impact pads, throat, and RH snorkels, and CR2 for RH lower vessel non-critical areas. Both are for high performance comparison available in the market as reference value of standard fired refractory bricks.

Tab. 1: Detailed description of samples used in this paper

| Samples: | U1 | CR1 | CR2 |
|---|---|---|---|
| **Components:** | | | |
| Fused Magnesia (-5,0 mm) | 80.5 | - | - |
| Magnesia Sinter (-1,0 mm) | 2.5 | - | - |
| Fused Spinel (-1,0 mm) | 12.5 | - | - |
| Ceramic Additive A | 2.0 | - | - |
| Ceramic Additive B | 0.5 | - | - |
| Chemical Binder | 2.0 | - | - |
| | | | |
| **Chemical Analysis (%)** | | | |
| MgO | 83.0 | 65.0 | 67.0 |
| $Cr_2O_3$ | <0.0 | 23.5 | 16.1 |
| $Al_2O_3$ | 9.3 | 3.3 | 7.9 |
| $SiO_2$ | 0.5 | 1.8 | 2.0 |
| $Fe_2O_3$ | 0.1 | 5.5 | 7.0 |
| Other | 7.1 | 0.9 | 0.0 |

Physicochemical properties measurements, presented on Table 2, were conducted on U1 sample after baking at 200 °C and after heat treatments at 1,000 °C and 1,450 °C, to analyze the evolution of properties at different temperatures. As CR1 and CR2 are commercial products, the samples taken as received were used as comparison for properties after 1,450 °C heat treatment. After each heat treatment conducted in reduced atmosphere, Bulk Density and Apparent Porosity were perfomed following the standard ABNT NBR 16661, Cold Crushing Strength follows standard ABNT NBR 10059, Modulus of Rupture follows standard ABNT NBR 5014 and Hot Modulus of Rupture standard ABNT NBR 9642.

Before thermal shock resistance characterization, samples were submitted at 1,450 °C in reduced atmosphere for 5 hours. Then 10 cycles of thermal shock at 1,000 °C for 1 hour each and air (forced convection) until reach room temperature were conducted with sonic elastic modulus measurement after cycles 1, 2, 4, 6, 8 and 10. All materials were compared considering the residual percentage of the original Young Modulus.

FactSage 8.0 software was selected to simulate the both F2 and C2 slags/refractory interface selecting FactPs, FToxid and Ftmisc databases for calculations. Equilibrium condition of a hypothetical interface varying from 100% of slag to a 100% of refractory was simulated, showing what phases could be expected for at a simulated condition considering an operation at 1,700 °C and 0.04 atm (approximately vacuum condition inside the RH).

The RH Degasser slag changes throughout the operating cycle, starting from a normal steel ladle slag, evolving into a FeO-rich slag, and ending up in a $CaO/Al_2O_3$ slag system [7]. Corrosion

resistance was then determined using a rotary slag test kiln, at 1,680 °C (±20 °C), using two slag compositions: a FeO rich slag (F2) and a CaO/Al$_2$O$_3$ slag (C2). For each trial, the slag was renewed, resulting in a two corrosion stages with new slag. The slag chemistry analysis is presented in Table 3.

Tab. 2: Physicochemical properties

| Properties | U1 | CR1* | CR2* |
|---|---|---|---|
| After baking (200 °C) | | | |
| Bulk Density (g/cm³) | 3.12 | - | - |
| Apparent Porosity (%) | 8.8 | - | - |
| Cold Crushing Strength (MPa) | 84.8 | - | - |
| Module of Rupture (MPa) | 18.3 | - | - |
| | | | |
| After firing (1,000 °C) | | | |
| Bulk Density (g/cm³) | 3.07 | - | - |
| Apparent Porosity (%) | 13.8 | - | - |
| Cold Crushing Strength (MPa) | 43.9 | - | - |
| Module of Rupture (MPa) | 4.4 | - | - |
| | | | |
| After firing (1,450 °C) | | | |
| Bulk Density (g/cm³) | 3.07 | 3.21 | 3.08 |
| Apparent Porosity (%) | 13.9 | 15.9 | 17.5 |
| Cold Crushing Strength (MPa) | 37.1 | 54.1 | 34.8 |
| Module of Rupture (MPa) | 5.0 | 5.9 | 4.4 |
| | | | |
| Hot Modulus of Rupture at 1,400 °C (MPa) | 2.2 | 7.6 | 5.9 |

*As CR1 and CR2 are commercial products used as reference, their samples were already fired.

Tab. 3: Chemical analysis of FeO rich slag (F2) and CaO/Al$_2$O$_3$ slag (C2)

| Compounds | F2 | C2 |
|---|---|---|
| Fe$_2$O$_3$ | 39.3 | - |
| CaO | 34.2 | 40.4 |
| Al$_2$O$_3$ | 16.8 | 55.8 |
| SiO$_2$ | 6.5 | - |
| MgO | 3.2 | 3.8 |

In addition, as the absolute values of wear at samples submitted to the rotary kiln corrosion trial was too low, a more agressive test was necessary tring to have a more representative of RH Degasser real operational conditions. The purpose of the lance erosion test was to evaluate FeO resistance at a high temperature (~2,000 °C) with an irradiation time of 30 seconds. The oxygen gas flows through a steel pipe which at high temperatures generates FeO that will erode the refractory brick. The volume of the eroded hole was measured by filling the eroded hole with silicon carbide grains and converting the volume from its weight.

**RESULTS AND DISCUSSION**
As previously presented, Tables 1 and 2 showed that the developed formulation of unfired brick has a lower porosity than commercial MgO-Cr$_2$O$_3$ products which can impact on slag penetration.
The different heat treatments applied to the developed product showed a good evolution of cold mechanical resistance, with the values after heat treatment at 1,450 °C at the same level as those observed for the MgO-Cr$_2$O$_3$ products. However, the developed product presented lower value of hot mechanical resistance when compared to commercial products containing chromium. As an isolated case, these lower values may not has great influence on refractory performance, but when associated with the resistance to thermal shock and to cracks appearance by thermomechanical stress, it becomes an important property to be achieved. These phenomena are very common in critical regions of RH Degasser, such as the throat and snorkels, especially in those cracks that occur at the interface between volumes impregnated with slag and volumes that still unaltered, which greatly contribute to the structural spalling of the bricks in operation.
As seen in Figure 1, the thermal shock resistance test showed that the developed unfired product (U1) showed a very similar behavior

to the commercial product containing chromium used in the critical parts of the RH furnace (CR1) and better performance than commercial chromium containing product used in the less noble regions (CR2). This shows the effectiveness of the ceramic additives on improving the thermal shock characteristics of the developed material.
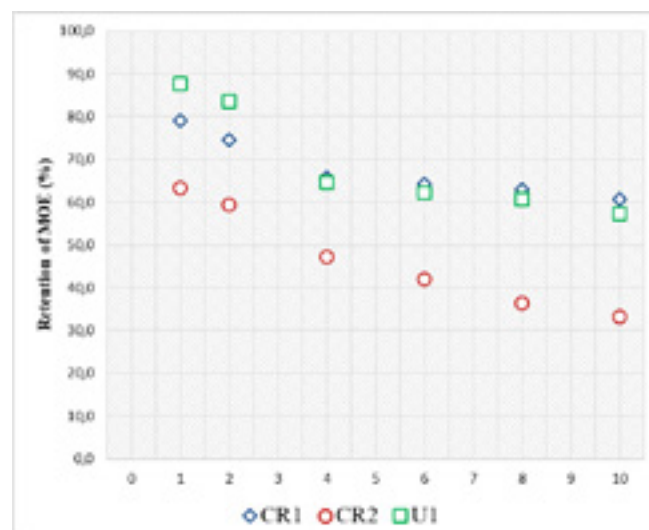


Fig. 1: Percentage values of Modulus of Elasticity/Young's Modulus after 10 cycles of thermal shock at 1,000 °C

In both cases, using F2 or C2 slags, the developed formulation proved to be more resistant in the corrosion test when compared to fired references as shonw in Figures 2 and 3.
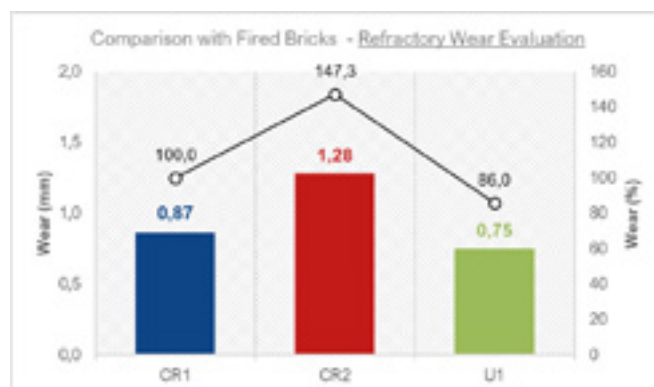


Fig. 2: Absolute and relative wear values after a FeO rich slag (F2) corrosion test in rotary kiln
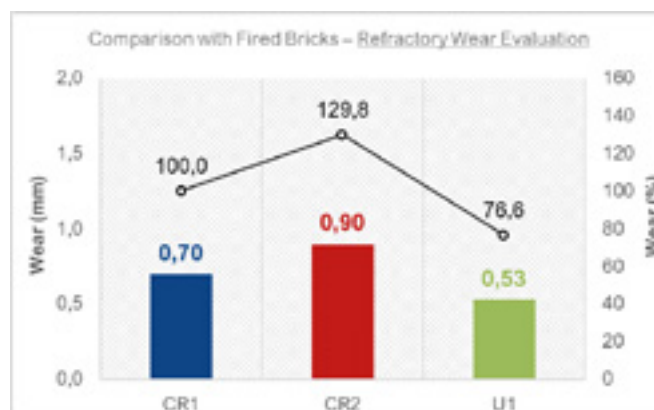


Fig. 3: Absolute and relative wear values after a CaO/Al$_2$O$_3$ rich slag (C2) corrosion test in rotary kiln

After achieving good results at thermal shock and corrosion resistance tests, U1 proposal formulation and CR1 reference were

409

selected for a simulation of phases in equilibrium at the slag/refractory interface, at temperature and pressure similar to the operating conditions, using Factsage 8.0 thermodynamic simulation software. The results are shown in Figures 4, 5, 6 and 7.

Simulation using the FeO-rich slag, shown in Figure 4, indicates that the interface of the commercial product containing chromium shows an initial solubilization of the refractory of about 17%. After this point, MgO saturation occurs becoming stable. The saturation of chromium spinel, on the other hand, occurs later, in a fraction around 20% of refractory. During all simulated fractions, there is a small evolution of the gas phase, rich in $O_2$. There is no precipitation, in equilibrium, of phases other than those initially present in the refractory.
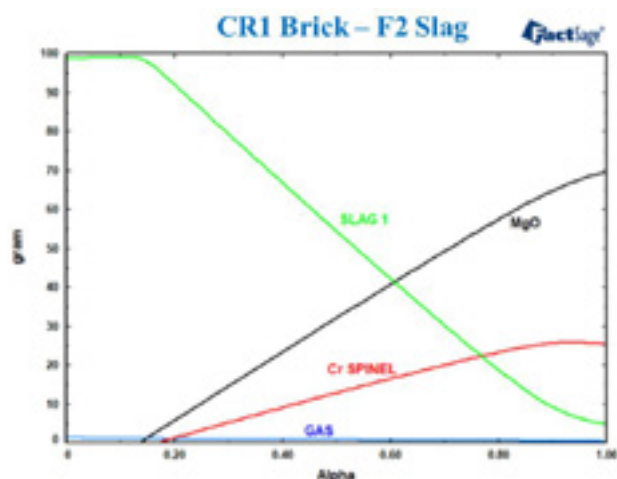


*Fig. 4: Equilibrium phases, at 1,700 °C and 0.04 atm, simulated by FactSage 8.0, considering chemical analysis of chromium containing CR1 brick, into hypothetical slag F2/brick interface, varying from 100% slag (Alpha=0) to 100% refractory (Alpha=1).*

The simulation (Figure 5) for U1 formulation results on initial refractory solubilization, at the FeO-rich slag interface, close to 15%. The additives ceramic phases A and B are completely solubilized, and the system, in equilibrium, presents, for proportions above 15% of refractory, 2 immiscible slags. The spinel phase only becomes stable in a proportion of above 90% refractory. There is also a presence of gas phase rich in $O_2$ in practically all refractory proportions.
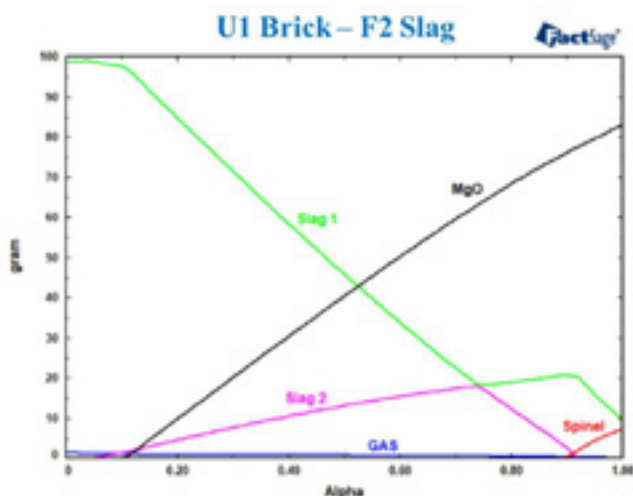


*Fig. 5: Equilibrium phases, at 1,700 °C and 0.04 atm, simulated by FactSage 8.0, considering chemical analysis of unfired chromium free U1 brick, into hypothetical slag F2/brick interface, varying from 100% slag (Alpha = 0) to 100% refractory (Alpha = 1).*

Figure 6 ilustrates the simulation of interface between CR1 brick with the C2 slag ($CaO/Al_2O_3$). The commercial refractory containing chromium (CR1) has a lower solubility when compared with the simulation done with F2 slag, with chromium spinel already saturating the slag from about 7% of refractory fraction. No gas phase was detected.
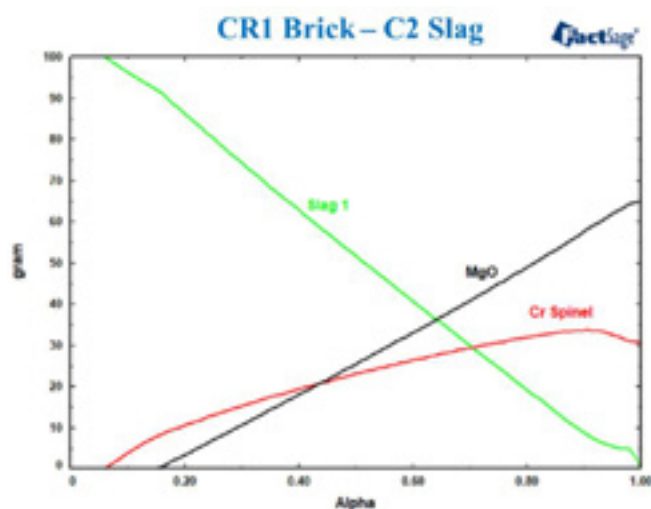


*Fig. 6: Equilibrium phases, at 1,700 °C and 0.04 atm, simulated by FactSage 8.0, considering chemical analysis of chromium containing CR1 brick, into hypothetical slag C2/brick interface, varying from 100% slag (Alpha=0) to 100% refractory (Alpha=1).*

In the case of the refractory/slag interface for formulation U1, showed at Figure 7, the initial solubilization is much higher than for the product containing chromium, around 18%. Again, the additive ceramic phases A and B are not stable at all refractory ratios, and two immiscible slags are present up to the 70% refractory ratio. No gas phase is present at equilibrium conditions, and the spinel phase only becomes stable from a proportion of 88% refractory.
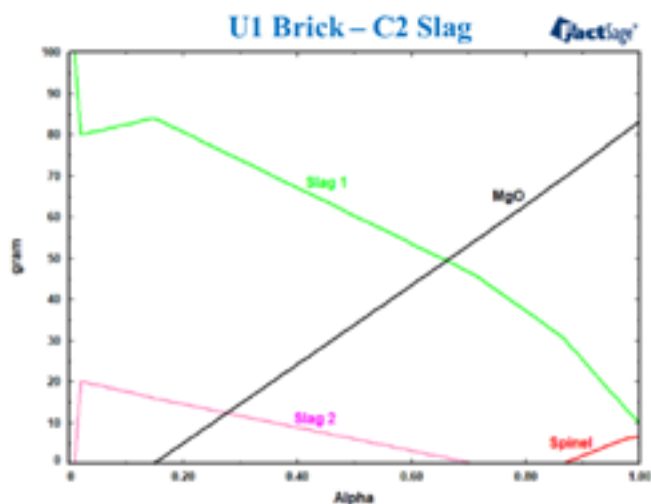


*Fig. 7: Equilibrium phases, at 1,700 °C and 0.04 atm, simulated by FactSage 8.0, considering chemical analysis of unfired chromium free U1 brick, into hypothetical slag C2/brick interface, varying from 100% slag (Alpha = 0) to 100% refractory (Alpha = 1).*

From achieved results at corrosion tests and in the phase equilibrium simulations, it is possible to indicate that the presence of two immiscible slag phases, present in the $MgO-Al_2O_3$ system, combined with the complete solubilization of additive ceramic phases A and B in these same slags, play a key role in the improved corrosion and slag penetration resistance.

410

Visual observation of the bricks after corrosion attack lance test, shows cracks in the holes of CR1 and CR2 bricks, but not in U1, according to the appearance and cross section surfaces. Figure 8 shows the detailed images of cross sections of the three products after lance teste and corresponding volume values caused by erosion.
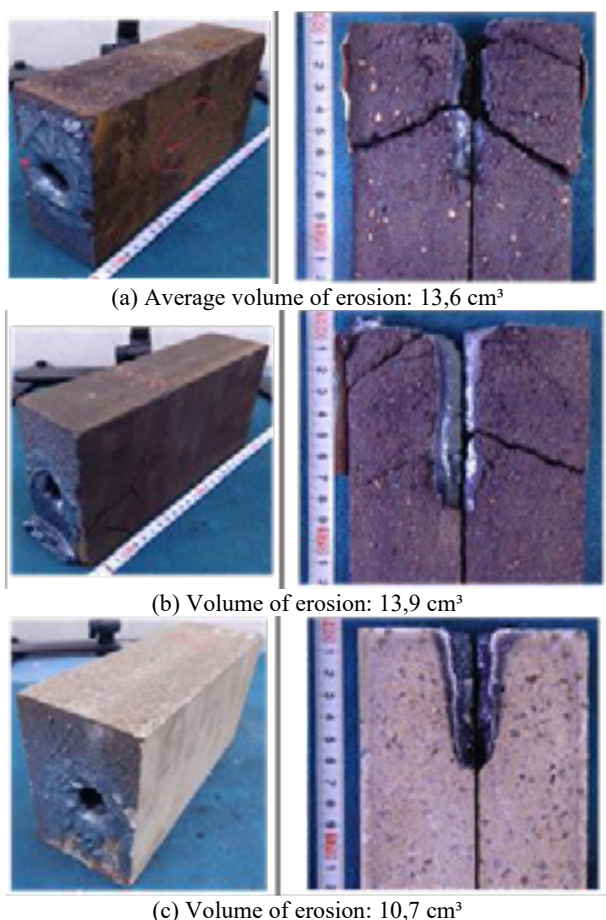


(a) Average volume of erosion: 13,6 cm³

(b) Volume of erosion: 13,9 cm³

(c) Volume of erosion: 10,7 cm³

Fig. 8: Cross section surfaces of (a) CR1, (b) CR2 and (c) U1 bricks after corrosion attack by lance test.

The depth and volume of melt loss was the lowest for U1 unfired bricks when compared to CR1 and CR2. The appearance and cross sections surfaces of the fired bricks CR1 and CR2 showed cracks around the melted holes unlikelly unfired bricks. The thermal shock is considered to be high because the lance melt damage test rapidly reaches very high temperatures, around 2,000 °C. Therefore, it is considered that the unfired bricks with excellent heat spalling resistance have not presented cracks.

In addition, the amount of erosion loss tended to be lower for unfired bricks than for fired ones which can be justified by lower porosity of unfired compared to the fired ones. Contrariwise, the porosity of unfired bricks increases when heat treatment is applied. Therefore, the FeO resistance of unfired bricks used and heated in an actual furnace may differ from the trend of the lance erosion test results. Although fired bricks were also included in the comparison, caution should be exercised in comparing the test results of this study.

Ultimately all performed tests results indicate the good performance of unfired new development as a potentail substitution of fired chromium-based standard bricks. When we remove the heat treatment at high temperatures from the production process of the refractory bricks, there is potential of reduction of 357,1 kg of $CO_2$ emission per ton of brick due to removal firing step maintaing only baking [8].

## CONCLUSIONS

Highlighting toxicological and environmental risks associated with hexavalent chromium in $MgO-Cr_2O_3$ fired bricks – widely used in steel degassing equipment, such as in the Ruhrstahl Henrichshutte (RH) process – refractories based on $MgO-Al_2O_3$ have been considered in the literature as potential substitutes. Throughout this work, several characterizations were carried out, seeking to evaluate the feasibility of a refractory based on $MgO-Al_2O_3$ for the lower vessel RH.

The present paper showed a successful development based on $MgO-Al_2O_3$ proposal suitable with some of the most important properties conferred by chromium-containing products currently applied in RH degasser. This new product was developed using a lower heat treatment temperature, reducing $CO_2$ emissions in comparison to traditional chromium containing materials.

Satisfactory levels of resistance to thermal shock were achieved, compatible with a commercial reference product containing chromium, used in critical regions of the RH furnace, such as throat and snorkel.

A major corrosion resistance was achieved by new product, mainly by the addition of ceramic additives that, through their solubilization, provided lower extension in the impregnation by the evaluated slags. Even in more harsh conditions trials, the new product performance exceeded fired bricks on thermal shock resistance associated with higher temperature corrosion resistance.

Future studies aiming at focusing on improvement of hot mechanical resistance, necessary to prevent the appearance of cracks in current commercial products, due to the very characteristic thermomechanical effects present during the operation of RH degasser.

## REFERENCES

[1] Buhr, A. Refractories for steel secondary metallurgy. CN-refractories 1999; 3:19–30.

[2] Zhang, L., Thomas, B.G. State of the art in evaluation and control of steel cleanliness. ISIJ international 2003; 43(3):271–291.

[3] Tong, S., Zhao, J., Zhang, Y., Cui, Q., Wang, R., Li, Y. Corrosion mechanism of Al-MgO-MgAl2O4 refractories in rh refining furnace during production of rail steel. Ceramics International 2020.

[4] Jones, P. Degradation mechanisms of basic refractory materials during the secondary refining of stainless steel in VOD ladles. Leuven: KU Leuven: 2001; 69–71.

[5] Malfliet, A., Lotfian, S., Scheunis, L., Petkov, V., Pandelaers, L., Jones, P.T., et al. Degradation mechanisms and use of refractory linings in copper production processes: a critical review. Journal of the European Ceramic Society 2014;34(3):849–876.

[6] Goto, K., Argent, B.B., Lee, W.E. Corrosion of MgO-MgAl2O4 spinel refractory bricks by calcium aluminosilicate slag. Journal of the American ceramic society 1997;80(2):461–471.

[7] M.K. Cho, M.A. Van End, T.H. Eun, I.H. Jung. "Investigation of slag-refractory interactions for the Ruhrstahl Heraeus (RH) vacuum degassing process in steelmaking". Journal of the European Ceramic Society, 32 (2012) 1503–1517.

[8] Strubel, S. "Developing a model to calculate the carbon footprint of refractory products". Master Thesis. Leoben: Institut für Nachhaltige, 2012.

411

# EFFECT OF SPECIAL CARBON ADDITIVE ON THE PROPERTIES OF DOLOMITE–CARBON REFRACTORIES FOR STEEL LADLE APPLICATION

T. Mahata*, V. Jha, S. Das, B. Ghosh, A. Acharya, H. Nagata, S. Sengupta and P. B. Panda

TRL Krosaki Refractories Ltd., India

## ABSTRACT

Dolomite is well known for its use as refractory to produce cleaner steel. High thermodynamic stability of its oxides at elevated temperature, excellent corrosion resistance towards corrosive slag and good refractoriness makes dolomite suitable for above applications. Carbon containing dolomite bricks (Dolo-C) used in steel ladle where silicon killed grade steel produced and low $Al_2O_3$ containing slag is generated. Performance of Dolo-C refractory restricts due to poor hydration resistance of the material and generation of vertical crack due to less strength at higher service life.

In this present investigation, an effort has been made to improve the physical and thermomechanical properties by strengthening the matrix of the bricks. A special carbon additive has been introduced to improve the brick properties. Various trial recipes were prepared with varying percentage of additives and compared with recipes having no additive. The optimized recipe was characterized thoroughly, like thermomechanical, physical properties, hydration and oxidation behavior and compared with recipe having no additive. Improvement in physical properties along with oxidation and hydration behavior was observed due to the addition of the special carbon additive. Recipe with optimized property was considered to supply bricks for application in steel ladle metal zone. Performance improvement was noted along with less premature down compared to regular quality bricks in steel ladle application.

## INTRODUCTION

Dolo-C refractories are majorly used in steel ladle applications for Si killed steels, as the doloma is more thermodynamically stable and helps in the production of cleaner steel with low carbon pickup. The focus of research community has been majorly in the field of MgO-C refractories, but Dolo-C refractories share a lot of same characteristics as former. Therefore, multiple new developments in the field of MgO-C refractories can be directly used in the field of Dolo-C bricks. The knowledge of low melting phases in case of Dolo-C refractories are important for this.

Carbon is added as graphite flakes to the refractories, due to its non-wetting characteristics, excellent slag corrosion resistance and improved thermal shock resistance. However, the use of high amount of carbon has its own problems. Oxidation of carbon increases the porosity of the bricks, which in turn make the structure weak and reduces corrosion resistance. Higher carbon content also results in higher carbon pickup in molten steel. Efforts have been made by several researcher to introduce different carbon source in MgO-C refractories to improve properties of the bricks. In some research people tried to reduce total carbon content in the bricks by adding different source of carbon and additives to improve performance and reduce carbon emission. In this investigation we have identified two fine carbon source which can be used in combination with flaky graphite. Purpose of these fine carbon additives were to coat the grains and dust particles properly during mixing with binder. It was expected to reduce small voids inside the brick matrix and hence enhance hydration resistance and improve thermomechanical properties.

## EXPERIMENTAL PROCEDURE

High purity natural sintered dolomite and natural flake graphite are the main constituents to produce test refractory bricks. Novolac resin was used as binder. One standard recipe of Dolomite-C refractory was selected to study the effect of new additives. Two types of fine carbon additives having different particle size were selected to study the effect in the bricks. Two series of test bricks were prepared with additives A and B. Amount of these two additives varies from 0.25 % to 2% in the recipe and compared the properties with the brick sample prepared without any additive. All the recipes with nomenclature are described in **Table-1**. Laboratory scale mixer machine was used to mix the materials with binder and pressed in hydraulic press (SACMI-1600 MT) with 2T/cm² specific pressure. After pressing brick samples were cured at 300°C in tunnel dryer for 14 hrs. Bricks were cut after curing in different dimensions to measure different physical and thermomechanical properties.

Table 1: Recipes used for the experiments.

| Sample Name | Sintered Dolomite | Graphite | Additive -A | Additive-B |
|---|---|---|---|---|
| R | 97% | 3% | - | - |
| A-1 | 97% | 3% | 0.25% | - |
| A-2 | 97% | 3% | 0.50% | - |
| A-3 | 97% | 3% | 1% | - |
| A-4 | 97% | 3% | 1.5% | - |
| A-5 | 97% | 3% | 2% | - |
| B-1 | 97% | 3% | - | 0.25% |
| B-2 | 97% | 3% | - | 0.50% |
| B-3 | 97% | 3% | - | 1% |
| B-4 | 97% | 3% | - | 1.5% |
| B-5 | 97% | 3% | - | 2% |

Apparent Porosity (AP) and Bulk Density (BD) testing were carried out as per ISO 5017:1998. Cold Crushing Strength (CCS) of the samples were tested as per ISO 10059-2:2003. Coking of the brick samples was carried out at 1000°C for 3 hours soaking in reducing atmosphere (fired inside coke bed) and AP, BD and CCS were again tested as per the same standards described above. Modulus of Elasticity (MOE) testing was conducted after coking according to IS 13311, which is used for calculation of dynamic young's modulus of elasticity in concrete. For this test, samples with dimensions 50x50x100mm were prepared, and the transit time (T) was measured using an ultrasonic pulse generator and transducer. Pulse velocity (V) was calculated from transit time(T) and path length (L=100mm). Dynamic young's modulus was calculated using the following equation:

$$E = \rho\, f(\mu)\, V^2$$

Where, $\rho$ is the density in $kg/m^3$

$f(\mu)$ is the function of poisson's ratio which has value of 0.9 for the refractories and V is the pulse velocity in m/s

Hot modulus of rupture (HMOR) was conducted as per ISO 2478:1987. Oxidation resistance testing was performed using cuboid samples with 50x50x100 mm dimensions. Samples were set vertically in laboratory furnace and fired at 1400°C with 3 hours soaking. After firing samples were cut and measured the % of decarburised area. Hydration resistance test was conducted in humidity chamber maintaining the constant humidity 70% at 35°C temperature. 50*50*50 mm brick samples were taken and kept in humidity chamber for four days. After four days weight gain of the samples was measured. Amount of weight gain (%) was considered as hydration %. Slag corrosion test was carried out in static induction furnace with synthetic ladle slag. Slag chemistry was shown in Table 2. Bricks were cut and lined inside the furnace in hexagonal shape. Six no of samples (2 from each brick) with 120 mm height and 35 mm thickness was used to make the hexagon. Cylindrical steel bar (diameter 90 mm and height 125 mm) was put inside the furnace. After melting the steel, slag was charged in

412

every 30 min interval for 4 hrs. After 4 hours molten slag and metal was discharged. Corroded brick samples collected after cooling and measured the thickness of maximum corroded area. Rate of corrosion was calculated from the initial and leftover thickness after corrosion test.

Table 2: Slag Chemistry (wt%).

| CaO | MgO | SiO2 | Al2O3 | Fe2O3 | MnO | Cr2O3 |
|------|------|-------|-------|-------|------|-------|
| 56.7 | 2.21 | 35.01 | 2.23 | 0.47 | 1.51 | 1.7 |

## RESULTS AND DISCUSSION
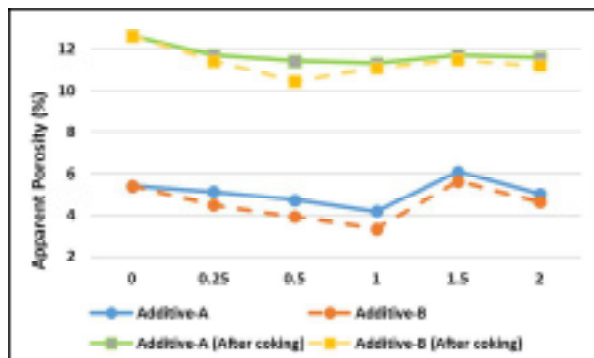


*Fig.1: Variation of Apparent Porosity and Coked Apparent Porosity with increase in additive %.*

Apparent porosity variation of as such sample and coked samples with increase in A and B type Carbon additives in the recipe is shown in **Fig.1.** It has been observed that AP of as such sample decreased up to addition of 1% additive for both the additives. But further increase of additives did not continue the decreasing trend of AP further. In fact, these values become inconsistent beyond 1% addition of additives. Coked samples also has shown similar trends of AP, but variation is very less. This initial reduction in AP up to 1% addition due to filling the small voids between grains and
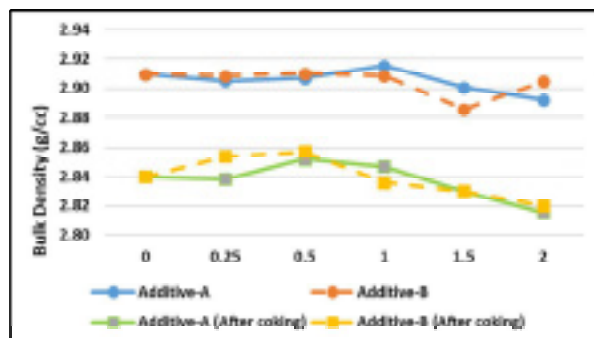


*Fig.2: Variation of Bulk Density and Coked Bulk Density with increase in additive %.*

matrix. This is possible as because fine particles of the additives distributed uniformly within the matrix. Beyond 1% addition of additives, AP increased due to agglomeration of excessive additives. During curing and coking of the bricks these agglomerates create fine pores and hence AP increases.

**Fig.2** shows the variation of Bulk Density with respect to the amount of additives A and B addition for as such and coked samples. There is no change in BD of the samples up to 1% addition of both the additives. But above 1% addition, BD decreased in both the cases. This indicates higher % of type A and B additives reduces the compactness of the bricks or not allow the brick matrix to get maximum compactness. BD of coked samples also showing the similar trend. Reduction of BD also due to low

density of the additives A and B. One point to be noted here that, compactness of bricks samples containing additive B shown better values compared to that of additive A.

**Fig.3** shows the variation of Cold Crushing Strength with respect to the amount of additives A and B addition for as such and coked samples. There is no such increase of CCS value was noted for additive A containing samples up to 0.5% addition. Addition of 1%
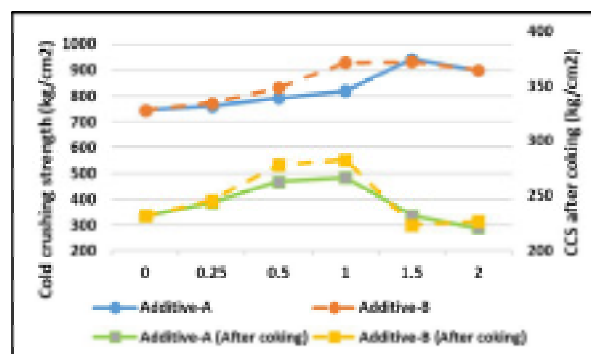


*Fig.3: Variation of Cold Crushing Strength (CCS) and Coked Cold Crushing Strength with increase in additive %.*

or more additive A, notable amount of CCS values has increased. Additive B containing samples showing improved CCS values upto 1% addition, further addition of additive B did not increase the CCS values further. This is due to better compactness and filling the smaller voids due to addition of fine additives. Coked CCS increases up to 1% and decreases above 1% addition of the additives. It is probably due to excessive addition of the additives, it got agglomerated and loosen during coking of the brick samples.

**Fig.4** shows the variation of HMOR/MOE ration of the brick samples. Higher value of this ratio indicates better thermal shock resistance of the bricks. This value increased up to 1% addition of additive A and for additive B added samples it increased up to
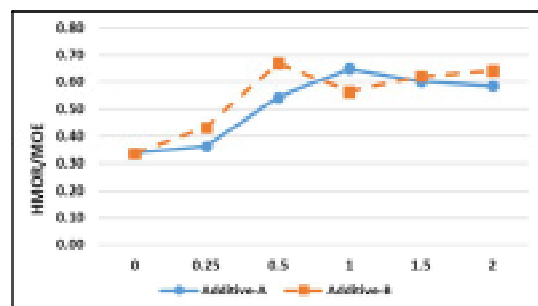


*Fig.4: Variation of HMOR/Modulus of Elasticity ratio.*

0.5% addition. After that this ratio of HMOR/MOE becomes constant.

**Fig.5** shows the cross section of the brick samples after oxidation test at 1400°C. Remaining black area measured and calculated the oxidised area (%) which is shown in **Fig.6.** Less oxidised area indicates better oxidation resistance. Oxidised area reduced initially due to small addition (0.25%) of both the additives. Addition of higher amount of additive does not improve the oxidation resistance further. This happens due to homogeneous distribution of fine additives and filling the void spaces.

413
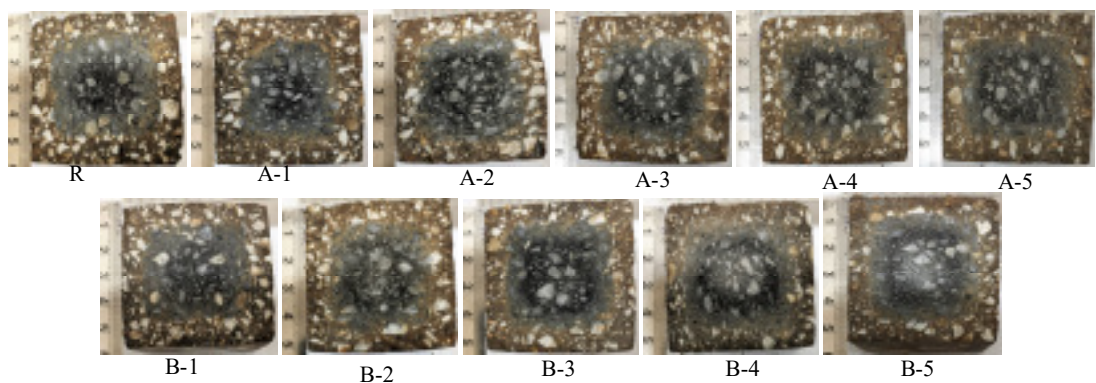
Fig.5:Cross Section of Brick samples after oxidation test.
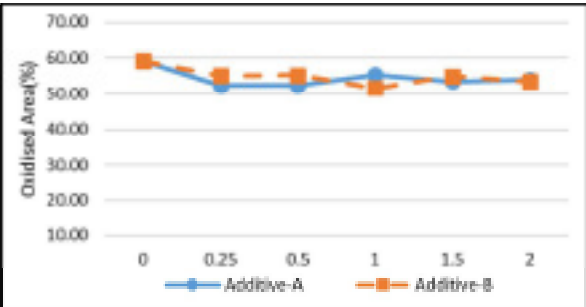


Fig.6: Variation of oxidised area with increase in additive %.

Table 3: Slag Corrosion rate.

| Sample Name | R | A-3 | B-3 |
|---|---|---|---|
| Corrosion Rate (mm/hr) | 4.5 | 2.5 | 4 |



Fig.8: Samples after slag corrosion test (a) R (b) A-3 (c) B-3

Hydration resistance improved due to addition of carbon additives, which is shown in **Fig. 7**. As the additives are very fine in nature and having high surface reactivity it is very easily adhere on the surface of grains. Also, small particles of the additives fill the small voids. It prevents the moisture to directly contact with dolomite grains up to some extent and improves hydration resistance.

Based on the findings in laboratory scale trial recipe A-3 was selected for commercial production for steel ladle metal zone application. Trial was conducted in one of the integrated steel plants, producing silicon killed steel in India. Spalling tendency of recipe A-3 bricks compared to regular (R) was reduced, which is evident in the photographs in Fig.9. and 10% performance improvement was reported.



Fig.7: Variation of hydration (%) with increase in additives %.

Analysis of physical and thermomechanical property indicates that 0.5-1.0% addition of both the additives (A & B) exhibits best results. Based on this analysis, 1% additive containing samples (A-3 & B-3) was considered for slag corrosion test along with the sample containing no additive. **Fig.8** shows the cross section of the samples after slag corrosion test. It was observed that sample A-3 has lowest corrosion rate (2.5 mm/hr) compared to sample B-3 (4 mm/hr) and R (4.5 mm/hr). Corrosion resistance of additive containing brick samples improved due to homogeneous distribution of fine carbon particles inside the matrix. It prevents the molten slag to penetrate the matrix. Although both the additives are showing similar type of improvement in physical and thermomechanical properties, but slag corrosion resistance is much superior in additive A containing sample (A-3). This is possibly due to more homogeneous distribution of additive A inside the brick matrix and better non-wetting property compared to additive B.



Fig.9: Ladle during repair of slag zone (a) with regular brick (b) brick with 1% additive A .

## CONCLUSIONS

In this study we have considered two types of carbon additives (A & B) to investigate their compatibility in Dolomite-C refractory. Initially physical and thermomechanical property of the bricks was studied with increase in additive content in the bricks (0.25% to 2%). Based on this study following conclusions were made:

- Optimum AP was observed in the bricks containing 0.5-1% of both the additives. There is no change in bulk density up to 1% addition, more than 1% addition of the additives reduce the bulk density. Which indicates that use of the additives is optimum up to 1%.

- CCS value of as such samples are showing higher value in 1% or more addition of both the additives. Coked CCS decreased due to more than 1% addition of the additives. It indicates 1% additive is the optimum quantity to get good brick strength.

- Oxidation resistance improved in both the cases with 0.25% addition. There is no further improvement due to extra addition of the additives.

- HMOR/MOE value increases in 0.5% or more additive containing (A & B both) brick samples, which indicates better thermal shock resistance in >0.5% additive containing bricks.

- Hydration (%) of bricks reduced gradually due to increase of additive additions, it indicates improvement of hydration resistance due to increase of additive %. It happens due to filling the small pores and coating of grain surfaced by the additives which prevents the moisture to react with the dolomite grains.

- Slag corrosion test of 1% additive (A-3 & B-3) containing bricks was conducted along with regular brick (R). It was observed that A-3 sample had significant improvement in corrosion rate (2.5 mm/hr) compared to regular sample (4.5 mm/hr). Whereas B-3 sample has corrosion rate (4.0 mm/hr) almost equivalent to regular sample.

- Plant scale trial conducted in ladle metal zone in one of the integrated steel plant in India with A-3 recipe and 10% performance improvement was reported.

## REFERENCES

[1]  Behera, S, Sarkar, R. Nano Carbon Containing Low Carbon Magnesia Carbon Refractory: An Overview. Protection of Metals and Physical Chemistry of Surfaces, 2016, Vol. 52, No. 3, p. 467–474.

[2]  Gheisari, D, H, Ghasemi-Kahrizsangi, S, Karamian, E, Addition impact of nano-carbon black on the performance of MgO.CaO compounds. Ceramics International, 44(5) 2018, p. 5524-5527.

[3]  Zhu, T, Li, Tianbin, et.al. Effect of nanocarbon sources on microstructure and mechanical properties of MgO–C refractories. Ceramics International, 40(3) 2014, p. 4333-4340.

[4]  Stein, V, Aneziris, C, G, Gueguen, E, New approach for the application of functional ceramic material in carbon bonded doloma refractories to reduce emissions. Advanced Engineering Materials, 2011, 13(12), p. 1135-1141.

[5]  S. Ghasemi-Kahrizsangi, Ebrahim Karamian, Hassan Gheisari Dehsheikh, Ahmad Ghasemi-Kahrizsangi, A review on recent advances on magnesia-doloma refractories by nano-technology, J. Water Environ. Nanotechnol. 2 (3) (2017) 206–222.

[6]  S. Gh. Kahrizsangi, A.Nemati, A. Shahraki and M. Farooghi "The effect of nano-additives on the hydration resistance of materials synthesized from the MgO-CaO system", International Journal of Engineering, 29(2016), 539-545.

[7]  Stein, V, Aneziris, C, G, Gueguen, E, The influence of titania on properties of doloma-carbon refractories. 53rd International Colloquium on Refractories. 2010, p.174-176.

415

# A STUDY ON THE FLUIDITY IMPROVEMENT OF QUICKLIME FOR DESULFURIZATION AGENT USED IN BOTTOM BLOWING FURNACE

Shin, Gil Jae of POSCO FUTURE M, Pohang-si , Korea, Lee, Nam Gil of POSCO FUTURE M, Sejong-si, Korea
Bae, In Kyung of POSCO FUTURE M, Pohang-si, Korea

## ABSTRACT

Extensive research is being carried out worldwide to reduce carbon dioxide ($CO_2$) emissions through various approaches. Even in the steel industry, which is one of the largest emitters of $CO_2$, research and development of steelmaking technologies to address this issue are being actively pursued. In order to reduce $CO_2$ emissions, the steel company is planning to achieve this through hydrogen reduction steelmaking, electric arc furnaces, and converter operations. The most practical and quickest solution to respond is considered to be reducing molten steel usage and increasing the amount of scrap, as this can effectively reduce $CO_2$ emissions. The technology involves injecting pure oxygen into the molten steel while adding quicklime to remove impurities such as carbon, silicon, manganese, sulfur, and titanium present in the molten steel inside the converter. For smooth injection, the quicklime used is coated with silicone oil on its surface to enhance its flow properties and water repellency. Research has been conducted on the dry coating technology of quicklime using silicone oil and its manufacturing processes.

## INTRODUCTION

This study investigates the processing method for the quicklime (CaO) powder used as a desulfurizing agent in the steelmaking process. Desulfurizing agents commonly used in the steelmaking process are classified into calcium carbide ($CaC_2$) based, sodium carbonate ($Na_2CO_3$) based, and quicklime (CaO) based. Calcium carbide has good reaction efficiency but is expensive to manufacture due to high power consumption. It also carries the risk of acetylene gas generation. Sodium carbonate has slightly lower reaction efficiency than calcium carbide but offers the advantage of desulfurization effect. However, it is more expensive than quicklime and has the disadvantage of generating white smoke during desulfurization and causing erosion of the refractory lining of the steelmaking vessel. Quicklime is inexpensive but has lower reaction efficiency. It reacts with moisture in the air to form calcium hydroxide ($Ca(OH)_2$) and has poor flowability in hoppers due to its high cohesiveness. It also causes clogging and circulation disturbances in the injection pipe. Therefore, increasing the pressure of the inflow gas is necessary, but it leads to waste of the gas and exacerbates the bubbling and rising velocity of the furnace, resulting in reduced desulfurization efficiency. Thus, this study aims to improve the reaction efficiency of the cheap quicklime-based desulfurizing agent, reduce the cohesiveness of the powder for easier injection, and prevent the generation of calcium hydroxide due to reaction with moisture during storage and handling. The approximate configuration of furnace is shown in Figure 1.



*Fig. 1-1: Top Blowing Furnace Process (Conventional Furnace)*
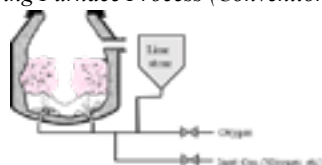


*Fig. 1-2: Bottom Blowing Furnace Processs*

In general, the conventional furnace is of the top blown type (Fig. 1-1). In the top blown type, quicklime is injected from the top. On the other hand, in a bottom blowing furnace, quicklime is injected from the bottom using high-pressure oxygen as a carrier medium(Fig- 1-2). If the quicklime particle size is large, there is a potential risk of sparks and explosions due to particle collisions in pipes and bends.

## EXPERIMENT

### Material

The materials used in this research are quicklime and silicone oil. The conditions for these materials are as follows. To achieve high-purity steel production, quicklime should meet the following properties as it is injected from the bottom

· High reactivity: The quicklime should have a high reactivity to Effectively remove sulfur and impurities from the steel.
· Low impurity content: The quicklime should have low levels of impurities such as silica, alumina, and iron oxide, as these impurities can negatively affect the steel quality.
· Proper particle size distribution: The quicklime particles should have a suitable and uniform size distribution to ensure effective mixing and reaction with the molten steel.
· Good flowability: The quicklime should have good flowability to ensure smooth injection.
· High thermal stability: The quicklime should exhibit high thermal stability to withstand the high temperatures in the furnace without significant decomposition or loss of reactivity.

These properties are essential to achieve efficient desulfurization and maintain high steel quality during the steelmaking process.

The specific desirable qualities of quicklime for injection from the bottom are as follows, as shown in Table 1

| Item | | Value, % |
|---|---|---|
| Chemical Properties | CaO | $\geq$ 90 |
| | $SiO_2$ | $\leq$ 3.0 |
| | S (Sulfur) | $\leq$ 0.05 |
| | Loss of ignition | $\leq$ 10.0 |
| Physical Porperties | $\leq$ 0.1 mm | $\geq$ 90.0 |
| | $\leq$ 1 mm | $\leq$ 100 |
| | water content | $\leq$ 1.0 |

*Table. 1: Quality data requirement for quicklime*

The silicon oil used in this study was a methylhydrogensiloxane product with reactive hydrogen groups. Conventional silicon oil, known as polydimethylsiloxane, was excluded from consideration as it lacks functional groups that can coat the surface of powders. The reactive hydrogen groups in methylhydrogen silicon oil act as functional groups that can chemically bond to the surface of powders, imparting hydrophobic properties to the coating material. Figure 2 shows the chemical structures of polydimethylsiloxane and methylhydrogen silicon oil and Table 2 provides details on the differences between them.

*Fig. 2: Chemical Structure of the Silicone oil*

| Silicone Oil | Properties |
|---|---|
| Polydimethylsiloxane | - Smoothing the surface , Enhancing color<br>- Water repellency , Compressibility, Compatibility<br>- Low environmental pollution and fire hazard<br>- Low surface tension, Excellent heat stability<br>- Odorless, tasteless, and non-toxic, water Solubility |
| Methylhydrogen Silicone Oil | - Water repellent treatment of powders and other particulate materials to achieve water repellency and excellent flowability while reducing agglomeration.<br>- Formulation of water repellent and hybrid coatings.<br>- Use of flexibilizers or water repellent treatments.<br>- Production of chemically reactive silicones and silicone copolymers.<br>- Acting as crosslinking agents and chain extenders |

*Table. 2: The Properties of Silicone Oil*

$$CaO + H_2O \rightarrow Ca(OH)_2 \qquad (1)$$
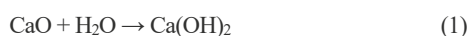
Calcium hydroxide causes scaling inside the injection pipeline, hindering accurate dosing and prolonging the injection time, thereby reducing operational efficiency. Moreover, it may result in significant accidents where the fluid overflows outside the furnace.

**Coating Device**

A typical equipment used for dry surface treatment of powders is a hansel mixer. The author also considered using a hansel mixer but due to insufficient productivity, a self-designed equipment was developed as follows.
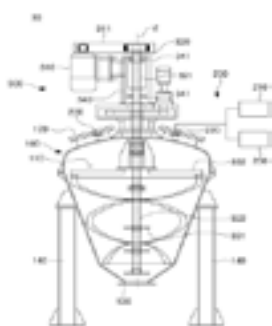


*Fig. 3: Dry coating device for quicklime*

| | | |
|---|---|---|
| 100: Chamber (2.5 m³) | 110: Interior space | 200: Spray unit |
| 210: Oil supply unit | 220: Spray nozzle | 230: Gas supply unit |
| 300: Mixing unit | 310: Drive motor | 320: Shaft |
| 330: Impeller unit | 340: Frame | |
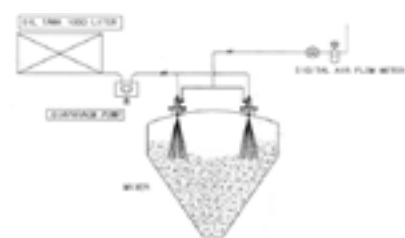


*Fig. 4: Silicone Oil Nozzle Spray System*

**Experimental method**

Put uncoated quicklime into chamber (100) and agitate while injecting silicone oil through a nozzle. Control the amount of silicone oil injection with the rotation speed of the diaphragm pump shown in Fig. 3. The injection pressure should be between 2 to 3 kgf/cm² and regulated by the air pressure. Operate the stirring speed (300) between 800 to 1,200 rpm. Below 800 ppm, the quicklime will not be properly agitated, resulting in uneven coating. Above 1200 rpm, the device will vibrate, produce noise, and overload.

After dry coating the powder with silicone oil, a curing process is necessary. Without the curing process, the oil will remain on the surface of the powder, making the coating film easily damaged even with light impact. Additionally, oil components can be adsorbed onto transfer pipes, leading to contamination issues. However, performing the curing process can reduce productivity and incur additional costs. In this study, during the dry coating process, the high stirring speed causes collisions between the quicklime particles, generating heat and naturally raising the chamber temperature above 80°C. This temperature increase allows for natural curing of the coated silicone oil, eliminating the need for a separate curing process. If necessary, the chamber can be thermally insulated to prevent heat dissipation.

The coating time is approximately 8 minutes when 0.3wt% silicone oil is injected. In order to provide curing functionality, an additional 32 minutes of stirring was performed for coating uniformity and stabilization purposes.

**RESULTS AND DISCUSSION**

**Viscosity of the silicone oil**

To ensure uniformity in spraying, the viscosity of silicone oil should be low. In one example, the viscosity of silicone oil can range from 20 to 100 cps. Viscosity above 100 cps can lead to poorer spray uniformity, while viscosity below 20 cps can result in reduced water repellency.

**Hydrogen Content (%) in the silicone oil**

The author investigated the moisture resistance of quicklime treated with surface-coated oil with varying hydrogen concentrations. The conclusion is that the minimum hydrogen concentration should be at least 1.4% to achieve adequate moisture resistance. Figure 5 demonstrates the impact of hydrogen concentration on the moisture variation of quicklime.
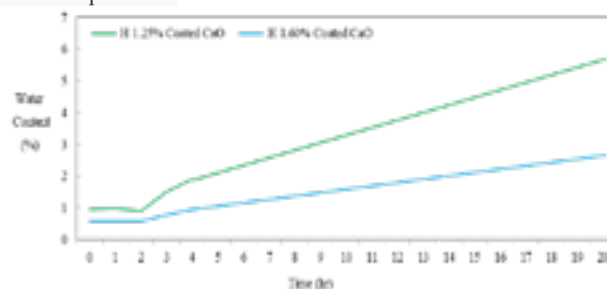


*Fig. 5: Moisture increase rate over time of quicklime according to hydrogen concentration. (25°C, Relative humidity 75%)*

**Flowability**

We have reviewed the amount of silicone oil coating on the quicklime. Insufficient coating of silicone oil leads to decreased flow characteristics

and moisture repellency. On the other hand, if it is excessive, it causes an increase in cost. The most appropriate oil coating amount for quicklime is 0.3~0.5wt%. If it is below 0.3 wt%, the moisture repellency decreases, and the quicklime absorbs moisture, converting to calcium hydroxide. This can result in process troubles such as pipe clogging when injected into the lower part of the furnace. Additionally, the flowability of the quicklime powder decreases. The flowability of the powder is evaluated using the angle of repose. The lower the angle of repose, the better the flowability of the powder. As the silicone oil coating amount increases, the angle of repose decreases, but it reaches a constant value at 0.5wt% or higher. Table 3 provides the data of the angle of repose according to the silicone oil coating amount.

| silicone oil coating amount, % | 0 | 0.1 | 0.3 | 0.5 | 0.7 | 0.9 |
|---|---|---|---|---|---|---|
| Angle of repose, ° | 61 | 55 | 43 | 42 | 41 | 41 |

*Table. 3: The change in angle of repose of limestone with respect to the amount of silicone oil coating.*

## CONCLUSIONS

Research is underway in various fields worldwide to reduce the emission of carbon dioxide, the main contributor to greenhouse gases. Among the industrial sectors, the steel industry is known to have the highest carbon dioxide emissions. It is generally understood that producing one ton of steel results in the emission of two tons of carbon dioxide. In the steel field, research is being conducted on technologies such as hydrogen reduction ironmaking and furnace modification to reduce carbon dioxide emissions. However, it is expected that it will take some time for these technologies to be fully developed. Therefore, reducing the use of molten steel and increasing the use of iron scrap are realistic alternatives to reduce carbon dioxide emissions. The silicon oil-coated quicklime, which is the result of this study, has excellent fluidity and water repellency compared to ordinary quicklime when used in a bottom blowing furnace

418

## REFERENCES

[1]   Journal of the Korean Applied Science and Technology, Vol. 36, No.2. June, 2019. 508~516

[2]   Appl.Chem.Eng., Vol.27, No.3, June 2016, 299~306

[3]   J. Of korean Inst. of Resources Recycling Vol. 12, No. 1, 2003, 41~47

# DEVELOPMENT OF AL$_2$O$_3$–MGO–C REFRACTORIES CONTAINING LIGHTWEIGHT TABULAR ALUMINA AGGREGATES USED FOR STEEL LADLES

Qilong Chen, Tianqing Li*, Jie Gao, Qixiu Zuo, Qian Zhang
Puyang Refractories Group Co., Ltd., Puyang, China

## ABSTRACT

The lightweight of ladle lining refractories is of great significance to energy saving and consumption reduction. In this work, the lightweight alumina aggregates were selected to partially replace traditional tabular alumina aggregates to prepare lightweight Al$_2$O$_3$-MgO-C refractories used for steel ladle linings. And, the influence of lightweight alumina aggregates on the comprehensive properties of Al$_2$O$_3$-MgO-C refractories was investigated in detail. The results illustrated that the introduction of lightweight alumina aggregates can improve the strength of Al$_2$O$_3$-MgO-C refractories, due to the optimized interface bonding between aggregates and matrix. In addition, the thermal shock resistance of Al$_2$O$_3$-MgO-C refractories was also enhanced after adding lightweight alumina aggregates, which should be attributed to that the addition of lightweight alumina aggregates reduced the thermal expansion coefficient of such refractories, and micron-sized pores of lightweight alumina aggregates absorbed partial thermal stresses during thermal shock test. Furthermore, the addition of lightweight alumina aggregates improved the slag corrosion resistance of Al$_2$O$_3$-MgO-C refractories remarkably, which can be ascribed to the formation of continuous CA$_6$ protective layer and densified matrix.

## INTRODUCTION

Al$_2$O$_3$-MgO-C (AMC) refractories are mainly used as the working linings of steel ladle due to their superior hot mechanical properties, thermal shock resistance and slag corrosion resistance [1]. Different from traditional MgO-C and Al$_2$O$_3$-C refractories, Al$_2$O$_3$-MgO-C refractories were able to close the joints of working linings effectively by sustainable in-situ formation of MgAl$_2$O$_4$ spinel during their service life, which impeded the further corrosion and penetration of aggressive slag and enhanced overall integrity of refractory linings [2].

In recent years, with the growing demand for reduction of ladle heat loss, lightweight ladle working lining refractories with low thermal conductivity and bulk density was proposed, which was expected to decrease the ladle heat loss and specific refractory consumption per ton of steel [3]. However, ladle working lining refractories were inevitable to suffer from slag erosion, frequent thermal shocks and mechanical impacts of hot metal during ladle operation. Thus, the lightweight refractories were required to possess better comprehensive properties, especially the slag corrosion resistance and thermal shock resistance to guarantee the safety of steel ladle.

Taking the large proportion of alumina aggregates in the composition of Al$_2$O$_3$-MgO-C refractories, it was feasible to prepare lightweight refractories by introducing lightweight alumina aggregates into such refractories. Nevertheless, very limited reports about the application of lightweight alumina aggregates in Al$_2$O$_3$-MgO-C refractories are available at present, especially the comprehensive study on the thermal shock resistance and slag corrosion resistance of lightweight AMC refractories. Therefore, lightweight alumina aggregates were chosen to replace common tabular alumina aggregates of the Al$_2$O$_3$-MgO-C refractories in the current work, and the effects on the phase compositions, microstructure, mechanical properties, thermal shock resistance and slag corrosion resistance were studied.

## EXPERIMENTAL

Common tabular alumina (Al$_2$O$_3$≥99wt%, namely TA, Haicheng, China) and lightweight porous alumina aggregates (Al$_2$O$_3$≥99wt%, namely PA, Haicheng, China) were used in this experiment. The phase compositions of two series of alumina aggregates were shown in Figure 1. It was found that the two types of alumina

aggregates possessed similar chemical composition and phase compositions. In addition to the main corundum phase, a small amount of β-Al$_2$O$_3$ phase can also be observed in XRD patterns of TA and PA aggregates. The SEM images of TA and PA aggregates were exhibited in Figure 2. As shown, more numerous micro-sized pores were uniformly distributed in PA aggregates, while relatively few pores were observed in TA aggregates. Meanwhile, the pore size of PA aggregates was slightly lower than that of TA aggregates. Compared to TA aggregates, PA aggregates showed higher apparent porosity (7.3%), lower bulk density (3.44 g/cm$^3$) and lower true density (3.85 g/cm$^3$) as listed in Table 1.
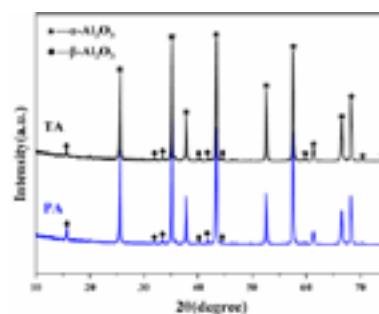


*Fig. 1: XRD patterns of tabular alumina and porous alumina aggregates.*
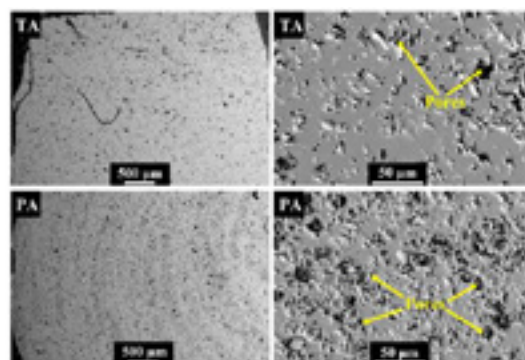


*Fig. 2: SEM images of tabular alumina and porous alumina aggregates.*

Tab. 1: The physical properties of alumina aggregates.

| Index | TA | PA |
|---|---|---|
| Apparent porosity (%) | 3.4 | 7.3 |
| Closed porosity (%) | 3.6 | 3.3 |
| Total porosity (%) | 7.0 | 10.6 |
| Water absorption (%) | 0.9 | 2.1 |
| Bulk density (g/cm$^3$) | 3.59 | 3.44 |
| True density (g/cm$^3$) | 3.86 | 3.85 |

Three series of Al$_2$O$_3$-MgO-C refractories containing different content of porous alumina aggregates were designed according to the initial particle grading. Specifically, 0, 15wt% and 32wt% PA aggregates were introduced to Al$_2$O$_3$-MgO-C refractories, and named them TC, LC1 and LC2 respectively. All series mentioned above are maintained the same particle grading, equal flake graphite (6wt% C) and antioxidant (1wt% Al). The liquid phenolic resin was chosen as the binder, and their amount was 3wt% (additionally added). Also, 5wt% magnesia aggregates were selected as the raw materials of specimens to provide MgO.

The raw materials were set in the mixer and mixed evenly for 20 min. Then, the rectangular bricks (300 mm×150 mm×100 mm) were fabricated by using friction press (600 t). After that, the bricks were tempered at 200 °C for 10 h and processed into standard specimens with required shape and size. Finally, the $Al_2O_3$-MgO-C samples were coked at 1600 °C for 3 h.

The apparent porosity and bulk density of $Al_2O_3$-MgO-C specimen after treating at different temperatures were measured based on the Archimedes' Principle with kerosene as medium. The cold compressive strength (CCS) of specimens was tested using an electronic digital control system. In order to obtain the hot modulus of rupture (HMOR), the bar specimens tempered at 200 °C were examined under coking atmosphere at 1450 °C for 0.5 h based on the three-point bending test.

The cubic specimens coked at 1600 °C were used to evaluate the thermal shock resistance of refractories by cyclic air-quenching method. These specimens were set in the 1100°C furnace for 30 min under air atmosphere. Then, these cubes were immediately placed at room temperature to cool for 5 min. After repeating the above process three times, the CCS and residual strength ratio of specimens were obtained. Also, the thermal expansion coefficient of $Al_2O_3$-MgO-C specimen tempered at 200 °C was determined according to push rod method using the thermal dilatometer.

Static cup method was adopted to determine the slag corrosion resistance of $Al_2O_3$-MgO-C refractories. 25 g of the slag ($CaO/SiO_2$=2.40) was placed into the hole of the crucible samples cured 200 °C. Then, the crucible samples were treated at 1600 °C for 3 h under air atmosphere.

## RESULTS AND DISCUSSION

### Phase compositions and microstructures

The phase compositions of different $Al_2O_3$-MgO-C specimens after treated at 200 °C and 1600 °C were shown in Figure 3. It was found that the phase evolution of all samples showed the same change with increase of the heating temperature, indicating that addition of PA aggregates had no obvious influence in the phase compositions of the $Al_2O_3$-MgO-C specimens. Specifically, $\alpha$-$Al_2O_3$, periclase, graphite, Al and a small amount of $\beta$-$Al_2O_3$ derived from the raw materials were found in all specimens tempered at 200 °C. When the heating temperature was increased to 1600 °C, the new $MgAl_2O_4$ phase was formed while the diffraction peaks of the original Al phase were not detected, indicating that the Al phase should be completely transformed to Al-containing ceramic phases under coking atmosphere, such as $MgAl_2O_4$ and AlN [4]. Meanwhile, the sustainable in-situ reaction between MgO and $Al_2O_3$ in $Al_2O_3$-MgO-C system was promoted, which also led to the formation of more $MgAl_2O_4$.
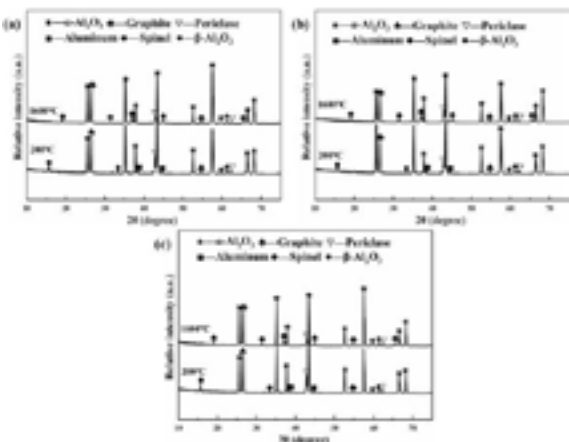


*Fig. 3: XRD patterns of the $Al_2O_3$-MgO-C specimens: (a)TC; (b)LC1 and (c) LC2.*

The microstructure of polished $Al_2O_3$-MgO-C specimen tempered at 200 °C were shown in Figure 4. The obvious difference lied in the bonding interface between the aggregates and matrix. In TC specimen, a number of gaps were found at the edges of common tabular alumina aggregates, indicating the poor bonding between TA aggregates and the matrix. Different from TC specimen, LC1 and LC2 specimen containing lightweight alumina aggregates showed optimized interface. Noteworthy, the indistinguishable interfaces between the aggregates and matrix were observed in such specimens, which was attributed that PA aggregates with rough surface were more likely to form interlocking structures with the matrix [5].
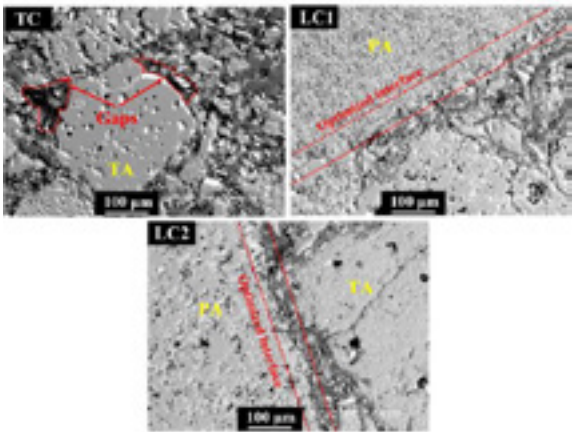


*Fig. 4: SEM images of polished $Al_2O_3$-MgO-C specimens tempered at 200 °C.*

### Physical properties and mechanical properties

The physical properties and strength of $Al_2O_3$-MgO-C refractories after treated at different temperatures were listed in Table 2. It was not difficult to find that all the specimen tempered at 200 °C showed the lowest apparent porosity and the highest bulk density. After heating treatment at 1600 °C, the apparent porosity of all the specimen increased sharply and their strength also decreased. Instead of organic bonding, a synergistic combination of graphite and ceramic reinforced phases was formed in AMC specimen, which was due to the pyrolysis of resin and in-situ chemical reactions [6]. As expected, both LC1 and LC2 specimen showed higher apparent porosity and lower bulk density due to addition of lightweight porous aggregates. Interestingly, the $Al_2O_3$-MgO-C specimen containing 32wt% PA aggregates had the highest strength, and their strength reached 63.4 MPa and 37.8 MPa after treated at 200 °C and 1600 °C, respectively. Similarly, the HMOR of different specimen exhibited the same change with the increase of PA aggregates content as depicted in Figure 5. Therefore, it can be believed that the introduction of lightweight alumina aggregates led to the enhanced mechanical properties of $Al_2O_3$-MgO-C refractories by forming optimized interface. Meanwhile, the larger contact area between porous alumina aggregates and matrix might contribute to the formation of the sintering neck at elevated temperatures, which facilitated the sintering process and ultimately improved the strength of such refractories [7].

Tab. 2: The physical properties and mechanical properties of $Al_2O_3$-MgO-C specimens.

| T | Index | TC | LC1 | LC2 |
|---|---|---|---|---|
| | AP (%) | 5.5±0.1 | 6.7±0.3 | 7.0±0.2 |
| 200°C | BD (g/cm³) | 3.25±0.01 | 3.20±0.01 | 3.19±0.02 |
| | CCS (MPa) | 57.7±3.6 | 59.7±1.6 | 63.4±0.8 |
| | AP (%) | 14.4±0.1 | 15.1±0.1 | 15.4±0.1 |
| 1600°C | BD (g/cm³) | 3.12±0.02 | 3.08±0.01 | 3.04±0.01 |
| | CCS (MPa) | 31.9±2.2 | 33.1±1.4 | 37.8±0.2 |
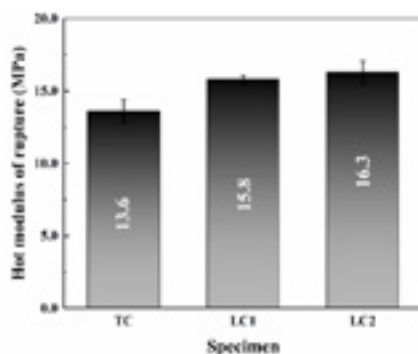
*Fig. 5: The HMOR (1450 °C×0.5 h) of Al₂O₃-MgO-C specimens.*

**Thermal shock resistance**

The thermal shock resistance of different Al₂O₃-MgO-C refractories coked at 1600 °C was provided in Figure 6. It can be clearly seen that the LC1 (29.1 MPa) and LC2 specimen (29.9 MPa) containing PA aggregates showed higher CCS than TC specimen (27.4 MPa) after thermal shocks. Meanwhile, the AMC specimen containing 15wt% lightweight alumina aggregates had the highest residual strength index (87.9%), indicating that the improved thermal shock resistance of AMC refractories could be obtained by adding proper content of lightweight alumina aggregates. However, AMC specimen with 32wt% PA aggregates showed poor thermal shock resistance, which might result from LC2 specimen with high apparent porosity suffered from the more aggressive oxidative damage during the thermal shock test.
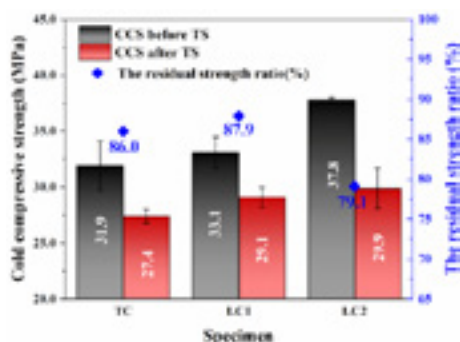


*Fig. 6: The CCS of Al₂O₃-MgO-C specimens before and after thermal shocks and their residual strength ratio.*

The expansion of different Al₂O₃-MgO-C specimens were given in Figure 7. It can be seen that there were little obvious differences in the thermal expansion rates between different AMC specimens below 1000 °C (Figure. 7(a)). As for the thermal expansion rates of AMC refractories from 1000 °C to 1250 °C (Figure. 7(b)), LC1 and LC2 specimen had lower thermal expansion rates than TC specimen. The above results demonstrated that the thermal expansion coefficient of AMC refractories was decreased effectively, which provided key evidence for the better thermal shock resistance of AMC refractories containing lightweight alumina aggregates. Meanwhile, a large number of micro-sized pores in PA aggregates might also be beneficial to absorbing the thermal stresses in the materials [8].
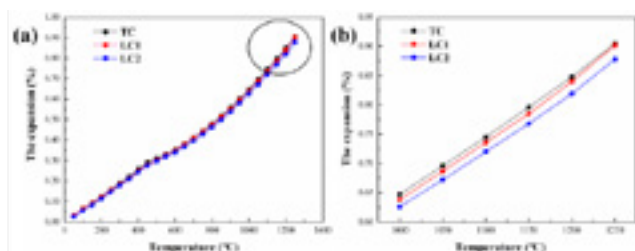


*Fig. 7: The thermal expansion of different Al₂O₃-MgO-C specimens.*

**Slag corrosion resistance**

In order to investigate the influence of lightweight aggregates on the slag resistance of AMC refractories, the cross-sections of specimens after slag corrosion test and corresponding slag corrosion index were diagrammed in Figure 8 and Figure 9, respectively. With the increase of lightweight alumina aggregate content, the slag corrosion index of the AMC specimen decreased first and then increased. The specimen containing 15wt% PA aggregates showed the lowest slag corrosion index (3.8%), indicating that the slag resistance of Al₂O₃-MgO-C refractories can be improved after adding proper content of lightweight alumina aggregates.
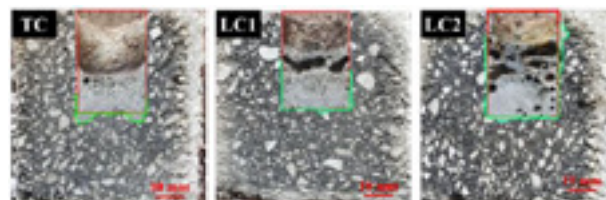


*Fig. 8: Cross-sections of different Al₂O₃-MgO-C specimens after slag corrosion test.*
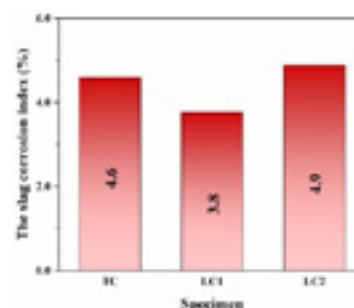


*Fig. 9: The slag corrosion index of Al₂O₃-MgO-C specimens.*

Figure 10 illustrated the microstructure of different Al₂O₃-MgO-C specimens after slag corrosion test. The EDS results of relevant points in Figure 10 were also listed in Table 3 to analyze the possible reaction products. As for the SEM images of corroded AMC specimens (Figure 10), the yellow circles and arrows referred to pores and cracks, respectively, and the obvious stratified structure was observed in all specimens. With the increase of distance from the hot face, it can be divided into slag layer, reaction layer and origin layer in all Al₂O₃-MgO-C specimens (as shown by the red and white lines). Apparently, the largest differences between such specimen lied in the following two aspects: (1) the continuity and densification of the reaction layer; (2) the distribution and the number of the pores and cracks in the origin layer. In TC specimen (Fig. 10(a)), the structure of some common alumina aggregates has been damaged seriously due to the dissolution of alumina to the slag. Meanwhile, the relatively dense protective CA₆ layer (Point 1) on the surface of alumina aggregates and MgAl₂O₄ spinel were formed by reacting with the slag, which prevented the further penetration of the slag. In addition, a large number of pores and cracks were found in TC specimen, especially at the interface between the common alumina aggregates and the matrix, indicating the poor bonding and relatively loose matrix. In LC2 specimen (Figure 10(b)), the number of cracks and pores in the origin layer decreased obviously due to the optimized interface. But many widely distributed pores were observed in the reaction layer, even though CA₆ layer (point 3) also formed at the surface of the lightweight alumina aggregates. It was considered that the loose decarburization layer containing numerous pores might weaken the isolation effect of CA₆ layer, leading to the poor slag resistance of LC2 specimen. Different from TC and LC2 specimen, LC1 specimen (Figure 10(c-d)) possessed the continuous and dense CA₆ isolation layer (Point 4). Combined with the mapping results, the CA₆ isolation layer formed on the surface of lightweight alumina aggregates bonded tightly with the slag layer, which effectively

421

impeded the penetration of slag into the relatively weak matrix. Considering the PA aggregates had relatively lower mean pore size demonstrated by the microstructure, $CA_6$ phase with high melting point was easier to precipitate during the interaction between the slag and PA aggregates [9], which provided favorable conditions for the formation of continuous dense protective layer at the hot face of the $Al_2O_3$-MgO-C refractories. Hence, the formation of continuous $CA_6$ isolation layer and the densified matrix should be responsible for the better slag resistance of $Al_2O_3$-MgO-C refractories containing 15wt% lightweight alumina aggregates.
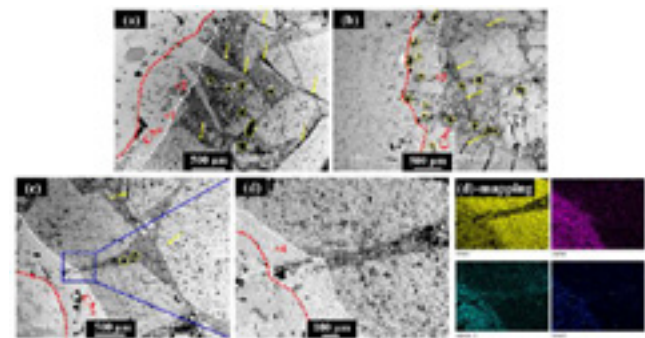


*Fig. 10: The SEM images of $Al_2O_3$-MgO-C specimens after slag corrosion test: (a) TC; (b) LC2 and (c-d) LC1.*

Tab. 3: EDS results of points in Figure 10 (wt%).

| Element | O | Al | Mg | Ca | Possible phase |
|---------|-------|-------|-------|------|----------------|
| Point 1 | 44.79 | 46.42 | - | 8.79 | $CA_6$ |
| Point 2 | 45.09 | 38.74 | 16.16 | - | MA |
| Point 3 | 44.91 | 46.75 | - | 8.34 | $CA_6$ |
| Point 4 | 44.92 | 46.77 | - | 8.31 | $CA_6$ |

## CONCLUSIONS

The effects of lightweight tabular alumina aggregates addition on the phase compositions, microstructure, mechanical properties, thermal shock resistance and slag corrosion resistance of $Al_2O_3$-MgO-C refractories were investigated. The following conclusions were made.

(1) The addition of lightweight aggregates had no obvious effect on the phase composition of AMC refractories, but they could effectively optimize the boding interface between the aggregates and matrix due to their rough surface and more pores, which enhanced the strength of the $Al_2O_3$-MgO-C refractories.

(2) The lightweight $Al_2O_3$-MgO-C refractories possessed better thermal shock resistance, which was related with the decrease of thermal expansion coefficient and thermal stress absorption of a large number of micron-sized pores.

(3) The dense and continuous $CA_6$ isolation layer was formed between the slag layer and the origin layer in lightweight $Al_2O_3$-MgO-C refractories after slag corrosion test. Moreover, lightweight alumina aggregates containing $Al_2O_3$-MgO-C refractories presented denser matrix, which could prohibit the further penetration of slag. Consequently, the lightweight AMC refractories achieved better slag corrosion resistance.

## REFERENCES

[1] S.M. Tabatabaie-Hedeshi, M. Bavand-vandchali, R. Naghizadeh. Characterization and post-mortem analysis of $Al_2O_3$-MgO-C refractories used in steelmaking ladle furnaces. Engineering Failure Analysis. 116, 2020, p. 104697-104712.

[2] V. Muñoz, P. Pena, A. G. T. Martínez. Physical, chemical and thermal characterization of alumina–magnesia–carbon refractories. Ceramics International. 40 (7), 2014, p. 9133-9149.

[3] M.F. Santos, M.H. Moreira, M.G.G. Campos, P.I.B.G.B. Pelissari, R.A. Angélico, E.Y. Sako, S. Sinnema, V.C. Pandolfelli. Enhanced numerical tool to evaluate steel ladle

thermal losses. Ceramics International. 44 (11), 2018, p. 12831-12840.

[4] T. Zhu, Y. Li, S. Sang, Z. Xie. Formation of nanocarbon structures in MgO–C refractories matrix: Influence of Al and Si additives. Ceramics International. 42 (16), 2016, p. 18833-18843.

[5] Z. Chen, W. Yan, S. Schafföner, S. Ma, Y. Dai, N. Li. Effect of SiC powder content on lightweight corundum-magnesium aluminate spinel castables. Journal of Alloys and Compounds. 764, 2018, p. 210-215.

[6] Y. Cheng, T. Zhu, Y. Li, S. Sang. Microstructure and properties of MgO-C refractory with different carbon contents. Ceramics International. 47 (2), 2021, p. 2538-2546.

[7] L. Fu, H. Gu, A. Huang, S. Or, Y. Zou, Y. Zou, M. Zhang. Design, fabrication and properties of lightweight wear lining refractories: A review. Journal of European Ceramic Society. 42 (3), 2022, p. 744-763.

[8] Q. Chen, Y. Li, T. Zhu, Y. Xu, Y. Li, X. Wang. Improved thermal shock resistance of MgO–C refractories with addition of calcium magnesium aluminate (CMA) aggregates. Ceramics International. 48 (2), 2022, p. 2500-2509.

[9] L. Fu, H. Gu, A. Huang, Y. Zou, H. Ni. Enhanced corrosion resistance through the introduction of fine pores: Role of nano-sized intracrystalline pores. Corrosion Science. 161, 2019, p. 108182-108193.

# ANALYSIS OF CORROSION MECHANISMS OF NON−CEMENT AND LOW−CEMENT ALUMINA−MAGNESIA GUNNING MIX WITH SPECIAL CALCINED ALUMINA IN ROTARY SLAG TEST

Y.T. Lee[1], L.T. Chao[1], Hsin Lian Hsin Enterprise Co. Ltd., Kaohsiung, TW
J. Lee[2], ALTEO Alumina, Business development, Taipei, TW
W. Liu[3], Wuhan Ruxing Technology Co., Ltd., Wuhan, CN

## ABSTRACT

$Al_2O_3$-MgO and $Al_2O_3$-spinel low cement castable (LCC-AM and LCC-AS) have been extensively used in steel ladles as working linings. Nevertheless, the use of alumina-magnesia gunning mixes has been mainly kept for maintaining these castable linings, because of high rebound loss, poor green strength, high porosity and short life-span.

Thanks to a MC-G (high BET alumina), it is now possible to develop a series of high-performance non-cement and low-cement alumina-magnesia gunning mixes (NCG-AM and LCG-AM). The paper focuses on the BOF slag resistance of NCG-AM, LCG-AM, LCC-AM and LCC-AS. The corrosion mechanisms of rotary slag specimens are studied by Scanning Electron Microscopy.

The results reveal different microstructure around MgO particles, depending on the four used compositions. Continuous and thicker spinel phases were formed in NCG-AM, which proved to have the best corrosion resistance. It resulted from MC-G made $J_{Al3+}$ larger and hence inhibited Kirkendall porosity around MgO particles. In addition, continuous spinel phase acts like a pinning nail to reinforce the matrix and thus decrease erosion by slag.

In contrast to NCG-AM, we found porous spinel phase around unreacted MgO particles and some particles had been were carried away near the interface of LCC-AM and slag.

The NCG-AM composition with MC-G had been tested in two steel plants, and it extended the service life of the ladles up to 50%. In addition, this study suggests the potential application of NCG-AM as steel ladle linings.

## MATERIALS AND METHODS

As shown in Tab. 1, different compositions were designed to investigate the effects of various factors on the performance of dynamic rotary slag corrosion test.

Tab. 1: General information of the specimen compositions.

| Designed composition | LCC-AM | LCC-AS | NCG-AM | LCG-AM |
|---|---|---|---|---|
| Raw materials | | | | |
| Tabular(d<6mm) | 71 | 59 | 75 | 72 |
| 97-grade fused MgO | 5 | - | 7.5 | 7.5 |
| Alumana rich spinel) | - | 23 | - | - |
| Bimodal Reactive alumina (PBR) (d50:2~4μm) | 19 | 13 | 10 | 5 |
| High BET alumina (MC-G) (d50=5.5μm) | - | - | 7.5 | 7.5 |
| Calcium aluminate cement | 5 | 5 | - | 7.5 |
| Silica fume | 0.2 | - | - | 0.5 |

Dynamic rotary slag corrosion test was carried out to compare the corrosion resistance in following sequence:



Fig. 1: Re-charging the slag

1. Test pieces were prepared using a special casting method and cured for 48 hours at 25°C, followed by drying at 110°C.
2. Converter slag was used for the test, and compotation was shown in Tab.2.
3. Test temperature was at ~1650℃ for 1 hour and re-charging the slag for 6 cycles.

5. After cool down, sample's cross section was then measured to evaluate the corroded depth.

Tab. 2: Converter slag composition(wt%)

| % | CaO | $Al_2O_3$ | $SiO_2$ | $Fe_2O_3$ | MgO | $MnO_2$ | $P_2O_5$ |
|---|---|---|---|---|---|---|---|
| % | 49.7 | 2.5 | 6.7 | 26.7 | 7.1 | 2.3 | 3.6 |

The specimen's physical properties were analysed followed in JIS R2205 and R2553. In order to discover the spinel formation and corrosion mechanism, scanning electron microscopy (JEOL JSM-6360) microstructure images and X-ray diffractometer figures (Rigaku miniflex300) of the specimens after dynamic rotary slag corrosion test were attained.

## RESULTS AND DISCUSSION

From Tab.3, NCG-AM gives an outstanding property, its low apparent porosity and high bulk density were similar to LCC-AM and LCC-AS.

Tab. 3: Physical properties of the specimen compositions.

| Designed composition | LCC-AM | LCC-AS | NCG-AM | LCG-AM |
|---|---|---|---|---|
| After dried: | Physical Properties | | | |
| Bulk density(g/cm³) | 3.12 | 3.01 | 3.00 | 2.79 |
| Open porosity (%) | 10 | 18 | 18 | 20 |
| CCS(MPa) | 51 | 30 | 29 | 36 |
| MOR(MPa) | 12 | 4 | 5 | 8 |
| After-firing at 1200℃: | | | | |
| Bulk density(g/cm³) | 3.05 | 3.00 | 3.01 | 2.73 |
| Open porosity (%) | 17 | 19 | 18 | 27 |
| CCS(MPa) | 82 | 91 | 99 | 26 |
| MOR(MPa) | 17 | 21 | 22 | 5 |
| PLC (%) | 0.15 | -0.16 | -0.20 | -0.01 |
| After-firing at 1550℃: | | | | |
| Bulk density(g/cm³) | 2.86 | 2.92 | 2.89 | 2.53 |
| Open porosity (%) | 23 | 20 | 21 | 31 |
| CCS(MPa) | 109 | 82 | 85 | 42 |
| MOR(MPa) | 30 | 24 | 26 | 13 |
| PLC (%) | 2.19 | 0.84 | 0.99 | 2.01 |

**Dynamic rotary slag corrosion test**

According to Fig. 2, the cross-section and thickness loss of the corroded samples are shown. The dotted line indicates the refractory-slag interface from the chamber to the feeding port. NCG-AM had by far the lowest thickness loss, at 7.7mm (85% residual thickness), and the dotted line is relatively straighter than the others.
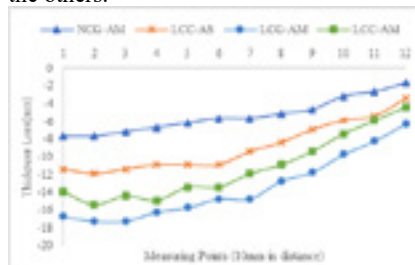


Fig.2: Dynamic rotary slag test result
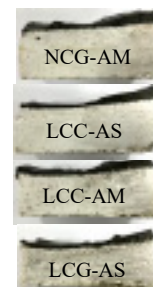
In contrast, LCG-AM and LCC-AM showed much worse corrosion resistance, with thickness losses of 17.24mm (66% residual thickness) and 15.44mm (70% residual thickness) respectively, and the curvature of the dotted line is larger, which indicates different corrosion mechanisms among these samples.

423

## Microstructure characterization
*Uncorroded microstructures*

In Fig. 3(a), the microstructure around the MgO particles of LCC-AM is shown. It consists of MgO particles, a porous spinel phase with an Al/Mg atomic ratio of 1.63:1, a spinel phase with an Al/Mg atomic ratio of 1.96:1 and a matrix phase. Based on the BEI figure, the MgO particles are trapped by a dark region, which is the porous spinel. The diffusion length of $Mg^{2+}$ from the particles is approximately 20μm.

In contrast, a clearly continuous structure was found in NCG-AM, as shown in Fig. 3(c), with $Mg^{2+}$ diffusing further from the MgO particles to the matrix, approximately 50μm. The spinel phase in NCG-AM, which had an Al/Mg atomic ratio of 2.18:1, appeared much brighter in the BEI image compared to LCC-AM, indicating a dense spinel phase.

Fig. 3(d) displays LCG-AM, which has a microstructure similar to NCG-AM but with a shorter $Mg^{2+}$ diffusion distance.
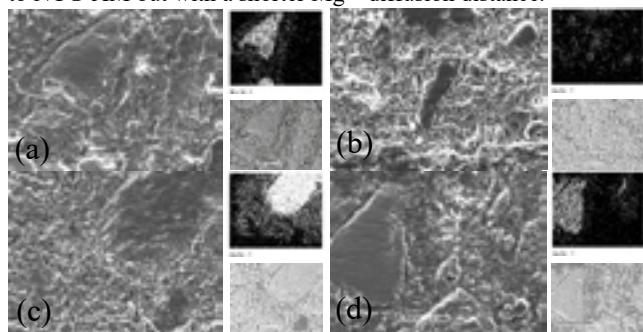


*Fig.3: SEM of uncorroded microstructures, (a)LCC-AM; (b)LCC-AS; (c)NCG-AM; (d)LCG-AM.*

*Corroded microstructures near slag line*

The microstructure of the refractory/slag interface after six rotary tests reveals different corrosion mechanisms among four compositions. These images focus on the reaction of MgO particle in the refractory and slag.

(1) LCC-AM: Fig. 4(a) shows that a MgO particle wrapped up by in-situ spinel was pulled out from the matrix and remained in a hole occupied by slag. The weak bonding between MgO particle and the matrix due to porous spinel was the cause of the evulsion of unreacted MgO particle.

(2) LCC-AS: Although the matrix with spinel grain and tabular alumina both have excellent corrosion resistance, there is relatively weak bonding between them, resulting in the slag penetrating along the interface.

(3) NCG-AM: The original MgO particle was dissolved into the matrix and formed a continuous reaction region that has strong bonding. It indicates that an alumina-rich spinel with an Al/Mg atomic ratio 2.65:1 was detected at the boundary, and higher levels of Si and Ca elements were found in the core compared to the boundary. This suggests that monticellite ($CaMgSiO_4$) may have formed.

(4) LCG-AM: Fig. 4(d) shows that corrosion was more severe in the matrix, and the MgO particle was taken away when the surrounding matrix was lost. The MgO particle was also wrapped up by in-situ spinel, but it was thinner than the others, leaving most of the unreacted particle in the slag.
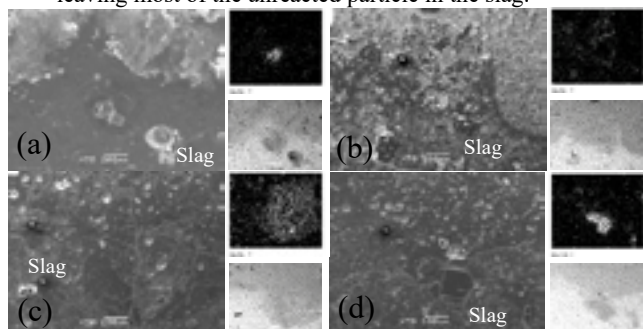


*Fig.4: SEM of corroded microstructures, (a)LCC-AM; (b)LCC-AS; (c)NCG-AM; (d)LCG-AM.*

## Corrosion Mechanisms Model

By comparing the appearance of slag corrosion among different samples, it can be inferred that the bonding strength between MgO particles and the matrix can affect the material's resistance to slag. In the case of the superior performing NCG-AM, the thickest dense spinel layer (~50um) was formed in the non-corroded region, which bound the unreacted MgO particles to the matrix and reduced the possibility of MgO particles detaching from the matrix during slag corrosion. The thicker spinel layer could absorb more manganese and iron ions from the slag, resulting in higher slag viscosity and reducing slag penetration, as shown in Fig. 5(a). Therefore, a distinct interface was maintained between NCG-AM and the slag. This phenomenon provides more time for the unreacted MgO particles to undergo ion diffusion, resulting in the formation of thicker spinel layers, further enhancing the slag resistance performance of NCG-AM.

On the other hand, due to the formation of porous spinel and a thinner spinel layer, LCC-AM experienced more pronounced slag infiltration, causing the MgO particles to be washed away and leaving behind holes. This led to a higher degree of erosion in LCC-AM compared to NCG-AM, as shown in Fig. 5(b).
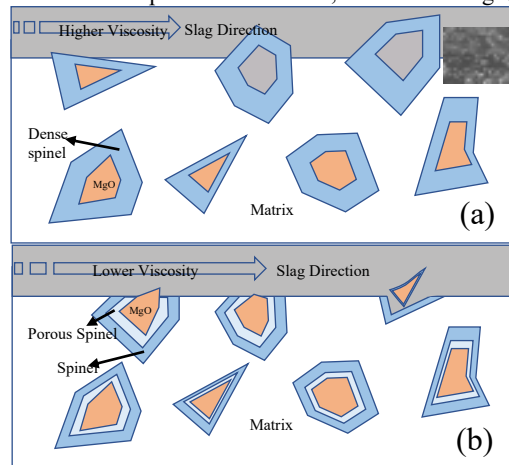


*Fig. 5: Corrosion mechanisms model of (a)NCG-AM; (b)LCC-AM*

## What is the main cause of the porous spinel in LCC-AM?

According to E.Y. Sako et al. [1], the faster mobility of $Mg^{2+}$ ions and their reaction with a higher thickness ratio seem to induce the Kirkendall effect during in-situ spinel formation, especially with MgO <45um. They finished the slag attack experiment using a cylindrical container after firing it at 1500°C for 5 hours, which relatively provided a homogeneous temperature field and sufficient time for ion diffusion to form in-situ spinel. Thus, they discovered remaining pores. On the other hand, a dynamic rotary slag corrosion test was carried out with dried specimens under quick heating, reaching 1450°C within 1 hour and kept around 1650~1700°C during the experiment. This may have made the ions diffuse rapidly, especially $Mg^{2+}$, thus resulting in a high-porosity spinel region around the MgO particles.

On the other hand, NCG-AM and LCG-AM, which had the addition of MC-G, do not exhibit such phenomenon. It is speculated that alumina with high specific surface area can provide a larger flux of $Al^{3+}$ in terms of kinetics, reducing the diffusion rate difference between $Mg^{2+}$ and $Al^{3+}$ ions to avoid the generation of high-porosity spinel region around MgO particles.

## CONCLUSIONS

NCG-AM had the superior performance with the thickest dense spinel layer (~50um) in the non-corroded region, which bound the unreacted MgO particles to the matrix and reduced the possibility of MgO particles detaching from the matrix during slag corrosion.

## REFERENCES

[1]  E. Y. Sako, Fundamentals and applications on in situ spinel formation mechanisms in Al2O3–MgO refractory castables, Ceramic International, 2012, pp. 2243~2251.

# MICROSTRUCTURAL EVOLUTION AND CORROSION BEHAVIOR OF REBOUNDED MAGNESIA–CHROMITE REFRACTORIES USED IN STEELMAKING RH FURNACES

M. Khanzadeh jouryabi[1,3], M. Bavand-vandchali[1,3], A. Kazemi-nafchi[1], S.M. Tabatabaie-hedeshi[2,3]

1.Department of Materials Engineering, Science and Research Branch, Islamic Azad University, Tehran, Iran.
2.Materials Engineering Department, Imam Khomeini International University, Qazvin, Iran.
3.Almas Alborz Refractory Co., Tehran, Iran.

## ABSTRACT

In the Ruhrstahl Heraeus (RH) furnaces during vacuum-degassing process, the amount of impurities such as solved gases and carbon decreased. The magnesia-chromite refractories used as lining of RH furnaces exposed to the severe thermo-mechanical and chemical stresses which can have a critical role in the final quality of molten steel[1-2].

In the present study, microstructure and corrosion behaviour of magnesia-chromite refractories used as working lining in the RH furnaces evaluated.
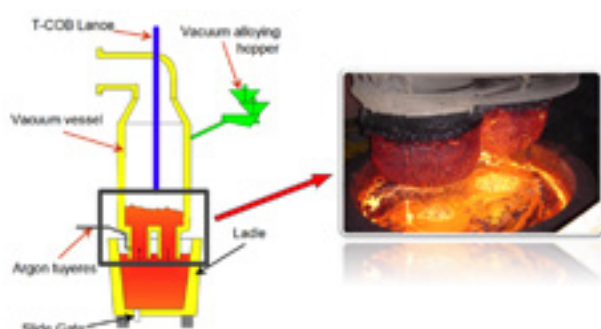
## Research materials and methods

chemical and phase analysis of the samples were taken from different reaction zone in the current research, a magnesia-chromite rebounded refractory produced by RHI Company used in the RH furnace of Mobarakeh Steel Company (MSCo.) has been considered.

## Chemical and phase analysis of refractory sample

The chemical analysis of the examined refractory from the RH furnace is given in Table 1.

*Tab. 1: Chemical analysis of refractory sample.*

| Oxide | MgO | $Cr_2O_3$ | $Al_2O_3$ | $Fe_2O_3$ | CaO | $SiO_2$ |
|-------|-----|-----------|-----------|-----------|-----|---------|
| % | 64 | 18 | 2.6 | 8.6 | 1.15 | 0.6 |

One of the important issues in the production of magnesia-chromite refractories is the low percentage of SiO2, which should be less than 1%. Regarding magnesia-chromite refractories that are used for furnaces such as the RH furnace of steelmaking. The high percentage of SiO2 above 1% due to the formation of calcium silicate phases causes the connection between periclase crystals in co-clinker aggregates, as well as the connection between coclinker particles and chromite particles to move towards quasi-silicate and silicate connections [3-5]. Due to the low melting temperature of these phases, this can cause a decrease in the thermomechanical properties of the refractory, such as hot bending strength, creep and finally increase the corrosion rate [6-7].

Fig. 1 shows the X-ray diffraction pattern of the rebounded magnesia-chromite refractory sample. Chemical analysis of this sample also showed that it contains 0.6% SiO2 (Table 1). Therefore, we cannot expect to detect a small amount of silicate phases in the XRD pattern. A closer examination of the peaks with high spinel intensity shows that the MgAl2O4 spinel ratio has some peak shift (2θ in the 100 MgAl2O4 peak is about 36.1° and in (Mg,Fe)(Cr,Al,Fe)2O4 spinel, 2θ is about 74/36°) which is due to

the dissolution of Fe, Al and Cr ions inside the normal spinel structure and the presence of complex spinel in the structure.
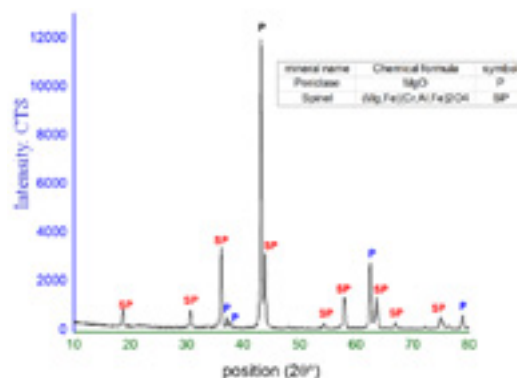


*Fig. 1: X-ray diffraction pattern of refractory sample.*

## Chemical and phase analysis of refractory sample

Fig. 2 shows the microstructure of the healthy refractory sample. As can be seen, the white chromite particles are placed between the large and small co-clinker particles and the interconnected background caused by the sintering of the fine magnesia co-clinker particles.
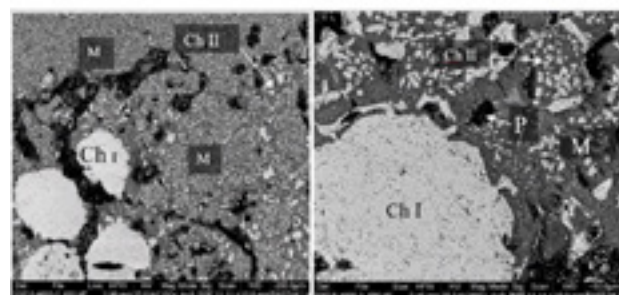


*Fig. 2: Microstructure of magnesia-chromite sample- M: MgO Coclinker; Ch I: primary chromite; Ch II: Secondary chromite.*
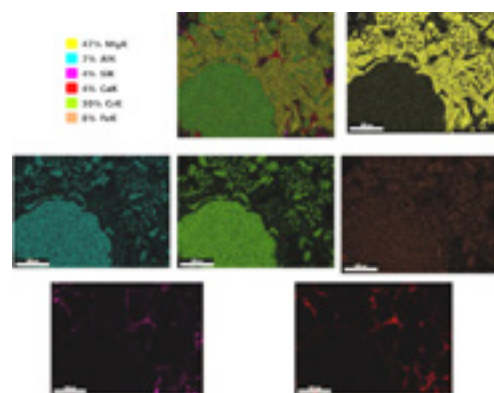


*Fig. 3: Map analysis of magnesia-chromite sample in Fig.2.*

Examining magnesia coclinker particles also shows that bright spots are formed in three separate areas. The EDS analysis performed on these areas shows that these areas have spinel complex compounds (Fe, Mg)(Fe, Al, Cr)2O4. SP2 and SP3 spinel

425

phases, in addition to being located in magnesia aggregates in the regions of grain boundaries and triple points, are also formed between magnesia and chromite particles and the boundary between them.
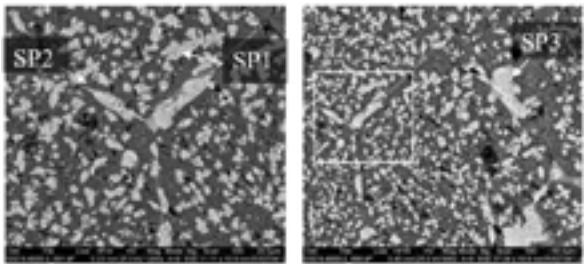


*Fig. 4: different types of spinel formed in microstructure. SP1: intragranular spinel, SP2: grain boundary spinel, SP3: triple zone spinel.*

The presence and accumulation of areas with a very bright and white contrast in the inner areas of the sample, as shown in Fig 6, indicates the penetration of molten steel into the refractory due to its low viscosity. The penetration of melt and slag into the refractories has been well done due to the presence of existing discontinuities in the refractories field, which leads to the filling of the pores, therefore, due to the penetration in the layer, the coefficient of thermal expansion will change compared to the healthy part of the refractories sample. In alternating thermal cycles and due to uneven expansion and contraction in this area, transverse cracks are created, which can be clearly seen in Fig 5.
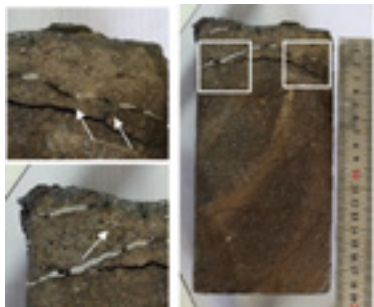


*Fig. 5: Corroded refractory sample of RH degassing furnace.*

Fig 6 shows the microstructure of the reaction interface between the slag refractory and the steel melt.
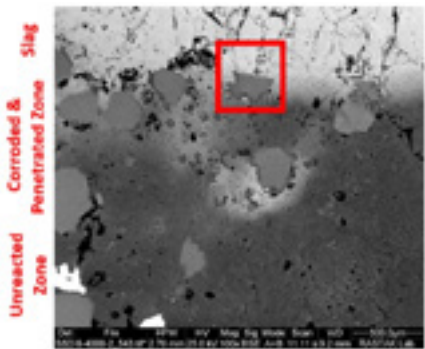


*Fig. 6: Micrograph of refractory/slag interact area*

Fig 7 shows this reaction interface at a higher magnification. As can be seen, on the left side of the image, a particle of chromite (Ch) and next to it a coclinker aggregate is shown, which has reacted with melt and slag.

Fig 8 shows the reaction between coclinker magnesia and molten slag in two different magnifications. As a result of the reaction of the aggregate with the molten slag, a continuous magnesian phase

has formed in the aggregate, and as a result of the reaction of the molten slag and the spinel phases.
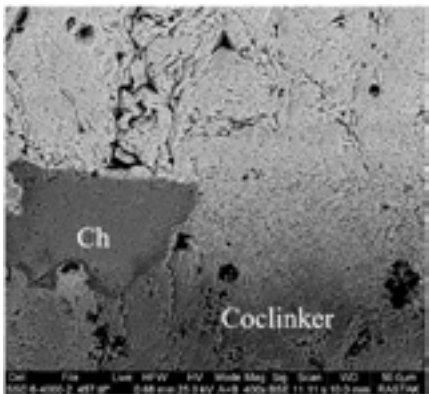


*Fig. 7: Co-clinker & chromite grains corrosion.*
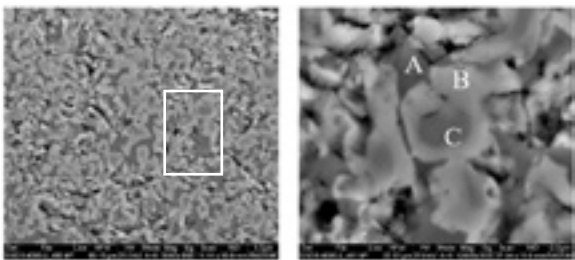


*Fig. 8: Reaction products due to chromite grains corrosion.*

*Tab. 2: Oxidative analysis of different areas marked in Fig. 8*

| Element | Wt % | | |
|---|---|---|---|
| | A | B | C |
| MgO | 59 | 17.01 | 17.9 |
| $Al_2O_3$ | - | 5.7 | 24.1 |
| $Cr_2O_3$ | 1.4 | 7.8 | 36.3 |
| MnO | 1.5 | 2.2 | 1.9 |
| $Fe_2O_3$ | 38.1 | 65.5 | 19.8 |
| $SiO_2$ | - | 1.3 | - |

Chemical analysis was done and the results are presented in Table 2. Fig 9 shows the image of a chromite aggregate in the reaction zone with melt and slag. Elemental analysis with the help of EDS showed that inside the chromite particle there is an accumulation of small white dots along with small hollow holes. The points with bright contrast are metallic Fe particles and possibly the small uniform holes can be caused by the decomposition of a component in the chromite structure.
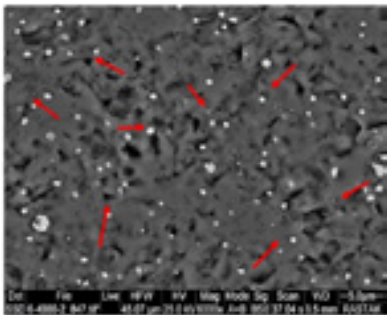


*Fig. 9: The formation of holes due to the evaporation of $Cr_2O_3$ and the formation of Fe metal particles due to the decomposition of FeO.*

According to the working conditions in RH furnaces, a very strong vacuum is created to remove impurities in the work process and causes the possibility of decomposition of FeO and Cr2O3 from inside the chromite aggregates. The decomposition of FeO and Cr2O3 depends on the temperature (T) and oxygen potential and the activity of FeOx and Cr2O3 in chromite spinel, so it can be concluded that the corrosion probability of chromite aggregate,

which actually has a (Mg, Fe)(Cr, Al, Fe)$_2$O$_4$ spinel structure, Generally, it is due to two reasons:

1)    The decomposition of FeOx or Cr2O3 inside the chromite aggregate at high temperatures.

2)    The penetration of melt and slag into the chromite aggregate and its dissolution. In general, the chemical decomposition of FeOx and Cr2O3 takes place through the following two reactions, which in the metallurgical conditions governing the refractory at the working temperature of the RH furnace are the thermodynamic conditions for the following reactions[2].

$$FeO\ (s) = Fe\ (l) + 1/2\ O_2\ (g) \qquad \Delta G = 287340 - 73/7\ T$$
$$Cr_2O_3\ (s) = 2Cr\ (s) + 3/2\ O_2\ (g) \qquad \Delta G = 1110000 - 247\ T$$
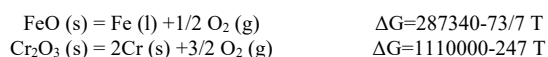
## CONCLUSIONS

1. The phase and microstructural studies of magnesia-chromite rebounding refractory showed that direct bonding prevails in this refractory and proper formation of spinel phases and very low amount of silicate phases are its prominent characteristics.

2. Due to the infiltration of slag and melt through the pores into the refractory structure, it leads to severe breakdown of the refractory during operation.

3. Corrosion of magnesia co-clinker aggregates due to the infiltration of molten iron into the structure of magnesia and complex spinel, lowering their melting temperature and dissolution, which takes place in the next step.

4. Corrosion of chromite aggregates occurs due to the decomposition of FeO and Cr$_2$O$_3$ in the structure and its weakening and chemical corrosion on its surface.

**REFERENCES**

[1].Ghosh, Secondary Steelmaking Principles and Applications. New York, 2001.

[2]. M. K. Cho, M. A. Van Ende, T. H. Eun, and I. H. Jung, "Investigation of slag-refractory interactions for the Ruhrstahl Heraeus (RH) vacuum degassing process in steelmaking," J. Eur. Ceram. Soc., vol. 32, no. 8, pp. 1503–1517, 2012.

[3]. C. Schacht, Refractories Handbook[1] C. Schacht, Refractories Handbook. CRC Press, 2004. CRC Press, 2004.

[4]. S. Li, et al "Identification of magnesia–chromite refractory degradation mechanisms of secondary copper smelter linings" J. Euro. Ceram. Soc. 2016.

[5].L. Schenunis, et al "Spinel saturation of a PbO based slag as a method to mitigate the chemical degradation of magnesia-chromite bricks", J. Euro. Ceram. Soc., 36(2016) 4291-4299.

[6].L. Chen, et al "Comparison of the chemical corrosion resistance of magnesia-based refractories by stainless steelmaking slags under vacuum conditions" Ceram. Int., 2017.

[7].A. Malfliet et al., "Degradation mechanisms and use of refractory linings in copper production processes: A critical review," J. Eur. Ceram. Soc., vol. 34, no. 3, pp. 849–876, 2014.

427

# IMPROVEMENT OF THERMO–MECHANICAL PROPERTIES OF DIRECT BONDED MAGNESIA CHROME REFRACTORIES FOR RH DEGASSER

S. Das*, A. Chakraborty, B. Ghosh, H. Nagata, S. Sengupta, P. B. Panda

TRL Krosaki Refractories Limited, India

## ABSTRACT

Due to increased demand for higher quality steel, RH degassing process gains importance in the secondary steel-making process for its higher productivity and low processing time. The performance of the refractories in the leg, bottom, snorkel, and lower vessel of the RH degasser is very crucial to reduce downtime and increase the degree of steel cleanliness. Direct bonded magnesia chrome brick is generally used in critical areas for a long time due to its excellent thermo-mechanical, and corrosion resistance properties. Refractories in these areas are facing high abrasion by liquid metal and hot gas, thermal shock, skull formation, attack of FeO and MnO-rich slag & oxidation-reduction reactions. In this paper, the effect of different additives in DBMC refractories with respect to thermo-mechanical properties has been studied. Different batches were made with fused magnesia chrome, chromite, and DBM and fired in different firing schedules. Physical and thermomechanical evaluations of different batches were done. Slag corrosion with different slag was also studied. SEM and XRD analysis was done to identify the formation of different phases and correlate with the use of different additive and firing schedules. A batch with novel spinel forming additive and fired at ultra-high temperature shows very good thermo-mechanical properties due to its high degree of direct bonding and fine pore size distribution.

428

## INTRODUCTION

Snorkel is the most critical part of the RH degasser, as it governed the downtime of the degasser. Direct bonded Magnesia chrome bricks are used in the snorkel lining. Circulation speed, lifting gas pressure, FeO%, and heat per day affect the performance of the DBMC bricks in the snorkel. The main degradation mechanism is FeO attack and spalling. So, refractories with very good hot strength are required for superior performance.

In this paper, the recipe for DBMC bricks is designed with varying percentages of spinel-forming additives and observed the effect in correlation with spalling and corrosion resistance. Developed bricks show very good strength at high temperatures and good corrosion resistance. Snorkels manufactured with newly designed bricks were sent to an integrated steel plant for performance evaluation.

## EXPERIMENTAL PROCEDURE

Different batches were made using Fused Magnesia Chrome (FMCR), Chromite Sand, Magnesia, and Spinel forming additives with varying percentages. All the batches are fired at high temperatures with prolonged cooling cycles. Batches are evaluated in terms of physical, mechanical, chemical, and thermal properties. A slag corrosion test was performed at 1650°C for 3 h in an induction furnace with RH degasser slag. SEM and XRD are also done to correlate the different properties.

## RESULTS AND DISCUSSION

All the batches show porosity of less than 16 and BD of more than 3.2 gm/cc. The lowest AP and highest BD are achieved through using of fused raw material and novel granulometry. The HMOR of all the compositions was measured using a three-point bending test at 1400°C and reported in Fig. 1. The composition C6 has shown the highest HMOR value compared to the others.
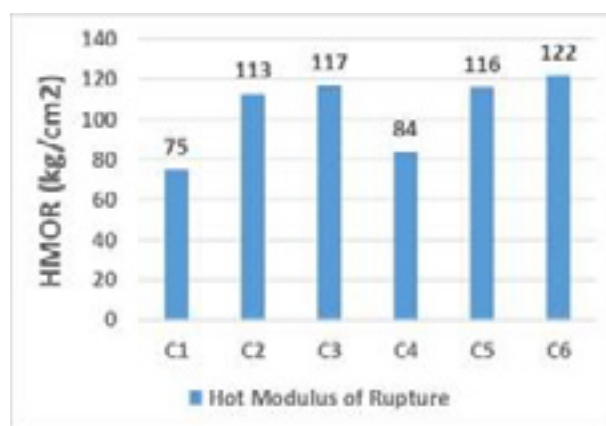


*Fig. 1: Hot Modulus of Rupture of all the composition measured at 1400 °C for 30 min.*

The MOE of all the compositions was measured by ultrasonic method, are reported in Fig. 2. Samples C5 has shown the highest MOE value whereas the C6 composition has shown the lowest MOE value. High MOE indicates the higher rigidity of the C5 refractory whereas low MOE indicates the high flexibility of the C6 material.
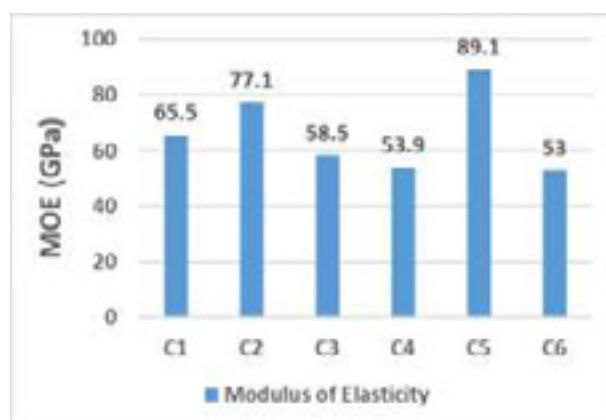


*Fig. 2: Modulus of elasticity of all the compositions.*

Fig. 3 represents the data obtained from the spalling test.

Composition C6 has shown the highest spalling resistance compared to the others. It is due to its low MOE value.
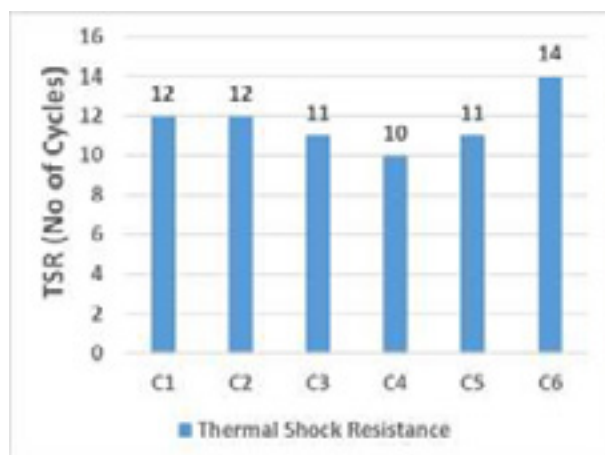


*Fig. 3: Thermal shock resistance tested at 950 °C.*

The slag corrosion test was performed at 1650 °C for 3h in an Induction furnace using RH slag. Fig. 4 represents the rate of slag corrosion of all the compositions. Composition C6 has shown the highest corrosion resistance. The microstructure of the C6 composition is examined after the slag corrosion test as represented in Fig. 5. All types of grains are distributed evenly. The compactness of the brick is good in unaffected areas.
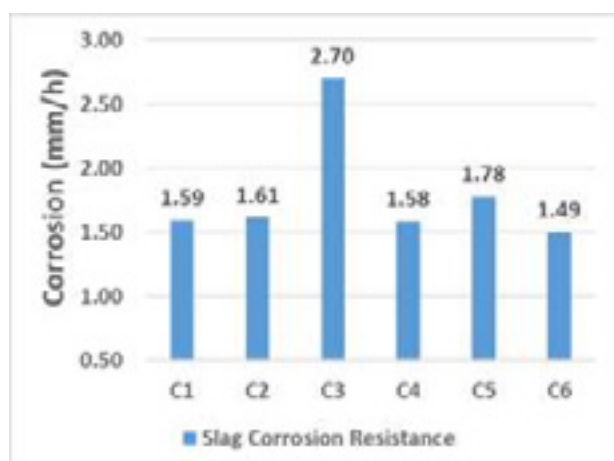


*Fig. 4: Slag corrosion resistance tested at 1650 °C for 3h.*

MgO and Cr2O3 both dissolved in the slags. FeO% increase in the slag-refractory affected area to 18% from 9.2%. Repeated heating and cooling cycles also faster the rate of slag corrosion. The high degree of direct bonding due to a higher percentage of secondary spinel, reduces the rate of slag corrosion in C6. Slag corroded area shows a large no of pores.

Snorkel made with C6 formulation was sent to integrated steel plant shows improvement in performance. No initial cheap-off is found in this snorkel and life improved to 126 heats. Previously, it was 90-102 heat. Where initial cheap-off is the major phenomenon and sometimes, snorkel down prematurely due to this reason. Which is absent in this revised recipe. Fig. 6 shows the regular vs trial situation in this integrated steel plant.
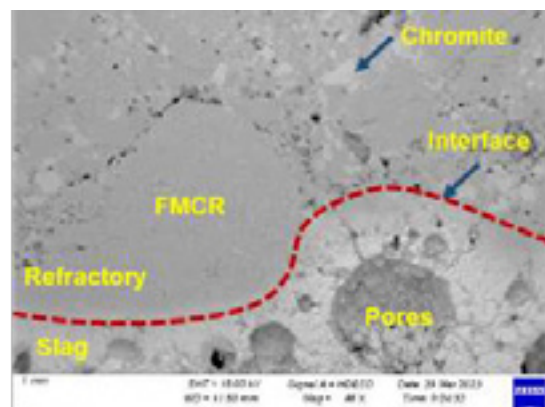


*Fig. 5: Evaluation of Microstructure of sample from C6 batch.*
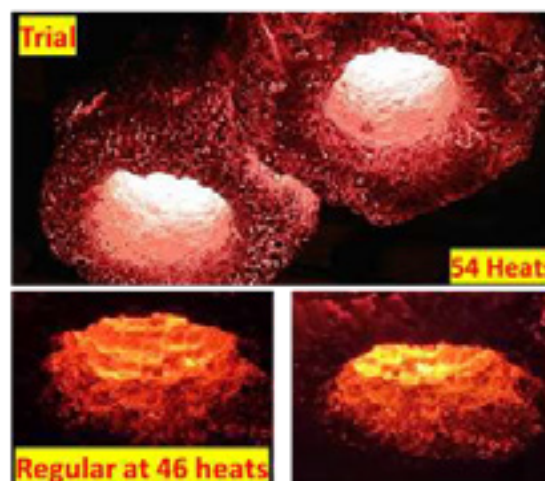


*Fig. 6: A few photographs of the field trial.*

## CONCLUSIONS

In the present work, attempts have been made to develop a novel refractory for the snorkel of RH degasser. The developed material possesses superior hot strength, high slag corrosion resistance, and good spalling resistance. A special spinel-forming additive was added to improve the spalling resistance. With a unique firing schedule, the degree of spinalization increases thus helping in developing the degree of direct bonding between periclase and primary chromite. This affects the actual performance in field trials.

## REFERENCES

[1] S Das et at. New generation semi-rebonded magnesia chrome refractories for RH degasser, UNITCER'21.

[2] Goto K, Lee WE. The direct bond in magnesia chromite and magnesia spinel refractories. J Am Ceram Soc 1995;78(7):1753–60.

429

# PERFORMANCE IMPROVEMENT OF STEEL LADLE MGO–C REFRACTORIES BY USING NOVEL CARBON ADDITIVES

S. Das*, A. Chakraborty, B. Ghosh, H. Nagata, S. Sengupta, P. B. Panda

TRL Krosaki Refractories Limited, India

## ABSTRACT

In the last few decades, the steel manufacturing industries have upgraded their technology to produce high-purity steel which is demanded by end customers in recent years. This has given severe challenges to the refractory industries for better performance without sudden failure. MgO-C refractory is generally used in the steel ladle as a major consumable refractory with respect to other steel-making furnaces. Different carbon-containing MgO-C refractories are used in different areas of the steel ladle as per process requirements. To increase the performance of the steel ladle refractory, different types of additives are used in MgO-C bricks to increase the oxidation & slag corrosion resistance. In this paper, the effect of a new novel carbon-bonded additive is studied with respect to slag corrosion and oxidation resistance. Different batches were made with varying carbon percentages and thermomechanical properties were evaluated. It is observed that the presence of novel carbon bonded additive alters the thermomechanical properties. SEM and XRD analysis was done to identify the different phases at high temperatures and correlated them with the different thermomechanical properties and slag corrosion resistance.

**Keywords:** MgO-C refractory, Low carbon refractories, Metal powder, antioxidants, Steel plant Refractory.

430

## INTRODUCTION

In Iron and Steel Industries, MgO-C (Magnesia Carbon) refractories are dominated because of the high thermal shock resistance, high slag corrosion resistance, excellent resistance to metal penetration, and good hot properties. Magnesia-carbon refractories typically contain between 8 to 20 weight percent of carbon. The primary reason for using graphite is to improve the thermal shock resistance of Magnesite-based refractories and to improve the slag corrosion resistance. However, low strength, oxidation, higher carbon peak up in steel, and heat loss limit its usage percentage. [1,2] Various metal powder and alloying elements are used as antioxidants to retard oxidation and improve strength at high temperatures. [3] The use of these antioxidants also imparts negative effects like high MOE etc. In the present work, attempts have been made to improve the slag corrosion resistance and oxidation resistance of MgO-C refractories by using a novel carbon-containing additive that fills the pore between the pores of graphite and the matrix and developed a stronger matrix that helps in increasing the slag corrosion resistance and also the thermal shock resistance by lowering the MOE.

In the present work, the properties of MgO-C refractories made with novel carbon additives are compared with the proven recipe of TRL Krosaki Refractories Ltd. Novel carbon additive is added through suspension in a liquid. The formulated composition has been characterized and found that the developed recipe shows better slag corrosion resistance compared to the existing composition.

## EXPERIMENTAL

Different batches were made using various grades of fused magnesia, graphite, antioxidants, additives, and binder (shown in Tab.1). All the materials were mixed thoroughly in an inclined mixer and pressed in a high-capacity electric screw press (650 MT) and tempered in a Tempering Kiln at a temperature of 200 °C.

Tab. 1: Batch Composition

| Components (%) | A1 | A2 | A3 | G1 | G2 | G3 |
|---|---|---|---|---|---|---|
| **Fused Magnesia** | * | * | * | * | * | * |
| **Graphite** | * | * | * | * | * | * |
| **Antioxidant** | * | * | * | * | * | * |
| **Novel Additive** | - | - | - | * | ** | *** |
| **Resin** | * | * | * | * | * | * |

After tempering, physical, chemical, and thermomechanical testing was performed on the bricks made of all the batches. XRD & SEM analysis was done to identify the phases present. A slag corrosion test was carried out using LRF slag at 1650°C for 3h in an Induction Furnace.

## RESULTS AND DISCUSSIONS

Among six numbers of batches, G3 shows the lowest AP, and A1 shows the highest BD. The lowest AP is achieved by filling the pores with microfine novel carbon additives. As the porosity is less, the lowest-coked AP and highest-coked BD are achieved by G3. AP and BD of different samples are shown in Fig, 1.
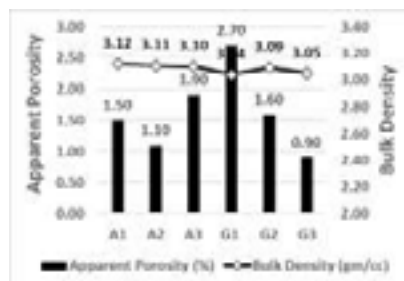


*Fig. 1: Hot Modulus of Rupture measured at 1400 °C for 30 min.*
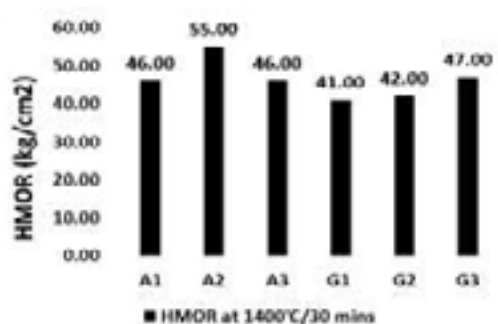


*Fig. 2: Hot Modulus of Rupture measured at 1400 °C for 30 min.*

Fig. 2 shows the HMOR of all the samples, measured at 1400degC. The highest strength is shown by A2 due to spinel-forming antioxidants and less graphite percentage. G3 shows average strength at high temperatures. Composition G3 has shown the least oxidation. The presence of less porosity is the reason for the highest oxidation resistance.
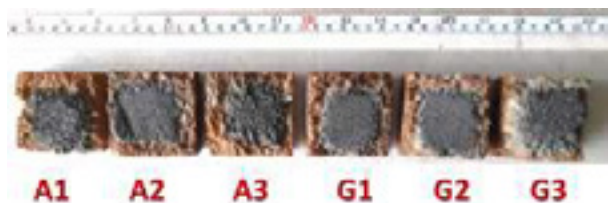


*Fig. 3: Photographs showing the oxidation test samples.*

The slag corrosion test was performed with LRF slag (Al killed) at 1650 °C for 3 h in an Induction furnace. The corrosion rate of all six MgO-C refractories is shown in Fig. 4. All the MgO-C samples have shown significant resistance against the slag. Although sample G3 shows better slag corrosion resistance among all the samples. Fig. 5 shows the photograph of the corroded samples.
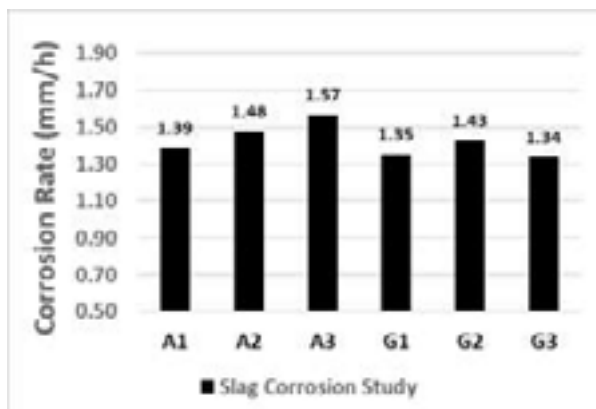


*Fig. 4: Slag corrosion rate of all the compositions in contact with LD slag at 1650 °C for 3 h.*



*Fig. 5: Photographs of the corroded samples after performing a slag corrosion test in the induction furnace.*

The microstructure of the novel carbon-added samples was seen using SEM. Fig. 6 shows the microstructure of sample G3. Corse fine and dust are uniformly distributed throughout the sample. Novel carbon additive and Graphite were evenly coated on the FM grains of the MgO-C samples. A dense matrix was seen in the samples. Due to less pore size, slag penetration is limited, and infiltration of the air is also less. So due to less oxygen partial pressure, oxidation of graphite is limited, and both this factor i.e. low pore and a higher percentage of residual carbon limits the slag corrosion. Also, the presence of a dense matrix with novel carbon additive shows low

MOE after cooking which explained the good spalling resistance also.
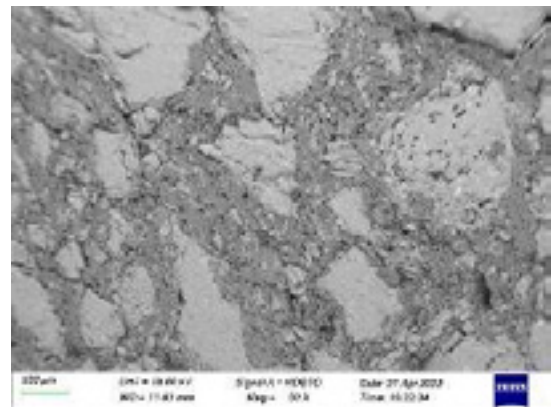


*Fig. 6: SEM microstructure of the MgO-C refractory of G3 composition.*

**CONCLUSIONS**

The developed recipe shows good corrosion and oxidation resistance due to low porosity. Also, the presence of highly conductive novel carbon additive, developed product shows good spalling resistance also. So due to the good spalling resistance and thermal shock resistance developed products can be used in the slag zone for betterment of service life.

**REFERENCES**

[1] Bag, M.; Adak, S.; Sarkar, R., Study on low carbon containing MgO-C refractory: Use of nanocarbon. Ceramics International 2012, 38 (3), 2339-2346.

[2] Zhang, S.; Lee, W., Influence of additives on corrosion resistance and corroded microstructures of MgO–C refractories. Journal of the European Ceramic Society 2001, 21 (13), 2393-2405.

431

# STUDY ON CHROME-FREE PURGING PLUG FOR STEEL LADLES

Sebastian Klaus, Andreas Buhr
Almatis GmbH, Frankfurt, Germany

Zhou Yunpeng, Tian Zhongkai, Wang Feng
Almatis Qingdao Ltd, Qingdao, China

Chatterjee Shankha
Almatis Alumina Pvt Ltd, Kolkata, India

## ABSTRACT

Purging plug refractories in China typically contain around 3% of super-fine chromium oxide in the matrix in order to improve the performance of the purging plugs, primarily, slag corrosion and wear resistance. Alternatives to chromium oxide containing refractories have gained interest due to health concerns related to the formation of soluble chromium compounds over long storage periods of refractory wastes. Super-ground reactive alumina can replace chromium oxide in purging plug refractories and this paper discusses the new reactive alumina E-SY 88 in comparison to chromium oxide in a typical purging plug castable. The results prove that E-SY 88 is an economically viable technical alternative to chromium oxide in purging plug refractories.

## 1 INTRODUCTION

Purging plugs in the steel ladle bottom are used for stirring the steel in the ladle during metallurgical treatment. Their use is essential for the process. Clogged purging plugs cannot perform their function and therefore the hot surface of the purging plug is examined after each heat to ensure the gas channels/slits are open. In the case of residual steel or slag being present on the surface, pure oxygen is blown through a lance onto the surface to melt and wash any residue. During that process an iron oxide slag is formed which attacks the refractories at temperature above 2000 °C [1-4].

Ultra-low cement bonded alumina-spinel-chromium oxide ($Cr_2O_3$) containing castables are dominantly used in purging plug for steel ladles in China due to performance demands, such as thermal stability, thermo-mechanical stability, thermal shock resistance, and erosion and corrosion resistance[5-7].

$Cr_2O_3$, reacting with other components in refractory castable forming solid solution with corundum or spinel, is used in various refractories applications such as for RH snorkel, as chromium ore grit in ladle filler sands in steel plants, coal gasifier furnace, sintering zone in cement kiln, etc. When chromium oxide containing refractory waste is deposited for long periods and exposed to e.g. alkalies, $Cr^{3+}$ can be transformed to water soluble and hazardous $Cr^{6+}$.

In Europe chromium oxide in purging plugs has been replaced after the introduction of alumina-rich spinel in most cases over the past 30 years due to health concerns and increasing problems to deal with chromium-containing refractory waste. In China the addition of around 3% $Cr_2O_3$ is still considered necessary for this application.

In this work, reactive alumina E-SY 88 is used as alternative to $Cr_2O_3$ in ultra-low cement bonded refractory castable and technical features like castable workability, strength development, bulk density, permanent linear change, hot modulus of rupture, thermal shock and slag corrosion resistance and creep behaviour are compared.

## 2 EXPERIMENTAL

### 2.1 Raw Materials

Tabular Alumina (T60/T64, Almatis), Spinel (AR 78, Almatis), reactive alumina with bi-modal particle size distribution (CL 370; Almatis), reactive alumina (E-SY 88; Almatis), Chrome oxide ultrafine (China source), alumina cement (CA-270; Almatis) and dispersing alumina (ADS 1 and ADW 1; Almatis) were used as the raw materials for the experiment.

Reactive alumina E-SY 88 is developed from Almatis Qingdao Co., Ltd for refractory castable applications. As reactive alumina and dispersing alumina became key products in the matrix, ongoing development took place with particular attention given to the ease of mixing, quick castable wet-out and straightforward on-site installation with easy workability at lowest castable dilatancy [8]. E-SY 88 was developed to fulfill the criteria for castable's robustness-in-use. Its non-dilatant rheology supports castable mixing and reduces the risk of excessive water addition to castables. Castable concepts based on E-SY alumina in the matrix have shown good thermal shock properties in other applications. Particle size distribution by CILAS laser granulometry and specific surface area by BET method of E-SY 88 and $Cr_2O_3$ used in the experiment are shown in **Table 1**.

**Table 1 Cilas PSD and specific surface area for $Cr_2O_3$ and E-SY 88**

| | Particle Size Distribution | | | BET/$m^2 \cdot g^{-1}$ |
|---|---|---|---|---|
| | D10/μm | D50/μm | D90/μm | |
| $Cr_2O_3$ | 0.20 | 1.10 | 2.82 | 2.2 |
| E-SY 88 | 0.23 | 1.57 | 12.59 | 3.9 |

### 2.2 Specimens preparation and testing

Dry castable mixes were prepared according to formulation given in **Table 2**. $Cr_2O_3$ 3% was included in first formulation (hereinafter named as Cr2O3), whereas 5% of E-SY 88 was added in chrome-free formulation (hereinafter named as ESY88). Meanwhile, 2% of T60/T64 -45micron was reduced in the ESY88 formulation to keep matrix weightage balance in both the formulations.

**Table 2 Experiment formulations**

| Raw materials | | Cr2O3 | ESY88 |
|---|---|---|---|
| T60/T64 aggregate | ≤ 6mm | 72 | 72 |
| T60/T64 fines | -45micron | 7 | 5 |
| Spinel AR78 | ≤ 0.5mm | 10 | 10 |
| Reactive alumina | CL 370 | 6 | 6 |
| | E-SY 88 | - | 5 |
| $Cr_2O_3$ | | 3 | - |
| Cement | CA-270 | 2 | 2 |
| Dispersing alumina | ADS1+ADW1 | 1 | 1 |

Another group of castable bar specimens with size 25mm×25mm×125mm were cast, cured and dried with the same procedure above, then pre-fired at 1500°C for 3 hours, and tested at 1500°C with dwelling time of 0.5 hour for hot modulus of rupture (HMoR).

Thermal shock resistance (TSR) was determined by water quenching method for specimens pre-fired at 1000°C for 3 hours and 1600°C for 3 hours respectively. The slag corrosion resistance was

evaluated by static crucible method filled with synthetic slag listed in **Table 3**.

**Table 3 Composition of synthetic stainless-steel slag**

| Items | CaO | SiO₂ | MgO | MnO | CaF₂ | Total | CaO/SiO₂ |
|---|---|---|---|---|---|---|---|
| WT/% | 53 | 28 | 7 | 2 | 10 | 100 | 2.1 |

Creep under compression was tested for 1600°C pre-fired specimens.

## 3 RESULTS AND DISCUSSION
### 3.1 Castable Workability
**Figure 1** shows the flow value at 10min,30min and 60min from the time of water addition in castables with Cr2O3 and ESY88 respectively. **Figure 2** shows the exothermal curve and **Table 4** shows the exothermal data.

Wet out time is the time it takes in mixing after water addition until a castable becomes homogeneously wet in appearance. Typical sequences during mixing process are: dust and fine fraction disappear, coarse fraction becomes visible, noise of mixing is reduced, dry pellets of about 8mm diameter are formed, and finally pellets form clusters or lumps and get a shiny surface. Shorter wet out times are preferred as they increase the confidence of the operator in the mixing process and prevent adding more respectively too much water to the mix.

The wet out time was 90 seconds for castable ESY88, a bit shorter than castable Cr2O3 whose wet-out time was 120 seconds. Both castables behaved good flow values around 170mm and very little flow decay up to one hour. The water addition was 3.6% for castable ESY88, 0.2% less compared to castable Cr2O3 to achieve comparable flow values. And during the experiment, it was observed that wet mix with E-SY 88 is very soft, while wet mix with Cr₂O₃ is much stiffer, thus increasing the risk of remaining air bubbles in the form during vibration. This clearly indicated that castable workability with E-SY 88 has significantly improved even water addition is reduced by 0.2%.
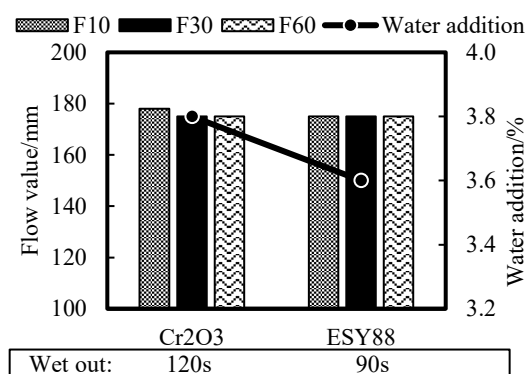


**Fig.1 Flow property of castables**

The time of exothermal curve reaching the peak was 358 minutes for castable ESY88; and 566 minutes for castable Cr2O3. For high temperature pre-fired purging plugs, the pieces need to be demoulded after curing for drying and firing. Therefore, shorter setting times are preferable for more frequent use of the moulds and higher productivity in manufacturing.
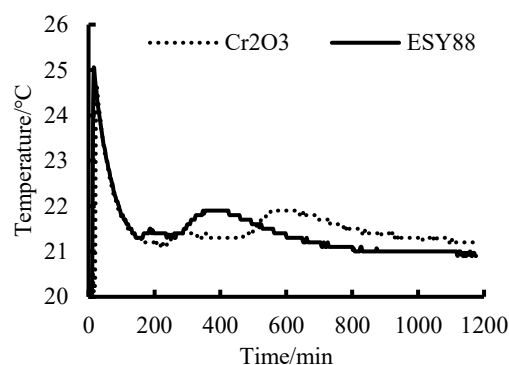


**Fig.2 Exothermal curve of castables**

**Table 4 Exothermal data of castables**

| | Cr2O3 | | ESY88 | |
|---|---|---|---|---|
| | Time/min | Temp./°C | Time/min | Temp./°C |
| Start1 | 236 | 21.1 | 164 | 21.3 |
| Start2 | 482 | 21.4 | 284 | 21.4 |
| Max | 566 | 21.9 | 358 | 21.9 |

### 3.2 Apparent Porosity and Bulk Density
**Figure 3** shows apparent porosity and bulk density for castable after treated at 110°C for 24 hours, 1000°C for three hours and 1600°C for three hours, respectively. After drying at 110°C, castable ESY88 showed apparent porosity of 8.1%; whereas it was 11.5% for castable Cr2O3. The dried bulk density was 3.29g/cm³ for castable ESY88 and 3.26g/cm³ for castable Cr2O3. The broad particle size distribution of E-SY 88 supported by its submicron distribution better fitted for optimized overall particle packing from the matrix and helped for effectively filling the pores formed by coarser particles. Accordingly, 0.2% lower water demand contributed to better castable densification and decreased apparent porosity for castable ESY88. After firing at 1000°C, apparent porosity of castable ESY88 was slightly lower than that of castable Cr2O3 – 12.2% against 13.5%; whereas bulk densities were comparable between the two castable. After firing at 1600°C, apparent porosity of castable ESY88 remained lower at 14.0% when compared to 14.7% for castable Cr2O3, whereas bulk densities remained comparable between the two castables.



**(a) Apparent porosity**
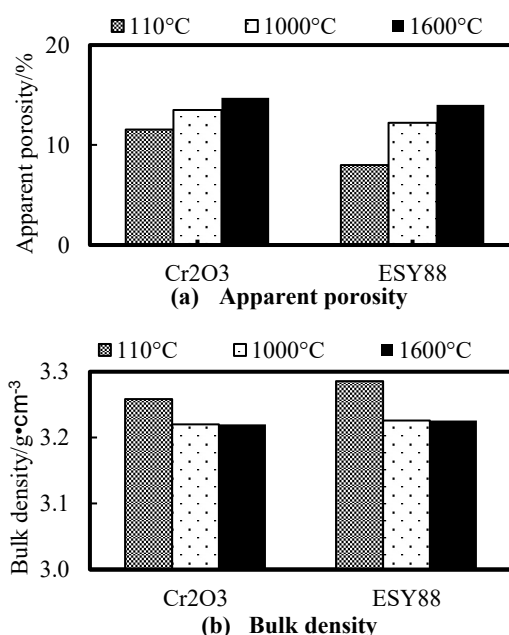


**(b) Bulk density**
**Fig. 3 Apparent porosity and Bulk density**

### 3.3 Permanent Linear Change

**Figure 4** gives permanent linear change of castables at different temperatures. After drying at 110°C, there was comparable minor shrinkage in both the castables. After firing at higher temperatures up to 1600°C, both castables showed comparable shrinkage due to sintering.
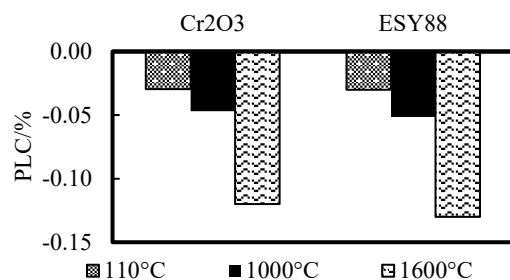


**Fig.4 Permanent linear change**

### 3.4 Strength Evolution

**Figure 5** shows cold modulus of rupture and cold crushing strength for castables after treated at 110°C, 1000°C, and 1600°C. **Figure 6** gives the hot modulus of rupture for castables at 1500°C.

Strengths after curing at 20°C and drying at 110°C were both slightly higher for castable ESY88. This is because of better particle packing arising from optimized particle size distribution in the matrix. Lower water addition contributed to better densification for castable ESY88 and also result in slightly higher castable strength.

After firing at 1000°C, CMoR and CCS of castable Cr2O3 were higher than that of castable ESY88. This is because $Cr_2O_3$ initiated solid solution reaction with corundum, which was also reflected from the faded green colour at the body inside and on the surface of castable specimens. Although strengths after firing at 1000°C from castable ESY88 were lower, they are considered sufficient for practical application as would apply for just tempered purging plugs (at 350 - 450°C) common in Europe. In China, where purging plugs are pre-fired at 1500-1650°C during production, the strength at 1000°C is not important anyways.

After firing at 1600°C, both castables were fully sintered for very high strength development with CMoR above 40MPa and CCS above 300MPa.
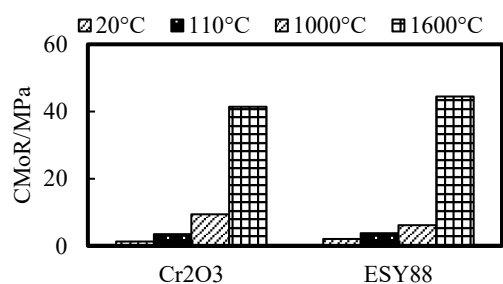


**(a) Cold Modulus of Rupture**
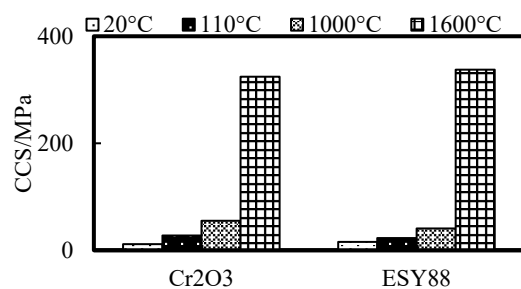


**(b) Cold Crushing Strength**
**Fig. 5 Cold strength development**
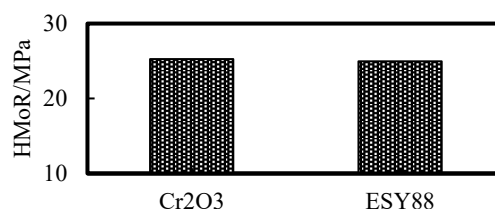


**Fig.6 Hot Modulus of Rupture**

**Figure 6** gives hot modulus of rupture for castable at 1500°C with dwelling time of 30 minutes, whose specimens were pre-fired at 1500°C for three hours. Result showed both castables had comparable HMoR of 25MPa, suitable for high erosion resistance during application in the steel ladle.

Pre-firing at high temperatures with strong sintering of the material is advantageous for the strength. However, the material is also becoming more brittle and sensitive against thermal shock, which is discussed in the following chapter.

### 3.5 Thermal Shock Resistant Property

**Figure 7** shows residual strength after one, three, and five cycles of quenching as described above. Both, absolute values and residual strength as percentage of starting strength are given.

Residual strength is higher when samples were pre-fired at 1000°C when compared to 1600°C. At both pre-firing temperatures, the residual strength is clearly higher for ESY88 than for Cr2O3. This indicates a higher resistance against thermal spalling of purging plugs based on ESY88 when compared to Cr2O3. And that can be considered a clear advantage of ESY88 vs. Cr2O3 especially for the high temperature pre-fired purging plugs in China.
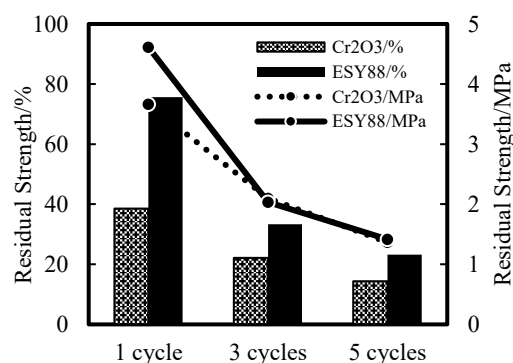


**(a) TSR for specimens pre-fired at 1000°C**
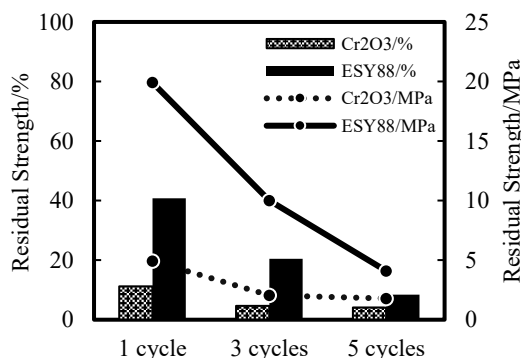


**(b) TSR for specimens pre-fired at 1600°C**
**Fig. 7 Residual strengths after thermal shock**

### 3.6 Slag Resistance

**Figure 8** shows slag resistance test crucibles for both castables with synthetic stainless-steel slag at 1600°C with dwelling time of five hours. Erosion percentage from crucible ESY88 is 8.5%, slightly lower than crucible Cr2O3 which is 9.0%. Overall slag corrosion resistant performance was slightly better for castable ESY88 than castable Cr2O3. But, having done only the static slag corrosion test,

434

it can be indicated as comparable between the two castables for actual dynamic conditions for purging plug application.

Overall, erosion pattern as visually observed, was comparable between the two castables. More severe erosion occurred on crucible body at the interface area between slag and air for both castables. There is no clear boundary between penetrated layer and slag, but clear boundary between penetrated layer and original layer is observed. Almost similar erosion among bigger grains and matrix part can be seen for both castables, especially at the bottom area.



| Cr2O3 | ESY88 |
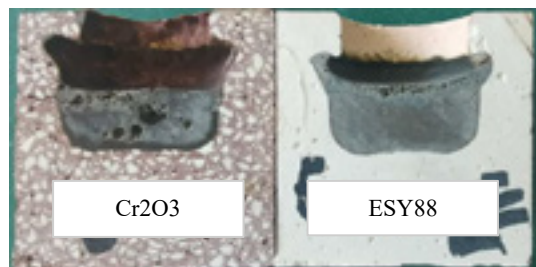
**Fig.8 Crucible slag test**

### 3.7 Creep Resistance

**Figure 9** shows creep under compressive curve of specimens under the load of 0.2MPa at 1550°C with dwelling time of 50 hours. **Table 5** shows the average creep rate from 25 to 50 hours at the later stage of the test. Result proves a higher creep resistance for castable ESY88. The average creep rate per hour was 0.0019%, almost half compared to castable Cr2O3 which was 0.0032% from 25-50 hours.
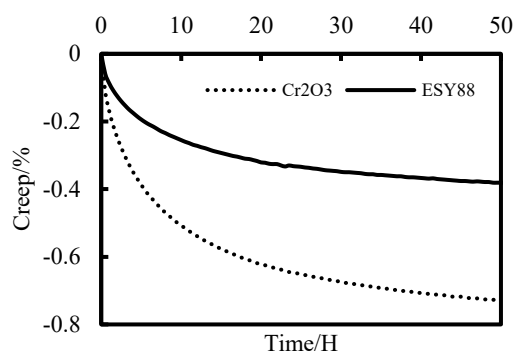


**Fig.9 Compressive creep resistance**

**Table 5 Creep rate at 25~50 hours**

|  | Cr2O3 | ESY88 |
|---|---|---|
| Creep rate 25~50H (%/H) | 0.0032 | 0.0019 |

### 4 CONCLUSIONS

Reactive alumina E-SY 88 replacing $Cr_2O_3$ in ULC based castable for purging plug application provided encouraging results.

- Castable workability has improved by replacing Cr2O3 with E-SY 88 alumina. Less water addition is required to achieve comparable flow value, while wet mix is much softer, which reduces the risk of air bubbles and inhomogeneity in the matrix. The shorter setting time with E-SY 88 is advantageous for higher productivity in manufacturing.
- Strength development meets purging plug application requirement. Cured and dried strength developments of E-SY 88 containing castable are comparable to $Cr_2O_3$ contained castable, so is high temperature fired strength.
- Permanent linear change is comparable for both types of castables.
- Usage of E-SY 88 alumina, replacing Cr2O3 has improved thermal shock resistance both for 1000°C and 1600°C pre-fired castables. This is beneficial for both high temperature fired and tempered purging plug.
- Slag corrosion resistance of E-SY 88 containing castable is comparable to $Cr_2O_3$ contained castable.
- Creep resistance has also improved by usage of E-SY 88 alumina replacing $Cr_2O_3$.

Overall, using E-SY 88 alumina to replace $Cr_2O_3$ in purging plug could improve purging plug performance and would eliminate the hazards related to chromium oxide usage. Besides this, the cost of reactive alumina E-SY 88 is lower than fine synthetic chromium oxide, and thus E-SY 88 is an economically viable technical alternative to chromium oxide in purging plug application.

### REFERENCES

[1] Long Bin, Xu Guiying, Li Yong, Andreas Buhr. Fracture behaviour and microstructure analysis of Al2O3-MgO-CaO castables for steel-ladle purging plugs. International Journal of Minerals, Metallurgy and Materials, 2016, 23(11), 1333-1339.

[2] Zhang Ju, Long Bin, Zhou Yunpeng, et al. Relation between Sintering Reactivity of Matrix and Thermal Shock Resistance of Ultra-low Cement Bonded Corundum-Spinel Castables for Fired Purging Plug. Refractories (CN), 2018,4: 13-19.

[3] Zhang Hui, Sun Jialin. Thermal shock damage behaviour of alumina-magnesia based ladle purging plug. Refractories (CN), 2009, 43(6): 409-411.

[4] Yang Wengang, Liu Guoqi and Wang Jianguo. Stress field distribution of purging plug for ladle in application process. Refractories (CN), 2013, 47(2): 107-110.

[5] Li Yuanbing, Li Nan, Peng Bing, et al. Develop-ment and application of Purging plug for steel ladle. China Refractories(CN), 2002, 36(2) 95-96.

[6] Kou Zhiqi, Fan Tianyuan, Zhang Limin, et al. Development and application of slit Purging plug. Refractories(CN), 2001,(02) 92-94.

[7] Chang Ya'nan, Zhang ling, Shao Zimin. Research and development direction of Purging plug for steel ladle. Journal of Liaoning University of Science and Technology, 2016,39(03): 191-197.

[8] R. Kockegey-Lorenz et al., E-SY alumina for easy to use high performance castable. 52. International Colloquium on Refractories, Aachen (2009), 86-88.

435

SHORT COMMUNICATIONS
# IMPROVEMENT OF GAS HOLDER SYSTEM

Takafumi Imaeda, Kimihiro Yasui, Takafumi Kaminishi,
Tomomi Soeda
TYK Corporation., Tajimi City, Japan

## ABSTRACT
Approximately 20 years ago, our company developed a gas holder system (hereinafter referred to as GHS) for securing serviceability of purging plugs used for stirring molten steel with inert gas in teeming ladle. In the business activities to supply GHS to many customers, varieties of improvements or modification works have been made on GHS. In recent circumstances in which achievement of SDGs and/or establishment of carbon-neutral society is called for, it is thought that improvement of purging plug's service life would contribute to the global environment. Improvement or modification works which have been made on GHS are reviewed in this report.

## Outline of GHS
GHS was developed for securing serviceability of purging plugs. That is, even when inert gas for molten steel stirring is not supplied from the main gas supply source to a purging plug, inert gas supply to the purging plug is continued from a gas storage tank in GHS so as to suppress molten steel penetration into the plug and to minimize purging plug damages caused by oxygen gas cleaning required for removing adhering steel. As schematically illustrated in Fig. 1, GHS is configured with a gas storage tank and a control unit. During secondary refining treatment in teeming ladle, inert gas provided from the main gas supply source is used for molten steel stirring through purging gas and is stored into the gas storage tank simultaneously. When inert gas supply from the main gas supply source is shut off during transportation or standby of teeming ladle, inert gas is automatically supplied to the purging plug from the gas storage tank for suppressing molten steel penetration into the purging plug.
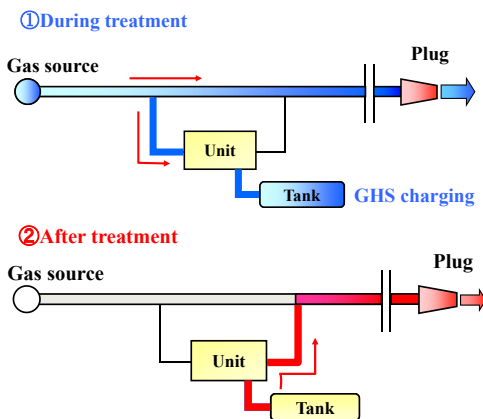


*Fig. 1: Concept of GHS*

## Problem of GHS
Various problems have been turned up in GHS operation. Typical examples are incidental change of needle valve opening by mechanical vibration during teeming ladle transportation, or damages to several components of needle valve by thermal load. When this situation occurs, it is impossible for the GHS to perform, so we decided to start improving it.

## Improvements of GHS
Fig. 2 shows a GHS unit of an old design that includes a needle valve.

This needle valve was damaged by vibration and thermal load, GHS often did not work well.
So we replaced the needle valve with a small pore tube joint, as shown in Fig. 3, to control unintended changes in needle valve opening and minimize thermal damage to the component.
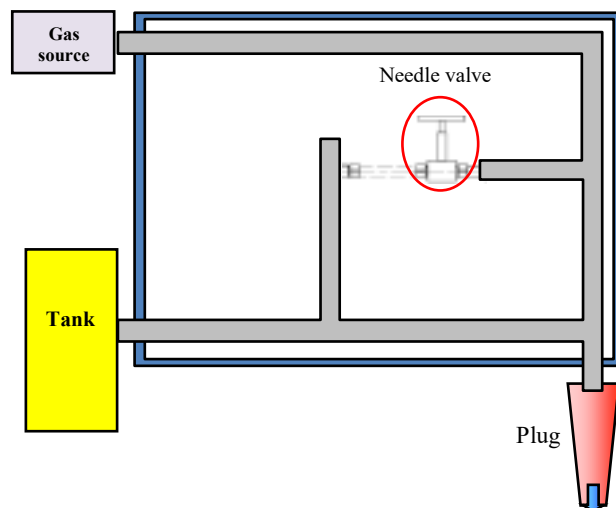


*Fig. 2:Old Design of GHS*
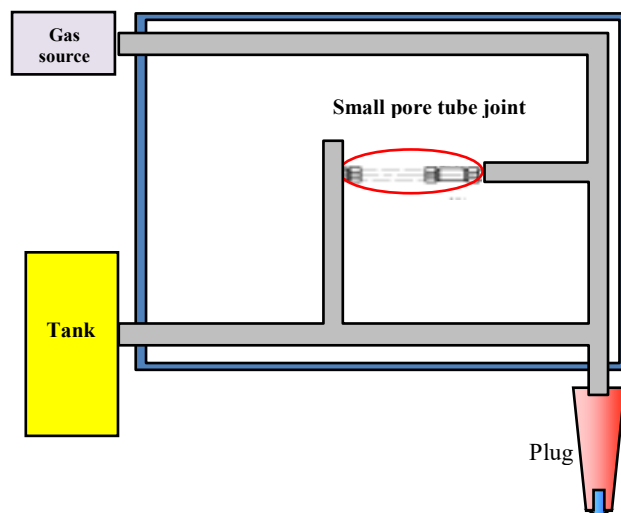


*Fig. 3:New Design of GHS*

## Result of dispensing test
We conducted having tests at room temperature and at 450°C to confirm the effect of the new design, which changed from a needle valve to a small pore tube.
As shown in the graphs in Fig. 4 and 5, the old designs with needle valves show a decrease in initial discharge flow rate at 450°C.
This is thought to be because the needle valve has been damaged by heat and is not functioning properly.
As shown in the graphs in Fig. 6 and 7, no change in the initial discharge flow rate was observed in the new design using the small pore tube joint, even at 450°C.
This is thought to be due to the fact that the change to a small pore tube suppressed thermal damage.
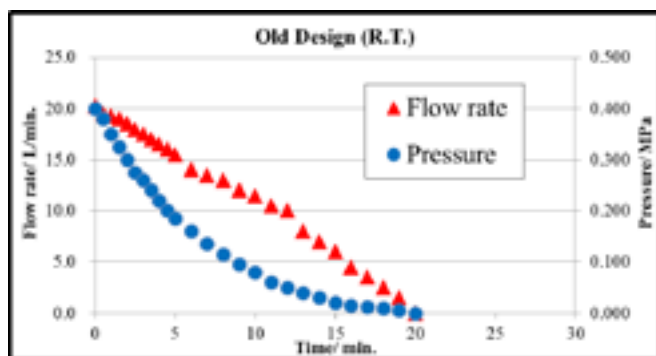
*Fig. 4: Pressure and flow rate curve of old design at R.T.*
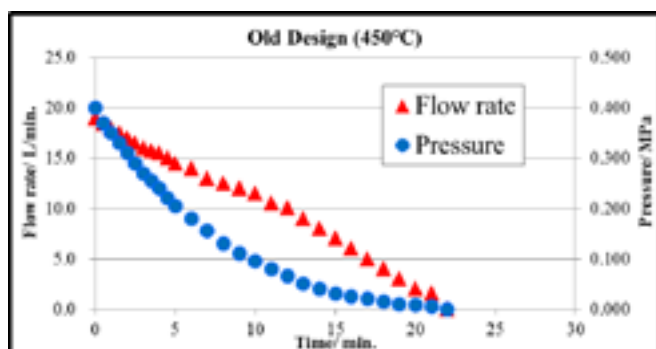


*Fig. 5: Pressure and flow rate curve of old design at 450℃*
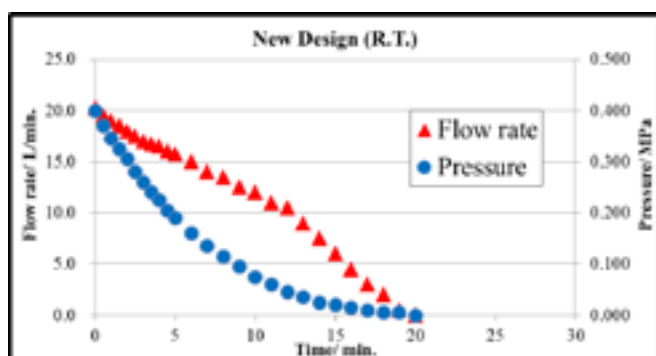


*Fig. 6: Pressure and flow rate curve of new design atR.T.*
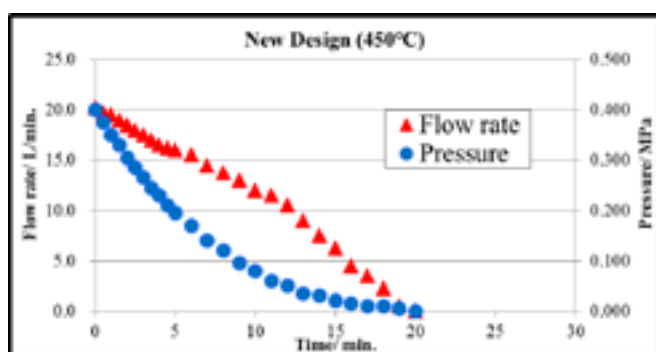


*Fig. 7: Pressure and flow rate curve of new design at 450℃*

## CONCLUSIONS

This improvement by changing from needle valves to small pore tube joint will greatly improve the serviceability of the GHS against vibration and high temperatures, and will enable the GHS to be used in a more stable condition.

In the future, we will continue to confirm the results of use under various conditions and consider further improvements to the GHS.

## REFERENCES

[1]  Kondo J, Nakakita K, Aramaki K, Morimoto S, Egashira H. DEVELOPMENT OF GAS PURGING SYSTEM. UNITECR '01, 2001, p. 1289-1294

[2]  Inoue M, Kondo J, Aramaki K, Morimoto S, Koike Y. DEVELOPMENT OF GAS HOLDER SYSTEM. UNITECR '03, 2003, p. 596-598

437

SHORT COMMUNICATIONS

# KUMAS'S NEW GENERATION MGO−C BRICK DEVELOPMENT

Nuri Sarioglu, KUMAS Refractories R&D Center, 43100, Kutahya, Turkey

Merve Ucak, KUMAS Refractories R&D Center, 43100, Kutahya, Turkey

## ABSTRACT

There is a need for adjustments across the entire steel industry due to competitive pressures such as global demand, high energy costs, environmental and safety laws, competing materials, consumer demand for high quality, and the high cost of capital. Therefore, it is important to reduce refractory material consumption. There are numerous studies regarding improving refractory materials' performance in this concept. In recent years, the limits of raw material quality have been pushed. The research to be done here is carried out in a very limited scope. Therefore, the studies on MgO-C-based bricks are generally based on additives rather than the raw material quality. In this context, KUMAS is working on additives in its MgO-C-based bricks. With the studies, it has been able to prevent the infiltrations that will occur by achieving to delay the oxidation of the MgO-C-based bricks under the working conditions, and the customers have observed increases in the brick performances. This work aims to present the properties of these newly designed MgO-C-based bricks compared to the KUMAS commercial product range with customer trials.

## INTRODUCTION

The steel industry is confronted with a variety of factors that necessitate adjustments to enhance competitiveness and operational efficiency. Among these factors are global demand fluctuations, escalating energy costs, stringent environmental and safety laws, increasing competition from alternative materials, consumer expectations for high-quality products, and the high cost of capital. In this context, reducing refractory material consumption has emerged as a critical area for improvement [1, 2]. Refractory materials play a crucial role in the steel industry, providing essential lining solutions for furnaces, ladles, and other high-temperature applications. Therefore, efforts to enhance the performance and durability of refractory materials can significantly impact overall operational efficiency and cost-effectiveness. To achieve this, previous research has mainly focused on exploring additives for MgO-C-based bricks, while the importance of improving the raw material quality has received limited attention [3, 4].

To address this research gap, KUMAS R&D Center has conducted studies on additives for MgO-C-based bricks, aiming to prolong their resistance to oxidation under operational conditions. By successfully delaying oxidation, KUMAS anticipates a reduction in unwanted infiltrations and improvements in brick performance. This paper presents the properties of the newly designed MgO-C-based bricks, comparing them with KUMAS' existing commercial product range, through customer trials.

## MATERIALS AND METHODS

The experimental investigation involved the preparation of newly designed MgO-C-based bricks using KUMAS' proprietary additives. The composition of the additives, along with the specific additives used, was optimized based on extensive laboratory testing and analysis. The production process adhered to industry standards and employed state-of-the-art equipment to ensure consistent brick quality. Customer trials were conducted in collaboration with steel manufacturers across different operational environments. The trial setups involved the installation of both the newly designed MgO-C-based bricks and the KUMAS commercial product range in relevant furnace and ladle applications. Operational parameters, such as temperature, duration, and working conditions, were carefully monitored throughout the trials. Key performance indicators, including refractory wear, oxidation resistance, thermal shock resistance, and mechanical strength, were measured and compared.

## RESULTS AND DISCUSSION

The results obtained from the customer trials demonstrated notable improvements in the properties of the newly designed MgO-C-based bricks compared to the KUMAS commercial product range. These improvements were observed across multiple performance indicators, validating the efficacy of the developed additives. The presence of residue carbon after coking plays a crucial role in the performance and properties of MgO-C-based bricks. In this study, residue carbon acts as a protective barrier against oxidation. When the bricks are exposed to high temperatures and oxidizing atmospheres, the residue carbon reacts preferentially with oxygen, forming a protective layer that shields the underlying matrix from direct oxidation. This delayed oxidation helps maintain the structural integrity and performance of the bricks over extended periods, reducing infiltrations and preventing premature failure. Also, the presence of residue carbon significantly improves the thermal shock resistance of MgO-C-based bricks. The carbonaceous material possesses a high coefficient of thermal expansion, which effectively absorbs and dissipates thermal stresses generated during rapid temperature changes. This characteristic allows the bricks to withstand thermal cycling conditions without experiencing cracks or structural damage, ensuring their durability and longevity. Overall, the additives provide enhanced resistance to oxidation, superior thermal shock resistance, and improved mechanical strength. These properties ensure the bricks can withstand harsh operating conditions, maintain their structural integrity, and deliver long-lasting performance.

The positive outcomes observed during customer trials highlight the potential of the newly designed MgO-C-based bricks to contribute to refractory material consumption reduction in the steel industry. By prolonging the service life of refractory linings, steel manufacturers can achieve cost savings and improve operational efficiency while maintaining high-quality standards.

## CONCLUSION

In conclusion, this study focused on the development of additives for MgO-C-based bricks to enhance their performance and reduce refractory material consumption in the steel industry. The customer trials conducted in collaboration with steel manufacturers revealed significant improvements in the properties of the newly designed bricks compared to the KUMAS commercial product range. The achieved delay in oxidation, attributed to the developed additives, resulted in reduced infiltrations and increased resistance to wear. Additionally, the newly designed bricks demonstrated superior thermal shock resistance and improved mechanical strength, indicating enhanced durability and longevity. These findings emphasize the potential of the newly designed MgO-C-based bricks as a viable solution for steel manufacturers seeking to optimize refractory material usage and improve operational efficiency. Further research and development in this area hold promise for advancing the field of refractory engineering and addressing the competitive challenges faced by the steel industry.

## REFERENCES

[1] Horckmans, Liesbeth, Peter Nielsen, Philippe Dierckx, and Antoine Ducastel. "Recycling of refractory bricks used in basic steelmaking: A review." Resources, Conservation and Recycling 140 (2019): 297-304.

438

[2] Madias, Jorge. "A review on recycling of refractories for the iron and steel industry." In Proceedings of the UNITECR. 2017.

[3] Lynch, Charles T. CRC Handbook of Materials Science: Material Composites and Refractory Materials. Vol. 2. CRC press, 2020.

[4] Goto, Kiyoshi, Seiji Hanagiri, Kohji Kohno, Tsuyoshi Matsui, and Tadashi Ikemoto. "Progress and perspective of refractory technology." Nippon steel technical report 104 (2013): 21-25.

# MECHANICAL AND CHEMICAL BEHAVIOR OF MGO–C BRICKS UNDER NEAR–SERVICE CONDITIONS

Delia Gutiérrez-Campos[1]; Pablo Galliano[2]; M.N. Moliné[3]; S.E. Gass[3]; A.G. Tomba Martínez[3]

[1]Universidad Simón Bolívar, Caracas, Venezuela; [2]Tenaris Siderca, Campana, Venezuela; [3]INTEMA, Argentina

In spite of the long use of MgO-C bricks in the steelmaking industry, there are still issues, regarding the influence of compositional variables on the behavior of this kind of refractories, that have to be better understood. For instance, the effect of graphite content or the addition of antioxidants has been extensively studied and well established; but less is known about the interactions between those components. With the aim of contributing to clearing up these relationships, different non-commercial MgO-C materials were tested under near-service conditions. The bricks were formulated with 83-85 wt% of magnesia (fused/sinter: 70/30), with various contents of graphite (8 and 12 wt.%) and types of binder (phenolic resin or soft binder). The addition of 2 wt.% of a metallic additive was also considered as a variable. A comprehensive characterization of bricks was performed by using several techniques (XRD, XRF, ICP-OES, DTA/TGA, density, porosity and permeability measurements, mercury intrusion porosimetry, and SEM/EDS). Compressive tests between RT and 1400°C (Ar atmosphere) were performed to study the mechanical behavior. The chemical response of bricks to the attack of a typical steelmaking ladle slag at 1600°C was determined by static and dynamic tests (cup and dipping tests), and the oxidation resistance was evaluated by thermal treatments at 1000°C using gaseous atmospheres with different oxygen contents.

440

SHORT COMMUNICATIONS

# THE CHOICE OF MAGNESIA–CARBON REFRACTORIES FOR STEEL LADLE LINING: A LIFE CYCLE PERSPECTIVE

Md Jubayed[1]; Rinus Siebring[2]; Angélique Léonard[1]

[1]PEPs, Laboratory of Chemical Engineering, Department of Applied Chemistry, University of Liège, Building B6a, Sart-Tilman, Liège, Belgium; [2]Ceramics Research Centre, Tata Steel, IJmuiden, Netherlands

Steet ladle is the single most consumer of refractories in the steel industry. Various magnesia-carbon refractory bricks are widely utilized for the slag line part of a steel ladle. Unfortunately, in literature, very few life cycle assessment (LCA) studies are found regarding magnesia-carbon refractories, most of which were focused on manufacturing while ignoring the use phase. Since the properties of refractories (such as density and thermal conductivity) have a significant effect on steel production volume and energy efficiency of steel ladle processes, it is essential to include the use phase when the choice of refractories is subject to question.

Therefore, this study aims to evaluate the environmental impacts of various magnesia-carbon refractories considering their use phase. Cradle-to-grave attributional LCA will be implemented to quantify the environmental impacts of refractories, maintaining a consistent system boundary. Data will be collected from industrial partners involved in the consortium of the CESAREF research project. Uncertainty will be investigated through Monte Carlo simulations and scenario analysis. The results of the study will help to choose magnesia-carbon refractories for steel ladle lining based on their environmental performance.

# FORMATION OF ISOLATION LAYER BETWEEN THE REFRACTORY LINING AND MOLTEN STEEL/SLAG: INDUSTRIAL TRIALS IN REFINING LADLE

Junfeng Chen[1]; Shaowei Zhang[2]; Nan Li

[1]Wuhan University of Science and Technology, The State Key Laboratory of Refractories and Metallurgy, Wuhan, China; [2]University of Exeter, College of Engineering, Mathematics and Physical Sciences, Exeter, United Kingdom; [3]Wuhan, China

Direct dissolution and corrosion during refractory service should be avoided because it leads to metal contamination and a lower service cycle. Forming a liquid phase isolation layer or high viscosity phase on a refractory surface against steel/slag's attack always be desired which has been observed and discussed in many cases. In this work, the corroded microstructures of two types used refractory lining in industrial ladles, including MgO/$Al_2O_3$-C brick and $Al_2O_3$-MgAl2O4 castable both for metal bath areas, were investigated. The formation of different liquid-phase/high-viscosity isolation layers was discussed based on chemical composition design and erosion process control. Furthermore, based on the microstructural characterizations, the interactions/reactions between the refractory lining and the molten steel/slag (rather than a single slag or steel) should also be considered to have a better understanding of the overall degradation mechanism of refractory lining served in an industrial trial

# EFFECT OF TUNDISH PLATE REFRACTORY EROSION ON STEEL QUALITY AND DEVELOPMENT OF EROSION MEASUREMENT SYSTEM

Janghoon Kim[1], Yonggu Lee[2]
POSCO Technical Research Lab.[1]
POSCO Gwangyang Refractory Group[2]

## ABSTRACT

In the recent years, to respond ever-growing demands in high quality steels, steel cleanliness during continuous casting process is one of main areas of focus in steelmaking. The presence of inclusions adversely affects the cleanliness of molten steel. Because these are considered to be detrimental to the mechanical properties of steel. Types of non-metallic inclusions include indigenous inclusions generated by reoxidation in molten steel and extrinsic inclusions introduced from the outside of molten steel. It is known that extrinsic inclusions are easy to remove by buoyancy because they have a large size.

In the present study, a method for measuring the amount of erosion to tundish plate refractories and its impact on the cleanliness of molten steel were investigated.

## Measuring the erosion of tundish plate

The plate refractory was scanned using a line laser and the distance was measured as shown Figure1.
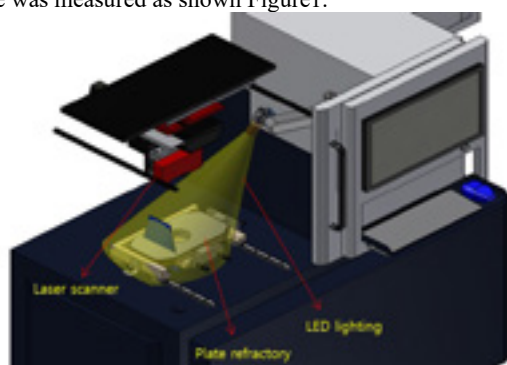


*Fig. 1: Schematic of Plate Erosion Measurement Device.*

The volume of the erosion part was measured by setting the zero point based on the non-contact area of molten steel, measuring the distance against the zero point, and then performing integration as shown Figure 2.
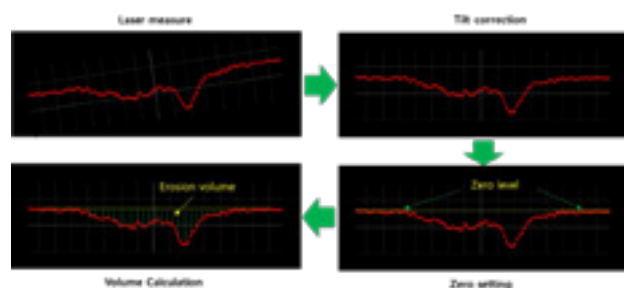


*Fig. 2: Schematic diagram of erosion volume measurement.*

To confirm the accuracy of the developed plate erosion measurement device, an experiment was conducted. A new plate was prepared and its weight was measured. Then, the plate was artificially damaged and weighed again to determine the damaged weight. The results from comparing the measured/calculated damaged weight obtained through the developed device with the actual damaged weight are presented in Table 1. The error between the actual and calculated damage values was found to be at the level of 0.4-1.4%.

Tab. 1: Caption for table 1.

| Number of experiments | Weight of damage(g) | | Mating rate (%) |
|---|---|---|---|
| | actual | Device measurement | |
| 1 | 1.3 | 1.28 | 98.54 |
| 2 | 2.7 | 2.69 | 99.59 |
| 3 | 3.6 | 3.58 | 99.50 |

As shown in Figure 3, 2D and 3D images of the scanned data are displayed on the monitor, and the calculated total erosion amount is presented together with the weight of the corrosive substance multiplied by the specific gravity, providing information on the weight of the damage.



*Fig. 3: Display of Measurement Results*

## A discussion on the measurement results of damages to plate

The used tundish middle plate was analyzed using the developed device. According to Figure 4, the upper surface of middle plate commonly experiences severe damages due to the significant force generated by steel pouring.
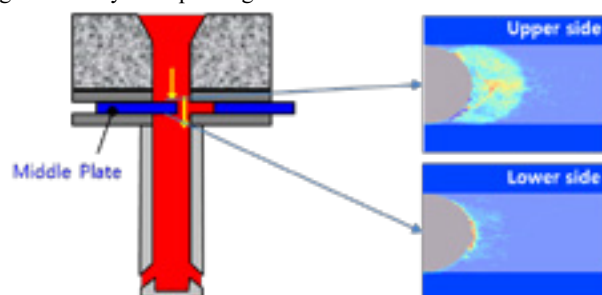


*Fig. 4: Measurement results of erosion on a used middle plate*

However, as shown in Figure 5, occasional cases have been observed where the lower side of the middle plate undergoes significant damage, and traces of air intrusion, along with big cracks, are found on the surface of the plates. It is suspected that gaps between the plates caused the intrusion of external air, which is believed to be the main cause of the damage to the lower side of the middle plate.
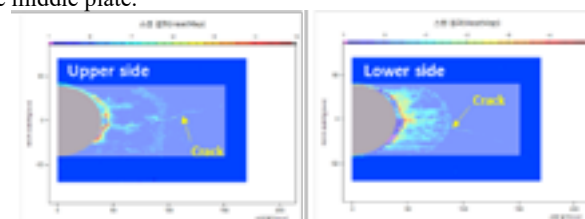


*Fig. 5: Example of lower side erosion on lower side of middle plate*

443

As illustrated in Figure 6, it can be observed that the lower carbon content in the steel results in higher damage on the middle plate. It is considered that this is caused by the decarburization of the refractory material due to the dissolution of C into the molten steel.
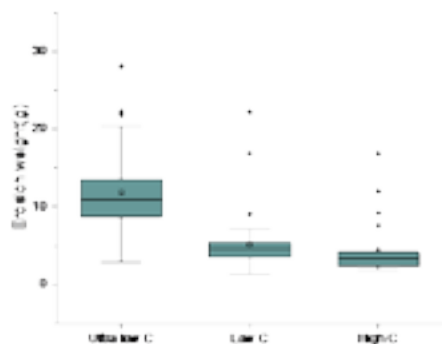


*Fig. 6: Middle plate erosion according to the level of carbon content in molten steel.*

**Molten steel cleanliness according to plate erosion**

Figure 7 demonstrates a clear connection between the amount of erosion in the plate refractory and the growing incidence of slab defects. It was evaluated based on the amount of plate refractory erosion measured by the above method. When the total erosion to the middle plate was categorized into three tiers: over 10g, 3-5g, and less than 3g, it was observed that cases with a erosion exceeding 10g exhibited a significantly higher occurrence of slab defects. As a result of these findings, it can be inferred that the erosion to the plate refractory can have a direct impact on the quality of the slab.
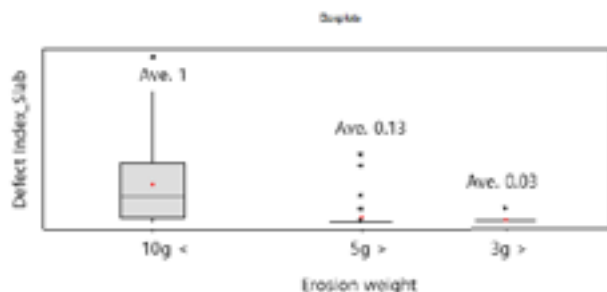
*Fig. 7: Relationship between TD plate erosion and slab defect.*

**CONCLUSIONS**

A device was designed to measure the extent of damage to the plate refractory and it was confirmed that the measurement accuracy is above 99%, indicating a reliable performance of the device. Damage to the middle plate refractory typically occurs more on the upper side. However, there are cases where the damage is more significant on the lower side, specifically in plates that exhibit traces of air inflow between the plates or have a big crack. After observing greater plate damage in the casting of alloys with lower carbon content, it has been confirmed that decarburization of the plate may also have a major impact on plate damage. And It was confirmed that as the erosion to the middle plate increases, the quality of the slab deteriorates.

From this result, it can be seen that the extrinsic inclusions originating from the tundish plate are difficult to remove from the mold. This means that inclusions introduced from the top of the mold do not have enough opportunities to separate and float, and it can be seen that the development of technology that can minimize damage to plate refractories can help improve steel quality.

# MINERALOGICAL FEATURES OF TUNDISH MGO–SPRAY AND THEIR INFLUENCE ON THE REOXIDATION OF AL–KILLED STEEL

C. Milot, C. Ganser, L. Loison, R. Belissont, J. Jactard,
ArcelorMittal Maizières Research, Maizières-les-Metz, France

## ABSTRACT

The tundish is the last vessel in contact with liquid steel before solidification into semi-finished products. The working lining of this container is usually a 30 mm thick layer of sprayed material which must achieve sufficient workability and dryability with simultaneously high insulative properties and low mechanical strength to allow deskulling. Its role is crucial in the steel quality since reoxidation inclusions generated in the tundish are hard to remove before steel solidification. With price increase of Chinese sintered Magnesia, steel plants tend to use lower MgO-content sprays to lower the cost, containing either lower quality of Magnesia, or higher Olivine content. After characterizing the mineralogy of different material formulations, the high temperature reactions were addressed thanks to XRD and quantitative Rietveld analysis. To assess the influence of the mineralogy and of the microstructural features, a lab test in contact with liquid steel was carried out Inclusion analysis was performed to reveal the reoxidation of killing aluminum and its dependance on lining material quality.

## INTRODUCTION

At the continuous caster for flat production, the tundish working lining can experience up to 3000t of steel during one casting sequence. Depending on sequence length, the sprayed refractory is in contact with liquid steel for duration from 4h up to 24h right before solidification in the mold. Added to the high contact surface with liquid steel, the refractory material exhibits a real risk of contamination of the steel. This refractory material is a blend of Magnesia and Olivine used to provide the thermal insulation, be easily disposable after use and at competitive price. It must also guarantee a low reactivity with the liquid steel because late reoxidation inclusions generated in the tundish are hard to remove and strongly impacts the semi-finished product quality. However, the price increase of Chinese Magnesia raw materials forced the suppliers to lower the MgO content and find alternatives to remain competitive. The strategy adopted consists in replacing the sintered Magnesia by Olivine which is a natural raw material mainly composed of a solid solution of Fayalite and Forsterite with the formula $2(MgO, FeO)SiO_2$.

Reactions between disposable MgO material and steel have been examined and different mechanisms are described in the literature. Beside Hydrogen pick up or contamination with other elements (Si, B, …), the main risk for steel quality is the generation of slivers due to reoxidation of Aluminum used for killing. For tundish refractory lining, reoxidation occurs mainly by transferring oxygen from reducible oxides contained in raw materials ($Fe_2O_3$ and $SiO_2$) to Aluminum dissolved in the steel. The reduction reaction forms additional Alumina inclusions which are difficult to remove before solidification. As observed by Lehmann et al. oxygen comes mainly from Iron oxide contained in the refractory rather than Silica [1]. The same study also showed that quality of the drying and of the preheating is crucial for steel reoxidation, with more reoxidation when the lining is only dried at 180°C instead of being preheated at 1200°C. This operation should be controlled carefully to reduce not only risk of H-pickup but also oxygen transfer to the steel. After alteration in contact with steel, reduction of Olivine generates Fe metal exsolution. Those droplets of metal are dispersed throughout the Olivine grains [2]. Although iron oxide and chemically bonded water are the two main sources of oxygen, Lehman et al. showed that the reoxidation of steel is activated by the formation of an interfacial liquid silicate phase which releases oxygen and speeds up the reactions between the refractory and the steel constituents. This silicate phase can be found between periclase grains in the magnesia raw materials or at the edge of Olivine which is enriched in lime [1][3].

According to Kalantar et al. the melt formation in the refractory microstructure, in the case of reaction with tundish slag, could be avoided by addition of Olivine [4]. In Olivine, the refractory phase Forsterite protects the grain from the formation of low melting phase like Monticellite. When slag penetrates into pores of lining, low melting point phases develop around MgO grains and provide continuous dissolution of Periclase during steelmaking process. Despite introducing reducible oxides, replacing part of the Magnesia by Olivine could have a positive influence to decrease dissolution of Periclase.

The present study aims at determining the differences found in the mineralogy of tundish lining products and their effect on the reoxidation of killing Aluminum contained in the steel. Therefore, several products were characterized with X-Ray Diffraction analysis before and after thermal treatment at 1600°C to enlighten the differences of mineralogy. Those mineralogical features were linked with a lab reoxidation study performed in contact with Al-killed steel

## MATERIALS AND METHOD

### Materials selection

The materials selected for this study have different chemistries measured with X-Ray Fluorescence (XRF). The product A has a high MgO content of 74,4% while the other ones have MgO contents between 62,1% et 67,5%. The product A has also a high CaO (6,0%) and a high $Na_2O$ (0,5%) content.

Tab. 1: X-Ray Fluorescence analysis of the tundish lining samples

| Sample # | A | B | C | D |
|---|---|---|---|---|
| $Fe_2O_3$ (%) | 3,4 | 4,4 | 4,9 | 3,9 |
| $SiO_2$ (%) | 14,3 | 28,9 | 30,5 | 25,3 |
| CaO (%) | 6,0 | 0,9 | 0,9 | 1,9 |
| $Al_2O_3$ (%) | 1,1 | 0,6 | 1,0 | 0,8 |
| MgO (%) | 74,4 | 64,8 | 62,1 | 67,5 |
| $P_2O_5$ (%) | 0,3 | 0,3 | 0,2 | 0,2 |
| $K_2O$ (%) | 0,1 | 0,1 | 0,1 | 0,0 |
| $Na_2O$ (%) | 0,5 | 0,1 | 0,2 | 0,3 |
| LOI (%) | 3,59 | 1,52 | 3,92 | 4,41 |

The materials were fired at two temperatures in a resistive furnace:
- 450°C/12h on 500g of powder material placed in a stainless steel plate
- 1600°C/6h on 100g of formed material (mixed with water, cast in a mold, dried at 110°C and demolded)

### X-Ray Diffraction (XRD)

The mineralogical composition and the origin of raw materials is determined using powder X-ray diffraction (XRD). The samples are milled to a 63µm top size using tungsten carbide vibrating disc mill. X-ray diffractograms, or scans, are collected using a Bruker D2 Phaser equipped with a Co source (Co Kα 1.789 Å) and a Lynxeye 1D silicon strip detector in Bragg-Brentano geometry. Primary and secondary beam focusing is performed using 2.5° Sollers and a 1mm divergence slit. A 3mm anti-scattering screen and a Fe-filter is set in front of the detector to reduce Co Kβ emission. Scans are acquired on the 7-80° 2θ range, with increments of 0.02 2θ. A dwell time of 1.5s is used for initial

445

qualitative mineralogical evaluation of the samples, while 0.5s is proven sufficient for phase quantification. Phase identification is performed using Bruker's EVA software with the ICDD PDF-2 database, and quantitative phase analysis is obtained using Rietveld refinement in Bruker's TOPAS software.

**Reoxidation test and inclusions analysis**
The samples were put in contact with a liquid steel grade containing 0,85 wt.% of Al. The test consisted in covering the bottom of an $Al_2O_3$ crucible with the tundish spray after mixing 200g of dry material with 27% water. After drying at 600°C for 2h in a resistive furnace, the crucible is used for steel melting. A reference crucible without any MgO spray is used as baseline. The assembly was heated in an induction melting furnace. For the beginning of the manipulation, a mass of electrolytic iron (90-99.99% of pure iron) is placed in the crucible. Vacuum is pulled and Ar is flushed to ensure the neutral atmosphere. The inductor is started to complete the melting. Afterwards, an addition of 1g of carbon is performed for deoxidizing the bath. The steel sample is alloyed to the targeted composition. A quartz sampling rod is used to sample the steel and check the chemical composition thanks to gas fusion and analysis for O, S, N and C and with spark spectrometry for all other elements. A residence time of 2h is completed at 1600°C before stopping the inductor and cooling down. After the melting, the ingot is extracted from the crucible to sample the solidified steel. A central slice of 1cm thickness is cut, and three parallelepiped samples are retrieved from this slice, according to Fig.1.
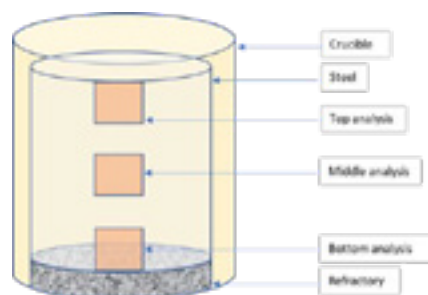


*Fig. 1: Sampling for Scanning Electron Microscopy for inclusions analysis.*

The samples are then coated with Bakelite-type conductive resin and polished to be observed with SEM Tescan Mira 3. The inclusion analysis was performed automatically via Intelissem automatic analysis software developed by the company RGLee Group to quantify and characterize the inclusions. The raw data of inclusions analysis are post-processed by an internally developed software using machine learning After a correction of the data considering the steel matrix composition, a clustering is performed to yield groups with similar features. This software is used to identify and quantify the $Al_2O_3$ inclusions. The quantity of the $Al_2O_3$ inclusions is compared to the total number of inclusions detected on each sample.

**RESULTS**
**Mineralogy after thermal treatment at 450°C**
The mineralogical composition after firing at 450°C is depicted in Fig.2 . The major phases were:
- Periclase (MgO) from the Magnesia
- Forsterite ($2MgO \cdot SiO_2$) and Enstatite ($MgO \cdot SiO_2$) from the Olivine

For simplification, other minor phases of Olivine were grouped under the category "Serpentines", namely:
- Talc ($3MgO \cdot 4SiO_2 \cdot H_2O$)
- Clinochlore ($5(Mg,Fe)O \cdot 3SiO_2 \cdot Al_2O_3 \cdot 4H_2O$)
- Lizardite ($3MgO \cdot 2SiO_2 \cdot 2H_2O$)

The category "Others" contains impurities from Magnesia as Quartz ($SiO_2$), Cordierite ($2MgO \cdot 2Al_2O_3 \cdot 5SiO_2$), Merwinite ($3CaO \cdot MgO \cdot 2SiO_2$), and even Larnite ($2CaO \cdot SiO_2$) for product A.
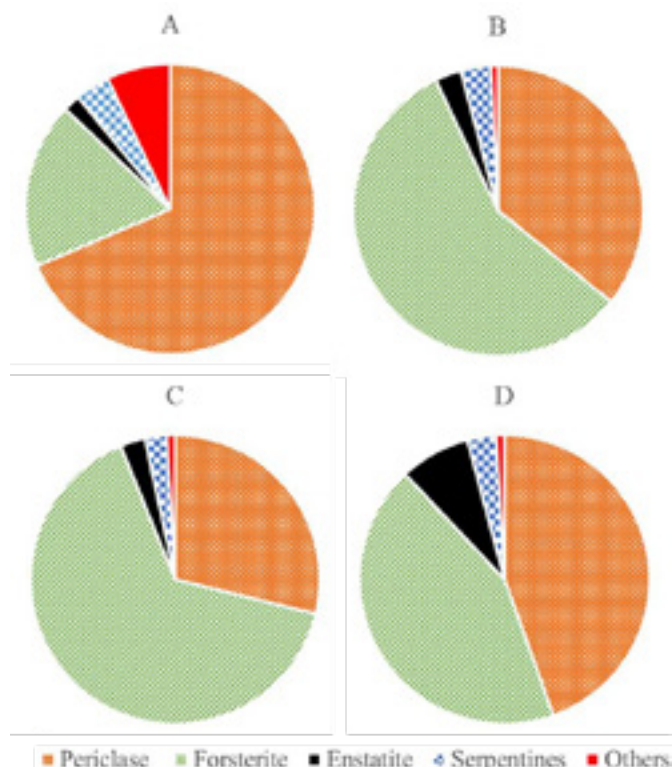


*Fig. 2: Mineralogical composition quantified from XRD analysis thanks to Rietveld analysis after firing at 450°C/12h*

The XRD revealed that only forsteritic Olivine is used in the investigated samples. No Fayalite was detected, but EDX analysis with Scanning Electron Microscopy (SEM) showed $Fe_2O_3$ in the Olivine grains:
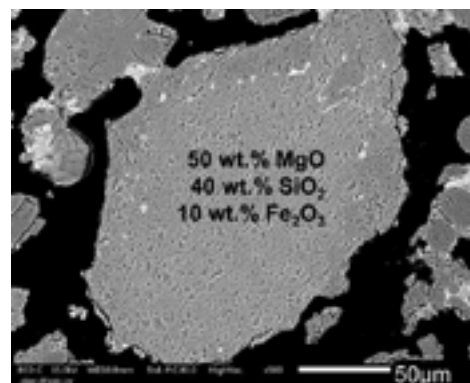


*Fig. 3: SEM micrograph of an Olivine grain with EDX analysis of its chemical composition*

The ratios Periclase/Forsterite is different between the products, in agreement with the chemical MgO content (Tab.1). The mineral impurities content is higher for the product A with "Others" containing mostly Merwinite and Larnite. The Enstatite content is the highest for the product D, but the Periclase content is high, indicating that the high Enstatite is due to the poor quality of the Olivine rather than its content.

**Mineralogy after thermal treatment at 1600°C**
Samples were cast in cylindrical molds before firing at 1600°C for 6h. After cooling down, a part of the sample was cut and grounded for XRD quantitative analysis.
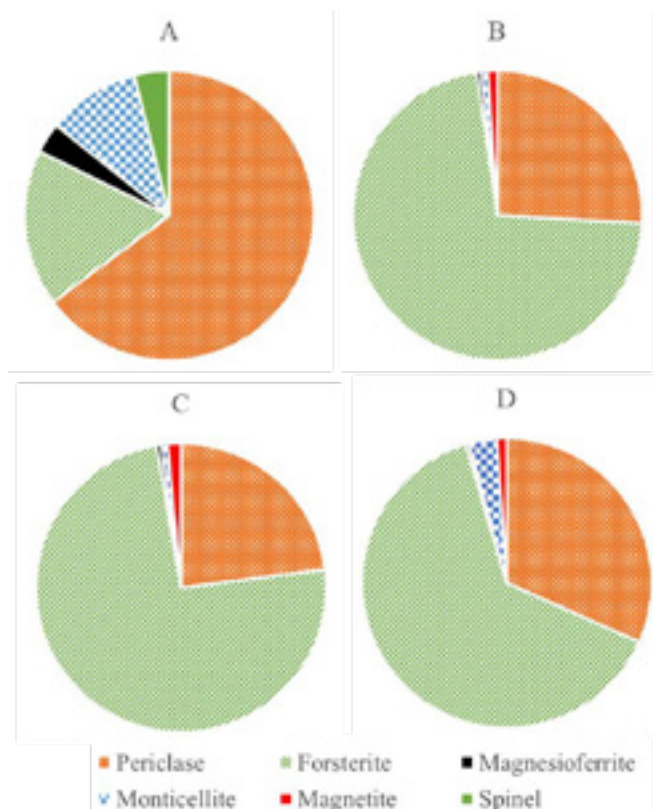
*Fig. 4: Mineralogical composition quantified from XRD analysis thanks to Rietveld analysis after firing at 1600°C/6h*

Tendencies in the evolution of the mineralogy are observed:
- Decrease of the Periclase content, due to the dissolution in low melting phases and reaction with Enstatite to form Forsterite
- Dehydration of the Serpentines to form Enstatite which further reacts with Periclase to form Forsterite
- Increase of Forsterite due to the above-mentioned reactions
- All impurities form Magnetite, Magnesioferrite and Monticellite

**Reoxidation of Al-killed steel lab test**

Based on the mineralogic characterization performed after firing at 1600°C, lab test was performed to assess the reoxidation of Al-killed steel in contact with the tundish lining materials. The four samples and a reference crucible without MgO spray were tested.
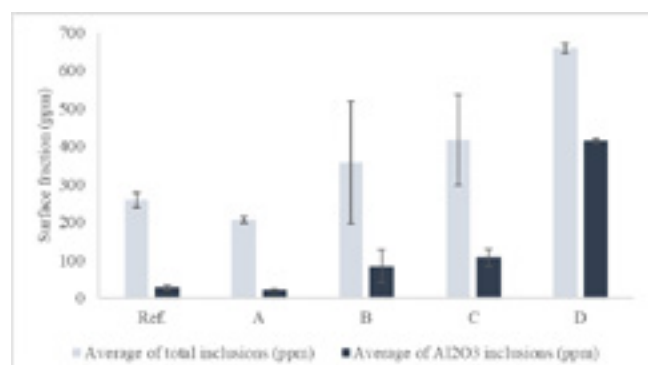


*Fig. 5: Inclusions quantification on steel samples retrieved after 2h in contact with refractory at 1600°C. The error lines represent the deviation between botton/middle/top samples. The bars are the average of inclusions quantity between bottom/middle/top samples.*

On Fig. 5, the total inclusions and the $Al_2O_3$ inclusions are depicted. The inclusions which are not $Al_2O_3$ were mainly MnS.

The formation of $Al_2O_3$ inclusions is depending on the refractory used. There is a strong difference between the product A (22 ppm), with reoxidation level comparable to the crucible without sprayed material, and the product D, which shows a strong reoxidation of the killing Aluminum (415 ppm). While the product with the highest MgO content shows the lowest reoxidation (product A), the product D with 67,5% MgO shows higher reoxidation (415 ppm) than the product C with 62,1% MgO (107 ppm). This emphasizes that the chemical MgO content is not reliable enough to estimate the risk of reoxidation in contact with liquid steel. The deviation between bottom, middle and top can give an indication on the speed of the reaction. For product D with low deviation, it can be estimated that the reaction is fast and that the liquid steel bath had time to be homogenized during the duration of the lab test (2h). However, for products B and C with high error bars, the oxygen transfer might still be ongoing at the end of the test, with strong discrepancy in the inclusions content between bottom, middle and top samples. Concerning the tundish residence time, not only the extent of the oxygen transfer but also the reaction kinetics should be considered.

A sample used for preliminary test was retrieved for examination with Scanning Electron Microscopy (SEM). The distribution of the mineral phases were observed:
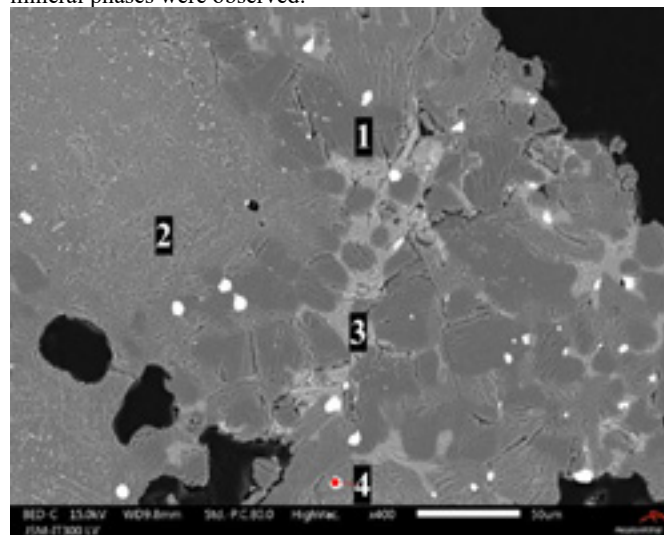


*Fig. 6: SEM micrograph of tundish lining after performing lab reoxidation test at 1600°C/2h in contact with Al-killed steel*

Tab. 2: EDX measurements from Fig.6:

| [wt.-%] | MgO | $SiO_2$ | FeO | $Al_2O_3$ | CaO | Constituent |
|---|---|---|---|---|---|---|
| 1 | 100 | | | | | Periclase |
| 2 | 49,5 | 43,8 | 6,6 | 0,1 | | Olivine |
| 3 | 26,4 | 36,2 | | | 36,3 | Monticellite |

| [wt.-%] | Fe | Mg | Al | $O_2$ | Constituent |
|---|---|---|---|---|---|
| 4 | 82,3 | 11,2 | 2,3 | 3,3 | Steel |

The micrograph shows both Olivine and Magnesia constituents. The solid solution of Fayalite and Forsterite is visible in the region 2. Metallic exsolutions can be observed at the periphery of the Olivine grain. In the region of the Magnesia, crystals of Periclase are embedded in a low melting phase matrix with Monticellite composition.

Considering the hypothesis of [1], $Fe_2O_3$ should be the main source of oxygen and the presence of a liquid silicate phase activates and speed up the oxygen transfer toward the steel. It was first decided to focus on the correlation between the [Monticellite%] formed at 1600°C and the reoxidation of killing aluminum. However, the product with the highest Monticellite content (product A with 10,4% Monticellite) shows low reoxidation (22 ppm of $Al_2O_3$ at the

same level than the reference crucible). This sample had also the specificity to exhibit no Magnetite ($Fe_2O_3$), which is suspected to be the main source of oxygen for reoxidation of Al-killed steel. Based on those considerations, the reoxidation $Al_2O_3$ inclusions were plotted depending on the content of both Monticellite and Magnetite after firing at 1600°C:
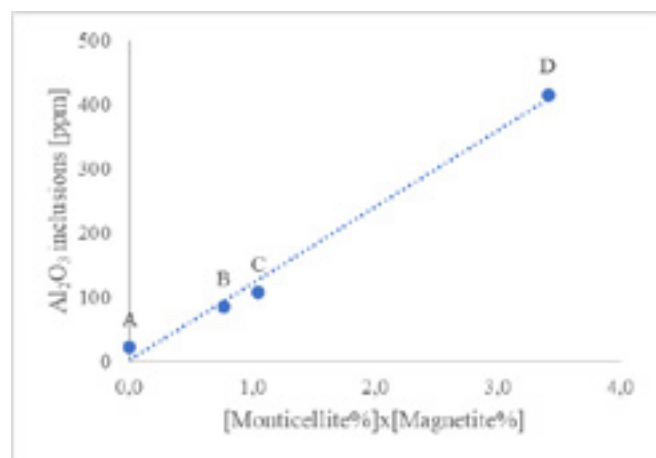


*Fig. 7: Correlation between the $Al_2O_3$ inclusions formed during lab reoxidation test and the product [%Monticellite] x [%Magnetite] contained in the product after firing at 1600°C/6h*

The formation of $Al_2O_3$ during lab test seems to be correlated with the mineral impurities quantified after thermal treatment [Monticellite%]x[Magnetite%]. This confirms the hypothesis enunciated by Lehman et al and this correlation could be a used to assess the risk of reoxidation without performing a test in contact with liquid steel.

**CONCLUSIONS**

Based on XRD analysis before and after lab firing at 1600°C, different features were retrieved to assess the mineralogical quality and high temperature stability of the tundish working lining. It was observed that after firing at 1600°C, the mineral impurities are reacting to form three phases: Monticellite, Magnetite and Magnesioferrite. During heating, while the Periclase peak decreases due to dissolution in low melting phase and reaction with minor phases from Olivine, the Forsterite peak increases, lowering the amount of molten phases generated in the material.

To understand further the link between the mineralogy and the reoxidation, lining materials were put in contact with Al-killed steel during lab experiment. The test showed that the mineral purity has a great influence on the reoxidation of the killing Aluminum. The determining factor to assess the risk of reoxidation based on the mineralogy of the lining is likely to be the product of Monticellite and Magnetite contents after firing at 1600°C. The Magnetite can be considered as the reservoir of oxygen to be transferred to the steel while the Monticellite activates and accelerates this transfer by forming liquid silicate phase. The knowledge of this parameter can support the reduction of cost for the raw material composition while ensuring the chemical inertia of the lining.

**REFERENCES**

[1] Lehmann J., Boher M. Kaerlé M. C., An experimental study of the interactions between liquid steel and a MgO-based tundish refractory, CIM Bulletin, Vol. 90 (1013), pp. 69-74, 1997

[2] Pack A., Tracing the origin of oxide inclusions in continuously casted steel using stable oxygen isotopes – an interdisciplinary approach, These, Bonn, 2000

[3] Moshtaghioun B. M. Monshi A., Analyze complex phases of slag-tundish plaster reactions by modified XRD ratio of slopes method for some kinetic considerations, Journal of materials processing technology 196, pp. 52-63, 2008

[4] Kalantar M., Moshtaghioun B. M., Monshi A., Developing two new tundish plasters and comparing with the magnesia plaster used in continuous casting of steel, Journal of Materials Engineering and Performance, Vol. 19 (2), pp.237-245, 2010.

# THE INFLUENCE OF CA, NA-, AND P-CONTENT OF MGO-BASED RESIN-FREE VIBRATEABLE DRY TUNDISH LININGS ON THE POPULATION OF NON-METALLIC INCLUSIONS IN A STEEL MELT

D. Veres, F. Kerber, S. Dudczig, C.G. Aneziris
Technical University Bergakademie Freiberg, Germany

S. Horn, C. Setzer, K. Lippold
Chemische Fabrik Budenheim KG, Germany

## ABSTRACT

The state-of-the-art magnesia-based dry vibrateable tundish linings are predominantly bonded by resin. However, besides high energy consumption, the pyrolysis of the resin-containing lining during the tundish heat-up process generates hazardous gases and carbon residues, resulting in an unwanted carbon pick by the molten steel after the finished ladle treatment. For water-based or spray-coated tundish linings, similar energy consumption can be anticipated since the remaining water of the hydraulic bonding need to be removed during the heat-up process to avoid damage of the lining by released steam or H2 dissolution by the steel melt. In contrast to resins or water-based binders needing a heat-up at high temperatures, there are binders with a cold or a low-temperature bonding behaviour such as sol/gel, acid-base, or thermally (low temperature) activated systems.

Hence, the aim of this study was to combine acid-based with thermally activated binder systems to develop new resin-free tundish linings. Therefore, Ca-, Na-, and P-containing chemicals/hydrates as well as organic acids were used to promote the thermally activated acid/base bonding reaction. Their influence on the physical and mechanical properties such as density and compressive strength of the lining was investigated. Additionally, utilizing a unique steel casting simulator, the influence of newly developed lining compositions on the steel quality compared to a reference binder system was tested and analysed. The influence on the inclusion population in the molten steel as well as the elemental composition of the steel was evaluated.

Results showed that the reaction time is strongly dependent from the solubility of the acids. Lower dissolution results in an increased strength development with increasing temperature. Newly developed compositions showed no significant influence on the steel cleanliness, only a minor change in the population could be detected.

## INTRODUCTION

Impurity and inclusion reduction in the steelmaking industry have become extremely important in the past few years [1–3]. To challenge this issue, filters can be used for melt filtration [4–7]. However, a significant reduction of inclusions can be also achieved by improved refractory lining materials[8], which also influence the service life. These improvements should fulfil the customer requirements.

Lately, the tundish in the continuous casting process has assumed the role of an inclusion removal device and metallurgical reactor [9]. Depending on the steel grade, inclusions in the form of alumina or spinel can be found. They influence the steel castability and cleanliness [8]. Beside, reducing the CO2 emission and footprint and lowering the energy demand is one of the key and challenging issues of the XXI century to follow the Kyoto protocol. Furthermore, health-related issues i.e. avoid the evolution of hazardous gases during the process, is of high importance. Therefore, refractory materials and systems with new developments are in continuous reconsideration.

MgO and/or olivine with a novolac or resin bond is state of the art for tundish linings. During the tundish heat up, with increasing temperatures resin releases smelly and hazardous gases. It undergoes pyrolysis, which leaves carbon residues in the lining, that later could cause unwanted carbon pickup in the steel. Novel bonding systems use a two component (2K) or cold binder system based on sodium silicate [10]. These systems allow both a cold and hot start. Spray linings are an alternative to the dry mixture, which, however, still need to be dried and cured between 150 and 250 °C.

Not only the binder system but the MgO quality of the tundish lining plays an important role for the steel quality. Reoxidation reactions between molten metal and the refractory according Lehmann et al. [11] increases when the MgO content of the refractories decreases. The triggering reaction for this reoxidation is the reduction of the iron, that is influenced in turn by the silica content. Furthermore, the water content is an important aspect. Refractories fired at 1200°C before liquid metal contact provide less reoxidation than dried at 180°. As an indirect prove, Kerber et al. presented immersion results for different MgO-C qualities, showing a decreasing size of Al2O3 inclusion with increasing MgO quality [12,13]. Furthermore, the overall inclusion chemistry was dependent on the MgO qualities. Many authors described the inclusions, their form and the influence on the steel properties [14–16]. Generally, it can be said that hard inclusions such as Al2O3 are the most detrimental for the steel quality and can lead to critical failure in the casted parts. Novel improvements try to fit the requirements for no carbon or silicate borate addition in the tundish lining mixtures. Since the last key process stage before casting occurs in the tundish, the requirements for the tundish lining simultaneously include short service time and long service life at a low price.

In this paper, the development of novel binder systems and their differences in comparison to a conventional resin-based tundish lining composition are presented. Beside of the basic properties, their contact with liquid steel was investigated and their influence on the steel quality in terms of the inclusion population

## EXPERIMENTAL PROCEDURE

MgO from Chinese source (CM) with fractions of 0-1 mm and fine <63 µm (F) fractions were used. The chemical analysis is given in Tab. 1. As binder system, acids Oxalic acid (Oxs) Adipic acid (Ads) and Salicylic acid (Salics) in combinations with different trisodium-phosphate -6 hydrates (NaPH6H) and -12 hydrates (NaPH) were tested. All components were supplied from the Chemische Fabrik Budenheim Kg. Furthermore, in perspective of the high temperature phase composition to avoid Phosphor contamination as far as possible, calcium source in form of calcium hydroxide and calcium carbonate was introduced. As reference, a state-of-the-art (SoA) MgO composition with 4 wt.-% of novolac powder resin and hexamethylentetramine as hardener was used.

The mixtures were prepared with an Eirich EL1 intensive laboratory mixer using the following settings: 15 m/s rotor speed and 5 minutes mixing time.

449

Tab. 1: Chemical composition of the used MgO

| GRAIN SIZE | content in % | | | | | |
|---|---|---|---|---|---|---|
| | $Al_2O_3$ | $CaO$ | $Fe_2O_3$ | $MgO$ | $MnO$ | $SiO_2$ |
| 0-1 MM | 0.7 | 1.9 | 1.1 | 92.5 | 0.1 | 3.4 |
| < 63 μM | 0.9 | 2.0 | 1.1 | 92.3 | 0.1 | 3.4 |

Cylindrical steel moulds with a diameter of 50 mm and a height of approx. 50 mm were used. The powder mixtures were filled and the samples were compacted with a compaction tool, adapted from a compressed air tamper. A defined weight was crushed onto the surface area from 50 cm height 5 times. The maximum applied compaction force was approx. 0.005 MPa.

For the steel casting simulator tests, bars with dimensions of 120x25x25 mm³ were prepared the same way.

The reference samples with powder resin were cured at 180 °C using the traditional heating schedule with 2 steps in between. The newly developed sample compositions were cured with a heating rate of 2 K/min and a final dwell time of 3 hours at 150 °C. The density and the cold crushing strength (CCS) (Tiratest 28100) of the specimens were then measured.

For "finger" tests, reference sample with resin binder were coked up to 1000 °C in coke grid. Samples with the newly composed binder system were preheated up to 1100 °C in oxidizing atmosphere.

Tests in the steel casting simulator were carried out while samples were immersed in approx. 38 kg of steel (42CrMo4) at 1600 °C with an immersion time of 20 minutes. The test took place under fully controlled argon atmosphere, see Fig 1.
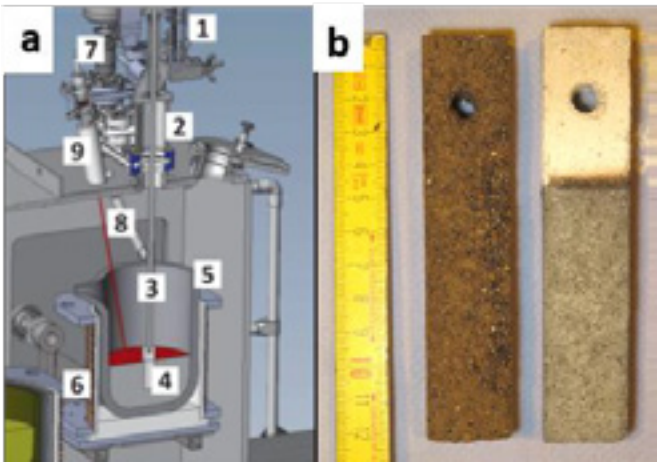


Fig. 1: Immersion test: a - Scheme of the steel casting simulator (1 – rotatable revolver system, 2 – chamber for sample handling, 3 – sample holder, 4 – sample in melt contact, 5 – melting crucible, 6 – induction coil, 7 – gas tight reservoir for additives, 8 – feeding mechanism, 9 – pyrometer) according to [17]; b – exemplary specimens before (left) and after (right) the immersion test.

For the generation of inclusions, the steel melt was firstly oxidized with 0.5 wt.% FeOx powder and then deoxidized with 0.05 wt.% aluminum chippings (both related to the total steel mass) prior the immersion of the refractory specimen. After the immersion, the steel was cooled down inside the crucible. For each specimen, a fresh steel sample and a fresh crucible was used.

Samples 50x50 mm2 with a height of approx. 10 mm were cut out form the solidified steel blocks, lapped and polished to identify the inclusions and its population in a defined area with the aid of automated feature analysis using an automated scanning electron microscope equipped with energy dispersive X-ray spectroscopy (ASPEX PSEM eXpress, FEI, USA). The inclusion size distribution was analyzed by means of population density functions relating the inclusion count in a bin to the corresponding bin width [18]. The steel quality was further analyzed via optical emission spectroscopy analysis (OES).

**CONCLUSION**

Temperature activated novel acid-base binder systems were developed for the tundish lining. The influence of the acid source and the influence of calcium addition were investigated. The solubility of the acid plays a major role for the strength development. Calcium addition up to a certain level also increases the strength. It was observed that the samples prepared with the novel binder systems present comparable results to the resin-bonded tundish linings. There was no increase irregularity for S and B content in the samples. Interestingly the raw steel sample and samples from the immersion experiment performed with the specimens containing the new binder system with CaCO3, NaPH6H and Ads/Oxs show the highest P and Al content, followed by the sample without Ca content. Despite, all result are within the tolerance.

The results of the quantitative inclusion analysis can be summarized as follows:

- The main inclusion types were alumina, and Mn-Si containing inclusions, either with pronounced Al-rich regions or without

- The frequency of Mn-Si containing inclusions appeared to be highly sensitive to oxygen content and also sensitive to the steel melt temperature.

- A higher initial oxygen content resulted in a higher frequency of Mn-Si containing inclusions indicating that such inclusions are formed by reoxidation of the steel melt.

- A higher steel melt temperature tends to reduce the number of Mn-Si containing inclusions, supporting the assumption of Mn-Si dissolution in the steel melt.

- Additional factors might affect the Mn-Si formation, which were not identified yet. Based on the collected data, no type-dependent influence of the immersed specimen on the Mn-Si inclusion formation was observed.

- The size distribution of Al2O3 appears to be highly sensitive to the steel melt temperature, showing an increasing size (larger right sided tail in the PDF curves) with increasing temperature.

- Despite, a type-related effect of the immersed specimen was identified, showing an increasing inclusion size with increasing proportion of Ca contained in the immersed specimen.

- Nevertheless, the inclusion size distribution was comparable or even shifted to a smaller inclusion size compared to the reference experiment performed with a resin-bonded specimen.

- Therefore, the usage of the new binder system containing CaCO3, NaPH6H and Ads/Oxs revealed no adverse effect on either inclusion size distribution or inclusion chemistry.

**ACKNOWLEDGEMENT**

**REFERENCES**

[1] P. Tassot, C. Turrel, Some trends for the tundish refractory lining, Refract. Worldforum. 3 (2011) 93–98.

[2] D.H. Lee, J.H. Lee, Y.M. Cho, C.J. Um, Refinable lining material for clean steel in tundish, UNITECR 2007. (2007) 354–357.

[3] I. Krausz, P. Tassot, C. Turrel, Element Pick-Up in Liquid Steel from Tundish Lining Refractories, in: UNITECR 2009, Salvador, 2009: pp. 1–4.

[4] M. Emmel, C.G. Aneziris, G. Schmidt, D. Krewerth, H. Biermann, Influence of the Chemistry of Surface Functionalized Ceramic Foam Filters on the Filtration of Alumina Inclusions in Steel Melts, Adv. Eng. Mater. 15 (2013) 1188–1196. https://doi.org/10.1002/adem.201300118.

[5] E. Storti, S. Dudczig, A. Schmidt, G. Schmidt, C.G. Aneziris, Filter Functionalization with Carbon Nanotubes and Alumina Nanosheets for Advanced Steel Filtration, Steel Res. Int. 88 (2017) 1700142. https://doi.org/10.1002/SRIN.201700142.

[6] E. Storti, M. Farhani, C.G. Aneziris, C. Wöhrmeyer, C. Parr, Calcium Aluminate Reactive Coatings on Carbon-Bonded Alumina Filters for Clean Steel Approaches, Steel Res. Int. 88 (2017). https://doi.org/10.1002/SRIN.201700247.

[7] E. Storti, S. Dudczig, M. Emmel, P. Colombo, C.G. Aneziris, Functional Coatings on Carbon-Bonded Ceramic Foam Filters for Steel Melt Filtration, Steel Res. Int. 87 (2016) 1030–1037. https://doi.org/10.1002/SRIN.201500446.

[8] M.C. Mantovani, L.R. Moraes, R. Leandro Da Silva, E.F. Cabral, E.A. Possente, C.A. Barbosa, B.P. Ramos, Interaction between molten steel and different kinds of MgO based tundish linings, Ironmak. Steelmak. 40 (2013) 319–325. https://doi.org/10.1179/1743281212Y.0000000035.

[9] P. Tassot, C. Turrel, O. Jonsson, J. Wang, Improvement in the productivity and steel quality by introducing innovative solutions for tundish, in: UNITECR 2011, 2011: pp. 453–456.

[10] E.Y. Sako, V.P.S. Ramos, A. Nascimento, S.M. Justus, S.C. Frasson, D.F. Galesi, M.T. Fadel, Novel dry mix technology for tundish refractory lining, Proc. Unified Int. Tech. Conf. Refract. UNITECR 2013. (2014) 559–564. https://doi.org/10.1002/9781118837009.ch96.

[11] J. Lehmann, M. Boher, M.C. Kaerlé, An experimental study of the interactions between liquid steel and a MgO-based tundish refractory, Cim Bull. (1997).

[12] F. Kerber, T. Zienert, J. Hubálková, V. Stein, T. Schemmel, H. Jansen, C.G. Aneziris, Effect of MgO Grade in MgO C Refractories on the Non-metallic Inclusion, Steel , Steel Res. Int. 93 (2022). https://doi.org/https://doi.org/10.1002/srin.202100482.

[13] F. Kerber, P. Malczyk, V. Stein, T. Schemmel, H. Jansen, C.G. Aneziris, Influnce of the MgO grade in MgO-C refractory material and steel melt, Intern. J. Ceram. Eng. Sci. (2022) 102–111. https://doi.org/https://doi.org/10.1002/ces2.10119.

[14] M. Emmel, Development of active and reactive carbon-bonded filters for steel melt filtration, Ph.D. thesis Technische Universität Bergakademie Freiberg, 2014.

[15] L. Zhang, B.G. Thomas, State of the Art in Evaluation and Control of Steel Cleanliness, ISIJ Int. 43 (2003) 271–291. https://www.jstage.jst.go.jp/article/isijinternational1989/43/3/43_3_271/_pdf/-char/en.

[16] L. Zhang, B.G. Thomas, X. Wang, K. Cai, Evaluation and control of steel cleanliness - Review, Steelmak. Conf. Proc. 85 (2002) 431–452.

[17] S. Dudczig, C.G. Aneziris, M. Emmel, G. Schmidt, J. Hubalkova, H. Berek, Characterization of carbon-bonded alumina filters with active or reactive coatings in a steel casting simulator, Ceram. Int. 40 (2014) 16727–16742. https://doi.org/10.1016/J.CERAMINT.2014.08.038.

[18] M.A. Van Ende, M. Guo, E. Zinngrebe, B. Blanpain, I.H. Jung, Evolution of non-metallic inclusions in secondary steelmaking: Learning from inclusion size distributions, ISIJ Int. 53 (2013) 1974–1982. https://doi.org/10.2355/isijinternational.53.1974.

# REDUCTION OF LARGE INCLUSIONS IN BILLETS BY IMPROVING THE CLEANLINESS OF TUNDISH MOLTEN STEEL

JungMin Lee[1*], Seockju Jang[1] , Jungwoon Bae[2], WoongGan Ki[1]

[1]Steelmaking refractories Team, Hyundai Steel Company, Rep. of Korea
[2]Continuous Casting Production Engineering Team, Hyundai Steel Company, Rep. of Korea
*ljm4805@hyundai-steel.com

**ABSTRACT**

In this study, a total of 4 improvements were made to reduce large inclusions in the billet. First, the opening rate of molten steel for ladle was improved by developing ladle filler components and shape. Second, oxygen concentration is reduced through Ar purging in the tundish before casting the molten steel from ladle to tundish. Third, erosion of stopper head is reduced by improving the material. Finally, tundish slag composition is improved to reduce the reoxidation of molten steel in the tundish. To evaluate the effect of this study after casting, the mold level, molten steel cleanliness (total O, N), and billet UT were conducted.

**Keywords** : Tundish, Stopper, TD Slag, opening rate of ladle, Re-oxidation, lancing(O2)

## INTRODUCTION

In general, not only steelmaking operation conditions, but also casting operation conditions and refractory material/shape are very important for automobile steel sheets and special steels that require high quality First, if the ladle opening is not properly performed, casting is performed through oxygen opening, and in this process, the molten steel is seriously reoxidized. Since ladle opening is generally affected by filler particle size, composition, shape of ladle well block, inner diameter of ladle SN nozzle, and steelmaking lead time, it is important to use an appropriate refractory material and filler for operating conditions. Second, the oxygen concentration in the tundish immediately before casting of molten steel from ladle to tundish is an important factor in re-oxidizing molten steel in tundish. This is affected by the tundish capacity, the Ar purging amount, and the purging position, and especially this is a technique used to improve the quality of first billet. Third, stopper erosion and clogging are the biggest factors that cause large inclusions in the final product, and it is important to select an appropriate shape and material depending on the molten steel composition and continuous casting conditions. In general, MgO material is selected for Ca treated steel, and Al2O3 material is used for high carbon and ultra-low carbon steel. In particular, in the case of steel with high carbon and high Ca content, it is very important to select an appropriate material through closely analysis. Lastly, it is very important to use rice ash and B-flux alone or properly mixed for tundish slag, which is used to block the air contact of tundish molten steel, considering the molten steel temperature and composition. In this study, the four factors mentioned above were evaluated and improved to reduce large inclusions in billets for special steel in manufacturing the automobiles.

## CONCEPT OF DEVELOPMENT, RESULTS AND DISCUSSION

1) Improve the opening rate of molten steel for ladle

Four improvements were conducted to improve the opening rate of molten steel for ladle (Fig.1). First, the fine particle was reduced

and the SiO2 component was reduced to suppress the sintering ability of the ladle filler. Second, the upper diameter of the ladle well block was enlarged so that the filler could more easily pass through the well block. Third, the lead time from steelmaking to continuous casting was reduced by adjusting the amount of steel tapping in the electric furnace. Lastly, after casting of ladle, the test was conducted by reinforcing the O2 washing of metal or slag in the well block. The evaluation was carried out by sampling the molten steel of the case with and without oxygen, respectively, and analyzing the total O and nitrogen pick-up. In the case of total O pick-up, it decreased by about 4ppm, and in the case of nitrogen pickup, the result was reduced by 5ppm. (Fig.2)
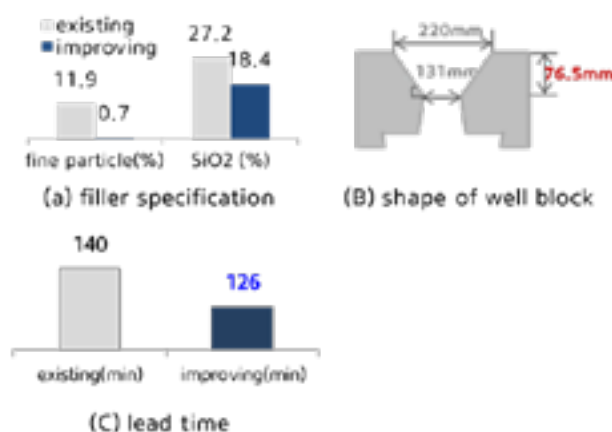


*Fig. 1. improvement of opening rate of Ladle*
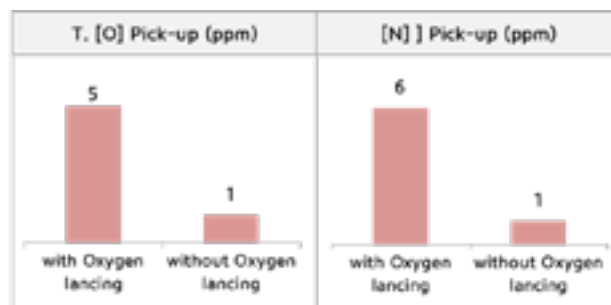


*Fig. 2. result of Total O, Nitrogen pick up*

2) Reduce the oxygen concentration in tundish immediately before casting of molten steel to tundish

Two improvements were conducted to reduce the oxygen concentration. First, the Ar purging flow rate was increased, and

second, hole on tundish cover was sealed. (Fig.3) In general, by controlling the oxygen concentration inside the tundish before casting of molten steel from ladle to tundish, the inclusion quality of first billet can be improved, and the oxygen concentration needs to be maintained at 1% or less. The oxygen concentration is mainly determined by the flow rate of Ar gas and the sealing method, and should be appropriately selected according to the capacity and shape of the tundish. We increased the Ar amount to about 3,500lpm, and sealed hole on the thudish cover. Results of the oxygen concentration measurement was controlled to about 0.1%, and amount of total O pick-up decreased by about 28% and the nitrogen pickup amount decreased by about 56%. (Fig. 4)
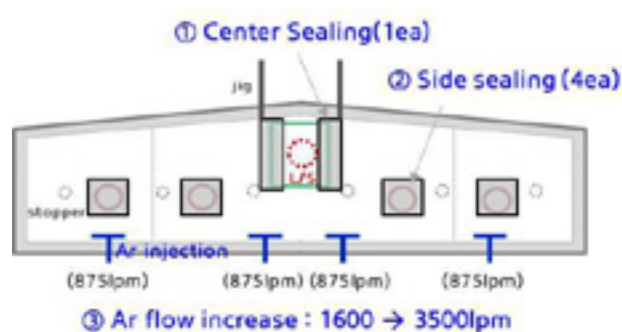


Fig. 3. improvement of Ar flow rate, sealing for tundish
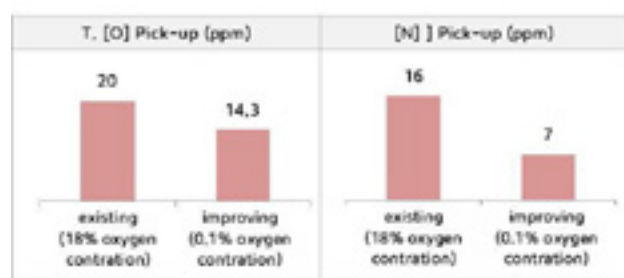


Fig. 4. result of Total O, Nitrogen pick up

3) Reduce the erosion of stopper tip

The refractory material was changed to reduce the erosion of the stopper head. In general, in the case of MgO refractory reacts with C (refractory/molten steel) and is decomposed into a gas and formed pore in the structure. during casting, molten steel penetrates the formed pores and refractory erosion is occured by structural spalling. In contrast, Al2O3 refractory reacts with CaO in molten steel and forms a liquid compound at casting temperature and refractory erosion is occured. In this study, as shown in Table.1, steel grades with high C content and high Ca content were evaluated.

Table . 1. chemical Composition of steel grade

| C | Si | Mn | Al | Ca |
|---|---|---|---|---|
| 0.36~0.39% | 0.1~0.4% | 0.7~1.1% | 0.02~0.06% | 10~15ppm |

As a result of this evaluation on the existing product, it was confirmed that erosion occurs due to the MgO decomposition reaction. As shown in Fig.5, the stopper material of MgO(50%)-Al2O3(30%)-C(15%) is changed to Al2O3(70%)-MgO(20%)-C(3%) to improve the erosion reaction with molten steel and an erosion improvement test was conducted. As a result of the test, it

was improved by about 60% compared to the conventional item, and as a result of billet MIDAS evaluation, it was As a result of tissue evaluation on the existing product, it was confirmed that erosion occurs due to the MgO decomposition reaction. As shown in Fig.5, the stopper material of MgO(50%)-Al2O3(30%)-C(15%) is changed to Al2O3(70%)-MgO(20%)-C(3%) to improve the erosion reaction with molten steel and an erosion improvement test was conducted. As a result of the test, it was improved by about 60% compared to the conventional item, and as a result of billet MIDAS evaluation, it was confirmed that large inclusions were also improved. (Fig.6)
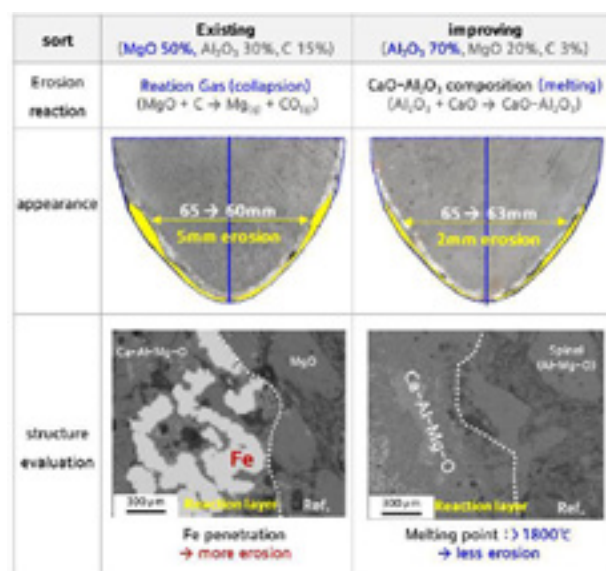


Fig. 5. Improvement Concept of materials and Erosion result of test.
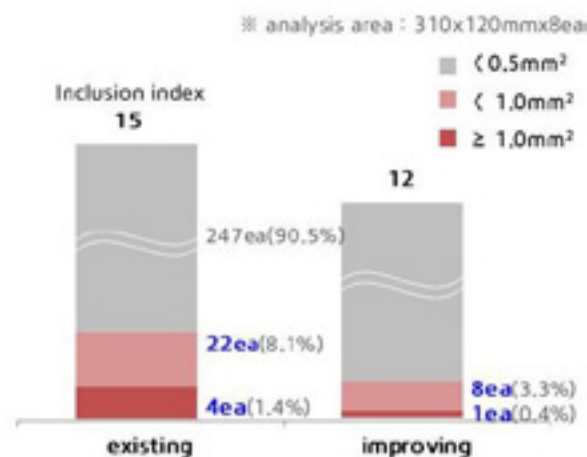
Fig. 6. Results of MIDAS after rolling billets

4) Improve the tundish slag composition

In order to block the contact between air and molten steel during casting, the tundish flux input standard was changed. Previously, the standard was to use only rice ash, but both rice ash and B-flux were put in the tundish and the improvement effect was confirmed through the FeO content in the slag after using. When only rice ash was used, FeO was detected at 9.8%. On the other hand, FeO was

detected at 1.8% when both rice ash and B-Flux were used. (Fig. 7) Rice ash and B-flux components are shown in Table.2.

Table . 2. chemical Composition of rice ash and B-Flux

| Sort | CaO | $Al_2O_3$ | $SiO_2$ | $Fe_2O_3$ | C |
|------|-----|-----------|---------|-----------|---|
| Rice ash | - | <5% | >75% | - | 10~20% |
| B-Flux | 53~59% | 30~38% | <4% | <1.5% | - |
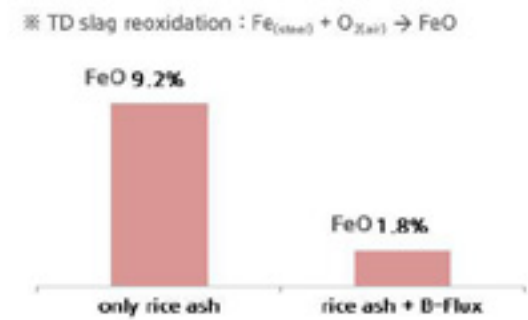


*Fig. 7. Results of FeO content analysis in TD slag*

## CONCLUSIONS

In this study, a total of 4 improvements were evaluated to reduce large inclusions in the billet (special steel for automobiles), and the results are as follows.

1) Improve the opening rate of molten steel for ladle

In the case of total O pick-up, it decreased by about 4ppm, and in the case of nitrogen pickup, the result was reduced by 5ppm.

2) Reduction of oxygen concentration in tundish immediately before casting of molten steel to tundish

Results of the oxygen concentration measurement was controlled to about 0.1%, and amount of total O pick-up decreased by about 28% and the nitrogen pickup amount decreased by about 56%.

3) Reduce the erosion of stopper tip

As a result of the test, it was improved by about 60% compared to the conventional item, and as a result of billet MIDAS evaluation, it was confirmed that large inclusions were also improved.

4) Improve the tundish slag composition

When only rice ash was used, FeO was detected at 9.8%. On the other hand, FeO was detected at 1.8% when both rice ash and B-Flux were used.

**REFERENCES**

[1] TAKANORI KOMINAMI, SHOZO WATANABE, KAZUKI SUMIDA, EIICHIRO MORI, NAKAMURA", EISHI IIDA* and TAKEO OHTAN :Taikabutsu Overseas, Vol. 18 No1

# DETERIORATION MECHANISM OF AL$_2$O$_3$−MGO REFRACTORY CASTABLE IN RH REFINING LADLE

Junfeng Chen[1], Yu Zhang[1]*, Wen Yan[1], Nan Li[1]*
The State Key Laboratory of Refractories and Metallurgy, Wuhan University of Science and Technology, Wuhan, China
Guangping Liu[2], Guoping Wei[2], Yi Zhao[2]
Zhejiang Zili Holdings Co. Ltd, Shaoxing, Zhejiang, China

## ABSTRACT

The purpose of this work was to compare and investigate the deterioration mechanism of Al$_2$O$_3$-MgO refractory castable under industrial condition. After structural optimization, the average corrosion rate of every cycle deceased to 0.31 mm/cycle from 0.46 mm/cycle. Corroded microstructure of the optimized Al$_2$O$_3$-MgAl$_2$O$_4$ refractory castable after server 195 cycles was explored. An adhered slag layer comprising mainly (Fe, Mg)Al$_2$O$_4$ spinel was observed on the refractory's surface. Iron beans and iron/manganese oxides mainly occurred in the reaction layer, and penetrating cracks occurred at the corroded interface which would cause potential structure spalling for refractory lining. Based on the observed microstructural characteristics, corrosion mechanism of refractory lining in a commercial ladle was proposed.

**Keywords:** Al$_2$O$_3$-MgO refractory; RH refining ladle; Corroded microstructure; Degeneration mechanism

## INTRODUCTION

The interaction between refractory lining and molten slag/steel in refining ladle is drawing much more attention from both refractory engineers and metallurgist. From a metallurgical point of view [1, 2], refractory lining in refine ladle is considered as the main sources of exogenous oxide inclusions. However, from the perspective of refractory, refractory lining in refining ladle is a typical complex steel/slag contact application and suffers from a harsh server environment [3-5]. Up to now, Al$_2$O$_3$-MgO system refractory castables are the mainstream choice for metal bath area and bottom in refining ladle, particularly large size ladles. Incorporation of aluminum-magnesium spinel powders and fine spinel particles into corundum based castables, corundum-spinel refractory castables processed a higher resistance to slag penetration and thermal shock when compared with pure corundum based castables [6].

One heat cycle of ladle treatment is compounded from three stages, including process of molten iron poured into ladle, refining and alloying process, and steel tapping. Hence at the different stages of ladle treatment, the Al$_2$O$_3$-MgO refractory lining needs to subject to chemical attack form molten slag/steel in the refining process, mechanical erosion from molten steel and intense thermal shock during tapping and pouring of steel processes [1, 2, 7]. For this reason, the degeneration process of Al$_2$O$_3$-MgO refractory castable during server in a commercial ladle is quite complex and dependent upon a large number of parameters. So it is difficult to achieve a deeper understanding of such degradation behavior with the laboratory scale testing, though it is contributed to estimate the service performance of potential refractory materials, assist further structure and composition optimization [8, 9].

Considering the above issues, Al$_2$O$_3$-MgO per-formed refractory bricks with alumina-silica gel powder as binder were fabricated and industrial trials in RH refining ladle after structural optimization. After that, a post-mortem analysis on the used Al$_2$O$_3$-MgO per-formed refractory brick was carried out, and compared with our previous work. Corroded microstructures were explored in detail, and degeneration mechanism governing the degeneration process was proposed and discussed in this work.

## 2. EXPERIMENTAL PROCEDURE

### 2.1 Service conditions the used refractory brick and testing process

Chemical composition of Al$_2$O$_3$-MgO refractory castable before/after structural optimization is shown in Table. 1. After pre-casting into refractory bricks (thickness: 210mm) and masonry construction, the above-preformed Al$_2$O$_3$-MgAl$_2$O$_4$ castable bricks lined the wall of a 300-ton industrial ladle. After 195 cycles in the ladle for RH operations, the residual Al$_2$O$_3$-MgAl$_2$O$_4$ refractory of trial sample was removed from the refining ladle.

Tab. 1: Chemical composition of Al$_2$O$_3$-MgO refractory castable

|  | Al$_2$O$_3$ | MgO | CaO | SiO$_2$ | FeO$_x$ | R$_2$O | TiO$_2$ | MnO |
|---|---|---|---|---|---|---|---|---|
| Trial sample | 91.92 | 5.35 | 0.28 | 1.08 | 0.86 | 0.02 | 0.04 | 0.02 |
| Contrast sample | 96.03 | 3.25 | 0.02 | 0.87 | 0.01 | 0.26 | 0.01 | - |

### 2.2 Examination of corroded microstructure

In order to obtain a whole corroded interface for microstructure analysis, the residual Al$_2$O$_3$-MgAl$_2$O$_4$ refractory was cut along corrosion direction using a diamond saw blade. A whole corroded sample (75mm in length and 25 mm in width) was characterized by a scanning electron microscope (SEM, Apreo S HiVac, ThermoFisher), along with energydispersive X-ray spectrometer (EDS, Oxford Ultim Max 100 EDS) and X-ray diffraction (XRD) analysis (Bruker D8 Advance; using Ni-filtered, Cu Kα radiation). Furthermore, the corroded interface of the used Al$_2$O$_3$-MgAl$_2$O$_4$ castable was examined by an X-ray computed tomography (CT, Phoenix v|tome|x s, GE Inspection Technologies, GmbH, Germany).

## 3. CORRODED MICROSTRUCTURES AND DISCUSSION

The residual thickness in this optimization work was approximately 150mm after 195 server cycles (initial thickness: 210 mm), which shown a g significant enhancement compared with the contract sample (residual thickness 126mm, 184 cycles). The average corrosion rate of every cycle deceased to 0.31 mm/cycle from 0.46 mm/cycle, it indicated that the corrosion resistance of optimized Al$_2$O$_3$-MgO castable improved by ~30%. For contract sample, a wide reaction layer and a through crack observed on the corroded interface which just located at the boundary of infiltration layer (figure 1).
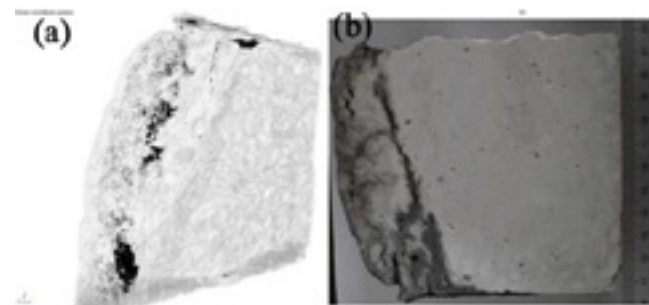


Fig. 1: *Cross-sectional image of the used Al$_2$O$_3$-MgAl$_2$O$_4$ castable after service in a commercial RH refining ladle for 184 cycles, (a) X-ray CT scanning images of the corroded sample, 3D reconstructed profile of overall corroded sample*

Compared with the previous work [10], a clearly visible difference was observed in the corroded microstructures of sample after 195 cycles after structural optimization, particularly the microstructure corroded in infiltration layer. Cross-sectional image of the used Al$_2$O$_3$-MgO per-formed bricks after 195 cycles in the refining ladle is presented in figure 2(a), revealing three main different regions

455

along the corrosion direction, reaction layer (black area), infiltration layer (gray area) and un-reaction layer. And there are several transverse and longitudinal cracks at corroded interface. The crystal phase composition in the surface layer (slag and reaction layer) and infiltration were confirmed by XRD and shown in figure 2 (b) and (c), indicating that the main phases in surface layer were gehlenite, spinel, iron oxide and calcium aluminum oxide. Moreover, it was confirmed that the infiltration layer was composed mainly of calcium magnesium aluminum silicate, gehlenite, calcium aluminum ($CA_6$), spinel and remained corundum. The detailed microstructures and phases morphology the corroded interface would be presented in the coming section.
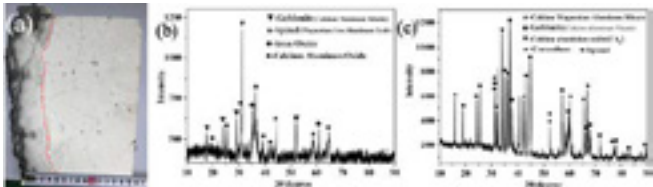


*Fig. 2: (a) Cross-sectional image of the $Al_2O_3$-MgO per-formed bricks after 195 cycles in the refining ladle, (b) XRD pattern of the surface layer (black area in (a)), (c) XRD pattern of infiltration layer (gray area in (a))*

The overall corroded microstructure of used $Al_2O_3$-MgO castable refractory is depicted in figure 3, showing four different regions including adhered slag layer, reaction layer, infiltration layer and original layer based on microstructural characterization. A thin slag layer with macro-pore structure adhered on the castable's surface, and there were many small iron beans and several iron belts in the dense reaction layer. The infiltrated slag had react with grains in the matrix and blurred the boundaries of aggregates/matrix and grains in the matrix. Besides, a through crack occurred in the boundary of the infiltration/original layer and closed to the latter.

Moreover, the chemical compositions of different regions in the used per-formed brick were analyzed by chemical titration method and the results showed in Table 2. Compared with the chemical compositions in different layers, the CaO and $SiO_2$ content in the infiltration layer is higher than that of original layer. And iron oxides as corrosive compositions main occurred in surface layer (reaction layer). The result indicated that CaO and $SiO_2$ possessed the strongest permeability in this case.
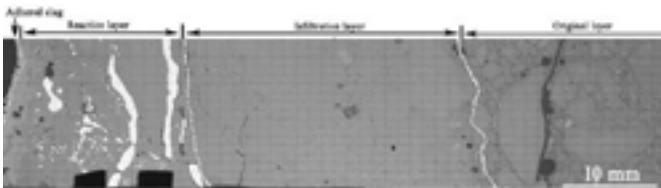


*Fig. 3: Backscattered electron image (BEI) of the overall corroded microstructure of used $Al_2O_3$-MgO castable refractory after 195 heats, showing four different layers*

Tab. 2: Chemical compositions of different regions at corroded interface (wt%)

|  | $SiO_2$ | $Al_2O_3$ | $FeO_t$ | CaO | MgO | $K_2O$ | $Na_2O$ | $TiO_2$ | MnO | LOI |
|---|---|---|---|---|---|---|---|---|---|---|
| Surface layer | 6.73 | 64.62 | 11.79 | 7.72 | 4.95 | 0.043 | 0.035 | 0.15 | 1.74 | 2.43 |
| Infiltration layer | 5.02 | 85.05 | 0.77 | 2.71 | 5.25 | 0.051 | 0.045 | 0.055 | 0.025 | 0.08 |

A high magnification BEI of refractory castable's surface is presented in Fig. 4 (a), revealing a continuous adhered layer with macro-pore structure on the surface. Based on the analysis of XRD (figure 2 (b)) and the corresponding EDS in Table.3, the main components in the adhered slag layer were ferrospinel ((Fe,

Mg)$Al_2O_4$), iron and manganese oxides and CaO-$SiO_2$-$FeO_t$-$Al_2O_3$ glass phase.

The microstructure of corroded aggregate in the reaction layer is shown in Fig.5, revealing that the calcium hexaaluminate ($CA_6$) with strip structure formed on the aggregate's surface and isolated island-liked alumina and spinel grains inside aggregate were surrounded by low-melting phase. The corroded microstructure indicated that the aggregate suffered an intergranular corrosion process which meant that slag infiltrated along the grain's boundaries in the aggregates and led to a further attack.
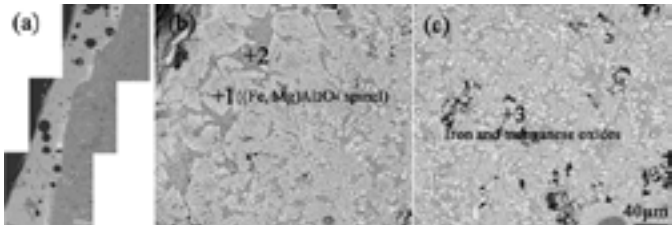


*Fig. 4: High magnification BEI of the slag layer in Fig. 2; (a) showing a continuous adhered layer*
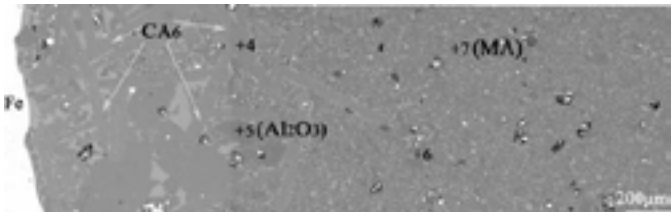


*Fig. 5: High magnification BEI of the aggregate in the reaction layer, showing the slag infiltrated along the grain's boundaries*

Tab. 3: EDS results in Fig.4 and Fig.5 (atomic %)

| Elements | Al | Mg | Ca | Fe/Mn | Si | O | Possible phase |
|---|---|---|---|---|---|---|---|
| Point 1 | 16.3 | 3.7 | - | 27.6 | - | 52.4 | (Fe,Mg)$Al_2O_4$ spinel |
| Point 2 | 4.4 | - | 15.3 | 8.5 | 9.9 | 61.9 | - |
| Point 3 | - | - | - | 48.2/4.1 | - | 47.7 | Iron and manganese oxides |
| Point 4 | 41.5 | - | 3.9 | - | - | 54.6 | $CA_6$ |
| Point 5 | 56.1 | - | - | - | - | 43.9 | $Al_2O_3$ |
| Point 6 | 42.2 | - | - | - | - | 57.8 | $Al_2O_3$ |
| Point 7 | 35.9 | 11.8 | - | 0.8/0.7 | - | 50.8 | (Fe,Mg,Mn)$Al_2O_4$ |

The generated cracks on the corroded interface can cause the structural spalling on refractory lining. The formed cracks in the infiltrated and original layer all grew along the interfaces of aggregates and matrix. The macro-image of the formed crack in the infiltrated layer shown in figure 6 (a), suggesting the infiltrated slag reacted with matrix compositions and caused densification and volume change in matrix structure. The aggregate/matrix bonding interface (weak-binding state) was prone to deterioration when suffering from the above densification and volume change process during slag infiltration. figure 6 (b) gives a high magnification image of the interface between the infiltration and the original layer, confirming that permeated slag led to a densification process with shrinkage pores structure in the matrix. The differences in the structural and chemical composition of infiltrated layer and the original layer led to various physicochemical properties. That was the primary reason for the formation and growth of cracks in corroded interface.
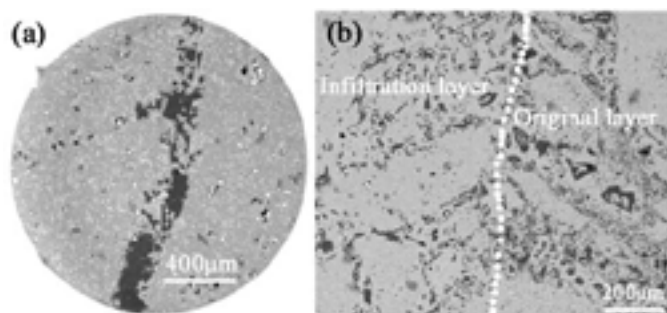
*Fig. 6: (a) Cracks generated in the infiltrated layer; (b) High magnification image (BEI) of the interface between the infiltrated layer and the original layer*

## CONCLUSIONS

A post-mortem analysis on preformed $Al_2O_3$-MgO castable with alumina-silica gel powder as binder after industrial trials was studied. Deterioration process and corrosion mechanism were discussed based on the observed microstructural characteristics. The main conclusions are as follows:

(1) After structural optimization, the trial $Al_2O_3$-MgO pre-cast bricks after server 195 cycles in RH refining ladle had a residual thickness of ~150 mm from the initial thickness of 210 mm. It indicated that the optimized one displayed a ~30% improvement in corrosion resistance after industrial application when compared with the conventional ones (184 cycles). It was attributed to the corroded behaviors and slag infiltration behaviors of $Al_2O_3$ based aggregates in the corroded interface.

(2) Four separate layers, including adhered slag layer, reaction layer, infiltration layer and original layer, was fully characterized on the used alumina-silica gel powder bonded $Al_2O_3$-MgO castable. A wide infiltration layer with ~30mm was observed on the corroded interface, the boundaries between aggregates and matrix are blurred because of slag infiltration.

(3) A penetrating crack formed on the corroded interface, which is located on the boundary between infiltration and original layer. The formation of that penetrating crack could be ascribed to the difference in physicochemical properties and sintering degree. Corroded microstructure indicated that slag infiltrated inside the $Al_2O_3$ aggregates along the grain boundaries and confirmed the aggregates suffered from an intergranular erosion process.

## REFERENCES

[1] K. Beskow, J. Jia, C. H. P. Lupis, Du Sichen, Chemical characteristics of inclusions formed at various stages during the ladle treatment of steel, Ironmaking & Steelmaking, 29:6, 427-435.

[2] K. Beskow, Du Sichen, Ladle glaze: major source of oxide inclusions during ladle treatment of steel, Ironmaking & Steelmaking, 31:5, 393-400,

[3] J. Chen, Y. Cheng, Y. Li, J. Xiao, Y. Zhang, G. Liu, Y. Wei, G. Li, S. Zhang, N. Li, Formation of ferrospinel layer at the corroded interface between $Al_2O_3$-spinel refractory and molten steel in RH refining ladle, J. Am. Ceram. Soc., 2021 104(11), 6044-6053.

[4] W.E. Lee, W. Vieira, S. Zhang, K.G. Ahari, H. Sarpoolaky, C. Parr, Castable refractory concretes, Int. Mater. Rev., 3[46](2001):145-167.

[5] M.A.L. Braulio, M. Rigaud, A. Buhrc, C. Parr, V.C. Pandolfelli, Spinel-containing alumina-based refractory castables, Ceram. Int., 37 (2011) 1705-1724.

[6] E. Y. Sako, M. A. L. Braulio, A. P. Luz, E. Zinngrebe, V. C. Pandolfelli, Slag resistance of $Al_2O_3$-MgO refractory castables in different environmental conditions, J. Am. Ceram. Soc., 96 [10](2013):3252-3257.

[7] J. Xiao, J. Chen, Y. Li, Y. Cheng, M. Nath, Y. Zhang, Corrosion mechanism of cement-bonded $Al_2O_3$-$MgAl_2O_4$ pre-cast castables in contact with molten steel and slag, Ceram. Int., 48 (2022) 5168-5173.

[8] H. Sarpoolaky, S. Zhang, W.E. Lee, Corrosion of high alumina and near stoichiometric spinels in iron-containing silicate slags, J. Eur. Ceram. Soc., 23 (2003) 293-300.

[9] P. Gehre, C.G. Aneziris, D. Veres, C. Parr, H. Fryda, M. Neuroth, Improved spinel-containing refractory castables for slagging gasifiers, J. Eur. Ceram. Soc., 33 (2013) 1077-1086.

[10] J. Wei, Z. Miao, Y. Li, J. Chen, et al., Chemical attack of $Al_2O_3$-$MgAl_2O_4$ refractory castables in the non-slag-tapping side of refining ladle, Ceram. Int., 48 (2022) 16832-16838.

457

# DEVELOPMENT OF UNFIRED AND NON-IMPREGNATED SLIDE GATE PLATES AS A CONTRIBUTION TO REDUCING EMISSIONS OF CARBON BONDED REFRACTORIES

Dominic Helmus, Sylvia Schwartz, Marcus Blumenberg, Peter Stein, Jochen Kattwinkel

Knöllinger Keramische Verschleißteile GmbH, Hillscheid, Germany

## ABSTRACT

Knöllinger Keramische Verschleißteile GmbH (Knöllinger) is a well-known and established supplier of alumina based, carbon bonded slide gate plates especially for the German steel market. Approx. 35.000 pieces are delivered annually, of which the biggest share belongs to the group of fired and tar pitch impregnated slide gate plates. In order to contribute towards reducing greenhouse gas emissions Knöllinger is going to launch a new product line of unfired and non-impregnated slide gate plate ceramics. Beside the lower energy consumption especially due to curing as the only thermal treatment, pitch tar free carbon bonded ceramics almost show no hazardous emissions during manufacturing and service. First trial results of unfired and non-impregnated slide gate plates in comparison to the standard products used in an electrical steelworks are presented in this paper.

## INTRODUCTION

Slide gate valves for steel ladles have been put in operation about 60 years ago. They essentially consist of a mechanical housing and several refractory components such as well block, sleeve, slide gate plates and nozzle (Fig. 1). For continuous casting slide gate valves containing two slide gate plates are the state of the art.
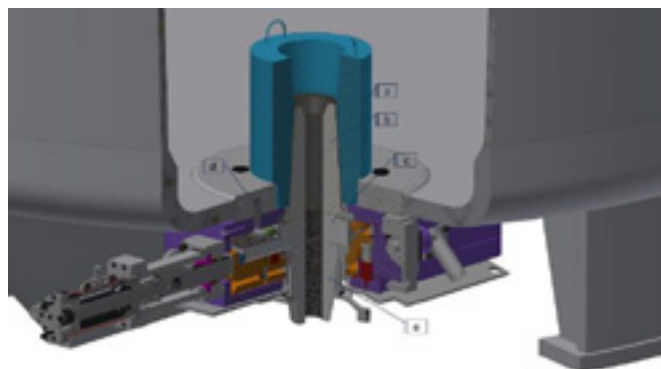


Fig. 1: refractory components of a ladle slide gate valve
a: well block; b: sleeve; c: upper slide gate plate, d: lower slide gate plate, e: nozzle

To open and close the slide gate valve, the lower slide gate plate is moved linearly against the upper plate by the help of a hydraulic or electric actuator. Thus, the steel flow rate from the ladle to the tundish is regulated. Fig. 2 illustrates the movable lower slide plate inside the slide gate valve's mechanical housing.
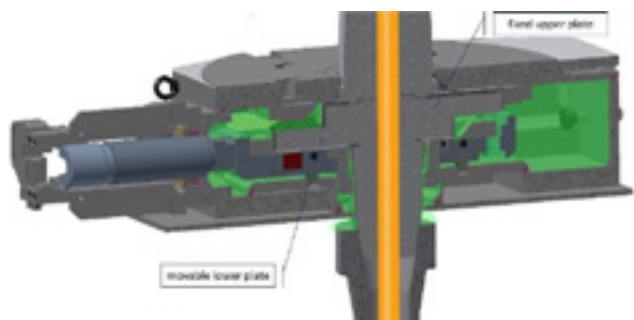


Fig. 2: detail of slide gate valve mechanism consistent of a fixed upper plate and a movable slide gate plate

## Refractory materials for slide gate plates

The chemical composition of slide gate plates can be regarded as the most important differentiating and selecting criterion for a particular application. The most commonly used grades are based on alumina due to their relatively good abrasion, thermal shock and corrosion resistance. Slide gate plates based on magnesia and zirconia normally show superior corrosion resistance along with reduced thermomechanical properties. Tab. 1 shows one possibility to group available slide gate plate materials:

| Raw material basis | Type of binding | |
|---|---|---|
| | Ceramic bonded | Carbon bonded |
| Alumina, fired | X | X |
| Alumina, unfired | | X |
| Magnesia | X | |
| Zirconia | X | |

Tab. 1: overview of slide gate plate materials

Fired and thus ceramic bonded slide gate plate materials regularly get impregnated with a carbon-based liquid, i.e., tar pitch, to further enhance mechanical and corrosion resistance properties. Unfired qualities may be impregnated as well. Also, to improve performance and to prevent the carbon bond and/or impregnation from oxidation, metallic and non-oxide compounds are added to the raw material mixes. Common additives are silicon, aluminium, silicon carbide, boron carbide etc. Other solid carbonaceous materials, i.e., graphite or carbon black, can be included as well.

## Processing of fired and unfired carbon bonded alumina plates

About two third of the slide gate plates distributed by Knöllinger belong to the group of alumina based, carbon bonded, fired and double pitch impregnated plates. These products are marketed under the brand "AC-Technology", the compositions of which were developed entirely by Knöllinger. Fig. 3 illustrates the processing route for this type of slide gate plates. During the production process four temperature treatments are carried out:

1. curing of the bonding agent at about 280 °C
2. firing of the slide gate plates at about 1200 °C
3. curing after first impregnation step at 400 °C
4. curing after second impregnation step at 400 °C

Another third of actually distributed slide gate plates are unfired and single impregnated alumina-based products. Their production process differs of course in the absence of the firing step (Fig. 4).
The processing of unfired and non-impregnated slide gate plates finally shows only one temperature treatment for the purpose of curing the carbon bond after shaping the slide gate plate bodies as displayed in Fig. 5. The curing temperature is slightly lower compared to both impregnated qualities.
Due to the lack of appropriate facilities Knöllinger collaborates with experienced European partners in the field of shaped refractories for the production of the ceramic slide gate bodies. The last step in the processing route, the assembly of the final slide gate plates, takes place at Knöllinger's plant located in Hillscheid, Germany. Assembly includes work steps as grinding, drilling, fitting in metal cans, casting of outlet nozzles etc. These steps are similar independent from the chosen processing route for the refractory bodies. Tab. 2 summarizes and compares the three described processing routes for fired and double impregnated plates, unfired and single impregnated plates and finally unfired and non-impregnated slide gate plates.
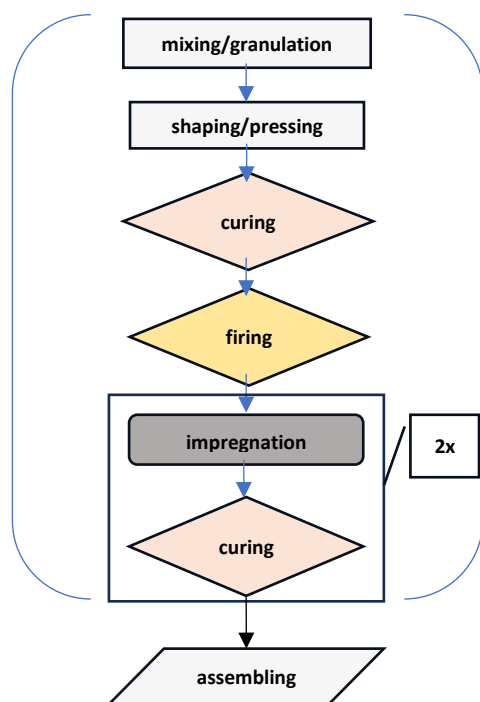
Fig. 3: processing route of alumina based, carbon bonded, fired and double impregnated slide gate plates
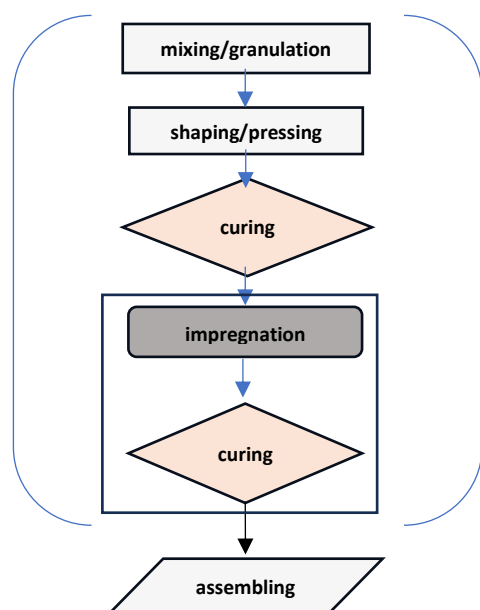


Fig. 4: processing route of unfired but single impregnated, carbon bonded alumina slide gate plates
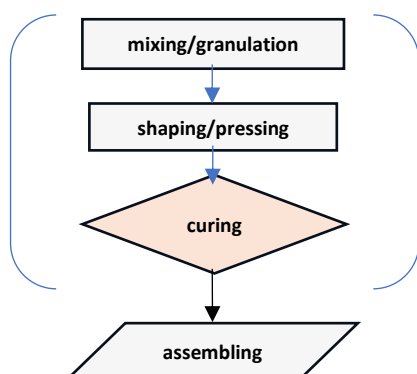


Fig. 5: processing route of unfired and non-impregnated, carbon bonded and alumina-based slide gate plates

| Processing steps | Type of carbon bonded alumina slide gate plates | | |
|---|---|---|---|
| | fired, 2x impregnated | unfired, 1x impregnated | unfired, not impregnated |
| mix./granul. | ✓ | ✓ | ✓ |
| shaping | ✓ | ✓ | ✓ |
| curing | ✓ (280 °C) | ✓ (280 °C) | ✓ (250 °C) |
| firing | ✓ | ✗ | ✗ |
| impregn. + curing | ✓, 2x | ✓, 1x | ✗ |

Tab. 2: summarized processing routes for fired + impregnated, unfired + impregnated and unfired + non-impregnated slide gate plate refractories delivered by Knöllinger

## COMPARISON OF ENVIRONMENTAL ASPECTS

Especially the differing number of thermal treatments and the use of pitch based impregnates have a significant impact on emissions of carbon dioxide related to energy consumption as well on potentially environmental harmful emissions during service and disposal of used slide gate plate refractories.

### Carbon dioxide emissions of different processing routes

Tab. 3 displays the actual carbon dioxide emissions related to production of slide gate plates following the above-described processing routes. The shown figures are determined for so-called scope I+II emissions connected to the production of fired + double impregnated (product class name "AC") and unfired + single impregnated plates ("93P", cf. Fig. 3+4, Tab. 2). As the production of unfired and non-impregnated slide gate plates ("GF") is about to get launched in Q4 of this year, the production related $CO_2$ emissions are estimated based on the verified numbers for the other two types of plates. It should be noted that the emissions associated with the assembly of the slide gate plates are not included in the figures given. Assembly includes one thermal treatment to dry-out water after wet-grinding and casting of nozzles in the same temperature range than

| | Type of slide gate plates | | |
|---|---|---|---|
| | AC | 93P | GF |
| kg $CO_2$ per ton of product | 6000 | 1800 | ≈ 350 |
| Relative emissions | 100 % | 30 % | 5-8 % |

Tab. 3: scope I+II $CO_2$-emissions related to the production of different slide gate refractories distributed by Knöllinger. Calculations based on assumptions of PAS 2050.

the curing step, namely around 250 °C. $CO_2$-emissions linked to slide gate plate assembly is assumed to be in the range of 300-350 kg $CO_2$ per ton of product. Considering this, it is expected that the total $CO_2$ emissions from the production of the unfired and non-impregnated slide gate plates will be about nine times lower compared to the fired and double impregnated plates.

### Potential for further environmentally harmful emissions

To check and compare further possible emissions of potentially harmful compounds especially during the service of slide gate plates, GC-MS-analyses of extractions made of crushed and ground "AC" and "GF" materials by hexane and methanol as solvents were conducted. These samples correspond to the materials as delivered. That means pyrolysis of the resin-based carbon bond of the "AC" sample took already place during the firing step within the production process whereas the pyrolysis of the carbon bond of the "GF" sample has not occurred yet. Other samples of these two materials were heated to 600 °C and 1200 °C in a nitrogen stream which was then guided through the same type of solvents and were analyzed by GC-MS as well. The received results are summarized in Tab. 4.

Comparing the results after extraction of the samples in the as-delivered state (column "original" in Tab. 4), it can be seen that the impregnated and fired "AC" material contains over 7000 mg/kg of

the so-called 16-PAHs (polycyclic aromatic hydrocarbons) which are classified by EPA (US Environmental Protection Agency) as priority environmental pollutants. As the "GF" sample does not show such values it can be concluded that they mainly originate from pitch impregnation. Some of these substances are partially released when the sample is heated to 600 °C, with an amount of 97 mg/kg and 30 mg/kg respectively detected in the rinsed nitrogen stream when further heated to 1200 °C.

The "GF" material shows phenol and derivates after extraction of the sample, which surely originates from the phenolic carbon bond. During degassing up to 600 °C the sample releases especially phenol by 554 mg/kg as well as benzene and bisphenol. Further heating to 1200 °C releases 116 mg/kg of benzene and 102 mg/kg of 16-PAHs. The appearance of these substances is linked to the pyrolysis of the cured phenolic resin bond as the "GF" material is not fired [1]. It can be assumed that the "AC" material shows these releases as well but already within the firing step during manufacturing. Tab. 5 summarizes the source and place of potential emissions originating from slide gate plate materials.

| | | GC-MS Analysis | | |
|---|---|---|---|---|
| | | original | 600 °C | 1200 °C |
| Benzene & derivates | AC | < 10 | < 10 | < 10 |
| | GF | < 10 | 80 | 116 |
| Phenol & derivates | AC | < 10 | < 10 | < 10 |
| | GF | 73 | 554 | < 10 |
| Bisphenol | AC | < 10 | < 10 | < 10 |
| | GF | < 10 | 74 | < 10 |
| 16-PAH's | AC | 7115 | 97 | 30 |
| | GF | < 20 | < 20 | 102 |
| additionals | AC | 3346 | 235 | 16 |
| | GF | < 10 | 12 | 30 |
| total | AC | 10461 | < 500 | < 500 |
| | GF | < 500 | 720 | < 500 |

Tab. 4: results of GC-MS analyses of slide gate plate materials "AC" (fired + double impregnated) and "GF" (unfired + non-impregnated) slide gate plate materials in state as delivered (orig.) and after degassing in nitrogen at 600 °C and 1200 °C. The candidates of the 16-PAH's can be found here: [2]. All values in units of mg per kg of product. Analyses conducted by Horn & Co. Analytics GmbH, Wenden-Hünsborn, Germany

| | "AC" material | "GF" material |
|---|---|---|
| refractory producer | resin bond | -- |
| refractory user | impregnation | resin bond |

Tab 5: source and place of PAH emissions for "AC" and "GF" materials

## CASE STUDY OF UNFIRED & NON-IMPREGNATED SLIDE GATE PLATE REFRACTORIES

First trials with Knöllinger's new "GF" materials have been conducted in a German electrical steel mill. This plant has been constantly delivered with AC qualities since 2015. Particularly, the quality in use is called "AC51". Besides being based on alumina this material also contains zirconia mullite resulting in a content of approx. 4,5% $ZrO_2$. The average service life time is 3,9 heats. In comparison, two "GF" type materials were tested under the same conditions. One quality is completely based on alumina ("GF1") whereas the second one includes zirconia mullite additions on the same level than the fired "AC51" quality ("GF2"). Both tested materials showed average service life times of approx. 3,7 to 3,8 heats. Tab. 5 summarizes the physical properties and achieved life times of all three materials. A commonly known disadvantage of only cured carbon bonded refractories is a significant loss of strength and related properties associated with pyrolysis of the phenolic resin binder [3]. This is also observed in both "GF" qualities, but in this case the degradation does not affect the service life of the slide gate

plates. Wear indicators are the widening of the casting hole and material losses on the plate surfaces next to the casting channel of slide gate plates. Fig. 6, 7 and 8 display slide gate plates with their typical appearance after having been used in the steel mill and no major differences in wear phenomena can be observed.

All plates show the same type of radial crack formation around the casting hole which are typical for thermal shock spalling as slide gate plates are not separately heated up before steel flow is initiated. The wear in the travel and working area appears to be on a similar level for all three qualities. Statistically proven statements on durability have to be drawn after a longer period of usage.

| Properties | | Slide gate plate qualities | | |
|---|---|---|---|---|
| | | AC51 | GF1 | GF2 |
| Raw material basis | | $Al_2O_3$+ZM | $Al_2O_3$ | $Al_2O_3$+ZM |
| CCS As delivered | MPa | 178 | 151 | 144 |
| CCS 500 °C | | 196 | 93 | 80 |
| CCS 1000 °C | | 234 | 137 | 159 |
| Open porosity | vol-% | 7.9 | 8,3 | 8,1 |
| Bulk density | g/cm³ | 3.17 | 3,14 | 3.11 |
| Service life time | No. of heats | 3.9 | 3.7 | 3.7 |

Tab. 5: physical properties of slide gate plate materials used in an electrical steel plant. AC51: standard quality, fired, impregnated; GF1 & GF2: trial qualities, unfired, non-impregnated; ZM: zirconia mullite
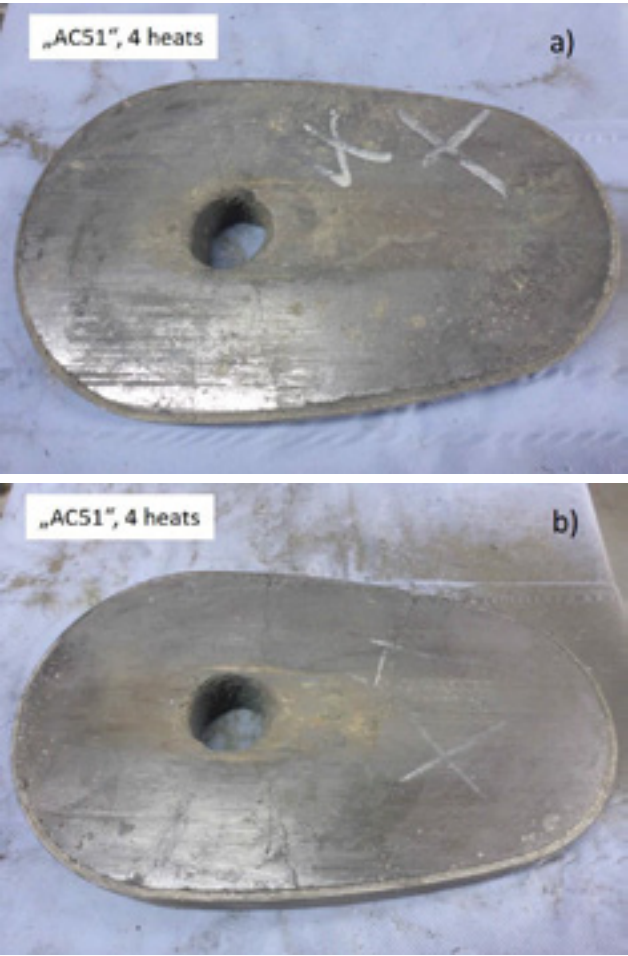


Fig. 6, a)+b): typical appearance of lower slide gate plates in quality "AC51" after 4 heats
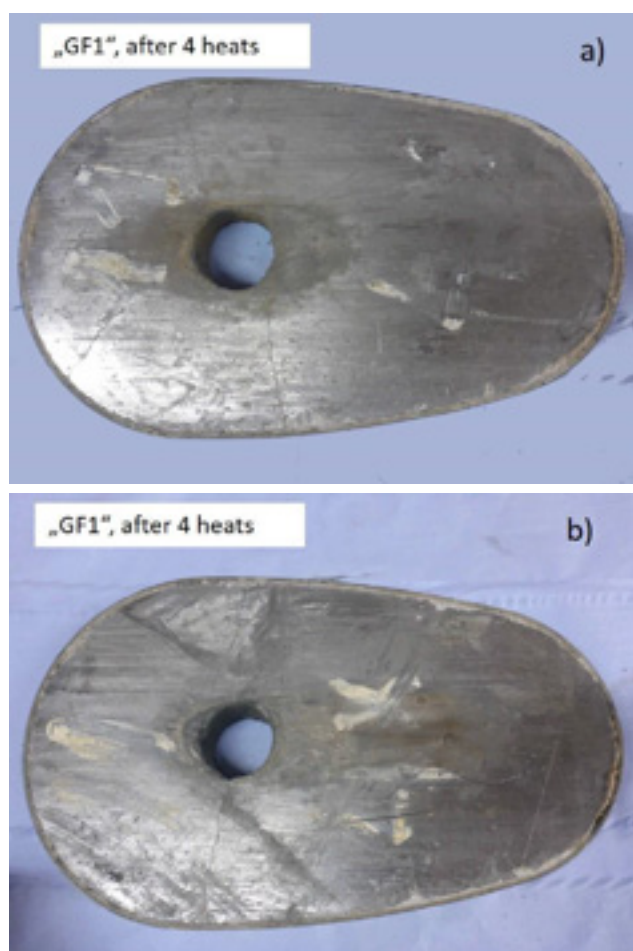
*Fig. 7, a)+b): appearance of quality "GF1" after 4 heats.*



*Fig. 8, a)+b): appearance of quality "GF2" after 4 heats*

## CONCLUSIONS

The widespread use of unfired and non-impregnated slide gate plate refractories has a huge savings potential of production related $CO_2$ emissions. First calculations show nine times lower scope I+II type emissions in comparison to fired and impregnated slide gate plates representing the actual state of the art.

By not using pitch-based impregnates, the emission of potentially harmful hydrocarbons is further reduced, although important steps have been taken to reduce hazardous compounds in these materials.

First industrial trials show that the newly developed unfired and non-impregnated slide gate plates can be able to perform on the same level as fired and impregnated ones. A stable and continuous supply should be realized by the end of 2023. For cases where fired and impregnated slide gate plates cannot be easily substituted, Knöllinger's R&D activities continue to further enhance the performance of unfired and non-impregnated slide gate plate refractories.

## REFERENCES

[1] A.P. Luz, R. Salomão, C.S. Bitencourt, C.G. Renda, A.A. Lucas, C.G. Aneziris, V.C. Pandolfelli, Thermosetting resins for carbon-containing refractories: Theoretical basis and novel insights, Open Ceramics, Volume 3, 2020

[2] https://sor.epa.gov/

[3] Yoshida, T., Koike, Y., Hattanda, H., Takagi, K. und Noguchi, H. Improvement of oxidation resistance of resin bonded SN plates. Taikabutsu Overseas, Vol. 16, No. 2, 20-25

461

# THE EFFECT OF SELECTED METALLIC ADDITIVES ON THE PROPERTIES OF THE AL$_2$O$_3$−C REFRACTORY MATERIAL

Robert Świerszcz, Zbigniew Czapka,
Zakłady Magnezytowe "Ropczyce" S.A, Ropczyce, Poland

Jacek Szczerba, Ilona Jastrzębska,
AGH University of Science and Technology, Cracow, Poland

## ABSTRACT

Alumina-carbon (Al$_2$O$_3$-C) refractory materials are widely used in the process of continuous casting of steel as flow control elements, including slide gate plates, nozzles, ladle shrouds, stoppers or submerged entry nozzles. Their task is to direct and regulate the flux of liquid steel and protect it against oxidation of the alloy additives. Decarburization at intermediate temperatures of 300-700°C, corrosion, abrasion and formation of cracks during operation are main wear factors determining the replacement of the Al$_2$O$_3$-C elements. In this work the influence of antioxidants and heat treatment temperature on the physico-chemical and strength parameters of materials was examined.

## 1. INTRODUCTION

The main advantage of Al$_2$O$_3$-C materials, predestining them to be used as flow control elements, is their high refractoriness, ability to withstand high thermal shocks, corrosion and erosion resistance. The presence of carbon in refractories lowers the contact angle of the material at the border refractory/liquid slag or steel, reducing the depth of infiltration. This in turn, causes better corrosion resistance.

Antioxidants are often used in Al$_2$O$_3$-C refractories, e.g., Si or Al. They can react directly, or indirectly, with carbon or nitrogen to form carbides and nitrides [1, 2, 3] which increase mechanical and resistance parameters of refractory materials.

Typically, Al$_2$O$_3$-C slide plates with the addition of Si, are heat treated at a temperature above 1000°C. The purpose of heat treatment is to carbonize the carbon and form a carbon bond. Carbides and other ceramic bonds are formed as a result of the thermally-activated reaction (e.g. between Si and C) and sintering process. Also, unfired Al$_2$O$_3$-C slide plates with the addition of Al on the resin bond heat-treated below 600°C are used. The refractory type is selected based on the metallurgical conditions, e.g., oxygen or calcium content in liquid steel, the presence of slag or the size of the slide gate plate. Fired materials are characterized by higher mechanical strength below 700°C, resistance to decarburization at intermediate temperatures of 300-700°C and dimensional stability. On the other hand, unfired Al$_2$O$_3$-C materials are characterized by higher corrosion resistance and increased mechanical strength above 700°C [3, 4]. The purpose of this work was to investigate the properties of Al$_2$O$_3$-C materials fired at an intermediate temperature of 600-1000°C and compare them with the properties of materials fired at higher temperatures.

## 2. MATERIALS AND METHODS

The isothermal predominance area diagrams for the Si-C-N-O and Al-C-N-O systems were determined using the FactSage 7.0 software applying *Predom* module. Al$_2$O$_3$-C refractory materials were industrially produced based on 7 different compositions, including reference material, materials with Si addition (1, 3 and 5 %) and materials with Al addition (1, 3 and 5 %), according to Tab. 1. Cylinders (35x35 mm) and beams (25x25x150 mm) were shaped at a forming pressure of 1000 kg/cm$^2$. Shapes were dried at 250°C, then fired at different temperatures of 800°C, 1000°C, 1200° and 1400°C in carbon bed to for the antioxidation protection.

Tab. 1: Starting composition of the Al$_2$O$_3$-C refractory materials

| Sample | Ref. | 1%Si | 3% Si | 5%Si | 1%Al | 3%Al | 5%Al |
|---|---|---|---|---|---|---|---|
| Tabular alumina | 86 | 86 | 86 | 86 | 86 | 86 | 86 |
| Reactive alumina | 11.6 | 11.6 | 11.6 | 11.6 | 11.6 | 11.6 | 11.6 |
| Carbon black | 2 | 2 | 2 | 2 | 2 | 2 | 2 |
| Si <0.045mm | - | 1 | 3 | 5 | - | - | - |
| Al <0.045mm | - | - | - | - | 1 | 3 | 5 |
| Novolac resin | 4.0 | 4.0 | 4.1 | 4.2 | 4.0 | 4.1 | 4.2 |

XRD diffractograms of fired materials were registered by Philips X-Ray PW 1730 diffractometer, and analyzed using PANalytical's X'pert High Score Plus software. Open porosity and bulk density were determined acc. to standard PN-EN-993-1:1998, cold crushing strength (CCS) acc. to EN-10059-1 and modulus of rapture (MOR) at room temperature acc. to EN 993-6. The JOEL JSM - JT500 LA scanning electron microscope was used for the microstructural analysis. Young's modulus (modulus of elasticity, MOE) was determined using the dynamic method by measuring the ultrasonic wave velocity with the use of ULTRATEST BP-700 PRO Ultrasonic Tester.

## 3. RESULTS AND DISCUSSION

The FactSage thermodynamic calculations for the Si-C-N-O system (Fig. 1) indicate that, after heat treatment the stable phases are SiC, SiO$_2$ and Si$_3$N$_4$. In addition, Si is the stable phase at 1400°C, while it does not occur at lower temperatures. As the temperature increases the region of SiC stability enlarges towards the CO lower partial pressure. Si$_3$N$_4$ is the stable phase within a limited range of partial pressures of CO and N$_2$.

For the Al-C-N-O system (Fig. 2), the calculations show that Al$_4$C$_3$, Al$_2$O$_3$ and AlN are the stable phases at all temperatures. As the temperature increases, the Al$_4$C$_3$ stability region enlarges towards the CO lower partial pressure. AlN is a stable phase in a limited range of partial pressures of CO and N$_2$. With increasing temperature, the stability region of AlN shifts towards the lower partial pressure of CO.
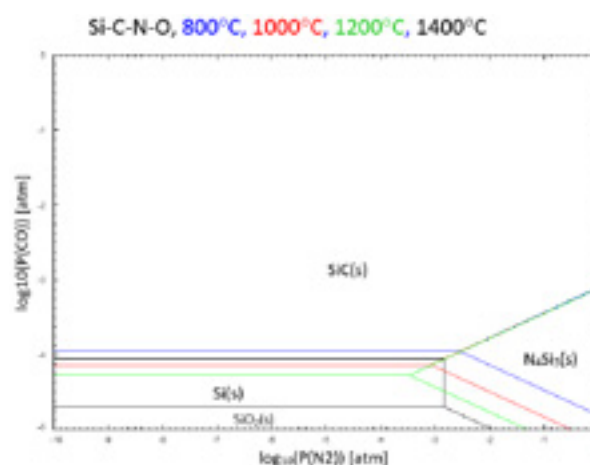


Fig. 1: Predominance diagram for Si-C-N-O system
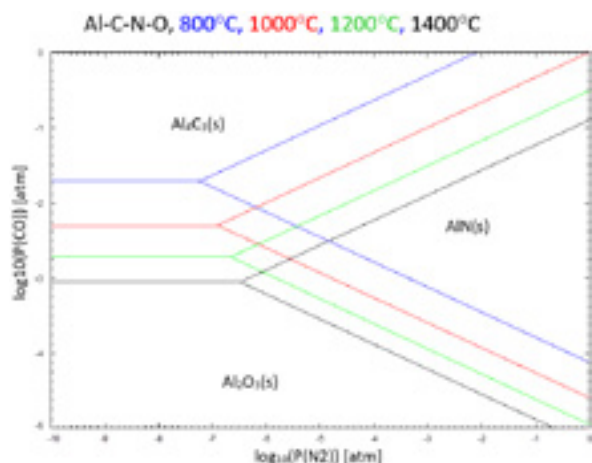
Fig. 2: Predominance diagram for Al-C-N-O system

XRD analysis for addition of Si showed that, heat treatment at 800°C and 1000°C is insufficient to form SiC as it was detected only after firing 1200°C and 1400°C (Fig. 3).

For Al addition, $Al_4C_3$ was detected in the samples 3% and 5% Al after treatment at 800°C and 1000°C. For sample 1%Al, $Al_4C_3$ was detected only after treatment at 1200°C and 1400°C. For 1%Al and 1400°C, metallic Al was not registered, probably due to its oxidation to $Al_2O_3$. In addition, after treatment at 1400°C, graphite was detected in all antioxidants-containing samples, which was most likely formed as a result of graphitization of amorphous C derived from carbon black and/or phenol-formaldehyde resin.
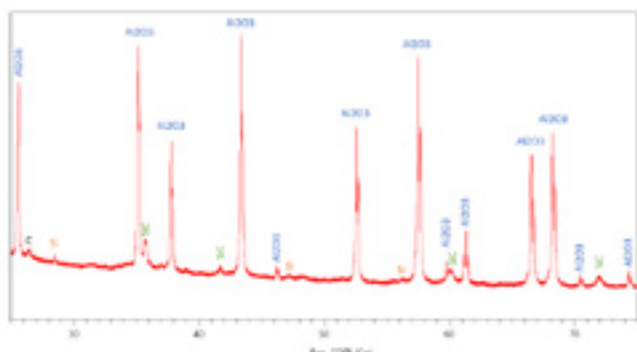


Fig. 3: Diffractogram for sample 5%Si after heat treatment at 1400°C
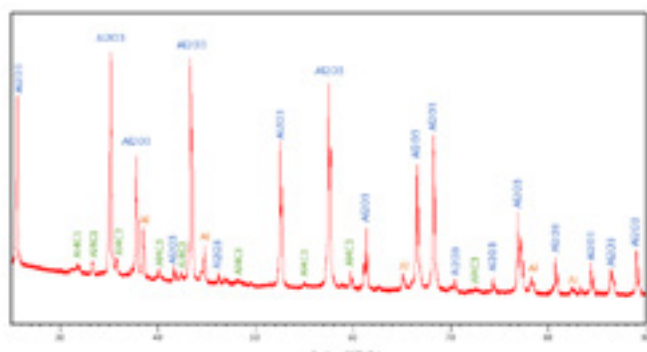


Fig. 4: Diffractogram for sample 5%Al after heat treatment in 800°C

Results of the modulus of elasticity (Fig. 5) shows that, Si addition decreases MOE. This tendency is very clear for samples after heat treatment at 800°C and 1000°C, while for samples after treatment at 1200°C and 1400°C this effect is slighter. On the other hand, for Al addition increases MOE. This effect is most pronounced for sample 5%Al after treatment at high temperatures of 1200°C and 1400°C. Raised temperature of heat treatment increases the MOE for both additives Si and Al.

The results of flexural strength (Fig. 6) and cold crushing strength (Fig. 7) follow the same trend as the results of the MOE (Fig. 5). MOE, MOR and CCS increase with the increased heat treatment temperature and Al addition, and decrease with Si addition. However, for SiC-containing samples (for 1200°C and 1400°C) greater amount of Si increases MOR and CCS. Znaczenie wysokiego MOE i MOR
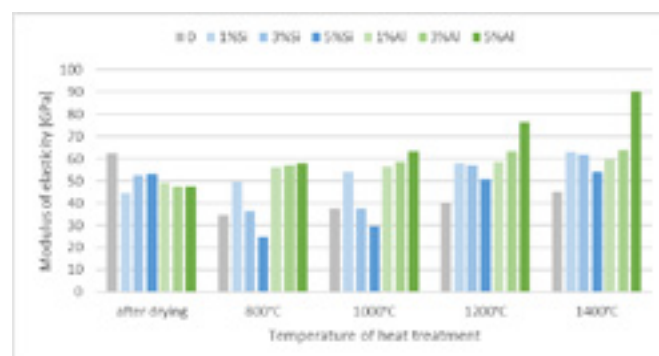


Fig. 5: Results of modulus of elasticity
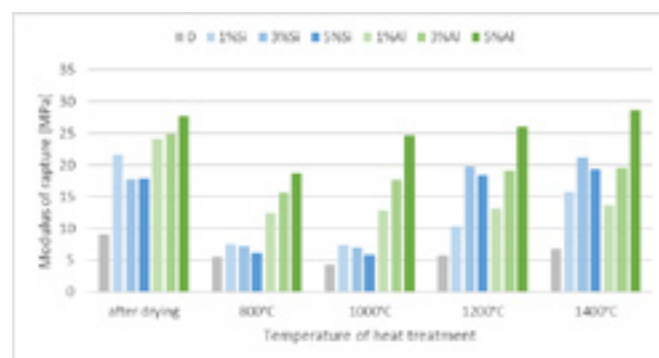


Fig. 6: Results of modulus of rapture
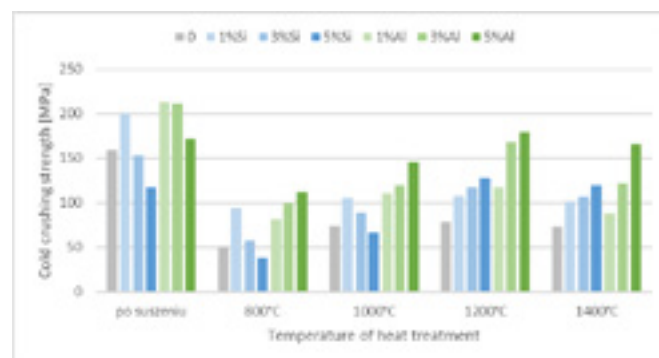


Fig. 7: Results of cold crushing strength

During the MOR test (three-point bending test), two types of stress arise in the sample: compressive in the upper parts of the sample and tensile in its lower parts, as presented in Fig. 8. The compressive stress strength of ceramic materials, including $Al_2O_3$-C refractory materials, is several times higher than the tensile stress strength. Hence, it can be assumed that the destruction of the sample in the three-point bending test occurs as a result of the tensile stresses generated in its lower parts. In the case of the CCS test, the destruction of the sample occurs as a result of the compressive stresses increased within the material with the raised load. For ductile materials, e.g. steel, the compressive stress strength is close to the tensile stress strength. However, as mentioned earlier, in the case of brittle materials like refractory materials the compressive strength is several times higher than the bending strength.

The CCS/MOR ratio (Fig. 9) allows for a general assessment of the material brittleness. The greater the CCS/MOR ratio the higher the brittleness of the material due to its high compressive strength

463

and low tensile strength. Based on Fig. 9 it can be concluded that, we can reduce the brittleness of the material via increasing the amount of Si or Al additions. Increasing the heat treatment temperature for both additives also increases brittleness. However, for Si addition after heat treatment at 1200°C and 1400°C, the modulus of elasticity decreases, and for Al addition it happens only after treatment at 1400°C.
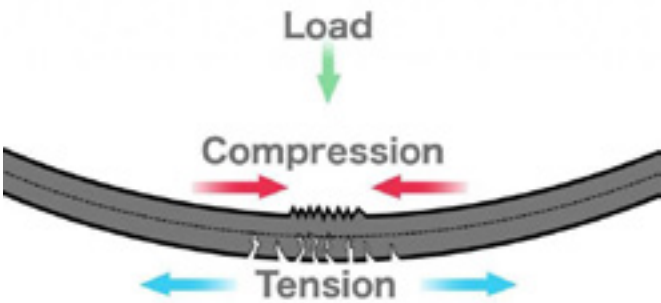


Fig. 8: Stresses created in the sample during bending test
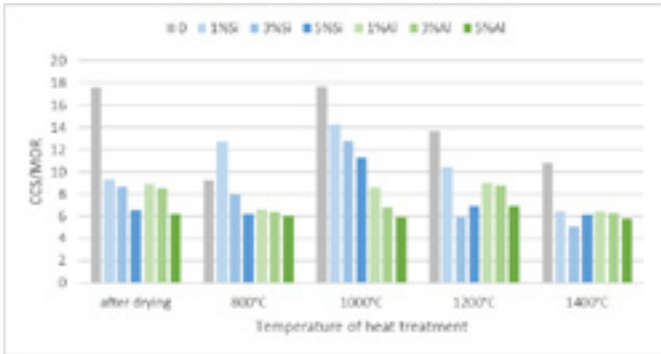


Fig. 9: Ratio of cold crushing strength to modulus of rapture (CCS/MOR)

For Si addition, the open porosity (Fig. 10) increases with increasing amount of this additive, and with increasing heat treatment to 1000°C. After heating at 1200°C and 1400°C, SiC whiskers were formed in the pores of the material, reducing open porosity. The opposite tendency was observed for bulk density (Fig. 11). For Si addition, bulk density decreased with increasing Si amount and with increased raised treatment temperature, while after heat treatment at 1200°C and 1400°C we observed a slight increase in density.

For Al addition, both open porosity (Fig. 10) and bulk density (Fig. 11) decrease with the increase of the Al amount and with the increased temperature.
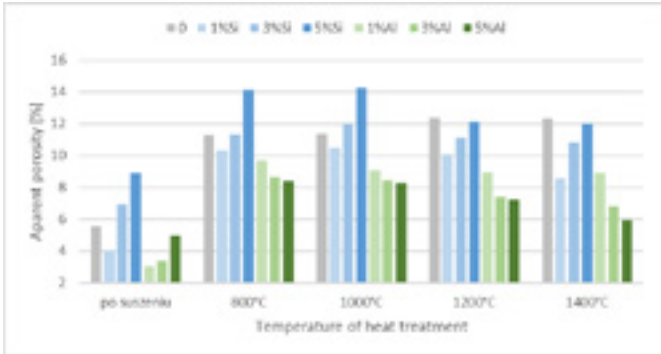


Fig. 10: Results of open porosity
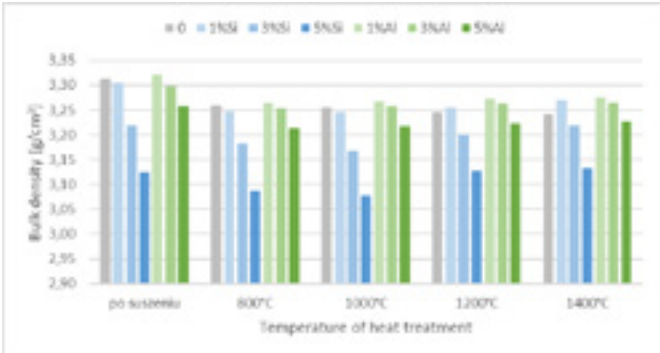


Fig. 11: Results of bulk density

## 4. CONCLUSIONS

Formation of SiC in $Al_2O_3$-C materials requires heat treatment at minimum 1200°C, while $Al_4C_3$ generates already at 800°C. Increasing the Si amount lowers MOE, while Al addition increases MOE. The formation of both carbides (SiC and $Al_4C_3$) is highly beneficial as it increases mechanical strength (both compression and bending) compared to the reference samples without Al, Si. The ratio CCS/MOR (expressing the brittleness of the material) shows that the formation of carbide bonds allows to decrease brittleness of material. It can also be assumed that by increasing the amount of carbide bonds in the material we reduce its brittleness.

## REFERENCES
[1] M.N. Khezrabadi, J. Javadpour, H. R. Rezaie, R. Nagihizadeh, The Effect of Additives on the Properties and Microstructure of $Al_2O_3$-C Refractories – Journal of Materials Science 41, 2006, p. 3027-3032
[2] C. Atzenhofer, S. Hschiel, H. Harmuth, Phase formation in $Al_2O_3$-C refractories with Al Addition – Journal of the European Ceramic Society 37, 2017, p. 1805-1810
[3] Kazuo Itoh, Kunio Hayamizu, Kazuhide Kawai, Hideo Uemoto, Development of Cermet Materials for Composite Silde Gate Plates, Journal of the Technical Association of Refractories, Japan, 21 (1), 2001, p. 26-29
[4] Keiichiro Akamine, Isao Sasaka, Arito Mizobe, Jyoki Yoshitomi, Keisuke Asano, Improving Thermal Shock Resistance of Aluminium-Added, Semi-Burnt SN Plante Refractories – Journal of the Technical Association of Refractories 24 (2), 2004, p. 135-140
[5] Tsuyoshi. Yoshida, Yasuta Koike, Hirokatsu Hattanda, Kazuhiro Takagi, Hironori Noguchi Improvement of Oxidation Resistance of Resin Bonded SN Plates – TAIKABUTSU OVERSEAS 16 (2), 1996, p. 20-25
[6] Vasileios Roungos, Christos G. Aneziris, Harry Berek, Novel $Al_2O_3$-C Refractories with Less Residual Carbon Due to Nanoscaled Additives for Continuous Steel Casting Applications, Advanced Engineering Materials 14 (4), 2012, p. 255-264
[7] J. M. Lihrmann, Thermodynamics of the $Al_2O_3$-$Al_4C_3$ system. I. Thermodynamical functions of Al oxide, carbide and oxycarbides between 298 and 2100K., Journal of the European Ceramic Society 28, 2008, p. 633-642
[8] Yuichi Kato, Tadashi Ikemoto, Kiyoshi Goto, Investigation of the Corrosion Mechanism of $Al_2O_3$-$ZrO_2$-C Slide Gate Plates for the casting of Ca-added Steel, UNITECR PROCEEDINGS, 2017, p. 13-16

# EFFECT OF RECYCLED REFRACTORY, PHENOLIC RESIN, AND SI POWDER ON THE AL$_2$O$_3$−C REFRACTORY FOR CONTINUOUS CASTING

PAN Lei*, GAO Zhi, WANG Zuochuang, YANG Qin

(1. Puyang Refractories Group Co., Ltd. Technology Research Institute Puyang 457100. Henan, China.)

## ABSTRACT

In this paper, a kind of Al$_2$O$_3$-C refractory was prepared with plate corundum, flake graphite, alumina powder and phenolic resin as raw materials. The influence of the amount of recycled refractory (mainly composed of Al$_2$O$_3$ and C) on mechanical properties was also studied. The results showed that, with the increase of recycled refractory addition, the apparent porosity of the Al$_2$O$_3$-C refractory increased and the strength decreased sharply. When the amount of recycled materials was 30 wt%, the hot modulus of rupture of the Al$_2$O$_3$-C refractory was 8.2 MPa. Subsequent studies found that the integral strength of Al$_2$O$_3$-C refractory with 30 wt% recycled refractory could be increased ~30% by supplement solid phenolic resin. Furthermore, the hot modulus of rupture of Al$_2$O$_3$-C refractory improved by ~12% by supplementing Si powder.

## 1.INTRUCTION

The steel industry is a critical industry in refractory material consumption and also the industry with the largest amount of waste refractory[1]. The waste of a large amount of refractory which had used not only leads to the waste of refractory resources, but also brings severe environmental pollution and land resource occupation through the landfill of refractory which had used. Fully utilizing the resources of refractory which had used by steel enterprises for research and utilization can not only significantly reduce the raw material cost of refractory, but also accelerate the construction of a steel circular economy system and build a green and environmentally friendly enterprise[2].

The recovery and utilization of solid waste refractory has also been a research hotspot for scholars at home and abroad. In addition, scholars have also used waste high alumina bricks, MgO-C bricks，MgO-Al$_2$O$_3$-C bricks fly ash, and other materials for effective utilization[3-5]. Continuous casting functional refractory materials mainly consist of alumina and carbon. Because of its harsh usage environment, the raw materials used are mostly high grade, such as fused corundum, high-purity flake graphite or fused magnesia alumina spinel, etc. Moreover, functional refractory materials have a short service life, rarely exceeding 24 hours. Therefore, steel mills consume a large amount of functional refractory materials every year. The parts of functional refractory materials that do not come into contact with molten steel suffer less oxidation damage and have high recyclability. If they are directly discarded, a large amount of high-quality alumina and graphite resources will be wasted[6-7]. But there are still few reports on its recycling research

This article first investigated the effect of adding functional refractory recycled materials for continuous casting on the performance of alumina carbon refractory materials for continuous casting. The phase composition, mechanical strength, and microstructure of the samples with added recycled materials were characterized. Then, by adjusting the amount of binder added and supplementing the Si powder operation, the room temperature strength and high temperature strength of the sample with 30 wt% recycled material were reinforced, laying the foundation for subsequent industrial experiments.

## 2 EXPERIMENTAL

### 2.1 raw materials

The raw materials used in this experimental sample were:
recycled refractory materials for continuous casting (refer to Table 2 for their chemical composition), and tabular corundum particles（0.6-0.2 mm，＜0.044 mm of powder，from Yingkou , China）、Flake graphite（C≥95 wt%，＜0.15 mm, from Shandong, China）、Industrial SiC powder（SiC≥98 wt%，＜0.045 mm, from Shandong, China）、Si powder (Si＞98 wt%，＜0.074 mm, from Shandong,

China) and Solid phenolic resin powder (＜0.106 mm, from Shandong, China). Industrial alcohol is a solid phenolic resin powder solvent. The purpose of adding industrial alcohol was to dissolve solid phenolic resin powder and make it act as a binder during the mixing process. During the subsequent drying process of the mud, alcohol will evaporate and be removed, which will not affect subsequent experiments. The selected part of the recycled refractory is not contact with the molten steel. That is, the part that is not contaminated by the molten steel and slag layer. After unified classification, crushing, ball milling and screening, the recycled material particles are crushed to a size of less than 1.5 mm. The specific particle size distribution is as follows Table 1. After crushing, the particle size range of 0.2-1 mm is relatively large in the recycled refractory. The obtained chemical analysis results of the recycled refractory were shown in Table 2.

**Table 1** Screening results after crushing of recycled materials

| Particle size range | ≥1.5 mm | 1.5 mm~1 mm | 1mm~0.5mm | 0.5mm ~0.1mm | ≤0.1mm |
|---|---|---|---|---|---|
| Mass fraction (wt%) | 0 | 16.3 | 26.31 | 49.2 | 8.15 |

**Table 2** Chemical composition of recycled refractory (wt%)

| SiO$_2$ | Al$_2$O$_3$ | MgO | ZrO$_2$ | SiC | Si | C | Others |
|---|---|---|---|---|---|---|---|
| 8.90 | 56.22 | 4.90 | 3.63 | 1.00 | 1.71 | 20.58 | 2.95 |

The main components of the recycled material are Al$_2$O$_3$, C, and SiO$_2$, in addition to a small amount of ZrO$_2$, SiC, and Si. However, even though its source and composition are similar to those of the three major refractory materials for continuous casting, after high-temperature sintering above 1500 °C, new phases such as mullite, spinel, and olivine may be formed in situ in the components of the refractory materials, including SiO$_2$, Al$_2$O$_3$, MgO, and other oxides. Because the recycled refractory originally contains Al$_2$O$_3$ and C, and the particle size distribution is relatively wide. when the recycled material is introduced into the original formula A0, the content of raw material plate corundum and flake graphite in A1, A2 and A3 will also change. The specific experimental formula is shown in Table 3.

**Table 3**. Formulation of raw materials for samples (wt%)

| Raw materials | specifications | A0 | A1 | A2 | A3 |
|---|---|---|---|---|---|
| Tabular alumina | 0.6-0.2 mm | 35% | 31% | 28% | 27% |
| Tabular alumina | ＜0.044 mm | 20% | 17% | 14% | 11% |
| α-Al$_2$O$_3$ powder | 5 μm | 5% | 4% | 3% | 2% |
| Flake graphite | ＜0.15 mm | 22% | 20 | 18% | 16% |
| Solid phenolic resin | ＜0.106 mm | 10% | 10% | 10% | 10% |
| Industrial SiC powder | ＜0.045 mm | 6% | 6% | 6% | 6% |
| Si powder | ＜0.074 mm | 2% | 2% | 2% | 2% |
| Industrial alcohol (plus) | | | 6% | 6% | 6% | 6% |
| Recycled refractory | | 0% | 10% | 20% | 30% |

The sample preparation method is to mix the solid raw materials evenly in a forced countercurrent mixer, add an appropriate amount of alcohol, and then the mud is granulated at high speed for about 15 min. Subsequently, the sample was compressed and formed into 220 mm× 160 mm × 80mm square bricks under 120 MPa isostatic pressure (equipped with LDJ830/2500-300YS static press machine from AVIC Chuanxi Machinery Factory, from China). Finally, each sample was dried at 200 ° C for 12 hours and coked in carbon

465

embedded atmosphere at 1000 °C for 3 hours.

## 2.2 Characterization and testing

With reference to the Chinese National Standard GB/T 2997-2015, the apparent porosity and bulk density of samples were separately measured by the vacuum method (water as the test medium). With reference to the Chinese National Standard GB/T 5072-2008, a universal testing machine (WDW-100, China; a loading rate of 0.5 mm·min⁻¹) was used to measure the cold compressive strength of the cured samples and the coked samples. Reference to the Chinese National Standard GB/T3001-2000, the cold modulus of rupture was measured by flexural testing machine. Reference to the Chinese National Standard GB/T3002-2017, the hot modulus of rupture was measured by high temperature flexural testing machine and the samples coked in carbon embedded atmosphere at 1450 °C for 0.5 hours during the test. The refractory samples after coking at 1000 °C were crushed, ground, and sieved (200 mesh) to prepare fine powder samples that meet XRD test standards, and the phase composition was analyzed by an X-ray diffractometer (XRD, Bruker D8, Germany; a scan rate of 4 °/min, from 15° to 75°). The micromorphology of the polished and fracture surfaces of the coked samples was characterized by a scanning electron microscope (SEM, JSM6360, Japan), and their microstructure and element distribution were analyzed by an energy dispersive spectrometer (EDS, Ultim Max, England).

## 3. RESULTS AND DISCUSSION

### 3.1 Effect of adding recycled refractory on phase and particle grading

The screening statistics of mud after mixing of sample A0, A1, A2, and A3 were shown in Table 4.

**Table 4**: Results of mud sieving for sample A0, A1, A2 and A3

| Sample | ≥1.5 mm | 1.5 mm~1 mm | 1 mm~0.5 mm | 0.5mm~0.1mm | ≤0.1mm |
|--------|---------|-------------|-------------|-------------|--------|
| A0 | 0 | 4.01 | 12.05 | 82.32 | 1.62 |
| A1 | 0 | 7.26 | 22.46 | 68.06 | 2.22 |
| A2 | 0 | 8.48 | 20.89 | 66.89 | 3.77 |
| A3 | 0 | 9.29 | 23.29 | 60.66 | 6.76 |
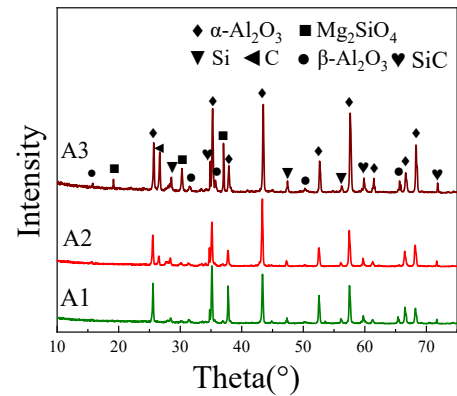


*Fig.1 XRD patterns of the refractory samples coked at 1000 °C for 3 h*

With the amount of recycled refractory added increases, the proportion of aggregate (2-1mm) and fine powder (≤ 0.1mm) in the mud were increased. This is related to the particle size distribution of the recycled refractory itself, even though the muds undergoes high-speed rotation granulation process, some fine powder still was residue.

After coking at 1000 °C, the XRD analysis of samples A1, A2, and A3 with added recycled refractory was carried out. In order to eliminate the influence of C peak, each ample was pre-oxidized at 800 °C for decarbonization.

The XRD analysis pattern is shown in Fig 1. The main components of the three samples are $\alpha$-$Al_2O_3$, with a small amount of Si and SiC. The three samples have a large amount of amorphous glass phase in the range of 10-20 °, which is due to the presence of amorphous $SiO_2$ of the recycled refractory. With the amount of recycled refractory added increases, the increase in peak intensity of $\beta$-$Al_2O_3$ and the appearance of magnesia alumina spinel phase in A3 sample indicate

an increase in the content of Na and Mg elements in the system. The introduction of recycled refractory makes the reaction more complex in the system at high temperatures.

Through SEM analysis which was shown in Fig 2, it can be seen that the particle distribution in sample A3 with added recycled refractory is uneven, and the resin wrapping situation of sample A3 is not as good as A0. Moreover, the particle size range in A3 is large, and it is obvious that there are more fine particles and some particle surfaces are irregular. There are still impurity phases between the particles.
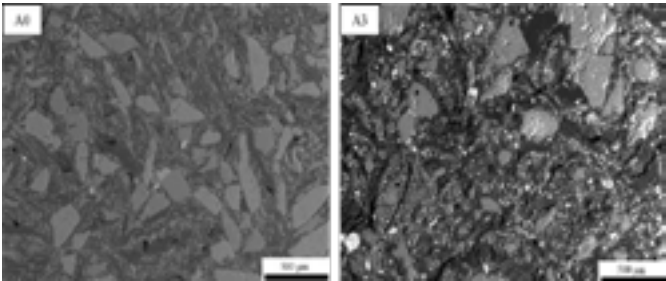


Fig 2 SEM images of polished surfaces of the refractory samples coked at 1000 °C for 3 h

### 3.2 Effect of adding recycled refractory on the performance of refractory
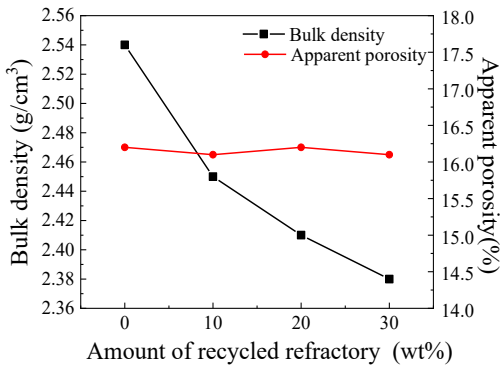


*Fig 3 Bulk density and apparent porosity of refractory samples coked at 1000 °C for 3h*

Fig 3 shows the bulk density and apparent porosity of samples A0, A1, A2, and A3 after coking at 1000 °C. The overall porosity is controlled between 16.0% and 16.5%. With the amount of recycled refractory added increases, the bulk density of the sample gradually decreases. The decrease in bulk density is due to the presence of other minerals such as $SiO_2$ and $Na_2O$ in the recycled refractory. Although the recycled material contains components with high bulk density such as MgO and $ZrO_2$, the total volume of the sample increases with the addition of recycled refractory under equal mass replacement.

The results of the amount of recycled refractory added and the mechanical strength are shown in Fig 4 and Fig 5. With the amount of recycled material added increases, the cold compressive strength (39.43 MPa, 35.19 MPa, 31.22 MPa, 24.56 MPa), cold modules of rupture (12.8 MPa, 11.7 MPa, 10.1 MPa, 8.8 MPa), and hot modules of rupture (14.1 MPa, 13.2 MPa, 11.9 MPa, 8.2 MPa) of the samples were all decreased.

The hot modules of rupture of samples A0, A1, and A2 have been improved compared to the cold modules of rupture. This may be due to the expansion of particles in the system at high temperatures, which enhances the internal structural stress. The main reason for the decrease in strength of A3 is that the recycled refractory contains many impurities, such as $SiO_2$, $Na_2O$, $K_2O$, etc. The impurity phase reduces the melting point of refractory, especially the formation of liquid phases at grain boundaries, leading to the generation of cracks. These two effects coexist, and as the amount of recycled refractory added increases, the decrease in strength caused by impurities dominates.
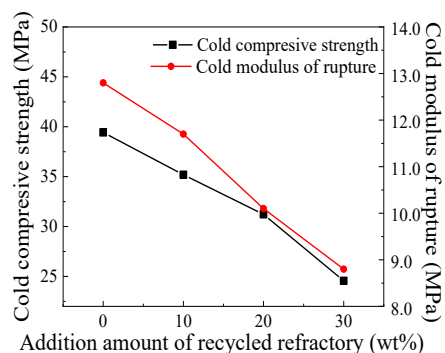
*Fig 4 Cold compressive strength and cold modulus of rupture of refractory samples coked at 1000 °C for 3h*

The introduction of impurities is an inevitable problem when using recycled refractory. Compared to the corundum-graphite system without recycled materials, the introduction of impurity phases increases the complexity of the components in the system. At the same time, these components are prone to react with the refractory system $Al_2O_3$, MgO, or $SiO_2$ to form a low melting point liquid phase, causing internal structural damage and thereby affecting the strength.
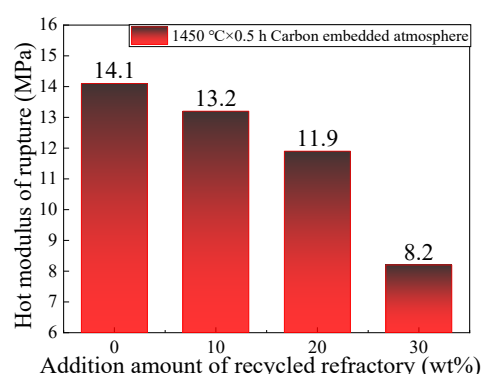


*Fig 5 Hot modulus of rupture of refractory samples coked at 1450 °C for 0.5 h*

When added 30 wt% recycled refractory (sample A3) in this experiment, compared with sample A0, the cold compressive strength decreased by ~37% and the cold modulus of rupture decreased by ~31%. hot modulus of rupture of A3 (8.2 MPa) has decreased by about 42% compared to A0 (14.1 MPa).
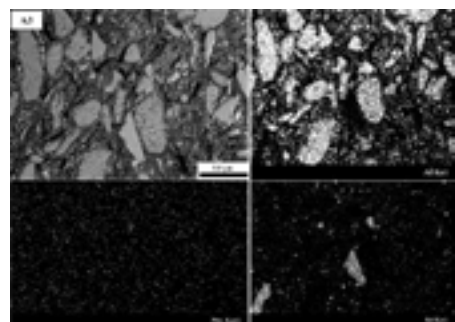


*Fig 6 SEM images and elemental distribution of polished surfaces of the refractory samples A3*

Through SEM and EDS analysis of sample A3 (refer to Fig 6). As is well known, with the increase of Na and Si content in refractory, the melting point of the system decreases sharply, and some areas are prone to the formation of low melting point phases that affect the strength. This can also explain why the high-temperature strength of A3 samples decreases more.

### 3.3 Effect of binder addition on strength of refractory sample

The addition of recycled materials will cause a decrease in the strength of the sample, and with the amount of recycled refractory added increase, the degree of weakening will also increase. The strength of refractory materials, especially high-temperature strength, is an important performance that affects the service life of refractory. The higher the high-temperature strength of the submerged entry nozzle slag line, the smaller the limit thickness of residual slag line damage. Research has shown that increasing the strength of carbon-containing refractory materials involves the addition of nanoscale additives[], nano carbon sources[], etc. Such additives are often highly effective but too expensive. The purpose of introducing

recycled refractory aim to scrap refractory for secondary utilization, mainly reflected in two aspects: environmental protection and cost reduction. Moreover, the main characteristics of continuous casting functional refractory materials are high carbon content and small particle size. On the one hand, the results in internal strength of A3 coming from the residual "carbon mesh" structure after resin curing, which is carbon bonding. The introduction of recycled materials has increased the proportion of coarse aggregate and fine powder in the formula. The difficulty of resin adhesion during material mixing and subsequent granulation processes has been increased. On the other hand, the specific surface area (roughness) and shape regularity of the particles in the raw material of the recycled refractory also different compared to conventional board corundum raw materials. It may have an impact on the bonding strength between particles. Therefore, based on sample A3, an experiment was designed to increase the amount of binder added, with the aim of improving the bonding strength between materials. Compared to A3, other samples only change the amount of resin added, without changing the amount of other raw materials added, and the increase in binder is based on A3 as a reference.

**Table 5** Supplement of solid phenolic resin in each sample

| Samples | A3 | A4 | A5 | A6 | A7 |
|---|---|---|---|---|---|
| Supplement the amount of phenolic resin | 0% | 0.5% | 1% | 1.5% | 2% |

The bulk density, mechanical properties at room temperature and hot modulus of rupture of the samples were tested. Samples A3~A7 were formed under the same conditions and tested simultaneously, rather than intentionally controlling the apparent porosity as in Experiment 1. The purpose is to minimize the impact of environmental factors on the experiment and further explore the impact of resin addition on the sample. The test results are as follows Fig 7, Fig 8 and Fig 9.
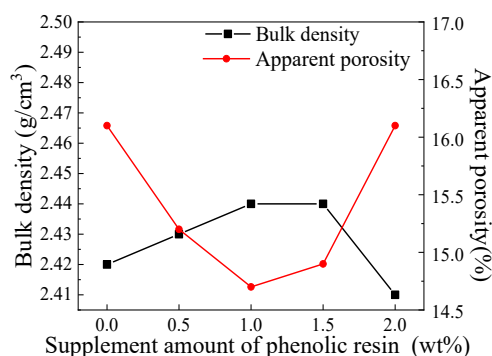


*Fig 7 Effect of phenolic resin addition on the apparent porosity and bulk density of the refractory samples*

The apparent porosity and strength of the sample first increase and then decrease with the increase of the amount of phenolic resin powder added. Bulk density decreases first and then increases.
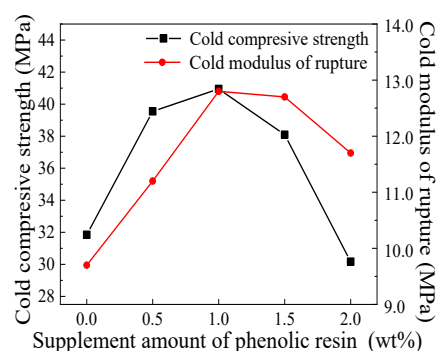


*Fig 8 Effect of phenolic resin addition on the mechanical properties of the refractory sample at room temperature*

The results confirm the previous hypothesis that the introduction of recycled refractory has increased the difficulty of material binding. Increasing the proportion of binder, it can make the binder more fully encapsulate particles. The decrease in apparent porosity also indicates that the sample particles are more tightly packed. The increase in strength comes from the tighter carbon mesh structure generated after resin heat treatment. However, excessive addition of phenolic resin can

affect the quality of the sample. The excess of phenolic resin, resulting in resin agglomeration during the mixing process, which is equivalent to mixing resin particles in the sample. After coking, the strength of the resin agglomeration area decreases significantly due to the lack of particle fixation, making it easier to generate cracks from inside.
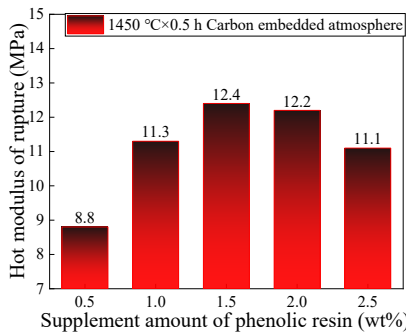


*Fig 9 Effect of phenolic resin addition on the hot modulus of rupture of the refractory samples*

In this experiment, sample A5 had the highest cold compressive strength, cold modulus of rupture, and hot modulus of rupture, which were 40.95 MPa, 12.8 MPa, and 12.4 MPa, respectively. Compared to sample A3, the strength of sample A5 has increased by ~30%.

## 3.4 The effect of supplementing Si powder

Si powder is a kind of commonly used additive for the industrial production of carbon-containing refractory. Previous studies have found that Si powder can improve the antioxidant and toughening effects of carbon-containing materials at high temperatures. Compared to high-end additives, it is easier to complete the conversion from laboratory to product by adding Si powder from a cost perspective. This formula contains Si powder (2 wt%), which is mainly added as an antioxidant. Therefore, under the material ratio of experimental sample A5 mentioned above, Si powder was added to it to explore the effect of Si powder addition on the high-temperature mechanical properties of the sample. Samples A5, A8, A9, and A10 were formed and tested under the same conditions.

**Table 6** Supplement amount of Si powder in each sample

| Samples | A5 | A8 | A9 | A10 |
|---------|----|----|----|-----|
| Si powder | 0% | 1% | 2% | 3% |
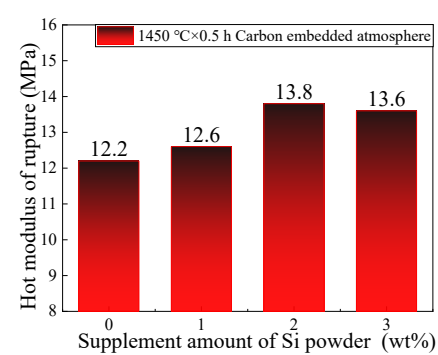


*Fig 10 Effect of supplement amount of Si powder on hot modulus of rupture of refractory sample*

From Fig 10, with the amount of Si powder increases, the hot modulus of rupture showed an upward trend. When the amount of Si powder is 2 wt%, the hot modulus of rupture is highest. During the heating and insulation process of Si powder at 1450 ℃, the internal Si and carbon components of the material react in situ to generate SiC, which enhances the strength of the sample. The reaction mechanism is based on formulas (4) and (5).

$$SiO_2(s)+3C(s) \rightarrow SiC(s)+2CO(g) \qquad (1)$$
$$\Delta G_{R1}=603150-331.98T+2RT\ln(P_{CO}/P_O) \qquad (2)$$
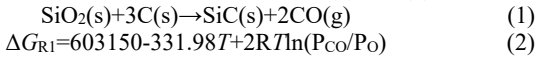
After adding 2 wt% Si powder to sample A9, the hot modulus of rupture increased to 13.8 MPa. The reason for continuing to supplement Si powder without improving its strength may be that the vacancies generated by SiC whiskers are allowed to approach saturation, while introducing more fine powder reduces the binding ability. Fig 11 shows the microstructure photos of the fracture surfaces of A5, A8, and A9 samples after the hot modulus of rupture test. There is no whisker formation between A5 grains, while shorter

whiskers are formed between A8 grains, and the length of A9 whiskers is significantly increased. The generated SiC is in the form of whiskers, which fixes the structural gaps of the matrix, suppresses crack propagation, and improves material strength. However, due to the high carbon content of the sample, particles are easily separated by graphite layers, which limits the space for whisker generation and does not significantly improve the high-temperature flexural strength. The experimental results are consistent with the previous experimental conclusions.

*Fig 11 SEM images of fracture surfaces of the refractory samples after hot modulus of rupture*
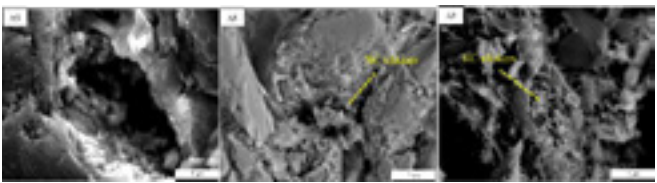


## 4. CONCLUSION

(1) Replacing raw materials with recycled materials to prepare alumina carbon refractory can cause a decrease in both cold strength and high temperature strength, and the degree of decrease increases with the addition of recycled materials. The main reasons are the irregular particles of recycled materials, large particle size distribution range and more impurities.

(2) In this experiment, increasing the amount of binder appropriately can improve the strength of alumina carbon refractory. When an additional 1wt% of solid phenolic resin is added, the strength improvement ~30%. However, excessive addition can cause a decrease in strength.

(3) After appropriate supplementation of Si powder, SiC whiskers are generated in situ in aluminum carbon refractory materials, and as the amount of Si powder supplementation increases, the amount of SiC whiskers generated increases. When the amount of Si powder added is 2wt%, the high-temperature flexural strength reaches its maximum, but the effect of excessive addition of Si powder may not be significant due to the limited vacancies that generate SiC whiskers.

## REFERENCES

[1] Luza A L, Simão L, Acordi J, et al. Synthesis of chemically bonded porous ceramics from MgO–C refractory bricks waste [J]. Ceramics International, 2022, 48(3): 3426−3434.

[2] Cheng X, Peng B, Zhang T H, et al. Cyclic thermal shock resistance for MgAlON–MgO composites obtained with additions of spent MgO–C brick: Microstructure characteristics, thermal shock parameter and thermal shock mechanism [J]. Ceramics International, 2022, 48(20): 29862−29872.

[3] Pagona E, Kalaitzidou K, Zaspalis V, et al. Effects of MgO and Fe2O3 addition for upgrading the refractory characteristics of magnesite ore mining waste/by-products [J]. Clean Technologies, 2022, 4(4): 1103–1126.

[4] Pilli V, Sarkar R. Study on the nanocarbon containing Al2O3-C continuous casting refractories with reduced fixed carbon content[J]. Journal of Alloys and Compounds, 2018, 781: 149-158.

[5] Si Y C, Fan Z, Li X. et al. Thermodynamic calculation and microstructure characterization of spinel formation in MgO-Al2O3-C refractories[J]. Ceramics International, 2022, 48(11):15525-15532.

[6] Roungos V, Aneziris C G. Improved thermal shock performance of Al2O3-C refractories due to nanoscaled additives[J]. Ceramics International, 2012, 38(2): 919-927.

[7] Bach M, Gehre P, Biermann H, et al. Recycling of carbon fiber composites in carbon-bonded alumina refractories [J]. Ceramics International, 2020, 46(8): 12574–12583.

# DEVELOPMENT AND IMPLEMENTATION OF HOLISTIC APPROACH TO ADDRESS CLOGGING PHENOMENA IN CONTINUOUS CASTING OF STEEL FOR VESUVIUS FLOW CONTROL CUSTOMER

Ata Fallah-Mehrjardi; Taigo Dos Santos; Andrzej Warchal; Camille Reynaert; David Dumont

VESUVIUS, Ghlin, Belgium

Fraction, size, type, and morphology of non-metallic inclusions (NMIs) in steel impact steel cleanliness i.e. steel quality (defects formation in semi-finished products) and productivity of continuous casting ( longer casting sequence for a given steel grade). Clogging in casting channels of tundish shrouds (SEN/SES/MTSP) are a complex phenomenon in Al-killed steel grades that was studied previously via characterization of industrial samples, experimental and modelling approach..

To ascertain information on the root causes of clogging phenomenon and to develop anti-clogging solutions consequently, a diagnostic approach was used in the present study to identify (1) reactions occurred in upstream & downstream processes, (2) sources of oxidative agents and (3) clogging mechanisms. To audit the casting process and build the baseline, industrial steel samples and compositions (mainly ultra-low carbon) from ladle/tundish/product and used nozzles (SEN/SES/MTSP) were recovered and analyzed iteratively.

Some steelmakers and refractory suppliers have approached the clogging problem via using solely a different SEN/SES/MTSP. This study, however, indicates the importance of applying the holistic approach to identify the contributing factors from ladle to mold/products and apply refractory solutions accordingly.

# SUBMERGED ENTRY NOZZLE PREHEATING EFFECT ON ITS PERMEABILITY

Emmanuel de Bilbao

CEMHTI UPR 3079 CNRS, Université d'Orléans, 45071Orléans Cedex 2, France

Mathilda Derensy, Christophe Ganser, Lise Loison, Chloé Milot.
ArcelorMittal Maizières Research, Maizières-les-Metz, France

## ABSTRACT

The submerged entry nozzle (SEN) plays a key role in continuous casting and its clogging has been discussed for a long time without converging to a real consensus about the reasons of the clogging and the effect on the steel quality. The preheating of this consumable materials is achieved thanks to air/natural gas burners placed inside the outlet ports of the nozzle. Due to the carbon content (>20%), those materials are sensitive to oxidizing atmosphere above > 500 °C. To avoid the decomposition of the graphite, the nozzle is coated with a borosilicate glass, which melts upon heating to form a viscous phase impermeable to gas to protect the graphite material from oxygen contact. However due to the abrasive flame of the burner, the protective glaze can be eroded and the core material decomposed in contact with surrounding oxygen. In this study, the effect of the preheating of the SEN on its permeability was addressed. The permeability of SEN refractory material was measured before and after preheating operations with preheating temperature ranging between 400 and 1000 °C and preheating period for 1 and 6 hours. It was found that permeability of preheated material at 400 °C was very close to not preheated material of 3-4 milli-Darcies while it increased up to 184 mD for the sample preheated at 1000 °C for 6 hours. The results confirmed air ingress through the SEN refractory material due to permeability increase may be one of the causes.

## INTRODUCTION

Submerged entry nozzle (SEN) clogging is a critical issue as it affects productivity of continuous casting process and quality of product. The causes of SEN clogging were extensively investigated and it has been now admitted clogging results in a combination of four mechanisms [1]:

- Agglomeration and sintering of deoxidation products,
- Freezing of liquid steel and build-up of solid steel
- Agglomeration of complex oxides
- Reaction products deposited in a film

The build-up of the reaction products results from the reaction between the deoxidant and i) oxygen from the steel, ii) oxygen produced by silica refractory decomposition, or iii) air flowing through nozzle porosity and driven by negative gauge pressure induced by liquid steel flow.

Very few studies focused on the air flow through nozzle refractory and the effect of the permeability. Poirier et al. observed that SEN permeability increased when the glaze coating which protects the nozzle during preheating contained defects. The authors also reported increased permeability allowed the air flow through the nozzle refractory and the oxidation of the carbon contained in the refractory, the aluminium which did not deoxidized the metal as well as the steel itself [2].

However other studies concluded that refractory permeability did play a role in nozzle clogging. For instance, Singh et al. argued accretions were found in the inner volume of the submerged part which is not in contact with air [3] and Tuttle et al. calculated the time it would take to grow the accretions observed in the lab-scale nozzle used in a casting simulator and observed it was much longer than the experimental time [4]. These latter concluded that air transport through the nozzle could not be the main raison of the clogging and permeability was not a relevant property.

The permeability role in the SEN clogging is still questionable in the case of a sound nozzle. However, if the preheating performed with natural gas burners generates hot spot in the material and local

decarburization, it can be assumed that the contribution of air ingress to clogging mechanisms becomes significant.

The preheating treatment requires to properly follow specific recommendations. In particular the temperature should not be higher than 1200 °C for the considered SEN and the nominal treatment should be at 1000 °C for 1h30. In practice these recommendations are hard to achieve and the temperature is not homogeneous in the height of the SEN, causing the glaze to be partially destroyed. Considering that permeability may have a significant impact on clogging process, the effect of the preheating of the SEN on this property was addressed.

## MATERIALS AND METHODS

### Sample preparation

Submerged entry nozzle (SEN) studied in this work was mainly made of corundum with graphite matrix. The 20 mm thick refractory body was coated outside with a glaze preventing decarburization during SEN preheating. The inner wall was protected by a liner mainly made of silica, alumina, and graphite and a thin vitreous phase-based layer.

The samples for permeability measurement were retrieved in the part of SEN in contact with air and had a diameter of 35 mm and a thickness of 25 mm (Fig. 1). The outer liner and the glaze based inner layer were removed to keep refractory body with the $SiO_2$-$Al_2O_3$-C liner.
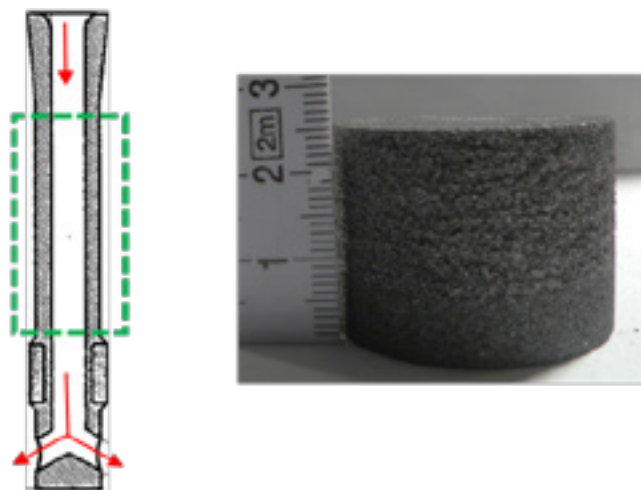


*Fig. 1: Samples for permeability measurement retrieved in SEN part in contact with air (dashed green rectangle)*

### Preheating treatment

Samples were preheated at different temperatures, no preheating, 400 °C, 600 °C, 800 °C, and 1000 °C, and for two different times, 1 and 6 hours. For each temperature/duration couple, 3 samples were tested.

The samples were put into the furnace before heating and removed after free cooling to avoid crack formation.

### Permeability measurement

Intrinsic permeability is the property inherent to the material relating the pressure drop to the flow rate according the Darcy law. Different techniques have been developed to measure it: with gas or liquid and

in unsteady state or steady state conditions. Gas permeability measurement in steady state conditions is the technique used in standards ISO 8841:1991, DIN EN 993-4, and ASTM C577- 7 [5,6]. It consists in measuring the inlet pressure Pi, the outlet pressure Po, and the volumetric flow rate Q of the gas flowing through the sample and to derive the permeability parameters (Fig. 2).
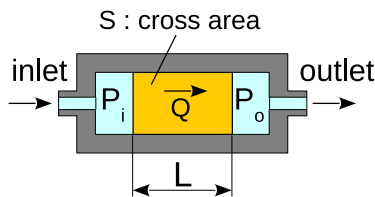


*Fig. 2: Principle of permeability measurement in steady state conditions*

The integrated form of gas flow equation applied to the test in steady-state conditions depends on the flow regime. According to Darcy, Klinkenberg, and Forchheimer [7–9], its general form writes:

$$\frac{P_i{}^2 - P_o{}^2}{2PL} = \frac{\mu}{k_\infty \left(1 + \frac{b}{P_m}\right)} v + \frac{\rho}{k_2} v^2 \qquad (1)$$

where $L$ is the sample thickness. Contrary to the standards, the pressure drop is expressed in function of the squared pressure due to the gas compressibility. The gas velocity $v$, or flow rate, varies from the entrance to the exit because of the pressure gradient and the gas compressibility. $P$ is the absolute gas pressure for which the flow rate $v$ is evaluated, that is $P_i$ or $P_o$ for $v_i$ or $v_o$ respectively. $v$ is derived from the volumetric flow rate $Q$ per cross-sectional area of the sample perpendicular to the flow. The dynamic viscosity of the gas $\mu$ is assumed to be constant within the applied pressure range. $k_\infty$ is called the intrinsic permeability and is expected to be the permeability one would measure with liquid. The slippage factor $b$ accounts for the slippage of gas molecules and depends on both the molecular mean free path and characteristic length of pore geometry. $P_m$ is the mean pressure of $P_i$ and $P_o$.

The second right-hand side term of the equation accounts for inertial effects due to dissipation of inertial energy as fluid particles accelerate through smaller pore throats and decelerate through larger area. Although $k_2$ has the dimension of a length, it is called the non-Darcian or inertial permeability.

The standards mentioned above recommend permeability measurement in atmospheric mode, for which the exit is left at atmospheric pressure and the gas leaving the sample is thereby allowed to flow directly at this pressure. The flow rate is measured at the outlet of the sample and $P = P_o$ in equation 1. In addition, it is assumed that the mean pressure equals 1 atm. as the pressure drop is very small. However, the methods proposed by the standards do not allow for determining the intrinsic permeability and the slippage factor. It is possible to extend the standard method by applying increasing inlet pressure to get different sets of triplets ($Pi$, $Po$, $v_o$). However, the determination of the three parameters is very inaccurate when increasing inlet pressure and letting the outlet at atmospheric pressure because inertial effect may be activated and it becomes impossible to properly determine the intrinsic permeability $k_\infty$ and the slippage factor $b$.

An improved gas permeameter has been then developed to fix this issue [10]. It includes a mass flow controller put at the inlet to control the flow regime and valves put at the outlet to apply a backpressure if needed (Fig. 3). Controlling the flow regime allows to make one of the right-hand terms of equation 1 predominant with respect to the other one and to determine therefore the selected parameter i.e., the intrinsic permeability $k_\infty$ and the slippage factor $b$ or the inertial factor $k_2$. Determining the Klinkenberg factor may require to apply backpressure at the outlet to increase the measurement accuracy.
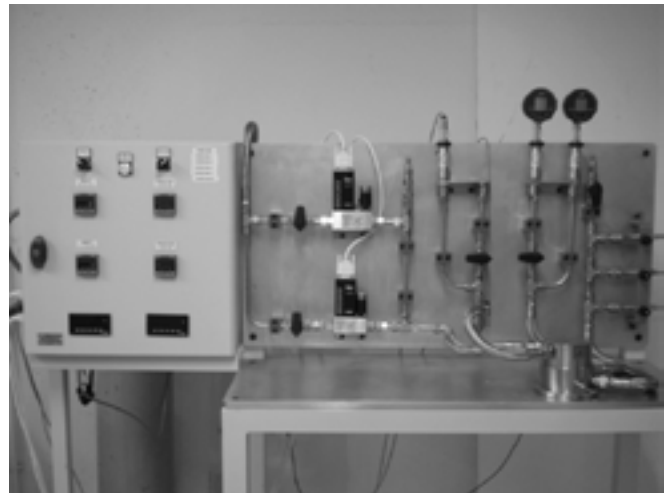


*Fig. 3: Gas permeameter developped for accurate measurement of intrinsic permeability*

## RESULTS AND DISCUSSION

The permeability measurement of the 3 not preheated samples was performed letting the outlet at atmospheric pressure as their permeability was low. The pressure drop followed a parabolic behaviour with the flow rate indicating inertial effect was significant for flow rate over 1 mm/s (red diamonds in Fig. 4).
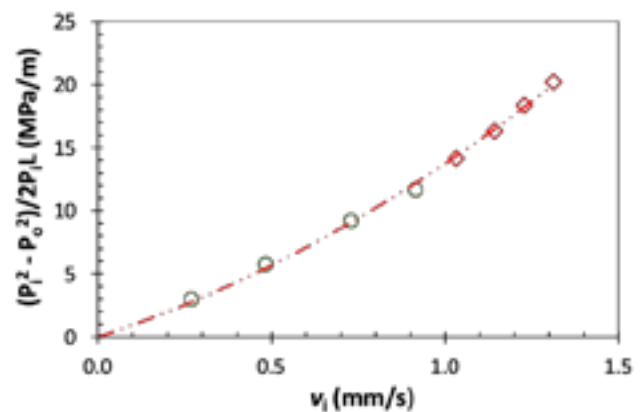


*Fig. 4: Darcy plot of one of the three not preheated samples*

Fig. 5 plots the apparent permeability $k_a$ calculated according to equation 2 which is derived from equation 1 but not taking into account the inertial term with the reciprocal mean pressure $P_m$.

$$k_a = \frac{2P_iL}{P_i{}^2 - P_o{}^2} \cdot \mu \cdot v = k_\infty \left(1 + \frac{b}{P_m}\right) \qquad (2)$$

The green circles correspond to the 4 lowest flow rates for which the turbulent flow in the porous network was negligible while the red diamonds were derived from measurements performed in turbulent regime. Indeed, the turbulent flow rate consumes flow energy without "helping" the gas to go toward the outlet and leads to an underestimated apparent permeability. The intrinsic permeability was derived with a linear regression using the measures obtained in Darcy-Klinkenberg flow regime i.e., from the green circles. For the sample presented in the figures the intrinsic permeability was 1.2 mD. Finally, the intrinsic permeability of the three not preheated samples ranged from 0.95 to 1.65 mD.
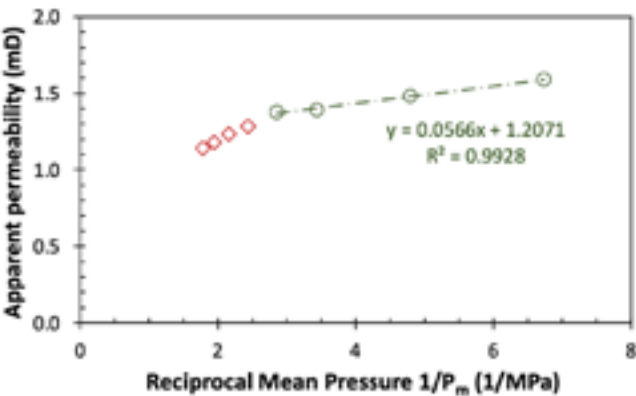
*Fig. 5: Apparent permeability of one the three not preheated samples*

Figure Fig. 6 shows the Darcy plot for a sample preheated at 1000 °C for 6 h. At low flow rate the measures do not follow the Darcy-Klinkenberg model as the point alignment does not seem to cross the origin. It can be explained either by a diffusive regime of by gaz creep contribution. On the other hand, measurements performed with higher flow do not present a parabolic shape characteristic of a turbulent flow. Trying to fit a parabolic function representative of equation 1 gave a negative quadratic coefficient which does not make sense. The Klinkenberg plot confirms that the points at low flow rate do not obey to a Darcian flow (Fig. 7, red diamonds). Performing measurements in back pressure mode using the valves located at the outlet of the permeameter and controlling the flow rate made it possible to increase the mean pressure in the sample and to activate the Klinkenberg effect (green squares). It was possible to include measures obtained in atmospheric mode for the linear regression (green circles). The derived intrinsic permeability was 146 mD. The permeability of the two other tested sample with the same treatment was 193 and 213 mD (Tab. 1)).

Additionally, the slippage factor *b* in equation 1 account for the gas slippage on the pore wall when the characteristic pore size is close to the molecular mean free path. For given flow rate and pressure drop the higher the pore size the higher slippage factor. The slippage factor of the preheated sample (1000 °C for 6 h) was 114 kPa, almost 25 times the one of not preheated sample, 4.69 kPa. It is clear that the slippage factor increase may be explained by the pore size increase induced by the oxidation. Another point confirming the pore size increase is the activation of the turbulent flow with the not preheated sample from 1 mm/s while the almost laminar Darcy-Klinkenberg flow still predominates with the flow rate of 15 mm/s.
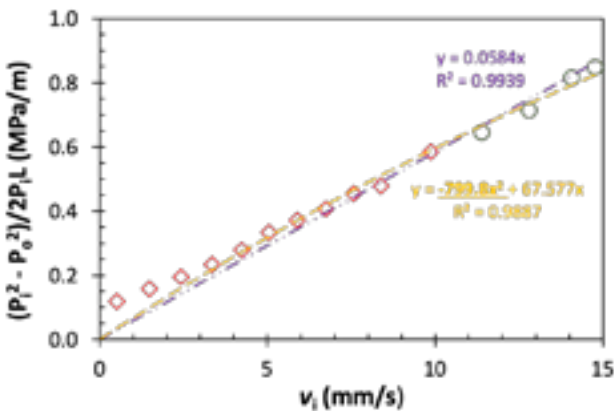


*Fig. 6: Darcy plot of one of the three samples preheated at 1000 °C for 6 h.*
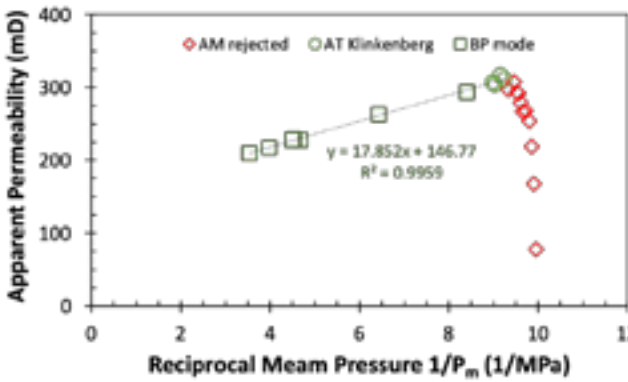


*Fig. 7: Apparent permeability of one the three samples preheated at 1000 °C for 6 h*
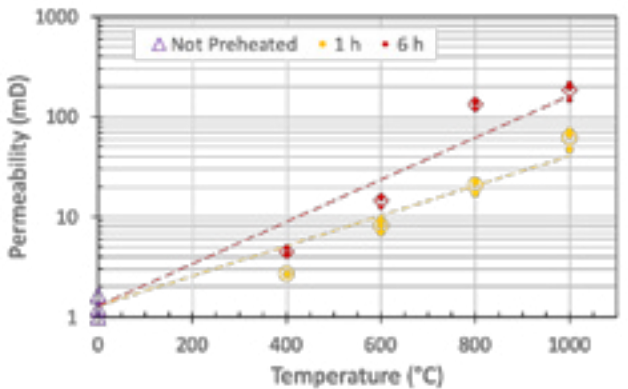


*Fig. 8: Evolution of the intrinsic permeability with temperature*

Finally figure Fig. 8 shows the evolution of the intrinsic permeability with the preheating temperature for the two durations. All the values are also summarized in Tab. 1. As expected, the permeability increases with treatment temperature assuming the oxidation rate also increases with temperature. The points do not lie on a straight line although the permeability increase seems to be thermally activated. Here the increase of the permeability is due to the decarburization of the material. As the graphite flakes burn, they generate porosity which contributes to the material gas permeability. The oxidation of the carbon content is starting >500°C.

*Tab. 1: Intrinsic permeability measured on not preheated samples and heated samples from 400 °C to 1000 °C for 1 and 6 hours*

| | | $k_\infty$ (mD) | | |
|---|---|---|---|---|
| | | Sample 1 | *Sample 2* | Sample 3 |
| | Not preheated | 1.21 | 1.61 | 0.95 |
| 1 h | 400 °C | 2.69 | | |
| | 600 °C | 8.23 | 9.22 | 7.02 |
| | 800 °C | 22.7 | 17.1 | 22.2 |
| | 1000 °C | 71.6 | 46.8 | 65.7 |
| 6 h | 400 °C | 4.31 | 4.25 | 4.87 |
| | 600 °C | 12.6 | 15.9 | 15.2 |
| | 800 °C | 137 | 119 | 141 |
| | 1000 °C | 146 | 193 | 213 |

## CONCLUSIONS

The permeability of refractory body of submerged entry nozzle was measured as a function of the preheating temperature and time. It was observed that the permeability increased significantly with temperature and time due to the decarburization of the graphite content. The highest value was obtained for the test at 1000 °C for 6 h and was two orders of magnitude higher than the one of material before preheating.

This work may help to determine the contribution of air transfer in clogging process with respect to the other causes. It can be expected that actual permeability at high temperature increase and make the air transfer even more significant. Measuring accurately the permeability at high temperature is still a challenge for the future work.

## REFERENCES

[1] Rackers KG, Thomas BG. Clogging in Continous Casting Nozzles. 78th Steelmaking Conference Proceeding, vol. 78, Nashville: Iron and Steel Society; 1995, p. 723–34.

[2] Poirier J, Verrelle D, Thillou B, Provost G, Taffin C, Tissot P. Study of Clogging Phenomena in Continous Casting Submerged Nozzles, 1991, p. 226–9.

[3] Singh SN. Mechanism of alumina buildup in tundish nozzles during continuous casting of aluminum-killed steels. Metallurgical Transactions 1974;5:2165–78. https://doi.org/10.1007/BF02643930.

[4] Tuttle RB, Peaslee KD, Smith JD. Effect of Nozzle Permeability on Clogging. AISTech Proceedings, Nashville: 2004.

[5] ISO. Dense, shaped refractory products - Determination of permeability to gases. 1991.

[6] ASTM. Standard Test Method for Permeability of Refractories. 2007.

[7] Darcy H. Les fontaines publiques de la ville de Dijon (Éd. 1856). 1856.

[8] Klinkenberg LJ. The Permeability Of Porous Media To Liquids And Gases. American Petroleum Institute; 1941.

[9] Forchheimer P. Wasserbewegung durch boden. Zeit Ver Deutsch Ing 1901;45:1781–8.

[10] de Bilbao E, Loison L, Hbiriq Y, Orgeur C, Brassamin S, Tonnesen T, et al. Intrinsic permeability of refractories from gas permeability measurements: Comparison of results. Ceramics International 2018;44:2900–10.

# INHIBITION OF ABNORMAL DAMAGE OF CAO–ZRO$_2$–C MATERIAL FOR SUBMERGED ENTRY NOZZLES

Hironobu Miura, Wei Lin, Takayuki Matsunaga and Toshio Horiuchi

Research Center, Shinagawa Refractories Co., Ltd., Bizen-city, Japan

## ABSTRACT

The CaO-ZrO$_2$-C (CZ-C) inner linings of submerged entry nozzles were found to be damaged abnormally fast in one actual continuous slab-casting process. A significant quantity of ZrC was formed and the original graphite disappeared in the CZ-C microstructure, so the microstructure deteriorated severely. It is considered necessary to find countermeasures to inhibit ZrC formation reaction even under conditions of low CO partial pressure in order to prevent the abnormal damage of CZ-C. For this purpose, fundamental research on the effects of adding Al$_2$O$_3$ and MgO compositions into CZ-C was implemented in the present study. In a heating experiment under Ar atmosphere, the quantity of ZrC formed in the spinel (5%)-added specimen, especially in the (spinel+Al$_2$O$_3$) (5% each)-added specimen was clearly smaller than that in the conventional CZ-C material. EPMA analysis indicated that low-melting phases of Al$_2$O$_3$-CaO system were formed in the above-mentioned two specimens, coating the CZ, ZrO$_2$ and ZrC grains and simultaneously enhancing the densification of the microstructure, whereas the conventional CZ-C exhibited a microstructure in which ZrC was present in isolation between the CZ grains. On the other hand, in a molten steel-dipping experiment, both specimens maintained good alumina deposition resistance, similar to the conventional CZ-C.

## INTRODUCTION

Submerged entry nozzles are applied to introduce molten steel from the tundish into mold in the continuous casting of steel. Alumina-silica-carbon (Al$_2$O$_3$-SiO$_2$-C), having excellent resistance to both spalling and corrosion, is commonly employed as the nozzle material. However, when using Al$_2$O$_3$-SiO$_2$-C nozzles in the casting of Al-killed steel, as is well known, the phenomenon of alumina deposition on the inner wall of the nozzles, i.e, nozzle clogging often occurs.

Since the alumina deposition greatly worsens the stability of the casting operations and steel quality, many studies have been carried out on the causes and preventive measures [1-5]. The measures include the Ca-treatment of Al-killed steel, blowing argon gas through the nozzles into the molten steel and optimization of the nozzle structures and materials. As an anti-alumina deposition material, CaO-ZrO$_2$-C (CZ-C) is frequently utilized for the nozzle inner wall, focusing on the fact that CaO composition reacts with the Al$_2$O$_3$ from the molten steel to form molten phases [6]. The major component of CZ-C material is calcium zirconate CaZrO$_3$ (CZ), which has a sufficient hydration resistance.

The CZ-C nozzles usually show high performance, e.g., neither abnormal damage nor alumina deposition occur even when casting steel for more than 20 heat. However, it was found that the CaO-ZrO$_2$-C (CZ-C) inner linings are damaged abnormally fast in one actual continuous slab-casting process; specifically, the inner linings with a thickness of several millimeters are almost completely washed away after only about 2 heats cast. It has become a technical challenge to prevent the abnormal damage of CZ-C inner linings.

Since the nozzle inner linings of other materials (e.g. Al$_2$O$_3$-C, spinel-C) do not show such abnormal damage during pouring various steel grades in the same casting process, the abnormal damage of CZ-C linings can be inferred to be not solely caused by the wear due to the molten steel flow. Analyzing the microstructure of the residual CZ-C on the nozzles after use, it was observed that a significant quantity of ZrC was formed and nearly all of the original graphite disappeared, and as a result the microstructure deteriorated severely (figure 1). This microstructure was totally different from the case where no abnormal damage occurred in the inner linings of CZ-C [6].
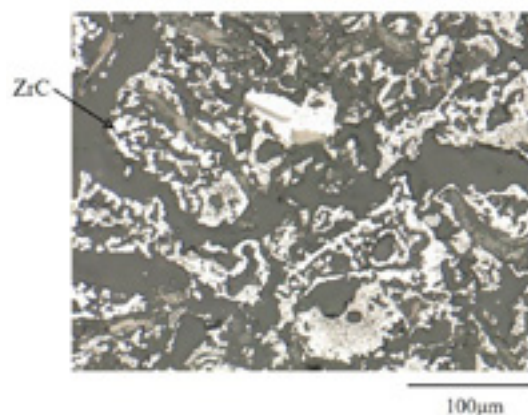


*Fig.1: Optical microstructure of CZ-C inner lining of a nozzle used in an actual continuous slab-casting.*

This abnormal damage is considered to be closely related to the ZrC formation reaction as shown in equation (1). That is, because the reaction results in the ZrC formation and graphite disappearance and therefore the microstructural deterioration, the CZ-C inner linings are easily worn by the molten steel flow.

$$(ZrO_2)_{\text{ in CZ}}+3C(s)=ZrC(s)+2CO(g) \tag{1}$$
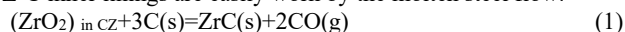
As equation (1) is a reaction producing CO gas, the lower the partial pressure of CO in the atmosphere relative to the equilibrium CO partial pressure of the reaction, the faster it will proceed. Therefore, the CO partial pressure in the CZ-C inner linings should be rather low in the casting process where abnormal damage has occurred in the inner linings of CZ-C.

Consequently, it is necessary to find countermeasures to inhibit the ZrC formation reaction even under the condition of extremely low CO partial pressure in order to prevent abnormal damage of CZ-C. For this purpose, fundamental research on the effects of adding Al$_2$O$_3$ and MgO compositions into the CZ-C was carried out in the present study.

## EXPERIMENTAL METHODS

Specimens included the conventional CZ-C material, spinel (MgAl$_2$O$_4$)-5% added Specimen 1, and both spinel and Al$_2$O$_3$-5% added Specimen 2 (table 1). All contained 25% graphite. The specimens were made through a process in which a mixture of the raw materials was molded by cold isostatic pressing (CIP) and then fired in a coke breeze at 1000 °C for 3 hours.

Tab. 1: Components of specimens (mass %).

| - | Conventional CZ-C | Specimen 1 | Specimen 2 |
|---|---|---|---|
| Graphite | 25 | 25 | 25 |
| CZ (CaZrO$_3$) | 75 | 70 | 65 |
| Spinel (MgAl$_2$O$_4$) | - | 5 | 5 |
| Al$_2$O$_3$ | - | - | 5 |

For the evaluation of the ZrC formation tendency at low atmospheric partial pressure of CO gas, a heating experiment in an Ar atmosphere was conducted using an electric furnace with high sealing performance, of which the heating element was graphite.

Specimens (20×20×35 mm) were set into the furnace, followed by vacuuming the furnace and introducing a high-purity Ar gas at a

flow rate of 1 L/min. Then the temperature was raised to 1560 °C at 10 °C /min and held for 3 hours. Next, the specimens were cooled rapidly in the furnace by turning off the furnace power. For the specimens after the heating experiment, the rate of change in weight was measured, and the mineral phases were identified with XRD analysis. The microstructure was also analyzed by means of EPMA.

Moreover, an experiment for evaluation of alumina deposition resistance was carried out by using a molten steel-dipping method. 22 kg of steel was melted under an Ar atmosphere in a high-frequency induction furnace, equipped with an MgO crucible, followed by adding 0.12% metal Al and stirring the molten steel. After the temperature was kept at around 1560 °C, the specimens (cuboid of 20×20 mm) were simultaneously dipped into the molten steel for 1 hour. For a comparison, a common $Al_2O_3$-$SiO_2$-C material ($SiO_2$: 20%, C: 25%) was also adopted as a dipping specimen. The alumina deposition state and microstructure of the specimens after the dipping experiment were observed. According to the experimental results so far, it has been known that ZrC does not formed in the conventional CZ-C specimen in the dipping experiment. Hence, the influence of the additives (spinel, $Al_2O_3$) on the alumina deposition resistance of CZ-C under conditions where no ZrC is generated can be investigated by this experimental method.

## RESULTS

### Evaluation of ZrC formation tendency

The apparent porosity of the specimens before the experiment (after the firing) was 14.8% (the conventional CZ-C), 14.7% (Specimen 1) and 15.1% (Specimen 2), respectively. The values were all within the normal range, and the differences among the specimens were small.

After the Ar atmosphere-heating experiment, the weight of each specimen was reduced compared to before the experiment. The rate of weight reduction of the conventional CZ-C was the largest, reaching 4.64%, followed by 4.19% for Specimen 1 and 2.10% for Specimen 2. The indexed values based on the conventional CZ-C were 100, 90 and 45, respectively (figure 2). Specimen 2 was 55% lower than the conventional.
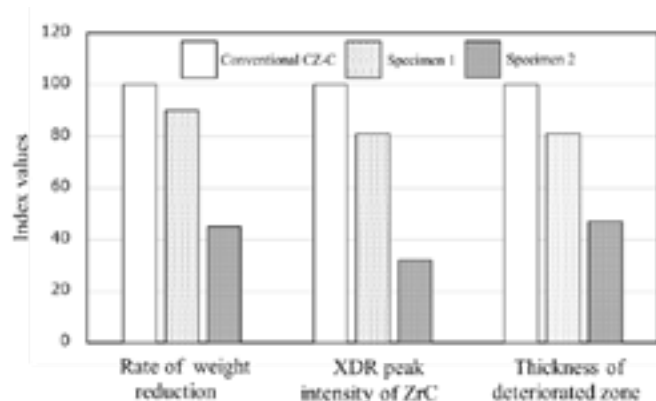


*Fig.2: Index values of characteristics of specimens after heating experiment (under Ar at 1560 $^0$C for 3 hours).*

The XRD analysis results of the samples taken from the longitudinal middle positions of the specimens after the heating experiment revealed that ZrC was formed in each specimen, and the phases except ZrC were mainly CZ ($CaZrO_3$), graphite and $ZrO_2$(c) (figure 3). The intensity of ZrC XRD strongest peak indexed based on the conventional CZ-C was 81 for Specimen 1, and 32 for Specimen 2, which was 68% lower than the conventional (figure 2). This was consistent with the above-mentioned variation tendency in the rate of weight reduction due to the spinel and $Al_2O_3$ addition.

Moreover, analyzing the microstructures (figure 4), a deteriorated zone was found to occur in the surface side of each specimen after the heating experiment, in which a part of the original graphite disappeared and ZrC (light-colored grains) was formed.
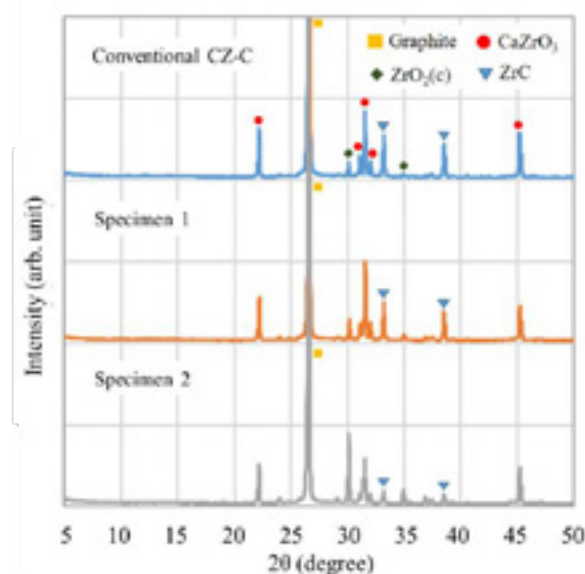


*Fig.3: XRD patterns of specimens after heating experiment.*
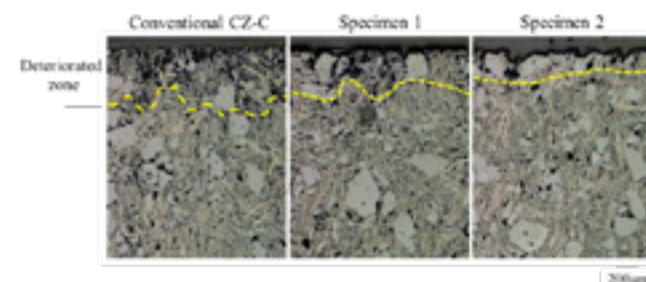


*Fig.4: Optical microstructure of specimens after heating experiment.*

The deteriorated zone had a thickness of approximately 470 μm (the conventional CZ-C), 380 μm (Specimen 1) and 220 μm (Specimen 2), respectively. The index values were 100, 81 and 47 (figure 2), which was also consistent with the variation tendency in the rate of weight reduction.

On the one hand, both Specimens 1 and 2 contained 1.4% MgO composition derived from the spinel according to table 1. The reaction between MgO and carbon (MgO(s)+C(s)=Mg(g)+CO(g)) also occurred as explained later. Nevertheless, even if all the MgO (1.4%) reacts with the carbon to transform into Mg and CO gases, it only consumes 0.4% carbon, negligible compared to the initial carbon (graphite) content (25%). Thereby, the weight reduction of the specimens during the heat was primarily due to the reaction between CZ and carbon (equation (1)) even in MgO-bearing Specimens 1 and 2.

The above results for the rate of weight reduction, the XRD-peak intensity and the thickness of the deteriorated zone all imply that the quantity of ZrC formed in Specimen 1, especially in Specimen 2 was less than the conventional CZ-C; that is, the ZrC formation reaction was retarded by the spinel and $Al_2O_3$ addition.

According to EPMA analysis for the deteriorated zone (figure 5), it was found that low-melting phases of $Al_2O_3$-CaO system (around 52% $Al_2O_3$, 46% CaO) were formed in Specimens 1 and 2, which were distributed on the surface of the CZ grains and also present between the CZ grains in the form of mixing with the small $ZrO_2$ and ZrC grains; i.e., the low-melting phases coated the CZ, $ZrO_2$ and ZrC grains and simultaneously enhanced the densification of the microstructure. Conversely, the conventional CZ-C exhibited a microstructure in which ZrC was present in isolation between the CZ grains.

475

Furthermore, MgO composition was hardly detected in the deteriorated zone of Specimens 1 and 2. This suggests that the MgO-C reaction generating the Mg evaporation indeed occurred during the heating.
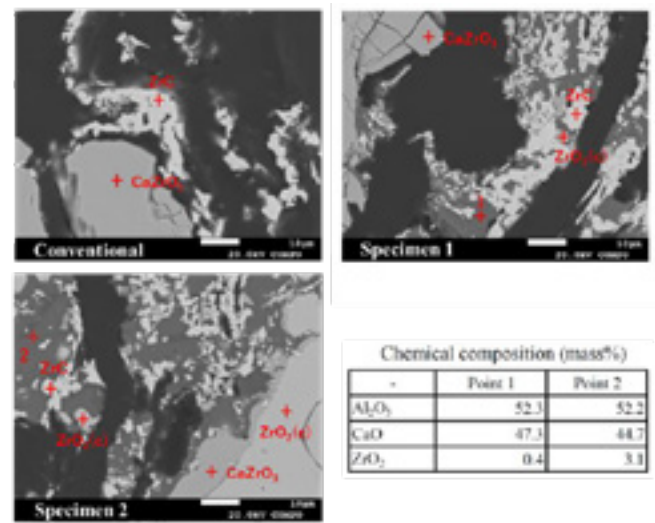


*Fig.5: EPMA analysis of deteriorated zone in specimens after heating experiment.*

On the other hand, the content of $ZrO_2$ composition (mainly $ZrO_2$ in CZ) in the specimens decreased relatively due to the addition of spinel and $Al_2O_3$ (table 1). The indexed $ZrO_2$ contents of the specimens were 100, 93 and 86, respectively. Accordingly, the $ZrO_2$ content decreased by only 14% at the maximum (Specimen 2), significantly smaller than the variation extent of the weight reduction, the ZrC XRD intensity and the thickness of the deteriorated zone described before. Therefore, the main reason for the inhibition of the ZrC formation by the spinel and $Al_2O_3$ addition is not the decrease of the $ZrO_2$ content, but the formation of the low melting point phases.

**Evaluation of alumina deposition resistance**

An adhesion layer (brown) with a maximum thickness of approximately 2 mm was observed on the surface of cross-section of the $Al_2O_3$-$SiO_2$-C specimen (as a comparative specimen) after the dipping experiment (figure 6). According to EPMA analysis, it was an $Al_2O_3$ system with over 80% $Al_2O_3$.

In contrast, almost no adhesion layer was formed on the conventional CZ-C, Specimens 1 and 2. They also did not display any corrosion. As with the conventional CZ-C, no ZrC was formed in Specimens 1 and 2 (see figure 7).

Consequently, under the condition that ZrC is not formed, Specimens 1 and 2 will exhibit a high alumina deposition resistance without corrosion, similar to the conventional CZ-C. In other words, spinel and $Al_2O_3$, within the amount of this experimental addition range, do not lower the alumina deposition resistance or corrosion resistance of CZ-C.
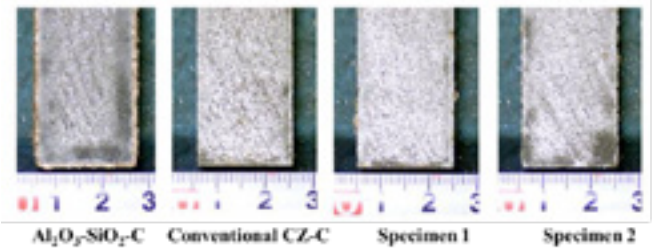


*Fig.6: Cross-section of specimens after molten steel-dipping experiment.*
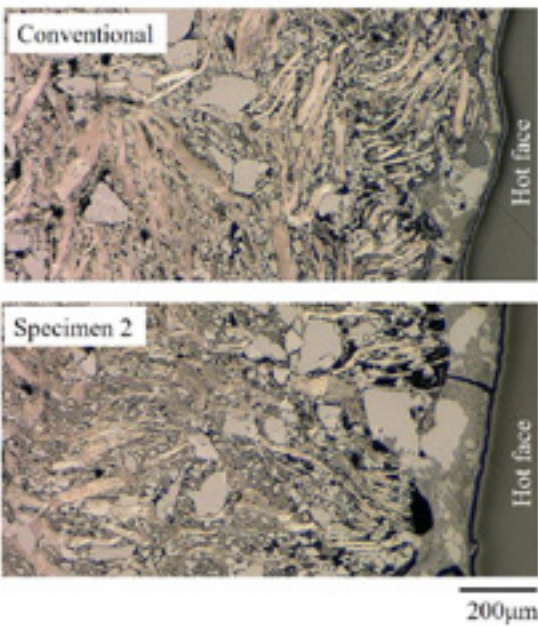


*Fig.7: Optical microstructure of specimens after molten steel-dipping experiment.*

**DISCUSSION**

The CZ raw material included a small amount of $ZrO_2(c)$ besides the CZ. The ZrC produced from the $ZrO_2(c)$ should be extremely low. ZrC formation reactions between CZ and carbon can be expressed as equations (2)-(4) in detail (equation (2) is effectively the same as equation (1)).

The reaction of equation (2) occurs between the CZ and carbon grains in contact with each other, while equations (3) and (4) occur between the CZ and carbon grains that are not in contact.

$$CaZrO_3(s)+3C(s)=ZrC(s)+CaO(s)+2CO(g) \quad (2)$$
$$CaZrO_3(s)+4CO(g)=ZrC(s)+CaO(s)+3CO_2(g) \quad (3)$$
$$CO_2(g)+C(s)=2CO(g) \quad (4)$$
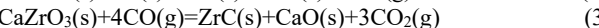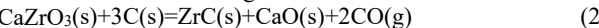
The reactions of equations (3) and (4) proceed in a chain, of which the total reaction takes the same form as equation (2). The standard Gibbs free energy change ($\triangle G^0$) of the reaction of equation (2) was calculated according to the reported standard formation Gibbs free energies of $ZrO_2$ [8], ZrC [8] and $CaZrO_3$ [9], as shown in the following equation.

$$\triangle G^0 = 674,000-318.44T, \quad J/mol \quad (5)$$

The relationship between the equilibrium CO partial pressure and temperature for the reaction of equation (2) obtained from equation (5) is illustrated in figure 8. When the partial pressure of CO in an actual atmosphere is lower than the equilibrium CO partial pressure, the reaction of equation (2) or equations (3) and (4) will proceed to the right, i.e., ZrC is generated.
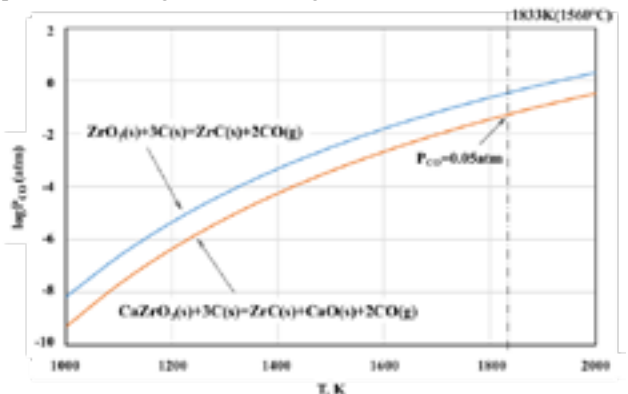


*Fig.8: Equilibrium CO partial pressure of ZrC formation reactions as a function of temperature.*

From figure 8, it can be seen that the equilibrium CO partial pressure increases with the rising temperature, reaching 0.05 atm at the experiment temperature 1560 °C (1833K). As the Ar gas was blown into the furnace at a relatively high rate (1 L/min), the CO partial pressure around the specimens should have been significantly lower than 0.05 atm, and the ZrC formation may have started during temperature rising.

The phase of $Al_2O_3$ 52%, CaO 46% in Specimens 1 and 2 (see figure 5) has a melting point of approximately 1455 °C according to the $Al_2O_3$-CaO phase diagram, 95 °C lower than the experiment temperature. This indicates that a molten phase of $Al_2O_3$-CaO system began to form during temperature rising and eventually existed stably. It is believed that the molten phase played a role in suppressing ZrC formation primarily by the following mechanism.

A part of the molten phase coats the CZ grains, blocking the contact of the CZ with the carbon and CO gas; the rest exists between the CZ grains in the form of a mixture with the small $ZrO_2$ and ZrC grains, improving the compactness of the CZ-C microstructure and thus hindering the diffusion of CO gas from the inside, thereby raising the CO partial pressure in the CZ-C.

The reason why the ZrC formation could not be completely prevented by adding the $Al_2O_3$ and MgO composition is inferred to be that sufficient time is required for the formation of appropriate amount of molten phase. The low amount of ZrC formed in Specimen 2 may be because of the short time required to form a suitable molten phase. Detailed investigation on this aspect is a future topic.

Regarding the effect of MgO composition, it is believed that contact between the CZ and carbon grains was hindered and the CO partial pressure was increased due to the MgO-C reaction, which also suppressed the ZrC formation reaction to some extent [7].

On the other hand, the reason why ZrC did not form in the CZ-C specimens in the molten steel-dipping experiment is considered to be that the diffusion of CO gas was slow due to the low flow of the molten steel under the experimental condition, allowing a high CO partial pressure in the specimens.

In actual casting, when the flow of molten steel through the SEN inner lining is fast (figure 9), the CO gas diffuses and dissolves quickly into the molten steel (equation (6)), therefore the partial pressure of CO inside the CZ-C becomes low, leading to the easy formation of ZrC, similar to the case of Ar atmosphere-heating in this study.

$$CO(g)=\underline{C}+\underline{O} \qquad (6)$$

In fact, the molten steel throughput in the continuous slab-casting process where the abnormal damage occurred in the CZ-C inner linings was several times higher than the casting processes where no abnormal damage occurred in the CZ-C inner linings.

The results of this basic investigation will be helpful in finding measures to prevent the abnormal damage of CZ-C material that occurs in actual steel casting. Under practical casting conditions, the material of Specimen 2 has the potential to significantly inhibit the ZrC formation reaction and so prevent the abnormal damage, and meanwhile, exhibit high alumina deposition resistance.

Additionally, the equilibrium CO partial pressure for the formation reaction of ZrC from $ZrO_2$ is higher than from CZ (see figure 8). For example, they are 0.34 and 0.05 atm at 1560 °C (1833 K), respectively. This suggests that it is also necessary not to use CZ raw materials containing too much $ZrO_2(c)$ for the inhibition of ZrC formation.

## SUMMARY

Submerged entry nozzles with the inner linings of $CaO-ZrO_2$-C (CZ-C) material are frequently utilized to prevent alumina deposition. However, it was found that the CZ-C inner linings with a thickness of several millimeters are almost completely damaged after casting only about 2 heats in one actual continuous slab-casting process. The investigation of the microstructure of the CZ-C inner linings remaining in the used nozzles revealed that a significant quantity of ZrC was formed and the original graphite disappeared, as a result its microstructure deteriorated severely.
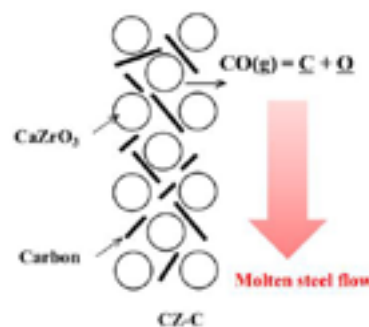


*Fig.9: Schematic diagram of CO gas movement from CZ-C into molten steel flow.*

It was considered necessary to find countermeasures to inhibit the ZrC formation reaction even under conditions of low CO partial pressure in order to prevent abnormal CZ-C damage. For this purpose, fundamental research on the effects of adding $Al_2O_3$ and MgO compositions into the CZ-C was implemented in the present study.

In a heating experiment under Ar atmosphere, the quantity of ZrC formed in the spinel (5%)-added specimen, especially in the (spinel+$Al_2O_3$) (5% each)-added specimen was clearly smaller than that in the conventional CZ-C material. For example, the XRD peak intensity index of ZrC was 81 for spinel-added specimen and 32 for spinel+$Al_2O_3$-added specimen, relative to 100 for the conventional CZ-C material.

EPMA analysis indicated that low-melting phases of $Al_2O_3$-CaO system were formed in the above-mentioned two specimens, coating the CZ, $ZrO_2$ and ZrC grains and enhancing the densification of the microstructure, whereas the conventional CZ-C exhibited a microstructure in which ZrC was present in isolation between CZ grains.

On the other hand, in a molten steel-dipping experiment, both specimens maintained a high alumina deposition resistance, similar to the conventional CZ-C.

## REFERENCES

[1] R. B. Snow and J. A. Shea. Mechanism of erosion of nozzles in open-hearth ladles. J. Am. Ceram. Soc. 32 (1949), p.187-194

[2] S. N. Singh. Mechanism of alumina buildup in tundish nozzles during continuous casting of aluminum-killed steels. Metall. Trans. 5 (1974), p.2165-2178

[3] K. Sasai and Y. Mizukami. Reaction Rate between Alumina Graphite Immersion Nozzle and Low Carbon Steel. ISIJ International 35 (1995). p. 26-33

[4] S.Ogibayashi. Mechanism and Countermeasure of Alumina Buildup on Submerged Nozzle in Continuous Casting. Taikabutsu overseas 15 (1995). p.3-14

[5] K.Mukai, R.Tsujino, I.Sawada, M.Zeze and S. Mizoguchi. Effect of refractory materials on inclusion deposition of immersion nozzle in continuous casting and mathematical modeling of inclusion deposition. Tetsu-to-Hagane 85 (1999), p.307-313

[6] W. Lin, Y. Ohkawa, T. Matsunaga and M. Iida. Inhibition effect of $CaO-ZrO_2$-C nozzles on alumina deposition in continuous casting of Al-killed steel. AISTech 2019-Proceedings of the Iron & Steel Technology Conference. p.2843-2850

[7] T. Matsunaga, W. Lin, Y. Ohkawa, E. Iida, A. Watazu and S. Tsutomu. Formation of ZrC and its effect of molten steel penetration in $ZrO_2$-C. Taikabutsu 60 (2008), p. 293-301

[8] The Iron and Steel Institute of Japan. Handbook of Iron and Steel (Tekkobinran) 4.1 Edition CD-ROM, Vol.1 (2002)

[9] J. Tanabe and K. Nagata. Use of solid-electrolyte Galvanic cells to determine the activity of CaO in the $CaO-ZrO_2$ system and the standard Gibbs free energies of formation of $CaZrO_3$ from CaO and $ZrO_2$. Metallurgical and Materials Transactions B 27 (1996), p.658-662

477

# EVALUATION OF OXIDE–BASED SEN AND OXIDE–LESS SEN ON NOZZLE CLOGGING

Jun-Hyun Kim[1], Min-Suk Kim[1*], Sang-Bae Choi[1], Chul-Young Park[1], Sang-Ahm Lee[1]
[1]Chosun Refractories Co., Ltd, Pohang, South Korea

Youn-Bae Kang[2], Dong-Jun Lee[2], Yong-Min Cho[2],
[2]Graduate Institute of Ferrous and Energy Materials Technology, Pohang University of Science and Technology, Pohang, South Korea

## ABSTRACT

One of the causes of nozzle clogging during continuous casting of molten steel is interfacial chemical reaction between the refractory and the molten steel. Several researches have been conducted on the interfacial reaction product. However, evaluation of the interfacial chemical reaction has been insufficient. Without evaluation of the interfacial reaction, it is difficult to find out the refractory material capable of reducing the nozzle clogging. Therefore, in the present study, the interfacial chemical reaction between the refractory and molten steel was assessed in various ways: volume of the gas released from the refractory, evolution of steel components during reaction between the refractory and molten steel, thickness of the interfacial reaction product. Also, various nozzle refractories composed of different constituents were employed: alumina-silica-C base, $SiO_2$-less, lime-zirconia-C base, C-less, and oxide-less refractories. Based on the evaluation results, the refractory material capable of reducing the nozzle clogging was suggested, which can also contribute to the design direction of the nozzle material. It was found that the oxide-less refractory was efficient to reduce clogging, followed by $SiO_2$-less refractory.

## 1. Introduction

The submerged entry nozzle (SEN) is a critical component in the continuous casting process of molten metal. It serves as a conduit for the smooth flow of liquid metal from the ladle into the mold. However, one of the persistent challenges in this process is the clogging of the SEN, which can significantly impact the productivity, quality, and stability of the casting operation [1-3].

Clogging of the SEN can occur due to various factors, including suspended materials in the molten steel, reactions between the refractory and molten steel, temperature reduction, and atmospheric contamination [4]. These clogs restrict the flow of molten metal, leading to disruptions in the casting process and necessitating frequent maintenance and downtime.

Addressing the issue of SEN clogging is crucial for the efficient and reliable operation of continuous casting systems. Over the years, researchers and industry practitioners have explored different methods and techniques to mitigate or prevent clogging. This paper focuses on presenting an innovative anti-clogging material for submerged entry nozzles.

In this study, various methods were employed to evaluate the interfacial chemical reactions between refractory materials and molten steel, including the amount of gas emitted from the refractory, the image of samples after the reaction between the refractory and molten steel. Additionally, various refractory compositions, such as alumina-silica-carbon (AGS), $SiO_2$-less (AG), lime-zirconia-carbon (CSG), C-less (CL), and oxide-free (ALBN) refractories, were utilized as nozzle refractories.

Based on the evaluation results, refractories capable of reducing nozzle clogging were proposed, which can also contribute to the design direction of nozzle materials. It was found that oxide-free refractories were efficient in reducing clogging, followed by refractories without SiO2.

## 2. Clogging mechanism: SEN Inner Wall Reoxidation as a Result of Carbothermic Reaction

In the case of low carbon (C) aluminum-killed steel, the formation mechanism of network alumina in the submerged entry nozzle (SEN) can be described as follows [5]:
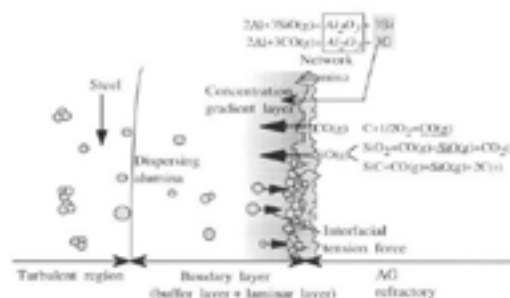


*Fig. 1: Reaction mechanism causing the early-stage clog deposit growth: low C Al-killed Steel [5]*

During the continuous casting process, carbothermic reactions occur within the SEN refractory, leading to the emission of carbon monoxide (CO) gas. This CO gas propagates through the interconnected pores present in the refractory material.

At the interface between the refractory and the liquid steel, the CO gas reacts with aluminum dissolved in the steel. This oxidation reaction results in the formation of alumina ($Al_2O_3$). The newly formed alumina adheres to the surface of the SEN, creating a network-like structure. This network alumina acts as a nucleation site for further alumina deposition. Simultaneously, alumina inclusions suspended in the liquid steel can also adhere to the existing network alumina. This accumulation of alumina inclusions on the network alumina is referred to as "build-up" alumina.

The presence of network alumina and build-up alumina can significantly affect the flow of molten steel through the SEN, leading to reduced flow area and potential clogging issues.

Understanding the network alumina formation mechanism is crucial for managing nozzle clogging in low carbon aluminum-killed steel. By implementing strategies to control the generation and deposition of alumina, such as refractory material selection, slag management, and control of oxygen levels in the steel, it is possible to mitigate clogging and ensure a smooth continuous casting process.

## 3. Evaluation of Gas Emissions from Refractory Materials

Previous studies have reported that the reaction between $SiO_2$ and C in the refractory materials leads to the release of CO(g) and SiO(g) [7-8]. However, it is observed that the formation of CO(g) and SiO(g) through Reaction (3.1) resulting from the reaction between $SiO_2$ and C is less spontaneous compared to the formation of CO(g) and SiC(s) through Reaction (3.2).

$$SiO_2(s) + C(s) = SiO(g) + CO(g) \qquad (3.1)$$
$$SiO_2(s) + 3C(s) = SiC(g) + 2CO(g) \qquad (3.2)$$
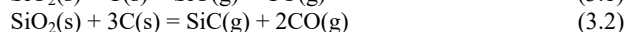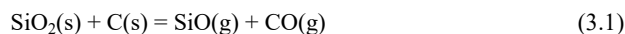
This indicates that only CO(g) is emitted from the refractory materials. Hence, there are discrepancies among different literature

sources regarding the gaseous emissions from refractory materials. Therefore, this study aims to verify the actual gas emissions from refractory materials through experimental validation based on thermodynamic calculations. Details of the experiental setup and test results can be found elsewhere [6].

## 3-1. Test Specimens and Testing Method
To enhance the reactivity of the refractory material at high temperatures, the refractory powder was formed into pellets (1 g, 4 pieces). The refractory material used in the experiments is shown in Table 3.1.

**Table 3.1: The refractory materials used for the submerged nozzle**

| Wt% | Oxide-based | | | | Non-Oxide | |
|---|---|---|---|---|---|---|
| | AGS | AG | CL | CSG | Wt% | ALBN |
| $SiO_2$ | 14.2 | 2.5 | 13.8 | 5.7 | AlN | 41.9 |
| $Al_2O_3$ | 54.8 | 64.8 | 78.5 | 1.8 | AlON | 29.5 |
| C | 28.8 | 27.4 | 5.5 | 22.9 | BN | 28.6 |
| $ZrO_2$ | - | - | - | 45.5 | | |
| CaO | - | - | - | 23.5 | | |

The high-temperature stability evaluation experiments of the refractory materials were conducted within an induction furnace, and the gas emissions from the refractory material were monitored using a quadrupole mass spectrometer (QMS) (Fig. 3.1). The experiments were carried out under controlled atmospheres by injecting purified Ar gas. Once the target temperature of 1600 °C was reached, the refractory materials were maintained at the temperature for 30 minutes, to induce high-temperature reactions of the refractory materials. Afterward, the power to the induction furnace was turned off, and the reactions were terminated. The volume of the emitted gases from the refractory material could be calculated.
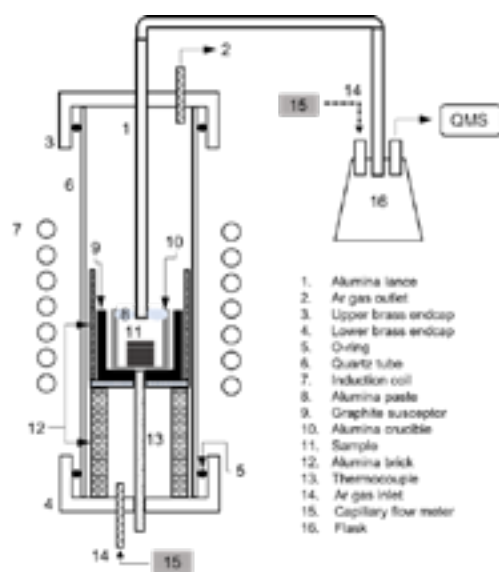


*Fig. 3.1 Schematic diagram of the experimental setup for detecting the gases emitted from the refractory pellet using a quadrupole mass spectrometer (QMS) [6].*

## 3-2. Experimental Results and Discussion
### 3-2-1. Mass Spectrometer Analysis Results
The gases emitted from all refractory materials were analyzed using the mass analyzer, and the results are presented in Fig. 3.2. For the oxide-based refractory materials, both the $N_2$ and $O_2$ flow rates decreased before 80 minutes of reaction time, but after 80 minutes, only the $N_2$ flow rate increased rapidly. A similar phenomenon was observed for the non-oxide-based refractory materials after 60 minutes. This indicates the emission of gases from the refractory

materials, and the emitted gases differ depending on whether it is an oxide-based or non-oxide-based material.

For the oxide-based refractory materials, only CO was emitted as a gas. The reaction between $SiO_2$ and C in the refractory material leads to the generation of CO. In the non-oxide-based refractory materials, since there is no $SiO_2$ and C, the emitted gas was $N_2$. As AlON, a component of the refractory material, is unstable at low temperatures, it decomposes into $Al_2O_3$ and AlN, resulting in the generation of $N_2$ [7].

The gases emitted from the refractory material were released into the induction furnace, initiating the interfacial reactions between the refractory material and the molten metal. The reactivity of the refractory material was evaluated based on the volume of the emitted gases, as a larger gas volume indicates a higher reactivity with the molten metal. In the case of non-oxide-based materials, as CO is not emitted, they exhibit the best refractory stability. Within the oxide-based materials, the lowest volume of CO emitted was observed in AG, where $SiO_2$ is reduced. This indicates that AG has the highest refractory stability, followed by CL, CSG, and AGS (Table 3.2).
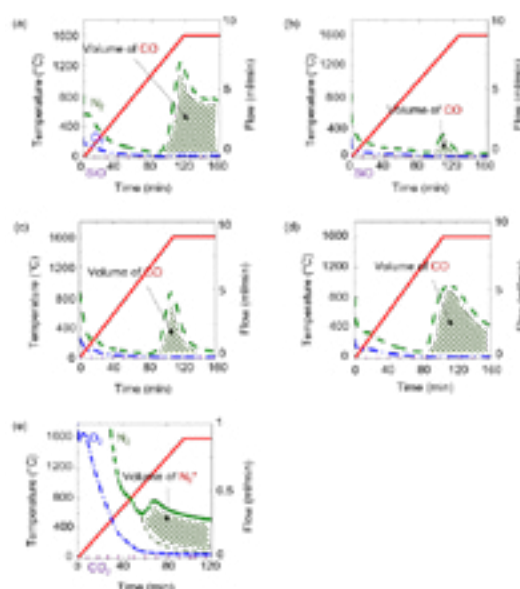


*Fig. 3.2. Confirmation of gases emitted from the refractory pellet: (a) AGS, (b) AG, (c) CL, (d) CSG, (e) ALBN ($N_2$: initial nitrogen in the crucible, CO: gas emitted from the refractory, $N_2^*$: gas emitted from the refractory). In (a) to (d), CO is emitted from the refractory around 1200 °C, while in (e), $N_2$ is emitted around 1000 °C.*

**Table 3.2: The Volume of gas emitted from 4g of refractory powder**

| ml | Oxide-based | | | | Non-Oxide |
|---|---|---|---|---|---|
| | AGS | AG | CL | CSG | ALBN |
| CO | 308 | 43.2 | 121.2 | 218 | |
| N2 | - | - | - | - | 22 |

### 3-2-2. Predicted CO Generation
Based on the mass analyzer experimental results, it was confirmed that the AG refractory material, in which $SiO_2$ was reduced, emitted the least volume of CO. However, it is generally expected that the CL refractory material, in which C is reduced, would emit the least volume of CO. Therefore, the mass of CO that can be emitted from the refractory material was calculated based on the reaction equation (Reaction (3.2)), where CO is generated. The purpose was to investigate the reason why $SiO_2$-reduced AG refractory material emits the least volume of CO, comparing it with the experimental results. The calculated masses of CO are presented in Table 3.3.

**Table 3.3: The mass of CO emitted from 100g of refractory material**

| g | Oxide-based | | | | Non-Oxide |
|---|---|---|---|---|---|
| | AGS | AG | CL | CSG | ALBN |
| CO | 13.5 | 2.3 | 12.8 | 5.3 | - |

Consistent with the mass analyzer experimental results, AG, with reduced $SiO_2$, exhibited the lowest mass of CO emitted from the refractory material. Fig. 3.3 represents the wt% and mole% of $SiO_2$ and C in the oxide-based refractory materials. Although CL had the lowest wt% of C, when converted to mole%, it still contained sufficient C to react with $SiO_2$ and emit CO. However, in the case of AG, the mole% of $SiO_2$ available for reaction with C was low. Therefore, to reduce the emission of CO from the refractory material, it is effective to decrease the wt% of $SiO_2$ rather than C, which aligns with the results of the refractory material reactivity.
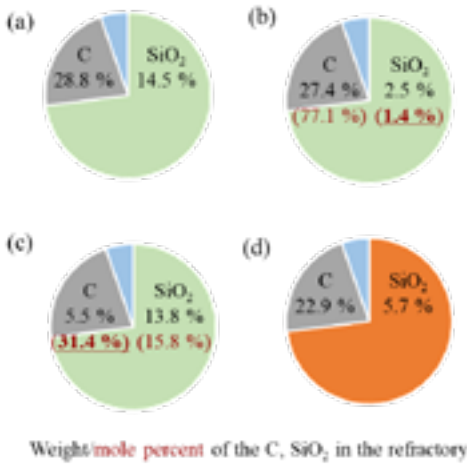


**Fig. 3.3.** *SiO$_2$ and C wt % and mole % in oxide-based refractories: (a) AGS, (b) AG, (c) CL, (d) CSG (green area corresponds to Al$_2$O$_3$, orange area corresponds to CaO, ZrO$_2$ as the main components).*

### 3-3. Test Results

The emission of gas species from refractory materials was investigated using quadrupole mass spectrometer. It was observed that CO(g) is emitted from oxide-based refractory materials, while $N_2$(g) is emitted from non-oxide-based refractory materials. The volume of CO emitted from the refractory material was used to evaluate its stability. It was found that non-oxide-based refractory materials exhibited superior stability compared to oxide-based materials, and among the oxide-based materials, AG with reduced SiO2 showed the best performance.

Overall, this study provides insights into the gas emissions from refractory materials and their relation to the thermodynamic properties and composition of the materials. The findings contribute to the understanding and evaluation of refractory material performance and can be valuable in the development and selection of refractory materials for high-temperature applications.

### 4. Evaluation of Reactivity at the Interface between Refractory Materials and Molten Steel

Research on the interfacial reaction between refractories and molten steel has been continuously conducted. However, most of the studies have focused on the deposits formed by interfacial reactions. It is difficult to identify refractory materials that can improve the clogging phenomenon in nozzles based solely on studies of deposits. Therefore, in this study, various commercially available refractory materials were immersed in molten steel during the casting process to evaluate their refractory reactivity. Based on the results of refractory reactivity, refractory materials that can

reduce nozzle clogging were proposed. Details of the experiental setup and test results can be found elsewhere [8].

### 4-1. Experimental Method

In actual operations, during continuous casting, molten steel flows at a constant velocity and reacts with the immersed nozzle. To simulate this phenomenon, a rotational immersion experiment called the Finger Rotating Method (FRM) was conducted to mimic the reaction between refractory materials and molten steel. The refractory materials used in the experiment and the composition of the molten steel are presented in Table 3.1 and Table 4.1, respectively.

To prepare the molten steel, 600 g of molten iron was poured into an $Al_2O_3$ crucible. The refractory material samples for immersion were prepared in a bar-type shape (10 ×10 ×160 mm). After reaching the target temperature (1565 °C), the additives (Al) were added at 10-minute intervals. Immediately after immersion, the refractory material was stirred at a speed of 100 rpm, which is similar to the speed at which molten steel passes through the inner wall of the nozzle during continuous casting [9]. The reaction time between the refractory material and molten steel was set at 30 minutes. Afterwards, the refractory material was separated from the stirrer and collected.

SEM analysis was conducted to examine the reaction product from the refractory materials. During SEM imaging, backscattered electron (BSE) mode was used to clearly distinguish different phases based on their composition. Energy-dispersive X-ray spectroscopy (EDS) mapping analysis was conducted for elemental analysis.

**Table 4.1 Target composition of molten steel used in refractory/molten steel interface reaction experiments.**

| Type | | Fe | Al |
|---|---|---|---|
| ULCAK steels | Mass(g) | 600 | 0.18 |
| | Conc.(ppm) | Bal. | 300 |

### 4-2. Test Results

The visual appearance of the refractory materials, both oxide-based and non-oxide-based, after immersion in the molten steel, is shown in Fig. 4.1. In both cases, a gray-colored deposit was observed in the immersed region. Previous literature reports have attributed the gray deposit formed on the refractory surface after immersion to $Al_2O_3$, a product of the reaction between the refractory material and the molten steel [12]. To confirm this, the morphology and composition of the deposit were examined through SEM analysis, and the results are presented in Fig. 4.2 in case of AGS and ALBN refractories.

In the non-oxide-based refractory materials, $Al_2O_3$ was also formed as a reaction product. However, the morphology of the deposits differed from that observed in the oxide-based refractory materials. While polygonal $Al_2O_3$ deposits were formed in the oxide-based refractory materials, spherical $Al_2O_3$ deposits were observed in the non-oxide-based refractory materials. Previous studies have reported that the morphology of the deposits is determined by the underlying mechanisms of their formation.

Polygonal deposits are formed as a result of interfacial reactions between the refractory material and the molten steel, while spherical deposits are attributed to residual desulfurization agents [5]. In oxide-based refractories, the generation of oxidizing gas leads to the formation of polygonal-shaped $Al_2O_3$ deposits as reaction products. However, non-oxide-based refractory materials do not produce oxidizing gases. Therefore, the spherical-shaped $Al_2O_3$ deposits observed in the non-oxide-based refractory materials are considered to be residual desulfurization agents. The absence of CO formation in the non-oxide-based refractory

materials further supports the observation of the deposit morphology.
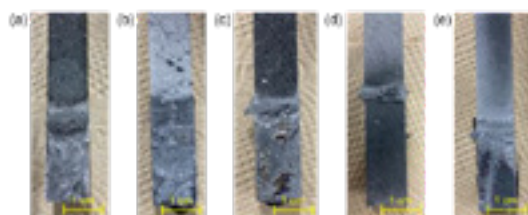


**Fig. 4.1** *Shape of refractories after refractory/molten steel interface reaction at 1565°C for 30 minutes with Al content of 300 ppm in the molten steel: (a) AGS, (b) AG, (c) CL, (d) CSG, (e) ALBN.*
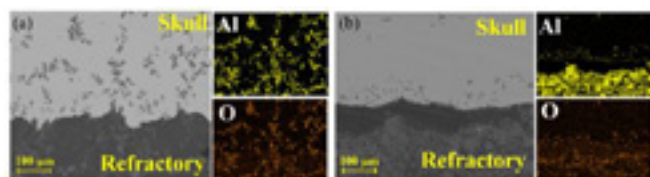


**Fig. 4.2** *Formation of deposits after refractory/molten steel interface reaction at 1565°C for 30 minutes with Al content of 300 ppm in the molten steel: (a) AGS and (b) ALBN. Deposits in (a) consist of polygonal $Al_2O_3$, while in (e, spherical $Al_2O_3$ is formed as a reaction product [8].*

## 5. Field Test

Based on the previous laboratory results, a field test was conducted to confirm the anti-clogging effect of non-oxide-based refractories. A comparison was made between the existing product with a calcium zirconate liner and an improved product with a non-oxide-based liner (Fig. 5.1). The test was conducted using a 20Ch H-beam caster, and the results are as follows.
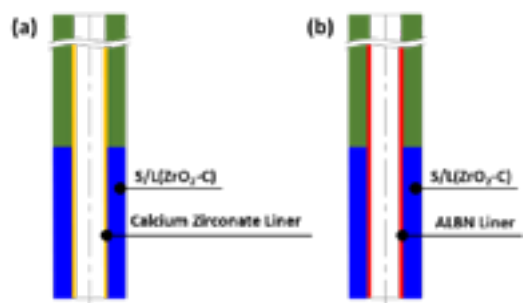


**Fig. 5.1** *Schematic diagram of the products used in field test. (a) Calcium Zirconate Liner SEN, (b) ALBN Liner SEN*
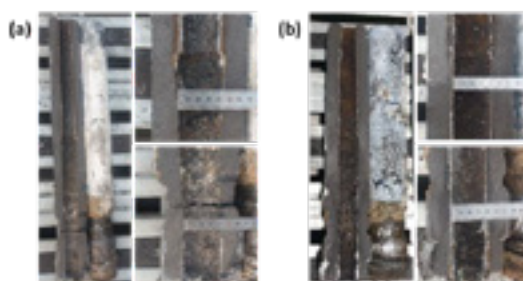


**Fig. 5.2** *Field Test Results (a) calcium zirconate liner SEN, (b) ALBN liner SEN*

In the existing SEN with the calcium zirconate liner, it was observed that there was an anti-clogging effect due to the formation of low-melting compounds during the casting process. However, In the long-term casting, the liner was consumed, leading to a decrease in refractory lining life and the occurrence of refractory wear. And another problem with calcium zirconate liner includes poor steel quality resulting from zirconia washed into the steel flow.

On the other hand, the newly developed non-oxide-based liner, demonstrated consistent results with its anticipated performance. It not only exhibited an anti-clogging effect, preventing the build-up of adhered materials, but also showed minimal refractory wear. Therefore, it is expected to enhance stability during extended casting process.

Furthermore, in order to validate the operational stability of non-oxide refractories, a large-scale slab caster test is currently scheduled. The results will be reported in future publications for reference and consideration.

## CONCLUSIONS

Among various factors that cause nozzle clogging, we focus on the reactions between refractory materials and molten steel to observe the phenomenon of nozzle clogging. Both commercially available oxide-based refractories and newly developed non-oxide-based refractories were utilized to identify refractory materials. The interface reactions between refractories and molten steel involve an initial interfacial reaction followed by the attachment of suspended materials. The reactivity of the refractories was evaluated through two experiments.

Firstly, gas emissions from the refractories were observed using a quadrupole mass analyzer, and subsequently, the interface reactions were simulated by immersing the refractories in molten steel. In oxide-based refractories, $CO(g)$ was emitted, while $N_2(g)$ was emitted in non-oxide-based refractories. The reactivity of the refractories was evaluated based on the volume of oxidizing gases emitted from the refractories and the SEM image of the reaction products at the interface.

The non-oxide-based refractories exhibited superior stability compared to the oxide-based refractories, while within the oxide-based refractories, refractories with reduced $SiO_2$ content showed improved stability.

Furthermore, based on laboratory test results, field tests confirmed. The SEN with the developed non-oxide-based liner exhibited a lower corrosion rate caused by molten steel compared to the existing calcium zirconate liner. Nozzle clogging was not observed upon inspection of the used SEN. It was confirmed that the product has an anti-clogging effect.

Therefore, to maximize the anti-clogging functionality by reducing the interface reactions between refractories and molten steel, non-oxide-based refractories should be used in non-oxide environments, while $SiO_2$-reduced refractories should be used in oxide-based environments.

## REFERENCES
[1] S. Ogibayashi, Taikabutsu Overseas, 15(1995), 3.
[2] Y. Vermeulen et al., Steel Research, 71(2000), 391.
[3] K.G. Rackers and B. Thomas, Steelmaking Conference Proceedings, 78(1995), 723.
[4] S. N. Singh, MMTB, 5(1974), 2165.
[5] Matsui et al. Taikabutsu Overseas 18(1998) 3.
[6] D.-J. Lee et al., Ceramics International (2023), in revision.
[7] S. Bandyopadhyay et al., Journal of the American Ceramic Society, 85(2002), 1010.
[8] D.-J. Lee et al., Proceedings of ICS 2023 (2023) 161.
[9] K. Sasai and Y. Mizukami, ISIJ International, 34(1994), 802.
[10] J.-H. Lee et al., ISIJ International, 58(2018), 1257.
[11] R. Tsujino et al., Testu-to-Hagane, 34(1994), 853.
[12] Y. Fukuda et al., ISIJ International, 32(1992), 164.
[13] J.-H. Lee et al., ISIJ International, 59(2019), 749.
[14] N.U. Girase et al., Ironmaking & steelmaking, 34(2007), 506.

# STUDY OF TYPICAL FAILURE PATTERN IN THIN SLAB CASTER SEN–INVESTIGATION & FINDING

Gautam Choudhury, Gaurav Pandey, Sahin Ali, Manish Kumar, Shubhashish Kumar,
Rupesh Kumar Gaurav, Ujjal Singha, Shubhashish Paul, Hiroshi Nagata, P.B. Panda
TRL Krosaki Refractories Ltd. Jharsuguda (Odisha), India

Brijender Singh, Navneet Sinha, Alok Kumar, Amit Banerjee
TATA Steel Limited, Jamshedpur, India

**ABSTRACT**

Thin Slab Casting & Rolling (TSCR) known as compact strip mill production (CSP) is an integrated technology of casting to enhance productivity, reduce energy consumption and lower the operating cost. In this facility, thin slabs are casted at high speed and directly hot rolled into strip of required dimensions. Mold thickness in thin slab caster ranges from 50-70 mm.

In Continuous Casting, tundish is placed over mould. SEN (Submerged Entry Nozzle) is fixed at bottom of Tundish and acts as a medium for flow of liquid steel. During casting Tundish refractories play very crucial role like prevention of re-oxidation of molten steel, control flow from Tundish to Mould & Safe casting operation. Tundish refractories used in Continuous casting are Ladle Shroud, Tundish Working lining, Mono Block Stopper (MBS), SEN etc.

Continuous casting operation in thin slab mould is highly influenced by SEN Design, Material quality, Application (due to manual installation process) and operational casting parameters. SEN performance and failure directly affects the productivity of shop and have process safety implications.

This paper covers various practical aspects regarding improving SEN reliability in a particular shop to improve overall productivity & safety aspect at caster. In this study SEN bottleneck has been identified & categorized as Crack on SEN face, Neck breakage, High erosion in slag line & Metal trickling. Last 5 years data is considered. Each phenomena probable cause has been analysed & studied. Countermeasure deployment & respective results are analysed.

Post this study & various actions, this shop has set benchmark in terms of productivity in global steel industry. It also includes additional learnings related to site application, operational parameters.

**Key Words:**

Continuous Casting, Submerged Entry Nozzle, Failure Analysis, Refractory, Field Study

**INTRODUCTION:**

This paper includes study & experiences at Thin Slab Caster and Rolling mill (a new energy efficient 'Compact Strip Processing' technology). Tata Steel LD3 TSCR is a steel melting & casting shop Jamshedpur works dedicated to Flat Products.

Submerged entry nozzle (SEN) has a key role in steel plant productivity & reliable operation as any failure may lead to interruption in production, in addition to this safety may also be impacted.

SEN is a refractory tube used for transfer of molten steel from Tundish to mould. Flow lines & laminarity of flow depends on SEN design & proper installation in Tundish. Any failure in SEN will put a break in continuous casting operation, may have a potential of safety hazard at caster floor & equipment damage.

SEN is designed based on inputs of casting parameters, customer requirement, casting duration etc.

Based on investigation & field study all possible causes were analysed & based on result most prominent causes with respect to each type is briefly explained.

This study focuses on the impact of field installation operations and customer operating conditions on the performance of Tundish refractories, including SEN. Therefore, as a rule, we assume that the refractories used are of a particular quality that satisfies the customer's required specifications.

This article summarizes all countermeasures taken in SEN to reduce sequence break ratio, enhance equipment availability and enhance shop safety.

**Caster Refractories Arrangement:**

In Continuous Casting, tundish is placed over mould. SEN is fitted at bottom of Tundish. During casting Tundish refractories play very crucial role like prevention of re-oxidation of molten steel control flow from Tundish to Mould, safe casting operation. Tundish refractories which play vital role during continuous casting are Ladle Shroud, Tundish Working lining, Mono Block Stopper (MBS), Submerged Entry Nozzle SEN etc. (As shown in figure 1).



A- Tundish
B- Tundish Working Lining
C- Shroud
D- MBS
E- SEN
F- Mold
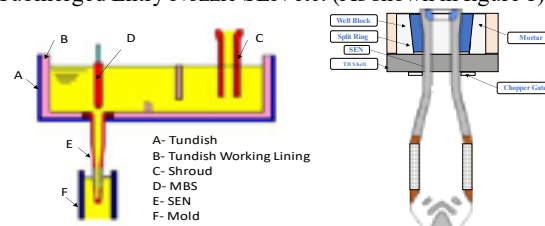
Figure 1: Schematic of Caster Refractory Arrangement

Tundish:

Its serves as buffer or intermediate vessel/ reservoir for the liquid steel during ladle change and therefore, makes sequential casting possible. The tundish is designed for optimum flow pattern such that inclusion separation into the top slag is supported.

Tundish Working lining:

Wear lining between liquid steel and permanent lining is a MgO monolithic layer. It resists erosive and corrosive attack of molten steel and slag.

Shroud:

It's role to Safely delivery of molten steel from Steel Ladle to tundish and prevention of re-oxidation of molten steel.

Mono Block Stopper (MBS):
It's role to control flow of molten steel from tundish to Mold. Safe and reliable stopper opening to allow transfer and shutting off.

Submerged Entry Nozzle (SEN):
Its role is to Safely delivery of molten steel from tundish to Mold and Prevention of re-oxidation of molten steel & allow streamline mould filling which results in smooth solidification in mould.

Split Ring (SR):
It's a part of Tundish refractories act as a key, and it helps to lock and hold the SEN with Tundish.

Well Block (WB):
It's a part of TD refractories and it holds the Split Ring within itself which in turn locks the SEN.

**SEN Material selection:**
Material selection for the SEN is highly crucial as its different zones in SEN which has a specific function & its performance depends on operational like preheating condition, mould flux etc. Based on experience and operational condition the following base material has been selected. Schematic of SEN body shown in figure 2.

Seat area: fired $ZrO_2$ ring.
To take care of mechanical strength as well as abrasion and corrosion.
Body: $Al_2O_3$-Graphite
Abrasion, corrosion and thermal spalling resistance.
Slag Line: $ZrO_2$-Graphite
High corrosion and thermal spalling resistance.
Bottom/ Port: $Al_2O_3$-Graphite
Abrasion, corrosion and thermal spalling resistance.
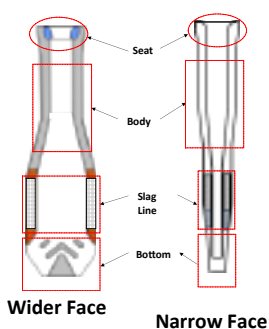
Figure2: Schematic of SEN Body

**SEN Failures History:**
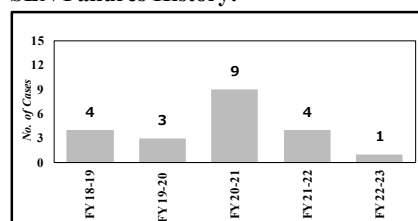
Figure 3: SEN Failure Summary Graph

Data for only TRL Krosaki SEN failure is considered. It has been observed that while there are some variations in terms of number of SEN failure in each year, It is confirmed that it occurs at a certain frequency.
Improvement actions started from 2021-2022 & some continued till 22-23.

These failures were categorized for a focussed investigation & troubleshooting.
SEN Failure are as follows: -
1. Crack on SEN Face,
2. Neck breakage,
3. High erosion in slag line,
4. Metal trickling
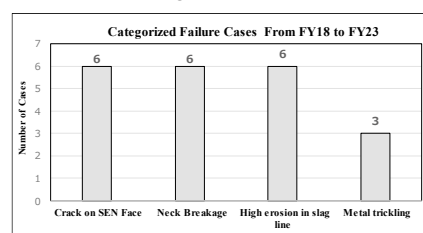
Figure 4: SEN Failure Cases Categorized from FY18 to FY23

**1) Crack on SEN face-**
This type of failure generally occurs in Narrow face of SEN, A vertical crack generates from port to Slag line (Zirconia Band) of SEN. As shown in Figure 5. This failure can lead to Casting interruption, disturbed flow in mould, Mould breakout etc.
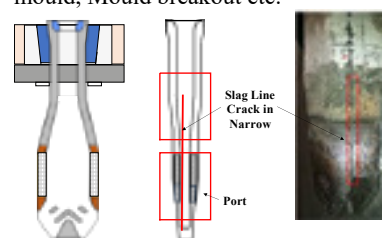
Figure 5: Crack on SEN face

Predominant probable causes for Crack on SEN are as follows:
a) Material/ Handling Issue - If any internal crack persists in SEN body during transfer of SEN may lead to crack formation in SEN during operation.
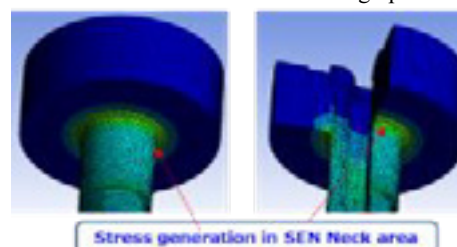
Figure 6: Stress in SEN neck area

b) Thermal Shock in SEN- SEN is made from $Al_2O_3$ Graphite must be preheated to temperature range between 1000°C and 1200°C to prevent thermal shock. Thermal shock can occur due to abnormal preheating of SEN OR more heat loss time from

483

preheating end to casting start. Preheating end to the cast start shall begin within 3 - 5 minutes to avoid instant cooling of SEN.

<u>Action taken for Crack on SEN face:</u>
a)   Stabilization of SEN preheating temperature. Earlier common line was there for compressed air supply for SEN preheating. To maintain stable pressure, a dedicated compressor air line for SEN preheating system.

b)   Real time monitoring of SEN preheating temperature. SEN preheating temperature monitoring at regular intervals to check real time condition of SEN preheating.

**2) Neck breakage**
During Casting if any SEN breakage from neck may have a potential of safety hazard at caster.
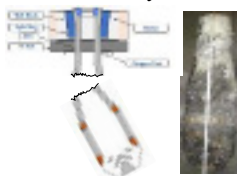


Figure 7: Breakage in SEN Neck

<u>Predominant probable cause of SEN neck breakage are as follows:</u>
a)   Excessive Stress in SEN Neck caused during fixing - Well Block and Split Ring which are main item responsible for holding & locking of SEN with Tundish. A special mortar is applied to fill the joints between Well block and Split ring, Split Ring and SEN. In Ideal condition, Well Block Split ring should be set in proper locking position to eliminate excessive stress in SEN neck (As shown in Figure 8.).
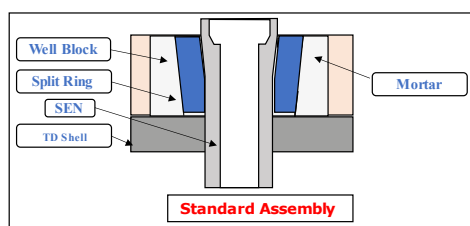


Figure 8: Standard assembly of Well Block, Split Ring and SEN

During installation if Split ring is not in proper position, Stress will increase on the neck area of SEN.

b)   Mechanical stress in SEN Neck during movement of SEN- During Tundish handling & transfer from Tundish preparation area to caster or placing of Tundish from Caster Car, there are chances of SEN interference, this may lead to generate stress in Neck of SEN.

c)   Thermal stress in SEN Neck due to thermal shock can be considered as a probable reason for crack on SEN face.

<u>Action taken for SEN Neck breakage:</u>
a)   Modification in SEN installation process turned out to be a positive one. Ensuring Split Ring & WB in proper locking position to counter stress in SEN Neck.

**3) High erosion in slag line (Zr Band)**
SEN puncture occurs due to high erosion of SEN in slag line (Zr band) As shown in figure 9.
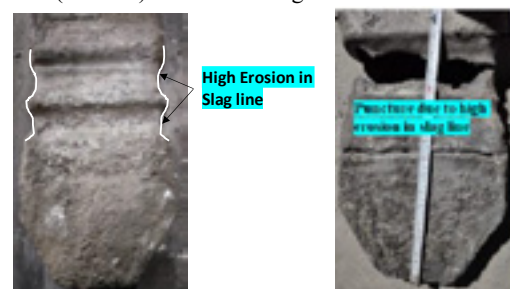


Figure 9: High erosion/ Puncture in Slag line (ZG band) of SEN

<u>Predominant Probable Cause of abnormal ZG band erosion:</u>
a)   Biased Flow in Mould can cause abnormal Zirconia band erosion or SEN breakage from Zirconia band. Biased flow from port of SEN can disturb mould meniscus which can cause mould powder entrapment, highly corrosive in nature causing ZG Band Erosion/ breakage.

b)   Abnormal Ramping pattern followed during casting operation- Ramping of Tundish/ SEN is done to prevent excess erosion in slag line of SEN. During Ramping Tundish is lowered or raised so that Mould meniscus level is not eroding a particular band of Zirconia.

<u>Action taken for abnormal ZG band erosion:</u>
a)   SEN body & port design is optimized for smooth flow of molten steel into mould. Design changed by modification in SEN port area was done. Modified SEN port design acts as a flow separator & ensure smooth streamline flow from SEN Body. As a result, reduction of slag line erosion is achieved by improvement of molten steel flow in the mould. Apart from this, Zirconia band was also strengthened by increasing thickness as a counter to solve excessive erosion.

b)   Improvement in ramping pattern: - Tundish ramping (upward and downward) is done by actuator (as shown in figure 10), chances of band overlapping due tundish ramping error is there.

Based on Field study & data collection we were able to investigate tundish ramping error condition. Ramping band length was optimized to prevent band overlapping during tundish ramping.
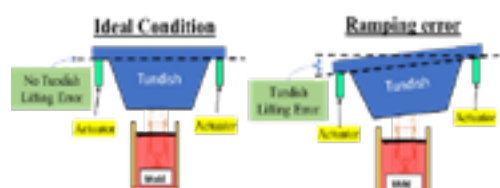


Figure 10: High erosion in slag line (ZG band) due to band overlapping by Tundish ramping error

**4) Metal Trickling**

Metal trickling or SEN breakage from neck occurs during continuous casting (As shown in Figure 11).



Figure 11: Metal trickling through SEN Neck

Predominant Probable Cause of Metal trickling through SEN Neck-

a)  Application error- Joint material application process is totally dependent on human skill. If joint material mortar and ramming mass are applied in wrong process then there is chance of metal trickling between joint of SEN, Well block and Split ring. (As shown in figure 12).
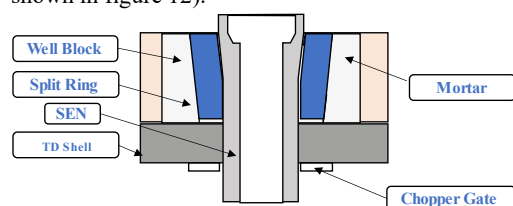


Figure 12: Assembly of SEN, Well block and Split ring

Action taken for Metal trickling through SEN Neck

a)  In earlier process ramming mass was being installed in one step process (one layer), due to which Ramming material was having less compactness due to which metal penetration occurred during casting. Step wise Ramming mass application process is introduced for more compactness which does not allow metal trickle.
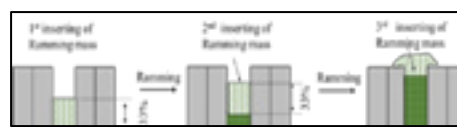


Figure 13: Step - Wise Layer Ramming for Proper Compactness

**CONCLUSION:**

Various SEN Failure troubles were investigated categorically through site study, data collection & analysis was carried out by data study, simulation, design & process parameters etc. Based on analysis, all possible causes were identified & counteractions were taken to minimize SEN Failure issue.

Results of countermeasures was also studied with an aim to minimize SEN Failure issues leading to unplanned sequence break, safety issues at caster, quality & productivity issues.

Emphasizing the results categorically –

Issue of Crack on SEN face was mainly due to abnormal preheating. Continuous monitoring SEN temperature can prevent from thermal shock during SEN preheating.

Issue of SEN Neck breakage- root cause was identified as improper application during SEN fixing, which was responsible for excessive stress generation, eventually leading to SEN neck breakage, the problem was eliminated by modification in SEN installation practice.

Issue of high erosion in slag line (ZG band) of SEN was mainly due to tundish ramping error & biased flow in mould. Better ramping discipline in case of high error can eliminate such issues.

Issue of Metal trickling from SEN neck is mainly due to improper installation of joint material mortar and ramming mass, this has been completely addressed by implementation of proper installation practice for SEN, well block and split ring.

**REFERENCES**

1.  Simulation of Fluid Flow In Thin Slab Casting Process M.I. El-Anwar, G.M. Megahed, M.K. Bedewy, M.G. El-Sherbiny and N.M. Chazly

2.  New Design of submerged Entry Nozzle Design in thin slab casting process, January 2006, Mohamed El-Anwar, Gamal M. Megahed, M.K. Bedewy, Mahmoud Elsherbiny

# CASTING OF CAFE TREATED STEEL AND ITS EFFECT ON RECRYSTALLIZATION AND LIFETIME OF ZRO$_2$ METERING NOZZLES

Mazyar Bahrami Samani[1],*, Mehdi Naeemi[1], Elham Rahimi[1], Hossein Rafiei Boroujeni[1]

1- Mehrgodaz Refractory Company, Sefiddasht, Chaharrmahal and Bakhtiari, Iran

## ABSTRACT

Zirconia metering nozzles play a crucial role in controlling the flow of liquid steel during continuous casting processes. The chemical composition, thermal properties, and mechanical characteristics directly impact the functionality and performance of these nozzles in steelmaking plants. This study focuses on the investigation of stabilized zirconia metering nozzles modified with magnesia and explores the effect of calcium input from CaFe additives on the surface recrystallization of these nozzles.

Industrial samples were prepared using zirconia with 99% purity and particle sizes less than 7 µm. After mixing, the samples were pressed at a pressure of 1200 Kgf/cm² and fired at a temperature of 1600°C, following a specialized heating cycle. Physical properties, including density, apparent porosity, and cold crushing strength (CCS), were determined according to DIN EN 993-1 and EN 993-5 standards. Microstructure and phase analysis were conducted using XRD, FESEM, and EDS techniques.

Optical microscopy revealed the growth of zirconia grains and an increase in the porosity size on the hot surface. FESEM and EDS analysis confirmed the occurrence of recrystallization on the hot surface, with higher concentrations of calcium (Ca) and magnesium (Mg) compared to the cold surface. The expansion during recrystallization and grain growth of ZrO directly influence the lifetime of zirconia metering nozzles.

This study provides valuable insights into the modification of stabilized zirconia metering nozzles with calcium input and its impact on surface recrystallization. The findings contribute to enhancing the understanding of casting processes and optimizing the performance and longevity of zirconia metering nozzles in steelmaking applications.

Keywords: Stabilized zirconia, metering nozzle tundish, recrystallization, casting rate

## INTRODUCTION

The continuous casting process relies on functional refractories with extended service life for optimal performance. Among these refractories, the metering nozzle system holds significant importance[1,2]. Partially stabilized zirconia (PSZ) is the primary raw material used in the production of metering nozzles due to its advantageous properties, including high thermal expansion coefficient, resistance to chemical corrosion, oxidation, and wear[3].

The similarity in radii between cations such as Mg²⁺, Ca²⁺, and Y³⁺ (common stabilizers) and Zr⁴⁺ in zirconia results in their high solubility, allowing their precipitation after rapid cooling from elevated temperatures. This unique characteristic enables the retention of the cubic phase of zirconia below its phase transformation temperature[1]. Previous studies by Primachenko et al.[1,4] and Roa and Anglada[1,5] have highlighted the correlation between damage to zirconia nozzles and the precipitation of stabilizers and slag. Furthermore, Li et al.[1,6] discovered that grain fracture contributes to the deterioration of zirconia metering nozzles.

Klaudia et al.[7] emphasized several key factors contributing to nozzle damage, including erosion from liquid steel, infiltration of molten steel and slag into the refractory material, slag composition, and rapid temperature changes[2,7]. Additionally, their research revealed the recrystallization of ZrO$_2$ grains along the hot face of zirconia nozzles, stabilized at high temperatures through the dissolution of oxides present in the slag and molten steel[7].

However, the maximum service life of metering nozzles is dependent on the grade of the steel products being cast. In this study, we investigated the cross-sectional properties of zirconia metering nozzles after 22 hours of service life in a steel plant to determine the primary mechanisms leading to nozzle damage. X-ray fluorescence (XRF), X-ray diffraction (XRD), field emission scanning electron microscopy (FESEM) with energy-dispersive X-ray spectroscopy (EDS), and optical microscopy techniques were employed to comprehensively analyze the zirconia metering nozzles.

This research provides valuable insights into the mechanisms of damage in partially stabilized zirconia metering nozzles and contributes to the understanding of their performance and service life in the continuous casting process.

## EXPERIMENTAL METHOD AND PROCESS

Zirconia of 99% purity, with a particle size diameter of less than 7 µm, was utilized in this study. The samples were prepared by mixing the zirconia powder, followed by pressing at a pressure of 1200 Kgf/cm². Subsequently, the specimens were fired at a temperature of 1600°C using a specific heating cycle.

To assess the physical properties of the prepared zirconia samples, several parameters were determined according to the DIN EN 993-1 and EN 993-5 standards. These included density, apparent porosity, and cold crushing strength (CCS).

In order to investigate the microstructure and phase analysis of the samples, X-ray diffraction (XRD), scanning electron microscopy (SEM), and energy-dispersive X-ray spectroscopy (EDS) techniques were employed.

Table 1 presents the chemical analysis of the zirconia raw materials used in the study, while Tables 2 and 3 provide the physical characteristics and chemical composition of the unused zirconia metering nozzles, respectively.

Tab. 1: Chemical analysis of zirconia raw materials

| ZrO$_2$ | Al$_2$O$_3$ | Fe$_2$O$_3$ | SiO$_2$ |
|---|---|---|---|
| 98.5 | <0.3 | <0.1 | <0.3 |

Tab. 2: Chemical analysis of sample

| ZrO$_2$ | MgO | SiO$_2$ |
|---|---|---|
| 95 | <3.0 | <0.3 |

Tab. 3: physical characteristics

| Bulk Density (g/cm³) | Apperant prosity (%) | CCS(Mpa) |
|---|---|---|
| 5.12 | 4.58 | 482 |

## RESULT AND DISCUSSION

Figures 1, 2, and 3 depict the optical microscopy images of the hot and cold surfaces of the sample after a service life of 22 hours in contact with liquid steel treated with CaFe cored wire additive.



*Fig.1: cross section of refractory metring nozzle*

Figure 1 illustrates two distinct zones in the corroded zirconia metering nozzles: a dark zone corresponding to the hot face and a bright zone associated with the cold face.
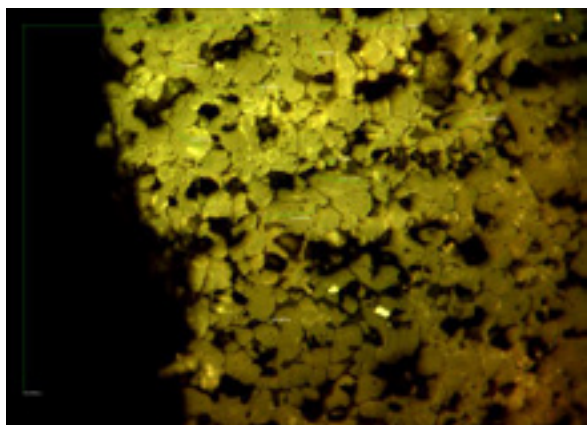
*Fig.2: Cross-section of the polished surface from hot face of refractory metring nozzle*
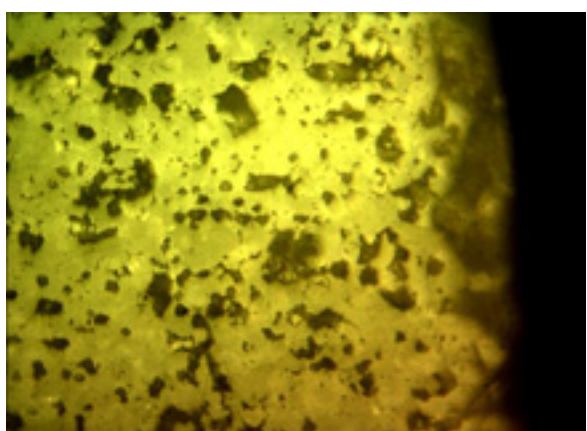


*Fig.3:Cross-section of the polished surface from cold face of refractory metring nozzle*
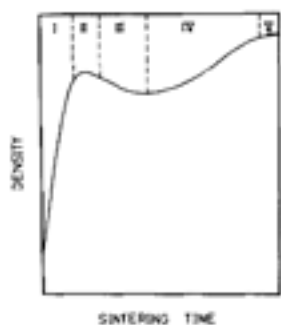


*Fig.4: Schematic diagram of the possible bulk density against sintering time curve for highly agglomerated ultrafine powder[8]*

The sintering of highly agglomerated ultrafine zirconia powders involves mechanisms like I- neck formation and shrinkage, II- fissure formation and growth, III- pore growth, IV-grain growth, V- pore rearrangement shrinkage, and pore entrapment. During sintering, a decrease in bulk density is observed in highly agglomerated powders due to fissure formation and pore growth. In zone I, efforts were made to achieve maximum density, but after 22 hours of service life, density reduction occurs, possibly due to fissure formation and growth. The low thermal conductivity and heat loss of PSZ contribute to grain growth on the hot face.
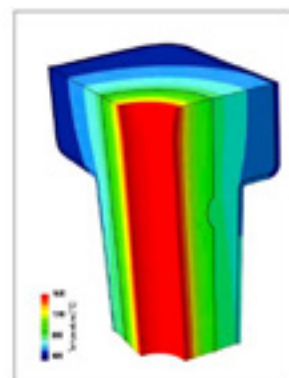


*Fig.5: Temperature profile of zirconia metering nozzle after one hour of casting [2].*

Based on Figure 5, the temperature in the hot face of the zirconia metering nozzles is approximately 1600°C, while in the cold face it is around 1200°C, indicating the low thermal conductivity of the nozzles. So the stage 3 in figure 4 will be started , which specifically affects the corrosion resistance of the zirconia metering nozzles in the hot face.

The composition analysis in Table 2 reveals that the main component of unused zirconia metering nozzles is 95% Zirconia. However, XRF analysis of used zirconia metering nozzles confirms a decrease in $ZrO_2$ content to 93.40%, along with the presence of other oxides such as $Fe_2O_3$, CaO, MgO, $SiO_2$, and $Al_2O_3$, as shown in Table 4.

Tab. 4: Chemical analysis of zirconia metering nozzle

| $ZrO_2$ | $Al_2O_3$ | $Fe_2O_3$ | $SiO_2$ | CaO | MgO | $TiO_2$ |
|---------|-----------|-----------|---------|------|------|---------|
| 93.40 | 1.68 | 0.18 | 0.91 | 0.61 | 2.80 | 0.07 |

The XRD analysis confirmed that the unused sample primarily consisted of monoclinic Zirconia and magnesia-stabilized zirconia (Magnesium Zirconium Oxide).
Further XRD analysis using Rietveld quantitative phase analysis revealed an increased content of stabilized Zirconia in the reacted layer (hot zone), indicating a higher concentration of stabilizer agents in the hot face. Previous research by Klaudia et al. [7] has reported that the addition of MgO and CaO stabilizes the high-temperature phase of zirconium oxide by dissolving in $ZrO_2$. This solid solution alters the internal structure of the $ZrO_2$ crystal, preserving the cubic phase at room temperature and resulting in a sample composed of both cubic and monoclinic zirconia phases [3]. Comparison of the XRD analysis between the hot and cold faces (Figures 6 and 7) showed the appearance of cubic phases and a decrease in the percentage of $ZrO_2$ monoclinic phase, indicating a recrystallization process during the service life. However, the subsequent grain growth process revealed the second stage of damage to the zirconia metering nozzles, leading to increased pore distribution and the potential penetration of other oxides.
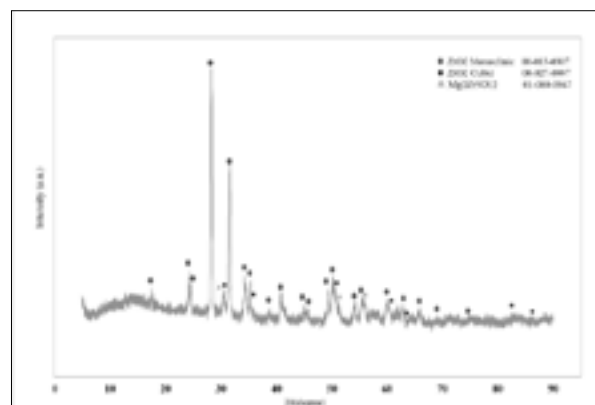


Fig. 6: XRD analysis of hot face from refractory metering nozzle
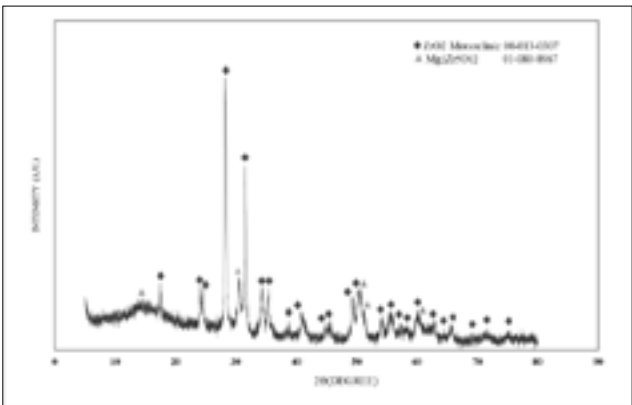
Fig. 7: XRD analysis of cold face from refractory metering nozzle

To investigate the aforementioned mechanism, microstructure analysis using FESEM and EDS was conducted, and the results are presented in Figures 8 and 9.

In Figure 8a, the observation of grain growth and an increase in pore size is evident. Furthermore, EDS analysis confirmed the presence of oxides such as $Fe_2O_3$, CaO, MgO, $SiO_2$, and $Al_2O_3$, indicating their penetration into the hot face from the liquid steel or slag. The significant quantity of these phases in the hot face can be attributed to the formation of a liquid phase at lower temperatures, thereby promoting corrosion of the metering nozzles.

On the other hand, the microstructure study and EDS analysis of the cold face, as shown in Figure 9, did not reveal any notable damages.
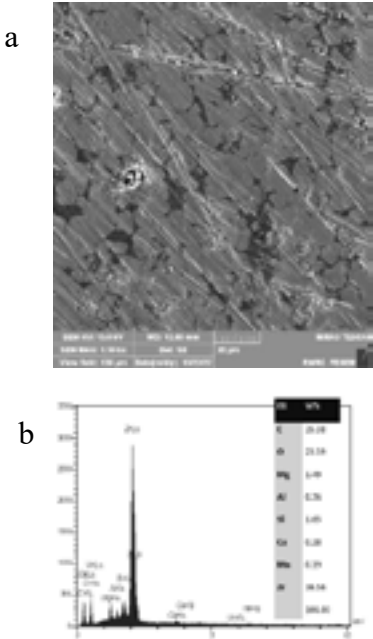




*Fig. 8a:* FESEM analysis of hot face from refractory metering nozzle
8b: EDS analysis of hot face from refractory metering nozzle
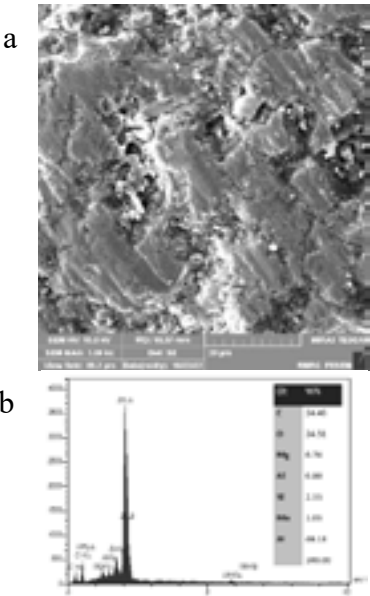




*Fig. 9a:* FESEM analysis of cold face from refractory metering nozzle
9b: EDS analysis of cold face from refractory metering nozzle

It is well known that during steel casting using zirconia metering nozzles, the casting speed remains relatively constant over time. This is attributed to the formation of solid solutions and recrystallization in the hot surface, as indicated by the $ZrO_2$-MgO-CaO phase diagram.

Initially, MgO and CaO contribute to recrystallization and grain growth. However, as the casting duration progresses, the presence of high porosity allows for the penetration of $SiO_2$, $Al_2O_3$, and $Fe_2O_3$. This can lead to the formation of low melting phases and an increase in the corrosion rate. By comparing the two mechanisms at the beginning and end of casting, it can be observed that the corrosion rate remains relatively constant, which is crucial for steel manufacturing (see Figure 10).
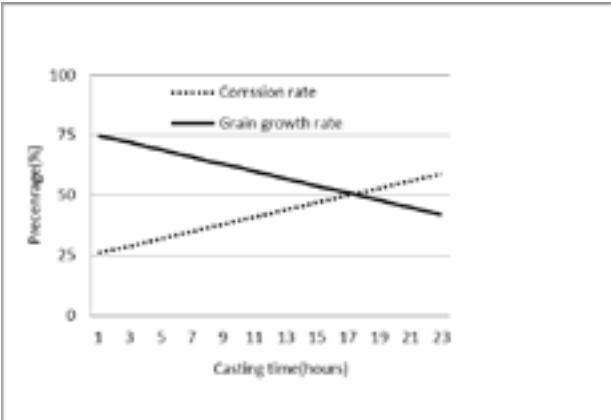


*Fig .10: the corrosion rates in contrast with grain growth in schematically*

**CONCLUSIONS**

The investigation results of Zirconia metering nozzles after a 22-hour trial in a steel plant have demonstrated that the damage process of these nozzles is characterized by three distinct steps: grain growth, recrystallization, and destabilization and decomposition of the material.

Interestingly, grain growth and recrystallization have the potential to mitigate the corrosion rate by inducing expansion and thereby extending the operational lifespan of zirconia nozzles. This effect, however, is contingent upon the effective control of steel liquid and slag oxides penetration during the service life of the nozzles.

**REFERENCES**

[1] Liang Zhao, Qun-hu Xue, and Dong-hai Ding, Effects of the precipitation of stabilizers on the mechanism of grain fracturing in a zirconia metering nozzle, International Journal of Minerals, Metallurgy and Materials Volume 23, Number 9, September 2016

[2] Neha Jain, Florian Bathmann and Ghufran Ansari, RHI Zirconia Nozzles in Tundish Application, RHI Bulletion>1>2016

[3] Liang Zhao, Qian Huang, Huayin Sun, Xiang Li,Corrosion Resistance of Partially Stabilized Zirconia Materials to Alkaline Steel Slag, *Key Engineering Materials, 1662-9795, Vol. 852, pp 119-128*

[4] V.V. Primachenko, A.G. Karaulov, I.G. Shulik, T.G. Gal'chenko, P.A. Kushchenko, and N. G. Privalova, Postservice analysis of zirconia nonswirl nozzles for intermediate ladles of a continuous casting machine, *Refract. Ind. Ceram.*, 44(2003), No. 1, p. 1.

[5] J.J. Roa and M. Anglada, Annealing aged zirconia: Study of surface mechanical properties at the micrometric length scale, *J. Eur. Ceram. Soc.*, 35(2015), No. 3, p. 1031.

[6] X. Li, Q.H. Xue, X.H. Ren, F.Q. Li, and L. Xu, Study on wearing mechanism of zirconia non-swirl nozzle,*Bull. Chin. Ceram. Soc.*, 31(2012), No. 6, p. 1523.

[7] Klaudia Wioeniewska, Dominika Madej, Jacek Szczerba, Corrosion of the refractory zirconia metering nozzle due to molten steel and slag, Original scientific article/Izvirni znanstveni ~lanek, UDK 666.76:620.193

[8] Jenn-Ming WU, Chih-Hsyong WU, Sintering behaviour of highly agglomerated ultrafine zirconia powders, journal of materials science 23 (1988) 3290-3299

# SIMULATING METHODS FOR AL$_2$O$_3$ CLOGGINGS ON SEN

Liu Guoqi, Li hongxia, Gu qiang, Ma Feixiang

Sinosteel Luoyang Institute of Refractories Research Co., Ltd., Luoyang 471039, China

Yuan Lei,School of Metallurgy, Northeastern University, Shenyang 110819, China

Zhi Jianjun, Gan Feifang, Fan Zhengjie, Gao Hua, Baoshan Iron and Steel Co., Ltd, Shanghai ,China

**Abstract**

Submerged entry nozzle (SEN) is an important functional refractory for high-efficient continuous casting. When casting high-quality steel, SEN is easy to be clogged, which will cause flow field instability, slag entrapment, adhesions, refractories falling off, etc., resulting in a significant increase in inclusions in the molten steel, deterioration of billet quality, and even interruption of continuous casting. Negative pressure in SEN will accelerate clogging. This factor is neglected in the design process of the existing Al$_2$O$_3$ clogging experimental method. Therefore, based on the SEN negative pressure, this paper innovatively designed an Al$_2$O$_3$ clogging experimental method under near working conditions, and verified its feasibility. Compared with the existing experimental methods, this new experiment method stimulates the working conditions, ensures the stable source, content, and size of Al$_2$O$_3$ inclusions around specimen. The composition and morphology of the clogging on the specimen obtained by the new simulating experimental method are the same as those on the inner wall of the SEN obtained by the factory. The new method was used to optimize the anti-clogging liner, and it was determined that the calcium stabilized ZrO$_2$ lining present good anti-clogging effects.

Keywords: SEN, clogging, Al$_2$O$_3$, negative pressure, experimental method

## 1 Introduction

SEN is an important functional refractory for high-efficient continuous casting, cooperating with mold fluxes to prevent molten steel oxidation, control the flow field and temperature field of molten steel in the mold, ensure slab quality and continuous casting process stability [1–3]. When casting high-quality steel, SEN is easy to be clogged, which will cause flow field instability, slag entrapment, adhesions, refractories falling off, etc., resulting in a significant increase in inclusions in the molten steel, deterioration of billet quality, and even interruption of continuous casting [4,5]. Therefore, it is imperative to anti SEN clogging.

SEN inner wall is generally Al$_2$O$_3$-C material, decarbonization will occur after contact with molten steel. The roughness of the SEN inner wall increases significantly after decarburization, which accelerates the adhesion of inclusions on its surface and eventually causes rapid clogging of the SEN. In order to prevent the SEN clogging, a variety of lining materials have been developed, which have good anti-clogging effect on some steel castings, but the universality is poor. The main reason is that there is a large deviation between the conditions of existing inclusions clogging experiment and the actual working conditions. Therefore, it is necessary to innovate the inclusions clogging experimental method. Researchers show that there is negative pressure in SEN during continuous casting [6-8]. Under the action of pressure difference, the external air or the oxidizing gas produced by the carbothermal reduction reaction may be transmitted to the SEN-molten steel interface, oxidizing the [Al] in the molten steel, resulting in SEN clogging. Therefore, the continuous oxidation of molten steel caused by negative pressure is an important reason for SEN clogging. However, the researchers ignored the role of negative pressure in Al$_2$O$_3$ clogging experiment.

From what has been discussed above, in this paper, new Al$_2$O$_3$ clogging experimental method under near working conditions based on negative pressure principle is designed and verified by high temperature simulation experiment. Then, the designed new Al$_2$O$_3$ clogging experimental method is used to optimize the anti-clogging lining materials.

## 2 Experiment

### 2.1 Design ideas

In this section, the innovative Al$_2$O$_3$ clogging experimental method under near working conditions is designed. Under the action of pressure difference, the external air will be sucked into the SEN (as shown in **Fig. 1a**). However, this situation cannot be achieved under laboratory conditions. In order to achieve the same effect, an equivalent experiment is designed here (as shown in **Fig. 1b**). A certain pressure of air is continuously introduced into the specimen. **Fig. 2** shows the shortcomings of the existing experimental methods and the advantages of the new method.

### 2.2 Specimen preparation

The raw materials used in this experiment are shown in **Table 1**, experimental formulations of Al$_2$O$_3$-C specimen and, anti-clogging lining materials are shown in **Table 2** and **3**. The specimens was prepared, firstly, mixture was prepared by mixing raw materials in Erich intensive mixer; secondly, the volatile matter of mixture was regulated by drying in electric drying oven (60 °C for ≈12 h); thirdly, crucible specimens (inner diameter is 25 mm; outer diameters is 40 mm; height is 350 mm) were obtained by isotactic pressing at 120 MPa; fourthly, the specimens were dried (at 120 °C for 12 h, at 180 °C for 6 h); finally, specimens were heat-treated under the carbon embedded condition (at 850 °C for 6 h).

### 2.3 Experimental device and process

The schematic diagram of Al$_2$O$_3$ clogging experimental method under near working conditions was shown in **Fig. 3**. The new experimental method was verified by high temperature simulation experiment. Firstly, the steel ingot was melted under argon protection. Then, the preheated specimens at 1100 ºC were slowly immersed in the molten steel. After the temperature was stabilized at 1550 ºC, the Al wire (0.20 wt % of total molten steel%) was fed into the molten steel. Subsequently, air was injected into or extracted from inside the specimens under the given pressure (−15000, 0, 15000 and 30000 Pa). Finally, the specimens were brought out of the molten steel after 10 min and the Al$_2$O$_3$ cloggings on the surface of the specimens were observed.
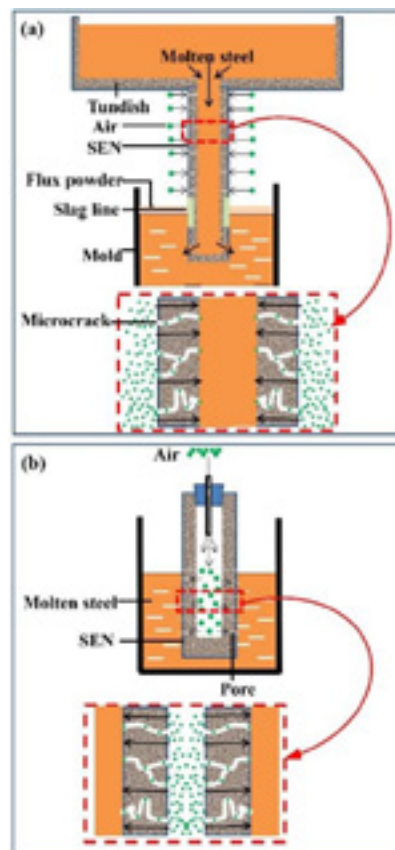


**Fig. 1** Mechanism diagram of equivalent experiment: (a) air flow direction under working conditions; (b) air flow direction under experiment conditions
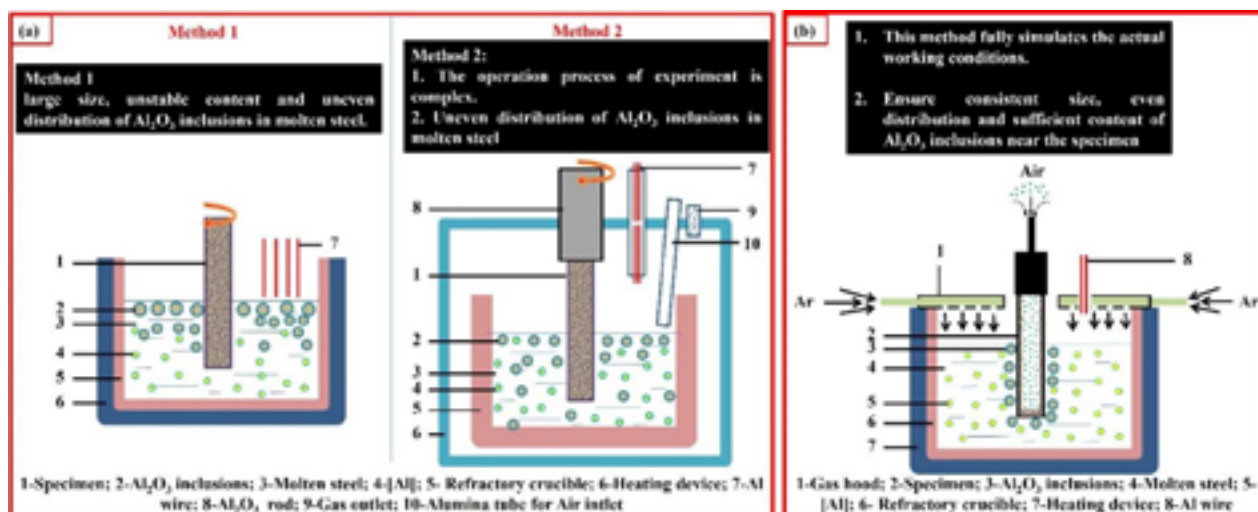
**Fig. 2** Comparison diagram of Al$_2$O$_3$ clogging experimental method under near working condition and traditional experimental method: (a) existing experimental method; (b) Al$_2$O$_3$ clogging experimental method under near working condition

**Table 1** Specifications of experimental materials

| Material | Specification | Manufacturer |
|---|---|---|
| Fused white corundum | 0.5-0.2 mm, 0.2-0 mm | Zhongtian Special Alumina Co., Ltd. |
| α-Al$_2$O$_3$ powder | D$_{50}$ = 10 μm | Zhongtian Special Alumina Co., Ltd. |
| Fused magnesium aluminate spinel | 0.5-0.2 mm, 0.2-0 mm, ≤0.045 mm | Zhengzhou Yufa High-tech Materials Co., Ltd. |
| Fused calcium stabilized zirconia | 40#, 100#, 350# | Zhengzhou Zhenzhong Fused New Material Co. Ltd. |
| Fused mullite | 0.5-0.2 mm, 0.2-0 mm, ≤0.045 mm | Ruishi New Material Technology Co.Ltd |
| Graphite | 99%, 149 μm | Qingdao Zhongkai graphite Co., Ltd. |
| Liquid phenolic resin | Thermoplastic | Shandong Shengquan Chemical Co., Ltd. |
| Solid resin powder | Thermoplastic | Zhengzhou Shuangge Resin Co., Ltd. |
| Absolute alcohol | Analytically pure | Dean Chemical Reagent Co., Ltd. |
| Si powder | >99%, ≤30 μm | Shanghai Baowei Ceramic New Materials Co., Ltd. |
| SiC powder | >98.5%, ≤100 μm | Weifang Huarong Ceramic Materials Co., Ltd. |

**Table 2** Experimental formulation of Al2O3-C specimen (wt%)

| Specimen | Fused white corundum aggregate (mm) | | Activated alumina powder | Graphite | SiC | Si |
|---|---|---|---|---|---|---|
| | 0.2-0.5 | 0-0.2 | | | | |
| Al$_2$O$_3$-C | 40 | 10 | 25 | 22 | 2 | 1 |

**Table 3** Experimental formulation of lining materials (wt%)

| Raw material | | lining materials | | | |
|---|---|---|---|---|---|
| | | Al$_2$O$_3$ | MgAl$_2$O$_4$ | Al$_2$O$_3$-SiO$_2$ | ZrO$_2$ |
| Fused white corundum | 0.2-0.5mm; 0-0.2mm | 40 10 | | | |
| α-Al$_2$O$_3$ powder | 10 μm | 50 | | | |
| Fused magnesium aluminate spinel | 0.2-0.5mm; 0-0.2mm; ≤0.045mm | | 40 10 50 | | |
| Fused mullite | 0.2-0.5mm; 0-0.2mm; ≤0.045mm | | | 40 10 50 | |
| Fused calcium stabilized zirconia | 40#; 100#; 350# | | | | 40 10 50 |
| Liquid phenolic resin | | 4 | 4 | 4 | 3 |

## 2.4 Characterization

Fracture and polished section morphology of specimens were observed by field-emission scanning electron microscopy (FE-SEM, JEOL JSM-700F) with an energy-dispersive X-ray spectroscopy (EDS).

## 3 Results and discussion

### 3.2 Verification of experimental method

Macrophotographs of specimens under different air pressures are shown in **Fig. 4**. It can be seen that when the air pressure is 0 Pa, a small amount of Al$_2$O$_3$ cloggings on the surface of the specimen (as shown in Fig. 8b). The main reasons are as follows: ① when the specimen was immersed in molten steel, due to the drastic temperature change (to 1550 °C), the air in the specimen would expand rapidly and diffuse to the specimen-molten steel interface, which will oxidize the metal [Al] near the specimen to form Al$_2$O$_3$ inclusions; ② decarburization of the molten steel increased the surface roughness of the specimen, which increases the contact area between the specimen and the Al$_2$O$_3$ inclusions.

When the air pressure is -15000 Pa, there was almost no $Al_2O_3$ cloggings on the surface of the specimen (as shown in **Fig. 4a**). The main reason is that most of the air inside the specimen is extracted, and the residual air cannot reach the specimen-molten interface, resulting in almost no $Al_2O_3$ cloggings near the specimen (as shown in **Fig. 5a**).
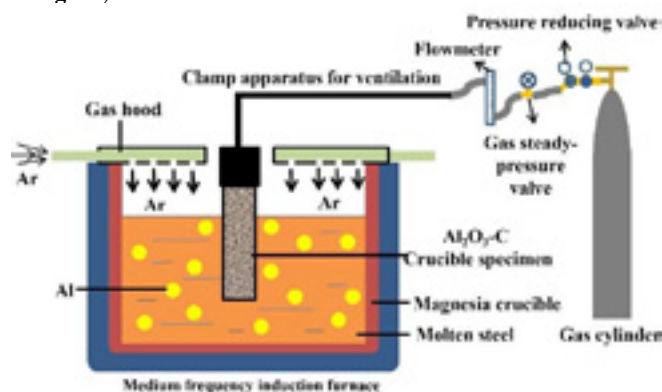


**Fig. 3** Schematic diagram of $Al_2O_3$ clogging experimental method under near working conditions
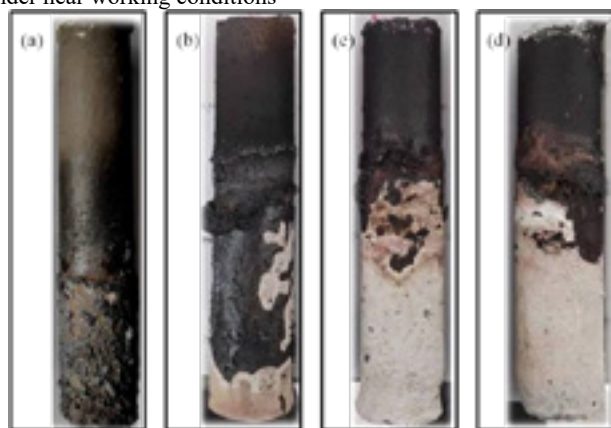


**Fig. 4** Macrophotographs of specimens under different air pressures: (a) -15000 Pa, (b) 0 Pa, (c) 15000 Pa, and (d) 30000 Pa

When the internal air pressure of the specimen is 15000 Pa and 30000 Pa, there are more $Al_2O_3$ cloggings on the surface of the specimens, and the higher the pressure is, the more the thickness of the cloggings is (as shown in **Fig. 4c** and **d**). Because under the action of pressure difference, air will continuously reach the specimen-molten steel interface (as shown in **Fig. 5b**) and oxidize Al in the molten steel to form a large number of $Al_2O_3$ inclusions. This shows that the new experimental method realizes the idea of $Al_2O_3$ clogging and can be used for the development of SEN anti-clogging lining materials.
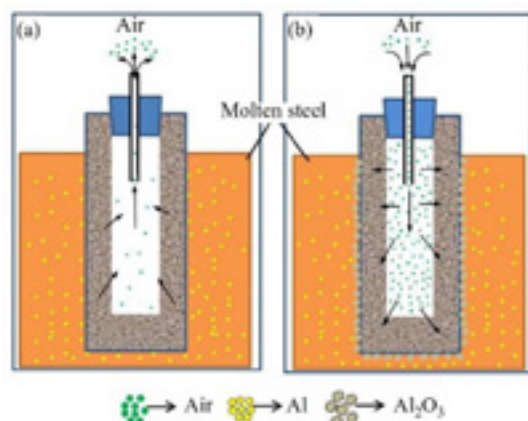


**Fig. 5** Clogging mechanism of specimens: (a) extracting air from inside the specimen (-15000 Pa); (b) injecting air into specimens (15000, 30000Pa)

When the internal pressure of the specimen is 30000 Pa, the fracture morphology of the cloggings is shown in **Fig. 6**. It can be seen that the cloggings are composed of $\alpha$-$Al_2O_3$ and $\beta$-$Al_2O_3$, and they are staggered distribution. The microstructure of the cloggings was shown in **Fig. 7**. It can be seen that the cloggings was mainly composed of $\alpha$-$Al_2O_3$, $\beta$-$Al_2O_3$, and cold steel, which is basically consistent with the microstructure of cloggings on the specimens obtain by $Al_2O_3$ clogging experimental method under near work conditions.
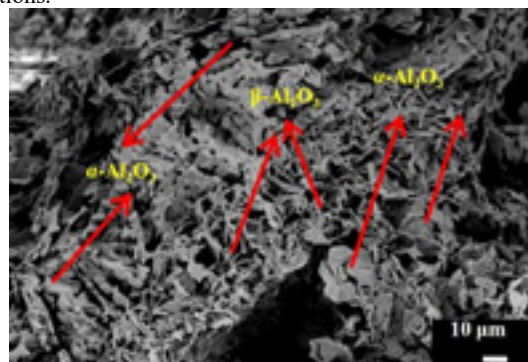


**Fig. 6** Fracture morphology of cloggings on $Al_2O_3$-C specimen when the inner pressure in specimen is 30000 Pa: (a) cross section fracture at the red line mark of specimen; (b,c) enlargement diagram of red box area in Fig. 11a
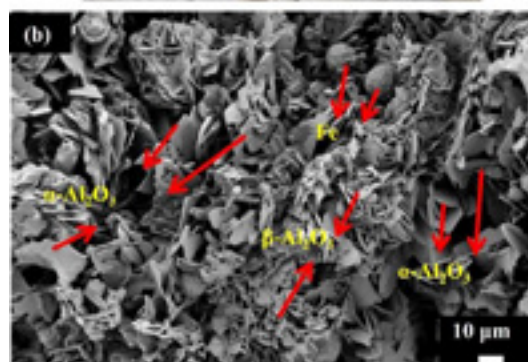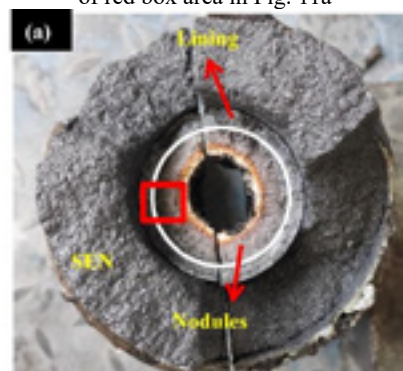


**Fig. 7** Fracture morphology of cloggings on SEN used by a domestic company: (a) macrophotograph of cross section of SEN; (b) enlargement diagram of red box area in Fig. 12a

**3.3 Application of experimental method**

**Fig. 8** is the macrophotographs of the specimens after the experiment (four materials are compounded on the same sample). It can be seen that there are more cloggings on the $Al_2O_3$-C specimen surface than those on the lining specimen surface, indicating that the graphite-free lining presents a better effect on preventing $Al_2O_3$ clogging. In addition, there are more cold steel on the surface of $MgAl_2O_4$ and $Al_2O_3$-$SiO_2$ lining materials. The cold steel on the $MgAl_2O_4$ material surface is distributed in clusters, and the cold steel on the $Al_2O_3$-$SiO_2$ material surface is uniformly dispersed. This shows that the anti-clogging effect of $MgAl_2O_4$ and $Al_2O_3$-$SiO_2$ materials are poor.
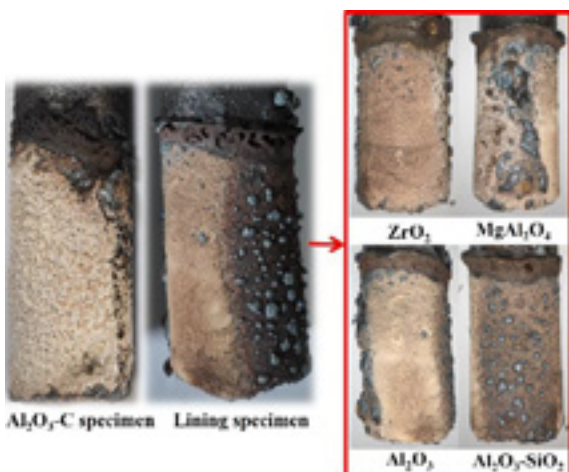
**Fig. 8** Clogging state of different lining materials
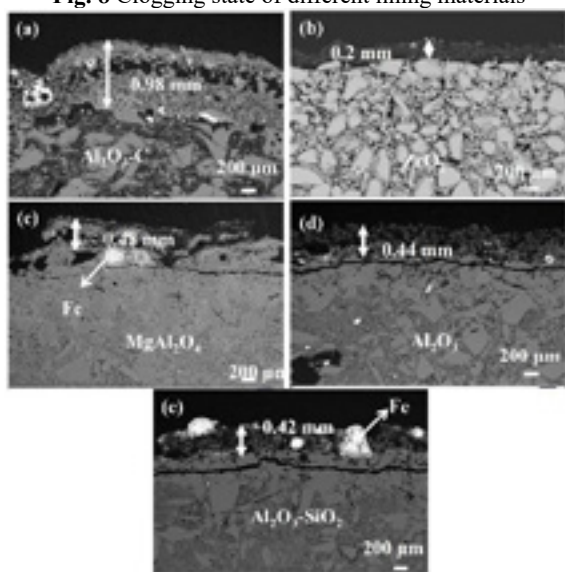


**Fig. 9** Microstructure of cloggings on the specimens surface: (a) Al₂O₃-C; (b) ZrO₂; (c) MgAl₂O₄; (d) Al₂O₃; (e) Al₂O₃-SiO₂

The microstructure of the above specimens were analyzed, and the results were shown in **Fig. 9**. It can be seen that the thickness of the cloggings on the lining specimen surface is much smaller than that on the Al₂O₃-C specimen surface. The thickness of the cloggings on the ZrO₂ material surface is the smallest (0.2mm), which is 1/5 of that on the Al₂O₃-C specimen surface, 2/5 of that on the MgAl₂O₄

material surface, and 1/2 of that on the surface of Al₂O₃ material and Al₂O₃-SiO₂ material. In addition, it can be seen that there is no Fe in the cloggings on the ZrO₂ material surface, which indicates that ZrO₂ material does not react with molten steel. Therefore, choosing ZrO₂ as SEN lining can improve the anti-clogging ability of SEN.

**4 Conclusions**

In this paper, an Al₂O₃ clogging experimental method under near working conditions was innovatively designed and verified. Then the optimization of anti-clogging lining material is studied by using this new method. The research conclusions are as follows:

(1) The new Al₂O₃ clogging experimental method simulates the actual working conditions, which ensures the stable source, content, and size of Al₂O₃ inclusions around specimen and makes the experimental results more reliable. It provides strong support for make up the shortcomings of the existing experimental method and further research and development of new anti-clogging SEN lining material.

(2) Fused calcium stabilized zirconia (ZrO₂) has poor reactivity with Al₂O₃ inclusions, non-wetting with molten steel, and possess excellent anti-nodulation properties.

**References**
[1] Hongxia L, Guoqi L, Bin Y. Development of functional refractories for continuous casting. Refractory 35(1), 2001, p. 45-49
[2] Mianguang X, Miaoyong Z. Transport phenomena in a beam-blank continuous casting mold with two types of submerged entry nozzle. ISIJ International 55(4), 2015, p. 791-798
[3] Sambasivam R. Clogging resistant submerged entry nozzle design through mathematical modelling. Ironmaking & steelmaking 33(6), 2006, p. 439-453
[4] Lifeng Z, Yufeng W, Xiangjun Z. Flow transport and inclusion motion in steel continuous-casting mold under submerged entry nozzle clogging condition. Metallurgical and Materials Transactions B 39, 2008, p. 534-550
[5] Lifeng Z, Brian G. T. State of the art in evaluation and control of steel cleanliness. ISIJ international 43(3), 2003, p. 271-291
[6] Hyunjin Y, Surya P. V, Brian G. T. Modeling argon gas behavior in continuous casting of steel. JOM 70, 2018, p. 2148-2156
[7] Hyunjin Y. Modeling of multiphase turbulent flow in continuous casting of steel. Ph.D. thesis, Urbana-Champaign: University of Illinois at Urbana-Champaign, 2018
[8] Go-Gi L, Brian G. T, Seon-Hyo K. Effect of refractory properties on initial bubble formation in continuous-casting nozzles. Metals and Materials International, 16, 2010, p. 501-506

493

# THE DEVELOPMENT OF THE THERMAL INSULATION COATING

Wataru Koide, Shigeru Morimoto, Noriaki Yamauchi, Masahiro Shinato, and Keisuke Kachi

TYK Corporation, Gifu, Japan

## ABSTRACT

The refractories for continuous casting such as submerged entry nozzle (SEN) are often preheated before casting.

To keep SEN temperature, it applies an insulation on.

In the past, RCF (Refractory Ceramic Fiber) used to be generally applied as an insulation, but due to concerns about its health effects, the shift to AES (Alkaline Earth Silicate) is progressing worldwide.

It has also been developed that the coating material does not contain fibers as an insulation. Fiber-type insulation sheets have a prickly feel on the skin, so non-fiber-type insulation coatings are preferred sometimes.

This non-fiber insulation coating has another effect that prevent the antioxidant glaze melt from the molten steel splashes during casting.

However, instead of high heat retention, the heat insulation inhibits heat transfer from the outer surface of the nozzle, which is a factor in inhibiting preheating in a short time.

In order to solve these issues, it's developed that the non-fiber insulation material that improves to make shorter the preheating time and keep the heat retention after preheating.

## INTRODUCTION

In general, SEN are preheated before using to reduce the risk of thermal spalling and the insulation is applied on the SEN to keep the preheating temperature.

RCF fiber used to be most usual insulation fiber, but due to concerns about its health effects, the shift to AES fiber is progressing worldwide.

On the other hand, non-fiber type insulation material has been developed for long time. It's preferred sometimes compared with fiber type insulation.

As one of issue, non-fiber type insulations is slightly higher thermal conductivity than fiber type insulations.

In this study, by adding carbon to the conventional heat insulating material, we have developed a heat insulating material that maintains the heat insulating effect after temperature rise while improving the heating rate and the cooling rate.

## EXPERIMENTAL METHODS

### Test sample

The refractory sample is used alumina-graphite, which is generally used the nozzle for the continuous casting, and applied the glaze on the surface. Tab. 1 shows the chemical composition of the refractory samples used in this test, and the thermal insulation coating materials. Sample A has no insulation on the refractory sample. 3 other samples are applied 3 types of insulation on each sample. Sample B is applied AES fiber sheet by inorganic adhesive and keep drying in the atmosphere for 24 hours. Sample C is applied the non-fiber insulation material (Insulation 1 on Tab. 1), which is conventional. Sample D is applied the new non-insulation material (Insulation 2 on Tab. 1). Sample C and Sample D are applied the insulation materials by spraying and keep drying at 100°C for 8hours, after drying in the atmosphere for 4 hours. Insulation 2 is added Carbon to Insulation 1.

Tab. 1: Chemical composition

| | | Alumina-graphite | Insulation 1 | Insulation 2 |
|---|---|---|---|---|
| Chemical composition / mass% | C | 32 | 5 | 20 |
| | $Al_2O_3$ | 66 | 65 | 55 |
| | $SiO_2$ | - | 26 | 21 |
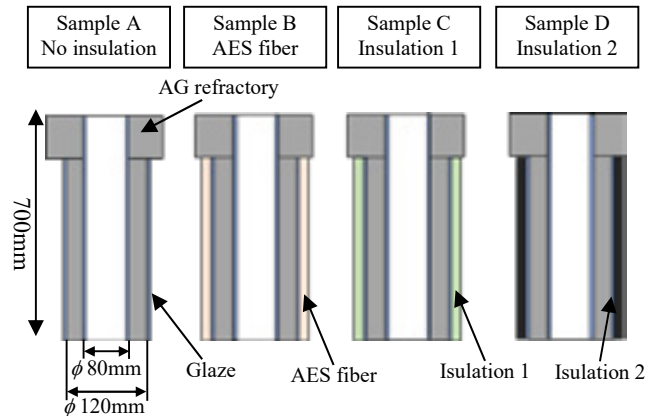


*Fig. 1: Appearance of each sample.*

### Test procedure

Fig. 2 shows the appearance of heating test. The sample put in the furnace, heat up to 1200°C and keep for 2hours. After that, the sample is brought out from furnace and keep in the atmosphere. While the testing, it is monitored the temperature. The K type thermocouple is inserted like Fig. 3 to measure the temperature of the sample.
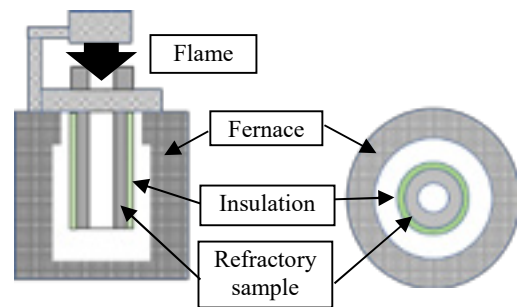


*Fig. 2: Appearance of heating test.*
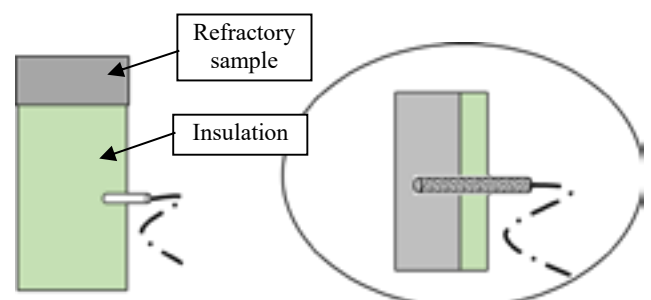


*Fig. 3: Temperature measurement.*

## RESULTS

### The appearance of non-fiber insulation

Fig 4 shows the appearance of non-fiber insulation coating.

The color of Insulation 1 is white before heating. The color is due to $Al_2O_3$ and $SiO_2$. The color of Insulation 1 is changed to ocher after heating.

The color of Insulation 2 is black before heating. It is due to carbon. The color is changed to ocher same as Insulation 1 after heating. After carbon oxidizes and vaporizes in heating, by leaving behind $Al_2O_3$ and $SiO_2$, the color of insulation 2 is changed ocher.

| Insulation 1 (Conventional) | | Insulation 2 (Carbon added) | |
|---|---|---|---|
| Before heating | After heating @ 1200°C | Before heating | After heating @ 1200°C |
| White | Ocher | Black | Ocher |

Fig. 4: The appearance of non-fiber insulation.

### The comparison of heating rate

At first, it's compared the heating rate of each sample while heating.

Tab.2 shows the result about the temperature of each sample for each 10 min while heating. Fig.5 shows the graph about the temperature of each sample for each 1min while heating.

The temperature of Sample B after heating for 10 minutes was more than 150°C lower than that of Sample A. The insulation sheet would make slow the heating rate.

On the other hand, the gap of the temperature after 10 minutes between Sample A and Sample C was less than 150°C, and between Sample A and Sample D was less than 100°C.

From these results, it was confirmed that the non-fiber insulation material has a higher temperature rise property than the AES fiber insulation sheet. And also, the addition of carbon raw material can further improve the temperature heating property.

Tab. 2: Temperature of each sample while heating.

| Heating time / min | Sample A | Sample B | Sample C | Sample D |
|---|---|---|---|---|
| 10 | 878 | 714 | 750 | 793 |
| 20 | 1090 | 990 | 1020 | 1050 |
| 30 | 1177 | 1109 | 1127 | 1145 |
| 40 | 1201 | 1158 | 1168 | 1187 |
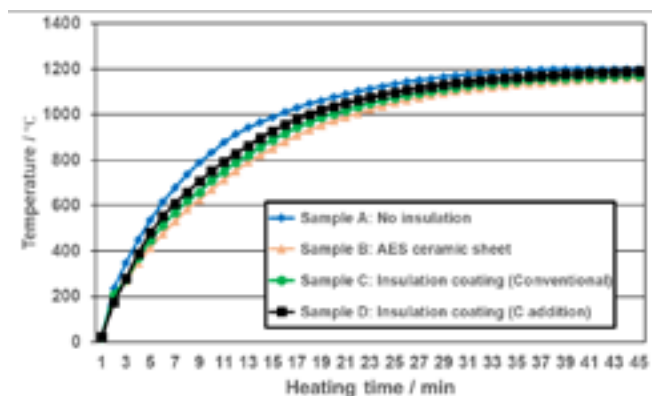


Fig. 5: Temperature of each sample while heating.

### The comparison of cooling rate

There is the comparison of cooling rate after the refractory temperature reach at 1200°C and keep for 2 hours.

Tab.3 shows the result about the temperature of each sample for each 10 min while cooling. Fig.6 shows the graph about the temperature of each sample for each 1min while cooling.

The temperature of Sample B after cooling for 10 minutes was approximately 200°C higher than that of Sample A. It's confirmed the AES fiber sheet has high thermal insulation.

The temperature of Sample C after cooling for 10 minutes was approximately 150°C higher than that of Sample A. It means the insulation material is lower insulating than the fiber sheet.

The temperature of Sample D after cooling for 10 minutes was approximately 350°C higher than that of Sample A. Sample D shows the highest insulation performance in 4 samples.

Tab. 3: Temperature of each sample while cooling.

| Cooling time / min | Sample A | Sample B | Sample C | Sample D |
|---|---|---|---|---|
| 5 | 618 | 792 | 768 | 958 |
| 10 | 485 | 685 | 639 | 837 |
| 20 | 324 | 536 | 476 | 666 |
| 30 | 214 | 435 | 384 | 538 |
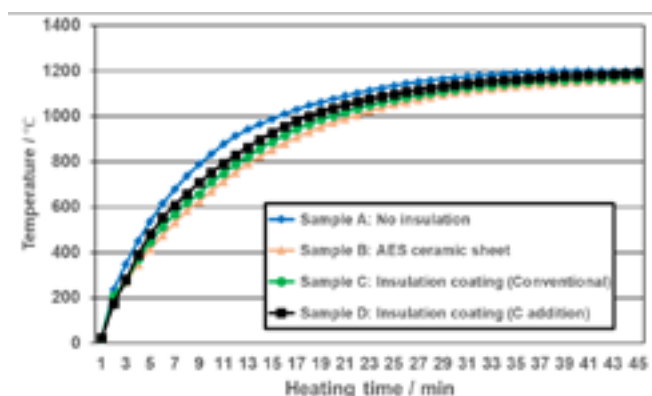


Fig. 6: Temperature of each sample while cooling.

495

**CONSIDERASIONS**

It's expected that the addition of carbon would improve the heating rate. As the result in "The comparison of heating rate", the temperature rising of Sample D (the insulation material including carbon) is slightly faster than that of Sample B (AES fiber) and Sample C (the conventional insulation material).

On the other hand, as mentioned in "The comparison of cooling rate", the temperature rising of Sample D is much slower than that Sample C.

At first, it is thought that the added carbon, which is high thermal conductivity, improved the heating rate of the insulation material during heating. When the sample was heated above a certain temperature, the carbon oxidized and vaporized, creating a large number of pores in the heat insulating material.

Tab.4 shows the physical properties of insulation material before and after heating.

Sample making method
- Mixed insulation material and dried at 100°C (Before heating)
- Heated above sample at 1200°C for 2 hours (After heating)

Tab. 4: The physical properties of insulation

|  | Insulation 1 (Conventional) | | Insulation 2 (Carbon added) | |
|---|---|---|---|---|
|  | Before heating | After heating | Before heating | After heating |
| Apparent porosity / % | 38.4 | 39.0 | 47.3 | 56.0 |
| Bulk density / g·cm⁻³ | 1.66 | 1.79 | 1.13 | 1.22 |
| Modulus of rupture / MPa | 2.9 | 6.8 | 1.0 | 2.8 |

The bulk density and modulus of rupture of Insulation 1 increased after heating, and the apparent porosity of one almost unchanged. It is considered the reason that the volatile matter content vaporizes during heating and the some of materials in insulation sinters.

On the other hand, not only the bulk density and modulus of rupture of Insulation 2 increased after heating, but also apparent porosity of one increased. It is thought the reason that the pore in insulation increases by carbon oxidizing and vaporizing during heating.

Fig.7 shows the observation results by Microscope for insulation materials before and after heating.

Insulation 1 was no significant difference between before and after heating. it was observed that the number of pores for Insulation 2 after heating increased compared to before heating. It is presumed that these pores were formed after the carbon disappeared as described above.

By adding carbon to insulation material, it was improved the heating rate at the start of heating, and by disappearing carbon during heating, it has higher heat insulation than the conventional, great improving the heat retention property of the refractory temperature after heating.
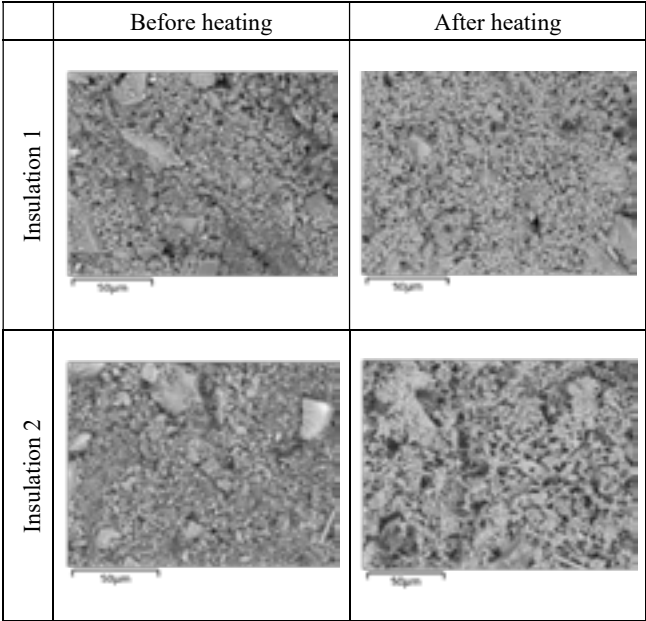


*Fig. 7: Microscope observation results.*

**CONCLUSIONS**

The non-fiber insulation coating, which have been developed so far, have been inferior to the AES insulation fiber in terms of thermal insulation.

In this development, by adding carbon, which is high thermal conductivity, to the insulation material, it was possible to ensure the heating rate during heating. In addition, by carbon vaporizing, the thermal insulation properties during cooling after heating can be improved compared to the conventional insulation material, and the thermal insulation performance exceeds that of the AES insulation sheet.

It is expected to improve the heat insulation (the resistance of the heat removal) of the refractory after preheating, without increasing the energy cost for preheating the nozzle.

As issue of the future, the workability of the insulation material application is worse than the conventional one. Moreover, it could be possible that the insulation coating peels off from the refractory due to weaker strength of the insulation material. Therefore, in order to maintain stable performance, selection of the optimum additive amount will be a future issue.

**REFERENCES**
S.Takahashi, N.Yamauchi, and M.Shinato - Taikabutsu 69 [2] p92-93 (2017)
K.Kachi, S.Takahashi, N.Yamauchi, and M.Shinato - Taikabutsu 74 [2] p72-73 (2022)

# YTTRIA MAGNESIA CO-STABILIZED ZIRCONIA REFRACTORIES FOR APPLICATION AS FUNCTIONAL COMPONENTS IN CONTINUOUS STEEL CASTING

Claudia Heuer, Steffen Dudczig, Nora Brachhold, Christos G. Aneziris,
Technische Universität Bergakademie Freiberg, Germany

Ratana Soth, Angelika Priese, Christoph Wöhrmeyer, Christopher Parr,
IMERYS S.A., France

## ABSTRACT

The increasing demands in iron and steel industry with regard to longer casting times and speeds as well as improved steel qualities require the constant further development and investigation of existing material systems. Zirconia is one of the most promising functional refractory materials in continuous steel casting and is mainly employed in areas with high thermal and chemical stresses such as the slag line and the nose of monoblock stoppers or the inlet area of submerged entry nozzles. The key for the application of zirconia based ceramics in such harsh application areas is a profound understanding of its thermomechanical and thermochemical properties that are mainly influenced by the type and the amount of stabilizer, the grain size as well as the thermal conditions during sintering and operation. Within the present contribution coarse grained (up to 5 mm) zirconia self-flowing castables based on a yttria stabilized zirconia co-stabilized by magnesia are developed and bars as well a model monoblock stoppers are cast. The mechanical and thermo-mechanical properties are evaluated after sintering at 1650 °C. The influence of different stabilizer variants as well as the contribution of the binder to the phase evolution of the zirconia during sintering and operation and thus the influence on the thermo-mechanical properties is investigated with the aid of EDS- and X-ray diffraction measurements.

## INTRODUCTION

In the continuous casting of steel zirconia refractories are employed in areas with high thermal and chemical stresses such as the slag line and the nose of monoblock stoppers or the inlet area of submerged entry nozzles since they offer excellent corrosion and erosion resistance and a unique combination of strength, toughness, hardness and thermal shock resistance [1]. Up to date and depending on the required steel quality carbon-bonded zirconia materials are employed among others because they offer an excellent thermal shock performance. Nevertheless, their application will be more limited in the future since they do not meet the quality requirements of low and ultra-low carbon steels due to dissolution processes [2]. In the present study a fuse cast yttria stabilized (2.46 wt.%) zirconia co-stabilized by 1.44 wt.% magnesia is introduced. The use of carbon as binder is consciously avoided for the above mentioned reasons. A good thermal shock resistance of the co-stabilized zirconia with residual strengths of >5 MPa, even after recurring thermal shock, is addressed by employing coarse grains (up to 5 mm) and tailoring a high metastable tetragonal phase proportion. Therefore, the impact of calcium magnesium aluminate cement (CMA) as hydraulic binder [3, 4] as well as of a hydratable alumina binder on the phase evolution during sintering is investigated. The development of self-flowing castables is presented not only for test specimen but also for application-oriented components. The physical and thermo-mechanical properties are evaluated. The microstructure as well as the phase compositions of the sintered materials are investigated with the aid of SEM and X-ray diffraction.

## MATERIALS AND METHODS

In the present study a fuse cast yttria stabilized zirconia co-stabilized with magnesia was employed. As binder 3-9 wt.% CMA72 provided by Imerys S.A. with a mean particle size of 15 µm was used. As an alternative binder, 1 wt.% Alphabond 300 (Almatis, Germany), hydratable alumina binder was used [5, 6]. Peramin AL 200 (Imerys S.A.) [4] was used as a dispersing agent for the CMA containing castables. For the castables prepared with Alphabond 300 as binder, ADW and ADS [7] were used as dispersants and for adjusting the setting behavior. The investigated self-flowing castables with the compositions given in Tab. 1 were designed according to the grain size distribution model of Dinger and Funk [8-10] with a distribution modulus of 0.28. Casting of the self-flowing masses was done in steel molds with the dimensions 25 x 25 x 150 mm³. Furthermore, the most promising composition was chosen to cast model monoblock stopper with a diameter of 40 mm and a length of 340 mm. All samples were demolded after 24 h and then dried stepwise up to 110 °C. Sintering was conducted at 1650 °C in oxidizing atmosphere with a heating rate of 1 K/min with a dwell time of 120 min at maximum temperature. For composition Z991AB an additional dwell of 60 min at 500 °C during heating was done.

Tab. 1: Composition of the zirconia refractory castables in wt.%

|  | Z97CMA3 | Z94CMA6 | Z91CMA9 | Z99AB1 |
|---|---|---|---|---|
| Grades in mm |  |  |  |  |
| 2 – 5 | 25 | 25 | 25 | 25 |
| 1 – 3 | 15 | 15 | 15 | 15 |
| 0.5 – 1 | 11 | 11 | 11 | 13 |
| 0 – 0.5 | 16 | 13 | 10 | 18 |
| 0 – 0.045 | - | - | - | 8 |
| Finest I | 29 | 29 | 29 | 9 |
| Finest II | 1 | 1 | 1 | 11 |
| Binder |  |  |  |  |
| Alphabond300 | - | - | - | 1 |
| CMA 72 | 3 | 6 | 9 | - |
| Additives |  |  |  |  |
| ADW/ADS | - | - | - | 0.5 / 0.5 |
| Peramin AL200 | 0.1 | 0.1 | 0.1 | - |
| Water | 4.3 | 4.4 | 4.6 | 5.8 |

The initial co-stabilized zirconia powder exhibits a partial stabilization since reflexes for all three phases were identified. The quantification using Rietveld refinement yields 56 % monoclinic, 16 % tetragonal and 27 % cubic phase. The sintering of the cast samples was conducted at 1650 °C in the phase field of the tetragonal solid solution (for yttria stabilized) and tetragonal/cubic solid solution (for magnesia stabilized). The results of the x-ray analysis after sintering are summarized in Tab. 2.

Tab. 2: Results of the quantitative phase analysis by Rietveld in %

| Phase | Z99AB1 | Z97CMA3 | Z94CMA6 | Z91CMA9 |
|---|---|---|---|---|
| Monoclinic | 84 | 46 | 34 | 21 |
| Tetragonal | 7 | 45 | 50 | 61 |
| Cubic | 4 | - | - | - |
| Spinel | 5 | 9 | 16 | 18 |
| Alumina | - | - | - | - |
| Others | - | - | - | - |
| Rwp | 10.0218 | 7.9558 | 7.6099 | 7.8855 |

Fig. 1 displays the microstructure of the composition Z94CMA6 after sintering, showing that an adequate densification of the matrix

took place. Grain boundaries, pores are visible as well as spinel agglomerates with sizes of up to 50 µm.
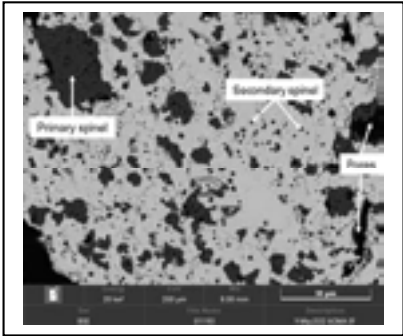


*Fig. 1: SEM micrograph (BSE mode) of the co-stabilized zirconia sintered at 1650 °C*
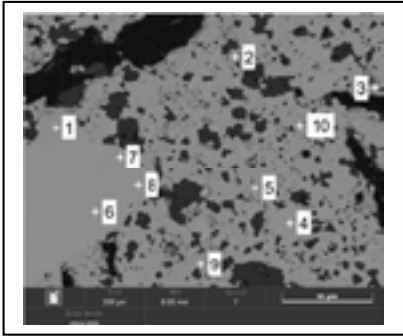


*Fig. 2: SEM micrograph (BSE mode) of composition Z94CMA6 sintered at 1650 °C with marked positions 1-10 of EDS point analyses.*
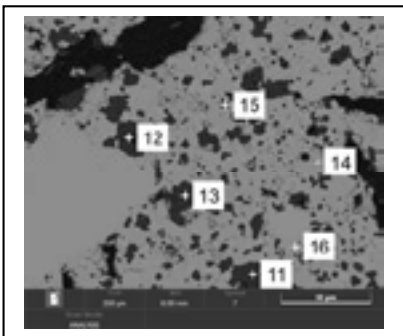


*Fig. 3: SEM micrograph (BSE mode) of composition Z94CMA6 sintered at 1650 °C with marked positions 11-16 of EDS point analyses.*

Detailed EDS analyses were carried out in order to investigate the interactions between zirconia and the binders. Fig. 2 and Fig. 3 displayed a polished cross-section of the sample Z94CMA6. The results of the EDS scans for the marked positions are summarized in Tab. 3 and Tab. 4.

Four different areas of the microstructure were investigated in detail. The EDS point analyses 2, 3, 5, 9 reveal a depletion of the fine zirconia matrix by magnesia. The co-stabilized powder in initial state contained 1.44 wt.% MgO; it decreased during sintering to 0.7 wt.%. In the fine zirconia matrix, a CaO-content of 2.4 wt.% was determined via EDS point analysis. During sintering calcium ions (present in the CMA binder) diffuse into the zirconia grains and lead to a stabilization of the zirconia. According to the phase diagram, this stabilization takes place in the phase field of tetragonal and tetragonal/cubic solid solution modification [11]. Close to the grain boundaries of the large zirconia grains (EDS scans 1, 7, 8) also a depletion by magnesia was registered. In addition to that, small precipitates are formed close to the grain boundaries of large (>1 mm) zirconia grains. These have also been identified as magnesium aluminate spinel. At distances >15 µm from the grain boundary the initial chemical composition of the co-stabilized zirconia was measured. The EDS point analyses 11-15 clearly identify magnesium aluminate spinel that was formed during sintering.

Fig. 4 shows the microstructure of the composition Z99AB1 with 1 wt.% Alphabond 300. It appears less densified as compared to the composition Z94CMA6 with 6 wt.% CMA. The open porosity was determined to be 17.4 % and the pores appear elongated with a span of up to 50 µm. Fig. 4 also contains position of EDS point analyses and the results are summarized in Tab. 5 and Tab. 6. In the EDS point analyses 1- 5 as well as 6-10, taken in the center or at the boundaries of large zirconia grains, a strong deviation in the chemical compositions with regard to magnesia content can be recognized, indicating the diffusion of magnesia and thus a severe destabilization. This was confirmed by x-ray analysis, where the monoclinic phase content was determined to be 84 %. In addition to that spinel was formed during sintering (EDS positions 11 and 12). Furthermore, smallest spinel precipitates (≤300 nm) start to grow within the zirconia grains.

Tab. 3: EDS point analyses of composition Z94CMA6 at the positions indicated in Fig. 2

| Scan no. | $ZrO_2$ | $Y_2O_3$ | MgO | CaO |
|---|---|---|---|---|
| **Fine zirconia matrix** | | | | |
| 2 | 93.0 | 2.0 | 0.8 | 2.0 |
| 3 | 92.1 | 2.4 | 0.6 | 2.7 |
| 5 | 92.1 | 2.4 | 0.6 | 2.7 |
| 9 | 93.2 | 2.1 | 0.9 | 1.7 |
| *MW ± SD* | *92.6 ± 0.6* | *2.2 ± 0.2* | *0.7 ± 0.2* | *2.3 ± 0.5* |
| **Close to the grain boundaries of large zirconia grains** | | | | |
| 1 | 93.3 | 2.1 | 0.9 | 1.5 |
| 7 | 94.7 | 1.8 | 0.9 | 0.5 |
| 8 | 95.0 | 1.7 | 0.9 | 0.3 |
| *MW ± SD* | *94.3 ± 0.9* | *1.9 ± 0.2* | *0.9 ± 0.0* | *0.8 ± 0.6* |
| **15-20 µm distance to grain boundaries of large zirconia grains** | | | | |
| 4 | 94.9 | 1.8 | 1.2 | 0.1 |
| 6 | 94.5 | 1.9 | 1.5 | 0.1 |
| *MW ± SD* | *94.7 ± 0.3* | *1.9 ± 0.1* | *1.4 ± 0.2* | *0.1 ± 0.0* |

Tab. 4: EDS point analyses of composition Z94CMA6 at the positions indicated in Fig. 3

| Scan no. | MgO | $Al_2O_3$ |
|---|---|---|
| 11 | 26.7 | 73.3 |
| 12 | 27.1 | 72.6 |
| 13 | 26.8 | 73.1 |
| 14 | 25.9 | 74.1 |
| 15 | 24.5 | 75.5 |
| 16 | 26.1 | 73.9 |
| *MW ± SD* | *26.2 ± 0.9* | *73.8 ± 1.0* |
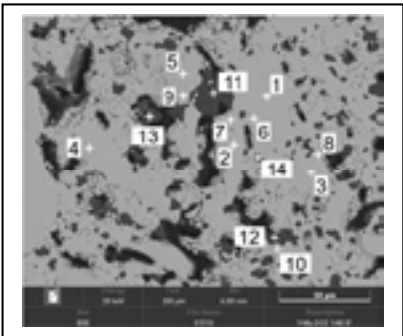


*Fig. 4: SEM micrograph (BSE mode) of composition Z99AB1 sintered at 1650 °C with marked positions 1-13 of EDS point analyses.*

Tab. 5: EDS point analyses of composition Z99AB1 at the positions 1-10 indicated in Fig. 4

| Scan no. | ZrO$_2$ | Y$_2$O$_3$ | MgO |
|---|---|---|---|
| **Close to the grain boundaries of large zirconia grains** | | | |
| 6 | 94.8 | 2.2 | 1.1 |
| 7 | 95.2 | 2.3 | 0.5 |
| 8 | 94.7 | 2 | 1.4 |
| 9 | 94.6 | 1.8 | 0.7 |
| 10 | 96.2 | 1.7 | 0.1 |
| *MW ± SD* | *95.1 ± 0.7* | *2.0 ± 0.3* | *0.8 ± 0.5* |
| **15-20 μm distance to grain boundaries of large zirconia grains** | | | |
| 1 | 94.8 | 2 | 1.3 |
| 2 | 95.3 | 2.3 | 0.4 |
| 3 | 94.5 | 2.2 | 1.4 |
| 4 | 94.6 | 2.4 | 0.9 |
| 5 | 94.7 | 2.2 | 1.2 |
| *MW ± SD* | *94.8 ± 0.3* | *2.2 ± 0.1* | *1.0 ± 0.4* |

Tab. 6: EDS point analyses of composition Z99AB1 at the positions 11-12 indicated in Fig. 4

| Scan no. | MgO | Al$_2$O$_3$ | FeO |
|---|---|---|---|
| 11 | 18.5 | 80.7 | 0.9 |
| 12 | 18.5 | 80.6 | 0.9 |
| *MW ± SD* | *18.5 ± 0.0* | *80.7 ± 0.1* | *0.9 ± 0.0* |

Tab. 7 summarizes the physical and mechanical properties of the co-stabilized zirconia castables. The linear shrinkage was small in all of the compositions. Thus, the formation of large stresses during sintering (responsible for crack formation) was prevented. This is one basic requirement for the fabrication of large-scale components.

Tab. 7: Physical, mechanical and thermomechanical properties of the castables after sintering at 1650 °C

| | Z99 AB1 | Z97 CMA3 | Z94 CMA6 | Z91 CMA9 |
|---|---|---|---|---|
| Shrinkage (%) | 0.65 ± 0.2 | 0.86 ± 0.2 | 0.85 ± 0.2 | 0.72 ± 0.1 |
| Bulk Density (g/cm³) | 4.4 ± 0.1 | 4.4 ± 0.1 | 4.3 ± 0.2 | 4.2 ± 0.2 |
| Open porosity (%) | 17.4 ± 0.2 | 17.7 ± 0.4 | 16.8 ± 0.2 | 16.8 ± 0.2 |
| Flexural strength (MPa) | 8.5 ± 1.7 | 12.6 ± 1.6 | 14.8 ± 1.8 | 11.2 ± 0.6 |
| Young´s Modulus (GPa) | 18.9 ± 2.2 | 32.4 ± 1.8 | 39.5 ± 0.9 | 22.2 ± 0.0 |
| Remaining strength after TS (MPa) | 4.5 ± 0.1 | 9.6 ± 0.8 | 9.3 ± 1.0 | 5.5 ± 0.2 |
| Young´s Modulus after TS (GPa) | 9.5 ± 0.4 | 21.5 ± 2.0 | 30.9 ± 0.0 | 12.5 ± 0.6 |

The open porosity of the castables was determined between 16.8 to 17.7 % and thus typical values for self-flowing castables were obtained [12]. The porosities for the compositions Z94CMA6 and Z91CMA9 with 6 or 9 wt.% CMA are lower as compared to the other compositions. This might be the result of the noticeable spinel formation during sintering, which was shown in Tab. 2. It was recognized that the spinel "grows" into the pores. The lowest flexural strength was determined for composition Z99AB1 with 8.5 MPa. During sintering a severe destabilization of the co-stabilized zirconia was registered and the monoclinic phase content significantly increased to 84 %. During sintering, upon cooling the phase transformation tetragonal to monoclinic is accompanied by a volume expansion of 3-5 % resulting in the damage of the microstructure and thus deteriorates the mechanical properties. This is also reflected in the remaining strength after thermal shock testing where a loss in strength of 47 % was registered. Composition Z94CMA6 had the highest flexural strength with 14.8 MPa. The calcia contained in the CMA cement stabilized the tetragonal zirconia phase during

sintering. Thus, a significant decrease in monoclinic phase was registered, see Tab. 2. This means, that on the one hand the tetragonal to monoclinic phase transformation upon cooling is inhibited and on the other hand that the tetragonal grains may undergo (depending on their size) a martensitic phase transformation during mechanical loading. Despite the high tetragonal phase content of 61 %, the composition Z91CMA9 has the lowest flexural strength in the group of CMA containing castables. In the x-ray analysis it was shown that a severe spinel formation (18 %) took place during sintering. The spinel grains grow to sizes >50 μm and thus weakened the zirconia matrix deteriorating the mechanical as well as thermo-mechanical properties. The compositions Z97CMA3 and Z94CMA6 show a very good thermal shock performance with losses in strength of only 24 % and 37 % after one thermal shock testing cycle.

In order to evaluate the thermal shock performance in an application-oriented manner, the composition Z94CMA6 was thermally cycled for 5 times and the remaining strength was determined after one, three and five thermal shock tests. The results are summarized in Fig. 5. As expected, the loss in strength is most pronounced after the first thermal shock. A remaining strength of 9.3 ± 1.0 MPa was determined after the first thermal shock. In the further tests, the loss in strength is less pronounced since the microstructure is characterized by a distinct micro-crack network (from transformation of tetragonal to monoclinic phase and due to spinel formation during sintering). In addition to that, the tetragonal zirconia phase is able to transform stress-assisted (martensitic) into monoclinic state. This leads to closure of cracks and prevents further crack propagation. After the third thermal shock a loss in strength of 27 % and after the fifth thermal shock a loss in strength of 20 % was determined. The remaining strength after five thermal shocks was measured to be 5.5 ± 1.5 MPa, which is a good value for coarse zirconia refractories.
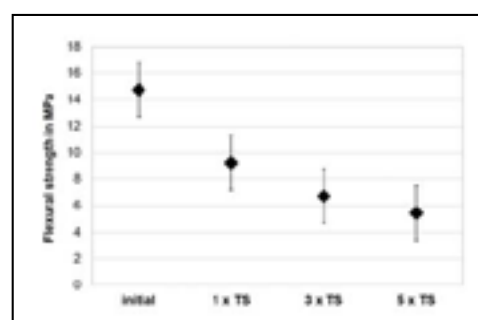


*Fig. 5: Flexural strength after thermal shock testing, composition Z94CMA6 with 6 wt.% CMA*

In the final part of this study, larger application-oriented components have been developed, e.g. for casting experiments in a steel casting simulator (Systec, Germany) [12-14]. Model monoblock stopper with a length of 340 mm and a diameter of 40 mm were successfully cast, see Fig. 6. For the preparation of the self-flowing castables the same compositions as shown in Tab. 1 were used without further modification. The mixing routine was also identical, but the casting itself had to be modified. Small portions of the self-flowing mass were filled into the stopper mold that consisted of two parts. During the filling of the mold, short breaks for the de-airing of the self-flowing mass were made. Demolding took place after 24 h. After drying the stopper was sintered on an alumina bed (2 mm) in a lying position with a heating rate of 1 K/min to 1650 °C and a dwell at maximum temperature of 120 min. Due to the small shrinkage during sintering as well as due to the tailored phase composition of the co-stabilized zirconia a defect-free stopper was successfully fabricated. In further studies the stopper/testing bars will be investigated in the above mentioned steel casting simulator.

*Fig. 6: Defect-free stopper rod prepared with coarse grained co-stabilized zirconia.*

## CONCLUSIONS

Within this paper a yttria stabilized zirconia co-stabilized by magnesia has been introduced for the preparation of coarse-grained self-flowing castables. The co-stabilized zirconia was composed of 56 % monoclinic, 16 % tetragonal and 27 % cubic phase. Traces of alumina and ytterbium silicate were also detected. The addition of calcium magnesium aluminate (CMA) cement as binder led to a stabilization of the tetragonal zirconia phase during sintering due to the replacement of magnesia as stabilizer by calcia. After sintering the tetragonal phase content was determined to be in the range of 45 and 61 % depending on the CMA content. With the aid of EDS measurements, it was shown that the stabilization of the zirconia involved all the different zirconia particle sizes. In large zirconia particles (up to 5 mm) the initial chemical composition was detected at distances of 15-20 μm from the grain boundary. The monoclinic phase content decreased significantly in all of the CMA containing compositions. In contrast to this, the compositions prepared with hydratable alumina binder showed a severe destabilization with a monoclinic phase content of 84 % after sintering. In all compositions the chemical reactions between magnesia (lost as stabilizer) with alumina (from binder) and the subsequent formation of magnesium aluminate spinel was recognized.

All of the prepared samples had a very small shrinkage during sintering, thus enabling the preparation of larger components. The flexural strength was the highest in compositions Z94CMA6 and Z97CMA3 with 14.8 ± 1.8 MPa and 12.6 ± 1.6, respectively. The flexural strengths of the compositions Z99AB1 and Z91CMA9 were low, due to the high monoclinic phase content and the high spinel content, respectively. For the composition Z94CMA6 the thermal shock performance was further evaluated by quenching the samples 5 times. As expected, the loss in strength was most pronounced after the first thermal shock test. A remaining strength of 9.3 ± 1.0 MPa was determined. The loss in strength was less pronounced in the further thermal shocks. A remaining strength after five thermal shocks of 5.5 ± 1.5 MPa was determined.

Finally, large application-oriented components were developed for casting experiments in a steel casting simulator (Systec, Germany). After a minor modification of the casting routine, model monoblock stopper with a length of 340 mm and a diameter of 40 mm were successfully cast and defect-free stoppers were obtained after sintering. In future work these stoppers will be tested in real-term conditions in the above mentioned steel casting simulator.

## ACKNOWLEDGEMENT

## REFERENCES

[1] I. Elstner, P. Jeschke, H. Leistner, Einsatz von ZrO2-Werkstoffen bei der Stahlerzeugung, Goldschmidt informiert, 59 (1983) 27-33.

[2] F. Cirilli, A.D. Donato, U. Martini, P. Miceli, P. Guillo, J. Simoes, Y.J. Song, Corrosion mechanisms of zirconia/carbon based refractory materials by slg in presence of steel, la metallurgia italiana, (2008) 43-50.

[3] C. Parr, G. Assis, H. Fryda, C. Wöhrmeyer, Castables with improved corrosion resistance for steel-making applications, UNITECR 2011Kyoto, Japan, 2011, pp. 1-D-4.

[4] C. Wöhrmeyer, C. Parr, H. Fryda, J.M. Auvray, S. Li, Castables with improved corrosion resistance based upon a novel calcium aluminate cement, refractories WORLDFORUM, 4 (2012) 99-105.

[5] Datasheet, Alphabond 300, Almatis Germany, 2012.

[6] I.R. Oliveira, V.C. Pandofelli, Dispersants and their effects on hydratable alumina containing castables, Refractories Worldforum, 1 (2009) 103-109.

[7] Datasheet, ADW, ADS, Almatis Germany, 2017.

[8] D.R. Dinger, J.E. Funk, Particle Packing II - Review of Packing of Polydisperse Particle Systems, Interceram, 41 (1992) 95-97.

[9] D.R. Dinger, J.E. Funk, Particle Packing III – Discrete versus Continuous Particle Sizes, Interceram, 41 (1992) 332-334.

[10] J.E. Funk, D.R. Dinger, Particle Packing, Part I - Fundamentals of Particle Packing Monodisperse Spheres, Interceram, 41 (1992) 10-14.

[11] D.G. Lamas, R.E. Juárez, A. Caneiru, N.E.W.d. Reca, Preparation of novel calcia-stabilized TZP ceramics, Nanostruct. Mater., 10 (1998) 1199-1207.

[12] S. Dudczig, Wekstoffentwicklung von Feuerbetonen für Schlüsselbauteile zur Erfassung von Wechselwirkungen zwischen Stahlschmelzen und Feuerfestmaterialien in einem Stahlgusssimulator, Fakultät für Maschinenbau, Verfahrens- und Energietechnik, Technische Universität Bergakademie Freiberg2017.

[13] C.G. Aneziris, S. Dudczig, M. Emmel, H. Berek, G. Schmidt, J. Hubalkova, Reactive Filters for steel melt filtration, Adv. Eng. Mater., 15 (2013) 46-59.

[14] S. Dudczig, C.G. Aneziris, M. Emmel, G. Schmidt, J. Hubalkova, H. Berek, Characterization of carbon-bonded alumina filters with active or reactive coatings in a steel casting simulator, Ceram. Int., 40 (2014) 16727-16742.

# EXTRUDED CELLULAR FILTER COMPONENTS FOR STEEL MELT FILTRATION IN INDUSTRIAL CONTINUOUS CASTING OF STEEL

T. Wetzig, M. Neumann, C. G. Aneziris

TU Bergakademie Freiberg, Institute of Ceramics, Refractories and Composite Materials, Freiberg, Germany

M. Schwarz, L. Schöttler

Deutsche Edelstahlwerke Specialty Steels GmbH & Co. KG, Siegen, Germany

## ABSTRACT

Different $Al_2O_3$-based materials were investigated as base materials for the extrusion of cellular filter components for the continuous casting of steel melts. The final filter component should be implemented at the tundish bottom. It has to withstand thermal shock and oxidation during preheating and at the first melt contact. Additionally, it has to survive the corrosive attack and mechanical stresses at high temperatures during the continuous casting process over several melt batches and a duration of several hours. Thus, the fine $Al_2O_3$ basis was modified regarding three major factors: Adding a coarser alumina fraction, adding a carbonaceous fraction and adding $ZrO_2$. The resulting eight combinations were mixed with methylene cellulose to form plastic mixes and extruded into bar-shaped samples. The samples were investigated regarding their shrinkage behaviour, density, porosity, mechanical strength and thermal shock behaviour. The oxidic material with the most promising property profile was $Al_2O_3$-$ZrO_2$ with 200 µm grain. The carbon-bonded material with the most promising property profile was $Al_2O_3$-$ZrO_2$-C with 200 µm grain. Both materials were successfully applied to generate large-scale filter tube prototypes.

## INTRODUCTION

Ensuring steel cleanliness is of ever-increasing importance with regard to increasing efficiency, performance and safety while reducing carbon footprint, scrap rates and the waste of energy and raw material [1]. When all technologies of modern steelmaking including advanced secondary metallurgy, the use of high-performance refractories, clever plant, ladle and tundish design as well as state-of-the-art process control systems, are utilized to full potential, steel melt filtration can provide a further way to remove remaining non-metallic inclusions shortly before the casting process.

While melt filtration is state of the art in batch processes, e.g. in foundries, it is quite challenging in continuous casting. The high duration of casting sequences and the amount of steel melt passing through filters increases the risk of filter blockage or failure substantially. Wetzig et al. [2,3] investigated the immersion of exchangeable foam filter systems in an industrial tundish in order to tackle these challenges. The immersion process allows for flexible removal and replacement of the filters after a defined casting time. In this way, filter blockage or failure and a premature termination of the casting process is avoided. Of course, this method is only possible if the tundish design allows for it. Some systems include covers, instruments or generally limited space above the tundish. In this case, classic fixed implementation of filters into the tundish prior to casting is the only possibility.

In this case, the following conditions have to be considered:

1. Preheating of the system prior to casting (oxidation, thermal shock)
2. Casting duration (high temperature creep, corrosion, erosion)
3. Filter position and tundish design (mechanical stresses depending on pressure and flow conditions)
4. Steel melt composition and temperature (corrosion, thermal shock)

The expected conditions should determine a) the applied filter type and b) the applied filter material. The target application in the present case was a filter tube at the bottom of the tundish, directly above the outlet to the moulds. The system is preheated with gas burners and then cast on directly with melt including first slag contact. After that the filter has to withstand constant melt flow and ferro-static pressure at temperatures greater than 1500°C for several hours. Due to the filter positioning and the severe conditions, foam filters were deemed too fragile and thus too risky. As an alternative, an extruded cellular chaotic structure like presented by Essock et al. [4] was proposed. Essock et al. extruded SiC "spaghetti" filters and successfully applied them in iron casting. A structure on this basis with comparatively dense and strong filter struts was also considered most suitable for the present investigation.

For the selection of the most suitable filter material, a fine alumina-based material (A) was modified using a combination 3 main factors:

- adding $Al_2O_3$ with < 200 µm grain size ($^b$),
- adding monoclinic $ZrO_2$ (Z) and
- adding carbonaceous material (C)

The 8 resulting compositions were analysed on their shrinkage, density, porosity, mechanical strength and thermal shock resistance. The materials with the most suitable property profile were applied to manufacture a filter prototype.

## EXPERIMENTAL

Table 1 shows the base composition the investigated compositions. The alumina portion of compositions including a second alumina faction was optimized based on a Dinger-Funk model using q = 0.2 as exponent. The material was dry-mixed together with 2 wt.% methyl cellulose derivative in an intensive mixer for 5 minutes. Afterwards, 0.3 wt.% of dispersing agent was added and water was introduced in a stepwise manner while mixing until the approximate consistency of a reference extrusion mix was achieved (see Fig. 1a). The final material was mixed for another 5 minutes. Since water may evaporate during mixing, a sample of each mix was analysed on their actual humidity in a moisture analyser. It ranged between 12.6 wt.% ($^b$AZ) and 19.7 wt.% (AZC) depending on the individual mix. The mixes were stored in air-tight plastic bags for 24 hours in order to let the methyl cellulose soak.

Tab. 1: Extrusion material compositions.

|  | A | $^b$A | AZ | $^b$AZ | AC | $^b$AC | AZC | $^b$AZC |
|---|---|---|---|---|---|---|---|---|
| Raw material composition in wt.% | | | | | | | | |
| $Al_2O_3$ (< 20 µm) | 100 | 17 | 80 | 5 | 70 | 33 | 56 | 26 |
| $Al_2O_3$ (< 200 µm) | - | 83 | - | 75 | - | 37 | - | 30 |
| $ZrO_2$ | - | - | 20 | 20 | - | - | 14 | 14 |
| Pitch binder | - | - | - | - | 20 | 20 | 20 | 20 |
| Graphite | - | - | - | - | 10 | 10 | 10 | 10 |

After the soaking time, the mixes were extruded into strands of approximately 300 mm length using a piston extruder (see Fig. 1b) with a rectangular nozzle of the dimension 4 x 5 mm². The strands were marked with a stamp in 50 mm distance sections to allow for the determination of the shrinkage after drying and the subsequent separation of bar-shaped samples.

After drying for 24 hours at room temperature, the dimensions and mass of 30 random bar-shaped samples per composition were measured to determine the geometric density, dry shrinkage and parameters for mechanical testing on 3-point bending strength

(CMOR). The mechanical testing was performed using a mechanical testing machine TIRA test 2420.
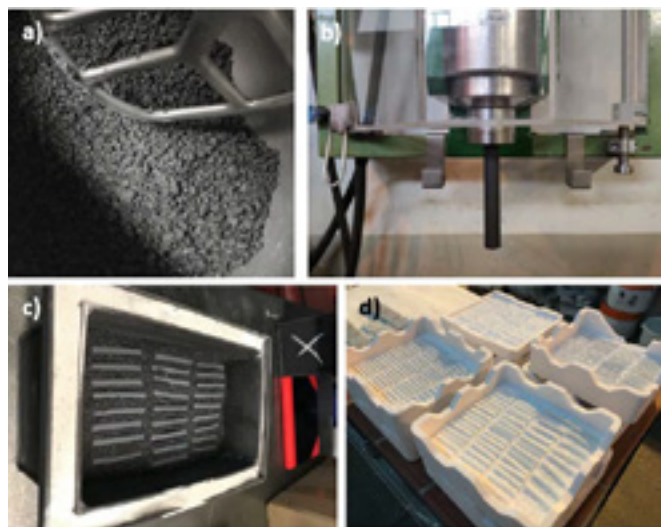


*Fig. 1: Sample preparation; a) Extrusion mix in intensive mixer; b) Piston extruder; firing preparation of bar-shaped carbon-bonded samples in pet-coke bed (c) and oxidic samples (d).*

The rest of the oxidic samples was fired for 5 hours at 1600 °C and the rest of the carbonaceous samples was fired in coke bed (reducing atmosphere) for 3 hours at 800 °C (Figure 1c-d). The measurement of the mass and dimensions, the determination of the geometric density and the shrinkage as well as the CMOR measurement of 30 random samples were again performed after firing. Furthermore, 10 samples of each composition were tested on their open porosity and raw density using the Archimedes principle. To disclose also the closed porosity, the true density of each material was also analysed by means of a helium pycnometer.

Finally, 30 more fired samples of each material were subjected to thermal shock in water (25 °C) from a temperature of 1000 °C. The CMOR of the shocked samples was measured to determine the residual strength of each material as a proxy for the thermal shock resistance.

The data was then analysed in comparison to find the most suitable materials in order to manufacture first filter prototypes.

## RESULTS AND DISCUSSION

All materials were extrudable without major issues regarding surface quality, tearing or deformation. However, there was some deformation after drying depending on the amount of water used. In this regard, the coarser oxide materials [b]A and [b]AZ were of advantage, whereas fine, carbon-bonded materials show more deformation after firing.

This directly correlated with the linear dry shrinkage of the investigated materials which ranged from about 1 to 2 % for [b]A and [b]AZ and was about 3 to 4 % for other materials.

Geometric density after drying was about 1.5 g/cm³ and very similar for carbon-bonded materials. For oxidic materials, the lower water demand of [b]A and [b]AZ, led to roughly 15-20% higher density implying lower porosity compared to their finer counterparts A and AZ.

The dry CMOR of most materials was in the range of 8 to 11 MPa. Materials [b]A and [b]AZ, which were preferred regarding their dry shrinkage showed much lower dry CMOR of about 5 MPa. This mainly originated from higher roughness and the coarser microstructure. This effect was not observed for the coarse carbon-bonded materials [b]AC and [b]AZC which suggests that the dry CMOR was dominated by the binding matrix, in this case carbonaceous material.

After firing, most materials shrank another 3 to 5 % with [b]A showing the lowest shrinkage in the test. The fine oxidic materials A and AZ both shrank over 17% in length after firing. This high

shrinkage already eliminates these materials for use as base materials of large-scale filter components as the expected degree of deformation and residual stress is critical.

Of course, the high shrinkage comes with high densification which made materials A and AZ the compositions with the highest geometric density after firing. For the fired materials, the density and porosity were investigated more comprehensively using the Archimedes principle in combination with helium pycnometry. In carbon-bonded materials, the carbonaceous matrix dominated the effect on the microstructure resulting in similar total porosity ranging from 44 to 50 % with negligible closed porosity. Coarse oxidic materials [b]A and [b]AZ had slightly lower porosity of about 35 % which was entirely open. Fine oxidic materials A and AZ had the lowest total porosity of 11 to 12 % with a majority of pores closed. In terms of corrosion, this would be favourable if the shrinkage behaviour of the fine materials were not so critical. Considering the similarity of the other materials in the study, the porosity was not a major selection point.

The CMOR after firing again showed that all carbon-bonded materials were rather similar ranging from 18 to 20 MPa. Zirconia-containing materials showed slightly lower CMOR than their zirconia-free counterparts. This originated from microcracks in the microstructure of the material introduced by the monoclinic zirconia and its phase transitions during firing. Naturally, the CMOR of fine materials was much higher with 149 MPa for AZ and 162 MPa for A compared to coarse materials (25 and 38 MPa). However, the most critical property for the intended application as filter material was the residual strength after thermal shock. Fine materials A and AZ only retained about 20 % of their CMOR after shocking. Material [b]A with 27% residual strength provided no major improvement of the thermal shock performance. All other materials retained above 35% of their CMOR after shocking with coarser materials outperforming slightly. [b]AZC showed the highest residual strength in the test with 46 %. Material [b]AZ retained 39 % of its strength making it the highest performing oxidic material in the test.

In summary, the critical shrinkage and low thermal shock resistance disqualified the materials A and AZ from further consideration. The carbon-bonded materials all performed similar, so due to its slightly higher residual strength, [b]AZC was chosen as carbon-bonded filter material. However, due to oxidation during the preheating, coatings will be necessary to apply the material in the final application for industrial continuous casting of steel. Hence, composition [b]AZ was chosen as most suitable oxidic alternative due to its low shrinkage and favourable thermal shock behaviour.
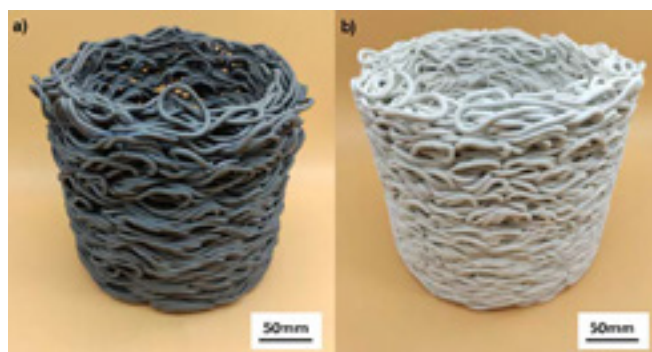


*Fig. 2: Filter prototypes using materials a) [b]AZC and b) [b]AZ [5]*

Both materials were used to extrude hollow cylindric filter prototypes with the height of 160 mm and a mean outer diameter of 200 mm. The geometry had a slight cone shape to allow for easy demoulding. The wall thickness of the cellular filter walls amounted to 30 mm. The manufacturing was performed by extruding a continuous strand into a constantly rotated cone-shaped polymer mould with a core in the middle. The rotation speed of the mould was chosen slightly slower than the extrusion speed to allow for a random swerving and stacking of the strand. The extrusion

was continued until the mould was filled. Figure 2 shows the resulting filter prototypes for both materials [5].

The prototypes showed no major cracks or deformation after drying. The strand contact points were strongly connected due to the strong cohesion of the cellulose in wet state. Due to its higher density and thus higher own weight, the [b]AZ cellular structure was slightly densified especially in the lower parts of the component. The lower-density carbon-bonded material [b]AZC allowed for a much more open pore structure. A next step to improve the open-celled structure will be to automate and control the movement of the strand and the mould to optimize the stacking process for maximum porosity and strand support. The shown filter prototypes will furthermore be tested in contact with molten steel.

## CONCLUSIONS

The material design has a major impact on the extrusion process, processing prior to firing and the component integrity and properties after firing. The most critical characteristics were the firing shrinkage, which made materials A and AZ unsuitable for upscaling as well as the residual strength after thermal shock based on which the materials [b]AZC and [b]AZ were preferable. Both materials were successfully applied to manufacture first filter prototypes for implementation at the tundish bottom in industrial continuous casting. The testing in contact with molten steel, the computer-controlled extrusion of ordered cellular structures as well as the investigation of even more coarse-grained materials will be next steps in the investigation.

## REFERENCES

[1]    Zhang, L, Thomas, B G Inclusions in continuous casting of steel. Proceedings of XXIV National Steelmaking, 2003, p. 138–183

[2]    Wetzig, T, Luchini, B, Dudczig, S, Hubálková, J, Aneziris, C G. Development and testing of carbon-bonded alumina foam filters for continuous casting of steel. Ceramics International 44 (15), 2018, p. 18143–18155

[3]    Wetzig, T, Baaske, A, Karrasch, S, Brachhold, N, Rudolph, M, Aneziris, C G. Application of exchangeable carbon-bonded alumina foam filters in an industrial tundish for the continuous casting of steel. Ceramics International 44 (18), 2018, p. 23024–23034

[4]    Essock, D M, Jaunich, H, Aneziris, C G, Hubálková, J. Novel foamless ceramic filters for advanced metal casting technologies. Proceedings of the Unified International Technical Conference on Refractories, 9th Biennal Worldwide, 2005.

[5]    Wetzig, T, Schwarz, M, Schöttler, L, Gehre, P, Aneziris, C G. Functionalized feeders, hollow-ware, spider bricks and starter casting tubes for increasing the purity in steel casting processes. Chapter 32. In: Aneziris, C G, Biermann, H. Multifunctional Ceramic Filter Systems for Metal Melt Filtration – Towards Zero-Defect Materials. Springer Series in Materials Science, 2023, ISBN: 978-3-031-40929-5

# DEVELOPMENT OF VIBROCAST ALUMINA−SPINEL INNER NOZZLES FOR VACUUM INGOT CASTING

Ph. D. Valeriy V. Martynenko*, Ph. D. Iryna G. Shulyk, Ph. D. Pavlo O. Kushchenko, Lyudmyla N. Zolotukhina

Ukrainian Research Institute of Refractories named after A.S. Berezhnoy, Kharkiv, Ukraine

## ABSTRACT

During the steelmaking process the steel must be degassed for removal gases from liquid. One type of vacuum degassing processes is stream degassing practice, in particular ladle to ingot mould degassing. Inner nozzles used in this method must have increased performance characteristics, because must be able to pass up to 500 MT of liquid steel at a rate of up to 10 MT/min. The refractory most suitable for such conditions is an alumina-spinel material based on fused alumina and magnesia-alumina spinel. The influence of grain composition of the coarse-grained batch on the properties of alumina-spinel vibrocast mass (moisture, flowing during vibration) and on the properties of unfired and fired at 1580 °C vibrocast samples has been studied. The optimum grain composition of vibrocast alumina-spinel mass and its moisture, which ensure the achievement of the highest properties of products, were determined. The industrial tests in service at one of metallurgical enterprises of Ukraine developed inner nozzles established that they provide non-stop casting of steel from 240 to 450 MT at temperature 1580-1650 °C and are characterized by high corrosion resistance (have insignificant wear of steel casting channel, which does not exceed ~ 3-5 mm). Petrographic studies of the inner nozzle sample after service have shown that, due to the contact of molten steel with refractory, a band of spinel up to ~ 0.2 mm wide is formed in it, which restrains the penetration of molten metal in the nozzle structure and prevents its wear, thereby increasing its corrosion resistance.

## INTRODUCTION

One of the methods for improving the metal quality during casting is vacuum metallurgy, which makes it possible to effectively fight harmful impurities to produce high-quality alloyed grades of steel. During the steelmaking process the steel must be degassed for removal gases from liquid. One type of vacuum degassing processes is stream degassing practice, in particular ladle to ingot mould degassing. Inner nozzles used in this method must have increased performance characteristics, because must be able to pass up to 500 MT of liquid steel at a rate of up to 10 MT/min. In world practice, the production of high-quality ladle refractories is based on the use of high-purity materials and, first of all, magnesia-alumina spinel (MA spinel), which has such properties as high corrosion resistance and high-temperature strength along with high refractoriness [1-3]. The refractory most suitable for such conditions is an alumina-spinel material based on fused alumina and magnesia-alumina spinel. In addition, an essential factor in the resistance of refractories in service to various aggressive reagents, along with their chemical and mineral composition, is the structure, the main characteristic of which is porosity (or density).

A large complex of works on production of plugs for steel casting in steel ladles, including the use of MA spinel, has been carried out by the Institute [4–7]. These studies were used as the basis for the development of vibrocast alumina-spinel inner nozzles for vacuum casting steel for ladles to ingot mould degassing. Developed inner nozzle is used in the processing of carbon-alloyed steel at its temperature in the steel ladle of 1580-1650 ºC. It is designed to form a jet of metal, regulate the rate of continuous casting, which reaches 450 MT of steel with metal flow rate through the channel of 10 MT/min. Residual pressure in the vacuum chamber during casting is not more than 2 mbar, the channel diameter wear of the inner nozzle should not be more than 5 mm. The design of the inner nozzle is shown in figure 1.
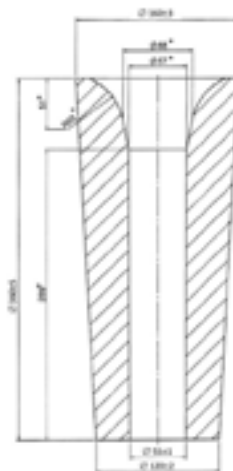


Fig. 1. Design of inner nozzle.

## EXPERIMENTAL PART

The following raw materials were used:
– fused alumina produced by Ukrainian Research Institute of Refractories named after A.S. Berezhnoy;
– fused MA spinel produced by Ukrainian Research Institute of Refractories named after A.S. Berezhnoy;
– alumina grade of "Salox M-S1 (ALO-Ex34)" (presented mainly α-$Al_2O_3$);
– powdery quartz;
– dispersing additives Castament FS-10 and FW-10.

The chemical composition of raw materials is given in Table 1.

Tab. 1. The chemical composition of raw materials

| Content, % wt. | Chemical composition of | | | |
|---|---|---|---|---|
| | fused alumina | fused MA spinel | alumina grade of "Salox M-S1 (ALO-Ex34)" | powdery quartz |
| L.O.I. | 0.04 | – | 0.02 | 0.13 |
| $SiO_2$ | 0.05 | 0.45 | 0.10 | 99.36 |
| $Al_2O_3$ | 99.50 | 85.61 | 99.70 | 0.42 |
| $TiO_2$ | <0.02 | – | 0.01 | – |
| $Fe_2O_3$ | 0.05 | 0.26 | 0.02 | 0.04 |
| CaO | 0.02 | 0.87 | 0.03 | 0.02 |
| MgO | 0.04 | 12.6 | 0.02 | 0.02 |
| $Na_2O$ | 0.32 | – | 0.13 | – |

As follows from the data in table 1, the initial raw materials were characterized by high content of main components and contained a small amount of impurities.

Fused alumina with a maximum grain size of 5 mm at a certain ratio of fractions 5-2, 2-1, 1-0.5, < 0.5 mm was used as a coarse-grained component of the batch. To obtain the matrix fused MA spinel and alumina were grained separately in a vibrating mill, and then these components were mixed with powdery quartz.

The particle size of finely dispersed materials is given in table 2.

Tab. 2. The particle size of finely dispersed materials.

| Material name | Particle size, μm | | Particle size content ≤ 10 μm, % |
|---|---|---|---|
| | Maximum | Prevailing | |
| Alumina grade of "Salox M-S1 (ALO-Ex34)" | 20 | < 4-8 | 90-92 |
| Fused MA spinel | 60 | <4-15 | 60 (≤ 4 μm ~ 25 %) |
| Powdery quartz | 130 | <4-30 | — |

The coarse-grained component was mixed with the fine-grained part of batch, in which dispersing additives were previously introduced, moistened with tap water. The moisture content of

grainy masses for vibrocasting was determined according to DSTU EN ISO 1927-3:2018. The actual moisture of batch was 4.1-4.4 %. The flowing of freshly prepared coarse-grained masses of alumina-spinel composition under vibration was carried out according to DSTU EN ISO 1927-4:2018.

Determination of the main properties of green samples was carried out on samples in the form of a cube with an edge size of 40 mm, fired ones at 1580 º C - on samples-cubes with an edge size of 40 mm, cut out of bricks with size 230x115x40 mm and manufactured by vibro-casting with the vibration amplitude of shake table 0.5 mm and frequency of 50 Hz, using removable plaster molds reinforced with metal. The green samples after mold disassembly were kept in natural conditions of the shop premises for 24 hours, and then dried in a desiccator at 110 ºC for 3 days. After drying, bricks were fired in a batch gas-flame oven at 1580 ºC with isothermal holding at this temperature for 8 hours.

Chemical composition of the materials was determined by chemical analysis according to the current standards of Ukraine.

Particle size of the fine-grained materials was determined under the MIN-8 microscope using an ocular micrometer. Petrographic study of samples microstructure was carried out under the microscope MIN-8 in immersion preparations in transmitted polarized light and on polished anshliffe in reflected light under the microscope Nu-2E. [1]

Open porosity and apparent density of fired samples were determined according to DSTU ISO 5017:2014, the cold crushing strength - according to DSTU ISO 10059-1:2018.

Linear dimensions change of samples during firing was determined as the ratio of linear dimensions difference before and after firing to their linear size before firing and expressed as a percentage.

To study the effect of the grain composition of coarse-grained component, four compositions were made (table 3).

Tab. 3. The composition of the studied vibrocasting MA samples, % wt.

| № of compo sition | Coarse fractions of fused alumina, mm | | | | Matrix: MA spinel, alumina, quartz |
|---|---|---|---|---|---|
| | 5-2 mm | 2-1 mm | 1-0,5 mm | < 0,5mm | |
| 1 | 30 | 10 | 10 | 15 | 35 |
| 2 | 25 | 10 | 10 | 20 | 35 |
| 3 | 20 | 10 | 10 | 25 | 35 |
| 4 | 15 | 10 | 10 | 30 | 35 |

**RESULTS AND DISCUSSION**
The properties of alumina-spinel masses and green vibrocast samples after drying at 110 °C are given in table 4.

Tab. 4. The properties of alumina-spinel masses and green vibrocast samples after drying at 110 °C

| Property name | № of composition | | | |
|---|---|---|---|---|
| | 1 | 2 | 3 | 4 |
| Moisture, % | 4.1 | 4.2 | 4.3 | 4.4 |
| Flowing, % | 85.0 | 90.0 | 100.0 | 100.0 |
| Properties of samples after drying at 110 °C: | | | | |
| - apparent density, g/cm$^3$ | 3.17 | 3.18 | 3.19 | 3.20 |
| - cold crushing strength, N/mm$^2$ | 6.8 | 7.0 | 7.8 | 8.6 |

The properties of vibrocast samples after firing at 1580 °C are shown in table 5.

Tab. 5. The properties of samples after firing at 1580 °C

| Property name | № of composition | | | |
|---|---|---|---|---|
| | 1 | 2 | 3 | 4 |
| Linear shrinkage, % | 0.9 | 0.8 | 0.9 | 0.9 |
| Open porosity, % | 15.0 | 14.7 | 14.5 | 14.3 |
| Apparent density, g/cm$^3$ | 3.28 | 3.30 | 3.31 | 3.33 |
| Cold crushing strength, N/mm$^2$ | 245 | 324 | 340 | 365 |

As is known [8], the porosity of refractory products resulting from various molding methods depends not only on the pressure and molding conditions, but is also determined by the ratio of grain sizes, i.e. the grain composition of batch. The data analysis shown in table 4 shows that changing the grain size distribution of fractions 5-2 mm and < 0.5 mm according to the row: 30 → 25 → 20 → 15 % and 15 → 20 → 25 → 30 %, while maintaining the constant grain size distribution of fractions 2-0.5 mm, leads to an increase in the mass flowing under vibration from 85 to 100 % with the moisture of these masses equal to 4.1-4.4 %. Thus the apparent density of unfired samples and cold crushing strength increase from 3.17 to 3.20 g/cm$^3$ and from 6.8 to 8.6 N/mm$^2$, respectively.

In the process of high-temperature firing at 1580 ºC all samples are sintered and their structure is compacted, this is evidenced by their property values; but the pattern of apparent density growth from 3.28 to 3.33 g/cm$^3$, as well as cold crushing strength from 245 to 365 N/mm$^2$, and open porosity reduction of vibrocast samples from 15.0 to 14.3 % remains the same, that is as decrease of grain fraction of 5-2 mm in the row: 30 → 25→20→15 % and increasing of the grains content of fraction < 0,5 mm in the row: 15 → 20 → 25 → 30 % at preservation of a constant content of grain fraction of 2-0,5 mm in the coarse-grained component of batch.

The samples made from the batch with coarse-grained component of the established optimum grain composition: 5-2 mm - 15 %, 2-0.5 mm - 20 %, < 0.5 mm - 30 % are characterized by the highest properties (open porosity 14.3 %, apparent density 3.33 g/cm$^3$, cold crushing strength 365 N/mm$^2$). This ratio of grains in the coarse-grained component of batch provides the most optimal packing in the vibrocasting process and contributes to the formation of a dense refractory structure.

Taking into account the obtained results of researches and with the purpose of industrial tests in the service in Institute a vibrocast alumina-spinel inner nozzles were produced, which are characterized by high property indicators: content, wt. %: Al$_2$O$_3$ - 96.0, MgO - 1.5, SiO$_2$ - 0.6; open porosity 14.0-14.5 %; apparent density 3.32-3.35 g/cm$^3$; cold crushing strength 320-360 N/mm$^2$.

The industrial tests in service at one of metallurgical enterprises of Ukraine these inner nozzles in vacuum casting of steel from tundishes established that they provide non-stop casting of steel from 240 to 450 MT at temperature 1580-1650 °C and have high corrosion resistance - the steel casting channel wear is insignificant (does not exceed ~ 3-5 mm).

Petrographic studies of the inner nozzle sample after service have established that under the influence of high temperature and molten steel in it formed three zones: the least changed, transitional and reactionary.

The least changed zone structure of the inner nozzle sample practically does not differ from its structure before the tests. It consists of angular-shaped grains of fused alumina filler and fine-dispersed binder, which is represented by crystals of magnesia-alumina spinel and sintered α-Al$_2$O$_3$.

The transitional zone with a width of ~ 0.6-1.0 mm tightly contacts the least changed one. This contact is clearly expressed and relatively even, differs from the least changed zone microstructure by a more compacted microstructure due to its sintering.

On the contact of the transitional zone with the reactionary zone under a microscope a band up to ~ 0.2 mm wide is observed, which mainly consists of a dense cluster of spinel crystals < 8 microns in size, close to isometric or elongated shape, and in a small amount

505

[1] Carried out by T. G. Tyshyna.

of sintered α-Al$_2$O$_3$, cemented by films and irregularly shaped glass-phase precipitates. This band has different widths and contains metallic inclusions.

The contact zone microstructure of the transitional and reactionary zones is shown in figure 2.
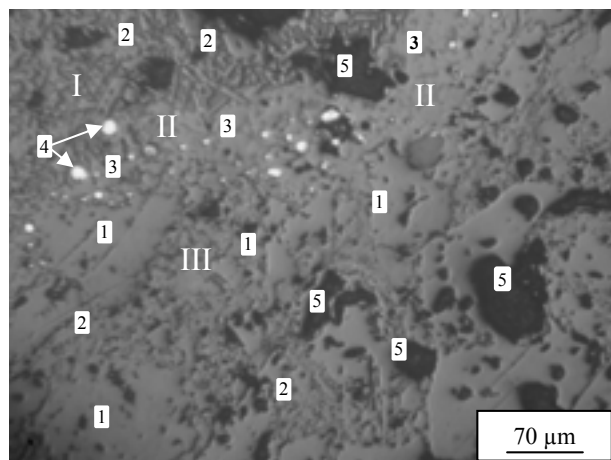


Fig. 2. The contact zone microstructure of the transitional and reactionary zones of the inner nozzle sample:
I – reactionary zones; II – spinel band; III - transitional zone;
1 – fused alumina; 2 - sintered α-Al$_2$O$_3$; 3 – MA spinel; 4 - metallic inclusions; 5 - pores.

The reactionary zone of the inner nozzle sample consists of single residual grains of fused alumina filler with traces of corrosion and a crystalline mass of idiomorphic elongated-prismatic crystals of sintered α-Al$_2$O$_3$ sized ~ 10-15 μm, cemented by a glass binder. In the reactionary zone, metallic inclusions up to ~ 0.5-0.6 mm in size are present, rounded and irregular in shape due to the filling of pores with molten metal.

Thus, the petrographic studies of the inner nozzle sample after service have established that due to the contact of molten steel with refractory, the spinel band up to ~ 0.2 mm wide is formed in it, which restrains the penetration of molten metal through pores and microcracks in the inner nozzle structure and prevents its wear, thereby increasing its corrosion resistance.

As a result of the research the technology of vibrocast alumina-spinel inner nozzles for vacuum casting steel from tundish ladles to ingot mould degassing was developed.

## CONCLUSIONS

The technology of inner nozzles for tundish ladles to ingot mould degassing has been developed. It is established that the highest property indicators (open porosity 14.3 %, apparent density 3.33 g/cm$^3$ and cold crushing strength 365 N/mm$^2$) are characterized by vibrocast samples made of batch with the coarse-grained component of established optimum grain composition.

For industrial tests a inner nozzles was made with the following properties: content, wt. %: SiO$_2$ - 0.6, Al$_2$O$_3$ - 96.2, MgO - 1.49, CaO - 0.19; open porosity - 15.2 %; apparent density - 3.30 g/cm$^3$; cold crushing strength - 174 N/mm$^2$.

Tests of the alumina-spinel inner nozzles during vacuum casting of steel showed that they provide non-stop casting of 240 to 450 MT of steel at a temperature of 1580-1650 °C in the tundish ladle. Wear of steel casting channel diameter did not exceed 3-5 mm.

Petrographic studies of the inner nozzles after service have established the formation of spinel "band" of up to 0.2 mm wide in the refractory at the contact with the molten steel, which restrains the melt penetration into the refractory and causes its insignificant wear.

## REFERENCES

[1] Ochagova I. Spinels as a refractory raw materials. New Refractories 2, 2002, p. 48-49

[2] Buchel, G, Girish, D, Buhr, A. Spinel aluminum-magnesium materials for resistant linings of steel-pouring ladles. New Refractories 4, 2009, p. 117-123

[3] Stinnensen, I, Buchel, G, Buhr, A. Magnesia-alumina spinel as a raw material for high-quality ladle refractories. Metallurgical and mining industry 4, 2004, p. 52-57

[4] Primachenko, VV, Martynenko, VV, Ustichenko, VA. Corundumspinel fired purging plugs of increased durability for the bottom blowing in steel ladles. Proceedings of Unified International Technical Conference on Refractories (UNITECR 05 Proceedings). 9th Biennial Worldwide Congress on Refractories (Orlando, Florida, 8-11 November). Orlando, USA, 2005, p.24-27

[5] Primachenko, VV, Martynenko, VV, Ustichenko, VA. Fired purging plugs for the bottom blowing of metal in steel ladles. 49th International Colloquium on Refractories. Refractories for Metallurgy (Aachen, 7-8 November). Aachen, Germany, 2006, p. 152-154

[6] Primachenko, VV, Martynenko, VV, Ustichenko, VA. Advanced Vibrocast Fired Corundumspinel Plugs for the Bottom of Metal in Steel Ladles. Berichte der Deutschen Keramischen Gesellschaft Ceramik forum international, 2008, p. 74-76

[7] Bottom metal blowing device. Patent 72322 (Ukraine), appl. 04.10.2002, publ. 15.02.2005.

[8] Strelov, KK. Theoretical foundations of refractory materials technology. Metallurgy, Moscow, 1985

# REFRACTORY HANDLING MANIPULATOR FOR SAFE & BETTER ERGONOMICS

Ujjwal Kumar, Gautam Kumar Choudhury, Deepak Kumar, Suchit Kumar Mahanta,
Kunal Kumar, Shubhashis Paul, Hiroshi Nagata, Sunanda Sengupta, P.B Panda.
TRL Krosaki Refractories Limited, Jamshedpur, India.

## ABSTRACT

In ladle preparation, Slide Gate refractory changing is a time taking & exhaustive process as it involves changing of refractories like Upper Nozzle, Slide Plate & Lower Nozzle. Changing of these refractories is human exhaustive process as these are heavy in weight and executed in heat & dusty environment and the entire process is done manually in every steel plant of India.

Refractory arrangement in slide gate system is in such a way that firstly upper nozzle is fixed in ladle well block (it is part of ladle lining) then slide plate and lower nozzle. One of the highly exhaustive processes is changing and fixing of upper nozzle, its weight is around 17 Kgs and after applying mortar its weight increases to 25-30 Kgs and operator has to lift and fix manually. The upper nozzle fixing process requires more time, human effort leading to fatigue to operators and sometimes delay in preparation of ladle. This is a controlled and precise operation; deviations can lead to failure. To eliminate these problems a mechanized manipulator was designed to reduce human effort, better ergonomics and to make the process easier and operator friendly. This mechanized manipulator consists of some mechanical & pneumatic components which allows operator to lift and handle such heavy load without any effort. The manipulator is provided with a pneumatic suspension system which carries the load of refractory which helps in lifting and fixing of nozzle with all degree of freedom. This system works completely with pneumatic, with this system operator has to give only 1-2 kgs of force for lifting 25-30 kgs of load as complete load is being nullified by the pneumatic suspension system. A special type of gripper was also provided to grip the refractory components without damaging it. This type of solution can serve to solve various weight handling issues in heat & dusty environment across steel industry.

## INTRODUCTION

In steel making, various process are being carried out from primary steelmaking to final casting shown in fig.1 and in this process liquid steel is transferred by steel ladle. First ladle is sent for to BOF (Basic oxygen furnace) for tapping, then the processed liquid steel is poured into the ladle and then ladle is sent for secondary refining station and then casting shown in fig.2


Fig. 1 Steel making process.
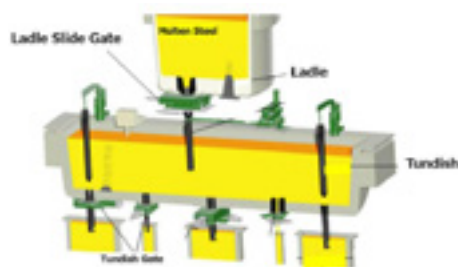

Fig. 2 Steel casting process.

where the casting is done by opening of ladle slide gate machine which is mounted underneath of steel ladle and actuated with the help of hydraulic cylinder. After operating of slide gate machine, the bore of slide plate inside the machine gets matched and casting starts. In the whole process of steelmaking ladle slide gate plays a very crucial role for casting of steel smoothly.

Ladle slide gate machine shown in fig.3 consist of various consumable refractories like slide plate, upper nozzle, lower nozzle. After casting is completed, ladle is sent to preparation area also known as ladle tilters to make the slide gate ready by cleaning the hole and changing the slide gate refractories based on operational requirements. The entire process of slide gate preparation and refractory changing is done manually almost in every steel plant in India and across the world.
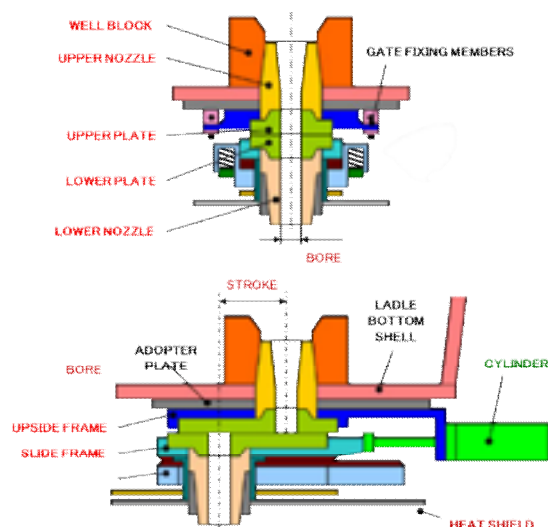

Fig. 3 Slide gate machine assembly.

## EXISTING CHALLENGES IN FIXING UPPER NOZZLE

During preparation of slide gate, its refractories upper nozzle, slide plates & lower nozzle is changed depending upon its life. These refractories are heavy in weight, specially upper nozzle. It weighs around 17 kgs and refractory arrangement in slide gate system is in such a way that first upper nozzle is fixed into well block (it's a part of ladle lining) and before fixing upper nozzle into well block, a thick mortar coating is applied to the outer surface of upper nozzle as a joint material between upper nozzle and well block and it is lifted by the help of jig for fixing into well block shown in fig.4.


Fig. 4 Manual Upper nozzle fixing process.

507

In total its weight reachs upto 30 kgs approx. then slide plates and lower nozzle is fixed which is later tightened by mechanical force.

## ASSOCIATED PROBLEMS

*Fatigue to Operators* - The entire process is done manually like lifting & fixing heavy weight and done in heat & dusty environent which makes the process more human exhaustive as its done multiple times (normally 10-12 in a day).

*Chances of Error* – As its done manually and the process requires precision in upper nozzle fixing, any deviation could lead to leakage of liquid steel.

*Delay in preparation*- Due to manual preparation and sometimes human error, preparation gets delayed and delay in slide gate prepration directly effects the shop production as delay in ladle supply causes productivity loss.

Challenge was taken to develop a mechanized system to solve the problem with manual process and to make the operator work easier.

## AVAILABLE OPTIONS

*Robotic System*- This system includes advanced robots and the entire process is done fully automatically with robots as shown in fig.5.
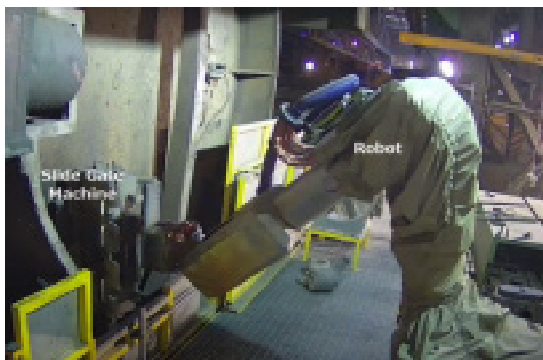


Fig. 5 Robot for slide gate preparation.

Only few steelmakers outside India has installed the system which is still under development stage. As this include advanced systems, requires high maintenance & more space for installation.

## SEMI-MECHANIZED MANIPULATOR

The objective of this design was to make a manipulator which will easily lift the heavy weight of refractories and will work in a challenging environment, i.e. heat & dusty area.

Manipulators weight lifting concept is based on pneumatic suspension system, this type of lifting devices are normally used in automotive industries but using same in steel industry was a bit challenging due to its working environment (Hot & dusty). Using pneumatic suspension concept, a semi-mechanized manipulator fully pneumatic based system was designed as shown in fig.6.

This Manipulator mainly consist of vertical pillar, primary arm, secondary arm, pneumatic suspension, clutch, gripper and other parts.

*Vertical Pillar*- Provide strength and holds the load of system it is mounted in the tilter platform.

*Arms*- Provide degree of freedom and movement to system so that upper nozzle can be moved within the range.

*Pneumatic suspension* - Lifts and balance the load with pneumatic cylinder operator only need to give 1-2 Kgs of force to lift 25-30 Kgs of load. This pneumatic suspension can lift upto 100 Kgs of load.

*Clutch*- Provides rotary provision for upper nozzle with the help of incorporated jig with very simple clutch mechanism.

*Gripper*- Grips the upper nozzle from inside by pneumatic force without damaging and works in High temperature.

The whole system (Pneumatic suspension & gripper) works with pneumatic line with minimum required pressure of 5 bars. Operator only needs to guide the upper nozzle for fixing & applying Mortar as load of upper nozzle is being nullified by the pneumatic suspension. For applying mortar rotary provision is also provided in the jig.
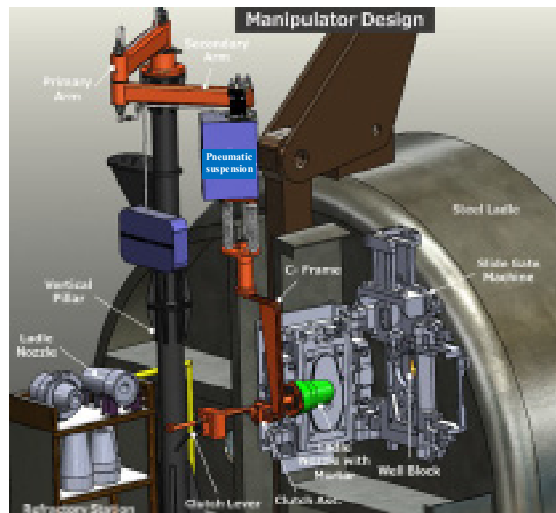


Fig. 6 TRLK Semi-mechanized manipulator.

## CONCLUSION

Effort required is now reduced by 96% with precise control. Process has become more standard now as load is lifted by the system, operator just needs to guide and push the jig into well block in order to fix upper nozzle which also take less time. With this semi-mechanized system process has became smoother & safer. It can be customized easliy and can be used as lifting & handling applications (upto 100 Kgs of load) across steel plant and other industries.

## REFERENCES

[1] The Making of Iron & Steel – SEAISI (Pg. 32 – 35)
[2] Making, Shaping & Treating of Steel, 11th Ed., A Cramb, ed., AISE Found., 2000, Chapter 4.3
[3] Human-Centered Robotic Development in the Steel Shop: Improving Health, Safety and Digital Skills at the Workplace STEEL 2021 Page- 9

# MODIFICATIONS IN LADLE SLIDE GATE SYSTEM FOR IMPROVING SAFETY & PRODUCTIVITY

Gaurav Pandey, Gautam Choudhury, Ujjwal Kumar, Deepak Kumar, Manishankar Mukherjee,
Shubhashish Paul, Sunanda Sengupta, Hiroshi Nagata, P.B. Panda
TRL Krosaki Refractories Ltd. Jharsuguda (Odisha), India

## ABSTRACT

In steel melting shop, teeming ladle is used for treatment & transfer of liquid steel for various operations. Finally at caster, liquid steel is shaped into semi-finished product through continuous casting process. Ladle slide gate (LSG) is fixed underneath the teeming ladle, it is a mechanical assembly having some refractory components. Function of LSG is to control the discharge of liquid steel from ladle to tundish.

Post casting at Caster machine, teeming ladle is transported to Ladle preparation area where various operations such as consumable refractory replacement is performed, this is a time intensive process. Any delay in ladle preparation, leads to direct productivity loss. This operation is performed in ladle running condition so safe operation is a concern.

This paper covers modifications in LSG & introduction of products used in LSG for safety & productive benefits.

A Backsplash cover was developed, it's a sacrificial component which saves LSG machine from damage & eliminates long ladle preparation time.

Modification in cylinder fixing area to ensure LSG cylinder removal in close condition only. With this there is no chance of LSG open position during tapping operation.

A mortar collecting tool was developed for use during ladle nozzle (LN) changing operation, this is installed in advance to ensure easy cleaning of excess mortar. This reduces ladle preparation time & effort.

A LN GO - NO GO gauge is developed as LN checking is crucial job as it indicates suitability to usage for further heats. With simple GO – NO GO gauge, it easy & quick checking.

## INTRODUCTION

Ladle slide gate machine which is mounted underneath of teeming ladle with the help of hydraulic cylinder. After operating of slide gate machine, the bore of the slide plates inside the machine gets matched and casting starts. In the whole process of steelmaking ladle slide gate plays a very crucial role for casting of steel smoothly. Ladle slide gate machine shown in (figure1) consist of various consumable refractories like Slide Plate, Ladle nozzle, Collector Nozzle and Mortar which is changed after certain life.
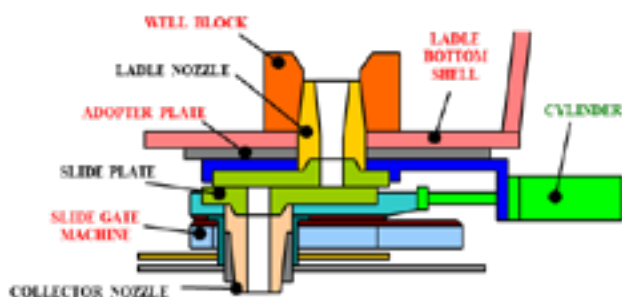


*Fig. 1: Slide gate refractory arrangement.*

After casting is completed then ladle is sent to preparation area to make the slide gate ready by cleaning the hole and changing the slide gate refractories if required. For this hydraulic cylinder is required to operate the slide gate which is fixed in preparation stand. It is attached in machine and after preparation it is detached. Some modifications and various tools were developed for easy and safe operation of slide gate.

## BACKSPLASH PROTECTION COVER

At caster ladle shroud is fixed in collector nozzle of slide gate to guide the flow of liquid steel from ladle to tundish and prevent steel from reoxidation. But due to improper fixing of ladle shroud or some other operational reasons backsplash occurs at caster.

During backsplash liquid steel penetrates in the slide gate machine causing damage to machine parts which leads to various problems.

1. Damage of machine parts increase of spare cost.
2. Increase in maintenance time at preparation area causing delay in supply of ladle and loss of production.
3. Unplanned ladle outage for changing slide gate causes shortage of ladle and loss of production.
4. Sometimes due to severe backsplashes machine sliding stuck at caster which causes uncontrolled discharge of liquid steel and it's a process safety hazard.

To prevent these issues and metal penetration in machine due to backsplash a backsplash protection cover was designed using some mechanical parts. This backsplash protection cover is fixed in the machine around collector nozzle using some screws. This cover itself gets damaged in case of backsplash and won't allow metal to penetrate into the machine as shown in (figure. 2).
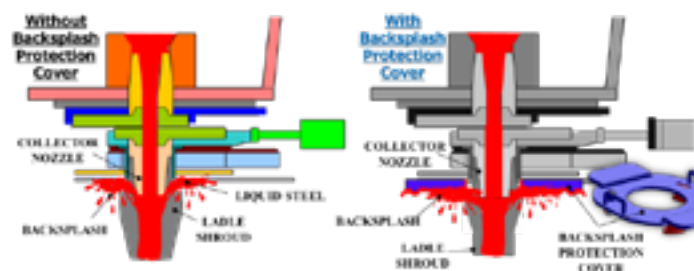


*Fig. 2: Backsplash at Caster with & without backsplash protection cover.*

Post implementation of Backsplash protection cover damage of machine parts were reduced and unplanned ladle outage cases were reduced by 40%.

## ENSURING EJECTION OF HYDRAULIC CYLINDER IN CLOSE POSITION OF SLIDE GATE

Slide gate after casting comes to preparation area for refractory change/bore cleaning etc. jobs. During preparation hydraulic cylinder is used to operate and sliding of machine which is disengaged from machine after the job is completed.
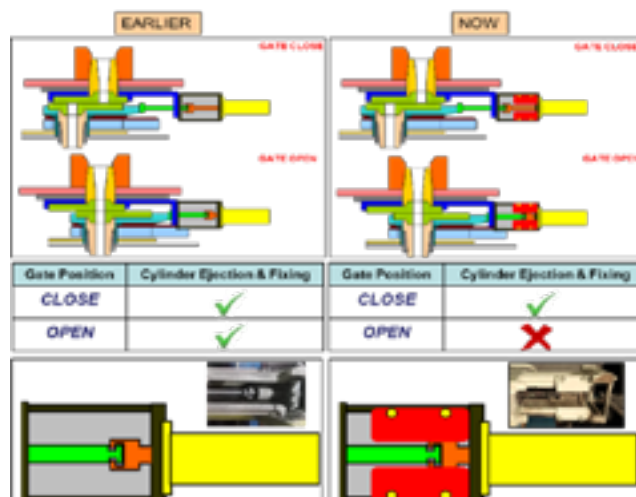


*Fig. 3: Fixing of stopper plate in LSG machine to ensure ejection of hydraulic cylinder in close position.*

If hydraulic cylinder is ejected in open position of slide gate than there are chances of drainage from slide gate during tapping from BOF, at one of the customer site this incident happened.

To prevent this mishappening, modification in slide gate machine was done, a stopper plate was fixed in the cylinder bracket of machine to ensure ejection of hydraulic cylinder in close position of slide gate as shown in (figure 3).

## MORTAR COLLECTING TOOL

Slide gate system has Ladle Nozzle which is fixed in the well block of ladle and mortar is used as a joint material. To ensure proper mortar in the joint excess mortar is applied intentionally over the ladle nozzle and fixing some excess mortar comes back and gets spread over the slide plate setting area as shown in (figure 4).
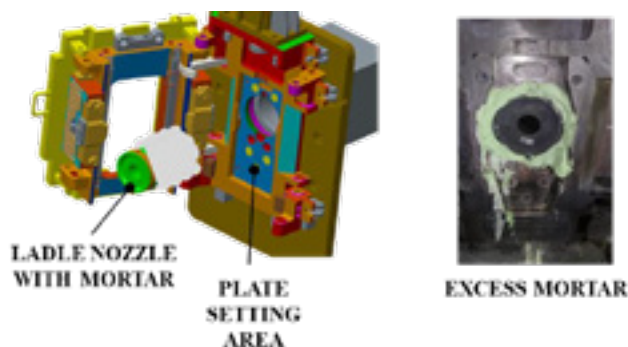


Fig. 4: Excess mortar after nozzle fixing.

If this spread mortar is not cleaned properly than it could lead to improper setting of slide plate resulting cracking ad failure between slide plate as shown in (figure 5). Also, this increases preparation time as cleaning mortar takes 2-3 mins of time.
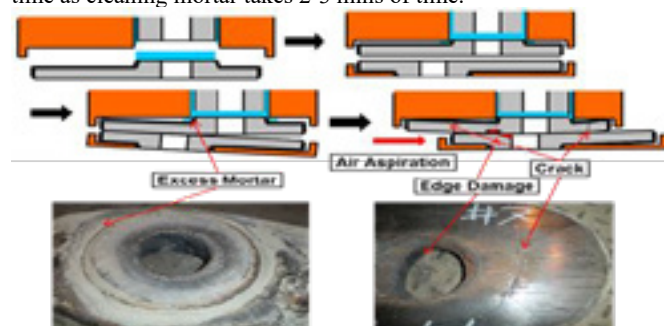


Fig. 5: Effect of excess mortar on slide plate.

To encounter these issues a mechanical template was designed which is fixed in the plate setting area before fixing of ladle into well block so that the excess mortar coming out of well block instead of getting spread over the plate setting area gets collecting in this template as shown in (figure 6).
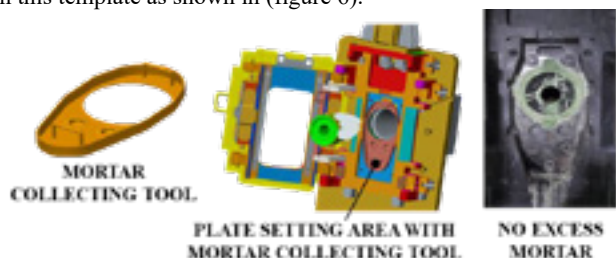


Fig. 6: Excess mortar condition with mortar collecting tool.

With implementation of this mortar collecting tool cleaning of excess mortar became easy and helped in reducing the preparation time.

## LADLE NOZZLE CONDITION CHECKING

Damage/erosion happens during the usage of side gate refractories, and it is important to keep checking the condition of refractory to prevent from failure or abnormality. One of the key checking is done at running condition of refractory is bore erosion of ladle nozzle as it goes for multiple heats. Earlier checking of ladle nozzle bore erosion was done with calliper & measuring tape. but it has some negative branches like.

1. Longer exposer to heat as it is performed multiple times
2. Chances of error in measurement

To overcome these challenges a GO NOGO gauge was designed considering erosion pattern and potential of ladle nozzle for further heats. With the help of gauge checking process and judgement became easy, operator only needs to insert the gauge in the bore of ladle nozzle and can make judgement as shown in (figure 7).



Fig. 7: Checking of Ladle Nozzle bore previous (with caliper and tape) VS now (with GO NOGO Gauge).

## CONCLUSION

Even a small change can make a big impact. Slide gate preparation is very crucial job a little deviation can lead to a big failure as it plays with $1600^0C$ liquid steel. Slide gate preparation still in India and many parts of the world is done manually due to its criticality and various checkpoints. It is important to make and design the process more user-friendly for better safety and safe operation.

With backsplash protection cover safety at caster was improved and helped in reducing preparation time and unplanned ladle outage.

With modification in slide gate to ensure ejection of hydraulic cylinder in close position the process was fool proofed, operator can't send ladle for tapping in open position of slide gate by mistake also.

With mortar collecting tool excess mortar cleaning became easy as excess mortar is now being collected in mortar collecting tool instead of spreading over plate setting area.

With ladle nozzle GO NOGO gauge checking of bore erosion very easy and safe also exposer to heat was reduced.

With all these ideas, process safety of slide gate was improved and improved productivity by reducing preparation time. This also helped in standardizing of checking and inspection process at slide gate preparation area by development of tools and gauges.

With slight modification in design applicability of these ideas are possible for different shops.

## REFERENCES

[1] The Making of Iron & Steel – SEAISI (Pg. 32 – 35)
[2] Making, Shaping & Treating of Steel, 11th Ed., A Cramb, ed., AISE Found., 2000, Chapter 4.3
[3] Human-Centered Robotic Development in the Steel Shop: Improving Health, Safety and Digital Skills at the Workplace-STEEL 2021, Page-9

# SHORT COMMUNICATIONS

# DEVELOPMENT OF OLIVINE BASED PRECAST CASTABLE FOR TUNDISH WEIR AND DAM

Shang-ru, Yeh, Ping-chum, Liu, Henry, Chen.
Good Furnace Refractory Industrial Co., Ltd, New Taipei City, Taiwan, R.O.C

## ABSTRACT

Forsterite, also known as olivine, is a natural wide ore and can be used as material directly for refractory. Its potential to produce refractory castable is possible. For the environment friendly and operation requirement of China Steel Corp., Kaohsiung, Forsterite based precast castable for tundish weir and dam must be developed and studied. Experiment results show that introducing alumina cement as a hardening accelerator or alumina lactate as an anti-hydration additive or both of them can reduce the HMOR of olivine based precast castable for tundish weir and dam. Slag erosion test indicates that the slag resistance of olivine based precast castable is better then that of high alumina low cement precast castable. Moreover, the slag resistance of olivine based precast castable containing olivine powder in matrix is worse than that of olivine based precast castable without olivine powder. Field test results demonstrate that less olivine aggregates content in Tundish weir and dam fulfills the continuous steel operation at the customer site in Kaohsiung.

## INTRODUCUION

Forsterite, also known as olivine, is a natural wide ore and can be used as material directly for refractory [1]. By the limited literature review, its potential to produce refractory castable is possible [2]. Moreover, for the environment friendly and operation requirement of China Steel Corp., Kaohsiung, Forsterite based precast castable for tundish weir and dam must be developed and studied. Otherwise, Forsterite is also a kind of basic refractory raw material. Refractory made by forsterite may help to produce clean steel while continuing operation [3]. Furthermore, refractory made by forsterite may reduce the risk of hydration damage of basic refractory. According to the requirement from R & D of China Steel Corp. in 2019, Good Furnace Refractory Industrial Co., Ltd. had an opportunity to develop olivine based monolithic refractory for tundish. The following is a simplified presentation of the whole development from the laboratory to the application at custom site.

## Materials and Experiments

■Materials

There are four testing recipes compositing by olivine aggregates and fines, dead burn magnesia (DBM), sea water magnesia, microsilica fume, specialty Mag, and silicon carbide powder. And silicon carbide powder, olivine and dead burn magnesia are from mainland China. Sea water magnesia is from Japan. Microsilica fume, specialty M are sold by Elkem and alumina cement is provided by Almatis. These four testing recipes are shown as follow in Table 1.

Table 1 Formula developed for tundish weir and dam precast

|  | A | B | C | D |
|---|---|---|---|---|
| Olivine aggregates | O | O | O | O |
| DBM 1-0 mm | × | × | O | O |
| DBM 100F |  | × | × | O |
| DBM powder |  | O | × | O |
| Sea water MgO flour |  | O | O | × |
| Microsilica fume | 8% | 5.5% | 8% | 6% |
| Olivine 200F | O |  | × | × |
| Specialty M | O | O | O | O |
| Alumina cement | O | × | × | × |

× means no using in formula.

■Sample preparation and Testing methods

Testing samples composited in Table 1 are adding and mixing appropriate amount of water, casting in a $40 \times 40 \times 160$ mm mould. Samples are removed from the mould, dried in 110°C for 24 hours and then detected their properties shown in Table 2.

Table 2 Testing mothed in this work

| Property | Standard |
|---|---|
| Bulk density (BD) | JIR R 2205 |
| Apparent porosity (AP) | JIS R 2205 |
| Modulus of rapture (MOR) | JIS R 2553 |
| Cold crush strength (CCS) | JIS R 2553 |
| Permanent liner change (PLC) | JIS R 2554 |
| Hot modulus of rapture (HMOR) | GB/T 3002 |
| Slag erosion | Crucible |

## RESULTS AND DISCUSSION

■Evaluation in laboratory

Table 3 presents the physical properties of every formula shown in Table 1 after 1500°C × 3 hrs firing and their HMOR results under 1500°C is also shown in the same table. According to Table 3, only BD and AP of recipe D are better than Currently but the mechanical properties of all olivine based formula, including A, B, C, and D, is worse than Currently due to the difference between the sintering property of olivine with dead burnt magnesia (no cement bonding) and high alumina material with high alumina cement.

Table 3 Physical properties after 1500°C firing and HMOR at 1500°C

|  | A | B | C | D | Currently* |
|---|---|---|---|---|---|
| BD, g/cm³ | 2.34 | 2.46 | 2.49 | 2.71 | 2.55 |
| AP, % | 28.5 | 24.6 | 24.5 | 17.1 | 18 |
| PLC, % | +0.41 | -0.47 | -0.25 | +0.06 | +0.5 |
| MOR, MPa | 9.0 | 6.5 | 8.0 | 4.9 | 15 |
| CCS, MPa | 46 | 32 | 43 | 38 | 85 |
| HMOR, MPa | 1.3 | 3.3 | 3.6 | 1.9 | 1.8 |

*Currently means the original alumina weir and dam recipe using at custom site currently

Figure 1 is the slag erosion test results of original high alumina weir and dam recipe using at custom site currently and developed recipe A. Apparently, figure 1 indicates that recipe B is much better than original high alumina recipe. Therefore, recipe B was decided to carry out the field test at custom site.



(A)       (B)
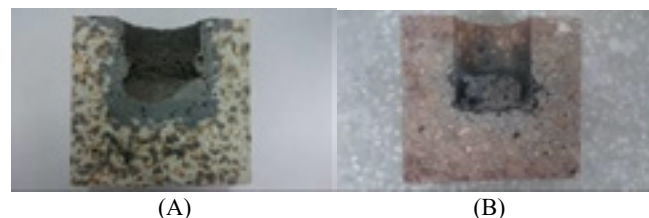
*Fig. 1: Comparison of slag erosion by crucible method (A) original high alumina recipe and (B) olivine based recipe B.*

Figure 2 is the slag erosion test results of Recipe B, C, D but A not including because HMOR of Recipe A is lower than the original high alumina weir and dam recipe. By the experience, HMOR of tundish weir and dam lower than 1.4 MPa means the risk of fracture by molten steel or slag during the continuous casting

511

operation, so we decide not to carry out the slag erosion test of Recipe A. From figure 2, small area of slag erosion can be observed both in the crucible cross section of recipe B and C but only slightly slag penetration exists in the crucible cross section of recipe D.



(A)                                  (B)

(C)
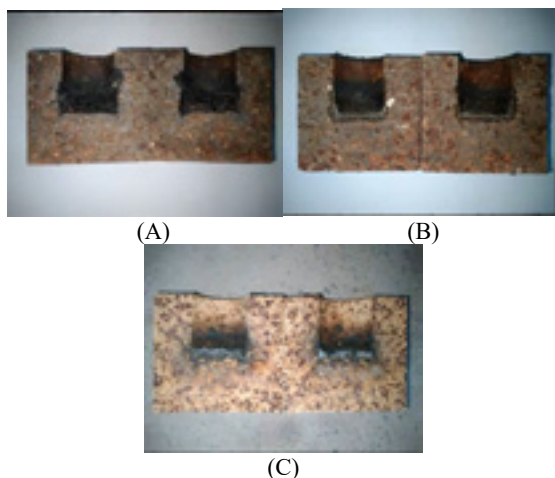
*Fig. 2: Comparison of slag erosion by crucible method (A) olivine based recipe B, (B) olivine based recipe C, and (C) olivine based recipe D.*

■Field test at custom site

Before the field test at custom site, all recipes pass the quality examination executed by China Steel Corp. Figure 3 shows the field test result of recipe B.

*Fig.  3: Field test at custom site of Recipe B*

From figure 3, it's clear that weir and dam made by recipe B was eroded by slag and nothing remained after continuous operation.

By discussion after knowing the trail result, recipe C was introduced to try. Comparing with recipe B, there is no DBM powder content but sea water magnesia flour replaced in recipe C. Figure 4 indicates that weir and dam made by recipe C is better than those made by recipe B after continuous operation. Unfortunately, from figure 4, there was one weir fabricated by recipe C eroded through by tundish slag.



*Fig. 4 Field test result of Recipe C*

Learning the result and experience from recipe B and C, to use higher quality of magnesia powder, avoid olivine 1 mm, and less microsilica fume are the keys to develop olivine based weir and dam precast well. Therefore, recipe D, containing DBM97 1-0 mm and powder, was the last chance for the field test at China Steel Corp. Figure 5 presents that weir and dam fabricated by recipe D are fulfill with the operation condition at custom site and remain whole block after 5 cycles of continuous casting of steel.
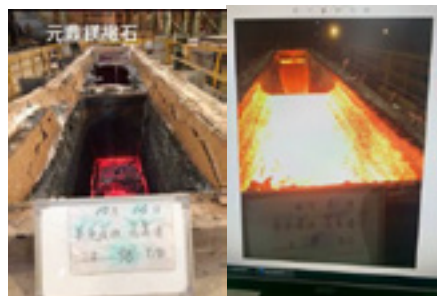


*Fig 5: Field test result of recipe D at custom site*

## CONCLUSIONS

Tundish weir and dam precast castable using olivine was developed and field test investigated at custom site. Results show as follows.

1. By using olivine coarse aggregates, 1-0 mm dead burn magnesia 97, dead burn magnesia 97 fines, and less microsilica fume, it is the better way to make the performance of olivine based tundish weir and dam suitable adapted well for the continuous casting operation at custom site.
2. Using some olivine fine aggregate and 200F in olivine based weir and dam pre cast give higher HMOR. But higher HMOR for olivine based does not give good slag or molten steel resistance for that at field test.
3. To achieve good tundish slag erosion resistance for olivine based tundish weir and dam precast during the continuous casting operation, it is important to not only choose good quality of dead burn magnesia fines in the matrix part of olivine based precast but also avoid to use olivine fine aggregate in coarse part.

## ACKNOWLEDGEMENT

## REFERENCES

[1] Ritwik Sarker, "Olivine - The potential industrial material: An overview." Transactions of the Indian ceramic society, volume62, 2002, Issue2, pp.80 – 82.
[2] Hong Peng, Bjorn Myhre, "New Insight on Developing MgO-SiO$_2$-H$_2$O Gel Bonded MgO Castables." REFRACTORIES WORLDFORUM 6 (2014) [3], pp.83 – 87.
[3] YU Shuzhong, WANG Dejun, LIU Zhenglong, DENG Chengji, "Effects of containing calcined forsterite tundish materials on steel cleanliness." Steel Making, v.35, No.197, 2019.

# CARBON BONDED RODS FOR MEASUREMENT OF MOLTEN STEEL VELOCITY AT THE MENISCUS LEVEL IN THE CONTINUOUS CASTER MOULD: FROM THE LAB TO THE PLANT TRIALS

Bruno Luchini[1]; Tony Wetzig[2]; Vasileious Roungos[2]; Marc Neumann[2]; Steve Verdier[1]; Pieter Put[1]; Laurens Jan Pille[1]; Christos G. Aneziris[2]; Sido Sinnema[1]

[1]Tata Steel Nederland, R&D, IJmuiden, Netherlands; [2]IKFVW/TU Bergakademie Freiberg, Freiberg, Germany

During continuous casting of steel, monitoring the velocity and direction of the melt flow is a crucial step for the process control. One of the methods used to perform such measurement is the so-called "rod deflection method". Refractory rods are mounted in a rotational pivot equipped with a potentiometer. The rods are then inserted into the copper mould and deflected in response to the molten steel flow. By monitoring their deflection, the flow pattern and velocity can be obtained in the region close to the meniscus. Due to the very harsh conditions such as high temperature, extremely reactive mould powder material and high melt velocity, selecting refractory materials able survive this scenario is a challenging task. In this study, TSN and IKFVW discuss the conceptual process and the testing procedures used to select and produce the carbon-bonded refractory rods used in the rod deflection device.

513

SHORT COMMUNICATIONS

# PUREBLOX 1400, HOW TRB TAKE UP THE ENERGY SAVING CHALLENGE WHILE USING SAFER PRODUCTS

Simon CHIARTANO*, Martial BARRET, Stéphane DUHAMEL, Benoît VANDENBON
TRB, Nesles, France.

## ABSTRACT

Currently, many heat treatment furnaces are made up of insulating linings composed of refractory ceramic fibers (RCF). This technology withstands temperatures theoretically up to 1400°C. However, the fibers that constitute this product are classified Carcinogenic, Mutagenic, or toxic to Reproduction (CMR) [1]. Two alternative technologies can be used today: polycrystalline fiber and high temperature bio fiber. The first one has a very high cost, the second does not withstand temperatures exceeding 1150°C, under certain favorable conditions.

Our approach was global to find a new solution with the same specifications in term of resistance and thermal performance but with a non-classified safer product: the Pureblox 1400.

## MATERIAL & METHODS

Context was the replacement of RCF which are often used in heat treatment furnace and unfortunately harmful for lungs because CMR classified. This study explores every step of a new product development, from design to manufacturing including mechanical and thermal behaviour calculated by simulation and checked by measurement, laboratory test and final installation at our customers.

## SIMULATION

Simulation was used to evaluate the energy balance and optimize insulation and material choice.
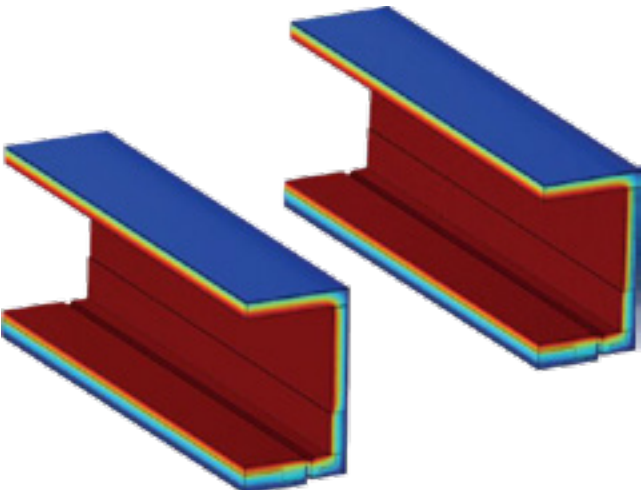


Figure 1: Temperature comparison in a reheating furnace – RCF design (l) Pureblox new design (r)

Figure 1 shows thermal profile on both RCF and Pureblox design. Results are very similar which validate the new design. Same conclusion can be made on energy balance with the heat flux magnitude comparison on Figure 2.
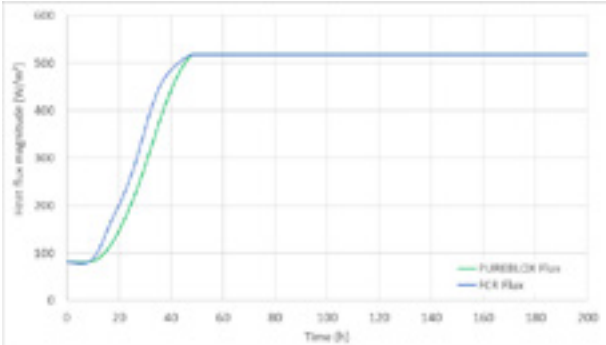


Figure 2: Heat flux magnitude comparison on both RCF and Pureblox design in a reheating furnace

## PRODUCT DEVELOPMENT

Specific laboratory tests including thermal conductivity and specific heat were also made to find the best formulation for this new material. See Table 1.

| Pureblox 1400 property | Value | Unity |
|---|---|---|
| Density | 830 | kg/m³ |
| Thermal conductivity[1] | 0.38 | W/m.K |
| Specific heat[2] | 1060 | J/kg.K |
| CCS[3] | 2 | MPa |

Table 1 : Pureblox 1400 material properties

## MEASUREMENT

On site measurement was implemented. First, IR Camera was used to measure temperature of external walls. Full mapping of the shell temperature is a powerful tool to estimate the global exchange of the furnace as shown on Figure 3. It also allows to compare one solution to another.
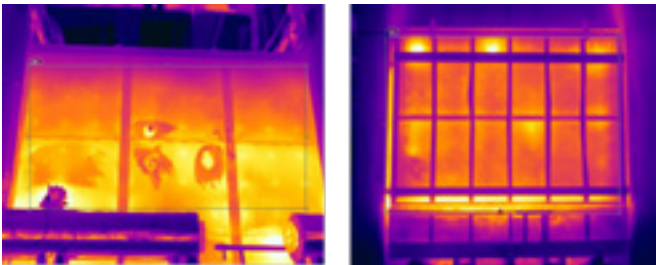


Figure 3: Thermographic view of a reheating forge furnace made of Pureblox 1400

A specific and tailor-made instrumentation was carried out with thermocouples located at different depth and position of a furnace made of Pureblox 1400, see Figure 4. Temperatures were recorded at every material interface, during several months of utilization, results are given on Figure 5.

---

[1] At 800°C
[2] At 1000°C
[3] After firing at 1200°C

Figure 4: Instrumentation system of a reheating forge furnace made of Pureblox 1400
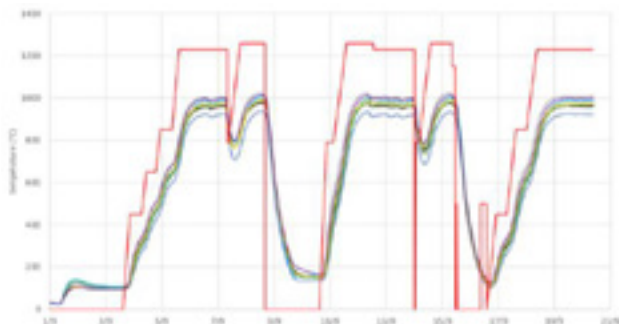


Figure 5: Temperature measurement inside the refractory lining of a reheating forge furnace made of Pureblox 1400

All these measurements are useful to evaluate accurately the true performance of our solution on site and check both simulation and laboratory results.

**DESIGN**

After few years of development and tests, our new Pueblox 1400 solution is ready to be installed at our customers: it is made of an advanced low-density material in precast shape (see Figure 6) and insulating back layers.
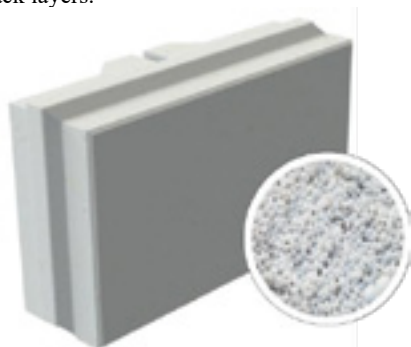


Figure 6: Pureblox 1400 precast shape

Precast shape is a huge advantage in term of assembly time: installation become faster and easier rather than other products (bricks, modules, …). The solution can be installed on both walls (Figure 7) and roof (Figure 8).



Figure 7: Pureblox 1400 precast shapes wall installation



Figure 8: Pureblox 1400 precast shapes roof installation

**CONCLUSIONS**

With a thickness equivalent to current installation, the solution developed by TRB with the PUREBLOX 1400 product offers a cumulative thermal insulation equivalent to CMR classified ceramic fibers using a safer product for the health of operators and withstands temperatures up to 1400°C.

This new solution is already implemented in 3 different customer furnaces and give excellent results as shown on Figure 9.
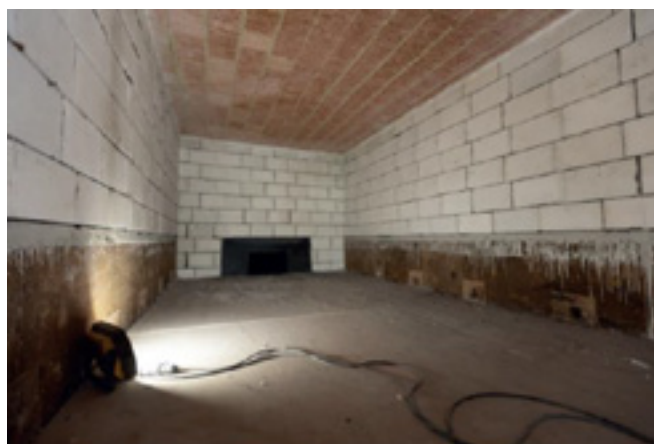


Figure 9: Reheating forge furnace made of Pureblox 1400

**REFERENCES**

[1] List of substances banned for use in cosmetic products - CMR substances of category 1A, 1B or 2, European commission, July 2015
https://ec.europa.eu/docsroom/documents/11382/attachments/1/translations/en/renditions/native

515

# THE INFLUENCE OF ALUMINA TYPE ON CORROSION RESISTANCE OF SMART AL$_2$O$_3$–MGO MONOLITHIC REFRACTORIES USED IN CRUCIBLE INDUCTION FURNACES

M. Bavand Vandchali[1], S. M. M. Tabatabaie Hedashi[1,2],
1. Almas Alborz Refractories Co., Tehran, Iran.
2. Material Science and Engineering Department, Faculty of Engineering, IKIU, Iran.

**ABSTRACT**

In the present paper, the influence of alumina type (white fused (WFA) and tabular (TA)) on corrosion behavior of two commercial DVM linings has been investigated based on the post-mortem analysis. The microstructural analysis results show that the nature, amount and rate of in-situ spinel formation is different according to the alumina type. Higher expansion amount in TA-based DVM is accompanied to higher crack formation in the hot face of refractory lining and extensive molten metal penetration and microstructural spalling, although corrosion is low. Al$_2$O$_3$-rich spinel structure has been detected in the matrix of both refractory that mainly enhance corrosion resistance in due to formation of complex spinel structure via accommodation of corrosive ions from slag in steelmaking process. As well as, according to microstructural evolution of grains corrosion, a continuous layer from CA$_6$ and CA$_2$ crystals forms around the alumina grains, WFA and TA, that decrease its corrosion rate due to indirect corrosion behavior.

## 1. INTRODUCTION

During the steelmaking process in crucible induction furnace (CIF), refractory lining is exposed to different aggressive condition and corroded by corrosive liquid molten steel and slag at high temperatures (1620-1700°C). Also, the further metallurgical demand due to above wear mechanism has resulted in the development of high-quality refractory lining to withstand the hard conditions of the furnace and create very safe environment for steelmakers. Due to steelmakers requirements choosing the right refractories for a given malting or holding application is very important and depends on many parameters such as melting temperature, holding time, volume, inductive stirring, additive & alloying agents, etc. As smart refractories, the Al$_2$O$_3$-MgO dry vibrating mixes (DVM) development has brought a significant evolution in the history of refractories as lining of modern CIF. The techno-commercial benefits of spinel bonded DVM refractories compare to traditional silica based ramming mixes showed significant service life and despite the high price, it is very economical due to its patching capability. DVM refractories mainly composed of Al$_2$O$_3$ and MgO addition in special grain sizes in the matrix, which results in-situ spinel formation at steel melting temperature. Also, the major advantage of these DVM is that they are installed in the dry form by compaction via vibration/ramming without any binders that need water for the formation of a green strength. A sufficient green strength is realized by an optimized particle size distribution and high strength in the front layer developed by an initial sintering step due to formation of in-situ spinel (MgAl$_2$O$_4$) phase via reaction of Al$_2$O$_3$ and MgO in the matrix. It has been well clarified that the basic challenge in the designing of DVM refractories is the kinetic and amount of in-situ spinel phase formation in the front layer (hot face) to resist against early corrosion, but also to remain unchanged layer at the back of the furnace refractory lining (cold face) for safety purposes. Ideally, a trisection of the lining develops with a contact zone between lining and coil of furnace that keeps its safety function during the whole furnace lifetime (Fig. 1).

-Very strong sintered layer with spinel bonded matrix should be formed on the hot face of refractory lining to resist against corrosive slag and molten metal.

-The succeeding semi-sintered layer with little in-situ spinel formation and higher porosity is a low sintered part of the furnace refractory lining and the unchanged layer of the DVM is a mechanically compacted mass without any ceramic bond.

-The existence of unchanged layer is important at the end of the furnace campaign as this is required in order to press the furnace out.
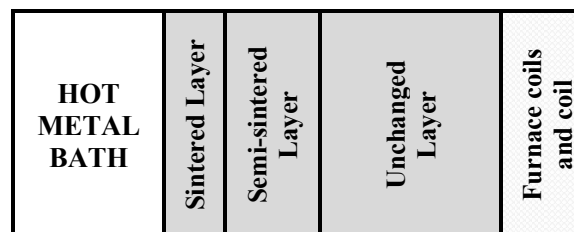


*Fig. 1: schematic of multi-layer concept of DVM lining in CIF.*

According to alumina based monolithic refractories designing, the different types of alumina such as tabular alumina (TA), fused alumina (WFA, GFA, BFA) and bauxite can be used. The difference in the structure, properties and reactivity of different types of alumina will change the final properties of the refractory and as a result its performance. The purpose of this paper is to outline the differences between TA based (TA sample) and WFA based (WF sample) DVM refractories as working lining of CIF and show their influence on the performance and corrosion behavior.

## 2. EXPERIMENTA PROCEDURE

In evolution of alumina type influence on the performance of the CIF refractory lining, the appearance of the furnace after a specified numbers of heat in similar metallurgical condition and also *post-mortem* scanning electron microscope (by FESEM technique) examination of corroded samples taken from lining of furnace were investigated. The samples were selected from top 1/3 of the furnace where the slag attack, thermal shock stresses and mechanical wear were predominant, usually.

The sample of refractory lining obtained from a 10mt CIF and DVM refractory of the lining was provided by Almas Alborz Refractories Co., the specific brand being coded as DiamoRam Al-Sp18-T (TA-based) and DiamoRam Al-Sp18-W (WF-based). With this lining the furnace was used to melt numerous heats of steel until the furnace demanded repair and patching due to refractory lining wear. Table 1. described the structure of the studied lining material from 10mt CIF.

*Tab. 1: CIF characteristics and structure of the linings breakout.*

| DVM Refractory Brand | DiamoRam Al-Sp 18-T | DiamoRam Al-Sp 18-W |
|---|---|---|
| Steel type | Carbon Steel | |
| Tapping temperature | 1650-1680 | |
| Number of heats | 65 | 85 |
| Initial lining thickness | 150 mm | |
| Remaining lining thickness | 55 mm | 60 mm |
| Dept of infiltration | 3-4 mm | 5-6 mm |
| Layers thickness<br>-sintered layer<br>-semi-sintered layer<br>-unchanged layer | 0-11<br>11-20<br>25-55 | 0-13<br>13-30<br>30-60 |
| Numbers of patching | 2 | 3 |

## 3. RESULT AND DISCUSSION

### 3.1. Lining appearance

The appearance of the refractory wear lining of the furnace with two different linings, TA and WF, after 60 heats is shown. Unlike the TA lining, which has many island expansion cracks on the surface of the hot face, the WF lining has a smooth surface without any cracks. (Fig. 2). This phenomenon can be attributed to the difference in structural characteristics, reactivity and expansion behavior of in-situ spinel phase formation between MgO with TA and WFA in the matrix of refractory lining. This is due to higher thermal reactivity of TA with fine MgO compared to WFA and fine MgO particles. Also, the results showed that the expansion rate after firing at 1600°C in TA sample is approximately 1.5 times that of the WF sample and thus the corresponding strength in TA lining reduced significantly and cracks formed on the lining.
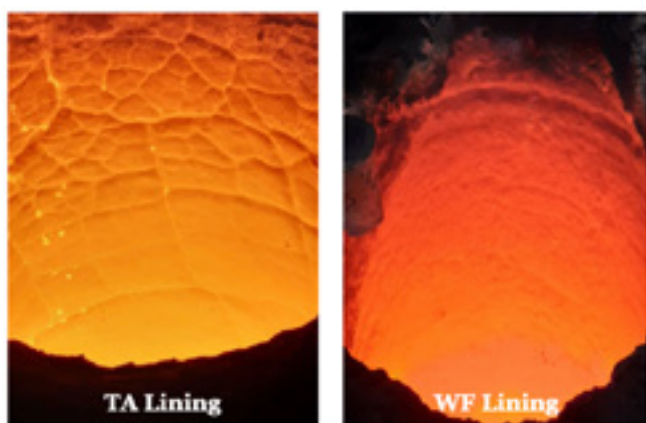


*Fig. 2: Furnace refractory lining after 50 heats.*

The picture of representative pieces from TA and WF linings used in post-mortem analysis is shown in Fig. 3. As seen, completely different appearance is observed in two samples. Despite the presence of different layers formed by the hot face of the refractory lining, the structure of each layer is different. (Table 1.). Also, a dense sinter layer is formed on the hot surface of the TA sample and the slag penetration in the TA sample is lower compared to WF sample. The notable point is the lack of continuity between the layers in the TA sample, which will cause the structural difference between sinter layer compared to the semi-sinter and unchanged layers. As a result, due to the thermal shocks and increasing tap to tap times, the possibility of cracks formation and thermal spalling increases.
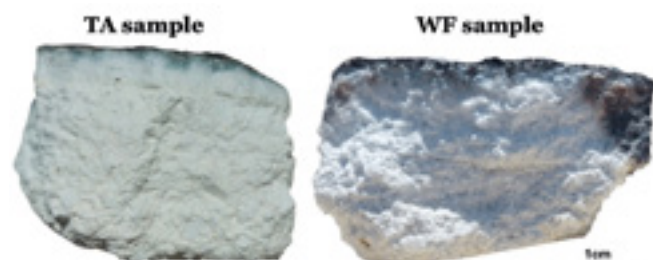


*Fig.3: Microscopical overview from.*

### 3.2. Microstructural evaluation by FESEM

According to the microstructural evolution of two TA-based and WFA-based samples after firing at high temperature at 1600°C (not shown here), the nature of in-situ formed spinel, i.e., MgO-rich, $Al_2O_3$-rich or stoichiometric spinel in the matrix of DVM refractories related to the $Al_2O_3$/MgO ratio, size, amount and spinalization behavior of alumina type. On the basis of two mentioned DVM formulations, only the type of alumina changed and thus the nature of spinel is same. But the speed and amount of spinel formation can be different. This fact is clearly visible in the appearance of the samples and difference in the thickness of sintered layer on the hot face.
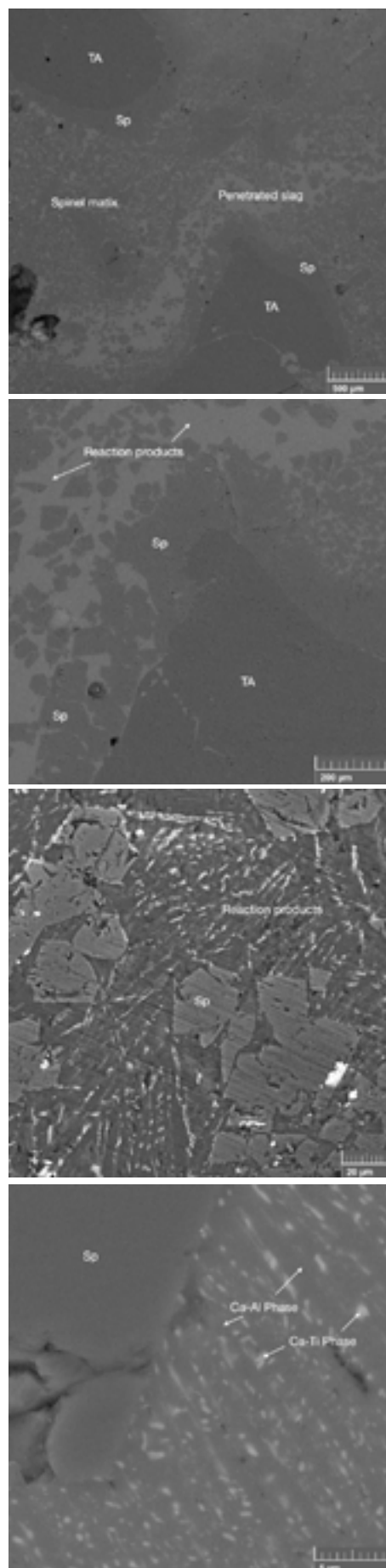


*Fig. 4: Slag penetration and spinel crystal separation.*

According to the in-situ formed spinel in the matrix and on the surface of alumina aggregates and its reaction with the slag composition, different phases according slag composition formed during corrosion process. Elemental analysis by EDX were done on the different phases in contrast that help to distinguished reaction phases. Higher magnification from reaction area shown in Fig. 4.
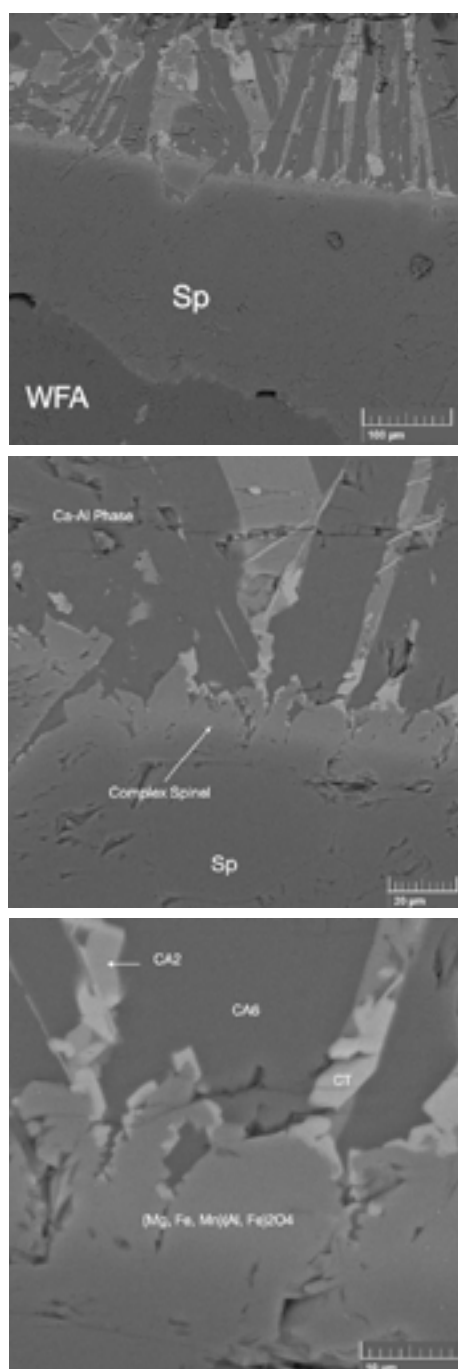
*Fig.5: Spinel formation on the surface of alumina aggregate and reaction with slag.*

The reaction of spinel matrix with slag shows the penetration of slag liquid phase into the spinel crystals that contain impurities such as Si, Ca and Ti. In this case, the reaction between the penetrated liquid slag and impurities in the spinel grains boundaries forms different calcium aluminates and calcium titanate phases. The formation of these phases, some of which are liquid at that temperature with low viscosities, separate the spinel crystals and moves them into the slag.

As well as, according to solid state reaction mechanism on the basis of Wagner theory, lower size and amount of MgO grains compare to alumina particles, causes the spinel phase to form on the surface and around of alumina particles. Therefore, TA-based sample show higher penetration and corrosion resistance compare to WFA-based sample due to higher spinel formation. Higher spinel formation in the matrix create denser structure and also enhance matrix capability to accommodation of $Fe^{+2}$ and $Mn^{+2}$ ions from corrosive slag and formation of dense complex spinel structure (Mg, Fe, Mn)(Al, Fe)$_2$O$_4$ (Fig. 5).

It is well known that the aggregates phase has a significant influence on the extend and mechanism of liquid slag corrosion on refractories. Therefore, the corrosion behavior of aggregates is usually important in order to evaluate the corrosion mechanism of refractories. As well as, spinel formation on the surface of alumina aggregates and create an indirect corrosion, other phases with different contrast in BSE micrograph also found near to hot face of refractory/slag as reaction products. This means $Al_2O_3$ aggregates and spinel layer formed on $Al_2O_3$ surface react with the refractory lining and new phases occur upon dissolution of $Al_2O_3$. As shown, a larger number of columnar crystals ($CA_6$ and $CA_2$ and calcium titanium phase (CT) confirmed by EDS results (Fig. 4.)), were completely formed on the surface of $Al_2O_3$ aggregate in contact with slag, and the growth direction of these phases is perpendicular to the surface of $Al_2O_3$. Therefore, different phases formed consecutively as a result of the reaction between the liquid slag and matrix and aggregates. It seems, when $Al_2O_3$ aggregates are exposed to the liquid slag, high melting calcium aluminate phases such as $CA_6$ and $CA_2$ (according to the $CaO$-$Al_2O_3$) phase diagram) precipitated. As a result, the proposed corrosion mechanism for $Al_2O_3$ is can be explained as a dissolution-precipitation process inside a liquid phase with formation of $CA_6$ layer. Therefore, the $Al_2O_3$ aggregate remained for the reaction with slag was reduced, resulting in the formation of a second layer of $CA_2$. Thus, the $Al_2O_3$ aggregate remained for the reaction with slag was reduced, resulting in the formation of a second layer of $CA_2$.

As reported according to thermodynamic data, different reactions involving the corrosion of the $Al_2O_3$ aggregates and the values of free energy of formation associated with each of them are described in Eqs. (1) and (2), respectively:

$$6Al_2O_{3(l)}+CaO_{(l)} \longrightarrow CaO.6Al_2O_{3(s)} \quad \Delta G° = -261.1 \text{ kJ/mol} \quad (1)$$
$$2Al_2O_{3(l)}+CaO_{(l)} \longrightarrow CaO.2Al_2O_{3(s)} \quad \Delta G° = -152.2 \text{ kJ/mol} \quad (2)$$
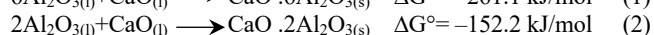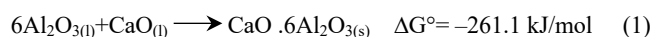
Both above reactions are possible, as their $\Delta G°$ values are negative. When comparing reaction (1) (precipitation of $CA_6$) and Eq. (2) (precipitation of $CA_2$), it is concluded that the former presents a lower $\Delta G°$ value than the latter and, therefore, it is the preferential product observed in the micrograph (Fig. 5).

As the slag attack and reaction increases, or in other words, as $CA_6$ dissolves within the slag, a continuous layer of $CA_2$ forms. In the following, as CaO concentration increases due to the slag attack, CA and $CA_2$ phases form. Given that the melting temperatures of them are below 1650°C, they dissolve in the slag at CIF working temperature. After the $CA_2$ layer, spinel crystals formed discretely, which could be due to the reaction between MgO and $Al_2O_3$ and the slag's enrichment of magnesia and alumina inside the slag.

## 4. CONCLUSIONS

1. The island cracks formation on the surface of TA-based DVM lining of CIF is the mainly create due to lower thermal shock resistance, thermal and structural properties of tabular alumina compare to fused alumina.

2. A dense spinel structure in the matrix of TA-based DVM decrease penetration depth of liquid slag into lining.

3. Corrosion of alumina aggregates and matrix accompanied to formation of calcium aluminate phase and is same in TA-based and WFA-based DVM lining.

## REFERENCES
[1] Uylas O, et al., Post mortem study on Al2O3-MgO induction furnace lining., IMMC 2016, p. 227-230.

[2]    Schnaized et al., Properties and characteristics of fused and sintered refractory aggregates., Refractories WORLDFORUM, 7 (4), 2015, p. 75-81.

[3]    Krause O., Kemnitz H., Behaviour of spinel-forming DVM using crucible induction furnaces. A case study on material failure., Ceramics International 42, 2016, p. 10645-10654.

[4]    Tabatabaie-Hedeshi S.M., Bavand-vandchali M., Naghizadeh R., Charactrization and *post-mortem* analysis of Al2O3-MgO-C refractories used in steelmaking ladle furnaces., Engineering Failure Analysis., 104697, (116), 2020, p: 1-16.

# PERFORMANCE OF NOVEL SILICA DRY VIBRATING REFRACTORY LINING MIXES WITHOUT PURE BORIC ACID OR BORON OXIDE IN CRUCIBLE INDUCTION FURNACES IN THE IRON FOUNDRIES

I. Hofmann, M. Schellhorn, A. Jelonnek, J. Hess, K. Rieke, Dr. U. Bach, Dr. Valetine Kubong Atanga*

Dörentrup Feuerfestprodukte GmbH & Co. KG, Lemgoer Strasse 9, D-32694 Dörentrup, Germany

## ABSTRACT

Silica ($SiO_2$) dry vibrating mixes with sintering additive boric acid ($H_3BO_3$) or diboron trioxide / Boron oxide ($B_2O_3$) are the standard refractory lining products used for crucible induction furnaces (CIF) in the iron foundries worldwide. The sintering agents are used to control the reaction with $SiO_2$ that forms a melt phase on the surface of the grains, which protect the refractory lining, reduces infiltration and extend the campaign life of the lining. Though, the sintering agents have shown a high performance of the refractory lining life, they are classified as reproductive toxicity "1B" to humans, present challenging health effects and environmental disposal problems. Currently, delivered products are labeled with 1B and regulatory institutions are proposing a further reduction in concentration of less than 0.3 % $B_2O_3$ in all products. This paper presents recent developments on a novel sintering agent combination for $SiO_2$ refractory lining products. The sintering additive is not classified by legislation and is envisaged to minimized health risks to humans and the environment. For a better evaluation of the suitability of the novel sintering agent for binding the $SiO_2$ matrix, a chemical and mineralogical analysis was performed with lining samples hammered from the furnace. Field applications revealed equivalent performance comparable to current sintering agents.

## 1.0 INTRODUCTION

The most common and well know sintering agents for binding $SiO_2$ dry vibrating mixes (DVM) used in lining the hot face of crucible induction furnaces (CIF) for melting recycled copper, iron and their alloys are boric acid ($H_3BO_3$) or boron oxide ($B_2O_3$) or frits and/or phosphate. In some special cases, additives such as chrome oxide and/or carbon are added to improve the slag resistance of the lining wall or the anti-wetting effect respectively. The $SiO_2$ content in the mixture varies from 94 – 99 % and the rest constitutes the sintering agents, converters and stabilitators. When mix and thermally heat treated, based on the additive ionic state, they can either interchange with the silicon ion in the crystal structure or stay unreacted within its interstitials/cavities. This alters the $SiO_2$ crystal structure and lower its melting point with the formation of a melt/sintered phase according to Fig. 1, suitable for resisting slag and liquid metal infiltration [1, 2].
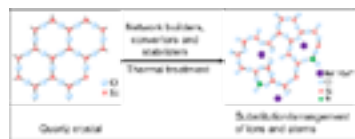


*Fig. 1: Reaction mechanism showing the influence of the network builders, converters and stabilizers on the quartz crystal structure* [2, 3]

The suitability and functionality of the sintering agent is based on certain properties. It should have a low melting temperature ($H_3BO_3$:170 °C, $B_2O_3$: 450 °C, phosphate: >200 °C, frits: >700 °C) couple with a high temperature stability up to 1700 °C. A desirable high expansion, softening and less sealing effects are reported during high temperature service life for frits or phosphate compared to low temperature consolidation and lower expansion when $B_2O_3$ or $H_3BO_3$ were used [1]. The suitable additives are currently classified as toxic material category 1B and are listed as substance of very high concern by REACH (Registration; Evaluation, Authorization and Restriction of Chemicals) and ECHA (European Chemicals Agency) with a maximum permitted concentration of C≥5.5 % for $H_3BO_3$ and C≥3.1 % for $B_2O_3$. Recently, in Europe a new legislation to label all products containing pure boron oxide concentration of C≥0.3 % $B_2O_3$ was adopted [4]. Some Asian countries have signed a regulation adopting a maximum concentration level of 0.3 % $B_2O_3$ in all $SiO_2$ products.

Novel $SiO_2$ products without pure $H_3BO_3$ and/or $B_2O_3$ bears a real potential for minimization of health and environmental hazards. The goal of this work is to develop a dry vibrating $SiO_2$ refractory product with a novel sintering agent that does not contain pure $H_3BO_3$ and $B_2O_3$. It is expected to have similar performance comparable to the $H_3BO_3$ and $B_2O_3$ sintering agents, which could possibly be use as an alternative in case of regulation enforcement in future.

### 1.1 Experimental and material processing routes

Silica raw materials of varying particle sizes were mixed separately with three different sintering agents [phosphate from Chemische Fabrik Budenheim KG; glass frit from Reimbold & Strick; and/or DFP high temperature combination binder (HTB)]. Obtained results are compared to the standard $SiO_2$-$B_2O_3$ concept as follows [2].

1. $SiO_2$ + Phosphate concept denoted as **SiO₂-P**
2. $SiO_2$ + Glass frit concept denoted as **SiO₂-GF**
3. $SiO_2$ + DFP „HTB"combination concept denoted as **SiO₂-HTB**
4. $SiO_2$ + $B_2O_3$ standard concept denoted as **SiO₂-B₂O₃**

Mixture 1 to 4 were homogenized separately, and cylindrical shapes of 50 X 50 mm were compacted from each system. The samples were subjected to a heat treatment with a constant heating rate of 5 K min$^{-1}$ to maximum temperature between 1200 °C and 1600 °C. Sawn cross-sections of some samples are represented in Fig. 2. The sintered samples were characterized in terms of physical properties and compared with the $SiO_2$-$B_2O_3$ concept. Industrial trials were carried out with iron foundries melting recycled cast and ductile iron. In this short overview, selected laboratory physical properties of the best results (Fig. 2 and Tab. 1), results of the industrial trials (Fig. 3) including the mineralogical analysis in Fig. 4 and Tab. 2 are presented.

## 2.0 RESULTS AND SUMMARY

### 2.1 Density, cold crushing strength and open porosity

In Tab. 1, the results of the cold crushing strength (CCS), bulk density, open porosity and permanent linear change (PLC) values for the $SiO_2$-HTB and $SiO_2$-$B_2O_3$ system are compared. The CCS values for both systems increase due to sintering and densification. The $SiO_2$-$B_2O_3$ system shows a higher strength and less porosity for sintered samples at 1600 °C. A possible reason is the start of early densification in the $SiO_2$-$B_2O_3$ system. The low strength value for the $SiO_2$-HTB sample sintered at 1200 °C is related to its high initial start melting temperature and late densification, which was observed to start at >700 °C compared to 450 °C for the $SiO_2$-$B_2O_3$ system [1].

### 2.2 Results and observation of the pushout crucibles

Fig. 3 represent the pushout crucibles and breakout lining samples from the different furnaces with some collected data listed. More wearing, erosion, less heat numbers and deep sintering were observed in the $SiO_2$-P and $SiO_2$-GF systems compared to the $SiO_2$-HTB system. In Fig. 3 (upper-left), it was observed that, above 1500 °C, the $SiO_2$-P system showed very high amount of blown-out melted surface view, suspected to originate from low melting eutectic aluminum phosphate formation with intensified erosion and infiltration compared to the other sintering agents [2]. Though, the $SiO_2$-GF achieved more heat numbers than the $SiO_2$-P system, its sintered and fritted layer showed less density, and the loose layer

was completely hardened after 100 heats (Fig. 3, top-right). This was suspected to be caused by the alkali ($Na^+$, $K^+$, $Ca^{2+}$) content of the glass frit, that is voluminous and capable of softening and forming low eutectic melting phases, weakening the lining microstructure at temperatures >1500 °C [1, 3]. Comparable sintered, fritted, and loose zones with higher heat numbers were observed with the $SiO_2$-HTB system similar to the $SiO_2$-$B_2O_3$ system. In Fig. 3 and Fig. 4, the $SiO_2$-HTB and $SiO_2$-$B_2O_3$ systems showed no infiltration observed beyond the sintered zones.
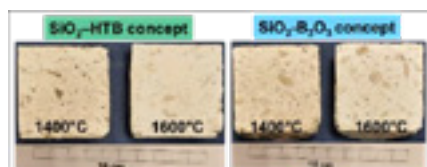


*Fig. 2: Matrix view of the cross-section of the sintered samples at 1400 °C and 1600 °C for 5 hrs*

Tab. 1: Physical properties of the $SiO_2$-HTB and $SiO_2$-$B_2O_3$ system

| Temperature [°C] | 1200 | | 1400 | | 1600 | |
|---|---|---|---|---|---|---|
| System | $SiO_2$-HTB | $SiO_2$-$B_2O_3$ | $SiO_2$-HTB | $SiO_2$-$B_2O_3$ | $SiO_2$-HTB | $SiO_2$-$B_2O_3$ |
| CCS [MPa] | 8 | 17 | 10 | 16 | 20 | 27 |
| Density [g/cm³] | 1,92 | 1,96 | 1,87 | 1,95 | 1,83 | 1,81 |
| OP [%] | 21 | 20 | 22 | 18 | 18 | 15 |
| PLC [%] | 0,6 | 0,3 | 1,7 | 0,2 | 3,1 | 3,6 |

Where CCS: cold crushing strength, PLC: permanent linear change, OP: open porosity



3t CIF, 90 heats, #: erosion and melt out, →: infiltration, wear: 3-4 cm

2,2t CIF, 100 heats, ø: deep sintered, →: erosion, infiltration, wear: 3-5 cm

8t CIF, ~ 880 heats, Δ: crack free, loose layer (→): 3-4 cm, wear: 2-3 cm.

8t CIF, ~ 880 heats, Δ: crack free, loose layer (α): 2-3 cm, wear: 1-2 cm.
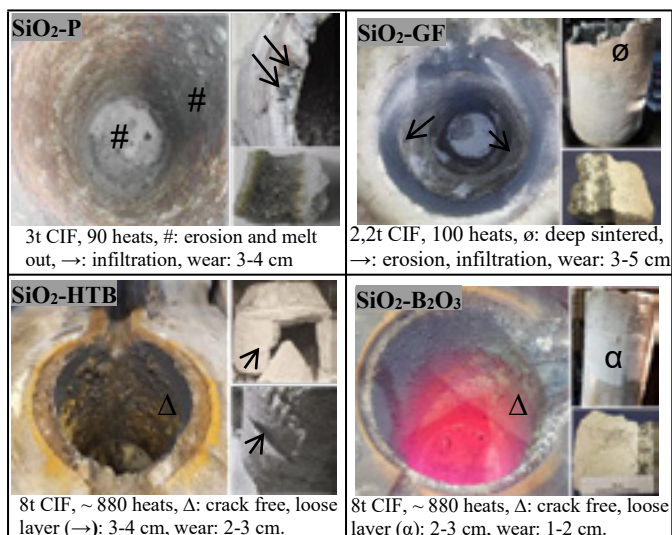
*Fig. 3: Crucible view; program: cast and ductile iron; operating temperatures: 1530 – 1600 °C; and discontinues melting.*
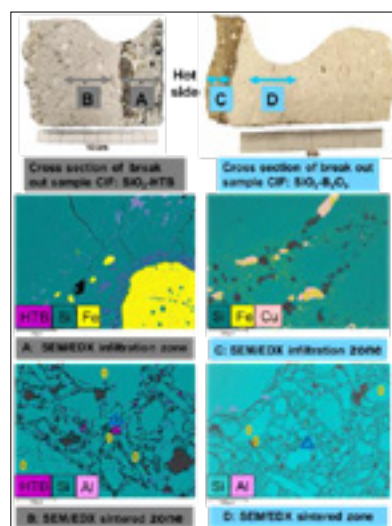


*Fig. 4: Breakout cross-section of the wall lining samples and SEM/EDX analysis of the infiltrated (A, C) and sintered zones (B, D). where 0: SiO2, Δ: amorphous.*

## 2.3 Chemical and mineral analysis of the lining samples

Breakout lining cross sections, SEM micrographs and EDX spot analysis for the $SiO_2$-HTB and $SiO_2$-$B_2O_3$ crucible samples are shown in Fig. 4, with corresponding mineral analyses in Tab. 2. The infiltration zones A and C of both systems

consist of slag and silica with dentritic crystallites of fayalite observed. In addition, CuO was analyzed in the infiltration zone of the $SiO_2$-$B_2O_3$ system (Tab. 1), suspected to be an impurity from the used scrap. Moving into zones B and D, the matrix densification is improved and shows a reduction in the impurities observed. The quartzite is totally cristobalized, showing cloudy structures with typical crack structures of the quartz at the beginning of transformation to tridymite/cristobalite. The glassy matrix with rest quartzite and large transformed grains are observed typically in B and D [4,5]. The matrix is made up of tridymite and cristobalite with some mullitization traces observed along the boundaries or in-between the tridymite and quartzite grain boundaries, which is suspected to have improved the strength of the $SiO_2$ product.

Tab. 2: Qualitative mineral analysis of the zones

| Samples | Zone | Major phase | Minor phase | Trace |
|---|---|---|---|---|
| $SiO_2$-HTB | Infiltration | Cristobalite | Tridymite, Fayalite, Amorphous, | Quartz |
| | Sinter | Quartz | Cristobalite, Mullite, amorphous | Tridymit |
| $SiO_2$-$B_2O_3$ | Infiltration | Tridymite | Cristobalite, Fayalite, Cu | Quartz |
| | Sinter | Quartz | Cristobalite, amorphous | Tridymit |

## 3.0 Summary

The introduction of the DFP "HTB" combination binder into the $SiO_2$ crystal, resulted in a reinforcement and stabilization of the $SiO_2$ structure with similar wear and heat numbers achieved comparable to the pure $SiO_2$-$B_2O_3$ system. Low melting eutectics and alkali content reduces the refractoriness of the $SiO_2$-P and $SiO_2$-GF system respectively. Until date, 20 iron foundries melting cast and ductile iron with medium and line frequency furnaces, having capacity of 1-16t have carried out successful trials with the novel sintering agent with greater than 85 % lifetime achieved. Since, little or no $B_2O_3$ erodes into the melt during the first two melting batches, customers discarding first two batches due to high boron content do not longer discard them. Improved operational safety and minimization of environmental contamination is possible. The $SiO_2$-$B_2O_3$ system starts melting at 450 °C compared to >700 °C for the $SiO_2$-HTB system, which requires a little more energy.

Ongoing investigations have shown that, the novel system is also suitable for melting recycled copper. Currently, prefabricated crucibles are being tested in the copper and iron foundries. Further work is based on analyzing the influence/distribution mechanism of the HTB combination sintering agent, and the replacement of the fine crystalline quartz as raw material for the silica product.

## REFERENCES

[1] Brunk F, Silica Refractories. CN Refractories special issues. Volume 5. 2001, P. 27-30

[2] Harders F, Kienow S. Feuerfestkunde, Herstellung, Eigenschaften und Verwendung feuerfester Baustoffe. Springer-Verlag, 1960

[3] Schackelford, J. F, Doremus R. H. Ceramic and glass materials, Springer, 2008

[4] https://echa.europa.eu/canidate-list-table

[5] Krause O, Wear of vibrating refractory materials on andalusite basis installed in crucible induction furnaces of iron-, steel- and copper industry, International Colloquium on Refractories. Aachen 2002, p. 79-80

# EFFECTS OF SPINEL-CALCIUM ALUMINATE ON PROPERTIES OF ALUMINA-MAGNESIA BASED DRY RAMMING MIXES

Hu Tang[1], Zhenggang Jia[3], Bing Li[3], Jianying Gao[4], Wenjie Yuan[1,2,*]

1 The State Key Laboratory of Refractories and Metallurgy, Wuhan University of Science and Technology, Wuhan 430081, China
2 National-Provincial Joint Engineering Research Center of High Temperature Materials and Lining Technology, Wuhan University of Science and Technology, Wuhan 430081, China
3 Hubei Annex Furnace Lining Material Co., Ltd., Xiangyang 441100, China
4 Imerys Technical Center China, Tianjin 300450, China
*yuanwenjie@wust.edu.cn

**ABSTRACT**

Due to high efficiency and energy-saving, induction furnaces are widely used in foundry and metallurgy industries. Spinel forming dry ramming mixes worked as the lining of induction furnaces for high quality alloy steel casting. Aiming at optimizing properties of alumina-magnesia based dry ramming mixes, white fused alumina and calcined magnesia particles were replaced partially with the novel porous multi-component materials of spinel-calcium aluminate (CaO-MgO-Al$_2$O$_3$, CMA) with the size of 0-1 mm. Properties including the bulk density, apparent porosity, strength and slag corrosion resistance of alumina-magnesia based dry ramming mixes containing CMA were evaluated contrastively. The results demonstrated that the incorporation of CMA can significantly improve manganese-bearing slag penetration resistance of dry ramming mixes, although companying with slight decrease in the bulk density. However, the permanent linear change of dry ramming mix first increased and then decreased with CMA additions. When the addition of CMA reached 8 wt%, the strength of dry ramming mixes was a little lower than the reference, and the slag penetration index was 38% lower than the latter.

**Introduction**

Due to their flexibility and other advantages, medium-frequency induction furnaces are widely used in the foundry industry. As one of the most important components of the induction furnaces, the linings work in an extremely harsh environment during the smelting process [1]. Because of its excellent chemical stability, thermal shock resistance and mechanical properties, spinel-forming dry mixes are suitable to induction furnaces for melting of high alloy steels [2]. During the service of alumina-magnesia based dry ramming mixes, the formation of in-situ spinel would lead to a certain volume expansion (8%) [3-4], which could seriously affect the performance of the linings and shorten the service life of the furnaces [5]. The expansion of refractories was controlled by the incorporation of preformed spinel, which was as the consequence of less in-situ spinel formation [6]. It was pointed out that preformed and in-situ spinel containing castables had immense potential to enhance properties such as strength, thermal shock resistance and corrosion resistance [7].

In the Al$_2$O$_3$-rich part of Al$_2$O$_3$-MgO-CaO ternary system, the first liquidus temperature is higher than 1730 °C. Recently, the novel calcium magnesium aluminate (CMA) materials containing 73% spinel and 25% calcium aluminate have been developed by Imerys. The aim of this study is to systematically investigate effects of CMA particles (1-0 mm) on properties of alumina-magnesia based dry ramming mixes.

**Materials and Methods**

The formulations of dry ramming mixes are listed in Table 1. Coarse white fused alumina (Yufa, Zhengzhou, China) was used as aggregates, and fine particles of white fused alumina and tabular alumina (Higiant, Binzhou, China) served as the matrix. Calcined alumina (Alteo, Gardanne, France) and magnesia (Jinding, Dashiqiao, China) were designed to form in-situ spinel at high temperatures. CMA particles (MagArmour, Imerys, Paris, France) were composed of MA (72.5%), CA (16.5%) and CA$_2$ (9.0%). Samples were marked as X0-X8 according to CMA additions.

Tab. 1: Formulations of alumina-magnesia based dry ramming mixes.

| Raw materials | Content (wt%) | | | | |
|---|---|---|---|---|---|
| | X0 | X2 | X4 | X6 | X8 |
| White fused alumina (<5 mm) | 72 | 71 | 70 | 69 | 68 |
| White fused alumina (<0.075 mm) | 7 | 7 | 7 | 7 | 7 |
| Tabular alumina (<0.045 mm) | 3 | 3 | 3 | 3 | 3 |
| Calcium alumina (AC34B5) | 3 | 3 | 3 | 3 | 3 |
| Calcined magnesia (<0.3 mm) | 8 | 8 | 8 | 8 | 8 |
| Calcined magnesia (<0.075 mm) | 7 | 6 | 5 | 4 | 3 |
| MagArmour (0-1mm) | − | 2 | 4 | 6 | 8 |

Raw materials were mixed for 10 min in a cement mortar mixer. The mixture was pressed into a cylinder with the dimension of Φ 50 mm×50 mm in molds with aluminum foils on the inner surface by a compression testing machine (TYE-2000B, Wuxi Jianyi, China). The pressure of 60 MPa was applied. All samples were dried at 110 °C for 24 h, and then calcined at 1600 °C for 3 h. Cylindrical samples for corrosion tests were also pressed under the pressure of 60 MPa as the following dimensions: Φ 50 mm×50 mm with the hole of 18 mm diameter and 24 mm depth in the center. The calcined cup samples were filled with slag (8 g), and then heated up to 1600 °C and soaked for 3 h.

Tab. 2: Chemical compositions of slag used for testing.

| Compositions | SiO$_2$ | Al$_2$O$_3$ | Fe$_2$O$_3$ | CaO | MgO | MnO | TiO$_2$ |
|---|---|---|---|---|---|---|---|
| Content (wt%) | 36.91 | 31.22 | 5.62 | 0.84 | 3.28 | 20.55 | 1.14 |

**Results**

*Phase composition*

The major phases were corundum and spinel, and unreacted magnesia was detected. The spinel contents in samples calculated by reference intensity ratio (RIR) method were listed in Table 3. It can be seen that the spinel in samples firstly increased and then decreases with the increase of CMA additions.
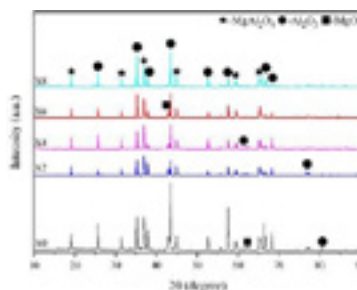


*Fig. 1: XRD patterns of dry ramming mixes with the addition of CMA after sintering at 1600 °C for 3 h.*

Tab. 3: Spinel content of different samples.

| Spinel | X0 | X2 | X4 | X6 | X8 |
|---|---|---|---|---|---|
| Content (wt%) | 48.7 | 48.3 | 50.7 | 44.3 | 37.9 |

*Physical and Mechanical Properties*

As shown in Fig. 2, the permanent linear change of samples after sintering firstly increased and then decreased. Apparent porosity and bulk density of samples are presented in Fig. 3. It can be seen
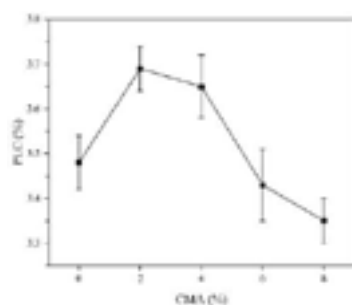
Fig. 2: Permanent linear change of specimens with the addition of CMA after sintering at 1600 °C for 3 h.

that the apparent porosity of samples first raised and then decreased after sintering at 1600 °C for 3 h with the increase of CMA contents, and the variation of the bulk density was opposite. Except for a certain decrease of the apparent porosity for the sample with 8% CMA addition, the use of up to 38% porous CMA aggregates (particles with 30% porosity) instead of dense white fused corundum leads to an increase in apparent porosity. The significantly lower bulk density of CMA particle than white fused corundum led to the decline of the bulk density.
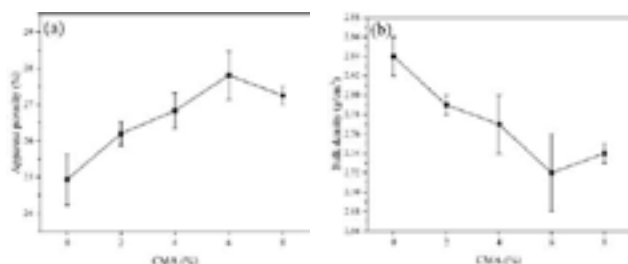


Fig. 3: Apparent porosity and bulk density of specimens with the addition of CMA after sintering at 1600 °C for 3 h.

Figure 4 shows the cold crushing strength of samples. As the increase of the content of CMA, the cold crushing strength of samples first decreased and then raised. The strength of the sample with 8% CMA addition is not significantly different from the reference.
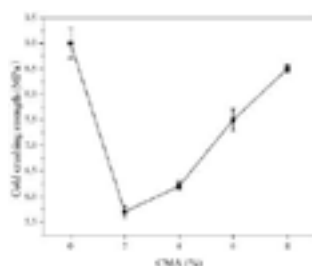


Fig. 4: cold crushing strength of specimens with the addition of CMA after sintering at 1600 °C for 3 h.

Figure 5 shows the microstructure of samples X0, X6 and X8. There were many pores in sample X0, X6. In contrast, the junction of aggregates and matrix in sample X8 was relatively denser because of the addition of CMA particles. In addition, 25% calcium aluminate from CMA could form $CA_6$ around the corundum aggregates over 1450 °C, which resulted in a strong bridging effect between aggregates and matrix.
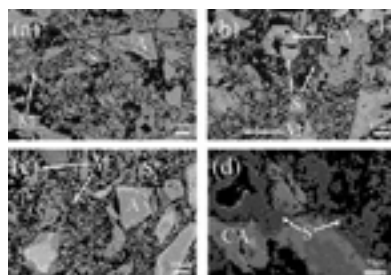


Fig. 5: SEM images of X0 (a), X6 (b) and X8 (c) (d) (A-Corundum, S-Spinel, M-periclase)

EDS mapping and the local magnified SEM images of sample X8 are shown in Fig. 6. It can be seen that a large amount of $CA_6$ was generated at the center of aggregate. Formed $CA_2$ as a bonding phase tightly connected $CA_6$ and spinel. A structure of $CA_6$-$CA_2$-MA with closely combined layers could eliminate pores, absorb stress and improve the mechanical properties of materials. The fracture toughness of this three-layer structure was greater than in MA-alumina region due to the crack-deflection and crack-bridging effects derived from $CA_6$ platelets.
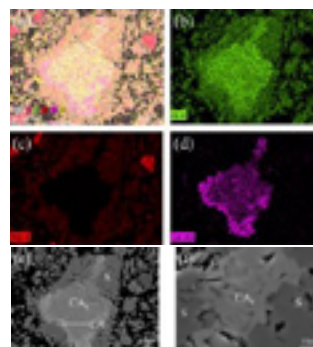


Fig. 6: EDS mapping of X8 (a), (b) Al, (c) Mg, (d) Ca and Partial enlarged images of X8 (e), (f) (S-Spinel)

Figure 7 presents the photos of the crucible samples after the cup tests. The penetration index of samples is listed in Table 4. The penetration index of samples basically decreases with the increase of CMA contents. In theory, slag penetrates into the matrix under the action of capillary force. When the slag comes into contact with CMA, the porous structure of CMA can absorb the slag through capillary force. In addition, the formation of a three-layer structure of $CA_6$-$CA_2$-MA may improve the slag corrosion resistance of ramming mixes.
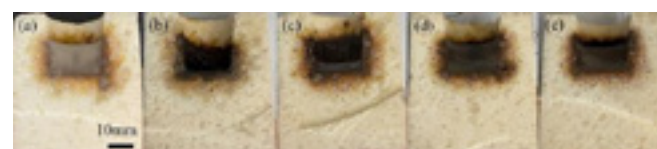


Fig. 7: Images of cross-section of the corroded samples X0 (a), X2 (b), X4 (c), X6 (d) and X8 (e)

Tab. 4: Penetration indexes of the corroded samples

| Samples | X0 | X2 | X4 | X6 | X8 |
|---|---|---|---|---|---|
| Penetration index (%) | 25.96 | 21.46 | 21.80 | 18.70 | 16.07 |

## CONCLUSIONS

Enhanced properties of alumina-magnesia based dry ramming mixes were achieved by incorporated a novel kind of multi-component materials of calcium magnesium aluminate (CMA) particles. The addition of CMA promoted the formation of the bond structure of $CA_6$-$CA_2$-MA in dry ramming mixes. Although the incorporation of CMA particles (0-1 mm) slightly reduced the physical properties of dry ramming mixes after sintering at 1600 ℃ for 3 h. But when 8 wt% CMA particles are introduced, the slag penetration resistance has been significantly improved.

## REFERENCES

[1] Zhang P.W.; Li X.C.; Zhu B.Q. Influence of α-Al$_2$O$_3$ micropowder addition on properties of corundum dry ramming mix. China's Refractories 22 (3), 2013, p. 28-31

[2] Routschka G. Pocket manual refractory materials, Vulkan-Verlag GmbH, Essen, 2004.

[3] Braulio M.A.L.; Martinez A.G.T.; Luz A.P. Luz; Liebske C.; Pandolfelli V.C. Basic slag attack of spinel-containing refractory castables. Ceramics International 37 (6), 2011, p. 1935-1945

[4] Braulio M.A.L.; Castro J.F.R.; Pagliosa C.; Bittencourt L.R.M; Pandolfelli V.C. From macro to nanomagnesia: designing the in situ spinel expansion. Journal of the American Ceramic Society 91 (9), 2008, p. 3090-3093

[5] Sako E.Y.; Braulio M.A.L.; Zinngrebe E.; Laan S.R. van der; Pandolfelli V.C. Fundamentals and applications on in situ spinel formation mechanisms in Al$_2$O$_3$-MgO refractory castables. Ceramics International 38 (3), 2012, p. 2243-2251

[6] Kang R.; Wang X.T.; Wang Z.F.; Ma Y.; Liu H. Effect of pre-synthesized spinel addition on alumina-magnesia dry vibration mix. Refractories (Naihuo Cailiao) 54 (3), 2020, p. 205-209

[7] Kumar S.; Sarkar R. Alumina-spinel castable for steel ladles: An overview. International Journal of Applied Ceramic Technology 20 (1), 2023, p. 410-423

523

# 4 REFRACTORIES FOR NON-FERROUS METALLURGY

# FLAME–SPRAYED CALCIUM ALUMINATE–BASED COATINGS FOR APPLICATION IN THE ALUMINIUM INDUSTRY

Patrick Gehre*, Christos G. Aneziris
TU Bergakademie Freiberg, Institute of Ceramics, Refractories and Composite Materials, Freiberg, Germany

Christoph Wöhrmeyer, Christopher Parr
Imerys S.A., Paris, France

## ABSTRACT

The aluminium industry is a major consumer of refractories. Today, most furnaces are lined with aluminosilicate-based materials. To reduce the penetration of Al into the refractory material, non-wetting additives such as barium sulphate, different types of fluorides, and CaO were used. The aim of this study was the investigation of different calcium aluminate-based coatings to reduce the wettability of a metallic substrate by molten aluminium. Feedstock composed of calcium magnesium aluminate CMA, calcium di-aluminate $CA_2$, and $CA/CA_2$ with and without $TiO_2$ were processed via powder and flame spraying to thin coatings on metal substrates. The phase composition, roughness, macro- and microstructure, porosity, and bending strength of the coatings have been analysed. Additionally, a casting test, has been performed by pouring 1.5 kg AlSi7Mg alloy at 800 °C over coated half-pipes using pure alumina as reference coating. The amount of residual Al sticking on the substrates after the casting test indicates the degree of wetting of the coatings. The thermally sprayed CMA and $CA_2$ powder feedstock showed the lowest degree of interaction with the aluminium melt.

## INTRODUCTION

Aluminium is the most important light metal with a consumption of 96.6 million tons in the year 2022 and a growth of 3.3 % compared to the previous year [1]. The aluminium industry is a major consumer of refractories, which are faced with increasing wear by fluxes, the use of oxy-fuel burners, higher furnace temperatures, higher amounts of alloying Mg and recycled Al metal, as well as a requirement for higher efficiencies. The wettability of alumina, silica, Be, $B_4C$, graphite as well as SiC by aluminium and Al alloys has been investigated by several researchers [2]. Today, alumina and aluminosilicate refractory castables are widely used for the lining of holding and melting furnaces due to their good thermomechanical properties and – in the case of the latter - low costs [3]. The castables are composed of coarse aggregates such as mullite, grog, bauxite, and tabular alumina, fumed silica and calcined alumina as fillers, and calcium aluminate cement with an $Al_2O_3$ content in the range of 60 to 80 wt.-% as a binder [4]. Above the metal line, the furnace can reach a temperature up to 1300 °C and the growth of corundum along the walls was observed degrading the lining material [5]. Below the metal line, the temperature is as low as 800 °C and the refractory is attacked by corrosion. Since aluminosilicate castables contain free silica as well as alkalis, they show poor corrosion resistance in contact with molten aluminium [6,7]. The metallic Al reduces the $SiO_2$ or mullite and an adhesive $Al_2O_3$ deposit is formed on the surface of the refractory, which acts as a protective barrier as long as it will not be decomposed by alkalis or a reducing atmosphere in the furnace [8]. Additives such as $BaSO_4$, $CaF_2$, $AlF_3$, $CeO_2$, and $La_2O_3$ promote the non-wettability of aluminosilicates by aluminium, but $AlF_3$ and $CaF_2$ deteriorate the corrosion resistance due to the formation of glassy phases [9,10]. Afshar et al. developed a high-alumina-based low-cement castable with fumed silica to reduce the porosity and pore size and added barite to counterbalance the low chemical resistance of $SiO_2$ [11]. Allaire and Guermazi added wollastonite $CaSiO_3$ to an alumina-based refractory to increase the resistance against corundum above the metal line and also the corrosion resistance against molten aluminium below the metal line by decreasing the penetration and increasing the mechanical properties [4]. Avraham and Kaplan investigated the reactive

wetting of $TiO_2$ by molten Al. The titania will be reduced by Al resulting in the formation of $Al_3Ti$ in the metal and a thin corundum layer at the interface leading to the reduction of the wetting angle [12]. Buhr et al. proposed the use of silica-free calcium hexaaluminate ($CA_6$) refractories for a low wettability and high temperature stability against molten aluminium [13]. Compared to refractories based on bauxite with $BaSO_4$ as anti-wetting agent and silica fume or high purity alumina, the $CA_6$ showed only slight discoloration, whereas the conventional bauxite refractories showed dark discoloration and a reaction with molten aluminium. Next to the low wettability, the enhanced aluminium resistance of $CA_6$ was explained with a micro porosity and lower pore size distribution. Siljan et al. have shown, that the density, porosity, and pore size distribution determines the contact and infiltration of a refractory next to its chemistry [14]. An optimized pore size distribution with a maximum pore size below 1–2 µm can improve materials, that are not thermodynamically stable towards molten aluminium.

Since the literature review has shown that the coarse aggregates are a weak point of the alumina and aluminosilicate castables, CaO was found to reduce the wettability of alumina-based castables by molten aluminium, and $MgAl_2O_4$ as well as calcium aluminates exhibited an enhanced corrosion resistance, the aim of this study was the development of fine-grained calcium aluminate-containing protective coatings for aluminium casting products produced by flame-spraying and the investigation of the interaction of the coatings in contact with molten aluminium.

## MATERIALS AND METHODS

### Materials and sample preparation

To determine the interaction of calcium aluminate-containing coatings with an aluminium melt, CA cement-based raw material mixtures as listed in table 1 were prepared to produce flame-spray feedstocks. Alumina was used as reference material.

Tab. 1: Composition of the feedstock for the flame-spray coatings

| Material | Sample (wt.-%) | | | | |
|---|---|---|---|---|---|
| | A100 | S71 | S71T2 | CA2 | CMA |
| $Al_2O_3$ | 100 | - | - | - | - |
| $TiO_2$ | - | - | 2 | - | - |
| Secar 71 | - | 100 | 98 | - | - |
| Non-standard product | - | - | - | 100 | - |
| CMA 72 | - | - | - | - | 100 |

As ceramic raw materials, Secar 71, a non-standard $CA_2$ product, CMA 72 0-1 mm (all Imerys S.A., Paris, France), $Al_2O_3$ powder spray feedstock (Amdry 6062, Oerlikon Surface Solutions AG, Pfaeffikon, Switzerland), and rutile $TiO_2$ (TR-HP-2, Sachtleben Chemie GmbH, Duisburg, Germany), were used. To generate the coatings, rod (sample S71, S71T2) and powder flame spraying (sample A100, CA2, CMA) have been performed. To produce the rods, the raw materials were mixed with 20 wt.-% of a thermoplastic injection moulding binder (Siliplast HO, Zschimmer&Schwarz, Koblenz, Germany) and a hot melt powder (abifor1625, Abifor AG, Zurich, Switzerland) for 5 minutes. The mixture was extruded at 120 °C using a heatable twin screw extruder from Brabender® OHG (Duisburg, Germany. After extrusion, the rods with a length of 600 mm were debinded and

sintered. The sintered rods of the samples S71 and S71T2 were fed to a Master Jet® flame-spray unit (Saint-Gobain Coating Solutions, Avignon, France) and processed to coatings. The sieved CMA 72 36-71 µm fraction (sample CMA), the CA2-rich powder (sample CA2), and the Amdry 6062 (A100) were automatically powder flame-sprayed with the MetcoTM 6P-II-A ThermoSprayTM gun, which is supplied with the process gases by the 6CE Combustion Control Unit (both Oerlikon Surface Solutions AG, Pfaeffikon, Switzerland) and guided by a robot arm (IRB 2600, ABB Ltd, Zurich, Switzerland). The powders were fed to the flame-spray gun by the 5MPE powder carrier (Oerlikon Surface Solutions AG, Pfaeffikon, Switzerland) using nitrogen as the carrier gas, which allows the processing of powders with low flowability. During the spraying processes, all raw materials were melted in an oxygen-acetylene flame with a maximum combustion temperature of 3160 °C.

## Methods

Free-standing band-shaped samples (approx. $10 \times 100 \times 1$ mm$^3$) for characterisation were produced by guiding the spraying gun perpendicular to a graphite substrate (GM-154e, Graphite Materials, Oberasbach, Germany), which was encircled by steel sheets. The characterisation of structural aspects such as the macro- and microstructure and the roughness was performed with a digital light microscope (VHX-2000 D, Keyence International, Mechelen, Belgium), a confocal laser scanning microscope (VK-X, both Keyence Deutschland, Neu-Isenburg, Germany), and a scanning electron microscope (SEM) (XL30 ESEM FEG D1511, Philips, Eindhoven, The Netherlands) equipped with an energy dispersive spectroscopy (EDS) detector. To obtain detailed information on the portion of open pores and the distribution of their size, mercury intrusion porosimetry, as comprehensively explained in DIN 66133, was applied with an assumed contact angle of 140° using an AutoPore V 9600 (Micromeritics Instrument, Norcross, USA). Three-point bending strength experiments were performed using a TiraTest 2420 machine (TIRA, Schalkau, Germany) according to EN 993-6 with a lower support roller span of 31.5 mm. Phase analysis was performed at milled and sieved (sieve aperture 20 µm) coating samples by XRD with qualitative and quantitative evaluation. To evaluate the interaction of the flame-sprayed coatings with molten aluminium, metal half-pipes were sandblasted and flame-spray coated with A100, S71, CA2, and CMA, respectively. 1.5 kg of solid AlSi7Mg alloy was portioned, filled in a crucible, and melted in a gas-fired furnace at 800 °C with a 2 h dwell time. Afterwards, the molten aluminium was slowly poured for approx. 1 min over the coated halfpipe, which was rested in 10° inclinations into another crucible, where the molten metal was collected. The setup of the casting test is depicted in figure 1.



Fig. 1: Setup of the casting test before (a) and during casting (b) of molten aluminium.

To evaluate the casting test, the mass of the coated halfpipes before and afterwards was detected. The resulting mass difference is the amount of aluminium, which remained in the halfpipe and is a degree of the wetting behaviour of the coating. Additionally, the coating and the cast aluminium melt were investigated in the digital light microscope as well as in the SEM.

## RESULTS AND DISCUSSION
### Coating characterisation

The rod flame-spraying of samples S71 and S71T2 resulted in a very homogenous but rough coating with a $R_a$ of 78.2 µm of sample S71. The addition of 2 wt.-% TiO$_2$ led to a significantly lower roughness of 44.9 µm. The powder flame-sprayed samples CA2

and CMA exhibited a loser structure. In the case of CA2, two different areas, a light grey and a dark grey one, could be identified. Sample CMA contained brownish impurities. The powder flame-spraying resulted in significantly smoother surfaces with a Ra of sample CA2 and CMA of 18.7 and 13.6 µm, respectively. In the SEM, the coatings S71 and S71T2 appear similar. Typically for rod flame-spraying, the coatings have a dense and homogenous character and are composed of overlaid splats with round or pancake-like shapes within a wide diameter range (5–200 µm) as well as pores. According to the XRD analyses, both samples S71 and S71T2 are composed of a very high amount of amorphous phases of 98 % as well as 1 % of CA and CA$_2$ each. In contrast, the coatings of samples CA2 and CMA are composed of molten particles in a narrower diameter range, indicating a good melting of the powder feedstock, but no flattening of the molten droplets and consequently no distinctive densification of the coating took place. EDS analyses of sample CA2 revealed CA$_2$ (37.5 mol.-% CaO, 62.5 mol.-% Al$_2$O$_3$) as a continuous phase. According to XRD, the coating consists of 83 % amorphous phases and 17 % CA$_2$. These two different phase portions were visible in the light microscope. The coating of sample CMA appears more porous with larger particles, which have on the hand a spherical and on the other hand a more edgy shape. According to EDS analyses, the edgy particles are spinel with CaO (26 mol.-% MgO, 54.5 mol.-% Al$_2$O$_3$, 19.5 mol.-% CaO), whereas the particles with a higher degree of melting additionally contain traces of Na$_2$O (0.3 mol.-%), SiO$_2$ (0.5 mol.-%), and P$_2$O$_5$ (0.4 mol.-%) next to MgO, Al$_2$O$_3$ (spinel), and CaO. An EDS mapping showed, that all of the elements Mg, Al, Ca, Si, Fe, and O are homogeneously distributed in the microstructure. The XRD analysis revealed that sample CMA is composed of 47 % MgAl$_2$O$_4$, 14 % CA, 37 % amorphous phases, and traces of Fe$_3$O$_4$ (1 %). Table 2 summarizes the open porosity as well as the $d_{10}$, $d_{50}$, and $d_{90}$ values of the pore size distribution of the as-sprayed coatings. The pore size distribution is additionally displayed in figure 2. The results of the mercury intrusion confirm the findings of the microstructure investigation in SEM. The rod flame-sprayed samples S71 and S71T2 had an open porosity of 7.1 and 5.9 %, respectively, and a $d_{50}$ pore size below 1 µm (44.7 % of the pores in sample S71 and 23.2 % of the pores in sample S71T2 are larger than 2 µm). Hence, both coatings should be proper materials for an application in contact with molten aluminium. The addition of 2 wt.-% TiO$_2$ have a positive effect on the microstructure by further reducing the open porosity and resulting in a narrower pore size distribution with lower pore sizes of coating S71T2 in figure 2.
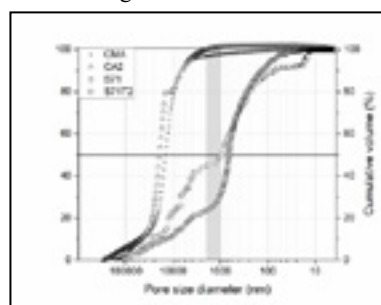


Fig. 2: Pore size distribution of the as-sprayed coatings with marked (grey) area of maximum pore size for aluminium melts.

The coatings CA2 and CMA, which appeared much more porous in the SEM also have a significant higher open porosity of 24.1 (CMA) and 32.6 % (CA2) analysed by mercury intrusion. With a $d_{10}$ of 6.55 (CMA) and 10.56 µm (CA2), both powder-sprayed coatings contain a high degree of pores (96.5 % in coating CMA and 99.8 % in CA2) being large enough to be infiltrated by an aluminium melt and may encounter a higher degree of infiltration and corrosion during application. However, CMA provides a lower porosity and lower pore sizes compared to CA2. The flame-sprayed alumina reference coating A100 has a porosity of 10.8 %, a low $d_{50}$ in the range of the rod flame-sprayed coatings of 0.62 µm, but a $d_{90}$ with very large pore sizes of 172 µm. Fig. 5 shows the bending strength of the free-standing coatings.

527

Tab. 2: Open porosity (OP), and $d_{10}$, $d_{50}$, and $d_{90}$ values of the pore size distribution of the as-sprayed coatings.

| Sample | OP (%) | $d_{10}$ (µm) | $d_{50}$ (µm) | $d_{90}$ (µm) |
|--------|--------|---------------|---------------|---------------|
| S71 | 7.1 | 0.03 | 0.99 | 26.47 |
| S71T2 | 5.9 | 0.14 | 0.73 | 14.12 |
| CA2 | 32.6 | 10.56 | 18.78 | 48.97 |
| CMA | 24.1 | 6.55 | 14.35 | 42.04 |
| A100 | 10.8 | 0.24 | 0.62 | 172.70 |

The reference alumina coating A100 exhibited the highest bending strength of 16.7 MPa but also a high standard deviation. The rod flame-sprayed samples S71 and S71T2 showed similar strength values (7.5 MPa for S71 and 7.1 MPa for S71T2). Hence, the titania content does not influence the strength of the coatings. The porous powder flame-sprayed samples CA2 and CMA exhibited a much lower strength, whereas sample CMA shows a higher strength of 3.1 MPa compared to CA2 (2.0), but a much higher standard deviation.

**Evaluation of the casting test**
The casting test revealed distinct differences in the behaviour of the coatings in contact with molten aluminium. In the case of the powder flame-sprayed coatings A100, CA2, and CMA, the solidified aluminium could have been torn off residual-free. This is a very important property, as the main degradation mechanism of e.g. furnace walls and refractory casting channels against molten aluminium isn't corrosion or erosion but the manual removal of residual solidified Al and dross that stuck at the wall or in the channel after the casting, which tears not only the aluminium from the wall or out of the channel but a lot of the refractory material, too. Macroscopically (figure 3a, j, and m) as well under the light microscope, no damage to the coatings could be detected.
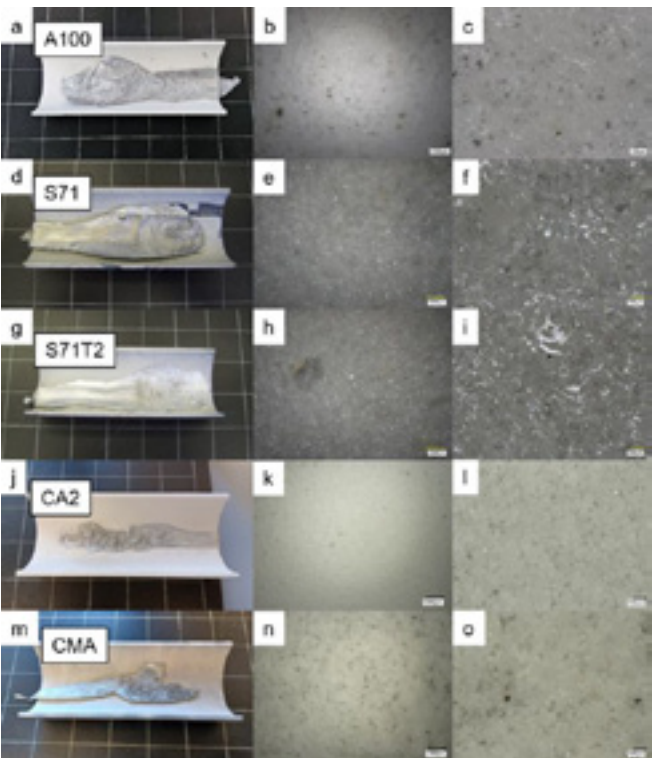


Fig. 3: Coated half-pipes of sample A100 (a-c), S71 (d-f), S71 (g-i), CA2 (j-l), and CMA (m-o) after the casting test and investigation under the light microscope at 30- (middle) and 200-times (right) magnification.

On top of the reference alumina sample A100, brownish-coloured spots after the casting test were visual (figure 3b and c), which is a sign of interaction with molten alumina. In contrast, the surface of the CA2 and CMA coating didn't show a change in the microstructure (see figure 3k, l, n, and o). At higher magnification (figure 3l and o), both coatings CA2 and CMA revealed their porous character but the molten Al didn't infiltrate the open pores of the coatings during the casting test. However, some Al splash could have been found.

After the casting test, parts of the coating S71 spalled from the metallic half-pipe (figure 3d) and the Al could not have been peeled off without tearing off parts of the coating from the substrate. But the majority of the surface of the coating stayed unaffected (figure 3e and f) and showed no differences in its character compared to the as-sprayed state but brownish-coloured impurities as well as locally residual solidified Al. The addition of 2 wt.-% $TiO_2$ prevented the spalling of the coating S71T2 from the metallic halfpipe after the casting test (figure 3g). Similar to sample S71, the majority of the surface of the coating S71T2 stayed unaffected by the casting test compared to its as-sprayed state.

Table 3 summarizes the casting test by listing the mass of the coated half-pipes before ($m_{coated}$) and after the test and hence, the amount of remaining Al ($m_{Al}$) on the coating. The wettability of the rod flame-sprayed samples S71 and S71T2, and the powder flame-sprayed reference sample A100 were at the same level with remaining Al in the halfpipe in the range of 7.8 to 8.1 g, whereat the newly developed $CA/CA_2$ samples showed slight advantages over the reference. In contrast, the powder flame-sprayed samples CA2 and CMA exhibited a very low wettability by molten Al with only a thin Al foil of 3.8 (sample CA2) and 2.4 g (sample CMA) remaining in the half-pipe after the casting of 1.5 kg AlSi7Mg at 800 °C.

Tab. 3: Mass of the coated half-pipes before ($m_{coated}$) and after ($m_{end}$) the casting test and amount of remaining Al.

| Sample | $m_{coated}$ (g) | $m_{end}$ (g) | $m_{Al}$ (g) |
|--------|------------------|---------------|--------------|
| S71 | 358.7 | 366.2 | 7.5 |
| S71T2 | 372.7 | 380.4 | 7.7 |
| CA2 | 368.2 | 372.0 | 3.8 |
| CMA | 379.1 | 381.5 | 2.4 |
| A100 | 378.6 | 386.7 | 8.1 |
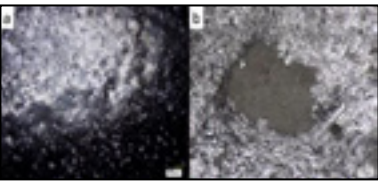


Fig. 4: Light microscope images of ceramic inclusions at the backside (Al-coating interface) of the Al after the casting test with coating S71 (a) and A100 (b).

Figure 4 displays the backside (Al-coating interface) of the Al after the casting test. At different magnifications in the light microscope, ceramic inclusions of different particle sizes embedded in the solidified aluminium could be found after the casting test with each coated halfpipe, exemplarily shown for coating S71 in figure 4a and A100 in figure 4b. The amount of particles which were removed during the casting test from the coating by the molten aluminium is hardly detectable but seems not to differ widely for each coating. However, the maximum grain size of the inclusions at the interface differs: up to 1 mm for coating A100, approx. 200 µm for the coatings S71 and S71T2, 100 µm for CA2, and 150 µm for the CMA coating.
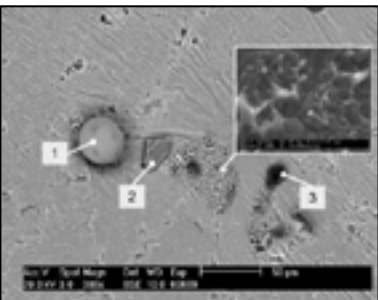


Fig. 5: SEM microstructure of the solidified Al after casting with the S71T2 coating with marked spots for EDS analysis.

In figure 5, the SEM microstructure of the solidified Al after the casting test can be found,

exemplarily for coating S71T2. The matrix consists of typical and characteristic textured Al. Within the solidified Al, several impurities are embedded. According to DIN EN 1706, the AlSi7Mg alloy can contain Al, Si, Mg, Fe, Ti, Mn, Zn, and Cu. An EDS spot analysis showed, that the very fine white particles (below 1 μm), which are homogeneously distributed in the Al matrix, are rich in CaO. The large spherical particle consists of $Al_2O_3$ (72 wt.-%), CaO (26 wt.-%), and $TiO_2$ (2 wt.-%) (spot 1) and represents a part of the coating that had been removed by molten Al during the casting test. Next to $Al_2O_3$-CaO-$TiO_2$, $SiO_2$ can be detected in spot 2. As the coatings don't contain silica, this impurity had been formed by oxidation of the Si portion of the Al alloy. Furthermore, an impurity containing $Al_2O_3$ (69 wt.-%) and $SiO_2$ (20 wt.-%) as well as a lot of trace compounds such as $Na_2O$, MgO, $K_2O$, CaO, S, and Cl was analysed (spot 3). Figure 5 shows another eye-catching part of the microstructure (SEM micrograph at higher magnification), which appears ripped and is only composed of Al (80 wt.-%) and Si (20 wt.-%) without MgO. This is an additional sign of diffusion of Mg from the Al alloy into the coating.

## CONCLUSIONS

More than the chemistry, the state of the feedstock and the spraying technology predetermined the properties of the coatings and hence their interaction with the aluminium melt. The rod flame-sprayed samples S71 and S71T2 are composed of densified overlaid splats and had a roughness $R_a$ in the range of 45–78 μm, a strength of approx. 7 MPa, a low open porosity, and smaller pore sizes. The addition of 2 wt.-% $TiO_2$ to CA/$CA_2$ resulted in an even narrower pore size distribution with 76.8 % of the pores being smaller than the critical pore size of 2 μm. In contrast, powder flame-spraying of CMA and CA2 resulted in a coating composed of spherical particles with a lower strength below 3 MPa but exhibited a lower roughness in the range of 13–18 μm. Both coatings showed a significantly higher open porosity and larger pores with 96.5 % (CMA) and 99.8 % (CA2) of the pores being larger than 2 μm. Even if their open porosity is higher and they have a larger pore size distribution, the powder-flame sprayed coatings composed of $MgAl_2O_4$ (CMA) and $CA_2$ (CA2) showed a better wetting behaviour against Al with less residual Al remaining in the coated half-pipe, which could be peeled-off residual-free after the casting test. However, in the microstructure of the solidified Al after the casting test, fine CaO particles, $Al_2O_3$-CaO-$TiO_2$ spheres (in the case of sample S71T2), and $SiO_2$ could be found. The latter had been formed by oxidation of the Si portion of the Al alloy. Furthermore, Mg from the Al alloy diffused into the coating. In summary, powder flame-sprayed coatings composed of $MgAl_2O_4$ and $CA_2$ are promising barriers to reducing the degradation of refractories by molten aluminium. This is a sustainable resource- and energy-saving approach, as less interaction with the molten aluminium will cause less rejected cast aluminium, which doesn't need to be melted again. Furthermore, the robot-guided automatically powder-flame-spray technology does not only allow the production of coatings but also of three-dimensional refractory components.

## REFERENCES

[1]    Alcircle. Global Aluminium Industry Outlook 2022, 2022.

[2]    Laurent V, Chatain D, Eustathopoulos N. Wettability of SiC by aluminum and Al-Si Alloys, Journal of Material Science 22, 1987, p. 244–250

[3]    Afshar S, Allaire C. The corrosion of refractory aggregates by molten aluminum, Journal of the Minerals Metals & Materials Society JOM 52, 2000, p. 43–46

[4]    Allaire C. Interfacial phenomena, n.d.

[5]    Wynn A, Coppack J, Steele T, Latter G. Improved monolithic materials for lining aluminium holding and melting furnaces – Roof, upper walls and flue, Materials Science Forum 693, 2011, p. 80–89

[6]    Dewing EW, Lindsay JG, Bakker WT. Chemical resistance of refractories to Al and Al-Mg alloys, Journal of the American Ceramic Society 47, 1961, p. 90–94

[7]    Koshy P, Gupta S, Sahajwalla V, Edwards P. Effect of silica on high-temperature interfacial phenomena of monolithic refractories with Al alloy, Metallurgical and Materials Transactions B: Process Metallurgy and Materials Processing Science 39, 2008, p. 331–339.

[8]    Allaire C, Desclaux P. Effects of alkalies and of a reducing atmosphere on the corrosion of refractories by molten aluminium, Journal of the American Ceramic Society 74, 1991, p. 2781–2785

[9]    O'Brien MH, Akinc M. Reduction in Aluminum Alloy Attack on Aluminosilicate Refractories by Addition of Rare-Earth Oxides, Journal of the American Ceramic Society 73, 1990, p. 491–495

[10]   Allahevrdi M, Afshar S, Allaire C. Additives and the Corrosion Resistance of Aluminosilicate Refractories in Molten Al-5Mg, Journal of the Minerals Metals & Materials Society JOM 50, 1998, p. 30–34

[11]   Afshar S, Gaubert C, Allaire C. The effects of fumed silica and barite on the aluminum resistance of alumina castables, Journal of the Minerals Metals & Materials Society JOM. 55, (2003, p. 66–69

[12]   Avraham S, Kaplan WD. Reactive wetting of rutile by liquid aluminium, Journal of Material Science. 40, 2005, p. 1093–1100

[13]   Buhr A, Gierisch D, Mcconnell RW. Raw material concepts for SiO2 free high strength and low wettability aluminium castables, in: UNITECR '05 - Proceedings of the Unified International Technical Conference on Refractories. 9th Biennial Worldwide Congress on Refractories., 2006, p. 635–641

[14]   Siljan O, Hydro N, Porsgrunn N-. Refractories for molten aluminum contact Part II : Influence of pore size on aluminum penetration., Refractories Application and News 8, 2003, p. 21–30

529

# NEW GENERATION CASTABLES – A CONTRIBUTION TO THE DISCUSSION OF H$_2$–ASSISTED SMELTING FURNACES FOR SECONDARY ALUMINUM

Daniel Cölle, Nicole Schlimm, David Schreiner, Bastian Vesenberg
EKW GmbH, Eisenberg, Germany

Frédéric Etienne, François Malandain
EKW France S.A.S., Paris, France

**ABSTRACT**

This paper is addressing the influence of hydrogen as an energy source of fuel-fired smelting furnaces within the processes for the production of secondary aluminum. General aspects of gas-fired & hydrogen-fueled burner technologies are touched upon and special features of handling hydrogen are addressed. The scope of relationships within the impacts of atmospheric effects, reflections and reactivities on the combustion of hydrogen, its reaction products and the effect on established refractory ceramics is illuminated in a particularly.

Advanced & complex application oriented tests & evaluations are discussed to determine and simulate loading conditions of refractory ceramics specified for aluminum alloys with reference to the H$_2$ induced operating conditions.

Hydrogen as critical factor

In principle, hydrogen absorption in aluminium melts is related to the surrounding water. The H2 that is formed is absorbed by the melt within a very short time. If the metal temperature drops, the solubility for hydrogen is reduced. In the liquidus-solidus transition, the H2 solubility decreases in a very small temperature interval over several orders of magnitude and leads to the precipitation of H2 and the generation of gas pores in the cast aluminium structure during the solidification of the aluminium melt. Basically, the proportion of H2 dissolved in the aluminium melt depends on the atmospheric pH2 (hydrogen partial pressure) and on the temperature and composition of the aluminium melt. For example, alloying elements such as Si, Zn or Cu slightly lower the hydrogen solubility, while Mg and sodium increase the H2 solubility.

The refractory material approach leads to a discussion about mineral exclusion criteria & the presentation of individual novel material designs to ensure the operation of the hydrogen-fueled (or mostly hydrogen-fueled) smelting furnace systems in a functionally appropriate state.

# COMPARATIVE POST–MORTEM RESEARCH ON THE CORROSION RESISTANCE OF CHEMICALLY BONDED CASTABLES IN CONTACT WITH MOLTEN ALUMINUM

**Paulina Sołtys**, **Rafał Janik**, **Monika Borowska**, **Wojciech Mikulski**, GÓRBET REFRACTORIES Wojciech Mikulski,
ul. Lipcowa 58, 32-540 Trzebinia, Poland
wojciech.mikulski@gorbet.com.pl

**Dominika Madej**, AGH University of Science and Technology, Faculty of Materials Science and Ceramics,
Department of Ceramics and Refractories, al. A. Mickiewicza 30, 30-059 Kraków, Poland
dmadej@agh.edu.pl

## ABSTRACT
The $Al_2O_3$-based castables are widely used as refractory lining for aluminium melting furnaces. These materials are susceptible to chemical reactions between molten aluminium and refractory compounds. In order to prevent those reactions, commercial additives such as barium sulphate, monoaluminium phosphate or calcium fluoride are generally added in castables. Reduced-density castables containing a highly lightweight aggregates are now an important part of monolithic refractories. Generally, these low-density monolithics are very necessary in terms of enhancing the role of refractories in energy saving and reducing material consumption under demanding working conditions. This article presents and analyses the effect of type of additives and aggregates on the corrosion behaviour of an $Al_2O_3$-based castables with liquid Al alloy.

*Keywords: castables, energy saving, lightweight castables, corrosion tests, a new technology of lightweight castables*

## INTRODUCTION
Aluminium industry is constantly growing and there is a permanent demand of better refractories, especially castables [1]. There are several needs for refractory materials in contact with molten aluminium, such as low wettability by molten aluminium, thermal shock resistance, chemical stability, and good mechanical and thermomechanical properties at temperatures below ca. 1000°C. Many types of aluminosilicate or bauxite refractories containing different additives are generally used in the aluminium industry due to their low cost and availability. Moreover, several anti-wetting additives like barium sulphate, calcium fluoride, zircon or chromium oxide are used to improve the resistance of the refractory to corrosion by molten aluminium [2]. Binder commonly used in these monolithic products is hydraulic i.e. calcium aluminate cement. Regarding the chemical-ones, the bond strength can be developed by the addition or in situ generation of phosphates in the castables fine grained matrix. Phosphoric acid, monoaluminium phosphate or combinations thereof are widely used in the refractory industries as an alternative binder source in castable compositions [3].

### Goal of this work
This study aims to investigate the effect of addition of different components (phosphoric acid, monoaluminium phosphate, barium sulfate and calcium fluoride) on the corrosion resistance of bauxite and lightweight refractory aggregates-based castables at temperature below 1000°C in contact with molten aluminum. For this purpose, the industrial-scale corrosion test in aluminum foundry plant was performed. Comparative post-mortem studies of wear and performance of hydraulically and chemically bonded-castables were conducted based on the results from the macroscopic observations and SEM-EDS.

### Experimental part
Two bauxite-based and one lightweight aggregate-based castables were chosen as the materials for the real-life industrial scale test (Table 1). All castables investigated for the wetting experiment were manufactured by Górbet Refractories company (Trzebinia, Poland) by the standard procedure. The castable compositions were dry and wet homogenized, poured in a mold and compacted through vibration. Then, samples were kept in the molds for 24 h to set completely and then they were removed from the molds, dried and heat treated at 370°C. Firstly, the samples were investigated in term of their physical properties including bulk density (BD), apparent porosity (AP) and cold cursing strength (CCS) according to the procedures presented in the PN-EN ISO 1927-6:2013-06 standard. Secondly, the preheated SAMPLES A, B and C were immersed into molten aluminum alloys at 720°C for durations ca. 6 months. For this purpose the holding furnace was used. The microstructures and chemical compositions of the corroded SAMPLE A were analyzed by scanning electron microscopy (SEM) and energy-dispersive X-ray spectroscopy (EDS) analyzer. SAMPLES B and C without adhesion and infiltration were not analyzed in this regard.

Table 1. The composition of the castables.

| CASTABLES | CASTABLES MAIN COMPONENT | MODIFYING AGENT / TYPE OF BONDING |
|---|---|---|
| SAMPLE A | Bauxite aggregates | Monoaluminium phosphate / chemically bonded |
| SAMPLE B | Bauxite aggregates | Barium sulphate / hydraulically bonded |
| SAMPLE C | Lightweight aggregates | Calcium fluoride / hydraulically bonded |

## RESULTS
### Physical properties of as-delivered materials
The physical and mechanical properties of the three castables heat-treated at 850°C are listed in Table 2. It can be seen that both the bulk density and apparent porosity of the bauxite-based materials (SAMPLES A and B) depends on the non-wetting additive type. Thus, the different apparent porosity of two refractories will affect the wettability of the molten aluminum. It can be also seen that the castables made of the microporous aggregates exhibit low bulk density and relatively high apparent porosity.

Table 2. Physical properties of the castables heat-treated at 850°C.

| CASTABLES | BD / g/cm$^3$ | AP / % | CCS / MPa |
|---|---|---|---|
| SAMPLE A | 2.71 | 20.5 | 60.7 |
| SAMPLE B | 2.91 | 16.6 | 135.7 |
| SAMPLE C | 2.01 | 42.1 | 38.4 |

### Comparative macroscopic observations of corroded samples
The macroscopic morphology of bauxite-based castables after corrosion by molten aluminium is shown in Figure 1. Obvious appearance differences were observed on the samples after the immersion corrosion test under industrial conditions in aluminium casting plant. According to the results obtained, it can be summarized that the chemically bonded SAMPLE A was infiltrated

531

by molten aluminium alloy and the corundum build-up was adhered to the refractory surface. On the other hand, two hydraulically bonded SAMPLES containing barium sulphate (B) or calcium fluoride (C) exhibit a superior resistance to aluminium attack since no adhesion and infiltration were observed.

**SAMPLE A. ADHESION VISIBLE, INFILTRATION.**
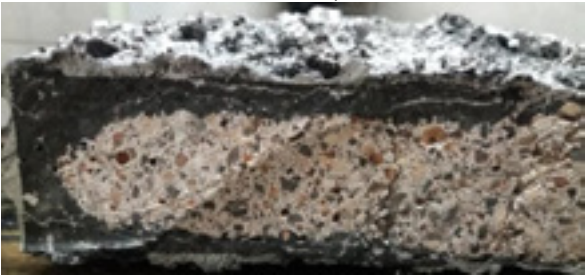


**SAMPLE B. NO ADHESION, NO INFILTRATION.**



**SAMPLE C. NO ADHESION, NO INFILTRATION.**



*Fig. 1. Macroscopic morphology of castables after corrosion by molten aluminium. SAMPLE A – phosphate bonded bauxite-based castables, SAMPLE B – hydraulically bonded bauxite-based castables, SAMPLE C – hydraulically bonded lightweight refractory aggregates-containing castables.*

**Results of microstructural investigations**

Photograph showing different regions analysed in the SAMPLE A is shown in Fig. 2. This figure shows the sample used for SEM/EDS analysis, and five regions (1 – metal area, 2 – metal area/corroded area interface, 3 – corroded area, 4 – corroded area/non-corroded area interface and 5 – non-corroded area) can be identified from this sample, and investigation of these zones was carried out.
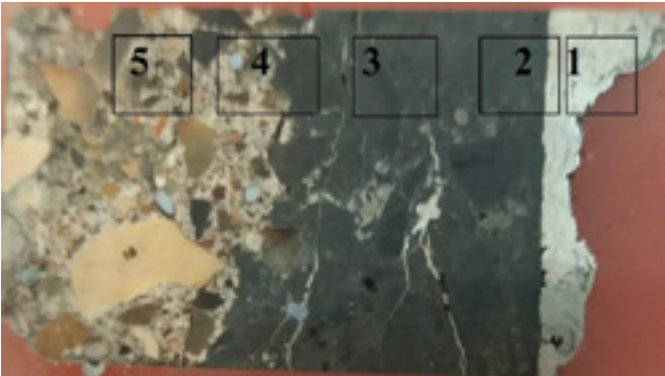


*Fig. 2. Photograph showing different regions analysed in the SAMPLE A. 1 – metal area, 2 – metal area/corroded area*

interface, 3 – corroded area, 4 – corroded area/non-corroded area interface and 5 – non-corroded area.

The cross-section of the corroded chemically-boned bauxite-based castables with phosphate additive (SAMPLE A) was analysed by SEM-EDS. The microstructure of interface between Al-alloy and castables is shown in Fig. 3-4. The chemical compositions the regions 1-5 are shown in Table 3. The microstructure of the region below the slag/refractory interface is shown in Fig. 5. The chemical compositions the regions 1-5 are shown in Table 4.

Figs 3-4 show the SEM images of the slag/refractory interface (from region 2 in Fig. 2). A deep infiltration/reaction zone can be seen below the metal area/corroded area interface. This part exhibits corrosion of both the coarse grains and refractory matrix. The bauxite grains of different sizes still are firmly embedded in the matrix. Moreover, a build-up was adhered to the refractory surface. Here, a high proportion of Mg can be detected using EDS analysis (Fig. 4, Table 3, Spot 3). Thus, the formation of spinel phase in the form of magnesium aluminate spinel ($MgAl_2O_4$) can be confirmed. Since the build-up contains also alumina ($Al_2O_3$), thus it can be considered as corundum-spinel build-up. Spinel was also detected in the region below the contact line (Fig. 4, Table 3, Spot 5). Fig. 5 presents the SEM image of the region below the slag/refractory interface (from region 3 in Fig. 2), where molten aluminium penetration pathway can be distinguished. A high proportion of Al can be detected using EDS analysis (Fig. 5, Table 4, Spot 4).

Table 3. Chemical composition of the regions 1-5 in atomic % (from Fig. 4).

| Spot | O$K$ | Mg$K$ | Al$K$ | Si$K$ | Cr$K$ | Mn$K$ | Fe$K$ | Cu$K$ | P$K$ | Ca$K$ |
|---|---|---|---|---|---|---|---|---|---|---|
| 1 | 8.47 | 1.84 | 64.79 | 11.82 | 0.44 | 3.80 | 7.66 | 1.18 | - | - |
| 2 | 7.46 | - | 65.95 | 12.10 | - | 1.24 | 10.92 | 2.33 | - | - |
| 3 | 51.82 | 17.62 | 29.62 | - | - | - | - | 0.94 | - | - |
| 4 | 59.64 | - | 40.36 | - | - | - | - | - | - | - |
| 5 | 50.17 | 12.01 | 32.69 | 2.68 | - | - | - | - | 1.69 | 0.76 |

Table 4. Chemical composition of the regions 1-5 in atomic % (from Fig. 5).

| Spot | O$K$ | Mg$K$ | Al$K$ | Si$K$ | Cr$K$ | Mn$K$ | Fe$K$ | Cu$K$ | P$K$ | Ca$K$ | Na$K$ |
|---|---|---|---|---|---|---|---|---|---|---|---|
| 1 | 60.06 | - | 39.94 | - | - | - | - | - | - | - | - |
| 2 | 50.80 | 5.99 | 40.36 | 0.42 | - | - | - | - | 0.25 | 1.04 | 1.14 |
| 3 | 8.08 | - | 67.63 | 11.64 | 1.50 | 3.54 | 7.61 | - | - | - | - |
| 4 | 8.28 | - | 90.64 | - | - | - | - | 0.41 | - | - | 0.67 |
| 5 | 59.23 | - | 40.22 | 0.55 | - | - | - | - | - | - | - |
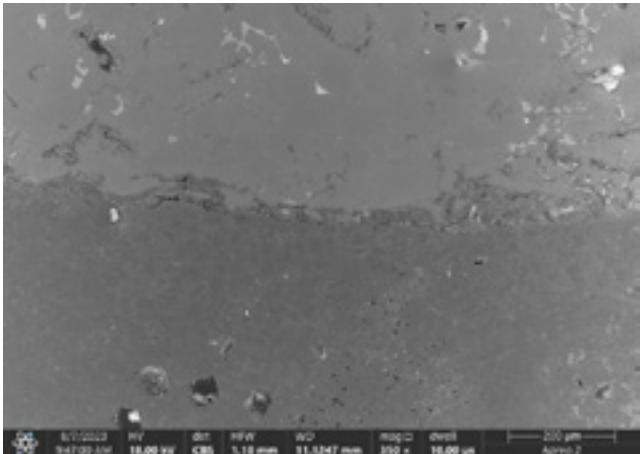


*Fig. 3. SEM image of the slag/refractory interface (region 1) of sample A corroded by Al-alloy. Backscattered electrons SEM micrograph on polished section.*
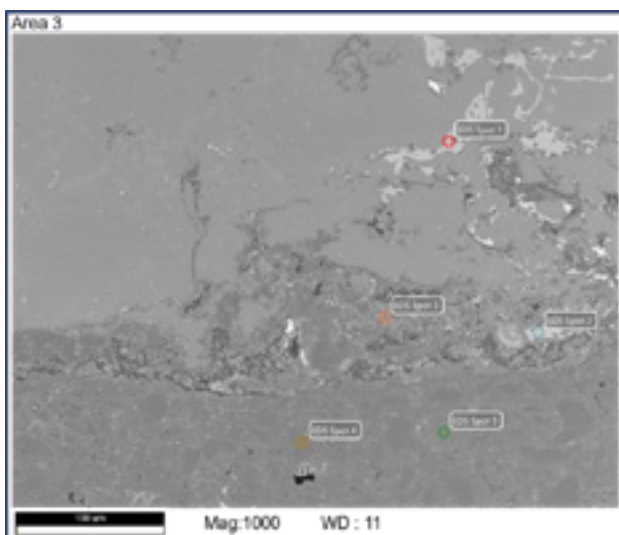
*Fig. 4. SEM-EDS analysis of the slag/refractory interface (region 1) of sample A corroded by Al-alloy. Backscattered electrons SEM micrograph on polished section. EDS results – Table 3.*
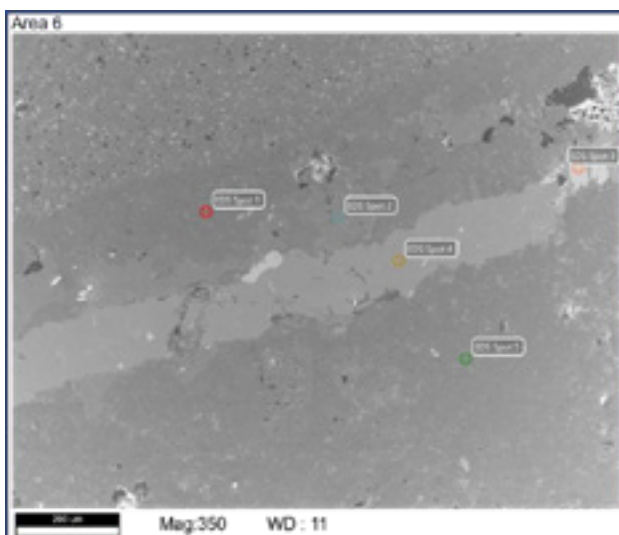


*Fig. 5. SEM-EDS analysis of the region below the slag/refractory interface (region 3) of sample A corroded by Al-alloy. Backscattered electrons SEM micrograph on polished section. EDS results – Table 4.*

## CONCLUSIONS

The reduced-density castables containing a highly lightweight aggregates were successfully obtained. These castables showed a better corrosion resistance in contact with molten aluminium than those of dense bauxite-based samples. There was a definite relationship between the type of both aggregates and non-wetting additives, and the corrosion resistance of castables. The chemically bonded sample made of bauxite aggregates and monoaluminium phosphate as an additive exhibits adhesion and extensive penetration zone. The hydraulically-boned samples made of bauxite or lightweight aggregates exhibit superior corrosion resistance. In these two materials barium sulphate or calcium fluoride were used, respectively.

## REFERENCES

[1] Reichert W., Kenn D., Sannikow V., Tonnesen T., Telle R., Influence of modern aluminium alloys on the reaction behavior of refractory linings, International Journal of Ceramic Engineering & Science 4, 2022, p. 180-185

[2] AdabiFiroozjaei E., Koshy P., Sorrell C. C., Effects of $AlPO_4$ addition on the corrosion resistance of andalusite-based low-cement castables with molten Al-alloy, Journal of the European Ceramic Society 33, 2013, p. 1067-1075

[3] Lopes S. J. S., Luz A. P., Gomes D. T., Pandolfelli V. C., Self-flowing high-alumina phosphate-bonded refractory castables, Ceramics International 43 (8), 2017, p. 6239-6249

533

# STEEL CERAMIC COMPOSITES RESISTANT TO LONG–TERM CONTACT WITH MOLTEN ALUMINUM ALLOYS

Piotr Malczyk, Tilo Zienert, Florian Kerber, Jana Hubálková, Gert Schmidt, Nora Brachhold, Christos G. Aneziris

Institute of Ceramics, Refractories and Composite Materials, Technische Universität Bergakademie Freiberg, 09599 Freiberg

## ABSTRACT

The development and evaluation of novel stainless steel-based composites for direct contact with liquid aluminum alloys has been carried out. The Steel Ceramic Composite consisted of 60 vol% 316L stainless steel powder and 40 vol% of MgO or $TiO_2$ ceramic powder. The sample were manufactured using uniaxial pressing and subsequent surface pre-oxidation at 850, 1000 °C for 24 h.

The corrosion resistance of composite was investigated against molten AlSi7Mg0.3 alloy using crucible corrosion tests. The tests were carried out at 850 °C for 24 h and 168 h. The influence of pre-oxidation on the corrosion resistance of the samples was analyzed using XRD and SEM/EDS. The corrosion phases formed in the aluminum alloy were investigated using SEM/EDS/EBSD and PSEM/ASPEX/AFA and included the assessment of aluminum alloy contamination by evaluation of corrosion precipitation content, quantity and size. The sample Steel-MgO exhibited excellent corrosion resistance with negligible contamination of the aluminum alloy.

## INTRODUCTION

Steels are very prone to corrosion during contact with liquid aluminum alloys. The reactivity of steel and their elements with molten aluminum alloys is well known and has already widely been reported. This phenomenon is to some extend used to form hard Fe-Al-based intermetallics on the steel parts for corrosion protection. Nevertheless, during the longer contact with liquid aluminum the rapid dissolution of steel takes part. This dissolution does not only refer to Fe but includes also another steel alloying elements like Cr, Mn, Ni and Mo. It leads to both, the damage of the steel product and the contamination of aluminum, and thus narrows the utilization of steel-based components in the aluminum industry to very short contact with molten aluminum. Even the application of protective coating on steel parts is extending the corrosion resistance of steel for only a short period, as the high affinity of aluminum to oxygen and its very low half-cell potential causes the reduction of most oxides [1-4].

Conventional refractory parts for contact with liquid alloys are based on coarse grained castables. For the aluminum industry it is commonly alumina-mulite with anti-wetting additives reducing the intrusion of the alloy melt in the refractory material. The production process of these widely used refractory materials, including drying and prefiring steps, is very time- and cost-consuming and can be prone to numerous failures through arising internal stresses and presence of micro-cracking. It is also well known, that thermal shock resistance of these castables is insufficient for demanding and rapidly changing conditions of metallurgical processes. Although, the incorporation of thermo-mechanical properties of steel would be very advantageous for refractory applications, it requires the elaboration of sophisticated multi-material components or the development of novel aluminum melt corrosion resistant material.

The beneficial influence of refractory ceramics on the corrosion resistance of Steel Ceramic Composites was already reported by the authors [2]. These composites, due to the presence of steel powder, are characterized by good machinability, advantageous thermo-mechanical properties, higher ductility and in consequence better thermal shock resistance. On the other hand, when carried out correctly, the addition of refractory ceramic powders significantly increases their corrosion resistance to molten aluminum alloys. Weigelt et al. [3] investigated the influence of addition of 10 vol% and 30 vol% of $TiO_2$ and $Al_2O_3$-$TiO_2$ to the CrMnNi TRIP-Steel on the corrosion resistance against molten aluminum alloy after 4h corrosion test. Although the low Ni-steel should exhibit higher stability to the aluminum alloy, no improvement for the Steel Ceramic Composites by application of these ceramic particles on the corrosion resistance against aluminum alloy as well as on the mechanical characteristics after the corrosion tests was reported. Malczyk et al. [4] reported the beneficial influence of addition of 40 vol% of $TiO_2$ to 316L stainless steel on the differential potential arising between molten aluminum alloy and the composite, resulting in the reduction of the corrosion potential. Nevertheless, the chemical reactivity of aluminum in contact with steel hampers the formation of a dual layer electrochemical interface. In order to benefit from electrochemical characteristics of this composite the interface between aluminum alloy and composite should be characterized with sufficient electrical impedance and partial chemical stability for the contact with aluminum. Basing on these conclusions, Malczyk et al. [2] reported very promising results regarding long-term corrosion resistance against molten aluminum alloy with 60 vol% 316L stainless steel and 40 vol% MgO composites after the pre-oxidation of their surface forming corrosion resistant FeO-MgO solid solution phases.

For the investigation of long-term corrosion in alloy melts finger immersion tests and crucible tests are commonly applied. For the immersion tests the contact with liquid aluminum alloy last mostly up to 12 h and use relatively high amount of aluminum. The crucible corrosion tests are characterized by significantly longer testing times with incorporation of a smaller amount of aluminum, giving the opportunity for in-depth analysis of not only the composite but also the aluminum and its contamination. Taking this into consideration, the samples discussed in this paper were investigated using crucible corrosion tests with the 24 h and 168 h contact duration to the molten aluminum alloy. This paper is a complementary work to the already reported newly developed molten aluminum corrosion resistant composites based on steel matrix with addition of both $TiO_2$ or MgO ceramic powders [7, 14]. The study focuses on the influence of the surface pre-oxidation process on the structure of composites and their corrosion resistance against the melt.

## EXPERIMENTAL

For the manufacturing of composite samples, the gas-atomized 316L-FeCr18Ni10Mo3 stainless steel powder (TLS Technik, Bittterfeld-Wolfen, Germany), electrofused MgO < 3 μm, 98% (Refratechnik Steel, Duesseldorf, Germany and TR HP-2 rutile $TiO_2$ (Sachtleben Chemie, Duisburg, Germany) were used. The composites consisted of 60 vol% of 316L steel and 40 vol% of ceramic powder, MgO or $TiO_2$ respectively.

Samples were pressed into prismatic and cylindrical samples with the aid of a uniaxial press (Rucks, Glauchau, Germany). The prismatic samples used for investigation of pre-oxidation had dimensions of 7 mm x 7 mm x 70 mm, whereas the cylindrical corrosion tests samples had diameter of 50 mm and height of 50 mm. For the pressing procedure two degassing steps at 30 MPa and 60 Mpa for 1 s were applied. The consolidation pressure of pressing was performed for 3 s at 100 MPa. After the pressing, all samples were dried in a convection drying oven at 40 °C for 24 h and

subsequently at 110 C for 24h. The cylindrical samples were hand drilled to prepare cylindrical crucibles with wall thickness of 7 mm and crucible depth of approx. 42 mm.

The binder removal was carried out in a debinding furnace (Xerion Berlin Laboratories, Berlin, Germany) with heating rates of 2 K·min⁻¹ to 200 °C, and 2 K·min⁻¹ from 200 °C to 500 °C, holding time of 30 minutes at 500 °C and cooling rate of 0.5 K·min⁻¹. The samples were sintered at 1350 °C for 2 h using sintering furnace with graphite lining (Xerion Berlin Laboratories, Berlin, Germany) under argon atmosphere, with heating and cooling rates of 5 K·min⁻¹. After the sintering, the 316L40MgO samples had 21.0% open porosity and 4.75 g·cm⁻³ bulk density, whereas 316L40TiO2 samples had 7.5% open porosity and 5.78 g·cm⁻³ bulk density – measured using an AutoPore V mercury intrusion porosimeter (Micromeritics, Unterschleissheim, Germany). The mean value of linear sintering shrinkage was 4.0% and 8.8% for 316L40MgO and 316L40TiO2, respectively.

To carry out the surface treatment, samples of both composite materials were split into two groups, which were pre-oxidized in two different temperatures – 850 °C and 1000 °C. The pre-oxidation was performed for 24 h with 10 K·min⁻¹ heating and cooling rate.

For the investigation of the influence of pre-oxidation on the phase formation at the surface of both composite materials the SEM/EDS aided X-ray diffraction (XRD) experiments were carried out. The measurements were performed on polished cross-sections of prismatic samples. By using divergence slit measuring 1/32°, a narrow area of approx. 0.3 mm × 10 mm was irradiated. The irradiation area was placed parallel and in the nearest vicinity to the sample surface, in order to investigate only the pre-oxidized part of the sample. The experiments were performed with a Bragg-Brentano geometry and with Cu-K$_\alpha$ radiation between 25° and 100° 2Θ using Empyrean DY1946 XRD diffractometer (Malvern Panalytical, Kassel, Germany). The phase analysis of the oxidized part of the composite samples was done using Rietveld analysis with the aid of the SEM/EDS microscopy analysis of the irradiated surface.

Static crucible corrosion tests were performed in a laboratory furnace (Nabertherm, Bremen, Germany). Pre-oxidized crucibles with prepared aluminum alloy inside were placed together in the furnace and heated up to 850 °C. The heating and cooling rate was 10 Kmin⁻¹. After reaching 850 °C the crucibles with molten aluminum alloy were held for 24 h or 168 h at this temperature. The 24 h crucible corrosion test was performed on the samples pre-oxidized at 850 °C only, whereas the longer 168 h test was performed on both 850 °C and 1000 °C pre-oxidized crucibles.

The evaluation of the crucibles after the corrosion tests was performed using images assembly of confocal laser scanning microscope (LSM) micrographs using Keyence VK/X-1000 laser scanning microscope with multifile analyzer (Keyence, Neu-Isenburg, Germany) as well as by SEM/EDS microscopical analysis performed using the XL 30 scanning electron microscope (Philips, Eindhoven, Germany). The analysis of the aluminum alloy after the crucible corrosion tests was performed on selected samples exhibiting sufficient corrosion resistance against aluminum melt. This test was carried out using ASPEX PSEM eXpress (FEI, Delmont, PA, USA) with automatic feature analysis (AFA) focusing on area fraction and composition of corrosion precipitations present in the solidified aluminum alloy after the corrosion tests.

## CONCLUSIONS

The steel ceramic composites with addition of TiO$_2$ and MgO have been successfully developed and the influence of their pre-oxidation performed for 24 h at 850 °C and 1000 °C on the structure of the composites surface has been analyzed. The evaluation of their corrosion resistance against AlSi7Mg0.3 aluminum alloy was performed using crucible corrosion test for 24 h and 168 h at a temperature of 850 °C. The investigations revealed formation of favorable protective FeO-MgO solid solution layer for the samples from 316L40MgO composite. Formed FeO-MgO layer was characterized as stable against molten aluminum alloy even for longer contact time with the melt. The best results were obtained in the case of 316L40MgO composite pre-oxidized at 1000 °C for 24 h. This composite was able to withstand 168 h of contact time with molten aluminum alloy revealing no significant damage of the surface and only minor contamination of the aluminum melt. The contamination of the alloy originated mainly from dissolved $(Fe,Cr)_3O_4$ and $(Fe,Cr)_2O_3$ phases from the composite surface. There are reasonable presumptions that, after dissolution of these phases, no further corrosion of the composite will be observed.

Although the 316l40TiO2 composite was able to withstand 24 h corrosion test with molten aluminum alloy, its protective layer, consisting mainly of mentioned Fe-Cr-O phases, dissolves in longer contact times with the melt leaving the composite exposed for further corrosion. Therefore, the 316L40TiO2 composite was not able to withstand the 168 h contact with molten aluminum alloy.

The analysis of the surface of the pre-oxidized 316L40MgO samples revealed the presence of phases with high Si-content. These Si-containing phases were placed at the boundary between the steel particle and the MgO particle or transforming MgO-FeO solid solution. The phase is based on the MgO-FeO-SiO$_2$ system, with Ni and Cr in its structure. It is assumed that this phase may remain partially liquid during the pre-oxidation process. It was concluded that the Si-containing boundary phase is responsible for diffusion of Fe-O from the steel particles during the pre-oxidation process into the MgO structure facilitating the transformation of MgO into corrosion resistant MgO-FeO. It was also revealed that the presence of this Si-containing phase led to the trapping of Ni-containing steel residuals (encapsulating Ni-Fe phase) in the structure of oxidized MgO-FeO solid solutions. This successfully hampered the contamination of aluminum alloy by detrimental Ni diffusion.

## REFERENCES

[1] Malczyk et al.: Investigation of interfacial phase formation during corrosion of stainless steel. *Interceram Int. Ceram.* Rev. 2020, 69, p. 42–51
[2] Malczyk et al.: Corrosion-Resistant Steel–MgO Composites as Refractory Materials for Molten Aluminum Alloys. Materials 2020, 13, 4737.
[3] Weigelt et al.: Metal-Matrix Materials for High-Temperature Applications with Liquid Aluminum. Adv. Eng. Mater. 2020, 22, 1–11
[4] Malczyk et al.: Electrochemical Studies of Stainless Steel and Stainless Steel-TiO2 Composite in Reference to Molten Aluminum Alloy Using a Solid-State BaCO3 Electrolyte. Materials 2022, 15, 6723

# INFLUENCE OF FILTER SURFACE ROUGHNESS ON THE PRESSURE DROP OF CERAMIC FOAM FILTERS

Claudia, Voigt, Jana Hubálková, Christos G. Aneziris

Technische Universität Bergakademie Freiberg, Institute of Ceramics, Refractories and Composite Materials, Agricolastr. 17, 09599 Freiberg, Germany

Eric Werzner

Technische Universität Bergakademie Freiberg. Institute of Thermal Engineering, Chair of Gas and Heat Technology. Gustav-Zeuner-Str. 7. 09599 Freiberg. Germany

Robert, Fritzsch, Ragnhild Aune

Department of Materials Science and Engineering, Norwegian University of Science and Technology (NTNU), Trondheim, Norway

Massoud Hassanabadi

Innovation & Technology, Hydro Extruded Solution AB, Kanalgatan 1, Finspång, Sweden

Murilo, D.M. Innocentini

University of Ribeirão Preto, Course of Chemical Engineering, Ribeirão Preto, SP, Brazil

## ABSTRACT

The pressure drop of a ceramic foam filter is an important characteristic indicating the resistance to fluid flow through the filter. Filtration experiments have shown that the filtration efficiency increases with decreasing functional pore size, however, this improvement comes at the cost of a higher pressure drop. Furthermore, trials with increased roughness of the filter struts showed an improved filtration behaviour. In order to compare these two measures with respect to their efficiency, i.e., in terms of filtration per pressure drop, the sensitivity of the pressure drop with respect to surface roughness needs to be known. In the study, the pressure drop of ceramic foam filters was measured for different functional pore sizes, porosity, and surface roughness with a water-based test facility at NTNU in Trondheim, Norway. The flow velocity was varied in the range of 0.6 - 80 cm/s.

## INTRODUCTION

Ceramic foams are used in the area of metal melt filtration for conditioning the melt flow and the removal of non-metallic inclusions [1]. For an existing industrial casting process, most of the influencing parameters are difficult to adjust, except for the parameters of the filter, which can be configured easily. Hence, efforts to improve filtration efficiency are focused on the parameters of the filter. Most geometrical features of filter structures that are beneficial for filtration (e.g., high ppi (pores per inch) number, low porosity, or presence of closed windows) are associated with an increased pressure drop. A higher pressure drop is detrimental to the financial viability and operational reliability of the filtration process. Such filters demand a higher pressure head or pumping power to maintain a desired flow rate. The junior research group PurCo funded by the BMBF (Federal Ministry of Education and Research) do research to understand whether the enhancement of filter surface roughness for improved filtration is advantageous with regard to the pressure drop, its influence on the flow resistance has to be understood. While the effect of the ppi number on the filtration efficiency [2] and pressure drop [3] has been extensively studied, the effect of filter roughness on flow resistance has not yet been reported for CFFs. To investigate the effect of surface roughness on the pressure drop during the flow of liquid metals through CFFs and to assess its magnitude compared to other geometry modifications, an experimental study using CFFs with different surface roughness, porosity, and ppi number was conducted. In the present study, the pressure drop experiments were performed using water instead of liquid metal. After dividing the pressure drop dp by the sample thickness, the pressure gradient dp/dx was obtained.

## MATERIALS AND METHODS

Ceramic foams made of alumina ($Al_2O_3$) with sintered sizes of length 50 mm, width 50 mm, and height 20 mm were prepared for the present study. The sintered $Al_2O_3$ skeleton foams were coated with the combined dip centrifugation procedure with different slurries (see Table 1) to obtain different foam surface roughness. The slurry 33 µm and slurry 70 µm are named according to the $d_{50}$ of the raw

material with the largest particle size. The filters coated with these slurries were labelled in the same way – reference filter, filter 33 µm, and filter 70 µm.

Tab. 1: Composition of the coating slurries for generating different foam surface roughness (* based on the sum of solids)

| | Slurry reference | Slurry 33 µm | Slurry 70 µm |
|---|---|---|---|
| $Al_2O_3$ CT 9 FG $d_{50}$=5 µm (Almatis. Germany) (mass%) | 33.3 | | |
| $Al_2O_3$ CT 3000 SG $d_{50}$=0.8 µm (Almatis, Germany) (mass%) | 33.3 | 50 | 50 |
| $Al_2O_3$ T60/T64 -45µm (Almatis, Germany) m(mass%) | 33.3 | | |
| $Al_2O_3$ P6 $d_{50}$=33 µm (Almatis, Germany) (mass%) | | 50 | |

The pressure drop was determined using a water-based test facility at the Norwegian University of Science and Technology (NTNU, Trondheim, Norway). A filter holder made of acrylic glass was used to keep the filter in place in the water channel. For the measurement of rectangular samples, a sample holder with rectangular openings of 47.5 x 47.5 mm² was used per measurement, and two rectangular filters were stacked above each other. The filter holder was connected to a water tank (970 x 670 x 1000 mm³) filled with 500 l of tap water at 16°C by smooth pipes with an inner diameter of 49.8 mm, which extended 1250 mm in both upstream and downstream directions and, thereby, provided a development length of 25 diameters. A vertical multistage centrifugal pump (maximum pressure 10 bar) with an integrated frequency converter (Grundfos, Denmark)) was employed to pump the water. The flow velocities varied between 0.006 m/s and approx. 0.8 m/s by using different valve settings (low flow velocities) and different power levels of the pump (high flow velocities). The flow velocity was indirectly determined from the mass gain using a balance (Flintab, Germany) that recorded the mass of the water, which was collected at the outlet with an interval of 1 s. Once 20 measurements were recorded, the mass flow rate ṁ (kg/s) was calculated, and the corresponding velocity u was determined.

## RESULTS

Figure 1 shows the variation of pressure gradients with velocities for rectangular ceramic foam filters with different ppi numbers, ranging from 10 to 40 ppi, whereby the porosity of the filters was established to be between 75.2% and 78.5%. The determination of the pressure drop was repeated at least once, whereby the stacked filters were removed and repositioned between measurements. The measurements show good repeatability, and significant differences in pressure drop values between different ppi numbers were obtained. Overall, it was established that the pressure drop was

higher for higher ppi numbers. This is an expected result and is in accordance with various publications [2, 3].
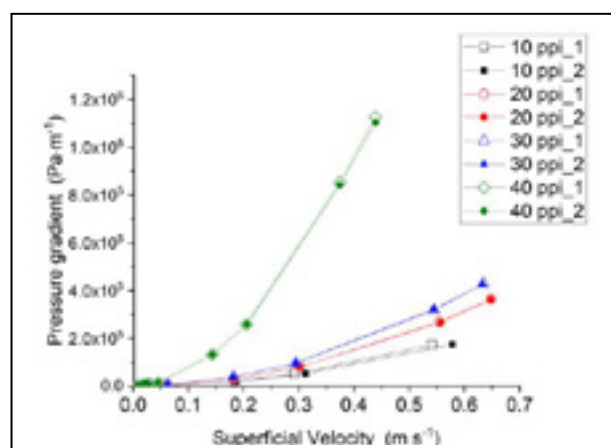


*Fig. 1: Pressure drop independence of the superficial velocity for ceramic foam filters of different ppi numbers*

The influence of the filter porosity on the pressure drop was also investigated for 40 ppi filters, Figure 2. The filter porosity of the stacked filters proved to vary between 72.8% (95 g) and 79.7% (70 g). The obtained differences in the pressure drop are believed to be a result of the interlinking of the pressure drop and the filter porosity. For the lower filter porosities, the pressure drop is higher, as the higher strut volume present in these filters acts as a flow resistor. However, it is notable that the obtained pressure drops for CFFs with 40 ppi, of higher filter porosities, i.e., 75%, 79%, and 80%, are relatively close to each other.
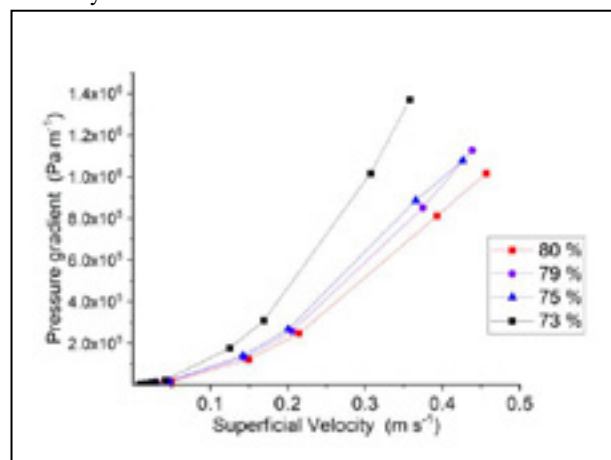


*Fig. 2: Pressure drop independence on the superficial velocity and filter porosity of 40 ppi samples*

In comparison, the lowest porosity of 73% (95 g) possesses a significantly higher pressure drop. This is believed to result from the higher proportion of closed pores with decreasing filter porosity. Overall, the significant influence of filter porosity on the filter performance is clearly shown by the presented experimental data.

Therefore, it must be taken into account during the investigation of the effect of filter roughness The pressure drop independence on the surface roughness was measured for 40 ppi (Figure 3) filters, and showed only small differences between the obtained data for the reference filters and the filters with rougher surfaces.

However, the difference was established to increase with an increasing superficial velocity of the fluid medium (water). The pressure drop differences between the reference filters and the filters with rougher surfaces proved to be significantly lower than the differences obtained between the different ppi numbers and filter porosities.
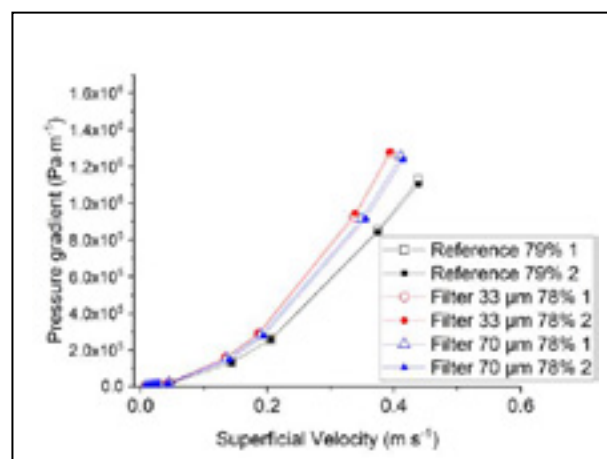


*Fig. 3: Pressure drop independence on the superficial velocity of 40 ppi filters with different surface roughness*

Further research will be conducted considering the significance of the observed differences. It is, however, notable that the pressure drop of the 33 μm and 70 μm filters were almost the same even if the grain distribution at the surface was different. The 33 μm filters had small but homogenously distributed grains at their surface whereas the 70 μm filters had larger particle sizes at lower numbers.

## CONCLUSIONS

The main objective of the present study was to assess the effect of the surface roughness of ceramic foam filters on the pressure drop compared to other geometrical modifications known to promote filtration. This was accomplished by measuring the variations of pressure gradients with respect to velocity, using a water-based test facility for filters with different ppi numbers, porosities, and surface roughness. The obtained values of the coefficients are in agreement with existing literature data for similar ceramic foam filters and showed the expected trends with respect to the influence of the ppi number and porosity. The surface roughness was, however, found to have only a minor impact on the pressure drop and the permeability coefficients.

## REFERENCES

[1]  Olson III R A, Martins L C, Cellular ceramics in metal filtration, Advanced Engineering Materials. 7, 4 (2005) 187-192.

[2]  Gauckler L J, Waeber M M, Conti C, Jacob-Duliere M, Ceramic foam for molten metal filtration, Journal of Metals September (1985) 47- 50.

[3]  Garrido G I, Patcas F C, Lang S, Kraushaar-Czarnetzki B, Mass transfer and pressure drop in ceramic foams: A description for different pore sizes and porosities, Chemical Engineering Science 63 (2008) 5202 – 5217.

537

# INTERACTIONS BETWEEN THE GAS PHASE IN A NICKEL FLASH SMELT– ING FURNACE AND THE REFRACTORY LINING

J. Lehmusto, L. Hupa
Åbo Akademi, Turku, Finland

S. Söyrinki, J. Lagerbom, T. Jokiaho, Z. Que, E. Huttunen-Saarivirta
VTT Technical Research Center of Finland, Espoo, Finland

J. Määttä
University of Turku, Turku, Finland

M. Lindgren
Metso, Pori, Finland

## ABSTRACT

Magnesia (MgO)-chromite ($MgCr_2O_4$) spinel-based refractories are applied as lining materials in copper and nickel flash smelting furnaces due to their excellent durability against thermal shocks, heat, and melt erosion forces. In smelters, the refractories experience high temperatures but also thermal gradients due to the cooling of the walls. In addition, the refractories are subjected to an aggressive gaseous environment on the gas-space side with more than 40 vol.% of $SO_2$. For optimal lining performance, more light needs to be shed on the interactions between the refractory and the smelter atmosphere, for example, the reaction mechanisms of refractory wear need to be understood. This work analyzed and compared the unused and reacted genuine refractories from a nickel flash smelting furnace to identify the reactive species and define the reaction mechanisms. The characterization was carried out with SEM-EDS, μ-CT, and XRD. The unused magnesia-chromite refractory had a two-phase microstructure consisting of MgO and $(Fe,Mg)(Al,Cr)_2O_4$ spinel. Compared to the unused material, the reacted refractory was denser and contained several zones with dissimilar chemical compositions, likely driven by the thermal gradient. For example, the hot zone of the refractory was depleted in MgO, whereas sulfur-containing species were identified deeper in the material, towards the cooled external wall of the smelter. Furthermore, the thermal gradient affected the inward diffusion of gaseous chemical species from the flash-smelting process, enabling their reaction with some refractory constituents. Interactions with slag revealed slight dissolution and the formation of silicates. The results from the microstructural characterization of the refractories will be presented and discussed. The results lay the basis for future activities: controlled lab-scale experiments and computational modeling of refractory behavior.

## BACKGROUND

Flash smelting refers to the pyrometallurgical processing of base metals, like nickel and copper, and utilizes the internal energy of the feed material for smelting, making the process very energy-efficient. Refractory lining in the flash smelting furnaces is one key enabler of the continuous operation of the process, as it acts as a thermal barrier between the hot smelting environment and the body of the furnace. However, the lining is exposed not only to high temperatures and thermal gradients but also to the smelter atmosphere and, occasionally, molten slag that is carried along the gas flow.

Magnesia-chromite ($MgCr_2O_4$) spinel-based refractories have been widely used as a lining material in smelters. Due to the harsh operation conditions, the lining gradually degrades over time. Plenty of research effort has been put into understanding the interactions between the operation environment and the refractory lining in copper flash smelting furnaces [1,2,3] in order to maximize the lining lifetime. The published results have acknowledged the important role of infiltration into the lining in the degradation process. In turn, studies on the performance of linings in nickel flash smelting furnaces are rare, yet the composition of the gas atmosphere with high $SO_2$ content is deemed aggressive. Previous work [4] revealed that microstructural changes that occurred in the lining during the service life likely originated from interactions between the lining and both the feed material constituents and the gas phase. However, based on purely examining the specimens taken from the operating nickel flash smelting furnace, the exact contribution by each of the components could not be defined. In this work, we report in parallel the results from the characterization of the as-received lining, spent lining from the nickel flash smelting furnace, and controlled laboratory "finger" experiments conducted for the lining specimens subjected to the slag. The results provide novel insights into the interactions between the gas phase in a nickel flash smelting furnace and the magnesia-chromite refractory lining.

## EXPERIMENTAL

The studied material was a magnesia-chromite product of type MCr50, ISO 10081-2, with a given composition of (in wt.%): 59.5 MgO, 19.0 $Cr_2O_3$, 13.5 $Fe_2O_3$, 6.0 $Al_2O_3$, 1.3 CaO, and 0.5 $SiO_2$, with an apparent porosity of 17.0 vol.%. The microstructure of as-received material was analyzed and compared to that of spent refractories from the roof lining of a nickel flash smelting furnace. The characterization was carried out with scanning microscopy (SEM), energy-dispersive spectroscopy (EDS), electron back-scattered diffraction (EBSD), micro-computed tomography (μ-CT), and X-ray diffraction (XRD) methods.

To understand better the effect of the gas phase on the refractory lining, a comparison was done to bricks with a nickel flash smelting slag contact. For this purpose, a so-called finger test was performed. Brick fingers were immersed into the slag at 1450°C and kept there, in an inert atmosphere, for six hours. After the holding period, the fingers were lifted above the melt and allowed to cool freely with the furnace. Afterwards, they were sliced in half and the samples were prepared for microscopy investigation. The main constituents of the slag were 7% MgO, 4% NiO, 31% $SiO_2$, and 52% of iron oxides.

## RESULTS AND DISCUSSION

Based on the XRD and EBSD results, the as-received material consisted of two phases; MgO (magnesia; periclase phase) and $(Fe,Mg)(Al,Cr)_2O_4$ (magnesia-chromite spinel; picotite phase). In SEM images, the former is seen in dark grey contrast, while the latter corresponds to the areas seen in light grey contrast, e.g., Fig. 1. EDS provided the following average compositions for the main phases: chromite ore particles 33% Cr-12% Fe - 14% Mg - 8% Al- 32% O, secondary chromite 28% Cr - 18% Fe - 15% Mg - 7% Al - 32% O, and magnesia 60% Mg – 35% O – 4% Fe – 2% Cr.

Compared to the intact material, the spent refractory was denser and contained several zones with dissimilar chemical compositions. On the process side of the refractory, a deposit layer existed that had constituents from both feed materials and refractory. It had a two-phase structure as presented in Fig. 2. The phase seen darker in the SEM image had an average composition (in wt%) of 32% O, 24% Ni, 20% Mg, 19% Si, and 4% Fe. The lighter phase was richer in metallic elements and lower in silicon consisting of 58% Fe, 19% Ni, and 18% O. No sulfur was detected in the deposit layer. Cross-sectional analysis revealed a noticeable gradient of silicon, with the hot side showing the highest concentration.

The colder part of the refractory had a chemical composition close to that of the as-received material, Fig. 2. However, the microstructure was less porous and the sub-grain surfaces seemed to contain less secondary chromite. The decrease in porosity originated most likely from the formation of $CaSO_4$, which was identified together with the original magnesia and chromite phases. The presence of sulfur inside the refractory indicates that the material is porous enough for the migration of gaseous species. Once inside the material, sulfur has reacted with CaO either as $SO_2$:

$$CaO\ (s) + SO_2\ (g) + \tfrac{1}{2}\ O_2\ (g) \rightarrow CaSO_4\ (s) \tag{1}$$

or as $SO_3$:

$$CaO\ (s) + SO_3\ (g) \rightarrow CaSO_4\ (s) \tag{2}$$

Reaction with Mg is also possible

$$MgO\ (s) + SO_3\ (g) \rightarrow MgSO_4\ (s) \tag{3}$$
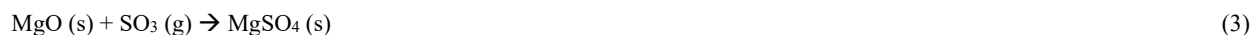
and $MgSO_4$ was also detected. Since the molar volume of $CaSO_4$ is roughly three times the molar volume of CaO, the pores are filled through the increase in the internal volume. Despite the formation of $CaSO_4$, no extensive microcracking was seen close to the $CaSO_4$-rich areas. Thus, the formation of $CaSO_4$ alone does not explain the degradation of the refractory material through cracking.
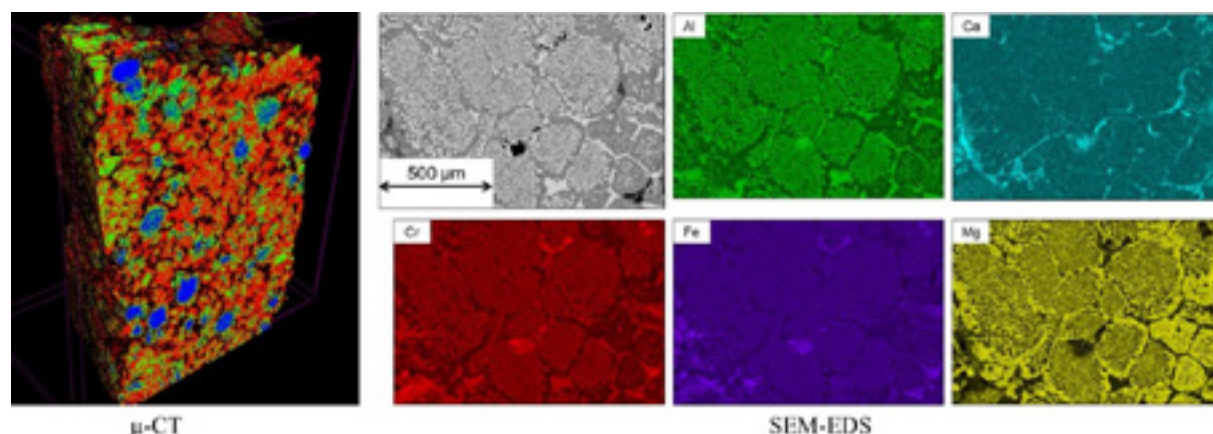


*Fig. 1: A three-dimensional density map (left) with an SEM image and corresponding elemental maps (right). The brighter areas in the SEM image are magnesia-chromite phase and the darker areas are magnesia.*
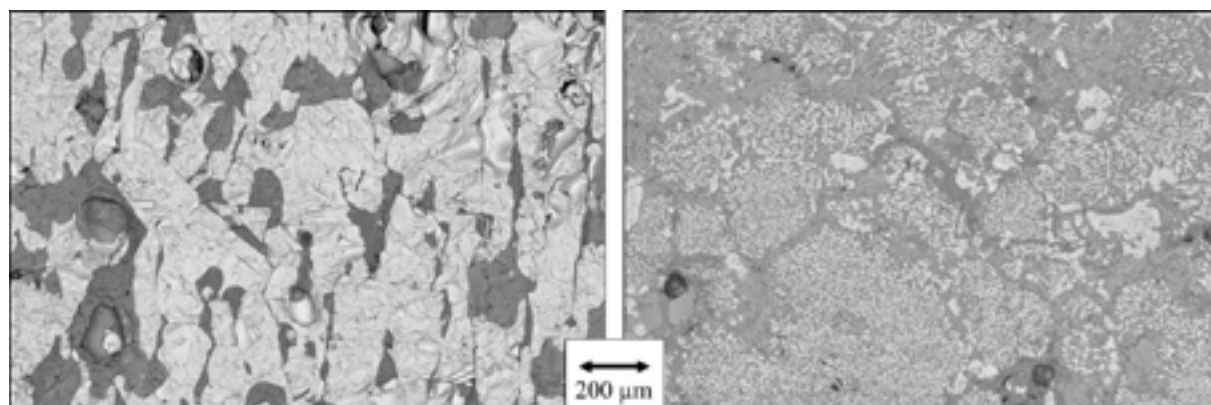


*Fig. 2: Two example SEM images of the microstructure of a spent refractory; close to the process environment (left) and in the colder end of the refractory (right).*

In slag contact, the refractory finger retained well its shape. However, reactions between the slag and the refractory had evidently taken place, with some slag being attached to the refractory surface, as shown in Fig. 3 The cross-sectional SEM/EDS analyses (Fig. 4) showed that, after slow cooling, the attached slag consisted of four phases: precipitates (that accounted for the majority of the slag structure) seen in light contrast, internal areas within the precipitates seen in light grey contrast, and two different types of areas within final slag, seen in

539

intermediate and dark grey contrast. The average chemical compositions of the phases are presented in Table 1. In comparison to the original slag composition, the precipitate phases dissolved plenty of chromium and aluminum from the refractory. The two types of areas in the final slag contained roughly the same elements as the original slag, yet with dissimilar proportions of magnesium, silicon, and iron, and with some calcium that likely originated from the refractory. It is further emphasized that the interface between the attached slag and the refractory was dense.



Fig. 3: Refractory finger after testing in slag contact and SEM image of the surface with slag reactions.
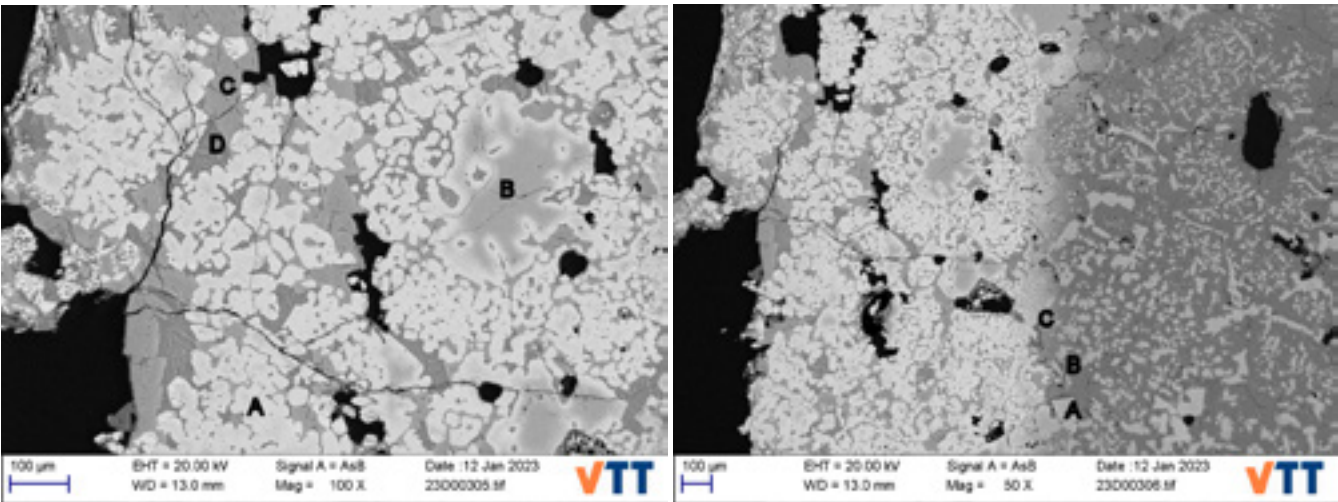


Fig. 4: SEM image of the cross-section of slag and slag-refractory interface after the finger test.

Tab. 1: Average chemical compositions of four different phases in the attached slag (in wt.%).

| Phase | O | Na | Mg | Al | Si | K | Ca | Ti | Cr | Fe | Ni |
|---|---|---|---|---|---|---|---|---|---|---|---|
| Precipitates (A) | 27.6 | | 3.7 | 6.2 | 0.7 | | | 0.2 | 17.2 | 39.7 | 5.3 |
| Precipitates, inside (B) | 31.6 | | 15.0 | 8.8 | 2.1 | | | 0.4 | 33.5 | 9.4 | 0.4 |
| Final slag 1 (C) | 40.7 | 0.5 | 1.8 | 6.9 | 27.2 | 0.9 | 3.4 | | 0.2 | 17.4 | 0.4 |
| Final slag 2 (D) | 35.1 | | 15.9 | 0.9 | 18.1 | 0.2 | 0.3 | | 0.4 | 24.7 | 4.4 |

Tab. 2: Chemical compositions measured from neighboring locations from the refractory gas interface.

| Location | O | Mg | Al | Si | Ca | Cr | Mn | Fe | Ni |
|---|---|---|---|---|---|---|---|---|---|
| Light grey (A) | 32 | 15.5 | 8.4 | 2.1 | | 30.4 | | 10.5 | 0.4 |
| Medium grey (B) | 30.3 | 44.1 | 0.6 | | | 5 | | 17.7 | 2.3 |
| Dark grey (C) | 38.5 | 35.4 | | 13.4 | 1.4 | 1.7 | | 7.7 | |

Three phases could be identified in the refractory material close to the slag contact: areas seen in light grey contrast, those seen in medium grey contrast, and finally areas with dark grey contrast. The phase seen in light grey contrast (area A in Table 2) corresponded to the magnesia-chromite phase, with a similar composition to that in the as-received material. The medium grey phase (area B in Table 2) was the MgO phase, yet with somewhat higher iron content than in the as-received condition. Presumably, FeO from the slag had diffused into MgO and formed $(Mg,Fe)O$ solid solution. The dark grey phase (area C in Table 2) contained oxygen and magnesium but was also rich in silicon. Such composition refers to magnesium silicates, possibly $Mg_2SiO_4$ reported in the literature in the connection of slag-refractory interaction in copper anode furnaces [5]. The refractory microstructure was also partially re-arranged: close to the slag-refractory interface, the secondary chromite phase at the grain boundaries seemed to have disappeared and a more uniform distribution of fine chromite precipitates, was observed. The likely reason for this is grain growth due to elevated temperatures rather than the interactions with the slag. Additionally, the refractory microstructure was densified. This may relate to the enhanced diffusion of elements described above. It is also

evident that the reason for densification is different from the one observed in the gas phase refractories, assigned to the reactions with sulfur-bearing gases and the subsequent formation of sulfates. However, in finger tests with slag, sulfur was not present.

Comparing the results from finger tests to those obtained for spent refractories, it is evident that the refractory may dissolve some elements from the slag, such as iron. However, this plays a minor role in the performance of the refractory. In turn, the slag may dissolve some elements from the refractory, like chromium, aluminum, and calcium. This may eventually influence the stability of the phases and contribute to the selection of elements, which are available to react with the gas phase. For example, if Ca from the refractory surface is dissolved in the slag, it is not available to react with the sulfur-containing gas phase to form $CaSO_4$, therefore, other sulfates, such as $MgSO_4$, will be favored. The results also revealed the development of a new phase, namely magnesium silicate, in refractory close to the slag contact. This phase was also occasionally detected in the spent refractory, but we did not detect any further interaction between the silicate phase and the sulfur-containing species.

## CONCLUSIONS

Based on the characterization of as-received and reacted refractory specimens, the following observations were made:

- The structure of a spent refractories was less porous than that of an as-received refractory.
- Thermal gradient clearly affects both the chemical structure and microstructure of the refractory.
- Thermal gradient clearly affects the diffusion of species.
- Even though $SO_2/SO_3$ clearly reacts with Ca and Mg, forming sulfates, other species diffuse into the refractory material as well, and especially as the feedstocks are becoming chemically more complex, the possible effect of these species on refractory degradation should be studied thoroughly in the future.
- Interactions with slag contribute to dissolution of elements from slag to the refractory and vice versa, yet this is foreseen to play only a minor role with respect to interactions with the gas phase. However, the possible transfer of Ca from the refractory to the slag may emphasize the role of Mg as the sulfate-forming species.
- $CaSO_4$ formation alone cannot explain refractory densification, as the same phenomenon is observed in slag contact without the presence of sulfur.
- Refractory densification is not directly related to spalling, since the main macroscopic cracks in the refractory are located elsewhere.

## ACKNOWLEDGEMENTS

## REFERENCES

[1] Malfliet, A., Loftian, S., Scheunis, L., Petkov, V., Pandelaers, L., Jones, P.T., Blanpain, B., Degradation mechanisms and use of refractory linings in copper production processes: a critical review. J. European Ceramic Soc. 34, 2014, 849-876.

[2] Xu, L., Chen, M., Wang, N., Gao, S., Chemical wear mechanism of magnesia-chromite refractory for an oxygen bottom-blown copper-smelting furnace: a post-mortem analysis. Ceramics International 47, 2021, 2908-2915.

[3] Chen, L., Li, S., Jones, P.T., Guo, M., Blanpain, B., Malfliet, A., Identification of magnesia-chromite refractory degradation mechanisms of secondary copper smelter linings. J. European Ceramic Soc. 36, 2016, 2119-2132.

[4] Lehmusto, J., Söyrinki, S., Lagerbom, J., Jokiaho, T., Que, Z., Määttä, J., Hupa, L., Huttunen-Saarivirta, E., Lindgren, M., Characterization of a magnesia-chromite refractory material: reactivity and reaction mechanisms in flash smelter gas atmosphere. Submitted to J. European Ceramic Soc.

[5] Perez, I., Moreno-Ventas, I., Rios, G., Fundamentals of the refractory wear in an industrial anode furnace used in the copper-making process. Ceramics International 45, 2019, 9788-9798.

# AL$_2$O$_3$–MGAL$_2$O$_4$ REFRACTORY MATERIAL AS A CR–FREE ALTERNATIVE DEDICATED TO THE COPPER INDUSTRY

Ilona Jastrzębska[1], Aleksandra Kalęba[1], Maciej Ludwig, Edyta Śnieżek, Paweł Drożdż[1], Jacek Szczerba[1]

[1]AGH University of Science and Technology
Faculty of Materials Science and Ceramics, al. Mickiewicza 30, 30-059 Kraków
email: *ijastrz@agh.edu.pl*

## ABSTRACT

The work is based on the previously published article [1]. In this work, we show the corrosion of novel Cr-free Al$_2$O$_3$-MgAl$_2$O$_4$ refractory material dedicated to the copper industry against PbO-rich copper slags. The FactSage simulations were conducted to reveal possible changes in the phase composition of the corroded material. Corrosion was tested experimentally by pellet and contact corrosion test at 1300ºC. Corroded materials were characterized in terms of phase composition by XRD and microstructure by SEM/EDS. The results showed that the passive corrosion mechanism predominates, with the formation of platelet-morphology PbAl$_{12}$O$_{19}$ and complex spinel (Mg,Fe,Cu,Zn)(Al,Fe)$_2$O$_4$. PbO-richest slag was found the most aggressive towards refractory.

## 1. INTRODUCTION

Copper is one of the most important metals among all non-ferrous metals, both in Poland and worldwide. In 2020, according to the International Copper Study Group [2], Poland was 13. the biggest producer of Cu worldwide in terms of copper mine production, 7. producer in smelted copper production, and 9. producer in refined copper production. Refractories are indispensable materials for the production of copper. They work as thermomechanical linings in all the heating devices for copper refining. According to statistics from the European Ceramic Industry Association [3], refractory materials account for 18.2 % in terms of the total value of the ceramic market in Europe, while 11 % of total refractory production is dedicated to the non-ferrous industry. With increased worldwide demand for copper, also, the raised demand for refractory materials for this industry is predicted. As copper production is very complex (the average Cu content in Polish copper sulfide ores is 1.99 % [4]) numerous refining devices are used, which are lined with refractories, e.g., fluidized-bed furnaces, electric-arc furnaces, converters or anode furnaces. Currently, magnesia-chromite (MgO-Cr) refractories are used in Cu devices, as they exhibit high thermal shock resistance and excellent corrosion and erosion resistance. However, the application of these refractories relates to the formation of hexavalent chromium compounds, which belong to 1. group of carcinogens, as classified by the International Agency for Research on Cancer (IARC) [5]. Hence, new Cr-free materials are sought worldwide [6][7][8][9][10][11]. In this work, we present the corrosion phenomena in Al$_2$O$_3$-MgAl$_2$O$_4$ refractory material, which can be one of the alternatives for MgO-Cr refractories.

## 2. MATERIALS AND METHODS

In this work, industrially-produced alumina-spinel refractory, Al$_2$O$_3$-MgAl$_2$O$_4$ (A-MA) was subjected to corrosion tests by three types of industrial PbO-rich copper slags. The slag samples, designated as S1, S2 and S3, were characterized by different chemical compositions, due to their different origin in three stages of converting process [12].

Equilibria simulations of high-temperature corrosion reactions between test refractory and slags were conducted based on the oxide composition of Al$_2$O$_3$-MgAl$_2$O$_4$ refractory and the composition of each slag S1, S2 and S3. The simulations were conducted applying FactSage thermochemical software version 7.3, using the *Equilib* module and the databases FactPS, FToxid and FTmisc. The applied proportion of refractory to slag was 50:50 g, and the simulation temperature range was 700-1400ºC.

In experimental route, the refractory material was subjected to corrosion tests against S1, S2 and S3 copper slags by powder and contact corrosion test. The pellet corrosion test was performed on powdered, homogenized mixtures of refractory and slag in a mass ratio of 3:1. The cylindrical samples of 20 mm in diameter and 10 mm in height, prepared by uniaxial pressuring under 65 MPa, were heat-treated in an electric furnace at 1300°C in air atmosphere with a heating rate of 5°C/min. After 3-h of soaking at maximum temperature, the samples were cooled down with the furnace, milled to grain size below 63 μm and subjected to XRD analysis. The application of the pellet test, with an increased surface area of a tested system, enabled the investigation of the liquid phase formation upon heating.

In the contact corrosion test, the refractory sample was prepared by cutting the cuboid out of the original material, while the slag sample was obtained by pressing the powdered slag into a cylindrical shape with its height below ½ of the height of the cut refractory. Then, the disc slag sample was placed on a cuboid refractory. The entire system was heat-treated in the electric furnace at 1300°C with a 3-h dwell time. After contact corrosion tests, SEM/EDS analysis was conducted to reveal the compositional and morphological changes at the cross-section of the corroded material.

## 3. RESULTS

### 3.1 Al$_2$O$_3$-MgAl$_2$O$_4$ refractory and corrosive slags

XRF of Al$_2$O$_3$-MgAl$_2$O$_4$ refractory showed that the dominant oxide component in the test refractory was Al$_2$O$_3$ (94 wt. %). The material also contained MgO (5 %) and SiO$_2$ (0.3 %). The rest oxides (Fe$_2$O$_3$ and Na$_2$O and others) constituted about 0.7 %. XRD identified the following phases: Al$_2$O$_3$, β-Al$_2$O$_3$, Mg$_{7.51}$Al$_{16.33}$O$_{32}$, MgAl$_2$O$_4$ and SiO$_2$ (α-quartz).



The microstructure of refractory consisted of Al$_2$O$_3$ grains with their size from 10 μm to even above 1 mm. The matrix of the material was composed of fine-grained spinel. As confirmed by the EDS analysis, it was primarily Al-rich spinel, where Al/Mg ratio was around 2.1, while it is 2.0 in a stoichiometric spinel.
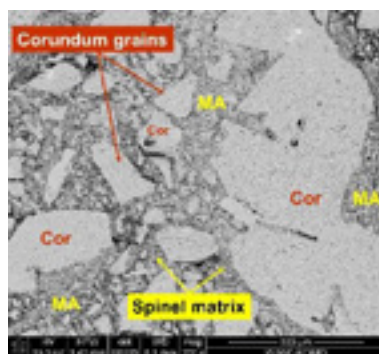
**Fig. 1**. *SEM image of Al$_2$O$_3$-MgAl$_2$O$_4$ refractory material.*

The corrosive media used in the test were copper converter slags S1, S2 and S3, characterized by the various chemical and phase composition. Corrosive slag S1 contained intermediate content of PbO (21 mol. %) and CuO (23 %) and an increased amount of Fe$_2$O$_3$ (14 %). Slag S2 was distinguished by the greatest amount of CuO (51 %), while S3 contained the greatest amount of PbO (29 %). All the slags were characterized by a low-melting nature, with the slag S2 (greatest CuO$_x$ content) melting as first at 680ºC, while S1 at 780ºC and S3 (greatest PbO content) at 800ºC according to FactSage equilibria simulations.

## 3.2 Simulations of high-temperature corrosion reactions



**Fig. 2.** Phase composition changes of $Al_2O_3$-$MgAl_2O_4$ refractory by slags.

Equilibria simulations of $Al_2O_3$-$MgAl_2O_4$ refractory in contact with copper slags in FactSage were shown in Fig. 2. Reactions of refractory under the influence of slag S1 were the least dynamic and produced the lowest amount of liquid phase (Fig. 2a). The intensive increase of liquid slag amount started at 1100°C and was directly related to $PbAl_{12}O_{19}$ phase decomposition (red curve for all slags). $Al_2O_3$, which was released to slag due to $PbAl_{12}O_{19}$ decomposition, was partly grabbed to form solid spinel phase (1100-1200°C) and partly liquid slag. Slag S1 of intermediate composition in terms of PbO (39 %) and CuO (16 %) content, seems the least detrimental for the work of refractory at 1120°C.

## 3.3 XRD after pellet corrosion



**Fig. 3.** Changes in phase composition of $Al_2O_3$-$MgAl_2O_4$ refractory by copper slag.

After pellet corrosion at 1300°C for 3h, $Al_2O_3$ was still the most abundant phase after corrosion (Fig. 3). The greatest decrease in alumina content was identified for slag S2. This sample contained the greatest amount of complex spinels, including ($Mg_{8.11}Al_{4.76}Fe_{1.12}O_{32}$-14%, $Cu_{0.08}Mg_{7.92}Al_{16.08}O_{32}$-19%). Spinel with copper ions was present only in sample with slag S2 (greatest Cu content). This sample also contained the greatest amonut of Pb, Ca, Al-silicates. Slight amounts of Cu were present in a form of $Cu_2O$ (0.8 %) and CuO (1.3 %).

## 3.4 SEM/EDS after contact corrosion

Fig. 4, Fig. 5 and Fig. 6 present microstructure from hot face to cold face of cross-sectioned $Al_2O_3$-$MgAl_2O_4$ refractory after 3h-contact corrosion at 1300°C corroded by slag S1, S2 and S3, respectively. Refractory was penetrated by slag which was liquid at the tested temperature. This penetration was initiated via open pores of refractory containing 18 % open porosity. The open pores present in the refractory material facilitated the diffusion of the ions as they increased the exposed surface area to corrosion reactions.



**Fig. 4.** SEM images of $Al_2O_3$-$MgAl_2O_4$ refractory after corrosion by slag S1.



**Fig. 5.** SEM images of $Al_2O_3$-$MgAl_2O_4$ refractory after corrosion by slag S2.
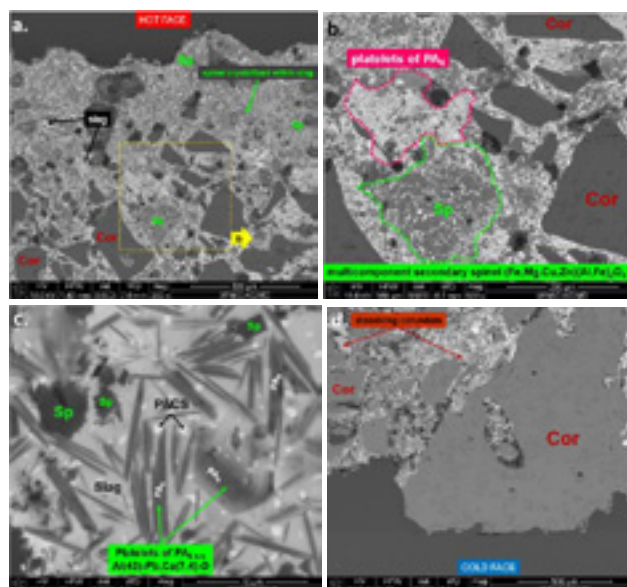


**Fig. 6.** SEM images of $Al_2O_3$-$MgAl_2O_4$ refractory after corrosion by slag S3.

543

The chemical composition of all the phases in corroded samples was attached in Tab. 1. After corrosion it was observed that the slag infiltrated mostly the spinel matrix at the hot face of refractory, which was seen for all slags. Interestingly, the newly formed spinel phase - crystallized out of the liquid phase - accepted numerous slag components into its structure, mostly di- and trivalent ions like $Cu^{x+}$, $Fe^{x+}$, $Zn^{2+}$, $Ni^{2+}$. This phenomenon allowed the material to partly inhibit further diffusion of aggressive components towards the inside of the refractory. The new spinel of multicomponent composition $(Fe,Cu,Mg,Ni,Zn)(Fe,Al)_2O_4$ most abundantly occurred at the contact zone (Fig. 4a, Fig. 5a, Fig. 6a).

The grains of corundum absorbed comparable amounts of Pb and Ca of about 2.5 %, which can be seen by the brighter colour of some $Al_2O_3$ grains (Fig. 4d, Fig. 5e, Fig. 6e). This phenomenon initiated the formation of new, platelet-morphology crystals which were clearly seen for all the slags, in Fig. 4b (S1), Fig. 5b (S2), Fig. 6b (S3). The average thickness and length of these small crystals were 1 and 10 μm, respectively. The numerous EDS analyses confirmed its relatively stable chemical composition, represented by Al (about 44 %) and comparable amounts of Pb and Ca (about 8 % as a sum) as shown in Tab. 1.

**Tab. 1.** *EDS analysis in selected microareas of refractory sample corroded by slag S1, S2 and S3, corresponding to Fig. 4, 5 and 6, respectively.*

| Name | Phase | Chemical composition, mol. %* | | | | | |
|---|---|---|---|---|---|---|---|
| | | Pb | Cu | Mg | Al | Fe | Others |
| Sp (S1) | Grey geometric spinel crystals | - | 9.7 | 3.8 | 16.0 | 29.2 | Ni 7.7 Zn 3.7 |
| Sp (S2) | | - | 12.0 | 9.7 | 43.8 | 1.4 | Ni 1.5 |
| Sp (S3) | | - | 4.9 | 7.6 | 36.5 | 9.9 | Zn 1.8 |
| PA6 (S1) | Platelet aluminate phase | 3.6 | - | 1.6 | 43.6 | 4.2 | Ca 3.6 Si 3.4 |
| PA6 (S3) | | 3.7 | - | - | 42.8 | 4.5 | Si 3.9 Ca 3.7 As 0.8 |
| PACS (S1) | Light needle-like crystals | 12.2 | 5.1 | - | 13.4 | 6.8 | Ca 15.9 Si 10.0 As 1.4 |
| PACS (S2) | | 16.8 | - | - | 14.7 | - | Ca 10.6 Si 5.8 As 3.3 |
| PACS (S3) | | 9.9 | 2.0 | - | 17.7 | 2.6 | Ca 10.4 Si 10.1 As 3.0 |
| Slag (S1) | Glassy phase | 9.6 | 3.8 | - | 19.7 | 5.9 | Si 17.7 Ca 6.3 |
| Slag (S2) | | 13.6 | 3.2 | - | 15.3 | - | Si 14.2 Ca 5.7 As 5.0 |
| Slag (S3) | | 10.7 | 2.1 | - | 18.2 | 2.9 | Si 20.6 Ca 6.4 As 1.2 Zn 0.9 |

P-PbO, A-$Al_2O_3$, S-$SiO_2$, C-CaO, *rest to 100 % is oxygen.

Slag S3 of greatest PbO content (51 %), infiltrated the refractory $Al_2O_3$-$MgAl_2O_4$ mostly, evidenced by the largest amount of bright-colour slag in the hot, middle and cold face of the sample, as shown in Fig. 6. In the area of the hot face, corundum grains were significantly dissolved by the slag, as the nearer to hot face the smaller alumina grains were observed (Fig. 6a).

In the middle part of all the samples additional Pb, Ca aluminosilicate phase of needle-like morphology, designated as PACS, crystallized within the glassy slag phase. This was the non-stoichiometric ternary phase from the system PbO-CaO-$SiO_2$.

Glassy silicate slag in the corroded samples was composed of multiple elements, including Al, Pb, Ca, Cu, As and Zn (Tab. 1). Cu did not diffuse into cold face, as spinel in this zone was of original composition (Mg-Al-O) with no other elements observed in the composition. Infiltration of Pb nearby $Al_2O_3$ grains was also confirmed, mostly for S1 and S3.

# 4. DISCUSSION

The refractory $Al_2O_3$-$MgAl_2O_4$ was composed mainly of corundum (α-$Al_2O_3$) and magnesia aluminate spinel ($MgAl_2O_4$, $Mg_{7.51}Al_{16.33}O_{32}$) with amounts of 77 % and 23 %, respectively. The microstructure of the material covered the large alumina grains located among the fine-grained Al-rich spinel matrix. The refractory was characterized by the bulk density of 3.1 g/cm³, while its open porosity reached 18.4 %. The typical Cr-containing magnesia refractory possesses a density of 3.3 g/cm³ and open porosity in the range of 14-17 % [13].

The fastest increase in liquid slag amount was observed for S3 of the greatest PbO-content, which is demonstrated in Fig. 7a,b. The amount of liquid phase for S3 raised from 700°C, with a maximum at 820°C reaching 0.3 g/°C. At 1120°C it reached the second maximum of 1g/°C. S1 possessed a similar maximum with 0.9 g/°C at the same temperature of 1120°C. Corrosion by S2 exhibited the lowest but most dynamic changes in a liquid phase formation with peaks at 1040°C (0.4 g/°C), 1120°C (0.3 g/°C) and 1240°C (0.4 g/°C).
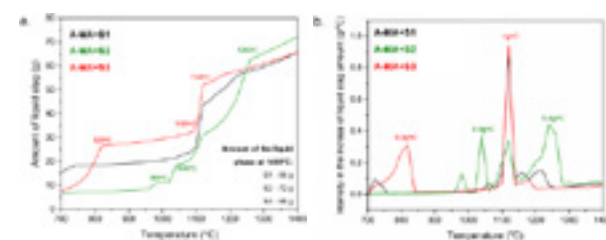


**Fig. 7.** a. Change in amount of liquid slag vs. T, b. change in the liquid slag amount at every 1°C, in the system refractory - copper slag.

Up to 1100°C, the formation of the liquid phase was the result of various silicates and aluminosilicates decomposition. Above about 1100°C, it was directly connected with the decomposition of $PbAl_{12}O_{19}$ (PA6, magnetoplumbite-like structure, hexagonal plate morphology). This is confirmed for all the slags, as the liquid phase started to be greatly enriched with PbO and $Al_2O_3$ from about 1100°C [1]. Decomposition of $PbAl_{12}O_{19}$ was also evidenced by SEM/EDS as the new, platelet-morphology corrosion product was characterized by Al/(Pb+Ca) ratio of 6.0 for S1 and 5.8 for S3 (Ca was assumed to substitute Pb, as $r_{Ca2+}$=100 pm and $r_{Pb2+}$=108 pm). PA6 was formed due to a reaction between PbO from slag and $Al_2O_3$ from refractory acc. to reaction (1):

$$PbO_{(slag)} + 6Al_2O_{3(refractory)} \rightarrow PbAl_{12}O_{19} \quad (1)$$

PA6 is one of three phases existing in the system PbO-$Al_2O_3$ acc. to [14], namely, PbO·6$Al_2O_3$ (PA6), PbO·$Al_2O_3$ (PA), and 2PbO·$Al_2O_3$ (P2A). PA6 melts the highest (>1000°C) among the rest of PA and PA2.

The PACS needle-morphology phase revealed at SEM images for all the slags is most probably the solid solution phase between two phases $C_2PS_3$ - $C_2P_3S_3$ from the system PbO-CaO-$SiO_2$, in which Si is partially substituted by 31 % larger Al ($r_{Si4+}$=32 pm, $r_{Al3+}$=42 pm) [15]. The three ternary phases exist in this system PbO-CaO-$SiO_2$ ($C_2PS_3$, $C_2P_3S_3$, $CP_8S_6$) [16].

The second interesting observation is that selected ions from the slag (Cu, Fe, Ni, Zn) are prone to interact with the starting refractory components of $Al_2O_3$ and $MgAl_2O_4$ and form secondary multicomponent spinels acc. to reaction (2) and (3):

$$Al_2O_{3(refractory)} + CuO_x + FeO_x + NiO + ZnO_{(slag)} \rightarrow (Mg,Fe,Cu,Zn)(Al,Fe)_2O_4 \quad (2)$$

$$MgAl_2O_{4(refractory)} + CuO_x + FeO_x + NiO + ZnO_{(slag)} \rightarrow (Mg,Fe,Cu,Zn)(Al,Fe)_2O_4 \quad (3)$$
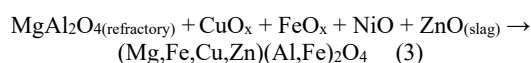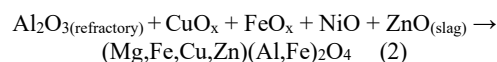
Spinel phase was confirmed in FactSage simulations, mostly in S1 and S3-corroded samples. Also, spinel phase was identified experimentally by XRD in samples after the powder test (closest to equilibria simulations). SEM/EDS analysis confirmed this finding, as demonstrated in Fig. 4a, 5a, 6a. Especially, this complex spinel

544

crystallized out of the liquid slag in the contact zone of the material. In general, spinel-structure compounds tend to crystallize in conditions of fast cooling, which is evidenced by the presence of spinels in meteorites [17]. Thus, the formation of spinels is favoured in a copper converter which works in a periodic work system, including loading, converting and unloading. This phenomenon partly blocks the slag ions against further penetration towards the inside of the refractory. The new dense spinel layer formed at the top of the test material which indicates that, the spinel phase can be potentially beneficial to improve the protection of refractory against progressing infiltration of specific ions which are present in the copper converting slag, like $Cu^{x+}$ or $Fe^{x+}$. Corrosion studies conducted previously for MgO-chromite refractories showed that, if Cu is present in the slag, it rather diffuses to MgO than to chromite spinel [18][19]. According to the phase diagram $MgO-CuO_x$ [20], the maximum solubility of $CuO_x$ in MgO is 20 % at 1050°C, and it lowers with the increased temperature up to 10 % at 1200°C and 7 % at 1300°C, with the latter temperature corresponding to the typical temperature in Cu processing devices. As can be seen from this work, Cu is not dissolved in $Al_2O_3$.

Moreover, the formation of complex spinels increases liquid slag viscosity and inhibits infiltration of the refractory. Also, precipitation of the needle-morphology PACS phase out of the liquid slag additionally increases viscosity at high temperatures, which has a dampening effect on slag penetration. In comparison to recently tested $MgO-Cr_2O_3$ refractory [18], in this work the slags penetrated significantly, but only part of the material.

In summary, the corrosion mechanism of $Al_2O_3-MgAl_2O_4$ refractory by Pb-rich copper slag (visualized in Fig. 8) can be described as follows: **1.** Entering the liquid copper slag into refractory via open pores, **2.** Penetration of refractory grain boundaries by the liquid slag, **3.** Formation of new products due to reaction between refractory and slag components, namely, attack of $Al_2O_3$ by PbO resulting in the formation of platelet-morphology $PA_6$, needle-morphology solid solution phase from the system $C_2PS_3$ - $C_2P_3S_3$ and complex spinel phase $(Mg,Fe,Cu,Zn)(Al,Fe)_2O_4$. This confirms mostly passive corrosion of $Al_2O_3-MgAl_2O_4$ refractory, resulting in the formation of new products which block diffusion of aggressive ions ($Cu^{x+}$, $Pb^{2+}$, $Fe^{2+}$) towards further zones of refractory.
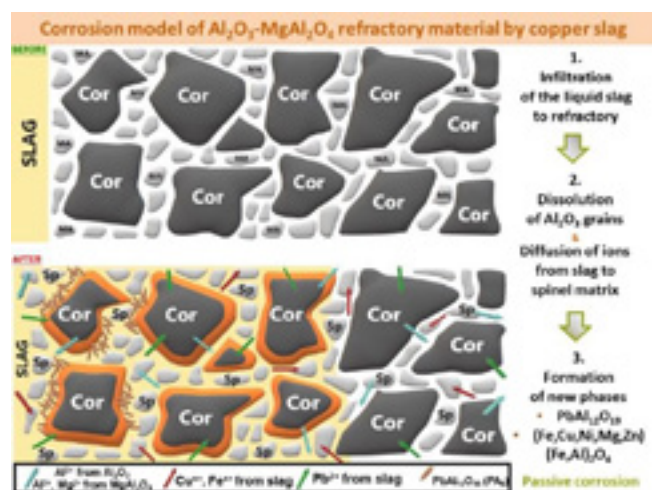


*Fig. 8. Corrosion mechanisms in the system $Al_2O_3-MgAl_2O_4$ refractory - PbO-rich copper slag.*

## 5. CONCLUSIONS

Passive corrosion mechanism predominates in the system $Al_2O_3$-$MgAl_2O_4$ – copper slag. XRD and SEM/EDS showed the formation of a complex spinel phase, via the incorporation of aggressive ions from slag ($Cu^{x+}$, $Fe^{x+}$, $Zn^{2+}$, $Ni^{2+}$) into the original spinel phase in a smart matrix, formation of platelet-morphology $PA_6$ and needle-morphology transitional phase from the system $C_2PS_3$ - $C_2P_3S_3$.

## REFERENCES

[1] Jastrzębska I., Ludwig M., Śnieżek E., Kalęba A., Drożdż P., Szczerba J., Corrosion study of novel Cr-free alumina-spinel refractory material dedicated to the copper industry, J Eur Ceram Soc, 42 (15), p. 7311-7327, 10.1016/j.jeurceramsoc.2022.08.038

[2] ICSG, The World Copper Factbook 2021, International Copper Study Group, 2021

[3] https://cerameunie.eu/topics/cerame-unie-sectors/sectors/refractories-key-technology-and-its-applications

[4] Polish Geological Instititute, The balance of mineral resources deposits in Poland as at 31.12.2021, M. Szuflicki, A. Malon, M. Tymiński, https://www.pgi.gov.pl/aktualnosci/display/13028-bilans-zasobow-zloz-kopalin-w-polsce-wg-stanu-na-31-12-2020-r.html

[5] IARC Working group on the evaluation of carcinogenic risks to humans, arsenic, metals, fibres, and dusts. in: IARC Monographs on the Evaluation of Carcinogenic Risks to Humans, 100C, International Agency for Research on Cancer, 2012, p. 11-465

[6] Jastrzębska I., Szczerba J., Stoch P., Błachowski A., Ruebenbauer K., Prorok R., Śnieżek E., Crystal structure and Mössbauer study of $FeAl_2O_4$, Nukleonika, 60 (1), 2015, p. 45-47, doi: 10.1515/nuka-2015-0012

[7] Jastrzębska I., Bodnar W., Witte K., Burkel E., Stoch P., Szczerba J., Structural properties of Mn-substituted hercynite, Nukleonika, 62 (2), 2017, p. 95-100, 10.1515/nuka-2017-00

[8] Jastrzębska I., Szczerba J., Stoch P., Structural and microstructural study on the arc-plasma synthesized (APS) $FeAl_2O_4-MgAl_2O_4$ transitional refractory compound, High Temp. Mater. Process. 63, 3, 2017, p. 299-303, 10.1515/htmp-2015-0252

[9] Crites M.D., Schlesinger M.E., Corrosion testing of chrome-free refractories for copper production furnaces, Proceedings of *4th International Conference COPPER 99-COBRE 99*, vol. 4, 1999, p. 187-194

[10] Mandal S., Hemrick J.G., Mahapatra M.K., Chrome-free qandilite ($Mg_2TiO_4$) refractory aggregates: Role of titania source and evaluation of thermal expansion coefficient, J Eur Ceram Soc, 42 (15), 2022, p. 7343–7351, 10.1016/J.JEURCERAMSOC.2022.08.012.

[11] Mandal S., Hemrick J.G., Mahapatra M.K., Zinc aluminate ($ZnAl_2O_4$) refractory aggregates: Dilatometric sintering studies and thermal expansion coefficient, J Eur Ceram Soc, 42 (13), 2022, p. 6244–6254, 10.1016/J.JEURCERAMSOC.2022.06.058

[12] Schlesinger M.E., Sole K.C., Davenport W.G., Alvear G.R.F., Extractive Metallurgy of Copper, 6th Edition, p. 191, Elsevier, 2021.

[13] Jastrzębska I., Szczerba J., Szlęzak J., Śnieżek E., Pędzich Z., Elastic behaviour of magnesia-chrome refractories at elevated temperatures, Materials and Technology, 49 (6), p. 913-918, 2015, 10.17222/mit.2014.186

[14] Kuxmann U., Fischer P., Lead monoxide-aluminium oxide, lead monoxide-calcium oxide, and lead monoxide-silicon dioxide phase diagrams, Erzmetall, 27 (11), 1974, p. 533-537.

[15] Shannon R.D., Prewitt C.T., Effective ionic radii in oxides and fluorides, Acta Crystallographica Section B Structural Crystallography and Crystal Chemistry, 25 (5), p. 925-946, 1969, 10.1107/s0567740869003220

[16] Chen S., Zchao B., Hayes P.C., Jak E., Experimental study of phase equilibria in the $PbO-Al_2O_3-SiO_2$ System, Metall. Mater. Trans. B 32, 6, 2001, p. 997-1005, 10.1007/s11663-001-0088-5

[17] Heuer A.H., Mitchell T.E., Further discussion on the space group of spinel, J. Phys. C Solid State Phys, 8 (23), 1975, p. 541-543, 10.1088/0022-3719/8/23/002

[18] M. Ludwig, E. Śnieżek, I. Jastrzębska, A. Piwowarczyk, A. Wojteczko, Y. Li, J. Szczerba, Corrosion of magnesia-chromite refractory by PbO-rich copper slags, Corrosion Science, 195, 2021, 10.1016/j.corsci.2021.109949

[19] Ludwig M., Śnieżek E., Jatrzębska I., Prorok R., Li Y., Liao N., Nath M., Vlček J., Szczerba J., Corrosion resistance of MgO and $Cr_2O_3$-based refractory raw materials to PbO-rich Cu slag determined by hot-stage microscopy and pellet corrosion test, Materials, 15 (3), 2022, 10.3390/ma15030725

[20] Assal J., Hallstedt B., Gauckler L.J., Thermodynamic evaluation of the Mg-Cu-O system, Zeitschrift Fur Metallkunde, 87 (7), 1996, p. 568-573

545

# CERAMIC FOAM FILTERS WITH A CARBON–BONDED ALUMINA COATING FOR ALUMINUM MELT FILTRATION

Claudia, Voigt, Jana Hubálková, Christos G. Aneziris
Technische Universität Bergakademie Freiberg, Institute of Ceramics, Refractories and Composite Materials, Agricolastr. 17, 09599 Freiberg, Germany
Are Bergin, Robert, Fritzsch
Department of Materials Science and Engineering, Norwegian University of Science and Technology (NTNU), Trondheim, Norway

## ABSTRACT

In the present study carbon-bonded alumina filters, have been investigated as a potential filter material for filtration of aluminium. The first time, short- and long-term pilot scale filtration trials were conducted, and the filter behaviour during filtration of aluminium alloy was determined by the use of PoDFA (Porous Disk Filtration Apparatus) for the short-term trials and LiMCA (Liquid Metal Cleanliness Analyzer) for the long-term trials with wrought alloy 6xxx aluminium. All applied filters were also investigated post-mortem by SEM (Scanning Electron Microscopy) analysis. Furthermore, sessile drop experiments with capillary purification were performed to evaluate the wetting behaviour.

## INTRODUCTION

The filtration of metal melt with ceramic foam filters is state of the art since the 1960s. Ceramic foam filters used for the filtration of aluminium and aluminium alloys are typically made of alumina ($Al_2O_3$) or silicon carbide (SiC). In comparison, for the filtration of steel melts ceramic foam filters predominantly based on zirconia ($ZrO2$) or carbon bonded alumina ($Al_2O_3$-C) are industrially applied. $Al_2O_3$-C is a refractory material with a low thermal expansion, negligible sinter shrinkage and improved slagging resistance caused by the low wetting (high contact angle) between carbon bonded alumina and metallic melts. The main drawback of $Al_2O_3$-C is the low resistance against oxidation at high temperatures. $Al_2O_3$-C materials are comprised of alumina, carbon fillers (e.g. carbon black and graphite) and carbon binders (e.g. pitch, tar, or phenolic resin) as well as appropriate additives [1]. The aim of this study was to test the suitability of $Al_2O_3$-C filters for the aluminium melt filtration. Furthermore, the wetting behaviour between aluminium and $Al_2O_3$-C was examined with the help of different test setups of sessile drop measuring devices. The sessile drop technique is often used due to the relatively simple experimental setup. The testing procedure comprises the placing of a piece of metal on the substrate and subsequent heating in a furnace. During the heating and dwelling time, the metal drop shape is recorded and analysed [7].

## MATERIALS AND METHODS

The measurement of the contact angle was conducted using bulk substrates in form of tablets having a diameter of 10 mm and a height of 6 mm prepared by uniaxial pressing.

Three types of sessile drop tests were conducted
- conventional sessile drop test and
- sessile drop test with capillary purification unit
- simplified sessile drop test with capillary purification unit

The conventional sessile drop test was performed at a high-temperature tube furnace with a high vacuum and an inert gas system (Carbolite Gero, Neuhausen, Germany) at the Institute for Nonferrous Metallurgy and Purest Materials (TU Bergakademie Freiberg, Germany). The aluminium alloy AlSi7Mg (Trimet Aluminium, Essen, Germany) was cut to masses between 90 mg to 95 mg, thereafter, placed on the substrates ($Al_2O_3$-C 800 °C and $Al_2O_3$ reference) at room temperature and positioned in the furnace. Before starting the heating procedure with 350 °C/h to the temperature of 950 °C, the furnace was evacuated to reach a pressure of $p \leq 1.5 \cdot 10^{-5}$ mbar. After a dwell time of 180 min, the pressure of $p < (2.8 \pm 0.4) \cdot 10^{-5}$ mbar was achieved.

For the evaluation of the contact angle $\theta_{cal}$, following equation valid for small droplets (m < 100 mg)

$$\theta_{cal}=2 \arctan(2h/d) \qquad (1)$$

was used [3]. The height h and the diameter d of the aluminium droplet were read off from the digital images recorded with a digital camera (The Imaging Source, Bremen, Deutschland).

The sessile drop tests with capillary purification unit were carried out at the Krakowski Instytut (Krakow, Poland). The aluminium alloy AlSi7Mg (Trimet Aluminium AG, Germany) was melted in a graphite syringe separately from the $Al_2O_3$-C substrate. At a temperature of 730 °C and a pressure $p < 1 \cdot 10^{-5}$ mbar, an oxide-free droplet was placed on the substrate. The shape of the drop was recorded by high-resolution CCD camera with a rate of 100 images per minute.

In the third test, a simple sessile drop setup with a dropping unit made off boron nitride (Henze Boron Nitride Products AG, Germany) was used. The dropping unit consists of a hopper for the melting of aluminium and a steel plunger pulling the melted aluminium through a bottleneck to retain the oxide skin. The hopper filled with a cylindrical piece of Al99.7 (Rheinfelden, Germany) was placed on the substrate and positioned in the hot stage microscope. The kiln was heated with 10 K/min to a temperature of 730 °C with a holding time of 10 min. During thermal treatment, the kiln chamber was flushed with argon to minimize the oxygen level.

For the filtration trials, $Al_2O_3$ skeleton filters coated with $Al_2O_3$-C slurry (compositions see [2]) were used. The coating was applied using a combined dip-spin technique where the $Al_2O_3$ skeleton was immersed completely in the slurry followed by a centrifugation step for the removal of excess slurry. In the next step the filters were sintered at 1600 °C ($Al_2O_3$) or coked at 800°C ($Al_2O_3$-C).

The short-term filtration trials were conducted at the metal foundry Georg Herrmann Metallgiesserei (Muldenhütten, Germany) with the aluminum alloy AlSi7Mg (EN AC-42100) from Rheinfelden Alloys (Rheinfelden, Germany) whereby the aluminum melt comprised 50 % ingots and 50 % scrap (recycled aluminum consisting of solidified feeders and runners) for the introduction of non-metallic inclusions.

The long-term filtration trials were conducted in a pilot filtration line at Hydro Aluminium AS primary aluminum plant (Sunndal, Norway), which consists of a melting furnace, a launder system, a filter box, and a lifting pump. The line is equipped with two LiMCA II units (ABB Ldt., Canada), which allow the continuous monitoring of inclusion number and size in the front and behind the filter box.

For every trial about 8 mT wrought aluminum alloy 6082 (main alloying elements of Si ~ 0.95 %, Fe ~ 0.2 %, Mn ~ 0.6 % and Mg ~0.65 %) were transferred to the melting furnace and circulated in the loop with the help of the lifting pump. Altogether two long-term filtration trials were conducted: one trial with a reference filter (labeled $Al_2O_3$) and one trial with carbon bonded alumina filters labeled as $Al_2O_3$-C. The aluminum melt temperature at the priming procedure was 740°C for both trials.

The employed filters were cut out and embedded in epoxy resin, ground, polished and analyzed with SEM/EDX.

## RESULTS

The contact angles determined with the different procedures possess discrepant results (Table 1). The underlying causes for the differences are manifold: The different testing temperatures, the intended flat deepening on the part of the substrate using the simplified dropping setup, a relative high mass of the aluminum

droplet. The contact angles measured using sessile drop measurement with capillary purification at 730 °C are therefore more reliable.

Tab. 1: Contact angles of the sessile drop experiments

|  | INEMET 950 °C Vacuum | Krakowski Instytut 730 °C Vacuum | IKFVW 730 °C Argon |
|---|---|---|---|
| $Al_2O_3$ | 100 | 108 | 132 |
| $Al_2O_3$-C | 92 | 157 | 132 |

The short-term filtration trial took approximately 16 s and showed an equal filling of the aluminum. The PoDFA index (given in area of inclusions per kilogram analyzed aluminum) yields the sum of total detected inclusions. The lower PoDFA index indicates a smaller number of non-metallic inclusions in the aluminum sample and hence the better is the melt quality. The PoDFA analyses found $Al_2O_3$ films, carbides, magnesium oxide, spinel, refractory material, iron and manganese oxides as well as grain refiners in the castings. The PoDFA indexes of 0.106 mm²/kg (trial 1) and 0.482 mm²/kg (trial 2) of the $Al_2O_3$-C filter samples were half of the PoDFA index of the $Al_2O_3$ reference filter samples [2]. This indicates an improved filtration when using $Al_2O_3$-C filter.

The SEM images of the used filters of the short-term filtration trials show large inclusions consisting of mainly Al, Mg, Si and O captured by the filters.

Tab. 2: PODFA results of short-term filtration trials

|  | PODFA / mm²kg⁻¹ | |
|---|---|---|
|  | Trial 1 | Trial 2 |
| $Al_2O_3$ | 0.246 | 1.06 |
| $Al_2O_3$-C | 0.106 | 0.482 |

The N20 values of the long-term filtration trials of the LiMCA measurements of the $Al_2O_3$ and the $Al_2O_3$-C filter possessed a comparable behaviour before and after the filter box. The N20 values before the filter box decreased at the beginning of the trial until they reached a relatively stable level [4].
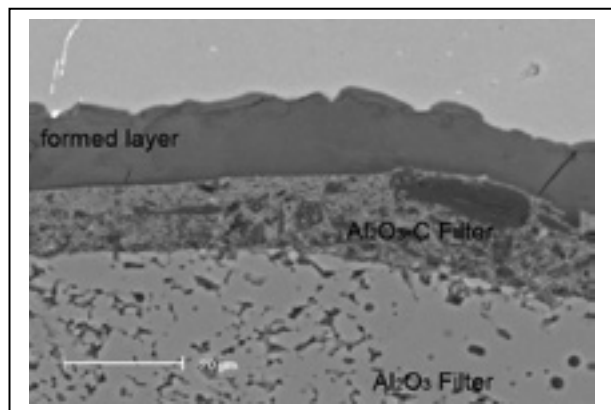


Fig. 1: SEM image (BSE) of filter coated with $Al_2O_3$-C used in short-term filtration trials

The N20 values after the filter box showed a decrease at the beginning of the experiment which is a common behaviour observed at other filtration experiments. It is obvious that the N20 values after the filter box possessed a higher standard deviation than the N20 values in the front of the filter. The N20 levels before and after the filter box are comparable for the $Al_2O_3$ and the $Al_2O_3$-C filtration trials. For the stable filtration areas, the filtration efficiency was calculated with 91.2 ± 6.7 % (for the $Al_2O_3$ between 23.1 and 45 min) and 88.8 ± 12.3 % (for the $Al_2O_3$-C between 15 and 25.9 min). So, the filtration behaviour of the two trials is comparable.



*Fig. 2:*
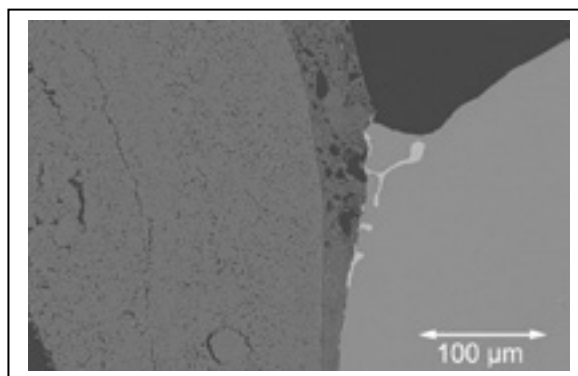
SEM image of $Al_2O_3$-C coating after long-term filtration trial

An intensive SEM investigation of the used filters revealed few typical inclusions captured in the filter.

Furthermore, it becomes evident that the $Al_2O_3$-C coating possessed different structures. Figure 2 shows areas with a very homogenous, dense, and compact coatings with nearly no pores or larger carbon structures. But there are also areas with $Al_2O_3$-C coating with large pores. No dependence on the location of the different structures in the filter was observed. It appears that only thinner areas of the coating have been affected of this phenomenon. EDX analysis implicates that in the denser structures the carbon is partly disappeared and left behind pores or a very dense structure made of mostly alumina particles. The latter is very surprising due to the high temperature needed to compact alumina grains (> 1400°C). The temperature during the filtration trials was not higher than 750°C, i.e., significantly lower than the required compaction temperature.

**CONCLUSIONS**

In the present overview carbon-bonded alumina filters have been investigated as a potential filter material for filtration of aluminum. In the first step, sessile drop test with different parameters were conducted yielding different results regarding the measured contact angle. In the next step, filtration trials were conducted - for the short-term filtration trials a better filtration behavior compared to $Al_2O_3$ reference filters was obtained. In contrast, the long-term filtration trials did not reveal a beneficial filtration effect of carbon-bonded alumina filters regarding the LiMCA results. An SEM analyses disclosed a partial transformation of the $Al_2O_3$-C coating layer from a heterogenous and porous layer into a dense and compact layer.

**REFERENCES**

[1] Routschka G., Wuthnow H., Handbook of Refractory Materials, Vulkan-Verlag GmbH (2012) The Technical Association of Refractories, Refractories Handbook, Tokyo 1998.

[2] Voigt C., Hubálková J., T. Zienert T., Fankhänel B., Stelter M., Charitos A., Aneziris C.G. Aluminum Melt Filtration with Carbon Bonded Alumina Filters, Materials, 13 (18) 2020, p. 20203962.

[3] Eustathopoulos N., Nicholas M. G., Drevet B., Wettability at High Temperatures, Amsterdam, New York 1999.

[4] Voigt C., Hubálková J., Bergin A., Fritzsch R., Akhtar S., Aune R., Aneziris C.G., Short- and long-term aluminum filtration trials with carbon-bonded alumina filters, Light Metals 2021, p. 785 – 793.

# IMCE

The Resonant Frequency and Damping Analyser (RFDA) identifies the mechanical material properties at room temperature and at elevated temperatures up to 1700 °C.

## Thermo-mechanical characterization by the Impulse Excitation Technique

- ✔ **Elastic properties, damping, microstructural behaviour, …**
- ✔ **Non-destructive, reliable and easy accessible measurements**
- ✔ **Continuous high temperature analysis**
- ✔ **Applicable to porous and brittle materials**
- ✔ **Quality control**

**UP TO 1700 °C**

**Scan for a FREE DEMO measurement on one of your own specimens**

**IMCE nv**
Slingerweg 52 - Poort Genk 5489
3600 Genk - Belgium
P: +32 89 41 00 70 | info@imce.net

**Visit our website**
for more information

**www.imce.net**

SHORT COMMUNICATIONS

# APPROACHES TO SOLVING ADVANCED PROBLEMS OF ESTABLISHED REFRACTORY DESIGNS IN NON−FERROUS METALLURGY

Alessio Vezzuli, Angelo G. Vezzuli
EKW Italia S.R.L., Concorezzo MB, Italy

Thomas Heikaus, Daniel Cölle
EKW GmbH, Eisenberg, Germany

**ABSTRACT**

The article outlines exemplary interactions between smelting technology and typical refractory ceramics within the non-ferrous metallurgy. In the context of this, the historical expertise is illuminated, critically questioned and compared with some essential of the more recent findings and resumed. One particular focus is on a comparative presentation illustrated by the specific example of the secondary metallurgy of copper-based alloys.

Thermomechanically complex stress conditions for the installed refractory structures are to be expected due to melting, transporting, but especially due to continuous casting by inductively actuated pouring systems. A contribution to accentuate and selectively illuminate thermally induced stress conditions is the identification of structural "mismatches" of complex linings, which are indicated step by step and are solved and discussed on the approach by applying specific thermomechanical calculations. The aim is to improve a refractory concept for a defined plant technology in such a way that the extrinsic and intrinsic conditions are counterbalanced by the best possible refractory structures, which is the perspective with which the article will conclude.

# 5 REFRACTORIES FOR NON-METAL INDUSTRIES

# CHALLENGES FOR A CEMENT PRODUCER

Dr. Volker Wagner, Heidelberg Materials AG, Heidelberg, Germany

## ABSTRACT

Refractories play a vital role for us as a cement producer. The yearly consumption of bricks and monolithic materials is causing significantly costs. Changing clinker production conditions, caused by continuously increasing alternative fuel rates or new production technologies, are the basis of new refractory developments. Based on a good cooperation between Heidelberg Materials and some refractory suppliers excellent solutions have been verified over the past few years.

However, old and solved problems are always replaced by new challenges. Our plants are looking for a continuous production without any unplanned stoppages. A reliable refractory lifetime predictability for any application area is required. But the tools available are still on a very basic level. So far, the detection of potential damages/pre-damages is not possible at all.

## Sudden unexpected failures

In an ideal world we would know exactly which part of the refractory lining must be replaced respectively repaired during a planned maintenance stop. For example, in the rotary kiln the remaining brick thickness is measured, and based on the wear rate a total lifetime can be predicted. Unfortunately, this is a view on the surface and valid only for certain brick sections. A brick which still looks good might fail shortly after start-up of the kiln, as it is infiltrated heavily by any kind of salts, resulting in the loss of roughly half of the brick. The more alternative fuels we are using, the heavier the degree of infiltration. And here we are not even talking about the additional effect of steel shell corrosion, which is another topic the cement industry must deal with [1].

## Blockages

Modern monolithic materials are showing an excellent behaviour towards the conditions inside the kiln. However, they are fixed with metallic anchors. And the major failure cause is the corrosion of these anchors. During operation we sometimes observe falling blocks in the cyclones, the cooler roof or other areas like for example inlet chamber. The blocks consist of a perfect lining, just the metallic fixation is gone completely.



*Pic. 1: Corroded anchors, roof section*

## Safety Issues

During a planned maintenance stop we always check the remaining refractory lining. It might look good, but we must be extremely careful. Safety nets are nowadays installed in almost all our kilns during inspection. This is done not only to prevent coating dropping down. There is a significant danger of complete monolithic blocks falling as the anchors are severely corroded. Of course, there is another mechanism leading to anchor failures, and that is the formation of σ-Phase, leading to embrittlement.

## What do we need?

Our target is clinker production within a certain timespan without unexpected interruption. This leads to an efficient planning and costs are under control. What is missing are tools which enable us predicting the remaining lifetime of refractory linings. Ideally, we install sensors of any type, which finally give us online information about the status of infiltration, corrosion, and phase transformation.

## CONCLUSIONS

In terms of refractory quality, we acknowledge the developments of the refractory industry. Modern bricks and monolithic materials can withstand the conditions in our production lines quite well. And for all problem areas some special solutions are available. It does not mean that we do not welcome further optimization based on innovative products. But our major problem are unpredictable failures. These failures do not only produce high costs, but they are also a major cause for safety issues. Traditional measures like the identification of remaining lining thickness are still necessary, but they are not sufficient. We need an "online" detection of upcoming refractory failures.

## REFERENCES

[1] F. L. Smidth A/S, Ebbe Jøns, MSc. Senior Research Chemist and Maria José L. Østergård, PhD. Metallurgist, 2001

SHORT COMMUNICATIONS

# NEAR–CUSTOMER ENGINEERING MANAGEMENT FOR ADVANCED APPLICATIONS IN THE CEMENT INDUSTRY

Bastian, Vesenberg, Nicole, Schlimm Daniel, Cölle
EKW GmbH, Eisenberg, Germany

Thomas, Weiss, Lennart, Hapke.
IKN GmbH, Neustadt, Germany

**ABSTRACT**

An engaging route to the realization of a technologically advanced alkali-resistant and particularly abrasion-resistant high-temperature material with reliable thermal shock behavior is outlined, from the idea through the development process to the final product. Novel testing methods are integrated into the development, which systematically assist the matrix optimisation of selected refractory castables in a targeted approach. Under implementation of a calculated, widely spread grain size interval, alkali tests at 1100 °C using potassium carbonate and sodium carbonate on the one hand and potassium sulfate and sodium sulfate on the other mark reliable results for the functional stability of the refractory ceramics in corrosive process routines. The design and prototyping of preformed components was used to successively optimize the material properties under real conditions close to the customer. A particular challenge was the adjustment of certain structural properties in order not to lose the resistance of the refractory ceramics to erosively acting particle streams and gases in favor of a robust behavior against abruptly occurring load peaks, for example abrupt temperature changes or locally occurring pressures. For this purpose, a test procedure was developed to test the so-called impact behavior under hot conditions, and both interventions in the bonding system of the refractory material and in construction elements led to improved robustness of impact zones.

The aim of optimizing the material, from an economical point of view in particular, was fulfilled, which was confirmed by the successful application on the customer's plant site. Last but not least, the potential transferability of the product solution to other industries is demonstrated, e.g. in the aluminum industry.

553

# EFFECTIVE CO$_2$–REDUCTION FOR ROTARY KILN BURNING PROCESSES BY USING ENERGY EFFICIENT LININGS

Hans-Jürgen Klischat*, Holger Wirsing, Peter Groger, Stefan Puntke
Refratechnik Cement GmbH, Göttingen, Germany

## ABSTRACT

The carbon challenge or carbon emission challenge is a major topic especially for cement and lime production, as carbon dioxide is released from the raw material and from the material burning process. To reduce the latter, new refractory lining concepts have been developed by designing a new finer-ceramic microstructure. These novel basic and non-basic brick grades with porosities up to 25% reduce the heat losses due to their exceptionally low heat transfer. All other properties, including refractoriness, strength, structural elasticity, permeability, and thermal shock resistance, are kept at values which are well-proven for the application in refractory rotary kiln linings. Emphasis is also laid on kiln linings which are exposed to increased alkali atmosphere, so silicon carbide containing high alumina bricks are an essential part of this emission- and energy-saving concept. The installation of these new products is as easy as for standard products, no additional effort like two-layer linings is necessary. The results of recent installations show a significant decrease of the kiln shell temperature. The reduction in overall CO$_2$ emission is calculated with approx. 5 kg/t clinker, the thermal energy input at the main burner comes down by 4-5% and the wall heat losses drop by up to 25%, which is enormous considering the already well-matured rotary kiln process. In addition to a lower lining weight, even reducing the necessary operating power, the reduction of 10% in refractory lining material use is responsible for an improved sustainability and reduced carbon footprint not only for the kiln operator, but also for the refractory producer and the environment: carbon challenge accepted.

## INTRODUCTION

At the latest since the first energy crisis in the recent century, high temperature processes required consideration of energy saving to keep the heat within the process, i.e., avoiding its escape to the environment. In the cement industry the effect of CO$_2$ emissions has to be considered, (1) which originates from the limestone and from the burning process. To increase the energy efficiency and reduce the impact of cement production on the environment, several measures have been taken, from the reduction of the amount of clinker in cement and development of technological solutions of the manufacturing equipment to measures on the refractory side, (2). For all these measures it has to be ensured that the cement quality is reliably stable. This paper deals with a novel refractory concept to minimize the energy consumption for cement clinker production.

## OVERVIEW ON CONCEPTS FOR ENERGY SAVING

Since the first oil crisis in the early 1970s, saving energy and improving energy efficiency in industrial (and private) sectors has become important. Especially in the cement industry, the carbon footprint and the reduction of gases presumably responsible for global warming have come more and more into focus, Fig. 1.
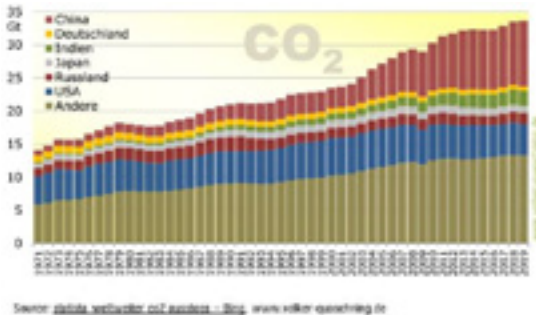


Fig. 1: Worldwide CO$_2$ emissions from 1971 until 2019 (in Gt)

The focus was not only laid on energy saving whilst maintaining operational performance, but even more emphasized on emission saving to counteract the harmful effect of CO$_2$ on the climate. Also costs for thermal fuels and their emissions, or for the prevention of emissions, have to be considered, as together with electricity they account for around 50-60% of operational production costs, Fig. 2.
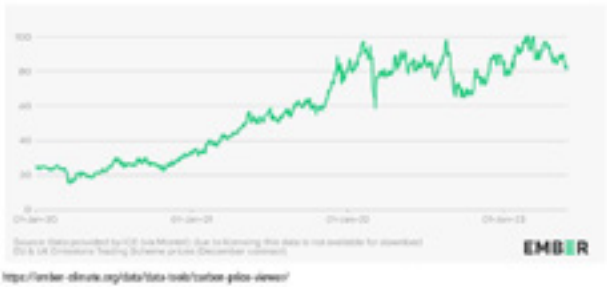


Fig. 2: Cost per ton of CO$_2$ produced (in €)

Therefore, the application of refractories to save energy has quite a long tradition, initially for non-basic refractories. For basic refractories, this was impossible due to technical reasons (a high porosity was connected to a low strength, insufficient for cement kiln applications). Still, several attempts were made to overcome this technical obstacle and develop a system to reduce thermal losses through the kiln shell, Fig. 3, (3).



Fig. 3: Various concepts for thermal insulation of basic lined zones in rotary kilns

Due to typical wear patterns, none of these concepts were successful, as the main requirement – similar performance as standard bricks – could not be achieved reliably. Only in the field of non-basic refractories, several brick grades performed satisfactorily, providing a reliable performance and the ability to reduce the heat losses through the kiln shell.

Due to the high temperatures in the sintering and transition zones and the high thermal conductivity of basic bricks, a specific development was needed to reduce energy consumption and emissions. To provide a wholistic concept and to decrease the emissions to a maximum, also the non-basic lined areas must be emphasized. This would bring advantages in energy and emission saving, CO$_2$ reduction and thus reduction of the carbon footprint, cost, stockkeeping, etc.

## BREAKTHRU IN EMISSION-SAVING REFRACTORIES
### Basic refractories

A major obstacle for the development of bricks is that density and porosity directly influence other properties like strength, elasticity, refractoriness under load etc., usually in a way that prevents

successful installation. Usually, strength and refractoriness were negatively affected when porosity was increased.

To overcome this limitation, a new brick structure, completely different from the ones used up to date, was developed. It is characterized by a fine-grained structure and a porosity in the range between 20 and 25%, up to now unfamiliar to the typical refractory materials for working linings of rotary kilns, Fig. 4.
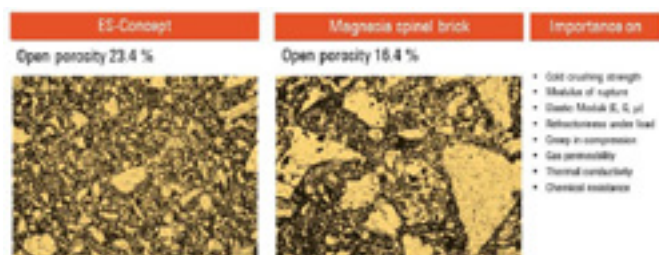


*Fig. 4: Structure of typical magnesia-spinel bricks and bricks with reduced thermal conduction (ES concept)*

To strengthen the performance and widen the application area, the modulus of elasticity was decreased by an increase of the alumina content, which resulted in a further decrease of alkali susceptibility and ability to deal with mechanical tensions in cement clinker and lime rotary kilns. Porosity and strength are barely influenced by this further structural modification, Fig. 5.



*Fig. 5: Properties of magnesia-spinel bricks with reduced heat transfer*

The successful proof has already been pointed out in [2].

**Non-basic refractories**

Due to the promising results for basic bricks, the so-called ES concept was also applied to non-basic materials. A special challenge were the requirements on these brick types, not only that their thermal conductivity is already lower, but they also have to withstand the chemical and mineralogical attacks taking place in modern rotary kilns fired with large amounts of alternative fuels. This means that the alkali resistance of these materials has to be similar to that of the already used high-performance SiC-containing products, despite their higher porosity and the concomitant higher inner surface.

It was figured out that by careful adjustment of the composition and a special firing regime, the high porosity concept known for basic bricks could be transferred to bricks based on mullite, andalusite, and fireclay as well. Fig. 6.
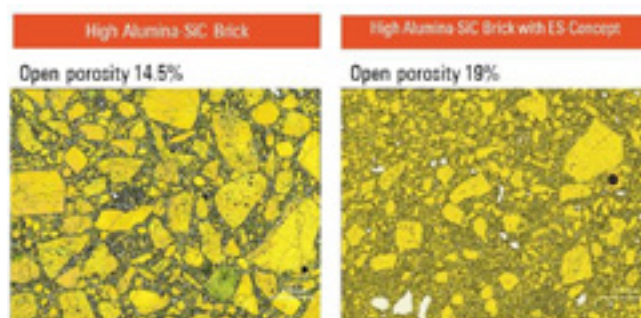


*Fig. 6: Structure of 60% alumina-SiC bricks and bricks with reduced heat transfer (ES concept)*

All necessary properties for a successful performance were met, while the porosity was adjusted at the required high level and the gas permeability at the required low level, Fig. 7.



*Fig. 7: Various high alumina-SiC bricks with reduced heat transfer*

As a result, density was also significantly lower than for the standard products, while strength levels and refractoriness were maintained.

An examination of the alkali resistance was performed with the well-known cup corrosion or crucible test at a temperature of 1100 °C and with $K_2CO_3$ as corrosive agent, Fig. 8.



*Fig. 8: Alkali resistance of high alumina-SiC bricks with and without application of the ES concept*

The results clearly show the formation of a protective layer that prevents the undesired alkali corrosion reaction.

**Installation in lime rotary kilns**

Kiln shell temperatures (providing a directly measurable parameter) of installations in lime rotary kilns, which include kilns in the pulp & paper industry, show the positive effect of an ES lining. A standard lining consisting of an andalusite working lining and an insulating fireclay lining result in a kiln shell temperature of 247 °C, Fig. 9.

555
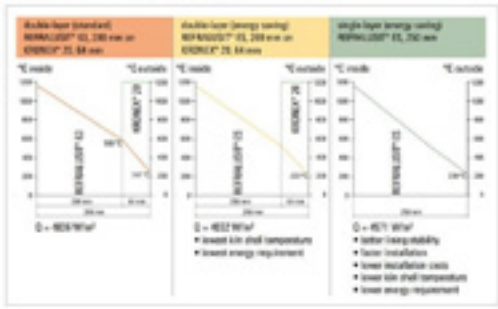
*Fig. 9: Reduction of kiln shell temperature in a lime kiln by application of the ES concept*

When exchanging the dense andalusite brick by an ES product, the shell temperature can be reduced to a value of 223 °C. At the same time, the heat loss through the wall is reduced by 17%.

It is well-known that a two-layer lining is susceptible to mechanical influences, possibly caused by a deformed kiln shell, ovality, or lack of skilled workers, as a proper installation is decisive for refractory performance, Fig 10. So, by installing a single-layer lining, compared to a classic double layer lining, the kiln shell temperature can be reduced to 239 °C. This stable single-layer lining still offers the saving of 5% energy.



*Fig. 10: Mechanical destruction of a two-layer lining*

**Conclusion for bricks with high porosity**
Due to the fact that the performance-relevant properties of bricks with high porosity are met, these refractories are currently being installed to qualify their performance, and to probably set a new standard for rotary kiln linings that counteract $CO_2$ emissions and energy losses. As the firing processes in the cement industry with varying raw materials and fuels prevent an experimental proof of the savings, mathematical simulations were performed by the Verein Deutscher Zementwerke, the VDZ (German Cement Manufacturer's association), (4), (5).

**CALCULATION OF THE SAVINGS WITH THE ES LINING**
For this calculation, a BAT (best available technique) state-of-the-art rotary kiln with a production capacity of 5000 $t_{clinker}$/day was chosen, with a single-string 5-stage precalciner and a grate cooler. Its length is 75 m, with a diameter of 5 m. The kiln is fired with a thermal substitution rate of 75% coal dust and 25% mix of alternative fuels. Whereas the kiln is fired with coal dust, the calciner is fired with a combination of coal dust and an alternative fuel mix (fluff, animal meal, mechanically dewatered sewage sludge).
For the calculation, two refractory lining patterns were evaluated.

**Calculation for a kiln with regular conditions**
This type of kiln represents the average of kilns which are not fired with alternative fuels, but with standard gas, oil, coal, or the like.
In the reference lining concept for conventional kiln operation conditions, fireclay bricks and high alumina bricks with 60% $Al_2O_3$ are installed in the calcining and safety zone, Fig. 11.
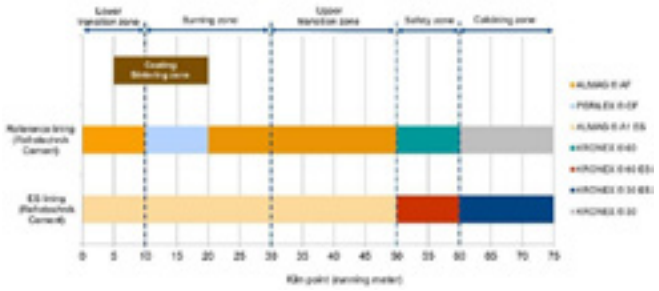


*Fig. 11: Conventional and ES lining for a kiln with regular conditions*

In the higher thermochemically stressed transition zones and burning zone, basic magnesia-spinel bricks, low iron as well as iron-rich grades (for coating-enhancing purposes) are applied.
In the ES lining concept, the calcining and safety zone are lined with KRONEX® 30 ES and KRONEX® 60 ES. The transition zones and the burning zone are lined solely with the magnesia-spinel brick ALMAG® A1 ES.

**Calculation for a kiln with demanding conditions**
Demanding kiln conditions are characterized by thermochemical influence due to use of alternative fuels and raw materials as well as elevated process requirements as such. Mostly, a mechanical strain influence is present as well, probably caused by kiln shell deformation, ovality, axial distortion, and the like. If there is a need for the installation of a special alkali-resistant AR lining, the use of an emission-saving ES AR lining is the installation of choice, Fig. 12.
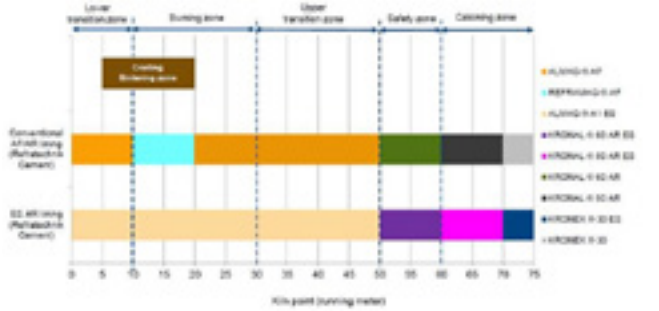


*Fig. 11: Conventional and ES lining for a kiln with demanding conditions*

Therefore, a mechanically and alkali-optimized lining concept includes high alumina alkali-resistant brick grades in the calcining and safety zones. In the transition zones and burning zone, basic brick grades are installed.
In the ES AR lining concept, the safety and calcining zones are lined with KRONAL® 50 AR ES, KRONAL® 60 AR ES, and even optimized fireclay KRONEX® 30 ES bricks. The transition zones and the burning zone are lined with ALMAG® A1 ES magnesia-spinel bricks.

**Results for emission savings**
The results for emission and energy saving are exceeding a value of 1% by far, Table 1.
Although this value seems to be not too high, it must be stated that the cement clinker burning process in terms of energy consumption is one of the best optimized processes in the industrial world.

Table 1: Calculated savings by application of the ES concept

| | Regular conditions | ES Concept | Severe Conditions | A1 ES Concept |
|---|---|---|---|---|
| Savings specific energy demand | | 1.8% | | 1.5% |
| Wall losses kJ/s | 11360 | 8832 | 12331 | 9256 |
| CO$_2$ emissions t CO$_2$/t clinker | 0.829 | 0.814 | 0.820 | 0.815 |
| Savings coal t/a | | 3429 | | 2875 |
| Savings CO$_2$ t CO$_2$/a | | 8580 | | 7331 |
| CO$_2$ emissions t CO$_2$/t.m. (for refractory production) | 19.6 | 17.0 | 18.3 | 17.3 |
| CO$_2$ emissions t CO$_2$/t.m. (cement clinker production) | 18022 | 17917 Δ=105 | 18032 | 17934 Δ=98 |

The CO$_2$ emissions are reduced, but also the savings of coal of up to 3500 t/a must be noted, coming along with emission savings of up to 8600 t/a.

From a cost and environmental perspective not only the emissions (including emission certificates) have to be noticed, but also the reduced purchase of coal and CO$_2$ certificates. With its high technology readiness level (TRL) over the all relevant refractory categories (basic and non-basic), the ES concept serves the industry pledge of compliance towards sustainability as well as cost competitiveness.

Overall, installation of products from the ES concept results in significant economic and ecological savings, which cannot be bypassed to meet the carbon challenge.

## CALCULATION OF THE CARBON FOOTPRINT

The carbon footprint is a parameter which may describe the emission impact on the environment as a new decisive KPI for the industry. Although it makes sense to have such a figure, it leaves room for misinterpretation and even wrong conclusions. The classical calculation considers the production emissions (Scope 1) as well as energy-related emissions (Scope 2). This usually results in a KPI which is reported as t CO$_2$/t refractory. This figure has to be compared to other figures, but fails miserably when various product groups are compared, e.g., dense refractories with porous materials. It is more meaningful and robust if pieces or linings (or emissions per running meter installed in the case of rotary kilns) are reported. Even more robust are statements when the whole Scope 3 is considered, which includes raw materials (essential for the carbon footprint of refractories) and the use and beneficial performance in the kiln.
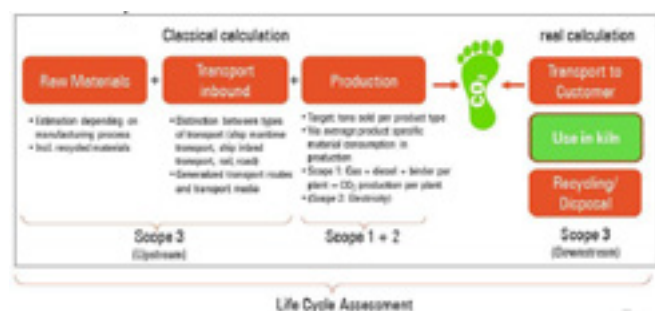
*Fig. 12: Definition of scopes for carbon footprint calculation*

While the CO$_2$ emissions per ton are comparable for dense and ES products, it has to be respected that for a given area, much less material is needed for the lining. This keeps the environmentally relevant carbon footprint much lower for ES products, Table 1. Not only the emission for the product is important, but even more the savings which are possible due to its use, as already pointed out in Table 1. A comprehensive overview is given in Table 2, where the savings in weight (contributing to a lower carbon footprint Scope 1, 2, and 3 upstream) as well as thermal conduction (contributing to a lower carbon footprint Scope 3 downstream) are shown.

Table 2: Weight reduction and reduced thermal conduction of bricks according to the ES concept

| | Density g/cm³ | | Thermal conduction W/m·K at 1000°C | | Savings by ES concept | |
|---|---|---|---|---|---|---|
| | ES | Standard | ES | Standard | Weight | Thermal conduction |
| ALMAG ES | 2.68 | 2.9 – 3.05 | 2.1 | 2.9 | 10 % | 28 % |
| ALMAG A1 ES | 2.76 | 2.9 – 3.05 | 2.1 | 2.8 | 7 % | 25 % |
| RETRALUSIT ES | 2.35 | 2.6 – 2.8 | 1.3 | 1.6 | 13 % | 19 % |
| KRONAL 60 AR ES | 2.4 | 2.5 – 2.7 | 1.5 | 2.5 | 8 % | 40 % |
| KRONAL 50 AR ES | 2.37 | 2.35 – 2.55 | 1.5 | 2.0 | 7 % | 25 % |
| KRONEX 60 ES | 2.22 | 2.4 – 2.6 | 1.5 | 1.8 | 11 % | 17 % |
| KRONEX 30 ES | 2.02 | 2.1 – 2.3 | 0.9 | 1.2 | 8 % | 25 % |

This explains the tremendous effect, which can be achieved by the application of the ES concept for refractory manufacturer and user.

CONCLUSION

In a comprehensive way, the following conclusions can be drawn:

- Through the application of the ES concept for refractory brick production and its application in the industry, significant saving of energy and reduction of CO$_2$ emissions is possible.
- Less use of coal and CO$_2$ certificates costs for kiln services can be achieved.
- Due to less material needed for brick production (density!) production becomes more sustainable.
- Brick performance-relevant properties (strength, refractoriness, chemical resistance, elasticity) are maintained.
- Lower weight of bricks facilitates the installation (health & safety aspects).
- Lower electricity costs due to less weight and less necessary cooling of the kiln shell.
- Protection of mechanical aggregates such as main drive and tyres by reduced kiln shell temperature.
- Lining of a two-layer brickwork possible, but not necessary, simplifying installation and reducing cost and installation time.
- Due to high TRL (technology readiness level) over the total refractory application categories, immediately applicable in global scale within the industry.

REFERENCES

[1] Birgi, O.; Janssn, R.: RE4Industry brochure Towards 100% Decarbonisation of Energy Intensive Industries with Renewable Energy. RE4Industry, WIP Renewable Energies, Munich 2023

[2] Weber, K.; Orujov, N.; Blanco Santos, D. J.; Matus Jara, C. P.: How refractory technologies can reduce costs and CO2 emissions. ZKG (2020) Nr. 9, p. 45-50

[3] Klischat, H.-J.; Puntke, S.; Groger, P.; Wirsing, H.: Sustainable Linings for Rotary Kilns, Proc. UNITECR 2022, Chicago

[4] Schäfer, S.; Fleiger, K.: Independent expert evaluation based on a simulation study of a novel refractory brick used in the cement clinker burning process of a rotary kiln; VDZ Technical Report No. A-2015/0657, March 2015, Düsseldorf, Germany

[5] Fleiger, K.; Joschko, D.: Independent expert evaluation on improvement of carbon footprint and energy usage by refractory technology; VDZ Technical Report No. A-2022/0921, March 2023, Düsseldorf, Germany

# ENERGY-SAVING REFRACTORY BRICKS FOR SUSTAINABLE LINING OF ROTARY KILNS

Ufuk Akkasoglu, Nuri Sarioglu

KUMAS Manyezit Sanayi A.Ş., Kutahya, Turkey

## ABSTRACT

Reducing carbon footprint is a significant challenge for energy-intensive industries- including cement and lime- due to the usage of extensive thermal processes in production. One possible way to decrease energy consumption is using an energy-saving lining in which the thermal conductivity is reduced by increased porosity. However, mechanical, chemical and thermal limitations of the rotary kilns should be considered in brick design since porosity will degrade relevant properties. In this study, novel basic refractory bricks with reduced thermal conductivity were developed to reduce kiln shell temperature and hence reduce energy consumption. In this study, a novel energy-saving basic refractory brick with reduced thermal conductivity by induced porosity is developed without compromising the refractoriness as well as mechanical and thermal properties.

## INTRODUCTION

The pursuit of net zero emissions has become a paramount goal in mitigating the impacts of climate change. With the target of achieving net zero emissions by 2050 gaining global momentum [1-3], there is an urgent need to explore sustainable and energy-efficient solutions across various industries. In the field of refractories, which play a vital role in high-temperature applications, the development of advanced materials with improved thermal insulation properties is of great significance.

One such material of interest is MgO-Spinel refractories, which possess excellent thermal stability, corrosion resistance, and mechanical strength, making them suitable for various industrial applications including steelmaking, cement production, and non-ferrous metal processing [4-6]. However, the high thermal conductivity of MgO-Spinel refractories limits their energy-saving potential, leading to increased heat losses and reduced overall efficiency in high-temperature processes.

A possible way to decrease thermal conductivity is to induce porosity in the microstructure. However, thermo-chemical and thermo-mechanical limitations of rotary kilns must be considered since induced porosity will degrade both infiltration resistance as well as thermal and mechanical properties.

There two types are porosity: Open pores and closed pores. Open pores have access to the surface and thus they are prone to the infiltration, while closed pores have no access to the surface and thus they can reduce thermal conductivity without sacrificing the infiltration resistance. Interconnected porosities degrade permeability and thus infiltration resistance. Therefore, non-permeable pores are desired (Fig. 1).
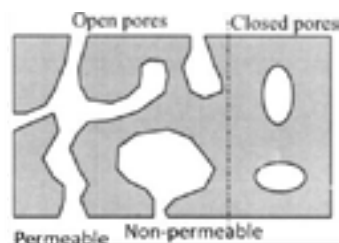


*Fig. 1: Schematic diagram showing the open, closed, permeable and non-permeable pores.*

The literature includes different studies about synthesis of porous aggregates (i.e., $MgAl_2O_4$) to reduce thermal conductivity of the refractories [7-10]. However, the mass production of porous aggregates is hindered due to the complex preparation conditions and significantly higher cost of raw materials involved in the majority of processes. Consequently, this poses considerable challenges to the economic viability of industrial production.

The aim of this study is to produce an energy-saving MgO-Spinel refractory brick, which is feasible to mass production, by inducing controlled and non-permeable porosity to decrease thermal conductivity without sacrificing physical, mechanical and thermal properties.

## EXPERIMENTAL PROCEDURE

A standard 85 wt.% MgO – 15 wt.% MA-Spinel composition is used to optimize the packing density, pore structure, and thermal conductivity. The raw materials are mixed in a mixer and then shaped by a uniaxial hydraulic press. Green compacts are fired by a tunnel kiln in mass production conditions. Produced bricks are characterized according to relevant ISO or ASTM standards.

## RESULTS & DISCUSSION

The microstructural analysis of the developed energy-saving bricks was conducted by using Scanning Electron Microscopy (SEM) to examine the pore characteristics and their impact on the thermal conductivity and mechanical properties of the samples. The SEM analysis revealed the presence of both large and sub-micron sized pores within the refractory matrix (Fig. 2). The presence of large pores in the refractory samples is beneficial for reducing thermal conductivity. Large pores act as thermal barriers by impeding the transfer of heat through the refractory material and lowering the overall thermal conductivity.

The development of sub-micron sized pores in the refractories plays a crucial role in maintaining the high mechanical strength and low permeability characteristics of the material. It is observed that the presence of sub-micron sized pores does not compromise the cold crushing strength of the developed refractories.

The combination of large and sub-micron sized pores in the refractory matrix provides a synergistic effect on thermal conductivity reduction without sacrificing mechanical strength and permeability. The large pores act as thermal barriers, while the sub-micron sized pores ensure low permeability and maintain the cold crushing strength. This dual porosity system optimizes the energy-saving potential of the refractory material for rotary kiln applications.
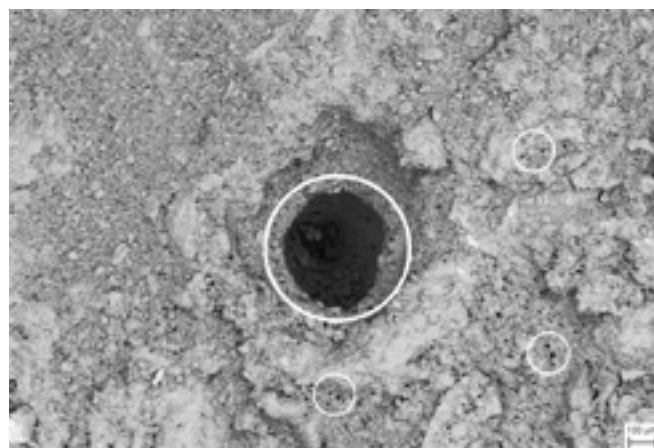


*Fig. 2: SEM image of the energy-saving brick. Large and sub-micron sized pores are shown with white circles.*

Table 1 summarizes the physical, mechanical and thermal properties of the commercialized energy-saving refractory bricks compared to the standard MgO-Spinel brick. It was observed that

the cold crushing strength remained within acceptable limits, indicating that the mechanical integrity of the refractories was maintained. Additionally, gas permeability values were comparable to those of standard MgO-Spinel bricks, ensuring adequate infiltration resistance within the kiln environment. The commercialized energy-saving bricks exhibited a lower thermal conductivity at 1000 °C, resulting in a 23-25% reduction compared to the standard brick. This reduction in thermal conductivity translates into significant energy savings in clinker production. Furthermore, the thermal expansion values of the developed bricks were within an acceptable range, ensuring their compatibility with the kiln system. Since the bulk density of the energy-saving bricks is ~5-10% lower than the standard MgO-Spinel bricks, the overall weight of the refractory lining is decreased by almost 10% which increases the kiln ring lifetime while decreasing the electricity consumption to rotate the kiln.

Tab. 1: Physical, mechanical and thermal properties of the commercialized energy-saving bricks in comparison to standard MgO-Spinel brick

| | Physical & Mechanical Properties | | | | Thermal Properties | | | |
|---|---|---|---|---|---|---|---|---|
| | Bulk Density | Apparent Porosity | Cold Crushing Strength | Gas Permeability | RUL ($T_{0.6}$) | Thermal Conductivity (1000°C) | Thermal Expansion (%) | |
| Unit | g/cm³ | % | N/mm² | cd | °C | Kcal/m.°C.h | 1000°C | 1400°C |
| Standard | ASTM C 830-00 | | ASTM C 133-97 | EN 993-4 | EN ISO 1893 | EN ISO 8894-2 | NETZSCH DIL 402 PC | |
| KÜM SP 87 LC | 2,70 | 23 | 60 | 32 | >1700 | 2,10 | 1,25 | 1,85 |
| KÜM SP 90 LC | 2,75 | 21 | 65 | 26 | >1700 | 2,15 | 1,29 | 1,89 |
| KÜM SP 87 A (Std) | 2,92 | 17 | 65 | 25 | >1700 | 2,80 | 1,28 | 1,87 |

The KÜM SP 90 LC brick is specially designed for RDF (Recycle Derived Fuel) burning kilns with higher alkali ratio, in which lower permeability and lower apparent porosity are required. Due to the higher MgO ratio and lower porosity, its thermal conductivity is slightly higher than the KÜM SP 87 LC brick, while KÜM SP 87 LC brick focuses more on thermal conductivity with its slightly higher porosity and permeability.

The thermal conductivity as a function of temperature graph is given in Fig 3. The thermal conductivity of the KÜM SP 90 LC brick is higher than the KÜM SP 87 LC brick at lower temperatures since it has higher MgO ratio and higher porosity. The gap between the thermal conductivity of KÜM SP 87 LC and KÜM SP 90 LC decreases with increasing temperature, since the pore size and distribution are similar between these two bricks and radiation mechanism plays a vital role at higher temperatures in thermal conductivity.
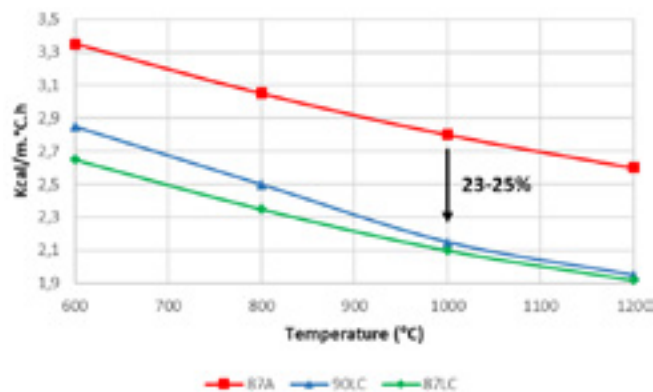
Fig. 3: Thermal conductivity as a function of temperature graph of commercialized energy-saving bricks in comparison to standard MgO-Spinel brick
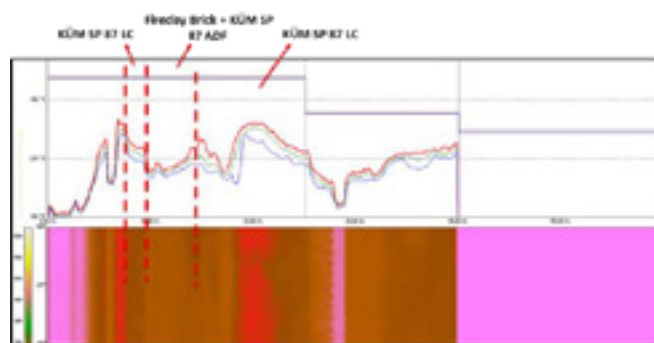
Fig. 4: Kiln shell temperature as a function of kiln meter showing both single layer and conventional double layer lining

Field tests were conducted to evaluate the performance of the developed refractories in actual kiln operations for white clinker production. The field test results showed that the single-layer lining of the low conductivity bricks reduced the kiln shell temperature even more than the conventional double-layer lining (Fig. 4). This improved insulation led to a total energy saving of approximately 0.8 kcal/kg clinker in a 5-meter area. Additionally, the developed refractories demonstrated better insulation properties over time compared to a competitor energy-saving brick, resulting in a difference of approximately 0.5-0.6 kcal/kg clinker in energy savings (Fig. 5). Moreover, after 8 months of operation, the developed low conductivity bricks remained 4-5 cm thicker than the competitor bricks, indicating better performance under high thermal loads in the combustion zone.
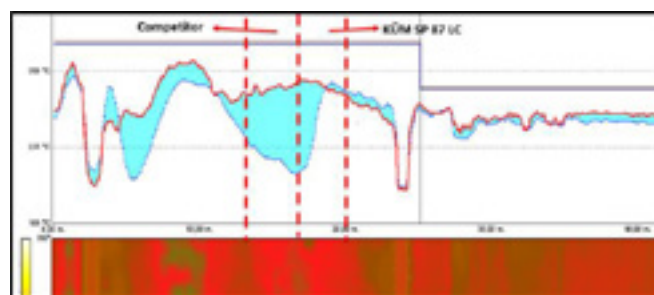
Fig. 5: Kiln shell temperature as a function of kiln meter showing single layer lining of both competitor and developed energy saving bricks

**CONCLUSION**

It has been concluded that:

1. The optimized brick design has no negative effect on refractoriness, and provides the ability to control the degree of the porosity, thus altering the relevant properties. The sub-micron sized porosity ensures no sacrifice on cold crushing strength as well as low permeability.
2. Comparable gas permeability to the standard MgO-Spinel bricks is achieved.
3. Thermal conductivity of the refractory brick is achieved to be decreased by 25% at 1000 °C by induced porosity.
4. Reduction in thermal conductivity resulted in 0,8 kcal/kg clinker energy saving in clinker production.
5. Single layer lining of the low conductivity brick decreased kiln shell temperature even more than the conventional double layer lining in white cement production.
6. The weight of the overall refractory lining is decreased by ~10% which would increase kiln ring lifetime and decrease electric consumption to rotate the kiln.
7. The weight reduction of the refractory lining provides less refractory consumption per meter lined.
8. Developed energy-saving bricks proved themselves in white cement production. The field tests are still ongoing in conventional rotary kilns.

**REFERENCES**

[1] International Energy Agency. (2021). Net Zero by 2050: A Roadmap for the Global Energy Sector. Paris: International Energy Agency.

[2] United Nations Framework Convention on Climate Change. (2015). Paris Agreement. Retrieved from https://unfccc.int/process-and-meetings/the-paris-agreement/the-paris-agreement

[3] European Commission. (2019). A Clean Planet for All: A European Strategic Long-Term Vision for a Prosperous, Modern, Competitive, and Climate-Neutral Economy. Retrieved from https://ec.europa.eu/clima/policies/strategies/2050_en

[4] I. Ganesh (2013) A review on magnesium aluminate (MgAl2O4) spinel: synthesis, processing and applications, International Materials Reviews, 58:2, 63-112, DOI: 10.1179/1743280412Y.0000000001

[5] Sarkar, R. (2010). Refractory applications of magnesium aluminate spinel. Interceram: Refractories Manual, 1, 11-14.

[6] Shi, M., Li, Y., & Shi, J. (2022). Fabrication of periclase and magnesium aluminate spinel refractory from washed residue of secondary aluminum dross. Ceramics International, 48(6), 7668-7676.

[7] F. Wang, J.K. Ye, G. He, G.H. Liu, Z.P. Xie, J.T. Li, Preparation and characterization of porous MgAl2O4 spinel ceramic supports from bauxite and magnesite, Ceram. Int., 41 (2015), pp. 7374-7380.

[8] J. Qiao, Y.B. Wen, Mechanical and dielectric properties of porous magnesium aluminate (MgAl2O4) spinel ceramics fabricated by direct foaming-gelcasting, Ceram. Int., 46 (2) (2020), pp. 1442-1447.

[9] Z.I. Chen, H.Z. Chen, H. Yang, et al., Characterization of spinel bubbles and preparation and properties of lightweight ceramics, Ceram. Int., 47 (2020), pp. 6513-6520.

[10] Effects of sintering temperature on the properties and the pore evolution of microporous MgAl2O4 aggregates

# CUSTOMIZED LININGS FOR UPPER TRANSITION ZONES OF ROTARY KILNS FOR CONTEMPORARY CEMENT CLINKER PRODUCTION CONDITIONS

Holger Wirsing, Carsten Vellmer, Hans-Jürgen Klischat
Refratechnik Cement GmbH, Göttingen, Germany

## ABSTRACT

Refractories for linings of cement clinker rotary kilns have been developed according to the process conditions resulting from the mineral phase transformations of the kiln feed and the kiln gas atmosphere. Even under standard conditions the requirements for refractory bricks used for linings in the upper transition zone are complex, and the increasing use of alternative fuels and raw materials intensifies the loads drastically. In kilns with thermal substitution rates exceeding 80 %, especially in the upper transition zone, burning conditions again became more severe. New combinations of inside temperature profile, kiln shell temperature, oxygen content, concentration of volatile compounds, new compounds and clinker melt activities never observed before in that area, are then constantly present or occur as temporary effects. Refractory lifetime monitoring, lining inspections, and post-mortem investigations showed that lining concepts must be reviewed and adapted. To meet this increasing demand, refractory brick materials have been developed to withstand these stress combinations in a better way. The refractory linings used today in the upper transitions zones of cement clinker kilns with high thermal substitution rates are designed to cope with the specific combinations of stresses. This includes not only new non-basic brick types with high resistance to sulfur oxide attack, but also linings for better performance that directly and indirectly contribute to a reduction of emissions and to energy savings.

## THE KILN PROCESS

In the kilns of the cement industry, cement clinker is burned from limestone, quartz sand, clay and components containing iron oxide. In addition to natural raw materials, alternative raw materials are also used for this purpose. Via the cyclones, the raw material is fed into the kiln as fine meal, which is heated until, at a sufficient temperature, calcination of the limestone begins. In the calciner, large amounts of energy are supplied for this highly energy-consuming reaction. Consequently, during the decomposition of the limestone in the kiln feed, its temperature rises only slowly, due to the endothermic reaction. After the raw meal has entered the rotary kiln, the reaction continues in the calcining zone and comes to an end in the safety zone. After complete calcination, the continuous energy input cause rapid heating of the material to be burned, and the clinker mineral phase formation begins. As an intermediate product of these phase formations, clinker melts are formed which are strongly basic, table 1. The kiln zone in which the clinker melts begin to occur in the material to be fired is referred to as the upper transition zone. Here, contact reactions of the clinker melt with the refractory material become possible. If a refractory lining made from acidic alumosilicate refractory materials would be affected by that basic clinker melts, a fast corrosion of the brickwork by erosion would be the consequence, figure 1.

Therefore, when planning the refractory lining of the rotary kiln, the change from aluminosilicate to basic products is usually made at this point.



| Typical chemical composition | | Cement clinker | Cement clinker melt |
|---|---|---|---|
| CaO | weight% | 63-70 | 57.0 |
| SiO$_2$ | weight% | 19-24 | 7.5 |
| Al$_2$O$_3$ (+ TiO$_2$) | weight% | 3-7 | 22.6 |
| Fe$_2$O$_3$ | weight% | 1-5 | 12.9 |
| Melt content (1450 °C) | weight% | 20-30 | - |

Tab. 1: Composition of cement clinker and clinker melt [1][2]

While in the later course of clinker phase formation in the central burning zone a coating layer can form on the lining, which reduces the interaction of refractory material with the material to be fired and with the kiln gas atmosphere, the bricks in the upper transition zone remain free from coating. They are in direct contact with the material to be fired and the kiln gas atmosphere. The thermal situation of the kiln shell therefore solely depends on the temperature reduction of the refractory lining.

Often, the upper transition zone is in the vicinity of the second tyre, which may add mechanical stresses. The materials used there must be sufficiently resistant to all the resulting stresses to enable effective kiln operation.
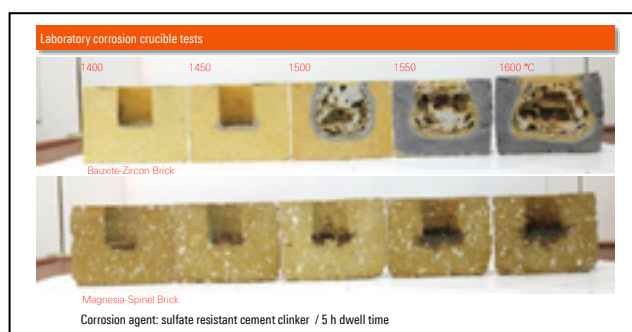
Fig. 1: Cut face sides of crucibles made from alumosilicatic (top) and basic bricks (bottom) after corrosion tests with sulfate resistant cement clinker as corrosive agent.

## EFFECT OF ALTERNATIVE FUELS ON THE PROCESS

An important aspect to be considered is the impact by an intensive use of alternative fuels. In some cement plants, the substitution rate has already reached 80 %. As a result, higher contents of volatile components, mostly alkali salts, are present in the kiln gas atmosphere. The alkali salts accumulate in the sulphate and chloride alkali cycles up to very high concentrations, figure 2. Depending on the type, quantity and feed location (main burner, calcinator, kiln inlet) of the alternative fuels, the temperatures in the different kiln sections are changing. Temporary, more unstable firing conditions become possible. An excess of sulfur in the kiln gas atmosphere can occur. Especially in plants without a tertiary air duct, which are operated with high feeding rates of alternative fuels at the kiln inlet
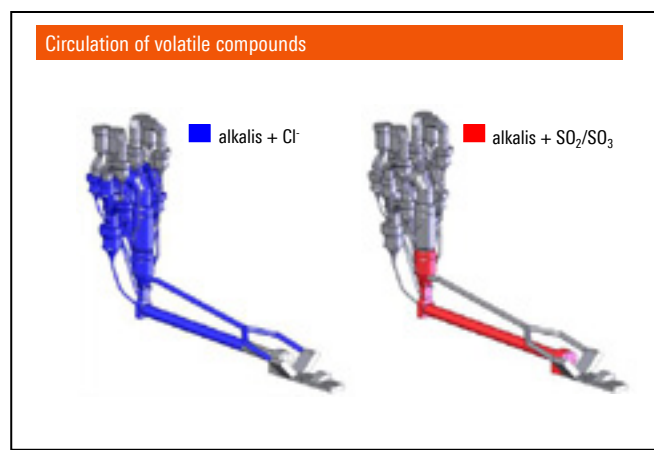
*Fig.2: Location of alkali circles in cement clinker kilns*

(e.g., tyres, sewage sludge), an extremely reducing atmosphere can result locally in the kiln gas atmosphere close to the surface of the lining of the upper transition zone.

**IMPACT ON THE REFRACTORY PRODUCTS**

Bricks used in linings of the upper transition zone interact with the kiln gas atmosphere via the surface and the inner surface, which is the open porosity. The changes in the composition of the kiln gas atmosphere thus have a direct influence on the refractory material.

In the open pores of the elastified magnesia bricks, condensation and crystallization of salt compounds occur when the atmosphere is highly alkaline, following the temperature gradient toward the cold side of the lining, figure 3. This zonal saturation of the pores leads to an increased stress sensitivity of the products. In interaction with additional mechanical stresses, spalling occurs when the structural strength is exceeded by these stresses. This can lead to premature wear of the refractory lining.

562
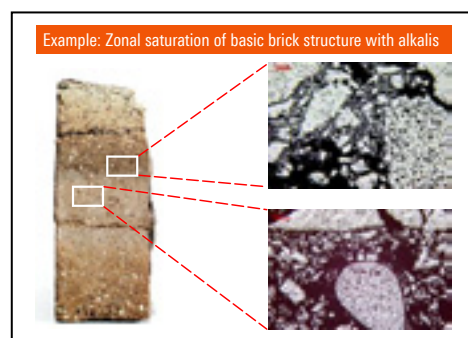


*Fig.3: Structural cut face side and microstructure of a magnesia-spinel brick after use in an alkali loaded cement clinker kiln.*

With zonal saturation of the pores, there may also be an increase in heat transfer. If this leads to kiln shell temperatures that can be harmful to the steel structure, countermeasures must be taken. Often, the furnace shell is cooled by means of external blowers or water spraying. These cooling measures do not reduce heat loss and only mitigate the effects of high thermal flow.

Excess sulfur in the kiln gas atmosphere can occur when sulfureous lignite and petroleum coke are used as fuel. Sulfur components in the flue gas which are not saturated by alkalis can lead to an attack on the calcium silicate secondary phases of the magnesia component of the basic bricks. The porosity in the affected brick horizons is reduced by the formation of anhydrite, due to the interaction with $SO_2$ from the flue gas as a first step of corrosion. An embrittlement of the bricks upper parts may occur. At the prevailing temperatures, the products from this reaction are mobile

in the microstructure of the refractories and migrate in a second step of corrosion toward the lower brick parts.



*Fig.4: Structural cut face side of a magnesia-spinel brick after use and lining showing signs of sulfur attack.*

This results in a formation of monticellite and forsterite and in a loss of strength of the hot side, figure 4. The embrittlement shifts to the middle part of the brick. As with saturation with alkali salts, these changes in the microstructure of the brick increase the risk that that mechanical loads will exceed the structural strength of the brick. Spalling of the affected areas may reduce the service life of the material.

Reducing atmosphere and redox conditions may change the valence state of the iron in iron oxide containing refractory compounds from trivalent to bivalent. This transformation can lead to volume changes of the iron oxide-containing mineral phases. The reducing atmosphere also can influences the salt compounds which turns to sulfites. Under conditions like this infiltration down to the kiln shell becomes possible.

If solid fuel burns off on the surface of the refractory lining, elemental carbon can be precipitated from the gas phase in accordance with the Boudouard equilibrium in the brick structure, figure 5. The microstructural stresses increase as a result. Iron oxide containing compounds have a catalytic effect on this reaction, and extreme mechanical stresses can occur due to localized deposition of carbon.
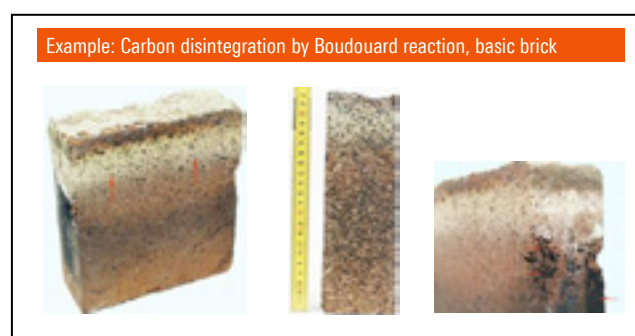


*Fig.5: Outside view and structural cut face side of a magnesia-hercynite brick after use in strongly reducing atmosphere.*

These specified types of stress can occur in different combinations and act on the refractory material. The refractory material must be selected according to the actual combination of stresses present.

**SELECTION OF REFRACTORY MATERIALS**

In kilns with low substitution rates, the thermodynamic parameters of the clinker burning process and the mechanical kiln specifics determine the choice of refractory material. In general, magnesia spinel, magnesia pleonast and magnesia hercynite bricks based on magnesia raw materials of varying purity are used.

Starting from these linings, which can be regarded as standard, the changes in the wear situation due to the intensive use of alternative fuels and possible ceramic solutions are discussed below.

In many cases, these effects can be compensated using elastic magnesia spinel bricks with a denser microstructure, which enhance infiltration resistance and offer higher resistance to spalling due to higher microstructural strength (AF products). By slowing down the speed of saturation with alkali salts, the critical stress sensitivity is delayed. The higher microstructural strength ensures that the strength limit is exceeded later or not at all. In the latter case, spalling is avoided even with zonal saturation of the brick.

| Refratechnik's product groups for application in the Upper Transition Zone of cement clinker rotary kilns | | | | | | |
|---|---|---|---|---|---|---|
| | magnesia bricks, elastified | additionally spalling resistant structure superelastified | | additionally emission reducing structure | and spalling superelastified | corundum-SiC bricks |
| conditions of operation | | AF and CF-products | A1-products | ES-products | ES A1-products | |
| standard clinker melt activity | X | X | X | X | X | X |
| standard alkali load | X | X | X | X | X | X |
| standard atmosphere | X | X | X | X | X | X |
| no excess of sulfur | X | X | X | X | X | X |
| standard mechanical stresses | X | X | X | X | X | X |
| standard kiln shell temperature | X | X | X | X | X | X |
| | | | | | | |
| emission control / fuel savings | (X) | | | X | X | |
| severe clinker melt activity | | X | | X | X | |
| severe alkali load | | X | X | X | X | X |
| severe atmosphere | X (such with low $Fe_2O_3$!) | X (such with low $Fe_2O_3$!) | X (such with low $Fe_2O_3$!) | X (such with low $Fe_2O_3$!) | X (such with low $Fe_2O_3$!) | X |
| excess of sulfur | X (such with low CaO!) | X (such with low CaO!) | X (such with low CaO!) | X (such with low CaO!) | X (such with low CaO!) | X |
| severe mechanical stresses | | | | | X | X |
| high kiln shell temperature | (X) | | | (X) | X | (X) |

Tab. 2: Characteristics of refractory brick types related to be used under specific conditions of kiln operation.

In case of additional mechanical stress, e.g., due to a higher ovality as well as deformation of the kiln shell or a strong influence of the tyre, it is more difficult to achieve this goal. In the case of combined loading of salt infiltrations and kiln mechanics, products as described above, which have been additionally superelastified, can be used (A1 products). With denser microstructure and higher elastifier content, the gain in elasticity outweighs slight strength losses compared to AF products. These superelastified bricks are also used in applications with increased mechanical stress without significant alkali load.

If a reduction of the kiln shell temperature is intended to protect the outer kiln structure or to specifically reduce heat losses, the use of the superelasticized products mentioned above can already be helpful. The higher content of elastifying minerals, which have a lower thermal conductivity compared to magnesia, already reduces the heat transfer.

Brick grades from another product group are targeting to reach lower kiln shell temperature (ES products). These magnesia spinel bricks have the characteristics of high resistance to infiltration and spalling as well as increased porosity [3]. Heat transfer can thus be reduced by 25% to 30% compared to dense products. Regardless of the salt load of a kiln, such products can be used to reduce heat loss, energy use, and hence the $CO_2$ emissions of the clinkering process. In the form of A1 ES products they can also be used in areas of kilns with high mechanical load.

A low content of calcium silicate secondary phases or a low CaO to $SiO_2$ ratio of approx. 1 are added as selection criteria to achieve the highest possible resistance to excess sulfur in the kiln gas atmosphere for basic brick grades. All the product groups listed in Table 2 are containing brick grades which meet this criterion.

If a locally strongly reducing atmosphere occurs in the upper transition zone, attention must also be paid to low iron oxide contents when selecting the elastified magnesia bricks in order to reduce the influence of redox conditions and the risk of carbon deposits and associated stress increase.

A more recent approach is the extension of the area of non-basic bricks with SiC reinforced corundum bricks including the upper transition zone and partly the central burning zone. The higher resistance to clinker melt compared to other aluminosilicate products is sufficient at low clinker melt activity, figure 6 on the right side. Other properties of these products are very suitable to lead to good service behavior under the complex stress situation. The alkali resistance is high and depends on the manufacturing conditions of the products. This is also given under highly reducing conditions, figure 6 on the left side. The alkali resistance of these bricks differs from the resistance of elastified magnesia bricks. Constituents of the SiC reinforced corundum bricks react with the alkalis in the pores near the surface, which results in the formation of a highly viscous and thus sealing melt phase. Further alkali penetration is prevented, the porosity of the deeper brick areas is not saturated with alkalis, and the porosity therefore continues to contribute to the reduction of heat transfer in favor of lower kiln shell temperatures.



Example KRONAL® 90 AR: Structural cut of crucibles after testing with…

…potassium carbonate/ reducing atm. /1100 °C /5 h dwell time    …sulfate resistant cement clinker/1500 °C /5 h dwell time
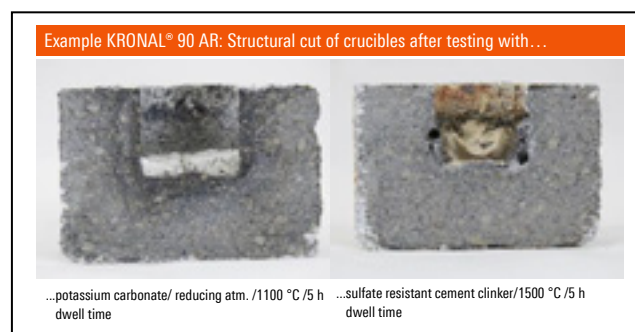
Fig.6: Cut face sides of crucibles made from corundum-SiC brick grade KRONAL® 90 AR after corrosion tests with potassium carbonate (left side) and sulfate resistant cement clinker (right side) as corrosive agents.

Since these products, including the binding matrix, are free of calcium silicates, unlike basic bricks, $SO_2$ resistance is high. Lower thermal expansion than in basic products and high strengths contribute to reduced stress in the lining and good thermomechanical resistance. If, on the other hand, the clinker melt activity is high, the neutral thermochemical character of the corundum is no longer sufficient and a change to the basic products already described must be made to avoid high wear rates.

**CONCLUSIONS**
Using the example of the upper transition zone, it was shown that especially modified basic, and under special conditions also corundum-SiC refractory materials are available for linings of this area even in complex stress situations. A suitable selection for a successful application can only be made if the existing stresses can be correctly assessed and the material is correctly installed. This requires intensive contact between kiln operators and refractory manufacturers. Furnace inspections and post-mortem analyses on the refractories provide important hints.

[1] Verein Deutscher Zementwerke – Tätigkeitsbericht 1993 -96, S. 56-57
[2] Seidel, G., Huckauf, H., Stark, J. – Technologie der Bindebaustoffe, Band 3. VEB Verlag für Bauwesen, 1978
[3] Klischat H.-J., Wirsing, H.; Basic refractories enabling ecological cement and lime production under difficult conditions, Proceedings UNITECR 2019

# REFRACTORY LININGS FOR CEMENT ROTARY KILNS CONTRIBUTING TO ENVIRONMENTAL IMPACT REDUCTION

Makoto Ohno*, Shiho Takeuchi and Yasutaka Yoshimi
MINO CERAMIC CO., LTD., JAPAN

## ABSTRACT

As one of the most carbon-intensive industries, the cement industry is required to reduce environmental impact in order to tackle climate issues. Refractory manufacturers can primarily contribute to the efficiency of cement burning process, in other words, environmental impact reduction by providing durable and energy-saving refractories. From the view point of environmental footprint reduction, many cement plants have been using a larger amount of alternative fuels (AFs) and alternative raw materials (ARMs) and consequently this has caused premature wear of refractories inside the kilns. Additionally, with regards to thermal energy released from the process it seems not much effort has been made about the reduction of heat radiation from the kiln shell surface, whereas a lot has been implemented about recovery of waste heat from exhaust hot gases.

This paper describes our latest progress on the development of a magnesia-spinel brick coping with the increasing use of AFs and ARMs and an alkali resistant alumina-silica brick contributing to shell temperature reduction.

## INTRODUCTION

Tackling climate change by reducing greenhouse gas (GHG) emissions is an urgent global challenge. The cement industry has been facing increasing pressure to reduce its carbon footprint due to its large contribution to greenhouse gas emissions. Currently, for reducing the emissions a great effort has been made on some CCUS projects and more breakthrough innovative projects have been attempted. The short-term measures include increasing the use of AFs, improving thermal and electric energy efficiency, and reducing the clinker-to-cement ratio by blending with mineral substitutes. Increasing the AF substitution rate is one of the most important measures and cement plants in many countries are attempting to enhance the substitution rate. However, the increasing use of AFs and ARMs has made the refractory lining in cement rotary kilns exposed to severe conditions such as unstable coating and high chemical load, often causing premature wear of lining bricks and high heat radiation eventually lowered efficiency and economic loss. As a refractory manufacturer, we believe we can contribute to environmental impact reduction by providing refractories that can cope with harsh conditions and lower the shell temperature.

In the cement industry in Japan, a large amount of wastes and byproducts have been used in the manufacturing process and the unit amount per ton of cement has reached around 470 kg/t-cement recently. Figure 1 shows the transition of the specific amount of wastes and byproducts per ton of cement and the usage of plastic waste. As seen in the graph, the specific consumption of wastes and byproducts has increased significantly from 1990 to 2010. Additionally, while the specific consumption of wastes and byproducts remained flat since 2010, the usage of plastic waste has increased continuously. For the plastic waste, it could make a local reducing atmosphere in part of burning zone and upper transition zone since a large amount of oxygen is consumed during combustion. Furthermore, it tends to have less uniformity in size and type, leading to temperature fluctuations especially when it is fed from the main burner. These characteristics can result in unstable coating conditions and enhancing circulation of volatile components such as alkali, chloride and sulfur, more adversely affecting the bricks.

In this study we present our latest progress on the development of a magnesia-spinel brick coping with the increasing use of AFs and ARMs and an alkali resistant alumina-silica brick contributing to shell temperature reduction.
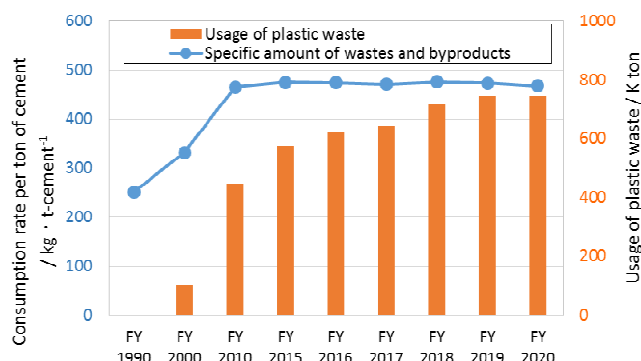


Fig. 1: Transition of specific amount of wastes and byproducts per ton of cement and usage of plastic waste.

## HIGH WEAR-RESISTANT BASIC BRICKS
### Postmortem analysis of conventional magnesia-spinel brick

Figure 2 shows the appearance and cross section of a concentional magnesia-spinel brick used for five months at L/D of 5.6 in a precalciner kiln. This precalciner kiln utilizes various kinds of AFs and ARMs such as waste plastics, wood chips and sewage sludge and its AF substitution rate is approximately 40%. The photo on the left side of Figure 2 shows that one of two bricks was severely damaged from the hot face to over 100mm depth while the other was kept its original thickness. As this brick was used near a tire section and found to be damaged in the actual kiln, it would have been subject to mechanical stress. Table 1 shows the results of measured physical properties and XRD identification of the magnesia-spinel brick divided into layers every 30mm. Intense densification was observed at the 3rd to 5th layer and a large amount of KCl and $CaSO_4$ was identified at the 3rd to 5th and the 4th to 5th respectively. It is evident that the densification was caused by the deposit of KCl and $CaSO_4$. The deposit at the deep part from the hot face is explained by the following; CaO components, which were contained in the brick and/or came from the outside, reacted with infiltrated $SO_X$ to form $CaSO_4$ and then the low temperature eutectic of KCl-$CaSO_4$ was formed by the existence of KCl and it moved toward the shell side. This will lead to the microstructure deterioration near the hot face and lack of flexibility at the densification part (3rd to 5th layer in this case). We believe the damage observed from the hot face to the 5th layer was caused by the microstructure deterioration by chemical attack, densification with infiltrated minerals and mechanical stress from the tire. Similar damages have been observed in several kilns, in some cases shortening the life of the lining bricks, which led to its necessity for improvement to enhance the process efficiency.
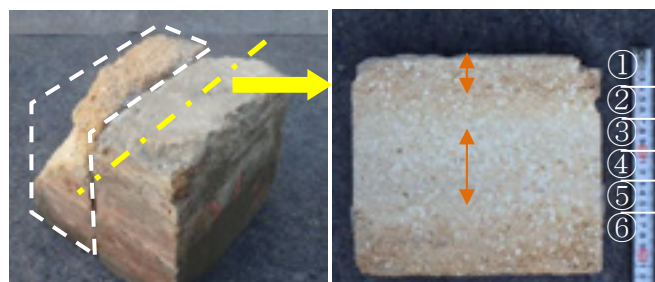


Fig. 2: Appearance and cross section of a conventional magnesia-spinel brick used for 5 months at L/D of 5.6 in a precalciner kiln.

Tab. 1: Results of measured physical properties and XRD identification of the magnesia-spinel brick as shown in Figure 2.

| | ① | ② | ③ | ④ | ⑤ | ⑥ |
|---|---|---|---|---|---|---|
| Distance from hot face / mm | 0-30 | 30-60 | 60-90 | 90-120 | 120-150 | 150-200 |
| App. Porosity/% B.D./ g/cm$^{-3}$ | 13.0 2.98 | 10.4 3.04 | 5.3 3.16 | 3.1 3.21 | 6.3 3.17 | 15.5 2.95 |
| Infiltrated mineral KCl NaCl CaSO$_4$ | x (-) | X - | XX - (-) | XXX X | XX - XX | (-) - |

X-ray Intensity: Strong XXXXX > XXXX > …> X > x > - > (-) Weak

**Development of high wear resistant magnesia-spinel brick**

<u>Characteristics required for magnesia-spinel bricks under chemical attack and mechanical stress</u>

1. Reinforced microstructure in the matrix with spinel (MgAl$_2$O$_4$) bonding

Controlling the amount of CaO and SiO$_2$ is an important factor in terms of bonding formation. Adjusting it to proper amount and ratio of CaO and SiO$_2$ makes the bonding in the matrix primarily formed with spinel bonding, contributing to hot strength, volume stability after repeated heating, and resistance to sulfur, chlorine, and alkali.

2. Low permeability for foreign components

Optimizing grain size distribution and firing conditions and using easily-sinterable raw materials makes the dense microstructure composed of smaller pores, contributing to low permeability.

3. High flexibility for mechanical stress

Adding some spinel materials of proper sizes and optimizing grain size distribution makes it possible to have high flexibility while achieving high strength.

Based on the required characteristics and determined product concept, we developed a magnesia-spinel brick that can overcome the harsh conditions. The properties of the developed magnesia-spinel brick are shown in Figure 3 as indexes with the properties of a conventional magnesia-spinel brick set at 100. Although the developed one has the same level of apparent porosity as the conventional one, it has lower permeability. Furthermore, it has lower volume change after repeated heating (700-1300ºC, 100 times) and high hot bending strength at 1200 ºC due to its reinforced microstructure. An increase in damage resistance parameter was also observed.
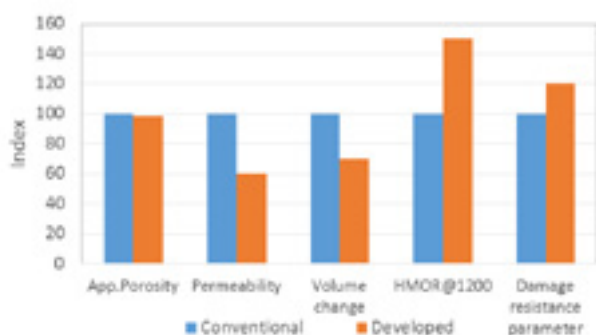
Fig. 3: Several quality characteristics of the developed magnesia-spinel brick as indexes with the properties of the conventional magnesia-spinel brick set at 100.

Figure 4 shows the appearance and cross section of the developed magnesia-spinel brick used for one year at L/D of 5.8 in the same precalciner kiln as Figure 2. The photo on the left side of Figure 4 shows that the hot face was almost flat and no significant damage was observed. In the cross section, although some tiny

deterioration was observed near the hot face, no definite cracks were found throughout the brick. Table 2 shows the results of measured physical properties and XRD identification of the magnesia-spinel brick divided into layers every 30mm. Infiltrated minerals identified are the same as shown in the conventional one (see Table 1) but the amount and depth of infiltration was reduced in this sample even though it was used for one year (2 campaigns). Figure 5 shows the apparent porosity of the developed one (Table 2) and the conventional one (Table 1). The result clearly shows that densification in the developed one was more reduced than in the conventional one. The developed magnesia-spinel brick achieved one year life, demonstrating no deep infiltration, severe densification and crack generation. The characteristics of reinforced microstrucure, low permeability and high flexibility in this brick can contribute to stable operations and process efficiency under harsh conditions due to increasing use of AFs and ARMs.
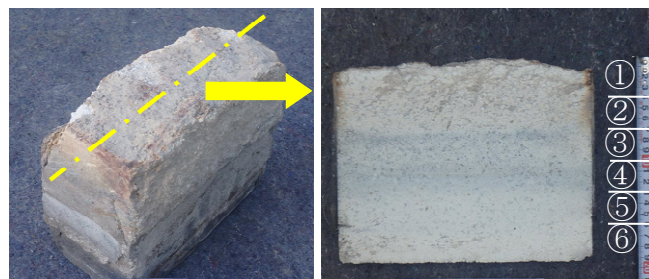
Fig. 4: Appearance and cross section of the developed magnesia-spinel brick used for one year at L/D of 5.8 in a precalciner kiln.

Tab. 2: Results of measured physical properties and XRD identification of the magnesia-spinel brick as shown in Figure 4.

| | ① | ② | ③ | ④ | ⑤ | ⑥ |
|---|---|---|---|---|---|---|
| Distance from hot face / mm | 0-30 | 30-60 | 60-90 | 90-120 | 120-150 | 150-200 |
| App. Porosity/% B.D./ g/cm$^{-3}$ | 12.0 3.01 | 7.4 3.11 | 6.7 3.09 | 9.4 3.08 | 14.1 3.00 | 16.1 2.94 |
| Infiltrated mineral KCl NaCl CaSO$_4$ | x (-) | XX (-) | XX (-) | x - (-) | - - (-) | |

X-ray Intensity: Strong XXXXX > XXXX > …> X > x > - > (-) Weak
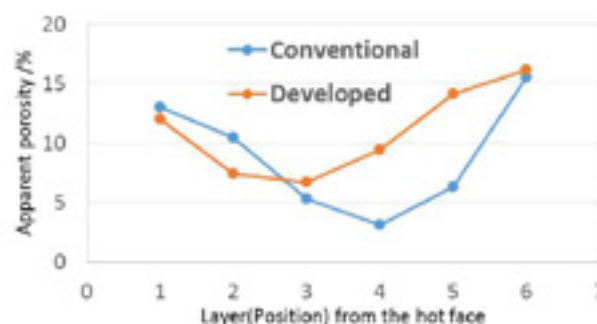
Fig. 5: Apparent porosity of the developed and conventional magnesia-spinel bricks used in the same area (Table 1 and 2).

**HIGH ALKALI-RESISTANT ALUMINA-SILICA BRICK WITH LOW THERMAL CONDUCTIVITY**

High alumina bricks containing over 50% alumina content are commonly used in the safety/calcining zone in many cement kilns worldwide. Particularly for the adjacent area to the upper transition zone where basic bricks are installed in most cases, high alumina bricks with higher alumina content tend to be installed due to concerns about erosion by reaction with CaO components. Recently, however, the increasing of AFs and ARMS has caused an

increase in volatile components including alkali and chlorine circulating through the lower temperature zone, leading to premature wear of the lining bricks. In general, alumina-silica bricks in this zone are worn by peeling-off near the hot face caused by alkali attack and the resistance to alkali attack increases as the alumina content decreases. Moreover, alumina-silica bricks with lower alumina content have lower thermal conductivity and thus if they have sufficient erosion resistance and mechanical strength, then they can satisfy the needs for reduced heat loss from the kiln shell along with longer service life. Therefore, we will propose a high alkali resistant alumina-silica brick with low thermal conductivity for the safety/calcining zone, even for the adjacent area to the upper transition zone. Table 3 shows the several quality characteristic values of the high alkali resistant alumina-silica brick with low thermal conductivity (hereinafter referred to as AS) in comparison with other alumina-silica bricks, which are measured by our laboratory based on JIS. AS has the following features, which allows it to be installed from the uphill side of upper transition zone depending on kiln conditions;

1. Prevent alkali infiltration with the formation of viscous liquid phase at the hot face by adding special raw materials
2. Prevent crack growth with absorbing stresses from the kiln by introducing microcracks and using raw materials with low thermal expansion

Tab. 3: Quality characteristic values of AS and other alumina-silica bricks.

| Type | AS | Typical High Alumina | Typical Fireclay | Two-layer combined | |
|---|---|---|---|---|---|
| | | | | Ref. | Ins. |
| Apparent porosity /% | 19.3 | 18 | 17.4 | 23.4 | 36.4 |
| Bulk density /g・cm$^{-3}$ | 2.12 | 2.57 | 2.27 | 2.28 | 1.82 |
| Cold crushing strength /MPa | 55 | 63 | 53 | 55 | 28 |
| Chemical compositions /% | | | | | |
| $Al_2O_3$ | 37 | 63 | 43 | 58 | 42 |
| $SiO_2$ | 57 | 31 | 52 | 37 | 54 |
| Thermal conductivity /W・m$^{-1}$・K$^{-1}$ | (measured by JIS hot-wire method) | | | | |
| 350ºC | 1.2 | 2.1 | 1.8 | 1.4 | 0.9 |
| 500ºC | 1.4 | 2.1 | 1.8 | 1.6 | 0.9 |
| 1000ºC | 1.6 | 2.2 | 1.9 | 2.0 | 1.1 |

Tab. 4: Thermal calculation results of AS and other alumina-silica bricks in case 30 m of bricks are installed respectively.

| Type | AS | Typical High Alumina | Typical Fireclay | Two-layer combined | |
|---|---|---|---|---|---|
| | | | | Ref. | Ins. |
| Brick thickness /mm | 220 | 220 | 220 | 160 | 60 |
| Hot face temperature /ºC | 1200 | | | | |
| Shell face temperature /ºC | 268.7 | 316.9 | 296.4 | 270.5 | |
| Radiation heat loss /W・m$^{-2}$ | 6,297 | 8,604 | 7,567 | 6,375 | |
| Radiation heat loss /kW 30m installed in 5.0m ID kiln | 2,968 | 4,055 | 3,566 | 3,004 | |
| Radiation heat loss /GJ・year$^{-1}$ 30m installed in 5.0m ID kiln One year [8,000hrs] operation | 85,478 | 116,784 | 102,701 | 86,515 | |
| Coal required for heat energy /ton・year$^{-1}$ | 3,213 | 4,390 | 3,861 | 3,252 | |
| Reduction of CO2 emission /ton・year$^{-1}$ | 2,835 | 0 | - | - | |

(Conditions)

Hot face temp.: 1200ºC, Ambient temp.: 20ºC, Wind speed: 0 m/s, Blackness: 0.85

Calorific value for coal: 26.6MJ/kg, $CO_2$ emission for coal: 2.409kg-$CO_2$/kg

In terms of environmental impact reduction, AS also has an advantage of light bulk density in addition to low thermal conductivity. In order to evaluate the $CO_2$ reduction by reduced shell temperature, we calculated hypothetical radiation heat losses and $CO_2$ emission reductions if we install a 30 linear meter of bricks in a 5.0m ID kiln. Table 4 shows the thermal calculation results of AS and other alumina-silica bricks on the conditions described in the below part of Table X. As you can see, AS is much more energy-efficient than typical high alumina/fireclay bricks and a little superior to two-layer combined bricks. Compared to typical high alumina bricks, AS can save 1,177 ton/year of coal and reduce $CO_2$ emissions by 2,835 ton/year.

Figure 6 shows the cross sections of AS used for five months (left) and two years (right) at 9.2 (left) and 9.7 (right) of L/D in a precalciner kiln, in which magnesia spinel bricks were installed downward from 9.2 of L/D. This precalciner kiln utilizes various kinds of AFs and ARMs such as waste plastics, waste tyres and construction soil and its AF substitution rate is approximately 30%. Since these bricks were installed at the same time and in close proximity to each other, there would be no issues with the assumption that they were used under the same conditions. Although some yellowish-brown discoloration was found at the shell face side due to iron content came from the kiln shell, no cracks and damage was observed inside the bricks. Table 5 shows the results of measured physical properties and XRD identification of AS divided into layers every 30mm. In the five-month sample, a large amount of lucite ($K_2O・Al_2O_3・4SiO_2$), which was formed by the reaction of brick with foreign alkali, was identified at the 1$^{st}$ layer and some alkali salts were identified up to the 4$^{th}$ layer.
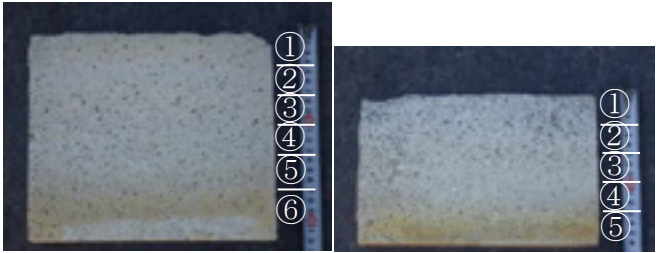


Fig. 6: Cross sections of AS used for five months (left) and two years (right) at 9.2 (left) and 9.7 (right) of L/D in a precalciner kiln.

Tab.5: Results of measured physical properties and XRD identification of AS as shown in Figure 6.

<For five months at 9.2 of L/D>

| | ① | ② | ③ | ④ | ⑤ | ⑥ |
|---|---|---|---|---|---|---|
| Distance from hot face / mm | 0-30 | 30-60 | 60-90 | 90-120 | 120-150 | 150-200 |
| App. Porosity/% B.D./ g/cm$^{-3}$ | 9.7 2.36 | 10.4 2.32 | 12.4 2.29 | 16.5 2.19 | 17.9 2.16 | 19.8 2.12 |
| Infiltrated mineral $K_2O・Al_2O_3・4SiO_2$ KCl NaCl | XXXx | X - | X (-) | - | | |

<For two years at 9.7 of L/D>

| | ① | ② | ③ | ④ | ⑤ |
|---|---|---|---|---|---|
| Distance from hot face / mm | 0-30 | 30-60 | 60-90 | 90-120 | 120-150 |
| App. Porosity/% B.D./ g/cm$^{-3}$ | 10.6 2.33 | 8.1 2.40 | 9.3 2.37 | 11.5 2.31 | 16.4 2.17 |
| Infiltrated mineral $K_2O・Al_2O_3・4SiO_2$ KCl NaCl | XXx | XX x | X - | X (-) | - |

X-ray Intensity: Strong XXXXX > XXXX > …> X > x > - > (-) Weak

Considering the infiltration of foreign components was inhibited in the shell face side (4th to 6th layer), this result implies that viscous liquid phase formed in operation prevented the infiltration. In the two-year sample, leucite is identified at the 1st layer and some alkali salts were identified up to the shell face side. Although some alkali salts infiltrated toward shell face side after two years of use, it was likely that the infiltration hardly affected the inside part of the brick. At the 1st layer in both samples, a large amout of leucite was identified, indicating a glassy protective layer was formed at the same time. In terms of erosion, no cement attack was confirmed in both samples, thus no excessive concern is likely to be needed. Judging from the comparison of these bricks, AS would be mainly worn out by about 20mm thick (structural spalling) from the hot face over time because leucite expands when it forms and its expansion coefficient is large. In many cement kilns, AS is gradually and stably worn by thin structural spalling and performs well for long periods. We believe this is because the formed viscous glassy phase prevents the infiltration of foreign components and inhibits the crack generation at the deep position.

Although AS has a lower alumina content, which may raise concerns about erosion by cement materials, it has been installed from the adjacent area to UTZs where magnesia spinel bricks have been installed in dozens of cement kilns in Japan. They have seldom shown erosion, significant wear or any issues concerning its material itself. Figure 7 shows the shell temperature profile at the boundary area between the upper transition zone and safety zone in a precalciner kiln. Magnesia-spinel bricks had a residual thickness close to original size after one year of use, while AS had a residual thickness of 50 to 60 mm thinner than the magnesia brick after two years of use. The average shell temperature was 313ºC and 231 ºC at 10.5 and 11.2 of L/D respectively. As the theoritical caliculations show the shell temperature difference between AS and magnesia-spinel bricks is approximately 100ºC on the conditions of 1200 ºC hot face, coating or other conditons may have been different in each zone. Despite the fact that AS has a lower residual thickness, the shell temperature was kept low due to its low thermal conductivity and its ability to inhibit the penetration of foreign elements, and no abnormal temperature changes were observed near the boundary. Furthermore, inside the kiln, no brick displacement and abnormal movement was observed neat the boundary area. The characteristics of high alkali resistant and low thermal conductivity in AS can contrubutes to the kiln operation with environmental impact reduction.
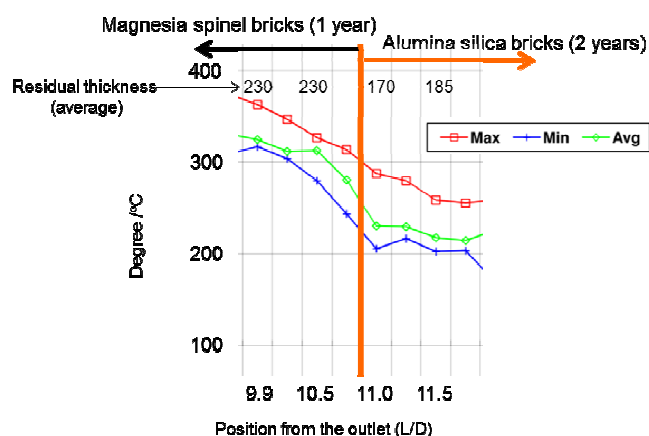
**CONCLUSION**

With the increasing pressure to reduce $CO_2$ emissions, the cement industy has been increasing the use of AFs and ARMs and working on improving the energy efficiency as short-term measures. However, the increasing use of AFs and ARMs has made the refractory lining in cement rotary kilns exposed to severe conditions such as unstable coating and high chemical load, often causing premature wear of lining bricks and high heat radiation eventually lowered efficiency and economic loss. This paper presented our latest progress on the development of a magnesia-spinel brick coping with the increasing use of AFs and ARMs and an alkali resistant alumina-silica brick contributing to shell temperature reduction. Based on the postmortem analysis, we developed a durable magnesia-spinel brick that features reinforced microstrucure, low permeability and high flexibility. The develoed brick has exhibited its features in the actual kiln, achieving a longer service life under harsh conditions due to increasing use of AFs and ARMs. We believe this developed magnesia-spinel brick can contribute to stable operations and process efficiency in cement plants. Likewise in the safety/calcining zone, volatile components such as alkali and chlorine are rising due to the increasing use of AFs and ARMS, exposing the refractory linings to alkali attack. Under the situations that high alumina bricks containing over 50% alumina content are commonly used in the safety/calcining zone in many cement kilns, we have proposed a high alkali resistant alumina-silica brick with low thermal conductivity for the safety/calcining zone, even for the adjacent area to the upper transition zone. It features preventing alkali infiltration and crack growth and has superiority in terms of $CO_2$ emission reduction to common high alumina and fireclay bricks. Our alumina-silica bricks have demonstrated their gradual and stable wear and thier energy-saving propoerties in actual kilns, contributing to the kiln operation with low $CO_2$ emissions

**REFERENCES**

[1] Cement Handbook 2022 – Use of wastes and by-products. Japan Cement Association, 2022
[2] M. Ohno, H. Toda, K. Tokunaga, Y. Mizuno "Development of Magnesia-Spinel Brick for Transition Zone in Cement Rotary Kilns Under the Vastly Increasing Use of Waste", Proc. UNITECR 2013, 2013, p.193-197
[3] H. Toda, M. Fujii, M. Ohno, F. Ozeki "Effect of Minor Components on the Properties of Magnesia-Spinel Brick for Cement Rotary Kilns", Proc. UNITECR 2019, 2019, p.238-241
[4] K. Inaba, K. Tokunaga, Y. Mizuno, Y. Tsuchiya, H. Kozuka, T. Honda, "Development of Calcining Zone Bricks for Cement Rotary Kilns, "Taikabutsu 53 (7), 2001, p.418

567



Fig. 7: Shell temperature profile at the boundary area between the upper transition zone and safety zone in a precalciner kiln.

# SOLIDIFICATION OF TWO FUSED CAST AL$_2$O$_3$–ZRO$_2$–SIO$_2$ MATERIALS IN AN AERO ACOUSTIC LEVITATOR

Jonas, Niessen; Dirk, Muehmer; Thorsten, Tonnesen; Rainer, Telle; Jesus, Gonzaelz-Julian

Institute of Mineral Engineering, Chair of Ceramics, RWTH Aachen University, Aachen, Germany

## ABSTRACT

Due to their excellent high-temperature properties and corrosion resistance, AZS ($Al_2O_3$-$ZrO_2$-$SiO_2$) materials are widely used as refractories. Especially in the glass industry, these products are essential to withstand the corrosive environment. Two industrially available fused cast AZS materials were chosen for this study. One composition was close to the ternary eutectic of zirconia, mullite, and corundum. The other material was close to mullite composition with approx. ten wt% $ZrO_2$. The microstructure and phase composition of the received material was analyzed. Additionally, the materials were remelted in an aero acoustic levitator. A pyrometer and a high-speed camera recorded the crystallization. The fused cast grains and the remelted samples showed significant microstructure and phase composition differences. Due to the high cooling rates and homogeneous nucleation under containerless conditions, both materials tended to form a glassy phase. Cooling samples with a pre-existent nucleus or controlled conditions yielded a fine-grained crystalline microstructure. For conventional cooling, the silica and alumina-rich material exhibited large corundum precipitates. In contrast, the containerless processed sample showed primary precipitation of mullite.

## Introduction

Refractories are essential for metal, glass ,or cement production. They have to resist corrosive media, mechanical loads ,and extreme temperatures. For an extended service lifetime, optimizing the refractories for the given process conditions is mandatory. Fused AZS products are state of the art in glass making due to good mechanical properties and corrosion resistance [1]. Despite the technological importance of the AZS system, there is still an ongoing controversy about a congruent[2,3] or incongruent melting mullite [4,5].

Due to their high melting point, studying the liquidus phase regions of ceramics is difficult. Finding a sufficient container material that resists such high temperatures is challenging. Moreover, dissolution of the vessel material can contaminate the melt. Containerless processing like aero acoustic levitation circumvents these problems. The contactless processing enables direct observation of the crystallization process via a high-speed camera, improving the understanding of the solidification process [6]. Moreover, high cooling rates and high undercooling are achievable. Therefore, the technique is excellently suited to study metastable processes. Most scientists used levitation techniques for high-purity materials. Here we want to study the solidification of refractory-grade AZS materials under containerless conditions.

## Experimental

Two different AZS aggregates were used for the study. One will be referred to as AZS-mullite, which is alumina-rich. The other contains more zirconia and will be referred to as AZS-Zirconia. The exact composition was determined by X-ray fluorescence spectroscopy (XRF) on fused glass discs using a PW2404, Malvern PANalytical B.V, Eindhoven, Netherlands. Both compositions' beads were produce by laser sintering the ground raw materials in a copper mold. A stirring motion yielded a spherical shape necessary for levitation.

Nordine et al. [7] describe the aero acoustic levitator (Pyhsical Property Measurements Inc., Evanston, Illinois, USA) used for this study in detail. The ceramic beads are levitated above a nitrogen gas stream. Additionally, three orthogonal ultrasonic transducer couples create a pressure node to stabilize the sample's position. Two 240W CO$_2$ lasers (SynradInc., Mukliteo, WA, USA) can heat the samples up to 3000°C. To induce solidification the lasers are switched off. A high-speed camera (V5.2, PhantomVision Research Inc., Wanyne, NJ, USA) and a pyrometer (Exactus BF 8402, Bayer Catalysts LCC, Rome, Italy) record the solidification process at1000 fps.

The experimental procedure begins with introducing the bead into the central position of the acoustic node with a vacuum chuck and carefully adjusting the gas flow. Then the laser power is gradually increased while controlling the sample's rotation. When the sample is completely molten, the laser is turned off to record the solidification. Repeating the process several times yields statistical temperature data.

The received and levitated samples were studied by X-ray diffraction using a D8 Advance, Bruker AXS Advances GmbH, Karslruhe Germany, copper tube 2θ 5-90°). The resulting microstructures were studied by scanning electron microscopy (SEM) and energy dispersive spectroscopy (EDS) (FESEM Gemini 500, Zeiss, Oberkochen, Germany; EDS detector XMax80, Oxford Instruments, Abingdon, Oxfordshire, UK).

## Results and Discussion

*Raw material characterization*

Table 1 gives the composition of both materials determined by XRF. Besides the main components, the products contain 2.3-2.5 wt.% impurities. Na$_2$O is the most prominent one.

*Tab. 1: Composition of refractories determined by XRF.*

| Component | Portion in wt.% | |
| --- | --- | --- |
| | AZS-ZrO$_2$ | AZS-mullite |
| SiO$_2$ | 14,5 | 18,4 |
| Al$_2$O$_3$ | 50,0 | 69,3 |
| Fe$_2$O$_3$ | 0,1 | 0,5 |
| TiO$_2$ | 0,1 | 0,1 |
| CaO | 0,0 | 0,1 |
| K$_2$O | 0,1 | 0,1 |
| Na$_2$O | 1,3 | 1,1 |
| ZrO$_2$ | 33,0 | 10,1 |
| HfO$_2$ | 0,7 | 0,1 |
| Co$_3$O$_4$ | 0,0 | 0,1 |
| Y$_2$O$_3$ | 0,2 | 0,1 |

The AZS-ZrO$_2$ material contains only corundum and baddeleyite as crystalline phases. In the SEM micrographs, large interpenetrating Al$_2$O$_3$-ZrO$_2$ grains with a eutectic-like structure are embedded in a silica-rich glassy matrix. Mullite, which would be expected according to the ternary phase diagram [4], is absent. However, various authors reported suppressed mullite precipitation for slow cooling rates [5,8]. Assuming an incongruent melting of mullite, corundum starts to precipitate from the melt. If the peritectic reaction kinetics are sluggish, the Al$_2$O$_3$ cannot be consumed to form mullite. Instead, the remaining silicarich melt solidifies as a glass.

The AZS-mullite material contain besides corundum and baddeleyite, also mullite and cristobalite. As both compositions are in the Al$_2$O$_3$-ZrO$_2$-mullite compatible triangle, cristobalite is not an

equilibrium phase. Again, sluggish peritectic kinetics is a suitable explanation.

*Levitation experiments*

Figure 1 depicts exemplary cooling curves of the AZS-ZrO$_2$ material. At zero seconds, the beads are molten. After approx. one second, the lasers are turned off, inducing rapid cooling. The blue curve cools approx. 300 K below the ternary eutectic temperature (1700-1710°C [4]) before recalescence leads to a temperature increase. In contrast, the orange curve does not reheat and belongs to a glassy completely transparent bead. Bot compositions yielded crystalline and amorphous beads after melting. Under containerless conditions, preferred nucleation sites are missing. Therefore, homogenous nucleation occurs. The statistical nature of homogenous nucleation and high silica content in the samples could explain, that some bead crystalize, while others do not.
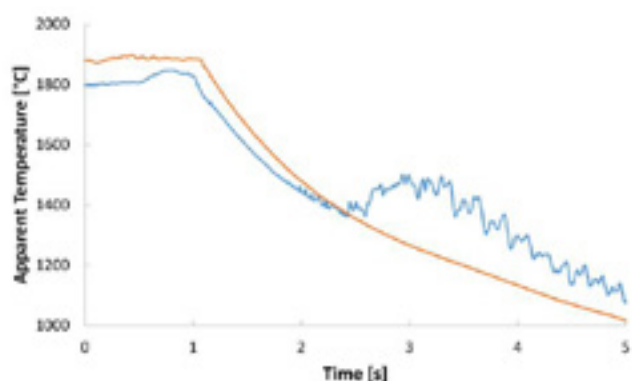


*Fig. 1: Cooling curves of AZS-ZrO$_2$; glass formation without crystallization (orange); recalescence after undercooling, indicating crystallization (blue)*

High-speed camera recordings revealed that several nuclei form in the samples. During crystallization, latent heat is released in proximity to the growth front. The interface between approaching nuclei becomes significantly brighter, indicating a local temperature increase due to heat accumulation. The solidification microstructure of the AZS-ZrO$_2$ is shown in figure 2. Compared to the crushed aggregates, the grain size is significantly refined due to the high undercooling prior to solidification. Around the nucleation sites a radiated structure forms. The interface between two nucleation cells becomes coarser (Fig. 2c) due to the local temperature increase promoting grain growth. Figure 2b shows a coarser structure in the center of a nucleation cell. We assume that it is an unmolten residue acting as a nucleation site. Besides the statistical nature of homogenous nucleation, unmolten solids could explain the different solidification behavior. The microstructure of the AZS-mullite material exhibits comparable features, like an overall small grain size and a coarsening at the interfacial regions.

XRD results of levitated AZS-ZrO$_2$ exhibit mullite and tetragonal zirconia as only crystalline phases. AZS-mullite contains monoclinic as well as tetragonal zirconia, mullite, and some traces that could not be identified. Tetragonal zirconia could be stabilized by the small grain size and pressure from surrounding grains. In contrast to the conventional cooled samples, both compositions do not contain corundum. Likely, due to the high undercooling prior to nucleation, mullite can nucleate directly from the melt [8].
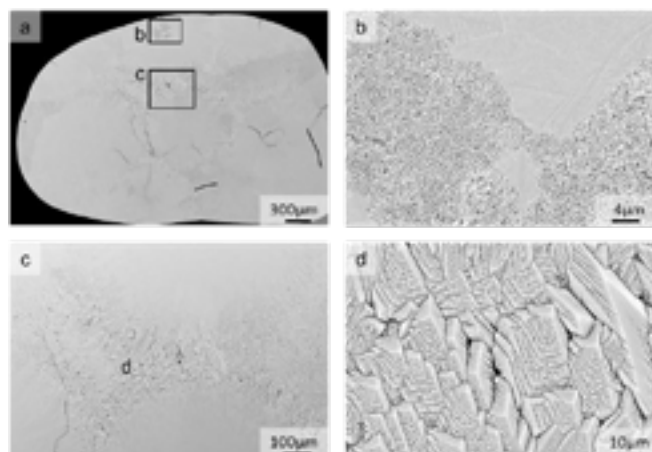


*Fig. 2: Corss-section of a solidified AZS-ZrO$_2$ bead; a) overview; b) coarse structure in the center of a nucleation cell, surrounded by a fine-grained matrix; c) transition zone; d) interfacial eutectic structure.*

**CONCLUSIONS**

The results show the high importance of cooling conditions on the phase selection in AZS materials. In conventional fused cast materials, corundum precipitation is favored above the mullite melting point. Sluggish peritectic reaction kinetics suppress mullite precipitation. The high cooling rate under levitation conditions promotes direct nucleation and precipitation of mullite from the supercooled melt. The results strongly support an incongruent melting of mullite, as it is the only explanation for the suppressed mullite formation in the refractory aggregates.

**REFERENCES**

[1] L.J. Manfredo, R.N. McNally, The corrosion resistance of high ZrO$_2$ fusion-cast Al$_2$O$_3$-ZrO$_2$-SiO$_2$ glass refractories in soda lime glass, J Mater Sci 19 (1984) 1272–1276.

[2] S. Aramaki, R. Roy, Revised Phase Diagram for the System Al$_2$O$_3$-SiO$_2$, J American Ceramic Society 45 (1962) 229–242.

[3] S.S. Ordan'yan, P.S. Gudovskikh, O.V. Pozhidaeva, Refining the phase diagram of the system 3Al$_2$O$_3$ 2SiO$_2$ZrO$_2$, Russian Journal of Applied Chemistry 74 (2001) 1390–1391.

[4] M.C. Greca, J.V. Emiliano, A.M. Segadães, Revised phase equilibrium relationships in the system Al$_2$O$_3$-ZrO$_2$-SiO$_2$, Journal of the European Ceramic Society 9 (1992) 271–283.

[5] S.H. Risbud, J.A. Pask, SiO$_2$-Al$_2$O$_3$ metastable phase equilibrium diagram without mullite, J Mater Sci 13 (1978)

[6] J. Niessen, D. Muehmer, T. Tonnesen, R. Telle, J. Gonzalez-Julian, Examination of the binary system Al2O3-ZrO2 by aero acoustic levitation melting, Int J Ceramic Engine & Sci 4 (2022) 10–15.

[7] P.C. Nordine, D. Merkley, J. Sickel, S. Finkelman, R. Telle, A. Kaiser, R. Prieler, A levitation instrument for containerless study of molten materials, Rev. Sci. Instrum. 83 (2012) 125107.

[8] W. Wisniewski, C. Thieme, C. Rüssel, The detailed microstructure of an alumina-zirconia-silica (AZS) fused cast refractory material from the cast skin into the bulk analyzed using EBSD, Journal of the European Ceramic Society 39 (2019) 2186–2198.

569

# STUDY OF THE MICROCRACKING EFFECT IN AN ALUMINA−MULLITE−ZIRCONIA  REFRACTORY CERAMIC

Amélie Bigeard, David Jauffres, Didier Bouvard
Univ. Grenoble Alpes, CNRS, Grenoble INP, SIMaP, 38000 Grenoble, France

## ABSTRACT

A complex alumina-mullite-zirconia refractory ceramic including a calcium aluminate cement binder was studied in terms of thermal and mechanical properties. The evolutions of the deformation (dilatometry) and of the elastic modulus (impulse excitation technique) during thermal treatments were investigated. Three successive phenomena were observed, namely dehydration, liquid phase sintering and microcracking. The latter one was studied more in details by examining separately the matrix and the aggregates of the material. It was demonstrated that the microcracking effect during cooling originates from the thermal expansion mismatch between the mullite zirconia aggregates and the matrix.

## INTRODUCTION

Refractory materials are used in industrial furnaces (e.g. steelmaking, cement, petrochemical and glass industries) thanks to their resistance to high temperatures, thermal gradients, thermal shocks and chemical attacks (leading to corrosion). Alumina castable refractories containing mullite zirconia aggregates and a calcium aluminate cement (CAC) binder, referred to as CAC bonded alumina mullite zirconia (AMZ) refractories, are an example of such refractories. Although they have an important industrial role, CAC-bonded AMZ refractories have not been widely studied in the literature. To improve the formulation and thermal treatments of these refractories, it is important to gain a better understanding of their thermomechanical behaviour and their microstructural evolutions during heating and cooling.

The thermal treatments applied to refractory materials are expected to improve their strength thanks to consolidation through sintering. Nevertheless, a possible consequence of these thermal treatments is the damage occurring during cooling, mainly in the form of microcracking. This damage can come either from the difference of coefficients of thermal expansion (CTE) between the phases or from the physicochemical transformations in the material [1].

Fogaing et al. [1] proposed a simplified microcracking model during cooling, that considers a biphase material containing spherical inclusions (CTE $\alpha_p$) surrounded by an isotropic homogeneous matrix (CTE $\alpha_m$). Three configurations are possible:

- $\alpha_m < \alpha_p$: partial or complete decohesion between the matrix and the inclusions is expected.
- $\alpha_m = \alpha_p$: no damage is expected.
- $\alpha_m > \alpha_p$: radial cracks are likely to appear in the matrix, around the inclusions.

This theoretical model was verified experimentally on industrial products. For instance, Chotard et al. [2] observed a thermal damage in a cordierite-mullite refractory due to the thermal expansion mismatch between the cordierite matrix and the mullite grains. Microcracking was also observed in refractory ceramics containing andalusite and bauxite aggregates [3].

In zirconia containing refractories, the zirconia phase change can also lead to microcracking. During heating, zirconia transforms from monoclinic to tetragonal around 1100°C and during cooling the reverse phase change occurs around 1000°C [4, 5]. Not only the intrinsic elastic modulus of the monoclinic phase is higher than that of the tetragonal phase [6] but this phase transformation can also lead to large volume changes (4% for pure zirconia). Therefore, it can favor microcracking as well [7-9].

In this context, the objective of this study is to understand the mechanisms of consolidation and damage during high temperature cycles of an alumina mullite zirconia refractory bonded with CAC. The evolution of the physical (density, porosity, crystal phases), thermal (thermal expansion) and mechanical (modulus of elasticity) properties as a function of temperature was studied. The analysis of the phenomena occurring during different temperature ranges will be described and the origins of the microcracking phenomenon will be specifically investigated in this paper.

## MATERIALS AND METHODS

Two refractory materials were designed with a mix of coarse particles, larger than 200 µm, referred to as aggregates, and a matrix containing particles smaller than 200 µm. The compositions are given in Table 1. The raw materials were mixed in a Perrier planetary mixer for 15 min. The mixture was then cast into bar-shaped molds of size 150*25*25 mm³. After 6 hours, the parallelepiped bars were demolded and cured at ambient temperature for approximately 24 hours. Finally, the specimens were oven-dried at 250°C. Unless mentioned otherwise, the considered refractory is the oven-dried mat_MZ material, referred to as 'green material'. An extra composition consisting in only the matrix particles was also prepared by adjusting the water level to be castable (viscosity lower than 20 Pa.s).

*Table 1: Composition of the studied materials.*

| | Mat-MZ (ref) | Mat-Al |
|---|---|---|
| **Aggregates (>200 µm, 70 wt%)** | Mullite zirconia (<3mm) | Tabular alumina (<3mm) |
| | Tabular alumina (<2mm) | Tabular alumina (<2mm) |
| **Matrix (<200 µm, 30 wt%)** | Alumina, silica, zirconia | Alumina, silica, zirconia |
| | Binder: CAC | Binder: CAC |

The density and apparent porosity were measured by Archimedes immersion technique with water as the immersion fluid (DIN EN 623-2). Dilatometry experiments up to 1350°C with 1h dwell time, using 100°C/h heating and cooling rates, were performed with specimens core drilled as cylinders of 50 mm height and external diameters and 12 mm central inner diameter (Afnor NF EN 993-19). The coefficient of thermal expansion of the materials was measured from the dilatometry experiments between 600 and 200°C during cooling. The Modulus Of Elasticity (MOE) was measured with bars of dimensions 150*25*25 mm³ by the impulse excitation technique, using a laser doppler vibrometer to capture the signal (ASTM E1816-01). Continuous measurements were performed up to 1350°C, with heating and cooling ramps of 200°C/h and a dwell time of 2h. Chemical analyses were carried out by X-Ray fluorescence and phase analyses by X-Ray powder diffraction.

## RESULTS AND DISCUSSION

### Composition of the material

The bulk density of the refractory is 2.991 ± 0.004 g/cm³ and the open porosity is 17.7 ± 0.1 %. The chemical composition and the phases of the refractory are presented in Table 2 and Table 3.

Table 2: Chemical analysis

| Compounds | Amount (wt%) |
|---|---|
| $Al_2O_3$ | 75 |
| $ZrO_2$ | 12 |
| $SiO_2$ | 10 |
| CaO | <1 |
| MgO | <1 |
| $Na_2O$ | <1 |

Table 3: Main phases

| Compounds | Amount (wt%) |
|---|---|
| Corundum | 67 |
| Mullite | 19 |
| Monoclinic zirconia | 11 |
| Alumina β | 3 |

It is worth noting that during a temperature cycle, 'liquid phases' might appear. In this paper, 'liquid phases' refer to:
- The phases formed by the reactions between the impurities and the raw materials that promote the formation of low melting-points eutectics.
- Amorphous phases that soften above their glass transition temperature.

**General material evolution scenario during a thermal cycle**

Different phenomena can be highlighted during a thermal treatment on the green material. They are illustrated in Figure 1 and specified below. A second MOE cycle, presented in Figure 2, was performed as well and provides additional information on the material. The evolution of the deformation of the material during a thermal treatment was followed by dilatometry and is presented in Figure 3.
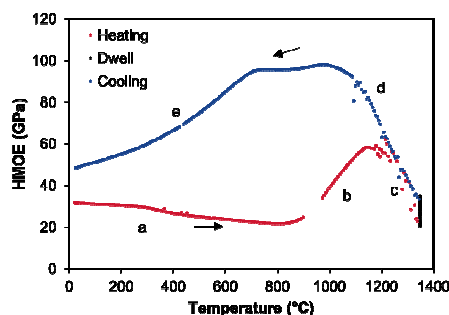


Figure 1: Evolution of the hot modulus of elasticity during a cycle up to 1350°C, with heating and cooling rates of 200°C/h and a dwell time of 2h.
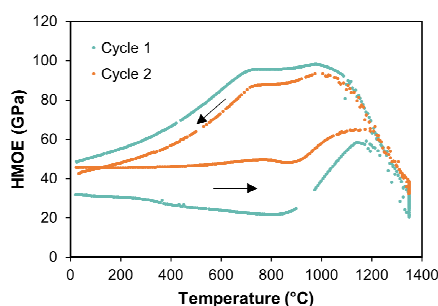


Figure 2: Evolution of the hot modulus of elasticity during two successive cycles up to 1350°C, with heating and cooling rates of 200°C/h and a dwell time of 2h.
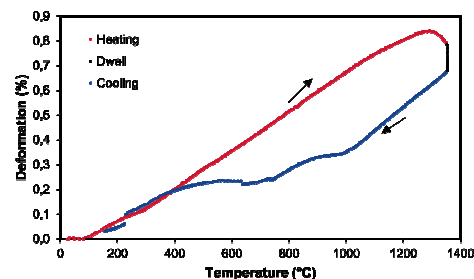


Figure 3: Deformation vs temperature, during two successive cycles, up to 1350°C, with heating and cooling rates of 100°C/h and a dwell time of 1h.

Phase a: heating from 25 to 800°C

The initial MOE value is 32 GPa. At room temperature, the calcium alumina cement in the material reacts with water to form hydrates, responsible for the consolidation of the material. At the beginning of heating, the elastic modulus slightly declines, reaching 22 GPa at 800°C. This loss is associated to a mechanical degradation of the material, explained by the dehydration of the previously formed hydrates. According to thermogravimetric measurements, the hydrates are fully decomposed after 800°C, which is coherent with the MOE stability during the second cycle between 25 and 800°C. During heating, the dilatometry test shows a continuous and linear thermal expansion of the refractory.

Phase b: heating from 800 to 1200°C

In this temperature range, the elastic modulus starts increasing. Dehydration is over and consolidation of the material by sintering begins, promoted by liquid phases. In this temperature range, according to Figure 3, the material continues its expansion without shrinkage.

Phase c: heating from 1200 to 1350°C

Above 1200°C, the MOE loss indicates that the consolidation effect of sintering is overcome by high temperature softening of the matrix due to the presence of a large amount of liquid phases. During the two-hour dwell time at 1350°C, the MOE increase confirms that the sintering still operates, this time with a low shrinkage (0.1%). The fact that the shrinkage observed is very limited is explained by the multiscale composition of the refractory. Indeed, while the matrix shows a high shrinkage due to sintering (4.5% measured by dilatometry), the aggregates do not sinter due to their large size, leading to the constrained sintering of the matrix. The matrix shrinkage generates tensile stresses between matrix and aggregates. These tensile stresses lead to the opening of mesoporosity between the sintering matrix and the skeleton formed by the aggregates [10, 11]. The sintering shrinkage of the matrix is thus not transferred to the aggregate skeleton but accommodated by the opening of mesoporosity, which leads to a very small macroscopic shrinkage.

Phase d: cooling from 1350 to 800°C

During this step, the elastic modulus increase is explained by the solidification or stiffening of the liquid phases. The inflection around 1000°C corresponds to the indirect effect of the tetragonal to monoclininc zirconia phase change. Indeed, the MOE of the tetragonal phase is higher than that of the monoclinic phase [6] but the volumetric expansion induced by the transformation explains the slight decrease of elastic modulus. The zirconia phase change also results in an expansion that is observed in the dilatometry test around 1000°C.

Phase e: cooling from 800 to 25°C

In this temperature range, the continuous decrease of the MOE can be attributed to damage or microcracking in the material. A second expansion occurs in the dilatometry test around 800°C, that can also be explained by microcracking in the material, as proposed by Mouiya et al [12]. The second MOE cycle shows a similar behavior than the first one after 800°C. This suggests that the microcracking phenomenon is reversible, with closing / healing of microcracks during heating and new opening during cooling. This was also verified with a third cycle.

**Origin of the thermally-induced damage**

Microcracking is expected to play a major role in the thermal shock resistance of the refractory. Therefore, it is worth studying in detail the origin of this phenomenon in order to be able to control it.

To begin with, the evolution of the MOE of the matrix alone is plotted as a function of temperature in Figure 4. At the beginning of heating, the modulus slowly decreases due to cement dehydration. From 800°C, the rise of the MOE shows a consolidation in the material due to sintering, facilitated by liquid phases. From 1200°C, the softening of the material is explained by the viscosity decrease of the liquid phases. During the dwell time and at the beginning of cooling, the elastic modulus continuously increases due to the solidification of the liquid phases. From 800°C to room temperature, unlike the composite refractory material, the modulus of the matrix is stable. It can be deduced that neither the physicochemical transformations in the matrix (sintering, mullitization, cement dehydration, phases cristallizations, zirconia phase change) nor the CTE difference between constituents of the matrix are responsible for microcracking in the refractory. The microcracking is either occurring in the aggregates or due to interactions between the matrix and the aggregates.
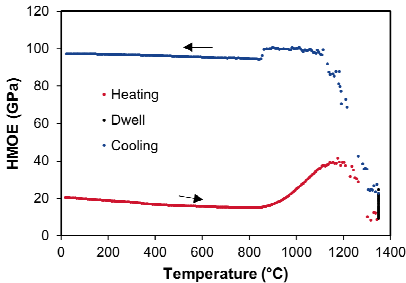
*Figure 4: Evolution of the hot modulus of elasticity of the matrix during a cycle up to 1350°C, with heating and cooling rates of 200°C/h and a dwell time of 2h.*

Next, the influence of the type of aggregates was specifically studied. Material mat_Al was prepared by replacing the mullite zirconia aggregates by alumina aggregates with the same particle size distribution. The evolution of the elastic modulus as a function of temperature for mat_MZ and mat_Al is shown in Figure 5. The behavior of both materials is similar during heating but strongly differs from 800 to room temperature during cooling. Indeed, no damage is observed in mat_Al, supporting that the alumina aggregates do not play a significant role in microcracking.
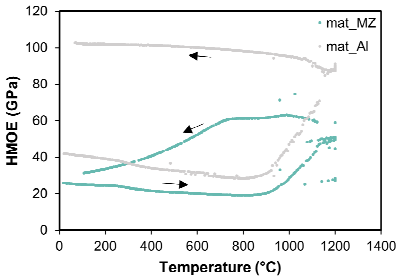


*Figure 5: Evolution of the hot modulus of elasticity mat_MZ (green) and mat_Al (grey) during a cycle up to 1200°C, with heating and cooling rates of 200°C/h and a dwell time of 2h.*

Then, the influence of the mullite zirconia aggregates, and more specifically of the zirconia phase change, was investigated. Four thermal treatments were applied on four mat_MZ samples:
- T1) Maximum reached temperature: 700°C (red curve).
- T2) Maximum reached temperature: 1000°C (orange curve).
- T3) Maximum reached temperature: 1100°C (blue curve).
- T4) Maximum reached temperature: 1200°C (green curve).

The curves are presented in Figure 6. The same behaviour than in Figure 1 can be underlined, with dehydration until 700 (T1) or 800°C (T2, T3, T4), liquid phase sintering until the maximum reached temperature (except for T1) and microcracking during cooling. It is worth underlining that this damage is observed, independently of the maximum reached temperature. Knowing that the monoclinic-tetragonal phase change of the zirconia occurs around 1100°C during heating, this graph suggests that this physicochemical transformation is not the main cause of microcracking in the material.
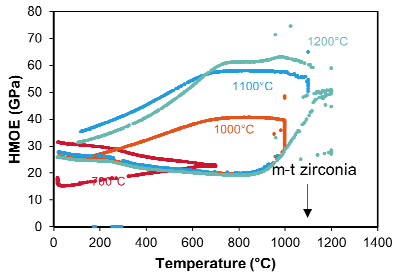


*Figure 6: Evolution of the hot modulus of elasticity mat_MZ during different thermal cycles with heating and cooling rates of 200°C/h and a dwell time of 2h.*

The last possible origin of microcracking lies in the thermal expansion mismatch between the phases. It was previously shown that such mismatch within the matrix constituents is not creating damage (see Figure 4). A thermal expansion mismatch between the matrix and the aggregates is thus suspected to be at the origin of the thermal damage. The dilatometry experiments allowed determining the coefficients of thermal expansion of the matrix, the alumina aggregates and the mullite zirconia aggregates. The values are presented in Table 4.

*Table 4: Coefficients of thermal expansion of the matrix, a mullite zirconia aggregate and an alumina aggregate, measured on the dilatometry tests between 600 and 200°C during cooling.*

|  | Matrix | MZ | Alumina |
|---|---|---|---|
| **CTE 600-200°C ($10^{-6}$/°C)** | 7.0 | 3.3 | 8.5 |

The CTE of the matrix is more than twice the CTE of the mullite zirconia aggregates, respectively 7.0 and 3.3 * $10^{-6}$/°C. Therefore, during cooling, the matrix tends to contract more than the MZ aggregates, likely leading to damage in the form of radial cracks,

according to the model developed by Fogaing et al. [1]. Furthermore, the coefficient of thermal expansion of the alumina aggregates is closer to the matrix one and less damage is therefore expected in mat_Al, which is coherent with Figure 5.

These results thus indicate that the thermal expansion mismatch between the matrix and the mullite zirconia aggregates is the main origin of microcracking in the AMZ refractory.

## CONCLUSIONS

A high alumina refractory castable was prepared with alumina and mullite-zirconia aggregates (particles larger than 200 μm) embedded in an alumina, zirconia and silica matrix (particles lower than 200 μm), bonded with calcium aluminate cement. The material was characterized with elastic modulus and dilatometry measurements during successive thermal cycles. Three main phenomena were observed during these thermal treatments:

- In the first cycle, dehydration at low temperatures, due to dehydration of the cement hydrates formed during setting at room temperature.
- Sintering promoted by liquid phases during heating, mainly in the first temperature cycle.
- Microcracking during cooling.

It was shown that microcracking was mainly driven by the thermal expansion mismatch between the matrix and the mullite zirconia aggregates. In addition, the reversibility of this phenomenon was observed with microcracks closing / healing and opening during a second cycle.

These investigations allowed in-depth understanding of the thermomechanical behavior of the material. The study of the microstructure of the material is on-going and will complete these first results. For instance, in-situ Xray tomography at the European Synchrotron Radiation Facility and SEM during different thermal treatments can provide complementary and novel information on sintering and microcracking in the material.

## REFERENCES

[1] E. Yeugo Fogaing, "Caractérisation à haute température des propriétés d'élasticité de réfractaires électrofondus et de bétons réfractaires," Limoges, 2006.

[2] T. Chotard, J. Soro, H. Lemercier, M. Huger, and C. Gault, "High temperature characterisation of cordierite–mullite refractory by ultrasonic means," Journal of the European Ceramic Society, vol. 28, no. 11, pp. 2129-2135, 2008, doi: https://doi.org/10.1016/j.jeurceramsoc.2008.02.029.

[3] M. G. Kakroudi, E. Yeugo-Fogaing, C. Gault, M. Huger, and T. Chotard, "Effect of thermal treatment on damage mechanical behaviour of refractory castables: comparison between bauxite and andalusite aggregates," Journal of the European Ceramic Society, vol. 28, no. 13, pp. 2471-2478, 2008.

[4] Y. Moriya and A. Navrotsky, "High-temperature calorimetry of zirconia: Heat capacity and thermodynamics of the monoclinic–tetragonal phase transition," The Journal of Chemical Thermodynamics, vol. 38, no. 3, pp. 211-223, 2006.

[5] D. Simeone, D. Gosset, J. Bechade, and A. Chevarier, "Analysis of the monoclinic–tetragonal phase transition of zirconia under irradiation," Journal of nuclear Materials, vol. 300, no. 1, pp. 27-38, 2002.

[6] E. Y. Fogaing, M. Huger, and C. Gault, "Elastic properties and microstructure: study of two fused cast refractory materials," Journal of the European Ceramic Society, vol. 27, no. 2-3, pp. 1843-1848, 2007.

[7] C. Patapy, C. Gault, M. Huger, and T. Chotard, "Acoustic characterization and microstructure of high zirconia electrofused refractories," Journal of the European Ceramic Society, vol. 29, no. 16, pp. 3355-3362, 2009.

[8] E. Y. Fogaing, Y. Lorgouilloux, M. Huger, and C. Gault, "Young's modulus of zirconia at high temperature," Journal of Materials science, vol. 41, pp. 7663-7666, 2006.

[9] A. Sibil, T. Douillard, C. Cayron, N. Godin, M. R'mili, and G. Fantozzi, "Microcracking of high zirconia refractories after t→ m phase transition during cooling: An EBSD study," Journal of the European Ceramic Society, vol. 31, no. 9, pp. 1525-1531, 2011.

[10] A. Evans, "Considerations of inhomogeneity effects in sintering," Journal of the American ceramic Society, vol. 65, no. 10, pp. 497-501, 1982.

[11] O. Sudre and F. F. Lange, "Effect of inclusions on densification: I, microstructural development in an Al2O3 matrix containing a high volume fraction of ZrO2 inclusions," Journal of the American Ceramic Society, vol. 75, no. 3, pp. 519-524, 1992.

[12] M. Mouiya, N. Tessier-Doyen, Y. Tamraoui, J. Alami, and M. Huger, "High temperature thermomechanical properties of a microcracked model refractory material: A silica-doped aluminium titanate," Ceramics International, 2023.

# FUSED CAST AZS BLOCKS AND THEIR MINERAL PHASES AFTER PRODUCTION, AFTER ANNEALING THE FURNACE AND IN USE

Bernhard Fleischmann
Hüttentechnische Vereinigung der Deutschen Glasindustrie (HVG) e.V. Offenbach am Main, Germany

Christian Thieme,
Fraunhofer-Institut für Mikrostruktur von Werkstoffen und Systemen IMWS, Halle / Saale, Germany

## ABSTRACT

Fused cast alumina-zirconia-silica (AZS) blocks are used in glass contact area as well as lining of the combustion room among other things.

The changes of their mineral phases during production and use (annealing of the furnace during glass production and during furnace shut down) are analysed in detail with modern microscopic techniques to learn about the interpretation of the presence of distinct phases.

If present, mullite is a crystalline phase that leads to discussion about its origin. The microscopic analysis of these materials with scanning electron microscopy in combination with elemental analyses (EDXS) as well as X-ray diffraction are primarily used for this purpose. Thermodynamic, kinetic considerations are made about the cooling of the blocks during production, during the annealing of the furnace and during usage regarding the equilibrium and semi stationary states that are reached within the single steps. Taking phase diagrams into account mullite may be present in AZS blocks after production, when annealing a block but may it originate from corrosion, too? The investigations with modern microscopic methods allow the detection of smallest amounts of crystalline and amorphous phases and will give evidence for the importance of the different corrosion and phase formation mechanisms and so help to decide whether the presence of a phase, especially mullite, is the consequence of failure in production or use or is just 'natural'.

## INTRODUCTION

The corrosion of AZS materials in glass melting tanks, with direct contact of these materials to the melt, may be summarized in a simplified way by the following process [1, 2]:

At the interface glass melt and refractory, alumina and the high silica vitreous phase of the blocks are dissolved and enriched in the glass melt near the refractory block. The viscosity near the interface glass/refractory increases and a highly viscous layer is formed, saturated with $Al_2O_3$. Due to a common solubility limit of alumina and zirconia, the solubility of $ZrO_2$ is decreased and the reason for the high corrosion resistance of the AZS fused cast refractories.

The typical AZS refractories produced in Europe consist of zirconia (baddeleyite), alumina (corundum) and a vitreous phase (aluminosilicate glass). If used blocks are examined for their mineral phases mullite often is present [3, 4]. The question of interest is, when and how the formation of mullite happens or why sometimes mullite is not found?

## TESTING PROCEDURE

A detailed description of the sample preparation and the testing program is given in [5]. The investigated samples, used for microscopic and mineralogical phase detection can be categorised as:

- Samples from an AZS block after production.
- Samples of the same block with a thermal treatment similar to the annealing of a typical container glass furnace.
- Samples that undergo the annealing process and emulate the temperature cycling of the combustion space of a regenerative furnace ($\Delta T= 50$ K, $\Delta t=20$ min.).
- Samples from dismantled furnaces.

## RESULTS AND DISCUSSION

### Production of AZS fused cast blocks

The raw materials (zirconia with traces of CaO or $Y_2O_3$; zircon; alumina, sodium carbonate) are molten in an arc furnace with graphite electrodes. Sub-stoichiometric $ZrO_2$ is oxidised by blowing oxygen into the melt which will also oxidise polyvalent impurities and helps to homogenise the melt. The melt is then cast into moulds made of sand. These moulds are removed as soon as the stable casting skin formed around the melt and allows further handling. The block is then placed into a cooling bed. The crystallization process is completed after some hours, but to reduce mechanical stresses slow cooling of the huge (soldier) blocks is necessary over weeks.

If the cooling rate is small enough so that the formation of the phases in equilibrium state is feasible (enough time is available for chemical reactions, diffusion and crystallisation), phase diagrams may help to discuss the process of crystallisation.

Fig. 1 focus on the subarea of the phase diagram of the main components of AZS soldier blocks [6] that helps to understand the cooling and crystallisation process of AZS materials.
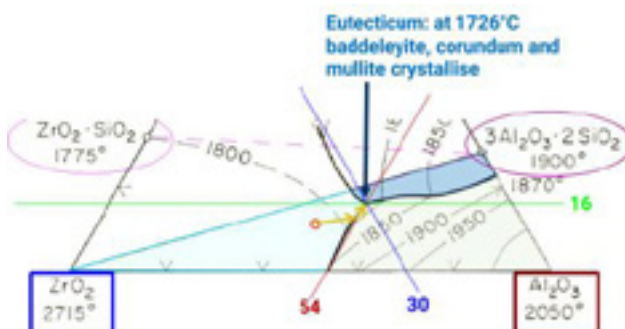


*Fig. 1: Part of the phase diagram $ZrO_2 – Al_2O_3 – SiO_2$, [6] that helps to understand the cooling process. Following the crystallisation path (golden yellow arrows) of specific fused cast AZS blocks from starting point (red circle) to phase border zirconia with alumina, following the phase border until eutectic point is reached*

The starting point (red circle in Fig. 1) marks a block with 42 wt.-% zirconia, 45 wt.-% alumina and 12 wt.-% silica as main components and disregarding sodium oxide and other trace components. Zirconia (at least baddeleyite as metastable low temperature phase) crystallises as the only phase during first cooling until the phase borderline with alumina is reached. The melt depletes zirconia until the phase border between the zirconia and the alumina region is reached. Now two phases crystallise simultaneously: zirconia and corundum. The crystallisation path follows now the border line in the direction of lower temperatures until the eutectic point is attained (golden yellow arrow in fig. 1). If equilibrium conditions (enough time, all components have the same temperature, no kinetic obstruction and pure composition) would be present all three phases would crystallise simultaneously that "meet" at the eutectic point: baddeleyite, corundum and mullite.

Instead, the relatively high viscosity of the aluminosilicate melt, the presence of impurities and intentional minor components prevent

the crystallisation of mullite more or less complete and only zirconia and corundum were built together with the vitreous phase.

To follow the crystallisation process an additional phase diagram would be necessary: alumina – silica – sodium oxide. Even though the equilibrium state is abandoned, the presence of the vitreous phase in the block is reasonable.

The phase diagram allows to determine the overall composition of the crystal phase and the changed composition of the residual melt as long as the cooling of the block represents the equilibrium state which is given for temperatures above the eutectic point.

The questions to be answered with this paper are:

- Does blocks with the typical composition of European AZS soldier blocks show reasonable mullite after production?
  Even the investigations with its high resolution in [5] showed no mullite in AZS blocks after production.

- Will the presence of mullite increase if heating up the furnace with newly installed soldier blocks? Is the temperature high enough so that reactions occur to serve the equilibrium state and are times long enough [7]?

**Annealing the furnace**

Neighbouring samples, cut from the block that was used to investigate the block after production, were used to run through a two-staged heat treatment. The first two weeks simulate the annealing curve of a typical container glass furnace (see Fig. 2). After reaching 1580°C samples were taken out of the furnace, cooled down quickly and investigated with the high resolution methods.
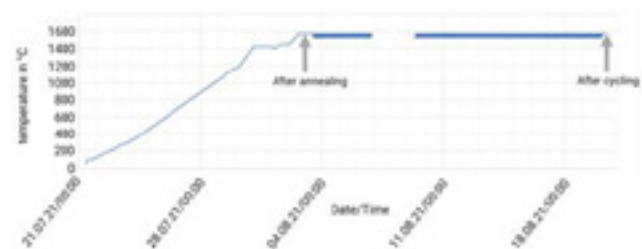


*Fig 2: Heat treatment of samples simulating the annealing of the furnace and the temperature cycling of regenerator furnaces. The continuous change between 1580 and 1530°C within 20 minutes is not visible. The missing part is due to a malfunction of the documentation software whereas the test continues without any problems.*

After annealing, a small amount of mullite is found. The mullite does not occur as needles but as blocky crystals [5].

**Temperature cycling of regenerative glass furnaces**

Samples that were investigated after running through the second heat treatment, i.e. thermal cycling between 1530 and 1580 °Ca (Fig. 2), that simulates the behaviour of superstructure blocks placed in the side wall of the combustion space of glass furnaces, showed a higher content of mullite than the merely annealed one.

Fig. 3 compares the results of XRD measurements of untreated samples after refractory production, of samples after annealing and of samples after temperature cycling. The XRD analyses showed the absence of mullite after production and increasing intensity of the mullite signal with increasing treatment time at high temperature. Even the signals height, i.e. the mullite concentration, increases with longer treatment.
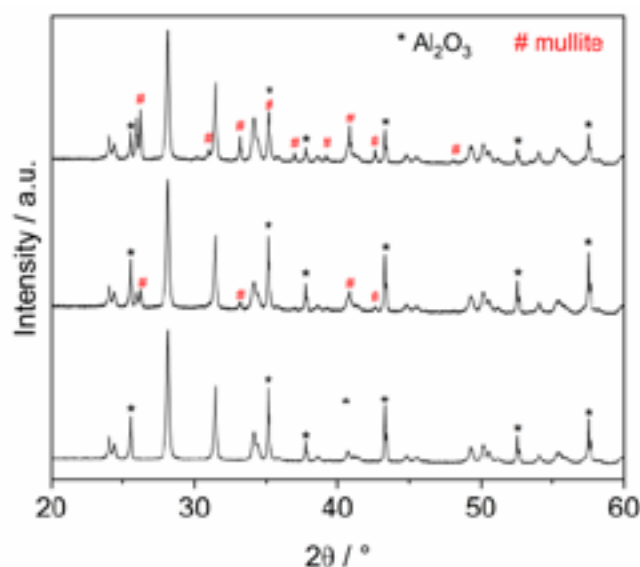


*Fig. 3: XRD of samples after refractories production (bottom curve), after annealing and 10 hours at 1580°C (center line) and after additional temperature cycling between 1530 and 1580°C for about 14 days (upper curve). The unlabelled peaks can be assigned to baddeleyite ($m\text{-}ZrO_2$).*

**Post mortem investigations**

Fig. 4 represents the top part of a corroded soldier block after years of glass contact. The results of XRD measurements on this material are summarised in Fig. 5.
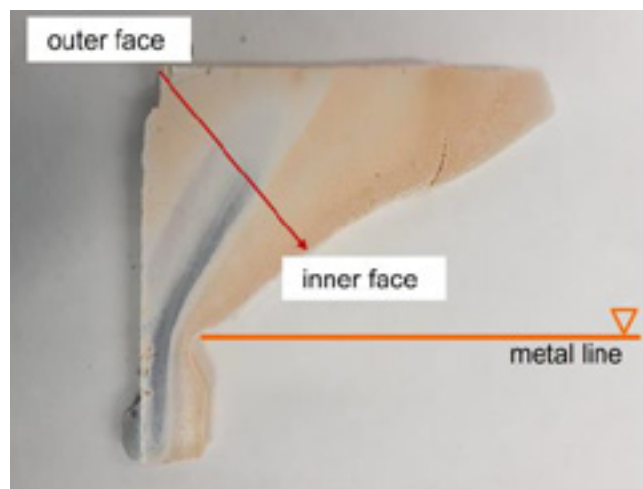


*Fig. 4: Slice of a top part of a soldier block after years of use in a glass furnace*

With XRD, mullite is not detected but nepheline ($Na_3K[AlSiO_4]_4$) is present. This alkaline aluminosilicate is found in areas where alkaline from the glass melt or evaporated alkaline infiltrated and could be proved with EDXS in the vitreous phase of the block. The parts of the block that show no diffusion of alkaline consist only of the crystalline phases baddeleyite and corundum beside the vitreous phase. The temperature gradient and the duration the sample was exposed to higher temperatures are unknown.
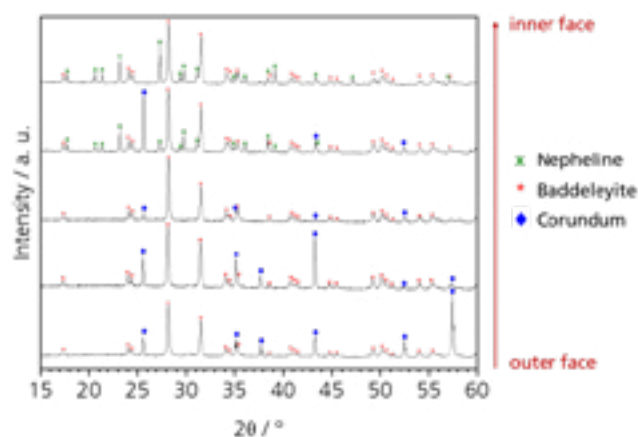
*Fig. 5: XRD results of the post mortem analyses of a soldier block*

## CONCLUSIONS

If investigating refractory materials after dismantling of a furnace or after breaking down, the presence of mullite may be the reason of intense discussions. The following questions arise:

- Which conditions lead to mullite formation?
- Does the presence of mullite give a hint for the failure of an AZS material?
- Is mullite a "natural" component of fused cast AZS blocks?

The investigation of refractory samples of AZS materials after production, after a temperature treatment that simulated the annealing of a glass furnace, after thermal cycling to imitate the behaviour of a regenerator furnace and after furnace lifetime with electron microscopy and XRD helps to find answers for these questions.

1. Typical European fused cast AZS soldier blocks for glass contact do not contain mullite after refractory production. They consist of baddeleyite, corundum and a vitreous aluminosilicate phase.
2. Phase diagrams representing the equilibrium state suggest that mullite should be present due to thermodynamic considerations. Kinetic aspects and the presence of impurities or trace elements inhibit the formation of mullite within the available time at elevated temperatures during AZS production.
3. Temperature treatment similar to annealing the furnace results in the formation of mullite crystals in fused cast AZS blocks. Temperature is high enough and time long enough to approximate equilibrium and to compensate kinetic constraints.
4. Longer times at temperatures above 1530°C enhance the number of mullite crystals and their size. The thermodynamic equilibrium is not yet reached.
5. Mullite is not mandatory in blocks with glass contact. It cannot be found if corrosion is faster than mullite formation. At temperatures below 1500°C, other phases might be more stable.
6. Small mullite (needles) may be found beside nepheline surrounded with vitreous phase in blocks after dismantling the furnace. These two crystalline phases may be formed as devitrifications from the vitreous phase of the block, saturated with glass and corrosion components, when cooling the furnace slowly. If sodium and/or potassium penetrates the block at temperatures below 1500°C, nepheline seems to be the more stable crystalline silicate.

## REFERENCES

[1] Manfredo, L.J. and R.N. Mcnally, Solubility of Refractory Oxides in Soda-Lime Glass. Journal of the American Ceramic Society, 1984. 67(8): p. C155-C158.

[2] Manfredo, L.J. and R.N. Mcnally, The Corrosion-Resistance of High $ZrO_2$ Fusion-Cast $Al_2O_3$-$ZrO_2$-$SiO_2$ Glass Refractories in Soda Lime Glass. Journal of Materials Science, 1984. 19(4): p. 1272-1276.

[3] Fleischmann, B.: Fused cast AZS refractory materials – structure and structural changes during application- refractories worldforum 2(2010)2, 63-68

[4] Fleischmann, B.: The microstructure of fused cast AZS materials before, during and after the use for glass melting. Verre 15(2009)2, 55-58]

[5] Thieme, Christian et al., Ceramics International, https://doi.org/10.1016/j.ceramint.2023.06.174

[6] Phase diagram $ZrO_2$ – $SiO_2$ – $Al_2O_3$ [Levin, E.M.; Robbins, C.R:; McMurdie H.F.: Phase diagrams for ceramists. The American Ceramic Society, Columbus, Ohio. 1964. Phase diagram No. 772: [Budnikov, P.P.; Litvakovskii, A.A.. Doklady Akad. Nauk S.S.S.R., 106,268(1956)]].

[7] Ratto, P.C.: Fused cast refractories: science or craft. Glass machinery &accessories 5(2014). P. 84 - 87

## Forschungsgemeinschaft Feuerfest e. V.

**FGF**
Forschungs-
Gemeinschaft
Feuerfest e.V.

### Research and Innovation

**Methods:**
- Development of in situ testing methods for High Temperature Properties
- High temperature thermal shock behaviour
- High temperature gas/liquid corrosion ($H_2$, $H_2O$-vapour, slags, metals)
- High temperature elasticity and dynamic creep
- FEM simulations

**Materials:**
- Refractories, binder systems, secondary raw materials

**Processes:**
- Optimisation of shaping and firing processes




Head of R&D: **Dr. Christian Dannert**

Rheinstr. 58
56203 Höhr-Grenzhausen
Germany

+49 2624 94 33 180

info@fg-feuerfest.de

www.fg-feuerfest.de

---

## Refractory Organisations in Höhr-Grenzhausen

**FGF**
Forschungs-
Gemeinschaft
Feuerfest e.V.



Pathways to Innovation



Scope · Pre-competitive research · Bi-lateral partnership · Consulting · Time to market
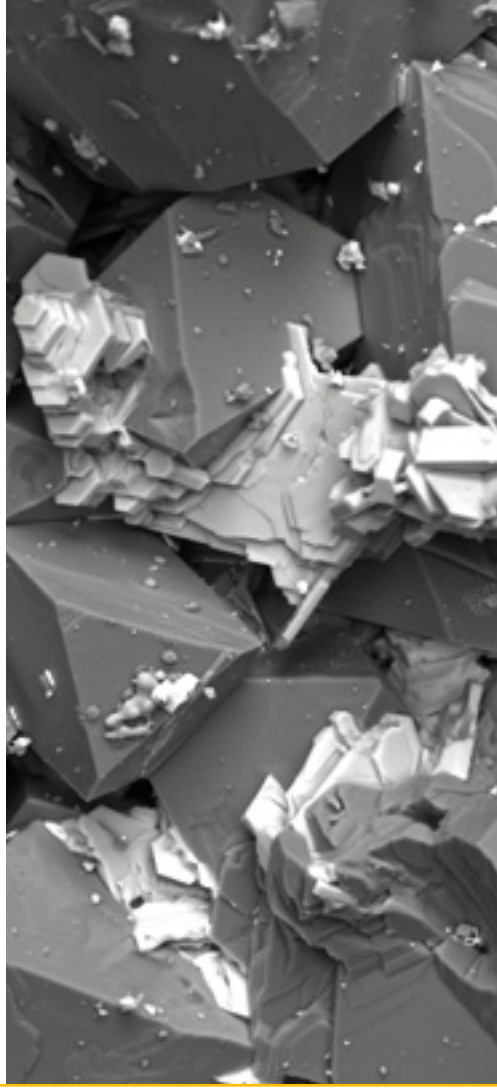


### Forschungsgemeinschaft Feuerfest e. V.

**Research and Innovation**

**Technology Transfer**
- Patent database and research service
- Training, Publications, Marketing
- Partnerships with the Process Industry

**Project Management**
- One stop shop – no hassle with funding agencies

**Funding Advisory Service**
- National and European R&D funding – for companies of all sizes

SHORT COMMUNICATIONS

# FUSED SILICA – THE ANSWER TO CHALLENGING FURNACE CONDITIONS

M. Dietrich[1]; S. Redik[2], S. Postrach[1]; A. Roncaglia[1]; G. Reif[2]

[1]RHI Glas GmbH, Wiesbaden, Germany; [2]Technologie Center, Leoben, Austria

Silica ($SiO_2$) dry vibrating mixes with sintering additive boric acid or boron oxide ($B_2O_3$) are the standard refractory lining products used for crucible induction furnaces in the iron foundries worldwide. The sintering agent is used to control the reaction with $SiO_2$ that forms a melt phase on the surface of the grains, which protect the refractory linin g, reduces infiltration and extend the campaign life of the lining. Though, the sintering agents have shown a high performance of the refractory lining life, they are classified as reproductive toxicity "1B" to humans, presents challenging health effects and environmental disposal problems. Currently delivered products are labeled with 1B and regulatory institutions are proposing a further reduction in concentration of less than 0.3 % $B_2O_3$ in all products.

This paper presents recent developments on a novel sintering agent for $SiO_2$ refractory lining products. The sintering additive is not classified by legislation and is envisaged to minimized health risks to humans and the environment. For a better evaluation of the suitability of the novel sintering agent for binding the $SiO_2$ matrix, a chemical and mineralogical analysis was performed with lining samples hammered from the furnace. Field applications revealed equivalent performance comparable to current sintering agents.

# DEVELOPMENT OF A HIGH–TEMPERATURE–TES SYSTEM USING REFRACTORY MATERIALS FOR LONG–TERM STORAGE OF RENEWABLE ENERGY

E. Hennemann-Hohenfried, T. Schemmel
Refratechnik Steel GmbH, Düsseldorf, Germany

J. Gonzalez-Julian, T. Tonnesen, T. Leber
Institute of Mineral Engineering – RWTH Aachen, Aachen, Germany

R. Kremer
Alpha Ceramics GmbH, Aachen, Germany

## ABSTRACT

With rising energy prices and the expansion of renewable energy sources, the ability to store energy reliably and cost-effectively is becoming increasingly important for homes and industry. Thermal energy storage (TES) is an option for storing thermal energy and converting it back to electricity. The advantage of this storage method is that it is comparatively inexpensive and poses no risk to the environment in the event of possible disasters such as fire, flood or earthquake [1].

This research is concerned with the design of a sensitive high-temperature TES system (Fig. 1) that can be further developed to provide a self-sufficient power supply for a four-person household using photovoltaics. There are no moving parts or other sensitive, complex components inside the TES, and recirculation is enabled solely by thermal radiation. To this end, computational fluid dynamics (CFD) simulations are being carried out and a demonstrator made of industrial refractory materials is being built. Two different refractory bricks for storage and four different insulation materials were used in the construction of the TES unit. The two refractory brick variants for the storage core are based on fireclay and corundum bricks, which have specific thermal conductivities and heat capacities. The wall insulation was made of two different microporous silicate boards and a high temperature insulation wool. The properties of these refractories were characterised to assess their suitability. Thermocouples were placed in different areas of the TES unit to record the temperature in the core and wall insulation during the initial heating process over a period of four weeks. This allowed the system-related heat capacity and thermal conduction to be determined. The data obtained was fed into the previous model and used in the CFD simulation for further optimisation.
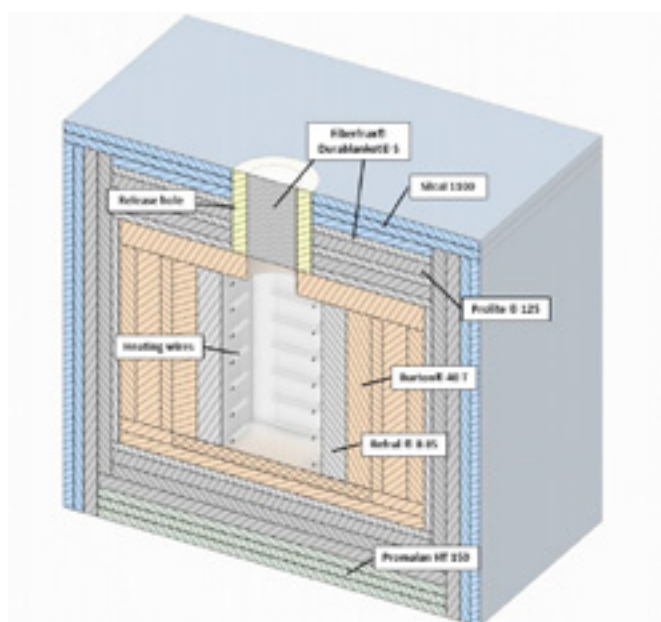
The results - after 4 weeks of cyclic heating - showed that the thermal energy was successfully delivered to the refractory storage core with the required temperature distribution. However, as expected, the wall insulation was too thin, so the thermal insulation was not sufficient for complete heating. The measured temperature values could be transferred to the CFD simulation and used for further virtual designs.

Energy storage options are an important aspect of the current energy transition. The focus is on cost, safety and versatility. In addition to electrical, mechanical and chemical energy storage systems, thermal energy storage systems are particularly well established. TES is divided into latent and sensible heat storage, with latent heat storage storing and releasing thermal energy via a change in aggregate state and sensible heat storage via a change in sensible temperature. For this project, a sensitive high-temperature solid state thermal storage system was chosen. Compared to the other storage options mentioned above, it is characterised by low cost, high storage density, almost unlimited application possibilities and low risk. For example, electrical or chemical storage systems such as batteries are very expensive [2]. Positional (mechanical) energy storage systems, such as pumped storage power plants, are not flexible or are tied to local conditions and are expensive to install. Latent thermal energy storage systems, for example molten salt storage, have high requirements for the materials used, which in turn lead to high costs and, in the event of damage, pose a certain potential risk to people and the environment [3].

The TES used here was initially designed for a 4-person household in a single-family house in Berlin in such a way that, after further optimisation of the thermal insulation, a permanent self-sufficient power supply is possible.

The thermal energy is fed via heating wires into a central cavity (furnace chamber), which is heated by the electricity fed supplied by the PV system and released for recirculation by pure radiation through an opening in the ceiling above. The storage core, which is divided into two sections (inner and outer), is located around the furnace chamber and is itself surrounded by wall insulation. The opening over the furnace chamber can be assumed to be a black body according to Planck's law of radiation if the temperature distribution in the cavity below is homogeneous [4]. Thus, a Stirling engine or a liquid to be heated for a steam turbine can be placed on top of this opening and heated by thermal radiation. The TES must not fall below a certain minimum temperature in order to ensure sufficient re-powering when required. Similarly, the TES must not be heated above a maximum temperature to protect the materials used from thermal failure.

At the same time, a CFD simulation was carried out to verify the design of the TES and to test the influence of various conditions such as ambient temperature and feed rate. Subsequently, the simulation allowed further dimensioning in relation to the wall insulation and application for future development.

## EXPERIMENTAL

For the experimental implementation, the dimensioning of the TES with the available materials was first determined based on solar irradiance and electricity consumption measurement values. With the CFD simulation, the functionality of the storage could be



*Fig. 1: CAD-Modell of the TES with the storage core and the surrounding insulation.*

mapped over a longer period of time. With the real measured temperature values and the thermal properties calculated from them, the simulation could be used for further optimisation of the TES.

**Calculation for TES dimensioning**
The TES should be of suitable size for a detached house while having a square base. The furnace chamber should be centred in the middle of the TES area with a square side length of approximately 50 cm (Fig. 2).
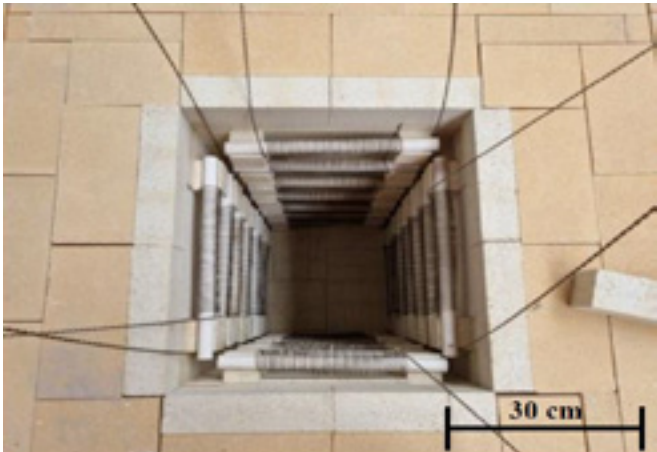


*Fig. 2: Top view of the central TES cavity.*

For the design of the heat storage system, the electricity consumption of a 4-person household was compared with the electricity production of a PV system of a single-family house. For this purpose, the measurement data of the solar irradiance (University of Applied Sciences Berlin) on a conventional photovoltaic system of a single-family house in Germany (south orientation, tilt angle: 35°, surface area: 45 m², PV efficiency: 0.2, maximum power: 240 Wp) over a period of two years were evaluated [5]. The measured values for the electricity consumption of this single-family house were taken from the standard load profile of the VDEW [6]. In this way, the exact amount of energy fed in or consumed could be determined at 15-minute intervals, with the respective differences in the course of the day and night, as well as the influence of the different seasons.
The efficiency of the re-conversion was set at ηws = 0.2 (e.g., Stirling engine) and the maximum operating temperature of the storage tank was set at 1100 °C, while the minimum temperature was set at 400 °C.

**Materials**
The storage core was built around the furnace chamber using two different types of bricks: Corundum bricks measuring 254 x 62 x 66 mm (REFRAL® B 85, REFRATECHNIK), which have a high thermal conductivity and heat storage capacity, were used inside the storage core, while fireclay bricks measuring 250 x 124 x 64 mm (BURTON® 40 T, REFRATECHNIK), which have a lower thermal conductivity and heat storage capacity, were used in the outer storage core. The fireclay bricks provide a thermally storage and insulating transition to the wall insulation. From the inside to the outside, the wall insulation around the storage core consists of high-temperature wool 2.5 cm thick (Fiberfrax® Durablanket® S, Unifrax), rice husk ash panels 0.8 x 0.8 x 0.07 m (Prolite® 125/26 LC-S, REFRATECHNIK) and highly porous calcium silicate panels 1500 x 1250 x 50 mm (Silcal 1100, Silca).
The inner storage core was made of corundum bricks and the outer one of fireclay bricks. Two (side walls) or three panels (ceiling) of rice husk ash and high temperature insulation wool were placed around the storage core. Finally, the outer wall was made of two layers of calcium silicate boards. The side wall panels were fixed with steel straps.

The thermal conductivity and heat capacity of each material are listed in the Tab. 1.

Tab. 1: Heat conductivity and Heat Capacity of the used materials.

| | Heat conductivity at 1000 °C [W/(m·K)] | Heat capacity At 1000 °C [kJ/(kg·K)] |
|---|---|---|
| REFRAL® B 85 | 2,45 | 1,25 |
| BURTON® 40 T | 1,40 | 1,22 |
| Fiberfrax® Durablanket® S | 0,28 | - |
| Prolite® 125 | 0,32 | 1,16 |
| Silcal 1100 | 0,18 | 1,09 |

During construction, more than thirty thermocouples (type K) were installed in the TES at various points in the cavity, storage core and wall insulation, and the temperature curves were recorded by a data recorder throughout the test procedure. From these measurements, the material data in Tab. 1 could then be used to determine the stored energy and the heat transport through the TES to the point of heat loss to the environment.
The TES was heated for 8 hours daily, except for holidays (Easter) and weekends, over a period of 32 days with 25 heating days (heating period: 12.04.-14.05.2022). To investigate the influence of highly reflective materials on the insulation effect within the wall insulation, two non-area-covering steel plates were installed in the ceiling and floor insulation. In addition, on the 18th heating day, the entire TES was wrapped in aluminium foil.
Theoretically, the TES was designed so that in its final state with optimised wall insulation, at a temperature of 1100°C in the storage core, it would emit 140 W/m² of thermal energy to the environment (25°C) via the wall insulation.

**Flow simulation**
For the flow simulation, the TES was made as a CAD model and the heating and holding process was simulated in a CFD simulation with the given dimensions and material data. The three heat transport variants of radiation, (natural) convection and conduction were considered in the calculation. Literature values were used for the emissivities [7]. Cyclic heating (8 hours per day) with different input powers up to the maximum temperature of 1100 °C and cooling at different ambient temperatures were then investigated. The simulation included simplifications, neglecting certain undesirable gap dimensions due to the construction, in order to represent a perfect construction of the TES without thermal bridges. The conductive influence of the steel sheets was also not taken into account in this simulation, as they were thermally too thin for the flow simulation. However, the surfaces of the steel sheets were included in the simulation for radiative heat transfer processes.

**RESULTS**
The calculation using the above specifications gave a maximum storage capacity of 2750 kWh for the TES, giving a width for the square storage core of 1.63 m at a height of 1.12 m for a self-sufficient power supply (Fig. 3).
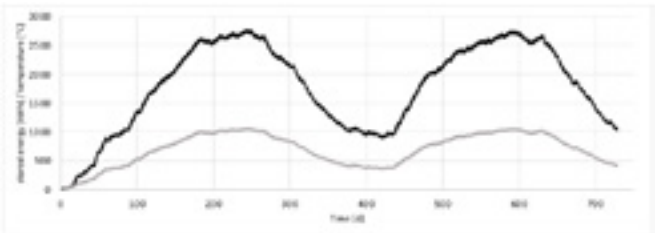


*Fig. 3: Curves of the amount of energy stored (black) and the temperature (grey) in the TES.*

The inner storage core around the square one, consisting of the REFRAL® B 85 bricks, had a thickness of 124 mm and that of the outer storage core built of the BURTON® 40 T bricks 435 mm. Overall, the storage tank had dimensions of 2.2 x 2.2 x 1.85 m at the outer edges.

After heating the TES for 8 hours on 25 days over a period of 32 days, the temperature curves in the storage core were as shown in Figure 4.
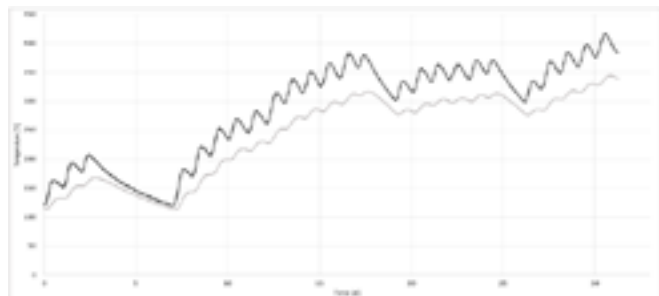


*Fig. 4: Temperature distribution after 25 heating days over a period of 32 days in the inner (black) and outer (grey) storage core.*

The temperature in the storage core stagnated at around 350 °C after 23 days, whereupon the TES was wrapped in aluminium foil after 24 days. This caused the temperature to rise to 420 °C within 3 days. Temperatures increased by an average of 19 °C per heating day during the heating process (8 hours), decreased by about 5 °C during the remaining 16 hours, and decreased by about 30 °C on cooling days. The stored heat energy in the storage core could be determined from the evaluation of further thermocouples. The curve of the stored heat energy over the 25 heating days is shown in Fig. 5.
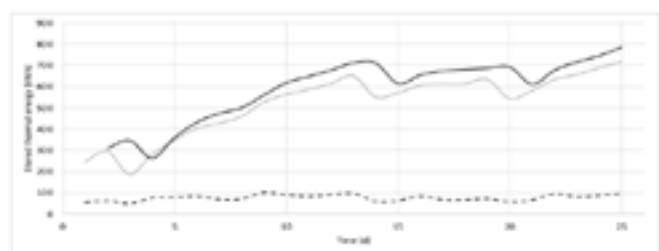


*Fig. 5: Curve of the stored thermal energy in relation to the 25 heating days in the inner (black) and outer (grey) storage core as well as the daily amount of electricity fed in (dotted black line).*

After 25 heating days with a daily input of about 80 kWh, the TES contains about 800 kWh of stored thermal energy and has reached about 25% of its maximum storage capacity. During this period, approximately 2000 kWh of electricity was fed into the TES. The losses through the wall insulation could be determined from the measured temperature distribution in the storage core and the wall insulation. For the emitted heat flux densities through the central ceiling area, the area through which the highest heat fluxes escape, the curve shown in Fig. 6 was obtained from the 10th heating day onwards.
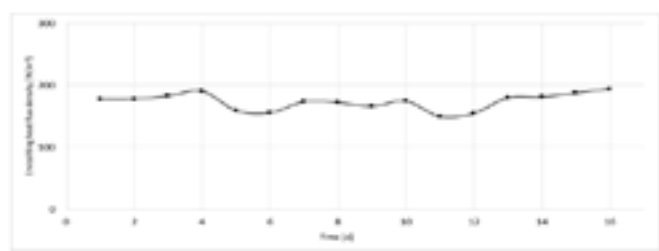


*Fig. 6: Heat flux densities through the ceiling insulation from the 10th heating day.*

At a storage core temperature of approximately 350 °C, the heat flux is approximately 180 W/m². At 400 °C the heat flux density increases to 200 W/m². The thermal conductivity coefficient is approximately 0.19 W/m·K at a thickness of 0.35 m through the entire ceiling insulation.

The influence of steel sheets could also be assessed by evaluating further thermocouples. Fig. 7 shows the heat flux density curves through the ceiling insulation. Square steel sheets with an edge length of 1.15 m were placed centrally in the ceiling insulation between the high-temperature rolls (central recess for the furnace chamber opening) and the heat transfer in this area and the edge area without steel sheets was measured with thermocouples. As the steel sheet ceiling area is centrally located and therefore in the immediate vicinity of the furnace chamber, higher temperatures prevail here, resulting in generally higher heat flux densities.
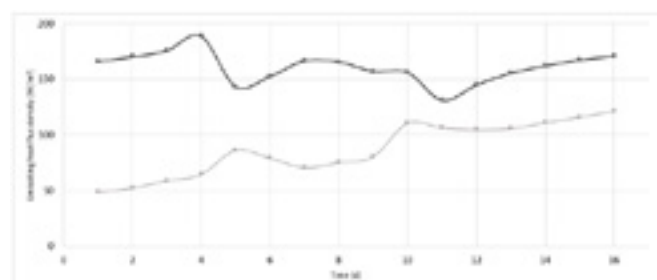


*Fig. 7: Course of heat flux densities through areas with (black) and without (grey) steel sheets in the ceiling insulation.*

While the heat flux density through the steel plates in the temperature range of 350 - 400 °C remains constant over time in the range of 165 W/m², the curve of the heat flux density without steel plates increases from 50 W/m² to 125 W/m². After wrapping the TES with aluminium foil, the heat flux through the steel plates increases less than the heat flux through the area without steel plates.

Using computational fluid dynamics (CFD), it was possible to set up the same heating cycle as the real one. Figure 8 shows the temperature distribution in the storage core (without wall and ceiling insulation) after the 2nd and 3rd heating days.
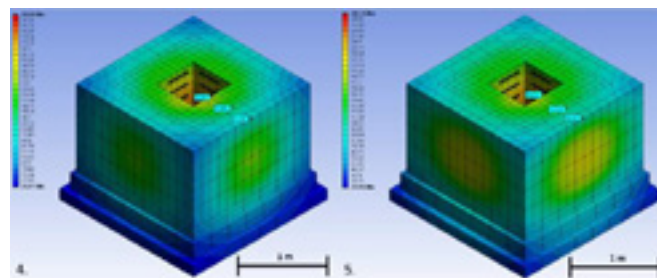


*Fig. 8: TES models with a CFD-simulated temperature distribution after two (left) and three (right) heating days.*

The temperatures in the TES storage core range from 73 °C to 138 °C after two heating cycles and are between 98 °C and 198 °C after three heating days. The actual measured values are approximately 20 °C lower than the simulated values with a similar distribution.

**DISCUSSION**

The results confirm, as expected, that the wall insulation of the TES is not sufficient to provide a self-sufficient energy supply for a 4-person detached house. However, the basic principle of storing thermal energy in refractory bricks seems to be an adequate method of energy storage, as the temperature is distributed centrally around the furnace chamber. The corundum and fireclay bricks absorb the thermal energy sufficiently to prevent the furnace chamber from

overheating. In addition, the heating cycles used here, where the maximum power (based on the PV system mentioned above) is fed into the TES for 8 hours a day, rarely occur in practice.

The wall insulation would have to be approximately 1.45 m thick at the calculated thermal conductivity coefficient of 0.19 W/m-K at a temperature of 1100 °C, if the thermal conductivity coefficients remained constant. However, with the materials used, the thermal conductivity coefficient increases with higher temperature, so it can be assumed that the wall thickness required for this design would have to be up to 2,3 m thick at 1100 °C in order to dissipate a maximum heat flux density of 140 W/m² to the environment.

The CFD simulation shows that for the same heating cycle, the temperatures in the virtual TES are higher than the measured temperature by thermocouples installed in the real TES. The heat flux densities in the simulation are also approximately 10 W/m² lower. These differences are due to the missing gap dimensions in the simulation, which were caused by design errors in the real TES.

Thermal energy loss was reduced by the aluminium foil, which acts as a reflector of thermal radiation. The aluminium foil also created gaps in the sheathing, offering potential for improving the insulation effect. The reflective effect of high emissivity surfaces was also evident in the use of steel sheets in the ceiling insulation.

If the wall insulation were increased to achieve a maximum average heat flux density of 140 W/m² from the TES, the TES demonstrator would be capable of providing electricity to a 4-person detached house all year round. The materials used for the wall insulation appear to be suitable for this application, in particular the transition from the high temperature resistant and mechanically stable Prolite® 125 panels to the Silcal 1100 panels placed on top, which have a lower strength and maximum operating temperature, but a lower thermal conductivity. Between the panels, the high temperature insulation wool act as a suitable filler for the gaps between the panels. In a gapless construction, the wall insulation consisting of these three layers would have to be approximately 2,3 m thick at an operating temperature of 1100 °C, making this TES unsuitable for use in a detached house. By using polished metal sheets, such as aluminium foil and steel sheet, the insulating effect of the wall insulation can be increased, thus reducing the required wall thickness.

The refractory materials used were able to deliver the expected performance at comparatively low cost, in particular the positioning along the TES brought the desired temperature distribution. To avoid the resulting gaps between the storage core and the insulation, a refractory cast concrete can also be used here, which would also simplify the one-off construction.

However, it is also useful to use a higher scaling for the TES, for example for a housing estate consisting of several houses, since the storage volume increases by a power of 3 and the area to be insulated increases by a power of 2. For this purpose, the CFD simulation generated with the real data can be used to determine the behaviour of the TES for different construction and environmental scenarios. The real TES can then be further developed and compared with the simulated values. In this way, different refractory materials - both shaped and unshaped - can be simulated to efficiently verify suitable materials that offer the best possible performance at a reasonable cost.

## CONCLUSIONS

Through this series of tests, a practical demonstrator has been built which can be used for further development for self-sufficient power supply by the TES. Especially in combination with flow simulation, this goal can be achieved as efficiently as possible.

Although this TES is not yet sufficiently insulated to make this possible, the principle of storing thermal energy in refractory bricks with subsequent storage based purely on radiation seems to be a useful alternative for the important issue of energy management today.

## REFERENCES

[1] I. Sarbu, C. Sebarchievici: A comprehensive Review of Thermal Energy Storage, Department of Building Services Engineering, Polytechnic University of Timisoara, Timosisoara, Romania, 2018.

[2] B. Diouf, R. Pode: Potential of lithium ion batteries in renewable energy, Kyung Hee University, Department of Physic, Seoul, South Korea.

[3] R. Jacob, W. Saman, F. Bruno: Capital cost expenditure of high temperature latent and sensible thermal energy storage systems.

[4] W. Pepperhoff: Die Gesetze der Hohlraumstrahlung, Springer Verlag, 1956.

[5] Hochschule für Technik und Wirtschaft Berlin: Messdaten Sonneneinstrahlungsinstensität Berlin, wetter.htw-berlin.de, 17.12.2021

[6] Verband der Elektrizitätswirtschaft: Repräsentatives Profil "Haushalt", BTU Cottbus – Lehrstuhl für Energiewirtschaft, 1999.

[7] S. Kabelac, D. Vortmeyer: Wärmestrahlung technischer Oberflächen, VDI Wärmeatlas, 2021.

582

# THE INFLUENCE OF FIRING PARAMETERS ON THE FORMATION OF NITRIDE PHASES IN NITRIDE BONDED SILICON CARBIDES

J. T. Kehren, M. Hauke, O. Krause

Koblenz University of Applied Sciences, Materials Engineering Glas & Ceramics, Höhr-Grenzhausen, Germany

T. Steffen, C. Linden, C. Dannert

Forschungsgemeinschaft Feuerfest e. V., Höhr-Grenzhausen, Germany

## ABSTRACT

In this study the influence of parameters like heating rate, $N_2$ gas flow and dwell time on the kinetics of the nitridation process were investigated. A combination of *in situ* and *ex situ* methods was used with special focus on the spatial formation of nitride phases. Centerpiece of the experiments was a new thermogravimetric nitridation furnace, capable of firing in $N_2$ atmosphere up to 1500 °C which was built at the Forschungsgemeinschaft Feuerfest e. V. Samples treated in this furnace were analyzed by Raman spectroscopy and scanning electron microscopy (SEM). Both methods provide details on the local formation of nitride phases. SEM analysis was used to determine the morphology of formed phases while Raman spectroscopy is capable of providing spatially resolved mineralogical data. Therefore, it was possible to differentiate between the various nitride phases and silicon nitride polymorphs. With this approach of combined *in situ* and *ex situ* methods, new insights into the formation process of nitride phases within nitride bonded silicon carbides were gained.

## INTRODUCTION

Nitride-bonded silicon carbides (NBSC) are important refractory materials used in various applications. They have high resistance to corrosion and wear and do not react with metal melts, making them an ideal material for the lining in aluminum electrolysis cells [1, 2]. In waste-to-energy plants, NBSC is preferred because of its excellent oxidation resistance and high thermal conductivity [3, 4]. The latter is particularly important for an efficient use of heat exchangers. Typically, the production of NBSC involves the direct nitridation of silicon carbide grains and silicon powder in a controlled nitrogen atmosphere at temperatures up to 1600 °C. This process results in the formation of a composite matrix of different silicon nitride (SN) phases through the highly exothermic reaction:

$$3\ Si_{met} + 2\ N_{2(g)} \rightarrow Si_3N_4 \ [5, 6] \qquad (1)$$
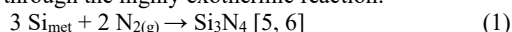
Due to recent crisis, energy prices have increased and there is a growing focus on reducing the environmental impact in almost all industrial sectors. As a result, energy consumption in high-temperature production lines has become a major concern. For the production of NBSC, it is essential to understand the factors that influence the formation of the matrix phases. Parameters such as nitriding temperature, heating rate and $N_2$ gas flow were identified to have a high potential in reducing the carbon footprint and cost of NBSC products. This study aims to investigate the effect of different firing profiles, including varying firing rates and $N_2$ gas flow rates on the silicon conversion and local phase composition. In addition, the influence of the exothermic reaction on these parameters was investigated.

## METHODS

Green bodies were prepared from metallurgical grade silicon powder (98.5 %, FeO: 0.7 %, metallpulver24.com) and different SiC grain sizes (98.5 %, ESK-SiC). For every green body the components were mixed in the ratios given in table 1. Uniaxial pressing was carried out with 300 kN to form cylindric bodies with a height of 50 mm and 50 mm diameter. Included within the pressing mold is a mandrel to later insert a thermocouple into the sample center.

The in-sample thermocouple is part of a set of thermocouples within the newly designed furnace and is intended to provide information on the exothermic heating within a sample during nitriding. A total of four thermocouples are included in the furnace for temperature control (Fig. 1). In addition to the thermocouples, the furnace was equipped with a unit for thermogravimetric (TG) measurements, comprising of a scale and a weighing plate for one cylindric sample. Prior to nitriding, samples were treated at 500 °C for 5 h to allow debinding.

Tab. 1: Standard composition of the green bodies.

| Components | Proportion in Ma.-% | Weigh-in in g |
|---|---|---|
| E-REFSIC98E 0 – 0,06 mm | 10 | 25.0 |
| E-REFSIC98 0 – 0,2 mm | 14 | 35.0 |
| E-REFSIC98 0,2 – 0,5 mm | 16 | 40.0 |
| E-REFSIC98 0,5 – 1 mm | 17 | 42.5 |
| E-REFSIC98 1 – 2 mm | 27 | 67.5 |
| Silicon 45 µm | 16 | 40.0 |
| SUM | **100** | **250.0** |
| Hoechst Wax C | | 1.0 |

Different firing profiles were carried out with heating rates of 1 K/min, 3 K/min and 5 K/min in the nitridation furnace (P1 - P3, Tab. 2). For each nitridation experiment, the heating rate was set to 3 K/min up to 1250 °C and then set to the respective rate. In order to hinder the formation of oxide bearing phases and focus on the formation of silicon nitride, oxygen concentration was kept at $10^{-18}$ % $O_2$ and monitored during the whole process. For P3 at 1 K/min the $N_2$ gas flow rate was varied between 25, 40, 45 and 50 l/h ($N_2$ 99.999 %). The accuracy of the new system was tested in a reproducibility test for which the samples were fired at 3 K/min to 1450 °C and then held at this temperature for 8 h. At the end of a profile, the furnace was switched off and no active cooling of the samples was performed. However, the $N_2$ gas flow was maintained to a temperature of 100 °C. After nitriding, open porosity was determined after DIN EN 993-1 and all samples had an open porosity between 19.6 and 19.8 Vol.-%.
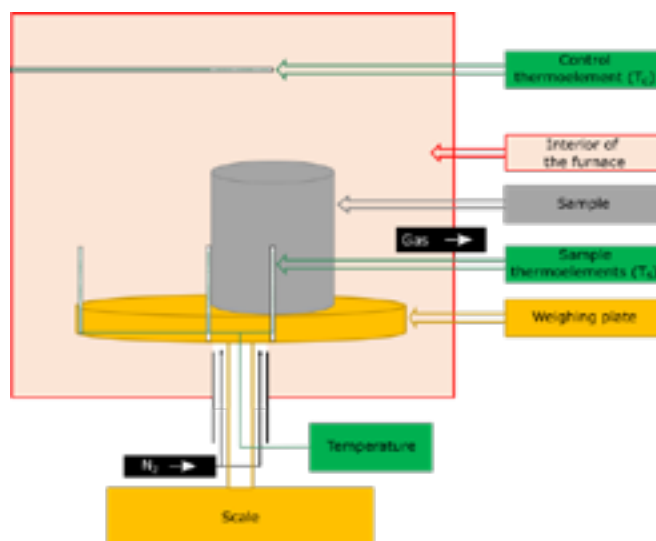


*Fig. 1: Schematic drawing of the test stand used in this study. A weighing unit and multiple encased thermocouples were placed inside the furnace. One of the thermocouples is inserted into the sample.*

The microstructure of the matrix was studied *ex situ* with a SEM running at 15 kV. To identify phases by their morphology SEM

images were taken on the surfaces of sawn samples. In addition, the mineralogical phase composition of the matrix was studied by Raman spectroscopy. For both methods, analyses were conducted at the center and edge of the samples.

Tab. 2: Overview of the different firing profiles with their respective steps and dwell times. Each profile was run at 1, 3 and 5 K/min.

|  | Step 1 [°C] | Dwell time 1 [h] | Step 2 [°C] | Dwell time 2 [h] | Step 3 [°C] | Dwell time 3 [h] |
|---|---|---|---|---|---|---|
| P1 | 1450 | 2 | 1400 | 6 |  |  |
| P2 | 1350 | 4 | 1450 | 4 |  |  |
| P3 | 1350 | 2 | 1400 | 2 | 1450 | 4 |

## RESULTS AND DISCUSSION
### Thermogravimetry and thermochemistry
The final mass gain for all combinations of different heating rates, $N_2$ gas flow settings and firing profiles, ranged from around $9.31 \pm 0.18\,\%$ to $10.00 \pm 0.18\,\%$. This equates to the conversion of approximately 87 to 93 % of the starting silicon. The onset of the nitridation reaction can be observed after 7 to 7.5 h in all experiments, corresponding to a temperature between 1300 and 1350 °C. In all profiles the rate of mass gain begins to slow down rapidly at the end of the last stage and drops to zero when cooling is initiated. After 18 to 19 h no further mass gain is detected in any of the profiles, indicating a complete stop of the nitridation reaction. The highest mass gains were measured for heating rates of 1 K/min and the highest mass gain overall was detected for P1 at 1 K/min. It is noticeable that every increase in temperature causes an increase in the rate of mass gain, whereas a temperature decrease has no influence on the mass gain rate. Furthermore, neither increase nor decrease of the mass gain were observed in experiments varying the nitrogen gas flow (Fig. 2).
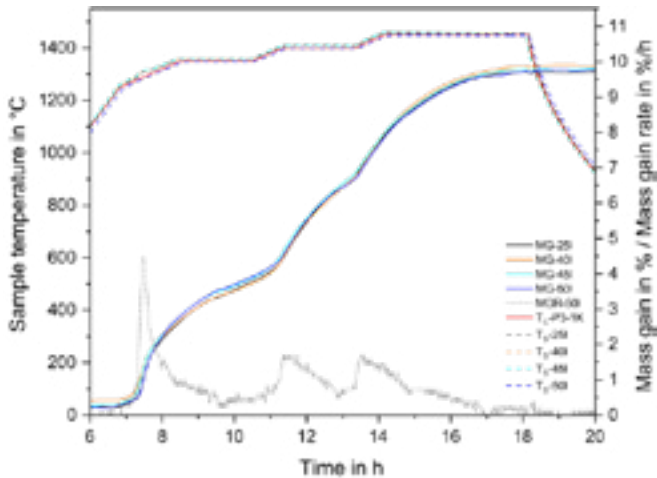


Fig. 2: The temperature at the sample center ($T_S$, dashed line) and the absolute mass gain (MG, solid line) are plotted for P3@1 K/min running at different $N_2$ gas flow rates with the furnace temperature ($T_c$) as a solid red line. In addition, the mass gain rate for a gas flow of 50 l/h is depicted as an example.

The temperature measurements at the sample center revealed the strongest exothermic peaks in P1 shortly after the transition from firing to the isothermal stage. Additionally, the other two profiles led to the observation, that smaller temperature steps at lower heating rates decrease the exothermic temperature peaks and at 1 K/min no exothermic peaks were detected at all.

A slight decrease of the sample temperature, indicative of an endothermic reaction, was recorded in all experiments at a temperature of 1400 to 1410 °C. This can be ascribed to the melting point of silicon at 1409 °C and the onset of a silicon melt formation.

## Microstructure
The matrix of all samples is dominated by $\alpha$-$Si_3N_4$ in its 'matte' morphology, while the presence of $\alpha$-$Si_3N_4$ whiskers as well as $\beta$-$Si_3N_4$ prisms depends on the spatial position and firing conditions. It was observed, that a high firing rate reduces the number of whiskers and decreases their size. Whiskers are still present at 5 K/min heating rate, but they appear primarily in larger pores. This is also the case when comparing the sample center and edge. Here, the number of whiskers decreases towards the edge of the sample. At the same time the amount of $\beta$-$Si_3N_4$ prisms increases (Fig. 3). The latter form by a liquid phase or a solid-gas reaction between silicon and nitrogen. Therefore, $\beta$-$Si_3N_4$ is often associated with a high grade of idiomorphism, because crystal growth takes place in the silicon with nitrogen diffusion through the hexagonal crystals [6]. The increased number of these idiomorphic $\beta$-$Si_3N_4$ prisms leads to the conclusion, that higher temperatures are attained at the sample edge and therefore more silicon has already transitioned to a liquid melt phase. The main finding with Raman spectroscopy was a higher amount of residual silicon at higher heating rates, especially at the sample center.
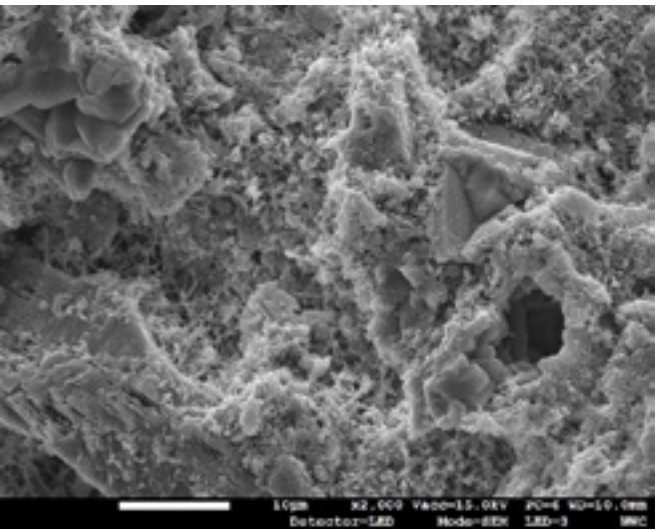


Fig. 3: SEM image of the matrix at the edge position in a sample fired with an $N_2$ gas flow of 45 l/h. $\alpha$-$Si_3N_4$ whiskers are present in larger pore spaces. In addition, $\beta$-$Si_3N_4$ prisms formed in areas where a silicon melt occurred.

## CONCLUSIONS
The $N_2$ gas flow rate has no influence on the overall silicon conversion in NBSC materials. However, lower heating rates increase the silicon conversion and SEM analysis revealed that the number of $\alpha$-$Si_3N_4$ whiskers increases at lower heating rates.

## REFERENCES
1. Reddy NK, Mukerji J (1991) Silicon Nitride-Silicon Carbide Refractories Produced by Reaction Bonding. J Am Ceram Soc 74(5): 1139–1141. doi: 10.1111/j.1151-2916.1991.tb04356.x
2. Wang Z, Skybakmoen E, Grande T (2009) Spent $Si_3N_4$ Bonded SiC Sidelining Materials in Aluminium Electrolysis Cell. TMS Light Metals: 353–358
3. Jacobson NS (1993) Corrosion of Silicon-Based Ceramics in Combustion Environments. J Am Ceram Soc 76(1): 3–28. doi: 10.1111/j.1151-2916.1993.tb03684.x
4. Zymla A, Zymla V, Biausser H (2001) Oxidation of Silicon Nitride Bonded Silicon Carbide Refractory Material in Air and Carbon Dioxide. KEM 206-213: 1655–1658. doi: 10.4028/www.scientific.net/KEM.206-213.1655
5. Messier DR, Wong P (1973) Kinetics of Nitridation of Si Powder Compacts. J Am Ceram Soc 56(9): 480–485. doi: 10.1111/j.1151-2916.1973.tb12529.x
6. Jennings HM (1983) On reactions between silicon and nitrogen. J Mater Sci 18(4): 951–967. doi: 10.1007/BF00551961

# DEVELOPMENT OF HIGH SIC FRACTION REFRACTORIES WITH SILICA SOL BINDER

Hirotaka Goto, Atsushi Sasaki and Kazuaki Komiya
Calderys Japan, Toyota city, Aichi, Japan

Bruno Touzo
Calderys, Paris, France

## ABSTRACT

Silicon Carbide (SiC) is a suitable material to be used in thermal exchangers, such as on the boiler walls in waste incinerators. Although SiC raw material is sometimes questioned due to its high carbon footprint and regulations, in the short term, there are no substitutes that can reach the high thermal efficiency and chemical resistance necessary in such applications.

Nowadays, in Japan, because of the lack of skilful bricklaying workers, and in order to reduce the maintenance downtime, castable lining is preferred over ready shaped lining such as bricks and tiles. Because of their high thermal conductivity property high SiC castables bonded with regular calcium aluminate cement require careful temperature control during the drying out process to avoid spalling which could occur because of the rapid water vapor pressure build up inside the castable. On the other hand, silica sol bonding technique gives refractories much higher permeability when heated up above the boiling point of water. Hence this bonding system gives a quick dry out feature to refractories, enabling shorter downtime than cement bonding system. Higher abrasion strength and higher duration than general cement bonded products can also be reached.

This paper reports the development of high SiC content refractories with silica sol binder. Results show that sol-bonded SiC showed a permeability record more than 20 times greater than the one of cement bonded products after drying out at 110 ℃, as a result, spalling was not observed on rapid heating tests. Regarding mechanical properties after sintering, sol-bonded SiC refractory achieved 30 % higher cold crushing strength compared to cement bonded castables.

## INTRODUCTION

Silica sol binder is a water solution of dispersed nanoscale silica particles, the particles are stabilized by pH control to prevent flocculation. Different from sodium silicate, which is commonly used as one of the alternative binders to alumina cement, the sol binder contains little alkaline elements, so it shows high refractoriness at high temperature when used as a binder. Refractory dry mix for sol-bonding does not require alumina cement, thus degradation of the dry mix during storage is less likely. For installation, in order to percolate the silica particles, alkaline powders are used as flocculators. They are mixed with the binder to shift the pH value. Cured strength of sol-bond castables is lower than cement castables because in cement bonded castables there are calcium aluminate hydraulic bonds between the castable particles. In other words, the sol-bonded matrix does not have chemically trapped crystalline water[1].

Hence, it does not need careful temperature control during the

first drying out[2], therefore a rapid drying out curve is applicable at the first heat up after installation. The downtime can then be reduced. For a 350-400mm thick lining, the dry out time can be reduced to about 12 hours, which is around half what is need for cement-bonded system.

Although there are many reports mentioning improvement of strength and usability of sol bonded refractories [3]-[6], discussions for anti-explosiveness used with high thermal conductive materials on rapid heating are very few. This report discusses the rapid heat up and spalling risk reduction of SiC based monolithic materials with silica sol binder. It shows the results of permeability measurement and moisture reduction dependency to drying temperature.

## EXPRIMENTAL

Five mixes are prepared for four types of measurements.

### Mix design

In order to evaluate the spalling risk reduction of silica sol-bonded SiC refractories which have high thermal conductivity, we prepared SiC low cement castables (LCC), bauxite LCC and sol-bonded bauxite as well as sol-bonded SiC. The mixes are compiled in Table 1. In this table, A, B are sol-bonded SiC, C is SiC LCC, D is sol-bonded bauxite and E is bauxite LCC. 0.03 wt% organic fibre is added into the sol-bonded mix, and 0.1 wt% fibre into the LCC mixes. For these five mixes, physical strength measurements, spalling tests and permeability measurements were determined.

### Physical strength

Kneading with either sol binder or water, the mix is casted in cuboid shapes according to JIS specification (40 x 40 x 160 mm$^3$), then cured for 24 hours in 90 %RH environment at 20 °C. After demoulding, the samples are dried out at 110 °C, then cold modulus of rupture (MOR) and cold crushing strength (CCS) is measured.

### Lab-scale explosion test

For this test the Chinese standard YB/T4117-2003 was used. The kneaded mix is casted into 50 mm diameter and 100 mm height cylinder shape, and cured for 24 hours. Then the demoulded sample is put into an electric furnace which is pre-set at 800 °C without dry-out step. The cylinder placed in the hot furnace experiences rapid heat up for 20 minutes. After exposure, inspection of appearance reports whether explosive spalling occurred.

### Permeability measurement

The same size cylinder as for the explosion test is prepared.

Tab. 1: The mixing design for the examination.

|  | A | B | C | D | E |
|---|---|---|---|---|---|
| SiC | 63 | 85 | 61 | 0 | 0 |
| Bauxite | 0 | 0 | 0 | 77 | 77 |
| Mullite | 13 | 0 | 10 | 0 | 0 |
| Calcined alumina and fume silica | 23 | 15 | 24 | 23 | 19 |
| Alumina cement | 0 | 0 | 5 | 0 | 4 |
| Water (%) | 0 | 0 | 7 | 0 | 6.5 |
| Silica sol (%) | 12 | 12 | 0 | 8 | 0 |

Tab. 2: Mechanical strength after drying at 110 °C, bulk density and thermal conductivity.

|  | MOR (MPa) | | CCS (MPa) | | BD | TC (W/(m·K)) |
|---|---|---|---|---|---|---|
| Fired at | 110 ℃ | 1200 ℃ | 110 ℃ | 1200 ℃ | 800 ℃ | 800 ℃ |
| A | 9 | 24 | 50 | 128 | 2.48 | 5.2 |
| B | 6 | 25 | 40 | 112 | 2.46 | 7.2 |
| C | 9 | 11 | 90 | 108 | 2.52 | 5.6 |
| D | 8 | 33 | 50 | 131 | 2.95 | 3.3 |
| E | 8 | 17 | 50 | 120 | 2.90 | 2.9 |

585

After demoulding, it is dried out at 200 °C for three hours, then cut into a 50 mm high cylinder. The permeability measurement is performed, following JIS R 2115. The flow rate of a nitrogen gas is recorded when the sample gets 10, 20 and 30 kPa differential pressure. The data is then converted into permeability values.

**Moisture reduction**

The physical properties after drying at 110 °C are described on Table 2. Modulus of rupture values for all samples are between 6 and 9 MPa, and CCS values are almost 50 MPa except for the SiC aggregate cement castable, which showed 90 MPa. The bulk densities (BD) for the SiC aggregate samples are approximately 2.5, and 2.9 for the bauxite ones. The thermal conductivity (TC) at 500 °C, which value depends on bulk density and SiC fraction, are on the right column, bauxite, SiC 60% and SiC 80 % are 3.0, 5.5 and 7.5 at 500 °C respectively.

**RESULTS AND DISCUSSION**

Explosive spalling occurs very fast, due to the surge of vapor pressure. The crack progression speed is related to the MOR. Thus, it is preferable that the MOR after drying at 110 °C is high. Among the samples tested on this set of experiment, MOR values are between 6 and 9 MPa regardless of the bonding system. Figure 1 shows the appearance of the SiC aggregate samples A, B and C after the explosion test. SiC LCC could not withstand this rapid heating and explosive spalling eventually happened. However, no cracks were found on the surfaces of the other four mixes. The explosion risk is strongly related to the balance of the thermal conductivity and the permeability.

Properties for A, B, D after firing at 1200 °C are superior to the conventional LCC C and E, particularly for the MOR results. Nanoscale colloidal silica and reactive alumina form a mullite matrix after firing. The matrix generates high strength for silica sol bonded refractory. In addition, the absence of lime prevents the formation of the low melting point components. Therefore a better abrasion resistance and a longer durability than the cement bonded SiC refractory can be expected at high temperature.

The heat curves for the samples of the explosion tests, in Figure 2, were estimated from the numerical calculation of a two dimensional heat conduction equation for cylindrical coordinates system under Crank-Nicolson Method. The equations are expressed as:

$$\frac{\partial T}{\partial t} = a\left(\frac{\partial^2 T}{\partial r^2} + \frac{\partial^2 T}{\partial z^2}\right) + \frac{Q}{c_p \rho} \tag{1}$$



Fig. 2: Calculated heat curves for three levels of thermal conductivities.

$$T_i^{n+1} = \frac{1}{2(1+c_r+c_z)} \cdot \left\{ c_r \left( \left(1+\frac{\Delta t}{2r_{i,j}}\right) T_{i+1,j}^{n+1} + \left(1-\frac{\Delta t}{2r_{i,j}}\right) T_{i-1,j}^{n+1} \right. \right.$$

$$\left. + \left(1+\frac{\Delta t}{2r_{i,j}}\right) T_{i+1,j}^n + \left(1-\frac{\Delta t}{2r_{i,j}}\right) T_{i-1,j}^n \right) + c_z \left( T_{i,j+1}^{n+1} + T_{i,j-1}^{n+1} \right.$$

$$\left. \left. + T_{i,j+1}^n + T_{i,j-1}^n \right) + 2(1-c_r-c_z)T_{i,j}^n \right\} + 2\frac{\Delta t}{c_p \rho} Q \tag{2}$$

$$a = \lambda/c_p \rho, \ c_r = a\Delta t/\Delta r^2, \ c_z = a\Delta t/\Delta z^2 \tag{3}$$

The differential equation was turned to the equation (2). Coefficients in the equations, $c_p$, $\lambda$, $\rho$, are material constants for heat transfer, $Q$ is radiation heat transportation between the kiln wall and the cylinder surface unit in Watt.

The sample cylinder in the calculation model, put in an electric kiln, receives heat from the kiln wall via radiation, then the heat flux flows inside the sample through conductive heat transfer. For these calculations, vaporization of the moisture and the moisture transfer is not considered. Calculation was done for 2 values of thermal conductivities, to mimic different SiC fractions. For the temperature at the center of the cylinder to reach 95 % of the pre-set furnace temperature (760 °C), it takes only 6.5 minutes for a thermal conductivity of 7.2 W/(m·K). This would correspond to a castable with 80 %SiC. When the thermal conductivity is 3.0



Fig. 1: Appearances of the samples after the explosion test.
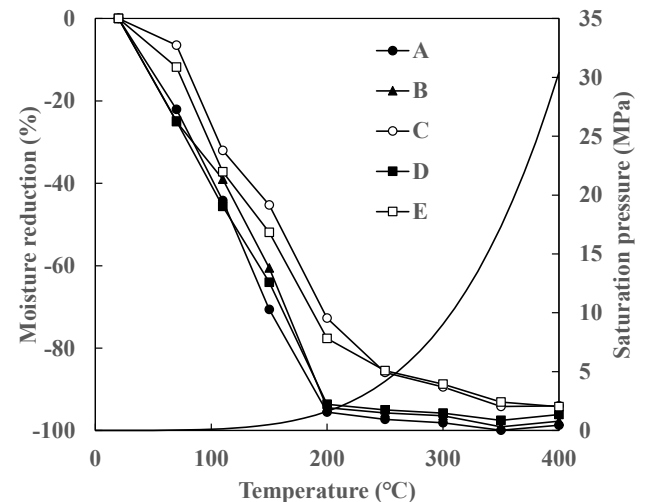


Fig. 3: The moisture reduction of the samples after putting for 1 hour at each temperature.

Tab. 3: Results for the explosion test and the permeability measurement.

| | Explosion | Permeability | |
|---|---|---|---|
| | | $(10^{-16}\ m^2)$ | X / C (%) |
| A | No | 78 | 3100 |
| B | No | 53 | 2120 |
| C | Yes | 2.5 | 100 |
| D | No | 150 | 6000 |
| E | No | 2.1 | 84 |

W/(m·K), as for bauxite castable, it would take 13 minutes, which is twice as long. For a thermal conductivity of 5.5 W/(m·K), corresponding to the 60 %SiC castable, an intermediate value of 8.5 minutes is calculated.

These calculations show that the thermal transfer from the surface to the center of the cylinder is slowed down in the bauxite LCC because of the relatively low thermal conductivity. The heating rate is slower compared to SiC contained sample C. The stresses generated by the vapor pressure during the rapid heating does not exceed the MOR of the E sample. On the other hand, the permeability contributes to the explosion avoidance for sol-bonded SiC A and B samples. Their high permeability value is the reason for their explosion resistance, although they have a high thermal conductivity.

On Table 3, the sol bonded refractory showed a very high permeability indenpendant of the type of aggregate. Indeed, after the drying out of samples SiC A, B and bauxite D, the measurement gave 31, 21 and 60 times greater permeability respectively than SiC LCC named C. The residual moisture of these castables formulations after heat treatment can also contribute to the explosion resistance. Figure 3 shows the residual moisture as a function of drying temperature together with the saturation water vapor pressure. For these measurements the same cylinder shapes as for the explosion test were used. They were put in the furnace pre-set at a given temperature for 60 minutes. The water loss is calculated from the sample weight loss, before and after heat treatment. . Below the temperature where vapor pressure begins to surge, almost all moisture has vaporized regardless of the aggregate type. However, after drying at 200 ℃, the LCC sample still has 25 % residual moisture compared to the initial. This residual moisture which comes from crystallized water in the alumina cement hydrates causes explosive spalling of the refractory during rapid heating.

For the sol-bonded lab-scale sample, almost all the moisture is vaporized when the temperature of the body reaches 200 ℃ because there is no crystallised water. Besides, the permeability is over 20 times higher than the one of LCC, which makes it easier for the transfer of the vaporized water from backward. This also applies for industrial scale refractory bodies, of several hundred of kilogram[7].

## CONCLUSIONS

Through this report, we introduced the performance of the silica sol-bonded SiC refractory and its anti-explosiveness in comparison to LCC and to another type of aggregate.
Sol-bonded refractory has over 20 times high permeability compared to LCC, it shows excellent explosion risk reduction at the lab-scale, even if high thermal conductive SiC aggregate is used.

Colloidal silica and reactive alumina form a high strength mullite matrix after firing, and the absence of lime in formula prevents the creation of the low melting point components that may induce poor abrasion resistance and weaken the structure at high temperature.

Hence, this bonding system assures quicker dry out properties for refractories than classic cement-bonding system, enabling short downtime as well as higher durable performance at high temperature, even with high SiC content castable.

## REFERENCES

[1] A. Kitahara, "Fundamentals of interface and colloid chemistry", Kodansha Scientific, 1-7 (1994).
[2] T. Makihara *et al*., Taikabutsu (Refractories) 61 [4], 165 (2009).
[3] M.R. Ismael *et al*., Refract. Appl. News, 11 [4] 16 (2006).
[4] M.R. Ismael *et al*., American Ceramic Society Bulletin, Vol. 86, No. 9, 58 (2007).
[5] D. Chen *et al*., Ceramics International Volume 43, Issue 12, 8850 (2017).
[6] M. Nouri-Khezrabad *et al*., Ceramics International Volume 41, Issue 2, 3051 (2015).
[7] H. Peng and B. Myhre, Refractories WORLDFORUM 9 (2017) [3], 61.

# A MAJOR STEP TOWARDS THE REPLACEMENT OF CHROMIUM OXIDE IN REFRACTORIES FOR INCINERATORS AND OTHER APPLICATIONS

R. Soth*, R. Jacquemot, C. Masgalides, M. Weissenbacher, F. Simonin, C. Wöhrmeyer, C. Liu, M. Szepizdyn, E. Frier

Imerys S.A., Paris, France

* Presenting author

## ABSTRACT

Alumina chromium refractories are still amongst the best performing materials for the application in special waste incinerators and other furnaces with for example a high load of alkalies. On the other hand, typically a significant amount of the compounds that contain initially trivalent chromium oxide, turn during application into hexavalent compounds. This requires a special refractory waste treatment to minimize the health and safety risks associated with the water soluble hexavalent Chromium compounds. While for very high temperature fired bricks some Cr-free new matrix compositions have been developed already based on a new in-situ formed mullite-zirconia microstructure, this paper investigates, how such a microstructure can also be employed in aggregates and fillers to enable the formulation of bricks and monolithics without the need for very high pre-sintering temperatures.

In this context, a new synthetic aggregate has been developed. Special focus is given on the different types of raw materials as well as the process conditions necessary to reach the desired characteristics and innovative microstructure. Performance tests in castable formulations have been conducted to verify their behavior in application conditions. It will be shown that this novel sintered aggregate keeps a kind of microstructural memory of its original raw materials which is very beneficial for its thermomechanical behavior compared to a standard zirconia mullite aggregate produced through the electrofusion route.

## INTRODUCTION

Althought the alumina chromium refractories still remain amongst the highest performing materials for the application in special waste incinerators and other furnaces with for example a high load of alkalies [1], the drawbacks linked to the necessary special treatment of refractory wastes due to the presence of water-soluble Cr VI motivate more and more the search for alternative Cr-free solutions. In particular, new zirconia-mullite based materials, obtained by electro-fusion or sintering, seem to have a high potential in this role as shown by Bouchetou et al. [2], Chotard et al. [3] and Rendtorff et al. [4], regarding the thermal shock resistance and/or corrosion tests.

The present paper deals with the synthesis at laboratory scale of sintered zirconia-mullite (SZM) materials dedicated to be used as aggregates in refractories. The effect of those SZM materials will be evaluated in terms of thermal shock resistance (TSR) and slag corrosion resistance of SZM-based refractories.

## MATERIALS AND METHODS

The raw materials and their characteristics are described in the following tables (Tab. 1). The zircon flour and alumina (smelter grade) materials were from external sources, while the andalusite (Kerphalite KA) was from internal Imerys SA materials. Samples of coarse materials were previously ground down to under 100 µm prior to analysis, either for the chemical composition measured by X-ray fluorescence (XRF) with the Panalytical Zetium device on fused beads, or for the X-ray diffraction (XRD) performed with the diffractometer Bruker D8 Advance equiped with Detector Lynxeye XE-T, using Cu radiation and analysis within the 2θ range of 5-80°. The mineralogical composition was quantified with the software Topas R V6. The particle size distribution (PSD) was determined by the laser granulometer Malvern Mastersizer 3000 using the Fraunhofer model and powder dispersion pressure of 3 bar.

Tab. 1: Chemical composition and fineness of the raw materials.

| Raw materials | SiO$_2$ (wt%) | Al$_2$O$_3$ (wt%) | ZrO$_2$ (wt%) | Fe$_2$O$_3$ (wt%) | Total (wt%) | Fineness D$_{90}$ (µm) |
|---|---|---|---|---|---|---|
| Zircon flour | 32.5 | 0.8 | 66 | 0.1 | 99.4 | 4.8 |
| Alumina | 0.1 | 99.7 | 0 | 0 | 99.8 | 100 |
| Andalusite | 38.3 | 59.8 | 0 | 0.8 | 98.9 | 90 |

## SYNTHESIS OF SZM MATERIALS

The sintered zirconia-mullite materials have been synthesized by sintering a raw material powder mix containing zircon flour, alumina and andalusite. The ratio of the raw material components was chosen to achieve a total weigth ratio (Al$_2$O$_3$/SiO$_2$) close to that of the 3:2 mullite, so that the mullite formation may be maximized either from andalusite mullitisation or as secondary mullite from the reaction between silica and alumina. The raw mix of materials was prepared following two different processes prior to calcination. On the one hand, a wet process consisted of milling the raw materials in a jar mill with a certain quantity of water to obtain a fluid slurry. Afterwards, the obtained final slurry was cast into parallelepipedic steel molds (2x2x10 cm$^3$) and dried for 24 hours in an oven at 110°C before demolding. On the other hand, the mix of raw materials was dry-milled and was submitted to granulation in an Eirich mixer for 60 minutes. During this mixing, water was progressively added in order to form granules of around 1 cm diameter. Those granules were then dried in an oven at 110°C for 24 hours.

The dried materials from the two preparation processes were then placed in alumina saggars and calcined in an electric muffle furnace Nabertherm HT 128-17 at the same very high temperature. The SZM materials (SZM-1 from wet milling process and SZM-2 from granulation process) thus obtained were characterized regarding the bulk density (d) and open porosity (OP) which were determined by water immersion according to Archimedes' principle method, and the microstructural observations by Scanning Electron Microscopy (SEM) coupled with elemental analysis by Energy Dispersive Spectroscopy (EDS) on polished surface sections.

## RESULTS

### Sintered zircon-mullite materials characteristics

Tab. 2: Mineralogical composition, density and open porosity of SZM materials. m-ZrO$_2$ and t-ZrO$_2$ stand for monoclinic and tetragonal zirconia respectively.

| SZM materials | Zircon (wt%) | Mullite (wt%) | m-ZrO$_2$ (wt%) | t-ZrO$_2$ (wt%) | α-Al$_2$O$_3$ (wt%) | d (g/cm$^3$) | OP (%) |
|---|---|---|---|---|---|---|---|
| SZM-1 Wet milling | traces | 80.4 | 18.3 | 1.2 | 0 | 3.21 | 6.1 |
| SZM-2 Granulation | traces | 80.6 | 18.2 | 1.0 | traces | 3.11 | 8.4 |

It is to note the amorphous phases were not considered in the quantification of the mineralogical composition by the Rietveld method shown in Tab. 2. Nevertheless, the quantities found were not far from the values theoretically expected as shown below.

Indeed, it can be observed that $Al_2O_3$ and $SiO_2$ have been almost completely combined during the calcination, leading to a maximum content of mullite. As the mullite quantified by the Rietveld method was considered as the 3:2 mullite (3 $Al_2O_3$ . 2 $SiO_2$), its theoretical weight ratio ($Al_2O_3/SiO_2$) equals to 2.55, quite close to that of the recipe which is 2.69 calculated from the chemical composition of raw materials and their respective proportions in the recipe. So, the content of $Al_2O_3$ of the recipe is slightly in excess in comparison to the needed quantity of $SiO_2$ with respect to the composition of 3:2 mullite. Likewise, the zircon has been nearly totally decomposed to $SiO_2$ and $ZrO_2$ during the heat treatment, and $SiO_2$ reacted with $Al_2O_3$ to form Mullite whereas $ZrO_2$ remained as m-$ZrO_2$ mainly. Finally, andalusite and zircon have been quasi completely decomposed to form mullite and zirconia, leaving a very low quantity of residual silica as a potential amorphous phase.

According to Tab. 2 the two types of SZM materials have similar mineralogical compositions but with a slight difference in density and open porosity.
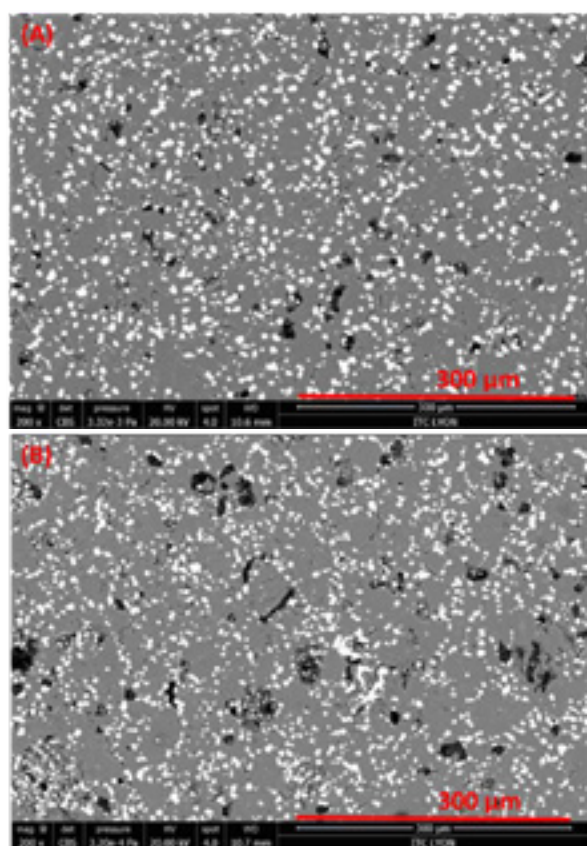

Fig. 1: SEM microstructure of (a) SZM-1 and (b) SZM-2 materials
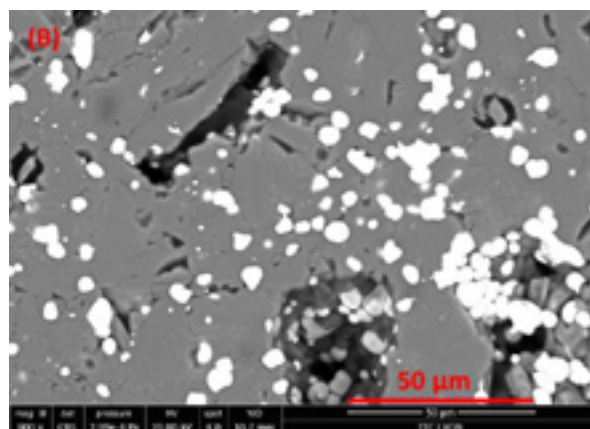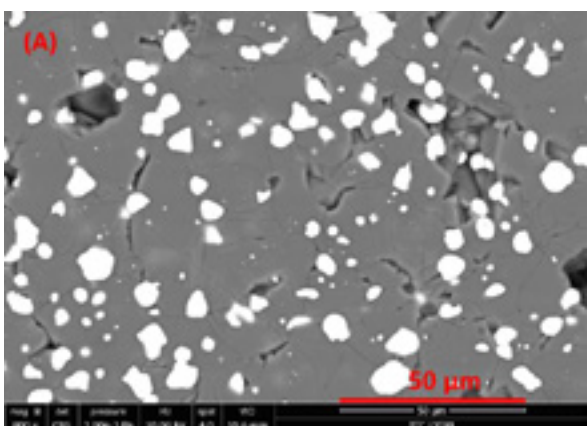

Fig. 2: SEM microstructure of (a) SZM-1 and (b) SZM-2 materials

The SEM images of Fig. 1 and Fig. 2 show an example of microstructure of SZM-1 and SZM-2 materials after calcination at 1700°C. Both types of microstructures exhibit a dispsersion of zirconia grains (small white grains) in a matrix of mullite (grey parts), with pores in black. In both cases, the zirconia grains appeared smaller than 4 µm. However, it can be observed that the SZM-1 shows a more homogeneous dispersion of zirconia grains and a lower porosity with smaller pores than in SZM-2.

**Corrosion and thermal shock tests**
The two sintered zirconia-mullite materials previously obtained (SZM-1 and SZM-2) have been sized in different grades in order to be used as aggregates in refractory castables for thermal shock and slag corrosion tests.

The castable compositions shown in Tab. 3 are the two reference formulations which contain tabular alumina aggregates and differ by the grade of fine zircon sand ($ZrSiO4$). In total, 65 wt% of different grades of tabular alumina were replaced with the SZM materials as shown in Tab. 4, and the combination of the remaining alumina and zircon sand ($ZrSiO_4$) is expected to form in-situ mullite and zirconia.

Tab. 3: Castable composition serving as references

| Raw Materials | | Ref 1 | Ref 2 |
|---|---|---|---|
| Tabular Alumina | wt% | 75 | 75 |
| Reactive alumina | wt% | 10 | 10 |
| Coarse zircon sand | wt% | 10 | |
| Fine zircon sand | wt% | | 10 |
| Silica binder | wt% | 5 | 5 |
| Total | wt% | 100 | 100 |
| Water | wt% | 5 | 5 |
| Additives | wt% | 0.08 | 0.08 |

Tab. 4: Castable composition containing SZM aggregates

| Raw Materials | | SZM-1 | SZM-2 |
|---|---|---|---|
| SZM-1 | wt% | 65 | |
| SZM-2 | wt% | | 65 |
| Tabular Alumina | wt% | 10 | 10 |
| Reactive alumina | wt% | 10 | 10 |
| Fine zircon sand | wt% | 10 | 10 |

589

| Silica binder | wt% | 5 | 5 |
|---|---|---|---|
| Total | wt% | 100 | 100 |
| Water | wt% | 5 | 5 |
| Additives | wt% | 0.08 | 0.08 |

Prior to thermal shock and corrosion tests, a pre-calcination at 1600°C was applied to the specimen according to the following thermal treatment profile after 24 hours drying at 110°C. The heating up was from 110°C to 500°C at 100°C/h, from 500°C to 1600°C at 300°C/h with a holding time of 6 hours. The cooling down was from 1600°C to 110°C at 300°C/h and then the specimens were exposed to ambient conditions.
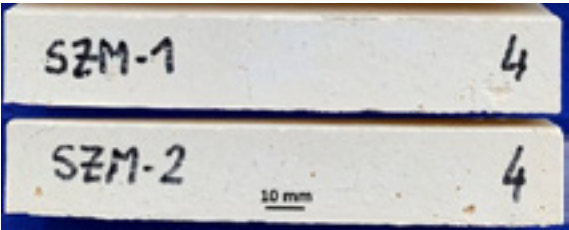


Fig. 3: Examples of specimen of SZM-based castables dedicated to the corrosion test.

The SZM-based castables were also compared to two commercial alumina-chromium bricks, A and B. The characteristics of the different materials are shown in Tab. 5 and Tab. 6.

Tab. 5: Phase composition of commercial products. Mull stands for mullite and Am stands for amorphous phase.

| Comm. product | Phase composition (wt%) | | | | |
|---|---|---|---|---|---|
| | α-Al$_2$O$_3$ | (Al,Cr)$_2$O$_3$ | Mull | Am. | Eskolaite_Cr$_2$O$_3$ |
| A | 50.0 | 31.8 | 13.3 | 4.9 | |
| B | 15.8 | 80.8 | | | 3.4 |

Tab. 6: Bulk density and open porosity of specimen

| Specimen | Bulk density (g/cm$^3$) | OP (%) |
|---|---|---|
| A | 3.1 | 15.7 |
| B | 3.4 | 14.8 |
| SZM-1 | 2.8 | 17.7 |
| SZM-2 | 3.0 | 13.9 |
| Ref 1 | 3.1 | 13.3 |
| Ref 2 | 3.2 | 11.8 |

For the dynamic corrosion test, a synthetic slag has been made in laboratory according to an average composition of real slags from incinerator of municipal wastes (Tab. 7).

Tab. 7: Slag composition in weight percent

| Al$_2$O$_3$ | CaO | SiO$_2$ | MgO | Fe$_2$O$_3$ | SO$_3$ | Na$_2$O | TiO$_2$ | P$_2$O$_5$ | K$_2$O | Cl | Tot. |
|---|---|---|---|---|---|---|---|---|---|---|---|
| 11.2 | 32.1 | 34.0 | 2.3 | 4.3 | 2.5 | 3.8 | 1.6 | 4.7 | 0.9 | 2.7 | 99.9 |

The corrosion was performed with a dynamic Finger test consisting of immersing 115x25x25 mm$^3$ specimen into fused slag at 1350°C

while rotating for 2 hours. The slag resistance was evaluated by the erosion size (width variation along the length of specimen after corrosion test) and penetration degree (visual examination of cross sections).
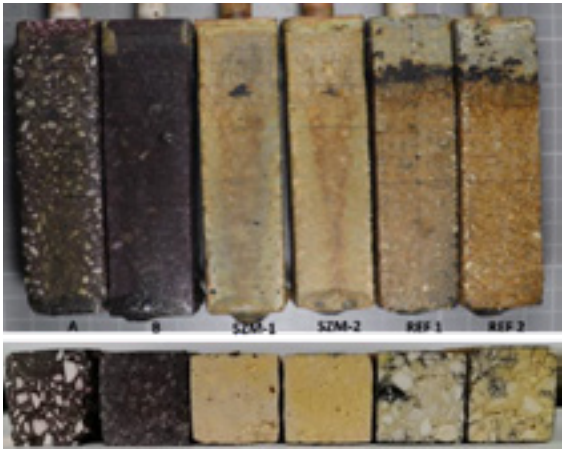


Fig. 4: Visual aspect of specimen after corrosion test, the up part shows the whole samples and the bottom part their cross-section.

The thermal shock test was performed on specimen of 160x40x(25~30) mm$^3$ at 950°C for 30 minutes and at 1, 3, 5, 7, 9 cycling times with 5 minutes air quenching followed by Young's modulus (E-Mod) determination by impulse excitation of vibration for E-Mod residual retention rate. For the modulus of rupture (CMOR) after thermal shock, the samples of 160x40x40mm$^3$ were submitted to 950°C for 30 minutes and 5 continuous cycling times with 5 minutes air quenching and evaluated by CMOR for residual retention rate.

The evaluation of erosion size and anti-penetration is much subjected to uncertainty and must be confirmed by microstructure analysis by SEM-EDS techniques. However, the values of Tab. 8 indicate that the SZM-based specimen have underwent the most important erosion, but had also the best anti-penetration.

Tab. 8: Width variation and visual examination of specimen after corrosion tests

| | Dimension before corrosion (mm) | | Residual dimension (mm) | | | | | Erosion size (mm) | | Anti-penetration |
|---|---|---|---|---|---|---|---|---|---|---|
| | | | A | B | C | D | Average | | | |
| A | width1 | 25.5 | 25.2 | 25.2 | 24.7 | 24.8 | 25 | 0.5 | 0.3 | **** |
| | width2 | 25.8 | 25.6 | 25.6 | 25.8 | 25.8 | 25.7 | 0.1 | | |
| B | width1 | 25.8 | 25.5 | 25.4 | 25.5 | 25.3 | 25.4 | 0.4 | 0.3 | *** |
| | width2 | 25.8 | 25.8 | 25.8 | 25.4 | 25.3 | 25.6 | 0.2 | | |
| SZM-1 | width1 | 25.2 | 23.8 | 23.8 | 23.8 | 23.4 | 23.7 | 1.5 | 1.3 | ***** |
| | width2 | 25.4 | 24.3 | 24.3 | 24.2 | 24.2 | 24.2 | 1.2 | | |
| SZM-2 | width1 | 25.2 | 23.4 | 23.5 | 23.4 | 23.5 | 23.4 | 1.8 | 1.8 | ***** |
| | width2 | 24.9 | 23 | 23 | 23.2 | 23.2 | 23.1 | 1.8 | | |
| Ref 1 | width1 | 25.1 | 24 | 24 | 24.3 | 24.4 | 24.2 | 0.9 | 1.1 | ** |
| | width2 | 25.1 | 23.8 | 23.8 | 24 | 24 | 23.9 | 1.2 | | |
| Ref 2 | width1 | 25.7 | 25.4 | 25.3 | 24.9 | 24.9 | 25.1 | 0.6 | 0.7 | ** |
| | width2 | 24.9 | 24.1 | 24.1 | 24.1 | 24.1 | 24.1 | 0.8 | | |
| **** : very good according to visual examination | | | | | | | | | | |
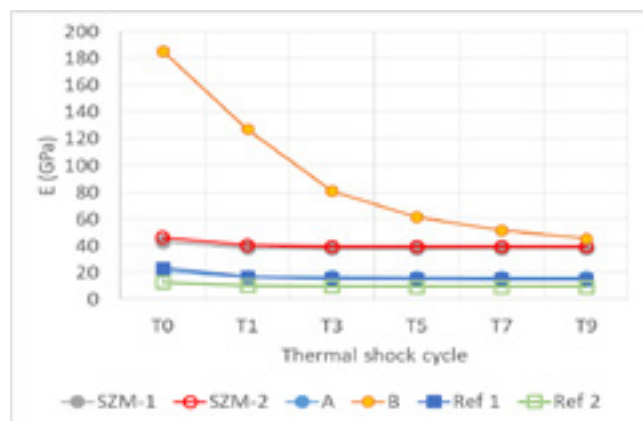
*Fig. 5: Young's modulus as a function of thermal shock cycle*
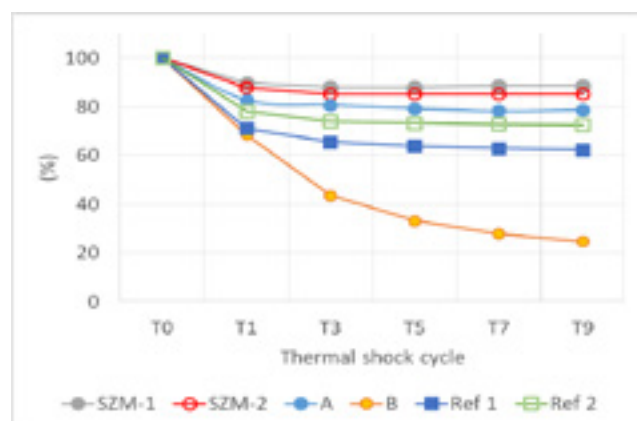


*Fig. 6: Young's modulus residual retention rate after thermal shocks*

It is noted that the B-specimen has shown the highest Young's modulus before thermal shock (Fig. 5), but also the most important loss of this modulus after each thermal shock cycling (Fig. 6). A remarkable performance of SZM-based specimen can be observed with the fact that their loss of Young's modulus is lower than that of the other samples from the first thermal shock, and that this elastic modulus remained stable along the thermal shock cycles.

Tab. 9: Mechanical strength and residual strength after 5 thermal shocks.

| | Before thermal shock CCS (MPa) | Before thermal shock CMOR (MPa) | After 5 thermal shock CMOR (MPa) | Residual CMOR rate (%) |
|---|---|---|---|---|
| **A** | 176 | 11.4 | 9.8 | 86% |
| **B** | >280 (*) | 40.4 | 6.6 | 16% |
| **SZM-1** | 121 | 19.5 | 15.3 | 78% |
| **SZM-2** | 125 | 17 | 19.8 | 116% (**) |
| **Ref 1** | 99 | 9.9 | 9.3 | 94% |
| **Ref 2** | 88 | 7.4 | 7.6 | 102% (**) |

(*) In Tab. 9, the cold compressive strength (CCS) of the specimen was higher than the value of the maximum limit of the device.
(**) The ratio between the modulus of rupture before and after the thermal shock is higher than 100% due to the uncertainty of the measure. In that case, the ratio may be considered equivalent to 100%.

The results show that the SZM-based formulations are only slightly impacted by the thermal shock cycles (Fig. 6, Tab. 9), indicating that their microstructure can cope very well with thermomechanical stresses preventing macroscopic damages.

**CONCLUSIONS**

Sintered zirconia-mullite (SZM) materials have been synthesized via two different processes regarding the raw materials preparation, either by wet milling or by granulation of fine andalusite, alumina and zircon sand. Both SZM materials exhibited a similar microstructure containing fine grains of zirconia well dispersed in mullite matrix. In addition, quantitative XRD has shown that the starting raw materials have been quasi completely reacted and combined during the high temperature calcination process, leading to a nearly maximum quantity of mullite and zirconia with traces of remaining uncombined materials. When submitted to thermal shock and corrosion tests, the castables containing SZM aggregates have shown high thermomechanical performances. In particular, a remarkable performance of SZM-based castables could be observed with the fact that their loss of Young's modulus is lower than that of the other samples from the first thermal shock, and that this elastic modulus remained stable along the thermal shock cycles.

Further characterizations on post-mortem samples will be conducted to investigate the phase composition and the texture of microstructure as a consequence of thermal shock cycles and of slag corrosion exposure.

**REFERENCES**

[1] Chan C.F., Ko Y.C., Effect of $Cr_2O_3$ on slag resistance of $Al_2O_3$-$SiO_2$ refractories. J. Am. Ceram. Soc. 75 (10), 1992, p. 2857–2861

[2] Bouchetou M.L., Poirier J., Morales A.L., Chotard T., Joubert O.R., Weissenbacher M., Synthesis of an innovative zirconia-mullite raw material sintered from andalusite and zircon precursors and an evaluation of its corrosion and thermal shock performance. Ceramics International 45, 2019, p. 12832-12844

[3] Chotard T., Morales A.L., Bouchetou M.L., Poirier J., Thermomechancial characterization of mullite zirconia composites sintered from andalusite for high temperature applications. Ceramics 9, 2019, p. 587-601

[4] Rendtorff N.M., Garrido L.B., Aglietti E.F., Effect of the addition of mullite-zirconia to the thermal shock behavior of zircon materials. Mater. Sci. Eng., A 498, 2008, p. 208–215

591

# OXIDATION BEHAVIORS AND MECHANISMS OF SIC REFRACTORY MATERIALS USED IN MUNICIPAL WASTE INCINERATORS CONTAINING ANTI-OXIDIZING ADDITIVES

C. Lang*, S. Abdelouhab, F. Delobel, P. Pilate
BCRC-INISMa, Belgian Ceramic Research Center, Mons, Belgium

**ABSTRACT**
An oxidation test, based on the ASTM C863-83 standard was developed, allowing a sequential follow-up of the oxidation by mass variation measurement. An oxide bonded SiC material, mixed with different boron-based additives and a nitride-bonded SiC material (commercial tile) were tested in this testing device. The characterizations before and after oxidation (mass variation, C-content analysis, open porosity) allowed for the mechanism identification responsible of the material oxidation behaviour. The comparison of oxidation resistance between the samples tested are discussed based on the adjuvant and the observed oxidation behaviour, in comparison with the reference material. Some additives enhanced the oxidation resistance, whilst being easy to prepare, making them interesting for an industrial upscaling.

## INTRODUCTION

Nowadays, the incineration process of municipal wastes with energy recovery is both a way to reduce waste volumes and a way to produce energy. Waste sorting and management lead to an increase in their calorific value, as well as an increase in the combustion temperature in the furnaces. The combination of high temperature, ashes and corrosive gases induces serious oxidative and corrosive conditions. Therefore, the steel tubes of the boilers need to be protected with refractory materials [1, 2, 3, 4, 5]. Silicon carbide (SiC) shaped materials (bricks or tiles) are mainly used and fixed to the metallic boiler walls with steel anchors. The main advantages of using SiC products for this process are the high thermal conductivity of SiC, associated to the low thermal expansion and the high corrosion resistance of this material. Even with these properties, the harsh conditions encountered in the furnaces justify the ongoing research for new solutions to improve the durability of the linings and the SiC oxidation resistance.

It is well known that the nitride bonded SiC presents better resistance to oxidation and corrosion than oxide bonded SiC, but these materials need firing under nitrogen atmosphere thus leading to more expensive production costs [6]. Their use can only be justified in the higher temperature area of the furnaces. Oxide bonded materials are preferred in the remaining part at lower temperature and with less active corrosion. However, the oxidation of SiC to $SiO_2$ leads to some disorders due to the associated expansion.

In this context, the aim of this work was to incorporate some anti-oxidizing additives in the oxide bonded phase, in order to improve the material oxidation resistance. Boron based additives ($B_2O_3$ or $B_4C$) were selected. Indeed, the literature reveals that for some materials (for example cutting tools made of SiC) [7] boron-based compounds can be used as sintering additives to obtain a higher density after firing [8, 9, 10] and therefore a lower porosity [11] of the material due to a liquid sintering at lower temperature. In addition, $B_4C$ addition is also well-known acting as an anti-oxidizing agent in carbon containing refractory materials by oxidizing first, therefore preventing the material from early oxidation [12].

The oxidation performances of the new compositions developed and tested in this study has been compared to those of a nitride bonded SiC.

## MATERIALS AND METHODS

### Materials

*Nitride bonded SiC tile (Si3N SiC):*

For the establishment of the oxidation behaviour of nitride bonded SiC material, the commercial material used in this study is a REFRAX plus material supplied by Saint Gobain (France).

*Oxide-bonded SiC raw material composition:*
For the evaluation of the corrosion resistance of oxide bonded SiC material containing boron based anti-oxidizing additives, a commercial SiC reference mixture was supplied by Fire Technic SA.
The boron-based additives used were: $B_2O_3$ (Merck) and $B_4C$ (grade HD15, Höganäs). The contents added in the starting mixture were 0.5 wt% or 1.0 wt% for $B_4C$ and 1.0 wt% for $B_2O_3$ with respect to the weight of the starting mixture.

### Sample preparation

All samples were prepared by mixing the SiC reference mixture powder with the selected additive compound. Boron based additives were directly incorporated in the starting composition of the commercial oxide bonded SiC composition for an easier further industrial implementation without process production modification. The samples were prepared by filling a cylindrical mould (50 mm diameter 50 mm height), followed by uniaxial pressing (RT, 2 min, 200 kN) in the mould. Finally, the cylindrical shaped samples were fired at 1400 °C for 4h.
The sample identifications and their composition are presented in table 1.

*Tab. 1 : Description of the samples*

| Sample name | Composition |
|---|---|
| Ref SiC | Reference SiC, oxide bond |
| Si3N SiC | SiC, Nitride bond $Si_3N_4$ (commercial tile) |
| SiC05B4C | SiC, oxide bond + 0.5 % $B_4C$ |
| SiC1B4C | SiC, oxide bond + 1.0 % $B_4C$ |
| SiC1B2O3 | SiC, oxide bond + 1.0 % $B_2O_3$ |

The pressed and fired samples were machined in 2.5×2.5×2.5 cm³ cubes for oxidation tests.

### Characterization method

Density/porosity
The density and the porosity were obtained according to the standards EN 993-1 (Archimedes' principle), for samples before and after oxidation.

C-analysis
Samples of materials before and after oxidation were finely ground before chemical analyses (≤5µm). Carbon content was determined using LECO spectrometer for the calculi of silicon carbide contents.

Mass variation
The samples were weighted before and after oxidation for each 100 h cycle, the mass variation ($m_v$) was calculated based on the initial mass before oxidation ($m_i$) and the final mass ($m_o$) after 100 h oxidation cycles:

$$m_v(\%) = 100 \times \left(\frac{m_o - m_i}{m_i}\right)$$

### Oxidation tests

For the evaluation of the oxidation and corrosion tendencies, a vertical tubular furnace was used (figure 1). The working temperature was 1000 °C. Each oxidation test was conducted for 500 h under oxidative atmosphere (5 cycles of 100 h). For that, a

pump linked to a water tank allows water injection in the bottom of the furnace. In this case, the ASTM C863-83 standard was followed leading to 32 kg.m$^{-3}$.h$^{-1}$ of water flow in the furnace.

As a mass variation occurs during the oxidation of SiC into $SiO_2$ [6] (mass variation directly linked to SiC oxidation), the oxidation was followed by measuring the mass variation of the samples after 100 h oxidation cycles.
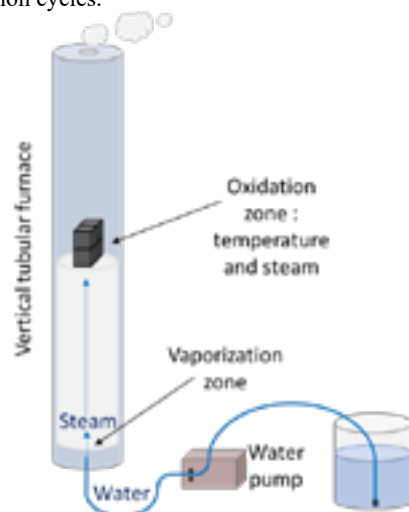


*Fig. 1: oxidation setup*

## RESULTS
### Oxidation tests
The results obtained during oxidation tests on reference samples and boron-containing samples are reported on figure 2.
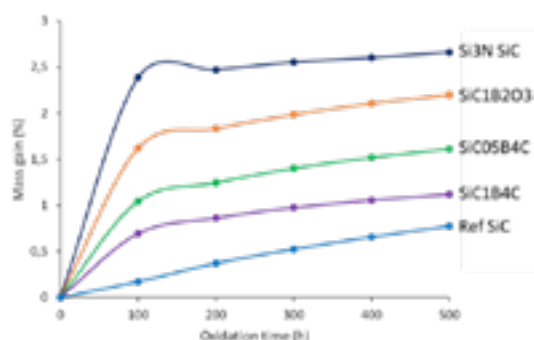


*Fig. 2: Oxidation results*: **Si3N SiC**, **Ref SiC**, **SiC1B2O3**, **SiC05B4C**, **SiC1B4C** *based on mass variation*

First, the Ref SiC oxidizes slowly in a nearly linear way as it is shown through the mass gain curve figure 2.

Regarding $Si_3N_4$-bonded SiC, $B_4C$ and $B_2O_3$ containing samples, the oxidation profile can be divided in two stages. During the first cycle (100 h), a high oxidation rate is observed, linked to a high mass gain. Then, during the other cycles, the mass variation decreases. The curve becomes nearly linear with a lower mass gain indicating a lower oxidation rate.

The oxidation rate was estimated from the slope of the mass variation in the linear zone (from 200 h to 500 h oxidation) and is presented table 2.

*Tab. 2: Mass gain slope*

| Sample | Mass gain slope (×1000) wt% / h |
|---|---|
| Ref SiC | 1.3 |
| Si3N SiC | 0.6 |
| SiC1B2O3 | 1.6 |
| SiC05B4C | 1.2 |
| SiC1B4C | 0.7 |

The different samples can be ranked according to their oxidation rate, from higher to lower oxidation rate:

SiC1B2O3 > Ref SiC ≈ SiC05B4C > SiC1B4C ≈ Si3N SiC

### Open porosity
Figure 3 reports the comparison between open porosities (%) before and after oxidation (500h). The porosity variation is calculated in % relative to the initial porosity (before oxidation) of each sample.
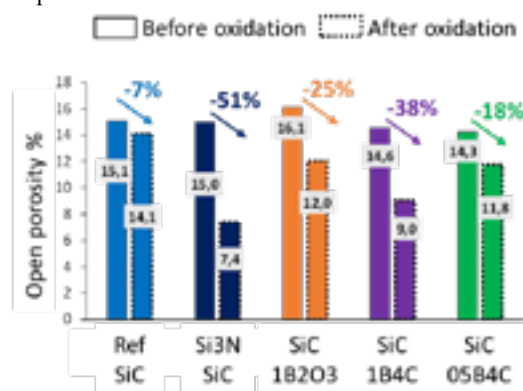


*Fig. 3: Open porosities before and after oxidation*: **Si3N SiC**, **Ref SiC**, **SiC1B2O3**, **SiC05B4C**, **SiC1B4C** *and porosity variation compared to initial porosity before oxidation*

First by comparing the samples before oxidation, it appears that the porosity is similar for oxide bonded reference SiC and $Si_3N_4$ bonded SiC, and higher for the sample containing $B_2O_3$. The porosity is lower for $B_4C$ containing samples, indicating a better densification during firing due to the presence of $B_4C$ [8, 9, 10, 11]. Except for the Ref SiC, where the porosity after oxidation is similar to that before oxidation, for all other samples the porosity decreases after oxidation, indicating a pore closure phenomenon which takes place during oxidation.

### C-Analysis
C-analysis allows to calculate the amount of SiC in the samples before and after oxidation during 500h (figure 4).
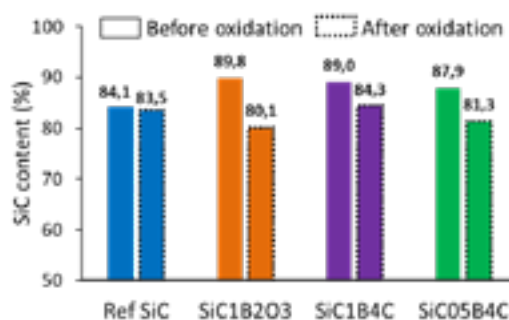


*Fig. 4: SiC contents before and after oxidation:* **Ref SiC**, **SiC1B2O3**, **SiC1B4C**, **SiC05B4C**

First, it is important to notice that the initial SiC content (before oxidation) is higher for samples containing additives than for the Ref SiC. During sample preparation, the firing at 1400 °C was performed under air, and some small part of the SiC easily accessible could have been oxidized during this process. The additives ($B_2O_3$ and $B_4C$) already have a protective effect on SiC during the first heating of samples (the firing step) and play a role in decreasing SiC oxidation during firing, leading to higher SiC content after firing.

It appears that for all samples, the SiC amount decreases after oxidation test, indicating an oxidation of SiC to $SiO_2$.

## DISCUSSION
First, as mentioned before, looking at the oxidation results (figure 2) of reference samples, it appears that the Ref SiC oxidizes in a

593

linear way whereas the oxidation profile of SI3N SiC sample is divided in two stages with a higher oxidation rate during the first 100 h and then a lower oxidation rate indicated by the slope of the curve in the time range 200 h – 500 h.

Also as mentioned in the result section, for Ref SiC sample, the open porosity after oxidation is similar to that before oxidation, with only a slight variation: 7% loss of porosity. For Si3N SiC sample, the open porosity after oxidation is very low compared to that before oxidation with a 51 % loss of porosity (figure 3). This could be explained by the preferential oxidation of $Si_3N_4$ phase (bonding phase, located in the matrix) to $Si_2ON_2$, leading to pore closure during the first hours of oxidation [13, 14]. This pore closure limits the gas access in the sample, thus limiting the SiC coarse grain oxidation beyond 100 h of test leading to a low oxidation rate, $0.6.10^{-3}$ wt%/h that is the smallest rate observed in this study (table 2).

The SiC1B2O3 sample presents a similar oxidation profile as the Si3N SiC sample, with two stages. The open porosity is also lower after oxidation test than before. These results indicate a similar oxidation behaviour as that of nitride bonded material, with a pore closure during test preventing from gas penetration and thus a further SiC coarse grain oxidation. However, the oxidation mechanism of SiC1B2O3 can differ in the first 100 h from Si3N SiC. Indeed, the $B_2O_3$ present in the composition could react with silica coming from the SiC oxidation [15] during the first 100 h of the test to form a borosilicate viscous phase filling then the pores. With the enrichment in silica of the borosilicate phase while the SiC oxidizes in $SiO_2$, this phase becomes more and more viscous [16, 17]. At the end, the viscous glassy phase may slow down the oxidation rate with the porosity closure and the decrease in oxygen diffusion in the material microstructure as the viscosity of the borosilicate phase increases [18].

For SiC05B4C and SiC1B4C, the oxidation is still divided in two stages, with a higher oxidation rate in the first stage. Nevertheless, the oxidation rate of the first stage is less important than for previous samples (Si3N SiC and SiC1B2O3). The B4C is an anti-oxidizing additive, meaning that it first oxidizes to $B_2O_3$ and thus partially prevents the SiC from oxidation. Then, as for the SiC1B2O3, the $B_2O_3$ that is formed can oxidize the SiC to $SiO_2$ and produce the viscous borosilicate phase leading to pore closure as the viscous phase filled them. The borosilicate phase is enriched in $SiO_2$ as the SiC oxidizes, increasing the viscosity. As before, the closure of the porosity and the increase in the borosilicate phase viscosity slows down the penetration of gases and leads to a decrease in the oxidation rate during the second phase. It appears that the lower B4C content (0.5 % instead of 1%, respectively for samples SiC05B4C and SiC1B4C) leads to the same mechanisms but less marked with a higher mass gain slope in the second stage of oxidation, related to a higher porosity after 500 h under oxidation. This may be related to the lower amount of glassy borosilicate phase formed because of the lower amount of B4C. The SiC05B4C sample is therefore less resistant to the oxidation than the SiC1B4C one.

The SiC oxidized calculated from C-analysis (in %, related to initial SiC content) and the total mass gain are presented in table 3.

*Tab. 3: % of oxidized SiC related to initial SiC (before oxidation) and mass gain after 500h under oxidation*

| Sample | SiC oxidation (%) | Total mass gain (%) |
|---|---|---|
| Ref SiC | 0.7 | 0.8 |
| SiC1B2O3 | 10.8 | 2.2 |
| SiC1B4C | 5.2 | 1.1 |
| SiC05B4C | 7.5 | 1.6 |

When the samples are ranked from least to most oxidized regarding SiC loss in C-analysis: Ref SiC > SiC1B4C > SiC05B4C > SiCB2O3. It corresponds to the total mass gain after oxidation (figure 2 and table 3). By comparing this result with the oxidation curves, it is clear that the C-analysis does not take into account the

oxidation rate occurring during the second stage (figure 2), but only reflects the oxidized SiC after the whole test (500h under oxidation). The effective oxidation resistance should be better described only by the mass gain in second stage of oxidation and an extension of the trial would lead to an inversion of the trends observed for C-analysis and directly linked to the oxidation rates (mass gain in second stage of oxidation).

The SiC1B2O3 sample presents a high amount of initial SiC but also the highest loss of SiC (SiC oxidation, table 3), in accordance with the high mass gain during the first stage of oxidation (figure 2). The SiC05B4C and SiC1B4C also present a higher initial SiC content compared to Ref SiC, and a higher SiC loss (table 3) that is also correlated to the first stage of oxidation. Their SiC oxidation is much lower than for SiC1B2O3 sample and can be due to the protection and oxidation mechanism previously described: first oxidation of B4C to $B_2O_3$ preventing an early SiC oxidation then SiC oxidation by $B_2O_3$ progressively formed and closing the porosity by the viscous glassy borosilicate phase thus decreasing oxidation rate. In the end, the oxidation resistance can be estimated here from the oxidation rates obtained from mass gain (table 2). The sample containing 1 % $B_2O_3$ seems to have a higher oxidation rate than the Ref SiC, attributed to the additional oxidation of SiC due to the presence of $B_2O_3$. On the opposite, the B4C seems to have a positive impact on SiC oxidation, and the sample containing 1% B4C presents an oxidation rate very close to that of Si3N SiC sample (respectively mass gain slopes of 0.7 and 0.6).

**CONCLUSIONS**

This work sought to improve the oxidation resistance of oxide bonded SiC materials through the incorporation, in the composition, of some additives such as boron compounds.

The whole results showed that different mechanisms are implicated in SiC oxidation in the presence of different boron additives. This study showed the presence of a two stages mechanism for SiC oxidation in the presence of boron additives as for nitride bonded SiC material. The first stage concerns the formation of a glassy borosilicate phase, that leads to close the porosity, decreasing the oxidation rate in stage two.

Based on the slopes of second oxidation stage and on the low SiC oxidation, the sample SiC1B4C containing 1 % B4C seems to present the most interesting tendencies. This additive helps closing the porosity through the progressive formation of the glassy borosilicate phase during the first hours of oxidation and also the B4C oxidation preventing of an early SiC oxidation, leading to a high decrease in the oxidation rate and thus protecting the SiC from further oxidation. The oxidation rate measured with this additive is close to that for Silicon nitride bonded materials. Trials with content higher than 1 wt% of B4C should be performed to determine an optimum adding value of B4C as anti-oxidizing agent for oxide bonded SiC refractory materials used for lining of waste incinerator furnaces.

**REFERENCES**

[1] K. H. Thoemen: "Contribution to the Control of Corrosion Problems on Incinerators with Water-wall Steam Generators", Proceedings of the 1972 National Incinerator Conference, New York, NY, June 1972, p. 310-18 (1972).

[2] H. H. Krause: "High temperature corrosion problems in waste incineration systems", Journal of Materials for Energy Systems, Vol.7, 4, p. 322-332 (1986).

[3] P. Prigent, M.L. Bouchetou, J. Poirier, J.M. Brossard: "Study of the corrosion mechanism of SiC refractory lining in

594

municipal waste to energy facilities", Proc Unitecr 2009, Salvador Brazil, p. 630-634 (2009).

[4] P. Prigent, M.L. Bouchetou, J. Poirier, E. De Bilbao, E. Blond: "Corrosion of oxide bonded silicon carbide refractories by molten salts in solid waste-to-energy facilities", Ceramics International, Elsevier, p.5643-5649 (2012).

[5] J. Poirier, P. Prigent, M. L. Bouchetou, E De Bilbao, E Blond, JM Brossard: "Mechanisms of SiC Refractory High Temperature Corrosion by Molten Salts (Na,K,Ca,Cl,S) in Waste to Energy Facilities", Advances in Science and Technology 92, p. 272-281 (2014).

[6] Munro R. G., Dapkunas S. J.: "Corrosion characteristics of silicon carbide and silicon nitride", Journal of Research - National Institute of Standards & Technology, 98, p.607-631 (1993).

[7] Abolhassan Najafi, F. Golestani-Fard, H.R. Rezaie, Saviz Parsa Saeb: "Sol-Gel synthesis and characterization of SiC–B4C nano powder", Ceramics International, 47, Issue 5, p. 6376-6387 (2021).

[8] Datta M. S., Bandyopadhyay A. K., Chaudhuri B.: "Sintering of nano crystalline α silicon carbide by doping with boron carbide", Bulletin of Materials Science, 25, p. 181-189 (2002).

[9] Liu M., Yang Y., Wei Y., Li Y., Zhang H., Liu X., Huang Z.: "Preparation of dense and high-purity SiC Ceramics by pressureless solid-state sintering", Ceramics international, 45, p.19771-19776 (2019).

[10] Liu J., Tian C., Xiao H., Guo W., Gao P., Liang J.: "Effect of B4C on co-sintering of SiC ceramic membrane", ceramics international, 45, p. 3921-3929 (2019).

[11] Clegg, William J.: "Role of Carbon in the Sintering of Boron-Doped Silicon Carbide", Journal of the American Ceramic Society, 83, p. 1039-1043 (2004).

[12] Zhuangjun Fan, Yongzhong Song, Jiangang Li, Lang Liu, Jinren Song, Junling Chen, Gengtai Zhai, Jingli Shi: "Oxidation behavior of fine-grained SiC–B4C/C composites up to 1400 °C", Carbon, 41, p.429-436 (2003)

[13] S. Abdelouhab, P. Pilate: "Relationship Between SiC Refractory Materials Characteristics Used in Municipal Waste Incinerators and Oxidation Behavior at High Temperature, Investigation of Material Improvement", Proceedings of ICR International Colloquium on Refratories, September 2019, Aachen Germany, 135-139.

[14] Pickrell Gary R., Sun Tawei, Brown Jesse J.: "High temperature alkali corrosion of SiC and Si3N4", Fuel Processing Technology, 44, p. 213-236 (1995).

[15] Maître A., Put A. Vande, Laval J. P., Valette S., Trolliard G.: "Role of boron on the Spark Plasma Sintering of an α-SiC powder", Journal of the European Ceramic Society, 28, p. 1881-1891 (2008).

[16] D. Aboutaleb, J. Douglad, B. Safi, O Jbara, A. Iratni: "Phase Separation and Chemical Durability in the $SiO_2$-$B_2O_3$-$Na_2O$ (SBN) Glass System", Asian Journal of Chemistry, 24 (2) p. 473-480 (2012).

[17] Ren Mengguo, Lu Xiaonan, Deng Lu, Kuo Po-Hsuen, Du Jincheng: " $B_2O_3$/$SiO_2$ substitution effect on structure and properties of $Na_2O$–$CaO$–$SrO$–$P_2O_5$–$SiO_2$ bioactive glasses from molecular dynamics simulations", Physical Chemistry Chemical Physics, 20, p. 14090-14104 (2018).

[18] Qiankun Xu, Qingliang Shan, Jianbao Hu, Yewei Wang, Yu Wang, Qian Ma, Changrong Chen, Yuqian Zhou, Anze Shui: " The oxidation resistance mechanism of SiC-B4C-xAl2O3 ceramics at 1400 °C in air atmosphere", Journal oft he European Ceramic Society, 42, p. 2618-2629 (2022).

595

# DEVELOPMENT OF HIGH CHROME OXIDE GASIFIER REFRACTORIES – ONE STEP AHEAD TOWARDS CARBON NEUTRALITY

J. P. Nayak, B. Ghosh, R. Adhikary, H. Nagata, S. Sengupta, P. B. Panda

TRL Krosaki Refractories Ltd., Jharsuguda, Odisha, India

## ABSTRACT

Shaped refractory making and its uses, both are high energy-intensive one. Manufacturing of refractory products involve a large section of raw materials; most of the refractory raw materials require a large capacity of energy for their production, as it is not possible to use as such and needed at least crushing and screening, which often requires thermal processing. Based on an application; different type of refractory products manufactured by refractory makers, which are required to process at different temperature ranges by using fossil fuel mainly. As a result, refractory industry also contributing environmental burden up to some extent apart from other manufacturing industries, although percentage is very less. Now, the refractory industries are increasingly attentive and motivated to promote the functionalities which is much needed to support carbon neutrality program. In this context, present work describes the development of high chrome oxide ($Cr_2O_3$) gasifier refractory product, $Cr_2O_3$ content is more than 85.0%, which has been fired at lower temperature i.e., 1450 to 1550 ºC compared to chrome based shaped refractory products generally sintered at high temperature i.e., >1650 ºC. By the developmental process; manufacturing process and firing temperature has been optimized. Chemical analysis, physical properties, and thermal shock resistance of the product has been evaluated. Slag corrosion resistance of the developed product has been also carried out by using slag of gasifier run with feed stock of pet coke + coal.

Key words: Refractory, Chrome, gasifier, environment, carbon neutrality, corrosion

## INTRODUCTION

Coal gasification is a process of producing syngas - a mixture of CO, $CO_2$, $H_2$ and water vapour from coal and water in presence of air/oxygen [1].

$$3C \text{ (Coal)} + O_2 + H_2O \longrightarrow H_2 + 3CO + H_2O \longrightarrow CO_2 + H_2$$
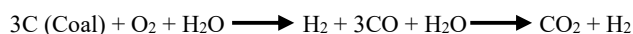
While coal gasification itself can be an efficient way to produce energy, it does have implications for carbon footprint. It also helps to reduce carbon footprint when combined with carbon capture and storage technologies. So, the need to reduce greenhouse gases emision to the environment become more intense for sustainable energy solutions for all kind of manufacturing industries. To achieve carbon neutrality $CO_2$ must be reduced as much as possible and for industries those are dealing with very high temperature processing like refractory inducstries, their role is very significant here. Gasifications, an advanced thermomechanical conversion process, offers the potential to transform carbonaceous feedstocks like coal, tar, petcoke into valuable products such as syngas, hydrogen and biofuels. $CO_2$ is generated during gasification as minority process by-product [2]. Gasifiers with high-performance refractories can operate at higher temperatures, which improves energy efficiency. Higher temperatures enable more complete carbon conversion and enhance the overall process effuciency, reducing carbon footprint per unit of energy generated. Gasifiers suffer a lot of problems which limit their wide use due to degradation of working lining refractory of the inner walls of gasifier. Lining loss is due to the severe gasification environment involving high temperature, high pressure, reducing environment, and both physical and chemical attack by impurities in the carbon feedstock [2]. Due to operational severity of gasifiers, high chrome oxide refractory has been chosen because of its excellent intrinsic properties like corrosion resistance, thermal shock resistance, and thermomechanical strength.

This article mainly focuses on the develpment of high chrome oxide gasifier refractory body sintered at low temperature compared to in general sintering temperature of $Cr_2O_3$-Corundum shaped refractory, which is an innovative approcah to address the challenges associated with gasification technology and emission of greenhouse gases. Developed product plays a crucial role in supporting sustainable and environmentally friendly industrial processes as well as towards carbon neutrality aspect.

## EXPERIMENTAL STUDY

This study mainly discusses the development of low temperature fired high chrome oxide bricks for coal/coke gassifier reactor application. Developed product is resulting similar or little bit better properties compared to bricks fired at high temperature (> 1700 ºC). As a result energy consumtion in low temperature fired bricks is less, thus emision of greenhouse gases are also less to the environment.

The main raw materials used to develop the high chrome oxide bricks were synthetic chrome corrundum grains and chrome oxide powder along with special additive and binders. A series of recipes i.e. trial 1 (T-1), trial 2 (T-2), and trial 3 (T-3) were formulated, as tabulated in Table 1 using said raw materials in varying proportions to manufacture the bricks.

Tab. 1: Batch composition of bricks.

| Raw Materials (wt.%) | T-1 | T-2 | T-3 |
|---|---|---|---|
| Synthetic Chrome Corrundum (1) | 25 | 30 | 35 |
| Synthetic Chrome Corrundum (2) | 60 | 55 | 50 |
| Chrome Oxide | 15 | 15 | 15 |
| Additive | 1.7 | 1.7 | 1.7 |
| Binders | 2 | 2 | 2 |

The mixes were made in high intensity mixer machine and bricks were given into perticular shape by using high capacity hydraulic press. After drying at 110°C for 24 hours, dried bricks were fired in tunnel kiln at two different temperature i.e., >1700°C with 5 hours soaking i.e., High Temperaure Fired (HTF), and >1450°C with 6 hours soaking i.e., Low Temperature Fired (LTF).

## CHARACTERIZATION OF PRODUCTS

Fired bricks were characterised to evaluate the apparent porosity (AP), bulk density (BD), cold crushing strength (CCS), refractoriness under load ($t_a$) according to DIN standard. Hot modulus of rupture (HMoR), and permanent linear change (PLC) of developed bricks also tested at 1400 °C (soaking 30 minutes) and 1500 °C (soaking 180 minutes) respectively. Reversible thermal expansion (RTE) behaviour of brick samples also checked at 1500 °C with Dilatometer. Thermal shock resistance (TSR) of brick samples were estimated by adopting DIN method (at 950°C by water quenching). Slag Corrosion test has been carried out by using rotary drum slag corrosion test method at 1550°C with 1 hour soaking. Coal/coke gassifier slag sample was used during slag corrosion test. Corrosion test samples were further analysed by using X-ray diffraction (XRD) technique to know the phases developed in the interface area of reafractory body after corrosion test, and to understand the reaction mechanism between slag and refractory mass; microstructural study and elemental analysis were being performed by using scanning electron microscopy (SEM) and energy dispersive X-ray analysis (EDAX).

## RESULTS AND DISCUSSION

Chemical and physical properties analysis of three trials have been evaluated and summarized in Table 2 and 3 respectively.

Tab. 2: Chemical analysis of the fired brick samples.

| Constituents (wt.%) | T-1 | | T-2 | | T-3 | |
|---|---|---|---|---|---|---|
| | .>1700°C | .>1450°C | .>1700°C | .>1450°C | .>1700°C | .>1450°C |
| $Cr_2O_3$ | 88.65 | 88.53 | 89.39 | 89.27 | 89.38 | 89.28 |
| $Al_2O_3$ | 6.21 | 6.23 | 6.33 | 6.34 | 6.33 | 6.35 |
| $SiO_2$ | 0.39 | 0.40 | 0.27 | 0.28 | 0.27 | 0.27 |
| $Fe_2O_3$ | 0.32 | 0.32 | 0.33 | 0.35 | 0.35 | 0.35 |
| $TiO_2$ | 1.32 | 1.37 | 1.31 | 1.36 | 1.29 | 1.34 |
| CaO | 0.10 | 0.10 | 0.11 | 0.12 | 0.10 | 0.10 |
| MgO | 2.01 | 2.01 | 2.02 | 2.01 | 2.01 | 2.0 |
| $Na_2O$ | 0.11 | 0.12 | 0.06 | 0.07 | 0.06 | 0.07 |
| $K_2O$ | 0.01 | 0.01 | 0.01 | 0.01 | 0.01 | 0.01 |

Tab. 3: Physical properties analysis of the fired brick samples.

| Properties | T-1 | | T-2 | | T-3 | |
|---|---|---|---|---|---|---|
| | >1700°C | >1450°C | >1700°C | >1450°C | >1700°C | >1450°C |
| AP (%) | 18.1 | 17.7 | 18.0 | 17.3 | 16.3 | 15.7 |
| | 17.9 | 17.8 | 17.8 | 17.7 | 16.7 | 16.0 |
| BD (g/cc) | 4.01 | 4.03 | 4.02 | 4.05 | 4.04 | 4.08 |
| | 4.02 | 4.04 | 4.01 | 4.06 | 4.05 | 4.10 |
| CCS (Mpa) | 647 | 687 | 655 | 707 | 723 | 779 |
| | 635 | 703 | 678 | 717 | 737 | 763 |

From the chemical analysis, it is concluded that all samples are resulting similar chemical purity, but physical properties of T-3 bricks are better than others. Thus, further high temperature studies were performed by considering T-3 brick samples only, and test results are tabulated in Table 4.

Tab. 4: High temperature properties of T-3 brick samples.

| Properties | Unit | T-3 | |
|---|---|---|---|
| | | .>1700°C | .>1450°C |
| RUL($t_a$) | °C | 1740+ | 1740+ |
| HMOR at 1400°C | MPa | 3.1, 3.2 | 3.1, 3.3 |
| PLC at 1500°C/3 hrs. | % | +0.81 | +0.79 |
| RTE at 1000°C | % | 1.23 | 1.35 |

From the test results mentioned in Table 2, 3 and 4, it is concluded that both temperature fired bricks of T-3 are giving better results as compared to other two trials. It may be due to selection of materials with proper granulometry; T-3 gives significant improved results compared to others. Phase analysis of T-3 brick samples has been performed to understand the reason being of attaining the improved properties. Fig.1 (a) and (b) depicts the XRD pattern of high chrome bricks fired at high and low temperature respectively. Both HTF and LTF bricks are resulting similar type of XRD pattern, and dominant phase is only Eskolite.

Fig. 1: XRD Pattern of high chrome brick (a) HTF, (b) LTF.
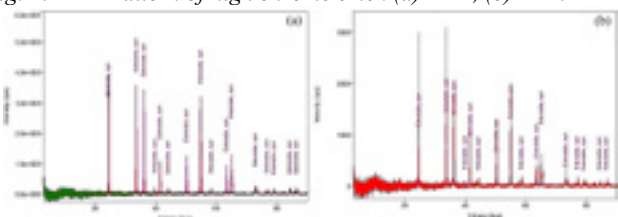


Due to the severe and harsh application conditions of coal gasifier reactor, alumina chrome refractory has been choosen because of its excellent slag corrosion resistance and thermal shock resistance. Rotary drum slag corrosion test method was adopted to check the corrosion resistance of high chrome bricks. In this study, a hexagon was made with T-3 brick samples. Six samples were considered, where three from LTF (Sample no. 1, 2, 3) and rest three samples (Sample no. 4, 5, 6) were from HTF bricks. Slag was collected from a reputed coal gasifier industry for slag corrosion test and analysis of slag is summarized in Table 5.

Tab. 5: Chemical composition of gasifier slag.

| Components | Wt. (%) |
|---|---|
| $Al_2O_3$ | 12.79 |
| $SiO_2$ | 17.02 |
| $Fe_2O_3$ | 6.53 |
| CaO | 10.89 |
| MgO | 0.79 |
| $Na_2O + K_2O$ | 0.90 |
| NiO | 3.08 |
| $V_2O_5$ | 38.75 |
| $SO_3$ | 6.15 |

Slag corrosion study detail has been described sequentitally in Fig.2. Hexagon builted with the fired bricks as per schematic design and lined in rotary drum furnace, after then corrosion test was conducted. After completion of test, hexagon structure was dismentled, and individual brick sample pieces were sliced down to estimate the slag corrosion percentage.

*Fig. 2: Rotary slag corrosion test: from making of hexagon to getting slicing part of individual tested brick sample specimen.*
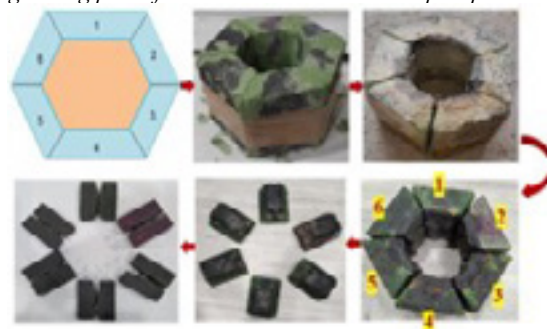


Slag corrosion test indicates that low temperature fired brick of T-3 is resulting better slag corrosion resistance due to formation of thicker interfacial area/band in between refractory body and attacking slag. Interfacial area is mainly dominated by the presence of vanadium-chromium (V-Cr) bearing spinel along with nickel, as confirmed by XRD analysis in Fig. 3. Formation of V-Cr spinel is more in LTF brick which enhances slag penetration resistance and limiting the ingress of corrosive slag components to the refractory matrix. Whereas in HTF high chrome brick interface band area as well as spinel formation is less compared to LTF high chrome brick, as a result penetration of slag is more. Slag corrosion test result is shown in Table-6.

Tab. 6: Slag corrosion test results.

| Sample ID | Sample No | % of Slag Corrosion (Avg.) |
|---|---|---|
| Low temperature fired high chrome brick | 1 | 5.41 |
| | 2 | 5.49 |
| | 3 | 5.43 |
| High temperature fired high chrome brick | 4 | 6.49 |
| | 5 | 6.51 |
| | 6 | 6.44 |

Porosity is a critical factor influencing both spalling and corrosion resistance. It is seen that LTF bricks are resulting little bit lower

porosity compared to HTF bricks. A low-porosity refractory material provides fewer pathways for the ingress of corrosive substances, such as gases or liquids, thereby improving corrosion resistance. On the other hand the reduced porosity minimizes the presence of voids or trapped pockets of gas, which can lead to spalling under thermal cycling conditions.

Fig. 3: XRD Pattern of interface portion of LTF high chrome brick sample after slag corrosion test.



Typical failure mechanisms found in gasifiers having a gas or liquid feedstock include thermal expansion or irreversible creep deformation, which occurs during rapid thermal cycling and leads to surface spalling or joint failure [3]. To estimate the potential of spalling resistance of developed bricks, thermal shosk resistance (TSR) test has been performed, and condition of tested brick sample specimen has been shown in Fig. 4. Both the samples are showing similar type of characteristics but it has been observed that LTF brick sample is resulting better TSR property as compared to HTF brick although having porosity slightly lesser than HTF one. This has happened may be due to rigidityness of HTF brick sample compared to LTF brick, since HTF bricks have been fired at quite high temperature. As a result, HTF test samples spalled after 15th cycle whereas, complete spalling occured after 17th cycle for LTF brick sample. High-temperature firing can induce significant thermal stress within the refractory material due to the large difference in temperature between the firing process and subsequent operational conditions. This thermal stress can promote crack initiation, propagation, and subsequently spalling. In contrast, low temperature firing minimizes the thermal stress generated, leading to improved resistance against spalling.

Fig. 4: Status of HTF and LTF brick samples after TSR test.



On the other aspect, during high-temperature firing, certain refractory materials may undergo undesired phase transformations, which can negatively affect their performance. By employing a low-temperature firing process, the phase transformations can be controlled, resulting in a more stable crystal structure within the refractory body. This results in better bonding between the refractory grains, leading to increased resistance against spalling,. The finer microstructure also hinders the penetration of corrosive agents into the material, enhancing its corrosion resistance.

From the above studies, it is clearly evidensed that low temperature fired brick is better as compared to high temeperature fired brick in terms of thermal shock resistance as well as slag corrosion resistance.

Fig. 5 represents the micrograph of interface area of HTF brick sample after corrosion test. Three different zones called refractory body (R), slag portion area (S), and slag/refractory interaface area separated by yellow lines in between R and S are being clearly distinguished from Fig. 5 (a) and (b). Magnifying view of interface area is shown in Fig. 5 (c) and (d). It is found that refarctory aggregates are sevely attacked by slag materials, and micro cracks are also developed within the aggregates.

Fig. 5: Microstructure of HTF high chrome brick sample after corrosion test (a) interface portion of test sample, (b) magnifying view of interface area, (c) and (d) further magnifying view of interface area.



It is understood from the SEM images of HTF brick sample that slag materials have penetrated into the refractory mass through grain boundary channel, and/or through voids network as shown in Fig. 6. It may be assumed that such type of phenomena might be enhancing the structural spalling of refractory body during application.

Fig. 6: slag penetrated into the refractory mass through grain boundary channel of HTF brick.



Fig.7 depicts the interface area of LTF brick sample after corrosion test mainly. Wide band of interface area between refractory mass and slag is being found, which is widener than interface area of HTF brick sample. Said widened interface area is mostly populated with V-Cr spinel material along with nickel, as confirmed from XRD analysis (previously described) and EDAX analysis of interface area as shown in Fig.8.

Fig. 7: Magnifying view of interface area and grain boundary of LTF brick sample after corrosion test.

Fig. 8 depicts EDAX analysis of R, S, and slag/refractory interaface area, wherein, R consists of chrome (major) and alumina (minor) along with some amount of magnesia. The slag (S) mainly consists of different elements like vanadium, iron, nickel, magnesium, sodium, silicon etc.

*Fig. 8: EDAX analysis of R, S, and slag/refractory interface area.*
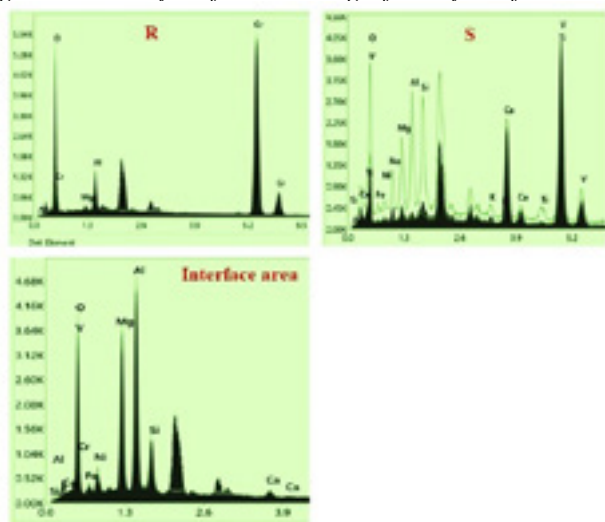


It can be corelated from slag corrosion test result with XRD, and SEM analysis that due to presence of more amount of V-Cr bearing spinel crystal in the interface area of LTF brick sample; better slag corrosion resistance resulted by LTF brick sample compared to HTF one. Spinel crystals are acting as protecting agent against slag components, as a result slag infiltration followed by penetration suppressed.

Summerarlly, it has been concluded that LTF high chrome containg brick is exhibiting not only good physical and chemical properties than HTF brick, but also resulting better TSR and slag corrosion rsistance property, which are much essential and awaited intrinsic property of gassifier refractory to achieve desired performance during application. By the process of low temperature firing of high chrome bricks, less fuel consumption is required, as a result less carbaneous gases emitted into atmosphere – which is directly accelerating carbon neutrality toward a sustainable future.

**CONCLUSIONS**
Developed brick exhibits exceptional slag corrosion resistance, and thermal shock resistance, which are desired to achieve better performance in gassifier reactor application. Development of low temperature fired high chrome refractories applicable for gasifier application is a significant step towards achieving carbon neutrality

and sustainable energy production. Firing at low temperature consumes lesser energy, which contributes towards lesser carbon emission into atmosphere.

**REFERENCES**
[1]  Bennet James P. The wear and corrosion of high chrome oxide linings used in air cooled slagging coal gasifiers. FE conference, 2008.
[2]  Nakano J. A Comprehensive Study of Modern Gasification Slags and Refractories Used in Gasifiers to Guide the Development of Novel/Improved Lining Materials. Refractories WORLDFORUM, 4 (2), 2012, p. 107-112.
[3]  Bennet James P, Kwong Kyei-Sing. Failure Mechanisms in High Chrome Oxide Gasifier Refractories. Metallurgical and Materials Transactions A 42, 2011, p. 888-904.

# PREMATURE REFRACTORY LINING INTEGRITY DETERIORATION IN A SYN-GAS REFORMING FURNACE

Manabendra Maity
Saudi Basic Industries Corporation (SABIC)
Kingdom of Saudi Arabia

## ABSTRACT

Reforming furnaces are the heart of synthesis gas (syn-gas) production processes in hydrogen, ammonia, and methanol plants. Revamping and modifications of these furnaces are ongoing strategies as part of the continuous improvement of aging plants. Revamping aged plants provide opportunities to enhance plant reliability, production capacity, energy, and operational efficiencies including complying with best practices and environmental regulations. Often, the conventional burners of furnaces are upgraded for higher firing capacity to add additional thermal energy and to improve combustion efficiencies and heat distributions inside the furnace. Also, in many cases, the quality of fuel and service condition of the furnace are changed significantly.

Refractory linings of furnaces are designed considering certain operating parameters and performances. Changes in operating conditions from the original design limitations including the replacement of the burner with a different flame size and/or increased heat release or any other significant modifications may negatively affect the performance and life of the existing refractory linings and structures. A premature refractory lining degradation occurred in a petrochemical plant within a short period of time after a major revamp that included the replacement of burners of a reforming furnace. Investigation revealed that the old refractory system was not compatible with the revamped operating conditions of the furnace. Therefore, the adequacy and limitations of the existing refractory systems should be carefully assessed in order to avoid any post-revamp reliability and performance uncertainties.

This paper discusses the potential refractory problems associated with furnace revamping. Mitigation measures are also discussed.

Keywords: Reformer, refractory, lining, burner, failure

## INTRODUCTION
### Reforming furnace
Main function of a reforming furnace is to convert a mixer hydrocarbon feedstock (e.g., natural gas) and steam into a mixture of $H_2$ and CO with the ratio varying depending on the desired final products [1-3]. This gas mixture of $H_2$ and CO is usually known as synthesis gas (syn-gas). Syn-gases have a wide range of applications including ammonia and methanol production, liquid fuel production in gas to liquid (GTL) plants, hydrogen production for the oil refining, iron ore reduction in steel productions, etc. Thus, reforming furnace is an integral part of many industries. The reforming reactions of hydrocarbon feedstocks usually take place in pressurized catalyst-filled alloy tubes disposed of vertically inside the furnace that operates at high temperatures in the range of 950°C to 1100°C. A reforming furnace could be used as a standalone syn-gas production unit or in combination with other reforming process units such as adiabatic pre-reforming, heat exchange reforming, auto thermal reforming, or secondary reforming. Reforming furnace is typically known as a hydrogen reformer when it is exclusively used for the production of hydrogen. It is known as a primary reformer in an ammonia or methanol plant when used in combination with a secondary reformer or auto-thermal reformer. Reforming furnace is one of the most complex and energy-intensive equipment to design, built, operate and maintain. Size of a reforming furnace can vary widely and plant capacity is typically in the range of 1000 to 5000 MT per day. A wide variety of proprietary reforming furnace designs and shapes are available. The main furnace is a large refractory-lined box (known as radiant chamber) containing hundreds of tubes disposed of vertically. A furnace is equipped with a large number of burners to supply the required heat for the endothermic steam reforming reaction of hydrocarbon feedstocks inside the tubes. The burners can be placed in different places- on the roof, on the floor, on levelled terraces on the walls, or on the walls. A rectangular shaped furnace with top-fired and side-fired types is most common. Fig. 1 shows a typical top-fired reformer. The heat from the hot flue gases leaving the radiant chamber is recovered in furnace convection box and flue-gas heat-recovery system to pre-heat the hydrocarbon feedstock, pre-heat combustion air, generate steam, and superheat steam and for other process requirements. The cooled flue gas after maximum possible heat recovery leaves the convection and waste heat recovery section and is vented to the atmosphere through the stack at 100-200°C. The reformed process syn-gas leaving from the catalyst tubes (at about 800°C to 900°C) is further processed in several downstream process units depending on the plant configuration and desired end products.
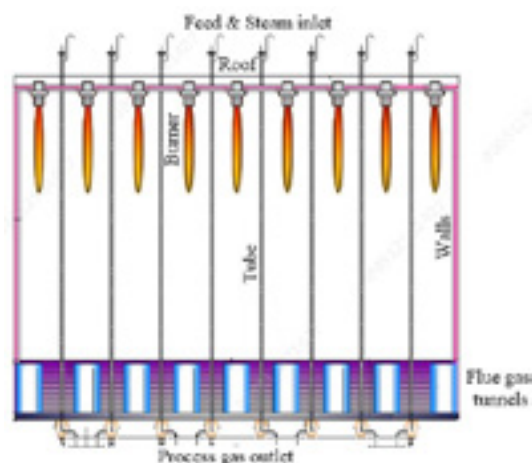


Fig. 1: Typical top-fired reforming furnace.

Syn-gas process plants including reforming furnaces usually operate continuously at the best possible efficiency for 3 to 4 years or more without a shutdown. Refractory lining design, material selection, installation and maintenance practices of a specific furnace are typically decided based on its design and operating parameters and performance objectives. It is expected that refractory linings and structures will continuously provide thermal protection and should not be the cause of an unplanned shutdown. Typical service life of radiant wall lining is around 10 to 15 years for such furnaces. However, life of the lining and its performance could vary significantly depending on the initial lining design, quality of installed refractories, installation workmanship, furnaces operation, and refractory repair & maintenance practices.

### Furnace revamp and upgradation
Many process plants are more than 25-30 years old. Such plants can't often continue yielding desired throughput, reliability, run-length, fuel efficiency and pollutant emission limits. Revamping or retrofitting the existing plant including the furnace is a good opportunity to make the plant economical and fit for continuing operation with improved reliability through the use of new

technologies. Therefore, during the long life-cycle of a process plant, often several changes are made in a plant in order to enhance the production capacity, reliability, risks, and environmental, health and safety (EHS) issues. However, changes made to equipment, process technology, operation variables, burner systems, quality and type of fuels could impact the integrity, reliability and life of existing refractory systems and associated structures. The consequences of such changes could be immediate or accelerated degradation that could occur over time resulting in reduced life, potential unplanned shutdown incidents and high maintenance costs. For example, furnace burner retrofitting from conventional to ultra-low NOx burners could cause problems associated with high heat-flux, flame instability and potential flame impingement on walls [4-5]. Relatively higher heat-flux, flame dimensions and possible impingement on refractory wall and tube could cause overheating and accelerated damage. Similarly, substituting alternate dirty fuels (e.g., waste gases and fuels with relatively high S, Na, and V content) in place of clean fuels could accelerate both high-temperature and low- temperature corrosion (e.g., acid gas dew point corrosion) and deterioration of refractory and metallic components.

## Management of change (MOC)

Regulatory codes and standards on process safety management (PSM) and asset integrity management require hydrocarbon and petrochemical plants to develop and implement an effective management of change (MOC) process in order to ensure that the potential risks associated with significant changes in an operating asset are carefully evaluated and controlled prior to implementation of the changes. While MOC requirements for implementing important changes and modifications are well integrated with plant integrity management programs, refractory integrity-related issues are often overlooked or misunderstood. Often significant changes are made assuming that such changes would not impact the existing refractory material and lining systems. However, premature refractory failures could take place directly or indirectly related to inadequate implementation of the MOC program. Incidents of accelerated refractory deterioration and unusual failures have been reported in the industries due to process and hardware changes in the furnaces without an effective MOC process to check the adequacy of existing refractories for the changed conditions. Following such incidents, the plants could require unplanned shutdowns for several days to restore the integrity of refractory and associated components.

In this article, a case history of an unusual post-revamp refractory deterioration of a reformer furnace of an ammonia plant is presented including remedial measures suggested for preventing recurrence of similar incidents.

## CASE STUDY
### Background information

Primary reformer of an ammonia plant was in service for more than 28 years. The Reformer is top-fired box type with process tubes arranged vertically in numbers of rows in the radiant section. Burners are fixed on the roof in multiple rows, with process tubes located between each burner row. The outermost rows of burners are located close to the side wall. Natural gas is used as fuel. Heat is radiated on the process tubes, both from the high-temperature refractory surfaces and directly from the flame. This is illustrated in Fig. 1 with the rows of process tubes identified as the vertical lines. The tunnels made of refractory bricks on the floor of radiant chamber collect hot gas and divert towards the convection section. The refractory linings of radiant box sidewalls consist of insulating fire brick and insulating board. Roof lining consists of ceramic fiber module and blanket. There were no incidents of major problems or failure of refractory lining except for usual aging. Overall, the original lining system performed well before revamping.

## Furnace revamp and burner retrofitting

Revamp and reliability improvement of the ammonia plant necessitated a change of the reformer furnace heat duty and burner retrofitting. The existing reformer was retained but burner types and heat duties were upgraded. All the burners were replaced and upgraded from conventional to relatively higher-capacity ultra-low NOx types. An MOC had been performed for tubes and associated structural supports to check their suitability and fitness for service for the changed heat duty and service conditions. However, a detailed adequacy check of the existing refractory for the changed service was overlooked. The refractory design and lining system of the reformer remained the same.

## Post-revamp refractory performance

Following the start-up of the plant, new burners were able to increase the heat duty for enhanced plant capacity, meet the reduced NOx emissions limit, and improve thermal energy efficiency. However, the furnace casing temperature was found to be relatively higher, particularly at the upper side walls. Higher casing temperatures and localized hotspot problems were mainly restricted to areas adjacent to burners. In-service visual inspection of the radiant box through peep-doors showed flames interactions and roll into adjacent refractory walls. Also, inspection through peep-doors indicated refractory deterioration locally around the burners. The hotspot problems were a major concern for the safe operation of the plant. Therefore, once the problems were noticed, some of the side row burners were switched off and the remaining side burners were operated with reduced firing load to restrict further deterioration of refractory and steel structures. Also, external steam cooling was provided locally on steel casing to control the hotspot temperature and continue plant operation safely till the next shutdown.

The nature of refractory damage was unusual as the same refractory system had performed satisfactorily for more than 28 years before the furnace revamp. Therefore, an investigation was performed to identify the possible causes of the problems. The findings and causes of deterioration are briefly discussed.
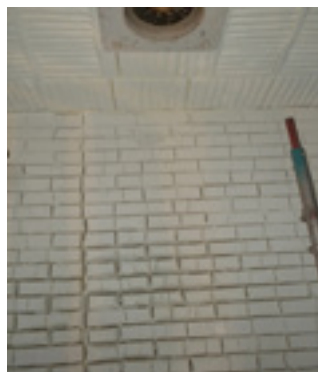


*Fig. 2: Deteriorated refractory wall.*



*Fig. 3: Deteriorated refractory around burners.*

An on-site inspection of the lining during shutdown revealed considerable deterioration of hot face insulating brick with severe shrinkage, cracks, and deformation. The deterioration was mainly restricted to the upper walls only and more severe around the burners as shown in Fig. 2. Bricks were found to be either displaced

or fallen locally and the back-up insulating board and brick hooks (anchors) were exposed, Fig.3. The lower brick walls and roof linings were found to be in satisfactory condition.

## DISCUSSION
**Burner retrofitting and potential impact on refractory integrity**
Burner locations, heat flux, flame shape (flame length and diameter), peak flame temperature, and flame stability could significantly impact the performance of refractory and tubes. Usually, radiant box outlet flue gas temperature is monitored to infer reformer internal temperature and operating severity. However, the radiant box outlet temperature usually does not reflect localized temperature variations within the box. Radiant box temperature could vary significantly at different regions depending on burner location, design, operation and heat release profiles. In the case of a top-fired reformer, the flue gas temperature is relatively higher at the upper half of the radiant box. As a result, the upper wall could be subjected to higher thermal exposure. Further, the outer row burners of a top-fired furnace are located very close to the side wall. Localized flame impingement on the refractory wall and/or higher heat flux could potentially raise the temperature of the wall above 1300$^0$C. In the original design, natural draft burners were used. The burner flames were compact and short which avoided damage to the refractory wall due to flame impingement. Therefore, no problem was experienced and the refractory performed satisfactorily. However, total heat release (heat flux) of burners and flame dimension has increased significantly after the burner revamp. Usually, a low NOx burner has a flame that is relatively longer and larger in cross-sectional area and volume than the flame in a standard conventional burner. Also, the flame of a low NOx burner is relatively less stable than a conventional burner. The risk of elongated flame is potential impingement and overheating of refractory wall. Further, operational upset tends to increase the flame length in low NOx burners, thereby increasing the chance of flame impingement [4-5] and flame rollover on the wall, Fig.4. Even though there is no flame impingement, the burners located adjacent to the walls, causes very high heat flux and overheating of wall locally.

Computational fluid dynamics (CFD) modelling and simulation allow performing detailed combustion analysis of burners to study the temperature profiles, flue gas flow pattern, flame impingement issues, heat flux distribution over radiant tubes and refractory [6]. The flame patterns and potential flame interactions were investigated through CFD analysis of the furnace radiant box to evaluate the performance before and after a furnace revamp. CFD analysis confirmed relatively higher heat flux on the refractory wall around the burner. The localized temperature of the wall is hotter than the surroundings by more than 100$^0$C. The overheating resulted in accelerated deterioration of refractory wall locally.
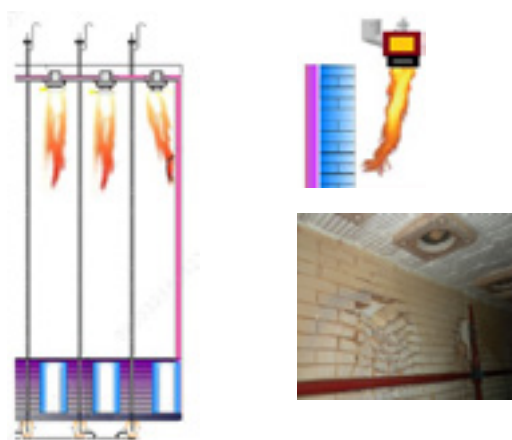


*Fig. 4: Flame impingement on wall and associated damage.*

## CORRECTIVE MEASURES
The nature of localized damage of lining suggests that the original refractory lining around the burner is not suitable for the changed operating conditions with the new burners. Therefore, the refractory design and anchor metallurgy was upgraded for all four walls. An optimum combination of a compatible superior grade insulating brick, insulating board and micro-porous material was used to enhance the performances without changing the total lining thickness, casing temperature and heat losses. Also, burner operations of outer rows, left and right sides of Fig. 1, were readjusted and fine-tuned to reduce firing load and improve flame stability. The problems were resolved after the successful implementation of the above changes.

## FINAL REMARKS
Furnace revamp and optimization efforts are often focused on capacity and efficiency improvement. However, improvement steps taken could result in subsequent issues that negatively impact the safety and reliability of critical components including the refractory system. Premature deterioration of refractory lining of a reforming furnace was investigated. Investigation revealed that the existing refractory lining around the burners was not suitable for the revamped operating conditions. The changes in burner design have resulted in relatively higher flame dimensions, heat flux and heat radiation. The refractory lining was subjected to high levels of heating from the intense radiation of high-capacity burners. Higher heat flux and potential flame impingement on the adjacent wall caused localized overheating and accelerated deterioration of refractory and components. Based on this investigation, modified refractory designs for the walls have been implemented to resolve the problems. The following suggestions are made in general:

- Furnace revamping and associated changes in operating temperature, thermal load and other critical parameters can have a negative effect on the life of the refractory linings and structures. Therefore, suitability and validation of fitness for service of the existing refractory system for revamped conditions should be analyzed carefully considering the changed service conditions.
- Refractory around the burners of fired furnaces can become hot locally due to the proximity of the flame. Major changes in burner design may require a refractory material upgrade and design modification of the entire lining and / or locally around the burners. A higher design margin for refractory materials and associated components around the burners should be considered.

## REFERENCES
[1] Gunardson: Industrial gases in petrochemical processing. Marcel Dekker, New York, 2010.
[2] Steynberg A, Dry M. Fischer-Tropsch Technology- Vol.152. Elsevier Science, 2004.
[3] Y.T. Shah: Chemical Energy from Natural and Synthetic Gas, 1st ed., CRC Press (2017).
[4] Gary R Martin, Barletta T. Avoiding unscheduled shutdowns. www.digitalrefining.com/article/1000286; PTQ Q2 2001; April 2021.
[5] Rex K Isaacs. Flame interaction and rollover solutions in ethylene cracking furnaces. www.digitalrefining.com/article/1000778; April 2013.
[6] Chilka A, Garg A. Use of computational fluid dynamic analysis to revamp fired heaters. Hydrocarbon Processing, May 2016, p. 67-73.

# REFRACTORY LINING CONDITION ASSESSMENT AND INTEGRITY MANAGEMENT OF HYDROCARBON PROCESS FURNACES AND REACTORS

Manabendra Maity
Saudi Basic Industries Corporation (SABIC)
Kingdom of Saudi Arabia

## ABSTRACT

Fired heaters, furnaces, reformers, reactors, incinerators, and boilers are amongst the most expensive and essential assets in the hydrocarbon process industries including oil-gas refineries, petrochemicals, fertilizers, and allied industries. Refractory linings and components play a significant role for managing the structural integrity, process safety, reliability and profitability of these high temperature assets. There are several factors over the life-cycle that affects the performances of refractory systems. The complex service conditions and operational upsets often make them vulnerable to risk of premature failure. Refractory performance left unchecked, could cause serious impact on reliability and run-length. The consequences of undetected refractory degradation or failure could be catastrophic.

Over the years, the qualities of refractory materials, design, installation and maintenance practices have been enhanced progressively with operational experiences and technological developments. Despite advances in refractory integrity management practices, premature failures still occur. Many of these problems could have been mitigated by following a systematic on-stream and off-line inspection and monitoring program in order to timely detecting the faults, predicting degradation of refractory and take corrective measures before loss of integrity or functional capability beyond the safety margins. Standards and codes for refractory inspection and maintenance are very few or non-existent. Further, each individual process furnace is unique to its operational environment and performance demand. Therefore, individual strategies should be formulated for a more proactive and tailored approach towards refractory integrity management backed by experience and driven by appropriate technologies and techniques.

This paper discusses the important aspects of refractory lining and structural inspection, performance monitoring, and the integrity management best practices that serves to increase reliability for the furnaces and vessels in hydrocarbon process industries.

## INTRODUCTION

### Process furnaces and reactors

Hydrocarbon and petrochemical industries typically involve processing of gaseous, liquid and solid feedstocks at elevated temperature and/or pressure within a broad range of fired heaters, furnaces, reformers, pressure vessel reactors, fluid catalytic and fixed bed reactors, carbon-black reactors, gasifiers, coke calciner, dryers, incinerators, oxidizers, boilers, hot gas transfer piping, and a host of other assets (hereinafter called furnaces). Operating conditions and process dynamics of furnaces typically range from hot-oxidizing atmospheres to processes that contain hot acidic & alkali gases or gases with entrained solid particles or extremely reducing conditions or highly corrosive and erosive slags, molten salts, and ashes. Typical operating temperatures in furnaces could be as low as 250°C to as high as 1950°C. Many of these assets are pressure vessels, operated at pressures as high as 8MPa or more. Safety and reliability is top priority for construction, operation and maintenance of these assets.

### Refractory linings, structures and components (RLSC)

Furnace casings and structures are usually made of carbon steel or alloy steel and designed based on several codes including ASME, API, etc. Objectives of the refractory linings are to protect the casing against thermal-mechanical-physical-chemical stresses and associated degradation. Also, the lining provides thermal insulation and reduces heat losses from the furnace. Refractory functions could be completely different between the furnaces and between the various zones of the same furnace. Therefore, a proper understanding of the purpose of the refractory is important for both the design and material selection, and also for subsequent maintenance and repair decisions. For example, fired heaters are designed to have substantial insulating capability in their linings, while others (e.g., Fluid catalytic cracking unit-FCCU) designed to withstand the extremely severe erosion caused by the flowing catalyst. Thus, several different refractory lining designs range from 25mm to 450mm thick or more are utilized depending on the operating severity and performance demands. Varieties of refractory materials are used like, brick, monolithics, ceramic fiber, insualting boards, etc. Also, there are many other internal structures and functional components made of refractory materials like catalyst support structures, domes, flue gas tunnels in syn-gas reformers, partition walls, bridge walls, ceramic ferrules, etc. Integrity and performance of these structures and components are equally important for a trouble free operation.

Process plants typically operate continuously for 2 to 5 years or more between planned maintenance shutdowns. Furnace outage frequency and refractory maintenance is accordingly combined with outage of upstream and downstream equipment. Life of refractory should not be a barrier in continuous plant operation. Therefore, refractory linings and structures must be fit for service and maintain their structural and functional performance over required levels to meet specific demands during its lifetime. This can be achieved both with adequate reliable design, construction and maintenance practices based on the concept of life-cycle management.

### Refractory failure and consequences

RLSC are susceptible to ageing and degradation by several mechanisms including overheating, melting, shrinkage, chemical wear, thinning due to corrosion, abrasion & erosion, thermal shock, cracking, thermo-mechanical stresses, creep, acid dew point corrosion, etc. Also, many of the refractory failures could be accelerated as a result of refractory design deficiencies, poor material quality, inadequate anchoring, installation quality deficiencies, operational upsets, and inadequate maintenance practices. Combined effect of many of these factors could give rise to susceptibility to an accelerated deterioration and early failure. Deteriorations of refractory lining can be continuous (e.g., corrosion or erosion) or discontinuous (e.g., cracking or spalling). Also, deterioration could differ by zones within the same furnace.

When a lining deteriorates or fails, the metallic containment structure could be exposed to service conditions and potentially overheated creating local hotspots. At high temperature, metallic structures are prone to several damage mechanisms including metallurgical degradation, thermal fatigue, creep, deformation, corrosion, sulfidation, metal dusting, hydrogen attack, reheat cracking, etc. In case of pressure vessels, the combined effect of high temperature and pressure can reduce the overall load carrying capacity due to lower yield strength of the region resulting from overheating. A ruptured vessel can be extremely dangerous, leading to potential loss of containment, leaks, fires, and even explosions. In general, once the lining integrity is lost, through-wall damage may not take very long time, Fig.1. Also, a deteriorated lining can reduce process thermal insulation efficiency and increase fuel costs and associated NOx emissions.

Further, furnaces in process plants are rarely built with a backup or stand-by equipment. Therefore, an unusual incident and unplanned shutdown in a plant can cost millions of dollars per day in lost production. For example, a FCC unit in oil refinery processes several hundred thousand barrels of crude oil a day. An unplanned FCC unit shutdown could be a very expensive incident and may lead to local fuel shortages. In case of an integrated complex chemical plant (e.g., refinery and petrochemical unit), the consequential impact of unplanned downtime could be serious on associated upstream or downstream operating units.

A permanent damage to the containment structure may take several weeks to repair and restore the integrity. In many cases, the refractory repair and replacement costs of a furnace could be insignificant compared to the cost of unscheduled stoppage. The magnitude of impact (in terms of safety, cost and time) of failure incident could vary significantly depending on whether the problem is identified and mitigated on time before major damage. Consequently, RLSC requires periodic inspection, assessment, maintenance and repair.



*Fig. 1: Refractory deterioration leading to shell overheating and puncture in a vessel.*

Many refractory failure and unplanned shutdown incidents have been reported in different process industries. Investigations revealed that such incidents could have been avoided, if there had been an effective refractory integrity management program including inspection maintenance for timely identification of the problems and implementation of corrective measures. This paper describes the importance of inspection and condition monitoring of RLSC in particular, in-service monitoring and typical approaches to assess refractory fitness for continued service.

**REFRACTORY INSPECTION AND ASSESSMENT**
Once a furnace is commissioned and placed into service, the RLSC integrity and performance should be monitored by periodic in-service inspection to detect any signs of emerging degradation and failure [1-3]. Also, RLSC should be inspected and repaired at each scheduled shutdown. Inspection and maintenance requirements for each specific equipment item should be included in a customized preventive and predictive maintenance program. Assessment can be made by condition-based and performance-based concept.

**In-service inspection and monitoring practices**
A variety of traditional and state-of-the-art non-destructive tests (NDT) and techniques could be utilized for assessment of condition of equipment and refractory integrity when the plant is in-service. Typical benefits of in-service assessment of refractory condition include but are not limited to
- Timely identification of anomalies, operational deviations and potential problems before they become major issues;
- Catastrophic lining failure, extent of damage to main containment structure, unplanned downtime and associated risks can be proactively prevented and / or reduced by effective mitigation measures and / or by a safe shutdown;
- Monitor ageing and degradation, damage progression, trending and decide fitness for continued service and assess remaining service life, reducing uncertainties;

- Plant run-length can be extended by interim mitigation measures(e.g., hot spot temperature control by steam sparging);
- Proactively schedule and prioritize maintenance rather than reacting to a catastrophic failure;
- Allow advanced shutdown scoping, planning, resourcing, and refractory spare management.

Common in-service inspection and monitoring practices include:
- Furnace casing temperature measurement and trending: Periodic monitoring of furnace casing temperatures could identify the onset of potential problems and provide an early indication of refractory damage and/ or any other abnormalities. Typical tools include: Infrared thermography (Fig.2), thermo-indicating paint (Fig.2), skin thermocouple (Fig.3).
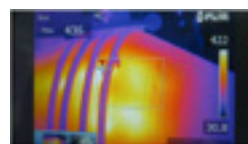


*Fig.2: Localized hotspot: Thermography view (left) and thermo-indicating paint discoloration (blue to white).*



*Fig.3: Skin thermocouple.*          *Fig. 4: Internal thermocouple.*
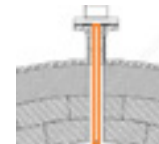
- Visual inspection of casing (paint burning, deformation, corrosion, cracks, and leaks caused due to overheating): Once abnormalities detected; affected area could be closely inspected and monitored by thermography or other techniques.
- Interior refractory wall-temperature measurements can be done through peepholes of fired heaters and furnaces (e.g., infrared spot pyrometer, infrared borescope and thermocouples, Fig.5).
- Infrared radiation pyrometer, contact thermocouples and IR emission sensors are commonly used tools to measure the internal temperature of thermal reactor of sulphur recovery unit (SRU), incinerators, etc. Also, thermocouples could be embedded at specified locations in the refractory wall to monitor temperature profile at any cross-section of the lining, Fig.4.
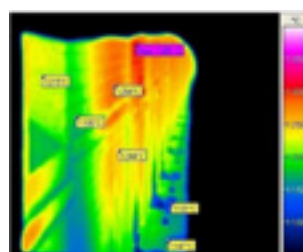


*Fig.5: Interior refractory wall-temperature measurements (wall overheated and caused accelerated deterioration of fiber lining).*

- Visual inspection of fired furnaces interior through peep-doors to check flame patterns, flame impingement on walls, broken, missing or displaced refractory (Fig.6 & 7).
- Ultrasonic thickness (UT) measurement of casing at suspected areas where erosion (Fig.8) or corrosion could occur due to refractory damage (e.g., FCC unit in oil refinery).
- Furnace operation and control: A well-established integrity operating windows (IOW) program would allow monitoring

604

key parameters (e.g., temperature, pressure, heating & cooling rate, burner malfunctioning, and operational upset) those have direct effect on refractory damage mechanisms. Periodic monitoring of major deviations of critical operating parameters could provide early sign of potential refractory problems so that the possible corrective measures could be initiated.



*Fig.6: Peep-doors.*



*Fig.7:-Internal view.*



*Fig. 8: FCCU Refractory deterioration leading to erosion of casing plate and through hole.*

- For water jacketed refractory lined vessels, water flow rate, deviations in water outlet temperature through jacket and steaming can be monitored to monitor lining integrity.

Also, a wide variety of advanced NDT inspection techniques, such as acoustic emission testing, impact-echo methods, ultrasonic, radiography, and microwave based techniques, optical and laser techniques are aviable. However, most of these methods have limitations and requires specific skills to perform and asses refractory integrity.

Frequency of in-service inspections is usually decided for each specific equipment based on the several factors including asset criticality, industry best practices, past experiences, severity of operation, existing or chronic problems or new problems, etc.

**Inspection & assessment during shutdown**
During a plant shutdown, a thorough internal inspection of refractory systems should be performed, especially at locations where thermography indicated elevated temperatures. This inspection helps in validating findings of in-service inspection. Inspection involves combination of activities including visual inspection, dimensional measurement, hammer test, photographing, sample testing, and engineering analyses. The integrity is assessed for general condition including existing or developing visible unusual damage, signs of any forms of deterioration, defects or deviations, crack, gap, shrinkage, leak, erosion, corrosion, thickness profile, discoloration, detachment or dislodgement, sagging, deformation, bowing, bulging, leaning structures, out of plane offsets, movement-out of plumb, instabilities that indicate a compromised structural integrity of the refractory systems, anchors, supports, etc. Where access is limited, borescopes can be used to perform the inspection.

**Refractory repair, replacement or alteration**
Fitness-for-service, repair or relining decision of RLSC should be made based on inspection findings, engineering assessment and analyses of useful data, and past experiences. It is important to address weaknesses with a scientific approach instead of "replace in-

kind" practices. Potential root causes, contributing factors and mode of failure of premature and chronic problems should be identified and ascertained in order to prevent reoccurrences. Interim and long term mitigation plan could be planned and implemented based on identified risks.

Inspection and maintenance records including all major findings and descriptions, operating history, basic data, field notes, pictures, sample test reports, failure investigation reports, location of the repairs, follow-up tasks, expected repair for next shutdown etc. should be maintained. These periodic inspection and maintenance records typically form the basis of scheduled maintenance programs.

**FINAL REMARKS**
An effective life-cycle and integrity management of furnaces and associated refractory systems is essential to ensure their fitness for service during the long campaign cycle. A typical refractory integrity management program involves several requirements including periodic in-service inspection, monitoring, surveillance, preventive and corrective maintenance. It is necessary to develop real-time diagnosis tools with capabilities of generating early warnings of hotspots or potential deteriorations. Each furnace and associated refractory system is unique with respect to its design, operational severity and performance requirements. Therefore, a customized refractory integrity monitoring program should be tailored to the specific equipment to suit the specific process condition and service. The plan should include what, how, where and when the inspection must be conducted and the what, how, where and when the appropriate action must be undertaken to address the concerns that may affect safety, reliability, and productivity.

**REFERENCES**
[1]   Pressure Vessel Inspection Code: In-service Inspection, Rating, Repair, and Alteration; API 510.
[2]   Piping Inspection Code: In-service Inspection, Rating, Repair, and Alteration of Piping Systems; API 570.
[3]   Inspection of Fired Boilers and Heaters, API recommended practice 573.

SHORT COMMUNICATIONS

# MICROPOROUS CALCIUM SILICATE HYDRATE–BASED THERMAL INSULATORS: A CRITICAL REVIEW

Rafael Salomão, Leandro Fernandes

São Carlos School of Engineering, Materials Engineering Department, University of São Paulo, São Carlos, Brazil

## ABSTRACT

Calcium silicate hydrate (CSH) is a synthetic microporous material used as a thermal insulator due to its low thermal conductivity, chemical resistance, and competitive costs. The production of porous CSH structures requires the hydrothermal dissolution of sources of CaO and $SiO_2$ and the precipitation of needle-like whiskers of Xonotlite ($Ca_6Si_6O_{17}(OH)_2$). The flocculated CSH paste is shaped by press-filtering and dried. Typical industrial applications of porous CSH involve thermal insulation between 300-1000ºC, as pre-shaped boards or pipe-covering in petrochemical units, non-ferrous metals casting operations, and steam-powered electric power plants. In civil construction, thin boards comprise fireproofing doors and roofs, and, in cold regions, reduce the loss of heat through external walls. This paper addresses a review of the technical and scientific literature on microporous CSH, focusing on the processing, microstructure, and properties of thermal insulation at high temperatures.

## ENERGY CONSUMPTION IN INDUSTRIAL PROCESSES

Three groups of human activities, namely transportation of people and goods, acclimatization and agriculture, and heating-based industrial processes are responsible for the greatest consumption of energy [1]. Together, they spent approximately 30,000-40,000 EJ of energy and generated over 500 million tons of $CO_2$ per year in the past decade (Fig. 1) [2]. One-third of this energy amount and approximately one-quarter of the $CO_2$ emissions originated in industrial operations that employ heat to produce or modify raw materials and goods (Fig. 2) [1]. Although most of their energy consumption is necessary, inevitably, all processes show a certain degree of unnecessary heat exchange and thermal losses. The use of thermal insulators based on microporous ceramics is a well-known strategy to improve thermal efficiency [3,4].
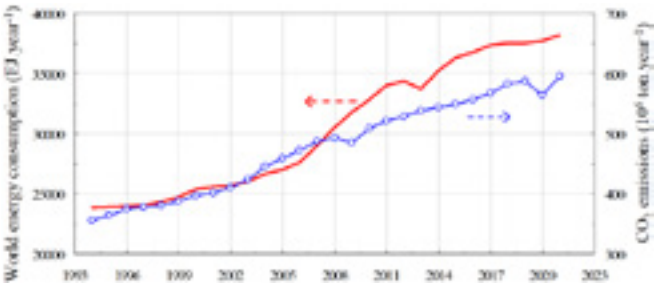

*Fig. 1: Word energy consumption and $CO_2$ emissions [2].*
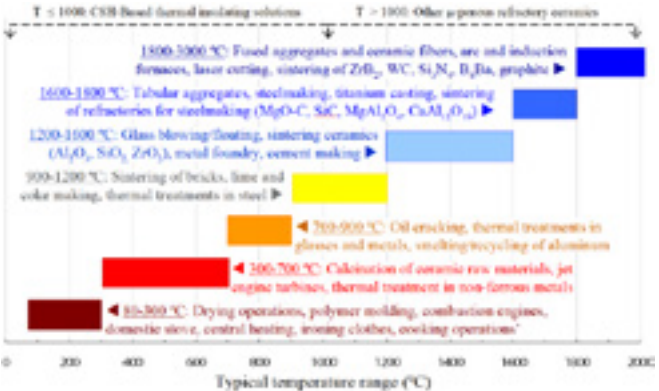

*Fig. 2: Temperature ranges found in industrial processes [3].*

Towards reductions in undesired heat exchange, microporous ceramics combine the high refractoriness of ceramic matrixes with a large fraction of thin pores (0.5-5 μm diameter) [5-7]. The lack of a permeable connection amongst them hinders the heat transfer by air convection. Moreover, they are very effective in scattering thermal waves (phonons and photons) whose mean free path and wavelength are similar to their average diameter and inter-pore distance [8,9]. Consequently, microporous ceramics such as calcium silicate hydrate (CSH) show very low thermal conductivity in a wide range of temperatures (Figs. 3-4), as well as enough strength to support compression loads [10].
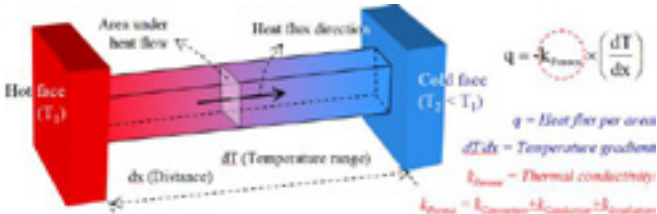

*Fig. 3: Thermal conductivity of porous materials [3,8,9].*
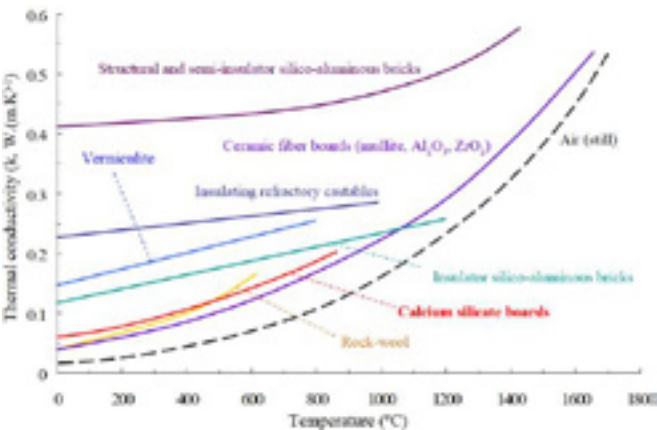

*Fig. 4: Thermal conductivity of microporous ceramics [3,4,10].*

## CALCIUM SILICATE HYDRATES INSULATORS (CSHI)

CSHI consists of structures of very low relative density (< 10 %) containing intermeshed 1-5 μm length by 50-100 nm diameter whiskers of xonotlite ($Ca_6Si_6O_{17}(OH)_2$) and tobermorite ($Ca_5Si_6O_{16}(OH)_2$) around 1-5 μm diameter pores (Fig. 5) [4,11,12].
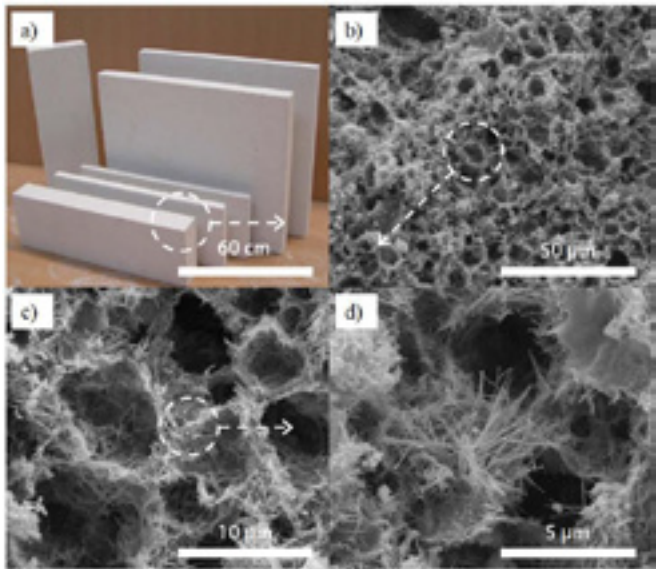

*Fig. 5: Microstructure of a CSH insulator (fracture surface) [4,10]*

The fabrication of CSHI structures begins with the production of an aqueous mixture of finely grounded raw materials and recycled shavings that will behave as templates for the growth of crystal nuclei [11]. Other elements such as foaming agents, inert filers, and fibrous reinforcement can be added at this step [13]. Intensive paddle mixers produce slurries containing 10-25 wt% of solids that are thickened by vacuum filtering and then pressed or extruded. Those shaping steps increase the solid content in the suspension to up to 70-80 wt% and define the geometry of the product. The humid compacts remain in autoclaves at 160-250ºC for up to 10 h. Under hydrothermal conditions, both hydroxylation and dissolution of CaO rapidly increase the suspensions' pH (Eq. 1), favoring the dissolution of silica into silicilic acid (Eq. 2) [15]. Because amorphous silica sources usually show higher chemical reactivity in comparison to crystalline ones, the replacement of micronized quartz with diatomaceous earth, for instance, reduces the total hydrothermal time-temperature schedule [15,16].

$$CaO + H_2O \rightarrow CaOH^+ + OH^- \rightarrow Ca + 2OH^- \qquad (1)$$
$$SiO_2 + OH^- \rightarrow (HSiO_3)^- \qquad (2)$$
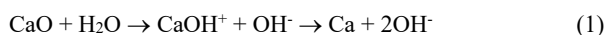
When the concentration of ions in the solution reaches the saturation point, calcium silicate hydrates are formed (Eq. 3) and begin to precipitate as weak agglomerates of elongated thin crystals.

$$xCa^{2+} + y(HSiO_3)^- + z(OH)^- \rightarrow xCaO.ySiO_2.zH_2O \qquad (3)$$
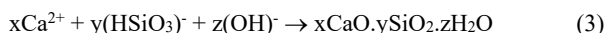
where $2 \leq x \leq 6$, $1 \leq y \leq 6$, and $1 \leq z \leq 5$. Such compounds that crystallize as needle-like whiskers belong to the Xonotlite and Tobermorite mineral family, whose ideal chemical formulas are $Ca_6Si_6O_{17}(OH)_2$ and $(Ca_5Si_6O_{16}(OH)_2)$, respectively [15]. Variations in the initial solid-water and CaO-SiO$_2$ ratios affect both formation and development of the CSH structure. As an example, higher contents of SiO$_2$ require longer autoclave times and produce longer and more rigid whiskers due to the lower mobility of the ions in the solution [12,15,17]. After cooling, the autoclaved structure is dried and trimmed in specific dimensions.

## APPLICATIONS OF CSHI
Different from other microporous ceramics that require thermal treatments at high temperatures to trigger pore formation [18], CSHI became fully functional soon after the evaporation of the remaining free-water. Moreover, exposures to temperatures above 350ºC lead to the dehydroxylation of CSI, even further increasing the total pore content of the structure [11,19]. Depending on the Xonotlite-Tobermorite ratio, the final composition can be a mixture of high refractoriness calcium silicates (Alite, $Ca_3SiO_5$, $T_M$=2150ºC; Belite, $Ca_2SiO_4$, $T_M$=2130ºC; $CaSiO_3$, Wollastonite, $T_M$=1544ºC) that withstand long-term working temperatures of up to 1100ºC [15]. Due to such excellent thermal insulation properties, mechanical strength, and chemical stability, CSHI finds a wide range of industrial applications. For instance, civil, marine, offshore, and automotive construction uses CSHI sheets for thermal insulation of walls, roofs, and floors, as well as for fire-resistant and soundproofing partitions [10,17]. Regarding high-temperature applications, glass fiber-reinforced CSH boards line the outer surface of urban waste incinerators (300-500ºC), primary aluminum smelters and runners (700-800ºC), pipes at petrochemical units (600-800ºC), and rotary cement kilns (700-1100ºC) [4-6,10].

## FUTURE DEVELOPMENTS
The major challenge for CSHI production is to reduce the time-temperatures employed in hydrothermal reactors [19]. The use of raw materials, which are more reactive due to their finer particles and higher specific surface area, would reduce both maximum temperature and pressure inside the vessels. On the other hand, the production of stable hetero-dispersions under such conditions would require the careful use of surfactant agents and powerful mixers.

CSHI are promising materials for reducing the carbon footprint of industrial processes not only due to their high energy-saving potential but also because of the possibility of being fully produced from biomass-based raw materials. Dried avian eggshell, for instance, contains approximately 92 wt% of calcium carbonate, which can be converted into CaO or Ca(OH)$_2$ at low calcination temperatures (720-800ºC) [20]. Similarly, the ashes of rice husks, currently employed as fuel for boilers furnaces, contain 98 wt% of amorphous SiO$_2$ [21]. Besides adjustments of processes and formulations to the intrinsic variability of natural products, the selective pick-up of such materials is another challenge.

## REFERENCES
[1] Andrews, R., Pearce, J.M. Environmental and economic assessment of a greenhouse waste heat exchange (2011) J. Cleaner Production, 19 (13), pp. 1446-1454.
[2] IEA (2020), World Energy Outlook 2020, IEA, Paris https://www.iea.org/reports/world-energy-outlook-2022.
[3] Salomão, R., Oliveira, K.S., Fernandes, L. Tiba, P., Prado, U.S. Porous refractory ceramics for high-temperature thermal insulation – Part 1: The Science behind energy saving (2021). Interceram 70 (3), pp. 38-45.
[4] Salomão, R., Oliveira, K.S., Fernandes, L. Tiba, P., Prado, U.S. Porous refractory ceramics for high-temperature thermal insulation – Part 2: The technology behind energy saving (2021). Interceram 71 (1), pp. 38-50.
[5] Ohji, T., Fukushima, M. Macro-porous ceramics: Processing and properties (2012) Int. Mat. Rev., 57 (2) 115-131.
[6] Hammel, E.C., Ighodaro, O.L.-R., Okoli, O.I. Processing and properties of advanced porous ceramics: An application based review (2014) Cer. Int., 40 (10) 15351-15370.
[7] Pelissari, P., Salvini, V.R., Vivaldini, D., Pandolfelli, V.C. Analysis of the pore size effect on the thermal conductivity of alumina foams for high temperature applications (2017) Ceram. Int. 43 (16) 13356-13363.
[8] Toberer, E.S., Baranowski, L.L., Dames, C. Advances in thermal conductivity (2012) Ann. Rev. Mat. Res., 42 179-209.
[9] Rathakrishnan E. Elements of Heat Transfer (2012) 1st Edition, Taylor & Francis Group, 45-91.
[10] Salomão, R., Fernandes, L. Tiba, P., Prado, U.S. Porous refractory ceramics for high-temperature thermal insulation – Part 3: Innovation in energy saving (2021). Interceram 71 (3), pp. 30-37.
[11] Zheng, Q., Wang, W. Calcium silicate based high efficiency thermal insulation (2000) Brit. Cer. Trans., 99 (4) 187-190.
[12] Li, M., Chen, Y. Relation of density and thermal conductivity of micro-porous calcium silicate insulation material (2005) J. Chin. Cer. Soc., 33 (11) 1414-1417.
[13] Koronthalyova, O., Matiasovsky, P. Thermal Conductivity of Fibre Reinforced Porous Calcium Silicate Hydrate-based Composites (2003) J. Build. Phys., 27 (1) 71-89.
[15] Nonat, A. The structure and stoichiometry of C-S-H (2004) Cem. Con. Res., 34 (9) 1521-1528.
[16] Schlegel, E., Hölscher, T., Schneider, H.-J., Aneziris, C.G. Alkali salt corrosion of calcium silicate thermal insulation materials (2015) Interceram 64 (4) 188-192.
[17] Ebert, H.-P., Hemberger, F. Intercomparison of thermal conductivity measurements on calcium silicate insulation material (2011) Int. J. Ther. Sci., 50 (10) 1838-1844.
[18] Costa, L.M.M., Sakihama, J., Salomão, R. Characterization of porous calcium hexaluminate ceramics produced from calcined alumina and microspheres of Vaterite (µ-CaCO$_3$) (2018) J. Eur. Ceram. Soc. 38 (15) 5208-5218.
[19] Whitaker, T.E., Myles, S., Gardner, I.P. Process for the manufacture of calcium silicate hydrate objects (1978) Denver, Colorado; U.S. Patent 4, 131,638, p. 1-8.
[20] Freire, M.N. Characterization of avian eggshell aiming its use in a ceramic wall tile paste (2006) Cerâmica 52 (324) p.38-47.
[21] Fernandes, L, Salomão, R. Characterization of synthetic amorphous silica (SAS) used in the ceramics industry (2014) Interceram 63(4) 220–224.

# 6   MODELLING AND DIGITALIZATION

# LIFE CYCLE ENVIRONMENTAL AND COST ASSESSMENT OF LADLE REFRACTORIES MANAGEMENT ACCORDING TO CIRCULAR ECONOMY CRITERIA

Ivan Muñoz, 2.-0 LCA consultants, Barcelona, Spain. E-mail: ivan.munoz@lca.net.com
Aintzane Soto, SIDENOR I+D, Basauri, Spain

**ABSTRACT**

Management of ladle refractories by a steel factory in Spain melting 1 million tonnes of steel scrap per year, is assessed by means of life cycle assessment (LCA) and life cycle costing (LCC). The case study addresses two situations, namely before and after implementing circular economy strategies. Such strategies include reduction of refractory waste generated in the ladles by optimising the ladle life, increasing amounts of worn bricks that can be reused in the production process or for other purposes, and increasing the amounts of waste refractories that can be recovered as secondary raw materials through recycling. The LCA and LCC studies consider the entire life cycle of refractory products and addressed a set of 14 environmental indicators, while the LCC is expressed in €. The results show both environmental and economic benefits by adopting the developed strategies. Life cycle costs are reduced by approximately 1 million €/year, while GHG emissions are reduced by 2,000 tonnes $CO_2$-eq/year.

## 1. BACKGROUND AND GOAL

Every year close to 20 million tonnes of spent refractory waste materials need to be managed globally, of which it is estimated that around 70% is landfilled and 30% recycled, the latter either as a secondary refractory raw material or in other applications such as roadbed aggregates [1]. However, management practices differ widely from country to country. In Spain, landfilling still constitutes a widespread practice [2], which constitutes the least preferred option from a waste hierarchy and sustainability perspective, due to the loss of potentially useful materials. In this paper we present the application of life cycle assessment (LCA) and life cycle costing (LCC) to the management of ladle refractories by a steel factory in Spain, melting 1 million tonnes of steel scrap per year.

## 2. The E-CO-ladleBrick PROJECT

This research was carried out as part of the EU RFCS-funded E-CO-LadleBrick project, aiming at implementing the environmental model of the 4R (reduce, reuse, remanufacture and recycle) to the management of refractories in the European steel sector. The developed strategies within the project, implemented in the above-mentioned steel factory in Spain, include:

- Reduction of refractory waste by optimising the ladle life
- Increasing amounts of worn bricks that can be reused internally at the factory
- Increasing waste recovery through off-site recycling
- Completely avoiding refractory waste landfilling

Table 1 below summarizes the ladle management achievements as a result of project E-CO-LadleBrick, when the situations before project (2018) and after project (2022) are compared.

Tab. 1: Key performance indicators for ladle management as a result of implementing E-CO-LadleBrick in a steel factory melting 1 million tonnes steel scrap per year.

| Reduction in refractory consumption | Additional waste refractories reused internally | Additional waste refractories valorised externally | Reduction in refractories sent to landfill |
|---|---|---|---|
| 237 tonne/year | 262 tonne/year | 228 tonne/year | 653 tonne/year |

## 3. Applying LCA and LCC

The LCA applied consequential inventory modelling principles (multifunctionality dealt with by substitution, constrained suppliers excluded), which is consistent with the ISO 14040 and ISO 14044 standards. The study included the entire life cycle of refractory products: mining of minerals, processing to obtain refractory raw materials, manufacturing of finished products, use phase and management as waste. Inventories (mass and energy balances) were built for production of 12 different raw materials and 17 finished shaped and unshaped products (see Fig.1). Data were also collected from the steel manufacturer in terms of refractories consumption, waste collection and treatment. As background database, the EXIOBASE v3 (https://simapro.com/products/exiobase-database/) was used in the LCA software SimaPro. The advantage of using an input-output based database as EXIOBASE is its high level of completeness, as well as the ability to cover processes in different countries with country-specific data. The main limitation of such a database, namely the level of aggregation of activities, is managed by disaggregating them whenever necessary, using process-specific data from other sources. In terms of environmental impact metrics, the LCA addressed a set of 14 environmental indicators by means of the Stepwise method developed by 2.-0 LCA consultants.

In parallel, LCC was applied following the principles by [3] and [4], where LCC is defined as an assessment of all costs associated with the life cycle of a product that are directly covered by any one or more of the actors in the product life cycle (supplier, producer, user/consumer and waste manager. This LCC approach addresses only 'internal' costs, that is, costs for which a price is paid by a particular actor in the supply chain. Costs and benefits must be taken into account even if the decision maker, in this case the steel factory, is not directly responsible for them. The calculation of the LCC was performed based on a wide variety of data sources, such as actual prices of refractories and estimated costs and benefits for waste collection, reuse, recycling and disposal.
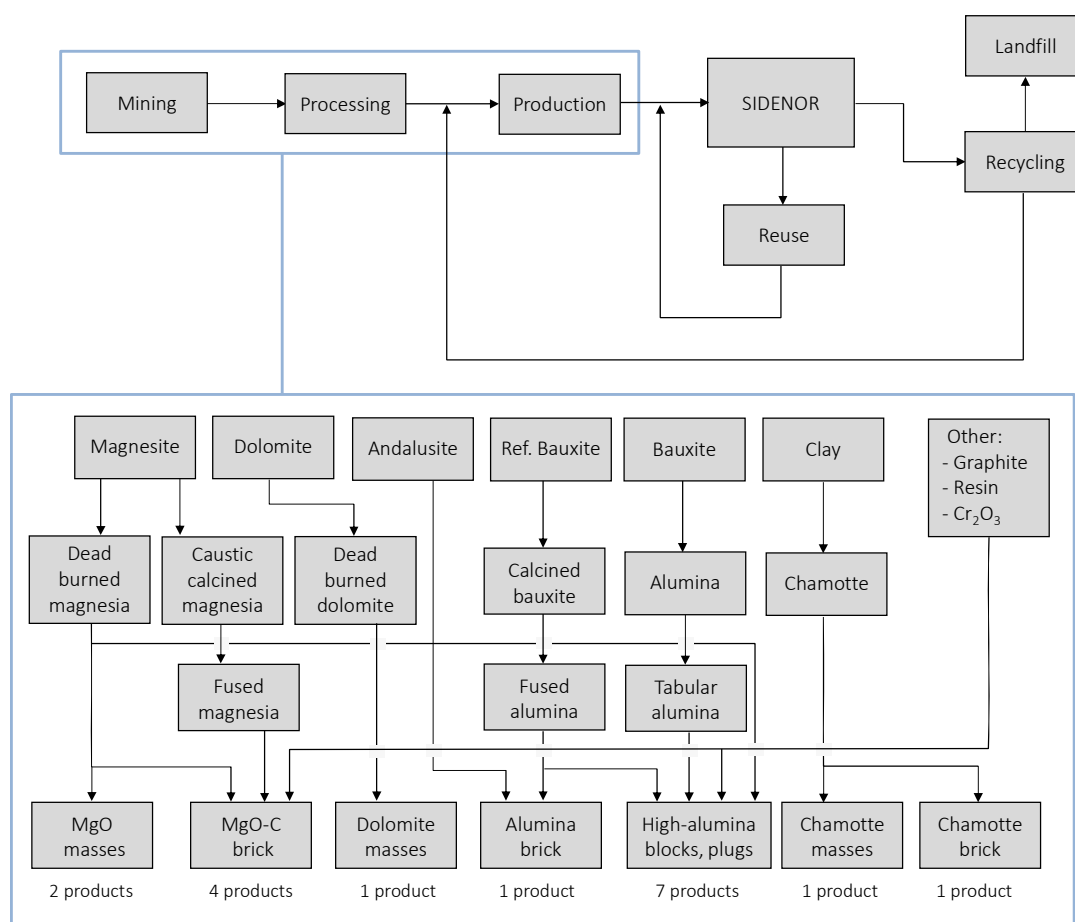
*Fig. 1: Boundaries of the LCA study.*

**Results: LCA**

Table 2 shows the impact assessment results for annual ladle management before and after E-CO-LadleBrick project implementation, for the 14 indicators included. Each indicator is expressed in different units and therefore they cannot be compared to one another. Besides the absolute scores for each scenario, the last column shows the reduction in impact score, expressed in percentages. The results clearly show a lower impact after project implementation, with reductions in impact that range from 19% in aquatic eutrophication (water pollution by nutrients) to 79% in mineral extraction.

Tab. 2: Life cycle impact assessment results before and after E-CO-LadleBrick implementation in a steel factory melting 1 million tonnes steel scrap per year. Indicators in physical units according to the Stepwise method.

| Indicator | Units[a] | Before E-CO-LadleBrick | After E-CO-LadleBrick | E-CO-LadleBrick reduction (%) |
|---|---|---|---|---|
| **Human toxicity, carcinogenic effects** | kg $C_2H_3Cl$-eq emitted to air/year | 246,502 | 192,576 | 22% |
| **Human toxicity, non-carcinogenic effects** | kg $C_2H_3Cl$-eq emitted to air/year | 34,688 | 26,428 | 24% |
| **Particulate pollution** | kg $PM_{2.5}$-eq/year | 15,281 | 12,375 | 19% |
| **Ecotoxicity, aquatic** | kg TEG-eq emitted to water/year | 15,903,823 | 12,583,435 | 21% |
| **Ecotoxicity, terrestrial** | kg TEG-eq emitted to soil/year | 34,576,994 | 27,606,864 | 20% |
| **Nature occupation** | PDF·$m^2$a/year | 122,869 | 101,571 | 17% |
| **Greenhouse-gas emissions** | kg $CO_2$-eq/year | 10,550,041 | 8,499,345 | 19% |
| **Acidification** | $m^2$ UES/year | 782,915 | 610,942 | 22% |
| **Eutrophication, aquatic** | kg $NO_3$-eq/year | 7,356 | 6,052 | 18% |
| **Eutrophication, terrestrial** | $m^2$ UES/year | 818,079 | 647,722 | 21% |
| **Respiratory organic effects on humans** | person·ppm·hour/year | 11,558 | 9,104 | 21% |
| **Photochemical ozone effects, vegetation** | $m^2$·ppm·hour/year | 106,912,340 | 84,109,634 | 21% |
| **Non-renewable energy demand** | MJ primary/year | 85,963,291 | 69,344,681 | 19% |
| **Mineral extraction** | MJ extra/year | 81,614 | 17,483 | 79% |

[a] $C_2H_3Cl$: chloroethylene; $PM_{2.5}$: fine particulates measuring 2.5 microns or less in width; TEG-eq: triethylene glycol; PDF: potentially disappeared fraction of species; $CO_2$: carbon dioxide; UES: unprotected ecosystem; $NO_3$: nitrate; ppm: parts per million; MJ: megajoule; eq: equivalents.

Fig. 2 below shows how emissions of greenhouse gases (GHG), measured in tonne $CO_2$-eq/year, are distributed across the life cycle of refractories, from production to waste management. The graph shows values with a positive sign, interpreted as emissions, as well as values with a negative sign, interpreted as emission savings or avoided emissions.
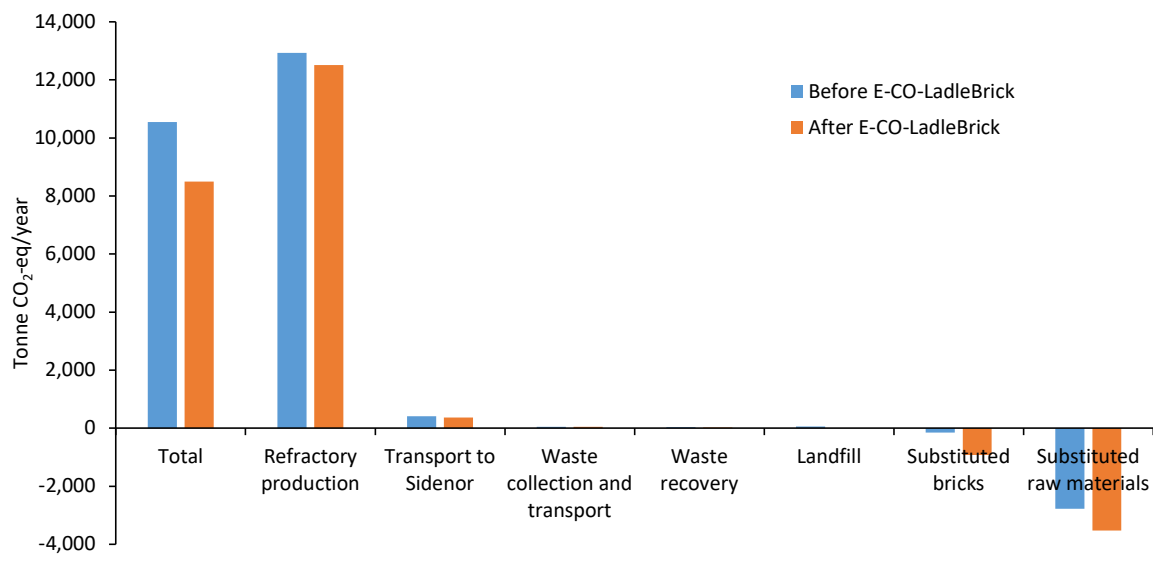
*Fig. 2– Life cycle GHG emissions for ladle refractory management before and after E-CO-LadleBrick implementation in a steel factory melting 1 million tonnes steel scrap per year.*

Fig. 2 shows that the major share of emissions is associated with refractory production (including the entire chain of mining and processing of raw materials into finished products), which justifies the E-CO-LadleBrick strategy of maximizing a ladle's useful life, thus reducing the consumption of refractories. This alone achieves a reduction in GHG emissions of 4%. Fig. 2 also shows how crucial waste management is. Reuse and recycling notably increase after project implementation, leading to the avoidance of emissions associated to producing new raw materials and final products. Altogether, reuse and recycling achieve a reduction in GHG emissions of 14%. Finally, the avoidance of landfilling after project implementation also contributes to the GHG reduction, by 1%. Overall, the life cycle GHG emission reduction is 19%.

**Results: LCC**
The results of the LCC study are shown in Table 3 below, where instead of showing the before project/after project situations separately, we show only the difference between these two situations. Results with negative values imply a benefit, that is, a cost reduction as a result of implementing E-CO-LadleBrick. The total LCC shows a negative value, indicating a benefit, that is, a lower cost after project implementation.

*Tab. 3: Life cycle costing results, in €/year: difference between before and after implementing E-CO-LadleBrick in a steel factory melting 1 million tonnes steel scrap per year.*

| Cost item | Cost, € |
|---|---|
| Refractory supply | -610,648 |
| Ladle reparation | -548 |
| Ladle demolition | -823 |
| Waste collection | 10,444 |
| Waste transport | -7,655 |
| Waste treatment | -40,869 |
| Substituted raw materials | -135,897 |
| Substituted refractories | -269,659 |
| **Total** | **-1,055,656** |

It can be seen that total annual life cycle costs are reduced by about 1 million € thanks to the implementation of E-CO-LadleBrick. All items in Tab. register cost reductions, with the exception of waste collection, where an increase is registered. This is mainly due to the increase in collection efforts for bricks destined for internal reuse in the factory. The volume of such bricks increases substantially, thus incurring in higher costs for manual sorting and internal transport. This cost increase is, however, largely compensated by the resulting avoided cost of purchasing new bricks, estimated at more than 269,000 €. Overall, the biggest cost reduction is associated to a reduced supply of refractories, thanks to the optimization of their useful life as a result of the prediction model developed in the project. These savings are estimated at 610,000 €. The second most important cost reduction is due to brick reuse, estimated, as already mentioned, at 269,000 €. Recycling also leads to substantial benefits, through avoided raw material production. Altogether, avoided raw materials amount to savings close to 136,000 €.

**Conclusions**
The main outcome of this parallel LCA and LCC study is that circular economy strategies such as the ones developed in the E-CO-LadleBrick lead to a reduction in life cycle impacts and costs associated to ladle refractory management. Even though this is only one case study in a single factory, the overall conclusions are likely to be valid for the general refractories sector.

**REFERENCES**

[1] Muñoz I, Soto A, Maza D, Bayón F (2020) Life cycle assessment of refractory waste management in a Spanish steel works. Waste Management, 111: 1-9.

[2] Ferreira G, López-Sabirón AM, Aranda J, Mainar-Toledo MD, Aranda-Usón A (2015) Environmental analysis for identifying challenges to recover used reinforced refractories in industrial furnaces. J. Clean. Prod. 88, 242–253.

[3] Hunkeler D, Lichtenvort K, Rebitzer G (2008) Environmental Life Cycle Costing. CRC Press.

[4] Hunkeler D, Rebitzer G (2005) The future of Life Cycle Assessment. International Journal of Life Cycle Assessment, 10 (5), pp. 305-308.

# INSULATING REFRACTORIES AS AN ENABLER TO CARBON SUSTAINABILITY, DEMONSTRATED THROUGH LIFE CYCLE ASSESSMENT.

R.S.Mottram, T.Steele, A.Williamson, B.K. Amin, R. Cantone
Morgan Advanced Materials, Bromborough, UK

## ABSTRACT

Legislation and market forces are necessitating an increasing range of products to declare their environmental impact, reverberating down the supply chain. This paper discusses the cradle-to-gate Life Cycle Assessment (LCA) for insulating refractories, including the challenges of obtaining accurate raw material data and attributing Scope 1 and Scope 2 emissions to individual products. Insulating refractory products reduce the amount of carbon emissions from thermal processes, a methodology of differentiating between best-in-class and consumer grades is presented. This utilises heat flow models, and fuel carbon intensity calculations over the full expected lifetime of a refractory lining.

## DRIVING FORCES FOR MEASURING CARBON FOOTPRINT THROUGH LIFE CYCLE ASSESSMENT

According to the United Nations Intergovernmental Panel on Climate Change (UN IPCC), climate change is causing global temperatures to increase[1], resulting in rising sea levels, and more frequent extreme weather events. The principal cause of global warming is the rise in man-made greenhouse gas (GHG) emissions.

Legislation is pushing the need to measure and declare an increasingly detailed amount of environmental impact data. Over the past several years and in many jurisdictions, there has been the requirement that the company's annual directors report must contain energy use and greenhouse gas emissions[2,3]. Recently, the EU introduced the Carbon Border Adjustment Mechanism (CBAM)[4] , which is a tool to put a fair price on the carbon emitted during the production of carbon-intensive goods that are entering the EU, and to encourage cleaner industrial production in non-EU countries. The CBAM will initially apply to imports of certain goods and selected precursors whose production is carbon intensive and at the most significant risk of carbon leakage: cement, iron and steel, aluminium, fertilisers, electricity, and hydrogen. These and other legislations are requiring companies to track, in detail, their Scope 1 (direct), Scope 2 (indirect energy emissions) and, increasingly Scope 3 (other indirect) environmental emissions. Knowledge of the environmental impact of raw materials and components is required for the accurate calculation of Scope 3.

As stakeholders' opinions shift towards a more vital environmental consciousness, it becomes critical for companies to prioritise sustainability against the three pillars of: environmental, social and governance (ESG). Therefore, a company cannot solely focus on one pillar (e.g., focusing on governance goals solely while disregarding environmental impact). Doing so may be profitable in the short term but detrimental to the company's long-term viability as regulatory penalties, investor or other stakeholder interests and public opinion can negatively impact the company. By contrast, every company will have an environmental footprint, and there is a limit to reducing the impact of that footprint before the price becomes so large that it impacts the governance pillar. As public concern grows, more customers ask about industries GHG emissions as part of the manufacturing process and request information on products' environmental impacts.

The above factors are driving the need for the measurement and declaration of the environmental impact of their products. Refractories are no exception to this. In fact, their influential role in the production of carbon intense goods mentioned in CBAM, put them in a group of high interest materials. The process for measuring the environmental impact of a product is called Life Cycle Assessment.

## LIFE CYCLE ASSESSMENT PROCESS

Life Cycle Assessment (LCA) is a systematically analyses the environmental impacts across a product's life[5]. The beginning of a refractory materials life is mineral extraction at many separate mines, followed by transportation and a first round of manufacturing steps. These intermediate products then undergo more transportation and get used by the refractory producer as raw materials in further manufacturing steps. When the product reaches the end user, it may have gone through numerous manufacturing and transportation stages. The product is then used, maintained, and eventually recycled or disposed of. The summation of the environmental impact, in numerous categories, across all these steps comprises the LCA.

A complete assessment of manufacturing a product, its use and recycling are referred to as "cradle-to-cradle" see Figure 1. An assessment including manufacturing and use, but not recycling is called "cradle-to-grave". An assessment of only the manufacturing level is called a "cradle-to-gate" assessment. Cradle-to-gate refers to all environmental impacts associated with a product until it leaves the refractory manufacturer's site; it includes the impact of:
- Raw materials
- Transportation of raw materials from the last manufacturing / processing site
- Manufacturing impacts

Environmental impact encompasses many categories, including, but not limited to: climate change ($CO_2e$) -often referred to as carbon footprint, ozone depletion, acidification, and resource use, to name a few out of more than 20 categories usually tracked.

To ensure uniformity in approach and comparison between manufacturers and industries, numerous standards cover the process such as ISO 140406, ISO 140447, EN 15804+A28.



*Fig. 1: the LCA process*

## LIFE CYCLE ASSESSMENT FOR REFRACTORIES

Below, a Cradle-to-Gate Life Cycle Assessment is discussed on materials from Morgan Thermal Ceramics. The Cradle-to-Gate method is selected because it is currently problematic for a manufacturer to predict use and disposal / recycling due to the myriad uses of each refractory, the high impact of various applications in different use environments (eg. Glass, Iron & Steel, Energy production, Petrochemicals, Ceramics.) on lifetime and variability in end of life due to contamination. As more industries adopt LCA, this will resolve by the integration of multiple assessments. The order and detail of the steps below are not intended to be instructional or comprehensive. Instead they are intended to highlight some of the important considerations and challenges experienced with specific reference to refractories.

### Software to calculate, analyse and present LCA

Multiple companies offer software and support for calculating Life Cycle Assessment. Most of these integrate databases of the environmental impact of standard raw materials, packaging, transportation, water usage, waste disposal and Scope 1 and Scope 2 emissions. The user interface guides the entry of data in the categories mentioned below and automatically generates a Life Cycle Assessment. Often the software has tools to help the user understand which materials or process steps have the largest impact. In the below assessment, Ecochain Helix[6] cloud-based LCA software tool was used, with integrated Ecoinvent v6.3 database. The quality and accuracy of the software output is highly dependent on the input's quality and accuracy; careful verification is required to avoid inappropriate selection of raw materials or order of magnitude errors in mass or energy allocations. To ensure sufficient LCA quality, adherence to the previously mentioned standards[6,7,8] is imperative.

### Raw Material Environmental Impact.

In the best-case scenario, the raw material suppliers can provide a Cradle-to-Gate LCA on each raw material. Currently for the specialist minerals grades used in refractory production, such information is quite rare. An alternative is using a standard materials database, such as Ecoinvent V6.3. Whilst these are very large and powerful, it is not always easy to identify the most appropriate entry. Common materials, such as Alumina, have many entries, some with similar descriptions and maybe none exactly matching to a specialist grade used in refractories. Where no close match can be found, read across from analogous product, or the combination of a base material with a process step can be used, e.g. a calcination step could be combined with a standard Alumina to yield the environmental impact data for calcined alumina. More complexity can result where the raw material is from a recycled source or is a by-product of another process. Detailed rules for considering these are available in relevant standards and texts[5,8]. For some refractories such as castables (see below), the raw materials constitute the majority of the finished product's environmental impact; therefore, errors in the supplier data can be very significant in the accuracy of Cradle-to-Gate LCA.

### Environmental impact of transportation.

In a cradle-to-gate LCA, the manufacturer must include the impact of all materials being transported to their site and waste removed. This will vary by distance and type / efficiency of vehicle used, e.g. truck type, size, Euro emissions rating and loading factor. The most accurate data for this would come from a LCA that had been carried out on that type of Vehicle (giving climate change potential per km per kg of material transported). Where this is not available, standard databases can provide relevant data. Generally, transportation is only a small component of refractory production, this is due to the high packing density of raw materials and the relatively high energy intensity of extraction and manufacturing steps.

### Emissions from energy used in manufacturing

It is required to consider both direct emissions, Scope 1, e.g. from burning natural gas, fuel oil, diesel etc. and Scope 2, where the energy is used on-site, but the emissions are made elsewhere, e.g. electricity. For Scope 1, it should be noted that in the calculation of the LCA, the environmental impact will be higher than that for just fuel combustion. This is because it is also necessary to include the fuel's life cycle, including its extraction, refining and transportation. This data can be taken from a supplier who has performed an LCA, or from a standard database. For Scope 2, many electricity suppliers do provide the carbon intensity of the supplied power (calculated through LCA). Although databases do have standard entries by geographic region, these are of limited use as each energy supplier will have its own, ever-changing mix of electricity sources, some with higher or lower environmental

impact. Even where a manufactures electricity comes from a 100% renewable source, the LCA will need to considered contributions from the manufacture of the production unit, its operation and electricity transmission etc.

### Emissions from process releases

Many processes in refractory manufacturing may lead to direct process emissions, such as $CO_2$ from calcination of carbonates. These need to be accurately calculated and included in the LCA. Other factory and office releases such as refrigerants, have a very high environmental impact by mass, so the amount used on a site needs careful monitoring and allocation. Waste and water leaving the site are also environmental emissions and need to be accounted.

### Allocation of resources to products

Presuming a manufacturing facility has multiple production lines and products, it is necessary to map all raw material and energy use onto those lines and products. Where there is metering and logging on each process, this can be a relatively simple task of data enquiry. A system for fair allocation will be required where metering covers multiple processes or lines.

### Calculation and reporting of LCA.

Once the raw materials have been identified, the transportation distances and methods measured, the energy sources identified, and each allocated to a process and product, then the LCA can be calculated. This is a mathematical process of ratioing the environmental impact of each input by the amount used to manufacture the product. Often it is easiest to calculate the LCA of a product in environmental impact per kg manufactured. However, end users may often work in terms of per unit area or unit volume of insulation or per box or bag of product purchased. When interpreting a LCA, paying attention to the reporting unit is important.

### COMPARISON OF THE OUTPUT OF A LCA ON FIBRE BLANKET, INSULATING FIRE BRICK (IFB) AND LIGHTWEIGHT CASTABLE

A LCA will report on many environmental impact categories. The most reported and compared is climate change ($CO_2e$) [EN15804+A2], often called carbon footprint. Figure 2 shows the relative climate change $CO_2e$ for 3 typical refractory products as calculated by Ecochain Helix software[9] (the actual values are not revealed as they are not yet verified for publication). The breakdown shows the contribution of raw materials, transportation, and manufacturing. This breakdown and their subcomponents are useful information for targeting improvements in environmental impact of products. It should be noted that this is at the manufacturer's level; at the supplier level, the raw materials themselves could be again subdivided into these 3 categories; this data is not carried through to the final assessment.
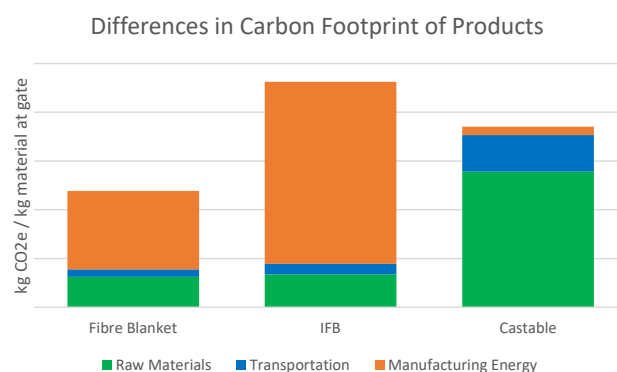


Differences in Carbon Footprint of Products

*Fig. 2: relative climate change impact of various refractories as calculated by LCA (Cradle-to-Gate).*

Figure 2 shows that per kg of product, Fibre blankets are accountable for about half the $CO_2e$ emissions compared to an Insulating Fire Brick (IFB), the major difference being the large Scope 1 emissions in firing the IFB compared to the Scope 2 electricity used in melting raw materials for fibres. The Castable has little energy input in manufacturing with the major contributor being the raw materials (although at the supplier level, manufacturing, transport and process emissions would have contributed most of their cradle-to-gate LCA).

When considering the effect of manufacturing location on LCA, typically the contribution from Scope 1 emissions will typically be very stable around the world, barring any variations in process efficiency. Hence the carbon footprint for an IFB from Europe will be largely similar to one from America. This is not necessarily the case for Scope 2 emissions; a fibre blanket from a country with predominantly green electricity may have a significantly lower carbon footprint than one from a country generating electricity from mostly fossil fuels.

## IMPACT OF REFRACTORY SELECTION ON PROCESS EFFICIENCY AND CARBON EMISSIONS

The selection of grade, quality, and thickness of an insulating refractory lining will greatly influence the efficiency of any high-temperature process and hence the environmental impact of any product manufactured by that process. Heat flow calculation, combined with the fuel cost and carbon footprint can demonstrate the payback of a lining selection, both financially and environmentally. Figure 3 compares three options for insulation on the walls of an ethylene cracker operating at 1250°C. Originally "Consumer grade" fibre refractories were installed; the customer was not happy with the heat loss; this is shown in the "Existing Lining" scenario. Two alternative systems were proposed, to prove performance, the customer chose to have both installed in different regions of the walls. System 1 comprises best in class Pyro-Bloc®[10] fibre modules and Superwool® Plus fibre blankets[11]. System 2 comprises the Pyro-Bloc with ultra low thermal conductivity WDS microporous board[12] replacing the fibre blanket. Figure 3 shows for each scenario a thermal image scan of the outside casing, and a thermal calculation using Morgan Heat Flow[13] calculator.

Using the supplier data for the "Consumer grade" refractory, the outside casing was calculated to have a temperature of 123°C and a heat loss of 1400W/$m^2$. In actuality, the thermal imaging showed the temperature, and hence heat loss to be even higher. With System 1, the casing was calculated to have a temperature of 104°C and a heat loss of 1041W/$m^2$, this was found to be accurate within measurement error. For system 2, the casing was calculated to have a temperature of 82°C and a heat loss of 663W/$m^2$, again the thermal imaging demonstrated the accuracy of the calculation.

Figure 4 shows a lifetime performance comparison of the three linings using, Thermal Efficiency and $CO_2$ Emissions (TECE) calculator software[14]. This calculates financial and environmental impacts over a 16 year life and gives a payback period in comparison to the existing lining. Typical market prices for the refractory, natural gas and carbon credits are used, as shown in the figure.

The TECE predicts that over the lifetime of the ethylene cracker wall lining (700$m^2$), the use of Pyro-Bloc and WDS instead of "Consumer grade" refractories would save 13,000 tons of $CO_2$ emissions and €3.9 Million in natural gas and carbon credits (based on 0.04€/kWh for natural gas and €85/ ton of $CO_2$). The upgrade in lining would have a payback period of 6 months. A future revision to the TECE, will take the carbon footprint from LCA (once available) and calculate a carbon payback time.

## CONCLUSIONS

Legislation and customer demand increasingly require all products, including refractories, to declare their environmental impact. The method for calculating this is through Life Cycle Assessment (LCA), for which there are defined standards. For refractories, there are complexities in calculation resulting from the use of specialist raw materials, which may not have had LCA performed upon them and for which it is not easy to identify analogous materials in standard databases. Where uncertainty exists in material flow and facility metering, emissions from manufacturing may be hard to map. The scope 2 emissions of electricity used in production can be location dependent; hence the LCA for refractory products consuming a large proportion of electricity in manufacture may vary by geography. A LCA both informs consumers about the environmental impact of a product and the manufacturer about which components have the largest influence on emissions. Thermal heat flow calculations combined with the cost and environmental impact of fuels can be used to demonstrate the payback time of additional high-quality insulation. Once LCAs are available on refractory materials, the environmental payback times can also be calculated

## REFERENCES

1. Masson-Delmotte, V., P. Zhai, A. Pirani, S.L. Connors, C. Péan, S. Berger, N. Caud, Y. Chen, L. Goldfarb, M.I. Gomis, M. Huang, K. Leitzell, E. Lonnoy, J.B.R. Matthews, T.K. Maycock, T. Waterfield, O. Yelekçi, R. Yu, and B. Zhou (eds.),. IPCC, 2021: Climate Change 2021: The Physical Science Basis. Contribution of Working Group I to the Sixth Assessment Report of the Intergovernmental Panel on Climate Change, Cambridge University Press, Cambridge, United Kingdom and New York, NY, USA.
2. Directive (EU) 2022/2464 of the European Parliament and of the Council of 14 December 2022 amending Regulation (EU) No 537/2014, Directive 2004/109/EC, Directive 2006/43/EC and Directive 2013/34/EU, as regards corporate sustainability reporting.
3. Environmental Reporting Guidelines: Including streamlined energy and carbon reporting guidance March 2019 (Updated Introduction and Chapters 1 and 2). HM Government.
4. Document L:2023:130:TOC, Official Journal of the European Union, L 130, 16 May 2023
5. M.Z.Hauschild, R.K.rossenbaum, S.I. Olsen, Life cycle Assessment: Theory and Practice Springer press (2017) ISBN 978-3-319-56474-6
6. ISO14040 Environmental management — Life cycle assessment — Principles and framework (2006), ISO copyright office, Case postale 56, Geneva.
7. ISO14044 Environmental management — Life cycle assessment — Requirements and guidelines (2006) ISO copyright office, Case postale 56, Geneva.
8. EN 15804+A2 Sustainability of Construction Works. Environmental Product Declarations. Core Rules For The Product Category Of Construction Products (2019). European standards.
9. Ecochain, Helix Cloud-based LCA software tool, (2014) https://helix.ecochain.com/
10. Pyro-Bloc fibre modules data sheet (2023) https://www.morganthermalceramics.com/media/9323/rcf-pyroblocmodules_eng.pdf
11. Superwool Plus data sheet (2023) https://www.morganthermalceramics.com/media/8946/superwool-plus-blankets_eng.pdf
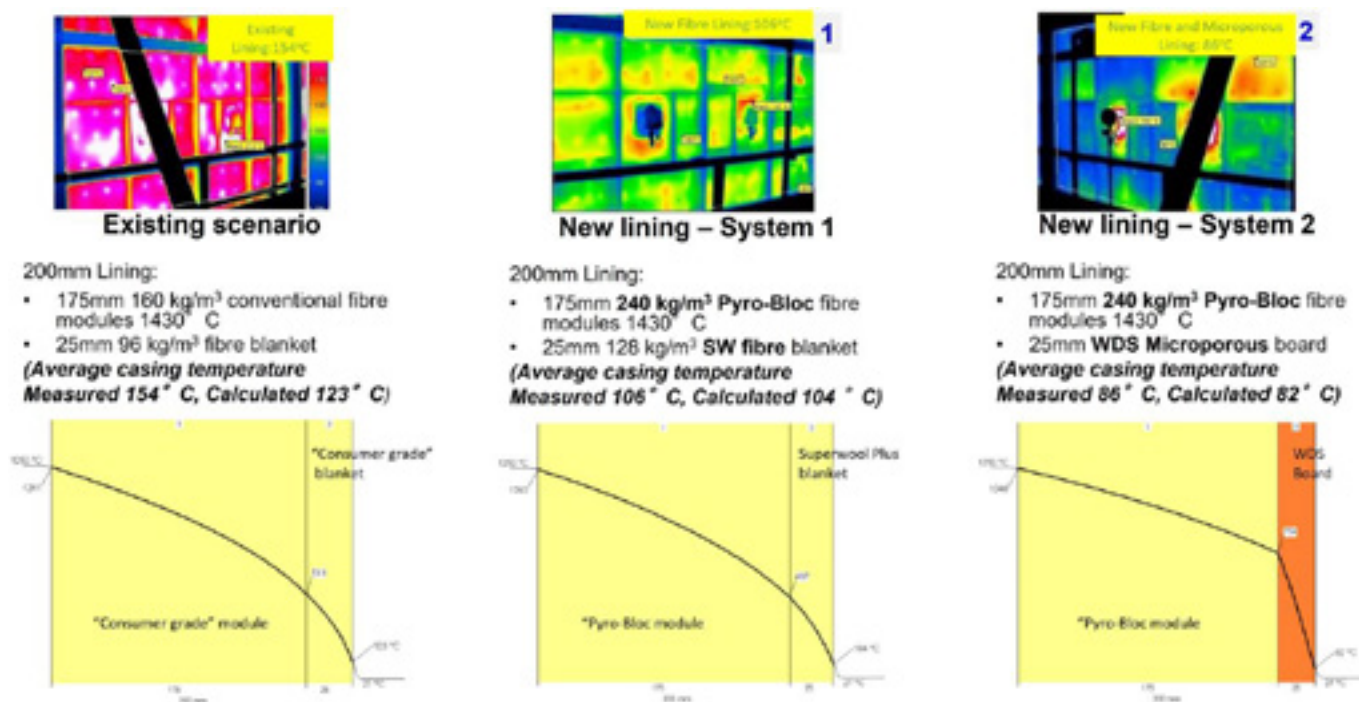
*Fig 3 Heat flow calculation of 3 alternative refractory linings for a 1250ºC Ethylene cracker wall*



*Fig 4 Thermal Efficiency and CO₂ Emissions (TECE) calculations for 3 alternative refractory linings for a 1250ºC ethylene cracker walls*

12. WDS Ultra Plus Board Datasheet (2023) https://www.morganthermalceramics.com/media/7564/wdsultraplusboard_eng.pdf

13. Morgan Thermal Ceramics HEAT FLOW calculator (2023) https://Morganheatflow.com

14. Morgan Thermal Ceramics TECE calculator: email marketing.tc@morganplc.com

# OVERVIEW ON LCA: CHALLENGES AND OPPORTUNITIES FOR THE REFRACTORY INDUSTRY

João V., MENEZES CUNHA
GeMMe – Georesources, University of Liège, Liège, Belgium
Environment & Energy Department, RHI Magnesita GmbH, Leoben, Austria

Eric, PIRARD
GeMMe – Georesources, University of Liège, Liège, Belgium

Thomas, DRNEK
Environment & Energy Department, RHI Magnesita GmbH, Leoben, Austria

## ABSTRACT

Organizations are now integrating life cycle thinking tools and techniques into decision-making to enable an analysis of the environmental impacts associated with all stages of a product's life. In this context, mining has been questioned by the widespread consensus that reducing resource consumption is a requirement for sustainable development. On the other side, it is clear that, due to dissipation, virgin raw materials will always be needed, and that circular economy thinking should integrate the mining industry and not oppose it. From this emerges the concern of resource depletion and the abiotic depletion potential (ADP) comes therefore as an attempt to assess the risk of depletion within life cycle assessment (LCA) methodology. However, when it comes to mineral resources, a lot of general assumptions are made, and the specificities of each element are often neglected. By attempting to include anthropogenic stocks in the calculations, some authors also neglect the singularities of each product. LCA has proven to be a powerful tool and its successful application within the refractory industry depends on collaboration between organisations in order to fill the numerous lacks of data availability and to overcome the challenges ahead. This paper is part of a PhD project that aims to build a database of magnesia production, from the mine to the kiln, to support LCA as well as to discuss resource depletion within the methodology and to account for the benefits and challenges of refractory recycling, focusing on magnesia bricks.

## INTRODUCTION

The Circular Economy (CE) concept is increasingly gaining ground in academia and industry. Sustainability is the key word of our times and is leading the trend to increase circularity throughout all the stages of the production processes (Fig. 1). To achieve such a bold goal, it is important to know well and have a systemic vision of the whole life cycle, from the raw materials to the end-of-life (EoL), accounting for the origin of the main dissipative flows and environmental impacts.



Fig. 1: Representation of a product life cycle, Source: EIT Raw Materials

Life Cycle Assessment (LCA) has gained relevance in many industrial sectors as a sustainability tool. The methodology is used in different maturity levels within the industries, but it is generally recent. It is a powerful tool to get a better picture of the whole production chain and to help decision-making and redesigning of a product or process. Knowledge has advanced through the development of scientifically valid life cycle inventory (LCI) databases and models (e.g., EcoInvent), but some industrial sectors have still no significant or reliable inputs. Therefore, this is an open field with plenty of opportunities to be developed and intensive work will be required to face the challenges that will come with it.

The refractory industry is not out of it, but the LCA of refractory products is still in its infancy. Refractory linings are required in a lot of high-temperature production processes (metals, glass, cement, etc.). Therefore, refractories are part of the production of many essential materials for the civilization. Additionally, refractories have a significant $CO_2$ footprint, especially due to the calcination of magnesite ($MgCO_3$) to produce magnesia ($MgO$), one of the main raw materials (Eq. 1). Furthermore, the harsh corrosive conditions to which refractories are often exposed during their service life result in high dissipation rates, which affects circularity.

$$MgCO_{3(s)} \rightarrow MgO_{(s)} + CO_{2(g)} \tag{1}$$

LCI databases have been created but seem still inconsistent and/or incomplete that professionals prefer not to use them and trust on their internal data, even though it may not represent a global extent. Additionally, relevant stakeholders are still not interested in overall environmental data, which limits the added value of LCA. Instead, customers are increasingly interested in Product Carbon Footprint (PCF) due to the growing pressure to decarbonise their whole value chain. Despite the given lack of interest in full environmental assessments, it can be expected that regulations can encompass an overall environmental impact of products in the near future. Therefore, given the importance of the refractory industry and the significant environmental impacts associated with it, efforts should be made to promote the use of LCA tools to provide a better picture and support decision-making towards sustainability.

## REFRACTORY INDUSTRY: A SPECIAL CHALLENGE

Refractories present a major challenge to LCA practitioners due to their complexity. There is a wide variety of refractory products with distinct compositions and production processes. Unlike ordinary clay bricks, refractories have a wide range of raw materials between aggregates, binders, and additives. RHI Magnesita, the global leader in refractories manufacturing, uses more than 6,000 raw materials from many types of sources to produce more than 200,000 different refractory products. This is the order of magnitude of the challenge that needs to be addressed.

Moreover, very often some steps of the production chain are neglected or poorly documented in the literature. For example, it is common to find simplified representations of the production chain of magnesia from magnesite that obliterate the mineral processing step right after mining. The availability of high-quality data is fundamental for the assertiveness of the LCA study and therefore, industrials should think more collaboratively to fill the lacks that actual databases have. In the complex context that the refractory industry presents, only collective and centralized efforts would produce satisfactory results.

## RAW MATERIALS SOURCING

Given that dissipation is inevitable in every step of a production process, many industries are often concerned about supply risk

since virgin raw materials will always be necessary to feed the loop. Getting to know the production process and its required inputs is a first step that, followed by a detailed study of the raw materials sources, can give a more accurate scenario to help strategic decisions. Abiotic Depletion Potential (ADP) is a method within LCA that aims to account for the risk of depletion of elements with characterisation factors based on the ratio of the annual extraction rate (DR) to the square of the assumed stock (R) of a given element [22]. Antimony was chosen arbitrarily as a reference element to make a normalization of the results as shown in Equation 2.

$$ADP_i = \frac{DR_i / (R_i)^2}{DR_{ref} / (R_{ref})^2}$$

(2)

Despite the simple calculation, the determination of the assumed stocks can be challenging, especially in the case of diverse potential sources and uses of the same element. In addition, since the methodology focuses on the very long run, an estimation of stocks should also consider a technological development that could make available some sources that are currently unavailable due to technical and economic constraints. To do so, there is no objective answer, and this subject is still an open discussion among experts.

Given that there may be more than one source and/or functional mineral of a given element, crustal content seems to be the best base for the calculation, since it refers to the element. Additionally, crustal content is the only reliable and stable base to estimate the stocks [3]. Regardless of the criteria used to determine the stocks in a long-term perspective, very often authors generalize it for different elements (e.g., same crustal depth). This is not geologically reasonable since different elements may have distinct origins, with different types of mineralization, varying the size, shape, and depth of the deposits. The generalization is also not economically supported, since elements may also have different values, not being able to afford the same extraction/processing costs. It is inconceivable to expect companies to dig as deep for limestone as they do for gold, due to the discrepant added values between these commodities. In the same way, it is unimaginable to find bauxite as deep as we find copper, given the differences in the geogenesis of these mineralisations.

Moreover, crustal content may mislead if applied disregarding the cut-off grade, i.e., the minimum concentration that allows the processing of a given element with the actual technology. Still, as ADP refers to a very long-term, technological development should be expected, enabling deeper mining and processing of poorer ores. Finally, economic, geological and technological constraints must be considered in the analysis.

**A closer look into Magnesia**

Due to its high melting point (2800°C), magnesia is one of the most important refractory aggregates. Mainly used in steelmaking, magnesia is obtained from the calcination of magnesite in most cases (Eq. 1). Developed countries without commercial magnesite resources typically produce magnesia from seawater, brines, or evaporitic deposits, which are common sources for the production of magnesium metal [19]. Magnesia produced from these sources is often called "synthetic magnesia", and "natural magnesia" is commonly the name given to the one obtained from magnesite. The concentration of magnesium in seawater is 1290 ppm [4] and high-purity magnesia can be obtained from it, but with significantly higher costs. Synthetic magnesia production requires up to twice the energy needed in natural magnesia production [18].

The share of synthetic magnesia in the global magnesia production capacity has decreased due to the tough competition with the Chinese market resulting in closures and a significant decrease in synthetic magnesia production capacity. However, due to the return of market growth, substantial investments were made in 2010, resulting in synthetic magnesia production capacity increasing, but remained a minor part of the share with magnesite source [19].

Figure 2 shows the global production capacity share between natural and synthetic magnesia in 2001 and 2013. Experts estimate that synthetic magnesia may represent around 10% of the actual global magnesia production capacity.
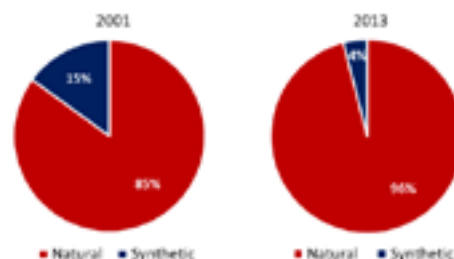


*Fig. 2: Global production capacity of Natural and Synthetic magnesia, 2001 and 2013 [19]*

With the increasing urgency of tackling climate change, alternatives to natural magnesia with a lower $CO_2$ footprint should now receive more attention. Besides seawater and brines, it has been shown to be possible to produce magnesia from Mg-bearing minerals either by mineral digestion followed by brucite ($Mg(OH)_2$) precipitation and further calcination [21] or by carbonation [11]. These processes are highly energy intensive and present higher $CO_2$ footprint than the natural magnesia mainly due to the available energy sources. Therefore, fostering green energy production could enable the production of magnesia from alternative sources with considerably lower $CO_2$ footprint. Combined with that, improvements are needed to achieve a production scale that would meet the industrial demand and increase the market share of synthetic magnesia.

**Anthropogenic Stocks**

With the growing stimulus to establish an industry that follows the principles of circular economy, it is important not to disregard anthropogenic stocks when evaluating resource depletion. Elements are not always used or dissipated, they can often still be available to be reused through recycling, which is also true for refractories. Therefore, Schneider et. al. (2015) [20] suggested that the ADP assessment should be broadened to encompass anthropogenic stocks in the calculation. The authors made no differentiation between the elements and a general dissipation rate was used. This is problematic because, in addition to the different behaviour of distinct elements, the same element may be used in multiple ways within the anthroposphere, resulting in multiple dissipation rates for the same element. That gives an idea of how complex the estimation of anthropogenic stocks can be.

Moreover, a point that must be highlighted is that not all the elements within the anthroposphere are available for eventual recycling due to long-term use. Consequently, occupation-in-use should be taken into account when trying to measure anthropogenic stocks [1].

Last but not least, in some cases the anthropogenic stocks may not be relevant because they may represent a minor part of the total stocks in the calculation of ADP. Thus, estimating the anthropogenic stocks to include in the ADP calculation may not be worthwhile for elements with high natural stocks and/or dissipation rates. Otherwise, it may be relevant in case of more scarce elements and/or with high recyclability.

**RECYCLING**

During the use phase, around 30-40 wt.% of the refractory is consumed [13], indicating that up to 35 million tons of spent refractories are generated every year from the 50 million produced [12]. The fact that refractories are corroded and dissipated during the use phase shows that primary raw materials will always be needed in the refractory industry because even with refractories completely made of recycled raw materials in a closed loop, the losses during the use phase would make it impossible to keep the production without using virgin raw materials.

Due to the abundance of virgin raw materials, in the past, recycling received little attention in refractories manufacturing. Added to this, the low disposal costs of the, largely inert, spent refractories was another reason to keep the refractories recycling out of focus. Instead, a lot of progress was made in the refractory consumption per ton of product. In the steel industry, refractory consumption has declined from 25-30 kg of refractory per ton of steel in the 1970s to 8 kg/t today in US and Japan [2]. Such progress could be seen also in other industries as the production of cement, which decreased the relative refractory consumption from more than 2 kg per ton of cement clinker to on average 0,9 kg/t [5].

With the increasing landfilling costs and environmental concerns, recycling has risen as a strategic alternative to guide the refractory industry towards a circular economy. Spent refractories have been largely used in open-loop recycling applications such as roadbed aggregates [2] and slag conditioners in the steel industry [8]. In these applications, the value of the recycled material is limited to the cost of the replaced material, which is much cheaper than refractories.

However, closed-loop recycling is still limited to an average of 7% of refractory raw material demand [15]. Recently, RHI Magnesita has increased the global recycling rate to 10.5% in 2022 [16]. Studies showed that the production with 20% of recycled refractories as raw material is achievable in the manufacturing of LC series [9]. Remanufactured MgO-C bricks containing up to 30% of recycled material were found to have almost the same properties and durability as low-grade MgO-C brick [13]. More recently, Kunanz et al. (2022) [10] reported a successful implementation of high recycling containing magnesia-carbon brick in steel ladles. The newly developed brick contains 87 wt.% of recycled material and reduced the long-term average consumption from 0.21 kg/tonne steel to 0.13 kg/tonne steel, a reduction of 38% of refractory material use.

The substitution of virgin raw materials for recycled spent refractories leads to a considerable reduction in the carbon footprint since the thermal treatment of magnesite and dolomite includes the most $CO_2$-intensive processes. The production of dead burned magnesia (DBM) and dead burned Doloma (DBD) is responsible for around 85% of RHI Magnesita's scope 1 emissions. In 2020, the production of DBM and DBD generated approximately 1.8 million tons of $CO_2$ scope 1 emissions, of which 60% were geogenic and 40% were fuel-based [17]. A standard magnesia-carbon brick has a $CO_2$ footprint of 3.95 tonne $CO_2$/tonne bricks, while an 87% recycled content magnesia-carbon brick has only 0.55 tonne $CO_2$/tonne bricks, an expressive reduction of 85% [10].

Nevertheless, refractories recycling can be challenging. During their lifetime, the refractories undergo some modifications in their physical and chemical properties, especially in their exposed surface, due to the usually hard operating conditions. Refractories may then have some inclusions of slag or metals and then, the content of CaO, $Fe_2O_3$ and $SiO_2$ also increases in the spent magnesia-based refractories used in steelmaking. Therefore, this increase can also be seen in recycled refractories [7]. The presence of these impurities typically leads to a decrease in durability because of melt formation between Ca/Si and Mg/Al [6]. Furthermore, recycled refractories aggregates tend to present higher porosity and lower density than virgin raw materials, which affects their physicomechanical properties and limits the amount of recycled refractory aggregates that can be introduced into the refractory mix [7].

In addition, as most of the furnaces use more than one type of refractory product, it becomes difficult to separate the different refractories when removing the spent lining and in most of cases they are indiscriminately mixed into a pile. Therefore, processing spent refractories to improve refractory recycling faces the challenge of sorting different types of refractories. The state-of-the-art recycling plant for refractory waste includes, therefore, a pre-sorting step, in which the different types of refractories are separated. This stage is usually done manually, and even after this sorting process different types of refractory materials are often mixed and contaminated with pieces of iron metal and slag [6]. This step is highly error-prone due to the presence of dust and other contaminants that limit the visual identification and because it is dependent on the operator's expertise [7].

Besides the lack of efficiency and objectivity of the manual pre-sorting of spent refractories, the dusty environment and the hostile working conditions are other concerns. Therefore, there is a strong demand for automation in the pre-sorting step within the industry to improve accuracy and speed as well as the working conditions. Some systems have been developed based on colour sorting, however, it is hindered by the dust layers as well as the similar appearance of chemically distinct refractories. In the last years, sorting systems were developed using LIBS (Laser Induced Breakdown Spectroscopy), which uses a pulsed laser to ablate the surface of a material, typically penetrating around 100 µm deep into the sample, eliminating then, most of the surface interference caused by dust [7].

The European project REFRASORT successfully developed a LIBS system that aims to separate the main refractory types used in the steel industry, such as MgO-C with and without antioxidants, carbon-bonded doloma, fired doloma, bauxite, andalusite and chamotte [14]. A test was carried out using the REFRASORT demonstrator (Figure 3) with 30 t of mixed magnesia, doloma and alumina-based spent refractories [7]. The accuracy was validated by analysis of the output fractions and the sorted fractions achieved the targeted contents, being the only exception a slightly higher $SiO_2$ content in the doloma fraction.



*Fig. 3: REFRASORT demonstrator system [7]*

Recycling is one of the best strategies to reduce carbon emissions within the refractory industry and therefore it is one of the priorities of many refractory producers. The increasing environmental concern may motivate customers to push the refractory industry to develop green alternatives. In this context, some kind of sustainability certification of refractories will be of interest, since refractory consumers will be concerned about the global environmental impacts the products have. LCA is the right tool to produce that kind of summary and enable a more conscient consumption.

**CONCLUSIONS**

LCA is an important tool that can contribute to a better understanding of a whole production process in terms of supply and environmental impacts. It is a powerful method to enable a systemic vision and therefore to identify the main bottlenecks in the environmental performance of a product, allowing the eco-designing. By giving the big picture of a product, LCA can help industries to know their products and processes well enabling a more assertive decision-making towards sustainability.

However, it has been proven challenging to implement LCA within the refractory industry. There is still low reliability in the few databases created and the high complexity and variability of refractory products pose difficulties. To accomplish such a tough goal, collaborative efforts would be necessary between raw materials suppliers, refractory producers, and end users since data availability is still of concern.

Moreover, there is a lack of interest in LCA data from relevant stakeholders, which limits the added value of such assessments. Instead, PCF is increasingly in demand as companies come under small but growing pressure to decarbonise their entire value chain. Thus, from a regulatory perspective, linking taxation with the whole environmental footprint could be a possibility in the near future to push the industries to reduce overall environmental impacts, and then the refractory industry should be prepared to overcome this challenge, possibly by implementing LCA analysis.

In terms of supply, there is evidence that the ADP should be reviewed to assess the risk of depletion of raw materials more accurately. Every element should be addressed individually, accounting for its specificities, and avoiding generalisations. The assumed stocks have been a concept under discussion and hard to determine, given the subjectiveness of envisioning economic and technological conditions in a very long-term perspective added to the complexity of geological analysis. Alternative sources should be considered to avoid supply shortages and, in the case of magnesia, can offer the environmental advantage of avoiding high $CO_2$ emissions by producing synthetic magnesia instead of natural magnesia. The inclusion of anthropogenic stocks in the calculation of ADP seems to be relevant since recycling has been fostered in many industries. However, some improvements are still needed to do this coherently.

Recycling has proven to be an effective strategy to reduce the carbon footprint of refractories and to make the refractory industry more sustainable and circular. A lot of progress has been done in the past few years and an overall recycling input rate of 10.5% was achieved in 2022 at RHI Magnesita. Magnesia-carbon bricks made with 87 wt.% of recycled material proved to be functional, reducing the PCF by 85%. Many projects have been developed to improve the recycling of refractories and the LIBS technique delivered good results in sorting different spent bricks. Recycling seems to be the way to revolutionise the refractory industry towards sustainability.

## OUTLOOK

This paper is part of a PhD thesis, within the CESAREF consortium, entitled *"Documenting the Upstream of Refractories Manufacturing to Support LCA"*. Since one of the challenges of implementing LCA within the refractory industry is the lack of availability of good quality data, the main goal of this project is to build a better knowledge about the production of refractory raw materials, more specifically, magnesia production. A description of the current and alternative production routes will be accompanied by an inventory of the main inputs and outputs of the production processes ($CO_2$ emissions, energy consumption, etc.). Parallelly, the project aims to discuss resource depletion within LCA, reviewing the ADP methodology and making an analysis focusing on magnesium. Finally, accounting for the benefits and challenges of magnesia bricks recycling with eco-design recommendations is another goal.

## REFERENCES

[1] Beylot, A., Ardente, F., Sala, S. & Zampori, L., 2021. Mineral resource dissipation in life cycle inventories. *International Journal of Life Cycle Assessment,* Volume 26, pp. 497-510.

[2] Domínguez, M., Romero-Sarria, F., Centeno, M. & Odriozola, J., 2010. Physicochemical Characterization and Use of Wastes from Stainless Steel Mill. *Environmental Progress & Sustainable Energy,* pp. 471-480.

[3] Drielsma, J. et al., 2015. Mineral Resources in Life Cycle Assessment - Defining the Path Forward. *Life Cycle Sustainability Assessment,* 9 November, Issue 12, pp. 85-105.

[4] Fontana, D. et al., 2022. Magnesium recovery from seawater desalination brines: a technical review. *Environment, Development and Sustainability,* 25 September.

[5] Guéguen, E., Hartenstein, J. & Fricke-Begemann, C., 2014. Raw Material Challenges in Refractory Application. *Proceedings Berliner Konferenz Mineralische Nebenprodukte und Abfälle,* pp. 489-501.

[6] Hanagiri, S. et al., 2008. Recent improvement of recycling technology for refractories. *Nippon Steel Techn. Rep.,* pp. 93-98.

[7] Horckmans, L., Nielsen, P., Dierckx, P. & Ducastel, A., 2019. Recycling of Refractory Bicks Used in Basic Steelmaking: A Review. *Elsevier,* pp. 297-304.

[8] Kek, F. et al., 2022. Refractory Waste to Slag Engineering Solution - Metallurgical Consulting Supports Steel Plant's Circular Economy Strategy. *RHI Magnesita Bulletin - 2022,* pp. 21-28.

[9] Klitzsch, M., Krischanitz, R. & Telser, H., 2021. RHI Magnesita is Leading the Way to a Circular Economy in the Refractory Industry. *RHI Magnesita Bulletin - 2021,* pp. 12-14.

[10] Kunanz, H., Nonnen, B., Kirowitz, J. & Schnalzger, M., 2022. Successful Implementation of a High Recycling Containing Magnesita-Carbon Brick in Steel Ladles. *RHI Magnesita Bulletin - 2022,* pp. 17-20.

[11] Maroto-Valer, M. et al., 2005. Activation of magnesium-rich minerals as carbonation feedstock materials for CO2 sequestration. *Fuel Processing Technology,* October, 86(14-15), pp. 1627-1645.

[12] Mordor Intelligence, 2021. *Refractories Market - Growth, Trends, COVID-19 Impact, and Forecasts (2022 - 2027).* [Online] Available at: https://www.mordorintelligence.com/industry-reports/refractories-market [Accessed 8 November 2022].

[13] Nakamura, Y. et al., 1999. Recycling of Refractories in the Steel Industry. *Indust. Ceram. ,* II(19), pp. 111-114.

[14] Noll, R. et al., 2018. LIBS analysis for industrial applications - an overview of developments from 2014 to 2018. *Anal. At. Spectrom.,* Volume 33, pp. 945-956.

[15] Odreitz, W., 2016. Recycling Refractories from an Enduser´s Viewpoint. *Proceedings Mineral Recycling Forum.*

[16] RHI Magnesita GmbH, 2022. *RHI Magnesita Annual Report,* s.l.: s.n.

[17] Ribeiro, T. et al., 2021. Alternatives to Reduce the Carbon Footprint in Refractory Raw Material Production Processes. *RHI Magnesita Bulletin - 2021,* pp. 16-21.

[18] Roskill, 2010. *Magnesium Compounds & Chemicals: Global Industry Markets & Outlook, Eleventh Edition,* London: Roskill Information Services Ltd.

[19] Roskill, 2013. *Magnesium Compounds and Chemicals: Global Industry Markets and Outlook, Twelfth Edition,* London: Roskill Information Services Ltd.

[20] Schneider, L., Berger, M. & Finkbeiner, M., 2015. Abiotic resource depletion in LCA—Background and update of the anthropogenic stock extended abiotic depletion potential (AADP) model. *Int. J. Life Cycle Assessment,* 12 February, Issue 20, pp. 709-721.

[21] Teir, S., Eloneva, S., Fogelholm, C. & Zevenhoven, R., 2009. Fixation of carbon dioxide by producing hydromagnesite from serpentinite. *Applied Energy,* February, 86(2), pp. 214-218.

[22] van Oers, L., de Koning, A., Guinée, J. & Huppes, G., 2002. Abiotic Resource Depletion in LCA: Improving Characterization Factors for Abiotic Resource Depletion as Recommended in the New Dutch LCA Handbook. *Road and Hydraulic Engineering Institute, Ministry of Transport and Water, Amsterdam.*

621

# THERMODYNAMICS OF INTERFACES IN THE REFINING OF CLEAN STEELS AND ITS IMPORTANCE TO THE DESIGN OF CERAMIC PLUGS

L. O. Z. Falsetti [a], R. Delfos [b], F. Charruault [c], B. Luchini [c], D. van der Plas [c], D. N. F. Muche [a], V. C. Pandolfelli [a]

[a] Federal University of Sao Carlos (UFSCar), Graduate Program in Materials Science and Engineering, São Carlos, Brazil

[b] Delft University of Technology (TUDelft), Delft, Netherlands

[c] Tata Steel Nederland, IJmuiden, Netherlands

## ABSTRACT

Refractory solutions go beyond thermal management during the secondary refining of liquid steel. For instance, refractory bubbling devices might be applied in the ladle to homogenise the molten bath (chemically and thermally) and to induce the floating of non-metallic inclusions to the slag phase. These inclusions are typically ceramic phases and have many origins along the steelmaking, e.g., the deoxidation step, the re-entrainment of slag and the erosion of refractories. Their effect on the mechanical properties of steels may be detrimental based on the severity of the processing step and the stresses during the application. To illustrate, inclusions could lead metallic axles to an early fatigue failure by acting as stress concentrators under cyclic loading. Therefore, the design of high-performance ceramic plugs and the production of cleaner steel grades rely on understanding the fundamentals of non-metallic inclusions captured by the gas bubbles. From a thermodynamic point of view, this attachment changes the system's energy related to the interfacial energies among the phases, which can drive the system to a meta-stable configuration where the detachment of the particle is unlikely, mainly for non-wettable particles. Thus, this work uses a thermodynamic model to discuss the influence of the particle's wettability on its removal rate and efficiency. Besides, it analyses the design of a flotation water model to conduct physical simulations assessing the theoretical calculations. Based on the results, suggestions are proposed to improve the removal of non-metallic inclusions during the secondary metallurgy of steels.

## INTRODUCTION

The removal of non-metallic inclusions (NMI) is one of the goals for the secondary refining of steels and is conducted by injecting inert gases through porous bubblers either in the ladle or in the tundish. From a macroscopical point of view, the bubble plume interacts with the molten metal to capture inclusions, carrying them to the slag layer. If properly adjusted (i.e., in chemical and rheological aspects), this top molten layer irreversibly dissolves the NMI, positively contributing to the cleanliness of the molten bath [1]. On the other hand, understanding the underlying microscopical mechanisms allows one to tune the process parameters and increase the removal rate and efficiency of the bubble-induced flotation which might also lead to the development of porous bubblers [2]. In this sense, the literature describes three mechanisms by which inclusions interact with bubbles: (A) they can be attached to the gas bubble's surface, (B) captured in the bubble wake region and/or (C) dragged by the flow pattern induced by the bubble plume, as represented in Fig. 1 [3,4]. It is worth noting that only mechanism "A" relies on a three-phase contact among the inclusion, gas bubble and liquid medium. Thus, it may become relevant to investigate the interface tensions and their influence on the attachment step.
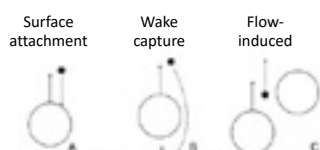


Fig. 1: Mechanisms involved in the bubble-induced flotation of particles in liquid media.

The thermodynamics of particle attachment has been previously investigated by the authors in a former paper [5] that could be summarised as depicted in Fig. 2. From the moment when the bubble-particle collision takes place, the three-phase contact line defines an angle for the particle on the bubble's surface ($\theta$). By increasing this angle, the particle moves towards the bubble, facing an energy barrier to its attachment ($\Delta E_a$). Thus, the magnitude of this energy barrier can be related to the easiness of capturing the inclusion. Once overcome, the system seeks a local minimum energy point, corresponding to the stable contact angle ($\theta_e$). In some cases, typically for liquidphobic inclusions, this point also corresponds to a global minimum, so the detachment of the inclusion back to the liquid phase is unlikely. If it was to occur, the particle would need enough energy to overcome a detachment barrier ($\Delta E_d$), which is higher than the attachment one ($\Delta E_a$) when the attachment represents a lowering in the system energy (i.e., $\Delta E_{att} < 0$). Instead, the detachment barrier is lower than the attachment one for liquidphilic particles, as $\Delta E_{att} > 0$. Then, the particle could still be attached to the bubble surface, though in a metastable condition as it does not represent a global minimum energy point.
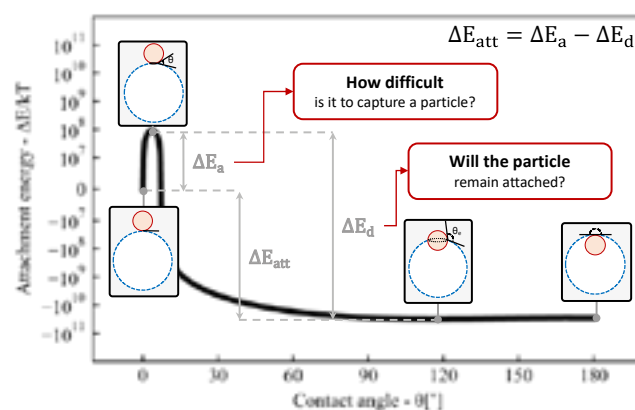


Fig. 2: Typical energy curve for the particle attachment [5].

Therefore, this work presents the design of experiments on a water model to assess the flotation of hydrophobic and hydrophilic particles. The particle concentration was measured timewise and the decay due to particle removal was exponentially fitted to get insights about the removal rate and process efficiency. The results suggest that bubble injection speeds up the flotation of hydrophobic particles and increases the removal efficiency.

## METHODS

Aiming at investigating the induced flotation of inclusions with different wettabilities, two grades of particles with similar size distributions were selected. Potters Q-Cel 7014 and 3M Glass Bubbles K-20 were employed as hydrophobic and hydrophilic particles, respectively. Both are spherical glass hollow spheres, with a density lower than the water one, as presented in Tab. 1. However, as the particle density is directly related to the ratio between its glass thickness layer and the hollow bulk, one could expect that smaller particles have a higher density, approaching the solid glass one. Thus, the particles were dispersed on a 3:2 water-isopropanol solution and wet-sieved down to 75 μm. The particles (as received) and the obtained suspensions were characterised in a Malvern

Panalytical Mastersizer 2000 to get their size distribution, coupled with a Hydro 2000S sample dispersion unit. In these analyses, the solvent phase was ethanol 96% v/v for the hydrophobic particle and deionized water for the hydrophilic particle. All samples were analysed according to Fraunhofer's theory of light scattering. Besides, SEM micrographs were obtained in a TESCAN MIRA electron microscopy under high vacuum, with an acceleration voltage of 25kV, a working distance of 15 µm, and a beam current of 300 pA. Samples were coated with a 10nm layer of AuPd alloy.

Tab. 1: Glass particles employed in the flotation experiments.

| Particle | Wettability | Density [g/cm³] |
|---|---|---|
| 3M Glass Bubbles K-20 | hydrophilic | 0.20 |
| Potters Q-Cel 7014 | hydrophobic | 0.14 |

The water model consisted of a 1000x400x40mm³ vessel with acrylic walls to allow the visualisation of the experiments, as illustrated in Fig. 3. The system is filled in with softened tap water and has a pump to recirculate the aqueous suspension and homogenise the concentration of particles. During the experiments, the pump is kept at 900 rpm, corresponding to a recirculating flow of 21 L/min or a velocity of roughly 22 mm/s when considering the model's cross-section. Besides, a porous bubbler was installed at the centre of the model's base, where compressed air was blown to generate bubbles of roughly 1.1 mm.
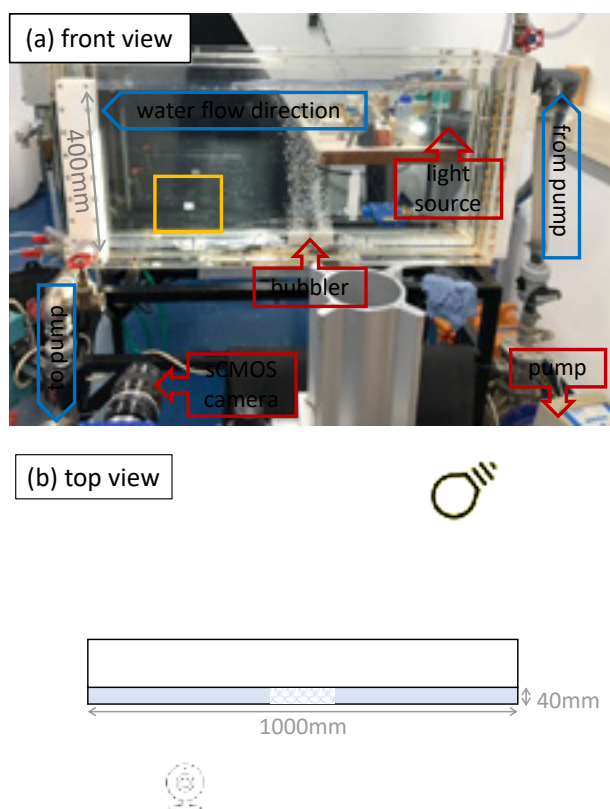


Fig. 3: Water model's (a) front view - highlighting the recirculation path (in blue), the various apparatus (in red) and the field of view (in yellow) - and (b) top view – illustrating the light scattering system.

The concentration of particles was indirectly measured by a light scattering technique, as represented in Fig. 3b. The system had been previously calibrated within the analysed range (700-9000 counts). A 250-watt tungsten-halogen lamp, located in the back part of the model, was used as a source of collimated light. The light rays are scattered by the particle and collected by a scientific CMOS camera (LaVision Imager) in front of the model, at 1 Hz. Each frame has 2160x2560 pixels, is 16-bit deep, and corresponds to a 1 ms exposure

time. The camera has a Nikon 55mm lens installed at full aperture (f/2.8).

Before starting the experiments, 80 mL of particle suspension was injected close to the water outflow, and the model was homogenised for 5 minutes. Then, the natural flotation of particles was recorded for 10 minutes and fitted by an exponential decay function ($I(t) = I_\delta \cdot \exp(TS^{-1} \cdot t) + I_\infty$), where TS stands for "time scale" and represents the mean lifetime of particles in suspension. Next, compressed air was injected through a porous bubbler at 100 NL/min, and the induced flotation of particles was recorded for 25 minutes and mathematically adjusted. Finally, particles were filtered out, and the system's background with bubbles was measured.

## RESULTS AND DISCUSSION

### Suspension characterisation
The hydrophilic and hydrophobic particle grades were characterised by their size distribution before and after the wet-sieving procedure, resulting in a suspension of fine particles. The results of size distribution are presented in Fig. 4 and summarised in Tab. 2. Based on the results, one can notice the similarity of size distribution between the hydrophilic and hydrophobic grades. It is also possible to infer that the sieving procedure not merely removed particles above 75 µm but generated a new distribution of smaller particles. For the hydrophilic grade, the values of $d_{10}$, $d_{50}$ and $d_{90}$ were cut down by two-thirds whereas these values decreased by roughly a half for the hydrophobic one.

Tab. 2: Particles diameters measured from their size distribution before and after the wet-sieving procedure.

| Sample | | $d_{10}$ [µm] | $d_{50}$ [µm] | $d_{90}$ [µm] |
|---|---|---|---|---|
| as received | 3M K-20 | 21.6 | 51.1 | 100 |
| | Potters 7014 | 20.2 | 57.6 | 114 |
| in suspension | 3M K-20 | 14.2 | 34.2 | 66.1 |
| | Potters 7014 | 10.1 | 28.5 | 64.3 |
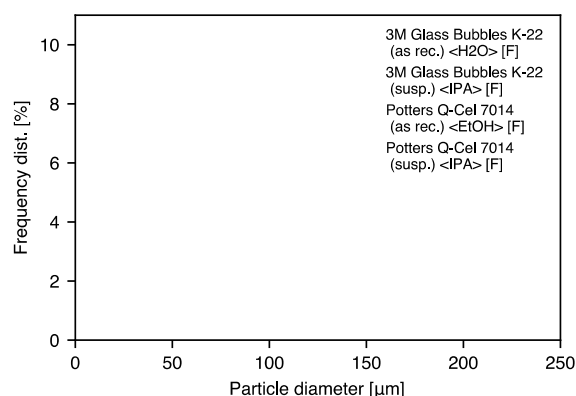


Fig. 4: Particle size distribution obtained by a Malvern analyser before and after the wet-sieving procedure.

The particles and their suspensions were also analysed by electron microscopy and the micrographs are presented in Fig. 5 a-d. The images show that the particles are perfectly round, and few fragments and debris are observed in the samples before sieving. There is a noticeable decrease in particle size after wet-sieving and preparing the suspensions, which confirms the results of Fig. 4. However, broken particles were also among the sieved fraction that was suspended, and the debris would tend to sediment during the experiments.

(a)

(b)

(c)

(d)
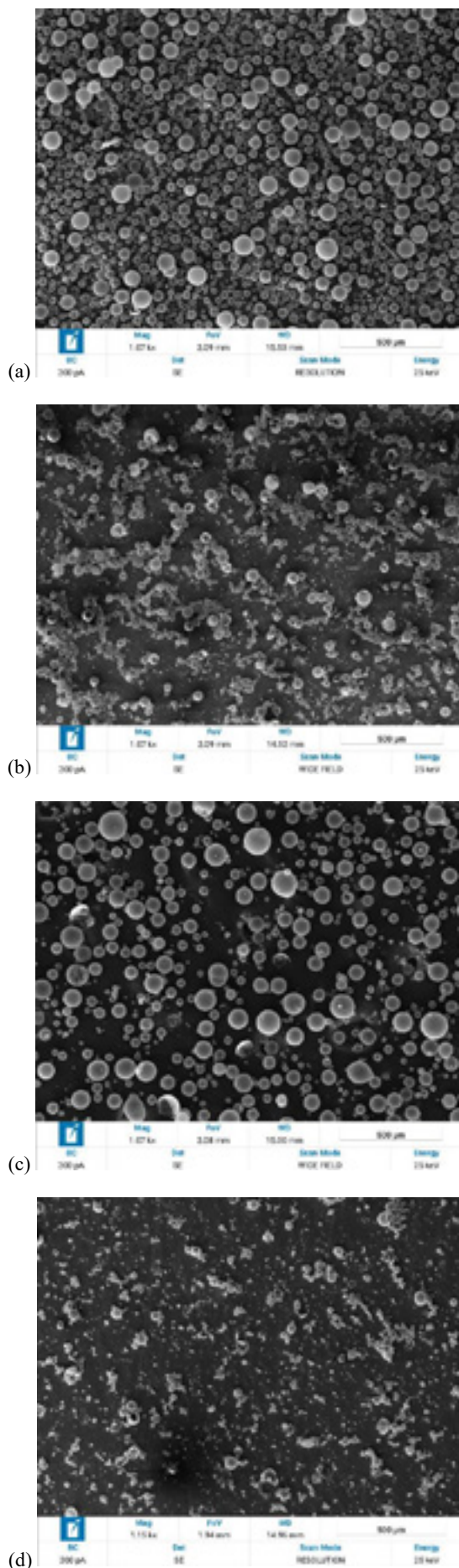
Fig. 5: Micrographs of (a,b) hydrophilic and (c,d) hydrophobic particles, before and after wet-sieving, respectively.

**Flotation experiments of hydrophobic and hydrophilic particles**

The sieved suspension of hydrophobic particles was employed in the flotation experiment, and the results are shown in Fig. 6, which presents the average pixel intensity in the obtained images as a function of time. The highest intensity in the beginning represents that more light rays were scattered by the particles, due to their higher concentration. After the homogenisation step, the average intensity of pixels (4640 counts) is taken as 100% for the concentration of particles. The first decay in Fig. 6 represents the particles' natural flotation (NF), as no gas bubbles were being injected into the system. The exponential fitting shows that particle concentration tends to 3127 counts at an infinite time, corresponding to a removal efficiency of 40.4 % (Eff. NF). When bubbles were injected into the system, the flotation speeded up as the TS parameter was reduced from 607 to 138 seconds. Besides the 3.4 times faster removal, the efficiency increased to 49.0 % (Eff. N&IF) when the mechanisms of induced flotation were coupled by the bubble plume.
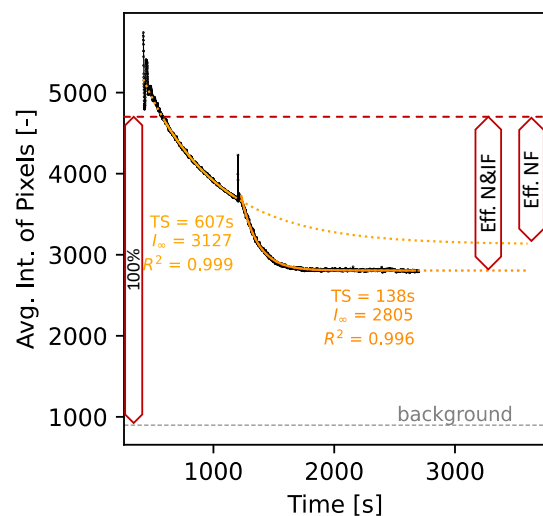


Fig. 6: Intensity of scattered light as a function of time for the flotation experiment of hydrophobic particles. The 100% concentration and the efficiencies are highlighted.

Even though the experiment with hydrophobic particles highlighted the higher removal rate and efficiency when bubbles were injected, it is not possible to correlate these results with individual mechanisms of induced flotation, as pointed out in Fig. 1. Thus, the same experiment was carried out with the sieved suspension of hydrophilic particles and the results are presented in Fig. 7. Under these conditions, the average intensity of 5089 counts was obtained after the system homogenisation and taken as the 100% concentration of particles. During the natural flotation step, the exponential fitting led to a TS parameter of 687 seconds and an efficiency of 56.5 %.

In contrast to the previous experiment, the injection of bubbles initially led to an increase in the average intensity, as highlighted in Fig. 7. This effect might be related to the re-entrainment of particles from the top surface of the system as the bubble plume locally increases the instability of this layer. After 10 minutes, the removal and the re-entrainment of particles came to a stable condition, and the results were fitted by an exponential decay equation. Although the removal rate decreased 2.4 times, with TS going from 607 to 2351 seconds, the efficiency was still higher when induced flotation mechanisms were coupled (64.5 %). However, these results were affected by the instability of the water model's top layer and do not represent the behaviour of a slag phase, in which inclusions could be dissolved when reaching the metal-slag interface.
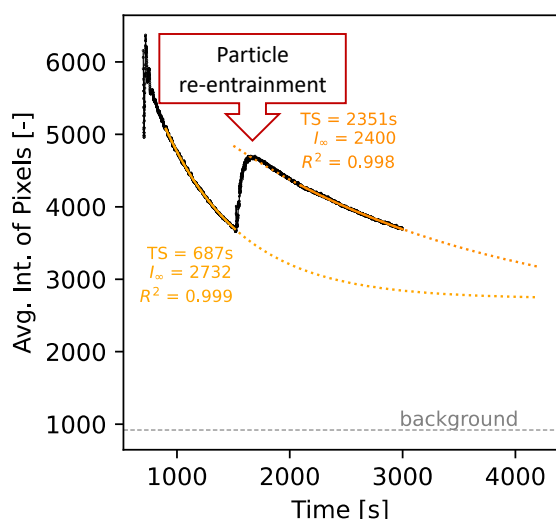
*Fig. 7: Intensity of scattered light as a function of time for the flotation experiment of hydrophilic particles, highlighting the particle re-entrainment after bubble injection starts.*

The instability of the floated particles layer at the water model's top region may be related to the thermodynamics of capturing particles at liquid-gas interfaces. As shown in Fig. 8, the change in energy due to the attachment depends on the macroscopic contact angle ($\theta_{slg}$) among the solid, liquid and gas phases, defining three scenarios:

– Non-wettable particles (90° or higher) show a negative $\Delta E_{att}$, causing the detachment barrier to be higher than the attachment one ($\Delta E_a < \Delta E_d$). Thus, particles are stable at the liquid-gas interface, as in the experiment with hydrophobic particles (Fig. 6);

– Slightly wettable particles (around 60°) can still be attached to the liquid-gas interface because a local minimum energy point is observed beyond the attachment barrier. However, it represents a meta-stable condition as $\Delta E_{att}$ is positive (and $\Delta E_d < \Delta E_a$), causing the particle to easily detach and return to the liquid phase;

– Highly wettable particles (30° or lower) do not even have a metastable condition of attachment, and the energy components ($\Delta E_{att}$, $\Delta E_d$ and $\Delta E_a$) are not applicable.
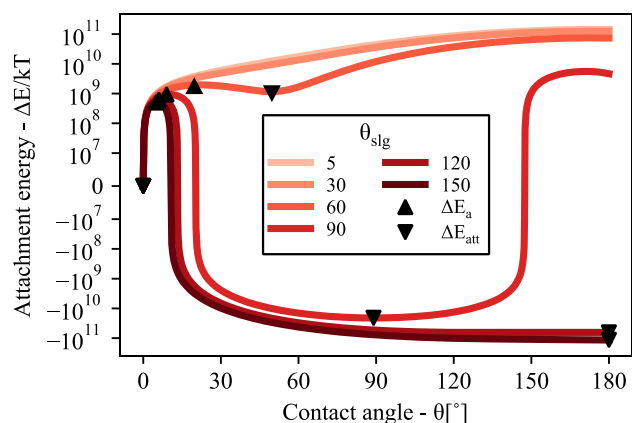


*Fig. 8: Change in energy caused due to the attachment of a particle at a liquid-gas interface as a function of its position for different values of macroscopic contact angles ($\theta_{slg}$).*

Considering that the hydrophilic grade of particles (3M Glass Bubbles K-20) was made of soda-lime-borosilicate glass, one could expect a low macroscopic contact angle in contact with aqueous solutions and, therefore, a condition close to the third scenario – where particles are not stable at the liquid-gas interface. Thus, the naturally floated particles remained at the model's top surface merely because of their low density (compared to the water phase) and re-entrained the system when the bubble plume was started, increasing the turbulence of the top layer. On the other hand, the additional

flotation mechanisms - related to either the particles captured by the bubble wake region or by the induced flow pattern – would still be activated, which explains the higher efficiency of removal when bubbles were injected (Fig. 7). Therefore, changes in the system to remove the floated particles right after reaching the top layer would be required for future experiments so that it suitably acts as a slag layer.

**CONCLUSIONS**

This work studied the flotation behaviour of hydrophobic and hydrophilic hollow glass particles by conducting experiments on a water model and measuring the particle concentration by a light scattering technique. Particles were pre-dispersed in an isopropanol-water solution and wet-sieved to generate inclusion-like suspensions. The natural flotation of both particles presented a similar removal rate. When 1.1 mm bubbles were injected, the removal rate for hydrophobic particles increased by 3.4 times, and the removal efficiency improved from 40.4 to 49.0 %. Conversely, the naturally floated hydrophilic particles re-entrained from the model's top region as bubbles were injected, and no conclusions could be drawn about the contribution of the bubble plume to the removal rate and efficiency. Such an effect was expected as these particles are highly wet by the liquid and not captured by the liquid-gas interface due to their low contact angle.

**REFERENCES**

[1] Ren Y, Zhu P, Ren C, Liu N, Zhang L. Dissolution of SiO₂ inclusions in CaO-SiO₂-based slags in situ observed using high-temperature confocal scanning laser microscopy. Metallurgical and Materials Transactions B 2022;53:682–92. https://doi.org/10.1007/s11663-021-02401-5.

[2] Falsetti LOZ, Ferreira Muche DN, Andreeta MRB, Moreira MH, Pandolfelli VC. Bubble generation in refractory porous plugs: The role of the ceramic surface composition. International Journal of Ceramic Engineering & Science 2022;4:199–210. https://doi.org/10.1002/ces2.10132.

[3] Zheng S, Zhu M. Physical modelling of inclusion behaviour in secondary refining with argon blowing. Steel Res Int 2008;79:685–90. https://doi.org/10.2374/SRI07SP134-79-2008-685.

[4] Yang HL, He P, Zhai YC. Removal behavior of inclusions in molten steel by bubble wake flow based on water model experiment. ISIJ International 2014;54:578–81. https://doi.org/10.2355/isijinternational.54.578.

[5] Falsetti LOZ, Ferreira Muche DN, Santos Junior T dos, Pandolfelli VC. Thermodynamics of smart bubbles: The role of interfacial energies in porous ceramic production and non-metallic inclusion removal. Ceram Int 2021;47:14216–25. https://doi.org/10.1016/j.ceramint.2021.02.006.

# THERMODYNAMIC SIMULATION OF SLAG–REFRACTORY–INTERACTIONS IN DIFFERENT METALLURGICAL SYSTEMS

E-P. Heikkinen, V-V. Visuri, R. Mattila
University of Oulu, Oulu, Finland

M. Lindgren
Metso, Pori, Finland

A. Laukkanen, E. Huttunen-Saarivirta, T. Andersson, M. Lindroos
VTT, Espoo, Finland

## ABSTRACT

Contact with molten slags is one of the key reasons for chemical wear of refractory materials used in the metallurgical industry. Computational thermodynamics and equilibrium simulations offer a fast method to estimate the driving force for chemical wear in situations in which refractory material is in contact with reactive fluids such as slags. The purpose of this study was to estimate the possible wear mechanisms based on thermodynamic simulations executed with commercial thermochemistry software FactSage and its databases. Interactions between different refractory materials and slags with compositions corresponding stainless steelmaking and flash smelting slags (both copper and nickel matte production) were studied. Based on the results of these simulations, the driving forces for direct and indirect dissolution, formation of new solid phases as well as other forms of chemical interaction were estimated. The results of the simulations were compared with the analyses of industrial samples as well as results of the laboratory experiments. Based on the results of the simulations, it is possible to predict the chemical wear of refractory materials caused by slags.

## INTRODUCTION

Depending on the conditions, the wear of the refractory materials in pyrometallurgical processes is caused by different combinations of thermal, mechanical and chemical stresses. In order to estimate the durability of different materials under different conditions, it is necessary to know the wear mechanisms caused by the stresses mentioned above. Although the characterization of materials either tested in laboratory experiments or used in actual processes can provide more reliable information on the behavior of materials, the computational simulation tools can offer a faster, cheaper, safer and more reproducible way to predict the possible wear mechanisms of different materials.

With a focus on the chemical stresses caused by molten slags, the wear mechanisms can be roughly divided into three categories: (1) direct dissolution, (2) indirect dissolution and (3) formation of new (solid) phases on the slag/refractory-interface. In the third mechanism the refractory material is not worn by the chemical reaction itself, but the formation of new phases may cause mechanical stresses which, in turn, can cause wear of the material.

The aim of this research was to estimate, whether the chemical wear mechanism caused by molten slags can be predicted from the results of thermodynamic simulations made with a commercial thermochemistry software (FactSage) and its databases. For this purpose, the simulation results were compared with the results of laboratory experiments as well as *post mortem* analyses of industrially used refractory materials.

## METHODS

Thermodynamic simulations were made for refractory-slag-systems in which the total composition of the system varied from 100% refractory material to 100% slag. Thermochemical software FactSage (version 8.0) and its FactPS, FToxid and FSstel databases were used in the simulations. As a result, thermodynamically stable phases for different refractory/slag-ratios in given conditions (*i.e.* temperature and pressure corresponding the conditions in chosen industrial processes) were obtained. These results illustrate what can happen when different portions of refractory material and molten slag are in contact with each other. For example, if the proportion of molten oxide phase in equilibrium is larger than its initial proportion, there is a driving force for dissolution. On the other hand, the existence of solid phases not present in the unused refractory material indicate the possibility for the formation of solid product layers on the slag/refractory-interface.

The studied refractory/slag-systems are shown in Table 1, whereas the chemical compositions of the considered refractory materials and slags are shown in Tables 2 and 3. The highest simulation temperatures were chosen to correspond the temperatures in studied industrial processes, whereas the lower temperatures simulate the conditions inside the refractory materials close to the interface. Atmospheric pressure was chosen for all studies except for the system, in which refractory/slag-interactions in steel ladle vacuum treatment were simulated. Magnesia-carbon-refractories with two different C-contents were studied: (1) one with lower carbon content for the chrome converter system and (2) one with higher carbon content for the steel ladle vacuum treatment system. The numbers (1) and (2) in Tables 1 and 2 indicate these two different materials. Three refractory materials studied in the flash smelting furnace systems were identical for both copper and nickel production systems.

Validation was made by comparing the simulation results with the results of the laboratory experiments (crucible tests) executed for similar systems as well as with the characterisation of used industrial refractory materials.

Tab. 1: Refractory/slag-systems studied in this research.

| Process | Refractories (main components) | Slag compositions | T (°C) | p (kPa) |
|---|---|---|---|---|
| Chrome Converter (CRC) (Stainless steelmaking) | MgO-C (1) $Al_2O_3$-$SiO_2$ | Corresponding industrial CRC-slag (3 different basicities; CRC1-3) | 1400-1650 | 101 |
| Flash Smelting Furnace (FSF) (Production of copper matte) | MgO-$Cr_2O_3$ $Al_2O_3$-$Cr_2O_3$ SiC-$Al_2O_3$ | Corresponding industrial FSF-slag in copper production (FSF1) | 1100-1350 | 101 |
| Flash Smelting Furnace (FSF) (Production of nickel matte) | MgO-$Cr_2O_3$ $Al_2O_3$-$Cr_2O_3$ SiC-$Al_2O_3$ | Corresponding industrial FSF-slag in nickel production (FSF2) | 1100-1400 | 101 |
| Vacuum Tank Degassing (VTD) (Steelmaking) * | MgO-C (2) MgO-$Al_2O_3$ | Corresponding ladle slag in steelmaking (reduced/unreduced; VTD1-2) | 1550-1700 | 101 / 0.7 |

* Simulations for the VTD-system were executed with an earlier version of the FactSage (7.2) and the results have been presented in [1].

Tab. 2: Normalized refractory compositions (in weight-%) studied in this research. Compositions of VTD-refractories taken from [1].

| Refr. | MgO | SiO₂ | Fe₂O₃ | CaO | Al₂O₃ | TiO₂ | Cr₂O₃ | K₂O | ZrO₂ | P₂O₅ | SiC | C |
|---|---|---|---|---|---|---|---|---|---|---|---|---|
| MgO-C (1) | 90.80 | 0.94 | 0.75 | 1.51 | | | | | | | | 6.00 |
| Al₂O₃-SiO₂ | | 13.13 | 1.62 | | 81.82 | 3.03 | | 0.40 | | | | |
| MgO-Cr₂O₃ | 59.62 | 0.50 | 13.53 | 1.30 | 6.01 | | 19.04 | | | | | |
| Al₂O₃-Cr₂O₃ | | 3.04 | 0.51 | | 80.12 | | 9.63 | | 5.58 | 1.12 | | |
| SiC-Al₂O₃ | | 3.05 | 0.10 | 0.61 | 6.10 | | | | | 1.63 | 88.50 | |
| MgO-C (2) | 85.88 | 0.53 | 0.53 | 1.06 | | | | | | | | 12.00 |
| MgO-Al₂O₃ | 4.00 | 1.00 | 0.20 | 1.00 | 93.30 | | | 0.50 | | | | |

Tab. 3: Normalized slag compositions (in weight-%) studied in this research. Compositions of VTD-slags taken from [1].

| Slag | MgO | SiO₂ | Fe₂O₃ | CaO | Al₂O₃ | TiO₂ | Cr₂O₃ | Fe₃O₄ | CoO | Cu₂O | FeO | NiO | MnO | S |
|---|---|---|---|---|---|---|---|---|---|---|---|---|---|---|
| CRC1 | 16.64 | 21.15 | | 33.89 | 18.09 | 0.26 | 7.07 | | | | 2.81 | 0.09 | | |
| CRC2 | 16.64 | 29.29 | | 25.75 | 18.09 | 0.26 | 7.07 | | | | 2.81 | 0.09 | | |
| CRC3 | 16.64 | 37.43 | | 17.61 | 18.09 | 0.26 | 7.07 | | | | 2.81 | 0.09 | | |
| FSF1 | 1.78 | 31.01 | | 3.90 | 9.14 | | | 7.20 | | 1.28 | 44.04 | | 1.04 | 0.62 |
| FSF2 | | 34.10 | 12.78 | | | | | 0.75 | 0.40 | | 45.99 | 5.99 | | |
| VTD1 | 6.52 | 7.43 | | 52.14 | 33.91 | | | | | | | | | |
| VTD2 | 6.19 | 4.12 | | 47.42 | 11.34 | | | | | | 20.62 | | 10.31 | |

## RESULTS AND DISCUSSION

A few examples of the results of thermodynamic simulations are shown in Figure 1. The examples in Figure 1 have been chosen to represent different kind of potential wear mechanisms. A more comprehensive summary of potential wear mechanisms for different slag/refractory-systems is shown in Table 4.

Results of the MgO-C (1) / CRC1 -system at 1650 °C (presented in Figure 1(a)) illustrate a system in which the phases existing in thermodynamic equilibrium correspond almost exactly with the initial phases. This represents a more or less "ideal" situation, in which there is no driving force for either dissolution (direct or indirect) or formation of new solid phases in the refractory/slag-interface. Small stability area of spinel solid solution in the lower right-hand corner of the Figure 1(a) indicates, that the slag is not homogeneously molten at 1650 °C.

Results of the MgO-C (2) / CRC3 -system at 1650 °C (presented in Figure 1(b)) illustrate a system in which the phases existing in thermodynamic equilibrium still correspond rather well with the initial phases, but in in which the stability area of the molten slag is larger in comparison to the situation presented in Figure 1(a). For instance, a system consisting of 50% of slag and 50% of refractory material has an equilibrium composition with approximately 40% of solid phases. This difference indicates the driving force for the dissolution of refractory material in these conditions. The lack of new solid phases (*i.e.* phases not existing in the initial system) suggests that the dissolution would be direct.

Results of the Al₂O₃-SiO₂ / CRC2 -system at 1650 °C (presented in Figure 1(c)) illustrate an example in which the driving force for the chemical wear of the refractory material is much larger than in the situations presented in Figures 1(a) and 1(b). A very large stability area of the molten slag phase indicates a strong driving force for the dissolution. If a smaller amount of molten slag is assumed to be in equilibrium with the refractory material (situation shown in the left-hand side of the Figure 1(c)), there is a driving force for direct dissolution of the corundum phase. If the amount of molten slag is increased, a new phase (spinel solid solution) is formed and dissolution is likely to occur indirectly. In addition to this severe chemical instability in studied conditions, it is also seen from Figure 1(c) that this refractory material does not have a sufficient thermal resistance at 1650 °C either, since the stability area of the molten slag extends all the way to the system consisting of 100% refractory material. According to the thermodynamic simulations, approximately one third of the material would melt at 1650 °C even when it is not in contact with slag at all.

Results of the MgO-Cr₂O₃ / FSF1 -system at 1350 °C (presented in Figure 1(d)) illustrate a system in which the stability region of the molten slag phase is smaller in comparison to previous three examples, but which contains a relatively large stability area for a new solid phase (olivine) in addition to the solid phases already existing in the original refractory material (spinel and monoxide). Similar to the system presented in Figure 1(a), there is no driving force for dissolution in this system, but unlike in Figure 1(a), the occurence of the olivine phase indicates a clear driving force for the interactions between the refractory material and molten slag. Instead of dissolution, a solid olivine phase is formed due to this reaction. From the perspective of refractory durability, this new phase could act as a protective layer (forming autogeneous lining) when formed on the interface, or it could cause mechanical stresses when formed in the pores of the refractory material.

Results of the Al₂O₃-Cr₂O₃ / FSF2 -system at 1400 °C (presented in Figure 1(e)) illustrates a system which also contains a large stability area for a new solid phase (in this case spinel) in addition to the solid phases existing in the original material (in this case corundum and ZrSiO₄). The magnitude of the molten slag phase stability region indicates that there is only a very small driving force for dissolution. A comparison of Figures 1(d) and 1(e) reveals that the major difference between these systems is related to the location of the stability region of the new phase. In the MgO-Cr₂O₃ / FSF1 -system (Figure 1(d)) this stability region of olivine decreases the size of the molten slag stability region, where as in the Al₂O₃-Cr₂O₃ / FSF2 -system (Figure 1(e)) the formation of the new phase (spinel in this case) decreases the size of the solid corundum stability region. This difference could indicate that in the MgO-Cr₂O₃ / FSF1 -system the forming olivine phase is more likely to form on the refractory/slag-interface (*i.e.* grow outwards), whereas in the Al₂O₃-Cr₂O₃ / FSF2 -system the forming spinel phase is likely to form inside the refractory material (*i.e.* grow inwards) as the original corundum phase reacts into spinel as a consequence of interaction with the molten slag.

Results of the SiC-Al₂O₃ / FSF1 -system at 1350 °C (presented in Figure 1(f)) illustrate a system with clear driving forces for various chemical reactions between the refractory material and molten slag. Even though there is no significant driving force for the dissolution in this system, the high reactivity makes the system very unstable for refractory purposes. It is seen from Figure 1(f) that the refractory material acts as a reductant and hence the conditions are reducing enough for oxidic iron (in the slag) to be reduced into metallic iron. Depending on how much carbon is dissolved into this metal phase, it may exist in either solid or liquid form, both of which are quite likely to cause severe stresses to the refractory materials. As FeO-content of the molten slag is decreased due to reduction of iron, some solid SiO₂ (not existing in the original refractory material) also precipitates as the slag composition changes and the solubility of SiO₂ is eventually exceeded. This formation of new solid phase may cause mechanical stresses if formed inside the refractory material. Furthermore, it is also possible for small amounts of gaseous reaction

products to form in the refractory/slag-interactions making the system even more reactive.

Examples of the results concerning steel ladle vacuum treatment system are not included in Figure 1, but the results of this case can be found in more detail in our previous paper [1] and the main results concerning these systems are also summarized in Table 4.

Phases described as "Others" in Figure 1 refer to phases, which exist in small quantities (between 0 and 2 wt-% of the total systems studied in this research) in the results of thermodynamic simulations, but which were estimated not to exist in real systems. The occurence

of these phases in the simulation results is mainly due to the lack of certain components in the used models. For instance, if a system is defined to contain small amounts of certain components which are likely to be dissolved in *e.g.* molten slag or some solid solution, but for which there is no thermochemical data available in the models used to describe these solutions, the results show these components as separate phases. However, these phases are included in the results shown in Figure 1 (especially 1(a) and 1(b)) in order to ensure that the total size of the system remains constant.

Tab. 4: Summary of conclusions based on the results of thermodynamic simulations. Systems also shown in Figure 1 are marked in **bold**.

| *Refractory* | *Slag* | *Potential wear mechanism* | *Observations concerning validation* |
|---|---|---|---|
| **MgO-C (1)** | **CRC1** | No driving force for chemical wear. | No dissolution in the laboratory experiments [2]. |
| MgO-C (1) | CRC2 | Very small driving force for direct dissolution. | No dissolution in the laboratory experiments [2]. |
| **MgO-C (1)** | **CRC3** | Small driving force for direct dissolution. | Minor direct dissolution in the laboratory experiments [2]. |
| $Al_2O_3$-$SiO_2$ | CRC1 | Large driving force for either direct (high refractory/slag -ratio) or indirect (low refractory/slag -ratio) dissolution. Indirect dissolution via spinel phase. Not enough thermal stability (melting). | Major direct dissolution in the laboratory experiments [2]. |
| **$Al_2O_3$-$SiO_2$** | **CRC2** | Large driving force for either direct (high refractory/slag -ratio) or indirect (low refractory/slag -ratio) dissolution. Indirect dissolution via spinel phase. Not enough thermal stability. | Major direct and indirect dissolution in the laboratory experiments [2]. |
| $Al_2O_3$-$SiO_2$ | CRC3 | Large driving force for either direct (high refractory/slag -ratio) or indirect (low refractory/slag -ratio) dissolution. Indirect dissolution via spinel phase. Not enough thermal stability. | Major indirect dissolution in the laboratory experiments [2]. |
| **MgO-$Cr_2O_3$** | **FSF1** | Clear driving force for the formation of olivine phase. Can form a protective layer (or cause mechanical stresses). No driving force for dissolution. | Calculation results in line with industrial experience. |
| $Al_2O_3$-$Cr_2O_3$ | FSF1 | Large driving force for the formation of spinel phase. Can cause mechanical stresses (or form a protective layer). Small driving force for indirect dissolution via spinel. | Calculation results consistent with laboratory experiments. |
| **SiC-$Al_2O_3$** | **FSF1** | Large driving force for the reduction of iron from slag (and formation of solid $SiO_2$ as slag composition changes). Potential gas formation. Highly reactive system. | Extensive reactions observed in laboratory experiments. |
| MgO-$Cr_2O_3$ | FSF2 | Large driving force for the formation of olivine phase. Can form a protective layer (or cause mechanical stresses). No driving force for dissolution. | Calculation results in line with industrial experience. |
| **$Al_2O_3$-$Cr_2O_3$** | **FSF2** | Clear driving force for the formation of spinel phase. Can cause mechanical stresses (or form a protective layer). Very small driving force for indirect dissolution via spinel. | Calculation results consistent with laboratory experiments. |
| SiC-$Al_2O_3$ | FSF2 | Very large driving force for the reduction of iron from slag (and formation of solid $SiO_2$ as slag composition changes). Potential gas formation. Highly reactive system. | Extensive reactions observed in laboratory experiments. |
| MgO-C (2) | VTD1 | No driving force for chemical wear in atmospheric pressure, but driving force for MgO+C-reaction in lowered pressure (not likely to occur in practice due to kinetic constraints) [1]. | No significant wear by dissolution based on the characterisation of industrial samples [1]. |
| MgO-C (2) | VTD2 | Driving force for several reactions: reduction of FeO (and MnO) from slag with carbon as a reductant; dissolution of carbon; precipitation of solid CaO (and MgO) from slag; formation of gaseous reaction products. Driving forces larger in the lowered pressure. Very reactive system (especially in lowered pressure). [1] | Increased wear of refractories when producing steel grades in which unreduced ladle slag is required [1]. |
| MgO-$Al_2O_3$ | VTD1 | Strong driving force for indirect dissolution via several new phases (CA2, CA6, C2M2A14). May cause layered structure close to the interface. Highly reactive system (not affected by pressure). [1] | Refractory material considered non-suitable for industrial slag-line applications due to high wear rate. Use of magnesia-carbon-bricks instead. [1] |
| MgO-$Al_2O_3$ | VTD2 | Very strong driving force for indirect dissolution via several new phases (CA2, C2M2A14). May cause layered structure close to the interface. Highly reactive system (not affected by pressure). [1] | Refractory material considered non-suitable for industrial slag-line applications due to high wear rate. Use of magnesia-carbon-bricks instead. [1] |
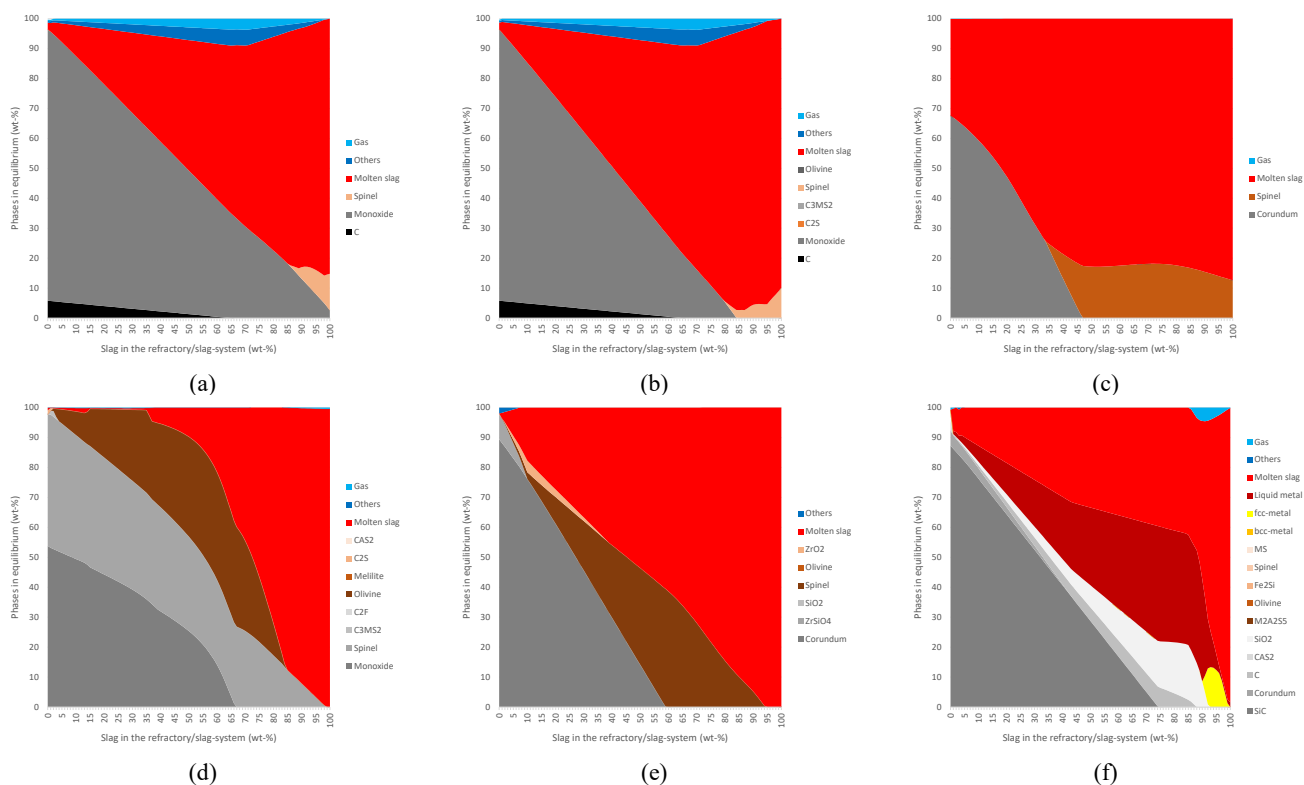
*Fig. 1: Examples of results of thermodynamic simulations:*
*(a) MgO-C (1) -refractory / CRC1-slag (1650 ℃).*
*(b) MgO-C (1) -refractory / CRC3-slag (1650 ℃).*
*(c) Al₂O₃-SiO₂-refractory / CRC2-slag (1650 ℃).*

*(d) MgO-Cr₂O₃-refractory / FSF1-slag (1350 ℃).*
*(e) Al₂O₃-Cr₂O₃-refractory / FSF2-slag (1400 ℃).*
*(f) SiC-Al₂O₃-refractory / FSF1-slag (1350 ℃).*

## CONCLUSIONS

Thermodynamic simulations provide a tool to predict to potential wear mechanisms of refractory materials caused by a contact with different kind of molten slags. Based on the simulation results it is possible to estimate the possibility for direct and indirect dissolution as well as formation of new phases on the refractory/slag-interface. The main results of the simulations made in this study for different pyrometallurgical refractory/slag-systems are as follows:

1.  MgO-C refractories used in the CRC process have a very good resistance against slags used in this process, but the driving force for direct dissolution increases as the slag basicity decreases.

2.  Al₂O₃-SiO₂-based refractories considered as a potential alternative for MgO-C-refractories proved to have neither sufficient thermal nor sufficient chemical resistance to be used in the CRC process.

3.  MgO-Cr₂O₃-based refractories used in the flash smelting furnaces in copper matte and nickel matte production have no driving force for dissolution, but nevertheless have a clear tendency to react with both copper and nickel production slags to form an olivine layer, which is likely to grow outwards from the refractory/slag-interface. This tendency is slightly larger for nickel production slags and smaller for copper production slags.

4.  Al₂O₃-Cr₂O₃-based refractories used in the flash smelting furnaces in copper matte and nickel matte production also have a tendency to react with slags and to form spinel phase, which in this case is likely to grow inwards inside the refractory material. There is also a small driving force for indirect dissolution (via formed spinel phase), which is slightly larger for copper matte production slags and slightly smaller for nickel slags.

5.  SiC-Al₂O₃-refractories considered as as an alternative for flash smelting furnaces proved to create a highly reactive system when in contact with flash smelting slags (both copper and nickel production). Refractory can act as a reductant and reduce oxidic iron

from the slag thus causing a new metallic phase (either solid or liquid) to form.

6.  MgO-C-refractories used in the steel ladle slag line have a very good resistance against reduced ladle slag, but can react aggressively with unreduced slags with higher FeO and MnO contents. Lowering the pressure creates a driving force for the reaction between MgO and C although this reaction is not likely to have a major role in the real process.

7.  Spinel-forming MgO-Al₂O₃-refractories used in steel ladles do not have a good chemical resistance against ladle slags.

The use of simulation tools may help to reduce the amount of required experiments and analyses, but it can never completely remove the need for validation. One should for example keep in mind, that the results of this study are based on thermodynamic simulations, which are not taking rate phenomena (*i.e.* reaction kinetics, transport phenomena) into account and are only indicative of the driving force for chemical wear.

## ACKNOWLEDGEMENTS

## REFERENCES

[1]  Heikkinen, E-P, Vatanen, J, Sihvonen, M, Pärkkä, H, Tähtilä, H, Mattila, R & Fabritius T. Proc. of the UNITECR 2019, Yokohama, Japan, Technical Association of Refractories, Japan. pp. 158-161.

[2]  Harju, A. Master's Thesis. University of Oulu, Finland, 2021.

# A COUPLED THERMO–CHEMO–MECHANICAL APPROACH TO SIMULATE THE OXIDATION OF SIC–BASED REFRACTORY CASTABLE

## J. Sayet, T. Sayet

*Univ. Orléans, LaMé (EA7494, Univ. Orléans, Univ. Tours, INSA CVL), Orléans, France*

**ABSTRACT**

Most of the industrial applications are subjected to severe work conditions in terms of heat, chemistry, and mechanical constraints. Nowadays, the existence of a numerical tool accounting for all the physics that take place is a major challenge for many industrial processes like steel and glass production, welding, nuclear fusion, etc. Some fully coupled theories exist in the literature [Hu and Shen 2013]. Rambert et al. [Rambert et al. 2006] developed a numerical tool accounting for thermal, transport, and mechanics but without the chemical reactions.

The goal of this study is to implement a coupled numerical tool within the framework of an irreversible thermodynamic process for reactive porous multiphase materials using a User-defined Element (UEL) subroutine. To validate the tool, an oxidation of a cylindrical shape SiC-based refractory castable under high temperature gradient is simulated in order to predict the swelling effects [Merzouki et al. 2014]. Note that some parameters are estimated due to the lack of reliable experimental data under high temperatures.

**INTRODUCTION**

In industrial applications, reactive porous multiphase materials are often encountered in processes where chemical reactions occur, such as combustion, catalysis, and chemical synthesis. The porous structure of these materials facilitates the exchange of reactants, products, and heat, making them suitable for various applications.

The behavior of reactive porous multiphase materials is governed by a mixture of physical and chemical factors. This comprises heat transfer, mass transfer, flow, chemical reactions, phase changes, and mechanical deformation. Modeling and simulating the various interactions and changes that occur within these materials necessitate the study of coupled thermo-chemo-mechanical processes. As a result, the requirement for a more improved knowledge of coupled multi-field phenomena has become increasingly critical, resulting in increased research interest in this area. Hence, fully coupled theories addressing thermo-chemo-mechanical interactions have been developed in the literature [Blond 2017; Hu and Shen 2013; Lemaitre et al. 2020]. Blond [Blond 2017] introduces the fully coupled problem using the irreversible thermodynamic process. Hu and Shen [Hu and Shen 2013] developed variational principles for coupled thermal-chemical-mechanical problems by applying the principles of non-equilibrium thermodynamics.

It is noted that numerous studies have been conducted on numerical simulation methods for solving coupled thermo-chemo-mechanical models. Rambert *et al* ([Rambert et al. 2006] examine the behavior of materials in which there is interaction between chemical species (chemical processes and diffusion), temperature, and elastic mechanical characteristics. Gigliotti and Grandidier [Gigliotti and Grandidier 2010] study the coupling of oxidation and mechanics in polymer matrix materials at high temperatures. Ulff *et al.* [Ulff et al. 2019] examine the impact of hydrogen diffusion on the thermomechanical behavior of nickel-titanium-based shape memory alloy structures. Loeffel *et al.* [Loeffel et al. 2013] investigate the oxidation of metal at high temperature. However, none of these models account for the effects caused by the chemical reaction, i.e., the link between mechanical deformation and reaction rate. On the other hand, many studies have exhibited the complicated relationship between chemical reactions and mechanical behavior [Craig 2012], i.e., it has been shown that the swelling is induced by oxidation of SiC-RC materials and leads to failure [Prigent et al. 2012; Rodrigues et al. 2011]. Thus, the full coupling between chemical processes and mechanical behavior must be considered.

In this paper, we derived the governing equations for fully coupled Thermo-chemo-mechanical system based on the irreversible thermodynamic process. Then, using a user-defined element (UEL) subroutine, we implement this model in a Abaqus finite element code. At last, we describe the application used to validate our tool. It consists of simulating the oxidation of SiC-based refractory material at high temperature [Merzouki et al. 2014].

**Coupled thermo-chemo-mechanical theory**

In order to define the thermo-chemo-mechanical model based on the irreversible thermodynamic process, it is necessary to determine the state variable, the balance equations, the behavior and evolution laws. A similar approach has been described in references [Blond 2017; Lemaitre et al. 2020].

The values of the state variables that maximize entropy S or decrease internal energy U while adhering to the system's mathematical restrictions related to equilibrium, laws of behavior, and laws of evolution describe the equilibrium state. Thus, it's crucial to select state variables carefully so that there are just enough independent variables to properly describe the model.

In this system, the state variables are as follows:
- The strain $\epsilon$
- The temperature T
- The mass title $x_i$
- The extent of the reaction $\xi_r$

According to the first principle of thermodynamics, the equilibrium equation is written as:

$$\rho\dot{u} - \dot{r} + div\,\vec{q} - \underline{\underline{\sigma}}{:}\underline{\dot{\epsilon}} - \sum_\alpha \frac{\rho\mu_\alpha}{M_\alpha}\dot{x}_\alpha + \sum_r \left(\sum_\alpha v_{\alpha r}\mu_\alpha\right)\frac{\dot{\xi}_r}{\Omega} + j^\alpha\,\vec{\nabla}\left(\frac{\mu_\alpha}{M_\alpha}\right) = 0 \qquad (1)$$

Where $\dot{u}$ is the internal energy, $\dot{r}$ is the external energy, q is the heat flux, $\sigma$ is the stress, $\mu_\alpha$ is the chemical potential, $v_{\alpha r}$ is the stoichiometric coefficient, $\Omega$ is the volume, $j^\alpha$ is the mass flux, $M_\alpha$ is the molar mass, $\alpha$ denotes the number of species and r denotes the number of reactions.

Furthermore, according to the 2nd law of thermodynamic, the inequality corresponds to:

$$\rho T\dot{s} \geq \dot{r} - Tdiv\left(\frac{\vec{q}}{T}\right) \qquad (2)$$

Next, the Helmoltz free energy depending on the four state variables is expressed as follows:

$$\psi = u - Ts \qquad (3)$$

Hence, substituting the first law of thermodynamics and the total derivative of the Helmoltz free energy in the 2nd law of thermodynamic, the Clausius-Duhem inequality becomes:

$$\left(\rho\frac{\partial\psi}{\partial\underline{\epsilon}^r} - \underline{\underline{\sigma}}\right)\underline{\dot{\epsilon}}^r + \rho\left(\frac{\partial\psi}{\partial T} + s\right)\dot{T} + \rho\sum_\alpha\left(\frac{\partial\psi}{\partial x_\alpha} - \frac{\mu_\alpha}{M_\alpha}\right)\dot{x}_\alpha + \sum_r\left(\rho\frac{\partial\psi}{\partial\xi_r} + \frac{\mathcal{A}_r}{\Omega}\right)\dot{\xi}_r - \underline{\underline{\sigma}}{:}\underline{\dot{\epsilon}} - T\vec{q}\overrightarrow{grad}\left(\frac{1}{T}\right)$$
$$+ \vec{j}^\alpha\vec{\nabla}\left(\frac{\mu_\alpha}{M_\alpha}\right) \leq 0 \qquad (4)$$

Where $\mathcal{A}_r = \sum_\alpha v_{\alpha r}\mu_\alpha$ is the affinity of the reaction.

Therefore, from the intrinsic dissipation, we can deduce the behavior laws of the reversible part $\left(\left(\rho\frac{\partial\psi}{\partial\underline{\epsilon}^r} - \sigma\right)\underline{\dot{\epsilon}}^r + \rho\left(\frac{\partial\psi}{\partial T} + s\right)\dot{T} + \rho\sum_\alpha\left(\frac{\partial\psi}{\partial x_\alpha} - \frac{\mu_\alpha}{M_\alpha}\right)\dot{x}_\alpha\right)$ and the evolution laws of the irreversible part $\left(\sum_r\left(\rho\frac{\partial\psi}{\partial\xi_r} + \frac{\mathcal{A}_r}{\Omega}\right)\dot{\xi}_r - \underline{\underline{\sigma}}{:}\underline{\dot{\epsilon}}\right)$. The remaining terms $\left(-T\vec{q}\overrightarrow{grad}\left(\frac{1}{T}\right) + \vec{j}^\alpha\vec{\nabla}\left(\frac{\mu_\alpha}{M_\alpha}\right)\right)$ are the exchange dissipation (thermal and mass dissipation).

Taking advantage of the Clausius-Duhem inequality and the separable form of the free energy $\psi(\underline{\epsilon}, T, x_\alpha, \xi_r)$, the stress, temperature, mass title, and rate of extent of the reaction [Merzouki et al. 2014] are written as:

$$\underline{\underline{\sigma}} = \rho\frac{\partial\psi}{\partial\underline{\epsilon}^r} = \rho(\lambda\,tr\underline{\epsilon}\,I + 2\mu\underline{\epsilon} - 3k\alpha'(T - T_{ref})I - 3k\beta\xi_r\,I)$$

$$\rho c\dot{T} = \dot{r} - div\,\vec{q} + T\frac{\partial\sigma}{\partial T}\underline{\dot{\epsilon}}^r + \frac{\rho T}{M_\alpha}\sum_\alpha\frac{\rho\mu_\alpha}{M_\alpha}\dot{x}_\alpha - \frac{T}{\Omega}\sum_r\frac{\partial\mathcal{A}_r}{\partial T}\dot{\xi}_r - \vec{j}^\alpha\vec{\nabla}\left(\frac{\mu_\alpha}{M_\alpha}\right)$$

$$(5)$$

$$\rho\dot{x}_\iota = -div\,\vec{J}_1 + \sum_{n=1}^r v_{in}M_i\dot{\xi}_n$$

$$\dot{\xi} = \frac{1}{2\xi}\,K_p\left(\frac{\rho x_i}{M_i}\right)^2\left(1 - \frac{Q}{K^{eq}}\right)^2$$

Where $\lambda$ and $\mu$ are Lamé parameters, $k$ is the bulk modulus, $\alpha'$ is the thermal expansion coefficient, $\beta$ is the chemical expansion coefficient, $\rho$ is the density, $K_p$ is the kinetic factor, $Q$ is the reaction product, and $K^{eq}$ is the reaction constant.

### Implementation of the numerical tool

Our model consists of three physics. Thus, we have three mechanical degrees of freedom, one thermal degree of freedom and n chemical degrees of freedom. The number of chemical degrees of freedom depends on the number of species and the number of reactions in the system. The standard elements in Abaqus cannot account for such number of degrees of freedom. However, it is possible to define our own element [Abaqus 2023] using the UEL subroutine (User-Defined Element). It enables the modeling of complex and non-linear material responses by allowing users to create their own constitutive models.

Chester *et al.* [Chester et al. 2015] use the UEL subroutine to implement a coupled diffusion-deformation problem for elastomeric gels. They define a new element to study their model. In contrary, inspired by the code of [Chester et al. 2015], we maintain the standard element of Abaqus C3D8T and add the chemical degrees of freedom (Fig. 1). Similar approach has been used in [Vasikaran et al. 2020; Charles et al. 2022]. Additionally, we include the coupled terms between the chemical and mechanical and thermal components. Hence, the stiffness matrix and the secondhand side of the equation (Fig. 1) are enlarged to account for the degrees of freedom associated with chemistry. Furthermore, Galerkin's method must be used to obtain the appropriate weak formulation from the governing equations in order to incorporate the additional terms in the UEL subroutine.
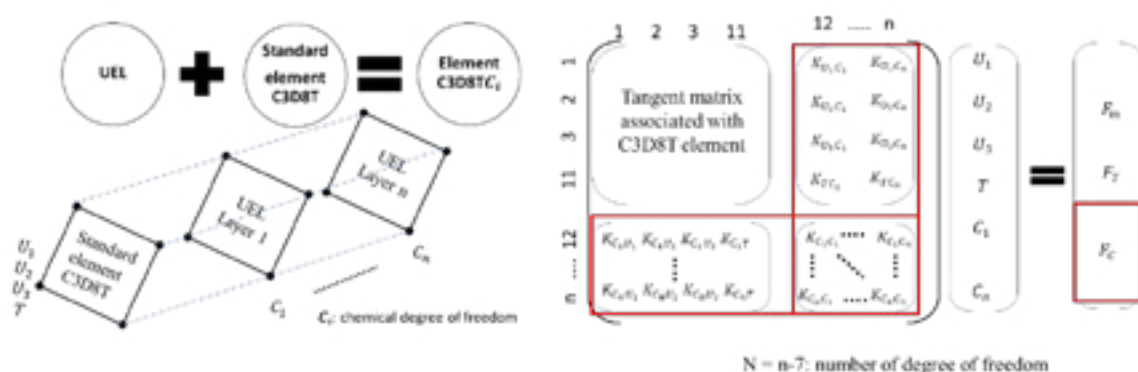
*Fig. 1 :The creation of the new element using UEL subroutine and the standard element of Abaqus and its corresponding matrix.*

### Validation of the model

Merzouki *et al*. [Merzouki et al. 2014] perform an experimental and numerical study to investigate the swelling induced by oxidation ( 6 ) of a cylindrical shape of SiC-based refractory castables. They show the expansion of the cylinder due to oxidation near the face exposed to high temperatures.
The reaction equation is defined by:

$$SiC_{(s)} + \frac{3}{2}O_{2_{(g)}} \rightarrow SiO_{2_{(s)}} + CO_{(g)} \qquad (6)$$

To solve their numerical model, the simulation is performed in three steps. First, the heat transfer equation is solved. Second, the mass balance equation is solved using the UMATHT subroutine. Finally, the mechanical behavior is addressed by employing the UEXPAN subroutines to incorporate thermal and chemical strains. This approach allows for the separation of the heat equation resolution from other physical phenomena, such as chemical and mechanical processes, thereby simplifying the energy balance equation. In other words, the coupling effect between chemical reaction and temperature is not included.

Therefore, the same model is simulated using our numerical tool in order to validate our implementation. In our model, must of the coupling effects are taken into consideration.

### CONCLUSIONS

In this work, completely coupled theories for three branches of physics — thermal, chemical, and mechanical — have been developed. A numerical tool is implemented thanks to the User-ELement subroutine. The chemical degree of freedom is activated in parallel with the mechanical and thermal degrees of freedom. Furthermore, all the coupling terms between chemical and other physics have been added to the extended matrix.

In the following, it is crucial to investigate the impact of each coupling term depending on the simulated model. Additionally, the time convergence of the numerical model must be evaluated. Also, due to the high number of degrees of freedom, the stability of the approach must be assessed.

Finally, this approach enables the consideration of all chemical reactions that can occur in a specific system. More chemical degrees of freedom can be added to the numerical tool, allowing for a comprehensive study of the model's behavior. Hence, understanding and accurately predicting the behavior of reactive porous multiphase materials is crucial for optimizing industrial processes and designing efficient systems.

## REFERENCES

[1] ABAQUS. 2023. ABAQUS/Standard User's Manual. https://help.3ds.com/2023/English/DSSIMULIA_Established/SIMULIA_Established_FrontmatterMap/sim-r-DSDocAbaqus.htm?contextscope=all&id=1b1ae51926d24938af0bc43d99e4735b.

[2] BLOND, E. 2017. Chapter 6 "Thermal, chemical and mechanical couplings". In: J. Poirier, ed., *Corrosion of refractories: the Fundamentals*. göller Verlag.

[3] CHARLES, Y., MOUGENOT, J., AND GASPÉRINI, M. 2022. Modeling hydrogen dragging by mobile dislocations in finite element simulations. *International Journal of Hydrogen Energy 47*, 28, 13746–13761.

[4] CHESTER, S.A., DI LEO, C.V., AND ANAND, L. 2015. A finite element implementation of a coupled diffusion-deformation theory for elastomeric gels. *International Journal of Solids and Structures 52*, 1–18.

[5] CRAIG, S.L. 2012. A tour of force. *Nature 487*, 7406, 176–177.

[6] GIGLIOTTI, M. AND GRANDIDIER, J.-C. 2010. Chemo-mechanics couplings in polymer matrix materials exposed to thermo-oxidative environments. *Comptes Rendus Mécanique 338*, 3, 164–175.

[7] HU, S. AND SHEN, S. 2013. Non-equilibrium thermodynamics and variational principles for fully coupled thermal–mechanical–chemical processes. *Acta Mechanica 224*, 12, 2895–2910.

[8] LEMAITRE, J., CHABOCHE, J.-L., BENALLAL, A., AND DESMORAT, R. 2020. *Mécanique des matériaux solides (3e édition) - Jean Lemaitre, Jean-Louis Chaboche, Ahmed Benallal, Rodrigue Desmorat - Dunod - Grand format - Dalloz Librairie PARIS*. .

[9] LOEFFEL, K., ANAND, L., AND GASEM, Z.M. 2013. On modeling the oxidation of high-temperature alloys. *Acta Materialia 61*, 2, 399–424.

[10] MERZOUKI, T., BLOND, E., SCHMITT, N., BOUCHETOU, M.-L., CUTARD, T., AND GASSER, A. 2014. Modelling of the swelling induced by oxidation in SiC-based refractory castables. *Mechanics of Materials 68*, 253–266.

[11] PRIGENT, P., BOUCHETOU, M.L., POIRIER, J., DE BILBAO, E., AND BLOND, E. 2012. Corrosion of oxide bonded silicon carbide refractories by molten salts in solid waste-to-energy facilities. *Ceramics International 38*, 7, 5643–5649.

[12] RAMBERT, G., JUGLA, G., GRANDIDIER, J.-C., AND CANGEMI, L. 2006. A modelling of the direct couplings between heat transfer, mass transport, chemical reactions and mechanical behaviour. Numerical implementation to explosive decompression. *Composites Part A: Applied Science and Manufacturing 37*, 4, 571–584.

[13] RODRIGUES, F., WEISS, R., AND KOCH, S.A. 2011. Refractory Linings in Waste-to-energy Plants – New Developments for Improved Oxidation Resistance. *refractories WORLDFORUM 3*, 63–68.

[14] ULFF, N., BOUBY, C., LACHIGUER, A., BOURAOUI, T., AND ZINEB, T.B. 2019. Simulation numérique des effets d'une distribution hétérogène d'hydrogène sur la réponse thermomécanique de structures en alliages à mémoires de forme à base nickel-titane. 12.

[15] VASIKARAN, E., CHARLES, Y., AND GILORMINI, P. 2020. Implementation of a reaction-diffusion process in the Abaqus finite element software. *Mechanics & Industry 21*, 5, 508.

# DESIGN OPTIMIZATION OF REFRACTORY CASTABLE PANELS FOR ALUMINA CALCINER LININGS VIA FINITE ELEMENT SIMULATIONS

C. I. Pereira[1], M. H. Moreira[1], M. F. Santos[2], R. A. Angélico[3], M. Braulio[4], T. Iwanaga[5], V. C. Pandolfelli[1]

[1] Federal University of São Carlos, São Carlos, Brazil

[2] REDLAB, São Carlos, Brazil

[3] University of São Paulo, São Carlos, Brazil

[4] 4CAST, São Carlos, Brazil

[5] Hydro Alunorte, Barcarena, Brazil

## ABSTRACT

It is well known that the performance of industrial processes operating under hostile mechanical, chemical or, especially, harsh thermal conditions depends majorly on refractory ceramics. Thus, studies on the optimization of these materials are of great relevance for the industry, as changing their composition, microstructure, or project design can increase the equipment lifetime and/or decrease its maintenance halts. So far, several studies have used computational simulations to model the thermomechanical behaviour of ceramic refractory linings with joints, usually for steel ladles. However, few of them have focused on design optimization such as the correct dimensioning of expansion joints, optimised size of monolithic panels and spatial distribution and quantity of anchors. The present study aims to fill this gap by modelling the castable lining of alumina calciners, which is a less complex system in terms of refractory requirements compared to the steel-making processes. The work was based on the Finite Element Method (FEM) to predict the expansion behaviour of refractory panels under different features, specifically focusing on the design of expansion joints. The results pointed out the significant impact of considering temperature-dependent properties and frictional effects on the expansion behaviour of refractory linings. The findings indicated that these factors can increase the required size of expansion joints by up to 33.3% for the specific materials and geometry studied. Thus, the insights gained from this research can assist in optimising the design and sizing of expansion joints, ultimately adding to the efficiency and longevity of industrial processes operating in challenging thermal environments.

## INTRODUCTION

Calcination is the final stage of the Bayer process in the production of aluminium oxide. It involves the heat treatment of gibbsite ($\gamma$-Al(OH)$_3$) to remove its structural hydroxyl groups, leading to the formation of alumina (Al$_2$O$_3$) [1]. The prevailing equipment used by most alumina refineries for this process is the fluidized bed calciner. This technology operates by fluidizing the aluminium hydroxide particles in an upward airflow, creating a fluidized bed that eases heat transfer. During this process, the maximum temperatures typically range from 900 to 1100°C for the production of smelting grade alumina (SGA) [2].

Given the harsh conditions within the calciner, the refractory lining material plays a critical role in ensuring the feasibility and efficiency of the process. Apart from providing thermal insulation to the structure and reducing energy consumption, the lining acts as a protection against the severe thermomechanical and erosive stresses imposed by the process. Consequently, any failure in the performance of the lining can lead to production halts and significant financial losses.

Over the past few decades, significant developments have been made in refractory technology to improve the performance and lifespan of calciner linings. Innovative materials have been developed to enhance thermomechanical properties and minimise downtime for maintenance and repairing [3-9]. However, there remains a relative lack of attention focused on optimising the geometric design of refractory linings, despite being as important as the intrinsic material properties in determining the lining's performance and lifespan.

One critical parameter in refractory lining design is the expansion joint between panels. This gap plays a crucial role as it directly affects the generation of stresses resulting from thermal expansion, which can lead to detrimental effects on the lining integrity. If the expansion joint between panels is narrow, the contact-induced stresses can reach high levels, thereby increasing the risk of damage. Conversely, a wide spacing between panels can ease the penetration of high-temperature erosive particles into the lining, thereby spoiling the integrity of the equipment's metallic vessel and requiring unscheduled maintenance shutdowns. Additionally, unplanned failures in refractory linings have a higher impact on production losses [7]. Past experiences with calciners have shown that substantial refractory failures lead to a downtime of at least 14 days [7, 10]. For a calciner such as Metso Outotec's 5th generation CFB, which has a capacity of 3,500 tons of alumina per day [11], the associated production loss during this period could reach 49,000 tons of alumina. This loss amounts to approximately $17 million in revenue, assuming a price of $350 per ton of alumina. Additionally, the installation costs for new refractories can range between $1.5 and $3 million [7]. Hence, selecting the right balance for the panel expansion joint is of utmost importance to ensure optimal performance and longer refractory lining's life in industrial applications.

One likely method to forecast them in panels exposed to temperature variations is using analytical mathematical equations. The linear thermal expansion equation represents the most basic approach for estimating the required spacing between panels to accommodate their thermal expansion [5, 12, 13]. However, this model exhibits limited accuracy due to its unrealistic assumptions, particularly when applied to processes carried out at elevated temperatures. The complexity of such processes, including temperature gradients across the lining thickness and variations in material properties with temperature, requires the development of more robust models.

Numerical analysis using tools as the Finite Element Method (FEM) enables the modelling of complex systems, such as the thermal analysis of steel ladles in the steel industry [14]. Several studies have employed these methodologies to model the thermomechanical behaviour of refractory linings containing expansion joints. Gasser et al. [15-17] analysed specific sections of the lining and successfully predicted the thermomechanical behaviour using homogenization techniques. These studies helped to improve the prediction of stress and deformation in linings by considering the presence of expansion joints. However, there is currently no literature available regarding applying these methodologies for selecting their appropriate size in refractory linings.

Within this context, the present study aims to address this gap by employing numerical modelling to better predict the expansion behaviour of a refractory panel, accounting for conditions not considered by the simplistic analytical model, such as non-uniform temperature variations, temperature-dependent properties and the friction between the lining components.

## MATERIALS AND METHODS

The structure of the calciner furnace consists of three layers of materials: an outer metallic shell, an insulating layer followed by a dense one known as the working layer. The working lining comprises castable panels that are apart by expansion joints and held in place by metallic anchors. In this study, the panel geometry considered was parallelepiped with a square faced cross-section 1000 mm wide and 150 mm thick. The insulating layer and the metallic shell were 200 mm and 10 mm thick, respectively. The presence of anchors was not considered.

The material behaviour was assumed to be isotropic and linearly elastic. Table 1 shows the property data obtained from the literature. It was considered a calcium aluminate cement (CAC) bonded refractory castable (pre-fired at 1400 °C for 5 h) for the working layer [18, 19], a generic 55% $Al_2O_3$ for the insulating layer [20], and carbon steel for the metallic shell [21].

The investigation of the lining thermomechanical behaviour was carried out in two steps, considering a one-way weakly coupling between the thermal and thermomechanical analyses. First, a steady-state heat transfer model estimated the thermal response of the lining. Following, mechanical analyses were performed to investigate the thermal expansion, displacements and stresses within the lining system considering a quasi-static loading. The numerical models were developed using a Finite Element Method (FEM) approach and implemented using Abaqus/CAE software. The geometry was assumed as a quarter of the panel, considering the symmetry of the problem, and discretized using 90,000 linear hexahedral finite elements with full integration. Figure 1 presents the geometry and surfaces considered to define the problems' boundary conditions.
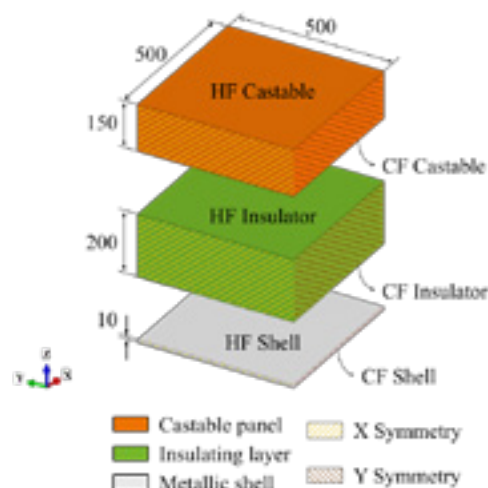


**Figure 1**. Geometry and surfaces of the numerical model. HF = Hot Face; CF = Cold Face. Dimensions in mm.

For the thermal analysis, a temperature of 1030 °C was imposed on the hot face of the castable. The transfer of thermal energy among the different layers was considered perfect. On the cold face of the metallic shell, both convection with a film coefficient of 4 W/m²K and radiation were taken into account considering an emissivity of 0.7. The surrounding air temperature outside the metallic shell was assumed to be 30°C, as well as the initial temperature throughout the lining volume.

For the mechanical analysis, the thermal profile obtained from the heat transfer was imposed as an initial condition. The cold face of the shell was constrained against displacement in the thickness direction (z-direction). The normal contact between the different layers was considered "hard" (following Abaqus/CAE manual), meaning that no penetration occurs between the parts and there is no transfer of tensile stresses across the interfaces. Two extreme scenarios were considered for the tangential contact between the parts (mechanical boundary conditions scenarios): (i) frictionless contact, where there is no resistance to sliding, and (ii) rough contact, where all relative sliding motion between two contacting

**Table 1.** Material's properties: density (ρ), thermal conductivity (k), coefficient of thermal expansion (α), elastic modulus (E), poisson's ratio (ν) and emissivity (ε). Sources: [18-21].

| Material | Property | Temperature [°C] | Value |
|---|---|---|---|
| **CAC Castable** <br><br> Working layer | ρ [kg/m³] | – | 3130 |
| | k [W/m·K] | 33 | 10.65 |
| | | 189 | 7.43 |
| | | 394 | 5.16 |
| | | 595 | 3.82 |
| | | 796 | 4.32 |
| | α [/°C] | 30 | $7.14 \times 10^{-6}$ |
| | | 400 | $7.75 \times 10^{-6}$ |
| | | 700 | $8.24 \times 10^{-6}$ |
| | | 1100 | $8.90 \times 10^{-6}$ |
| | E [GPa] | 30 | 156 |
| | | 400 | 151 |
| | | 700 | 145 |
| | | 1100 | 137 |
| | ν | – | 0.2 |
| **Insulator** <br><br> Insulating layer | ρ [kg/m³] | – | 1361 |
| | k [W/m·K] | – | 0.4 |
| | α [/°C] | – | $7.38 \times 10^{-6}$ |
| | E [GPa] | 30 | 4.14 |
| | | 260 | 2.07 |
| | | 538 | 2.76 |
| | | 677 | 2.76 |
| | | 815 | 1.38 |
| | ν | – | 0.2 |
| **Carbon Steel** <br><br> Metallic shell | ρ [kg/m³] | – | 7850 |
| | k [W/m·K] | 30 | 53.00 |
| | | 100 | 50.67 |
| | | 200 | 47.34 |
| | α [/°C] | 30 | $12.24 \times 10^{-6}$ |
| | | 100 | $12.80 \times 10^{-6}$ |
| | | 200 | $13.60 \times 10^{-6}$ |
| | E [GPa] | 30 | 210 |
| | | 100 | 210 |
| | | 200 | 189 |
| | ν | – | 0.3 |
| | ε | – | 0.7 |

surfaces is prevented. Gravity was considered in the negative z-direction. The thermo-mechanical behaviour of the lining was evaluated by examining the impact of two parameters: (i) temperature-dependent properties (property scenarios), and (ii) mechanical constraints arising from friction between the lining components (mechanical boundary conditions scenarios).

The influence of temperature-dependent properties was evaluated by comparing the results of the analyses considering such scenarios with those that assumed constant constitutive laws. For the latter case, the material properties were considered to be equivalent to those at room temperature (30°C).

Finally, the displacement results for the numerical models were compared with those obtained with the classical linear thermal expansion model, commonly used to estimate the expansion joint between refractory panels, expressed as:

$$\Delta L(z) = L_0 \, \alpha \, (T(z) - T_0) \tag{1}$$

where $\Delta L$ represents the change in length of the material, $L_0$ is the original length, $\alpha$ is the coefficient of linear thermal expansion, T the temperature, and z represents the position along the thickness of the panel. For the temperature-dependent material properties case, $\alpha(T)$ was considered for each position at the lining thickness.

## RESULTS AND DISCUSSION

Table 2 presents the thermal profile obtained across the lining thickness for the two property scenarios considered. It was evident that when temperature-dependent properties were taken into account, the temperature at each interface, as well as that at the cold face of the metallic shell, decreased. This behaviour can be attributed to the decrease in thermal conductivity of the CAC castable with the temperature, which was the only property considered in the steady-state heat transfer analysis. Consequently, the thermal gradient within the castable, considering temperature-dependent properties, was higher (56.3°C) compared to the case with constant properties (23.7°C). Conversely, the thermal gradient in the insulating layer was lower when temperature-dependent properties were considered. This was because the thermal conductivity of the insulation was assumed to be constant in both scenarios.

**Table 2.** Temperature profile obtained from finite element analysis for the two property scenarios. Thermal gradient is presented for constant properties | temperature-dependent properties.

| Position | Temperature (°C) | | Thermal gradient (°C) |
|---|---|---|---|
| | Constant properties | Temperature-dependent properties | |
| HF – Castable | 1030 | 1030 | – |
| CF – Castable | 1006.3 | 973.7 | 23.7 \| 56.3 |
| CF – Insulator | 166.3 | 162.9 | 840 \| 810.8 |
| CF – Shell | 165.8 | 162.4 | 0.5 \| 0.5 |

Table 3 shows the in-plane displacement (x and y directions) results for the two property scenarios according to the linear thermal expansion model (equation 1), and along with the results obtained from finite element analyses for the two mechanical boundary conditions. Firstly, it is evident that, across all cases, the expansion at the hot face of each refractory layer is consistently greater than at the cold face. This indicates a wedge-shaped trend in the lining after experiencing temperature variation. Furthermore, when examining the case of constant properties, the impact of friction between the different layers of the lining becomes apparent. Assuming zero friction led to a behaviour that closely resembles that predicted by the analytical model of linear thermal expansion. However, when maximum friction between the layers was considered, the expansion of the system undergoes a significant change. In this case, the interface between the castable and insulating layer (i.e., the cold face of the castable and the hot face of the insulator) experienced smaller displacements compared to both surfaces in the frictionless contact case. Conversely, the extremes of the refractory lining (i.e., the cold face of the insulator

**Table 3.** In-plane displacement (mm) results for the two property condition cases according to the linear thermal expansion model and the two mechanical boundary condition scenarios.

| | Position | Linear thermal exp. model | FE Analysis | |
|---|---|---|---|---|
| | | | Friction-less contact | Rough contact |
| Constant properties | HF – Castable | 3.57 | 3.57 | 3.70 |
| | CF – Castable | 3.48 | 3.49 | 3.32 |
| | HF – Insulator | 3.60 | 3.59 | 3.31 |
| | CF – Insulator | 0.50 | 0.51 | 0.86 |
| | HF – Shell | 0.83 | 0.83 | 0.87 |
| | CF – Shell | 0.83 | 0.83 | 0.87 |
| Temperature - dependent properties | HF – Castable | 4.40 | 4.64 | 4.76 |
| | CF – Castable | 4.10 | 4.34 | 4.18 |
| | HF – Insulator | 3.48 | 3.46 | 4.18 |
| | CF – Insulator | 0.49 | 0.51 | 1.04 |
| | HF – Shell | 0.88 | 1.04 | 1.06 |
| | CF – Shell | 0.88 | 1.04 | 1.06 |

and the hot face of the castable) experienced larger displacements. This phenomenon occurred because the condition of rough contact between the surfaces prevented relative sliding and detachment between the parts, even when warping caused by the thermal gradient was presented, as depicted in Figure 2. The frictional forces acting between the surfaces effectively prevented the trend to slide the plates or separate them, resulting in a more constrained and interconnected system.
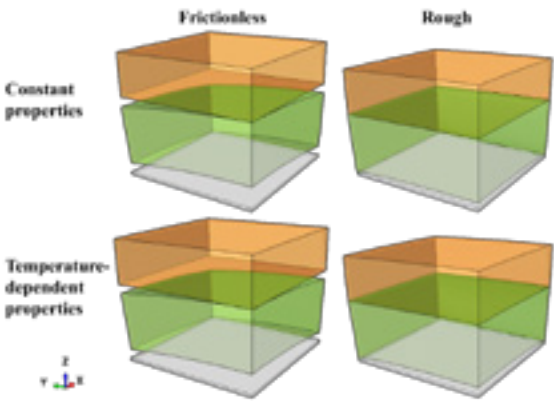


**Figure 2.** Deformed shape of the lining for the analysed cases.

The impact of temperature-dependent properties on the behaviour of the lining was even more contrasting. Firstly, there was an increase in the in-plane displacement of the castable due to its higher thermal expansion coefficient at elevated temperatures. The lower displacement of the insulator was not due to a decrease in its thermal expansion coefficient but was influenced by the lower temperature at the interfaces, resulting from temperature-dependent properties. When comparing the results of the analyses without friction versus rough contact, a similar behaviour was observed at the extremes of the refractory lining. These surfaces underwent an increased displacement in the case of maximum friction, whereas the interface castable–insulator showed an intermediate pattern between the behaviour of the two surfaces in the frictionless contact case.

It is also important to note that even in the case of frictionless contact, the results from finite element analysis considering

temperature-dependent properties significantly differed from those obtained using the linear thermal expansion equation. This highlights the complex and non-linear nature of the thermo-mechanical behaviour, which cannot be accurately captured by a simple linear expansion model.

The numerical model implemented using the finite element method not only enabled the estimation of displacements but also made the evaluation of the stresses generated within the refractory lining easier, providing valuable insights for project decision-making. The results of the analyses conducted for the cases considered highlighted that the maximum principal tensile stresses were higher when there was friction between the layers of the lining, as depicted in Table 4. Furthermore, in general, the stresses generated were lower when temperature-dependent properties were taken into account. This indicated that considering the variation of material properties with temperature can help to mitigate the magnitude of stresses induced within the lining system.

**Table 4.** Maximum principal stresses in each lining material for the property and mechanical boundary condition scenarios analysed.

| | Lining component | Max. principal stress (MPa) | |
|---|---|---|---|
| | | Frictionless contact | Rough contact |
| **Constant properties** | Castable | 0.91 | 83.97 |
| | Insulator | 25.08 | 62.07 |
| | Shell | 20.45 | 173.0 |
| **Temperature - dependent properties** | Castable | 2.51 | 72.90 |
| | Insulator | 14.44 | 48.60 |
| | Shell | 9.71 | 108.6 |

## CONCLUSIONS

The analyses presented in this study highlighted the necessity of revising the design approach for expansion joints in refractory linings. The conventional linear expansion model, commonly used for joint design, does not accurately predict the expansion behaviour of materials subjected to high-temperature process conditions.

The analyses conducted in this study highlighted that incorporating temperature-dependent properties along with friction between the layers can lead to a substantial increase in the required size of an expansion joint compared to calculations based on the linear thermal expansion model considering material properties at room temperature. The increase in joint size can reach up to 33.3% in certain cases, a value that can be further amplified by other factors such as the presence of anchors, increased panel size, different material properties, among others.

These findings emphasise the importance of considering the non-linear and complex nature of thermo-mechanical behaviour in refractory linings, and the necessity to develop more comprehensive design methods that account for temperature-dependent properties and mechanical constraints such as frictional effects. By doing so, the accuracy of joint design can be significantly improved, ensuring the structural integrity and longevity of refractory linings in high-temperature applications.

## REFERENCES

[1] Wefers K, Misra C. Oxides and hydroxides of aluminum. Alcoa Technical Paper nº 19. Revised. Pennsylvania: Aluminum Company of America, 1987.

[2] Raahauge BE. Production of Smelter Grade Alumina (SGA) by calcination. In: Raahauge BE, Williams FS. Smelter Grade Alumina from bauxite. Springer Ser. Mater. Sci. 320, 2022.

[3] Lopes DA, Pandolfelli VC. Fluid bed alumina calciner refractory lining: a systemic approach [in Portuguese]. MSc Dissertation, UFSCar, S. Carlos, SP, 2005.

[4] Gonçalves LRG, Tiba PRT, Teider BH, Brandt C, Gallo JB, Pandolfelli VC. Refractories materials selection for fluid flash calciners [in Portuguese]. Proceedings of the 53rd Brazilian Ceramic Congress, Guarujá, SP, 2009.

[5] Teider, BH. The refractory lining and its effect on the lifetime and energy consumption of alumina calciners [in Portuguese]. MSc Dissertation, UFSCar, S. Carlos, SP, 2012.

[6] Braulio MA, Morbioli GG, Medeiros J, Gallo JB, Pandolfelli VC. Nano-bonded wide temperature range designed refractory castables. J. Am. Ceram. Soc. 95 (3), 2012, p. 1100-4.

[7] Teider BH, Graham B, Braulio MA, Gallo JB, Pandolfelli VC. Lifetime critical analysis of alumina calciner refractories. Refractories Worldforum 5 (3), 2013, p. 101-106.

[8] Leicht N. Shinagawa Refractories Australasia Pty. Ltd. Product selection for alumina calciner applications. Shinagawa Technical Report 58, 2015, p. 105-12.

[9] Braulio MA, Cunha JR, Maxwell AJ, Whiteman D, Pandolfelli VC. Improving the reliability of fluidized bed alumina calciners by suitable refractory lining selection. In Light Metals 2019, p. 27-32.

[10] Hiltunen P, Bligh R, Klett C, Missalla M, Schmidt H. How to achieve high availability with large calciners and avoid unforseen downtime. In Light Metals 2008, p. 63-68.

[11] Metso Outotec. Smelter grade alumina CFB calcination plant solution [accessed on May 21, 2026].

[12] Plibrico Japan Co. Ltd.: Technology of monolithic refractories. Tokyo 1999, 314-339.

[13] Sengupta P. Refractory design, installation, and maintenance. Refractories for the Cement Industry 2020, p. 99-134.

[14] Santos MF, Moreira MH, Campos MG, Pelissari PI, Angélico RA, Sako EY, Sinnema S, Pandolfelli VC. Enhanced numerical tool to evaluate steel ladle thermal losses. Ceram. Int. 44 (11), 2018, p. 12831-40.

[15] Gasser A, Terny-Rebeyrotte K, Boisse P. Modelling of joint effects on refractory lining behaviour. Proc. Inst. Mech. Eng. L: J. Mater.: Des. Appl. 218 (1), 2004, p. 19-28.

[16] Ali M, Sayet T, Gasser A, Blond E. Transient thermo-mechanical analysis of steel ladle refractory linings using mechanical homogenization approach. Ceramics 3, 2020, p. 171-189.

[17] Ali M, Sayet T, Gasser A, Blond E. Computational homogenization of elastic-viscoplastic refractory masonry with dry joints. Int. J. Mech. Sci. 196, 2021, p. 106275.

[18] Cunha TM, Moreira M., Santos MF, Angélico RA, Pandolfelli VC. Numerical analysis of drying schedules of refractory castables by using computing simulations. Proceeding 11, XLII ALAFAR Congress, Foz do Iguaçú, Brazil, 2022.

[19] Luz AP, Consoni LB, Pagliosa C, Aneziris CG and Pandolfelli VC. Sintering effect of calcium carbonate in high-alumina refractory castables. Ceram. Int. 44(9), pp. 10486-10497, 2018.

[20] Potter RA. Improvement of the mechanical reliability of monolithic refractory linings for coal gasification process vessels. Final report. No. LRC-5258. Babcock and Wilcox Co., Lynchburg, 1981.

[21] European Committee for Standardisation, Eurocode 3 – EN 1993-1-2 (2005) (English): Eurocode 3: Design of Steel Structures - Part 1-2, General rules - Structural fire design, Brussels, Belgium, 2005. EN 1993-1.2.

637

SHORT COMMUNICATIONS

# A NOVEL DESIGN FOR FLOW STABILIZER OF TUNDISH BY CFD AND WATER MODEL SIMULATION

Qi Li[1], Hang Ye*, Yumin Ma[1], Tianfei Ma[1], Gernot Hackl[2], Yong Tang[2],

1 RHI Magnesita (Dalian) Co., Ltd., Dalian 116600, China;2 RHI Magnesita, Leoben 8700, Austria

*Corresponding author: E-mail: Hang.Ye@rhimagnesita.com

## ABSTRACT
The flow in the impact region of a tundish is known to be highly turbulent. High wear rates of the refractory lining can be associated with this phenomenon. Particularly, T- or delta-T-shaped tundishes are prone to this problem. Turbulence inhibitors are often incorporated to weaken turbulent flow and are therefore an effective measure to counteract the localised wear problem. In this study, an isothermal transient model of a tundish was established using CFD to simulate the flow performance of molten steel in a seven-stranded T-shaped tundish using the ANSYS Fluent software. Two types of flow stabilisers were designed and compared, focusing on the flow characteristics in the impact region. Additionally, a 1:3 water scale model was adopted. Dye injection tests with associated video recordings were completed to demonstrate the flow trajectories in the tundish. The residence time distribution curve and dead zone volume fraction were analysed using the CFD method and the water model. The results of the water model verified the accuracy of the CFD simulations; the newly designed turbulence inhibitor had a lower scouring velocity near the pouring area. Simultaneously, the dead zone volume decreased, the plug zone volume increased, and the flow in the tundish was optimised.
**Keywords:** Water model, CFD simulation, Tundish, flow stabilizer, RTD

## INTRODUCTION
With the increasing demand of steel users for steel quality, obtaining high-purity liquid steel effectively has become a core issue of great concern to enterprises. A tundish is the last metallurgical container before the solidification of liquid steel, and its metallurgical function is self-evident. Particularly in the production of clean steel, the role of the tundish is increasingly important, as it is no longer used as a simple shunt container, but it will also carry the function of further removal of inclusions, preventing the secondary refining of liquid steel from being contaminated during high-quality steel production [1–3].
Owing to the high turbulence in the middle region of the tundish, local wear may be caused, and flow-control devices such as retaining walls and turbulence inhibitors are generally employed to weaken the turbulence. Turbulence inhibitors, as important flow control devices in tundishes, can effectively prevent liquid-level fluctuations caused by high-speed injection flows and improve the quality of the billet [4,5].
Many scholars have studied different types of flow control devices and their combinations, such as flow control combination of upper and lower retaining walls, swirl turbulence inhibitors with square eaves, curved retaining walls, diversion holes or flow steel holes, among others [6–8]. This study was primarily based on an actual situation in a steel mill. In this study, a turbulence inhibitor with a baffle on the inner wall was designed, and a retaining wall with a 30° up-dip diversion hole was added to the outside so that the liquid steel would not cause more wear on the T-tundish. Good results were achieved, as described herein.
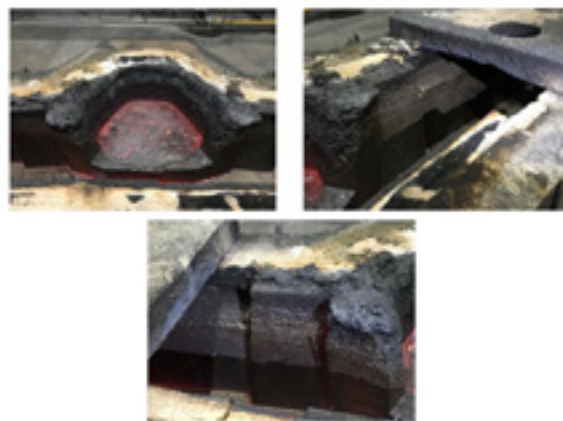


*Fig. 1: Local wear situation*

## OPTIMISATION MODEL DESCRIPTION
### Fundamental assumption
(a) Effects of the surface fluctuation of the molten steel, slag layer, and secondary oxidation of the stainless-steel liquid on the flow field of the tundish were ignored.
(b) The fluid was regarded as an incompressible Newtonian fluid with fixed physical properties.
(c) The flow of liquid steel in the entire tundish was turbulent with a low Reynolds number.
(d) The effect of temperature change on the flow of the tundish fluid was ignored.

### Governing equation
The basic, continuity, and momentum equations for the flow field simulation of the tundish are:

$$\frac{\partial \rho_m}{\partial t} + \nabla \cdot (\rho_m \overrightarrow{u_i}) = 0 \qquad (1)$$

$$\frac{\partial \rho_m}{\partial t} + \nabla \cdot (\rho_m \overrightarrow{u_i u_j}) = -\nabla p + \frac{\partial}{\partial x_i}\left[\mu_{eff}\left(\frac{\partial u_r}{\partial x_r} + \frac{\partial u_i}{\partial x_i}\right)\right] \qquad (2)$$

where $\rho_m$ is the fluid density, $u_i$ is the velocity of the fluid flowing in direction $i$, $u_j$ is the velocity of the fluid flowing in direction $j$, $p$ is the static flow pressure, and $\mu_{eff}$ is the effective viscosity.
In the process of tundish casting, the turbulence behaviour of molten steel is characterised by the standard low Reynolds number k-ε model.
The equation of turbulent kinetic energy ($k$) is:

$$\frac{\partial(\rho_m k)}{\partial t} + \frac{\partial(\rho_m k u_i)}{\partial x_i} + \rho_m \varepsilon = \frac{\partial}{\partial x_i}\left[\left(\mu_{eff} + \frac{\mu_t}{\sigma_k}\right)\frac{\partial k}{\partial x_i}\right] + G_k \qquad (3)$$

The turbulent kinetic energy dissipation ($\varepsilon$) is expressed as:

$$\frac{\partial(\rho_m \varepsilon)}{\partial t} + \frac{\partial(\rho_m u_i \varepsilon)}{\partial x} = \frac{\partial}{\partial x_i}\left[\left(\mu_{eff} + \frac{\mu_t}{\sigma_j}\right)\frac{\partial \varepsilon}{\partial x_i}\right] + \frac{1}{k}(\varepsilon C_{1\varepsilon} G_k - \varepsilon^2 C_{2\varepsilon}\rho_m) \qquad (4)$$

$$\mu_{eff} = \mu_m + \mu_t \qquad (5)$$

$$\mu_t = \rho_m C_\mu \frac{k^2}{\varepsilon} \qquad (6)$$

Here, $\mu_m$ is the viscosity of mobile molecules; $\mu_t$ is turbulence viscosity; $C_{1\varepsilon}$, $C_2$, $C_\mu$, $\sigma_k$, $\sigma_\varepsilon$ are constants corresponding to 1.44, 1.92, 0.09, 1.3, and 1.0.

To calculate the residence time of the liquid steel in the tundish, a certain amount of tracer is added into the inlet, and the following user-defined scalar (UDS) function is solved.

$$\frac{\partial(\rho\varphi)}{\partial t} + \nabla \cdot (\rho\varphi\vec{u_j}) = \nabla \cdot \left(\left(\rho D_0 + \frac{\mu_t}{Sc_t}\right)\nabla\varphi\right) + S_\varphi \qquad (7)$$

where $\varphi$ is the tracer concentration, $Sc_t$ is the turbulent Schmidt number, $S_\varphi$ is a source term for the concentration, $\mu_t$ is the eddy viscosity, and $D_0$ is the kinematic diffusivity of the tracer.

After the flow field was calculated, a residence time distribution (RTD) analysis was conducted to characterise the flow according to the definitions of the plug volume, dead volume, and mix volume[9].

The formula for the average residence time $T_a$ of each first-class liquid steel in the tundish is:

$$T_a = \frac{\sum t_i c_i \Delta t_i}{\sum c_i \Delta t_i} \qquad (8)$$

where $\Delta t_i$ indicates the time interval of the monitoring value, $t_i$ is the sampling time, and $c_i$ is the tracer concentration at the outlet corresponding to $t_i$ time.

In this study, the analytical model proposed by Pan et al. [10] was adopted to describe the deviation between the actual flow and ideal piston flow with variance as follows:

$$\sigma_j^2 = \int_0^\infty (t_j - \bar{t_j})^2 c_j(t_j)\,dt = \int_0^\infty (\theta_j - 1)^2 c_j(\theta_j)\,d\theta = \int_0^\infty \theta_j^2 c_j(\theta_j)\,d\theta - 1 \qquad (9)$$

$$\sigma^2 = \sum_{i=1}^n \sigma_i^2 \qquad (10)$$

The dead zone volume fraction is given by:

$$\frac{V_d}{V} = \int_{2t_a}^\infty c_j\,dt \qquad (11)$$

The total mixed flow volume fraction is expressed as:

$$\frac{V_{mj}}{V} = \sigma^2 - \frac{V_d}{V} \qquad (12)$$

The plug flow volume fraction is written as:

$$\frac{V_{pj}}{V} = \frac{1}{N} - \frac{V_{dj}}{V} - \frac{V_{mj}}{V} \qquad (13)$$

where $V_{dj}$ is the dead zone volume, $V_{mj}$ is the full mixing zone volume, $V_{pj}$ is the volume of the piston region, and $V$ is the volume of the liquid steel in the intermediate envelope.

**Boundary condition**

The following boundary conditions of the mathematical model for the seven-stranded tundish were determined based on the actual flow of the tundish:

(a) Liquid steel flows into the tundish from the ladle through the ladle nozzle. The velocity of the liquid steel in the ladle nozzle was vertically downward and the velocity distribution at the entrance section was the same. The entrance boundary was set as the velocity boundary, and the size was determined by the steel throughput and section size, according to the law of conservation of mass. $v_{in}=Q/S$, where $Q$ is the volume flow rate of the ladle nozzle, $S$ is the cross-sectional area of the ladle nozzle, and the turbulent kinetic energy and turbulent energy dissipation rate at the entrance are $k=0.01v_{in}^2$, $\varepsilon=2k^{1.5}/D_{in}$; $D_{in}$ is the inner diameter of the ladle nozzle.

(b) The liquid level of the tundish was set as the free surface, and the shear force was set to 0.

(c) The outlet type was set as the pressure outlet.

(d) The solid wall surface of the tundish was set as the nonslip wall surface.

The calculated grids used in this study were all hexahedral grids, and the main technological parameters of the continuously cast tundish are listed in Table 1. To reduce the calculation time, half of the model was processed in this study, and only the left part was calculated. Figure 2 shows the turbulence inhibitor design and mesh division used in this study.

Tab. 1: Main technological parameters of continuous casting tundish.

| Process parameter | Value |
|---|---|
| Tundish working capacity (t) | 37.2 |
| Tundish throughput (t/min) | 3.5 |
| Tundish bath level (mm) | 900 |
| Inside diameter of ladle nozzle (mm) | 80 |
| Immersion depth of ladle nozzle (mm) | 265 |
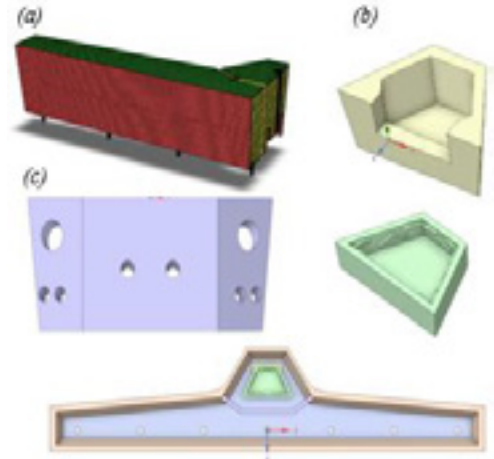


*Fig. 2: Design of (a) mesh, and (b) original and (c) proposed turbulence inhibitors.*

In the calculation, the liquid flow inside the tundish is considered to be an isothermal incompressible fluid, and the density and viscosity of the steel are constant. The specific values are listed in Tab. 2.

Tab. 2: Physical parameters of liquid steel.

| Density (kg·m$^{-3}$) | Viscosity (Pa·s) | Molar mass (g·mol$^{-1}$) |
|---|---|---|
| 7000 | 0.0061 | 55.85 |

**RESULTS AND DISCUSSION**

**Flow field of tundish under different turbulence inhibitors**

Fig.3 presents flow diagrams of the $y=0$ sections and the free surface of the two turbulence-inhibitor schemes. As can be seen in the case of the original turbulence inhibitors, because there is no flow control device, a higher speed will be generated from the two nearest outlets, which will reduce the residence time of the liquid steel in the tundish to a certain extent, resulting in short-circuit flow. The velocity of the liquid steel near the turbulence inhibitors will reach more than 0.1 m/s, which causes slag rolling. When the newly designed turbulence inhibitors and retaining wall are used for flow control, under the action of a turbulence controller, the liquid steel only has a large velocity in the small part above the turbulence inhibitors, while the velocity in other areas of the tundish is small. In addition, the liquid steel diffused around the impact zone and generated a flow to the liquid surface of the tundish. When the liquid steel flowing along the liquid surface hits the sidewall of the tundish, it generates a downward circumferential flow, which is conducive to inclusions floating up. Compared with the original turbulence inhibitors, the velocity of the newly designed turbulence inhibitors at the free liquid surface is relatively small, with the maximum of only 0.05 m/s, and slag rolling probability decreases.
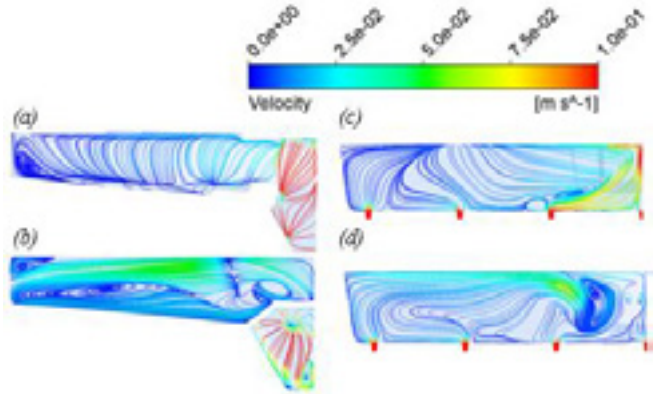
*Fig. 3: Flow diagrams of the free surface and y=0 sections of free liquid surface under (a) (c) original and (b) (d) new turbulence inhibitor design schemes.*

Fig. 4 displays velocity contour plot of the original and the newly designed turbulence inhibitors at the free surface. Compared with the original turbulence inhibitors, when the new turbulence inhibitors were applied to the retaining wall, the liquid steel flowing from the ladle nozzle to the bottom of the inhibitors was blocked by the baffle on the turbulence inhibitors. Therefore, the velocity in the impact zone of the tundish is relatively low, which helps reduce the local wear in the impact zone, as shown in subfigures (a) and (b). The velocity reduction at the wear position can be as much as 50% (0.2–0.1 m/s).
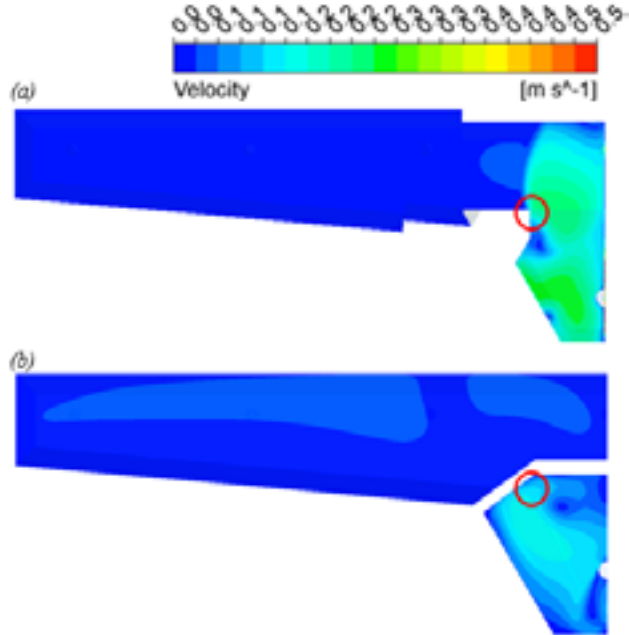
*Fig. 4: Velocity contour plot at the free liquid surface under (a) original and (b) new turbulence inhibitor design schemes.*

Fig. 5 presents the velocity cloud diagrams of the different sections in the impact zone under the two turbulence inhibitor schemes. It is clear that the newly designed turbulence inhibitors combined with the retaining wall with a diversion hole effectively reduced the turbulence velocity in the impact zone and helped reduce the original local wear phenomenon.
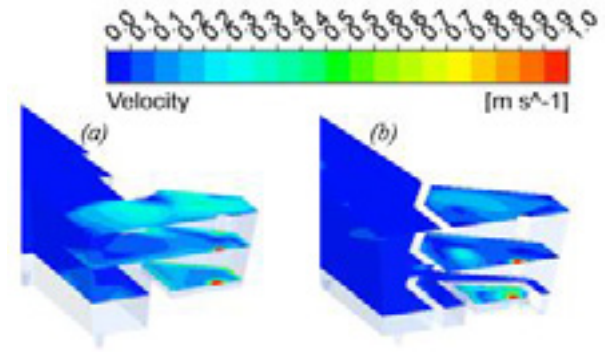


*Fig. 5: Velocity clouds for different sections at the impact zone of the (a) original and (b) new turbulence inhibitors designs.*

Fig. 6 displays the cloud diagrams of the turbulent kinetic energy at the free surface and $x=0$ section for the two schemes. Compared with the original turbulence inhibitor, the turbulent kinetic energy of the molten steel in the impact zone of new turbulence inhibitor was mainly concentrated in the interior. When the original turbulence inhibitors were used, the turbulent kinetic energy of the molten steel in the impact zone of the entire tundish was generally large, and the turbulent kinetic energy of the free liquid surface near the impact zone of the tundish reached 0.0015 $m^2/s^2$, which easily caused slag and molten steel exposure. Simultaneously, the turbulent kinetic energy in the impact zone with the new turbulence inhibitors was lower than that with ordinary turbulence inhibitors.
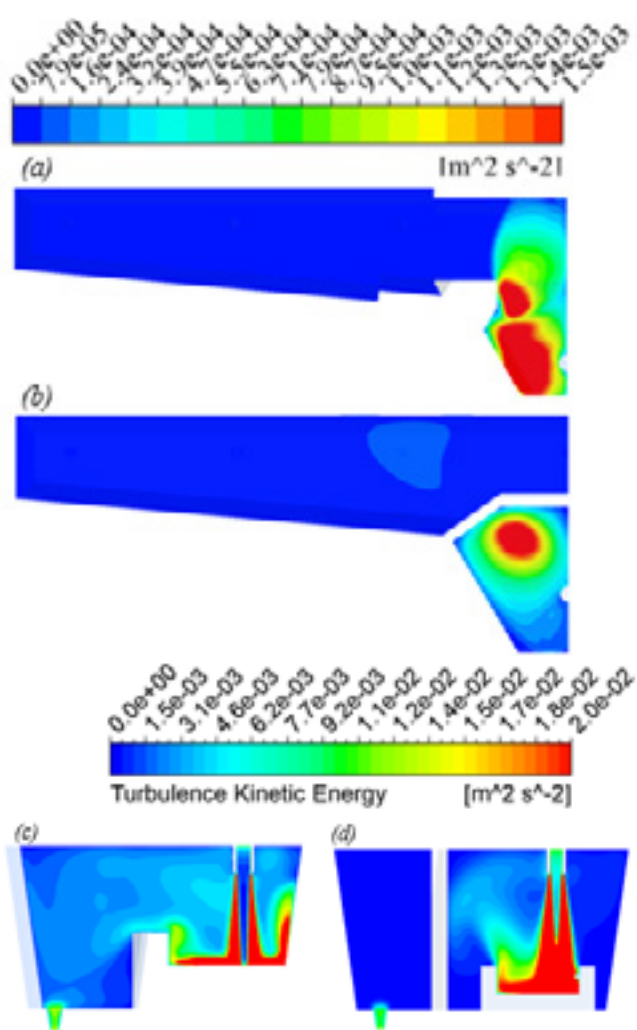


*Fig. 6: Turbulent kinetic energy distributions at the free surface and x=0 section of the (a) (c) original and (b) (d) new turbulence inhibitors designs.*

**RTD curve analysis**

Fig.7 presents the RTD curves of the tundish for the different schemes, and Tab.3 provides the analysis results corresponding to the RTD curves for the different schemes. According to Figure 8 and Tab.3, the response time of the newly designed turbulence inhibitors and the flow control device of the retaining wall increased by 35.7 s, the average residence time increased by 200 s, the dead zone volume decreased by 22%, and the plug zone volume increased by 17%. As shown in the figure and table, the RTD curves of the newly designed turbulence inhibitors significantly differ from those of the original turbulence inhibitors. The newly designed turbulence inhibitors can not only reduce local wear, but also promote the floating of inclusions. Thus, the new turbulence inhibitors can improve the flow state of molten steel in the tundish impact zone as well as reduce the local wear.
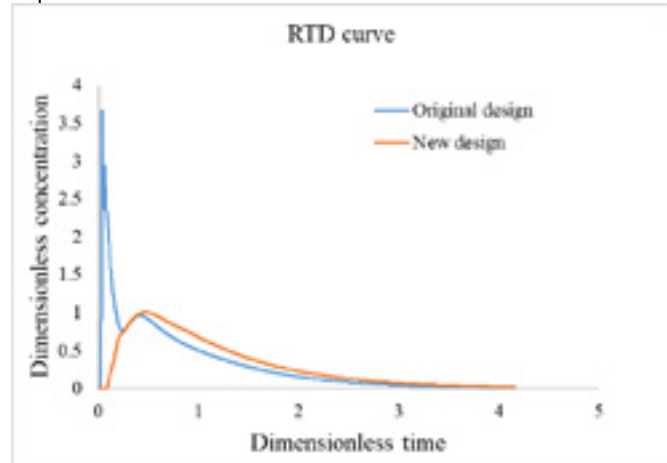


Fig. 7: RTD curves for tundish under different designs.

Tab. 3: Results of RTD curves under different designs

| Design | $t_r$/s | $t_p$/s | $t_a$/s | $v_p$/% | $v_d$/% | $v_m$/% |
|---|---|---|---|---|---|---|
| Original | 37.3 | 159.3 | 531.8 | 15.4 | 24.2 | 60.3 |
| New | 77 | 333.6 | 716.8 | 32.5 | 14.1 | 53.4 |

where $t_r$ is the tundish response time; $t_p$ is the tundish peak time; $t_a$ is the average residence time; $v_p$ is the plug zone volume ratio; $v_d$ is the dead zone volume ratio; and $v_m$ is the mixing zone volume ratio. In summary, the flow state of the liquid steel in a tundish impact zone can be improved with a new design of turbulence device.

**Water model and model validation**
Based on the original design scheme, a water model experiment was conducted considering the ratio of 1:3 using a similarity criterion. During the experiment, Kcl solution was selected as the tracer. After the flow field was stabilised for 3 min, the tracer was injected through the ladle water outlet for 1 s. The obtained distribution trend of the red tracer in the tundish at different times was similar to the mathematical simulation results. In addition, the "stimulus response" technique was adopted to measure the RTD of the liquid steel in the tundish, and the electrical conductivity corresponding to the Kcl concentration at each outlet was monitored by the conductance electrode inserted at the outlet. Finally, the RTD curve was drawn. Through comparison and analyses, the RTD curves for the tundish measured via numerical simulation calculations under various flow control devices and water model experiments had good consistency in variation. The error in the overall average residence time in the tundish was maintained at approximately 5%. This shows that the model can accurately calculate the RTD curve for a tundish. However, the turbulence model, tracer diffusion model, and RTD analysis method adopted in this study are consistent with the above research. Therefore, the simulation results of the influence of different turbulence inhibitors on the flow of molten steel in the tundish, as well as the RTD curve using this model are credible. Figure 9 shows camera snapshots of original design water model from 0 to 180 s.



Fig. 9: Images of original design for tundish at 0–180 s.

**CONCLUSION**
(a)Compared with the original turbulence inhibitors, use of the newly designed turbulence inhibitors to reinforce the retaining wall significantly improved the local wear problem. The velocity reduction at the wear position can be as much as 50% (0.2–0.1 m/s).

(b)Using the new design turbulence inhibitors compared with the original turbulence inhibitors, the response time of the newly designed turbulence inhibitors and the flow control device of the retaining wall increased by 39.7 s, the average residence time increased by 185 s, the dead zone volume decreased by over 40% and the plug volume was more than doubled. Thus, the flow field in the tundish was effectively improved.

**REFERENCES**
[1] Hackl, G., Tang Y., Lukesch, G., Meurer, D., Shivaram, P. and Resende, A. Impact Zone Solutions for an Improved Flow Performance in the Tundish. Presented at the AISTech 2019 Conference and Exhibition, Pittsburg, USA, 6–8 May 2019, 2851–2858.
[2] Mazumdar D. Review, analysis, and modeling of continuous casting tundish systems. Steel Research International 90 (4), 2019, p. 1800279.
[3] Sahai Y. Tundish technology for casting clean steel: A review. Metallurgical and Materials Transactions 47B (4), 2016, p. 2095.
[4] Zhang H, Fang Q, Luo R, et al. Effect of ladle changeover condition on transient three-phase flow in a five-strand bloom casting tundish. Metallurgical and Materials Transactions 50B (3), 2019, p. 1461.
[5] Yang B, Lei H, et al. Quasi-symmetric transfer behavior in an asymmetric two-strand tundish with different turbulence inhibitor. Metals 9 (8), 2019, p. 855.
[6] Fang Q, Zhang H, Luo R, et al. Optimization of flow, heat transfer and inclusion removal behaviors in an odd multistrand bloom casting tundish. Journal of Materials Research and Technology 9 (1), 2020, p. 347.
[7] Jiangsu Yonggang Group Co. Ltd. A Swirling Type Turbulence Inhibitor for the Tundish: China, CN201310185641.4[P]. 2013-5-20.
[8] Ai F. Simulation of the Effect of the New Type of Control Devices on the Single-Strand Caster Tundish. Wuhan: Wuhan University of Science and Technology, 2018.
[9] Ai X G, Han D, li S l, et al. Optimization of flow uniformity control device for six-stream continuous casting tundish. Journal of Iron and Steel Research International 27 (9), 2020, p. 1935.
[10] Pan H, Cheng S. Mathematical model of flow characterization in multi-strand continuous casting tundishes. Journal of University of Science and Technology Beijing 31 (7), 2009, p. 815.

# REMAINING USEFUL LIFE AND WEAR ESTIMATION OF THE REFRACTORY BRICKS OF THE LADLE LININGBY ARTIFICIAL INTELLIGENCE

Maria Arostegi, Diana Manjarrés
TECNALIA, Basque Research and Technology Alliance (BRTA), 48160 Derio, Bizkaia, Spain

Aintzane Soto Larzabal
Sidenor, Barrio Ugarte s/n, 48970 Basauri, Spain

## ABSTRACT

The steel industry is a key driver of new developments in the refractory industry due to its high market share (>70%) and the harsh conditions involved in the steelmaking processes. In addition, the annual refractory consumption in a special steel plant that produces more than 750.000 ton of steel per year, can reach around 10.000 ton. The RFCS European E-CO-LadleBrick project aims to develop an ecological and economic waste management of the ladle refractory bricks by implementing circular economy criteria (Reduce, Reuse, Re-manufacture and Recycle). Due to the higher impact, it is very important to promote the reduction in the waste generation by optimizing the use of the refractories. Could AI help, in this sense, to the first of these R's and reduce the refractory consumption in the ladles?

To answer this question, this work proposes a methodology by using two sources of information: First, refractory remaining thickness measurements obtained through a 3D laser equipment, and second, the information of the operation variables with the greatest influence on refractory degradation, collected heat-by-heat by a steelmaker. By means of using this information, this paper presents a Machine Learning tool with the main purpose of optimizing the refractory consumption: 1) by estimating the Remaining Useful Life with the information of the operation variables and 2) by estimating the wear of the MgO-C refractory lining that a specific heat can suppose. The work has been validated in a real application with data from a relevant steel company of the Basque Country (Spain).

**Keywords:** 3D Laser Data; Reduce Thickness; Refractory Bricks of Ladle Lining; Machine Learning Techniques

## INTRODUCTION

Around 35 to 40 million tons per year of refractory are produced worldwide [1], of which the steel industry is responsible for up to 70% of the total demand [2]. In this context, Artificial Intelligence (AI) techniques have been applied to Industry 4.0 and more specifically to different fields of application in Steel Making [3-5]. For instance, authors in [3] give a general but basic overview of the possibilities of AI in different fields of application in Steel Making. [4] presents a "playbook" in an early stage to guide/design effective advances in AI have the potential to impact innovation. Finally, [5] examines the relevance of Industry 4.0 related opportunities and challenges as drivers for Industry 4.0 implementation in the context of sustainability, taking a differentiated perspective on varying company sizes, industry sectors, and the company's role as an Industry 4.0 provider or user.

Regarding specific Machine Learning (ML) approaches, in [6] a temperature prediction model to be used as an advisory system for the casting process is presented. The used methodology transforms empirical expertise on the casting process into a model of qualitative nature. Moreover, in [7] a literature review related to heat transfer in steel-making ladle refractories is shown. The reviewed works are classified into experimentally and theoretically focused researches and besides some strategies for improving temperature control have been considered. In [8] the factors which affect temperature

variations between furnace tapping and teeming are analysed, and a procedure to determine the probable temperature change is posed. Similarly, authors in [9] propose the use of an Artificial Neural Network (ANN) to obtain an estimation of the slag Corrosion of MgO-C in ladle refractories, with several input features such as: %CO(g) in test atmosphere, Brick-slag exposure time, Test temperature (ºC) and CaO/SiO2 ratio of the slag. Finally, [10] obtains decisive factors that have great relevance in the determination of the wear, namely: basicity excursions versus MgO-C Refractory Lining Life, impacts of temperature fluctuations on lining life, residual thicknesses and non-uniform wear of bricks and micrographs of last working surfaces of residual bricks, among others.

Motivated by the growing interest and awareness of both the scientific community and society in applying more sustainable models in the Steel Industry, this paper focuses on a key aspect that will lead us unequivocally to Best Available Technology (BAT) methodology to follow: *Optimization of the use of steel ladles by AI*. This optimization is approached in two different ways: 1) Estimating the Remaining Useful Life (RUL) in order to maximize it, i.e., by providing information of the possible remaining heats that a specific ladle can support. 2) Estimating the wear of the most limiting areas of the ladle, i.e., the areas of maximum affection of the ladle.

Finally, the work is structured as follows: Section 2, focuses on detailing how the optimization problem, named *Optimization of the use of steel ladles by AI*, is approached. Section 3 analyses the results obtained and finally, Section 4 presents the conclusions of the work.

## OPTIMIZATION OF THE USE OF THE STEEL LADLES BY ARTIFICIAL INTELLIGENCE TECHNIQUES

### Data collection and pre-processing

*RUL estimation model*

Currently, in our real case study the remaining brick thicknesses are manually registered by the steel maker and are performed twice throughout the ladle life: at reparation and at demolition phases (in cold conditions).

On the other hand, the operation variables that are used heat by heat, i.e., *Sulphur in vacuum, KWh, Lime, Alumina Sulphur to overturn, time of vacuum, spar, argon, nitrogen, Oxygen overturn, slag, Desulphurisation speed, steel liquid*, are automatically collected. Both sources of information are used in this work to estimate the RUL of the ladle.

Firstly, an integration of both sources of information is done by splitting the information of the operation variables before reparation and between reparation and demolition phases. With all the variables collected in those two groups, new statistical variables have been built to be the input for the ML models. Specifically, the statistical variables that have been considered, are *mean*, *standard deviation* and *accumulated sum* of the variables for both groups which are considered as inputs, "x", of the RUL estimation model. Moreover,

the number of useful lives reached in the two phases of the campaigns (at reparation and demolition) is also obtained and used as "y" for the RUL estimation model.

*Ladle wear estimation model*

Regarding the data for the Ladle wear estimation model, a total amount of 12 campaigns is analysed, 10 of which will serve to train the model, and 2 to validate it. These campaigns integrate a total of 368 thickness measurements (311 for training and 57 for validation) performed with a commercial laser equipment, the LaCam Mobile unit by Ferrotron-Minteq. Four zones are selected as areas of maximum affection (Figure 1): Plug Transition Zone, Plug Wall Zone, Nozzle Transition Zone and Nozzle Wall Zone for which the Ladle wear estimation model is executed.
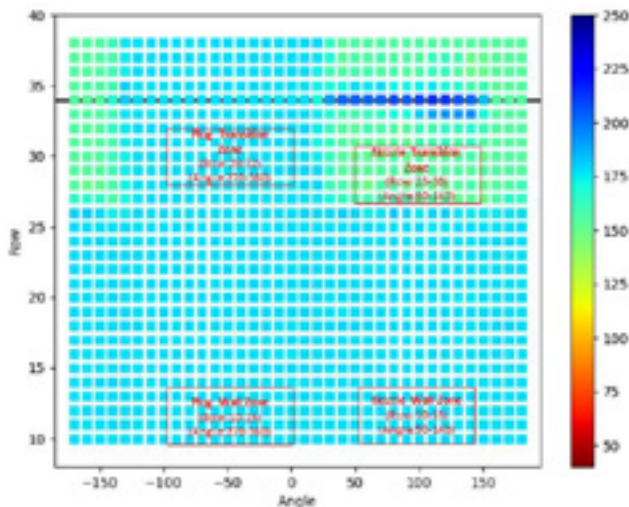


*Figure 1: Areas of maximum affection of the ladle, i.e., Plug Transition Zone, Plug Wall Zone, Nozzle Transition Zone and Nozzle Wall Zone (in red colour).*

In order to obtain a quality dataset by using the 3D points cloud the following methodology has been accomplished:

– Data cleaning: Transformation and Alignment of measurements: To achieve spatial coherence to obtain a time series in which the degradation is reflected, a grid is built with specific dimensions. Then, the 3D point clouds are placed on the corresponding grid element. Besides this, to analyse and compare the degradation of the thickness at specific locations, the position of the elements of the grid should be consistent throughout all the measurements. Therefore, a procedure for aligning the measurement files that contain the point clouds is done chronologically (from heat zero to 80, for example) according to the number of heats performed between corresponding measurements.

– Treatments of NaNs and Slag: In both cases it is quantified and located the areas of maximum affection of each phenomenon. In both cases the zones are very well defined, and two specific methodologies were designed to maximize the amount of the elements of the grid.

– Selection of areas of maximum affection: In order to select these areas, each and every one of the pre-processed ladles are analysed. The result of this comparison pointed out systematic similarities located in four areas: Plug Transition Zone, Plug Wall Zone, Nozzle Transition Zone and Nozzle Wall Zone (Figure 1).

– Obtaining the time series: In order to achieve the training process the information that comes from the 3D laser measurements in the grids included in the selected areas; instead of using the "Minimum

thickness of the area" in each of the measurements carried out per campaign, the "Percentile Q5 of the thicknesses of the area" is used, because the minimum one is reached in a very abrupt way on many occasions, which does not help the aforementioned learning process (Figure 2).
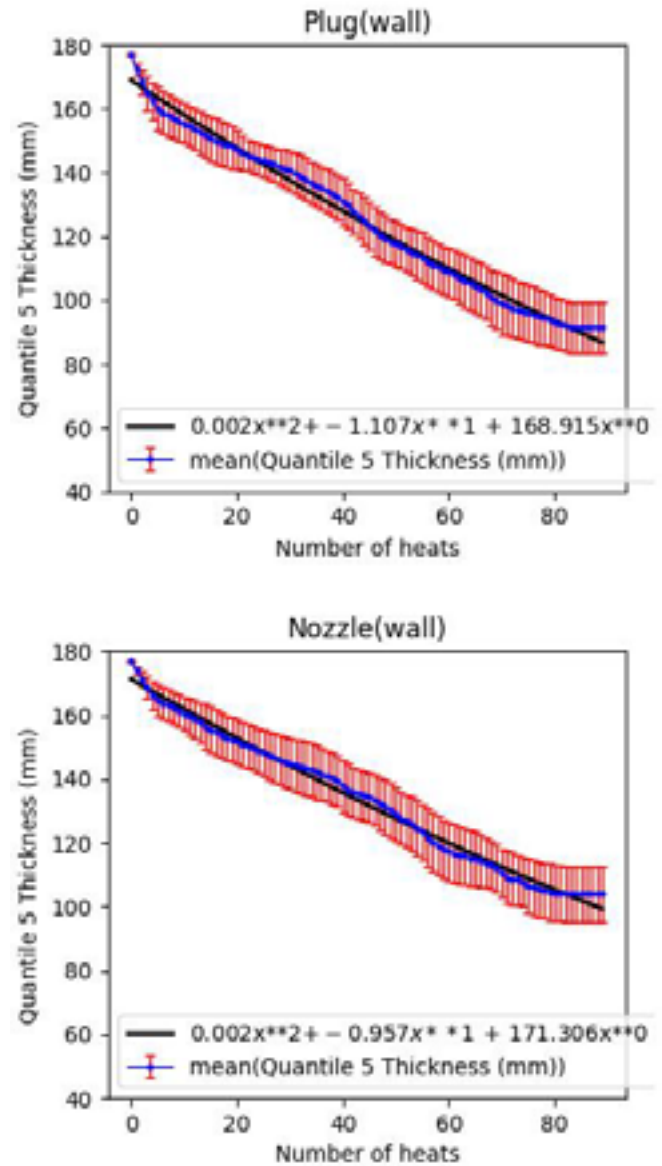


*Figure 2: Graphical representation of the regression curves (black), and mean values of the Q5(blue) of the thickness ± std(red) in the Plug Wall Zone.*

– Integration with the operation variables: For each instance in which there is a measurement, the remaining thickness is transformed to be integrated with the operation variables This process has been done for those four areas of maximum affection, the Wear Rate (Equation 1) "y" is computed as:

$$WR_i = \frac{(t_{(i-1)} - t_i)}{f_i}, \qquad (1)$$

being
$\begin{cases} t_i: \text{Remaining Percentile } Q_5 \text{ thickness at time } i. \\ f_i: \text{Number of heats integrated between measurements } i \text{ and } (i-1). \\ WR_i: \text{Wear Rate at time } i. \end{cases}$

Regarding the operation variables: Each instance must bring together the information of the heats performed up to that moment. In this use case, this transformed information has been obtained through the average and the accumulated value of all the operation variables of the performed heats. Moreover, the average and the accumulated value of all the operating variables "x" are considered as input for the models.

**Artificial Intelligence Techniques**

For both models, different AI algorithms have been used: 1) Random Forest (RF), XGBoost (XGB) and K-Nearest Neighbours (KNN).

– "Ensembling" is the technique to build a "model of models", that is, a few models are trained, and the final model does not depend on the prediction of a single scheme, but on several assemblies. The assembly concept is a good way to reduce the variance in the prediction, which is, extracting the most stable statistical component (least variance). There are two kind of ensemble methodology:

–*Bagging* is a way to decrease the variance in the prediction by generating additional data for training from dataset using combinations with repetitions to produce multi-sets of the original data. For example, **Random Forest**.

–*Boosting* is an iterative technique which adjusts the weight of an observation based on the last classification. If an observation was classified incorrectly, it tries to increase the weight of this observation. For example, **XGBoost** (Figure 3).
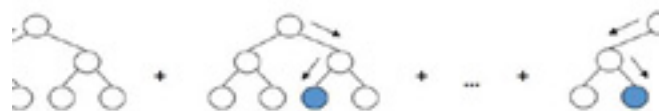


*Figure 3:XGBoost Boosting example.*

– **KNN**: KNN algorithm uses 'feature similarity' to predict the values of any new data points. This means that the new point is assigned a value based on how closely it resembles the points in the training set. And K, is the number of nearby points that the model will look at when evaluating a new point. The reason of comparing the IA models by using KNN, is because the number of instances is not very high so techniques such as KNN can be favoured by this fact.

**RESULTS**

In this section the results obtained for both estimation ML models (RUL and Ladle wear) are shown.

In order to evaluate the precision of both models, different test datasets reserved for this purpose are used. In the case of the RUL estimation model, the campaigns carried out during 2021 from January to December are reserved for this purpose. In the case of the Ladle wear estimation model 2 campaigns from a total of 12 are reserved to be used as test.

The metrics used to validate the performance of both models are the following: RMSE, MAE, Maximum committed error, Minimum committed error, and finally R-squared, $R^2$, which is a statistical measure that represents the proportion of the variance for a dependent variable that is explained by an independent variable(s) in a regression model.

Figure 4 presents the results of the RUL estimation model obtained by the XGBoost (in number of heats). Note that the x-axis represents several test campaigns, and the y-axis represents the number of heats supported by the ladles. The real RUL is shown in blue colour while the prediction is in cyan colour. The error metrics obtained are: RMSE of 2.295, MAE of 1.579, maximum error of 4.639, minimum error of 0.005 and $R^2$ of 0.067. The error distribution of the RUL estimation model is presented in Figure 5.
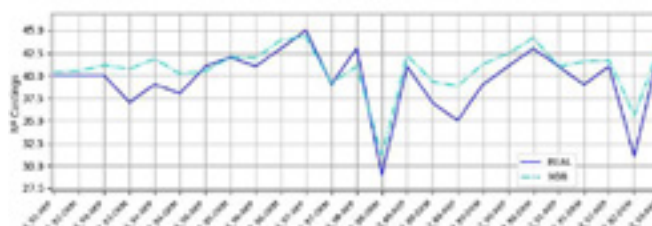


*Figure 4: Results of the RUL estimation model. The real value is represented in blue and the predicted in cyan.*
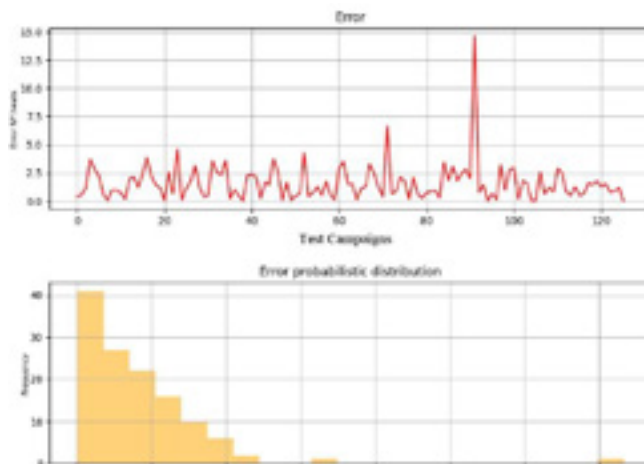


*Figure 5: Error distribution of the RUL estimation model.*

Similarly, Figure 6 presents the wear estimation results (in mm) obtained by different algorithms per validation campaigns: Random Forest (Rf) in red line, XGBoost (XGB) in cyan dashed line, 4-Nearest Neighbours (4NN) in black dotted line. The real wear rate is shown in solid blue line. Note that the y-axis is the error rate (mm), and the x-axis shows a detail of the campaigns used for the validation. On the other hand, given that the best results have been obtained by the XGB algorithm, Figure 7 shows the punctual error obtained in each prediction, and the histogram of the distribution of the error is presented. The metrics obtained are RMSE of 1.119, MAE of 0.710, maximum error of 5.1874 and minimum error of 0.055.
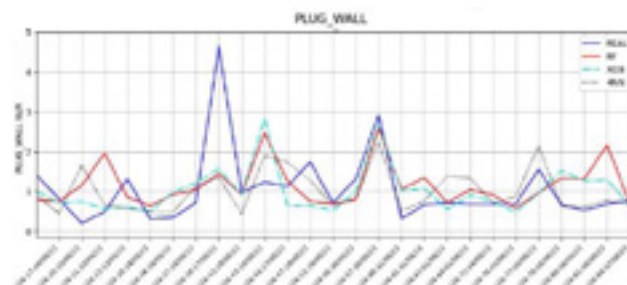


*Figure 6: Results of the wear estimation model per validation campaign in the PLUG wall Zone.*

644
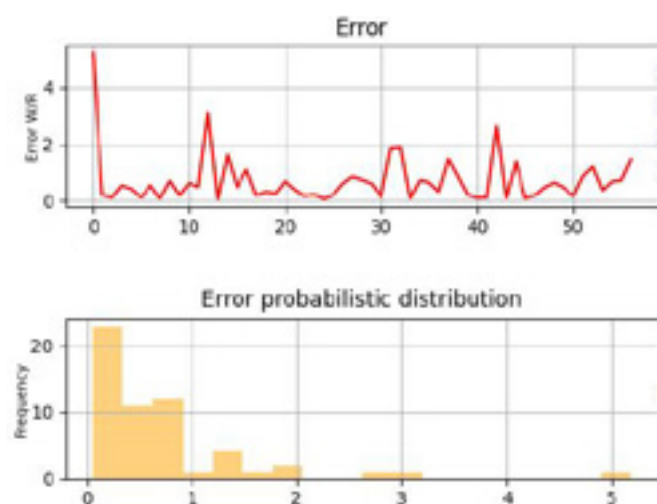
*Figure 7: Error distribution for the XGB algorithm in the PLUG wall Zone.*

## CONCLUSIONS

This paper presents a ML tool with the aim at optimizing the refractory consumption. Specifically, RUL and ladle wear rate estimation models are proposed for optimizing the use of steel ladles by AI techniques. It shows promising results, with a MAE of 1.5 heats for the RUL estimation model and 0.7 mm for the wear rate estimation model.

Future work will be delved in improving the results by including other relevant features as the composition of the steel. In this sense and continuing with the line of research, a hybridization of different methodologies to increase accuracy maintaining the speed of computation is proposed. Also, the implementation and testing of several multi-layer (deep) random vector functional link neural networks variants as straight-forward implementations is part of future work.

## AKNOWLEDGEMENTS

## REFERENCES

[1] Nakamura, Y., Hirai, N., Tsutsui, Y., Uchinokura, K., & Tamura, S. I. (1999). Recycling of refractories in the steel industry. *Advances in science and technology*, D693-D700.

[2] Horckmans, L., Nielsen, P., Dierckx, P., & Ducastel, A. (2019). Recycling of refractory bricks used in basic steelmaking: A review. *Resources, Conservation and Recycling*, *140*, 297-304.

[3] Naujok, N., & Stamm, H. (2017, June). Industry 4.0 in steel: Status, strategy, roadmap and capabilities. In *Future Steel Forum*.

[4] Cockburn, I. M., Henderson, R., & Stern, S. (2018). The impact of artificial intelligence on innovation: An exploratory analysis. In *The economics of artificial intelligence: An agenda* (pp. 115-146). University of Chicago Press

[5] Müller, J. M., Kiel, D., & Voigt, K. I. (2018). What drives the implementation of Industry 4.0? The role of opportunities and challenges in the context of sustainability. *Sustainability*, *10*(1), 247.

[6] Saxén, H., & Sillanpää, M. (1994). A model for decision support in continuous steel casting. *Modelling and Simulation in Materials Science and Engineering*, *2*(1), 79.

[7] Fredman, T. P. (2000). Heat transfer in steelmaking ladle refractories and steel temperature. *Scandinavian Journal of Metallurgy(Denmark)*, *29*(6), 232-258.

[8] Samways, N. L., & Dancy, T. E. (1960). Factors affecting temperature drop between tapping and teeming. *JOM*, *12*(4), 331-337.

[9] Akkurt, S. (2004). Prediction of the slag corrosion of MgO-C ladle refractories by the use of artificial neural networks. In *Key Engineering Materials* (Vol. 264, pp. 1727-1730). Trans Tech Publications Ltd.

[10] Otunniyi, I. O., Theko, Z. V., Mokoena, B. L. E., & Maramba, B. (2019, October). Major determinant of service life in magnesia-graphite slagline refractory lining in secondary steelmaking ladle furnace. In *IOP Conference Series: Materials Science and Engineering* (Vol. 655, No. 1, p. 012003). IOP Publishing.

# ARTIFICIAL INTELLIGENCE APPLIED TO ENHANCE THE THERMAL MANAGEMENT OF TORPEDO LADLE CARS

MGG Campos, B. Luchini, P. van Beurden, T. van der Velde, S. Sinnema
Tata Steel Netherlands, Velsen-Noord, Netherlands

H. Kuiken
Quantillion Technologies, Amsterdam, Netherlands

## ABSTRACT

The steel industry is highly complex. Steel manufacturers have to monitor all kinds of processes, maintain the operation and reduce the emission of $CO_2$. Advanced digitalization tools are vital to evolve toward a more sustainable, optimized, integrated, and agile operating model. Representing processes and systems as a digital twin with artificial intelligence-based optimization and scheduling models greatly enhances the decision-making on logistics, refractory maintenance, and energy efficiency. In this context, the thermal management of the torpedo ladle cars (used to transfer hot metal from the blast furnace to the steelmaking plant) has an important role. In this paper, the development of an artificial intelligence system to support decision-making on selecting the most energetically favorable torpedo car is presented. The application uses a simulation-based digital twin consisting of reduced order models of validated FEM models to forecast the torpedoes' refractory lining and pig iron temperatures. In addition, the system includes the refractory wear, location, and number of the torpedoes to indicate the most suitable to be selected for hot metal transportation. This increases the life of the equipment and avoids unnecessary heat losses, thereby reducing production costs and energy consumption. Thus, these new technologies lead us to solve existing logistics management challenges, improve process control, and prepare steel companies for the future.

## INTRODUCTION

The digital transformation in the steel industry provides the potential to reduce costs, improve profit margins and create more sustainable processes. Advanced analytics, machine learning, artificial intelligence, cloud solutions and digital twins are some of the technologies present in the ongoing digital transformation. In particular, applying the related technologies to the production processes allows the industry to become greener.

In this context, the hot metal route significantly impacts this challenge. The torpedo cars transport hot metal from the blast furnace to the steelmaking. The hot metal temperature affects the steel plant process as this can introduce a reheating step or reduce the amount of scrap in the converter if the temperature is too low. Therefore, the thermal management of torpedo cars is essential for green steel transformation [1].

This complex and ambiguous procedure involving several variables requires a multi-disciplinary solution [2]. An artificial intelligence system to support real-time decision-making on selecting the most energetically favourable torpedo car is being developed. The application uses a digital twin based on reduced-order models from complex finite element (FEM) thermal simulations. The refractory lining age, thermal conditions, and the torpedo's location define the most suitable torpedo to be filled and emptied.

The insights and capabilities of the AI solution provide a scenario planning for more dynamic and long-term decision-making clearness reducing the accumulative thermal losses during operation. We present the first results on the hot metal temperature losses by applying the artificial intelligence system.

## APPROACH

The torpedoes are responsible for transferring the hot metal from the blast furnace to the steel plant and its operation is described in Figure 1. The torpedoes are pre-heated and the cycle begins at the blast furnace, where the liquid metal is poured into the torpedo car. The hot metal resides in the car for transportation and treatment (BOS buffer). After it reaches the BOS plant, the vessel is emptied into a hot metal ladle. After that, the empty car returns and waits in the blast furnace buffer until the next cycle (aging).
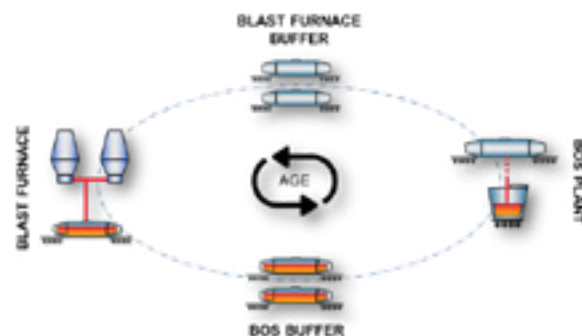


*Fig. 1: Operation and cycle of the torpedo cars from the blast furnace to the basic oxygen steel plant (BOS).*

Nowadays, the decision of which torpedo from the blast furnace buffer should be filled is based on the first-in-first-out principle (FIFO) [3]. This methodology is rather simplistic and does not include energy efficiency, refractory lifetime and hot metal temperature and quality. Therefore, the development of an artificial intelligence model combined with the digital twins can enhance the multifactorial analysis, improving energy efficiency in the ironmaking procedures.

## METHODOLOGY

### Finite element model

Finite element model is a powerful tool for simulating and analyzing the behavior and the physical aspects of complex scenarios under various conditions. These models can be used to develop new equipment, verify the temperature distribution at certain heat conditions, and analyze failures and non-linear problems.

A three-dimensional 1/4th symmetric transient model of the torpedo was used to calculate the thermal condition, see Figure 2. Natural convection on the external shell and radiation and convection on the internal surfaces were included as boundary conditions. In addition, temperature dependent for the materials properties and the age of the torpedoes were considered.
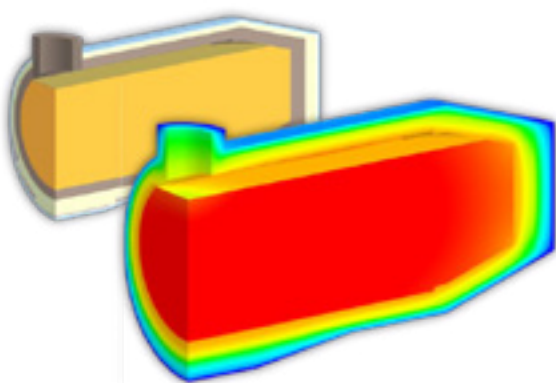
*Fig. 2: Finite element model of the torpedo car.*

A thermocouple measurement campaign was conducted to monitor the torpedo ladle car's refractory lining temperatures and validate the finite element model [1]. The agreement between the FEM model and the thermo-couples was very good, see Figure 3.
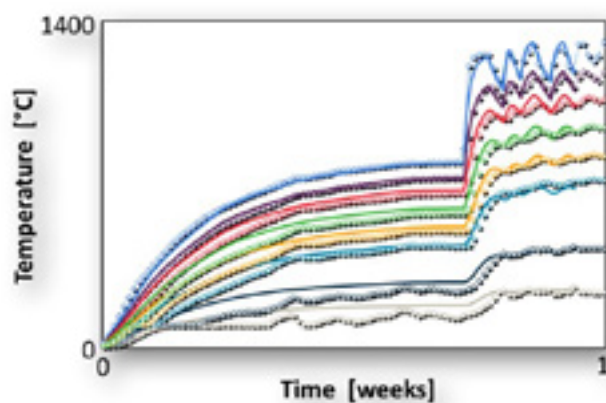


*Fig. 3: Thermocouple measurements. The diamonds are the measured temperatures, the solid lines are the calculated temperatures by FEM.*

One of the main disadvantages of FEM models is that they require a lot of computational resources and time. Therefore, using these models in real-time applications and daily operation is difficult. The reduced order model can be used in this context, described in the next section.

**Reduced order model**

A reduced order model (ROM) is a simplified representation of a complex system that captures its essential dynamics while reducing computational complexity [4]. Creating a reduced order model involves the following general steps (Figure 4):



*Fig. 4: General steps to create a reduced order model [5].*

The first step is to define the problem to solve, identifying the system's essential variables, parameters, and governing equations. In this case, the problem's output parameters are the refractory and hot metal temperatures.

To create a reduced order model, you need either experimental data or a high-fidelity numerical model of the system. However, a design of experiments is essential to define the training dataset and optimize the model's accuracy. The finite element model of the torpedo described in the previous section was used to generate the data. The singular value decomposition theory is used to develop the reduced order model itself and the dataset is split into training and validation [5,6]. Creating accurate reduced order models can be a complex task. It might be necessary to iterate through the steps above, considering different parameters, model forms, or refining the data used for training.

The digital twin was generated, and it can be deployed. It was also necessary to assess the accuracy of the digital twin by comparing its predictions with independent simulations, Figures 5 and 6.
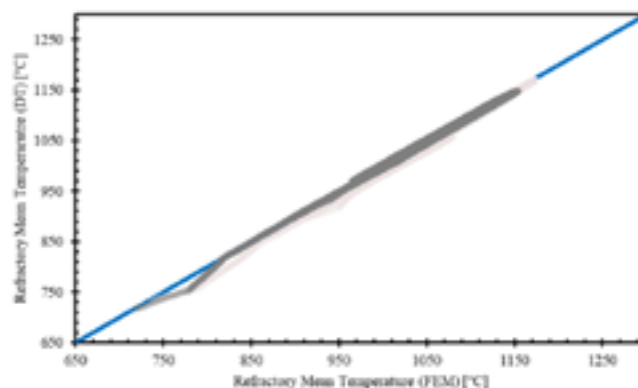


*Fig.5: Comparison between the predicted refractory temperatures using the DT and the FEM model.*
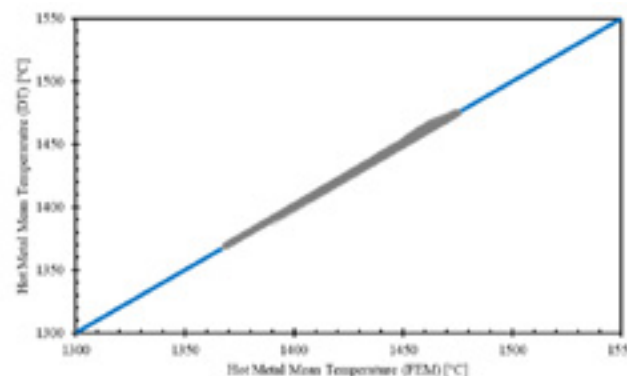


*Fig. 6: Comparison between the predicted hot metal temperatures using the DT and the FEM model.*

The digital twin showed high agreement with the FEM modeling. The accuracy of the digital twin was 99% for both refractory and hot metal temperatures when compared with FEM results. Therefore, using the digital twin during production and having a thermal state for each torpedo car in operation is possible.

By associating the digital twin with artificial intelligence algorithms it is possible to optimize the decision making on the torpedo management and selection.

**Artificial Intelligence**

Artificial intelligence (AI) systems can be highly effective in solving multi-factorial problems due to their ability to process large amounts of data, analyze complex patterns, and make optimized decisions.

AI algorithms can analyze various factors, constraints, and objectives related to scheduling, such as how many torpedoes are in the fleet, productivity, refractory temperature, empty time and full time. By formulating scheduling as an optimization problem, the AI system can reduce the hot metal temperature losses and $CO_2$ emission.

There are several types of AI and optimized algorithms. Customized heuristic algorithms (CH) and reinforcement learning (RL) are two approaches to solving problems, including scheduling issues.

Heuristic algorithms are designed based on domain-specific knowledge and problem understanding. They rely on predefined rules, heuristics, or algorithms crafted by human experts. These algorithms often exploit specific problem characteristics to find good solutions quickly. On the other hand, RL approaches do not rely on predefined rules or problem-specific knowledge. Instead, they learn optimal policies through interactions with the environment. RL algorithms can adapt to various problem domains without requiring explicit human expertise.

CH generally requires manual design and tuning by experts. They may adapt well to changing environments or new problem instances with additional modifications. Therefore, they may only explore within established heuristics, limiting their ability to discover novel and potentially better solutions.

RL algorithms learn through trial and error, continuously improving their performance over time. They can adapt to new situations and handle changing environments. RL models are trained using reward signals to guide the learning process and optimize long-term performance, see Figure 7.
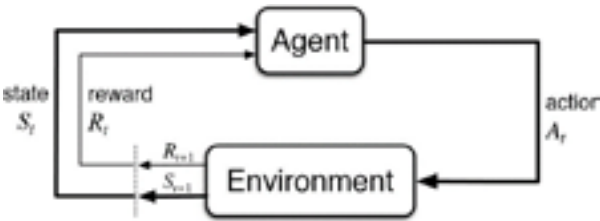
Figure 7. Reinforcement Learning agent-environment interaction

RL algorithms inherently balance exploration and exploitation. They explore different actions and strategies to discover optimal policies while gradually shifting towards exploiting the learned knowledge to maximize rewards. RL can potentially find new, improved solutions beyond what human-designed heuristics may have considered. However, the convergence to optimal policies may take time and unexpected action can happen depending on the problem's complexity and the training process.

Both algorithms were used to compare the hot metal temperature losses by optimizing the thermal management of the torpedo cars.

## RESULTS

The estimated algorithms' performance was defined by computing hot metal temperature loss based on average values (means). The hot metal temperature loss is calculated by subtracting the average temperature of the hot metal that arrives at the BOS plant from the temperature of the hot metal that comes from the blast furnace to a torpedo.

First, the customized heuristic algorithm was compared with the FIFO methodology over one week, see Figure 8 and Table 1.
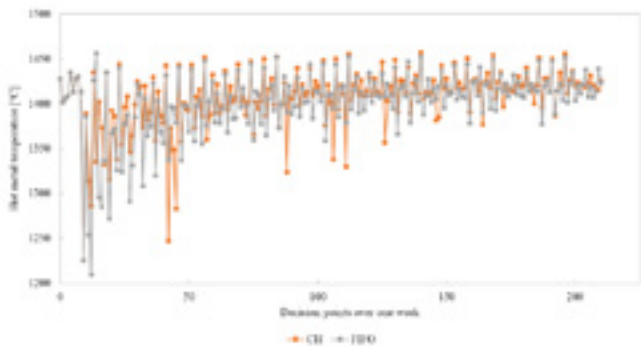


Fig. 8: Hot metal temperature for CH and FIFO over one week.

Tab. 1: Comparison of the mean hot metal temperature loss after one week.

| Algorithm | Hot metal temperature loss (°C) |
|-----------|--------------------------------|
| FIFO | 0 |
| CH | -7 |

The CH performed better than the actual methodology used in current operations, reducing 7°C in the mean hot metal temperature loss.

The RL was modelled only over two days due to its complexity, it requires a long computation time. The hot metal temperature results of RL, FIFO, and CH are shown in Figure 9 and Table 2. In addition, a random agent was included as a baseline for comparison with the other algorithms. The random agent facilitates seeing if the RL is simply with unexpected or optimal behavior.
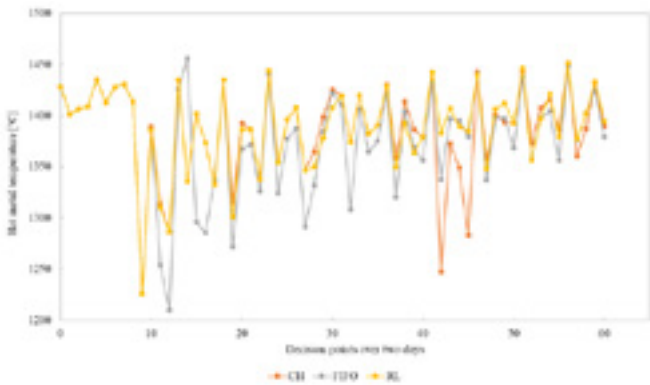


Fig. 9: Hot metal temperature for RL, CH and FIFO over two days.

Tab. 2: Comparison of the mean hot metal temperature loss after two days.

| Algorithm | Hot metal temperature loss (°C) |
|-----------|--------------------------------|
| FIFO | 0 |
| CH | -9 |
| RANDOM AGENT | -3 |
| RL | -12 |

The results show the potential of using the RL algorithm to optimize the thermal management of the torpedoes, minimizing the hot metal temperature losses and maximizing the production control.

## CONCLUSIONS

Digitalization is essential for the steel industry as it allows for real-time monitoring and control of manufacturing processes, leading to improved operational efficiency and more sustainable operation. Additionally, by leveraging AI capabilities, scheduling problems can be solved more efficiently, accurately, and adaptively. AI systems can help optimize resource utilization, reduce costs, improve process control, and make the steel industry greener.

In this context, an artificial intelligence system based on a digital twin was developed to select the most energetically favourable torpedo car. The digital twin is created from reduced order models (ROM) of complex finite element models.

Two optimization algorithms were used to compare the results. The customized heuristic algorithms are based on human expertise and problem understanding, while reinforcement learning learns optimal policies through environmental interactions. Customized heuristics can be efficient and effective for specific problem instances or classes, whereas reinforcement learning offers adaptability, scalability, and potential for generalization across different domains.

In summary, both algorithms showed the significant potential of the solution in reducing the accumulative thermal losses during torpedo cars operation and reducing $CO_2$ emissions. CH reduced 7 °C of the hot metal temperature loss over one week. On the other hand, the reinforcement learning reduced 12 °C over two days. However, optimizing the reinforcement learning algorithm to model long periods is necessary.

In addition, this methodology can be expanded to other installations, for instance, hot metal and steel ladles. It will drive to solve existing and future logistics management challenges, improving process control and refractories life, and reducing $CO_2$ emissions.

## REFERENCES

[1] Van Beurden P, Liefhebber J, Sentveld P, Kerkhoven F. On the Thermal Management of Torpedo Ladle Car Logistics of Tata Steel in IJmuiden. Proc. UNITECR 2019, 2019, pp.365-368.

[2] Goldwaser A, Schutt A. Optimal torpedo scheduling. Journal of Artificial Intelligence Research 63, 2018, p.955-986.

[3] Luchini B, Campos MGG, Van Beurden B, Sinnema S. AISTech 2023 - Proceedings of the Iron & Steel Technology Conference, 2023, Detroit, Mich., USA.

[4] Hurkamp A et al., Simulation-based digital twin for the manufacturing of thermoplastic composites. Procedia CIRP 100, 2021, p.1-6.

[5] Calka M et al., Machine-learning based model order reduction of a biomechanical model of a human tongue, Computer Methods and Programs in Biomedicine 198, 2021, 105786.

[6] Hu et al., A transient reduced order model for battery thermal management based on singular value decomposition, IEEE Energy Conversion Congress and Exposition, 2014.

649

# THE USE OF NUMERICAL MODELLING FOR REFRACTORIES OPTIMISATION IN THE REHEATING FURNACES AT TATA STEEL NEDERLAND

Bruno Luchini, Frank van Sikkelerus, Florus Beukema, Ed Wortel, Sido Sinnema.
Tata Steel Nederland, IJmuiden, The Netherlands

**ABSTRACT**

Tata Steel in IJmuiden (NL) produces approx. 7 million tons of steel per year. In order to cope with such volume, the IJmuiden site makes use of 4 slab reheating furnaces. Refractories are crucial components for a stable operation and a high quality end product. With energy prices in historical peak, reducing heat-losses in the furnaces became an even stronger objective. In this study, we discuss how numerical simulation based on finite element method (FEM) assists Tata Steel in the decision-making process, from materials selection up to geometry optimisation of refractory components like support walls and anchor bricks. The study also sheds light on the trade-off between using an 1D simplified model and a more detailed 3D FEM model.

**INTRODUCTION**

Slab reheating furnaces are crucial components in the steel manufacturing process. They are used to reheat slabs to the desired temperatures before the hot rolling stage. The reheating furnaces operate in temperatures up to 1350°C. Tata Steel produces approx. 7 million tons of steel per year. In order to cope with such volume, the IJmuiden site makes use of 4 slab reheating furnaces (Fig. 1). Last year furnace 21 was replaced by the walking beam furnace 25 at Tata Steel in IJmuiden, reducing energy consumption by 1.0 PJ/year. Refractory materials play a vital role in this installation due to the extreme temperatures involved. They are designed to withstand the intense heat and minimise the heat losses to the surroundings. The refractories act as a protective barrier, resisting thermal shock, corrosion and thermo-mechanical stresses, thus maintaining the structural integrity of the furnace and optimising its performance.

Numerical modelling has emerged as a valuable tool for optimising refractory performance in various industrial applications, including reheating furnaces [1,2]. The models are used in the materials' selection, heat losses estimations and geometry optimisation during the design phase of furnace 25. Through computational simulations, one can simulate the behaviour of distinct refractory materials under specific operating conditions, enabling for informed decision making. These models can be rather simple, like 1D thermal analysis, or very complex, taking into account multiple factors such as thermal conductivity, heat capacity and corrosion, allowing for a comprehensive evaluation of the refractory's performance. Additionally, numerical simulations can identify design issues and easily evaluate different mitigation strategies. By leveraging numerical modelling techniques, industries can optimise the refractories performance, reduce the energy consumption and extend the lifespan of the refractory linings, ultimately leading to improved operational efficiency and cost savings.
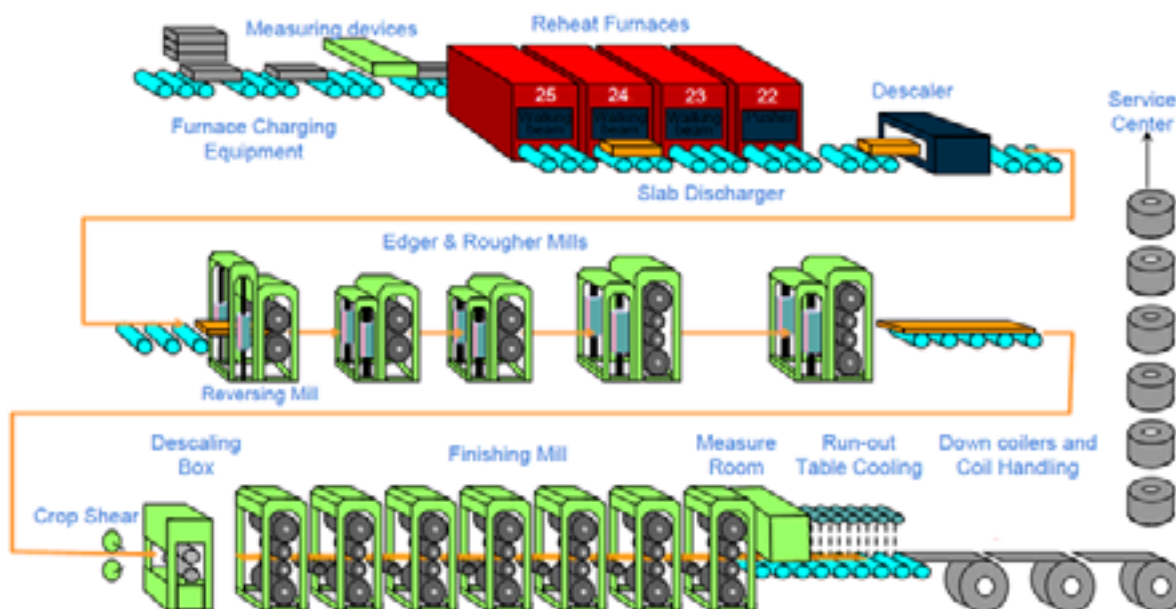
*Fig. 1: Downstream route – Tata Steel in IJmuiden*

## THE USE OF NUMERICAL MODELLING AT TATA STEEL'S REHEATING FURNACES

Furnace 25 is the newest walking beam furnace at Tata Steel in IJmuiden. During its design phase, several models were created to select the most suitable materials and design strategies. One good example where numerical modelling was useful is the simulation of the thermo-mechanical behaviour of the roof. As it can be seen on Fig. 2a, part of the roof of furnace 25 has an inclined slope. This design feature was not present in any of the other furnaces in IJmuiden. A numerical model was used in order to understand the behaviour of this design before installation. The model represents only a section of the roof and makes use of symmetry planes to reduce computational costs while maintaining physics fidelity. The model was used to evaluate the temperature (Fig, 2b), deformation (Fig. 2c) and stress over strength ratio <SSR> (Fig. 2d and 2e) in the roof components. The stress over strength ratio <SSR> is a temperature dependant failure criterion which takes into account the measured max principal strengths at different temperatures. The equation for this criterion is given by equation 1. One of the main concerns in such structure is related to the level of stress the anchors would be subject during operation. The models have shown medium levels of SSR in the anchors. To be even safer, the expansion allowances were revised based on the outcome of the model, reducing the SSR level of the anchors.

$$SSR(T) = \frac{\sigma_1(T)}{\sigma_{measured}(T)} \qquad \text{Equation 1}$$

a)



b)



651

c)



d)



e)
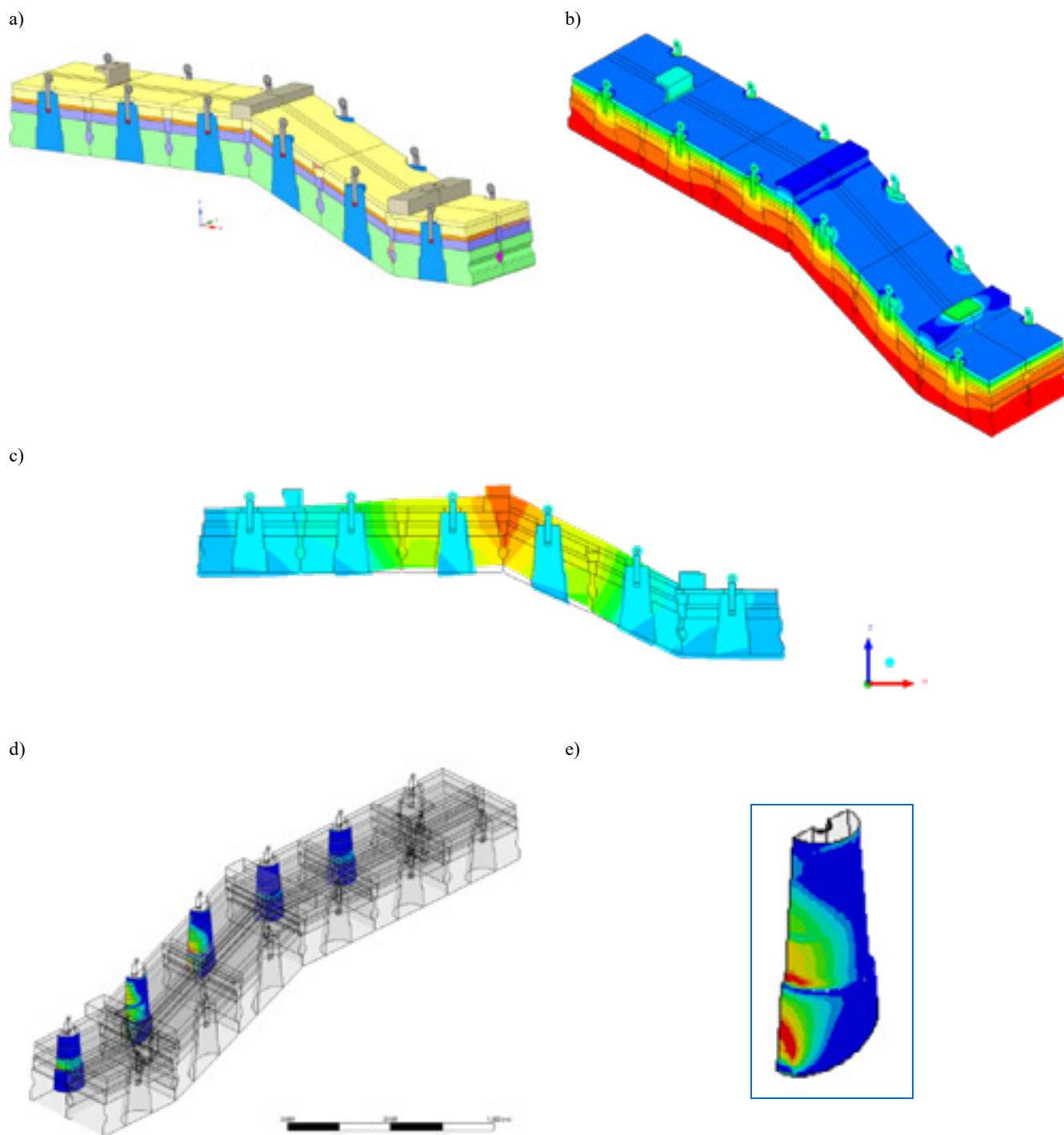


*Fig. 2: Roof's model (a), temperature distribution(b), deformation distribution <magnified 5x>,(c) and stress over strength distribution on anchors (d and e).*

**NECESSITY OF 3D MODELS**

1D simulation is typically appropriate when the thermal behaviour is predominantly one-dimensional, such as in structures with uniform thickness and when heat flow occurs primarily in one direction. On the other hand, 3D simulation is necessary when the thermal behaviour of the structure is inherently three-dimensional or if it involves complex geometries, complex heat flow paths and varying material properties. 3D simulations provide a more detailed representation of the system capturing localized variations.

Therefore, in a reheating furnace project, if one is interested in the temperature distribution along a flat wall, where the refractory and insulating lines present constant thicknesses, and when the heat flow is predominantly unidirectional, a 1D calculation can result in a good approximation.

An interesting example where 3D simulation had to be employed in the design evaluation of reheating furnace is the materials' specification behind the anchor bricks. The anchor has a rather complex geometry and the bolt act as a heat sink. Therefore, a 1D approximation in this location is imprecise. With the 3D model it was possible to verify that the insulation material initially selected would be subject to temperatures higher than its working specification. The 1D model of the wall (not considering the bolt's heat sink effect) predicted that all materials were within working specifications.

Based on the results a redesign of the refractory construction was made (Fig. 4). The two main target were to keep temperatures below the working temperature for each material and to reduce the heat loss. The results showed that all materials have met this criteria and heat loss was reduced by 19%. Thus, 3D simulation is recommended for a finer and optimized design in those situations.
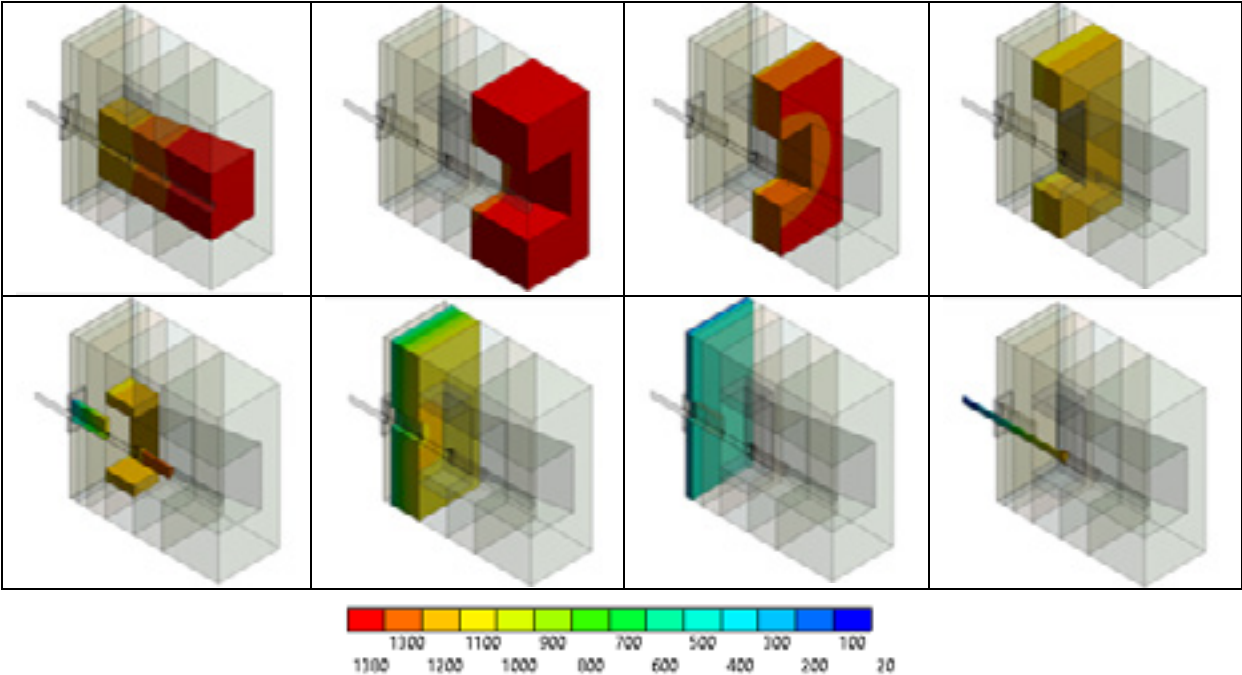
Fig. 3: Temperature distribution in the different structures behind the anchor brick
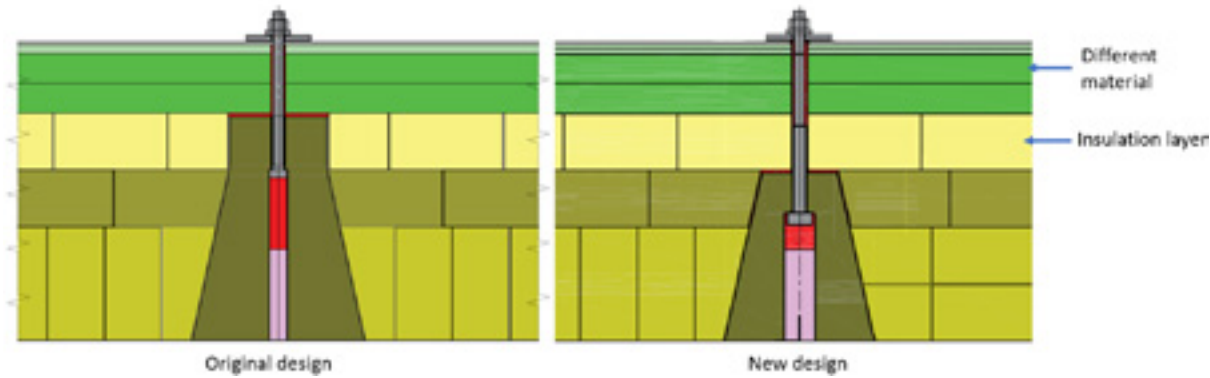


Fig. 4: Re-design of the the anchor brick construction of the furnace wall

As previously mentioned, 1D simulation is appropriate when the thermal behaviour is predominantly one-dimensional. In this case, using a 3D simulation would result in increased expensed resources without much added value. In Fig. 5a, one can see that the results attained by the 3D model far from the anchor bolt (line AB), where the heat flux is mainly unidirectional. The 1D (Fig, 5b - green line) and 3D (Fig, 5b - black line) results are very much comparable.

a)

b)
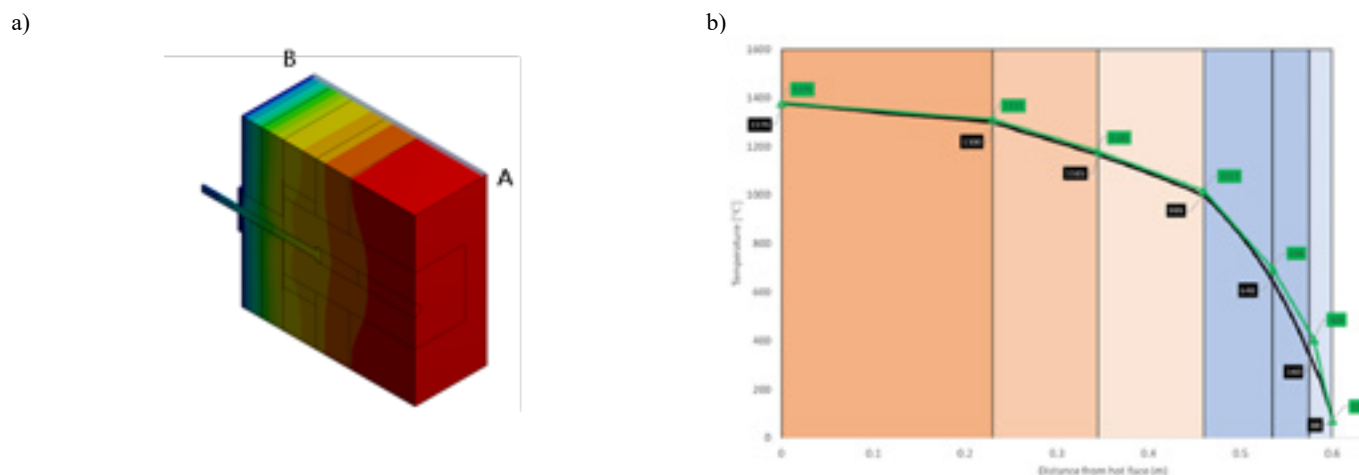


*Fig. 5: a) Temperature distribution in the anchor brick and surroundings, b) 1D and 3D results comparisons*

## CONCLUSIONS

The article underscores the significant role of numerical simulation, particularly finite element method (FEM), in optimizing refractory performance in Tata Steel Nederland's slabs' reheating furnaces. Through simulations, materials selection, geometry optimization, and informed decision-making processes are facilitated, ultimately leading to stable operation, high-quality steel production, and minimized heat losses. The study showcases the application of numerical modelling in evaluating the thermo-mechanical behaviour of the furnace roof and anchor bricks, highlighting the necessity of 3D models for complex geometries and three-dimensional thermal behaviour. Additionally, the article emphasizes the value of comparing 1D and 3D models, noting that while 1D simulations provide a good approximation for predominantly one-dimensional thermal behaviour, 3D simulations offer a more detailed representation of the system, capturing localized variations and enabling a finer and optimized design. Furthermore, the article highlights the example of anchor bricks where the use of a 3D model was essential to accurately assess temperature specifications and facilitate a redesign of the refractory construction, resulting in reduced heat loss. Overall, numerical modelling proves to be a valuable tool in achieving optimal design and operational outcomes, reducing energy consumption, and prolonging the lifespan of refractory linings.

## REFERENCES

[1]  Steinboeck A., Wild D., Kiefer T., Kugi, A., A mathematical model of a slab reheating furnace with radiative heat transfer and non-participating gaseous media. International Journal of Heat and Mass Transfer 53 (25-26), 2010, p.5933-5946.
[2]  Zaaquib A., Lecompte S., Raad T, Paepe, M., Steady State model of a Reheating Furnace for determining slab boundary conditions. Ernergy Procedia 158, 2019, p.5844-5849

653

# A NEW STANDARD FROM WRA FOR DIGITAL EXCHANGE OF REFRACTORIES DATA

Alexander Platzer, Bernardo Gosaric de Barros,
RHIMagnesita, Vienna, Austria and Contagem/Brasil
and
WRA, Bruxelles, Belgium

## ABSTRACT

Bringing product information for customers to describe refractory products is done daily thousands of times, but in many different ways and forms, some being safer than others and many of them not digital. The data transfer process in B2B transactions defines quality, speed and mostly trust. As the world is more and more digital and many other industries further up in the value chain are using digital standards to exchange product information the World Refractory Association (WRA) has supported the development of a digital refractory exchange data standards (REDS) to also facilitate this development, which can become a requirement soon down the value chain. The paper presents the approach, the structure and also a way to generally exchange refractory product information.

## INTRODUCTION

Imagine you want order food online. You open one of the apps that allows you to select between a variety of different styles of cooking, Indian, Italian, Chinese, or Thai for example. You select the one you feel in the mood for, then you continue your select one of several different restaurants serving your favoured food style. Once you have selected your trusted food supplier you scroll through a list of different dishes, with nice pictures and descriptions that allow you to pick what you hunger for. Life can be so easy, right? But did you ever consider what allows you to do that? All the different restaurants are having a pre-specified way to enter their food information, in other words the food delivery service uses a specific data standard to provide the information the restaurant wants to supply over the food-app. So while the food names, descriptions and pictures my vary in stile and depth, the structure of the presentation remains the same, irrespectively if it is Thai or Italian. As a (hungry) user this allows us quick absorption of the information and focus on the details of product of interest. We want clear information on the product, not a different structure of presentation when we change from one restaurant to another one and we clearly have to always find out if the selected dish contains a compound that might cause an allergic reaction. After we've found our dinner of the day we're ready to press the order-button, but wait, there's also this restaurant, where you know the food is really good, because you already ate there before, unfortunately it is in a different part of the city so walking there is taking too long and it's not on the food-app. However, you're sure that you still have their folder lying around to order by phone, so you start searching your apartment for it. 20 minutes later you give up the search, because you couldn't find their folder and you go back to the food-app, order and online. This shows the second benefit, digitally available online data cannot be misplaced, you just go on the dedicated platform and retrieve it from there.

As users of a food- or any other kind of commercial app we like this type of comfort, more so, we take it for granted. The question is why we as refractory producers are not aiming to provide a comparable comfort when dealing with our product information to our customers. Consequently, the question arises: "how are we exchanging information on our products in the refractory industry?". While the author was not able to draw a statistically reliable sample to answer this question scientifically, his gut feeling makes him believe the refractory industry behaves in most cases like the normal, average person, dealing with data. The German newspaper "Die Zeit" has evaluated early this year the most common formats to exchange data in Germany in 2023. Surprisingly DIN A4 (the most common paper format in central Europe) is still ruling data exchange, followed by the well-known
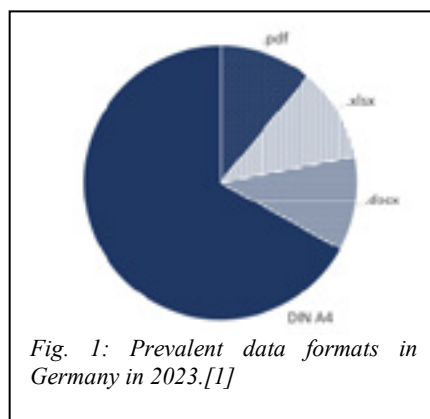


*Fig. 1: Prevalent data formats in Germany in 2023.[1]*

office PC-file-formats. Now unsurprisingly this also matches the author's daily work experience. While it is not fair to extrapolate this pattern to an entire industry, conversations with representatives of refractory suppliers as well as customers revealed this was also their normal way of handling data. This is somewhat bewildering as there's a shared understanding that data has value, so handling it carefully and efficiently would be the logic thing to do. On the other side it is only human to use what is there (paper, word and pdf) and make the most out of it, but it is equally human to ask the fundamental question of any innovation, "Can we do this in a better way?". Improvement however comes with the effort to change something, and change can make people feel uncomfortable. "Why do I need this?" is the classic defence mechanism we always perceive at others but never at ourselves. So let's answer the question.

## WHY THE REFRACTORY INDUSTRY SHOULD HAVE A PRODUCT OR RFRACTORY DATA EXCHANGE STANDARD

Søren Kierkegaard is believed to have said "Comparison is the end of happiness and the beginning of dissatisfaction.". Still comparing is necessary to understand where you are in a process, into which direction you can improve or what could hit you unprepared if you don't understand how others dealt with a comparable challenge. So, once you start comparing you find out that there are thousands of different data standards in use today. These standards cater to various sectors, including finance, healthcare, manufacturing, telecommunications, transportation, energy, retail, and more. Each industry and domain may have multiple standards specific to their needs. Here are a few examples:

1. EDIFACT (Electronic Data Interchange for Administration, Commerce, and Transport): EDIFACT is a widely used international standard for electronic data interchange. For example, in the automotive industry, it is utilized for various business processes, including purchase orders, shipping notices, and invoicing, enabling seamless data exchange between automotive manufacturers and suppliers. Alternatively, the North American region would be the equivalently working ANSI ASC X12 standard.
2. SWIFT (Society for Worldwide Interbank Financial Telecommunication): SWIFT is a messaging network used by banks and financial institutions to securely send and receive financial transactions globally. It provides a standardized format for international payments, messages, and instructions.
3. XBRL (eXtensible Business Reporting Language): XBRL is a standard for electronic communication of business and financial data. It enables the exchange and analysis of financial statements, regulatory filings, and other business reports.

4. HL7 (Health Level Seven): HL7 is a set of international standards for the exchange, integration, sharing, and retrieval of electronic health information. It facilitates interoperability and data exchange between different healthcare systems.

5. XML (eXtensible Markup Language): XML is a widely used standard for structuring and organizing data. It is platform-independent and allows for the exchange of structured information between systems.

6. JSON (JavaScript Object Notation): JSON is a lightweight data interchange format. It is widely used for representing structured data and is particularly popular for web-based applications and APIs.

Data standards have become the norm in the B2B-world. They come in many types and sizes, and all have one goal, to provide the customer/receiver with the data set needed. Handling data efficiently, allows for simplification, transparency and can become a service through the right technology.



Fig. 2: with the customer in focus, data and technology can create value through more transparency, service delivered and simplification of handling [2]

The requirements of vertical data-integration and circular economy drive towards the availability and accessibility of product data as one element in the digital chain.

The refractory industry could benefit significantly from a product exchange data standard. Here are some ways the industry could profit from implementing such a standard:

1. Streamlined Procurement Process: A product exchange data standard would provide a common format and structure for exchanging information related to refractory products, such as specifications, material compositions, dimensions, and performance characteristics. This would simplify the procurement process by enabling seamless communication between buyers and suppliers, reducing errors, and speeding up the ordering and fulfilment cycle.

2. Enhanced Product Information: By adhering to a data standard, refractory manufacturers can provide detailed and standardized product information, including technical specifications, testing data, safety certifications, and usage guidelines. This would enable customers to make informed decisions and compare different products more easily, leading to improved purchasing decisions and higher customer satisfaction.

3. Improved Supply Chain Efficiency: With a product exchange data standard, the refractory industry can achieve better supply chain integration and efficiency. The standard would enable automated data exchange and integration between suppliers, manufacturers, distributors, and end-users, resulting in faster order processing, improved inventory management, and reduced lead times.

4. Facilitated Equipment Integration: Refractory products are often used in conjunction with other equipment and systems in industrial processes. A product exchange data standard could include information on compatibility, installation requirements, and maintenance procedures, enabling better integration of refractories with other equipment. This would simplify installation and maintenance processes, reduce downtime, and enhance overall system performance.

5. Compliance and Traceability: A product exchange data standard can incorporate regulatory requirements and traceability features. This would assist the refractory industry in complying with industry regulations, environmental standards, and safety guidelines. It would also enable tracking and documentation of product origins, materials used, and performance history, ensuring transparency and accountability in the supply chain.

## WHAT THE WRA REDS-TEAM HAS CREATED

In early 2021 (shortly before Covid started) the WRA formed a taskforce to work on Refractory Exchange Data Standards (REDS). The taskforce was formed by employees of RHIMagensita, Refratechnik, Vesuvius, Harbison Walker International and later joined by Almatis and Calderys. Two workstreams were defined. The first focuses on refractory product data which should be shared
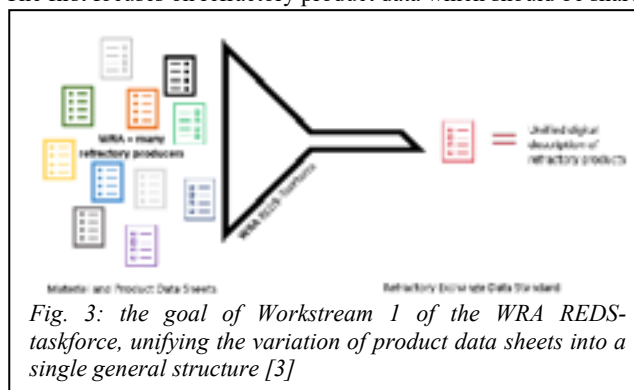


Fig. 3: the goal of Workstream 1 of the WRA REDS-taskforce, unifying the variation of product data sheets into a single general structure [3]

with the customer, the second should define how data around the usage of a refractory product at customer site can be shared with the refractory producer. The group decided to focus on the first workstream to start with. Covid restrained progress heavily in the beginning, later the different views on how structure of the standard should look like, what it should contain and how certain information should be shared took quite some time and effort. The result is (at least for the author) almost unbelievable: for the first time, a group of some of the largest refractory suppliers agreed on a unified, single way to generally describe refractory products. The developed standard allows equally to describe a brick, a castable or a functional product. While it is of course necessary to have a unified way of describing to form a standard, the fact that this level of agreement could be reached across all products classes and participating producers, is remarkable. The taskforce worked hard together to get to this point. When the result was then finally presented to a group of selected customers, the taskforce learned, that some customers where already thinking beyond the intended idea of how the product data could/should be provided, while others were not so easily convinced. Therefore, the WRA decided to create an MVP (Minimum Viable Product = pilot project) of an exchange platform, which uses the Product REDS inside. While this platform is only the conveying framework, allowing for the data exchange, it is extremely necessary and helpful to understand the process and benefits.

## HOW THE PRODUCT REDS IS STRUCTURED

The content of the REDS is not bearing any surprised for anyone making or using refractory products, and it shouldn't. The product data standard is like a universal translator, allowing to describe and understand the qualities of a product on a digital level, or, like back in school, it is the structure that grammar is providing to make meaning out of what one is saying. And of course, like every country has their own specific words and sentence structures, refractory products require special descriptions which are rooted in the material property descriptions, the way these products need to be packed and shipped, and where they can finally be used. All of this the REDS holds in the following structure presented in Tab 1.

Tab. 1: Structure of the Product REDS

| Section | Description | Number of categories | Number of sub-categories/ fields | „Must" fields |
|---|---|---|---|---|
| Application | Area, purpose, function of application | 3 | 10 | 1 |
| Logistic | Origin, storage, packing, quantity, brand name | 5 | 21 | 4 |
| Manufacturing | Fabrication, on-site processing for unshaped and shaped products | 4 | 79 | 9 |
| Product Family | Refractory categories | 1 | 3 | 1 |
| Classification & Certificates | Health and safety, environm., & production requirement | 5 | 23 | 2 |
| Chemistry & Mineralogy | Chemical composition & containing minerals | 22 | 74 | 0 |
| Chemical Resistance | CO-resistance, alkaline resistance, etc. | 5 | 12 | 0 |
| Physical Properties | Density, porosity, CCS, MoR, RuL, CiC, etc. | 28 | 130 | 4 |

The standard should allow to describe every refractory product. As visible in Tab 1. every section contains a lot of individual fields ("number of subcategories/fields"), some of them being mandatory to be filled ("must fields"). This is necessary to allow for a minimum description. It has also to be noted that not every product can contain information in all of the non-mandatory fields, as e.g. it does not make sense to specify a mixing liquid or additive, which is necessary for a castable, for a brick. In other cases, the specific data point may not be available for a specific product because it has never been generated up to this point in time.

With a defined structure in place the pathway for a secure, efficient, and automatable data exchange is clear.

**An MVP to convey the Product REDS**

For most people data transfer process is not a very tangible subject, while the benefits as described in the Introduction are naturally more accessible. Like the benefits help to capture the "Why", it is equally important to understand the "How", how is the data standard put to use to allow for the benefits realization. The task force therefore decided to develop a simple data exchange platform as an MVP (minimum viable product). The MVP concept in a simple form defines the basic functional version of a solution, aiming to:

1. Validate a project viability.
2. Reduce costs for a solution release.

Both converging to validate if the proposed solution covers "the job to be done" which means the desirable problem to solve with the current proposal. It allows stakeholders to experience the product and collaborate for better versions through constant feedback. The MVP concept was created back in 2001 by Frank Robinson CEO of the American IT consulting company SyncDev Inc., but got its notoriety with the best-seller: "The Lean Startup" from Eric Ries only in 2011. For the REDS-Task force team it was equally important to create the desired exchangeability of the data standard but also to keep the character of the refractory business. This means that the exchange of product information via the Product REDS must remain between one customer and one refractory producer only. Further, to make the standard be used by all potential refractory producers, the entrance barrier needs to be low. Therefore, different file formats and structures needs to be accepted for upload a product description/specification, reducing this way complexity and simplifying user journey and experience. While the original product description is uploaded, inside the platform it is converted into the REDS model, and encrypted before being stored into the database, which makes it not possible for someone hosting the exchange platform to read the data. To access, download and decrypt the product information in the WRA-RDX (Refractory Data eXchange) platform the customer uses the unique access key only valid for this individual data transaction. The exchange platform must provide a "4 eyes only" data exchange working with data and environment security to avoid data leaks. Security measures must be considered not only in the back-end but also in the front-end to guarantee the deliver and access for data only to respective parts involved.



*Fig. 4: Schematic of the data exchange to convey the Product REDS over the MVP, on the left the refractory producers upload with a specified pass-key, at the storage area the data is fully encrypted, and only with a unique pass key on the customer side the data can be downloaded and decrypted [4]*
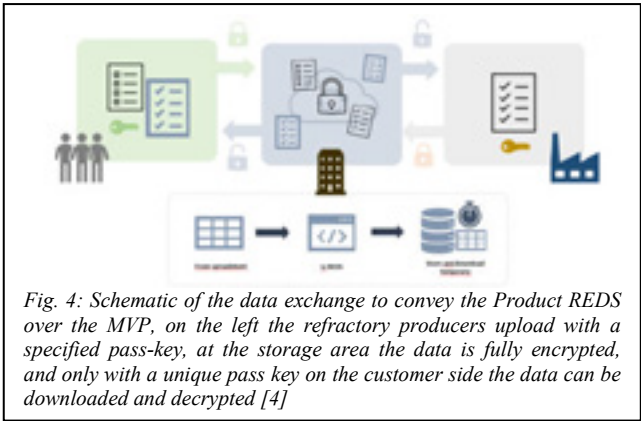
WRA-RDX platform will follow 3 pillars: Usability, Security and Reliability. Usability refers to the user experience, with focus on a easy-to-use interface and journey through each process. Security to guarantee the deliver and access only for those authorized and involved into exchange transactions which will be applied individually and environmentally. Reliability represents the transparency history within the environment allowing the trace of transactions between parts involved and total volume by WRA. To achieve this several features are required to work together within the MVP:

- Access will only be possible through authentication.
- Distinct functional areas designed based on entities roles and needs: Suppliers (S), Customers (C), WRA (W)
- Exchanges transactions directly between entities.
- Data stored encrypted, accessible and readable by entities related to transaction.
- Upload functions responsible to convert data to REDS.
- "Limited-time" availability control per transaction
- Exchanges history volume collected to support resources usage and possible re-dimensioning.
- WRA has no access to content delivered or stored.

- WRA will only manage access to platform and KPIs related to usage history.

**THE FEAR OF COMMODITIZATION**

Does this data standard make us more comparable and by that make refractories a commodity? There are two counter questions to raise, first "are our customers not already comparing our products today?" and second "what is a commodity product in the refractory world?" The first question can be answered with a clear yes, but of course we make it a little easier to compare products from different suppliers. That is customer service. But it will not change the quality of our products or their performance in the field, which is what our customers are buying. The second question is also easy to answer, as like in most other industries, some refractories are commodities fulfilling an "easy task", while others are tailormade to withstand a harsh chemical attack or optimized to enhance the transfer of liquid metals. You can also compare this to coffee for example. You can buy it in an industrialized form but also from small independent local farms/producers. The quality and flavour of the local farm/producer can in many cases excel the industrialized product even if is organic but the consumer will choose the option which fit it´s taste and pocket.

So, nothing will change in the performance or quality of our products because we can convey product details to single customer in a unified digital way, we only help our customer to make that decision, which products he prefers to buy. Also, sending a product description does not take away the personal exchange which is central in an industry where building trust into the quality and performance of a product is so crucial.

**CONCLUSIONS**

Most changes are often perceived as critical or even unnecessary, but change is the only constant in our lives and digitalization has brought us a lot of beneficial changes over the last decades. Our customer industries are faced by their customers to use digital data standards, and this will trickle down to our industry, so why not being ahead of the curve and setting a Product Refractory Exchange Standard out of our industry to serve our customers today? Therefore, we must embrace the change as an opportunity to improve our processes, products and mainly new ways of serving our customers with them at the center of our process which will add value to the chain through a simplified operation through digital communication that adds value as well to their daily routines with fast integration and also as a result of our industry improvement in its customer-centricity maturity levels. Soon everyone will understand that data standards will help to make the refractory industry more efficient and consistent.

**REFERENCES**

[1]    Die Zeit", issue 13, 2023, page 4
[2]    Platzer A. "How to Speed Up Digitalization in the refractory industry?" PRE-presentation, Barcelona, 14.10.2021
[3]    Platzer A. "Refractory Exchange Data Standards", WRA-online presentation for selected customers, 13.4.2023
[4]    de Barros Gosaric B. "MVP/Pilot for REDS", WRA-online presentation to the REDS taskforce, 7.6.2023

# CONVERTER ON LIFE–SUPPORT: A STRUCTURED APPROACH TO DETERMINE THE GOVERNING PARAMETERS OF REFRACTORY WEAR TO STABILISE AND PROLONG THE LINING LIFETIME

F. Vermeulen, W. Tesselaar,  E. Gisolf

Tata Steel Nederland, Velsen-Noord, Netherlands

**ABSTRACT**

The average wear and the spread in total lifetime of the refractory linings of the converters at Tata Steel IJmuiden has been increasing under the influence of alterations in both the BOS process and the refractory maintenance strategy. To minimise the risk of premature failure and loss of production, a stable and predictable lifetime of the converter refractory lining is required. Laser scanning is of vital importance for the prediction of refractory wear and the influence of refractory maintenance on it, but is difficult to interpret. This study provides a case study in which through data processing, data analysis and Mood's median testing, slag washing (SW) and slag splashing (SS) are found to significantly reduce converter vessel lining refractory wear.

**INTRODUCTION**

Converter availability is an important parameter for many BOS plants to minimise costs and maximise production. Converter availability is strongly influenced by refractory life. The life of a converter is depending on three main parameters: refractory material and construction, process parameters and maintenance strategy (Siebring et. al, 2008). Multiple process parameters influence the refractory wear and can potentially be optimised to reduce wear: thermal cycling, slag composition, temperature etc. Next to influencing process parameters, performing refractory maintenance potentially reduces the wear rate as well. However, maintenance of refractory takes time, which means it can have a negative effect on the production level of steel.

Tata Steel IJmuiden has three converter vessels. Under favourable market conditions all three converters are used simultaneously (except when one undergoes a reline). Generally, when three converters are available, sufficient time is available for maintenance. However when a converter is in reline, performing maintenance can have a direct effect on the production rate. The planning for a reline depends on the expected life of the converter vessel. The life can be significantly influenced by refractory maintenance.  At Tata Steel IJmuiden there are currently four main refractory maintenance techniques in use for the converter: 1) slag washing (SW), 2) slag splashing (SS), 3) brick patching and 4) gunning. Brick patching is a technique where a small portion of slag is left in the converter and recycled refractory is added. The converter is tilted so that the material is positioned at the desired spot. The slag mixture is left there for several hours to cool and is believed to form a protective layer. Slag splashing and slag washing are both based on the idea that if the slag has the right composition and temperature (and therefore the right viscosity), it will stick to the lining forming a protective layer. SW is a technique where the remaining slag after tapping is moved along the refractory lining by rocking the converter back and forth. With slag washing it is not possible to cover the trunnion areas with a protective slag layer. SS requires the use of the oxygen lance. After tapping, the oxygen lance is lowered into the converter in the upright position and starts blowing nitrogen. The flow of nitrogen causes the slag to splash up against the lining. The nitrogen is believed to have an additional cooling effect and SS is assumed to cover a larger area of the vessel than SW.

Between two production heats different refractory maintenance techniques can be used to prolong the life of the refractory lining Depending on production pressure (=time available), slag composition, temperature, wear rate, planning, number of converters in use,  availability of equipment in the case of gunning, reblows, remaining thickness of the lining and/or reline planning, no maintenance is done or  one or multiple maintenance techniques can be used, e.g. SS followed by SW.  This may be used in several subsequent heats or as a single event. In IJmuiden, the frequency of refractory maintenance increases with the age of the lining.  In IJmuiden SW is done in ~18% of the heats and SS in ~10%. To follow the wear of the linings, IJmuiden uses one mobile laser scanner for all three converters. The use of a mobile scanner (instead of a fixed scanner per converter) means extra time for positioning the scanner and position finding (knowing the exact location and angle of the converter relative to the scanner), resulting in time loss that can't be used for production and/or maintenance and as well as the risk of a deviation in the measurement or measuring error. As a result,  laser scans, to follow the wear of the converter are roughly made in ~15% of the heats.  The frequency of the scanning slightly increases with the age of the refractory lining to approximately 18-20% in the last 10% of its life, but never to 100% of the heats. Performing refractory maintenance and making laser scans are not synchronised, which means that different combinations of maintenance techniques could precede a single laser scan. The same applies for the process conditions. The laser scanner scans the lining surface including slag, skull and possible remnants of refractory maintenance. To assess the effectiveness of refractory maintenance on the refractory wear rate, multiple consecutive laser scans are required to minimise the effects of other process conditions and reduce the influence of the measuring error on the scans. Multiple laser scans can cover dozens, even hundreds of heats and this means that the resulting refractory wear rate assessment corresponds to a plethora of different combinations of refractory maintenance.

In the past, the effectiveness of different refractory maintenance techniques was analysed by looking at a long period of a certain maintenance technique and to find a correlation with the average wear rate in that period. However, the results of this approach were not very conclusive and were often even contradictory. Even though we are convinced that SW and SS are effective techniques to lower the refractory wear, this simple linear approach sometimes led to the conclusion that they have a neutral to negative effect. Therefore more complex data analysis methods were explored.

This research proposes to use a segmentation-method based on moving averages in combination with Mood's median test to analyse the effectiveness (Mood, 1950). It will focus on SW and SS, and will not include brick patching or gunning.

**METHODS**

Data analysis was performed within the Data Science & Engineering environment in Azure Databricks from Microsoft. The data consisted of minimum residual thicknesses from laser scans, converter, campaign and heat identifications and refractory maintenance techniques derived from logged process phase data. Minimum residual lining thickness is obtained by determining the lowest point of a predefined area in a laser scan (see fig. 1). These predefined areas include among others: the charge pad and sections of the knuckle and tapping breast. The lowest point is preferred instead of average, modus or median because it represents the distance to a potential breakout. Minimum residual thickness versus heat number leads to a wear line as seen in figure 2.
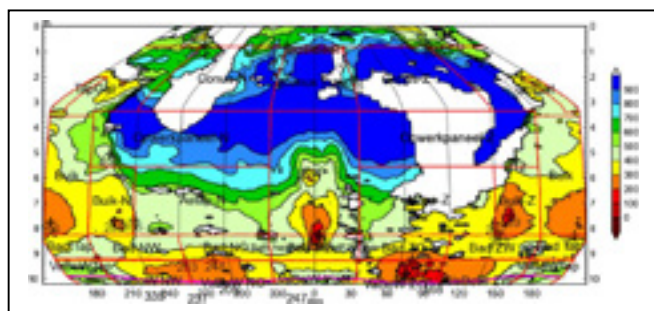
*Fig. 1: Laser scan of converter vessel 23Q after 3181 heats. Colours represent minimum residual thickness. Red grit shows the predefined areas.*
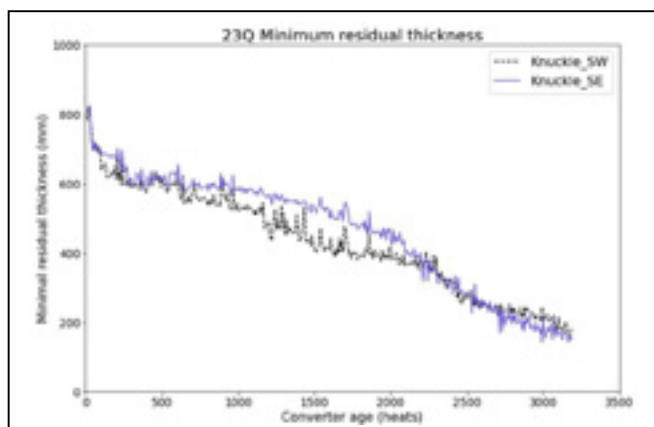


*Fig. 2: Wear lines based on minimum residual thickness measurements for two knuckle areas during converter campaign 23Q.*

## Segmentation-method

The segmentation-method is a method in which time periods are defined from a large data set in which specific conditions are met. These periods or segments are analysed and subsequently collected in a new dataset that forms a uniform hypothetical subset. Generally, more datapoints within a dataset will lead to less variance in predictions. By using the segmentation-method it is possible to use short segments/ periods that are normally rejected because of sample size by combining them with longer segments. It should be noted that in the case of the laser scans of the converter lining, shorter segments have a lower probability to unveil a true trend in wear rate. The segmentation-method handles this problem by normalising. Longer segments carry more datapoints, and trends found in these segments therefore weigh proportionally more. Moreover, it is assumed that deviations caused by short segments are normally distributed. Nonetheless, to prevent outliers from contaminating the dataset, segments must consist of at least ten consecutive scans in order to be approved. In this research the segmentation-method was applied to a dataset comprising all converter campaigns from three converter vessels over the period 2018 – 2023. This results in a dataset covering 67,126 heats, 30 campaigns and 9506 laser scans.

Table 1: The four types of segments defined by the fraction of SW and SS over the previous 100 heats.

|  | Void | SS only | SW only | SW or SS* |
|---|---|---|---|---|
| SW | $\leq 0.2$ | $\leq 0.2$ | $\geq 0.5$ | $\geq 0.5$ |
| SS | $\leq 0.2$ | $\geq 0.5$ | $\leq 0.2$ | $\geq 0.5$ |
| *In the case of the SW or SS segments, either the MA SW or the MA SS must be equal or greater than 0.5 (can be both as well). | | | | |

## Segmentation definition

Segment conditions were chosen to define periods in which the refractory maintenance consisted of only SS, only SW, SW or SS (or both) or nothing (Void). For each converter campaign moving averages were calculated. This resulted in fractions of heats over the preceding 100 heats that had a specific type of refractory maintenance. Generally, there is no refractory maintenance performed during the first 100-200 heats of a campaign. Segment

definitions consist of minimum and maximum value for the fraction of both SS and SW. The segment definitions can be found in table 1. Because the fractions of SS and SW are based on a rolling average of 100 heats prior, the start and end of each segment was shifted 50 heats into the past.

## Linear regression and Mood's median test

After the segments have been determined, the corresponding wear lines are used to determine the average change in minimum residual thickness per heat per segment (slope). These slopes are obtained performing linear regression on the segments with the Scikit-learn module in Python (Pedregosa et al., 2011). A new dataset is formed in which each laser scan in each segment corresponds with a slope. Consequently, each laser scan within a segment will yield the same slope. From the new dataset boxplots are made per segment type per area and Mood's median tests are applied on these sample populations to establish whether the difference is significant. Mood's median tests were performed using the SciPy module in Python, settings were set to default.

## RESULTS

Visualisations of data processing can be seen in figures 2 through 5. Keep in mind that these visualisations are subsets of the complete data set. Figure 2 shows the rolling averages of SS and SW of converter campaign 23Q. It can be seen that periods of SS and SW alternate and near the end of the converter lifetime they were performed both. Figure 3 shows how the data from figure 2 was translated into segment types. It should be noted that undefined data remains between these segments. This data was deemed ambiguous because of lack of strong preference for a specific maintenance strategy and was not used for further analysis.

Table 2 contains the number of segments per segment type and the combined number of datapoints (laser scans) withing these segments per type. It can be seen that the SS only type yields far less segments (9) than for example the SS or SW type (53). It should also be noted that even though the Void type has fewer segments than the SS or SW type (37 and 53 resp.), the total number of datapoints within these segments is more than tripled (4166 and 1162 resp.). Thus, void segments contain more datapoints per segment.
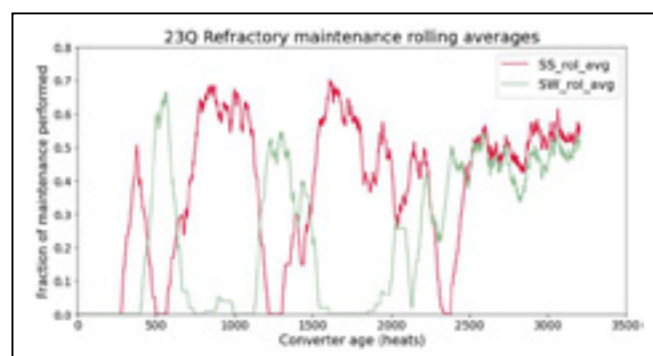


*Fig. 2: Rolling averages for Super Slag Splashing (SS) and Slag Washing (SW) over 100 heats during converter campaign 23Q.*
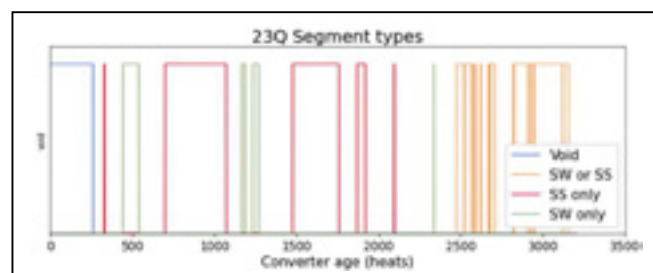


*Fig. 3: Segment periods based on the rolling averages from fig. 2 for converter campaign 23Q. Note that SS and IS segments types are per definition an IS or SS type segment as well.*

Table 2: Number of segments per segment type and total number of datapoints (laser scans) within these segments.

|          | Void     | SW only  | SS only  | SW or SS  |
|----------|----------|----------|----------|-----------|
| segments | n = 37   | n = 9    | n = 30   | n = 53    |
| datapoints | n = 4166 | n = 170 | n = 732 | n = 1162  |

A visualisation of the minimum residual thickness of a section of the knuckle area for SS segments is shown in figure 4. Although a trend can be seen, it is also apparent that the variability in change between two scans is large. After performing linear regression (fig. 5), only the calculated trend (slope) is left. Note that longer segments tend to have intermediate slopes. Slopes are given in mm change per heat. The more negative the slope, the higher the refractory wear.
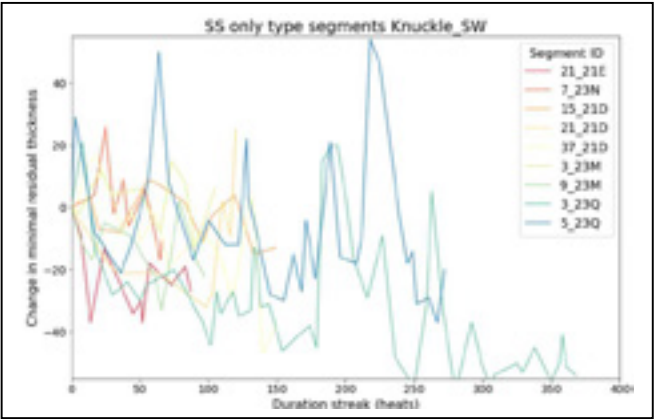


*Fig. 4: Super slag splashing streak segments from the Knuckle_SW area. Segments are from multiple campaigns and are presented as change in minimum residual thickness compared to the first scan in the segment.*
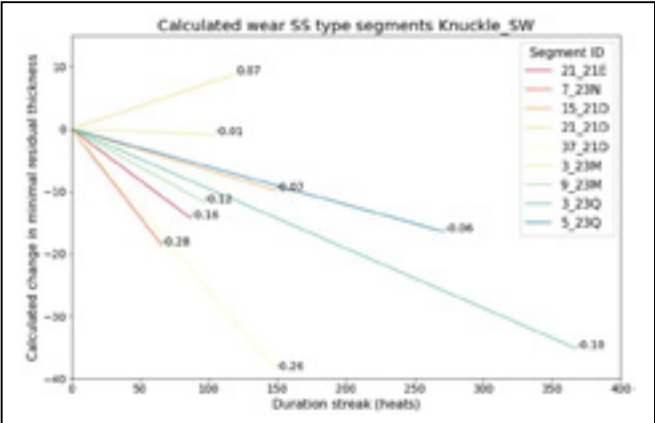


*Fig. 5: Super slag splashing streak segments from the Knuckle_SW area. Segments are from multiple campaigns and are presented as calculated minimum residual thickness. Slopes are shown.*
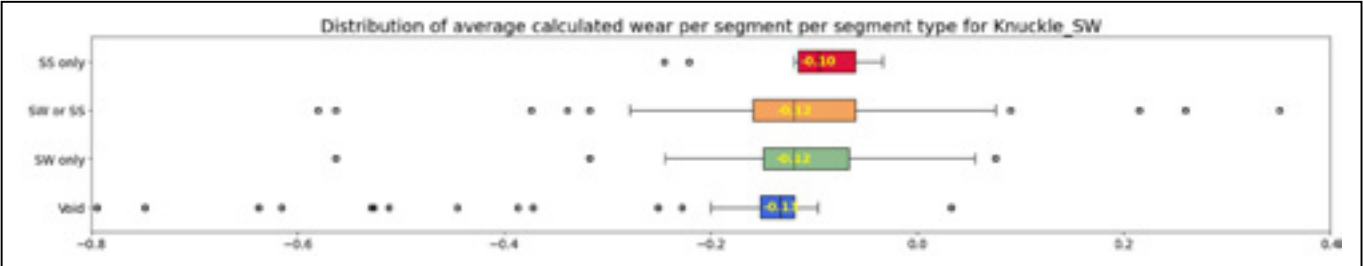


*Fig. 6: Boxplot visualising the distribution of the average calculated wear per segment (slope) per segment type for the Knuckle_SW area.*

Boxplots of the slopes per segment type for the Knuckle_SW area are shown in figure 6. Void segments yield the steepest negative slopes for all areas. In almost all cases either SW only or SS only type segments have the least negative slopes. This can be seen in table 3 as well. Table 3 shows that any type of refractory maintenance results in lower median wear rates compared to no refractory maintenance.

The outcomes of the Mood's median tests for each segment type against the Void segment type for the knuckle areas are presented in Table 4. The results are presented in P-values. The lower the P-value, the higher the chance that the median of the two sample groups differs significantly. It is generally accepted that P-values should be lower than 0.05 to detect a significant difference (this translates to a 95% certainty that the sample groups are different).

Table 3: Medians per segment type per test per area. Results for knuckle areas are shown.

|              | Void  | SS only | SW only | SW or SS |
|--------------|-------|---------|---------|----------|
| Knuckle char | -0.15 | -0.08   | -0.05   | -0.08    |
| Knuckle NE   | -0.14 | -0.12   | -0.09   | -0.10    |
| Knuckle NW   | -0.13 | -0.07   | -0.09   | -0.08    |
| Knuckle tap  | -0.10 | -0.06   | -0.09   | -0.09    |
| Knuckle SE   | -0.14 | -0.10   | -0.11   | -0.11    |
| Knuckle SW   | -0.12 | -0.10   | -0.10   | -0.10    |

Table 4: Results from Mood's median test per area. P-values are given for void segments against maintenance segments. Results for knuckle areas are shown.

|              | SS only  | SW only  | SW or SS  |
|--------------|----------|----------|-----------|
| Knuckle char | 6.25E-20 | 1.00E-43 | 2.58E-50  |
| Knuckle NE   | 4.47E-17 | 1.78E-41 | 3.18E-65  |
| Knuckle NW   | 1.82E-02 | 1.27E-25 | 9.72E-48  |
| Knuckle tap  | 2.88E-04 | 4.73E-03 | 2.23E-14  |
| Knuckle SE   | 1.08E-12 | 3.45E-66 | 3.88E-68  |
| Knuckle SW   | 4.87E-13 | 1.61E-09 | 6.10E-11  |

**DISCUSSION**

Based on the medians it can be concluded that performing refractory maintenance (either SS or SW) results in lower wear rates (gentler or even positive slopes for the segments). These results can be statistically justified trough Mood's median tests. This is a great improvement compared to previous trials and is the first time that the influence of refractory maintenance on refractory wear is isolated from all other process parameters. Moreover, this approach has a generic set-up and can be applied to future trials consisting of other variables. However, there are some points of attention:

1. The quality of all hypotheses, calculations, models and conclusions are ultimately based on the quality of the data. In the case of refractory wear rates of a converter vessel, it is dependent on the quality of the laser scans. Even if the accuracy of the scan itself is suffucient, the question often remains: 'What is it that we scanned?'. This research aimed to bypass that question by compiling data, using moving averages and looking at larger trends. On the other hand, it cannot be disregarded that these techniques have their own shortcomings and that relations may stay hidden by reducing the variability. Using moving averages poses a challenge in particular. They carry information of multiple datapoints but are presented as a single one. In this research a large window of 100 datapoints was chosen. This enabled segments to yield relatively stable averages during an increased amount of heats. More heats within a segment increases the probability that a segment contains enough laser scans to be approved. But moving averages covering a large window lead to a diminished influence of a single datapoint

660

and its direct neighbours. Consequently, the chances of creating false positives/ negatives increase. Risk of creating false positives/ negatives is highest at the beginning and end of segments. To reduce this risk, the duration of the segments was shifted 50 heats towards the past. In this new definition the moving averages are better aligned with the observed wear. In future studies this could be optimised further.

2. The data is heavily modified to mute the influence of process, outliers and the limitations of laser scanning in general. The dataset on which Mood's median tests were applied consisted of slopes. A single slope was obtained per segment and to keep the original sample size and to account for the length of each segment, this single value was duplicated for each of the datapoints withing the segment. Although this helps transforming seemingly incoherent data into a more robust dataset, it does so by creating many duplicates. Performing any form of statistics on such a dataset poses its own unique challenges. For example: The Mood's median test calculates a grand median between two sample groups. All data is then divided into groups larger and smaller than the grand median. Values that correspond to the grand median are either grouped below or above the grand median. They could also be ignored and discarded. This research used default settings for the Mood's median test from the Python SciPy module which classifies them as below the grand median. However, with the introduction of many duplicates in the dataset this setting has a much greater effect. Simply ignoring this data is not an option either because this implies discarding a large portion of you data which is in agreement with the grand median (up to hundreds of datapoints for Void type segments). Using the right statistics is key for understanding the outcomes of refractory trials, optimising process conditions or performing maintenance. Therefore, optimising and applying the right type of statistics should be a priority for BOS plants.

3. It is assumed that the influence of the process can be disregarded due to the large dataset (assuming occurrence of process conditions and refractory maintenance are independent variables and that the doseffect of process conditions consequently evens out in a large dataset). In reality the relation might be more complicated. Process conditions ultimately all lead to refractory wear. And refractory maintenance, although intended to be done preventively, is often carried out reactively. This cause-and-effect relationship between harsh process conditions and subsequently increased frequency of refractory maintenance in combination with moving averages will influence the outcomes. On top of that, it could also be argued that more refractory maintenance is performed when production pressure is low. Low production pressure could be accompanied by larger temperature fluctuations or specific steel grades. Which in return influence refractory wear as well. When carrying out data analysis, it is important to identify these relations and correct the analysis accordingly.

4. It is assumed that the settings for refractory maintenance were constant throughout the dataset (or were at least randomly distributed). In reality there is a large variety in amount and composition of slag, nitrogen flow, nitrogen flow duration, lance height etc., and they are prone to trends in time. Further research will investigate the influence and significance of these settings.

Despite these opportunities for optimisation and improvement this research demonstrates that structured and statistical assessment of refractory wear of converter linings is possible. Current and future analysis of trials at Tata Steel IJmuiden BOS2 will be performed similarly. It helps to optimise the choices for refractory maintenance. This will help to make the optimum choice between production (yes or no time for maintenance) and life (availability of converters due to relines). A further improvement will be fixed scanners that will be installed at each converter. It will result in more scans and a higher scan accuracy which will be used in the above data analysis for further improvement of the availability of the converters.

## CONCLUSIONS

Through statistics, data processing and analysis on a large dataset it is possible to confirm effectiveness of refractory maintenance in reducing refractory wear of a converter.

Super Slag Splashing (SS) and Slag Washing (SW) are statistically proven effective refractory maintenance techniques that reduce refractory wear and can prolong converter lifetime. Overall SS is effective in reducing median refractory wear. With the more detailed knowledge it is possible to improve the maintenance strategy for the converters in IJmuiden

## REFERENCES

Mood, A. M. (1950). Introduction to the Theory of Statistics.

Pedregosa, F., Varoquaux, G., Graford, A., Michel, V., Thirion, B., Grisel, O., ... & Duchesnay, E. (2011). Scikit-learn: Machine learning in Python. the Journal of machine Learning research, 12, 2825-2830.

Siebring, R., Andreev, K., Heijboer, W., Everstein, S., Schmidt, A., Brockhoff, J. (2008). Integrated approach on improving converter linings; focus area thermo-mechanical improvements for the bottom. International conference on Refractories for iron and steel, 10th and 11th November 2008, Jamshedpur, India

# INTO THE UNKNOWN: EXPLAINING AND PREDICTING SLAG LINE WEAR BASED ON PROCESS PARAMETERS

Ana Gil, Warbout Tesselaar, Elizabeth Gisolf, Tata Steel, IJmuiden, The Netherlands

**ABSTRACT**
Steel ladles are an essential tool for steel production and are "exposed" to a wide variety of chemical and physical reactions which lead to the wearing of the refractory lining. Thus, being able to predict the effect of operating conditions on wear is critical to ensure high and stable life and, consequently, high ladle availability and minimum refractory cost. Over the past year, wear rate at slag line, as well as transition area between slag line and wall, has become the bottleneck for ladle life. Therefore, understanding, predicting and controlling wear at the slag line has become critical for the ladle life stability and performance. The aim of this project is to create a descriptive model capable to identify the key process variables which affect the wear at slag line level. An advanced analytics approach was followed due to the complexity and sizeable number of process parameters. Prior to diving in, both the target areas and target function (wear rate based on minimum remaining thickness) were defined. Hypotheses generation and prioritization were carried out by a team of experts, followed by identification, transformation, visualization and cleaning of corresponding process variables. The modelling was carried out using a histogram-based gradient boosting regression tree estimator. The results indicate an overfitted model, describing well the training set ($R^2$=0.82) and poorly the test set ($R^2$=-0.1). The accuracy of the inputs for the target function was of concern since a MSA revealed lack of reliability and repeatability on the laser scanning measurement. A descriptive model based on a per-heat-basis is therefore not possible using the currently available data. The inaccuracy of the measurement can, however, be minimized by performing analysis on a per-campaign-basis. An example is the study on increased wear at the transition area between wall and slag line wear linings. The outcome of the study has led to a change in slag line wear lining design which enabled a wear reduction of around 25%, a decrease in frequency of ladles out-of-service at this location and an increase in ladle life of about 2.5 heats.

**INTRODUCTION**
Steel ladles are an essential tool for steel production. Therefore, the security, the availability and the reliability of steel ladles are critical to ensure a safe and smooth operation. During a complete campaign, A-campaign and B-campaign, the ladle is "exposed" to a wide variety of chemical and physical reactions under harsh conditions. In order to withstand the treatments and guarantee a safe working environment, refractory materials are carefully selected for each part of the ladle. Selecting the right refractory, i.e. with adequate chemical and thermo-mechanical properties, for all areas enables a balanced wear and, consequently, the full use of the wear linings.
The steel plant of Tata Steel Ijmuiden has a fleet of 23 steel ladles of which, under normal operating conditions, 12 are in production and 2 in stand-by. When in service, the refractory lining is monitored by performing visual inspections on a heat-basis as well as measuring the remaining thickness by laser scanning in roughly 50% of the heats.
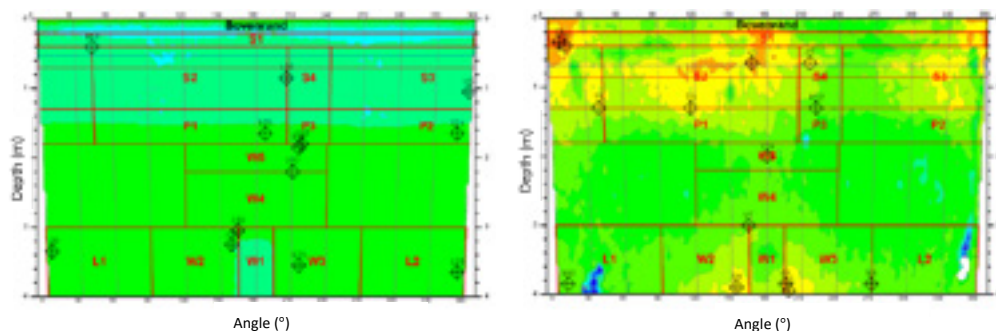


*Fig. 1: Remaining thickness of the refractory lining in mm at beginning and end of campaign, measured by laser scanner. S1 to S4 are slag line subareas.*

The monitoring of the remaining thickness of the wear lining provides insight to the operators so that informed decisions can be made and safe operation can be ensured. Furthermore, the collected data is the basis for a life prediction dashboard used for daily planning. The effect of process conditions is not yet incorporated in the ladle life prediction and, therefore, process variability is not accounted for.
Furthermore, an increase in ladle life requires understanding of wear [1].

**PROBLEM STATEMENT**
The performance of the steel ladle is mainly defined by the worst performing wear lining refractory area. In ideal conditions, the wear lining at all areas wears uniformly and, consequently, end of life can be predicted and planning can be made. However, in the majority of the cases, increased wear at a single location culminates in the relining of the ladle without fully utilizing the complete wear lining.
Over the past years, wear rate at slag line level has become a bottleneck for ladle life as 32% of the ladles are removed from service due to low residual thickness at this location. Moreover, an additional 8% of the ladles show increased wear at the transition area between slag line and wall (barrel).
In addition to the non-optimal ladle life, the variability and unpredictability of wear has led to logistical maintenance challenges and lower ladle availability. Thus, understanding, predicting and controlling wear at the slag line has become critical for the ladle performance, e.g. life and availability.
The first steps of developing a logistic ladle model, able to understand, predict and control wear, have been taken [1]. The end findings and outcomes of part of the project described in this paper will be incorporated into the logistic ladle model as a descriptive model for slag line wear.

**APPROACH**

Over the past decade, the increasing amount of data collected and available in industrial plants has facilitated the transition from an empirical to a data driven problem solving approach. Furthermore, tools such as practical problem solving (PPS), 6-sigma and advanced analytics (AA) have been fomented as the desired approach to find suitable and sustainable solutions promptly.

Even though wear at slag line and wear at the transition area slag line-wall are similar in concept, the complexity of the problems has required different approaches. The high number of process variables potentially affecting the wear at slag line qualifies the investigation for an AA approach, using Microsoft Databricks as a Python programming platform. On the other hand, a simpler and faster methodology could be used for investigating the root cause for increased/variable wear at the transition area, i.e. 6-sigma with support of Minitab software.

**Defining target area**

The first step in the project was to identify the target area(s) within the slag line, i.e. determining the set of coordinates (angle and depth) containing the points with lowest remaining thickness at the end of the campaign. As shown in Fig 2, the location of the thinnest point at end of the campaign is spread over all the slag line subareas (S1, S2, S3 and S4) with occasional overlapping of multiple campaign points. The definition of a single well defined area is not possible based on this information alone. Instead the frequency of campaigns with the thinnest points at a specific set of coordinates (depth and angle) is required and described using a heat map (Fig 3).
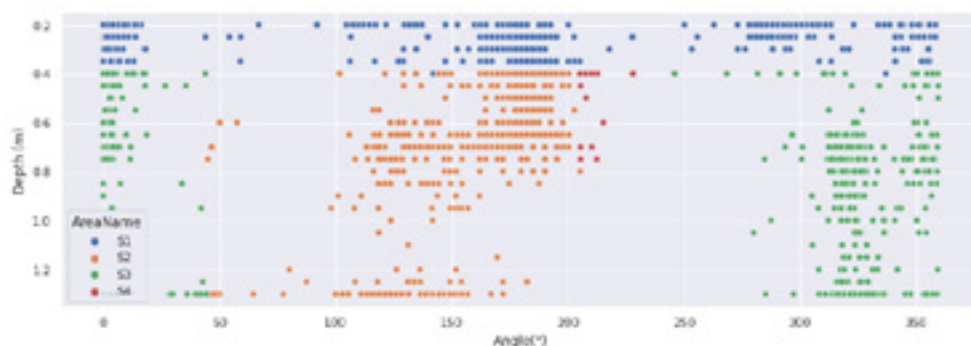


*Fig. 2: Location of the minimum remaining thickness at slag line level at the end of campaign (depth is measured from the top of the ladle). One dot represents one or more campaigns.*
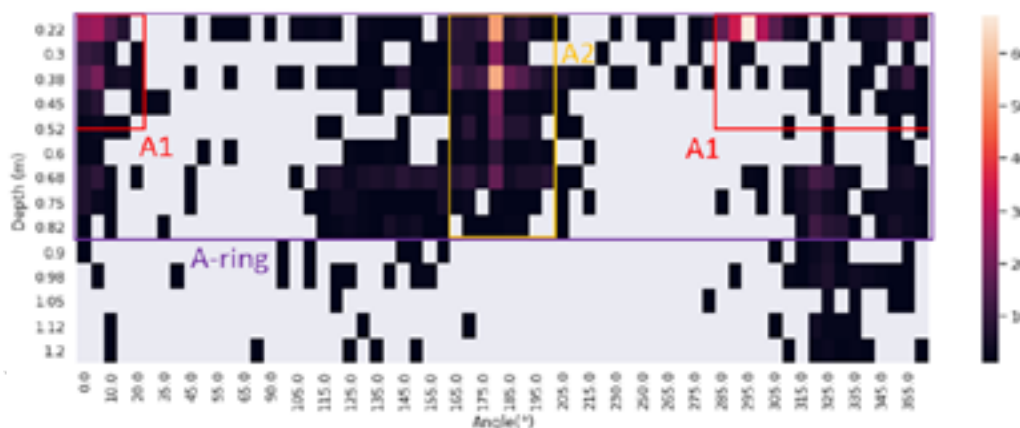


*Fig. 3: Number of steel ladles with lowest remaining thickness at end of campaign per set of coordinates. Identification of target areas A1, A2 and A-ring.*

Two critical areas, A1 and A2, and a reference area (A-ring) have been defined. A1 and A2 are small areas containing 27% and 32% of the data set, respectively. A-ring is a reference area containing both A1 and A2 and representing 81% of all campaigns.

**Target Function**

Defining the correct target function is crucial to ensure a successful outcome. Even though the objective of this project has been clearly identified as slag line wear rate, it was still to define if the determination of wear would be based on the minimum or average remaining thickness, and if all laser scans or only data acquired between consecutive heats would be considered. Aiming to select the best option, the distribution of the data was visualized with histograms and boxplots (Fig 4).

Wear rate calculated based on the minimum remaining thickness presents higher intensity distributions as extreme values are more often observed. Furthermore, the box plots suggest a narrower distribution, in particular, to the wear at A2 area. Opting for a determination based on the minimum remaining thickness also prevents averaging of combined effects of build up (skull formation) and wear.

At Tata Steel IJmuiden, steel ladles are used to produce all steel grades at any given time. Thus, a steel ladle undergoes all secondary steel treatments, e.g. stirring station, ladle furnace and RHOB, in a random sequence during its life. As scanning of the remaining refractory thickness is not performed every heat, the target function includes points based on multiple heats that underwent different secondary treatments. In order to include these data points, aggregation of the process data of these heats is needed. Hence, effect of process parameters (treatment dependent) on wear are averaged and relationships can be missed. However, averaging over several heats does enable the reduction of the noise-to-signal ratio.

Upon weighing pros and cons, the target function is to be determined based on minimum thickness and only data from consecutive heats is to be included.
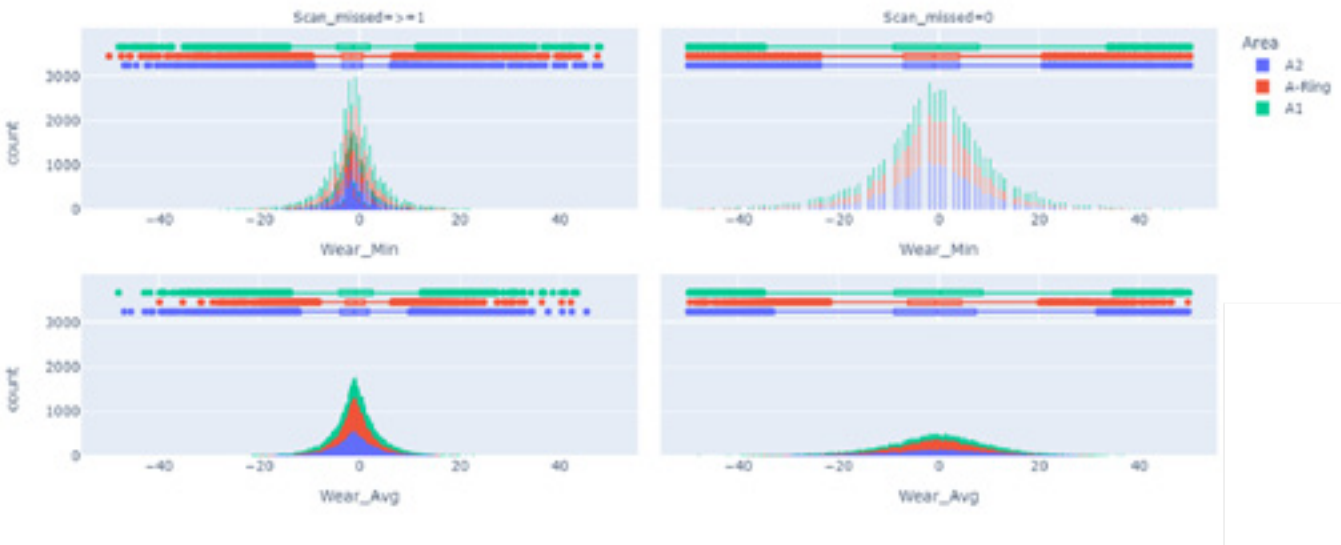
*Fig. 4: Distribution of minimum and average wear for consecutive and non-consecutive heats.*

**Selection of process variables**

Identification, collection, determination and cleaning of variables are a fundamental and cyclical process to achieve a suitable descriptive model. In the attempt to identify all potential causes of wear variation at slag line level, the hypotheses, a brain storming session was held with a team of experts from the different departments (i.e. production, maintenance and technical). After listing and prioritizing the hypotheses, the corresponding process variables were identified, collected and visualized. Unfortunately, not all hypotheses could be tested as some process data was not available or could not be extracted.

Depending on the type of data, a different set of descriptive statistics (e.g. median, mean, standard deviation, count of nulls, etc.) and graphical representations (e.g. boxplots, time series) were done. The aim was to facilitate the data cleaning by identifying time dependent changes, boundaries and outliers. An example for a numerical variable can be seen in Fig. 5.
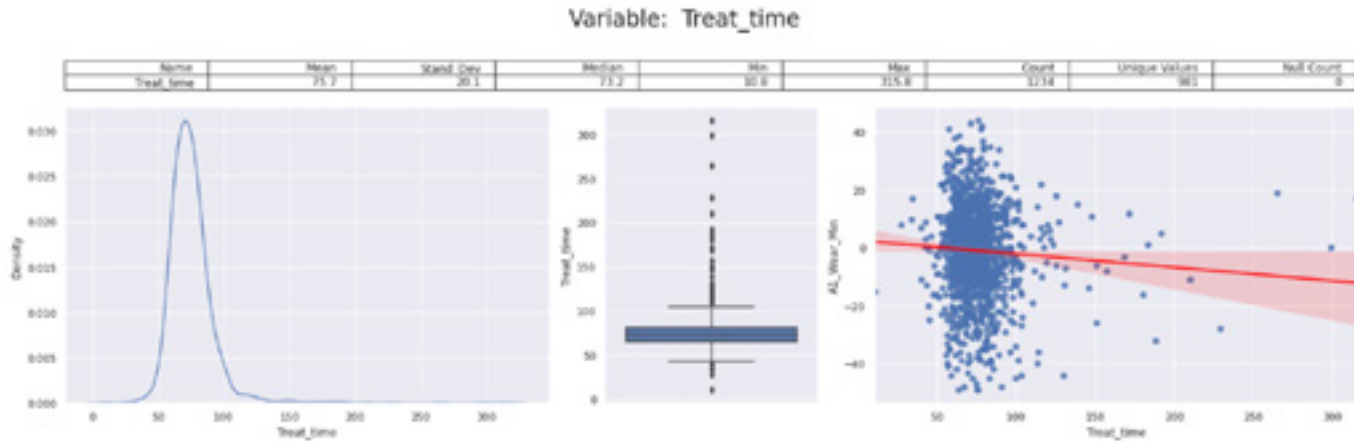
*Fig. 5: Example of the descriptive statistics and graphical representations for a numerical variable.*

For some of the proposed hypotheses, none of the process variables were on their own representative of the parameter to test. As a result, synthetic variables were created based on the already cleaned process variables and a similar set of descriptive statistics and graphical representations was made. Furthermore, categorical variables of interest were converted to numerical using OneHotEncoder.

Despite the overlap in general process variables, such as tapping or casting conditions, each secondary treatment installation (ladle furnace, stirring station and RHOB) has a distinctive set of variables reflecting its own operations and parameters. In order to minimize the amount of data lost as well as to ease potential correlations, the data was split per route.

The last step prior to modelling is to eliminate highly correlated variables, which was carried out for each data set using a correlation matrix. Fig. 6 provides an example for the ladle furnace data set.
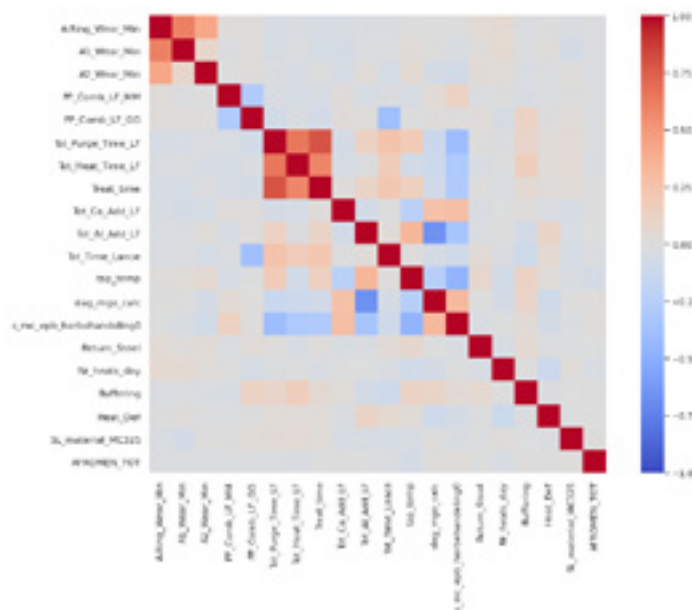
*Fig. 6: Correlation matrix for a reduced set of variables for ladle furnace route.*

**Modeling**

After the failure of the linear regression and random forest estimator in generating a meaningful model, the histogram-based gradient boosting regression tree estimator was attempted. As shown in Fig 7, the model is overfitted as it describes well the training set ($R^2$=0.82) but poorly the test set ($R^2$=-0.1). Potential causes are: the number variables is high for the data set size, a critical process variable(s) has not been included or wear at slag line is not accurately represented by the target function. As the target function is determined based on the minimum residual thickness measured by laser scanner, the capability of the measuring system must be assessed. A Measurement System Analysis (MSA) was performed, revealing a lack of reliability and repeatability across the different steel ladle areas. As the measurement error can be within the same range as the wear between two consecutive heats, a descriptive model based on a per-heat-basis is not possible.
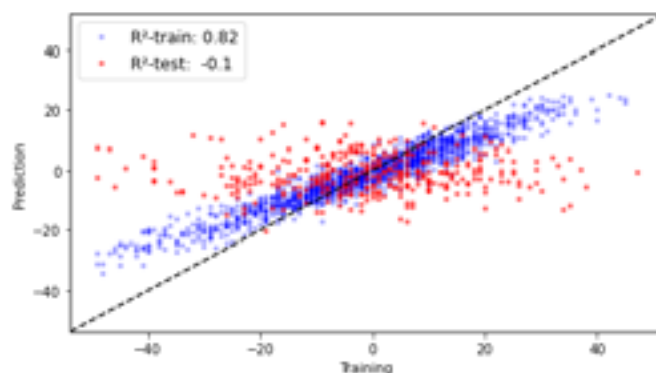


*Fig. 7: Outcome of the* histogram-based gradient boosting model

The inaccuracy of the measurement can, however, be minimized by performing analysis on a per-campaign-basis. An example is the investigation on increased wear at the transition area between wall and slag line wear linings. Following a similar methodology but a 6-Sigma approach, frequency of ladle furnace heats, stirring efficiency, treatment time and amount of MgO added were identified as root causes for the increase in wear. Based on these findings and aiming to mitigate the effects, the design of the slag line wear lining was adjusted by increasing the height by 10cm. In addition to a reduction in wear of around 25%, the new design reduced significantly the frequency of ladles out-of-service at this location and enabled an increase in ladle life of about 2.5 heats comparing with standard design ladles.

**CONCLUSIONS**

In spite of a suitable working model for slag line wear not being achieved, this study has revealed the challenges of establishing relationships between wear rate and process parameters on a per-heat-basis using the data acquired by a low accuracy laser scanner. That was further supported by the successful outcome, i.e. decrease in wear and increase in life, of the per-campaign-basis analysis performed on the increase wear at the transition area study.

To enable further steps in the development of the logistic ladle model at Tata Steel IJmuiden, a capable laser scanner with high accuracy is required as well as an increase of scanning frequency to a per-heat-basis.

**REFERENCES**

[1]    W. Tesselaar, S. Allard, M. Peekel. Optimizing steel ladle logistics by predicting and understanding refractory wear., METEC, 2019

665

# REFRACTORY PERFORMANCE TRACKING: FROM MATERIALS DEVELOPMENT TO APPLICATION MONITORING

Santos, M. F.
Federal University of Sao Carlos, Sao Carlos, Brazil

Braulio, M. A. L.
4Cast, Sao Carlos, Brazil

Cunha, J.
Alcoa Brazil, Sao Luis, Brazil

Macedo, T.
Hydro Alunorte, Barcarena, Brazil

Pandolfelli, V. C.
Federal University of Sao Carlos, Sao Carlos, Brazil

## ABSTRACT

Refractory linings perform an essential role in most of the metallurgical processes, acting as thermal energy barriers and ensuring structural integrity. The refractory selection and lining design must consider the main wear mechanisms, the interaction between the refractory and liquid metals or slags, the costs, and the environmental impacts associated with its production and application. Maintaining the best performance of the materials in use requires good operational practices, the quality of the refractory products during installation, the quality and control of the application practices, and the continuous tracking of each step. In the case of refractory castables, the evaluation of the production and application aspects of the products were carried out by collecting samples during the maintenance/repairing of the linings along the overhaul of an alumina calciner and comparing the fundamental properties of the castables with the standard values previously obtained during the selecting/development steps. The analysis pointed out which were the expected properties of the refractories, and the differences with reference indicators, pointing out potential regions of the calciner that could undergo earlier repair or anticipated failure. The variability of the properties with application features, such as the quantity of water during mixing, time of mixing, temperature, etc, were detected. In conclusion, the study validated and showed the importance of tracking the performance of refractories, fostering the systematization of the methodology for higher productivity and lower costs.

## INTRODUCTION

Refractories play a crucial role in high-temperature processes such as alumina calciners and furnaces. The performance of refractory materials directly affects the efficiency and productivity



*Fig . 1: Main steps for tracking the performance and quality of refractory linings in industrial applications.*

of these processes. Any downtime required for repairing and maintenance of refractories can have a significant financial impact on the overall accounting and management of such operations. Therefore, it is essential to have a reliable method to track the condition of refractories before and during their use and to predict their performance over time.

The difficulty in predicting the actual condition of refractories during operation arises from the harsh environment they are exposed, including extreme temperatures, thermal cycling, chemical reactions, and mechanical stresses. These factors contribute to the gradual degradation of refractory materials, leading to their eventual failure. Traditional approaches to monitoring and tracking refractory condition often rely on visual inspection and empirical decisions, which is subjective and lacks quantitative data.

Usually, the process of guaranteeing the performance of refractory lining in industrial process is based on three steps: those activities that occur prior, during and after the installation [1], specially for the case of castable refractories. The process cycle is summarized in Fig. 1.

### Pre-installation

Pre-installation activities for refractory applications in industrial sites involve analysis of previous failures and meticulous planning. These activities assess the existing condition, determine the causes of failure (i.e., predominantly abrasion or thermal shock for alumina calciners), and select the appropriate refractory materials and installation techniques.

The overhaul team need to prepare a detailed specification, which shall include the several materials and project features of the products to be used, the thicknesses of each region, the methods of application, the use of anchor materials, geometry and welding details, etc. The contractor, companies that deal with the installation of refractories, should provide a comprehensive execution plan in accordance with the industry requirements. It must account for the suitable material storage, possible substitutions and challenges, the procedure for sampling the refractories for material qualification, the time required to finish the work, etc. The refractory manufacturer should delivery the materials properly, on-time, and provide sufficient technical information for analysis of the overhaul team.

### Installation

The process is shutdown during installation and the overhaul execution plan starts. After demolition, the surfaces are prepared for good adhesion and bonding between the substrate and the new refractory material. The substrate surface is typically cleaned by removing any loose debris, dust, or contaminants. It may also involve roughening the surface to enhance the mechanical interlocking between the substrate and the refractory castable. Pre-wetting the substrate with water is often carried out to prevent rapid water absorption from the castable (when this is the case), which can cause

drying shrinkage and result in cracks. It is important to highlight that the water quality plays a fundamental role during the installation of refractory castables. Additionally, formwork or molds may be used to shape the refractory material during installation, especially for complex lining geometries.

Following the surface preparation, the refractory castable or monolithic material is mixed and then applied using various methods such as gunning, casting, or shotcrete. The specific application method depends on factors like the size and shape of the area to be lined, access restrictions, and the desired thickness of the refractory lining. During installation, it is important to achieve proper packing of the material to minimize the presence of voids or air pockets, which can lead to reduced performance and susceptibility to damage. Vibrators or manual tamping may be used to ensure adequate compaction.

The temperature of the water, the environment, the substrate, and the mix are fundamental to guarantee the time and efficiency of the material properties, specially when the lining is curing, during dry out (in case of castables) and heating. Those heat treatment steps shall meet the requirements of the manufacturer and the ones stablished prior to installation. If not carried out adequately, the structural properties can be affected, and the safety and cost efficiency ruined.

**Post-installation**

Monitoring the performance of refractories after installation in industrial processes involves tracking various parameters, including wear of the lining, shell temperatures, spalling occurrence, and process data. These monitoring activities are essential for assessing the condition of the refractory lining, identifying potential issues, and implementing timely maintenance or repair measures.

The wear of the refractory lining is a critical aspect to monitor as it indicates the material's degradation over time. Wear can result from factors such as abrasion, erosion, chemical attack, or thermal cycling. Regular inspections, visual assessments, and measurements of lining thickness are conducted to evaluate the extent of wear and determine if it is within acceptable limits. Monitoring wear allows for proactive planning of maintenance schedules, including repairing or replacing worn sections of the refractory lining before it affects the performance or integrity of the industrial process [1, 2]. Alves et al [3] showed that using ultrasound techniques for evaluation, selection and classification of ceramic anchors applied in reheat furnaces roof and walls allowed the identification of main defects and the thermal shock resistance of the anchors. The decay on the elastic modulus and thermal shock resistance of the anchors enabled the prediction of the lining lifespan, showing the actual performance of the refractory.

Monitoring shell temperatures can be another crucial aspect of refractory performance tracking, for industrial processes that inspection and lining thickness measurement take place only prior to installation or repairing, during an overhaul. Excessive shell temperatures indicate potential failure of refractory material and temperature sensors, or thermal imaging techniques, could be employed to measure and monitor the temperature distribution across the metallic shell. By closely monitoring these temperatures, any anomalies or hotspots can be detected, indicating areas of potential concern. Actions can then be taken to mitigate the effects, such as adjusting operating conditions, optimizing insulation, or implementing localized repairs to prevent further damage.

In the case of alumina calciners each of these steps is adjusted to fit the specific requirements and the downtime for installation takes approximately 14 days or even more. According to Teider et al [4], depending on the calciner's capacity and the economic conditions, this downtime can represent a potential loss of between USD 5–15 million in revenue. The pre-installation step is critical to avoid delays, which would increase the revenue losses. Usually, it can last more than one year of planning, qualification of materials and analyzing historical data, for the overhaul success. The authors also stated the lack of studies relating the in-situ observations, post-mortem analyses and selection based on quantitative requirements, pointing out that the refractory performance could be significantly improved. That would depend on carrying out these main steps in a systematic methodology to produce meaningful information, fostering the performance of refractories and helping high temperature industries optimize the lifespan of their refractory linings, leading to improved thermal efficiency, reduced downtime, and increased overall productivity.

Therefore, this study aims to present a practical method for tracking the refractory performance, showing its use on a real case scenario of an alumina calciner. The method points out the activities from the main three steps that were tracked, the data that was collected and the analyses that were carried out. The comparison of the refractory properties evaluated in two occasions, on the qualification step (pre-installation) and on samples collected during the overhaul (installation), showed a significant discrepancy. This was associated with the selection key indicators, used to identify the differences found, and to the region of the calciner in which the material was applied. Enabling the overhaul team to anticipate actions for preventing further downtime.

**METHODOLOGY**

The main goal of this study was to establish a simple and effective refractory tracking performance methodology specifically tailored for alumina calciners. The methodology encompasses various steps that ease on comprehensive monitoring and evaluation of refractory materials throughout their lifecycle. The key steps involved in the methodology are as follows:

*Material selection (pre-installation)*

The method of material selection involves several steps to ensure the appropriate choice of materials for a specific project or application. The steps involved were:

1. Identification of the main failure mechanism: understanding and evaluating the historical refractory damage/wear and crack's behavior of previous visual inspection reports. These activities drive the material selection to high thermal shock, corrosion, or abrasion resistance materials, to meet the specific requirements that guarantee the process integrity.

2. Evaluation of performance improvements: exploring new refractory technologies for optimizing the refractory lining, as low cost, fast-drying, low energy consumption, or fast-application products.

3. Prospection of suppliers: searching for the available manufacturers and materials that could fulfil the defined refractory requirements.

4. Qualification of material samples: characterization of the product properties to compare the different available refractories, aiming the selection of the most suitable and the acquisition of quality data for further tracking analysis (standard value). In this study, two tests were carried out: one to evaluate the abrasion/erosion resistance (ASTM C704-15 [5]) and other to check the refractoriness under load (DIN 51053 Standard [6]).

5. Overhaul planning definition: purchasing the refractory materials and scheduling the downtime with the contractor, according to regions to be repaired during the overhaul. Herein, three regions of the calciner were analyzed: pre-heater (PF), furnace (FR) and holding vessel (HV).

*Material application (installation)*

During the refractory application a series of steps need to be carefully handled to provide appropriate data for the tracking analysis:

1. Compeling of mixing parameters: acquiring several data from the castable mixing step as the water content, pH and temperature, powder temperature, mix temperature, dry

667

mixing time, wet mixing time, and the room temperature during the installation day.

2. Overhaul sampling during installation: two distinct moments for sampling the material: firstly, as received by the manufacturer (CPR) and, secondly, as prepared for each region of the calciner (CPA). The procedure consisted of gunning or casting the castable in brick-shaped molds to ship it for testing in the laboratory.

3. Overhaul sample qualification: characterization of the overhaul samples properties according to testing during the material selection step.

4. Tracking analysis: comparison of the standard and overhaul samples results to identify material nonconformities and the regions of the calciner that would require careful attention.

*Material inspection (post-installation)*

After starting of the calciner, the steps that follow consist in monitoring the key indicators of the refractory performance, specially for the regions where the overhaul samples showed nonconforming results.

1. Verification of hot spots: periodically monitoring the shell temperatures to identify the regions where the refractory failure might have happened, which would increase the heat transfer from the interior of the calciner to the vessel shell (as the refractory act as an insulator of the process).

2. Visual inspection: analyzing the lining condition during any downtime to check whether the condition of the refractory has changed unexpectedly.

*Tab. 1: Sample labeling for the overhaul, for qualification step and for the technical datasheet to the high-alumina castable in different preparation conditions.*

| Samples | Calciner | Region |
|---------|----------|--------|
| CPA 12 | #2 | Preheater - PF |
| CPA 14 | #2 | Furnace - FR |
| CPA 17 | #2 | Holding Vessel - HV |
| CPR 03 | Prepared by the contractor as received | |
| LAB | Prepared by 4Cast/UFSCar | |
| TDS | Prepared by the supplier | |

In this study, one refractory material was analyzed. It consisted of an alumina low cement castable, which main components were tabular alumina and mullite. The installation method was gunning and the amount of water suggested by the supplier was in the range of 5.8 to 6.6 liters/100kg of dry powder. All the sample labelling is presented in Tab. 1. Four samples were prepared by the contractor on site (CPA 12, 14 and 17, CPR 03), one was prepared by 4Cast (LAB) and one consisted of the properties from the material technical datasheet (TDS).

**RESULTS AND DISCUSSION**

The results of tracking the refractory performance presented in this study yielded the following discussions. First, the increase of the predictability of the material lifespan, optimizing the repair planning and driving special attention to specific regions of the calciner, and second, the identification of the mostly likely cause of deteriorated properties of the refractory.

Based on the previous results, the calciner's regions preheater, furnace and holding vessel had specific areas that required a refractory with a high erosion resistance. Fluidized bed calciners are driven by an air flow of alumina particles that leads to high abrasion on the surface of the refractories. The material selection considered the process conditions of the calciner and the previous inspection data, that had unveiled the scratched surface of the refractory panels. The material selection step considered a gunning application
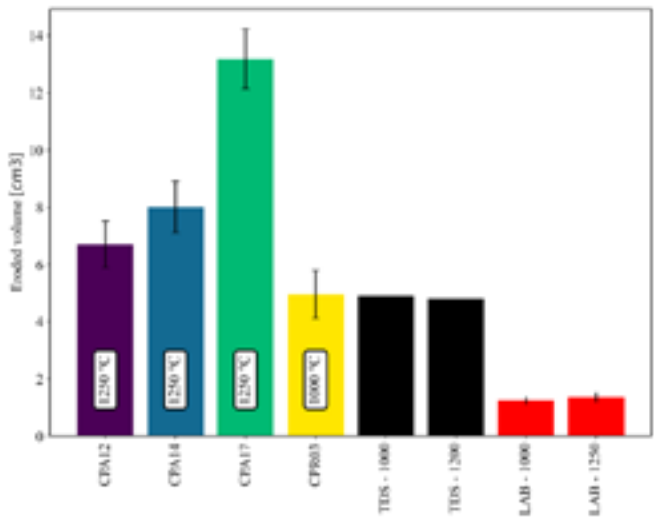


*Fig . 2: Abrasion/erosion resistance for the different samples.*

method, for shortening the installation time and reducing the overhaul downtime. The requirements of main wear mechanism and installation method were used to search the available materials and suppliers. After lab testing several of them, the best one was selected and it was set as the standard value for tracking analysis. In Fig. 2, the values of the abrasion/erosion resistance of standard sample are shown by the red bars in two firing temperatures 1000 ºC and 1250 ºC.

Also in Fig. 2, the eroded volume of other samples is also presented. The black bars (TDS) are the technical datasheet values and the colored ones are the values for the samples prepared on site. The overhaul samples were taken for each of the repaired regions, defined during planning. They were prepared by the contractor and shipped for lab analysis. One can note that all the samples diverged from the standard one. In special, sample CPA 17 that showed a high eroded volume, almost ten times higher than the standard value. The CPA 17 was sampled during installation of the material in the holding vessel. Due to the low erosion resistance, it could be expected that that region would certainly require a repair and a special monitoring during operation. Knowing in advance which region would demand a specific action, save time and material waste during the overhaul.

Although CPA 17 showed the lowest erosion resistance, CPA 12 and 14 had similar analysis and probably would have its lining lifespan reduced. The sample prepared as received by the refractory manufacturer, CPR 03, showed similar erosion resistance as the technical datasheet, but still higher eroded volume than the standard one.



*Fig . 3: Refractoriness under load for the different samples.*

In Fig. 3, the refractoriness under load of the samples were investigated. Note that the softening temperature, $T_{soft}$, for the overhaul samples were approximately 150 ºC lower than the standard one. In the case of some uncontrolled operational time t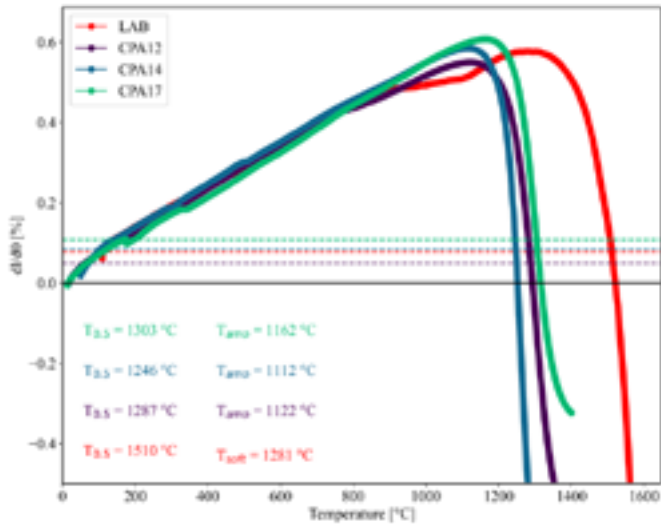hat increases the average operational temperature of the firing zones (usually around 950 ºC), the refractory could already undergo critical deformation, as it is usually recommended to operate at temperatures below $T_{soft}$ and maximum at $T_{0.5}$ (also presented in Fig. 3). If that is the case, the material could melt, decreasing its thickness and lifespan. Again, acknowledging this information right after the installation drove attention to monitor this regions and better planning of the overhaul. Note that both erosion resistance and refractoriness of the CPA samples were downgraded compared to the standard properties.
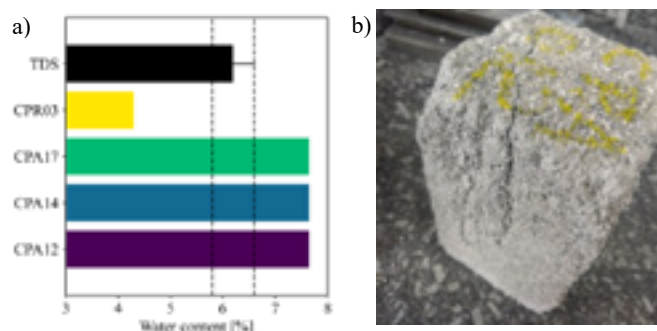
*Fig . 4: a) Water content of the overhaul samples compared to the recommended in the technical datasheet (TDS). b) Overhaul sample as received for properties characterization highlighting a macro crack in the refractory block.*

The amount of water of the samples were compared with the amount suggested by the manufacturer to find one explanation for the results. Fig. 4 a) showed that all the samples were out of the range specified. The one prepared as received required or used less water than the specification and the ones prepared during installation required higher amount. The increase of water content from 1 to 2 % higher than the specified can significantly affect the properties of the refractories after firing. Higher porosity leads to lower elastic modulus and, consequently, decrease the erosion resistance and refractoriness under load of the material. That could explain why the qualification of the overhaul samples was downgraded as shown. The quality of the bricks when received for analysis in the laboratory already contained some macro cracks due to the shaping process, as can be observed in Fig. 4 b). However, note that sample CPR 03 that used less water than the suggested by the supplier had a similar erosion resistance as the technical datasheet. It was clear that during application of the high alumina castable some irregularities appeared and that revealed that the material in use had completely different properties than the one made in the laboratory. The qualification of the material diverged from its desired performance due to application issues.

Tracking the performance of the refractories by analyzing key parameters helped to predict the lining lifespan after the overhaul. The post-installation step consisted of monitoring and doing visual inspections when available. During the analysis of the shell temperatures, it was identified a hotspot at the holding vessel region that needed repairing. Due to other problem with the calciner that resulted in shutdown, the contractors were able to repair the region while the problem was being fixed. This shows the potential of the methodology to provide data for better decision making concerning the lifecycle of the refractory lining.

Running the same methodology to all calciner regions and materials for an overhaul requires effortful work and produces a lot of data. It is important to have well-qualified people collaborating in all steps, to ensure the best tracking analysis, and to have a system and method to process all the information rapidly. Nowadays, there is a lot of opportunity for digital solutions for helping the refractory end-users and manufacturers along the tracking of the refractory performance, by using cameras, lasers and sensors, software and modules, machine learning and modeling, etc. It a step to meet on-going desires of modern refractory industrial practices.

**CONCLUSIONS**

The establishment of a simple refractory performance tracking methodology for alumina calciners, furnaces, and other high temperature processes is essential for effective maintenance and improved operational efficiency. The proposed methodology encompasses various stages, including planning, sample collection, material analysis, and data analysis. Implementing this methodology enables better monitoring of the refractory condition and decision-making regarding repairing.

The results obtained through the methodology highlighted the importance of considering factors such as water content, the erosion resistance and refractoriness, in selecting and evaluating the refractory performance. The information gathered through the methodology facilitates the repair planning and optimization of maintenance strategies, reducing the time and mostly the cost involved in an overhaul.

Ultimately, this study showed that tracking the refractory performance development to application can improve reliability, reduce downtime, and enhance financial indicators. Further research and implementation of this methodology across various regions and installation can contribute to advancements in refractory performance and maintenance practices, including better digitalization throughout the steps.

**ACKNOWLEDGMENTS**

669

**REFERENCES**

[1] Harbison-Walker Handbook of Refractory Practices, First Edition, 1992, ANH Refractories, 400 Fairway Drive, Moon Township, Pennsylvania 15108, www.hwr.com.

[2] Vierthauer, A., Mutsam, N., Pernkopf, F. Gantner, f., Grimm, G., Winkler, W., Lammer, G., Ratz, A., Refractory Condition Monitoring and Lifetime Prognosis for RH. AISTech Proceding of the Iron & Steel Technology Conference, 2019, p. 1081-1089.

[3] Alves, G. S., Duarte, A. K., Lins, V. F. C., Silva, D. G. M., "Metodologia para previsão da vida útil de âncoras refratárias aplicadas em fornos de reaquecimento," Rev. Mater., vol. 21, no. 4, pp. 906–920, 2016, doi: 10.1590/S1517-707620160004.0084.

[4] Teider, B.H., Graham, B., Braulio, M. A., Gallo, J. B., Pandolfelli, V. C.. Lifetime critical analysis of alumina calciner refractories. Refractories Worldforum 5 (3), 2013, p. 101-106.

[5] American Society for Testing and Materials (2022), Standard Test Method for Abrasion Resistance of Refractory Material at Room Temperature, ASTM C704/C704M-15(2022).

[6] German Institute for Standardisation (2013), Testing of Ceramic Materials, Determination of Creep in Compression, Determination of the Deformation of a Refractory Product Subject to a Constant Temperature and a Constant Load, DIN 510053-1, Testing of Ceramic Materials.

# APPLICATION OF MACHINE LEARNING IN THE ASSESSMENT OF THE WEAR RATE OF MGO−C REFRACTORY MATERIALS DEDICATED FOR STEEL INDUSTRY

S. Sado, W. Zelik,

Zakłady Magnezytowe ROPCZYCE, S.A., Research and Development Centre of Ceramic Materials, Ropczyce, Poland,

I. Jastrzębska, J. Szczerba

AGH University of Science and Technology, Faculty of Materials Science and Ceramics, Cracow, Poland

**ABSTRACT**

MgO-C refractories are zonally installed in the heating units of steel and iron production. In these conditions, refractory materials are exposed to multiple corrosive factors. The interaction with aggressive liquid slags of variable basicity is one of the main factors which determine the wear rate of MgO-C refractories. In this work, we show the unusual attempt for selecting the MgO-C refractories of various properties, but comparable corrosion resistance to specific conditions. The designed and industrially produced MgO-C products were characterized by different ratios of the sintered to fused magnesia raw materials and variable forming pressure. 20 laboratory corrosion tests were conducted in an induction furnace. Then, corrosion resistance of MgO-C refractories was assessed using Self Organizing Maps (SOM). The input variables in the used algorithm were: apparent porosity of materials before and after coking, decarburization rate of MgO-C materials after tests at 900°C and 1100°C, chemical composition of designed materials, temperature of the corrosion test and slag basicity. Physicochemical properties of MgO-C materials and their wear rates were used to classify the materials of different starting composition into groups of comparable corrosion resistance.

## 1. INTRODUCTION

MgO-C refractories are used as linings of heating devices in steel and iron metallurgy processes. Manufacturers and end-users of refractories must provide safe and the longest possible operation of refractories in exploitation conditions. The operation time of heating devices is determined by the intensity of the corrosive wear rate of refractories and ranges in steel convertors approximately from to ….. The most critical corrosive factors for MgO-C refractories are the decarburization of the material's hot face, associated with the oxidation of carbon contained in MgO-C materials and slag corrosion [1]. The decarburized hot face of MgO-C material is loose, and porous, thus, exposed to liquid flow and erosion. For this reason, slag may infiltrate easily into the matrix, thus, promoting corrosion.

Several studies describe the corrosion mechanism of MgO-C refractories by a liquid slag [2]-[8]. In the context of corrosion resistance, the authors mainly underline the importance of raw materials' chemical purity ($CaO/SiO_2$ ratio, concentration of selected impurities $Fe_2O_3$, $Al_2O_3$, $B_2O_3$), size of MgO crystals and quality of graphite used for MgO-C bricks production.

Scarce information can be found in literature concerning the impact of fused/sintered MgO (primary raw material in MgO-C production) on the corrosion resistance of MgO-C bricks. Lao *et al.* [9] conducted a comparative study of the wetting and corrosion behaviour of fused magnesia and microporous magnesia aggregates by molten slags of different $CaO/SiO_2$. Benavidez *et al.* [10] compared the corrosion resistance of three commercial bricks composed of fused magnesia, fused and sintered magnesia, and only sintered magnesia in the composition, describing its wear mechanism.

Currently, statistical tools and machine learning (ML) techniques becomes more widely applied in the field of refractory materials. The application of selected ML-supervised techniques was reported to effectively predict the wear rate of refractories installed in heating devices [11]-[14]. ML-unsupervised techniques are also applied, e.g., for extraction the comparable groups of data in large data sets [15].

ML algorithms are expected to allow engineers to select materials with an optimized cost-to-quality ratio by substituting fused raw materials with sintered ones. Therefore, the aim of this work was the application of ML-unsupervised algorithm to identify the groups of refractory materials of comparable corrosion resistance among 10 variants of MgO-C refractories composed of different ratios of fused/sintered magnesia raw materials.

## 2. MATERIALS AND METHODS

### 2.1. Materials

MgO-C materials were industrially produced based on ten different formulations (designated as 1-10) and using different ratios of fused-to-sintered magnesia raw materials, as presented in Tab. 1. The grain composition of mixtures was designed with the use of the Dinger–Funk model using a distribution coefficient $q$=0.37. Bricks were shaped with the use of hydraulic pressing machines to obtain the rectangular shapes (400x150x100 mm), and applying two different final shaping pressures of 120 MPa and 180 MPa. Finally, twenty variants of MgO-C materials were obtained (ten formulations and two values of final shaping pressure applied), with 8 bricks for each variant which gives 160 bricks produced in total. After shaping, bricks were tempered for 36 h at 180°C. The following magnesia raw materials were used in starting composition: fused magnesia FMI (MgO min. 97.5 wt. %, $Al_2O_3$ 0.1 %, $Fe_2O_3$ 0.1%, $CaO/SiO_2$ min. 3.5), fused magnesia FMII (MgO 97.0 wt. %, $Al_2O_3$ 0.3 %, $Fe_2O_3$ 0.8 %, $CaO/SiO_2$ min. 2.0), sintered magnesia SMI (MgO 94.0 %, $Al_2O_3$ 0.6 %, $Fe_2O_3$ 2.9 %, $CaO/SiO_2$ min. 0.4), sintered magnesia SMII (MgO 98.0 %, $Al_2O_3$ 0.12 %, $Fe_2O_3$ 0.5 %, $CaO/SiO_2$ min. 3.0) and sintered magnesia SMIII (MgO 97.0 wt. %, $Al_2O_3$ 0.2 %, $Fe_2O_3$ 0.85 %, $CaO/SiO_2$ min. 1.8). FMI, FMII, SMI and SMII were used in different proportions in compositions while SMIII was fixed at constant amount of 12 wt. %. Flake graphite constituted 10 wt. % for all compositions. Phenol-formaldehyde resin was used as a binder in each formulation (liquid - 2 wt. %, powder - 1 wt.%).

Table 1. Composition of designed MgO-C refractory materials, wt. %.

| Formulation | FMI | FMII | SMI | SMII |
|---|---|---|---|---|
| 1 | 77.00 | - | - | - |
| 2 | - | 77.00 | - | - |
| 3 | 50.00 | - | - | 27.00 |
| 4 | - | 50.00 | - | 27.00 |
| 5 | 12.00 | - | - | 65.00 |
| 6 | - | 12.00 | - | 65.00 |
| 7 | 50.00 | - | 27.00 | - |
| 8 | - | 50.00 | 27.00 | - |
| 9 | 12.00 | - | 65.00 | - |
| 10 | - | - | 77.00 | - |

### 2.2. Methods

#### 2.2.1 Physicochemical properties

Apparent porosity (*AP*) and bulk density (*BD*) of specimens were measured acc. to standard PN-EN 993:1, apparent porosity ($AP_k$) and bulk density ($BD_k$) after coking acc. to PN-ISO10059/PN-EN 993:3. Decarburization tests at 900°C ($u_1$) and 1100°C ($u_2$) were conducted separately. The heating rate was 50°C/h to achieve the assumed temperature in both decarburization tests. The dwell time in maximum temperature in both tests was 3 h. The average $O_2$ concentration in a chamber during a decarburization test at 900°C was 15.37 % (standard deviation of 0.75 %) and 16.12 % (standard deviation of 0.93 %) at 1100°C. Decarburization rate (*u*) was

estimated with the use of Eq. 1, where $D$ is the initial diameter of the cylindrical specimen (before heat treatment), while $d$ is an average of four diameters of the unreacted core (after heat treatment).

$$u = \left[1 - \left(\frac{d}{D}\right)^2\right] \cdot 100\% \qquad (1)$$

### 2.2.1. Corrosion tests

Corrosion tests of produced MgO-C refractory materials were conducted in a medium-frequency induction furnace. The furnace chamber was covered with a steel lid at the top. The non-alloy structural steel S235JR (PN-EN 10025-2:2007) was used as a source of liquid melt during the test. After achieving the assumed temperature of the liquid melt (1650°C/1720°C, depending on test number), the synthetic slag was added at the top of the liquid melt. The temperature of a liquid was measured during the test with the use of thermocouples immersed directly in the melt. The crucible made of prepared refractory shapes was shown in Fig. 1a, and the induction furnace during operation in Fig. 1b.
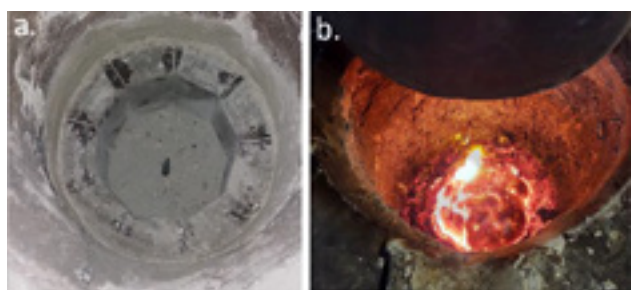


*Fig. 1 a. Refractory crucible after installation in an induction furnace, b. corrosion test with slag at the top.*

Overall, 160 shapes were selected for corrosion tests out of all 20 variants of produced MgO-C refractory materials (8 shapes for every variant). Corrosion tests were conducted in 4 Blocks, namely, Block I: slag with CaO/SiO₂ of 0.8 and temperature 1650°C; Block II: slag with CaO/SiO₂ of 0.8 and temperature 1720°C; Block III: slag with CaO/SiO₂ of 1.6 and temperature 1650°C; Block IV: slag with CaO/SiO₂ of 1.6 and temperature 1720°C. In each test block, 9 shapes were installed in a furnace: 8 shapes for measuring the wear rate, and 1 shape at the casting side, which was not taken into consideration. The wear rate ($w$) of tested materials was determined acc. to Eq. 2:

$$w = \frac{S_c}{S_i} \cdot 100\% \qquad (2)$$

where $S_i$ is the initial cross-section surface of the test material, and $S_c$ is the corroded surface of the test material, as demonstrated in Fig. 2.



*Fig. 2. Cross section of MgO-C refractory shape after a corrosion test in an induction furnace.*

The results of the wear rate measurements were normalized to obtain values in the range of 0 to 1, where 0 means the lowest wear rate and 1 is the highest wear rate.

### 2.2.2. Analysis after corrosion tests

After corrosion in the induction furnace, statistical analysis and machine learning evaluation were conducted for tested materials. The analysis was developed with the use of the "R" programming language. Assessment of differences in obtained values of properties between tested materials was performed by the Kruskal-Wallis test and 'kruskal.test()' function. For determining the normality of data distribution 'shapiro.test()' function was used. All mentioned functions are assigned to the library *stats*. Self Organizing Maps (SOM) algorithm was applied, with the use of 'som()' function assigned to the *kohonen* library, to find the groups of materials of comparable corrosion resistance. The quality of clustering was assessed with the use of 'somQuality()' function from the *awSOM* library.

## 3. RESULTS AND DISCUSSION

### 3.1. Chemical composition of produced MgO-C refractories

Chemical analysis of produced refractories was presented in Tab. 2. The main differences between formulations refer to the CaO/SiO₂ ratio of the magnesia part. The highest CaO/SiO₂ was registered for formulation 1 of 2.28, while the lowest for formulation 10 of 0.40. Significant differences were also detected in the amounts of impurities in produced materials, including Fe₂O₃ and Mn₃O₄ which affects the high-temperature performance.

Table 2. Chemical characteristics of MgO-C refractory materials wt. %.

| Formulation | MgO | Al₂O₃ | SiO₂ | CaO | Mn₃O₄ | Fe₂O₃ | CaO/SiO₂ * |
|---|---|---|---|---|---|---|---|
| 1 | 96.73 | 0.40 | 0.74 | 1.69 | 0.09 | 0.29 | 2.28 |
| 2 | 96.46 | 0.41 | 0.81 | 1.45 | 0.04 | 0.71 | 1.79 |
| 3 | 97.07 | 0.30 | 0.68 | 1.40 | 0.09 | 0.39 | 2.06 |
| 4 | 96.81 | 0.35 | 0.74 | 1.19 | 0.10 | 0.74 | 1.61 |
| 5 | 97.34 | 0.30 | 0.57 | 1.11 | 0.08 | 0.54 | 1.95 |
| 6 | 96.64 | 0.43 | 0.72 | 0.98 | 0.24 | 0.93 | 1.36 |
| 7 | 95.71 | 0.43 | 1.19 | 1.18 | 0.40 | 1.02 | 0.99 |
| 8 | 95.83 | 0.46 | 1.09 | 1.10 | 0.30 | 1.13 | 1.01 |
| 9 | 94.84 | 0.49 | 1.43 | 0.75 | 0.70 | 1.71 | 0.52 |
| 10 | 94.15 | 0.74 | 1.60 | 0.64 | 0.77 | 2.00 | 0.40 |

*in the magnesia part of the starting composition (refers to raw materials in Tab. 1).

### 3.2. Physical properties

Alternations in the physical properties of MgO-C refractory materials were presented in Fig. 3 – Fig. 6. For shaping pressure of 120 MPa, apparent porosity ($AP$) of produced MgO-C refractories varied from 4.20 % to 13.80 %, while for 180 MPa it ranged from 2.30 % to 12.40 % (Fig. 3). Comparable trend in apparent porosity was registered after coking ($AP_k$) where results varied from 8.50 % to 17.90 % (120 MPa) and 7.40 % to 15.70 % (180 MPa) (Fig. 4). Decarburization rate at 900ºC ($u_1$) ranged from 54.95 % to 87.02 % (120 MPa) and 49.79 % to 85.73 % (180 MPa) (Fig. 5). Decarburization rate at 1100ºC ($u_2$) was higher for 120 MPa shaping pressure of 64.08 % to 91.88 %, and lower for 180 MPa of 59.90 % to 87.5% (Fig. 6).
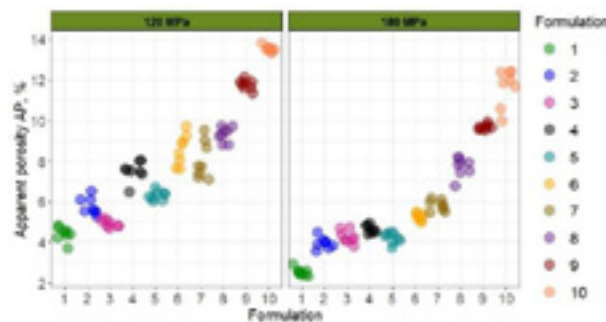


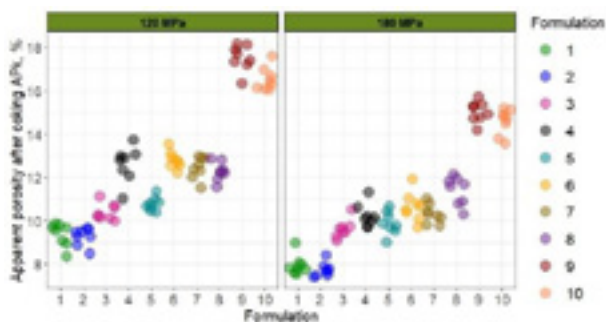*Fig. 3 Apparent porosity of MgO-C materials.*

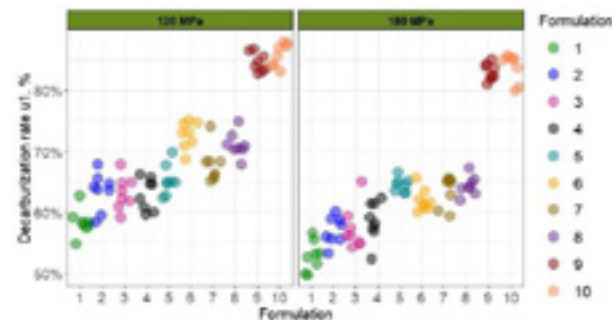*Fig. 4 Apparent porosity after coking of MgO-C materials.*



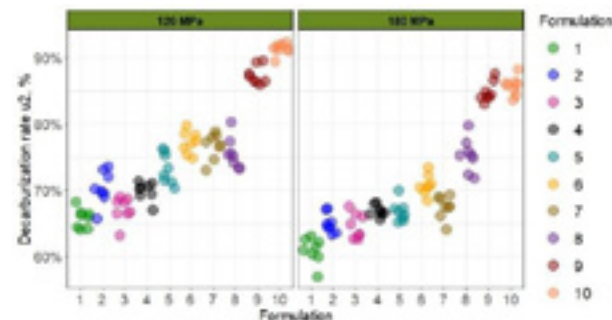*Fig. 5 Decarburization rate at 900℃ of MgO-C materials.*



*Fig. 6 Decarburization rate at 1100℃ of MgO-C materials.*

### 3.3. Wear rate

Results of the wear rate of MgO-C materials were presented in Fig. 7. Wear rate was found to depend on the temperature of the corrosion test and CaO/SiO$_2$ ratio in slag. 7-10 formulations-based materials containing sintered magnesia SMI (MgO 94.0 %, CaO/SiO$_2$ min. 0.4) exhibited the lowest corrosion resistance. 3-6 formulations-based refractories were reported to possess comparable corrosion resistance.
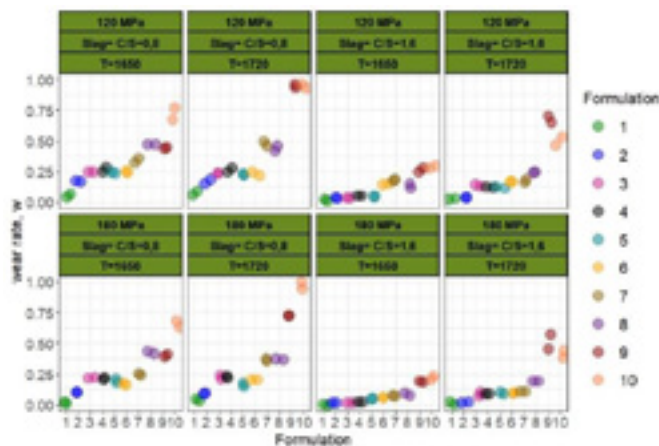


*Fig. 7 Wear rate of MgO-C materials.*

Application of Shapiro-Wilk statistics showed that measured temperatures during the corrosion test as well as the wear rates are not normally distributed. For this reason, Kruskal-Wallis test was applied to reveal if the wear rate is significantly influenced by temperature. Moreover, it was checked if the CaO/SiO$_2$ in the used slag influences the measured wear rates. For the measured temperatures during corrosion, Kruskal-Wallis statistics showed *chi-squared* of 50.41 and *p-value* of $6.534 \cdot 10^{-5}$, while for the CaO/SiO$_2$ ratio in slag *chi-squared* equalled 103.6 with *p-value* of $1.487 \cdot 10^{-13}$. These results clearly indicate that, wear rates are significantly differentiated by both temperature and CaO/SiO$_2$ ratio in slag.

### 3.4. Self-Organizing Maps

For the application of the SOM algorithm, the following properties of designed MgO-C bricks were used: apparent porosity (*AP*); apparent porosity after coking (*AP$_k$*); CaO/SiO$_2$ ratio (*CS*) and MgO content (*MgO*) of magnesia part in starting composition; decarburization rate at 900°C (*u$_1$*); decarburization rate at 1100°C (*u$_2$*) and wear rate after corrosion test (*w*). All initial data were normalized to obtain values in the range of 0 - 1. The analysis was divided into 4 groups, according to the corrosion tests blocks (1650°C and 1720°C, and 2 slags of different basicity, refer to *2.2.1*).

The analysis aimed to identify the groups of refractory materials of comparable corrosion resistance among 10 variants of produced MgO-C refractories composed of different ratios of fused/sintered raw materials.

SOM maps for the corrosion tests were presented in Fig. 8 (Block I), Fig. 9 (Block II), Fig. 10 (Block III) and Fig. 11 (Block IV). The codes plot on the left side of each figure corresponds to values of selected properties (the larger the quarter the greater the value of the property), and the wear rate map on the right side of each figure corresponds to the average wear rate assigned to each cluster, containing specific MgO-C variant of materials. For the map with the wear rate, the deepest-red colour refers to the clusters containing materials with the lowest wear rate, while the lightest-yellow clusters correspond to the materials with the highest values of the wear rate. Tab. 3 lists the materials assigned to the clusters in each of the maps. Materials located in the same cluster are considered materials of comparable corrosion resistance.
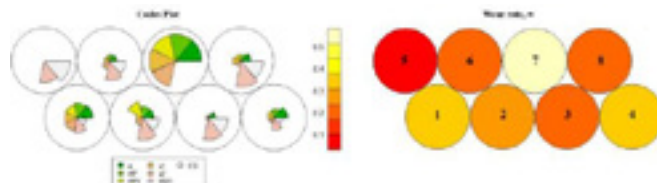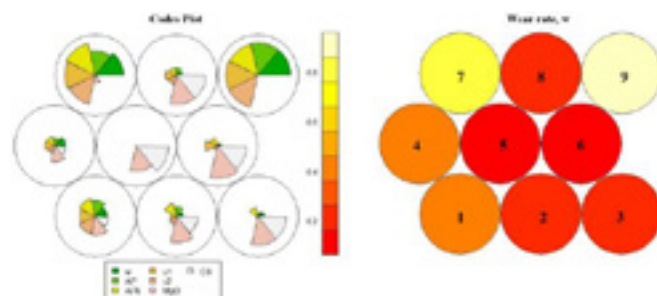


*Fig. 8 SOM maps for corrosion results in Block I.*



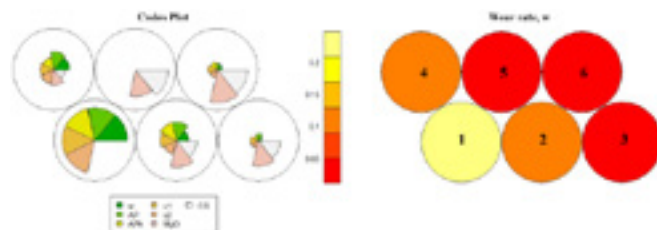*Fig. 9 SOM maps for results of corrosion test in Block II.*



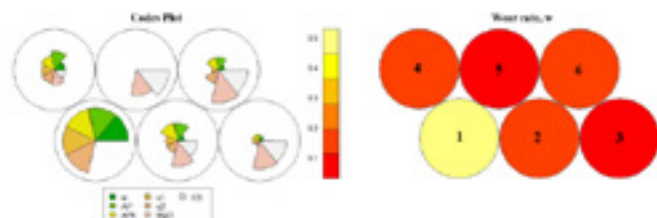*Fig. 10. SOM Maps for results of corrosion test in Block III.*

*Fig. 11. SOM maps for results of corrosion test in Block IV.*

After the results in Tab. 3, we can conclude that it is possible to substitute fused magnesia with sintered one in MgO-C materials with no loss of corrosion resistance. For example in tests of Block I, cluster 3 contains formulation 2 and 4-based MgO-C materials, shaped at 180 MPa. According to the composition of starting mixture Tab. 2, formulation 2-based material contains 77 % of fused magnesia (FMII) while and formulation 4-based material contains 50 % of fused magnesia (FMII) and 27 % of sintered magnesia (SMII). Such interchangeability of raw materials would be economically beneficial for both manufacturers of refractory and end-user as well as would contribute to a more sustainable utilization of currently strategic raw materials.

Table 3. MgO-C materials assigned to clusters of comparable wear rates.

| Cluster | Block I | Block II | Block III | Block IV |
|---|---|---|---|---|
| 1 | 6_120; 7_120; 8_120 | 6_120; 7_120; 8_120 | 9_120; 9_180; 10_120; 10_180 | 9_120; 10_120; 9_180; 10_180 |
| 2 | 4_120; 4_120 | 6_180; 4_120 | 4_120; 6_120 | 4_120; 6_120 |
| 3 | 2_180; 4_180 | 3_1280; 4_180 | 2_120; 4_180; 6_180 | 2_120; 3_120; 3_180; 4_180; 5_180 |
| 4 | 8_180; 7_180 | 7_180 | 7_120; 8_120; 7_180; 8_180 | 7_120; 8_120 |
| 5 | 1_120; 1_180 | 1_120; 1_180; 2_180 | 1_120; 1_180; 2_180; 3_180 | 1_120; 1_180; 2_180; |
| 6 | 2_120; 6_180 | 5_180 | 3_120; 5_120; 5_180 | 5_120 |
| 7 | 9_120; 9_180; 10_120; 10_180 | 9_120; 9_180 | - | - |
| 8 | 3_120; 5_120; 5_180 | 2_120; 3_120 | - | - |
| 9 | - | 10_120; 10_180 | - | - |

Block I-IV (refers to the corrosion test described in 2.2.1)

## 4. CONCLUSIONS

- 20 variants of MgO-C refractory materials were designed and industrially produced, based on different contributions of sintered and fused magnesia raw materials in a starting composition.
- After conducting 20 corrosion tests, high differentiation in the wear rate of materials was observed which was subsequently assessed with the aid of machine learning tools.
- The application of Self-Organizing Maps algorithm enabled classifying the materials (containing different amounts of fused and sintered magnesia) of comparable corrosion resistance
- It is recommended to always check the algorithm's results and compare them to the expert knowledge and experience.

## REFERENCES

[1] F. Nadachowski, A. Kloska, „Refractory Wear Processes". AGH, Kraków, Poland, 1997; pp. 17-27, 38-39.
[2] S-H. Heo, K. Lee, Y. Chung, "Reactive wetting phenomena of MgO-C refractories in contact with CaO-SiO$_2$ slag". *Trans. Nonferrous Met. Soc. China*, vol. 22, no.3, 2012, pp.870-875.
[3] J. Liu, H. Sheng, X. Yang, Z. He, X. Hou, "Research on the Wetting and Corrosion Behavior Between Converter Slag with Different Alkalinity and MgO-C Refractories". *Oxid.Met.,* 97, no.13, 2022, pp.157-166.
[4] S. Lee, Y. Chung, "The effect of C content in MgO-C on dissolution behavior in CaO- SiO$_2$-Al$_2$O$_3$ slag". *Ceram. Int.,* vol.48, no.18, 2022, pp. 26984-26991.
[5] A. Yehorov, G. Ma, O. Volkova, "Interaction between MgO-C bricks and ladle slag with a 1:1 CaO/Al$_2$O$_3$ ratio and varying SiO$_2$ content". *Ceram. Int,* vol. 47, no.8, 2021, pp. 11677 – 11686.
[6] M. K. Kujur, I. Roy, K. Kumar, P. Chintaiah, S. Ghosh, and N. K. Ghosh, "Raw materials for manufacturing of Superior quality MgO-C bricks". *Interceram – Int. Ceram. Rev,* vol.5, no. 1, 2018, pp. 2359-2366.
[7] R. Kundu and R. Sarkar, "MgO-C Refractories: A Detailed Review of These irreplaceable Refractories in Steelmaking". *Interceram – Int. Ceram. Rev,* vol. 40, 2021, pp. 46-55.
[8] S. Nanda, A. Choudhury, K. S. Chandra, and D. Sarkar, "Raw materials, microstructure, and properties of MgO–C refractories: Directions for refractory recipe development". *J. Eur. Ceram. Soc,* vol. 43, no. 1, 2023, pp. 14–36.
[9] Y. Lao, G. Li, Y. Gao, and C. Yuan, "Wetting and corrosion behavior of MgO substrates by CaO–Al2O3–SiO2–(MgO) molten slags". *Ceram. Int,* vol. 48, no. 10, 2022, pp. 14799–14812.
[10] E. Benavidez, E. Brandaleze, L. Musante, and P. Galliano, "Corrosion Study of MgO-C Bricks in Contact with a Steelmaking Slag". *Procedia Mater. Sci.,* vol. 8, 2015, pp. 228–235.
[11] A. Hou, S. Jin, D. Gruber, H. Harmuth, "Modelling of a steel ladle and prediction of its thermomechanical behaviour by finite element simulation together with artificial neural network approaches". Congress of Numerical Methods In Engineering. Guimaraes, Portugal, 2019. Available online: https://www.researchgate.net/publication/334304593_Modelling_of_a_steel_ladle_and_prediction_of_its_thermomechanical_behavior_by_finite_element_simulation_together_with_artificial_neural_network_approaches.
[12] A. Hou, S. Jin, H. Harmuth, and D. Gruber, "Thermal and Thermomechanical Responses Prediction of a Steel Ladle Using a Back-Propagation Artificial Neural Network Combining Multiple Orthogonal Arrays". *Steel Res Int*, vol. 90, no. 7, 2019, 1900116.
[13] A. Hou, S. Jin, D. Gruber, and H. Harmuth, "Influence of variation/response space complexity and variable completeness on BP-ANN model establishment: Case study of steel ladle lining". *Appl. Sci.,* vol. 9, no. 14, 2019, 2835.
[14] S. Sado, W. Zelik, and R. Lech, "Use of Machine Learning for modelling the wear of MgO-C refractories in Basic Oxygen Furnace Ceramic Processing Research Use of Machine Learning for modelling the wear of MgO-C refractories in Basic Oxygen Furnace". *J. Ceram. Process. Res.*, vol. 23, no. 4, 2022, pp. 1–9.
[15] R. A. A. Borges, N. P. Antoniassi, L. E. Klotz, C. de Carvalho Carneiro, and G. F. B. Lenz e Silva, "A Statistical and Self-Organizing Maps (SOM) Comparative Study on the Wear and Performance of MgO-C Resin Bonded Refractories Used on the Slag Line of Ladles of a Basic Oxygen Steelmaking Plant".*Metall. Mater. Trans. B*, vol. 53, no. 5, pp. 2852–2866.

# EXPERIMENTAL AND NUMERICAL INVESTIGATION OF A PILOT STEEL LADLE

Pratik N. Gajjar, João M. Pereira, Paulo B. Lourenço
University of Minho, ISISE, ARISE, Department of Civil Engineering, Guimarães, Portugal

Pieter Put, Bruno Luchini, Sido Sinnema
Ceramics Research Centre, Tata Steel, 1951MD Velsen Noord, The Netherlands

## ABSTRACT

Masonry refractory linings are commonly employed in industrial vessels to protect against extreme working environments. Mortarless refractory masonry is frequently used in the working lining of steel ladles to contain the molten steel and limit heat losses. During operation, such masonry lining undergoes high thermo-mechanical loads, primarily due to the complex thermal and mechanical boundary conditions. Therefore, large-scale experiments are required to characterise the behaviour of such structures, leading up to their optimisation. This work presents a novel approach for the experimental characterisation of refractory linings using a laboratory-scaled pilot steel ladle. This 3D pilot model is a scaled representation of a ladle that includes all the linings as an industrial ladle. The pilot ladle was tested under transient thermal loads, and its behaviour was assessed through thermocouples, strain gauges and DIC (digital image correlation). The experimental observations describe a complex and nonlinear global behaviour of the pilot ladle due to thermal gradient, creep of the refractories and damage. Finally, the results obtained from these experiments were used to validate numerical models using a 3D meso-modelling approach. The numerical simulations revealed a good agreement with the experimental outcome that can further be employed to investigate and design an industrial steel ladle.

## 1. INTRODUCTION

Steel ladles play a crucial role in the steelmaking industry. They are employed as industrial vessels to transport and refine molten steel and are exposed to a harsh operating environment. Normal operating conditions of these vessels include high temperatures, high thermal stresses, slag attack, and degradation of layers in contact with molten steel [1]. Steel ladles are often built with multiple layers of refractory masonry linings enclosed within a thick steel shell to withstand extreme operating conditions. Each layer comprises refractory materials with different thermal, mechanical, and chemical properties. The selection of refractory materials for these layers depends on their designed purpose, such as thermomechanical behaviour, thermal insulation, and chemical stability. Therefore, knowledge of the thermal, mechanical, and chemical behaviour of the refractories becomes essential to optimise their consumption in extreme working environments.

The working lining of a steel ladle is usually constructed with mortarless masonry. The joints of such masonry provide a physical break in continuous media, which can reduce the stress build-up. These dry joints show a high nonlinear behaviour affected by material type, contact area distribution, and the spatial and size distributions of the asperities on the surfaces [2]. Therefore, large-scale experimental campaigns are required to evaluate the global behaviour of refractory masonry under varying thermal and mechanical boundary conditions. These campaigns also validate the material properties derived from experiments at material levels, noting that limited work is available in the literature regarding the large-scale experimental evaluation of such masonry.

Oliveira et al. [3] experimentally investigated the mechanical behaviour of mortarless refractory masonry under uniaxial compression with various loading conditions at ambient and high temperatures (900°C). Their work highlights the heterogeneity in mortarless refractory due to dry joints and its influence on thermomechanical behaviour, which is widely used in steel ladles. Further, Ali et al. [4] evaluated the mechanical behaviour of the mortarless refractory masonry in a biaxial press under various loading and boundary conditions at ambient and high temperatures (1500°C). They observed permanent deformation of bricks due to viscoplastic behaviour. This experimental campaign shows the presence of viscoplasticity in alumina spinel bricks at high temperatures and its impact on refractory masonry under different loading conditions. Gasser and Poirier [5] investigated the thermomechanical behaviour of mortarless refractory masonry in a laboratory pilot that resembles a steel ladle. The test was conducted with only one layer of refractory lining and was performed under transient thermal loading with a maximum temperature of 1000°C. They observed that the elastic strains observed from the steel shell reveal the thermomechanical behaviour of the refractory lining. The behaviour of the lining was influenced by the dry joints present and the contact between the bricks and steel shell.

Finite element models are often used to investigate or design industrial installations such as steel ladles with different linings of refractory masonry. The data obtained through experimental campaigns are used to calibrate models with varying degrees of complexity from linear thermo-elastic to more complex models, including viscoplasticity and damage [1,6,7]. However, the behaviour obtained through such models for a steel ladle is not validated due to a lack of experimental investigations. Therefore, experimental work must be carried out to validate numerical models on an assembly representing an industrial ladle subjected to a thermal loading similar to normal operating conditions (around 1500°C).

This work presents a novel experimental setup for large-scale refractory masonry to characterise a pilot steel ladle that undergoes similar thermomechanical loadings as an industrial ladle to gather data to validate numerical models.

## 2. DEVELOPMENT OF THE PILOT LADLE

The scale of the pilot ladle should be such that it is small enough to be handled at the laboratory level and big enough to represent the global behaviour of an industrial ladle. The other difficulties involved with the scale are the thickness of the steel shell and the size and shape of the refractory bricks. To tackle these challenges, preliminary numerical investigations were developed, assisting with the design and, ultimately, contributing to the choices made regarding the installation itself. From the design optimisation process, only the barrel part of the ladle with 1500 mm diameter and 500 mm in height was made, as shown in Fig. 1. This configuration contains all refractory linings with identical lining thickness as in industrial ladle enclosed within a 6 mm thick steel shell.
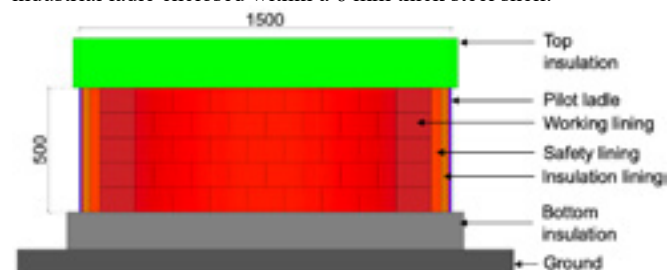


*Fig. 1: Graphical illustration of the pilot steel ladle showing pilot ladle, refractory linings, and top and bottom insulation.*

The working lining is made of mortarless masonry with alumina spinel bricks, providing good thermal, chemical and mechanical stability at high temperatures. The safety lining is constructed with bauxite brick, offering better thermal insulation than working linings with good mechanical behaviour. Insulation lining is used to reduce the heat losses in the ladle. The material used in this lining is aluminium silicate which has low thermal conductivity. The insulation board is an additional lining component to further reduce

heat losses. This microporous material offers excellent thermal properties while it is highly compressible.

For the measurement of thermal fields, thermocouples were used. An assembly of thermocouple placement was installed at three different locations and layers of the pilot ladle (spaced at about 120° in the plan view), as shown in Fig. 2 (total of 18 thermocouples). Six type K thermocouples were installed in different refractory linings at one location. One type S thermocouple was placed near the innermost part of the working lining. Additional thermocouples were placed inside the bottom insulation layers to monitor the heat losses.
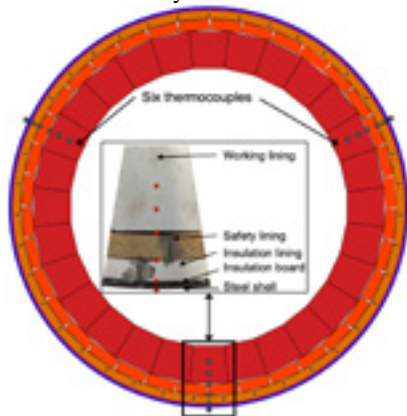


*Fig. 2: Placement of thermocouples to measure thermal fields.*

DIC was employed to monitor displacement and strains in the working lining through a cut window in the top lid and on the exterior section of a steel shell. Additionally, three high-temperature spot welding foil strain gauges from Kyowa (self-temperature compensating) were placed on the structure's cold face, close to the thermocouples shown in Fig. 2.

## 3. EXPERIMENTAL RESULTS

Fig. 3 shows the final experimental setup of the pilot steel ladle with all components and measurement devices. Two tests were performed on a pilot with new working linings (NWL) by applying thermal load through 18 heating elements. Once the target temperature was achieved, an eight-hour dwell time was used for all the tests. The test specimen NWL-01 was tested till 1250°C to check the structural safety of the pilot ladle, while the other test reached 1400°C. This experimental device was constructed and tested at the Ceramics Research Centre (CRC) of Tata Steel in Ijmuiden, Netherlands.



*Fig. 3: Experimental setup of the pilot ladle.*

Fig. 4 shows the average temperature evolution observed in the installed thermocouples at various heights. At the beginning of the thermal loading through heating elements, the whole assembly of the pilot ladle was at room temperature of around 16°C. The thermal loading was applied at a rate of 4°C/minute. It is possible to notice that the applied rate of thermal loading was sustained till 500°C of the furnace temperature. Afterwards, the rate of loading decreased due to increased power requirement. However, at the 20th hour, the furnace temperature reached 1250°C for both tests. For the test specimen NWL-01, the applied temperature was kept constant for the next eight hours, and for the other test specimen, the applied

temperature was increased to 1400°C. Once the 1400°C desired temperature was achieved at the 36th hour, the same was kept constant for the next eight hours.

For both specimens, temperature evolution observed in the linings is very similar. Moreover, irregular temperature evolution can be observed at the different linings at 100°C, which can be attributed to the evaporation of free water. The temperature evolution and distribution in the ladle linings exhibit the expected thermal behaviour of a steel ladle. Temperature measurement data provides insight into the behaviour of different layers in the lining when applying thermal loads. Considering the selection of materials used in the linings and their different thermal properties, a complex temperature distribution from the hot face to the exterior of the steel shell can be observed.
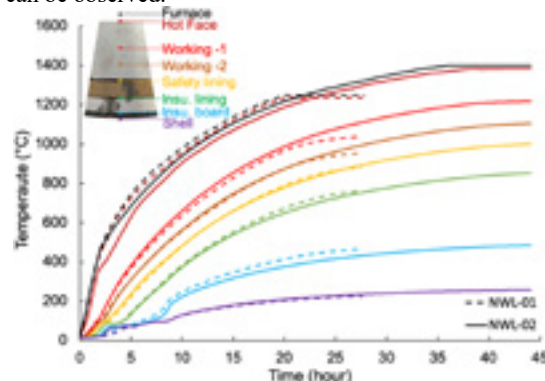


*Fig. 4: Average temperature evolution observed during experiments.*

As mentioned, the working lining is built with dry joints. Therefore, measurements were taken before and after the experiments on both specimens to observe the change in the joint thickness. Tab. 1 presents the measurements taken for the head joint at the hot face. The influence of the dry joint on the global behaviour can be observed through the strain gauges installed on the outer steel shell.

*Tab. 1:Change in the thickness of head joints.*

|  | NWL-01 | | NWL-02 | |
|---|---|---|---|---|
|  | Before | After | Before | After |
| Mean joint thickness (mm) | 0.32 | 0.40 | 0.23 | 0.47 |
| Standard deviation (mm) | 0.30 | 0.26 | 0.27 | 0.31 |
| Largest joint (mm) | 1.68 | 1.46 | 1.77 | 1.25 |

The performance of the steel shell is a critical issue in the behaviour of the refractory linings subjected to thermal loads. Fig. 5 shows the average mechanical strain observed in the circumferential direction through strain gauges on the exterior surface of the steel shell. The strain evolution confirms a highly nonlinear behaviour during thermal loading. During the early stage of the test, a slight increase in the strain can be observed. This increase can be attributed to the closing of the head joints in the working lining as well as the closing of the gap between the linings. Once these joints are closed, a steady growth in the strain can be observed till about the 20th hour. The effect of the joint thickness can also be noticed from the maximum strain observed. NWL-02 exhibits stiffer behaviour compared to NWL-01. This difference was expected as the average head joint thickness in the working lining is smaller for NWL-02 (0.23 mm) compared to NWL-01 (0.32 mm). After the 20th hour, strain reduction can be observed till the end of the test. In NWL-01, the maximum applied temperature was lower (1250°C) than NWL-02 (1400°C). Therefore, during the dwelling period for NWL-01, no significant drop in strain was observed. However, for NWL-02, despite a rise in applied temperature after the 20th hour (consequently an increase in thermal expansion), a gradual reduction in the strain was observed (from 0.57 to 0.48 mm/m). This reduction is due to the viscoplastic behaviour of the alumina spinel bricks in the working lining that becomes prominent after 1200°C.
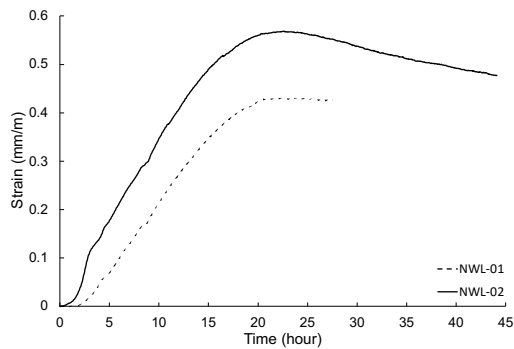
*Fig. 5: Average circumferential strain evolution.*

DIC analysis measures the total strain on an inspected surface. Under thermomechanical loading, the total strain comprises of elastic, thermal and inelastic strain. Fig. 6 shows the evolution of circumferential strain observed from DIC analysis on the steel shell. The figure also shows the expected thermal strain due to temperature rise in the steel shell and total strain (calculated thermal strain plus measured average strain from strain gauge). The total strain observed from the DIC shows similar behaviour as the calculated strain. The differences observed between the observed and calculated strain may be partly due to the hot air draft that affects the image captured by the camera, particularly when DIC values are lower.
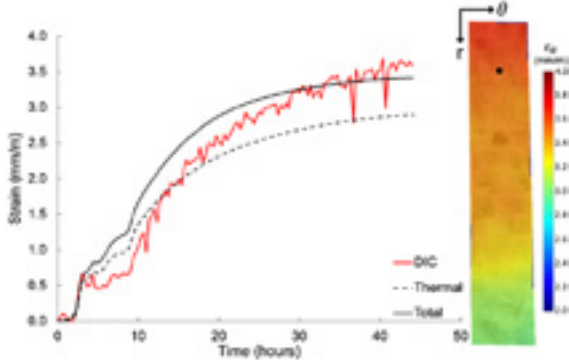


*Fig. 6: Circumferential strain evaluation at 250mm height of the shell and strain distribution at the 44th hour.*

Fig. 7 shows the evolution of the strains in the circumferential direction, measured at 25 mm and 130 mm from the hot face of the working lining brick. The values presented are the average strains observed from virtual extensometers at both bricks. The strain evolution shows an increase in strain at both locations as the temperature increases due to thermal expansion. The strain level observed at 25mm from HF is low compared to the expected 12 mm/m thermal strain. The difference is due to the combination of thermal expansion, onset of viscoplasticity and joint closing. However, the strain observed at 130 mm from HF is comparable with the thermal strain due to expansion at that location, 8.8 mm/m expected vs 7 mm/mm measured. This lower difference suggests less relevance of joint closing and no viscoplasticity at that location.
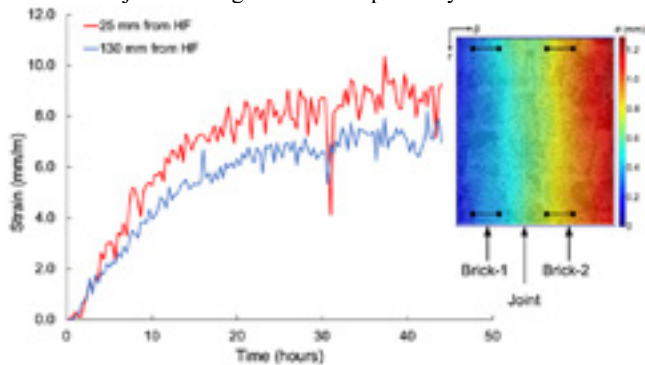


*Fig. 7: Circumferential strain evaluation at 25mm and 130mm from the hot face and displacement distribution at the 44th hour.*

## 4. VALIDATION OF NUMERICAL MODEL

Finite element models are often used to design or analyse steel ladles. Meso and macro modelling approaches are often used for this purpose. This work employed the meso modelling approach, where units (bricks) and joints are modelled separately. The model was made by taking advantage of the periodic geometry of the pilot ladle to reduce computational costs. Fig. 8 presents the 3D view of the meso model used and a plan view of the geometry showing the thicknesses of linings (mm).
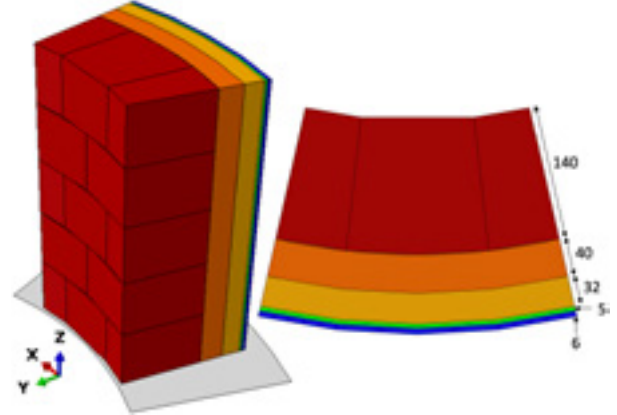


*Fig. 8: FE meso model of pilot ladle showing the 3D and top view.*

The analysis was performed using coupled thermal and mechanical analysis. The observed value of the furnace temperature was used as the thermal load at HF with a heat transfer coefficient of 600 W/m²K. The exterior face of the steel shell was exposed to room temperature with a heat transfer coefficient of 50 W/m²K. The thermal and mechanical properties of the materials were taken from [1,6]. For all the materials, temperature-dependent elasticity was used. Additionally, the viscoplastic behaviour of the working lining was used. The measured value of head and bed joints from test NWL-02 was used in the model for the working lining masonry. These joints follow an exponential closure behaviour as described in [2]. The model was supported in gravity by a rigid plate (allowing separation in tension) and a friction coefficient of 0.7. The temperature distribution obtained with the numerical model shows good agreement with the experimental result, as shown in Fig. 9. The result validates the thermal properties of the materials used in the model.
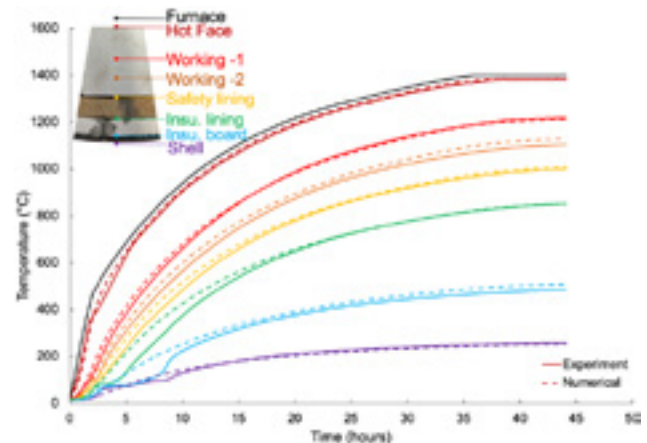


*Fig. 9: Temperature evolution in the FE model along with the experimental result of NWL-02.*

The evolution of circumferential strain in the steel shell of the FE model shows a good agreement with the experimental result, as shown in Fig. 10. The strain evolution can be expressed by the closing of the joints in working linings and gaps between the linings in the beginning. After joint closure, a steady rise in strain till the 20th hour, when the temperature at HF reaches 1200 °C. Afterwards, strain reduction can be observed. However, the drop in strain in the numerical model is not as prominent as in the experimental result.

This difference could be due to creep parameters used in the model, which requires further investigation.

Nevertheless, the obtained behaviour is well within the bounds of the experimental outcome. Fig. 10 presents the distribution of maximum principal creep strain in the working linings of the pilot. A strain concentration can be observed near the joints at HF, which is expected due to high-stress concentration. Higher creep strain can generally be noticed near the HF, and no creep at the CF of the working lining due to temperature distribution which influences the creep parameters.
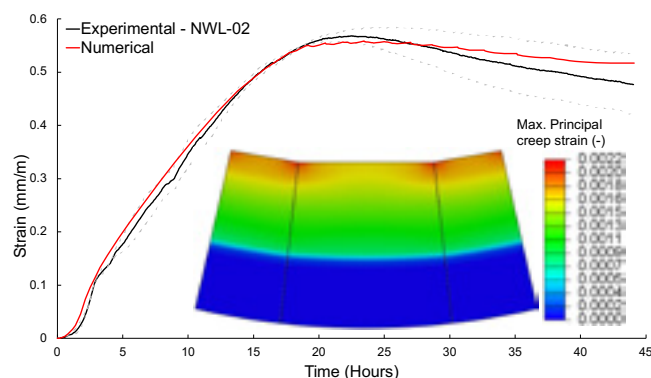


*Fig. 10: Circumferential strain evolution in steel shell in FE model and experiment along with distribution of creep strain in working lining at the 44th hour.*

Fig. 11 shows the evolution of total strain observed at the 25 mm from HF in working linings and the results obtained from the DIC analysis at that location. A good agreement between the results can be noticed. The figure also presents the total strain's thermal, elastic and creep strain components. As the applied temperature increases, a rise in thermal strain can be observed due to thermal expansion. After the joint closure, a build-up of elastic strain can be observed. An increase in the creep strain and, consequently, a reduction in the elastic strain can be observed once the temperature at that location reaches 1200 °C.



*Fig. 11: Evolution of circumferential strain and DIC result.*

## 5. CONCLUSION

Mortarless refractory masonry exhibits complex behaviour when subjected to high thermal loading, particularly with complex and multi-material industrial applications. Thus, characterising refractory masonry behaviour is essential for designing or investigating industrial vessels using it. Moreover, limited e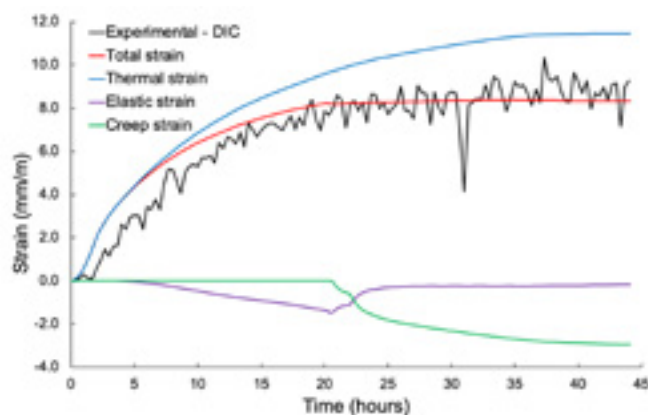xperimental works focusing on the thermomechanical characterisation of refractory masonry are available in the literature. This experimental campaign describes a novel simplified approach for the thermomechanical characterisation of a steel ladle's cylindrical shell without the constraints of ladle bottom and molten steel.

The thermal behaviour observed through various thermocouples presents a similar distribution of temperatures between the refractory linings for all tests. Tests performed on specimens with new working linings show the influence of evaporation of free water around 100 °C. The effect of the dry joint thickness can be observed by measuring mechanical strain in the circumferential direction on the exterior side of the steel shell. The working lining with a larger mean thickness of joints demonstrates lower strain on the steel shell than the lining with a small joint thickness. The effect of viscoplasticity that becomes prominent around 1200°C in working lining bricks was also observed through strain gauges on the steel shell.

The result presented here shows that the meso modelling approach provides a reliable response of the structure. This result also validates the various thermal and mechanical properties of the materials found in the literature. Moreover, this approach can be used to perform parametric analysis to identify critical material and geometric properties. Furthermore, the experimental and numerical outcome of this work can be used to validate other modelling approaches, such as homogenised macro models.

## REFERENCES
[1]     M. Ali, T. Sayet, A. Gasser, E. Blond, Transient Thermo-Mechanical Analysis of Steel Ladle Refractory Linings Using Mechanical Homogenization Approach, Ceramics 2020, Vol. 3, Pages 171-189. 3 (2020) 171–188. https://doi.org/10.3390/ceramics3020016.

[2]     P.N. Gajjar, P. Put, J.M. Pereira, B. Luchini, S. Sinnema, P.B. Lourenço, Characterisation of mortarless refractory masonry joints under elevated temperatures, Eng Struct. 275 (2023). https://doi.org/10.1016/J.ENGSTRUCT.2022.115234.

[3]     R.L.G. Oliveira, J.P.C. Rodrigues, J.M. Pereira, P.B. Lourenço, H.U. Marschall, Thermomechanical behaviour of refractory dry-stacked masonry walls under uniaxial compression, Eng Struct. 240 (2021). https://doi.org/10.1016/j.engstruct.2021.112361.

[4]     M. Ali, R.L.G. Oliveira, J.M. Pereira, J.P. Rodrigues, P.B. Lourenço, H. Ulrich Marschall, T. Sayet, A. Gasser, E. Blond, Experimental characterization of the nonlinear thermomechanical behaviour of refractory masonry with dry joints, Constr Build Mater. 364 (2023) 129960. https://doi.org/10.1016/J.CONBUILDMAT.2022.129960.

[5]     A. Gasser, J. Poirier, Thermomechanical testing of a laboratory pilot containing refractory masonries without mortar, Open Ceramics. 13 (2023). https://doi.org/10.1016/J.OCERAM.2022.100325.

[6]     P.N. Gajjar, M. Ali, T. Sayet, A. Gasser, E. Blond, J.M. Pereira, P.B. Lourenço, Numerical study on the nonlinear thermomechanical behaviour of refractory masonry with dry joints, Eng Struct. 291 (2023) 116468. https://doi.org/10.1016/J.ENGSTRUCT.2023.116468.

[7]     S. Samadi, S. Jin, H. Harmuth, Combined damaged elasticity and creep modeling of ceramics with wedge splitting tests, Ceram Int. 47 (2021) 25846–25853. https://doi.org/10.1016/J.CERAMINT.2021.05.315.

677

# DIGITALIZATION TO REALIZE AN AUTOMATIC AND CONTINUOUS REFRACTORY MAINTENANCE SYSTEM SCANTROL™ 4.0 FOR THE EAF

Rolf Lamm, Minteq International GmbH, Duisburg Germany

## ABSTRACT

The new requirements and challenges brought about by the transformation to "Green Steel" call for intelligent concepts in the production of steel. The increasing number of electric arc furnaces, accompanied by high competitive pressure, require steel producers to introduce innovative measures to reduce costs, CO2 emissions and improve safety.

The paper presents the latest development in digitalization to realize an automatic and continuous refractory maintenance system for the electric arc furnace (EAF), which is tailored to the requirements of contemporary steel production in a modern steel mill. The automatic system has eliminated the disadvantages of intermittent, personnel-intensive refractory maintenance and follows the "no person on the floor" safety philosophy. The functionality of the SCANTROL™ 4.0 system (laser scanner-controlled measurement of refractory thickness, visual display of scan results and intelligent material application of repair compound) has significantly improved productivity, working conditions and the decision-making ability of steelworkers.
The overall effect at the EAF steelplant has included:

- Reduction in total refractory consumption
- Increased furnace availability by reducing "Power Off" delays
- Improved operational safety
- Integration of the determined data into an "Industry 4.0" environment

## THE CONCEPT

The use of refractory materials is one of the main causes of downtime in electric steel plants. This applies both to the relining of the furnace and to the maintenance of the refractory materials by spraying and fettling. Classic maintenance by spraying requires very hard manual work with a hand lance in front of the furnace, which requires two employees. Already in 2003, the first fully automated refractory maintenance system from Minteq® was installed in a German steel mill. From then until today, a lot has happened technologically in laser scanning technology, analysis of measurement data, digitalization of results and repair spraying robots.
Today, a modern maintenance system for refractory linings consists of four main components (Fig. 1).



Fig. 1 Components of the fully automatic maintenance system

- LaCam® Laserscanner measures the residual refractory thickness of the furnace.
- SCANTROL™ interface module, linking the above-mentioned components, to evaluate the measurement data, analyse the application strategy and control the robotic maintenance unit.
- MINSCAN™ robotic maintenance system to repair the refractory lining in different areas of the EAF.
- High temperature video cameras provide additional safety, improved performance, and visual inspection capability.

These four components are combined in a mechanical robotic system, the LaCam® - MINSCAN™ manipulator. The spray materials, which are stored in silos and transported into the MINSCAN™ by batch guns, are specifically designed for improved flowability, wettability and plasticity. The unique particle size and binder package provide excellent adhesion to the furnace substrate, improving density at the wall and minimizing rebound. This increases the durability of the material, which in turn reduces maintenance and increases furnace availability.

## THE TECHNOLOGY

### LaCam® Laserscanner

The 5th generation LaCam® laser scanner technology, with more than 10 million measurement points per scan in one furnace, makes it possible to determine wear with a very high degree of accuracy. The laserscanner (Fig. 2) is designed to measure the refractory lining from the inside of the metallurgical vessel, by inserting the laser head into the metallurgical vessel itself. A huge improvement is that the laser scanner is inserted into the metallurgical vessel and scans the wall and at the same time the bottom of the vessel with a 360° rotation. This reduces the overall measuring time to less than a minute. The laser scanner, using the Time-of-Flight principle (TOF), sends out a series of short laser pulses organised in a highly collimated beam, in a well-defined direction. The pulses are partially and diffusely reflected by

targets and the receiver gathers backscattered optical echo signals and converts them into electrical signals. The receiver's electronics detects the targets even in the presence of dust and smoke thanks to the echo digitization with full waveform analysis (DSP-Technology).



**Laserscanner Specifications**

**Real Number of Range Points per Scan:** <10 Million
**Measuring Time per Frame (360°/120°):** < 16 sec. (selectable)
**Scan Angle:** vertical 120°; horizontal 360°
**Scan Frequency:** <900 kHz
**Max. Surface Temperature:** 1700°C /3092°F
**Dual Wavelength Pyrometer for Temperature Detection of Lining**

*Figure 2: Technical specification of the 5th generation LaCam® laser scanner with protection enclosure*

As a result, the distance between the scanner and the target points is computed with high accuracy. Additional measurement values, like laser echo amplitude and surface heat radiation, are recorded for each measurement point too. The heat radiation is measured at two separate wavelengths, which allows to take the full advantage of the high measurement accuracy offered by the two-colour (ratio) pyrometry. In combination with a high-sensitivity long-wavelength channel, a wide temperature range between 500 °C (932°F) and 1700 °C (3092°F) can be measured accurately and displayed in the form of a high-resolution thermographic image. Using the measurement data, a program precisely calculates the critical areas that need to be repaired. It also suggests the quality and required quantity of repair spray material. The information thus obtained is used to automatically control a spraying robot for repairing the refractory lining. This machine applies the repair mixes exactly where they are needed in the furnace.

**MINSCAN™ Gunning Head**
The gunning head can perform a continuous 360° rotational and simultaneous vertical movement from the furnace centre to the upper edge of the furnace water-cooling panels. (Fig. 3). Incorporated inside the gunning head is an eccentric jet mixing Minteq®'s patented nozzle designed to thoroughly wet the material at high speeds whilst preventing clogging and pipe drip. The gunning Capabilities are up to 250 kg/min wet material and up to 350 kg/min dry material. Advanced cooling technique ensures that the maintenance operation can operate continuously without any temperature restrictions. Maintenance of EAF is possible immediately after tapping and even possible with remaining steel in the furnace. The system enables precise, efficient, safe, and fast application of the gunning material.



*Fig. 3 MINSCAN™ Gunning Head in operation*

**High Temperature Video cameras**
During the gunning process, four video cameras film the performance of the gunning mix application. All camera images are displayed on a monitor in the control station for continuous observation. This provides additional information for monitoring the quality of the spraying process.

**LaCam® - MINSCAN™ Manipulator**
Two types of design are available: A system where the laser scanner and the gunning head are mounted on the same manipulator arm, which is attached to a tower column (Fig. 4), and a solution where one tower column supports two independent manipulator arms. Depending on the location and available space the selection is made. In both alternatives is the tower column located next to the furnace on the ground. The one manipulator arm set up with main components is shown in Fig. 4. The compact design does not require a big footprint on the floor. All movements of the manipulator are detected by high-precision sensors to enable reproducible movement.
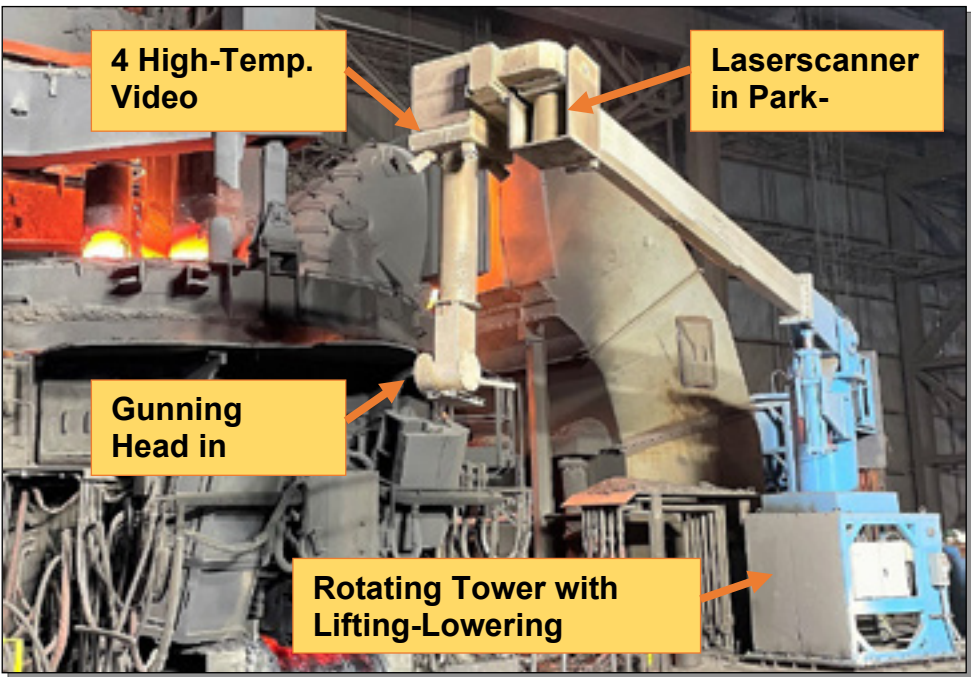
*Fig. 4: One manipulator arm set up*

**Interface between laser and manipulator: Scantrol™**
The SCANTROL™ interface module converts the measurement data from the laser scanner in such a way that this information is evaluated, and a maintenance strategy is derived from it to control the robotic maintenance unit (Fig.5).

**Evaluation**
The operator at the EAF triggers the measuring process. After the exact position of the furnace has been automatically determined from the laser measurement by means of 3D structure, the working lining measuring points are filtered out and transformed into a coordinate system for the furnace. The calculation of the residual brick thickness is based on a comparison profile (permanent lining).
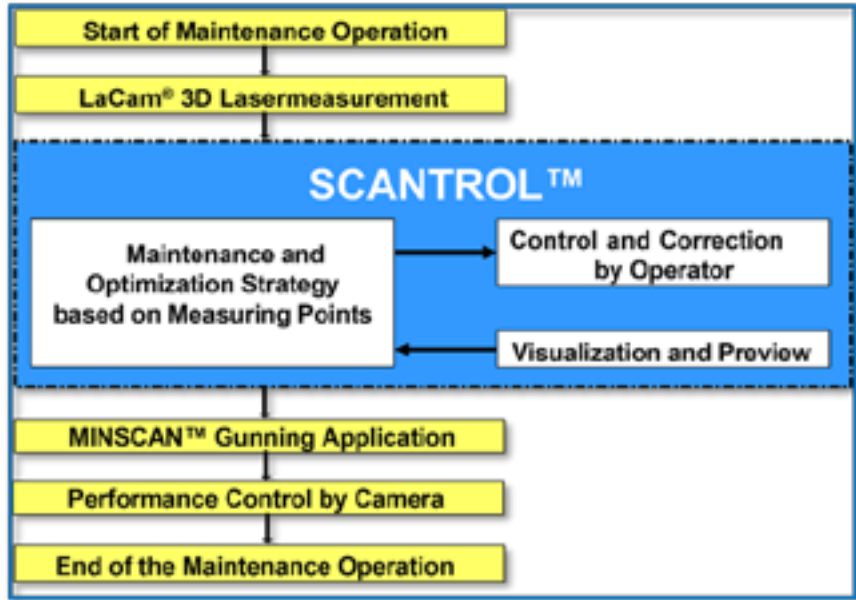


*Fig. 5 The maintenance process including Scantrol™*

The individual measurement points in high-resolution subfields, defined by cylindrical coordinates and evenly distributed over the area of the vessel potentially to be repaired, are then merged. The system determines the coordinates with minimum residual thickness in relation to sectors displayed in three dimensions. Based on thresholds defined by the operator for the allowable residual wall thicknesses per sector, the matrix of areas in need of repair is derived where the residual wall thickness is less than the respective threshold. The operator sets the optimisation sequence (duration, material consumption, degree of restoration) and starts the calculation of the optimised maintenance procedure so that the system carries out the maintenance automatically:
- Special matrix formulas combine the fragmented, high-resolution structures of the fields to be repaired into three-dimensionally coherent, compact structures.
- The size and sequence of the rectangular areas to be repaired, as well as the type of repair materials and the application quantity (application thickness), are determined using strategies for optimizing the time required, material consumption and degree of restoration,

and considering the physical properties of the mixtures used for the repair (application from bottom to top, setting time, maximum application thickness).
- The manipulator coordinates for the areas to be repaired are transmitted to the PLC unit of the MINSCAN™ system in the form of a telegram.
- The MINSCAN™ system performs its maintenance routine fully automatically, i.e., the correct product is applied "expertly" at the exact location in the desired layer thickness.

These parameters are integrated in the preventive maintenance programme, thereby harmonising consumption, and operating efficiency.

**Visualisation**

A monitor in the control pulpit is used for the visualisation of the measured residual refractory thicknesses and the parameters for the fully automatic maintenance process in the EAF. The measured residual refractory thicknesses are shown in the left-hand half of the display (Fig. 6). Visible on the right-hand side are the maintained areas or the thicknesses of the refractory after a pre-calculated, automatic maintenance process.
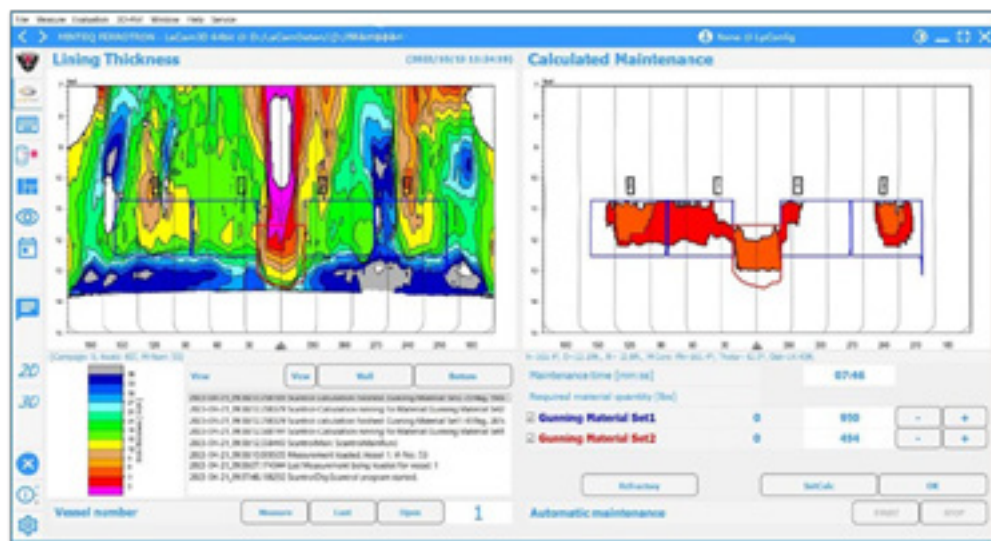


*Fig. 6 Main Screen of Scantrol™*

Here you can also read the proposed repair product, the required amount and the time needed for the application of the mass. The operator has the possibility at any time to adjust the maintenance process to the situation at the furnace. If he agrees with the proposed procedure, he can trigger the fully automatic repair from the control station. The exact measurements of the residual thickness in the whole furnace provide the operator with versatile information about the state of the refractory in wall and bottom. Profiles of the refractory wear in the EAF are being determined and evaluated online. The various colours symbolise the diverse residual thicknesses. Horizontal or vertical sectional images can be displayed at all angles. See Fig. 7
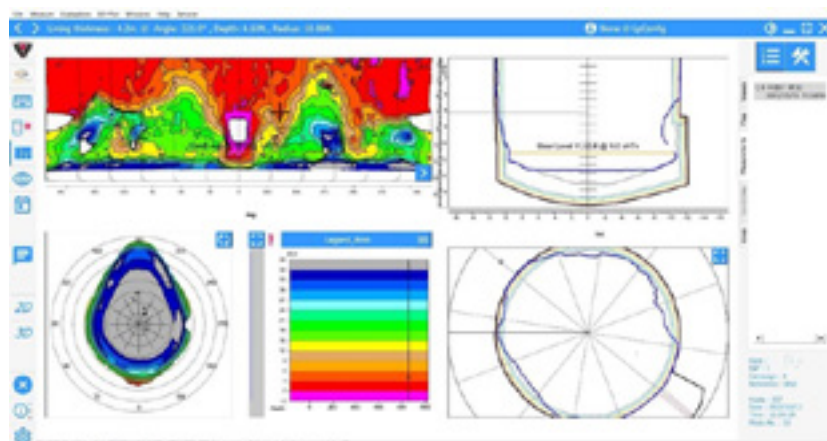


*Fig. 7 Presentation of measurement results (Wall, Bottom, Bathlevel) in different form*

**CONCLUSIONS**

The new generation of automatic and continuous refractory maintenance system SCANTROL™ 4.0 for the EAF takes subjectivity in gunning away from the operator as material applications governed by quantitative laser measurements. This more efficient refractory application reduces number of bricks relines and patches. It reduces the repairing time and refractory (kg/ton of steel) consumption. It provides increased furnace availability by reducing "Power Off" delays. Extra Power On time leads to increased heats and steel production. Due to remote operation safety conditions will improve – "NO PERSON ON THE FLOOR" Philosophy. Collecting and analyzing data from measurement systems and databases using the INDUSTRY 4.0 standards will allow steelplants to optimize production- and procurement processes to save on material-, energy- and $CO_2$ Emission-cost.

SHORT COMMUNICATIONS

# ADVANCED ANALYTICS APPLIED TO IMPROVE THE ENERGY EFFICIENCY OF STEEL LADLE LOGISTICS

V.S.P. Ruela[1,2], P. van Beurden[1], S. Sinnema[1], R. Hofmann[2], F. Birkelbach[2]

[1]Tata Steel Nederland, Velsen-Noord, The Netherlands
[2]TU Wien, Vienna, Austria

## ABSTRACT

Steelmaking is a highly complex and energy-intensive industry. With ever-increasing production demand, steel manufacturers must anticipate challenges and use innovative approaches to remain competitive while contributing to a sustainable future for the industry. Hence, leveraging advanced analytics tools has become vital to achieving more agile, integrated, optimized, and sustainable operations. Within the available tools, prescriptive analytics techniques can significantly enhance decision-making within steelmaking operations. In this context, one of the main levers to reduce the $CO_2$ emissions of steelmaking processes is to optimize the steel ladle logistics. We review current technologies and outline how advanced analytics can support this task.

Moreover, we discuss that to make good decisions on ladle deployment, precise predictions for the thermal state of the ladle for a given sequence of processing steps are required. Furthermore, the condition of the ladle lining and its remaining useful lifetime must be considered. A prescriptive analytics tool currently in development is presented. It enables the calculation of energy-efficient ladle schedules considering the lifetime and thermal state of the ladles. This initial contribution from the CESAREF European Project allows us to understand how to make better decisions and contribute toward more sustainable use of refractories in the steelmaking industry.

## INTRODUCTION

Steel ladles play an essential role in operating a steel plant, being responsible for moving hot metal from tapping at primary refining, undergoing secondary metallurgy treatment, and finally reaching the casting machines for producing the steel slabs. After casting, the ladles undergo several treatment processes until they are ready again to receive the hot metal. These operations define the so-called ladle cycle, depicted in Figure 1. Proper ladle availability and logistics management are critical aspects of the steelmaking process.
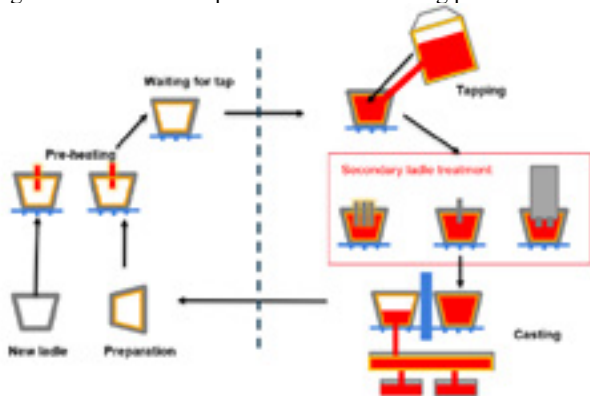


*Fig. 1: The steel ladle cycle*

Ladles are built with special refractory linings to transport molten steel at high temperatures. Three layers usually separate the molten steel from the ladle steel shell: the working, insulating, and safety linings. The working lining's choice of material and thickness is vital to achieving a trade-off between ladle capacity and its thermal capability [1]. The working lining is exposed to chemical, mechanical, and thermal sources of wear during its lifetime. This results in a reduction of its volume, which leads to different thermal properties over time. Thus, understanding the correlation between the remaining lifetime and heat-transfer mechanisms is a crucial aspect of achieving better control of the ladle's temperature and improving the overall energy efficiency of the steel plant.

## Motivation

The consideration of sustainability objectives, such as reducing the carbon footprint and energy consumption, has recently received much attention in industrial optimization applications [2]. In the steelmaking sector, optimizing the steel ladle logistics can be leveraged to improve energy efficiency. Inefficient ladle management can yield undesired results, such as (i) failure to achieve the production and quality targets, (ii) excessive energy losses, and (iii) reduction of the lifetime of the refractory lining. Hence, incorporating advanced analytics tools into the decision-making process is essential to achieve higher production demands while being energy efficient during the entire lifetime of the ladles.

## LITERATURE REVIEW

A relevant problem in the literature is the so-called steelmaking-continuous-casting (SSC) scheduling [3]. It can determine in what sequence, at what time, and on which device molten steel should be processed at the various production stages involved [4]. The usual formulation and solution of this problem are done within a static schedule for a given time horizon.

[3] presents a systematic review of the static SCC scheduling literature. The available methods differ mainly concerning the mathematical approach to their solution. They can be classified as:

1. Exact algorithms: These include branch & bound variants and decomposition approaches
2. Heuristics: These are mainly used to find a feasible solution quickly. It entails the use of greedy, local, and global search approaches.
3. Meta-heuristics: usually capable of obtaining good solutions, although they cannot guarantee optimality. Evolutionary computing techniques are often employed for this task.

Ladles are essential to the SCC scheduling problem since one must use them to transport the molten steel until it reaches the casting machines. However, the literature often overlooks their critical role in a steel plant [3]. Thus, more effort is required to advance the ladle scheduling problem, especially regarding energy efficiency. The most relevant ladle scheduling references are now briefly discussed. The SCC problem with ladle allocation decisions is described in [5]. Constraints regarding ladle maintenance, such as sanding and sliding plate change, are considered in the problem. A hybrid method that combines a meta-heuristic algorithm with a MIP solver was developed to tackle this problem. [6] presents an energy-efficient integrated SCC and ladle scheduling optimization problem. It considers the heating and waiting times during empty ladle operations. A tailor-made meta-heuristic was designed for its solution. [7] proposes and integrated planning and scheduling problem formulation. It includes a complete set of operational constraints and ladle allocation decisions. The Simulated Annealing (SA) algorithm is applied for its solution. Finally, [8] studies the ladle scheduling problem focusing on empty-ladle operations. It assumes that a production schedule is given and tries to optimize the allocation of ladles for that scenario. A genetic algorithm is proposed to solve the optimization problem.

## LADLE SCHEDULING OPTIMIZATION

A continuous-time mixed-integer linear programming (MILP) formulation of the ladle scheduling problem was developed to extend the existing related literature. It aims to minimize waiting times, heating times, and full ladle temperature losses while respecting the production plan and the stages a ladle must undergo after casting:

maintenance, warming, and waiting for tap. A steel ladle's reduced order model (ROM) calculates the refractory temperature. This model is an internal development of the Ceramics Research Center in Tata Steel IJmuiden, which has been extensively validated and is currently in use by other applications. The optimizer was developed using Python and the Pyomo modeling language [9]. Gurobi [10] is currently being employed for its solution. It requires a small amount of time to solve small to medium-sized instances. A web application was developed to allow the configuration and execution of different instances of the problem. It is then possible to evaluate other initial ladle conditions, such as the initial thermal state, lifetimes, and production plans. The application saves the optimization results of each instance in a database for later analysis.

A reporting section is also available, where users can quickly inspect the results of a single instance for the optimal schedule and predicted thermal profile of the ladles, as shown in Figure 2. For example, it is possible to identify the recommended operational practices within the resulting schedule and correlate them with the ladle temperature predictions. Moreover, constraints on the refractory temperature can be added to see how the logistics must be adapted to keep the refractory temperature in a particular range.
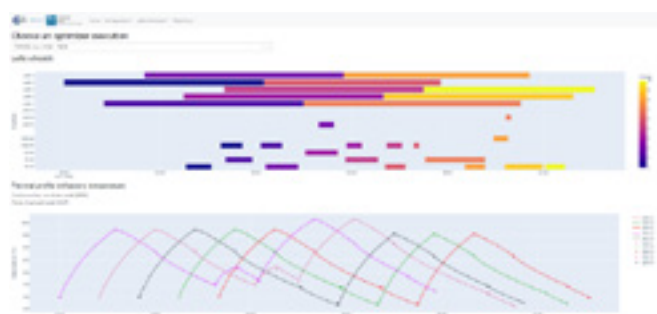


*Fig. 2: The schedule results view*

In a scenario comparison report (Figure 3), it is also possible to compare the potential savings between several instances regarding energy-efficiency metrics, such as heating times and ladle temperature losses. Furthermore, a visualization of the thermal model predictions enables the quick assessment of the ladle's average temperature over the scheduling horizon. Considering the current lifetime of a ladle fleet, it is possible to quickly compare the effect of the initial temperature and choose a ladle pre-heating practice that increases the process' energy efficiency.



*Fig. 3: The results comparison view*

## CONCLUSIONS

A prescriptive analytics tool to support the ladle scheduling was developed as an initial contribution of the CESAREF European Project. It solves a complex MILP scheduling problem incorporating the ladle's energy balance by leveraging a refractory temperature model developed in Tata Steel IJmuiden. Through a scenario-driven approach, evaluating and comparing the energy-efficiency metrics for different ladle configurations and production plans is possible. After this initial development, the tool already enables a step towards more sustainable ladle management regarding energy consumption and refractory usage. Future developments include improvements to the solution approach and User interface, optimization regarding

$CO_2$ emissions, and evaluation of the optimization model against production data.

## REFERENCES

[1] Tesselaar, W., Sluiter, A., & Peekel, M. (2019). Optimizing steel ladle logistics by predicting and understanding refractory wear. METEC-ESTAD proceedings.

[2] Li, M., & Wang, G. G. (2022). A review of green shop scheduling problem. Information Sciences, 589, 478–496. https://doi.org/10.1016/j.ins.2021.12.122

[3] García-Menéndez, D., Morán-Palacios, H., Ortega-Fernández, F., & Díaz-Piloñeta, M. (2020). Scheduling in Continuous Steelmaking Casting: A Systematic Review. ISIJ International, 60(6), 1097–1107. https://doi.org/10.2355/isijinternational.ISIJINT-2019-574

[4] Tang, L., Liu, J., Rong, A., & Yang, Z. (2000). A mathematical programming model for scheduling steelmaking-continuous casting production. European Journal of Operational Research, 120(2), 423–435. https://doi.org/10.1016/S0377-2217(99)00041-7

[5] Y. Tan, M. Zhou, Y. Zhang, X. Guo, L. Qi and Y. Wang, "Hybrid Scatter Search Algorithm for Optimal and Energy-Efficient Steelmaking-Continuous Casting," in IEEE Transactions on Automation Science and Engineering, vol. 17, no. 4, pp. 1814-1828, Oct. 2020, doi: 10.1109/TASE.2020.2979079.

[6] D. Han, Q. Tang, Z. Zhang and J. Cao, "Energy-Efficient Integration Optimization of Production Scheduling and Ladle Dispatching in Steelmaking Plants," in IEEE Access, vol. 8, pp. 176170-176187, 2020, doi: 10.1109/ACCESS.2020.3027018.

[7] Armellini, D., Borzone, P., Ceschia, S., di Gaspero, L., & Schaerf, A. (2020). Modeling and solving the steelmaking and casting scheduling problem. International Transactions in Operational Research, 27(1), 57–90. https://doi.org/10.1111/itor.12595

[8] Hong, Y. jie, Liu, Q., Yang, J. ping, Wang, J., Gao, S., & Li, H. hui. (2022). Genetic optimization of ladle scheduling in empty-ladle operation stage based on temperature drop control. Journal of Iron and Steel Research International, 29(4), 563–574. https://doi.org/10.1007/s42243-021-00668-1

[9] Hart, William E., Jean-Paul Watson, and David L. Woodruff. "Pyomo: modeling and solving mathematical programs in Python." *Mathematical Programming Computation* 3(3) (2011): 219-260.

[10] Gurobi Optimization, L.. (2023). Gurobi Optimizer Reference Manual.

# SHORT COMMUNICATIONS

# PREDICTION OF PERFORMANCE AND ASSESSMENT OF REUSABILITY AND RECYCLING OF REFRACTORY MATERIALS USING NON−DESTRUCTIVE ONLINE EVALUATION AND MACHINE LEARNING ALGORITHMS

Amit Kumar GOPE[1, 2] Alexandre Boulle[1], Marc Huger [1]
Johan Richaud[2], Severine Romero Baivier[2]
Felix Birkelbach[3], Lionel Rebouillat[4]

[1]University of Limoges, IRCER, UMR CNRS 7315, 12 rue Atlantis, Limoges 87068, France
[2]Vesuvius group plc, Department of Advanced Refractories, 17, Rue de Douvrain, B-7011 Ghlin, Belgium
[3]TU Wien, Institute for Energy Systems and Thermodynamics, Getreidemarkt 9/E302, 1060 Vienna, Austria
[4]Pyrotek Inc, Mineral Processing, Iron &amp; Steel Department, 2400 Bd Lemire, Drummondville, QC J2B 6X9, Canada

**ABSTRACT**

With short service life from tens of minutes to a few months due to the harsh conditions in Iron and Steel (I&S) making process, the refractory material consumption is substantial, leaving companies with significant challenges in the use, recycling, and disposal of these materials. In the current context of the European Green Deal, a Concerted European action on Sustainable Applications of REFractories (Doctoral Network CESAREF, www.cesaref.eu), has been launched in 2022 [1]. In order to develop better knowledge around refractory materials with regards to the new operating conditions requested by the drastic reduction of greenhouse gas emissions, improved energy efficiency, and by life cycle assessment requirements. The presented PhD study aims to predict refractory materials' evolution in service and determine their reusability (to optimize material lifetime) and reduce operational costs. For that purpose, the existing online sensoring systems will help obtain real-time data. Whereas the non-destructive evaluation methodologies will obtain the thermo-chemical-mechanical properties through experimentation, both the collected data and the experimental data will be analyzed by machine-learning algorithm. The final global target of this new approach is to develop an artificial intelligence model that can assess the reusability and recyclability of refractory parts. Such tools can, in the future, assist the end user in planning regarding the 4Rs (Reduce, Reuse, Recycle and Replace).

**Keywords:** Non-destructive evaluation**,** machine learning (ML) refractories, recycling, sensoring, sustainability.

## INTRODUCTION

Digitization has become a prominent trend across various industries, driven by ongoing technological advancements. The steel industry is no exception, as digitalization has started playing a significant role in its operations. In high-temperature industries, such as steel production, refractory linings for industrial vessels serve as a vital foundation for its working. Each industrial revolution has progressively enhanced the overall industrial process, leaving a significant impact on our daily lives and work environments. Now, we stand at the brink of the fourth industrial revolution, known as Industry 4.0, which aims to leverage smart technology for automating traditional manufacturing and industrial activities. This concept is still in development but encompasses technologies like digital twins, the Internet of Things (IoT), big data analytics, advanced robotics, cloud computing, machine learning (ML), and artificial intelligence (AI) [2].

Steel is a broad category of iron alloys with carbon content ranging from 0.002 to 2.14 wt%. The casting process is used to create steel, and today continuous casting is the most used technique, accounting for more than 96% of all steel produced [3]. The ladle, the tundish, and the cooling zone are the three essential components of a contemporary continuous casting system. The ladle is a large container for liquid steel that may hold tens to hundreds of tons of steel and is used to pour the liquid steel into the tundish. One heat is equal to the weight of the ladle, and one sequence is equal to the amount of heats one tundish can accomplish. The tundish serves as a molten steel reservoir and disperses the liquid metal into several casting molds where steel solidification is initiated. In the steel industry, tundish, which are crucial for providing molten steel at high temperatures during the continuous casting process, require specific refractory linings. These linings typically consist of three layers: working lining, insulating lining, and safety lining, serving as a barrier between the molten steel and the tundish shell.

The tundish is used to control flow and provide a constant output from irregular inputs by holding a tiny amount of molten steel while dispersing some of it elsewhere. The tundish serves several crucial functions in the process of molten steel handling, including molten steel distribution, buffering, flow control, purification, and heat loss mitigation. To effectively fulfill these functions, various refractory materials are employed within the tundish:

o To control and homogenize the flow of liquid metal inside the tundish, refractories are used. These components include purging plugs, wires, impact pads, and dams that help regulate the flow of the molten steel.

o Using refractories reduces energy waste and oxidation during the secure transfer of steel between reservoirs. These parts, which ensure the steel flows smoothly, include submerged entrance nozzles, submerged entry shrouds, and sliding gates.

o To ensure safety and save energy, refractories are used to separate and isolate the exterior steel shell from the molten steel. These set of refractories, also known as lining refractories, which form a barrier between the environment and the molten steel in order to protect it.

Combining large-scale machine-to-machine communication and IoT enables improved automation, connectivity, and self-monitoring. The selection of the working lining's material and thickness is of utmost importance. Over its lifespan, the working lining undergoes wear due to thermal, mechanical, and chemical factors, resulting in a reduction in volume and changes in its thermal characteristics over time. To effectively control the tundish's temperature and enhance overall energy efficiency in a steel plant, understanding the relationship between the remaining lifespan of the working lining and heat-transfer processes becomes crucial.

## MOTIVATION

Industrial optimization programs have recently paid a lot of attention to environmental goals, such as reducing carbon footprints and energy usage [4]. In the steelmaking sector, predicting the parameters of tundish, which will be leveraged to improve energy efficiency. Refractories are essential in high-temperature operations in today's industrial environment, assuring the durability and effectiveness of furnaces. Refractories need to be checked and maintained because of the constant wear and tear they undergo during the process in order to increase their efficacy and a long lifespan. Our project's goals are to investigate various online sensing tools for refractories, apply cutting-edge A.I. methods to forecast

refractory wear, use non-destructive testing techniques for data collection, and use monitoring and modeling techniques to make educated decisions about reduction, reuse, recycling, and recreation in order to address this challenge. We want to transform refractory management methods and promote sustainability in industrial operations by integrating these multidisciplinary techniques.



*Fig. 1: Process methods.*

**Goal 1:** Non-Destructive Testing for Experimental Data Collection to augment the accuracy and reliability of our predictive models, our project will incorporate non-destructive testing (NDT) methods for data collection. Techniques such as ultrasonic testing, laser vibrometer and magnetic particle inspection will be employed to obtain crucial information about refractory properties, including microstructural changes, material integrity, and the presence of defects. By integrating NDT into our data collection processes, we aim to enhance the fidelity and comprehensiveness of our predictive models [5].

**Goal 2:** Understanding Different Online Sensing Instruments for Refractories the initial purpose of our study is to completely examine and comprehend the array of online sensing techniques available for monitoring refractory conditions. We will explore technologies such as infrared thermography, acoustic emission sensors, and optical coherence tomography, among others, to collect real-time data on refractory health and performance. By gaining a deep understanding of these tools, we aim to enhance our ability to capture accurate and timely information about refractory wear [6].

**Goal 3**: Implementation of A.I. for Refractory Wear Prediction Utilizing machine learning algorithms and artificial intelligence, our project seeks to develop predictive models for refractory wear. By training these models on historical data collected from online sensors and non-destructive testing, we aim to create accurate and reliable predictions of refractory degradation patterns. These predictive insights will empower operators to proactively plan maintenance activities, minimize downtime, and optimize the lifespan of refractory materials, leading to substantial cost savings and increased operational efficiency [7].

**Goal 4**: Monitoring and Modeling Techniques for Informed Decision-Making The final objective of our project revolves around leveraging advanced monitoring and modeling techniques to derive valuable insights for decision-making. By continuously monitoring refractory conditions and analyzing data collected from online sensors and NDT methods, we aim to generate actionable information regarding the reduction, reuse, recycling, and recreation of refractory materials. These insights will facilitate evidence-based decision-making processes, enabling industrial stakeholders to adopt sustainable practices, optimize resource utilization, and minimize environmental impact [8].

We hope to revolutionize refractory management through our initiative by utilizing online sensing, artificial intelligence, non-destructive testing, and sophisticated modeling methods. We aim to

transform conventional refractory management practices and promote sustainable approaches in industrial operations by gaining a thorough understanding of refractory conditions, accurately forecasting wear patterns, using NDT for data collection, and making informed decisions about reduction, reuse, recycling, and recreation. The results of our experiment might fundamentally alter how refractories are used, monitored, and maintained, ultimately leading to greater operational effectiveness, lower costs, and a more sustainable future.

## LITERATURE STUDY

Machine learning, a component of artificial intelligence, enables computer systems to think as people do by learning from the past and improving on it. It operates by investigating data, spotting patterns, and formulating hypotheses. Data-driven strategies are what are used to classify AI today [9]. Data availability and accessibility are a result of the expansion of our technological infrastructure, which includes sensors, system logs, user logs, storage availability, etc. This information might include an image, a sound, text, machine RPM, the thickness of the refractory lining, campaign lengths, chemical components, etc.

For instance, a smart factory may generate different photographs of the product parts that are categorized as normal or faulty. The residual thickness of the refractory, which can be measured with a laser, production parameters like tapping temperature, processing time, lancing time, blowing time, maintenance data like the amount of mix used during gunning, and refractory lining like the type of material used can all be considered as input data in the case of refractory maintenance. A typical AI/ML model follow the following steps as depicted below;
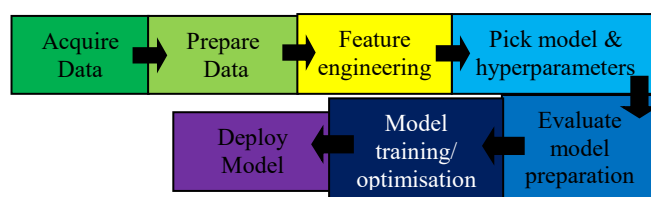


*Fig. 2: AI/ML Model.*

The quality of AI/ML outputs is determined by this crucial stage, which is highly significant. It controls how well the AI/ML model performs, determines its capacity to produce valuable insights, and ultimately determines how well the model can address the business issue.

Feature engineering is the following stage after data has been gathered and arranged in a certain way. The method of feature engineering, which draws on domain knowledge, is used to acquire features from unstructured data using data mining techniques. [10].



*Fig. 3: Sample data.*

In the context of refractory maintenance, characteristics of refractories like cold crushing strength at different temperatures, apparent porosity, bulk density, refractories, hot modulus of rupture, and thermal expansion of coefficient, workability, water addition percentage, Alkali resistance, and particular process parameters could be the features that have an impact on the refractory wear. The next step is to choose the appropriate machine learning algorithm model, where features are used as input data, such as linear classification, support vector machines (SVM), artificial neural

685

networks (ANN), convolution neural networks (CNN), logistic regression, K-mean, decision trees, random forests, etc [11].



*Fig. 4: Flowchart of proposed method.*

## RESEARCH FOCUS

Although the literature study describes several studies about the refractory from ladle and furnaces not from tundish, which gives us opportunity to explore through this project. The primary focus of this project is following:

1.  The use of Pearson's correlation coefficient assessment to lower the number of factors needed for tundish lining wear prediction to avoid data fitting.
2.  This doctoral study proposes an approach of the application of machine learning in the field of steelmaking industry.
3.  This study will end-up with an algorithm modal for evaluation of the online monitoring tool verified with an experimentation data for its accuracy.

## CONCLUSIONS

In order to meet the sustainability, circularity, and environmental impact objectives for 2050, the European Green Deal [12] has set significant technological and scientific challenges for the steel manufacturing industry. The CESAREF collaboration seeks to contribute to innovations in refractory materials for steelmaking that are transferable to other industries. The refractory materials used in the tundish linings will be the subject of this study. The determination of the crucial features to be evaluated in accordance with the criteria of the refractory application might be one of the potential solutions to address the European concerns while using the waste hierarchy as a reference point. This doctoral study focuses on the advancement of online sensing tools for refractories in the steel industry, utilizing artificial intelligence (AI) and machine learning techniques to develop a robust predictive model for refractory wear. The development of refractory wear models, accurate identification of the major wear affecting parameters, refractory benchmarking, and automated maintenance are all made possible by modern smart technologies. This model provides insights into the performance and lifespan of refractories, enabling proactive decision-making in reducing, reusing, recycling, or recreating refractory materials. Non-destructive testing techniques are also emphasized, providing

reliable and accurate data for informed analysis. The integration of monitoring and modeling tools enhances research findings, enabling informed decision-making processes. The findings have substantial implications for the sustainable operation of the steel industry, as predicting refractory wear and making well-informed decisions aligns with the industry's commitment to circular economy principles.

Maximizing refractory material utilization can boost resource efficiency and environmental performance. This increases safety, decreases refractory consumption, and enables plant operators to forecast the lifetime of the lining. These insights gained through monitoring and modeling approaches are help in deciding about the positive influence in decision-making processes, driving the transition towards a circular economy and responsible resource management.

## ACKNOWLEDGEMENT

## REFERENCES
[1]. CESAREF, Concerted European action on Sustainable Applications of REFractories, https://www.cesaref.eu/project/

[2]. Hou A, Jin S, Harmuth H, Gruber D. A method for steel ladle lining optimization applying thermomechanical modeling and Taguchi approaches. Jom. 2018 Nov; 70:2449-56

[3]. World Steel Association. Steel Statistical Yearbook 2022. (2022).

[4]. European Parliament, C. of the E. U. Directive 2008/98/EC of the European Parliament and of the Council of 19 November 2008 on waste and repealing certain Directives (Text with EEA relevance). (2008).

[5]. Williams, Royson Vaughan. Control and analysis in iron and steelmaking. Elsevier, 2016.

[6]. Yenus, Jaefer, Geoffrey Brooks, Michelle Dunn, and Rohini Kadam. "Application of vibration and sound signals in monitoring iron and steelmaking processes." Ironmaking & Steelmaking (2018).

[7]. Gao, C., Min, X., Fang, M., Tao, T., Zheng, X., Liu, Y., Wu, X. and Huang, Z., 2022. Innovative materials science via machine learning. Advanced Functional Materials, 32(1), p.2108044.

[8]. Backman, J., Kyllönen, V. and Helaakoski, H., 2019. Methods and tools of improving steel manufacturing processes: Current state and future methods. IFAC-PapersOnLine, 52(13), pp.1174-1179.

[9]. Kano, M. and Nakagawa, Y., 2008. Data-based process monitoring, process control, and quality improvement: Recent developments and applications in steel industry. Computers & Chemical Engineering, 32(1-2), pp.12-24.

[10]. Turner, C.R., Fuggetta, A., Lavazza, L. and Wolf, A.L., 1998, April. Feature engineering [software development]. In Proceedings Ninth International Workshop on Software Specification and Design (pp. 162-164). IEEE.

[11]. Mahesh, B., 2020. Machine learning algorithms-a review. International Journal of Science and Research (IJSR). [Internet], 9(1), pp.381-386.

[12]. Szpilko, D. and Ejdys, J., 2022. European Green Deal–research directions. a systematic literature reviews. Ekonomia i Środowisko, (2).

# MICRO-MECHANICAL MODELLING OF HETEROGENOUS MATERIALS CONTAINING MICROCRACKS WITH DISCRETE ELEMENT METHOD

Q. Pledel; M. Huger, D. André

IRCER / University of Limoges, Limoges , France

Refractories are ceramic materials resistant to very high temperatures. Used in environments with harsh solicitations, a better understanding between the macroscopic physical properties and the micro structural aspects is necessary to optimize their use. This work proposes to focus on the resistance to thermal shocks by micro mechanical modelling.

To do this, numerical simulations are performed to model the microcracking caused by the thermal expansion mismatch between the constituents and its influence on the non linear stress strain behavior of such materials. The work has been performed with GranOO, a soft ware using the discrete element method (DEM), to which is added a periodic homogenization method to consider the phenomena at microscopic scale on the macroscopic properties. The damage process is studied during the cooling of refractories materials in order to reproduce a multi cracked state and to understand the mechanisms depending on parameters such as the proportion of the constituents, their thermal expansion anisotropies and the geometry of the model. From these simulations, the main macroscopic mechanical properti es involved in the resistance to thermal shocks can be analyzed and related to the microcracking state of the system. These results are then compared with analytical models and experimental results. These developments allow a better understanding between microstructure and macroscopic behavior. This work envisages the potential of the discrete element method to predict the thermome chanical behavior of microcracked media.

Keywords: Refractories, Microcracks, DEM modelling, Thermal shock, Periodic homogenisation.

# DEVELOPMENT OF AN ORTHOTROPIC ELASTIC–VISCO–PLASTIC BEHAVIOUR LAW FOR THE THERMOMECHANICAL MODELLING OF REFRACTORY MASONRIES

Z. El-Alami, T. Sayet, A. Gasser

*Univ. Orléans, Univ. Tours, INSA-CVL, LaMé (EA 7494), 45072 Orléans, France*

**ABSTRACT**

Some refractory linings that protect metallic vessels from the hot temperature of the products they contain are made of masonries with dry joints (*i.e.* without mortar). The presence of these joints makes the behaviour of the masonry non-linear and orthotropic, allowing a free expansion during the first part of the temperature increase, reducing the stresses in the masonries. Since bricks have an elastic-visco-plastic behaviour at high temperature, it is necessary to develop an orthotropic elastic-visco-plastic behaviour law for the homogeneous material that has a behaviour equivalent to that of the brick and dry joint assembly. This non-linear behaviour is the origin of creep, that could be represented at the mesoscopic scale (brick and joint scale) by the well-known Norton-Bailey creep law. This law was in a previous study adapted to the macroscopic scale (masonry scale) for orthotropic secondary creep (with a constant creep strain rate). This study presents the adaptation of this law to primary creep for which the strain rate is not constant. The parameters of this new law are determined by a non-linear full-field homogenization technique. The identified law is then validated by comparing the results obtained by meso-modelling (bricks and joints are simulated) and macro-modelling (bricks and joints are replaced by the equivalent material) of an elementary periodic cell subjected to different loads.

## I. INTRODUCTION

Refractory materials are the best candidates for application in steel ladles due to their low thermal conductivity and thermal, chemical, and mechanical stability at elevated temperatures. In order to meet the mechanical, thermal and operational requirements, various refractory layers are used for ladle construction. Each layer serves a specific function and possesses unique thermophysical and mechanical properties. The layers include a work lining, a safety lining (also known as a permanent lining) and a steel shell (see Fig. 1a). The working lining is often made of mortarless refractory masonry. The safety lining consists of two layers: a dense refractory masonry with a mortar joint layer with low thermal conductivity, and a porous layer with lower thermal conductivity (insulation layer).
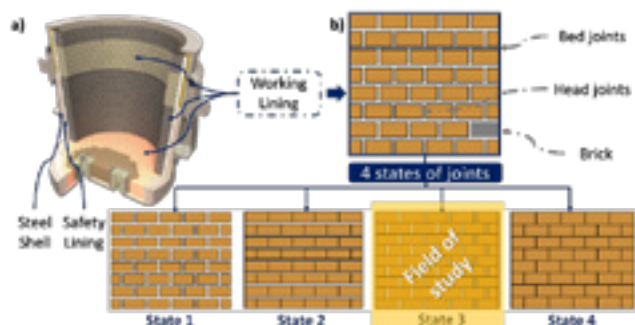


**Fig. 1:** (a) Schematic of a simplified steel ladle showing the different layers. (b) Schematic of the four states of dry joints.

### 1. Joint states

In this work, we are interested in the study of the working layer of the steel ladle, which consists of hundreds of refractory bricks, which are arranged periodically forming a periodic masonry with dry joints separating the bricks from each other. Often, these joints result from the shape, dimensional tolerances, and irregularities of brick surfaces. Two types of joints can be defined according to their orientation: head joints, and bed joints. These joints can close and

reopen, making the mechanical response of the mortarless refractory masonry variable under cyclic loading and unloading.

In order to consider the impact of joint closure and reopening on the behaviour of the brick and joint assembly, four possible joint states are predefined according to the closure or opening of head and bed joints (see Fig. 1b): the 1st state is characterized by open head and bed joints, the 2nd state is characterized by open bed joints and closed head joints, the 3rd state is the opposite of the 2nd, and the 4th state corresponds to the closure of all joints.

Each case corresponds to a different periodic structure and therefore to a different equivalent macroscopic behaviour. It is necessary to determine this equivalent macroscopic behaviour for each state. There are three out of four states which are extremely easy to identify:

- The 1st state: there is no stiffness in the plan of the masonry, since all the joints are open. However, in the direction perpendicular to the plane, the stiffness of the brick is present since there is only one brick in the thickness.
- The 2nd state: there is no stiffness in the vertical direction, but there is stiffness in the horizontal direction, which is equal to that of the brick.
- The 4th state: since all the joints are closed, the behaviour of the equivalent homogeneous medium is simply the same as that of the brick.

The only state for which it is not trivial to identify all the material parameters of the equivalent homogeneous medium of the masonry, is the 3rd state for which it will be necessary to use a homogenization technique in order to determine the parameters of the equivalent homogeneous medium.

### 2. Scale of study

No matter what material is considered, there is always a scale where its structure is heterogeneous. Refractory masonry can be presented in three scales of size (macroscopic, mesoscopic, and microscopic) as indicated in Fig. 2:

- Microscopic scale: at this scale, the heterogeneity of the brick is considered.
- Mesoscopic scale: at this scale, the interaction between bricks and joints is investigated on the assumption that the brick is made of a continuous material.
- Macroscopic scale: at this scale, the refractory masonry is considered as a continuous material, it is then modelled by a homogeneous solid.

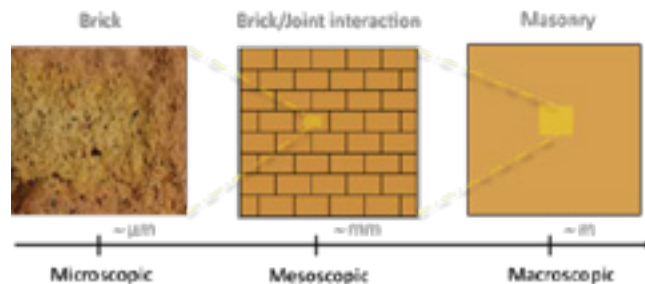

**Fig. 2:** The three characteristic scales of the studied masonry.

The benefit of the mesoscopic scale is that it can obtain both global results, such as the deformed state of the masonry, and local results, such as the deformations of bricks.

### 3. Full-field homogenization technique

When calculating a structure comprising a refractory masonry with dry joints and several hundreds or thousands of bricks, it is difficult to model every brick and every joint (problems of convergence and computation time). It is a homogenization technique that makes it possible to determine the behaviour of a homogeneous material that will have the same behaviour as all bricks and joints[1].
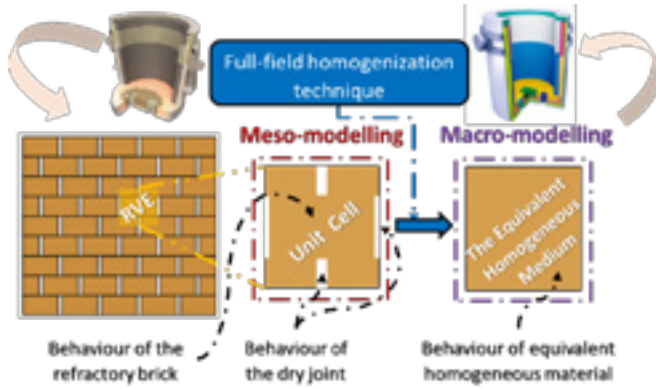


**Fig. 3:** Switch from meso to macro with full-field homogenization technique.

In order to study the homogeneous mechanical behaviour of refractory masonry in the 3$^{rd}$ state of dry joints (bed joints are closed and head joints open), the full-field homogenization technique based on the finite element method can be adopted. This homogenization technique allows us to go from meso-modelling (at the level of bricks and dry joints) to macro-modelling (at the level of the homogeneous medium equivalent to the studied masonry). It has the advantage of predicting both the effective properties of heterogeneous materials and the local-fields of stress and strain. This technique is based on the finite element simulation of a representative volume element (RVE).

First, we need to select a RVE of the masonry. In the case of a regular periodic masonry, the RVE is replaced by a unit cell (UC) which will reproduce periodically in both directions of the masonry plane (see Fig. 3). This unit cell is modelled using the meso-modelling approach (hence the need to describe the mechanical behaviour of the refractory brick) and subjected to boundary conditions resulting from the periodicity and a number of solicitations.

## II. CREEP MODELLING

In this section, the laws of creep behaviour in transient and steady state are presented in the form of the following two types of formulations:

- Local formulation: is used in meso-modelling to simulate the creep behaviour of the refractory brick for the purpose of identifying the parameters of the homogenized behaviour of the masonry.
- Macroscopic or homogenized formulation results from the full-field homogenization technique, it is used in the macro-modelling for simulating the behaviour of a homogeneous material equivalent to the set of bricks and joints.

### 1. Secondary creep
#### a. Local formulation

Secondary creep or steady-state creep is a period of time in which the rate of creep is constant. Bailey and Norton[2] have developed a model widely used to model secondary creep, which relates the creep strain rate $\dot{\varepsilon}_{ij}^{vp}$ to stresses using the following equation:

$$\dot{\bar{\bar{\varepsilon}}}^{vp} = \frac{3}{2}\bar{\bar{s}}\, A\, \sigma_{eq}^{n-1} \quad (1)$$

With $\dot{\varepsilon}_{ij}^{vp}$ is the viscoplastic strain rate

$\bar{\bar{s}}$ is the deviatoric component of the stress tensor $\bar{\bar{\sigma}}$

$\sigma_{eq}$ is the equivalent Von Mises stress

A, n are temperature-dependent material parameters

### b. Macroscopic or homogenized formulation

Due to the presence of open head joints, the macroscopic elastic-visco-plastic behaviour law of UC must be orthotropic. There is a homogenized orthotropic steady-state creep law of heterogeneous solids developed by Tsuda and al.[3]. The main advantage of this behaviour law is that by using the same creep parameters of the base material, the orthotropic homogenized viscoplastic behaviour of heterogeneous solids can be found. The behaviour law is obtained by averaging the local fields on the UC volume and using a stress concentration tensor based on the following equation:

$$\dot{\bar{\bar{E}}}^{vp} = \frac{1}{2}\,A\,(\Sigma_{eq})^{n-1}\bar{\bar{\bar{N}}}:\bar{\bar{\Sigma}} \quad (2)$$

Where A and n are the material parameters of the bricks, reported in Tab. 3, and:

$\bar{\bar{\Sigma}}$ is the macroscopic stress

$\Sigma_{eq}=\sqrt{\frac{1}{2}\,(\bar{\bar{\Sigma}})^{T}:\bar{\bar{\bar{N}}}:\bar{\bar{\Sigma}}}$ is the equivalent macroscopic stress

$\bar{\bar{\bar{N}}}$ is the stress concentration tensor that can be represented by a second order tensor $\bar{\bar{N}}$ using the vector notations of stress and strain tensors:

$$\bar{\bar{N}}=\begin{bmatrix} N_{11} & N_{12} & N_{13} & 0 & 0 & 0 \\ N_{12} & N_{22} & N_{23} & 0 & 0 & 0 \\ N_{13} & N_{23} & N_{33} & 0 & 0 & 0 \\ 0 & 0 & 0 & N_{44} & 0 & 0 \\ 0 & 0 & 0 & 0 & N_{55} & 0 \\ 0 & 0 & 0 & 0 & 0 & N_{66} \end{bmatrix} \quad (3)$$

The tensor $\bar{\bar{N}}$ is symmetric and is characterized by 9 non-zero components, which can be determined (Tab. 1) by combining the uniaxial tensile loads along the 3 directions of space and simple shear loads within the three planes of space.



**Tab. 1:** Expressions of concentration tensor $\bar{\bar{N}}$ constituents in secondary creep.

### 2. Primary creep
#### a. Local formulation

Primary or transient creep is a period in which the creep rate drops. Bailey and Norton have developed a model currently used to model

primary and secondary creep, which links the creep strain rate to the stresses by means of the following equation:

$$\overline{\dot{\varepsilon}}^{vp} = \frac{3}{2}\,\overline{\overline{s}}\,mA^{\frac{1}{m}}\,\sigma_{eq}^{\frac{n}{m}-1}\left(\int\sqrt{\frac{2}{3}\dot{\varepsilon}_{ij}^{vp}\dot{\varepsilon}_{ij}^{vp}}\,dt\right)^{\frac{m-1}{m}} \quad (4)$$

Where A, n and m are temperature-dependent material parameters (for the case of secondary creep, $m = 1$).

### b. Macroscopic or homogenized formulation

The behaviour law that has been developed at the LaMé laboratory to account for primary creep is written as follows:

$$\overline{\overline{E}}^{vp} = \frac{1}{2}\,mA^{\frac{1}{m}}\,(\Sigma_{eq})^{\frac{n}{m}-1}\overline{\overline{\overline{N}}}:\overline{\Sigma}\left(\int\sqrt{2\left(\overline{\overline{E}}^{vp}\right)^T:\left(\overline{\overline{\overline{N}}}\right)^{-1}:\overline{\overline{E}}^{vp}}\,dt\right)^{\frac{m-1}{m}} \quad (5)$$

With A, n and m are the material parameters of the bricks, reported in Tab. 3 (the secondary creep macroscopic formula may be recovered for m=1).

Tab. 2 summarizes the expressions of the tensor $\overline{\overline{\overline{N}}}$ components identified for each of the six applied loads, based on the macroscopic viscoplastic strain rate $\dot{E}_{ij}^{vp}$ and the macroscopic viscoplastic strains $E_{ij}^{vp}$.



**Tab. 2:** Expressions of concentration tensor $\overline{\overline{\overline{N}}}$ constituents in primary creep.

| Mechanical parameters of the brick forming the UC | | |
|---|---|---|
| Elasticity parameters | E=11000 MPa | υ=0.2 |
| Norton Bailey creep law parameters at 1000°C | A=2.77×10⁻⁸ s⁻¹ MPA⁻ⁿ | n=2.8 m=0.8 |

**Tab. 3:** Elasticity and creep parameters of the studied brick.

### 3. Principle of homogeneous formulation of primary and secondary creep

Considering that the local creep law of Norton Bailey only depends on the time and the applied stress, by analogy, the macroscopic creep law will also depend only on time and the applied macroscopic stress (see Fig. 4a).

The homogenization theory provides a tensor which links mesoscopic stresses to macroscopic stresses, called stress concentration tensor $\overline{\overline{\overline{N}}}$. This tensor has an orthotropic form since the masonry itself has an equivalent orthotropic behaviour due to the closure and opening of the head and bed joints. It should be noted

that the tensor $\overline{\overline{\overline{N}}}$ has 9 unknowns, which means that 9 loading cases need to be applied in order to identify its components.

However, the viscoplastic incompressibility condition of macroscopic viscoplastic strains ($\text{tr}\left(\overline{\overline{E}}^{vp}\right) = E_{11}^{vp} + E_{22}^{vp} + E_{33}^{vp} = 0$) makes it possible to reduce the number of unknowns from 9 to 6 (see Fig. 4b).

The viscoplastic incompressibility condition does not matter for pure
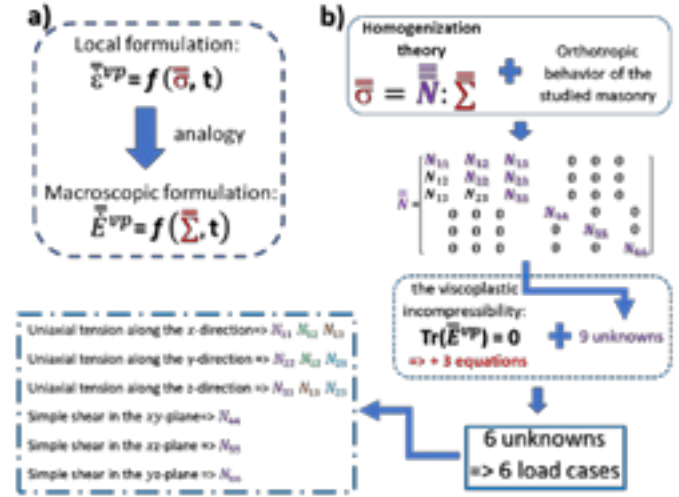


**Fig. 4:** (a) Similarity between local and homogenized creep formulations. (b) Principle of homogeneous formulation of primary and secondary creep.

shear tests. However, it must be checked and taken into account for uniaxial tensile tests in the 3 directions of space.

### 4. Methodology for evaluating effective meso-model behaviour

To implement the law of macroscopic creep in a finite element code, it is first necessary to determine by six load cases the 6 components of the tensor $\overline{\overline{\overline{N}}}$ for transient and permanent creep. All six load cases are simulated using meso-modelling (see Fig. 5a), with a UC subjected to the conditions resulting from the periodicity and a number of uniaxial stresses of 1.5MPa based on each of the six load cases.

The presence of open dry joints in the UC model leads to a discontinuity in the displacement field, given that the local strains within the placement of these joints are unknown (due to lack of viscosity and stiffness in the volume corresponding to dry joints). Therefore, the homogenized (or macro) strains $E_{ij}$ cannot be computed by integrating the local (or meso) strains $\varepsilon_{ij}$ over the volume of the unit cell ($V_{UC}$) according to [4]:

$$E_{ij} = \frac{1}{V_{UC}}\iiint \varepsilon_{ij}(x, y, z)\,dv \quad (6)$$

For this reason, in the current study, the homogenized strains are calculated from the average variation of the displacements of the corners of the UC [5], i.e. by dividing the variation of the displacements of the corners by the initial dimensions of the UC.
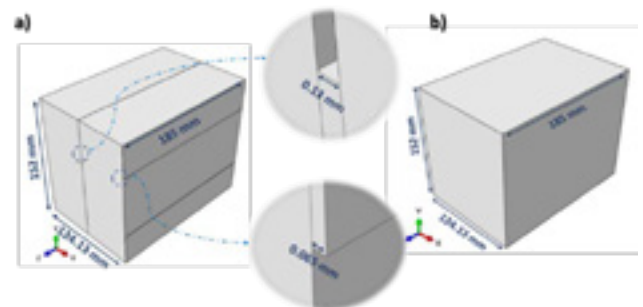


**Fig. 5:** UC geometry modelling: (a) Meso-model, (b) Macro-model.

Once the individual tensor $\overline{\overline{N}}$ components have been identified for both creep rates, macroscopic modelling can be used to simulate the equivalent homogeneous behaviour of the masonry (see Fig. 5b).

derivation have a considerable influence on the values of the stress concentration tensor components.
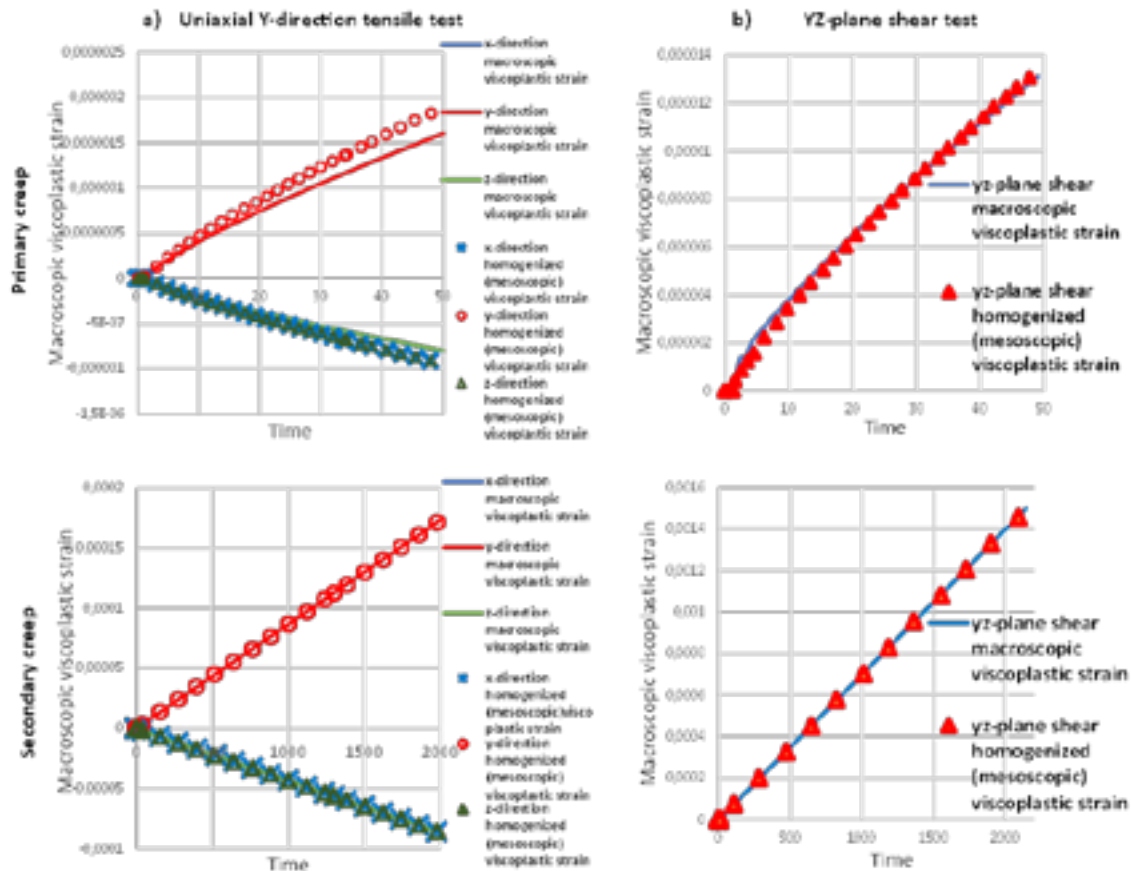


**Fig. 6:** Comparison of the macroscopic viscoplastic strain field between the Meso/Macro model for primary and secondary creep: (a) uniaxial Y-direction tensile test, (b) YZ-plane shear test.

## III. RESULTS AND DISCUSSION

With the aim of verifying the robustness and relevance of the macroscopic creep behaviour law in transient and stationary mode, a comparison is carried out between the simulation results of macro-modelling and meso-modelling for a uniaxial y-direction tensile test and an yz-plane simple shear test (see Fig. 6). By visualizing the curves obtained, it can be seen that the viscoplastic incompressibility is respected, and a very good correlations are obtained using the secondary macroscopic creep law, whereas less good correlations are obtained with the primary macroscopic creep law. This due to errors generated by the numerical derivation of homogenized viscoplastic strains $E_{ij}^{vp}$ in order to obtain homogenized viscoplastic strain rates $\dot{E}_{ij}^{vp}$. It should be noted that the numerical derivation problem was not encountered during the secondary creep simulation, because it is characterized by a steady rate of homogenized viscoplastic strain, whereas for primary creep, the homogenized viscoplastic strain rate gradually decreases over time. Subsequently, the error in the numerical derivation accumulates as time goes by, causing fluctuations of the identified components of the tensor $\overline{\overline{N}}$.

It must be noted that the tensor $\overline{\overline{N}}$ components are constant in secondary creep because they depend only on the macroscopic viscoplastic strain rate $\dot{E}_{ij}^{vp}$, which is constant during this period (Fig. 4). In addition, the tensor $\overline{\overline{N}}$ components evolve in the primary creep, because they depend on both the macroscopic viscoplastic strain $E_{ij}^{vp}$ and the macroscopic viscoplastic strain rate $\dot{E}_{ij}^{vp}$, which, in turn, change within that period (Tab. 2).

The error of the numerical derivation decreases as the simulation accuracy increases. It is a matter of finding the critical time step: $\Delta t_{crtical}$, above which the fluctuations caused by the numerical

## IV. CONCLUSIONS

A homogenized orthotropic creep behaviour law was proposed to model the primary and secondary creep behaviour of masonries without mortar at high temperature. It was identified using a meso-modelling of the periodic cell. The proposed law gives good correlations for primary creep and slightly poorer correlations for secondary creep. This is due to the fluctuations generated during the numerical derivation of the homogenized viscoplastic strain field, which are on the one hand high and increasing in primary creep, and on the other hand stable in secondary creep, because the viscoplastic strain rate is constant in the stationary creep regime and decreasing in the transient creep regime.

## REFERENCES

[1] M. A. A. Ali, Nonlinear thermomechanical modelling of refractory masonry linings, PhD thesis, University of Orléans, France, 2021. https://www.theses.fr/2021ORLE3197

[2] J. Betten, Creep Mechanics, in Applied Mechanics Reviews, Springer, 2004. doi: 10.1115/1.1584417.

[3] M. Tsuda, T. Asada, N. Ohno, T. Igari, Homogenized elastic-viscoplastic behavior of plate-fin structures at high temperatures, Int. Conf. Comput. Exp. Eng. Sci., 10 (3), 2-2, 2009, doi: 10.3970/icces.2009.010.097.

[4] C. T. Sun, R. S. Vaidya, Prediction of composite properties from a representative volume element, Compos. Sci. Technol., 56 (2), p. 171-179, 1996, doi: 10.1016/0266-3538(95)00141-7.

[5] N. Ohno, K. Narita, D. Okumura, Homogenized elastic–viscoplastic behavior of plate-fin structures with two pore pressures, Int. J. Mech. Sci., 86, p. 18-25, 2014, doi: 10.1016/j.ijmecsci.2013.10.015.

# FE MODELLING OF REFRACTORIES' MATERIAL PROPERTIES BASED ON 3D MICROSTRUCTURAL ANALYSIS

S. Pirkelmann, S. Sharba, G. Seifert, H. Friedrich, F. Raether
Fraunhofer HTL, Bayreuth, Germany

## ABSTRACT

This paper presents a simulation-based approach to evaluate the mechanical strength of refractory materials by investigating the influence of the material's structural composition on component failure. A neural network is trained and applied for image segmentation of 3D computed tomography images of refractory samples, enabling the identification of different material components. Structural properties, such as phase fractions, porosity, grain sizes, and their spatial distributions, are extracted from the segmented images. Finite element analyses are then conducted to assess the impact of mechanical loads on the material. The relationship between the identified structural properties and the probability of failure is evaluated, providing insights into material reliability. The approach is demonstrated using commercially available B80 and SP78 refractory materials.

## INTRODUCTION

The drive towards climate neutrality necessitates the quick optimization of thermal processes in terms of energy and material efficiency. Refractories play a crucial role in achieving these goals not only by enhancing functionality and prolonging service life but also by improving performance with reduced wear, and increased strength. These improvements enable the construction of lighter and more efficient structures, further contributing to energy savings and sustainability. In the systematic development of sustainable refractory materials, simulation-based methods offer significant advantages by reducing time and experimental effort. Consequently, understanding the behavior of refractory materials under stress becomes paramount, as it provides essential insights for optimizing their performance and reliability in a wide range of applications.

This paper aims to address the challenge of evaluating the mechanical strength of refractory materials by investigating the influence of material composition on component failure. By employing simulation-based techniques, it becomes possible to identify critical structural elements that contribute to component failure under various loads. The goal is to improve the reliability of new refractory materials by avoiding these critical elements.

The paper is structured as follows. The methodology begins with the acquisition of computed tomography (CT) imagery of refractory samples, allowing for non-destructive characterization of the material's microstructure. Subsequently, an image segmentation approach using a neural network is employed to accurately identify and classify the main structural components of the refractory material.

Following the segmentation, representative volume elements (RVEs) are extracted from the segmentation data and converted into meshes, enabling their utilization in finite element simulations. Finite element simulations are then conducted to analyze the stress increase within the RVEs when subjected to externally applied tensile strain, providing insights into the material's response to mechanical loading. Furthermore, macroscopic simulations of damage are performed using a 3-point bending simulation, allowing for an assessment of the material's behavior at a larger scale.

## NON-DESTRUCTIVE ANALYSIS OF REFRACTORY SAMPLES

### Computed Tomography imagery of B80 and SP78 refractories

We demonstrate our method using commercially available refractories: a dense refractory brick made of Bauxite B80 and a dense high alumina brick made of synthetic magnesia spinels with a high clay content Alurath SP 78. Cylindrical samples of 5 mm height and 33 mm diameter have been cut from the as-received refractory bricks. The resolution of the CT images is 24µm. Figure 1a) shows a slice through the CT image of a B80 material. The image clearly shows the very inhomogeneous microstructural compositions of the refractory material. The total volume of the samples is about 4.3cm$^3$ which is sufficiently large to be representative of the material at hand.
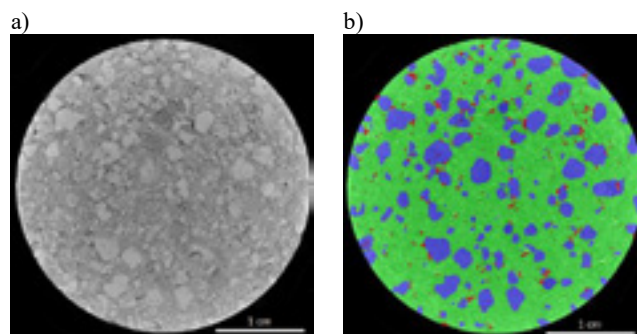


*Fig. 1a): Computed tomography image of a sample of B80 refractory material with a resolution of 1518 x 1483 x 276 voxels. A single slice of the image in the z-axis is displayed. b) Segmentation image as generated by nnUNet algorithm. Different colors indicate the distinct structural components of the material: pores are shown in red, course-grained inclusions in blue, fine-grained matrix in green, background in black.*

### Material analysis and 3D-image segmentation using convolutional neural networks

From the CT images, three main structural components of the refractory samples can be distinguished: pores (dark regions), coarse-grained inclusions (distinct light regions), and a fine-grained matrix in between. The structural and chemical composition of the various components of the B80 refractory was determined through scanning electron microscope (SEM) and X-ray diffraction (XRD) analysis. The analysis revealed that the B80 material consists of 61.8% Al2O3 (Corundum), 33.5% 3Al2O3-2SiO2 (Mullite), 4.6% Al2TiO5 (Tialite), with traces of other compounds. The material exhibits a complex structural composition, with distinct coarse grains made up primarily of Corundum with inclusions of either Mullite or Tialite, and varying degree of porosity. The matrix phase essentially shares the same composition but has a high degree of micro-porosity below the threshold resolution of the CT imaging.

A convolutional neural network has been trained to automate the process of generating 3D-segmentations of the CT images, assigning to each voxel of the input image a corresponding class (background, pore, distinct coarse grain, or matrix). nnUNet has been chosen for its proven effectiveness in image segmentation tasks [1]. The algorithm was trained using manually generated training data from a single B80 image, consisting of a volume of 1152×1152×64 voxels. Despite the relatively small training volume, the implementation of data augmentation strategies in nnUNet ensured the generation of high-quality segmentations. Additionally, custom variations of the input data were incorporated to replicate common CT image artifacts, enhancing the algorithm's robustness to diverse imaging conditions. The resulting segmentation, showcased in Figure 1b), demonstrates the effectiveness of the approach in accurately identifying and classifying the structural components within the B80 refractory material. The segmentation model was also applied to CT

images of the SP78 material. Despite not being specifically trained on this material, the model demonstrates excellent segmentation performance, yielding accurate results.

**Analysis of structural composition**

The segmentation data is used to analyze the structural composition of refractory materials. We can derive various quantities from the segmentation results such as the volume fractions of grains, pores and matrix phase, the size and local distribution of inclusions, and the orientation of particles within the matrix phase. This information can be used to compare different samples and materials based on their microstructure. To illustrate this, Figure 2 shows the volume fractions, porosity and average grain size for the B80 and SP78 samples, respectively. Note that the reported porosity only includes critical macroscopic pores that are detectable in the CT images and does not capture the much higher micro-porosity of > 10% according to density measurements.
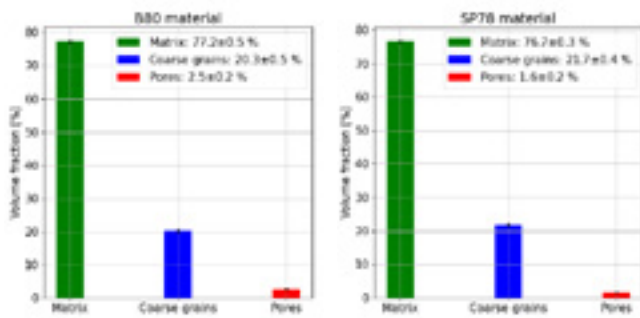


*Fig. 2: Volume fractions of pores, distinct coarse grains and matrix for B80 and SP78 material.*

Homogenized mechanical properties of the main structural components of the B80 material were estimated using mixture rules, as listed in Table 1. to ensure the accurate modelling of the material's behaviour under stress in the simulations.

*Tab. 1: Material data used in microstructure simulations as estimated by mixture rules based on input data from the Material Property Database (MPDB) [2].*

| Component | Young's modulus [GPa] | Poisson ratio |
|---|---|---|
| Coarse grains | 320 | 0.22 |
| Matrix phase | 95 | 0.22 |

**FINITE-ELEMENT-BASED CHARACTERIZATION OF MATERIAL STRENGTH**

To quantify the failure probability of a given refractory material under external load we apply finite element simulations. The analysis is focused on the B80 material, but similar investigations could be conducted for SP78.

We follow a multi-scale approach: on the micro-scale we calculate an approximate distribution of fracture stress using microstructure simulations based on representative volume elements (RVEs) extracted from the CT image segmentation data from above. The resulting distribution then serves as an input to a macro-scale simulation of a three-point bending experiment from which we can estimate the failure probability of the material.

**Mesh generation from volumetric data**

For the simulations on the micro-scale, we cut out numerous RVEs with a resolution of 125 x 125 x 125 voxels, each corresponding to a volume of 27 mm³, from the segmentation image of the refractory, cf. Figure 3. For each RVE, the volumetric data is converted to a mesh for use in finite element (FE) analysis using the CGAL library [3] and subsequent simulation in Ansys APDL.
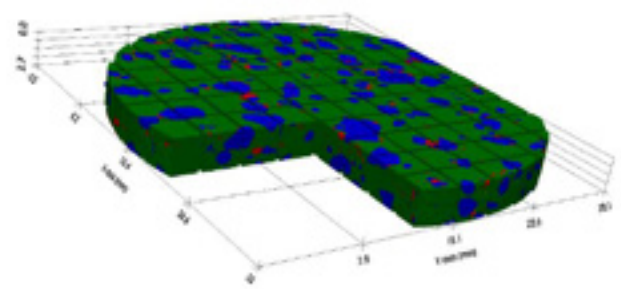


*Fig. 3: Illustration of multiple representative volume elements cut from the segmented CT image of a B80 sample.*

**Tensile strain simulations on micro-scale**

For each RVE, finite element simulations of linear elasticity were performed to determine the relative stress-increase factor compared to a defined external stress. In these simulations, a specified tensile strain was applied to the RVE, corresponding to a reference stress of 1 MPa. If structural defects such as pores are present within the RVE, the surrounding material has to bear the additional stress, resulting in localized regions of elevated stress within the material. To quantify the stress increase, the 99th percentile of the volume-weighted first principal stress in the matrix phase of each RVE was measured. This value was then used to compute a local stress increase factor by calculating the ratio between this percentile and the reference stress. In addition to the stress increase, an equivalent local stiffness is calculated for each RVE structure. By employing automated scripting, this procedure was iteratively applied to all RVEs, enabling the computation of a representative distribution of local stress increases across the material. Figure 4 shows the resulting distribution of stress increase from the simulation of approx. 400 RVEs of the B80 material.

The distribution of local stress increase is mapped to a distribution of fracture stresses which is used in damage simulations as discussed in the following section.
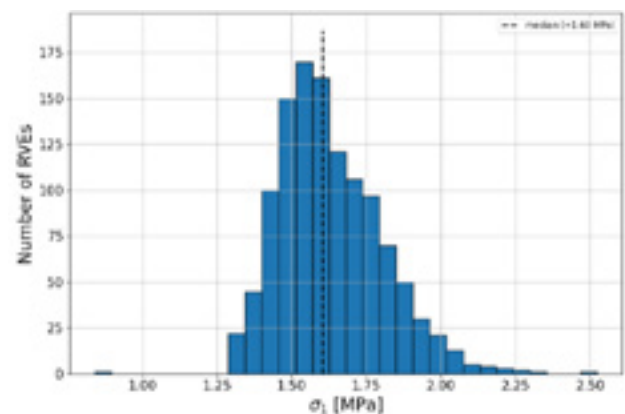


*Fig. 4: Histogram of the stress increase of individual RVEs when applying an external tensile strain corresponding to a stress of 1 MPa to opposite faces of the RVE.*

**Macro-scale simulation of 3-point-bending**

The scatter of bending strength of the refractory material is evaluated using a virtual three-point bending test as illustrated in Figure 5. The bending strength is computed using finite element analysis (FEA) with the goal of comparing it with experiments and eventually using FEA directly to evaluate the failure distribution of complex structures. The model accounts for microscopic elasticity via coupling the effective properties of the microscopic representative volume elements with a macroscopic model of a three-point bending test.

*Fig. 5: Illustration of a finite element model of the three-point bending test.*

On the macroscopic scale, an isotropic damage model that influences the stress-strain relationship is implemented as a user programmable feature (UPF) in Ansys [4, 5, 6]. The stress-strain relation is represented as

$$\boldsymbol{\sigma} = (1 - D)\,\mathbb{C}\,\boldsymbol{\varepsilon}\,,$$

where $\boldsymbol{\sigma}$ is the Cauchy stress tensor, $\boldsymbol{\varepsilon}$ denotes the strain tensor, $\mathbb{C}$ represents the fourth-order elasticity tensor and $D \in [0,1]$ is the damage variable, $D = 0$ corresponds to the undamaged state and $D = 1$ represents the fully damaged states.

The damage evolution is implicitly expressed by the following equation:

$$D(\kappa) = 1 - \frac{\kappa_0}{\kappa} e^{-\frac{\sigma_F h_e}{G_F}(\kappa - \kappa_0)},$$

where $\kappa$ is the maximum value of the equivalent strain experienced during the loading history, $\kappa_0$ represents the critical equivalent strain beyond which damage is initiated, $h_e$ represents the characteristic length associated with the element size in the FEA, $\sigma_F$ represents the fracture stress, and $G_F$ represents the fracture energy. A key point here is to use a modified equivalent von Mises strain from [5, 7] to evaluate $\kappa$. The modified version differentiates between tensile and compressive scenarios on the top and lower surfaces of the beam. This strain is given by the following expression:

$$\kappa = \frac{k-1}{2k(1-2v)} I_1 + \frac{1}{2k}\sqrt{\left(\frac{k-1}{1-2v} I_1\right)^2 + \frac{12k}{(1+v)^2} J_2}\,,$$

where $v$ represents the Poisson ratio, $k$ represents the ratio of tensile to compressive strength, $I_1$ represents the first invariant of the strain tensor, and $J_2$ represents the second invariant of the deviatoric strain tensor. Moreover, the critical equivalent strain $\kappa_0$ is determined by

$$\kappa_0 = \sigma_F \frac{(1+v)(1-2v)}{E(1-v)}.$$
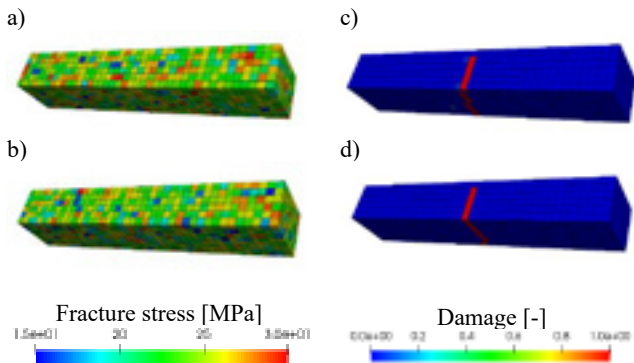


*Fig. 6): a, b) fracture stress distribution of two randomly chosen beam models, where fracture stress in each element is coming from the underlying RVE. c, d) the corresponding damage evolution pattern given identical loading conditions.*

To study the scatter of the bending strength and the effect of the microstructure on this scatter, various simulations are carried out with RVEs assigned in a random manner to each element of the beam model in order to reflect the inhomogeneous material/pore distribution. In other words, the material properties of each element come from a pool of RVEs resulting in beams with different fracture stress distributions, as seen in Figure 6a and Figure 6b.

Examining the corresponding damage distribution and crack path in Figure 6c and Figure 6d, the effect of the fracture stress distribution on the failure pattern and consequently on the bending strength (15.2 MPa and 14.9 MPa) can be seen. The fracture stress distribution around the center of the lower surface has a profound effect on the results as this is the location of the highest tensile stress. The simulation is run 45 times to allow statistical evaluation of the results. A Weibull distribution is fitted to the resulting bending stresses with a mean of 14.6 MPa and a standard deviation of 0.66 MPa. The mean is in good agreement with experimentally observed values of 14.8 MPa from in-house data. However, the standard deviation is further away from the experimental value of 1.25 MPa. The difference may be due to a limited fracture stress distribution that does not fully reflect reality. Further investigation could, for example, directly calculate the fracture stress in each RVE by simulation, thus reducing the dependence on the available experimental data.

**CONCLUSIONS**

We have presented a simulation-based approach to evaluating the failure probability of refractories for mechanical loads based on their microstructure composition. Using this method, it becomes possible to rapidly compare different refractory materials based on data from CT imagery, eliminating the need for costly and time-consuming destructive testing. This will enable more rapid iterations when designing new refractory materials. In a future work, more detailed investigation on the scatter of bending strength will be carried out and then the resulting failure distribution obtained using FEA will be validated against an experimental setup.

**REFERENCES**

[1] Isensee, F., Jaeger, P. F., Kohl, S. A., Petersen, J., & Maier-Hein, K. H. (2021). "nnU-Net: a self-configuring method for deep learning-based biomedical image segmentation." Nature methods, 18(2), 203-211.

[2] MPDB (Material Properties Database) v9.17, 2022. [Online], https://www.jahm.com/ (accessed 14 July 2023).

[3] P. Alliez, C. Jamin, L. Rineau, S. Tayeb, J. Tournois, and M. Yvinec, "3D Mesh Generation," in CGAL User and Reference Manual, 5.5.2 edition, CGAL Editorial Board, 2023. [Online], https://doc.cgal.org/5.5.2/Manual/packages.html#PkgMesh3 (accessed 14 July 2023).

[4] Ozaki, S., Nakamura, M., & Osada, T. (2020). Finite element analysis of the fracture statistics of self-healing ceramics. Science and Technology of Advanced Materials, 21(1), 609-625.

[5] Kurumatani, M., Terada, K., Kato, J., Kyoya, T., & Kashiyama, K. (2016). An isotropic damage model based on fracture mechanics for concrete. Engineering Fracture Mechanics, 155, 49-66.

[6] Oliver, J. (1989). A consistent characteristic length for smeared cracking models. International Journal for Numerical Methods in Engineering, 28(2), 461-474.

[7] Ozaki, S., Yamagata, K., Ito, C., Kohata, T., & Osada, T. (2022). Finite element analysis of fracture behavior in ceramics: Prediction of strength distribution using microstructural features. Journal of the American Ceramic Society, 105(3), 2182-2195.

# MULTISCALE MODELING OF GAS–SLAG–REFRACTORY INTERACTIONS AND DEGRADATION MECHANISMS

A. Laukkanen, T. Andersson, M. Lindroos, E. Huttunen-Saarivirta
VTT Technical Research Centre of Finland Ltd., Espoo, Finland

E-P. Heikkinen, R. Mattila, V-V. Visuri
University of Oulu, Oulu, Finland

M. Lindgren
Metso, Pori, Finland

**ABSTRACT**
Refractories interacting with molten slags and gaseous process environments can be unexpectedly compromised with respect to their durability and display complex failure modes. We focus particularly on degradation mechanisms resulting in catastrophic refractory brick failure due to formation of multiple reaction zones and chemical reactivity taking place within its respective microstructure. In order to address this complex micromechanism, we propose and demonstrate a multiscale modeling approach which accounts for the various mechanistic couplings between the material and the operating environment at the scale of the material microstructure. Focus of the work is in full field representation of material microstructure that is seen critical in order to be able to reproduce the observed failure mechanisms computationally. Use case work with bricks seen use in flash smelting operation is presented and the modeling results are compared to experimental and characterization results, the outcome is seen to be overall in compliance and comparable to the respective findings. The work demonstrates how addressing the refractory degradation modeling problem as a multiphysical and multiscale one yields improved ability to evaluate performance against challenging durability and lifetime limiting process conditions.

**INTRODUCTION**
Degradation of refractory materials in pyrometallurgical processes involves a complex set of mechanisms including loadings that are typically multiphysical in nature, from a modeling perspective it can involve chemo-transport, thermomechanics and material damage in a strongly coupled manner over the refractory lining's lifetime. Similarly, the problem can be argued to be multiscale, several of the mechanisms and resulting effects having their origins in the microstructural scale of the materials. However, presently the most successful approaches in addressing refractories interacting with molten slags or gaseous process environments are typically based on thermodynamical Calphad methods, which albeit have proven reliable in estimating, e.g., chemical wear behavior, are forced to simplify the problem considerably as far as accounting for the complex interplay of different physical phenomena at different scales. In order to be able to address complex failure models and investigate the interactions between the different coupled phenomena, we present a full field modeling concept and toolset which can incorporate many of the features typically neglected by thermodynamical equilibrium approaches. The aim the work is to improve the prediction of refractory degradation and failure and followingly provide a sound basis for refractory selection for new designs and process conditions.

695

**COMPUTATIONAL METHODS**
The concept of the multiscale modeling framework is summarized in Fig. 1. The objective is to enable the implementation and deployment of numerical high-performance computing (HPC) workflows which are able to address refractory degradation in a multiscale and multiphysical context. In this sense, it means that coupled problems can be addressed which involve interactions between transport, chemistry, thermomechanics and degradation (e.g., by cracking) of refractories in conditions of relevance to industrial processes. The implementation of the respective material behaviors and evolution laws is performed in a full field microstructural setting, by making use of microstructural modeling toolsets presented in more detail in [1-2]. Fig. 1 if interpreted as a sequential modeling workflow presents the simplest analysis scenario where no complex interrelations between the solutions steps are present, but the analysis is in essentially a sequence of data transfers between the modeling solvers addressing the differing physical phenomena. If divided to such a sequence, typically the analysis initiates from the evaluation of transport mechanisms, chemistry and phase transformations taking place within the refractory domain. Process conditions and their evolution in time, i.e., the conditions at the outer surface of the brick exposed to the respective environment and thermal histories arising from operation, are considered given by either other types of models or measurements.
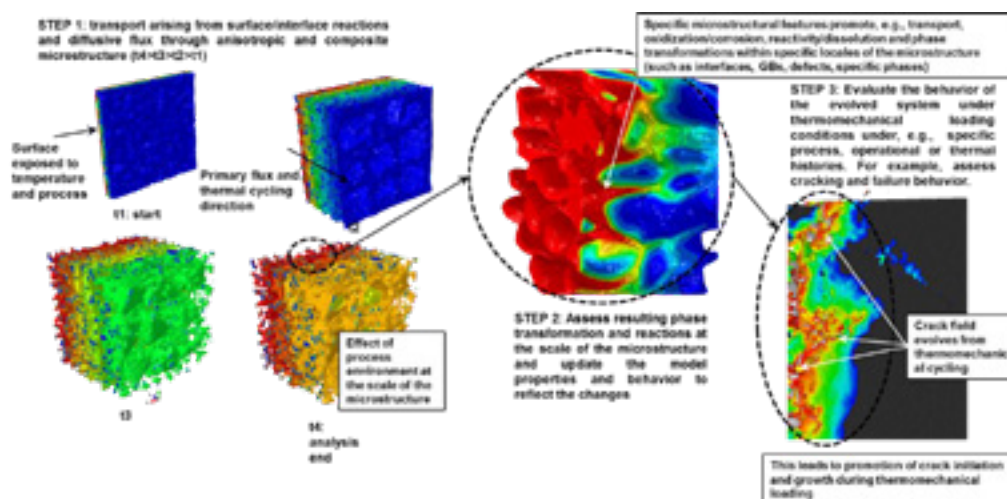


*Fig. 1: Modeling concept and simplified sequential analysis sequence between the different physical phenomena.*

As a tightly coupled problem the thermal solution is typically performed for process initial and boundary conditions and over the smelter wall to establish the respective conditions influencing the transport problem. The transport problem is addressed as a multi-phase one as all the other steps as well, i.e., microstructural and phase specific characteristics are included. During the solution of the transport problem, local elemental concentrations are utilized to address phase changes and formation of new compounds due to process species interacting with the refractory phases. Parallel to addressing the evolution and transport within the microstructure, the thermomechanical problem is solved to address thermally induced stresses and those arising from mechanical loading. This solution is updated and fed into the effects arising from the solution of the chemo-transport problem. This stage necessitates typically a coupling to experimental work to address the mechanical properties of the updated microstructure, typically by way of incorporating the results of small scale mechanical tests (or alternatively, lower scale model couplings). Followingly, damage and possible cracking are addressed, typically by way of cleavage fracture models seen compatible with the behavior of the rather brittle ceramic phases. If nucleation and growth of cracks is predicted, this typically necessitates a model update as cracks couple strongly to the chemo-transport and thermomechanical problems. This is carried out by adaptively remeshing the solution domain and remapping the last time increment results to the new, modified, material microstructure. In practise, the model update can be done in steps by specifying criteria for model changes or updates over time which constitute significant enough couplings to push interactions within the co-simulation (e.g., coupling the selection to species and thermal diffusivity).

Typically, this form of modeling where the degradation process is interpreted as a unidirectional sequence of events is not sufficient to consider the degradation process with the necessary physical consistency, but rather, interactions between chemo-transport, phase transformations and the formation of new compounds, thermomechanics and degradation via crack nucleation and growth arise. For example, it is easy to see that if new compounds are formed this influences the respective properties across the physics being solved, or, if cracking takes place, it significantly influences transport mechanisms within the microstructure, let alone further accumulation of damage. To enable the solution of the degradation problem in a sufficiently realistic setting, the different physics-solutions can be coupled and time-integrated differently in time. This can mean direct coupling of solvers (although this leads to a prohibitively costly numerical computation) or a co-simulation type of an approach adopted in current work, where the different solutions are propagated in time and enabled to frequently interact during the solution process. As an example, the phase distribution arising from the solution of chemo-transport and evolving over solution is updated for the thermomechanical solution to capture the respective effects to, e.g., mechanical behavior of the refractory microstructure. The toolset is implemented primarily by making use of the Moose framework [3] as a basis, which as a multiphysical and adaptive mesh refinement finite element (FE) development environment enables one to develop different levels and types of couplings making also use of its build-in capabilities for linking different physics kernels. Computational workflows can be executed sequentially or with stronger degrees of coupling and concurrency. The outcomes can be upscaled to engineering material properties by way of, e.g., numerical homogenization methods as in present work, and data from lower scale methods can be included to specifics of microstructure scale models if seen of benefit. Methods such as Calphad calculations can be coupled directly or indirectly by making use of the APIs of the respective tools, current implementation interfaces to [4-5]. With respect to many of the inputs, thermodynamical and mobility databases are utilized [4-5] for the solid phases, additionally, the influence of the pore network is accounted for. In addition, the experimental and characterization activities contributing the current work are summarized in [6-7].

## RESULTS AND DISCUSSION

The studied magnesia-chromite refractory and its microstructure obtained by way of micro-computed tomography (µCT) imaging is presented in Fig. 2, further details of the characterization are provided in [6-7]. The primary phases that are resolved by segmenting the µCT image with the aid of scanning electron microscopy (SEM) and X-ray diffraction (XRD) results are the magnesia MgO and spinel $(Mg,Fe)(Al,Cr)_2O_4$ phases. Additionally, porosity is included explicitly in the imaging-based models as in the µCT results. Multiples of the microstructure are utilized in modeling as synthetic microstructures to obtain domains of large enough in size to extract results comparable to experimental ones.
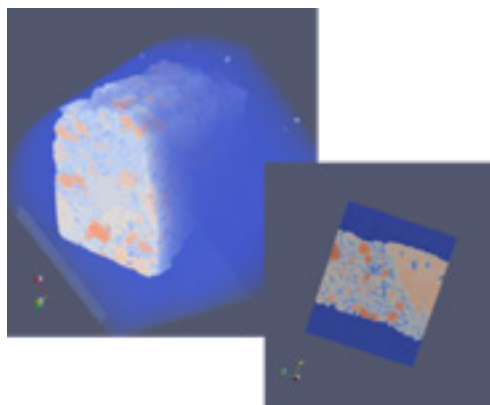


*Fig. 2: Segmented model input of magnesia-chromite refractory based on µCT results.*

The aim of the simulation is to evaluate the degradation and failure of refractories, in current case addressing particularly a case where gaseous species from process atmosphere can exhibit transport over the microstructure and pores particularly considering sulfur dioxide, leading to the formation of reactions zones consisting of calcium and magnesium sulfates. Different analysis cases have been investigated: loading of the refractories at operational temperatures uniformly and investigating failure behavior, assessing the infiltration and development of reaction zones within the brick, and lastly, assessing fracture of reacted bricks subjected to the gaseous atmosphere during fast thermal cycling. The results for micromechanical modeling of refractory failure and the development of reaction zones are summarized in following. For comparing the reaction zones and distribution of compounds across the refractory a process boundary condition is defined exposing the microstructure to a gaseous environment and the changes within the microstructural domain can subsequently be investigated.

Firstly, results are presented in Fig. 3 when the refractory is loaded at an operational temperature of 1350°C (corresponding roughly to, e.g., copper and nickel flash smelting furnaces) by uniform applied tensile loading. The mismatch in properties between the magnesia and spinel phases yields a heterogeneous distribution of stress within the microstructure (stresses given in MPa). It is also noted that the pores within the refractory contribute to the local stress concentrations, as can be expected. The damage in current case is particularly promoted by the pore network in relation to the spinel phases running across the refractory microstructure and contributing to the localization of damage. Results of an analysis simulating the formation of reaction zones is presented in Fig. 4, the chemo-transport and resulting microstructure infiltration leading to a formation of calcium and magnesium sulfates. The outermost region is considered to primary correspond to a reaction zone already within the refractory brick, as the formation of the outer deposit layer visible in experiments [6-7] and containing elements of the feed materials is partially neglected with the current set of initial and boundary conditions.
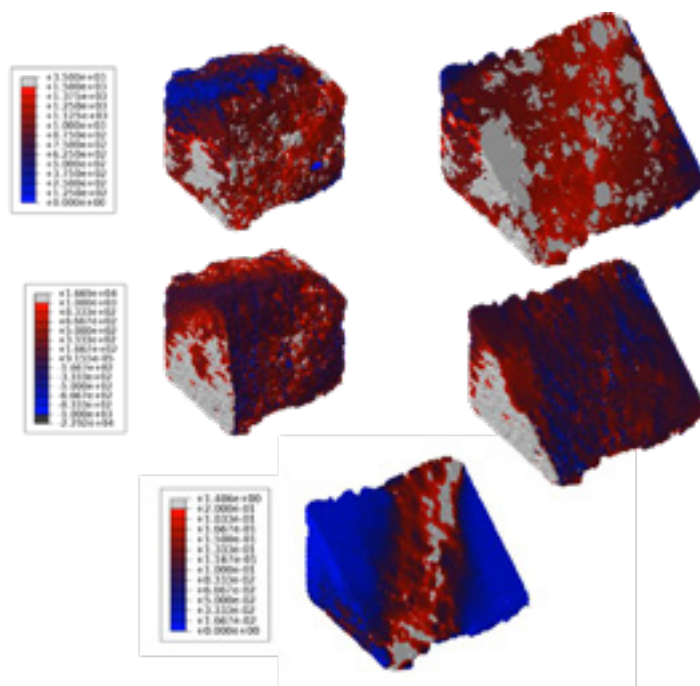


*Fig. 3: Uniform loading of the refractory at a temperature of 1350°C: equivalent stress (top), first principal stress (middle) and damage when reaching failure (bottom).*
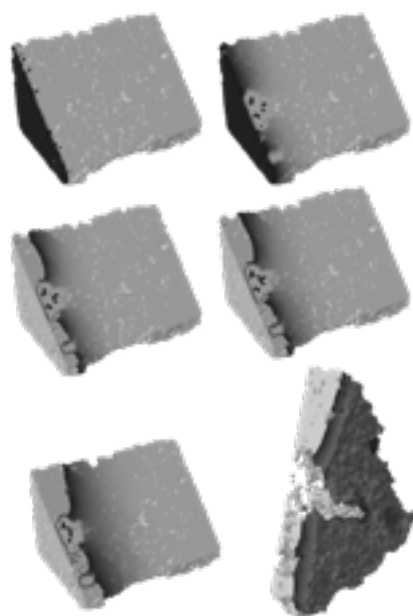


*Fig. 4: Simulating the formation of reaction zone and the respective evolution as a function of time (final figure segmentation of the sulfate containing reaction zone).*

The experimental work related to measurement of reaction zone dimensions from the studied refractory system is presented in Fig. 5 related to work in [6-7]. The numerical values are homogenized over full field microstructures to yield comparable values and zones are differentiated by changes in elemental chemistry and the specific phases, although the segmentation of phase distributions over the experimental and computational results is a source of uncertainty. What is deemed zone 3 is best aligned with the experimental work and model formulation as far as the comparison is concerned as it includes the formation of new phases. Zone 1, the face of the brick open to the

gas-space of the smelter, is underestimated in the model compared to experiments, although as the elements and richer deposit chemistry is not accounted for thoroughly in the model as is this is to be expected. Thus, the computational results for the gas-space end are lower than the most comparable experimental findings. For the zone 3, where the formation of calcium and magnesium sulfates is the primary difference, the model yields a bit of a lower bound for the zone thickness, although the results are comparable to what has been obtained experimentally. For zone 2 the changes in the brick are rather limited based on experimental findings, the model produces somewhat greater dimensions to this region over the experimental results.
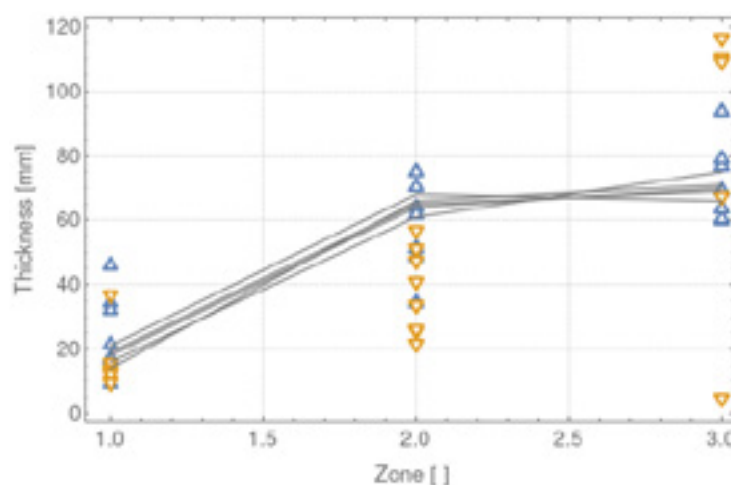


*Fig. 5: Comparison of the three reaction zone thicknesses: simulation (solid lines) vs. experimental measurements (triangles which correspond to different furnace measurement locations).*

## SUMMARY AND CONCLUSIONS

We present a multiphysical and multiscale modeling concept for assessing the degradation mechanisms of refractories interacting with molten slags and gaseous process environments. The focus is particularly on degradation mechanisms resulting in catastrophic refractory brick failure due to formation of multiple reaction zones and chemical reactions taking place within its respective microstructure. We emphasize the full field representation of material microstructure to be able to reproduce complex failure mechanisms and study interactions with industrial process environments and various multiphysical behaviors taking place within the refractory microstructure.

The performed use case work against experimental findings focusing on refractory bricks seen use in flash smelting operation suggests the proposed approach appears viable and can address scenarios beyond classical chemical wear models, although further work is required to perform comparisons to experimental and characterization results in order to establish proper validation of the computational approaches. The comparisons as far as the principal refractory behavior are concerned are promising as the findings for the reaction zones are similar, but the model sensitivities and quality of inputs needs to be investigated further to ensure the predictive abilities being targeted can be reached. The work demonstrates how formulating the refractory degradation as a multiscale and multiphysical problem enables better evaluation of the performance against challenging durability and lifetime limiting process conditions. This is foreseen as an important step towards better evaluating the performance of refractories in novel and complex process environments, which is to enable the systematic design and selection of the respective material solutions by making the most out of state-of-the-art computational methods.

## ACKNOWLEDGEMENTS

## REFERENCES
[1] Laukkanen, A., Uusikallio, S., Lindroos, M., Andersson, T., Komi, J., Porter, D., Micromechanics driven design of ferritic–austenitic duplex stainless steel microstructures for improved cleavage fracture toughness. Engineering Fracture Mechanics 253, 2021, 107878.
[2] Lindroos, M., Laukkanen, A., Andersson, T., Vaara, J., Mantyla, A., Frondelius, T., Micromechanical modeling of short crack nucleation and growth in high cycle fatigue of martensitic microstructures. Computational Materials Science 170, 2019, 109185.
[3] Lindsay, A.D, Gaston, D., Permann, C., Miller, J., Andr, D., Slaughter, A., Kong, F., Hansel, J., Carlsen, R., Icenhour, C., Harbour, L., Giudicelli, G., Stogner, R., German, P., Badger, J., Biswas, S., Chapuis, L., Green, C., Hales, J., Hu, T., Jiang, W., Jung, Y., Matthews, C., Miao, Y., Novak. A., Peterson, J., Prince, Z., Rovinelli, A., Schunert, S., Schwen, D., Spencer, B., Veeraraghavan, S., Recuero, A., Yushu, D., Wang, Y., Wilkins, A., Wong, C., MOOSE: Enabling massively parallel multiphysics simulation, SoftwareX 20, 2022, 101202.
[4] Andersson, J.O., Helander T., Höglund L., Shi P.F., Sundman B., Thermo-Calc and DICTRA, Computational tools for materials science, Calphad, 26, 2002, 273-312.
[5] Bale, C., Bélisle, E., Chartrand, P., Decterov, S. A., Eriksson, G., Gheribi, A.E., Hack, K., Jung, I. H., Kang, Y. B., Melançon, J., Pelton, A. D., Petersen, S., Robelin., C., Sangster, J., Spencer, P., Van Ende, M-A., FactSage Thermochemical Software and Databases -2010-2016. Calphad, 54, 2016, 35-53.
[6] Lehmusto, J., Hupa, L., Söyrinki, S., Lagerbom, J., Jokiaho, T., Que, Z., Huttunen-Saarivirta, E., Määttä, J., Lindgren, M., Interactions between the gas phase in a nickel flash smelting furnace and the refractory lining, UNITECR, 2023.
[7] Lehmusto, J., Söyrinki, S., Lagerbom, J., Jokiaho, T., Que, Z., Määttä, J., Hupa, L., Huttunen-Saarivirta, E., Lindgren, M., Characterization of a magnesia-chromite refractory material: Reactivity and reaction mechanisms in flash smelter gas atmosphere. Submitted to J. European Ceramic Soc.

# ESTIMATION OF REFRACTORY CASTABLE THERMAL CONDUCTIVITY: A MANUFACTURER'S PERSPECTIVE

Chia-Yuan Chang
China Ecotek Corporation, Kaohsiung, Taiwan

**ABSTRACT**
Thermal conductivity ($\lambda$) is one of the most important parameters for refractory lining. We have purposed a practical procedure by following existing models to estimate thermal conductivity of castable. The results showed for room temperature estimation, the maximum deviation is less than 30%. By considering factors which might affect the estimation, the accuracy of estimation could be further improved.

**BACKGROUD**
**Ribaud's expression**
Among different models for $\lambda$ estimation, Ribaud's expression has been found fairly accurate and relatively simple [1][2]. According to the expression, apparent porosity (A.P.) and thermal conductivity of mass ($\lambda_s$) are the only needed parameters (1).

$$\lambda = (1-P^{2/3}) \lambda_s + (P^{1/3}) \lambda_g \qquad (1)$$

in (1) where, $P$(%):apparent porosity of castable; $\lambda_s$(W/mK):thermal conductivity of mass; $\lambda_g$(W/mK):thermal conductivity of air, which value can be found at relevant literature.

**Geometric mean model**
As a refractory manufacture, quality control is extremely critical for castable production. Therefore, apparatus for A.P. measuring might not be a problem. On the other hand, $\lambda_s$ in Ribaud's expression is difficult to know.

By introducing Geometric mean model (2), $\lambda_s$ of castable can be calculated by its raw materials [3]. However, since volume fraction of constituent is inconvenient for manufacture, we purposed to replace volume fraction to weight fraction. Therefore, Geometric mean model can be used easily (3).

$$\lambda s = \Pi \lambda_i^{voli} \qquad (2)$$

$$\lambda s = \Pi \lambda_i^{wi} \qquad (3)$$

where, $\Pi$ is notation of repeated multiplication; $\lambda_i$(W/mK) is the conductivity of ith constituent (solid); $voli$ is the volume fraction of constituent; $wi$ is the weight fraction of raw material.

**PROCEDURE**
**Case A: $\lambda_s$ of all raw materials of castable are known**
To begin with, the proportion of raw materials of castable should be listed. Then, according to the weight proportion of raw materials, using Geometric mean model to calculated $\lambda_s$ of castable. Additionally, refer to ISO 1927-6:2012 measuring the castable's A.P.. Finally, according to Ribaud's expression, the $\lambda$ of castable can be estimated.

**Case B: $\lambda_s$ of raw materials are unknown**
When confronted with this situation, the database of $\lambda_s$ of each raw material should be established first. Only at here, the thermal conductivity measuring meter is required.

First of all, $\lambda_s$ of binder (ex: cement) is an entry point. By mixing binder with suitable water, after forming, measuring it's $\lambda$ at desired temperature. Then, following ISO 1927-6:2012 measuring the mixture's A.P..

Secondly, transposed Ribaud's expression, $\lambda_s$ of binder can be found. Thirdly, mixing previous binder with 1st raw material (same weight of binder and 1st raw material is suggested), then adding suitable water. After forming, measuring this mixture's $\lambda$ at desired temperature. Lastly, following ISO 1927-6:2012 measuring the mixture's A.P..

So far, 1st raw material's $\lambda_s$ can be calculated by transposed Geometric mean model with Ribaud's expression. The procedures are simplified listed as follow (4-6).

transposed of Ribaud's expression:
$$\lambda_{s\ of\ binder} = [\lambda - (P^{1/3}) \lambda_g] / (1 - P^{2/3}) \qquad (4)$$
$$\lambda_{s\ of\ 1st\ raw\ material\ with\ binder} = [\lambda - (P^{1/3}) \lambda_g] / (1 - P^{2/3}) \qquad (5)$$
transposed Geometric mean model with same weight of binder and raw materials:
$$\lambda_{s\ of\ 1st\ raw\ material} = (\lambda_{s\ of\ 1st\ raw\ material\ with\ binder} / \lambda_{s\ of\ binder}^{0.5})^2 \qquad (6)$$

Repeated with previous step, until all raw materials $\lambda_s$ have been found. Then, follow case A situation. The details can be referred to figure 1.



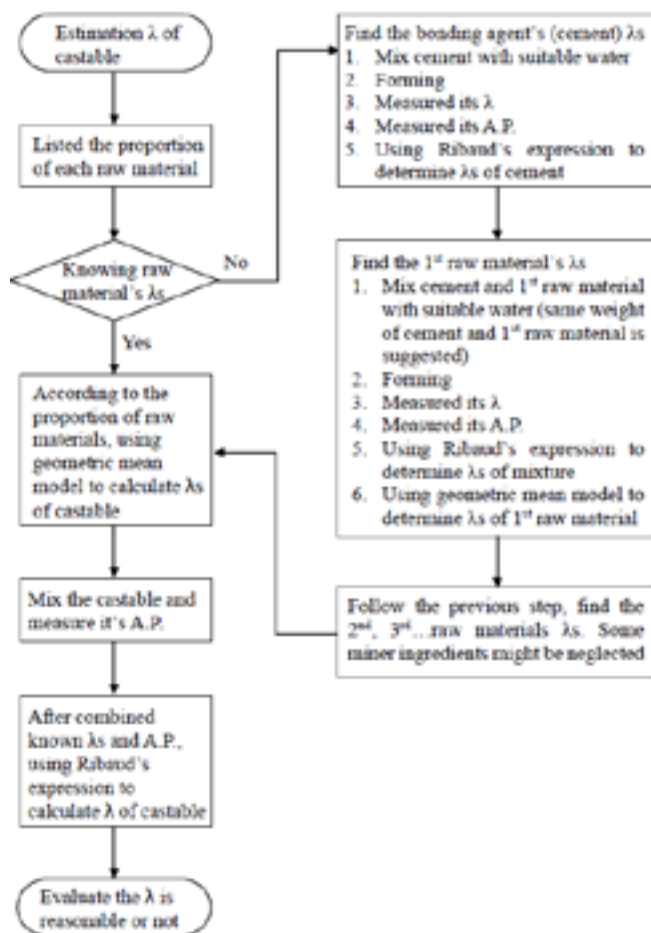*Fig. 1: Procedure of $\lambda$ estimation.*

**DISCUSSIONS**
According to the procedure as we purposed, the database of $\lambda_s$ of each raw material at different temperature has been constructed (not shown at here). In addition, by using Ribaud's expression to estimate $\lambda$ of castable, the actual $\lambda$ has been measured by thermal conductivity meter as well. The deviations are listed at Table 1

Tab. 1: Results of λ estimation and actual value.

| | | Commercial Castable | | Gunning Material | | FCWFA | | AWFA | |
|---|---|---|---|---|---|---|---|---|---|
| | composition | Cement A: 10%<br>F.C. 5-3: 20%<br>F.C. 3-1: 25%<br>F.C. 1-0: 15%<br>F.C. 200F: 24%<br>etc.: 6% | | Cement A: 10%<br>Cement B: 10%<br>M47 3-1: 34%<br>M47 1-0: 30%<br>F.C. 200F: 10%<br>A34: 5%<br>etc.: 2.5% | | Cement A: 20%<br>WFA 1-0: 40%<br>F.C. 3-1: 40% | | Cement A: 20%<br>WFA 1-0: 40%<br>WFA 3-1: 30%<br>WFA 325F: 10% | |
| Test Temp. | | Thermal Conductivity (λ) measured and estimation value (W/mK) | | | | | | | |
| Room temp. | Actual λ[2] | 1.51[2] | A.P.= 20.6% | 1.44 | 21.0 | 2.87 | 18.4 | 5.31 | 17.6 |
| | Estimation λ[3] | 1.68[3] | | 1.47 | | 3.55 | | 4.98 | |
| | Deviation(%)[4] | +11.3[4] | | +2.1 | | +23.7 | | -6.2 | |
| 400°C | Actual λ | 1.25 | 25.2 | 0.95 | 29.7 | 1.25 | 29.4 | 2.88 | 24.5 |
| | Estimation λ | 0.71 | | 0.91 | | 1.41 | | 1.73 | |
| | Deviation(%) | -43.2 | | -4.2 | | +12.8 | | -39.9 | |
| 600°C | Actual λ | 1.17 | 25.6 | 0.85 | 30.3 | 1.13 | 32.0 | 2.07 | 29.2 |
| | Estimation λ | 0.91 | | 0.95 | | 1.38 | | 1.69 | |
| | Deviation(%) | -22.2 | | +11.8 | | +22.1 | | -18.4 | |
| Sintered 1000°C measured at room[1] | Actual λ | 1.19 | 24.2 | 1.22 | 27.3 | No data | | No data | |
| | Estimation λ | 0.85 | | 0.94 | | | | | |
| | Deviation(%) | -28.6 | | -23.0 | | | | | |
| Sintered 600°C measured at room[1] | Actual λ | 1.15 | 25.6 | 1.01 | 30.3 | 1.26 | 32.0 | 2.11 | 29.2 |
| | Estimation λ | 0.93 | | 0.86 | | 1.33 | | 1.71 | |
| | Deviation(%) | -19.1 | | -14.9 | | +5.6 | | -19.0 | |

1: The sample has been either sintered at 600 or 1000°C*3hr then furnace cooling, λ is measured at room temperature.
2: Measured by thermal conductivity meter QTM-710.
3: Calculated by Ribaud's expression, trace additives are neglected.
4: [(Estimation λ)-(Actual λ)]/(Actual λ)

As the results shown, for room temperature, the deviation between estimation and actual λ is small. The maximum deviation is -28.6% for commercial castable after sintered at 1000°C. This might be the effects of low melting elements, trace additives we neglected for calculation or other reasons. Nevertheless, for manufacturer, this deviation should be acceptable and can be improved by knowing the factors which might affect the results.

Moreover, the density difference of raw materials might also influence the results. As Table 1 listed, the FCWFA and AWFA both containing white fused alumina (WFA) and flint clay (F.C.). Since we have modified Geometric mean model from volume fraction to weight fraction, the density difference of ingredients might be non-negligible. Furthermore, concentration difference should also be considered. For Table 2, over diluted castable, its λ might be overestimated. On the other hand, castable with less water content, its λ might be underestimated. In sum, despite lots of factors might affect the results, the estimation method we purposed is still be considered as a good approximation for λ of real castable.

**CONCLUSIONS**
1. By combining Ribaud's expression and modified Geometric mean model, a relatively simple and accurate method has been provided for λ estimation.
2. Once the database of $\lambda_s$ has been created, the thermal conductivity meter is no longer needed. Only A.P. apparatus and simple calculation are needed for λ estimation.
3. The estimated value might be affected by temperature, concentration and density weight difference of raw materials.
4. This method is worth to be promoted due to simplicity, low cost and high accuracy.

**REFERENCES**
[1] Ribaud, M. Theoretical study of thermal conductivity of porous and pulverulent materials. Chaleur and Industry, 18, 1937.
[2] Plibrico, Technology of monolithic refractories revised, Plibrico Japan, Tokyo, 1999.
[3] Brigaud, F., David, S., Chapman, S. and Douaran, S.L. Estimating thermal conductivity in sedimentary basins using lithologic data and geophysical well logs. The American Association of Petroleum Geologists, 74, 1990, p. 1459-1477.

Tab. 2: Effect of concentration on λ estimation

| Water content (%) | A.P. (%) | Measured λ (W/mK) | Calculated λ (W/mK) | Deviation (%) |
|---|---|---|---|---|
| Commercial castable measured at room temp. ($\lambda_s$ = 1.91) | | | | |
| 11.0 | 17.6 | 1.45 | 1.32 | -9.0 |
| 12.0 | 19.1 | 1.36 | 1.29 | -5.1 |
| 13.0 | 20.4 | 1.38 | 1.26 | -8.7 |
| 14.0 | 21.9 | 1.24 | 1.23 | -0.8 |
| 15.0 | 22.8 | 1.20 | 1.21 | +0.8 |
| Commercial castable sintered at 1000°C, after cooling measured at room temp. ($\lambda_s$ = 1.37) | | | | |
| 11.0 | 24.2 | 1.19 | 0.85 | -28.6 |
| 12.0 | 25.2 | 1.17 | 0.84 | -28.2 |
| 13.0 | 26.3 | 1.12 | 0.82 | -26.8 |
| 14.0 | 27.8 | 1.06 | 0.80 | -24.5 |
| 15.0 | 28.6 | 0.97 | 0.79 | -18.6 |
| FCWFA measured at room temp. ($\lambda_s$ = 3.95) | | | | |
| Insufficient water | 16.2 | 2.82 | 2.79 | -1.1 |
| Suitable water | 19.6 | 2.44 | 2.63 | +7.8 |
| Over diluted | 21.2 | 2.29 | 2.56 | +11.8 |
| FCWFA sintered at 1000°C, after cooling measured at room temp. ($\lambda_s$ = 2.54) | | | | |
| Insufficient water | 26.1 | 1.64 | 1.52 | -7.3 |
| Suitable water | 29.5 | 1.32 | 1.43 | +8.3 |
| Over diluted | 31.8 | 1.17 | 1.38 | +17.9 |

# DISCRETE ELEMENT METHOD (DEM) TO SUPPORT MICROSTRUCTURE DESIGN OF REFRACTORIES

Harikeshava RANGANATHAN (1,2), Ratana SOTH (1), Christoph WÖHRMEYER (1)
Damien ANDRE (2), Marc HUGER (2)
(1) Imerys Technology Center, 1 Rue le Chatelier, 38090 Vaulx-Milieu, France
(2) University of Limoges, IRCER, UMR CNRS 7315, 12 rue Atlantis, Limoges 87068, France

## ABSTRACT
The CESAREF project is a Doctoral Network (DN), supported by the European Commission, to generate a Concerted European action on Sustainable Applications of REFractories. In the current context of the European Green Deal, this ambitious project has been launched in 2022 in order to develop a better knowledge around refractory materials with regards to the new operating conditions requested by the drastic reduction of greenhouse gas emissions, improved energy efficiency, and by life cycle assessment requirements. The present PhD study is focused on developments of numerical tools based on the discrete element method (DEM) for investigation of the relationships between microstructure and thermomechanical properties of model materials. This original numerical approach includes debounding, thermomechanical coupling, crack-closure and anisotropic behaviours. These developments will lead to a "virtual numerical lab" able to provide tensile, dilatometry, fracture mechanics or thermal shock virtual tests for virtual characterizations. The related achievements will be integrated to the free DEM software GranOO. Obtained numerical results will be validated in regard to experimental observations in terms of (i) mesoscopic thermomechanical quantities such as CTE, Young's modulus, Poisson's ratio, stress-strain law and fracture energy and (ii) microscopic observations such as fracture coalescence under thermal and mechanical loadings dynamically observed in SEM.
Keywords: Discrete Element Method (DEM), Microstructure, Refractories and Thermomechanics

## INTRODUCTION
Refractory materials are advanced materials with high thermomechanical properties and chemical stabilities. Refractory materials are used as insulating linings of equipment in steel, glass, and cement manufacturing. When exposed to an environment with fast temperature variations, refractory materials experience thermal shocks leading to thermal stress introduced over the material's surface, which causes critical failures of the material leading to environmental damage and pollution.

Past researchers have summarised that the critical failure of refractory materials can be enhanced by improving the material's Thermal Shock Resistance (TRS). According to several experimental studies, introducing thermal expansion mismatches between constituents of a refractory material can increase its thermal shock resistance. Micro-cracks promoted by an imbalance in thermal expansion might result in a refractory material exhibiting a non-linear mechanical behavior (figure 1a) [4].

On the other hand, past Doctorates Asadi [1] and Nguyen [2] have incorporated modelling platforms to give experimental insights for improving TSR. The modelling field has not yet fully covered every aspect of study regarding thermo-mechanical behavior for refractory materials. Modelling the complex behaviors of refractory has become an objective and the current Ph.D. focuses on investigating the relationship between microstructure and thermomechanical properties of model materials using the Discrete Element Method (DEM).

The developed tool will set up a virtual lab to characterize the material failure virtually. The numerical tool will help us perform the process from 3➔4 in the Youngs modulus evolution graph (Figure 1b). In this paper, we will address the basics of DEM, choice of model material of interest, boundary conditions and material routines to achieve the first set of results.
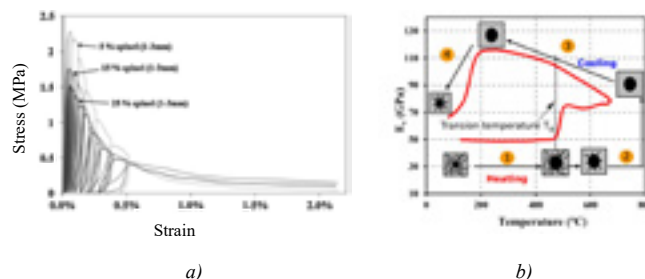


*Fig. 1: a) The non-linear stress-strain curve with microcrack promotion [4] b) Youngs modulus evolution w.r.t temperature [2]*

## DISCRETE ELEMENT METHOD (DEM)
The DEM is widely used for investigating the discontinuity behaviors in rocks, ceramics, and refractories [6]. The principles of discrete elements method are described as follows:
- The elements are rigid body that can move freely in a defined 3D space;
- The interaction between the elements is defined using interaction laws;
- It incorporates explicit numerical technique;
- The elements can have a translational and rotational movement determined using Newton's second law.

The benefits of incorporating DEM are listed down below ([1], [5] & [7]):
- It allows considering overlapping of the discrete elements; it is computationally efficient in GPU aspects, and the elements have mass and geometry as shown in figure 2a;
- It helps us perform mesoscale analysis of quasi-brittle failure, preserve real natural phenomena using rheology (example: spring), and simulate multiple crack nucleation, propagation, branching, and failure analysis, as shown in figure 2b.
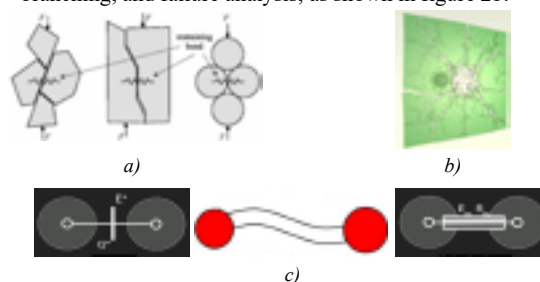


*Fig. 2: a) The realistic phenomena is preserved [8], b) Multiple crack nucleation and propagation c) Flat joint [1], Beam model [2] & Cohesive beam [3]*

## PROBLEM STATEMENT
Past doctorate had chosen different interaction models like a cohesive beam [2], Flat joint [1], and beam models [3] (figure 2c) with discrete elements of spherical form.

The current Ph.D. incorporate the lattice spring model (figure 4a) generated using the voronoi tessellation technique. The computational study of the model can be performed by directly using the continuum mechanics laws, and the crack surface is visible, as shown in figure 4b. In addition, the lattice model does not require a calibration step as the continuum laws are well established [7].

Fig. 4: Description of a) Lattice spring model b) Surface crack with polyhedral element [7]

## Preprocessor

The Voronoi discretization technique is generated using the granoo preprocessing package named cook-project.

## Model Material

Incorporating complex microstructures of refractories (figure 6a) to study the relationship of its microstructure with thermomechanical properties, computationally is difficult. The ideology of defining a simplistic model material was the primary objective of the current study. The model material of interest is as defined below:

1. Model material 1:
   - Single-phase system (figure 6b);
   - 1-set of material parameters;
   - Homogenic system with just the matrix material.
2. Model material 2:
   - Bi-phase system (figure 6c);
   - 2-set of material parameters;
   - FCC packing will be incorporated to have very low anisotropy.
3. Model material 3:
   - Polycrystalline system (figure 6d);
   - n-sets of material parameters;
   - High in anisotropy → more related to realistic refractory behavior.
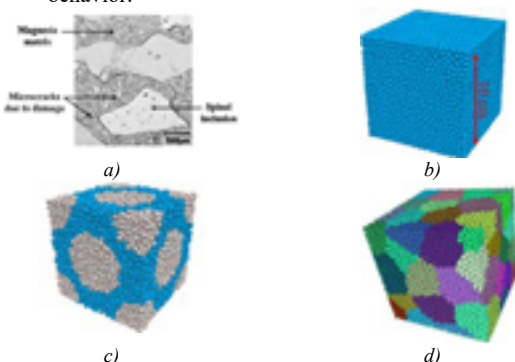


Fig 6: Description of the material model a) Example microstructure [4] b) Single-phase system [1] c) Bi-phase system [1] d) Polycrystalline system [3]

## Boundary conditions

The homogenization aspect of the study in DEM is still not as familiar as in the FEM. Recent past doctorate students have shown that applying the periodic boundary condition (figure 7a) will give us better results than the Free boundary condition [1]. The model material is chosen as the Representative Volume Element (RVE), and the copy of the RVE is arranged around the master element to bring the most simplistic microstructure arrangement replicating the realistic microstructure. The free boundary condition (figure 7b) is also incorporated for the following study to cross-verify the proven study by past doctorate students.



Fig. 7: Boundary condition a) Free boundary [8] b) Periodic boundary [1]

## Material routines

In the current Ph.D., the Elastic model and Fracture model are incorporated.

Local failure criteria: $\sigma_{(I)} \geq \sigma_{(max)}$

## Failure test

The current Ph.D. study focuses on the refractory material's tensile loading and mode-I fracture analysis.

## Validation

The developed numerical tool will be quantitatively validated using the results (experimental data) of a colleague from the CESAREF group. In addition, analytical solutions are also utilized as supportive data for the current Ph.D.

## CONCLUSIONS

The following Ph.D. incorporates further study by using:

a) Discretization technique: Voronoi tessellation DEM model
b) Boundary conditions: Free boundary model and periodic boundary model
c) Model/systems: Single-phase, bi-phase and polycrystalline system
d) Material routine: Elastic and Fracture model (Mode I)
e) Thermomechanical model with tensile loading

## REFERENCES

[1] F. Asadi, "Micro-mechanical modelling of heterogeneous materials containing microcracks with Discrete Element Method (DEM)," Limoges, 2021.

[2] Nguyen, Truong Thi. Numerical modeling of microstructure-properties relationships of refractories: micro-mechanical approach with the discrete element method. Diss. Limoges, 2019.

[3] PLEDEL Quentin (PhD Student), "Modélisation de l'endommagement thermique de la microstructure de matériaux réfractaires modèles par la méthode des éléments discrets"

[4] R. Grasset-Bourdel et al, "Influence of thermal damage occurrence at microstructural scale on the thermomechanical behaviour of magnesia–spinel refractories", Journal of the European Ceramic Society, Volume 32, Issue 5, 2012, Pages 989-999

[5] M. H. Moreira et al., "Discrete element modelling—A promising method for refractory microstructure design," Am. Ceram. Soc. Bull, vol. 99, pp. 22–28, 2020.

[6] D. André, I. Iordanoff, J. Charles, and J. Néauport, "Discrete element method to simulate continuous material by using the cohesive beam model," Comput Methods Appl Mech Eng, vol. 213–216, pp. 113–125, 2012, doi: https://doi.org/10.1016/j.cma.2011.12.002.

[7] D. André, J. Girardot, and C. Hubert, "A novel DEM approach for modeling brittle elastic media based on distinct lattice spring model," Comput Methods Appl Mech Eng, vol. 350, pp. 100–122, 2019, doi: https://doi.org/10.1016/j.cma.2019.03.013.

[8] Potyondy, David O., and P. A. Cundall. "A bonded-particle model for rock." International journal of rock mechanics and mining sciences 41.8 (2004): 1329-1364.

# COMBUSTION CHARACTERISTICS OF METHANE AIR PREMIXED FUEL IN ORDERED POROUS BURNERS

Liping PAN [1,2*], Yawei LI [1], Xiong Liang [1], Bowen XU[1]

[1]Wuhan University of Science and Technology, The State Key Laboratory of Refractories and Metallurgy, Wuhan 430081, China
[2]Geotechnical Institute, TU Bergakademie Freiberg, Freiberg 09596, Germany

**ABSTRACT**
Inside porous medium burners, the holes exhibit a variable size due to the sponge template, leading to uneven combustion intensity and exacerbating thermal shock damage. With the equivalent cell, an ordered lattice structure is proposed as a replacement for the disordered structure of the sponge template. By incorporating the two-step reaction mechanism of $CH_4$/air, radiative heat transfer and turbulence models, comprehensive calculations are performed to analyze the combustion kinetics and heat transfer within both solid and gaseous domains. The finite volume method is utilized to fully simulate the impact of cell structure parameters on fluid flow and combustion characteristics in porous media. The results indicate that increasing the cell side length while reducing the pore diameter enhances the porosity of the porous medium, resulting in reduced pressure resistance. Moreover, this adjustment leads to a more uniform temperature distribution, contributing to improved combustion efficiency, higher $CH_4$ conversion rate, and reduced CO emissions.

## 1 Introduction

Porous Media Combustion (PMC) technology involves combustion of fuel and oxidizer within a three-dimensional porous medium, resulting in high combustion efficiency, low emissions, and uniform heat release. However, traditional porous materials, like foam ceramics, have uncontrolled pore structures, limiting their application in low-calorific value fuels. To overcome this limitation, this study utilizes 3D-printed porous resin templates to design and optimize the cell body structure of the porous medium. By investigating the influence of the cell body structure on stress and flow fields, as well as studying the correlation between cell body structure and combustion characteristics, this research aims to optimize the parameters for enhanced combustion efficiency in porous media combustors.

## 2 Experimental and Simulation Methods

The complex structure of foam material (Fig. 1(a)) is geometrically simplified using a simplified equivalent unit channel (single cell), resulting in a cubic framework structure (Fig. 1(b)). The calculation of porosity in the lattice cell structure is as follows:

$$\varepsilon_c = \frac{V_p}{V} = \frac{a^3 - \frac{3\pi d^2}{4}(a - 0.6d)}{a^3} \tag{1}$$

$\varepsilon_c$, $V_p$ and $V$ represents porosity, pore volume, and cell volume, respectively. $a$ means the edge length of the cell, and $d$ is the diameter of the cell.

The modified momentum equation takes into consideration the porous structure and seepage effects. It can be expressed as:

$$\frac{\partial(\rho_m\varepsilon)}{\partial\tau} + \nabla\cdot(\rho_m\varepsilon\vec{v}_m) = \nabla\cdot[(\mu_m + \rho_m C_\mu\frac{k^2}{\varepsilon\sigma_\varepsilon})\nabla\cdot\varepsilon] \tag{2}$$

$$+ \rho_m C_1\nabla\vec{v}_m\varepsilon - \rho_m C_2\frac{\varepsilon^2}{k + \sqrt{v_m\varepsilon}}$$

where $\rho_m$ is the density of the fluid, $\vec{v}_m$ is the velocity vector, t is time, $k$ is the turbulent kinetic energy, $\varepsilon$ is the turbulent dissipation rate, $v_m$ is the dynamic viscosity coefficient of the mixture gas $\sigma_k$ =1.0, $\sigma_\varepsilon$ =1.2, $C_\mu$ =0.09, $C_1$ =0.43 and $C_2$ =1.9.
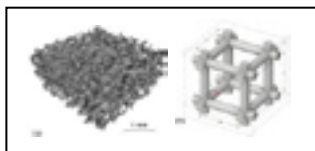


*Fig.1: PMC Diagram: (a) Foam type, (b) Lattice cell type.*

To investigate the relationship between cell structureparameters, porosity, and combustion characteristics, a structure was designed with different edge lengths (a=4-8mm) and a regular hexahedron shape (D=2R=0.25-0.9mm). Mechanical simulation analysis was conducted to evaluate the strength of the lattice cell structure, and a model was established to analyse its flow characteristics in the combustion field. The designed structure was 3D-printed using porous resin material, and a two-step process involving slurry coating and vacuum impregnation was used to prepare ordered SiC porous ceramics. Combustion experiments were conducted to study their combustion characteristics. Temperature measurements were conducted by an infrared thermal imager and a flue gas analyser after the methane combustion experiment, which was at an equivalence ratio of 0.65 ($CH_4$%= 6.4%), the methane flow rate of 0.82 NL/min, and air flow rate of 12 NL/min.

## 3 Results and discussion

The variation in pore size during the impregnation process is shown in Fig.2. The results indicate that as the cell edge length decreases from 8 mm to 4 mm, the increment in pore size (ΔR) gradually diminishes. This trend highlights the increasing difficulty of reducing porosity during the slurry coating process with smaller cell dimensions.
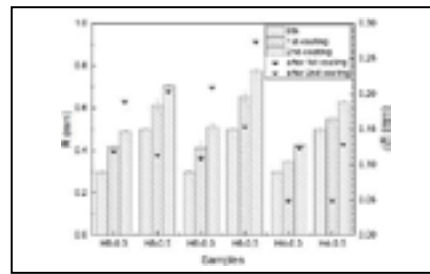


*Fig.2: The variation in pore size during the impregnation process.*

The analysis revealed significant relationships between the geometric parameters of the lattice cell and both porosity and pressure drop, as depicted in the graph. Increasing the lattice cell edge length led to higher porosity, while increasing the strut radius resulted in lower porosity. Interestingly, as the cell edge length decreased, the impact of increasing strut radius on porosity became more pronounced. For instance, with an increase in edge length from a=4 mm to a=8 mm, the difference in porosity for a strut radius of R=0.25 mm was only 2.74%. However, as the strut radius increased to 0.9 mm, the porosity difference soared to 24.45%.
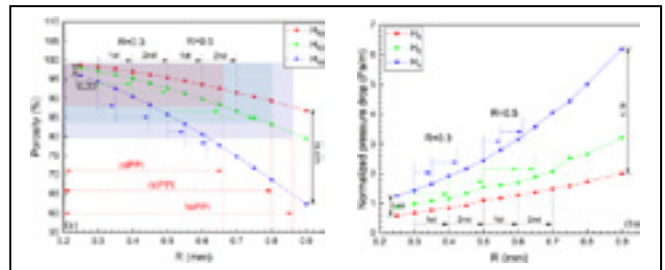


*Fig.3: The porosity and pressure drop with cell size.*

Regarding pressure drop, larger lattice cell edge lengths were associated with reduced pressure drop, whereas increasing strut radius led to higher pressure drop. Notably, as the cell edge length decreased, the influence of increasing strut radius on pressure drops intensified. For example, as the edge length increased from a=4 mm to a=8 mm, the difference in pressure drops for a strut radius of R=0.25 mm was merely 0.68 Pa/m. However, with an increase in strut radius to 0.9 mm, the pressure drop difference surged to 4.19 Pa/m. It is worth highlighting that when the strut radius exceeded

0.5 mm, the impact of cell edge length and pore size on porosity and pressure drop became even more pronounced.
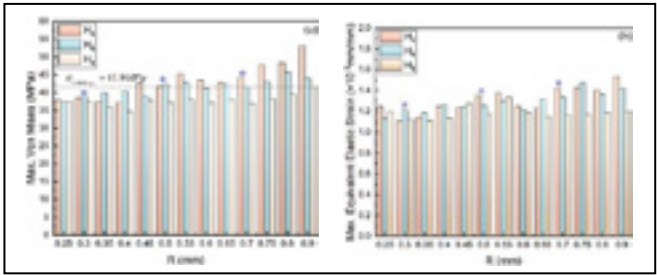


*Fig.4: The equivalent stress and strain with cell size.*

The investigation of H-system ordered cell structures subjected to a 0.02 mm (0.1% strain) displacement loading highlighted important findings. It was observed that larger cell edge lengths contributed to reduced maximum equivalent stress and strain within the structure, while larger pore sizes led to increased stress and strain. Remarkably, based on the critical flexural strength of SiC (CMOR = 41.9 MPa), optimal design dimensions for structural stability were identified: a cell edge length of 4 mm required a pore radius (R) below 0.45 mm, a cell edge length of 6 mm necessitated R to be below 0.5 mm or equal to 0.6 mm, and a cell edge length of 8 mm demanded an R below 0.9 mm.
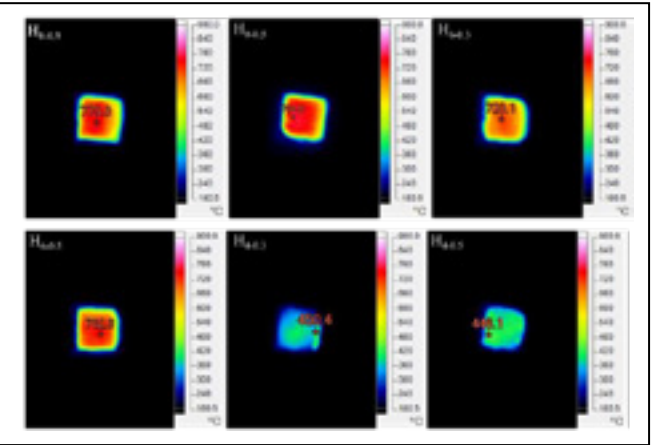


*Fig.5: Temperature distribution of different structures.*

The temperature distribution within the combustion chamber was uniform, as shown in Fig.5. Notably, the combustor with a strut radius (R) of 0.5 mm and a cell length (a) of 8 mm exhibited the highest peak temperature, reaching 784°C. In contrast, the combustor with a cell length of 4 mm had the lowest peak temperature, a significant 337.9°C lower than the maximum temperature observed in the combustor. This disparity in temperature arises from incomplete combustion at a cell length of 4 mm, leading to considerably lower temperatures compared to conditions of complete combustion.
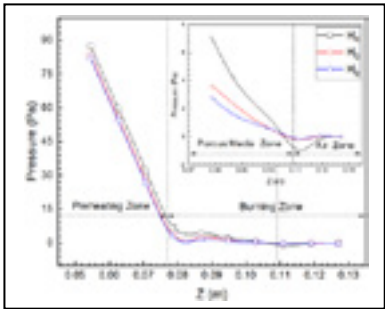


*Fig.6: Static pressure distribution along the flow direction.*

Tab. 1: Pollunt products of *different structures*.

| | $H_{8\_0.3}$ | $H_{8\_0.5}$ | $H_{6\_0.3}$ | $H_{6\_0.5}$ | $H_{4\_0.3}$ | $H_{4\_0.5}$ |
|---|---|---|---|---|---|---|
| CO/ppm | 100 | 106 | 203 | 284 | 253 | 872 |
| NO/ppm | 0 | 0 | 0 | 0 | 0 | 0 |
| NO$_2$/ppm | 0 | 0 | 0 | 0.3 | 0 | 0.2 |
| NO$_X$/ppm | 0 | 0 | 0 | 0.3 | 0 | 0.2 |
| 烟温/°C | 310.6 | 272.7 | 348.9 | 329.9 | 324.7 | 312.6 |

The sufficient combustion of gas in PMC significantly reduces pollutant emissions. The exhaust gas composition during stable combustion is summarized in Table 1. Generally, lower CO content in the exhaust gas signifies a higher degree of combustion. It is worth noting that the cell structure with a=8 mm enhances the combustion of fuel gases within the combustor, resulting in more complete combustion compared to a=6 mm and a=4 mm. Regarding NOx emissions, four of the combustors showed no NOx production, while the remaining two had low emissions of approximately 0.2-0.3 ppm, significantly below those of randomly distributed porous media combustors. These findings indicate that, at a constant strut radius (R), a decrease in cell pore length reduces porosity and diminishes the combustion performance of silicon carbide porous ceramics.

## CONCLUSIONS

The irregularity of hole sizes caused by the sponge template leads to uneven combustion intensity and increased thermal shock damage in PMC. An ordered lattice structure is proposed as a substitute for the disordered sponge template. The findings of the present study reveal that increasing the cell side length and reducing the pore diameter enhance the porosity of the porous medium, resulting in reduced pressure resistance. Additionally, this adjustment leads to a more uniform temperature distribution, ultimately improving combustion efficiency, increasing the conversion rate of CH$_4$, and reducing CO emissions. These results demonstrate the significance of optimizing cell structure parameters in achieving enhanced combustion performance in PMB.

## REFERENCES

[1] Chalia S, Bharti M, Thakur P, et al. An overview of ceramic materials and their composites in porous media burner applications. Ceramics International, 2021, 47(8): 10426-10441.
[2] Samoilenko M, Seers P, Te Rriault P, et al. Design, manufacture and testing of porous materials with ordered and random porosity: Application to porous medium burners. Applied Thermal Engineering, 2019, 158: 113724-113724.
[3] Huo W, Zhang X, Chen Y, et al. Mechanical strength of highly porous ceramic foams with thin and lamellate cell wall from particle-stabilized foams. Ceramics International, 2018, 44(5): 5780-5784.
[4] Hwang J, Hwang G, Yeh R, et al. Measurement of interstitial convective heat transfer and friction drag for flow across metal foam. Journal of Heat Transfer, 2002, 124(1): 120-129.
[5] Pusterla S, Barbato M, Ortona A, et al. Numerical study of cell morphology effects on convective heat transfer in reticulated ceramics. International Journal of Heat & Mass Transfer, 2012, 55(25-26): 7902-7910.
[6] Schaedler T, Carter W. Architected cellular materials. Annual Review of Materials Research, 2016, 46(1): 187-210.
[7] Hammel E, Ighodaro L, Okoli O. Processing and properties of advanced porous ceramics: An application-based review. Ceramics International, 2014, 40(10): 15351-15370.
[8] Mingjian L, Shuyuan J, Qiang Wang, et al. Numerical simulation of methane combustion in Two-Layer porous media under oxy-fuel condition. Flow, Turbulence and Combustion, 2023, 110: 649-670.

# TRANSMISSION CONDITIONS ACROSS A THIN THERMOELASTIC INTERPHASE

Shubhra Pade[1]; Andrea Piccolroaz[2]; Séverine Romero Baivier[3]

[1]Università degli Studi di Trento, Tento, Italy; [2]University of Trento, Department of Civil, Environmental and Mechanical Engineering, Trento, Italy; [3]Vesuvius group plc, Department of Advanced Refractories, Ghlin, Belgium

Refractory devices composed of ceramics are employed wherever there is contact with molten metals as in crucible, filters, furnaces or systems for flow control. These devices are composed as a mixture of two or more materials, and thus have varying elastic and thermal properties. As these devices operate at very high temperatures, the mixture undergoes thermal expansion at different rates, which can lead to crack initiation, and ultimately the failure of the materials.

The work mainly focuses on the development of transmission conditions across a thin thermoelastic interphase. The interphase is modeled as a thin, „spring-type" elastic layer of constant thickness, whose properties are different from those of the surrounding media, and is subjected to a high thermal load. This interphase is then reduced to „zero thickness" leading to imperfect interface conditions. An asymptotic approach is used to derive the non-linear transmission conditions across the interface, and results are analyzed using finite element methods.

# PRODUCT RANGE

## Natural Minerals
- Alumo Silicates
- Bentonite
- Calcite, Marble
- Chalk
- Colemanite
- Coke
- Dolomite
- Feldspars
- Fluorite, Fluorspar
- Graphite
- Green Earth
- Ilmenite
- Iron Oxides
- Iron Spar, Siderite
- Kaolin, China Clay
- Magnesite
- Manganese Ore, Hausmannite
- Mica, Muscovite
- Pumice
- Pyrite
- Quartz
- Rutile
- Talc
- Wollastonite
- Zirsio® - Zirconium Silicate

## Fused and Sintered Products
- Carbides (Cr, Si, W...)
- Chamottes
- Fumed Silica
- Fused Oxides (Mg, Zr, Cr)
- Fusil® - Fused Silica
- Malox® - Alumina (Calcined, Fused, Tabular, Light Weight)
- Mullites
- Spinel
- Titanates (K, K-Mg, Ca)

## Chemical Products
- Alginates (K, Na, Ca)
- Alkasil® - Sodium Silicate, Potassium Silicate (liquid, milled, spray-dried)
- Alkali Silicate Stabilizer
- Carbonates (Ba, Sr, K, Na, Li...)
- Carboxymethyl Cellulose (Na)
- Cellulose Powder
- Cryolite (Na, K)
- Fluorides (Al, Ba, K, Li, Mg, Na, Sr...)
- Guar Gum, Gum Tragacanth
- Metal Oxides (Al, Bi, Cr, Fe, Mg, Mn, Ni, Ti, Zr...)
- Methyl Hydroxyethyl Cellulose
- MLR-MX® - Application-optimized Mixed Products
- Oxalates (Na, K)
- Phosphates (Na, Ca)
- Potassium Tetrafluoroborate

## Metal and Alloy Powders
- Kovosil® - FeSi 45
- Minoal® - Co, Cu, CuSn (Bronze), FeCo, FeMo, FeNb, FeNi, FeV, FeW, Mo, Ni, Sn, Ti, W, ...
- Mipral® - Al, AlMg, CaSi, Cr, Fe, FeAl, FeB, FeCr, FeMn, FeSi 15, FeSi 50, FeSi 65, FeSi 75, FeTi, Mg, Mn, Si, SiMn, ...

## Processing Services
- Crushing
- Milling
- Classification
- Blending
- Drying
- Dedusting
- Magnetic-Seperation
- Octical Sorting
- Packing

Our core competence is sourcing, production, processing and supplying of customized Minerals, Chemicals and Alloys

# 7 EDUCATION

# REIMAGINING REFRACTORIES: HOW PROFESSIONAL SOCIETIES INFLUENCE THE PERCEPTION OF REFRACTORY TECHNOLOGY AND ENGINEERING

Eileen J. De Guire, Mark J. Mecklenborg

The American Ceramic Society, Westerville, Ohio, USA

## ABSTRACT

Refractory ceramics are essential to industrial heat-intensive processes but generally are used in environments that hide them from view. However, they fill a vital role in achieving sustainable manufacturing, improving efficiency, reducing carbon emissions, adapting to hydrogen fuels, adapting to new high-performance alloy compositions, and more. As such, the refractory industry offers straight-to-the-bottom line opportunities for engineers to impact today's grand challenges. However, the industry competes for talent with emerging materials science technologies, and it suffers from an outdated perception as a dusty, staid industry. The American Ceramic Society and its Refractory Ceramics Division have taken on the challenge of raising the visibility of this "invisible" industry and of presenting the industry as an innovative discipline that solves urgent problems with global impact.

## INTRODUCTION

According to the World Refractories Association (WRA), 70% of all refractory products are sold to the steel industry. Thus, as the steel industry goes, so also goes the refractory industry. [1]

The steel industry is changing, as are other processing industries that rely on heat and heat-treatment processes. Energy-intensive industries are embracing their roles as global citizens, acknowledging their corporate responsibility to mitigate climate change by transitioning to sustainable production methods, among other steps. Plus, these companies' customers are challenging them to make not just refractory products sustainably but also to develop new products that will help the customers make their own products sustainably. For example, automakers need high-strength, lightweight steel alloys that will reduce the weight of cars and thereby make room for large battery packs in electric vehicles.

New steel, aluminum, glass, etc. compositions change the hot face reaction chemistries inside furnaces. Additionally, experiments with hydrogen fuel by steelmakers, glassmakers, and others change the combustion chamber chemistries and melt–refractory reactions.

The refractory industry, as the literal "holders of the heat," is an essential partner in the drive toward sustainable manufacturing. And, in turn, refractory manufacturers are embracing sustainable manufacturing of their products across the entire value chain.

The UNITECR 2022 and 2023 programs point to some of the new science, engineering, and skills that the refractory industry needs: nanoscale microstructure engineering, modelling and artificial intelligence, recycling, slag and mine tailing reclamation, and more.

Despite the essential role refractories have in all heat processing—from steelmaking to glassmaking to pizza ovens—they have low visibility. Few people entering their career decision-making pathway are aware of refractories.

The refractory industry faces stiff competition for engineering talent. Based on data the Society of Women Engineers compiled from the United States Bureau of Labor Statistics job outlook for engineers, between 2021–2031, demand for materials engineers in the U.S. is expected to grow 6.1%. Demand also will increase for other manufacturing-related engineering disciplines: chemical, health and safety, industrial, and mechanical engineers. [2]

Within the refractory ceramic engineering subdiscipline, other end uses such as hypersonic vehicles compete for materials scientists trained in high-temperature ceramic materials, their synthesis, properties, and applications.

However, for those motivated by the urgency of the impact they can have—and the speed at which they can affect that impact—a refractory engineering career offers a rewarding pathway.

Many factors influence career choice. This paper presents some actions The American Ceramic Society is taking to promote STEM careers broadly and careers in the ceramic and glass industry specifically through outreach, community building, publications, multi-media communications, and workforce development. Several examples that pertain specifically to refractory engineering careers will be presented.

## CAREER DECISIONS START EARLY

Young children are often asked what they want to be when they grow up. As students approach the end of their secondary school years, they are asked again, but this time the question carries more importance. Students who choose university are asked to refine the question further: What major will you study? Will you go to graduate school, medical school, law school, etc.?

Recent research shows that the first inquiry—what you want to be when you grow up—may be the most important gateway.

In 2020 Ph.D. research [3], Ralph C. Tillinghast asked about 2,500 working science and engineering professionals the following questions:

1. In what grade did you first become interested in science and/or engineering?
2. In what grade did you first see yourself as a scientist and/or engineer?
3. In what grade did you decide to become a scientist or engineer?
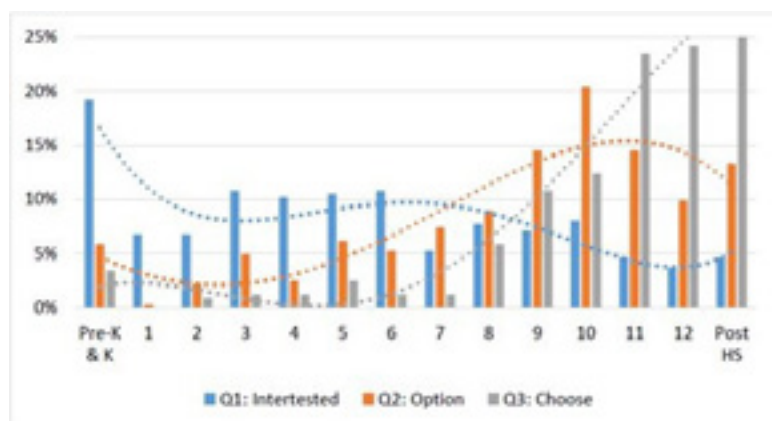
The responses, summarized in Figure 1, show that awareness and interest start in the preschool years. Interest declines in first and second grade, but by third grade—the age at which most students have become skilled readers—interest in science and engineering undergoes a steep increase. The incidence of first interest in science and engineering is approximately constant through sixth grade, when it starts to wane in middle school and high school. Presumably, as students advance through the elementary and middle school curriculum, most will have been introduced to science and/or engineering (S&E).

The orange line represents the grade at which students first imagined the possibility of becoming scientists or engineers. This line shows that students first begin to consider S&E careers in third grade—the same age at which a more informed awareness of S&E begins. Students' openness to S&E careers continues to increase into high school and begins to decline as students make career path decisions during the second half of high school. This research shows that there are key points at which outreach and intervention will take root.

The Ceramic and Glass Industry Foundation (CGIF) was established by ACerS in 2014 to advance the educational outreach of the American Ceramic Society and serve as ACerS's philanthropic arm. Its mission is to "attract, inspire, and support the next generation of ceramic and glass professionals," which it does through the outreach activities listed in Table 1. [4]

CGIF's programs intervene at key points on the career pathway: K–12, undergraduate, and graduate levels. The CGIF Materials Science Classroom Kits (Figure 2) and Mini Materials Kits leverage the natural curiosity of young students in the context of materials. Undergraduate and graduate students are supported by scholarships, travel grants, and professional development programs. The reach of these programs is significant, as highlighted in the table.

Tab. 1: CGIF outreach programs

| Program | Target audience | Program goal | 2022 impact |
|---|---|---|---|
| Materials Science Kit Mini Materials Kit Glass Science Kit | K–12 students | Toolkits of hands-on experiments for K–12 teachers | 691 kits distributed 99 teachers 39,440 students |
| President's Council of Student Advisors | Undergraduate students Graduate students | Student leadership development | 46 students 28 universities 8 countries |
| Scholarships | Underrepresented college students | Reduce cost barriers to underrepresented students interested in MSE | 3 awards $10k distributed |
| Student travel grants | Undergraduate students Graduate students | Travel support | 107 students $37k distributed |
| Outreach in a Box | Adults, including college students | Toolkit for volunteer-based MSE outreach | N/A (Launched in 2023) |
| IGNITE MSE (International Gathering and Networking for Individuals to Explore Materials Science and Engineering) | Undergraduate students Graduate students | Professional development for students about to enter the workforce | N/A (To launch in late 2023) |
| Ceramic and Glass Career Center | Undergraduate students Graduate students Working professionals | Employment | |
| University–Industry Networks/Keramos | Undergraduate students Graduate students | Promote interest in ceramic engineering, technology, and science professions | |



*Fig. 2: The "Hot or Not" lesson in CGIF's Materials Science Classroom Kit teaches K–12 students about refractories. Teachers can learn how to teach MSE concepts using the kits by attending a teacher workshop or by watching YouTube demonstrations. All kits come with Next Generation Science Standards aligned lesson plans.*

## COMMUNITY BUILDING

ACerS' Refractory Ceramics Division (RCD) is among the oldest of the Society's 11 Divisions. In collaboration with ACerS St. Louis Section (SLS), RCD has organized the Refractory Ceramics Symposium for 52 consecutive years. Recent themes and prese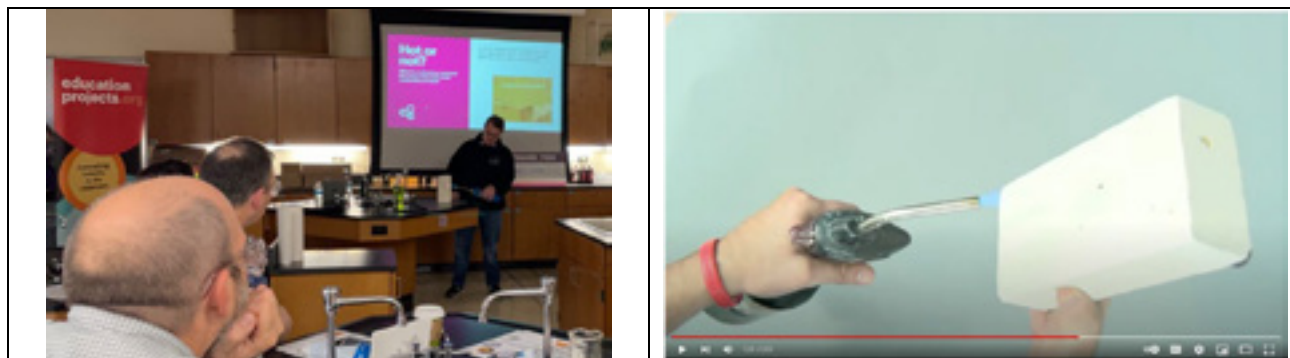ntations reflect the evolving grand challenge issues for refractory engineers to solve: sustainability, hydrogen firing, recycling, nanoscale effects, and more. RCD and the SLS intentionally recruit and nurture young professionals to organize the symposium and give presentations. Nearly 40% of the 200 people who attended the 2023 Symposium were attending for the first time. Anecdotally, many of those first-timers were early career engineers (Figure 3). RCD also organizes sessions at ACerS Annual Meeting at MS&T and is a founding member of UNITECR.



Taylor Perrey and Austin Scheer, both of Zircoa, are representative of the new generation of refractory engineers attending the Refractories Symposium.

Anthony Williamson of Morgan Advanced Ceramics recently earned a B.S. in chemical engineering before entering the refractoryindustry.

*Fig. 3: The proportion of young professionals attending the St. Louis Section/Refractory Ceramics Division meeting has increased in recent years. About 40% of attendees at the 2023 Symposium were first-timers.*

## CONTENT

The Society has published authoritative content in the form of books, journals, and magazines for more than 100 years. Modern internet and social media tools provide new opportunities to showcase the refractory industry. ACerS's *Ceramic Tech Chat* podcast, for example, which is hosted by *ACerS Bulletin* editors, showcases leaders in ceramic and glass science, including the refractory industry. The refractory professionals talk about the industry, as well as their personal career stories (Table 2). Additionally, the High Temperature Times podcast, which is published by HarbisonWalker International and promoted on the ACerS website, provides an excellent insight into the refractory industry. [5]

Each March issue of the *ACerS Bulletin* magazine focuses on refractories. Themes, which come from ACerS members in the refractory industry, reflect the evolution of refractory technology as the industry responds to new requirements. Some recent themes include Refractory solutions for sustainability, Innovations in refractory technology, Going green: Ceramics in renewable energy, Refractory lifecycles, and Refractories as engineered ceramics for industry. The Society promotes *Bulletin* content through email to a global audience of 13,000. The audience expands with promotion of *Bulletin* content over LinkedIn, Facebook, and Twitter. The new digital-based *Bulletin* ensures optimal discoverability of *Bulletin* content. This publishing format allows collection of metrics and will allow *Bulletin* editors to tailor future content.

The Society publishes a thrice-weekly blog called *Ceramic Tech Today* (*CTT*). Through *CTT*, the Society curates content from around the world for the ceramic and glass community. In addition, each issue contains original reporting on developments in the industry. *CTT* is distributed to a global audience of about 11,000, which provides excellent visibility of topics to a targeted audience. Recent blog posts related to refractory topics include

- Effects of expanded graphite content on the performance of magnesia carbon bricks,
- Singling out discrepancies: The effect of magnesium source on a ceramic's final properties,
- New test method for aluminosilicate refractories offers better insight into real-world alkali attack mechanisms,
- Ensuring safe production of metal goods: A review of alumina spinel castables for steel ladles,
- Ceramics processing—are we using the correct sintering and creep models?
- Refractories Symposium resumes in St. Louis with sustainability theme.

Tab. 2: *Ceramic Tech Chat* podcast guests and topics relevant to the refractory industry

| Guest | Affiliation | Podcast topic |
|---|---|---|
| Dana Goski | Allied Mineral Products | Why we like two-year tech degrees |
| Matt Creedon | Washington Mills | Local manufacturing in a global economy |
| Carol Jackson | HWI (formerly) and WRA (formerly) | Leading a global refractories company |
| Scott McCormack | University of California, Davis | Thermodynamics in the classroom and lab |
| Christopher Berndt | Swinburne University of Technology, Australia | Engineering surfaces using thermal spray |
| Jürgen Rödel | Technical University of Darmstad, Germany | Actions for a sustainable future |
| Rita Baranwal | Westinghouse Electric | New technologies for nuclear energy |

## WORKFORCE DEVELOPMENT

Many engineers entering the refractory industry today have general MSE or nonmaterials backgrounds. ACerS partnered with the Edward Orton Jr. Ceramic Foundation to create two certificate programs to train new hires; up-skill non-MSE engineers; and train technicians, production staff, and other personnel, such as purchasing agents and sales engineers.

The Basic Refractory Technology and Intermediate Refractory Technology certificate programs are taught primarily online and conclude with an onsite, hands-on course. Table 3 summarizes the certificate curricula, plus additional refractory courses. Participants may take the full sequence of courses to earn a certificate, or they may enroll in individual courses to build specific skills. Students may purchase a prerecorded course option if attending a live course is impractical. [6]

Since establishing the program in 2020, eight courses have been taught to 180 students, with about one-fourth attending from outside the U.S. Students have said, "It helped me make connections to the work I do daily and understand the background of the materials I work with" and "It was great that the course attacks the knowledge from first principles. Exactly what I needed to help my understanding of refractory. Magnifique."

Tab. 3: Orton–ACerS Refractory Technology program courses.

| Course | Formats |
|---|---|
| **Basic Refractory Technology Certificate** | |
| Refractory Fundamentals | Live, online<br>Prerecorded |
| Characterization of Refractory Microstructures | Live, online<br>Prerecorded |
| Properties of Refractories | Live, online<br>Prerecorded |
| Property Measurements of Refractories | In-person with onsite lab experience at Orton |
| **Intermediate Refractory Technology Certificate** | |
| Manufacturing/Processing of Refractories | In development<br>Live, online |
| Drying and Firing of Refractory | In development<br>Live, online |
| **Course (continued)** | **Formats (continued)** |
| Design and Failure of Refractories | In development<br>Live, online |
| Processing of Refractories Laboratory Instruction | In development<br>In-person with onsite lab experience at Orton |
| **Other refractory technology courses** | |
| Introduction to Refractories | Live, online<br>Prerecorded |
| Introduction to Properties of Refractories | Live, online<br>Prerecorded |
| Introduction to Refractory Compositions | Live, online<br>Prerecorded |
| Advanced Thermal Properties of Refractories | Live, online |

**SUMMARY**

As a professional society, The American Ceramic Society has many tools in its arsenal for promoting careers in STEM and for highlighting careers in the refractory industry. Outreach through student programs, podcast interviews, and publications (blog, magazine, journals, books) communicates the impact of refractory engineering careers to address urgent grand challenges in impactful ways. ACerS's workforce partnership with the Edward Orton Jr. Ceramic Foundation provides practical, immediate, high-quality education for the refractory industry's incumbent workforce and for those new to the industry.

**REFERENCES**

[1]    World Refractories Association, "About Refractories." https://www.worldrefractories.org/about-refractories. Accessed July 5, 2023.
[2]    Society of Women Engineers, "Job Outlook for Engineers." https://swe.org/research/2023/job-outlook. Accessed July 5, 2023.
[3]    R. C. Tillinghast, "The STEM career pipeline system: Optimizing stem outreach through the identification of key development stages from past success indicators," Ph.D. dissertation, Stevens Institute of Technology, 2022.
[4]    Ceramic and Glass Industry Foundation, "Programs." https://foundation.ceramics.org/programs. Accessed July 5, 2023.
[5]    HWI, a member of Calderys, "High-Temperature Times." https://thinkhwi.com/category/podcast/high-temperature-times. Accessed July 5, 2023.
[6]    The American Ceramic Society, "Orton-ACerS Refractory Technology Program." https://ceramics.org/professional-resources/career-development/refractory-technology-program. Accessed July 5, 2023.

**ADDITIONAL RESOURCES**

| | |
|---|---|
| The American Ceramic Society | https://ceramics.org |
| *ACerS Bulletin* | https://ceramics.org/publications-resources/the-bulletin-of-the-american-ceramic-society |
| *Ceramic Tech Today* blog | https://ceramics.org/feature/ceramic-tech-today |
| *Ceramic Tech Chat* podcast | https://ceramics.org/publications-resources/ceramic-tech-chat |
| Ceramic & Glass Industry Foundation | https://foundation.ceramics.org |
| ACerS Learning Center | https://ceramics.org/professional-resources/career-development/learning-center |
| Edward Orton Jr Ceramic Foundation | https://www.ortonceramic.com |

# ON REFRACTORY ENGINEERING EDUCATION EVOLUTION

Michel Rigaud, Ecole Polytechnique, Montreal, Canada

Jacques Poirier, CEMHTI-CNRS, University Orleans, France

**ABSTRACT**

This paper provides answers to stay tune with the "Conceptual Age" refractory producers, users and service providers are already facing for the coming years. This New Age is a major change of paradigm.

Some answers are given to consider how the new research and innovations for new refractory solutions should be conducted with the adequate human resources required for the purposes.

After a review of the education tools now available, those to be the further developed are

then presented, which will involve the participation of all the refractory constituency.

## 1. INTRODUCTION

It took two centuries for the factory workers to outnumber the farmer workers, but then less than one century for the knowledge worker to become the predominant ones.

To-day many of the changes in our societies are propelled by the technological efficiency of the communication networks, to facilitate technology transfers to support the commercial exchanges and the global economy. Just realize how fast the use of the Artificial Intelligence(A.I) and the CHAT-GPT have spread!

This is impacting the entire educational system. Yes, the refractory engineering education has evolved. However, to provide the required knowledge workers with the required technical expertise, it is required to train more engineers to become ''creators" of long term solutions, with a broad vision of our contemporary world.

After a brief review about the FIRE network as a starting block, the needs for innovations and innovators, then of creators will be clarified, so that the need to extend the CDIO approach will be made apparent. To conceive the future with a positively built-thinking mind, acting in a competitive spirit (i.e., keeping competition and collaboration in balance) will lead to the conclusion. It is a matter of education and collaboration.

## 2. THE FIRE'S NETWORK

Fire has been able to develop into a non-bricks and mortars network with 10 academic institutions (Austria, Brazil, China, France (2), Germany (2), Korea, Spain, United-States) with 14 industrial partners. Details of the FIRE mission, goals, research, and education programs have been described at different times of its evolution [1-2-3]and presented on its web-page (http://fire-refractory.org). In short FIRE does fund international studies and research activities associated to allow graduate students to obtain a degree in refractory materials. FIRE pools the expertise, the experience and the

712

willingness of some worldwide most competent persons and the availability of their installations to tackle some innovative research programs at the precompetitive level. In the last 15 years, FIRE has delivered over 50 diplomas to FIRE'S alumni, most of them still strongly related to our industrial sector, including manufacturers, raw materials providers, all others service providers, and users of refractories.

## 3. INNOVATIONS AND INNOVATORS

To appreciate fully what innovations involved, it is important to deal with patent rights, technology transfer limits, business laws, foreign exchanges policies, technology forecasting, strategic planning, including the economical, environmental and ethical aspects.

From an educational point of view to train 'innovator' this constitute an immense challenge to learn, to learn to learn, to teach, to use in a rapidly changing world.  But there is no reason not to tackle the task, challenging partners, and the students to develop bit by bit some of the needed innovations at our disposal right now: such as better high temperature insulting materials, others with ultra high temperature corrosion and erosion resistance, and for to-morrow refractories for new carbon free processes, and also near-net-shaped casting of steels. FIRE'S contribution into such projects as ATHOR and CESAREF [4] are valuable steps forward in that direction.

## 4. CREATORS

In order to benefit from technical innovations such as robotization, virtual reality, artificial intelligence, etc.…to bring the trained refractory engineers to be more at ease into the 'Conceptual Age' [5] it is time to educate new potential refractory leaders to realize that the human cultural values are deeply influenced by the objects being manufactures in our surroundings. It does require to develop candidates with personal and interpersonal skills.

Then FIRE'S students should be confronted with different aspects of: i) knowledge discovery along with data mining, ii) system thinking and discussion about the abstraction necessary to define and model systems and to use metaphoric thoughts, taking on account that the brain rules, iii) professional skills and the attitudes to assert the social and technical impact of new discoveries and innovations.

To incorporate such preoccupations into a graduate a cursus on refractories do require team-teaching with colleagues of cognitive sciences faculties such psychology of learning and/or sociology. The goal is to facilitate the development of the right side of our brain. To distinguish between objective (left-brain) and subjective (right-brain) knowledges, in order to move into 'Conceptual Age' had been considered recently with other academic refractory colleagues (4) in some more details.

## 5. THE CDIO APPROACH IN THE FUTURE

CDIO approach stands for Conceive, Design, Implement and Organize. This is a road-map well defined, in details, in [6]. FIRE'S alumni have been trained. as graduate students, at the M.Sc. and Ph.D. levels, to accomplished experimental research projects focus on industrial needs, defined collaboratively in within the FIRE network. In order to meet perceivable future needs, more emphasis on imaginative rationality must be implemented.

At the end, FIRE alumni should have learned how to implement efficient changes at 4 levels: i) the technical efficiency based on solid STEM core, ii) the production efficiency based on pragmatism and memorable experiences, iii) the organizational efficiency based on some management know-how, iv) the economical efficiency based on financial and political analysis.

It is necessary to insist on the personal and interpersonal skills required to grasp the impact of new technological innovations and a certain awareness of the discovers made by the human cognitive sciences.

To finally benefit from such an approach, for the immediate future, it would still be necessary to conclude an evaluation procedure, to be followed by the academic institutions with the accepted standards, approved by the network members, to provide the proper feed-back, to appreciate the evolution over time.

## 6. CONCLUSION

Under the hospices of the Unified Technical Conference on Refractories it is good to notice that since 2003, Education has always been considered as an issue of concern. It is essential to keep such an interest on educational aspects to be able to seduce and recruit the human ressources required to surf on the E-waves. E for economy, E for ethic (a key determinant in the 'Conceptual Age' we do need to adjust to).

All our leaders need to coordinate their efforts and join forces to induce university administrators and politicians at all levels, to sustain refractory engineering education as a needed activity in the globalized world education system.

It is essential to define broad enough vision to allow for new initiatives to emerge. And yes networking in a competitive way is surely a way to prosper. Again, it is a matter of education and collaboration.

## 7. ACKNOWLEDGEMENTS

## 8. REFERENCES

[1] Rigaud, M. Education and research: their relevance to the future prosperity of the refractory industry. Proceedings UNITECR 2005, Orlando, Fl., USA, pp.118-121.

[2] Rigaud, M., FIRE: progress and outcome on education. Proceedings UNITECR 2011, Kyoto, Japan, pp 104-107

[3] Rigaud, M., Poirier, J., presented at UNITECR 2022, Chicago, USA, published in International Journal of Ceramic Engineering & Science. 2022; 1-5. https://doi./10.1002/ces.10121

[4] Rigaud, M., Poirier. J., Huger, M., Tonnesen, T., Pandolfelli., A Refractory Engineering Program for the 21 Century. ECRS Open Source, accepted May 2023.

[5] Pinker, D., A whole new mind: moving from the information age to the conceptual age. Why the right-brainers will rule the future. River Head Books, New York, USA, 2005

[6] Crawley, E., Malmqvist, J., Soren, O., Brodeur, D., Rethinking Engineering Education The CDIO approach. Springer Science, New-York, USA, 2007

# The European Center of Refractories
## future – systemrelevant – sustainable – unique
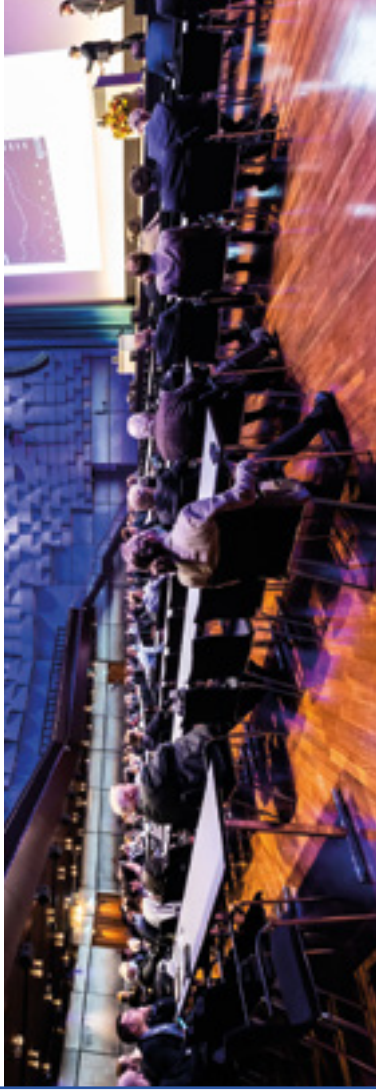


### Knowledge – Education – Training

The Integrated Refractory Education System (IRES) supports the development of young school leavers across all levels of vocational education and training, from basic apprenticeship courses through to graduate and doctorate programmes. The Koblenz University of Applied Sciences offers a complementary vocational programme that leads to the qualification of Ceramic Technician ("Keramiktechniker") as well as an academic programme leading to the degree of Bachelor of Engineering which, in cooperation with the University of Koblenz and Landau, can be crowned with the degree of Master of Ceramic Science and Engineering. This cluster of expertise in conjunction with the close collaborative relationship maintained with the University and the Ceramics Education and Research Centre (Bildungs- und Forschungszentrums Keramik e.V. / BFZK) enables the wealth of knowledge about refractory products, their manufacture and use to be imparted and shared in a well-condensed way across all levels, up to the university-awarded doctoral degree.

**European Centre for Refractories**

### Bildungs- und Forschungszentrum Keramik (BFZK)

BFZK offers with its 8 institutes in Höhr-Grenzhausen a combination of facilities that is unique in the world, all of which deal with the topic of training and further education as well as research within ceramics. The Montabaur vocational school, with its ceramics branch, is one of the dual partners in ceramics initial training and teaches the necessary theoretical knowledge for successful completion as a skilled worker in industry or as a journeyman in the trade. Further training as a ceramics technician or ceramics designer at the technical colleges for ceramics technology and ceramics design is then just as possible as studying for a bachelor's or master's degree in engineering – materials engineering, ceramics and glass – on the Westerwald Campus. Furthermore, with the Bachelor or Master of Fine Arts at the Institute for Artistic Ceramics and Glass, which also belongs to the Koblenz University of Applied Sciences, there are opportunities for further training in areas of art. Information about the 8 members of the education and research center: www.bfzk.de



---

# The European Center of Refractories

## Study Guide "Materials Engineering Glass & Ceramics"



**NEW**

The Koblenz University of Applied Sciences offers an application-oriented, engineering Bachelor of Engineering, Bachelor of Engineering dual, Ceramics Industrial Engineer and a consecutive Master of Ceramic Science and Engineering on the Westerwald campus. The range of courses: broadly based, clearly focused on ceramics and glass, unique. The location can look back on a 150-year tradition in training and is the oldest location of the Koblenz University of Applied Sciences. Together with the local research institutions, the European Center for Refractories (ECREF) and the Research Institute for Inorganic Materials-Glass-Ceramics (FGK), the location forms a unique concentration of training and research in a small radius. All those involved benefit from research and teaching, which also directly benefit training through joint projects with industry-related research. Due to the close and exceptionally good networking with the refractory or ceramic industry, contacts are made at an early stage, which enables the students to write their theses in the companies where they later find their professional start. Both bachelor's and master's students have excellent opportunities on the job market.

## Master's degree "Refractory Engineering" Tandem professorship at Koblenz University of Applied Sciences



**Prof. Dr. Amin El Gammal**

The German refractory industry is a world leader in product quality and in the application areas of high-temperature processes for steel, cement or glass. The processing of refractory materials is of particular importance. That is why the German refractory industry is supporting the establishment of a professorship "Refractory Engineering" at the Koblenz University of Applied Sciences.as an industrial partner. On the professorship Dr. Amin El Gammal appointed. This tandem professorship between the Koblenz University and the refractory industry will be connected in the European Refractory Center and the Westerwald-Campus and organized by ECREF gGmbH. The development of the part-time English-language master's degree program "Refractory Engineering" is aimed in particular at international bachelor's graduates in materials science or civil engineering who are about to or after starting their business careers. The content will be divided into the three areas of "Refractory Engineering", "Refractory Materials" and "Services". Aspects such as building law, construction site management or approval procedures are also dealt with in the curriculum.

Managing Directors: **Dr. Christian Dannert | Thomas Kaczmarek**

📍 Rheinstr. 58
56203 Höhr-Grenzhausen
Germany

📞 +49 2624 94 33 130

✉ info@ecref.eu

🌐 www.ecref.eu

# EU ATHOR PROJECT (2017–2022) – DIRECT IMPACTS ON INTERNATIONAL REFRACTORY COMMUNITY

Marc HUGER, University of Limoges, Institute of Research for Ceramics (IRCER), UMR 7315, Limoges, France

**ABSTRACT**

ATHOR (Advanced THermomechanical multiscale mOdelling of Refractory linings) was an innovative, collaborative and interdisciplinary European project that brought together 6 academic beneficiaries and 8 private partners. The main objective was to develop high-end engineering technologies in material engineering and numerical simulations thanks to an intensive cooperation between academia, raw materials suppliers, refractory producers and end-users. Starting from material characterization, all significant properties were investigated, including fracture behaviour, tension and compression creep behaviour, corrosion and thermal shock resistance. The interdisciplinary aspects have been addressed thanks to a multiscale approach looking at the influences of micro-, meso- and macro-characteristics on each other. To conduct their research and interlink the different topics, the 15 recruited researchers have taken advantage of the most sophisticated numerical tools to model, design and predict the life of different lining configurations in critical operation conditions. The ATHOR network was deeply committed to provide a combination of research and training activities which has supported and strengthened the initiative of the Federation for International Refractory Research and Education (FIRE). The different key impacts, achieved on several levels in the international refractory community, of this EU project, will be highlighted here.

## INTRODUCTION

Refractories are heat-resistant materials used as inner linings of high temperature furnaces, reactors and processing units. Unique and advanced ceramic materials, refractories sustain complex combinations of thermomechanical stresses and chemical/physical wear generated by fluids and chemical agents used during high temperature fluid processing. As the only low-cost family of materials able to sustain operating conditions, at temperatures typically above 1000°C, refractories are widely used in energy intensive industries such as Iron and Steel production. Vessels commonly lined with refractories include the steel ladle which, due to the harsh environment, typically require the lining to be changed every 8 weeks. Extending the lifetime of refractories under such conditions is thus of importance both economically and environmentally.

ATHOR was a H2020 MSCA European Training Network combining seven academic and eight industrial partners across Europe. The project, which has run from October 2017 to March 2022, focussed on the training of 15 young researchers in multi engineering required fields for a better understanding of thermomechanical behaviour of refractory linings. The research was aimed at the design of more robust and reliable refractory linings, undertaken through the combination of advance numerical modelling with both small- and large-scale laboratory research (from the micro to the 10-meter scale). This will allow the development of innovative numerical simulations that will form the basis of future research as well as monitoring form a safe location. Ultimately, it represents a reduction of the refractory costs, an increase of the equipment's availability and an enhanced process control. In total, 16 milestones have been past, and 43 deliverables have been submitted to the European Commission. This paper is an overview of the project, the achieved results and the socio-economic impact.

## ATHOR APPROACH TO REFRACTORIES RESEARCH

The European steel industry is a world leader in innovation and environmental sustainability. A constant engineering of refractories is needed to cope with new and more demanding requirements in the steel making process. The steel ladle forms the hearth of the steel making process and is a major refractory using facility accounting for about ¼ of all refractory consumption. Dependent on its purpose and position in the steel ladle, the requirements for the refractory materials are various ranging from high thermal stability to high erosion resistance, high corrosion resistance, penetration resistance, thermomechanical stability, impact resistance, flexibility and creep resistance. The concerted work in the ATHOR program was therefore be focused on the steel ladle as model installation.

The main scientific goals of ATHOR were to adapt and develop the most advanced modelling strategies and experimental technologies to the refractories field such that reliable computations and measurements, in the temperature range of the applications of these materials, could be performed. ATHOR targets the development of high-end engineering technologies in the fields of material's science and numerical simulations to give a substantial contribution through the design of more robust and reliable refractory linings.

The main training objective was to prepare the 15 Early-Stage Researchers (ESRs) to be the next generation of highly employable scientists and engineers in the refractory and related sectors. With the evolution of industry towards digital twins and the use of advanced numerical simulations based on real world data, the ESRs needed a basis in both numerical simulations and fundamental materials science. This was achieved through a series of Refractory Training Courses (RTCs) and online webinars, which were recorded and stored in a database such that future interested PhD students can benefit from the time and energy given by the ATHOR industrial and academic experts. The highly interconnected and international nature of this project meant that the ESRs were required to communicate extremely precisely with each other as well as the industrial and academic partners to determine the exact nature of the data required for the numerical simulations and the parameters used in the lab to generate this information. Communications skills were thus also developed as well as soft-skills important for the future employability of the ESRs such as leadership skills. The training was provided at both the local universities and via centrally organised activities.

The specific objectives of the ATHOR network were defined as:
- Deliver the best training to young researchers to reach a scientific level by addressing their scientific and transversal needs.
- Enable young researchers, through their tailored training and regular mobility, to "cross-pollinate" industry and academia;
- Give the young researchers the opportunity to be close to the industry and to face the actual engineering challenges;
- Support the development of new characterization devices and modelling methods to offer solutions to current S/T challenges;
- Create a multidisciplinary environment where industries and academia can share ideas and find solutions together.
- Explore the capability of advanced numerical modelling in order to design better materials and better refractory linings, consequently improving energy efficiency and thermomechanical properties of products.
- Assist the European refractory and steelmaking industries to identify technological improvements by providing high performance characterization and modelling tools which can improve their competitiveness.

To guarantee a maximum economic impact when ATHOR methodologies were implemented in practice, the consortium decided to carry out research on different refractory materials, in well organised Work Packages. These Work Packages:
- involved materials with different chemical composition and microstructure so as to cover a wide diversity of end-user applications;
- involved different key scientific topics sufficiently critical and/or of economically importance;

717

- were sufficiently generic for the European market to cover the different current interests of the industrial partners.

## ORGANISATION OF THE SCIENTIFIC WPS

The ATHOR project brought together 7 academic and 8 industrial partners to carry out cutting-edge research, using state-of-the-art technology, in highly specialized areas including materials science, structural engineering and numerical modelling. Research ranged from, the development of techniques to initiate, track and analyse small scale crack formation, to the construction and analysis of large-scale structures, such as a 3D pilot steel ladle, which were subjected to various heating and loading regimes.

The scientific work program consisted of 4 highly interconnected, scientific Work Packages, Figure 1.



*Figure 1 : The four highly interconnected, scientific Work Packages of the ATHOR project.*

WP1 was dedicated to the improvement of measurements tools through the development of experimental methods (contactless optical techniques, high temperature strain gauges…). These tools were then employed in the collection of the mechanical data necessary to study refractory materials in service conditions (temperature up to 1500°C, large structures, industrial environment). Previously, these techniques were mainly used for different materials in a laboratory environment up to 500 °C and for small structures. The aim of WP1 was thus to improve these experimental optical methods in order to accurately quantify low level of strain fields and to make measurements possible in extreme conditions associated with the environment of in service refractory materials.

WP2 was dedicated to the characterization of selected materials, at room and elevated temperatures, in a virgin or corroded state by conventional and specific experimental techniques. This WP has provided all the experimental results needed for characterisation and understanding of the materials behaviour. Furthermore, the input parameters for the finite element simulation have been determined for the modelling from micro to macro scale. WP2 took advantage of the ATHOR network to apply the most appropriate experimental device to each task. Where available, different methods within the ATHOR network were used to validate the experimental results and improve the testing procedures.

WP3 was dedicated to the production of dedicated modelling methods and numerical tools to optimize the design of industrial refractory linings. The different proposed approaches cover all the scales that impact the thermomechanical refractory lining behaviour: from the material scale (i.e. microstructure) to the industrial lining (structural computation). The multiscale approach was developed from micro to macro to establish the models and then, inversely, from macro to micro to optimize each scale from the final vessel requirements point of view.

WP4 was dedicate to advanced measurements for numerical validation. As such, it closely interacted with WP1 and WP3, the improved and newly developed methodologies for thermal and mechanical characterization of refractories within WP1 were used in WP4. Using a multiscale approach, measurements were performed to validate the advanced numerical models developed in WP3.

## KEY SCIENTIFIC RESULTS

### Improvement of measurements tools

Expertise developed by ATHOR partners, for example on Digital Image Correlation, mark tracking in 2D and stereovision configuration, were applied to monitor deformation and temperature of the steel shell of the industrial ladle to validate the results of numerical modelling based on mesoscopic characterization. Moreover, a bi-axial high temperature testing device, for a 1 m² masonry wall, available through ATHOR network, was improved thanks to additional instrumentation. A second laboratory pilot device, at around 2 m in diameter, was designed to reproduce the stress state induce by the cylindrical shape of industrial vessels. They were used to validate, at mesoscopic level, the results of numerical modelling based on new mathematical and numerical method taking into account mesoscopic materials and contact properties. All the different experimental technologies used for the characterization of individual materials, subsystems (e.g. bricks with or without mortar, castable-based linings, bed joints…) and the overall thermomechanical behaviour of selected industrial devices, were strongly enhanced through WP1. These included thermal and strain fields instrumentation as well as devices for thermo-physical properties characterisation, thermomechanical characterisation and validation of masonry and vessels.

### Advanced characterization of raw materials, refractories and joints

The experimental results, of the refractory materials under investigation, that were required to characterise and understand the materials behaviour were obtained here. The microstructure and its evolution were described, thermal and mechanical characterisations were carried out, fundamental corrosion mechanisms were described as well as the mechanical characterisation of corroded samples and finally the behaviour of the joints was defined. Thermal expansion and thermal conductivity were tested by laser flash or hot wire method, Young's modulus by ultrasonic echography or by Resonance Frequency and Damping Analyser (RFDA), damage monitoring by acoustic emission, stress-strain and creep laws were determined for tension and compression and work of fracture by wedge splitting test.

### Innovative modelling from microstructure to industrial scale

Different modelling techniques were used depending on the material being modelled. The Discrete Element Method (DEM) was used for the modelling of the microstructure and thermomechanical behaviour. When regarding the modelling of bricks and joints, the multi-surface plasticity theory and nonlinear homogenisation method were used and compared. For the full-scale industrial steel ladle, the simulation of a representative volume element was also compared with the multi-surface plasticity theory and nonlinear homogenisation method.

### Advanced measurements for numerical validation

Refractory masonries were characterized experimentally, in order to obtain data for the validation of advanced analysis methods, as well as for subsequent simulation of industrial problems to allow industrial device optimization. The selected materials and structures were characterized under different conditions, and their thermal and mechanical properties investigated under complex limit conditions. A large and comprehensive experimental campaign was implemented, wallets were constructed and subjected to uniaxial and biaxial loading from room temperature to high temperature. A 3D pilot steel ladle was designed, constructed and tested. The 3D pilot scale and the full-scale models investigated have provided unique and valuable data for the calibration and validation of the advanced numerical macro-models developed in WP3.

## RESULTS DISSEMINATION AND EXPLOITATION

As part of the ATHOR training program, the 15 ESRs have had the opportunity to disseminate the results of their cutting-edge research through workshops, summer schools, international journals and

international conferences across the globe. The ATHOR ESRs have participated in conferences in Japan, China, America and Europe and have published their work in Rank A journals such as the Journal of the European Ceramic Society, Ceramics International and the International Journal of Mechanical Sciences. These published results are openly available via the ATHOR website and on the Zenodo platform, the list of published articles is presented below:

VITIELLO Diana, NAIT-ALI Benoit, TESSIER-DOYEN Nicolas, TONNESEN Thorsten, LAÍM Luís, REBOUILLAT Lionel, SMITH David,
Thermal conductivity of insulating refractory materials: Comparison of steady-state and transient measurement methods,
Open Ceramics 2021, 6, 100118.
https://doi.org/10.1016/j.oceram.2021.100118

VITIELLO Diana, NAIT-ALI Benoit, TESSIER-DOYEN Nicolas, REBOUILLAT Lionel, SMITH David,
Thermal conductivity of porous refractory material after aging in service with carbon pick-up,
Open Ceramics 2022, 11, 100294.
https://doi.org/10.1016/j.oceram.2022.100294

KACZMAREK Robert, DUPRÉ Jean-Christophe, DOUMALIN Pascal, POP Octavian, TEIXEIRA Lucas, HUGER Marc,
High-temperature digital image correlation techniques for full-field strain and crack length measurement on ceramics at 1200°C: Optimization of speckle pattern and uncertainty assessment,
Optics and Lasers in Engineering 2021, 146, 106716.
https://doi.org/10.5281/zenodo.6556728.
https://doi.org/10.1016/j.optlaseng.2021.106716

ASADI Farid, ANDRÉ Damien, EMAM Sacha, DOUMALIN Pascal, HUGER Marc,
Numerical modelling of the quasi-brittle behaviour of refractory ceramics by considering microcracks effect,
Journal of the European Ceramic Society 2022, 42(3), 1149-1161.
https://doi.org/10.5281/zenodo.5877203
https://doi.org/10.1016/j.jeurceramsoc.2021.11.016

ASADI Farid, ANDRÉ Damien, EMAM Sacha, DOUMALIN Pascal, KHLIFI Imad, HUGER Marc,
Investigation of different discrete modeling strategies to mimic microstructural aspects that influence the fracture energy of refractory materials,
Open Ceramics 2022, 11, 100288.
https://doi.org/10.1016/j.oceram.2022.100288

ASADI Farid, ANDRÉ Damien, EMAM Sacha, DOUMALIN Pascal, HUGER Marc,
Advances in Micro-Mechanical Modeling Using a Bonded-Particle Model and Periodic Homogenization Within Discrete Element Framework Applied to Heterogeneous Ceramics,
Journal of the European Ceramic Society 2023, 43, 1205-1219.
https://doi.org/10.1016/j.jeurceramsoc.2022.10.073

REYNAERT Camille, SNIEZEK Edyta, SZCZERBA Jacek,
Corrosion tests for refractory materials intended for the steel industry – a review,
Ceramics-Silikáty 2020, 64 (3), 278 - 288.
https://doi.org/10.13168/cs.2020.0017.

KIELIBA Ilona, DOMINIK Ireneusz, LALIK Krzysztof, TONNESEN Thorsten, SZCZERBA Jacek, TELLE Reiner,
Self-Excited Acoustical System Frequency Monitoring for Refractory Concrete under Uniaxial Compression,
Energies 2021, 14, 2222.
https://doi.org/10.3390/en14082222

TADAION V., ANDREEV K., ZHU Q., WANG W., YIN Y., TONNESEN T.,
Thermal and mechanical cyclic tests and fracture mechanics parameters as indicators of thermal shock resistance - case study on silica refractories,
Journal of the European Ceramic Society 2019, 39(4), 1650-1659.
https://doi.org/10.1016/j.jeurceramsoc.2018.12.062

TEIXEIRA Lucas, GILLIBERT Jean, SAYET Thomas, BLOND Eric,
A creep model with different properties under tension and compression - Applications to refractory materials,
International Journal of Mechanical Sciences 2021, 212, 106810.
https://doi.org/10.1016/j.ijmecsci.2021.106275

TEIXEIRA Lucas, SAMADI Soheil, GILLIBERT Jean, JIN Shengli, SAYET Thomas, GRUBER Dietmar, Blond Eric,
Experimental investigation of the tension and compression creep behavior of alumina-spinel refractories at high temperatures,
Ceramics 2020, 3, 372-383.
https://doi.org/10.3390/ceramics3030033

ALI Mahmoud, SAYET Thomas, GASSER Alain, BLOND Eric,
Computational Homogenization of Elastic-Viscoplastic Refractory Masonry with Dry Joints,
International Journal of Mechanical Sciences 2021, 196, 106275.
https://doi.org/10.1016/j.ijmecsci.2021.106275

ALI Mahmoud, SAYET Thomas, GASSER Alain, BLOND Eric,
Transient thermo-mechanical analysis of steel ladle refractory linings using mechanical homogenization approach,
Ceramics 2020, 3, 171-189.
https://doi.org/10.3390/ceramics3020016

ALI Mahmoud, OLIVEIRA Rafael, PEREIRA João, RODRIGUES João, LOURENÇO Paulo; MARSCHALL Hans Ulrich, SAYET Thomas, GASSER Alain, BLOND Eric,
Experimental characterization of the nonlinear thermomechanical behaviour of refractory masonry with dry joints,
Construction and Building Materials 2023, 364, 129960.
https://doi.org/10.1016/j.conbuildmat.2022.129960

OLIVEIRA Rafael, RODRIGUES João, PEREIRA João, LOURENÇO Paulo, LOPES Rúben,
Experimental and numerical analysis on the structural fire behaviour of three-cell hollowed concrete masonry walls,
Engineering Structures 2021, 228, 111439.
https://hdl.handle.net/1822/69519
https://doi.org/10.1016/j.engstruct.2020.111439

OLIVEIRA Rafael, RODRIGUES João, PEREIRA João, LOURENÇO Paulo, MARSCHALL Ulrich,
Thermomechanical behaviour of refractory dry-stacked masonry walls under uniaxial compression,
Engineering Structures 2021, 240, 112361.
https://hdl.handle.net/1822/72527
https://doi.org/10.1016/j.engstruct.2021.112361

OLIVEIRA Rafael, RODRIGUES João, PEREIRA João, LOURENÇO Paulo, MARSCHALL Ulrich,
Normal and tangential behaviour of dry joints in refractory masonry,
Engineering Structures 2021, 243, 112600.
https://hdl.handle.net/1822/73394
https://doi.org/10.1016/j.engstruct.2021.112600

OLIVEIRA Rafael, RODRIGUES João, PEREIRA João,
**Numerical simulations on refractory linings for steel casting vessels**,
**Fire Safety Journal** 2023, 138, 103794.
https://doi.org/10.1016/j.firesaf.2023.103794

DARBAN Sina, REYNAERT Camille, LUDWIG Maciej, PROROK Ryszard, JASTRZĘBSKA Ilona, SZCZERBA Jacek,
Corrosion of alumina-spinel refractory by secondary metallurgical slag using coating corrosion test,
Materials 2022, 15(10), 3425.
https://doi.org/10.3390/ma15103425

SAMADI Soheil, JIN Shengli, GRUBER Dietmar, HARMUTH Harald, SCHACHNER Stefan,
Statistical study of compressive creep parameters of an alumina spinel refractory,
Ceramics International 2020, 46(10), Part A, 14662-14668.
https://doi.org/10.1016/j.ceramint.2020.02.267

SAMADI Soheil, JIN Shengli, HARMUTH Harald,
Combined damaged elasticity and creep modeling of ceramics with wedge splitting tests,
Ceramics International 2021, 47(18), 25846-25853.
https://doi.org/10.1016/j.ceramint.2021.05.315.

SAMADI Soheil, JIN Shengli, GRUBER Dietmar, HARMUTH Harald,
A comparison of two damage models for inverse identification of modeIfracture parameters: Case study of a refractory ceramic,
International Journal of Mechanical Sciences 2021, 197, 106345.
https://doi.org/10.1016/j.ijmecsci.2021.106345

SAMADI Soheil, JIN Shengli, GRUBER Dietmar, HARMUTH Harald,
Thermomechanical finite element modeling of steel ladle containing alumina spinel refractory lining,
Finite Elements in Analysis and Design 2022, 206,103762.
https://doi.org/10.1016/j.finel.2022.103762

GAJJAR Pratik, ALI Mahmoud, SAYET Thomas, GASSER Alain, BLOND Eric, PEREIRA João, LOURENÇO Paulo,
Numerical study on the nonlinear thermomechanical behaviour of refractory masonry with dry joints,
Engineering Structures 2023, 291, 116468.
https://doi.org/10.1016/j.engstruct.2023.116468

GAJJAR Pratik, PUT Pieter, PEREIRA João, LUCHINI Bruno, LOURENÇO Paulo, SINNEMA Sido,
Characterisation of mortarless refractory masonry joints under elevated temperatures,
Engineering Structures 2023, 275, 115234.
https://doi.org/10.1016/j.engstruct.2022.115234

This list of publications will continue to be added to as the ESRs finalise their PhDs which is standard for this type of project. However, while the PhDs have come to an end, the work that has been produced during ATHOR will continue to be exploited. For example, measurement tools that have been developed and improved, such as the ATHORNA device, bi-axial press and 3D pilot plant, will continue to be used by the industrial partners to generate data for future projects. A database of thermomechanical behaviour of large-scale specimens has also been developed for different testing configurations. The advanced characterisation of raw materials, refractories and joints has led to a plethora of information being made available to partners to use as a baseline against which future products can be compared. This work also demonstrated how microstructures can improve resistance against thermomechanical loads by, for example, inducing a dedicated microcrack formation. This phenomenon has the potential to be exploited in other refractory applications such-as in the aluminum, foundry, cement and petrochemical industries. Several numerical models have been developed over the course of ATHOR to determine material parameters and simulate the thermomechanical behaviour of refractory materials. These models are now being employed in both academic and industrial partners in various ongoing projects.

**SOCIO-ECONOMIC IMPACT OF THE PROJECT**
ATHOR was built on an international network of academic and industrial institutes (Federation for International Refractory research and Education - FIRE) focused on the development of the refractory industry. This network aims to promote the refractories industry and provide training to young researchers. This solid basis for the ATHOR project has led to a free-flowing exchange between the

partners from the very beginning of the project and this strong foundation has enabled the consortium to adjust to the changes to the initial planning due to the COVID-19 pandemic. This has limited the effect the pandemic has had on the project and resulted in high impact achievements on several levels.

**Direct impact of ATHOR on the ESRs**
The employability of the ATHOR ESRs has been greatly impacted through participation in this project. They have received training on cutting-edge research projects using state-of-the-art technology, and on transferable skills. Simultaneously, the ESRs have developed an international network and have gained experience working in an interdisciplinary and intercultural environment. This was achieved, for example, by the completion of at least one secondment, per ESR, with a project partner. Currently 11 out of 15 ESRs are employed as postdocs, engineers or R&D professionals with the four remaining ESRs writing their theses.

The communication skills of the ESRs have also benefitted from ATHOR in several ways. The ESRs have all presented work at international conferences and "ATHOR industrial feedback events" to scientific audiences, improving their presentation skills and increasing their networks at the same time. On top of this, communication with the general public was achieved through making personal videos for the website, as well as contributing to a short video, drawmylife and a short documentary produced by the BBC. ESRs were also face-to-face with the general public in events such-as the European researchers night and during the presentation of the ATHOR travelling exhibition "CeramiK".

The "CeramiK" exhibition is aimed at 11-18 year old students and combines technical concepts, presented in plain language (English and the corresponding translation depending on the location), visually impressive imagery and hands-on experiments and games. The ESRs were all implicated to some extent in the production of the text, images and suggestions of experiments that could capture the imagination of younger students.

All of these activities have enhanced different aspects of the ESRs communication skills while at the same time increasing the visibility of the project on both the scientific stage and to the general public.

Over the course of the project, eight ESRs were also chosen by their peers to represent the ESRs on the ATHOR Supervisory board. This provided ESRs with first-hand experience on how an international, interdisciplinary and intercultural project is managed as well as actively participating in the decisions and actions that were addressed.

**The impact of ATHOR at a local level**
The refractories industry is known within the industry as the "hidden industry". This is because, while refractories are fundamental to the production of materials at high temperature (steel, cement, glass etc.) the general public are unaware of their existence. The lack of visibility has resulted in difficulties recruiting talented research engineers who are required to modernise a business that is relied on by industries across Europe. As such, 15 ATHOR ESRs have been trained with the skills needed to directly respond to this need for high quality engineers in the short term and the visibility of the industry amongst future R&D engineers has been increased to respond to this need over the long term.

This new group of highly skilled, young professionals will induce a new movement in the industry towards new technologies and scientific approaches. They will act as light-towers, multiplicators through their social networks, and be the ambassadors to attract new talents to the refractory industry in the near future. The training received by the ESRs, at the ATHOR Refractory Training Courses and a series of webinars by academic and industrial experts, was recorded and stored on the database ELEANOR. Different levels of access can be granted (ranging from "general public" to "ATHOR consortium only" depending on the preference of the author of the content) that can be accessed by future refractories students free of charge. Thus, local universities have access to high quality,

industrially relevant teaching materials, which will continue to be updated after ATHOR, to provide to future students. It will also be used in an industrial context to train new generations of researchers, engineers, and for those who want to refresh their knowledge.

Regarding the long-term, two main tools were developed during the project, the dedicated videos and the "CeramiK" exhibition. These tools will be used to attract new students in the domain of refractory materials and structures. They will most likely be the best marketing tools to attract people far beyond the four years of the project itself. They will give visibility of the refractory industry to all levels of the society including policy makers, young talent looking to choose their career paths, and to researchers and engineers in industries beyond refractories. Those tools will definitely facilitate the attraction of excellent talent to join the relatively unknown and small refractory community that is so essential to all high temperature processes and to our daily lives.

**The impact of ATHOR on a scientific level**
From refractory producers through to end users, all sections of the refractories value chain have benefitted from the research carried out during the ATHOR project.

New and improved measurement tools have been developed including the ATHORNA device, a bi-axial high temperature testing device and a 3D pilot steel ladle. These were used to validate, at mesoscopic level, the results of numerical modelling based on new mathematical and numerical method taking into account mesoscopic materials and contact properties. Both the measurement tools and models will continue to be exploited by both the industrial and academic partners.

A large database of data, generated from the advanced characterisation of raw materials, used in refractories manufacture has been developed. This will remain available to the project partners for future use.

The optimisation of industrial devices will be made possible through future simulations of industrial problems. In order to obtain data for the validation of advanced analysis methods, refractory masonries were characterized experimentally under different, complex conditions. A large and comprehensive experimental campaign was implemented, wallets were constructed and subjected to uniaxial and biaxial loading from room temperature to high temperature. A 3D pilot steel ladle was designed, constructed and tested. The 3D pilot scale and the full-scale models investigated have provided unique and valuable data for the calibration and validation of the advanced numerical macro-models developed and will continue to be exploited by our partners.

One of the most significant and direct impacts is without a doubt that made by the direct employment of ERSs by the industrial partners. With their expertise on modelling and characterization, the ESRs will be part of new development activities to reduce cost and time required for the development of new materials and technologies.

The scientific and technical exchanges in the ATHOR consortium will continue beyond the life of the project and will facilitate future cooperation between refractory suppliers and steel producers. In addition, having some academic partners beyond the classical ceramic/refractory domain was very useful as the transfer of knowledge was possible and very efficient, specifically in the case of expertise on joints and mortar from the civil engineering field. New ideas have been triggered by the mix of expertise.

This network has already and will continue to foster collaboration and procurement of funding towards the development of other research projects. For example, the recently awarded Horizon Europe MSCA-DN-ID project CESAREF has several original partners from the ATHOR project.

# EU CESAREF PROJECT (2022–2026) – A COMING CONTRIBUTION TO EUROPEAN GREEN DEAL

Marc HUGER, University of Limoges, Institute of Research for Ceramics (IRCER), UMR 7315, Limoges, France

## ABSTRACT

The movement of the Iron & Steelmaking (I&S) industry towards Net-Zero emissions and digitalized processes through disruptive, breakthrough technologies will be achieved through the use of Hydrogen. The biggest challenge for the refractory industry is to continue to meet the performance expectations while, at the same time, moving to a more sustainable production direction. The complexity and urgency of these technological changes, highlighted by the European Green Deal, requires a Concerted European Action on Sustainable Applications of REFractories (CESAREF). A consorted and coordinated European network, with steel, refractory and raw material producers collaborating with key academic poles, will tackle the following key topics: efficient use of raw materials and recycling, microstructure design for increased sustainability, anticipation of hydrogen steelmaking, energy efficiency and durability.

While creating new developments in the I&S and refractory industries, the network will train highly skilled doctoral candidates capable of communicating and disseminating their acquired knowledge. CESAREF will create a core team across the European refractory value chain, accelerating the drive of the European refractory industries towards sustainable materials and processes, as well as Net-Zero emission steel production. This will help to create and secure sustainable employment in the European refractory and I&S industries.

## INTRODUCTION

Refractories are unique ceramic materials used in vessel linings and components to contain and process fluids, solids and/or gases at high temperature. They can sustain complex combinations of thermomechanical stresses and chemical/physical wear generated by fluids and chemical agents. Being the only materials able to sustain operation conditions at temperatures typically above 1000 °C, refractories are identified as advanced materials and key enablers of the production of essential products for everybody's daily life across Europe.

CESAREF (Concerted European action on Sustainable Applications of REFractories) is a Horizon Europe MSCA Doctoral Network combining nine academic and fourteen industrial partners across Europe. The project, which will run from October 2022 to September 2026, aims firstly to train researchers in multi-engineering areas and expose them to the academic and non-academic sectors through international and inter-sectoral mobility combined with an innovation-oriented mind-set. They will receive a combination of research-related and transferable competences in the full production-to-the-end-of-life cycle of refractory materials applied to I&S processes. These processes include new operation conditions required to reduce GHG emissions drastically, improved energy efficiency and life cycle assessment requirements. An important part of the project will be dedicated to the sustainability of refractories, including recycling issues, using the Life Cycle Assessment (LCA) methodology. The 15 doctoral candidates (PhDs) recruited will take advantage of the most sophisticated numerical tools and laboratory equipment to model, design and predict the life of refractory materials in critical operational conditions. Being trained in scientific, technical, and transferable skills, these PhDs are the next generation of highly employable scientists and engineers in the refractory sector and related areas. New testing methods and models will be developed to address the Scientific/Technological (S/T) challenges for these applications and help to design better performing and sustainable refractory materials and linings.

## CESAREF APPROACH TO REFRACTORIES RESEARCH

Steel, cement, glass and super alloys are essential materials of our society. The competition in and out of the European territory is intense. Due to rising costs related to $CO_2$ emissions and to the European Green Deal, the urgent challenge for the industry is to stay competitive and invest in breakthrough technologies for decarbonization.[1,2] The European Iron & Steel (I&S) industry is a world leader in innovation, environmental sustainability and a pioneer in the development of new technical solutions to enhance resource efficiency and meet the "Net-Zero emission of Green House Gas" (GHG) target by 2050.[3,4] 84 % of the European Steel producers have already committed themselves to be fully Net Zero by 2050, compared to 67 % in Japan and 19 % in China.[5] Steel production is very highly energy intensive and accounts for 25 % of Europe's industrial $CO_2$ emissions and 7 % of the global industrial GHG emissions. Every ton of steel produced in 2018 emitted on average 1.85 tons of $CO_2$. As shown in Figure 2, Net-Zero emissions by 2050 entails alternative breakthrough technologies and processes. The European I&S industry has numerous decarbonisation projects in the works, at various levels of technical readiness, either on the Smart Carbon Usage and/or the Direct Carbon Avoidance technological pathways. By dealing with energy efficiency through new refractory materials and technologies, the CESAREF network will target research topics not presently covered. Other key initiatives are dedicated to steelmaking by enlarging the use of hydrogen based-Direct Reduced Iron (DRI) as feeding material in Electric Arc Furnaces or by developing low-carbon footprint iron production technologies.[6] The conversion from carbon-based fuels to clean burning hydrogen-based mixes is a major change in the industry. DRI is expected to be a major decarbonization lever and offers the potential for truly green steel, particularly in Europe where 70 % of steel is still produced through integrated process. However, the current refractory materials are not designed to perform as well with such new operation practices.[7]
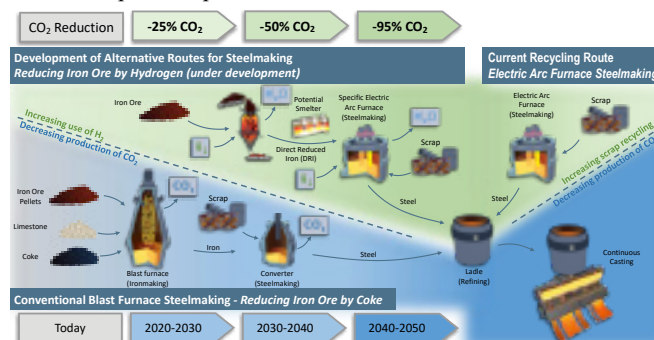


*Figure 1: Overview of upcoming evolutions in steelmaking.*

Competitiveness must also be based on innovative technologies like advanced analytics, digitalization, and digital twin. Simulations don't benefit from having real-time data. On the other hand, digital twins are designed around a two-way flow of data and can itself run any number of simulations to study multiple processes and reach a global effectiveness. Model-based optimization for efficient use of resources and energy have started to be developed but not directly related to the refractory performances yet.[8] In this context, the European Refractory industry is a vital pillar of the European I&S industry. The raw material suppliers and refractory producers are part of the global production cycle of steel and a key part of the solution to reach Net-Zero emissions.

## ORGANISATION OF THE SCIENTIFIC WPS

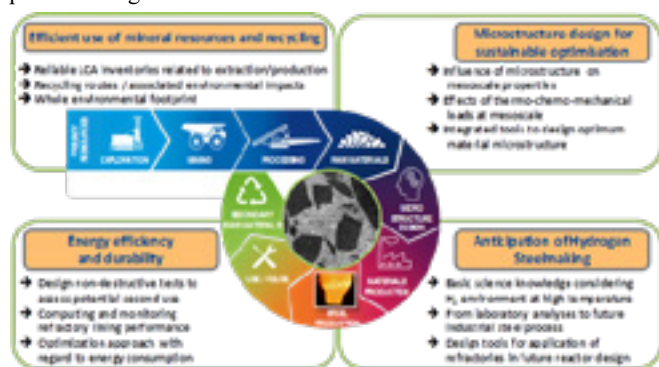CESAREF's objectives are identified through four scientific WPs presented Figure 2.



*Figure 2: Overarching research and industrial objectives of CESAREF within the circular economy challenges and using a multiscale approach.*

**WP 1 - Efficient use of mineral resources and recycling** will deal with the 4 challenges associated with circular economy: feed the loop, design the loop, slow down the loop and close the loop. The Life Cycle Assessment methodology (LCA), which has become a standard environmental evaluation tool (ISO 14040 - 14044:2006), will play a key role in this WP. Feeding the loop in a sustainable way requires knowledge about raw materials extraction (including secondary raw materials) to build robust inventory databases. Designing the loop means having access to relevant production routes of several types of refractories (bricks, precast blocks, unshaped products), to optimize them in an eco-design perspective. Slowing down the loop refers to the value of the environmental footprint of the refractories once applied in the steel industry. The impact of several operating parameters has to be assessed to both reduce the environmental impact and costs associated to refractories for the steel industry. Closing the loop means working on recycling routes and the associated environmental impacts, including the recycling process and re-use of secondary materials, relying namely on model material systems. WP1 will benefit from the CESAREF industrial network, to access the required primary resources allowing relevant inventory databases to be built, calculate the environmental impacts (climate change and resource depletion among many others), and propose eco-design strategies so the sector contributes to the EU Green objectives.

**WP 2 - Microstructure design for increased sustainability** will deal with the characterization of selected materials at room and high temperature in virgin state, after service, or after exposure to $H_2$ or other combustion atmospheres. Conventional and specific experimental techniques, based on the use of European large-scale facilities such as synchrotron radiation sources, will be used to determine the relationships between structure, microstructure and macroscopic properties. Alongside thermal expansion, thermal conductivity will be tested, as well as the Young's modulus by ultrasonic echography or the resonant frequency method. X-ray tomography and diffraction under synchrotron radiation source will be applied to investigate structural and microstructural evolutions of refractories in service or due to $H_2$ containing atmospheres. Stress-strain relationships and creep laws will be determined from tension and compression tests and work of fracture by wedge splitting tests. WP2 will take advantage of the CESAREF network to apply complementary experimental devices useful for each task. If different methods are available within the network, the most appropriate will be used to obtained key experimental results and improve the global outputs of the project.

**WP 3 - Anticipation of Hydrogen Steel Making** will deal with the acquisition of science-based knowledge on the long-term behaviour of refractory materials in the new emission-free processes. The conversion to emission free industrial processes, as requested by the European Green Deal, will lead to the replacement of carbon-based by hydrogen-based fuels. Several options for hydrogen-based ironmaking are presently being tested on a pilot scale level. The most promising breakthrough technologies need to be tested and implemented on an industrial scale between 2020 and 2030 and beyond.[9] The time pressure to ensure the process changes, and consequently change enabling process parameters such as refractories, is enormous and research is needed. The application of refractories has to be revised due to drastically changed process conditions in both iron- and steelmaking, and in more downstream processes. Extensive characterization of the relevant refractories materials (WP2) is urgently needed, and the results thereof will form the backbone of this work package.

**WP 4 - Energy efficiency and durability** will deal with leveraging advanced digital methods to reduce heat losses in the steel making process and prolong the useful lifetime of refractory linings and components. The basis for the novel methods to be developed in WP4, is accurate real-time data on the thermal state of steel ladles and the condition of the refractory lining. To collect the required data new monitoring methods aided by machine learning and data driven approaches will be developed. Experimental data will be augmented with data from detailed simulation models. The insights gained from these monitoring and modelling methods will be transferred to the steelmaking process to support the decision making regarding reduce/reuse/recycle/recreate and employing the steel ladles. To incorporate the process perspective in the decision support, an optimization model for the ladle logistics is set up, which not only takes the thermal state and the remaining useful lifetime of the refractory lining into account, but also considers the limitations of the steel making process. Incorporating this new information in the decision-making process will result in a reduction of resource consumption (gas, refractories, hot metal) and greenhouse gas emissions, thus directly contributing to the objectives of the European Green Deal. For validation, dedicated experiments in a steelmaking plant will be conducted.

## TRAINING ASPECTS, DISSEMINATION AND OUTREACH

Being built on an interdisciplinary and inter-sectoral approach, the CESAREF value chain (cf. Figure 3) will dramatically increase the transfer of scientific knowledge to the refractory users in EU, ensuring their progress on societal, economic, and environmental aspects.
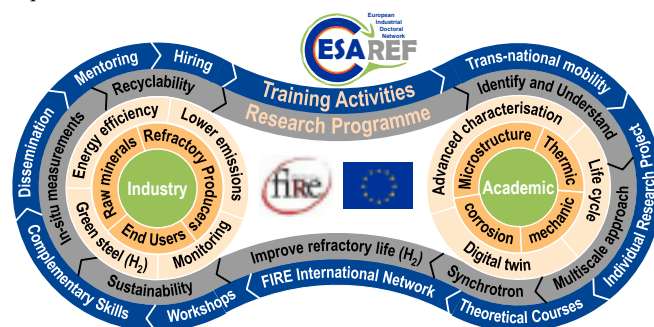


*Figure 3: CESAREF value chain global overview.*

CESAREF targets the development of high-end engineering technologies in the fields of material's science and numerical simulations to give a substantial contribution through the design of more sustainable, robust, and reliable refractory linings. Ultimately, it represents a reduction of the refractory costs, an increase of the equipment's availability and enhanced process control. In addition to the significant energy savings that meet the interest of the industrial partners, CESAREF contributes to tackling environmental issues, namely through the focus on refractory recycling at their end of life, in a circular economy perspective.

### Overview of the doctoral training programme

Today, refractory companies experience ever-expanding economic and environmental challenges that hinder the continuous development of innovative approaches in material design, process,

and product functionality. Their competitiveness and sustainability are related to the availability of industrial-oriented, well-educated young engineers whose inter-disciplinary and inter-sectoral skills drive the development and improvement of refractories as advanced materials enabling essential material production, e.g., steel, cement, or glass. CESAREF will provide unique training of 15 PhDs for 540 researcher months. WP 5, dedicated to training, mobility, sustainable recruitment, and transfer of knowledge, will offer them continuous and discrete training activities that contribute to the development of refractories science globally and the innovation system for the I&S industry. The 15 PhD positions are distributed among 15 Beneficiaries (6 academics and 9 industrials) in 6 countries. In total, CESAREF represents 9 countries with 15 Beneficiaries and 10 Associated Partners, most of whom are members of the Federation for International Refractory Research and Education (FIRE). This worldwide network constitutes a valuable assembly of complementary expertise for these training activities. All CESAREF academic partners have extensive expertise in post-graduate and post-doctorate research training. The PhDs will be fully integrated in the existing local research teams and related activities. Thus, each PhD participates in local Doctoral training programs (scientific and transversal lectures) and also benefits from the integration activities (welcome parties, administrative help and language courses) which are regularly organised for foreign students. A member of the academic research team will be appointed as the primary supervisor for each PhD. The supervision will be managed by both academic supervisors as well as one dedicated industrial supervisor. Thus, each PhD capitalizes on the interdisciplinary expertise available. To meet the objective of increasing the training level of European researchers in the field of Refractories, and thus their employability, CESAREF will provide advanced training in research methods and engineering skills, as well as industrial experience. The PhDs will develop their own network, during events and promote collaboration between academia and the industry. This combination of research-related and transferable competencies will enhance career perspectives in both academic and non-academic sectors.

The 13 companies of the network, in collaboration with FIRE, will contribute to interdisciplinary and intersectoral research training and to outreach activities (talks at internal and external events, organisation of training lectures and webinars, and industrial site visits, etc.). They will identify main industrial needs and regularly inform the consortium. They will provide materials and relevant data to facilitate the successful completion of the Individual Research Projects. All will participate in network-wide training events and/or host secondments. They will also guide training through participation in the Industrial Advisory Committee (IAC) and Steering Board (SB) meetings. They will play a vital role in strengthening the connections between academia and industry, and in accelerating knowledge transfer and adoption of innovative solutions. Every 6 months, the CESAREF network will organise 2 days of scientific virtual workshop during which PhDs are expected to prepare dedicated oral presentations to present their work progress and results to the overall consortium. Such a training program will foster interaction of the trainees with a truly exceptional inter-sectoral community to arm them with all the skills required to realise their professional life and their entrepreneurial ambitions.

**Dissemination activities**

Considering the impact of the activities under the scope of this network, the dissemination and exploitation of the results obtained throughout the project is of paramount importance. Measures will be implemented within a WP6 dedicated to "Dissemination and proactive knowledge transfer to industry" led by S. Sinnema (TATASTEEL/FIRE). The Plan for Exploitation and Dissemination of Results (PEDR) is outlined below.

Depending on the targeted audiences, the dissemination of CESAREF results will comprise many different channels. The communication to the industrial sector will be based on the strong capability of FIRE as a multiplier to disseminate among its network's members and beyond. In parallel, CESAREF is expecting to organize regular dedicated scientific workshops and two specialist industry seminars to promote knowledge transfer. These events will allow to present/discuss and develop a knowledge database for the expertise generated within the consortium.

Another far-reaching platform for the dissemination of CESAREF (especially for WP4) will be the IEA IETS Annex XVIII[10] on "Digitalization, Artificial Intelligence and Related Technologies for Energy Efficiency and GHG Emissions Reduction in Industry", which is a worldwide network of academia and industry. In Annex XVIII, TU Wien leads Task 2 on "Methods and Applications of Digital Twins" and TataSteel leads Task 4 "Road mapping the implementation of digitalization in the energy-intensive process industries".

High-performance refractory materials and applications are not typically used directly by the general public. Thus, CESAREF PhDs and their supervisors will also ensure that research activities are made known to society at large in ways that they can be understood by non-specialists, thereby improving the public's understanding of science.

CESAREF Website: dedicated to non-confidential research and network-related communications will target three types of audience: general public without a strong technical background, experts in the field interested in the project results, and participants of the project. PhDs and all the network partners will be encouraged to contribute to the website, which will also feature a social networking portal, blogs, forums, a "FAQ" section and wikis for the general public. A dedicated section with restricted access will serve for internal communication to the project partners. Information such as S&T field of activity, patents, publications, and positions will be regularly updated for every PhD. The website will thus be an excellent indicator of the success of the initial training of the PhDs, connecting them and promoting careers in refractory products. The coordinating institution is responsible for the website's design and maintenance (until at least 8 years after the end of the project).

During the first year of the project, a short video project will be produced in which the CESAREF's goals, the team and the collaborating partners will be presented in a comprehensive way. This video will be accessible via YouTube as well as via CESAREF and FIRE websites. During the last 6 months of the project, other promotional videos will be made to showcase the project results.

In close collaboration with Centre Sciences[11] an interactive exhibition called "Cerami°K" dedicated to "The World of High Temperature Science" (in the context of European Green Deal) will be used at each academic pole for general public awareness (notably for secondary schools) at the occasion of yearly open days at universities. Interviews in mass media will be organized to target the general public through the local press.

A newsletter will be published every semester in the CESAREF website and disseminated by email. This will be directed to the general public, but links will be given to the website for experts to obtain further technical information. Researchers' informal wikis and monthly blogs to showcase their research work to a non-technical audience. Specialised Press releases and joint articles will be submitted to magazines and websites linked to the refractory industries. Advice and contacts with existing stakeholder groups (e.g. potential investors, advisory groups, competitiveness clusters, etc.) will be sought to prepare at least one broad audience article published in each country represented in the CESAREF consortium. Regular Press releases, through the collaboration of the communication offices of CESAREF partner institutions, will be published on the network results.

Scientific results will be disseminated through oral communications during international congress and publications in rank A international peer reviewed journals. The organization of dedicated sessions in selected conferences will also be promoted to show the project results to large audiences. Since academic partners in CESAREF are editors of relevant journals and/or organizers of key conferences, the dissemination will be highly efficient. An average

723

target of three Open-Access, peer-reviewed papers per PhD is expected.

## EXPECTED IMPACTS

### Contribution to the European Doctoral Training structuration

Industrial partners in CESAREF participate at the highest level of the training programme and are directly (and strongly) involved in the supervision of all the PhDs (Industrial Doctorate) and can be additionally involved by specific mentoring (closely monitoring an area of a given PhD work) in case of secondments. CESAREF fosters a tight interconnection of cutting-edge European research institutions, several world leading scientists and leading companies in the fields of raw minerals, refractory materials producers, and end-users (in steelmaking or superalloy casting). The inputs of industrial partners in the training activities will enable the creation of a pool of well-trained researchers. At the end of the project, this industry will be looking to recruit them.

The CESAREF network covers the full supply chain for these critical materials required in steel-making industries, which urgently need to drastically change their industrial process (increasing hydrogen use) to reduce $CO_2$ emissions. The industrial partners will also be able to lead research activities and ensure that the research projects are relevant to the refractory applications. They will be able to directly use the results of the CESAREF projects and exploit them to increase their competitiveness in the EU and the international market. The reputation of the industrial partners will also be improved by their participation in CESAREF as this will increase their visibility, both within the Network's academic partnership, and out of the Network. Long lasting collaborations are expected to be developed between industry and academia during the four years of the network.

Furthermore, the results obtained in CESAREF are transferrable to other essential domains like cement or glass. CESAREF assembles expertise within the EU, leading to scientific exchange and knowledge transfer, thereby overcoming fragmentation within European research. In this fruitful collaborative context, PhDs are offered the rare possibility for international, interdisciplinary and intersectoral training, characterised by 1) an individual, scientifically ambitious, research project well connected to other researchers and disciplines, 2) close collaboration with academic and industrial partner labs working in a complementary research field where they are supervised for a period of 18 months (9 months at the beginning and end of the PhD), and 3) training in core and advanced research skills and transferrable skills. The non-academic partners will participate in the courses (WP5) via presentations and case studies. Industrial site visits and direct access to R&D facilities will be provided. This structured training stimulates the creativity and entrepreneurial mindset of researchers at a doctoral level.

### Expected scientific impact(s)

Scientific impact is expected through materials development triggered by the combined application of methods such as synchrotron radiation sources, thermochemical simulation and advanced material testing at temperatures up to 1600 °C. In addition, life cycle analysis, in conjunction with simulation methods, will show further potential for developments. The research on life cycle analysis will address some of the key recommendations recently published by a working group of members from the "task force mineral resources" participating in the "global guidance for LCIA indicators and methods"[12] hosted by UN Environment. CESAREF will significantly contribute to covering a broader range of inventory flows which are currently under-represented, namely minerals and aggregates. It will also develop characterization models including both natural stocks and anthropogenic stocks (secondary resources). The depletion of resources considered in CESAREF will also consider flows of material ending up in tailings, waste rock, or as emissions to nature. It will promote the identification of "dissipative resource use". Some PhD students will be strongly involved in the use of synchrotron radiation sources, use of such facilities and a related training period will be built-up. Due to the very high X-ray flux and the tunability of the beam energy, synchrotron radiation allows in-situ and operando diffraction and tomography measurements that are not possible without these types of sources. At the end of the project, PhDs able to use, for industrial purpose, such equipment will disseminate their knowledge to the industrial community. Building scientific relationships with other users of such facilities, they will be able to lead industrial projects including the use of such facilities.

### Expected economic/technological impact(s)

The industrial partners will directly benefit from the training of the network and the dedicated industrial doctorate programs ensuring that the research projects are relevant to the refractory and steel industries as well as others committed to Net-Zero emissions. Their inputs in the training activities and supervision of the PhDs will enable the creation of a pool of well-trained, highly employable researchers. The industrial partners will make direct use of the obtained results during the project and increase their competitiveness by implementing new technological solutions. On completion of CESAREF the industrial partners will be bolstered by life cycle analysis, refractory design for hydrogen technology and enhanced energy efficiency by using advanced digitalization methods. This will enable the realisation of maximum recyclability, zero $CO_2$ emissions and lower energy consumption. The visibility, and thus reputation, of the industrial partners' will be improved by their participation to the project, increasing the potential for future collaborations leading to continued innovation and/or patents for the years to come. The proposed network will help to establish long-term partnerships between the researchers and industry in the areas of research, training and development, which will promote the creation of new refractory solutions. The structured training programme will create synergies from the expertise of all participants and can only be offered through a network such as the one proposed. The network will also reinforce the critical mass of researchers in the European Research Area able to compete with other international actors.

### Expected societal impact(s)

CESAREF will contribute to circularity, energy efficiency and $CO_2$ reduction and as such contribute to environmental and social well-being. The collective willingness to put the energy transition into operation as soon as possible has led to this urgent concerted action of all academic and industrial partners. With the attention on development of robust refractory materials, unwanted breakouts of installations can be prevented, leading to safer working conditions. Educating PhD's on themes with high environmental added value will also lead to a generation of researchers and future decision makers with enhanced awareness of social responsibility.

[1] EUR-lex, The European Green Deal, COM final, 2019.
[2] EUR-lex, Delivering the EU's 2030 Climate Target, COM final, 2021.
[3] EUR-lex, A Clean Planet for all, COM final, 2018.
[4] EUR-lex, A Union of Vitality in a World of Fragility, COM final, 2020.
[5] Green Revol. built on a Very Dirty Industry, www.bloomberg.com, 2021.
[6] H2020 project LoCO2Fe, Development of a Low $CO_2$ Iron and Steelmaking Integrated Process Route for a Sustainable European Steel Industry, 2018.
[7] P. Sengupta, Refractories for the Chemical Industries, Springer, 2020.
[8] H2020 project MORSE, Model-based optimisation for efficient use of resources and energy, 2017-2022.
[9] A plan of action: A Green Deal on Steel, www.eurofer.eu, 2020.
[10] Annex XVIII about "Digitalization, Artificial Intelligence and Related Technologies for Energy Efficiency and GHG Emissions Reduction in Industry", Industrial Energy-Related Technologies and Systems, iea-industry.org
[11] Centre Sciences, Center for Scientific, Technical and Industrial Culture.
[12] Global Guidance for Life Cycle Impact Assessment Indicators, www.lifecycleinitiative.org, 2019.

# WETTING BEHAVIOR OF CAO–AL₂O₃–SIO₂ MOLTEN SLAGS ON MAGNESIA REFRACTORY UNDER WEEK STATIC MAGNETIC FIELD

Xuechun Huang, Ao Huang, Shenghao Li, Huazhi Gu, Ziyao Shen
The State Key Laboratory of Refractories and Metallurgy, Wuhan university of science and technology, Wuhan, China

Zhiyong He
Central Iron and Steel Research Institute Group, Beijing, China

**ABSTRACT**

The wettability between refractory and slag is a crucial property for assessing their resistance to slag. This study investigates the slag wetting behavior of magnesia refractories with varying basicity (C/S ratio), magnetic induction intensity and different atmospheres. It aims to uncover the influence of weak static magnetic field on the wetting behavior of the slags. The findings reveal that the reaction involving superoxide radical significantly impacts the contact angle between the slags and magnesia under different atmospheric conditions. Moreover, the application of a weak static magnetic field can effectively suppress the free radical reaction, leading to an improved contact angle between the slags and magnesia, and can enhance the slag resistance of magnesia refractories.

Keywords: magnesia refractory; molten slag; static magnetic field; superoxide radical

## 1. INTRODUCTION

Magnesia refractory not only has high refractoriness, strong resistance to the corrosion of alkaline slag and high iron slag, but also has the ability to purify molten steel without pollution. Because of these properties, it is widely used in oxygen converters, electric furnaces, off-furnace secondary refining, ladles and other industrial vessels [1]. Lao et al. [2] studied the wettability between CaO-Al₂O₃-SiO₂-(MgO) slags and magnesia. It was found that a high C/S ratio in the slag and a higher MgO content could help enhance the slag resistance.

With the development of electromagnetic metallurgy technology, the application of external electric and magnetic fields to the interface reactions between slags and refractory materials has attracted the attention of researchers. Christos G et al. [3] found that applying an electric field can change the wettability between the slag and magnesium oxide, promote electron transfer and exchange, thus promoting the interfacial reaction and accelerating the dissolution of magnesium oxide in the slag. Wang et al. [4] found that the effect of alternating electromagnetic field increased the diffusion coefficient of $Fe^{2+/3+}$ and $Mn^{2+}$, as well as the substitution ability with $Mg^{2+}$ in magnesia, which contributed to the formation of solid solution of magnesium oxide and iron oxide or manganese oxide, and intensified the corrosion of magnesia carbon refractory by slag. Ren et al. [5-6] investigated different magnesia-based refractories (MgO-MgAl₂O₄, MgO-CaO, and MgO-C) under static slag resistance and dynamic rotational corrosion tests in a vacuum electromagnetic field environment. Both types of slag corrosion tests demonstrated that the electromagnetic field can promote interface reactions between slags and refractory materials, accelerating the corrosion and infiltration of slags into the refractories. Lian et al. [7] found that under a static magnetic field, the viscosity and contact angle of the slag increase with the increase of magnetic induction intensity, and electromagnetic damping phenomenon can be formed to inhibit the penetration of the slag. Zou et al. [8] discovered a "magnetic braking effect" on slag under a static magnetic field, reducing the wettability between slag and magnesia-based refractories. The introduction of alternating magnetic fields exacerbates refractory corrosion, while a static magnetic field can effectively inhibit slag infiltration corrosion. Moreover, weak static magnetic fields have important prospects for application in high-temperature smelting processes due to their adjustability and cost-effectiveness. However, there is

still a lack of in-depth research on the wetting behavior of slag on magnesia refractories under high-temperature weak magnetic fields. This paper aims to investigate the wetting phenomenon between slag and magnesia refractories under weak static magnetic field conditions, elucidating the influence of magnetic induction intensity, temperature, and slag composition on the wetting behavior of slag. It provides a theoretical basis for the application of high-temperature weak static magnetic fields in regulating and improving the resistance of magnesia refractories to slag corrosion.

## 2. EXPERIMENTAL

### 2.1 Experimental materials

Large crystalline fused magnesia (average crystallite size is 283 μm, chemical composition is shown in Table 1) was used in the wetting experiment. Al₂O₃ powder (analytical pure, Al₂O₃≥99 wt%), CaO powder (analytical pure, CaO≥98 wt%) and SiO₂ powder (analytical pure, SiO₂≥98 wt%) were used for synthetic slag (following the mass ratio shown in Table 1). Alumina ceramic balls were used as the mixing medium. CaO-Al₂O₃-SiO₂ oxide powders with different C/S ratio were prepared by mixing and grinding.

After the oxide powders were evenly mixed following the specifications in Table 2, they were pre-melted in an induction furnace for 15 min, quenched, and then placed in a Muffle furnace for 8 h at 1000 ℃ for decarbonization. Subsequently, the powders were finely ground into slag powder and pressed into small cylindrical samples with a height and diameter of 3 mm.

Tab. 1: Chemical composition of the fused magnesia (wt%)

| MgO | CaO | SiO₂ | Al₂O₃ | LOI |
|---|---|---|---|---|
| 97.81 | 0.60 | 0.65 | 0.18 | 0.34 |

Tab. 2: Chemical composition of the synthetic slags (wt%)

| No. | CaO | Al₂O₃ | SiO₂ | C/S ratio |
|---|---|---|---|---|
| S1 | 32.5 | 35 | 32.5 | 1 |
| S2 | 48.75 | 35 | 16.25 | 3 |
| S3 | 54.16 | 35 | 10.84 | 5 |

### 2.2 Experimental process

The wetting behavior experiment was carried out with the ultra high temperature confocal laser observation system VL200DX-SVF18SP. The polished fused magnesia samples were successively polished with 200, 400, 800, 1000, 1200, and 1500 grit sandpaper. The samples were placed in alumina crucibles, and a cylindrical slag sample was placed in the center of the magnesia surface before being placed in the furnace.

The heating regime was as follows: the temperature was raised to 1600 ℃ at a heating rate of 50 ℃/min from room temperature ~200 ℃, 300 ℃/min from 200 ℃ ~1400 ℃, and 50 ℃/min from 1400~1500 (1550 and 1600 ℃), and then decreased to room temperature at 200℃/min. At the same time, the furnace chamber was subjected to different static magnetic intensities: no static magnetic field, as well as static magnetic fields of 0.5 mT, 1.0 mT and 1.5 mT. After the experiment was completed, the sample was photographed using an optical microscope, and the apparent wetting angle between molten slag and fused magnesia was analyzed using Image J software (National Institutes of Health, America). Subsequently, the samples were quenched, cut along the

center line of the slag, polished, gold-plated through vacuum ion sputtering, and analyzed using scanning electron microscopy (SEM; JSM-6610, JEOL, Tokyo, Japan) and Energy Spectrometer (EDX; QUANTAX, Bruker, Berlin, Germany) for comparative analysis of the interfacial microstructure and composition of the slag and fused magnesia.

The slag was ground into fine powder with a particle size below 0.074mm, and electron spin resonance spectroscopy (ESR, A300, Bruker, Salbrucken, Germany) was used to quantitatively measure superoxide radicals in a light-free environment. The ESR settings were as follows: central magnetic field 3500.00 G, field sweep width 150.00 G, sweep time 30.00 s; microwave power 3.99 mW, modulation amplitude 1.000 G; conversion time 40.0 ms, using DMPO as the trapping agent.

## 3. RESULTS AND DISCUSSION
### 3.1 Effect of slag basicity and static magnetic field under air
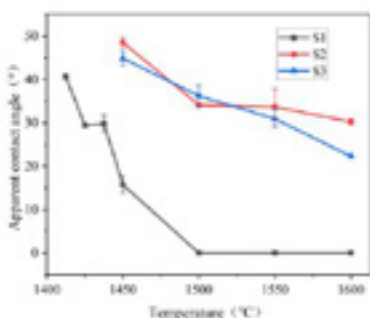


*Fig. 1 Apparent contact angle of slag with different basicity under temperature variation situation and air*

It can be seen from Fig.1 that at 1450 ℃, the contact angle between slag S1 and magnesia is much lower than that between slag S2 and S3. This discrepancy can be attributed to the low basicity and acidic nature of slag S1, which easily corrodes and penetrates magnesia and certain basic refractories. Consequently, the contact angle of S1 is much smaller than that of S2 and S3 slags. At 1600 ℃, the contact angle of S2 is greater than that of S3. This variation occurs due to the reaction between S2 slag and magnesia, resulting in the formation of spinel (as depicted in Fig.2). The spinel formation inhibits further penetration and corrosion of the slag, thereby increasing the contact angle.
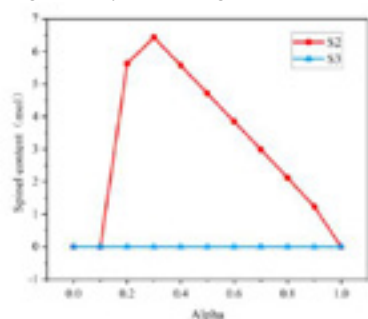


*Fig. 2 Thermodynamic simulation of the amount of spinel generated by the reaction between slag S2 and S3 and magnesia (Alpha is the ratio, when it is 0, it is the pure slag, when it is 1, it is the pure fused magnesia)*

From the Fig.3, it can be observed that the application of a static magnetic field has a significant effect on the contact angle between the slags and the magnesia. Within the temperature range of 1425 to 1462.5 ℃, the introduction of a static magnetic field of 1.0 and 1.5 mT results in a notable decrease in the contact angle between slag S1 and magnesia. However, at 1450 and 1462.5 ℃, a static magnetic field of 0.5 mT can increase the contact angle. Specifically, at 1450 ℃, the contact angle is 23.7° with a magnetic field, while without the magnetic field, the contact angle is 15.7°, indicating an increase of up to 50.8%. For the contact angle between S2 slag and magnesia, it initially decreases and then stabilizes as the temperature rises. The magnetic field can reduce the contact angle between S2 slag and magnesia. Additionally, at 0.5 mT, the effect of accelerating slag infiltration and corrosion is the greatest. The contact angle between S3 slag and magnesia gradually decreases with increasing temperature. At temperatures between 1450 to 1550 ℃, the application of a 1.5 mT static magnetic field increases the contact angle. At 1500 ℃, the contact angle is 45 ° at 1.5 mT, compared to 36.2 ° at 0 mT, representing an increase of 24.3%. Conversely, st 0.5 mT and 1mT, the contact angle decreases. At 1600 ℃, the external static magnetic field has little effect on the contact angle.
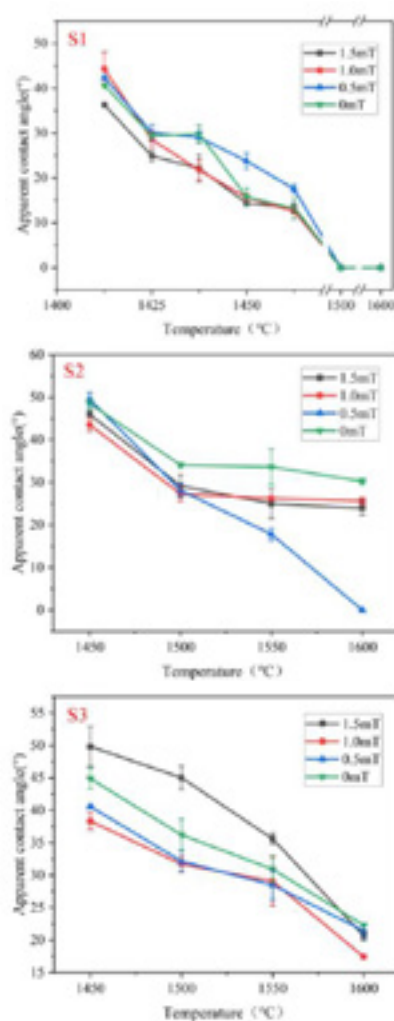


*Fig. 3 The apparent contact angle of the slags with different basicity and the magnesia under air*

### 3.2 Effect of atmosphere and temperature

From the results of the contact angle between the slags with different basicity and magnesia, it can be observed that the contact angle of slag S3 is reduced by applying a static magnetic field. Additionally, slag S1 exhibits high permeability, making it difficult to investigate its wetting behavior with fused magnesia at higher temperatures. As a result, the experiment on wetting behavior under different atmospheres selected slag S3.
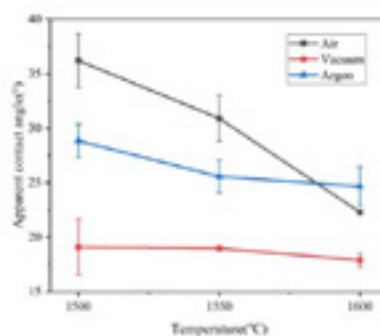


*Fig. 4 The apparent contact angle between slag S3 and magnesia varying with atmosphere and temperature*

As shown in Fig.4, in the temperature range of 1500~1600 ℃, the contact angle between air and argon is consistently larger than that under vacuum condition. Specifically, at 1500 and 1550 ℃, the contact angle in air is greater than that under argon atmosphere. However, when the temperature reaches 1600 ℃, the contact angle between air and argon shows no significant difference.

### 3.3 Effect of atmosphere and temperature under static magnetic field

It can be seen from Fig. 5 that with the increase of temperature in the air, the contact angle between slag S3 and magnesia gradually decreases, and the degree of wetting gradually increases. The

introduction of a static magnetic field will change the wetting behavior between the slags and magnesia. The static magnetic field with an intensity of 0.5 mT and 1.0 mT results in a smaller contact angle compared to the contact angle without a magnetic field. However, a static magnetic field with an intensity of 1.5 mT significantly improves the contact angle between the two materials at 1500 ℃ and 1550 ℃. At 1500 ℃, the contact angle is 45° with the magnetic field, whereas it is 36.2° without the magnetic field, representing a 24.3% increase. At 1550 ℃, the contact angle is 35.6° with the magnetic field, while it is 31° without the magnetic field, resulting in a 15.1% increase. As the temperature increases further, reaching 1600 ℃, the contact angle without a magnetic field becomes similar to that with a 1.5 mT magnetic field. Under vacuum conditions, the static magnetic field with intensities of 0.5 mT and 1.0 mT effectively improves the contact angle at 1500 ℃ and 1550 ℃. The contact angle of 1.0 mT at 1500 ℃ is the highest, measuring 26.3°, which is a 37.7% increase compared to the contact angle of 19.1° without a magnetic field. Similarly, at 1550 ℃, the contact angle of 0.5 mT is the highest at 23.1°, representing a 21.5% increase compared to the contact angle of 19° without a magnetic field. However, at 1600 ℃, the contact angle of 0.5 mT becomes significantly smaller than that without a magnetic field. Under argon atmosphere at 1500 ℃, applying a static magnetic field with intensities of 0.5 mT and 1.5 mT can improve the contact angle. The contact angle with a 0.5 mT magnetic field is the largest, measuring 39.7°, while the contact angle without a magnetic field is 28.8°, resulting in a 37.9% increase. However, applying a static magnetic field at higher temperatures has little effect on the contact angle.
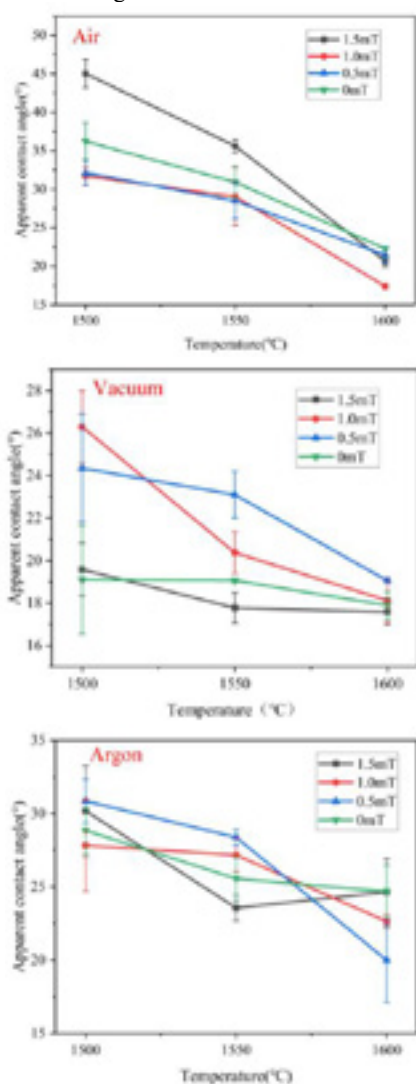


*Fig. 5 The apparent contact angle of S3 slag and magnesia in different atmospheres*

## 3.4 Microstructure and analysis of the interface

One control group was selected for microstructure analysis. The group was subjected to a vacuum atmosphere of 1550 ℃, a static magnetic field of 1.0 mT, and another group without a static magnetic field (0 mT). Analysis of Fig. 6 reveals that under the vacuum atmosphere of 1550 ℃ and a static magnetic field of 1.0 mT, there is weaker slag corrosion between magnesia particles compared to conditions without a magnetic field. Furthermore, the corrosion between particles is reduced, and there is no difference in composition between the slag and particles under both 1.0 mT and 0 mT. The primary components identified are calcium aluminite and cacoclasite phases (Table 3).
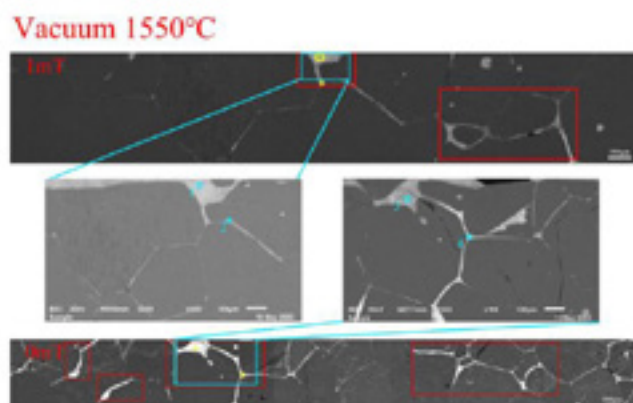


*Fig. 6 Microstructure and composition of the interface between slag and magnesia under vacuum atmosphere in 1550 ℃*

Tab. 3: EDS analysis results (at%)

| Element | Ca | Al | Si | Mg | O |
|---------|-------|-------|------|------|-------|
| Area 1 | 20.94 | 14.8 | 3.59 | 3.29 | 57.38 |
| Area 2 | 19.71 | 14.30 | 3.39 | 2.48 | 60.12 |
| Area 3 | 20.90 | 13.84 | 4.41 | 2.23 | 58.62 |
| Area 4 | 22.36 | 15.48 | 3.69 | 2.20 | 56.27 |

The influence of the static magnetic field at the Gauss level on the energy change of the reaction process can be ignored [9,10] , However, it is believed that the magnetic field at this intensity may have an effect on the reaction rate. Li et al. [11-13] proposed that there are abundant superoxide radicals in oxide smelt, and expounded their formation mechanism. The static magnetic field of Gauss level may inhibit the free radical reaction.
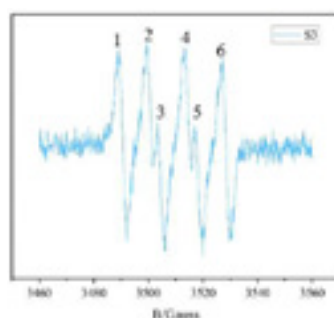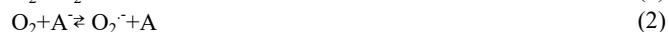


*Fig. 7 ESR/EPR test results of S3 slag after quenching*

The ESR/EPR spectrum of slag S3 after quenching at 1600 ℃ is shown in Fig.7. There are 6 absorption peaks in the spectrum, among which the peak intensity at 1, 2, 4, and 6 is higher, and the peak intensity at 3 and 5 is lower, with a g value of about 2.006. The detection result shows that they are superoxide radicals, indicating the existence of superoxide radicals in the slag. In high-temperature air, $O_2$ melts into the slag to form singlet oxygen, and then superoxide radical (see equation (1) and (2)) [14]. In the melt, non-brig oxygen (NBO) will react with ion clusters to form superoxide radicals (see equation (3)) [15]. With the participation of $O_2$, the concentration of superoxide radical will be greater. The advancement of equation (3) is impeded under high-temperature air conditions, resulting in a reduction in the degree of

reaction between the slag and magnesia. As a consequence, the contact angle at 1500 ℃ and 1550 ℃ is decreased. However, at 1600 ℃, the accelerated diffusion rate leads to an intensified free radical pair bonding reaction. As a result, the contact angle under air is not much different from that in argon. Due to the vacuum environment, the oxygen generated in the reaction is continuously pumped away, which prevents the equilibrium between free radicals and oxygen conversion reaction from being reached. As a result, the reaction proceeds towards oxygen generation, intensifying slag corrosion and reducing the contact angle.

$$O_2 \rightleftarrows {}^1O_2 \tag{1}$$
$$O_2 + A^- \rightleftarrows O_2^{\cdot -} + A \tag{2}$$
$$M^{2+} + 2O^- \rightleftarrows M^{\cdot +} + O_2^{\cdot -} \tag{3}$$

Where ${}^1O_2$ is singlet oxygen, $O_2^{\cdot -}$ is superoxide radical, $O^-$ is NBO, $A^-$ is on cluster : $[SiO_4]^{4-}$, $[Si_2O_7]^{6-}$, $[Si_2O_6]^{4-}$, $[Si_2O_5]^{2-}$, $[AlO_4]^{5-}$, etc. $M^{2+}$ is Mg, Ca, etc.
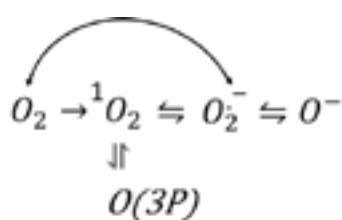


*Fig. 8 Mechanism of free radical reaction under air, where O(3P) is Triplet oxygen.*

Superoxide radicals are mainly involved in reactions as shown in Fig. 8 under air. With the increase of magnetic induction intensity, the contact angle decreases first and then increases. This is because magnetic field makes the triplet states ($T_+$ and $T_-$) and singlet state (S state) level become non-degenerate. The probability of S→$T_±$ intersystem channeling is reduced, so the total S→T intersystem channeling rate decreases with the increase of the magnetic induction intensity [10,16] , thus inhibiting the transformation of singlet oxygen to triplet oxygen, increasing the concentration of singlet oxygen, promoting the reaction with ion clusters in the slag to generate more superoxide radicals, and facilitating the reaction wetting. When the magnetic induction intensity reaches 1.5 mT, The degree of magnetic field inhibiting free radical reaction is greater than the degree of promoting reaction wetting. Thus, the contact angle is increased to inhibit the corrosion and penetration of slag. But the static magnetic field has a certain threshold for inhibiting the bond of free radical pairs, the inhibition effect of 0.5mT is the best when the vacuum and argon are 1550 ℃. When the temperature reaches 1600 ℃, the increase of diffusion rate will reduce the recombination probability of free radicals, so the effect of magnetic field on the apparent contact angle of slag will gradually decrease, and magnetic field will also accelerate the reaction wetting to reduce the contact angle.

## CONCLUSION

The wetting behavior of the magnesia was analyzed and studied with variations in slag C/S ratio, atmospheres, and magnetic induction intensity. Based on the research, the following conclusions were drawn:
(1) The contact angle of S1 is much smaller than that of S2 and S3 slags. The spinel formation inhibits further penetration and corrosion of the slag, thereby increasing the contact angle. The influence of the weak static magnetic field on the wettability of the slags with different C/S ratio and magnesia is completely different, weak static magnetic field has a significant impact in the temperature below 1600 ℃.
(2) The atmosphere was found to have a significant influence on the apparent contact angle between slag and magnesia. In vacuum environment, the conversion reaction from free radicals to oxygen intensifies the slag corrosion and reduces the contact angle.
(3) The magnetic field affects the reaction degree between slag and refractory by inhibiting the reaction of free radicals, thereby

reducing the reaction rate between slag and magnesia, and improving the contact angle and reducing the wettability of the slags to magnesia refractory especially in vacuum condition.

## REFERENCES

[1] Li N, Gu H, Zhao H, Refractory Technology [M]. Beijing: Metallurgical Industry Press, 2012

[2] Lao Y, Li G, Gao Y, et al. Wetting and corrosion behavior of MgO substrates by CaO–Al₂O₃–SiO₂–(MgO) molten slags, Ceramics International 48(10), 2022, p. 14799-14812

[3] Christos G. Aneziris, Michael H. Microstructured and electro-assisted high-temperature wettability of MgO in contact with a silicate slag-based on fayalite, International Journal of Applied Ceramic Technology 5(5), 2008, p. 469~479

[4] Wang T, Li X, Jiang X, et al. Study on the influence of electromagnetic field on slag corrosion performance of low-carbon MgO-C refractory. Journal of Materials Engineering z2, 2010, p. 421-424

[5] Ren X, Ma B, Li S. Slag corrosion characteristics of MgO-based refractories under vacuum electromagnetic field, Journal of the Australian Ceramic Society 55, 2019, p. 913~920

[6] Ren X, Ma B, Li S. Comparison study of slag corrosion resistance of MgO-MgAl₂O₄, MgO-CaO and MgO-C refractories under electromagnetic field, Journal of Iron and Steel Research International 28, 2020, p. 38~45

[7] Lian P. Study on interface behavior of alumina-magnesia refractory and slag under electromagnetic field [D]. Master's thesis, Wuhan University of Science and Technology, 2018

[8] Zou Y, Huang A, Wang R. Slag corrosion-resistance mechanism of lightweight magnesia-based refractories under a static magnetic field, Corrosion Science 167, 2020, p. 108517

[9] Li Z, Wang E, Zhang L, Xu Y, et al. Influence of vertical electromagnetic brake on the steel/slag interface behavior in a slab mold, Metallurgical and Materials Transactions B 48, 2017, p. 2389–2402

[10] Pan H. Study on magnetic field effect in solution based on free radical reaction [D]. Huazhong University of Science and Technology, 2015, p. 1-29

[11] Li S, Huang A, Gu H, et al. Corrosion resistance and anti‐reaction mechanism of Al₂O₃‐based refractory ceramic under weak static magnetic field. Journal of the American Ceramic Society 105(4), 2022, p. 2869-2877

[12] Li S, Huang A, Gu H, et al. Revealing of rich living radicals in oxide melts via weak magnetic effect on alumina dissolution reaction, Journal of Molecular Liquids 375, 2023, p. 121391

[13] Li S, Huang A, Gu H, et al. Corrosion resistance and anti‐reaction mechanism of Al₂O₃‐based refractory ceramic under weak static magnetic field. Journal of the American Ceramic Society 105(4), 2022, p. 2869-2877.

[14] A preparation method of high temperature oxide melt containing superoxide free radical: CN202210619484.2 [P]. 2022-08-12.

[15] Peng Y, Huang A, Li S, et al. Radical reaction-induced Turing pattern corrosion of alumina refractory ceramics with CaO–Al₂O₃–SiO₂–MgO slags. Journal of the European Ceramic Society 43(1), 2023, p. 166-172

[16] Hayashi, Introduction to dynamic spin chemistry: magnetic field effects on chemical and biochemical reactions [M]. World Scientific, 2004

# FROM UNPOPULAR MATTER TO SMART SUBJECT:
# PUBLIC FUNDING OF REFRACTORY RESEARCH AND PHD EDUCATION BY DFG RESEARCH PROGRAMS AT TU FREIBERG

Patrick Gehre*, Jana Hubálková, Christos G. Aneziris

TU Bergakademie Freiberg, Institute of Ceramics, Refractories and Composite Materials, Freiberg, Germany

## ABSTRACT

The imparting of knowledge, as well as hard and soft skills to young PhD scientists by close supervision as well as by workshops and training courses, are important instruments for acquiring not only scientific and technical but also social competencies in the environment of interdisciplinary research work. The German Research Foundation DFG has established long-term research programs such as the Collaborative Research Center CRC 920, the Research Unit FOR 3010, and the Research Training Group GRK 2802 at the TU Freiberg, in which more than 60 PhD students explore basics framing multiple actual challenges in the field of refractory materials such as the manufacturing and interaction of ceramic foam filters with steel and aluminium melts for cleaner metal parts, electrically heatable refractory composites based on refractory metals and refractory oxides, and the recycling of MgO-C in new bricks the and upcycling of metal-ceramics as carbon-free electrodes. But also team and leadership competence questions were educated to the PhD students. For an interdisciplinary, international, and industrial-related education, all the research programs involve mentors from the industry, foreign universities, and three departments of Freiberg University (plasto-mechanics, fluid dynamics, iron and steel, and materials science), who guide the PhD students during workshops, internships, and bilateral discussions. The presentation will summarise key scientific outputs and will give insights into the tools and experience of more than ten years of activities in focused research programs and structured training strategies of PhD students.

## COLLABORATIVE RESEARCH CENTER CRC 920: MULTI-FUNCTIONAL FILTERS FOR METAL MELT FILTRATION - A CONTRIBUTION TOWARDS ZERO DEFECT MATERIALS

### Vision

There are increasing requirements in the metal-making and metal-using industry to remove solid and liquid inclusions such as deoxidation products, sulfides, nitrides, carbides etc., and thereby improve metal cleanliness. It is well known that the size, type and distribution of non-metallic inclusions in metal exert considerable effects on the mechanical properties of the cast products. The vision of the collaborative research centre (CRC) 920 is to create a new generation of metal qualities via melt filtration with superior mechanical properties for use in lightweight structures and high-demand construction materials. The aim of the collaborative research centre is an enormous reduction of non-metallic inclusions in the metal matrix by the use of intelligent filter materials as well as filter systems with a functionalised filter surface. Especially in the third funding period, a new generation of combined refining filter systems will be the focus. The metal melt comes first in contact with a reactive filter which generates gas bubbles in the melt as well as activates gas bubbles on the surface of the inclusions. As a result, a kind of flotation of the inclusions towards the slag on the surface of the melt takes place. Further, the high reactivity, as well as the gas bubbles, contribute to the agglomeration of the fine inclusions to big clusters, which flow due to buoyancy forces to the surface of the melt or are filtrated on the surface of active filters, which do not form gas bubbles but provide on their functionalised surfaces the same chemistry as the inclusions for a sufficient adhesion and as a result for a sufficient filtration of the inclusions. With this approach, a purification higher than 95 % can be achieved. The modelling focuses mainly on the several contributions of the gas bubbles and on the in situ formed reactive layers on the surface of the reactive filters as well as they generate codes with respect to the thermomechanical and functional properties of the filters for a 3D-printing of filter structures which are then end shaped with the aid of a robot-assisted flame spraying technique. The dynamic flow conditions in the filter during casting are of great importance for the proper design of the filter macrostructure. A material, as well as a flow computer-aided micro- and macrostructure filter design based on investigated filtration mechanisms, will lead to high purification efficiencies with superior properties – strength, fracture toughness, fatigue- of the cast steel, iron, aluminium and magnesium components. In addition, other applications, such as the electronic industry via filtration of copper or thin aluminium foil production, will profit from the scientific results. The target for higher material efficiency and reduction of energy and $CO_2$ emissions is coming closer in the near future.
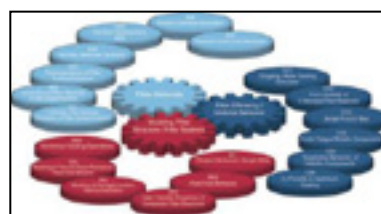


*Fig. 1: Research program of the CRC 920*

### Project areas

The CRC 920 is divided into three project areas, which include 19 scientific subprojects (figure 1). There is also a graduate program, three service projects, transfer projects and a central administration project. The three project areas of CRC 920 are constantly interacting with each other in terms of exchanging information about their results. Together they create an innovative cycle of research, material design and understanding of the main mechanisms of active and reactive filter materials. This cycle enables the CRC to transfer the results on other metal melts to the point of their application.

Project area A - Filter materials - consisting of 6 subprojects, researches active filter materials. Especially the surface tension at the junction of the filter wall - solid inclusion - metallic melt is set up. The main goal is to raise the filter efficiency for primary and secondary inclusions with a size of 1 to 100 μm from currently about 70 % for steel melts and about 75 % for aluminium melts to over 90 %. Another focus of this project area is the examination of the reaction mechanism and the filtering potential of reactive filter materials. That means that the filter material reacts with the gases which are included within the melt. This can help to reduce the primary and secondary inclusions but also can be a substantial contribution to reducing tertiary and quaternary inclusions. Project area B - Modelling of filter structures and filter systems - consisting of 5 subprojects, is considered to be a prerequisite both for a precise geometrical and material design of filter structures and the evaluation of the material behaviour under operation conditions. Understanding the micro-processes of particle deposition, meaning inclusions, on an active and reactive inner surface of a functional cavity is the main focus of this project area. To understand the effects of filter mechanisms as a function of filter structure, filter process and filter systems, physical and stochastic models are developed. Those models include deposition, agglomeration and heat conduction. Based on those models, simulations are being run. The stochastic distribution of inclusions within the melt has to be

determined to allow a theoretical prediction of the probability of occurrence of those inclusions. Project area C - Filter efficiency and material properties - consisting of five subprojects, researches the efficiency of the produced filter materials. With the now improved mechanical properties, this project area will demonstrate how these new filters will help to create new generations of highly stressable cast iron parts. Filter technologies and efficiencies, as well as the properties of the filtered end product, a metal cast iron part, will be examined extensively within the course of this project area. Based on these examinations, conclusions can be drawn considering the filter materials (project area A) and structural filter design (project area B). An important aspect is the creep resistance of ceramic filter bodies in mould casting under extreme temperature changes. This project area will also determine the necessary material parameters that are essential for the modelling in project area B and are also important for designing and dimensioning.

## RESEARCH UNIT FOR 3010 - MULTIFUNCTIONAL, COARSE-GRAINED, REFRACTORY COMPOSITES AND MATERIAL COMPOUND FOR LARGE-VOLUME KEY COMPONENTS IN HIGH-TEMPERATURE PROCESSES
### Motivation

Materials for high-temperature applications contribute essentially to our society. Without them, there would be no light, no car, no turbine, and no wind and solar energy. They are not seen, but they are directly or indirectly needed everywhere. The increasing demands on environmentally friendly and resource-saving processes as well as on higher efficiency lead to increasing requirements regarding high-temperature materials. The Research Unit FOR 3010, supported by the German Research Foundation DFG, has the aim to research and develop a new generation of coarse-grained refractory composites based on pre-synthesised aggregates from refractory metals and refractory ceramics.

Limited resources and an imperative need to reduce energy requirements challenge the material research to develop more powerful yet more material and energy-efficient materials and manufacturing processes. Modern high-temperature composite materials undertake a pacemaker function for the industry and are thus key for future technologies and products. The Research Unit FOR 3010 "Refrabund" has set itself the goal to develop an entirely new generation of high-temperature composite materials, which should replace the previously used refractory ceramics and refractory metals. The fundamental idea evolves the merging of both material classes as well as the expertise of both research institutions, the TU Bergakademie Freiberg and the Karlsruhe Institute of Technology KIT.

## RESEARCH TRAINING GROUP GRK 2802 - "REFRACTORY RECYCLING: A CONTRIBUTION FOR RAW MATERIALS, ENERGY AND CLIMATE EFFICIENCY IN HIGH TEMPERATURE PROCESSES"
### Motivation

Every year, approximately 28 million tons of used refractories are generated worldwide. The majority of the consumed refractories are primarily used for foreign applications, such as aggregates for road construction (downcycling) or deposited in landfills. The recycling of such materials played a rather subordinate role until now. For ecological reasons and due to the risen landfill costs, an increased research potential to deal with the application of refractory recyclates was identified in the last few years. The objective of the Research Training Group GRK 2802 is to research and develop new sophisticated recycling options for used refractories. Within the scope of the Research Training Group, fundamental knowledge should be developed, allowing both the recycling (re-utilisation in similar high-temperature materials) and the upcycling (material upgrading) of refractories in metallurgical processes.
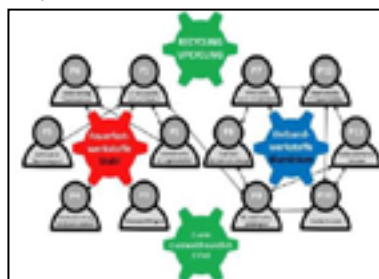
## Objectives



*Fig. 2: Scheme of the interconnectivity of the projects.*

The main objectives of the GRK 2802 are an interdisciplinary and structured training of PhD students in the fields of recycling and upcycling of refractories as well as the research and development of a new generation of coarse-grained high-temperature materials based on refractory recyclates with particular functional properties for high-temperature processes in the metallurgy (figure 2).

This will be applied in 2 core ideas:
1.  Core idea I: Recycling - Novel refractories based on refractory recyclates and environmentally friendly binders (resin-free, pitch-free) with an application as lining material for steel ladles
2.  Core idea II: Upcycling - Novel composites based on refractory recyclates with an application as electrode material for aluminium fused-salt electrolysis

The interdisciplinary team of the Research Training Group GRK 2802 comprises 12 PhD students, 1 Mercator Fellow, 12 Principal Investigators and several Associated Members. The training and qualification programme of the Research Training Group GRK 2802 is being developed and organised by a scientific coordinator. The administrative coordinator is responsible for the fund management and accounting.

## CONCLUSIONS

All refractory research activities at the TU Freiberg are supported and supervised by industrial advisory boards ensuring a direct linking to the topics of the real-world industry. Moreover, the developed materials and technologies can be directly tested and approved under real conditions in the end users industry. Therefore, the whole chain, from the raw materials up to the development of particular component as well as the understanding of the properties, needs to be explores in a multiscale approach. Besides the research skills, the main emphasis is on fostering of hard and soft skills in order to develop analytical, organisation and communication competences of the involved PhD-students. The qualification concept is based on lectures, soft skill workshops, networking, industrial internships as well as stays abroad. Consequently, the PhD-students are equipped with knowhow and capabilities to face the challenges of the professional work and to contribute to finding of appropriate scientific solutions. Inspiring environment, passion for innovation and continuous exchange of experiences allow for generations of new ideas, networks and perspectives in the engineering disciplines.

730

# BACHELOR OF CERAMIC SCIENCE (DUAL) AT KOBLENZ UNIVERSITY OF APPLIED SCIENCE – AN OPPORTUNITY FOR THE INDUSTRY TO OVERCOME SKILLS SHORTAGE

Olaf Krause

Koblenz University of applied Science, Höhr-Grenzhausen, Germany

## ABSTRACT

The challenges facing the ceramics industry today are many and varied. In addition to the supply of raw materials, environmental issues and the energy crisis, the lack of well-trained employees will lead to stagnation in the ceramics industry. The situation will become even worse in the near future if demographic factors are taken into account: Even today, old, experienced engineers cannot be replaced by young, well-educated engineers when they retire. One of the main reasons for this situation is that young people are not interested in materials science because it is not taught in schools. Young people are unaware of the importance of materials and their ongoing development for our ecological and sustainable community. In order to alleviate the still worsening situation, Koblenz University of Applied Sciences with its location in Höhr-Grenzhausen has opened a practice-integrated course in close cooperation with industry in 2018. This course is aimed at industrial partners and offers the opportunity to further qualify employees and also to attract school leavers from the region, with the latter receiving intensive practical insights at the industrial sites while the theoretical basics are taught at the university. This presentation summarises the educational system in general in Höhr-Grenzhausen and with special regards towards the first experiences with the novel and cooperative form of praxis integrated education.

## HÖHR-GRENZHAUSEN A HOTSPOT FOR CERAMICS

Based on excellent clay deposits in the Westerwald region Höhr-Grenzhausen looks back on a long tradition in ceramics. Beside the ceramic industry education and research in ceramics build a hotspot that is unique in Germany and Europe. All levels of education, vocational school for ceramics, state college for ceramics and Koblenz University of Applied Science are situated in Höhr-Grenzhausen. Apprentices and students from all over Germany join in the educational system for Ceramics.

Education in ceramics is closely connected to the Educational and Research Centre for Ceramics (BFZK), which brackets education, research and economy in the broad field of ceramic materials in Höhr-Grenzhausen. It guarantees the close and steady interchange with the ceramic industry that guarantees up-to-date contents and developments in teaching and research.

BFZK makes the educational system permeable for every young people committing themselves for a carrier in the ceramic Industry (figure 1).

Since its foundation in 1991, the Education and Research Centre in Höhr-Grenzhausen has developed very efficient in view of common and successful work of various research and educational institutions. The thereby achieved penetration in teaching and research in the field of ceramics is unique worldwide. Through continuous close contacts with the industry, research and teaching facilities the ceramic materials should even stay what it had always been - a material of the future.

Here, the competence centre provides even more than just research and teaching. So, at Höhr-Grenzhausen one can go through all facets of professional training, from the initial training in the ceramic field (an apprenticeship) to the doctor's degree in materials engineering. Similarly, the aforementioned institutes are closely working together with the industry, the trade, the art scene and with all other representatives of the ceramics sector. Thus, numerous national and international co-operations of manifold types have emerged in recent decades. Content references are available in silicate and high-tech ceramics and refractories, as well as in the technical and artistic applications with design and art issues.

Members of the Education and Research Centre are today eight institutions: the University of Applied Sciences at Koblenz with the Department of Materials Engineering, specializing in ceramics and glass, the Institute of Ceramic and Glass Arts, the State College of Ceramic Engineering and Ceramic Design, the Vocational School of Montabaur with the Department of Ceramics at Hoehr-Grenzhausen, the Research Institute Glass and Ceramics, the Westerwald Ceramics Museum, the centre for business start-up CeraTechCenter and the European Centre for Refractories ECREF. This integrated system enables the institutions to respond quickly to the needs of the industry with respect to the quality of education for the graduates.

The uniqueness of this network is the close connection of practical research (FGK, ECREF and University of Applied Sciences Koblenz), foundation activities (CTC), teaching at University (Bachelor and Master of Engineering "Ceramic Science" degree), the State college (State-certified ceramics engineer, State-certified ceramic Designer) and at the vocational school as well as the steady interchange amongst all of them.

In doing so BFZK aims for two main goals. One particular interest is to make the various fields of applications of this fascinating material group Ceramics available to the public and to unveil its (already existing but hardly seen) tremendous influence on the quality of all our lives.

In addition, the close and steady interchange with the industry guarantees up-to-date contents and developments in teaching and research.

The industry, ranging from primary materials to finished end production, utilizes the affiliate network of the BFZK for its own further development. To benefit from research and teaching experience and to access innovative research achievements clearly is a win-win-situation.

At the same time, the BFZK is an important point of contact for globally working graduates in terms of professional cooperation and exchange of knowledge. Joint projects, conferences, symposia, seminars and advanced trainings are conducted regularly.
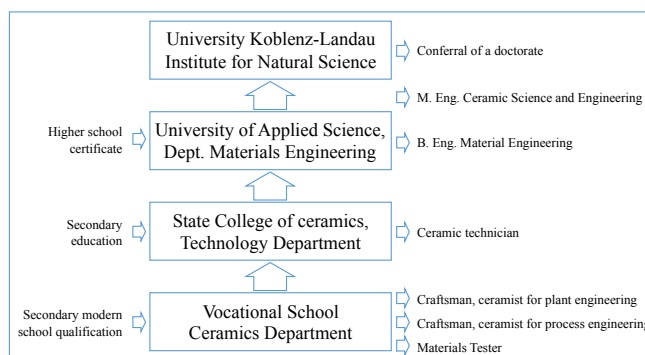


*Fig. 1: With the help of BFZK the educational system is permeable for every young people committing themselves for a carrier in the ceramic Industry.*

## KOBLENZ UNIVERSITY OF APPLIED SCIENCE, WWC CAMPUS IN HÖHR-GRENZHAUSEN

Founded in 1879 as a technical school for ceramics design, with a primarily arts and crafts orientation - Ernst Barlach, for example, was a teacher at the institution in 1904. As early as 1901, with the founding of the state technical school for ceramics, it was seen as necessary to place significantly more emphasis on engineering

ceramics in the training, in order to provide adequately trained specialists for the continuing industrialisation of the ceramics industry. In 1946, the school was recognised as an engineering school, which in 1971 was transformed into the ceramics department of the University of Applied Sciences Rhineland-Palatinate and organisationally affiliated to the regional department, Koblenz as the ceramics department. With around 300 students enrolled, one can speak of a heyday of education in Höhr-Grenzhausen in the 1980s, which, however, collapsed to around half in the 1990s and is still decreasing until today. The institution is designed for 350 students, divided among four degree programmes: A basic 7-semester Bachelor's degree with a consecutive Master's degree (3 semesters), a dual Bachelor's degree (10 semesters) and an industrial engineering and business degree in cooperation with the Department of Business and Economics at Koblenz University of Applied Sciences (7 semesters). For the Master's programme, the University of Applied Sciences and the University of Koblenz cooperate so that graduates have both a university and a college degree, which makes them eligible for doctoral studies without restrictions. Since 2018, the two institutions have maintained a research college, Max-von-Laue Institute of Advanced Ceramic Material Properties Studies (CerMaProS), which supports 11 doctoral students in their pursuit of a PhD. Funding was provided by the Rhineland-Palatinate Ministry of Research, and both institutions are among the first three in the state to receive this funding.

The focus of the training is traditionally in the field of ceramic raw materials and materials and deals with all industrially manufactured ceramic products. Höhr-Grenzhausen thus has a unique selling point, as professorships are specifically occupied in the fields of building ceramics, silicate fine ceramics, structural ceramics, functional ceramics, and refractory ceramics and pursue application-oriented training concepts. It is a living tradition that the course content is closely aligned with the needs of industry, so that graduates are typically put in a position to start adding value in companies immediately upon entering the profession. Entry is also facilitated by the fact that 99.5 % of all final theses are written in industrial companies, which gives students an important first insight into production processes and applied research.

In general, all study programmes in materials science suffer from a lack of demand from young people willing to study, which is generally the subject of much discussion by the study day MatWerk, of which we are a member, as this phenomenon is independent of the materials system. The lack of students in Höhr-Grenzhausen has repeatedly caused discussions in the past and even led to consideration of closure. In the end, it was the companies in the ceramics industry that were able to prevent the worst through intervention. What could not be prevented, however, was that personnel cuts thinned out the number of permanent staff. For example, the number of professors was reduced from 9 to 6, and the number of research assistants was halved from 4 to 2. In principle, the closure of the site is now off the table, as it has been recognised that the Höhr-Grenzhausen site is unique in Germany in the breadth of its orientation. Since mid-2021, the site has been officially recognised as a small subject by the Centre for Quality Assurance and Development (ZQ) in Mainz.

The Höhr-Grenzhausen location of Koblenz University of Applied Sciences is extremely well networked regionally through the Bildungs- und Forschungszentrum Keramik e. V. (BFZK). This institution brackets all training areas in ceramics (vocational school, technical school and university), which are in constant dialogue about this. This makes the training system vertically very permeable. In cooperation with the University of Koblenz, even doctorates are possible for those who have worked their way up through training. Also represented are the European Centre for Refractories as a professional training centre and the Forschungsinstitut für Glas | Keramik GmbH.

The environment and the good contacts in industry also prove to be extremely fruitful in the application and execution of industrial joint projects, which enable research and transfer of research results

in an outstanding directness. Both sides benefit equally from this. Since 2010, third-party funding amounting to 10 million euros has been successfully acquired, making the Höhr-Grenzhausen campus by far the strongest research campus at Koblenz University of Applied Sciences.

**DEGREE PROGRAMME AT KOBLENZ UNIVERSITY OF APPLIED SCIENCE, DEPARTMENT OF MATERIALS ENGINEERING, GLASS AND CERAMICS**

In principle, the dual study programme can be derived from the basic Bachelor's degree, whereby the scope of the specialisation subjects in the ceramic disciplines was greatly reduced in order to increase the studyability, as around 70 % of the time is spent in the industrial companies. On the one hand, the study programme is aimed at high school graduates, but on the other hand, it is particularly aimed at industrial ceramists with work experience who have been identified by the companies as future managers (figure 2).
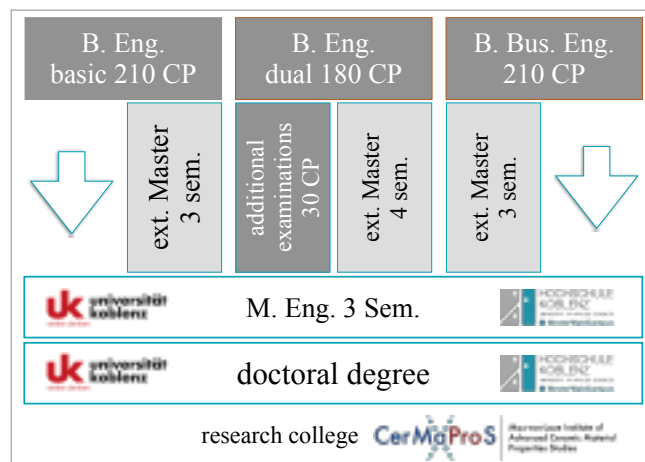


*Fig. 2: The education system is based on three Bachelor's degree programmes, one of which is dual or practice-oriented and requires cooperating companies. In cooperation with the University of Koblenz, a Master's degree can be added. Further qualification with the completion of a doctorate is also possible, whereby support can be provided by a research college.*

**Entrance requirements**

German students registering for the Bachelor of Engineering degree course need to reach "Fachhochschulreife" or equivalent. In terms of British qualifications, this level of attainment would normally be obtained after one year of 'A' level study in England and Wales or at Scottish Higher level. Applicants from England and Wales would therefore need to have 'A' level qualifications with the recommendation that Mathematics and German have been studied at this level.

Current admission requirements of the University require that prospective students provide evidence of their language skills in German (either DSH-2; or TestDaF with TDN 4 in all parts; or Goethe-Institute Certificate C2 (ZOP)).

**Bachelor of Material Engineering**

Within 3.5 years the students gain 210 ECTS (European Credit Transfer System) credit points and finish their degree program as bachelor of material science that enables to take up a master course of studies at any university in Europe that offers a similar apprenticeship. The curriculum as shown in figure 3 can be divided in five sections starting with the basic knowledge in natural science and ceramics that is followed by a deep-in study that provides special lectures in silicate ceramics, ceramics for civil engineering, functional and structural ceramics, refractories, and glazes. The students gain further expertise in general process technology and business and administration. In the 7th semester they complete their

studies with the bachelor thesis that is typically executed in cooperation with industrial partners.



| Bachelor of Engineering | | | | | | |
|---|---|---|---|---|---|---|
| Sem 1 | Sem 2 | Sem 3 | Sem 4 | Sem 5 | Sem 6 | Sem 7 |
| Basic natural science | | | | | | Bachelor thesis |
| Basics in ceramics | | | Ceramic in-depth study | | | |
| | | Process technology | | | | |
| | | | Business and administration | | | |

*Fig. 3: The curriculum of the Bachelor of Material Engineering*

**Master of ceramic Science and Engineering**

The bachelor-degree programme is followed by a consecutive Master that is executed in cooperation with the University Koblenz-Landau. The students gain further expertise in material physics, materials chemistry, thermochemistry. The courses are provided by the University of Koblenz-Landau. Further in-depth studies in ceramics as listed in figure 4 are given at Koblenz University of Applied Science. After the 2nd semester the students elaborate their master thesis that is again executed in cooperation with the I industry. In total the graduation as Master of Engineering – Ceramic Science and Engineering takes five years as it is common practice beyond the Bologna Process within the European Union. Students who join in the Master after three year's bachelor education must account for supplementary modules in order to gain further 30 credit points that are necessary to finish the master.

| Master of engineering - Ceramic Science and Engineering | | |
|---|---|---|
| Sem 1 | Sem 2 | Sem 3 |
| Materials physics | Materials for Aeronautics | Master thesis |
| Materials chemistry / Korrosion | Thermochemistry | |
| Glass materials | Energy process engineering | |
| Structural and functional ceramics | Further elective modules | |
| Silicate ceramics | | |
| Bio ceramics | | |

*Fig. 4: The curriculum of the Master of Ceramic Science and Engineering*

**Bachelor of Materials Engineering (dual / praxis integrated)**

A praxis integrated curriculum was launched in 2018. It combines on the job training with the curriculum. Instead of seven semesters the curriculum is extended to eight semesters. That is necessary to provide a co-operative education concept that enables students to accomplish a course of studies that is equal to the bachelor as described above (figure 5).

The target group for this co-operative education concept is identified beyond materials testers, craftsman (ceramist for process engineering and ceramist for plant engineering) as well as beyond ceramic technician who work in the ceramic industry and fulfil the entrance requirements reported above. A second target group are pupils that already passed their higher school degree who transact training contracts with industrial enterprises.

Both target groups persist or get recruited as employees in the enterprises and accomplish their course of studies in terms of apprenticeship training. In the 3rd and 5th semester the education is performed in co-operating enterprise, where defined scientific projects are elaborated. From the sight of the industrial partners this educational concept is very beneficial for at least four reasons:

- It is capable of being integrated in the internal qualification structure,
- Offers the opportunity to promote talented workers in a period of life in which they cannot resign their positions,
- the co-operation can obligate talented workers to the company and
- the concept has a high potential to attenuate the oppressive

skills shortage that is especially a problem for enterprises that are in out-of-way regions.

**Bachelor of Materials Engineering (dual) – first experiences**

Currently, 12 students have taken up their practice-integrated studies and some have already completed them. We would like to see a much greater response here in the future and hope to at least triple the number of students. So far, the cooperating companies have only sent employees from their own ranks. An acquisition at local schools seems to fail due to similar problems, which also have to be mentioned with regard to the currently low student numbers in the undergraduate Bachelor's programme. Lack of interest in materials engineering due to a lack of awareness of the subject in schools.

The experiences of the past 5 years have been consistently positive, although some students who have already been working in companies for a longer period first have to relearn goal-oriented learning and easily feel overwhelmed by the high theoretical part of the training. Here we provide individual support if needed and by holding tutorials in which the students' wishes can be specifically addressed. From the beginning of the training, the students are assigned to professors who supervise the respective specialist discipline of the companies in-house and who also maintain communication with the supervising companies. They also accompany the practical semesters and the associated project phases.



| Sem 1 | Sem 2 | Sem 3 | Sem 4 | Sem 5 | Sem 6 | Sem 7 | Sem 8 |
|---|---|---|---|---|---|---|---|
| Koblenz University of App. Sci. | Koblenz University of App. Sci. | On the job training | on the job training follow-up / Koblenz University of App. Sci. | Koblenz University of App. Sci. | On the job training | on the job training follow-up / Koblenz University of App. Sci. | Bachelor thesis |
| | on the job training preparation | | | on the job training preparation | | | |

*Fig. 5: The curriculum of the praxis integrated Bachelor of Engineer*

**CONCLUSIONS**

In Höhr-Grenzhausen, we have a tradition of offering high-quality training in all ceramic professions, from industrial ceramists to doctoral graduates. We attach great importance to a good mix of theoretical and practical training focal points, which enables graduates to contribute profitably to the company from day one. Ceramists from Höhr-Grenzhausen are successfully pursuing their professions all over the world and are always welcome at their former training centres.

# Preparation Technology
# for Refractory Materials

From the initial consultation to the turnkey system, we are your competent partner with broad know-how and decades of experience.

**Mixers and complete systems for:**

- Castables
- Prefabricated parts
- Granules for isostatic pressing

- Granules, e. g. ZrO2
- Press bodies for all types of bricks, including hot mixture

**eirich.com**

# 8 TESTING AND STANDARDIZATION

# IN SITU HIGH–TEMPERATURE RAMAN SPECTROSCOPY: A POWERFUL TOOL FOR STUDYING REFRACTORY MATERIALS

Sinje Zimmer, Johannes Kehren, Olaf Krause

Koblenz University of Applied Sciences, Höhr-Grenzhausen, Germany

## ABSTRACT

In the last decades, Raman spectroscopy has become an important analytical tool in various research areas such as physics, chemistry, biology, medicine, and geosciences. Initially, the technique was very complex and time-consuming and, therefore, limited to scientific applications. The development of new technologies has opened up Raman spectroscopy to a broader audience. Some companies are already using it to monitor and control quality. Raman spectroscopy enables non-destructive analysis to identify crystalline and amorphous phases and to distinguish polymorphs with a spatial resolution of the order of 1 μm.

Raman spectroscopy in combination with a furnace opens entirely new insights into the thermal evolution of mineral phases in terms of phase reactions and their reaction kinetics, whereat all measurements can be performed space-resolved and *in situ* up to 1500 °C. It speaks for itself that this method allows completely new insights into the sintering behavior of refractory materials and also opens the possibility to observe reactions temperature-, time-, and space-resolved in contact with corrosive media.

This paper gives an overview of *in situ* Raman spectroscopy at high temperatures in general, as well as the information that can be obtained with this method and the challenges that have to be overcome. Furthermore, initial results on the high temperature behavior in the CaO-Al₂O₃ system are presented. These experiments show that high temperature Raman spectroscopy is a promising method for refractory materials.

## INTRODUCTION

Raman spectroscopy is a powerful non-destructive tool for the mineralogical and chemical investigation of various materials. By performing *in situ* Raman measurements at high temperatures, a better understanding of the structure and behavior of refractory materials under these extreme conditions can be gained. This can help optimize their performance and extend their service lifespan.

Using commercially available heating stages, Raman spectra can be measured at temperatures up to 1500 °C. In addition, pressure and different environments can be applied depending on the desired objective [1]. To gain spatially resolved information of mineral reactions and interactions, Raman images have to be recorded instead of point measurements. The first time this was done *in situ* at high temperatures, was by Stange et al. [2] and the method itself was published in Hauke et al. [3]. Since then, several other studies have used it to investigate the high temperature behavior of ternisite [4], Rhenish lignite ashes [5], and silica/calcium phosphate ceramics [6].

This work reports on the application of *in situ* Raman spectroscopy at high temperatures to study refractory materials. Furthermore, it was investigated if the method can provide information to better understand mineral interactions and reactions through spatially resolved measurements. The $CaO-Al_2O_3$ system was chosen as the basis for these investigations because it has already been examined by other methods, and, therefore, the reactions and mineral phases ($CA$, $CA_2$, $C_{12}A_7$, and $C_3A$) during heating are well known [7, 8]. Furthermore, this system is very important in refractory materials as it is the basis for calcium aluminate cement, which is a major component in refractory castables.

## MATERIALS & METHODS

### Sample preparation

Calcite from Merck KGaA (Germany) with at least 99% $CaCO_3$ and corundum from Almatis (The Netherlands) with 99.8% $Al_2O_3$ were used as starting materials for the experiment. The powders were mixed in a weight ratio of 1:1 and pressed into a tablet with a diameter of 3 mm and a height of 3.44 mm. It was then placed in a heating stage (TS1500V, Linkam Scientific Instruments Ltd., United Kingdom) which was mounted onto the x-y-stage of the Raman spectrometer. A schematic drawing of the heating stage is shown in figure 1. The stage can be heated up to 1500 °C with a temperature stability of < 1 °C and a heating and cooling rate of 0.1 to 200 °C/min. Due to the placement of the thermocouple at the bottom of the heating cup and a temperature gradient within the sample, the temperature at the surface (were the measurement takes place) deviates from the temperature recorded. To adjust for this gradient, the temperatures are corrected according to Stange et al. (2018) [2].
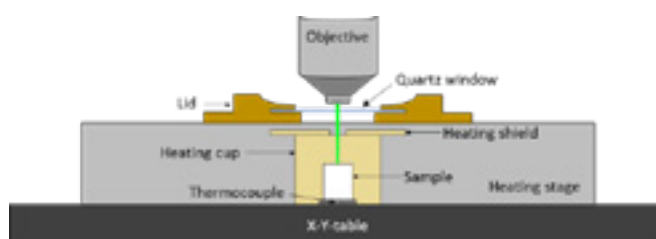


*Fig. 1: Schematic drawing of the Linkam TS1500V heating stage. The sample cup size is 7 mm in diameter and 6 mm in height.*

### Raman spectroscopy

The experiments were carried out with a confocal Raman spectrometer (Apyron, WITec GmbH, Germany) equipped with a deep-depletion detector and a 532.06 nm laser at 460 mW under a microscope. A 600 l/mm grating was used for all measurements, resulting in a spectral resolution of up to 2 cm⁻¹ and covering a spectral range from -80 to 4140 cm⁻¹. Furthermore, a 50x LD objective with a working distance of 9.1 mm and a numerical aperture of 0.55 was chosen. With these parameters, the theoretical lateral resolution ($d_1$) was about 1.2 μm and the axial resolution ($d_a$) was about 7.0 μm. The resolutions are given by $d_1 \approx 1.22 \lambda/NA$ and $d_a \approx 4\lambda/NA^2$, where $\lambda$ is the wavelength of the incident laser [9].

### Experimental detail

In the experiment, a total of six Raman images were recorded, two of which were measured at room temperature before (RTs) and after heating (RTe). The remaining images were measured at 1000, 1100, and 1200 °C. The surface temperatures corrected after Stange et al. [2] are 907, 992, and 1078 °C and are used to refer to the images in the following text. At each of these temperature steps, a Raman image was taken, and only at 1078 °C a second one was taken to see if there were any isothermal reactions taking place. The sample was fired to the different temperature steps with 10 K/min and cooled with 100 K/min. The full heating curve is depicted in figure 2.

The Raman images RTs and RTe cover an area of 200 x 200 μm² with 1 μm steps. At elevated temperatures, the images were smaller with 60 x 60 μm² and 1 μm steps, so a Raman image takes less time to measure (about 1 h). A larger area was chosen for the room temperature images because the mineral phases move during heating and can therefore be followed. All images were recorded with an acquisition time of 1 s per spectrum, instead of RTs, which was acquired with 0.1 s.

The Raman spectra of the images were measured in a grid from top left to bottom right, which must be considered when interpreting the data, as time passes during the measurement and mineral reactions proceed.

Before each Raman image, a manual focus was performed at the center position of the Raman image. However, the volume of the sample expanded during the high temperature measurements, resulting in defocusing. Therefore, only the first 20 to 30 min of each high temperature Raman image can be used for interpretation.
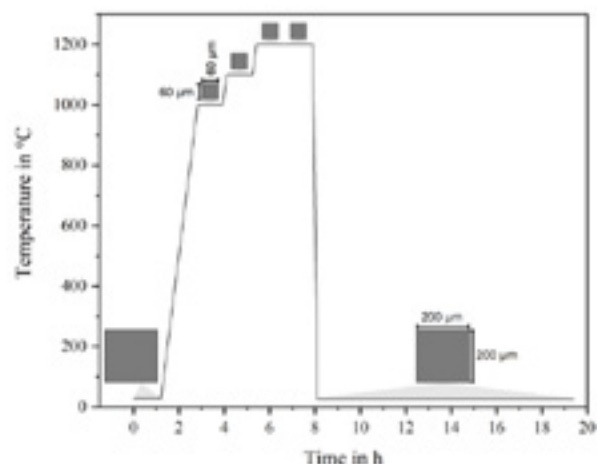


*Fig. 2: Heating ramp of the experiment. A Raman image was taken before and after the heating process at room temperature. One Raman image was measured at each temperature step, except at 1200 °C at which two Raman images were taken.*

## Data processing & analysis

The Raman images were first corrected for spikes caused by cosmic rays hitting the detector. Not all spikes could be removed automatically, therefore the remaining ones had to be fixed manually. The spectra were then cropped to a range of about 90 to 1200 cm$^{-1}$ to reduce computational time and improve further processing and analysis. Furthermore, the Raman data was smoothed using the Savitzky-Golay filtering algorithm to correct for noise and 2$^{nd}$ order polynomial was fitted and subtracted from the data to correct the background.

After data processing, the images were analyzed using the True Component Analysis of the WITec Project SIX software. This procedure extracts reference spectra of each phase from within the image to create intensity distribution images, which can then be combined to create a false-color image that includes all phases. The extracted reference spectra were obtained by averaging 9 individual spectra. For some phases no single phase spectrum could be extracted, therefore, interfering Raman bands of other phases were removed with the demixing tool in the project SIX software.

It is important to note that Raman spectra change at high temperatures due to crystal lattice changes, phase transformations, and blackbody radiation. These influences lead to increasing backgrounds, position shifts and broadening of the Raman bands, and an overall weaker signal. Although the Raman spectra of calcite, corundum and the expected CA phases are known at room temperature, the high temperature spectra have to be reassigned due to the shift of the Raman bands. However, it is still possible to correlate the high temperature spectra with the room temperature spectra.

## RESULTS & DISCUSSION

The Raman images of the experiment are shown in figure 3. Initially, calcite can be observed in RTs as well as weak signals from corundum, although both phases are present in the sample in equal amounts. This is due to the higher total Raman band intensities of calcite compared to corundum.

## Decarbonation of calcite

After heating to 907 °C, calcite is still present in the first 3 min of the and then decomposes to CaO. This is the result of the decarbonation of calcite according to the following reaction:

$$CaCO_3 \rightarrow CaO + CO_2$$

CaO can also be detected at 992 °C, but in smaller amounts than at 907 °C. At 1078 °C and in RTe, CaO cannot be clearly identified in the Raman spectra. However, the Raman spectrum of CaO is only a secondary Raman spectrum, which means that the spectrum has a weak signal and only broad Raman bands. Therefore, it is possiblethat CaO is not seen at higher temperatures because the blackbody response increases with temperature and superimposes the CaO signal. After cooling to RT, calcite and portlandite can be observed, which must have formed from unreacted CaO. The recrystallization of calcite follows the reverse reaction of decarbonation:

$$CaO + CO_2 \rightarrow CaCO_3$$
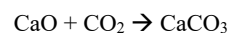
In this process, CaO reacts with the remaining CO$_2$ trapped in the heating stage. The decarbonation and recrystallization of calcite during *in situ* Raman measurements was also observed by Hauke et al. [3]. However, it appears that not all CaO reacts with CO$_2$ to form calcite, but instead reacts with atmospheric moisture to form portlandite:

$$CaO + H_2O \rightarrow Ca(OH)_2$$
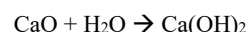
Portlandite is only present in the lower part of the Raman image, which is either because the remaining CaO was only present in the lower part of the Raman image, or the CaO took at least 7 h to react to portlandite, although the reaction should be quite rapid.

Corundum can be observed in all Raman images, but its amount seems to decrease with time to form other mineral phases.

## Formation of CA phases

During heating, the formation of three phases can be observed: Phase A, B and C. Phase A forms at 907 °C and appears to crystallize in large amounts at the expense of CaO. Phase B and C appear only at 1078 °C. At RT after heating the calcium aluminates CA, CA$_2$, C$_3$A and C$_{12}$A$_7$ and an unknown phase (Phase D) can be detected. Due to the temperature dependent band shift and broadening, the assignment of the unknown phases at high temperatures cannot be done with certainty. However, first assumptions can be made. According to the CaO-Al$_2$O$_3$ phase diagram, mainly CA and C$_{12}$A$_7$ are formed in the temperature range between 900 and 1100 °C [7]. In figure 4, the unknown phases A, B, and C are compared with reference spectra of CA, CA$_2$, C$_3$A, and C$_{12}$A$_7$ synthesized by the author. Phase A and B both have an intense band at about 500 cm$^{-1}$ and a smaller band between 700 and 800 cm$^{-1}$, whereas the Raman band of Phase A is less intense compared to that of Phase B. However, for Phase A this band is at about 758 cm$^{-1}$ and for Phase B at about 730 cm$^{-1}$. The main band of the reference CA is at 519 cm$^{-1}$. In addition, the spectrum has two sets of Raman band groups, between 100 and 160 cm$^{-1}$, and 770 and 810 cm$^{-1}$. In particular, the second group of bands is much smaller than the main band. The Raman bands of C$_{12}$A$_7$ are located at about 309, 521 and 774 cm$^{-1}$. The second one has the highest intensity. It can be assumed that Phase A is the high temperature Raman spectrum of CA and Phase B is that of C$_{12}$A$_7$. because although the two main bands of the Phase A and B have similar positions, the second band of Phase B at about 734 cm$^{-1}$ has a higher intensity compared to the corresponding main band and correlates with the reference spectrum of C$_{12}$A$_7$. Comparing Phase C with the calcium aluminate spectra, no correlation can be observed. However, the Raman bands at about 500 and between 705 and 790 cm$^{-1}$ are similar to those of Phase B and mainly only one additional band appears at about 585 cm$^{-1}$. In RTe another spectrum (Phase D) was detected, which could not be identified yet. The main band of this phase is at about 601 cm$^{-1}$ (figure 5). Considering the band shift caused by high temperatures, it is possible that Phase C is a mixed spectrum of Phase B and D.

Although CA$_2$ and C$_3$A are present at room temperature after the experiment, there is no evidence of these phases are present in the high temperature images. It could be that the phases were formed during heating but are not within the measured area.
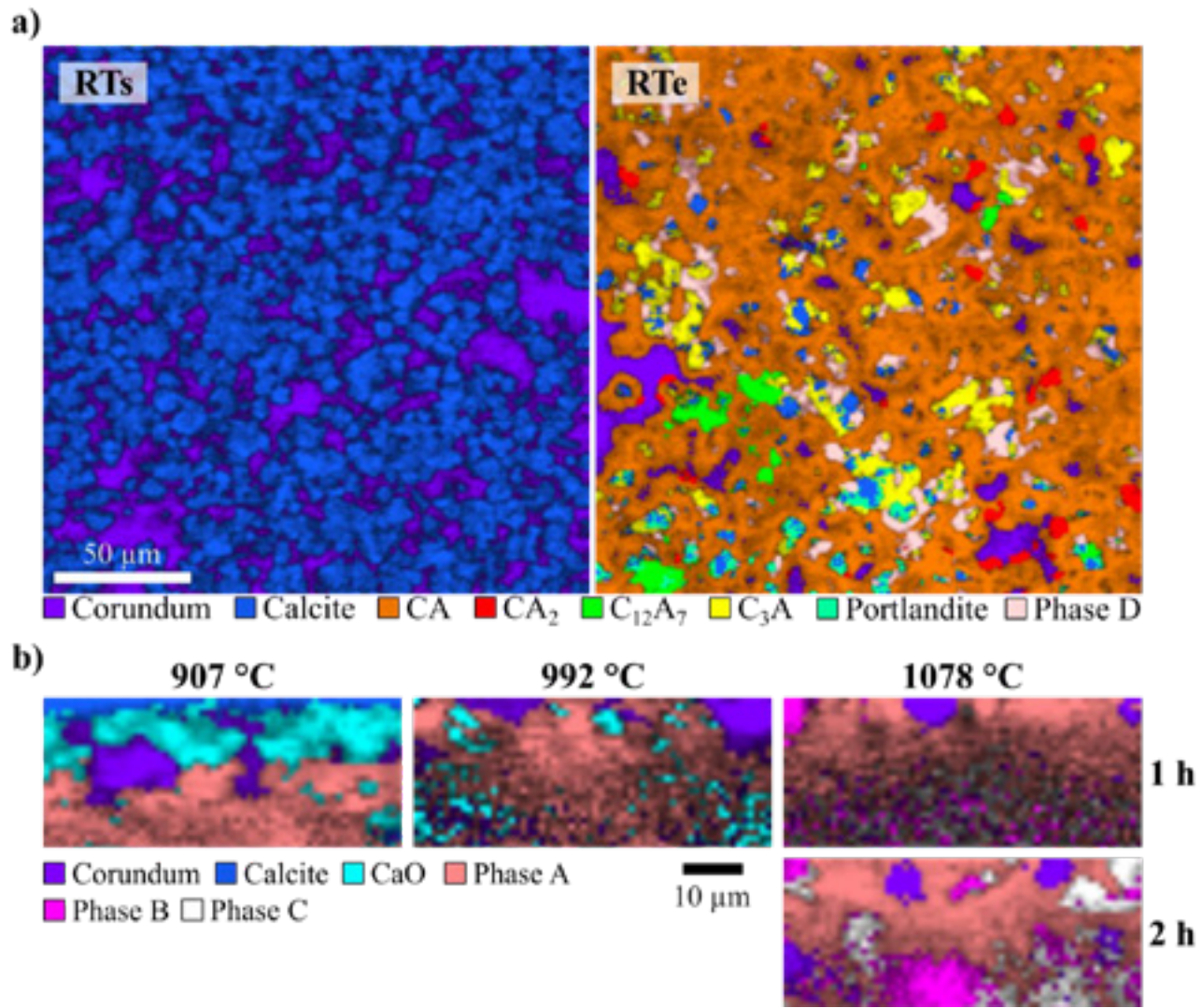
**a)**

RTs · RTe

50 µm

■ Corundum ■ Calcite ■ CA ■ CA₂ ■ C₁₂A₇ □ C₃A ■ Portlandite □ Phase D

**b)**

907 °C · 992 °C · 1078 °C

1 h

■ Corundum ■ Calcite ■ CaO ■ Phase A
■ Phase B □ Phase C

10 µm

2 h

Fig. 3: a) Raman images at room temperature before (RTs) and after heating (RTe). The images were recorded over an area of 200 x 200 µm² with 1 µm steps between the Raman spectra. b) Raman images at 907, 992 and 1078 °C. Due to the defocusing caused by the dilatation of the sample, the images have been cropped to areas of 25 x 60 µm².
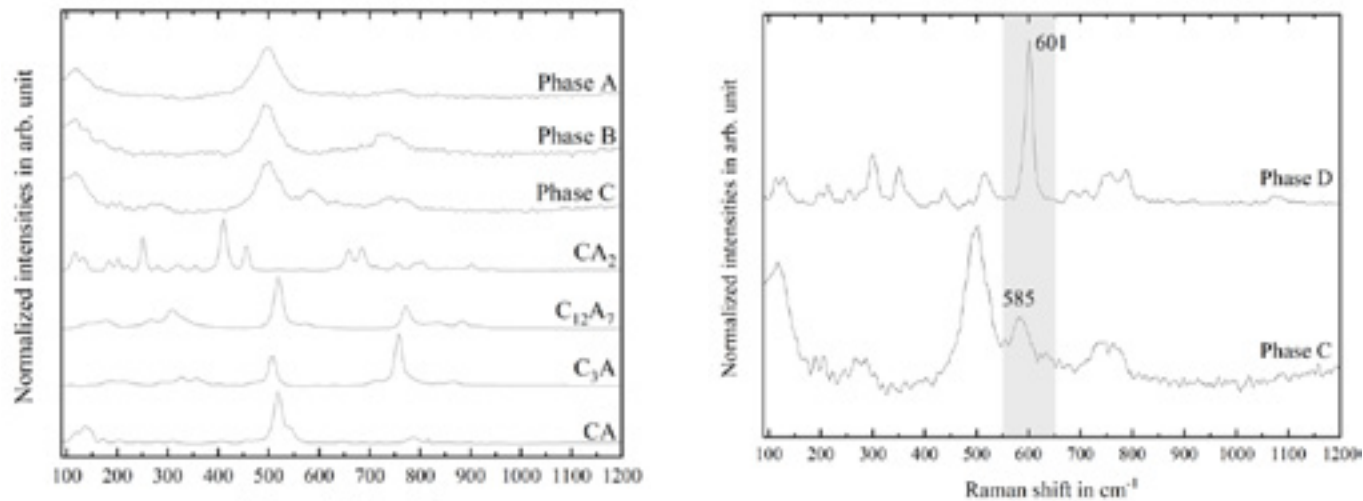


Fig. 4: Normalized Raman spectra of Phase A, B, and C extracted from the Raman image at 1078 °C and reference spectra of CA, $CA_2$, $C_3A$, and $C_{12}A_7$ obtained from previous synthesis at Koblenz, University of Applied Sciences. The reference spectra were measured with a 532 nm laser (50 mW), a 600 l/mm grating, an acquisition time of 1 s and 100 accumulations.



Fig. 5: Normalized Raman spectra of Phase D, derived from RTe and Phase C extracted from the Raman image at 1078 °C. The highlighted area depicts the Raman bands, which could belong to the same mineral phase, by taking the temperature shift into account.

## CONCLUSIONS

In this study, we have shown that Raman spectroscopy performed *in situ* at high temperatures can be a powerful tool for studying refractory materials.

The decarbonation and recrystallization of calcite could be observed, as well as the reaction of CaO to a calcium aluminate during firing at 907 °C and to portlandite at RT. Although we cannot yet identify the unknown phases with certainty, we were able to show that first approaches can be made.

In future experiments, high temperature measurements of pure calcium aluminates will be performed to study the Raman band changes of each phase. This will help to identify the unknown phases in this study. In addition, experiments with other materials such as nitride bonded silicon carbide are planned to further investigate the mineral reactions during heating and to show that this method can also be applied to other refractory materials.

## REFERENCES

[1]    Daniel, I, McMillan, P F, Gillet, P, Poe, B T. Raman spectroscopic study of structural changes in calcium aluminate ($CaAl_2O_4$) glass at high pressure and high temperature. Chemical Geology 128 (1–4), 1996, p. 5-15

[2] Stange, K, Lenting, C, Geisler, T. Insights into the evolution of carbonate-bearing kaolin during sintering revealed by *in situ* hyperspectral Raman imaging. Journal of the American Ceramic Society. 101 (2), 2018, p. 897-910

[3]    Hauke, K, Kehren, J, Böhme, N, Zimmer, S, Geisler, T. *In Situ* Hyperspectral Raman Imaging: A New Method to Investigate Sintering Processes of Ceramic Material at High-temperature. Applied Sciences 9 (7), 2019, p. 1310

[4] Böhme, N, Hauke, K, Neuroth, M, Geisler, T. *In Situ* Hyperspectral Raman Imaging of Ternesite Formation and Decomposition at High Temperatures. Minerals. 10 (3), 2020, 287.

[5] Böhme, N, Hauke, K, Neuroth, M, Geisler, T. *In situ* Raman imaging of high-temperature solid-state reactions in the $CaSO_4$–$SiO_2$ system. Int J Coal Sci Technol 6, 2019, 247–259.

[6] Böhme, N, Hauke, K, Dohrn, M, Neuroth, M, Geisler, T. High-temperature phase transformations of hydroxylapatite and the formation of silicocarnotite in the hydroxylapatite–quartz–lime system studied *in situ* and *in operando* by Raman spectroscopy. J Mater Sci. 57, 2022, p. 15239–15266

[7]    Hussain, A, Mehmood, S, Rasool, M N, Aryal, S, Rulis, P, Ching, W Y. Electronic structure, mechanical, and optical properties of $CaO \cdot Al_2O_3$ system: a first principles approach. Indian Journal of Physics. 90, 2016, p. 917–929

[8] Kohatsu, I, Brindley, G W. Solid State Reactions between CaO and α-$Al_2O_3$. Zeitschrift für Physikalische Chemie. 60 (1-6), 1968, p. 79-89

[9] Vandenabeele P. Practical Raman Spectroscopy – An Introduction, John Wiley & Sons, Ghent; 2013. p. 91-95

# MATERIAL CHARACTERIZATION & PRODUCT ANALYSIS OF REFRACTORIES VIA X–RAY COMPUTED TOMOGRAPHY

D. Lüftner, P. Seitz, R. P. Rana
RHI Magnesita, Leoben, Austria

**ABSTRACT**

X-ray analysis is a standard approach to investigate all kinds of materials and is well established for refractories (e.g., X-ray diffraction, X-ray fluorescence, and X-ray adsorption). X-ray computed tomography is used to get a sample's three-dimensional (3D) density distribution by capturing X-ray absorption images while the sample is rotating (CT). This provides the opportunity to view the sample's inside in three dimensions with a resolution that ranges from around 100µm down to the submicron range. The capabilities of the CT system at RHI Magnesita's Technology Center Leoben (TCL), which makes it possible to collect precise information about a sample's internal structure, will be illustrated in this article utilizing a few chosen investigations in the field of flow control products.

**INTRODUCTION**

X-ray radioscopy is an indispensable tool for many industrial applications, especially in the field of quality control and has been in use at RHI Magnesita for many years. However, because it yields a two-dimensional (2D) representation of a 3D object, it is often difficult to interpret [1]. In the last two decades the field of industrial CT has been steadily increasing [2]. During an industrial CT scan more than thousand X-ray transmission measurements of a rotating object are performed and then this data is converted into a 3D representation of the object using various reconstruction algorithms. As such, the drawbacks of pure X-ray radioscopy can be overcome because firstly, CT provides a map of the radiation absorption coefficient (i.e., density) for each point in space. Secondly, the dimensions are absolute values, and the 3D tomogram represents the real shape of the object [1]. Therefore, defects or flaws can be detected with high accuracy and their dimensions can be extracted.

In the area of flow control, products such as refractory slide gate plates, ladle shrouds, monoblock stoppers, and SENs are used in the continuous casting process to transfer molten steel from the ladle to the tundish and then into the mould [3,4]. These products are used to regulate the steel flow and protect the molten metal stream from reoxidation. Due to their direct contact with the high-velocity liquid steel stream, they need to resist elevated temperatures, corrosive and abrasive attack by steel and slags, as well as high-temperature gradients during application. To fulfil the rising customer demands (e.g., clean steel and anti-clogging), these refractories are becoming more and more complex. Consequently, improving the product performance is challenging and time consuming. Hence, there is an increasing demand for innovative technologies to support product development in the flow control area. CT, which gives the opportunity to have a detailed look inside the full volume of an uncut product, enables fast optimisation of the manufacturing process, product design, as well as excellent quality control.

In this paper, the capability of CT in the world of refractories is demonstrated using various examples of flow control product ranging from post-mortem investigations of a SEN and slide gate plate, over the development and of 1500 mm long TS-SENs to the characterization of the material used for these products.
.

**X-RAY COMPUTED TOMOGRAPHY DEVICE**

The new tailor-made CT device at RHI Magnesita's TCL (Austria) is depicted in Figure 1a. It is a dual X-ray source device, equipped with a 225 kV direct beam and a 190 kV transmission beam source. While the former has a higher penetration depth and may be used for larger samples, the latter is limited in power but with a focus spot size in the sub-micron range, which enables high-resolution measurements of small samples. As an example, the result of scanning a single MgO grain is shown in Figure 2b, where the light colour corresponds to higher density material and the dark regions are low density areas. A voxel size resolution of approximately 2 µm offers a precise determination of a crack's thickness (i.e., 40 µm in this case) and length. Furthermore, the system is comprised of a 3000 x 3000-pixel flat panel detector with a pixel pitch size of 150 µm, a manipulator with seven independent axes of movement, a maximum focus detector distance of more than 1400 mm (necessary to achieve the geometrical magnification for high resolutions), and a vertical travel distance of the X-ray source and detector of about 800 mm.
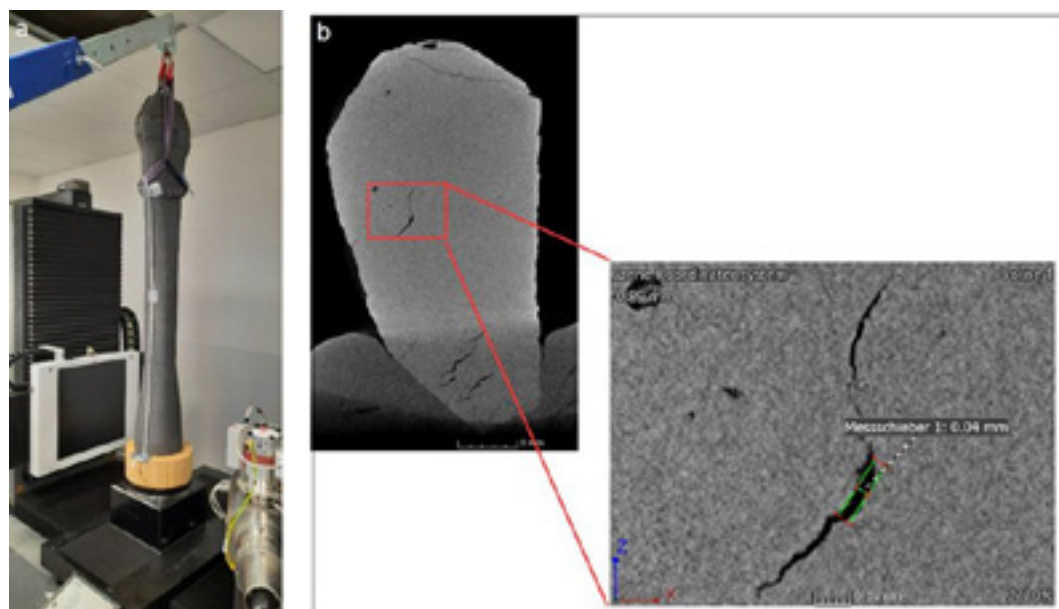


*Fig. 1 (a) TS-SEN standing upright on the system's turning table and (b) vertical cut through the 3D CT data set of a single MgO grain with a detailed dimensional measurement of the crack (i.e., 40 µm)*

**APPLICATION OF X_RAY SCANNING TECHNOLOGY**

**Postmortem analysis**
The first postmortem example described in this section is the analysis of a used SEN that showed rather high wear after use.

A full 3D CT measurement of the piece was accomplished, and an image of the sample surface is shown in Figure 2a. A slice through the 3D data is depicted in Figure 2b. The slag band area, which has a high amount of ZrO2 and therefore a higher density, was easily identified at the bottom of the sample and the following conspicuous regions can be observed in the data.

Inside the bore remaining droplets of steel could be detected (whitish because of their high density). The following changes to the body material above the slag band during operation of the product were also identified. Firstly, local densification of the product due to steel and/or slag infiltrating pores was observed in the CT measurements, with the infiltrations leading to a brighter colour that can be seen in the regions indicated with a green arrow (see Figure 2b). Secondly, at the elevated temperatures during casting, oxidation (i.e., decarburisation) of the body material can occur that locally lowers the density and therefore appears darker in the CT data. In this case, it was evident that a large part of the sample above the infiltrations had undergone oxidation. Thirdly, and most importantly, the nozzle was affected by chemical attack from the mould powder above the meniscus, which caused material wear. The wear is clearly visible in Figure 2c, where the red-purple horizontal lines show deviation of the surface of the used SEN from the CAD drawing of an unused product. It can be concluded from the CT images that the root cause of the high product wear was a too deep immersion of the product during casting and/or an insufficiently long slag band.
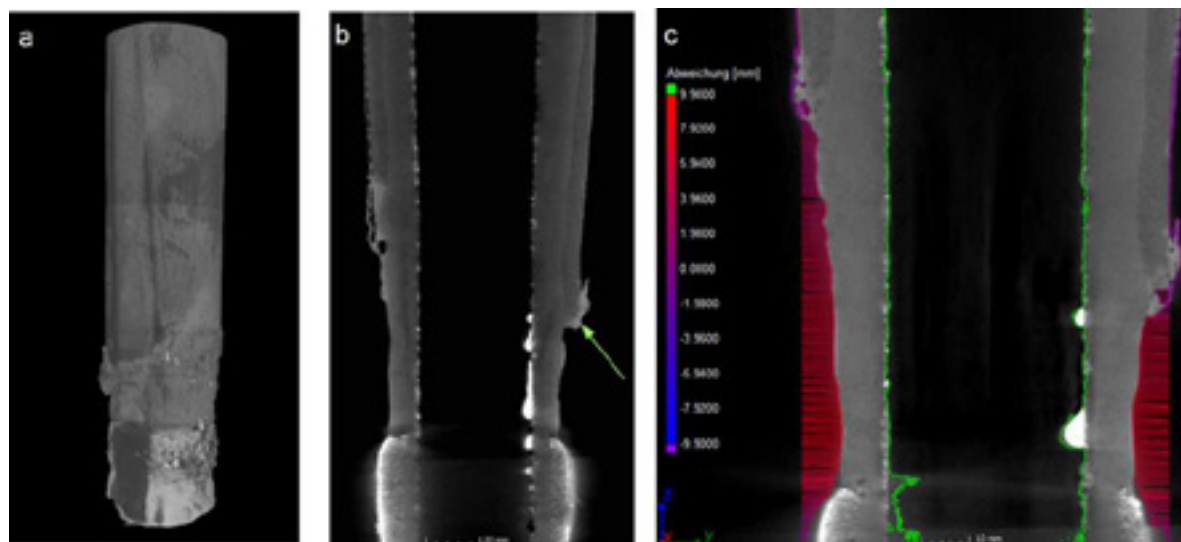


*Fig. 2. (a) 3D view of the SEN surface obtained by CT, (b) vertical cut through the SEN CT data, and (c) difference between the used SEN's surface and the CAD drawing of the product. The inner bore profile of the used SEN is indicated in green.*

For certain flow control products, a 3D CT measurement may not be applicable, for example in the case of slide gate plates. This is primarily due to the aspect ratio of the piece as well as the metal can covering a proportion of the refractory surface. However, the CT device at TCL can also be used to perform 2D radioscopy measurements and this was the approach used in the following post-mortem investigation. In this example, a slide gate plate showed cracks on its surface after application (Figure 3a). The question in this case was whether the cracks occurred during cool down or if they had formed at an earlier stage during application. The 2D radioscopy image of the used slide gate plate is shown in Figure 3b. It should be noted that the radioscopy images directly show the information from the detector, meaning that light grey values correspond to a high radiation intensity and hence a low linear absorption, while dark values indicate a higher density/thickness. Thus, the black area surrounding the grey circle is the steel jacket around the slide plate and the bore hole appears white. The cracks can be seen as white lines radiating from the bore hole. Because there are no visible steel infiltrations, which would have appeared dark, it can be concluded that the cracks formed during cool down of the product due to thermal shrinkage of the material. The darker areas indicated by the red arrow are due to the remaining mortar located on the backside of the plate.
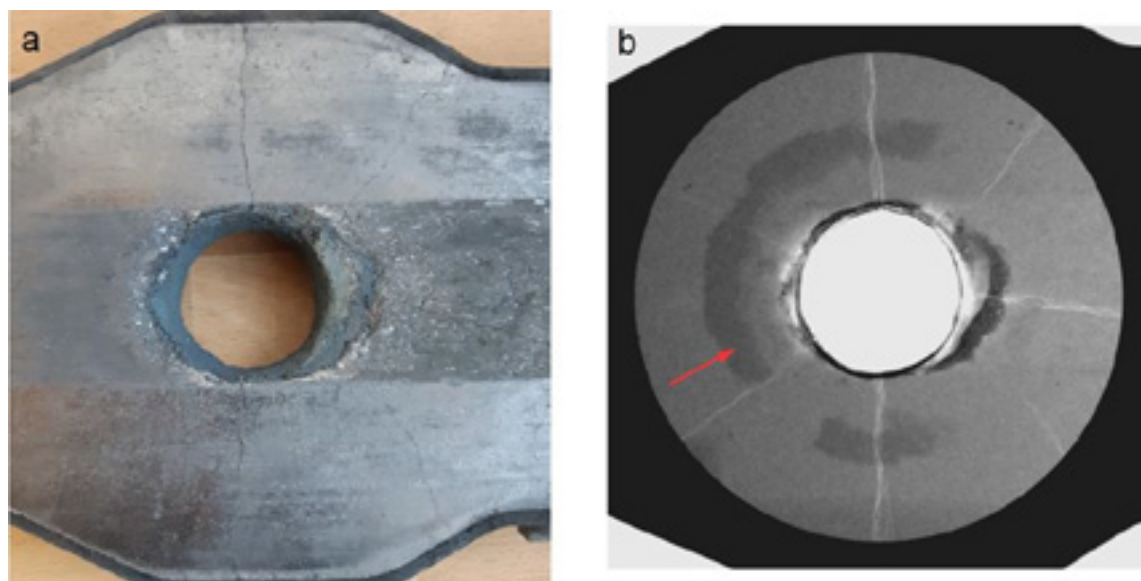


*Fig. 3. (a) image of the used slide plate and (b) 2D radioscopy measurement of the corresponding slide gate plate.*

In addition to these examples, the CT equipment has been pivotal for the post-mortem analysis of many other flow control products such as monoblock stoppers and ladle shrouds. Furthermore, if the root cause of a sample failure cannot be determined directly from the CT scan, the images can be used to identify the ideal location for sampling so that further analyses can be performed, such as microscopic investigations.

**Product development and process improvement**

Another important application for the CT technology is supporting new product developments or improving existing ones. This is particularly important for flow control products with an elaborate design, consisting of multiple different materials, and/or a complex shape and therefore requiring an expensive production process. One example for which these criteria hold true are TS-SENs, which are used for thin slab casting where a well-controlled flow of the steel from the tundish to the mould is essential. Here, the potential of CT lies in a fast analysis of any change in the production process and/or material recipe for the whole volume of a piece in a non-destructive way. This enables a direct link to be established between implemented changes and their effect on the product in terms of defects or imperfections. As such the CT can significantly reduce the development time for this kind of product in the prototype stage.

The following is an example of how the CT equipment was used to expedite the development of a TS-SEN design. Due to the large size of the TS-SEN, a full 3D CT scan of the whole volume would have been more time consuming and expensive compared to a 2D scan. Therefore, only the most critical parts, namely the slag band and port area are 3D-scanned. Because of the TS-SEN's rotational symmetry along a high proportion of the shape, it was sufficient to measure these sections three times in 2D with a 60° rotation selected between each image. Thereby any defect could be detected in the entire sample volume. The remaining TS-SEN volume, namely a proportion of the slag band region and the nozzle outlet, was investigated using 3D CT measurements and several anomalies were identified that occurred while trying new production routes or alternative recipes. For example, Figure 4a shows the outcome of a new production approach that led to scratches and zirconia contamination at the outlet and Figure 4b depicts the results of a trial where significant intermixing of the slag band and body material occurred. Only with the fast and direct feedback from the CT measurements, could such trials be done efficiently and economically. The images in Figure 4c, which show vertical cuts in three orientations (i.e., top, front, and side view) demonstrate two more imperfections. Firstly, there are white lines which are, as already discussed above for the 2D measurements, due to the zirconia material migrating down from the slag band area. This indicates an improper filling of both the alumina graphite and zirconia graphite materials. Secondly, a crack is visible in all three Figure 4c images, which can be identified from the typical nonlinear shape and the sharp contrast to the surrounding material. Based on these results the necessary improvements were made.
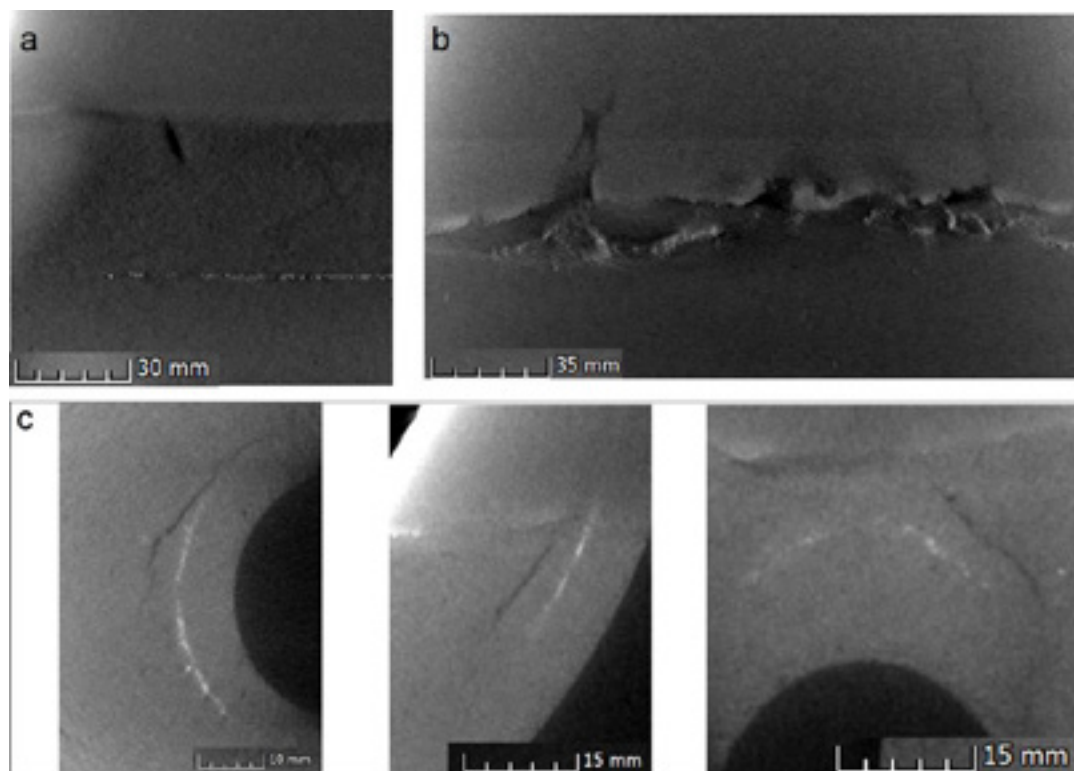
*Fig. 4. Compilation of anomalies found in TS-SENs. The images show vertical and horizontal cuts through the 3D CT data. (a) scratch on the inner surface and zirconia contamination at the outlet, (b) intermixing of slag band and body material, and (c) crack close to the slag band material in three orientations (top, front, and side view) and zirconia material migration (white).*

**Material characterization**

The last example of an application of X-ray CT is the characterization of the refractory material. Because the resolution which can be obtained in the CT measurement depends on the size of the investigated sample, it is necessary to take samples from the products. Figure 5 shows an example of such an investigation for the body material of an isostatically pressed product. In this case a cylindric sample with a diameter of 8 mm has been utilized allowing for a voxel size and, due to the low power, a resolution of about 3 μm. Clearly, different components can be recognized, however, for a further analysis of such kind of data, it needs to be segmented into the different components of interest. Different algorithms can be applied to perform the segmentation, from very simple ones like global threshold, which is often sufficient if only the pore space is needed for further investigations, to more complex ones like convolutional neural networks, which have been used in this work [5] and can be seen in Fig. 5c. Here, the red colour corresponds to the coarse grains, the green to graphite, yellow to the remaining matrix (e.g., fine grains) and grey to the porosity. To have a reference for the annotation of the different components the sample has been cut after the CT measurement and has been investigated using an optical microscope, Fig. 5b shows the corresponding image. Clearly, apart from a small misalignment and the different contrast, the slice corresponding to the cut plane has been found in the 3D CT data, which can be seen best when considering the coarse grain fraction.
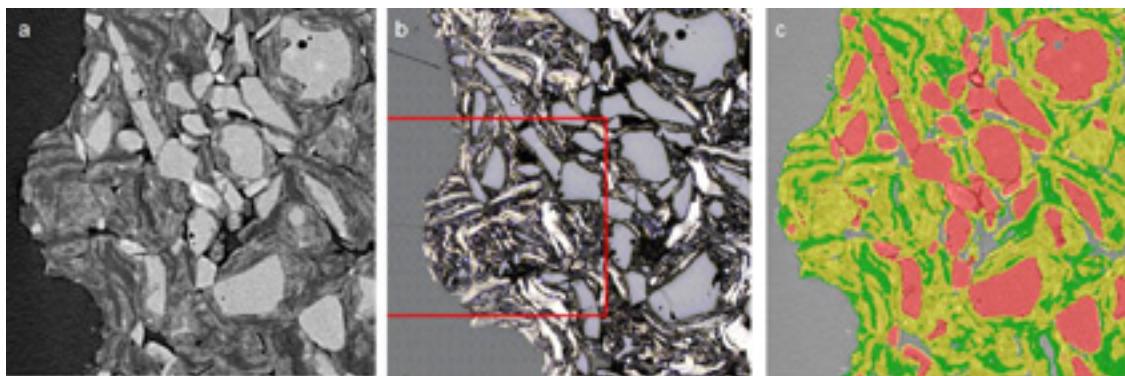
*Fig.5 (a) Slice through the 3D CT data of a high resolution (<5µm) µ-CT scan. (b) Microscopy image of the same sample at the plane indicated in panel a. (c) Slice through the segmented CT data, at which red corresponds to the coarse grains, green to graphite, grey to the porosity and yellow to the remaining matrix of the refractory.*

Once the computed tomography data is correctly segmented (Fig. 5c), various further analyses can be done on such kind of data. From the three-dimensional characterization of the microstructure, i.e., the size- and geometric distribution of pores and grains and the orientation of different components, over the calculation of integral properties of the investigated material like the permeability or the thermal- or the electrical conductivity, to the prediction of e.g., elastic properties by using the segmented data as input for thermomechanical simulations.

## CONCLUSIONS
In conclusion, with the possibility to get a rapid and complete picture of a sample's inner structure, ranging from a single grain to the full dimensions of a complex product in a non-destructive way, CT is an indispensable tool for refractory investigations. In this article the following uses of an industrial CT system were discussed:

- Raw material characterisation.
- Post-mortem analysis.
- Dimensional measurement/wear measurement.
- Quality control.
- Process optimisation.
- Product development.
- 3D Microstructure characterization.

Besides these applications, there are several other possibilities for the CT system within the world of refractories. Among them are 3D microstructure characterisation, for example the geometric and size distribution of pores or inclusions (material characterisation), use as a reference method for other non-destructive testing methods, and generating input data for subsequent mechanical or thermomechanical simulations such as finite element method and discrete element method. In the future, it is planned to perform in-situ measurements at elevated temperatures or with applied stresses. Finally, it can be concluded that the new X-ray equipment significantly supports refractory developments, especially in the area of flow control. It has become a key technology for detecting all kinds of anomalies and leads to a better understanding of their origin, thereby increasing the product and process quality and hence refractory performance.

## REFERENCES
[1] Carmignato, S., Dewulf, W. and Leach, R. Industrial X-Ray Computed Tomography; Springer International Publishing AG: Switzerland, 2018.

[2] De Chiffre, L., Carmignato, S., Kruth, J.P., Schmitt, R. and Weckermann A. Industrial Applications of Computed Tomography. CIRP Annals-Manufacturing Technology. 2014, 63(2), 655–677.

[3] Routschka, G. and Wuthnow, H. Praxishandbuch Feuerfeste Werkstoffe (5. Auflage); Vulkan-Verlag GmbH: Germany, 2011.

[4] Hackl, G., Nitzl, G., Tang, Y., Eglsäer, C. and Chalmers, D. Innovative Flow Control Refractory Products for the Continuous Casting Process. AISTech 2015 Proceedings, Cleveland, USA, 4–7 May, 2015; pp. 2436–2442.

[5] Ronneberger, O., Fischer, P., Brox, T. (2015). U-Net: Convolutional Networks for Biomedical Image Segmentation. In: Navab, N., Hornegger, J., Wells, W., Frangi, A. (eds) Medical Image Computing and Computer-Assisted Intervention – MICCAI 2015. MICCAI 2015. Lecture Notes in Computer Science(), vol 9351. Springer

# FRACTURE ENERGY DETERMINATION OF CARBON–CONTAINING REFRACTORIES WITH CONSIDERATION OF THE CREEP BEHAVIOUR

Dietmar Gruber, Martin Stückelschweiger, Shengli Jin, Harald Harmuth

Montanuniversität Leoben, Leoben, Austria

## ABSTRACT

A carbon-containing magnesia refractory product (MgO–C) as it is applied in steel ladles of the secondary steel metallurgy was investigated for the Mode I fracture behaviour. Usually, it is determined with the wedge splitting test to quantify the thermal shock behaviour, the materials' brittleness or to gain input parameters for thermomechanical Finite Element (FE) simulations. For high-temperature testing of carbon-containing refractories, gas purging, for example, with argon, is required to avoid carbon oxidation in the sample. Laser speckle extensometers measure the displacement in a contactless manner. Based on the results obtained from the tests, fracture mechanical parameters such as the specific fracture energy and the nominal notch tensile strength were calculated. An inverse FE simulation yielded tensile strength, the total specific fracture energy, and the strain-softening behaviour. As refractories often show significant creep rates at application temperatures, the creep behaviour was also considered in the inverse evaluations. Finally, the contribution of creep to the determined area under the load-displacement curve was quantified and a corrected specific fracture energy was determined.

## INTRODUCTION

The wedge splitting test is commonly used to characterise the fracture mechanical behaviour of refractory materials [1,2]. The advantages are the relatively stable crack propagation and the possibility of developing a large fracture process zone [3]. When testing carbon-containing materials at high temperatures, protection against carbon burnout is essential. This may be achieved by gas purging. At elevated temperatures, the results of wedge-splitting tests could be influenced by creep; this means the results will depend on the loading velocity. A decrease in the loading speed will increase the effect of creep [4]. An approach to quantify the contribution of creep is to determine the creep behaviour in advance and conduct a Finite Element inverse evaluation considering creep and fracture. The procedure and results for a Magnesia carbon material are explained in this paper.

## MATERIAL AND SAMPLE PREPARATION

A resin-bonded magnesia carbon brick consisting of fused magnesia, magnesia clinker and graphite was tested. After coking at 1000°C for 5h under a reducing atmosphere, the residual carbon content was 10%. The C/S weight ratio was 3.8.

## EXPERIMENTAL

The wedge splitting test according to Tschegg was applied for the fracture mechanical investigations [1]. The samples are prismatic, with a starter notch and additional crack-guiding notches at the lateral surfaces. The specimen dimensions and a schematic of the wedge-splitting test setup are shown in Fig. 1. The relatively high ratio of the fracture surface area to the specimen volume and the decrease in the elastically stored strain energy in the testing machine by the action of the wedge favour stable . A vertical load is applied to the wedge during the test, resulting in a horizontal reaction force and crack propagation in the vertical direction. The test is performed with a 0.5 mm/min vertical loading rate. A laser extensometer detects the horizontal displacement at the measuring points during the test. The displacement is measured at the height where the rolls contact the load transmission elements.
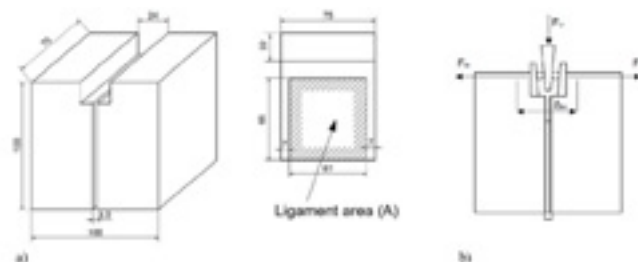


*Fig. 1: (a) Wedge splitting test shape and dimension in mm and (b) testing setup*

The sample is supported by a corundum piece (prismatic, $3\cdot3\cdot90mm^3$) to allow sample deformation (Fig. 1 (b)). The vertical force $F_V$ is measured, and the horizontal force is calculated according to eq 1.

$$F_H = \frac{F_V}{2tan\frac{\alpha}{2}} \tag{1}$$

$\alpha$ is the angle of the wedge (10°). The specific fracture energy $G_f'$ and the nominal notch tensile strength $\sigma_{NT}$ were calculated according to eq. 2 and 3.

$$\sigma_{NT} = \frac{F_{H,max}}{bh}\left(1 + \frac{6y}{h}\right) \tag{2}$$

$$G_f' = \frac{1}{A}\int_0^\delta F_H d\delta_H \tag{3}$$

$b$ and $h$ are the width and height of the ligament area, respectively, and $y$ is the vertical distance of the horizontal force from the centre of gravity of the ligament area. The measured horizontal displacement is defined with $\delta_H$, and the horizontal displacement at 15% of the maximum load is $\delta$.

Usually, the material brittleness is characterised by the characteristic length $l_{ch}$ (eq. 4) [5]:

$$l_{ch} = \frac{G_f E}{f_t^2} \tag{4}$$

Here, $E$ is the Young's modulus and $f_t$ the tensile strength. To avoid oxidation of carbon in the sample at elevated temperatures, the tests were carried out in an argon-purged furnace (10-70 l/h). The horizontal displacement was measured on the front and rear sides with laser speckle extensometers (LSE) through quartz glass windows [6]. The resolution of the displacement measurement is 0.11μm.

## SIMULATION MODEL

It is impossible to directly determine tensile strength, the complete specific fracture energy, and the contribution of creep to the testing result. For this reason, an inverse evaluation method was applied to a two-dimensional finite element model of the wedge-splitting test [7]. The commercial software package ABAQUS was applied for the simulations. Fracture was assumed to happen in the ligament area (Fig. 2).
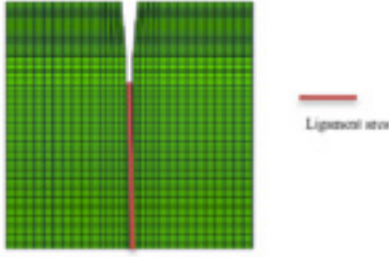
*Fig. 2. Finite element model and ligament area*

According to eq. 5, an exponential softening was applied to simulate the Mode I fracture.

$$\sigma = f_t \left\{ 1 - \left( \frac{1 - e^{-\varphi \frac{x}{x_{ult}}}}{1 - e^{-\varphi}} \right) \right\} \qquad (5)$$

$f_t$ is the tensile strength of the material, the parameter $x_{ult}$ is the ultimate crack opening and $\varphi$ is a non-dimensional parameter that defines the strain softening behaviour [8]. An adaptive nonlinear least-squares algorithm was applied to inversely determine the fracture parameters by fitting the finite element simulation results to those of laboratory wedge splitting tests. To evaluate the influence of creep on the results, inverse evaluations were carried out with and without consideration of creep. The Norton-Bailey creep was applied (eq. 6):

$$\dot{\varepsilon}_{cr} = K(T)\sigma^n \varepsilon_{cr}^a \qquad (6)$$

$\sigma$ is the von Mises stress, $\dot{\varepsilon}_{cr}$ is the creep strain rate, $\varepsilon_{cr}$ is the creep strain, $K(T)$ is a temperature-dependent function, and the parameters $n$ and $a$ are the stress and strain exponents, respectively. Creep was considered in the whole sample volume.

**RESULTS AND DISCUSSION**
Fig. 3. Shows the load-displacement curves from experiments carried out at 20°C, 1100°C, 1370°C and 1470°C.
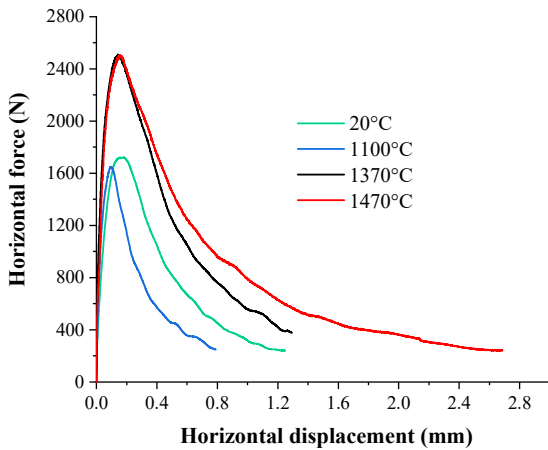


*Fig. 3. Load/displacement curves of the magnesia carbon material measured at different temperatures.*

Tab. 1 shows the maximum horizontal force $F_{Hmax}$, the specific fracture energy $G_f'$ and the nominal notch tensile strength $\sigma_{NT}$

according to equations 1, 2 and 3.

Tab. 1: Fracture mechanical parameters determined from tests performed at 20°C, 1100°C, 1370°C and 1470°C

|  | 20°C | 1100°C | 1370°C | 1470°C |
|---|---|---|---|---|
| $F_{Hmax}$ [N] | 1720 | 1646 | 2508 | 2510 |
| $G_f'$ [N/m] | 240 | 125 | 362 | 513 |
| $\sigma_{NT}$ [MPa] | 2.71 | 3.13 | 4.02 | 4.35 |
| $G_f'/\sigma_{NT}$ [mm] | 0.09 | 0.04 | 0.09 | 0.12 |

For the tests above 1000°C the specific fracture energy $G_f'$ and the nominal notch tensile strength $\sigma_{NT}$ show an increase with temperature. The test at room temperature shows the smallest nominal notch tensile strength $\sigma_{NT}$, but the specific fracture energy $G_f'$ was higher than that at 1100°C and lower than that at 1370°C. The ratio between the specific fracture energy $G_f'$ and the notch tensile strength $\sigma_{NT}$ was applied to indicate the brittleness, showing the highest brittleness at 1100°C. After the test at 1470°C, the weight loss was below 1% for a purging rate of 70 l/h. The weight loss after the test at 1370°C was 0.8%. For the test at 1100°C the weight loss decreased to 0.5%.

**Results from the inverse evaluation**
A comparison of measured and in the inverse evaluation determined load-displacement curves for the high-temperature tests are given in Fig. 4-6. The black curves show the laboratory experiments. The red curves were simulated without the consideration of creep and the blue ones were simulated considering creep.
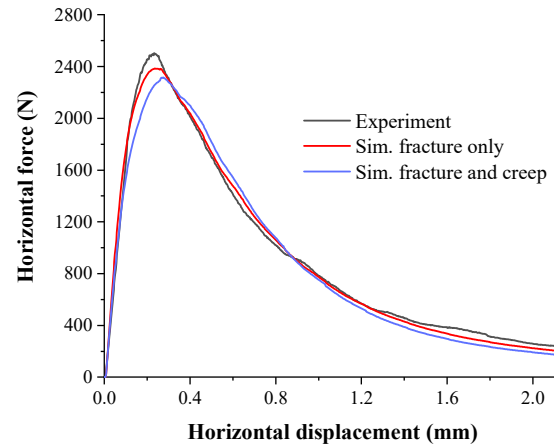


*Fig. 4: Load-displacement curves at 1470°C.*

The curves show in general good fits, especially in the pre-peak and post-peak regions. Slight deviations appear around the maximum loads.
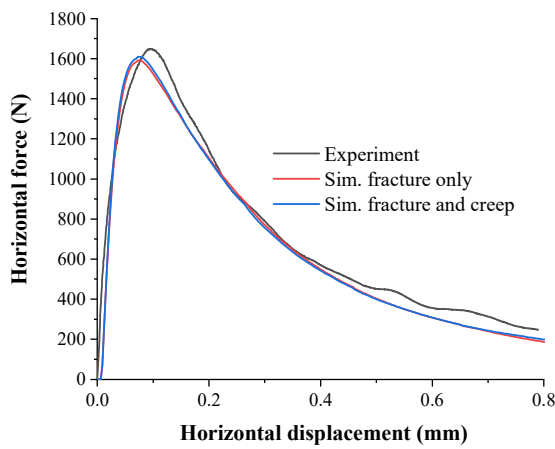
745
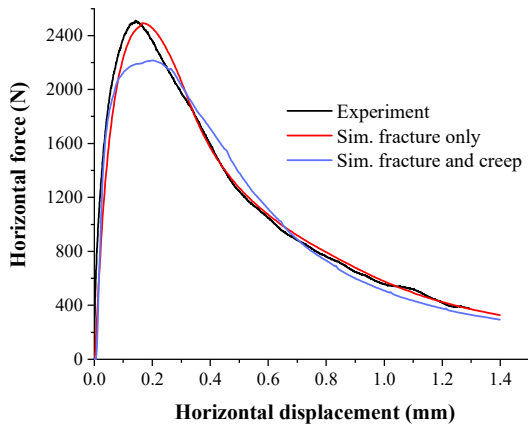
Fig. 5: Load-displacement curves at 1370°C.



Fig. 6: Load-displacement curves at 1100°C.

Fig. 7-9 show the inverse evaluation results for the strain softening behaviour. In the cases where creep was considered (blue curves), the area under the curves (representing total specific fracture energy $G_f$), is smaller and the strength is higher. The ultimate displacement increases with the temperature.
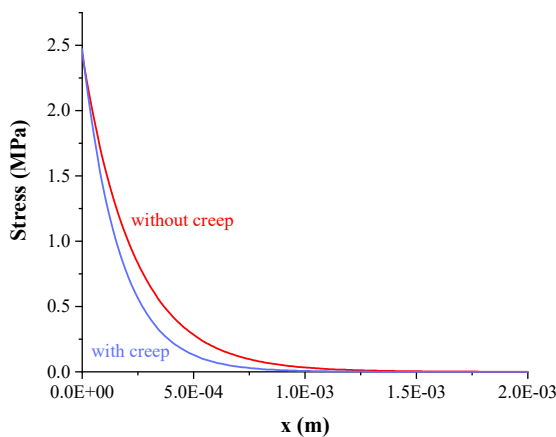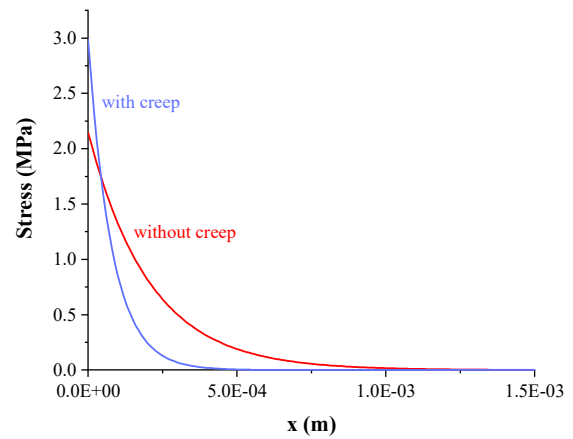


Fig. 7: Strain softening behaviour at 1470°C.



Fig. 8: Strain softening behaviour at 1370°C.

Fracture mechanical parameters and brittleness indicators from the inverse evaluation without consideration of creep are summarised in Tab. 2. Here creep contributes to fracture characteristics. $G_f$ is in all cases higher than $G_f'$ (Tab.1), because for $G_f'$ the integration was stopped at 15% of the maximum force on the post-peak side. $G_f'/\sigma_{NT}$ and $G_{ff}/f_t$ show the same trend but higher values for $G_{ff}/f_t$, the minimum of $l_{ch}$ was detected for 1370°C and the maximum at 1470°C.
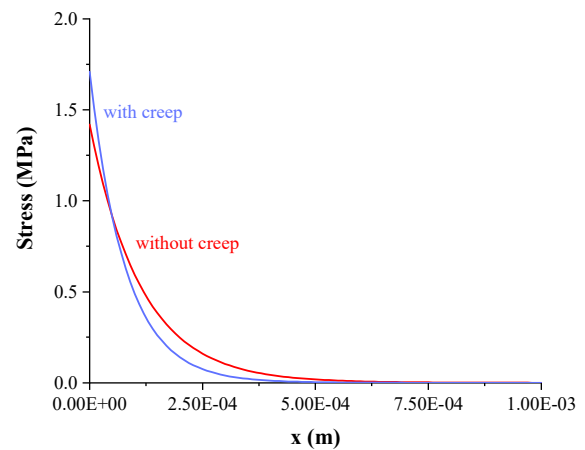


Fig. 9: Strain softening behaviour at 1100°C.

Tab. 2: Fracture mechanical parameters and brittleness indicators at different temperatures calculated from ABAQUS simulations without consideration of creep.

|  | 1100°C | 1370°C | 1470°C |
|---|---|---|---|
| $G_f$ [N/m] | 162 | 453 | 563 |
| $f_t$ [MPa] | 1.42 | 2.26 | 2.40 |
| $\sigma_{NT}/f_t$ | 2.2 | 1.77 | 1.83 |
| $G_{f}/f_t$ [mm] | 0.11 | 0.20 | 0.23 |
| $l_{ch}$ [m] | 2.00 | 1.91 | 2.93 |

Fracture mechanical parameters and brittleness indicators from the inverse evaluation with consideration of creep are summarised in Tab. 3. Here creep does not contribute to fracture chartacteristics. Further this table shows the differences caused by the action of creep. The influence on $G_f$ is significant and has a maximum at 1370°C with ann increase of 47% by creep. $f_t$ is higher with a maximum increase of 0.73 MPa for 1370°C by creep. The higher strength and the lower $G_f$ result in a higher brittleness (shown by the lowest $l_{ch} = 0.57$ m) for pure fracture without creep.

Tab. 3: Fracture mechanical parameters at different temperatures calculated considering creep and the influence on fracture mechanical parameters.

| | 1100°C | 1370°C | 1470°C |
|---|---|---|---|
| $G_f$, creep considered [N/m] | 137 | 238 | 417 |
| $\Delta G_f$ [N/m] | 25 (15%) | 215 (47%) | 146 (26%) |
| $f_t$, creep considered [MPa] | 1.71 | 2.99 | 2.47 |
| $\Delta f_t$ [N/mm²] | 0.29 | 0.73 | 0.07 |
| $G_f/f_t$, creep considered [mm] | 0.08 | 0.08 | 0.17 |
| $l_{ch}$ [m] | 1.17 | 0.57 | 2.05 |

## CONCLUSIONS

With the applied procedure it was possible to:
- determine the fracture mechanical parameters $G_f'$, $\sigma_{NT}$ for a carbon-containing refractory at elevated temperatures with minimised carbon burnout,
- determine the parameters for an exponential strain softening behaviour as well as the tensile strength $f_t$ and $G_f$ with finite element simulations coupled with the inverse evaluation procedure,
- assess the influence of creep during the high-temperature tests on the determined parameters.

As expected, $G_f$ is raised by creep because it contributes to energy consumption (even without crack propagation, a displacement could be recorded after load application). Creep further leads to lower inverse evaluated $f_t$, because creep decreases the loads in the sample in general and around the maximum force in the load-displacement diagram. Lower $l_{ch}$ indicates higher brittleness due to the action of creep originating mainly from the higher $f_t$, especially for 1370°C the lower $G_f$ has a further significant influence.

## Acknowledgments

## REFERENCES

[1]   Tschegg E. Equipment and appropriate specimen shapes for tests to measure fracture values. Austria Patent 390328 1986, 31

[2]   Harmuth H, Rieder K, Krobath M, Tschegg E. Investigation of the nonlinear fracture behaviour of ordinary ceramic refractory materials. Mat. Sci. Eng. A-Struct 214 (1), 1996, p. 53-61

[3]   Dai Y, Gruber D, Jin S, Harmuth H. Observation and quantification of the fracture process zone for two magnesia refractories with different brittleness. Journal of the Europen Ceramic Society 37, 2017, p. 2521-2529

[4]   Stueckelschweiger M, Gruber D, Jin S, Harmuth H. Creep testing of carbon containing refractories under reducing conditions. Ceramics Int. 45, 2019, p. 9776-9781

[5]   Bache, H H. Durability of concrete – fracture mechanical aspects. Nordic Concrete Research, Oslo, 1985, p. 7-25.

[6]   Stueckelschweiger M, Gruber D, Jin S, Harmuth H. Wedge-Splitting Test on Carbon-Containing Refractories at High Temperatures. Appl. Sci. 9(16), 2019, p. 3249

[7]   Jin S, Gruber D, Harmuth H. Determination of Young's modulus, fracture energy and tensile strength of refractories by inverse estimation of a wedge splitting procedure. Eng. Fracture Mechanics 116, 2014, p. 228-236

[8]   Abaqus 6.13 Documentation. Available online: http://dsk.ippt.pan.pl/docs/abaqus/v6.13/index.html (accessed on 26 May 2023)

747

# INVESTIGATION OF THE SIMULTANEOUS INFLUENCE OF MECHANICAL LOADING AND THERMAL GRADIENT AS OCCURRING IN REFRACTORY LININGS ON THE REFRACTORY MICROSTRUCTURE AND PHYSICAL PROPERTIES

Erwan Brochen, Michael Kaminski and Christian Dannert
Forschungsgemeinschaft Feuerfest e. V. at the European Centre for Refractories, Höhr-Grenzhausen, Germany

Laura Erbar, Katharina Sarnow and Olaf Krause
Koblenz University of Applied Sciences, Höhr-Grenzhausen, Germany

Karolina Dudek, Magdalena Kujawa, Robert Kusiorowski and Jacek Podwórny
Institute of Ceramics and Building Materials, Refractory Division, Gliwice, Poland

## ABSTRACT

Whenever a refractory product is used in a lining of an industrial vessel at high temperatures, it simultaneously experiences a thermal gradient and mechanical loading. In operation, each part of the lining expands, as do all the neighbouring parts, resulting in substantial compressive stresses parallel and near to the hot face of the lining. As a result, specific microstructural changes that condition the behaviour of the refractory material in service take place. Such changes could, until now, not be reproduced at laboratory scale. The closest commonly used method to experimentally simulate the impact of temperature and load is the determination of refractoriness under load, which only applies stresses of 0,2 MPa in a single direction.

With a new testing system, refractory materials can be restrained or subjected to loads at the hot face of a prismatic test piece (54 x 54 230 mm), which is heated up to 1700 °C though one of its small end faces (54 x 54 mm) and accordingly experiences a thermal gradient. Stress levels of up to 30 MPa were assessed or applied to the test piece in either one or two directions perpendicular to the thermal gradient near to the hot face. High load and high temperatures trigger typical microstructural changes, especially a coarsening of the matrix near the hot face.

With the new testing device, the evolution of refractory materials used as linings can be understood better, which opens new perspectives for material development.

## INTRODUCTION

The common denominator for most refractory product applications is that they must withstand high temperatures and substantial loads [1]. In case of refractory linings, only one side of the structure is typically exposed to the process heat, resulting in a steep thermal gradient within the lining. With regards to the mechanical loadings of the refractory linings, these have two main origins. Firstly, individual parts of typical refractory structures support the weight of the parts which are above them. For example, in a brickwork lining, the bricks in the lower part support the weight of all the other bricks above them. Secondly, as temperatures rise in the lining, the hot part of the structure expands and, when at last the expansion joints are closed and/or the cold part of lining cannot follow anymore the thermal expansion of the hot part, the free thermal expansion of the hot part is retrained and significant compressive stresses arise near to the hot face of the lining. The combined effect of the thermal gradient and compressive stresses near to the hot face leads to an inhomogeneous evolution of the microstructure and properties of the refractory materials. This is expected to play a critical role and significantly impact the high temperature and long-time performance of refractory linings.

## BACKGROUND

Currently, unless considering the thermal shock resistance, the characterization of refractory materials in the laboratory is mostly limited to test procedures in quasi-isothermal conditions. Some information on the behaviour of refractories experiencing thermal gradient might be obtained from thermal shock tests. However, standardized tests imply a dwell time at elevated temperature, which homogenises the temperature in the test piece and accordingly does not allow for a practice-relevant temperature gradient. The main focus of these tests is, of course, to trigger damage in order to appraise the resistance of the test pieces against thermomechanical stresses, not simulating the behaviour of the test piece as part of refractory lining. In fact, a testing procedure where test pieces are simply heated from one side and experience a thermal gradient comparable to those occurring in service for refractory lining is not challenging to implement, but fails to consider the impact of the compressive stresses at the hot face of a refractory lining. Neither the obtained microstructures, nor the observed deformations, would reflect accurately the evolution of the material as part of a refractory lining. On the other hand, test procedures that apply a compressive load on test pieces, especially the testing standards EN ISO 1893: Determination of refractoriness under load, and EN 993-9: Determination of creep in compression, rely on quasi-isothermal conditions. Both testing standards are carried out with the same testing equipment and similar testing procedure. A cylindrical refractory test piece (50 x 50 mm) is subjected to a constant load (0,2 MPa) while increasing the temperature (5 °C.min$^{-1}$). The deformation (height) of the test piece is recorded continuously. For the determination of refractoriness under load (RuL), the test is stopped once a prescribe deformation is attained, typically 5 % of its initial length [2]. In contrast, for the determination of creep in compression (CiC), once a specified temperature is reached, the heating is maintained constant for a given time. While both methods are prominently used to investigate the behaviour of refractory materials at high temperature, namely their refractoriness and the creep rate, the exerted load is actually very low and applied in one direction only. In service, much higher levels of stresses are expected and a biaxial loading state in the plane parallel to the hot face of refractory linings prevails [3].

## NEW TESTING SYSTEM

### Experimental setup

In order to simulate the behaviour of refractory products as part of a lining in service, a new testing system has been developed (Fig. 1). The testing system triggers a realistic thermal gradient in a prismatic test piece (54 x 54 x 230 mm). This has been achieved by heating the test piece through one of its small end faces (54 x 54 mm), later called hot face, thanks to a laboratory furnace with a fitting opening (Fig. 3 and 4).
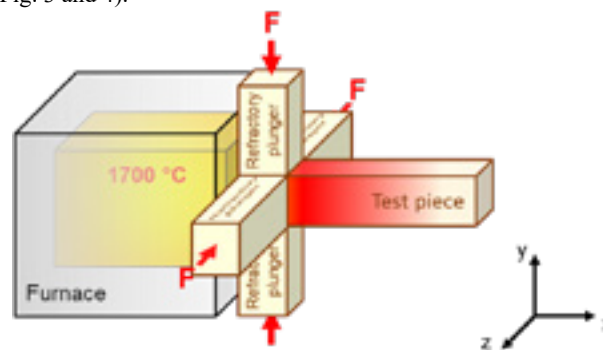


Fig. 1: Schematic representation of the new testing system and the testing procedure to investigate the combined effect of mechanical loading and thermal gradient.

The maximum operating temperature of the laboratory furnace, and accordingly the maximum temperature at the hot face of the test piece, is 1750 °C. During heating, temperature differences of several hundred Kelvin arise between the two small end faces of the test piece (x-direction). Simultaneously, the testing system mimics the thermomechanically induced compressive stresses at the hot face of refractory linings (in the y-z-plane). This was accomplished by applying a load F onto the test piece or constraining the free thermal expansion of the test piece perpendicular to the thermal gradient near to the hot face (Fig. 1). These loads or constraints are applied to the test piece through four refractory "plungers" (54 x 54 x250 mm), two of those fixed and the other two mobile. Each of the two mobile plungers is connected to a servomotor that is fixed to a robust frame made of high-strength aluminium and can build up compressive forces up to 4 kN (Fig. 4). The displacements of the mobile plungers are monitored by Linear Variable Differential Transformer (LVDT).
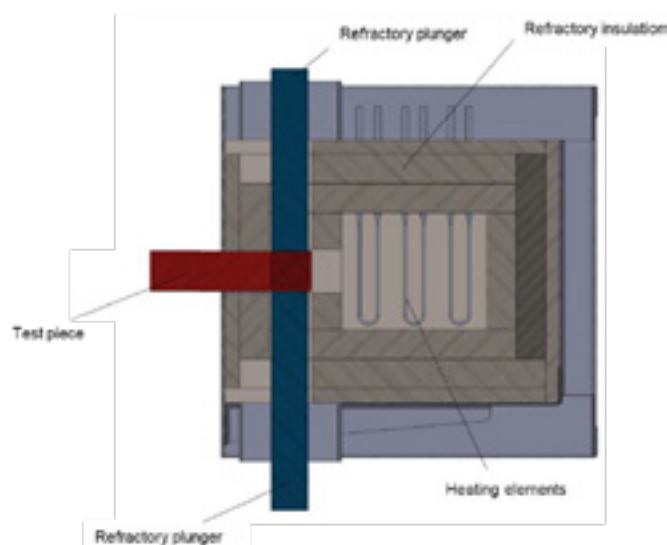


Fig. 2: Design model of the furnace to heat a test piece through one of its smaller end faces (hot face) and apply load or constraint near to the hot face.
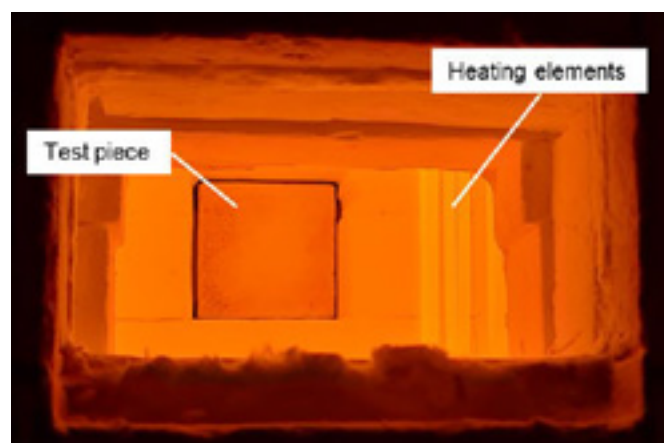


Fig. 3: Inside of the furnace during heating.

**Testing strategy**
Test pieces made of hydratable alumina (HA) bonded high alumina castable were heated from one end face with a rate of 5 K.min⁻¹. Two different loading conditions were considered:
– applying a constant load/force near to the hot face of the test piece and following the displacement of the mobile refractory plungers,
– restricting the free thermal expansion of the test piece by blocking the displacement of the mobile refractory plungers and following the evolution of the resulting force.
These two loading configurations can be applied separately on each of the two directions perpendicular to the hot face. Hence, it is

possible to just exert a uniaxial loading or perform a biaxial loading. In the case of a biaxial loading, the same configuration can be used in both direction (i.e. constant load or restriction of the free thermal expansion) or a combination of the two different loading combinations (i.e. constant load in one direction and restriction of the free thermal expansion in the other direction) can be applied.
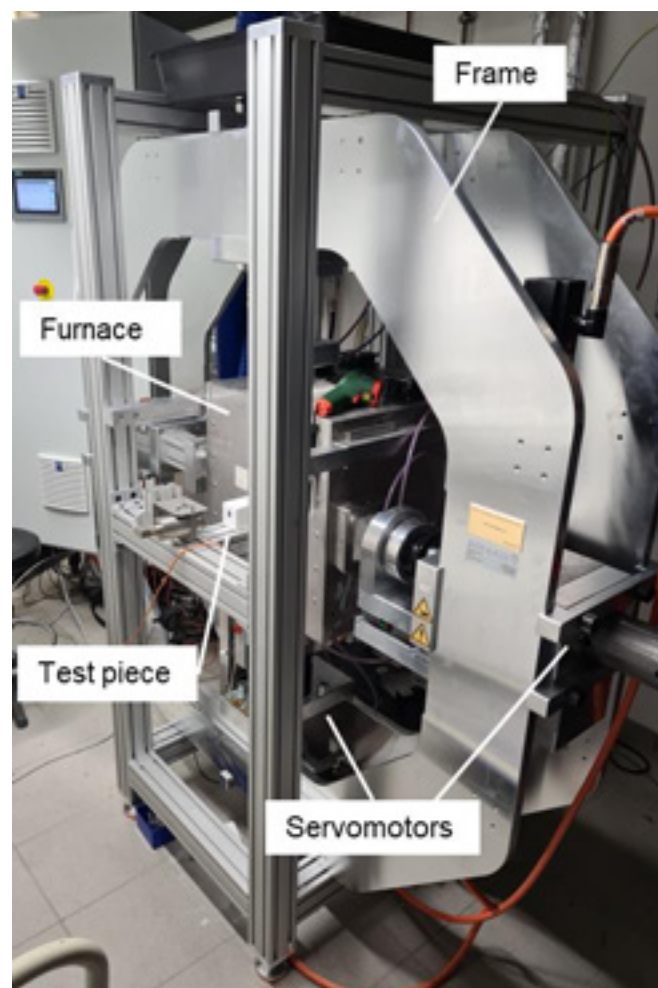


Fig. 4: New testing system to investigate the combined effect of mechanical loading and thermal gradient.

**RESULTS AND DISCUSSION**

**Development of stresses in test pieces with restrained free thermal expansion**
To examine the development of stresses in a test piece, the laboratory furnace was heated up to 1200 °C while the free thermal expansions in both directions y and z (see Fig. 1) are being restrained. As the temperature increases at the hot face, the heated part of the test piece strives to expand under the fixed refractory plungers and as a result stresses built up. Since the refractory castable is mostly anisotropic, very similar levels of stresses are assessed in the two perpendicular y and z directions, reaching almost 20 MPa (Fig. 5). The increase of the stresses is not directly proportional to the temperature inside of the furnace, nor linear. The two main reasons for this behaviour are: 1) the part of the test piece in contact with the plungers is not homogenously heated (thermal gradient) and accordingly does not expand linearly, and 2) the refractory plungers themselves heat up as heat from test piece is transferred to the plungers at the contact surfaces. Accordingly, the plungers do also expand, but again not linearly. The second effect also means that the plungers do not only restrain the thermal expansion of the test piece but also compress it further, in a comparable way as neighbouring bricks or parts of a refractory lining would do in service.
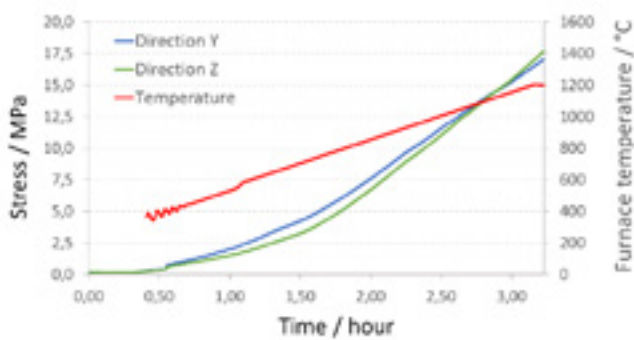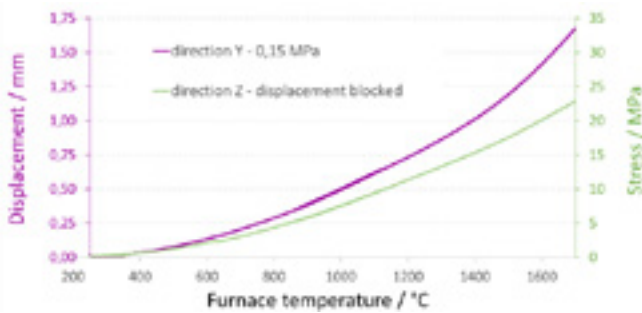
*Fig. 5: Evolution of the furnace temperature and induced stresses for a test piece made of HA bonded high alumina castable with restrained free thermal expansion in the directions y and z near to the hot face.*

Following that, the laboratory furnace was heated to 1700 °C with the displacement of the mobile plunger again blocked in one direction (z), i.e. restraining the free thermal expansion, but the free thermal expansion in the other direction (y) allowed. Actually, a comparably small load of 0,15 MPa is always applied in the y-direction to guarantee the contact between the plunger and the test piece, as well as maintaining the test piece in position, while still allowing the free thermal expansion of the test piece. A stress level of about 23 MPa was assessed in the z-direction and the non-linearity of the expansion of the test piece and plungers confirmed (Fig. 6). It is also worth noticing that, as the test piece was allowed to expand in the y-direction and because of the Poisson effect, the deformation in the y-direction (perpendicular to the applied load) is slightly higher than the free thermal expansion. This also means that, in case of the restriction of the free thermal expansion in both directions perpendicular to the thermal gradient (y and z-directions), the level of achieved stresses after heating the laboratory furnace to 1700 °C should be significantly higher. By extrapolating the combined results from two experiments (Figures 5 and 6), stresses larger than 30 MPa could be expected in the case of the complete restriction of the free thermal expansion in both directions perpendicular to the thermal gradient and accordingly near to the hot face of refractory linings in services.



*Fig. 6: Evolution of induced stresses for a test piece made of HA bonded high alumina castable with restrained free thermal expansion in the z-direction and displacement of the refractory plunger in the y-direction near to the hot face.*

### Displacement and creep of test pieces under load

Another important aspect of interest is the creep of refractory materials at high temperature. To investigated this, a series of measures was performed in which the laboratory furnace was heated to 1700 °C and the load kept constant in both the y and z-directions. Again, a load of only 0,15 MPa was applied in the y-direction to guarantee a contact between the plungers and the test piece. In the z-direction, the load was first set to 0,15 MPa, but then increased to 10 MPa, 20 MPa or 30 MPa.

Under a load of 0,15 MPa applied in both directions, the displacement of the mobile refractory plungers was found to be almost identical in both directions, which is further evidence of the anisotropic behaviour of the castable under examination. The obtained

displacement curve for a load of 0,15 MPa was considered to represent the almost free thermal expansion of the test piece and partially heated refractory plungers. By increasing the load in the z-direction, the corresponding displacement of the plunger in the z-direction followed closely the thermal expansion previously observed for a load of 0,15 MPa, at least up to a furnace temperature of 1200-1300 °C. Above these temperatures, the displacements stay significantly below the displacement previously observed for a load of 0,15 MPa, namely was partially restrained (Fig. 7). More than just the consequence of a mechanical compression that impedes the free thermal expansion, it is likely that creep occurred near the hot face. Indeed, creep is a function of the temperature and applied load. In the present case, it seems to begin at a furnace temperature of 1200-1300 °C and its contribution increase with increasing temperature and higher applied load, namely the higher the temperature and applied load were, the more limited the displacement in the z-direction was. It is also worth noting that the displacement in the y-direction, in contrast, tended to increase with increasing load in the z-direction (not shown in the figure 7 to avoid overloading the graph with too much information). This is also likely the result of the creep process. As the test piece is compressed and irreversibly deformed (due to creep) in the z-direction, this deformation is at least partially accommodated by an expansion in the y-direction.
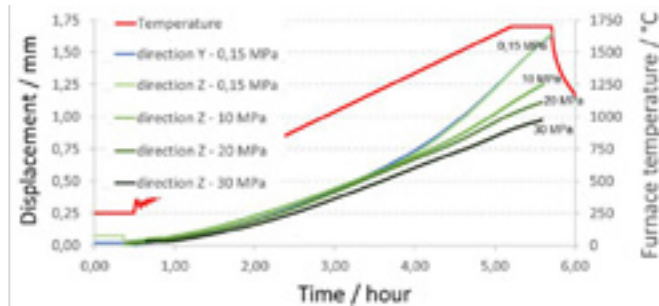


*Fig. 7: Evolution of the furnace temperature and displacement of the mobile refractory plungers applying different load on a test piece made of HA bonded high alumina castable near to the hot face (the displacement in the y-direction corresponds to the measurement where a load of 0,15 MPa was applied in both directions).*
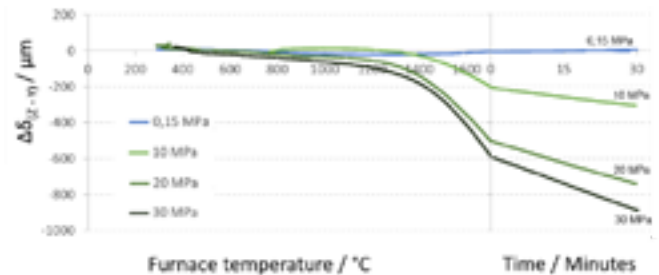


*Fig. 8: Difference between the displacement ($\Delta\delta$) of the mobile refractory plungers in the z-direction and y-direction as a function of the furnace temperature and time after having reached 1700 °C.*

Although not perfectly depicting creep (because of the above-mentioned phenomenon), the difference between the displacement of the mobile refractory plungers in the y-direction and z-direction ($\Delta\delta_{(z-y)}$) provides a valuable information on the creep process (Fig. 8). Under a load of 0,15 MPa applied in both directions, the displacement of the mobile plungers is almost the same in both directions, and $\Delta\delta_{(z-y)}$ is accordingly almost constant (near to zero). Increasing the load (in the z-direction) resulted in $\Delta\delta_{(z-y)}$ that increases (in terms of absolute value) with increasing furnace temperature. Higher temperatures as well as higher loads in one direction promote the creep process that results in an increased difference between the displacement of the mobile refractory plungers in the y-direction and z-direction. This is also reflected in a higher apparent creep rate ($\Delta\delta(z-y)/\Delta t$) with increasing load in the z-direction at a furnace temperature of 1700 °C (Tab. 1).

Tab. 1: Difference between the displacement of the mobile refractory plungers in the y-direction and z-direction over time ($\Delta\delta(z\text{-}y)/\Delta t$ – apparent creep rate) at a furnace temperature of 1700 °C for test pieces made of HA bonded high alumina castable.

| Load / MPa | apparent Creep rate / $\mu m.min^{-1}$ |
|---|---|
| 0,15 | -0,38 |
| 10 | 3,32 |
| 20 | 8,00 |
| 30 | 9,97 |

SEM micrographs revealed the manifest influence of the compressive stresses near to the hot face on the microstructure of the test pieces (Fig. 9). The higher the applied load, the more advanced the coarsening of the matrix is. In light of these results, it is unlikely that simple pre-firing of test pieces or the load imposed by the standards EN ISO 1893: Determination of refractoriness under load, and EN 993-9: Determination of creep in compression, namely 0,15 MPa, are sufficient to promote the formation of the microstructure that can be found near the hot face of refractory linings in service. Furthermore, the observed microstructural changes are expected to impact the properties, behaviour, and performance of the refractory materials at high temperature, such as their strength and resistance to corrosion, erosion and thermal shocks. This aspect can be studied in subsequent investigations on test pieces after being exposed to high temperatures and load in the new testing system.

## CONCLUSIONS

A new testing system was developed to simulate the thermal gradient and compressive loading that refractory materials experience as a part of linings in industry furnaces and vessels in service. The thermal gradient resulted from the heating of a prismatic test piece from one side (hot face). The loading was applied through refractory plungers connected with servomotors, either by restricting the free thermal expansion or applying a constant load. Stress levels of up to 30 MPa were assessed or applied near to the hot face, in either one or the two directions perpendicular to the thermal gradient. Such level of stress should definitely be expected near to the hot face of refractory linings.

High load and high temperatures promoted specific microstructural changes in the test piece near to the hot face, especially a coarsening of the matrix that cannot be achieved by a simple pre-firing or moderate load as prescribed in the standards EN ISO 1893: Determination of refractoriness under load, and EN 993-9: Determination of creep in compression.

A better insight into the behaviour of refractory materials exposed to thermal gradient and high compressive stresses as occurring in refractory linings was gained and should open up new perspectives for material development.

## ACKNOWLEDGEMENTS

## REFERENCES

[1] Schacht CA. Refractories Handbook. Taylor & Francis Inc, Boca Raton, 2004.

[2] Routschka G, Krause O. Normen-Handbuch: Feuerfest Werkstoffe und Feuerfestbau, 2. Auflage. Vulkan Verlag, 2010. p. 457-472

[3] Oliveira RG, Rodrigues JPC, Pereira JM. Numerical simulations on refractory linings for steel casting vessels. Fire Safety Journal 138, 2023, 103794
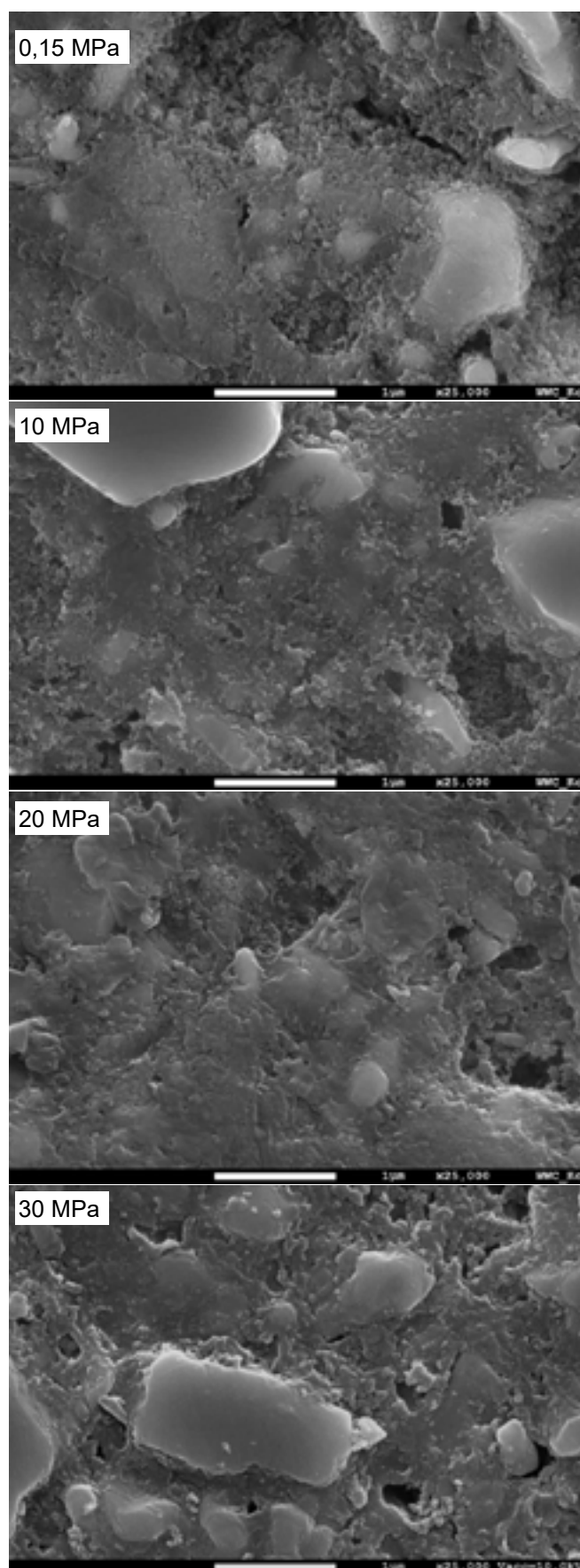


Fig. 9: Evolution of the microstructure (SEM micrographs, 25.000-fold magnification) of test pieces made of HA bonded high alumina castable near to the hot face and with increasing load applied in the z-direction.

# APPLICATION OF ULTRA−HIGH SPEED HEATING TEST SYSTEM − EVALUATION OF THERMAL CONDUCTIVITY −

Kazuya Nakabo
Shinagawa Refractories co., ltd., Bizen, Okayama, Japan

Tomoyuki Maeda, Hatsuo Taira
Okayama Ceramics Research Foundation, Bizen, Okayama, Japan

Seiji Ohashi, Norihito Mitani
Nissin Kikai co., ltd, Takamatsu, Kagawa, Japan

Norihisa Tsuda
Nippon Steel Technology co., ltd., Kimitsu, Chiba, Japan

## ABSTRACT

Our group is developing a new test system called "Ultra-high speed heating test system". This apparatus is a hot observation system with the advanced features of ultra-high-speed and ultra-high-temperature heating. Currently, we are examining various applications of this system as a multi-purpose evaluation system. In this paper, we will report about the thermal property evaluation methods used to investigate refractories materials used with this system. One of the structural features of this system is that the specimen is placed on the heater directly. This heating method can be applied for estimation of thermal conductivity, and examining the evaluation method.

We prepared pellet specimens of various raw material powders for refractories. As a simple comparing test, we placed these specimens on the heater of the system and measured the top and bottom temperatures while heating. The temperature gaps between top and bottom showed different temperature dependency according to the sample. This result suggest that this test method can be used to evaluate the relative thermal conductivity and its temperature dependence at high temperature. In addition, we will report on the investigation of measurement of the thermal conductivity as a physical property evaluation. Numerical analysis suggested that the effect of heat transfer from heater to specimen should be excluded, and we are considering improvements in the specimens setting and temperature measurement methods.

## INTRODUCTION

The newly developed testing system called "Ultra-high speed heating test system" [1-3] is shown in fig. 1. This system was developed primarily to focus on the observations at high temperature and to be operational at ultra–high temperatures and ultra–high speeds of heating. For this purpose, the system employed a distinctive heating method in which the specimens are placed on the heater directly. This method reduces the volume to be heated and enables extreme heating. The maximum achievable temperature is 2,800 °C, and the temperature rate reaches 100,000 °C/min [1]. Moreover, this method can reduce the heat quantity, thus this facility requires no insulation for the enclosure and can be installed with observation windows.

We are now examining the utilization of this facility for various applications. For example, taking advantage of the ability to observe heating in this facility, we measured the contact angles between oxides and melts [2], and we also tried experiments of rapid rate sintering by ultra–high speed heating [3]. As a part of this examining, we tried to measure thermal conductivity. Thermal conductivity is one of the most important parameters in the design of refractories
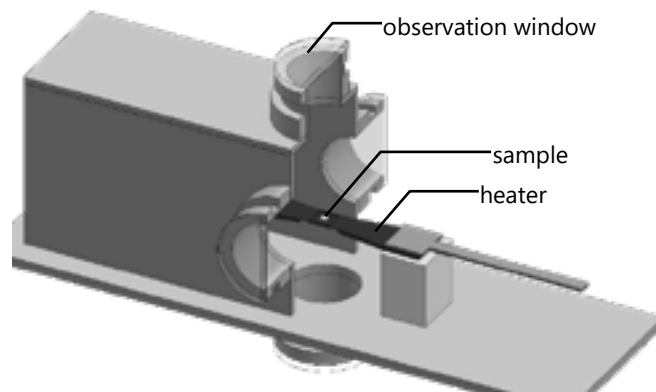


*Fig. 1: Schematic view of ultra–high speed heating test system.*

and kiln furnace linings with effects on energy conservation and durability of products.

Thermal conductivity is difficult to measure under the conditions in which refractories are actually used. Specifically, the hot wire method, the most commonly used method for refractory bricks, is insufficient for measuring temperatures, on the other hand, the flash method used for fine ceramics assumes a uniform texture and is limited in its application to refractories specimens. The new system has fewer sample limitations and can be raised to high temperature, so if it can be used to measure thermal conductivity, it will provide more useful data. In this paper, we will report about the consideration of measurement methods and discussion of results.

## EXPERIMENTS

### Simple relative evaluation test

First, we attempted a simple experimental method of relative evaluation of thermal conductive behaviour by continuous temperature measurements of pellet samples of refractories raw material powders. We prepared the specimens by pressing the powder materials into ⌀20 mm samples, sintering them at 1600 °C, and grinding them to a thickness of 3 mm. The sample properties are shown in table 1. A schematic image of measurement system is shown in Fig. 2. The temperatures were measured by two-color radiation thermometer (Chino, IR-CZH8N3, 900-3000 °C, spot size 1.7 mm) at the top center of the specimens and the bottom center of the heater. The test temperature was set to 1500 °C, and the

*Table 1: Properties of samples used for simple relative evaluation test.*

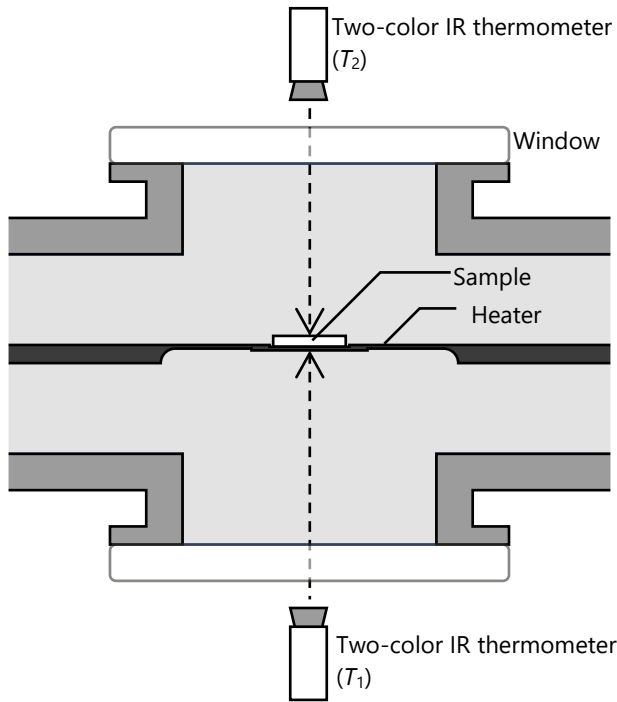| Sample | | A | AS1 | AS2 | AS3 | M |
|---|---|---|---|---|---|---|
| Chemical composition / % | Al₂O₃ | 99 | 87 | 61 | 47 | |
| | SiO₂ | | 7 | 36 | 50 | 2 |
| | MgO | | | | | 95 |
| Apparent porosity / % | | 26 | 0.96 | 11 | 0.75 | 16 |
| Material type | | Fused alumina | Chinese bauxite | Mullite | Chamotte | Magnesia crinker |

*Fig. 2: Schematic view of measurement system for simple relative evaluation test.*

temperature was increased by 1 °C/s. The internal atmosphere was substituted with Ar.

**Evaluation of thermal conductivity**

We attempted to estimate thermal conductivity as a physical property with the alumina sample. Specimens, $\varnothing20$ mm cylindrical alumina ceramic (Nikkato, SSA-S) were prepared with various thicknesses. We set the specimens on the heater, substituted the atmosphere with Ar, and held them at each test temperature until steady. The test temperatures were set in 100 °C increments to 1600 °C. From the temperature measurement results and sample thickness $t$, the temperature gradient in the sample $\nabla T$ was calculated under the assumption that the temperature of the sample bottom and the heater were the same. The thermal conductivity was calculated by Fourier's law;

$$q = -\lambda \cdot \nabla T \tag{1}$$

where, $q$ is the heat flux density and $\lambda$ is the thermal conductivity. The heat flux $q$ was calculated from the current $I$, the resistance of the heater $R$ and heating area of the heater $A$.
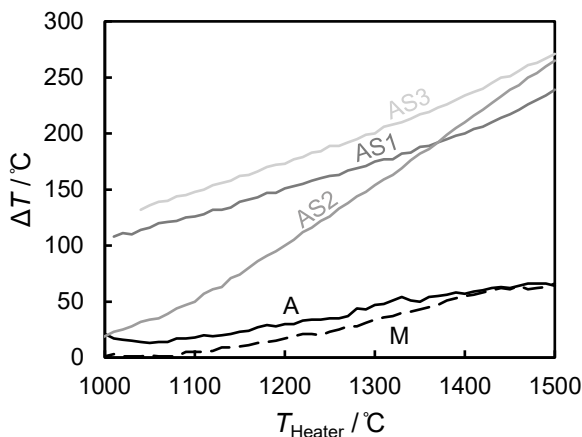


*Fig. 3: Temperature gap $\Delta T$ in specimens in simple test.*

$$q = I^2 R / A \tag{2}$$

In additon, we considered improvements for the measurement methods from the obtained results. We examined the results by simulation with a one-dimensional steady heat transfar model to evaluate the influence of the factors. And based on the results, we considered the improvements in the sample setting and the temperature measuring methods.

**RESULTS AND DISCUSSION**
**Simple relative evaluation test**

Figure 2 shows the measurement results of temperature gap $\Delta T$ between the top and the bottom of the specimens in the simple tests. $\Delta T$ can be used as a rough indicator of thermal conductivity with larger values of $\Delta T$ corresponding to less thermal conductivity. The measured $\Delta T$ showed different behaviour depending on the sample, with the sample M sowing the smallest value over the whole test temperature rage, followed by sample A, AS1, and AS3 in the order of decreasing value. The temperature dependence of $\Delta T$ for sample AS2 differed significantly from the other samples, with $\Delta T$ for S being as small as sample A at low temperature, but as large as sample AS3 at high temperature.

From these results, it was found that this testing method can evaluate the relative magnitude and temperature dependence of the thermal conductivity of the specimens. This method allows measurement at high temperatures where refractories are actually used, and is considered to be an effective technique that complements the existing measurement methods.
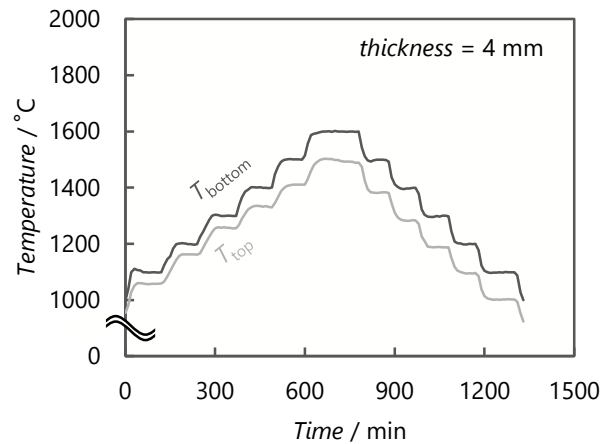


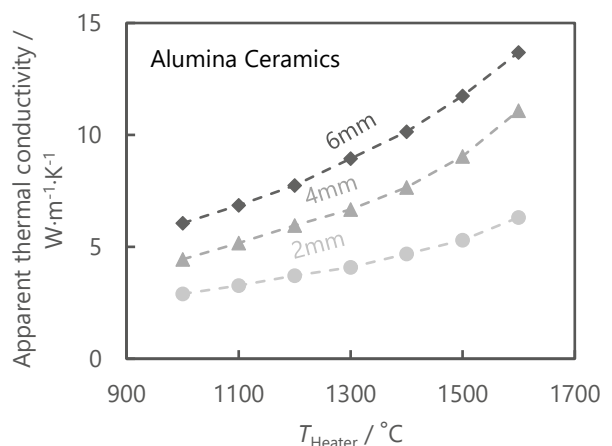*Fig. 4: Measured temperature with alumina ceramics sample.*



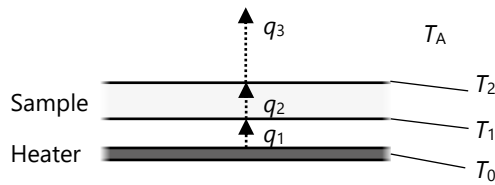*Fig. 5: Measured temperature with alumina ceramics sample.*

*Fig. 6: Model for simplified investigation.*

## Evaluation of thermal conductivity

Figure 4 shows the temperature measurement results for the alumina ceramics specimen. The apparent thermal conductivities calculated from the measured temperatures of the specimens at each thickness are shown in fig. 5. This evaluation method resulted in the apparent thermal conductivity being dependent on the thickness of the specimen. As a physical property, thermal conductivty is essentially independent of specimen geometry. So it is considered that factors other than thermal conductivity had some effects.

## Simplified model investigation

We examined the factors that seemed to influence the thermal conductivity results with a simplified model. The calculation model is shown in fig. 6. The model is an infinite flat plate steady-state heat transfer model with the assumption that the temperatures are measured on the central axis of the sample. The heat transfers in the model are expressed eq. 3.

$$q_1 = \sigma \cdot (T_0^4 - T_1^4) / (\varepsilon_H^{-1} - (\varepsilon_S^{-1} - 1)) + H \cdot (T_0 - T_1) \quad (3a)$$
$$q_2 = -\lambda \cdot (T_2 - T_1) / t \quad (3b)$$
$$q_3 = \sigma \cdot \varepsilon_S \cdot (T_2^4 - T_A^4) \quad (3c)$$
$$q = q_1 = q_2 = q_3 \quad (3d)$$

Where, $q$ is the heat flux density, $q_1$ is due to heat transfer from heater to sample, $q_2$ is due to heat conduction within the sample, and $q_3$ is due to heat radiation from the top of the sample. Moreover, $\sigma$ is the Stefan–Boltzmann constant, $\varepsilon$ is the emissivity, $t$ is the sample thickness, $H$ is the coefficient of heat transfer between heater and sample, and $\lambda$ is the thermal conductivity. In the investigation, $\lambda_0 = 5.0$ W·m$^{-1}$·K$^{-1}$ was assumed as the true value for thermal conductivity. We solved the simultaneous equations by Newton's method to obtain $q$, $T_1$, and $T_2$, and calculated the apparent thermal conductivity. And we evaluated the effect on the sample thickness dependence of the apparent thermal conductivity for varying $\varepsilon_S$, $H$ and $T_A$.

The results of apparent thermal conductivity calculation with the simplified model are shown in fig. 7. Fig. 7(a) shows the effect of the ambient temperature $T_A$, and (b) shows the effect of the sample emissivity $\varepsilon_S$. Tentative values were set for parameters other than those of interest. We could find no significant effect of $T_A$ and $\varepsilon_S$ on the results of apparent thermal conductivity. On the other hand, $H$, shown in fig. 7(c) exhibited significant influence on the apparent thermal conductivity and its sample thickness dependence. When the $H$ value was sufficiently large, the apparent thermal conductivity $\lambda_A$ was close to the set true value $\lambda_0$; when the $H$ value was small, the value of $\lambda_A$ became smaller than the true value $\lambda_0$, and the sample thickness dependence increased, with smaller sample thickness $t$ showed a tendency for the value of $\lambda_A$ to be smaller. The small $H$ value correspond to high thermal resistance and heat loss between the heater and the sample. The calculation of apparent thermal conductivity approximated that the temperatures of the heater $T_0$ and the bottom of the sample $T_1$ were the same, however it was suggested that there was actually a significant temperature difference. Furthermore, when the sample thickness $t$ was small, the deviation of the apparent value $\lambda_A$ from the true value $\lambda_0$ was considered to be lager because the ratio of contact thermal resistance in the total thermal resistance was larger. In summary, the approximation of $T_0 = T_1$ was inappropriate.

## Reduction of heat transfer influence

The heat transfer coefficient depends on various conditions such as the materials and surface properties of samples and the heater, the
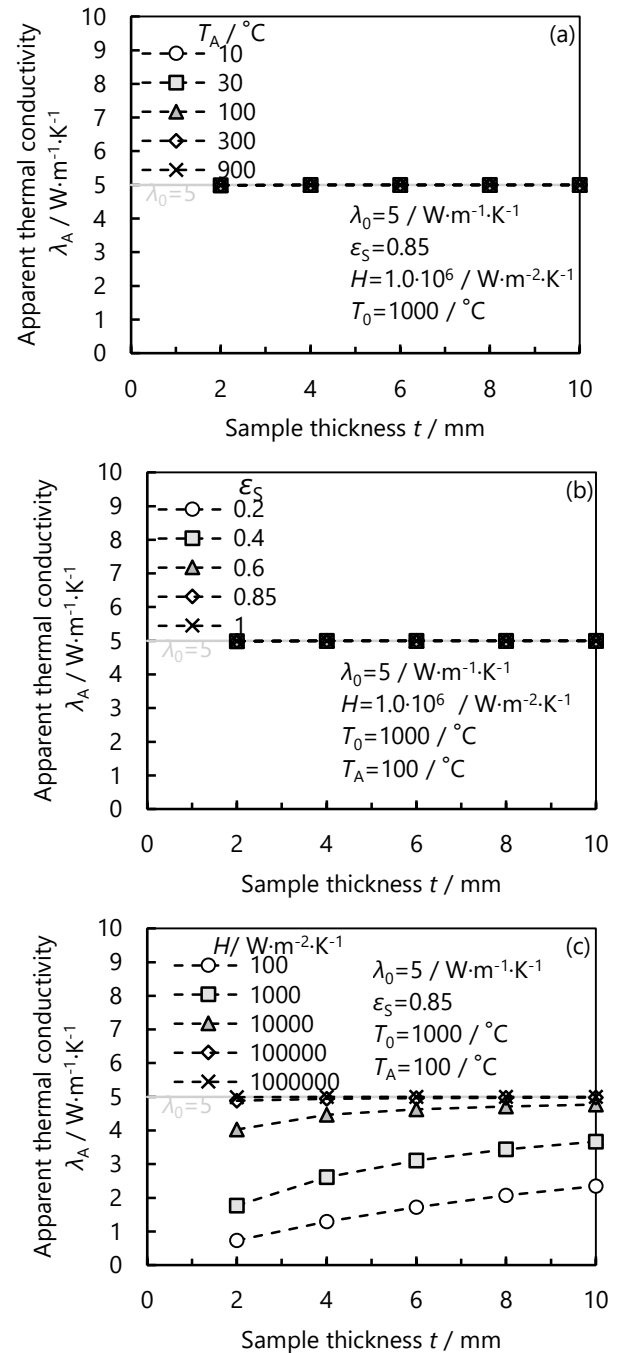


*Fig. 7: Calculation results of apparent thermal conductivity in simplified model with varying parameters; (a) ambient temperature $T_A$, (b) sample emissivity $\varepsilon_S$, (c) coefficient of thermal transfer H between heater and sample.*

atmosphere composition, and the temperature of each part, making it difficult to accurately determine. Therefore, the contact thermal resistance is considered to be a cause of systematic errors and inhibit reliable measurements. Therefore, we have investigated reducing the influence of contact thermal resistance. The coefficient of contact thermal heat transfer between two solid phases in no load contact is expressed by eq. (4).

$$H = \lambda_g / \delta \quad (4)$$

Where, H is the coefficient of contact thermal heat transfer, $\lambda_g$ is the thermal conductivity of the atmosphere, $\delta$ is the distance between the phases. Assuming that $\delta$ is 10 μm when the sample is in direct contact with the heater, and $\lambda_g$ is 0.01 W·m$^1$·K$^{-1}$ when the atmosphere is Ar, H is 1000 W·m$^{-2}$·K$^{-1}$. In reference to fig. 7, this value of H
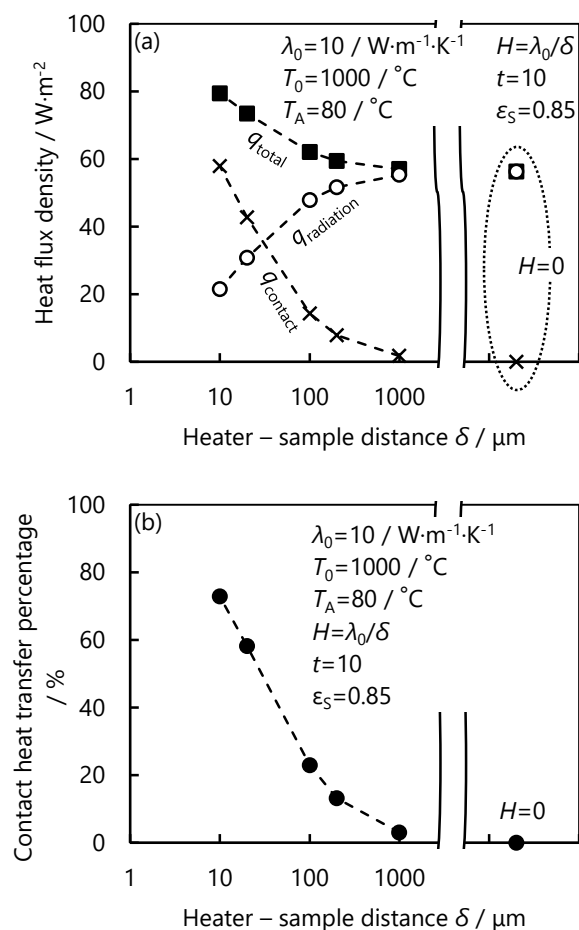
*Fig. 8: Culculation results of heat flux in simplified model with varying distance between heater and sample δ; (a) heat flux density (b) fraction of contact heat transfer to total heat flux density.*
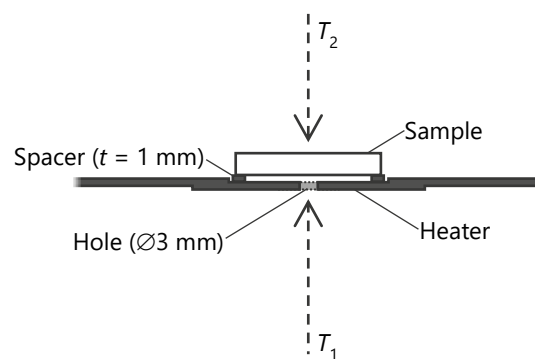


*Fig. 9: Schematic image of improved measuring system.*



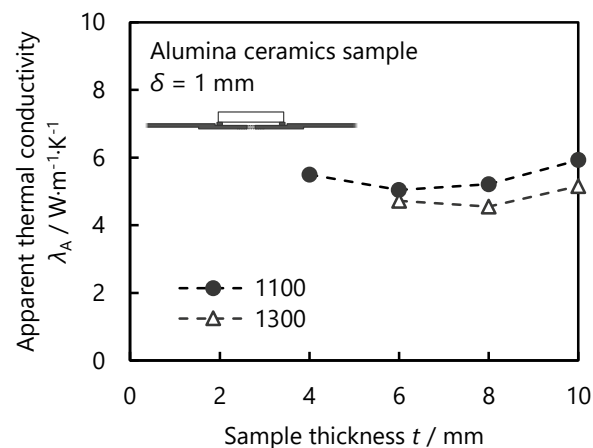*Fig. 10: Estimated apparent thermal conductivity with measured temperatures by improved measurement method..*

corresponds to a condition where the sample thickness dependence of apparent thermal conductivity is large. The calculated heat flux density with varying values of $\delta$ is shown in fig. 8(a). As $\delta$ increased, the value of heat flux density due to radiation $q_{radiation}$ increased, and $q_{contact}$ due to contact decreased. The variation of the percentage of contact heat transfer to the total as $\delta$ was varied as shown in fig. 8(b). As $\delta$ reduced, the percentage became smaller, and the percentage fell below 3 % at $\delta$ = 1 mm. From this result, it was considered that heating with a distance of 1 mm between the heater and the sample would make it possible to supress the influence of the heat transfer coefficient.

**Improvement of heating method**

A schematic image of the improved measurement method based on the investigation is shown in fig. 9. To create a gap between the heater and the specimen, we placed spacers under the specimen. Moreover, for more accurate measurements, we made a hole in the centre of the heater to directly measure the temperature of the bottom of the specimen $T_1$. The apparent thermal conductivities estimated from the temperatures measured by the improved measurement method are shown in fig. 10. The dependence on sample thickness of the data was drastically supressed. By this improvement, the accuracy of thermal conductivity estimation has been increased and it enabled the thermal conductivity measurement of alumina ceramics samples by the ultra–high speed heating test system.

**CONCLUSIONS**

We tried to estimate thermal conductivity with the newly developed "Ultra–high speed heating test system". By simple tests, it was able to carry out relative evaluation of thermal conductivity. This test can be done rapidly, easily, and under high temperature. It should be utilize to approximate estimations which complements existing standard tests.

To estimate thermal conductivity as a material property, it was necessary to consider the heat loss in heat transfer from heater to sample. To reduce the influence of the loss, it was effective to make a gap between the heater and the sample. Simplified model calculation revealed that the heat loss should be suppressed by separating the heater and the sample by 1 mm. We confirmed experimentally, the improved accuracy of the thermal conductivity estimation. This improvement made measuring thermal conductivity in alumina ceramics samples by Ultra–high speed heating test system possible.

**REFERENCES**

[1]   K. Nakabo, T. Maeda, H. Taira, S. Ohashi, N. Mitani: Application of Ultra–High Speed Heating Test System (1) — Observation of thermal behavior, Proc. of 9th Symposium on Refractories for Iron and Steel, TARJ (2021).

[2]   K. Nakabo, T. Maeda, H. Taira, S. Ohashi, N. Mitani: Application of Ultra–High Speed Heating Test System (2) — Contact Angle Measurement Results, Proc. of 9th Symposium on Refractories for Iron and Steel, TARJ (2021).

[3]   K. Nakabo, T. Maeda, H. Taira, S. Ohashi, N. Mitani: Application of Ultra–High Speed Heating Test System (3) — Rapid Rate Sintering, Proc. of 9th Symposium on Refractories for Iron and Steel, TARJ (2021).

[4]   F. Tachibana: Nippon Kikai Gakkai Shi, 55 [397] 102-107, JSME (1952).

[5]   K. Sanokawa: Transactions of the Japan Society of Mechanical Engineers, 33 [251] 1131-1137, JSME (1967).

# EUROPEAN AND INTERNATIONAL STANDARDIZATION WORK IN REFRACTORIES

Franziska Baensch of DIN, Berlin, Germany

## ABSTRACT
The topics and contents of standardization in the refractory industry are mainly influenced at international and European level. For success, the personal commitment of the experts and delegates is indispensable. Afterall, for those who do not standardize, they will be standardized and must ultimately use rules that others shaped according to their own interests. A prerequisite for participation in European and international standardization bodies is the involvement in the corresponding national mirror committees of the national standards institutes, which mirror the European and international activities and authorize the technical experts to participate at ISO and/or CEN.
The relevant committee structure at international level (ISO/TC 33 Refractories) and at European level (CEN/TC 187 Refractory products and materials) and the function of the national mirror committees, the interaction of these committees, and the possibilities for exerting influence are shown.

## ISO/TC 33 REFRACTORIES
The technical committee (TC) of international standardization on *Refractories*, ISO/TC 33, was established in 1947 and is currently held by the British Standards Institution (BSI). Current chairperson is the German expert Prof. Olaf Krause. The scope of ISO/TC 33 is the standardization of raw materials and products of the refractories industry and their properties [1].
The 15 voting participants are Austrailia (SA), Austria (ASI), Belgium (NBN), China (SAC), Egypt (EOS), France (AFNOR), Germany (DIN), India (BIS), Japan (JISC), Republic of Korea (KATS), Poland (PKN), Russian Federation (GOST R), Spain (UNE), Ukraine (SE UkrNDNC) and United Kingdom (BSI). Moreover, 22 members observe the activity of ISO/TC 33. National and multinational raw material suppliers and producer companies provide technical experts to advance the work. ISO/TC 33 is substructured with 5 working groups (Fig. 1), whose experts create the standard documents:

- WG 17, Chemical analysis
- WG 25, Refractory test piece preparation – Gunning techniques
- WG 27, Refractory mortars – Determination of permanent change in dimension on heating
- WG 31, Phase quantitative analysis of residual quartz in silica bricks
- WG 32, Dense shaped refractory

However, WG 26 (Thermal shock resistance), WG 28 (Determination of Young's modulus at elevated temperatures), WG 29 (Determination of compressive strength at elevated temperatures) and WG 30 (Determination of bulk density of granular materials, grain density) are currently disbanded.
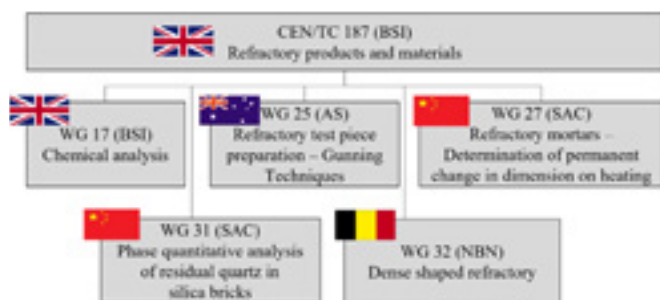About 93 standards are published and in the responsibilty of ISO/TC 33. Currently under development are 9 standards.

This committee contributes with 20 standards to the Sustainable Development Goals SDG9, "Industry, innovation and infrastructure" and SDG 12, "Responsible consumption and production", which are defined by the united nations (UN). Improvements have included a reduction in energy consumption and the use of cleaner energy resources. While there has been a reduction in the consumption of raw materials, there has also been an increased emphasis on reducing the amount of material finally going to land fill as a result of the activities of the refractories and related user industries.

## CEN/TC 187 REFRACTORY PRODUCTS AND MATERIALS
The technical committee (TC) of European standardization on *Refractory products and materials,* CEN/TC 187, was established in 1989 and is currently held by the British Standards Institution (BSI). Current chairperson is the German expert Prof. Olaf Krause. The scope of CEN/TC 187 includes classification, methods of test and sampling for refractory products and materials, including shaped and unshaped products and ceramic fibres [2].
CEN includes the 34 voting participants Austria (ASI), Belgium (NBN), Bulgaria (BDS), Croatia (HZN), Cyprus (CYS), Czech Republic (UNMZ), Denmark (DS), Estonia (EVS), Finland (SFS), France (AFNOR), Germany (DIN), Greece (NQIS/ELOT), Hungary (MSZT), Iceland (IST), Ireland (NSAI), Italy (UNI), Latvia (LVS), Lithuania (LST), Luxembourg (ILNAS), Malta (MCCAA), Netherlands (NEN), Norway (SN), Poland (PKN), Portugal (IPQ), Republic of North Macedonia (ISRSM), Romania (ASRO), Serbia (ISS), Slovakia (UNMS SR), Slovenia (SIST), Spain (UNE), Sweden (SIS), Switzerland (SNV), Türkiye (TSE) and United Kingdom (BSI).
CEN/TC 187 aims to contribute to the elimination of technical barriers to trade and to facilitate the European Union's internal market for refractory materials. To this end, standards are developed for characterizing refractory materials by classifying and determining their chemical and physical properties. Additional work items are related to product requirements, dimensions and quality assurance of items delivered in bulk. National and multinational raw material suppliers and producer companies provide technical experts to advance the work. The technical work is managed in two active working groups (Fig. 2):

- WG 1, Dense shaped refractory materials
- WG 4, Chemical analysis.

However, WG 2 (Unshaped refractory materials), WG 3 (Insulating materials and high temperature insulation wools) and WG 5 (Chemical attack on refractory products) are currently disbanded.
About 70 standards are published and in the responsibilty of CEN/TC 187. Currently under development are 8 standards. All CEN member countries participate in the development of refractories standards.



*Fig. 1: Structure of ISO/TC 33, year 2023*



*Fig. 2: Structure of CEN/TC 187, year 2023*

CEN systematically addresses environmental issues in standardization to reduce the environmental impacts of products and services. CEN/TC 187 is aware that some of its methods have an impact on the environment. Thus, wherever feasible, the use of

toxic chemicals is avoided. Also methods for the determination of hazardous compounds such as hexavalent chromium (chromium V!) are standardized. There is a gradual move to instrumental methods such as X-ray fluorescence analysis XRF not requiring corrosive acids and potentially toxic spectrophotometric colouring agents. Furthermore, the reduction in energy consumption and the use of cleaner energy resources are focussed by CEN/TC 187.

The objectives of CEN/TC 187 are to contribute to the elimination of technical barriers to trade and to facilitate the internal European Union market for refractory materials. Through the liaison with ISO/TC 33 the aim is to give standards an international diffusion and thus develop further the global market.

## NATIONAL STANDARDIZATION ORGANIZATION

All members of ISO and/or CEN are entitled to nominate delegates to Technical Committees and experts to Working Groups, ensuring a balance of all interested parties (Fig. 3). Participation as observers of recognized European or international organizations is also possible under certain conditions. To participate in the activities of ISO and/or CEN, please contact the national standards organization in your country.



*Fig. 3: Secondment of delegates and experts to European and international committees*

## CHALLENGES FOR ISO/TC 33 AND CEN/TC 187

The large work programme in ISO/TC 33 and in CEN/TC 187, besides the development of new standards, includes regular review and appropriate action, i.e. confirmation, amendment, revision or withdrawal of each standard. Additionally, work programmes and the development of standards in the area of refractories are frontated with further challenges, f.e. the limited number of experts, which often results in an imbalance of relevant stakeholders. A lack of expertise would result in standards not up-to-date and state-of-the art, and consequently, in withdrawing standards. In addition, international as well as European committees have no budget for hosting meetings. This and the fact, that attending any meeting are becoming more prohibitive, may result in difficulties finding a member to host a TC or WG meeting and in reduced levels of participation.

Moreover, lack of funding obviously affects the number of laboratories able to participate in interlaboratory trials. Thus, some standards already lack on precision data from an interlaboratory test, which actually are required for validating any test methods.

All issues together have the effect of keeping responsible personnel at full capacity and create a number of several competing priorities.

## ADVANTAGES OF STANDARDIZATION

International standards are the common denominator and shared language of suppliers and customers. By international standardization the transfer of technologies and trade are facilitated and the technical compatibility is ensured. Regulation in health, safety, security and environmental matters are supported by being at the cutting edge of science and technology, and trade agreements are successfully implemented by international standardization.

European standardization is fundamental in ensuring free trade and an effective European Single Market. For business, harmonized standards are a reliable indicator of conformity with relevant EU legislation and legal certainty is increased through a technical interpretation of unspecific legal terms.

## REFERENCES

[1]  ISO/TC 33, information see
https://www.iso.org/committee/47812.html
[2]  CEN/TC 187, information see
https://standards.cencenelec.eu/dyn/www/f?p=205:7:0::::FSP_ORG_ID:6168&cs=126A961E89A546A9C170F0DF98F49E173

757

# YOUNG'S MODULUS OF REFRACTORIES AT HIGH TEMPERATURES: COMPARISON OF DIFFERENT TESTING METHODS AS BASE FOR MASONRY MODELLING

Thorsten Tonnesen, Jesus Gonzalez-Julian
RWTH Aachen University, Institute of Mineral Engineering (GHI), Aachen, Germany

Michel Henze, Gerhard Hirt
RWTH Aachen University, Institute of Metal Forming (IBF), Aachen, Germany

## ABSTRACT

Comprehensive knowledge about thermomechanical behavior is mandatory for an accurate prediction of occurring stresses to design load-optimized linings. Refractory linings are, in addition to loads due to corrosion and creep processes, particularly affected by thermo-mechanical stresses caused by the restricted thermal expansion of the lining. These stresses can occur within individual components as well as in bricks and can lead to plastic deformation, cracks, and material failure.

This study compares methods for determination of Young's Modulus at different temperatures for the use in refractory modelling of lining systems. In three point bending tests the deflections of different refractory materials was examined during loading by means of digital image correlation (DIC) up to high temperatures. The achieved data allows to evaluate static Young's Modulus values respectively. In parallel refractoriness under load (RUL) tests with higher loads up to 1.5 MPa have been carried. The measured data of change in temperature and length are then corrected by the thermal expansion and used to construct elastic lines for several temperatures, where the elastic slope is determined using the change in length and the respective load. Thus, Young's modulus for several temperatures can be determined.

These obtained values for static Young's modulus are then compared to values which have been determined by the dynamic resonant frequency damping analysis (RFDA) measurements without load apply. Finally a validation for refractory linings using a Finite Element (FE) model by means of these data is discussed.

## INTRODUCTION

Nowadays numerical modelling of refractory lining concepts are in favourable use for the prediction of thermo-mechanical stresses. Thus better description of material behaviour leads to better calculation of relevant technical parameters by means of Finite Element Modelling (FEM). E.g. the non-homogenous material properties due to brick-mortar linings with joints increase the modelling efforts. This leads to the concept of the homogenization of material properties and the characterization of the behaviour of complete systems. The simulations will support the plant design since the determination of static load cases can be realized. For this accurate material data such as thermal properties, creep behaviour and elastic-plastic behaviour are essential. To determine the dynamic elastic behaviour Resonance Frequency Damping Analysis (RFDA) is state of the art and allows a standardized calculation [1]. Nevertheless static values representing the elastic behaviour under load are desirable for the modelling of refractory lining concepts. Therefore an approach using the standardized method for determination of the Refractoriness under Load (RUL) is in focus of these studies [2].

## EXPERIMENTAL

Analogous to the bending tests, Young's moduli were determined by means of 3-point bending tests according to DIN EN 993-6 using DIC (Digital Image Correlation). According to this method, the modulus of elasticity is determined from the ratio of stress and strain or the deformation. In addition to the test forces that occur, the deflection of the specimen must also be measured during the test. Experience has shown that the crosshead travel of the testing machine is usually subject to significant measurement inaccuracies, since setting effects and system stiffness are included in the measurement data. Therefore, the measurement record of the testing machine does not represent the elastic behavior of the test specimen. To determine the Young's modulus as accurately as possible, the change in displacement or deflection was therefore measured directly on the specimen. For this purpose, an optical strain measurement was used. This was also used to determine the system stiffness, i.e. the difference in displacement measurement between specimen and system. The optical measurement system requires high contrast, approximately 50% black and 50% white areas, and sample dots with a size of 3-5 pixels. This was ensured by the refractory materials used. The principle of stochastic pattern detection is shown in Figure 1. First, individual facets are defined in the reference image (Fig. 1 left). Within a facet, a gray value distribution is then performed. Thus, even with perspective distortion (Fig. 1 right) and a stretching, the gray value distribution is almost the same.
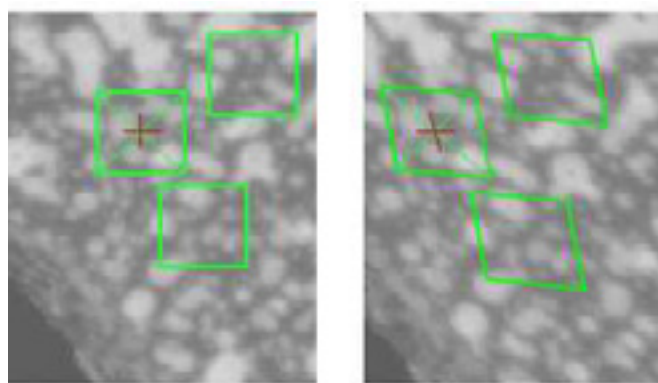


*Fig. 1: Individual facet in the reference image (left) and distortion (right).*

Refractoriness under load (RUL) tests without load were performed on specimens according to DIN 993-19 for the refractory materials investigated in the project to determine the thermal expansion of the materials. At least three test repetitions were carried out for each material. The thermal expansion as a function of temperature was then determined on the basis of the determined temperature-displacement records.

Subsequently, RUL tests were carried out on cylinder specimens with load according to DIN EN ISO 1893, initially with the standard load of 0.2 MPa, then also with loads of 0.3, 0.4 and 0.45 MPa, and on average-reduced cylinders with loads of 0.7 and 1.3 MPa. Using the averaged curves for constant stresses at increasing temperature, elastic straight lines at constant temperature for increasing stresses were created from corresponding measurement points. The slope of these straight lines can be used to determine the E-Modulus of the material. In parallel, resonant frequency measurements were carried out to determine the dynamic modulus of elasticity according to DIN EN ISO 12680-1 and ASTM C1548-02 for the first materials in order to obtain a comparative value for the moduli of elasticity determined.

Based on the measurement data provided, the coefficients of thermal expansion as well as Young's moduli could be calculated or validated for the tests performed. For the validation, the material data used were stored in corresponding FE models of 3-point bending and RUL, and the deflection or change in length calculated

758

by the solver was compared with the experimental measurement data. In addition, values for the Young's modulus could be determined by means of inverse modeling; for this purpose, the Young's modulus values stored in the simulations were adjusted until the deviation of the change in length or deflection between simulation and experiment reached a minimum.

**RESULTS AND DISCUSSION**

*Determination of different E-moduli by means of 3-point bending test and DIC*

To visualize the crack propagation and deformation of the specimen during the three-point bending test, the strain of the specimen is displayed in the horizontal x-direction (Figure 2). About 100 frames in 2 seconds are recorded by the measuring system. The evaluation of the bending tests is then carried out using the bending line method according to the following formula:

$$w = \frac{F \cdot L_s^3}{16E \cdot I} \cdot \frac{x}{l} \cdot \left[ 1 - \frac{4}{3}\left(\frac{x}{L_s}\right)^2 \right], x \leq \frac{l}{2}$$

(1)

F: Maximum force; $L_s$ : span; E: E-modulus; l: specimen length
I: Area moment of inertia

Two different materials were used to determine the elastic modulus by means of a bending line model. On one hand, the deflection was recorded on a metallic aluminum prism and the Young's modulus was calculated according to the bending line. On the other hand, bauxite material also used for the RUL determinations was tested. Figure 2 shows the time-displacement measurements and the deflections of the refractory bauxite specimen. The values determined for the deflections are very different, so that the deflection of the aluminum sample is four times as large as that of the refractory bauxite sample. However, the different deformation behavior and the resulting crack formations in the refractory specimens must also be taken into account here. The values determined for bending force, deflection and modulus of elasticity are summarized in Table 1:

Tab. 1: Bending force, deflection and modulus of elasticity determined by three-point bending and DIC

| Material | Deflection [mm] | Bending Force [MPa] | E-Modulus [GPa] |
|---|---|---|---|
| Aluminium | 0.172 | 9879 | 70.7 |
| Bauxite Brick | 0.042 | 1623 | 47.5 |
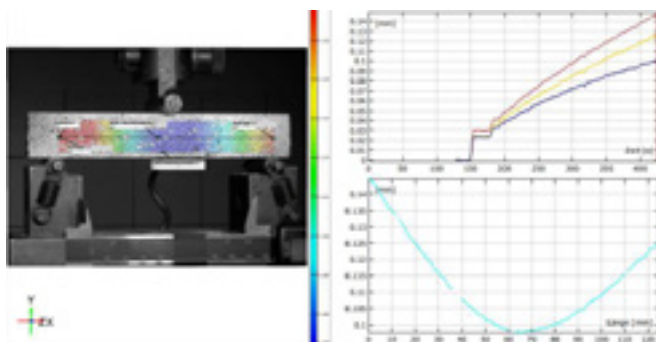


Fig. 2: Time dependant deformation of a refractory bauxite brick specimen in the three-point bending test and determined deflection

FE model of the 3-point bending test was set up as a 2D model; in order to represent the machine stiffness of the system mentioned above, additional springs were modeled at the two lower supports (Fig. 3). With the modulus of elasticity values previously determined by means of various evaluation methods in the 3-point bending test, simulations were carried out in each case and then the force-displacement diagram of the laboratory experiment was compared with the simulation results. It was found that the

evaluation by means of bending line theory provided the best agreement between simulation and experiment.
A Young's modulus determined inversely on the basis of the force-displacement relationship deviates only slightly from the Young's modulus of bending theory, as can be seen in Figure 4.
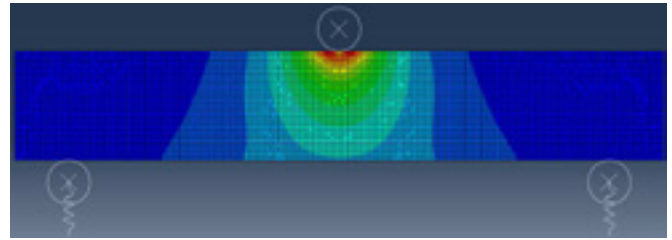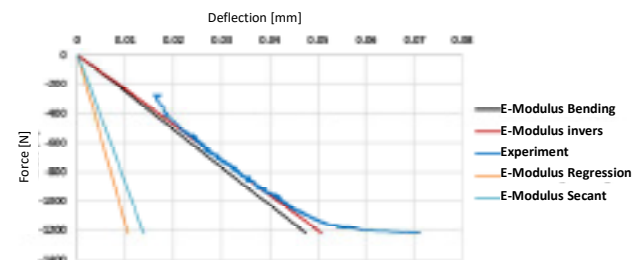


Fig. 3: FE model of the 3-point bending test



Fig. 4: Comparison of the force-displacement curves calculated by the 3-point bending model with experimental measurement results for different Young's modulus values

*Determination of thermal expansion and Young's modulus*

Temperature-strain data from RUL tests of refractory lightweight bricks with 99% $Al_2O_3$ (ASTM Group 34) have been measured and documented. For validation of the determined temperature-dependent Young's modulus, the corresponding Young's modulus data from the RUL tests and RFDA measurements were each deposited in a model of RUL (1.3 MPa load). The comparison of the temperature-strain data from simulation and experiment show very good agreement between simulation and experiment for the Young's modulus data determined by RUL for the refractory lightweight bricks. In contrast, the simulation using the Young's modulus data from the RFDA measurement significantly overestimates the strains that occur, so that the simulation results are closer to experimental data from RUL test at 0.01 MPa than to the 1.3 MPa actually simulated. These results suggest that the static modulus of elasticity determined by means of RUL tests represents the static load case occurring the practical conditions significantly better than the dynamic modulus of elasticity of the RFDA measurements [3].

Industrial shaped refractory material based on bauxite represents another reference refractory material for the evaluation of the modulus of elasticity from measurement data of the RUL tests. Compared with the lightweight refractory, it has a significantly higher density and strength and is used for refractory structures subjected to higher thermal and, above all, mechanical loads.

Initially, cylindrical bauxite brick specimens were used for the determinations during this project period. The entire RUL tests have been measured at loads between 0.7 MPa and 1.3 MPa. It should be noted that such refractory materials have been engineered and microstructured in terms of mechanical loading capacity. High load rates are thus necessary to achieve the corresponding elastic behavior. Figure 5 and 6 show all measurements and following determinations of stress strain curves of the bauxite material with the increasing load rates. It should be noted that a Y-offset at the beginning of the measurements is already considered in this plot. The general trend line is clearly visible. Nevertheless, there are small deviations between 0.7 MPa and 1 MPa resp. 1 MPa and 1.3 MPa. It should be noted that these are not repeat measurements but always new measurements. Figure 10 shows the elastic curves

required to determine the static modulus of elasticity of the bauxite brick for different temperatures. Significantly higher and also more realsitic Young's modulus determinations are now recorded than before the Y-offset. Turning points as in the determinations before are only recognizable at 1200°C in these measurements. The determined values before and after the Y-correction are listed in Table 2. With regard to the static Young's modulus values, the value for 600°C shows the highest deviations with 1.8 GPa.

The determined measurement results for thermal expansion of the bauxite brick specimens (0.01 MPa) and the measurement results for higher loads up to 1.3 MPa showed slight differences among them, but the tendency was observed. The series of measurements at 0.01 MPa showed the largest relative change in length, and the series up to 1.3 MPa the smallest. In contrast to earlier measurements, straight lines can now be constructed from the available measurement results to determine the Young's modulus. As described above, the material group of lightweight refractory bricks and the bauxite bricks show that the measurement principle is suitable for determining the Young's modulus. The assumption that higher superimposed loads are required for this purpose was thus also confirmed independently of previously conducted compression tests.

Tab. 2: Young's modulus determinations from the straight lines constructed for different temperatures from fig. 4 (RUL), initial measurement as well as correction after Y-offset adjustment

| Temperature [°C] | E-Modulus (RUL test) [GPa] | E-Modulus after Y-Offset [GPa] |
|---|---|---|
| 200 | 4.0 | 20.1 |
| 400 | 3.5 | 7.6 |
| 600 | 2.7 | 1.8 |
| 800 | 2.6 | 3.8 |
| 1000 | 2.3 | 4.4 |
| 1200 | 0.8 | 0.9 |

Inverse modeling of the individual measurements was then recognized as a solution for this, since the Young's modulus of the refractory bauxite material is known from previous measurements. A variation of the Young's modulus values of the mortar was performed until the applied simulation and the applied experiment were in good correlation. This was done by three tests per material to check the reproducibility of the method.
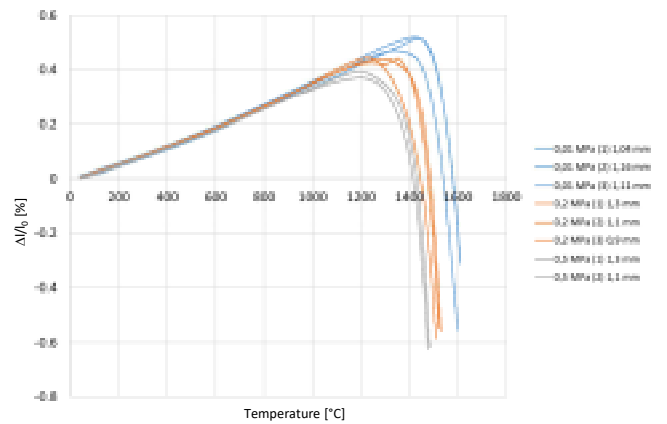


Fig. 5: RUL tests with different loads between 0.01 and 1.3 MPa for bauxite bricks (multiple measurements)



Fig. 7: RUL tests with different loads between 0.01 and 0.5 MPa of bauxite-mortar samples (multiple measurements)

**CONCLUSIONS**

In these studies a new approach for the determination of $E_{static}$ (T) values using RUL tests was examined. Therefore different RUL tests on refractory lightweight bricks as well as bauxite bricks have been performed leading to $E_{static}$ values using isothermal lines. The comparison with $E_{dynamic}$ data achieved by means of RFDA shows reasonable deviations. Finally FEM validation using model of RUL test lead to a good agreement for determined $E_{static}$ values.

For comparison with the results of the RUL tests, 3-point bending tests at elevated temperature are planned in the future in order to be able to determine a temperature-dependent static modulus of elasticity here as well.

For both refractory materials the measurement principles using RUL and DIC are suitable for the determination of mechanical behavior.

For future works a modification of the RUL test setup to achieve higher stresses would be favourable. Higher loads are then essential. In regard of the examination of brick-mortar lining systems at higher temperatures these studies support the utilized method to test multi-layer specimen of refractory and mortar as an experimental homogenization technique.



Fig. 6: Elastic straight lines for different temperatures generated from RUL tests of bauxite material (from Fig. 5)

Measurement results of RUL determinations for multipart bauxite specimens with mortar joints are shown in Figure 7. The load here was initially increased from 0.01 MPa to 0.5 MPa. However, it is not possible to determine the static modulus of elasticity by isotherm from these measurements because the thickness of the applied mortar layer was highly influencing.

760

## REFERENCES

[1] ASTM C 1548-02: Standard Test Method for Dynamic Young's Modulus, Shear Modulus, and Poisson's Ratio of Refractory Materials by Impulse Excitation of Vibration: 2002

[2] DIN EN 993-8: Methods of testing dense shaped refractory products - Part 8: Determination of refractoriness-under-load; German version prEN 993-8:2006

[3] Henze M, Reichert W, Tonnesen T, Telle R, Hirt G. Determination of temperature dependent static Young's modulus of refractory ceramics using RUL tests. Int J Ceramic Eng Sci. 2022; 4:77–83. https://doi.org/10.1002/ces2.101223

# STATISTICAL EVALUATION OF INFLUENCING FACTORS ON VARIOUS COLD CRUSHING STRENGTH DETERMINATION METHODS

Gerhard Urbanek*, Hans-Jürgen Klischat, Manuel Miranda-Martinez,
World Refractories Association, Brussels, Belgium

## 1  ABSTRACT

Measurement of cold crushing strength (ASTM C133) strength resp. cold compressive strength (ISO 10052-1) (CCS) has been used over 100 years as a test method for characterizing refractory products. Although CCS describes in a limited way the performance of a refractory, it is widely used as a key parameter in data sheets and product definitions. Moreover, there are several different CCS standards, each with different influences, a circumstance leading to different and sometimes hardly comparable results which may cause complex trade issues.
For these reasons, a Task Force on Testing Methods and Standards of the World Refractory Association (WRA) has investigated precision data and the comparability of the different CCS standards. More than 1000 individual tests were performed by seven renowned laboratories on six different refractory grades.  This work presents the statistically assured results.
The standards ASTM C133 and ISO 10059-1 differ mainly in the load rate applied and the usage of an interlayer (packing) between the plunger and the test specimen. The results have shown that ASTM C133 gives on average around 24% lower values, this is attributed to the use of the packing.  The influence of the geometry of the test specimens (be it cylindrical or cubic) was also investigated and showed only a minor effect on the values.
The precision data collected in this study have shown for both ASTM C133 and ISO 10059-1 a relative repeatability interval of around 20%. Regarding reproducibility, ASTM C133 performed slightly worse than ISO 10059-1 (40% compared to 30%).
In a further step, the integration of the precision data and the comparative results into ISO/TC 33 for ISO 10059-1 will be proposed.

## 2  OBJECTIVE: THE COMPARISON AND ESTABLISHMENT OF CORRELATIONS BETWEEN STANDARDS ISO, EN (I.E.: DIN, ETC), ASTM, AND GB/T

CCS measurements have always been the subject of controversy. Unfortunately, there is not a single standard but several national and international ones.  They produce a significant scattering of results, generally known up to 20 % standard deviation.

This is a foregone result of the heterogeneous structure of refractories, whose microstructure consist of grains and pores, each of different size and distribution. As a matter of fact, even small deviations in their production process - like the pressure applied during forming, the temperature distribution in the kiln during firing, etc. - may contribute to the unevenness of the resulting material, and thus to the scattering of measured CCS values.

Several CCS testing methods have been standardized, applying various possible influencing factors (section 6).

Tab. 1: Roundup of various international CCSstandards

| Standard | Country | Sample Shape | Sample Size | Packing | Load Rate |
|---|---|---|---|---|---|
| ISO 10059-1 | International | cylinder | 50 mm or 36 mm | No | 1,0 MPa/s |
| ISO 10059-2 | International | cylinder or cube | cylinder 50 or 36 mm<br>cube 75 mm or half standard brick | Yes<br>3-7 mm | 1,0 MPa/s |
| EN 993-5 | Europe | cylinder or cube | 50 mm or 36 mm | No | 1,0 MPa/s |
| ASTM C133-97 | USA | cylinder or cube | 51 mm | Yes<br>6,4 mm | 0,2 MPa/s |
| GOST 4071.1-94 | Russia | cylinder or cube | 20 - 100 mm | No | 1,0 - 2,0 MPa/s |
| JIS R2206 based on ISO 10059-1 | Japan | cylinder | 50 mm or 36 mm | No | 1,0 MPa/s |
| JIS R2206-2 based on ISO 10059-2 | Japan | cylinder or cube or half of a standard brick | cylinder 50 or 36 mm<br>cube 75 mm or half standard brick | Yes<br>3-7 mm | 1,0 MPa/s |
| IS 1528;4 | India | cubes, cylinder or standard brick or half of a standard brick | 50 mm or standard brick or half of a standard brick | No and Yes<br>3-7 mm | 1,0 MPa/s |
| GB/T 5072-2008 | China | cylinder | 50 mm or 36 mm | No | 1,0 MPa/s |

## 3  FOCUS OF THE INVESTIGATION

The focus of our investigation has been the evaluation of the most important influencing parameters on CCS testing.

Various types of refractory brick grades, both basic and non-basic, covering a wide range of CCS values, from very high to low ones, were studied (MgO-C, magnesia spinel, bauxite, andalusite, fireclay, lightweight fireclay).

For each grade the evaluation has included several testing scenarios, those a priori considered having an influence on the dispersion of the CCS values measured, namely:

– Testing the influence of the testing standard employed: ASTM C133-97 (2021) and ISO 10059-1.  The latter chosen as it is matchable with several other standards (Table 1).
– Testing within each brick and each laboratory separately (repeatability).
– Testing in different laboratories (reproducibility).
– Testing the influence of specimen shape (cylinder or cube) for each grade and each laboratory, as sample preparation for both standardized shapes is different.
– Testing the influence of load rate (0.2 and 1.0 MPa/s).
– Testing the influence of using packing or not.

The aim has been the determination of reproducibility and repeatability of standards, and to find systematic deviations that may be harmonized by a distinct factor to convert values from one standard into another.

## 4 LABORATORIES AND MATERIALS

### 4.1 Laboratories
Seven internationally well-respected laboratories were selected for the investigations:
– Laboratories in Germany, Poland and Spain all specialized in measurements on refractory and ceramic materials.
– Refractory manufacturer's laboratories: In the United States of America, Great Britain, Austria (which also created the design, performed data preparation and statistical analysis) and in Germany (which also acted as coordinating laboratory).

### 4.2 Refractory brick grades
Six industrially, on hydraulic high-performance presses formed brick grades were selected to cover the whole range of dense refractory materials and expected material strengths.

### 4.3 Design of tests and sample description

#### 4.3.1 General
To achieve significant and meaningful results, a sophisticated procedure was elaborated to determine possible correlations among the influencing parameters.

The population constituted by all samples was used to carry out:
– An interlaboratory tests for each standard method and brick grade (round robin test),
– A comparison of the tests carried out following ASTM C133-97 (onwards ASTM) and ISO 10059-1 (onwards ISO), where the results obtained testing by each method were compared to those obtained for 50 mm cylinders tested according to ISO.

The Spanish laboratory and the two refractory manufacturers laboratories in Austria and Germany also carried out some additional tests intended for determining the influence of load speed on ISO cylinders (1 MPa/s vs. 0.2 MPa/s) and the effect of packing on ISO cylinders separately, and not only both together in the combinations defined by ASTM and ISO.

#### 4.3.2 Sample preparation
All samples for the comparative tests were wet drilled and/or cut in a single laboratory, using the same equipment that was operated by one person. The final sample preparation (cutting/grinding) was completed in each laboratory separately, so that the influence of sample preparation is as it is in real business.
For each refractory grade three bricks were selected from a higher initial population. In order to avoid deviations in CCS results that are caused by inhomogeneities typical for the brick production, bricks were selected according to fit in a 0.01 g/cm$^3$ interval.
From these three bricks, cylinders as well as cubes were prepared. The samples were dried immediately after cutting to prevent hydration (most important for basic bricks) or influence from the filling of pores with water.
The sampling was designed to compare each type of test specimen and condition with that of the ISO cylinders taken as reference, Fig. 1.
– On brick #1: ISO cylinders (A,D,E,H) as reference for ISO cubes (B,C,F,G)
– On brick #2: ISO cylinders (A,D,E,H) as reference for ASTM cubes (B,C,F,G)
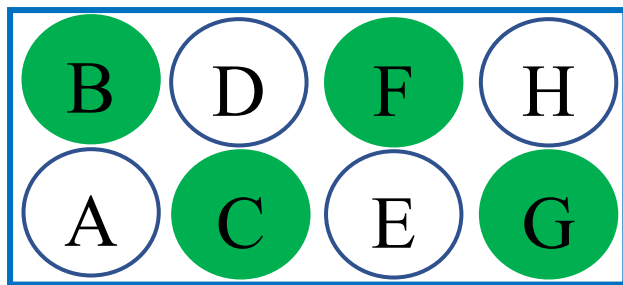– On brick #3: ISO cylinders (A,D,E,H) as reference for ASTM cylinders (B,C,F,G)



Fig. 1: Design pattern of specimens' extraction for comparison test for both: i) ASTM cylinders and cubes and ii) ISO cylinders and cubes.

## 5 DETERMINATION OF PRECISION (ISO 5725-2)
Based on the results of the interlaboratory study, the precision of the different tests methods was calculated according to ISO 5725-2.

Precision was evaluated under the following conditions:

1. Repeatability: one equipment, tests carried out by one operator, with the same material in one laboratory.
2. Reproducibility: different equipment, tests done by different operators with the same material in different laboratories).
3. According to ISO 5725-1 the repeatability (r) reflects the closeness of agreement, that is, the maximum permissible difference due to the test error between two test results under repeatable conditions (ASTM C133). As such, two test results that do not differ by more than the repeatability interval will be from the same population. The reproducibility (R) has the same definition under reproducibility conditions.

Tab. 2: Precision data for the different methods and grades. The color marking indicates very good precision values in green and lowest precision values in red, and intermediate precision values in yellow.

| method | interval | A Andalusite | B Bauxite | C Magnesia Carbon | F Fireclay | R Low density Fireclay | S Magnesia Spinel | all grades |
|---|---|---|---|---|---|---|---|---|
| ILS 1 repeatability interval | | | | | | | | |
| ISO 10059-1 | r [%] | 25.2 | | 15.0 | | | | |
| ILS 2 repeatability interval | | | | | | | | |
| ISO 10059-1 | r [%] | 18.4 | 18.1 | 14.7 | 14.4 | 13.9 | 27.6 | 17.9 |
| ISO_cub | r [%] | 19.0 | 18.3 | 20.6 | 15.8 | 20.3 | 36.2 | 21.7 |
| ASTM_cyl | r [%] | 27.7 | 23.8 | 18.9 | 17.6 | 16.3 | 25.4 | 21.6 |
| ASTM_cub | r [%] | 30.6 | 24.2 | 21.8 | 20.5 | 15.3 | 32.0 | 24.1 |
| ASTM C133 repeatability interval | | | | | | | | |
| ASTM C133 | r [%] | | 12.2 | | | 5.9 | | |
| | | | | | | | | |
| ILS 1 reproducibility interval | | | | | | | | |
| ISO 10059-1 | R [%] | 33.4 | | 23.6 | | | | |
| ILS 2 reproducibility interval | | | | | | | | |
| ISO_cyl | R [%] | 30.9 | 23.7 | 21.1 | 26.7 | 15.9 | 33.9 | 25.4 |
| ISO_cub | R [%] | 43.0 | 43.4 | 30.7 | 46.2 | 27.2 | 46.0 | 39.4 |
| ASTM_cyl | R [%] | 46.9 | 48.9 | 25.3 | 32.3 | 30.5 | 37.9 | 36.9 |
| ASTM_cub | R [%] | 48.1 | 42.9 | 28.3 | 36.9 | 34.5 | 51.1 | 40.3 |
| ASTM C133 reproducibility interval | | | | | | | | |
| ASTM C133 | R [%] | | 45.0 | | | 18.1 | | |

## 6 COMPARISON OF THE MAIN DIFFERENT FACTORS OF THE STANDARDS

The main differences of the standards are:
- shape (cube, cylinder)
- packing (with/without)
- load rate (0.2 or 1.0 MPa/s, see Table 1)

A statistical evaluation on so called "twin" samples (as close as possible sample positions at the bricks – see fig.1 like A-B or C-D) shows table 3.

Tab. 3: ANOVA for all variated parameter based on all differences of pairs
Horizontal data (red): Parameter has significant influence on CCS (p-value < 0.05)

| effect | step of effect | parameter | standard error | t | p | -95% confidence | +95% confidence |
|---|---|---|---|---|---|---|---|
| Constant | | -8,70 | 0,52 | -16,82 | 0,00 | -9,72 | -7,69 |
| Laboratory (reference 6) | 3 | 1,84 | 1,11 | 1,65 | 0,10 | -0,35 | 4,02 |
| | 1 | 0,54 | 1,13 | 0,48 | 0,63 | -1,67 | 2,75 |
| | 7 | -0,07 | 1,02 | -0,07 | 0,94 | -2,07 | 1,92 |
| | 2 | -0,95 | 1,02 | -0,92 | 0,36 | -2,95 | 1,06 |
| | 4 | -0,24 | 1,11 | -0,21 | 0,83 | -2,42 | 1,95 |
| | 5 | -0,78 | 1,13 | -0,70 | 0,49 | -2,99 | 1,43 |
| Grade (reference R) | S | 0,17 | 0,90 | 0,18 | 0,85 | -1,60 | 1,93 |
| | C | 1,25 | 0,84 | 1,48 | 0,14 | -0,40 | 2,90 |
| | A | -1,15 | 1,12 | -1,03 | 0,30 | -3,34 | 1,04 |
| | B | -1,23 | 1,12 | -1,10 | 0,27 | -3,42 | 0,96 |
| | F | 0,07 | 1,12 | 0,07 | 0,95 | -2,12 | 2,26 |
| Sample shape | cylinder | 2,33 | 0,50 | 4,69 | 0,00 | 1,36 | 3,31 |
| packing | no | 11,41 | 0,75 | 15,20 | 0,00 | 9,94 | 12,88 |
| load rate | 1.0 MPa/s | 3,86 | 0,75 | 5,13 | 0,00 | 2,39 | 5,33 |

This ANOVA is calculated based on twin samples. All three parameters are significant: cylinder, without (no) packing, and load rate 1.0 MPa/s give higher results, with the main effect by packing, as also may have been proposed by theoretical considerations.

A calculated linear regression of absolute values and differences of twin specimen shows that a conversion between the test methods according to Fig. 2 is possible and reasonable. More tests would increase the accuracy due to statistical reasons

764
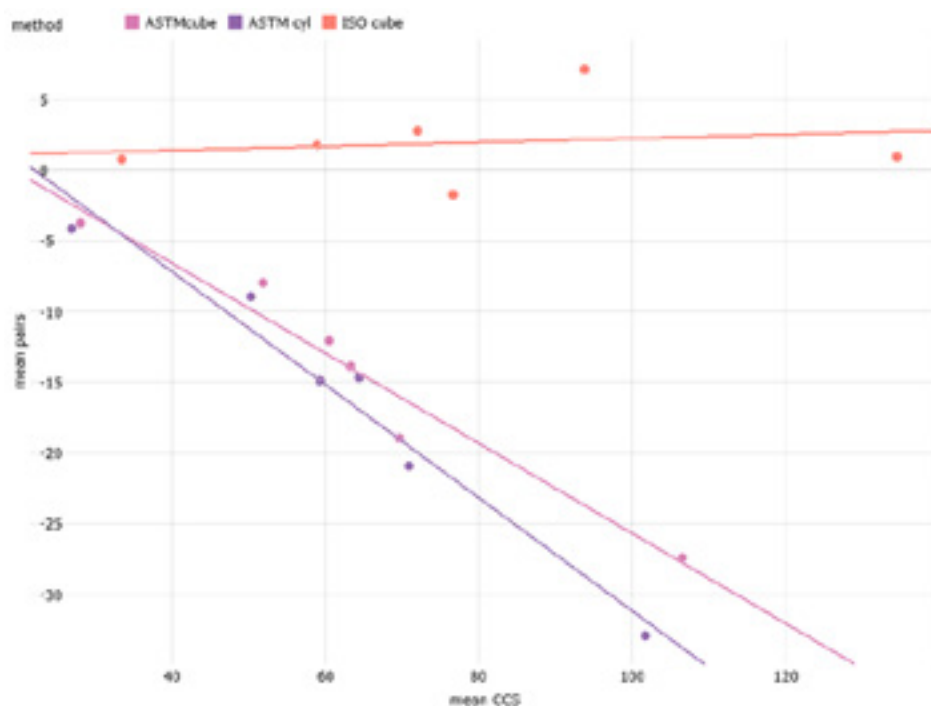
Fig. 2: Linear regression for the different methods compared on twin specimens for ISO cylinder specimens. One point is the mean value of all results of all laboratories for one grade.

## 7   CONCLUSION

In conclusion, more than 1000 single CCS tests have been performed from seven leading refractory laboratories (producer and independent laboratories) on six different refractory grades according to different standards to provide a closer look on this very common test method for refractories. The goal was to statistically compare the results of the different standards (ASTM and ISO) to establish a basis and allow a conversion between the methods and to obtain precision data for all considered test methods. A special drilling schema, which ensures a direct comparison of the different methods with samples from one brick (twin or pair specimen), has been applied to avoid possible differences in the CCS of different bricks and to avoid unknown influencing parameters. Both standards differ mainly in the load rate applied and the usage of an interlayer (packing) between the plunger and the test specimen. ASTM C133 gives around 24 % lower values, attributed to the use of the packing. The influence of the geometry of the test specimens (be it cylindrical or cubic) was also investigated and showed only a minor effect on the values. The precision data collected in this study have shown for both standards a relative repeatability interval of 20 %. Regarding reproducibility ASTM C133 performed slightly worse than ISO 10059-1 (40 % compared to 30 %). In a further step, the integration of the precision data and the comparative results into ISO/TC 33 for ISO 10059-1 are proposed

REFERENCES

[1] Jarvis, D. A.: Refractories Testing and the Significance of Chemical and Physical Characteristics. Part 2: The Physical Properties of Refractory Materials. Refractories Worldforum, 13 (2021) No. 3, p. 15-18
[2] Konopicky, K.; Lohre, W.: Die Kaltdruckfestigkeit feuerfester Baustoffe. Tonind. Ztg. 80 (1956), p, 299-292
[3] Sharma, V.: Influence of Sample Geometry and Contact Properties on Cold Crushing Strength. Master Thesis, Montanuniversität Leoben, June 30, 2014
[4] Czechowski, J.; Podwórn, J.; Gerle, A.; Dahlem, E.; Investigating the factors that influence the Cold Crushing Strength results of shaped refractories. XVI International Scientific Conference "Refractory materials: manufacture, methods of testing, application", Wista-Jawornik, Poland, May 20-22, 2015
[5] ISO 10059-1:1992-02 Dense, shaped refractory products; determination of cold compressive strength; part 1: referee test without packing
[6] EN 993-5:2019-03 Prüfverfahren für dichte geformte feuerfeste Erzeugnisse - Teil 5: Bestimmung der Kaltdruckfestigkeit; Deutsche Fassung EN 993-5:2018 (Methods of test for dense shaped refractory products - Part 5: Determination of Cold Crushing Strength)
[7] GB/T 5072-2008 Refractories – Determination of cold compressive strength
[8] ASTM C133-97 (reapproved 2021) Cold Crushing Strength and Modulus of Rupture of Refractories
[9] Majdic, A.; Hagemann, L.; Lichomski, H.: Einfluss der Güte der Probekörperdruckflächen und der Druckplattenrauheit auf Mittelwert und Streubreite der Kaltdruckfestigkeit feuerfester Steine (The influence of the quality of the specimen surface and the roughness of the pressure platens on the mean value and the dispersion in the cold-crushing-strength test of refractory bricks). Tonind.-Ztg. 97 (1973) Nr. 9, p. 237-243
[10] ISO 5725-2: 2019-12 Accuracy (trueness and precision) of measurement methods and results - Part 2: Basic method for the determination of repeatability and reproducibility of a standard measurement method
[11] ASTM E691:2022 Standard Practice for Conducting an Interlaboratory Study to Determine the Precision of a Test Method

# EVALUATION OF COLD CRUSHING STRENGTH METHODS ON STATISTICAL VALUES OF VARIOUS REFRACTORY BRICK GRADES

Hans-Jürgen Klischat*, Gerhard Urbanek, Manuel Miranda-Martinez,
World Refractories Association, Brussels, Belgium

## ABSTRACT
The cold crushing strength (CCS) test is a standard test method for refractory products, which is indicated in nearly all data sheets of refractory materials. The measurement, although theoretically quite simple, often produces a wide variety of results, which sometimes raise unnecessary discussions between refractory producers and refractory users. A statistical evaluation of precision data and the comparability of different standards, encompassing seven laboratories and the application of Mandel's statistics for all laboratories and materials tested, was carried out by the Task Force "Testing Methods and Standards" of the World Refractory Association. The results gathered show the influence of application of the standards ASTM C133 and ISO 10059-1 not only regarding the influence of testing parameters, but also some material dependencies. So, a higher scatter of values with increasing strength values was observed. Specific features were also observed mainly for magnesia spinel bricks which may be explained by the presence of microcracks, which certainly influence the strain field within the specimen. Furthermore, the values of all brick grades are also affected by the laboratory measurements conditions themselves, as various influences are considered to result in lower values. Therefore, it would be desirable that more statistical data on CCS are reflected into standards (ISO/TC 33 for ISO 10059 and ASTM C133), as should also be the results for different refractory grades.

## INTRODUCTION
Although the measurement of cold crushing strength seems rather simple at first sight, the results can differ to a great extent due to several influencing factors, mostly speed of load increment, shape and size of specimen, and use of an interlayer between sample and plungers of the testing machine. Although the latter is used mainly to compensate unevenness of plates and sample, the stress distribution changes dramatically from compressive stresses to tensile stresses. Ceramic materials are more sensitive to tensile than compressive stresses, so this interlayer or packing leads to lower values of the cold crushing strength, (1), (2), Fig. 1.
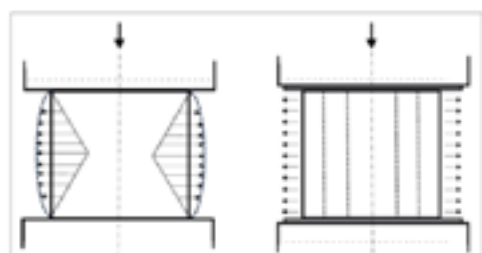


Fig. 1 Types of strain induction on a specimen during measurement of cold crushing strength without (left) and with packing (right)

Unfortunately, the most well-known standards use variations in test methods, which will inevitably result in differing values. From a statistical approach, an attempt was made to determine the precision and reproducibility of data, which gave mostly satisfying results for the overall data, and concluded that a conversion between the test methods according is possible and reasonable. The precision data have shown for both ASTM C133 and ISO 10059-1 a relative repeatability interval of around 20%. Regarding reproducibility, ASTM C133 performed slightly worse than ISO 10059-1 (40% compared to 30%). Still, more tests would increase the accuracy. To complete the statistical evaluations, material behaviour under the differing conditions of the two main standards

is discussed. Repeatability standard deviations and relative repeatability standard deviations are given in Figs. 5 and 6. They reflect the dependency of scatter under repeatability conditions and reproducibility, being ordered by the grades with increasing strength values.

## MATERIALS AND TEST PROCEDURE
Basic and non-basic refractory bricks grades, covering a wide range of CCS values, were studied. The properties of magnesia carbon (C), magnesia spinel (S), bauxite (B), andalusite (A), fireclay (F), and lightweight fireclay (R) bricks are shown in Figure 2.

| Brick grade | Brick C | Brick S | Brick B | Brick A | Brick F | Brick R |
|---|---|---|---|---|---|---|
| Raw materials | magnesia carbon | magnesia spinel | bauxite | andalusite | fireclay | fireclay |
| Density [g/cm³] | 2.96 | 3.01 | 2.88 | 2.67 | 2.24 | 1.78 |
| Porosity [%] | 2.45 | 14.1 | 17.50 | 13.40 | 56.00 | 26.70 |
| MgO [%] | 95.50 | 88.10 | 0.10 | 0.10 | 0.25 | 0.35 |
| Al2O3 [%] | 1.10 | 10.50 | 82.80 | 61.10 | 41.45 | 22.30 |
| SiO2 [%] | 0.80 | 0.2 | 10.71 | 36.30 | 53.20 | 68.70 |
| Fe2O3 [%] | 0.70 | 0.50 | 1.50 | 0.80 | 1.40 | 2.00 |

Fig. 2: Properties of the investigated brick grades

For each grade several testing scenarios with an influence on the dispersion of the CCS values were measured. These were (i) influence of the testing standard employed: ASTM C133-97 (2021) and ISO 10059-1, (ii) testing within each brick and each laboratory separately (repeatability), (iii) testing in different laboratories (reproducibility), (iv) influence of specimen shape (cylinder or cube), (v) influence of load rate (0.2 and 1.0 MPa/s), (vi) influence of using packing (or not).

Due to the expected high scatter of results, Mandel's statistics for interlaboratory testing were used to retrieve a correlation with material properties as well as material's response. The specific values are the h-statistics for comparison of mean values of all laboratories and grades (and to determine the consistency of interlaboratory tests, and to confirm if a laboratory is an outlier) and the k-statistics for the repeatability performance of each laboratory (comparing the standard deviation of a laboratory with the average of the standard deviation of all laboratories). The Mandel's statistics are recommended by ISO 5725-2, (3) as well as ASTM E691, (4).

## RESULTS OF INTERLABORATORY TESTS
### Tests according to ISO 10059-1 with cylinders
Reference tests containing all precision data were carried out with cylinders for all laboratories and brick grades, Fig. 3.



Fig. 3: Results of the interlaboratory study based on ISO cylinders with separate precision data for grades (outliers eliminated) as an example for all performed tests

All collected laboratory data were evaluated. As an example, the data for magnesia carbon bricks are given in Fig. 4, showing the single CCS values as well as their scatter, the median value, and the tolerance limits.

Laboratory 3 is characterized by a significantly too wide range of values as single results (red dots). These results were eliminated for further precision calculation.
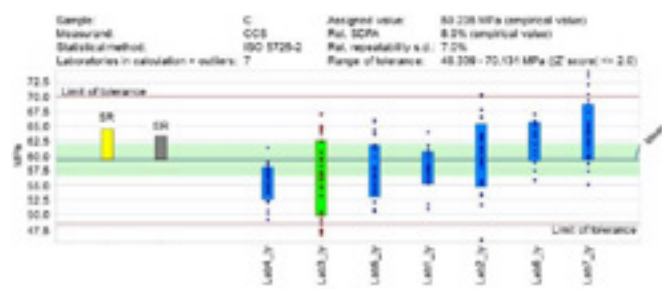


*Fig. 4: Detailed graph for the magnesia carbon brick C with all single results of each laboratory, grouped with increasing strength values by laboratory*
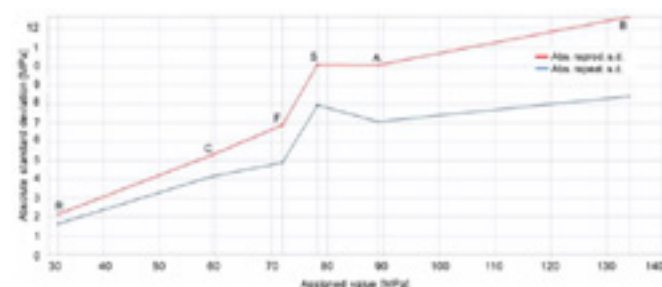


*Fig. 5: Increase of repeatability standard deviation with increase of absolute CCS values and reproducibility standard deviation*
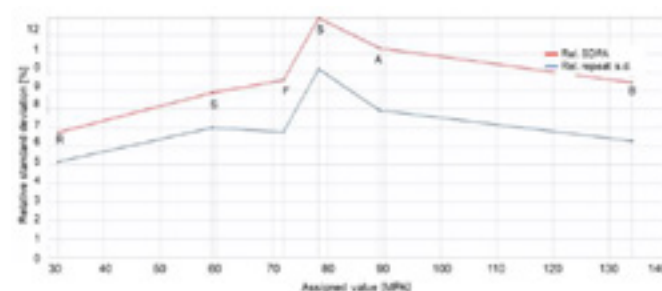


*Fig. 6: Relative repeatability standard deviation (MPa) with increase of absolute CCS values*

Figs. 5 and 6 reflect the dependency of scatter regarding repeatability conditions and reproducibility, respectively, with ordering points of grades. The peaks in both diagrams are related to grade S (magnesia spinel brick).

For magnesia carbon bricks C, an amount of 188 samples were tested. The mean value was calculated for all tested samples excluding outliers. For this grade, 7 laboratories conducted the test, but one laboratory was an outlier. The absolute and relative reproducibility intervals are similarly descriptive than other precision parameters like repeatability standard deviation. Two single results under repeatability or reproducibility conditions should not differ more than these intervals. Otherwise, it is not the same sample, or the methods are different. A graphically overview for comparison of mean values of all laboratories and grades are given by the two figures of Mandel's h- and k-statistics for the repeatability performance of each laboratory, Figs. 7, 8.

The bars are grouped by the laboratories, each bar represents the standardized results of each grade. The "h" statistics displays positive values for higher results than the mean of all laboratories vice versa. The "k" statistics displays the repeatability: bars, yellow or red, mark "significant" to "high" variations. Fig. 7 shows that laboratories 6 and 7 measure predominantly higher values, while laboratories 1, 2, and 3 measure values which are generally lower than the overall mean value. Laboratories 4 and 5 measure values

which correspond to the mean value but show a wide scattering of values for the different brick grades. All laboratories are within the critical value. A systematic dependence on special brick grades cannot be derived.
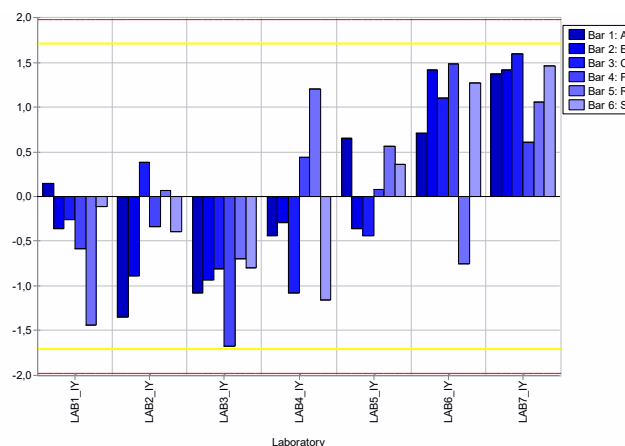


*Fig. 7: Mandel's h statistics for ISO cylinder method*
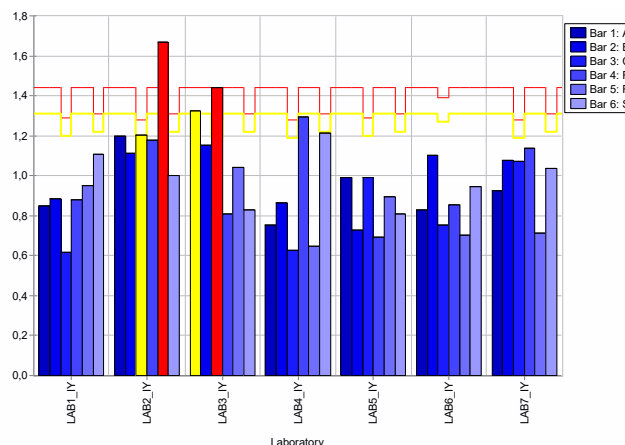


*Fig. 8: Mandel's k statistics for ISO cylinder method*

For Mandel's statistics, a red or yellow bar (a result is significantly different to the other grades/samples and laboratories) is defined as outlier and erased for further calculations of the precision data. In this case, laboratories 2 and 3 show outliers (above the critical value), but only for some brick grades (Lab 2: C, R; Lab 3: A, C), Fig. 8.

**Tests according to ISO 10059-1 with cubes**

The test procedure was similar to the one with cylinders, but the results varied between the two geometrical shapes.

Several values for laboratory 2 regarding cubes are outside of the critical value (andalusite, bauxite, and fire clay), while all other values show a similar trend as for cylinders. Remarkably labs 6 and 7 continue the trend of high Mandel's h values, which means they measure higher values than the mean of all laboratories, Fig. 9.

Laboratory 2 had once again a significantly too high scatter in its results.

For the geometrical parameter "cube" the similar results as for "cylinder" are found also for Mandel's k, Fig. 10. Laboratory 2 shows statistically differing results compared to the other ones, mainly for magnesia carbon, fireclay, and magnesia spinel bricks. Still, the other values are also higher. It has to be noted that the outliers for Mandel's h and Mandel's k statistics affect different brick grades, still belonging to laboratories 2 and 3.
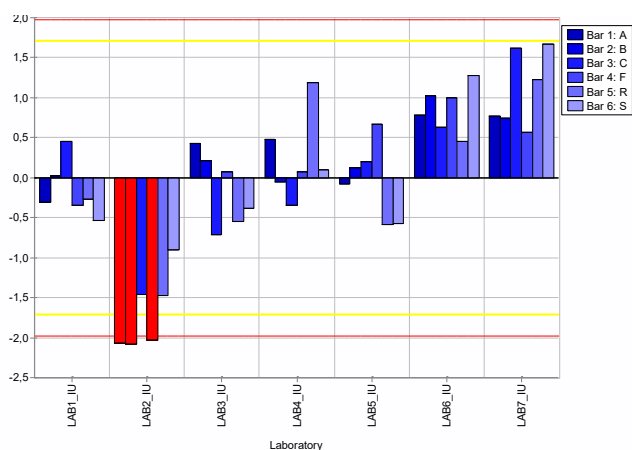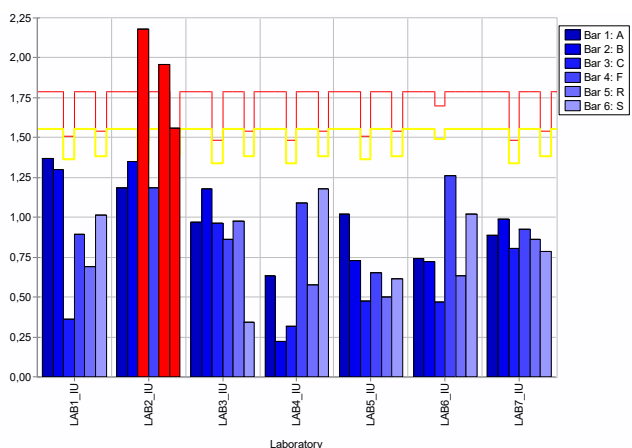
*Fig. 9: Mandel's h statistics for ISO cube method*



*Fig. 10: Mandel's k statistics for ISO cube method*

**Tests according to ASTM C133 with cylinders**

As a comparison to ISO 10059-1, tests according to ASTM C133 were performed to investigate the influence of the lower load rate and, more significantly, the influence of the packing layers between plungers and specimen on the results, Figs. 11, 12.
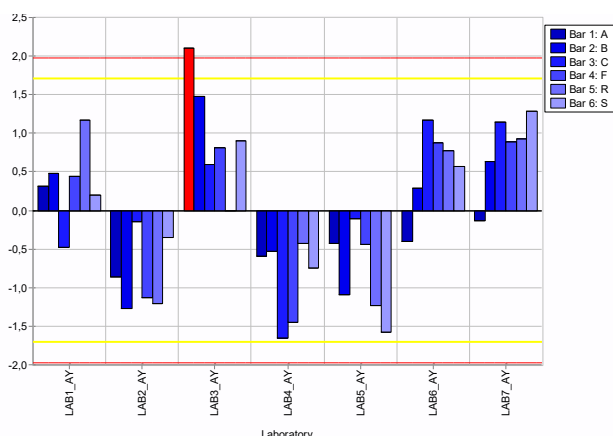


*Fig. 11: Mandel's h statistics for ASTM cylinder method*

For ASTM cylinders the trend for Mandel's h-statistics is similar as for ISO data, Laboratories 6 and 7 always show values above the average, but contrarily to previous results, laboratory 3 also shows high values. Remarkable is the very high effect of andalusite bricks in this laboratory, indicating the effect of tensile stresses on the result especially for this brick grade, which, on the other hand, is not observed by the other laboratories.

Here, also laboratory 2 shows significant effects on repeatability. It is worth noting that lab 2 exceeds the critical value for three brick grades, magnesia carbon, insulating fireclay and magnesia spinel bricks.
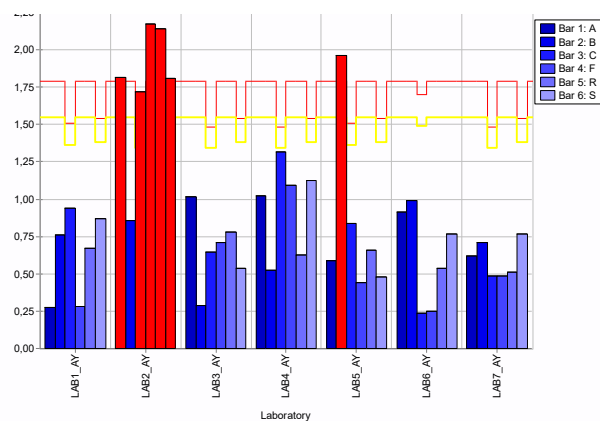


*Fig. 12: Mandel's k statistics for ASTM cylinder method*

## VIEW ON BRICK GRADES

**Magnesia carbon bricks C**

Generally, the measurements on ISO cylinders show that Laboratories 2, 6, and 7 show the highest values, while laboratory 4 measures the lowest values, Fig. 7. Laboratory 3 is characterized by a high standard deviation, which exceeds the lower tolerance limit, which is ± 2 standard deviations from the mean value of all laboratory results.

The measurements on ISO cubes show a different picture, Fig. 9, while laboratories 6 and 7 still homogeneously show the highest values, Laboratory 2 shows an unacceptable high variation, while the other laboratories show intermediate values with a low scatter of results.

The measurements on ASTM cylinders result in a very high scatter of values from Laboratories 2 and 4, while laboratories 6 and 7 again measured the highest values with a low standard deviation, Figs. 9, 10.

All in all, there is no systematic dependence on the measurements of the MgO-C bricks. Laboratories 6 and 7 measure the highest values, while all other laboratories sometimes measure values with a very high standard deviation exceeding or undercutting the tolerance limits, but this cannot be assigned to a special laboratory. An assignment to material properties, e. g. the orientation of plate-like graphite grains which can align themselves during the pressing process of brick production, is not obvious.

**Magnesia spinel bricks S**

For magnesia spinel bricks, there is also no systematic dependence of the values on the measurements. ISO measurements give higher values than ASTM measurements. Cylinders give tighter tolerance limits only for ISO cylinders, for ASTM there is no significant difference. Laboratories 6 and 7 measure the highest values. An assignment to material properties by Mandel's statistics is not obvious. With regard to Fig 5 and 6, the influence of the microcrack system (caused by the thermal expansion mismatch between magnesia and spinel to reduce Young's modulus and increase brick elasticity) has to be considered as an influence on the brick behaviour.

**Bauxite bricks B**

The results for ISO cylinders show for all laboratories values within the tolerance limit, Figs. 7, 8. Taken the high strength values into account (one reason why bauxite bricks were chosen), the scattering is not increased but remains stable below 10%. Again, Laboratories 6 and 7 measure the highest values.

This is confirmed for ISO cubes, except for Laboratory 2, where significantly lower values are measured, Fig. 9. A reason from material's point of view is not obvious.

ASTM measurements give lower values compared to ISO measurements. For ASTM cylinders, Laboratory 5 is characterized by low values of CCS, accompanied by a high scattering of the

standard deviation, Figs. 11, 12. Laboratory 2 also gives low values, Fig. 11.

Although bauxite bricks, in this case with an additional phosphate bond, are characterized by a very high strength (median value 134 MPa), there are no material characteristics obvious which influence their statistical behaviour.

### Andalusite bricks A

The results for ISO cylinders show for all laboratories values within the tolerance limit, although strength levels are very different for all the laboratories, they increase from 78 MPa to 99 MPa, but very consistently and with typical standard deviations. For this brick grade this could be a hint for a systematic influence of the testing conditions. It is obvious that Laboratory 2 measures again the lowest values, but at a similar level as Laboratory 3, Fig. 7. Again, Laboratories 6 and 7 measure the highest values.

This is confirmed by measurements of cubes, with the exception that Laboratory 2 measures all values significantly below the lower tolerance limit, Fig. 3, confirming the results of bauxite bricks.

The values for cubes are well below the ones of the cylinders.

For measurements on ASTM cylinders, all laboratories measure similar strength values of ca. 68 MPa, Fig. 6, except laboratory 3, where all measured values are located above the upper tolerance limit. Also here, a special material specific correlation cannot be found regarding an influence on CCS.

### Fireclay bricks F

Contrarily to the other products, the tolerance limits and the standard deviations for the different laboratories are less pronounced. All standard deviations are below 6.5 MPa. Laboratories 6 and 7 show again the highest values but are not far apart from the other laboratories, Fig. 7. A clear explanation for this behaviour is not obvious, as also fireclay bricks consist of several mineral phases (mullite, glass phase, cristobalite), which would theoretically result in a behaviour comparable to the other brick grades.

All other values for ISO cube measurements confirm the already known results. Laboratory 2 still measures the highest scattering of results, Fig. 9, which cannot be directly related to material properties.

### Insulating fireclay bricks R

The standard deviation of insulating fireclay bricks is, like fireclay bricks, comparatively small, with a maximum standard deviation of 3.3 MPa. Laboratory 6 does not measure the highest values, while laboratory 7 again measures the second highest values

The results are roughly confirmed by ISO cube measurements, but a higher scatter of values (standard deviation maximum 4.75 MPa of Laboratory 2), Figs. 9. 10. This high value contributes also to the comparatively high limits of tolerance.

Regarding material properties of this unburnt brick grade, there is also no direct influence on the cold crushing strength values obvious.

### CONCLUSIONS

Various refractory brick grades covering a wide variety of cold crushing strength values were investigated to get information on their influence on CCS testing reproducibility and repeatability in seven laboratories with the aim of possibly finding a correlation to brick composition.

As a helpful tool, Mandel's statistics were applied to detect differences between samples measured by different laboratories to examine if a material contains outliers in comparison to others. The h statistic is relevant for differences between mean values, the k statistic is relevant for differences between variances.

Most of the evaluated influencing factors had a high dependency on the grades. Still, a direct influence of the material's structure to the scattering of values was not obvious, neither to the h-value nor the k-value. The pure ceramically bonded magnesia spinel brick behaves different to the other brick grades, as can be read from the repeatability standard deviation and the relative repeatability standard deviation, Figs. 5, 6. This is most probable due to the special microstructure intentionally created by the installation of a microcrack system to reduce Young's modulus. These microcracks are created by a thermal expansion mismatch between magnesia and spinel. This may result in a different stress and strain pattern in these bricks during the tests, being responsible for the unique behavior.

For further measurements, to minimize the effect of laboratory influences, the application of knowledge of Mandel's h and k values is advantageous, and its application would also be advisable when updating international standards.

Measurement values being too high can only be explained by a not centric location of the ancillary adaptor. This can result in the pick-up of forces which results in higher values, especially at low forces. On the other hand, there are several possibilities for explaining too low measurement values:

o   Uneven face surfaces of the cylinders and cubes resulting in uncontrollable stress peaks.
o   Not rectangular preparation of the specimen.
o   Not parallel surfaces of specimen.
o   Pop-outs of the sample surfaces.

Some laboratories may also have more experience in preparation of cylinders instead of cubes, and therefore may be more prone to failures when testing cubes.

Furthermore, uneven steel plates, be it worn or scratched, result in uncontrollable stress peaks. Roughness decreases by permanent measurements. Due to the lack of the hardness, a faster wear may occur.

A number of hints may be taken from this work for revision of CCS standards. Generally speaking, it would be advisable to include precision data, consider advancement in the conversion between test methods, establish of the number of specimens for one sample (n=4) and for more precise comparison the special drilling scheme.

### REFERENCES

[1]   Urbanek, G., Klischat, H.-J., Miranda-Martinez, M.: Statistical evaluation of influencing factors on various cold crushing strength methods, Unitecr 23, Frankfurt 2023

[2]   Urbanek, G., Klischat, H.-J., Miranda-Martinez, M.: Evaluation of Test Methods for Refractory Bricks: A Comparison and Validity Study of some Cold Crushing Strength Standards. Part 1: Procedure and Determination of Precision. Refractories Worldforum 15 (2023) No. 2

[3]   ISO 5725-2: 2019-12 Accuracy (trueness and precision) of measurement methods and results - Part 2: Basic method for the determination of repeatability and reproducibility of a standard measurement method

[4]   ASTM E691:2022 Standard Practice for Conducting an Interlaboratory Study to Determine the Precision of a Test Method

# BULK DENSITY DETERMINATION OF REFRACTORY RAW MATERIALS – FASTER AND BETTER WITH A SPIN-DRYER

Andreas Buhr, Almatis GmbH, Frankfurt, Germany

Geert Wams, Almatis BV, Rotterdam, The Netherlands

John Stevenson, Almatis Inc., Benton/AR, USA

Gerhard Urbanek, RHI Magnesita, Leoben, Austria

Jerry Dutton, Stourbridge, United Kingdom

## ABSTRACT

In order to determine the bulk density of refractory raw materials, the so-called water method following the Archimedes principle is normally used. This is where the effect of water displacement on the weight of the sample is used to determine the bulk volume of the sample grains. During this test procedure, the surface of water infiltrated sample grains must be dried with a wet towel. Experience shows, that this drying step is the main root cause for variation in reproducibility of results and even repeatability of tests. A new spin dryer (centrifuge) was developed and introduced to automate this surface drying step, and is now included as a new method in ISO 8840:2021. The paper discusses the improvement of measurement with the new approach and industrial experiences from two big industrial players in the raw material business.

## INTRODUCTION

The bulk density is an important property for refractory raw materials and the apparent (open) porosity is also an essential part of the specification. It is measured frequently as in-process control in refractory aggregate production. During tabular production, Almatis performs about 28,000 bulk density measurements per year over its six sites in the USA, The Netherlands, Germany, India, China, and Japan.

The different standard methods for determination of bulk density are briefly and comprehensively described by Lorenzoni [1] and will not be discussed in detail here. Popular methods such as DIN-EN 993-18 [2] and ASTM C357-07 [3] include sample volume determination by weighing the immersed sample in water following the Archimedes principle with buoyancy related to the volume of the immersed body. An important part of that procedure is weighing the water - infiltrated sample without excess water on the surface of the sample. This would lead to grain bulk density appearing lower. However, undesired removal of water from open pores at the grain surface would give apparently higher bulk density.

Therefore a wet cotton towel is wrung and then used to manually blot the grains to dry the surface until the wet sheen on the grains has disappeared (figure 1). It is clear that this procedure adds variability to the results because of slight differences between operators and their subjective judgements. This has been proven by multiple round robin tests both internally and externally at Almatis and RHI Magnesita. A bulk density variation of +/- 0.02g/cm³ is commonly accepted for tabular alumina or other refractory aggregate grain density measurements.

RHI Magnesita has developed a new method for this critical step in grain bulk density measurement, This replaces the manual and subjective method by the use of a centrifuge (spin dryer), to give an automated and more reproducible process [1]. It has been included in ISO 8840:2021 [4]. Almatis, at first, tested the centrifuge and then purchased six machines from RHI Magnesita for use in all worldwide tabular alumina sinter plants. The current status of experiences and results is described as follows.



*Fig. 1: Surface drying of immersed tabular alumina grains by blotting with wet towel (cotton cloth).*

## CENTRIFUGE METHOD

### Centrifuge for surface drying

Fig. 2 shows the centrifuge with five baskets for carrying the immersed, water-infiltrated grain samples. If less than five samples are to be tested, dummies should be used in the other baskets to ensure balance during the spinning process. The rotation speed and time can be adjusted based on calibration experiments depending on the requirements of specific materials. However, Almatis found the setting of 680 RPM for 90 secs as recommended by RHI Magnesita was also suitable for tabular alumina. This figure was defined by RHI Magnesita after an extended series of tests over a broad range of raw materials but with a particular focus on magnesia.

For each bulk density measurement Almatis uses three 90 g tabular alumina samples, crushed and sized to 5 - 8 mm. This is coarser than the figure in ISO 8840:2021 where 2 – 5.6 mm or 3 – 4 mm is recommended for the centrifuge method. Tabular alumina is a very hard material and lab-crushing of the 19 mm diameter sintered balls down to 3 – 4 mm for bulk density testing would be inappropriately cumbersome for the high number of samples in daily processing in the plants. The high homogeneity of tabular alumina as a granulated and sintered product allows that deviation from the norm.

Fig. 3 shows the bulk density of tabular alumina samples comparing surface drying with the towel with the centrifuge method. The correlation found in this and multiple other tests was very good and triggered the decision to equip all tabular alumina sintering plants within Almatis with centrifuges for bulk density measurement. With regard to nomenclature some clarification is

needed here. Historically, bulk density of tabular alumina was always referred to as bulk specific gravity (BSG) which strictly speaking is a unitless figure relating the gravity to that of water with 1 g/cm³. Nevertheless, BSG was and is used with g/cm³ as unit in data sheets and all technical communication.

The process of establishing the centrifuge method and qualifying it as a replacement of the towel method for drying is ongoing in Almatis sinter plants..The plants that started first have already implemented this change.



*Fig. 2: Centrifuge (spin dryer) built at the RHI Magnesita Technology Center Leoben, Austria.*
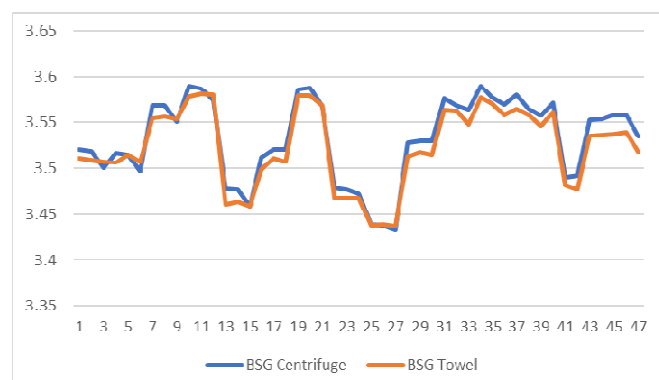


*Fig. 3: Bulk Specific Gravity (BSG) of tabular alumina - centrifuge vs. towel drying.*

## Centrifuge for grain infiltration

The centrifuge provides another interesting opportunity for improving the bulk density measurement of raw material aggregates. RHI Magnesita has successfully tested grain infiltration with the centrifuge. In the standard methods, the sample is infiltrated with water either by the vacuum method [2] or by boiling in water [3]. Both procedures require a minimum of 45 minutes to achieve the required infiltration of the grains. At Almatis, boiling the sample in water is the common way for infiltration. When the dry sample is put into a plastic container with water and then into the centrifuge basket (figure 4), the spinning can be used to infiltrate the sample grains. Here, rotation speed and time have to be increased when compared to the surface drying step later in the procedure. For Almatis tabular alumina samples, 880 RPM for 220 seconds was established as the standard setting for achieving stable infiltration results. This is significantly faster than the boiling method.

With this new approach, using the centrifuge for infiltration and drying the surface, results from bulk density measurement are already available after about 15 minutes. This compares to about 90 minutes using the old approach. It also means that the lab analysts can perform the testing in one operation instead of having interruptions, waiting for the infiltration to be finished.
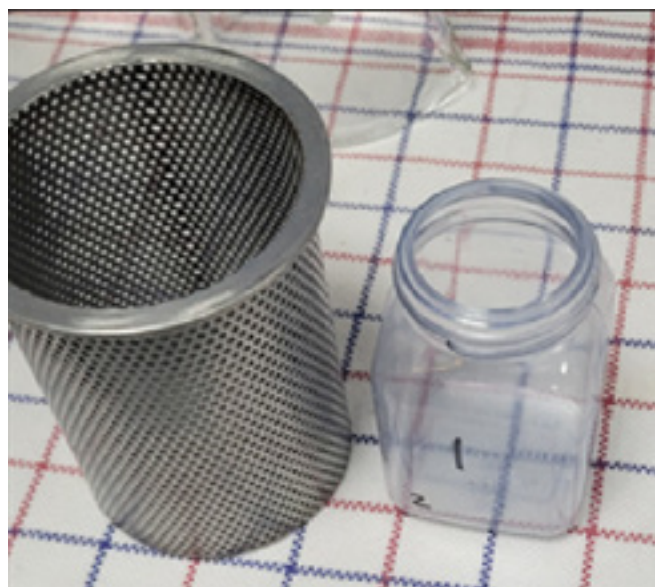


*Fig. 4: Basket with plastic container for infiltration of tabular grains by centrifuge.*

## Results from new method with tabular alumina

Test series were started in different locations to compare results using the new method (centrifuge for infiltration and surface drying) with the old method (boiling in water and surface drying with wet towel). Fig. 5 shows good correlation of BSG between both methods from a test series of 48 samples and six different analysts at Almatis Rotterdam. There were only slight differences in apparent porosity (AP), and water absorption (WA). Fig. 6 shows box plots from the same comparison at Almatis Benton, AR with 30 samples and 4 different analysts. In addition, correlation for BSG is good here, and differences in AP and WA are small. More test series are ongoing in all Almatis tabular alumina sinter plant locations including a global Gage R&R test for establishing the new method as the future standard within Almatis.
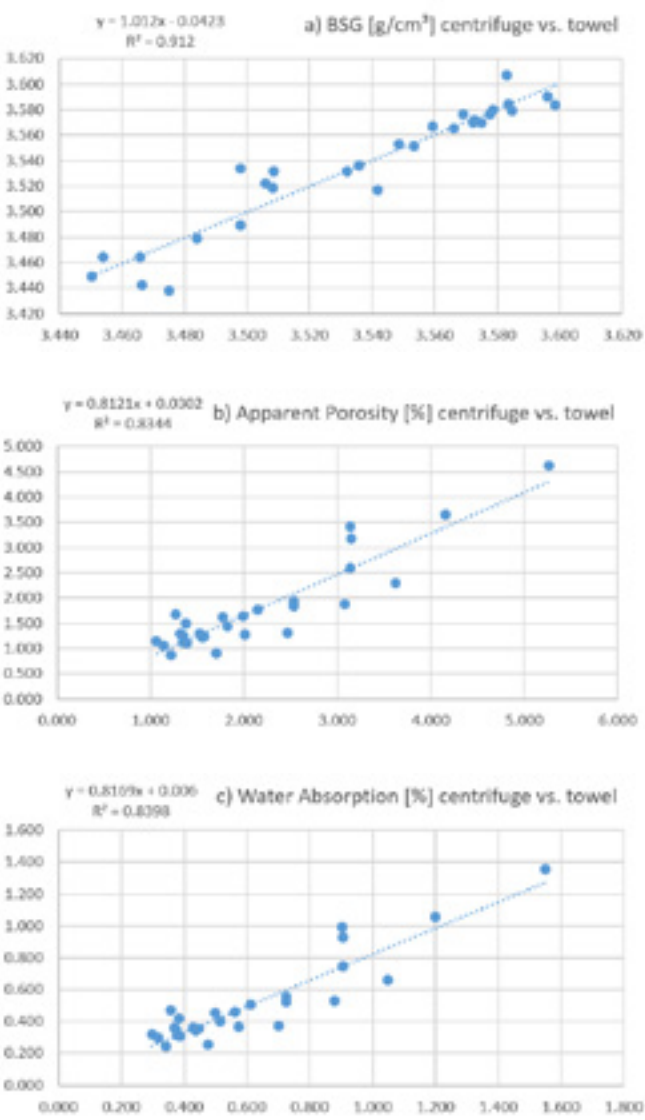
*Fig. 5: Correlation of BSG, AP, and WA - centrifuge vs. towel method at Almatis Rotterdam, The Netherlands.*



*Fig. 6: Box plot of BSG, AP, and WA results Almatis Benton, USA.*

## CONCLUSION AND OUTLOOK

The centrifuge enables automation of the surface drying step in bulk density measurement based on the water method. It can help to reduce human element variation in lab work. This will improve repeatability and reproducibility in bulk density measurement in the laboratory and between different laboratories. The extension of centrifuge usage for the infiltration of the grains replacing the vacuum or boiling method leads to significantly reduced times for the entire measurement. Intensive work is ongoing to qualify this new approach as the future standard within Almatis.

## REFERENCES

[1]   Lorenzoni, B. Bulk Density Determination of Granular Refractory Materials, RHI Magnesita Bulletion 74 (2020), 74-76

[2]   DIN EN 993-18 - 2002 Methods of test for dense shaped refractory products - Part 18: Determination of bulk density of granular materials by the water method with vacuum

[3]   ASTM C357-07  Standard test method for bulk density of granular refractory materials

[4]   ISO 8840:2021 Refractory materials – Determination of bulk density of granular materials (grain density)

# THERMAL CONDUCTIVITY: A MODIFIED HIGH TEMPERATURE PANEL METHOD TO SPEED UP MEASURES FOR LIGHTWEIGHT AND DENSE REFRACTORY MATERIALS

S. Cappuzzo, S. Sanchetti.
Stazione Sperimentale del Vetro S.c.p.A, Venice, Italy.

L. Folco, A. Tomc.
Seven Refractories d.o.o., Divaca, Slovenia

J. Laing
Delta Thermal Systems, Liverpool, UK.

## ABSTRACT

There are many direct and indirect ways to measure thermal conductivity, a property that is becoming increasingly essential for energy-efficient projects. While some indirect methods can speed up measurement times, only real direct methods, such as the one defined by ASTM C201, are adequate to measure the real heat transfer in refractory linings. A new test method has been developed by SSV in collaboration with DTS: said method allows to significantly reduce analysis time and costs compared to ASTM panel ones, while still relying on direct method. Earlier results with the first version of this new method were found to be extremely comparable with results from ASTM C201 standard, within laboratory deviation. Such findings have been topic for scientific publications in 2022. A new version of SSV thermal conductivity has been developed, with capability of reaching higher temperatures. In this article, findings of these results on dense, insulating and castable materials, together with a deeper study on earlier results, will be discussed and compared with results obtained from standard ASTM C201 Thermal conductivity instrument.

## INTRODUCTION

Thermal conductivity is an essential property in refractory materials. Their ability to insulate or to conduct heat is, in many cases, their primary function. Thermal conductivity coefficient ($k$) determines the heat flow for a given temperature gradient, or inversely, determines the temperature gradient when a specific heat flow is given.

If heat can be defined as the energy required to raise the temperature of a standard substance, heat transfer is described as the flow of heat due to temperature differences and its subsequent distribution. The heat transfer occurs in three different modes – conduction, radiation and convection- and generally two or all three of these modes are simultaneously involved in every actual case[1].

For all high temperature heat enclosures, an accurate calculation for the refractory lining is essential to reach a high reliability, thermally efficient refractory lining. Although there are mathematic models that can predict $k$ by correlating it with some physical properties of the refractory, these fit poorly when combining more parameters simultaneously, giving as a consequence less accurate results[2].

Insulating refractories have a pore structure as a major component of its microstructure. The main mechanisms that govern the phenomena are radiation and solid conduction, as well as pore convection if the pores' diameter is considerable. As radiation increases as the fourth power of the absolute temperature, the higher the overall temperature is, the more significant the heat transfer by radiation becomes. This is particularly important over 800°C with highly porous insulation [3]. Additionally, the more heterogeneous the refractory is, the more complex the interaction between true conductivity (by conduction) and apparent conductivity (by radiation) within the internal pores and the grains[4] [5] will be.

**Most diffused test methods for refractories**

Thermal conductivity measurements based on Fourier's law are determined by temperature gradients and heat flow. These methods can be based in steady or dynamic-state measurements, as we will briefly describe and compare in this study.

Suitable for isotropic homogeneous ceramics, the Laser Flash Method [6] is a quick and practical measurement for the characterization of technical ceramics, with good repeatability and accuracy. The method consists of rapidly heating the front side of a sample surface with a short laser pulse and to measure the time evolution of the back surface temperature variation using an infrared detector. The major downside of this technique is that it is not suitable to test most common refractory types, as typical heterogeneities of refractories brings discrepancies in the results: the small dimension of the test specimen (a few cubed millimeters) are not in-line with the refractories internal structure, and highly porous materials such as ultra-lightweight or ceramic-fiber refractories renders the measure impossible due to major laser's scattering [7]. Lastly, the measuring equipment can be very expensive.

Hot-wire method, defined in the ASTM Standard C1113 [8] is considered adequate for most isotropic refractory materials, but is not suitable for anisotropic materials or materials with large pores, since the underlying assumptions behind the method does not take into account heat transfer by radiation[9] [10]. The hot-wire method uses a furnace to heat the sample to a specified temperature; embedded in the sample, an additional heating source (the hot-wire) is used to introduce a local controlled heat, and the temperature rise is recorded by a thermocouple embedded at a defined distance. This technique can be used to determine thermal conductivity in a broad range of temperatures and materials, though with the above stated limitations.

A steady-state method developed for the fiberglass Industry that can be applied to determine thermal conductivity is the ASTM C177's Guarded-Hot-Plate [11]. The apparatus is adequate to measure fiber mats and boards to up to 650°C [9], but is not suitable for thicknesses higher than 2". Besides, it requires certain level of expertise to operate, maintain or repair the apparatus [11] compared to other methodologies.

ASTM C201 water-calorimeter method [12] is based on the hot wall principle, simulating the exposure of insulating bricks to a hot environment and measuring thermal conductivity coefficient (k) using Fourier's equation (1) [13] that establishes that thermal conductivity coefficient (k) is equal to the heat flow (Q) by a given thickness (x) per unit of area (A) and temperature gradient (ΔT).

773

$$k = \frac{Q \cdot x}{A \cdot \Delta T} \quad (1)$$

It is an accurate method to determine thermal conductivity of dense, insulating and castables materials, of ceramic fiber boards and mats[7], but it has the disadvantage of the long duration of the test itself: not only for being a steady-state method, but also because of the practical difficulty to stabilize the water calorimeter. The apparatus consists in a furnace that heats one face of the sample, distributing the heat uniformly with a SiC plate diffusor, and a calorimeter on the opposite side of the test specimen. The temperature on the hot face and the cold face is measured, the thickness of the specimen is registered, and the heat flux is determined by measuring the temperature rise in the water and its flow.

The main disadvantage of the ASTM 201's apparatus is operational: to obtain a trustable value of thermal conductivity is necessary to perfectly balance the main and secondary fluxes of water passing through the calorimeter circuit to assure temperature homogeneity all over the plane. A minor fluctuation leads to changes in the measurement of the heat flux and the analysis loses accuracy. For this reason, a new model was developed eliminating the necessity of a water calorimeter altogether.

**Modification to ASTM C201 Method**

To address ASTM C201 limitations and improve the robustness of the thermal conductivity measurements, a variant of this direct method has been developed both for lower and higher temperatures. Similarly to ASTM C201, this method uses an electric furnace and a SiC plate to uniformly heat-up the hot-face of the test specimen. The temperature gradient is obtained and registered by means of a pair of thermocouples at the hot and the cold faces too.

This method relies on determining the heat flux by placing a black plate and calculating its heat transfer coefficient.
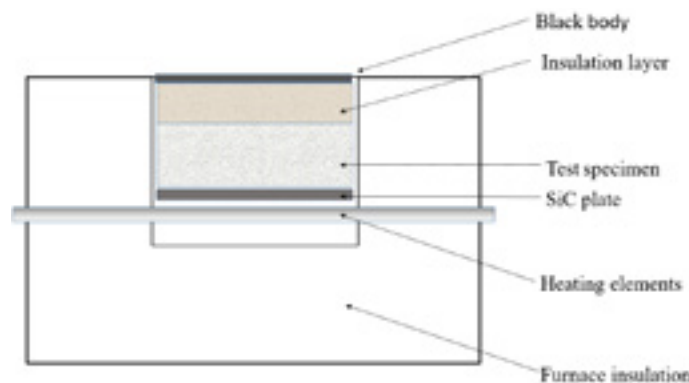


*Figure 1: Schematic design of the apparatus*

The heat transference between a horizontal black plate with its upper face exposed and air in a steady environment can be calculated by determining the amount of heat emitted by radiation and the heat by convection [14]–[16]. A back-up layer of insulating material is set between this plate and the test specimen to reach more convenient temperature gradients, allowing to work with reasonably low heat emissions. The test specimen is positioned on a Silicon Carbide refractory plate that transfers the heat of the furnace in a uniform way all over its contact area. Finally, sets of thermocouples are placed on both horizontal faces of the test specimen (the so called hot-face and cold-face), in the interface between the back-up layer and the black plate, and near the latter to register the air temperature.

All the temperatures are to be recorded once the system reaches its steady state at the desired temperature.

The higher temperature model differs from its counterpart of lower temperatures by employing thicker layers of insulating material around the heating chamber, to ensure the heat flux stays vertical. Verifications of the verticality of the heat flux have been performed by placing 2 thermocouples at a defined distance between 2 layers of refractory and checking the difference in temperature is not greater than 0,5°C.

**MEASURES**

For the purposes of this study and the validation of the developed method, a series of refractory materials with different bulk densities (*BD*) were prepared: two different monolithic refractories with BD from 2150 kg/m³ to 2300 kg/m³ after firing and three insulating firebricks (BD 412 kg/m³ to 825 kg/m³). The same samples had previously been sent to an accredited European laboratory for an inter-laboratory comparison. An additional test for castables was conducted in-house to evaluate the extended repeatability of the developed method: a sample composed by three test specimens of a monolithic refractory with a bulk density of 1100 kg/m³ was cast in the manufacturer's facilities, at Seven Refractories d.o.o. After curing and firing to 815°C, the specimens were tested for thermal conductivity and the variation between triplicates was analyzed.

**RESULTS AND DISCUSSIONS**

Firstly, the results of the set of three specimens with a BD equal to 1100kg/m³ was analyzed (fig. 2) to check for repeatability of the method. The tests have been conducted with the same isothermal conditions, same operator and same accessory instrumentation. The variance between tests was calculated giving as result a mean coefficient of variation of 2,10% with the maximum discrepancy at the lower isotherm of 225°C equal to 2,57%. This value enters within the range of variability given for the ASTM C201 apparatus in the international standard, validating the method.
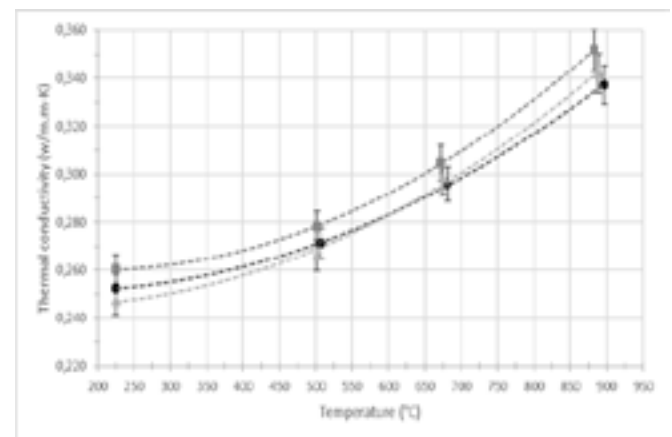


*Figure 2: In-lab thermal conductivity analyses of a castable monolithic refractory (BD = 1100 kg/m³) with the developed apparatus. Three test specimens of the same sample tested separately to determine the repeatability of the method with this kind of matrix. Reported temperatures are mean of sample.*

Secondly, the method was checked to be comparable to the results obtained from the third-party laboratory using ASTM C201 testing methods. In absence of an experimental calculation of variance for the reference laboratory's data, a coefficient of variation within laboratories of 3.4% reported in the standard method has been used to establish the error bars of the series. For the series of data produced with the apparatuses, a coefficient of variation of 2.4% has been

determined by repeating eight times a measure using an internal standard.

The adherence to the results produced by the 2 apparatuses was thus tested against the ones made according to the material specific ASTM norms based on ASTM C201. Considering the variance reported in the ASTM C201 standard, expressed as coefficients of variations of 9.0% and a precision of 26.6% between laboratories [12], there is an acceptable correlation for all the three different insulating firebricks studied (Figure 3).
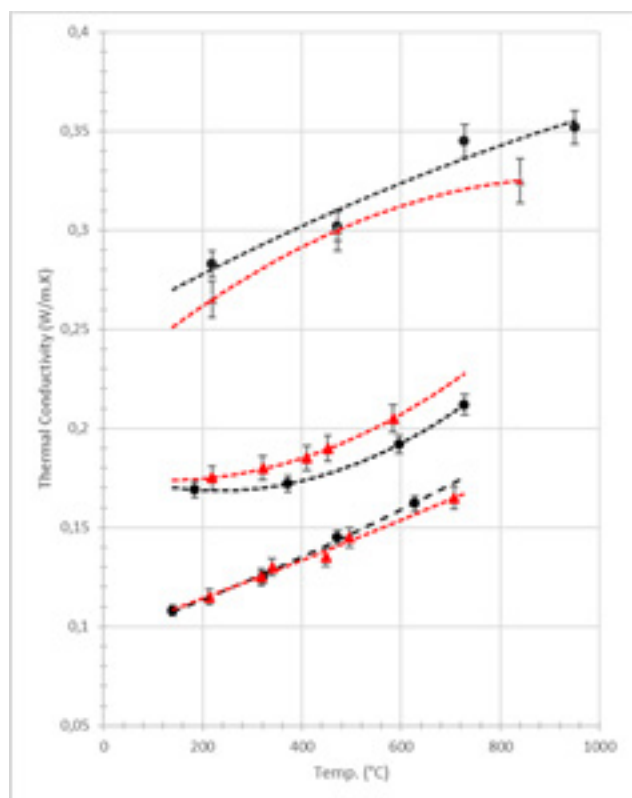


*Figure 3: Inter-laboratory thermal conductivity analyses of three insulating firebricks: the developed apparatus (black series) compared to the standard ASTM C201 apparatus of an external laboratory (red series). Reported temperatures are mean of sample.*

For the case of the monolithic castables analyzed between laboratories, bigger discrepancies were generally found regarding the dispersion of the thermal conductivity value as a function of temperature, and the correlation between both methods used. The results obtained for the first of the two test specimens (BD = 2280 kg/m$^3$) are well aligned between both labs and follow a good correlation respect to their tendency line (see fig. 4). Even though the trend is to increase the k proportionally with the increase of temperature, it is expected to start decreasing gradually with the higher temperature ranges as the curve begins to show.

This phenomena is due that for dense refractories heat transportation is attributed to phonon conduction (lattice vibration waves) and since the scattering of this lattice vibrations increases with temperature, the thermal conductivity coefficient lowers [2].
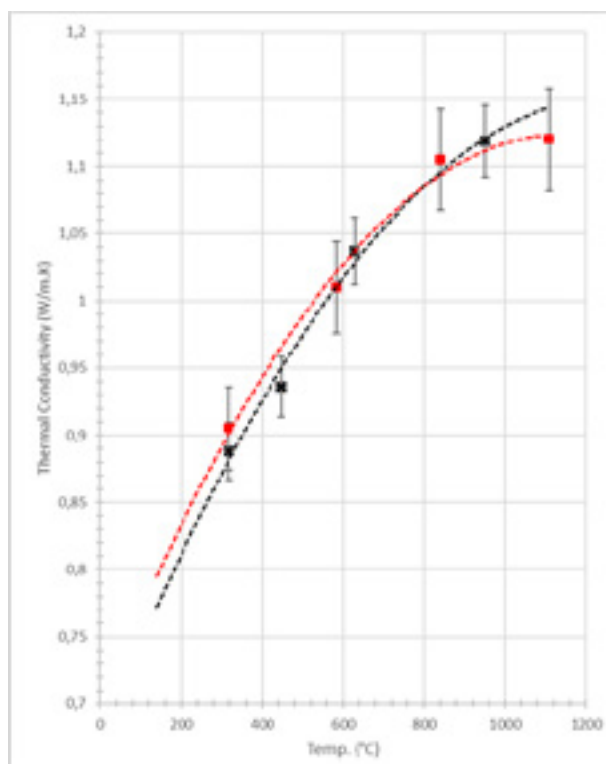


*Figure 4: Inter-laboratory thermal conductivity analyses of a castable monolithic refractory (BD = 2280 kg/m$^3$): the evaluated apparatus (black series) compared to the standard ASTM C201 apparatus of an external laboratory (red series). Reported temperatures are mean of sample.*

An extensive number of tests was finally performed on a range of products with Bulk Densities ranging from 0,71 g/cm$^3$ to 3,02 g/cm$^3$ (fig. 5) at temperatures up to 1200°C. Different behaviors were observed, as different refractory types were tested, but a general increase in conductivity with Bulk Density and a correlation with chemical composition were found as expected.

775
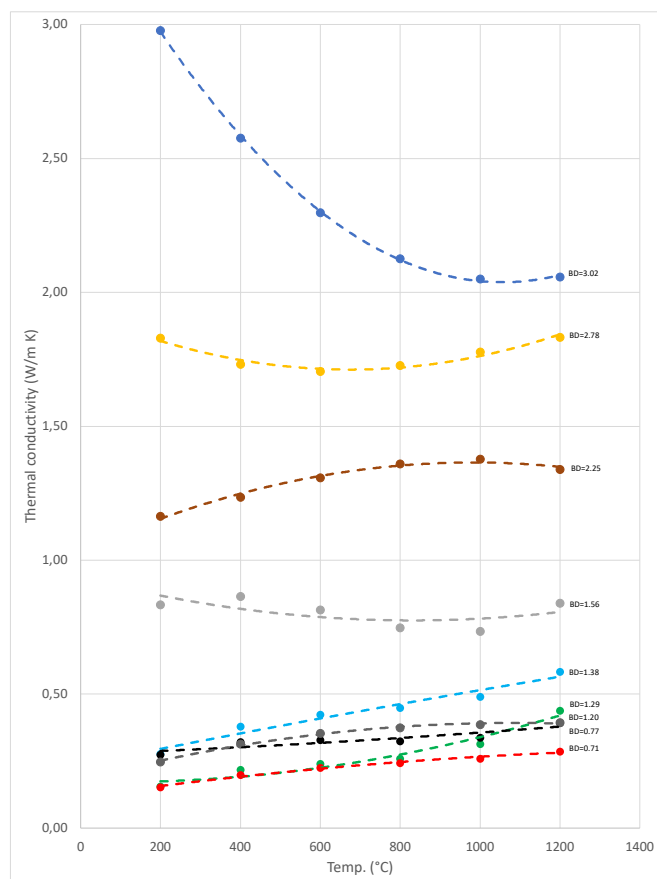
*Figure 5: Conductivity curves of refractories with different Bulk Densities. Reported temperatures are mean of sample.*

776

## CONCLUSIONS

The main methods available to measure thermal conductivity of different refractory materials have been compared highlighting their strengths and disadvantages. Based on this, ASTM C201 water-calorimeter method was taken as a reference, analyzing its operative bottlenecks and weaknesses. A variant of the water-calorimeter method has been developed successfully obtaining the heat flux of the system by means of a black plate with known radiation emissivity and thermocouples to determine the temperature gradients. A series of materials with different BDs and chemical compositions were analyzed to compare the obtained thermal conductivity values with reference values from ASTM C201 standard apparatus.

With this new method, thermal conductivity could be measured in a broad range of densities, compositions and thermal conductivities, reaching an accuracy that suits within the repeatability and reproducibility given by the ASTM C201 reference standard [12]. The second apparatus, able to reach temperatures of 1450°C in the hot face, was successfully produced and tested and allowed to measure conductivities at higher mean temperatures.

## REFERENCES

[1]     W. D. KINGERY and M. C. McQUARRIE, "Thermal Conductivity: I, Concepts of Measurement and Factors Affecting Thermal Conductivity of Ceramic Materials," *J. Am. Ceram. Soc.*, vol. 37, no. 2, pp. 67–72, 1954, doi: 10.1111/j.1551-2916.1954.tb20100.x.

[2]     M. M. Akiyoshi, A. L. Christoforo, A. P. Luz, and V. C.

Pandolfelli, "Thermal conductivity modelling based on physical and chemical properties of refractories," *Ceram. Int.*, vol. 43, no. 6, pp. 4731–4745, 2017, doi: 10.1016/j.ceramint.2016.11.091.

[3]     K. Daryabeigi, G. R. Cunnington, and J. R. Knutson, "Combined heat transfer in high-porosity high-temperature fibrous insulation: Theory and experimental validation," *J. Thermophys. Heat Transf.*, vol. 25, no. 4, pp. 536–546, 2011, doi: 10.2514/1.T3616.

[4]     H. W. Russell, "Principles of Heat Flow in Porous Insulators," *J. Am. Ceram. Soc.*, vol. 18, no. 1–12, pp. 1–5, 1935, doi: 10.1111/j.1151-2916.1935.tb19340.x.

[5]     W. E. Lee, W. Vieira, S. Zhang, K. Ghanbari Ahari, H. Sarpoolaky, and C. Parr, "Castable refractory concretes," *Int. Mater. Rev.*, vol. 46, no. 3, pp. 145–167, 2001, doi: 10.1179/095066001101528439.

[6]     A. International, "ASTM E1461-13 (2022): Standard Test Method for Thermal Diffusivity by the Flash Method." 2022.

[7]     F. Modarresifar, P. A. Bingham, and G. A. Jubb, "Thermal conductivity of refractory glass fibres: A study of materials, standards and test methods," *J. Therm. Anal. Calorim.*, vol. 125, no. 1, pp. 35–44, 2016, doi: 10.1007/s10973-016-5367-0.

[8]     A. International, "ASTM C1113-09(2019): Standard Test Method for Thermal Conductivity of Refractories by Hot Wire (Platinum Resistance Thermometer Technique)." .

[9]     T. Viverito, "Comparison of Thermal Conductivity Test Methods," *Morgan Therm. Ceram. 2016 Fall Refin. Equip. Stand. Meet. Proj. Gr.*, 2016.

[10]    D. Vitiello *et al.*, "Thermal conductivity of insulating refractory materials: Comparison of steady-state and transient measurement methods," *Open Ceram.*, vol. 6, no. May, p. 100118, 2021, doi: 10.1016/j.oceram.2021.100118.

[11]    A. International, "ASTM C177-19: Standard Test Method for Steady-State Heat Flux Measurements and Thermal Transmission Properties by Means of the Guarded-Hot-Plate Apparatus." 2019.

[12]    A. International, "ASTM C201-93 (2019): Standard Test Method for Thermal Conductivity of Refractories." .

[13]    J. B. J. Fourier, *The Analytical Theory of Heat*, 2009th ed., vol. 15, no. 2. New York: Cambridge University Press, 1877.

[14]    R. D. Cess, "The interaction of thermal radiation with free convection heat transfer," *Int. J. Heat Mass Transf.*, vol. 9:11, pp. 1269–1277, 1966.

[15]    C. E. Mendenhall and W. E. Forsythe, "High Temperature Measurements With the Stefan Boltzman Law," *Dep. Physics, Univ. Winsconsin*, no. 4, pp. 63–70, 1914.

[16]    M. Kaviany and A. M. Kanury, "Principles of Heat Transfer," *Appl. Mech. Rev.*, vol. 55, no. 5, pp. B100–B102, Sep. 2002, doi: 10.1115/1.1497490.

# CHARACTERIZATION OF INCLUSION POPULATIONS IN METAL MATRIX USING AUTOMATED FEATURE ANALYSIS

Florian Kerber, Marc Neumann, Jana Hubálková, Gert Schmidt, Christos G. Aneziris,
TU Bergakademie Freiberg, Institute of Ceramics, Refractories and Composite Materials, Freiberg, Germany

Thomas Schemmel, Volker Stein, Helge Jansen,
Refratechnik Steel GmbH, Research and Development, Düsseldorf, Germany

## ABSTRACT

Since decades the presence of non-metallic inclusions within steel products is of high interest. Because of their detrimental impact on the processing technologies and the properties of fabricated metallic components, their population has to be under complete control. Therefore, suitable characterization methods for non-metallic inclusions are indispensable. One of them, presented in this work, is automated feature analysis, which automatically determines non-metallic inclusions based on grayscale differences. However, to achieve the greatest possible benefit from this method, proper data evaluation and interpretation of the obtained raw data is required. The paper introduces the key principles of evaluating AFA data, emphasizing its capabilities and constraints by utilizing four large datasets obtained from solidified steel blocks, each containing a minimum of 4000 features.

## INTRODUCTION

Current research still aims to improve the steel quality with regard to non-metallic inclusions (NMIs) as they drastically reduce the properties of the final metallic components. Contamination of the steel melt must be avoided, especially in the steel ingot casting process, where the focus is on steel quality rather than production quantity [1]. Therefore, there is in ongoing demand for improving the refractory lining materials used in such applications [2,3]. Recently, a newly developed refractory material based on rice husk ashes functionalized by a flame-sprayed alumina coating was presented potentially used in the steel ingot casting process [4]. However, its influence on the steel quality needs to be evaluated. In the end, it is usually the mechanical properties of the produced metallic components that are of highest interest. However, characterizing such properties is time-consuming and expensive. A simplified approach is therefore the indirect evaluation of the steel quality taking the NMIs into account.

NMIs are commonly analyzed via image analysis on polished samples extracted from the melt or from solidified components [5]. The impact of NMIs on steel properties is closely related to their specific characteristics, including size, chemical composition, hardness, and morphology. Therefore, a comprehensive characterization of the NMI population supported by an appropriate statistical tool is essential.

Automated feature analysis (AFA), a threshold-based method for identifying NMIs in a continuous matrix, is a suitable approach that meets such requirements. The method utilizes an automated scanning electron microscope equipped with energy-dispersive X-ray spectroscopy (EDS) and detects areas of interest, called features, by their contrast to the matrix in BSE micrographs (Fig. 1a). Therefore, the AFA method is applicable to any material system that provides a continuous matrix with a sufficiently high contrast to the features of interest in the BSE contrast. The output of the AFA is a large dataset including positional parameters, elemental composition, size, and shape of each feature. However, in order to draw meaningful conclusions, the following issues must be considered during the analysis.

AFA detected features within a steel matrix inherently contain a certain amount of Fe. For example, pure alumina inclusions detected in a steel matrix appear to contain Fe, see Fig 1c. This issue is based on interactions of the electron beam during EDS analysis with the volume of the surrounding matrix. The Fe content increases with decreasing feature area as the perimeter to volume ratio of the feature increases. Consequently, the fraction of the adjacent matrix volume

of a feature interacting with the electron beam increases. As a result, the alumina inclusions appear with different elemental composition, which not only correspond to reality and must be taken into account when interpreting the data. In addition, AFA unintentionally also detects non-relevant features (artifacts) caused by pores or scratches, resulting in dust accumulation and/or a corroded surface. It is crucial to address such artifacts adequately in order to obtain accurate results. Subsequently, the absolute number of an inclusion total population already gives an indication of the steel cleanliness. However, not all NMIs are equally detrimental to the steel properties, making their species also relevant. Studying different inclusion species in an inclusion total population requires a clustering of the features based on their elemental composition

The paper introduces the fundamental concepts of assessing AFA raw data while emphasizing its potential and limitations. To demonstrate the practical application of AFA, the paper utilizes four extensive datasets acquired from solidified steel blocks resulting from immersion experiments conducted with various refractory materials.
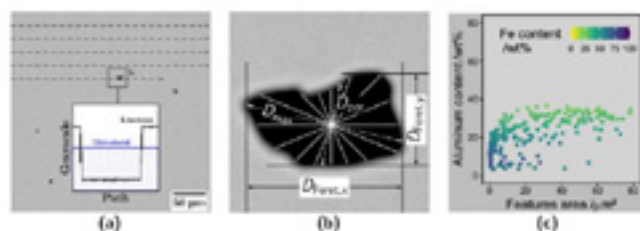


*Figure 1. Detection of non-metallic inclusions (dark areas) in a steel matrix (gray areas) via AFA; search mode (a), feature characterization (b), results (c) [6].*

## EXPERIMENTAL

Automated feature analysis (AFA) was conducted using a scanning electron microscope equipped with energy dispersive X-ray spectroscopy (ASPEX PSEM eXpress, FEI, USA) to analyze four polished steel samples, resulting in four separate datasets. Specifically, two datasets were acquired from immersion tests involving composite materials comprising rice husk ash and a flame-sprayed alumina coating (datasets D1 and D2), while the other two datasets (D3 and D4) originated from immersion tests with different MgO-C refractory materials.

## CONCLUSIONS

Automated feature analysis is a highly effective tool for analyzing inclusions and assessing the cleanliness of metals. This study demonstrated the practical application of automated feature analysis using four extensive datasets, which provided essential principles for data evaluation. The analysis of these datasets focused on identifying characteristic inclusion species and quantifying their presence.

The fundamental approach for data analysis can be summarized as follows:

- Removal of non-relevant features such as scratches, pores, and dirt/dust.
- Composition normalization based on the elements of interest.
- Classification of relevant features using appropriate rulefiles based on their chemistry.

777

To cluster inclusions, scatter plots of the elements of interest can be employed to identify distinct gaps in the data. The process of defining proper conditions is iterative process includes the following steps:

- Defining conditions based on distinct gaps between data points.
- Conducting an inclusion classification.
- Evaluating the proper assignment of features through scatter plotting.

Furthermore, each rulefile must include an "Others" class to account for features that do not meet the criteria of any the defined classes. The proportion of inclusions assigned to the "Others" class relative to the total number of inclusions serves as a measure of the rulefile's suitability for the underlying data, and it should ideally be minimized.

In general, a rulefile can accommodate an unlimited number of classes with varying complexity. Allocating inclusions into more specific classes allows for a more detailed description of the inclusion population in terms of their species. However, for an overview analysis, a simplified rulefile may suffice. The level of detail required in the rulefile depends on the analysis purpose and the variation in the total populations of inclusions being compared. Therefore, the development of the rulefile and the definition of conditions should always be done in conjunction with the responses, including scatter plots of assigned features, the proportion of features assigned to the "Others" class, and the results of the inclusion classification. Consequently, it is crucial to use the same rulefile for inclusion classification when comparing multiple datasets.

The application of automated feature analysis requires a sample with a continuous matrix and a significant contrast between the matrix and the features of interest. Therefore, AFA is not restricted to the analysis of inclusions in solidified metals but can be applied to any other material system that fulfills these requirements.

**REFERENCES**

[1] L. Zhang, B.G. Thomas, State of the art in the control of inclusions during steel ingot casting, Metallurgical and Materials Transactions B 37 (2006) 733–761.

[2] F. Kerber, P. Malczyk, V. Stein, T. Schemmel, H. Jansen, C.G. Aneziris, Influence of the MgO grade in MgO-C refractory material and steel melt temperature on the inclusion population in Al-treated steel, Int J Ceramic Engine & Sci 4 (2022) 102–111. https://doi.org/10.1002/ces2.10119.

[3] F. Kerber, T. Zienert, J. Hubálková, V. Stein, T. Schemmel, H. Jansen, C.G. Aneziris, Effect of MgO Grade in MgO–C Refractories on the Non-metallic Inclusion Population in Al-Treated Steel, steel research international 93 (2022) 2100482. https://doi.org/10.1002/srin.202100482.

[4] F. Kerber, M. Hollenbach, M. Neumann, T. Wetzig, T. Schemmel, H. Jansen, C.G. Aneziris, On the Statistics of Mechanical Failure in Flame-Sprayed Self-Supporting Components, Ceramics 6 (2023) 1050–1066. https://doi.org/10.3390/ceramics6020062.

[5] Y. Murakami, Metal Fatigue: Effects of Small Defects and Nonmetallic Inclusions, Elsevier, 2002.

[6] F. Kerber, M. Neumann, S. Dudczig, G. Schmidt, J. Hubálková, G. C. Aneziris, Automated feature analysis as a tool for non-metallic inclusion analysis in solidified metals, Submitted to *Open Ceramics*, Special issue: *Refractories for the Carbon Challenge*, 2023

# IMPROVING THE REFRACTORIES SELECTION REGARDING THEIR THERMAL SHOCK RESISTANCE (TSR) BY USING PRACTICE–ORIENTED INVESTIGATIONS PROMOTING EXPERIMENTAL THERMAL LOADING CLOSE TO THEIR SERVICE CONDITIONS

Erwan Brochen, Tim Waldstädt, Michael Kaminski and Christian Dannert

Forschungsgemeinschaft Feuerfest e. V. at the European Centre for Refractories, Höhr-Grenzhausen, Germany

**ABSTRACT**

In service, refractories undergo thermal shocks, which magnitudes and ranges of temperature depend on the processes in which they are being used. The suitability of refractory products to serve in a given process, and more especially their ability to sustain thermal shocks, is, however, still widely established by using standardised testing methods that hardly represent their actual service conditions. As a result, refractory products may be selected despite not being the best fit for a given application. A refractory product could perform well at medium temperatures, even when faced with thermal shocks of high magnitude, but fail at higher temperatures despite experiencing thermal shocks of smaller magnitude.

A new testing system for thermal shock resistance (TSR) was used to assess the response of different refractory products (high alumina, andalusite and fused silica bricks) to different thermal cycling conditions. Different temperature ranges (moderate or high temperatures), different magnitudes of thermal shocks and different thermal shock modalities (ascending/descending) were investigated. The resulting damaging was assessed using ultrasonic measurements. For the investigated refractory products, the damaging was found to be more severe for thermal cycling applied at high temperature (above 900 °C) than at moderate temperature (below 900°C) despite having the same magnitude ($\Delta T$ of at least 580 K). Additionally, the resistance to thermal shocks was found to be dependent of the applied testing conditions, and even reversed in different temperature ranges.

Practice-oriented investigations, promoting experimental thermal loading close to their service conditions, lead to more relevant claims about the TSR of refractory products and help achieving better predictions of the lifetime of refractory linings.

**INTRODUCTION**

Depending on the processes in which they are being used, refractory products encounter different thermal loading conditions. For instance, in refractory linings of tunnel kilns in the tableware industry temperatures rarely exceed 1350 °C and mild, steady heat flow conditions prevail, whereas in the steel industry, linings in process units must withstand severe temperature changes with temperatures exceeding 1700 °C. Consequently, the response of refractory products to these thermal loading conditions, and the corresponding thermal stresses, vary considerably. A specific material might exhibit satisfactory performance at moderate temperatures when experiencing substantial temperature differences, but the very same material could fail when exposed to higher temperatures, even with smaller temperature differences and comparable heat transfers. Conversely, another material might behave differently, performing better at higher temperatures than at a lower temperature range.

In this regard, assessing the thermal shock resistance of refractory products using the common standardized testing conditions may result in inaccurate conclusions regarding the selection of the most suitable refractory solution for a specific application. Hence, there is a definite requirement for a testing approach that adjusts to the varied thermal shock conditions encountered by refractory products during their service.

**DETERMINATION OF THE THERMAL SHOCK RESISTANCE OF REFRACTORY PRODUCTS**

By the very nature of their function, refractory products, which serve as linings in high-temperature vessels and furnaces, are exposed to more or less severe transient or steady-state thermal gradients. One side of a refractory lining faces high temperatures as it comes into direct contact with the process heat that needs to be contained within the system. The opposite side of the lining remains at much lower temperatures, so that heat losses are minimized and the immediate vicinity of the structure is being protected. However, the presence of such a thermal gradient within a massive solid body is not without consequences, as thermal stresses arise that pose a threat to the material's structural integrity.

While, depending on the application, thermally-induced damage (thermal spalling) may not always be the primary wear mechanism, refractory materials will almost inevitably suffer from the formation of cracks. However, modern well-designed refractory materials and linings exposed to thermal stresses typically do not experience catastrophic failure but instead undergo a gradual wear process, maintaining their structural stability despite significant damage. Even severely cracked refractory linings do not disintegrate into fragments. Yet, the presence of cracks is very likely to increase the susceptibility to other wear mechanisms (corrosion and erosion), and the determination of the resistance to thermal-induced damage is therefore of particular relevance for many refractory applications.

Unfortunately, when it comes to testing the thermal spalling resistance of refractory products, more commonly referred to as their thermal stress/shock resistance (TSR), there is no such thing as a "one-size-fits-all" method [1]. The performance of refractory products exposed to thermal stresses is not an intrinsic material property [2]. Instead, the thermal stress resistance of refractory products is influenced by various factors, most of them varying significantly with the application. In addition to the thermomechanical and thermal properties of the material (thermal expansion coefficient, thermal conductivity, modulus of elasticity, mechanical strength, and specific fracture energy), which are highly dependent on temperature, the geometry of the refractory components (including shape, presence of edges, and dimensions) and the specific thermal conditions (process temperature, heat transfer coefficient, thermal cycling or steady-state) play a significant role.

Typically, a set of narrowly specified testing conditions are applied to test refractory pieces of well-defined geometry to evaluate the TSR of refractory products. The most common standardised test methods are DIN 51068, EN 993-11 and ASTM-C-1171. All these standardised procedures describe quenching cycles between either 950 °C (DIN and EN) or 1200 °C (ASTM) and room temperature with water (DIN) or compressed air (EN and ASTM). Such test conditions are relatively straightforward to perform in the laboratory and efficient in inducing thermal stresses and damage to refractory materials, but they are not particularly consistent with actual service conditions of refractory products and can therefore lead to misleading conclusions. As a result, testing procedures that are more focused on the refractory's service conditions have been developed over the last decades. In particular, the melt immersion test, in which test pieces are at least partially immersed in a melt (e.g. pig iron, steel, aluminium), is particularly proficient to simulating the service conditions encountered in steel and metal manufacturing processes [3]. Open flame burners are sometimes used to reproduce the heating process in tunnel kilns, rotary kilns or glass melting furnaces as well as to mimic the pre-heating process of metallurgical vessels for the steel production, or simply as heat source to provide more efficient heat transfer into a test piece as compared to a cold test piece that is simply placed into a hot laboratory furnace [4-5]. More exotic testing procedures are occasionally reported, such as the use of a laboratory furnace with two chambers at different temperatures to perform hot temperature cycling [6-7], or the direct irradiation of test pieces by focusing artificial light or by an intensively radiating susceptor that is induc-

779

tively heated to incandescence, [8]. However, these procedures are time consuming and labour intensive. In order to advance the testing procedures, Forschungsgemeinschaft Feuerfest e. V. has developed a new, fully automated thermal shock testing system.

## PRACTICE-ORIENTED THERMAL SHOCK TESTING SYSTEM

### Description of the new thermal shock testing device

A crucial aspect of the new system is to enable thermal cycling at different ranges of temperatures for both ascending and descending thermal shocks. To achieve this, the testing system uses three chambers, through which a test piece (50 x 50 mm cylinder) is conveyed (Fig. 1). The middle chamber serves as a standby furnace with the ability to heat or cool the test piece to a predetermined temperature (Fig. 1 (b)). Ascending thermal shocks are achieved in the upper chamber by transporting the test piece into a carbon ring which is inductively heated to incandescence (chamber 2). The intensive radiation emitted by the carbon ring (susceptor) is particularly efficient to raise the surface temperature of the test piece inside the carbon ring quickly up to 1800 °C (Fig. 1 (a)). Descending thermal shock takes place in the lower chamber by gas quenching (Fig. 1 (c)). A lifting device carrying a tube made of alumina assures the transport of the test piece through the three chambers

that are stacked on top of each other. The system is continuously flushed with inert gas to protect the carbon ring in the chamber 2.

### Assessment of the thermally induced damage

During the thermal cycling, stresses of sufficient magnitude to damage the test piece are generated. The impact of the thermal shocks is assessed quantitatively by measuring the decrease of the ultrasonic velocity inside the test piece, which reflects the deterioration of the mechanical properties of the test piece after having undergone a specified number of thermal cycling. Finally, for a better insight, the thermal damage is quantified using the dimensionless damage parameter according to Kachanov [9]:

$$D = 1 - \left( \frac{v}{v_0} \right)^2 \qquad (1)$$

where v is the ultrasonic velocity as it propagates through the test piece after thermal cycling and $v_0$ is the initial ultrasonic velocity as it propagates through the undamaged test piece before thermal cycling. D = 0 means therefore no damage, while the value of D increases with increasing damage.
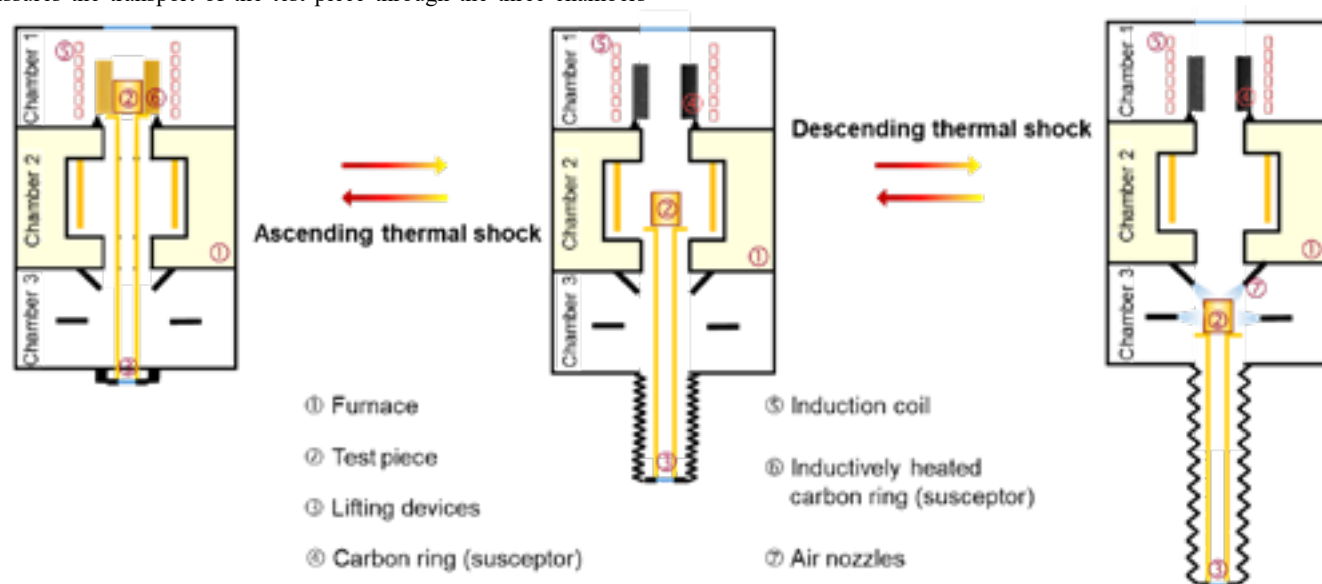


Fig. 1: Schematic representation of the new thermal shock testing system and the testing procedure. Preheating and tempering in the chamber 1 *(b, middle)*, ascending thermal shock through driving the test piece into an inductively heated carbon ring in the chamber 2 *(a, left)* or descending thermal shock by gas quenching in the chamber 3 *(c, right)*.

## TESTING STRATEGY

### Materials under investigation

Three refractory materials were investigated:

*High-Alumina bricks* with a content of $Al_2O_3$ above 99 % and ceramic bonded. Especially resistant to atmospheres containing CO and hydrogen up to very high temperature, they are typically used in the petrochemical and chemical industry (e.g. soot reactor).

*Fused Silica bricks* with a content of amorphous $SiO_2$ above 99 %. Because of their great resistance to acid environments, they are used in the chemical industry, as well as in the glass industry and as a hot repair material (for glass melters and coke oven plants).

*Andalusite bricks* with an $Al_2O_3$ content of 60 % and ceramic bonded. A versatile product presenting good resistance to creep, slag corrosion as well as to thermal shocks, and accordingly is a fitting solution for many applications in furnace engineering, iron and steel industry, waste incineration and glass melting furnace.

### Thermal shock procedure

Either 5 or 10 ascending or descending thermal shock cycles were applied to test pieces as described above. A dwell time of 30

minutes in the middle chamber (chamber 2) was implemented to ensure the temperature homogeneity of the test pieces. Since thermal stresses tend to quickly reach a maximum during thermal shocking, which roughly corresponds to the maximal temperature difference in the test piece i.e. before its core starts to heat up and the thermal gradient inside of the test pieces gradually flattens out, there is no need to reach temperature homogeneity after applying the thermal shocks. Accordingly, a shorter dwell time (15 minutes) was used in the upper and lower chambers (chambers 1 and 3).

To quantify the resulting damage, the ultrasonic velocity inside the test pieces was measured at room temperature by pulse technique of ultrasonic (C.S.I. Concrete Tester, Type RBT 2-A) before and after the thermal cycling.

## RESULTS AND DISCUSSION

On the whole and as expected, the damage increases with increasing temperature difference applied to the surface of the test pieces, i.e. increasing thermomechanical load. While small temperature differences (e.g. 380 K) cause little or no damage, large temperature differences (e.g. 880 K) almost systematically cause significant damage.

Tab. 1: Results from the TSR investigations with the new testing system on the test pieces made from high-alumina bricks.

| Test | Temperature / °C | | | ΔT / K | Number of thermal shock cycles | D / - |
|------|------------------|--------|-------|--------|--------------------------------|-------|
| | Lower chamber | Middle chamber | Upper chamber | | | |
| **1** | RT (~20 °C) | 900 | - | 880 | 10 | 0,24 |
| **2** | RT | 800 | - | 780 | 10 | 0,21 |
| **3** | RT | 600 | - | 580 | 10 | 0,04 |
| **4** | RT | 400 | - | 380 | 10 | 0,00 |
| **I** | | RT | 900 | 880 | 5 | 0,00 |
| **II** | | RT | 800 | 780 | 5 | 0,00 |
| **III** | | RT | 600 | 580 | 5 | 0,00 |
| **A** | - | 900 | 1280 | 380 | 5 | 0,09 |
| **B** | - | 900 | 1480 | 580 | 5 | 0,27 |
| **C** | - | 900 | 1680 | 780 | 5 | 0,33 |
| **C*** | - | 900 | 1680 | 780 | 5 | 0,30 |
| **A'** | - | 900 | 1280 | 380 | 10 | 0,13 |
| **B'** | - | 900 | 1480 | 580 | 10 | 0,34 |
| **C'** | - | 900 | 1680 | 780 | 10 | 0,44 |

*Duplicate to check the repeatability*
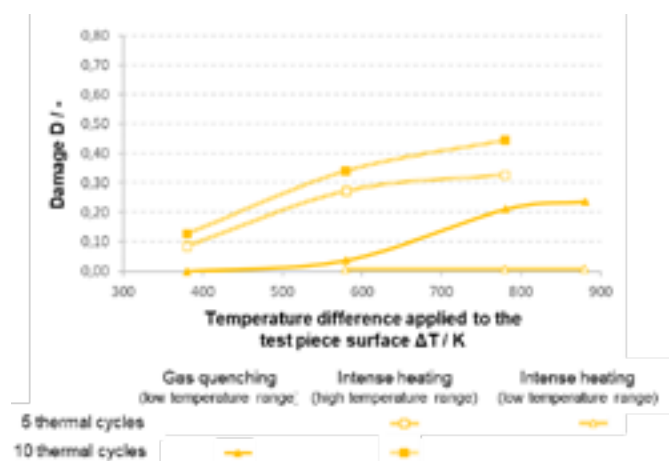


Fig. 2: Evolution of the damage for test pieces made from high-alumina bricks in function of the temperature difference applied to the surfaces of the test pieces for different testing conditions (low temperature range = below 900 °C, high temperature range = above 900 °C).

In the case of high-alumina bricks (Tab. 1 and Fig. 2), in the low temperature range (< 900 °C), gas quenching (descending thermal shocks) is more efficient to induce damage in the test pieces than intense heating with radiation (ascending thermal shocks). Quite surprisingly, no damage could even be detected as a result of ascending thermal shocks with intense radiation below 900 °C. Descending thermal shocks (quenching) on homogeneously heated test pieces promote more intense tensile stresses, to which refractory materials are notoriously more susceptible, while ascending thermal shocks promote initially more intense compressive stresses. Additionally, the applied gas quenching may lead to a more effective heat transfer than applying intense radiation.
However, in contrast, even a small applied temperature difference (380 K) resulted in significant damage during thermal cycling above 900 °C by means of intensive radiation. As expected, the extent of the damage increased with increasing applied temperature difference at the surface of the test pieces and with increasing the number of thermal cycles. Finally, significantly higher levels of damages due to thermal cycling were observed in the high temperature range than in the low temperature range, indicating a higher thermal shock sensitivity of the high-alumina bricks at high temperatures.

Tab. 2: Results from the TSR investigations with the new testing system on the test pieces made from andalusite bricks.

| Test | Temperature / °C | | | ΔT / K | D / - |
|------|------------------|--------|-------|--------|-------|
| | Lower chamber | Middle chamber | Upper chamber | | |
| **1** | RT (20 °C) | 900 | - | 880 | 0,13 |
| **2** | RT | 800 | - | 780 | 0,02 |
| **3** | RT | 600 | - | 580 | 0,03 |
| **4** | RT | 400 | - | 380 | 0,01 |
| **A** | - | 900 | 1280 | 380 | 0,18 |
| **B)** | - | 900 | 1480 | 580 | 0,53 |

*Number of thermal shock cycles: 5*

Tab. 3: Results from the TSR investigations with the new testing system on the test pieces made from fused silica bricks.

| Test | Temperature / °C | | | ΔT / K | D / - |
|------|------------------|--------|-------|--------|-------|
| | Lower chamber | Middle chamber | Upper chamber | | |
| **1** | RT (20 °C) | 900 | - | 880 | 0,00 |
| **2** | RT | 800 | - | 780 | 0,01 |
| **3** | RT | 600 | - | 580 | 0,00 |
| **4** | RT | 400 | - | 380 | 0,00 |
| **A** | - | 900 | 1280 | 380 | 0,05 |
| **B)** | - | 900 | 1480 | 580 | 0,76 |

*Number of thermal shock cycles: 5*
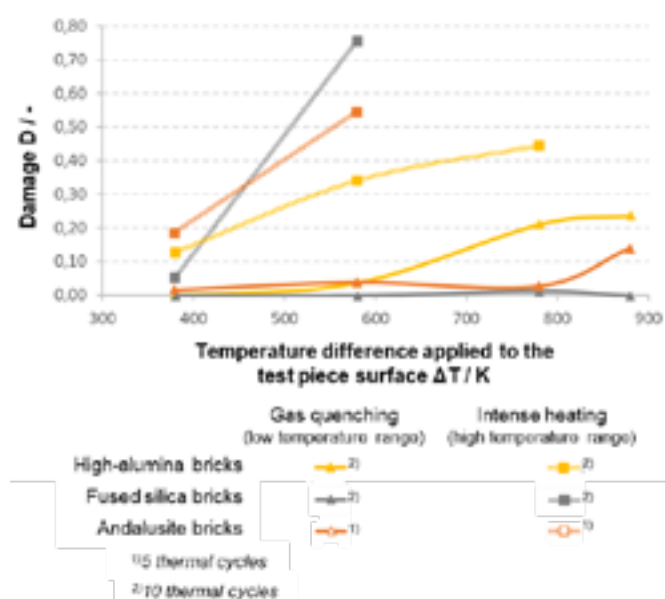


Fig. 3: Evolution of the damage for test pieces made from high-alumina bricks, fused silica bricks and andalusite bricks in function of the applied temperature difference to the surface of the test pieces for different testing conditions (low temperature range = below 900 °C, high temperature range = above 900 °C).

When comparing the three refractory materials, significant damage occurs as a result of gas quenching (i.e. low temperature range) for temperature differences applied to the test piece surface (ΔT) of 780 K and 880 K in the test pieces made from high-alumina bricks and andalusite bricks respectively. Test pieces made from fused silica bricks remained virtually undamaged by every gas quenching performed. Fused silica bricks are indeed well-known for their excellent thermal shock resistance up to approx. 1000 °C.
For ascending thermal shocks in the high temperature range (intense radiation heating), the previous classification is reversed, i.e. test pieces from fused silica bricks were already severely damaged

for a ΔT of 580 K (inhomogeneous transformation of quartz glass to cristobalite), andalusite bricks displayed slightly less damage and high-alumina suffered the least damage under these test conditions. Besides, these test conditions result in higher damage for all investigated materials compared to gas quenching in the low temperature range. This illustrates the great importance of TSR investigations that reflect the service conditions as much as possible to ensure a fair and application-oriented classification of the performance of refractory materials.

Visual inspection of the cut test pieces makes the extent of the damage even clearer. However, macrocracks could only be unequivocally detected in specimens whose dimensionless damage parameter D exceeded approximately 0,3 (Fig. 4). Furthermore, in materials such as andalusite bricks, which displays a network of cracks from the beginning (i.e. as a part of their microstructure), the increase and growth of the cracks is very difficult to assess visually. While helpful to gain an initial impression of the state of the test piece after thermomechanical loading, optical assessment does not allow an objective and quantitative assessment of the damage. However, the combination of optical inspection with ultrasonic measurements and calculation of the dimensionless damage parameter is particularly suitable for quantifying specific features and patterns resulting from thermomechanical loading.

## CONCLUSIONS

In service and depending of their application, refractory products are subjected to thermal stresses and shocks of different magnitudes, and in different ranges of temperatures. Their suitability to sustain thermal stresses for a specific application is usually assessed using standardized testing conditions regardless of their actual service conditions, thus increasing the likelihood of coming to erroneous conclusions, or at least, to a suboptimal solution. On the contrary, thermal shock experiments tailored to the service conditions applied to refractory products are needed to obtain relevant information about the performance of refractories in their intended applications.

Thanks to a three chambers testing system, descending (gas quenching) as well as ascending (fast irradiation heating) thermal shocks of different intensity can be applied automatically and repeatedly to refractory test pieces previously heated to a defined temperature. Hence the temperature changes triggered at the surface of a test piece are controlled and a tailored automatic investigation of refractory product's resistance to thermal shocks in the application relevant temperature range is being achieved.

For the investigated products (high alumina, andalusite and fused silica bricks), the damaging was found to be more severe for thermal cycling applied at high temperature (above 900 °C) than at moderate temperature (below 900 °C) despite having the same magnitude (ΔT of at least 580 K). Additionally, while test pieces made of fused silica bricks outperformed the two other materials during descending thermal shocks in the lower temperature range, the classification obtained was completely reversed for ascending thermal shocks at high temperature.

As a result, the suitability of a given refractory product and/or the selection of refractory products for a given application can be assessed with enhanced reliability and a better prediction of the lifetime of refractory linings is expected.

## ACKNOWLEDGEMENTS
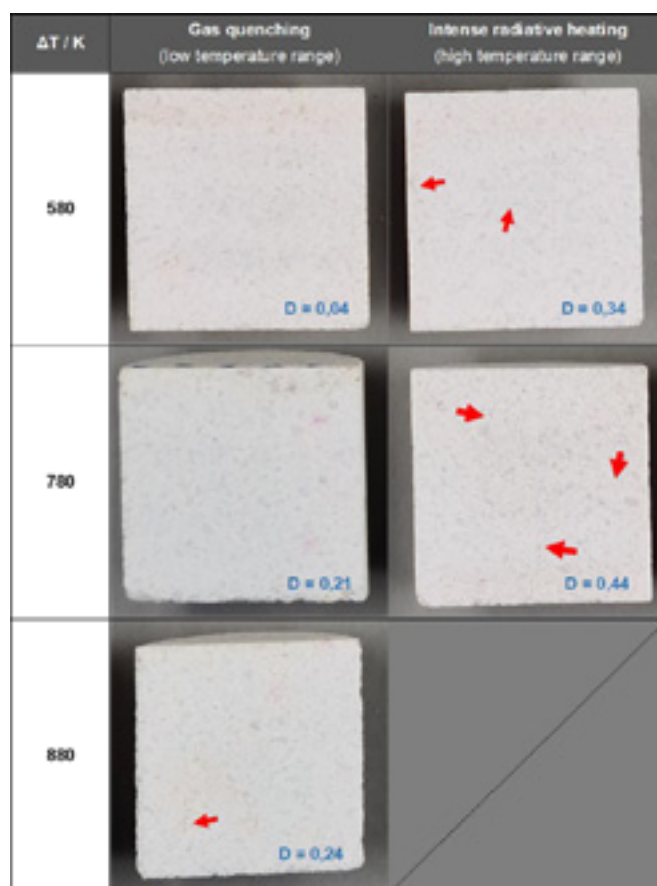
*Fig. 4: Cross-sections of test pieces made from high-alumina bricks for different combinations of testing conditions after 10 thermal cycles (visible cracks are marked with arrows).*

## REFERENCES

[1] Harada T. Thermal Shock Resistance Equipment, Taikabutsu. Overseas, 13(1), 1993, p. 44–51

[2] Brochen E, Pötschke J, Aneziris CG. Improved Thermal Stress Resistance Parameters Considering Temperature Gradients for Bricks in Refractory Linings. Int. J. Appl. Ceram. Technol. 11(2), 2014, p. 371-383

[3] Dienst W, Scholtz H, Zimmermann H. Thermal shock resistance of ceramic materials in melt immersion test. J. Eur. Ceram. Soc. 5(6), 1989, p. 365-370

[4] Elstner I, Jeschke P, Krönert W, Protogerakis E. Thermoschockverhalten feuerfester Baustoffe aus Zirkoniumdioxid, Teil III: Experimentelle Untersuchungen. Sprechsaal 115, 1982, p. 542-556

[5] Semler CE. Thermal shock testing of refractories – Revisited: Part II. Refractories Applications and News 13(2), 2008, p 18-24

[6] Quintela M, Melo T, Lage I, Rodrigues J, Pandolfelli VC. Thermal shock of carbon-containing refractories. Interceram / Refractman 52(1), 2003, p. 40-44

[7] Traon, N. Thermal shock resistance characterization of high alumina castable containing stabilized zirconia through Resonant Frequency Damping Analysis. Dissertation, RWTH Aachen, 2019

[8] Brochen E, Clasen S, Dahlem E, Dannert D. Determination of the Thermal Shock Resistance of Refractories. refractories Worldforum 8 (1), 2016, p. 79-85

[9] Kachanov LM. Introduction to Continuum Damage Mechanics. Mechanics of Elastic Stability. Dordrecht, Boston, Lancaster: Martinus Nijhoff Publishers, 1986

# THERMAL SHOCK RESISTANCE OF ALUMINA FOAM FILTERS – A COMPARATIVE STUDY

Celaida Gayle Gumban, Alexandros Charitos
Technische Universität Freiberg, Institute of Nonferrous Metallurgy and Purest Materials, Leipziger Str. 34, 09599 Freiberg, Germany
Jana Hubálková, Christos G. Aneziris, Claudia Voigt
Technische Universität Freiberg, Institute of Ceramics, Refractories and Composite Materials, Agricolastr. 17, 09599 Freiberg, Germany

## ABSTRACT

Among the many properties of ceramic foams used in metal melt filtration, thermal shock resistance is one of the most critical features. In contrast to dense refractory materials, there is no thermal shock resistance testing standard available for ceramic foam filters at the moment. This work aims to investigate the influence of the different test parameters such as temperature and quench medium when testing ceramic foam samples. Reference alumina ($Al_2O_3$) foams and commercially- available ceramic foam filters ($ZrO_2$, $Al_2O_3$-$ZrO_2$, $Al_2O_3$-P, and SiC) were subjected to thermal shock tests with water and air as quenching medium. The thermal shock performance was evaluated by estimating the mechanical strength and elastic modulus before and after the thermal shock. The experimental results were compared with the calculated values using the Gibson and Ashby equation.

## INTRODUCTION

Thermal shock resistance is an important feature of ceramic foams used in metal melt filtration [1]. Although there are existing standards for testing the thermal shock resistance of refractories, i.e. DIN 51068:2008-11 (Determination of resistance to thermal shock - Water quenching method for refractory bricks) [2] and DIN EN 993-11: 2008-3 (Methods of test for dense shaped refractory products - Part 11 Determination of resistance to thermal shock) [3], there are none specific to ceramic foams for melt filtration applications. The typical porosity of ceramic foams ranges from 70- 90% [4] places it out of the standard´s scope [2]. In the first part of the study, the thermal shock tests were conducted on reference $Al_2O_3$ foam and bulk samples wherein the influences of the thermal shock parameters were investigated.

Aside from experimental thermal shock tests, the thermal shock behavior can also be estimated through the material properties by the calculation of the thermal shock resistance. Gibson and Ashby developed Equation (1) for the thermal shock resistance of ceramic foams [5].

$$R_{foam} = \Delta T = \frac{\sigma_{fs} \cdot (1 - \nu)}{E_S \cdot \alpha_S \cdot \rho_{rel}^{0.5}} \quad (1)$$

Where $R_{foam}$ is the thermal shock resistance of the foams, $\sigma_{fs}$ is the bending strength of the strut, $E_S$ is the elastic modulus of the strut, $\rho_{rel}$ is the relative density given by the ratio of the foam´s geometric density to its strut density, $\alpha_S$ is the thermal expansion coefficient of the struts, and $\nu$ is the Poisson ratio.

The second part of the study compares the calculated thermal shock resistance of the commercially available filters ($ZrO_2$, $Al_2O_3$-$ZrO_2$, $Al_2O_3$-P, and SiC) to the experimental data.

## MATERIALS AND METHODS

The samples used in the study is comprised of $Al_2O_3$, $ZrO_2$, $Al_2O_3$-$ZrO_2$, $Al_2O_3$-P, SiC foam and bulk samples. The $Al_2O_3$ samples served as reference for preliminary testing. $Al_2O_3$ foams (150 x 50 x 22 $mm^3$ and 50 x 50 x 22 $mm^3$) were prepared by means of the Schwartzwalder process [6] whereby polyurethane foams were coated two times with an $Al_2O_3$ slurry through a dip-spin coating procedure and sintered at 1600 °C [7]. The commercially-available foam filters (75 x 75 x 22 $mm^3$) were supplied by the industrial manufacturers.

Additionally, bulk samples (70 x 7 x 7 $mm^3$) were uniaxially pressed from the dried slurries which are used to produce the ceramic foams. The pressed $Al_2O_3$ samples were then sintered at 1600 °C while the pressed industrial filter materials followed a sintering procedure similar to that used for the industrial foams.

The bulk and foam samples were characterized with regard to their bulk density, foam relative density $\rho_{rel}$, and thermal expansion coefficient α. Whereas Equation (1) was used to determine the theoretical thermal shock resistance, the experimental values are taken from the results of the thermal shock tests and are characterized by residual mechanical properties.

For an evaluation of the thermal shock resistance, the elastic modulus, crushing strength, and bending strength were measured before and after the thermal shock. The residual values were calculated from the values measured at the as received ($P_{pre\ thermal\ shock}$) and thermal shocked samples ($P_{post\ thermal\ shock}$) with Equation (2) [3].

$$P_{residual} = \frac{P_{post\ thermal\ shock}}{P_{pre\ thermal\ shock}} \cdot 100\% \quad (2)$$

## RESULTS AND DISCUSSIONS

### Influence of the thermal shock parameter

Figure 1 illustrates the impact of the thermal shock test parameters on the residual elastic modulus and residual strengths of the different reference $Al_2O_3$ samples. The difference between the measured elastic modulus and strength of the pre-heated samples (preheated 950 °C air) and directly heated samples (950 °C air) is within the standard deviation so the difference is marginal. The only exception is the elastic modulus measured for the 50 x 50 x 22 $mm^3$ foams. The reason for this exception is not known at the moment.

The quench medium clearly has a more pronounced impact, with water-quenched samples showing a lower residual elastic modulus and strength compared to air. This indicates that the thermal shock in water was more severe, explainable by the better heat transfer of water compared to compressed air.

The difference in the elastic modulus and strength between the samples shocked from 950 °C and those shocked from 1200 °C to room temperature is less pronounced as it is within the standard deviation.
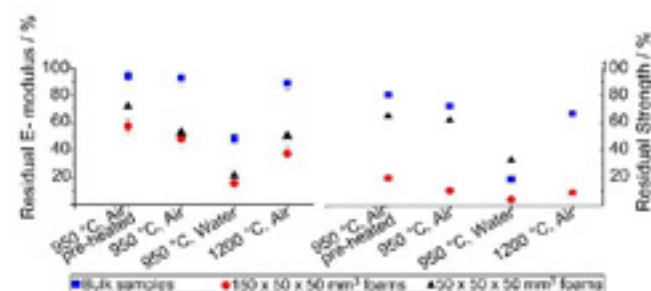


*Figure 1. Residual elastic modulus and strength of $Al_2O_3$ samples after thermal shock*

As the quench medium proved to be the parameter with the highest impact, the next part of the study utilizing industrial samples only had the quench medium as a variable.

### Thermal shock of industrial filter materials

For the industrial filter materials, the water quenching procedure resulted in lower values of elastic modulus (Figure 2) and strength (Figure 3) compared to the air quenching procedure indicating a more pronounced thermal shock when using water. Thermal shock through air-quenching only had a small impact as shown in the residual elastic moduli (Figure 2) of > 76 % for foams and > 93 % for bulk materials and residual strength (Figure 3) of > 80 % for

foams and >83 % for bulk samples. The reason for the small impact is the small size of the samples – the foam samples possess struts with a diameter of < 1 mm and the bulk samples of 70 x 7 x 7 mm³ causing a fast cooling of the whole volume and consequently only marginal stresses due to low temperature gradients.
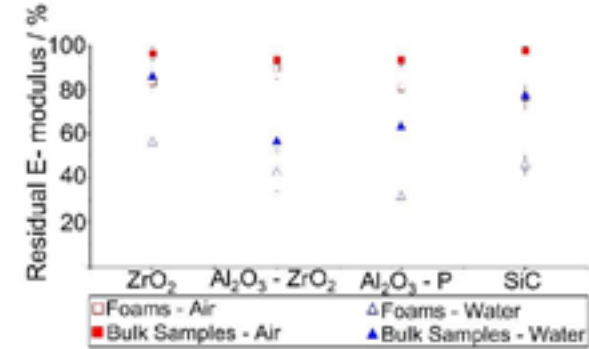


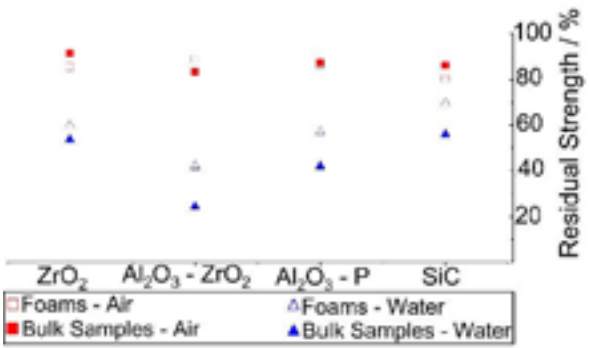*Figure 2. Residual elastic modulus of industrial foam and bulk samples*



*Figure 3. Residual strength of industrial foam and bulk samples*

In the next step, the ranking of the materials was assigned. As quenching with water is the most severe thermal shock, the results of this procedure were chosen.

An important question is if the chosen material should have a high strength after quenching or a high residual strength after quenching. The former means that with a high initial strength despite a major change, the strength after thermal shock is still sufficient, ensuring no failure of the sample. The latter represents a low level of damage. The rankings regarding crushing and residual strength can be found in Table 1. $ZrO_2$ ranks high in both cases, which is consistent with the fact that $ZrO_2$ filters are typically used for steel filtration with operating temperatures of up to 1650 °C. SiC also shows a high residual strength. Surprisingly, the crushing strength of SiC after quenching is the lowest even with its typical use in aluminum, copper and iron melt.

*Table 1. Ranking of measured and calculated thermal shock resistance of foams using different criteria.*

| Sample | Ranking of residual strength | Ranking of crushing strength | Thermal expansion coefficient of the struts $\alpha_S$ ($10^{-6}$ K$^{-1}$) | Thermal shock resistance $R_{foam}$ (K) |
|---|---|---|---|---|
| Al$_2$O$_3$ | 5 | 5 | 10.1 | 50 |
| ZrO$_2$ | 2 | 1 | 4.4 | 226 |
| Al$_2$O$_3$-ZrO$_2$- | 4 | 2 | 7.0 | 107 |
| Al$_2$O$_3$-P | 3 | 3 | 7.6 | 131 |
| SiC | 1 | 4 | 4.7 | 217 |

With Equation (1) [5] the thermal shock resistance (Table 1) was estimated. Due to the low thermal expansion coefficients, SiC (4.7 $10^{-6}$ K$^{-1}$) and $ZrO_2$ (4.8 $10^{-6}$ K$^{-1}$) possess the highest calculated thermal shock resistance $R_{foam}$. In contrast, the reference Al$_2$O$_3$ sample has a low-thermal shock resistance, $R_{foam}$ of 50 K due to a thermal expansion coefficient of 10.1 $10^{-6}$ K$^{-1}$. The thermal expansion coefficient is the decisive factor in Equation (1). Comparing the results of the calculated $R_{foam}$ and the residual crushing strength results in a coefficient of determination of $R^2$=0.84 which is not a very good correlation, but it shows a certain linking. Thermal expansion causes mechanical stresses during heating and cooling when temperature differences are present in the sample. As shown before, this is not necessarily the case for ceramic foams as the struts are very thin and the temperature increase and decrease proceed very fast.

## CONCLUSIONS

Among the hot thermal shock test parameters, heating mode, thermal shock temperature, and quench medium, the latter has the highest impact on the residual mechanical properties (thermal shock resistance). Due to the low thermal expansion coefficients of SiC (4.7 $10^{-6}$ K$^{-1}$) and $ZrO_2$ (4.8 $10^{-6}$ K$^{-1}$), the two materials possess the highest thermal shock resistance $R_{foam}$. The SiC and $ZrO_2$ foams also have the highest residual strength after quenching in water. $ZrO_2$ and SiC ranked the highest which is consistent with the fact they are typically used in high-temperature metal melt filtration.

## ACKNOWLEDGEMENT

## REFERENCES

[1] Brockmeyer, J., Aubrey, L., Application of Ceramic Foam Filters in Molten metal Filtration, in *Ceramic Engineering and Science Proceedings*, The American Ceramic Society, 2019, pp. 63-74.

[2] German Institute for Standardisation, *DIN 51068 ( Testing of ceramic raw materials-Determination of resistance to thermal shock - Water quenching method for refractory bricks,* 2008.

[3] German Institute for Standardisation, *DIN EN 993-11 (Methods of test for dense shaped refractory products - Part 11: Determination of resistance to thermal shock,* 2008.

[4] Adler, J., Standke, G. , Offenzellige Schaumkeramik Teil 1, *Keramische Zeitschrift* 55 (9), pp. 694-703, 2003.

[5] Gibson, L. J., Ashby, M.F., Cellular Solids: Structure and Properties, 2nd ed., Cambridge: University Press, 2010.

[6] Schwartzwalder, K., Somers, A. V., Method of Making Porous Ceramic Articles. USA Patent US3090094A, 21 05 1963.

[7] Voigt, C., Zienert, T., Schubert, P., Hubálková J., Aneziris, C., Reticulated Porous Foam Ceramics with Different Surface Chemistries, *Journal of the American Ceramic Society* 97 (7), pp. 2046-2053, 2014.

[8] Schneider, G., Thermal Shock Criteria for Ceramics, *Ceramics International* 17, pp. 325-333, 1991.

[9] Orenstein, R. M., Green, D. J., Thermal Shock Behavior of Open-Cell Ceramic Foams, *Journal of the American Ceramics Society* 75 (7), pp. 1899-1905, 1992.

[10] Grabenhorst, J. , Luchini, B. , Fruhstorfer, J. , Voigt, C. , Hubálková, J., Chen, J. , Li, N. , Yawei, L., Aneziris, C. G. , Influence of the Measurement Method and Sample Dimensions on the Young's Modulus of Open Porous Alumina Foam Structures, *Ceramics International* 45 (5), pp. 5987-5995, 2018.

# DEVELOPMENT OF A NOVEL THERMAL SHOCK PROTOCOL OF EXPERIMENT OF CARBON–BASED REFRACTORY MATERIALS

Kaoutar Anrhour[1]; Séverine Romero Baivier[2]; Andrea Piccolroaz[3]

[1]VESUVIUS/Trento university, Mons, Belgium; [2]Vesuvius group plc, Department of Advanced Refractories, Ghlin, Belgium; [3]University of Trento, Department of Civil, Environmental and Mechanical Engineering, Trento, Italy

Ladle shrouds, tundish nozzles, slide gates, and other flow control refractory materials play an important role in ensuring good production and quality of products in the continuous casting of steel; however, their chemical, mechanical, and thermal degradation and wear mechanism can lead in some cases to disastrous social, environmental, and financial effects in the steel-making plants. Therefore, it is both important and challenging to understand and characterize their behavior at a laboratory scale. This study aims to show the primary steps of investigating the thermal shock resistance of flow control products and mainly carbon-based ladle shroud mixes. The adopted approach for the novel testing protocol is to use induction as a heating source to produce an ascending thermal shock and assess the resultant damage. The preliminary results confirm the experimental protocol feasibility and ability to measure strain evolution and crack initiation as a function of time and temperature; furthermore, the microstructure of the tested specimens will be inspected to allow a better and complementary understanding of their behavior under thermal shock test.

# SHORT COMMUNICATIONS

# APPLICATION OF ULTRA–HIGH SPEED HEATING TEST SYSTEM – HIGH TEMPERATURE OBSERVATION OF SIC/FE/SLAG SYSTEMS –

Tomoyuki Maeda, Hatsuo Taira
Okayama Ceramics Research Foundation, Bizen, Okayama, Japan

Kazuya Nakabo
Shinagawa Refractories co., ltd., Bizen, Okayama, Japan

Seiji Ohashi, Norihito Mitani
Nissin Kikai co., ltd, Takamatsu, Kagawa, Japan

## ABSTRACT

Our group is developing a new test system called "Ultra-high speed heating test system". This apparatus is a hot observation system with the greatest feature of ultra-high-speed, ultra-high-temperature heating. Currently, we are examining various applications of this system as the multi-purpose evaluation system. As part of this work, we will report about the investigation of the wettability of refractories/metal/slag systems with this system.

Blast furnace slag formed the spherical liquid phase at 1450 °C on Fe powder. At 1550°C, Fe started to melt and the temperature decreased for the endotherm reaction. Molten Fe moved on slag until the end of the test. On the other hand, the spherical liquid phase slag wetted with the SiC brick and spread.

As a result of observed the three phase interface of brick/Fe/slag, it was found that iron reacted with SiC grains to decompose the brick, and Slag reacted with the liquid phase in the brick to penetrate the brick. From the above results, the developed new test system may be able to visualize Marangoni convection.

## INTRODUCTION

Fig.1 show the photograph of newly developed testing system called "Ultra-high speed heating test system". This system was primarily to focus on the observations at high temperature and to be operational at ultra–high temperatures and ultra–high speeds of heating[1-3]. For this purpose, the system employed a distinctive heating method in which the specimens are placed on the carbon heater directly. In addition, this test system was equipped with four observation windows so that temperature measurement and state changes of sample could be observed from various angles. In this study, the wettability of SiC bricks/Fe/blast furnace slag system was observed with this test system.

## EXPERIMENTS

Fig.2 show the schematic diagram of test method. □15×t2mm of SiC bricks (table 1) set on bottom carbon heater. Reagent-grade electrolytic iron powder (purity of >99.99%) set on the brick, and blast furnace slag powder (table 1) set on the iron. The volume ratio



*Fig.1 the photograph of newly developed testing system.*
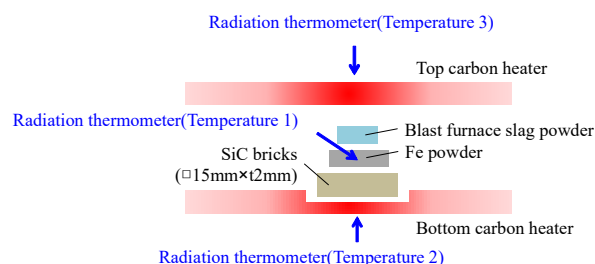


*Fig.2 Schematic diagram of test method.*

*Tab. 1 : Chemical compositions of SiC bricks and Blust furnace slag.*

|  | SiC brick | Blast furnace slag |
|---|---|---|
| SiC | 80.3 |  |
| $SiO_2$ | 16.5 | 34.7 |
| $Al_2O_3$ | 2.49 | 14.2 |
| CaO | 0.07 | 45.0 |
| MgO | 0.06 | 2.8 |
| $TiO_2$ | 0.11 | 0.66 |
| T.Fe | 0.52 | 0.13 |
| S |  | 1.09 |
| Other |  | 0.83 |

Mass%
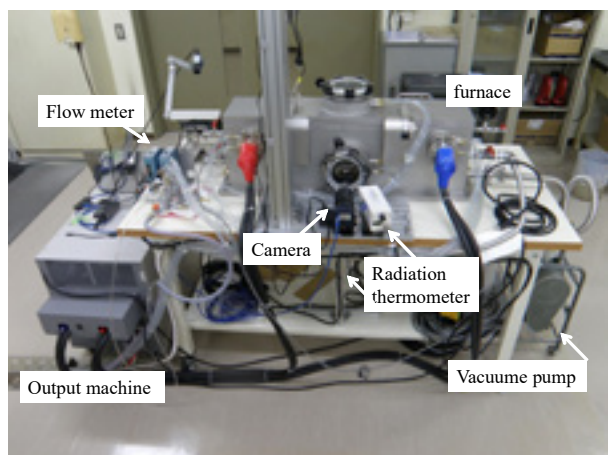
of iron and blast furnace slag were 1:9-9:1. The samples were heated to 1600°C at a rate of 500°C/min for 30s in Ar using top and bottom carbon heaters. The Temperatures were measured at the 3point of Fe powder area (temperature 1), bottom heater (temperature 2) and top heater (temperature 3) during test. In addition, the state change of samples were photographed from the side throughout with a digital camera.

After heating, the center of the test samples were cut and embedded in epoxy resin. After mirror polishing, the cross sections were observed by SEM-EDS.

## RESULTS AND DISCUSSION

Fig.3 show the photographs of the SiC brick/30vol%-Fe/70vol%-blast furnace slag system at various test temperature. The slag deformed by the formation of liquid phase from 1250°C formed spherical at 1450°C on the Fe powder. Spherical slag on Fe powder indicates poor wetting of both. At 1550°C, Fe started to melt and

the temperature decreased for the endotherm reaction. Molten Fe moved on slag until the end of the test. On the other hand, the spherical liquid phase slag wetted with the SiC brick and spread. This behavior suggests that the wettability between slag and brick is better than that between Fe and brick. And, Although the true density of slag is lower than that of Fe, Fe floats on the slag. We reaffirmed that the repulsive force (interaction force) due to the poor wetting is greater energy than imagined energy.

Fig.4 show the microstructure of tested sample. At the three phase interface, the disintegration of the brick structure and the decomposition of SiC grains were observed. In the EDS analysis(Fig.5), Al, Si and Ca were detected in the disintegrated part, and Fe and Si were detected in the decomposed part. From these results, it is seemed that the disintegration of the brick structure was caused by slag penetration through the sintering additive (liquid phase), and that the decomposition of SiC grains was caused by Fe erosion. This phenomenon is similar to the Marangoni convection, and it is thought that the visualization of the Marangoni convection is possible with this test system.
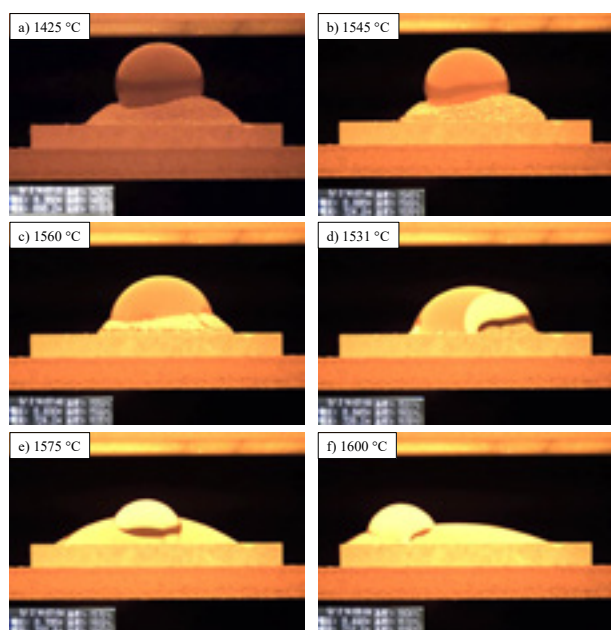


*Fig.3 Photographs of the sample at various test temperature.*
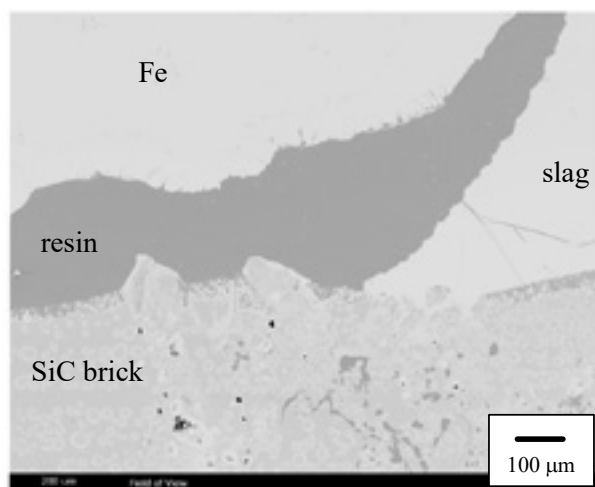


*Fig.4 microstructure of tested sample.*
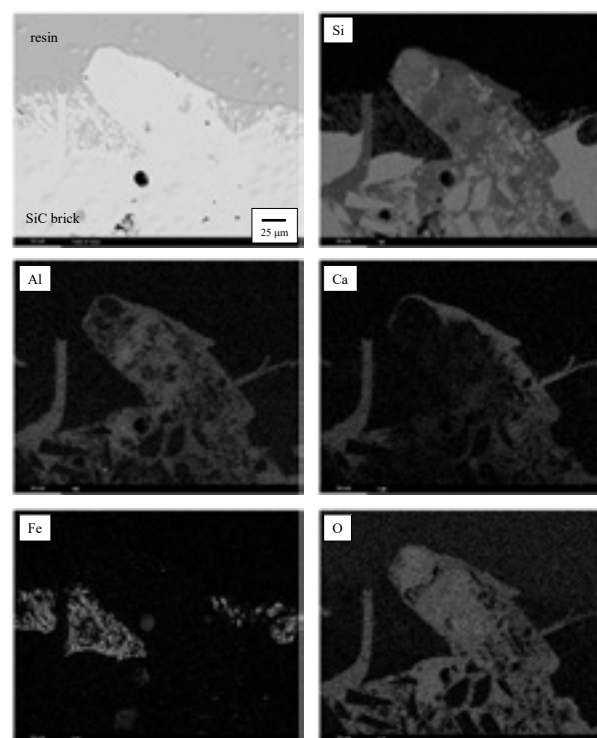


*Fig.5 Element mapping images of tested sample.*

## CONCLUSIONS

Our group is developing a new test system called "Ultra-high speed heating test system". From the investigation of the wettability of refractories/metal/slag systems with this system, the developed new test system may be able to visualize Marangoni convection.

## REFERENCES

[1]    K. Nakabo, T. Maeda, H. Taira, S. Ohashi, N. Mitani: Application of Ultra–High Speed Heating Test System (1) — Observation of thermal behavior, Proc. of 9th Symposium on Refractories for Iron and Steel, TARJ (2021).

[2]    T. Maeda, K. Nakabo, H. Taira, S. Ohashi, N. Mitani: Application of Ultra–High Speed Heating Test System (2) — Contact Angle Measurement Results, Proc. of 9th Symposium on Refractories for Iron and Steel, TARJ (2021).

[3]    T. Maeda, K. Nakabo, H. Taira, S. Ohashi, N. Mitani: Application of Ultra–High Speed Heating Test System (3) — Rapid Rate Sintering, Proc. of 9th Symposium on Refractories for Iron and Steel, TARJ (2021).

787

# HOT THERMAL SHOCK TESTING USING TOM_WAVE

Kirsten Schulze, Jens Baber, Holger Friedrich

Fraunhofer-Centre for High Temperature Materials and Design HTL, Bayreuth, Germany

## ABSTRACT

The capability of refractories to withstand thermal shock is usually tested by a series of rapid cool downs from high temperature (ASTM-C-1171). In these so-called cold thermal shock tests, however, the local cooling conditions are so imprecisely defined that no material properties usable for a simulation can be derived or model predictions verified. More controlled temperature changes can be introduced via hot thermal shock: e.g. by means of metal melts applied to the test specimens [1] or by means of burners [2]. After thermal shock, the damage is evaluated by fracture mechanics tests or non-destructively. Precisely quantifiable heating of samples is possible via induction, IR/halogen lamps and especially lasers [3, 4, 5]. In addition, the later conditions during usage are often better represented by a hot thermal shock. For example, in melting metallurgy hot metal is poured into the refractory which could be already at an elevated temperature.

Knowledge about the behaviour of refractories under operating conditions is important to choose the material that will have the longest life time in the production line. A well-chosen material can both reduce the cost for material replacement and machine down time and reduce the $CO_2$ footprint of the production line.

The thermo-optical measuring system TOM_wave developed as part of the EnerTHERM project has the option of using lasers to generate a hot thermal shock at a controlled furnace temperature [6]. Int this paper we present results for laser induced hot thermal shock measurements at high temperature for two commercial refractory materials.

## EXPERIMENTAL PROCEEDURE

For a laser induced thermal shock at high temperature, the sample is heated in a furnace to the chosen target temperature. In-situ laser radiation on the sample induces an additional hot thermal shock on the sample. Different parameter can be used to customize the experimental conditions to specific needs: Furnace temperature, laser diameter, laser pulse and relaxation time and the laser power.

### TOM_wave

The TOM_wave is a thermo-optical measuring device equipped with a $CO_2$ laser. The furnace can reach a base temperature up to 1750 °C in a controlled atmosphere (Air, $N_2$, Argon).

*Fig. 1: View into the muffle of TOM_wave. Visible in the centre is a sample that is heated to glow by laser radiation. This picture is taken at room temperature.*
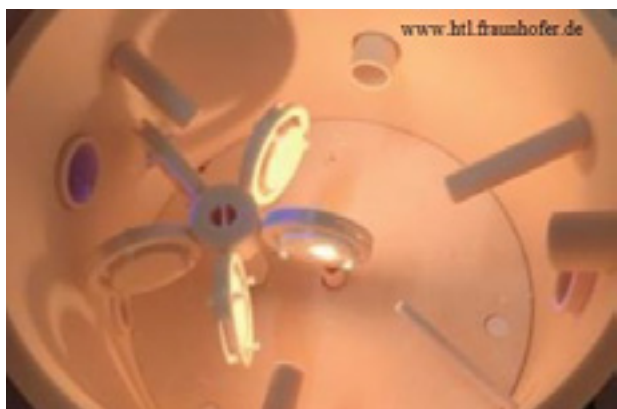


Up to five samples can be placed in a special rotatable holder. This allows the user to make comparative measurements in terms of material or thermal shock. The temperature profile of the furnace during heating, experiment and cool down is identical for all samples. The samples used are disk-shaped, and the laser is directed on the bases (figure 1). Sample dimensions can vary with a maximum of 15 mm in height and 40 mm in diameter. These sample volumes are big enough for representative measurements on heterogenous materials. The Laser diameter can be varied between 3 and 16 mm. From the laser power and the laser pulse time (milliseconds to several minutes), the energy applied to the sample can be calculated and can be varied with these two parameters. Thermal shocks can be applied either from both sides or on either of the bases. The sample position is optically observed, and the formations of cracks or the destruction of the sample can be detected. The change in temperature on the sample is measured with two pyrometers on the base and the circumference of the sample.

## ACCOMPANYING ANALYTICS

Besides the standard parameters such as mass, dimensions und density, several other experiments and analysis methods are used in our lab before and after the thermal treatment for evaluation. The following techniques are ex-situ measurement at room temperature. The list can be extended to all techniques that are applicable on disk-shaped samples.

### Computed tomography

Computed tomography (CT) as a non-destructive 3D imaging method is used for the detection of structural defects induced by thermal shock. Crack propagation can be followed throughout the entire volume.

### Impulse excitation techniques

Impulse excitation techniques is used to analyse changes of the vibration modes of the sample due to thermal shock treatment. For disk-shaped samples, this method can also be used to measure the E- and G-Modulus.

### Mechanical tests

Destructive mechanical tests are performed in reference to samples that have not been thermally treated. Examples for such tests on disc-shaped samples are ball on ring or ball on three balls.

## RESULTS

Three laser induced thermal shock experiments conducted in TOM_wave on refractory materials will be presented in the following. The materials used are one Bauxite-type refractory and one based on synthetic magnesia spinel, they will be referred to as B80 and SP78 in the following. All samples had a diameter of 33 ± 0.2 mm and a thickness of 5 ± 0.2 mm.

### Comparative hot thermal shock measurements on B80 and SP78 at room temperature

Two refractory materials were thermally treated with the same laser conditions. On both bases of the sample, 80 W of laser power were radiated on a laser spot of 10 mm in diameter simultaneously. Five thermal shocks with a duration of 0,5 s were applied. Between the shocks, the laser was blocked for 1 s. The furnace was at room temperature.

The temperature was monitored on one base with a pyrometer, and the data is presented in figure 2. For the first two laser pulses (black), the change in temperature for B80 (blue) and SP78 (red) show a similar progression. From the third pulse on, the temperature of SP78 increases more compared to B80. This is related to crack formation in the sample during the third thermal shock. During the experiment, the crack formation could be observed both optically and acoustically. The lower thermal shock resistance of SP78 compared to B80 is in accordance with the manufacturer's specifications.

*Fig 2: The change in temperature on B80 and SP78 refractory material during five rounds of laser induced thermal shock.*
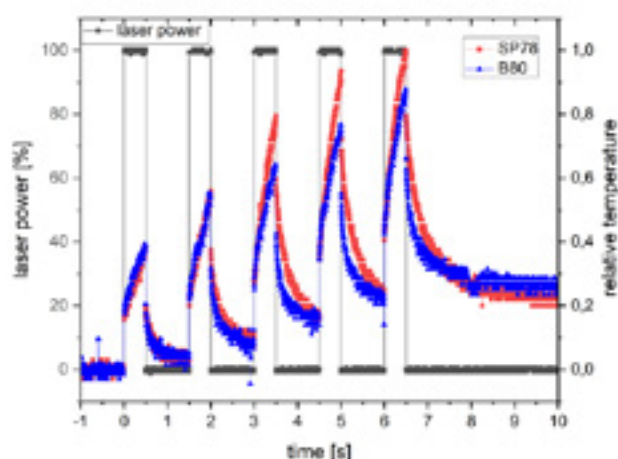


## CT analysis of thermal shock damage of SP78 at room temperature

For CT analysis another sample of SP78 was treated with a single thermal shock of 17 s and 80 W on both of the bases of the sample. The laser spot was 10 mm in diameter, and the furnace was at room temperature. During the experiment, crack formation in the sample could be observed both acoustically and optically. After recovery, the sample showed signs of melting on the point where it was hit by the laser. A crack from one of the melting spots to the rim of the sample is also visible. CT images of the sample were made before and after the thermal treatment, figure 3.

*Fig 3: Three slices of CT images of SP78 before and after thermal shock treatment. At the top, the direct comparison of the base of the sample before (left) and after (right) the thermal treatment is shown. The area of plastplatication from the laser spot highlighted in red is also visible in the cross section shown below.*
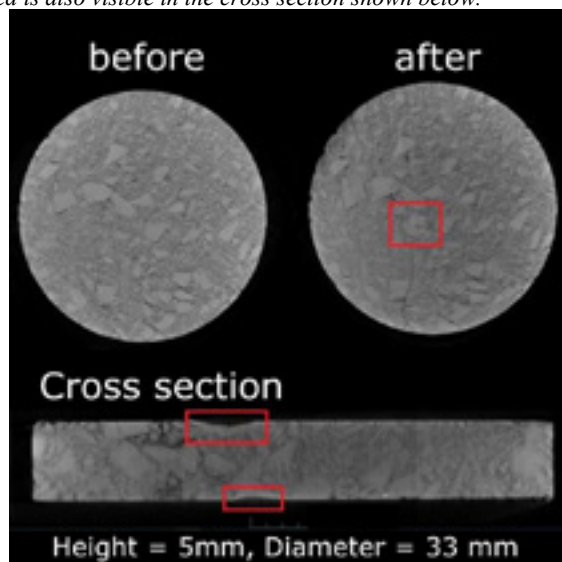


The direct comparison of the images shows the areas of melting (marked in red) and in the cross section their depth profile. The crack is also well visible and propagates downwards from the melted area to the rim in the top right image. In the 3D visualisation of the CT images, the crack can be followed through the entire sample. Its path goes, as expected, trough the matrix and bypassing the larger grains of the refractory.

## Hot thermal shock of B80 at 1500 °C

A hot thermal shock experiment at 1500 °C furnace temperature in air was performed on a sample of B80. Three laser pulses of 17s duration were applied on both sides with a power of 80 W and a laser diameter of 10 mm. Between the pulses, a 120 s laser dead time was set to let the sample cool down to the furnace temperature. During and after the experiment, no signs of cracks could be detected.

The temperature at the location of the laser spots has reached well beyond 1700 °C, as the sample shows extensive melting features (figure 4) on both sides. The pattern of the melted area suggests that during the laser heating this part of the sample was molten and quenched to a solid phase after the thermal treatment.

*Fig 4: A B80 sample after three rounds of thermal shocks at 1500 °C furnace temperature. At the laser spot, the sample is molten during laser impact and quenched to an amorphous phase after the thermal shock.*



## CONCLUSIONS

TOM_wave was used to treat samples with well-defined and reproducible laser induced hot thermal shocks at 1500 °C furnace temperature. The relatively large sample size of almost 20 mm$^3$ is representative also for heterogeneous materials. The application can range from thermal cycling with low laser power and large diameters of the heated area to concentrated thermal shocks with small laser spots and high energy input. The laser parameters can be selected in such a way that they simulate the conditions of the application. The well-defined heating condition enables the usage of data for simulations and model prediction verification. With the rotatable sample holder, comparative measurements of up to five samples are possible.

Well defined heat treatments in combination with further characterization of the sample can be used to choose the optimal refractory for a specific application and help to understand the cause of material failure and how to prevent it.

## REFERENCES

[1] Dienst, W., Scholtz, H., Zimmermann, H. J., Thermal shock resistance of ceramic materials in melt immersion test, J. Europ. Ceram Soc. 5, 1989, p. 365-370

[2] Semler, C. E., Thermal shock testing of refractories – Revisited: Part II, Refractories Applications and News 13, 2008, p. 132-140

[3] Merklinger, V., Martin, C., A New Thermal Shock Application-Related Testing Method for Ceramic Components, Interceram-International Ceramic Review 68.1, 2019, p. 22-25

[4] Putz, R. Rehmer, B., Schneider, G. A., Skrotzki, B. Thermal Shock on Different Advanced Ceramics by Laser Irradiation in Different Media, Advanced Engineering Materials 18.1, 2016, p. 132-140

[5] Seifert, G., Raether, F., Baber, J., A New Device for Maesuring Hot Thermal Shock, Thermal Cycling and Other High Temperature Properties of Refractories, refractories worldforum 1/2018, p.77-80

[6] Raether, F. (editor), Nachhaltige Wärmebehandlungsprozesse systematisch entwickeln, ISBN 978-3-8163-0728-0, VDMA-Verlag, Frankfurt, 2018.

789

# 9 BASIC REFRACTORY SCIENCE AND TECHNOLOGY TRANSFER

# MGO–C REFRACTORIES BASED ON REFRACTORY RECYCLATES AND ENVIRONMENTALLY FRIENDLY BINDERS

Till M. J. Stadtmüller, Enrico Storti, Nora Brachhold, Jana Hubálková, Patrick Gehre, Christos G. Aneziris.
Institute of Ceramics, Refractories and Composite Materials, TU Bergakademie Freiberg, Agricolastraße 17, 09599 Freiberg, Germany

Anna-Marie Lauermannová, Ondřej Jankovský
University of Chemistry and Technology Prague, Department of Inorganic Chemistry, Technická 5, 166 28 Prague 6, Czech Republic

Thomas Schemmel
Refratechnik Steel GmbH, Am Seestern 5, 40547 Düsseldorf, Germany

## ABSTRACT

This study focused on the development of an an environmentally friendly binder system based on lignin and collagen for uniaxially-pressed MgO-C refractories. The aim was to explore sustainable alternatives to resin and pitch binders commonly used in refractory materials. Additionally, were partially utilized as raw materials MgO-C recyclates obtained from steelmaking plants. The physical and mechanical properties of the developed refractory materials were compared with those of reference batches containing only fresh (no recyclates) magnesia. The results showed that the binder system is characterized by reliable binding properties of the MgO-C, although the recycled MgO-C exhibited higher porosity, slightly lower density, and lower strength compared to the reference batches without recyclates. However, the application of antioxidants significantly improved the properties of the recyclate containing MgO-C samples. Scanning electron microscopy (SEM) analysis coupled with energy-dispersive X-ray spectroscopy revealed the formation of whiskers, as well as oxidation and nitridation of aluminum particles. This research highlights the potential of environmentally friendly binders and the utilization of recycled materials in MgO-C refractories to mitigate their environmental impact and enhances the environmental performance of carbon containing refractory materials.

## INTRODUCTION

Refractory materials used in contact with molten metal require particular properties such as high thermal shock resistance, corrosion and erosion resistance and sufficient mechanical strength at high temperatures[1, 2, 3, 4, 5]. Magnesia-carbon (MgO-C) bricks were initially developed for electric furnaces in the 1970s and later adopted as working linings for converters (BOF) and secondary refining processes. Traditional MgO-C bricks typically contain 10 wt.% or more carbon (graphite) and are bonded by phenolic resin or pitch [6]. Graphite plays a crucial role in inhibiting slag penetration into the brick structure due to its low wettability by slag. Moreover, the addition of graphite significantly enhances the thermal shock resistance compared to pure magnesia, due to its high thermal conductivity and low coefficient of thermal expansion [7, 8]. The choice of binder is essential for all refractory ceramics. A binder for carbon-containing refractories should meet following requirements [9]:

– environmental and health safety of both the binder and its reaction products
– good wetting of both the refractory grain and the carbon carrier
– long time stability storage
– stable viscosity behavior within the processing temperature range
– good processability (no sticking)
– high bonding strength after pressing (low springback during pressing)
– high strength after curing and after coking
– low thermal expansion during coking
– long coking range to keep the stresses within the brick low
– no softening during coking
– high residual carbon content (ratio between the mass of the coke residue after coking and the initial mass of the binders)

– graphite like structure after carbonization for better oxidation resistance [10]

A large variety of organic binders have been tested for carbon containing refractories. Apart from a few special applications, pitches and phenol formaldehyde resins nowadays dominate the market in the bonding of carbon-bonded products [11]. Their pyrolysis deliveres a three-dimensional cross-linked lattice, which is very hard, insoluble, and stable [12, 6]. There are two types of phenolic resins: a resol type, which is thermosetting, and a novolac type, which is thermoplastic. The curing process is based on the reaction of hydroxymethyl groups (-$CH_2OH$) in the system. Resol based binders already contain these groups and can be simply activated by heating, while novolac resins contain fewer phenol groups and thus require an additional hardening agent such as hexamethylenetetramine to promote the polymerization reaction. The polymerization process takes place at temperatures higher than 160 °C with the splitting off of water molecules (resol) or ammonia (novolac). None the less, it is well known that compounds such as phenol-formaldehyde resins and pitches are highly harmflul for human health and the environment as well. Formaldehyde has carcinogenic as well as suppressive effects on the nervous system. Phenol formaldehyde resins have harmful effects on the skin, causing dermatitis and eczema [13, 14, 15]. The pyrolysis of coal tar pitches results in the release of hazardous compounds, such as benzo[a]pyrene, benzoanthracene, and others. Such compounds are dangerous even at low concentrations because of their bioaccumulation properties [16, 17, 18]. In addition, the European REACH regulations impose strict protocols for transporting and processing of all polycyclic aromatic hydrocarbons (PAHs).

Consequently, current research aims at reducing the toxicity of binders while maintaining the relevant properties of the components. There a is great interest in developing new uses for biomass and its derivatives that can offer sustainable alternatives to petroleum-based materials [19]. In particular, a high coke yield [20], cross-linking of PAHs [21], and a high atomic C/H ratio [22] are desired. Considering naturally occurring materials, lignin is the second most abundant aromatic polymer which has been traditionally relegated to use as a low-grade fuel. However, clean lignin represents a novel candidate for the manufacturing of high-temperature binders and carbonized materials due to its appropriate structure and behavior [23, 24]. Lignin pyrolyzes through a free-radical chain-reaction mechanism, similar to the liquid-phase carbonization of coal tar pitch [25]. Free radical precursors, generated during the heat treatment of lignin, undergo crosslinking, aromatization, and rearrangement reactions leading to the formation of highly condensed aromatic rings and consequently heterogeneous carbon structures of graphitic nature [26]. Collagen is derived from the hides and residues from the meat-packing industry. Owing to its ampholytic character with ionizable groups and active sites for crosslinking reactions, collagen acts as a strong binder. Early studies revealed that it can be used in combination with other additives as a core binder for iron casting in foundries [27, 28, 29]. Collagen maintains favorable physical and mechanical

properties even at elevated temperatures. It also releases far fewer volatile organic compounds, hazardous air pollutants, and greenhouse gas emissions than conventional phenolic urethane-based binders [27, 28, 29]. Lignin and collagen were already used to bind anthracite fines into bricks, which exhibited superior unconfined compression strength in all thermal stages (up to 1400 °C) found in cupola foundry furnaces [30, 31]. Zhao et al. [19] have also used a system consisting of lignin and collagen as a binder for specialty graphites and electrodes.

The focus of the Research Training Group GRK 2802 ``Refractory Recycling: A contribution for raw material-, energy-, and climate-efficiency in high-temperature processes'' is to explore the material property spectrum as well as the limitations of new high-temperature materials based on refractory recyclates and enviromentally friendly binders with special thermo-mechanical, chemical, and functional properties in high-temperature processing in the metallurgy [32]. In particular, a reduction of $CO_2$ emission shall be achieved by refractory material recycling ($CO_2$-free approaches due to the removed need for calcination of new raw materials) and on the other hand by the development of new metal/ceramic composite materials, enabling the development of $CO_2$-poor metallurgical technologies. The recycling and upcycling of materials for high-temperature applications offer a great potential for the direct reduction of greenhouse gas emissions together with more economical production processes. In this study, the combination of lignin and collagen was investigated as binder system. The design of the batches corresponds to the patent with file number 10 2023 002 367.1 [33].

## MATERIALS AND METHODS
### Raw materials
The raw materials used for the preparation of the pressed samples included both fresh MgO and recycled MgO-C. The fresh MgO was sourced from Refratechnik Steel GmbH (Düsseldorf, Germany). Fused magnesia, with purity exceeding 97.5 %, was utilized in three different size fractions: 3-7 mm, 1-3 mm, and 0-1 mm. As for the recycled material, three fractions of MgO-C (3-6 mm, 1-3 mm, and 0-1 mm) were obtained from Refratechnik Steel GmbH (Düsseldorf, Germany). Obviously, the recycled MgO-C materials exhibited varying content of residual carbon and other impurities, depending on size fraction. To further enhance the properties of the refractory samples, fine fractions of either fused cast MgO (F, purity >97.5 %) or dead burnt magnesia (DBM, purity >97 %) were added. Both types of fines MgO, with particle sizes below 45 μm, were acquired from Refratechnik Steel GmbH (Düsseldorf, Germany). Additionally, the coarse natural flake graphite NFL 92/94 (Graphit Kropfmühl AG, Hauzenberg, Germany) served as a carbon source. Dealkaline lignin (L0045) and alkaline lignin (L0082) obtained from TCI Deutschland GmbH (Eschborn, Germany) and collagen (100 % pure bovine collagen hydrolysate) from FNW International GmbH (Horb am Neckar, Germany) were used as binders. Ethylene glycol with a purity of 99% from Grüssing GmbH (Filsum, Germany) was used as a substitute for deionized water. Several additives were employed to enhance the properties of the MgO-C refractory batches. Aluminum powder with a purity of ≥ 99% and a grain size below 160 μm was obtained from Carl Roth GmbH + Co. KG (Karlsruhe, Germany). Silica (purity 96% ± 1.5%) was purchased from RW silicium GmbH (Pocking, Germany) and consisted of primary particles (approximately 63%) with sizes ranging from 0.1 to 0.3 μm, along with 1.5% coarser grains with a maximum size of 45 μm. Finally, $TiO_2$ (purity >99%, particle size <0.045 mm) was obtained from Crenox GmbH (Krefeld, Germany).

### Batch design
The batches developed and investigated in this study are summarized in Table 1. The majority of the batches were formulated using MgO-C recyclates. However, to assess their influence, four additional batches were prepared using only fresh magnesia (referred to as 100-A-F, 100-A-D, 100-A-D-E, and 100-A-D-E2). All batches were produced with environmentally friendly binders. Furthermore, additives with the same proportion were incorporated into most of the batches to enhance the properties of the coked samples. To evaluate their impact, two batches (50-F and 50-D) were prepared without any additives.

The compositions of the individual batches were designed according to the state-of-the-art MgO-C bricks produced in the industry. For batches consisting completely of fresh MgO, a constant graphite content of 10 wt.% was applied, in compliance with current industrial practice. Since the recycled fractions already contained carbon, the graphite content was reduced to 5 wt.% in order to achieve a comparable carbon content after coking. A total of 3 wt.% enviromentally friendly binder (lignin and collagen) was added, reflecting the typical binder amounts used in the industry. Initial tests indicated that coked samples bonded with a lignin-to-collagen ratio of 4:1 exhibited superior cold crushing strength compared to samples bonded solely with lignin. The batches 50-A-D and 50-A-F presented in Table 1 correspond to the batches described in a recent patent by Aneziris et al. [33].

### Sample preparation
The batches were mixed using a conventional mortar mixer ``ToniMIX'' (Toni Baustoffprüfsysteme GmbH, Berlin, Germany) while maintaining a consistent mixing order to ensure reproducibility. The mixing process started with the dry mixing of the coarse grains (3-7 mm and 1-3 mm), followed by the addition of half of the deionized water or the ethylene glycol (0.5 wt.% relative to total solids). Subsequently, the graphite and fine magnesia (0-1 mm) were incorporated into the mixture. Next, the binders (lignin and collagen) and, when applicable, additives (Al, $TiO_2$, and $SiO_2$) were pre-mixed and added to the mortar mixer. The remaining deionized water or the ethylene glycol was then introduced, followed by the finest MgO fraction (<0.045 mm), which could be either fused MgO (F) or DBM (D). The batch was mixed for 5 minutes, and the walls of the mixing container were scraped to ensure thorough mixing. An additional stirring of 5 minutes followed. Cylindrical samples (50 mm in diameter 50 mm in height) were pressed with a uniaxial press ``ES 270'' (RUCKS Maschinenbau GmbH, Glauchau, Germany). To minimize the risk of cracks due to entrapped air, the chamber was degassed twice at 1/3 and 2/3 of the maximum pressure of 150 MPa. After the pressing, the samples were dried at a temperature of 85,°C with a heating rate of 10 K/min and a holding time of 2 h, in a drying furnace ``P330'' (Nabertherm GmbH, Lilienthal, Germany). Subsequently, the samples were subjected to a curing process at 300 °C with a heating rate of 55 K/h and a dwell time of 1 h, allowing the lignin to soften and fill the gaps during the curing treatment. To approach reducing conditions, all samples were then coked inside retorts filled with calcined petcoke. The schedule involved a heating rate of 100 K/h up to the maximum temperature of 1000 °C, which was maintained for 3 h before free cooling.

793

Tab. 1: Developed and investigated of MgO-C samples.

| Raw mat. | Fra, | 50-F | 50-D | 100-AF | 100-AD | 50-AF | 50-AD | 100-ADE | 100-ADE2 |
|---|---|---|---|---|---|---|---|---|---|
| | | Amount in wt.% | | | | | | | |
| FM | 3-7 | 13.9 | 13.9 | 26 | 26 | 13.9 | 13.9 | 26 | 26 |
| | 1-3 | 13.3 | 13.3 | 25 | 25 | 13.3 | 13.3 | 25 | 25 |
| | 0-1 | 13.3 | 13.3 | 25 | 25 | 13.3 | 13.3 | 25 | 25 |
| | <0.045 | 14 | - | 14 | - | 14 | - | - | - |
| DBM | <0.045 | - | 14 | - | 14 | - | 14 | 14 | 14 |
| Recy. | 3-6 | 13.9 | 13.9 | - | - | 13.9 | 13.9 | - | - |
| | 1-3 | 13.3 | 13.3 | - | - | 13.3 | 13.3 | - | - |
| | 0-1 | 13.3 | 13.3 | - | - | 13.3 | 13.3 | - | - |
| Grap. | | 5 | 5 | 10 | 10 | 5 | 5 | 10 | 10 |
| | | wt.% relative to total solids | | | | | | | |
| Lig.D | | 2.4 | 2.4 | 2.4 | 2.4 | 2.4 | 2.4 | 2.4 | - |
| Lig.A | | - | - | - | - | - | - | - | 2.4 |
| Coll. | | 0.6 | 0.6 | 0.6 | 0.6 | 0.6 | 0.6 | 0.6 | 0.6 |
| H2O | | 1 | 1 | 1 | 1 | 1 | 1 | - | - |
| Ethy. gly. | | - | - | - | - | - | - | 1 | 1 |
| Al | | - | - | 2.5 | 2.5 | 2.5 | 2.5 | 2.5 | 2.5 |
| SiO2 | | - | - | 0.5 | 0.5 | 0.5 | 0.5 | 0.5 | 0.5 |
| TiO2 | | - | - | 0.4 | 0.4 | 0.4 | 0.4 | 0.4 | 0.4 |

**Sample characterization**

After coking, the MgO-C refractory samples were subjected to various characterization procedure to assess their properties. The open porosity and bulk density of cylindrical samples were determined using the toluene immersion method, following the European Standard DIN EN 993-1. The cold crushing strength (CCS) of the refractory samples was measured in accordance with the European Standard DIN EN 993-5 using a testing machine ``TIRAtest 2280'' (TIRA GmbH, Schalkau, Germany). 10 cylinders from each batch were subjected to compression testing after the coking process. The collagen and lignin binders were analyzed using simultaneous thermal analysis (STA-MS) combined with mass spectroscopy. Setsys Evolution apparatus (Setaram, Mougins, France) under dynamic air atmosphere conditions. The samples were heated with a rate of 5 K/min up to a temperature of 800 °C, and the gases evolved during heating were analyzed using a mass spectrometer OmniStarTM (Pfeiffer Vacuum, Asslar, Germany). In addition, thermogravimetry was conducted on cylindrical samples to determine their oxidation resistance. Flat alumina disks were placed on the cylindrical end faces of the samples, to minimize edge effects during oxidation and account for the anisotropic orientation of graphite flakes resulting from the pressing process. This setup ensured that the oxidation predominantly occurred from the lateral surface of the samples. The evaluation of the oxidation resistance was performed on cylindrical samples coupled with a laboratory scale. The samples was continuously recorded throughout the thermal cycle, which involved heating the samples in air up to a temperature of 1000 °C at a rate of 5 K/min. Subsequently, the samples were cooled to room temperature at a rate of 10 K/min, without any dwell time. In order to estimate the oxidation depth, the cylinders were broken lengthwise in the center after the oxidation tests. The Images of fractured surface were taken and the oxidation depth (OD) was measured digitally, using the software ``ImageJ''. 10 individual measurements per sample were carried out to determine the oxidation depth. To exclude the influence of edge effects, the oxidation depth was not measured directly at the edges. As specimens ``50-F'' and ``50-D'' failed during the cutting process, only photographs of the front surface, taken in advance, are available for both samples. To determine the oxidation depth for these two samples, the measured oxidized thickness on the face was subtracted from the total radius. Furthermore, differential scanning calorimetry (DSC) with thermogravimetry (TG) was performed on ground samples using simultaneous thermal analysis STA 409 PC/PG (Netzsch-Gerätebau GmbH, Selb, Germany). The samples were heated up to 1400 °C under an artificial air atmosphere, utilizing a heating rate of 10 K/min. Finally, fracture surfaces of the 100-A-D sample (taken as exemplary sample) were glued to sample holders and sputtered with Pt/Pd. In addition, a similar sample was embedded in epoxy resin, vibration polished for 20 h, and finally sputtered with Pt/Pd. SEM analysis ``AMBER'' (Tescan, Brünn, Czech Republic) combined with EBSD (Bruker Nano GmbH, Berlin, Germany) was performed on the prepared sample to gain information about morphology and phase composition.

**CONCLUSIONS**

In the present study, an environmentally friendly binder system based on lignin and collagen was developed to achieve effective bonding in MgO-C refractory samples. Moreover, as raw materials MgO-C recyclates obtained from steelmaking plants were partially used. The physical and mechanical properties of the developed refractories were comprehensively investigated and compared to reference batches with the same binders but without any recyclates. Batches comprising recycled MgO-C generally exhibited higher open porosity, slightly lower bulk density, and reduced cold crushing strength (CCS) in comparison to the reference batches. However, the application of antioxidants significantly improved the mechanical strength of the samples and provided effective resistance against oxidation in an air atmosphere. Scanning electron microscopy analysis revealed the presence of whiskers in the coked samples containing antioxidants. Oxidation of antioxidants resulted in the formation of an alumina layer on the surface of the aluminum particles, while specific regions were identified as AlN, indicating the reaction between aluminum and the surrounding atmosphere. Furthermore, replacing ethylene glycol in preliminary investigations yielded promising findings, relating to higher CCS. This alternative approach should be pursued in further studies. Generally, the successful development of the lignin and collagen binder system, along with the utilization of MgO-C recyclates and antioxidants, shows a clear potential for the development of sustainable and high-performance MgO-C refractories. Other research should focus on increasing the proportion of recycled materials, and exploring alternative typed of lignin and collagen binder systems to further enhance the properties and performance of enviromentally friendly refractories. By combining environmentally friendly with advanced material design, it is feasible to achieve sustainable and cost-effective refractory materials, contributing to the decarbonization of the steel industry.

**REFERENCES**

[1] Lee, W., Zhang, S.. Melt corrosion of oxide and oxide–carbon refractories. International Materials Reviews 1999;44:77–104.

[2] Carniglia, S.C., Barna, G.L.. Handbook of Industrial Refractories Technology. Noyes Publications; 1992.

[3] Rigaud, A.R.V.P.C.A.M.. Correlation between thermal shock and mechanical impact resistance of refractories. Br Ceram Trans 1997;96:225–230.

[4] Poirier, J., Qafssaoui, F., Ildefonse, J., Bouchetou, M.. Analysis and interpretation of refractory microstructures in studies of corrosion mechanisms by liquid oxides. Journal of the European Ceramic Society 2008;28:1557–1568.

[5] Refractories handbook. 1998.

[6] Aneziris, C.G., Borzov, D., Ulbricht, J.. Magnesia-carbon bricks – a high-duty refractory material. 2003.

[7] Pierson, H.O.. Handbook of Carbon, Graphite, Diamond and Fullerenes. Noyes Publications; 1993.

[8] Ewais, E.M.M.. Carbon based refractories. Journal of the Ceramic Society of Japan 2004;112:517–532.

[9] Hampel, M., Aneziris, C.G.. Herstellung und eigenschaften von magnesia-kohlenstoff-erzeugnissen. 2007.7

[10] Luz, A.P., Renda, C.G., Lucas, A.A., Bertholdo, R., Aneziris, C.G., Pandolfelli, V.C.. Graphitization of phenolic resins for carbon-based refractories. Ceramics International 2017;43:8171–8182.

[11] Luz, A.P., Salomão, R., Bitencourt, C.S., Renda, C.G., Lucas, A.A., Aneziris, C.G., et al. Thermosetting resins for carbon-containing refractories: Theoretical basis and novel insights. Open Ceramics 2020;3.

[12] Brachhold, N., Fruhstorfer, J., Mertke, A., Aneziris, C.G.. Carbon-bonded alumina refractories with reduced carbon content due to the addition of semi-conductive silicon and/or nanoparticles. Journal of Ceramic Science and Technology 2016;7:209–222.

[13] Saha, N.C., Bhunia, F., Kaviraj, A.. Toxicity of phenol to fish and aquatic ecosystems. Bulletin of Environmental Contamination and Toxicology 1999;63:195–202.

[14] Babich, H., Davis, D.. Phenol: A review of environmental and health risks. Regulatory Toxicology and Pharmacology 1981;1:90–109.

[15] TIŠLER, T., ZAGORC-KONČAN, J.. Comparative assessment of toxicity of phenol, formaldehyde, and industrial wastewater to aquatic organisms. Water, Air, and Soil Pollution 1997;97:315–322.

[16] Bukowska, B., Mokra, K., Michałowicz, J.. Benzo[a]pyrene—environmental occurrence, human exposure, and mechanisms of toxicity. International Journal of Molecular Sciences 2022;23:6348.

[17] Kasimov, N.S., Kosheleva, N.E., Nikiforova, E.M., Vlasov, D.V.. Benzo[a]pyrene in urban environments of eastern moscow: pollution levels and critical loads. Atmospheric Chemistry and Physics 2017;17:2217–2227.

[18] Verma, N., Pink, M., Rettenmeier, A.W., Schmitz-Spanke, S.. Review on proteomic analyses of benzo[a]pyrene toxicity. PROTEOMICS 2012;12:1731–1755.

[19] Zhao, Z., Cannon, F.S., Nieto-Delgado, C., Pena, L.. Lignin/collagen hybrid biomaterials as binder substitute for specialty graphites and electrodes. Carbon 2016;108:303–317.

[20] Hatano, H., Suginobe, H.. Improvement and control of the quality of binder pitch for graphite electrodes. Fuel 1989;68:1503–1506.

[21] Pérez, M., Granda, M., Santamaría, R., Morgan, T., Menéndez, R.. A thermoanalytical study of the co-pyrolysis of coal-tar pitch and petroleum pitch. Fuel 2004;83:1257–1265.

[22] Wagner, M., Jäger, H., Letizia, I., Wilhelmi, G.. Quality assessment of binder pitches for carbon and graphite electrodes. Fuel 1988;67:792–797.

[23] Vázquez, G., Antorrena, G., González, J., Mayor, J.. Lignin-phenol-formaldehyde adhesives for exterior grade plywoods. Bioresource Technology 1995;51:187–192.

[24] Kijima, M., Hirukawa, T., Hanawa, F., Hata, T.. Thermal conversion of alkaline lignin and its structured derivatives to porous carbonized materials. Bioresource Technology 2011;102:6279–6285.

[25] Britt, P.F., Buchanan, A., Thomas, K.B., Lee, S.K.. Pyrolysis mechanisms of lignin: surface-immobilized model compound investigation of acid-catalyzed and free-radical reaction pathways. Journal of Analytical and Applied Pyrolysis 1995;33:1–19.

[26] Rodríguez-Mirasol, J., Cordero, T., Rodríguez, J.. High-temperature carbons from kraft lignin. Carbon 1996;34:43–52.

[27] Wang, Y., Cannon, F.S., Salama, M., Goudzwaard, J., Furness, J.C.. Characterization of hydrocarbon emissions from green sand foundry core binders by analytical pyrolysis. Environmental Science and Technology 2007;41:7922–7927.

[28] Fox, J.T., Cannon, F.S., Brown, N.R., Huang, H., Furness, J.C.. Comparison of a new, green foundry binder with conventional foundry binders. International Journal of Adhesion and Adhesives 2012;34:38–45.

[29] Allen, J.F., Cannon, F.S., Nieto-Delgado, C., Voigt, R.C., Fox, J.T., Lamonski, J., et al. Full-scale air emissions monitoring and casting quality demonstration of a hybrid hydrolyzed collagen-alkali silicate core binder. International Journal of Metalcasting 2016;10:172–189.

[30] Lumadue, M.R., Cannon, F.S., Brown, N.R.. Lignin as both fuel and fusing binder in briquetted anthracite fines for foundry coke substitute. Fuel 2012;97:869–875.

[31] Nieto-Delgado, C., Cannon, F.S., Paulsen, P.D., Furness, J.C., Voigt, R.C., Pagnotti, J.R.. Bindered anthracite briquettes as fuel alternative to metallurgical coke: Full scale performance in cupola furnaces. Fuel 2014;121:39–47.

[32] Aneziris, C.G., Volkova, O., Gehre, P., Hubálková, J.. Graduiertenkolleg GRK 2802: Feuerfest Recycling. ACAMONTA 2022;:73–76.

[33] Aneziris, C.G., Gehre, P., Veres, D., Dudczig, S., Hubálková, J., Stadtmüller, T.M.J.. Feuerfeste Erzeugnisse aus der Basis von umweltfreundlichen Bindemitteln und Feuerfest-Rezyklaten. Patent 10 2023 002 367.1. 2023.

# THE ROLE OF ANDALUSITE IN REFRACTORY CASTABLES AND POSSIBLE SUBSTITUTIONS PART 1: THERMAL BEHAVIOUR OF ANDALUSITE BEARING CASTABLES

Ralf Simmat[1]; Christian Dannert[1]; Kerstin Hauke[1]; Juliane Paul[2]; Kariman Abdelgawad[2]; Olaf Krause[2]

[1]Forschungsgemeinschaft Feuerfest e. V. at the European Centre for Refractories, Höhr-Grenzhausen, Germany;
[2]Hochschule Koblenz, Höhr-Grenzhausen, Germany

Natural andalusite is an important refractory raw material that is widespread in use for manufacturing industrial refractory unshaped products and fired brick materials. However, andalusite cannot be synthesized for refractory purposes and natural ressources are limited. FGF, Hochschule Koblenz and InisMa together investigate in depth the thermal phase evolution and, in parallel, the thermomechanic properties to understand the outstanding properties of andalusite bearing refractory castables. It is well known that andalusite decomposes at temperatures above ~1300 °C, resulting in dense, felted aggregates of mullite and a highly viscous silica phase. Theses aggregates still provide high refractoriness and mechanical strength. The volume increase of about 4.5 % during this transformation works against high temperature shrinkage.

The phase changes occuring with increasing temperatures, involving the andalusite transformation that can be influenced by other components of the castables, as well as reactions of transformed andalusite with the surrounding matix, influence the thermomechanical properties of the castables. With the aim to develop alternatives to andalusite bearing castables, these processes must be entirely understood.

The method of monotonic heating reveals important mineralogical phase changes in two commercial castables (ULCC and silica-gel bonded) in the temperatures up to 1620 °C, including transformation of andalusite and melt formation.The nature of observed phase transformations is verified by XRD and SEM using samples of the castables that were treated between 900 and 1600 °C at a step size of 100 K. RUL and CREEP was determined for correlating the thermal softening of the castables with the described phase evolution.

796

# THE ROLE OF ANDALUSITE IN REFRACTORY CASTABLES AND POSSIBLE SUBSTITUTIONS PART 2: CHANGES IN CERAMIC STRUCTURE DURING HEAT–UP

J. Paul[1], O. Krause[1], K. Abdelgawad[1], R. Simmat[2], K. Hauke[2], C. Dannert[2]

[1]Koblenz University of Applied Science, Höhr-Grenzhausen, Germany; [2]Forschungsgemeinschaft Feuerfest e. V. at the European Centre for Refractories, Höhr-Grenzhausen, Germany

Andalusite bearing castables are widely used in the process industry due to their outstanding corrosion resistance and thermo mechanical properties. Typical applications are biomass and waste incineration and permanent linings of vessels in the steel industry.

However, andalusite is a natural raw material with limited supply. An approach to mitigate this risk is to develop alternative refractory castables which have the same outstanding properties like andalusite refractory castables, but do not contain andalusit e. However, the high temperature behaviour of andalusite refractory castables is not fully understood yet. Especially, a better understanding of the role of andalusite in the matrix of refractory castables is necessary to develop suitable substitution refr actories.

To better understand the behaviour of andalusite in refractory castables, two commercial castables (ULCC and silica gel bonded) were investigated by scanning electron microscopy and X ray diffraction analyses after thermal treatment at different temperatures and for different durations. The results diverge significantly from former data reported in the literature. Unexpectedly, mullite is not a stable high temperature phase in the matrix of the ULCC. In the presence of CaO from the cement binder, anorthite and liquid phase are being formed instead.

This paper presents SEM and XRD investigations of the heating experiments and shows mineralogical and chemical differences during thermal treatment.

# THE ROLE OF ANDALUSITE IN REFRACTORY CASTABLES AND POSSIBILITIES FOR ITS SUBSTITUTION.
# PART 3: FIRST ATTEMPT TO REDESIGN REQUIRED PROPERTIES WITHIN THE PARAMETERS OF  ANDALUSITE FREE CASTABLES

Kariman Abdelgawad[1]; Olaf Krause[1]; Juliane Paul[1]; Ralf Simmat[2]; Christian Dannert[2]

[1]Koblenz University of Applied Sciences, building-art-materials (materials technology glass and ceramics), Höhr-Grenzhausen, Germany; [2]Research Association Refractory e.V., Höhr-Grenzhausen, Germany

The andalusite transformation and accompanied thermal induced phase transformations in ultra-low cement and no-cement-high alumina refractory castables are described in the first part of this joint contribution. The andalusite transformation is accompanied by volume expansion and the formation of an amorphous silica-rich phase. Observation by SEM anticipatesa great benefit of the silica-rich phase by hampering crack propagation, thus improving the mechanical properties and of the castables at high temperatures.

Nevertheless, the high demand for andalusite in refractory markets raises concerns regarding long-term supplies. The observed mechanisms guide the way in developing alternative, andalusite-free and sustainable castables.

In this work, model low cement castables based on tabular alumina with additions of SiC, kyanite or luting sand (as a fine particle < 45 um) were developed to achieve a similar microstructures and thermo-mechanical properties as andalusite based castables. SiC enhances the formation of mullite through oxidiation and in the presence of alumina in the matrix . The role of kyanite is 1. to support the mullite formation and 2. To compensate shrinkage by the volume expansion during transforms to mullite + $SiO_2$ during heating.

The model castables were fired at 1000, 1200, 1300, 1400, and 1500 °C for 8 hrs. The refractoriness under load and creep under compression in combination with mineralogical and microscopic analysises were used to investigate the influence of SiC, Kyanite and luting sand on the microstructural and thermo-mechanical properties of the castables

# REFRACTORY INK-COATED POROUS INSULATORS TO PREVENT MICROWAVE PLASMA DISCHARGES FOR HIGH-TEMPERATURE MICROWAVE HEATING

A. L. F. Cardoso[*,1], D. N. F. Muche[1], V. R. Salvini[2], V. C. Pandolfelli[1], R. F. K. Gunnewiek[1]

[1] Federal University of Sao Carlos, Graduate Program in Materials Science and Engineering, São Carlos, São Paulo, Brazil.
[2] College of Technology (FATEC), Jordão Borghetti Street 480, Sertãozinho, SP, 14160-050, Brazil.
[*] **andre.l.f.cardoso93@gmail.com**

## ABSTRACT

The refractory industry known for its high energy consumption, can greatly benefit from the implementation of microwave processing techniques to reduce energy usage. Nevertheless, a proper insulating system is of paramount importance for microwave sintering. Careful selection of its composition and structure impact directly the performance of the insulator. A plain alumina porous insulator is a suitable candidate to fulfill some of the requirements. However, this type of insulator may cause plasma discharges during microwave sintering, hindering the process's effectiveness. In this study, the use of a refractory ink coating on a commercial plain alumina foam insulator was evaluated. The performance of the ink-coated insulator was compared to the uncoated one, under the same microwave heating conditions. A coated insulator promoted a more homogeneous and controlled heating, displacing the effect of plasma discharges for higher temperatures.

## INTRODUCTION

The discovery and utilization of ceramics are one of the most relevant accomplishments in human history, and firing is a crucial step in their processing to achieve a dense and resistant ceramic body. Microwave heating was conceived in the last century, around the 1950s, and developed mainly as a technique to heat food, however ceramic materials were explored more extensively in microwave processing around the late 1980s [1]. Several aspects must be considered to implement microwave heating on an industrial scale for ceramic sintering. One of the most challenging aspects to overcome is to find a suitable thermal insulator system that is transparent to microwave (at room and high temperatures) while simultaneously withstand high temperatures without melting or deforming and presenting high resistance to thermal shock damage. To solve this issue, a plain alumina ($Al_2O_3$) porous insulator is a potential candidate for the application. Alumina is transparent to microwave radiation in a wide temperature range. Alumina foam insulators can fulfill two out of three requirements: transparency to microwave and refractoriness [2,3]. However, using porous materials might lead to the generation of plasma discharges within the pores. This phenomenon occurs when a high-frequency electromagnetic field is applied to a porous material with a pore size close to the microwave wavelength [4]. The presence of plasma discharges hinders the heating effectiveness of the target because the plasma absorbs a substantial amount of the input power, and the larger the plasma region generated through this phenomenon, the larger the power absorbed by the plasma. This work aims to develop a refractory aluminum oxide-based ink to coat a thin layer of the porous insulator, preventing the formation of plasma discharges on the surface pores of the insulator during the sintering process in microwave ovens while maintaining its insulating properties, microwave transparency, and refractoriness.

## EXPERIMENTAL PROCEDURE

In this work, the material used to produce the refractory ink is alumina (CT3000SG, Almatis). The ink was produced by mixing the alumina with distilled water, surfactant (Castament FS60, BASF), polyvinyl alcohol (PVA 72000, Synth), and polyethylene glycol (PEG 8000, Union Carbide). After mixing in a mechanical stirrer for 15 minutes, the suspension was milled using zirconia spheres for 3 hours to ensure complete homogenization.

The insulator used for the deposition of the produced ink is a lightweight plain aluminum oxide foam (Norfoam, Saint-Gobain) designed for high-temperature applications [5].

Two sintering methods were applied to consolidate the ink onto the insulator surface: conventional or microwave sintering (Cober Electronics MS6K, 2.45 GHz, 6kW). In the former, the heating ramp is as follows: 300 °C for 1h with a 3 °C/min heating rate, followed by heating to 500 °C for 1h with a 3 °C/min heating rate, and after, heating up to 1600 °C for 2h with a 5 °C/min heating rate. In the latter, the samples were sintered while in use as insulators in the microwave cavity, with a 50 °C/min heating rate up to 1100 °C, and with a scheduled 20 °C/min heating rate up to 1450 °C with no holding time. The temperature measurement in the microwave oven was carried out using an optical pyrometer (Raytek MA2S Marathon Series).

The deposition of the produced ink on the insulator surface was made by dipping the insulator in a 1-millimeter-deep bath of the produced ink, ensuring that only a thin layer of the insulator surface would be coated by the ink. After the deposition, the ink-coated insulator was left to dry at room temperature for 24 hours.

The microwave oven cavity view is shown in Fig. 1. The grey piece in the center of the image is silicon carbide used as a microwave susceptor material to absorb the microwave and heat the system, and the red dot is the pyrometer target pointer. After sintering, the coated insulator surfaces were analyzed in an optical microscope (Zeiss Stemi 2000-C).
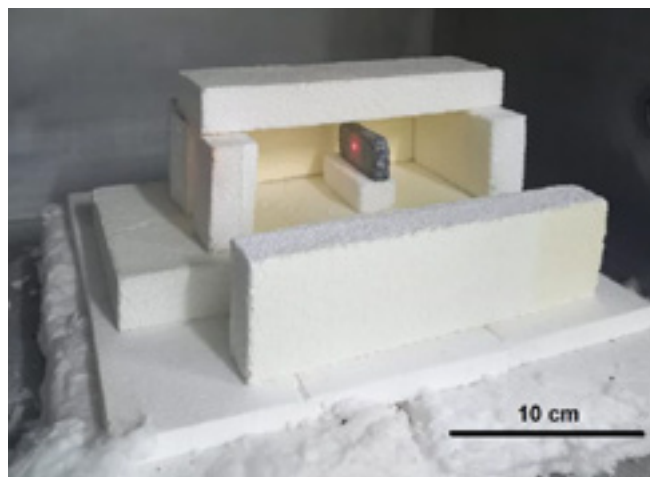


*Fig. 1: Side view of the inside of the microwave oven cavity.*

## RESULTS AND DISCUSSION

After sintering, the coating was well attached to the porous scaffold, as seen in Figure 2. It is possible to observe that different sintering methods resulted in changes on the surface morphology of the ink layer. For the 78% solid content ink microwave sintered composition (Fig. 2a), it is noticed the smaller size of plate-like surfaces with a higher number of cracks. This was expected [6,7] given the much shorter time to thermally decompose the additives used for the ink preparation (due to the high heating rates and no holding times) and the sample's lower temperature in the microwave sintering process. The same can be accounted for the 80% solid content ink microwave sintered (Fig. 2b). However, changing the formulation of the ink has given rise to a slightly

different surface morphology. The latter depicted more homogeneous sized although bigger plates, and slightly larger crack widths. For the 80% solid content ink conventionally sintered composition (Fig. 2c), the same trend happened to a higher extent, resulting in even bigger plates and crack widths. However, comparing the different formulations of the depositions over the insulator surface during use in the microwave oven, the different morphologies of the plates and crack widths did not seem to affect the heating or the unfolding of plasma discharges (what is not desirable in this case) during the process.
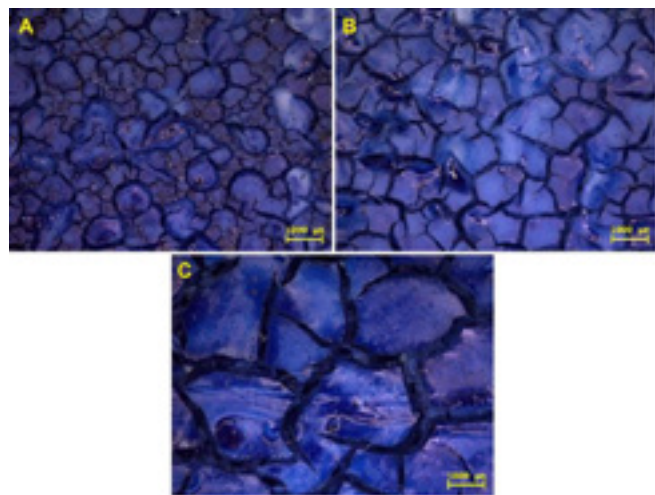


*Fig. 2: Optical microscopies of (a) 78 microwave sintered, (b) 80 microwave sintered, and (c) 80 conventionally sintered.*

The microwave sintering time of the refractory ink coating was significantly lower compared to the conventional sintered one (approximately 10x lower, comparing 55 minutes to 600 minutes, respectively). The surface morphologies obtained did not present outstanding differences regarding the sintering method (except for the size of the plates). This suggests the potential of sintering this type of coating already in use during the thermal treatment in the microwave oven. It might lead to substantial energy savings likewise the already-known benefits of microwave sintering related to this aspect [8,9].

Using the insulator with no ink deposition in the microwave sintering system usually generated plasma discharges between 950~1020 °C. When a stable plasma forms, the measured temperature decreases by approximately 100 to 150 °C, resulting in an increase in the incident power rise to 4 kW. One would expect a significant temperature rise because the silicon carbide susceptor is an excellent microwave absorber [10] and would absorb most of the incident power, however, this does not occur promptly. After the temperature drops and stabilizes, it rises at a slightly lower rate after a couple of minutes. The reason behind this is that the plasma absorbs a significant amount of microwave power, as alumina is mostly transparent to microwaves at this temperature range. This absorption of the microwave power by the plasma can be described by equation (1), which highlights the electric energy absorbed by the electrons and ions in the plasma [11].

$$P_{abs} = n_e . A_{eff} . E^2 \qquad (1)$$

where $P_{abs}$ is the power absorbed in the plasma in watts, $n_e$ is the plasma electron density, $A_{eff}$ is the effective area for power absorption and depends on the plasma properties such as the electron and ions temperature, and $E$ is the electric field intensity.

In the aforementioned event (using an insulator with no ink deposition), the maximum temperature reached was 1350~1370 °C. When the insulator used in microwave heating is coated with the refractory ink, the maximum temperature achieved is 1430~1450 °C. This is accompanied by a considerably higher heating rate once the temperature recovers from the initial decline caused by the

absorption of the microwave power by the plasma. Using the coated insulator, the plasma discharges begin above 1180 °C (at least 160 °C higher) with the temperature falling approximately 70 °C (at least 30° less).

**CONCLUSIONS**

The results obtained pointed out that using ink-coated insulators enabled reaching a higher temperature in the microwave oven system. The plasma discharges could not be avoided or prevented as expected, but in addition to being displaced to a higher temperature, the overall heating speed was better controlled and presented a higher recovery heating rate after the plasma discharges were initiated. The use of ink-coated porous ceramics can be a promising technological improvement for cheap and easy-produced insulators used for microwave sintering in addition to shielding the insulator and increasing its lifespan.

**REFERENCES**

[1] D.E. Clark, W.H. Sutton, Microwave processing of materials, Annu. Rev. Mater. Sci. 26 (1996) 299–331.

[2] S.-T. Oh, K. Tajima, M. Ando, T. Ohji, Fabrication of porous Al2O3 by microwave sintering and its properties, Mater. Lett. 48 (2001) 215–218.

[3] C. Sadik, I.-E. El Amrani, A. Albizane, Recent advances in silica-alumina refractory: A review, J. Asian Ceram. Soc. 2 (2014) 83–96.

[4] Y.-R. Zhang, K. Van Laer, E.C. Neyts, A. Bogaerts, Can plasma be formed in catalyst pores? A modeling investigation, Appl. Catal. B: Environ. 185 (2016) 56–67.

[5] M. Schumann, L. San-Miguel, Fiber-Free Ceramic Insulation Foam for Highest Temperatures – a New Generation of HSE-Friendly Refractory Products with Multiple Application Possibilities, Refract. Worldforum 9 (2017) 50–58.

[6] S. Akpinar, I.M. Kusoglu, O. Ertugrul, K. Onel, In situ mullite foam fabrication using microwave energy, J. Eur. Ceram 32 (2012) 843–848.

[7] S. Akpinar, İ.M. Kuşoğlu, O. Ertugrul, K. Onel, Microwave assisted sintering of in-situ cordierite foam, Ceram. Int. 41 (2015) 8605–8613.

[8] J.D. Katz, Microwave sintering of ceramics, Annu. Rev. Mater. Sci. 22 (1992) 153–170.

[9] K.I. Rybakov, E.A. Olevsky, E.V. Krikun, Microwave Sintering: Fundamentals and Modeling, J. Am. Ceram. Soc. 96 (2013) 1003–1020.

[10] S. Kumari, R. Kumar, P.R. Agrawal, S. Prakash, D.P. Mondal, S.R. Dhakate, Fabrication of lightweight and porous silicon carbide foams as excellent microwave susceptor for heat generation, Mater. Chem. Phys. 253 (2020) 123211.

[11] M.A. Lieberman, A.J. Lichtenberg, Principles of Plasma Discharges and Materials Processing, second ed, John Wiley & Sons Inc., Hoboken, New Jersey, 2005.

# HIGH–TEMPERATURE DAMAGE AND MECHANICAL BEHAVIOR OF NIOBIUM–ALUMINA REFRACTORY COMPOSITES UNDER COMPRESSION AND BENDING

G. Günay, T. Zienert, C. G. Aneziris, H. Biermann, A. Weidner
TU Bergakademie Freiberg, Germany

B. Kraft, S. Wagner
Karlsruhe Institute of Technology, Karlsruhe, Germany

## ABSTRACT

In the present study, $Nb-Al_2O_3$ refractory composite materials produced by slip casting and extrusion methods were studied in terms of their mechanical behaviour at high temperatures under compressive and bending loading conditions. In addition, materials with lower porosity manufactured by field-assisted sintering technique (FAST) were tested to explore the effect of porosity on mechanical behaviour of these composites. Within the scope of this study, compression tests were performed up to 1300 °C. To understand damage behaviour, bending tests were performed together with acoustic emission measurements. Fractured surfaces were characterized with stereo microscopy and scanning electron microscopy. The results show that temperature has a significant effect on brittle to ductile transition associated with deformation in these materials. As the temperature increased, these composites exhibited higher plasticity and showed more pronounced creep behaviour, in particular at 1500 °C. Furthermore, acoustic emission measurements were applied at RT and for the first time also at high temperatures.

## INTRODUCTION

Refractory composites have become increasingly popular in recent years as promising candidates owing to their ability to withstand extreme temperatures, mechanical stresses, and corrosive atmospheres [1-4]. Refractory composites typically consist of a combination of refractory materials, such as alumina ($Al_2O_3$), together gathered with refractory metals like tantalum and niobium. Among these composites, $Nb-Al_2O_3$ composites have gained significant attention due to their unique combination of properties, including high strength, thermal stability, low shrinkage, and high resistance to harsh operating conditions [1-2]. Nb, with its high melting point, excellent mechanical properties, and notable chemical stability, presents an ideal candidate for improving the overall performance of refractory materials. Forming a composite of Nb together with $Al_2O_3$ can lead to synergistic effects, resulting in enhanced high-temperature mechanical properties and improved dimensional stability.

$Nb-Al_2O_3$ composites are particularly effective when combined with various coating technologies, owing to their ability to provide good bonding between the metal particles and the ceramic matrix [5-7]. Furthermore, the shrinkage behaviour of these composites during the sintering process plays a crucial role in hot temperature applications [2]. Given these inherent benefits, these materials are expected to see increased utilization in the near future, particularly in applications where exposure to high temperatures is a critical factor while minimizing the environmental impact.

The performance and reliability of refractory composites at elevated temperatures heavily rely on their mechanical behaviour. To effectively employ these composites in demanding applications, a comprehensive understanding of their high-temperature mechanical properties is crucial. Previous studies of the authors group [3, 8] have focused on conducting compression experiments to evaluate the high-temperature properties of $Nb-Al_2O_3$ composites in various compositions for the first time. Thorough understanding of the properties and performance of these composites can provide valuable insights for designing and implementing environmentally sustainable materials in different applications.

In the present study, we aim to investigate the mechanical properties of $Nb-Al_2O_3$ composites in a more comprehensive manner. This study provides the high-temperature damage and mechanical behaviour of $Nb-Al_2O_3$ composites, which are produced through slip casting and FAST (Field-Assisted Sintering Technique). The utilization and effects of different alumina powders in two different grain sizes will also be evaluated, considering their contributions to costs and the mechanical behaviour of these composites. Mechanical properties, such as strength, hardness, and deformation behaviour of the composites, were assessed through compression tests. Furthermore, we performed bending experiments on the composites produced through two different sintering regimes for comparison. These experiments were supplemented by acoustic emission measurements in order to evaluate the damage and fracture behaviour. It is essential to conduct these experiments, including acoustic emission measurements, at high temperatures to gain comprehensive insights into the material's behaviour under extreme conditions.

## EXPERIMENTAL PROCEDURE

### Materials

Within the scope of these studies, $Nb-Al_2O_3$ refractory composite materials, containing 60 vol % refractory metal niobium and 40 vol % alumina, were investigated. These composites were fabricated using slip-casting and FAST, utilizing the raw materials with particle sizes provided in Table 1.

Tab. 1: Particle size distributions of the raw materials.

| Production | Raw materials | Particle Size [µm] | | |
|---|---|---|---|---|
| | | $d_{10}$ | $d_{50}$ | $d_{90}$ |
| SLIP-CASTING | Niobium powder | 9.1 | 31 | 64.7 |
| | Alumina CT9FG | 2 | 5.5 | 20.6 |
| | Alumina CL370 | 0.2 | 0.5 | 5.8 |
| | Alumina Alodur | 42.3 | 96.3 | 163.7 |
| FAST | Niobium powder | 10.8 | 37.6 | 75.6 |
| | Alumina CT9FG | 0.8 | 4.4 | 11.9 |
| | Alumina Alodur | 44.8 | 95.8 | 162.4 |

*Castables*

The slip-cast refractory composites were produced by two different sintering processes, namely single-sintered and double-sintered. Single-sintered refractory composites were produced using Nb powder (EWG Wagner, Germany) and alumina powders (CT9FG, Almatis, Germany, and Treibacher Alodur WRG, Imerys Fused Minerals Zschornewitz, Germany). Before the experiments, open porosity and density of each specimen were measured using the Archimedes method. Detailed information regarding the production process can be found in a recent study of Zienert et al. [2].

The double-sintered $Nb-Al_2O_3$ composites were produced by a two-step manufacturing process. In the first step, single-sintered refractory composite prisms were produced and sintered. Subsequently, these prismatic materials underwent a crushing

process, and Nb-Al₂O₃ aggregates were classified to different grain size through the process of sieving. During this process, CL370, a finer-grained alumina powder, was added to aid in better sintering and improved interlocking. After selecting the proper grain size, the mixture was sintered at 1600 °C for 4 hours under an argon atmosphere. The resulting materials were referred to as double-sintered refractory composites. Detailed information related to the process is given in [9].

*FAST*

In the FAST technique, the materials were produced with the aid of different-sized alumina powders, namely the fine-grained CT9FG and the coarse-grained Alodur. The process entailed a dry mixing of Nb powder and alumina powder using a Turbular Tumbler type T2C (WAB AG Maschinenfabrik, Switzerland). The mixture was transferred into a polyethylene (PE) bottle and mixed for 10 minutes without any further additions. Subsequently, the powder mixture was processed using a FAST system type HP D25/1 (FCT Systeme GmbH, Germany). The samples were sintered at a controlled temperature with a heating rate of 100 K/min and then held for 5 minutes. During this process, an axial pressure of 50 MPa was applied. After this period, the axial pressure was released, and the samples were cooled down to RT at a cooling rate of 100 K/min. Before the mechanical testing, open porosity and density measurements were conducted on each specimen using the Archimedes method. For comprehensive details regarding the production route, refer to the study conducted by Kraft et al. [10].

**Specimen preparation**

For the compression tests, the materials produced using two different techniques were investigated. Single-sintered castable cylindrical samples in dimensions of Ø 12 mm × 20 mm height were used for compression tests. These materials were prepared by drilling of the single-sintered castable prismatic bars used for bending tests (in dimensions of 25 mm × 25 mm × 150 mm). Fig 1 shows the castable specimens utilized for the compression (Fig. 1a) and bending tests (Fig. 1b), respectively.



*Fig 1. Single-sintered castable refractory composite specimens used for the compression tests (a) and bending tests (b).*

The specimens produced via FAST technique had a size of Ø 2.5 mm × 2.5 mm height and were used for the compression tests. These specimens were prepared using waterjet cutting method from the composite discs produced with FAST technique.

Table 2 shows the initial open porosities of the materials used for the compression and the bending tests.

Table 2: Specimens and the initial open porosities.

| Type of test | Material | Open porosity [%] |
|---|---|---|
| Compression | 60/40 (Nb/CT9FG) FAST | 0.1 |
| | 60/40 (Nb/Alodur) FAST | 0.6 |
| | 60/40 (Nb/CT9FG) Cast | 36.5 |
| | 60/40 (Nb/Alodur) Cast | 41.9 |
| Bending | 60/40 (Nb/CT9FG) Cast Single-sintered | 37.1 |
| | 60/40 (Nb/CT9FG) Cast Double-sintered | 34.8 |

**Mechanical testing**

The experimental investigation of the mechanical properties of the test specimens was carried out at an elevated temperature of 1300 °C using an electromechanical high-temperature testing machine (Z020, Zwick Roell, Germany) equipped with a protective gas chamber (Maytec, Germany). The heating process was conducted by inductive heating via a medium-frequency induction generator (Hüttinger HF 5010, Germany) with a heating rate of 30 K/s. In order to measure the temperature of the specimen directly, a pyrometer (Sensortherm Metis MS09, Germany) with a wavelength of 0.9 µm attached to the chamber and assuming an emission coefficient of 0.93 was used. The system was evacuated twice to a pressure of 0.7 mbar and swept twice with argon gas at ambient pressure to prevent oxidation. In addition, all experiments were carried out in an argon environment, and the presence of oxygen level in the system was monitored using an O₂ sensor (Stange Elektronik, Germany).

The compression tests and 4-point bending tests were conducted using two different testing setups shown in Figure 2. The cylindrical single-sintered castable and FAST specimens were used for the compression tests. The test specimen was placed between susceptor plates and in a susceptor cage made of Mo alloy TZM. The strain measurement was carried out using a short Al₂O₃ rod integrated to the upper susceptor and two long Al₂O₃ rods. The heating process was accomplished using an induction coil around the testing area. The loading on the specimen was applied through Si₃N₄ punches. Prior to the experiments, the lower piston was raised at a rate of 0.1 mm/min, and a pre-load of 5 N was applied to the specimen. Before all experiments, the test specimens were held for 5 minutes at the test temperature to achieve a homogeneous temperature distribution throughout the specimens. All compression tests were conducted at an initial strain rate of $7.5 \times 10^{-4}$ s$^{-1}$.
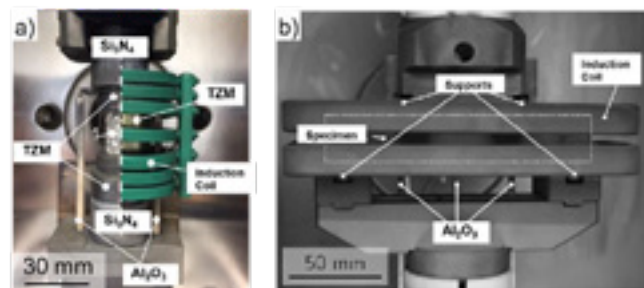


*Fig. 2: Testing setups used for the compression tests (a) and 4-point bending tests (b).*

4-point bending tests were conducted using the testing setup depicted in Figure 2b. The specimen was positioned in the region where the heating process takes place using the induction coil, and the bending tests were performed using four supports, two on the top and two on the bottom, shown in Fig 2b. The bending was measured using three Al₂O₃ rods in contact with the test specimen. Prior to the experiments, the lower piston was raised up at a rate of 2 mm/min, and then a pre-load of 10 N was applied to the specimen. It is important to note that, prior of all HT bending tests, the specimens were subjected to a holding period of 15 minutes at the test temperature, to ensure that a homogeneous temperature distribution was achieved throughout the specimen.

Acoustic emission measurements were conducted simultaneously with 4-point bending tests to better understand the damage behaviour of the materials both at RT and at high temperatures. For this study, two different types of transducers were selected. Both are piezo-electric resonant sensors, however, with different frequency response ranges. The two sensors (both from MISTRAS, USA) are low frequency narrow band sensors, R15S and R6S. Both sensors have a very high sensitivity and a good frequency response over the range of 50-400 kHz (R15S) and 35-100 kHz (R6S), respectively.

They are, therefore, ideal candidates for applications requiring high sensitivity to AE signals at medium (R15S) and low frequencies (R6S). Both sensors feature a rugged steel construction with an integrated coaxial cable exiting on the side with a BNC connector. The temperature application range is -65 °C to 177 °C. The size of the sensors (Ø 16.5 mm for R15S and Ø 19 mm for R6S) makes them suitable for application at RT directly on the bending specimens with a width of 25 mm ensuring that the entire sensor area is connected to the specimen surface. The areas of sensor location were manually smoothed by grinding with SiC paper. Small droplet of vacuum oil was used as a coupling medium. The sensors were securely mechanically clamped at the specimen using two alumina cases. Figure 3a and 3b show the 4-point bending testing setup for acoustic emission measurement at 1300 °C. Since the operating temperature range of the sensors was significantly lower than the test temperature, two $Al_2O_3$ waveguides of the same length were connected to the specimen using ceramabond (Kager GmbH, Germany) to ensure signal transmission. In addition, two identical adapters were used to transmit the signals from the waveguides to the sensors and vacuum oil was applied between the sensor surfaces and the adapters as a coupling medium. This allowed the sensors to be kept far away from the high-temperature region, and the signals from the specimens could be obtained through this setup.
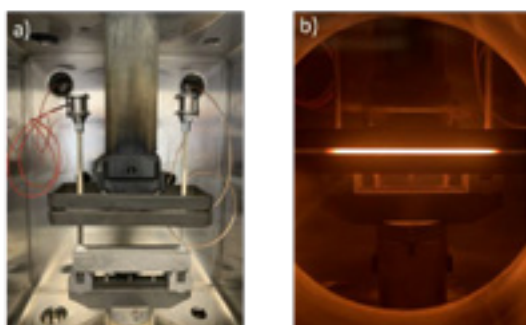


*Fig. 3: Acoustic emission measurements; testing setup (a) and a specimen during high-temperature test (b).*

## RESULTS AND DISCUSSION

Figure 4 shows the results obtained from the compression test conducted at 1300 °C. The specimens, which were fabricated using the FAST technique, showed superior strength when compared to the single-sintered castable materials. This is expected, as it is in accordance with the initial porosity values of the specimens, given in Table 2. The materials produced using the FAST technique possessed a lower level of porosity, thereby leading to an overall higher level of strength. Conversely, the castable materials exhibited a lower level of strength due to their higher initial porosity of about 40%. However, after surpassing the yield strength, these materials did not undergo any significant damage or failure. Once the maximum strength was achieved, a significant softening became noticeable, in particular in the material that contained fine-grained alumina of type CT9FG. Moreover, the materials that contained fine-grained alumina CT9FG displayed higher strength when compared to those containing coarse-grained alumina Alodur, regardless of the production techniques employed.

Figure 5 depicts the results of the 4-point bending tests carried out at a temperature of 1300 °C. It is evident that the single-sintered composite exhibited superior bending strength in comparison to its double-sintered counterpart.
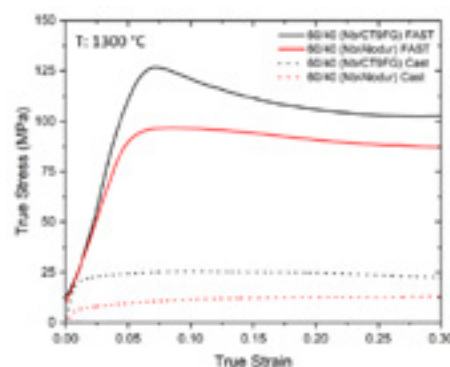


*Fig 4: Compression test results for cast single-sintered composites and FAST Nb-Al₂O₃ composites with two different chemical compositions each.*

A critical observation from these findings is that the initiation of damage in the double-sintered material occurred at significant lower stress levels compared to the single-sintered material. The double-sintered composite showed minimal bending before suffering damage and failure. Conversely, the single-sintered composite exhibited different behaviour, as it did not fail abruptly after achieving the maximum bending strength but continued to exhibit bending before finally failing at higher bending limits than the double-sintered composite. These results indicate that the single-sintered composite possessed higher bending strength, even if it had similar porosity levels before the bending tests, as given in Table 2. A more comprehensive analysis would be worthwhile to investigate the regions where damage occurred and crack propagation took place. This would provide valuable insights into the specific locations where crack initiation occurs and contribute to a better comprehension of the influence of grain size on bending strength, and is planned for future work.
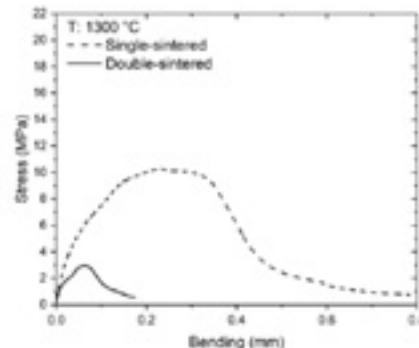
*Fig 5: Results of bending tests at 1300 °C.*

RT bending tests were performed in combination with AE measurements on notched bending bars of both single and double-sintered Nb-Al₂O₃ composites. Figure 6a shows the load vs. time plot of both bending tests, whereas Figure 6b shows, in addition to the load vs. time curve of the double-sintered material, the two AE data streams of the two AE transducers R15 (black) and R6 (red), respectively. Similar picture was obtained also for the single-sintered specimen. Both AE data streams consisted of a huge number of transient signals throughout the entire loading process. Moreover, high amplitude AE signals of both sensors corresponded well with the serrations in the load vs. time curve caused by damage of the material. The AE data streams were transferred from the time domain into the frequency domain via a Fast Fourier Transformation (FFT) [11]. As a result, power spectral density functions with different characteristics were obtained resembling that throughout the bending process different AE sources were activated. It is clearly visible that clusters with different values of the parameters 'energy' and "median frequency' were separated (Figure 7a).
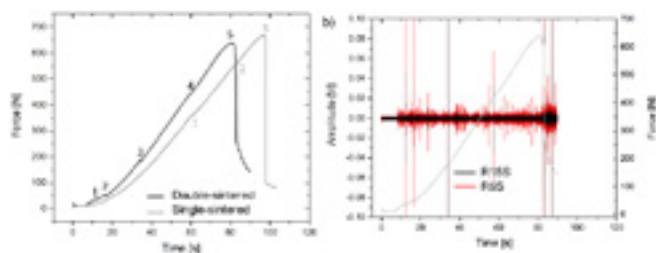
*Fig 6: Compression tests at RT on notched bending bars of single- and double sintered Nb-Al₂O₃ composite (a) in combination with acoustic emission measurements exemplarily shown for double-sintered specimen (b).*

Two of these clusters contain signals with a very low energy and a wider range of median frequencies (black, red). Two other clusters contain high energy signals in a very narrow band of median frequencies. From the evolution of these clusters during the entire bending experiment it turned out that the red and black cluster are related to different levels of noise starting right before the bending experiment: (i) machine noise in load-free condition (black), (ii) machine noise under preload of 10 N. The two high-energy clusters are related to friction (blue) and to cracks (green). The signals related to friction start directly at the beginning of the bending tests, whereas signals related to cracks appear somewhat later pronounced jump in the cumulative energy of signals belonging to this cluster appears together with severe serrations in the load vs. time curve (Figure7b).
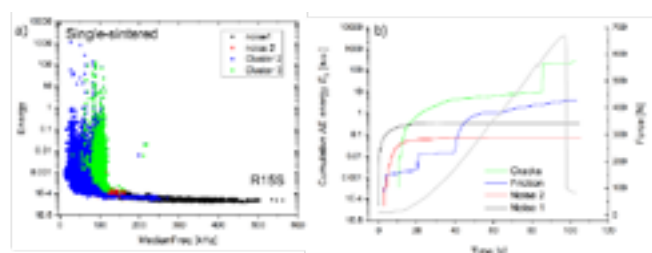


*Fig 7: Results of the AE data analysis in terms of median frequency and AE power as a result of power spectral density functions obtained from the Fast Fourier analysis. Exemplarily for single-sintered material and AE sensor R15S.*

The first high-temperature bending test at 1300 °C on a single sintered material was accompanied by in-situ acoustic emission measurements. As the RT measurements revealed different sources of acoustic emission such as (i) machine noise, (2) friction during bending, and (3) initiation and propagation of cracks, the situation at high temperature, however, is much more complex due to the damping of the acoustic emission signals at high temperatures, the application of wave guides as well as thermal expansion of material during heating up to 1300 °C. Thus, Fig. 8 shows the complete HT deformation test including the heating and the bending part of the experiment. Thus, the black curve gives the load vs. time, whereas the red curve shows the temperature vs. time and the green curve the tool separation vs. time. The continuously recorded AE data stream is plotted in blue. It is obvious that prior to the bending test, significant number of transient signals occurred, already in the heating regime. However, it is not yet clear what is the reason of these in parts high-amplitude signals. AE sources could be either (friction between specimen and bending tool or processes in the material caused by the heating itself. Here, further tests had to be done for clarification.

## CONCLUSIONS

The high-temperature mechanical behaviour of Nb-Al₂O₃ composites (60 vol.% Nb + 40 vol.% Al₂O₃) manufactured via castable and FAST techniques was studied. Compression as well as bending tests were performed at 1300 °C in order to study the influence of temperature on mechanical behaviour.
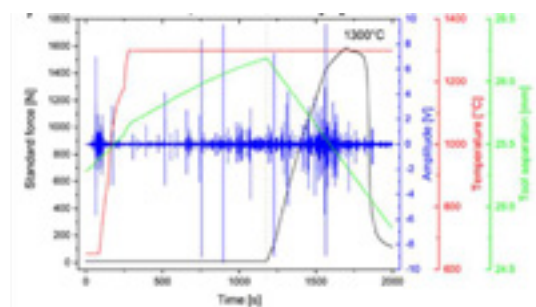


*Fig 8: Bending test at 1300 °C on single-sintered Nb-Al₂O₃ composite in combination with acoustic emission measurements.*

It is observed that the initial open porosity of composites produced using different manufacturing methods significantly influences the mechanical properties. Composites produced using the FAST technique exhibited higher strength due to the low porosity being less than 1%. Additionally, material produced using the same manufacturing method but containing different grain sizes exhibited different behaviour at high temperature. Despite having the lower open porosity, the single-sintered refractory composite demonstrated superior strength and plasticity at high temperatures than the double-sintered composite.

## REFERENCES

[1]   del Rio, E., Nash, J. M., Williams, J. C., Breslin, M. C., Daehn, G. S. Co-continuous composites for high-temperature applications. Materials Science and Engineering: A, 463 (1-2), 2007, p. 115-121.

[2]   Zienert, T., Farhani, M., Dudczig, S., Aneziris, C. G. Coarse-grained refractory composites based on Nb-Al₂O₃ and Ta-Al₂O₃ castables. Ceramics International, 44 (14), 2018, p. 16809-16818.

[3]   Xiangchong, Z., Hailei, Z. High-temperature properties of refractory composites. American Ceramic Society Bulletin, 78 (7), 1999, p. 98-101.

[4]   Günay, G., Zienert, T., Endler, D., Aneziris, C. G., Biermann, H., Weidner, A. High-Temperature Compressive Behavior of Refractory Alumina–Niobium Composite Material. Advanced Engineering Materials, 24 (8), 2022, p. 2200292.

[5]   Kuwabara, M., Spence, J. C. H., Ruhle, M. On the atomic structure of the Nb/Al₂O₃ interface and the growth of Al₂O₃ particles. Journal of Materials Research, 4 (4), 1989, p. 972-977.

[6]   Rühle, M., Backhaus-Ricoult, M., Burger, K., Mader, W. Diffusion Bonding of Metal/Ceramic Interfaces - A Model Study at the Nb/Al₂O₃ Interfaces. Ceramic Microstructures' 86: Role of Interfaces, 1987, p. 295-305.

[7]   Burger, K., Rühle, M. Material transport mechanisms during the diffusion bonding of niobium to Al₂O₃. Ultramicroscopy, 29 (1-4), 1989, p. 88-97.

[8]   Weidner, A., Ranglack-Klemm, Y., Zienert, T., Aneziris, C. G., Biermann, H. Mechanical high-temperature properties and damage behavior of coarse-grained alumina refractory metal Composites. Materials, 12 (23), 2019, p. 3927.

[9]   Zienert, T., Endler, D., Hubálková, J., Gehre, P., Eusterholz, M., Boll, T., Aneziris, C. G. Coarse-Grained Refractory Composite Castables Based on Alumina and Niobium. Advanced Engineering Materials, 24 (8), 2022, p. 2200296.

[10]  Kraft, B., Wagner, S., Schell, K. G., Hoffmann, M. J. Field-Assisted Sintering of Nb–Al₂O₃ Composite Materials and Investigation of Electrical Conductivity. Advanced Engineering Materials, 24 (8), 2022, p. 2200063.

[11]  Pomponi, E., Vinogradov, A. A real-time approach to acoustic emission clustering, Mech. Syst. Signal Proc. 40 (2), 2013, p 791.

# COMPARISON OF SOLIDIFICATION BEHAVIOR OF SYNTHETIC MULLITE AND MULLITE-FORMING RAW MATERIALS BY AERO-ACOUSTIC LEVITATION

Dirk Mühmer, Jonas Niessen, Thorsten Tonnesen, Jesus Gonzalez-Julian
Chair of Ceramics, Institute of Mineral Engineering, RWTH Aachen University, Germany

## ABSTRACT

Fused mullite is used in refractories and as an abrasive due to its suitable properties. Mullite is formed over a wide range in the $Al_2O_3$-$SiO_2$ phase system, preferably as 3:2 or 2:1 mullite. There are several options to tailor the features of fused mullite, and consequently its properties. In that sense, solidification at different $Al_2O_3$:$SiO_2$ ratios, undercooling, and impurity content have a major influence on the microstructure.

This report focuses on the difference between synthetic high-purity fused mullite and mullite-forming raw materials kyanite and andalusite, which are commonly used in refractories. The synthesis of high-purity samples is possible by applying containerless levitation. The used aero-acoustic levitator allows the melting and solidification of samples in a gas stream without any contamination from the crucibles. A high-speed camera enables the observation of molten samples and their solidification, while a pyrometer monitors the apparent temperature of the sample. This allows the continuous monitoring of the solidification process in terms of temperature, crystallization, and reaction during the whole process, including the release of latent heat. Further analysis is carried out by Scanning Electron Microscope (SEM) to examine the microstructure of the mullite phases and X-ray diffraction (XRD) to confirm the presence of mullite. Thermodynamic considerations are used to discuss these results.

## INTRODUCTION

Refractory materials play a critical role in the energy transition, as they are required in any heat-intensive production process. Especially for the steel industry, which is facing new challenges in providing hydrogen technologies for the decarbonization of industrial heating processes. In that sense, some of the most used compositions are mullite and mullite-forming raw materials due to their determinant response at high temperatures and under aggressive environments such as creep resistance, chemical stability, and thermal shock resistance [1].

In the mid-1900s, mullite was processed by reaction sintering of mixed minerals. This resulted in poor homogeneity. The use of high-purity powders increased the technical applications of mullite [1]. So far, mullite can be synthesized in many different forms, such as single crystals, fibers, or fused bricks. [2]. Rodrigo et al. [3] studied the reaction sintering of amorphous silica and α-alumina, emphasizing the important role of the alumina-to-silica ratio. They obtained almost dense ceramics (97%) by firing the samples up to 10 h at 1600°C. The highest density and the finest microstructure were observed with the molar ratio of 3:2 $Al_2O_3$ to $SiO_2$.

Andalusite and Kyanite are anhydrous minerals containing mainly alumina and silica. They have the same molar ratio (1:1) of $Al_2O_3$ to $SiO_2$, which results in an ideal composition of 62,92 wt% $Al_2O_3$ and 37,08 wt% $SiO_2$ [4]. In natural deposits, impurities are found in these aluminosilicates. Besides their same chemical composition, they have different crystallographic structures. Both aluminosilicates are not stable at 1 atm pressure. They are in equilibrium at high pressures and elevated temperatures. These conditions are found inside the earth. Therefore, they can be found in many parts of the world. [4]. On the contrary, mullite is at equilibrium at atmospheric pressure. However, it is rarely found in nature and then only as an intrusion [4][5]. Mullite is the only stable compound at higher temperatures in the $Al_2O_3$- $SiO_2$ phase system [6]. This leads to the industrial relevance of andalusite and kyanite. At higher temperatures, they decompose to mullite and silica. Since the molar ratio of alumina to silica of andalusite and kyanite compared to 3:2 mullite is shifted to silica, there has to be

residual $SiO_2$ after the phase transition. Andalusite transforms to mullite in the range of 1500 – 1600°C [7]. Kyanite decomposes at lower temperatures between 1150 – 1350°C [8]. Both phase transitions result in a microstructure of mullite and mostly amorphous $SiO_2$. At high temperatures, these $SiO_2$ precipitations are the weak spot of the microstructure due to the lower melting point of 1713°C [9] in contrast to mullite (1890±10°C) [6]. Mullite precipitates over the entire range between pure $SiO_2$ and pure $Al_2O_3$. The $Al_2O_3$- $SiO_2$ phase system has a peritectic reaction at the stoichiometric composition of 2:1 mullite (77 wt% $Al_2O_3$, 23 wt% $SiO_2$), where liquid and $Al_2O_3$ react to form mullite [6].

The use of pure powders is problematic for experiments at elevated temperatures. Ceramics are known to have a very high melting point. Therefore, crucibles that can withstand very high temperatures are required. Even if they do not melt at the melting point of the ceramic used, some of the crucible material will diffuse into the ceramic melt. By incorporating impurities into the melt of the pure powders, the advantage of working with expensively produced pure powders is diminished. Therefore, to explore ceramic systems at high temperatures, even in the molten state, a containerless heating device is required. To meet this challenge, we used an aero-acoustic levitator to study synthetic mullite down to the liquid phase.

## EXPERIMENTAL

The synthetic mullite was made of high-purity alumina and amorphous silica: $Al_2O_3$: Baikowski, Malakoff works, United States; BMA15, >99.99 wt% $Al_2O_3$; Amorphous $SiO_2$: pyrogene silica Aerosil 90, Evonik; crystalline >99.8 wt% $SiO_2$. These powders were mixed to the composition proportion of $3Al_2O_3$ $2SiO_2$. For the mullite-forming raw materials were Virginia Kyanite from Kyanite Mining Corporation and Andalusite from Imerys, South Africa, used.

The mixtures were processed into beads up to 3 mm in diameter with the help of a water-cooled copper hearth and $CO_2$-laser beam by melting. The round shape is necessary for the experiments in the aero-acoustic levitator.



*Fig. 1: Aero-acoustic Levitator in operation. An inserted sample is levitating in front of the pyrometer. The golden tubes are ultrasonic transducers.*

The aero-acoustic levitator (Fig. 1) enables the levitation of the ceramic bead. The position of the ceramic bead is fixed above the Bernoulli nozzle by a nitrogen gas stream and by the acoustic waves of ultrasonic transducers. The transducers get feedback from

a diode laser positioning system to settle the turbulence of the levitated sample. Two 240W $CO_2$ lasers (SynradInc, Mukilteo, WA, USA) heat the oxide samples above their liquidus temperature. The power of the lasers is adjustable to control the temperature of the samples, which is recorded by a pyrometer (Exactus BF 8402, Bayer Catalysts LCC, Rome, Italy) at a frequency of 1000 Hz. The experiments are observed by a high-speed camera (V 5.2, PhantomVision Research Inc., Wayne, NJ, USA) with a sampling rate of up to 2600 frames per second. It is equipped with a long-distance lens to capture full-scale images of the samples.

## RESULTS AND DISCUSSION
### Chemical composition
Tab. 1 shows the oxide chemical compositions of the used materials. Andalusite and kyanite were analyzed by X-ray fluorescence. The raw materials were mixed appropriately to a 3:2 $Al_2O_3$:$SiO_2$ ratio for the synthetic mullite material. In addition to the main constituents, andalusite contains smaller amounts of $Fe_2O_3$ and $K_2O$. In kyanite, these are $TiO_2$ and $Fe_2O_3$. No XRF was performed on the synthetic mullite because the raw materials have a purity of >99.99 wt% and 99.80 wt%, respectively.

*Tab. 1: Chemical composition by X-ray fluorescence analysis in wt%. The 3:2 mullite sample, marked with an asterisk, was not measured, but its initial composition is shown.*

| Oxide | Andalusite | Kyanite | 3 2 Mullite* |
|---|---|---|---|
| $SiO_2$ | 36,80 | 40,60 | 28,20 |
| $Al_2O_3$ | 62,05 | 57,16 | 71,80 |
| $Fe_2O_3$ | 0,60 | 0,75 | 0,00 |
| $TiO_2$ | 0,16 | 1,13 | 0,00 |
| $CaO$ | 0,06 | 0,00 | 0,00 |
| $MgO$ | 0,01 | 0,02 | 0,00 |
| $K_2O$ | 0,23 | 0,10 | 0,00 |
| $Na_2O$ | 0,05 | 0,02 | 0,00 |
| $P_2O_5$ | 0,00 | 0,13 | 0,00 |
| $ZrO_2$ | 0,01 | 0,03 | 0,00 |
| $ZnO$ | 0,03 | 0,04 | 0,00 |
| $SrO$ | 0,00 | 0,02 | 0,00 |

### Surface morphology
The samples were placed in the aero-acoustic levitator and heated by the lasers until they were completely molten. For solidification, the lasers were turned off and the temperature dropped. Due to homogeneous nucleation, the molten sample undergoes high undercooling before crystallization starts. During the solidification, latent heat is released and raises the temperature for a period of time.
Fig. 2 shows the surface of a kyanite sample. The highlighted areas (1-3) define different surface morphologies. Solidification begins in area 1 and progresses through areas 2 and 3. The surface of the initial solidification stage shows a smooth but uneven surface. The images taken by the high-speed camera showed a highly viscous melt before solidification began. This type of shape could be the result of crystallization in a highly viscous melt. During further solidification, associated with an increase in temperature due to the release of latent heat, the surface morphology changes into small branched needles. The facetted needles are randomly oriented. In area 3, the surface structure has changed to larger needles growing in the same direction. This structure solidified at the highest temperature.
The results are consistent with the findings of Li et al. [10]. They stated that for a smaller undercooling the solute redistribution can occur during growth, resulting in facetted rods without any branching. This needle morphology is similar to area 3. As the melt is further undercooled, the atomic diffusivity decreases, and the

crystal growth rate increases. This results in the growth of feathery, facetted dendrites, comparable to area 2.
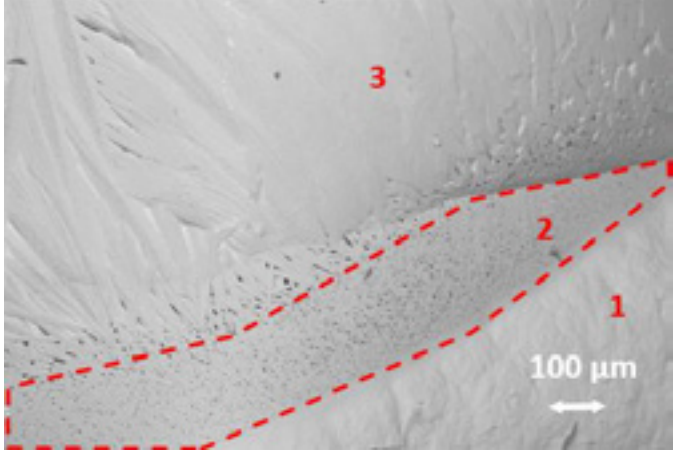


*Fig. 2: Backscattered electron scanning microscope image of the surface of kyanite. The surface is divided into three different areas with different morphologies.*

## CONCLUSIONS AND OUTLOOK
The undercooling determines the surface morphology of the levitated samples. The exceptional experimental conditions in the aero-acoustic levitator lead to a large undercooling of the samples due to the homogeneous nucleation. The differences are shown by three different surface structures: (1) higher undercooling, smooth but uneven surface, (2) medium undercooling, small branched needles, (3) smaller undercooling, larger needles growing in one predominant direction.

A detailed elaboration of the topic as a scientific article can be found in the journal "Open Ceramics".

## REFERENCES
[1] Aksay, I. A., Dabbs, D. M., & Sarikaya, M. (1991). Mullite for structural, electronic, and optical applications. Journal of the American Ceramic Society, 74(10), 2343-2358.
[2] Schneider, H., Schreuer, J., & Hildmann, B. (2008). Structure and properties of mullite—A review. Journal of the European Ceramic Society, 28(2), 329-344.
[3] Rodrigo, P. D. D., & Boch, P. (1985). High purity mullite ceramics by reaction sintering. International Journal of High Technology Ceramics, 1(1), 3-30.
[4] J.F. Shackelford and R.H. Doremus (eds.), Ceramic and Glass Materials: 41 Structure, Properties and Processing. Springer 2008.
[5] Bowen, N. L., Greig, J. W., & Zies, E. G. (1924). Mullite, a silicate of alumina. J. Wash. Acad. Sci., 14(9), 183–191. http://www.jstor.org/stable/24531487.
[6] Klug, F. J., Prochazka, S., & Doremus, R. H. (1987). Al2O3-SiO2 system in the mullite region. J. Am. Ceram. Soc., 70(10), 750-59.
[7] Hülsmans, A., Schmücker, M., Mader, W., & Schneider, H. (2000). The transformation of andalusite to mullite and silica: Part I. Transformation mechanism in [001] A direction. American Mineralogist, 85(7-8), 980-986.
[8] Schneider, H., & Majdič, A. (1980). Kinetics of the thermal decomposition of kyanite. Ceramurgia international, 6(2), 61-66.
[9] Harders, F., Kienow, S., Harders, F., & Kienow, S. (1960). Die Eigenschaften feuerfester Stoffe und ihre Prüfung. Feuerfestkunde: Herstellung, Eigenschaften und Verwendung feuerfester Baustoffe.
[10] Li, M., Nagashio, K., & Kuribayashi, K. (2002). Containerless solidification of highly undercooled mullite melts: Crystal growth behavior and microstructure formation. Metallurgical and Materials Transactions A, 33, 2677-2683.

# CARBON-FREE ELECTRICALLY HEATABLE COARSE-GRAINED COMPOSITE MATERIALS CONSISTING OF (NB/TA)-AL$_2$O$_3$ AND ALUMINA

Patrick Gehre, Dirk Endler, Nora Franke, Tilo Zienert, Jana Hubálková, Christos G. Aneziris
TU Bergakademie Freiberg, Institute of Ceramics, Refractories and Composite Materials, Freiberg, Germany

## ABSTRACT

Due to actual challenges such as the way to carbon neutrality and limited access to raw materials and fossil fuels, material researchers have to develop environmentally friendly, efficient materials and resource-saving processes. Moreover, modern high-temperature processes require smart refractories with, e.g. electric properties besides a superior thermo-mechanical behaviour. The Research Unit FOR 3010, supported by the German Research Foundation DFG, investigates and develops a new generation of coarse-grained refractory composites based on the electrically conductive and ductile refractory metals niobium and tantalum with the corrosion- and thermal shock-resistant refractory ceramic Al$_2$O$_3$ [1]. A concept of a carbon-free electrically heatable functional component implies a coarse-grained core based on the (Nb/Ta)-Al$_2$O$_3$ refractory composites protected by a coarse-grained alumina shell with excellent stability even in hydrogen- and steam-containing atmospheres up to 1700 °C. The shaping of such a heat shield or stopper component was realised by utilising slip casting and sequential pressure slip casting. In dependence on the water and binder content, the rheological behaviour of the slips was investigated with a rheometer and a pressure strainer. With 1.0 wt.% binder (konjak flour and welan gum) and 15 wt.% water, sufficient dewatering with an applied pressure of 6 bar was achieved. After shaping and sintering, the microstructure and interface of the (Nb/Ta)-Al$_2$O$_3$ core and Al$_2$O$_3$ shell were investigated. After sintering at 1600 °C, no makrocracks along the interface could be detected due to a low shrinkage and a similar thermal expansion of the Al$_2$O$_3$ and Nb-Al$_2$O$_3$ (60 vol.% Al$_2$O$_3$) components.

## MATERIAL AND METHODS

Coarse-grained aggregates with 60 vol.% metal were produced from fine-grained castables based on commercially available standard raw materials, e.g. the alumina CT9FG from Almatis and an Nb-powder with -325 mesh particle size distributions as shown in figure 1.
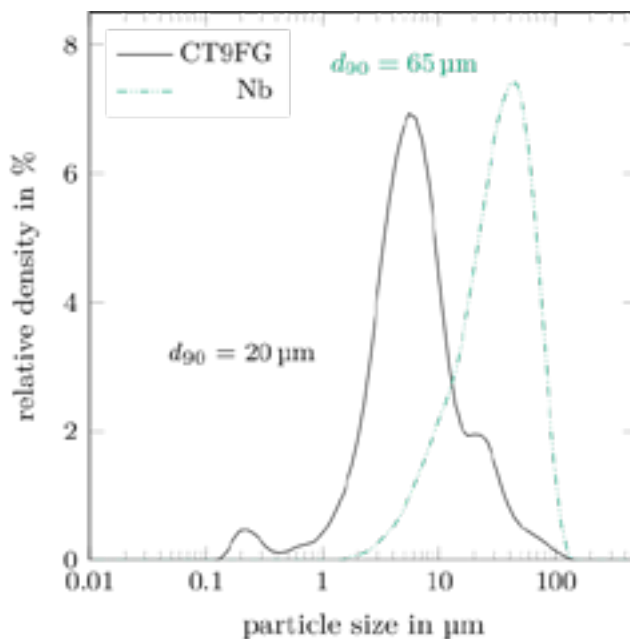
After sintering at 1600 °C and crushing, the aggregates were sieved to particle sizes <3150 μm and were characterised by means of porosity (Archimedes method, mercury intrusion porosimetry), chemistry (XRD, SEM/EDS/EBSD) and morphology (laser scanning microscopy) [2]. For the latter, a statistical approach [3] was used to identify the morphology parameters radius $r_0$, ovality $o$, the height of first-order peaks $h_p$ and the number of peaks $n_p$ defined by

$$r(phi) = r_0 * (1 + h_p*\cos(phi*n_p) + o*\cos(2phi)) \qquad (1)$$

## RESULTS

An example of one fit of equation (1) to a determined outer contour of a synthesised particle can be seen in figure 2 and the derived statistics on the example of the particle radii in figure 3.



$r_0 = 493.1 \ \mu m$     $n_p = 6$
$h_p = 0.033$     $o = 0.147$
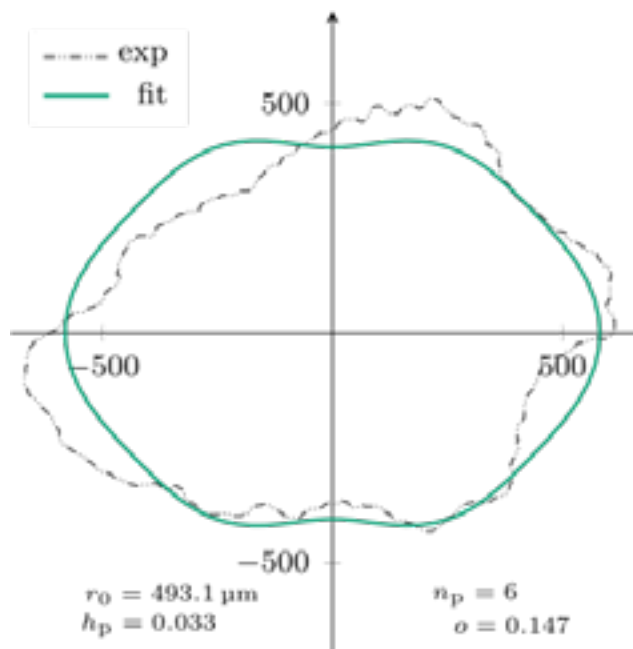
Fig. 2: Morphology fit on the outer contour of a synthesised particle.

X-ray powder diffraction revealed the presence of NbO and beta-Nb$_2$C after sintering the Nb-Al$_2$O$_3$ composite material. Due to sintering in a graphite-based furnace, the formed sintering atmosphere was Ar with traces of CO/CO$_2$, which caused the formation of the mentioned intermediate phases. Niobium carbide formed especially on the free surfaces of the aggregates, which is more pronounced on particles with a large value of open porosity like the alginate-based beads [4]. Such chemical reactions were proven by EBSD measurements after focused ion beam preparation of the sample, as shown in figure 4.



Fig. 1: Particle size distribution of the used raw materials.

807
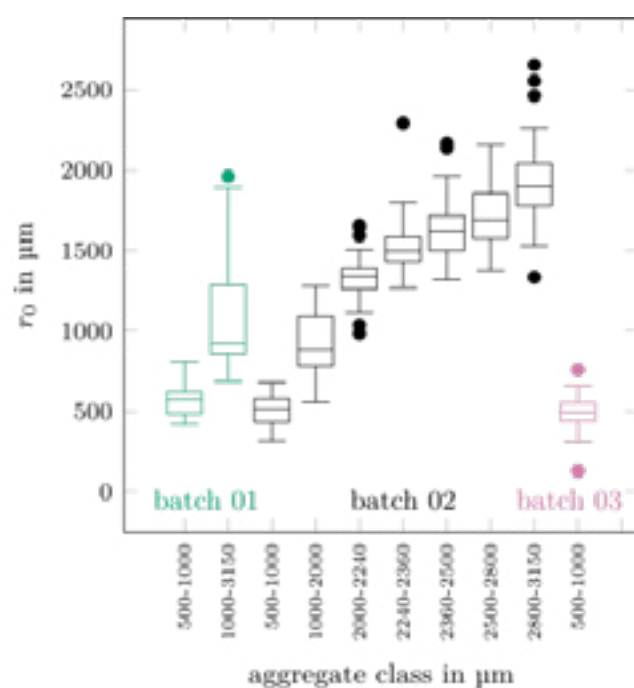
Fig. 3: Obtained particle radii distribution using the statistical approach.

808
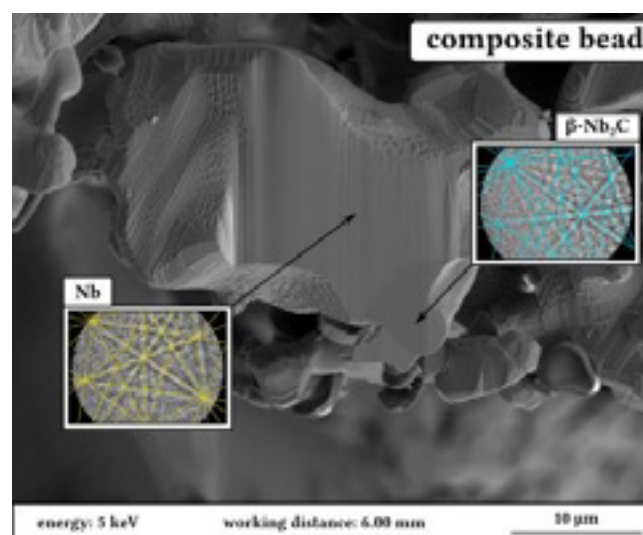


Fig. 4: SEM micrograph of a Nb-Al$_2$O$_3$ composite bead showing the formation of beta-Nb$_2$C at the particle surface.

The electrical conductivity of the casted composite material was 40-60 S/cm, which is only three orders of magnitude below the values of pure niobium [1], whereas the dense-sintered material (using SPS) showed values of 5-10 kS/cm [5].

**CONCLUSIONS**

An electrical and thermal conductive composite material based on Nb-Al$_2$O$_3$ for refractory application was developed. The refractory composite is especially suitable for heating cores in typical ceramic-based refractory applications.

**REFERENCES**

[1]  Zienert, T.; Endler, D.; Hubálková, J.; Günay, G.; Weidner, A.; Biermann, H.; Kraft, B.; Wagner, S.; Aneziris, C.G.: Synthesis of Niobium-Alumina Composite Aggregates and Their Application in Coarse-Grained Refractory Ceramic-Metal Castables, Materials 14 (2021) 6453

[2]  Zienert, T.; Endler, D.; Brachhold, N.; Weiner, M.; Schmidtchen, M.; Prahl, U.; Aneziris, C.G.: Characterisation of niobium-alumina refractory aggregates synthesised by castable technology, Advanced Engineering Materials 24 (2022) 2200407

[3]  Weiner, M.; Zienert, T.; Schmidtchen, M.; Hubálková, J.; Aneziris, C. G.; Prahl, U.: A New Approach for Sintering Simulation of Irregularly Shaped Powder Particles-Part II: Statistical Powder Modeling, Advanced Engineering Materials 24 (2022) 2200443

[4]  Storti, E.; Neumann, M.; Zienert, T.; Hubálková, J.; Aneziris, C.G.: Metal-Ceramic Beads Based on Niobium and Alumina Produced by Alginate Gelation, Materials 14 (2021) 5483

[5]  Kraft, B.; Wagner, S.; Hoffmann, M.J.: Field Assisted Sintering of Nb-Al$_2$O$_3$ Composite Materials and Investigation of Electrical Conductivity, Advanced Engineering Materials 24 (2022) 2200063

# STEEL CERAMIC COMPOSITE ANODES BASED ON RECYCLED MGO−C LINING BRICKS FOR APPLICATIONS IN CRYOLITE/ALUMINUM MELTS

S. Yaroshevskyi, C. Weigelt, P. Malczyk, V. Roungos, J. Hubalkova, T. Zienert, C.G. Aneziris

Institute of Ceramics, Refractories and Composites, TU Bergakademie Freiberg, Agricolastr. 17, 09599 Freiberg, Germany

B. Kraft, S.Wagner

Institute for Applied Materials - Ceramic Materials and Technologies, Karlsruhe Institute of Technology, Haid-und-Neu-Straße 7, 76131, Karlsruhe, Germany Germany

## ABSTRACT

Development and utilization of novel manufacturing route for composite inert anodes containing 60:40 volumetric ratio of 316L stainless steel and MgO powder obtained from spent MgO-C lining bricks has been conducted. After burning residual carbon from recycled MgO-C powder, MgO and steel were granulated and pre-sintered in order to create agglomerates of composite material that played the role of coarse grains of composite material, hindering sintering-related shrinkage. These granules were mixed with raw steel and MgO powders in order to form dense particle distribution and subsequently cold isostatically pressed in the form of electrodes. All manufactured anode samples underwent sintering at 1350 °C and pre-oxidation under different temperatures – 800 °C, 900 °C, and 1000 °C. Mechanical and electrical properties of the manufactured electrodes were characterized. The results show that upcycling of the spent MgO-C bricks enables manufacturing of sophisticated electrode products, which can be applied in the aluminum industry.

## INTRODUCTION

Refractories are commonly used in high-temperature applications in particular, production of metal, cement, glass, and ceramics. Despite significant amounts of refractory materials being used every year, recycling of such products gained attention only during recent years, recycling rate for refractories is estimated to be only 7% of raw material demand. It is expected that recycling rate of refractory materials to have increased up to 10% by 2025. Production costs of refractory materials rise every year, as well as energy prices, moreover, necessity of environmental protection becomes more and more clear. Besides recycling of the refractory materials, another possible way to decrease disposal rate of refractories is utilization of the spent materials (ones that came to the end of their life cycle), is to produce more profound and complicated functional parts, specifically, upcycle the refractories.

In metal industry the largest part of refractories is dolomite, followed by magnesite, fireclay and bauxite. MgO-C lining bricks have been gaining more and more attention over recent decades and nowadays they are widely used in basic oxygen furnaces, electric arc furnaces, and steel ladle furnaces due to their excellent resistance to thermal shock, slag penetration, and corrosion; as well as their outstanding properties at elevated temperature. Around 40% of the original converter lining is wearing out, and approximately half of the remaining material is recyclable refractory material. According to Moritz et al., MgO-C bricks that contain recyclate perform comparatively good in comparison with the fresh MgO-C bricks in terms of thermal shock resistance, even with content of recyclates up to 80 % by mass. However, due to decrease in CMOR and RUL at high content of recyclate, such material could be suitable for applications with relatively low refractory requirements [1]. Among the application fields of MgO-containing materials that do not require outstanding refractoriness there are composite materials that were studied recently: in field of plasma resistance for semiconductors application, and in field of corrosion resistance against molten aluminium alloys. According to Malczyk et al., steel-ceramic composite material based on 316L stainless steel with addition of MgO powder after certain thermal treatment exhibited outstanding corrosion resistance against molten aluminium alloys [2], due to the formation of MgO-FeO solid solution on their surface [3]. Thus, it might be possible to utilize spent MgO-C bricks for aluminium production, where corrosion resistance is of more importance than refractoriness of the material, specifically for inert electrodes for the alumina-cryolite electrolytic cell process.

There are few metal oxides which do not co-deposit in the aluminum by electrochemical deposition or chemical displacement. Preferred metal oxides are MgO, SrO, La2O3, CaO, etc. However, these oxides have significant solubility in cryolite. Nowadays, most commonly used electrodes for production of aluminum-silicon alloys in cryolitic melts are consumable graphite anodes. Galasiu and Thonstad give comprehensive overview of inert anodes for electrowinning of aluminium [4], dividing them into three categories:

1. Ceramic inert anodes, especially based on SnO2 with doped with CuO and Sb2O3, which are being prepared from oxides and therefore do not oxidize during electrolysis.

2. Cermet inert anodes, which combine two phases: ceramic phase which is resistant to oxidation, however lacks electrical conductivity; and metallic phase added to increase conductivity. The major disadvantage of such materials is the oxidation of the metallic part during the electrolysis process.
3. Metallic inert anodes that utilize specific alloys that undergo a surface oxidation during electrolysis, forming oxide layers with low solubility in the electrolyte. The surface layer of such electrodes has to be electrically conductive and impermeable to oxygen.

There is an increasing argument that the introduction of inert anodes would have a little to none environmental benefits due to higher DC energy consumption with inert anodes. However, research studies continue in present. For production of such electrodes it is important to note that fine-grained metal ceramic composites suffer from the high shrinkage during sintering process, which drastically limits dimensions of the manufactured body. A concept of coarse-grained composite materials was recently introduced [5]: fine powders of raw materials are used to create aggregates of desired size. Such aggregates then undergo pre-sintering process, forming an analogue of coarse grains of the composite material. These sintered aggregates have already experienced shrinkage caused by sintering process. Therefore, after mixing with fine powders to form a dense body, they will significantly decrease shrinkage of the manufactured product.

This research focuses on the utilization of the crushed spent MgO-C lining bricks to manufacture cermet inert composite anodes for the aluminium cryolite electrolytic cells. Furthermore, this research studies further implementation of the novel manufacturing process, namely, pre-sintering of coarse-grains (aggregates) of composite materials in order to decrease the sintering-related shrinkage of the products. The research also includes characterization of the produced parts, including E-modulus, splitting tensile strength, electrical conductivity at room temperature, as well as

809

microstructural analysis by means of REM and EDS analysis of the manufactured electrode samples.

## METHODS AND MATERIALS

### Materials

Crashed MgO-C bricks were provided by Refratechnik Steel GmbH with particle size of 0-1 mm. For the manufacturing of the anode samples as well as for the granulate production, the finest MgO-C fraction – less than 125 μm – was sieved out and only this fraction was used throughout the whole research. Carbon content of the powder was estimated to be approximately 19.3 % by mass during the oxidation test: Nabertherm LHT 04/16 SW oven (Nabertherm GmbH, Lilienthal/Bremen, Germany) is equipped with weigh that allows to continuously measure mass of the sample during the heating process to desired temperature. 12.5 g of the sieved fine fraction of MgO-C material were slowly heated up with heating rate of 2.5 K/min until mass of the sample stabilizes (approximately 6.5 h, reaching 950 °C). Therefore, 24 h at 1000 °C was chosen as the sufficient thermal treatment to burn out all the residual carbon (conducted in Nabertherm N 20/14 ventilated oven under air). The true density of MgO powder is 3.58 g/cm3, particle size D90 < 109 μm.

The steel powder of gas-atomized 316L-FeCr18Ni10Mo3 stainless steel (TLS Technik, Bitterfeld-Wolfen, Germany) was used as a metallic part for ceramic metal composite. Chemical composition of the steel is provided in Table 1. True density of the 316L stainless steel is 7.62 g/cm3, particle size D90 < 51 μm.

Table 1. Chemical composition of the 316L stainless steel in wt.%.

| Steel | Fe | Cr | Ni | Mo | Mn | S | Al |
|-------|---------|------|------|-----|-----|------|------|
| 316L | Balance | 16.9 | 10.5 | 2.1 | 0.9 | 0.01 | 0.07 |

Carbonless recyclate powder was then used to produce steel-ceramic composite material with volumetric ratio 60 vol.% 316L stainless steel powder + 40 vol. % carbonless MgO recyclate powder. For the coarse-grain aggregates formation, granulation process was chosen. Binder material for the granulation process was water solution of the fructose syrup 70% (Gellmi, Hanseatische Zuckerraffinerie GmbH & Co. KG, Hamburg, Deutschland) in proportion 30 wt.% fructose syrup to 70 wt.% deionized water. Such binder was chosen due to the fact that fructose is environmentally friendly binder material and this correlates with the concepts of the sustainability and upcycling of the conducted research.

### Aggregates preparation

Eirich EL-1 laboratory mixer (Maschinenfabrik Gustav Eirich, Hardheim) was used to mix and to granulate the mixture of the powders of carbonless MgO-recyclate, 316L stainless steel, water and binder material. Granulation process included addition of 1 wt.% of de-ionized water and seven consecutive steps of addition of 1 wt.% of binder material, with one minute mixing at 300 min$^{-1}$ between each step, followed by granulation for 100 seconds at 600 min$^{-1}$.

After the granulation, the material was dried at 110 °C for 24 hours, with further debinding at 500 °C under air for 30 minutes in Xerion Entbinder- und Sinter Sonderofen (XERION ADVANCED HEATING Ofentechnik GmbH, Freiberg, Germany). Parameters of the debinding process were: heating rate 2 K/min to 200 °C, 0.5 K/min to 500 °C and cooling rate 0.5 K/min to 100 °C followed by free cooling to room temperature. After debinding, material was directly transferred to Xerion XGRAPHIT Hochtemperatur-Vakuum-Ofensystem sintering oven, and sintered at 1350 °C for 2 h. Sintering was conducted under argon atmosphere with heating rate 5 K/min to 1350 °C, cooling rate 5 K/min to 300 °C followed by free cooling to room temperature.

### Electrodes manufacturing and testing

Sintered granules of composite material were sieved through the sieving tower with mesh-sizes 8 mm – 6.3 mm – 3.15 mm – 2 mm – 1 mm – 500 μm – 250 μm. Small amount of sintered granulate material was embedded in epoxide and polished in order to conduct XRD analysis. Results for granulate that contains carbonless MgO were then compared to the results of XRD analysis of granulate prepared in the same way, with the same composition 60 vol.% 316L stainless steel powder + 40 vol.% MgO powder, but with fresh fused MgO powder (Refratechnik GmbH, D90 < 100 μm), used instead of recycled material.

After sieving, the sintered granulate was split into three categories, coarse particles in range 2 - 6.3 mm, medium size particles in range 0.5 - 2 mm, and fine particles containing mixture of 316L stainless steel powder with carbonless MgO recyclate powder in a respective volumetric ratio 60:40. Mass ratio coarse:meduim:fines was chosen to be 2:1:2 in order to obtain sufficient densification of the material during pressing. As a pressing aid, Zusoplast G63 (Zschimmer & Schwarz GmbH & Co KG Chemische Fabriken, Lahnstein, Germany) in an amount of 0.5 wt.% of the material mixture was added. Electrodes were pressed in a latex form with diameter 35 mm and height 155 mm under 150 MPa pressure using EPSI CIP 300-250*1000 Y cold isostatic press (Engineered Pressure Systems International NV, Temse, Belgium). After the pressing electrodes were debinded and sintered with the same thermal treatment regimes and in the same Xerion ovens as granulated composite material.

Four cylindrical specimens with height of 70 mm and diameter around 35 mm (depending on the diameter of the parts after pressing) were cut from the sintered electrodes (Fig. 1). Three specimens were pre-oxidized under 800 °C, 900 °C, and 1000 °C. Reference specimen in the as-sintered state and three pre-oxidized specimens were used for E-modulus acoustic measurement with UltraTest Ultrasonic Tester BP-700 (UltraTest GmbH, Achim, Germany) before and after oxidation process. After non-destructive E-modulus test, the same set of specimens was tested for splitting tensile strength at Toni Technik 40-4000 kN testing press (Toni Technik Baustoffprüfsysteme GmbH, Berlin, Germany). Tests were conducted with speed of 0.06 N/mm2/s according to DIN EN 12390-6.

Electrical conductivity was measured with a Keithley 220 Programmable Current Source (Keithley Instruments, Cleveland, OH, USA) and a Keithley 2000 Multimeter (Keithley Instruments, Cleveland, OH, USA) using four-point-measurement setup. Testing was performed by applying electrical currents of 1 mA, 10 mA, and 100 mA and measuring the resulting voltages. For application of the sputter coated layer of gold a Quorum Q150T ES was used. To reduce the influence of surface roughness and to ensure a continuous electrode over the whole sample surface, an additional layer of Pelco Colloidal Silver (Plano GmbH, Wetzlar, Germany) was added. For this setup, four prisms with dimension of 8 mm in height and 9 mm x 9 mm in cross-section were cut from the sintered electrode samples. A set of four prisms was prepared in the same way – reference prism in the as-sintered state and the three other prisms pre-oxidized under 800 °C, 900 °C, and 1000 °C.

Due to the fact that new MgO-FeO based phases appear on the surface of the specimens during pre-oxidation test, none of the specimens underwent grinding or polishing of the surface.
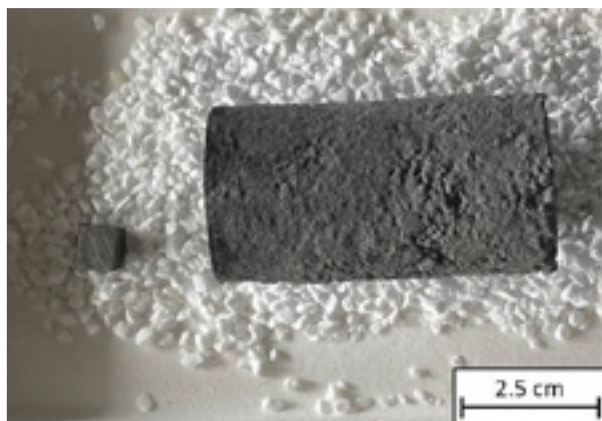
*Fig. 1: Prism for electrical conductivity test (left) and cylinder for spitting tensile test (right) prior to oxidation.*

Another set of four disks with height of 8 mm were cut from the sintered electrode. Three of the disks were pre-oxidized under 800 °C, 900 °C, and 1000 °C, fourth was used as a reference as-sintered sample. After pre-oxidation, all four disks were cut in half, embedded into epoxide and vibro-polished for REM and EDS analysis in order to estimate surface oxidation rate and depth.

## CONCLUSIONS

Spent MgO-C lining bricks after burning residual carbon can be utilized to produce inert anodes based on metal-ceramic composite with 60 vol.% of 316L stainless steel and 40 vol.% of recycled MgO material. In order to manufacture comparatively large parts, additional step of agglomerating and sintering fine powders in an analogue of coarse-grains has to be taken. Such step decreases shrinkage caused by sintering from around 4 % for fine powders up to 0.75% in length direction for mixture of fine-powders (40 wt.%) with pre-sintered agglomerates (60 wt%).

Described composite material forms protective inert oxides layer during pre-oxidation thermal treatment. Such protective layer mostly contains FeO-MgO solid solution phases. Results of the mechanical tests as well as electrical conductivity showed that the most suitable pre-oxidation temperature for the material studied is 900 °C. Anodes pre-oxidized at such temperature had electrical conductivity at the room temperature almost 150 S/cm, which lays in range of inert anodes for aluminium-cryolite electrolytic cells. Since oxide phases created during oxidation thermal treatment are semi-conductive and metal matrix composite of inner volume is electrically conductive, it is believed that at elevated temperatures conductivity of the system will decrease less compared to graphite.

The research is still ongoing, for the nearest future electrical conductivity tests under elevated temperatures and electro-chemical analysis of the results of the corrosion tests are planned.

## REFERENCES

[1] Moritz K, Brachhold N, Hubálková J, Schmidt G, Aneziris C.G. Utilization of Recycled Material for Producing Magnesia–Carbon Refractories. Ceramics. 2023; 6(1):30-42. https://doi.org/10.3390/ceramics6010003

[2] Malczyk P, Zienert T, Kerber F, Weigelt C, Sauke S-O, Semrau H, G. Aneziris C. Corrosion-Resistant Steel–MgO Composites as Refractory Materials for Molten Aluminum Alloys. Materials. 2020; 13(21):4737. https://doi.org/10.3390/ma13214737

[3] Fabrichnaya O. The assessment of thermodynamic parameters for solid phases in the Fe-Mg-O and Fe-Mg-Si-O systems, Calphad, 1998, 22, 1, 85-125.

[4] Galasiu, I., Galasiu, R., Nicolescu, C., Thonstad, J. and Haarberg, G.M. The Behaviour of Phosphorus and Sulfur in Cryolite-Alumina Melts: Thermodynamic Considerations. In Molten Salts and Ionic Liquids (eds M. Gaune-Escard and K.R. Seddon). 2010 https://doi.org/10.1002/9780470947777.ch10

[5] Zienert T., Farhani M., Dudczig S., Aneziris C.G. Coarse-grained refractory composites based on Nb-Al2O3 and Ta-Al2O3 castables. Ceram. Int. 2018, 44, 16809–16818.

# ENGINEERED REFRACTORY AGGREGATES COMPRISING HIGHER GRADE SHELL AND LOWER GRADE CORE

Dengrunyu Xie, Shaowei Zhang
University of Exeter, Exeter, UK

**ABSTRACT**
Aimed to save the expensive high-grade refractory raw materials and/or improve properties, in particular, corrosion resistance, of low- or medium grade refractory raw materials, a novel strategy has been proposed in this work, i.e., developing a new class of core-shell structured refractory aggregate comprising a higher grade/purer material shell and a lower grade/ less pure material. Based on this, a range of refractory aggregates with various shell and core combinations can be prepared, including, for example, alumina covered bauxite, spinel covered magnesia, higher-grade bauxite covered lower-grade bauxite, higher-grade magnesia covered lower-grade magnesia, and magnesia, $CaZrO_3$, or $CaTiO_3$ covered doloma or lime. To illustrate the feasibility of such an aggregate design/engineering strategy, in this work, a new type of aggregate with a higher-grade bauxite shell covering a lower-grade bauxite was used as a working tool. Its slag penetration resistance was tested and compared with that of the counterpart aggregate made of solely lower-grade bauxite or higher-grade bauxite. The results indicated that the conventional "naked" lower-grade bauxite aggregate exhibited the worst slag resistance whereas the core-shell structured bauxite aggregate exhibited much better slag resistance, similarly to the "naked" higher-grade bauxite aggregate.

## INTRODUCTION

As multifunctional materials, refractories are used extensively to line many important high temperature industrial vessels. Except for electrocast ones, refractory materials from powder processing typically contain large amounts of relatively large sized aggregates which are bonded together by much less amounts of fine matrix phase (Fig. 1[1]). The structure and quality of these two constituent parts have great effects on microstructure, property, and performance of refractory materials, although traditionally the matrix has been paid considerably more research attention than its aggregate counterpart. To make a refractory more corrosion resistant, highly pure high- grade raw materials are often preferentially used to make both constituent parts, which not only leads to increased production cost but also hinders the proper use of low- and medium-grade raw materials. This is actually not always necessary. As well known, in a refractory system, the matrix is much weaker than the aggregate, so when a refractory is exposed to a corrosive environment during its service, the matrix part would be attacked preferentially, after which the aggregate part which have only partially corroded will be simply washed away by the liquid slag/metal and then wasted. This has been confirmed by both lab corrosion test and post-mortem analysis of spent refractories [2 &3]. Given this, it might not be necessary to make the entire aggregates by using highly pure high-grade materials.
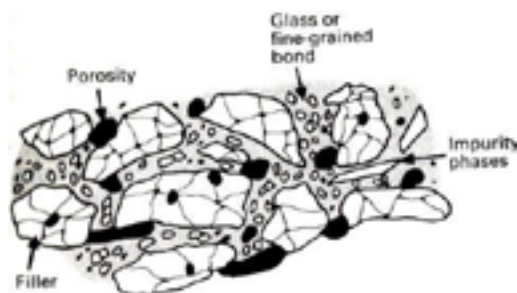
Based on this, a novel designing concept has been proposed in the present work, i.e., developing core-shell structured aggregates comprising a higher-grade/purer material shell and a lower-grade/less pure material core. It would be expectable that such a core-shell structured aggregate, in terms of slag corrosion resistance, would perform at least equivalently to its counterpart entirely made of the higher-grade material, and perform much better than its another counterpart entirely made of the lower-grade material. The benefits of making and using such an engineered type of aggregate are obvious, including: 1) enabling the comprehensive utilisation of low- and medium-grade raw materials; 2) leading to reduced production cost of both aggregates and refractory product; 3) applicability to a range of combinations of core and shell materials; and 4) potential in solving or alleviating some longstanding problems, e.g., hydration of doloma and lime based materials.

Several types of such core-shell structured refractory aggregates have been designed and preliminarily prepared via granulation and subsequent firing at an appropriate temperature for requisite time, including alumina covered bauxite, higher-grade bauxite covered lower-grade bauxite, higher-grade magnesia covered lower-grade magnesia, and magnesia, $CaZrO_3$ or $CaTiO_3$ covered doloma or lime. In this paper, the results from a proof-concept study on core-shell structured aggregates composed of a higher-grade bauxite shell and a lower-grade bauxite core are presented and discussed.

## EXPERIMENTAL

### Raw Materials

Two grades of bauxite powders (~45μm in size) were used as the main raw materials and pure water was used as the temporary binder for the granule formation. The higher-grade bauxite used to form the shell contained 85.7% $Al_2O_3$ (referred to as "85-bauxite") and the other lower-grade one contained about 75.8% $Al_2O_3$ (referred to as "85-bauxite"), as provided by the supplier.

### Aggregate Preparation

– Core or conventional "naked" aggregate

The bauxite powder was added to a Ø300mm disc granulator rotating at 45 rpm, and an appropriate amount (typically ~15wt% in total) of water was sprayed to assist in granules formation. The whole process, involving wetting and nucleation, consolidation and growth, breakage and attrition [4], lasted for 60 min, after which, reasonably high-quality green granules were prepared (Fig. 2).

– Core-shell structured aggregate

After sieving to remove the residual powder, the core granules made of the lower-grade 75-bauxite were reintroduced into the granulator still rotating at 45 rpm. Water was then sprayed to wet granules surface before the higher-grade 85-bauxite powder was introduced to further form the shell. The total processing time for this step was about 30min.



*Fig. 1: A schematic of typical microstructure of a refractory resultant from powder processing [1].*
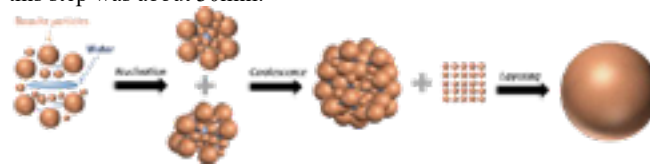


*Fig. 2: A flow chart of formation process of green bauxite granules entirely made of 75-bauxite or 85-bauxite.*

– Drying and sintering process

The prepared green aggregates were left in air at room temperature for 8 h and then dried in a convection oven at 110ºC for 12 h.  The

dried aggregate samples were contained in an alumina crucible and then placed in the centre of an electronic chamber furnace. The furnace was heated at a rate of 8ºC/min to the target temperature between 1600-1650ºC and held at the temperature for 3 h.

**Corrosion Test**

– Model slag

A model slag with the composition shown in Table 1 was prepared using reagent-grade $CaCO_3$, $MgCO_3$, $Al_2O_3$, $Fe_2O_3$, and $SiO_2$ powders which were pre-mixed in a ball-mill for 3h. The resultant mix was then fired/melted at 1450ºC for 1 h to form the model slag.

Tab. 1: Batch Composition of Model Slag

| Oxide | $Al_2O_3$ | $SiO_2$ | CaO | $Fe_xO$ | $CaO/SiO_2$ |
|---|---|---|---|---|---|
| Content (wt%) | 13.72 | 25.8 | 35.57 | 19.21 | 1.38 |

– Slag test

As-prepared aggregates were placed into an alumina crucible containing premelted slag (aggregate:slag=1:3 (weight ratio)) and heated at 10ºC/min to 1450ºC and held for 1 h before cooling to room temperature at 10ºC/min.

**Microstructural Characterisation and Slag Resistance Evaluation**

The aggregates before and after the corrosion test were mounted in cold-setting epoxy resin, and then ground and polished using different grades of SiC grinding paper and diamond paste. After chromium coating, the cross-sectional microstructures of the aggregate samples were observed by using a scanning electron microscope (SEM) linked with an Energy Dispersive X-ray Spectroscope (EDS). To assist in the phase identification and slag resistance comparison, apart from secondary electron image (SEI), backscattered electron image (BEI) was taken, along with EDS. Based on the SEIs and BEIs, and correspondong EDS, the slag penetration depth was evaluated.

**RESULTS AND DISCUSSION**

**Microstructure of As-prepared Aggregates**

Fig. 3, as an example, shows the low magnification image of an individual aggregate composed of a higher-grade 85-bauxite shell and a lower-grade 75-bauxite core. The shell appeared to be continuous and the core appeared to be homogeneous, and both were overall integrated well, showing no obvious gap between them, though some pores were seen at their interface. As the main purpose of the present work was to compare the relative slag resistance of the three types of aggregates. No further detailed phase and microstructural characterisation on high magnification was carried out at this stage.
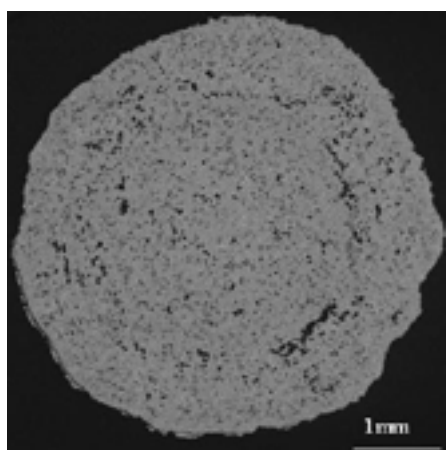


Fig. 2: Low magnification SEM image of an individual fired aggregate composed of an 85-bauxite shell and a 75-bauxite core.

**Corroded Microstructure**

Fig. 3 shows SEM images of the three corroded aggregate samples. The part on the left was the residual slag, and that on the right was the corroded aggregates. To reveal more clearly the slag penetration into the aggregate samples, the corresponding EDS mapping of Ca

element (indicated by pink coloured spots) is also shown together with (overlapped with) the microstructural images (Fig. 3). As seen from Fig. 3a, slag Ca penetrated most deeply into the "naked" 75-bauxite aggregate, with a penetration depth of ~230µm. However, the aggregate sample comprising an 85-bauxite shell and a 77-bauxite core, and the "naked" 85-bauxite aggregate suffered from much less slag penetration, with a similar penetration depth of <100µm. These results suggested that a core-shell structured aggregate comprising a higher-grade material shell and a lower-grade material core could have a much better slag resistance than an aggregate comprising solely the lower-grade material, and perform equivalently to its counterpart comprising entirely the higher grade material, confirming preliminarily the feasiblity of the strategy proposed in this work, although lots of future work are still required to verify it further.
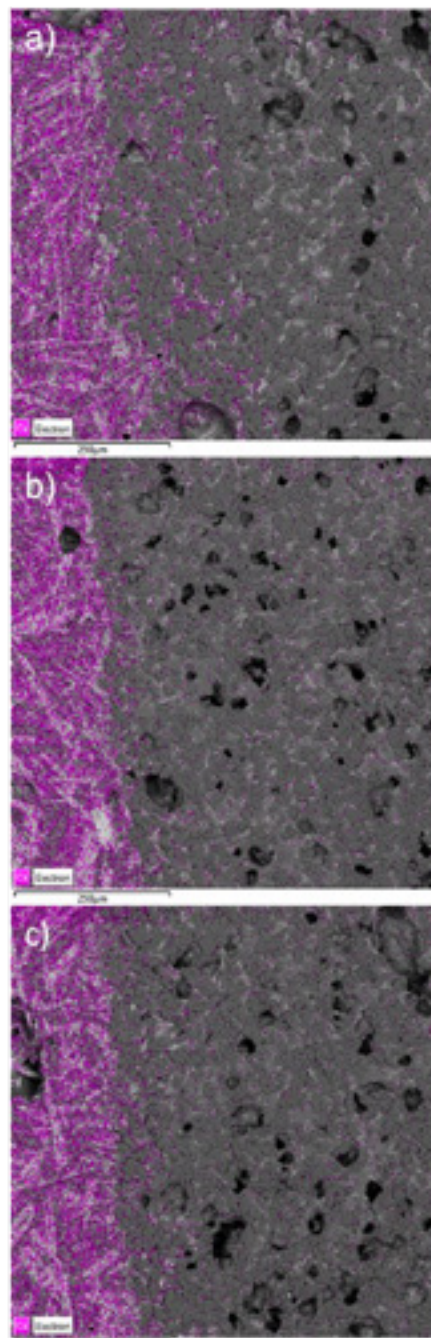


Fig. 3: SEM images (along with EDS mappings of Ca element) of corroded microstructures: a) "naked" 75-bauxite aggregate; b) "naked" 85-bauxite aggregate; c) core-shell structured aggregate comprising an 85-bauxite shell and a 75-bauxite core.

813

## CONCLUSIONS

In summary, a novel designing strategy has been proposed for the first time for developing new types of core-shell structured aggregates comprising a higher grade/purer material shell and a lower grade/less pure material core. A proof-concept work was carried out by using aggregate composed of a higher-grade bauxite material (85-bauxite) shell and a lower-grade bauxite core (75-bauxite) as a working tool. Such core-shell structured bauxite aggregates were prepared via granulation and subsequent high temperature firing. To compare, aggregates entirely made of the lower-grade bauxite or higher-grade bauxite were also prepared. These three types of as-prepared aggregates were exposed to a model slag with a CaO/SiO$_2$ of 1.38 at 1450°C for 1h, and their slag resistance were evaluated and compared. The results indicated that after 1h slag attack at 1450°C, the "naked" lower-grade bauxite aggregate suffered from the most severe slag penetration (up to ~230μm), whereas the core-shell structured bauxite aggregate suffered from much less penetration, performing equivalently/ similarly to its "naked" counterpart comprising solely the higher-grade bauxite. These results confirmed preliminarily the feasibility of the proposed aggregates design strategy, although lots of future work be still required to verify it further.

## REFERENCES

[1] Ceramic Microstructures; Property Control by Processing. William E. Lee and W. Mark Rainforth. Published by Chapman & Hall, London, 1994

[2] S. Zhang and W. E, Lee, Influence of additives on corrosion resistance and corroded microstructures of MgO–C refractories, J. Euro. Ceram. Soc., 21[13]2393-2405(2001).

[3] Y. Li, G. Li, G. Liu, Y. Zhao, N. Li, J. Chen, A post-mortem analysis of the used gel-bonded Al$_2$O$_3$–MgAl$_2$O$_4$ castables in an industrial steelmaking ladle. Int J Appl Ceram Technol. 20,1978–1989(2023).

[4] V. D. Simone, D. Caccavo, A. Dalmoro, G. Lamberti, M. d'Amore, and A. A. Barba, 'Inside the Phenomenological Aspects of Wet Granulation: Role of Process Parameters', Granularity in Materials Science. InTech, Oct. 24, 2018.

# PREPARATION AND PROPERTIES OF FIBER/WHISKER COMPOSITE MAGNESIA–ALUMINA SPINEL REFRACTORY BY *IN–SITU* CHEMICAL VAPOR DEPOSITION

Ruiqi Cao[1], Hang Ye[1*], Hang Li[2], Hilmar Schulze-Bergkamen[1], Haijun Zhang[2]

1 RHI Magnesita (Dalian) Co., Ltd., Dalian 116600, China

2 The State Key Laboratory of Refractories and Metallurgy, Wuhan University of Science and Technology, Wuhan 430081, China

*Corresponding author: E-mail: Hang.Ye@rhimagnesita.com

## ABSTRACT

Magnesium aluminate spinel (MAS) based refractories are widely used in the linings of high temperature industrial equipment because of their special performance. In this study, MAS powder, flake graphite, silica powder, phenolic resin and an iron-containing catalyst were used as main raw material for the preparation of whiskers and crystal carbon by *in-situ* chemical vapour deposition (CVD) at 1273 K for 3 h in a reducing atmosphere. The results showed that the carbon content of samples increased by 4%, their porosity after heat treatment decreased by 4%, and their modulus of rupture increased by 10%. Additionally, their cold compression strength (CCS) increased by 10%. In high-temperature performance investigations, the reinforced samples exhibited no cracks after five cycles of thermal shock resistance testing and the cold compression strength retention rate was 93%. The hot modulus of rupture of trial samples increased by about 8% compared to standard ones. The results of the study could be extended to commercial use and the applied method increase the performance of products.

## INTRODUCTION

In the process of steel smelting, slag and molten steel are the two most common corrosive components that are in direct contact with refractory materials. MAS based refractories are used in the lining of high temperature industrial equipment such as ladles, electric furnaces, and cement rotary kilns due to their high hardness, high mechanical strength, good thermal shock resistance and excellent slag corrosion resistance [1]. Besides, MAS enhanced material has been used in flow control refractories recently because of its better performance than that of original alumina-based refractory [2][3]. With the development of the steel industry, longer service life and lower material cost are required and become a target for all refractory practitioners [4].

As a kind of inorganic non-metallic material, refractory material can improve its strength in a similar way than other types of ceramic. In MAS-based carbon-containing refractories designed for the steel industry, fibre-strengthening has been widely researched for achieving better performance. A commonly used strengthening method for carbon-containing refractories is characterized by catalytic formation of whiskers and carbon nanotubes (CNTs) whereas the catalysts are various compounds of members of the iron group (Fe, Ni & Co) [5]. However, different heat treatment processes and carbon sources lead to gaps in the understanding of the mechanism of fibre-reinforced MAS-based refractories [6].

In this study, a phenolic resin and an iron-group compound were used as carbon source and catalyst, respectively. The sample investigation focused on the formation of whiskers and other fibre-structured matter and the MAS-based refractories' physical and chemical properties. Results of the study indicate the opportunity of using fibre-reinforced refractories for continuous casting in the steel industry.

## EXPERIMENTAL METHOD

### Experimental material

All raw material used in this study were sourced from local enterprises. Table 1 and 2 show their typical physical and chemical properties. In general, samples were prepared by using fused MAS, anti-oxidation additives, graphite, and phenolic resin. The catalysts used stem from iron-group elements among which an iron-type was predominantly chosen due to being eco-friendly when compared to other choices.

Table 1: Typical chemical properties of a refractory sample [wt.%]

| Item | $SiO_2$ | $Al_2O_3$ | MgO | C | LOI |
|---|---|---|---|---|---|
| Typical value | 4.5 | 72 | 22 | 14.5 | 12.5 |

Table 2: Typical physical properties of a refractory sample

| Item | Bulk density, BD [g/cm$^3$] | Apparent porosity, AP, [Vol%] | Cold Modulus of Rupture, CMoR, [N/mm$^2$] |
|---|---|---|---|
| Typical value | 2.57 | 18.0 | 6.0 |

### Experimental methods

*Mixing and forming*

At the beginning of the experimental session, a quantitative study was necessary to determine the optimal catalyst content in the resin. Previous research has shown amounts of about 1 wt. % of the resin by molar mass calculation seem to be appropriate. Hence, in this study, the catalyst's molar mass content was designed to be 0.5%, 0.75%, 1% and 1.25% of the resin mass to investigate the material properties and to determine the quantity of catalyst. In addition, a standard batch with no catalyst was prepared for comparison. The catalyst was added to the resin and stirred after being fully dissolved in water.

All raw material was dosed into the mixer for high-speed mixing. The mixing process could be divided into dry mixing with no resin and wet mixing after dosing the resin. The resin was preheated to a certain temperature for better fluidity. To investigate the property differences between standard and catalyst-containing grade, all mixing parameters were kept the same. The material was tested on the day of mixing and 24 h after mixing for green properties, then isostatically pressed into a standard design test stopper.

*Heat treatment*

The subsequent heat treatment was the same for all trial samples and could be divided into two parts. First, the green test stopper was cured in a kiln at 515 K for inducing initial strength by the reaction between resin and hexamine. Afterwards, samples were fired in a shuttle kiln at 1273 K.

*Sample investigation*

Cold modulus of rupture (CMoR) and cold compression strength (CCS) were measured by using standard device equipment, bulk density (BD) and apparent porosity (AP) were measured by vacuum method under water (ISO 18754:2020).

X-ray fluorescence (XRF) and loss on ignition (LOI) were used for element determination and carbon content. Besides, Energy Dispersive Spectroscopy (EDS) and X-ray diffraction (XRD) were also used to determine the phase of samples. For microstructural investigations, scanning electron microscopy (SEM) and transmission electron microscopy (TEM) were used as techniques.

For use in continuous casting, the performance of all products in a high temperature environment needs to be investigated. Therefore, thermal shock resistance (TSR) testing and hot modulus of rupture (HMoR) were applied. The TSR followed a national standard cycle test method which requires a 20 min-heating of samples at 1373 K, then cooling for 10 mins in water at 298 K and subsequent drying for 5 mins in air at 298 K. In addition, the CCS of samples after the TSR test were also used for a comparison with standard samples to monitor the situation between heats during casting.

## RESULTS AND DISCUSSION
### Chemical properties
The chemical analysis of all investigated samples with and without catalyst revealed no significant difference among them (Fe-catalyst 0.50%-1.25%). However, samples with catalyst showed a higher LOI and a lower mass loss than standard samples without catalyst. The details are listed below in Table 3.

Table 3: Chemical properties of samples [wt.%]

| Item | Standard sample | Sample with 0.5% Fe-catalyst | Sample with 0.75% Fe-catalyst | Sample with 1.0% Fe-catalyst | Sample with 1.25% Fe-catalyst |
|---|---|---|---|---|---|
| $SiO_2$ | 4.58 | 4.52 | 4.56 | 4.49 | 4.65 |
| $Al_2O_3$ | 72.37 | 71.98 | 72.87 | 72.49 | 72.61 |
| MgO | 22.16 | 22.43 | 22.19 | 22.30 | 22.81 |
| C | 13.00 | 13.32 | 13.31 | 13.17 | 13.39 |
| LOI | 11.74 | 11.81 | 12.31 | 12.14 | 12.08 |
| Mass loss | 3.72 | 3.67 | 3.53 | 3.59 | 3.61 |

Samples with catalyst appeared to have a higher carbon fixation than those without catalyst.

### Physical properties
*Physical properties at room temperature*
The investigation showed that properties like AP, CMoR and CCS were optimised when catalyst amounts of 0.75 and 1% were used, whereas bulk density results remained within the margin of error of measurements (table 4). All samples with catalyst had a lower AP and better mechanical properties compared to standard ones, which indicates their potential superior performance in slag resistance and long-life casting.

Table 4: Room temperature physical properties of samples

| Item | Standard sample | Sample with 0.5% Fe catalyst | Sample with 0.75% Fe catalyst | Sample with 1.0% Fe catalyst | Sample with 1.25% Fe catalyst |
|---|---|---|---|---|---|
| BD, g/cm³ | 2.71 | 2.69 | 2.70 | 2.69 | 2.68 |
| AP, % | 16.25 | 16.24 | 14.51 | 14.28 | 15.95 |
| CMoR, MPa | 5.61 | 6.32 | 6.48 | 6.53 | 6.81 |
| CCS, MPa | 20.35 | 22.57 | 22.83 | 23.59 | 22.63 |

*Physical properties at high temperatures*
Results of high temperature investigation showed that the CCS of samples before and after the TSR treatment was significantly higher than for samples without catalyst. Higher CCS values of catalyst samples even persisted after the TSR test. HMoR tests revealed an optimal catalyst amount of 0.5% and 0.75%, respectively. Details of the high temperature physical properties are listed below in Table 5.

Table 5: High temperature physical properties of samples [MPa]

| Item | Standard sample | Sample with 0.5% Fe catalyst | Sample with 0.75% Fe catalyst | Sample with 1.0% Fe catalyst | Sample with 1.25% Fe catalyst |
|---|---|---|---|---|---|
| CCS before TSR | 20.21 | 22.39 | 22.49 | 23.37 | 21.48 |
| CCS after TSR | 19.82 | 21.45 | 21.11 | 21.88 | 19.98 |
| HMoR | 5.13 | 5.53 | 5.53 | 4.87 | 5.01 |

### Phases and microstructure
*Phase investigation*
Phase investigation by XRD revealed expected mineral phases like MAS, graphite and antioxidant (Fig.1).
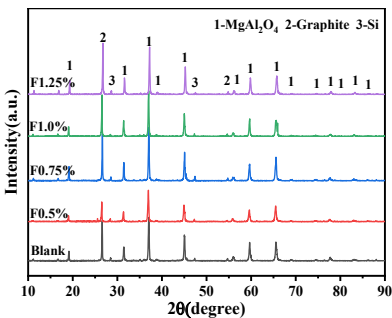


*Fig. 1: XRD results*

*Microstructural investigation*
All samples were analysed by means of SEM and TEM. Results as summarized below:

- No fibre structure and crystalline carbon appeared in samples without catalyst (Fig. 2).
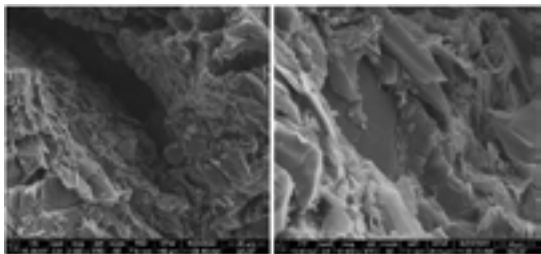


*Fig. 2: TEM images of samples with no catalyst*

- All samples with catalyst exhibited a whisker structure. By means of EDS, the whiskers were identified as MAS-whiskers.
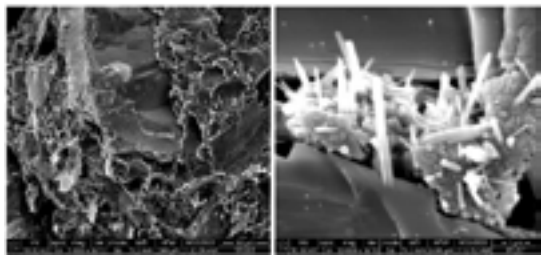


*Fig.3: TEM result of samples with 0.75% Fe-catalyst*
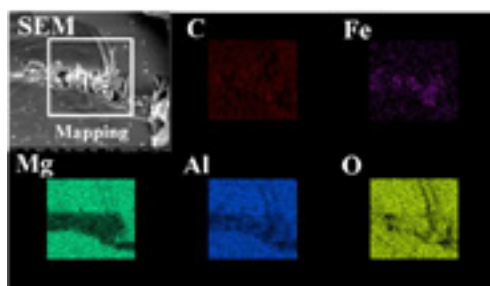
*Fig.4: Mapping results of samples with 0.75% Fe-catalyst*

The TEM and EDS results indicate that a large amount of iron was enriched at the bottom of the whiskers. It was assumed that the MAS whiskers were generated after heat treatment at 1273K, and catalyst nanoparticles reduced the activation energy of the whiskers' nucleation. The whiskers in matrix could act as bridge in the refractory material matrix and reduce its porosity, which means they would not only improve the mechanical strength of the material but also its refractoriness and resistance during casting. The carbon fixed in the matrix was identified as crystalline carbon (Fig. 5 and Table 6).
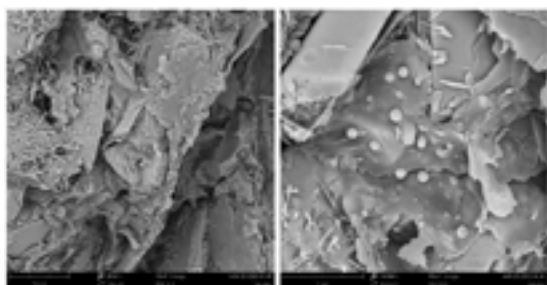


*Fig. 5: TEM image of crystalline carbon*

Table 6: crystalline carbon [wt.%]

| Element | C | O | Si | Al | Mg |
|---|---|---|---|---|---|
| Atomic concentration percentage | 59.89 | 24.00 | 10.33 | 4.61 | 1.17 |

The use of the Fe-catalyst improved the residual carbon rate of the resin via *in-situ* chemical vapour deposition (CVD) and transformed it to crystalline carbon. Fine crystalline carbon could be considered as an additional phase that was well distributed in the matrix. Moreover, it may also play a role in high-temperature melt resistance by lowering the AP of materials. Future investigations will also focus on the role of the crystalline carbon.

## CONCLUSIONS

The *in-situ* catalysis as described can be used for the formation of MAS-whiskers and crystalline carbon in the matrix of carbon-containing refractories. The mechanism of catalysis and strength improvement of refractories were analysed and explored, respectively. The assumption was made that whiskers and crystalline carbon from *in-situ* catalysis and CVD may deflect microcracks, thus improving the strength of refractory material. Moreover, the whiskers deposited in the matrix might delay crack formation. The well-distributed crystalline carbon in the matrix may also act as material reinforcement (Fig. 6). Both factors combined led to an improvement of mechanical properties at room and elevated temperature. Moreover, improved mechanical properties will have a better resistance to material washout during casting.
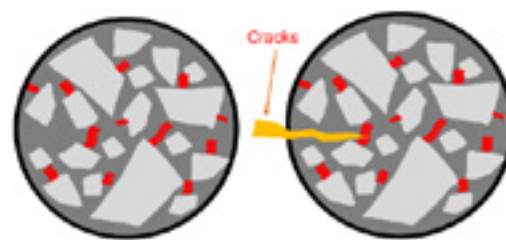


*Fig. 6 Schematic of strengthening mechanism*

During casting, the Marangoni effect [7] can lead to the erosion on the boundary of steel, slag and refractory, especially in carbon-containing refractories. Also, alkali metal can infiltrate into the matrix with pores, which leads to an expansion during new phase formation and structure peeling from matrix to grains [8]. A matrix with whiskers and crystalline carbon could better withstand the wash-out from the structure. In addition, low porosity means less infiltration by alkali metal vapor and lower volume expansion thus increasing the product's life expectation during continuous casting.

## REFERENCES

[1] Himpel, G., Herrmann, M. and Höhn, S. (2015). Comparison of the high-temperature corrosion of aluminium nitride, alumina, magnesia and zirconia ceramics by coal ashes. Ceramics International, 41(7), pp. 8288–8298.

[2] Ganesh, I. et al. (2008). Formation and Densification Behavior of $MgAl_2O_4$ Spinel: The Influence of Processing Parameters. Journal of the American Ceramic Society, 91(6), pp. 1905–1911.

[3] Luz, A.P. et al. (2012). Slag attack evaluation of in situ spinel-containing refractory castables via experimental tests and thermodynamic simulations. Ceramics International, 38(2), pp. 1497–1505.

[4] Wen, Y. et al. (2017). Effect of heat treatment conditions on the growth of MgAl2O4 nanoparticles obtained by sol-gel method. Ceramics International, 43(17), pp. 15246–15253.

[5] Ghosh, A.K. et al. (2004). Effect of spinel content on the properties of magnesia–spinel composite refractory. Journal of the European Ceramic Society, 24(7), pp. 2079–2085.

[6] Li, S. et al. (2018). Fabrication of graphitic carbon spheres and their application in $Al_2O_3$-SiC-C refractory castables. International Journal of Applied Ceramic Technology, 15(5), pp. 1166–1181.

[7] Fagerlund, K., Sun, S. and Jahanshahi, S., 2002. Effect of Marangoni-induced flow on the rate of refractory dissolution in molten slags. Scandinavian Journal of Metallurgy, 31(6), pp.359-366.

[8] Fan, X., Jiao, K., Zhang, J., Cao, R., He, R. and Wang, K. (2019). Study on physicochemical properties of $Al_2O_3$-SiC-C castable for blast furnace. Ceramics International, 45(11), pp.13903–13911.

817

# COMPOSITIONAL COMPLEX CERAMIC COATINGS FOR CORROSION RESISTANCE OF REFRACTORIES

Jonathan Maier, Holger Friedrich
Fraunhofer Institute for Silicate Research ISC / Center HTL, Bayreuth, Germany

Jihad Zraibi, Marzuk Kamal
AeonX AI SAS, Paris, France

Ana Mezuqita, Encarna Blasco
Instituto de Tecnologia Ceramica ITC, Castellon, Spain

Alvise Bianchin
MBN Nanomaterialia S.p.A. / MATRES Scrl, Vascon di Carbonera TV, Italy

## ABSTRACT

Compositionally Complex Ceramics (CCC) are a relatively new class of materials with promising properties, including strong corrosion stability. Therefore, CCC are interesting for corrosion-resistant coatings. CCC are an extension of the also quite new material class of High Entropy Ceramics (HEC) and extend them by medium entropy and non-equimolar compositions.

As part of the EU project FORGE, a corrosion-resistant CCC coating has been developed for refractory materials in a continuous roller kiln for firing ceramic tiles. The development was based on a combination of Machine Learning (ML) assisted high throughput material development. A large number of bulk samples with different elemental compositions were prepared from oxide powder mixtures to form medium or high entropy ceramics. The CCC were sintered and subsequently characterized by XRD, CT, SEM and EDS. The results from the CCC development were then transferred to the development of a corrosion-resistant coating. The coatings were applied on refractory bricks using a slurry coating technique. Corrosion tests were carried out on coated refractories under laboratory conditions, but also directly in the kiln. The results of the corrosion tests are presented.

## INTRODUCTION

Compositionally Complex Ceramics (CCC) were first proposed in 2020 by Wright et al. as an extension of the new material class, the High Entropy Ceramics (HEC) [1, 2].

The HEC are defined as single-phase ceramics consisting of at least four different anions or cations in equimolar composition [3, 4]. In their unit cell, the same number of different elements is uniformly distributed. As a result of the high number of different elements in the unit cell, the configurational entropy is maximized leading to an additional stabilization of the equimolar mixture [4]. The first HEC was produced in 2015 from the oxides MgO, NiO, CoO, CuO and ZnO and had a rocksalt structure [4, 5]. In addition to oxides, HEC can also be produced from borides, carbides, nitrides, boron carbides, carbonitrides, sulfides and fluorides, and in addition to the rocksalt structure, spinel, perovskite, fluorite, pyrochlores, bixbyite, rutile and garnet are also potential structures for HEC [1, 6, 7].

The reason for the increased interest in HEC is their unique properties, such as high hardness, high lithium-ion conductivity, tunable magnetism, high dielectric constant and low thermal conductivity [1, 8, 9]. As a result, there is a large number of potential applications for HEC, such as the use as catalysts, as battery materials, in thermoelectronics, as thermal barrier coatings and as wear and corrosion resistant coatings [4, 10].

As noted above, CCC are an extension of the HEC. Besides high entropy compositions, the CCC also include medium entropy compositions with non-equimolar compositions [1]. This allows an even broader range of possible compositions and thus the potential for a more specific adjustment of the various properties that can be achieved by entropy stabilization [1]. Compared to the HEC, the CCC can achieve further improved properties, such as lower thermal conductivities or better mechanical properties [2, 11]. Due to the wide range of applications and outstanding properties of CCC, they are a promising area for the development of new materials.

In the EU project Forge, CCC coating materials have been developed for the use as corrosion protective coatings on refractory bricks for an industrial gas-fired roller kiln for ceramic tiles. Corrosive atmospheres occur in this kiln at temperatures between 650 °C and 1200 °C, which lead to impairment of the refractory bricks, as can be seen in Figure 1. In some parts of the furnace a protective coating mainly composed of zirconia is applied on the refractories. However, corrosion due to combustion gases and gases coming from the decomposition of the ceramic product was observed in all refractories, with and without protective coating. The corrosion is mainly attributed to Na and K cations and Cl and $SO_3$. As corrosion advances, delamination of the refractory materials occurs, and small pieces and dust fall onto the tiles, causing defects in the fired product.



*Fig. 1: Appearance of a JM26 wall refractory after operating at 1185°C for 5 years.*

Due to the corrosion, regular maintenance of the roller kiln is necessary to replace the wall and vault refractory bricks. This means long downtimes and also high energy consumption due to the slow start-up of the relatively large kiln. A suitable coating for corrosion protection can ensure that the refractory bricks have a longer service life and thus the kiln has longer periods of use; currently applied state of the art coatings do not yet achieve the expected improvement.

In the following, the results of the development of CCC with a spinel crystal structure for the use as a corrosion protection coating will be presented. The properties of the CCC coatings, such as corrosion resistance, coefficient of thermal expansion etc. are adjusted in such a way that the service life of the refractories in the roller kilns will be significantly increased. To achieve this, the development was done with high throughput experiments combined with machine learning to narrow down the wide range of possible elements and compositions to find a suitable coating material for refractory bricks.

### CCC development using machine learning

Oxide CCC with spinel structure should be produced using the elements that are already present in the kiln. This means that the elements of the refractory materials as well as elements present in the furnace atmosphere are responsible for the corrosion. A screening for possible cations in literature and databases was done for oxide spinels. The candidates obtained were narrowed down to cations with similar ionic radii. The restriction to equal ionic radii was made because it is known that HEC and CCC form preferentially with equal ionic radii of the individual cations [6]. For the selection of the cations, availability, price and environmental compatibility were also considered. The following cations were selected:

Li, Mg, Al, Si, Ti, Cr, Fe, Cu, Zn, Sn

The CCC coatings are designed to protect the refractories from corrosion at high temperatures. Therefore, the coating material must meet several requirements. These include corrosion stability in the furnace process, matching coefficient of thermal expansion CTE to the aluminosilicate refractory materials JM23 and JM26, high temperature stability, phase stability, chemical compatibility with the refractory materials etc.

In order to find a previously unknown material from a very large compositional range of elements that covers all these properties, high-throughput experiments were combined with machine learning. Since CCC is a relatively new field, there is only a limited amount of published data available. For this reason, the ML was first trained with information from the literature and databases (COD) on normal spinels and in a later step with experimental data on CCC spinels [12-19].

In parallel to setting up an ML model, high-throughput experiments were carried out. For this, however, the CCC were not prepared as coatings but as bulk samples. This was done to save time time for sample preparation and characterization. Based on the experimental and the ML results, one material was later selected for testing as a coating. Starting from the selected cations, an experimental matrix was set up for all possible compositions, with the following preconditions:

- The charges of the cations are balanced to give an AB$_2$O$_4$ type spinel
- Each variant consists of at least 6 cations
- Cation amounts are multiples of 0.25 mole-%

This resulted in a matrix of 22,236 compositions. 67 compositions were randomly selected from the matrix for preparation, following the processing steps shown in Figure 2. Oxide or hydroxide powders were used as starting material. These were first milled to a mean particle size of d$_{50} \leq 5$ μm. Subsequently, the milled powders were weighed and mixed in a SpeedMixer® according to the experimental matrix. After mixing, the powders were pressed into compacts. For a good pressing result and to protect the pressing tool from abrasive wear, pressing aids were added. The samples were pressed with 5 tons to samples with a diameter of 15 mm. The sintering was carried out in a batch furnace up to 1500 °C. The heating rate was 2 K/min, the dwell time was 1 hour and the cooling rate was 5 K/min. During the sintering process, the samples were placed on ZrO$_2$ sand.
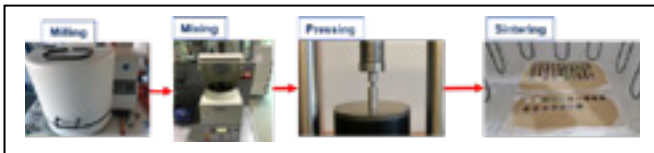


*Fig. 2: Processing steps for CCC sample preparation.*

The crystal phases of the sintered CCC samples were analyzed using an X-ray diffractometer (XRD, SmartLab, Rigaku, Japan) with CuKα radiation. Figure 3 shows exemplary diffractograms of two samples with different compositions.
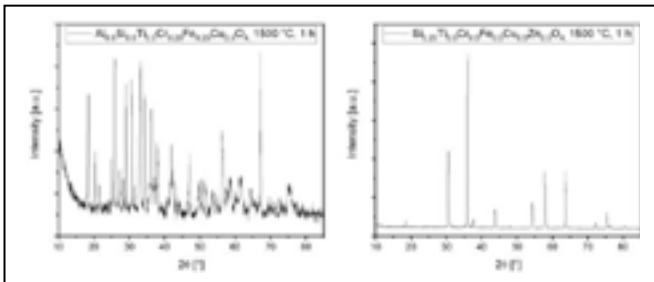


*Fig. 3: X-ray diffractograms of CCC samples with different compositions: Al$_{0.5}$Si$_{0.5}$Ti$_{0.5}$Cr$_{0.25}$Fe$_{0.25}$Cu$_{0.5}$O$_4$ (left) and Si$_{0.25}$Ti$_{0.5}$Cr$_{0.5}$Fe$_{0.5}$Cu$_{0.5}$Zn$_{0.5}$O$_4$ (right) after sintering at 1500 °C.*

The sample in Figure 3 on the left with the composition Al$_{0.5}$Si$_{0.5}$Ti$_{0.5}$Cr$_{0.25}$Fe$_{0.25}$Cu$_{0.5}$O$_4$ consisted of multiple phases after sintering. In contrast, the sample with composition Si$_{0.25}$Ti$_{0.5}$Cr$_{0.5}$Fe$_{0.5}$Cu$_{0.5}$Zn$_{0.5}$O$_4$, in Figure 3 on the right, is composed only of spinel. I.e., a CCC with the spinel structure can be successfully obtained by using the right composition. The phase content was determined for all 67 prepared samples by Rietveld analysis using the SmartLab Studio II program (Rigaku, Japan). The samples were then evaluated for their degree of spinel formation. Hereby, a total of 32 samples showed a spinel content of more than 95 %. The spinel contents for a selection of the samples are shown in Figure 4.

In addition, the CTE was measured from room temperature to 1200 °C or until softening using a push rod dilatometer (NETZSCH DIL 402 C, NETZSCH-Gerätebau GmbH, Germany). This evaluation was focused on selected compositions with a spinel content of > 95 %. Figure 4 shows the CTE from room temperature up to 1000 °C and up to 1200 °C for a selection of the 67 samples prepared. Part of the samples showed softening above 1000 °C. For these specimens, no CTE could be determined for 1200 °C. In this case, an "x" is shown. As can be seen, the different spinel compositions show a wide range of CTE values. This means that spinels are available for different types of substrates with different expansion behavior. This is often a problem, as the difference in the CTE of the coating and the substrate should be $\leq 1 \times 10^{-6}$ K$^{-1}$. The composition Mg$_{0.5}$Al$_{0.5}$Si$_{0.25}$Ti$_{0.5}$Fe$_{0.5}$Cu$_{0.5}$O$_4$ is highlighted in green, because its CTE is closest to that of the refractory material used in the industrial roller kiln.



| Composition Oxides | 95-100% Spinell | CTE 1000 °C [10$^{-6}$ K$^{-1}$] | CTE 1200 °C [10$^{-6}$ K$^{-1}$] |
|---|---|---|---|
| Mg0.5Al0.5Si0.5Ti0.5Cr0.25Fe0.25O4 | < 95% | | |
| Al0.5Si0.5Ti0.5Cr0.25Fe0.25Cu0.5O4 | < 95% | | |
| Si0.25Ti0.5Cr0.5Fe0.5Cu0.5Zn0.5O4 | 100 | 8,7 | x |
| Ti0.25Cr0.5Fe0.5Cu0.5Zn0.5Fe0.5O4 | 100 | 7,8 | x |
| Cr0.5Fe0.5Cu0.5Zn0.5Fe0.5Li1O4 | < 95% | | |
| Mg0.5Al0.5Si0.25Ti0.5Cr0.5Fe0.5O4 | < 95% | | |
| Mg0.5Al0.5Si0.25Ti0.5Cr0.5Fe0.5O4 | < 95% | | |
| Mg0.5Al0.5Si0.25Ti0.25Cr0.5Fe0.5Mn0.5O4 | 97 | 7,3 | 7,4 |
| Mg0.25Al0.5Si0.5Ti0.5Cr0.5Li0.5O4 | < 95% | | |
| Al0.5Si0.25Ti0.5Cr0.5Fe0.5Zn0.25O4 | < 95% | | |
| Al0.5Si0.25Ti0.5Cr0.25Fe0.25Fe0.25Cu0.5O4 | < 95% | | |
| Al0.5Si0.25Ti0.5Cr0.5Fe0.5Li0.5O4 | < 95% | | |
| Si0.25Ti0.5Cr0.5Fe0.5Cu0.5Zn0.5O4 | < 95% | | |
| Si0.5Ti0.5Cr0.5Fe0.5Cu0.5Zn0.25Li0.5O4 | < 95% | | |
| Mg0.5Si0.25Ti0.5Cr0.5Fe0.5Cu0.5O4 | < 95% | | |
| Ti0.5Cr0.5Fe0.5Cu0.5Zn0.5Li1O4 | 100 | 9,6 | 9,8 |
| Mg0.5Ti0.5Cr0.5Fe0.5Cu0.5Zn0.5O4 | 97 | 9 | x |
| Al0.5Ti0.5Cr0.5Fe0.5Cu0.5Zn0.5O4 | < 95% | | |
| Si0.25Cr0.5Fe0.5Cu0.5Zn0.5Fe0.5O4 | 100 | 8,1 | x |
| Mg0.5Cr0.5Fe0.5Cu0.5Zn0.5Zn0.5O4 | 100 | 8,7 | 8,9 |
| Al0.5Cr0.5Fe0.5Cu0.5Zn0.25Zn0.5O4 | 100 | 8,3 | 8,4 |
| Mg1Fe0.5Cu0.5Zn0.5Zn0.5Li0.5O4 | 99 | 10,4 | 11,1 |
| Mg0.5Al0.5Si0.25Ti0.5Fe0.5Cu0.5O4 | 98 | 6,3 | 6 |

*Fig. 4: Spinel phase fraction and CTE of CCC samples with different compositions.*

The experimental results together with literature and database information were used to train the ML to predict spinel formation, as mentioned above.



*Fig. 5: Selected physical input parameters for ML.*

Compositional data and physical properties of the spinel components were selected as design parameters. Out of 22 possible physical properties, 10 physical properties were selected, because

they showed minimum intercorrelation. The 10 selected physical properties are shown in Figure 5.

Besides the ML-model for predicting spinel formation, an additional ML-model was set-up to calculate the CTE of the spinels. However, in the experimental tests, only 26 samples of the 32 spinels were found without a softening up to 1200 °C. Because of this limited number of data, a simple linear model with the squared error as the cost function was used to predict the CTE. Despite these limitations on the input data, a good accuracy of $0.81 *10^{-6}$ $K^{-1}$ was achieved (see Figure 6).
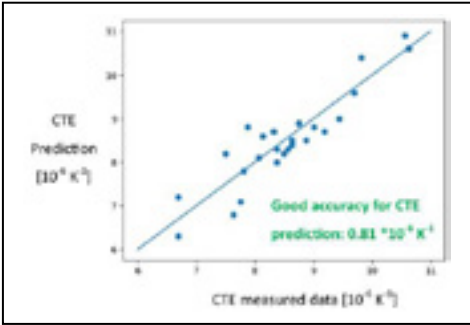


*Fig. 6: CTE machine learning model precision graph.*

The two ML models were then used to calculate new compositions for the CCC. In this context, a CTE between $5 *10^{-6}$ $K^{-1}$ and $6 *10^{-6}$ $K^{-1}$ and the highest possible spinel phase fraction of at least 94 % should be obtained. The predicted compositions are shown together with their predicted spinel phase fraction and CTE and their experimentally determined values in Figure 7. It was found that a relatively high proportion of spinel was formed in all samples, confirming the high quality of the developed ML model. A comparison of the predicted and the measured CTE (performed only for compositions with more than 95 % spinel) also showed good results, although only limited data was available for ML training. This model can probably be further refined with additional experimental data.



*Fig. 7: ML predicted compositions with predicted and measured CTE and spinel content.*

To facilitate future CCC development, two API assisted tools were developed to calculate the probability of spinel phase formation for a given composition on the one hand and its coefficient of thermal expansion on the other hand. These two methods were then combined in one tool to retrieve a specific composition with the respective amounts of preselected cations to achieve a given target CTE.

Corrosion tests based on the elements in the gases coming from the decomposition of the ceramic product were carried out on all samples. For this purpose, a compound consisting of the elements K, Na, Cr, Fe and Zn was applied to the specimen top surface. The prepared samples were placed in a batch oven and heated to 1200 °C at a heating rate of 5 K/min. The dwell time was 10 h. After heat treatment, the samples were characterized by CT, SEM and EDS. It should be noted, that a very high amount of the different cations was applied to the samples to accelerate possible reactions, since the samples were exposed to short dwell times compared to the roller kiln. Figure 8 shows examples of SEM images of a corrosion resistant and a corroded material. No significant vi-sible changes in the microstructure were detected in the sample with the composition

$Mg_{0.5}Al_{0.5}Si_{0.25}Ti_{0.5}Fe_{0.5}Cu_{0.5}O_4$, even directly below the position where the corrosion compound was placed. In comparison, a sample with the composition $Al_{0.25}Si_{0.5}Ti_{0.5}Cr_{0.25}Sn_{0.5}Li_{0.5}O_4$ and without spinel phase, thus no CCC, is shown in Figure 8 on the left. In this case, a clear change in the microstructure was observed, indicating insufficient corrosion stability.
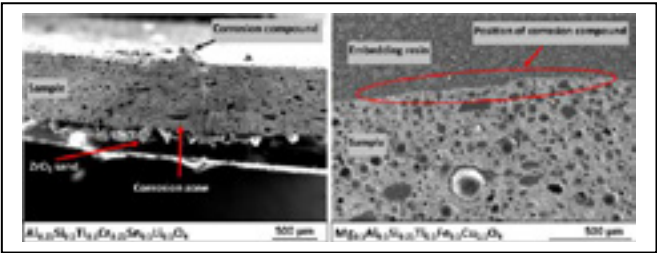


*Fig. 8: SEM images of CCC samples after a corrosion test up to 1200 °C.*

Of all the samples available, the CCC with the composition $Mg_{0.5}Al_{0.5}Si_{0.25}Ti_{0.5}Fe_{0.5}Cu_{0.5}O_4$ showed the best properties for the application as a coating material. The CCC meets the essential requirement that the coefficient of thermal expansion of this material is within the range of the CTEs of the substrates. The CTE of the CCC is $6 *10^{-6}$ $K^{-1}$. The CTE of the refractories JM23 and JM26 are $5 *10^{-6}$ $K^{-1}$ and $7 *10^{-6}$ $K^{-1}$, respectively. Due to the low deviation of the CTE, the CCC material is suitable as a coating for the refractory bricks. In addition, the CCC also showed no signs of corrosion in the lab corrosion test. Therefore, coatings were made from this material and are presented below.

**CCC coating application**

The coatings were applied by slurry spray coating. Various wall and vault refractory materials which are used in the ceramic kiln were coated. Figure 9 shows a wall and a vault material, respectively, and also the coating process.



*Fig. 9: Refractory materials and coating application procedure.*

Initially, a water-based CCC slurry for the oxide mixture $Mg_{0.5}Al_{0.5}Si_{0.25}Ti_{0.5}Fe_{0.5}Cu_{0.5}O_4$ was developed for its application on the refractory substrates. The raw materials for the selected composition were milled and mixed. To achieve stable slurries with defined rheological properties the viscosity and flow behavior was adapted for spraying using different dispersants and binders. The slurry stabilized in this way was applied to the substrates by spraying followed by subsequent drying and sintering.

Coatings without any cracking could be applied, dried and sintered in the case of the vault material by spraying and sintering at 1200 °C with a dwell time of 10 h. In the case of the wall material, an additional bond layer had to be developed and applied to the substrate. Otherwise, the coating thickness was too inhomogeneous due to the high surface roughness and the open porosity of the refractory material. By application of the bond coat, the open porosity was closed and a smoother surface could be achieved. The bond coat itself could be applied without any problems. Afterwards, the spray coating was greatly improved and only small cracks were detected after drying and sintering at 1200 °C with a dwell time of 10 h.

**Corrosion test in roller kiln**

After the successful application of the CCC coatings, their performance should be tested under real operating conditions in an

industrial roller kiln for production of ceramic tiles. For this purpose, the samples were prepared on a laboratory scale. The kiln and the samples placed in the kiln for testing are shown in Figure 10. The CCC coated samples are compared with uncoated refractory samples. As soon as the test phase is completed, the samples will be removed from the kiln and analyzed. In parallel, the coated samples will be subjected to thermal cycling tests, because the refractories are affected by thermal cycles that occur every time the kiln is heated up and down, and also when there is a gap in the production rate that causes some disturbances on the thermal stability of the kiln.

According to the results of the lab scale samples, the coatings will be applied and sintered directly in the furnace for further testing.



*Fig. 10: Industrial roller kiln and coated samples that were introduced into the kiln.*

## CONCLUSIONS

A Compositionally Complex Ceramic coating was developed for refractory bricks of a roller kiln.

It was possible to prepare CCC materials with spinel structure by using a simple powder mixing route. In addition, the development of an ML model to estimate the probability of spinel formation for ceramics and a linear model to estimate the CTE could be implemented. The ML models are used in a distributed computing backend that can be accessed via a REST API (https://forge.aeonx.ai/docs).

The sample with the composition $Mg_{0.5}Al_{0.5}Si_{0.25}Ti_{0.5}Fe_{0.5}Cu_{0.5}O_4$ was identified as a suitable material for the use as a protective coating for the refractories. A spinel was formed without significant other phases and the coefficient of thermal expansion was $6 *10^{-6}$ $K^{-1}$. Therefore, a CCC was formed with a CTE to match the refractories. In addition, laboratory corrosion tests showed no signs of corrosion of this material.

Water-based slurries for applying a CCC coating with the composition $Mg_{0.5}Al_{0.5}Si_{0.25}Ti_{0.5}Fe_{0.5}Cu_{0.5}O_4$ by spraying were successfully prepared and applied on refractories. However, it was found that bond coats are required for the application of spray coatings on the wall refractory with relatively high open porosity. The coatings are tested under real operating conditions in an industrial roller kiln.

## ACKNOWLEDGMENT

## REFERENCES

[1] Wright, Andrew J.; Luo, Jian (2020): A step forward from high-entropy ceramics to compositionally complex ceramics: a new perspective. In J Mater Sci 55 (23), 9812–9827. DOI: 10.1007/s10853-020-04583-w.

[2] Wright, Andrew J.; Wang, Qingyang; Huang, Chuying; Nieto, Andy; Chen, Renkun; Luo, Jian (2020): From high-entropy ceramics to compositionally-complex ceramics: A case study of fluorite oxides. In Journal of the European Ceramic Society 40 (5), 2120–2129. DOI: 10.1016/j.jeurceramsoc.2020.01.015.

[3] Zhang, Rui-Zhi; Reece, Michael J. (2019): Review of high entropy ceramics: design, synthesis, structure and properties. In J. Mater. Chem. A 7 (39), 22148–22162.

[4] Oses, Corey; Toher, Cormac; Curtarolo, Stefano (2020): High-entropy ceramics. In Nat Rev Mater 5 (4), 295–309. DOI: 10.1038/s41578-019-0170-8.

[5] Rost, Christina M.; Sachet, Edward; Borman, Trent; Moballegh, Ali; Dickey, Elizabeth C.; Hou, Dong et al. (2015): Entropy-stabilized oxides. In Nature communications 6, 8485. DOI: 10.1038/ncomms9485.

[6] Albedwawi, S. H. et al.: High entropy oxides-exploring a paradigm of promising catalysts: A review. Materials & Design 202 (2021), 109534.

[7] Fu, M. et al.: High-entropy materials for energy-related applications. iScience 24 (2021) 3, 102177.

[8] Ma, J. et al.: High-entropy spinel ferrites $MFe2O4$ (M = Mg, Mn, Fe, Co, Ni, Cu, Zn) with tunable electromagnetic properties and strong microwave absorption. Journal of Advanced Ceramics 11 (2022) 5, 754-768

[9] Bérardan, D. et al.: Colossal dielectric constant in high entropy oxides. physica status solidi (RRL) - Rapid Research Letters 10 (2016) 4, 328-333.

[10] Dong, Y. et al.: High-entropy environmental barrier coating for the ceramic matrix composites. Journal of the European Ceramic Society 39 (2019) 7, 2574-2579.

[11] Wright, Andrew J.; Huang, Chuying; Walock, Michael J.; Ghoshal, Anindya; Murugan, Muthuvel; Luo, Jian (2021): Sand corrosion, thermal expansion, and ablation of medium- and high-entropy compositionally complex fluorite oxides. In J. Am. Ceram. Soc. 104 (1), 448–462. DOI: 10.1111/jace.17448.

[12] Merkys, A., Vaitkus, A., Grybauskas, A., Konovalovas, A., Quirós, M. & Gražulis, S. (2023). Graph isomorphism-based algorithm for cross-checking chemical and crystallographic descriptions. Journal of Cheminformatics, 15(25). DOI: 10.1186/s13321-023-00692-1

[13] Vaitkus, A., Merkys, A. & Gražulis, S. (2021). Validation of the Crystallography Open Database using the Crystallographic Information Framework. Journal of Applied Crystallography, 54(2), 661-672. DOI: 10.1107/S1600576720016532

[14] Quirós, M., Gražulis, S., Girdzijauskaitė, S., Merkys, A. & Vaitkus, A. (2018). Using SMILES strings for the description of chemical connectivity in the Crystallography Open Database. Journal of Cheminformatics, 10(23). DOI: 10.1186/s13321-018-0279-6

[15] Merkys, A., Vaitkus, A., Butkus, J., Okulič-Kazarinas, M., Kairys, V. & Gražulis, S. (2016). COD::CIF::Parser: an error-correcting CIF parser for the Perl language. Journal of Applied Crystallography, 49. DOI: 10.1107/S1600576715022396

[16] Gražulis, S., Merkys, A., Vaitkus, A. & Okulič-Kazarinas, M. (2015). Computing stoichiometric molecular composition from crystal structures. Journal of Applied Crystallography, 48, 85-91. DOI: 10.1107/S1600576714025904

[17] Gražulis, S., Daškevič, A., Merkys, A., Chateigner, D., Lutterotti, L., Quirós, M., Serebryanaya, N. R., Moeck, P., Downs, R. T. & LeBail, A. (2012). Crystallography Open Database (COD): an open-access collection of crystal structures and platform for world-wide collaboration. Nucleic Acids Research, 40, D420-D427. DOI: 10.1093/nar/gkr900

[18] Grazulis, S., Chateigner, D., Downs, R. T., Yokochi, A. T., Quiros, M., Lutterotti, L., Manakova, E., Butkus, J., Moeck, P. & Le Bail, A. (2009). Crystallography Open Database – an open-access collection of crystal structures. Journal of Applied Crystallography, 42, 726-729. DOI: 10.1107/S0021889809016690

[19] Downs, R. T. & Hall-Wallace, M. (2003). The American Mineralogist Crystal Structure Database. American Mineralogist, 88, 247-250.

# DISPERSION OF SURFACE MODIFIED NANO ADDITIVES BY SILANOL GROUPS AND ITS EFFECT ON PROPERTIES OF OXIDE AND OXIDE−C REFRACTORIES

AmirAbbas Nourbakhsh[1], Najmeh Lotfian[1], Mozhdeh Malekpour[1], Mahsa Masoud[1], Amirhossein Nourbakhsh[1], Elham Rahimi[2], Yalda Keramat[1], Marzieh Nourbakhsh [3]

1-Arvin Dirgodaz Vijeh Sepano Company, Isfahan Science and Technology Town, Isfahan, Iran.
2-Mehrgodaz Refractory Company, Sefiddasht, Chaharrmahal and Bakhtiari, Iran.
3-Institute Für Ziegelforschung Essen Am Zehnthof 197, 45307 Essen, Germany.

## ABSTRACT

This work addresses a novel approach to improve the dispersion of nano $MgCr_2O_4$ and MWCNT- $Al_2O_3$ nanocomposite additives by functionalizing with silanol groups in Mag-chrome and Alumina-C refractories, respectively. In this way, Firstly, surface of nano additives have been modified with 3-(thriethoxsilyl) propyl amine (APTES) silanol group. Afterwards, 1% wt of nano additives (with and without functionalizing with silanol group) were added to matrix and compressed under a uniaxial press. Mag-chrome refractories were treated at firing temperature between 1400 and 1600 °C, and the firing temperature of Alumina-C refractories were 1450°C under reduced atmosphere. The presence of the silanol groups on the nano additives was approved by XRD, FTIR, and UV-visible spectroscopy. The physical and mechanical properties, such as permanent linear change, bulk density, apparent porosity, Cold crushing strength, and hot modulus of rupture were determined according to DIN standards. The results indicated that the surface modification and well distributed nano additives through the matrix of refractories not only promoted the secondary spinel phase formation in Mag-Chrome refractories, but also increased SiC formation in Alumina-C refractories. The mentioned phase formation increased CCS (from 886 kgf/cm$^2$ to 997 kgf/cm$^2$) and HMOR increased (from 57.5 kgf/cm$^2$ to 59.5 kgf/cm$^2$) of Mag-chrome sample due to higher secondary spinel formation. Also, it reduced 200°C of sintering temperature. In Alumina- C samples the CCS increased from (1370 kgf/cm$^2$ to 1560 kgf/cm$^2$), and HMOR (from 60 to 75 kgf/cm$^2$) due to promotion of higher SiC whiskers formation.

Keywords: Dispersion, Mag-chrome, Alumina-carbon, Nano Composite

## INTRODUCTION

Magnesia-chrome refractories have many potential uses including non-ferrous furnace linings, cement kiln linings and secondary metallurgy applications due to their high-temperature stability, low thermal expansion, and outstanding erosion-corrosion performance at high temperatures. Also, $Al_2O_3$-C refractories have been widely used as functional materials in a continuous casting process of iron and steel industry due to their excellent mechanical properties, thermal shock resistance, and corrosion resistance. However, despite these positive features in both refractories , a main drawback is their high sintering temperature and low mechanical properties specially at high temperature. This disadvantages could be solved by the use of suitable Nano-additives. Aneziris et al. [1] and Luo et al. [2] found that $Al_2O_3$-C refractories containing carbon nanotubes (CNTs) revealed better mechanical properties than those without CNTs. These achievements of superior properties originated from a combination of the nature of various nanocarbons and the in situ formation of ceramics in the specimens [3]. Azhari

also reported enhanced mag-chrome direct bonding in the presence of nano-sized iron oxide and attributed the enhancement to a drop-down in the liquid silicate phase viscosity, facilitating solid-state sintering and the formation of magnesioferite spinel at a lower temperature [4]. Despite many researches have been done in the field of nano additives of Oxide and Oxide-C refractories, there are two main problems with the use of nano additives: (1) the high-cost of their synthesis, and (2) the difficulty of homogeneously dispersing them in the refractory matrix. The first problem can be overcome by choosing a simple and inexpensive process such as the citrate-nitrate route as well as the lower consumption of nano materials. But the second problem requires a novel solution; one possibility is to functionalize the nano-additives with silanol groups. The use of silane groups to assist the dispersion of various nano-additives has previously been reported. Sabzi [5] used amino propyl triethoxy silane to modify the surface of $TiO_2$ nano-particles and reported their improved dispersion and mechanical properties. Dincer et.al [6] modified the surface of nano-$Fe_3O_4$ using various silane compounds and showed that the presence of silanol groups on the surface of the nano-particles could stabilize them and decrease their tendency for agglomeration. In another study, Peng [7] modified carbon nanotube particles with (3-aminopropyl) triethoxysilane (APTES) and reported the improvement of dispersion and chemical bonding in ceramic bodies based on the above literature [5-7].

The present study was undertaken to functionalize nano-$MgCr_2O_4$ and MWCNT-$Al_2O_3$ nanocomposite with silanol groups in order to facilitate its dispersion into a magnesia-chrome and Alumina-c matrix. Moreover, the effect of surface silanol treatment on the physical properties, mechanical properties and microstructure changes were investigated.

## EXPERIMENTAL PROCEDURE

### Functionalization of $MgCr_2O_4$ and MWCNT-$Al_2O_3$ nanoparticles

The $MgCr_2O_4$ nano-spinel particles were synthesized by the solution-combustion method and the MWCNT-$Al_2O_3$ nano composite were synthesized through the sol-gel method which was reported previously [8] The surfaces of these nano structures were then functionalized with (3-aminopropyl) triethoxysilane (APTES) silanol groups as follows: 1g of the $MgCr_2O_4$ and MWCNT- $Al_2O_3$ nanoparticles was dispersed in deionized water using an ultrasonic bath and magnetic stirrer for 2 h. The appropriate amount of silane was dispersed in water and acidified with HCl to assist chemical bonding and stirred for 1 h. This solution was then added to the solution containing the $MgCr_2O_4$ and MWCNT- $Al_2O_3$ nanoparticles, sonicated for more than 2h and stirred for 3h at 60 °C. Subsequently, the as prepared solution washed with ethanol and water, then dried at 100 °C for 12 h in a vacuum dryer. This procedure is shown schematically in (figure 1).
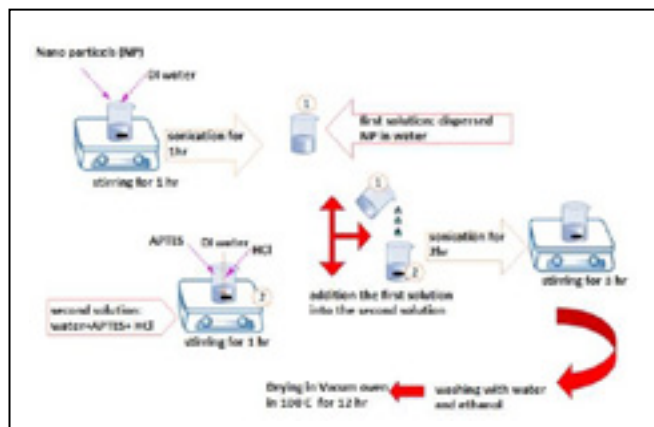
*Fig. 1: Schematic representation of the functionalization of MgCr₂O₄ and MWCNT- Al₂O₃ nanoparticles with APTES.*

**Preparation of the Magnesia-Chrome and Al₂O₃-C matrix containing functionalized MgCr₂O₄ and MWCNT-Al₂O₃ nanoparticles**

For Magnesia-Chrome refractories 1 wt.% of the functionalized and, for comparison, non-functionalized $MgCr_2O_4$ , nanoadditive were added to the calcium lingosulfonate solution and stirred for 30 min at added to the matrix of Mag-Chorme samples. Also 1wt.% of the functionalized and, for comparison, non-functionalized MWCNT-Al₂O₃, nanocomposite were added to the ethanol solution and stirred for 30 min. Then the obtained solution was added to the resin at 45 °C before its addition to the matrix. Finally, all samples compressed under a uniaxial pressure at 120 Mpa and dried overnight. Mag-Chrome samples fired at 1400 and 1600 °C for 5h and Alumina-C samples fired under reduced atmosphere at 1450 °C for 5h. The prepared sample labeled as table 1.

Tab. 1: Designation of samples.

| | Sample |
|---|---|
| Matrix formulation with 1% MgCr₂O₄, fired at 1600°C | M1-1600 |
| Matrix formulation with 1% functionalized MgCr₂O₄, fired at 1600°C | S1-1600 |
| Matrix formulation with 1% MgCr₂O₄, fired at 1400°C | M1-1400 |
| Matrix formulation with 1% functionalize MgCr₂O₄, fired at 1400°C | S1-1400 |
| Matrix formulation with 1% MWCNT-Al₂O₃, fired at 1450°C | CA-1450 |
| Matrix formulation with 1% functionalize MWCNT-Al₂O₃, fired at 1450°C | SCA-1450 |

**Characterization of the samples**

Determination of the cold crushing strength (CCS) and hot modulus of rupture (HMOR) was carried out according to DIN standards 993-5 and 993-7 respectively, using a Universal testing machine (model GT-7001-L100) for the CCS measurement and an HMOR15-610p machine to determine the hot modulus of rupture. Bulk densities (BD) and apparent porosities (AP) were measured according to DIN 993-1 and the permanent linear change (PLC) was determined according to DIN 993-10. The presence of silane groups on the surface of the nanoparticles was studied by XRD (Asenware AW-DX300 diffractometer with Cu Kα radiation (λ = 1.54184 A°) in the 2θ range from 10 to 100 and FTIR using an Impact 400D spectrometer (NICOLET) on samples embedded in KBr discs. The effect of silane functionalization on the dispersion of the nanoparticles was observed at 190-2700 nm using a UV-visible spectrometer (JASCO V-670, Japan). Since the modified and unmodified MgCr₂O₄ & MWCNT-Al₂O₃ nanoparticles were added to the refractory matrix in a binder, their dispersion was characterized by UV-visible spectroscopy in water and ethanol. The

refractory matrices containing both the silanol-modified and unmodified nanoparticles were examined by SEM/EDS on gold-coated samples at an operating voltage of 20 kV using a Zeiss SEM and an FEI Quanta 200 electron microscope.

**RESULTS AND DISCUSSION**
**Investigation of the presence of the functionalizing groups in the MgCr₂O₄ & MWCNT-Al₂O₃ additive**

FTIR spectra of MgCr₂O₄ & MWCNT-Al₂O₃ nanoparticles and functionalized MgCr₂O₄ (MgCr₂O₄-S) & (MWCNT-Al₂O₃-S) depicted in (figure 2-a) between 500 to 4000 $cm^{-1}$. The peak at 615 $cm^{-1}$ in MgCr₂O₄ is attributed to the Cr(III)-O vibration mode and that at about 536 $cm^{-1}$ to the Mg(II)-O bond. These two peaks in MgCr₂O₄-S are not clearly resolved due to the presence of the silane groups on the surface of the nanoparticles. The peak at 1087 $cm^{-1}$ in MgCr₂O₄-S confirms the presence of the Si-OH group and that at about 641 $cm^{-1}$ corresponds to the silanol Si-O group on the surface of the nanoparticles. The NH₂ stretching peaks of the functionalizing APTES groups are present at 3300 and 3500$cm^{-1}$ in the MgCr₂O₄-S sample, but the broadness and intensity of these peaks obscures the OH vibration which is also present, as can be distinguished at 3300-3400 $cm^{-1}$, in the spectrum of unfunctionalized MgCr₂O₄ (figure 2-a). The increased intensity of the peak at 1603 $cm^{-1}$ in the MgCr₂O₄-S sample and the presence of an associated shoulder is also attributed to the NH₂ bending vibration of this group. These spectra confirm the successful incorporation of silanol groups on the MgCr₂O₄ nanoparticles.
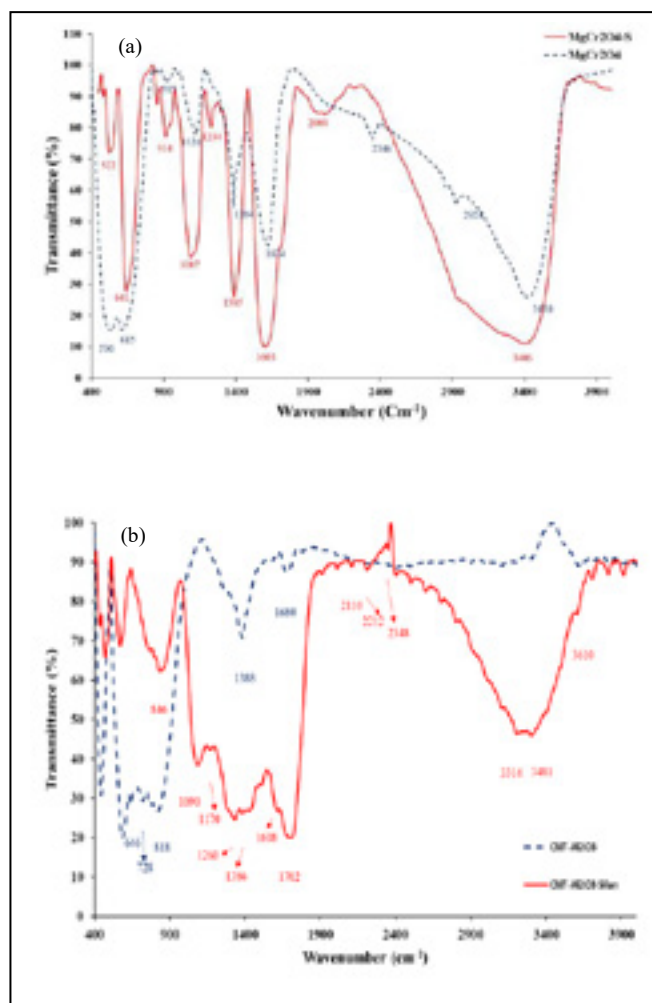


*Fig. 2: FTIR spectra of a) MgCr₂O₄, MgCr₂O₄-S, b) MWCNT-Al₂O₃ and MWCNT-Al₂O₃-S samples.*

Considering the functionalization of MWCNT-Al₂O₃ with 3-aminopropyltriethoxysilane (APTES) groups, the presence of NH2

and Si-OH groups in nanoparticles is obvious. As can be seen in (figure 2-b), the stretching peaks from 3300 cm$^{-1}$ to 3500 cm$^{-1}$ of MWCNT-Al$_2$O$_3$ sample related to the NH$_2$ group, on the other hand, the 1608 cm$^{-1}$ peak indicates the presence of NH$_2$ bending groups. The presence of a peak at 1090 cm$^{-1}$ in the functionalized MWCNT-Al$_2$O$_3$ sample is related to the Si-OH stretch bond which is an evidence for the presence of silane groups on the surface of the nanoparticles. This peak does not appear in the non-functionalized sample. The peak at 646 cm$^{-1}$ can be ascribe to Si-O bending mode. The peaks between 1170 cm$^{-1}$ and 1260 cm$^{-1}$ are related to the Si-C bond.

**The effect of silane treatment on the dispersion of MgCr$_2$O$_4$ & MWCNT-Al$_2$O$_3$ nanoparticles by UV-visible spectroscopic**
UV-visible spectroscopy at 200-330 nm is an appropriate method to investigate the dispersion of the silanol-functionalized nanoparticles. A great absorbance peak at the UV-visible region indicates better dispersion of nanoparticles in solution. MgCr$_2$O$_4$-S and MWCNT-Al$_2$O$_3$-S shows the remarkable UV-visible absorbance (figure 3), confirming the distinguished dispersion of functionalized sample in comparision to the others.
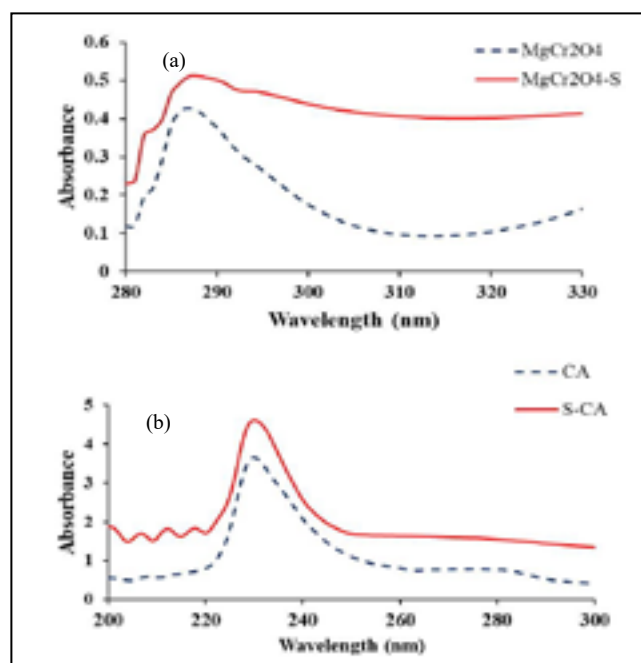
*Fig. 3: UV-visible spectra of samples a)MgCr$_2$O$_4$ , MgCr$_2$O$_4$-S, b)MWCNT-Al$_2$O$_3$ and MWCNT-Al$_2$O$_3$ –S.*

**Effect of the nano-additives on the magnesia-chrome and Alumina-C matrix properties**
*XRD patterns of magnesia-chrome and Alumina-C samples*

The XRD patterns of M1 and S1 fired at different temperatures (figure 4) show an increased intensity of the secondary spinel phase (Mg,Fe)Cr$_2$O$_4$ and (Mg,Fe)Al$_2$O$_4$ in sample S. This may result from the improved dispersion of nanoparticles which encourage spinel formation by the silanol groups as nucleating agents for the spinel phase. This will influence the high-temperature mechanical properties that is the same for both samples.
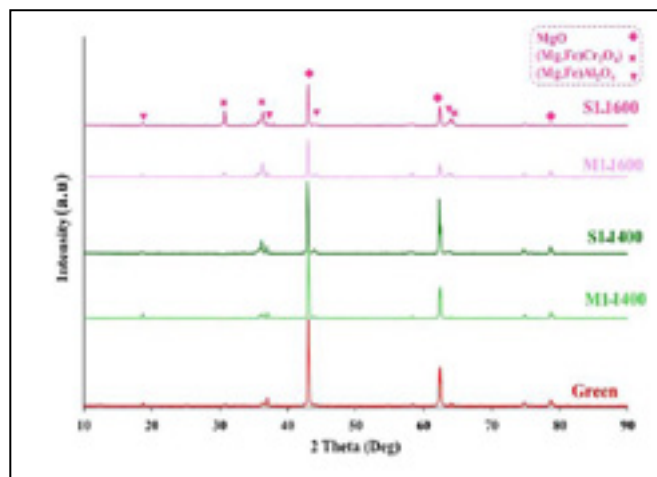


*Fig. 4: XRD patterns of magnesia-chrome samples fired at different temperatures.*

XRD pattern of Alumina-C samples is depicted in (figure 5). The sample functionalized with APTES, due to the better dispersion and uniform distribution of nanoparticles, the intensity of SiC peaks is higher and Si peak decreased. It could be concluded that the presence of MWCNT-Alumina nanocomposite and proper distribution increased the SiC phase which plays important role to improve mechanical properties.
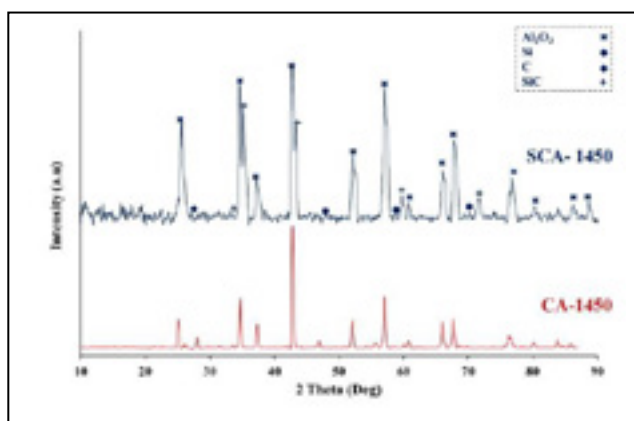


*Fig. 5: XRD pattern of CA-1450 & SCA-1450*

*Physical and mechanical properties*

The physical and mechanical properties of the magnesia-chrome samples containing MgCr$_2$O$_4$ and MgCr$_2$O$_4$-S nano-additives fired at 1400 and 1600 °C (Table 2) show that the samples containing silanol-modified nanoparticles (samples S1) are superior to those with unmodified nano-additive (samples M1). Since the content of the additives is the same in all the samples, this improvement can probably be the result of improved dispersion and effectiveness of the silanol-modified nano-additive. On the other hand, the permanent linear change (PLC) results suggest that two mechanisms may be involved: 1- Shrinkage due to sample sintering, and 2- Expansion of the secondary spinel phase which was formed during the process. Thus, decrease of shrinkage may be a reflection of the greater expansion associated with secondary spinel formation.
The standard deviation of the cold crushing strength (CCS) results (about 60 Kgf/cm$^2$) indicates that these values for S1-1400 are similar to those of M1-1600 within the limits of error, suggesting that the addition of the silanol-functionalized nanoparticles could decrease the sintering temperature up to 200 °C. For further investigation, the hot modulus of rupture values (HMOR), determined for S1-1600 and S1-1400 samples. The result of HMOR

were the same for both samples (about 59.5 kgf/cm$^2$ and 57.5 kgf/cm$^2$ respectively). This confirmed that the presence of the silanol-functionalized MgCr$_2$O$_4$ additive can produce similar physical and mechanical results for sample S1-1400 which compatibale with sample S1-1600. In Aumina- C samples, the CCS is higher in SCA-1450 which could be related to better distribution and higher amount of SiC formation through the matrix. Nourbakhsh etal [9] reported that in nitride bonded SiC refractories ,the presence of fibrous phases and the proper distribution could increase the strenghth of the sample and specially CCS and CMOR, although the density decreased and the percentage of open porosity costant or slightly increased. In fact ,the results of both researches pointing out the fact that higher ratio of length to diameter of the fibrous phase will have a good effect on improving the mechanical properties.Therefore, the longe length of the fibers with suitable distribution process could be the main reason of CCS increase. Additionally, absence of low melting phase, may result in high HMOR. The above results confirmed by labaratory investigation and shown in Table(2).

Tab. 2: Physical and mechanical properties of magnesia-chrome and Alumina-C containing nanoadditives samples with and without silanol groups.

| Sample | Permanent linear change(%) | Cold crushing strength (Kgf/cm$^2$) | Apparent porosity (%) | Bulk density (g/cm$^3$) | HMOR (kgf/cm$^2$) |
|---|---|---|---|---|---|
| M1-1400 | -1.172±0.005 | 759±20.23 | 25.79±0.05 | 2.73 | - |
| S1-1400 | -0.611±0.003 | 886±14.17 | 25.89±0.15 | 2.73 | 57.5 |
| M1-1600 | -1.991±0.056 | 932±75.52 | 19.41±0.94 | 2.96 | - |
| S1-1600 | -1.537±0.108 | 997±85.64 | 22.70±0.64 | 2.86 | 59.5 |
| CA-1450 | - | 1370±19.1 | 11/89±0.48 | 2.94 | 60 |
| SCA-1450 | - | 1560 ±27 | 10.47±0.21 | 2.81 | 75 |

*SEM of magnesia-chrome and Alumina-C refractories with and without APTES*
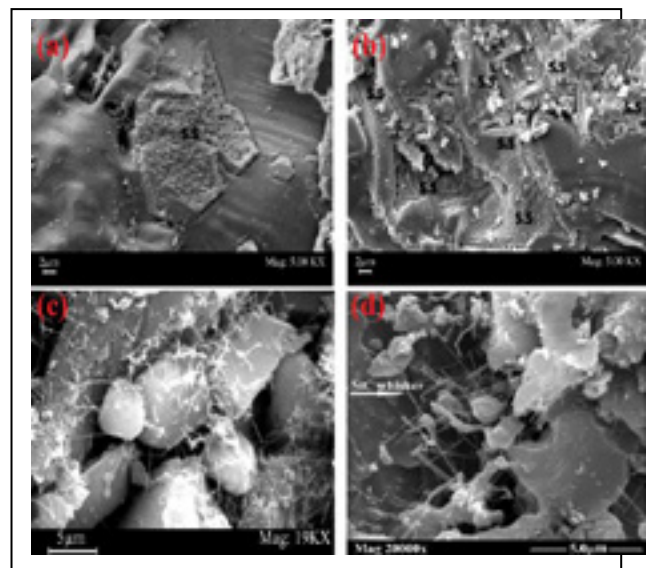


*Fig. 6: SEM of a) M1-1600, b) S1-1600, c)CA-1450, and d) SCA-1450 samples.*

Comparison of the SEM micrographs of M1-1600 and S1-1600 (figure 6-a,b) shows that silanol modification of the surface of the MgCr$_2$O$_4$ nano additive facilitates the formation and dispersion of the secondary spinels which are responsible for the development of mechanical strength specially at high temperature (HMOR).
Also, the SEM images of Alumina-C with and without silanized surface group (figure 6-c,d) containing 1%wt MWCNT-Al$_2$O$_3$ nano-composite confirmed the higher amount and more appropriate distribution of the SiC phase ,which plays an essential role to improve the high temperature mechanical properties (HMOR).

## CONCLUSIONS

The results approved the surface modification and well distributed nano additives through the matrix of refractories promoted both the secondary spinel phase formation in Mag-Chrome refractories and SiC formation in Alumina-C refractories. The mentioned phase formation increased CCS (from 886 kgf/cm$^2$ to 997 kgf/cm$^2$ ) and HMOR from (57.5 kgf/cm$^2$ to 59.5 kgf/cm$^2$) of Mag-Chrome sample due to higher secondary spinel formation. Also, it reduced 200°C of sintering temperature. In Alumina-C samples the CCS increased from (1370 kgf/cm$^2$ to 1560 kgf/cm$^2$), and HMOR (from 60 to 75 kgf/cm$^2$ ) due to promotion of higher SiC whiskers formation through the matrix.

## REFERENCES

[1] C.G Aneziris, S.L. Jin, Y.W. Li Roungos, Interaction of carbon nanotubes in Al$_2$O$_3$-C refractories for sliding gate applications, in: Proceeding of the summary Booklet (Abstract) of the Unified International Technical Conference on Refractories Brazil, 2009, p.8.

[2] M. Luo. Y.W. Li, S.L.Jin, S.B.Sang, L.Zhao, T.B.Li, Microstructure and Mechanicalo properties of Al$_2$O$_3$-C refractories with addition of multi walled Carbon nanotubes, Mater. Sci. Eng. A 548 (2012) 134-141.

[3] P. Hvizdos, J. Dusza. C. Balazsi, Tribological properties of Si$_3$N$_4$ graphene nanocomposites, J. Eur. Ceram. Soc. 33 (2013) 2359-2364.

[4] A. Azhari, F. Golestani-Fard, H. Sarpoolaki, Effect of nano iron oxide as an additive on phase and microstructural evolution of Mag-Chrome refractory matrix, J. Eur. Ceram. Soc. 29 (2009) 2679-2684.

[5] M. Sabzi, S.M. Mirabedini, J. Zohuriaan-Mehr, M. Atai, Surface modification of TiO$_2$ nano-particles with silane coupling agent and investigation of its effect on the properties of polyurethane composite coating, Progr. Org. Coat. 65 (2009) 222–228.

[6] C.A. Dinçer, N. Yıldız, N. Aydoğan, A. Çalımlı, A comparative study of Fe$_3$O$_4$ nanoparticles modified with different silane compounds, Appl. Surf. Sci. 318 (2014) 297-304.

[7] B. Peng, C. Takia, H. Razavi-Khosroshahi, M. Fuji, Effect of silane modification on CNTs/silica composites fabricated by a non-firing process to enhance interfacial property and dispersability, Adv. Pdr. Technol. 29 (2018) 2091-2096.

[8] Lotfian, Najmeh, et al. "A comparison of the effect of nanostructured MgCr2O4 and FeCr2O4 additions on the microstructure and mechanical properties of direct-bonded magnesia-chrome refractories." *Ceramics International* 46.1 (2020): 747-754.

[9] Nourbakhsh, A. A., F. Golestani-fard, and H. R. Rezaie. "The effect of Si content, firing temperature, and urea additive on the properties of nitride-bonded SiC refractories." *Refractories and Industrial Ceramics* 48.5 (2007): 383-386.

# THERMOPHYSICAL PROPERTIES OF CA$^{2+}$−CR$^{3+}$−FE$^{3+}$ DOPED LAALO$_3$ HIGH EMISSIVITY CERAMIC

Qu Wang, Gang Wang*, Yifan Zhang, Penghui Du

State Key Laboratory of Advanced Refractories, Sinosteel luoyang institute of refractories research co.,ltd, Luoyang 471039

## ABSTRACT

Pure LaAlO$_3$ and Ca$^{2+}$-Cr$^{3+}$-Fe$^{3+}$ co-doped LaAlO$_3$ ceramic materials were prepared by high temperature solid-state reaction. The microstructure, infrared emissivity, thermal expansion coefficient and thermal conductivity of the samples were studied. The results reveal that 10 mol% Ca$^{2+}$, 5 mol% Cr$^{3+}$, and 5 mol% Fe$^{3+}$ co-doped LaAlO$_3$, namely La$_{0.9}$Ca$_{0.1}$Al$_{0.9}$Cr$_{0.05}$Fe$_{0.05}$O$_3$, has a greater NIR emissivity of 0.91 in the wavelength range of 0.76–2.50 μm, which is 296% greater than that of pure LaAlO$_3$ The thermal conductivity of LaAlO$_3$ can be reduced by Ca$^{2+}$-Cr$^{3+}$-Fe$^{3+}$ co-doping. The minimum thermal conductivities of LaAlO$_3$ and La$_{0.9}$Ca$_{0.1}$Al$_{0.9}$Cr$_{0.05}$Fe$_{0.05}$O$_3$ both appear at 1200 °C, and the minimum thermal conductivity of La$_{0.9}$Ca$_{0.1}$Al$_{0.9}$Cr$_{0.05}$Fe$_{0.05}$O$_3$ is 3.707 W·m$^{-1}$·K$^{-1}$, which is 20% lower than that of pure LaAlO$_3$. Ca$^{2+}$-Fe$^{3+}$ co-doping can improve the TECs of LaAlO$_3$. The mean TEC of La$_{0.9}$Ca$_{0.1}$Al$_{0.9}$Cr$_{0.05}$Fe$_{0.05}$O$_3$ was 10.86×10$^{-6}$ K$^{-1}$.

## INTRODUCTION

High emissivity energy-saving materials are a new type of material that is being widely used in high-temperature energy-saving fields. To improve the thermal efficiency of high energy-consuming equipment such as thermal furnaces, it is necessary to improve their radiation heat transfer capacities [1-4]. According to Wien's law and Plan's law, radiant heat at temperatures above 800 °C should be mainly concentrated in the near-infrared band of 0.76-2.5 μm. Therefore, research into the high-temperature energy-saving field pays special attention to the emissivity of the near-infrared band.

According to the optical absorption theory of semiconductors, introducing suitable impurities into a semiconductor matrix can form impurity energy levels corresponding to the infrared spectral region [5,6]. This will enhance the absorption property of the semiconductor in the infrared range. Kirchhoff's law of thermal radiation states that, for a body in thermal equilibrium, absorptivity and emissivity are equal in the same wavelength range. Therefore, one potential method for increasing near-infrared emissivity is to form an impurity level locally by doping ions of different valence states and valence bonds. This will enhance the possibility of free carriers from a given valence band to undergo band transition, and will therefore promote the valence band. This process will increase the concentration of free carriers (electrons, holes, etc.) and the transition between the band gaps, thereby increasing near-infrared radiance [7,8]. LaAlO$_3$ is a perovskite-type semiconductor with a high melting point (2180 °C), a high temperature stability, and a typical indirect transition band structure. The valences of its A and B ions are not necessarily limited to its positive trivalent. This is in line with the doping conditions for the preparation of near-infrared high-emissivity ceramic materials, and this semiconductor has therefore received extensive attention [9,10]. In this study, Ca$^{2+}$-Cr$^{3+}$-Fe$^{3+}$ co-doping LaAlO$_3$ with excellent infrared emissivity was successfully prepared. This material has the potential to foster a new generation of infrared radiation energy-saving materials with high emissivity, high temperature resistance, and oxidation resistance.

## MATERIALS AND METHODS

### Sample preparation

In this paper, La$_2$O$_3$ (purity ≥99.95 %), Al$_2$O$_3$ (purity ≥99 %), CaCO$_3$ (purity ≥99 %), Cr$_2$O$_3$ (purity ≥99 %), Fe$_2$O$_3$ (purity ≥99 %) were used as experimental materials, and the ingredients were weighed according to the stoichiometric ratio of LaAlO$_3$ and La$_{0.9}$Ca$_{0.1}$Al$_{0.9}$Cr$_{0.05}$Fe$_{0.05}$O$_3$. The detailed synthesis process is shown in Ref. [11].

### Sample characterization

The phase composites of the samples were identified using X-ray diffractometer (XPert Pro, Philips) with Cu Kα radiation. The X-ray diffractometry (XRD) data were refined using the Rietveld refinement method to calculate the unit cell parameters. The microstructure of the sample was observed using field emission scanning electron microscopy (FESEM, GeminiSEM 300, German Zeiss) equipped with energy-dispersive X-ray spectroscopy (EDS). Before the SEM observation, the samples were thermally etched at 1400 °C for 2 h to ensure clear grain boundaries. The spectral absorptivity of samples in the wavelength range 0.2–2.5 μm was indirectly measured by recording the intensity of infrared reflection using an ultraviolet-visible-NIR (UV-Vis-NIR) spectrophotometer (Lambda 750 S, PerkinElmer, USA) equipped with a barium sulfate integrating sphere. The average linear TEC was obtained from the changes in the length of the specimen from 300 to 1200 °C in an air atmosphere using a thermal dilatometer (RPZ-04P, China) with sample dimensions of Φ10 mm × 50 mm. The thermal diffusivity and specific heat capacity of the ceramic samples were tested using a laser thermal conductivity meter (Netzsch LFA 467, Germany) in the temperature range 25–1200 °C with a sample size of Φ12.7 mm×2.5 mm. The thermal conductivities of the samples were then calculated using the formula $\lambda = C_p \cdot k \cdot \rho$, where $\lambda$ is the thermal conductivity (W/m·K), $k$ is the thermal diffusion coefficient (mm$^2$/s), $C_p$ is the specific heat capacity (J/g·K), and $\rho$ is the bulk density (g/cm$^3$).

## RESULTS AND DISCUSSION
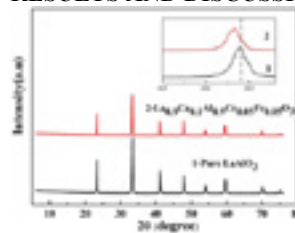


Fig. 1 XRD patterns of LaAlO$_3$ and La$_{0.9}$Ca$_{0.1}$Al$_{0.9}$Cr$_{0.05}$Fe$_{0.05}$O$_3$.

Fig. 1 shows the XRD patterns of LaAlO$_3$ and La$_{0.9}$Ca$_{0.1}$Al$_{0.9}$Cr$_{0.05}$Fe$_{0.05}$O$_3$. It can be seen from Fig.1 that the prepared samples have an orthorhombic perovskite structure with a space group of R-3c (167). No CaO, Cr$_2$O$_3$, Fe$_2$O$_3$ or other impurity phases were observed, indicating that most of Ca$^{2+}$, Cr$^{3+}$ and Fe$^{3+}$ ions were doped into the LaAlO$_3$ lattice. Compared with the peak of LaAlO$_3$, the diffraction peak of La$_{0.9}$Ca$_{0.1}$Al$_{0.9}$Cr$_{0.05}$Fe$_{0.05}$O$_3$ shifts to a lower angle, which is due to the increase of crystal plane spacing and lattice distortion after Ca$^{2+}$, Cr$^{3+}$ and Fe$^{3+}$ co-doping. This is consistent with the Rietveld refinement results of LaAlO$_3$ and La$_{0.9}$Ca$_{0.1}$Al$_{0.9}$Cr$_{0.05}$Fe$_{0.05}$O$_3$ cell parameters in Table 1.
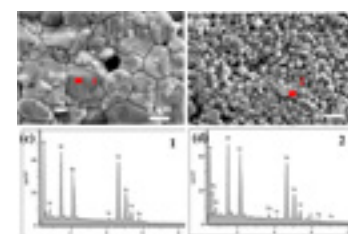


Fig. 2 SEM images of (a) LaAlO$_3$, (b) La$_{0.9}$Ca$_{0.1}$Al$_{0.9}$Cr$_{0.05}$Fe$_{0.05}$O$_3$ and EDS spectra of points (c)1 and (d)2.

Fig.2 shows the microstructure of LaAlO$_3$ and La$_{0.9}$Ca$_{0.1}$Al$_{0.9}$Cr$_{0.05}$Fe$_{0.05}$O$_3$. The grain shape of ceramics is irregular and the grain boundary is clearly visible. Compared with LaAlO3, Ca$^{2+}$-Cr$^{3+}$-Fe$^{3+}$ co-doping makes the grain size of the sample smaller, indicating that Ca$^{2+}$-Cr$^{3+}$-Fe$^{3+}$ co-doping promotes grain refinement.

Table1 Lattice parameters and tolerance factor of LaAlO$_3$ and La$_{0.9}$Ca$_{0.1}$Al$_{0.9}$Cr$_{0.05}$Fe$_{0.05}$O$_3$

| | Lattice parameter/Å | | Unit cell volume/Å$^3$ | Tolerance factor(t) |
|---|---|---|---|---|
| | a=b | c | | |
| LaAlO$_3$ | 5.36698 | 13.13549 | 327.67 | 0.8294 |
| La$_{0.9}$Ca$_{0.1}$Al$_{0.9}$Cr$_{0.05}$Fe$_{0.05}$O$_3$ | 5.37975 | 13.15183 | 329.64 | 0.8274 |
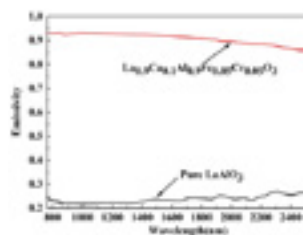
*Fig. 3 Infrared emissivity of LaAlO₃ and La₀.₉Ca₀.₁Al₀.₉Cr₀.₀₅Fe₀.₀₅O₃.*

Fig. 3 shows the emissivity of $LaAlO_3$ and $La_{0.9}Ca_{0.1}Al_{0.9}Cr_{0.05}Fe_{0.05}O_3$ in 0.76-2.50 μm. It can be seen from Fig.3 that $Ca^{2+}$-$Cr^{3+}$-$Fe^{3+}$ co-doping can greatly improve the emissivity of lanthanum aluminate materials in 0.76-2.50 μm. The average emissivity of $La_{0.9}Ca_{0.1}Al_{0.9}Cr_{0.05}Fe_{0.05}O_3$ is 0.91, which is 296 % higher than that of pure $LaAlO_3$. According to the infrared radiation mechanism, infrared radiation in the near-infrared region (0.76-2.5 μm) is mainly related to free carrier absorption, impurity level, and electronic transition [7]. When $Ca^{2+}$, $Cr^{3+}$ and $Fe^{3+}$ ions enter the $LaAlO_3$ lattice, $Ca^{2+}$ occupies the $La^{3+}$ position, $Cr^{3+}$ and $Fe^{3+}$ ions occupy the $Al^{3+}$ position. Since the valence of Ca is lower than that of La, the compensation mechanism is mainly the valence change and oxygen vacancy of B-site ions in order to maintain the valence balance of the system. The valence change of ions and the generation of oxygen vacancies will form impurity levels in the band gap of the material.
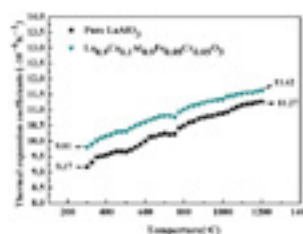


*Fig. 4 Thermal expansion coefficient patterns of LaAlO₃, and La₀.₉Ca₀.₁Al₀.₉Cr₀.₀₅Fe₀.₀₅O₃ ceramics at different temperature.*

It is well known that the mismatch of TEC will lead to large interfacial thermal stress between the substrate and the ceramic coating, which is the main reason for the cracking and spalling of the ceramic coating. Therefore, it is very important to study the TEC of doped $LaAlO_3$ high emissivity ceramics. Fig. 4 shows the TECs of pure $LaAlO_3$ and $La_{0.9}Ca_{0.1}Al_{0.9}Cr_{0.05}Fe_{0.05}O_3$ ceramics at different temperatures. It can be seen from Fig.5 that $Ca^{2+}$-$Cr^{3+}$-$Fe^{3+}$ co-doping can improve the TECs of $LaAlO3$ ceramics. The mean TECs of $LaAlO_3$ and $La_{0.9}Ca_{0.1}Al_{0.9}Cr_{0.05}Fe_{0.05}O_3$ are $10.33×10^{-6}$ $K^{-1}$ and $10.86×10^{-6}$ $K^{-1}$, respectively. It is well known that the thermal expansion coefficient is inversely proportional to the lattice energy. The relationship between thermal expansion coefficient and lattice energy can be expressed as [12]:

$$U = \frac{N_0 M z^+ z^- e^2}{r_0}\left(1 - \frac{1}{n}\right), \qquad (1)$$

where $N_0$, $M$, $z$, $r_0$, $e$, and $n$ represent Avogadro's number, the Madelung constant, ionic charge, inter-ionic distance, electron charge, and Born exponent, respectively. It can be seen from Table 1 that the unit cell expands slightly after $Ca^{2+}$-$Cr^{3+}$-$Fe^{3+}$ co-doping, indicating that the average ion distance $r_0$ increases, which will lead to the decrease of lattice energy of $La_{0.9}Ca_{0.1}Al_{0.9}Cr_{0.05}Fe_{0.05}O_3$. Therefore, TEC of $La_{0.9}Ca_{0.1}Al_{0.9}Cr_{0.05}Fe_{0.05}O_3$ is higher than that of pure $LaAlO_3$.
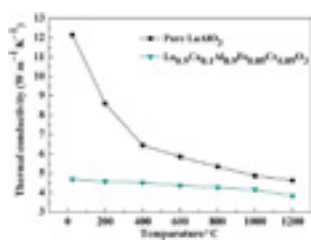


*Fig. 5 The thermal conductivity patterns of LaAlO₃ and La₀.₉Ca₀.₁Al₀.₉Cr₀.₀₅Fe₀.₀₅O₃ ceramic bulks at different temperature.*

Fig.7 shows the temperature dependence of thermal conductivity of $LaAlO_3$ and $La_{0.9}Ca_{0.1}Al_{0.9}Cr_{0.05}Fe_{0.05}O_3$ ceramics. From 25 °C to 1200 °C, the thermal conductivity of $LaAlO_3$ and $La_{0.9}Ca_{0.1}Al_{0.9}Cr_{0.05}Fe_{0.05}O_3$ ceramics decreased with the increase of temperature, and the thermal conductivity of $La_{0.9}Ca_{0.1}Al_{0.9}Cr_{0.05}Fe_{0.05}O_3$ ceramics was significantly lower than that of pure $LaAlO_3$. The thermal conductivity of $La_{0.9}Ca_{0.1}Al_{0.9}Cr_{0.05}Fe_{0.05}O_3$ ceramics is 3.707-4.910 $W·m^{-1}·K^{-1}$ in the temperature range of 25 °C to 1200 °C, which is lower than that of pure $LaAlO3$ ceramics. At 1200 °C, the thermal conductivity of $LaAlO_3$ and $La_{0.9}Ca_{0.1}Al_{0.9}Cr_{0.05}Fe_{0.05}O_3$ has the lowest value. The lowest thermal conductivity of $La_{0.9}Ca_{0.1}Al_{0.9}Cr_{0.05}Fe_{0.05}O_3$ is 3.707 $W·m^{-1}·K^{-1}$, which is about 20 % lower than that of pure $LaAlO_3$ (4.628 $W·m^{-1}·K^{-1}$), indicating that $Ca^{2+}$-$Cr^{3+}$-$Fe^{3+}$ co-doping can effectively reduce the thermal conductivity of lanthanum aluminate ceramics.

## CONCLUSIONS

$Ca^{2+}$-$Cr^{3+}$-$Fe^{3+}$ co-doped lanthanum aluminate infrared radiation material was successfully prepared by high temperature solid state reaction method. The infrared emissivity of $La_{0.9}Ca_{0.1}Al_{0.9}Cr_{0.05}Fe_{0.05}O_3$ doped with 10 mol% $Ca^{2+}$, 5 mol% $Cr^{3+}$, and 5 mol% $Fe^{3+}$ in 0.76 ~ 2.5 μm is 0.91, which is 296 % higher than that of pure $LaAlO_3$. The lowest thermal conductivity of $La_{0.9}Ca_{0.1}Al_{0.9}Cr_{0.05}Fe_{0.05}O_3$ is 3.707 $W·m^{-1}·K^{-1}$, which is 20 % lower than that of pure $LaAlO_3$. The mean TECs of $LaAlO_3$ and $La_{0.9}Ca_{0.1}Al_{0.9}Cr_{0.05}Fe_{0.05}O_3$ ceramics are $10.33×10^{-6}$ $K^{-1}$ and $10.86×10^{-6}$ $K^{-1}$, respectively.

## REFERENCES

[1] W. Tan, C.A. Petorak, R.W. Trice. Rare-earth modified zirconium diboride high emissivity coatings for hypersonic applications, Journal of the European Ceramic Society 2014; 34: 1–11.

[2] J.K. Ye, C.H. Bu, Z. Han, F. Wang, X.W. Li, Y.X. Chen, J.T. Li. Flame-spraying synthesis and infrared emission property of $Ca^{2+}$/$Cr^{3+}$ doped $LaAlO_3$ microspheres, Journal of the European Ceramic Society 2015; 35 (11): 3111–3118.

[3] Y. Su, X. Li, H. Ji, Z. Zhao, P. Zhang. Effect of $Ca^{2+}$ and $Mn^{2+}$ ions on the radiation properties of $LaAlO_3$, Ceramics International 2018, 44(16): 20427-20431.

[4] Zhang J Y, Fan X A, Lei L, et al. Ferrites based infrared radiation coatings with high emissivity and high thermal shock resistance and their application on energy-saving kettle[J]. Applied Surface Science, 2015, 344: 223-229.

[5] J.K. Ye, C.H. Bu, Z. Han, et al, Microstructural evolution and infrared radiation property of $Ca^{2+}$-$Cr^{3+}$ doped $LaAlO3$ in the presence of $SiO_2$, Materials Letters. 171(2016)55-58.

[6] N. Wakiya, J.K. Wang, A. Saiki, et al, Synthesis and dielectric properties of $Ba_{1-x}R_{2x/3}Nb_2O_6$ (R: Rare Earth) with tetragonal tungsten bronze structure, Journal of the European Ceramic Society. 19(6)(1999)1071-1075.

[7] J.P. Huang, C.L. Fan, G.P. Song, et al, Enhanced infrared emissivity of $CeO_2$ coatings by La doping, Applied Surface Science. 280(9)(2013)605-609.

[8] Wu X Y, Yu H B, Dong H, et al. Enhanced infrared radiation properties of $CoFe_2O_4$ by single $Ce^{3+}$-doping with energy-efficient preparation[J]. Ceramics International, 2014, 40(4): 5905-5911.

[9] Z. Han, X.W. Li, J.K. Ye, et al, Significantly enhanced infrared emissivity of $LaAlO_3$, by co-doping with $Ca^{2+}$, and $Cr^{3+}$,for energy-saving applications, Journal of the American Ceramic Society. 98(8)(2015)2336–2339.

[10] Q.S. Liu, Q. Chang, J.L. Li, Z. You, J.Q. Peng, J.A. Chen, Infrared radiation performance and calculation of B-site doped lanthanum aluminate from first principles, Ceramics International 44 (10) (2018) 11570-11575.

[11] Q. Wang, S.W Yan, B. Dong, et al. Preparation of environmentally friendly high-emissivity $Ca^{2+}$-$Fe^{3+}$ co-doped $LaAlO_3$ ceramic[J]. International Journal of Applied Ceramic Technology,2023, 20:1785–1792.

[12] W.D. Kingery, H.K. Bowen, D.R. Uhlmann, Introduction to Ceramics, 2nd ed., Wiley, New York, 1976.

# HIGH ENTROPY TRANSITION METAL DIBORIDES POWDERS SYNTHESIZED VIA MOLTEN SALT METHOD

Haijun Zhang

Wuhan University of Science and Technology, The state Key Laboratory of Refractories and Metallurgy, Wuhan, Hubei Province, China

$(Hf_{0.2}Ti_{0.2}Ta_{0.2}Nb_{0.2}Mo_{0.2})B_2$, $(Ti_{0.2}Mo_{0.2}W_{0.2}Ta_{0.2}Nb_{0.2})B_2$, $(Hf_{0.167}Zr_{0.167}Ti_{0.167}Ta_{0.167}Nb_{0.167}V_{0.167})B_2$ powders were synthesized by molten salt/ boro-carbothermal reduction method. Compared with the temperatures (about 2000 °C) required by conventional methods, the firing temperature and energy consumption demanded by the present method were remarkably the milder. $(Hf_{0.2}Ti_{0.2}Ta_{0.2}Nb_{0.2}Mo_{0.2})B_2$ powders can be synthesized by the method at 1300 °C, by using $HfO_2$, $TiO_2$, $Ta_2O_5$, $Nb_2O_5$, $MoO_3$ $B_4C$ and amorphous carbon as reactants and NaCl-KCl salt mixture as reacting medium. $(Ta_{0.2}Ti_{0.2}Mo_{0.2}W_{0.2}Nb_{0.2})B_2$ powders with a uniformly distributed elemental composition were synthesized via the method at 1473 K/3 h with salt/reactant weight ratio of 5/1. $(Hf_{0.167}Zr_{0.167}Ti_{0.167}Ta_{0.167}Nb_{0.167}V_{0.167})B_2$ six-principle-component high-entropy powders can be synthesized at 1400 °C/20 min by using $HfO_2$, $ZrO_2$, $TiO_2$, $Ta_2O_5$, $Nb_2O_5$, $V_2O_5$, $B_4C$ and amorphous carbon as reactants and NaCl-KCl salt mixture as reacting medium, with a $(n(HfO_2/ZrO_2/TiO_2/Ta_2O_5/Nb_2O_5/V_2O_5/B_4C/C))$ molar ratio of 2.0:2.0:2.0:1.0:1.0:1.0:9.6:21.0 and a salt/reactants weight ratio of 2.0. The as-synthesized six-principle-component high-entropy powders had high elemental distribution uniformities, well-defined hexagon-platelet-like morphology.

# REFRACTORY COMPOSITE AGGREGATES BASED ON NB–AL$_2$O$_3$ USING 3D PRINTING TECHNOLOGY

Tilo Zienert,  Dirk Endler, Jana Hubálková, Christos G. Aneziris
TU Bergakademie Freiberg, Institute of  Ceramics, Refractories and Composite Materials, Freiberg, Germany

**ABSTRACT**

Refractory composites based on Nb-Al$_2$O$_3$ or Ta-Al$_2$O$_3$ are promising functional materials, regarding their thermal and electrical conductivity, used for refractory applications at temperatures above 1500 °C [1]. The composites show ductile behaviour at application temperature. In addition, large components with low shrinkage on sintering can be produced using standard technology, e.g. castables with aggregate sizes up to 3 or 5 mm. Using 3D printing, the shape and materials composition of the aggregates can be produced in a defined way.

The work demonstrates how 3D-printing can be used to produce layered composite material of Al$_2$O$_3$/Nb-Al$_2$O$_3$ that combines the corundum refractoriness with the metal's thermal and electrical conductivity in combination with ductility to increase the thermal shock resistance of the composite material.

**MATERIAL AND METHODS**

Paste extrusion is used in combination with a modified clay printer for utilising the samples (figure 1). Standard refractory raw materials (e.g. the alumina CT9FG from Almatis) with particle sizes up to 100 µm (figure 2) are mixed with an organic binder based on cellulose, xanthan and oelic acid with a total water content of 50 vol.% water to obtain a extrusion-ready mass. By applying dual-extrusion, it is possible to fabricate coarse particles with layered morphologies.



*Fig. 2: Particle size distribution of the used raw materials.*

**REFERENCES**

[1]    Zienert, T.; Endler, D.; Hubálková, J.; Eusterholz, M.; Boll, T.; Heilmaier, M.; Günay, G.; Weidner, A.; Biermann, H.; Kraft, B.; Wagner, S. & Aneziris, C.G. Coarse-grained refractory composite castables based on alumina and niobium, Advanced Engineering Materials 24 (2022) 2200296

*Fig. 1: Utilised clay printer (StoneFlower 3.1).*

SHORT COMMUNICATIONS

# USE OF METALLURGICAL RESIDUES AS POTENTIAL RAW MATERIALS FOR HIGH PERFORMANCE REFRACTORY CASTABLES

Mathilda Derensy

RWTH Aachen University, Institute of Mineral engineering , Marsac-sur-l'Isle, France

Extractive metallurgy processes are not suitable for lower-grade resources with impurities. Therefore this study aims at advanced metal-extraction and recovery methods of slags from metallurgical processes. In order to produce nearly zero-waste results, it focuses on upcycling the residual matrices into engineered refractory products, namely alternative calcium aluminate binders and alumina-spinel castables for refractory linings. In order to test the engineered refractory materials into industrial conditions, assessment of thermomechanical behaviour of the refractory castables in service conditions is in regard. This work is just currently starting and it is part of the CESAREF European Project focusing on sustainable applications of refractories

# SHORT COMMUNICATIONS

# ENHANCED INFRARED RADIATION OF LAALO₃ CERAMICS VIA CO²⁺ DOPING

Qinghu Wang[1]; Xueqing Wang[2]; Yawei Li[3]; Jiangtao Li[4]; Shaobai Sang[1]; Liping Pan[5]

[1]Wuhan University of Science and Technology, The State Key Laboratory of Refractories and Metallurgy, Wuhan, China;
[2]Wuhan University of Science & Technology, The State Key Laboratory of Refractories and Metallurgy, Wuhan, China;
[3]Wuhan University of Scie

Infrared radiation ceramics are generally recognized as energy-saving material for thermal equipments. In this work, as novel infrared radiation ceramics, $Co^{2+}$ doped $LaAlO_3$ ceramics were synthesized via a solid-phase reaction method, and the influence of the $Co^{2+}$ doping concentration on the infrared emissivity of ceramics was systematically investigated. The original Al element position was replaced by Co element in $Co^{2+}$-doped $LaAlO_3$, leading to lattice distortion, oxygen vacancy generation and "$Co^{2+} \rightarrow Co^{3+}$" transformation. The increase of doped Co content leads to enhanced impurity absorption, freecarrier absorption and lattice vibration absorption, which significantly improve infrared emissivity. The average emissivity values in the 0.76-2.5 μm and 2.5-14 μm bands of the $LaAl0.6Co0.4O3$ specimen (40 mol% Co) are 0.89 and 0.86, respectively, which are 324% and 28% higher than those of pure $LaAlO_3$. This kind of infrared ceramic with high infrared emissivity has significant application prospects for energy-saving applications of thermal equipment. This $Co^{2+}$-doped $LaAlO_3$ ceramic is a potential candidate material of high-temperature furnaces (< 1700 °C) for energy-saving applications.

# EFFECT OF THE IMPREGNATION WITH LIQUID GLASS ON THE PROPERTIES OF REFRACTORY CASTABLE

Jurgita Malaiskiene, Valentin Antonovic, Renata Boris, Rimvydas Stonys

Institute of Building Materials, Laboratory of Composite Materials, Vilnius Gediminas Technical University, Vilnius, Lithuania

## ABSTRACT

In this study, the impact of liquid glass (sodium silicate) impregnation under vacuum on the physical, mechanical properties, and alkali resistance of fireclay-based conventional castable (CC) and medium cement refractory castable (MCC), which are using in boilers for biomass combustion, was analysed. In research standard test methods for physical and mechanical properties (EN ISO 1927-6), as well as scanning electron microscope (SEM), testing methods for alkali resistance (ASTM C 454–83) and thermal shock resistance by evaluating changes in ultrasound pulse velocity were used.

The results of the investigation have shown that the alkali resistance of CC as well as MCC can be improved by impregnation with liquid sodium silicate glass under vacuum. Impregnated refractory castables have lower porosity (7–9%), higher cold crushing strength (up to 18%). The structure of impregnated samples is denser compared with that of nonimpregnated refractory castables. The SEM images showed that the impregnated samples pores are partially filled with the sodium silicate.

Alkali resistance tests showed that a glassy protective layer (width approximately 1 mm) formed on the surfaces of refractory castables, thus reducing further penetration of alkali (potassium) into deeper layers of the samples. However, impregnated refractory castables are less resistant to thermal shock cycles.

## INTRODUCTION

In biofuel combustion boilers, the operating temperature is usually less than 1100°C, so refractory castables with aluminosilicate fillers for example fireclay could be used in their lining [1]. One of the main reasons for the disintegration of the refractory castable layer of the linings of these boilers, when burning conventional and especially alternative biofuels, is their low resistance to the effects of alkali at sufficiently low temperatures. It has been established [2] that potassium carbonate begins to decompose into $K_2O$ and $CO_2$ and forms new compounds at a temperature of 600°C. At higher temperature, $K_2O$ reacts with components of refractory castables, forming a low viscosity melt that penetrates deep into the layers of the refractory castables and such corrosion products as leucite, kalsilite, and other compounds with volume exceeding the initial volume of the material are formed [3-5]. In order to reduce the harmful effects of alkalis, refractory castable can be impregnated with special coatings to reduce surface porosity and prevent the penetration of potassium compounds into the deeper layers of refractory castable [6]. The penetration of alkalis into the structure of the refractory castable depends especially on its porosity parameters: the degree of corrosion is significantly lower in materials with lower porosity and gas permeability [7-9]. The impregnation material should be selected considering the potential compounds formed at a certain temperature and their possible viscosity, which should be quite high. In our previous works [6, 10], positive results were obtained in reducing the disruptive alkaline effect in the refractory castable when milled quartz sand (2.5%) was used in the composition of the refractory castables, and these castables were additionally impregnated with $SiO_2$ sol. However, especially when a larger amount of milled quartz sand was used (5-7.5%), the thermal shock resistance of the samples decreased by up to 70% [3].

This paper aims to evaluate the change in the main properties of refractory castables (cold crushing strength, porosity, microstructure, alkali and thermal shock resistance) when the refractory castable is impregnated with a liquid sodium silicate glass under vacuum. It is known that liquid glass, when used as a binder in refractory castables, acts as a flux at high temperatures and lowers the operating temperature of aluminosilicate refractory castables up to 200-300°C. However, research results show that the operating temperature of refractory castables with a liquid glass binder can be 1100-1300°C and higher [11].

## MATERIALS AND METHODS

For castable CC, the calcium aluminate cement Istra40 (ISTR) produced by Calucem GmbH and for MCC the G70 cement produced by Gorka Cement Company and different types of fireclays aggregate FA35 (~35% of $Al_2O_3$, $Al_2O_3/SiO_2$ (A/S) ratio 0.68 (CC-1, MCC-1) and $Al_2O_3$ content ~45%, A/S ratio 0.89 FA45 (CC-2, MCC-2)) were used in this investigation. Additionally, microsilica MS, RW-Fuller; RW Silicon GmbH, reactive alumina RA, CTC 20, Almatis containing 99.7% $Al_2O_3$ and calcined alumina CA, CT 19 containing 99.8% $Al_2O_3$, milled quartz sand MQS from SC Anykščių kvarcas were used for samples preparation. The compositions of the refractory castables are presented in Table 1.

Tab 1. The composition of refractory castables

| Composition,% | Cement G70 | Cement ISTR40 | MS | FA 35 <0.14 mm | FA45 <0.14 mm | FA35 <4 mm | FA45 <4 mm | RA | CA | MQS | Water |
|---|---|---|---|---|---|---|---|---|---|---|---|
| CC-1 | - | 25 | 2.5 | 10 | - | 60 | - | - | - | 2.5 | 11.3 |
| CC-2 | - | 25 | 2.5 | - | 10 | - | 60 | - | - | 2.5 | 7.4 |
| MCC-1 | 12 | - | 5 | 8 | - | 60.5 | - | 5 | 7 | 2.5 | 8.9 |
| MCC-2 | 12 | - | 5 | - | 8 | - | 60.5 | 5 | 7 | 2.5 | 7.1 |

*Water - up to 100%

The castables were labelled CC-1, CC-2 and MCC-1, MCC-2 respectively. The specimens 70×70×70mm of refractory castable were prepared, dried (105±2°C) and burnt (1100±2°C for 5h) according to the LST EN ISO 1927-5:2013 requirements. The burnt samples were impregnated under vacuum (1atm) in liquid sodium silicate glass, the density of which is 1.33g/cm³. Physical mechanical characteristics were established according to LST EN ISO 1927-6:2013 and thermal shock resistance was determined by evaluating changes in ultrasound pulse velocity, when samples are cyclically heated (1100 ° C) and cooled (between 2 metal plates filled with water). Before testing ($U_o$), after 3 ($U_{3c}$) and 7 ($U_{7c}$) cycles, the ultrasound pulse velocity was measured and the relative thermal shock resistance $R$ was calculated according to the formula:

$$R = \frac{\sqrt{U_{3c} \times U_{7c}}}{U_o} \times 100\% \qquad (1)$$

The crucible method ASTM C 454-83:2007 was chosen to assess the influence of alkali attack on the structure of the castable [6] using 9 g $K_2CO_3$ and firing at a temperature of 1100°C for 5 hours. After 6 cycles (upon adding 9 g of $K_2CO_3$ for each test), the samples were cut vertically, visually inspected and an appearance of microcracks and penetrated zone depth in them were recorded.

A SEM JEOL JSM-7600F scanning electron microscope device (Japan) was used for control and impregnated sample microstructure comparison tests.

## RESULTS AND DISCUSION

The results of the cold crushing strength CCS (Fig. 1) show that the strength of all types of refractory castables impregnated in liquid sodium silicate glass increased from approximately 10% to 18%. The increase in CCS of the impregnated samples was determined due to the formation of a denser structure and a decrease in porosity. It was found that after impregnation the porosity of all types of refractory castables decreased by about 10%, because the pores were filled with sodium silicate and the sintering of material at 1100°C temperature also took place more intensively. The influence of refractory castable porosity on the cold crushing strength, presented in Fig. 2, is significant because the determination coefficient $R^2$ is very close to 1 [12]. The porosity of the refractory castables, as can be seen, is quite different when comparing between the refractory castable compositions and varies from approximately 16% to approximately 29%. This difference in the compositions of refractory castables was chosen to evaluate the effectiveness of impregnation for different refractory castables.
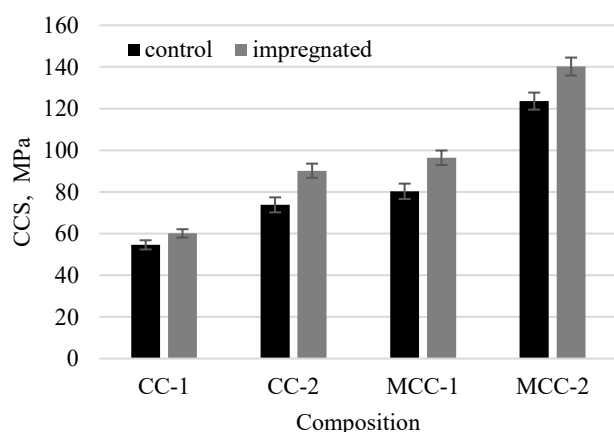
Fig. 1. CCS of control and impregnated samples after firing at 1100°C
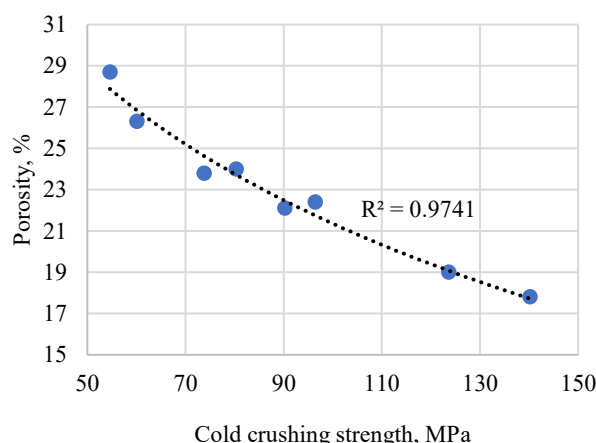
Fig. 2. Influence of CC and MCC porosity on the CCS

SEM images (Fig. 3 and Fig. 4) show that the microstructure of the impregnated samples, regardless of composition and initial porosity, especially on the surface (Fig. 3), is denser. The porosity was reduced when the refractory castable was exposed to liquid glass under vacuum, and the resulting sodium silicate partially filled the pores and capillaries. Such a densification of the microstructure also led to a higher cold crushing strength of the impregnated samples [13].
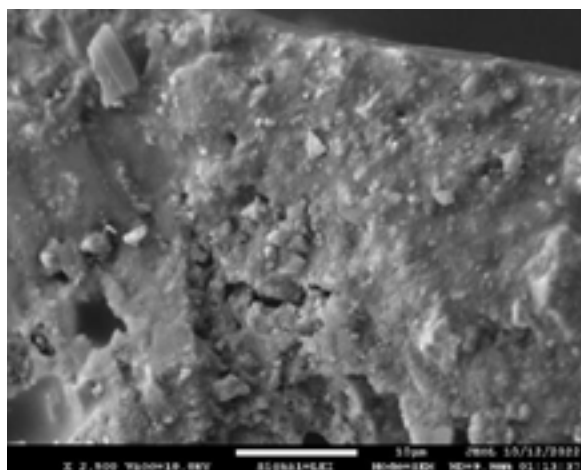


Fig. 3. The surface of the impregnated MCC-1 sample

Comparing the refractory castables of each composition (Fig. 4), it can be seen that after impregnation the microstructure of the samples became denser and the diameter of many pores decreases, because the sodium silicate partially filled them. The most visible changes in the microstructure were established for the MCC-2 impregnated samples, the zones of blowed sodium silicate in pores are visible.

The densified microstructure of the surface, taking into account the conclusions presented in the literature [14-16], should increase the alkali resistance of refractory castables with fireclay fillers at high temperatures. In Fig. 5 images of cut impregnated and control refractory castable samples are presented after 6 cycles of alkaline exposure.
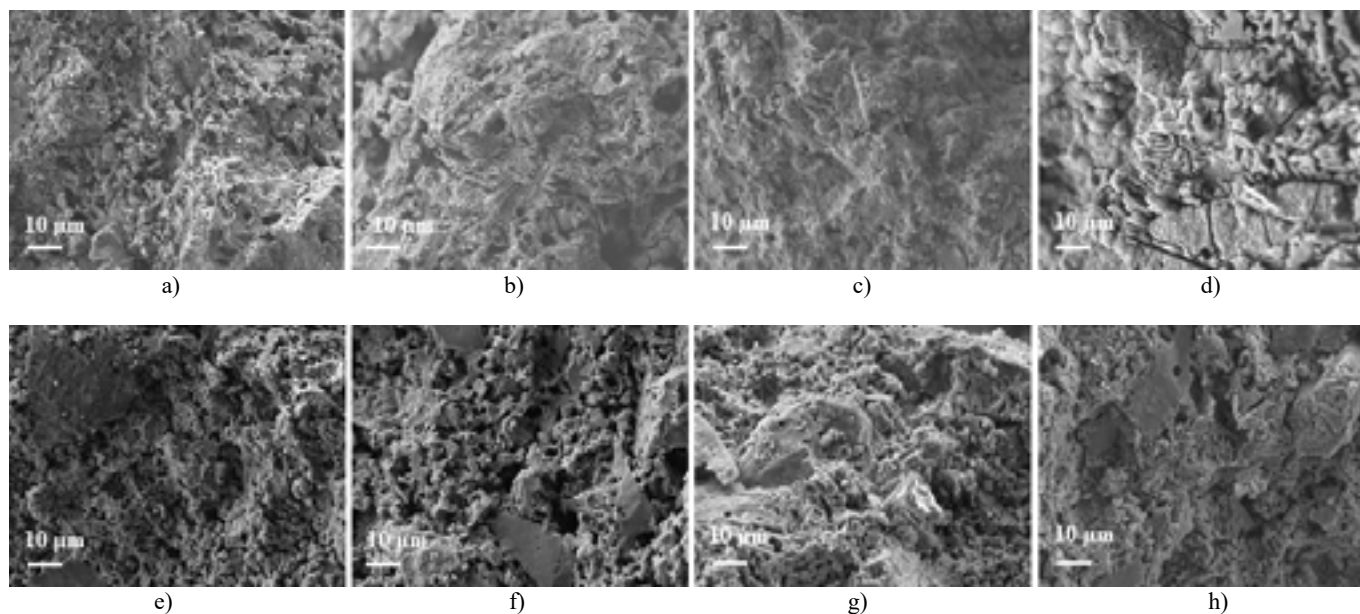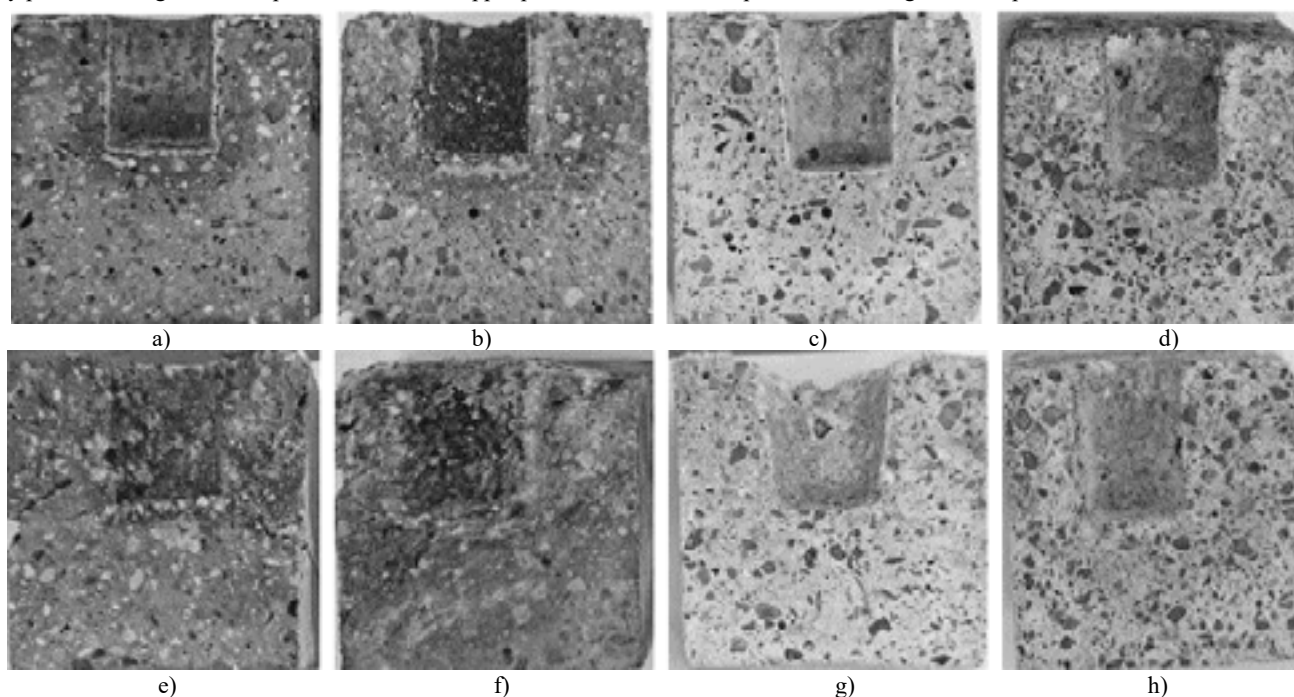
Fig. 4. The images of control and impregnated samples: a) CC1- impregnated, b) CC2- impregnated, c) MCC1- impregnated, d) MCC2- impregnated, e) CC-1 control, f) CC-2 control, g) MCC-1 control, h) MCC-2 control

A clearly visible glassy barrier with a width of about 1mm was formed on the surface of the impregnated samples holes into which the $K_2CO_3$ reagent was added. At high temperatures, sodium and potassium compounds react with the refractory compounds and form a sodium alumina silicate and potassium alumina silicate layer. According to the $Na_2O−Al_2O_3−SiO_2$ phase diagram [17], liquid sodium silicate can further react to form albite ($NaAlSi_3O_8$) and nepheline ($NaAlSiO_4$). It was determined [18], that $Al_2O_3$ can influence the viscous glass melting temperature and its viscosity; therefore, the melting temperature and viscosity values tend to increase. Then the formed glassy layer became higher in viscosity and could not penetrate deeper to the material and also work as a protective barrier. In the control samples, such a barrier was also formed due to the addition of milled quartz sand; only of the CC samples after 6 cycles this barrier was already damaged and became ineffective: the corrosion products penetrated deep into the sample and melted the outer layer. The damage of the control MCC samples is insignificant; only partial melting of the sample is visible in the upper part of the MCC-1 samples, which changed the shape of the hole.

834



Fig. 5. The images of control and impregnated samples: a) CC1- impregnated, b) CC2- impregnated, c) MCC1- impregnated, d) MCC2- impregnated, e) CC-1 control, f) CC-2 control, g) MCC-1 control, h) MCC-2 control

Impregnation of refractory castables with liquid sodium silicate glass increased the cold crashing strength, reduced porosity, compacted the microstructure, increased modulus of elasticity and increased resistance to alkali, but impregnation of refractories often leads to a lower resistance to thermal shock [6]. Thermal shock resistance (Fig. 6) of impregnated samples compared to control samples decreased from approximately 8% (CC-2, MCC-2) to 12% (CC-1, MCC-1). In article [19] it was established that material with a high modulus of elasticity will have lower thermal shock resistance and the thermal shock resistance of castables improves by reducing the modulus of elasticity.
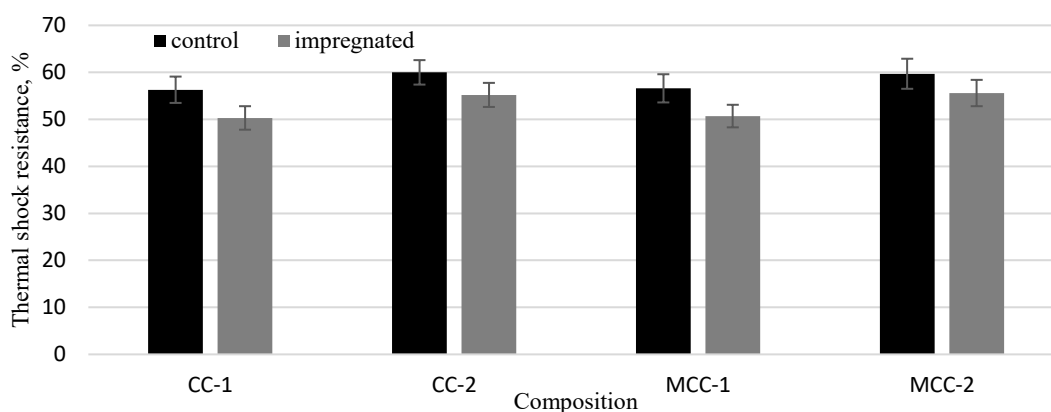
Fig. 6. The comparison of thermal shock resistance of control and impregnated samples

## CONCLUSIONS

Research of refractory castables in the resistance to alkali attack at 1100°C temperature showed that the use of 2.5% of milled quartz sand and the impregnation of the samples with a liquid sodium silicate glass (density 1.33g/cm$^3$) resulted in the development of a pronounced barrier of about 1mm width that prevented further penetration of alkali and stopped further disintegration of the refractory castables.

The cold crushing strength and resistance to alkali attack of refractory fireclay castables can be improved by impregnation of refractory castables with liquid sodium silicate glass. Sodium silicate densifies the microstructure and decreases the porosity of refractory castables by partially filling the pores and connecting capillaries through which liquid and/or gaseous-phase potassium (and sodium) can easily penetrate. The cold crushing strength of the impregnated samples increased by 10-18% according to composition and porosity decreased by approximately 10%.

The thermal shock resistance of the impregnated samples compared to the control samples decreased about 10%.

## REFERENCES

[1] Antonovič, V. Refractory materials for biofuel boilers: Chapter 22/ Antonovič, V, Szczerba, J, Kerienė, J, Stonys, R, Boris, R. Frontiers in bioenergy and biofuels. Rijeka (Croatia): InTech, 2017, p. 443-464

[2] Antonovič, V, Stonys, R, Zdanevičius, P, Mačiulaitis, R, Boris, R, Malaiškienė, J. Analysis of the formed protective layer inhibiting alkali corrosion in aluminosilicate refractory castables. Ceramics 5 (4), 2022, p. 1051-1065

[3] Antonovič, V, Stonys, R, Boris, R, Malaiškienė, J. Effect of quartz sand on the properties and alkali resistance of refractory aluminosilicate castables. Construction and building materials 351, 2022, p. 1-11

[4] Schlegel, E. Evaluation of phase diagrams with regard to the alkali corrosion of refractories. Proc. XVIth Int. Conf. on Refractories, 2008, p. 23-30

[5] Stjernberg, J, Olivas-Ogaz, MA, Antti, ML, Ion, JC, Lindblom, B. Laboratory scale study of the degradation of mullite/corundum refractories by reaction with alkali-doped deposit materials. Ceramics International 39 (1), 2013, p. 791-800

[6] Malaiškienė, J, Antonovič, V, Boris, R, Stonys, R. Improving the physical and mechanical properties and alkali resistance of fireclay-based castables by modifying their structure with SiO$_2$ sol. Ceramics international 48 (15), 2022, p. 22575-22585

[7] Poirier, J, Rigaud, M. Corrosion of Refractories: The Fundamentals. FIRE Compendium Series 2A, 2017

[8] Ren, B, Sang, S, Li, Y, Jin, S. Correlation of pore structure and alkali vapour attack resistance of bauxite-SiC composite refractories. Ceramics International 41, 2015, p. 14674-14683

[9] Xu, Y, Sang, S, Li, Y, Ren, B, Zhao, L, Li, Y, Li, S. Pore structure, permeability, and alkali attack resistance of Al$_2$O$_3$-C refractories. Metallurgical and materials transactions A 45A, 2014, p. 2885-2893.

[10] Malaiškienė, J, Antonovič, V, Boris, R, Stonys, R. The analysis of the change in the structure and properties of refractory refractory castables impregnated with SiO$_2$ sol. UNITECR 2022 proceedings. The 17th unified international technical conference on refractories (UNITECR 2022), March 15–18, 2022 Chicago, Illinois, USA. Westerville: The American Ceramic Society, 2022, p. 1-6.

[11] Goberis, S, Stonis, R. An air-setting refractory mortar using a composite binder. Refractories and Industrial Ceramics, 42 (7-8), 2001, p. 300-303

[12] Freund, RJ, Wilson, WJ, Sa, P. Regression Analysis: Statistical Modeling of a Response Variable 2nd Edition. Academic Press; 2nd edition, 2006

[13] Magliano, MVM, Prestes, E, Medeiros, J, Veiga, JLBC, Pandolfelli, VC. Colloidal silica selection for nanobonded refractory castables. Refractories Applications and News 15(3), 2010, p. 14-17

[14] Ren, B, Shaobai, S, Yawei, L, Shengli, J. Correlation of pore structure and alkali vapor attack resistance of bauxite-SiC composite refractories. Ceramics International 41 (10), 2015, p. 14674-14683

[15] Ren, B, Shaobai, S, Yawei, L, Yibiao, X. Effects of oxidation of SiC aggregates on the microstructure and properties of bauxite-SiC composite refractories. Ceramics International 41 (2), 2015, p. 2892-2899

[16] Butzbach, K. Hasle have a long tradition for producing highly alkali resistant refractory castables. Hasle Refractories, 2019

[17] Li, N, Vainio, E, Hupa, L, Hupa, M, Zabetta, EC. Interaction of high Al$_2$O$_3$ refractories with alkaline salts containing potassium and sodium in biomass and waste combustion. Energy Fuels 32, 2018, p. 12971-12980

[18] Niu, Y, Wang, Z, Zhu, Y, Zhang, X, Tan, H, Hui, S. Experimental evaluation of additives an K$_2$O-SiO$_2$-Al$_2$O$_3$ diagrams on high temperature silicate melt-induced slagging during biomass combustion. Fuel 179, 2016, p. 52-59

[19] Szczerba, J, Pedzicha, Z, Nikiel, M, Kapuscinska, D. Influence of raw materials morphology on properties of magnesia-spinel refractories. Journal of European Ceramics Society 27, 2007, 1683-1689

# NUMERICAL ANALYSIS OF MOLTEN STEEL INFILTRATION IN POROUS BRICKS

Shigefumi Matsumoto[(1), (2)], Keisuke Yamada[(1)], Tetsuo Igata[(1)], Ryohei Kometani[(1)], Masaki Yamamoto[(1)], Koji Goda[(1)], Katsumi Morikawa[(1)] and Hiroyuki Fukuyama[(2)]

(1) Krosaki Harima Corporation, Kitakyushu, Japan; (2) Tohoku University, Sendai, Japan

## ABSTRACT

The infiltration of the molten steel into the porous bricks was simulated in terms of the finite volume method (FVM) using a three-dimensional pore structure obtained by the X-ray computed tomography (CT). The effect of structure of the porous bricks on the infiltration phenomenon of the molten steel into the pores was discussed kinetically with comparing the results to those obtained in the analysis performed by simplifying the pore to a cylindrical shape using both Washburn's and Hagen-Poiseuille's equations. In the simulation, the rate of infiltration of the molten steel for four kinds of porous bricks correlated well to the mean pore size determined by the X-ray CT image analysis among the other structure parameters like the porosity or the maximum pore size. The infiltration rate and labyrinth coefficient both determined also in the simulation were about one-third (34 to 45%) and about half, respectively, of those in the analysis using the simplified pore shape. The simulation results facilitating to understand the infiltration of the molten steel into the bricks were obtained with a great assist of an accurate structure of the porous bricks. Further validation with improvements of the analysis enables to a prolonged life of the porous bricks for the plug.

## INTRODUCTION

Porous bricks are refractories used for porous plugs, which are attached to the bottom of the molten steel ladle during the steelmaking process. Porous plugs are used to blow gas into the molten steel, but there are intervals when the gas supply is stopped, such as during casting. It is known that the pores of the bricks are infiltrated with metal due to the molten steel head pressure. Since the infiltrated metal blocks gas blow, operations to remove the infiltrated layer in the brick, such as oxygen cleaning, are required when the porous plug is reused [1]. Therefore, it is important to control metal infiltration in order to improve the total performance of the porous plugs.

In this study, we discussed phenomenon of metal infiltration in simplified model and examined the difference from the actual infiltration in the porous bricks. Furthermore, the mechanism of a molten steel infiltration into actual porous bricks was investigated by a numerical fluid analysis using the finite volume method (FVM), on the three-dimensional structure of porous bricks obtained by the X-ray computed tomography (CT).

## THEORETICAL BACKGROUND

It is generally known that oxide raw materials used for porous bricks, such as $Al_2O_3$ and $MgO$, are less wettable by molten steel with contact angles higher than 90 degree. Therefore, molten steel cannot infiltrate into the pores of the porous bricks without external force. Assuming that the pores are simple cylindrical shape, the external force $P$ can be written using the Washburn equation [2], with the surface tension of the molten steel $\gamma$, the contact angle between the molten steel and the refractory material $\theta$, and the maximum pore diameter $D$ without molten steel infiltration as follows:

$$P = -\frac{4\gamma}{D}\cos\theta \qquad (1)$$

Since the head pressure of the molten steel acts as an external force in the actual ladle, the external force $P$ can be also written as:

$$P = \rho g h \qquad (2)$$

Where $\rho$ is the density of the molten steel, $g$ is the gravitational acceleration, and $h$ is the height of the molten steel level in the ladle.

Thus, from equations (1) and (2):

$$D = -\frac{4\gamma}{\rho g h}\cos\theta \qquad (3)$$

is found to be the relation between $D$ and $h$. Applying the $\rho$ and $\gamma$ for the molten steel as 7000 $kg \cdot m^{-3}$ and 1.8 $N \cdot m^{-1}$, respectively [3], together with the value of $\theta$ for the molten steel against refractory material (ex. $Al_2O_3$) as 110 degree [4] and $g$ as 9.8 $m \cdot s^{-2}$, the relation between the $h$ and the $D$ is shown as an asymtotic curve in Fig. 1. In the figure, the quadrant area expressed by the $h$ and the $D$ is divided by the curve into the infiltration and the non-infiltration areas for upper and lower of the curve, respectively.

In general, to ensure the gas flow rate required for refining, the average pore diameter of the porous bricks is often larger than 100 μm, while the molten steel level of the steel ladle in the actual operation (shown as zone in Fig. 1) is often higher than 1 m, depending on the ladle capacity. Therefore, it is difficult to inhibit completely the infiltration of molten steel by reducing the pore size of the brick.

On the basis of the knowledge thus obtained we consider rate of infiltration. Although the infiltration phenomenon is a passing phase itself actually, for simplicity we assume a Hagen-Poiseuille flow for it. In this case, from the Hagen-Poiseuille equation,

$$\Delta P = \frac{32\mu l u}{D^2} \qquad (4)$$

where $\Delta P$ is the pressure difference, $\mu$ is the viscosity of the molten steel, $l$ and $u$ are the depth and the rate of the infiltration, respectively. Since $l$ and $u$ are both time-dependent quantities, they are denoted hereafter as $l(t)$ and $u(t)$, respectively. Then, the pressure difference $\Delta P$, at both ends of pores can be expressed by the static pressure of molten steel $P_h$, the pressures caused by gas bubbling $P_g$ and wetting $P_c$, respectively, as follows;

$$\Delta P = P_h - P_g - P_c \qquad (5)$$

Now, for the sake of simplicity, we assume a state that the gas bubbling is completely stopped as $P_g = 0$. Thus, from the equations (1) and (2) it can be written as:
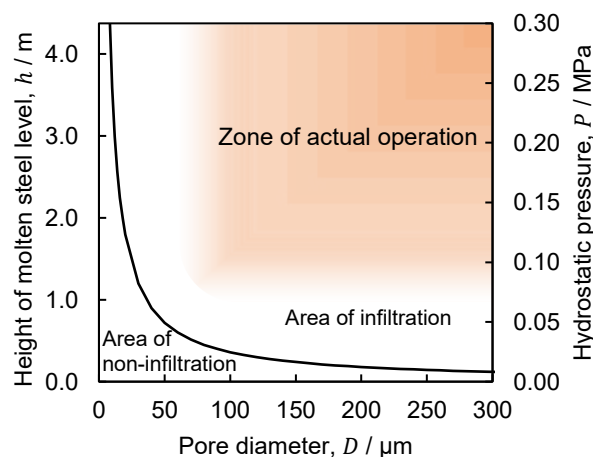


*Fig. 1: Relationship between the height of the molten steel level and the diameter of the pore through which the molten steel can infiltrate into the pore.*

$$\Delta P = \rho g\big(h - l(t)\big) + \frac{4\gamma}{D}\cos\theta \qquad (6)$$

and from the equations (4) and (6),

$$u(t) = \frac{D^2}{32\mu l(t)}\left[\rho g\big(h - l(t)\big) + \frac{4\gamma}{D}\cos\theta\right] \qquad (7)$$

is held. In general, since $h \gg l(t)$, we can simplify as $\rho g\big(h - l(t)\big) \cong \rho g h$, therefore,

$$u(t) = \frac{D^2}{32\mu l(t)}\left(\rho g h + \frac{4\gamma}{D}\cos\theta\right) \qquad (8)$$

is held. Now, the $u(t)$ is also expressed by the following equation:

$$u(t) = \frac{dl(t)}{dt} \qquad (9)$$

and from the equations (8) and (9), we can express $l(t)$ as follows;

$$l(t) = \frac{D}{4}\sqrt{\frac{\rho g h + \frac{4\gamma}{D}\cos\theta}{\mu}} \cdot \sqrt{t} \qquad (10)$$

The equation (10) shows that under this assumption, the infiltration depth is expressed as $l(t) \propto \sqrt{t}$. Figure 2 (a) and (b) shows examples of the calculated infiltration profiles with the time for the heights of the molten steel levels, $h = 2$ and $4$ m respectively, for the pore diameters $D = 50, 100, 150, 200$ and $250$ μm respectively.

The results of these calculations show that the amount of infiltration is about 10 mm even at the time of about 0.05 s for the condition of $h = 2$ m and $D = 50$ μm, where infiltration is difficult to occur. Matsushita et al. have conducted the experiments that molten steel, silver, and mercury were infiltrated into the porous bricks by pressurizing [5], and observed in situ the infiltration by X-ray radiography images. They introduced the labyrinth coefficient $\xi$ for the infiltration rate to correct the structure difference in the porous brick, and proposed the following modified equation:

$$u(t) = \frac{D^2}{32\mu l(t)}\left[\left(\rho g h + \frac{4\gamma}{D}\cos\theta\right)\xi - \rho g l(t)\right] \qquad (11)$$

Note that the term $\rho g l(t)$ has a negative sign because the direction of infiltration in their experiment is opposite to gravity. Now, as same as the former case, assuming that $h \gg l(t)$ and the term $\rho g l(t)$ is negligibly small,

$$u(t) = \frac{D^2}{32\mu l(t)}\left(\rho g h + \frac{4\gamma}{D}\cos\theta\right)\xi \qquad (12)$$

is held, and $u(t)$ is $\xi$ times that in equation (8). In addition, they have expressed $\xi$ as a function of porosity $\varepsilon$ [6]:

$$\xi = 0.04 + 0.238\varepsilon \qquad (13)$$

The equation (13) agreed with the experimental results for silver, but did not with those for both steel and mercury. Because the size and the morphology of the pore have also a significant influence on the infiltration, the equation (13) is insufficient to explain the effect of the structure of refractories on the infiltration. In their experiment, the applied pressure was about 0.01-0.06 MPa, which is 0.15-0.88 m in terms of molten steel head, which is too small to compare to the heights for the molten steel level in the actual ladle. Therefore, $h \gg l(t)$ does not necessarily to hold, and the term $\rho g l(t)$ is not negligible. Thus, they attempted to estimate the labyrinth coefficient $\xi$ by experimentally measuring $l(\infty)$, the height at which the infiltration rate $u$ becomes zero and the infiltration stops [5][7]. In their experiment, applied pressure is defined as $\Delta P_o$ and the infiltration height $l(0) = 0$ at the time of $t = 0$, from the equation (11),

$$l(\infty) = \frac{\Delta P_o}{\rho g} + \frac{4\gamma\cos\theta}{\rho g D_{\max}}\xi \qquad (14)$$

where $D_{\max}$ is the maximum pore diameter. Furthermore, they determined as $\xi = 1$ when the path through which the molten metal can infiltrate due to the applied pressure $\Delta P_o$ are connected from one end of the specimen to the other, the infiltration behavior is the same as the simple cylindrical shape pores with the narrowest channel diameter in that path. However, in the actual use of the porous bricks, the infiltration occurs downward, the gravity never stop infiltration, and the hydrostatic pressure on the bricks is about one order of magnitude higher than the pressure in their experiment. As shown in Fig. 2, the infiltration rate is considered to be very high. Therefore, a kinetic discussion of the process of the infiltration is important.

Yamada et al. have also conducted the experiment in which porous bricks shown in Table 1 were immersed in the molten steel and infiltration depth was only about 20mm under the vacuum evacuation with the pressure difference equivalent to molten steel head $h = 1.5$ m [8]. If $\xi = 1$, the result shows the lower infiltration depth compared to the calculation in Fig. 2.

Therefore, in order to discuss a kinetics on the molten steel infiltration phenomenon in porous bricks with considering the effect of the structure of the bricks, we have analysed numerically by the FVM to simulate the infiltration of molten steel into the three-dimensional structure of the actual porous bricks by X-ray CT.
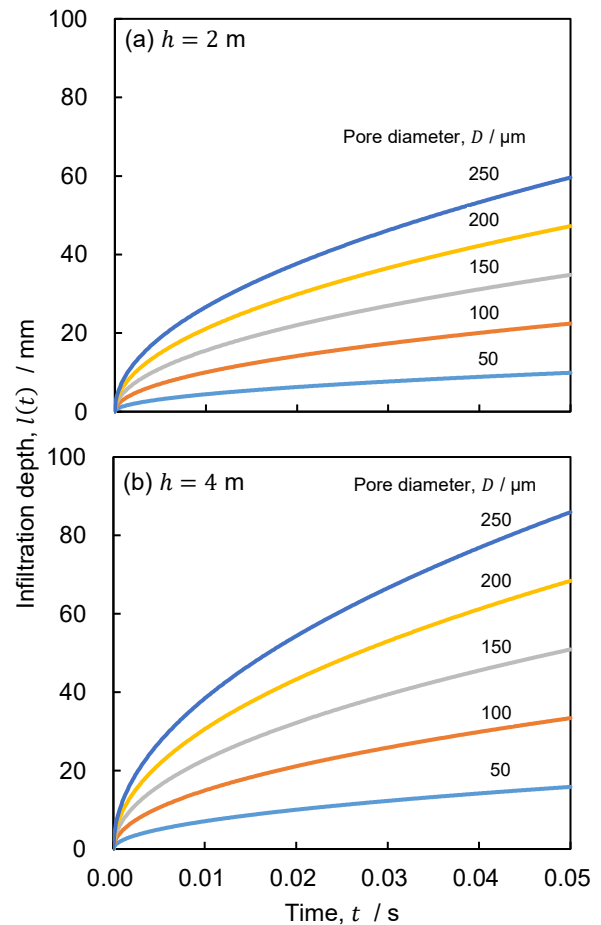
837



*Fig. 2: Calculated relationship between penetration depth and time with Hagen-Poiseuille equation for the heights of the molten steel level at $h = 2$ m (a) and $h = 4$ m (b).*

## NUMERICAL CALCULATION

The calculations were carried out using the porous brick samples 1 to 4 shown in Table 1 with same porosity data determined both by experiment and image analysis using the X-ray CT. Figure 3 shows the schematic diagram of the X-ray CT measurements system.

The radiography image measured by the X-ray CT was reconstructed into a three-dimensional tomographic image. An example of the tomogram is shown in Fig. 4 (a). The tomogram was binarized by the brightness value to distinguish the pores from refractory materials (Fig. 4 (b), (c)). The resulting 3D pore structures are shown in Fig. 5 for samples 1 to 4, respectively. As described previously, Table 1 showed the calculated porosity by image analysis based on the X-ray CT data which agreed well to the measured apparent porosity by the Archimedes method. Therefore, the structure obtained by the X-ray CT is considered to be a representative of the entire structure.

The numerical calculation was performed with OpenFOAM 4.x [9] using the Volume of Fluid (VOF) method. The density and kinematic viscosity of the air are set to $1 \ \mathrm{kg \cdot m^{-3}}$ and $14.8 \ \mathrm{mm^2 \cdot s^{-1}}$, respectively, while the density $\rho$, surface tension $\gamma$ and kinematic viscosity $\mu/\rho$ of the molten steel are set to $7000 \ \mathrm{kg \cdot m^{-3}}$, $1.8 \ \mathrm{N \cdot m^{-1}}$ and $1.0 \ \mathrm{mm^2 \cdot s^{-1}}$, respectively, and contact angle $\theta$ between molten steel and refractory material is set to 110°, and the gravity is not considered. The boundary conditions are shown in Fig. 6. The molten steel was infiltrated from the left side of the figure by applying a pressure difference of 0.1 MPa (equivalent to the molten steel head height of 1.5 m) to an air-filled pore. The sides and the contact area with the refractory were assumed to be non-slip walls. The non-steady state analysis was performed with the computation time of 1 ms.

*Tab. 1: Properties of porous brick samples*

| | Sample No. | 1 | 2 | 3 | 4 |
|---|---|---|---|---|---|
| Apparent porosity / % | | 20.2 | 29.6 | 30.7 | 29.5 |
| 3D-CT image analysis | Porosity / % | 21.2 | 30.7 | 31.6 | 28.5 |
| | Mean pore diameter / μm | 170 | 135 | 130 | 184 |
| | Maximum pore diameter / μm | 500 | 318 | 354 | 380 |
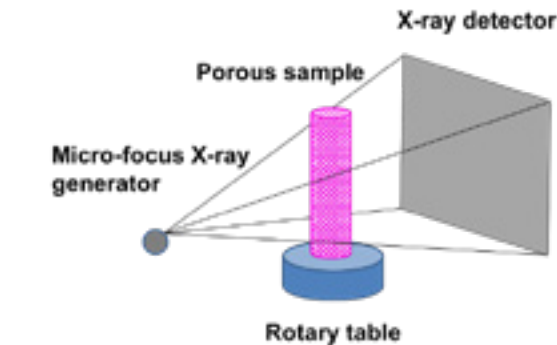


*Fig. 3: Schematic image of 3-dimensional X-ray CT.*
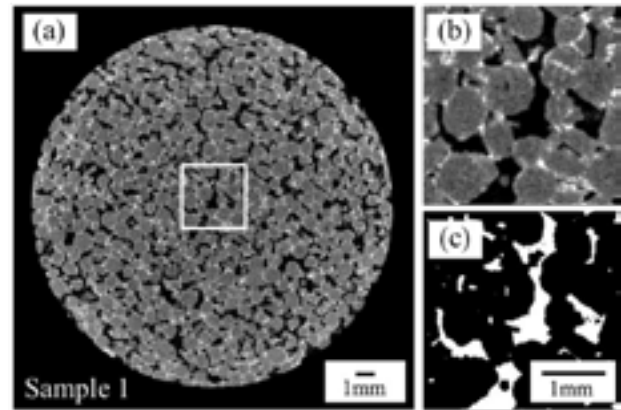


*Fig. 4: 2D-CT images of porous brick sample 1, showing raw image (a), cropped image (b), and binarized image (c).*
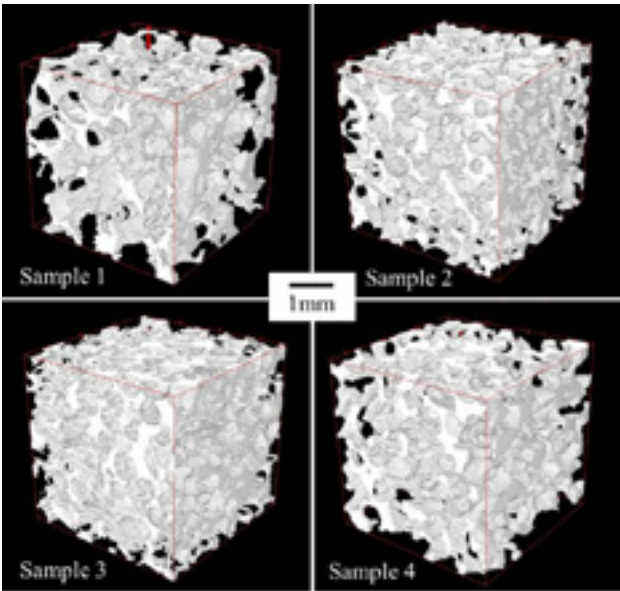


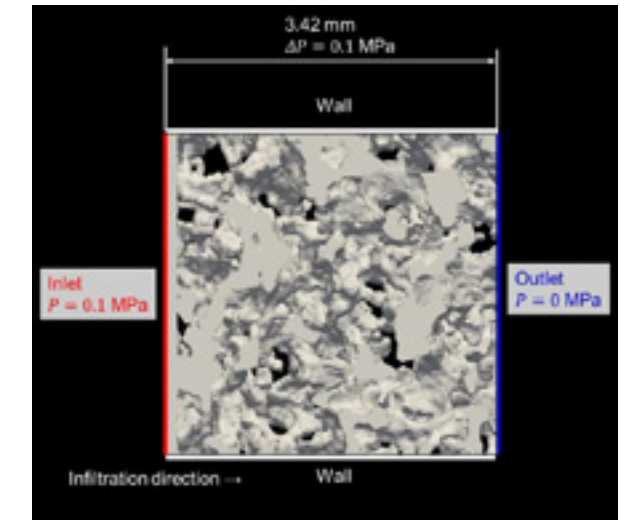*Fig.5: 3D-CT images for porous bricks for samples 1 to 4.*



*Fig. 6: Schematic illustration of the boundary conditions for numerical analysis using the finite volume method.*

## RESULTS AND DISCUSSION

The simulation results of molten steel infiltration by fluid analysis are shown in Fig. 7, as the state of the infiltration after 1 ms.

The infiltration morphology into the pores and the rate of infiltration seems different from sample to sample. For example, in the sample 1 infiltration proceeds in the selective pores with heterogeneous front where as in the sample 3 the infiltration proceeds rather uniformly. Figure 8 shows the analytical data on the relation between the apparent depth of the infiltration and time for each material obtained by the present simulation. Where the apparent depth of the infiltration is defined as the value of the deepest infiltration. As shown in the figure, the rate of infiltration is same for all samples up to 0.1 ms, but exceeding the time, the rate differs for each sample, with the order of the samples 4-1-3-2. In Fig. 9, the calculated infiltration rates at 1 ms were plotted against mean pore size determined by the 3D-CT image analysis for each sample, showing some correlation between the infiltration rate and the pore diameter. The orange dotted line in the figure is the infiltration rate determined by the flow equation (8) (Hagen-Poiseuille) for a simple cylindrical shape pore. Comparing the plots with the line, the infiltration rate by numerical simulation with the 3D-CT is roughly 1/3 of the infiltration rate for the simple cylindrical shape pore. Now, the labyrinth coefficient $\xi$ is also determined for comparison with equation (13). For simplicity, since the molten steel head height $h$ is
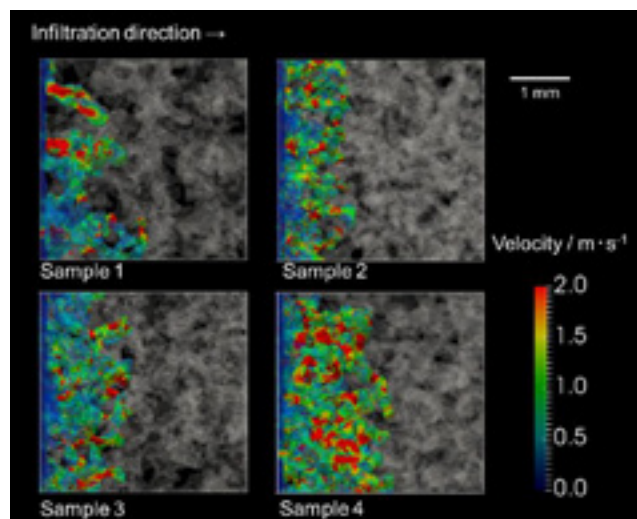
*Fig. 7: Calculation results of molten steel infiltration simulation of porous material samples with 3D-CT images.*
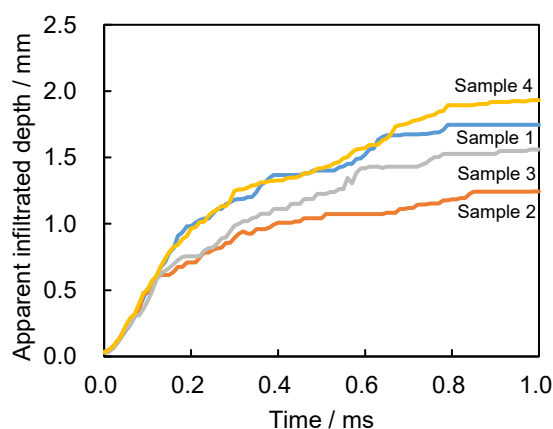


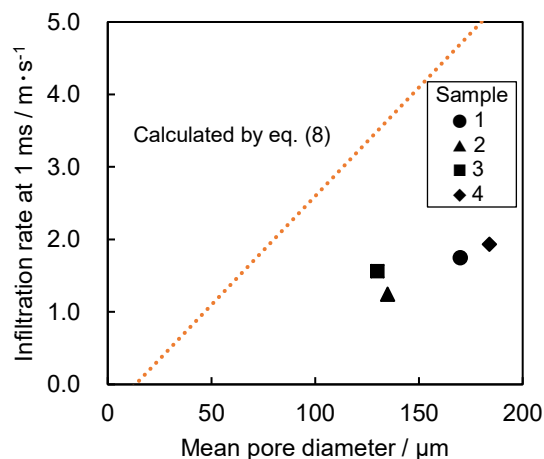*Fig. 8: Calculated infiltration profiles.*



*Fig.9: Relationship between calculated infiltration rate and mean pore diameter for each sample comparing calculated results by equation (8).*

equivalent to 1.5 m, the equation (12) holds with negligibly small effect of the $\rho gl(t)$ term. In this case, since the rate calculated by the equation (12) is $\xi$ times of that calculated by the equation (10), the labyrinth coefficient $\xi$ for each sample is calculated as shown in Table 2. From Table 2, the labyrinth coefficients calculated in the present work were about 0.34-0.45 times higher than those by the equation (13) [6]. In the model of Matsushita et al. in which the coefficient $\xi$ was calculated from the height at which infiltration stops due to gravity, $\xi = 1$ when the sample was applied the pressure

*Tab. 2: Calculated labyrinth coefficient $\xi$ for each sample*

| | Sample | 1 | 2 | 3 | 4 |
|---|---|---|---|---|---|
| Infiltration rate at 1 ms / m·s⁻¹ | Simulation with 3D-CT | 1.75 | 1.24 | 1.56 | 1.93 |
| | Eq. (8) | 4.70 | 3.65 | 3.50 | 5.12 |
| Labyrinth coefficient, $\xi$ / - | Present work | 0.37 | 0.34 | 0.45 | 0.38 |
| | Eq. (13) | 0.54 | 0.77 | 0.79 | 0.72 |

difference that can infiltrate from one end to the other, but in the present work, the $\xi$ calculated by the infiltration rate obtained by the numerical simulation results in different values. In addition, the magnification factor is about half of that obtained by using equation (13). The present method is considered to be simulated more closely to the actual molten steel infiltration phenomenon because the calculations are performed using the more realistic structures of the refractory materials obtained by the 3D-CT method. The validity of numerical analysis deployed in the present work, however, has not yet been fully verified, and further extended study will be required for more quantitative discussions.

## CONCLUSIONS

In order to discuss kinetically the effect of structure of the porous bricks on the infiltration of the molten steel into the pores of the bricks, the infiltration in the case of pores of a simple cylindrical shape was analyzed at first using both Washburn's and Hagen-Poiseuille's equations. Then, the finite volume method (FVM) was applied to simulate the infiltration of the molten steel into the porous bricks using a three-dimensional (3D) pore structure obtained by the X-ray computed tomography (CT). The results of the simulation were compared to those of analysis using the simplified model of pores.

The rate of infiltration obtained by the simulation correlated more intensively to the mean pore size determined by the 3D-CT image analysis than the other parameters of both porosity and the maximum pore size. Values of both infiltration rate and labyrinth coefficient determined in the simulation were respectively about one-third (34 to 45%) and about half of those in the anaysis using the simplified pore shape.

A realistic structure of the porous bricks determined by the X-ray CT has highly contributed to obtain more accurate simulation results for the infiltration of molten steel into the bricks superior to the results obtained in the conventional analytical works carried out previously in this field. There are, however, still susceptible to further improvements for validation of the numerical analysis deployed in the present work.

## REFERENCES
[1] Ouchi, T. Wear and countermeasures of porous plugs for ladle. Taikabutsu Overseas 21 (4), 2001, p. 290–295
[2] Washburn, E. D. The dynamics of capillary flow. Phys. Rev. 17 (3), 1921, p. 273-283
[3] The Iron and Steel Institute of Japan. Physical Properties of Molten Iron and Molten Slag. 1972, p. 6-95
[4] Verein Deutscher Eisenhüttenleute. Slag Atlas (2nd edition). Verlag Stahleisen GmbH. 1995, p. 522-524
[5] Matushita, T. et al. Direct observation of molten steel penetration into porous refractory. Taikabutsu Overseas 23 (1), 2003, p. 15-19
[6] Xihu, H. The Principles of Ironmaking and Steelmaking. Metallurgy Industrial Press Beijing. 1990, p. 234
[7] Matushita, T. et al. In-situ observation and analysis on metal penetration behavior into porous refractories. Taikabutsu Overseas 24 (2), 2004, p. 108-113
[8] Yamada, K. et al. Three-dimensional analysis of porous plug structure using X-ray CT. Proc. UNITECR 2019 p. 584-587
[9] OpenFOAM Foundation. https://openfoam.org

# CAO ATTACK ON REFRACTORY MATERIALS OF THE SYSTEM SIO$_2$–AL$_2$O$_3$

S. Uhlendorf, K. Weber*, X. Ritter, H. Wirsing, H.-J. Klischat
Refratechnik Cement GmbH, Goettingen, Germany

## ABSTRACT

The thermochemical attack of CaO-rich kiln feed on refractory materials of the system SiO$_2$-Al$_2$O$_3$ is a major cause of wear in e. g. cement clinker and lime kilns, and often limits the use of these refractories. Nevertheless, refractory materials of this system could gain in importance compared to basic products due to their lower CO$_2$ footprint, lower thermal conductivity, and their potential for lower firing temperature products, e.g. belite cement. Results are reported on reaction tests between CaO and SiO$_2$-Al$_2$O$_3$-based refractory material to contribute to the understanding of the thermochemical CaO attack. Bauxite and tabular alumina based mixtures with SiC addition were chosen, representing state of the art refractory products with increased alkali resistance.

The reaction tests showed that while corundum remains comparatively stable, the component most reactive to CaO is the matrix phase consisting of a finely grained mixture of mullite and glass phase/cristobalite. The susceptibility of the matrix phase to corrosion results from the high diffusion rates of Ca$^{2+}$ ions and their high potential of forming eutectic melting phases, as soon as CaO is added to SiO$_2$-Al$_2$O$_3$.

The findings support further development of enhanced high alumina and SiC-enriched high alumina refractory products with increased CaO and alkali resistance.

## INTRODUCTION

One of the major shares of well-known refractory materials is built on the system SiO$_2$-Al$_2$O$_3$ and includes fireclay, andalusite, mullite, bauxite, or corundum products. Technical data sheets often list excellent refractoriness (refractoriness under load) of the high alumina refractories (defined as Al$_2$O$_3$ > 45 % by mass) in the range of 1500-1800 °C, which would be sufficient for most industrial processes. However, in reality, increased thermal wear begins at much lower temperatures and is the result of the kiln feed and volatile components attacking the refractory material. In cement clinker kilns, the thermal application limit of SiO$_2$-Al$_2$O$_3$ refractory materials is often given as approximately 1300-1350 °C, which coincides with the occurrence of the first cement clinker melts. In most cement clinker rotary kilns, this is the case in the upper transition zone. Similar observations were made in lime kilns, in waste burning kilns, hot gas generators, steel treatment aggregates in contact with slags, etc. By visual inspection, smooth, wavy, or concave eroded hot surfaces are visible and indicate a softening and erosion of the hot face of the refractory lining (figure 1). In most cases, only a thin reaction layer is visible at the eroded hot face surface. The structural cut usually reveals no melt infiltration (figure 2).
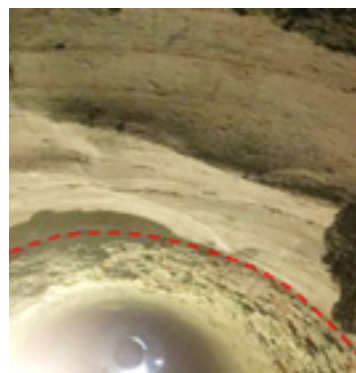
*Fig. 1: Thermally eroded alumina lining in the safety zone of a cement clinker rotary kiln. Smoothly and wavy eroded brick surfaces can be observed in the foreground. Transition to the basic lining in outlet direction is marked with a dashed line.*

*Fig. 2: Bauxite-based high alumina bricks subjected to thermal erosion after usage in a lime rotary kiln. The concavely eroded surface is covered with a very thin reaction layer. Thermochemical alteration is limited to the uppermost hot face horizon.*

After analysing such reaction layers mineralogically in many case studies, the minerals anorthite (CAS$_2$) and gehlenite (C$_2$AS) were pointed out as main reaction products between kiln feed/slag/ashes and non-basic refractory material. In the case of silica-rich refractory material, wollastonite (CS) was found, too. In the case of corundum-based material, calcium aluminates such as hibonite (CA$_6$) and grossite (CA$_2$) were detected. These findings indicate that calcium is mainly responsible for the thermal/thermochemical wear of the SiO$_2$-Al$_2$O$_3$ refractory materials. While the fundamental principle of the chemical reaction of basic components, such as CaO, with non-basic refractory components (SiO$_2$-Al$_2$O$_3$) is relatively easy to understand, little is published on the details of the reaction mechanism and the kinetics. This paper shall contribute to the understanding of the CaO attack on refractory materials of the system SiO$_2$-Al$_2$O$_3$, as this attack defines the thermal application limit of the non-basic refractory lining in most cases.

The typical measure to prevent CaO attack is the use of a basic refractory lining based on magnesia, magnesia-spinel, or magnesia-carbon, as a similar basicity of refractory material and CaO reduces the chemical reaction potential. However, basic refractories may carry a higher CO$_2$ footprint due to their higher thermal conductivity and their composition if produced from magnesite.

Therefore, an expansion of the application limits of SiO$_2$-Al$_2$O$_3$ refractories by optimisation of their CaO resistance can be seen as one forward-looking measure to reduce the carbon footprint of the processes, especially when a similar or even longer refractory service life can be achieved as well.

## EXPERIMENTAL

To characterize the reaction mechanism between CaO and refractory material, a crucible test was performed as described in DIN CEN/TS 15418. Bauxite and tabular alumina-based refractory mixtures with 10 % SiC and 5 % bonding clay were chosen since they represent state of the art refractory materials for high temperature applications with enhanced alkali resistance thanks to the SiC (table 1). The mixtures were formed in moulds and fired at 1460 °C. The main mineralogical difference between both mixtures after firing is that mullite is the main phase in the bauxite mixture, while in the tabular alumina mixture corundum is the main phase and mullite is only formed in the matrix due to the presence of bonding clay (tables 2-3). Crucibles were cut out from both mixtures for reaction tests with a sulphate-resistant cement clinker (SRC clinker) as reactant (table 1). When compared to ordinary Portland cement clinker, the SRC clinker has a higher iron oxide content and forms a more reactive, low-viscosity clinker melt above 1300 °C. The crucible tests were carried out in an electric laboratory furnace with a

heating rate of 5 K/min, a dwell time of 5 hours at test temperature and free cooling. Test temperatures were 1300 °C, 1350 °C, 1400 °C, 1450 °C, and 1550 °C.

The mineral phase composition of the refractory material, the cement clinker, and the reaction zone at each testing temperature was obtained by X-ray powder diffraction using a PANalytical X´Pert Pro diffractometer (Cu-Kα-radiation, step size: 0,017°, time per step: 20 s; tables 2-3) and analysed using the X´Pert HighScorePlus software. The reaction zone was analysed by reflected light microscopy on polished sections (figures 3-4). The element distribution was determined using a µ-XRF Tornado M4 from Bruker Corporation (figures 5-12).

Tab. 1: Chemical composition (XRF, fused bead) of the refractory mixtures after firing and the SRC clinker as reactant.
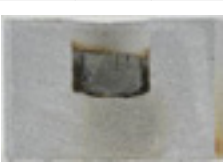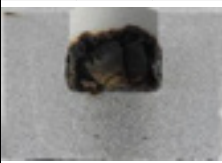
| | Al₂O₃ | SiO₂ | SiC | CaO | Fe₂O₃ | K₂O |
|---|---|---|---|---|---|---|
| Bauxite mixture (85 % bauxite, 10 % SiC, 5 % bonding clay) | 66,7 % | 20,8 % | 6,5 % | 0,6 % | 1,5 % | 0,4 % |
| Tab.alumina mixture (85 % tab.alumina, 10 % SiC, 5 % bonding clay) | 86,3 % | 5,8 % | 7,3 % | 0,1 % | 0,1 % | 0,0 % |
| Sulphate-resistant cement clinker (SRC clinker) | 4,2 % | 21,1 % | - | 65,2 % | 7,3 % | 0,4 % |

## RESULTS AND DISCUSSION

Tab. 2: XRD analyses of the bauxite + SiC crucible (brick) after tests with SRC clinker. Semiquantitative presentation: - = not determined, ? = not exactly determinable, ± = trace, + = determined, ++ = significant contents, +++ = considerable contents, ++++ = main phase

| Temperature [°C] | 1300 | | | 1350 | | | 1400 | | | 1450 | | | 1550 | | |
|---|---|---|---|---|---|---|---|---|---|---|---|---|---|---|---|
| Zone | Brick | Contact | Clinker | Brick | Contact | Clinker | Brick | Contact | Clinker | Brick | Contact | Clinker | Brick | Contact | Clinker |
| **Refractory Phases** | | | | | | | | | | | | | | | |
| Mullite (A₃S₂) | ++++ | + | - | ++++ | - | - | ++++ | +++ | - | ++++ | ++ | - | ++++ | ++ | - |
| Corundum (A) | +++ | ++ | - | +++ | ++ | - | +++ | +++ | - | +++ | +++ | +++ | +++ | +++ | +++ |
| SiC | + | ± | - | + | - | - | + | - | - | + | + | - | + | + | - |
| Cristobalite (S) | + | - | - | ± | - | - | ± | - | - | ± | - | - | ± | - | - |
| Rutile (T) | ± | - | - | ± | - | - | ± | - | - | ± | - | - | ± | - | - |
| amorphous | + | ? | - | + | ? | - | + | ? | - | + | ? | - | + | ? | ? |
| **Reaction Phases** | | | | | | | | | | | | | | | |
| Grossite (CA₂) | - | - | - | - | - | - | - | - | - | - | - | - | - | - | - |
| Hibonite (CA₆) | - | - | - | - | - | - | - | + | - | - | - | - | - | - | - |
| Perowskite (CT) | - | - | - | - | - | - | - | - | - | - | - | - | - | - | ± |
| Gehlenite (C₂AS) | - | ++ | - | - | +++ | - | - | ++++ | - | - | +++ | +++ | - | +++ | + |
| Anorthite (CAS₂) | - | - | - | - | ++ | - | - | +++ | - | - | ++++ | ++++ | - | ++++ | ++++ |
| **Clinker Phases** | | | | | | | | | | | | | | | |
| Alite (C₃S) | - | ++++ | ++++ | - | ± | ++++ | - | - | ++++ | - | - | - | - | - | - |
| Belite (C₂S) | - | ++ | + | - | ++++ | + | - | + | + | - | - | - | - | - | - |
| Brownmillerite (C₄AF) | - | + | ++ | - | + | ++ | - | - | ++ | - | - | - | - | - | - |
| Crucible cross section Bauxite + SiC |  | | |  | | |  | | |  | | |  | | |

Tab. 3: XRD analyses of the tabular alumina + SiC crucible (brick) after tests with SRC clinker. Semiquantitative presentation: - = not determined, ± = trace, + = determined, ++ = significant contents, +++ = considerable contents, ++++ = main phase

| Temperature [°C] | 1300 | | | 1350 | | | 1400 | | | 1450 | | | 1550 | | |
|---|---|---|---|---|---|---|---|---|---|---|---|---|---|---|---|
| Zone | Brick | Contact | Clinker | Brick | Contact | Clinker | Brick | Contact | Clinker | Brick | Contact | Clinker | Brick | Contact | Clinker |
| **Refractory Phases** | | | | | | | | | | | | | | | |
| Mullite (A₃S₂) | + | + | - | ++ | + | - | ++ | + | - | ++ | ++ | - | ++ | - | - |
| Corundum (A) | ++++ | ++++ | - | ++++ | ++++ | - | ++++ | ++++ | - | ++++ | ++++ | ± | ++++ | ++++ | ± |
| SiC | ++ | ++ | - | ++ | ++ | - | ++ | + | - | ++ | + | - | ++ | + | - |
| Cristobalite (S) | ± | - | - | + | ± | - | + | ± | - | + | ± | - | ± | - | - |
| Rutile (T) | - | - | - | - | - | - | - | - | - | - | - | - | - | - | - |
| amorphous | | | | | | | | | | | | | | | |
| **Reaction Phases** | | | | | | | | | | | | | | | |
| Grossite (CA₂) | - | - | - | - | - | - | - | - | - | ± | ± | - | - | ++ | +++ |
| Hibonite (CA₆) | - | - | - | - | - | - | - | - | - | - | + | - | - | ++ | +++ |
| Perowskite (CT) | - | - | - | - | - | - | - | - | - | - | - | - | - | - | - |
| Gehlenite (C₂AS) | - | ± | - | - | ± | - | - | ++ | - | - | ++ | ++++ | - | +++ | ++++ |
| Anorthite (CAS₂) | - | - | - | - | ± | - | - | + | - | - | ++ | + | - | +++ | +++ |
| **Clinker Phases** | | | | | | | | | | | | | | | |
| Alite (C₃S) | - | ++ | ++++ | - | - | ++++ | - | - | ++++ | - | - | - | - | - | - |
| Belite (C₂S) | - | ± | + | - | - | + | - | ± | + | - | - | - | - | ++ | ± |
| Brownmillerite (C₄AF) | - | ± | ++ | - | - | ++ | - | - | ++ | - | - | ± | - | - | - |
| Crucible cross section Tabular alumina + SiC |  | | |  | | |  | | |  | | |  | | |

The crucibles tests with the SRC clinker showed a reaction layer that formed between the refractory material and the clinker. The reaction layer is slag-like and thus indicates the presence of a liquid phase. The thickness of the reaction layer increased with the test temperature, while the clinker filling is consumed. The refractory material in the contact area was subsequently dissolved and became part of the reaction

layer. At 1450 °C and above, most of the clinker has already reacted and melted. The crucible filling became more homogenous with increasing temperature due to melting and approaching equilibrium conditions. At 1550 °C, the molten reaction product partially infiltrated the texture of the unreacted crucible in the case of the tabular alumina material. In the case of the bauxite material, no infiltration beyond the reaction layer in the contact zone was observed. Gehlenite ($C_2AS$) was determined by XRD as first reaction phase at 1300 °C test temperature in both refractory material mixtures. At 1350 °C and 1400 °C, anorthite ($CAS_2$) was found as well.

The contact reaction was significantly more intense in the bauxite + SiC mixture, where hibonite ($CA_6$) was additionally detected as reaction phase at 1400 °C. At 1450°C, the clinker almost fully reacted with the bauxite + SiC mixture, no clinker phases remained at this temperature. The mullite was completely consumed by the reaction, while SiC and considerable corundum contents survived. Anorthite was the main reaction phase at 1550 °C. This already leads to the assumption that mullite is the weaker phase in bauxite regarding CaO attack, compared to corundum.

In the case of the tabular alumina mixture, the reaction with clinker is slower so that clinker phases still exist at 1450 °C. The reason for slower reaction is most likely the limited amount of mullite here. Main reaction products are still gehlenite and anorthite at 1450 °C, while grossite ($CA_2$) and hibonite appear as well. The calcium aluminates indicate that corundum also starts corroding at higher temperatures. At 1550 °C, gehlenite is the main reaction phase beside significant amounts of anorthite, grossite, and hibonite. Mullite was consumed by the reaction, while SiC and considerable corundum contents remained in the contact area.

The microscopic investigation confirms the advancing melting processes in the reaction layer. It was also confirmed that corundum and SiC partially resist the corrosion and melting process in the reaction zone. Bauxite is more affected by disintegration than tabular alumina as the mullite phase reacts entirely. Tabular alumina grains exhibit a higher resistance to the corrosion and melting process. Since the matrix contains also mullite due to the bonding clay, the melt phase proceeds through the matrix. Finally, mainly intact tabular alumina grains were incorporated into the melt phase as a whole as soon as they are surrounded by the melt.
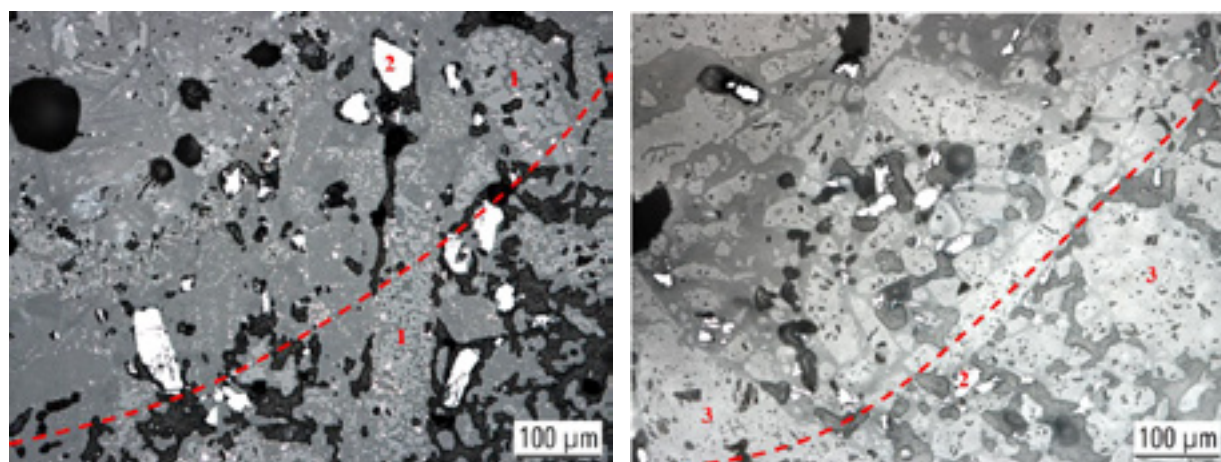
*Fig. 3-4: Reflected light micrographs of the contact area in the crucibles after reaction with SRC clinker at 1450 °C, bauxite + SiC mixture (left), tabular alumina + SiC mixture (right). A melt phase formed and propagated through the refractory matrix, which is thereby densified. The approximate front line of the reaction zone is marked with the dashed line. The bauxite grains (1) essentially consist of corundum crystals embedded in a mullite matrix. This mineral assembly was dissolved by the advancing melt phase, the corundum crystals partially survived. SiC (2) also partially survived in the reaction layer. In the case of the tabular alumina (3), the grains remained mainly intact but were subsequently incorporated into the melt phase as soon as they were surrounded by melt.*
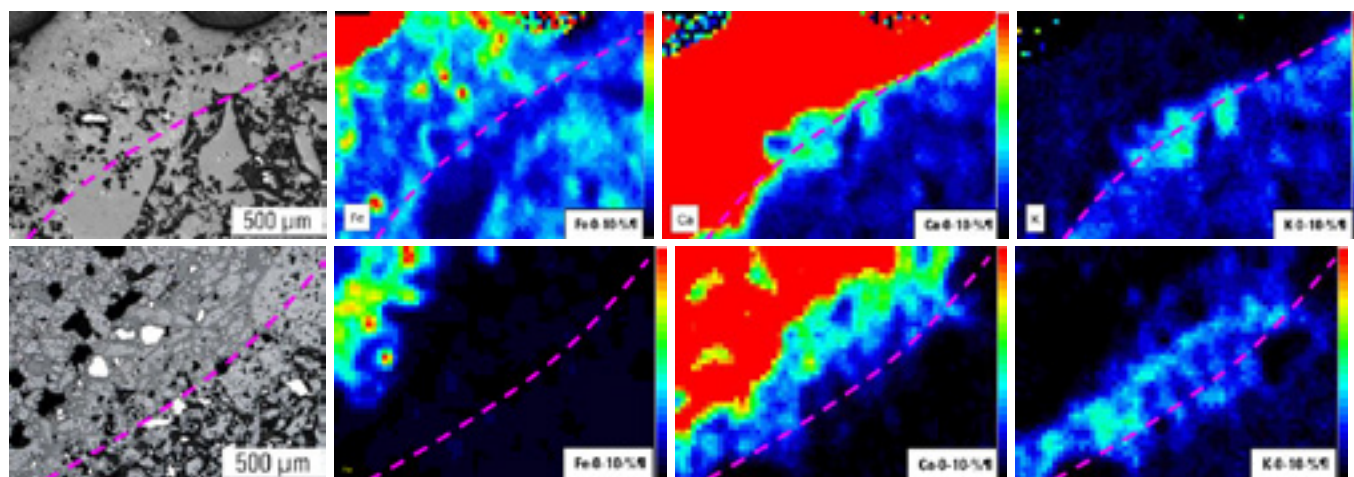


*Fig. 5-12: Reflected light micrographs and element mappings (μ-XRF) of the contact area in the crucibles after reaction with SRC clinker at 1450 °C, bauxite + SiC mixture (top), tabular alumina + SiC mixture (bottom). The approximate position of the microscopically visible melting front is marked with the dashed magenta line. Fe is a typical constituent of eutectic cement clinker melt but not present in the reaction front area. The Ca content decreases gradually in direction of the refractory material. K from the SRC clinker and the bonding clay is significantly enriched in the reaction zone. Map data: Rh- Kα-radiation, 20 μm pixel size, 500 ms time per pixel.*

Element mappings by μ-XRF of the contact area revealed that the proceeding melt phase in the reaction zone does not contain significant amounts of iron. Hence, this melt phase cannot be referred to as a eutectic cement clinker melt, which would be enriched in iron(oxide). This

is of special interest since the melt phase may otherwise be misinterpreted as an infiltrating clinker melt. The calcium content decreased gradually in the reaction zone in direction of the refractory material. This gradual transition indicates a diffusion-driven migration process of calcium ions. It can also be stated that the $Ca^{2+}$ diffusion front is closely ahead of the melting. Despite the low potassium content in the SRC clinker of 0.4 %, a strong enrichment of potassium took place in the reaction area. Potassium, along with calcium, will have contributed significantly to melt formation.

## CONCLUSIONS

The results of laboratory reaction tests showed a good consistency when compared with the results of post-mortem analyses of used refractory materials subjected to CaO-containing kiln feed or slags at high temperatures. It was confirmed that CaO is mainly responsible for the liquid phase formation in the contact area. The results indicate that the CaO attack can be characterized by a diffusion process of $Ca^{2+}$ ions into the refractory material. High diffusion coefficients of $Ca^{2+}$ were determined by other authors in cement clinker systems before [1]. The diffusion of $Ca^{2+}$ into the refractory material leads to melt formation if a certain level of Ca is reached and the temperatures are high enough. The mineralogically determined reaction phases finally crystallize out of the melt phase. The liquid phase formation is furthermore enhanced by the presence of $K^+$, which is known to act as a flux in refractories.

Mullite or a mixture of mullite, cristobalite, and glass phase were found to be attacked first. The higher degree of structural disorder in these phases favours the diffusion of $Ca^{2+}$ and other ions. The mullitised bonding clay itself is therefore prone for CaO attack and a refractory matrix-containing bonding clay acts as a pathway for the diffusion processes and melt propagation. Diffusion of $Ca^{2+}$ into the refractory material of the binary phase system $Al_2O_3$-$SiO_2$ necessitates consideration of the ternary system CaO-$Al_2O_3$-$SiO_2$ for further description of the processes in more detail (fig. 13)



fig. 13: Ternary system CaO-$Al_2O_3$-$SiO_2$ [2] with plotted composition of the used materials and a typical clinker melt composition at 1450 °C [3] (circles). First reactions were assumed and observed between the refractory matrix (red circle) and CaO coming from the eutectic clinker melt, which is formed in every clinker [3] (light blue circle). Considering a diffusion of $Ca^{2+}$, all compositions between the tie lines (yellow dashed) of both materials exist at the same time. These coexistent compositions in the reaction zone plot in the systems belite-calcium aluminates-gehlenite (blue area), gehlenite-anorthite (purple area) and anorthite-mullite-cristobalite/glass (red area). Relevant eutectics of the locally formed composition are in the range of 1270 - 1350 °C (purple arrows).

843

With the theoretical approach, the constantly determined formation of gehlenite and anorthite as first reaction phases is understandable since these minerals are in the tie line between the composition of the reactive refractory matrix and the composition of clinker melt or pure CaO. Relevant eutectic points are between 1270 °C and 1350 °C and hence agree with the determined occurrence of first liquid phases and the formation of the characteristic reaction minerals around 1300 - 1350 °C.

It can be concluded that the temperatures that are necessary for a significant $Ca^{2+}$ diffusion into the refractory matrix are in the same range as the eutectic melting temperatures. Melting of the refractory material therefore takes place closely behind the diffusion front. This mechanism is apparently the reason why in practice only a thin reaction layer and no deeper infiltration is observed. The melt formation itself further accelerates the diffusion of $Ca^{2+}$, which is a positive feedback reaction. Alkalis, like potassium or sodium, enrich in the reaction zone and most likely worsen the situation by increased glass phase formation, lowering the melting points and increased diffusivity.

## PROSPECTS

With reference to the results of numerous post-mortem analyses, the here described reaction mechanisms between $SiO_2$-$Al_2O_3$ refractory materials and CaO is similar over a wide product range from acidic fireclay to corundum-based bricks or concretes. There will be no magic bullet that can overcome the chemical reaction potential between both media. However, with the aid of understanding the corrosion processes in detail, new refractory products of the system $SiO_2$-$Al_2O_3$ and $SiO_2$-$Al_2O_3$-SiC with a higher buffer for thermochemical resistance have been developed, which currently prove themselves in the application and already led to significantly prolonged service life such as an entire additional campaign. It should be highlighted that a prolonged refractory service life is a very efficient way to reduce cost and $CO_2$ emissions. A substitution of a basic with a non-basic refractory lining is locally possible after a careful revision of the still limiting thermal loads and corrosion by process melts. Positive effects of replacing a basic lining include a lower thermal conductivity, higher resistance to sulphur attack, nearly unlimited shelf life, resistance to hydration, lower expansion coefficient, a more predictable wear pattern, and a lower product carbon footprint.

## REFERENCES

[1]    Rechmeier, H. – Reactions during Cement Clinker Firing. VI. International Congress on the Chemistry of Cement, Moscow 1974
[2]    Osborn, E.F., Muan, A. – Phase Equilibrium Diagrams of Oxide Systems. Published by the Am. Cer. Soc. and the Edward Orton, Jr., Cer. Foundation, 1960
[3]    Seidel, G., Huckauf, H., Stark, J. – Technologie der Bindebaustoffe, Band 3. VEB Verlag für Bauwesen, 1978

# IMPACT OF HYDROGEN ON CARBON MONOXIDE DISINTEGRATION OF REFRACTORIES

Joeri Liefhebber, Rinus Siebring
Tata Steel, IJmuiden, The Netherlands

**ABSTRACT**
In many critical installations for the steel industry, refractory materials are (locally) exposed to carbon monoxide (CO) gas. The reaction of CO gas to solid carbon and carbon dioxide ($CO_2$), the Boudouard reaction, has been studied by many authors over the past decades. The reaction results in the deterioration of refractory materials, which can influence the lifetime and availability of production installations. To evaluate the resistance of materials to CO disintegration, the standard test method uses a 100% CO atmosphere. However, various studies have shown that the use of a few percent $H_2$ together with the CO gas significantly increases the reaction rate. Current process gases (like in the Blast Furnace) already contain 2 - 8 vol% $H_2$ and this influences the reaction rates. In future processes, to reduce greenhouse gas emissions, this will further increase when more hydrogen containing gases, like $H_2/CH_4$, are used. Also, from a testing perspective it makes more sense to include hydrogen as faster reaction kinetics are observed to enhance the relative differences between materials' resistance. Tata Steel uses an inhouse testing method for the evaluation of the resistance of refractory materials to CO disintegration. Clear differences are observed when comparing the same samples, which are tested with and without H2 in the gas mix. This approach and method is being discussed with refractory suppliers and used by both sides for the selection of refractory materials where appropriate for the application.

**INTRODUCTION**
When refractories are exposed to carbon monoxide gas for a long period of time this could lead to the disintegration of the material structure, damaging the integrity of the refractory lining.
The reaction of carbon monoxide to solid carbon and carbon dioxide (1) is known as the Boudouard reaction. This reaction has been studied for many years over the past decades [1][2][3].

$$2CO_{(g)} \leftrightharpoons CO_{2(g)} + C_{(s)} \tag{1}$$

The reaction is catalysed by the presence of cementite particles formed from metallic iron and iron oxide particles in reaction with CO gas. These particles are introduced in the refractory products as impurities of the raw materials that are used for its production. The temperature range at which the reaction occurs is between 400 and 900ºC, the maximum rate of carbon deposition is around 500 to 700ºC, depending on the gas composition [2][3].
The resistance to CO gas is usually controlled by selection of low iron raw materials for the refractories production and/or sufficiently high firing temperature. Especially in alumina-silicate refractories the higher firing temperature leads to the formation of iron-silicate phases (like fayalite), which are stable in contact with CO gas. In other refractory materials, like carbon blocks for the Blast Furnace (BF) hearth, a higher firing temperature does not contribute to a better CO resistance. Recent work reveals that sulphur, in the solid and gaseous states, is an efficient inhibitor to limit the carbon formation [5][6].
There are many studies of carbon deposition in a 100% CO atmosphere, but it has been demonstrated that the rate of carbon deposition is strongly influenced by the presence of hydrogen ($H_2$) [2][3][4]. In ironmaking installations where the resistance against CO is relevant, $H_2$ is often present in the gas atmosphere. But the current test methods for determination of resistance of refractory materials to carbon monoxide are done with a 100% CO gas atmosphere (ISO 12676 and ASTM C288). For many materials, especially those with limited carbon deposition during the test, the standard test suffers from poor reproducibility. Even samples cut from the same piece show different results [7].
The role of hydrogen ($H_2$) in the test atmosphere is not fully understood, but it is seen as an accelerator for carbon deposition [3]. For many years Tata Steel has worked with an internal test method, that includes $H_2$ in the gas mixture, to compare the relative resistance of refractory materials against CO gas and select the most suitable materials for the application. More recently this method is discussed with refractory suppliers and used for quality control purposes.
With increasing levels of hydrogen in existing processes, like the Blast Furnace, but also in Direct Reduction Plants (DRP) one should not ignore its effect on carbon monoxide disintegration of refractories. For the selection of refractory materials that are resistant to CO, the inclusion of hydrogen in the test is required.

**CO DISINTEGRATION IN PRACTICE**
Also at Tata Steel in IJmuiden, multiple cases exist of refractory materials that have been damaged by decomposition of carbon monoxide. One of these examples is the torpedo safety lining. The torpedoes are used to transport hot metal from the blast furnaces to the steel plant. The lining consist of an insulation board against the shell, a chamotte (alumina-silicate) safety lining and a carbon bonded ASC (Alumina-SiC-C) wear lining. The gas atmosphere behind the carbon containing wear lining is reducing and CO gas can attack the lining. Figure 1 shows the internal structure (picture taken on a broken brick surface) of the safety lining with many black spots that were identified as deposited carbon in the matrix porosity. The carbon deposition causes the brick to fracture and weakens the structure. It results in damage to the safety lining and more frequent repairs.
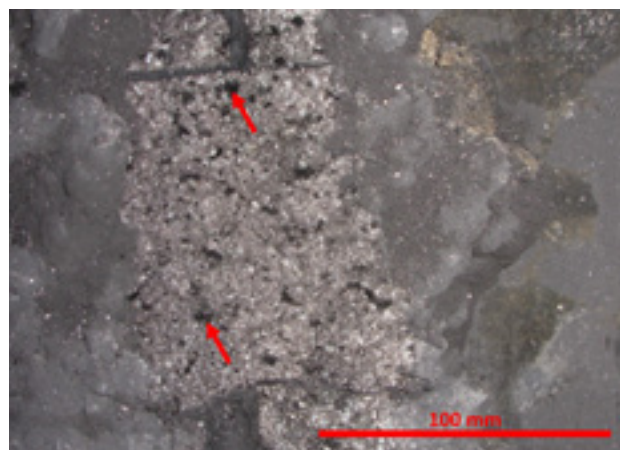


*Fig. 1: Broken surface of a safety lining refractory brick in the torpedo. Black spots of deposited carbon have formed (see also red arrows).*

Another installation where CO disintegration of the refractories is observed is the blast furnace hearth. Samples of the carbon and graphite blocks in the hearth have shown crack formation, microstructural evaluation confirmed that the cracks were generated by local growth of carbon in the matrix (figure 2). Once a nucleation site (iron particle) is present and the conditions for the Boudouard reaction are there, the process of carbon deposition continues and creates sufficient forces to break the refractory.
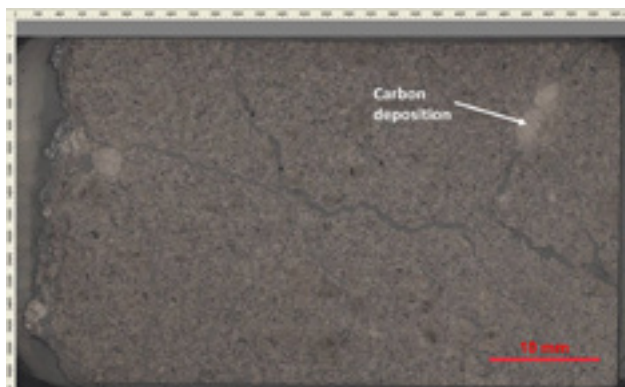
Fig. 2: cross section of the hot face of a carbon block from the blast furnace hearth, showing cracks generated by carbon deposition.

## TEST METHOD
### Historic development
At Tata Steel in IJmuiden, internal reports date back to the 1970's (at that time the company was called Koninklijke Hoogovens) where the CO resistance of refractory materials was tested using gas mixtures that not only consist of 100% CO. Initially trials were set up to resemble a gas composition close to process gases. Samples were ground to powder and heated under inert gas atmosphere to 600ºC, then the sample was exposed to a gas mixture of 65% $N_2$, 33% CO and 2% $H_2$ for a duration of 5 hours. The off gas was analysed to determine how much $CO_2$ formed during the test. At that time there was already information from literature describing the effect of $H_2$ on the decomposition of CO gas [2][3].

In the 1990's the test was adapted and the use of the inert gas ($N_2$) was eliminated and instead of powdered samples fixed rectangular samples were used. Based on several experiments the gas composition was set at 95% CO and 5%. This corresponds to the observation of Turkdogan et al. [2] that a small addition of hydrogen has a considerable effect on the rate of decomposition of carbon monoxide. The addition of a few percent increases the rate drastically but further increase of hydrogen has not much more effect. The temperature was set at 700ºC and the duration of the test was extended to 96 hours.

For many years this has been the internal test method for evaluating refractory materials for their carbon monoxide resistance.

### Current method
The test equipment consists of an electrically heated furnace with 4 horizontal gastight tubes through which the test gas is lead. Samples have a dimension of 15 x 15 x 50 mm and are weighed before the test on a balance with 0.01 gram accuracy. For each tube one sample is placed on a ceramic tray and pushed in the hot zone after which the tube ends are closed gas tight. One end with the gas entry the other for the gas outlet. A gas mixing facility provides the gases (N2, CO and/or H2) in the right quantities. The gas flow is controlled by mass flow controllers.

After placement of the samples the gas flow is switched on with 100% $N_2$ at 5 litre/hr for each tube. The furnace is heated to 700 ºC with 4 ºC/min, after this temperature is reached the gas is switched to a gas mixture of 95% CO and 5% $H_2$, again with a flow of 5 litre/hr per tube.

The test duration is 96 hours (4 days) after which the gas is switched to $N_2$ and the furnace heating is stopped for natural cooling of the furnace. The tube ends are opened when the temperature dropped below 100ºC after which the samples are extracted .



Fig. 3: horizontal tube furnace with gas mixing facilities

### Sample evaluation after the test
After extraction from the furnace the sample is weighed again to determine the weight change. However, most attention is paid to the visual appearance of the samples. Similar to the ASTM C288 standard, the most affected face(s) of the samples are photographed and the extend of the degree of disintegration is described according to the following classifications:

- Unaffected, no particles spall and no cracking occurs. Some degree of discoloration can be observed.
- Affected – surface popouts, popout of small refractory pieces (less then 13 mm) or growth of carbon on the surface.
- Affected – cracked, when sample is cracked and/or larger pieces (more than 13mm) are popped out.
- Destructive, sample breaks is several pieces apart.

Samples that are affected sometimes show very little weight change (mainly in case of popouts), which can be even less than samples that are unaffected. Therefore, weight change is not seen as the determining factor in this test.

## COMPARISON RESULTS WITH AND WITHOUT $H_2$
It has been demonstrated before that the formation of carbon by the reverse Boudouad reaction becomes much more efficient when hydrogen ($H_2$) is present. In the absence of $H_2$ the amount of carbon deposited at a given time is proportional to the amount of catalyst present. On the other hand in a $H_2$-CO atmosphere carbon deposition increases to a lesser extend with an increasing amount of catalyst [2]. Nolan et al. have shown significant effect of $H_2$ present in a CO atmosphere on the formation of carbon [7]. The type of structure appears to be an essential point that leads to the weakening and destruction of refractory materials [2][4][9]. As was also observed in the carbon block of the BF hearth (fig. 2) the build-up of carbon concretions eventually results in the formation of cracks. The presence of $H_2$ in the gas influences how the size of the Fe-catalyst evolves over time and is a key point for the growth and the morphology of the resulting carbon.

In a mixture of CO and $H_2$ gas there are different reactions taking place, such as (1) the reduction of iron oxides by either CO or $H_2$ (2) carbon deposition and (3) water and carbon formation via the reverse water-gas reaction.

In the presence of $H_2$ the catalyst particles are fragmented into much smaller pieces, each being able to form their own filament. In the absence of $H_2$ the catalyst particle is being encapsulated in carbon, which may slow down the reaction and forms less carbon.
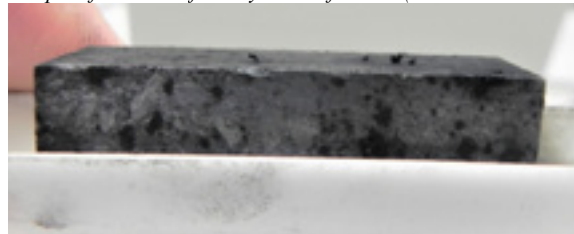
*Sample of chamotte fireclay brick after test (100% CO)*

*Sample of chamotte fireclay brick after test (95% CO an 5% H₂)*

*Sample of micropore carbon after test (100% CO)*

*Sample of micropore carbon after test (95% CO an 5% H₂)*

*Fig. 4: Result of CO resistance test on a fireclay brick and micropore carbon brick. The test was performed under a 100% CO atmosphere and a gas mixture of 95% CO and 5% H₂.*

Studies are often done on well-defined/pure catalyst particles to eliminate side effects.

At Tata Steel we use our internally developed method on commercially available refractory materials. Tests that were done to compare the influence of $H_2$ on the test result reveal clear differences. In fig. 4 the result of two different brick types that can be exposed to reducing gases in practice are shown, a) a chamotte based fireclay brick and b) a micropore carbon block. On the left side the result after the test under a 100% CO atmosphere is shown and on the right the result after exposure to a gas mixture of 95% CO and 5% $H_2$. There is a clear difference in visual appearance of samples from the same brick that are exposed to the different atmospheres. The samples exposed to a 100% CO atmosphere are judged as unaffected. The samples that are exposed to a mixture of CO and $H_2$ on the other hand are affected, at various locations across the samples carbon has deposited and accumulated. This results in popouts from the samples, likely the catalyst particles are fragmented which allows more abundant growth of carbon.

**Increasing H₂ level**

Tests have also been done with different CO/$H_2$ ratios by increasing the level of $H_2$ in the gas mix to test the impact on the test result. Fig. 5 shows the result of 4 different test conditions ranging from 100% CO to 85% CO with 15% $H_2$. With changes in the equipment setup higher levels of $H_2$ could be possible in the future. For this test an andalusite brick (60% $Al_2O_3$) was selected of which it was known to be not resistant to CO in our internal test. Again it is seen that with 100% CO there is no significant effect detected in terms of carbon deposition. When $H_2$ is present in the gas mix, popouts are observed on the sample surface. There is no visual difference in the test with 5 or 10 % $H_2$, both showing black dots and surface popouts. With 15% $H_2$ one could argue that the surface looks to have more black spots, but in terms of surface popouts there is not much difference.

**APPROACH IN MATERIAL SELECTION**

At Tata Steel in IJmuiden it has been the protocol for a long time to use a different method for testing the CO resistance of refractory materials than the ISO 12676 and ASTM C288. The lack of $H_2$ in these test methods makes it much more difficult to distinguish between the relative CO resistance of similar products. For selection of new products (especially for the BF lining) the internal test method of Tata Steel with 95% CO and 5% $H_2$ is used.

When a suitable material is found, it is important to guarantee similar resistance to CO in future deliveries. Most commonly, the iron content gets a guaranteed upper limit on the product definition. More recently we have discussed the test method for CO resistance with refractory suppliers for materials for the BF, such that they understand the approach. Some are also setting up own equipment in order to run the CO resistance test in an CO/$H_2$ atmosphere themselves. Ultimately, Tata Steel in IJmuiden is requesting the resistance to CO according to this method to be guaranteed on the product definition. In some cases this has been proven to be successful.

Not many companies (refractory producers and users) have their own facilities to perform such tests, but there are also third party labs in Europe that can perform these tests when necessary.
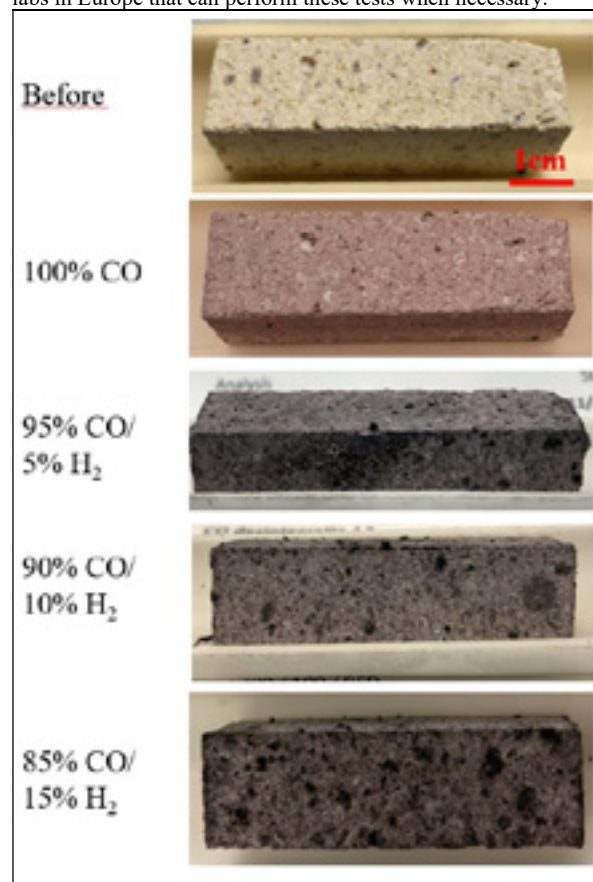


*Fig. 5: Result of CO resistance test with increasing level of H₂ in the gas mix*

## IMPLICATION FOR (FUTURE) IRON- AND STEELMAKING PROCESSES

One of the important installations where the mechanism of CO disintegration can damage the refractories is the Blast Furnace. Even though the trend for future ironmaking is to phase out Blast Furnaces and replace it by other processes, there will still be many blast furnaces in operation in the coming years. There are many trials (ongoing and planned) to increase hydrogen in the blast furnace process. Effects on refractory wear should be carefully monitored, if accelerated wear is observed the role of hydrogen in the decomposition of CO and subsequent deterioration of the refractories shouldn't be underestimated.

In the torpedoes (used for hot metal transport) it has been shown that CO disintegration can play a role in the deterioration of the refractory permanent/safety lining. However, the role of hydrogen here is very small or even not there. The only time when hydrogen is present is directly after repairs (from castables and mortars) or after a cold standby (moisture from air or rain). Of course CO disintegration can still take place, but without the contribution of hydrogen.

Various projects worldwide are underway to eliminate $CO_2$ emissions from the traditional BF-BOF route [10]. One of the trends for future ironmaking is the development of hydrogen based DRI production followed by melting the DRI. The existing way of DRI production is based on natural gas, for future DRI production this will then gradually be replaced by $H_2$. This is dependent on the availability of green hydrogen. In any case the reductant gases will be a combination of CO and $H_2$ until the process would run on 100% $H_2$. CO disintegration under the presence of hydrogen can potentially contribute to the wear of the refractories. Evaluating the suitability of refractory materials for this process would therefore be most relevant in the presence of hydrogen during the test.

Depending on the selected process route the hydrogen based DRI can be further used in an EAF or a reducing melting furnace. The EAF is an oxidising environment where CO disintegration is expected not to play an important role in the wear mechanism in the refractories. For melting DRI under reducing conditions it is expected that CO disintegration can play role in the deterioration of the refractories. However, the influence of $H_2$ is probably very limited again. There is no active source of $H_2$ (as gas or water vapour) in these processes that can influence the Boudouard reaction.

## CONCLUSIONS

The current standard test methods for determination of resistance of refractory materials to carbon monoxide use a 100% CO gas atmosphere (ISO 12676 and ASTM C288). It has been demonstrated before that the formation of carbon by the reverse Boudouad reaction becomes much more efficient when hydrogen ($H_2$) is present.

For many years Tata Steel has worked with an internal test method, that includes $H_2$ in the gas mixture, to compare the relative resistance of refractory materials against CO gas and select the most suitable materials for the application. More recently this method is now also discussed with refractory suppliers and used for quality control purposes.

## REFERENCES

[1] O. Boudouard, Les phénomènes de combustion dans les foyers industriels, Rev. Phys. Chim. 15 (1901) 385-400.

[2] E.T. Turkdogan, J.V. Vinters, Catalytic effect of iron on decomposition of carbon monooxide: I. carbon deposition in H2-CO mixtures, Metall. Trans. 5 (1974) 11– 19.

[3] P.L. Walker, J.F. Raiczawski, G.R. Imperial, Carbon formation from carbon monoxide-hydrogen mixtures over iron catalysts. II. Rates of carbon formation, J. Phys. Chem. 63 (1959) 140–149.

[4] N. Bost, M.R. Ammar, M.-L. Bouchetou, J. Poirier, The catalytic effect of iron oxides on the formation of nanocarbon by the Boudouard reaction in refractories, J. Eur. Ceram. Soc. 36 (2016) 2133–2142

[5] Kadok, J., Bost, N., Coulon, A., Ammar, M. R., Brassamin, S., Genevois, C., Etienne, A., Canizarès, A., Poirier, J.. Inhibiting the sp 2 carbon deposition by adjunction of sulphurous species in refractory ceramics subjected to CO and H2 reducing atmosphere. Journal of the European Ceramic Society (2019), p. 2960–2972.

[6] J. Poirier, N. Bost, A. Coulon, S. Brassamin, A. Canizares, M.R. Ammar, Some good news: inhibition of the boudouard reaction in refractory materials subjected to CO and $H_2$ reducing atmosphere, Proceedings of Unitecr 2017, p 549-552

[7] Krause, O., Pötschke, The predictability of CO resistance of refractory materials by state-of-the-art test methods – A technical and scientific approach. Interceram Vol 57 (2008), p. 176 – 180.

[8] P.E. Nolan, M.J. Schabel, D.C. Lynch, Hydrogen control of carbon deposit morphology, Carbon 33 (1995) 79-85.

[9] N. Bost, A. Canizarès, M.R. Ammar, N. Raimboux, P. Melin, P. Simon, J. Poirires, bing the structural organisation of $sp^2$ carbons obtained by the Boudouard reaction using in situ Raman scattering in reducing conditions, Vibrational Spectroscopy 87 (2016) p 157-163

[10] Shahabuddin, M., Brooks, G., Rhamdhani, M. A. Decarbonisation and hydrogen integration of steel industries: Recent development, challenges and technoeconomic analysis. Journal of Cleaner Production Vol. 395 (2023).

# KNOWLEDGE ABOUT THE CARBON DEPOSITION IN THE MICROSTRUCTURE OF REFRACTORY MATERIALS

Alexandra Koch, Olaf Krause
Koblenz University of applied Sciences, Höhr-Grenzhausen, Germany

Tobias Steffen, Christian Dannert
Forschungsgemeinschaft Feuerfest e. V. at the European Centre for Refractories, Höhr-Grenzhausen, Germany

## ABSTRACT

Carbon nanotubes (CNT) are graphene sheets in cylindric structure and have exceptionally qualities. The single-walled CNT, for example, depict excellent thermal and electrical properties. Whereby multi-walled CNT present extraordinary mechanical qualities and a high aspect ratio. On the other hand, it is well known that carbon nanotubes build a remarkable tabular structure which expands enormously during formation in refractory castables. Hence, the CNT are an unwanted and well documented by-product in refractory materials by exposure in CO atmosphere at intermediate temperatures. Solutions for CO resistance for refractory materials and, consequently, a better understanding of the decomposition and production process is desired and inevitable.

In this paper the knowledge of the development and destruction of the microstructure of refractory castables due to carbon deposition is given. For the first time an imaging method for the deposition of carbon in the microstructure of castables is presented. By varying the number of impurities in the refractory castables under CO atmosphere the progression of the carbon deposition was analyzed and displays the influence of crack formation, built by the carbon nanotubes. The results were gathered by using a Field Emission Scanning Electron Microscope (FESEM).

## INTROCUTION

The mechanism of carbon monoxide decomposition in refractory castables is a well-known issue by the refractory industry, whereas the microstructural process and mechanism is not fully understood till today.

So far two main mechanisms are analyzed and known to be the cause for the CO decomposition. The availability of a catalytic reactive phase in liquid form is required, which promotes the so-called vapor-liquid-solid (VLS) mechanism [1]. The vaporous phase, here CO, dissolves on the liquid catalyst, often iron, and generates fusible cementite ($Fe_3C$) until an oversaturation is reached. The result is the precipitation of the pure, whisker-shaped carbon. The other inevitable process is a shift of the Boudouard equilibrium ($2\ CO \leftrightarrows C + CO_2$) [2] to the reactant at around 500 – 600 °C, providing the necessary free carbon for the dissolution on the catalyst. In refractory products the crucial catalytical substances are Fe and $Fe_2O_3$, which are present as impurities in the (refractory) raw materials [3, 4].

The carbon generated in the process precipitates in $sp^2$ hybridization as carbon nanotubes or similar structures which lead to an enormous volume expansion with a crystallization pressure of 63 kbar. This leads to drastic destruction in the refractory products [5].

The standard corrosion test for CO bursting delineated in ISO 12676 and ASTM C 288 and is not reproducible and leads to divergent results which is confirmed by several studies [1, 3, 6]. Therefore, a proper testing method is aspired. In 2022 a newly designed furnace including a thermogravimetric test stand was presented after the conclusion of IGF project 21408N [7]. During the heating under CO-atmosphere the weight of a cylindric specimen is constantly measured, resulting in a time-depending weight gain analysis. The benefits are tremendous, because the evaluation of carbon deposition in the refractory materials during the heating process is now based on actual data. In comparison the corrosion test ISO 12676 is a superficial assessment of the treated samples categorizing them into groups of "A" to "D". The new, quantitative and reliable testing method was verified using scanning electron microscopy (SEM) in which the generated carbon species and their amount were determined. The new test method opens up new possibilities for testing the influence of different factors such as the number of catalysts, the gas flow rate and the permeability. The previously established relationship between a higher number of impurities (catalyst) and increased carbon deposition in the refractory material was confirmed by both thermogravimetric and SEM analysis [3, 5, 7, 8]. However, the dependency of the gas flow rate and carbon deposition in Krause and Pötschke was refuted with both analysis methods. In addition to the standard gas flow rate of 60 l/h, four different gas flow rates (10, 20, 30 and 40 l/h) were examined and yielded no weight gain or rising amount of carbon nanotubes with increasing gas flow rate. However, the porosity of the refractory castables affects the carbon deposition. Even a 1.5 % increase in open porosity doubles the weight gain of the cylindrical refractories [9]. The influence in open porosity goes along with the development of the microstructure, in particular the formation of cracks and the ingress of CO gas, which is inevitable for the formation of carbon nanotubes in the core and back of samples of refractory applications in the industry.

## METHOD

A model refractory castable was designed for the in-situ analysis in the newly designed furnace and ex-situ studies by other analytical methods. It primarily consists of CA-bonded alumina and has been spiked with varying amounts of hematite ($Fe_2O_3$) ranging from 0.1 to 0.3 wt.-% (table 1), provided by Thyssenkrupp Steel Europe AG with a purity level > 99,5 % iron oxide. The samples were manufactured in accordance with the standard procedure described in DIN EN ISO 12676. After mixing, the cylindrical castables were placed in a climate chamber for 24 h, followed by 24 h drying at 110 °C. The cylinders were then preheated for 5 h at 540°C in an oxidizing atmosphere in accordance with DIN EN ISO 12676. The pretreated samples were cut in half to form cylinders of 50 mm diameter and height. Afterwards, they were heated for 25 h in the newly constructed CO furnace, except for the sample V1 which was heated for 50 h.

Tab. 1: Compositions of the refractory material with various concentrations of iron oxide in wt.-%.

| Component wt.% | V1 | V2 | V3 | V4 | V5 |
|---|---|---|---|---|---|
| Tabular Alumina | | | | | |
| 1.0-3.0 mm | 25 | 25 | 25 | 25 | 25 |
| 0.5-1.0 mm | 21 | 21 | 21 | 21 | 21 |
| 0.2-0.6 mm | 11 | 11 | 11 | 11 | 11 |
| 0.0-0.2 mm | 12 | 12 | 12 | 12 | 12 |
| 0.0-0.045 mm | 9 | 9 | 9 | 9 | 9 |
| Calcined alumina | 10 | 10 | 10 | 10 | 10 |
| Reactive alumina | 7 | 7 | 7 | 7 | 7 |
| Dispersing agent (PCE) | 0.15 | 0.15 | 0.15 | 0.15 | 0.15 |
| CA cement | 5 | 5 | 5 | 5 | 5 |
| Iron oxide | 0.2 | 0.3 | 0.2 | 0.1 | 0.1 |
| Fibers | - | - | - | 0.01 | - |
| Water | 4.5 | 4.5 | 5 | 4.5 | 5 |

For understanding the microstructural texture and their influence on the carbon deposition microscopical analyses were conducted. Therefore, polished sections, fragments and sawn discs of the cylindric samples were prepared. The analyses for the distribution of the iron oxides and carbon depositions occurred using a Digital Microscope VXH 7000 from Keyence. SEM images of the specimen microstructure were taken at 10 kV using a JEOL JSM 7200F field emission scanning electron microscope. It was necessary to have a conductive surface for which reason the samples were coated with differing layers of iridium in a range of 0.5 – 2 nm. The analyses were conducted at the center and edge of the samples. In addition, the sawn discs provided information about how deep the reaction infiltrated the samples. For this reason, the reacted edge of the sample was related to the lesser affected center of the samples.

## RESULTS AND DISCUSSION
### Textural results
In a reduced atmosphere, the stress on the refractory materials is intensive. The more the refractory material is contaminated, the more carbon is deposited on the iron oxide particles and the more stress is placed on the material. [3, 5, 8]. The homogeneous distribution of the hematite in the cylinders produced ensures good accessibility for the CO gas and the subsequent carbon dissolution (figure 1a), resulting in good research conditions. In industry, the distribution of the impurities is more localized and not as dispersed as in the cylinder produced.

As shown in figure 1b the entire matrix of the castables discolors into different shades of gray, due to the precipitation of carbon. The darker an area the more carbon was deposited. The progression of the amount of carbon formed decreases from the edge to the core, respectively to the accessibility of the iron particles. Naturally with high amounts of hematite the amount of carbon deposited rises. The more affected edge of the cylinder presents the penetration depth of the CO gas. The comparison of affected edge to core is measured and presented in table 2. Once again, the dependency of the available iron oxide for the carbon disposition becomes apparent and gives a new approach to determine the CO resistance.
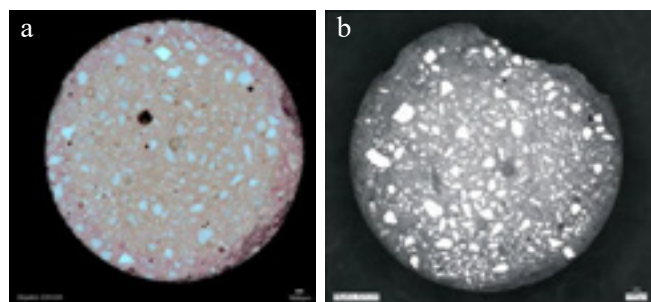


Fig. 1: a) Homogenous distribution of the hematite in the preheated cylinder. b) Cut disk of a heated cylinder of V2 (highest iron oxide content) in CO atmosphere. The edge of the sample is highly attacked presenting a high carbon deposition compared to the inner zone.

Tab. 2: Relation of the more CO-affected edge toward the center of the samples V1-5.

| Sample | Edge [mm] | Center [mm] | Ratio | Percent [%] | Iron oxide [wt.-%] |
|---|---|---|---|---|---|
| V1 | 7.2±0.3 | 17.8±0.3 | 2.5 : 1 | 29.0 | 0.2 |
| V2 | 10.2±0,3 | 14.8±0.3 | 1.5 : 1 | 40.8 | 0.3 |
| V3 | 6.7±0.4 | 18.3±0.4 | 2.7 : 1 | 26.8 | 0.2 |
| V4 | 2.9±0.2 | 26.9±0.2 | 7.5 : 1 | 11.8 | 0.1 |
| V5 | 23.0±0.2 | 22.0±0.3 | 7.4 : 1 | 12.0 | 0.1 |

V4 and V5 were spiked with as little as 0.1 wt.-% of hematite and have the smallest of the more affected zones with less than 2.5 mm. By increasing the iron content to 0.2 wt.% (V1 and V3) the affected zone rises to 6.2 – 9.6 mm. At last, in the castable with 0.3 wt.-%

hematite (V2), a highly carbon precipitated zone of more than 10 mm is produced.

On closer examination the integration of the particles in the matrix has changed after the heating in CO atmosphere. Depending on the hematite content, many particles broke out of the matrix and are not interlocked anymore, as depicted in figure 2a. In addition, circular cracks appear around the particles in the samples. Both are typical indicators of an enormous volumetric expansion. The crack evolution is shown in figure 2b and displays a gradient from outside inwards. During the heating, these cracks facilitate the CO gas to reach the inner iron oxide particles and precipitate more carbon. As a result, the volumetric expansion continues to increase, providing a constant space for the CO gas to infiltrate the refractory castables, which corresponds to an increase in permeability.
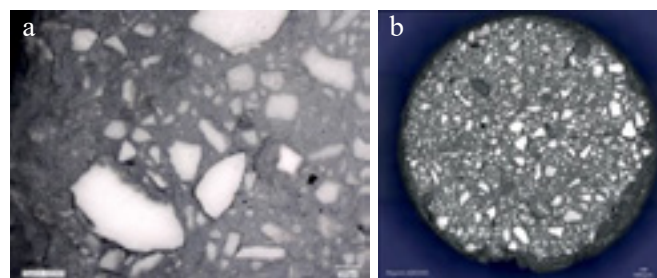


Fig. 2: a) Incoherent Particles in carbon rich matrix of the refractory castable V3 containing the highest amount of iron oxide (0.3 wt.-%). b) crack evolution from the outside inwards in the same sample.

### Microscopic results
SEM analysis of the heated samples gave a further, deeper impression of the interlocking of the carbon allotropes, in this case mostly represented by CNT, in the matrix of the castables. Depending on the amount of hematite the cylinders were already destroyed after 15 h of CO exposure with a gas flow rate of 10 lh$^{-1}$, as for example the cylinder of the castable of V2 containing 0.3 wt.-% of iron oxide. In figure 3 the fragment of the specimen V3 is displayed with an enormous amount of CNT interlocking in the matrix of the castable. Consistently, the amount of hematite affects the number of produced CNT, as the comparison of figure 3 and 4 illustrates.
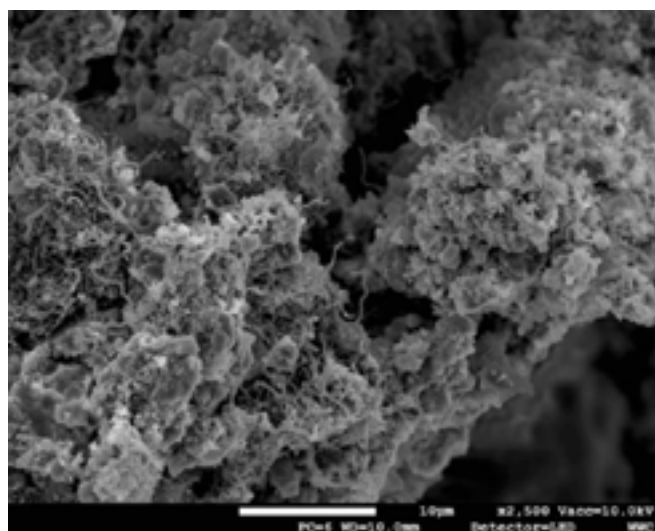


Fig. 3: SEM image of a fragment of the specimen V3. The CNT are present in a large quantity in the matrix. There are many different shapes of the CNT – plain and curly with variable length and thickness.

Although, the number of CNT is lower with less hematite, the increase in volume, which facilitates the circular cracks around the alumina particles, is apparent in the SEM images (figure 4). The
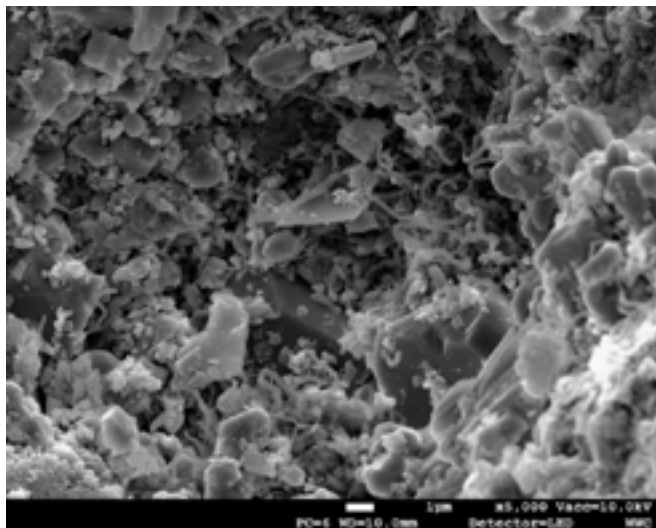
849

*Fig. 4: SEM image of a fragment of the specimen V5. The amount of the CNT is locally elevated. In addition, the CNT, as in the other specimen, are interlocked in the matrix and have a variety of different shapes.*

SEM examinations of edge and core fragments from one specimen confirm the before stated relation of more affected zones of the CO gas. In the fragments of the outer rim more CNT were detected than in the fragments of the core of the cylinders. Generally, the CNT were scattered in the matrix and regularly occurred in clusters. Compared to this, the centered CNT seem to form more often in clusters of varying sizes (figure 5).

Besides the CNT and hydrate phases as binding elements, calcite was found every now and then in various fragments and polished sections. As shown in figure 6, the calcite is predominant in its rhomboedric shape. In one specimen a rather scarce examples of full-grown calcite crystals as trapezohedrons were detected. The $CaCO_3$ polymorph originated from relictic cement phases, which were formed during the preheating phase at 540 °C in oxide atmosphere. As visible in figure 6, sparse CNT are in between the calcite crystals. This appears in other specimens (V5) in the opposite way, so that seldom calcite crystals are present at CNT clusters and in matrix phases or pores.

However, there is no correlation between CNT formation, iron content and calcite formation, as calcite was found in each specimen independent of the iron oxide content.
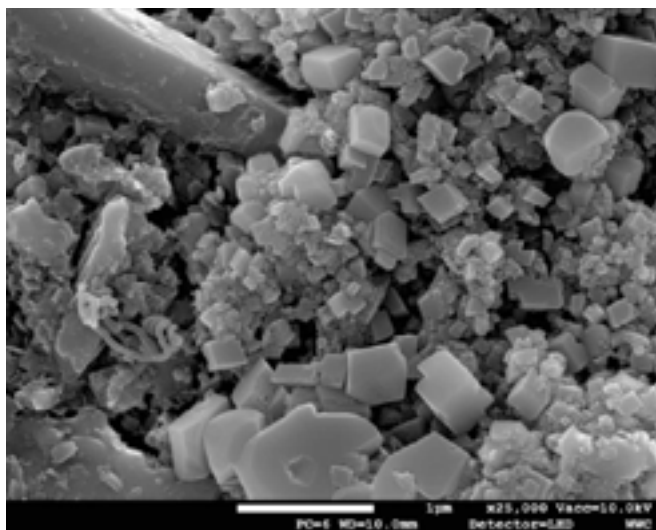


*Fig. 6: SEM image of a polished section of the specimen V4. The typical rhombohedron of calcite appear in a bulk within the matrix.*
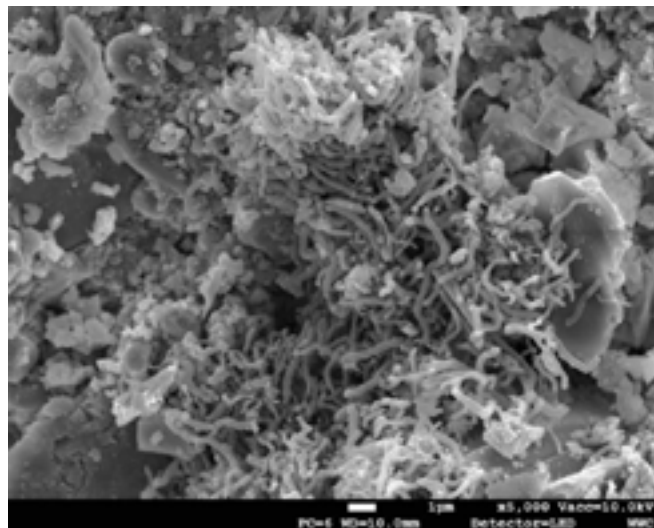


*Fig. 5: SEM image of a CNT cluster in an edge fragment of the sample V4. This is a fairly large example of a CNT cluster, given the hematite content of only 0.1 wt.-%.*

**CONCLUSIONS**

The analysis of the microstructure sheds light on the intensity of the carbon infiltration and its influence on the refractory castables. It is possible to correlate the destruction of a refractory castable to impurities and duration of heating in CO atmosphere. As a result, the higher the level of impurity is, in our case hematite, the greater the area of refractory castables affected and the greater the degree of destruction. The same assumption applies for the heating time in CO atmosphere.

Cracking during heating is a fatal process as the CO gas can infiltrate further into the sample, leading to more carbon deposition. On the one hand, the observed cracks leading from outside inward, promote this process. On the other hand, the second type of cracks detected (circular around the particles) is typical of an increase in the volume expansion of the matrix. This is the result of the built carbon nanotubes, which are known for their high volumetric expansion in refractory castables, causing a large increase in porosity and permeability. Whereby, the refractory castable loses consistency until its complete destruction. The formation of scattered CNT in the matrix as well as clusters could be confirmed using the generated SEM and microscopical images. The variation of length and diameter of the CNT is keen. The number of CNT depends mostly on the content of impurity and duration of firing in CO atmosphere. Additionally, other fullerene as well as calcite were found in the varying specimens.

This approach offers a good opportunity to determine the penetration of carbon deposition; however, more data is needed to verify the work done so far and to ensure reproducibility and consistency. Furthermore, the next steps will be to analyze different refractory castables with varying open porosity and subsequently permeability using imaging methods (e.g. SEM).

**ACKNOWLEDGEMENTS**

**REFERENCES**

[1]  Krause, O., Dannert, C., & Redecker, L. (2012). TECHNOLO-GIE-FORUM-Neue Ergebnisse zum Verhalten von feuerfesten Erzeugnissen in CO-Atmosphäre—Vorschläge zur

Verbesserung der aktuellen Prüfnormen, Teil 1. Keram. Z., Nr. 64[6], 348.

[2] Boudouard, O. (1901). Les phénomènes de combustion dans les foyers industriels. Rev Phys Chim, 25, 6.

[3] Krause, O. & Pötschke, J. (2008) „The Predictability of CO Resistance of Refractory Materials by State-of-the-art Test Methods – A Technical and Scientific Approach". In: Interceram Vol. 57 (3), S. 176-180.

[4] Krause, O., Dannert, C., & Redecker, L. (2014). Refractory Industry Suffers Financial Damages Through Imprecise Test Procedures for the Determination of the Coresistance of Refractory Materials-Time to Review ISO 12676 and ASTM C 288. In Proceedings of the Unified International Technical Conference on Refractories (UNITECR 2013) (pp. 89-94). Hoboken, NJ, USA: John Wiley & Sons, Inc..

[5] Bost, N., Ammar, M. R., Bouchetou, M. L., & Poirier, J. (2016). The catalytic effect of iron oxides on the formation of nano-carbon by the Boudouard reaction in refractories. Journal of the European Ceramic Society, 36(8), 2133-2142.

[6] Walker Jr, P. L., Rakszawski, J. F., & Imperial, G. R. (1959). Carbon formation from carbon monoxide-hydrogen mixtures over iron catalysts. I. Properties of carbon formed. The Journal of Physical Chemistry, 63(2), 133-140

[7] Steffen, T. (2022). Testing the CO resistance of refractory materials – a new technological approach to de-liver reliable results in shorter testing times. Proceedings 65nd ICR 2022.

[8] Turkdogan, E. T., & Vinters, J. V. (1974). Catalytic effect of iron on decomposition of carbon monoxide: I. carbon deposition in $H_2$-CO Mixtures. Metallurgical and Materials Transactions B, 5, 11-19.

[9] AIF Schlussbericht N 21408. "Entwicklung einer zu-verlässigen und aussagekräftigen Prüfsystematik zur Prüfung der CO-Beständigkeit feuerfester Werkstoffe ".

# THE INFLUENCE OF THE GAS PERMEABILITY OF REFRACTORY MATERIALS ON CARBON DEPOSITION IN CO CONTAINING ATMOSPHERES

T. Steffen, C. Dannert

Forschungsgemeinschaft Feuerfest e. V. at the European Centre for Refractories, Höhr-Grenzhausen, Germany

A. Koch, O. Krause

Koblenz University of Applied Sciences, Höhr-Grenzhausen, Germany

## ABSTRACT

The disintegration of refractory materials in CO containing atmospheres, due to the deposition of carbon in the microstructure in the presence of reducible iron phases, is a relevant issue for both refractory manufacturers and users.

With a new testing method, developed previously by Forschungsgemeinschaft Feuerfest e. V., reproducible and quantifiable in situ information on the reaction kinetics of this destruction process in unshaped refractory materials can be determined. With this method, the reaction kinetics of the carbon deposition was investigated in dependency of the pore structure of the refractory material by measuring the open porosity together with thermogravimetrical analysis to collect data on reaction kinetics of the carbon deposition in CO containing atmospheres.

The results of these investigations are helpful to develop new CO resistant refractory materials and to optimize already existing material systems for the application in reducing conditions.

## INTRODUCTION

The Boudouard reaction ($2CO \leftrightarrow CO_2 + C_{(solid)}$) and the accompanied carbon deposition due to the catalytic effect of iron and iron containing phases has been investigated for a long time [1]. In the relevant temperature range of 500 to 600 °C, the Boudouard reaction is thermodynamically shifted towards $C + CO_2$. However, the deposition of carbon is kinetically inhibited without the presence of catalytically active particles like iron oxide, nickel oxide or manganese oxide [2]. Since refractory materials often contain iron of metallic or oxidic nature, they are particularly affected by this effect when they are being used in reducing, carbon monoxide containing atmospheres. The damaging process of refractories can be summarized by [3]:

1. Diffusion of CO into the open pores of the refractory structure
2. Reduction of iron oxides into metallic iron (Fe)
3. Conversion of Fe into $Fe_3C$ as a result of saturation with carbon
4. Growth of elemental carbon in the material with a crystallisation pressure of 64 kbar
5. Formation of cracks and complete disintegration of the refractory material over time

The iron containing phases are either brought in via natural impurities from refractory raw materials or through mechanical processing. Earlier work was able to show that hematite ($Fe_2O_3$), as an iron containing phase, shows the highest catalytic effect in the deposition of elemental carbon in refractory materials. Under CO atmosphere, hematite is converted to magnetite with a decrease in density and an increase in surface area due to crack formation because of volume expansion through recrystallization [4]. As a result, the remaining hematite is converted more rapidly, leading to a cascading increase in surface area of the catalyst material. The reactions occurring during the conversion of iron containing phases under CO atmosphere can be summarized as:

$$3Fe_2O_3 + CO = 2Fe_3O_4 + CO_2 \quad (1)$$

$$Fe_3O_4 + 4CO = 2Fe + 4CO_2 \quad (2)$$

$$3Fe + 2CO = Fe_3C + CO_2 \quad (3)$$
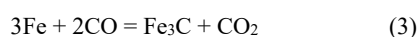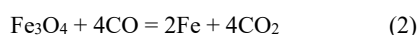
The resulting cementite ($Fe_3C$) is then supersaturated with elemental carbon from the atmosphere and further separated carbon is deposited on the cementite surface in the form of graphite. This leads to the instability of the cementite which decomposes according to:

$$Fe_3C \rightarrow 3Fe + C \quad (4)$$
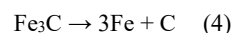
The graphite growing in the cementite during this process acts as an adhesion surface for additional carbon atoms, which in turn act as a catalyst for further carbon deposition. The carbon deposition can be qualitatively described as [5]:

$$Fe_3C \rightarrow C_{(graphite)} + \text{oversaturated solution } (Fe + C) \quad (5)$$
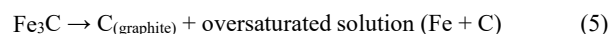
As the carbon deposition within the Boudouard reaction requires liquid iron or carbide droplets, shaped refractory materials are usually pre-treated at higher temperatures to increase the resistance of the material against destruction in carbon monoxide atmospheres. As a result, existing iron is bound in silicate form and no longer has a catalytic effect in the relevant temperature range between 500 and 600 °C. Since unshaped refractories are not pre-treated at sufficiently high temperatures, they are particularly susceptible to CO bursting – the destruction caused by the deposition of elementary carbon.

Previous work suggests that the CO bursting is a diffusion-controlled process that depends heavily on the open porosity and the associated gas permeability of the material [4]. The reason for this assumption is an observed re-increase in the carbon deposition rate after initial crack formation on the surface of the material. This results in new diffusion paths for CO gas and previously unreachable catalytically reactive particles are reduced and thus promote the further deposition of carbon in the refractory material.

To further understand this process, the influence of open porosity and thus the gas permeability of refractory materials on the carbon deposition by the Boudouard reaction using $Fe_2O_3$ catalyst and a CO atmosphere at 500 °C was investigated. The open porosity was varied by increasing the water content during preparation of unshaped refractory samples, by the addition of organic fibres and by changes in pore size distribution. The carbon deposition was investigated using a new test stand using thermogravimetrical analysis.

## METHODS AND MATERIALS
### Model materials

In order to investigate the influence of open porosity on carbon deposition, a reference refractory castable was developed and specifically contaminated with hematite as the catalytically active phase. Since the proportion of catalytically active material also plays a significant role for carbon deposition, this was also varied for two selected materials (V1 and V3) [7].

This reference material was a high-alumina based (all aluminas were provided by Almatis), CA-cement bonded (CAC was provided by Imerys Aluminates) refractory castable (table 1).

Based on this reference material, the open porosity was varied by adding organic fibres that are burnt out before testing (V2), increasing the water content of the mixture (V3) and changing the pore size distribution by increasing the proportion of coarse grains (V4). In addition, three materials were produced in which the proportions

of reactive alumina particles and the finest proportion of tabular alumina were varied (V5, V6 and V7).

Using the recipes shown in table 1, cylindrical test samples with a height and diameter of 50 mm were produced and thermally pretreated according to DIN EN ISO 12676 (5 hours at 540 °C under oxidizing conditions) For each material, four cylindrical samples were produced. Three of these samples were used to determine the open porosity, while one sample was subjected to thermogravimetric analysis and scanning electron microscopy after exposing the material to CO.

*Tab. 1: Composition of the high-alumina and CA-cement bonded refractory castables (all data given in wt.-%), TA = tabular alumina, RA = reactive alumina, CAC = calcium aluminate cement. Digits highlighted in red mark the differences compared to the reference material V1.*

| | V1a V1b | V2 | V3a V3b | V4 | V5 | V6 | V7 |
|---|---|---|---|---|---|---|---|
| TA T60 1-3 mm | 25 | 25 | 25 | 30 | 25 | 25 | 25 |
| TA T60 0.5-1 mm | 21 | 21 | 21 | 19 | 21 | 21 | 21 |
| TA T60 0.2-0.6 mm | 11 | 11 | 11 | 10 | 11 | 11 | 11 |
| TA T60 0-0.2 mm | 12 | 12 | 12 | 11 | 12 | 12 | 12 |
| TA T60 0-0.045 mm | 9 | 9 | 9 | 8 | 7 | 11 | 11 |
| RA RG4000 | 7 | 7 | 7 | 7 | 7 | 7 | 5 |
| RA CTC 20 | 10 | 10 | 10 | 10 | 12 | 8 | 10 |
| CAC Secar 71 | 5 | 5 | 5 | 5 | 5 | 5 | 5 |
| Dispersant FS 60 | 0.15 | 0.15 | 0.15 | 0.15 | 0.15 | 0.15 | 0.15 |
| Hematite | 0.1 0.25 | 0.1 | 0.1 0.25 | 0.1 | 0.1 | 0.1 | 0.1 |
| Distilled water | 4.5 | 4.5 | 5.0 | 4.3 | 4.5 | 4.5 | 4.5 |
| Organic fibres | | 0.01 | | | | | |

**Measuring the open porosity**

The open porosity of the refractory castables was measured according to DIN EN 993-1 (Archimedean principle in water). Therefore, three samples from each batch were measured in order to ensure the uniformity of the measurements.

**Determining the carbon deposition**

The time dependent carbon deposition was measured with the help of a new test stand that was developed at Forschungsgemeinschaft Feuerfest e. V. [7]. This test stand is based on thermogravimetrical analysis and measures the mass gain of refractory materials due to carbon deposition under a constant flow of carbon monoxide gas (figure 1). This test stand was designed with the help of fluid dynamic simulations to ensure uniform and homogeneous flow conditions around the samples and thus provides a high reproducibility of the tests [6].

For each test, a cylindrical sample (height and diameter of 50 mm) is being placed on an alumina sample plate and is then heated up to 500 °C at a rate of 5 °C min$^{-1}$ under 60 l h$^{-1}$ of nitrogen inert gas to eliminate remaining oxygen in the reaction chamber and thus to prevent oxidation reactions. After holding the sample temperature at 500 °C for 1 h under a constant flow of nitrogen to allow thermal influences on the weighing signal and the associated apparent changes in mass to subside, the sample is exposed to CO gas for either 50 h (samples with 0.25 wt.-% hematite) or 25 h (samples with 0.1 wt.-% hematite) at a constant flow rate (10 l h$^{-1}$).
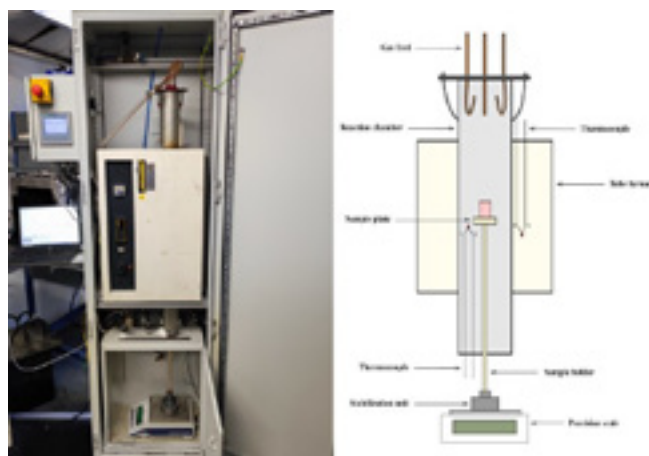


*Figure 1: Test stand to determine the carbon deposition in refractory materials under CO atmosphere; left: new test stand at Forschungsgemeinschaft Feuerfest e. V., right: schematic cross-sectional drawing of the developed test stand.*

## RESULTS

### Open porosity of the model materials

Table 2 shows the results of the investigations on the open porosity and bulk density of the materials. The deviations from average for both material parameters are also shown. Both the material with an increased water content (V3) and the one doped with fibres (V2) showed the highest open porosities of the materials measured (V3 with an open porosity of 15.1 vol.-% and V2 with an open porosity of 13.8 vol.-%). The material with an increased proportion of coarse grain and a lower water content showed the lowest open porosity of all materials of 11.5 vol.-%. All the other materials, including the reference material (V1a/b) and the comparison materials with differing finest fractions, showed very similar open porosities between 13.0 and 13.4 vol.-%.

*Tab. 2: Overview of the measured open porosities and bulk densities of the refractory castables.*

| Material | Bulk density in g cm$^{-3}$ | Deviation from average | Open porosity in vol.-% | Deviation from average |
|---|---|---|---|---|
| V1a/b | 3.136 | 0.002 | 13.1 | 0.6 |
| V2 | 3.107 | 0.005 | 13.8 | 0.7 |
| V3a/b | 3.141 | 0.003 | 15.1 | 0.1 |
| V4 | 3.137 | 0.011 | 11.5 | 0.7 |
| V5 | 3.151 | 0.004 | 13.0 | 0.3 |
| V6 | 3.127 | 0.002 | 13.4 | 0.4 |
| V7 | 3.131 | 0.003 | 13.3 | 0.4 |

### Thermogravimetrical analysis

The results from the thermogravimetric measurements with the reference material, a hematite content of 0.25 wt.-% and differing open porosities (V1b and V3b) are shown in figure 2. The samples were exposed for 50 hours in a CO atmosphere with a constant supply of CO gas (10 l h$^{-1}$) at 500 °C. The material with a higher open porosity is shown in red (V3b), the material with lower open porosity in blue (V1b). The rate of carbon deposition of V3b (open porosity of 15.1 vol.-%) was found to be significantly higher than the deposition rate of V1b (open porosity of 13.1 vol.-%). Both materials showed an initial strong weight gain due to carbon deposition, followed by a continuous decrease in the carbon deposition rate until an almost linear course of carbon deposition set in. Aside from that, both materials showed a re-increase of the carbon deposition rate after several hours of linear progression. However, the two materials differed significantly in terms of the point in time where the re-increase began. While V1b showed a re-increase in the carbon deposition rate after an exposure time of around 40 hours, the re-increase occurred after an exposure time of around 20 hours

for V3b. Due to the overall higher carbon deposition rate of V3b, after 50 hours of exposing the material to CO, the material showed an increase of 1.74 wt.-% due to carbon deposition, while V1b showed an increase of only 0.98 wt.-%. Since the samples no longer had structural stability after CO treatment and were therefore unsuitable for microscopic structural investigations, all further investigations were carried out on materials with a reduced hematite content of 0.1 wt.-% and a reduced exposition time of 25 h.
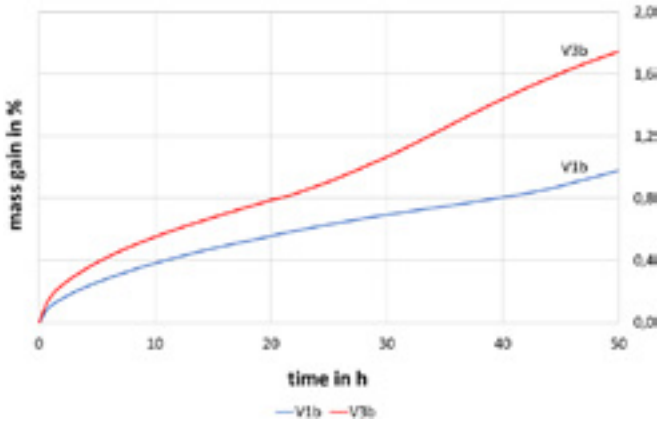


*Figure 2: Overview of the carbon deposition in high alumina refractory castables with different open porosities (V1b: 13.1 vol.-%, V3b: 15.1 vol.-%) and a hematite content of 0.25 wt.-%. The tests were carried out for 50 h at 500 °C and a CO flow rate of 10 l h$^{-1}$.*

Figure 3 shows the results of the thermogravimetric measurements with the reference and comparison material, 0.1 wt.-% hematite and differing porosities. The samples were exposed for 25 h in CO atmosphere with a constant supply of CO gas (10 l h$^{-1}$) at 500 °C. Right at the beginning of the exposition in CO, all the materials showed the same strong increase in mass. All the samples examined as part of these measurements showed a steady decrease in the carbon deposition rate after the first strong increase in mass. This was followed by the transition into an almost linear progression of carbon deposition from a test duration of about 10 h onwards. It is noticeable that V3a (highest open porosity of 15.1 vol.-%) showed a significantly higher carbon deposition rate after one hour of exposition to CO in comparison to all other materials. This trend continued for V3a until the end of the test duration and resulted in the highest mass increase of 0.41 wt.-%. In addition to V3a, V2 (open porosity of 13.8 vol.-%) also clearly stood out from the other materials regarding the carbon deposition rate after about 5 h of testing time. As a result, V3a and V2 showed the highest mass gains after 25 h of exposing them to CO. The increase in mass was 0.41 wt.-% for V3a and 0.39 wt.-% for V2. The lowest carbon deposition rate and thus the lowest mass increase with 0.33 wt.-% after 25 h in CO atmosphere was observed for the material with an increased proportion of coarse grain and a lower water content (V4, open porosity of 11.5 vol.-%). Both the reference material (V1a, open porosity of 13.1 vol.-%) and the materials with modified finest fraction (V5, V6 and V7, open porosities between 13.0 and 13.4 vol.-%) showed very similar final mass gains after testing. V1a and V6 showed a mass gain of 0.36 wt.-%. For V5 the mass gain was 0.33 wt.-% and for V7 0.35 wt.-%.
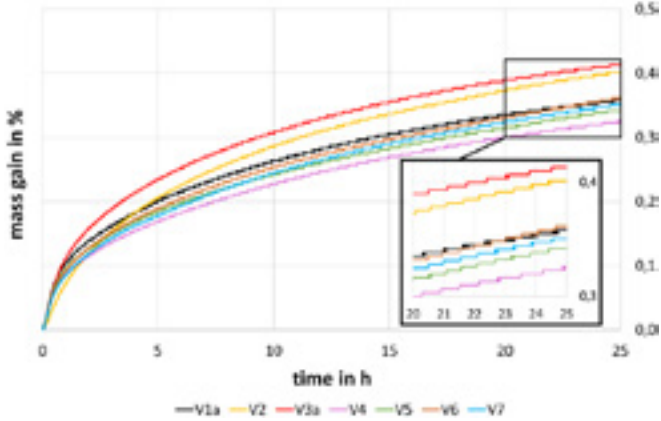


*Figure 3: Overview of the carbon deposition in high alumina refractory castables with different open porosities and a hematite content of 0.1 wt.-%. The tests were carried out for 25 h at 500 °C and a CO flow rate of 10 l h$^{-1}$. The enlarged area shows a more legible view of the differences of the studied materials in terms of their mass gain due to carbon deposition.*

**Correlation of open porosity and carbon deposition**

The data of open porosity and carbon deposition of the examined refractory castables are compared in table 3 and visually presented in figure 4. The refractory castable with an increased water content and the highest measured open porosity of 15.1 vol.-% (V3a) also shows the highest mass gain after exposing it to CO (0.41 wt.-%), followed by V2, the refractory castable with organic fibre material and the second highest values for open porosity (13.8 vol.-%) and mass gain due to carbon deposition (0.39 wt.-%). The materials V1a, V5, V6 and V7 (reference material and materials with variations in finest fraction) differ only slightly in terms of their open porosity (in a range between 13.0 and 13.4 vol.-%) and carbon deposition (in a range between 0.33 and 0.36 wt.-%). V4, the material with an increased proportion of coarse grains and reduced water content, shows both the lowest open porosity and the lowest mass gain with 11.5 vol.-% and 0.33 wt.-%. In general, it should be noted that the measurement of the open porosity of refractory castables has an error that is not negligible. Within the measurements carried out, this error is up to 0.7 vol.-% (deviation from average according to table 2). A determined deviation from average of max. 5 % (related to the mass gain in wt.-%) applies to the carbon deposition [8]. Under consideration of the possible errors for both measurement methods, a linear correlation between the open porosity and the tendency to carbon deposition of refractory castables can be assumed for the test results obtained so far.

*Table 3: Overview of the mass gain in refractory materials after exposition in CO for 25 h at 500 °C and the open porosities of the respective materials after thermal pre-treatment at 540 °C and prior to the exposition to CO.*

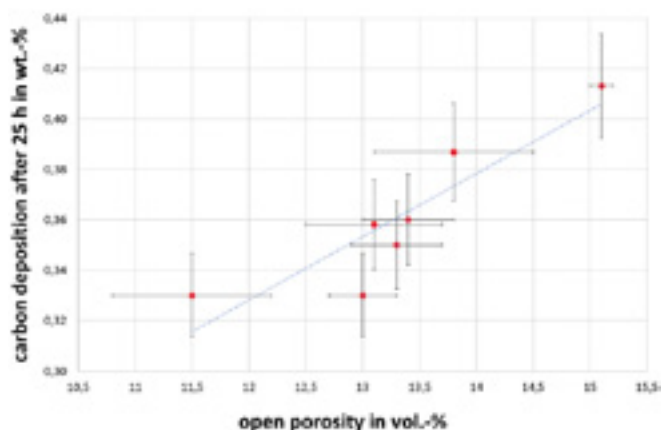|  | V1a | V2 | V3a | V4 | V5 | V6 | V7 |
|---|---|---|---|---|---|---|---|
| Mass gain in wt.-% | 0.36 | 0.39 | 0.41 | 0.33 | 0.33 | 0.36 | 0.35 |
| Open porosity in vol.% | 13.1 | 13.8 | 15.1 | 11.5 | 13.0 | 13.4 | 13.3 |

*Figure 4: Correlation of the thermogravimetric data for the final carbon deposition in all comparison materials after 25 h in a CO atmosphere at 500 °C and the open porosity of the materials after thermal pre-treatment and before the exposition in the CO test stand. The error indicators for the open porosity correspond to the deviation from average from table 2, the error indicators for the carbon deposition correspond to the maximum error from repeatability tests with the test stand [8].*

## CONCLUSIONS

Experimental results on the open porosity of refractory castables (after thermal pre-treatment) and the carbon deposition (after exposing the material to a CO atmosphere at 500 °C) are reported and correlated with each other. The refractory castables used in the test series were specifically contaminated with hematite to promote the carbon deposition within the Boudouard reaction.

For refractory castables with an increased degree of contamination (in this case 0.25 wt.-% hematite), increasing the open porosity by 2 vol.-% (due to an increased water content) led to a significant change in the reaction kinetics of the carbon deposition. While the carbon deposition rate of the refractory castable with a porosity of 13.0 vol.-% did not start to re-increase again until after 40 hours of exposition in a CO atmosphere, the rate of carbon deposition of the comparative material with a porosity of 15 vol.-% already started to re-increase after 20 hours. As a result, the increase in open porosity leads to a shortening of the time until the structural destruction of the refractory material due to cracking begins.

In a direct comparison of the open porosity of thermally pre-treated refractory castables with a reduced hematite content (0.1 wt.-%) and their mass increase due to carbon deposition after exposition in CO atmosphere, an almost linear correlation was observed. However, when assuming this linear correlation, the comparatively large measurement error of the open porosity measurement must be considered.

In summary, the results so far indicate a clear influence of the open porosity and thus the permeability of the material on its carbon deposition in CO containing atmospheres. The trend here is that materials with higher open porosities tend to have a much higher carbon deposition than those with lower open porosities. However, the assumption of a linear correlation between open porosity and carbon deposition needs to be investigated more intensively.

## OUTLOOK

Due to the promising results and the clear influence of the open porosity of refractory castables on carbon deposition, these investigations will be extended in the future. This includes the further adaption of the test materials in order to be able to map a larger area of the open porosity and to be able to describe the correlation with the mass increase due to carbon deposition more precisely.

## ACKNOWLEDGEMENTS

## REFERENCES

[1] Boudouard, O., "Les phénomenès de combustion dans les foyers industriels", Rev. Phys. Chim. 15, 1901, p. 385-400

[2] Baukloh, W.; Hieber, G., "Der Einfluss verschiedener Metalle und Metalloxyde auf die Kohlenoxydspaltung", Zeitschrift für anorganische und allgemeine Chemie 226 (4), 1936, p. 321-332

[3] Poirier, J.; Kadok, J.; Bost, N.; Coulon, A.; Ammar, M. R.; Brassamin, S.; Genevois, C., "Inhibiting the Carbon Deposition from the Reverse Boudouard Reaction in Refractories Submitted to CO-$H_2$ Atmosphere", Refractories Worldforum 11, 2019 [2], p. 83-91

[4] AiF Schlussbericht 14161 N, "Ursachen für den Verschleiß feuerfester Werkstoffe, insbesondere ungeformter feuerfester Erzeugnisse, unter CO-Atmosphäre", 2007, available through Forschungsgemeinschaft Feuerfest e. V., Rheinstraße 58, 56203 Höhr-Grenzhausen, Germany

[5] AiF Schlussbericht 21408 N, "Entwicklung einer zuverlässigen und aussagekräftigen Prüfsystematik zur Prüfung der CO-Beständigkeit feuerfester Werkstoffe", 2022, available through Forschungsgemeinschaft Feuerfest e. V., Rheinstraße 58, 56203 Höhr-Grenzhausen, Germany

[6] Steffen, T.; Dannert, C.; Krause, O., "Understanding CO bursting: the possibilities of thermogravimetrical measurements", Refractories Worldforum 2022 (3), p. 12-13

[7] Steffen, T.; Dannert, C.; Fischer, J.; Krause, O.; Koch, A., "Testing the CO resistance of refractory materials – a new technological approach to deliver reliable results in shorter testing times", ICR International Colloquium on Refractories 2022, Proceedings, p. 34-37

[8] Steffen, T., "Evaluation eines neuartigen, auf Thermogravimetrie basierenden Prüfverfahrens zur Erfassung der Kohlenstoffabscheidungsrate in feuerfesten Werkstoffen unter Kohlenstoffmonoxid-Atmosphäre bei 500 °C", Master thesis, available through Hochschule Koblenz – WesterWaldCampus, Rheinstraße 56, 56203 Höhr-Grenzhausen

855

# EXCEPTIONAL "HIGHLIGHTS" OF EXTREME WEAR OF REFRACTORIES

Jasper Neese, Thomas Schemmel, Bertram Kesselheim, Steffen Rollmann
Refratechnik Steel GmbH, Duesseldorf, Germany

## ABSTRACT

It is hard to imagine modern industrial high temperature processes without refractories. All of these processes cause a high load on the wear materials. The typical edges of the wear triangle are erosion, thermomechanical wear and corrosion. Various groups of refractories can be found in the industrial field depending on the profile of requirements of the particular process. For example, MgO-C bricks in steel making, Magnesia-Chromite bricks in non-ferrous metal making and so forth. Thermal stability, corrosion resistance, erosion resistance as well as thermal shock resistance are necessary properties. Each industry, each process and each furnace have their own requirements concerning the material properties. The present work points out some "highlights" of extreme refractory wear that we have collected during the last years. The given cases derive from different industrial processes and represent various failure modes that may occur in modern industrial high temperature processes.

## INTRODUCTION

In the steel and non-ferrous industry different refractory materials are used. In the most common cases a wear lining of refractory materials is produced, which reacts directly with melt, slag, process materials or gases. Therefore, a resulting wear is no surprise, the objective is to keep the wear as low as possible. In order to understand the wear mechanisms, post-mortem tests on heavily used bricks or components are useful. In this way, a broad knowledge can be generated, which subsequently helps in the most suitable material selection. The range of refractory materials is versatile - the following examples include products with different raw materials and different bond types. From the steel industry, a wear case from the steel ladle is shown using the example of $Al_2O_3$-MgO-Carbon (short "AMC") bricks. Common challenges have their origin in modern steel making practice: e.g. very high process temperatures, aggressive slags, intensive treatment and strong thermal cycling [1]. In the copper industry, fired magnesia chrome bricks (short "Mg-Cr") are often used, here an example from the copper recycling process is presented. In the case of castables, in addition to wear in use, installation and heating are also critical points. Therefore, a large-scale test is shown, which demonstrates the explosion potential during heating. Finally, a look into the future follows - laboratory tests on the attack of andalusite bricks by hydrogen-containing atmospheres are presented. Wear caused by gas attack is already frequently the cause of damage, for example due to CO gas. Hydrogen is already present in today's plants, but the concentration will increase significantly soon.

## WEAR MECHANISM OF REFRACTORIES

Typically, every type of wear found in practice can be attributed to three general mechanisms: corrosion and oxidation, abrasion and erosion and thermomechanical wear. In general, wear is always a combination in various portions of these basic mechanisms (Fig. 1) [2]. In the rarest of cases, only one factor is responsible for the wear. Figure 2 therefore shows the approximate areas in which the following examples are based. The areas of corrosion and oxidation and thermomechanical wear are dealt with in detail below. The shown examples are mainly from this area of the wear triangle.

### Corrosion and Oxidation

This mechanism is based on a result of chemical reactions. The reaction potential between slag and refractory material (based on the chemical composition) determines whether a reaction takes place. The reaction grade is driven by the total number and concentration of components, reaction space, reaction time, oxygen activity and temperature. To show the reaction potential commonly the c/s-ratio is used. Between CaO (basic) and $SiO_2$ (acidic) a high reaction potential is known for example. The complete calculation is shown in eq. 1 [3]. However, simplified forms also exist (CaO/$SiO_2$) and are often used.

$$c/s = ([CaO]+[MgO]/([SiO_2]+[Al_2O_3]+[TiO_2]+[Fe_2O_3])) \quad (1)$$

Temperature is a decisive factor in all reactions. In addition to the influence on the reaction kinetics, there are also process-related problems that lead to higher stress. An increase in temperature reduces the viscosity of the slag, which makes it more difficult to build up a protective layer on the refractory. This significantly increases corrosion, since fresh reactants can be added more and more. Kinetically accelerated oxidation leads to carbon burn-off by air oxygen and FeO.

The first example is a classic case of oxidation with subsequent thermomechanical wear. This mechanism is especially critical for carbon-bonded and carbon-containing products. In a steel casting ladle, AMC bricks were used as wear lining in the wall area. After only a few heats, a massive layer formed on the bricks. In figure 3, the layer on the AMC bricks can be clearly seen. This had to be removed at great expense after cooling down the ladle.
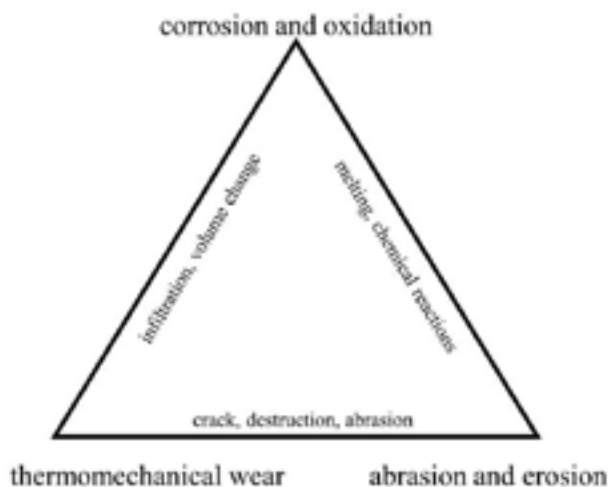
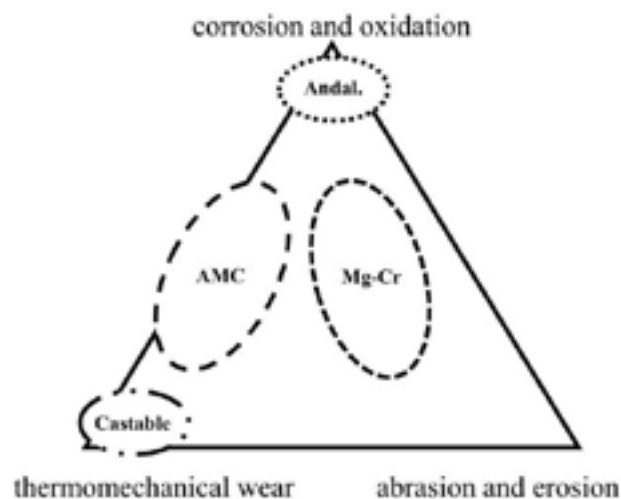

Fig. 1: General wear triangle



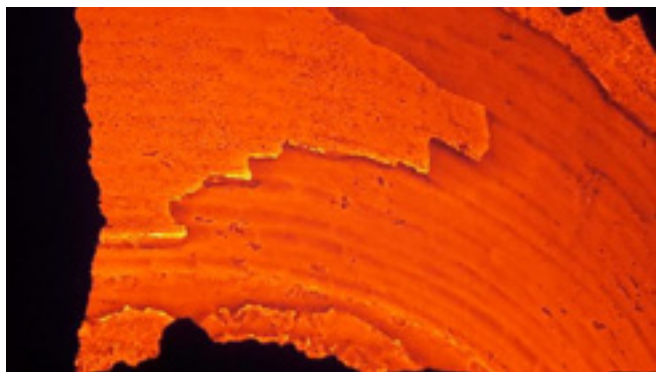Fig. 2: Wear triangle. Examples are located inside the triangle.

*Fig. 3: Detail of hot build-up on AMC bricks in the side wall of a steel ladle*
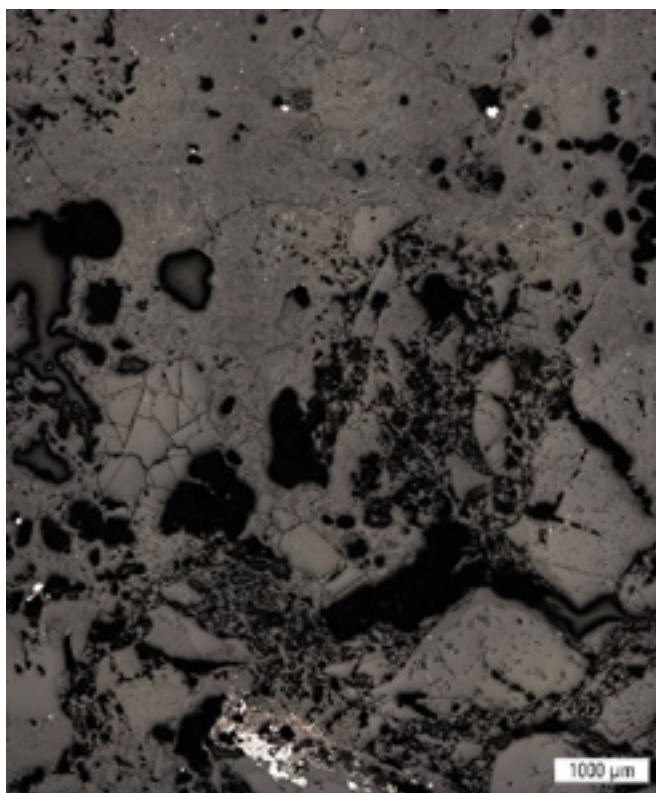


*Fig. 4: Microscopic examination of the AMC brick. Slightly attacked original AMC structure at the bottom, decarburized structure in the middle and slag deposit on the upper side*

In this case, a good impression of the wear progress could be obtained from the microscopic examination (figure 4). The original structure of the AMC brick was damaged by oxidation of the carbon. This phenomenon is often evident when the ladle has been pre-heated for a long time at high temperatures before its first use or in the case of oxidative wear during the process. The damaged and porous structure allows the calcium-aluminate slag to penetrate the brick while tapping and has a large surface area for chemical attack. Formation of new phases also occur (e.g. spinel). The reacted zone shows completely different hot properties such as melting behaviour and thermal expansion compared to the original material. The infiltrated layer therefore remained as a separate material and had to be removed manually.

**Thermomechanical Wear**

All types of damage that are caused by a temperature related increase in volume are summarized under the generic term of thermomechanical wear. One of the most important material properties in high-temperature processes is thermal expansion. The thermal expansion is a combination of the reversible thermal

expansion coefficient and irreversible expansion by physical-chemical reactions (after-contraction/after-expansion) [4]. Thermal expansion leads to stresses due to the increasing load in the ring network or if temperature inside the refractory is inhomogeneous or if material reactions result in a changed expansion behaviour (e.g. filled pores or chemical reactions). Also, the temperature gradient, the volume of the refractory and the ability to balance stresses without degradation determine the level of wear. Furthermore, all damages through mechanical strain (impacts, flexural stress, pressure) are important for thermomechanical wear.

The second example is a combination of corrosive and thermomechanical wear. The Peirce Smith Converter is a melting unit from the copper recycling process. The lining is made with magnesia-chrome bricks, for example. In this case the brick was attacked by an acidic fayalite slag. The proportion of sintered magnesia (approx. 50%) in the brick was strongly attacked by the acidic slag. Mixed spinels $(Mg,Fe,Cu)O*(Fe,Cr,Al)_2O_3$, monticellite and olivine were formed as a product from brick and slag. These mineral phases have changed melting and expansion behaviour, which has led to premature wear of the lining. During operation, the front layer is densified due to the lowering of the melting point and when the temperature changes, the infiltrated areas spall off due to the changed thermal expansion.

The increase in the $SiO_2$ proportion can be made visible in the bricks cross-section using µ-XRF. From the cold side (below) to the hot side (above), the proportion of $SiO_2$ increases significantly (figure 5). Deep penetration into the brick matrix takes place especially with such aggressive and low-viscosity slags. The reaction mechanism can be understood in the microscopy image in figure 6. The adherend slag on the hot side can be seen in the upper part of the picture. The fayalite slag has decomposed into magnetite and $SiO_2$ glass under oxidizing conditions. The acidic $SiO_2$ glass attacks the basic components, especially the magnesia. The relic of a partially dissolved DBM grain can be seen on the left. The chrome is incorporated into the slag without being dissolved.

857
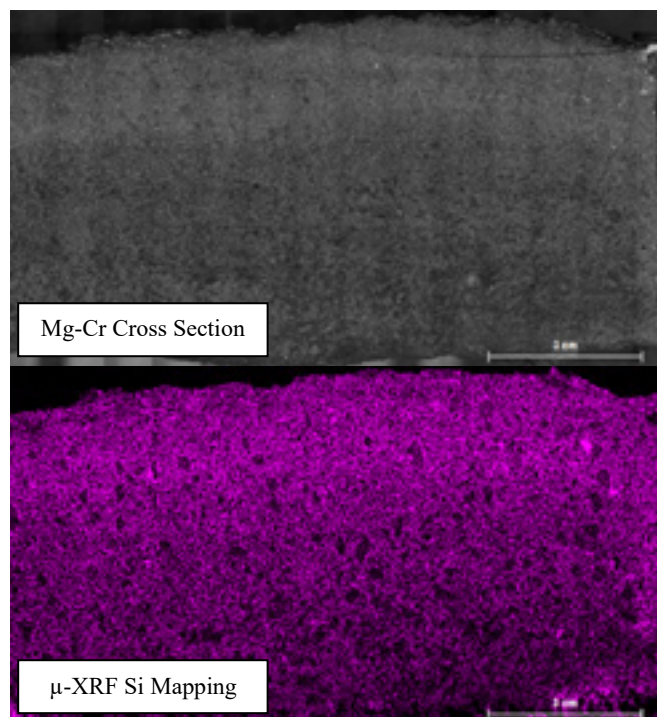


*Fig. 5: Investigation of Mg-Cr bricks cross section with µ-XRF. Enrichment of $SiO_2$ towards the hot face (above), due to infiltration of aggressive acidic slag.*
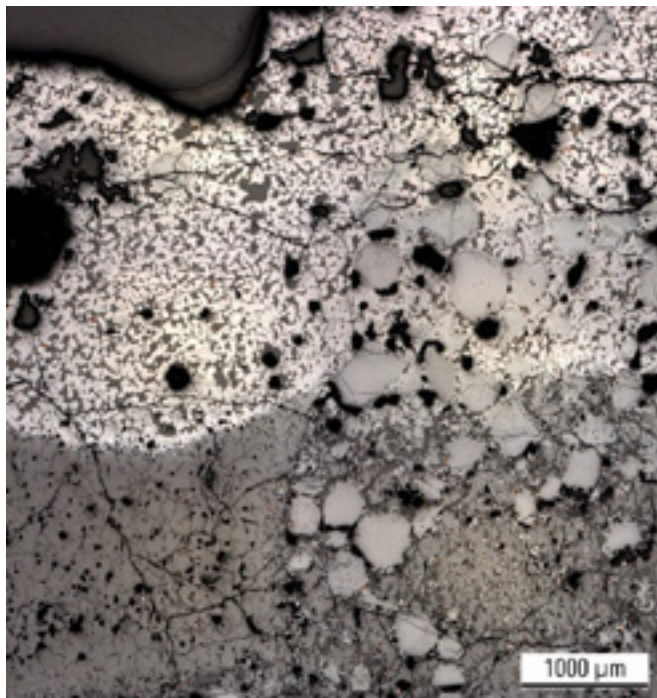
*Fig. 6: Microscopic view on Mg-Cr hot face (above). Adhering slag on the hot side, it has decomposed into magnetite and SiO₂ glass under oxidizing conditions. The relic of a partially dissolved DBM grain can be seen on the left. The chrome is incorporated into the slag without being dissolved.*

In addition to this frequent combination of mechanisms, there are also phenomena that are more clearly based on just one of the two wear mechanisms presented. In this case, heating damage to a castable pre-shape component is considered. Since it is a case of spalling caused by volume expansion under the influence of temperature, one can speak of thermomechanical wear in the broadest sense. Even if no process medium such as steel or slag was involved. The increase in volume of the chemically bound water in the component alone leads to explosive destruction of the refractory material if it is heated up too quickly. In a large-scale trial, two pre-shaped components, each weighing one ton, were placed in a furnace operated at 800 °C. The sudden increase in volume of the water builds up an enormous pressure. If the structure cannot dissipate the water vapor and withstand the pressure, the component abruptly fails. The result of such damage is shown in figure 7. A cement-free castable with high strength can cope with the high heating rate, while the reference material cannot withstand the pressure increase.



*Fig. 7: Result of a large-scale fast heating test with different pre-shaped castable to 800 °C. Increasing steam pressure led to a total collapse of the sample on the right side.*

## OUTLOOK

One last highly discussed example in the field of corrosion is the attack of hydrogen gas at high temperatures. In the course of decarburization in the steel industry, the use of large amounts of hydrogen at temperatures > 900 °C is being increasingly examined. When hydrogen is burned, the $H_2$ content in the atmosphere is still low, in the case of direct reduction processes with hydrogen, the doses can be very high. A critical refractory oxide is $SiO_2$. It reacts with hydrogen even at relatively low temperatures according to equation 2.

$$SiO_{2(s)} + 2\ H_{2(g)} = Si_{(s,l)} + 2\ H_2O_{(g)}$$
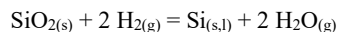
That this is not just theory is confirmed by exposure tests in a 100% hydrogen atmosphere. In this example, a fired CO-resistant andalusite brick was subjected to corrosive attack by hydrogen at 1400°C for 200 hours. In addition to the measured weight loss, the chemical analysis of the sample is interesting. Figure 8 shows μ-XRF recordings of the sample cross-section. A significant reduction in $SiO_2$ was determined in the edge area. This leads to a complete change in the structure. Thus, in use, thermomechanical or abrasion wear would have to be expected in the next step. Corrosion of gases is not a new topic but is becoming an intense subject for the future due to the use of high amounts of hydrogen.
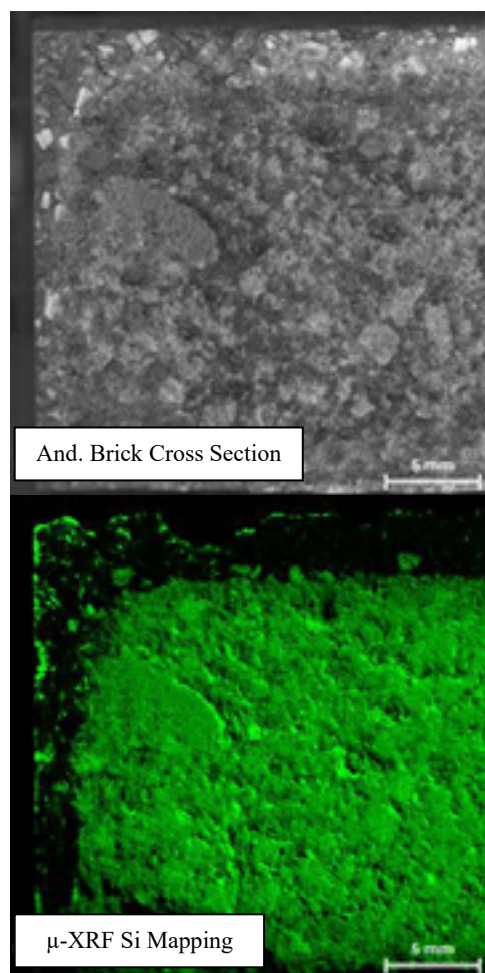


*Fig. 8: Laboratory trial with Andalusite brick in pure hydrogen atmosphere at 1400 °C. μ-XRF measurements are showing the strong reduction of SiO₂ in the edges.*

## CONCLUSIONS

The cases presented in this publication are intended to show how diverse the corrosion mechanisms on refractory products can be. Almost all refractory products are subject to wear over their lifetime. Basically, the mechanisms can be found in the corrosion triangle. However, the areas of application for refractory products

are exactly where other materials do not have sufficient properties. Many processes and industries depend on refractory products. In times with a focus on efficiency and sustainability, the longest possible service life of refractory linings should be striven for. This requires a detailed understanding of how corrosion mechanisms work and what the critical factors are. This means that there are special requirements for each application which must be understood in order to be able to carry out the optimal lining.

**REFERENCES**
[1]  Aneziris, C.G.; Borzov,D.; Ulbricht, J.: Magnesia-Carbon Bricks – A High-Duty Refractory Material. Refractories Manual (2003) pp. 22-27
[2]  Jansen, H.; Große Daldrup, H.: Refractory Wear in Steelmaking Processes. AISTech 2005, USA, 2005.
[3]  Trojer, F.; Obst, K.H.; Münchberg, W.: Mineralogy of basic refractory products. Springer-Verlag, Vienna-New York, 1981.
[4]  Stein, V., Schemmel, T., Jansen, H.: Varios Ways to kill MgO-C bricks in Steel Making practice. ICR Aachen, 2014.

SHORT COMMUNICATIONS

# DEGRADATION BEHAVIOR OF MGO−C REFRACTORY BY AR BLOWING IN CONTACT WITH LIQUID STEEL

Jaewoo Myung, Hana Lee, Byoungkwon Choi, Yongsug Chung[*]
Tech University of Korea, Siheung, Korea

## ABSTRACT

Degradation behavior of a MgO-15wt%C refractory by Ar blowing in contact with liquid steel was studied using a high frequency induction furnace at a temperature range between 1550 and 1650℃. When Ar was blown through the refractory, surface degradation was observed over 1600℃ compared to the no degradation without blowing. Internal degradation was observed in all specimens even though without blowing. It progressed from the interface between liquid steel and refractory to the inside of the refractory. Ar blowing and increasing temperature increased degradation of specimen. The degradation can be thought to be the carbothermic reduction reaction of MgO. The carbon content in the liquid steel increased with time by immersion of MgO-C, and it increased continuously with Ar blowing. The Mg content did not change significantly with time. It seems that Mg was consumed during the formation of the MgO layer and inclusions.

## Introduction

MgO-C materials are being considered for the purging plugs in EAFs [1], converters [2,3]. MgO-C gives strong stirring by injecting gas directly into the liquid steel through stainless pipes inserted inside the refractory. MgO-C is an appropriate material when cold gas is injected through it into liquid steel because of its excellent thermal shock resistance due to the carbon.

However, when MgO-C is in contact with liquid steel, chemical reactions occur. The MgO-C is degraded, which generates Mg and CO vapors by carbothermic reduction of MgO above 1400℃ [4]. The degraded MgO-C is easily damaged by liquid steel. Mg and CO vapors generated by degradation of MgO-C can be dissolved into liquid steel and affect the composition of the liquid steel. Carbon content in the liquid steel can be increased by the reaction between MgO-C and liquid steel [5,6]. Dissolved Mg can react with oxygen in liquid steel to form MgO layer and/or inclusions [7]. In particular, this contributed to formation of spinel inclusions in the case of Al killed steel [8].

In this study, for the case when Ar gas is passes through MgO-15wt%C into liquid steel, we conducted a fundamental study based on the degradation of MgO-C, interfacial reaction between MgO-C and liquid steel at a temperature range between 1550 and 1650℃.

## Experimental procedure

Experiments were carried out using a high-frequency induction furnace. Pure steel (99.97% in purity) and commercial MgO-15wt%C brick were used in this experiment. Tables 1 and 2 show the compositions of the MgO-C and steel, respectively. High purity Ar gas (99.999%) was used for gas injection into liquid steel. When the MgO-C specimen was immersed into the liquid steel, Ar gas was uniformly injected into the liquid steel at a flow rate of 1 NL/min by a Mass Flow Controller for 4 hr after immersion time of 20 min. After the experiment, the specimen was removed from the liquid steel and cooled. The steel samples were collected at the main experiment times (0, 5, 10, 15, 20, 30, and 80 min) without and with Ar blowing at 1600℃ to analyze the changes in the content in the liquid steel.

## Results and discussion
### Degradation of MgO-C in contact with liquid steel without/with Ar blowing

Fig. 1 shows the appearance, vertical cross-section, X-ray CT images of MgO-C specimen after the experiment at the condition of 1550℃ and Ar blowing. In the case without blowing, there was no surface degradation of the MgO-C. However, in the case with Ar blowing, the surface of the MgO-C slightly burst at 1600℃, and more severely at 1650℃. As seen in eq. 1, the surface degradation ratio was calculated as the degraded surface area ($A_d^s$) among the immersed area ($A_0^s$) in the liquid steel. The surface degradation ratios with Ar blowing were 9 and 29% at 1600 and 1650℃, respectively.

$$\text{Surface degradation ratio} = A_d^s/A_0^s \qquad (1)$$

As seen in Fig. 1 (c), density distribution inside the MgO-C was determined from 3D reconstructed X-ray CT scanning images based on differences in density; the grey phase of high density and the black & white phase of low density. As seen in Fig. 1 (a) and (b), even though no surface degradation was observed, difference in density was observed by this technique as seen in Fig. 1 (c). It was also seen in all MgO-C specimens without blowing where no
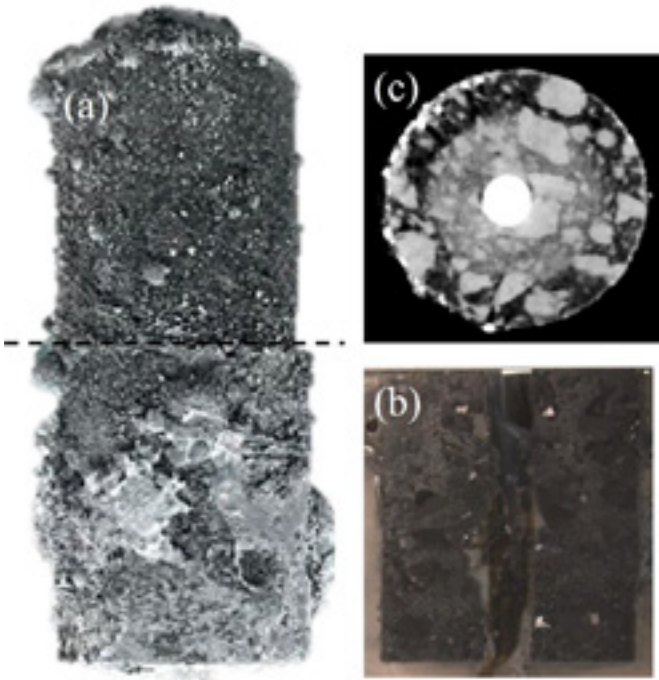


*Fig. 1. Analysis images of MgO-C specimen after the experiment at the condition of 1550℃ and Ar blowing (a) appearance, (b) optical image of vertical cross-section (c) X-ray CT image*

Tab. 1: Chemical composition of MgO-C

| Element | MgO | Carbon | Antioxidant(Al) | Others (CaO, SiO$_2$,etc) |
|---|---|---|---|---|
| Pct in Weight | 78.2 | 15.5 | 3.6 | 2.7 |

Tab. 2: Chemical composition of pure steel

| Element | C | Si | S | P | Mn | Ni | Al | O | etc | Fe |
|---|---|---|---|---|---|---|---|---|---|---|
| Pct in ppm | < 20 | < 10 | 10 | 12 | < 25 | < 5 | < 5 | 145 | < 10 | Bal. |

surface degradation was observed. As seen in eq. 2, the internal degradation ratio was calculated as the black & white phase area ($A_d^I$) from the X-ray CT image among the total area ($A_0^I$) of the cross-section of the specimen. In the case without blowing, the internal degradation ratios were 8, 31, and 58% at 1550, 1600, and 1650℃, respectively. In the case with Ar blowing, the internal degradation ratios were 47, 100, and 100% at 1550, 1600, and 1650℃, respectively. At the same temperature, the internal degradation always increased with Ar blowing.

$$\text{Internal degradation ratio} = A_d^I/A_0^I \tag{2}$$

It is well known that MgO and carbon react at temperatures above 1400℃, which forms Mg and CO vapor [4]. It can be explained by chain reactions of carbothermic reduction reaction of MgO by eq. 3 of the solid-solid reaction (direct reaction) and eqs. 2 and 3 of the solid-gas reaction (indirect reaction) [9,10].

$$MgO_{(s)} + C_{(s)} = Mg_{(g)} + CO_{(g)} \tag{3}$$
$$MgO_{(s)} + CO_{(g)} = Mg_{(g)} + CO_{2(g)} \tag{4}$$
$$C_{(s)} + CO_{2(g)} = 2CO_{(g)} \tag{5}$$
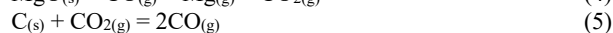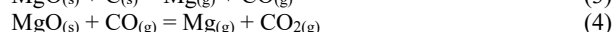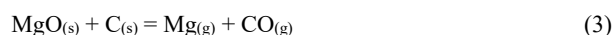
Several studies have been conducted on the degradation mechanism of MgO-C in an inert atmosphere. As seen in Fig. 2, Lee et al.[10] reported that the degradation mechanism of MgO-C. In their observation by X-ray CT, the degraded matrix of MgO-C was generated at the outside of the surface and progressed inward. Compared to their X-ray CT results, the degradation behavior of present study was similar in this study.
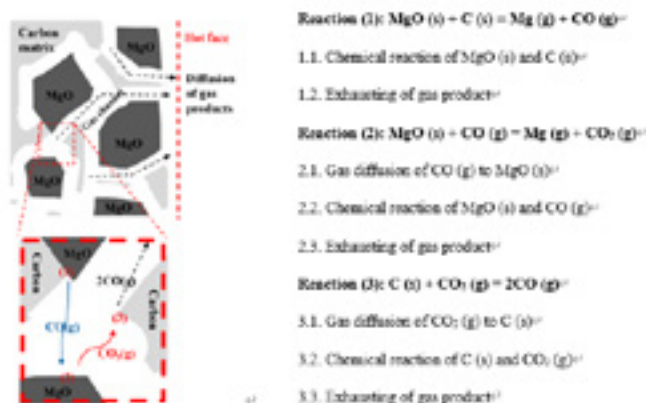


*Fig. 2. Kinetic steps of degradation of MgO-C [10]*

**Interfacial reaction between MgO-C and liquid steel without/with Ar blowing**

The composition changes in liquid steel were analyzed as a function of time. As seen in eqs. 6 and 7, CO and Mg vapors generated from MgO-C can be dissolved into liquid steel [11].

$$CO_{(g)} = C_{(in\ Fe)} + O_{(in\ Fe)} \tag{6}$$
$$Mg_{(g)} = Mg_{(in\ Fe)} \tag{7}$$
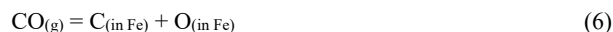
In the case without blowing, carbon content increased from about 20 ppm to about 120 ppm at 20 min and then it remained unchanged until 80 min. In the case with Ar blowing, carbon content increased from about 20 ppm to about 45 ppm at 20 min before Ar blowing, and then continuously increased until about 340 ppm after 80 min during Ar blowing. An increase in carbon content during Ar blowing can be reasonably explained by C-O deoxidation equilibrium in liquid steel as seen in eq. 8 [11]. The oxygen content was 12 ppm at 80 min with Ar blowing. The $P_{CO}$ was obtained 0.11 atm based on equation 1 at 1600℃. The equilibrium carbon content was calculated to be 0.18%. It can be though that carbon content was increased by the CO vapor.

$$K = ([\%C][ppmO])/(P_{CO}(atm)) = 20 \tag{8}$$

The Mg content did not changed without/with Ar blowing, which can be explained by Mg-O deoxidation equilibrium in liquid steel as seen in eq. 9 [12].

$$Mg_{(in\ Fe)} + O_{(in\ Fe)} = MgO_{(s)} \tag{9}$$

Brabie reported the formation of a MgO-based oxide layer at the interface between MgO-C and liquid steel [7]. As seen in Fig. 3, MgO layer was formed at the interface between MgO-C and liquid steel. The thickness increased with an increasing temperature and Ar blowing. However, there was no MgO layer with Ar blowing at 1650℃, which was due to the bursting of the specimen.
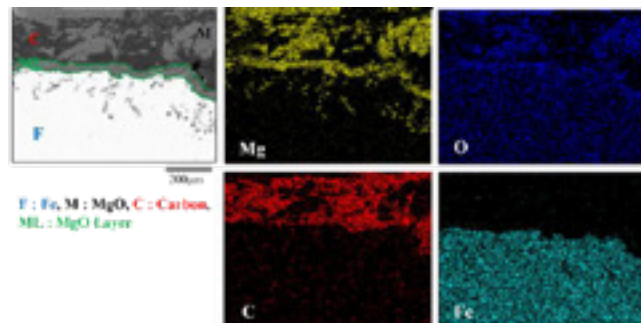


*Fig. 3. FE-SEM/EDS mapping images of the interface at 1600℃ without blowing*

**Conclusion**

We studied the degradation behavior of a MgO-15%C by Ar blowing in contact with liquid in experiments using a high frequency induction furnace for 4 hr at a temperature range between 1550 and 1650℃. The results are as follows.

1. No surface degradation of MgO-C was observed without blowing at the experimental temperatures, but it was observed with Ar blowing over 1600℃. The surface degradation ratios with Ar blowing were 9 and 29% at 1600 and 1650℃, respectively.

2. Internal degradation of MgO-C was observed using X-ray CT. In the case without blowing, the internal degradation ratios were 8, 31, and 58% at 1550, 1600, and 1650℃, respectively. In the case with Ar blowing, the internal degradation ratios were 47, 100, and 100% at 1550, 1600, and 1650℃, respectively.

3. The degradation reaction can be though to be the chain reactions of carbothermic reduction reaction of MgO.

4. The carbon content in the liquid steel increased with time. Ar blowing continuous increased the carbon content. The Mg content in the liquid steel did not change significantly with time regardless of Ar blowing, as a MgO layer was formed at the interface.

**REFERENCES**

[1] Kirschen M, Hanna A, Ehrengruber R and Zettl K. Latest developments in gas purging systems for EAF. In AISTech 2015 Conference Proceedings Vol. 2, 2015, pp. 1974-1983

[2] Kakihara M, Yoshioka H, Hashimoto M & Inoue K. Development of a New Spalling Test Method for Bottom Blowing Tuyeres for BOFS. In Proceedings of the Unified International Technical Conference on Refractories (UNITECR 2013), 2014, p. 83, John Wiley & Sons

[3] Lin L, Xiaoyan P Fei G and Hewei D. Improvement and Maintenance of MgO-C Bottom-Blowing Tuyere in BOF Converter for Prolonging Service Life. In Proceedings of the Unified International Technical Conference on Refractories (UNITECR 2013), 2014, p. 721, John Wiley & Sons

[4] Leonard R J and Herron R H. Significance of oxidation-reduction reactions within BOF refractories. Journal of the American Ceramic Society, 55(1), 1972, pp. 1-6.

[5] Jansson S, Brabie V and Jönsson P. Magnesia–carbon refractory dissolution in Al killed low carbon steel. Ironmaking & steelmaking, 33(5), 2006, pp. 389-397

[6]   Russo A A, Smith J D, O'Malley R J and Richards V L. Mechanism for Carbon Transfer from Magnesia-Graphite Ladle Refractories to Ultralow-Carbon Steel. Iron Steel Technol, 2016, pp. 134-143

[7]   Brabie V. A study on the mechanism of reaction between refractory materials and aluminium deoxidised molten steel. Steel research, 68(2), 1997, pp. 54-60

[8]   Liu C, Huang F, Suo J and Wang X. Effect of magnesia-carbon refractory on the kinetics of $MgO \cdot Al_2O_3$ spinel inclusion generation in extra-low oxygen steels. Metallurgical and Materials Transactions B, 47, 2016, pp. 989-998

[9]   Hino Y and Takahashi K. Effects of Temperature and Carbon Content in Brick on MgO–C Reaction Behaviour. ISIJ International, 61(10), 2021, pp. 2513-2523

[10]  Lee J, Myung J and Chung Y. Degradation kinetics of MgO-C refractory at high temperature. Metallurgical and Materials Transactions B, 52, 2021, pp. 1179-1185

[11]  Turdogan E T. Fundamentals of steelmaking. The Inst. of Materials, 1996

[12]  Itoh H, Hino M and Banya S. Thermodynamics on the formation of non-metallic inclusion of spinel ($MgO \cdot Al_2O_3$) in liquid steel. Tetsu-to-Hagané, 84(2), 1998, pp. 85-90

# HYDROGEN: AN ISSUE AND A NEW CHALLENGE FOR THE DURABILITY OF REFRACTORIES

**Jacques Poirier, CEMHTI-CNRS / University of Orléans, France**

## ABSTRACT

To achieve the objectives of the energy transition, green and renewable hydrogen could contribute to decarbonizing many industrial sectors: steel, glass, cement, ceramic industry.

However, the deployment of hydrogen technologies requires removing of barriers concerning the durability and corrosion of refractory materials.

Refractory industrial issues for decarbonated steelmaking, new energies (production of bio syngas), hydrogen enrichment of the atmosphere of furnaces will be approached with an innovative perspective. Approaches combining experimental methods and digital tools and making it possible to provide industrial solutions will be detailed in this paper:

- "Post-mortem" observations
- Thermodynamic calculations
- Experiments (corrosion tests) and high temperature characterizations (Raman, HT-DRX, HR-TEM, SEM) on a laboratory scale to identify key parameters and deduce reaction kinetics
- Evolution of microstructures at the micro and nanometric scale

Examples concerning the durability and corrosion of refractories will illustrate this approach.

- Volatilization, reduction, or fusion of refractory oxides ($SiO_2$, $Fe_2O_3$, alkaline)
- Boudouard reaction under $CO/H_2$
- Degradation by $H_2O$
- Other effects (Marangoni effect, ….)

## CONTEXT

Global greenhouse gas emissions produced by industry represent respectively 21% in 2010 and 18% in 2022 of total emissions. Table 1 shows the quantities of $CO_2$ produced to manufacture one ton of steel, glass, cement, or aluminum.

Tab. 1: $CO_2$ produced per ton of materials.

| Aluminum | Steel | Cement | Glass (packaging) |
|----------|-------|--------|-------------------|
| 8,6 t | 1,85 t | 0,86 t | 0,9 t |

The use of green hydrogen is a major challenge to decarbonize the high temperature industry:
- Supply carbon-free energy to industrial units
- Contribute to the decarbonization of high-temperature processes to replace the fossil fuels currently used.

The reduction of iron ores by green hydrogen for steelmaking is the most emblematic example.

Consequently, hydrogen is an issue and a new challenge for the durability of refractories.

The objectives of this research are:
- Understand the effect of $H_2$ on the damage of refractory ceramics at high temperature
- Provide recommendations to increase their durability in use
- Present the example of hydrogen for steel making.

## MECHANISMS OF REFRACTORY DAMAGE BY $H_2$

In contact with hydrogen, 5 main corrosion/damage reactions can occur (Figure 1).
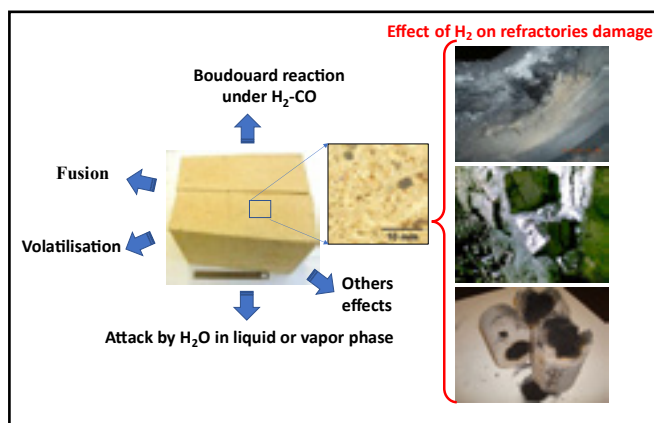


Fig. 1: Main mechanisms of damage by $H_2$ [1]

## FUSION OF REFRACTORY OXIDES

Under $H_2$, a refractory such as a fire clay brick with <1% $Fe_2O_3$ can melt locally (Figure 2). This degradation, which occurs at high temperatures > 1000°C, is explained by the reduction of iron oxides by hydrogen :

$$Fe_2O_3(s) + H_2(g) = 2FeO(s,l) + H_2O(g)$$
$$FeO(s,l) + H_2(g) = 2Fe(s,l) + H_2O(g)$$
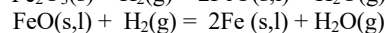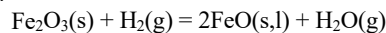
$Fe_2O_3$ particles are present in the refractories as impurities in raw materials and by attrition of the mixing devices while blending the refractory formulation.
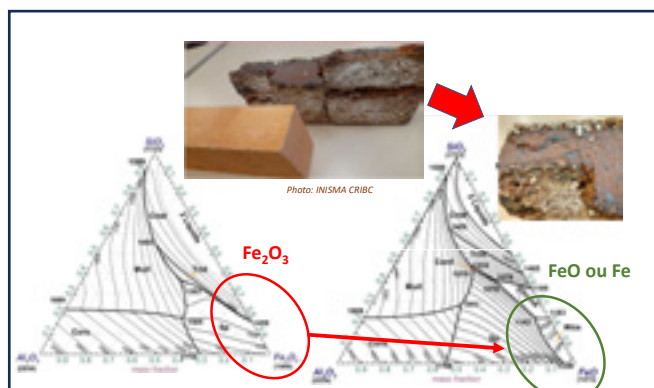


Fig. 2: Partial fusion of $Al_2O_3$-$SiO_2$ refractory due to hydrogen [1]

The phase diagrams $Al_2O_3$-$SiO_2$-$Fe_2O_3$ and $Al_2O_3$-$SiO_2$-$FeO$ confirm this hypothesis and show that temperatures of the liquidus fall under reducing conditions.

Refractory performance can be improved by the selection of raw materials with a low content of iron particles and by raising the refractory sintering temperature.

## VOLATILIZATION OF REFRACTORY OXIDES

Figure 3 shows the effect of hydrogen containing 5 ppm $H_2O$ at 1300°C for 500h on the microstructure of a high alumina refractory. After testing, the EDS mapping of the silicon shows the partial disappearance of the silica in the matrix. The open porosity increases, and the vitreous phase is corroded.

There is a reduction of the oxides by $H_2$ and the volatilization of $SiO(g)$ according to the reactions:

$$SiO_2(s) + H_2(g) = SiO(g) + H_2O(g)$$

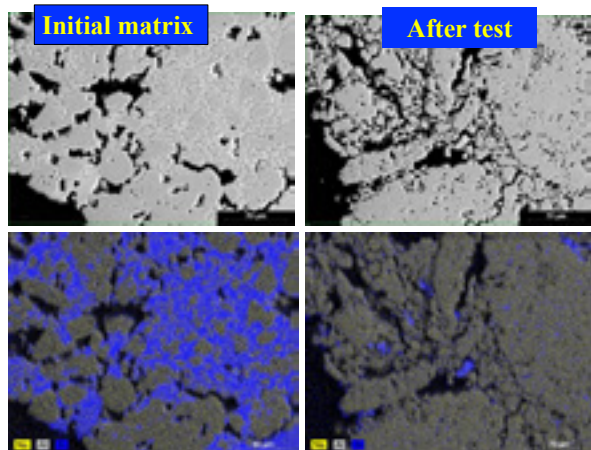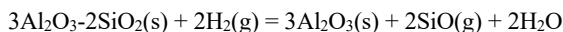$$3Al_2O_3-2SiO_2(s) + 2H_2(g) = 3Al_2O_3(s) + 2SiO(g) + 2H_2O$$
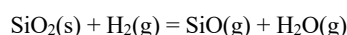


Fig. 3: Evolution of the microstructure of a high alumina refractory after 500h at 1300°C under $H_2$ containing 5 ppm $H_2O$.

The reduction by $H_2$ concerns the oxides which are thermodynamically the least stables: $SiO_2$, $Fe_xO_y$, alkali.

The partial pressure of $H_2O$ plays a major role. As an example, the Ellingham diagram (Fig. 4) shows that, at 1300°C, $SiO_2$ is reduced by $H_2$ if $P(H_2)/P(H_2O) > 10^5$.

Practical recommendations can be proposed:

- Increasing the partial pressure $P(H_2O)$ inhibits the reducing effect of $H_2$
- Avoid "free" silica for T > 1000°C. Mullite $3Al_2O_3$ -$2SiO_2$ is less sensitive to $H_2$
- Favor stable oxides $Al_2O_3$, $ZrO_2$, $MgO$
- Optimize microstructures.
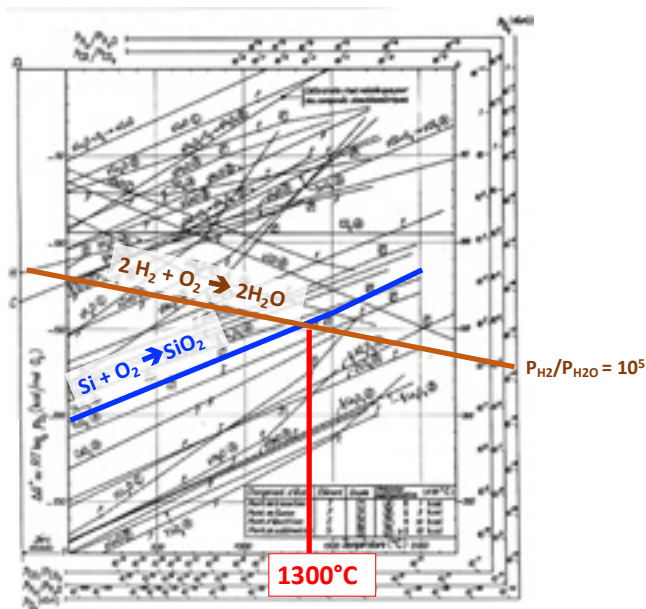
Fig. 4: Determination of silica reduction conditions using the Ellingham diagram.

**BOUDOUARD REACTION UNDER CO/$H_2$**

The mechanism of carbon monoxide decomposition: $2CO(g) \rightarrow CO_2(g) + C(s)$ results in the deposition of solid carbon. It causes premature degradation of refractories (Fig.5). This reaction occurs at temperature ranging between 400 to 900°C with a maximum intensity around 600 °C and is highly favored by the presence of catalytic particles such as iron and iron oxides [2].
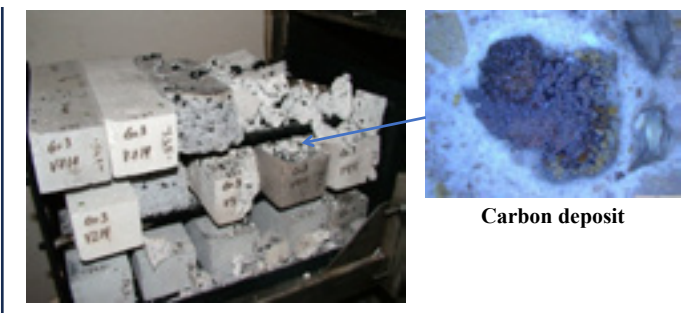


Fig. 5: Degradation of refractories by Boudouard reaction

When refractories are subjected to CO and $H_2$ reducing atmospheres (Biomass and Coal Gasification, Steam Methane Reformers, Direct Reduction shafts.....), the Boudouard reaction becomes more efficient. $H_2$ favours the nucleation and growth of carbon filaments on the iron-carbide particles.

Raman spectroscopy is an ideal technique to characterize in situ $sp^2$ carbon materials. It is the most sensitive to explore the full range of the structural states from perfectly crystalline to amorphous [3].

The typical Raman spectrum of "$sp^2$ carbon" is reported in Fig. 6 and shows three prominent features. The so-called G band located at approximately 1580 $cm^{-1}$ and corresponds to the in-plane bond stretching of carbon atoms ($E_{2g}$ symmetry). When defects are present, the crystal symmetry breaks down and additional bands appear at specific frequencies depending on the excitation energy used. These bands are called the defect bands: D ($\approx$1250-1400 cm-1) and D' ($\approx$1600-1630 cm-1). At relatively low defect density, the intensity ratio of the defect-induced D band and the symmetry-allowed G band increases with disorder.

Pure iron and iron oxides powders were submitted for 30 minutes at 600°C under reducing atmosphere: 100% CO and CO+$H_2$ mixture (industrial gas).

Fig. 6 summarizes the results obtained using Raman spectroscopy and TEM. Raman spectra of the carbon formed in the two types of gas are totally different. G band is observed in the carbon formed under 100% CO and D and G bands are observed when the gas is a mixture of CO and $H_2$.
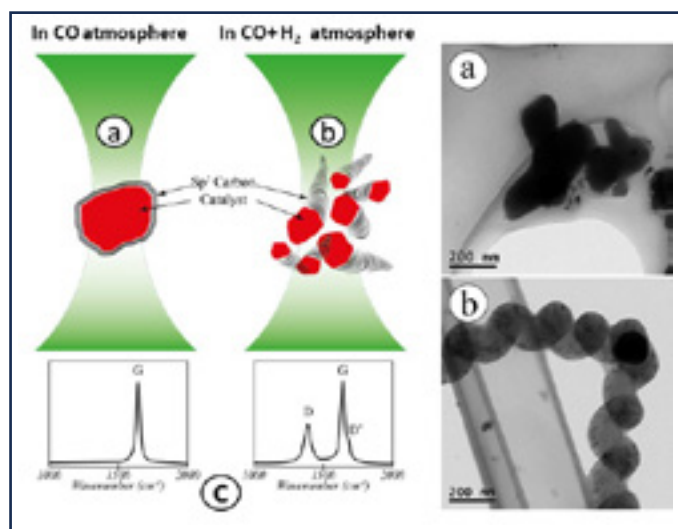


Fig. 6: Schematic representation of the interaction of the Raman excitation laser and the carbon particles in shell around catalyst particles in 100% CO and in nano-fibers in CO + $H_2$ atmosphere. TEM micrographs of nano-carbon shells and filaments formed à 600°C in a- 100%CO and b- 70.0% CO, 3.0% $CO_2$, 10.0% $H_2$ and 17.0% $N_2$ from $Fe_2O_3$ nanometer size catalyst.

In CO atmosphere, well organized sp² carbon is formed around the catalyst particles and the defect-induced D bands are not observed. Only chemical reduction of the catalyst particle occurs without significant size reduction. Therefore, poly-aromatic layers are formed around the catalyst particles in the form of encapsulating shells. These layers are sufficiently large with regards to the laser diameter which explains the no activation of the defect-induced D band in the corresponding Raman spectrum [4]. In CO + H₂ atmosphere, the corresponding Raman spectrum exhibits the defect induced D band suggesting disordered carbon. Catalyst particles are chemically reduced and highly fragmented. Therefore, small-sized carbon nanofibers are formed exhibiting a large amount of poly-aromatic boundaries. This eventually leads to the activation of the defect induced D band without the local structural order being necessarily disturbed [5].

Figure 7 reports the different steps of the formation of carbon nanofibers by the Boudouard reaction in CO-H₂ atmosphere:

- Step 1: Fragmentation of iron oxides to nanometer-sized grains and reduction by H₂ with formation of suboxides of iron (Fe₂O₃ ➔ FeO ➔ Fe)

- Step 2: Formation of Fe₃C nanoparticles

- Step 3: grow of polyaromatic carbon nanofibers.
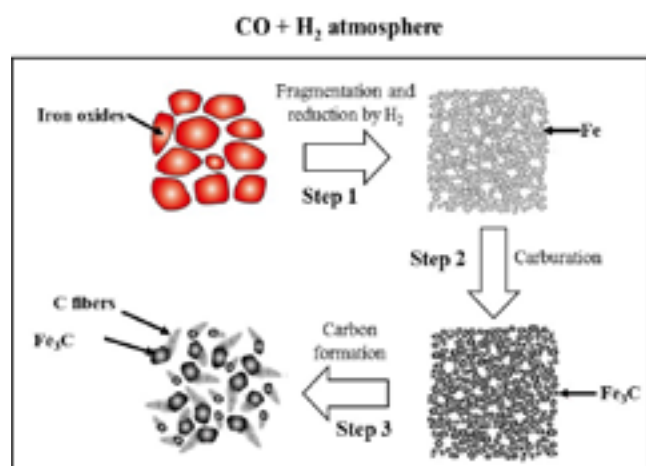


Fig. 7: Mechanism of carbon nanofibers formation by the reverse Boudouard reaction in CO-H₂ atmosphere

Sulphur is an efficient inhibitor to limit the carbon formation [6]. From 100 ppm of $SO_2(g)$, the carbon growth rate decreases by a factor of 70 compared to an experiment without inhibitor. In a CO/H2 atmosphere at 600 °C, iron oxide particles are chemically reduced to $Fe_3C$ and their sizes decrease. With the addition of sulphur such as 100 to 1000 ppm of $SO_2(g)$, the size of iron oxide particles ($Fe_2O_3$) decreases to a lesser extent but are still reduced to cementite ($Fe_3C$) and to Hägg iron carbide ($Fe_5C_2$). The sulphur intake has contributed to the formation of a very thin FeS layer (0.5–1 nm) around the iron carbide particles, preventing the catalytic effect of the Boudouard reaction (Fig. 8).
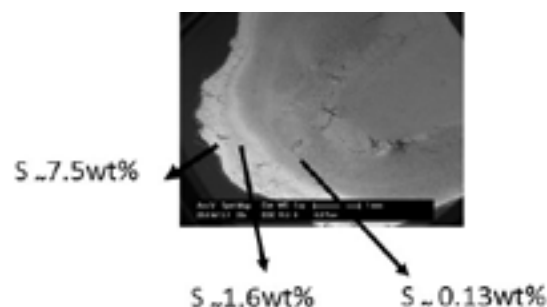


Fig.8: SEM micrograph of iron sulphides at the surface of catalytic iron particles.

Sulfur stabilizes iron carbides so that it can be heated above 600°C without decomposition.

Sulfur does not prevent the reduction of $Fe_2O_3$ by $H_2$ and the fragmentation of the $Fe_2O_3$ grains. Nevertheless, it prevents the formation of sp2 carbon. Sulfur diffuses into the crystallite structure or through the grain boundaries. Moreover, it is not necessary to transform all the iron into iron sulphides to inhibit the reverse Boudouard reaction. Figure 9 reports the mechanism of carbon inhibition in CO-H₂ atmosphere.

To sum up, lab experimentations show

- In the presence of pure CO gas, a carbon with a high structural organization and an important coherent domain diameter is produced in the form of shells around the catalyst particles.
- In the presence of a CO and H₂ mixture, a carbon with a nanofiber morphology is favored.
- In the presence of CO and H₂ mixture with an addition of S, the catalytic effect of the iron oxide particles is prevented.
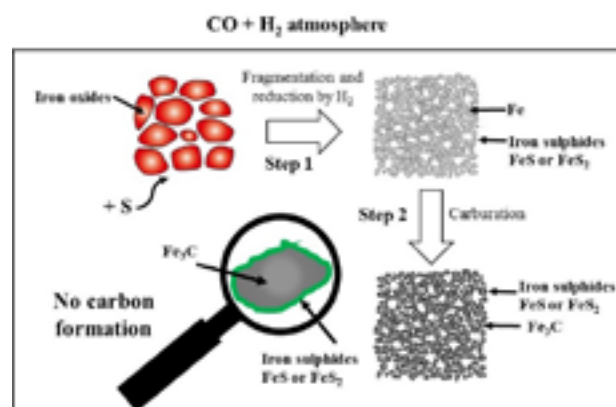


Fig. 9 Inhibition of carbon formation by S in CO-H₂ atmosphere.

### ATTACK BY H₂O IN LIQUID OR VAPOR PHASE

The combustion of hydrogen produces $H_2O(g)$ which can corrode the refractories.

Silica (in the presence of NaOH, HBO₂, SO2 vapors) forms hydroxides at a temperature T> 1000 – 1200°C.

- $SiO_2(s) + H_2O(g)$ ➔ $SiO(OH)_2(g)$
- $SiO_2(s) + 2 H_2O(g)$ ➔ $SiO(OH)_4(g)$
- $SiO_2(s) + 3 H_2O(g)$ ➔ $SiO(OH)_6(g)$
- $SiO_2(s) + 0,5 H_2O(g)$ ➔ $SiO(OH)(g)+ 0,25 O2(g)$

Silicon carbide is protected by a surface layer of silica which is vulnerable to H₂O and at high temperatures (Fig. 10)
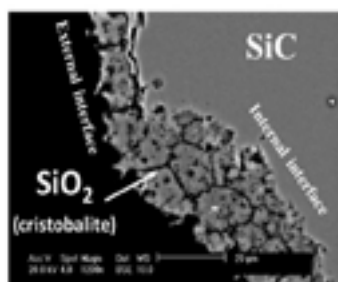
865

*Fig.10 Damage to the projective silica layer in a hydrogenated atmosphere in the presence of alkali chloride vapors*

Sulphur combines with water vapor to form acidic compounds. These acidic compounds condense at low temperatures (<600°C) and attack the ceramic fibers (Fig. 11)



*Fig.11. Alteration of ceramic fibres by sulphuric acid after 3 months*

## OTHER EFFECTS

Corrosion mechanisms at the triple point – refractory/bath/ atmosphere (Marangoni effect) can be modified due to a modification of the surface tension in presence of a hydrogen atmosphere.

## AN EMBLEMATIC EXAMPLE OF THE FUTURE USE OF $H_2$: THE STEEL MAKING

Hydrogen is of great interest, replacing the fossil fuels currently used, to supply industrial units with carbon-free energy and contribute to the decarbonization of processes. The most emblematic example is the manufacture of steel: why not reduce iron ores with green hydrogen?
The basics of iron and steel are based on two chemical reactions: the oxidation of carbon by oxygen which produces CO and the reduction of iron oxides by carbon monoxide to form iron with a little carbon, with the production of $CO_2$.

$2 C(s) + O_2 \rightarrow 2 CO$
$Fe_2O_3 + 3 CO \rightarrow 2 Fe_{(l)} + 3 CO_2$
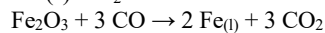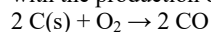
For one ton of steel, 1.8 tons of $CO_2$ are produced, and in 2022 the world steel industry produced 2.6 billion tons of $CO_2$, i.e. between 7 and 9% of global emissions, which is colossal.

The future challenge is a 30% reduction in the $CO_2$ produced by 2030 to achieve carbon neutrality by 2050, thanks to "green" steel.
Instead of reducing the iron oxides by carbon monoxide, a reduction by hydrogen is used:
$Fe_2O_3 + 3 H_2 \rightarrow 2 Fe(s) + 3 H_2O$
The steel plant will be then totally transformed, without blast furnaces and BOF convertors, but industrial units called the direct reduction and electric furnaces associated with a hydrogen production unit. The hydrogen is introduced into a preheater and sent to the reactor, the temperature of which is between 500 and 1200°C. Iron ore is introduced and pre-reduced iron ores, known as DRI
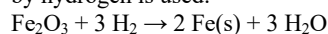
(Direct Reduction Iron), are obtained through the hydrogen reduction of iron oxide.
These new processes will impact the refractories, in particular the corrosion of refractories by hydrogen occurs (Fig.13). $H_2$ reduces silica. The $H_2$ corrosion will be associated with attacks by acids, abrasion, and thermomechanical stresses [7].
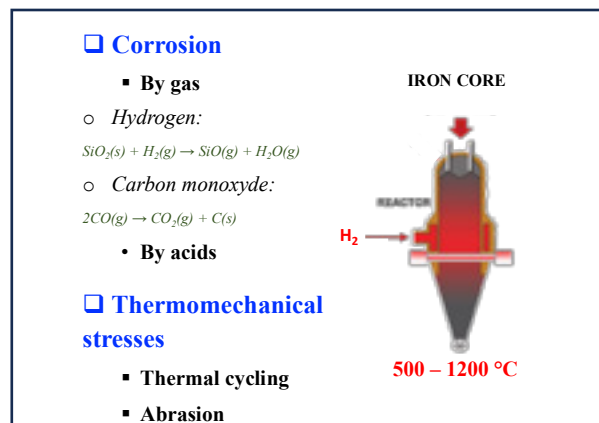


*Fig.12 Solicitations of refractories for DRI technology (direct reduction*

## CONCLUSIONS

Green hydrogen is a promising avenue for the energy transition. A wide field of scientific and technological progress remains to be made for the optimal choice of refractories and lead to mature and competitive high temperature processes.

## REFERENCES

[1] T. Poirier, Impact of adding H2 to fuel on refractory materials Conference : Materials used in extreme conditions, May 24 and 25, 2022 in Moncel-les-Luneville

[2] Krause O., Pötschke J., The predictability of CO resistance of refractory materials by state-of-the-art test methods - a technical and scientific approach, Interceram 57, 2008: 176-180.

[3] Bost N., Ammar M.R., Bouchetou, Poirier J, The catalytic effect of iron oxides on the formation of nanocarbon by the Boudouard reaction, J. Eur. Ceram. Soc. 2016; 36: 2133–2142

[4] Walker P.L., Raicszawski J.F., Imperial G.R, Carbon formation from carbon monoxide-hydrogen mixtures over iron catalysts. J. Phys. Chem. 1959; 63:140–149.

[5] Turkdogan E.T., Vinters J.V., Catalytic Effect of Iron on Decomposition of Carbon Monooxide: I. Carbon Deposition in $H_2$-CO Mixtures, Metall. Trans. 1974; 5: 11–19.

[6] Bost N., Canizares A., Ammar M.R, Raimboux N, Melin P., Simon P., Poirier J. Probing the structural organization of sp2 carbons obtained by the Boudouard reaction using in situ Raman scattering in reducing conditions, Vibrational Spectroscopy 2016; 87: 157-163

[7] Van Beudeen P. The new face of the steel industry & its effect on refractory management, Fire Summer School Aachen 2022

# STATUS AND CHALLENGES OF HYDROGEN CONTAINING FUELS ON POROUS CERAMIC MATERIALS AND PROTECTIVE SYSTEMS IN THE ENERGY INDUSTRY

Holger Grote[1]; Reiner Anton[1]; Arturo Flores Renteria[2]; Christian Nikasch[1]; Ivo Krausz[2]

[1]Siemens Energy, Ceramic and Coatings, Mülheim an der Ruhr, Germany; [2]Siemens Energy, Ceramic and Coatings, Berlin, Germany

As the world continues to move forward with ambitious decarbonization targets, the European Union has set goals to cut $CO_2$ emissions by 55% by 2030.

One opportunity to achieve this goal is blending green hydrogen with natural gas as fuel for power generation.

However, there is no siginificant contribution of hydrogen to the electricity generation as of today.

Siemens Energy is leading the way by providing the world's first proof of concept for hydrogen co-firing and hydrogen fireing in gas turbines in combined cycle application. The presentation highlights challenges and possible solutions for the use of porous ceramic protection systems in power plants. Furthermore, we will address alternative applications in the future of the hydrogen and energy industry.

# H₂-CHANGE: REFRACTORIES UNDER ATTACK OF CHALLENGING ATMOSPHERES DURING TRANSFORMATION PROCESS

Dipl.-Ing. Jens Sperber*, Technical Director
Franz-Josef Duennes, Head of Engineering/Design Department

STEULER Linings
Georg-Steuler-Str., 56203 Höhr-Grenzhausen, Germany
Phone: +49 2624 13367
Email: jens.sperber@steuler-kch.de

## INTRODUCTION

Our modern industrialised society is focussing on a new challenge regarding our own living environment. Therefore a change in mind and a change in economy is unavoidable. We can call this a global green deal as a basis for a sustainable economy.

To reach this aim the emissions of greenhouse gases have to be reduced. Only one part but of very high importance. Consequently a lot of transformation of industrial processes is needed. Caused by a long existing alternative process and therefore a high possible decrease of emissions the steel industry gets into this focus of transformation. Namely the direct reduction process will be one of the major production routes for iron and steel in the future.

In this paper common and advanced lining materials for gas driven DRI shaft furnaces are discussed. Based on more than 15 years of experience STEULER Linings shows some examples of lining solutions for the different major processes. Based on reformed natural gas as a standard we will take a closer look to the transformation route via hydrogen boosted coke oven gas in an integrated steel plant up to the pure hydrogen use in a pilot plant.

Especially by using different gases such as hydrogen, methane, carbon monoxide and water vapour and mixtures of these gases as attacking agent. Therefore we are will show the first result of tests made in a STA equipment where we are able to use these different gases under different pressures up to app. 72 psi and temperatures up to 2550 F. Whereas the transformation process with different gas compositions will be the real challenge we will focus in the first step on the hydrogen attack of standard and advanced brick material.

In another part of the paper the usual wear of lining materials for DRI shaft furnaces will be discussed. This will be done for both gas driven DRI processes.

## LINING CONCEPTS

### Improvement of gas inlet area

In this paper we will focus on the two major gas driven processes. One in a non-pressurised and the second one in a pressurised vessel. Both types of DRI shaft furnaces were lining with more or less a comparable refractory material. Most critical lining areas are the lower and upper shaft lining and especially the gas inlet area. The lining of this area in a non-pressurized reactor was always done with some special shaped so called port blocks. This area in a pressurized vessel were originally done by using small-format special shapes with small-size interlocking. Due to high mechanical loads, damage often occurs in this area because the "noses" break off and the brickwork loses stability. On the following pages we show the steps of improvement during a time frame of 5 years starting with the insufficient original lining design.

During a certain time of design review and inspections of old and new lining design we finally installing nowadays only the below mentioned lining design shown in pictures 4 to 6.

Very impressive to see was the behaviour of the old design after app. 18 month of operation. The brick arrangement in the gas inlet area was shifted by around 2 inch inside the reactor. Usually not possible but indeed it happened. On the other side it can be seen that the brick material itself shows fortunately more or less no wear. Anyway we came to the conclusion to provide a new design for the repair work based on special shaped bricks in a double layer design corresponding to the usual lining

concept of a pressurized vessel. Installation was done in 2016 and the inspection after 2 years in 2018 showed no issues regarding the design and the material used for this modification.
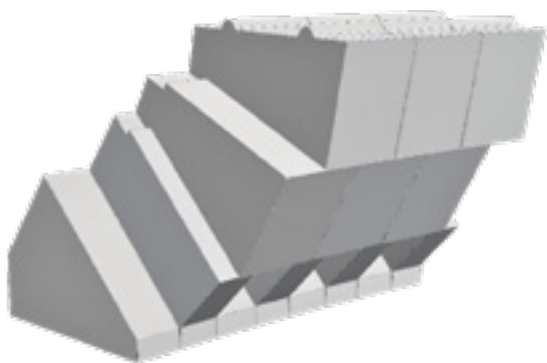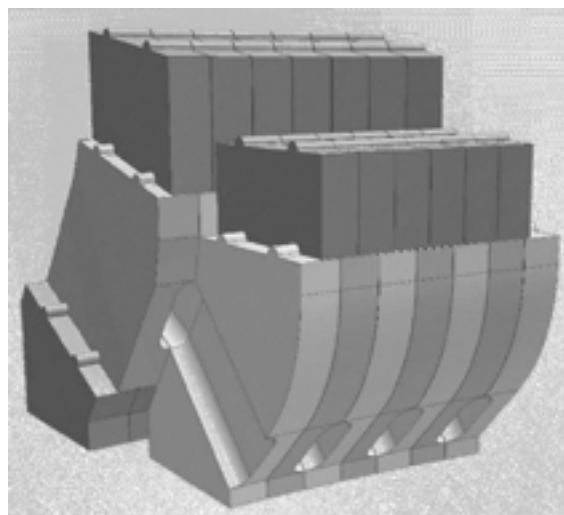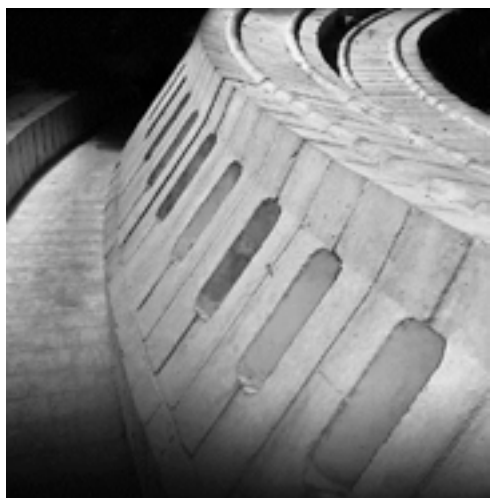


Picture 1. Design gas inlet area 2013



Picture 2. Gas inlet area 2013 during installation



Picture 3. Gas inlet area 2014 shifting of the lining



Picture 4. Gas inlet area redesign 2016



Picture 5. Gas inlet area installation 2016



Picture 6. Gas inlet area inspection 2018

869

Table 1. Properties of different types of lining material for DRI shaft furnaces

| | Unit | Fireclay brick | Mullite fireclay brick | Mullite/Corundum brick |
|---|---|---|---|---|
| Chemical Analysis | | | | |
| $Al_2O_3$ | [wt%] | 45 - 55 | 60 – 75 | 88 – 92 |
| $SiO_2$ | [wt%] | 40 – 50 | 20 – 35 | 9 – 11 |
| $TiO_2$ | [wt%] | 1.5 - 2 | 0.5 – 1.5 | 0 – 0.1 |
| $Fe_2O_3$ | [wt%] | 1 – 1.5 | 0.6 – 1.2 | 0 – 0.2 |
| $P_2O_5$ | [wt%] | 0 - 4 | 0 - 4 | < 0.05 |
| Physical Properties | | | | |
| Bulk Density | [g/cm³] | 2.35 – 2.45 | 2.55 – 2.75 | 2.95 – 3.03 |
| Apparent Porosity | [vol. %] | 14 – 18 | 14 – 18 | 14 - 18 |
| Cold Crushing Strength | [MPa] | 45 – 65 | 60 - 100 | 80 - 100 |
| Youngs' Modulus | [MPa] | 20,000 – 30,000 | 15,000 – 25,000 | 15,000 – 20,000 |
| Thermal Expansion Coefficient | $[*10^{-6}/K]$ | 5.5 – 6.5 | 5.8 – 6.5 | 5.8 – 6.2 |

The original brick material was a kind of Mullite fireclay brick whereas the special shaped gas inlet bricks of the new design were made as high fired Mullite/Corundum brick.

**Expansion joint and support rings**
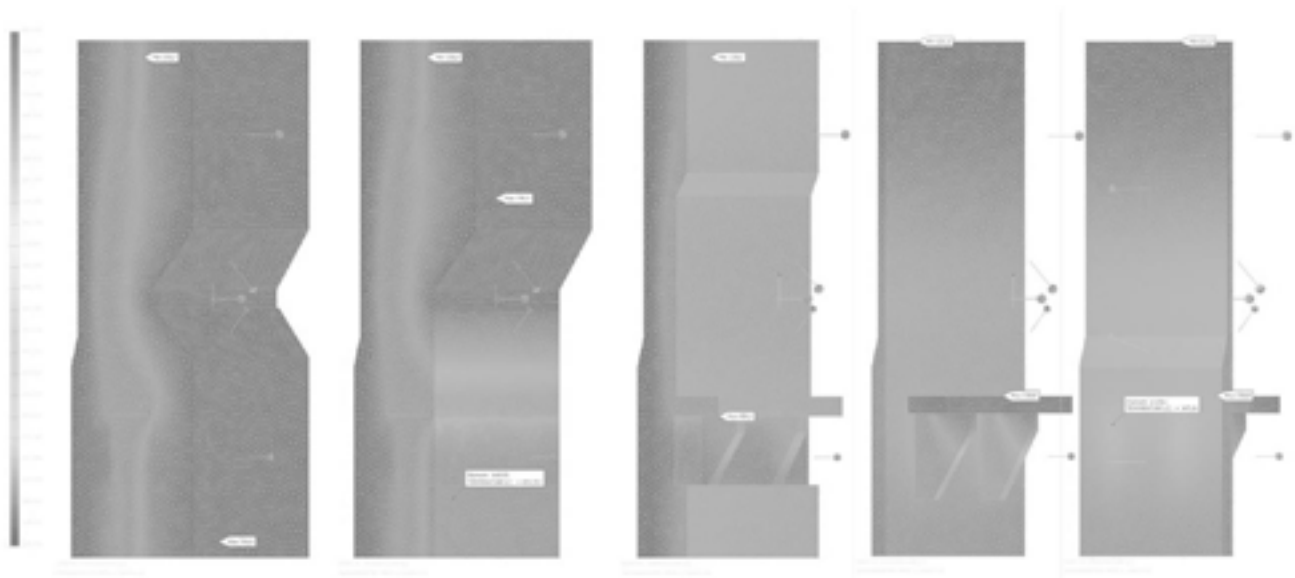


Picture 7. 3D Visualization of temperature distribution at expansion joint and steel support ring

Due to the thermal conductivity of the support ring made of steel we see a higher temperature on the steel shell outside. The areas with an increased risk for hotspots are clearly visible. Detailed adjustments to the lining concept of these areas can

be implemented and evaluated on the 3D model in order to minimize these hotspot areas.

**Reducing gas transfer line inlet**
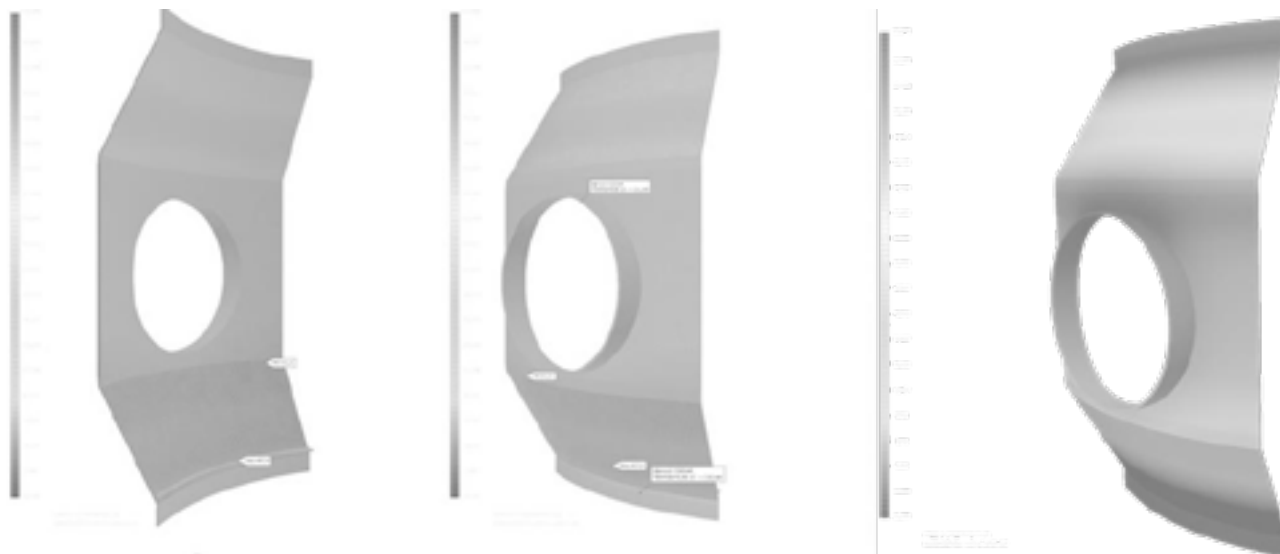


Picture 8. Transfer line connection to vessel upper half with a higher shell temperature

Due to the inlet hot gas stream the temperature on the upper half of the transfer line inlet increases. Therefore the installation of the inside refractory material has to be done very carefully to get a lining with sufficient tightness. Experience shown in the last paper let to the best solution by implementing a ring of special shaped bricks for the connection of transfer line and ring channel of the reactor.

## TYPICAL WEAR OF LINING

**Wear of shaft lining**

On the following pictures 9-10 we see the typical wear of a shaft lining based on mullite-fireclay bricks. Sometimes this happens when a chemical reaction of the pellets and or the coating of the pellets lead to a sticking of the feed to the lining material. Usually only in areas where there is a minor movement of the pellet bed accompanied with a possible temperature excursion. In the area with the highest gas velocity and therefore most turbulence this usually does not occur. So at least the area of the gas inlet nozzle bricks and app. half a meter below we don't see an impact.



Picture 9. Shaft lining with rough surface
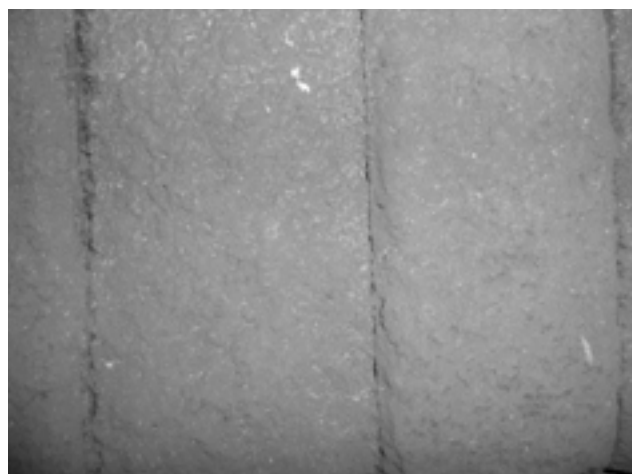
Picture 10. Closer look to the brick surface
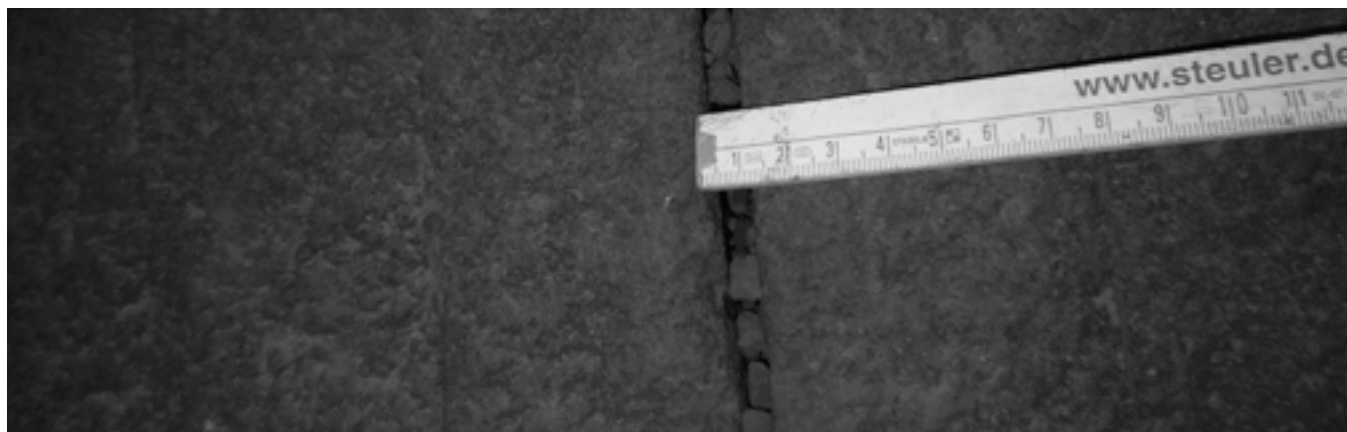
Picture 11. Shaft lining with open joint/expansion joint after shutdown, filled with pellets

Above picture 11 shows a possible situation after a shutdown for maintenance issues. Before restart it is necessary to clean up these joints and remove the pellets. If this happens some measures have to be obtained to avoid a refilling with pellets during the restart operation.

**Mechanical impact**

Another impact may occur if thermal expansion of the lining is not calculated in the right way. Due to uncompensated expansion of the lining the thermal stress can induce a spalling effect on the top surface of the brick lining. On the following picture 12 we see beside this effect above the gas inlet area. And of course above this spalled area we see also an advanced wear of the joints. To avoid such an impact the alignment of mortar and brick material has to be done in a proper way.
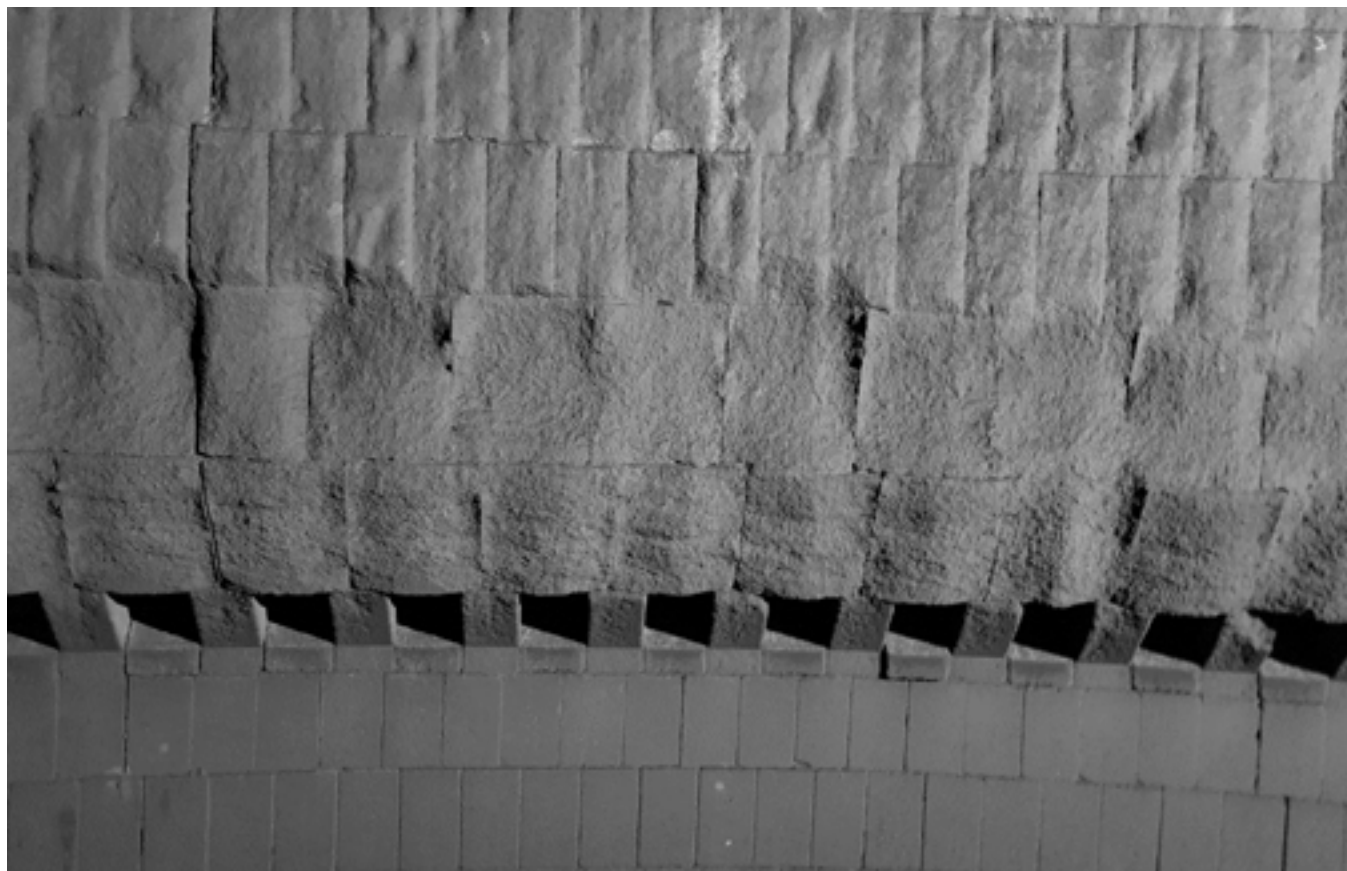
Picture 12. Gas inlet area (old design) with spalled area above and advanced wear of the joints in the upper part

## POST MORTEM ANALYSIS

### Analysis of upper shaft material

The samples for the analysis were taken out of the upper shaft lining above the gas inlet area. In this case the lining was done with a usual blast furnace brick based on fireclay (super duty). The following pictures 13-15 show the pieces for the analysis get out of partially spalled material which was already attached to the brick surface. Beside the brick material we see also a lot of metallic material attached to the brick surface.
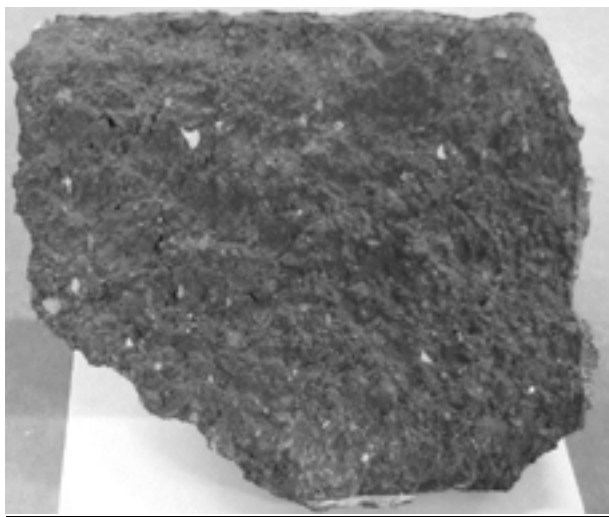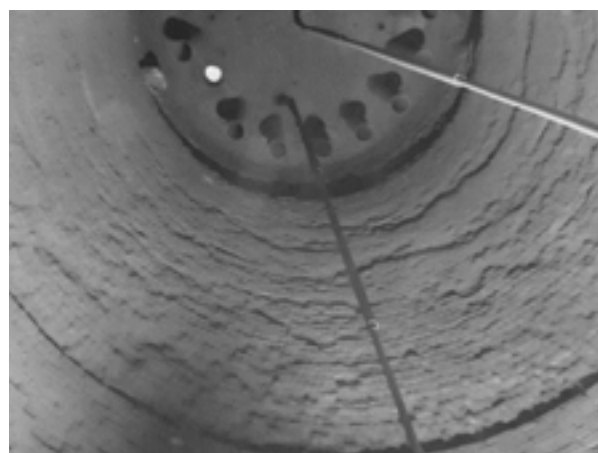


Picture 13. Spalled brick sample – Lab No. 6705-18



Picture 14. Big flake, metallic – Lab No. 6708-18
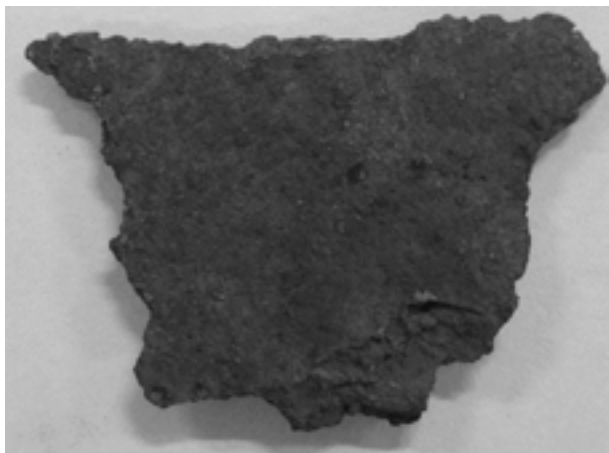


Picture 15. Small flake, metallic – Lab No. 6709-18



Picture 16. View into the upper shaft

Based on the chemical analysis in table 2 below we are able to state that there is no real chemical impact on the upper shaft lining due to the process and due to the possible occurring reduction gases in this area. Analysis of Lab No. 6705-18 compared to the mean value of this brand out of production are more or less the same. Definitely the difference in the major components based on alumina and silica show more or less no deviation. Therefore we can be very sure that there is no real attack by the reducing gases like carbon monoxide or hydrogen. Remaining reducing gases should also occur in this area, nevertheless they should reacted in the reducing part of the shaft which is in a lower part of the vessel. Seen from the point of chemical analysis the iron content of the spalled piece is slightly higher which is not really surprisingly.

On the other side we see very interesting analysis of the metallic flakes. It was not possible to separate the metal completely from the remaining brick material and therefore we got also alumina and silica in the analysis. The proportion of alumina and silica is contrary to the proportion in the brick. This may be related to the forming of iron silicates which will be attached in a very small amount to the metallic flakes. This may explain the small difference in alumina and silica analysis between the mean value of production and the spalled brick part out of the reactor.

Furthermore we have to accept a temperature excursion in this area with the effect of creating molten metal flakes. There is still no idea how this could happen in this area but it is a fact. Seen from the point of molten metal the temperature should have reached a level close to 2350 °F which is far away from a supposed temperature of app. 1900-1950 °F in the gas inlet area which is several meters below the investigated area.

Additionally the chemical analysis of the metallic flakes shows especially also a higher content of lime (CaO) and magnesia (MgO) which can be lead back to the use of cement as coating material for the pellets.

Table 2. Chemical analysis of the above mentioned samples

| | Unit | Lab No. 6705-18 fireclay brick | Mean value production fireclay brick | | Lab No. 6708-18 Big flake, metallic | Lab No. 6709-18 Small flake, metallic |
|---|---|---|---|---|---|---|
| Chemical Analysis (XRF) | | | | | | |
| $Al_2O_3$ | [wt%] | 49.21 | 49.78 | | 8.27 | 6.52 |
| $SiO_2$ | [wt%] | 46.10 | 45.39 | | 10.80 | 8.84 |
| $TiO_2$ | [wt%] | 1.71 | 1.59 | | 0.16 | 0.12 |
| $Fe_2O_3$ | [wt%] | 1.38 | 1.03 | $Fe_2O_3/Fe$ | 78.19 | 82.33 |
| CaO | [wt%] | 0.18 | 0.22 | | 1.19 | 0.96 |
| MgO | [wt%] | 0.19 | 0.27 | | 0.46 | 0.46 |
| $K_2O$ | [wt%] | 0.73 | 0.65 | | 0.31 | 0.21 |
| $Na_2O$ | [wt%] | 0.25 | 0.27 | | 0.24 | 0.24 |
| $Mn_3O_4$ | [wt%] | 0.01 | n.d. | | 0.05 | 0.04 |
| $Cr_2O_3$ | [wt%] | 0.03 | 0.03 | | 0.01 | 0.01 |
| $P_2O_5$ | [wt%] | 0.09 | 0.09 | | 0.27 | 0.22 |
| $ZrO_2$ | [wt%] | 0.08 | 0.19 | | 0.01 | 0.01 |

**STARTING NEW INVESTGATIONS**



Picture 17. New STA-equipment at Steuler-Lab
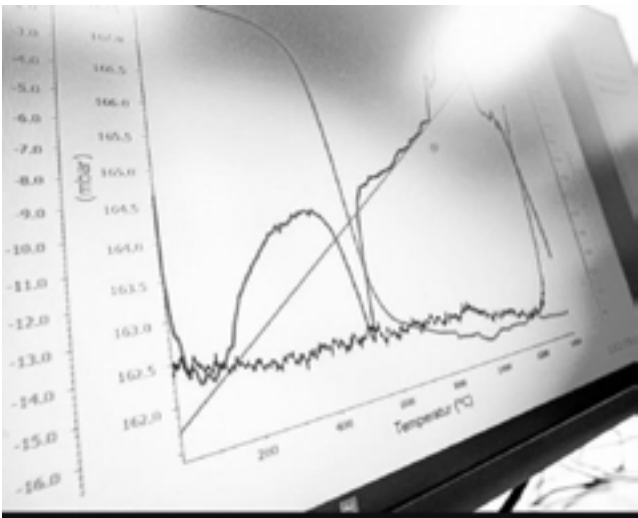


Picture 18. Example of online measured

**STA analysis in different atmospheres**

The testing of raw materials and refractory material in atmospheres containing hydrogen, carbon monoxide, methane and water vapour needs a fully new equipment which we have already installed this year. Additionally to the possibility for testing in different atmospheres it is also possible to apply different pressures up to 72 psi. The system is able to run at temperatures up to 2550 F and flexible heating up rates and holding ramps. During the first testing period we tested only in 100 % hydrogen atmosphere at atmospheric pressure to get a first impression on the effectiveness of the new equipment. An example of a measurement given as TG analysis is shown in the picture 19 below.
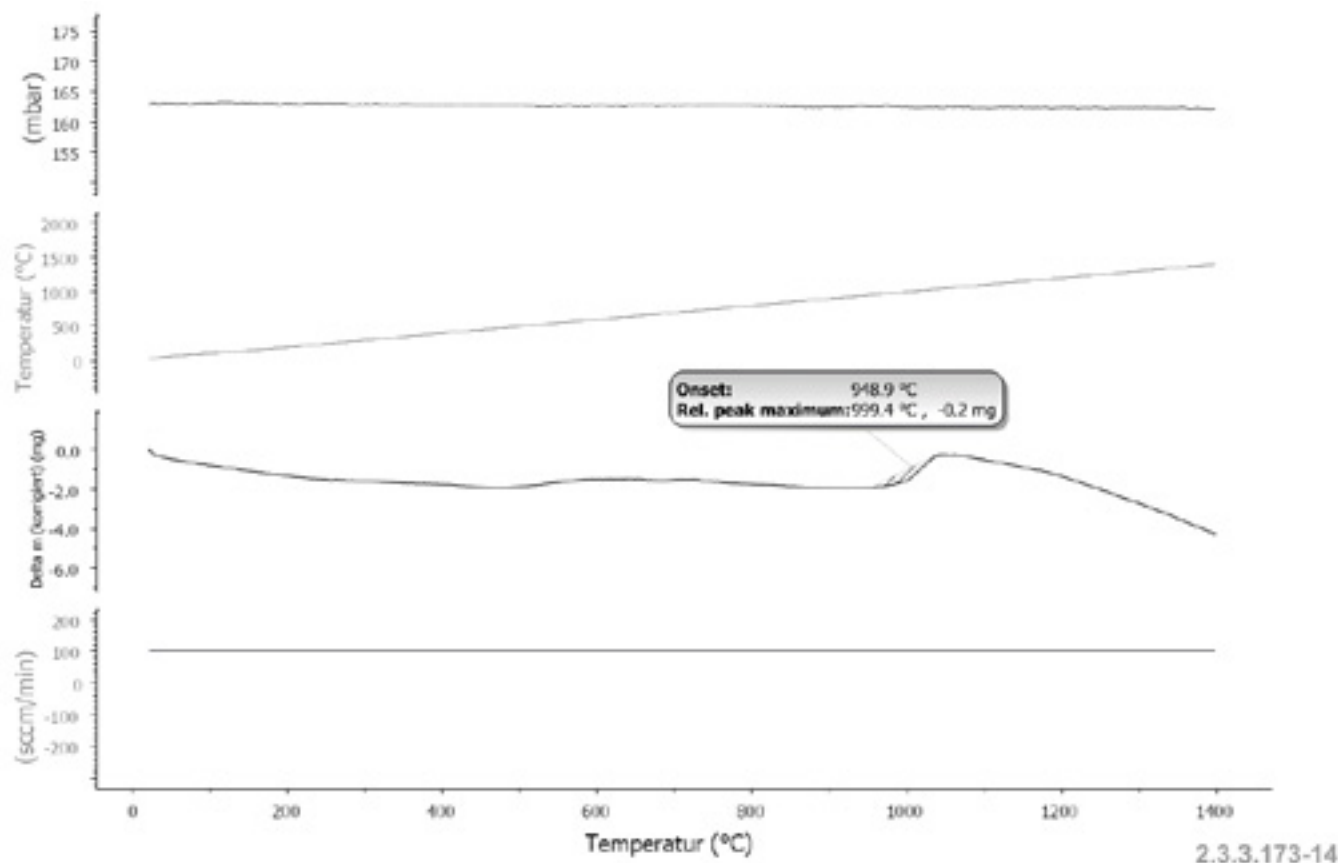


Picture 19. TG diagram of a mullite fireclay material

The above mentioned diagram shows the graphs of the measurement of a mullite fireclay brick. The brick material was milled and then fractionized. 2000 mg of this powder was given into the TG-crucible. The graphs show from up to down the pressure, the temperature, the weight difference and the hydrogen throughput in cm³ per minute. Additionally it is also possible to run a DSC analysis of such a sample. Between 1740 and 1830 F we see a weight increase of app. 0.01 wt.%, whereas afterwards up to 2550 F we are determining a slight weight loss of app. 0.2 wt.%. Currently we have no idea regarding the first effect, but maybe we see more after DSC running. The second effect shows a minor affected material. This slight effect is not really surprisingly cause this material is currently used in a lot of DRI plants and is obviously a suitable material for this kind of application.

**CONCLUSION**

This paper shows the importance of a careful consideration of the refractory engineering and design. Calculations of thermal stresses etc. are very helpful for getting a suitable lining concept. Combined with the experience of the use of especially developed refractory material for this kind of application we see currently no difficulties in the built up of DRI plants for the hydrogen case. Common systems based on reformed natural gas are running with more or less the same lining material and design.

For the transformation process with a lot of different possible gas atmospheres we are now able to run specialized tests. And one of the most important components in this field could be the addition of water vapour. Due to current knowledge this could change the measured attack in the lab. With pure hydrogen we see a minor effect but pure hydrogen will never go to the DRI-shaft. Also some water will be in the gas due to the heating up of the reducing gas. But we will also take this challenge.

# SWITCHING TO HYDROGEN BASED FUELS AND THEIR EFFECT ON REFRACTORY LININGS AND PROCESSES

Philip Walls

Hitech Materials Pty Ltd, Wollongong, Australia

## ABSTRACT

As we transition from carbon to hydrogen-based fuels to reduce carbon dioxide emissions to stem climate change. Many of the materials contained in the products we use every day at some stage during their manufacture rely on high temperature processes which are in turn directly reliant on "refractory" materials.

This paper summarises the main properties of hydrogen compared to natural gas fuels. It looks at the effect of hydrogen on refractory lining materials and provides some comment on the steps that need to be taken to ensure the transition to a reduced carbon economy proceeds as rapidly as possible.

## INTRODUCTION

Protective refractory linings are required to attain high process temperatures and when hydrogen-based fuels are used in place of natural gas, the refractories must be able to withstand the modified atmosphere and process conditions.

Such atmospheric modification must also be considered with respect to the affect they have on the material being processed in the plant.

Thoughtful refractory material selection and lining design, and/or development of "modified" refractory materials will be required to ensure lining durability and extended plant operation as this fuel transition progresses.

The shift from a "carbon" to a 'hydrogen" based fuel can affect burner design / material selection and alteration of hot zone position, the heat distribution within the process vessel and heat transmitted through the refractory lining. These all affect the durability of the refractories used.

As a reducing agent, at temperatures more than 1000°C, hydrogen attacks normally stable refractory oxides, causing them to decompose by release of volatile species. Such corrosion has a deleterious effect on lining strength and durability, creating headaches for plant managers.

Fortunately, refractories engineers are already on notice and significant research is being conducted to help mitigate potential issues.

Finally, the effect of additional steam generation during the combustion of hydrogen fuels needs to be accounted for. If this is not accommodated by process modifications, condensation in cooler regions can lead to corrosion of metallic components.

## HYDROGEN VERSUS NATURAL GAS FUELS

When comparing hydrogen ($H_2$) as a fuel source, to natural gas (~90% $CH_4$), various factors arising from the difference in their properties need to be considered [1]. These are briefly outlined below and include.

– *Flammability Limit*
  The amount of fuel required for the fuel air mixture to ignite. This is between 4 - 75% for hydrogen, and 7 - 20% for natural gas. This means that hydrogen has a much larger range of fuel/air mixtures that can combust compared to natural gas making hydrogen firing more difficult to control.

– *Flame Temperature*
  For natural gas this is approximately 1950°C and for hydrogen it is 2097°C, almost a 150°C hotter for the hydrogen flame, see (figure 1) below.
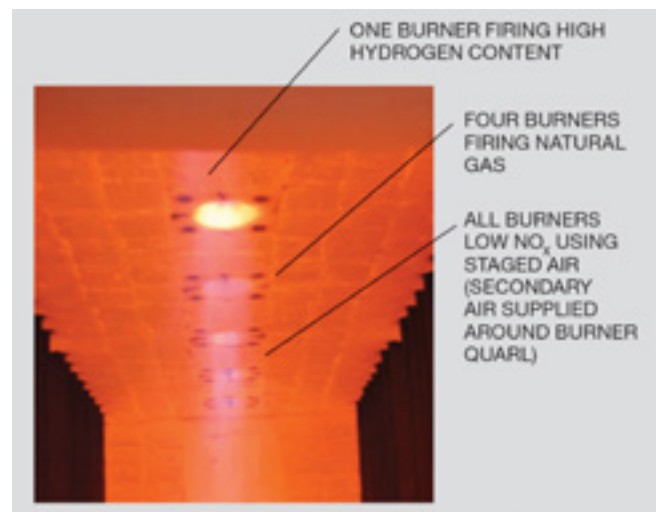


Fig. 1: Higher burning temperature for hydrogen.

– *Flame Speed*
  The speed at which a flame travels through an unburnt fuel air mixture. For hydrogen this is about 0.3 m/s about 7 times higher than for natural gas at 0.04 m/s. This makes control of where combustion occurs within the process vessel upstream when using hydrogen compared to natural gas fuels. This directly affects refractory lining, design, and material choice.

– *Energy Density*
  Hydrogen an energy density ~2.5 times that of natural gas, however as its density is lower, for the same amount of energy ~3 times the volume of hydrogen to natural gas is required.

– *Fuel flow rate*
  Because more hydrogen is required due to its low volumetric density, the flow rate for hydrogen fuels is significantly higher than for natural gas.

The comparisons above show there to be significant differences in the combustion behaviour of hydrogen over natural gas. This would require design changes to some existing process vessels if hydrogen is to be used as a replacement fuel.

## MICROSTRUCTURE OF REFRACTORY MATERIALS

Refractory materials for high temperature applications come in two forms, either as pressed bricks (or other shapes), or as monolithic refractory concretes. The latter are either preformed, dried and fired, or are installed in-situ by casting, gunning or ramming processes.

In both shaped and monolithic refractories, the main components include.

– Refractory aggregate grains of various size and/or composition, either straight from the mine or processed to control size, shape

and composition. Aggregates often contain finer particles and phases bonded either chemically or by an amorphous phase.

– A bond phase, which is initially cementitious in nature, before conversion to amorphous or crystalline grain boundary phases at operating temperatures. These are mainly silicate, aluminosilicate, or phosphate in composition.

There are therefore several potential sites where hydrogen can attack the surface of the refractory. These include the primary aggregate particles, the bond phase in general and the grain boundary phases between and within the primary aggregate particles.

These sites will have different compositions and so will be affected by hydrogen attack in different ways.

Now to look at the refractory phases in more detail.

## HYDROGEN CORROSION OF SILICATE AND ALUMINOSILICATE CONTAINING REFRACTORIES

Numerous studies [1-6] have shown that silica, silicate, and aluminosilicate glass phases are attacked by hydrogen via a reduction/corrosion process. Above 1000°C the sub-oxide of silica, SiO is generated in gaseous form together with the generation of water vapour. This is shown by equation (1) below.

$$SiO_2 \text{ (s)} + H_2 \text{ (g)} \rightarrow SiO \text{ (g)} + H_2O \text{ (g)} \tag{1}$$
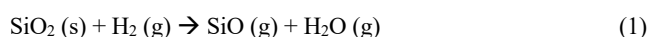
The silica component of aluminosilicate grain boundary phases and aggregates (such as mullite [7]) are also attacked by hydrogen as shown by equation (2).

$$Al_2Si_2O_{13} \text{ (s)} + 2H_2 \text{ (g)} \rightarrow 3Al_2O_3 \text{ (s)} + 2SiO\text{(g)} + 2H_2O \text{ (g)} \tag{2}$$
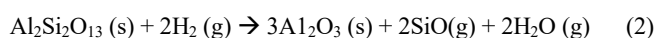
The SiO extracted from the refractory lining then either re-deposits further down the process line where the temperature is cooler causing build-up and eventual clogging of components or can interact with other refractory material or the material being processed.

Elimination or reduction of silica containing material in the refractories is necessary to assist hydrogen combustion.

## ALTERNATIVE COMPONENTS FOR REFRACTORIES

Work by Misra [8] on the chemical stability of ceramic materials, showed the upper temperature limits for different ceramics in pure hydrogen (figure 2), as well as in hydrogen/water environments (figure 3).

This work suggested that lime (CaO), alumina, yttria and zirconia were the most stable oxide materials and titanium diboride and carbide were the best performing non-oxides.

Interestingly both silicon carbide and silicon nitride did not perform well in Misra's evaluation. This is most likely due to the presence of a silica surface layer on these ceramics. They therefore would not be recommended to include in a hydrogen resistant refractory material.
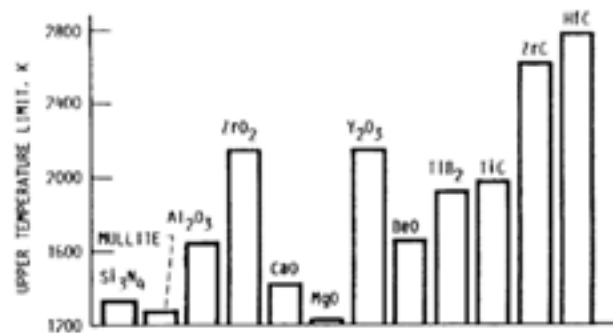


Fig. 2: Upper temperature limits for different ceramic materials in pure hydrogen.
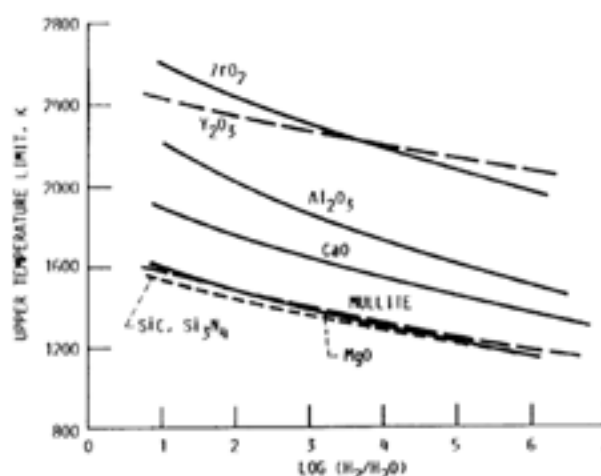


Fig. 3: Upper temperature limits for different ceramic materials in $H_2 / H_2O$ environments.

## CONCLUSIONS

At temperatures exceeding 1000°C, hydrogen attacks silica, silicate and aluminosilicate components of refractory materials as well as other refractory oxides to lesser degrees. Hydrogen also appears to attack the thin silica surface coating present on silicon nitride and carbides.

Alumina is stable in hydrogen and hydrogen water environments up to approximately 1340°C.

Zirconia and yttria are the most resistant to hydrogen attack and so yttria stabilised zirconia can be used at temperatures up to ~2000°C.

Titanium boride and carbide are also stable to approximately 1550°C in pure hydrogen.

Both silicon, carbide, and silicon nitride should be avoided as the thin silica layer on their surface, can be attacked by hydrogen in a similar way to silicates and aluminosilicates.

I also note in conclusion that there is little mention of the performance of phosphate bonded refractories. A phosphate rather than a silicate bond may well be beneficial regarding hydrogen attack resistance.

The complex microstructure of refractory materials containing multiple crystalline and amorphous phases, both complicates assessment of their stability in hydrogen containing atmospheres and offers possibilities for tailoring their composition and microstructure to improve their resistance to attack by hydrogen.

A recent review by Hemrick [9] highlighted that *"significant resources and attention are being devoted to the use of hydrogen as an alternative fuel source to fossil fuels…. (but) less information is available regarding the effects of hydrogen firing on processes and process vessels."*

If the transition from carbon to hydrogen-based fuels is to be successful in the timeframe stipulated by the United Nations Framework Convention on Climate Change. Then significant resources are needed to both develop refractory materials and convert existing process vessels to enable this change.

Further, during development of new refractory materials for hydrogen fired processes, it is necessary to develop new standards for assessing the durability of refractories in hydrogen atmospheres.

Such standards will hopefully be developed under the guidance of the ISO/TC 33 technical committee on refractories.

## REFERENCES

[1] *"Fuels,"* C. Baukal (editor), The John Zink Hamworthy Combustion Handbook, Vol. 1: Fundamentals, CRC Press, Boca Raton, Fla., (2013).

[2] Wright, R.E.; Wolff, H.I.: Refractory problems in production of hydrogen by pyrolysis of natural gas. J. Am. Ceram. Soc. 31 (1948) [2] 31–38

[3] Crowley, M.S.: Hydrogen-silica reactions in refractories. Am. Ceram. Soc. Bull. 46 (1967) [7] 679– 682

[4] Crowley, M.S.: Hydrogen-silica reactions in refractories, Part II. Am. Ceram. Soc. Bull. 49 (1970) [5] 527–530

[5] Gardner, R.A.: The kinetics of silica reduction in hydrogen. J. of Solid State Chem. 9 (1974) 336–344

[6] Sohn H.Y., "Overall rate analysis of the gaseous reaction of stable oxides incorporating chemical kinetics, mass transfer, and chemical equilibrium," *Journal of the American Ceramic Society*, 89:3, 1006–1013, (2005).

[7] Herbell, T.P.; Hull, D.R.; Garg, A.: Hot Hydrogen Exposure Degradation of the Strength of Mullite.
https://ntrs.nasa.gov/citations/19960045817

[8] Misra, A.K.: Thermodynamic analysis of chemical stability of ceramic materials in hydrogen-containing atmospheres at high temperatures. NASA 3459 Contractor Rept. No. 4271. National Aeronautics and Space Administration, Cleveland, OH, 1990.

[9] Hemrick J.G.: Refractory issues related to the use of hydrogen as an alternative fuel American Ceramic Society Bulletin, Vol. 101, No. 2

# PHOSPHATE–BONDED REFRACTORIES IN HYDROGEN CONTAINING ATMOSPHERE

T. Leber, D. Kenn, F. Matt, M. Scheller, T. Tonnesen, J. Gonzalez-Julian

Chair of Ceramics, Institute of Mineral Engineering, RWTH Aachen University, Germany

## ABSTRACT

In the transition to a $CO_2$-neutral industry, traditional carbon fuel-based systems must be replaced by sustainable fuel systems such as hydrogen. This change implies a different atmosphere during the operation at high temperature, which is a big challenge for refractory lining materials. This study focuses on four different phosphate-bonded refractories, which are generally characterised by fast drying times, adequate refractoriness, and excellent abrasion and slag resistances. Two phosphate-bonded industrial refractory masses, one based on corundum and the other on fireclay, are tested under corrosive conditions. Two model systems are considered to provide a fundamental view of the behaviour. These focus on smaller grain sizes, reduced silica content and proportionally contain higher amounts of different phosphate-based binders. The first model system contains mainly magnesia and is bound by sodium polyphosphate. The other consists of alumina and is bonded with monoaluminium phosphate. All materials are exposed in a dilute, $9Ar\ 1H_2$, hydrogen atmosphere at various temperatures and holding times.

Corrosion experiments up to 1500 °C have been carried out using a tube furnace with the above conditions. The microstructure, and in particular the binder phase, was characterized by SEM and EDS. Microstructural components undergoing reaction or loss will be identified and their behaviour and movement in the system will be considered. Particular attention is paid to the phosphorus components, their possible reduction and their influence on the binder phase.

## INTRODUCTION

Society, our life standards and the exponential growth of population require a considerable increase of energy consumption and raw materials. Briefly, this has some consequences such as global warming and $CO_2$ contamination, among others. Particular attention is being paid to the steel industry, as it accounts for the largest share of greenhouse gas emissions (around 30 % of the total $CO_2$ emissions) compared to other sectors and 6 % of total emissions in Germany. As a result, low-$CO_2$ and long-term climate-neutral process technology is a key area within the industry. [1] For example, the use of hydrogen in industry, which has a low $CO_2$ footprint depending on the source, can help to reduce substantially the carbon footprint of steel products by minimising the need for carbon-based reducing agents. [2] In addition, the non-ferrous industry is also exploring the potential of hydrogen to reduce greenhouse gas emissions in this sector. One current application is the deoxidation of copper melts in the anode furnace. [3] These changes in turn affect the process enablers, such as refractory materials. These must demonstrate their ability to withstand the changed process conditions, such as increased gas flow and higher levels of hydrogen and water vapour in the reactor atmosphere.

## EXPERIMENTAL PART

Four types of samples were processed and tested in this study. The first two, designated RM1 and RM2, are refractory masses bonded with phosphates. Sample RM1 is mainly based on fireclay and corundum as raw materials, while sample RM2 is mainly composed of corundum. Both samples have a maximum grain size of up to 6 mm. Prior to the tests, the samples were fired at 1500 °C for 8 h to minimise temperature related effects on the samples.

The other two sample types, labelled M1 and M2, are model systems designed to highlight specific effects within the matrix. The grain size distribution of these samples is limited to 1 mm and the amount of binder is significantly increased. Sample M1 is based on sintered magnesia grains with a maximum diameter of 1 mm, 5 wt.-% sodium polyphosphate binder and 1 wt.-% microsilica to prevent brucite formation. Sample M2, on the other hand, consists of a mixture of tabular alumina with a maximum grain size of 1 mm, bound with 8 wt.-% monoaluminium phosphate. Both model materials were sintered at 1100 °C. While the first two samples give an insight into the behaviour of commercial refractories, the latter two materials emphasise the effects within the matrix to a greater extent.

While the first two types of samples give an insight into the behaviour of commercial refractories, the two model systems were chosen to focus on more isolated effects. Sodium polyphosphates can be used as binders for basic refractory materials such as magnesia and as additives for cementitious castings. Their behaviour is observed in the first model system, M1. The second model system, M2, is used to observe the reaction of monoaluminium phosphate binders in more detail. The use of tabular alumina reduces the amount of impurities, which, combined with a low silica content, allows the binder to react with less interference from competing reactions. A tube furnace, Figure 3a, was used to expose the samples to a defined atmosphere at specific temperatures.

The tests were carried out at two temperatures: 1100 °C, representing the upper end of direct reduction technology for iron extraction, and 1500 °C to facilitate corrosive mechanisms. Two different time periods were chosen to assess the effects at the given temperatures and gaseous atmosphere. The gas used in all tests was a hydrogen-argon mixture (1:9 ratio). Control runs were performed to understand the behaviour of the samples in an oxidising atmosphere.

## RESULTS AND DISCUSSION

The behaviour at high temperature of the four different compositions was firstly determined by the mass balance, weighing the samples before and after each test. In addition, to the temperature, the position within the tubular furnace also plays a determinant role. Figure 1 shows the mass changes of all material systems and their respective samples. The first observation is the difference in the magnitude of the mass losses of the material systems RM1 and RM2 on the one hand and M1 and M2 on the other. The losses reach maximum values of 1.2% to 1.6% for the two refractory masses, whereas the two model systems show losses of up to 6%. This seems to correspond very well with the increased binder content of the model systems of 5 wt% for M1 and 8 wt% for M2.

Another notable result for all materials is that the mass losses generally increase at higher temperatures, i.e. from 1100 °C to 1500 °C. The two masses RM1 and RM2 only lose a maximum of about 0.4% at 1100°C and up to 1.6% at 1500°C. This shows the enhanced effect of increased activation energies and kinetics as well as the shifted equilibrium towards a higher proportion of gaseous species. The influence of increased holding time is of minor consequence.

Another aspect which is evident for all samples is that the mass loss of the sample exposed to air at 1500°C for 72 h is consistently lower than that of the samples at comparable temperature conditions from the corrosion tests. This generally demonstrates the influence of the corrosive conditions of the applied testing atmosphere. When looking at the positions of the individual samples and their respective mass

losses, it can be seen that the mass losses of the last sample in the test setup, i.e. the outlet sample, viewed from the direction of gas flow, are the lowest. In contrast, the first two samples, inlet and middle, show a comparably high mass loss. The middle samples of RM2, Figure 1b, show a slightly higher loss than the corresponding inlet samples in all tests. Similar behaviour occurs with M1, Figure 1c, where only the test at 1500 °C for 24 h results in a higher mass loss of the gas inlet sample than the middle sample.

In principle, it would be expected that the mass loss of the inlet samples should be the highest as the introduced reaction gas has not yet reacted at this point and therefore the hydrogen partial pressure is significantly higher in relation to the oxygen content. This should result in a correspondingly significant reduction and therefore mass loss of the inlet samples. The equilibrium should then shift away from the reducing conditions, resulting in less severe corrosion conditions for the intermediate and outlet samples.
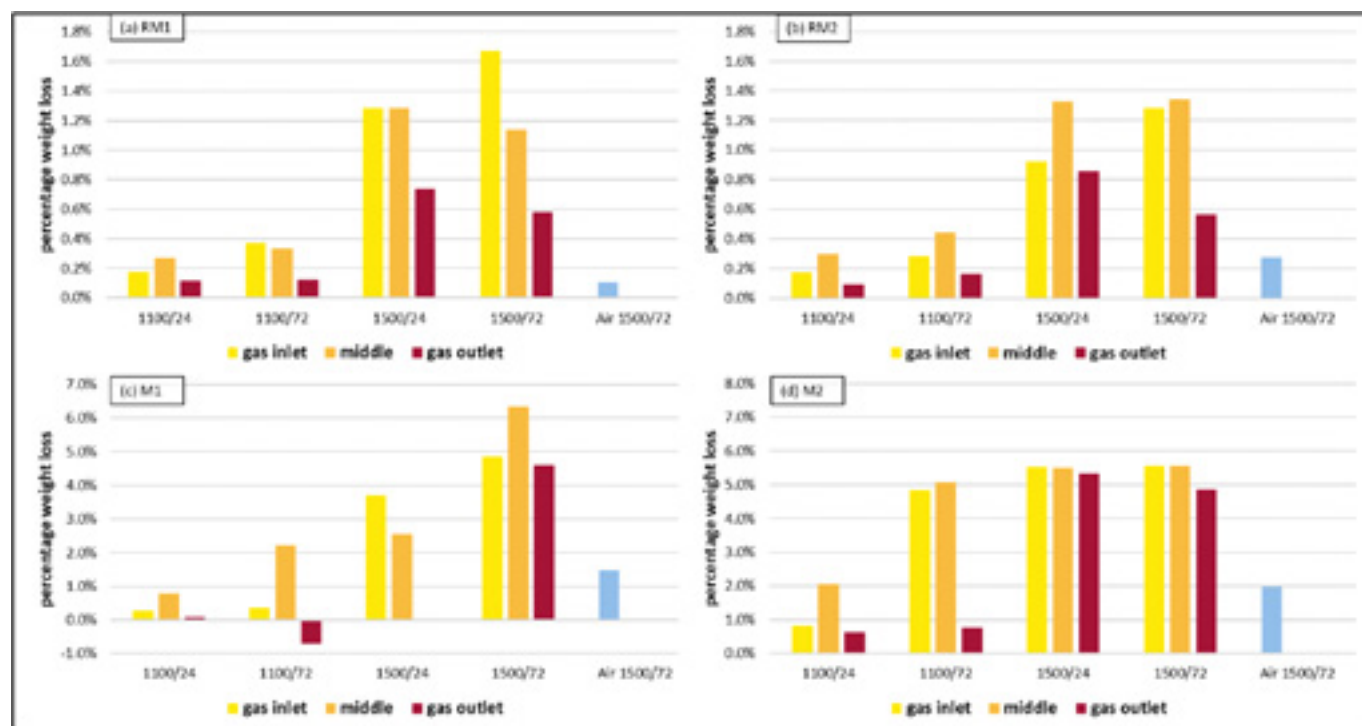


*Figure 1: Mass changes of the different materials in dependence of the test conditions and sample positions*

The reason for the deviating behaviour may be explained by the design of the tube furnace. An insufficiently developed homogeneous heating zone of the furnace could lead to a shifted temperature field. This would result in a higher temperature in the centre, i.e. for the middle sample, compared to the inlet and outlet samples. This in turn would cause a shift in the equilibrium, resulting in a higher proportion of gas phase for the middle sample due to the higher temperature.

The reason why the outlet sample has the lowest mass loss is due to the composition of the reduction gas. It can be assumed that the gas is already enriched with products from reactions with the other two samples, resulting in a less pronounced reduction for the outlet sample. However, this would not explain the mass increase observed for M1 at 1100 °C for 72 h Figure 1c. It is known that silicon monoxide is formed from silica under reducing conditions. In this case, this reaction is already happening at the inlet and the middle sample. This gas can then act as a reducing gas for oxides with less affinity for oxygen, such as disodium oxides or phosphorus trioxide. As a result, silica is deposited on the last sample, while more volatile components pass into the gas phase and are removed with the stream. Another aspect that could explain the different mass behaviour of the outlet sample and favour the previously described back reaction of products from the other two samples on the outlet sample is a possible lower sample temperature. As already described, this could be due to the temperature field of the furnace, which would then favour condensation of the gas phase on the samples.

In the case of M2, Figure 1d, particularly in contrast to RM1 and RM2, an increased mass loss can be observed for the inlet and middle sample in the test at 1100 °C for 72 hours. At just under 5 %, the losses here already reach the level of the two tests at 1500 °C of 5.5 %. This indicates that the phosphorus oxides are reduced, transferred to the gas phase and removed in the 1100 °C temperature range as long as there are only minor competitive reactions.

## OUTLOOK
This is only an extract from the complete article. For more details on the experimental setup, results and discussion, please refer to the article of the same title in the Refractories Special Issue of "Open Ceramics".

## REFERENCES
[1]    Spitzengespräch zur Stahlindustrie: Wege zur Umstellung auf CO2-arme und langfristig klimaneutrale Produktion., Bundesministerium Für Wirtschaft Und Klimaschutz. (2021). https://www.bmwk.de/Redaktion/DE/Pressemitteilungen/2021/06/20210621-spitzengespraech-der-stahlindustrie.html (accessed June 5, 2023).

[2]    J. Töpler, J. Lehmann, E.U. von Weizsäcker, eds., Wasserstoff und Brennstoffzelle: Technologien und Marktperspektiven, 2., aktualisierte und erweiterte Auflage, Springer Vieweg, Berlin [Heidelberg], 2017. https://doi.org/10.1007/978-3-662-53360-4.

[3]    T. Edens, J. Steindor, Using Hydrogen as a Reductant in Fire Refining at Aurubis Hamburg's "Down-town" Smelter, in: Metallurgy and Materials Society of CIM (Ed.), Proceedings of the 61st Conference of Metallurgists, COM 2022, Springer International Publishing, Cham, 2023: pp. 211–228. https://doi.org/10.1007/978-3-031-17425-4_31.

# HYDROGEN CORROSION OF REFRACTORY MINERALS AND THE IMPACT OF SIO-GAS

J. Astoveza, E. Frier, R.M. Mineau, L. Thomas, C. Wöhrmeyer

Imerys S.A., Paris, France

## ABSTRACT

In this study, the resistance of andalusite, mullite, tabular alumina, and stabilized zirconia against hydrogen attack was tested for 240 h in a laboratory furnace. At 900°C, no evidence of reaction was detected for all the minerals. This was not the case at 1400°C where significant mass losses were measured in direct proportion to the silica content. Microstructural analysis highlighted the influence of the unique morphology of mullite and andalusite to their corrosion resistance. A progressive conversion of mullite and glass phase into α-alumina was observed on the sample surface, where silica was preferentially consumed from the glass phase over the silica structurally-bonded in mullite. On the other hand, mullitized andalusite characterized by the dense, ordered capillary network of mullite and glass phase could potentially hinder hydrogen infiltration. Beside hydrogen itself, the effect of the by-product SiO-gas revealed that cross-reactions can be triggered in the presence of calcium resulting in the formation of a calcium silicate phase and subsequently leading to the destabilization of the calcia-stabilized zirconia at 1400 °C, while yttria-stabilized zirconia remained stable.

## INTRODUCTION

The major European steelmakers are on a race towards the green steel transition propelling paramount technological investments prompted by government subsidies to cut their industrial emissions. A target reduction by at least 55 % by 2030 was established under the European Green Deal to align with the 1.5 °C warming mark trajectory [1]. This has driven unprecedented technological disruptions in iron and steel-making, including the substitution of coal by hydrogen as the main reductant and energy source in blast- and direct reduction (DRI) furnaces. As expected, principal stakeholders including the refractory industry are faced with the challenge of identifying and addressing the impact of this technological shift to the market.

Theoretically, it is known that hydrogen at elevated temperatures reacts with free silica, or silicates in refractory linings to produce gaseous SiO and water, depicted primarily by the equation below:

$$SiO_2(s) + H_2(g) \rightleftharpoons SiO(g) + H_2O(g) \qquad (1)$$
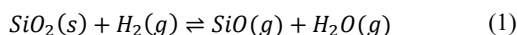
The gaseous products can be carried off in the process stream. When temperatures decrease downstream, the reaction reverses and silica is deposited as a solid. The result can be heat-exchanger fouling and product contamination [2]. Although limited in number, recent studies [3, 4, 5] demonstrated the resistance of conventional alumino-silicates and high alumina refractories at conditions pertinent to green steel processes.

This study aims to explore the fundamental mechanism of hydrogen attack on refractory minerals under pure hydrogen atmosphere at temperatures up to 1400°C. A cross-reaction effect by the SiO gas originating from the reduction of the silicate-rich phases and its impact to the stabilization of zirconia is also highlighted.

## METHODOLOGY

Pressed cylindrical samples as shown in figure 1 were obtained using a 3R hydraulic press applying 80 kN of force for 20 s on 100 g of pure refractory minerals. The raw materials were selected within the product portfolio of Imerys including Mulcoa®, Durandal™, Kerphalite™ KA and Zionic™, except the Tabular Alumina T60 from Almatis. Size distributions were obtained following the Andreasen packing model with the distribution (q) modulus of 0.35. Conpac500 superplasticizer and Solvitose FP7 starch were added to aid the dispersion and bond. Pre-firing at 1400 °C for 6 hours proved to be necessary to aid the compaction before subjecting the samples to the corrosion test.
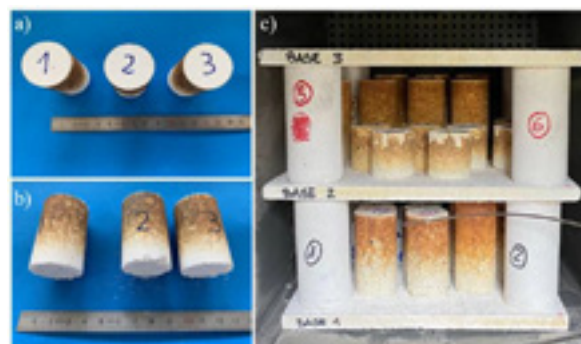


*Fig. 1: Photos of pressed refractory samples before the corrosion test. The arrangement of samples inside the furnace is shown in (c).*

The codes along with the properties of the pressed samples measured after pre-firing are presented in table 1. Five duplicates were prepared per formulation with the following representation: a sample before pre-firing; one after pre-firing; and the other three were subjected to the corrosion test. All the samples were loaded together in a single batch as shown in figure 1 (c).

*Tab. 1: Sample codes and general characteristics including alumina content, aggregate type, apparent porosity (AP), and bulk density measured after pressing and pre-firing at 1400 °C.*

| Code | Al₂O₃ (%) | Aggregate Type | AP (%) | ρ (g/cm3) |
|---|---|---|---|---|
| Mul-47 | 47 | Mullite | 24 | 2.17 |
| Mul-60 | 60 | Mullite | 25 | 2.31 |
| And-60 | 60 | Andalusite | 19 | 2.45 |
| TA-99 | 99 | Tabular Alumina | 24 | 2.38 |
| YSZ | Zirconia – 8% Y₂O₃ | | 29 | 4.21 |
| CSZ | Zirconia – 4% CaO | | 26 | 4.46 |
| 900-sample code | subjected to corrosion test at 900 °C | | | |
| 1400-sample code | subjected to corrosion test at 1400 °C | | | |

The corrosion tests were performed in a muffle-type laboratory furnace under 100 % hydrogen atmosphere both at 900 °C and 1400 °C, respectively, for a total duration of 240 h divided into three 80-h segments. Pure hydrogen gas was injected at a constant flow rate of 200 l/h throughout the tests. At each 80-h interval, a duplicate sample was taken out for weighing and further analysis.

To evaluate the impact of SiO gas, 230 g of CSZ fines (<325 mesh) was subjected to thermal treatment at 1400°C under pure hydrogen atmosphere using the Setsys™ TGA device. The focus on this paper is given to the XRD-Rietveld analysis of the end product and not to the details of the thermogravimetric study.

## RESULTS AND DISCUSSION

### Physical observations

Photos of the cross-sections of the pressed samples obtained using an optical microscope are shown in figure 2. Note that the sections were taken from the mid-region of the cylinders such that only their outer rims were directly exposed to hydrogen. A layer of reacted zone, 1-3 mm thick, is visible on the surfaces of mullite and andalusite after the test at 1400 °C. Polished sections were prepared for Scanning Electron Microscopy (SEM) with scan areas marked in red (figure 2). At this scale, no physical change was discernible for the other minerals tested at 1400 °C. No reaction zone was detected for all the formulations tested at 900 °C.
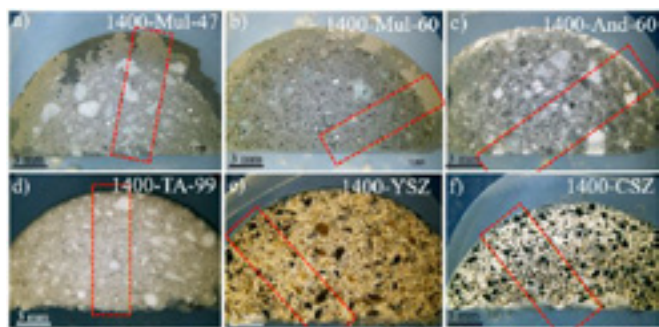
*Fig. 2: Cross-sections of samples after 240 h of hydrogen corrosion test at 1400 °C. SEM scan areas are marked in red.*

**Weight changes**

Consistent with the physical observations, all samples tested at 900 °C did not exhibit weight change beyond 0-0.50 %. On the other hand, a weight loss proportional to the silicate content was obtained at 1400°C, as shown in figure 3. Additionally, the calcia-stabilized-zirconia gained 1.15% of mass after 240 h. While a stable weight in some of the samples could already be an indication of their resistance against hydrogen attack, mineralogical verification is needed as weight re-gain due to oxidation during cooling, transfer of ions from the gaseous state, and the formation of new phases could counter-balance the weight loss from hydrogen reduction [2, 5].
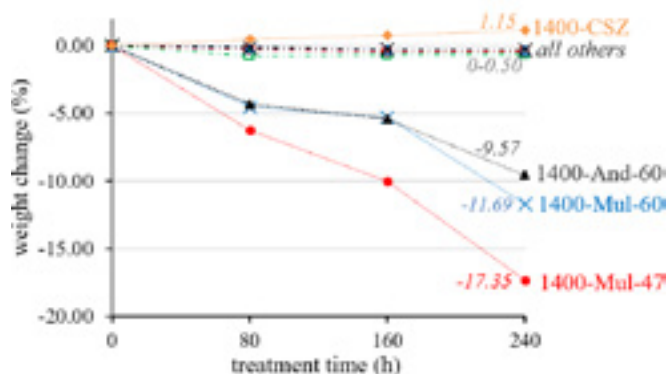


*Fig. 3: Weight changes measured every 80 h*

**Microstructure**

This section is focused on the results obtained from the 1400 °C test, where notable changes in physical properties were observed. The association of mineralogy to the microstructures presented here is supported by the results of energy dispersive X-ray spectroscopy (EDS) analyses.

*Mullite*

Having obtained the highest weight loss, a clear reaction zone with significantly lower Si content is visible on the exposed surface of 1400-Mul-47, as shown in its micro-XRF scan in figure 4.
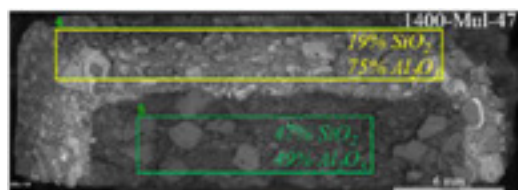


*Fig. 4: Cross-section and chemical analysis by area of the mullite sample obtained using micro-XRF*

A closer look at the morphology of the altered zone in figure 5 (a-d) reveals the complete absence of Si in the outermost regions. Instead, only hexagonal plates of α-alumina remained on the surface (a). The conversion of mullite + glass phase into mullite + degraded matrix[1] (d), then subsequently into α-alumina becomes more evident in the transition zones (b, c). It is therefore proposed that the silica from the

grain-boundary liquid phase was preferentially consumed over the silica structurally-bonded in mullite. This mechanism is consistent with that previously reported [6] in mullite test bars subjected to dry hydrogen atmospheres at 1050°C and 1250°C for 500 h. The same study also reported a reduction in the mechanical strength (up to 53% reduction at higher temperatures) attributed to the removal of the glassy matrix.
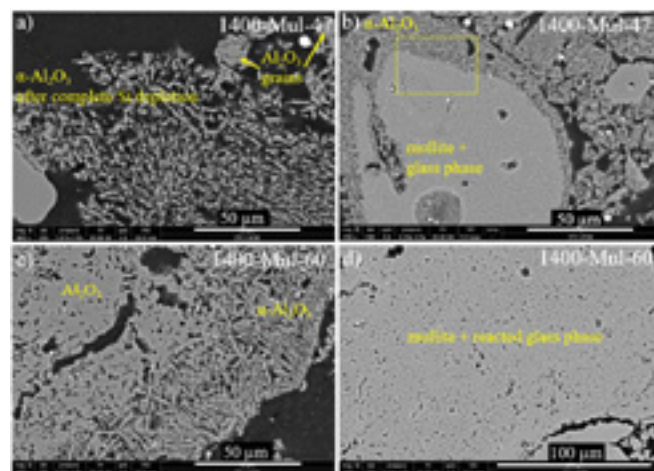


*Fig. 5: SEM-BSE images of the mullite samples after the corrosion test at 1400 °C. Shown here are areas from the reacted surface.*

*Andalusite*

The SEM images of the andalusite in figure 6 demonstrate how its dense, homogeneous single-crystal structure can somehow constrain the infiltration of hydrogen. It can be seen that the altered zones were deeper in regions of the fine-aggregate matrix, while the attack on the denser crystals were more concentrated along the borders and cracks.
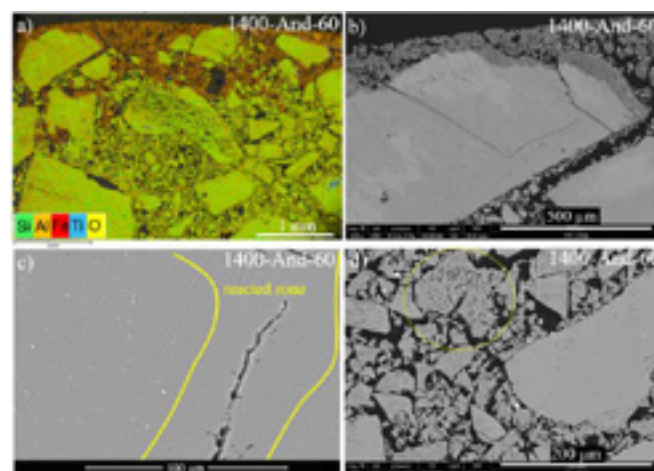


*Fig. 6: SEM images of mullitized andalusite after corrosion test at 1400 °C. Highlighted are areas with visible reaction.*

The total weight loss for 1400-And-60 is noted to be slightly lower than that of 1400-Mul-60 (figure 3) despite its slightly higher silicates content: 38 % $SiO_2$ for And-60 vs. 35 % for Mul-60 estimated using XRD-Rietveld analysis. The unique microstructure of mullitized andalusite reflected in its significantly lower apparent porosity (table 1) is postulated to contribute to an improved resistance against hydrogen attack. Evidence of corrosion appear to be concentrated along the cracks and the prismatic cleavages of andalusite in figure 6. It is important to note that after pre-firing at 1400°C, only 51 % of the andalusite has been converted into mullite and glass phase based on Rietveld analysis. Once mullitization is complete, the cracks are expected to close potentially eliminating the problem of hydrogen infiltration in these localized zones.

---

[1] where the glass phase is either partially or completely depleted due to the volatilization of silicates

*Tabular Alumina*

The SEM images of tabular alumina in figure 7 after the test at 1400 °C demonstrate its excellent resistance to hydrogen attack. The microstructure remained intact displaying no altered zone unlike the other refractory minerals tested. A magnified image (b) with its Fe map (c) marks a thin layer of reduced Fe in the outermost regions, signifying that hydrogen has anyway penetrated through, displacing Fe towards the surface – a phenomenon previously observed in bauxite samples subjected to hydrogen attack (90% Argon - 10% $H_2$) at 1500 °C for 72 h [5]. In their study, agglomerates of reduced Fe, Ti and P oxides were detected in castable surfaces.
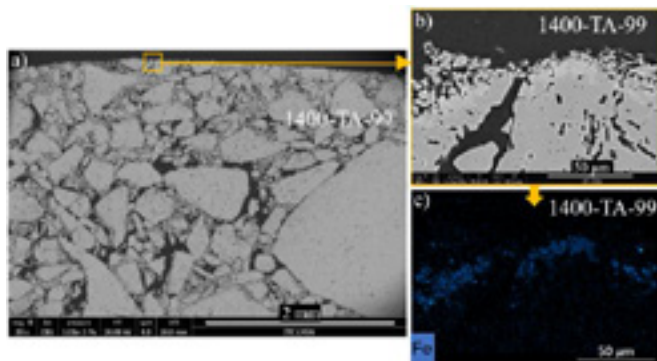


*Fig. 7: SEM-BSE images (a,b) of tabular alumina and Fe chemical map (c) of (b) after the corrosion test at 1400 °C.*

Even in the 900 °C test, the migration of reduced impurities notably Fe and P to the surface was evident in figure 8. This marks the importance of the level and type of impurities even in high-alumina aggregates and even at lower temperatures under hydrogen-rich atmosphere. A question is raised whether other alumina-rich alternatives such as fused alumina with larger crystals and less inter-crystal boundaries [7] could better resist the infiltration of hydrogen. Furthermore, sintered alumina is known to have networks of closed micro pores while its fused counterpart has rather local clusters of big pores, where impurities are likely concentrated in some clusters rather than homogenously distributed.
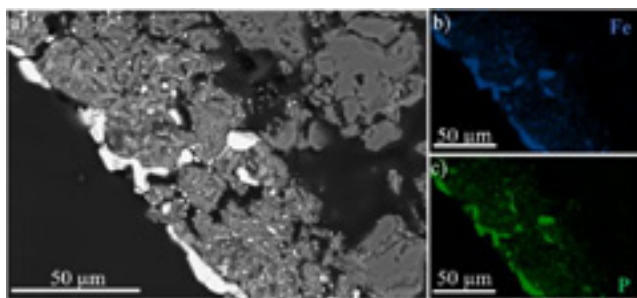


*Fig. 8: SEM-BSE image of tabular alumina (a) and its Fe and P chemical maps, after the 900 °C test.*

*Stabilized Zirconia*

Yttria-stabilized zirconia (YSZ) displayed excellent resistance to hydrogen attack characterized by its stable weight (figure 3), intact microstructure (figure 9 a-b), and unaltered mineralogy (figure 10 a). On the contrary, the stabilization of zirconia with CaO proved to be ineffective under the test conditions. The globular microstructure characteristic to monoclinic zirconia (figure 9 c-d; figure 10 a) has been broadly detected even within the innermost regions of the samples indicating destabilization. This is further supported by the Rietveld estimations for 1400-CSZ in figure 10 b.

**The impact of SiO gas**

EDS analysis on the destabilized CSZ after the test at 1400 °C points to a cross-reaction with the $SiO_{(gas)}$ resulting in the uptake of Si in CSZ. Even with the 200 l/h constant hydrogen flow assumed to provide sufficient gas replenishment, cross-contamination among the samples was not prevented.
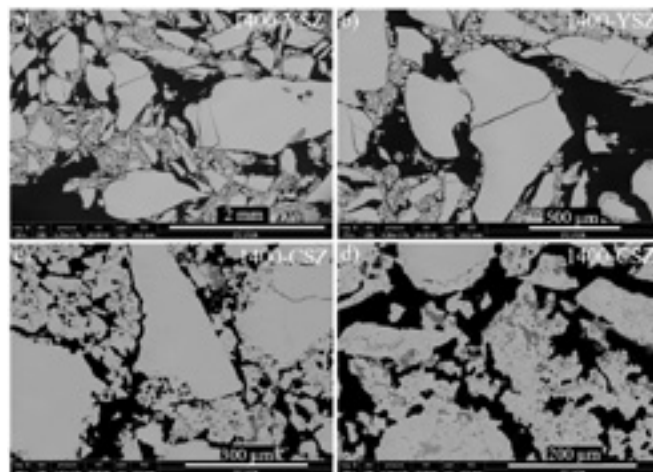


*Fig. 9: SEM-BSE images of stabilized zirconia after the corrosion test at 1400 °C. The globular morphology of monoclinic zirconia was largely observed for CSZ signaling destabilization.*
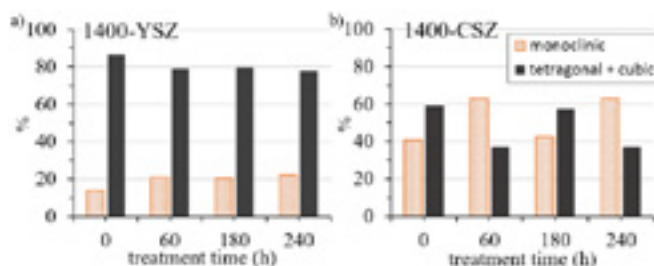


*Fig. 10: Compositions estimated using XRD-Rietveld analysis*

The formation of a calcium silicate phase (figure 11 b) was detected on various zones with the following molar composition: 10-20 % Ca; 5-16 % Si; 5-7% Zr; 60% O. XRD analysis was not able to establish the exact identity of the new phase, having no distinct contribution to the X-ray diffraction patterns. Furthermore, it could be inferred that the volumetric instability, notably shrinkage, expected due to the transformation of the tetragonal and cubic zirconia into its monoclinic structure may have facilitated the infiltration of hydrogen reaching the innermost regions of the sample.
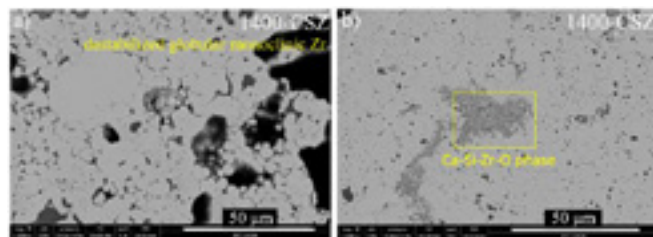


*Fig. 11: SEM-BSE images of CSZ for which destabilization was demonstrated by the extensive conversion to monoclinic zirconia (a) and the formation of a new calcium silicate phase (b).*

To verify whether the destabilization of CSZ was triggered by the $SiO_{(gas)}$ rather than by the corrosion due to hydrogen attack at 1400°C, thermogravimetric analysis on CSZ fines was performed. This time, no other refractory minerals were co-loaded and only raw powder was used. After the 5.5 h of thermal treatment with isotherms at 950 °C and 1400 °C under pure hydrogen atmosphere, the composition of the end product was estimated using Rietveld analysis and compared to previous results in figure 12.

The result shows that CSZ remained stable in the absence of $SiO_{(gas)}$. No significant change in the proportion of monoclinic, tetragonal and cubic zirconia was observed, unlike in the presence of $SiO_{(gas)}$ for the pressed samples. One important implication of this result could be that calcium has a role to play in triggering corrosion by hydrogen in these conditions. This finding, if validated with further tests, would

883

influence the selection of stabilizer for zirconia in applications involving hydrogen-rich atmospheres at very high temperatures.
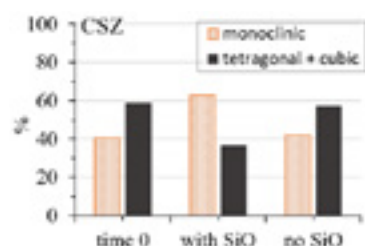


*Fig. 12: Composition based on XRD-Rietveld estimation of 1400-CSZ (with SiO) and CSZ fines (no SiO) from the thermogravimetric analysis.*

## Perspectives

In the end, it is important to underline that the test conditions used in this study may not even correspond to those in the actual application, notably to the industrial hydrogen-reduced iron processes. For instance, direct reduction using the Midrex® or the Tenova HYL® technologies is expected to be operated at temperatures below 1050 °C and with a pressure between 2-5 bars [3]. The practicality of easing the transition with mixed-gas atmospheres (natural gas, CO and hydrogen) would be taken advantage of. In any case, the atmosphere could theoretically not be purely hydrogen given the co-generation of steam and potentially of other by-product gases. More importantly, the role of the binder in minimizing the porosity to limit hydrogen infiltration is an indispensable factor unaccounted for in this study.

Nonetheless, the fundamental mechanism of corrosion demonstrated in this study contributes to a better understanding of the resistance of common refractory minerals against hydrogen. The excellent resistance of all the samples tested at 900 °C is already a promising prelude for DRI application. Trials involving a wider selection of refractory minerals incorporated in bricks and monolithics are on the way. Investigations on multi-component models based on standard industrial formulations is expected to bring results closer to those anticipated in actual applications as the effects of the binder-matrix systems, porosity distribution, gas permeability and impurity levels are factored in. In the end, all these efforts are directed towards predicting and achieving a well-balanced techno-economic and sustainable refractory solution to enable the green steel transition.

## CONCLUSIONS

This study validates the excellent resistance of common refractory phases against hydrogen attack at 900 °C. When the temperature is increased to 1400 °C, the mechanism of corrosion can be demonstrated:

– Silica volatilization in alumino-silicate minerals is manifested as weight loss and degradation of the sample surface. For mullite and andalusite, the total depletion of Si on the exposed surface resulted in complete transformation into α-alumina. This process was progressive with the preferential consumption of Si from the glass phase over the silica structurally-bonded in mullite.

– The unique microstructure of mullitized andalusite characterized by the dense, ordered capillary network of mullite and glass phase could potentially hinder hydrogen infiltration.

– The cross-reaction triggered by the SiO by-product gas in the presence of calcium resulted in the formation of a calcium silicate phase and led to the destabilization of the calcia-stabilized zirconia.

– Yttria-stabilized zirconia showed excellent resistance against hydrogen, kept a high degree of cubic/tetragonal stabilization and was not impacted by any cross-creation with SiO-gas.

## REFERENCES

[1] European Commission. European Green Deal: 2030 Climate Target Plan. https://climate.ec.europa.eu/.

[2] Palmer G. Volatilization of Refractory Silica in Hydrogen Water Vapour Gas Streams. Refractories World Forum, pp. 63-70, 2012.

[3] Bertrand B, Eliazord N, Lemaistre H, Touzo B. Evaluation of the possible changes of refractory linings for green steel processes. UNITECR, Chicago, Illinois, 2022.

[4] Sperber J, Duennes FJ. H2 Change: Refractory Technologies to Master the Challenge of H2 Atmospheres. Refractories World Forum, pp. 47-52, 2022.

[5] Leber T, Madeo S, Tonnesen T, Telle R. Corrosion of bauxite-based refractory castables and matrix components in hydrogen containing atmosphere. International Journal of Ceramic Engineering & Science, pp. 16-22, 2021 (4).

[6] Herbell T, Hull D, Garg A. Hot hydrogen exposure: degradation of the strength of mullite. NASA, Lewis Research Center, Technical Memorandum 107153, 1996.

[7] Schafföner S, Dietze C, Möhmel S, Fruhstorfer J, Aneziris C. Refractories containing fused and sintered alumina aggregates: Investigations on processing, particle size distribution and particle morphology. Ceramics International, pp. 4252-4262 (43), 2017.

# PHYSICAL PROPERTIES OF REFRACTORY BRICKS AND CHANGES OF OXIDE MATERIALS AFTER HEAT TREATMENT AT A HYDROGEN ATMOSPHERE

Rae-Hyeong Park[1], Sang-Bae Choi[1], Hyeon-Oh Song[1], Kee-Deok Yang[1]
[1]Chosun Refractories Co., Ltd., Republic of Korea

Sang-Chae Jeon[2], Eun-Hee Kim[2], Jong-Won Woo[2], Sung-Hyun Kim[2], Jong-Won Kim[2]
[2]School of Materials Science and Engineering, Changwon National University, Republic of Korea

## ABSTRACT
This study aims to provide the basic knowledge for furnace refractory design by investigating refractory property changes occurred in hydrogen atmosphere. Since refractory bricks are thermodynamically stable in hydrogen atmosphere at 1100°C, we tried to find out the minute changes. In this experiment, refractory brick is prepared by andalusite, mullite chamotte, and clay as raw materials and heated to 1100°C in 100% hydrogen atmosphere for 72 hours. In this experiment we found out the brick's strength was decreased and the color was changed into black by the reduction of impurities.

## INTRODUCTION
In order to achieve carbon neutrality, research is being conducted to convert the existing coke reduction iron method to hydrogen reduction iron[1]. Accordingly, the research is required to identify changes of refractories used in hydrogen atmosphere and the factors that cause the change. A lot of researches have reported that when refractories are exposed to hydrogen atmosphere at a high temperature, silica is reduced by hydrogen and decomposed into $SiO(g)$, reducing the strength of refractories[2,3,4,5]. Our research reports phase changes, weight changes, color changes, and physical properties shown when refractory bricks are exposed to hydrogen atmosphere at around 1,100°C. And further reports the effect of components that cause changes in the state of refractories based on thermodynamic theoretical calculations. We expect that this study is to be used as basic data to design refractories for hydrogen reduction steelmaking.

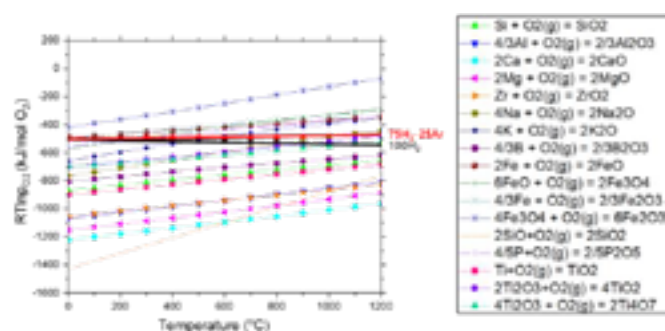## PREDICTION OF THERMODYNAMIC REACTIONS IN HYDROGEN ATMOSPHERE



*Fig. 1: Ellingham diagram*

HSC Chemistry 10 was used to predict the thermodynamic reaction of refractories in hydrogen atmosphere. As a result, the Ellingham diagram is shown in Figure 1. In the case of pure hydrogen atmosphere ($100(H_2)$), an oxygen potential was calculated by the partial pressure of hydrogen and water vapor. Among the oxide raw materials, $SiO_2$, $Na_2O$, $K_2O$, $Fe_2O_3$ and $TiO_2$ are predicted to be reduced at 1100°C.

## CHANGES OF REFRACTORY BRICK IN HYDROGEN ATMOSPHERE

### Refractory brick specimen preparation
As a specimen, we use a refractory brick which is composed of Andalusite, Mullite chamotte, and Clay as raw materials. After kneading raw materials with binder in a mixer, the mixture is molded with a uniaxial pressing press, dried at 110°C for 24 hours, and heat treated at 1,350°C for 6 hours in the air atmosphere. Table 1 shows the compositions of refractory brick.

Tab.1: The raw materials & composition of refractory brick

| Raw material (particle size, mm) | Composition (wt%) |
|---|---|
| Andalusite (1~0.3) | 30 |
| Mullite chamotte (3~0.3) | 60 |
| Clay (1) | 10 |

### Heat treatment conditions
A refractory brick fired in the air atmosphere was prepared in a size of 20×20×70mm. And the specimen brick is charged into an alumina tube which is capable of controlling the atmosphere, and heat-treated at 1100°C for 72 hours while injecting hydrogen and argon gas at a flow rate of 200cc/min. The heating rate was 5°C/min, and the pressure in the furnace was about 1 bar. Table 2 shows the heat treatment conditions of the specimen.

Tab.2: The heat treatment conditions of the specimen

| Specimen | A | B | C | D | E |
|---|---|---|---|---|---|
| 1st | Fired at 1350°C*6hrs (Air atmosphere) | | | | |
| 2nd | - | Heat-treated at 1100°C*72hrs | | | |
| | - | Atmosphere (Gas ratio) | | | |
| | - | Air | $H_2$ : Ar | | |
| | - | 100 | 25:75 | 75:25 | 100 |

### Color change of refractory brick
As shown in specimen "E" of Figure 2, after the specimen's heated in hydrogen atmosphere, the color is changed to dark. And the blackened specimen could be also returned to the bright color like specimen "A" when it is heated in the air. This reversible reaction is considered that some of the refractory brick components, especially, $K_2O$, $Na_2O$, and $Fe_2O_3$, are reduced to metal having dark color and be oxidized in the air to cause a bright color again.



*Fig. 2: Specimen before and after hydrogen heat treatment*

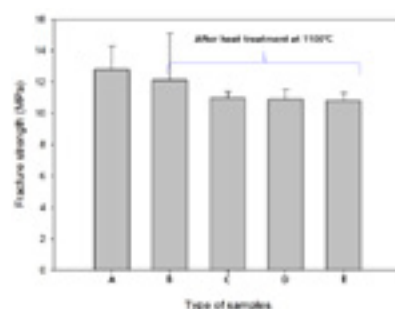### Strength changes (Modulus of Rupture)



*Fig. 3: Strength changes by heating atmosphere*

Figure3 shows that refractory's strength changes due to hydrogen reduction. Even though the strength of specimen "B" heat-treated in the air decreased slightly by 6% (1MPa), but specimen(C, D, F)'s strength, heated in the hydrogen atmosphere, decreased by more than 15% (2MPa). The strength change among specimen "C", "D", and "F" was similar to one another indicating that the decreasing strength is influenced by lack of oxygen not by hydrogen concentration.

**Phase changes (XRD)**
The XRD analysis shows that $Fe_2O_3$ in the refractory brick component was reduced to $Fe_3O_4$ and Fe after heat treatment. In particular, metal Fe was detected in specimens(C, D, F), and it seems to have caused a color change of the specimen after heat treatment[4].

Tab.3: XRD results of refractory brick (main peak +++, traces +)

| Specimen | A | B | C | D | E |
|---|---|---|---|---|---|
| Mullite | +++ | +++ | +++ | +++ | +++ |
| Andalusite | +++ | +++ | +++ | +++ | +++ |
| Cristobalite | ++ | ++ | ++ | ++ | ++ |
| Quartz | + | + | + | + | + |
| Fe2O3 | + | + | | | |
| Fe3O4 | | + | + | + | + |
| Fe | | | + | + | + |
| Fe(OH)3 | | + | + | + | + |

**Microstructure Changes (SEM)**
Figure 4 shows the microstructure observations before and after heat treatment in hydrogen atmosphere. Cracks were observed between and within the raw materials regardless of the atmosphere.
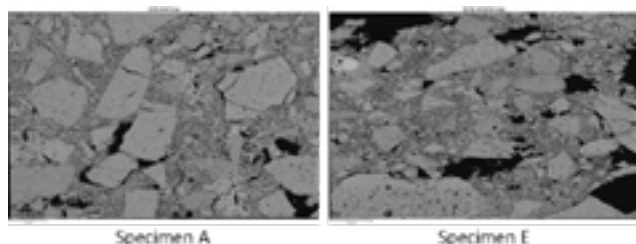

*Fig. 4: SEM image before and after hydrogen heat treatment*

**CHANGES OF RAW MATERIALS**

**Preparation of Raw Material Specimens**
To identify which material causes the color changes and strength reduction of refractory bricks in hydrogen atmosphere. The raw material specimens are prepared by the same procedures described in refractory brick. Afterwards, these specimens were heat-treated in 100% $H_2$ atmosphere. The six types of raw materials and their compositions are shown in Table 4.

Tab.4: **Raw materials composition of refractory brick**

| Raw material (particle size, mm) | Composition (wt%) | | | | | | |
|---|---|---|---|---|---|---|---|
| | $SiO_2$ | $Al_2O_3$ | $Fe_2O_3$ | $TiO_2$ | $P_2O_5$ | $Na_2O$ | $K_2O$ |
| Mullite chamotte(3-1) | 43.5 | 51.6 | 1.2 | 2.5 | 0.1 | 0.0 | 0.2 |
| Mullite chamotte(1) | 43.9 | 50.8 | 1.4 | 2.5 | 0.1 | 0.0 | 0.2 |
| Mullite chamotte(0.3) | 41.6 | 52.4 | 1.4 | 2.6 | 0.1 | 0.0 | 0.2 |
| Andalusite(1) | 40.7 | 57.1 | 0.8 | 0.2 | 0.0 | 0.1 | 0.2 |
| Andalusite(0.3) | 39.3 | 58.3 | 0.9 | 0.2 | 0.0 | 0.0 | 0.3 |
| Clay (1) | 51.2 | 33.1 | 1.2 | 0.8 | 0.1 | 0.0 | 0.1 |

**Color changes of raw materials**
As shown in Figure5, color changes were observed in all specimens after heat treatment. The color changes were more noticeable in

Mullite chamotte with smaller particle sizes. Referring to Table 4, we found out the fact that the higher $Fe_2O_3$ content caused the darker color. The degree of color change is increased in the order of Mullite chamotte, Clay and Andalusite which can be explained by the $Fe_2O_3$ content.
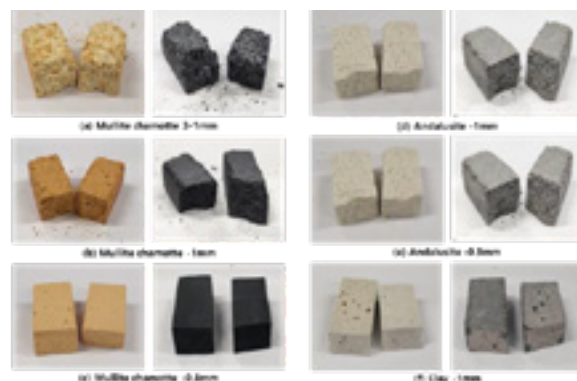

*Fig.5: Specimen before and after hydrogen heat treatment*

**Weight changes**
Weight changes after heat treatment are shown in Table 5. The weight loss was greater in smaller particle sizes. Weight loss of mullite chamotte and andalusite is attributed to the reduction of silica and $Fe_2O_3$.

Tab.5: Weight changes before and after hydrogen heat treatment

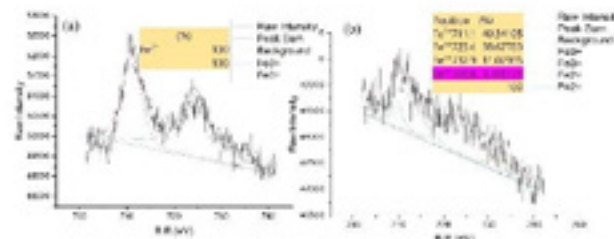| Raw material (particle size, mm) | Weight (g) | | $\triangle$g (%) |
|---|---|---|---|
| | Before | After | |
| Mullite chamotte (1) | 13.30 | 13.27 | -0.22% |
| Mullite chamotte(0.3) | 9.76 | 9.73 | -0.29% |
| Andalusite (1) | 13.65 | 13.62 | -0.19% |
| Andalusite (0.3) | 8.77 | 8.75 | -0.21% |
| Clay (1) | 6.97 | 6.97 | -0.03% |

**Phase Changes (XPS)**


*Fig.6: XPS of Fe peak in mullite chamotte(0.3)*
*(a)Before hydrogen heat treatment*
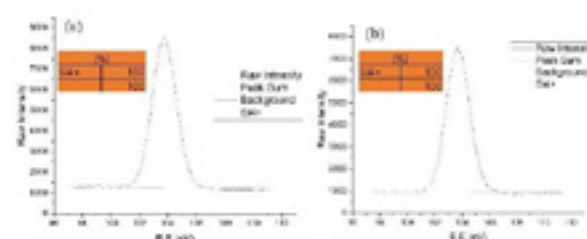*(b)After hydrogen heat treatment*


*Fig.7 XPS of Si peak in mullite chamotte(0.3)*
*(a)Before hydrogen heat treatment*
*(b)After hydrogen heat treatment*

The phase change of mullite chamotte(0.3), which has the largest color change and strength reduction, was observed by XPS. $Fe^{3+}$ and $Fe^{2+}$ were detected in the Fe peak after heat treatment, indicating that Fe and $Fe_3O_4$ were generated through the reduction

reaction of $Fe_2O_3$ impurities in the specimen by hydrogen, resulting in the observed color change. While silica reacts with hydrogen to produce SiO, it evaporates as a gas and none of the reduced Si species such as $Si^{3+}$ or $Si^{2+}$ were detected after heat treatment.

**Changes in silica in hydrogen atmosphere**
To demonstrate the relationship between the generation of SiO through the reaction of silica with hydrogen and the resulting strength reduction, the reaction of silica alone with hydrogen was performed. Amorphous and crystalline silica were compared under the same conditions as the raw material experiments.

Tab.6 Composition and content of silica

| Material | Composition (wt%) | | | |
|---|---|---|---|---|
| | $SiO_2$ | $Al_2O_3$ | $Fe_2O_3$ | LOI |
| Amorphous | 99.90 | 0.04 | 0.01 | 0.00 |
| α-Quartz | 99.05 | 0.34 | 0.13 | 0.13 |

**Color Changes**
Color changes were observed in the specimens after heat treatment in hydrogen atmosphere, both externally and internally. Similarly, color changes were more pronounced with higher $Fe_2O_3$ content.



*Fig.8 Specimen before and after hydrogen heat treatment*
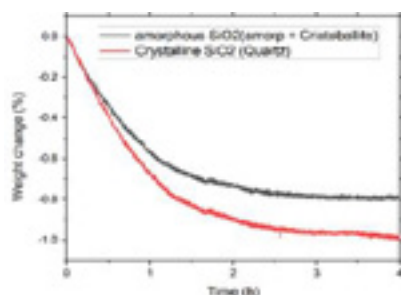
**Weight changes (TGA)**



*Fig.9 TGA results of Silica*

The TGA results representing the volatilization loss of silica shows that the weight of the specimens decreased by approximately 1.0% over time for both amorphous and crystalline specimens (Figure 9). The data is based on isothermal time right after reaching 1100°C. In both cases, the weight loss was greater than the amount of impurities contained in silica. This indicates the generation of SiO through the reduction of iron oxide as well as the reduction of silica. The evaporation of water vapor generated by the reduction reaction of iron oxide and the volatilization of gaseous SiO formed through the hydrogen reaction of silica occurred simultaneously. In accordance with literature[6], assuming an equilibrium state with the Gibbs free energy for the volatilization reaction of silica, the calculated volatilization loss(equilibrium pressure) at 1100°C is very small, approximately $2.14 \times 10^{-3}$Pa. However, as it is proportional to time, the volatilization loss of refractory materials increases linearly with longer exposure to hydrogen reduction [6].

**Microstructure (SEM)**
The microstructure changes of silica particles are shown in Figure 10. For Quartz with a high impurity content (Table 6), exposure to hydrogen for more than 4 hours at 1100°C resulted in a change from the original smooth surface to a rough surface. On the other hand, if the impurity content is low, the degree of surface damage is much milder.
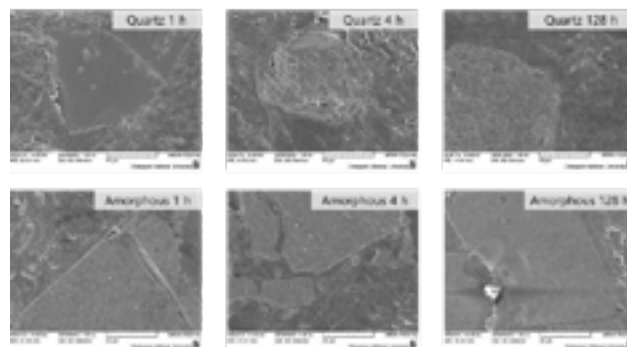


*Fig.10 Microstructure of Silica*

These defects eventually lead to a decrease in strength. Although the calculated volatilization loss (equilibrium pressure) of silica is minimal, even when silica is exposed to hydrogen for 72 hours at 1100°C, it demonstrates the formation of pores and a potential decrease in mechanical strength.

**CONCLUSION**
In hydrogen atmosphere, $SiO_2$ and impurities such as $Na_2O$, $K_2O$, and $Fe_2O_3$ among the refractory material raw materials are reduced under low oxygen partial pressure, resulting in the weakening of refractory bricks.

Refractory bricks show reversible color changes after heat treatment in reduction atmosphere. Since the degree of color change is determined by the impurity content, $Fe_3O_4$ and Fe, the reduction products of $Fe_2O_3$, were observed as major color change factors.

Silica components are prone to damage due to the evaporation of SiO, which leads to the weakening of refractory bricks. The damage to silica in the hydrogen atmosphere is accelerated by the presence of impurities.

In addition, oxides such as $TiO_2$ and $P_2O_5$ are likely to be reduced by hydrogen. The vulnerability of refractories in the hydrogen atmosphere can be also prevented by lowering the content of the impurities.

**REFERENCES**
[1] Development and Progress on Hydrogen Metallurgy, Int. J. Miner. Metall. Mater,27, 713-23(2020).
[2] Hot Hydrogen Exposure Degradation of the Strength of Mullite, Journal of the American Ceramic Society, 81, 910–16(1998).
[3] Andalusite Transformation and Properties of Andalusite-bearing Refractories Fired in Different Atmospheres, Ceramics International 45, 3186–3191 (2019).
[4] The Kinetics of Silica Reduction in Hydrogen, Journal of Solid State Chemistry, 9, 336-344 (1974).
[5] Reaction of Fused Silica with Hydrogen Gas, Journal of the American Ceramic Society, 65, 457-460(1982).
[6] Phase Equilibria and Stability of Mullite, WILEY-VCH Verlag GmbH & Co. KGaA, Weinheim p. 227–249(2005).

# CHARACTERIZATION OF REFRACTORIES WITH REGARD TO THE APPLICATION IN H$_2$−CONTAINING ATMOSPHERES

Cristian Daniel Bohorquez-Moreno[1]; Dietmar Gruber[2]; Sido Sinnema[1]

[1]Tata Steel IJmuiden, Ceramics Research Centre, Velsen Noord, Netherlands;
[2]Montanuniversität Leoben, Chair of Ceramics, Leoben, Austria

In search of mitigation solutions to avoid the effects of fossil fuel-based production, industries have been encouraged to understand new ways to reduce their carbon footprint during production. As a result, the major trend in the steelmaking industry is the transition from the blast furnace to direct reduction of iron based on the use of hydrogen. Especially the effect of H2-containing atmospheres on the degradation of thermo-mechanical behaviour is less investigated. Existing refractory solutions and designs for the direct reduction process (DRP) reactors use materials that are already available, for which only empirical and no detailed information is known about their interaction with atmospheres rich in hydrogen and water vapour. The present work shows challenges and limitations for testing under H2-containing atmospheres. Furthermore, results for common refractory materials are presented. For this purpose, samples were exposed to H2-rich atmospheres for at least 24 h, 48 h, and 72 h at high temperatures, showing that the prolonged exposure caused changes in the morphological, thermophysical and mechanical properties. The results are expected to serve as a basis for future DRP-reactor design or as preventive measures in the maintenance of existing reactors. This project is part of the cooperation between members of the Concerted European action on Sustainable Applications of REFractories (Cesaref), which aims to give new insights and support in the transition and anticipation of tomorrow's problems related with the green production.

# HYDROGEN INDUCED ATTACK OF AL$_2$O$_3$–SIO$_2$ REFRACTORIES – APPLICATION OF SEM TECHNIQUES AND THERMODYNAMICS

Isabelle Henn[1]; Almuth Sax[2]; Peter Quirmbach[2]

[1]University of Koblenz, Institute for Integrated Natural Sciences – Chair of Technical Chemistry and Corrosion Sciences, Koblenz, Germany; [2]University of Koblenz, Institute for Integrated Natural Sciences – Chair of Technical Chemistry and Corrosion Scie

In order to reduce $CO_2$ emissions, a change is currently taking place within the steel industry towards hydrogen-based steel production. For this purpose, the requirement profile for the refractory materials is thus being extended to include a resistance to hydrogen. The aim of this poster is to characterize the structural changes respectively the corrosion mechanism occurring in an Al2O3-SiO2 refractory material, which experienced a hydrogen induced attack. SEM techniques were applied and the results were verified with thermochemical calculations. First, a corrosion test was conducted. Therefore, the refractory material was exposed to 100 % H2 for 200 h at 1400°C. Subsequently, an elemental analysis by SEM of the hydrogen-induced corrosion zone of the refractory was performed. The corrosion mechanism was described by thermodynamic modeling using the software FactSage.

# IMPRINT

# OUR REFRACTORY INFO-TRAILER

Deutsche Feuerfest Industrie e.V. — **DFFI**

Deutsches Institut für Feuerfest und Keramik GmbH — **DIFK**

European Centre for Refractories gGmbH — **ECREF**

Forschungs-Gemeinschaft Feuerfest e.V. — **FGF**

# ICR® International Colloquium on Refractories

**SCIENTIFIC CONFERENCE AND TRADE FAIR**

18-19 Sept 2024 — Aachen, Germany

JOIN IN!

SCIENTIFIC CONFERENCE
TRADE FAIR
SOCIAL EVENT

www.ic-refractories.eu